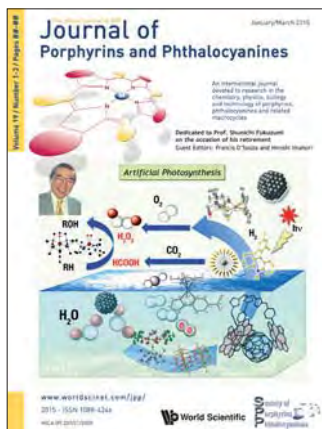


## About the Cover



Guest Editors: Francis D'Souza and Hiroshi Imahori

This special issue of JPP is dedicated to **Professor Shunichi Fukuzumi** on the occasion of his retirement from the Osaka University, Osaka, Japan. The cover images are taken in part from Prof. Fukuzumi's publications and website, and illustrates his research activities covering different areas of photochemistry and photocatalysis, in recent years. The current issue of JPP contains 52 papers from researchers, friends and collaborators alike, from all around the world.

## Reviews

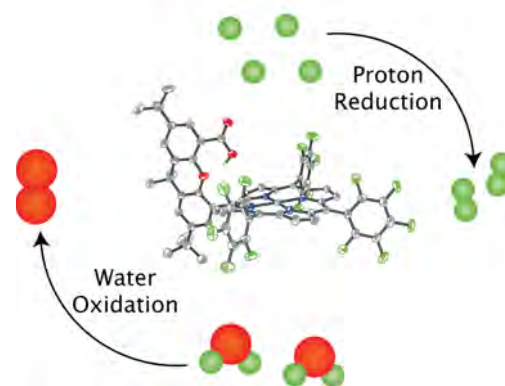
### pp. 1–8

#### Proton-coupled electron transfer chemistry of hangman macrocycles: Hydrogen and oxygen evolution reactions

Dilek K. Dogutan, D. Kwabena Bediako, Daniel J. Graham, Christopher M. Lemon and Daniel G. Nocera\*

The half reactions of water splitting, the hydrogen evolution reaction (HER) and oxygen evolution reaction (OER), requires the efficient management of electrons and protons. The use of hangman catalysts provides detailed mechanistic insight into the proton-coupled electron transfer (PCET) processes that underpin HER and OER. This review summarizes our efforts to use hangman porphyrins and corroles to develop a unified mechanistic PCET framework to describe O–O, O–H and H–H bond-breaking and bond-making processes, as they pertain to HER and OER.

### Hangman Catalysts

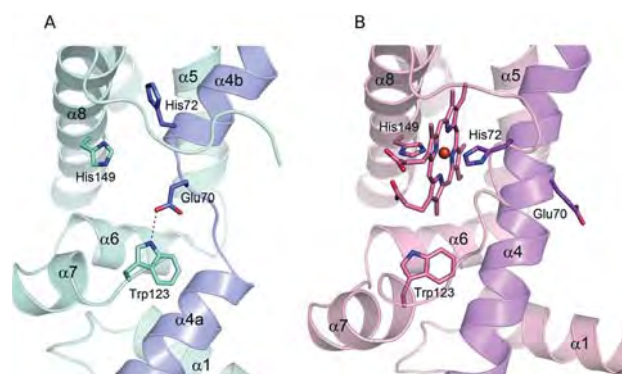


### pp. 9–20

#### A new biological function of heme as a signaling molecule

Norifumi Muraki, Chihiro Kitatsuji and Shigetoshi Aono\*

As free heme molecules are cytotoxic, the intracellular concentrations of biosynthesized or uptaken heme should be strictly controlled. In this mini review, the authors summarize the biochemical and biophysical properties of the transcriptional regulators and heme-sensor proteins responsible for these regulatory systems to maintain heme homeostasis.

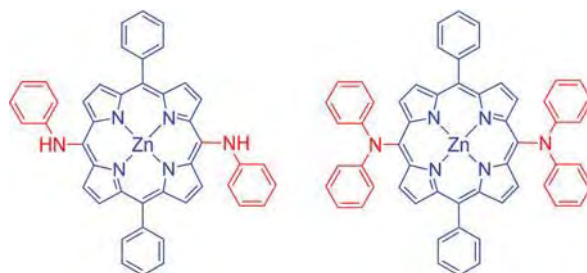


pp. 21–31

**Meso-*N*-arylamino- and *N,N*-diarylamino porphyrinoids: Syntheses, properties and applications**

Ryota Sakamoto\*, Suzaliza Mustafar and Hiroshi Nishihara\*

This review is devoted to porphyrinoids with *N*-arylamino groups tethered directly to their *meso*-positions, the study of which has significantly progressed in the past two decades. The present review contains a brief introductory description, various synthetic procedures for these compounds, their valuable photochemical and electrochemical properties induced by synergetic effects between the porphyrinoids and the *N*-arylamino groups, potential applications such as dye-sensitized solar cells (DSSCs), and conclusions.

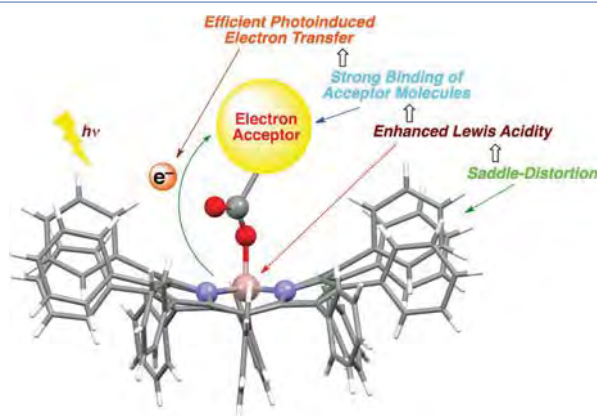


pp. 32–44

**Molecular assemblies based on strong axial coordination in metal complexes of saddle-distorted dodecaphenylporphyrins**

Tomoya Ishizuka, Shunichi Fukuzumi and Takahiko Kojima\*

Works on metal complexes, having saddle-distorted dodecaphenylporphyrin (DPP) and its derivatives as ligands, have been highlighted in the light of enhancement of the Lewis acidity of a metal center coordinated by the porphyrin. The enhanced Lewis acidity of the central metal ions enabled the construction of stable molecular complexes through axial coordination using metal-DPP moieties and molecular or ionic entities with Lewis-basic coordination sites.

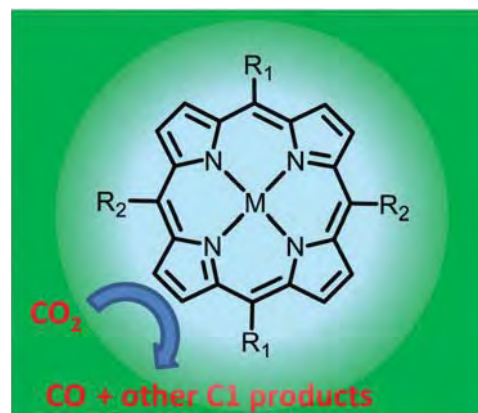


pp. 45–64

**A review of iron and cobalt porphyrins, phthalocyanines, and related complexes for electrochemical and photochemical reduction of carbon dioxide**

Gerald F. Manbeck\* and Etsuko Fujita\*

This review summarizes research on the electrochemical and photochemical reduction of CO<sub>2</sub> using a variety of iron and cobalt porphyrins, phthalocyanines, and related complexes. While remarkable progress has been made in carrying out coupled proton-electron transfer reactions for CO<sub>2</sub> reduction, ground-breaking research has to be continued to produce renewable fuels via low-energy pathways using durable and selective earth-abundant catalysts for creating carbon-neutral energy sources.

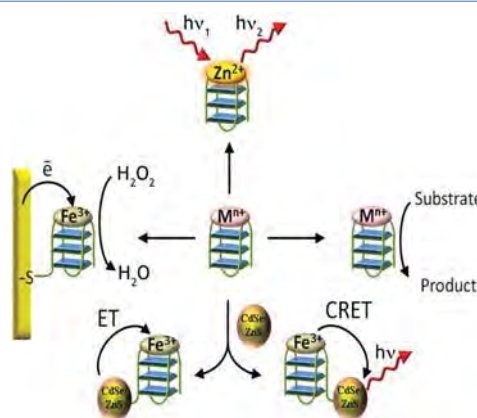


pp. 65–91

**Metalloporphyrin/G-quadruplexes: From basic properties to practical applications**

Eyal Golub, Chun-Hua Lu and Itamar Willner\*

Metal porphyrin/G-quadruplex supramolecular nanostructures exhibit unique catalytic, electrocatalytic and photocatalytic properties. These features of metal porphyrin/G-quadruplexes are extensively implemented to develop synthetic transformations and to use the nanostructures as electrochemical or optical labels for a variety of sensing platforms.



## pp. 92–108

**Effect of axial ligands on electronic structure and O<sub>2</sub> reduction by iron porphyrin complexes: Towards a quantitative understanding of the “push effect”**

Subhra Samanta, Pradip Kumar Das, Sudipta Chatterjee and Abhishek Dey\*

Differences in bonding interactions between imidazole, phenolate and thiolate axial ligands tune the electronic structure and kinetics of electrochemical O<sub>2</sub> reduction by synthetic iron porphyrin complexes.

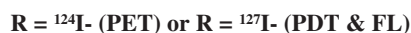


## pp. 109–134

**Porphyrin-based photosensitizers and the corresponding multifunctional nanoplateforms for cancer-imaging and photo-therapy**

Avinash Srivatsan, Joseph R Missert, Santosh K. Upadhyay and Ravindra K. Pandey\*

An overview on some of the recent approaches to improve the tumor-specificity of porphyrin-based multifunctional agents (theranostics) for cancer-imaging and photodynamic therapy is discussed.



## Articles

## pp. 135–139

**Macrocyclic dipyrin dimer bridged by ethylene and dioxyphenylene linkers**

Ji-Young Shin\*, Satoru Hiroto and Hiroshi Shinokubo

A tetrapyrrolic macrocycle containing ethylene and dioxyphenylene bridges was obtained through the reaction of a dipyrin-DDQ adduct with triethylamine. The structure of the macrocycle was elucidated by X-ray diffraction analysis. The macrocycle exhibited solvent-dependent absorption spectra due to intramolecular charge transfer interactions.

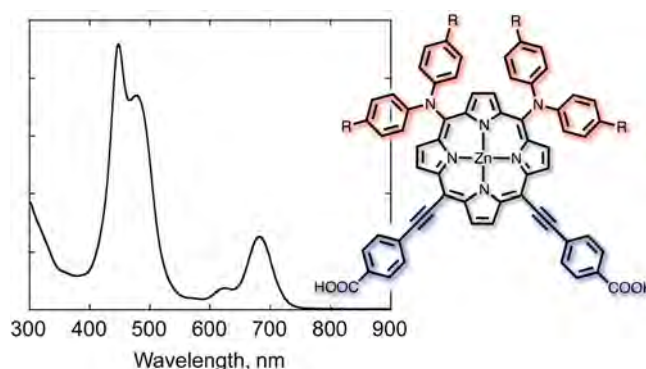


## pp. 140–149

**Synthesis of push–pull porphyrin with two electron-donating and two electron-withdrawing groups and its application to dye-sensitized solar cell**

Tomohiro Higashino, Yamato Fujimori, Kenichi Sugiura, Yukihiro Tsuji, Seigo Ito and Hiroshi Imahori\*

Introduction of multiple electron-donating groups and electron-withdrawing groups into a porphyrin core achieved a panchromatic light-harvesting in visible and NIR regions. The preliminary photovoltaic performance is moderate, but the extensive photocurrent generation matches with the excellent light-harvesting property.

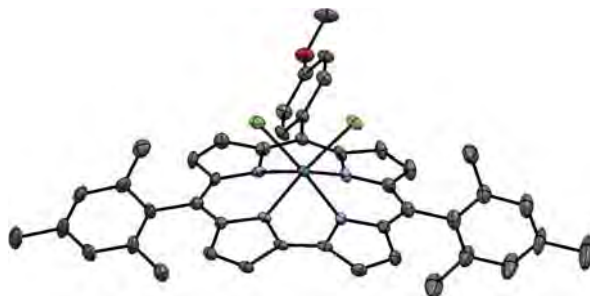


pp. 150–153

**Preparation and characterization of a tungsten(V) corrole dichloride complex**

Rosa Padilla, Heather L. Buckley, Ashleigh L. Ward and John Arnold\*

The first example of a tungsten(V) corrole complex,  $(\text{Mes}_2(p\text{-OMePh})\text{corrole})\text{WCl}_2$ , has been prepared through a metathesis reaction of a lithium corrole  $(\text{Mes}_2(p\text{-OMePh})\text{corrole})\text{Li}_3 \cdot 6\text{THF}$  and  $\text{WCl}_6$ . The product constitutes the first example of a tungsten(V) corrole complex synthesized under mild conditions and only the second example of a tungsten corrole complex.

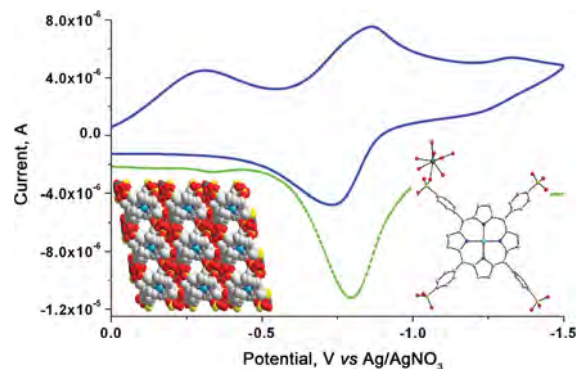


pp. 154–159

**A novel terbium-cobalt tetra(4-sulfonatophenyl)porphyrin: Synthesis, structure and photophysical and electrochemical properties**

Wen-Tong Chen\*, Jian-Gen Huang, Qiu-Yan Luo, Ya-Ping Xu and Hong-Ru Fu

A novel terbium-cobalt porphyrin has been synthesized *via* a hydrothermal reaction and structurally characterized by X-ray single crystal diffraction. It is characterized by a 3-D porous open framework. It displays an emission band in the blue region and the fluorescence lifetime is 1.14 ms. The CV and DPV discovers one reversible wave with  $E_{1/2} = -0.80$  V.

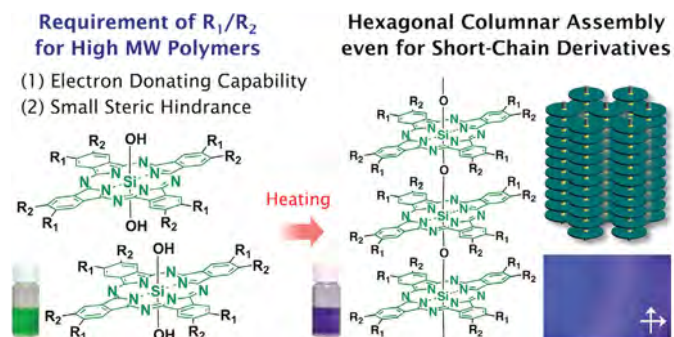


pp. 160–170

**Systematic studies on side-chain structures of phthalocyaninato-polysiloxanes: Polymerization and self-assembling behaviors**

Satoru Yoneda, Tsuneaki Sakurai\*, Toru Nakayama, Kenichi Kato, Masaki Takata and Shu Seki\*

A series of phthalocyaninato dihydroxysilicon having various types of side chains were synthesized and their bulk-state polymerization capability was investigated. Comprehensive studies disclosed that strong electron donating ability and small steric hindrance of the peripheral substituents are the dominant factors to afford high molecular weight polymers. Due to the siloxane covalent bonds, the obtained phthalocyaninato-polysiloxanes with enough degree of polymerization all form hexagonal columnar liquid crystals even for the derivatives with small peripheral chains.

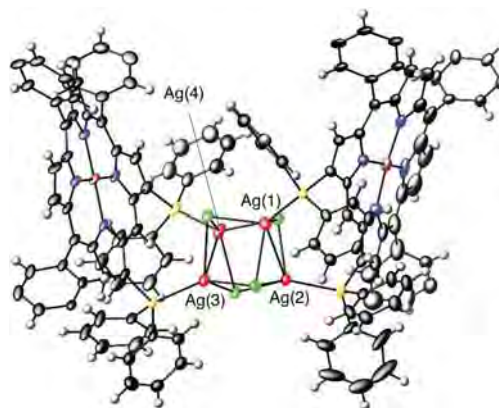


pp. 171–174

**Dimeric 1:2 adduct of  $\beta,\beta'$ -bis(diphenylphosphino)porphyrin with silver(I) chloride**

Keisuke Fujimoto, Hideki Yorimitsu\* and Atsuhiko Osuka\*

A 2,18-bis(diphenylphosphino)porphyrin ligand undergoes complexation with silver(I) chloride to afford a stable phosphine-silver complex. X-ray crystallographic analysis of the complex revealed a dimeric structure of a 1:2 adduct of the diphosphine and silver(I) chloride, where each phosphorus atom coordinates a silver atom. The four AgCl units construct a distorted cubic cluster with small metallophilic interaction. Variable temperature  $^{31}\text{P}$  NMR study exhibited a slow ligand exchange process between  $^{107}\text{Ag}$  and  $^{109}\text{Ag}$  at high temperature.

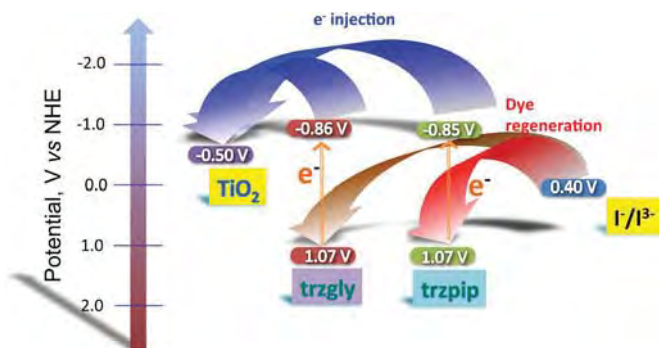


## pp. 175–191

**Donor- $\pi$ -acceptor, triazine-linked porphyrin dyads as sensitizers for dye-sensitized solar cells**

Ganesh D. Sharma\*, Galatea E. Zervaki, Kalliopi Ladomenou, Emmanuel N. Koukaras, Panagiotis P. Angaridis and Athanassios G. Coutsolelos\*

Two porphyrin dyads with the donor- $\pi$ -acceptor molecular architecture, which consist of a zinc-metalated porphyrin unit and a free-base porphyrin unit covalently linked at their peripheries to a central triazine group, that is substituted either by a glycine or a *N*-piperidine group, have been synthesized *via* consecutive amination substitution reactions of cyanuric chloride.

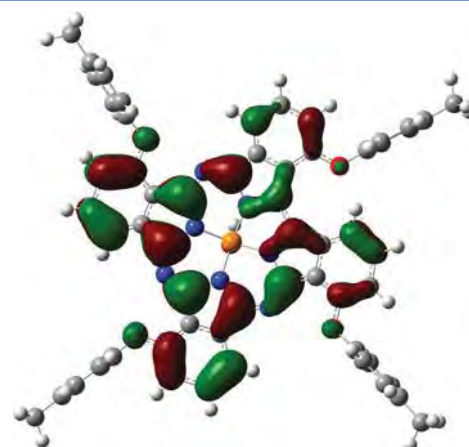


## pp. 192–204

**Optical limiting and singlet oxygen generation properties of phosphorus triazatetrabenzcorroles**

Colin Mkhize, Jonathan Britton, John Mack and Tebello Nyokong\*

Novel phosphorus triazatetrabenzcorrole (TBC) tetrasubstituted at the  $\alpha$ - and  $\beta$ -positions of the peripheral fused benzene rings with *t*-butylphenoxy substituents have been prepared and characterized. The effect of the substituents on the electronic structures and optical spectroscopy is investigated with TD-DFT calculations and MCD spectroscopy. The optical limiting properties have been investigated to examine whether the lower symmetry that results from the direct pyrrole-pyrrole bond and hence the permanent dipole moment that is introduced result in higher safety thresholds, relative to the values that have been reported for phthalocyanines. The suitability of the compounds for singlet oxygen applications has also been examined.

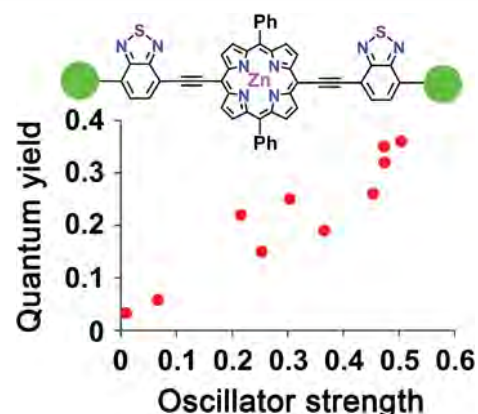


## pp. 205–218

**Design of diethynyl porphyrin derivatives with high near infrared fluorescence quantum yields**

Kimihiro Susumu and Michael J. Therien\*

A design strategy for (porphinato)zinc-based fluorophores that possess large near infrared fluorescence quantum yields is described. These fluorophores are based on a (5,15-diethynylporphinato)zinc(II) framework and feature symmetric donor or acceptor units appended at the *meso*-ethynyl positions *via* benzo[*c*][1,2,5]thiadiazole moieties. The measured radiative decay rate constants track with the integrated oscillator strengths of their respective *x*-polarized Q-band absorptions, and thus define an unusual family of high quantum yield near infrared fluorophores in which emission intensity is governed by a Strickler-Berg dependence.



## pp. 219–232

**Synthesis and photodynamics of diphenylethynyl-bridged porphyrin-quinoidal porphyrin hybrids**

Shuhei Sakatani, Takuya Kamimura, Kei Ohkubo, Shunichi Fukuzumi and Fumito Tani\*

Zinc complex and free-base of a porphyrin-quinoidal porphyrin dyad linked by a diphenylethynyl bridge were prepared as new donor-acceptor hybrids. The considerable quenching of the porphyrin fluorescence in the dyads was observed. Femtosecond laser flash photolysis of the dyads showed ultrafast energy and electron transfer from the porphyrin units to the quinoidal porphyrin ones.

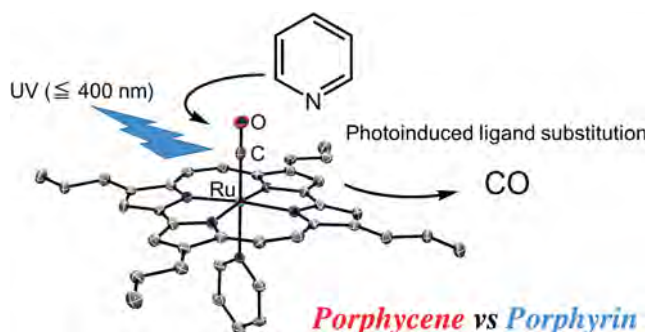


pp. 233–241

**Molecular structures, redox properties, and photo-substitution of ruthenium(II) carbonyl complexes of porphycene**

Toru Okawara, Masaaki Abe\*, Shiho Ashigara and Yoshio Hisaeda\*

Two ruthenium(II) carbonyl complexes of porphycene have been structurally characterized by single-crystal X-ray diffraction analysis. UV-light irradiation of a benzene solution of the ruthenium porphycene complexes leads to the dissociation of a carbonyl ligand from the ruthenium(II) centers to give the corresponding bis-pyridine complexes. The first-order kinetic analysis has revealed that the photosubstitution proceeds faster for complexes of porphycene than that of porphyrin.

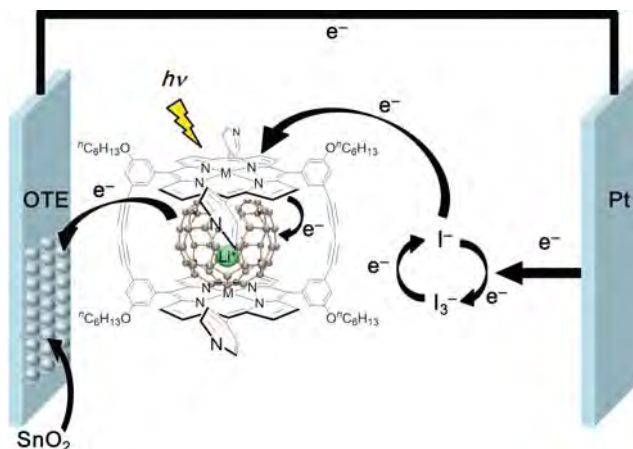


pp. 242–250

**Supramolecular photovoltaic cells utilizing inclusion complexes composed of Li<sup>+</sup>@C<sub>60</sub> and cyclic porphyrin dimer**

Hayato Sakai, Takuya Kamimura, Fumito Tani\* and Taku Hasobe\*

Supramolecular photovoltaic cells using inclusion complexes of lithium-ion-encapsulated [60]fullerene (Li<sup>+</sup>@C<sub>60</sub>) and cyclic porphyrin dimers (M-CPD<sub>Py</sub>, M = H<sub>4</sub> and Ni<sub>2</sub>) were newly constructed. The photoelectrochemical solar cells composed of these assemblies on SnO<sub>2</sub> electrode were fabricated by electrophoretic deposition. The photoelectrochemical behavior of Li<sup>+</sup>@C<sub>60</sub> and M-CPD<sub>Py</sub> assemblies on nanostructured SnO<sub>2</sub> film is higher than Li<sup>+</sup>@C<sub>60</sub> or M-CPD<sub>Py</sub> films and supramolecular complexes of C<sub>60</sub> and M-CPD<sub>Py</sub>.

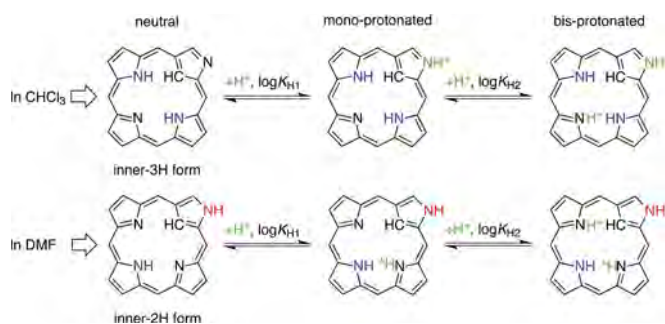


pp. 251–260

**N-confused meso-tetraaryl-substituted free-base porphyrins: Determination of protonation and deprotonation constants in nonaqueous media**

Zhongping Ou\*, Xueyan Chen, Lina Ye, Songlin Xue, Yuanyuan Fang, Xiaoqin Jiang and Karl M. Kadish\*

The protonation and deprotonation reactions for a series *N*-confused meso-tetraaryl-substituted free-base porphyrins was monitored in CHCl<sub>3</sub> and DMF by UV-visible spectroscopy during titrations with trifluoroacetic acid or tetra-*n*-butylammonium hydroxide and the spectroscopic data was then used to calculate equilibrium constants for these reactions.

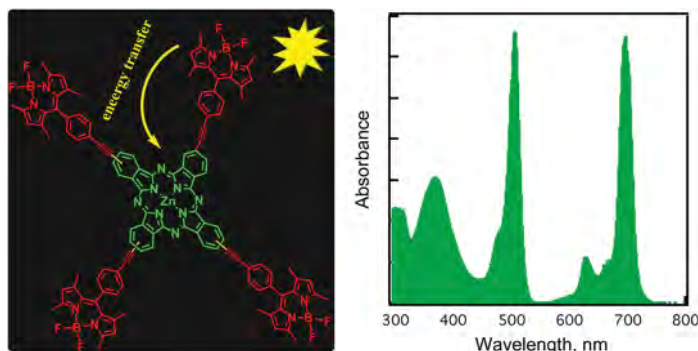


pp. 261–269

**Energy-transfer studies on phthalocyanine–BODIPY light harvesting pentad by laser flash photolysis**

Mohamed E. El-Khouly\*, Cem Göl, Morad M. El-Hendawy, Serkan Yeşilot and Mahmut Durmuş\*

Efficient energy transfer for symmetrical pentad bearing four BODIPY units connected to the phthalocyanine core via an ethynyl linkage at peripheral positions was investigated by femtosecond and nanosecond laser flash photolysis to explore photoinduced intramolecular events of the light harvesting pentad.

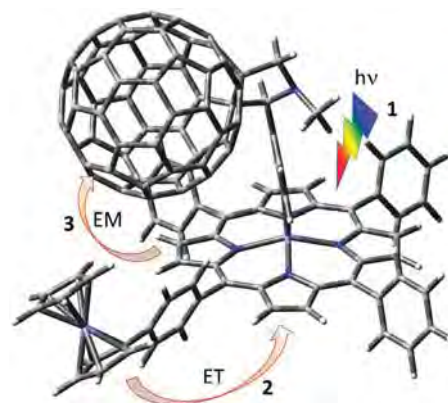


## pp. 270–280

**Charge separation in supramolecular ferrocene(s)-zinc porphyrin-fullerene triads: A femtosecond transient absorption study**

Gary N. Lim, Whitney A. Webre and Francis D'Souza\*

Using femtosecond transient absorption spectroscopy, mechanistic details of photoinduced charge separation in supramolecular triads, constructed using covalently linked zinc porphyrin-ferrocene(s) dyads — self-assembled *via* axial coordination to either pyridine or phenylimidazole appended fulleropyrrolidine is reported. Charge separation from ferrocene to  $^1\text{ZnP}^*$  to yield the initial  $\text{Fc}^+-\text{ZnP}^{\bullet-}:\text{C}_{60}$  radical ion-pair or charge separation from  $^1\text{ZnP}^*$  to  $\text{C}_{60}$  to yield the initial  $\text{Fc}-\text{ZnP}^{\bullet+}:\text{C}_{60}^{\bullet-}$  radical ion-pair, depending upon the ferrocene-zinc porphyrin intermolecular distance, is observed. These radical ion-pairs resulted in the formation of distantly separated  $\text{Fc}^+-\text{ZnP}:\text{C}_{60}^{\bullet-}$  radical ion-pairs either *via* an electron migration or hole shift process, as the ultimate electron transfer products.

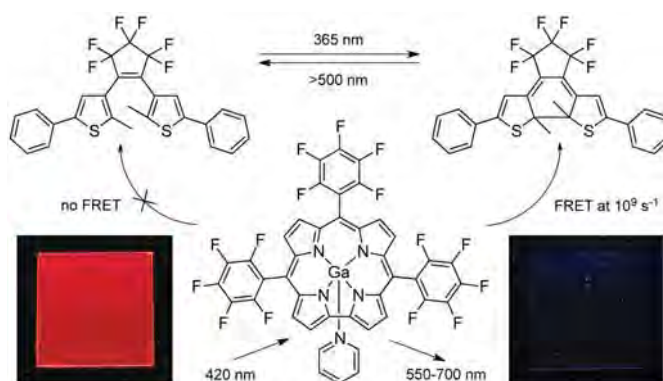


## pp. 281–287

**Nondestructive readout fluorescence memory based on a gallium(III) corrole complex and photochromic *cis*-1,2-dithienylethene**

Jijoon Kang and Youngmin You\*

Photochromic gating of fluorescence emission from a gallium(III) corrole complex provides a novel strategy for creation of fluorescence memory. The all-optical memory features advantages, including a high fluorescence on/off ratio and nondestructive readout capability. Transient photoluminescence experiments revealed effective modulation of intermolecular energy transfer from a fluorescent gallium corrole complex to photochromic *cis*-1,2-dithienylethene.

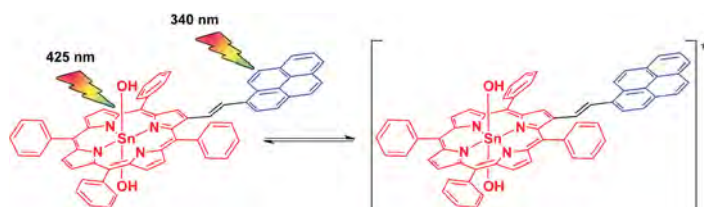


## pp. 288–300

**Photophysical properties of Sn(IV)tetraphenylporphyrin-pyrene dyad with a  $\beta$ -vinyl linker**

P. Silviya Reeta\*, Adis Khetubol, Tejaswi Jella, Vladimir Chukharev, Fawzi Abou-Chahine, Nikolai V. Tkachenko, L. Giribabu\* and Helge Lemmetyinen\*

A Sn(IV)tetraphenylporphyrin-pyrene dyad has been synthesized and its photophysical properties has been investigated by ps and fs time-resolved spectroscopy. Besides the occurrence of efficient excitation energy transfer (EET) from pyrene to porphyrin, the influence of conformational flexibility on the formation and decay of the excited dyads with increasing solvent polarity has been inferred by fs-ps transient absorption measurements.

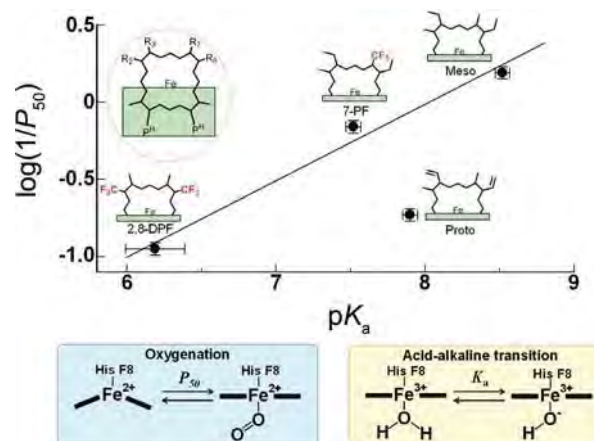


## pp. 301–307

**Effects of heme modification on oxygen affinity and cooperativity of human adult hemoglobin**

Tomokazu Shibata, Eisuke Furuichi, Kiyohiro Imai, Akihiro Suzuki and Yasuhiko Yamamoto\*

The  $\text{O}_2$  affinity of a reconstituted Hb exhibiting low cooperativity decreases with decreasing electron density of the heme Fe atom in such a manner that the  $P_{50}$  value increases by a factor of  $\sim 3$  with a decrease of 1  $\text{pK}_a$  unit. On the other hand, the native Hb deviated from the linear  $\text{pK}_a$ - $\log(1/P_{50})$  relationship, suggesting the significance of the heme vinyl side chains in the control of the  $\text{O}_2$  binding properties of the protein.

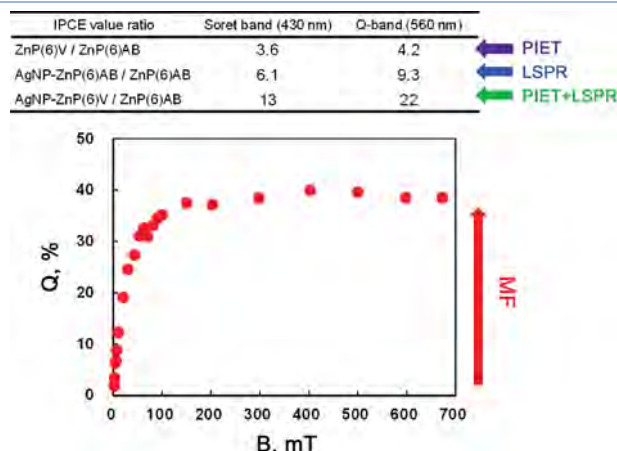


pp. 308–319

**Photocurrent enhancements in a porphyrin-viologen linked compound under plasmonic and magnetic fields**

Hiroaki Yonemura\*, Tomoki Niimi and Sunao Yamada

A remarkable increase in photocurrent for a zinc-porphyrin(ZnP)-viologen(V<sup>2+</sup>) linked compound (ZnP(6)V)-silver nanoparticle (AgNP) composite films was observed because of localized surface plasmon resonance (LSPR) from the AgNPs and photoinduced intramolecular electron-transfer (PIET) upon linking to a V<sup>2+</sup> moiety in the presence of a magnetic field (MF), when compared with ZnP derivative without V<sup>2+</sup> moiety (ZnP(6)AB) films as a reference in the absence of a MF.

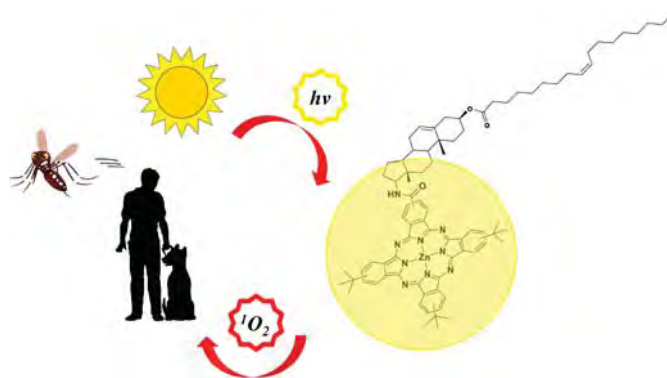


pp. 320–328

**Cholesteryl oleate-appended phthalocyanines as potential photosensitizers in the treatment of leishmaniasis**

Laura E. Sánchez Contreras, Johannes Zirzmeier, Sabrina V. Kirner, Francesca Setaro, Fernando Martínez, Stefany Lozada, Patricia Escobar, Uwe Hahn, Dirk M. Guldi\* and Tomás Torres\*

Two phthalocyanines (Pcs), of zinc and ruthenium, have been functionalized by cholesteryl oleate groups as potential photosensitizers (PSs) for photodynamic therapy (PDT) against leishmania. The photophysical characterization and their ability to photosynthesize singlet oxygen (<sup>1</sup>O<sub>2</sub>) of these potentially new photosensitizers (PSs) is provided. Their incubation into LDL particles and their toxicity and phototoxic activity have been assessed by *in vitro* preliminary studies on intracellular amastigotes of *L. panamensis* parasites and mammalian tumoral human monocytic cell line THP-1.



pp. 329–334

**Highly efficient hydroxylation of gaseous alkanes at reduced temperature catalyzed by cytochrome P450BM3 assisted by decoy molecules**

Norifumi Kawakami, Zhiqi Cong, Osami Shoji\* and Yoshihito Watanabe\*

Cytochrome P450BM3 functions as a small-alkane hydroxylase upon the addition of perfluorocarboxylic acids as decoy molecules. The coupling efficiency for the hydroxylation of small alkanes was improved by reducing the reaction temperature to 0 °C.

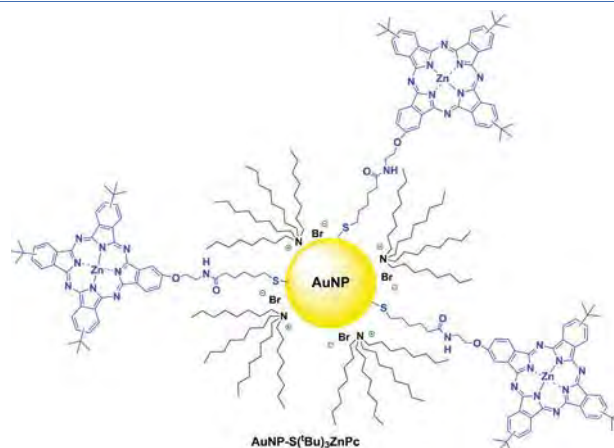


pp. 335–343

**Synthesis and characterization of a sulfur-containing phthalocyanine-gold nanoparticle hybrid**

Vicente M. Blas-Ferrando, Javier Ortiz, Fernando Fernández-Lázaro and Ángela Sastre-Santos\*

The synthesis and characterization of a new gold nanoparticle-zinc phthalocyanine system, AuNP-S(tBu)<sub>3</sub>ZnPc is reported. A solid configuration of TiO<sub>2</sub>-lipoic acid-AuNP-S(tBu)<sub>3</sub>ZnPc has been also prepared.



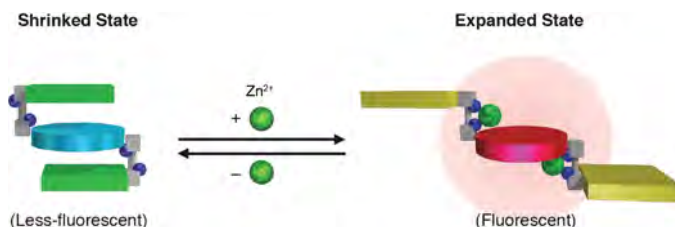


## pp. 344–351

**Metal-induced dynamic conformational and fluorescence switch of quinone-appended Zn-porphyrin**

Yasuyuki Yamada, Kosuke Hiraga and Kentaro Tanaka\*

We have designed and synthesized a novel switching molecule whose fluorescence can be switched via dynamic conformational change between expanded and shrunk states induced by metal complexation and decomplexation. It was revealed that metal complexation of the bipyridine units of the molecule with  $Zn^{2+}$  ions induced the dynamic structural change of the molecular shape and simultaneous enhancement of fluorescence of the  $Zn^{2+}$ -porphyrin fluorophore.

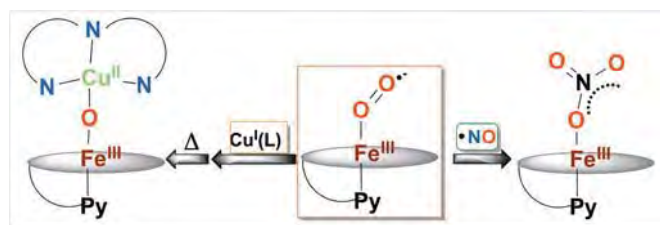


## pp. 352–360

**Reactions of a heme-superoxo complex toward a cuprous chelate and  $\bullet NO_{(g)}$ : CcO and NOD chemistry**

Savita K. Sharma, Patrick J. Rogler and Kenneth D. Karlin\*

A synthetically designed ferric heme superoxo complex displays cytochrome *c* oxidase reactivity in the presence of a copper(I) complex or nitric oxide dioxygenase reactivity in the presence of  $\bullet NO_{(g)}$ .

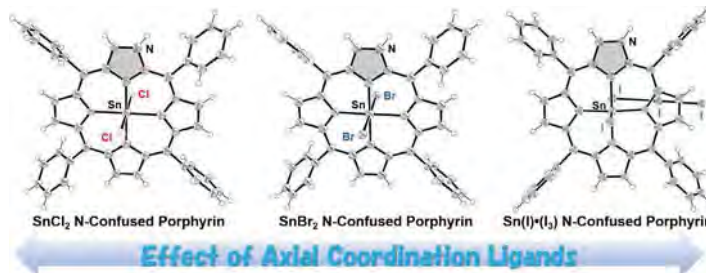


## pp. 361–371

**Near-infrared luminescent Sn(IV) complexes of N-confused tetraphenylporphyrin: Effect of axial anion coordination**

Arghya Basu, Motoki Kitamura, Shigeki Mori, Masatoshi Ishida, Yongshu Xie and Hiroyuki Furuta\*

Tin(IV) complexes of N-confused tetraphenylporphyrin with different axial halide ligands,  $SnX_2-2$  ( $X = Cl, Br, I/I_3$ ), have been synthesized and their X-ray crystal structures were determined. Among the complexes, unsymmetrically coordinated  $Sn(I)(I_3)-2$  showed the longer emission lifetimes and a smaller singlet-triplet energy gap.

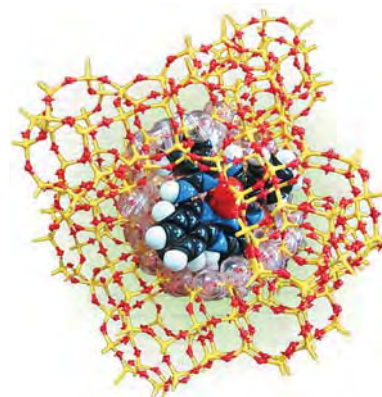


## pp. 372–376

**Preparation and characterization of cobalt(II) phthalocyanine complex-encapsulated zeolite-X**

Nayumi Ohata, Yurie Ito, Daisuke Nakane, Hideki Kitamura and Hideki Masuda\*

Cobalt(II) phthalocyanine complex encapsulated into the supercage of X-type zeolite, CoPc-X, and its secondary ion-exchanged zeolite ( $M^{n+} = Na^+, Ag^+, Cu^{2+}, Zn^{2+}$ ), CoPc- $M^{n+}$ -X, were prepared and characterized spectroscopically. They showed a unique deodorant behavior for smell gasses, 2-nonenal and indole.

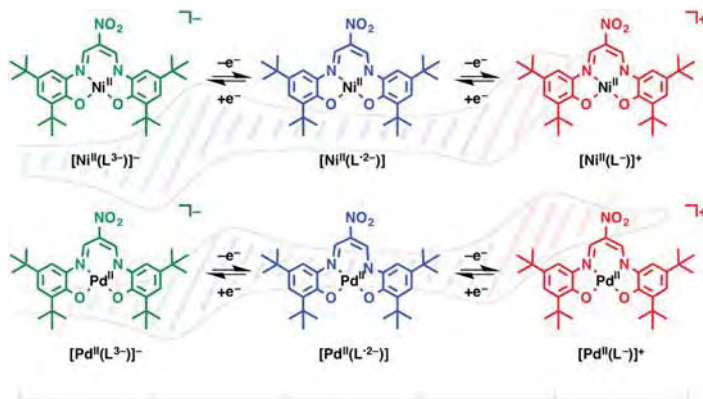


pp. 377–387

**Redox behavior of novel nickel and palladium complexes supported by trianionic non-innocent ligand containing  $\beta$ -diketiminato and phenol groups**

Yuma Morimoto, June Takaichi, Shinichi Hanada, Kei Ohkubo, Hideki Sugimoto, Nobutaka Fujieda, Shunichi Fukuzumi and Shinobu Itoh\*

A new type of nickel and palladium complexes with non-innocent  $\beta$ -diketiminato ligand having redox active phenol groups ( $LH_3$ , fully protonated form) have been developed, and the structure, physical properties, and reactivity of their one-electron and two-electron oxidized complexes,  $[M^H(L^{2-})]$  and  $[M^H(L^-)]^+$  ( $M = Ni^{II}$  or  $Pd^{II}$ ) have been examined in detail.

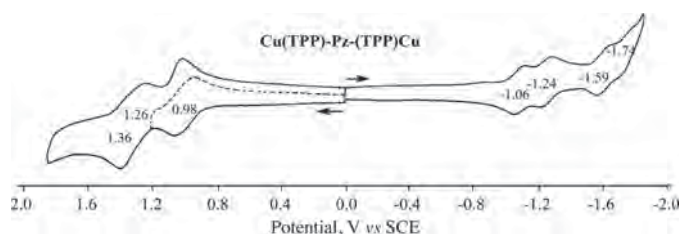


pp. 388–397

**Electrochemistry and spectroelectrochemistry of  $\beta$ -pyrazino-fused tetraarylporphyrins in non-aqueous media**

Yuan Yuan Fang, Federica Mandoj, Lihan Zeng, Rajesh Pudi, Manuela Stefanelli, Roberto Paolesse\* and Karl M. Kadish\*

Bis-porphyrins containing a  $\beta,\beta'$ -fused pyrazino (Pz) linking group were examined by electrochemistry and thin-layer UV-visible spectroelectrochemistry in PhCN containing 0.1 M tetra-*n*-butylammonium perchlorate (TBAP) as supporting electrolyte. The investigated compounds are represented as  $M(TPP)-Pz-(TPP)M$ , where TPP is the dianion of tetraphenylporphyrin and  $M = Zn(II)$ ,  $Cu(II)$  or  $Ag(II)$ .

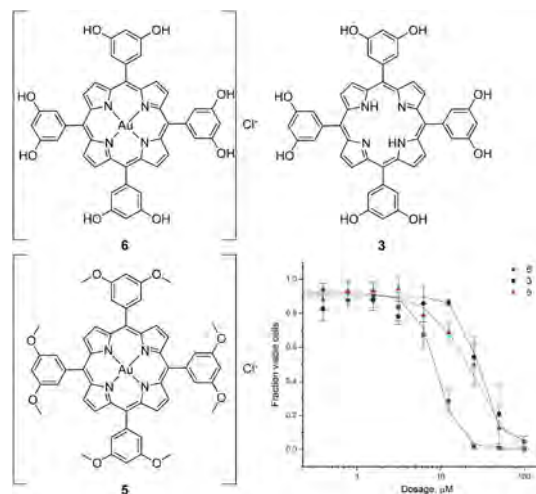


pp. 398–403

**Synthesis and anti-cancer activities of a water soluble gold(III) porphyrin**

Aaron D. Lammer, Melissa E. Cook and Jonathan L. Sessler\*

A recognized limitation of gold(III) as an anticancer agent is susceptibility to reduction under physiological conditions to produce the more labile gold(I) state. The use of porphyrins is an attractive solution to this potential problem. Typically, however, the stabilization provided by the use of a strongly chelating porphyrin is offset by the poor solubility of the resulting complex in aqueous media. In this work the synthesis and *in vitro* anti-cancer activity of a gold(III) porphyrin complex (**6**) with relatively good aqueous solubility is described. As judged from standard antiproliferation assays, this complex displays an  $IC_{50}$  of 9  $\mu M$  for the A2780 human ovarian cancer cell line. This activity is statistically enhanced relative to two control systems (compounds **3** and **5**).

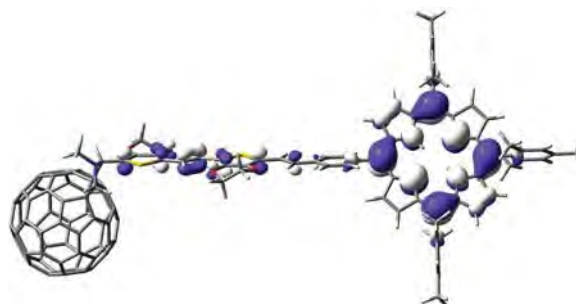


pp. 404–410

**Free-base porphyrin and [60]fullerene linked by oligomeric ethylenedioxythienylenevinylene bridge**

Beatriz Pelado, Julieta Coro, Pilar de la Cruz and Fernando Langa\*

The synthesis and structural characterization and the study of the electronic properties of two novel porphyrin-bridge-fullerene molecules, where a free-based porphyrin and [60]fullerene are connected through one and two units of ethylenedioxythienylenevinylene  $\pi$ -conjugated bridges, is reported. The absorption studies, voltamperometric measurements and theoretical calculations at DFT level are presented.

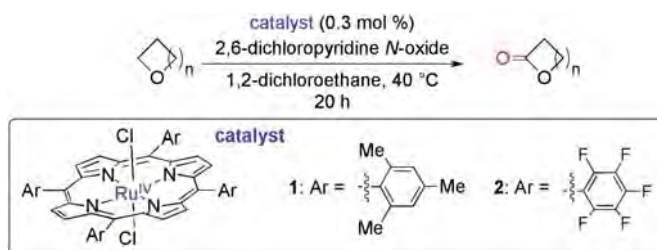


## pp. 411–416

**Efficient oxidation of ethers with pyridine *N*-oxide catalyzed by ruthenium porphyrins**

Nobuki Kato, Yu Hamaguchi, Naoki Umezawa and Tsunehiko Higuchi\*

It was found that oxidation of cyclic ethers with this reaction system gave lactones or/and ring-opened oxidized products with regioselectivity. A relatively high kinetic isotope effect was observed in the ether oxidation, suggesting that the rate-determining step is the first hydrogen abstraction.

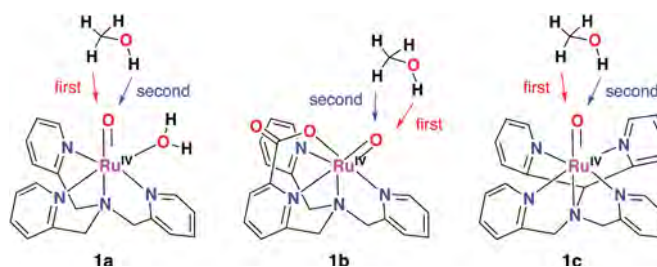


## pp. 417–426

**Mechanistic study of methanol oxidation by Ru<sup>IV</sup>-oxo complexes**

Yoshihito Shiota\*, Shoya Takahashi, Shingo Ohzu, Tomoya Ishizuka, Takahiko Kojima and Kazunari Yoshizawa\*

The catalytic conversion of methanol to formaldehyde by three kinds of non-porphyrin Ru<sup>IV</sup>-oxo complexes is discussed by using DFT calculations. There are two possible reaction pathways for the oxidation of methanol to formaldehyde with respect to the first hydrogen abstraction from the methyl group and the hydroxyl group. The rate-determining step is the H-atom abstraction from the CH<sub>3</sub> group of methanol, being in good agreement with kinetic analysis of the reactions.

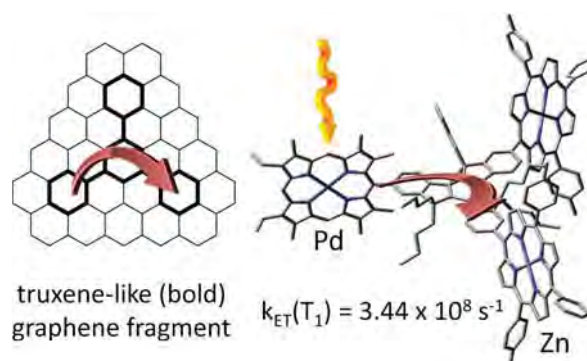


## pp. 427–441

**Very fast singlet and triplet energy transfers in a tri-chromophoric porphyrin dyad aided by the truxene platform**

Adam Langlois, Hai-Jun Xu, Paul-Ludovic Karsenti, Claude P. Gros\* and Pierre D. Harvey\*

A truxene-containing dyad with an octa- $\beta$ -alkyl-palladium(II)porphyrin (donor) and two tri-*meso*-aryl-zinc(II)porphyrins (acceptors) exhibits very fast rates for triplet energy transfers at 77 K ( $k_{ET}(T_1) = 1.63 \times 10^8$ ) and 298 K ( $k_{ET}(T_1) = 3.44 \times 10^8$  s<sup>-1</sup>). The energy transfer processes proceed *via* a through bond Dexter mechanism with evidence for a moderate MO coupling between the donor and acceptors in the frontier MOs.

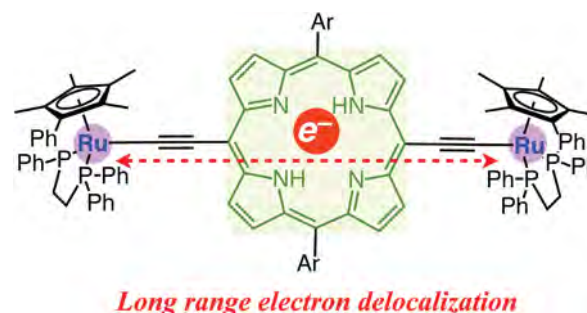


## pp. 442–450

**Synthesis and wire-like performance of diruthenium molecular wire with a C≡C-porphyrin-C≡C linker**

Yuya Tanaka, Masanori Ono and Munetaka Akita\*

A bis-ruthenium complex with a free-base porphyrin linker **1** is synthesized and characterized. By electrochemical and spectroscopic measurements, complex **1**<sup>2+</sup> is assigned as a Class III compounds according to Robin-Day classification. DFT calculation also supports strong electronic coupling between the two metal ends.

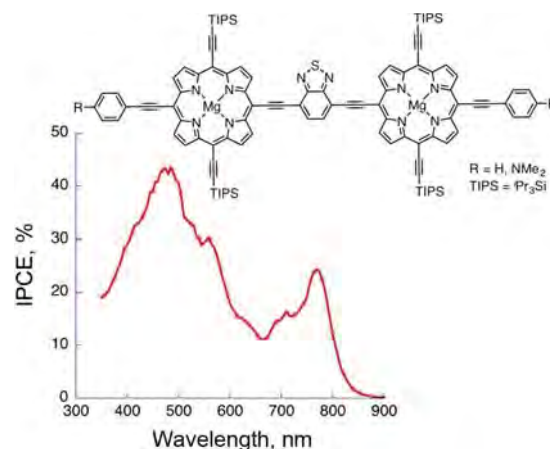


pp. 451–458

**Diporphyrin magnesium complex with long-wavelength light absorption for organic solar cells**

Takenari Sato, Takafumi Nakagawa, Hiroshi Okada and Yutaka Matsuo\*

Magnesium complexes of donor–acceptor–donor-type diporphyrin compounds containing two tetraethynylporphyrin units and one benzothiadiazole unit were synthesized and used in solution-processed organic thin-film solar cells. Long-wavelength light absorption due to low-bandgap nature contributed to photocurrent conversion in the near infrared region.

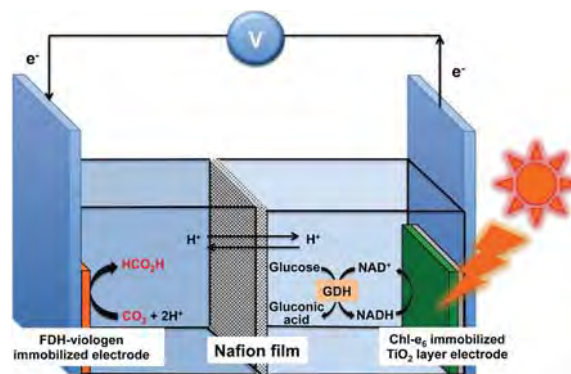


pp. 459–464

**Formate dehydrogenase catalyzed CO<sub>2</sub> reduction in a chlorin-e<sub>6</sub> sensitized photochemical biofuel cell**

Yutaka Amao\* and Naho Shuto

The new visible-light operated CO<sub>2</sub>-glucose biofuel cell consisting of chlorin-e<sub>6</sub> immobilized on TiO<sub>2</sub> thin layer film onto optical transparent conductive glass electrode as an anode, formate dehydrogenase and viologen with long alkyl chain co-immobilized onto electrode as a cathode, and the solution containing glucose, glucose dehydrogenase and NAD<sup>+</sup> as a fuel is developed. During visible light irradiation, the photocurrent was generated and formic acid was produced in the cell. Thus, CO<sub>2</sub> reduces and formic acid produces while generating electricity with visible light irradiation to this biofuel cell.

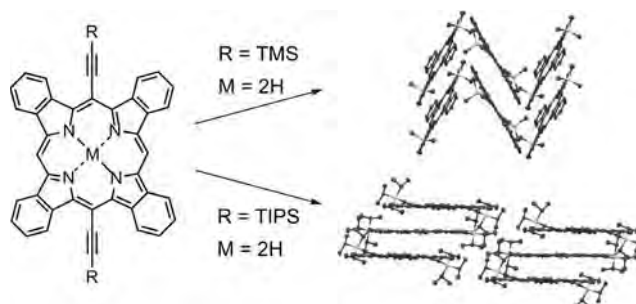


pp. 465–478

**Effect of alkyl substituents: 5,15-bis(trimethylsilylethynyl)- vs. 5,15-bis(triisopropylsilylethynyl)-tetrabenzoporphyrins and their metal complexes**

Kohtarō Takahashi, Naoya Yamada, Daichi Kumagai, Daiki Kuzuhara, Mitsuharu Suzuki, Yuji Yamaguchi, Naoki Aratani, Ken-ichi Nakayama\* and Hiroko Yamada\*

Crystal structures of 5,15-bis(trimethylsilylethynyl)tetrabenzoporphyrin (**TMS-H<sub>2</sub>BP**), 5,15-bis(triisopropylsilylethynyl)tetrabenzoporphyrin (**TIPS-H<sub>2</sub>BP**) and their metal complexes have been carefully studied. Bulk heterojunction organic solar cell based on **TMS-ZnBP** as p-type and PC<sub>71</sub>BM as n-type material fabricated by solution process attained the power-conversion efficiency (PCE) of 1.49%.



pp. 479–491

**Corrole–imide dyads — Synthesis and optical properties**

Roman Voloshchuk, Mariusz Tasiar, Adina I. Ciuciu, Lucia Flamigni\* and Daniel T. Gryko\*

Two rarely seen building blocks have been incorporated into light absorbing arrays: corroles and 2,3-naphthalimides. General synthetic strategy consisting in direct condensation of formyl substituted aromatic imides with dipyrroles led to diverse range of *trans*-A<sub>2</sub>B-corroles in acceptable yields. In small, strongly polarized amino-cyano-phthalimide neither efficient energy- nor electron-transfer could be detected and excitation leads to fluorescence from both components.

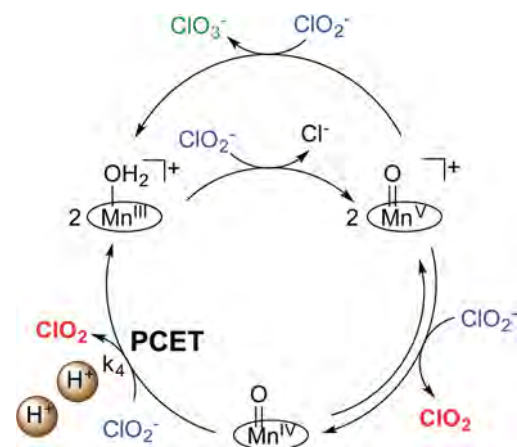


pp. 492–499

**Mechanistic study of a manganese porphyrin catalyst for on-demand production of chlorine dioxide in water**

Scott D. Hicks, Silei Xiong, Curt J. Bougher, Grigori A. Medvedev, James Caruthers and Mahdi M. Abu-Omar\*

A water-soluble manganese porphyrin complex was examined for the catalytic formation of chlorine dioxide from chlorite under ambient temperature at pH 5.00 and 6.90. Catalysis is initiated via an OAT (Oxygen Atom Transfer) reaction resulting in formation of a putative manganese(V) oxo species, which undergoes ET (Electron Transfer) with chlorite to form chlorine dioxide. As chlorine dioxide accumulates in solution, chlorite consumption slows down and  $\text{ClO}_2$  reaches a maximum as the system reaches equilibrium. The  $\text{ClO}_2$  product can be collected from the aqueous reaction mixture via purging with an inert gas, allowing for the preparation of chlorine dioxide on-demand.

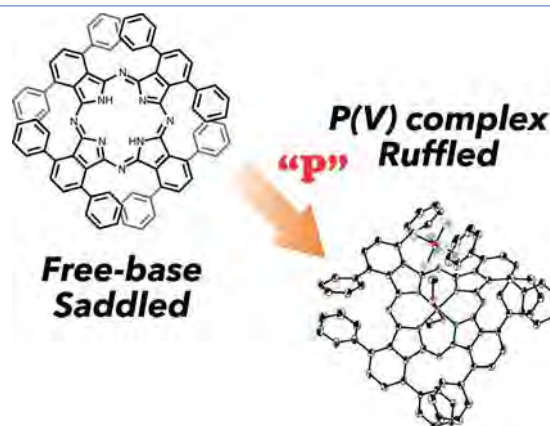


pp. 500–509

**Structural changes in non-planar octaaryl substituted phthalocyanine phosphorus complexes**

Taniyuki Furuyama, Ryosuke Harako and Nagao Kobayashi\*

Phosphorus complexes of non-planar  $\alpha$ -octaaryl phthalocyanine derivatives ( $(\alpha\text{-Ar})_8\text{Pc}$ ) have been synthesized by introduction of phosphorus(V) ions into free-base Pcs. The solid state structure of phosphorus complex indicated a ruffled Pc structure due to the small atomic radius of phosphorus, although the corresponding free-base Pc has a saddled Pc structure.

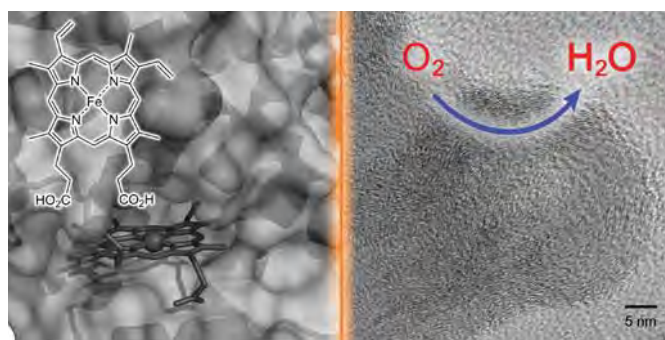


pp. 510–516

**Myoglobin-based non-precious metal carbon catalysts for an oxygen reduction reaction**

Akira Onoda\*, Yuta Tanaka, Toshikazu Ono, Shotaro Takeuchi, Akira Sakai and Takashi Hayashi\*

A non-precious metal catalyst promoting an oxygen reduction reaction was synthesized by heat-treatment of myoglobin (Mb) containing a heme. The Mb-based catalyst prepared at 940 °C catalyzes four-electron ORR and the onset potential is  $0.84 \pm 0.01$  V.

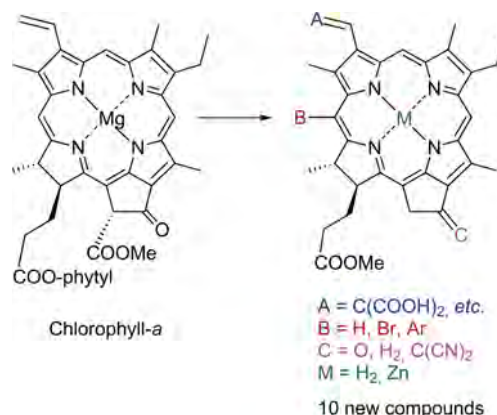


pp. 517–526

**Synthesis of carboxylated chlorophylls and their application as functional materials**

Shin-ichi Sasaki, Xiao-Feng Wang, Toshitaka Ikeuchi and Hitoshi Tamiaki\*

A series of carboxylated chlorophylls were synthesized and their application as components for dye-sensitized solar cells as well as sensing reagents were investigated. The detection of additional amine in THF was demonstrated by both visible absorption and fluorescence emission spectroscopies, while the photovoltaic performance of DSSCs were evaluated using chlorophyll-adsorbed  $\text{TiO}_2$  films.

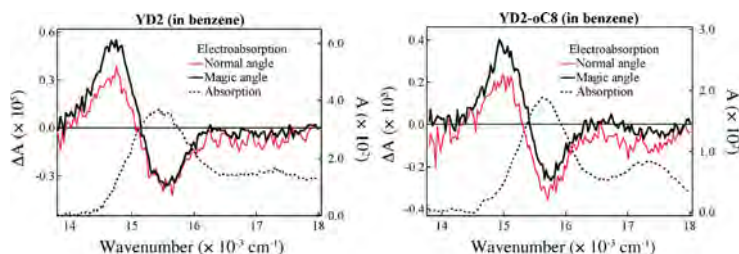


pp. 527–534

**Electroabsorption spectra of push–pull porphyrins in solution and in solid films**

Kamlesh Awasthi, Hung-Yu Hsu, Hung-Chu Chiang, Chi-Lun Mai, Chen-Yu Yeh\*, Eric Wei-Guang Diau\* and Nobuhiro Ohta\*

Polarized electroabsorption spectra of push–pull porphyrins which were used as dye-sensitizer in solar cells have been measured in solution and in solid films. Based on the results, the magnitudes of the electric dipole moment both in the ground state and in the excited state have been determined. These values are strongly related to the efficiency of dye-sensitized solar cells.

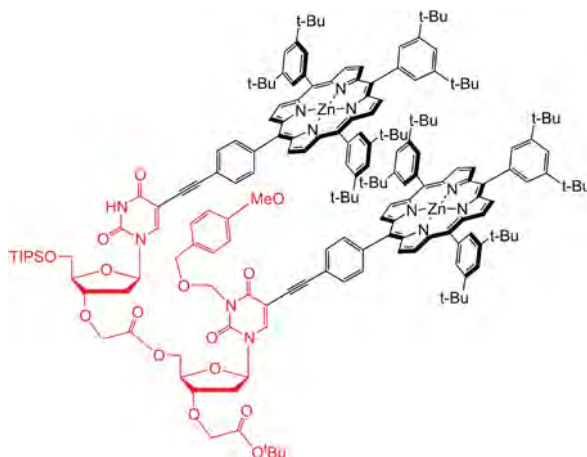


pp. 535–546

**Pre-organized dinucleosides with pendant porphyrins for the formation of sandwich type complexes with DABCO with high association constants**

Sonja Merkas, Souhaila Bouatra, Régis Rein, Ivo Piantanida, Mladen Zinic and Nathalie Solladié\*

The synthesis of a dinucleotide bearing pendant porphyrins dedicated to adopt a pre-organized conformation with face-to-face porphyrins is reported herein. We document the fact that some well-chosen nucleosidic linkers offer an interesting option for the synthesis of devices capable to self-organize in a stable sandwich type complex and enhance significantly the association constant with bidentate bases such as DABCO.



# AUTHOR INDEX (cumulative)

JPP Volume 19 - Numbers 1–3 - Pages 1–546

- 
- A**  
Abe, Masaaki 233  
Abou-Chahine, Fawzi 288  
Abu-Omar, Mahdi M. 492  
Akita, Munetaka 442  
Amao, Yutaka 459  
Angaridis, Panagiotis P. 175  
Aono, Shigetoshi 9  
Aratani, Naoki 465  
Arnold, John 150  
Ashigara, Shiho 233  
Awasthi, Kamlesh 527
- B**  
Basu, Arghya 361  
Bediako, D. Kwabena 1  
Blas-Ferrando, Vicente M. 335  
Bouatra, Souhaila 535  
Bougher, Curt J. 492  
Britton, Jonathan 192  
Buckley, Heather L. 150
- C**  
Caruthers, James 492  
Chatterjee, Sudipta 92  
Chen, Wen-Tong 154  
Chen, Xueyan 251  
Chiang, Hung-Chu 527  
Chukharev, Vladimir 288  
Ciuciu, Adina I. 479  
Cong, Zhiqi 329  
Cook, Melissa E. 398  
Coro, Julieta 404  
Coutsolelos, Athanassios G. 175
- D**  
Das, Pradip Kumar 92  
de la Cruz, Pilar 404  
Dey, Abhishek 92  
Diau, Eric Wei-Guang 527  
Dogutan, Dilek K. 1  
D'Souza, Francis 270  
Durmuş, Mahmut 261
- E**  
El-Hendawy, Morad M. 261  
El-Khouly, Mohamed E. 261  
Escobar, Patricia 320
- F**  
Fang, Yuanyuan 251, 388  
Fernández-Lázaro, Fernando 335  
Flamigni, Lucia 479  
Fu, Hong-Ru 154  
Fujieda, Nobutaka 377  
Fujimori, Yamato 140  
Fujimoto, Keisuke 171  
Fujita, Etsuko 45  
Fukuzumi, Shunichi 32, 219, 377  
Furuichi, Eisuke 301  
Furuta, Hiroyuki 361  
Furuyama, Taniyuki 500
- G**  
Giribabu L. 288  
Göl, Cem 261  
Golub, Eyal 65  
Graham, Daniel J. 1  
Gros, Claude P. 427  
Gryko, Daniel T. 479  
Guldi, Dirk M. 320
- H**  
Hahn, Uwe 320  
Hamaguchi, Yu 411  
Hanada, Shinichi 377  
Harako, Ryosuke 500  
Harvey, Pierre D. 427  
Hasobe, Taku 242  
Hayashi, Takashi 510  
Hicks, Scott D. 492  
Higashino, Tomohiro 140  
Higuchi, Tsunehiko 411  
Hiraga, Kosuke 344  
Hiroto, Satoru 135  
Hisaeda, Yoshio 233  
Hsu, Hung-Yu 527  
Huang, Jian-Gen 154
- I**  
Ikeuchi, Toshitaka 517  
Imahori, Hiroshi 140  
Imai, Kiyohiro 301  
Ishida, Masatoshi 361  
Ishizuka, Tomoya 32, 417
- Ito, Seigo 140  
Ito, Yurie 372  
Itoh, Shinobu 377
- J**  
Jella, Tejaswi 288  
Jiang, Xiaoqin 251
- K**  
Kadish, Karl M. 251, 388  
Kamimura, Takuya 219, 242  
Kang, Jijoon 281  
Karlin, Kenneth D. 352  
Karsenti, Paul-Ludovic 427  
Kato, Kenichi 160  
Kato, Nobuki 411  
Kawakami, Norifumi 329  
Khetubol, Adis 288  
Kirner, Sabrina V. 320  
Kitamura, Hideki 372  
Kitamura, Motoki 361  
Kitatsuji, Chihiro 9  
Kobayashi, Nagao 500  
Kojima, Takahiko 32, 417  
Koukaras, Emmanuel N. 175  
Kumagai, Daichi 465  
Kuzuhara, Daiki 465
- L**  
Ladomenou, Kalliopi 175  
Lammer, Aaron D. 398  
Langa, Fernando 404  
Langlois, Adam 427  
Lemmetyinen, Helge 288  
Lemon, Christopher M. 1  
Lim, Gary N. 270  
Lozada, Stefany 320  
Lu, Chun-Hua 65  
Luo, Qiu-Yan 154
- M**  
Mack, John 192  
Mai, Chi-Lun 527  
Manbeck, Gerald F. 45  
Mandoj, Federica 388  
Martínez, Fernando 320  
Masuda, Hideki 372  
Matsuo, Yutaka 451

- Medvedev, Grigori A. 492  
 Merkas, Sonja 535  
 Missert, Joseph R. 109  
 Mkhize, Colin 192  
 Mori, Shigeki 361  
 Morimoto, Yuma 377  
 Muraki, Norifumi 9  
 Mustafar, Suzaliza 21
- N**  
 Nakagawa, Takafumi 451  
 Nakane, Daisuke 372  
 Nakayama, Ken-ichi 465  
 Nakayama, Toru 160  
 Niimi, Tomoki 308  
 Nishihara, Hiroshi 21  
 Nocera, Daniel G. 1  
 Nyokong, Tebello 192
- O**  
 Ohata, Nayumi 372  
 Ohkubo, Kei 219, 377  
 Ohta, Nobuhiro 527  
 Ohzu, Shingo 417  
 Okada, Hiroshi 451  
 Okawara, Toru 233  
 Ono, Masanori 442  
 Ono, Toshikazu 510  
 Onoda, Akira 510  
 Ortiz, Javier 335  
 Osuka, Atsuhiko 171  
 Ou, Zhongping 251
- P**  
 Padilla, Rosa 150  
 Pandey, Ravindra K. 109  
 Paolesse, Roberto 388  
 Pelado, Beatriz 404  
 Piantanida, Ivo 535  
 Pudi, Rajesh 388
- R**  
 Reeta, P. Silviya 288  
 Rein, Régis 535  
 Rogler, Patrick J. 352
- S**  
 Sakai, Akira 510  
 Sakai, Hayato 242  
 Sakamoto, Ryota 21  
 Sakatani, Shuhei 219  
 Sakurai, Tsuneaki 160  
 Samanta, Subhra 92  
 Sánchez Contreras, Laura E. 320  
 Sasaki, Shin-ichi 517  
 Sastre-Santos, Ángela 335  
 Sato, Takenari 451  
 Seki, Shu 160  
 Sessler, Jonathan L. 398  
 Setaro, Francesca 320  
 Sharma, Ganesh D. 175  
 Sharma, Savita K. 352  
 Shibata, Tomokazu 301  
 Shin, Ji-Young 135  
 Shinokubo, Hiroshi 135  
 Shiota, Yoshihito 417  
 Shoji, Osami 329  
 Shuto, Naho 459  
 Solladié, Nathalie 535  
 Srivatsan, Avinash 109  
 Stefanelli, Manuela 388  
 Sugimoto, Hideki 377  
 Sugiura, Kenichi 140  
 Susumu, Kimihiro 205  
 Suzuki, Akihiro 301  
 Suzuki, Mitsuharu 465
- T**  
 Takahashi, Kohtarō 465  
 Takahashi, Shoya 417  
 Takaichi, June 377  
 Takata, Masaki 160  
 Takeuchi, Shotaro 510  
 Tamiaki, Hitoshi 517  
 Tanaka, Kentaro 344  
 Tanaka, Yuta 510  
 Tanaka, Yuya 442  
 Tani, Fumito 219, 242  
 Tasior, Mariusz 479
- Therien, Michael J. 205  
 Tkachenko, Nikolai V. 288  
 Torres, Tomás 320  
 Tsuji, Yukihiko 140
- U**  
 Umezawa, Naoki 411  
 Upadhyay, Santosh K. 109
- V**  
 Voloshchuk, Roman 479
- W**  
 Wang, Xiao-Feng 517  
 Ward, Ashleigh L. 150  
 Watanabe, Yoshihito 329  
 Webre, Whitney A. 270  
 Willner, Itamar 65
- X**  
 Xie, Yongshu 361  
 Xiong, Silei 492  
 Xu, Hai-Jun 427  
 Xu, Ya-Ping 154  
 Xue, Songlin 251
- Y**  
 Yamada, Hiroko 465  
 Yamada, Naoya 465  
 Yamada, Sunao 308  
 Yamada, Yasuyuki 344  
 Yamaguchi, Yuji 465  
 Yamamoto, Yasuhiko 301  
 Ye, Lina 251  
 Yeh, Chen-Yu 527  
 Yeşilot, Serkan 261  
 Yoneda, Satoru 160  
 Yonemura, Hiroaki 308  
 Yorimitsu, Hideki 171  
 Yoshizawa, Kazunari 417  
 You, Youngmin 281
- Z**  
 Zeng, Lihan 388  
 Zervaki, Galatea E. 175  
 Zinic, Mladen 535  
 Zirzmeier, Johannes 320



# KEYWORD INDEX (cumulative)

JPP Volume 19 - Numbers 1–3 - Pages 1–546

- 
- A**  
acid-alkaline transition 301  
air sensitive 150  
anti-cancer 398  
aptamer 65  
axial coordination 32
- B**  
benzo[c][1,2,5]thiadiazole 205  
benzoporphyrin 465  
binding studies 535  
biofuel cell 459  
biomass 459  
bipyridine 344  
bisporphyrin 388  
boron dipyrromethene (BODIPY) 261  
 $\beta$ -vinyl pyrene donor 288
- C**  
cancer-imaging 109  
carbon catalyst 510  
catalysis 492  
catalyst 1, 65  
catalytic mechanism 417  
C–H activation 417  
charge separation 270  
chemiluminescence 65  
chlorin 517  
chlorin-e6 459  
chlorine dioxide 492  
cholesterol 320  
CO<sub>2</sub> reduction 45, 459  
cobalt 45  
cobalt phthalocyanine 372  
cobalt phthalocyanine–encapsulated zeolite 372  
columnar phase 160  
cooperativity 301  
corrole 1, 150  
corroles 281, 479  
crystal structure 154, 465  
crystal structures 233  
cubic cluster 171  
cytochrome P450 329
- D**  
DDQ oxidation 135  
decoy molecules 329  
deodorant behavior 372  
deprotonation 251  
determination of equilibrium constants 251  
Dexter mechanism 427  
DFT calculation 417  
DFT calculations 361  
diethynylporphyrin 205  
diphosphine 171  
dipyrranes 479  
dipyrrin 135  
DNA 65  
DNAzyme 65  
dodecaphenylporphyrin 32  
donor–acceptor 219  
DSSC 175  
dye-sensitized solar cell 517, 527  
dye-sensitized solar cells 21
- E**  
early transition metal 150  
EDOT 404  
electric dipole moment 527  
electrochemistry 21, 388  
electronic structure 500  
electron transfer 219, 442  
endohedral fullerene 242  
energy transfer 219, 261, 281, 427  
ether 411
- F**  
femtosecond transient spectroscopy 270  
ferrocene 270  
fluorescence 154, 65, 109, 479  
fluorescence memory 281  
fluorescence switching 344  
folding 344  
formate dehydrogenase 459  
framework 154  
fs transient absorption 288  
fullerene 270, 404
- G**  
gaseous alkanes 329  
glycine 175  
gold 398  
gold nanoparticle 335
- H**  
hangman effect 1  
heme 9, 510  
heme-copper-m-oxo 352  
heme electronic structure 301  
heme regulatory motif 9  
heme-superoxo 352  
hemin 65  
hemoglobin 301  
high spin heme-copper peroxo 352  
hydrogen evolution 1  
hydrothermal reaction 154
- I**  
imide 479  
intramolecular charge transfer 135  
ion-exchange method 372  
iron 45  
iron porphyrin 92
- K**  
kinetics 288, 492
- L**  
laser photolysis 261  
leishmaniasis 320  
Lewis acidity 32  
light harvesting 261  
liquid crystal 160  
localized surface plasmon resonance 308  
low-bandgap 451
- M**  
magnesium 451  
magnetic field effect 308  
magnetic resonance imaging 109  
manganese 492  
MCD spectroscopy 192  
metal center effect 388  
metal complexes 465  
methanol oxidation 417

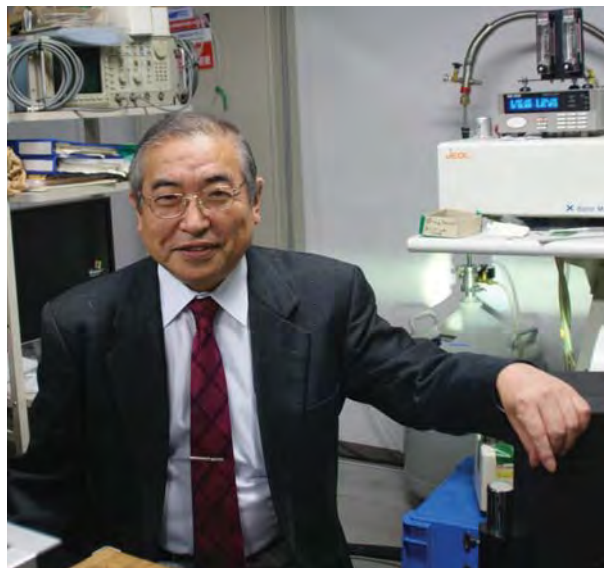
- mixed valence 442  
 MO coupling 427  
 molecular wire 404, 442  
 multimodality agents 109  
 myoglobin 510
- N**
- nanoparticles 109  
 nanoplatfoms 109  
*N*-arylamino porphyrinoids 21  
*N*-confused free-base porphyrins 251  
*N*-confused porphyrin 361  
 near infrared 205  
 near-infrared absorption 500  
 nickel complex 377  
 nitrate 352  
 non-innocent ligand 377  
 non-precious metal catalyst 510  
 nucleosides 535  
 nuclear imaging 109
- O**
- one-dimensional polymer 160  
 optical limiting 192  
 optical properties 288  
 organic solar cells 451, 465  
 ORR 92  
 oxidation 411  
 oxygen affinity 301  
 oxygen evolution 1  
 oxygen reduction reaction 510
- P**
- palladium complex 377  
 palladium(II)porphyrin 427  
 perfluorocarboxylic acids 329  
 peroxy nitrite 352  
 phosphorus phthalocyanine 500  
 photochemistry 21  
 photochromism 281  
 photocurrent 308  
 photodynamic therapy 109
- photoinduced electron transfer 32  
 photoinduced intramolecular  
   electron-transfer 308  
 photophysical properties 361  
 photosubstitution 233  
 photovoltaic cell 242  
 photovoltaics 451  
 phthalocyanine 160, 261, 45  
 phthalocyanines 320  
 piperidine 175  
 polyoxometallates 32  
 porphycene 233  
 porphyrin 1, 140, 154, 160, 219,  
   242, 45, 171, 344, 398, 404, 411,  
   451, 492, 535  
 porphyrin dyad 175  
 protonation 251  
 proton-coupled electron transfer  
   (PCET) 1  
 push effect 92  
 push-pull porphyrins 527  
 pyridine *N*-oxide 411
- Q**
- quantum yield 205  
 quinoidal porphyrin 219  
 quinone 344
- R**
- radical pair mechanism 308  
 redox properties 233  
 renewable 1  
 ruffled structure 500  
 Ru-oxo complex 417  
 ruthenium 233, 442  
 ruthenium catalyst 411
- S**
- saddle-type distortion 32  
*s*-diketiminato ligand 377  
 sensor 65  
 sensor proteins 9  
 ship-in-bottle synthesis 372
- silver complex 171  
 silver nanoparticle 308  
 singlet oxygen 192, 320  
 Sn(IV)tetraphenylporphyrin  
   288  
 solar cell 140  
 solar energy 459  
 solar fuels 1  
 solubility 398  
 spectroelectrochemistry 388  
 stark shift 527  
 steroids 320  
 Strickler-Berg 205  
 supramolecular assembly 242  
 supramolecular complexes 535  
 supramolecular triad 270  
 synthesis 479
- T**
- telomerase 65  
 tetrapyrrole 517  
 theranostics 109  
 tin(IV) complex 361  
 titanium oxide 140  
 transcriptional regulator 9  
 triazatetrazabenzcorrole 192  
 triazine 175  
 tungsten 150  
 two-component system 9
- U**
- ultrafast fluorescence lifetime  
   427
- V**
- visible absorption spectrum 517
- X**
- X-type zeolite 372
- Z**
- zinc(II)porphyrin 427  
 zinc phthalocyanine 335  
 zinc porphyrin 270

## Preface — Special Issue in Honor of Professor Shunichi Fukuzumi

We are very much pleased to dedicate this special issue of *Journal of Porphyrins and Phthalocyanines* to **Prof. Shunichi Fukuzumi** on his retirement from Osaka University in March, 2014. The main research topic that pervades all of the scientific research activities of Shunichi Fukuzumi spanning 42 years is “electron-transfer chemistry” focusing on “artificial photosynthesis” in which porphyrins and phthalocyanines have played important roles. **52 articles** contributed by collaborators and colleagues to this special issue attest to scientific significance of this field as well as the important role Prof. Shunichi Fukuzumi and his groups have played in this area of science.

Shunichi Fukuzumi was born in 1950 in Nagoya, which is one of the major cities in Japan. He moved to Tokyo and graduated from Tokyo Institute of Technology from which he received Ph.D. in 1978. The title of his first scientific paper is “The Electronic Spectrum of *p*-Benzo-semiquinone Anion in an Aqueous Solution” published in *Bull. Chem. Soc. Jpn.* 1973; **46**: 3353–3355. *p*-Benzo-semiquinone anion was produced by proton-coupled electron transfer (PCET) oxidation of hydroquinone with  $\text{MnO}_2$ . This is his start to explore the field of electron-transfer chemistry. In his doctoral thesis work, he studied catalytic mechanisms of heterogeneous and homogenous oxidation of substrates based on kinetics and detection of radical intermediates by EPR. His field was expanded to electron transfer chemistry of organometallic compounds under guidance of Prof. Jay K. Kochi at Indiana University, where he worked as a postdoctoral fellow from 1978–1981. He reported a unified view of Marcus electron transfer and Mulliken charge transfer theories in *J. Am. Chem. Soc.* 1980; **102**: 2928, which enabled him thereafter to clarify a variety of electron-transfer mechanisms including bond cleavage and formation of organic and organometallic compounds.

After hard work for three years at Indiana University, which enabled him to publish 21 papers, he went back to Japan as an assistant professor at Osaka University in April 1981. He was promoted to a full professor at Osaka University in 1994. In 2013, he was selected as the first distinguished professor at Osaka University. He retired from Osaka University on March 31, 2015. At Osaka University, he started exploring electron-transfer chemistry of metal complexes including metalloporphyrins at the excited states as well as the ground states. He has determined the reorganization energies of electron transfer of metalloporphyrins and fullerenes based on the Marcus theory of electron transfer. The small reorganization energies of electron transfer metalloporphyrins and fullerenes have led him to rational design and synthesis of a variety of photosynthetic reaction center models



composed of metalloporphyrins and fullerenes (*vide infra*).

Based on his research background covering electron-transfer chemistry of organic and inorganic compounds as well as homogeneous and heterogeneous redox catalysis, he started developing artificial photosynthetic systems composed of the light-harvesting (LH) unit, the charge-separation (CS) unit, the catalytic units for water oxidation and reduction, and the catalytic  $\text{CO}_2$  fixation unit in 1999 when he obtained a big fund called CREST (Core Research for Evolutional Science and Technology). Bioinspired artificial photosynthesis stayed in his focus for many years thereafter. His CREST project (five years) on artificial photosynthesis was extended as a SORST (Solution Oriented Research for Science and Technology) project from Japan Science and Technology Agency (JST). From 2011 he has been a director of Advanced Low Carbon Technology Research and Development Program (ALCA) from JST.

With regard to the CS systems, Prof. Shunichi Fukuzumi and his groups have successfully developed a series of multi-step photoinduced electron-transfer systems composed of porphyrins and fullerenes, which can well mimic functions of the photosynthetic reaction center. Prof. Fukuzumi's groups have further developed CS systems to attain long-lived and high-energy charge-separated states without significant loss of excitation energy by fine control of the redox potentials and geometry of simple organic donor–acceptor dyads based on the Marcus theory of electron transfer (*J. Am. Chem. Soc.* 2004; **126**: 1600). The combination of the LH unit and the CS unit has also been achieved by the rational

design of supramolecular electron donor–acceptor ensembles, which has significant advantages with regard to synthetic feasibility, providing a variety of applications including efficient photocatalytic systems for the solar energy conversion and organic solar cells. His rational development of excellent photosynthetic reaction center models based on the Marcus theory of electron transfer has been summarized in a series of feature and account articles (*Org. Biomol. Chem.* 2003; **1**: 609; *Bull. Chem. Soc. Jpn.* 2006; **79**: 177; *Phys. Chem. Chem. Phys.* 2008; **10**: 2283; *J. Mater. Chem.* 2008; **18**: 1427; *Chem. Commun.* 2012; **48**: 9801; *J. Mater. Chem.* 2012; **22**: 4575; *Acc. Chem. Res.* 2014; **47**: 1455).

The efficient CS unit has been successfully combined with the catalytic water reduction unit to attain the most efficient photocatalytic hydrogen evolution system. The activation of hydrogen has also been achieved by developing the structural and functional model of hydrogenases, which will enable to replace precious Pt catalysts by much cheaper metal catalysts for hydrogen evolution as summarized in *Energy Environ. Sci.* 2011; **4**: 2754. Prof. Fukuzumi's groups have utilized CS molecules as organic photocatalysts to develop a variety of photocatalytic organic transformations as summarized in *Chem. Sci.* 2013; **4**: 561.

Because the development of an efficient catalytic system for water oxidation remains the most important step to realize artificial photosynthesis, Prof. Fukuzumi's groups have clarified the electron-transfer properties of high-valent metal-oxo species, which are responsible for the water oxidation, to develop efficient water oxidation catalysts using earth-abundant metal oxides nanoparticles by fruitful collaboration with Prof. Wonwoo Nam's groups. The electron transfer chemistry of high-valent metal-oxo species has been summarized in review and account articles (*Coord. Chem. Rev.* 2013; **257**: 1564; *Acc. Chem. Res.* 2014; **47**: 1146).

With regard to CO<sub>2</sub> fixation catalysts, Prof. Fukuzumi's groups have developed efficient catalysts for the reduction of CO<sub>2</sub> to formic acid by hydrogen in water as well as the reverse reaction as summarized in *Dalton Trans.* 2013; **42**: 18; *Eur. J. Inorg. Chem.* 2008; 1351. The interconversion between NADH (dihyronicotinamide adenine dinucleotide, which is a natural electron source) and H<sub>2</sub> has also been achieved at ambient temperature and pressure.

Prof. Fukuzumi's groups have also developed a variety of efficient catalysts for O<sub>2</sub> reduction inspired by cytochrome *c* oxidase in respiration. Not only proton-coupled electron transfer (PCET) but also metal ion-coupled electron transfer (MCET) has been shown to play very important roles in the catalytic reduction of O<sub>2</sub>. The general concept of MCET as well as PCET has been summarized in a series of review and account articles (*Bull. Chem. Soc. Jpn.* 1997; **70**: 1; *Coord. Chem. Rev.* 2002; **226**: 71; *Prog. Inorg. Chem.* 2009; **56**: 49; *Coord. Chem. Rev.* 2010; **254**: 372; *Phys. Chem. Chem. Phys.* 2012; **14**: 8472; *Coord.*

*Chem. Rev.* 2013; **257**: 1564). The two-electron reduction of O<sub>2</sub> has been combined with the photocatalytic water oxidation to achieve production of hydrogen peroxide (H<sub>2</sub>O<sub>2</sub>) from H<sub>2</sub>O and O<sub>2</sub> using solar energy for the first time (*Energy Environ. Sci.* 2013; **6**: 3756). Aqueous H<sub>2</sub>O<sub>2</sub> can be used as a promising renewable solar fuel, which is more valuable than gaseous H<sub>2</sub>, in H<sub>2</sub>O<sub>2</sub> fuel cells that Prof. Fukuzumi's groups have been developing as summarized in *Electrochim. Acta* 2012; **82**: 493 and *Aust. J. Chem.* 2014; **67**: 354.

Throughout four decades of teaching and research, Prof. Shunichi Fukuzumi actively collaborated with scientists from all over the world. His international collaboration has been expanded rapidly ever since he started collaboration with Prof. Karl M. Kadish in 1994 when Fukuzumi was promoted to a full professor at Osaka University. He actively collaborated with Professors Karl M. Kadish (USA), Francis D'Souza (USA), Jonathan L. Sessler (USA), Ravindra K. Pandey (USA), Kenneth D. Karlin (USA), Roger Guilard (France), Maxwell J. Crossley (Australia), Dirk M. Guldi (Germany), Ángela Sastre-Santos (Spain) and Wonwoo Nam (Korea). The full list of his international collaborators is shown in this special issue. Prof. Fukuzumi served as the leader of a GCOE (Global Center of Excellence) program at Osaka University from 2007 to 2011, funded by MEXT (Ministry of Education, Culture, Sports, Science and Technology), Japan. The GCOE program provided funding support for establishing education and research centers to elevate the international competitiveness of the Japanese universities. He organized many international GCOE symposiums to facilitate international collaborations. He was invited to many international conferences, giving more than 40 plenary lectures.

Professor Shunichi Fukuzumi has published over 1000 papers, reviews and books in the area of electron-transfer chemistry focusing on bioinspired artificial photosynthesis. His research publications have been cited over 29,000 times, with an h-index of 81. The curriculum vitae of Prof. Fukuzumi also included in this special issue lists the awards and honors he has received in recognition of his contributions. It has been a great personal privilege and honor to be associated with Prof. Shunichi Fukuzumi for many years. We take this opportunity to thank all of the authors who contributed papers for this special issue.

## CURRICULUM VITAE OF PROFESSOR SHUNICHI FUKUZUMI

### Education

Ph.D. in Applied Chemistry, Tokyo Institute of Technology, 1978

Master's Degree in Applied Chemistry, Tokyo Institute of Technology, 1975

Bachelor's Degree in Applied Chemistry, Tokyo Institute of Technology, 1973

### Positions Held

*Professor*, National University of Singapore, Singapore, 2015–

*Designated Professor*, Meijo University, Nagoya, Japan, 2015–

*Professor Emeritus*, Osaka University, Osaka, Japan, 2015–

*Director*, ALCA, Japan Science and Technology Agency, 2011–

*Distinguished Professor*, Osaka University, Japan, 2013–2014

*Full Professor*, Department of Material and Life Science, Graduate School of Engineering, Osaka University, Japan, 1995–2014

*Full Professor*, Department of Applied Chemistry, Faculty of Engineering, Osaka University, Japan, 1994–1995

*Associate Professor*, Department of Applied Chemistry, Faculty of Engineering, Osaka University, Japan, 1992–1994

*Assistant Professor*, Department of Applied Chemistry, Faculty of Engineering, Osaka University, Japan, 1981–1992

*Post Doctoral Fellow*, Department of Chemistry, Indiana University, Indiana, USA, 1978–1981

### Awards and Academic Distinctions

2015 The Siedle Lectureship Award, Indiana University, USA

2014 Robert Burns Woodward Career Award in Porphyrin Chemistry, The Society of Porphyrins and Phthalocyanines

2014 Physical Organic Chemistry Award, The Society of Physical Organic Chemistry, Japan

2013 Distinguished Professorship, Osaka University, Japan

2013 Presidential Award of Osaka University, Japan

2012 KAIST Lectureship Award, Korea

2012 Presidential Award of Osaka University, Japan

2012 MMS Award, Japan

2012 Roseman Lectureship Award, Johns Hopkins University, USA

2011 Medal with Purple Ribbon from the Emperor, Japan

2011 Special Lectureship Award, The Japanese Photochemistry Association, Japan

2010 The Commendation for Science and Technology by the Minister of Education, Culture, Sports, Science and Technology, Japan

2007 Honorary Ph.D., Tampere University of Technology, Finland

2005 Osaka University Award, Japan

2005 Chemical Society of Japan Award, Japan

### International Invited Professorships

Ewha Womans University, Korea, 2008–2013

University of Strasbourg, France, 2010

Université de Bourgogne, France, 2001–2004

Ecole Normale Supérieure, France, 1998

Université de Droit, D'Economie et des Sciences d'Aix-Marseille, 1989

### Professional Assignments

Titular Member of International Union of Pure and Applied Chemistry (IUPAC), 1998–

Member of Japan Science Council, Japan, 2007–

President of The Society of Physical Organic Chemistry, Japan, 2011–2013

Program Officer, Research Center for Science Systems, Japan, 2004–2008

### Editorial Board Memberships

*Journal of Porphyrins and Phthalocyanines*

*Chemical Society Reviews*

*Recent Patents on Nanotechnology*

*Fullerenes, Nanotubes, and Carbon Nanostructures*

*Inorganic Chemistry*

*Journal of Bioinorganic Chemistry*

*Advances in Physical Organic Chemistry*

*Journal of Physical Organic Chemistry*

*Bulletin of Chemical Society of Japan*

*Chemistry Letters*

### Professional Society Memberships

*Chemical Society of Japan*

*American Chemical Society*

*International Union of Pure and Applied Chemistry (IUPAC)*

*The Society of Porphyrins and Phthalocyanines*

*The Society of Physical Organic Chemistry, Japan*

*Japan Society of Coordination Chemistry*

*The Japanese Photochemistry Association*

*The Kinki Chemical Society, Japan*

### Publications/Bibliometry

970 research papers in peer-reviewed scientific journals and 83 reviews or book and over 40 patents. Some 29,000 citations as of November 4, 2014, h-index = 81.

## RESEARCH COLLABORATORS OF PROFESSOR SHUNICHI FUKUZUMI (1981–2015)

### Collaborators

#### *Associate Professor* (chronological order)

Shinobu Itoh, Hiroshi Imahori, Seiji Ogo, Takahiko Kojima, Yusuke Yamada

#### *Assistant Professor*

Tomoyoshi Suenobu

#### *Professor*

Kei Ohkubo

#### *Postdoctoral Fellow* (chronological order)

Matthias Patz, Hiroko Yamada, Mohamed E. El-Khouly, Ryo Yamahara, Tsutomu Abura, Saija C. Menon, Hideki Hayashi, Hidetaka Nakai, Ryosuke Harada, Wentong Chen, Jung Hei Choi, Dipanwita Das, Mihoko Yamada, Shafiqul Islam

#### *External* (chronological order)

Kunio Mochida, Junzo Otera, Michel Chanon, Lucidieo Greci, Akito Ishida, Herbert Mayr, Karl M. Kadish, Ryuichi Arakawa, Koichi Mikami, Koichi Narasaka, Roger Guilard, Claude P. Gros, Jean-Michel Barbe, Osamu Ito, Mamoru Fujitsuka, Yoshihito Watanabe, Joseph P. Dinnocenzo, Teizo Kitagawa, Francis D'Souza, Osamu Yamauchi, Helge Lemmetyinen, N. V. Tkachenko, Christian Amatore, Prashant V. Kamat, Dirk M. Guldi, Iwao Yamazaki, Ravindra K. Pandey, Hideki Masuda, Maxwell J. Crossley, Olga V. Boltalina, Nobuhiro Ohta, Joe Otsuki, Yasuteru Urano, Tetsuo Nagano, Kohei Morikawa, Fumito Tani, Yoshinori Naruta, Kenneth P. Ghiggino, Paul J. Sentic, Dongho Kim, Yuji Wada, Shozo Yanagida, Ángela Sastre-Santos, Fernando Fernández-Lázaro, Yasuhiro Kobori, Yoshihiko Morooka, Takeshi Akasaka, Yoshizo Takai, Nathalie Solla-dié, Jonathan L. Sessler, Daoben Zhu, Thomas Torres, Hiromi Akahori, Jeffrey R. Reimers, Seigo Yamauchi, Wonwoo Nam, Yong-Min Lee, Kazunari Yoshizawa, Nagao Kobayashi, Tapan Ganguly, Hideyuki Murata, Panče Naumov, Masatatsu Suzuki, James M. Mayer, Jonathan P. Hill, Katsuhiko Ariga, Shu Seki, Shigenobu Yano, Kwang-Yol Kay, Kenneth D. Karlin, Peter Comba, Nobuo Suzuki, Dennis K. P. Ng, David P. Goldberg, Ali El-Agamey, Takashi Ogura, Youngmin You, Tetsuro Murahashi, Hidehiro Uekusa, Fernando Langa, Antoni Llobet, Pierre D. Harvey, Hidehiro Sakurai, Guido H. Clever, Mahdi M. Abu-Omar, Akihiko Tsuda, Yutaka Matsuo, Donglin Jiang

#### **Students** (chronological order; **bold: Ph.D.; 1981–2015**)

Nobuaki Yamada (Nishizawa), Katsuhiko Hironaka, Yuji Kondo, Sadaki Kuroda, Michito Tsunomori, **Kunio**

**Ishikawa, Masashi Ishikawa**, Shintaro Koumitsu, Seiji Mochizuki, Tatsushi Goto, Makoto Chiba, Kumiko Tanii, Toshiaki Kitano, Tomohiro Yorisue, Yoshihiro Tokuda, **Morifumi Fujita**, Toshihiko Okamoto, Souta Noura, Junichi Maruta, Tsutomu Urano, Takashi Komori, Yasuyo Seko, Yutaka Chiba, Naoki Takada, Kiyomi Yasui, Shigehisa Takayama, Kei Takegami, Keiko Tanaka, **Ikuo Nakanishi**, Hajime Nakao, Hirokatsu Kawakami, Shuichiro Kawamura, Kenichi Miyamoto, Takeomi Hirasaka, **Masayasu Taki**, Yoshihiro Kuwahara, Hideki Bandoh, Hideyuki Kumei, Yasuji Hashimoto, Masato Taniguchi, **Hideki Ohtsu**, Hisahiro Mori, **Taku Hasobe**, Naoya Satoh, Kanji Shimo-Osako, Kouta Kato, Yoshinori Fujii, Yutaka Yoshida, Hisahiro Mori, Shunsuke Fujita, Ichiro Takimoto, **Ken Okamoto**, **Hironori Kitaguchi**, Yoshito Endo, Ichiro Amasaki, Shinichi Teramae, Osamu Inada, Tetsuya Ojiri, **Junpei Yuasa**, **Kyou Suga**, **Yukiyasu Kashiwagi**, Mari Nishimine, Makoto Kimura, Junko Sonoda, Yoshiyuki Endo, **Hiroaki Kotani**, Yuji Sekiguchi, **Keiji Uehara**, Hiromi Nishida, **Bunsho Kure**, **Shigeki Hattori**, Kazusa Yukimoto, **Tomonori Kawashima**, Toshio Miyagawa, Hiroshi Miyao, **Makiko Tanaka (Shoji)**, Yusuke Murata, Takuya Mizuno, Takashi Nishimura, Takashi Nanjo, Daisuke Inoki, Yoshitaka Takebe, **Kenji Saito**, **Masataka Ohtani**, Shunsuke Yamada, Ryosuke Iwata, Yuto Okada, **Hironobu Kanemitsu**, **Atsuro Takai**, **Tatsuaki Nakanishi**, Ryota Kabe, Toshiya Ono, **Soushi Miyazaki**, Takahiro Yanagimoto, **Atsuyoshi Yokoyama**, Takashi Kishi, Yuichirou Hirai, **Tatsuhiko Honda**, Kakeru Hanabusa, Naofumi Fujioka, Norihisa Hirasa, Takeshi Morimoto, **Takashi Tachiyama**, Akinori Itoh, **Motonobu Murakami**, Takashi Kobayashi, **Mustafa Supur**, **Yuji Inui**, Kaoru Doi, **Yuma Morimoto**, Ryo Hanazaki, Yurie Fukunishi, Kentaro Yano, **Jiun Park**, Kentaro Mizushima, Atsushi Fujimoto, Yuichi Yano, Masato Murakami, Kazuya Nakayama, **Dachao Hong**, **Kentaro Mase**, Sho Yoshida, **Yuki Kawashima**, Takamitsu Miyahigashi, Satoshi Kato, Masanori Kanematsu, Yuta Maenaka, Takaki Kobayashi, **Jieun Jung**, Kazunori Maeda, Akifumi Nomura, Yusuke Nishida, Saya Kakuda, **Heejung Yoon**, Yuta Matsuoka, Shinya Shikano, Masaki Yoneda, Satoshi Shibata, Hideyuki Tadokoro, Naoki Kohno, Soichiro Matsumoto, Tetsuya Hasegawa, Kensaku Hirose, Takeshi Tsudata, Yusuke Isaka, Yusuke Aratani, Shoko Aoi, Kohei Oyama

## LIST OF MAIN PUBLICATIONS OF PROFESSOR SHUNICHI FUKUZUMI

1. A Unified Mechanism for Thermal and Photochemical Activation of Charge-Transfer Processes with Organometals. Steric Effects in the Insertion of Tetracyanoethylene, Fukuzumi S, Mochida K and Kochi JK. *J. Am. Chem. Soc.* 1979; **101**: 5961–5972.

2. Charge-Transfer Mechanism for Electrophilic Reactions.  $S_E2$  Cleavage of Alkylmetals with Iodine, Fukuzumi S and Kochi JK. *J. Am. Chem. Soc.* 1980; **102**: 2141–2152.
3. Unified View of Marcus Electron Transfer and Mulliken Charge-Transfer Theories in Organometallic Chemistry. Steric Effects in Alkylmetals as Quantitative Probes for Outer-Sphere and Inner-Sphere Mechanisms, Fukuzumi S, Wong CL and Kochi JK. *J. Am. Chem. Soc.* 1980; **102**: 2928–2939.
4. Electron Transfer Activation in Electrophilic Mechanisms. Cleavage of Alkylmetals by Mercury(II) Complexes, Fukuzumi S and Kochi JK. *J. Am. Chem. Soc.* 1980; **102**: 7290–7297.
5. Electrophilic Additions to Olefins. A New Approach to Unifying the Mechanisms of Bromination and Oxymercuration, Fukuzumi S and Kochi JK. *J. Am. Chem. Soc.* 1981; **103**: 2783–2791.
6. Electrophilic Aromatic Substitution. Charge-Transfer Excited States and the Nature of the Activated Complex, Fukuzumi S and Kochi JK. *J. Am. Chem. Soc.* 1981; **103**: 7240–7252.
7. Transition-State Barrier for Electrophilic Reactions. Solvation of Charge-Transfer Ion Pairs as the Unifying Factor in Alkene Addition and Aromatic Substitution with Bromine, Fukuzumi S and Kochi JK. *J. Am. Chem. Soc.* 1982; **104**: 7599–7609.
8. Photoreduction of Alkyl Halides by an NADH Model Compound. An Electron-Transfer Chain Mechanism, Fukuzumi S, Hironaka K, and Tanaka T. *J. Am. Chem. Soc.* 1983; **105**: 4722–4727.
9. Flavin Analogue-Metal Ion Complexes Acting as Efficient Photocatalysts in the Oxidation of *p*-Methylbenzyl Alcohol by Oxygen under Irradiation with Visible Light, Fukuzumi S, Kuroda S and Tanaka T. *J. Am. Chem. Soc.* 1985; **107**: 3020–3027.
10. Energetic Comparison between Photoinduced Electron-Transfer Reactions from NADH Model Compounds to Organic and Inorganic Oxidants, and Hydride-Transfer Reactions from NADH Model Compounds to *p*-Benzoquinone Derivatives, Fukuzumi S, Koumitsu S, Hironaka K and Tanaka T. *J. Am. Chem. Soc.* 1987; **109**: 305–316.
11. Acid-Catalyzed Electron-Transfer Processes in Reduction of  $\alpha$ -Haloketones by an NADH Model Compound and Ferrocene Derivatives, Fukuzumi S, Mochizuki S and Tanaka T. *J. Am. Chem. Soc.* 1989; **111**: 1497–1499.
12. Oxygenation and Oxidative Coupling Processes of Alkyl Ligands of *cis*-Dialkylcobalt(III) Complexes with Dioxygen, Catalyzed by Coenzyme Analogues in the Presence of Perchloric Acid, Ishikawa K, Fukuzumi S, Goto T and Tanaka T. *J. Am. Chem. Soc.* 1990; **112**: 1577–1584.
13. Selective One-Electron Reduction of a Cationic Substrate, 10-Methylacridinium Ion by Group 4B Dimetals,  $\text{Me}_3\text{Sn-MMe}_3$  ( $\text{M} = \text{Sn, Ge, Si}$ ) via Radical Chain Reactions, Fukuzumi S, Kitano T and Mochida K. *J. Am. Chem. Soc.* 1990; **112**: 3246–3247.
14. 10-Methylacridine Dimer Acting as a Unique Two-Electron Donor in the One-Electron Reduction of Triphenylmethyl Cation, Fukuzumi S, Kitano T, Ishikawa M. *J. Am. Chem. Soc.* 1990; **112**: 5631–5632.
15. 10-Methylacridine Derivatives Acting as Efficient and Stable Photocatalysts in Reductive Dehalogenation of Halogenated Compounds with Sodium Borohydride via Photoinduced Electron Transfer, Ishikawa M and Fukuzumi S. *J. Am. Chem. Soc.* 1990; **112**: 8864–8870.
16. Importance of Lewis Acid-Mediated Electron Transfer in Mukaiyama-Michael Reaction of Ketene Silyl Acetals, Sato T, Wakahara Y, Otera J, Nozaki H and Fukuzumi S. *J. Am. Chem. Soc.* 1991; **113**: 4028–4030.
17. Quinone/Hydroxide Ion Induced Oxygenation of *p*-Benzoquinone to Rhodizonate Dianion ( $\text{C}_6\text{O}_6^{2-}$ ), Accompanied by One-Electron Reduction to Semiquinone Radical Anion, Fukuzumi S and Yorisue T, *J. Am. Chem. Soc.* 1991; **113**: 7764–7765.
18. Electron Transfer Oxidation of Ketene Silyl Acetals and Other Organosilanes. The Mechanistic Insight into Lewis Acid Mediated Electron Transfer, Fukuzumi S, Fujita M, Otera J and Fujita Y. *J. Am. Chem. Soc.* 1992; **114**: 10271–10278.
19. Electron-Transfer Oxidation of 9-Substituted 10-Methyl-9,10-dihydroacridines. Cleavage of C-H vs C-C Bond of the Radical Cations, Fukuzumi S, Tokuda Y, Kitano T, Okamoto T and Otera J. *J. Am. Chem. Soc.* 1993; **115**: 8960–8968.
20. Magnesium Perchlorate-Catalyzed Diels-Alder Reactions of Anthracenes with *p*-Benzoquinone Derivatives: Catalysis on the Electron Transfer Step, Fukuzumi S and Okamoto T. *J. Am. Chem. Soc.* 1993; **115**: 11600–11601.
21. Addition of Organosilanes with Aromatic Carbonyl Compounds via Photoinduced Electron Transfer in the Presence of Magnesium Perchlorate, Fukuzumi S, Okamoto T and Otera J. *J. Am. Chem. Soc.* 1994; **116**: 5503–5504.
22. Charge-Transfer Complexes Acting as Real Intermediates in Hydride Transfer from Michler's Hydride to 2,3-Dichloro-5,6-dicyano-*p*-benzoquinone via Electron Transfer, Zaman KM, Yamamoto S, Nishimura N, Maruta J and Fukuzumi S. *J. Am. Chem. Soc.* 1994; **116**: 12099–12100.
23. A Model Compound of Novel Cofactor TTQ of Bacterial Methylamine Dehydrogenases. Synthesis and Physicochemical Properties, Itoh S, Ogino M, Haranou S, Terasaka T, Ando T, Komatsu M,

- Ohshiro Y and Fukuzumi S. *J. Am. Chem. Soc.* 1995; **117**: 1485–1493.
24. Functional Model of Dopamine  $\beta$ -Hydroxylase. Quantitative Ligand Hydroxylation at the Benzylic Position of a Copper Complex by Dioxygen, Itoh S, Kondo T, Komatsu M, Ohshiro Y, Li C, Kanehisa N, Kai Y and Fukuzumi S. *J. Am. Chem. Soc.* 1995; **117**: 4714–4715.
  25. Reactions of Carbocations with  $\pi$ -Nucleophiles: Polar Mechanism and No Outer-Sphere Electron Transfer, Patz M, Maruta J and Fukuzumi S. *Angew. Chem., Int. Ed. Engl.* 1995; **34**: 1225–1227.
  26. Addition of Ketene Silyl Acetals to the Triplet Excited State of C<sub>60</sub> via Photoinduced Electron Transfer Leading to the Fullereneacetates, Mikami K, Matsumoto S, Ishida A, Takamuku S, Suenobu T and Fukuzumi S. *J. Am. Chem. Soc.* 1995; **117**: 11134–11141.
  27. Addition vs. Oxygenation of Alkylbenzenes with 10-Methylacridinium Ion via Photoinduced Electron Transfer, Fujita M, Ishida A, Takamuku S and Fukuzumi S. *J. Am. Chem. Soc.* 1996; **118**: 8566–8574.
  28. Modeling of the Chemistry of Quinoprotein Methanol Dehydrogenase. Oxidation of Methanol by Calcium Complex of Coenzyme PQQ via Addition-Elimination Mechanism, Itoh S, Kawakami H and Fukuzumi S. *J. Am. Chem. Soc.* 1997; **119**: 439–440.
  29. Direct Observation of Radical Intermediates While Investigating the Redox Behavior of Thiamin Coenzyme Models, Nakanishi I, Itoh S, Suenobu T and Fukuzumi S. *Angew. Chem., Int. Ed. Engl.* 1998; **37**: 992–994.
  30. Electron Transfer Mechanism of Organocobalt Porphyrins. Site of Electron Transfer, Migration of Organic Groups, and Cobalt-Carbon Bond Energies in Different Oxidation States, Fukuzumi S, Miyamoto K, Suenobu T, Van Caemelbecke E and Kadish KM. *J. Am. Chem. Soc.* 1998; **120**: 2880–2889.
  31. Mechanistic Studies of Aliphatic Ligand Hydroxylation of a Copper Complex by Dioxygen: A Model Reaction for Copper Monooxygenases, Itoh S, Nakao H, Berreau LM, Kondo T, Komatsu M and Fukuzumi S. *J. Am. Chem. Soc.* 1998; **120**: 2890–2899.
  32. Formation of Radical Anions in the Reaction of *p*-Benzoquinone and C<sub>60</sub> with Alkoxide Ions, Fukuzumi S, Nakanishi I, Maruta J, Yorisue T, Suenobu T, Itoh S, Arakawa R and Kadish KM. *J. Am. Chem. Soc.* 1998; **120**: 6673–6680.
  33. Electrochemical Behavior and Characterization of Semiquinone Radical Anion Species of Coenzyme PQQ in Aprotic Organic Media, Itoh S, Kawakami H and Fukuzumi S. *J. Am. Chem. Soc.* 1998; **120**: 7271–7277.
  34. Selective One-Electron and Two-Electron Reduction of C<sub>60</sub> with NADH and NAD Dimer Analogues via Photoinduced Electron Transfer, Fukuzumi S, Suenobu T, Patz M, Hirasaka T, Itoh S, Fujitsuka M and Ito O. *J. Am. Chem. Soc.* 1998; **120**: 8060–8068.
  35. Formation of C<sub>60</sub> Adducts with Two Different Alkyl Groups via Combination of Electron Transfer and S<sub>N</sub>2 Reactions, Fukuzumi S, Suenobu T, Hirasaka T, Arakawa R and Kadish KM. *J. Am. Chem. Soc.* 1998; **120**: 9220–9227.
  36. Mechanisms of *N*-Demethylations Catalyzed by High Valent Intermediates of Heme Enzymes: Novel Use of Isotope Effects and Determination by Direct Observation of Intermediates, Goto Y, Watanabe Y, Fukuzumi S, Jones JP and Dinnocenzo JP. *J. Am. Chem. Soc.* 1998; **120**: 10762–10763.
  37. Decreased Electron Transfer Rates of Manganese Porphyrins with Conformational Distortions of the Macrocycle, Fukuzumi S, Nakanishi I, Barbe JM, Guillard R, Van Caemelbecke E, Guo N and Kadish KM. *Angew. Chem., Int. Ed. Engl.* 1999; **38**: 964–966.
  38. Oxidation of Benzyl Alcohol with Cu(II) and Zn(II) Complexes of the Phenoxyl Radical as a Model of the Reaction of Galactose Oxidase, Itoh S, Taki M, Takayama S, Nagatomo S, Kitagawa T, Sakurada N, Arakawa R and Fukuzumi S. *Angew. Chem., Int. Ed. Engl.* 1999; **38**: 2774–2776.
  39. Electron-Transfer Kinetics for Generation of Organoiron(IV) Porphyrins and the Iron(IV) Porphyrin  $\pi$  Radical Cations, Fukuzumi S, Nakanishi I, Tanaka K, Suenobu T, Tabard A, Guillard R, Van Caemelbecke E and Kadish KM. *J. Am. Chem. Soc.* 1999; **121**: 785–790.
  40. ESR Spectra of Superoxide Anion-Scandium Complexes Detectable in Fluid Solution, Fukuzumi S, Patz M, Suenobu T, Kuwahara Y and Itoh S. *J. Am. Chem. Soc.* 1999; **121**: 1605–1606.
  41. Electron-Transfer Properties of C<sub>60</sub> and *tert*-Butyl-C<sub>60</sub> Radical, Fukuzumi S, Nakanishi I, Suenobu T and Kadish KM. *J. Am. Chem. Soc.* 1999; **121**: 3468–3474.
  42. Mechanisms of Sulfoxidation Catalyzed by High-Valent Intermediates of Heme Enzymes: Electron Transfer vs Oxygen Transfer Mechanism, Goto Y, Matsui T, Ozaki S, Watanabe Y and Fukuzumi S. *J. Am. Chem. Soc.* 1999; **121**: 9497–9502.
  43. Aliphatic Hydroxylation by a Bis( $\mu$ -oxo)nickel(III) Complex, Itoh S, Bandoh H, Nagatomo S, Kitagawa T and Fukuzumi S. *J. Am. Chem. Soc.* 1999; **121**: 8945–8946.
  44. Aliphatic Hydroxylation by a Bis( $\mu$ -oxo)dicopper(III) Complex, Itoh S, Taki M, Nakao H, Holland PL, Tolman WB, Lawrence Que L Jr and Fukuzumi S. *Angew. Chem., Int. Ed.* 2000; **39**: 398–400.
  45. The Essential Role of a Zn<sup>II</sup> Ion in the Disproportionation of Semiquinone Radical Anion



- by an Imidazolate-Bridged Cu<sup>II</sup>-Zn<sup>II</sup> Model of Superoxide Dismutase, Ohtsu H and Fukuzumi S. *Angew. Chem., Int. Ed.* 2000, **39**: 4537-4539.
46. Electrosynthesis and Structural Characterization of Two (C<sub>6</sub>H<sub>5</sub>CH<sub>2</sub>)<sub>4</sub>C<sub>60</sub> Isomers, Kadish KM, Gao X, Van Caemelbecke E, Suenobu T and Fukuzumi S. *J. Am. Chem. Soc.* 2000; **122**: 563-570.
  47. Hydride Transfer from 9-Substituted 10-Methyl-9,10-dihydroacridines to Hydride Acceptors via Charge-Transfer Complexes and Sequential Electron-Proton-Electron Transfer. A Negative Temperature Dependence of the Rates, Fukuzumi S, Ohkubo K, Tokuda Y and Suenobu T. *J. Am. Chem. Soc.* 2000; **122**: 4286-4294.
  48. Stepwise Bond Formation in Photochemical and Thermal Diels-Alder Reactions of C<sub>60</sub> with Danishefsky's Dienes, Mikami K, Matsumoto S, Okubo Y, Fujitsuka M, Ito O, Suenobu T and Fukuzumi S. *J. Am. Chem. Soc.* 2000; **122**: 2236-2243.
  49. Resonance Raman Spectroscopy as a Probe of the Bis(μ-oxo)dicopper Core, Holland PL, Cramer CJ, Wilkinson EC, Mahapatra S, Rodgers KR, Itoh S, Taki M, Fukuzumi S, Que L Jr and Tolman WB. *J. Am. Chem. Soc.* 2000; **122**: 792-802.
  50. Synthesis and Characterization of Imidazolate-Bridged Dinuclear Complexes as Active Site Models of Cu, Zn-SOD, Ohtsu H, Shimazaki Y, Odani A, Yamauchi O, Mori W, Itoh S and Fukuzumi S. *J. Am. Chem. Soc.* 2000; **122**: 5733-5741.
  51. Photochemical Reactions of Coenzyme PQQ (Pyrroloquinolinequinone) and Analogs with Benzyl Alcohol Derivatives via Photoinduced Electron Transfer, Fukuzumi S, Itoh S, Komori T, Suenobu T, Ishida A, Fujitsuka M and Ito O. *J. Am. Chem. Soc.* 2000; **122**: 8435-8443.
  52. Effects of Metal Ions on the Electronic, Redox, and Catalytic Properties of Cofactor TTQ of Quinoprotein Amine Dehydrogenases, Itoh S, Taniguchi M, Takada N, Nagatomo S, Kitagawa T and Fukuzumi S. *J. Am. Chem. Soc.*, 2000; **122**: 12087-12097.
  53. Effects of Metal Ions on Physicochemical Properties and Redox Reactivity of Phenolates and Phenoxyl Radicals: Mechanistic Insight into Hydrogen Atom Abstraction by Phenoxyl Radical-Metal Complexes, Itoh S, Kumei H, Nagatomo S, Kitagawa T and Fukuzumi S. *J. Am. Chem. Soc.* 2000; **123**: 2165-2175.
  54. Light-Harvesting and Photocurrent Generation by Gold Electrodes Modified with Mixed Self-Assembled Monolayers of Boron-Dipyrin and Ferrocene-Porphyrin-Fullerene Triad, Imahori H, Norieda H, Yamada H, Nishimura Y, Yamazaki I, Sakata Y and Fukuzumi S. *J. Am. Chem. Soc.* 2001; **123**: 100-110.
  55. Photoactive Three-Dimensional Monolayers. Porphyrin-Alkanethiolate-Stabilized Gold Clusters, Imahori H, Arimura M, Hanada T, Nishimura Y, Yamazaki I, Sakata Y and Fukuzumi S. *J. Am. Chem. Soc.* 2001; **123**: 335-336.
  56. Catalytic Effects of Dioxygen on Intramolecular Electron Transfer in Radical Ion Pairs of Zinc Porphyrin-Linked Fullerenes, Fukuzumi S, Imahori H, Yamada Y, El-Khouly ME, Fujitsuka M, Ito O and Guldi DM. *J. Am. Chem. Soc.* 2001; **123**: 2571-2575.
  57. Modulating Charge Separation and Charge Recombination Dynamics in Porphyrin-Fullerene Linked Dyads and Triads: Marcus-Normal vs. Inverted Region, Imahori H, Tamaki K, Guldi DM, Luo C, Fujitsuka M, Ito O, Sakata Y and Fukuzumi S. *J. Am. Chem. Soc.* 2001; **123**: 2607-2617.
  58. Fine Tuning of the Interaction between the Copper(I) and Disulfide Bond. Formation of a Bis(μ-thiolato)dicopper(II) Complex by Reductive Cleavage of the Disulfide Bond with Copper(I), Itoh S, Nakagawa M and Fukuzumi S. *J. Am. Chem. Soc.* 2001; **123**: 4087-4088.
  59. C-H Bond Activation of External Substrates with a Bis(μ-oxo)dicopper(III) Complex, Taki M, Itoh S and Fukuzumi S. *J. Am. Chem. Soc.* 2001; **123**: 6203-6204.
  60. Charge Separation in a Novel Artificial Photosynthetic Reaction Center Lives 380 ms, Imahori H, Guldi DM, Tamaki K, Yoshida Y, Luo C, Sakata Y and Fukuzumi S. *J. Am. Chem. Soc.* 2001; **123**: 6617-6628.
  61. Oxygenation of Phenols to Catechols by a (μ-η<sup>2</sup>:η<sup>2</sup>-Peroxo)dicopper(II) Complex: Mechanistic Insight into the Phenolase Activity of Tyrosinase, Itoh S, Kumei H, Taki M, Nagatomo S, Kitagawa T and Fukuzumi S. *J. Am. Chem. Soc.* 2001; **123**: 6708-6709.
  62. Change in Spin State and Enhancement of Redox Reactivity of Photoexcited States of Aromatic Carbonyl Compounds by Complexation with Metal Ion Salts Acting as Lewis Acids. Lewis Acid-Catalyzed Photoaddition of Benzyltrimethylsilane and Tetramethyltin via Photoinduced Electron Transfer, Fukuzumi S, Satoh N, Okamoto T, Yasui K, Suenobu T, Seko Y, Fujitsuka M and Ito O. *J. Am. Chem. Soc.* 2001; **123**: 7756-7766.
  63. Photoalkylation of 10-Alkylacridinium Ion via a Charge-Shift Type of Photoinduced Electron Transfer Controlled by Solvent Polarity, Fukuzumi S, Ohkubo K, Suenobu T, Kato K, Fujitsuka M and Ito O. *J. Am. Chem. Soc.* 2001; **123**: 8459-8467.
  64. Photochemical and Electrochemical Properties of Zinc Chlorin-C<sub>60</sub> Dyad as Compared to Corresponding Free-Base Chlorin-C<sub>60</sub>, Free-Base Porphyrin-C<sub>60</sub>, and Zinc Porphyrin-C<sub>60</sub> Dyads, Fukuzumi S, Ohkubo K, Imahori H, Shao J, Ou Z, Zheng G, Chen Y, Pandey RK, Fujitsuka M, Ito O and Kadish KM. *J. Am. Chem. Soc.* 2001; **123**: 10676-10683.

65. Metal Ion-Catalyzed Cycloaddition vs Hydride Transfer Reactions of NADH Analogues with *p*-Benzoquinones, Fukuzumi S, Fujii Y and Suenobu T. *J. Am. Chem. Soc.* 2001; **123**: 10191–10199.
66. Formation, Characterization, and Reactivity of Bis( $\mu$ -oxo)dinickel(III) Complexes Supported by A Series of Bis[2-(2-pyridyl)ethyl]amine Ligands, Itoh S, Bandoh H, Nakagawa M, Nagatomo S, Kitagawa T, Karlin KD and Fukuzumi S. *J. Am. Chem. Soc.* 2001; **123**: 11168–11178.
67. Extremely Slow Long-Range Electron Transfer Reactions across Zeolite-Solution Interface, Fukuzumi S, Yoshida Y, Urano T, Suenobu T and Imahori H. *J. Am. Chem. Soc.* 2001; **123**: 11331–11332.
68. Scandium Ion-Promoted Photoinduced Electron Transfer Oxidation of Fullerenes and Derivatives by *p*-Chloranil and *p*-Benzoquinones, Fukuzumi S, Mori H, Imahori H, Suenobu T, Araki Y, Ito O and Kadish KM. *J. Am. Chem. Soc.* 2001; **123**: 12458–12465.
69. Thermal Intramolecular Electron Transfer in a Ferrocene-Naphthoquinone Linked Dyad Promoted by Metal Ions, Fukuzumi S, Okamoto K and Imahori H. *Angew. Chem., Int. Ed.* 2002, **41**: 620–622.
70. Comparison of Reorganization Energies for Intra- and Intermolecular Electron Transfer, Imahori H, Yamada Y, Guldi DM, Endo Y, Shimomura A, Kundu S, Yamada K, Okada T, Sakata Y and Fukuzumi S. *Angew. Chem., Int. Ed.* 2002; **41**: 2344–2347.
71. Large Photocurrent Generation of Gold Electrodes Modified with [60]Fullerene-Linked Oligothiophenes Bearing a Tripodal Rigid Anchor, Hirayama D, Takimiya K, Aso Y, Otsubo T, Hasobe T, Yamada H, Imahori H, Fukuzumi S and Sakata Y. *J. Am. Chem. Soc.* 2002; **124**: 532–533.
72. Oxo-transfer Reaction from A Bis( $\mu$ -oxo) dicopper(III) Complex to Sulfides, Taki M, Itoh S and Fukuzumi S. *J. Am. Chem. Soc.* 2002; **124**: 998–1002.
73. Stepwise Charge Separation and Charge Recombination in Ferrocene-*meso*, *meso*-Linked Porphyrin Dimer-Fullerene Triad, Imahori H, Tamaki K, Araki Y, Sekiguchi S, Ito O, Sakata Y and Fukuzumi S. *J. Am. Chem. Soc.* 2002; **124**: 5165–5174.
74. Fine-Tuning of Copper(I)-Dioxygen Reactivity by 2-(2-Pyridyl)ethylamine Bidentate Ligands, Taki M, Teramae S, Nagatomo S, Tachi Y, Kitagawa T, Itoh S and Fukuzumi S. *J. Am. Chem. Soc.* 2002; **124**: 6367–6377.
75. Hydrogen-Bonding Dynamics in Photoinduced Electron Transfer in a Ferrocene-Quinone Linked Dyad with a Rigid Spacer, Fukuzumi S, Yoshida Y, Okamoto K, Imahori H, Araki Y and Ito O. *J. Am. Chem. Soc.* 2002; **124**: 6794–6795.
76. Exciplex Intermediates in Photoinduced Electron Transfer of Porphyrin-Fullerene Dyads, Kesti TJ, Tkachenko N, Vehmanene V, Yamada H, Imahori H, Fukuzumi S and Lemmetyinen H. *J. Am. Chem. Soc.* 2002; **124**: 8067–8077.
77. Asymmetric Sulfoxidation and Amine Binding by H64D/V68A and H64D/V68S Mb: Mechanistic Insight into the Chiral Discrimination Step, Kato S, Yang HJ, Ueno T, Ozaki S, Phillips GN, Fukuzumi S and Watanabe Y. *J. Am. Chem. Soc.* 2002; **124**: 8506–8507.
78. Significant Enhancement of Electron Transfer Reduction of NAD<sup>+</sup> Analogues by Complexation with Scandium Ion and the Detection of the Radical Intermediate-Scandium Ion Complex, Fukuzumi S, Inada O, Satoh N, Suenobu T and Imahori H. *J. Am. Chem. Soc.* 2002; **124**: 9181–9188.
79. Fluorescence Maxima of 10-Methylacridone-Metal Ion Salt Complexes: A Convenient and Quantitative Measure of Lewis Acidity of Metal Ion Salts, Fukuzumi S and Ohkubo K. *J. Am. Chem. Soc.* 2002; **124**: 10270–10271.
80. A Negative Temperature Dependence of the Electron Self-Exchange Rates of Zinc Porphyrin  $\pi$  Radical Cations, Fukuzumi S, Endo Y and Imahori H. *J. Am. Chem. Soc.* 2002; **124**: 10974–10975.
81. Scandium Ion-Promoted Reduction of Heterocyclic N=N Double Bond. Hydride Transfer vs Electron Transfer, Fukuzumi S, Yuasa J and Suenobu T. *J. Am. Chem. Soc.* 2002; **124**: 12566–12573.
82. Metal Ion-Catalyzed Diels-Alder and Hydride Transfer Reactions. Catalysis of Metal Ions in the Electron-Transfer Step, Fukuzumi S, Ohkubo K and Okamoto T. *J. Am. Chem. Soc.* 2002; **124**: 14147–14155.
83. Direct Detection of Radical Cations of NADH Analogues, Fukuzumi S, Inada O and Suenobu T. *J. Am. Chem. Soc.* 2002; **124**: 14538–14539.
84. A Ruthenium-Pterin Complex Showing Proton-coupled Electron Transfer: Synthesis and Characterization, Kojima T, Sakamoto T, Matsuda Y, Ohkubo K and Fukuzumi S. *Angew. Chem., Int. Ed.* 2003; **42**: 4951–4954.
85. Excited-State Deprotonation and H/D Exchange of an Iridium Hydride Complex, Suenobu T, Ogo S and Fukuzumi S. *Angew. Chem., Int. Ed.* 2003; **42**: 5492–5495.
86. Effects of Hydrogen Bonding on Metal Ion-Promoted Intramolecular Electron Transfer and Photoinduced Electron Transfer in a Ferrocene-Quinone Dyad with a Rigid Amide Spacer, Fukuzumi S, Okamoto K, Yoshida Y, Imahori H, Araki Y and Ito O. *J. Am. Chem. Soc.* 2003; **125**: 1007–1013.
87. Isolation and Crystal Structure of Water-Soluble Iridium Hydride. A Robust and Highly Active Catalyst for Acid-Catalyzed Transfer Hydrogenations of

- Carbonyl Compounds in Acidic Media, Abura T, Ogo S, Watanabe Y and Fukuzumi S. *J. Am. Chem. Soc.* 2003; **125**: 4149–4154.
88. Mechanisms of Electron Transfer Oxidation of NADH Analogues and the Chemiluminescence. Detection of the Keto and Enol Radical Cations, Fukuzumi S, Inada O and Suenobu T. *J. Am. Chem. Soc.* 2003; **125**: 4808–4816.
  89. Metal Ion-Promoted Intramolecular Electron Transfer in Ferrocene-Naphthoquinone Linked Dyad. Continuous Change in Driving Force and Reorganization Energy with Metal Ion Concentration, Okamoto K, Imahori H and Fukuzumi S. *J. Am. Chem. Soc.* 2003; **125**: 7014–7021.
  90. Rational Design Principle for Modulating Fluorescence Properties of Fluorescein-based Probes by Photoinduced Electron Transfer, Miura T, Urano Y, Tanaka K, Nagano T, Ohkubo K and Fukuzumi S. *J. Am. Chem. Soc.* 2003; **125**: 8666–8671.
  91. Mechanisms of Hydrogen-, Oxygen-, and Electron-Transfer Reactions of Cumylperoxy Radical, Fukuzumi S, Shimoosako K, Suenobu T and Watanabe Y. *J. Am. Chem. Soc.* 2003; **125**: 9074–9082.
  92. Photovoltaic Properties of Self-Assembled Monolayers of Porphyrins and Porphyrin-Fullerene Dyads on ITO and Gold Surfaces, Yamada H, Imahori H, Nishimura Y, Yamazaki I, Ahn TK, Seong Kim SK, Kim D and Fukuzumi S. *J. Am. Chem. Soc.* 2003; **125**: 9129–9139.
  93. Role of Electron Transfer Processes in Reactions of Diarylcarbenium Ions and Related Quinone Methides with Nucleophiles, Ofial AR, Ohkubo K, Fukuzumi S, Lucius R and Mayr H. *J. Am. Chem. Soc.* 2003; **125**: 10906–10912.
  94. Oxidation Mechanism of Phenols by Dicopper-Dioxygen ( $\text{Cu}_2/\text{O}_2$ ) Complexes, Osako T, Ohkubo K, Taki M, Tachi Y, Fukuzumi S and Itoh S. *J. Am. Chem. Soc.* 2003; **125**: 11027–11033.
  95. Highly Self-Organized Electron Transfer from an Iridium Complex to *p*-Benzoquinone Due to Formation of  $\pi$ -Dimer Radical Anion Complex Triply Bridged by Scandium Ions, Yuasa J, Suenobu T and Fukuzumi S. *J. Am. Chem. Soc.* 2003; **125**: 12090–12091.
  96. Self-Promoted Electron Transfer from Cobalt(II) Porphyrin to *p*-Fluoranil to Produce Dimer Radical Anion-Cobalt(III) Porphyrin Complex, Okamoto K and Fukuzumi S. *J. Am. Chem. Soc.* 2003; **125**: 12416–12417.
  97. Selective Oxygenation of Ring-Substituted Toluenes with Electron Donating and Withdrawing Substituents by Molecular Oxygen via Photoinduced Electron Transfer, Ohkubo K, Suga K, Morikawa K and Fukuzumi S. *J. Am. Chem. Soc.* 2003; **125**: 12850–12859.
  98. Accelerating Effect of a Proton on the Reduction of  $\text{CO}_2$  Dissolved in Water under Acidic Conditions. Isolation, Crystal Structure, and Reducing Ability of a Water-Soluble Ruthenium Hydride Complex, Hayashi H, Ogo S, Abura T and Fukuzumi S. *J. Am. Chem. Soc.* 2003; **125**: 14266–14267.
  99. Quaternary Self-Organization of Porphyrin and Fullerene Units by Clusterization with Gold Nanoparticles on  $\text{SnO}_2$  Electrodes for Organic Solar Cells, Hasobe T, Imahori H, Kamat PV and Fukuzumi S. *J. Am. Chem. Soc.* 2003; **125**: 14962–14963.
  100. Metal-Centered Photoinduced Electron Transfer Reduction of a Gold(III) Porphyrin Cation Linked with a Zinc Porphyrin to Produce a Long-Lived Charge-Separated State in Nonpolar Solvents, Fukuzumi S, Ohkubo K, E W, Ou Z, Shao J, Kadish KM, Hutchison JA, Ghiggino KP, Sintic PJ and Crossley MJ. *J. Am. Chem. Soc.* 2003; **125**: 14984–14985.
  101. Ultra-Long Lived Charge-Separated State in Zinc Chlorin- $\text{C}_{60}$  Dyad Produced by One-Step Photoinduced Electron Transfer, Ohkubo K, Kotani H, Shao J, Ou Z, Kadish KM, Chen Y, Zheng G, Pandey RK, Fujitsuka M, Ito O, Imahori H and Fukuzumi S. *Angew. Chem., Int. Ed.* 2004; **43**: 853–856.
  102. A Dramatic Elongation of the Lifetime of Charge-Separated State by Complexation with Yttrium Triflate in Ferrocene-Anthraquinone Linked Dyad, Okamoto K, Araki Y, Ito O and Fukuzumi S. *J. Am. Chem. Soc.* 2004; **126**: 56–57.
  103. Electron-Transfer State of 9-Mesityl-10-methyl-acridinium Ion with a Much Longer Lifetime and Higher Energy than that of Natural Photosynthetic Reaction Center, Fukuzumi S, Kotani H, Ohkubo K, Ogo S, Tkachenko NV and Lemmetyinen H. *J. Am. Chem. Soc.* 2004; **126**: 1600–1601.
  104. pH-Dependent Chemoselective Synthesis of  $\alpha$ -Amino Acids. Reductive Amination of  $\alpha$ -Keto Acids with Ammonia Catalyzed by Acid-Stable Iridium Hydride Complexes in Water, Ogo S, Uehara K, Abura T and Fukuzumi S. *J. Am. Chem. Soc.* 2004; **126**: 3020–3021.
  105. Scandium Ion-Catalyzed Photoinduced Electron Transfer from Electron Donors to Pyrene and Acridine. Photocatalytic Oxygenation of Alkylbenzenes, Fukuzumi S, Satoh N, Yuasa J and Ohkubo K. *J. Am. Chem. Soc.* 2004; **126**: 7585–7594.
  106. Four-Electron Reduction of Dioxygen to Water by Ferrocene Derivatives in the Presence of Perchloric Acid in Benzonitrile, Catalyzed by Cofacial Dicobalt Porphyrins, Fukuzumi S, Okamoto K, Gros CP and Guillard R. *J. Am. Chem. Soc.* 2004; **126**: 10441–10449.
  107. DNA Cleavage Induced by Thermal Electron Transfer from a Dimeric NADH Analog to Acridinium Ions in the Presence of Oxygen, Fukuzumi S, Yukimoto K and Ohkubo K. *J. Am. Chem. Soc.* 2004; **126**: 12794–12795.

108. An Yttrium Ion-Selective Fluorescence Sensor Based on Metal Ion-Controlled Photoinduced Electron Transfer in Zinc Porphyrin-Quinone Dyad, Okamoto K and Fukuzumi S. *J. Am. Chem. Soc.* 2004; **126**: 13922–13923.
109. Rational Principles for Modulating Fluorescence Properties of Fluorescein, Ueno T, Urano Y, Setsukinai K, Takakusa H, Kojima H, Kikuchi K, Ohkubo K, Fukuzumi S and Nagano T. *J. Am. Chem. Soc.* 2004; **126**: 14079–14085.
110. Efficient Photocatalytic Oxygenation of Anthracene with Dioxygen via Selective Radical Coupling between Anthracene Radical Cation and Superoxide Anion using 9-Mesityl-10-methylacridinium Ion as an Effective Photocatalyst, Kotani H, Ohkubo K and Fukuzumi S. *J. Am. Chem. Soc.* 2004; **126**: 15999–16006.
111. pH-Selective Isolation of Alkynyl, Acyl, and Ketonyl Intermediates in *anti*-Markovnikov and Markovnikov Hydrations of a Terminal Alkyne, Ogo S, Abura T, Uehara K, Watanabe Y and Fukuzumi S. *J. Am. Chem. Soc.* 2004; **126**: 16520–16527.
112. Dehydrogenation vs Oxygenation in Two-Electron and Four-Electron Reduction of O<sub>2</sub> by 9-Alkyl-10-methyl-9,10-dihydroacridines Catalyzed by Monomeric Cobalt Porphyrins and Cofacial Dicobalt Porphyrins in the Presence of Perchloric Acid, Fukuzumi S, Okamoto K, Tokuda Y, Gros CP and Guillard R. *J. Am. Chem. Soc.* 2004; **126**: 17059–17066.
113. Characterizing Primary Charge-Recombination Accompanying Efficient Stepwise Charge-Separations in an Artificial Photosynthetic Reaction Center, Kobori Y, Yamaguchi S, Akiyama K, Tero-Kubota S, Imahori H, Fukuzumi S and Norris JR Jr. *Proc. Natl. Acad. Sci., U. S. A.* 2005; **102**: 10017–10022.
114. Photovoltaic Cells using Composite Nanoclusters of Porphyrins and Fullerenes with Gold Nanoparticles, Hasobe T, Imahori H, Kamat PV, Ahn TK, Kim D, Hanada T, Hirakawa T and Fukuzumi S. *J. Am. Chem. Soc.* 2005; **127**: 1216–1228.
115. Direct ESR Detection of Pentadienyl Radicals and Peroxyl Radicals in Lipid Peroxidation: Mechanistic Insight into Regioselective Oxygenation in Lipoxygenases, Kitaguchi H, Ohkubo K, Ogo S and Fukuzumi S. *J. Am. Chem. Soc.* 2005; **127**: 6605–6609.
116. Blue Copper Model Complexes with Distorted Tetragonal Geometry Acting as Effective Electron-Transfer Mediators in Dye-Sensitized Solar Cells, Hattori S, Wada Y, Yanagida S and Fukuzumi S. *J. Am. Chem. Soc.* 2005; **127**: 9648–9654.
117. Ordered Assembly of Protonated Porphyrin Driven by Single Wall Carbon Nanotubes. J- and H-Aggregates to Nanorods, Hasobe T, Fukuzumi S, and Prashant V. Kamat, *J. Am. Chem. Soc.* 2005; **127**: 11884–11885.
118. Synthesis and Crystal Structure of an Open Capsule-Type Octanuclear Heterometallic Sulfide Cluster with a Linked Incomplete Double Cubane Framework without an Intramolecular Inversion Center, Ogo S, Kure B, Inoki D, Nakai H, Isobe K and Fukuzumi S. *J. Am. Chem. Soc.* 2005; **127**: 14366–14374.
119. Stacked-Cup Carbon Nanotubes for Photoelectrochemical Solar Cells, Hasobe T, Fukuzumi S and Kamat PV. *Angew. Chem., Int. Ed.* 2006; **45**: 755–759.
120. Host-Guest Complexation of Endohedral Metalofullerene with Azacrown Ether and Its Application, Tsuchiya T, Sato K, Kurihara H, Wakahara T, Nakahodo T, Maeda Y, Akasaka T, Ohkubo K, Fukuzumi S, Kato T, Mizorogi N, Kobayashi K and Nagase S. *J. Am. Chem. Soc.* 2006; **128**: 6699–6703.
121. Reductive DNA Cleavage Induced by UVA Photoirradiation of NADH without Oxygen, Tanaka M, Ohkubo K and Fukuzumi S. *J. Am. Chem. Soc.* 2006; **128**: 12372–12373.
122. Electron-Transfer Reduction of Cup-Stacked Carbon Nanotubes Affording Cup-Shaped Carbons with Controlled Diameter and Size, Saito K, Ohtani M, Sakata T, Mori H and Fukuzumi S. *J. Am. Chem. Soc.* 2006; **128**: 14216–14217.
123. Mechanistic Borderline between One-Step Hydrogen Transfer and Sequential Transfers of Electron and Proton in Reactions of NADH Analogs with Triplet Excited States of Tetrazines and Ru(bpy)<sub>3</sub><sup>2+\*</sup>, Yuasa J and Fukuzumi S. *J. Am. Chem. Soc.* 2006; **128**: 14281–14292.
124. Spin-Site Exchange System Constructed from Endohedral Metallofullerenes and Organic Donors, Tsuchiya T, Sato K, Kurihara H, Wakahara T, Maeda Y, Akasaka T, Ohkubo K, Fukuzumi S, Kato T and Nagase S. *J. Am. Chem. Soc.* 2006; **128**: 14418–14419.
125. Persistent Electron-Transfer State of  $\pi$ -Complex between a Cofacial Bisporphyrin and Acridinium Ion, Tanaka M, Ohkubo K, Gros CP, Guillard R and Fukuzumi S. *J. Am. Chem. Soc.* 2006; **128**: 14625–14633.
126. A Mechanistic Dichotomy in Scandium Ion-Catalyzed Hydride Transfer of an NADH Analog: Delicate Balance between One-Step Hydride-Transfer and Electron-Transfer Pathways, Yuasa J, Yamada S and Fukuzumi S. *J. Am. Chem. Soc.* 2006; **128**: 14938–14948.
127. An OFF-OFF-ON Fluorescence Sensor for Metal Ions in Stepwise Complex Formation of 2,3,5,6-Tetrakis(2-pyridyl)pyrazine (Tppz) with Metal Ions, Yuasa J and Fukuzumi S. *J. Am. Chem. Soc.* 2006; **128**: 15976–15977.
128. A Dinuclear Ni( $\mu$ -H)Ru Complex Derived from H<sub>2</sub>, Ogo S, Kabe R, Uehara K, Kure B, Nishimura T,

- Menon SC, Ryosuke Harada R, Fukuzumi S, Higuchi Y, Ohhara T, Tamada T and Kuroki R. *Science* 2007; **316**: 585–587.
129. Modulation of Characteristics of a Ruthenium-Coordinated Flavin Analogue that Shows an Unusual Coordination Mode, Miyazaki S, Kojima T, Ohkubo K and Fukuzumi S. *Angew. Chem., Int. Ed.* 2007; **46**: 905–908.
  130. Direct ESR Detection of a Hydrogen-Bonded Complex between a Semiquinone Radical Anion and a Protonated Amino Acid and Electron Transfer Driven by the Hydrogen Bond, Yuasa J, Yamada S and Fukuzumi S. *Angew. Chem. Int. Ed.* 2007; **46**: 3553–3555.
  131. Porphyrin-Diones and Porphyrin-Tetraones: Reversible Redox Units being Localized within the Porphyrin Macrocycle and Their Effect on Tautomerism, Kadish KM, E W, Zhan R, Khoury T, Govenlock LJ, Prashar JK, Sintic PJ, Ohkubo K, Fukuzumi S and Crossley MJ. *J. Am. Chem. Soc.* 2007; **129**: 6576–6588.
  132. Intramolecular Electron Transfer within the Substituted Tetrathiafulvalene-Quinone Dyads: Facilitated by Metal Ion and Photomodulation in the Presence of Spiropiran, Wu H, Zhang D, Su L, Ohkubo K, Zhang C, Yin S, Mao L, Shuai Z, Fukuzumi S and Zhu D. *J. Am. Chem. Soc.* 2007; **129**: 6839–6846.
  133. Design and Synthesis of Polymetallic Complexes based on *meso*-Calix[4]pyrrole: Platforms for Multielectron Chemistry, Cuesta L, Gross D, Lynch VM, Ou Z, Kajonkijya W, Ohkubo K, Fukuzumi S, Kadish KM and Sessler JL. *J. Am. Chem. Soc.* 2007; **129**: 11696–11697.
  134. Reversible Formation and Dispersion of Chiral Assemblies Responding to Electron Transfer. Yuasa J and Fukuzumi S. *J. Am. Chem. Soc.* 2007; **129**: 12912–12913.
  135. Monooxygenase Activity of Type-3 Copper Proteins, Itoh S and Fukuzumi S. *Acc. Chem. Res.* 2007; **40**: 592–600.
  136. Spectroscopic Characterization of Photolytically Generated Radical Ion Pairs in Single-Wall Carbon Nanotubes Bearing Surface-Immobilized Tetrathiafulvalenes, Angeles HM, Ehli C, Campidelli S, Gutierrez M, Hug GL, Ohkubo K, Fukuzumi S, Prato M, Martin N and Guldi DM. *J. Am. Chem. Soc.* 2008; **130**: 66–73.
  137. Fundamental Electron-Transfer Properties of Non-Heme Oxoiron(IV) Complexes, Lee YM, Kotani H, Suenobu T, Nam W and Fukuzumi S. *J. Am. Chem. Soc.* 2008; **130**: 434–435.
  138. OFF-OFF-ON Switching of Fluorescence and Electron Transfer Depending on Stepwise Complex Formation of a Host Ligand with Guest Metal Ions, Yuasa J and Fukuzumi S. *J. Am. Chem. Soc.* 2008; **130**: 566–575.
  139. Photochemical and Thermal Isomerization by Pseudo-Rotation of Alloxazine Ligand with Unusual Coordination to a Ruthenium(II) Center, Miyazaki S, Kojima T and Fukuzumi S. *J. Am. Chem. Soc.* 2008; **130**: 1556–1557.
  140. One-Step vs Stepwise Mechanism in Protonated Amino Acid-Promoted Electron-Transfer Reduction of a Quinone by Electron Donors and Two-Electron Reduction by an NADH Analogue. Interplay between Electron Transfer and Hydrogen Bonding, Yuasa J, Yamada S and Fukuzumi S. *J. Am. Chem. Soc.* 2008; **130**: 5808–5820.
  141. Androgynous Porphyrins. Silver(II) Quinoxalino-porphyrins Act as Both Good Electron Donors and Acceptors, Fukuzumi S, Ohkubo K, Zhu W, Sintic M, Khoury T, Sintic PJ, E W, Ou Z, Crossley MJ and Kadish KM. *J. Am. Chem. Soc.* 2008; **130**: 9451–9458.
  142. Corrole-Fullerene Dyads: Formation of Long-Lived Charge-Separated States in Non-Polar Solvents, Chitta R, Ohkubo K, Tasiar M, Subbaiyan NK, Zandler ME, Gryko DT, Fukuzumi S and D'Souza F. *J. Am. Chem. Soc.* 2008; **130**: 14263–14272.
  143. Highly Selective Synthesis of the Ring-B Reduced Chlorins by Ferric Chloride Mediated Oxidation of Bacteriochlorins: Remarkable Effects of the Fused Imide vs. Isocyclic Ring in Photophysical and Electrochemical Properties, Liu C, Dobhal MP, Ethirajan M, Missert JR, Pandey RK, Balasubramanian S, Sukumaran DK, Zhang M, Kadish KM, Ohkubo K and Fukuzumi S. *J. Am. Chem. Soc.* 2008; **130**: 14311–14323.
  144. Sequential Electron-Transfer and Proton-Transfer Pathways in Hydride-Transfer Reactions from NADH Analogs to Non-Heme Oxoiron(IV) Complexes and *p*-Chloranil. Detection of Radical Cations of NADH Analogs in the Acid-Promoted Hydride-Transfer Reactions, Fukuzumi S, Kotani H, Lee YM and Nam W. *J. Am. Chem. Soc.* 2008; **130**: 15134–15142.
  145. “Umpolung” Photoinduced Charge Separation in an Anion-bound Supramolecular Complex, Sessler JL, Karnas E, Kim SK, Ou Z, Zhang M, Kadish KM, Ohkubo K and Fukuzumi S. *J. Am. Chem. Soc.* 2008; **130**: 15256–15257.
  146. Isolation and Crystal Structures of Both Enol and Keto Tautomer Intermediates in a Hydration of an Alkyne-Carboxylic Acid Ester Catalyzed by Iridium Complexes in Water, Kanemitsu H, Uehara K, Fukuzumi S and Ogo S. *J. Am. Chem. Soc.* 2008; **130**: 17141–17147.
  147. Metal Quinolinolate–Fullerene(s) Donor-Acceptor Complexes: Evidence for Organic LED Molecules Acting as Electron Donors in Photoinduced Electron Transfer Reactions, D'Souza F, Maligaspe E, Zandler ME, Subbaiyan NK, Ohkubo K and

- Fukuzumi S. *J. Am. Chem. Soc.* 2008; **130**: 16959–16967.
148. Detection of a Radical Cation of an NADH Analogue in the Thermal Reaction with a Protonated *p*-Quinone Derivative, Yuasa J, Yamada S and Fukuzumi S. *Angew. Chem., Int. Ed.* 2008; **47**: 1068–1071.
  149. Ruthenium-Catalyzed Selective and Efficient Oxygenation of Hydrocarbons with Water as an Oxygen Source, Hirai Y, Kojima T, Mizutani Y, Shiota Y, Yoshizawa K and Fukuzumi S. *Angew. Chem., Int. Ed.* 2008; **47**: 5772–5776.
  150. A Discrete Supramolecular Conglomerate Composed of Two Saddle-Distorted Zinc(II)-Phthalocyanine Complexes and a Doubly Protonated Porphyrin with Saddle-Distortion Undergoing Efficient Photoinduced Electron Transfer, Kojima T, Honda T, Ohkubo K, Shiro M, Kusukawa T, Fukuda T, Kobayashi N and Fukuzumi S. *Angew. Chem., Int. Ed.* 2008; **47**: 6712–6716.
  151. Hydrogen Atom Abstraction and Hydride Transfer Reactions by Iron(IV)-Oxo Porphyrins, Jeong YJ, Kang Y, Han AR, Lee YM, Kotani H, Fukuzumi S and Nam W. *Angew. Chem., Int. Ed.* 2008; **47**: 7321–7324.
  152. Proton Shift upon One-Electron Reduction in Ruthenium(II)-Coordinated Pterin, Miyazaki S, Ohkubo K, Kojima T and Fukuzumi S. *Angew. Chem., Int. Ed.* 2008; **47**: 9669–9672.
  153. Reorganization Energies of Diprotonated and Saddle-Distorted Porphyrins in Photoinduced Electron-Transfer Reduction Controlled by Conformational Distortion, Nakanishi T, Kojima T, Ohkubo K and Fukuzumi S. *J. Am. Chem. Soc.* 2009; **131**: 577–584.
  154. Long Lived Charge-Separated Configuration of a Push-Pull Archetype of Disperse Red 1 End-Capped Poly[9,9-Bis(4-diphenylaminophenyl) Fluorene], El-Khouly ME, Chen Y, Zhuang X, He N, Zhang B and Fukuzumi S. *J. Am. Chem. Soc.* 2009; **131**: 6370–6371.
  155. Topochemical Limits for Solid-State Photoreactivity by Fine Tuning of the  $\pi$ - $\pi$  Interactions, Yang SY, Naumov P and Fukuzumi S. *J. Am. Chem. Soc.* 2009; **131**: 7247–7249.
  156. Tuning Charge Transfer in Reaction Center Mimics Based on Th-Functionalized Fullerenes, Spaenig F, Kovacs C, Hauke F, Hartnagel U, Ohkubo K, Fukuzumi S, Guldi DM and Hirsch A. *J. Am. Chem. Soc.* 2009; **131**: 8180–8195.
  157. Photosynthetic Reaction Center Mimicry: Low-Reorganization Energy Driven Charge Stabilization in Self-Assembled Co-facial Zinc Phthalocyanine Dimer — Fullerene Conjugates, D'Souza F, Maligaspe E, Ohkubo K, Zandler ME, Subbaiyan NK and Fukuzumi S. *J. Am. Chem. Soc.* 2009; **131**: 8787–8797.
  158. Aliphatic C–H Bond Activation by a  $(\mu\text{-}\eta^2\text{:}\eta^2\text{-Peroxo})\text{dicopper(II)}$  Complex in Comparison with Cumylperoxyl Radical, Takahiro Matsumoto, Ohkubo K, Honda K, Yazawa A, Furutachi H, Fujinami S, Fukuzumi S and Suzuki M. *J. Am. Chem. Soc.* 2009; **131**: 9258–9267.
  159. Structure and Spectroscopy of Oxyluciferin, the Light Emitter of the Firefly Bioluminescence, Naumov P, Ozawa Y and Fukuzumi S. *J. Am. Chem. Soc.* 2009; **131**: 11590–11605.
  160. Proton-Coupled Electron Transfer of Ruthenium(III)-Pterin Complexes: A Mechanistic Insight, Soushi Miyazaki, Kojima T, Mayer JM and Fukuzumi S. *J. Am. Chem. Soc.* 2009; **131**: 11615–11624.
  161. Metalloporphyrines: Synthesis and Characterization of (Pentamethylcyclopentadienyl)ruthenium “Sitting-a-top” and  $\pi$ -Complexes, Cuesta L, Karnas E, Lynch VM, Zhang M, Kadish KM, Ohkubo K, Fukuzumi S and Sessler JL. *J. Am. Chem. Soc.* 2009; **131**: 13538–13547.
  162. Dioxygen Activation by Mononuclear Nonheme Iron(II) Complexes Resulting in the Generation of Iron(III)-Hydroperoxo and Iron(IV)-Oxo Intermediates, Hong S, Lee YM, Shin W, Fukuzumi S and Nam W. *J. Am. Chem. Soc.* 2009; **131**: 13910–13911.
  163. Mechanistic Insights into Hydride-Transfer and Electron-Transfer Reactions by a Manganese(IV)-Oxo Porphyrin Complex, Fukuzumi S, Fujioka N, Kotani H, Ohkubo K, Lee YM and Nam W. *J. Am. Chem. Soc.* 2009; **131**: 17127–17134.
  164. Anion-Complexation-Induced Stabilization of Charge Separation, D'Souza F, Subbaiyan NK, Xie Y, Hill JP, Ariga K, Ohkubo K and Fukuzumi S. *J. Am. Chem. Soc.* 2009; **131**: 16138–16146.
  165. Water as an Oxygen Source in the Generation of Mononuclear Nonheme Iron(IV)-Oxo Complexes, Dhuri SN, Sawant SC, Cho J, Lee YM, Kubo M, Ogura T, Fukuzumi S and Nam W. *Angew. Chem., Int. Ed.* 2009; **48**: 1803–1806.
  166. Unusually Large Tunneling Effect on Highly Efficient Generation of Hydrogen and Hydrogen Isotopes in pH-Selective Decomposition of Formic Acid Catalyzed by a Heterodinuclear Iridium-Ruthenium Complex in Water, Fukuzumi S, Kobayashi T and Suenobu T. *J. Am. Chem. Soc.* 2010; **132**: 1496–1497.
  167. Efficient Photoinduced Electron Transfer in a Porphyrin Tripod–Fullerene Supramolecular Complex *via*  $\pi$ - $\pi$  Interactions in Nonpolar Media, Takai A, Chkounda M, Eggenpiller A, Gros CP, Lachkar M, Barbe JM and Fukuzumi S. *J. Am. Chem. Soc.* 2010; **132**: 4477–4489.
  168. Mononuclear Copper Complex Catalyzed Four-Electron Reduction of Oxygen, Fukuzumi S, Kotani H, Lucas HR, Doi K, Suenobu T, Peterson R

- and Karlin KD. *J. Am. Chem. Soc.* 2010; **132**: 6874–6875.
169. Structure and Photoinduced Electron Transfer Dynamics of a Series of Hydrogen-Bonded Supramolecular Complexes Composed of Electron Donors and a Saddle-Distorted Diprotonated Porphyrin, Honda T, Nakanishi T, Ohkubo K, Kojima T and Fukuzumi S. *J. Am. Chem. Soc.* 2010; **132**: 10155–10163.
  170. Dioxygen Activation by a Nonheme Iron(II) Complex: Formation of an Iron(IV)-Oxo Complex via C-H Activation by a Putative Iron(III)-Superoxo Species, Lee YM, Hong S, Shin W, Morimoto Y, Fukuzumi S and Nam W. *J. Am. Chem. Soc.* 2010; **132**: 10668–10670.
  171. Synthesis and Photodynamics of 9-Mesitylacridinium Ion-Modified Gold Nanoclusters, Fukuzumi S, Hanazaki R, Kotani H and Ohkubo K. *J. Am. Chem. Soc.* 2010; **132**: 11002–11003.
  172. Formic Acid Acting as an Efficient Oxygen Scavenger in Four-Electron Reduction of Oxygen Catalyzed by a Heterodinuclear Iridium-Ruthenium Complex in Water, Fukuzumi S, Kobayashi T and Suenobu T, *J. Am. Chem. Soc.* 2010; **132**: 11866–11867.
  173. Stopped-Flow Kinetic Analysis of the Interaction of Cyclo[8]pyrrole with Anions, Karnas E, Kim SK, Johnson KA, Sessler JL, Ohkubo K and Fukuzumi S. *J. Am. Chem. Soc.* 2010; **132**: 16617–16622.
  174. Electron-Transfer Properties of an Efficient Nonheme Iron Oxidation Catalyst with a Tetradentate Bispidine Ligand, Comba P, Fukuzumi S, Kotani H and Wunderlich S. *Angew. Chem., Int. Ed.* 2010; **49**: 2622–2625.
  175. A Low-Spin Ruthenium(IV)-Oxo Complex: Does the Spin State Have an Impact on the Reactivity? Kojima T, Hirai Y, Mizutani Y, Ikemura K, Ogura T and Fukuzumi S. *Angew. Chem., Int. Ed.* 2010; **49**: 8449–8453.
  176. Reversible Cation- and Anion-Controlled Electron Transfer Using a Supramolecular Donor-Acceptor Ensemble, Park JS, Karnas E, Ohkubo K, Chen P, Kadish KM, Fukuzumi S, Bielawski C, Hudnall TW, Lynch VM and Sessler JL. *Science*, 2010; **329**: 1324–1327.
  177. Crystal Structure of a Metal Ion-Bound Oxoiron(IV) Complex and Implications for Biological Electron Transfer, Fukuzumi S, Morimoto Y, Kotani H, Naumov P, Lee YM and Nam W. *Nature Chem.* 2010; **2**: 756–759.
  178. Efficient Photocatalytic Oxygenation Reactions Using Water as an Oxygen Source, Fukuzumi S, Kishi T, Kotani H, Lee YM and Nam W. *Nature Chem.* 2011; **3**: 38–41.
  179. Photocatalytic Production of Hydrogen via Disproportionation of One-Electron Reduced Species of Rhodium and Iridium-Ruthenium Complexes in Water, Fukuzumi S, Kobayashi T and Suenobu T. *Angew. Chem., Int. Ed.* 2011; **50**: 728–731.
  180. Crystal Structures and Electronic Properties of Saddle-Distorted and Protonated Phthalocyanines, Honda T, Kojima T, Kobayashi N and Fukuzumi S. *Angew. Chem., Int. Ed.* 2011; **50**: 2725–2728.
  181. Reply to the Comments by Dr. D. Schröder and Prof. Dr. S. Shaik, Kojima T and Fukuzumi S. *Angew. Chem., Int. Ed.* 2011; **50**: 3852–3853.
  182. Direct Oxygenation of Benzene to Phenol Using Quinolinium Ions as Homogeneous Photocatalysts, Ohkubo K, Kobayashi T and Fukuzumi S. *Angew. Chem., Int. Ed.*, 2011; **50**: 8652–8655.
  183. Metal Ion-Coupled Electron Transfer of a Nonheme Oxoiron(IV) Complex: Remarkable Enhancement of Electron-Transfer Rates by  $\text{Sc}^{3+}$ , Morimoto Y, Kotani H, Park J, Lee YM, Nam W and Fukuzumi S. *J. Am. Chem. Soc.* 2011; **133**: 403–405.
  184. Post-translational His-Cys Cross Linkage Formation in Tyrosinase Induced by Copper(II)-Peroxo Species, Fujieda N, Ikeda T, Murata M, Yanagisawa S, Aono S, Ohkubo K, Nagao S, Ogura T, Hirota S, Fukuzumi S, Nakamura Y, Hata Y and Itoh S. *J. Am. Chem. Soc.* 2011; **133**: 1180–1183.
  185. Cupric Superoxo-Mediated Intermolecular C-H Activation Chemistry, Peterson RL, Himes RA, Kotani H, Suenobu T, Tian L, Siegler MA, Solomon EI, Fukuzumi S and Karlin KD. *J. Am. Chem. Soc.* 2011; **113**: 1702–1705.
  186. Electron- and Hydride-Transfer Reactivity of an Isolable Manganese(V)-Oxo Complex, Fukuzumi S, Kotani H, Prokop KA and Goldberg DP. *J. Am. Chem. Soc.* 2011; **133**: 1859–1869.
  187. Photocatalytic Generation of a Nonheme Oxoiron(IV) Complex with Water as an Oxygen Source, Kotani H, Suenobu T, Lee YM, Nam W and Fukuzumi S. *J. Am. Chem. Soc.* 2011; **133**: 3249–3251.
  188. Metal Ion Effect on the Switch of Mechanism from Direct Oxygen Transfer to Metal Ion-Coupled Electron Transfer in the Sulfoxidation of Thioanisoles by a Nonheme Iron(IV)-Oxo Complex, Park J, Morimoto Y, Lee YM, Nam W and Fukuzumi S. *J. Am. Chem. Soc.* 2011; **133**: 5236–5239.
  189. Disproportionation of Dipyrrolylquinoxaline Radical Anions with Internal Protons of the Pyrrole Moiety, Fukuzumi S, Mase K, Ohkubo K, Fu Z, Sessler JL and Kadish KM. *J. Am. Chem. Soc.* 2011; **133**: 7284–7287.
  190. An Efficient Fluorescence Sensor for Superoxide with an Acridinium Ion-Linked Porphyrin Triad, Kotani H, Ohkubo K, Crossley MJ and Fukuzumi S. *J. Am. Chem. Soc.* 2011; **133**: 11092–11095.
  191. Catalytic Mechanism of Water Oxidation with Single-Site Ruthenium-Heteropolytungstate Complexes, Murakami M, Hong D, Suenobu T and Fukuzumi S. *J. Am. Chem. Soc.* 2011; **133**: 11605–11613.

192. Formation of a Ruthenium(IV)-Oxo Complex by Electron-Transfer Oxidation of a Coordinatively Saturated Ruthenium(II) Complex and Detection of an Oxygen-Rebound Intermediates in C-H Bond Oxygenation, Kojima T, Nakayama K, Ikemura K, Ogura T and Fukuzumi S. *J. Am. Chem. Soc.* 2011; **133**: 11692–11700.
193. Reversible Photoredox Switching of Porphyrin-Bridged Hydroquinone, Ishihara S, Hill JP, Shundo A, Richards G, Labuta J, Ohkubo K, Fukuzumi S, Sato A, Elsegood M, Teat S and Ariga K. *J. Am. Chem. Soc.* 2011; **133**: 16119–16126.
194. Ion-Controlled On-Off Switch of Electron Transfer from Tetrathiafulvalene Calix[4]pyrroles to Li<sup>+</sup>@C<sub>60</sub>, Fukuzumi S, Ohkubo K, Kawashima Y, Kim DS, Park JS, Jana A, Lynch VM, Kim D and Sessler JL. *J. Am. Chem. Soc.* 2011; **133**: 15938–15941.
195. Photocatalytic Hydrogen Evolution under Highly Basic Conditions by Using Ru Nanoparticles and 2-Phenyl-4-(1-naphthyl)quinolinium Ion, Yamada Y, Miyahigashi T, Kotani H, Ohkubo K and Fukuzumi S. *J. Am. Chem. Soc.* 2011; **133**: 16136–16145.
196. Photochemical Activation of Ruthenium(II)-Pyridylamine Complexes Having a Pyridine-N-Oxide Pendant toward Oxygenation of Organic Substrates, Kojima T, Nakayama K, Sakaguchi M, Ogura T, Ohkubo K and Fukuzumi S. *J. Am. Chem. Soc.* 2011; **133**: 17901–17911.
197. Phosphorescent Sensor for Biological Zinc Ions, You Y, Lee S, Kim T, Ohkubo K, Chae WS, Fukuzumi S, Jhon GJ, Nam W and Lippard SJ. *J. Am. Chem. Soc.* 2011; **133**: 18328–18342.
198. Proton-Coupled Electron Shuttling in a Covalently Linked Ruthenium-Copper Heterodinuclear Complex, Ishizuka T, Tobita K, Yano Y, Shiota Y, Yoshizawa K, Fukuzumi S and Kojima T. *J. Am. Chem. Soc.* 2011; **133**: 18570–18573.
199. Protonated Iron-Phthalocyaninate Complex Used for Cathode Material for a Hydrogen Peroxide Fuel Cell Operated under Acidic Conditions, Yamada Y, Yoshida S, Honda T and Fukuzumi S. *Energy Environ. Sci.* 2011; **4**: 2822–2825.
200. Catalytic Mechanisms of Hydrogen Evolution with Homogeneous and Heterogeneous Catalysts, Fukuzumi S, Yamada Y, Suenobu T, Ohkubo K and Kotani H. *Energy Environ. Sci.* 2011; **4**: 2754–2766.
201. Homogeneous Catalytic O<sub>2</sub> Reduction to Water by a Cytochrome *c* Oxidase Model with Trapping Intermediates and Mechanistic Insights, Halime Z, Kotani H, Fukuzumi S and Karlin KD. *Proc. Natl. Acad. Sci. U.S.A.* 2011; **108**: 13990–13994.
202. Redox-induced Reversible Metal Assembling through Translocation and Reversible Ligand Coupling in Tetranuclear Metal Sandwich Frameworks, Murahashi T, Shirato K, Fukushima A, Takase K, Suenobu T, Fukuzumi S, Ogoshi S and Kurosawa H. *Nature Chem.* 2012; **4**: 52–58.
203. Catalytic Application of Shape-Controlled Cu<sub>2</sub>O Particles Protected by Co<sub>3</sub>O<sub>4</sub> Nanoparticles for Hydrogen Evolution from Ammonia Borane, Yamada Y, Yano K and Fukuzumi S. *Energy Environ. Sci.* 2012; **5**: 5356–5363.
204. Water Oxidation Catalysis of Active Species Derived from [Ir<sup>III</sup>(Cp\*) (4,4'-bishydroxy-2,2'-bipyridine)(H<sub>2</sub>O)]<sup>2+</sup>, Hong D, Murakami M, Yamada Y and Fukuzumi S. *Energy Environ. Sci.* 2012; **5**: 5708–5716.
205. Photocatalytic hydrogen Evolution with Ni Nanoparticles by Using 2-Phenyl-4-(1-naphthyl)quinolinium ion as a Photocatalyst, Yamada Y, Miyahigashi T, Kotani H, Ohkubo K and Fukuzumi S. *Energy Environ. Sci.* 2012; **5**: 6111–6118.
206. Catalytic Interconversion between Hydrogen and Formic Acid at Ambient Temperature and Pressure, Maenaka Y, Suenobu T and Fukuzumi S. *Energy Environ. Sci.* 2012; **5**: 7360–7367.
207. Photocatalytic Water Oxidation by Nanoparticles Derived from Water-Soluble Mononuclear Cobalt Complexes with Organic Ligands with Organic Ligands, Hong D, Jung J, Park J, Yamada Y, Suenobu T, Lee YM, Nam W and Fukuzumi S. *Energy Environ. Sci.* 2012; **5**: 7606–7616.
208. Regulation of Redox Potential of a Pterin Derivative Bound to a Ruthenium(II) Complex by Intermolecular Hydrogen Bonding with Nucleobases, Inui Y, Miyazaki S, Ohkubo K, Fukuzumi S and Kojima T. *Angew. Chem., Int. Ed.* 2012; **51**: 4623–4627.
209. Electronic Properties of Trifluoromethylated Corannulenes, Schmidt BM, Seki S, Topolinski B, Ohkubo K, Fukuzumi S, Sakurai H and Lentz D. *Angew. Chem., Int. Ed.* 2012; **51**: 11385–11388.
210. Photoelectrocatalysis Greatly Improves Cycloreversion Quantum Yields of Photochromic Dithienylethene Compounds, Lee S, You Y, Ohkubo K, Fukuzumi S and Nam W. *Angew. Chem., Int. Ed.* 2012; **51**: 13154–13158.
211. Efficient Catalytic Interconversion between NADH and NAD<sup>+</sup> Accompanied by Generation and Consumption of Hydrogen with a Water-Soluble Iridium Complex at Ambient Pressure and Temperature, Maenaka Y, Suenobu T and Fukuzumi S. *J. Am. Chem. Soc.* 2012; **134**: 367–374.
212. Control over Photoinduced Energy and Electron Transfer in Supramolecular Polyads of Covalently linked azaBODIPY-Bisporphyrin ‘Molecular Clip’ hosting Fullerene, D’Souza F, Amin AN, El-Khouly ME, Subbaiyan NK, Zandler ME and Fukuzumi S. *J. Am. Chem. Soc.* 2012; **134**: 654–664.
213. Proton-Promoted Oxygen Atom Transfer vs Proton-Coupled Electron Transfer of a Non-Heme Iron(IV)-Oxo Complex, Park J, Morimoto Y, Lee YM,



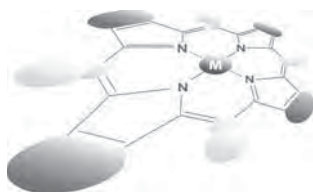
- Nam W and Fukuzumi S. *J. Am. Chem. Soc.* 2012; **134**: 3903–3911.
214. Proton-Coupled Electron-Transfer Reduction of Dioxygen Catalyzed by a Saddle-Distorted Cobalt Phthalocyanine, Honda T, Kojima T and Fukuzumi S. *J. Am. Chem. Soc.* 2012; **134**: 4196–4206.
215. Structural Change upon Photoinduced Electron Transfer of a Donor-Acceptor Dyad Detected by X-ray, Hoshino M, Uekusa H, Tomita A, Koshihara S, Sato T, Nozawa S, Adachi S, Ohkubo K, Kotani H and Fukuzumi S. *J. Am. Chem. Soc.* 2012; **134**: 4569–4572.
216. Utilization of Photoinduced Charge-Separated State of Donor-Acceptor Linked Molecules for Regulation of Cell Membrane Potential and Ion Transport, Numata T, Murakami T, Kawashima F, Morone N, Heuser JE, Takano Y, Ohkubo K, Fukuzumi S, Mori Y and Imahori H. *J. Am. Chem. Soc.* 2012; **134**: 6092–6095.
217. Factors that Control Catalytic Two- vs Four-Electron Reduction of Dioxygen by Copper Complexes, Fukuzumi S, Tahsini L, Lee YM, Ohkubo K, Nam W and Karlin KD. *J. Am. Chem. Soc.* 2012; **134**: 7025–7035.
218. Hydrogen Evolution from Aliphatic Alcohols and 1,4-Selective Hydrogenation of NAD<sup>+</sup> Catalyzed by a [C,N] and a [C,C] Cyclometalated Organoiridium Complexes at Room Temperature in Water, Maenaka Y, Suenobu T and Fukuzumi S. *J. Am. Chem. Soc.* 2012; **134**: 9417–9427.
219. Catalytic Four-Electron Reduction of Dioxygen via Rate-Determining Proton-Coupled Electron Transfer to a Dinuclear Cobalt- $\mu$ -1,2-Peroxo Complex, Fukuzumi S, Mandal S, Mase K, Ohkubo K, Park H, Benet-Buchholz J, Nam W and Llobet A. *J. Am. Chem. Soc.* 2012; **134**: 9906–9909.
220. Catalysis of Nickel Ferrite for Photocatalytic Water Oxidation Using [Ru(bpy)<sub>3</sub>]<sup>2+</sup> and S<sub>2</sub>O<sub>8</sub><sup>2-</sup>, Hong D, Yamada Y, Nagatomi T, Takai Y and Fukuzumi S. *J. Am. Chem. Soc.* 2012; **134**: 19572–19575.
221. Formation of a Long-Lived Electron-Transfer State in Nanosized Mesoporous Silica-Alumina Enhances Photocatalytic Oxidation Reactivity with a Copper Complex, Fukuzumi S, Doi K, Suenobu T, Ohkubo K, Yamada Y and Karlin KD. *Proc. Natl. Acad. Sci. U.S.A.* 2012; **109**: 15572–15577.
222. Energy and environment policy case for a global projection artificial photosynthesis. Faunce TA, Lubitz W, Rutherford AW, MacFarlane D, Moore GF, Yang P, Nocera DG, Moore TA, Gregory DH, Fukuzumi S, Yoon KB, Armstrong FA, Wasielewski MR and Styring S. *Energy Environ. Sci.* 2013; **6**: 695–698.
223. Production of Hydrogen Peroxide as a Solar Fuel from Water and Dioxygen, Kato S, Jung J, Suenobu T and Fukuzumi S. *Energy Environ. Sci.* 2013; **6**: 3756–3764.
224. Charge Dynamics in a Donor–Acceptor Covalent Organic Framework with Periodically Ordered Bicontinuous Heterojunctions, Jin S, Ding X, Feng X, Supur M, Furukawa K, Takahashi S, Addicoat M, El-Khouly ME, Nakamura T, Irle S, Fukuzumi S, Nagai A, and Jiang D. *Angew. Chem., Int. Ed.* 2013; **52**: 2017–2021.
225.  $\eta^5$ -Cyclopentadienyl-Iron(II)-[14]Triphyrin(2.1.1) Sandwich Compounds: Synthesis, Characterization, and Stable Redox Interconversion, Xue Z, Kuzuhara D, Ikeda S, Sakakibara Y, Ohkubo K, Aratani N, Okujima T, Uno H, Fukuzumi S and Yamada H. *Angew. Chem., Int. Ed.* 2013; **52**: 7306–7309.
226. Assembly and Stepwise Oxidation of Interpenetrated Coordination Cages based on Phenothiazine, Frank M, Hey J, Balcioglu I, Chen YS, Stalke D, Suenobu T, Fukuzumi S, Frauendorf H and Clever GH. *Angew. Chem., Int. Ed.* 2013; **52**: 10102–10106.
227. Direct Synthesis of Hydrogen Peroxide from Hydrogen and Oxygen with a Water Soluble Iridium Complex and a Flavin Analog in Water, Shibata S, Suenobu T and Fukuzumi S. *Angew. Chem., Int. Ed.* 2013; **52**: 12327–12331.
228. Protonation-coupled Redox Reaction in Planar Antiaromatic meso-Pentafluorophenyl-substituted Phenylene Bridged Annulated Rosarins, Ishida M, Preihs C, Ohkubo K, Lim JM, Lee BS, Lynch VM, Roznyatovskiy VV, Kim SJ, Lee CH, Fukuzumi S, Kim D and Sessler JL. *Nature Chem.* 2013; **5**: 15–20.
229. Efficient Two-Electron Reduction of Dioxygen to Hydrogen Peroxide with One-Electron Reductants with a Small Overpotential Catalyzed by a Cobalt Chlorin Complex, Mase K, Ohkubo K and Fukuzumi S. *J. Am. Chem. Soc.* 2013; **135**: 2800–2808.
230. Temperature Independent Catalytic Two-Electron Reduction of Dioxygen by Ferrocenes with a Copper (II) Complex with Tris[2-(2-pyridyl)ethyl]amine in the Presence of Perchloric Acid, Das D, Lee YM, Kei Ohkubo K, Nam W, Karlin KD and Fukuzumi S. *J. Am. Chem. Soc.* 2013; **135**: 2825–2834.
231. Acid-Induced Mechanism Change and Overpotential Decrease in Dioxygen Reduction Catalysis with a Dinuclear Copper Complex, Das D, Lee YM, Ohkubo K, Nam W, Karlin KD and Fukuzumi S. *J. Am. Chem. Soc.* 2013; **135**: 4018–4026.
232. Brønsted Acid–Promoted C–H Bond Activation via Electron Transfer from Toluene Derivatives to a Protonated Non-Heme Iron(IV)-Oxo Complex with No Kinetic Isotope Effect, Park J, Lee YM, Nam W and Fukuzumi S. *J. Am. Chem. Soc.* 2013; **135**: 5052–5061.

233. Visible Light Induced Oxygenation of Benzene by the Triplet Excited State of 2,3-Dichloro-5,6-dicyano-*p*-benzoquinone, Ohkubo K, Fujimoto A and Fukuzumi S. *J. Am. Chem. Soc.* 2013; **135**: 5368–5371.
234. Helicity Selective Photoreaction of Single-walled Carbon Nanotubes with Organosulfur Compounds in the Presence of Oxygen, Maeda Y, Higo J, Amagai Y, Matsui J, Ohkubo K, Yoshigoe Y, Hashimoto M, Eguchi K, Yamada M, Hasegawa T, Sato Y, Zhou J, Lu J, Miyashita T, Fukuzumi S, Murakami T, Tohji K, Nagase S and Akasaka T. *J. Am. Chem. Soc.* 2013; **135**: 6356–6362.
235. Enhanced Catalytic Four-Electron Reduction of Dioxygen with a Copper(II) Complex with a Pendant Ligand Pivalamido Group, Kakuda S, Peterson RL, Ohkubo K, Karlin KD and Fukuzumi S. *J. Am. Chem. Soc.* 2013; **135**: 6513–6522.
236. A Mononuclear Nonheme Manganese(IV)-Oxo Complex Binding Redox-Inactive Metal Ions, Chen J, Wu X, Davis KM, Lee YM, Seo MS, Cho KB, Yoon H, Park YJ, Fukuzumi S, Pushkar YN and Nam W. *J. Am. Chem. Soc.* 2013; **135**: 6388–6391.
237. Much Enhanced Electron-Transfer Reactivity of Nonheme Manganese(IV)-Oxo Complexes by Binding One and Two Scandium Ions, Yoon H, Lee YM, Wu X, Cho KB, Pushkar YN, Nam W and Fukuzumi S. *J. Am. Chem. Soc.* 2013; **135**: 9186–9194.
238. Porphyrins Fused with Strongly Electron Donating 1,3-Dithiol-2-ylidene Moieties. Redox Control by Metal Cation Complexation and Anion Binding, Bill NL, Ishida M, Bähring S, Lim JM, Lee S, Davis CM, Lynch VM, Nielsen KA, Jeppesen JO, Ohkubo K, Fukuzumi S, Kim D and Sessler JL. *J. Am. Chem. Soc.* 2013; **135**: 10852–10862.
239. Protonation Equilibrium and Hydrogen Production by a Dinuclear Co-Hb<sub>pp</sub> Complex Reduced by Cobaltocene with Trifluoroacetic Acid, Mandal S, Shikano S, Yamada Y, Lee YM, Nam W, Llobet A and Fukuzumi S. *J. Am. Chem. Soc.* 2013; **135**: 15294–15297.
240. The Stepwise Protonation and Electron-Transfer Reduction of a Primary Copper-Dioxygen Adduct, Peterson RL, Ginsbach JW, Cowley RE, Qayyum MF, Himes RA, Siegler MA, Moore CD, Hedman B, Hodgson KO, Fukuzumi S, Solomon EI and Karlin KD. *J. Am. Chem. Soc.* 2013; **135**: 16454–16467.
241. Angewante Author Profile, Fukuzumi S. *Angew. Chem., Int. Ed.* 2014; **53**: 6854–6855.
242. Redox-Inactive Metal Ions Modulate the Reactivity and Oxygen Release of Mononuclear Non-Haem Iron(III)-Peroxo Complexes, Bang S, Lee YM, Hong S, Nishida Y, Seo MS, Sarangi R, Fukuzumi S and Nam W. *Nature Chem.* 2014; **6**: 934–940.
243. Tuning Reactivity and Mechanism in Oxidation Reactions by Mononuclear Nonheme Iron(IV)-Oxo Complexes, Nam W, Lee YM and Fukuzumi S. *Acc. Chem. Res.* 2014; **47**: 1146–1154.
244. Long-Lived Charge Separation and Applications in Artificial Photosynthesis, Fukuzumi S, Ohkubo K and Suenobu T. *Acc. Chem. Res.* 2014; **47**: 1455–1464.
245. Autocatalytic Formation of an Iron(IV)-Oxo Complex via Scandium Ion-Promoted Radical Chain Autoxidation of an Iron(II) Complex with Dioxygen and Tetraphenylborate, Nishida Y, Lee YM, Nam W and Fukuzumi S. *J. Am. Chem. Soc.* 2014; **136**: 8042–8049.
246. Mechanistic Insights into the Oxidation of Substituted Phenols via Hydrogen Atom Abstraction by a Cupric Superoxo Species, Lee JY, Peterson RL, Ohkubo K, Garcia-Bosch I, Himes RA, Woertink J, Moore CD, Solomon EI, Fukuzumi S and Karlin KD. *J. Am. Chem. Soc.* 2014; **136**: 9925–9937.
247. Photoinduced Electron Transfer through Curved  $\pi$ -Surfaces in a Supramolecular  $\pi$ -Complex between Corannulene with  $\text{Li}^+@C_{60}$ , Yamada M, Ohkubo K, Shionoya M and Fukuzumi S. *J. Am. Chem. Soc.* 2014; **136**: 13240–13248.

*JPP Guest Editors***Francis D'Souza**University of North Texas  
Denton (TX), USA

December 2014

**Hiroshi Imahori**Kyoto University  
Kyoto, Japan



# Proton-coupled electron transfer chemistry of hangman macrocycles: Hydrogen and oxygen evolution reactions

Dilek K. Dogutan<sup>◇</sup>, D. Kwabena Bediako, Daniel J. Graham,  
Christopher M. Lemon and Daniel G. Nocera<sup>\*◇</sup>

Department of Chemistry and Chemical Biology, Harvard University, 12 Oxford Street, Cambridge, Massachusetts 02138, United States

*Dedicated to Professor Shunichi Fukuzumi on the occasion of his retirement*

Received 23 September 2014

Accepted 6 October 2014

**ABSTRACT:** The splitting of water into its constituent elements is an important solar fuels conversion reaction for the storage of renewable energy. For each of the half reactions of the oxygen evolution reaction (OER) and hydrogen evolution reaction (HER), multiple protons and electrons must be coupled to avoid high-energy intermediates. To understand the mechanistic details of the PCET chemistry that underpins HER and OER, we have designed hangman porphyrin and corrole catalysts. In these hangman constructs, a pendant acid/base functionality within the secondary coordination sphere is “hung” above the macrocyclic redox platform on which substrate binds. The two critical thermodynamic properties of a PCET event, the redox potential and  $pK_a$  may be tuned with the macrocycle and hanging group, respectively. This review outlines the synthesis of these catalysts, as well as the examination of the PCET kinetics of hydrogen and oxygen evolution by the hangman catalysts. The insights provided by these systems provide a guide for the design of future HER and OER catalysts that use a secondary coordination sphere to manage PCET.

**KEYWORDS:** porphyrin, corrole, catalyst, hangman effect, proton-coupled electron transfer (PCET), hydrogen evolution, oxygen evolution, renewable, solar fuels.

## INTRODUCTION

The generation of fuels from solar energy requires the rearrangement of stable chemical bonds with light as the impetus for the fuel-forming reaction. All such transformations of energy consequence require the coupling of protons to an overall multi-electron event. When such coupling is not achieved, large kinetic penalties are associated with the fuel-forming reaction. This is most easily seen for the seemingly simplest of chemical transformations, the reduction of protons to dihydrogen. If this reduction proceeds by sequential *one*-electron steps that are *uncoupled* from the proton, then the reaction confronts

a large energetic barrier. On the NHE reference scale, the first reduction proceeds with an uphill potential of 2.3 V; the addition of a second electron and proton then proceeds with a downhill potential of 2.3 V [1, 2]. This is schematically illustrated in Fig. 1. Despite an overall thermodynamic potential of 0 V, the half-reaction confronts a 2.3 V energy barrier if the protons are not coupled to the two-electron process. A catalyst can mediate the coupling of protons to electrons; the ability of the catalyst to do so, leads to a reduction of the barrier shown in Fig. 1. More generally, this is true of any PCET reaction involving a small molecule substrate. Hence the efficiency of a solar-to-fuels transformation effectively reduces to an issue of catalyst design and the ability of the catalyst to manage PCET.

The coupling of the electron to the proton is difficult because, unlike electrons, which can tunnel over long distances, the 2000-fold more massive proton can only

<sup>◇</sup> SPP full member in good standing

\*Correspondence to: Daniel G. Nocera, email: [dnocera@fas.harvard.edu](mailto:dnocera@fas.harvard.edu), tel: +1 617-495-8904, fax: +1 617-496-0265

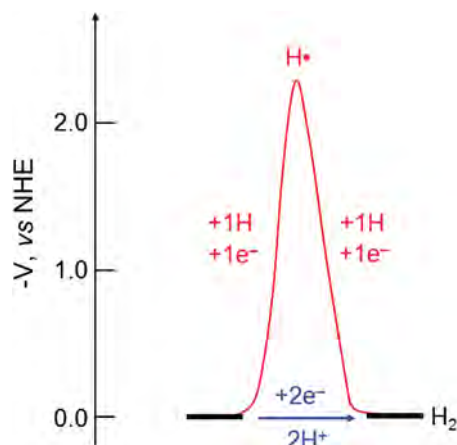


Fig. 1. Energetics for  $H_2$  generation in the absence of PCET

tunnel over very short distances [3]. Despite this inherent quantum mechanical difference between the two particles, they must both tunnel together for their coupling [3–8]. To achieve this coupling, we have developed catalysts in which the secondary coordination sphere is engineered to manage protons and the primary coordination sphere is engineered to manage electrons. By coupling short proton hops to substrates bound to a redox cofactor, PCET activation of the bound substrate may be achieved.

We have designed the hangman macrocycles shown in Fig. 2 to examine the hydrogen evolution reaction (HER), the oxygen evolution reaction (OER) and the oxygen reduction reaction (ORR). The hangman constructs utilize a pendant acid/base functionality within the secondary coordination sphere that is “hung” above the redox platform onto which substrate binds. In this way, we can precisely control the delivery of a proton to the substrate, thus ensuring efficient coupling between the proton and electron. We have examined hangman catalysis with electrochemical techniques to construct a unified mechanistic PCET framework to describe O–O, O–H

and H–H bond-breaking and bond-making processes as they pertain to HER and OER processes. This article will present a summary of our efforts to: (1) adapt and elaborate synthetic methods to enable the delivery of hangman macrocycles in sufficiently high yields and quantities to enable PCET studies to be undertaken with facility; (2) design hangman macrocyclic platforms that promote HER with an emphasis on elucidating key intermediates *via* the construction of mechanistic models; and (3) design a hangman macrocycle that promotes OER.

## EFFICIENT SYNTHESIS OF HANGMAN PLATFORMS

High yielding syntheses of hangman porphyrins and corroles are needed if PCET studies are to be performed with facility. Our methods have transformed hangman catalyst platforms from difficult-to-make substances, obtained in milligram quantities, to high yielding compounds that can now be made on the hundreds of milligram scale. These compounds thus have been transformed from isolated curiosities to compounds of sufficient quantity for us to undertake PCET studies that are not encumbered by the availability of catalyst.

### Hangman porphyrins

The library of metalated hangman porphyrins shown in Fig. 3 was synthesized [9–11] using refined high-dilution Lindsey reaction conditions [12] and modifications to established procedures. A mixed aldehyde condensation of pyrrole in chloroform in the presence of a Lewis acid furnished the corresponding porphyrinogen intermediate as a result of intermolecular cyclization. *In situ*  $6e^-/6H^+$  chemical oxidation of the latter with DDQ afforded the hangman porphyrin with a methyl ester hanging group. Acidic or basic hydrolysis of the methyl ester to the corresponding carboxylic acid with conventional

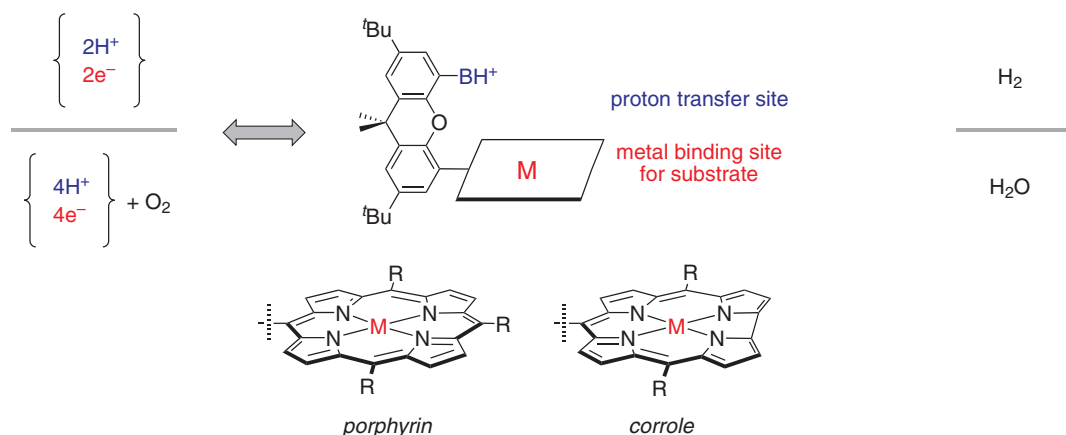


Fig. 2. Hangman platforms permit the study of PCET mechanisms of HER and OER processes

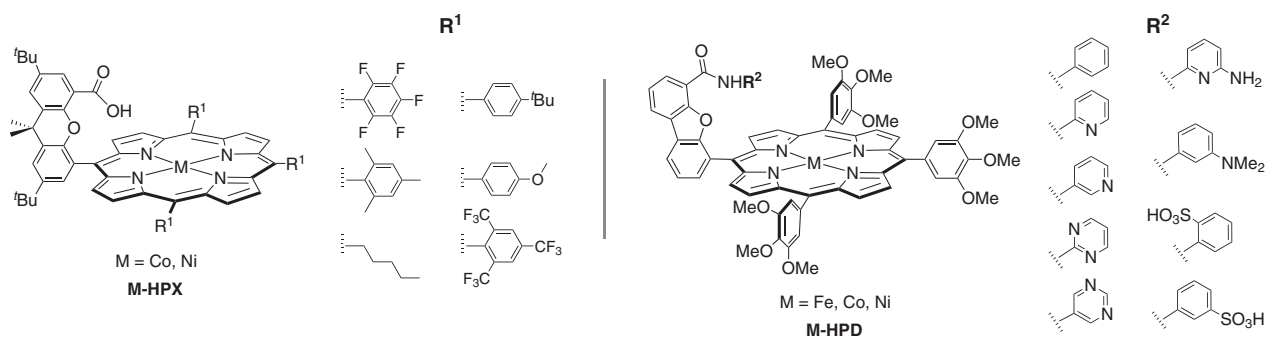


Fig. 3. Hangman porphyrins used in PCET studies for HER and ORR

heating proceeded with extremely poor yields [13,14]. We found that the introduction of microwave irradiation promoted hydrolysis to overcome this major hurdle confronting general hangman synthesis [15]. Deprotection of the methyl ester group with microwave irradiation was achieved in 6 N NaOH solution with more than 90% yield for the porphyrins shown in Fig. 3. Microwave irradiation also promoted the metalation of free base porphyrins in nearly quantitative yield. The statistical synthesis afforded the target metalloporphyrins in more than 35% overall isolated yield, which is 9× greater yield than our previous methods [15].

Hangman studies have recently been expanded from a xanthene spacer (**HPX**, Fig. 3) to include a dibenzofuran backbone (**HPD**, Fig. 3) [11]. The larger cleft allowed for the accommodation of a diverse set of hanging groups possessing different steric and acid/base properties. The key step in obtaining the **HPD** library relied on the synthesis of a dibenzofuran precursor that contained an aldehyde functionality and a protected carboxylic acid (methyl ester). The chemistry was carried out in four steps on a decagram scale in 37% overall isolated yield. Using this precursor, the corresponding hangman porphyrins with a hanging carboxylic acid can be obtained in gram quantities. The hanging carboxylic acid on the free base hangman porphyrin was post-synthetically modified to form a carboxamide linker to which the acid/base group was attached. Microwave-assisted metalation furnished the **M-HPD** compounds in good yields.

### Hangman corroles

Hangman corroles are attractive candidates for OER chemistry because the  $\pi$ -rich trianionic corrole platform stabilizes metals in higher oxidation states better than porphyrins do [16, 17]. Furthermore, electron-withdrawing substituents shift the reduction potential of the metal positively. This motivated us to synthesize a new class of compounds — hangman corroles bearing fluorinated  $\beta$ -pyrrolic positions (**Co-H<sup>BF</sup>CX**) [18] *via* the Lindsey [12] and Gryko [19] methods outlined in Scheme 1. The Gryko conditions were also used to deliver

the non-fluoro analog (**Co-HCX**) and had the added advantage of allowing us to enforce the *trans*-A<sub>2</sub>B isomer, thus enabling us to establish the regiochemistry of the corrole [20–22]. Deprotection and metalation steps were driven efficiently by microwave irradiation conditions, allowing us to obtain the corroles in 29% overall yield.

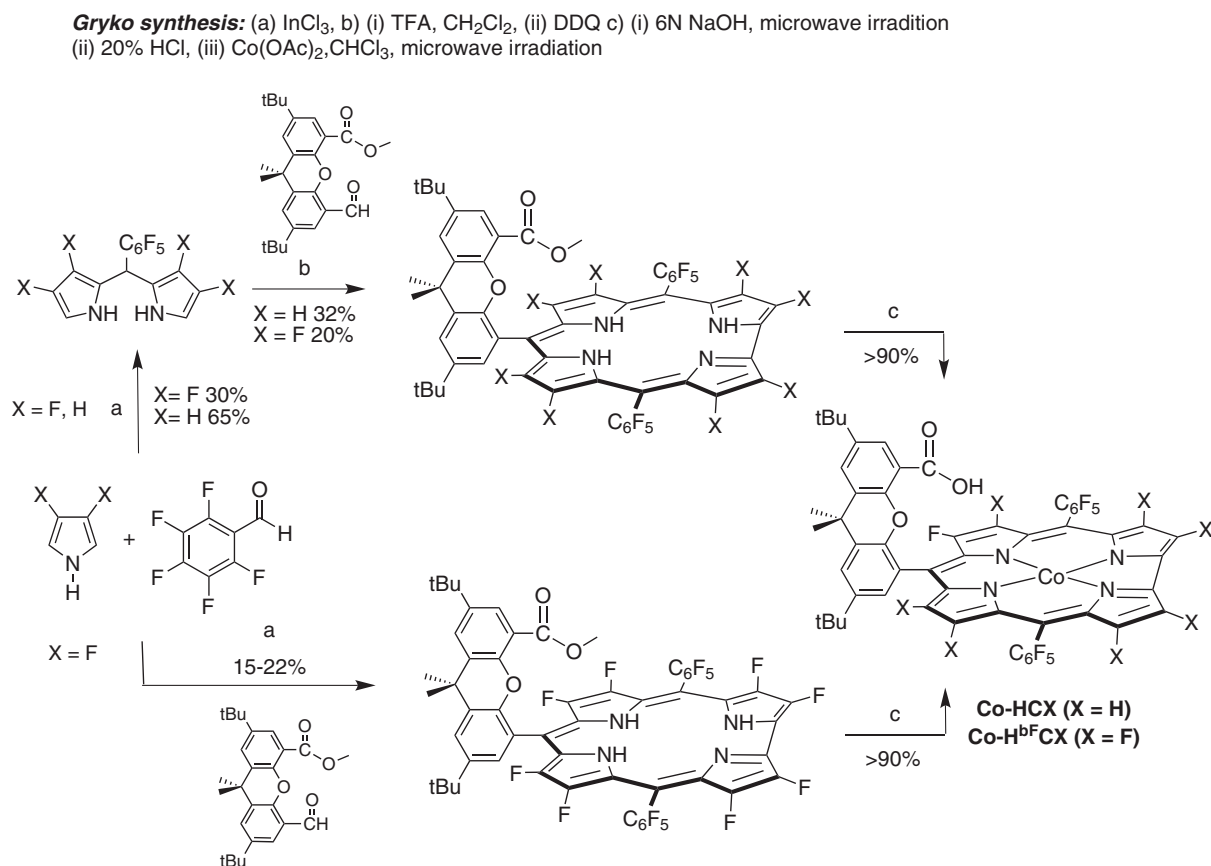
### HER BY HANGMAN PORPHYRINS

Proton relays are an emerging theme in HER catalysis [23–29]. Key factors that define the kinetics associated with the proton relay are: (i) the pK<sub>a</sub> of the metal ion, (ii) the pK<sub>a</sub> of the pendant hangman relay, and (iii) the proton transfer distance. The proton can participate in the PCET reaction by stepwise ET and PT steps during catalysis or in a concerted proton-electron transfer (CPET).

We have ascertained the PCET mechanism from electrochemical studies of catalysis, complemented by CV simulation. Heterogeneous ET rate constants ( $k_{ET}^\circ$ ) associated with the electron transfer to the hangman porphyrins have been obtained from “trumpet plots” [30]. Increasing separation between cathodic and anodic peak potentials with scan rate is indicative of deviation from strictly Nernstian (reversible) behavior. Accordingly, the degree of separation for a given scan rate relies on  $k_{ET}^\circ$ . In the strictly electrochemically irreversible region, the cathodic peak potential is defined by [31]:

$$E_{p,c} = E^\circ - 0.78 \frac{RT}{\alpha F} \ln \left( k_{ET}^\circ \sqrt{\frac{RT}{\alpha F \nu D}} \right) \quad (1)$$

where  $\alpha$  is the transfer coefficient. Complete electrochemical irreversibility is occasionally not attained because of instrumental limitations or the presence of a very fast ET process. In this case, no explicit analytical expression exists for the transitional behavior, but CV simulation software, such as DigiElch [31] provides a reliable means of determining  $k_{ET}^\circ$ . Beyond simple ET from the electrode, the current and potential dependencies of the catalytic HER wave sheds light on the PCET mechanism for H<sub>2</sub> evolution. There are



Scheme 1. Synthesis of hangman corroles

two major regimes for catalysis [31]: (i) total-catalysis and (ii) no-substrate-consumption regimes. Case (i) is revealed by a sharp catalytic peak, with a peak potential,  $E_p$ , that relates to the catalytic rate constant,  $k_{cat}$  by:

$$E_p = E_{cat}^0 - 0.409 \frac{RT}{F} + \frac{RT}{F} \ln \left( \frac{RTk_{cat}[\text{cat}]^2}{Fv[\text{acid}]} \right) \quad (2)$$

where [cat] and [acid] are the bulk concentration of the catalyst and acid, respectively,  $v$  is the scan rate, and  $R$ ,  $T$ , and  $F$  have their usual meaning.  $E_{cat}^0$  represents the reversible catalyst redox couple. In contrast, when catalysis is governed by case (ii), the kinetics parameters may be extracted from the plateau current  $i_{plat}$

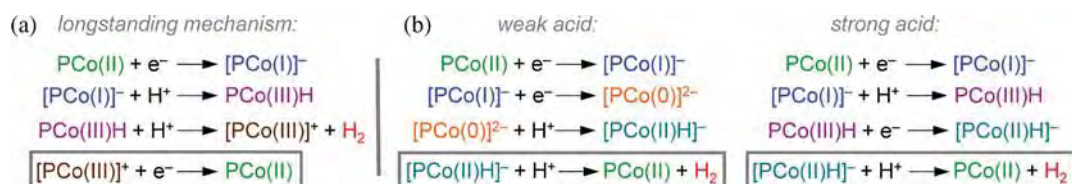
$$i_{plat} = FA[\text{cat}] \sqrt{Dk_{cat}[\text{acid}]} \quad (3)$$

where  $D$  represents the diffusion coefficient of the acid. By using Equations 1–3, together with CV simulation of catalytic data, we have identified the catalytic PCET mechanism with accompanying rate constants of HER for Co, Ni and Fe hangman porphyrins, and begun unveiling the precise role of the proton relay in HER conversions.

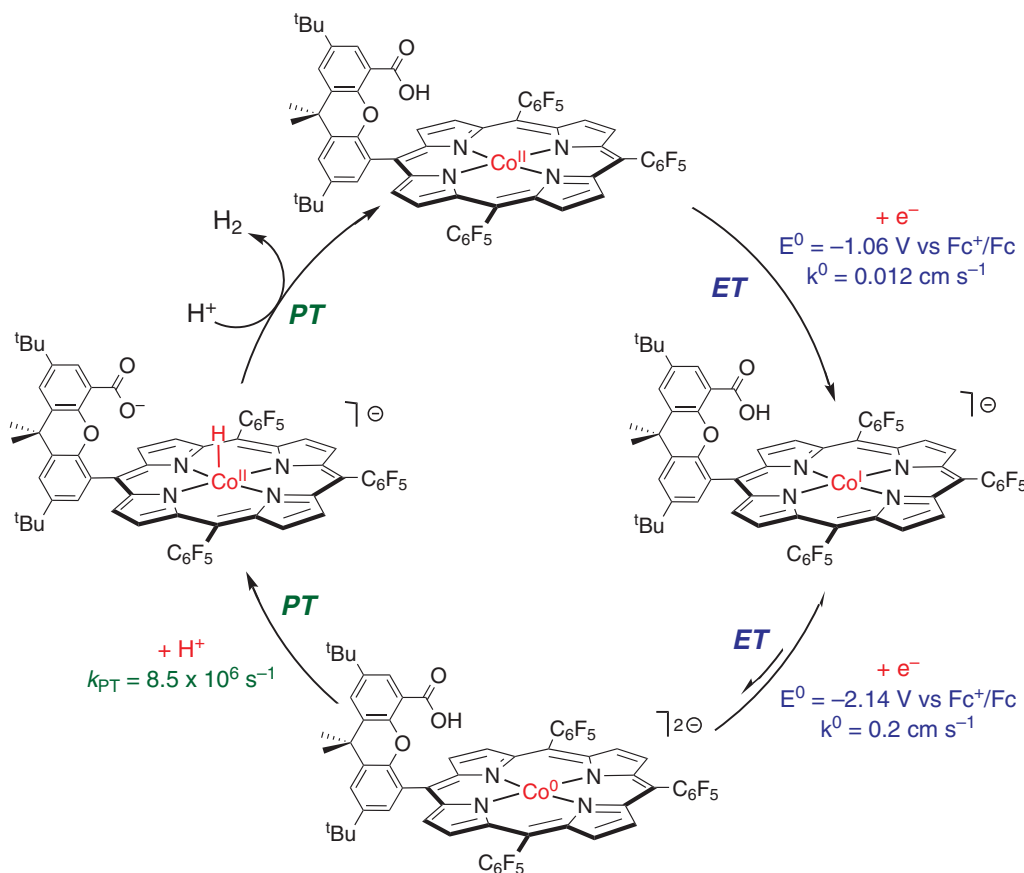
### Co hangman porphyrins

We have shown that **Co-HPX** (Fig. 3) catalyzes HER from weak (benzoic) and strong (tosic) acids in acetonitrile solutions [33]. Electrochemical analysis indicated that, regardless of the strength of acid,  $\text{Co}^{\text{II}}-\text{H}$  is exclusively involved in the generation of H<sub>2</sub>. As summarized in Fig. 4, in weak acid, a  $\text{Co}^0$  center is protonated; in strong acid, the  $\text{Co}^{\text{I}}$  center is protonated and subsequently reduced to deliver the  $\text{Co}^{\text{II}}-\text{H}$ . The same result was obtained for other Co macrocycles (*i.e.* tetraazamacrocyclic) as well [34]. The mechanisms on the right side of Fig. 4, at odds with the more common notion that H<sub>2</sub> is produced from a  $\text{Co}^{\text{III}}-\text{H}$  [35], is in line with recent experimental [36, 37] and theoretical [38] findings that  $\text{Co}^{\text{II}}-\text{H}$  is the critical intermediate for H<sub>2</sub> generation.

Electrokinetic mechanistic studies of HER are consistent with formation of the  $\text{Co}^{\text{II}}$  hydride by stepwise electron-transfer followed by proton transfer (ET-PT) [39]. The rate constants for the heterogeneous electron transfer to the hangman porphyrin are summarized in Fig. 5. Catalytic enhancement by the hangman moiety arises from a rapid intramolecular rate-limiting PT (*ca.*  $8.5 \times 10^6 \text{ s}^{-1}$ ). This is the first *direct* measure of a proton



**Fig. 4.** (a) Typical mechanism proposed for H<sub>2</sub> generation from Co centers. (b, c) Mechanism for H<sub>2</sub> generation by **Co-HPX** complexes, as determined from electrochemical kinetics analysis



**Fig. 5.** The rate constants for the PCET mechanism of HER by **Co-HPX**

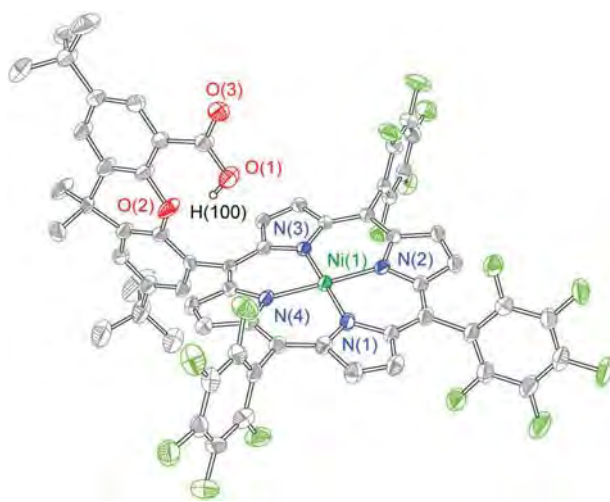
transfer rate for HER conversion. Moreover, construction of working curves for a non-hangman congener revealed that the intermolecular (2nd order) proton transfer from benzoic acid to a porphyrin lacking the hanging group proceeded with a rate constant of 1000 M<sup>-1</sup>.s<sup>-1</sup>. These results indicate that the presence of the pendant proton relay proximate to the metal center gives rise to a rate enhancement that is equivalent to an effective benzoic acid concentration >3000 M. This is the first quantitative measurement of the benefits of a pendant proton transfer in the secondary coordination sphere of a HER catalyst.

### Ni hangman porphyrins

The PCET mechanism may be altered owing to the differences in the d-electron count and hence the

thermodynamics of proton transfer as has been computationally discussed [40]. Accordingly, we have targeted Ni hangman porphyrins in order to interrogate the manner in which metal substitution impacts the PCET pathway and kinetics of H<sub>2</sub> production [41]. Because we are able to make the compounds on large scale, we have been able to crystallize the porphyrins, allowing for their structural characterization; the **Ni-HPX** (*meso*-C<sub>6</sub>F<sub>5</sub>) crystal structure is shown in Fig. 6. Thus structural metrics are available for interpreting the PCET kinetics with this system.

Cyclic voltammetry (CV) of **Ni-HPX** (*meso*-C<sub>6</sub>F<sub>5</sub>) reveals a shift of the catalytic wave by more than 100 mV to lower overpotential when compared to **Co-HPX** (*meso*-C<sub>6</sub>F<sub>5</sub>) [33]. This result is indicative of significantly faster catalysis. The CV data and attendant



**Fig. 6.** Crystal structure of Ni-HPX with thermal ellipsoids set at 50% probability; hydrogen atoms and crystallization solvents have been omitted for clarity

simulations, together with density functional theory (DFT) computational studies, are consistent with the occurrence of a stepwise PT followed by ET (PTET) pathway, involving the formation of a formally  $\text{Ni}^{\text{III}}\text{H}$ , which is subsequently reduced to  $\text{Ni}^{\text{II}}\text{H}$ . Operation *via* this pathway (involving the protonation of the metal(I) complex as opposed to the metal(0) complex) explains the improved activity of this catalyst relative to its cobalt analog. DFT calculations show that upon reduction of the  $\text{Ni}^{\text{II}}$  complex by one electron, the spin density on Ni is near unity, suggesting that the unpaired electron is localized on the Ni center [41]. Similar calculations on the doubly reduced (formally  $\text{Ni}^{\text{0}}$ ) molecule, however, show that only one electron is localized on Ni, and that the other electron is transferred to orbitals predominantly on the porphyrin ring. The non-innocence of the porphyrin ligand in this particular reduction reaction prompted us to consider that the proton may transfer to the ligand prior to  $\text{H}_2$  generation and that a transient phlorin intermediate may be involved in HER. This contention is currently under investigation.

### Fe hangman porphyrins

We have expanded our studies to the **Fe-HPD** hangman porphyrins shown in Fig. 3 because they enabled the modular installation of a wide range of pendant acid/base moieties, which are sterically imposing. With a phosphine coordinating to the distal face of the reduced porphyrin, these hangman porphyrins channel protons from solution to the catalyst active site *via* the pendant acid/base group. In our study of the catalytic efficacy of these new hangman porphyrins [10], we employed the foot-of-the-wave analysis (FOWA), developed by Costentin and Savéant [42]. Previously, FOWA had been used to analyze the electrocatalytic reduction of  $\text{H}^+$  to

$\text{H}_2$  [43] and  $\text{CO}_2$  to  $\text{CO}$  and  $\text{H}_2\text{O}$  using Fe porphyrins in the presence of a Brønsted–Lowry acid [42, 44–46]. The application of FOWA to **Fe-HPDs** allowed us to gain insight into the rate of proton transfer from solution to the active site, turnover frequency, and the effect of a pendant proton donor. We found that the steric bulk of the hanging group modulates its  $\text{pK}_a$  effect. Specifically, the sulfonic acid derivative (strongest acid) was the most active at high acid concentrations. However, at low acid concentrations, the hanging *N,N*-dimethylanilinium, though a weaker proton donor, showed higher activity because it was protonated and hence effectively increased the local acid concentration at the Fe center. These results are interesting because in cases where  $\text{H}_2$  evolution represents a parasitic side reaction, such as carbon dioxide reduction [47, 48], nitrite reduction [49–51] and olefin reduction [52] in acidic solutions, the rate of proton transfer to the catalyst active site might be tailored in order to minimize HER.

### OER BY HANGMAN CORROLES

We sought to develop a hangman platform that would allow us to undertake PCET studies of OER. Electrochemical measurements of electron-rich macrocycles, such as mesityl substituted hangmans, showed that they barely had sufficient potential for OER. In order to boost the oxidizing power of the porphyrin subunit, we sought to modify the hangman macrocycle with electron-withdrawing groups. It was known that the introduction of fluorinated phenyl groups onto the *meso*-positions of the porphyrin frameworks increased the reduction potential of oxidized porphyrins by more than 0.4 V [53, 54]. The oxidizing power of the macrocycle can be further augmented by an additional 0.4–0.6 V through fluorination of the  $\beta$ -pyrrole positions [55, 56]. We therefore targeted the design and synthesis of hangman corrole **Co-H<sup>BF</sup>CX** (Scheme 1).

Electrochemical experiments established that **Co-<sup>BF</sup>H<sub>2</sub>CX** catalyzes water oxidation [18]. The CV (Fig. 7) exhibits two reversible oxidation processes corresponding to the oxidation of the metal center and the corrole ring to produce the corrole cation radical ( $\text{corr}^{+\bullet}$ ). Formation of the corrole cation at a redox level of +2 beyond  $\text{Co(II)}$  corrole was established from EPR studies of an isolated “ $\text{Co}^{\text{IV}}\text{Cl}(\text{corr})$ ”, which exhibits hyperfine coupling that is consistent with a  $\text{Co}^{\text{III}}\text{Cl}(\text{corr}^{+\bullet})$  formulation for the compound [20]. Introduction of a third hole equivalent into the system leads to a catalytic wave for OER. GC traces revealed that only  $\text{O}_2$  was produced, and the absence of  $\text{CO}_2$  established that the porphyrin did not oxidatively decompose during OER. A steady decrease in pH with no observation of an anomaly also indicated that the catalyst did not decompose to cobalt oxide-like materials, since such species are unstable in acidic solutions. At 1.4 V vs. Ag/AgCl, the turnover frequency per Co atom of **Co-<sup>BF</sup>H<sub>2</sub>CX** is  $0.81 \text{ s}^{-1}$ . This



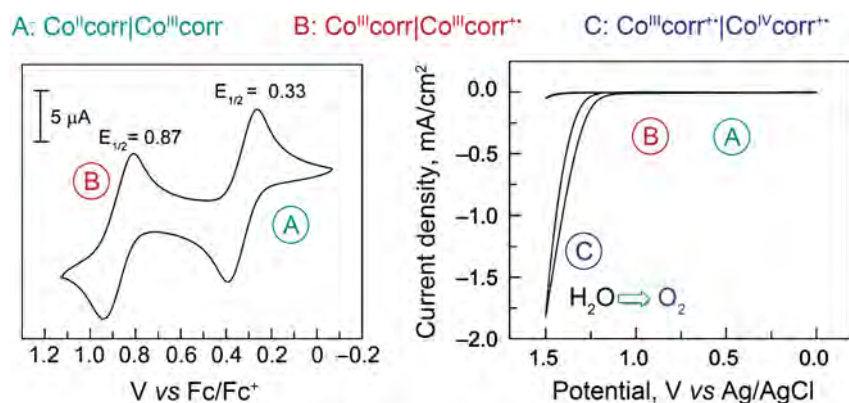


Fig. 7. Cyclic voltammogram of Co-H<sup>F</sup>CX in aqueous solution

number compares favorably with regard to heterogeneous cobalt-based water oxidation catalyts [57].

## CONCLUSIONS

Hangman catalysts were created to allow control over proton-coupled electron transfer (PCET) reactions. The hangman constructs utilize a pendant acid/base functionality within the secondary coordination sphere that is positioned above the redox platform onto which substrate binds. On a mechanistic front, the hangman system orthogonalizes PCET and, in doing so, the catalyst permits control of proton transfer over short distances and electron transfer over longer distances. In this way, we can precisely control the delivery of a proton to the substrate, thus ensuring efficient coupling between the proton and electron. Moreover, the two critical thermodynamic properties of a PCET event, the reduction potential and  $pK_a$  may be tuned with the macrocycle and hanging group, respectively. By constructing kinetics rate laws using electrochemistry accompanied by simulation, we have begun to develop a unified mechanistic PCET framework to describe O–O, O–H and H–H bond-breaking and bond-making processes, as they pertain to the hydrogen evolution reaction (HER) and the oxygen evolution reaction (OER), the two constituent reactions of the water-to-hydrogen/oxygen fuel forming reaction. To this end, the hangman catalysts offer a unique inroad to providing a succinct framework to guide the design of future HER and OER catalysts that use a secondary coordination sphere to manage PCET.

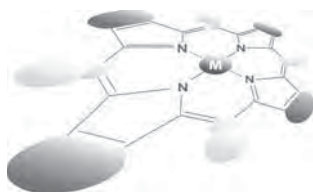
## Acknowledgements

This material is based upon work supported by the U.S. Department of Energy Office of Science, Office of Basic Energy Sciences program under Award Number DE-SC0009758. DJG and CML acknowledge the National Science Foundation (NSF) for Graduate Research Fellowship Program (GRFP) Fellowships.

## REFERENCES

1. Stanbury DM. *Adv. Inorg. Chem.* 1989; **33**: 69–138.
2. Schwarz HA. *J. Chem. Ed.* 1981; **58**: 101–105.
3. Cukier RI and Nocera DG. *Annu. Rev. Phys. Chem.* 1998; **49**: 337–369.
4. Mayer JM. *Annu. Rev. Phys. Chem.* 2004; **55**: 363–390.
5. Huynh MVH and Meyer TJ. *Chem. Rev.* 2007; **107**: 5004–5064.
6. Reece SY and Nocera DG. *Annu. Rev. Biochem.* 2009; **78**: 673–699.
7. Hammes-Schiffer S. *Acc. Chem. Res.* 2009; **42**: 1881–1889.
8. Hammes-Schiffer S and Stuchebrukhov AA. *Chem. Rev.* 2010; **110**: 6939–6960.
9. Lemon CM, Dogutan DK and Nocera DG. In *Handbook of Porphyrin Science*, Vol. 21, Kadish KM, Smith KM and Guillard R. (Eds.) World Scientific Publishing: Singapore, 2012; Chapter 99, pp 1–143.
10. Graham DJ and Nocera DG. *Organometallics* 2014; **33**: 4994–5001.
11. Graham DJ, Zheng S-L and Nocera DG. *ChemSusChem* 2014; **7**: 2449–2452.
12. Lindsey JS and Wagner RW. *J. Org. Chem.* 1989; **54**: 828–836.
13. Rosenthal J, Chng LL, Fried SD and Nocera DG. *Chem. Comm.* 2007; 2642–2644.
14. Chang CJ, Yeh C-Y and Nocera DG. *J. Org. Chem.* 2002; **67**: 1403–1406.
15. Dogutan DK, Bediako DK, Teets TS, Schwalbe M and Nocera DG. *Org. Lett.* 2010; **12**: 1036–1039.
16. Gross Z and Gray HB. *Comm. Inorg. Chem.* 2007; **27**: 61–72.
17. Aviv-Harel I and Gross Z. *Chem. Eur. J.* 2009; **15**: 8382–8394.
18. Dogutan DK, McGuire Jr. R and Nocera DG. *J. Am. Chem. Soc.* 2011; **133**: 9178–9180.
19. Guillard R, Gryko DT, Canard G, Barbe J-M, Koszarna B, Brandès S and Tasior M. *Org. Lett.* 2002; **4**: 4491–4494.

20. Dogutan DK, Stoian SA, McGuire Jr. R, Schwalbe M, Teets TS and Nocera DG. *J. Am. Chem. Soc.* 2011; **133**: 131–140.
21. Schwalbe M, Dogutan DK, Stoian SA, Teets TS and Nocera DG. *Inorg. Chem.* 2011; **50**: 1368–1377.
22. Graham DJ, Dogutan DK and Nocera DG. *Chem. Commun.* 2012; **48**: 4175–4177.
23. Helm ML, Stewart MP, Bullock RM, DuBois MR and DuBois DL. *Science* 2011; **333**: 863–866.
24. Appel AM, Pool DH, O'Hagan M, Shaw WJ, Yang JY, DuBois MR, DuBois DL and Bullock RM. *ACS Catal.* 2011; **1**: 777–785.
25. O'Hagan M, Ho M-H, Yang JY, Appel AM, DuBois MR, Raugai S, Shaw WJ, DuBois DL and Bullock RM. *J. Am. Chem. Soc.* 2012; **134**: 19409–19424.
26. Wiedner ES, Appel AM, DuBois DL and Bullock RM. *Inorg. Chem.* 2013; **52**: 14391–14403.
27. Barton BE, Olsen MT and Rauchfuss TB. *J. Am. Chem. Soc.* 2008; **130**: 16834–16835.
28. Wiese S, Kilgore UJ, Ho M-H, Raugai S, DuBois DL, Bullock RM and Helm ML. *ACS Catal.* 2013; **3**: 2527–2535.
29. Barton BE, Olsen MT and Rauchfuss TB. *Curr. Opin. Biotech.* 2010; **21**: 292–297.
30. Costentin C, Robert M, Savéant J-M and Teillout AL. *Proc. Natl. Acad. Sci. U.S.A.* 2009; **106**: 11829–11836.
31. Savéant J-M. *Elements of molecular and biomolecular electrochemistry: An electrochemical approach to electron transfer chemistry*, John Wiley & Sons Inc.: Hoboken, NJ, 2006; Chapter 1, pp 1–75.
32. Rudolf M. *J. Electroanal. Chem.* 2003, **543**: 23–39. DigiElch from Elchsoft under <http://www.elchsoft.com>.
33. Lee CH, Dogutan DK and Nocera DG. *J. Am. Chem. Soc.* 2011; **133**: 8775–8777.
34. Lee CH, Villagrán D, Cook TR, Peters JC and Nocera DG. *ChemSusChem* 2013; **6**: 1541–1544.
35. Dempsey JL, Winkler JR and Gray HB. *J. Am. Chem. Soc.* 2010; **132**: 1060–1065.
36. Lazarides T, McCormick T, Du P, Luo G, Lindley B and Eisenberg R. *J. Am. Chem. Soc.* 2009; **131**: 9192–9194.
37. Dempsey JL, Brunschwig BS, Winkler JR and Gray HB. *Acc. Chem. Res.* 2009; **42**: 1995–2004.
38. Muckerman JT and Fujita E. *Chem. Commun.* 2011; **47**: 12456–12458.
39. Roubelakis MM, Bediako DK, Dogutan DK and Nocera DG. *Energy Environ. Sci.* 2012; **5**: 7737–7740.
40. Small YA, Dubois DL, Fujita E and Muckerman JT. *Energy Environ. Sci.* 2011; **4**: 3008–3020.
41. Bediako DK, Solis BH, Dogutan DK, Roubelakis MM, Maher AG, Lee CH, Chambers MB, Hammes-Schiffer S and Nocera DG. *Proc. Natl. Acad. Sci. U.S.A.* 2014; **111**: 15001–15006.
42. Costentin C, Drouet S, Robert M and Savéant J-M. *J. Am. Chem. Soc.* 2012; **134**: 11235–11242.
43. Quentel F and Gloaguen F. *Electrochim. Acta* 2013; **110**: 641–645.
44. Costentin C, Drouet S, Robert M and Savéant J-M. *Science* 2012; **338**: 90–94.
45. Costentin C, Robert M and Savéant J-M. *Chem. Soc. Rev.* 2013; **42**: 2423–2436.
46. Costentin C, Drouet S, Passard G, Robert M and Savéant J-M. *J. Am. Chem. Soc.* 2013; **135**: 9023–9031.
47. Rail MD and Berben LA. *J. Am. Chem. Soc.* 2011; **133**: 18577–18579.
48. Kang P, Cheng C, Chen Z, Schauer CK, Meyer TJ and Brookhart M. *J. Am. Chem. Soc.* 2012; **134**: 5500–5503.
49. Buffington LA, Blackburn DW, Hamilton CL, Jarvis TC, Knowles JJ, Lodwick PA, McAllister LM, Neidhart DJ and Serungard JL. *J. Am. Chem. Soc.* 1989; **111**: 2451–2454.
50. Brylev O, Sarrazin M, Roué L and Bélanger D. *Electrochim. Acta* 2007; **52**: 6237–6247.
51. Uyeda C and Peters JC. *J. Am. Chem. Soc.* 2013; **135**: 12023–12031.
52. Rasnoshik H, Masarwa A, Cohen H, Zilbermann I, Maimon E and Meyerstein D. *Dalton Trans.* 2010; **39**: 823–833.
53. Neya S and Funasaki N. *J. Heterocyclic Chem.* 1997; **34**: 689–690.
54. Woller EK and DiMugno SG. *J. Org. Chem.* 1997; **62**: 1588–1593.
55. Kadish KM, Van Caemelbeck E and Royal G. In *The Porphyrin Handbook*, Vol. 8, Kadish KM, Smith KM and Guillard R. (Eds.) Academic Press: San Diego, 2000; pp 1–114.
56. Steene E, Dey A and Ghosh A. *J. Am. Chem. Soc.* 2003; **125**: 16300–16309.
57. Jiao F and Frei H. *Angew. Chem. Int. Ed.* 2009; **48**: 1841–1844.



# A new biological function of heme as a signaling molecule

Norifumi Muraki, Chihiro Kitatsuji and Shigetoshi Aono<sup>\*◇</sup>

Okazaki Institute for Integrative Bioscience & Institute for Molecular Science, National Institutes of Natural Sciences, 5-1 Higashiyama, Myodaiji, Okazaki 444-8787, Japan

Dedicated to Professor Shunichi Fukuzumi on the occasion of his retirement

Received 21 October 2014

Accepted 11 November 2014

**ABSTRACT:** This mini-review presents a recent development of a new function of heme as a signaling molecule especially in the regulation of gene expression. Heme is biosynthesized as a prosthetic group for heme proteins, which play crucial roles for respiration, photosynthesis, and many other metabolic reactions. In some bacteria, exogenous heme molecules are used as a heme or an iron sources to be uptaken into cytoplasm. As free heme molecules are cytotoxic, the intracellular concentrations of biosynthesized or uptaken heme should be strictly controlled. In this mini-review, we summarize the biochemical and biophysical properties of the transcriptional regulators and heme-sensor proteins responsible for these regulatory systems to maintain heme homeostasis.

**KEYWORDS:** heme, heme regulatory motif, sensor proteins, transcriptional regulator, two-component system.

## INTRODUCTION

Heme is one of the most widely used prosthetic groups in biological systems in both prokaryotes and eukaryotes, which acts as the active site for oxygen transport/storage, electron transfer, and a variety kinds of enzymes. In these heme proteins, the change in the oxidation state of heme iron between  $\text{Fe}^{2+}$  and  $\text{Fe}^{3+}$  or/ and the binding of substrates to heme plays an important role for their functional regulation. Some heme proteins are also involved in biological signal sensing and signal transduction, in which heme acts as the active site for sensing gas molecules [1–3]. In these heme-based sensor proteins, the binding of a gas molecule such as  $\text{O}_2$ , CO, or NO to heme triggers conformational changes of proteins, which result in their functional regulation. For another biological role of heme, it is also used as an iron source in some bacteria, especially pathogenic bacteria that infect mammals. In addition to these biological functions of heme, heme itself can act as a signaling molecule to regulate gene expressions. In this mini-review, we

focus on recent developments of selected systems in which heme is involved as a signaling molecule for their functional regulation.

## HrtR

Though a lactic acid bacterium *Lactococcus lactis* cannot biosynthesize heme due to an incomplete set of genes responsible for heme biosynthesis, it can grow by oxygen respiration with cytochrome *bd* as a terminal oxidase under aerobic conditions when heme is supplied exogenously [4, 5]. Exogenous heme molecules are imported into *Lactococcus lactis* cells by an unidentified transporter system to mature cytochrome *bd* as a prosthetic group [6–8]. While heme is an essential cofactor of cytochrome *bd* for oxygen respiration of *L. lactis*, a free heme is cytotoxic because it generates reactive oxygen species that react with proteins, nucleic acids, and lipids to cause dysfunction. Therefore, intracellular concentrations of free heme molecules should be controlled strictly under a threshold level. An ABC-type transporter HrtAB that works as a heme efflux system plays an crucial role for the regulation of intracellular concentrations of heme in *L. lactis* [6]. When intracellular concentrations of heme increase above a

<sup>◇</sup>SPP full member in good standing

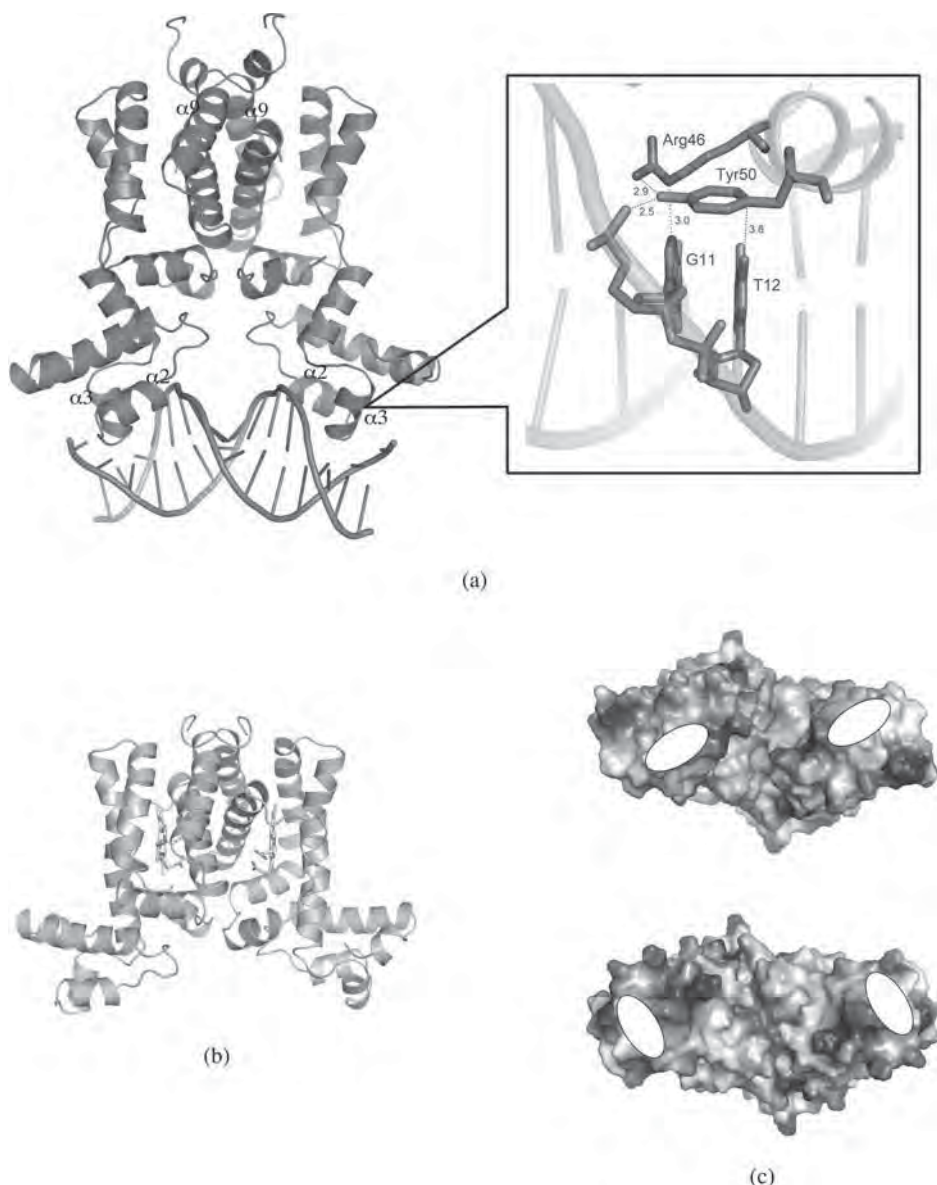
\*Correspondence to: Shigetoshi Aono, email: aono@ims.ac.jp, tel: +81 564-59-5575, fax: +81 564-59-5576

threshold level, the expression of HrtAB is induced to efflux excess heme molecules out of cells. The expression of HrtAB is regulated at the transcriptional level with a transcriptional regulator HrtR in response to excess heme. In this regulatory system, HrtR and heme act as a heme sensor and a signaling molecule, respectively, as described in detail below.

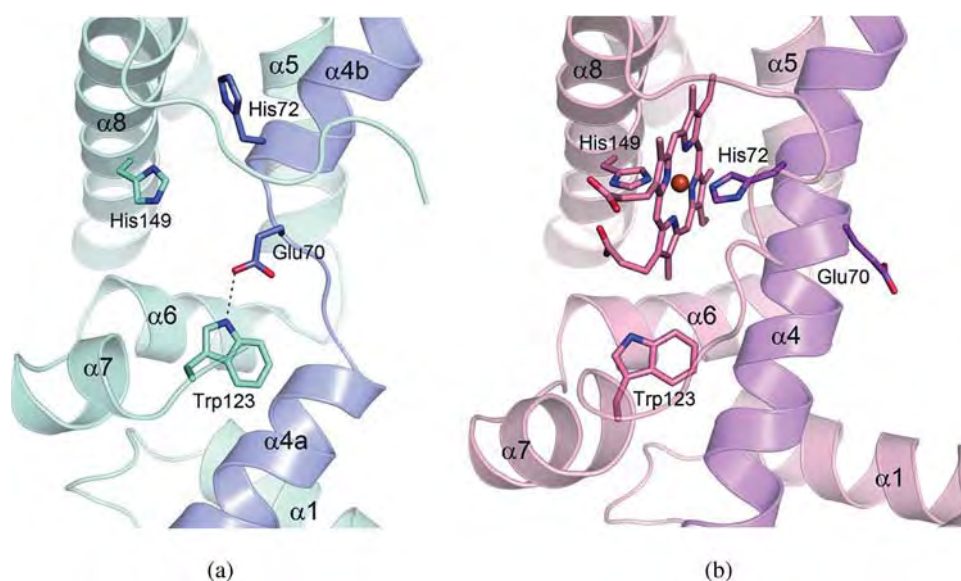
HrtR consists of 189 amino acid residues and belongs to TetR family of transcriptional regulators, which forms a homodimer both in the apo- and holo-forms [9, 10]. Heme is its physiological effector molecule that regulates the DNA-binding activity of HrtR. Apo-HrtR binds to its target DNA that is overlapped with -10 region of the

promoter for the *hrtRBA* operon with  $K_d$  of 0.2 nM, by which HrtR acts as a repressor of the *hrtRBA* operon [9]. HrtR forms a 1:1 complex with heme, upon which it dissociates from the DNA to result in the derepression of the *hrtRBA* operon in response to heme.

The crystal structures of HrtR are reported for apo-HrtR/DNA complex, apo-HrtR, and holo-HrtR at the resolution of 2.0, 2.9, and 1.9 Å, respectively [9]. HrtR is a homodimer in apo- and holo-forms, and the monomer consists of two domains, the *N*-terminal DNA-binding and the *C*-terminal heme-sensing (heme-binding) domains (Fig. 1). The DNA-binding domain and the heme-sensing domain consist of  $\alpha_N$ ,  $\alpha_1$ ,  $\alpha_2$ , and  $\alpha_3$  helices, and  $\alpha_4$ ,



**Fig. 1.** Crystal structures of (a) apo HrtR/DNA complex (PDB 3VOK) and (b) holo HrtR (PDB 3VP5). A close-up view of the interaction site between HrtR and DNA is shown in the inset of Fig. 1(a), in which dotted lines show the interactions between the amino acid side chains and DNA bases with the distance (Å). (c) The protein surface on which the DNA recognition helices (shown as white ellipses) are exposed for (top) apo-HrtR/DNA complex and (bottom) holo-HrtR. The distance between these helices increases upon heme binding



**Fig. 2.** The coil-to-helix transition induced by heme-binding to HrtR. The  $\alpha 4a$  and  $\alpha 4b$  helices with the intervening loop in apo HrtR (a) forms the single  $\alpha 4$  helix upon heme binding as shown in (b)

$\alpha 5$ ,  $\alpha 6$ ,  $\alpha 7$ ,  $\alpha 8$ ,  $\alpha 9$ , and  $\alpha_c$  helices, respectively. Though the global fold of HrtR is similar to that of TetR family transcriptional regulators that possess nine conserved helices, within which helices 1 to 3 comprise the DNA-binding domain, and helices 4 to 9 comprise the ligand-binding domain, HrtR possesses extra short helices ( $\alpha_N$  and  $\alpha_c$ ) at the *N*- and *C*-termini in addition to the nine conserved helices.

The  $\alpha 8$  and  $\alpha 9$  helices in each monomer form a four-helix bundle that constitutes a dimer interface. The  $\alpha 2$  and  $\alpha 3$  helices in the DNA-binding domain of each subunit constitute the helix-turn-helix motif that is responsible for the recognition of and specific binding to the target DNA. Only two amino acid side chains of Arg46 and Tyr50 are involved in the sequence specific interaction between HrtR and DNA, though there are several hydrogen bonding interactions between HrtR and the phosphate group of DNA [9]. While Arg46 forms a hydrogen bonding interaction with a guanine base, there is a Tyr50 CH- $\pi$  interaction between the methyl group of thymine and Tyr50 [9]. The orientation of these two residues is fixed by a hydrogen bonding interaction between each other, which results in a pairwise interaction of Arg46 and Tyr50 with the target DNA responsible for the specific DNA-binding [9].

A large cavity formed in HrtR dimer accommodates heme molecules, in which one heme molecule is bound with His72 and His149 as the axial ligands in one subunit [9]. The absorption peaks of the Soret,  $\alpha$ , and  $\beta$  bands of holo-HrtR are observed at 413, 562, and 536 nm in the ferric form and at 425, 560, and 530 nm in the ferrous form, respectively, which are consistent with the six-coordinate structure of the heme with two axial histidines observed in the crystal structure of holo-HrtR [9].

Heme-binding causes conformational changes of HrtR, which is triggered by a coil-to-helix transition of the  $\alpha 4$  helix, the first helix of the heme-binding domain [9]. While a loop intervenes between two helices ( $\alpha 4a$  and  $\alpha 4b$ ) in the apo-form, the coil-to-helix transition takes place in this region to form a single  $\alpha 4$  helix upon heme-binding (Fig. 2). The helical axis of the  $\alpha 4a$  helix is inclined by about 25 degrees upon the coil-to-helix transition with re-orientation of the  $\alpha 3$  helix in the DNA-binding domain, which results in a rigid-body translation and rotation of the DNA-binding domain [9]. Thus, the change in relative orientation of the DNA-binding domain is induced upon heme-binding, which causes a change in the distance between the recognition helices in the helix-turn-helix DNA-binding motif of each subunit. The distance between the  $C\alpha$  atoms of Tyr50 in the  $\alpha 3$  helix (the recognition helix) of each subunit increased from 35 to 47 Å upon heme-binding [9]. As the distance between two consecutive major grooves in B-DNA is 34 Å, the inter-helical distance between the recognition helices in holo-HrtR (47 Å between the  $C\alpha$  atom of Tyr50 in the  $\alpha 3$  helix) is too wide for the recognition helices to fit into two consecutive major grooves and to bind to the target DNA. Thus, the conformational changes triggered by the coil-to-helix transition of the  $\alpha 4$  helix upon heme-binding shifts HrtR from a DNA-binding competent conformation to one that is not.

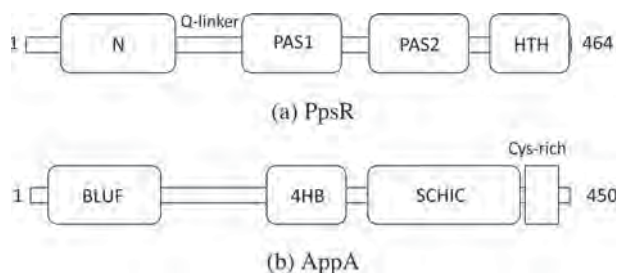
Both axial ligations of His72 and His149 are required for the heme-dependent regulation of the DNA-binding activity of HrtR. Although the mutational change of His72 or His149 to Ala does not affect the DNA-binding activity of these variants, these variants do not respond to heme at all [9]. Though the H72A and H149A variants bind heme with 1:1 ratio as wild-type does, their holo-forms still

bind to the target DNA [9]. CD spectroscopy reveals that the coil-to-helix transition of the  $\alpha 4$  helix upon heme-binding does not take place in H72A and H149A variants even though these variants bind heme to form a five-coordinate heme. In wild-type HrtR, it is proposed that His149 and His72 act as an “anchor” to fix the heme at the proper position, and as a “switch” to trigger the coil-to-helix transition, respectively [9].

HrtR adopts a unique heme-sensing motif except for the heme-regulatory motif (HRM), which is also called as cysteine-proline (CP) motif, that consists of a Cys-Pro sequence which is known to be a heme-sensing and heme-binding motif in heme-responsive signal transducers and regulators, as described below. HrtR adopts *bis*-His ligation to the heme as the heme-sensing and heme-binding motif instead of the CP motif, which is the first example of a heme-responsive regulatory protein that does not adopt the CP motif for heme-sensing and heme-binding.

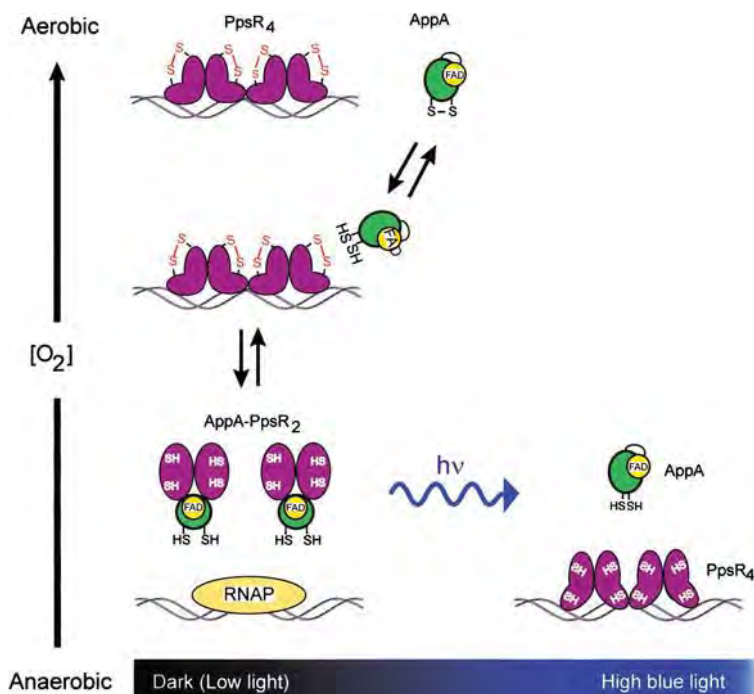
### AppA and PpsR

High-intensity blue light represses photosynthesis genes expression in *R. sphaeroides* [11]. The AppA/PpsR system is responsible for this light-dependent regulation of gene expression. PpsR acts as a repressor of photosynthesis and tetrapyrrole-synthesis genes expression, which consists of three PAS domains (N, PAS1, and PAS2) and a C-terminal DNA-binding domain. A glutamine-rich linker (Q-linker) intervenes between

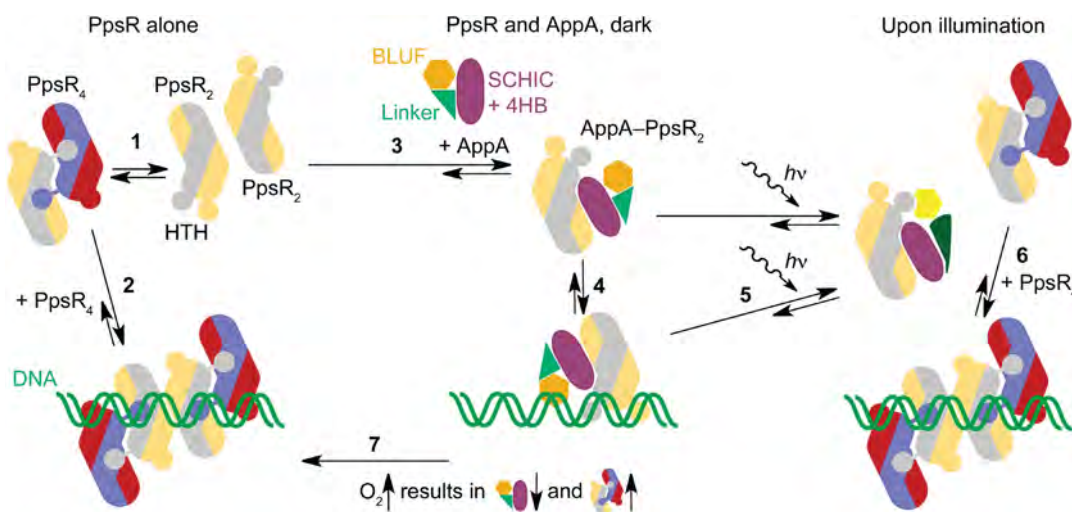


**Fig. 3.** Domain arrangements of (a) PpsR and (b) AppA. PpsR consists of the N, PAS1, and PAS2 domains followed by the C-terminal DNA-binding domain (HTH) containing the helix-turn-helix motif as a DNA-binding motif. In AppA, four helix-bundle motif (4HB) is present between the N-terminal BLUF and the SCHIC domains

the N and PAS1 domains (Fig. 3(a)). The biological function of PpsR as a repressor in *R. sphaeroides* is regulated by the antirepressor AppA. Masuda and Bauer [12] propose a model shown in Fig. 4 for the oxygen- and light-dependent regulation of gene expression with AppA and PpsR in *R. sphaeroides*. Under aerobic conditions, while AppA is functionally inactive as an antirepressor due to the formation of an intramolecular disulfide bond, PpsR tetramer binds to the target DNA to repress photosynthesis gene expression [12]. The disulfide bond in AppA is reduced under anaerobic conditions, which results in the formation of AppA/PpsR<sub>2</sub> complex that cannot bind to the target DNA [12]. While AppA acts as an O<sub>2</sub> sensor in this process, it acts as a blue-light



**Fig. 4.** A model depicting the action of PpsR and the role of AppA for controlling photosynthetic gene expression in response to oxygen and light. Reproduced with permission [12]



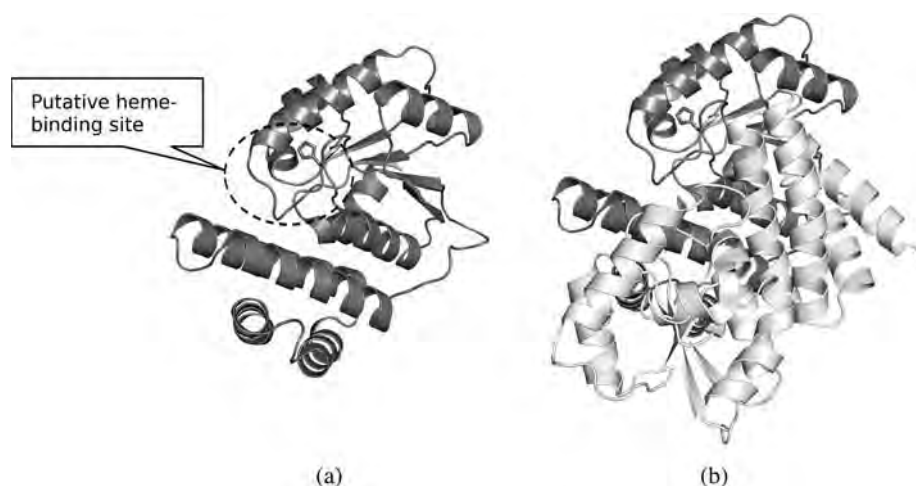
**Fig. 5.** A new model for controlling photosynthetic-gene expression of AppA and PpsR in a light- and oxygen-dependent manner. (1) PpsR exists in a dimer-tetramer equilibrium and (2) binds to promoter regions of regulated genes as an octamer. (3) Addition of AppA leads to the formation of AppA–PpsR<sub>2</sub>. (4) This species also interacts with the promoter region to form a ternary protein–DNA complex. (5) Illumination of this complex does not lead to dissociation of AppA and PpsR but reduces the affinity for DNA. Depending on the relative concentrations of AppA and PpsR (6), excess PpsR competes successfully with AppA–PpsR<sub>2</sub> for promoter regions under light conditions but is not able to replace the ternary complex in the dark. (7) The levels of AppA and PpsR are inversely regulated in response to oxygen availability. An increase in oxygen concentration favors the formation of the PpsR<sub>8</sub>–DNA species, thus leading to enhanced repression of photosynthesis-gene transcription. The model depicted accommodates *in vivo* results presented for anaerobic, semiaerobic and higher-oxygen conditions. Reproduced with permission [13]

sensor as well. As flavin adenine dinucleotide (FAD) in the BLUF (sensor of blue light using FAD) domain in AppA senses blue light, a conformational change of AppA is induced to result in the dissociation of AppA from the AppA/PpsR<sub>2</sub> complex [12]. The conformational change induced by light is responsible for the regulation of photosynthetic gene expression in response to light.

Based on the crystal structures of PpsR, AppA, and their complex, Winkler *et al.* [13, 14] have recently proposed a different model as shown in Fig. 5. PpsR exists in a dimer-tetramer equilibrium with a  $K_d$  of 0.9  $\mu\text{M}$  and forms an octamer to bind the target DNA [13]. When AppA is present, the AppA/PpsR<sub>2</sub> complex is formed, that also binds to the promoter region of regulated genes in dark. The AppA/PpsR<sub>2</sub>-DNA complex is proposed to show a reduced repressive strength compared to PpsR<sub>8</sub>-DNA complex and thereby promotes photosynthesis genes expression [13]. The AppA/PpsR<sub>2</sub> complex shows the higher kinetic stability compared to the PpsR tetramer [13]. Upon illumination, the DNA-binding affinity of AppA/PpsR<sub>2</sub> complex is reduced in addition to the subtle light-induced dissociation of AppA/PpsR<sub>2</sub>, which is caused by allosteric structural changes triggered by light [13]. In this model, it is proposed that the dissociation of AppA from the complex does not proceed upon illumination. Excess PpsR competes successfully with the AppA/PpsR<sub>2</sub> complex for promoter region under illumination, which results in the repression of photosynthesis genes expression in response to light [13].

In addition to the light- and oxygen-dependent regulation of AppA/PpsR regulatory system, it is proposed recently that heme-binding also regulates the function of this system [15]. AppA consists of the BLUF, the 4 helix bundle, and the SCHIC domains followed by the C-terminal Cys-rich domain (Fig. 3(b)). The full-length AppA binds ferric ( $\text{Fe}^{3+}$ ) heme to show the Soret peak at 412 nm with broad peaks in the 500 to 600 nm region [15]. The heme-binding affinity is estimated to be 1.25  $\mu\text{M}$  of  $K_d$ . Upon reduction, the Soret peak shifts to 424 nm and a well resolved  $\alpha$  and  $\beta$  peaks are observed at 558 and 528 nm, respectively [15]. These spectra are characteristic of six-coordinate heme proteins with two axial ligands. Though His284 is proposed to be one of the axial ligands as described below, the other axial ligand is not obvious at present.

The SCHIC (sensor containing heme instead of cobalamin) domain shows a similar overall structure to the vitamin B<sub>12</sub>-binding domain of *E. coli* methionine synthase (MetH) (Fig. 6). In vitamin B<sub>12</sub>-bound MetH, His759 in a loop located in the B<sub>12</sub>-binding cleft is coordinates to cobalt ion. Given that heme binds to the corresponding cleft in the SCHIC domain, the coordination structure of the heme bound to AppA could be estimated, though the crystal structure of a heme-bound SCHIC is not obtained. Based on the structural homology, it is proposed that His284 is an axial ligand of heme bound to AppA [15]. His284 is located at a loop corresponding the His-loop in MetH in a putative heme-binding cleft in the SCHIC domain of AppA. Heme-binding to AppA is



**Fig. 6.** Structures of the SCHIC domain in AppA (PDB 4HEH). (a) A putative heme-binding site is shown with a dotted ellipse in one subunit. His284 is shown as a stick model. (b) The SCHIC domain exists as a homodimer

proposed to push the BLUF domain toward the dark state conformation, which increases the antirepression activity of AppA on PpsR for photosynthesis genes expression [15]. The involvement of heme in the regulation of AppA antirepressor activity ensures that photosynthesis genes expression increases under the conditions of that sufficient heme is available [15].

PpsR is also reported to bind heme with a molar ratio of  $0.85 \pm 0.08$  PpsR/heme, and the affinity of PpsR for heme is estimated to be a  $K_d$  of  $1.9 \mu\text{M}$  [16]. While the Soret peak is observed at 372 nm with peaks in the 500–700 nm in the ferric state, the Soret peak is shifted to 420 nm with the appearance of clear  $\alpha$  and  $\beta$  peaks in the 500–600 nm region upon reduction [16]. Based on site-directed mutagenesis and UV-vis studies, Yin *et al.* [16] propose that Cys424 is an axial ligand of the ferric heme to form a five-coordinate heme, and that Cys424 and His275 are the axial ligands of the ferrous heme to form a six-coordinate heme. Heme inhibits the formation of a higher ordered PpsR/target DNA supercomplex [16]. Cys424 is located close to the helix-tern-helix motif in PpsR, which suggests that heme-binding to Cys424 would cause conformational changes of the DNA-binding domain including the helix-tern-helix motif to change interactions between PpsR and DNA [16]. Though the crystal structure is determined for a truncated form of PpsR lacking the C-terminal DNA-binding domain including the helix-turn-helix motif without heme, the structure of full-length PpsR is not obtained yet. To elucidate the molecular mechanisms of heme-sensing and heme-dependent functional regulation of PpsR in detail, the structural determination of full-length PpsR is required in both the apo- and holo-forms.

### Irr

Irr (iron response regulator) regulates the expression of *hemB*, which encodes amino levulinic acid (ALA)

dehydratase in heme biosynthesis pathway, in response to iron availability in *Bradyrhizobium japonicum* [17, 18]. Irr was initially discovered as a transcriptional regulator of heme biosynthesis, but it becomes clear that Irr in *B. japonicum* (Bj-Irr) is a global regulator of iron homeostasis and metabolism including the regulation for the expression of iron-regulated genes and iron transport genes [19, 20]. A mutation on the *irr* gene results in loss of normal iron responsiveness of iron-regulated genes and a lower total cellular iron content, which suggests Bj-Irr is required for the correct perception of the cellular iron status [19]. Bj-Irr interacts with ferrochelatase, the enzyme catalyzing iron ion insertion into protoporphyrin IX at the final step of heme biosynthesis, to sense the cellular iron status *via* the status of heme and protoporphyrin in bacterial cells [22]. Irr and ferrochelatase interact directly, and Irr responds to heme localized at the site of synthesis, not to a free heme pool [22]. Thus, ferrochelatase provides the input signal to Bj-Irr in mediating iron-dependent regulation of target genes, in which heme is a signaling molecule [22]. The direct interaction between ferrochelatase and Bj-Irr will prevent free heme molecules from exerting cytotoxicity.

Though Bj-Irr belongs to Fur family of transcriptional regulator, its functional properties are distinct from the canonical Fur protein. The canonical Fur protein senses and binds a transition metal ion  $\text{Fe}^{2+}$  as its physiological effector, and the binding/dissociation of  $\text{Fe}^{2+}$  is reversible, by which DNA-binding activity of Fur is regulated. Bj-Irr adopts heme as its physiological effector and the heme-dependent protein degradation plays an important role for the functional regulation of Bj-Irr [23]. Reactive oxygen species, probably  $\text{H}_2\text{O}_2$ , is involved in the heme-dependent degradation of Bj-Irr [24]. The oxidation (carbonylation) of Irr proceeds when Bj-Irr is incubated with hemin, dithiothreitol (DTT) as a reductant, and  $\text{O}_2$ , which would be a trigger of the degradation of Bj-Irr. Heme-binding to Bj-Irr is required for its degradation [22]. These results



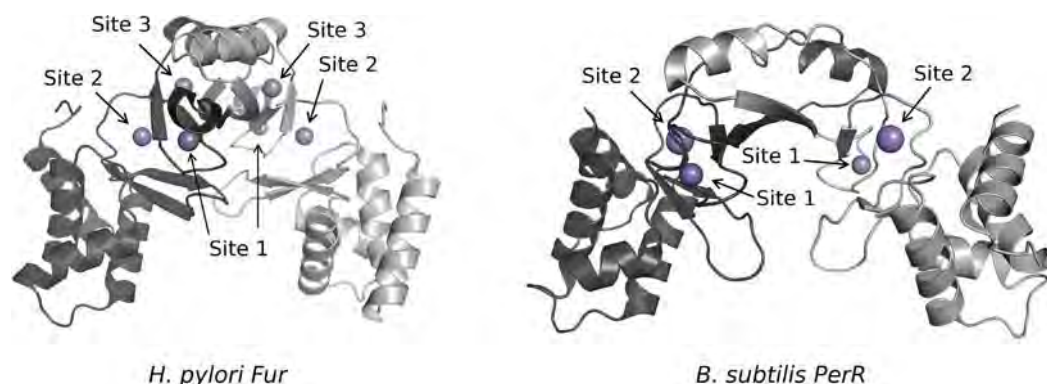
suggest that Irr mediates a cellular response not only to the cellular iron status but also to oxidative stress to regulate heme biosynthesis [24]. A similar protein modification in response to  $H_2O_2$  is observed in PerR, which is also Fur family of transcriptional regulator [25]. PerR senses  $H_2O_2$  by  $Fe^{2+}$  or  $Mn^{2+}$  at the regulatory metal-binding site, upon which the oxidation of His residues coordinated to the effector metal ion takes place [25]. The oxidation of the metal ligands in PerR results in conformational changes, by which the DNA-binding activity is regulated.

Bj-Irr can bind two equivalents of heme in two heme-binding sites, which is revealed by mutagenesis and spectroscopic studies including UV-vis, resonance Raman, and electron paramagnetic resonance (EPR) spectroscopy [26, 27]. The primary heme-binding site in Bj-Irr is assigned to be the *N*-terminal heme regulatory motif (HRM) consisting a Cys-Pro dipeptide motif. The heme in the HRM is in a five-coordinate, high-spin state with Cys29 as the axial ligand [27]. The Fe-S stretching mode is observed at  $333\text{ cm}^{-1}$ , which is lower compared with other thiolate-bound hemes like cytochrome P450 ( $351\text{ cm}^{-1}$ ) and chloro-peroxidase (CPO) ( $347\text{ cm}^{-1}$ ) [27]. The heme bound at the primary heme-binding site shows the  $\nu_3$  band at  $1492\text{ cm}^{-1}$  typical of the Cys-ligated five-coordinate high-spin heme in the high-frequency region. Due to the absence of hydrogen bonding interactions to the heme-bound thiolate, the labile and multiple configurations is proposed to be present in the ligation of Cys29 to the heme in the primary heme-binding site [27]. The heme-binding affinity ( $K_d$  for heme) is estimated to be *ca.* 10 nM by measuring the changes in the anisotropy of the intrinsic fluorescence of Trp31 adjacent to Cys29, the axial ligand of the heme in Irr [28]. In the secondary heme-binding site, two histidines are coordinated to the heme as the axial ligands to form a six-coordinate low-spin heme, which shows the  $\nu_3$  Raman band at  $1503\text{ cm}^{-1}$  and EPR signals at  $g = 2.98, 2.29, \text{ and } 1.53$ . As the crystal structure of Irr is not reported yet, it is not identified which histidines are the axial ligands of the heme [28].

The crystal structures of several Fur family proteins are reported [29], among which *Helicobacter pylori* Fur (Hp-Fur) and *B. subtilis* PerR are shown in Fig. 7. In *H. pylori* Fur, three metal-binding sites are present, in which Cys102, Cys105, Cys142, and Cys145 for site1, His42, His97, His99, Glu90, and Glu110 for site 2, and His96, His134, Glu117, and Gln120 for site 3 provide for ligands of metal ions bound in these sites. The sites 2 and 3 are thought to be the regulatory metal-binding sites responsible for the metal-dependent functional regulation of Fur, while the site 1 is the binding site of the structural zinc responsible for stabilizing the dimeric form of the regulator [29]. In *B. subtilis* PerR (Bs-PerR), while four Cys residues at the position of 96, 99, 136, and 139 provide for the ligands of the structural zinc, His37, Glu85, His91, His93, and Asp104 are coordinated to manganese ion in the regulatory metal-binding site.

Amino acid sequence alignment among Hp-Fur, Bs-PerR, and Bj-Irr shows that His63, His117, His119 are conserved in Bj-Irr at the corresponding locations to the regulatory metal ion-binding sites of Hp-Fur and Bs-PerR (Fig. 8), suggesting that two of these histidines could be the axial ligands of the heme bound at secondary heme binding site in Bj-Irr. A truncated Bj-Irr mutant lacking the *C*-terminal 47 amino acids (amino acids 117 to 163) unable to bind ferrous heme does not degrade *in vivo*, and is not oxidized *in vitro* [24].

*Rhizobium leguminosarum* and its close relatives such as *Brucella*, *Agrobacterium*, and *Bartonella* also contain Irr as an iron-responsive transcriptional regulator [30–35]. As Irr proteins from these bacteria including Irr from *Rhizobium leguminosarum* (RI-Irr) lack the *N*-terminal HRM, they show the molecular mechanism for the regulation of gene expression in response to heme distinct from that for Bj-Irr. While heme-binding to Bj-Irr promotes protein degradation, RI-Irr binds heme to form a stable heme-bound form, by which its DNA-binding affinity is regulated [30]. Irr from *Rhizobium leguminosarum* (RI-Irr) binds the target DNA in apo form, but heme-bound RI-Irr does not [30].



**Fig. 7.** Crystal structures of *H. pylori* Fur (PDB 2XIG) and *B. subtilis* PerR (PDB 3F8N). Spheres represent metal ions bound to the proteins

RI-Irr binds ferric heme to show the Soret,  $\alpha$ , and  $\beta$  bands at 412, 562, and 533 nm, respectively. The reduction of RI-Irr results in a red shift of the Soret peak to 426 nm and the sharp  $\alpha$  and  $\beta$  bands at 559 and 528 nm, respectively [30]. These UV-vis spectra are typical of six-coordinate low-spin heme proteins. Though RI-Irr is proposed to have two heme-binding sites, these two sites can not be distinguished from each other in its UV-vis spectra probably due to similar coordination structures of these sites, as described below.

RI-Irr has two heme-binding sites in its monomer with  $K_d$  values of  $1.0 \times 10^{-7}$  M and  $1.0 \times 10^{-6}$  M [30]. The higher affinity heme-binding site is proposed to be located in the sensory domain at the HxH motif at the position of 93–95 close to the monomer–monomer interface, where two histidines in this motif are coordinated to the heme to form a six-coordinate low-spin heme. The heme bound at the HxH motif is EPR silent probably due to magnetic coupling between two closely located hemes bound in the RI-Irr dimer [30]. The HxH motif is highly conserved among Irr proteins including Bj-Irr and RI-Irr (Fig. 8), suggesting that this motif is conserved as a heme-binding site in Irr proteins. The HxH motif is absolutely required for RI-Irr to bind the target DNA *in vitro* and to function as a transcriptional regulator *in vivo* [30]. While heme-binding to the HxH motif results in the loss of DNA binding activity, replacing the HxH motif with Ala residues also causes the same result [30]. Thus, heme-binding to the HxH motif causes conformational changes of RI-Irr to result in the loss of DNA binding activity, which can be mimicked by the mutations on the HxH motif.

EPR and UV-vis spectroscopy along with mutagenesis studies suggest that His46 and His66 are involved in coordinating heme in the second heme-binding site with a lower affinity [36]. The heme bound at the lower affinity site is in a low-spin state with two axial ligands (His46 and His66), showing the EPR signals at  $g = 2.95, 2.26,$  and  $1.55$  [30]. Though these histidines are not conserved between Bj-Irr and RI-Irr, they are conserved among Irr homologs lacking the *N*-terminal HRM [36].

Heme-binding to the lower affinity site, not to the HxH motif, promotes a change in the oligomerization states [36]. While heme-free RI-Irr exists as an equilibrium mixture of a dimer and hexamer, heme-binding promotes RI-Irr oligomerization [36]. The functional roles of the oligomerization induced by heme-binding to the lower affinity site remain unclear.

### HbrL

HbrL is LysR-type transcriptional regulator (LTTR) in *Rodobacter capsulatus*, which consists of the *N*-terminal DNA-binding domain containing a helix-turn-helix motif followed by a LTTR coinducer binding motif [37]. HbrL binds the promoter region of *hemA*, *hemB*, and *hemZ* to regulate the expression of these genes in response to the availability of heme, among which the expression of *hemA* and *hemZ* encoding 5-aminolevulinic synthase and coproporphyrinogen III, respectively, is strongly activated in the absence of heme while *hemB* encoding porphobilinogen synthase is moderately repressed in the presence of heme [37, 38]. In addition to these genes responsible for heme biosynthesis, HbrL acts as

Bj-Irr	<u>MSENTAPHHDDDVHAAALLSGRQPAL</u> <u>TGCP</u> WHDVNEMLQ <sup>S</sup> AGLRP <sup>T</sup> RQRMALG	53
RI-Irr	-----MMTGAFPIAIEVRLRGAGLRP <sup>T</sup> RQ <sup>R</sup> VALG	29
Bs-PerR	-----MAAHELKEALE <sup>T</sup> LKETGVRI <sup>T</sup> PQRHAIL	28
Hp-Fur	-----MRRLETLESILERLRMSIKKNGLKNSKQREEVV	33
Bj-Irr	WLLFGKGARHLTAEMLYEEATLAKVPVSLATVYNTLNQLTDAGLLRQVSDGT	106
RI-Irr	DLLFAKGDRHLTVEELHEEAVAAGVPVSLATVYNTLHQFTEAGLIRVLAVESA	82
Bs-PerR	EYLVN-SMAHPTADDIYKALEGKFPNMSVATVYNNLRVFR <sup>E</sup> SGLVKELTYGDA	80
Hp-Fur	SVLYR-SGTHLSPEEITHSIRQKDKNTSIS <sup>S</sup> VYRILN <sup>F</sup> LEKEN <sup>F</sup> ICVLETSKS	85
	*	
Bj-Irr	KTYFDTNV <sup>T</sup> THH-HYYLENSHELVDIEDP-HLALSKMPEVPEGYE <sup>I</sup> ARI <sup>D</sup> DMVV	158
RI-Irr	KTYFDTNVSDHH-HFFVEGDNEVLDIPVS-NLTIANLPEPPEGMEIAHVDVVI	134
Bs-PerR	SSRFDFVTS <sup>D</sup> HY-HAICENCGKIVDFHYPGLDEVEQLAAHVTGFKVSHHRL <sup>E</sup> I	132
Hp-Fur	GRRYEIAAKEH <sup>H</sup> DIICLHCGKII <sup>E</sup> FADPEIEHRQNEVVKYQAKLISHDMKM	138
	*** * * * + + +	
Bj-Irr	RLRKKR-----	163
RI-Irr	RLRAKQG-----	140
Bs-PerR	YGVCQECSK <sup>K</sup> ENH	145
Hp-Fur	FVWCKECESDD-	150

**Fig. 8.** Amino acid sequences of Bj-Irr, RI-Irr, Bs-PerR, and Hp-Fur. A CP motif in Bj-Irr is underlined. The ligands of regulatory metal ions at site 2 and site 3 for Hp-Fur are shown with \* and + under its sequence, respectively. The histidine residues in the HxH motif are shown in bold

a transcriptional activator of multiple ferrous and ferric iron uptake system and a heme uptake system, which indicates that HbrL plays a central role for regulating both iron transport and heme biosynthesis as a function of iron availability [38].

Though it is reported that HbrL binds heme showing the Soret peak at 413 nm, the coordination structure of the heme in HbrL is not known [37]. It is proposed that *hemB* expression would be reduced by repressive binding of an HbrL-heme complex and that only HbrL-heme complex activates the expression of *hemA* and *hemZ* though HbrL binds the target DNA in the presence and absence of heme [37]. However, as no structural information of HbrL is available at present, detail mechanisms of the heme-sensing and the heme-responsive regulation of gene expression for HbrL remains to be elucidated.

### Bach1

Bach1 is a mammalian transcriptional repressor that regulates the expression of heme oxygenase-1 (HO-1), ferritin, and  $\beta$ -globin in response to heme, by which it plays an important role for iron homeostasis [39–42]. Heme-free Bach1 forms a heterodimer with small Maf proteins such as MafK, and the resulting heterodimer binds to the target DNA, Maf recognition elements (MAREs) to act as a repressor. Bach1 consists of 739 amino acids, in which the *N*-terminal BTB/POZ and the bZip domains are responsible for mediating dimer formation and DNA binding with heterodimer formation with small Maf proteins, respectively. Though there are six CP motifs (Cys224, 301, 438, 464, 495, and 649 for CP1, CP2 CP3, CP4, CP5, and CP6, respectively) in Bach1, only CP3–CP6 bind heme, but CP1 and CP2 do not [40, 43].

When Bach1 binds heme, DNA-binding activity of the Bach1/MafK heterodimer is inhibited resulting in the dissociation the heterodimer from Maf recognition elements [44]. Transcription reporter assays and mutagenesis studies suggest that CP5 and/or CP6 may be involved in the regulation of the DNA-binding activity of Bach1 [43]. Heme-binding to Bach1 also controls the subcellular localization of Bach1, by which Bach1 is excluded from the nucleus. Deletion of CP3 or CP4 completely abolishes heme-induced nuclear exclusion, which reveals that CP3 and CP4 are critical in the heme-induced cytoplasmic relocalization of Bach1 [43]. It is proposed that heme-binding to CP3 and CP4 induces a conformational change around these CP motifs, resulting in an exposure of the putative nuclear export signal, a stretch of hydrophobic amino acids between CP3 and CP4, on the surface of the protein and thus in activation of the nuclear export of Bach1 [39].

In addition to the heme-induced regulation of DNA-binding activity and subcellular localization of Bach1, it is proposed that heme within a cell regulates the polyubiquitination and degradation of Bach1 [45].

While mutations in all of the CP motifs significantly reduce the HOIL-1 mediated polyubiquitination of Bach1, the addition of heme increases the levels of polyubiquitination of wild-type Bach1 but not Bach1 variant with mutations in the CP motifs [45]. A central region (amino acids 426 to 503) containing the CP3, CP4, and CP5 motifs is proposed to be a binding site for HOIL-1, suggesting that the heme-binding to these CP motifs causes a conformational change in this region, which results in the increased polyubiquitination [45].

Heme titrations with UV-vis spectroscopy reveal that Bach1 binds five equivalents of heme [39]. One molecule of heme binds to each of the cysteine residues in CP3, CP4, CP5, and CP6 in Bach1 to form a five-coordinate high-spin heme (Type 2 site), which show the Soret peak at 371 nm and the Raman bands at 343, 1569, and 1490  $\text{cm}^{-1}$  for the Fe-S stretching,  $\nu_2$ , and  $\nu_3$  modes, respectively [39]. A six-coordinate low-spin heme (Type 1 site) is also present in heme-bound Bach1, which shows the Soret peak at 423 nm and the Raman bands at 1584 and 1501  $\text{cm}^{-1}$  for the  $\nu_2$  and  $\nu_3$  modes, respectively [39]. Though a histidine and a non-CP motif cysteine residues are thought to be the axial ligands of the heme at Type 1 site, these residues are not assigned yet. While the hemes bound at Type 2 site are responsible for the functional regulation of Bach1 as described above, it is unclear if heme-binding at Type 2 site is involved in any physiological regulation of Bach1.

In addition to Bach1, there are some other eukaryotic heme-sensing proteins, including HAP1, Rev-Erb $\alpha$ , and Rev-Erb $\beta$ . HAP1 is a transcriptional regulator in yeast, which is activated by binding heme in its HRM, especially HRM7 located at the *C*-terminal region, to activate the expression of the genes for respiration and oxidative damage control [46, 47]. Rev-Erb $\alpha$  and Rev-Erb $\beta$  belong to the nuclear hormone receptor superfamily and are involved in the regulation of the circadian rhythm [48, 49]. Though they uses heme as their physiological ligand, the detail mechanisms of how heme-binding regulates their physiological functions remain to be elucidated.

### Heme-sensing histidine kinases in bacterial two-component systems

Bacterial two-component systems consists of sensor histidine kinases (SKs) that sense a wide variety of physical and chemical signals, including light, pressure, temperature, nutrients such as sugars and amino acids, metal ions, *etc.* and response regulator proteins (RRs) that are phosphorylated by the cognate sensor kinases to elicit a response, usually the regulation of gene expression in response to external signals sensed by sensor histidine kinases [50, 51]. Heme acts as an external signal in several bacterial two-component systems, as summarized in Table 1.

A heme sensing two-component system, HssR/HssS, is responsible for the regulation of the expression of an

**Table 1.** Heme-sensing two-component systems

SK/RR <sup>a</sup>	Microorganisms	References
HssS/HssR	<i>S. aureus</i> , <i>B. anthracis</i>	53–55
ChrS/ChrA	<i>C. diphtheriae</i> , <i>C. glutamicum</i>	57, 64
HrrS/HrrA	<i>C. diphtheriae</i> , <i>C. glutamicum</i>	59, 64
SaeS/SaeR	<i>S. aureus</i>	65
VirS/VirR	<i>C. perfringens</i>	66
Hklep/Rrlep	<i>L. biflexa</i>	67
HaeS/HaeR	<i>P. gingivalis</i>	68

<sup>a</sup>SK: sensor kinase, RR: response regulator.

ABC type transporter HrtA/HrtB in response to heme to maintain cellular heme homeostasis in a pathogenic bacterium *Staphylococcus aureus* [52]. Unlike the HrtAB transporter that export heme in *L. lactis*, it is proposed that the HrtAB transporter in *S. aureus* does not export heme itself from the cytoplasm, but exports by-products of heme toxicity or heme metabolites that accumulate in bacterial cells upon heme acquisition to overcome heme toxicity [52]. When the sensor histidine kinase HssS senses heme, autophosphorylation at His249 in HssS takes place followed by transphosphorylation of Asp52 in HssR. Phosphorylated HssR binds to the *hrtAB* promoter, which results in the activation of the expression of the *hrtAB* genes [53, 54]. *Bacillus anthracis* also encodes functional HssRS and HrtAB systems similar to those of *S. aureus*, which are required to cope with heme toxicity [55, 56].

Amino acid sequence analyses predict that HssS proteins from *S. aureus* and *B. anthracis* have two transmembrane regions with a long periplasmic loop and the C-terminal histidine kinase domain [53, 55]. Although HssS may sense heme by direct binding, there is neither any HRM nor conserved amino acids that typically engage in axial ligation to the heme iron among the potential HssS orthologs [52].

In *Corynebacterium diphtheriae*, a two-component system, ChrA/ChrS, regulates the expression of the *hmuO* and the *hrtAB* genes that encode a heme oxygenase and a putative ABC type transporter, respectively. When the sensor histidine kinase ChrS senses heme, the autophosphorylation activity of ChrS is significantly stimulated [57]. Phosphorylation of ChrS results in the activation of the expression of the *hmuO* and the *hrtAB* genes via intermolecular signal transduction between ChrS and ChrA [58–61]. While HmuO is important for iron acquisition by degradation of heme, HrtAB system is required for protection from heme toxicity [61].

Amino acid sequence analysis predicts that ChrS contains six transmembrane regions and the histidine kinase domain in the N-terminal sensor domain and the C-terminal region, respectively [57]. This structure is different from HssS proteins, suggesting distinct mechanisms of heme recognition [57]. Though it is

reported that ferric heme-bound ChrS shows the Soret peak at 405 nm, the coordination structure of heme in ChrS remains to be determined [57].

SenS and SenR, which are a histidine kinase and a response regulator, respectively, and an accessory protein HbpS in *Streptomyces reticuli*, form a novel sensing system consisting of a typical two-component system (SenS/SenR) and a third component. In this system, HbpS is proposed to bind heme to regulate the autokinase activity of the histidine kinase SenS in response to hemin or oxidative stress [62, 63]. In this system, the sensor histidine kinase SenS does not sense heme, but the third component acts as a heme sensor.

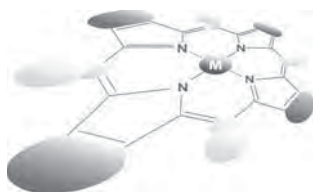
Though genetic and microbiological studies clearly reveal that heme acts as a signaling molecule in these heme-sensing two-component systems, detail molecular mechanisms remain to be elucidated for heme sensing and heme-induced signal transductions. To answer these questions, spectroscopic and structural analyses are required for the heme-sensing histidine kinases.

## REFERENCES

1. Aono S. *Acc. Chem. Rev.* 2003; **36**: 825.
2. Aono S. *Dalton Trans.* 2008; 3137.
3. Aono S. *Adv. Microbiol. Physiol.* 2013; **63**: 273.
4. Yamamoto Y, Poyart C, Trieu-Cuot P, Lamberet G, Gruss A and Gaudu P. *Mol. Microbiology* 2005; **56**: 525.
5. Lechardeur D, Cesselin B, Fernandez A, Lamberet G, Garrigues C, Pedersen M, Gaudu P and Gruss A. *Curr. Opin. Biotechnol.* 2011; **22**: 143.
6. Pedersen MB, Garrigues C, Tophile K, Brun C, Vido K, Bennedsen M, Mollgaard H, Gaudu P and Gruss A. *J. Bacteriol.* 2008; **190**: 4903.
7. Duwat P, Sourice S, Cesselin B, Bamberet G, Vido K, Gaudu P, Le Loir Y, Violet F, Loubiere P and Gruss A. *J. Bacteriol.* 2001; **183**: 4509.
8. Brooijmans RJ, Poolman B, Schuurman-Wolters GK, de Vos WM and Hugenholtz J. *J. Bacteriol.* 2007; **189**: 5203.
9. Sawai H, Yamanaka M, Sugimoto H, Shiro Y and Aono S. *J. Biol. Chem.* 2012; **287**: 30755.
10. Lechardeur D, Cesselin B, Liebl U, Vos MH, Fernandez A, Brun C, Gruss A and Gaudu P. *J. Biol. Chem.* 2012; **287**: 4752.
11. Shimada H, Iba K and Tkamiya K. *Plant Cell Physiol.* 1992; **33**: 471.
12. Masuda S and Bauer CE. *Cell* 2002; **110**: 613.
13. Winkler A, Heintz U, Lindner R, Reinstein J, Shoeman RL and Schlichting I. *Nat. Struct. Mol. Biol.* 2013; **20**: 859.
14. Heintz U, Meinhart A and Winkler A. *Acta Cryst.* 2014; **D70**: 863.
15. Yin L, Dragnea V, Feldman G, Hammad LA, Karty JA, Dann CE 3rd and Bauer CE. *MBio.* 2013; **4**: e00563.

16. Yin L, Dragnea V and Bauer CE. *J. Biol. Chem.* 2012; **287**: 13850.
17. Hamza I, Chauhan S, Hassett R and O'Brian MR. *J. Biol. Chem.* 1998; **273**: 221669.
18. Hamza I, Qi Z, King ND and O'Brian MR. *Microbiology* 2000; **146**: 669.
19. Yang J, Sangwan I, Lindemann A, Hauser F, Hennecke H, Fischer HM and O'Brian MR. *Mol. Microbiol.* 2006; **60**: 427.
20. Rudolph G, Semini G, Hauser F, Lindemann A, Friberg M, Hennecke H and Fischer HM. *J. Bacteriol.* 2006; **188**: 733.
21. Small SK, Puri S and O'Brian MR. *Biometals* 2009; **22**: 89.
22. Qi Z and O'Brian MR. *Mol. Cell* 2002; **9**: 155.
23. Qi Z, Hamza I and O'Brian MR. *Proc. Natl. Acad. Sci. U.S.A.* 1999; **96**: 13056.
24. Yang J, Panek HR and O'Brian MR. *Mol. Microbiol.* 2006; **60**: 209.
25. Lee JW and Helmann JD. *Nature* 2006; **440**: 363.
26. Yang J, Ishimori K and O'Brian MR. *J. Biol. Chem.* 2005; **280**: 7671.
27. Ishikawa H, Nakagaki M, Bamba A, Uchida T, Hori H, O'Brian MR, Iwai K and Ishimori K. *Biochemistry* 2011; **50**: 1016.
28. Ishimori K and Watanabe Y. *Chem. Lett.* 2014; doi: 10.1246/cl.140787, in press.
29. Fillat MF. *Arch. Biochem. Biophys.* 2014; **546**: 41.
30. Singleton C, White GF, Todd JD, Marritt SJ, Cheesman MR, Johnston AW and Le Brun NE. *J. Biol. Chem.* 2010; **285**: 16023.
31. Anderson ES, Paulley JT, Martinson DA, Gaines JM, Steele KH and Roop RM 2nd. *J. Bacteriol.* 2011; **193**: 5359.
32. Martínez M, Ugalde RA and Almirón M. *Microbiology* 2005; **151**: 3427.
33. Ngok-Ngam P, Ruangkiattikul N, Mahaviahakanont A, Virgem SS, Sukchawalit R and Mongkolsuk S. *J. Bacteriol.* 2009; **191**: 2083.
34. Martínez M, Ugalde RA and Almirón M. *Microbiology* 2006; **152**: 2591.
35. Parrow NL, Abbott J, Lockwood AR, Battisti JM and Minnick MF. *Infect. Immun.* 2009; **77**: 307.
36. White GF, Singleton C, Todd JD, Cheesman MR, Johnston AW and Le Brun NE. *FEBS J.* 2011; **278**: 2011.
37. Smart JL and Bauer CE. *J. Bacteriol.* 2006; **188**: 1567.
38. Zappa S and Bauer CE. *Mol. Microbiol.* 2013; **90**: 1277.
39. Hira S, Tomita T, Matsui T, Igarashi K and Ikeda-Saito M. *IUBMB Life* 2007; **59**: 542.
40. Igarashi K and Watanabe-Matsui M. *Tohoku J. Exp. Med.* 2014; **232**: 229.
41. Igarashi K, Hoshino H, Muto A, Suwabe N, Nishikawa S, Nakauchi H and Yamamoto M. *J. Biol. Chem.* 1998; **273**: 11783.
42. Sun J, Hoshino H, Takaku K, Nakajima O, Muto A, Suzuki H, Tashiro S, Takahashi S, Shibahara S, Alam J, Taketo M, Yamamoto M and Igarashi K. *EMBO J.* 2002; **21**: 5216.
43. Suzuki H, Tashiro S, Hira S, Sun J, Yamazaki C, Zenke Y, Ikeda-Saito M, Yoshida M and Igarashi K. *EMBO J.* 2004; **23**: 2544.
44. Ogawa K, Sun J, Taketani S, Nakajima O, Nishitani C, Sassa S, Hayashi N, Yamamoto M, Shibahara S, Fujita H and Igarashi K. *EMBO J.* 2001; **20**: 2835.
45. Zenke-Kawasaki Y, Dohi Y, Katoh Y, Ikura T, Ikura M, Asahara T, Tokunaga F, Iwai K and Igarashi K. *Mol. Cell. Biol.* 2007; **27**: 6962.
46. Hach A, Hon T and Zhang L. *Mol. Cell. Biol.* 1999; **19**: 4324.
47. Hon T, Hach A, Lee HC, Cheng T and Zhang L. *Biochem. Biophys. Res. Commun.* 2000; **273**: 584.
48. Raghuram S, Stayrook KR, Huan P, Rogers PM, Nosie AK, McClure DB, Burris LL, Khorasanizadeh S, Burris TT and Rastinejad F. *Nat. Struct. Mol. Biol.* 2007; **14**: 1207.
49. Yin L, Wu N, Curtin JC, Qaananani M, Szwergold NR, Reid RA, Waitt GM, Parks DJ, Pearce KH, Wisely GB and Lazar MA. *Science* 2007; **318**: 1786.
50. Laub MT and Goulian M. *Annu. Rev. Genet.* 2007; **41**: 121.
51. Jung K, Fried L, Behr S and Heermann R. *Curr. Opin. Microbiol.* 2012; **15**: 118.
52. Stauff DL and Skaar EP. In *Bacterial Sensing and Signaling*, Collin M and Schunch R. (Eds.) Karger: Basel, 2009; pp 120-135.
53. Stauff DL, Torres VJ and Skaar EP. *J. Biol. Chem.* 2007; **282**: 26111.
54. Torres VJ, Stauff DL, Pishchany G, Bezbradica JS, Gordy LE, Iturregui J, Anderson KL, Dunman PM, Joyce S and Skaar EP. *Cell Host Microbe.* 2007; **1**: 109.
55. Stauff DL and Skaar EP. *Mol. Microbiol.* 2009; **72**: 763.
56. Mike LA, Choby JE, Brinkman PR, Olive LQ, Dutter BF, Ivan SJ, Gibbs CM, Sulikowski GA, Stauff DL and Skaar EP. *PLoS Pathog.* 2014; **10**: e1004044.
57. Ito Y, Nakagawa S, Komagata A, Ikeda-Saito M, Shiro Y and Nakamura H. *FEBS Lett.* 2009; **583**: 2244.
58. Bibb LA, King ND, Kunkle CA and Schmitt MP. *Infect. Immun.* 2005; **73**: 7406.
59. Bibb LA, Kunkle CA and Schmitt MP. *Infect. Immun.* 2007; **75**: 2421.
60. Bibb LA and Schmitt MP. *J. Bacteriol.* 2010; **192**: 4606.
61. Burgos JM and Schmitt MP. *J. Bacteriol.* 2012; **194**: 1717.
62. Ortiz de Orué Lucana D, Zou P, Nierhaus M and Schrempf H. *Microbiology* 2005; **151**: 3603.

63. Bogel G, Schrempf H and Ortiz de Orué Lucana D. *Amino Acids* 2009; **37**: 681.
64. Heyer A, Gätgens C, Hentschel E, Kalinowski J, Bott M and Frunzke. *J. Microbiol.* 2012; **158**: 3020.
65. Schmitt J, Joost I, Skaar EP, Herrmann M and Bischoff M. *Microbiol.* 2012; **158**: 2619.
66. Hassan S, Ohtani K, Wang R, Yuan Y, Wang Y, Yamaguchi Y and Shimizu T. *J. Microbiol.* 2010; **48**: 96.
67. Louvel H, Betton JM and Picardeau M. *BMC Microbiol.* 2008; **8**: 25.
68. Scott JC, Klein BA, Duran-Pinedo A, Hu L and Duncan MJ. *PLos One* 2013; **8**: e73351.



# Meso-*N*-arylamino- and *N,N*-diarylamino porphyrinoids: Syntheses, properties and applications

Ryota Sakamoto<sup>\*◇</sup>, Suzaliza Mustafar and Hiroshi Nishihara<sup>\*</sup>

Department of Chemistry, Graduate School of Science, The University of Tokyo, 7-3-1, Hongo, Bunkyo-ku, Tokyo 113-0033, Japan

Dedicated to Professor Shunichi Fukuzumi on the occasion of his retirement

Received 4 November 2014

Accepted 24 November 2014

**ABSTRACT:** This review is devoted to porphyrinoids with *N*-arylamino groups tethered directly to their *meso* positions, the study of which has significantly progressed in the past two decades. After a brief introductory description, various synthetic procedures for these compounds are described. The third section focuses on their photochemical and electrochemical properties, and reviews the synergetic effects that arise between the porphyrinoids and the *N*-arylamino groups. Potential applications are then discussed, focusing on dye-sensitized solar cells (DSSCs).

**KEYWORDS:** *N*-arylamino porphyrinoids, electrochemistry, photochemistry, dye-sensitized solar cells.

## INTRODUCTION

Arylamines are one of the most important and useful groups of organic molecular fragments. For example, the *N,N'*-bis(3-methylphenyl)-*N,N'*-diphenylbenzidine (TPD) [1] and *N,N'*-bis(3-methylphenyl)-*N,N'*-diphenyl-9,9-spirobifluorene-2,7-diamine (spiro-TPD) [2] families are good hole-transport materials in organic electronics. Several arylamine-based organic dyes are also used in organic photovoltaics (OPVs) [3] and dye-sensitized solar cells (DSSCs) [4]. Arylamines have various useful features such as donor ability [5], reversible redox properties [6], fluorescence [7], and donor–acceptor interactions (when combined with an acceptor) [8] that allow them to be valuable and versatile functional molecular fragments with a wide variety of applications. Therefore, adding *N*-arylamino or *N,N*-diarylamino groups to the *meso*-position of porphyrinoids is a promising method of enhancing and tuning the photo- and electro-functionalities of the combined components. This review examines the syntheses, basic photo- and

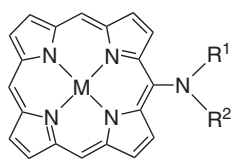
electrochemical properties, and applications of a series of *meso-N*-arylamino porphyrinoids (Fig. 1).

## SYNTHESES

The first synthesis of *meso-N*-arylamino porphyrin was reported by Gold [9], who used the nucleophilic addition of *N*-arylacetamido (generated from the corresponding *N*-arylacetamide and sodium hydride) to the cationic zinc(II) octaethylporphyrin radical with subsequent deacetylation using sodium methoxide to achieve yields of up to 40% (**1** in Fig. 2a). Zhang *et al.* achieved yields of up to 99% by using Buchwald–Hartwig amination (**2** in Fig. 2b) [10] to couple 5-bromo- or 5,15-dibromo-10,20-diphenylporphyrin (freebase or zinc) with monoaryl- and diarylamines in the presence of a palladium acetate and bis(2-diphenylphosphinophenyl) ether (DPEphos) catalyst and a base (cesium carbonate or sodium *tert*-butoxide). The protocol has been frequently used by other researchers, giving rise to slight variations. Metal-free *N*-arylamination of 5-bromo-10,20-bis(3,5-di-*tert*-butylphenyl)porphyrin was also reported by Balaban (yield: 36%) [11]. Recent work contributed by Devillers and Richeter has described aromatic nucleophilic substitution ( $S_NAr$ ) of nickel(II)

<sup>◇</sup>SPP full member in good standing

\*Correspondence to: Ryota Sakamoto, email: sakamoto@chem.s.u-tokyo.ac.jp; Hiroshi Nishihara, email: nisihara@chem.s.u-tokyo.ac.jp

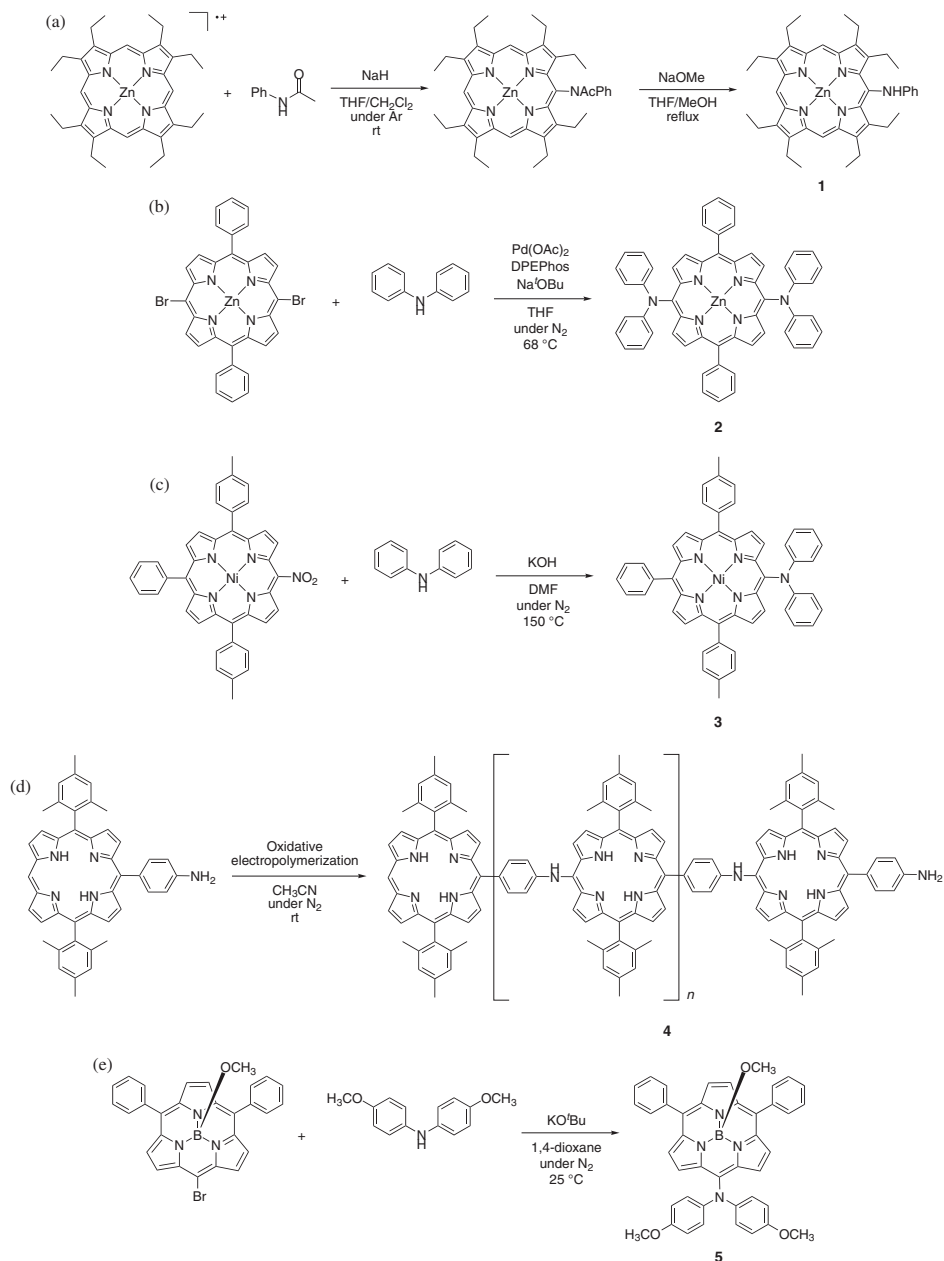


M = 2H, Zn, Ni...  
 R<sup>1</sup> = aryl  
 R<sup>2</sup> = H, alkyl, aryl

**Fig. 1.** Structure of the simplest *meso*-*N*-aryl- and *meso*-*N,N*-diarylamino porphyrins

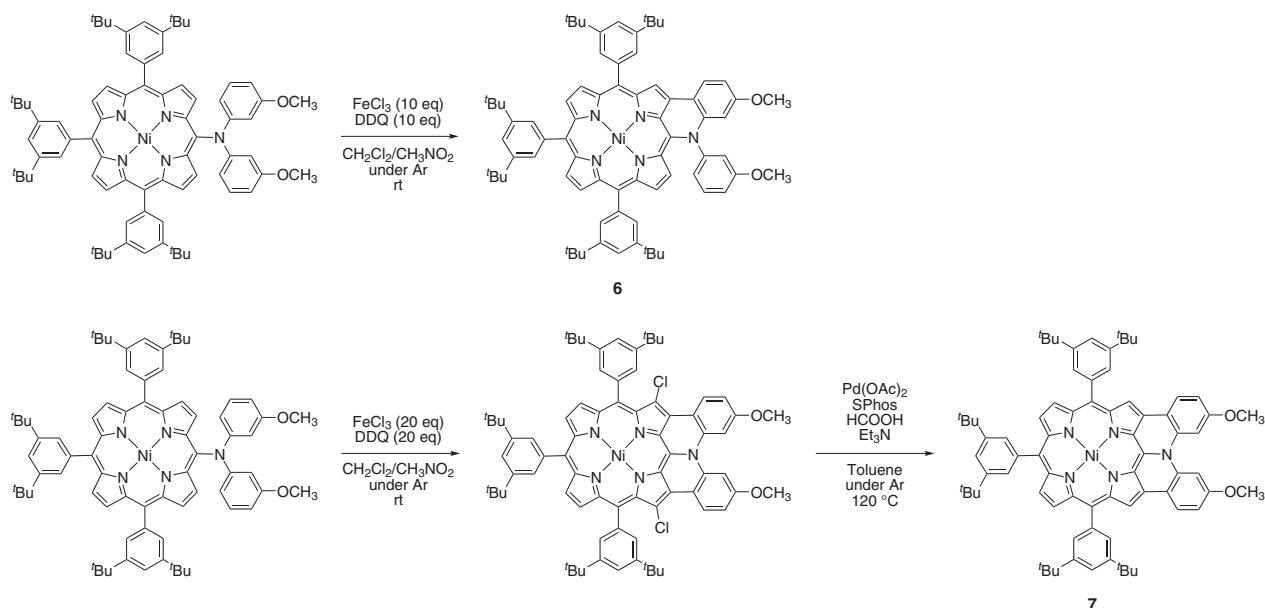
5-nitro-10,20-di-*p*-tolyl-15-phenylporphyrin, including the introduction of arylamines or diarylamines in the presence of a potassium hydroxide base (**3** in Fig. 2c, yield: up to 66%) [12]. In every case, *N,N*-diarylamination was more difficult than *N*-arylation.

Moore and Gust synthesized a polymeric material based on *meso*-*N*-arylamino porphyrin by means of a strategic procedure. An oxidative electrochemical polymerization of zinc(II) or free-base 5-(4-aminophenyl)-10,20-bis(2,4,6-trimethylphenyl)porphyrin was conducted in dry and deoxygenated 0.1 M Bu<sub>4</sub>NPF<sub>6</sub>/CH<sub>3</sub>CN (Fig. 2d),



**Fig. 2.** Synthetic procedures for *meso*-*N*-aryl- and *meso*-*N,N*-diarylamino porphyrinoids. (a) Nucleophilic addition of *N*-arylacetylamine to [octaethylporphyrinato]zinc(II) and subsequent deacetylation [9]. (b) Buchwald-Hartwig amination to [5,15-dibromo-10,20-diphenylporphyrinato]zinc(II) [10]. (c) S<sub>N</sub>Ar of [5-nitro-10,20-di-*p*-tolyl-15-phenylporphyrinato]nickel(II) [12]. (d) Oxidative electrochemical polymerization of 5-(4-aminophenyl)-10,20-bis(2,4,6-trimethylphenyl)porphyrin [13]. (e) S<sub>N</sub>Ar of methoxo(5-bromo-10,15-diphenylsubporphyrinato)boron(III) [15, 16]





**Fig. 3.** Oxidative fusion reaction of [5-*N,N*-bis(3-methoxyphenyl)amino-10,15,20-tris(3,5-di-*tert*-butylphenyl)porphyrinato] nickel(II) [17]

which led to the formation of polymer **4** (Fig. 2d) [13]. Moore also conducted chemical oxidation using  $\text{Cu}(\text{BF}_4)_2$ , obtaining oligomers with a mean degree of polymerization of 6.8 [14].

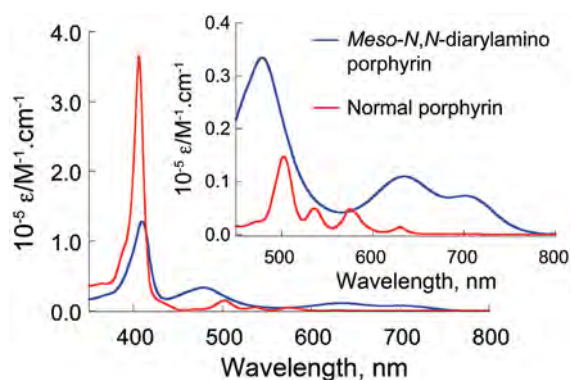
Osuka and Kim reported the *meso*-amination of boron-centered subporphyrins. Their first synthesis employed a technique similar to Zhang's, which gave rise to *meso-N*-arylamino-subporphyrin (yield: up to 78%) [15]. They then found that a  $\text{S}_{\text{N}}\text{Ar}$  reaction of 5-halo-10,15-diphenylsubporphyrin using potassium *tert*-butoxide as a base was more effective, obtaining not only *meso-N*-arylamino-subporphyrin (yield: up to 82%) but also *meso-N,N*-diarylamino-subporphyrin (**5** in Fig. 2e, yield: up to 80%) [16].

A valuable post-synthetic modification for *meso-N,N*-diarylamino porphyrin was reported by Kim, Yorimitsu and Osuka [17], who conducted a ring-closure reaction under oxidative conditions ( $\text{FeCl}_3$  and 2,3-dichloro-5,6-dicyano-*p*-benzoquinone, DDQ) between the arene of the amino group and the  $\beta$ -position of the porphyrin macrocycle. Either one or two fused six-membered rings including the amine center were generated (**6** and **7** in Fig. 3). The most important result of this modification was the planarization. The dihedral angle between the  $\text{sp}^2$  amino group and porphyrin ring was  $69.5^\circ$  (from single-crystal X-ray structure) for nickel(II) 5-*N,N*-bis(3-methoxyphenyl)amino-10,15,20-tris(3,5-di-*tert*-butylphenyl)porphyrin, which is induced by the steric hindrance between the two components. The dihedral angle, however, was significantly reduced in the singly- and doubly-fused products ( $10.4^\circ$  and  $19.1^\circ$ , respectively). In combination with the expanded  $\pi$ -system induced by the ring fusion, the porphyrin

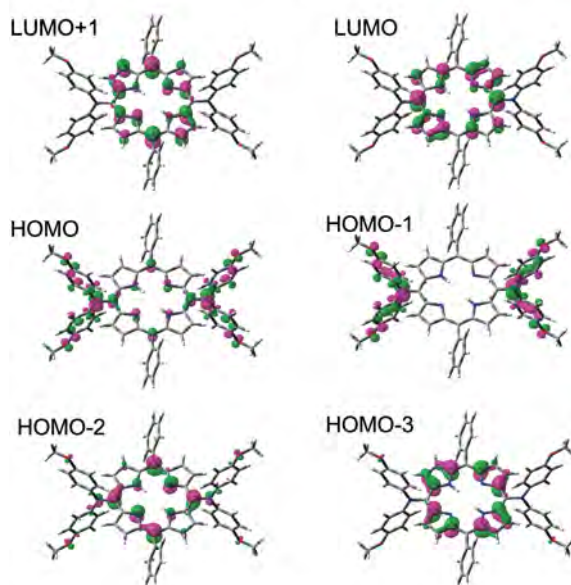
moiety may enjoy better communication with the diarylamino group. The fused compounds exhibited cathodic shifts in their oxidation potentials and red-shifts in the absorption bands.

## PHOTOCHEMICAL AND ELECTROCHEMICAL PROPERTIES

Their highly developed  $\pi$ -orbitals mean that porphyrinic compounds produce  $\pi$ - $\pi^*$  absorption bands in the visible region. Typically, there is a very strong and sharp absorption (B-band) at around 400–450 nm, and also a set of weak absorptions (Q-band) at 500–650 nm. As an example, the absorption spectrum of free-base 5,15-diphenylporphyrin is shown in Fig. 4a. The efficient acquisition of solar radiation requires strong absorptivity at  $\lambda > 450$  nm, which can be achieved through the introduction of arylamino and diarylamino groups. Figure 4a also shows the electronic spectrum of free-base 5,15-bis[(*N,N*-bis(4-methoxyphenyl)amino)-10,20-diphenyl]porphyrin synthesized by Sakamoto [18]. The intensity of the B-band is decreased (but still strong enough), whereas the absorptivity at  $\lambda > 450$  nm is increased and red-shifted. DFT calculations indicated that the *n*-orbital of the diarylamino group couples with one of the  $\pi$ -orbitals of the porphyrin moiety, giving rise to significant contributions to the HOMOs (Fig. 4b). Therefore, the expression of charge transfer bands and the weakening of the configuration interaction in the  $\pi$ - $\pi^*$  transitions [19] may account for the enhancement of absorptivity at long wavelengths.



(a)

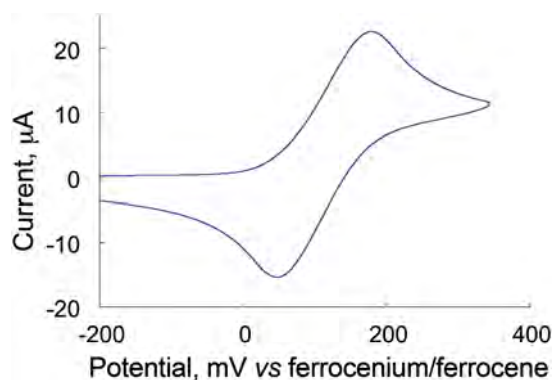


(b)

**Fig. 4.** (a) UV-vis/NIR spectra of 5,15-diphenylporphyrin (solid red line) and 5,15-bis[(*N,N*-bis(4-methoxyphenyl)amino)-10,20-diphenyl]porphyrin **8** (solid blue line) in dichloromethane. (b) Frontier orbitals of **8** estimated by DFT calculation (B3LYP/LanL2DZ) [18]

An aggregation-induced red-shift was excluded by the fact that a zinc analog with an addition of pyridine also underwent a red-shift [20]. The fluorescence was not quenched, but red-shifted in *N,N*-diarylaminoporphyrin [20]. Osuka and Kim demonstrated that the Q-band-like absorption and fluorescence of subporphyrin may also be red-shifted upon the introduction of arylamino and diarylamino substituents at the *meso*-position [16].

Sakamoto also reported that *N,N*-diarylaminoporphyrin displays good redox behavior [18]. Free-base porphyrin tends to show irreversible oxidation in cyclic voltammetry [21]. However, free-base 5,15-bis[(*N,N*-bis(4-methoxyphenyl)amino)-10,20-diphenyl]porphyrin **8** featured a reversible two-electron one-step oxidation process (Fig. 5). This result indicates that the positive charges upon oxidation are distributed chiefly on the



**Fig. 5.** Cyclic voltammogram of 5,15-bis[(*N,N*-bis(4-methoxyphenyl)amino)-10,20-diphenyl]porphyrin **8** (solid blue line) in 0.1 M  $\text{Bu}_4\text{PF}_6$ -dichloromethane at a sweep rate of  $100 \text{ mV}\cdot\text{s}^{-1}$ . Half-wave potential  $E_{1/2}$  is 107 mV ( $2e^-$ ) [18]

diaryl amino substituents, leading to the good stability of the cationic form. This is consistent with the DFT study (Fig. 4b).

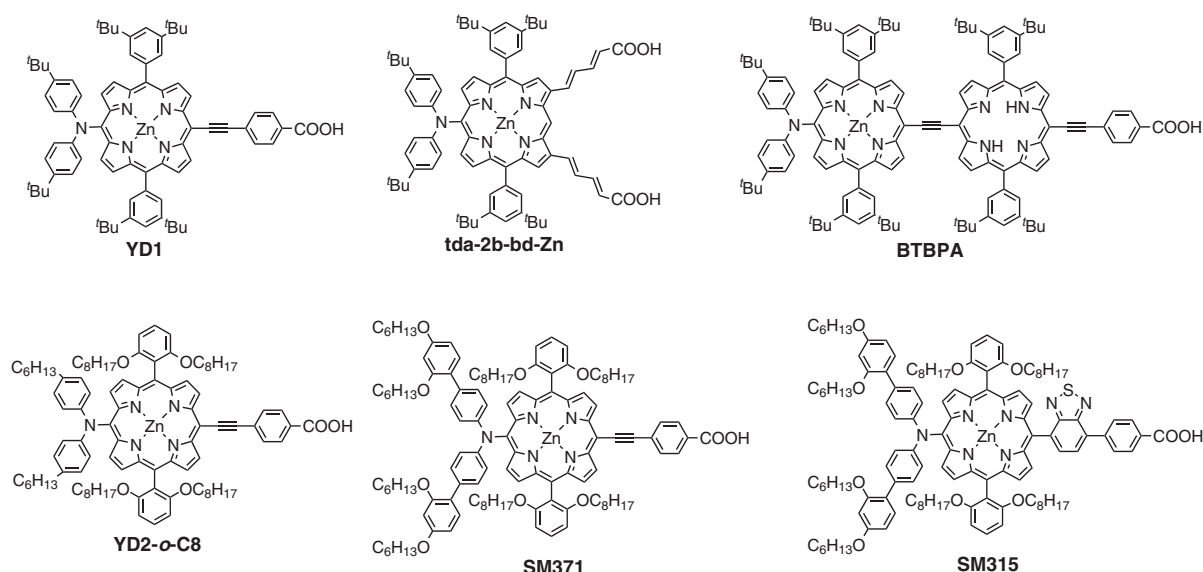
Therefore, arylamino and diarylamino groups are good partners for porphyrinoids, and the reinforced photochemical and electrochemical properties are useful for certain applications, which are described next.

## APPLICATIONS

Extensive studies by Fukuzumi and Imahori have found that porphyrinic compounds are useful for photoinduced charge-separation multiads and photoelectric conversion systems [21]. Porphyrins and related derivatives have also long been studied as potential sensitizers for dye-sensitized solar cells (DSSCs) [22]. As noted in the previous section, an unsubstituted porphyrin shows an intense B-band at 400–450 nm, but only moderate Q-bands at 500–650 nm. Compared with ruthenium complexes, which are often used as sensitizers of DSSCs [23], these narrow bands limit the light harvesting of porphyrin-based dyes. Insufficient light-harvesting and dye aggregation account for the low efficiencies of most of these porphyrin-based dyes. A rational approach to improve the performance of a cell with porphyrin dyes is to extend the  $\pi$ -systems, which broadens and red shifts these absorptions, and thus enhances solar energy acquisition [24].

The organic dyes used in DSSCs often possess donor- $\pi$ -bridge-acceptor (D- $\pi$ -A) molecular structures, and elaborated D- $\pi$ -A structures have been shown to affect the performance of DSSCs [25]. This strategy is also valid in porphyrinic systems [26–28]. Here we focus on D- $\pi$ -A porphyrins with diarylamines as the donor site, and their outstanding performance as DSSC dyes [27, 28].

The application of arylamine-appended porphyrins to DSSCs was initiated by Diau and Yeh [27a,o], who fabricated 12 types of porphyrinic dye. They found that



**Fig. 6.** DSSC dyes based on *N,N*-diarylaminoporphyrim [27a–27e]

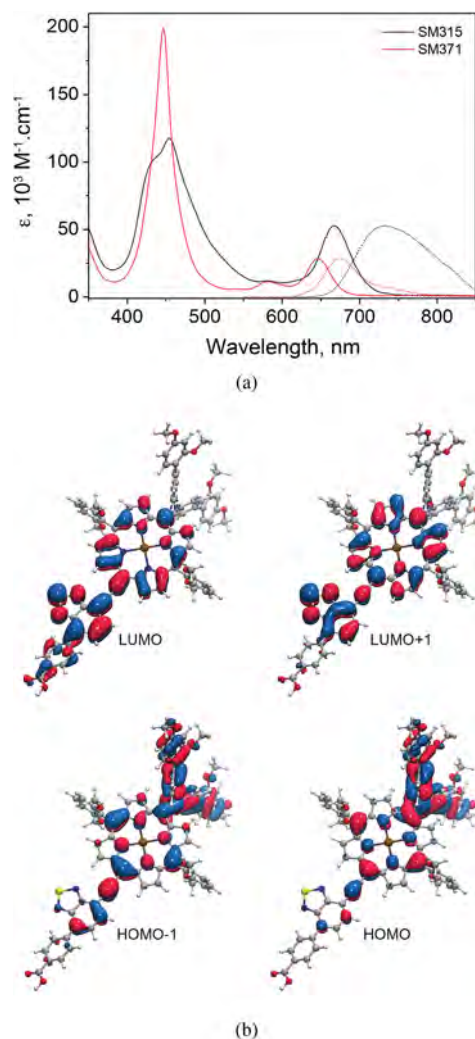
**Table 1.** DSSC parameters for pigments shown in Fig. 6 [27a–27e]

	$J_{SC}$ , mAcm <sup>-2</sup>	$V_{OC}$ , mV	$FF$	PCE, %	Redox mediator
<b>YD1</b>	13.60	701	0.629	6.0	$I_3^-/I^-$
<b>Tda-2b-bd-Zn</b>	18.4	710	0.57	7.47	$I_3^-/I^-$
<b>BTBPA</b>	13.15	541	0.68	4.83	$I_3^-/I^-$
<b>YD2-o-C8</b>	17.3	965	0.71	11.9	[Co(bpy) <sub>3</sub> ] <sup>3+</sup> /[Co(bpy) <sub>3</sub> ] <sup>2+</sup>
<b>SM371</b>	15.9	960	0.79	12.0	[Co(bpy) <sub>3</sub> ] <sup>3+</sup> /[Co(bpy) <sub>3</sub> ] <sup>2+</sup>
<b>SM315</b>	18.1	910	0.78	13.0	[Co(bpy) <sub>3</sub> ] <sup>3+</sup> /[Co(bpy) <sub>3</sub> ] <sup>2+</sup>

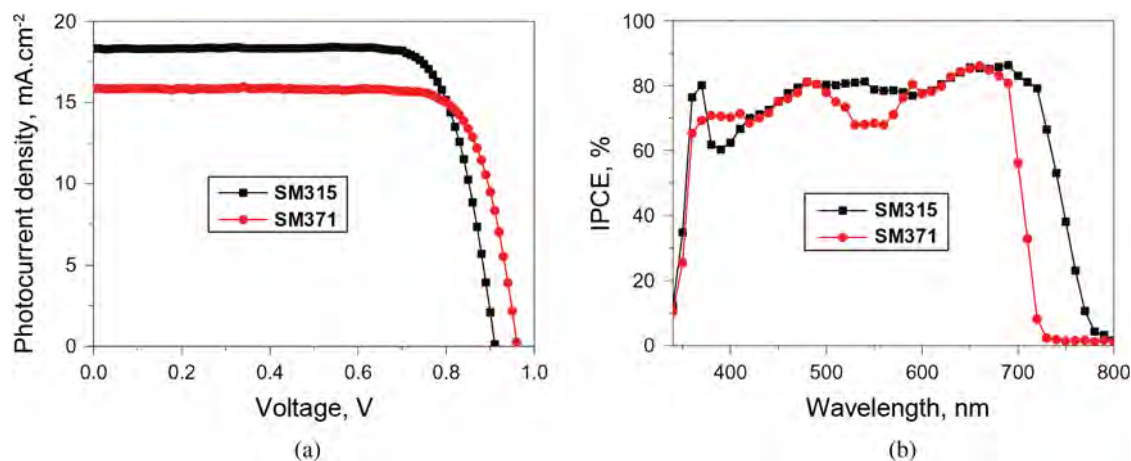
the pull–push porphyrin, **YD1**, comprising a diarylamino group donor at the 5 position and 4-(carboxylphenyl) ethynyl group acceptor at the 15 position (Fig. 6), produced a power conversion efficiency (PCE) of 6.0%, comparable to that of a ruthenium-based N3 dye system. The studies published by Diau and Yeh founded a new area of porphyrinic DSSC dye research that stimulated much subsequent research [27b–z, 28]. Important studies are described here and their DSSC parameters are summarized in Table 1. Sessler, Kim, and Kim introduced 2-propenoic or 2,4-pentadienoic acid at the  $\beta$ -positions, which served as both acceptor and anchoring groups (e.g. **Tda-2b-bd-Zn** in Fig. 6) [27b]. In combination with a scaffold film of anatase TiO<sub>2</sub> spheres, **Tda-2b-bd-Zn** exhibited a PCE of 7.47%. Lin and Segawa fabricated porphyrin dimers, which included the *N,N*-diarylaminoporphyrim motif (e.g. **BTBPA** in Fig. 6) [27c]. Dramatic progress was made by Diau, Yeh, Zakeeruddin and Grätzel [27d], who employed a redox couple of [Co(bpy)<sub>3</sub>]<sup>3+</sup>/[Co(bpy)<sub>3</sub>]<sup>2+</sup> as a redox shuttle (bpy = 2,2'-bipyridine), instead of frequently used I<sub>3</sub><sup>-</sup>/I<sup>-</sup>. As a result, **YD2-o-C8** (Fig. 6) showed a PCE of 11.9% at an incident intensity of AM1.5 solar light of 99.5 mW

cm<sup>-2</sup>. The best result was obtained by Grätzel [27e], and is discussed here in detail. Figure 7a shows the UV-vis/NIR and fluorescence spectra of the dyes **SM371** and **SM315** in THF (Fig. 6). Both pigments feature red-shifted bands in the Q-band region compared with normal porphyrin. The absorption edge of **SM315** reached 750 nm. The authors conducted DFT calculations to elucidate the red-shifted absorptions, and the frontier orbitals of **SM315** are depicted in Fig. 7b. The HOMOs have a substantial contribution from the diarylamino group, while the 4-(benzo[*c*][1,2,5]thiadiazol-4-yl)benzoic acid moiety plays a chief role in the LUMOs. Thus, **SM371** and **SM315** feature a fine D– $\pi$ –A structure: It increased the absorptivity at long wavelengths through charge transfer transitions, and also afforded efficient charge injection. The insertion of proquinoidal, electron-withdrawing 2,1,3-benzothiadiazole in **SM315** efficiently provided stronger D–A interaction than in **SM371**. In addition, 2,1,3-benzothiadiazole broadened the B-band, which then filled the valley between the B and Q-bands, thereby providing more efficient solar acquisition.

The introduction of bulky a diarylamino group and long alkoxy chains in the pigments was expected to reduce



**Fig. 7.** (a) UV-vis/NIR and fluorescence spectra of **SM371** and **SM315** in THF. (b) Frontier orbitals of **SM315** estimated by DFT calculation (M06/IEF-PCM/THF). Reproduced with permission from [27e]. Copyright 2014, Nature Publishing Group



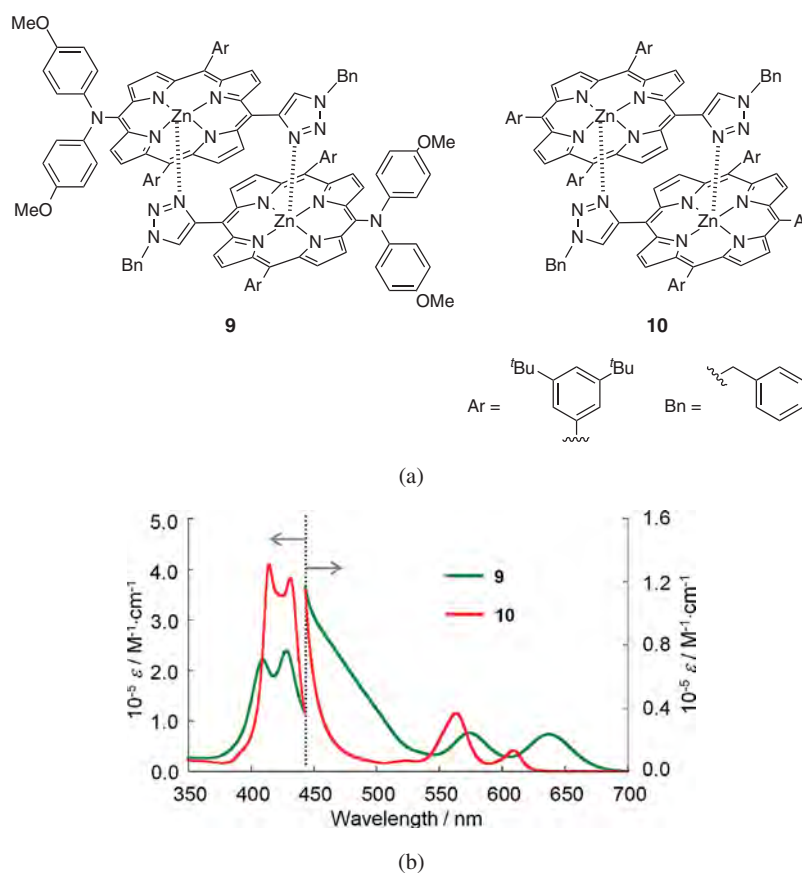
**Fig. 8.** Photovoltaic performance of devices made with **SM371** and **SM315**. (a)  $J$ - $V$  curve under AM 1.5G illumination ( $1000 \text{ W}\cdot\text{m}^{-2}$ ). (b) Photocurrent action spectra for **SM371** (red) and **SM315** (black). Reproduced with permission from [27e]. Copyright 2014, Nature Publishing Group

dye aggregation, which severely degrades the conversion efficiency of a porphyrinic-DSSC system [27f, 28a]. The dye loading on the mesoporous  $\text{TiO}_2$  film was estimated to be  $8.35 \times 10^{-7} \text{ mol}\cdot\text{cm}^{-2}$  for **SM315**. If uniform coverage without aggregation was realized, one **SM315** molecule occupied a  $\text{TiO}_2$ -surface area of  $1.98 \text{ nm}^2$ .

A DSSC cell employing **SM315** or **SM371**, chenodeoxycholic acid as a co-adsorbent,  $[\text{Co}(\text{bpy})_3]^{3+}/[\text{Co}(\text{bpy})_3]^{2+}$  as a redox shuttle, and 0.1 M lithium bis(trifluoromethanesulfonyl)imide and 0.5 M 4-*tert*-butylpyridine in acetonitrile as an electrolyte solution performed well (Fig. 8 and Table 1). Notably, **SM315** achieved an outstanding PCE of 13.0%, which remains, to the best of our knowledge, the best value reported for any type of sensitizer.

Beside the experimental research, theoretical and spectroscopic work has involved computational quantum chemistry for better pigment design, quantification of electron injection and charge recombination kinetics, and elucidation of the electron-injection mechanism upon photoexcitation.<sup>28</sup> Lee proposed that the substitution of a surface-anchoring group with stronger acceptors such as 3-(benzo[*c*][1,2,5]thiadiazol-4-yl)-2-cyanoacrylic acid could afford sensitizers better than **YD2-*o*-C8** [28b]. They would possess a broader absorption range up to 1100 nm due to their smaller HOMO-LUMO gaps. The acceptor group would also lead to a greater contribution to the LUMO, which would aid smooth electron injection to the  $\text{TiO}_2$  electrode.

The reaction center of the photosynthetic system contains a characteristic chlorophyll or bacteriochlorophyll dimer, known as the special pair, which undertakes the initial charge separation in the photosynthesis [29]. The special pairs of some species have slipped cofacial configurations with plane distances of approximately twice the van der Waals radius of an aromatic carbon ( $\sim 3.4 \text{ \AA}$ ) [29a-29d]. Sakamoto fabricated a functional model for



**Fig. 9.** (a) Zinc(II) *N,N*-diarylamino porphyrin dimer **9** and normal zinc(II) porphyrin dimer **10**. UV-vis/NIR spectra of **9** and **10** in dichloromethane [20]

the special pair employing *N,N*-diarylamino porphyrin (**9**, Fig. 9a) [20]. Compared with earlier structure models based on normal porphyrin (e.g. **10** in Fig. 9a) [30], the absorptivity at 450–700 nm was increased and extended (Fig. 9b); this feature is more suitable as a special pair functional model, because the natural pigments, chlorophyll and bacteriochlorophyll, collect light with long wavelengths (600–800 nm) more efficiently than does normal porphyrin. Taking advantage of the stability of the oxidized form of *N,N*-diarylamino porphyrin, the authors reported that there was charge delocalization between the two porphyrin macrocycles in the cationic mixed-valence state  $\mathbf{9}^{+\bullet}$ : They also quantified the off-diagonal coupling matrix element  $H_{ab}$  and the reorganization energy ( $\lambda = 192\text{--}483 \text{ cm}^{-1}$  and  $4600 \text{ cm}^{-1}$ , respectively). Positive charge delocalization after charge separation has been reported for the special pairs in natural systems [31]; however, no such study has been devoted to their structural models. Therefore, the special pair structural model **9** could be a potential functional model.

## CONCLUSION

This review summarized the progress made in the past 15 years in the study of the chemistry of

*meso-N*-arylamino- and *N,N*-diarylamino porphyrinoids. After an introductory note, Section 2 described the preparation procedures of these molecules *via* such as nucleophilic addition of *N*-arylaceto to octaethylporphyrin and subsequent deacetylation, Buchwald–Hartwig amination to *meso*-bromoporphyrin,  $S_NAr$  reactions of *meso*-nitroporphyrin and *meso*-halosubporphyrin, and oxidative electrochemical polymerization of 5-(4-aminophenyl) porphyrin. Oxidative ring-fusion of *meso-N,N*-diarylamino porphyrin to realize better conjugation between the porphyrin macrocycle and diarylamino group was also described. Section 3 discussed the enriched photochemical and electrochemical properties of *meso-N*-arylamino- and *N,N*-diarylamino porphyrinoids. Porphyrin and subporphyrin often suffer from weak absorptivity at longer wavelengths, but the introduction of arylamino and diarylamino groups is shown to improve this drawback. *N,N*-diarylamino porphyrin is also noted to show good durability against oxidation. These characteristics are of significant use in photo- and electro-functional applications. Potential applications using *meso-N,N*-diarylamino porphyrin were examined in Section 4. In combination with the push-pull D– $\pi$ –A molecular structures, *meso-N,N*-diarylamino porphyrin-based pigments have performed very well in DSSCs, and have given rise to the best observed conversion efficiency of 13%. A

slipped cofacial *meso-N,N*-diarylamino porphyrin dimer has been demonstrated to be a structural and functional model for the photosynthesis special pair; it collects solar radiation well and shows good charge delocalization upon oxidation, which is associated with the charge separation event.

### Acknowledgements

The authors acknowledge Grants-in-Aid from MEXT of Japan (nos. 21108002, 24750054, 25107510, 26708005, 26107510, 26620039, areas 2107 [Coordination Programming], 2406 [All Nippon Artificial Photosynthesis Project for Living Earth], 2506 [Science of Atomic Layers]). R.S. is grateful to Ogasawara Foundation for the Promotion of Science & Engineering, The Kao Foundation for Arts and Sciences, The Asahi Glass Foundation, The Noguchi Institute, and Japan Association for Chemical Innovation.

### REFERENCES

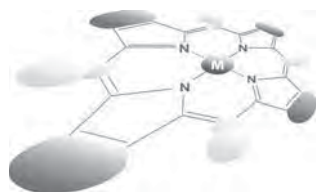
- (a) Kido J, Kimura M and Nagai K. *Science* 1995; **267**: 1332–1334. (b) Grice AW, Bradley DDC, Bernius MT, Inbasekaran M, Wu WW and Woo EP. *Appl. Phys. Lett.* 1998; **73**: 629–631.
- (a) Bach U, Cloedt KD, Spreitzer H and Grätzel M. *Adv. Mater.* 2000; **14**: 1060–1063. (b) Saragi TPI, Spehr T, Siebert A, Fuhrmann-Lieker T and Salbeck J. *Chem. Rev.* 2007; **107**: 1011–1065.
- (a) Chen Y-H, Lin L-Y, Lu C-W, Lin F, Huang Z-Y, Lin H-W, Wang P-H, Liu Y-H, Wong K-T, Wen J, Miller DJ and Darling SB. *J. Am. Chem. Soc.* 2012; **134**: 13616–13623. (b) Wang S, Hall L, Diev VV, Haiges R, Wei G, Xiao X, Djurovich PI, Forrest SR and Thompson ME. *Chem. Mater.* 2011; **23**: 4789–4798.
- (a) Qin H, Wenger S, Xu M, Gao F, Jing X, Wang P, Zakeeruddin SM and Grätzel M. *J. Am. Chem. Soc.* 2008; **130**: 9202–9203. (b) Satoh N, Nakashima T and Yamamoto K. *J. Am. Chem. Soc.* 2005; **127**: 13030–13038.
- (a) Reynolds R, Line LL and Nelson RF. *J. Am. Chem. Soc.* 1974; **96**: 1087–1092. (b) Sandanayaka ASD, Ikeshita K-I, Rajkumar GA, Furusho Y, Araki Y, Takata T and Ito O. *J. Phys. Chem. A* 2005; **109**: 8088–8095.
- (a) Lambert C, Nöll G and Schelter J. *Nat. Mater.* 2002; **1**: 69–73. (b) Sakamoto R, Katagiri S, Maeda H and Nishihara H. *Chem. Lett.* 2013; **42**: 553–555.
- (a) Field JE, Muller G, Riehl JP and Venkataraman D. *J. Am. Chem. Soc.* 2003; **125**: 11808–11809. (b) Hayashi M, Toshimitsu F, Sakamoto R and Nishihara H. *J. Am. Chem. Soc.* 2011; **133**: 14518–14521.
- (a) Rao KP, Kusamoto T, Toshimitsu F, Inayoshi K, Kume S, Sakamoto R and Nishihara H. *J. Am. Chem. Soc.* 2010; **132**: 12472–12479. (b) Sakamoto R, Kume S and Nishihara H. *Chem. Eur. J.* 2008; **14**: 6978–6986.
- Jayaraj K, Gold A, Ball LM and White PS. *Inorg. Chem.* 2000; **39**: 3652–3664.
- Chen Y and Zhang XP. *J. Org. Chem.* 2003; **68**: 4432–4438.
- Balaban MC, Chappaz-Gillot C, Canard G, Fuhr O, Roussel C and Balaban TS. *Tetrahedron* 2009; **65**: 3733–3739.
- Devillers CH, Hebié S, Lucas D, Cattet H, Clément S and Richeter S. *J. Org. Chem.* 2014; **79**: 6424–6434.
- (a) Liddell PA, Gervaldo M, Bridgewater JW, Keirstead AE, Lin S, Moore TA, Moore AL and Gust D. *Chem. Mater.* 2008; **20**: 135–142. (b) Gervaldo M, Liddell PA, Kodis G, Brennan BJ, Johnson CR, Bridgewater JW, Moore AL, Moore TA and Gust D. *Photochem. Photobiol. Sci.* 2010; **9**: 890–900.
- Brennan BJ, Kenney MJ, Liddell PA, Cherry BR, Li J, Moore AL, Thomas A. Moore TA and Gust D. *Chem. Commun.* 2011; **47**: 10034–10036.
- Kitano M, Hayashi S-Y, Tanaka T, Aratani N and Osuka A. *Chem. Eur. J.* 2012; **18**: 8929–8933.
- Shimizu D, Mori H, Kitano M, Cha W-Y, Oh J, Tanaka T, Kim D and Osuka A. *Chem. Eur. J.* 2014; **20**: 16194–16202.
- Fukui N, Cha W-Y, Lee S, Tokuji S, Kim D, Yorimitsu H and Osuka A. *Angew. Chem. Int. Ed.* 2013; **52**: 9728–9732.
- Sakamoto R, Sasaki T, Honda N and Yamamura T. *Chem. Commun.* 2009; 5156–5158.
- Gouterman M. *J. Mol. Spectrosc.* 1961; **6**: 138–163.
- Sakamoto R, Nishikawa M, Kume S, Yamamura T and Nishihara H. *Chem. Commun.* 2010; **46**: 2028–2030.
- (a) Wolberg A and Manassen. *J. Am. Chem. Soc.* 1970; **92**: 2982–2991. (b) Fukuzumi S and Ohkubo K. *Dalton Trans.* 2013; **42**: 15846–15858. (c) Bill NL, Ishida M, Kawashima Y, Ohkubo K, Sung YM, Lynch VM, Lim JM, Kim D, Sessler JL and Fukuzumi S. *Chem. Sci.* 2014; **5**: 3888–3896. (d) Bill NL, Ishida M, Bähring S, Lim JM, Lee S, Davis CM, Lynch VM, Nielsen KA, Jeppesen JO, Ohkubo K, Fukuzumi S, Kim D and Sessler JL. *J. Am. Chem. Soc.* 2013; **135**: 10852–10862. (e) Wijesinghe CA, El-Khouly ME, Zandler ME, Fukuzumi S and D'Souza F. *Chem. Eur. J.* 2013; **19**: 9629–9638. (f) Das SK, Chandra BKC, Ohkubo K, Yamada Y, Fukuzumi S and D'Souza F. *Chem. Commun.* 2013; **49**: 2013–2015. (g) Chandra BKC, Ohkubo K, Karr PA, Fukuzumi S and D'Souza F. *Chem. Commun.* 2013; **49**: 7614–7616. (h) Bandi V, Ohkubo K, Fukuzumi S and D'Souza F. *Chem. Commun.* 2013; **49**: 2867–2869. (i) Kamimura T, Ohkubo K, Kawashima Y, Nobukuni H, Naruta Y, Tani F and Fukuzumi S. *Chem. Sci.* 2013; **4**: 1451–1461.

- (j) El-Khouly ME, Wijesinghe CA, Nesterov VN, Zandler ME, Fukuzumi S and D'Souza F. *Chem. Eur. J.* 2012; **18**: 13844–13853. (k) Chandra BKC, Sushanta KD, Ohkubo K, Fukuzumi S and D'Souza F. *Chem. Commun.* 2012; **48**: 11859–11861. (l) Urbani M, Ohkubo K, Islam DMS, Fukuzumi S and Langa F. *Chem. Eur. J.* 2012; **18**: 7473–7485. (m) Fukuzumi S, Amasaki I, Ohkubo K, Gros CP, Guillard R and Barbe J-M. *RSC Advances*. 2012; **2**: 3741–3747. (n) Ohkubo K, Kawashima Y and Fukuzumi S. *Chem. Commun.* 2012; **48**: 4314–4316. (o) El-Khouly ME, Gutiérrez AM, Sastre-Santos A, Fernández-Lazaro F and Fukuzumi S. *Phys. Chem. Chem. Phys.* 2012; **14**: 3612–3621. (p) Lee S-H, Larsen AG, Ohkubo K, Cai Z-Li, Reimers JR, Fukuzumi S, Maxwell JC. *Chem. Sci.* 2012; **3**: 257–269. (q) Céspedes-Guirao FJ, Ohkubo K, Fukuzumi S, Fernández-Lazaro F and Sastre-Santos A. *Chem. Asian J.* 2011; **6**: 3110–3121. (r) Kanematsu M, Naumov P, Kojima T and Fukuzumi S. *Chem. Eur. J.* 2011; **17**: 12372–12384. (s) Honda T, Nakanishi T, Ohkubo K, Kojima T and Fukuzumi S. *J. Phys. Chem. C*. 2010; **114**: 14290–14299. (t) Takai A, Chkounda M, Eggenspieler A, Gros CP, Lachkar M, Barbe J-M and Fukuzumi S. *J. Am. Chem. Soc.* 2010; **132**: 4477–4489. (u) El-Khouly ME, Ryu JB, Kay K-Y, Ito O and Fukuzumi S. *J. Phys. Chem. C*. 2009; **113**: 15444–15453. (v) El-Khouly ME, Kim J, Kay K-Y, Choi C, Ito O and Fukuzumi S. *Chem. Eur. J.* 2009; **15**: 5301–5310. (w) Céspedes-Guirao FJ, Ohkubo K, Fukuzumi S, Sastre-Santos A and Fernández-Lazaro F. *J. Org. Chem.* 2009; **74**: 5871–5880. (x) Sessler JL, Karnas E, Kim SK, Ou Z, Zhang M, Kadish KM, Ohkubo K and Fukuzumi S. *J. Am. Chem. Soc.* 2008; **130**: 15256–15257. (y) Lee C-H, Guo J, Chen LX and Mandal BK. *J. Org. Chem.* 2008; **73**: 8219–8227. (z) Curiel D, Ohkubo K, Reimers JR, Fukuzumi S and Crossley M. *J. Phys. Chem. Chem. Phys.* 2007; **9**: 5260–5266.
22. (a) Mane SB and Hung C-H. *New J. Chem.* 2014; **38**: 3960–3972. (b) Ohkubo K, Kawashima Y, Sakai H, Hasobe T and Fukuzumi S. *Chem. Commun.* 2013; **49**: 4474–4476. (c) Jia H, Schmid B, Liu S-X, Jaggi M, Monbaron P, Bhosale SV, Rivadehi S, Langford SJ, Sanguinet L, Levillain E, El-Khouly ME, Morita Y, Fukuzumi S and Decurtins S. *ChemPhysChem*. 2012; **13**: 3370–3382. (d) D'Souza F, Amin AN, El-Khouly ME, Subbaiyan NK, Zandler ME and Fukuzumi S. *J. Am. Chem. Soc.* 2012; **134**: 654–664. (e) Zeng Z, Zhang B, Li C, Peng X, Liu X, Meng S, Feng Y. *Dyes and Pigments*. 2014; **100**: 278–285. (f) Hamamura T, Dy JT, Tamaki K, Nakazaki J, Uchida S, Kubo T and Segawa H. *Phys. Chem. Chem. Phys.* 2014; **16**: 4551–4560. (g) Gou F, Jiang Xu, Fang R, Jing H and Zhu Z. *ACS Appl. Mater. Interfaces*. 2014; **6**: 6697–6703. (h) Palomaki PKB, Civic MR and Dinolfo PH. *ACS Appl. Mater. Interfaces*. 2013; **5**: 7604–7612. (i) Sharma GD, Daphnomili D, Angaridis PA, Biswas S and Coutsolelos AG. *Electrochim. Acta*. 2013; **102**: 459–465.
23. (a) Funaki T, Otsuka H, Onozawa-Komatsuzaki N, Kasuga K, Sayama K and Sugihara H. *Inorg. Chem. Commun.* 2014; **46**: 137–139. (b) Funaki T, Kusama H, Onozawa-Komatsuzaki N, Kasuga K, Sayama K and Sugihara H. *Eur. J. Inorg. Chem.* 2014; **2014**: 1303–1311. (c) Shahroosvand H, Abbasi P, Mohajerani E and Janghour M. *Dalton Trans.* 2014; **43**: 9202–9215. (d) Singh SP, Gupta KSV, Chandrasekharam M, Islam A, Han L, Yoshikawa S, Haga M, Roy MS and Sharma GD. *ACS Appl. Mater. Interfaces*. 2013; **5**: 11623–11630. (e) Kinoshita T, Dy JT, Uchida S, Kubo T and Segawa H. *Nature Photonics*. 2013; **7**: 535–539. (f) Koyyada G, Botla V, Thogiti S, Wu G, Li J, Fang X, Kong F, Dai S, Surukonti N, Kotamarthi B and Malapaka C. *Dalton Trans.* 2014; **43**: 14992–15003. (g) Shoker TA and Ghaddar TH. *RSC Adv.* 2014; **4**: 18336–18340. (h) Abrahamsson M, Hedberg JHJ, Becker H-C, Staniszewski A, Pearson WH, Heuer WB and Meyer GJ. *ChemPhysChem*. 2014; **15**: 1154–1163. (i) Hu F-C, Wang S-W, Chi Y, Robertson N, Hewat T, Hu Y, Liu S-H, Chou P-T, Yang P-F and Lin H-W. *ChemPhysChem*. 2014; **15**: 1207–1215. (j) He M, Ji Z, Huang Z and Wu Y. *J. Phys. Chem. C*. 2014; **118**: 16518–16525. (k) Chitumalla RK, Gupta KSV, Malapaka C, Fallahpour R, Islam A, Han L, Kotamarthi B and Singh SP. *Phys. Chem. Chem. Phys.* 2014; **16**: 2630–2640. (l) Wood CJ, Robon KCD, Elliott PLP, Berlinguette CP and Gibson EA. *RSC Adv.* 2014; **4**: 5782–5791. (m) Chandrasekharam M, Kumar CHP, Singh SP, Anusha V, Bhanuprakash K, Islam A and Han L. *RSC Adv.* 2013; **3**: 26035–26046. (n) Zhang B, Xu X, Zhang X, Huang D, Li S, Zhang Y, Zhan F, Deng M, He Y, Chen W, Shen Y and Wang M. *ChemPhysChem*. 2014; **15**: 1182–1189.
24. (a) Ohkubo K, Mase K, Karnas E, Sessler JL, Fukuzumi S. *J. Phys. Chem. C*. 2014; **18**: 18436–18444. (b) Yamada H, Ohkubo K, Kuzuhara D, Takahashi T, Sandanayaka ASD, Okujima T, Ohara K, Ito O, Uno H, Ono N and Fukuzumi S. *J. Phys. Chem. B*. 2010; **114**: 14717–14728. (c) Lu J, Zhang B, Yuan H, Xu X, Cao K, Cui J, Liu S, Shen Y, Cheng Y, Xu J and Wang M. *J. Phys. Chem. C*. 2014; **118**: 14739–14748. (d) Chae SH, Yoo K, Lee YS, Cho MJ, Kim JH, Ko MJ, Lee SJ and Choi DH. *J. Porphyrins Phthalocyanines*. 2014; **18**: 569–578. (e) Kwok EC-H, Chan M-Y, Wong KM-C and Yam VW-W. *Chem. Eur. J.* 2014; **20**: 3142–3153. (f) Chen B, Li X, Wu W, Zha Q and Xie Y. *RSC Adv.* 2014; **4**: 10439–10449. (g) Chen P, Fang Y, Kadish KM, Lewtak JP, Koszelewski D, Janiga A and Gryko DT. *Inorg. Chem.* 2013; **52**: 9532–9538. (h) Campbell MW, Jolley KW, Wagner P, Wagner K, Walsh

- PJ, Gordon KC, Schmidt-Mende L, Nazeeruddin MK, Wang Q, Grätzel M and Officer DL. *J. Phys. Chem. C*. 2007; **111**: 11760–11762. (i) Hayashi S, Tanaka M, Hayashi H, Eu S, Umeyama T, Matano Y, Araki Y and Imahori H. *J. Phys. Chem. C*. 2008; **112**: 15576–15585. (j) Zems Y, Moiseev AG and Perepichka DF. *Org. Lett.* 2013; **15**: 5330–5333. (k) Wang C-L, Hu J-Y, Wu C-H, Kuo H-H, Chang Y-C, Lan Z-J, Wu H-P, Diao EW-G and Lin C-Y. *Energy Environ. Sci.* 2014; **7**: 1392–1396.
25. (a) Fuse S, Sugiyama S, Maitani MW, Wada Y, Ogomi Y, Hayase S, Katoh R, Kaiho T and Takahashi T. *Chem. Eur. J.* 2014; **20**: 10685–10694. (b) Barpuzary D, Patra AS, Vaghasiya JV, Solanki BG, Soni SS, Qureshi M. *ACS Appl. Mater. Interfaces*. 2014; **6**: 12629–12639. (c) Li S-R, Lee C-P, Yang P-F, Liao C-W, Lee MM, Su W-L, Li C-T, Lin H-W, Ho K-C and Sun S-S. *Chem. Eur. J.* 2014; **20**: 10052–10064. (d) Haid S, Marszalek M, Mishra A, Wielopolski M, Teuscher J, Moser J-E, Humphry-Baker R, Zakeeruddin SM, Grätzel M and Bäuerle P. *Adv. Funct. Mater.* 2012; **22**: 1291–1302. (e) Chen H, Huang H, Huang X, Clifford JN, Forneli A, Palomares E, Zheng X, Zheng L, Wang X, Shen P, Zhao B and Tan S. *J. Phys. Chem. C*. 2010; **114**: 3280–3286. (f) Zhao J, Yang X, Cheng M, Li S and Sun L. *ACS Appl. Mater. Interfaces*. 2013; **5**: 5227–5231. (g) Pastore M, Mosconi E and Angelis FD. *J. Phys. Chem. C*. 2012; **116**: 5965–5973. (h) Yella A, Humphry-Baker R, Curchod BFE, Astani NA, Teuscher J, Polander LE, Mathew S, Moser J-E, Tavernelli I, Rothlisberger U, Grätzel M, Nazeeruddin MK and Frey J. *Chem. Mater.* 2013; **25**: 2733–2739. (i) Zhao J, Yang X, Hao Y, Cheng M, Tian J and Sun L. *ACS Appl. Mater. Interfaces*. 2014; **6**: 3907–3914. (j) Katono M, Bessho T, Wielopolski M, Marszalek M, Moser J-E, Humphry-Baker R, Zakeeruddin SM and Grätzel M. *J. Phys. Chem. C*. 2012; **116**: 16876–16884. (k) Wang Z, Wang H, Liang M, Tan Y, Cheng F, Sun Z and Xue S. *ACS Appl. Mater. Interfaces*. 2014; **6**: 5768–5778.
26. (a) Caprasecca S and Mennucci B. *J. Phys. Chem. A*. 2014; **118**: 6484–6491. (b) Oswald F, Islam D-MS, El-Khouly ME, Araki Y, Caballero R, de la Cruz P, Ito O and Langa F. *Phys. Chem. Chem. Phys.* 2014; **16**: 2443–2451. (c) Duvanel G, Grilj J and Vauthey E. *J. Phys. Chem. A*. 2013; **117**: 918–928. (d) Göransson E, Boixel J, Fortage J, Jacquemin D, Becker H-C, Blart E, Hammarström L and Odobel F. *Inorg. Chem.* 2012; **51**: 11500–11512. (e) Hasobe T, Fukuzumi S, Hattori S and Kamat PV. *Chem. Asian J.* 2007; **2**: 265–272. (f) Ince M, Yum J-H, Kim Y, Mathew S, Grätzel M, Torres T and Nazeeruddin MK. *J. Phys. Chem. C*. 2014; **118**: 17166–17170. (g) Hart AS, Chandra BKC, Gobeze HB, Sequeira LR and D'Souza F. *ACS Appl. Mater. Interfaces*. 2013; **5**: 5314–5323.
27. (a) Lee C-W, Lu H-P, Lan C-M, Huang Y-L, Liang Y-R, Yen W-N, Liu Y-C, Lin Y-S, Diao EW-G and Yeh C-Y. *Chem. Eur. J.* 2009; **15**: 1403–1412. (b) Ishida M, Park SW, Hwang D, Koo YB, Sessler JL, Kim DY and Kim D. *J. Phys. Chem. C*. 2011; **115**: 19343–19354. (c) Liu Y, Lin H, Li J, Dy JT, Tamaki K, Nakazaki J, Nakayama D, Nishiyama C, Uchida S, Kubo T and Segawa H. *Phys. Chem. Chem. Phys.* 2012; **14**: 16703–16712. (d) Yella A, Lee H-W, Tsao H-N, Yi C, Chandiran AK, Nazeeruddin MK, Diao EW-G, Yeh C-Y, Zakeeruddin SM and Grätzel M. *Science* 2011; **334**: 629–633. (e) Mathew S, Yella A, Gao P, Humphry-Baker R, Curchod BFE, Ashari-Astani N, Tavernelli I, Rothlisberger U, Nazeeruddin MK and Grätzel M. *Nat. Chem.* 2014; **6**: 242–247. (f) Reddy NM, Pan T-Y, Rajan YC, Guo B-C, Lan C-M, Diao EW-G and Yeh C-Y. *Phys. Chem. Chem. Phys.* 2013; **15**: 8409–8415. (g) Yella A, Mai C-L, Zakeeruddin SM, Chang S-N, Hsieh C-H, Yeh C-Y and Grätzel M. *Angew. Chem. Int. Ed.* 2014; **53**: 2973–2977. (h) Barea EM, González-Pedro V, Ripollés-Sanchis T, Wu H-P, Li L-L, Yeh C-Y, Diao EW-G and Bisquert J. *J. Phys. Chem. C*. 2011; **115**: 10898–10902. (i) Yeh M-H, Lin L-Y, Sun C-L, Leu Y-A, Tsai J-T, Yeh C-Y, Vittal R and Ho K-C. *J. Phys. Chem. C*. 2014; **118**: 16626–16634. (j) Wang Y, Xu L, Wei X, Li X, Agren H, Wu W and Xie Y. *New J. Chem.* 2014; **38**: 3227–3235. (k) Pellejà L, Kumar CV, Clifford JN and Palomares E. *J. Phys. Chem. C*. 2014; **118**: 16504–15509. (l) Mathew S, Tijima H, Toude Y, Umeyama T, Matano Y, Ito S, Thachenko NV, Lemmetyinen H and Imahori H. *J. Phys. Chem. C*. 2011; **115**: 14415–14424. (m) Chandiran AK, Yella A, Stefik M, Heiniger L-P, Comte P, Nazeeruddin MK and Grätzel M. *ACS Appl. Mater. Interfaces*. 2013; **5**: 3487–3493. (n) Kang SH, Choi IT, Kang MS, Eom YK, Ju MJ, Hong JY, Kang HS and Kim HK. *J. Mater. Chem. A*. 2013; **1**: 3977–3982. (o) Hsieh C-P, Lu H-P, Chiu C-L, Lee C-W, Chuang S-H, Mai C-L, Yen W-N, Hsu S-J, Diao EW-G and Yeh C-Y. *J. Mater. Chem.* 2010; **20**: 1127–1134. (p) Ishida M, Hwang D, Koo YB, Sung J, Kim DY, Sessler JL and Kim D. *Chem. Commun.* 2013; **49**: 9164–9166. (q) Kang MS, Choi IT, Kim YW, You BS, Kang SH, Hong JY, Ju MJ and Kim HK. *J. Mater. Chem. A*. 2013; **1**: 9848–9852. (r) Favereau L, Warnan J, Anne FB, Pellegrin Y, Blart E, Jacquemin D and Odobel F. *J. Mater. Chem. A*. 2013; **1**: 7572–7575. (s) Kurotobi K, Toude Y, Kawamoto K, Fujimori Y, Ito S, Chabera P, Sundström V and Imahori H. *Chem. Eur. J.* 2013; **19**: 17075–17081. (t) Bessho T, Zakeeruddin SM, Yeh C-Y, Diao EW-G and Grätzel M. *Angew. Chem. Int. Ed.* 2010; **49**: 6646–6649. (u) Chang Y-G, Wu H-P, Reddy NM, Lee H-W, Lu H-P, Yeh C-Y and Diao EW-G. *Phys. Chem. Chem. Phys.* 2013; **15**: 4651–4655. (v) Kang



- MS, Kang SH, Kim SG, Choi IT, Ryu JH, Ju MJ, Cho D, Lee JY and Kim HK. *Chem. Commun.* 2012; **48**: 9349–9351. (w) Lu H-P, Mai C-L, Tsia C-Y, Hsu S-J, Hsieh C-P, Chiu C-L, Yeh C-Y and Diau EW-G. *Phys. Chem. Chem. Phys.* 2009; **11**: 10270–10274. (x) Liu Y, Lin H, Dy JT, Tamaki K, Nakazaki J, Nakayama D, Uchida S, Kubo T and Segawa H. *Chem. Commun.* 2011; **47**: 4010–4012. (y) Lu H-P, Tsai C-P, Yen W-N, Hsieh C-P, Lee C-W, Yeh C-Y and Diau EW-G. *J. Phys. Chem. C.* 2009; **113**: 20990–20997. (z) Imahori H, Matsubara Y, Iijima H, Umeyama T, Matano Y, Ito S, Niemi M, Tkachenko NV and Lemmetyinen H. *J. Phys. Chem. C.* 2010; **114**: 10656–10665.
28. (a) Hsu H-Y, Chiang H-C, Hu J-Y, Awasthi K, Mai C-L, Yeh C-Y, Ohta N and Diau EW-G. *J. Phys. Chem. C.* 2013; **117**: 24761–24766. (b) Karthikeyan S and Lee JY. *J. Phys. Chem. A.* 2013; **117**: 10973–10979. (c) Ørnsø KB, Garcia-Lastra JM and Thygesen KS. *Phys. Chem. Chem. Phys.* 2013; **15**: 19478–19486. (d) Pratik SM and Datta A. *Phys. Chem. Chem. Phys.* 2013; **15**: 18471–18481. (e) Ju M-G and Liang W. *J. Phys. Chem. C.* 2013; **117**: 14899–14911. (f) Ørnsø KB, Pedersen CS, Garcia-Lastra JM and Thygesen KS. *Phys. Chem. Chem. Phys.* 2014; **16**: 16246–16254. (g) Santhana-moorthi N, Lo C-M and Jiang J-C. *J. Phys. Chem. Lett.* 2013; **4**: 524–530. (h) Bahers TL, Brémond E, Ciofini I and Adamo C. *Phys. Chem. Chem. Phys.* 2014; **16**: 14435–14444. (i) Han L-H, Zhang C-R, Zhe J-W, Jin N-Z, Shen Y-L, Wang W, Gong J-J, Chen Y-H and Liu Z-J. *Int. J. Mol. Sci.* 2013; **14**: 20171–20188. (j) Yang F, Zhang Z and He X. *Dalton Trans.* 2013; **42**: 13874–13881. (k) Liu Y, Lin H, Dy JT, Tamaki K, Nakazaki J, Nishiyama C, Uchida S, Segawa H and Li J. *J. Phys. Chem. C.* 2014; **118**: 1426–1435.
29. (a) Deisenhofer J, Epp O, Miki K, Huber R, Michel H. *Nature.* 1985; **318**: 618–623. (b) Deisenhofer J and Michel H. *Science.* 1989; **245**: 1463–1473. (c) Feher G, Allen JP, Okamura MY and Rees DC. *Nature.* 1989; **339**: 111–116. (d) Jordan P, Fromme P, Witt HT, Kukas O, Saenger W and Krauss N. *Nature.* 2001; **411**: 909–917. (e) Zouni A, Witt H-T, Kern J, Fromme P, Krauss N, Saenger W and Orth P. *Nature.* 2001; **409**: 739–743.
30. (a) Kobuke Y and Miyaji H. *J. Am. Chem. Soc.* 1994; **116**: 4111–4112. (b) Kobuke Y and Ogawa K. *Bull. Chem. Soc. Jpn.* 2003; **76**: 689–708. (c) Ozeki H, Nomoto A, Ogawa K, Kobuke Y, Murakami M, Hosoda K, Ohtani M, Nakashima S, Miyasaka H and Okada T. *Chem. Eur. J.* 2004; **10**: 6393–6401. (d) Morisue M, Haruta N, Kalita D and Kobuke Y. *Chem. Eur. J.* 2006; **12**: 8123–8135. (e) Nakagawa H, Ogawa K, Satake A and Kobuke Y. *Chem. Commun.* 2006; **14**: 1560–1562. (f) Stibrany RT, Vasudevan J, Knapp S, Potenza JA, Emge T and Schugar HJ. *J. Am. Chem. Soc.* 1996; **118**: 3980–3981. (g) Matano Y, Matsumoto K, Terasaka Y, Hotta H, Araki Y, Ito O, Shiro M, Sasamori T, Tokitoh N and Imahori H. *Chem. Eur. J.* 2007; **13**: 891–901. (h) Maeda C, Yamaguchi S, Ikeda C, Shinokubo H and Osuka A. *Org. Lett.* 2008; **10**: 549–552.
31. (a) Lin X, Murchisson HA, Nagarajan V, Parson WW, Allen JP and Williams JC. *Proc. Natl. Acad. Sci. U.S.A.* 1994; **91**: 10265–10269. (b) Artz K, Williams JC, Allen JP, Lenzian F, Rautter J and Lubitz W. *Proc. Natl. Acad. Sci. U.S.A.* 1997; **94**: 13582–13587. (c) Müh F, Lenzian F, Roy M, Williams JC, Allen JP and Lubitz W. *J. Phys. Chem. B* 2002; **106**: 3226–3236. (d) Reimers JR and Hush NS. *J. Am. Chem. Soc.* 2004; **126**: 4132–4144. (e) Kanchana-wong P, Dahlbom MG, Treynor TP, Reimers JR, Hush NS and Boxer SG. *J. Phys. Chem. B.* 2006; **110**: 18688–18702.



# Molecular assemblies based on strong axial coordination in metal complexes of saddle-distorted dodecaphenylporphyrins

Tomoya Ishizuka<sup>a</sup>†, Shunichi Fukuzumi<sup>b</sup>† and Takahiko Kojima<sup>\*a</sup>†

<sup>a</sup> Department of Chemistry, Graduate School of Pure and Applied Sciences, University of Tsukuba, 1-1-1 Tennoudai, Tsukuba, Ibaraki 305-8571, Japan

<sup>b</sup> Department of Material and Life Science, Graduate School of Engineering, Osaka University and ALCA, Japan Science and Technology Agency (JST), 2-1 Yamada-oka, Suita, Osaka 565-0871, Japan

*Dedicated to Professor Shunichi Fukuzumi on the occasion of his retirement*

Received 20 November 2014

Accepted 15 December 2014

**ABSTRACT:** In this mini-review, we have highlighted our works on metal complexes having saddle-distorted dodecaphenylporphyrin (DPP) and its derivative as ligands in the light of enhancement of the Lewis acidity of a metal center coordinated by the porphyrin. The important point through this mini-review is ill-overlap of the out-of-plane lone pairs of pyrrole nitrogen atoms with  $\sigma$ -orbitals of the metal center bound to the saddle-distorted porphyrin core. The enhanced Lewis acidity of the central metal ions enabled us to construct stable molecular complexes through axial coordination using metal–DPP (M(DPP)) moieties (M = Mo<sup>V</sup> or Sn<sup>IV</sup>) and molecular or ionic entities with Lewis-basic coordination sites, including Keggin-type polyoxometallates (POM), which are known to have weak Lewis basicity and thus hard to coordinate to metal ions. A discrete 1:2 complex with a Ru-substituted POM performs catalytic substrate oxidation reactions in organic solvents. A 1:1 complex between Sn<sup>IV</sup>(DPP) and a Keggin-type POM exhibited photoinduced electron transfer, in which the Sn<sup>IV</sup>(DPP) moiety acts as an electron donor and the POM as an electron acceptor. Besides POM, other electron acceptors, including  $\mu_3$ -oxo trinuclear Ru<sup>III</sup> clusters and anthraquinone, having carboxyl groups as a linker unit also formed stable complexes with DPP-metal complexes as axial ligands to perform photoinduced electron transfer. Successful photoreactions of the M(DPP)-acceptor complexes are mainly enabled by the enhanced Lewis acidity of the DPP-metal complexes for the stabilization of the assemblies and also by lowering the oxidation potential of the porphyrin ligand to gain larger driving force of electron transfer to form an electron-transfer state with avoiding intersystem crossing. The stability and photochemical behavior are in sharp contrast to those for metal complexes with planar porphyrins as ligands.

**KEYWORDS:** dodecaphenylporphyrin, saddle-type distortion, Lewis acidity, axial coordination, polyoxometallates, photoinduced electron transfer.

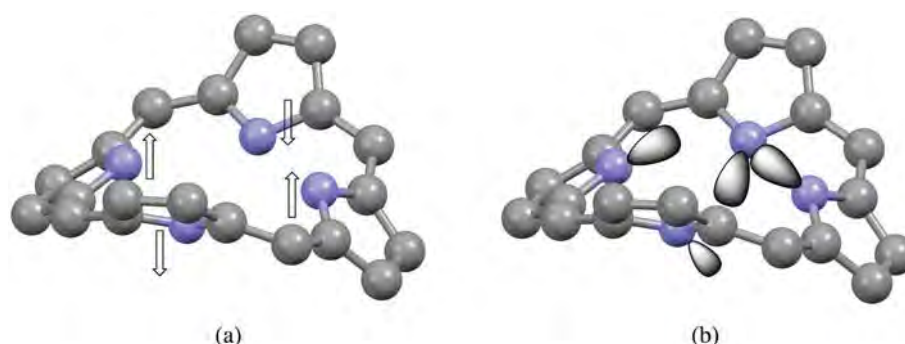
## INTRODUCTION

Porphyrin molecules are generally considered to be rigid and highly planar. However, the introduction

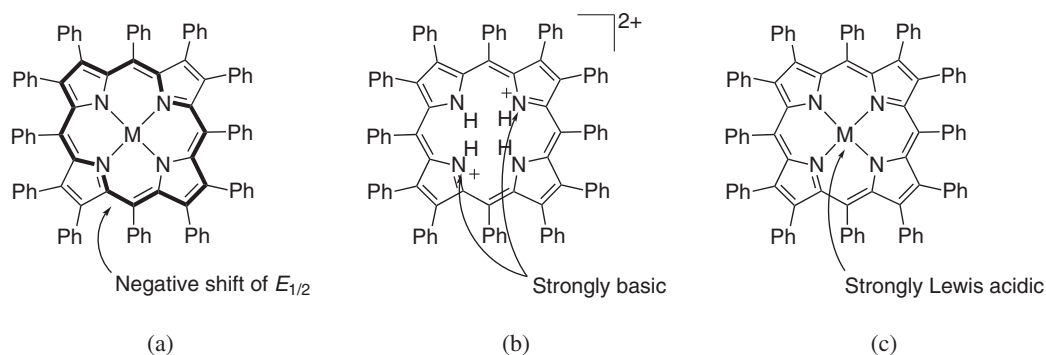
of substituents at the periphery or insertion of size-mismatched metal ions into the core can cause conformational distortion of the porphyrin ring. Among the various distortion types of the porphyrin skeleton, distortion showing the alternatively tilting of the four pyrrole rings is classified to saddle-type distortion (Fig. 1a) [1]. Saddle-distorted porphyrins have been intensively investigated due to relevance

†SPP full member in good standing

\*Correspondence to: Takahiko Kojima, e-mail: kojima@chem.tsukuba.ac.jp



**Fig. 1.** (a) Schematic description of the distortion manner of saddle-type porphyrins relative to a planar conformation. (b) Schematic description of the lone pairs of pyrrole nitrogen atoms lying out-of-plane directions



**Fig. 2.** Schematic description of characteristics of saddle-distorted porphyrins

of heme proteins [2], whose porphyrin rings mainly exhibit the saddle distortion [3]. The most facile method to obtain deeply saddle-distorted porphyrins is introduction of eight substituents at the eight  $\beta$ -positions of 5,10,15,20-tetraphenylporphyrin (TPP) [4, 5]. Among the octa- $\beta$ -substituted TPPs, 2,3,5,7,8,10,12,13,15,17,18,20-dodecaphenylporphyrin (DPP) is the representative and most intensively studied [6, 7].

Saddle-distortion of porphyrins causes various characteristics of the porphyrin properties on the basis of the out-of-plane lone pairs of pyrrole nitrogen atoms (Fig. 1b). For example, negative shifts of the redox potentials of the porphyrin ligands were observed for metal complexes (Fig. 2a) [8], due to ill-overlap of the lone-pair orbitals of the pyrrole nitrogen atoms with empty  $\sigma$ -orbitals of the metal center to reduce the electron donation to the central metal ion, making the porphyrin ring more electron-rich than the planar counterpart. The negative shift of the redox potentials of the porphyrin ring significantly affects the electron-transfer rates [9] — the metal-DPP complex moiety can act as a good electron donor due to lower oxidation potentials than those of metal complexes with usual planar porphyrins. In addition, the inner pyrrolic nitrogen atoms turn to be highly basic by the saddle distortion and the  $pK_a$  was reported to reach over 13 (Fig. 2b) [10].

The diprotonated saddle-distorted porphyrin ( $H_4DPP^{2+}$ , Fig. 2b) can strongly bind anions such as chloride ion and carboxylate ions by the hydrogen bonding and we utilized the hydrogen bonds to construct supramolecular systems to observe photoinduced electron transfer [11–13].

The saddle-distortion of a porphyrin ligand caused by the peripheral substituents affords discrepancy between the direction of the lone pairs of pyrrolic nitrogen atoms and that of the  $\sigma$ -orbitals of the central metal ions (Fig. 1b). As a result, the  $\sigma$ -donation from the pyrrolic nitrogen to the central metal ions becomes weak, and consequently, the Lewis acidity of the central metal ions should be enhanced (Fig. 2c). By virtue of the enhanced Lewis acidity of the central metal ions, various metal complexes can be formed even with relatively weak Lewis bases as axial ligands. In addition, photoinduced electron transfer occurs from the DPP-metal complex as an electron donor to the axially ligated electron acceptor without the dissociation reaction due to the strong binding. In this article, among various interesting properties of saddle-distorted porphyrins, we focus on the enhancement of the Lewis acidity of the central metal ions due to the saddle-distortion toward construction of unique discrete molecular assemblies based on the strengthened axial coordination.

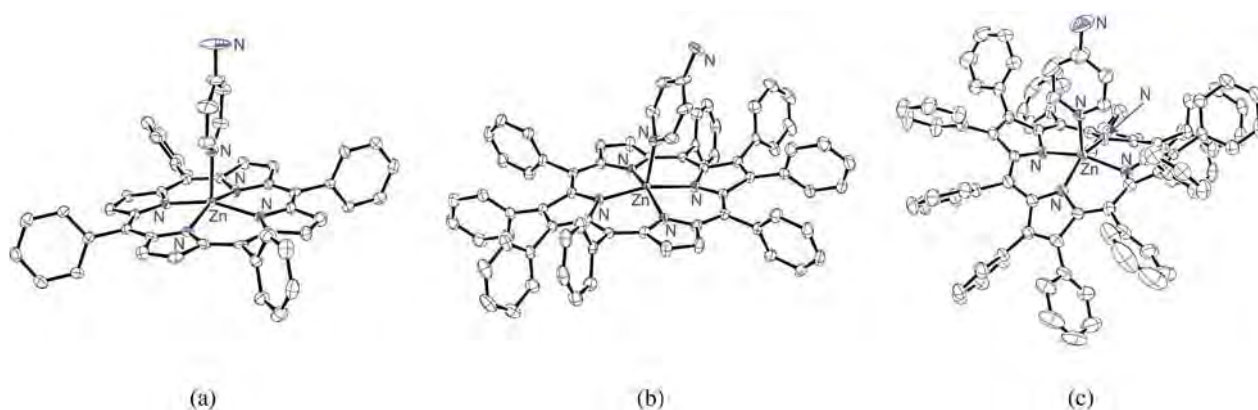
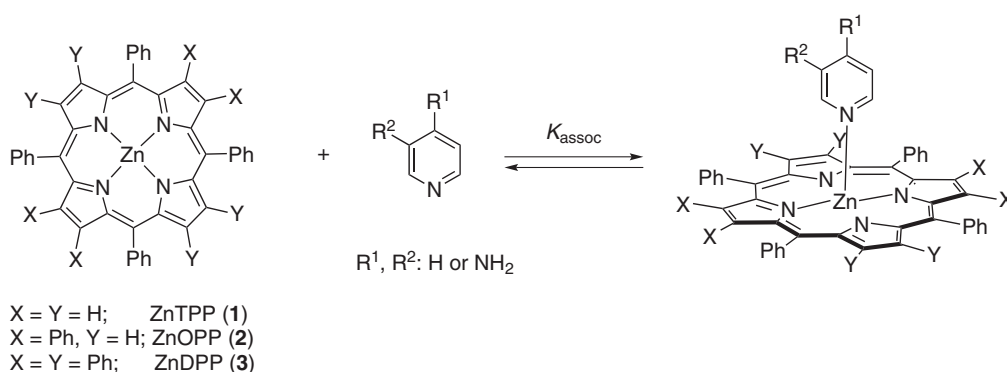


Fig. 3. Crystal structures of 1-4-AP (a) 2-4-AP (b) and 3-4-AP (c)



Scheme 1. Binding of pyridine derivatives to Zn(II)-porphyrins

Table 1. Binding constants ( $K_{\text{assoc}}$ ) between  $\text{Zn}^{\text{II}}$ (porphyrinato) complexes and pyridine derivatives [14]

$\text{Zn}^{\text{II}}$ (porphyrinato)	$K_{\text{assoc}}, \text{M}^{-1}$		
	py	3-AP	4-AP
1	$(1.1 \pm 0.1) \times 10^4$	$(1.8 \pm 0.1) \times 10^4$	$(9.2 \pm 0.4) \times 10^4$
2	$(1.4 \pm 0.2) \times 10^4$	$(3.2 \pm 0.5) \times 10^4$	$(2.5 \pm 0.2) \times 10^5$
3	$(4.6 \pm 0.2) \times 10^4$	$(1.1 \pm 0.0) \times 10^5$	$(6.2 \pm 0.0) \times 10^5$

## ENHANCEMENT OF THE LEWIS ACIDITY OF THE CENTRAL METAL IONS WITH SADDLE-DISTORTED COORDINATION ENVIRONMENT

In order to confirm the effect of the saddle-distortion of porphyrin ligands on the Lewis acidity of the central metal ions, spectroscopic titration has been performed to the  $\text{CH}_2\text{Cl}_2$  solutions of the  $\text{Zn}^{\text{II}}$  complexes of three types of porphyrin ligands with pyridine derivatives to observe the axial ligation (Scheme 1) [14]. Here, TPP, 2,3,5,10,12,13,15,20-octaphenylporphyrin (OPP), and DPP have been employed as the porphyrin ligands, and

pyridine (py), 3-aminopyridine (3-AP), and 4-aminopyridine (4-AP) as the axial ligands. The mean deviations of the core 24 atoms from the least-square plane, estimated from the crystal structure of each the 4-AP-adduct (Fig. 3), were 0.008 Å for ZnTPP (1), 0.011 Å for ZnOPP (2), and 0.049 Å for ZnDPP (3) [14]. Thus, the degree of distortion of the porphyrin core is in the order of  $1 \sim 2 \ll 3$ . Additionally, the central  $\text{Zn}^{\text{II}}$  ions deviate from the porphyrin plane to the direction of the axial ligand and the displacements are calculated to be 0.364, 0.314, and 0.471 Å for 1, 2 and 3, respectively.

The structures of the pyridine adducts of three kinds of  $\text{Zn}^{\text{II}}$ (porphyrinato) units were elucidated by  $^1\text{H}$  NMR

spectroscopy at low temperatures and the up-field shifts of the  $^1\text{H}$  NMR signals for the pyridine derivatives were observed due to the ring current effect of the porphyrin ligands [14]. The association constants ( $K_{\text{assoc}}$ ) between the three  $\text{Zn}^{\text{II}}$  complexes and the three pyridine derivatives are summarized in Table 1. The  $K_{\text{assoc}}$  values are in the order of  $1 < 2 < 3$  commonly for all of the three axial ligands, and the ratio of the  $K_{\text{assoc}}$  values is roughly estimated as  $1:2:3 = 1:2.1:5.9$ . The slight difference in the  $K_{\text{assoc}}$  values between **1** and **2** probably derives from the electron-withdrawing effect of the  $\beta$ -phenyl groups of the OPP ligand, because the planarity of the porphyrin core is not altered significantly between **1** and **2**. In contrast, the larger  $K_{\text{assoc}}$  values for **3** can be ascribed to the enhanced Lewis acidity of the  $\text{Zn}^{\text{II}}$  center caused by the saddle distortion of the porphyrin core [15].

## CONSTRUCTION OF DISCRETE MOLECULAR ASSEMBLIES BASED ON STRENGTHENED AXIAL COORDINATION

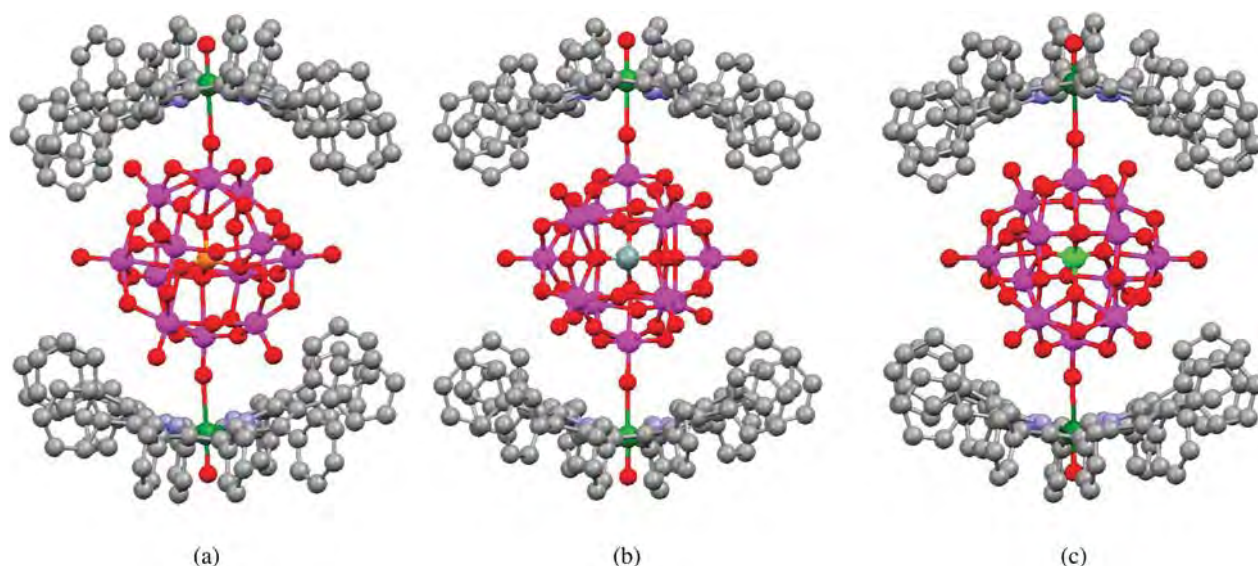
### Discrete 2:1 complex with Keggin-type polyoxometallates: porphyrin hamburgers

Polyoxometallates (POMs) have attracted considerable attention for decades due to the interests in the catalytic and optoelectronic applications [16, 17]. Although POMs generally bear large negative charges, the Lewis basicity is not quite high [18], because the negative charge is delocalized on the several oxo ligands in the POM framework. Recently, we have applied the enhanced Lewis acidity of the central metal ions bound

to DPP to construction of stable and discrete molecular assemblies including POMs as axial ligands of the  $\text{M}(\text{DPP})$  complexes (*vide infra*).

A class of POMs, which can be depicted with the general formula of  $[\text{XW}_{12}\text{O}_{40}]^{n-}$  (X represents a heteroatom), are known as Keggin-type POMs. The Keggin-type POMs have been used to construct nano-structured ionic crystals for guest sorption, catalysts, and molecular magnets [19]. Upon condensation of the  $[\text{Mo}^{\text{V}}(\text{DPP})(\text{O})(\text{H}_2\text{O})]^+$  (**4**) with  $[\text{XW}_{12}\text{O}_{40}]^{n-}$  (X = P,  $n = 3$  (**5**); X = Si,  $n = 4$  (**6**); X = B,  $n = 5$  (**7**)) in an ethyl acetate/ $\text{CH}_3\text{CN}$  mixed solvent, crystals of discrete 2:1 complexes with  $[\text{Mo}^{\text{V}}(\text{DPP})(\text{O})]^+$  cation and  $[\text{H}_m\text{XW}_{12}\text{O}_{40}]^{n-}$  anions (X = P,  $m = 1$ ,  $n = 2$  (**8**); X = Si,  $m = 2$ ,  $n = 2$  (**9**); X = B,  $m = 1$ ,  $n = 4$  (**10**)). For the case of the complex **10** with  $[\text{HBW}_{12}\text{O}_{40}]^{4-}$ , the charge valance was completed by including two TBA cations [20]. The structures of 2:1 complexes **8–10** were explicitly determined by the X-ray diffraction analysis (Fig. 4). The discrete 2:1 complexes composed of two of curved  $[\text{Mo}^{\text{V}}(\text{DPP})(\text{O})]^+$  units and one sandwiched Keggin-type POM have been named as *Porphyrin Hamburgers*. The conformational distortion of the DPP ligand in the *Porphyrin Hamburgers* has been changed from the saddle-type distortion to the ruffle one due to steric repulsion among the peripheral phenyl groups and terminal oxo groups of POMs. In the *Porphyrin Hamburgers*, the polyoxometallates coordinate directly to the  $\text{Mo}^{\text{V}}$  centers in the  $[\text{Mo}^{\text{V}}(\text{DPP})(\text{O})]^+$  units through two of terminal oxo groups by replacing the aqua ligand, where the strengthened Lewis acidity of the  $\text{Mo}^{\text{V}}$  center in the DPP coordination environment stabilizes the complexation.

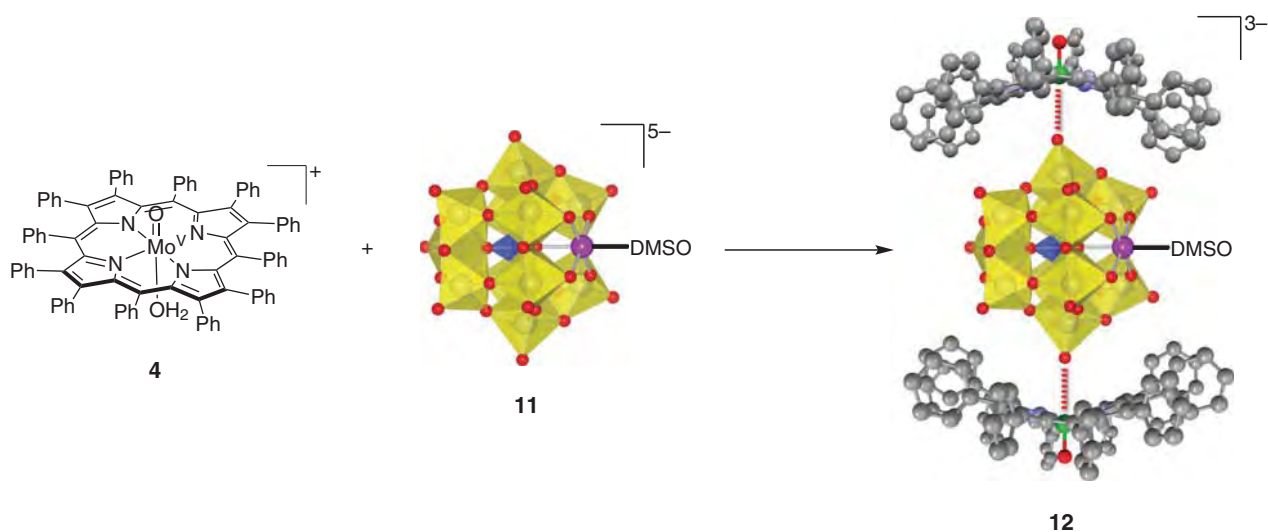
To confirm whether the 2:1 complexes maintain the structures even in solution, MALDI-TOF-MS spectra of the solutions in  $\text{CH}_2\text{Cl}_2$  were measured in the negative



**Fig. 4.** Crystal structures of *Porphyrin Hamburgers*: **8** (a), **9** (b), and the anion moiety of **10** (c). Gray, carbon; blue, nitrogen; red, oxygen; green, molybdenum; pink, tungsten; orange, phosphorus; dark gray, silicon; light green, boron

**Table 2.** Redox potentials of the 2:1 complexes **8–10** in PhCN in the presence of 0.1 M TBAPF<sub>6</sub> at room temperature [20b]

Compound	$E_{1/2}$ , V vs. SCE						
	POM <sup>6-</sup> /POM <sup>5-</sup>	P <sup>4-</sup> /P <sup>3-</sup>	P <sup>3-</sup> /P <sup>2-</sup>	POM <sup>5-</sup> /POM <sup>4-</sup>	POM <sup>4-</sup> /POM <sup>3-</sup>	Mo <sup>V</sup> /Mo <sup>IV</sup>	P <sup>2-</sup> /P <sup>•-</sup>
<b>8</b>		-1.47	-1.12	-0.82	-0.31	+0.06	+1.29
<b>9</b>		-1.41	-1.04	-0.87		0.00	+1.26
<b>10</b>	-1.49 <sup>a</sup>	-1.49 <sup>a</sup>	-1.12			-0.10	+1.16
(TBA) <sub>3</sub> - <b>5</b>				-1.04	-0.49		
(TBA) <sub>4</sub> - <b>6</b>	-1.51			-0.97			
(TBA) <sub>5</sub> - <b>7</b>	-1.52						
<b>4</b> -ClO <sub>4</sub>		-1.42	-1.03			+0.03	+1.28

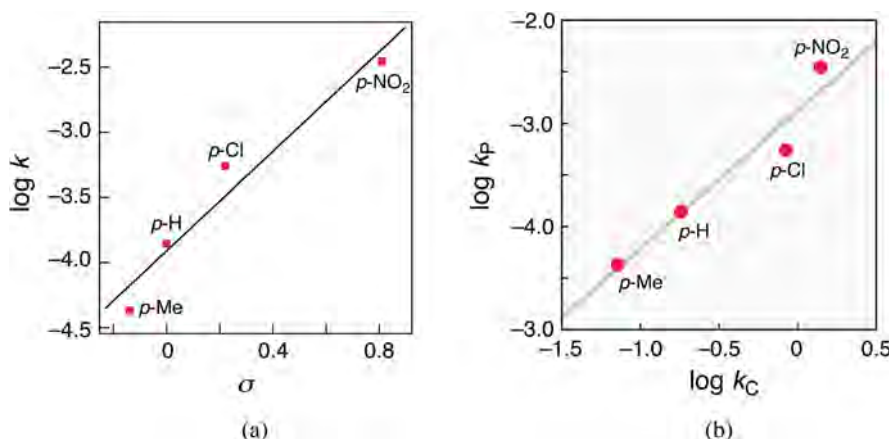
**Fig. 5.** Synthesis of the 2:1 complex **12**. Gray, carbon; light blue, nitrogen; red, oxygen; green, molybdenum; blue, silicon; purple, ruthenium. The tungsten atoms sit at the centers of yellow octagons consisting of oxygen atoms

mode. Peak clusters were observed at 5543.9 for **8** (calcd. for [M – H]: 5544.55), 5542.1 for **9** (calcd. for [M – H]: 5542.00), and 5525.8 for **10** (calcd. for [M + H – 2TBA]: 5526.36). Additionally, the redox potentials of the *Porphyrin Hamburgers* in PhCN exhibited slight shifts relative to those of the components, *i.e.* **4** and POMs used. These results also support the formation of the 2:1 complexes in solution (Table 2). For example, complex **9** exhibited five reversible redox waves at -1.41, -1.04, -0.87, -0.00, and +1.26 V vs. SCE; the first and the second waves are assignable to the reduction processes of the DPP moieties (DPP<sup>4-</sup>/DPP<sup>3-</sup> and DPP<sup>3-</sup>/DPP<sup>2-</sup>), the third is 1e<sup>-</sup> reduction of the [H<sub>2</sub>SiW<sub>12</sub>O<sub>40</sub>]<sup>2-</sup> moiety, the fourth is derived from the Mo<sup>V</sup>/Mo<sup>IV</sup> couple in the [Mo<sup>V</sup>(DPP)(O)]<sup>+</sup> unit, and the last is due to the DPP<sup>2-</sup>/DPP<sup>•-</sup> couple. To compare the redox potentials of the components, the reduction potentials of the DPP moieties in **9** were negatively shifted by 50~90 mV relative to those of the Mo<sup>V</sup>(DPP) complex, whereas the first reduction potential of the POM moiety was positively shifted by 100 mV

in comparison with that of (TBA)<sub>4</sub>-**6**. These shifts indicate that the POM moieties donate the lone pairs to the Mo<sup>V</sup>(DPP) moieties to form the 2:1 complex, and consequently, the POM moiety becomes electron-poor and the Mo<sup>V</sup>(DPP) moieties turns to be electron-rich [20].

### Substrate oxidation with a Ru-substituted polyoxometallate in the discrete 2:1 complex

Insertion of a transition metal into a lacunary-type POM has been intensively studied due to interest for preparation of efficient catalysts [21]. However, such POMs are generally insoluble in organic solvents and thus they are not usable for the reactions in organic solvents. Recently, we have succeeded in the incorporation of a Ru-substituted Keggin-type POM, [SiW<sub>11</sub>O<sub>39</sub>Ru<sup>III</sup>(DMSO)]<sup>5-</sup> (Ru-POM, **11**) [22], into the *Porphyrin Hamburger* structure to generate (TBA)<sub>3</sub>[{Mo(DPP)(O)}<sub>2</sub>{SiW<sub>11</sub>O<sub>39</sub>Ru(DMSO)}] (**12**) (Fig. 5) [23]. The condensation reaction of **4** and **11** was performed in a mixed solvent of CH<sub>2</sub>Cl<sub>2</sub>/CH<sub>3</sub>CN



**Fig. 6.** (a) A Hammett plot for the pseudo-first-order rate constants of oxidations of benzyl alcohol derivatives by **12** as a catalyst and PhIO in  $\text{CDCl}_3$ . (b) Plot of logarithm of the pseudo-first-order rate constants of the catalytic oxidation of benzyl alcohols with **12** ( $k_p$ ) at room temperature vs. logarithm of the second-order rate constants of H-atom abstraction from benzyl alcohols by CumOO ( $k_c$ ) at 183 K

and the MALDI-TOF-MS spectrum of the recrystallized sample of **12** from the solution in a  $\text{CH}_2\text{Cl}_2$ /hexane mixed solvent exhibited a peak cluster at 5444.7, ascribable to the signal derived from  $[\mathbf{12} - \text{DMSO} - 3\text{TBA} + 2\text{H}^+]^-$  ion (calcd. 5444.30). In complex **12**, the DMSO molecule is still coordinated to the  $\text{Ru}^{\text{III}}$  center as evidenced by the IR spectra showing a band at  $1100\text{ cm}^{-1}$  assignable to the S=O stretching. In the EPR spectrum of **12** in  $\text{CH}_2\text{Cl}_2$  at 5 K, two signals were observed around  $g = 2.00$ ; one of the two exhibited an anisotropic splitting at  $g_x = 2.297$  and  $g_y = 2.206$  ( $g_z$  signal was overlapped on the other signal and thus not to be determined the  $g$  value), which is typical for a  $\text{Ru}^{\text{III}}$  ( $S = 1/2$ ) species, and the other is isotopic signal observed at  $g = 1.964$ , assignable to the  $\text{Mo}^{\text{V}}$  ion ( $S = 1/2$ ) in the  $[\text{Mo}^{\text{V}}(\text{DPP})(\text{O})]^+$  moieties. The double integration of each the EPR signal indicates the existence ratio of the  $\text{Ru}^{\text{III}}$  and  $\text{Mo}^{\text{V}}$  ions as 1:2.

Upon addition of iodobenzene (PhIO) to the solution of **12** in  $\text{CH}_2\text{Cl}_2$ , EPR spectroscopy at 5 K allowed us to observe that the signal assigned to the  $\text{Ru}^{\text{III}}$  center completely disappeared and only the signal derived from the  $\text{Mo}^{\text{V}}$  centers remained. This EPR spectral change suggests that the reaction of **12** with PhIO gives the corresponding  $\text{Ru}^{\text{IV}}=\text{O}$  ( $S = 1$ ) species (**13**), which should be EPR-silent. To explore the reactivity of **13** in substrate oxidation reactions, catalytic oxidation reactions of benzyl alcohol and the derivatives were performed in  $\text{CDCl}_3$  in the presence of **12** as the catalyst and PhIO as the sacrificial oxidant. As a result, after stirring for 6 h, the  $^1\text{H}$  NMR signals of the corresponding benzaldehyde were observed as the sole product. In contrast, in the absence of **12** or with using  $4\text{-ClO}_4$  or  $(\text{TBA})_5\text{-11}$  as catalysts instead of **12**, the signals assignable to benzaldehyde were not observed and those of benzyl alcohol were intact. Thus, the reactivity of the Ru-substituted POM in the substrate oxidation in an organic solvent has been enhanced by

strong binding of the cationic  $[\text{Mo}^{\text{V}}(\text{DPP})(\text{O})]^+$  units to the POM unit, as represented by large anodic shifts of the redox potentials of the Ru center in the Ru-POM unit [23].

The kinetics of the catalytic oxidation of the benzyl alcohol derivatives in the presence of **12** as the catalyst was investigated to gain a mechanistic insight into the catalytic reaction. The pseudo-first-order rate constants ( $k_{\text{obs}}$ ) exhibited saturation behaviors relative to the concentration of the substrates, indicating that the pre-equilibrium process may exist prior to the oxidation reaction on the basis of the adduct formation between the reactive  $\text{Ru}^{\text{IV}}=\text{O}$  species and the substrates. In addition, the kinetic isotope effects on the oxidation reaction were studied by using a benzyl alcohol derivative deuterated at the benzyl position or at the hydroxyl groups at 293 K; consequently, the ratios of the pseudo-first-order rate constants,  $k_{\text{CH}_2}/k_{\text{CD}_2}$  and  $k_{\text{OH}}/k_{\text{OD}}$ , were determined to be 10 and 1, respectively. The KIE values indicate that the rate-determining step of the benzyl alcohol oxidation involves H-atom abstraction from the benzylic C–H bond, not from the O–H group. Interestingly, the reaction time to consume a substrate to afford an oxidation product became shorter with increasing electron-withdrawing properties of the  $p$ -substituent of benzyl alcohol derivative: The logarithm of the reaction rate constants for the four substrates having different  $p$ -substituents were plotted against the Hammett's parameters (Fig. 6a) [24] to obtain a linear correlation with the  $\rho$  value of 1.9. In addition, the logarithm of the catalytic rate constants ( $k_p$ ) of oxidation of benzyl alcohols by **12** and that of the rate constants ( $k_c$ ) for the corresponding oxidation reactions using cumyl peroxy radical as an oxidant showed a good linear correlation (Fig. 6b), indicating that the substituent effect on the oxidation reactions results from that on the rate-determining H-atom abstraction step [23].

## INTRAMOLECULAR PHOTOINDUCED ELECTRON TRANSFER FROM A $\text{Sn}^{\text{IV}}$ -DPP UNIT TO AN AXIALLY-COORDINATED ELECTRON ACCEPTOR

In this study, we utilized a  $\text{Sn}^{\text{IV}}$ (DPP) unit as an electron donor in photoinduced electron transfer and simultaneously as an anchor to hold an electron acceptor with a coordinating functional group through axial coordination. Comparing the crystal structure of  $\text{Sn}^{\text{IV}}$ (DPP) $\text{Cl}_2$  (**14**) [25] with that of  $\text{Sn}^{\text{IV}}$ (TPP) $\text{Cl}_2$  (**15**) [26], the bond length of Sn–Cl bond in **14** (2.391(3) Å) exhibits shortening relative to that of **15** (2.421(1) Å) (Fig. 7). This shortening indicates the increase of the Lewis acidity of the central  $\text{Sn}^{\text{IV}}$  ion in the DPP coordination environments relative to that in the TPP counterpart to strengthen the axial binding toward the construction of stable donor–acceptor assemblies. Furthermore, upon performing electron transfer from the  $\text{Sn}^{\text{IV}}$ (DPP) moiety to the axially ligated electron acceptor one, the interaction between the  $1e^-$ -oxidized  $\text{Sn}^{\text{IV}}$ (DPP) moiety and the  $1e^-$ -reduced axial ligand should become stronger than that in the ground state. This is also advantageous for forming donor–acceptor complexes to perform photoinduced electron transfer toward the emergence of photofunctionality. Importantly, the assemblies can form electron-transfer (ET) states at lower energy levels than those of their triplet excited states, by virtue of the lower first oxidation potential of the DPP ligand due to the saddle-distorted conformation to make the porphyrin ring electron-rich on the basis of the ill-overlap of the pyrrole lone pairs with the  $\sigma$ -orbitals of the central metal ions.

### A discrete molecular ensemble composed of $\text{Sn}^{\text{IV}}$ (DPP) and a trinuclear ruthenium cluster

A  $\text{Sn}^{\text{IV}}$ (DPP) complex having two of oxygen-bound 4-pyridine carboxylate (PyCOO<sup>-</sup>) as axial

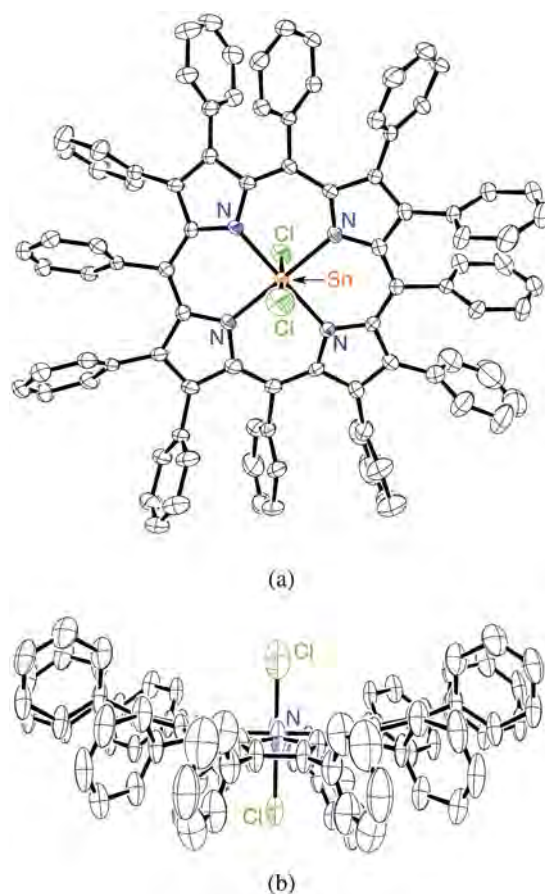
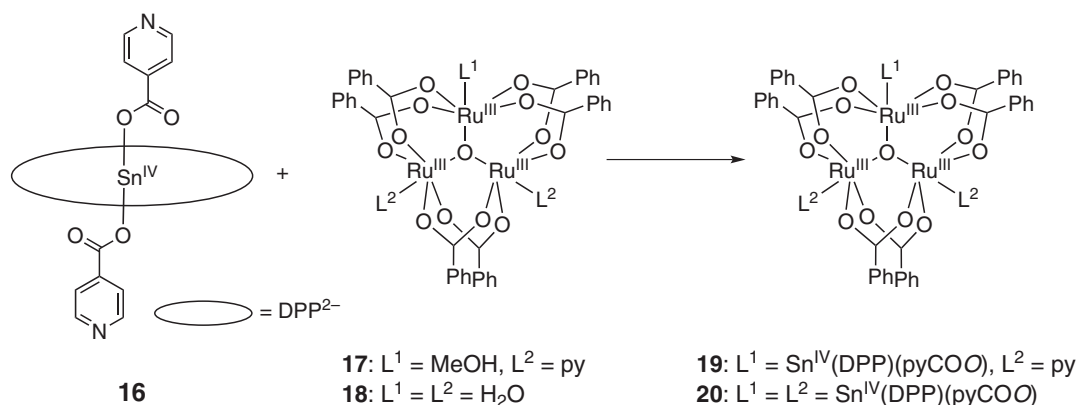


Fig. 7. Crystal structure of **14**: top (a) and side views (b)

ligands (**16**) reacted with a trinuclear  $\text{Ru}^{\text{III}}$ -oxo cluster,  $[\text{Ru}_3(\mu_3\text{-O})(\text{O}_2\text{CPh})_6(\text{py})_2(\text{MeOH})]^+$  (**17**) or  $[\text{Ru}_3(\mu_3\text{-O})(\text{O}_2\text{CPh})_6(\text{H}_2\text{O})_3]^+$  (**18**), in a mixed solvent of  $\text{CH}_2\text{Cl}_2$  and acetone to give molecular  $\text{Sn}^{\text{IV}}$ (DPP)-( $\text{Ru}^{\text{III}}$  cluster) assemblies, a 1:1 complex (dyad) and a 3:1 complex (tetrad) (**19** and **20**) as shown in Scheme 2 [25]. To clarify the structures of the complexes, the  $^1\text{H}$  NMR spectra of the  $1e^-$ -reduced complexes were

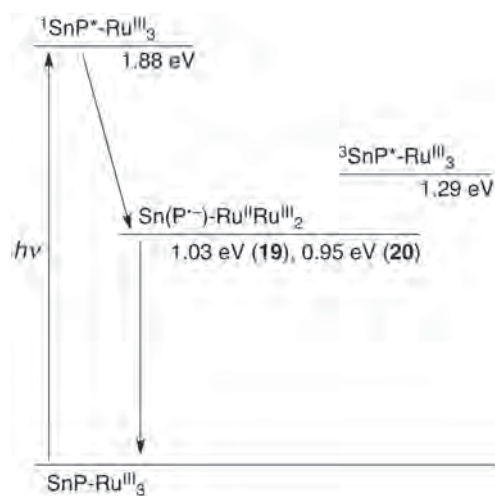


Scheme 2. Complexation of a  $\text{Sn}^{\text{IV}}$ (DPP) complex with trinuclear  $\text{Ru}^{\text{III}}$  clusters



measured in  $\text{CDCl}_3$ , because the trinuclear  $\text{Ru}^{\text{III}}$  cluster is paramagnetic but the  $1e^-$ -reduced  $\text{Ru}^{\text{II}}\text{Ru}^{\text{III}}_2$  species shows diamagnetic character due to the strong antiferromagnetic coupling between the two  $\text{Ru}^{\text{III}}$  centers [27]. The  $^1\text{H}$  NMR spectrum of  $1e^-$ -reduced mono-porphyrinic **19** in  $\text{CDCl}_3$  indicated that **19** should be a 1:1 complex of  $\text{Sn}^{\text{IV}}(\text{DPP})(\text{PyCOO})_2$  and the trinuclear Ru cluster in the two-fold symmetry. On the other hand, the complex **20** is composed of three  $\text{Sn}^{\text{IV}}(\text{DPP})(\text{PyCOO})_2$  moieties and one trinuclear Ru cluster in the three-fold symmetry, judging from the  $^1\text{H}$  NMR spectrum of the  $1e^-$ -reduced species. The electrochemical studies on the complexes were performed in PhCN at room temperature. The first reversible reduction waves for the  $\text{Ru}^{\text{III}}_3$ -cluster moieties were observed at +0.03 V vs. SCE for **19** and +0.11 V for **20**. The  $\text{Sn}^{\text{IV}}(\text{DPP})$  moieties showed the reversible first oxidation waves at +1.06 V vs. SCE for **19** and +1.06 V for **20**, which were overlapped on the oxidation wave of the Ru-cluster moieties. Therefore, the energy levels of the ET states were calculated to be 1.03 and 0.95 eV for **19** and **20**, respectively, and those energy levels were lower than those of the triplet excited states.

To elucidate the photodynamics of **19** and **20**, femtosecond transient absorption spectra were measured in PhCN upon photoexcitation at 430 nm. The fast decay of the singlet excited state was observed, due to the occurrence of intramolecular photoinduced electron transfer from the  $\text{Sn}^{\text{IV}}(\text{DPP})$  moiety to the Ru-cluster moiety. In fact, an absorption band of **19** was observed around 900 nm at 100 ps after laser flash photolysis, which derived from the  $\text{Sn}^{\text{IV}}(\text{DPP}^{\cdot-})$  moiety, indicating the formation of an ET state, a  $\text{Sn}^{\text{IV}}(\text{DPP}^{\cdot-})\text{-Ru}^{\text{II}}\text{Ru}^{\text{III}}_2$  species. Analysis of decay of the absorbance at 850 nm for **19** gave the rate constants of electron transfer and back electron transfer as  $8.6 \times 10^{10}$  and  $3.3 \times 10^9 \text{ s}^{-1}$ , respectively. On the other hand, the rate constants of electron transfer and back electron transfer for **20** were determined to be  $8.6 \times 10^{10}$  and  $3.3 \times 10^9 \text{ s}^{-1}$ , respectively. The energy diagrams for the photodynamics of **19** and **20** are schematically summarized in Fig. 8. The rate constants of electron transfer were analyzed on the basis of the Marcus theory of electron transfer to indicate that all of the rate constants fall in the Marcus inverted region. This should be due to the small reorganization energy of electron transfer of the molecular assemblies ( $\lambda = 0.58 \text{ eV}$ ,  $V = 28.2 \text{ cm}^{-1}$ ) [26]. Similar experiments were performed with a planar  $\text{Sn}^{\text{IV}}$ -porphyrin, and then, the photoexcitation of the corresponding 1:1 and 3:1 complexes with the  $\text{Sn}^{\text{IV}}(\text{TPP})$  and the Ru-cluster exhibited photodissociation to give  $\text{Sn}^{\text{IV}}(\text{TPP})(\text{OH})_2$  and the free Ru-cluster. Therefore, the strengthened axial coordination bonds achieved by the enhanced Lewis acidity of the central metal ions binding to distorted porphyrins should be indispensable to construct photostable donor-acceptor assemblies for performing intramolecular photoinduced electron transfer.

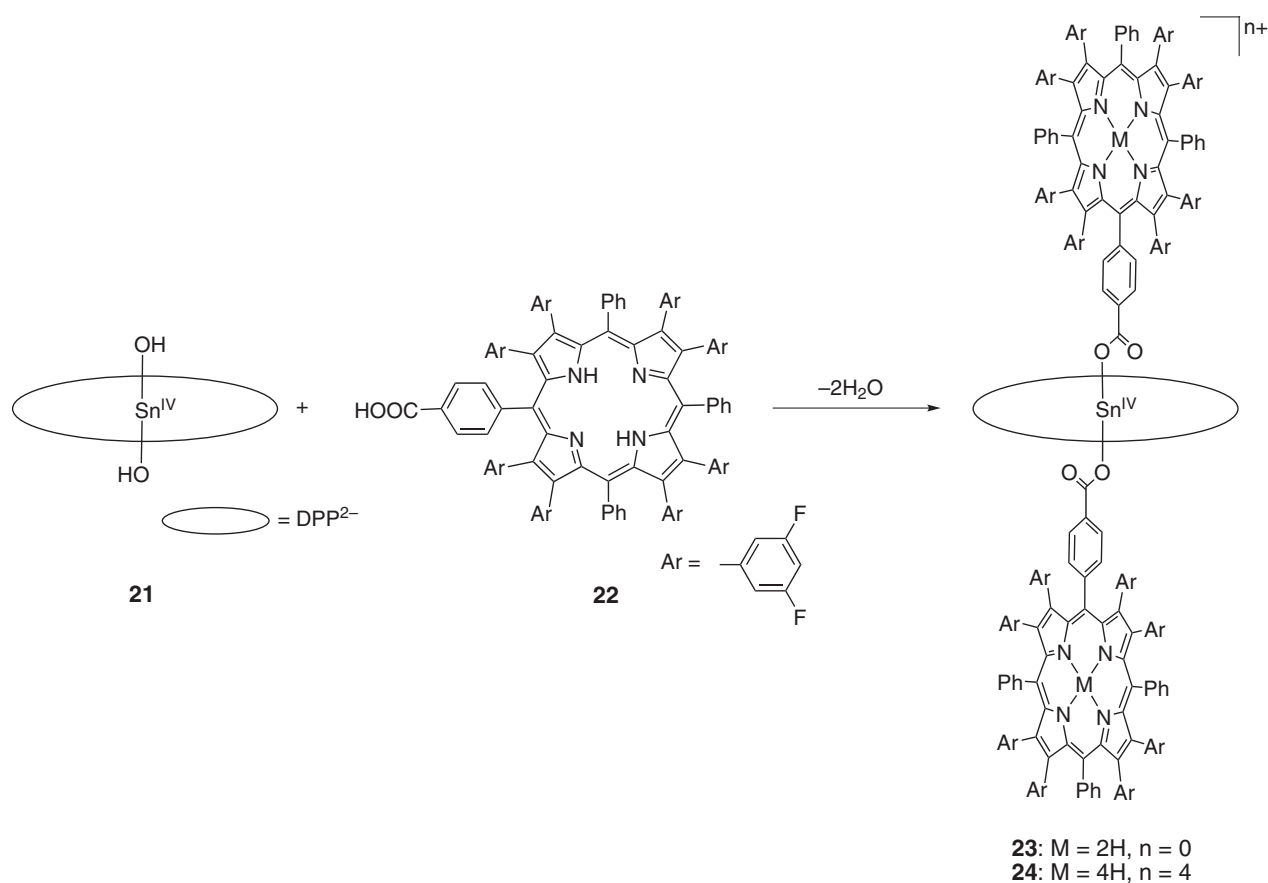


**Fig. 8.** Energy diagram of the photodynamics of **19** and **20** in PhCN. P denotes the dedecaphenylporphyrinate dianion and  $\text{Ru}^{\text{III}}_3$  does the Ru-trinuclear cluster

#### Construction of a DPP triad with axial coordination to the $\text{Sn}^{\text{IV}}(\text{DPP})$ moiety

Reaction of a  $\text{Sn}^{\text{IV}}(\text{DPP})$  complex,  $\text{Sn}^{\text{IV}}(\text{DPP})(\text{OH})_2$  (**21**), with a mono-carboxylated DPP,  $\text{H}_2\text{TPP}(3,5\text{-F}_2\text{Ph})_8(\text{COOH})$  (**22**) in toluene gave a porphyrin triad,  $\text{Sn}^{\text{IV}}(\text{DPP})\{\text{H}_2\text{TPP}(3,5\text{-F}_2\text{Ph})_8(\text{COO})\}_2$  (**23**), where the carboxylate groups of **22** strongly coordinated to the central  $\text{Sn}^{\text{IV}}$  ion of **21** (Scheme 3), *via* ligand substitution together with releasing water molecules [28]. The moieties of **22** in **23** can be easily protonated with addition of trifluoroacetic acid (TFA) to afford  $\text{Sn}^{\text{IV}}(\text{DPP})\{\text{H}_4\text{TPP}(3,5\text{-F}_2\text{Ph})_8(\text{COO})\}_2(\text{CF}_3\text{COO})_4$  (**24**), which exhibited a characteristic red-shifted Q-band at 740 nm for a diprotonated porphyrin. The electrochemical studies of **23** and **24** in PhCN indicated that the reduction potential of the moieties of **22** was positively shifted from -0.97 V vs. SCE for **23** to -0.27 V for **24** by protonation and the oxidation potential of the  $[\text{Sn}^{\text{IV}}(\text{DPP})]^{2+}$  moiety was also positively shifted from +0.63 V vs. SCE for **23** to +1.03 V for **24**. Therefore, the energy level of the ET state in **24** was determined to be 1.30 eV.

The photodynamics of **23** and **24** was investigated by femtosecond laser flash photolysis in PhCN. The singlet excited state of the  $[\text{Sn}^{\text{IV}}(\text{DPP})]^{2+}$  moiety (1.85 eV) of **23** was formed at first by photoexcitation at 430 nm, and then energy transfer occurred to the axially ligated **22** to form the singlet excited state (1.63 eV). The analysis of decay of the absorbance at 900 nm indicated that the rate constant of the energy transfer ( $k_{\text{EN}}$ ) was  $3.0 \times 10^{10} \text{ s}^{-1}$ . In addition, the direct intersystem crossing (ISC) of the singlet excited state to form the triplet excited state in the  $[\text{Sn}^{\text{IV}}(\text{DPP})]^{2+}$  moiety can be ignored, judging from the slow ISC rate constant of **21** ( $k_{\text{ISC}} = 1.2 \times 10^8 \text{ s}^{-1}$ ). The singlet excited state of the axially bound **22** decayed to the triplet excited state with the rate constant ( $k_{\text{ISC}}$ )



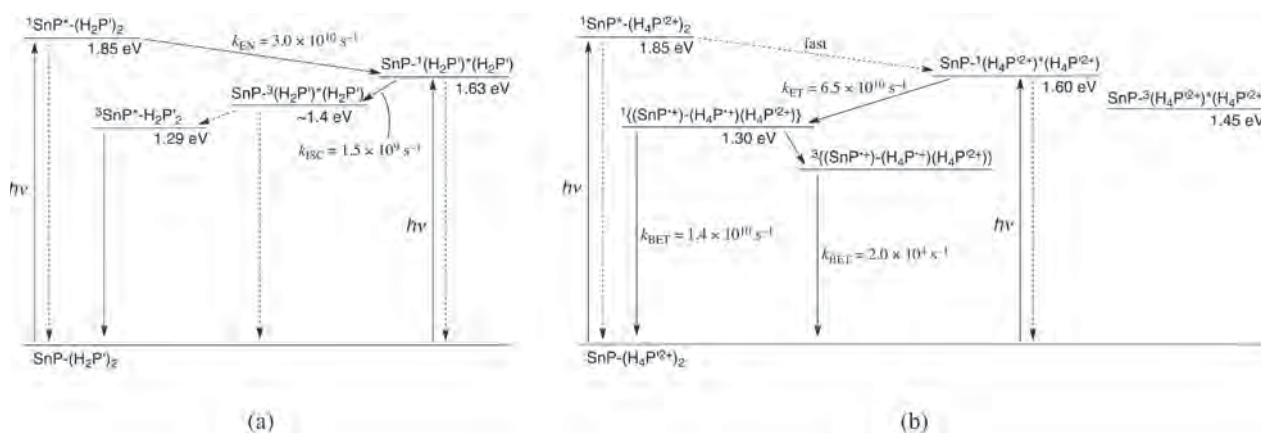
**Scheme 3.** Formation of a porphyrin triad through axial ligation to the Sn<sup>IV</sup> center

of  $1.5 \times 10^9 \text{ s}^{-1}$ . The nanosecond transient absorption spectra indicated that the absorption bands assignable to the triplet excited state of the  $[\text{Sn}^{\text{IV}}(\text{DPP})]^{2+}$  moiety disappeared within 10  $\mu\text{s}$ , suggesting that the energy transfer should occur from the triplet excited state of the moiety of **22** to that of the  $[\text{Sn}^{\text{IV}}(\text{DPP})]^{2+}$  moiety. On the other hand, femtosecond transient absorption spectra of **24** in PhCN clearly exhibited the absorption bands derived from the intramolecular ET state. The excitation of **24** irradiated at 430 nm mainly afforded the singlet excited state of the deprotonated moieties of **22** at first, and at 30 ps after photolysis, the absorption bands with the maxima at 540 and 1030 nm, which derives from the  $1e^-$ -reduced deprotonated moiety of **22** and the  $1e^-$ -oxidized  $[\text{Sn}^{\text{IV}}(\text{DPP})]^{2+}$  moiety formed by ET from the  $[\text{Sn}^{\text{IV}}(\text{DPP})]^{2+}$  moiety to the diprotonated moieties of **22**, were observed. The rate constants of the electron transfer and the back electron transfer were determined to be  $6.5 \times 10^{10}$  and  $1.4 \times 10^{10} \text{ s}^{-1}$ , respectively, on the basis of double-exponential fitting analysis of the absorbance change at 540 nm. The absorption bands showing similar spectral features to those of the ET state were observed at 3 ns after photoexcitation. Based on the absorption bands disappeared in the presence of oxygen, the bands were assigned to the triplet ET state, which exhibited the lifetime of 50  $\mu\text{s}$ . To further confirm the

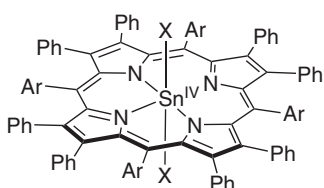
formation of the triplet ET state, the EPR spectrum of **24** under photoirradiation at 4 K was measured; a clear signal due to the triplet species was observed at  $g = 4.25$  and  $g = 2.00$ , and on the basis of the zero-field splitting parameter,  $D = 55 \text{ G}$ , the distance between the two unpaired electrons in the triplet state was determined to be 8.0  $\text{\AA}$ , which matches to the distance of the Sn<sup>IV</sup> center in the  $[\text{Sn}^{\text{IV}}(\text{DPP})]^{2+}$  moiety and the closest *meso*-carbon in the diprotonated moiety of **22**. The photodynamics of **23** and **24** is schematically summarized in Fig. 9.

#### A Keggin-type polyoxometallates as an axially bound electron acceptor for photoinduced electron transfer

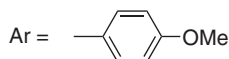
A related Sn<sup>IV</sup>(DPP) complex, Sn(TMPP(Ph)<sub>8</sub>)(X)<sub>2</sub> (X = Cl (**25**) or OMe (**26**); Fig. 10), having four methoxy groups at the *p*-positions of the *meso*-phenyl groups of the DPP ligand, was used as an anchor to bind a polyoxometallate anion as an electron acceptor [29]. To compare the crystal structures of **25** and **26**, the porphyrin plane of **25** exhibited saddle-distortion, typical for DPP-metal complexes, whereas that of **26** was in the wave-distortion mode. The difference mainly derives from the steric repulsion between the axial methoxy ligands and the porphyrin  $\pi$ -cloud. As a result of the steric repulsion,



**Fig. 9.** Energy diagrams of the photodynamics of **23** (a) and **24** (b) in PhCN. P denotes the dedecaphenylporphyrinate dianion and P' does  $\{\text{TPP}(3,5\text{-F}_2\text{Ph})_8(\text{COO})\}^{3-}$



**25** (X = Cl)  
**26** (X = OMe)

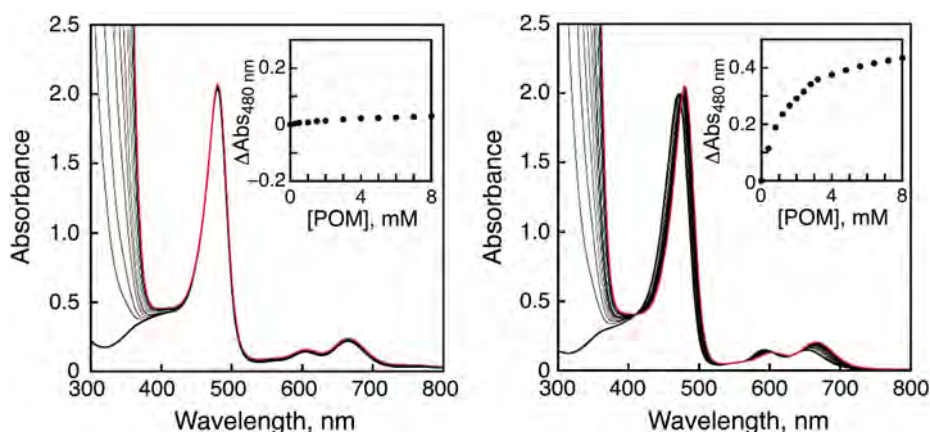


**Fig. 10.** Schematic description of nonplanar  $\text{Sn}^{\text{IV}}$ -porphyrins,  $[\text{Sn}(\text{TMPP}(\text{Ph})_8)\text{Cl}_2]$  (**25**) and  $[\text{Sn}(\text{TMPP}(\text{Ph})_8)(\text{OMe})_2]$  (**26**)

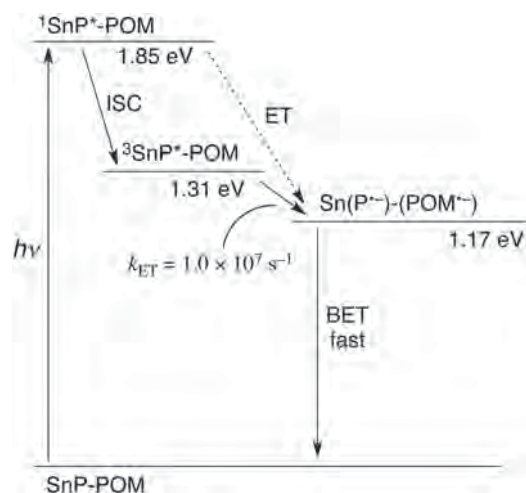
the methoxy ligands of **26** exhibit relatively facile dissociation; on the basis of a van't Hoff plot for the dissociation equilibrium constants, the  $\Delta H$  and  $\Delta S$  values for the equilibrium between the neutral and monocationic

species derived from the methoxo-ligand dissociation were determined to be  $2.7 \text{ kJ mol}^{-1}$  and  $30 \text{ J K}^{-1} \text{ mol}^{-1}$ , respectively.

The solution of **25** or **26** in PhCN was titrated by adding the solution of  $(\text{TBA})_3\cdot\mathbf{5}$  in PhCN. The spectrum of **25** did not show any change, whereas the Soret and Q-bands of **26** exhibited clear red-shifts upon increasing the concentration of **5** (Fig. 11). This difference in the association behavior between **25** and **26** is probably ascribed to the weak interaction of the methoxo ligand in **27** due to the aforementioned steric repulsion. On the basis of the MALDI-TOF-MS measurements, the association complex between **5** and **26** was assigned to the 1:1 complex (**27**). The association constant for the formation of **27** was determined to be  $7.4 \times 10^2 \text{ M}^{-1}$  by the curve-fitting of the absorbance change at 672 nm. The electrochemical studies of **27** in PhCN revealed that the first oxidation potential of the  $\text{Sn}^{\text{IV}}$ (DPP) moiety exhibited a negative shift by 50 mV relative to that of **26**, whereas the reduction potential of the POM moiety



**Fig. 11.** UV-vis spectral titrations of (a) **25** and (b) **26** with POM, **5** in PhCN ( $[\text{por}] = 1.0 \times 10^{-5} \text{ M}$ ). The spectrum changed from a black solid line to a red solid line



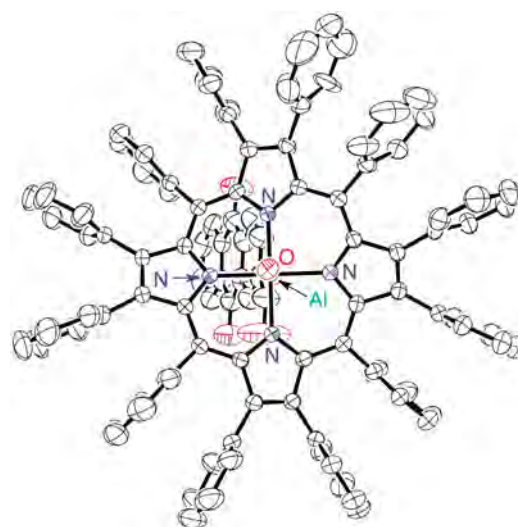
**Fig. 12.** Energy diagram of the photodynamics of **27** in PhCN. SnP denotes the Sn(TMPP(Ph)<sub>8</sub>(OMe) moiety and POM does the [PW<sub>12</sub>O<sub>40</sub>]<sup>3-</sup> anion

showed a slight positive shift by 10 mV relative to that of **5**. Therefore, the energy level of the intramolecular ET state was determined to be 1.17 eV.

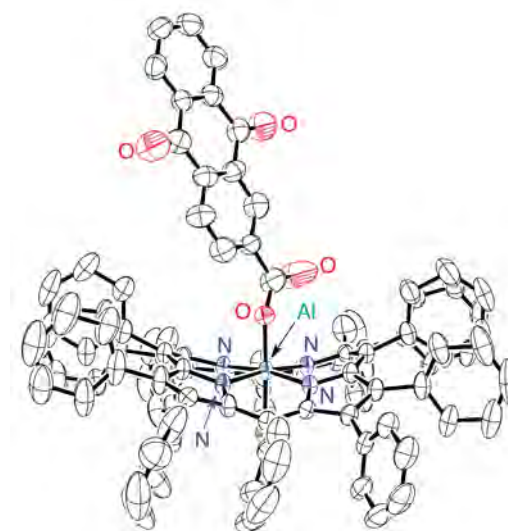
Femtosecond laser flash photolysis of **27** in PhCN was performed to reveal the photodynamics. The photoexcitation of **27** at 430 nm gave rise to absorption bands assigned to the singlet excited state of the Sn<sup>IV</sup>(DPP) moiety and exhibited the decay to the triplet excited state, without showing the sign of the formation of the ET state. However, comparing the rate constants of the ISC processes ( $k_{ISC}$ ) between **26** and **27**, the acceleration of the ISC process was recognized in **27**;  $k_{ISC} = 1.3 \times 10^{10} \text{ s}^{-1}$  for **27** and  $8.1 \times 10^9 \text{ s}^{-1}$  for **26**. This acceleration probably derives from the heavy atom effect of the POM moiety. On the other hand, the decay profile of the triplet excited state of **27** was monitored with nanosecond transient absorption spectroscopy and the decay rate constant of the triplet excited state ( $k_T$ ) of **27** was determined to be  $1.6 \times 10^7 \text{ s}^{-1}$ , which was also larger than that of **26**. The  $k_T$  values of **27** increased with increasing the concentration of **5** in the solution and reached to the constant value. This behavior can be analyzed by the ET reaction having a pre-equilibrium process based on the complexation between **26** and **5** to form **27**. As a result, the pre-equilibrium constant ( $K$ ) and the first-order rate constant ( $k_{ET}$ ) were determined as  $6.9 \times 10^2 \text{ M}^{-1}$ , which matches well to the association constant obtained by the analysis of the spectral change, and  $1.0 \times 10^7 \text{ s}^{-1}$ , respectively. The photodynamic of **27** is schematically summarized in Fig. 12.

#### Intramolecular photoinduced electron transfer in a 1:1 complex of Al<sup>III</sup>(DPP) with an electron acceptor

Axial coordination of an electron-acceptor entity with a coordinating functional group to a Al<sup>III</sup>(DPP)



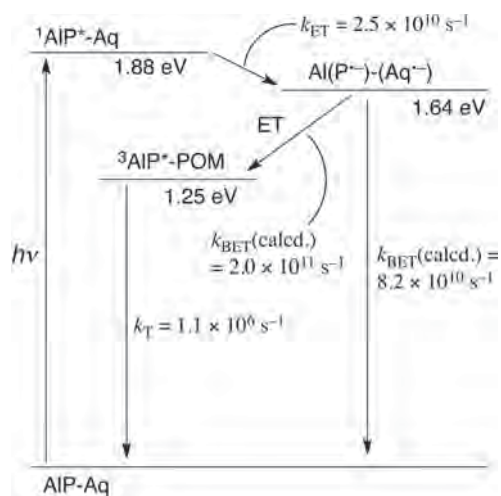
(a)



(b)

**Fig. 13.** Crystal structure of **29**: top (a) and side views (b)

complex can be also used to construct donor-acceptor dyads to perform photoinduced ET [30]. Condensation of [Al<sup>III</sup>(DPP)(OH)] (**28**) with anthraquinone-2-carboxylic acid (AqCOOH) in CHCl<sub>3</sub> gave a complex of [Al<sup>III</sup>(DPP)(AqCOO)] (**29**). The structure of the complex was revealed by <sup>1</sup>H NMR spectroscopy, MALDI-TOF-MS spectrometry, and single-crystal X-ray diffraction analysis (Fig. 13). The photodynamics of **29** in PhCN was investigated by femtosecond laser flash photolysis. In the transient absorption spectrum of **29** at 3 ps after photoexcitation at 455 nm, an absorption band derived from the singlet excited state of the Al<sup>III</sup>(DPP) moiety was observed. The singlet excited state of **29** exhibited very fast decay to the triplet excited state with the decay rate constant of  $2.5 \times 10^{10} \text{ s}^{-1}$ , in comparison to



**Fig. 14.** Energy diagram of the photodynamics of **29** in PhCN. P denotes the dedecaphenyl-porphyrinate dianion and Aq does the anthraquinone-2-carboxylate ligand

the decay rate constant of the singlet excited state of  $\text{Al}^{\text{III}}(\text{DPP})(\text{PhCOO})$  via intersystem crossing ( $k_{\text{ISC}} = 1.2 \times 10^9 \text{ s}^{-1}$ ). This acceleration suggests the occurrence of the photoinduced ET, i.e. the singlet excited state of the  $\text{Al}^{\text{III}}(\text{DPP})$  moiety was converted to an ET state of ( $\text{Al}^{\text{III}}(\text{DPP}^{\bullet-})\text{-AqCOO}^{2-}$ ) and the ET state performed the back electron transfer with a faster rate constant than that of the forward electron transfer. On the basis of the Marcus theory of ET, the rate constant of the back electron transfer occurring in the aforementioned ET state of **29** was calculated to be  $2.0 \times 10^{12} \text{ s}^{-1}$  to afford the triplet excited state. The photodynamics of **29** is summarized in Fig. 14.

## SUMMARY

Here, we have overviewed our recent progress in construction of stable molecular assemblies using metal complexes with non-planar DPP and its derivatives under the concept of the enhancement of Lewis acidity of a metal center trapped in the porphyrin core. The enhanced Lewis acidity of the central metal ions, which is gained by ill-overlap of the out-of-plane lone pairs of pyrrole nitrogen atoms with  $\sigma$ -orbitals of the metal center, allows us to attain strengthened axial coordination to stabilize molecular assemblies with a variety of electron-accepting entities bearing coordination sites. Concomitantly, the ill-overlap of the out-of-plane lone pairs of pyrrole nitrogen atoms renders the porphyrin ring electron-rich to attain a lower oxidation potential of the porphyrin ligand, facilitating intramolecular photoinduced ET process over intersystem crossing.

Based on the concept mentioned above, for example, we succeeded in construction of stable complexes using  $\text{M}(\text{DPP})$  moieties ( $\text{M} = \text{Mo}^{\text{V}}$  or  $\text{Sn}^{\text{IV}}$ ) and polyoxometallates, which are known to have weak Lewis

basicity [18] and thus hard to coordinate to metal ions. The discrete  $\text{Mo}^{\text{V}}(\text{DPP})(\text{O})\text{-Ru-POM}$  complex performs catalytic substrate oxidation reactions in organic solvents due to the elevation of the oxidation potential of the Ru center as the active site. The  $\text{Sn}^{\text{IV}}(\text{TMPP}(\text{Ph})_8)\text{-POM}$  assembly exhibited photoinduced electron transfer, in which the non-planar  $\text{Sn}^{\text{IV}}$ -porphyrin complex acts as an electron donor and the axially bound POM ligand accepts an electron from the  $\text{Sn}^{\text{IV}}$ -porphyrin unit. In addition, besides POM, other electron-accepting entities, such as  $\mu_3$ -oxo trinuclear Ru clusters, diprotonated DPP derivatives, and anthraquinone, having carboxylate group as a binding site also form stable complexes with  $\text{M}(\text{DPP})$  complexes as axial ligands and perform photoinduced ET reactions. Successful photoreactions of the  $\text{M}(\text{DPP})\text{-acceptor}$  complexes mainly result from the enhanced Lewis acidity of the  $\text{M}(\text{DPP})$  complexes. In fact, the similar coordination complexes of a TPP-metal complex and an electron acceptor with axial ligation exhibited dissociation under light irradiation due to the weak coordination bonds. The concept presented here will provide a useful strategy to construct a number of porphyrin-based photofunctional molecular assemblies.

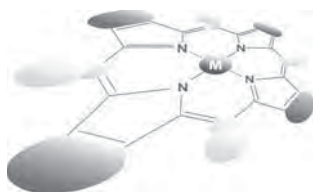
## Acknowledgements

The authors gratefully acknowledge the contributions of collaborators and co-workers mentioned in the references. The authors also appreciate financial supports provided by Grants-in-Aid (Nos. 20108010, 21111501, 23111703 and 24245011) from Japanese Society of Promotion of Science (JSPS).

## REFERENCES

1. Nurco DJ, Medforth CJ, Forsyth TP, Olmstead MM and Smith KM. *J. Am. Chem. Soc.* 1996; **118**: 10918–10919.
2. Shelnutt JA, Song XZ, Ma JG, Jia SL, Jentzen W and Medforth CJ. *Chem. Soc. Rev.* 1998; **27**: 31–41.
3. Pellicena P, Karow DS, Boon EM, Marletta MA and Kuriyan J. *Proc. Natl. Acad. Sci. USA* 2004; **101**: 12854–12859.
4. (a) Shelnutt JA, Medforth CJ, Berber MD, Barkigia KM and Smith KM. *J. Am. Chem. Soc.* 1991; **113**: 4077–4087. (b) Medforth CJ, Senge MO, Smith KM, Sparks LD and Shelnutt JA. *J. Am. Chem. Soc.* 1992; **114**: 9859–9869.
5. (a) Ikeue T, Saitoh T, Yamaguchi T, Ohgo Y, Nakamura M, Takahashi M and Takeda M. *Chem. Commun.* 2000; 1989–1990. (b) Ikeue T, Ohgo Y, Yamaguchi T, Takahashi M, Takeda M and Nakamura M. *Angew. Chem. Int. Ed.* 2001; **40**: 2617–2620. (c) Ogura H, Yatsunyk L, Medforth CJ, Smith KM, Barkigia KM, Renner MW, Melamed D and Walker FA. *J. Am. Chem. Soc.* 2001; **123**: 6564–6578.

6. (a) Medforth CJ and Smith KM. *Tetrahedron Lett.* 1990; **31**: 5583–5586. (b) Kadish KM, Van Caemelbecke E, D'Souza F, Lin M, Nurco DJ, Medforth CJ, Forsyth TP, Krattinger B, Smith KM, Fukuzumi S, Nakanishi I and Shelnutt JA. *Inorg. Chem.* 1999; **38**: 2188–2198. (c) Retsek JL, Drain CM, Kirmaier C, Nurco DJ, Medforth CJ, Smith KM, Sazanovich IV, Chirvony VS, Fajer J and Holten D. *J. Am. Chem. Soc.* 2003; **125**: 9787–9800.
7. (a) Takeda J, Ohya T and Sato M. *Chem. Phys. Lett.* 1991; **183**: 384–386. (b) Takeda J and Sato M. *Chem. Lett.* 1995; 971–972. (c) Ono N, Miyagawa H, Ueta T, Ogawa T and Tani H. *J. Chem. Soc., Perkin Trans. 1* 1998; 1595–1601.
8. (a) Takeda J and Sato M. *Chem. Lett.* 1995; 939–940. (b) Kadish KM, Lin M, Van Caemelbecke E, De Stefano G, Medforth CJ, Nurco DJ, Nelson NY, Krattinger B, Muzzi CM, Jaquinod L, Xu Y, Shyr DC, Smith KM and Shelnutt JA. *Inorg. Chem.* 2002; **41**: 6673–6687.
9. Fukuzumi S, Nakanishi I, Barbe JM, Guillard R, Van Caemelbecke E, Guo N and Kadish KM. *Angew. Chem., Int. Ed.* 1999; **38**: 964–966.
10. Takeda J, Ohya T and Sato M. *Inorg. Chem.* 1992; **31**: 2877–2880.
11. (a) Kojima T, Nakanishi T, Honda T and Fukuzumi S. *J. Porphyrins Phthalocyanines* 2009; **13**: 14–21. (b) Fukuzumi S, Honda T, Ohkubo K and Kojima T. *Dalton Trans.* 2009; 3880–3889.
12. (a) Kojima T, Honda T, Ohkubo K, Shiro M, Kusukawa T, Fukuda T, Kobayashi N and Fukuzumi S. *Angew. Chem. Int. Ed.* 2008; **47**: 6712–6716. (b) Honda T, Nakanishi T, Ohkubo K, Kojima T and Fukuzumi S. *J. Am. Chem. Soc.* 2010; **132**: 10155–10163.
13. (a) Harada R and Kojima T. *Chem. Commun.* 2005; 716–718. (b) Kojima T, Nakanishi T, Harada R, Yamauchi S, Ohkubo K and Fukuzumi S. *Chem.–Eur. J.* 2007; **13**: 8714–8725.
14. Kojima T, Nakanishi T, Honda T, Harada R, Shiro M and Fukuzumi S. *Eur. J. Inorg. Chem.* 2009; 727–734.
15. In contrast to the spectroscopic titration experiments of ZnDPP, the stretching bands of the V=O bonds for V(porphyrinato)(O) complexes are not severely affected by the saddle distortion of the porphyrin ligand. Harada R, Okawa H and Kojima T. *Inorg. Chim. Acta* 2005; **358**: 489–496.
16. (a) Sadakane M and Steckhan E. *Chem. Rev.* 1998; **98**: 219–237. (b) Kozhevnikov IV. *Chem. Rev.* 1998; **98**: 171–198.
17. (a) Yamase T. *Chem. Rev.* 1998; **98**: 307–325. (b) Katsoulis DE. *Chem. Rev.* 1998; **98**: 359–387.
18. Izumi Y, Matsuo K and Urabe K. *J. Mol. Catal.* 1983; **18**: 299–314.
19. (a) Uchida S and Mizuno N. *Coord. Chem. Rev.* 2007; **251**: 2537–2546. (b) Mirzaeia M, Eshtiagh-Hosseinia H, Alipoura M and Frontera A. *Coord. Chem. Rev.* 2014; **275**: 1–18.
20. (a) Yokoyama A, Kojima T, Ohkubo K and Fukuzumi S. *Chem. Commun.* 2007; 3997–3999. (b) Yokoyama A, Kojima T, Ohkubo K and Fukuzumi S. *Inorg. Chem.* 2010; **49**: 11190–11198.
21. (a) Neumann R and Gara M. *J. Am. Chem. Soc.* 1995; **117**: 5066–5074. (b) Mizuno N, Nozaki C, Kiyoto I and Misono M. *J. Am. Chem. Soc.* 1998; **120**: 9267–9272. (c) Nakazawa Y, Kamata K, Kotani M, Yamaguchi K and Mizuno N. *Angew. Chem., Int. Ed.* 2005; **44**: 5136–5141.
22. (a) Neumann R and Abu-Gnim C. *J. Chem. Soc., Chem. Commun.* 1989; 1324–1325. (b) Neumann R and Abu-Gnim C. *J. Am. Chem. Soc.* 1990; **112**: 6025–6031.
23. Yokoyama A, Ohkubo K, Ishizuka T, Kojima T and Fukuzumi S. *Dalton Trans.* 2012; **41**: 10006–10013.
24. Pine SH. In *Organic Chemistry, 5th ed.*, McGraw-Hill: New York, 1987.
25. Kojima T, Hanabusa K, Ohkubo K, Shiro M and Fukuzumi S. *Chem.–Eur. J.* 2010; **16**: 3646–3655.
26. Collins DM, Scheidt WR and Hoard JL. *J. Am. Chem. Soc.* 1972; **94**: 6689–6696.
27. Kobayashi H, Uryu N, Mogi I, Miyamoto R, Ohba Y, Iwaizumi M, Sasaki Y, Ohto A and Ito T. *Bull. Chem. Soc. Jpn.* 1995; **68**: 2551–2558.
28. Honda T, Nakanishi T, Ohkubo K, Kojima T and Fukuzumi S. *J. Phys. Chem. C* 2010; **114**: 14290–14299.
29. Yokoyama A, Kojima T, Ohkubo K, Shiro M and Fukuzumi S. *J. Phys. Chem. A* 2011; **115**: 986–997.
30. Kanematsu M, Naumov P, Kojima T and Fukuzumi S. *Chem.–Eur. J.* 2011; **17**: 12372–12384.



# A review of iron and cobalt porphyrins, phthalocyanines and related complexes for electrochemical and photochemical reduction of carbon dioxide

Gerald F. Manbeck\* and Etsuko Fujita\*<sup>‡</sup>

Chemistry Department, Brookhaven National Laboratory, Upton NY 11973, USA

*Dedicated to Professor Shunichi Fukuzumi on the occasion of his retirement*

Received 14 November 2014

Accepted 23 December 2014

**ABSTRACT:** This review summarizes research on the electrochemical and photochemical reduction of CO<sub>2</sub> using a variety of iron and cobalt porphyrins, phthalocyanines and related complexes. Metalloporphyrins and metallophthalocyanines are visible light absorbers with extremely large extinction coefficients. However, yields of photochemically-generated active catalysts for CO<sub>2</sub> reduction are typically low owing to the requirement of a second photoinduced electron. This requirement is not relevant to the case of electrochemical CO<sub>2</sub> reduction. Recent progress on efficient and stable electrochemical systems includes the use of FeTPP catalysts that have prepositioned phenyl OH groups in their second coordination spheres. This has led to remarkable progress in carrying out coupled proton-electron transfer reactions for CO<sub>2</sub> reduction. Such ground-breaking research has to be continued in order to produce renewable fuels in an economically feasible manner.

**KEYWORDS:** CO<sub>2</sub> reduction, porphyrin, phthalocyanine, cobalt, iron.

## I. INTRODUCTION

The global carbon cycle is a closed system with all fossil fuels currently burned originating from photosynthetic carbon dioxide fixation over millions of years. An imbalance in the rates of consumption vs. natural fixation with increasing human demand for energy leads to two major concerns: the rising concentration of atmospheric CO<sub>2</sub>, and the inevitable decline of extractable fossil fuels. The problem of atmospheric concentrations can be alleviated to some extent through CO<sub>2</sub> capture/sequestration technology [1]; however, a conversion/utilization or recycling scheme is perhaps more ideal since the need for energy is also addressed. If the recycling technology is ultimately powered by inexhaustible, although intermittent, solar energy, CO<sub>2</sub> is then viewed as a redox mediator in which diffuse solar energy is stored in

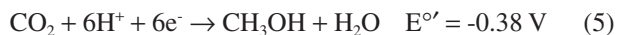
the form of chemical bonds by its reduction and electrical energy is obtained by oxidation of the reduced products.

The foremost challenge to CO<sub>2</sub> recycling is its chemically inert nature. Direct electrochemical reduction to CO<sub>2</sub><sup>•-</sup> (Equation 1) is highly unfavorable due in part to the geometric rearrangement from linear to bent. This difficulty is reflected by the standard potential of -1.90 V vs. NHE [2]. Energy requirements for proton assisted multi-electron reductions at pH 7 (Equations 2–6) are substantially lower; however, catalysts are necessary to mediate the microscopic steps involved in the multi-proton, multi-electron reductions. Transition metal complexes with a variety of accessible oxidation states (including ligand-localized reductions) are well-suited for this task and often provide product selectivity and tunable activity [3–5]. Nevertheless, reduction beyond formic acid or CO remains rare and further developments are needed.



<sup>‡</sup> SPP full member in good standing

\*Correspondence to: Gerald F. Manbeck, email: [gmanbeck@bnl.gov](mailto:gmanbeck@bnl.gov), Etsuko Fujita, email: [fujita@bnl.gov](mailto:fujita@bnl.gov)

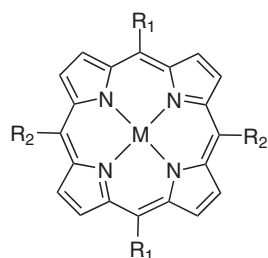


The conversion and utilization of carbon dioxide is an area of intense current research interest, and several recent review articles [6–12] provide a broader scope and overview than is possible in this minireview. We have limited the scope of this review to articles pertaining to catalytic  $\text{CO}_2$  reduction using iron and cobalt porphyrins, phthalocyanines, and related complexes (Chart 1). The Fe and Co centers exist from the +3 to 0 oxidation states while the macrocyclic ligand framework provides chemical stability and storage of a reducing equivalent and/or a proton. Characteristic electronic absorption spectra provide a probe into oxidation states and reaction kinetics, and mechanisms or structure-activity relationships are deciphered through the large variability in available ligands.

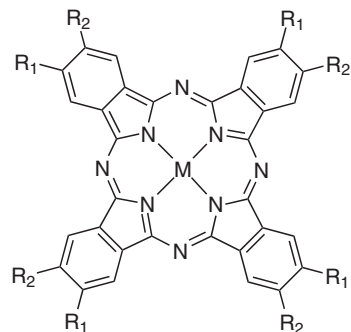
In this review, the papers discussed are separated into heterogeneous and homogeneous catalysis. The heterogeneous experiments employ complexes adsorbed onto or covalently bound to electrode surfaces. This technique can enhance efficiency by eliminating diffusion and mass transport, which are inevitable in

solution electrocatalysis. Catalysis in media in which the compound is poorly soluble (usually water) is then possible. The surface modification should not impede conductivity, block catalytic sites, or decrease catalyst reactivity. Two common methods of surface confinement are non-covalent adsorption and covalent anchoring to a surface through axial ligands, usually through pyridine or other monodentate ligands. The stability of an axial pyridine linkage could be problematic considering the known dissociative reactions of monodentate nitrogen ligands from  $\text{Co}^{\text{II}}\text{TPP}$  upon reduction in polar solvents [13]. Conversely, ligand based reductions of  $[\text{Co}(\text{pTMPyP})]^{3+}$  trigger the coordination of pyridine to the Co center [14]. It is likely that high local concentrations of linker ligands on the electrode along with complex insolubility contribute to stabilization of catalysts covalently bound to electrodes through axial ligands.

The discussion of homogeneous catalysis is separated into purely electrochemical systems, in which cyclic voltammetry (CV) and bulk electrolysis are the primary analytical techniques, and photocatalysis, in which photochemistry, radiolysis, and chemical reduction in conjunction with visible spectroscopy identify species that react with  $\text{CO}_2$  and provide rate constants for relevant reactions.



- R1 = R2 = C<sub>6</sub>H<sub>5</sub> MTPP
- R1 = R2 = C<sub>6</sub>H<sub>4</sub>(4-SO<sub>3</sub><sup>-</sup>) MTPPS
- R1 = R2 = C<sub>6</sub>H<sub>4</sub>(4-CO<sub>2</sub><sup>-</sup>) MTCPP
- R1 = R2 = C<sub>5</sub>H<sub>4</sub>(4-N<sup>+</sup>-CH<sub>3</sub>) M-pTMPyP
- R1 = R2 = C<sub>5</sub>H<sub>4</sub>(3-N<sup>+</sup>-CH<sub>3</sub>) M-mTMPyP
- R1 = R2 = C<sub>5</sub>H<sub>4</sub>(2-N<sup>+</sup>-CH<sub>3</sub>) M-oTMPyP
- R1 = R2 = C<sub>6</sub>H<sub>4</sub>(4-OCH<sub>3</sub>) MTMeOPP
- R1 = R2 = C<sub>6</sub>H<sub>3</sub>(2,6-Cl) MTCIPP
- R1 = R2 = C<sub>6</sub>H<sub>3</sub>(2,6-OCH<sub>3</sub>) MTDMP
- R1 = R2 = C<sub>6</sub>H<sub>3</sub>(2,6-OH) MTDHPP
- R1 = C<sub>6</sub>H<sub>3</sub>(2,6-OCH<sub>3</sub>) R2 = C<sub>6</sub>F<sub>5</sub> MTDHPPF<sub>10</sub>
- R1 = R2 = C<sub>6</sub>H<sub>2</sub>(2,4,6-CH<sub>3</sub>) MTMP
- R1 = R2 = C<sub>6</sub>H<sub>5</sub> + 2H (chlorin) MTPC
- R1 = R2 = H MPor
- R1 = R2 = C<sub>6</sub>H<sub>4</sub>(4-NH<sub>2</sub>) MTAPP
- R1 = R2 = C<sub>6</sub>H<sub>4</sub>(4-N<sup>+</sup>(CH<sub>3</sub>)) MTNMPP
- R1 = R2 = C<sub>6</sub>F<sub>5</sub> MTPFPP
- R1 = R2 = C<sub>6</sub>H<sub>4</sub>(3-F) MT3FPP
- R1 = R2 = C<sub>6</sub>H<sub>4</sub>(3-CF<sub>3</sub>) MT3CF<sub>3</sub>PP
- R1 = R2 = C<sub>6</sub>H<sub>4</sub>(3-CH<sub>3</sub>) MT3CH<sub>3</sub>PP
- R1 = R2 = H (2,3,7,8,12,13,17,18-CH<sub>2</sub>CH<sub>3</sub>) MOEP



- R1 = R2 = H MPc
- R1 = H R2 = SO<sub>3</sub><sup>-</sup> MTSPc
- R1 = R2 = CN MPc(CN)<sub>8</sub>
- R1 = H R2 = <sup>t</sup>Bu MTBPC
- R1 = H R2 = NH<sub>2</sub> MTAPc
- R1 = R2 = C<sub>6</sub>H<sub>4</sub>(4-SO<sub>3</sub><sup>-</sup>) MTPPS
- R1 = R2 = OBU MPc(OBU)<sub>8</sub>
- R1 = R2 = Benzo MNc

**Chart 1.** Porphyrins and Phthalocyanines studied as  $\text{CO}_2$  reduction catalysts



In all examples, we include practical parameters such as methods of electrode preparation and catalyst loading, while we highlight issues of scientific merit including Faradaic efficiency (FE), product distribution, turnovers, and kinetics. One consistently controversial issue is the nature of the active catalyst. This is especially problematic for surface bound catalysts with low loading relative to the electrode surface because of the inability to view characteristic redox couples of the catalyst. Deposition of metal colloids should always be considered, though in many cases it is not even discussed despite the occasional preparation of electrodes under harsh conditions (*e.g.* high temperature and pressure). Chart 1 contains most of the porphyrin and phthalocyanine ligands used for Fe and Co catalyzed CO<sub>2</sub> reduction. The structures of a few special cases will appear later.

## II. HETEROGENEOUS CATALYSIS

### A. Catalysts adsorbed onto electrodes

Non-covalent adsorption is the simplest method of electrode modification. In this discussion, we use “dip coated” to describe electrodes prepared by soaking in a solution of the catalyst (usually in organic solvent) for a given time followed by drying. “Drop coating” refers to electrodes prepared by dropping a concentrated solution onto the surface and evaporating the organic solvent. The catalyst loading is usually easier to determine using the drop coating method although integration of CV current or dissolution followed by concentration determination can be used in any case. Catalyst evaluation is most easily performed by cyclic voltammetry (CV) in CO<sub>2</sub>-saturated solvent and comparison to the current without CO<sub>2</sub>. Relevant data are summarized in Table 1.

In early work in 1974, CoPc adsorbed on graphite was studied in a CO<sub>2</sub>-saturated aqueous solution. The voltammogram exhibited a peak at *ca.* -1.6 V *vs.* SCE, which was about 200 mV more positive than the proton reduction reaction under N<sub>2</sub> [15]. A control scan in 0.1 M Na<sub>2</sub>CO<sub>3</sub> or NaHCO<sub>3</sub> solution showed no current in the absence of CO<sub>2</sub> indicating that dissolved CO<sub>2</sub> is reduced. When a quaternary ammonium salt was used for the electrolyte under CO<sub>2</sub> (*i.e.* pH ~ 4.5), oxalate and glycolate were detected by color reactions of thiobarbituric acid and 2,7-dihydronaphthalene (Table 1 entry 1). No formate was detected as a CO<sub>2</sub> reduction product in this early paper. In contrast, an electrode prepared by precipitation of CoPc onto glassy carbon produced formate with 60% FE during continuous electrolysis at 1 mA.cm<sup>-2</sup> for 72 h with 10 μg.cm<sup>-2</sup> loading (Table 1 entry 2) [16]. The CV was stable for several cycles if the switching of the potential remained positive of -1.55 V, otherwise activity was reduced to that of bare carbon. In both cases (CoPc on graphite or glassy carbon), the current was proportional to [CO<sub>2</sub>] and  $v^{1/2}$ , consistent with a diffusion controlled

process whereas the peak height of a redox couple immobilized on an electrode should be proportional to  $v$  (scan rate). On glassy carbon, the Tafel slope of ~120 mV/decade indicated that transfer of the first electron to CO<sub>2</sub> was the rate-limiting step.

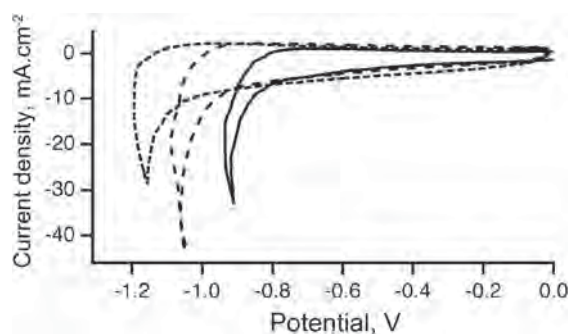
Carbon monoxide was reported as yet another product of electrocatalysis using CoPc. In this case, the catalyst was adsorbed onto pyrolytic graphite or carbon cloth by dip coating or drop coating from THF [17]. Electrolysis experiments from -0.95 to -1.2 V *vs.* SCE (pH 5, citrate buffer) produced CO and H<sub>2</sub> (1.5:1) with 55–65% FE for CO and 3.7 × 10<sup>5</sup> turnovers (entry 3) at an overpotential of 300 mV. Trace amounts of oxalate and formate were detected. A control experiment with 3 mM Co(ClO<sub>4</sub>)<sub>2</sub> yielded only 0.14 turnovers of products implicating the intact complex as the active catalyst. In solution, the CoPc was unstable to prolonged electrolysis due to hydrogenation of the Pc ligand, but deactivation was minimized on the electrode surfaces. The mechanism was investigated by CV experiments. First, binding of CO<sub>2</sub> to the one-electron-reduced species, [CoPc]<sup>-</sup>, was ruled out since there was no change in the first redox couple under N<sub>2</sub> or CO<sub>2</sub>. Aqueous CVs under N<sub>2</sub> showed two proton-coupled reductions, implying protonation of [CoPc]<sup>-</sup> followed by further reduction and reaction with CO<sub>2</sub>. Additional support for this mechanism was obtained in an *in-situ* FTIR study during electroreduction of CO<sub>2</sub> by CoPc-coated graphite electrodes [18]. The results indicate that (1) the first reduction of CoPc occurs on the Pc ligand to produce [Co<sup>II</sup>(Pc<sup>-</sup>)]; (2) the second reduction produced [Co(H)(Pc<sup>-</sup>)]<sup>-</sup> *via* protonation of [Co<sup>I</sup>(Pc<sup>-</sup>)]<sup>2-</sup>; (3) neither free nor adsorbed CO on the electrode were detected due to the relatively short-term spectroelectrochemical experiments; and (4) CO<sub>2</sub> reacted irreversibly with the doubly-reduced species by formation of products. The surface properties were related to electrode preparation as H<sub>2</sub> was generated from a film prepared from THF but not from pyridine. The assignment of the first reduction product as [Co<sup>II</sup>(Pc<sup>-</sup>)], is controversial as seen below.

The activity and stability of a CoPc film on glassy carbon was impacted by the method of preparation. By using vacuum deposition with intermittent plasma assistance, a uniform 40 nm film of CoPc on glassy carbon was prepared [19]. The CV showed one major peak at *ca.* -1.6 V *vs.* SSCE with stable current for multiple scans. In contrast, a film produced by traditional vacuum deposition showed two peaks which decreased after polarization at -1.85 V. The reduction of CO<sub>2</sub> seems to be controlled by a surface chemical reaction involving adsorbed H<sup>+</sup> and/or H and carbon-containing surface intermediates, but products of reduction were not determined.

Ligand effects were explored using CoPc(OBu)<sub>8</sub> or CoPc(CN)<sub>8</sub>. A film of CoPc(OBu)<sub>8</sub> (1.2 × 10<sup>-10</sup> mol.cm<sup>-2</sup>) was prepared by drop casting onto a basal-plane pyrolytic graphite electrode from DMF [20]. The first reduction couple was observed at -0.58 V *vs.* Ag/AgCl but the second

reduction was obscured by proton reduction. Interestingly, assignments of the first and second reduction couples are  $\text{Co}^{\text{III}}$  and a ligand reaction, respectively, which is inconsistent with a previous report on CoPc [18]. At mild potentials where  $\text{H}^+$  reduction does not dominate the CV response, the  $\text{CoPc}(\text{OBU})_8$  modified electrode greatly outperformed CoPc with turnover frequencies of  $1.1 \times 10^6 \text{ h}^{-1}$  vs.  $5.5 \times 10^4 \text{ h}^{-1}$  for  $\text{CO}_2$  reduction (entry 5). Spectral changes during electrolysis of a homogeneous pyridine solution showed stepwise  $\text{Co}^{\text{III}}$  and  $\text{Pc}^{0-}$  reduction under  $\text{N}_2$  while the doubly-reduced species could not be detected under  $\text{CO}_2$ . A mechanism was proposed in which the doubly-reduced, protonated species reacts with  $\text{CO}_2$  and CO release is triggered by reduction of the putative  $\text{Co}(\text{II})\text{-COOH}$  species.  $\text{CoPc}(\text{CN})_8$  was active for  $\text{CO}_2$  reduction to CO at  $-1.20 \text{ V}$  vs.  $\text{Ag}/\text{AgCl}$  at pH 10. In this case the ratio of CO to  $\text{H}_2$  was 10 whereas it was 4.2 for  $\text{CoPc}(\text{OBU})_8$  (pH 6.8) [21].

Gas diffusion electrodes (GDE) [22] impregnated with CoPc were prepared by precipitation of CoPc onto carbon black from sulfuric acid. Polytetrafluoroethylene (PTFE) was added, and the paste was spread onto lead-plated nickel gauze, cured at  $300 \text{ C}$  and compressed at  $10^5 \text{ kPa}$  [23]. CO was the only carbon product of reduction (entry 6) and its partial current density was independent of applied potential; however,  $\text{H}_2$  production increased with increasingly negative potentials. Similar experiments with Mn, Cu or Zn phthalocyanine produced varying amounts of formate suggesting differing mechanisms dependent on the metal ion. One trend is that Mn, Cu, and Zn Pc are first reduced at the ligand while CoPc first undergoes a  $\text{Co}^{\text{III}}$  reduction. The proposed mechanism entailed reaction of  $\text{CO}_2$  with  $\text{Co}(\text{I})$  followed by protonation and a second electron transfer in contrast to the mechanism proposed above for  $\text{CoPc}(\text{OBU})_8$  in which the doubly reduced species is first protonated and then reacts with  $\text{CO}_2$ . Examination of GDEs with 17 different MPc showed 100% FE for CO with Co (entries 7 and 8) and Ni, while others produced formate or methane [24]. FePc produced CO but with low FE and decreasing activity for repetitive experiments. Theoretical analysis based on the Hückel model suggested CO desorption occurs for metal ions with a doubly occupied  $d_{z^2}$  orbital while further reduction is possible if CO is  $\sigma$ -bound to the metal [25]. The effect of  $\text{CO}_2$  pressure was studied using GDEs impregnated with CoTPP or FeTPP [26]. The reduction wave of  $\text{Co}^{\text{III}}\text{TPP}$  ( $> -1.0 \text{ V}$  vs.  $\text{Ag}/\text{AgCl}$ ) was unobservable under Ar due to low concentration of adsorbed CoTPP, but the catalytic wave for  $\text{H}_2$  production was observed. The effect of pressure on catalytic potential was evident in a ca. 100 mV positive shift for 20 atm  $\text{CO}_2$  vs. 1 atm (Fig. 1). The CVs of CoTPP supported GDE show the unusual curvature toward the low-voltage especially under high  $\text{CO}_2$  pressure, however, the authors did not give a clear explanation except that the waves were caused by electrocatalytic reduction around the potential where  $\text{Co}^{\text{II}}\text{TPP}$  is reduced to  $\text{Co}^{\text{I}}\text{TPP}$  ( $-0.8 \text{ V}$  vs.  $\text{Ag}/\text{AgCl}$  in

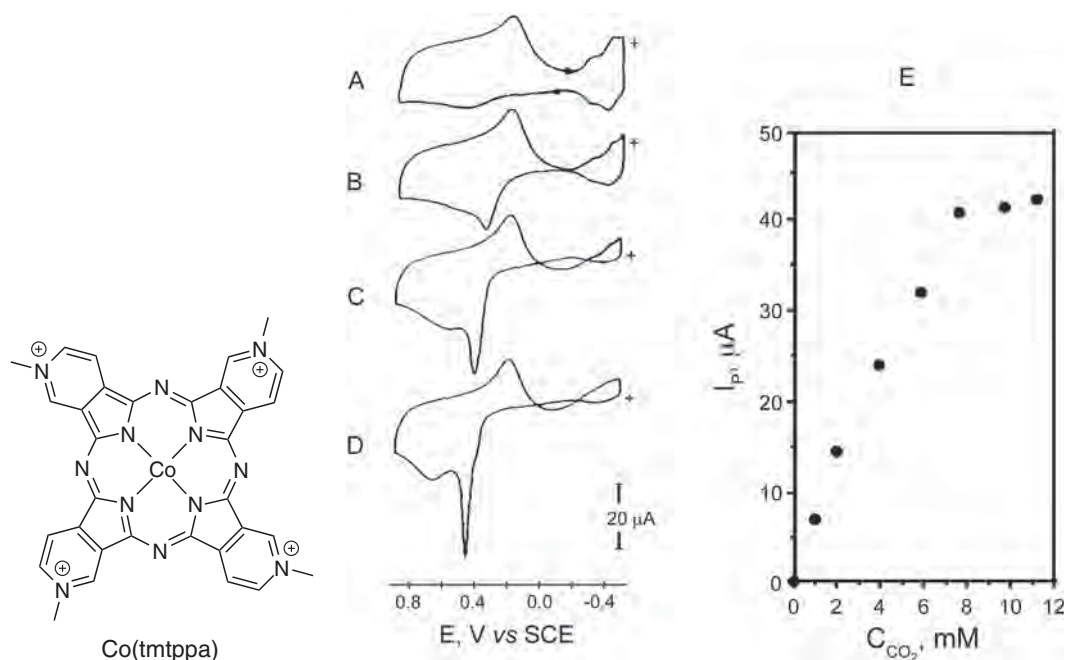


**Fig. 1.** Effect of  $\text{CO}_2$  pressure on the cathodic CVs at a CoTPP supported GDE: under Ar (small dash), atmospheric  $\text{CO}_2$  (large dash), and 20 atm  $\text{CO}_2$  (solid line). The reference electrode was  $\text{Ag}/\text{AgCl}$  and scan rate was  $50 \text{ mV}\cdot\text{s}^{-1}$ . Reprinted from Ref. 26 with permission from Elsevier, Copyright 1999

DMSO or DMF). Faradaic efficiencies for CO were also increased at a  $100 \text{ mA}\cdot\text{cm}^{-2}$  current density. For CoTPP, the FE increased from 75% to 97% while for FeTPP an increase from 42% to 75% was observed (entry 9). Catalysis occurred near the  $\text{M}^{\text{III}}$  potentials in DMF, and reactivity of the  $\text{M}(\text{I})$  oxidation state was presumed.

Gas diffusion electrodes with CoTMPP, CoPc, or  $\text{Co}(\text{tBuPc})$  adsorbed on activated carbon fibers produced CO with 70% FE (entry 10) in a  $\text{KHCO}_3$  aqueous solution under  $\text{CO}_2$  [27]. The carbon fibers were loaded from organic solutions of the catalysts, and the adsorption limit for CoTPP was found to be 9 wt% of the catalyst on the carbon fiber surface which is 16% of the theoretical coverage. Loading was found to agree with the wetted area suggesting the catalysts are absorbed up to a certain depth upon which full pore width is occupied. Maximum current densities for CO production were achieved from  $-1.35$  to  $-1.40 \text{ V}$  vs. SCE. Current efficiencies for CO production with cobalt catalysts adsorbed on activated fibers, which have slit-shaped pores of ca. 2 nm width, showed an inverse dependence on catalyst dimensions and electrocatalytic performances as expected from the benefit of the so-called nanospace effect. However,  $\text{Co}(\text{tBuPc})$  adsorbed on an activated carbon support, which has a much wider distribution in pore size dimension, was more effective with 85% FE for CO production.

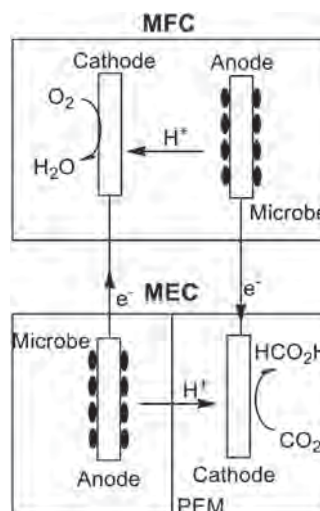
An interesting application of  $\text{CO}_2$  electroreduction by CoPc-type catalysts is quantitative  $\text{CO}_2$  analysis using the rotating ring-disk electrode and  $N,N',N'',N'''$ -tetramethyltetra-3,4-pyridoporphyrazino $\text{Co}(\text{II})$  ( $\text{Co}(\text{tmtppa})$ ) on a Nafion® protected carbon disk (entry 11) [28]. The film exhibited a  $\text{Co}^{\text{III}}$  couple at  $+0.25 \text{ V}$  vs. SCE and two pH dependent ligand based reductions near  $-0.25$  and  $-0.7 \text{ V}$ . At potentials more negative than  $-1.0 \text{ V}$ , proton reduction began and obscured any surface redox processes. While  $\text{CO}_2$  reduction was assumed to occur after formation of the doubly-reduced  $\text{Co}(\text{I})$  Pc radical anion, the possible involvement of a  $3e^-$  reduced species was considered. CO was detected at the Pt ring by its oxidation at  $0.4 \text{ V}$



**Fig. 2.** Ring electrode cyclic voltammograms of a rotating ring (Pt)-disk (EPG/Co(tmtpa)/Nafion®) electrode recorded at a disk potential of -1.1 V in a solution at pH 5.5 containing various concentrations of CO<sub>2</sub>: (a) 0.0 M; (b)  $2.0 \times 10^{-3}$  M; (c)  $5.9 \times 10^{-3}$  M; and (d)  $1.13 \times 10^{-2}$  M. Supporting electrolyte Britton-Robinson buffer, continuous scan, ring potential scan rate  $100 \text{ mV}\cdot\text{s}^{-1}$ , rotation rate 900 rpm. (e) Ring CO oxidation peak currents near 0.4 V as a function of CO<sub>2</sub> concentration. Reprinted from Ref. 28 with permission from Elsevier, Copyright 1996

with current proportional to scan rate, implicating surface oxidation of CO at Pt. A linear response was observed for CO<sub>2</sub> concentrations ranging from 0.1 to 32 mM using a disk potential of -1.08 V (Fig. 2).

A microbial electrolysis cell (MEC) driven by current from a microbial fuel cell (MFC) [29] has been studied for CO<sub>2</sub> reduction (Fig. 3) [30]. In an MEC, oxidation of organic compounds provides protons and electrons for cathodic reactions. The active composite cathode was prepared by layer-by-layer dip coating of multiwalled carbon nanotubes (MWCNT) and FeTPP on indium tin oxide (ITO) or graphite. Scanning electron microscope (SEM) images showed an even surface distribution of the MWCNTs with nano-sized clusters of CoTAPc, and the presence of the catalyst was verified by electronic absorption spectroscopy. The CV showed a CO<sub>2</sub> reduction peak at -0.5 V with current proportional to the number of adsorbed layers. The open circuit anode potential of the MEC was -0.3 V implying only 0.2 V external input was needed to drive CO<sub>2</sub> reduction. This input was generated by a single MFC with a cathode potential of 0.275 V and anode potential of -0.305 V across a  $1000 \Omega$  resistor. When connected to the MEC in series with a  $10 \Omega$  resistor, formic acid was produced with 74% FE. A maximum FE of 78% was achieved by controlling the anode potential to match the peak potential by CV (entry 12). The rate of formate production using the composite electrode was about three times that observed in the absence of MWCNTs and stable catalysis was measured for 10 consecutive



**Fig. 3.** Schematic representation of a microbial electrolysis cell (MEC) for CO<sub>2</sub> reduction using a MWCNT/CoTAPc cathode. The device is driven by electrons transferred from a microbial fuel cell (MFC). PEM = proton exchange membrane. Reprinted with permission from Ref. 30, Copyright 2012 American Chemical Society

4 h batches. For more negative potentials, side reactions such as H<sub>2</sub> production competed with CO<sub>2</sub> reduction. While the authors claimed that this self-driven device is promising for CO<sub>2</sub> electrolysis since no external energy is needed, MFCs are producing a large amount of CO<sub>2</sub>

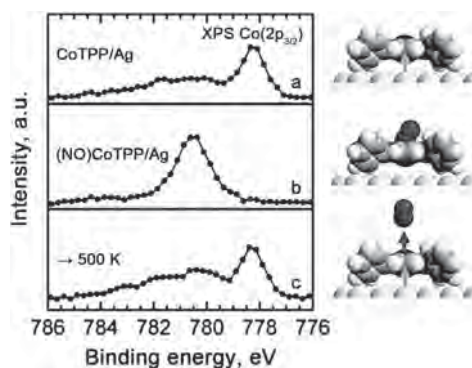
together with electrons and protons from the oxidation of organic substrates (e.g. if sugar is used as a consumable substrate, then  $C_{12}H_{22}O_{11} + 13H_2O \rightarrow 12CO_2 + 48H^+ + 48e^-$ ). Thus, while elegant in concept, practical application in  $CO_2$  reduction chemistry will require a system which does not generate  $CO_2$  as a byproduct.

In another example using MWCNTs as support on glassy carbon, adsorbed FeTPP showed higher activity and lower overpotential relative to drop coated FeTPP [31].  $CO_2$  was reduced to formic acid; however, the additives methyl viologen ( $MV^{2+}$ ) as a redox mediator, formic dehydrogenase (FDH), and nicotinamide adenine dinucleotide (NADH) were required. The authors attributed efficient electrocatalysis of  $CO_2$  by FeTPP adsorbed on MWCNT to (1) a decreased overpotential for reducing  $CO_2$  to formic acid due to the interaction between MWCNTs and FeTPP, and (2) the excellent electrical conductivity of MWCNTs improved the electron transfer between  $CO_2$  and the FeTPP active site to increase formic acid formation. However, the production of formate contrasts with the typical production of CO using FeTPP. Since this system requires  $MV^+$ , FDH and NADH, FeTPP may not be the active catalyst for formic acid production. It is known that FDH can catalyze not only oxidation of formate to  $CO_2$ , but also a hydride transfer from NADH to  $CO_2$  to produce formate (not CO). Interestingly, reversible interconversion of  $CO_2$  and formate by an electroactive FDH enzyme system with  $MV^{2+}$  and NADH has been achieved without any additional metal catalyst [32].

As pointed out above, the identity of surface adsorbed active species is difficult to assess, especially at low catalyst loadings. While the onset of catalytic behavior (by CV) is often compared to solution data, it is possible that the adsorbed catalyst exhibits different potentials and/or substrate binding affinity. Indeed, the electronic structure of MTPP changes upon surface adsorption [33–40]. On Ag(111), X-ray photoelectron spectroscopy (XPS) showed charge transfer from FeTPP and CoTPP due to interaction with the surface (Fig. 4). A new valence state in the UV photoelectron and scanning tunneling spectra (UV and STS) showed covalent character between the MTPP and the surface. This coordinative character was reversed by axial coordination of NO corresponding to an increase in the metal oxidation state. DFT data supported the mutual interference of NO and Ag as axial ligands. The implication for catalysis of  $CO_2$  reduction using adsorbed species is that electrode-catalyst surface interactions may increase electron density at the catalyst metal center in such a way that the transfer of a single electron may enhance substrate binding or even trigger catalysis at lower overpotentials compared to solution experiments.

## B. Catalysts covalently grafted to electrodes

**Amide linkages.** There are several disadvantages to simple non-covalent adsorption of catalysts onto



**Fig. 4.** Reversibility of the changes in the electronic structure induced by NO coordination: Co( $2p_{3/2}$ ) XP spectra of CoTPP and (NO)CoTPP on Ag(111). (a) CoTPP monolayer, (b) (NO)CoTPP monolayer, (c) after heating the (NO)CoTPP monolayer to 500 K for thermal desorption of the NO ligand. Reprinted with permission from Ref. 33, Copyright 2011 American Chemical Society

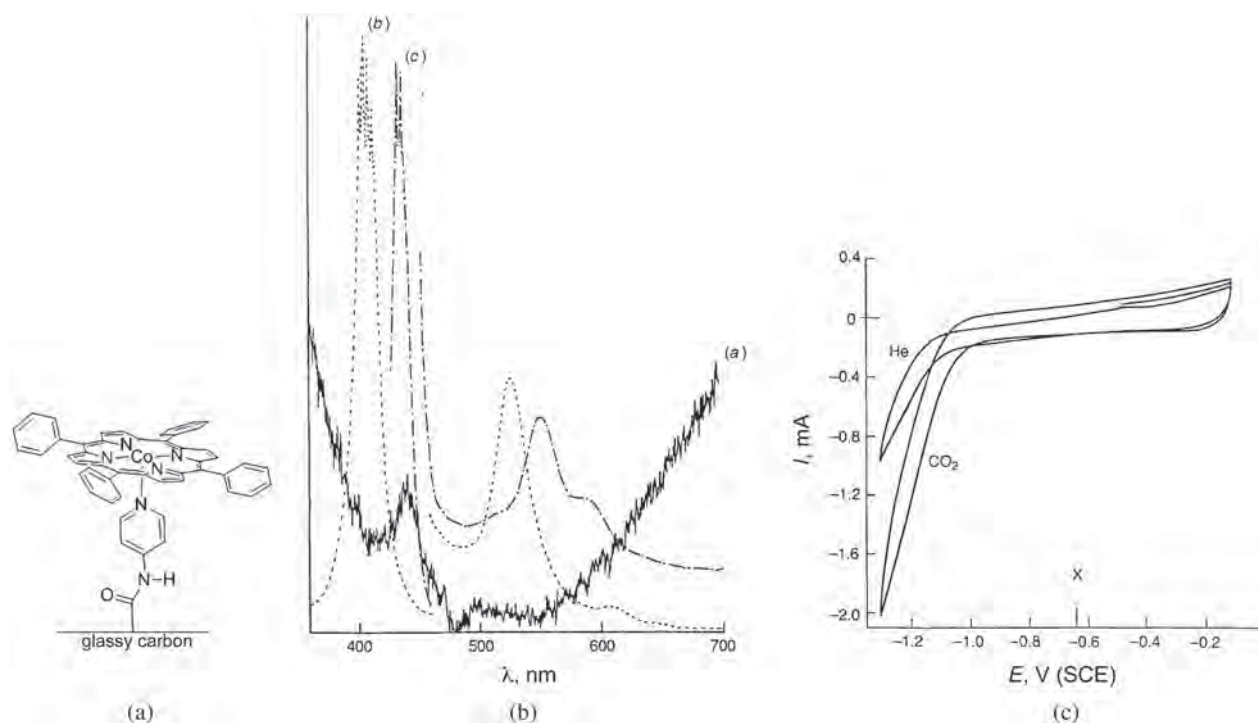
electrode surfaces. Stability of the modified electrode is a forefront concern while the impact of adsorption on catalytic properties is difficult to predict. Structure-activity relationships are difficult to surmise since solution properties may not be conserved on a surface. The following discussion summarizes experiments using covalent linkage of the catalyst to the electrode. These methods allow more direct translation of solution properties to the surface, and often better control of catalyst loading, film thickness, and local pH environment. Relevant data are summarized in Table 2.

A CoTPP-pyridine complex immobilized on a glassy carbon electrode (Fig. 5a) exhibited high electrocatalytic activity and stability for  $CO_2$  reduction [41]. The covalent linkage of pyridine to glassy carbon through amide bonds is achieved by oxidation of the carbon surface with  $H_2SO_4$ , treatment with  $SOCl_2$  and then 4-aminopyridine [41]. The presence of the amidine pyridine linker was confirmed by the C=O stretch at  $1665\text{ cm}^{-1}$  and pyridine C=C and C=N stretches at  $1610$  and  $1537\text{ cm}^{-1}$ . CoTPP was bound to the pyridine ligand in axial sites from benzene and its coordination to pyridine on the surface was confirmed by the matching of the Soret band at 440 nm in the diffuse reflectance spectrum to the visible spectrum of CoTPP in pyridine (Figs 5a and 5b). In water, the modified electrode showed catalytic waves for  $H_2$  and CO formation under He and  $CO_2$ , respectively, near the  $Co^{III/I}$  couple in pyridine (Fig. 5c). Extended electrolysis at  $-1.2\text{ V}$  produced CO with  $>50\%$  FE and  $10^5$  turnovers (Table 2, entry 1). Under optimized conditions (entry 2), CO was evolved with 92% FE, 300 mV overpotential, and over  $10^7$  turnovers [42]. The surface coverage, assuming a monolayer, was  $10^{-12}\text{ mol.cm}^{-2}$ . In solution, formate was produced with only 10% FE and rapid decomposition occurred thus validating the surface confinement as a method to stabilize the catalyst.

**Table 1.** Electrocatalytic CO<sub>2</sub> reduction using catalysts non-covalently adsorbed onto electrodes

Complex	Electrode	Product (FE)/TON or TOF	Catalytic species	E, V
1 CoPc <sup>a</sup>	Dip coated from benzene on graphite	oxalic acid, glycolic acid, but no formate	[Co(Pc <sup>•-</sup> )] <sup>2-</sup>	-1.6 (SCE)
2 CoPc <sup>b</sup>	Precipitated from sulfuric acid with water on glassy carbon	formate (60) methanol (5)	—	-1.2 to -1.4 (SCE)
3 CoPc <sup>c</sup>	Dip coated or drop cast from THF on glassy carbon	formate (55–60)/TON = 3.7 × 10 <sup>5</sup> H <sub>2</sub> (35–30)	[CoPcH] <sup>-1</sup>	-1.15 (SSCE)
4 CoPc <sup>d</sup>	Plasma assisted vacuum deposition on glassy carbon	—	—	-1.6 (SSCE)
5 CuPc(OBu) <sub>8</sub> <sup>e</sup>	Drop cast from DMF on basal plain pyrolytic graphite	CO/H <sub>2</sub> ~4.2/TOF = 1.1 × 10 <sup>6</sup> h <sup>-1</sup>	[CoPcH] <sup>-1</sup>	-1.3 (Ag/AgCl)
6 CoPc <sup>f</sup>	Gas diffusion electrode on carbon black with PTFE	CO (100) H <sub>2</sub> (14)	[Co'(Pc <sup>•-</sup> )] <sup>2-</sup>	-1.5 (SCE)
7 CoPc <sup>g</sup>	Gas diffusion electrode on carbon black with PTFE	CO (100)	[CoPc] <sup>2-</sup>	-1 to -1.75 (NHE)
8 FePc <sup>g</sup>	Gas diffusion electrode on carbon black with PTFE	CO (80)	[FePc] <sup>2-</sup>	-1.5 (NHE)
9 CoTPP <sup>h</sup> FeTPP <sup>h</sup>	Gas diffusion electrode on carbon black with PTFE	CO (97) CO (85)	[Co'TPP] <sup>-m</sup> [Fe'TPP] <sup>-m</sup>	-0.96 -1.01 (Ag/AgCl)
10 CoTMPP <sup>i</sup>	Activated carbon fiber, dip coated	CO (70)	—	-1.3 (SCE)
11 Co(tmippa) <sup>j</sup>	Dip cast on graphite disc, protected with Nafion	—	[Co'(Pc <sup>•-</sup> )] <sup>2-</sup>	-1.1 (SCE)
12 CoTAPc <sup>k</sup>	MWCNT/Co composite, layer by layer	formate (78)	—	-0.5 (Ag/AgCl)

<sup>a</sup> [15], 0.05 M Et<sub>4</sub>NClO<sub>4</sub>, <sup>b</sup> [16], bicarbonate pH 3–7, <sup>c</sup> [17], 0.05 M citrate, pH 5, <sup>d</sup> [19], 0.5 M Na<sub>2</sub>SO<sub>4</sub>/HCO<sub>3</sub><sup>-</sup> pH 6.65, <sup>e</sup> [20], pH 4, [23], sodium sulfate pH 2, <sup>f</sup> [24], 0.5 M bicarbonate pH 7.6, <sup>h</sup> [26], 0.5 M KHCO<sub>3</sub>, [27], 0.5 M KHCO<sub>3</sub>, [28], Britton-Robinson buffer pH 5.5, <sup>k</sup> [30], 0.1 M KHCO<sub>3</sub>, While [CoPcH]<sup>-1</sup> means a protonated [Co(Pc<sup>•-</sup>)]<sup>2-</sup> species, it is not clear the species is [H-Co(Pc)]<sup>-1</sup> or [Co(PcH)]<sup>-1</sup> from the original literature. <sup>m</sup> High pressure CO<sub>2</sub>.

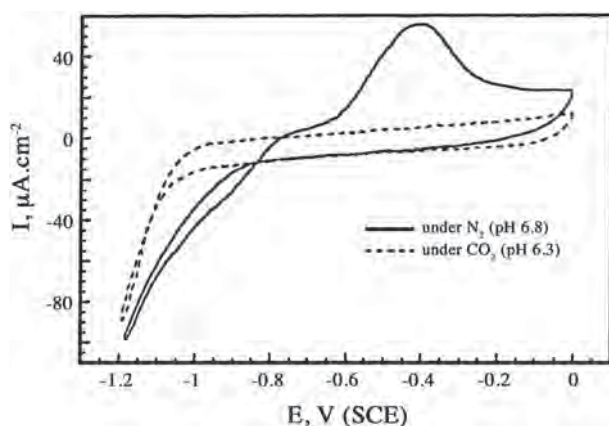


**Fig. 5.** (a) Schematic of CoTPP linked to glassy carbon through a 4-amide pyridine ligand. (b) Diffuse reflectance UV-vis spectrum of the CoTPP modified electrode (a), UV-vis spectrum of CoTPP (b) and CoTPP(pyridine) in  $\text{CH}_2\text{Cl}_2$  (c). (c) CV of the CoTPP electrode in pH 6.86 phosphate buffer in the presence of  $\text{CO}_2$  (a) or He (b) at room temperature. Scan rate  $1 \text{ mV}\cdot\text{s}^{-1}$ . Reproduced from Ref. 41 with permission from The Royal Society of Chemistry

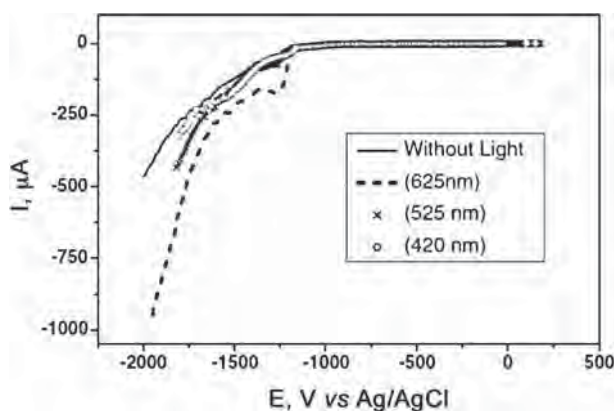
The same immobilization technique was extended to CoPc, CoNc, CoTMeOPP and hydrophobic vitamin B12 [43]. Catalytic activity for  $\text{H}_2$  evolution was observed together with  $\text{CO}_2$  reduction. An insightful observation regarding the mechanism was made using CV experiments: if the switching potential was negative of proton reduction current under  $\text{N}_2$ , the anodic return sweep exhibited a wave with potential varying from -0.35 to -0.78 V among these complexes. This feature was not observed if the switching potential was kept positive of the  $\text{H}_2$  evolution potential and also disappeared for CVs under  $\text{CO}_2$ . These observations suggest that the anodic wave under  $\text{N}_2$  is due to re-oxidation of a  $\text{H}_2$ -producing intermediate (*i.e.* a cobalt hydride), which is also consumed by the reaction of  $\text{CO}_2$  (and thus not re-oxidized at the electrode). The oxidation peak was thus assigned as oxidation of a Co hydride that reacts with  $\text{CO}_2$ . The authors proposed that the produced Co-COOH species converts to Co(II), CO, and  $\text{H}_2\text{O}$  by further addition of  $\text{H}^+$  and an electron. According to the CV data in DMSO, the complexes could be reduced by a second electron. Therefore, the loss of the anodic feature could be due to a preferential interaction of  $\text{CO}_2$  with the doubly-reduced species to produce CO. Furthermore, a product of the reaction of M-H with  $\text{CO}_2$  is normally considered to be M-OCHO (*i.e.* a precursor of  $\text{HCOO}^-$ ), not M-COOH (a precursor of CO). During electrolysis

under  $\text{CO}_2$ , the CoNc and CoPc (with the most positive potentials) exhibited the highest current densities (for mainly  $\text{H}_2$  production) while CoTPP showed the highest current efficiency for CO (Table 2 entry 3).

**Aminopyridine radicals.** A second approach to covalent linkage of a pyridine ligand to an electrode as a tether for Fe and Co catalysts is electrooxidation which triggers chemical bonding of the radical cation to glassy carbon. The method was investigated with 4-aminopyridine, 4-aminoethylpyridine, and imidazole. CoTPP was introduced from hot benzene/ $\text{CH}_2\text{Cl}_2$  [44]. The amount of immobilized ligand was estimated as  $9 \times 10^{-11} \text{ mol}\cdot\text{cm}^{-2}$ . The reductive CV in pH 6.8 phosphate buffer exhibits the same anodic return wave discussed above for amide-linked pyridine electrodes (Fig. 6). Again, the feature is absent under  $\text{CO}_2$  or for CoTPP adsorbed directly on glassy carbon. The good agreement found between the charge density of the anodic wave and the surface loading of CoTPP ( $1.6 \times 10^{-8} \text{ mol}\cdot\text{cm}^{-2}$ ) obtained by ultrasonic dissolution suggested a  $1e^-$  oxidation process for the anodic return wave. Notably the ultrasonic dissolution measurements revealed the presence of 100-fold more CoTPP than available ligand sites suggesting that a monolayer of CoTPP was bound through pyridine coordination and additional catalyst was stacked upon the base layer of CoTPP. Heavy rinsing with  $\text{CH}_2\text{Cl}_2$  removed the stacked molecules as



**Fig. 6.** Cyclic voltammograms at 50 mV.s<sup>-1</sup> of CoTPP bonded to glassy carbon in N<sub>2</sub> and CO<sub>2</sub> atmospheres in pH 6.8 phosphate buffer. The bridging compound is 4-aminopyridine. Reprint from Ref. 44 with permission from Elsevier, Copyright 1997



**Fig. 7.** Cyclic voltammograms at 5 mV.s<sup>-1</sup> showing the response of the supramolecular electrode toward the reduction of CO<sub>2</sub> with and without illumination at different wavelengths. Reprint from Ref. 46 with permission from Elsevier, Copyright 2009

shown by the absence of the anodic hump and increased the efficiency for CO production during electrolysis. Faradaic efficiencies of 39–59% were reported with the remaining current reducing H<sup>+</sup> (entry 5).

The amino-pyridine methodology has been extended to Co(benzoPor) (benzoPor = tetrabenzoporphyrin) with no effort to remove the stacked molecules from the pyridine-bound surface layer [45, 46]. Adsorbed Co(benzoPor) was inactive for electrochemical CO<sub>2</sub> reduction, but showed enhanced photoelectrochemical current. The authors viewed the Co(benzoPor) excited state as a source of reductive driving force and examined the CVs during illumination of the Soret band at 420 nm and Q bands at 525 and 625 nm. Irradiation of the electrode at 625 nm produced a significant positive shift in the CV under CO<sub>2</sub> (Fig. 7). The same shift was obtained using [Ru(bpy)<sub>3</sub>]<sup>2+</sup> as a sensitizer in solution for 420 and 525 nm. Product analysis was not reported.

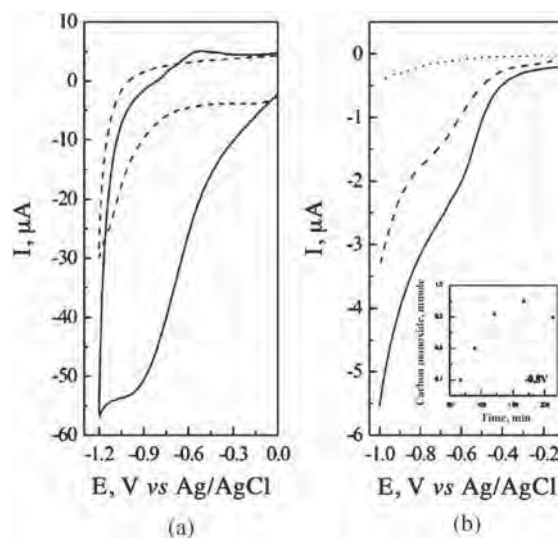
**Polymerized ligands.** A third approach to electrode preparation involves formation of a film by electropolymerization of monomers such as 4-vinylpyridine or pyrrole and drop casting CoPc onto the film or casting a mixture of dissolved polymer and catalyst directly onto the electrode [47–49]. A CoPc/PVP (poly-4-vinylpyridine) film exhibited similar UV-vis properties to those observed in pyridine suggesting a surface Co-pyridine interaction. The sharp bands of CoPc/PVP compared to the broadened features of a CoPc solid layer imply homogeneous dispersion within the film. A reactive surface coverage of  $5.0 \times 10^{-12}$  mol.cm<sup>-2</sup>, corresponding to a monolayer was determined. The Co<sup>III</sup> couple was found to exhibit 1H<sup>+</sup>/1e<sup>-</sup> pH dependence below pH 5.3 from -0.62 to -0.38 V vs. SCE attributed to protonation on the peripheral ring nitrogen. The ligand-based reduction in the film was observed at -0.7 V at pH 2.1 and showed a 75 mV/decade dependence on pH attributed to a second protonation. The CV of the CoPc/PVP electrode under CO<sub>2</sub> showed much larger catalytic current than CoPc adsorbed on graphite under the same conditions and CoPc/PVP produced more CO with better selectivity. Since proton reduction was observed concurrent with CO<sub>2</sub> reduction, the dependence on pH and applied potential were investigated to improve selectivity. Initially, the best CO/H<sub>2</sub> selectivity (~3) was found at pH 6.8 with turnover numbers *ca.*  $6 \times 10^5$ . In this case, a mechanism involving reaction of [Co<sup>I</sup>(PcH<sup>\*</sup>)] (*i.e.* the doubly-reduced species with the protonated Pc ligand) with CO<sub>2</sub> to form HOOC-CoPc *via* a proton transfer reaction from the protonated ligand was invoked. Later, the system was optimized with  $1.2 \times 10^{-10}$  mol.cm<sup>-2</sup> at pH 5 and -1.2 V vs. Ag/AgCl providing CO/H<sub>2</sub> = 6 (entry 8) [48]. The pH-dependent behavior was attributed to partial protonation of pyridine residues surrounding the catalyst functioning as proton donors and acceptors, possibly functioning *via* a concerted proton transfer mechanism. A steady state concentration of [Co<sup>I</sup>Pc] was found by electronic spectra measured during reduction under CO<sub>2</sub> confirming the reactivity of [Co<sup>I</sup>(Pc<sup>\*</sup>)]<sup>2-</sup> (or [Co<sup>I</sup>(PcH<sup>\*</sup>)]) since the later species did not accumulate during catalytic conditions in which it reacts rapidly with CO<sub>2</sub>.

An electrode prepared by electropolymerization of pyrrole followed by drop casting a solution of CoPc from THF (CoPc/PPy, PPy = polypyrrole) exhibited an onset potential for CO<sub>2</sub> reduction 160 mV more positive than a PPy film without catalyst [49]. SEM imaging showed smooth surface coating of the PPy film and a crystalline porous structure with cast CoPc. The CV under CO<sub>2</sub> in MeCN/H<sub>2</sub>O exhibited catalysis at -0.18 V vs. Ag/AgCl, and extended electrolysis produced formic acid with ~72% Faradaic efficiency (entry 9) compared to 59% for the PPy electrode. CO<sub>2</sub> reduction at such mild potentials even without the catalyst is somewhat suspicious and points to a major role of the PPy film even without catalyst coating. Furthermore, production of formate

in this system (vs. CO and H<sub>2</sub>) [47–49] illustrates that *a priori* prediction of product distribution for a given catalyst is not possible since electrode preparation and catalytic conditions are clearly important elements in the reduction of CO<sub>2</sub>.

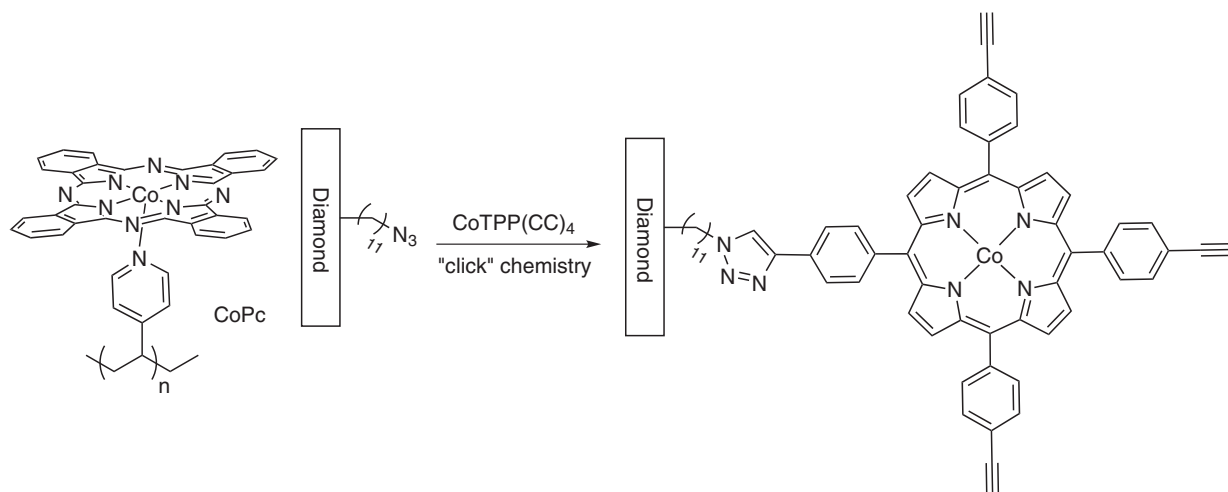
**Functionalized ligands.** The fourth category for preparing functionalized electrodes involves direct electrode modification using specialized ligands designed with functional groups for polymerization or covalent reactions with electrode surfaces. In this regard, Co Ni, and Fe complexes with aminophthalocyanines (TAPc) were electropolymerized on glassy carbon [50]. CoTAPc produced formic acid while FeTAPc produced formaldehyde and H<sub>2</sub>. No carbon products were detected using the polymerized free ligand. Poorly defined peaks were observed in the CV but the current discharge due to CO<sub>2</sub> reduction occurred cathodic of the doubly-reduced species, invoking injection of a third electron to trigger catalysis. Electrolysis of the CoTAPc polymer at -1.0 V yielded  $7.9 \times 10^4$  turnovers of formate after 1.5 h. The FeTAPc polymer was not stable and small amounts of formaldehyde were detected. Electrochemical impedance spectroscopy revealed important morphological differences among polymers with varied metal ions.

Recently, a Co tetrakis(4-aminophenyl)porphyrin (TAPP) was electropolymerized on ITO and catalysis was examined in the room temperature ionic liquid 1-butyl-3-methylimidazolium tetrafluoroborate (BMImBF<sub>4</sub>) [51]. The ionic liquid functions as solvent and electrolyte in this experiment. The film was prepared by 50 anodic cycles in DMF and any remaining NH<sub>2</sub> groups were electro-oxidized in water. SEM showed a heterogeneous distribution due to localized formation of oligomers. Stabilization in BMImBF<sub>4</sub> produced a more homogeneous surface due to intercalation of ions in the surface. The absorption spectrum of the film confirmed retention of the CoTAPP structure. Under N<sub>2</sub>, a quasi-reversible Co<sup>III</sup> couple was observed at -0.75 V vs. Ag/AgCl. Under CO<sub>2</sub>, a current increase at the



**Fig. 8.** (a) Cyclic voltammetry of the bare ITO electrode (dashed line) and the ITO/Poly-CoTAPP modified electrode (solid line) in BMImBF<sub>4</sub>; scan rate 100 mV.s<sup>-1</sup>. (b) Electrochemical behavior measured by linear sweep voltammetry at 5 mV.s<sup>-1</sup> of the bare ITO electrode (dots) and the Poly-CoTAPP modified electrode under N<sub>2</sub> (dashed line) and CO<sub>2</sub> (solid line) in BMImBF<sub>4</sub>. Inset: CO production over time. Reproduced from Ref. 51 with permission from The Royal Society of Chemistry

Co<sup>III</sup> couple prompted assignment of Co(I) as the active species; however, the Co<sup>III</sup> wave is visible in the catalytic current suggesting further reduction accelerates catalysis (Fig. 8). Electrolysis at -0.8 V produced CO with 65% FE (entry 12). After 4 h, about 25% of the activity was lost (by CV). Impedance spectroscopy suggested CO<sub>2</sub> inclusion in the electric double layer decreases charge transfer resistance due to deformation and loss of density. The oxide acceptor for production of CO was not discussed. Presumably CO<sub>2</sub> is the oxide acceptor since protons should be scarce in the medium.



**Fig. 9.** Representation of covalent CoTPP modified boron-doped diamond electrodes [52]



**Table 2.** Electrocatalytic CO<sub>2</sub> reduction using catalysts covalently bound to electrodes

Complex	Electrode	Product (FE)/TON of TOF	Catalytic species	E, V
1 CoTPP	4-aminopyridine amide linked to glassy carbon	CO (>50)/TON 10 <sup>5</sup>	[Co <sup>I</sup> (tpp)(py)] <sup>-</sup>	-1.2 (SCE)
2 CoTPP	4-aminopyridine amide linked to glassy carbon	CO (92)/TON 10 <sup>7</sup>	[Co <sup>I</sup> (tpp)(py)] <sup>-</sup>	-1.1 (SCE)
3 CoTPP	4-aminopyridine amide linked to glassy carbon	CO (45)	[Co <sup>I</sup> (tpp)(py)] <sup>-</sup> with H <sup>+</sup> and CO <sub>2</sub>	-1.3 (SCE)
4 CoTPP	Aminopyridine radical bound to glassy carbon	CO (60)	[H-Co(TPP)]	-1.1 (SCE)
5 Co(benzoPor)	4-aminopyridine radical bound to glassy carbon	—		-1.6 (Ag/AgCl)
6 CoPc	Poly-4-vinylpyridine on graphite	CO (69) H <sub>2</sub> (20) TOF 6.12 × 10 <sup>5</sup>	[Co <sup>I</sup> (PcH)] <sup>1</sup>	-1.5 (SCE)
7 CoPc	Poly-4-vinylpyridine on graphite			-1.2 (Ag/AgCl)
8 CoPc	Neat coating on graphite	CO/H <sub>2</sub> = 6	[Co <sup>I</sup> (PcH)] <sup>1</sup>	-1.2 (Ag/AgCl)
9 CoPc	Polypyrrole on glassy carbon, Co drop cast from THF	formate (72)	[Co <sup>I</sup> Pc] with H <sub>adsorbed</sub>	-1 (Ag/AgCl)
10 CoTAPc	Electropolymerized on glassy carbon	Formate/TOF 7.9 × 10 <sup>4</sup> h <sup>-1</sup>	Further reduced species of [Co <sup>I</sup> (TAPc*)] <sup>2-</sup>	-1 (Ag/AgCl)
11 CoTPC(CC) <sub>3</sub>	Click reaction on modified boron-doped diamond	CO/TOF 0.8 s <sup>-1</sup>		-1.55 (Ag/AgCl)
12 CoTAPP	Electropolymerized on ITO	CO (65)/TON 69 Ionic liquid	[Co <sup>I</sup> TAPP] <sup>-</sup>	-0.8 (Ag/AgCl)

<sup>a</sup>[41], phosphate pH 6.86. <sup>b</sup>[42], phosphate, pH 6.0. <sup>c</sup>[43], phosphate pH 6.3. <sup>d</sup>[44], phosphate pH 6.8. <sup>e</sup>[46], phosphate pH 6.3–6.8. <sup>f</sup>[47], phosphate pH 6.8. <sup>g</sup>[48], phosphate pH 5. <sup>h</sup>[49], LiClO<sub>4</sub>, CH<sub>3</sub>CN/H<sub>2</sub>O. <sup>i</sup>[50], NaClO<sub>4</sub>. <sup>j</sup>[51], BMImBF<sub>4</sub>. <sup>k</sup>[52], CH<sub>3</sub>CN, Bu<sub>4</sub>NPF<sub>6</sub>. <sup>1</sup>[Co<sup>I</sup>(PcH)]<sup>-</sup> is the doubly reduced and the protonated ligand species formed from [Co<sup>II</sup>(Pc)].

Co porphyrin has been attached to boron-doped diamond electrodes through triazolyl linkages (Fig. 9) [52]. Following functionalization of the diamond surface with alkyl azides, the 4-phenyl acetylene functionalized CoTPP(CC)<sub>8</sub> was attached *via* Cu-catalyzed cycloaddition. Its presence was verified by a decrease in azide IR signatures and observation of the Co(2p) region by X-ray photoelectron spectroscopy. The surface coverage was 3.8 × 10<sup>13</sup> Co cm<sup>-2</sup>. Electrocatalytic CO<sub>2</sub> reduction in acetonitrile was stable for >1000 cycles at -1.8 V with an estimated turnover frequency of 0.8 s<sup>-1</sup>. The doubly reduced species was suggested as the active catalyst and CO was the only product detected.

### III. HOMOGENEOUS CATALYSIS

#### A. Electrochemical CO<sub>2</sub> reduction

The reduction of CO<sub>2</sub> by water soluble tetrasulfonated CoPc (CoTScPc) at an amalgamated Pt plate electrode was carried out as early as 1977 [53]. Catalytic current was observed around -1.3 V *vs.* SCE but the current

depended on the initial potential and holding time, suggesting varied adsorption onto the electrode. Under similar conditions, CoTPPS reduced CO<sub>2</sub> to formate at -1.3 V while the Fe complex was not active [54].

A cofacial dinuclear metalloporphyrin CoTPPS//Co-pTMPyP (Fig. 10) prepared by self-assembly of the cationic and anionic porphyrins is catalytically active in aqueous DMSO at -1.8 V *vs.* Ag/Ag<sup>+</sup> [55]. The equilibrium constant for formation of the dinuclear structure was estimated as 10<sup>6</sup> M<sup>-1</sup> in aqueous DMSO. The CV is essentially the sum of CVs for each individual complex and CO<sub>2</sub> reduction was attributed to Co(I) of Co-pTMPyP although the exact oxidation state at this stage was difficult to determine due to the presence of several ligand-based reductions. Based on the CVs, the CoTPPS functioned only as an “electron mediator,” a term which the authors previously used to describe it as a redox-active electron donor to accelerate electron transfer to the catalytic metal [56]. In this case the metal ion identity of the mediator component was not essential, and similar catalytic results were achieved with CuTPPs.

Co porphyrins with phenylazomethine dendrimers catalyze CO<sub>2</sub> reduction in DMF assisted by lanthanide

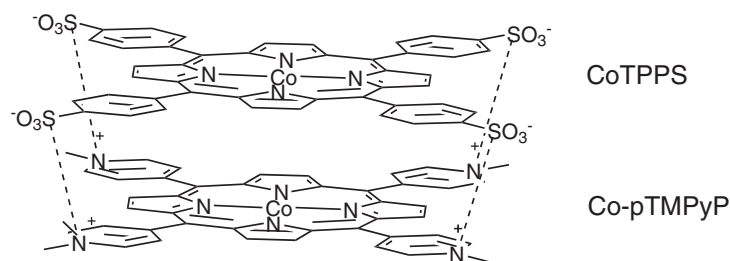


Fig. 10. Cofacial dinuclear porphyrin complex prepared by self-assembly [55]

ions as strong Lewis acids [57]. Under  $N_2$ , the CV showed characteristic  $Co^{III}$  waves near  $-1.3$  V vs.  $Fe^{+/0}$ , and a catalytic current was triggered at this wave under  $CO_2$ . Comparison among different generations revealed a maximum efficiency for the third generation dendrimer and a decrease in activity of the fourth generation structure attributed to steric effects. A non-symmetric third generation dendrimer showed the greatest current attributed to accessibility of the Co center to  $CO_2$  while maintaining the function of the dendrimer such as binding sites for  $Ln^{3+}$ . No product analysis was reported.

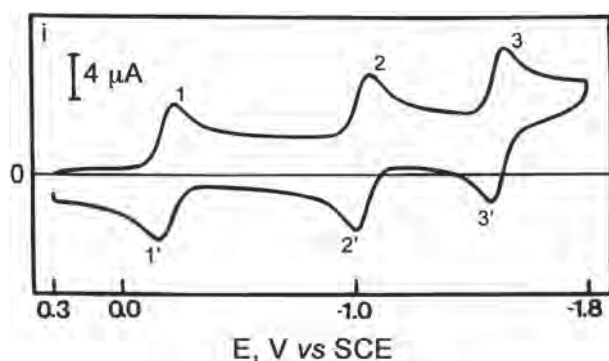
Iron tetraphenylporphyrins have received considerable attention as homogeneous electrocatalysts for reduction of  $CO_2$  to CO in DMF due in part to product selectivity, stability, and impressive rates. Early experiments revealed catalysis and the product CO as indicated by the  $Fe^{III}$  (CO) wave on the return scan [58] while advancement in the system understanding is revealed by recent experiments showcasing the concerted nature of electron transfer, proton transfer, and C–O bond cleavage [59]. The FeTPP exhibits clear  $Fe^{III/II}$ ,  $Fe^{III}$ , and  $Fe^{I/0}$  couples (Fig. 11), the last of which (at  $-1.64$  V vs. SCE) develops a catalytic current under  $CO_2$ . The active catalyst is best described using the  $Fe(0)TPP$  resonance structure in agreement with experimental reactivity and Raman spectroscopy [60–62]. In dry solvent,  $CO_2$  is proposed as the oxide acceptor thereby generating  $CO_3^{2-}$  and few catalytic turnovers are achieved due to destruction of the TPP ligand by carboxylation. The rate of catalysis and durability were enhanced by the addition of  $Mg^{2+}$ ,  $Na^+$ ,  $Li^+$ ,  $Ba^{2+}$ , or  $Al^{3+}$  ions, although  $Mg^{2+}$  was the most effective [63]. Two mechanisms were proposed to explain the temperature-dependent cyclic voltammograms. At  $-40$  °C the carbene type complex,  $[Fe^{II}(TPP)(CO_2^-)]^{2-}$ , formed *via* the reaction of  $Fe(0)$  with  $CO_2$  reacts first with another carbon dioxide molecule. Decomposition of this species into  $Fe^{II}(TPP)CO$  and carbonate is accelerated by a Lewis acid. At room temperature,  $Mg^{2+}$  reacts directly with  $[Fe^{II}(TPP)(CO_2^-)]^{2-}$ . For monovalent Lewis acids, the catalysis is second order in  $[CO_2]$  and  $[M^+]$ , suggesting a mechanism in which  $[Fe^{II}(TPP)(CO_2^-)]^{2-}$  reacts with  $CO_2$  and the intermediate is stabilized in two separate steps by  $Li^+$ . This species decomposes to  $Fe^{II}(TPP)CO$  and  $Li_2CO_3$  [64]. Deviation of the catalytic

wave from S-shape was explained by precipitation of carbonates on the electrode.

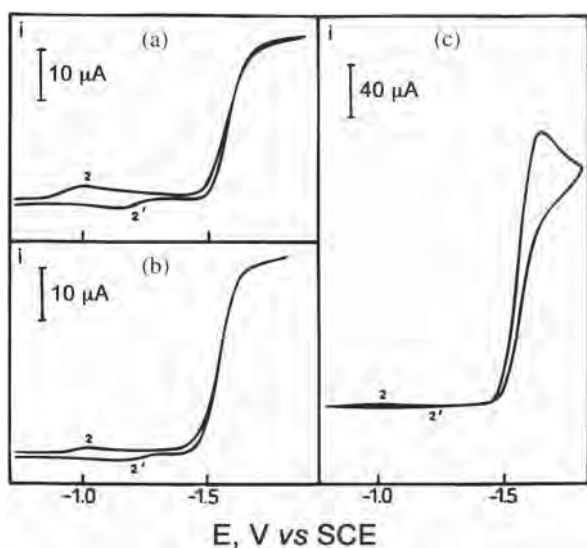
A major breakthrough in FeTPP catalysis was realized by the addition of weak Brønsted acids such as  $CF_3CH_2OH$  [65]. In DMF containing 0.1 M  $Et_4NClO_4$  at a hanging mercury drop electrode, the ratio of catalytic current ( $i_c$ ) to the  $Fe^{I/0}$  current in the absence of  $CO_2$  ( $i_p$ ) was only 1.8 but reached 131 with 1.47 M  $CF_3CH_2OH$ . The FE for CO production was 94% whereas it was only 70% with Lewis acid additives. In preparative scale experiments, current is limited by cell geometry, not the rate of catalysis. About 75% of the catalyst remained intact after passage of 225 C during bulk electrolysis. The scope of acid synergy was expanded to 2-pyrrolidone, 1-propanol, and mixtures of water in 1-propanol (Fig. 12) [66]. It was found that selectivity for CO and stability both increased as the acid becomes more acidic although FeTPP will catalyze proton reduction if stronger acids ( $pK_a < \sim 9$ ) are added. Kinetic analysis revealed first-order dependence on  $[CO_2]$  and second-order dependence on  $[CF_3CH_2OH]$ , at least in the low concentration region where the voltammetric response exhibits the S-shape characteristic of large substrate excess which remains unchanged from the bulk concentration (Fig. 13). At higher concentrations, the appearance of a peak-shaped wave was attributed to self-inhibition by the CO product through adsorption on the Hg thus inactivating portions of the electrode. In agreement with theory is the scan-rate dependence in which the peak shape becomes less pronounced at higher sweep rates. Notably, the turnover number in preparative scale electrolysis is significantly less than that calculated from voltammetry, suggesting the interference of ohmic drop in bulk experiments.

The catalytic response of FeTPP in the presence of water, phenol, trifluoroethanol, and acetic acid was further analyzed to reveal an intimate detail of the catalytic mechanism, namely, the concerted C–O cleavage with electron and proton transfer as the rate determining step [67]. There is a  $pK_a$  dependence on the rate determining step and stepwise proton/electron transfer was ruled out assuming protonation of a  $CO_2$  radical anion should be near the diffusion limit regardless of  $pK_a$ .

Further remarkable advancement of FeTPP electrocatalysis in DMF was achieved by introduction of phenol

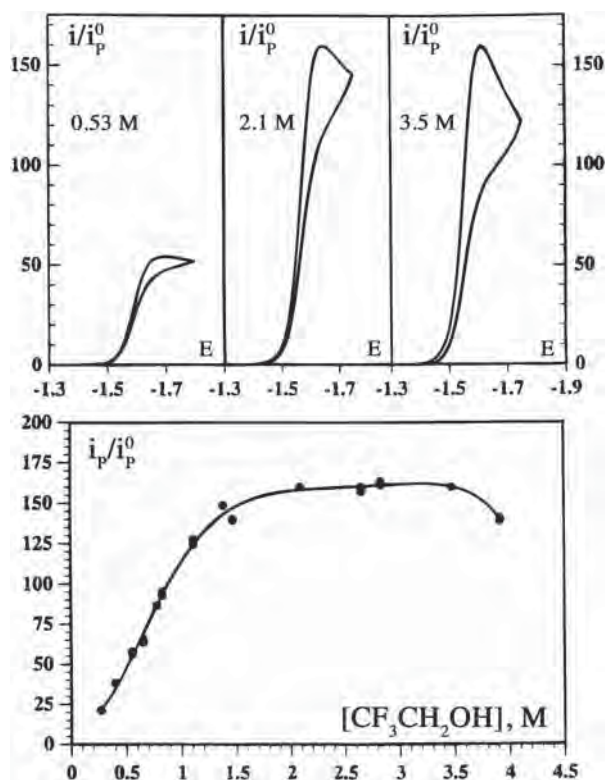


**Fig. 11.** Cyclic voltammetry of FeTPP (1 mM) in DMF at a glassy carbon electrode. Scan rate = 100 mV.s<sup>-1</sup>. Reprinted with permission from Ref. 66, Copyright 1996 American Chemical Society



**Fig. 12.** Cyclic voltammetry of FeTPP (0.5 mM) in DMF under 1 atm CO<sub>2</sub> in the presence of 0.51 M 2-pyrrolidone (a), 6.66 M 1-propanol (b), and 1.47 M CF<sub>3</sub>CH<sub>2</sub>OH (c) at Hg, scan rate 100 mV.s<sup>-1</sup>. Reprinted with permission from Ref. 66, Copyright 1996 American Chemical Society

groups in *ortho* positions of the TPP phenyl groups (TDHPP) to speed up CO<sub>2</sub> reduction by providing a pre-positioned proton source for the 2e<sup>-</sup>/2H<sup>+</sup> conversion of CO<sub>2</sub> to CO [68]. Comparison of the catalytic rate constant ( $k_{\text{cat}} = 2k[\text{CO}_2]$ ) of  $1.6 \times 10^6 \text{ s}^{-1}$  for FeTDHPP with that for FeTPP with external 3 M phenol ( $3.2 \times 10^4 \text{ s}^{-1}$ ) suggested the proximal proton source in FeTDHPP is equivalent to 150 M phenol. The authors describe that the exact mechanism of the phenol influence in CO<sub>2</sub> reduction is not known, however, it is likely to be a push-pull type interaction between a proton and an electron as previously proposed for other acids [66]. Electrolysis at -1.16 V (well below the Fe<sup>II</sup> couple at -1.33 V) produced CO with 90% FE and 0.31 mA.cm<sup>-2</sup> with 50 million turnovers over 4 h of electrolysis. Comparison to the



**Fig. 13.** Cyclic voltammetry of the reduction of CO<sub>2</sub> (1 atm) in DMF catalyzed by 1 mM FeTPP with varied concentrations of CF<sub>3</sub>CH<sub>2</sub>OH. Scan rate 100 mV.s<sup>-1</sup>. Reprinted with permission from Ref. 66, Copyright 1996 American Chemical Society

methylated catalyst FeTDMPP, which was less active, further supported the involvement of internal protons in the catalysis.

A related catalyst with prepositioned phenol groups and perfluorination of the remaining phenyl groups (FeTDHPPF<sub>10</sub>) is more active than FeTDHPP while its Fe<sup>II</sup> couple is less negative [59]. In this case, the catalytic response is preceded by a one-electron wave indicating that the “Fe(0)–CO<sub>2</sub>” adduct is stabilized by phenolic hydrogen bonding that is also confirmed with DFT calculations. However, injection of a third electron is required to commence catalysis. The rate constants for CO<sub>2</sub> adduct formation were estimated as  $>5 \times 10^6 \text{ M}^{-1} \cdot \text{s}^{-1}$  and  $3 \times 10^5 \text{ M}^{-1} \cdot \text{s}^{-1}$  for FeTDHPP and FeTDHPPF<sub>10</sub>, respectively, from the scan-rate dependent behavior of the pre-wave. Since the adduct is protonated by internal phenolic groups, the potential for the second electron transfer is only slightly cathodic of the Fe<sup>II</sup> couple. It was suggested that concerted re-protonation of internal OH groups by phenol with electron transfer, proton transfer, and C–O bond cleavage is also possible. The remarkable roles of the prepositioned phenol groups resemble the 2nd coordination-sphere effect previously found for interconversion of H<sup>+</sup>/H<sub>2</sub> and CO<sub>2</sub>/HCOO<sup>-</sup> using other molecular metal catalysts [69–71].

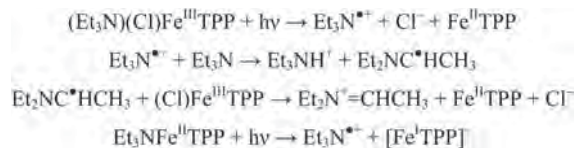
## B. Photochemical CO<sub>2</sub> reduction

Photochemical experiments are useful probes for studying Fe and Co porphyrins, phthalocyanines, corroles, and corrins and their reactions with CO<sub>2</sub> since the absorption spectra of each oxidation state exhibit distinct features which are readily monitored. Additionally, pulse radiolysis with a short electron pulse is used to determine reaction kinetics by monitoring differential absorption spectra. Photocatalytic CO<sub>2</sub> reduction is possible if the photo-produced species reacts with CO<sub>2</sub>, releases product, and re-enters the catalytic cycle. Pertinent photochemical systems for CO<sub>2</sub> reduction are summarized in Table 3 and relevant equations are collected in Table 4.

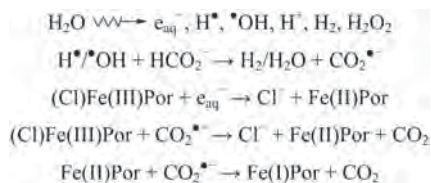
First, iron porphyrins are considered [72]. Photolysis of ClFe<sup>III</sup>TPP with 325 nm < λ < 385 nm in DMF containing 5% triethylamine (Et<sub>3</sub>N) as an electron donor yielded Fe<sup>II</sup>TPP through electron transfer with a quantum efficiency of *ca.* 0.05 (Scheme 1).

Continued photolysis generated [Fe<sup>I</sup>TPP]<sup>-</sup> with low efficiency suggesting weaker interaction with Et<sub>3</sub>N. The reaction was not quantitative and peaks due to hydrogenation products were observed. Under CO<sub>2</sub>, the reduced [Fe<sup>I</sup>TPP]<sup>-</sup> was converted to the Fe(II)–CO complex, which releases CO upon photolysis [73]. Throughout extended photolysis (>150 h) CO was quantified by gas chromatography and the overall turnover number reached ~70 [72]. During photolysis, the chlorin was observed as a green solution which remained catalytically active. CO production ceased when the solution turned yellow indicating destruction of the ligand. Decomposition was slowed at lower concentrations since its primary path is presumed to be the reaction of [Fe<sup>0</sup>TPP]<sup>2-</sup> with other porphyrin species.

Radiolytic reduction of various water soluble Fe porphyrins (FePor) also produced the Fe(I) complexes (Scheme 2) with small amounts of the phlorin anion and chlorin. In alkaline solution, the Fe(I) porphyrins are



**Scheme 1.** Photochemical reduction of Fe<sup>III</sup>TPP



**Scheme 2.** Radiolytic reduction of water-soluble Fe porphyrins showing the formal Fe-oxidation states, but ignoring the total charges due to complication of the peripheral charges

stable for many hours but decay more rapidly at lower pH. Pulse radiolysis of Fe(II) porphyrins was used to analyze short-lived species in aqueous solution. Bleaching of the Soret band along with formation of absorptions below 520 nm and 600–840 nm indicated formation of Fe(I) Por as the first product. Interestingly, the Fe(I) complex of oTMPyP (see Chart 1) exhibits complicated decay behavior attributed to varied reactivity among the four atropisomers of the ligand. The decay obeyed a second-order rate law with  $k = (1.5 \pm 0.5) \times 10^8 \text{ M}^{-1}\cdot\text{s}^{-1}$  for the first step. Results are explained by a disproportionation reaction of Fe(I)Por to produce Fe(II)Por and Fe(0)Por. The Fe(0)Por reacts with water, protons, or CO<sub>2</sub> to produce intermediates which are protonated to yield H<sub>2</sub> or CO, and the Fe(0) state is implicated as the reactive species in photolysis experiments.

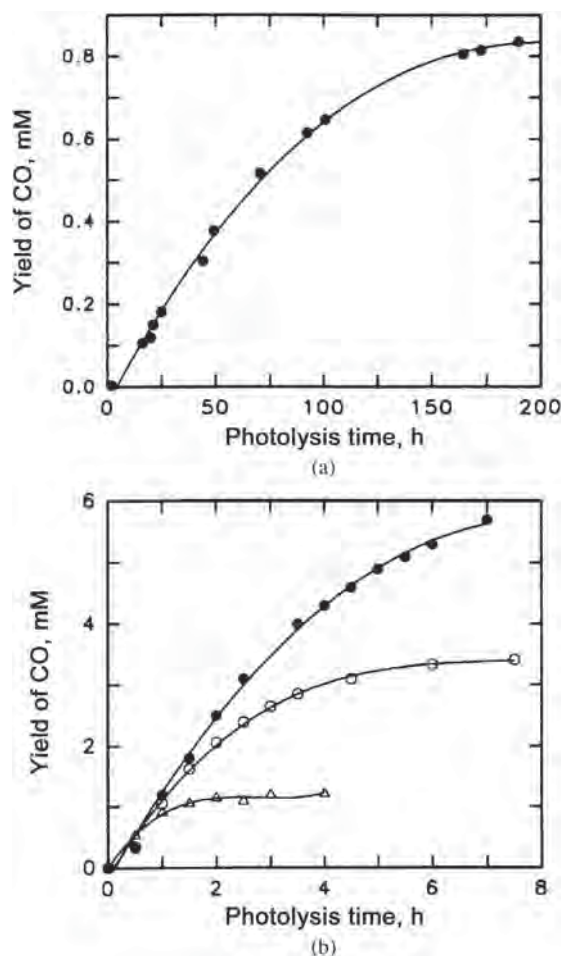
Photochemical and radiolytic studies of Co porphyrins were undertaken to characterize reduced species and examine their reactions with CO<sub>2</sub> [74]. In aqueous solution, radiolytic reductions of Co(III) to Co(II) and then to Co(I) were quantitative reactions yielding a stable Co(I) product at high pH. Pulse radiolysis of the Co(I) solution showed bleaching of the Co(I) absorption at 550 nm and broad absorptions from 640–800 nm, different from spectra of π-radical anions of Zn, Al and Sn [75–77] suggesting the product is Co(0) formed by reaction of Co(I) with e<sub>aq</sub><sup>-</sup> (Table 4, Equation 7). A slower reaction of Co(I)-mTMPyP with CO<sub>2</sub><sup>•-</sup> ( $k \sim 5 \times 10^9 \text{ M}^{-1}\cdot\text{s}^{-1}$ ) yielded a spectrum with features different from the Co(0) species suggestive of adduct formation followed by decomposition to CO and Co(II). Cyclic voltammetry in butyronitrile showed catalytic current under CO<sub>2</sub> upon reduction to Co(0) [74, 78]. The reaction is first order in [catalyst] and [CO<sub>2</sub>]. Since the Co(0) species are short-lived in water, sodium reduction was undertaken under static vacuum using dry THF. Smooth reduction to Co(I) and Co(0) was observed. While Co(I) did not react with CO<sub>2</sub>, the Co(0) solution quickly produced the spectrum of Co(I) upon introduction of CO<sub>2</sub> and gradually changed to the spectrum of Co(II). Since the reaction of CO<sub>2</sub> with Co(0) should release CO and Co(II), the persistence of a Co(I) spectrum is attributed to comproportionation of Co(II) with Co(0). Photochemical reduction with Et<sub>3</sub>N produced Co(II) and Co(I) while continued photolysis under CO<sub>2</sub> yielded CO with >300 turnovers.

Inefficient reduction to the reactive species of [Co<sup>0</sup>TPP]<sup>2-</sup> or [Fe<sup>0</sup>TPP]<sup>2-</sup> using Et<sub>3</sub>N is a major limitation of photochemical reduction with the Co and Fe porphyrins discussed above. Two drawbacks are weak interactions of Et<sub>3</sub>N with the Co or Fe centers and highly negative M<sup>II/0</sup> reduction potentials. Photochemical reduction efficiency was improved using *p*-terphenyl (TP) as a sensitizer [79]. The TP excited state is quenched by Et<sub>3</sub>N to produce the TP<sup>•-</sup> radical anion with a -2.45 V vs. SCE reduction potential which is sufficiently negative to produce Fe(0) and Co(0) [80]. Production of CO during photolysis was six times greater and ten times faster than in the absence

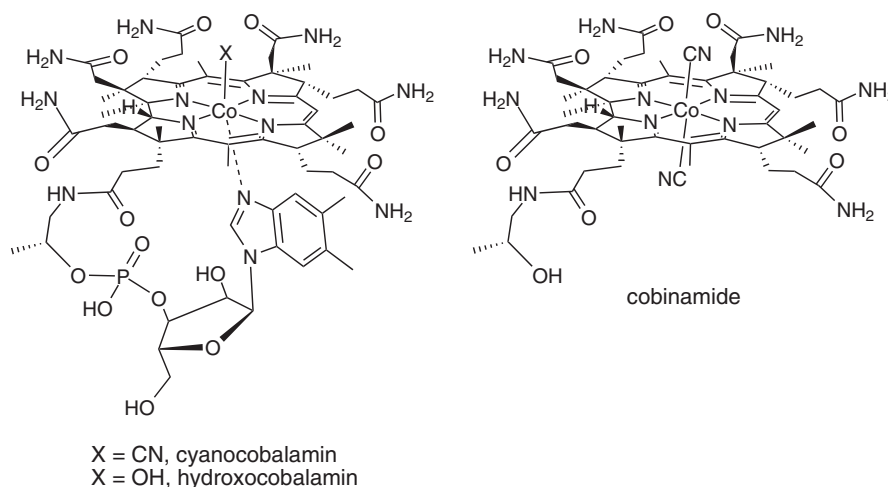
of TP (Fig. 14) indicating efficient reactions of Co(II) and Co(I) with TP\*. These reactions (Table 4, Equations 11 and 12) were nearly diffusion controlled as measured by pulse radiolysis. Control experiments in the absence of porphyrin produced formate from the reaction of TP\* with CO<sub>2</sub>; however the rate of formate production at early times was low with porphyrin and reached the same concentration at later times. Accumulation of CO was found to limit catalysis and experiments with larger headspace produced more CO and for longer times. Catalysis resumed if CO was purged from the system and slowed if CO was initially introduced. Fe<sup>III</sup>T3CF<sub>3</sub>PPCl was reduced by Na under static vacuum in THF to the Fe(0) state. CO does not bind to Fe(0) but binds to Fe(II) and Fe(I) in a reversible equilibrium. The spectrum of Fe<sup>II</sup>CO was also obtained by the reaction of CO<sub>2</sub> with Fe(0). No reactions of CO with Co(II), Co(I), or Co(0) were observed.

Since hydrogenation of porphyrin rings during photochemical experiments is a degradation pathway, Co corrins (B<sub>12</sub>) (Chart 2) with fewer double bonds, were examined as photocatalysts for CO<sub>2</sub> reduction using TP as a sensitizer and Et<sub>3</sub>N as the sacrificial reductant [81]. Similar to Co porphyrins, reduction to the Co(0) state was necessary and CO, formate, and H<sub>2</sub> were produced at higher rates than CoTPP in parallel experiments. Pulse radiolysis of Co(I) showed rapid decay of e<sub>aq</sub><sup>-</sup> and a slower reaction of CO<sub>2</sub>\* with Co(I) to form an adduct. Transient Co(0) reacts with water to form the hydride but decay of this species could not be observed separately.

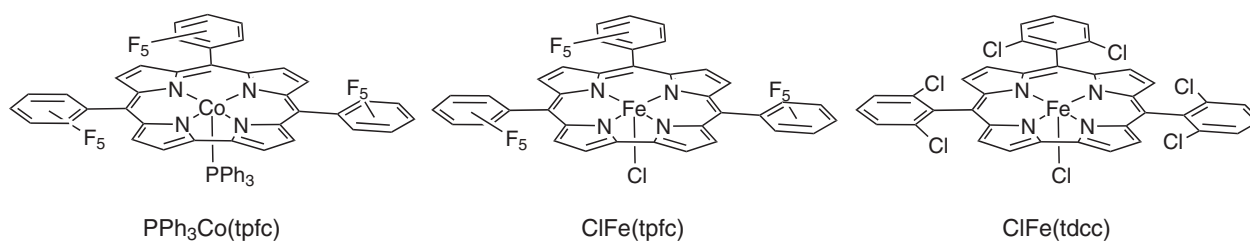
Photochemical and radiolytic techniques were also used to characterize the reduced species of Fe and Co phthalocyanines together with their tetra(*tert*-butyl)- and tetrasulfonated derivatives (Chart 1), and to determine reactivity toward CO<sub>2</sub> [82]. Radiolytic reduction of the Co(II) complex with TSPc produced the corresponding Co(I) (mixture of monomers and dimers) in quantitative yield. Likewise, the Fe(I) complex with TSPc was



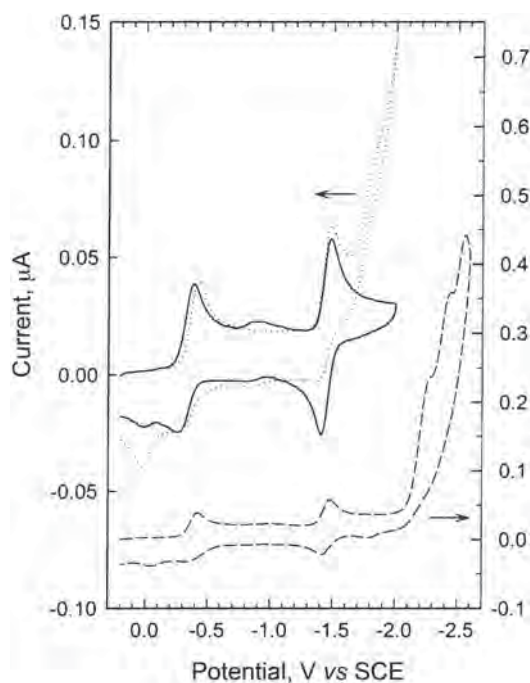
**Fig. 14.** Photochemical production of CO in CO<sub>2</sub>-saturated acetonitrile containing 5% Et<sub>3</sub>N: (a) 1 × 10<sup>-5</sup> M Co<sup>II</sup>-TPP with no TP; (b) with 3 × 10<sup>-3</sup> M TP and various concentrations of Co<sup>II</sup>-T3FPP: 9 × 10<sup>-5</sup> M (solid circles), 2.4 × 10<sup>-5</sup> M (open circles), and 7 × 10<sup>-6</sup> M (open triangles). The yield of CO refers to the total amount per unit volume of solution. Reprinted with permission from Ref. 79, Copyright 1999 American Chemical Society



**Chart 2.** Co corrins studied for photoreduction of CO<sub>2</sub>



**Chart 3.** Fe and Co corroles studied for photochemical  $\text{CO}_2$  reduction



**Fig. 15.** Cyclic voltammograms of  $\text{PPh}_3\text{Co}^{\text{III}}(\text{tpfc})$  in  $\text{CH}_3\text{CN}$  solution saturated with Ar (solid line) and  $\text{CO}_2$  (dotted line). A wider scan of the Ar-saturated solution is shown by the dashed line. Scan rate  $100 \text{ mV}\cdot\text{s}^{-1}$ . Reprinted with permission from Ref. 83, Copyright 2002 American Chemical Society

**Table 3.** Photocatalytic  $\text{CO}_2$  reduction

Complex	Product	TON	Additives	Oxidation state	Solvent
$\text{FeTPP}^{\text{a}}$	CO	70			DMF, 5% $\text{Et}_3\text{N}$
$\text{Fe-oTMPyP}^{\text{a}}$	CO	~70		Fe(0)	Water, 5% $\text{Et}_3\text{N}$
$\text{CoTPP}^{\text{b}}$	CO	300		Co(0)	DMF, 5% $\text{Et}_3\text{N}$
$\text{CoTmFP}^{\text{b}}$	CO	~150		Co(0)	DMF, 5% $\text{Et}_3\text{N}$
$\text{CoTM}(\text{CF}_3)\text{PP}^{\text{b}}$	CO	~150		Co(0)	DMF, 5% $\text{Et}_3\text{N}$
$\text{FeTPP}^{\text{c}}$	CO	230	TP 3 mM	Fe(0)	DMF, 5% $\text{Et}_3\text{N}$
cobinamide <sup>d</sup>	CO	60	TP 3 mM	Co(0)	9:1 MeCN/MeOH, 5% $\text{Et}_3\text{N}$
$\text{Co}(\text{TBPc})^{\text{e}}$	CO	50	TP 3 mM	Co(I)Pc <sup>*</sup>	DMF, 5% $\text{Et}_3\text{N}$
$\text{Co}(\text{tpfc})^{\text{f}}$	CO	100	TP 3 mM	Co(I)	MeCN, $\text{Et}_3\text{N}$ (5%)
	$\text{H}_2$	60			
$\text{Fe}(\text{tpfc})^{\text{f}}$	CO	100	TP 3 mM	Fe(I)	MeCN, $\text{Et}_3\text{N}$ (5%)
	$\text{H}_2$	190			

<sup>a</sup>[72]. <sup>b</sup>[74]. <sup>c</sup>[79]. <sup>d</sup>[81]. <sup>e</sup>[82]. <sup>f</sup>[83].

**Table 4.** Select reactions relevant to photocatalytic CO<sub>2</sub> reduction and mechanistic studies

	Reaction	Rate
1 <sup>a</sup>	$[\text{ClFe}^{\text{III}}\text{P}] + \text{Et}_3\text{N} \rightarrow \text{Fe}^{\text{II}}\text{P} + \text{Cl}^- + \text{Et}_3\text{N}^{*+}$	
2 <sup>a</sup>	$\text{Fe}^{\text{II}}\text{P} + \text{Et}_3\text{N} \rightarrow [\text{Fe}^{\text{I}}\text{P}]^- + \text{Et}_3\text{N}^{*+}$	
3 <sup>a</sup>	$[\text{ClFe}^{\text{III}}\text{-oTMPyP}] + \text{Et}_3\text{N} \rightarrow \text{Fe}^{\text{II}}\text{-oTMPyPH}_2 + \text{Cl}^- + \text{Et}_3\text{N}^{*+}$	
4 <sup>a</sup>	$\text{Fe}^{\text{II}}\text{-oTMPyP} + e_{\text{aq}}^- \rightarrow [\text{Fe}^{\text{I}}\text{-oTMPyP}]^-$ $\text{Fe}^{\text{II}}\text{-oTMPyP} + \text{CO}_2^{*\cdot} \rightarrow [\text{Fe}^{\text{I}}\text{-oTMPyP}]^-$	
5 <sup>a</sup>	$2[\text{Fe}^{\text{I}}\text{-oTMPyP}]^- \rightarrow \text{Fe}^{\text{II}}\text{P} + [\text{Fe}^{\text{0}}\text{P}]^{2-}$	$(1.5 \pm 0.5) \times 10^8 \text{ M}^{-1} \cdot \text{s}^{-1}$
6 <sup>b</sup>	$\text{Co}^{\text{II}}\text{Por} + e_{\text{aq}}^- \rightarrow [\text{Co}^{\text{I}}\text{Por}]^-$ $\text{Co}^{\text{II}}\text{Por} + \text{CO}_2^{*\cdot} \rightarrow [\text{Co}^{\text{I}}\text{Por}]^- + \text{CO}_2$	
7 <sup>b</sup>	$[\text{Co}^{\text{I}}\text{TPPS}]^- + e_{\text{aq}}^- \rightarrow [\text{Co}^{\text{0}}\text{TPPS}]^{2-}$ $[\text{Co}^{\text{I}}\text{-mTMPyP}]^- + e_{\text{aq}}^- \rightarrow [\text{Co}^{\text{0}}\text{-mTMPyP}]^{2-}$	$(2.1 \pm 0.4) \times 10^{10} \text{ M}^{-1} \cdot \text{s}^{-1}$ $(4 \pm 1) \times 10^{10} \text{ M}^{-1} \cdot \text{s}^{-1}$
8 <sup>b</sup>	$[\text{Co}^{\text{I}}\text{-mTMPyP}]^- + \text{CO}_2^{*\cdot} \rightarrow [\text{Co}^{\text{0}}\text{-mTMPyP}]^{2-} + \text{CO}_2$	$5 \times 10^9 \text{ M}^{-1} \cdot \text{s}^{-1}$
9 <sup>b</sup>	$[\text{Co}^{\text{I}}\text{TPPS}]^- + e_{\text{aq}}^- \rightarrow \text{chlorin, phlorin anion}$	
10 <sup>c</sup>	$\text{M}^{\text{II}}\text{Por} + \text{TP}^{*\cdot} \rightarrow [\text{M}^{\text{I}}\text{Por}]^- + \text{TP}$ $[\text{M}^{\text{I}}\text{Por}]^- + \text{TP}^{*\cdot} \rightarrow [\text{M}^{\text{0}}\text{Por}]^{2-}$	
11 <sup>c</sup>	$\text{Co}^{\text{II}}\text{TPP} + \text{TP}^{*\cdot} \rightarrow [\text{Co}^{\text{I}}\text{Por}]^- + \text{TP}$	$(1.0 \pm 0.2) \times 10^{10} \text{ M}^{-1} \cdot \text{s}^{-1}$
12 <sup>c</sup>	$\text{Co}^{\text{I}}\text{TPP} + \text{TP}^{*\cdot} \rightarrow [\text{Co}^{\text{0}}\text{Por}]^- + \text{TP}$	$(7 \pm 2) \times 10^9 \text{ M}^{-1} \cdot \text{s}^{-1}$
13 <sup>d</sup>	$[\text{Co}^{\text{I}}\text{B}_{12}]^+ + \text{CO}_2^{*\cdot} \rightarrow [(\text{CO}_2)\text{CoB}_{12}]^{2-}$	$(1.2 \pm 0.3) \times 10^8 \text{ M}^{-1} \cdot \text{s}^{-1}$
14 <sup>d</sup>	$[\text{Co}^{\text{I}}\text{B}_{12}]^+ + e_{\text{aq}}^- \rightarrow [\text{Co}^{\text{0}}\text{B}_{12}]^{2-}$	$1 \times 10^{10} \text{ M}^{-1} \cdot \text{s}^{-1}$
15 <sup>e</sup>	$\text{Co}^{\text{II}}\text{TSPc} + e_{\text{aq}}^- \rightarrow [\text{Co}^{\text{I}}\text{TSPc}]^-$ $\text{Co}^{\text{II}}\text{TSPc} + \text{CO}_2^{*\cdot} \rightarrow [\text{Co}^{\text{I}}\text{TSPc}]^- + \text{CO}_2$	
16 <sup>e</sup>	$\text{Co}^{\text{II}}\text{TSPc} + e_{\text{aq}}^- \rightarrow [\text{Co}^{\text{I}}\text{TSPc}]^-$	$2 \times 10^{10} \text{ M}^{-1} \cdot \text{s}^{-1}$
17 <sup>e</sup>	$[\text{Co}^{\text{I}}\text{TSPc}]^- + \text{CO}_2^{*\cdot} \rightarrow [\text{Co}^{\text{0}}\text{TSPcCO}_2]^{2-}$	$5.5 \pm 0.8 \times 10^7 \text{ M}^{-1} \cdot \text{s}^{-1}$
18 <sup>e</sup>	$\text{Co}^{\text{II}}\text{TSPc} + \text{TP}^{*\cdot} \rightarrow [\text{Co}^{\text{I}}\text{TSPc}]^-$	
19 <sup>e</sup>	$\text{Co}^{\text{II}}\text{Pc} + \text{TP}^{*\cdot} \rightarrow [\text{Co}^{\text{I}}\text{Pc}]^- + \text{TP}$ $\text{Co}^{\text{I}}\text{Pc} + \text{TP}^{*\cdot} \rightarrow [\text{Co}^{\text{0}}\text{Pc}]^- + \text{TP}$	$2 \times 10^{10} \text{ M}^{-1} \cdot \text{s}^{-1}$ $(7.8 \pm 1.2) \times 10^9 \text{ M}^{-1} \cdot \text{s}^{-1}$

<sup>a</sup>[72]. <sup>b</sup>[74]. <sup>c</sup>[79]. <sup>d</sup>[81]. <sup>e</sup>[82].

obtained in high yield and both compounds were stable for hours. The Co(I) complex was further reduced by CO<sub>2</sub><sup>•−</sup> to form the CO<sub>2</sub> adduct. To clarify the intermediates of CO<sub>2</sub> reduction, stepwise reduction of Co<sup>II</sup>TBPc was carried out using sodium mirror in THF. The doubly-reduced species, [Co<sup>I</sup>(TBPc<sup>•−</sup>)]<sup>2−</sup>, reacted rapidly with CO<sub>2</sub> to form a complex that decomposes to Co<sup>II</sup>TBPc and CO. The decomposition seems to be enhanced by CO<sub>2</sub> acting as an oxide acceptor. Photoreduction in CH<sub>3</sub>CN with Et<sub>3</sub>N and TP produced Co(I) and Fe(I) but further reduction led to bleaching. Photochemical production of CO and formate was not as effective as with phthalocyanines due to hydrogenation of the ligand.

To complete the series of photochemical CO<sub>2</sub> reduction experiments, Fe and Co corroles were investigated (Chart 3) [83]. Lacking one *meso* bridge and bearing three anionic nitrogen ligands, corroles stabilize higher metal oxidation states. Thus it was proposed that the M(I) state could react with CO<sub>2</sub>. Indeed, CV data

confirmed the reaction of CO<sub>2</sub> at slightly more negative potentials than the Co<sup>III</sup> wave with Ph<sub>3</sub>PCo(tpfc) (Fig. 15) or at the Fe<sup>III</sup> potential with ClFe<sup>IV</sup>(tdcc) showing catalytic current. Spectroscopic characterization showed the reaction of CO<sub>2</sub> with the Fe(I) state to produce Fe(II) and CO together with a small amount of Fe<sup>II</sup>CO. The Fe(II) species are produced by comproportionation of Fe(III) and Fe(I). Extended photoreduction of the M(II) state with Et<sub>3</sub>N and TP produced peaks different from sodium reduction which first decreased and then were completely lost. Under CO<sub>2</sub>, H<sub>2</sub> and CO are evolved showing that the reaction of M(I) with H<sup>+</sup> competes with CO<sub>2</sub>. Total turnovers were about 300.

## IV. CONCLUSIONS AND OUTLOOK

In this review, we summarized electrochemical and photochemical CO<sub>2</sub> reduction with a variety of iron

and cobalt complexes incorporating porphyrins and phthalocyanines. While CO<sub>2</sub> can bind to one-electron-reduced cobalt(I) complexes with partially saturated tetraaza-macrocycles such as a cobalt(I) complex with 5,7,7,12,14,14-hexamethyl-1,4,8,11-tetraazacyclotetradeca-4,11-diene [84], those of metalloporphyrins and metallophthalocyanines cannot because the electron densities on these species are partially distributed on the conjugated ligands. Although there are some conflicting reports of CO<sub>2</sub> activation by one-electron-reduced Co(I) and Fe(I) porphyrins/phthalocyanines (without the ligand anion radicals), the active catalysts with metalloporphyrins are further reduced species as identified by cyclic voltammetry to have the metal in the formal oxidation state of zero. In the case of phthalocyanine complexes, the metal oxidation state is +1 with the ligand anion radical. Fe and Co corroles are lacking one *meso* bridge and bearing three anionic nitrogen ligands, therefore, metal(I) corrole complexes can react with CO<sub>2</sub>. In each case, the species which react with CO<sub>2</sub> in solution have been identified in recent years using radiolytic or chemical reduction techniques.

Metalloporphyrins and metallophthalocyanines are visible light absorbers with extremely large extinction coefficients. However, yields of photochemically-generated active catalysts for CO<sub>2</sub> reduction are low due to the requirement of a photoinduced 2nd electron. This situation can be ignored in the case of electrochemical CO<sub>2</sub> reduction. Recent progress on efficient and stable electrochemical systems using FeTPP catalyst repositioning of proton-donating phenol groups in the 2nd coordination sphere to carry out coupled proton-electron transfer within the catalytic cycle is remarkable. The incorporation of Lewis or Brønsted acids in the catalysts seems an outstanding direction not only to reduce overpotential but also to speed up the reaction.

Selectivity of the products (*i.e.* CO, HCOO<sup>-</sup>, H<sub>2</sub>, *etc.*) and long-term durability of cobalt and iron catalysts can be problematic especially when water is used as a solvent. Reduced Fe and Co porphyrins react with protons to produce metal hydride species, which are considered as intermediates for H<sub>2</sub> and HCOO<sup>-</sup> production, and in some cases even for CO production. Also, hydrogenation of the ligand due to the electron rich nature of the reduced catalysts may decrease the catalytic activity for CO<sub>2</sub> reduction. Advances in experimental techniques have revealed a wealth of mechanistic information in recent years, yet detailed thermodynamic and kinetic studies of proton and CO<sub>2</sub> binding to the reduced metal catalysts would help to understand the mechanisms for CO<sub>2</sub> reduction.

Ground-breaking research has to be continued to produce renewable fuels (CO, and ultimately further reduced species such as methanol and methane) *via* low-energy pathways using durable and selective earth-abundant catalysts for creating carbon-neutral energy sources.

## Acknowledgements

We thank Drs. James T. Muckerman and David C. Grills for careful reading of this manuscript. The work at Brookhaven National Laboratory was carried out under contract DE-AC02-98CH10886 with the U.S. Department of Energy, Office of Science, Office of Basic Energy Sciences.

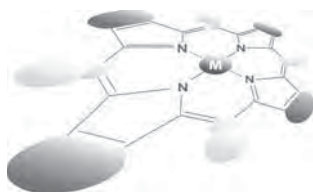
## REFERENCES

1. D'Alessandro DM, Smit B and Long JR. *Angew. Chem. Int. Ed.* 2010; **49**: 6058–6082.
2. Schwarz HA and Dodson RW. *J. Phys. Chem.* 1989; **93**: 409–414.
3. Benson EE, Kubiak CP, Sathrum AJ and Smieja JM. *Chem. Soc. Rev.* 2009; **38**: 89–99.
4. Morris AJ, Meyer GJ and Fujita E. *Acc. Chem. Res.* 2009; **42**: 1983–1994.
5. Windle CD and Perutz RN. *Coord. Chem. Rev.* 2012; **256**: 2562–2570.
6. Qiao JL, Liu YY, Hong F and Zhang JJ. *Chem. Soc. Rev.* 2014; **43**: 631–675.
7. Lim RJ, Xie MS, Sk MA, Lee JM, Fisher A, Wang X and Lim KH. *Catal. Today.* 2014; **233**: 169–180.
8. Izumi Y. *Coord. Chem. Rev.* 2013; **257**: 171–186.
9. Costentin C, Robert M and Saveant J-M. *Chem. Soc. Rev.* 2013; **42**: 2423–2436.
10. Appel AM, Bercaw JE, Bocarsly AB, Dobbek H, DuBois DL, Dupuis M, Ferry JG, Fujita E, Hille R, Kenis PJA, Kerfeld CA, Morris RH, Peden CHF, Portis AR, Ragsdale SW, Rauchfuss TB, Reek JNH, Seefeldt LC, Thauer RK and Waldrop GL. *Chem. Rev.* 2013; **113**: 6621–6658.
11. Sakakura T, Choi JC and Yasuda H. *Chem. Rev.* 2007; **107**: 2365–2387.
12. Aresta M and Dibenedetto A. *Dalton Trans.* 2007: 2975–2992.
13. Truxillo LA and Davis DG. *Anal. Chem.* 1975; **47**: 2260–2267.
14. Arauillomcadsams C and Kadish KM. *Inorg. Chem.* 1990; **29**: 2749–2757.
15. Meshitsu S, Ichikawa M and Tamaru K. *J. Chem. Soc. Chem., Commun.* 1974: 158–159.
16. Kapusta S and Hackerman N. *J. Electrochem. Soc.* 1984; **131**: 1511–1514.
17. Lieber CM and Lewis NS. *J. Am. Chem. Soc.* 1984; **106**: 5033–5034.
18. Christensen PA, Hamnett A and Muir AVG. *J. Electroanal. Chem.* 1988; **241**: 361–371.
19. Tanabe H and Ohno K. *Electrochim. Acta.* 1987; **32**: 1121–1124.
20. Abe T, Taguchi F, Yoshida T, Tokita S, Schnurpfeil G, Wohrle D and Kaneko M. *J. Mol. Catal. A: Chem.* 1996; **112**: 55–61.



21. Abe T, Imaya H, Yoshida T, Tokita S, Schlettwein D, Woehrl D and Kaneko M. *J. Porphyrins Phthalocyanines* 1997; **1**: 315–321.
22. Motoo S, Watanabe M and Furuya N. *J. Electroanal. Chem.* 1984; **160**: 351–357.
23. Mahmood MN, Masheder D and Harty CJ. *J. Appl. Electrochem.* 1987; **17**: 1223–1227.
24. Furuya N and Matsui K. *J. Electroanal. Chem.* 1989; **271**: 181–191.
25. Furuya N and Koide S. *Electrochim. Acta.* 1991; **36**: 1309–1313.
26. Sonoyama N, Kirii M and Sakata T. *Electrochem. Commun.* 1999; **1**: 213–216.
27. Magdesieva TV, Yamamoto T, Tryk DA and Fujishima A. *J. Electrochem. Soc.* 2002; **149**: D89–D95.
28. Zhang JJ, Pietro WJ and Lever ABP. *J. Electroanal. Chem.* 1996; **403**: 93–100.
29. Logan BE, Hamelers B, Rozendal RA, Schrorder U, Keller J, Freguia S, Aelterman P, Verstraete W and Rabaey K. *Environ. Sci. Technol.* 2006; **40**: 5181–5192.
30. Zhao HZ, Zhang Y, Zhao B, Chang YY and Li ZS. *Environ. Sci. Technol.* 2012; **46**: 5198–5204.
31. Zhao HZ, Chang YY and Liu C. *J. Solid State Electrochem.* 2013; **17**: 1657–1664.
32. Reda T, Plugge CM, Abram NJ and Hirst J. *Proc. Natl. Acad. Sci. U.S.A.* 2008; **105**: 10654–10658.
33. Hieringer W, Flechtner K, Kretschmann A, Seufert K, Auwarter W, Barth JV, Gorling A, Steinruck HP and Gottfried JM. *J. Am. Chem. Soc.* 2011; **133**: 6206–6222.
34. Seufert K, Auwarter W and Barth JV. *J. Am. Chem. Soc.* 2010; **132**: 18141–18146.
35. Auwarter W, Seufert K, Klappenberger F, Reichert J, Weber-Bargioni A, Verdini A, Cvetko D, Dell'Angela M, Floreano L, Cossaro A, Bavdek G, Morgante A, Seitsonen AP and Barth JV. *Phys. Rev. B.* 2010; **81**: 245403.
36. Gottfried JM and Marbach H. *Z. Phys. Chemie-Int. J. Res. Phys. Chem. Chem. Phys.* 2009; **223**: 53–74.
37. Buchner F, Warnick KG, Wolffe T, Gorling A, Steinruck HP, Hieringer W and Marbach H. *J. Phys. Chem. C.* 2009; **113**: 16450–16457.
38. Bai Y, Buchner F, Kellner I, Schmid M, Vollnhals F, Steinruck HP, Marbach H and Gottfried JM. *New J. Phys.* 2009; **11**: 125004.
39. Lukasczyk T, Flechtner K, Merte LR, Jux N, Maier F, Gottfried JM and Steinruck HP. *J. Phys. Chem. C.* 2007; **111**: 3090–3098.
40. Flechtner K, Kretschmann A, Steinruck HP and Gottfried JM. *J. Am. Chem. Soc.* 2007; **129**: 12110–12111.
41. Atoguchi T, Aramata A, Kazusaka A and Enyo M. *J. Chem. Soc. Chem., Commun.* 1991: 156–157.
42. Atoguchi T, Aramata A, Kazusaka A and Enyo M. *J. Electroanal. Chem.* 1991; **318**: 309–320.
43. Aga H, Aramata A and Hisaeda Y. *J. Electroanal. Chem.* 1997; **437**: 111–118.
44. Tanaka H and Aramata A. *J. Electroanal. Chem.* 1997; **437**: 29–35.
45. Ramirez G, Lucero M, Riquelme A, Villagran M, Costamagna J, Trollund E and Aguirre MJ. *J. Coord. Chem.* 2004; **57**: 249–255.
46. Ramirez G, Ferraudi G, Chen YY, Trollund E and Villagra D. *Inorg. Chim. Acta.* 2009; **362**: 5–10.
47. Yoshida T, Kamato K, Tsukamoto M, Iida T, Schlettwein D, Woehrl D and Kaneko M. *J. Electroanal. Chem.* 1995; **385**: 209–225.
48. Abe T, Yoshida T, Tokita S, Taguchi F, Imaya H and Kaneko M. *J. Electroanal. Chem.* 1996; **412**: 125–132.
49. Zhang AJ, Zhang WM, Lu JX, Wallace GG and Chen J. *Electrochem. Solid State Lett.* 2009; **12**: E17–E19.
50. Isaacs M, Armijo F, Ramirez G, Trollund E, Biaggio SR, Costamagna J and Aguirre MJ. *J. Mol. Catal. A: Chem.* 2005; **229**: 249–257.
51. Quezada D, Honores J, Garcia M, Armijo F and Isaacs M. *New J. Chem.* 2014; **38**: 3606–3612.
52. Yao SA, Ruther RE, Zhang LH, Franking RA, Hamers RJ and Berry JF. *J. Am. Chem. Soc.* 2012; **134**: 15632–15635.
53. Hiratsuka K, Takahashi K, Sasaki H and Toshima S. *Chem. Lett.* 1977: 1137–1140.
54. Takahashi K, Hiratsuka K, Sasaki H and Toshima S. *Chem. Lett.* 1979: 305–308.
55. Enoki O, Imaoka T and Yamamoto K. *Macromol. Symp.* 2003; **204**: 151–158.
56. Imaoka T, Nakazawa S and Yamamoto K. *Chem. Lett.* 2001: 412–413.
57. Imaoka T, Tanaka R and Yamamoto K. *J. Polym. Sci., Part A: Polym. Chem.* 2006; **44**: 5229–5236.
58. Hammouche M, Lexa D, Saveant JM and Momen-teau M. *J. Electroanal. Chem.* 1988; **249**: 347–351.
59. Costentin C, Passard G, Robert M and Saveant JM. *J. Am. Chem. Soc.* 2014; **136**: 11821–11829.
60. Lexa D, Saveant JM, Su KB and Wang DL. *J. Am. Chem. Soc.* 1988; **110**: 7617–7625.
61. Lexa D, Saveant JM, Schafer HJ, Su KB, Vering B and Wang DL. *J. Am. Chem. Soc.* 1990; **112**: 6162–6177.
62. Anxolabehere E, Chottard G and Lexa D. *New J. Chem.* 1994; **18**: 889–899.
63. Hammouche M, Lexa D, Momen-teau M and Saveant JM. *J. Am. Chem. Soc.* 1991; **113**: 8455–8466.
64. Bhugun I, Lexa D and Saveant JM. *J. Phys. Chem.* 1996; **100**: 19981–19985.
65. Bhugun I, Lexa D and Saveant JM. *J. Am. Chem. Soc.* 1994; **116**: 5015–5016.
66. Bhugun I, Lexa D and Saveant JM. *J. Am. Chem. Soc.* 1996; **118**: 1769–1776.
67. Costentin C, Drouet S, Passard G, Robert M and Saveant JM. *J. Am. Chem. Soc.* 2013; **135**: 9023–9031.

68. Costentin C, Drouet S, Robert M and Saveant JM. *Science*. 2012; **338**: 90–94.
69. Rakowski DuBois M and DuBois DL. *Chem. Soc. Rev.* 2009; **38**: 62–72.
70. Hull JF, Himeda Y, Wang WH, Hashiguchi B, Periana R, Szalda DJ, Muckerman JT and Fujita E. *Nature Chemistry* 2012; **4**: 383–388.
71. Fujita E, Muckerman JT and Himeda Y. *Biochim. Biophys. Acta-Bioenerg.* 2013; **1827**: 1031–1038.
72. Grodkowski J, Behar D, Neta P and Hambright P. *J. Phys. Chem. A*. 1997; **101**: 248–254.
73. Hoshino M, Ueda K, Takahashi M, Yamaji M, Hama Y and Miyazaki Y. *J. Phys. Chem.* 1992; **96**: 8863–8870.
74. Behar D, Dhanasekaran T, Neta P, Hosten CM, Ejeh D, Hambright P and Fujita E. *J. Phys. Chem. A*. 1998; **102**: 2870–2877.
75. Neta P. *J. Phys. Chem.* 1981; **85**: 3678–3684.
76. Baral S, Neta P and Hambright P. *Radiat. Phys. Chem.* 1984; **24**: 245–255.
77. Baral S, Hambright P and Neta P. *J. Phys. Chem.* 1984; **88**: 1595–1600.
78. Qiu AM and Sawyer DT. *J. Porphyrins Phthalocyanines* 1997; **1**: 125–134.
79. Dhanasekaran T, Grodkowski J, Neta P, Hambright P and Fujita E. *J. Phys. Chem. A*. 1999; **103**: 7742–7748.
80. Matsuoka S, Kohzuki T, Pac C, Ishida A, Takamuku S, Kusaba M, Nakashima N and Yanagida S. *J. Phys. Chem.* 1992; **96**: 4437–4442.
81. Grodkowski J and Neta P. *J. Phys. Chem. A*. 2000; **104**: 1848–1853.
82. Grodkowski J, Dhanasekaran T, Neta P, Hambright P, Brunschwig BS, Shinozaki K and Fujita E. *J. Phys. Chem. A*. 2000; **104**: 11332–11339.
83. Grodkowski J, Neta P, Fujita E, Mahammed A, Simkhovich L and Gross Z. *J. Phys. Chem. A*. 2002; **106**: 4772–4778.
84. Fujita E, Creutz C, Sutin N and Szalda DJ. *J. Am. Chem. Soc.* 1991; **113**: 343–353.



# Metalloporphyrin/G-quadruplexes: From basic properties to practical applications

Eyal Golub, Chun-Hua Lu and Itamar Willner\*

*Institute of Chemistry, The Center for Nanoscience and Nanotechnology, The Hebrew University of Jerusalem, Givat Ram, Jerusalem 91904, Israel*

*Dedicated to Professor Shunichi Fukuzumi on the occasion of his retirement*

*Received 20 November 2014*

*Accepted 28 December 2014*

**ABSTRACT:** Guanine-rich single-stranded nucleic acids self-assemble into G-quadruplex nanostructures (predominately in the presence of  $K^+$ -ions). Metalloporphyrins bind to the G-quadruplex nanostructures to form supramolecular assemblies exhibiting unique catalytic, electrocatalytic and photophysical properties. This paper addresses the advances in the characterization and the implementation of the metalloporphyrin/G-quadruplexes complexes for various applications. Out of the different complexes, the most extensively studied complexes are the hemin/G-quadruplex horseradish peroxidase-mimicking DNAzyme and the Zn(II)-protoporphyrin IX-functionalized G-quadruplex. Specifically, the hemin/G-quadruplex was found to act as a catalyst for driving different chemical transformations that mimic the native horseradish peroxidase enzyme, and, also, to function as an electrocatalyst for the reduction of  $H_2O_2$ . Also, the hemin/G-quadruplex stimulates interesting photophysical and photocatalytic processes such as the electron-transfer quenching of semiconductor quantum dots or the chemiluminescence resonance energy transfer to semiconductor quantum dots. Alternatively, Zn(II)-protoporphyrin IX associated with G-quadruplexes exhibit intensified fluorescence properties. Beyond the straight forward application of the metalloporphyrin/G-quadruplexes as catalysts that stimulate different chemical transformations, the specific catalytic, electrocatalytic and photocatalytic functions of hemin/G-quadruplexes are heavily implemented to develop sophisticated colorimetric, electrochemical, and optical sensing platforms. Also, the unique fluorescence properties of Zn(II)-protoporphyrin IX-functionalized G-quadruplexes are applied to develop fluorescence sensing platforms. The article exemplifies different sensing assays for analyzing DNA, ligand-aptamer complexes and telomerase activity using the metalloporphyrins/G-quadruplexes as transducing labels. Also, the use of the hemin/G-quadruplex as a probe to follow the operations of DNA machines is discussed.

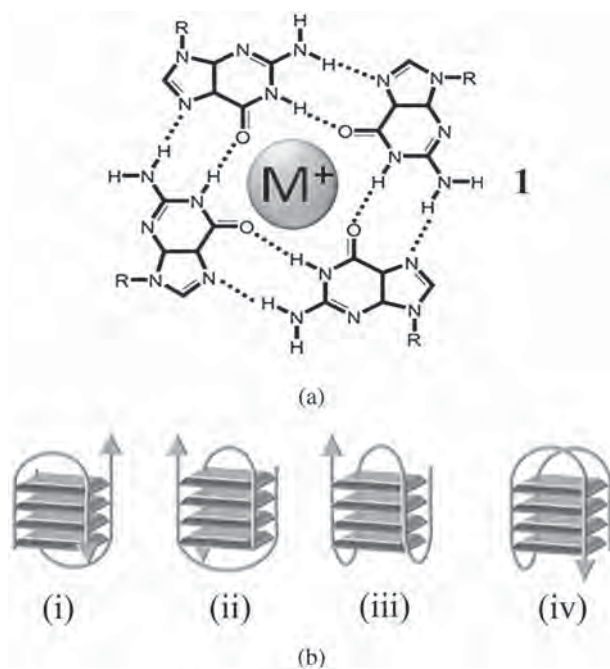
**KEYWORDS:** hemin, DNA, sensor, DNAzyme, fluorescence, telomerase, aptamer, catalyst, chemiluminescence.

## INTRODUCTION

Guanine-rich nucleic acids stimulate the formation of planar, Hoogsteen hydrogen bonds-stabilized G-quartet (1), Fig. 1(a). The following  $\pi$ - $\pi$  stacking of G-quartets, leads to the self-assembly of G-quadruplexes. These G-quadruplexes reveal cation-induced stabilization by

means of coordination, mainly in the presence of monovalent ions, generally in the order of stabilization of  $K^+ > NH_4^+ > Rb^+ > Na^+ > Cs^+ > Li^+$  [1]. The resulting G-quadruplexes may adopt various topologies, such as parallel, anti-parallel or mixed strand configurations [2]. For example, Fig. 1(b) outlines various forms of four-layer guanine-quartets exhibiting different configurations: (i) edge-loop dimeric hairpin structure, (ii) diagonal-loop dimeric hairpin, (iii) unimolecular single strand with diagonal central loop, and (iv) unimolecular edge-type

\*Correspondence to: Itamar Willner, email: willnea@vms.huji.ac.il, tel: +972 2-6585272, fax: +972 2-6527715



**Fig. 1.** (a) The Hoogsteen hydrogen-bonded stabilized G-quartet. (b) Different folding motives of layered G-quadruplex nanostructures

central loop configuration. Many studies were performed to characterize the thermodynamic properties of different G-quadruplexes [3–5], the kinetics of assembly of different structures [6, 7], the inter-conversion between distinct G-quadruplex topologies [8–10] and the equilibria existing between G-quadruplex configurations [11, 12]. These properties, as well as the effects of salt, pH and temperature on the stabilities and structures of G-quadruplexes were already extensively reviewed elsewhere [13, 14].

Apart from interesting structural motives of G-quadruplexes, G-quartet complexes have important biological implications. For example, the telomeric chains at the edges of the chromosomes consisting of a (TTAGGG) repeating unit self-assemble into a 3-layered G-quadruplexes [15, 16]. These telomeric chains were found to protect the chromosomes from oxidative damage, and to participate in the signaling of the cellular death cycle, thus playing a central role in the aging mechanism [17–19]. Also, the telomerase-stimulated synthesis of the telomere chains is a key process in the production of immortal malignant or cancerous cells [20–22]. An intriguing biological function of other G-quadruplexes is the regulation of protein transcription [23]. A detailed computational analysis of the human genome predicted the existence of ~370,000 G-rich sequences that, in principle, are capable of adopting the G-quadruplexes structures [24]. These sequences were found to be more common in the beginning of the promoter region for various protein-encoding genes, such as B cell lymphoma 2 (Bcl-2), hypoxia-inducible

factor 1a (HIF1a), platelet-derived growth factor  $\alpha$  polypeptide (PDGFA), and human telomerase reverse transcriptase (TERT). Several of these G-quadruplex structures were located in proto-oncogens, including MYC, KIT and KRAS, thus marking them as desirable targets for G-quadruplex-stabilizing anti-cancerous drugs that would disrupt the transcription process [25, 26]. Furthermore, many sequence-specific substrate-binding non-coding nucleic acids (aptamers) were found to self-assemble into G-quadruplexes upon the formation of the aptamer-ligand complexes. For example, the thrombin binding aptamer, TBA,  $d(G_2T_2G_2TGTG_2T_2G_2)$  folds into an edge-type central loop G-quadruplex structure upon binding to thrombin [27, 28].

The G-quartet-stacked quadruplexes can provide functional nanostructures for the association of guest molecules *via* cooperative electrostatic and/or  $\pi$ - $\pi$  interactions. For example, Fig. 2 outlines examples of molecular ligands that bind to G-quadruplexes. One specific class of molecules that bind to G-quadruplexes are metal porphyrins. Specifically, Fe(III)-protoporphyrin IX, hemin, binds to G-quadruplex nanostructures and the resulting complex can act as a catalytic DNA (DNAzyme) that mimics the functions of the native horseradish peroxidase (HRP) enzyme [29–31]. In fact, many different G-quadruplexes and aptamer G-quadruplex-ligand complexes bind hemin and, as a result, yield the catalytic HRP-mimicking DNAzyme structures [32–36]. The activities of the resulting DNAzymes are controlled by the structural and spatial folding features of the complexes, and by the number of G-quartets in the stacked quadruplexes [37–39]. Besides the catalytic properties of hemin/G-quadruplexes, the association of various dyes to the G-quadruplexes was found to affect the photophysical functions of the dyes and to control their luminescence properties [40–42].

The present feature article aims to survey the unique catalytic, electrocatalytic and photochemical properties of metalloporphyrin/G-quadruplex assemblies. It will detail the potential applications of these systems for novel catalytic synthesis, as well as optical and electrochemical sensing, and exemplify their use as functional units for the synthesis of new materials, and the assembly of DNA machines.

## 1. Synthetic applications of metal porphyrin-functionalized G-quadruplexes

The Fe(III)-protoporphyrin IX, (2), hemin, is known to bind to G-quadruplexes. It was found that the hemin/G-quadruplex complex is a HRP mimicking DNAzyme, Fig. 3. For example, in analogy to the characteristic reactions of HRP, the hemin/G-quadruplex was found to catalyze, in the presence of  $H_2O_2$ , the oxidation of 2,2'-azino-bis(3-ethylbenzothiazoline-6-sulphonic acid), ABTS<sup>2-</sup>, (3), to form the radical colored product ABTS<sup>-</sup> [29, 30], (4), to catalyze the oxidation of Amplex

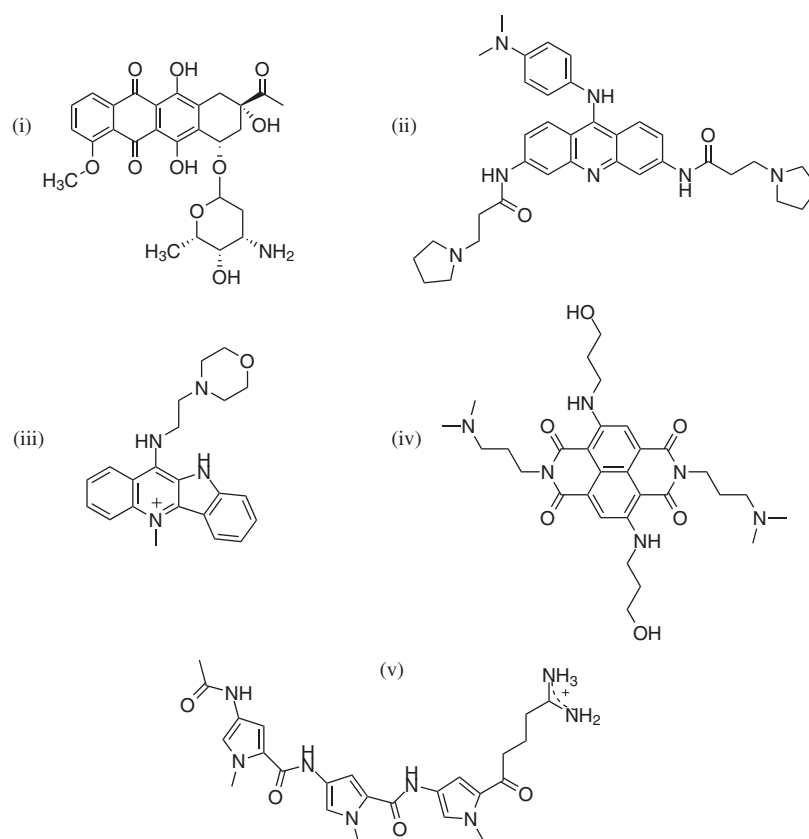


Fig. 2. Examples of molecules that bind to G-quadruplexes

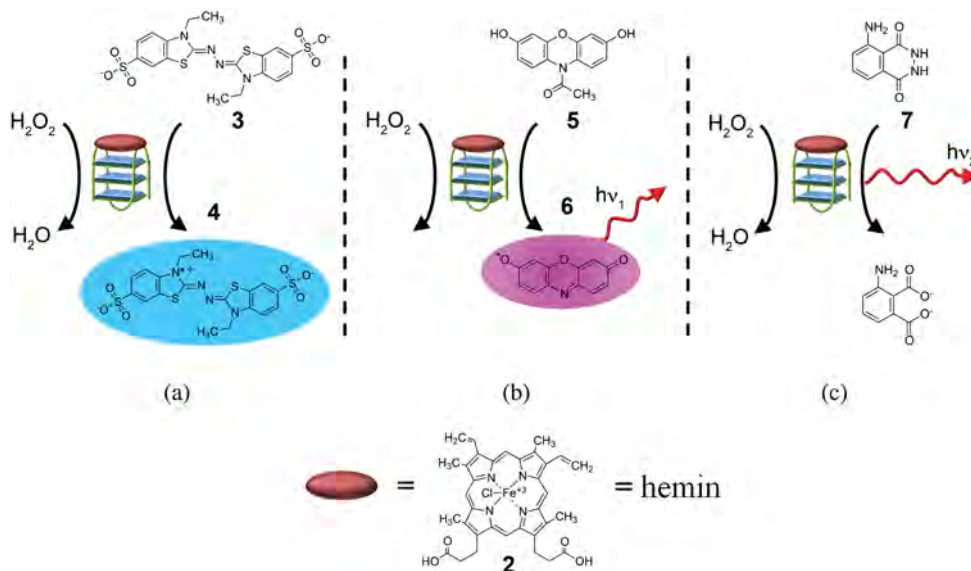
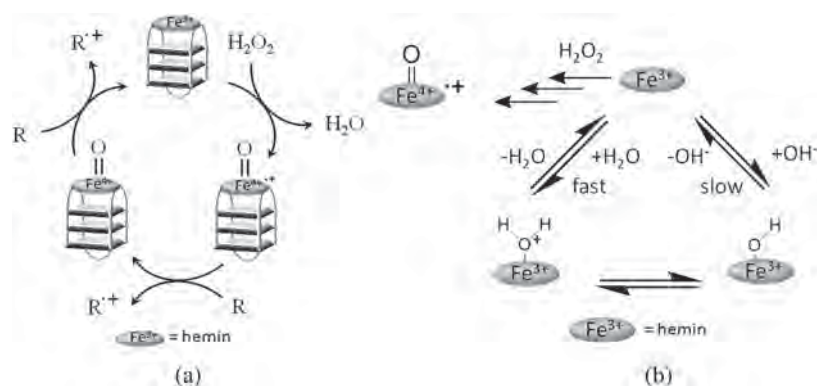


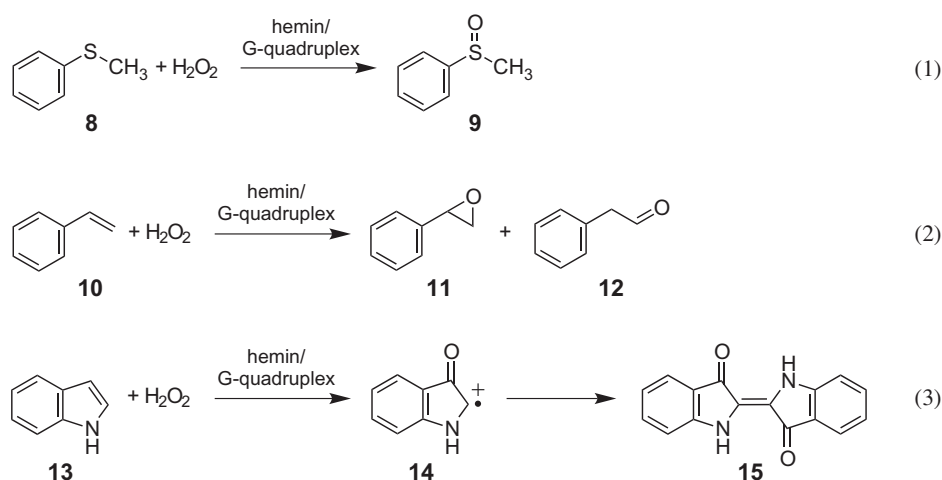
Fig. 3. Hemin/G-quadruplex-catalyzed  $\text{H}_2\text{O}_2$ -mediated oxidation of: (a)  $\text{ABTS}^{2-}$  to form the colored radical product  $\text{ABTS}^{\bullet+}$ , (b) Amplex Red to the fluorescent resorufin product, (c) oxidation of luminol to 3-aminophthalate and the concomitant generation of chemiluminescence

Red, (5), to the fluorescent product resorufin [43], (6),  $\lambda_{\text{em}} = 580 \text{ nm}$ , and to generate chemiluminescence by the oxidation of luminol [44, 45], (7),  $\lambda_{\text{max}} = 430 \text{ nm}$ , Fig. 3, routes (a)–(c), respectively. These reactions were substantially implemented in the development of optical

or chemiluminescent biosensors (see Section 3.1). These catalytic reactions of hemin/G-quadruplexes are attributed to a peroxidation cycle, Fig. 4(a), where in the primary step for the peroxidation cycle,  $\text{H}_2\text{O}_2$  catalyzes the two-electron oxidation of hemin to the



**Fig. 4.** (a) The activation of the hemin/G-quadruplex DNAzyme by  $\text{H}_2\text{O}_2$  to yield the intermediates for the peroxidation cycle. (b) Effect of alkaline transition on the kinetics of formation of the oxo- $\text{Fe}^{4+}$  radical-cation reactive species in the peroxidation cycle



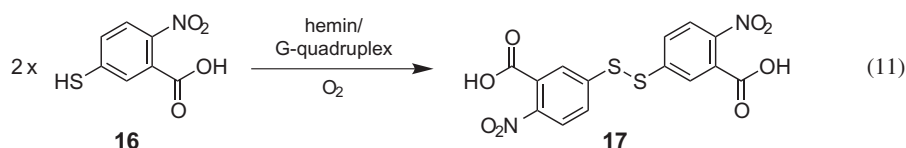
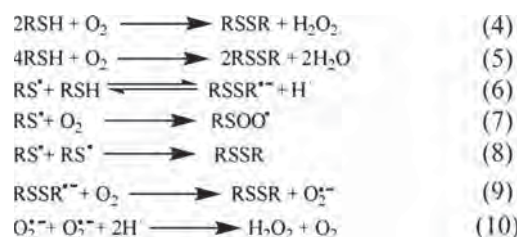
**Scheme 1.** Hemin/G-quadruplex-catalyzed 2-electron oxygen-transfer reactions

oxo- $\text{Fe}^{4+}$ -radical-cation intermediate, and the sequential two-electron oxidation of the dyes or luminol lead either to colored or fluorescent products or, alternatively, generates light. It should be noted that the association of hemin with the G-quadruplex structure is a key-step for the peroxidation cycle. The alkaline transition pKa value for free hemin corresponds to  $\text{pK}_a < 4.0$ . Thus, water molecule that acts as an axial ligand for hemin, Fig. 4(b), is deprotonated at neutral pH, resulting in a tightly-bound hydroxide complex that inhibits the association of the  $\text{H}_2\text{O}_2$  molecule to the hemin. In contrast, the hemin/G-quadruplex complex exhibits a pKa value of 8.7 that enables the water molecule to remain protonated at  $\text{pH} = 7$ . As a result, the exchange of the labile water ligand by  $\text{H}_2\text{O}_2$  at neutral pH, is facilitated in the hemin/G-quadruplex nanostructure. This enhances the formation of the catalytically-active oxo- $\text{Fe}^{4+}$ -radical-cation species through the oxidation of hemin by  $\text{H}_2\text{O}_2$ .

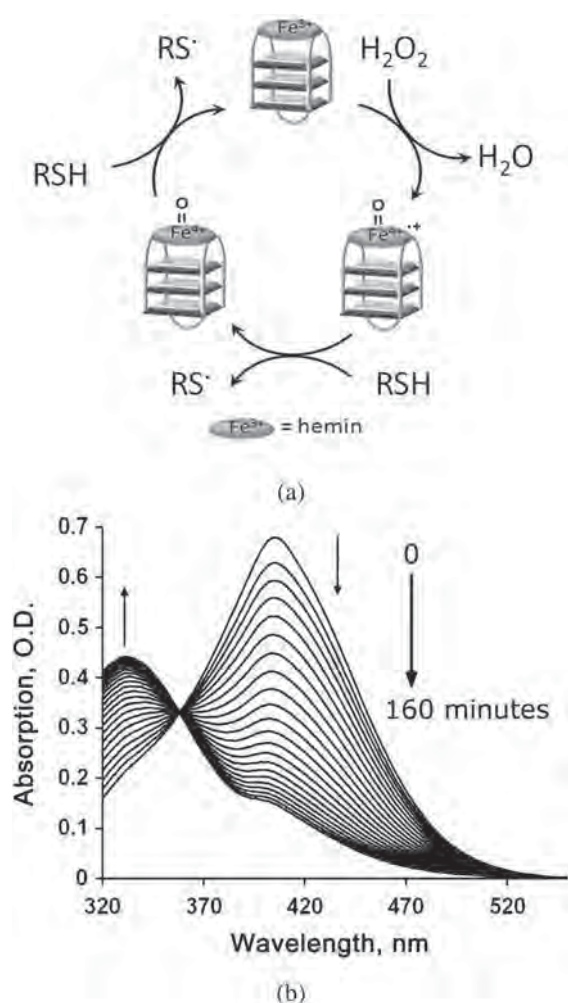
Similarly to native chloroperoxidase, CPO, or cytochrome P450, the hemin/G-quadruplex can also catalyze a two-electron oxidation processes that are characterized by an oxygen atom transfer to the substrate

[46]. Examples of these reactions are outlined in Scheme 1, Equations 1–3, where  $\text{H}_2\text{O}_2$  stimulates the oxidation of thioanisole, (**8**), to thioanisole sulfoxide, (**9**), Equation 1, the epoxidation of styrene, (**10**), to styrene oxide, (**11**), (with the phenylacetaldehyde coproduct, (**12**)), Equation 2, and the oxygen transfer to indole, (**13**), followed by the C–C coupling of the oxo-indole radical cation, (**14**), intermediate to indigo, (**15**), Equation 3.

Although the hemin/G-quadruplex-catalyzed oxidation of organic substrates is chiefly mediated by the  $\text{H}_2\text{O}_2$ , several reports describe that oxygen may, also, act as an oxidant. In these systems the reduced substrate was able to mediate the reduction of  $\text{O}_2$  to  $\text{H}_2\text{O}_2$ , with the resulting peroxide functioning as a co-oxidant for the hemin/G-quadruplex-catalyzed oxidation of the substrate. For example, Scheme 2 and Fig. 5(a) outline the mechanism for the aerobic oxidation of thiols, in the presence of a hemin/G-quadruplex [47]. The non-catalyzed, inefficient, aerobic oxidation of thiols to disulfides yields either  $\text{H}_2\text{O}_2$  or  $\text{H}_2\text{O}$ , Scheme 2, Equations 4 and 5, respectively. The trace amounts of  $\text{H}_2\text{O}_2$  generated by the autooxidation process act as an oxidant for the concomitant hemin/G-quadruplex-catalyzed oxidation



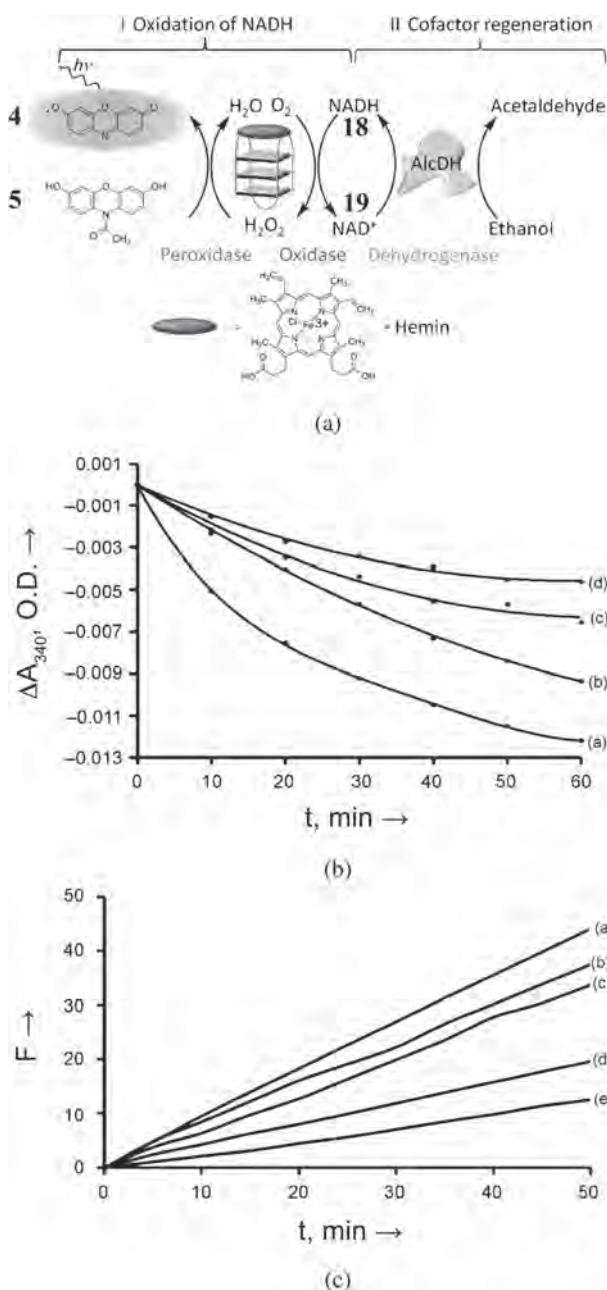
**Scheme 2.** The mechanism for the aerobic oxidation of thiols, in the presence of a hemin/G-quadruplex



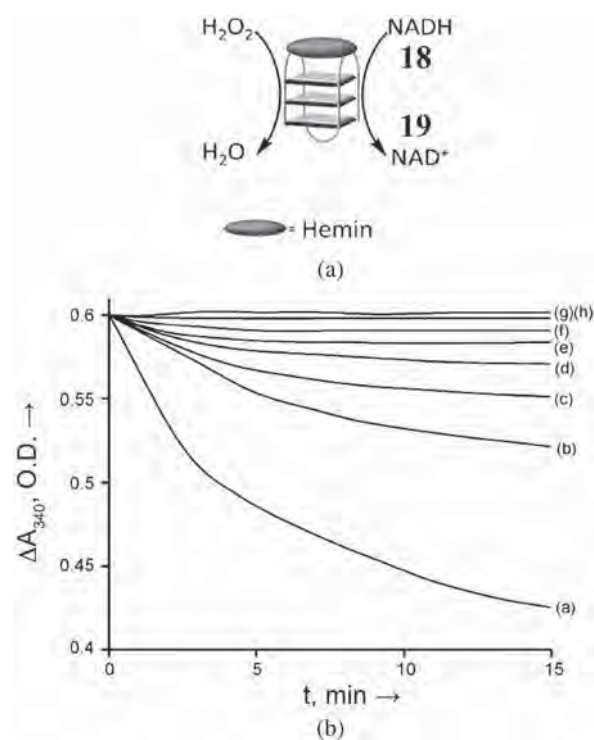
**Fig. 5.** (a) The hemin/G-quadruplex-catalyzed oxidation of thiols to thiol radicals by the peroxidase cycle leading to the formation of disulfides. (b) Time-dependent absorbance spectra upon the hemin/G-quadruplex-catalyzed oxidation of TNB, (**16**), to DTNB, (**17**), by  $\text{H}_2\text{O}_2$  (Reprinted with permission from Ref. 47. Copyright (2013) American Chemical Society)

of the thiol to a thiol radical,  $\text{RS}^\bullet$ , that is generated in two subsequent reactions, Fig. 5(a). Apart from the dimerization of  $\text{RS}^\bullet$  to the respective disulfide, the  $\text{RS}^\bullet$  also initiates an autocatalytic process involving the aerobic oxidation of  $\text{RS}^\bullet$  to the disulfide product and  $\text{H}_2\text{O}_2$ , Scheme 2, Equations 6–10. For example, Fig. 5(b) depicts the time-dependent spectral changes accommodating the hemin/G-quadruplex-catalyzed aerobic oxidation of 2-nitro-5-thiol-benzoic acid, TNB, (**16**) to 5,5'-dithio-bis-(2-nitrobenzoic acid), DTNB, (**17**), Scheme 2, Equation 11, according to the depicted mechanism [47]. The hemin/G-quadruplex-catalyzed oxidation of thiols was extensively implemented for the development of various sensing assays (see Section 3.1).

A related study has introduced the hemin/G-quadruplex as a catalyst for the aerobic oxidation of NADH or the  $\text{H}_2\text{O}_2$ -mediated oxidation of NADH, (**18**), to  $\text{NAD}^+$  [**19**], Fig. 6(a). The study demonstrated that the hemin/G-quadruplex DNAzyme mimics the catalytic activities of the native NADH-oxidase and NADH peroxidase biocatalysts. Although the mechanism is not fully understood, it was suggested that the hemin/G-quadruplex catalyzed a two-electron oxidation of NADH to  $\text{NAD}^+$  yielding  $\text{H}_2\text{O}_2$ . The generated  $\text{H}_2\text{O}_2$  acts also as an oxidant for the oxidation of NADH to  $\text{NAD}^+$ . The aerobic hemin/G-quadruplex-catalyzed oxidation of NADH was followed spectroscopically through the depletion of NADH upon the formation of  $\text{NAD}^+$ , Fig. 6(b) and by the concomitant monitoring of the fluorescence generated by the system *via* the conjugation of a reporter cycle of hemin/G-quadruplex-catalyzed oxidation of Amplex Red, (**4**), to resofurin (**5**) by  $\text{H}_2\text{O}_2$ , Fig. 6(c). From the time-dependent depletion of NADH, at different concentrations of the cofactor, the values of  $k_{\text{cat}} = (1.1 \pm 0.06) \times 10^{-4} \text{ s}^{-1}$  and  $K_M = (5.7 \pm 0.3) \times 10^{-5} \text{ M}$  for the hemin G-quadruplex were derived (as compared to  $k_{\text{cat}} = 5.1 \text{ s}^{-1}$  and  $K_M = 4.1 \times 10^{-6} \text{ M}$  for the native FAD-dependent NADH oxidase). Similarly, under anaerobic conditions, and in the presence of  $\text{H}_2\text{O}_2$



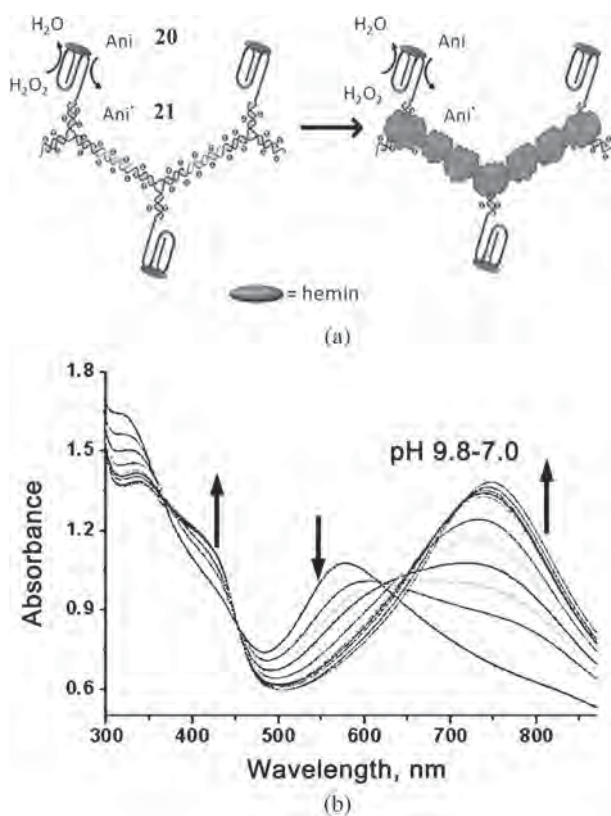
**Fig. 6.** (a) The aerobic hemin/G-quadruplex-catalyzed oxidation of NADH regenerated by the AlcDH/ethanol system, using  $O_2$  as the oxidant. The generated  $H_2O_2$  is used to activate the hemin/G-quadruplex-catalyzed oxidation of Amplex Red to the fluorescent resorufin, acting as a reporter system for the hemin/G-quadruplex NADH-oxidase mimicking DNAzyme. (b) Time-dependent absorbance changes upon the aerobic hemin/G-quadruplex-catalyzed oxidation of NADH, followed at  $\lambda = 340$  nm, in the presence of variable concentrations of NADH: (a) 1 mM, (b) 0.5 mM, (c) 0.1 mM, (d) 0.01 mM. (c) Time-dependent fluorescence changes upon the aerobic hemin/G-quadruplex-catalyzed oxidation of NADH, followed by the DNAzyme-catalyzed oxidation of Amplex Red to the fluorescent resorufin by the intermediate  $H_2O_2$  product, in the presence of variable concentrations of NADH: (a) 1 mM, (b) 0.5 mM, (c) 0.05 mM, (d) 0.01 mM, (e) 0 mM (Reprinted with permission from Ref. 48. Copyright (2011) Wiley-VCH)



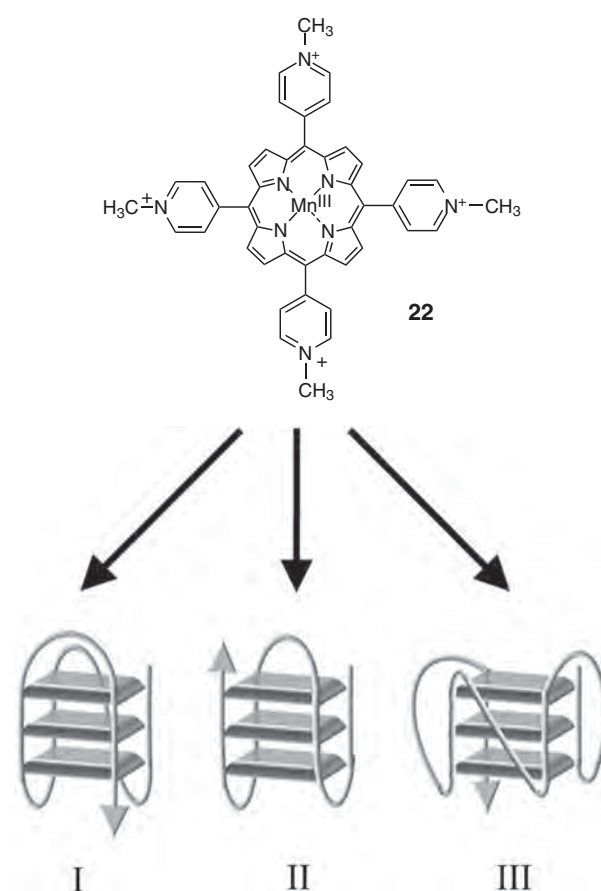
**Fig. 7.** (a) Hemin/G-quadruplex anaerobic-catalyzed oxidation of NADH by  $H_2O_2$ . (b) Time-dependent absorbance changes, followed at  $\lambda = 340$  nm, upon the hemin/G-quadruplex-catalyzed oxidation of NADH, 0.1 mM, in the presence of variable concentrations of  $H_2O_2$ : (a) 50  $\mu$ M (b) 20  $\mu$ M, (c) 10  $\mu$ M, (d) 6  $\mu$ M, (e) 3  $\mu$ M, (f) 20  $\mu$ M in the presence of a foreign DNA and hemin, (g) 20  $\mu$ M in the presence of a hemin only, (h) 0  $\mu$ M (Reprinted with permission from Ref. 48. Copyright (2011) Wiley-VCH)

as oxidant, the hemin/G-quadruplex-catalyzed oxidation of NADH to  $NAD^+$  occurred, Fig. 7(a). The oxidation of NADH under anaerobic conditions was characterized spectroscopically by following the depletion of the NADH absorbance at  $\lambda = 340$  nm, in the presence of different concentrations of  $H_2O_2$ , Fig. 7(b). From these results the values of  $k_{cat} = (4.6 \pm 0.2) \times 10^{-3} s^{-1}$  and  $K_M = (6.0 \pm 0.3) \times 10^{-6} M$  were derived as the biocatalytic features of the hemin/G-quadruplex as an NADH peroxidase (as compared to  $k_{cat} = 3.0 s^{-1}$  and  $K_M = 1.0 \times 10^{-6} M$  for the native FAD-dependent NADH peroxidase). Albeit the catalytic activities of the hemin/G-quadruplex as NADH oxidase or NADH-peroxidase are substantially lower than the respective native enzymes, the results demonstrate a new catalytic, non-enzymatic route to regenerate the  $NAD^+$  cofactor. The regeneration of the  $NAD^+$  cofactor is a key-step to drive numerous  $NAD^+$ -dependent biotransformations. In fact, enzyme-driven biotransformations using  $NAD^+$ -dependent enzymes attract substantial interest for the synthesis of valuable products, e.g. amino acids,  $\alpha$ -hydroxycarboxylic acids and chiral ketones for the pharmaceutical and food industries. Indeed, the NADH-oxidase mimicking activities of the hemin/G-quadruplex were implemented to regenerate the

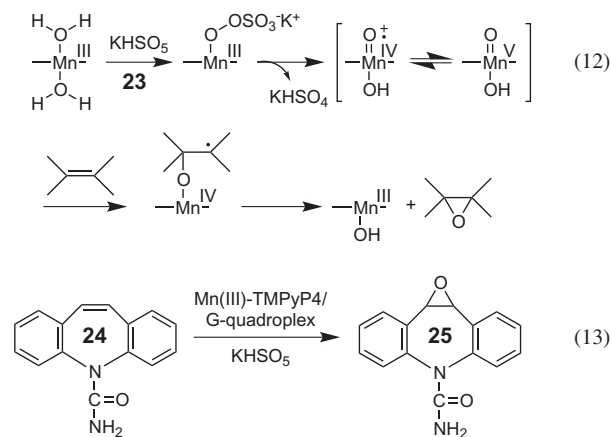




**Fig. 8.** (a) DNA template modified with hemin/G-quadruplex units acting as catalysts for the oxidation of aniline by H<sub>2</sub>O<sub>2</sub> to form polyaniline-coated DNA templates (b) Absorbance spectra changes upon the pH-induced doping of the polyaniline wires to form emeraldine salt (Reprinted with permission from Ref. 49. Copyright (2013) American Chemical Society)



**Fig. 9.** The association of Mn(II)-*meso*-tetramethylpyridinium porphyrin to different folding motives of G-quadruplexes (Reprinted with permission from Ref. 50. Copyright (2013) Wiley-VCH)



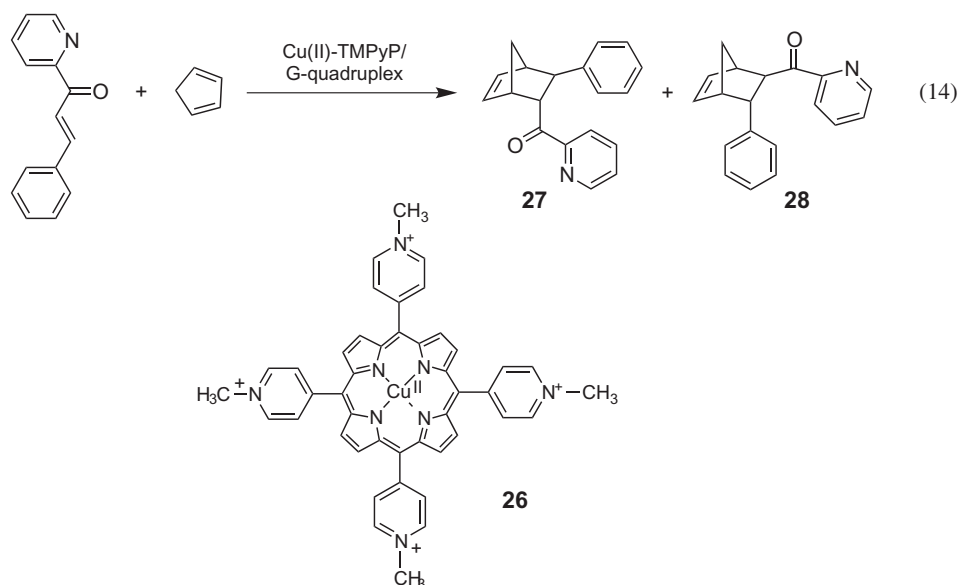
**Scheme 3.** Mn(III)-TMPyP4/G-quadruplex-catalyzed epoxidation of carbamazepine, (22), to carbamazepine-10,11-oxide, (23)

NADH cofactor by coupling it to the NAD<sup>+</sup>-dependent alcohol dehydrogenase (AlcDH) mediated cyclic oxidation of ethanol to acetaldehyde, Fig. 7(a).

In analogy to the HRP-catalyzed oxidation of aniline by H<sub>2</sub>O<sub>2</sub> to polyaniline, hemin/G-quadruplexes were found

to catalyze the oxidation of aniline (20) to radical aniline (21) by H<sub>2</sub>O<sub>2</sub> that subsequently polymerizes to polyaniline [49]. The resulting positively charged polyaniline was deposited on the DNA template. Figure 8(a) depicts the Y-shaped DNA template that was functionalized with hemin/G-quadruplex. The structure revealed linear *para*-substituted chains that were doped under acidic conditions to the emeraldine salt state, Fig. 8(b). Circular dichroism spectra indicated that the polyaniline chain generated a helical structure that wrapped the DNA template.

Apart from hemin, additional positively charged metal-substituted porphyrins were reported to bind to G-quadruplex nanostructures and to catalyze different reactions. For instance, the cationic Mn(III)-tetramethylpyridinium porphyrin, Mn(III)-TMPyP4, (22), bound to the G-quadruplex nanostructure was found to catalyze oxygen transfer reactions to olefins using persulfate, (23), as an oxygen source, to yield epoxides [50], Scheme 3, Equation 12. Specifically, the epoxidation of carbamazepine, (24), to carbamazepine-10,11-oxide, (25), Equation 13, was examined using different Mn(III)-TMPyP4-functionalized G-quadruplexes as catalysts [50], Fig. 9, configurations I-III. The oligonucleotide sequence



**Scheme 4.** Cu(II)-TMPyP<sub>4</sub>/G-quadruplex-catalyzed enantioselective Diels-Alder reaction

of 5'-d[TT(GGGTTA)<sub>3</sub>GGGA] corresponds to the human telomere sequence, and it adopts, in the presence of K<sup>+</sup>-ions, a parallel G-quadruplex configuration I, whereas in the presence of the Na<sup>+</sup> ions the configuration switches to the anti-parallel structure II. A related oligonucleotide sequence, 5'-d(TGAGGGTGGGGAGGGTGGGGAA), corresponding to the c-Myc oncogene promoter that forms, in the presence of K<sup>+</sup>-ions, a propeller-type parallel G-quadruplex structure, III, and provides a third scaffold for the formation of the complex. Mn(III)-TMPyP4-I and the Mn(III)-TMPyP4-II revealed similar catalytic activities toward the epoxidation of (**24**) to (**25**), while the Mn(III)-TMyPyP4-III showed a 30-fold lower catalytic activity toward the epoxidation process.

A Cu(II)-tetramethylpyridinium cationic porphyrin, Cu(II)-TMPyP<sub>4</sub>, (**26**), associated with the telomeric G-quadruplex, acted as a catalyst for the enantioselective Diels-Alder reaction [51], Scheme 4, Equation 14. Using a series of different G-quadruplex oligonucleotide variants it was demonstrated that the yields of the processes were ~98%, with a 98:2 ratio of *endo/exo* isomers, (**27**) and (**28**) respectively. The enantiomeric excess (*ee*%) for the formation of the *endo* enantiomer in the catalyzed reaction was in the range of 40% to 65%, depending on the sequence of the G-quadruplex.

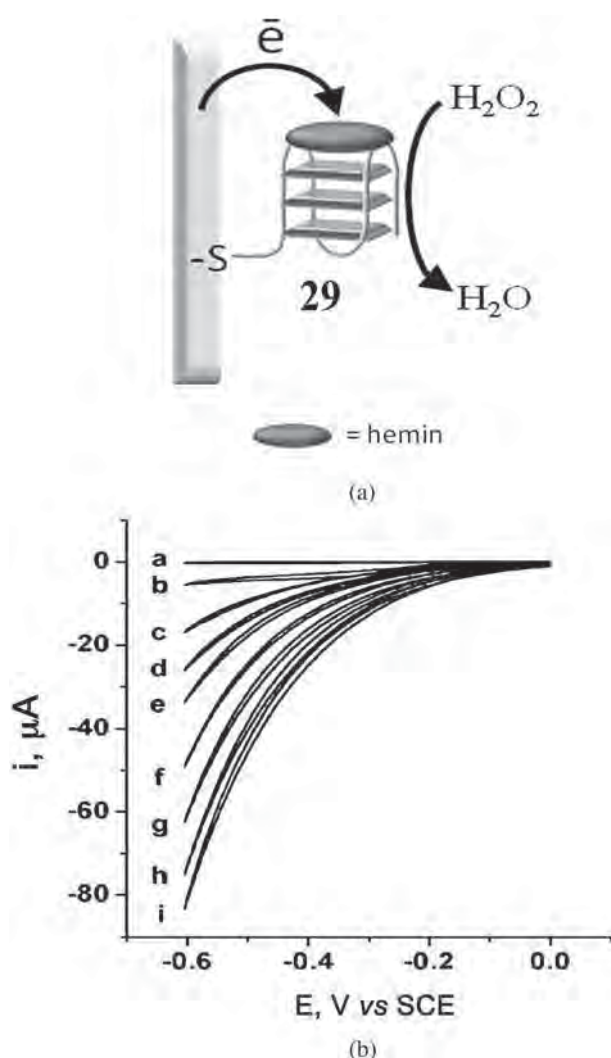
## 2. Photophysical, photochemical and electrocatalytic features of metalloporphyrin/G-quadruplexes

Hemin/G-quadruplex exhibits quasi-reversible redox features [52]. A thiolated G-rich nucleic acid (**29**) was assembled on a Au electrode, and assembled in the presence of K<sup>+</sup>-ions into the G-quadruplex structure. Hemin bound to the G-quadruplex yielded the

hemin/G-quadruplex HRP-mimicking DNAzyme, and this exhibited a quasi-reversible redox-wave at  $E = -0.27$  V vs. SCE. The hemin/G-quadruplex monolayer acted as an electrocatalytic surface for the electrochemical reduction of H<sub>2</sub>O<sub>2</sub>, Fig. 10(a). The monolayer-functionalized electrode was applied for the quantitative analysis of H<sub>2</sub>O<sub>2</sub>, with a detection limit that corresponded to 0.5 mM, Fig. 10(b).

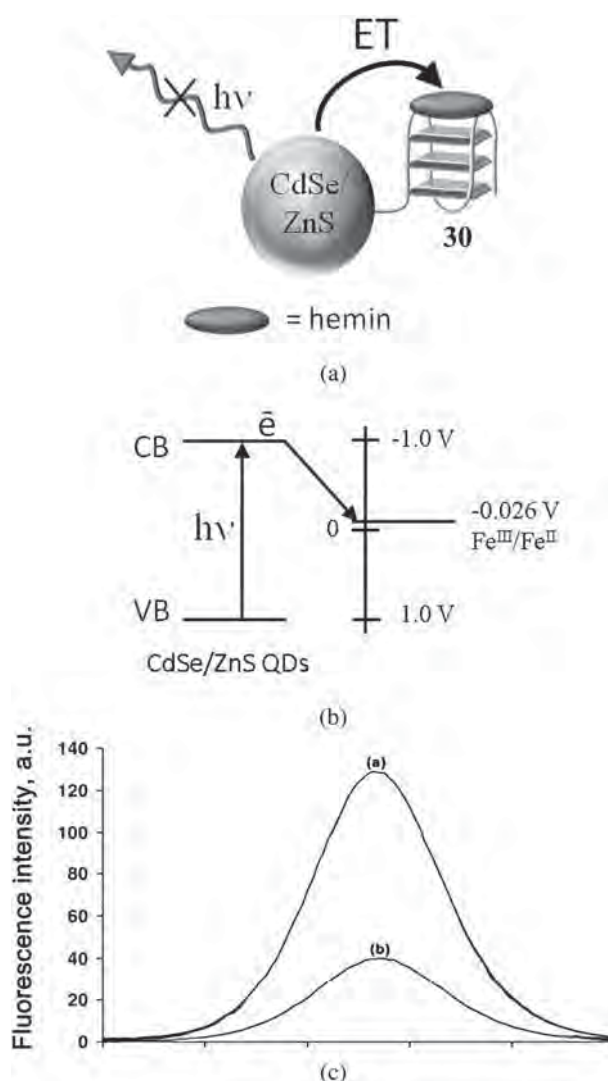
Different dyes coordinate to G-quadruplex nanostructures by cooperative electrostatic and  $\pi$ - $\pi$  interactions. The fluorescence of these dyes is significantly enhanced upon association to the G-quadruplexes due to restricted rotation and decrease in the polarity of the environment of the dyes. Specifically, Zn(II)-protoporphyrin IX binds to G-quadruplexes and the resulting complex exhibits a substantially higher fluorescence as compared to the metalloporphyrin molecule [53]. Indeed, this property was implemented for the development of various fluorescent biosensors (see Section 3.1).

Apart from driving biocatalytic reactions, the diverse catalytic and non-catalytic chemistry exhibited by the hemin/G-quadruplex allows it to participate as an active component in various photophysical mechanisms. For example, the luminescence of semiconductor quantum dot (QDs), such as CdSe/ZnS QDs modified with hemin/G-quadruplex units, (**30**), Fig. 11(a) is quenched *via* an electron-transfer, ET, quenching mechanism [54]. The energy levels corresponding to the CdSe/ZnS-hemin/G-quadruplex conjugates suggest that photoexcited conduction-band electrons generated in the QDs may be transferred to the hemin/G-quadruplex, Fig. 11(b). This process prohibits the radiative electron-hole recombination in the QDs, but instead proceeds *via* the subsequent dark, non-radiative, back-electron



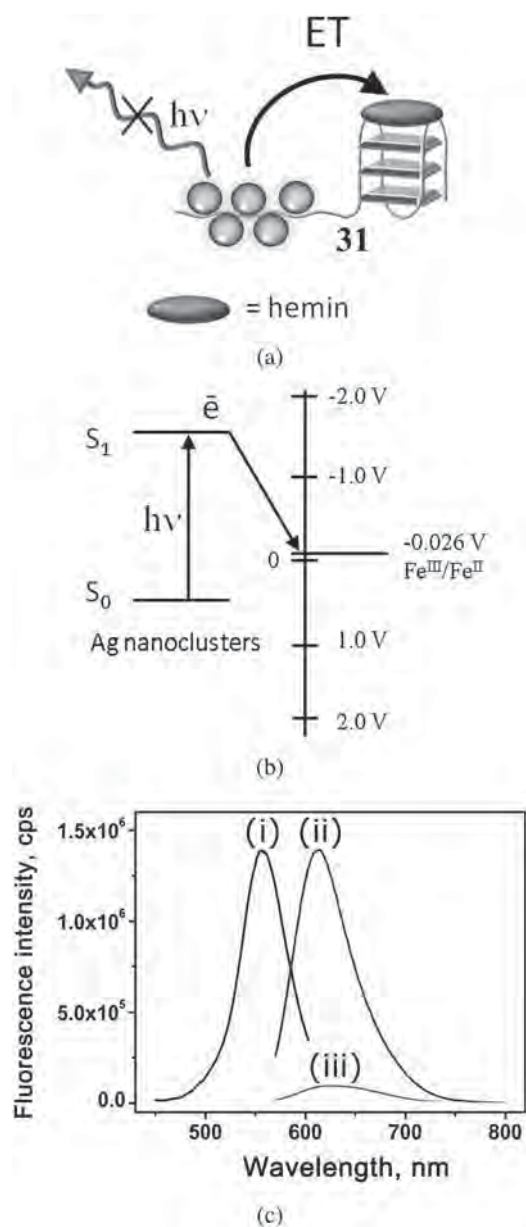
**Fig. 10.** (a) Electrocatalyzed-reduction of  $\text{H}_2\text{O}_2$  by a hemin/G-quadruplex monolayer associated with an Au electrode. (b) Electrocatalytic cathodic currents observed upon the electrocatalytic reduction of variable concentration of  $\text{H}_2\text{O}_2$  by the hemin/G-quadruplex-modified electrode: (a) 0 mM, (b) 0.5 mM, (c) 1.0 mM, (d) 1.5 mM, (e) 2.0 mM, (f) 3.0 mM, (g) 4.0 mM, (h) 5.0 mM, (i) 6.0 mM (Reprinted with permission from Ref. 52. Copyright (2010) American Chemical Society)

transfer from the reduced heme site to the holes present in the valence-band of the QDs, thus leading to quenching of the luminescence of the QDs, Fig. 11(c). Similarly, luminescent nucleic acid-stabilized Ag nanoclusters conjugated to a hemin/G-quadruplex, (31), are quenched by the hemin/G-quadruplex units [55], Fig. 12(a). The energy-levels diagram reveals a similar quenching mechanism to the QD-hemin/G-quadruplex system, *via* an electron-transfer, Fig. 12(b), resulting in the hemin/G-quadruplex-stimulated quenching of the Ag nanoclusters fluorescence, Fig. 12(c). A further interesting photophysical mechanism that involves semiconductor QDs and hemin/G-quadruplexes is the chemiluminescence resonance energy transfer (CRET)



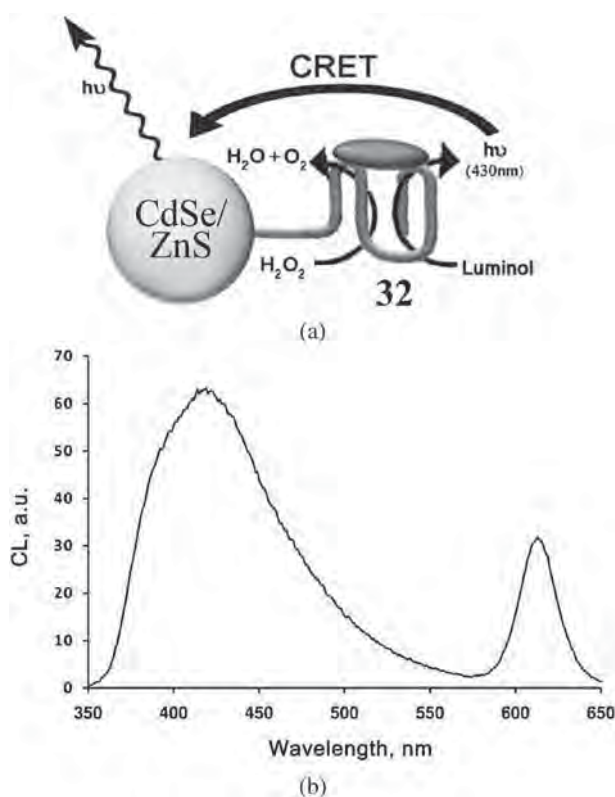
**Fig. 11.** (a) Electron-transfer quenching of the luminescence of CdSe/ZnS QDs by surface-associated hemin/G-quadruplex units. (b) Energy level diagram corresponding to the electron-transfer quenching mechanism of photoexcited CdSe/ZnS QDs by the surface-bound hemin/G-quadruplex. (c) Luminescence spectra of the G-quadruplex-modified QDs: (a) without hemin. (b) In the presence of hemin,  $1\ \mu\text{M}$  (Reprinted with permission from Ref. 54. Copyright (2010) American Chemical Society)

mechanism [56]. As mentioned, the hemin/G-quadruplex catalyzes the  $\text{H}_2\text{O}_2$ -mediated oxidation of luminol and the accompanied generation of chemiluminescence at  $\lambda_{\text{em}} = 430\text{ nm}$ . The generated light might act as a localized radiative source for the QDs, exhibiting absorbance that overlaps with the chemiluminescence spectral region. Indeed, it was found that hemin/G-quadruplex, (32), structures conjugated to semiconductor QDs lead to a chemiluminescence resonance energy transfer (CRET) where the chemiluminescence energy excites the semiconductor QDs, thus leading to their luminescence without external irradiation, Fig. 13(a). Indeed, treatment of CdSe/ZnS-hemin/G-quadruplex conjugates with luminol/



**Fig. 12.** (a) Schematic electron-transfer quenching of the luminescence of nucleic acid-stabilized Ag nanoclusters (NCs) by the hemin/G-quadruplex. (b) Energy levels corresponding to the Ag NCs and the conjugated hemin/G-quadruplex. (c) The photophysical properties of Ag NCs/G-quadruplex hybrids: (i) The excitation spectrum of the hybrid. (ii) The luminescence spectrum of the hybrid in the absence of hemin. (iii) The luminescence spectrum of the hybrid in the presence of the hemin/G-quadruplex (Reprinted with permission from Ref. 55. Copyright (2013) American Chemical Society)

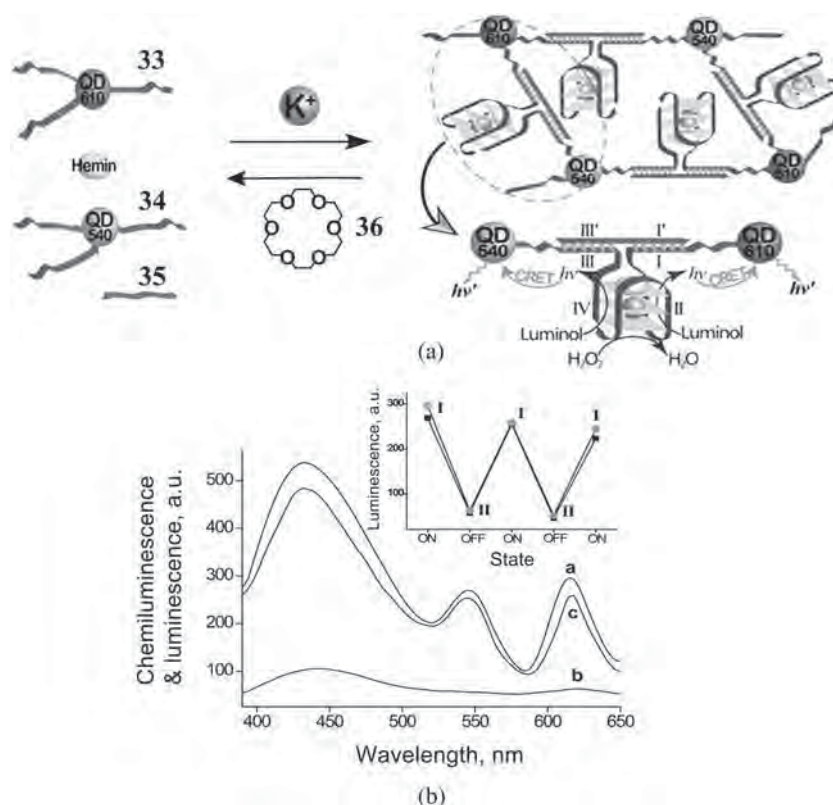
H<sub>2</sub>O<sub>2</sub> activated the CRET process [56]. Figure 13(b) shows the resulting broad chemiluminescence spectrum, centered at  $\lambda_{em} = 430$  nm, accompanied by the luminescence of the CdSe/ZnS QDs at  $\lambda_{em} = 610$  nm. It should be noted that the apparent contradicting features of hemin/G-quadruplex in semiconductor conjugates (ET quenching vs. CRET mechanisms) requires a delicate



**Fig. 13.** (a) A hybrid consisting of hemin/G-quadruplex and CdSe/ZnS quantum dots (QDs) and the chemiluminescence resonance energy transfer (CRET) in the hybrid nanostructure. (b) Chemiluminescence spectrum ( $\lambda_{max} = 425$  nm) generated by the hemin/G-quadruplex-catalyzed oxidation of luminol by H<sub>2</sub>O<sub>2</sub>, and the luminescence spectrum of the CdSe/ZnS QDs ( $\lambda_{max} = 610$  nm) generated by the CRET process (Reprinted with permission from Ref. 56. Copyright (2011) American Chemical Society)

tuning of the structural features of the QD-hemin/G-quadruplex. To minimize the quenching of the CRET-stimulated emission of the QDs the G-quadruplex should be spatially separated from the QDs.

The control of the photophysical properties of metalloporphyrins, semiconductor QDs, and metal nanoclusters provides versatile means to develop many different optical sensing platforms that will be addressed in Section 3.1. The hemin/G-quadruplex-catalyzed CRET process to semiconductor QDs was implemented to design switchable aggregation/deaggregation processes of CdSe/ZnS quantum dots, accompanied by the ON-OFF switching of the luminescence of two-sized CdSe/ZnS quantum dots (QDs) [57], Fig. 14(a). Two-sized QDs emitting at  $\lambda_{em} = 610$  nm and 540 nm were functionalized with nucleic acids (33) and (34), respectively, consisting of the G-quadruplex subunits, and an additional domain that hybridizes with a linking strand (35). The DNA hairpin-modified QDs were added to a solution containing hemin and (35), and in the presence of K<sup>+</sup>-ions, the self-assembly of the K<sup>+</sup>-stabilized G-quadruplex was



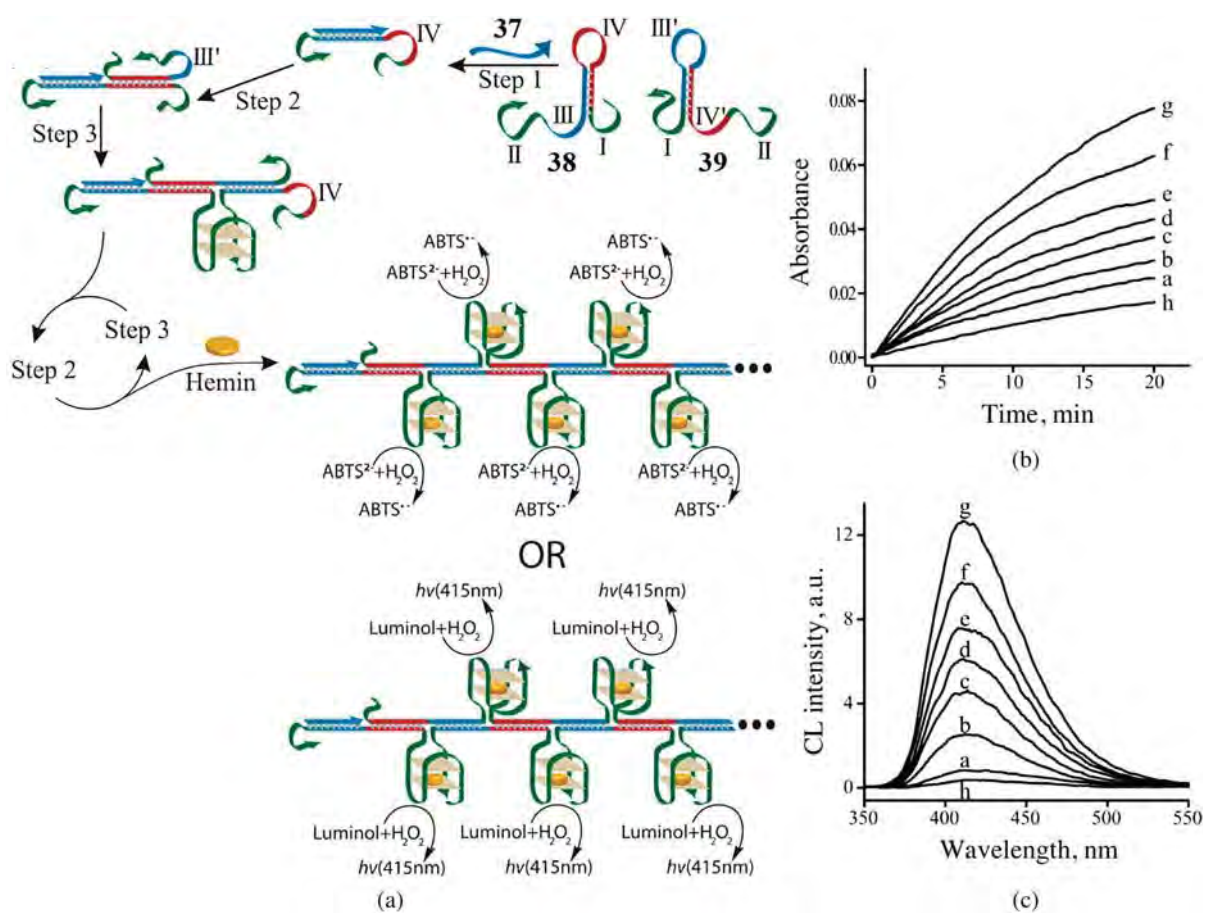
**Fig. 14.** (a) Switchable aggregation and deaggregation of CdSe/ZnS QDs in the presence of added K<sup>+</sup> ions or 18-crown-6 ether, respectively. (b) Switchable ON-OFF CRET-stimulated generation of the luminescence of the QDs: (a) CRET-stimulated luminescence spectrum of the hemin/G-quadruplex-bridged CdSe/ZnS QDs in the presence of the K<sup>+</sup>-ions stabilizing the G-quadruplex. (b) Luminescence spectrum of the system generated upon the 18-crown-6-induced deaggregation of the QDs and the separation of the bridging units due to elimination of the K<sup>+</sup>-ions from the G-quadruplex bridges. (c) Luminescence spectrum of the aggregated, hemin-G-quadruplex-bridged CdSe/ZnS upon the re-addition of K<sup>+</sup>-ions and the regeneration of the hemin/G-quadruplex catalytic bridges. Inset: Cyclic ON-OFF activation and deactivation of the luminescence properties of (●) 610 nm emitting QDs (■) 540 nm emitting QDs, upon the: (I) The K<sup>+</sup>-induced aggregation of the QDs by the hemin/G-quadruplex bridges. (II) The deaggregation of the QDs upon addition of 18-crown-6 (Reprinted with permission from Ref. 57. Copyright (2014) American Chemical Society)

cooperatively stabilized by the bridging strand (35), Fig. 14(a). Crosslinking of the different-sized QDs by the (35)-bridged G-quadruplex units led to the aggregation of the QDs and to the binding of hemin to the G-quadruplex bridges. The resulting hemin/G-quadruplex DNAzyme catalyzed the generation of chemiluminescence through the DNAzyme-catalyzed oxidation of luminol by H<sub>2</sub>O<sub>2</sub>. The resulting chemiluminescent process stimulated the CRET process to the adjacent two-sized QDs, resulting in their luminescence at  $\lambda_{em} = 540$  nm and  $\lambda_{em} = 610$  nm, without external excitation, Fig. 14(b), curve (a). Treatment of the QDs aggregates with 18-crown-6, (36), eliminated the K<sup>+</sup>-ions from the G-quadruplex units, resulting in the dissociation of the hemin/G-quadruplex bridging units and to the deaggregation of the QDs structure. The resulting mixture of the separated QDs did not possess any significant catalytic activity and the chemiluminescence process as well as the accompanying CRET process were switched-off, Fig. 14(b), curve (b). By the cyclic treatment of the system with K<sup>+</sup>-ions and

18-crown-6, the QDs are switched between hemin/G-quadruplex-functionalized catalytic aggregates and a deaggregated non-catalytic configuration. This resulted in the switchable cyclic activation of the dual luminescence features of the two-sized QDs to ON and OFF states, Fig. 14(b), inset.

### 3. Applications of metalloporphyrins-functionalized G-quadruplexes

The unique recognition and catalytic functions of sequence-specific nucleic acids may be implemented to develop a large variety of sensing platforms. The formation of duplex DNA nanostructures, ligand-aptamer complexes or of metal-assisted, cooperatively-stabilized, duplex nucleic acids provides versatile recognition elements for the sensing platforms. The conjugation of enzymes or DNAzymes to this recognition element may then provide effective means to amplify the recognition events that yields sensitive sensing modules. Indeed, in



**Fig. 15.** (a) Schematic analysis of a DNA analyte by the target-stimulated initiation of the hybridization chain reaction (HCR), leading to hemin/G-quadruplex catalytic wires. (b) Time-dependent absorbance changes observed upon analyzing different concentrations of the DNA analyte (37) using the HCR amplification scheme shown in (a) and by following the hemin/G-quadruplex-catalyzed oxidation of ABTS<sup>2-</sup> by H<sub>2</sub>O<sub>2</sub> to form the colored product, ABTS<sup>•-</sup> ( $\lambda = 420$  nm). (c) Chemiluminescence spectra generated upon analyzing different concentrations of the analyte (37) according to the scheme shown in (a), and using the hemin/G-quadruplex-catalyzed oxidation of luminol by H<sub>2</sub>O<sub>2</sub> and the generation of chemiluminescence. For both systems shown in (b) and (c) the analyte concentrations correspond to: (a) 0 M, (b)  $1 \times 10^{-13}$  M, (c)  $1 \times 10^{-12}$  M, (d)  $1 \times 10^{-11}$  M, (e)  $1 \times 10^{-10}$  M, (f)  $1 \times 10^{-9}$  M, (g)  $1 \times 10^{-8}$  M (Reprinted with permission from Ref. 65. Copyright (2012) American Chemical Society)

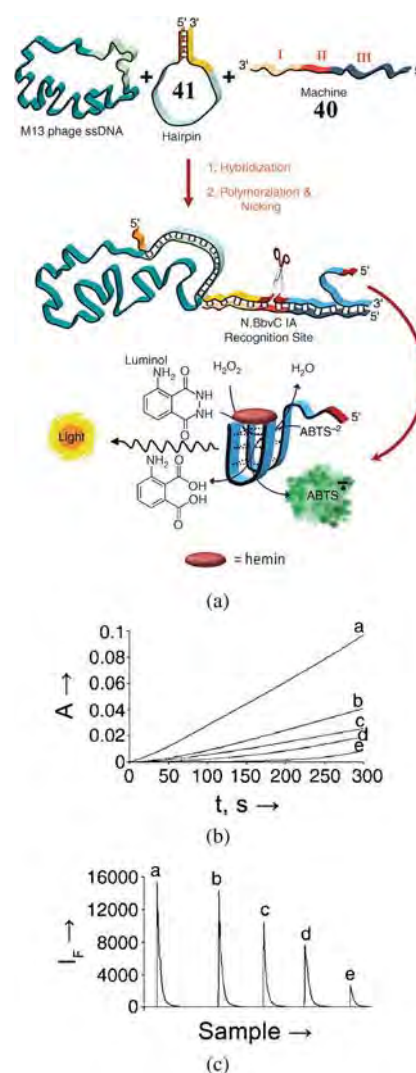
the past two decades, numerous studies have used nucleic acids and aptamers as recognition probes [58–62] and coupled enzymes [63, 64] or DNAzymes [65–71] as amplifying labels for the sensing events. Furthermore, the formation of DNA duplexes of controlled stabilities, the cooperative stabilization of nucleic acid nanostructures by metal ions (*e.g.* Ag<sup>+</sup>, Hg<sup>2+</sup>), the ion-stimulated stabilization of G-quadruplexes [72], the pH-induced formation of i-motif structures, or the stabilization of aptamer-ligand complex, provide means to control the reconfiguration of DNA nanostructures [73], and these may lead to switchable DNA devices or to functional DNA structures mimicking DNA machines [74].

**3.1 Metalloporphyrins as catalytic, electrocatalytic and optical labels for sensing.** Ultra-sensitive sensing platforms involving the hemin/G-quadruplex as a catalytic label have been developed using enzyme-free or enzyme-aided DNA machineries, capable of synthesizing autonomously the hemin/G-quadruplex

label as a result of recognition events [65]. Figure 15(a) depicts the enzyme-free ultra-sensitive detection of a DNA analyte (37) using the hybridization chain reaction (HCR) as DNA machinery [65]. In this system, the DNA hairpins 38 and 39 function as the DNA machinery. Hairpin 38 includes at the 5'-end of the stem region I the encodes the sequence that corresponds to three-fourths of the G-quadruplex and programmed domains IV and III, where the sequence II that is associated with III is complementary to a part of domain IV, thus forming the hairpin structure. Importantly, the hairpin 38 includes in domain III the recognition sequence for the analyte (37). The hairpin 39 is engineered to include at the 5' and 3' ends of the stem region one-fourth of the G-quadruplex sequences, respectively, where the three-fourths G-quadruplex domain II is conjugated to domains IV' and III', that are complementary to domains IV and III of hairpin 38. In the presence of the analyte (37), hairpin

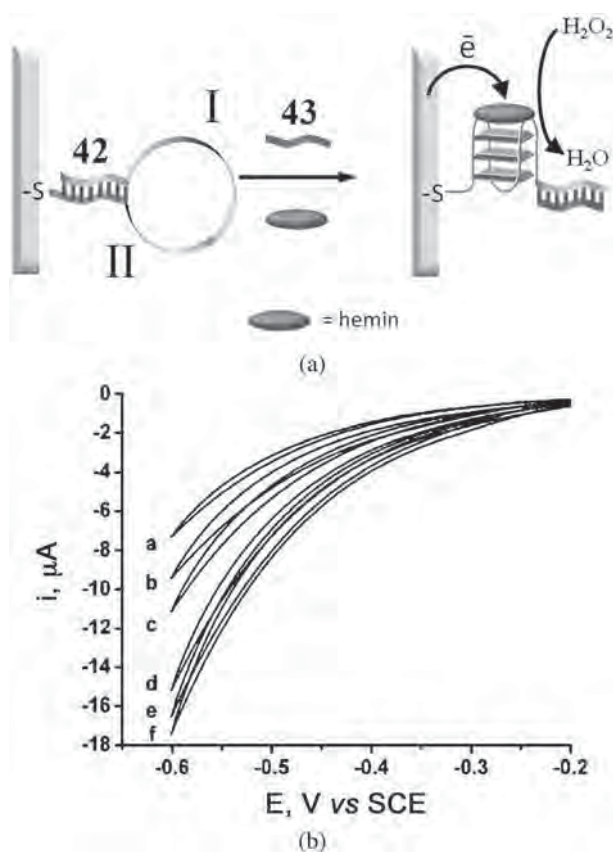
**38** opens, resulting in the free domain IV (step 1), and the latter open hairpin **39** through binding to domain IV', thereby releasing domain III', (step 2), that is complementary to domain III of hairpin **38**. The cross-opening of hairpin **38**, (step 3), releases the domain IV, while allowing the self-assembly of the tethers I and II to the G-quadruplex. By the autonomous cross-opening of hairpins **38** and **39**, (step 2 and step 3) long chains of the G-quadruplex DNAzyme units associated with the HCR wires are formed. The subsequent binding of hemin to the G-quadruplex polymer wires resulted in chains of the hemin/G-quadruplex DNAzyme labels as a result of a single recognition event. The resulting DNAzyme wires enabled, then, the colorimetric detection of the analyte through the catalyzed oxidation of ABTS<sup>2-</sup> by H<sub>2</sub>O<sub>2</sub> to form the colored product, ABTS<sup>•+</sup>, Fig. 15(b), or the chemiluminescence detection of the analyte (**37**) by the DNAzyme catalyzed oxidation of luminol by H<sub>2</sub>O<sub>2</sub>, Fig. 15(c). This sensing platforms enabled the analysis of the target DNA with a detection limit corresponding to  $1 \times 10^{-13}$  M within an isothermal reaction time interval of 4–6 h.

Enzyme/hemin/G-quadruplex DNA machineries were similarly applied for amplified biosensing. This is exemplified in Fig. 16(a) with the amplified detection of DNA [75]. The nucleic acid scaffold (**40**) provides the functional sensing module. Domain I is complementary to the analyte, whereas the domain III is complementary to the G-quadruplex sequence. The bridging domain II includes a programmed sequence that upon replication yields a duplex where the replication domain includes the specific sequence that is nicked by the enzyme N.BbvC IA. The sensing system includes polymerase, the nicking enzyme N.BbvC IA, and the oligonucleotide mixture, dNTPs. The analyte M13 phage opens the appropriate hairpin probe, (**41**), that yields a versatile primer that activates the DNA machinery. Hybridization of the phage M13/hairpin primer with the recognition site, in the presence of polymerase/dNTPs stimulate, results in the replication of the scaffold. This process replicates domain II and III, where the replicated sequences correspond to the nicking domain and the G-quadruplex, respectively. The nicking of domain II provides an opening for polymerase, resulting in the re-replication of the scaffold, while displacing the G-quadruplex sequence (conjugated to a short tether of domain II). That is, the recognition of the target DNA (**41**) by the scaffold (**40**) initiates the autonomous cyclic release of the catalytic G-quadruplex strand. The association of hemin to the displaced site yields the catalytic hemin/G-quadruplex DNAzyme that catalyzes the H<sub>2</sub>O<sub>2</sub>-stimulated oxidation of ABTS<sup>2-</sup> to the colored product ABTS<sup>•+</sup>, or catalyzes the oxidation of luminol by H<sub>2</sub>O<sub>2</sub> while generating chemiluminescence. These two processes provide readout signals for the sensing of (**41**), Figs 16(b) and 16(c). The method enabled the detection of (**41**) with a detection limit that corresponds



**Fig. 16.** (a) The analysis of the M13 phage analyte using an autonomous replication/nicking machinery synthesizing the hemin/G-quadruplex as an amplification catalyst. (b) Time-dependent absorbance changes upon analyzing different concentrations of the M13 phage using the amplification machinery shown in (a) and the hemin/G-quadruplex-catalyzed oxidation of ABTS<sup>2-</sup> to ABTS<sup>•+</sup> ( $\lambda_{\max} = 415$  nm) as readout signal: (a)  $1 \times 10^{-9}$  M, (b)  $1 \times 10^{-11}$  M, (c)  $1 \times 10^{-12}$  M, (d)  $1 \times 10^{-14}$  M, and (e) analysis of the foreign calf-thymus single stranded DNA,  $1 \times 10^{-8}$  M. (c) Chemiluminescence spectra corresponding to the analysis of different concentrations of M13 phage using the amplification machinery shown in (a) and the hemin/G-quadruplex-catalyzed oxidation of luminol by H<sub>2</sub>O<sub>2</sub> and the generation of chemiluminescence at  $\lambda = 420$  nm. (a)  $1 \times 10^{-9}$  M, (b)  $1 \times 10^{-11}$  M, (c)  $1 \times 10^{-12}$  M, (d)  $1 \times 10^{-14}$  M, and (e) analysis of the foreign calf-thymus single stranded DNA,  $1 \times 10^{-8}$  M (Reprinted with permission from Ref. 75. Copyright (2006) Wiley-VCH)

to  $1 \times 10^{-14}$  M. Similar DNA machineries were applied for the colorimetric and/or chemiluminescence detection of aptamer-ligand complexes or metal ions, e.g. Hg<sup>2+</sup>-ions [76]. Other DNA machineries such as the rolling circle amplification (RCA) process were similarly applied to



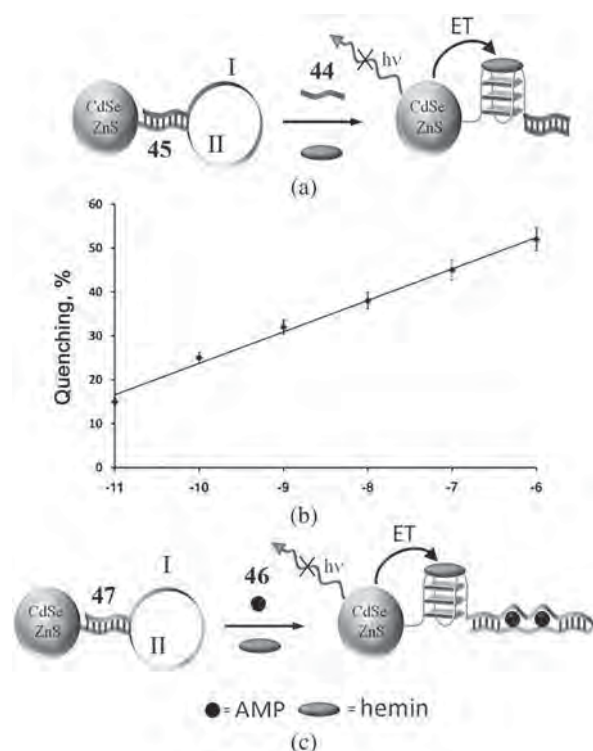
**Fig. 17.** (a) Amplified analysis of a target DNA by a hairpin-modified electrode using the hemin/G-quadruplex as an electrocatalytic label. (b) Electrocatalytic cathodic current generated upon the treatment of the hairpin-functionalized electrode with variable concentrations of the target DNA. Electrocatalytic currents are produced by the hemin/G-quadruplex-electrocatalyzed reduction of  $\text{H}_2\text{O}_2$ . The concentrations of the analyte correspond to: (a) 0 pM, (b) 20 pM, (c) 40 pM, (d) 60 pM, (e) 80 pM and (f) 100 pM (Reprinted with permission from Ref. 52. Copyright (2010) American Chemical Society)

autonomously synthesize the hemin/G-quadruplex as a catalytic label for the amplified detection of DNA or of aptamer-substrate complexes [77].

The electrocatalytic functions of the hemin/G-quadruplex toward the electrocatalyzed reduction of  $\text{H}_2\text{O}_2$  have been implemented to develop different DNA sensing platforms [52]. For example, Fig. 17(a) depicts the principle for the electrocatalyzed detection of DNA. The thiolated hairpin structure, (42), was assembled on an Au electrode. The hairpin included in domain I the recognition sequence for the analyte DNA, (43), while domain II is composed of the G-quadruplex sequence in an inactive caged configuration. In the presence of the analyte DNA, the hairpin opens and the G-quadruplex sequence is released. As a result, the hemin, present in the electrolyte solution, binds to the G-quadruplex, generating the electrocatalytic hemin/G-quadruplex that mediates the electrocatalyzed reduction of  $\text{H}_2\text{O}_2$ . As the amount of the hemin/G-quadruplex electrocatalytic units

is controlled by the concentration of the analyte, (42), the resulting electrocatalytic cathodic currents provide a quantitative measure for the concentration of the analyte, Fig. 17(b).

The unique photophysical properties of the hemin/G-quadruplexes that enable it to quench the luminescence of semiconductor quantum dots (QDs) *via* an electron-transfer mechanism, have been applied to develop different nucleic acid-based luminescent sensing platforms [54]. Figure 18(a) exemplified the analysis of a nucleic acid target (44) by the hairpin nucleic acid, (45)-functionalized CdSe/ZnS QDs. Domain I of the hairpin includes the recognition sequence for the target DNA (44) while domain II of the hairpin, partially hybridized with domain I, includes the G-quadruplex sequence in an inactive caged configuration. Treatment of the (45)-modified QDs with the target DNA, (44), and in the presence of hemin, results in the opening of the hairpin and the concomitant self-assembly of the hemin/G-quadruplex quenching units. As the concentration of the DNA target dictates the degree of opening of the hairpin units, the



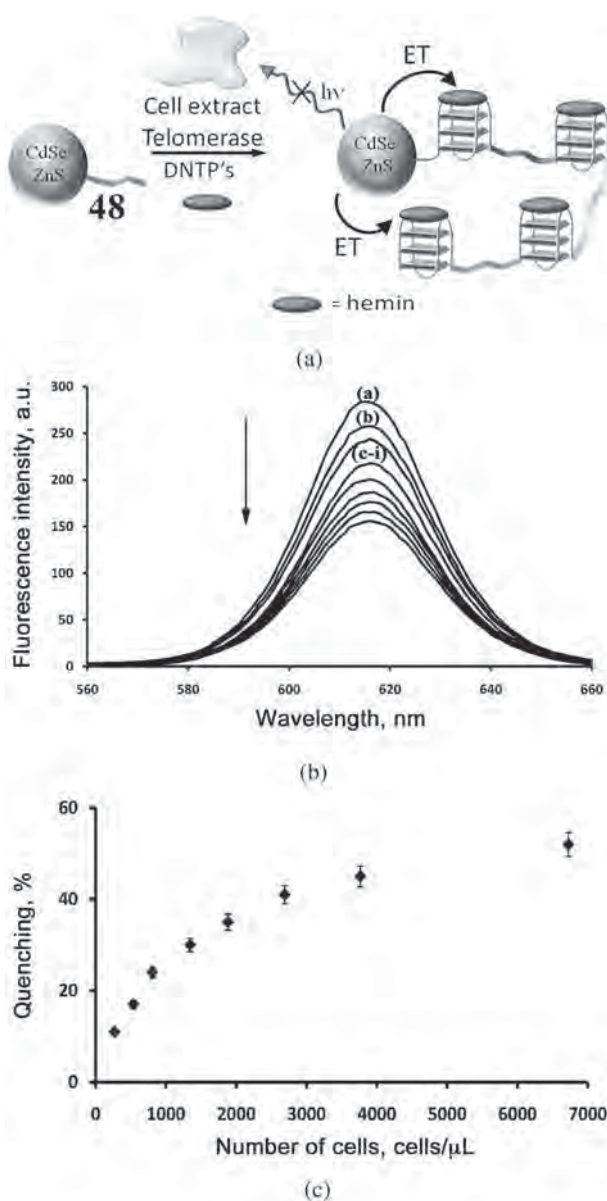
**Fig. 18.** (a) Analyzing a target DNA by a hairpin probe-modified CdSe/ZnS QDs through the electron-transfer quenching of the QDs by the hemin/G-quadruplex generated upon the opening of the hairpin probe. (b) Calibration curve corresponding to the analysis of different concentrations of the target DNA according to (a). (c) Analyzing the formation of an aptamer-ligand (AMP) complex through the application of hairpin-modified CdSe/ZnS QDs and the electron-transfer quenching of the QDs by the aptamer-ligand-stimulated formation of the hemin/G-quadruplex quencher (Reprinted with permission from Ref. 54. Copyright (2010) American Chemical Society)



resulting quenching-degree of the QDs is proportional to the concentration of the DNA analyte. Figure 18(b) shows the derived calibration curve corresponding to luminescence quenching efficiency as a function of the analyte concentration. This sensing platform enabled the sensing of the target DNA with a detection limit corresponding to  $1 \times 10^{-11}$  M. This paradigm was further applied to develop an adenosine monophosphate, AMP, (46), aptasensor, Fig. 18(c). The hairpin nucleic acid (47) included the sequence I that encoded the aptamer sequence for binding two AMP ligands, and sequence II, partially hybridized with sequence I, that consisted of the G-quadruplex sequence, in a caged inactive configuration. Subjecting the (47)-modified QDs to AMP, in the presence of hemin, resulted in the opening of the hairpin by forming the AMP-aptamer complex with a concomitant release of domain II and the self-organization of the hemin/G-quadruplex quenching units. As the concentration of AMP controls the opening of hairpin (47), the degree of quenching is thus dictated by the concentration of the AMP analyte. This sensing module enabled the analysis of AMP with a detection limit that corresponded to  $1 \times 10^{-6}$  M.

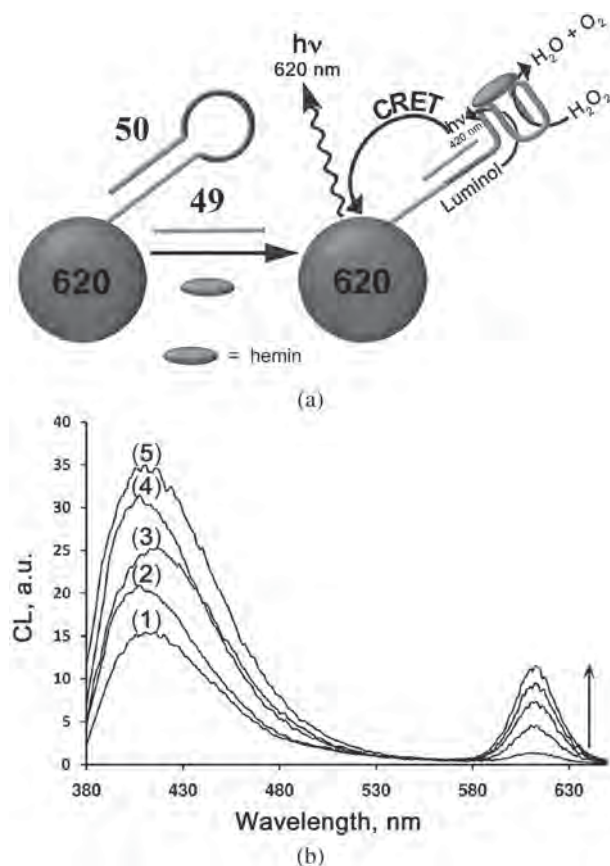
In a related study [78], the electron-transfer quenching of semiconductor CdSe/ZnS QDs phenomena was applied to sense the cancer biomarker telomerase, Fig. 19(a). The QDs were modified the nucleic acid, (48), that acts as primer for telomerase. In the presence of a cancer cell lysate containing telomerase, and in the presence of a nucleotide mixture of dNTPs and hemin, the telomerization process is initiated, yielding the G-rich telomeric chains. The biosynthesized telomeres self-assemble into the hemin/G-quadruplex chains, and these units quench the luminescence of the QDs. Figure 19(b) depicts the time-dependent quenching of the QDs upon treatment of the CdSe/ZnS QDs with a 293T cancer cell extract. As the duration of the telomerization process is prolonged, the level of the QDs' quenching is enhanced, consistent with the increase in the number of the hemin/G-quadruplex quencher units. Figure 19(c) presents the resulting calibration curve depicting the degree of quenching of the QDs upon stimulating the telomerization process by telomerase originating from different numbers of cell extracts for a fixed time-interval of 70 min. The method enabled the detection of telomerase originating from  $270 \pm 20$  293T cells/ $\mu$ L.

The chemiluminescence resonance energy transfer (CRET) process stimulated by hemin/G-quadruplexes linked to semiconductor CdSe/ZnS QDs, in the presence of luminol/ $H_2O_2$  (see Section 2), was applied to develop luminescent sensing platforms for DNA [56] and for the analysis of aptamer-ligand complexes. Specifically, these CRET-based sensing modules were applied for the multiplexed analysis of DNA analytes or of aptamer-ligand complexes [35]. Figure 20(a) exemplifies the sensing of analyte (49) by the hairpin (50)-modified 620 nm luminescent QDs. The hairpin (50) includes



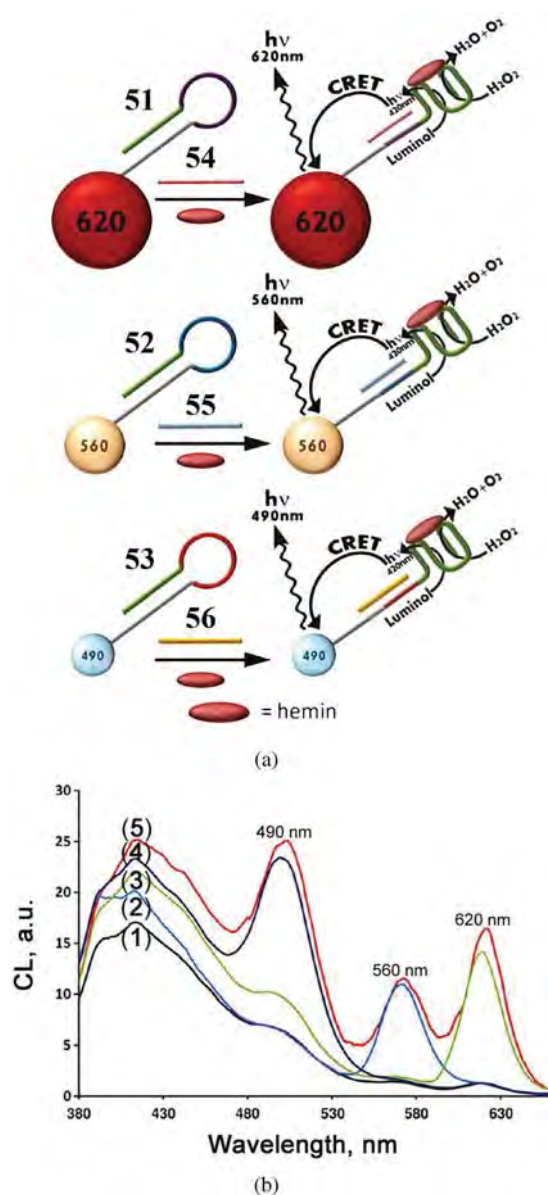
**Fig. 19.** (a) Analyzing the activity of telomerase in cancer cells using the electron-transfer quenching mechanism of CdSe/ZnS QDs by telomeric hemin/G-quadruplex chains as an optical readout. (b) Time-dependent electron-transfer quenching of CdSe/ZnS QDs by the telomerase-stimulated generation of telomeric hemin/G-quadruplex chains. The telomerase was extracted from a 293T cancer cell lysate. (c) Calibration curve corresponding to the quenching efficiency of the QDs by telomeric hemin/G-quadruplex chains generated after a fixed time-interval of 1 h by telomerase extracted from different numbers of 293T cancer cells (Reprinted with permission from Ref. 78. Copyright (2010) American Chemical Society)

the recognition sequence I for the selective binding of the target DNA, and domain II that is composed of the G-quadruplex sequence in a caged, inactive structure. In the presence of the target DNA (49), and hemin, the probe hairpin (50) opens, resulting in the formation of the catalytic hemin/G-quadruplex. The subsequent addition



**Fig. 20.** (a) Analyzing a target DNA by a hairpin probe-modified 620 nm-luminescent CdSe/ZnS QDs using the chemiluminescence resonance energy transfer (CRET) mechanism as readout signal. (b) Luminescence spectra corresponding to the analysis of variable concentrations of the DNA analyte by the CRET-stimulated mechanism: (1) 0 nM, (2) 10 nM, (3) 25 nM, (4) 50 nM, (5) 100 nM. The luminescence at  $\lambda_{em} = 620$  nm, generated by the CRET mechanism, provides the readout signal for the analysis of the DNA target (Reprinted with permission from Ref. 56. Copyright (2011) American Chemical Society)

of luminol/ $H_2O_2$  leads to the hemin/G-quadruplex-catalyzed generation of chemiluminescence, and this stimulates the CRET process to the QDs, resulting in the triggered luminescence of the QDs at  $\lambda_{em} = 620$  nm, Fig. 20(b). The degree of opening of the probe hairpin (50) is controlled by the concentration of the analyte, and hence the resulting chemiluminescence intensities and the subsequent CRET-stimulated intensities of the QDs are dictated by the concentration for the analyte, Fig. 20(b). This sensing module was further implemented for the multiplexed analysis of three different genes, Fig. 21(a). Three different-sized QDs emitting at  $\lambda_{em} = 620$  nm,  $\lambda_{em} = 560$  nm and  $\lambda_{em} = 490$  nm were functionalized with three different hairpin probes (51), (52) and (53), respectively. The loops of the hairpins included specific recognition sequences for the DNA analytes (54), (55), and (56), respectively, and the stem regions of all hairpins included the G-quadruplex sequence in the caged,

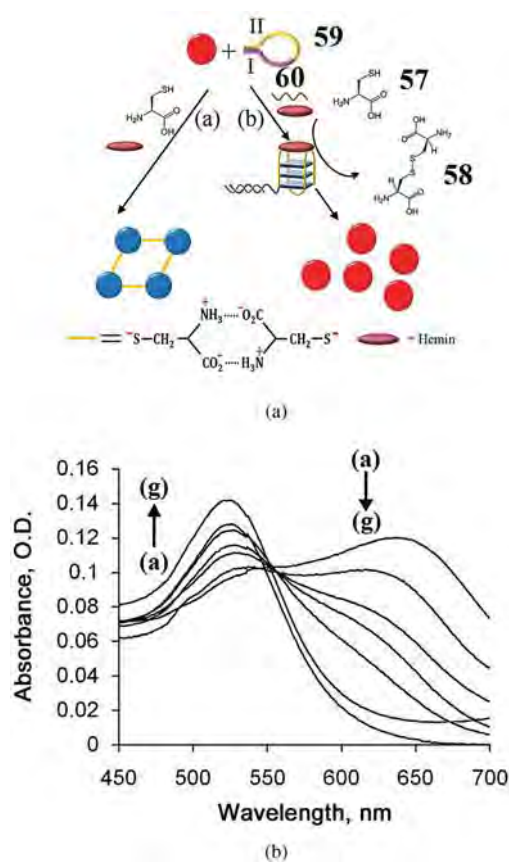


**Fig. 21.** (a) Multiplexed analysis of three genes using different-sized CdSe/ZnS QDs modified with three different DNA hairpin structures. The hairpins include in the loop regions specific recognition sequences for the different genes, and inactive caged G-quadruplex sequences in the stem regions. The hairpin structures, opened by the respective analytes, lead to the formation of catalytic hemin/G-quadruplexes that trigger-on the luminescence of the respective QDs by a chemiluminescence resonance energy transfer (CRET) mechanism. (b) Luminescence spectra of the composite three QDs mixture (1) in the absence of DNA analytes, or upon analyzing different analytes: (2) (55) (3) (54) (4) (56) (5) (54), (55) and (56) (Reprinted with permission from Ref. 56. Copyright (2011) American Chemical Society)

inactive configuration. The mixture of the three-sized QDs provided a functional assembly for the multiplexed analysis of the three genes through the hemin/G-quadruplex-catalyzed CRET-stimulated luminescence of the QDs, Fig. 21(b). Treatment of the QDs mixture

with either of the target genes, in the presence of hemin and luminol/H<sub>2</sub>O<sub>2</sub>, resulted in the selective opening of the hairpins associated with the specific QDs, thus leading to the luminescence of the respective QDs. Treatment of the QDs mixture with a combination of any of the two analyte genes, in the presence of hemin and luminol/H<sub>2</sub>O<sub>2</sub>, led to the CRET-stimulated luminescence of only the respective QDs. Introducing all three genes to the mixture of the QDs triggered-on the luminescence of all three-sized QDs, thus enabling the selective parallel detection of all three genes. Similarly, different-sized QDs, modified with hairpin probes composed of loops that include sequence-specific aptamers, as recognition elements, and caged G-quadruplex domains in the stem regions of the hairpin structures, have been implemented for the multiplexed analysis of the respective aptamer ligands, using the CRET mechanism as a transduction signal [35].

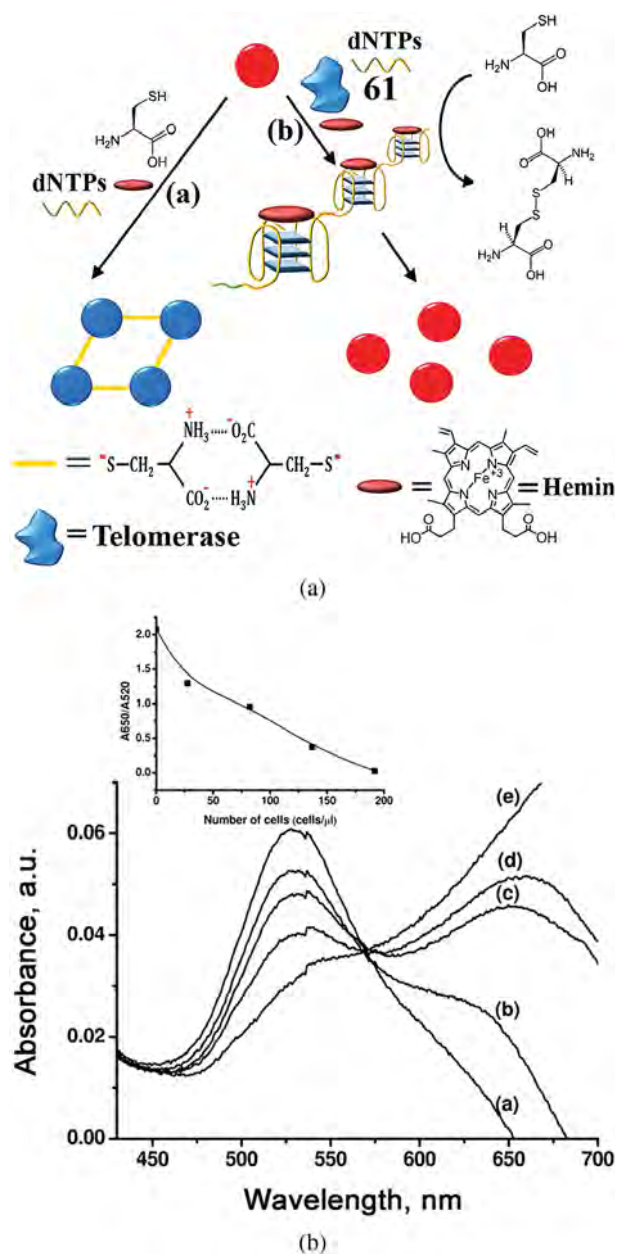
The aerobic hemin/G-quadruplex-catalyzed oxidation of thiols (L-cysteine, (**57**)) to disulfide (cystine, (**58**)) [47] has been applied to develop DNA analyte and aptamer-ligand sensing platforms by coupling the DNAzyme catalytic process to the cysteine-controlled aggregation of Au nanoparticles, Au NPs, Fig. 22(a) [79]. While individual Au NPs reveal size-controlled localized surface plasmon absorbance-bands in the region of  $\lambda = 525\text{--}550$  nm, their aggregation leads to inter-particle plasmon coupling, resulting in a red-shifted absorbance-band in the region of  $\lambda = 600\text{--}700$  nm. Accordingly, the sensing module is based on the aerobic hemin/G-quadruplex-catalyzed oxidation of L-cysteine to cystine, and the use of the cysteine-mediated aggregation of Au NPs as an auxiliary optical readout mechanism. Cysteine binds through its thiol functionality to Au NPs, and the surface-associated cysteine monolayer induces the aggregation of Au NPs through inter-particle H-bonds. In contrast to cysteine, its oxidation product cystine (disulfide) does not bind to Au NPs, and thus the aggregation of Au NPs, in the presence of cystine, is prohibited. Accordingly, the hairpin (**59**) was designed to include in domain I the recognition sequence for the target gene (**60**) and in domain II the G-quadruplex sequence in a stem-caged, inactive configuration. In the absence of the target gene cysteine is not effectively oxidized to cystine, and thus upon the addition of Au NPs the cysteine-stimulated aggregation of the NPs proceeds, leading to the disappearance of the localized plasmon band of individual NPs at  $\lambda = 520$  nm, and to the formation of the coupled plasmon-band of the aggregate at  $\lambda = 650$  nm, path (a). However, in the presence of hemin and the target DNA, (**60**), the hairpin probe (**59**) opens, resulting in the formation of the hemin/G-quadruplex. In the presence of cysteine, the aerobic hemin/G-quadruplex-catalyzed oxidation of cysteine to cystine proceeds and upon the addition of Au NPs their aggregation is prohibited, giving rise to the localized plasmon based of individual Au NPs at  $\lambda = 520$  nm, path (b). Since



**Fig. 22.** (a) The schematic analysis of a target DNA by a probe hairpin nanostructure using the hemin/G-quadruplex-controlled cysteine-mediated aggregation of Au NPs as readout mechanism. The opening of the hairpin probe by the analyte leads to the self-assembly of the hemin/G-quadruplex catalyst. (b) Absorption spectra corresponding to the analysis of different concentrations of the DNA analyte through the hemin/G-quadruplex-controlled cysteine-mediated aggregation of the Au NPs: (a) 0 M, (b)  $1 \times 10^{-9}$  M, (c)  $1 \times 10^{-8}$  M, (d)  $5 \times 10^{-8}$  M, (e)  $1 \times 10^{-7}$  M, (f)  $5 \times 10^{-7}$  M, (g)  $1 \times 10^{-6}$  M (Reprinted with permission from Ref. 79. Copyright (2014) Wiley-VCH)

the concentration of the hemin/G-quadruplex catalyst is controlled by the concentration of the analyte gene, (**60**), the extent of aggregation of the NPs is dominated by the analyte concentration. As the concentration of the analyte increases, the degree of aggregation decreases and the ratio of the absorbance bands at  $\lambda = 650$  nm and  $\lambda = 520$  nm ( $A_{650}/A_{520}$ ) provides a quantitative measure for the analyte DNA, Fig. 22(b). The method enabled the analysis of the target gene with a detection limit that corresponded to  $4.5 \times 10^{-9}$  M. The same platform was implemented to develop aptasensors where G-quadruplex aptamer-ligand nanostructures bind hemin and yields the catalytic DNAzyme for the aerobic oxidation of cysteine, and the subsequent controlled aggregation of Au NPs.

The hemin/G-quadruplex-catalyzed oxidation of cysteine to cystine and the subsequent cysteine-induced aggregation of Au NPs was further applied to develop an

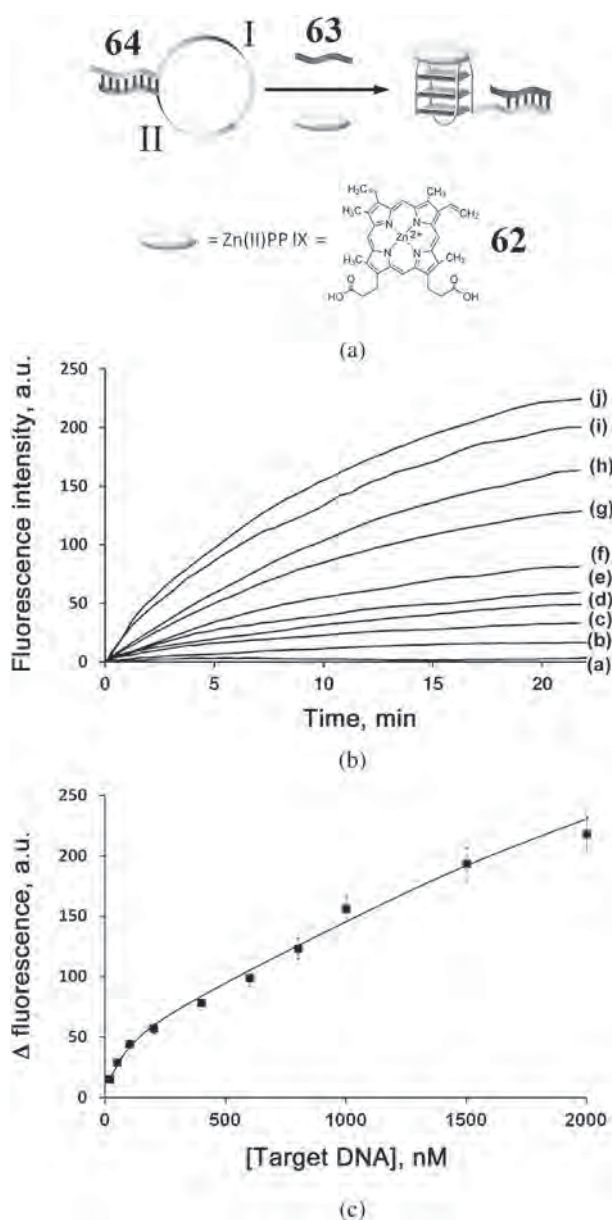


**Fig. 23.** (a) Schematic analysis of telomerase activity through the hemin/G-quadruplex telomeric chains-controlled cysteine-mediated aggregation of Au NPs. (b) Absorption spectra corresponding to the cysteine-mediated aggregation of Au NPs in the presence of (a)–(d) telomerase extracted from variable numbers of 293T cancer cells: (a) 192 cells/ $\mu$ L, (b) 137 cells/ $\mu$ L, (c) 82 cells/ $\mu$ L, (d) 27 cells/ $\mu$ L and (e) a fibroblast cell lysate (274 cells/ $\mu$ L) that lacks telomerase. Inset: Derived calibration curve corresponding to the analysis of variable numbers of cancer cells (Reprinted with permission from Ref. 80. Copyright (2014) American Chemical Society)

optical assay for analyzing telomerase in cancer cells, Fig. 23(a) [80]. The system included the telomerase primer, (61), the nucleotide mixture of dNTPs and hemin. In the absence of telomerase the added cysteine is not oxidized to cystine, and upon the addition of Au

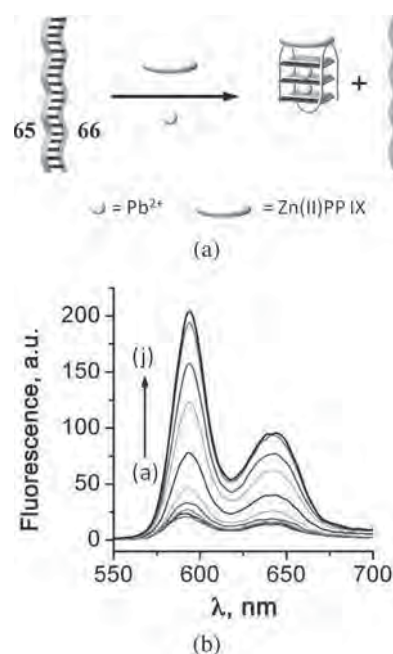
NPs to the system, an effective aggregation process of the NPs proceeds, path (a). However, treatment of the sensing module with telomerase, extracted from cancer cells, stimulates the telomerization of the primer and the formation of hemin/G-quadruplex telomere chains. These catalytic chains catalyze the oxidation of cysteine to cystine, thus prohibiting the aggregation of the added Au NPs, path (b). As the degree of telomerization is controlled by the concentration of telomerase extracted from cancer cells, the extent of Au NPs aggregation is dominated by the telomerase concentration. Figure 23(b) depicts the absorption spectra of the Au NPs system upon analyzing telomerase originating from different numbers of 293T cancer cell extracts. As the concentration of the cells increases, the degree of aggregation decreases, reflected in the decrease of the absorbance ratio of  $A_{650}/A_{520}$ . From the derived calibration curve, Fig. 23(b), inset, the sensing platform enabled the detection of telomerase originating from 27 293T cells/ $\mu$ L.

The enhanced fluorescence properties of Zn(II)-protoporphyrin IX, (62), associated with G-quadruplex nanostructures has been used to develop various nucleic acid-based sensing platforms [81]. Figure 24(a) exemplifies the fluorescent detection of a DNA analyte, (63), by the Zn(II)-protoporphyrin IX/G-quadruplex fluorescence label. The hairpin (64) functions as a probe for analyzing the target DNA, and includes domain I that provides the recognition sequence for the analyte and domain II that includes the caged structure of the G-quadruplex. The hairpin probe, in the presence of Zn(II)-protoporphyrin IX, reveals minute fluorescence. In the presence of the target DNA (63) the hairpin opens, and the association of the Zn(II)-protoporphyrin IX to the uncaged G-quadruplex leads to the generation of a fluorescent label that provides a reporter signal for the sensing events. As the concentration of the analyte, (63), controls the degree of opening of the hairpin probe, the resulting fluorescence provides a quantitative readout signal for the analysis of (63). Figure 24(b) depicts the time-dependent fluorescence changes of the system upon analyzing different concentrations of the target DNA. The fluorescence intensities reach a saturation value after *ca.* 25 min, a time interval that reflects the kinetics of the opening of the hairpin probe. The derived calibration curve corresponding to the fluorescence intensity generated by the system, after a fixed time interval of 20 min, upon analyzing different concentrations of the target DNA is depicted in Fig. 24(c). This sensing platform enables the analysis of the target DNA with a detection limit corresponding to  $5 \times 10^{-9}$  M. Similarly, the formation of ligand-induced G-quadruplex aptamer-ligand complexes and the fluorescence generated upon the association of Zn(II)-protoporphyrin IX to the aptamer-ligand complex was used to develop fluorescent aptasensors [81]. Also, the  $Pb^{2+}$ -ion stabilization of G-quadruplex nanostructures and the binding of Zn(II)-protoporphyrin IX to the resulting G-quadruplex provided a means to develop a fluorescent sensor for  $Pb^{2+}$ -ions



**Fig. 24.** (a) Analysis of analyte DNA by a hairpin nucleic acid probe and the Zn(II)-protoporphyrin IX/G-quadruplex as a fluorescent label. (b) Time-dependent fluorescence changes upon analyzing different concentrations of the analyte DNA according to (a): (a) 0 nM, (b) 20 nM, (c) 50 nM, (d) 100 nM, (e) 200 nM, (f) 400 nM, (g) 800 nM, (h) 1  $\mu$ M, (i) 1.5  $\mu$ M, and (j) 2  $\mu$ M. (c) Derived calibration curve (Reprinted with permission from Ref. 81. Copyright (2012) American Chemical Society)

[82], Fig. 25(a). The sequence (65) that consists of the  $\text{Pb}^{2+}$ -aptamer recognition sequence was blocked by the complementary sequence (66). The G-quadruplex domain in the duplex (65)/(66) exists in an inactive configuration that does not bind the fluorescence label. In the presence of  $\text{Pb}^{2+}$ -ions the formation of the energetically favored  $\text{Pb}^{2+}$ -G-quadruplex displaces (66). The binding of Zn(II)-protoporphyrin IX to the resulting  $\text{Pb}^{2+}$ -stabilized G-quadruplex leads to a fluorescence intensity that

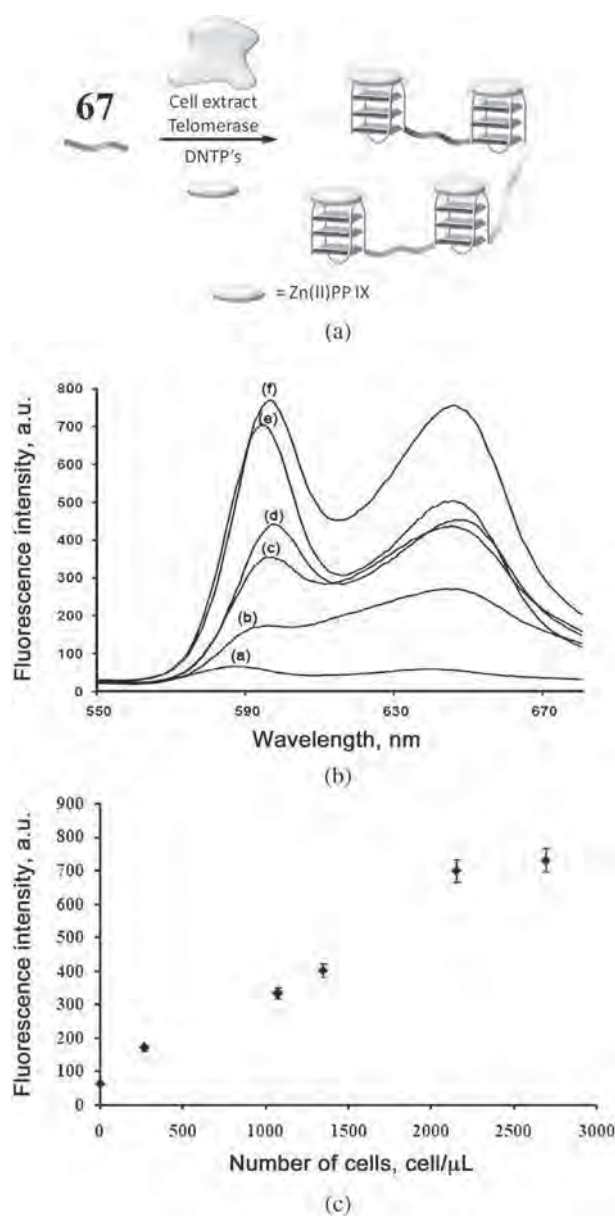


**Fig. 25.** (a) Analysis of  $\text{Pb}^{2+}$ -ions by the  $\text{Pb}^{2+}$ -ion-triggered reconfiguration of a duplex DNA probe into the fluorescent Zn(II)-protoporphyrin IX/ $\text{Pb}^{2+}$ -stabilized G-quadruplex. (b) Fluorescence spectra of the Zn(II)-protoporphyrin IX/G-quadruplex generated in the presence of variable concentrations of  $\text{Pb}^{2+}$ : (a) 0  $\mu$ M (b) 0.02  $\mu$ M (c) 0.05  $\mu$ M (d) 0.1  $\mu$ M (e) 0.2  $\mu$ M (f) 0.5  $\mu$ M (g) 1  $\mu$ M (h) 2  $\mu$ M (i) 5  $\mu$ M (j) 10  $\mu$ M (Reprinted with permission from Ref. 82. Copyright (2010) American Chemical Society)

provides a quantitative measure for the concentration of  $\text{Pb}^{2+}$ -ions, Fig. 25(b). The system enabled the analysis of  $\text{Pb}^{2+}$ -ions with a detection limit that corresponds to  $2 \times 10^{-8}$  M.

The unique fluorescence features of Zn(II)-protoporphyrin IX associated with G-quadruplexes were also implemented to detect the cancer cell biomarker telomerase [81], Fig. 26(a). The nucleic acid, (67), acts as primer that is recognized by telomerase. In the presence of the 293T cancer cell extract that contains telomerase and of the dNTPs oligonucleotide mixture, the telomerization of the primer proceeds to yield the G-quadruplex telomere chains. The association of Zn(II)-protoporphyrin IX to the generated G-quadruplex units provides a fluorescence signal that reflects the activity of telomerase present in the cell lysate. Accordingly, the resulting fluorescence intensity provides a quantitative measure for the number of cancer cells in the lysates. Figure 26(b) depicts the fluorescence spectra of the Zn(II)-protoporphyrin associated with the telomere chains generated upon telomerization of the (67) by telomerase originating from variable number of cell extracts, and the resulting calibration curve, Fig. 26(c). The method enabled the analysis of telomerase extracted from 380 293T cells/ $\mu$ L.

The present section has addressed different optical and electrical sensing platforms involving



**Fig. 26.** (a). Analysis of telomerase activities by the fluorescence of Zn(II)-protoporphyrin IX associated with the G-quadruplexes of telomeric wires. (b) Fluorescence spectra corresponding to the Zn(II)-protoporphyrin IX (a) in the presence fibroblast cell extract in a concentration of 2690 cells/μL, or when associated with telomeric chains generated by telomerase for a fixed time-interval of 1 h, where telomerase was extracted from variable number of 293T cancer cells: (b) 269 cells/μL, (c) 1076 cells/μL, (d) 1345 cells/μL, (e) 2152 cells/μL, (f) 2690 cells/μL. (c) Derived calibration curve (Reprinted with permission from Ref. 81. Copyright (2012) American Chemical Society)

metal-porphyrin-functionalized G-quadruplexes as labels. These included the development of DNA-sensors, ligand-aptamer sensors, and sensors for telomerase. Tables 1, 2 and 3 compare the performance of the metalloporphyrin/G-quadruplex-based DNA sensors, aptasensors and telomerase sensors to other sensing

platforms, respectively. One may realize that the optical or electrochemical metalloporphyrin/G-quadruplex-based sensors reveal comparable or even superior sensitivities as compared to other sensing platforms. Specifically, the amplified sensing platforms that include the horseradish peroxidase mimicking hemin/G-quadruplexes reveal superior or comparable sensitivities when compared to other DNAzymes (*e.g.* the Mg<sup>2+</sup>-dependent DNAzyme), or to systems that implement horseradish peroxidase, HRP, as amplifying label (due to the possibility to implement DNA machineries for the synthesis of the hemin/G-quadruplex DNAzyme).

### 3.2 Metalloporphyrins as labels for DNA machines.

The base-sequence encoded in nucleic acids has been broadly applied for the development of DNA switches and DNA machines [101–105]. Different DNA switching devices [106] or machines, such as tweezers [107, 108], walkers [109, 110], rotors [111, 112] or gears [113] were developed and their potential utilization as optoelectronic devices [114–116], as dictated molecular carriers [117, 118], and as functionalized units for programmed synthesis and biocatalysis [119–121] were reported. By conjugating metal-ion-functionalized G-quadruplex nanostructures to DNA machines, the unique catalytic and optical properties of the G-quadruplexes may be used to follow the switchable operation of the DNA machines or, alternatively, allow the use of the DNA machines as scaffolds for programmed synthesis or for switchable photonics. The switchable tweezers-stimulated activation and deactivation of the hemin/G-quadruplex DNAzyme [122] is presented in Fig. 27(a). The tweezers included two arms, (68) and (69), bridged by two nucleic acids, (70) and (71), to yield the closed tweezers configuration, T<sub>1</sub>. The arms of the tweezers include domains I and II that consist of the G-quadruplex sequences that are caged in an inactive configuration *via* hybridization with the complementary domains of the bridging strand (71). In the presence of K<sup>+</sup>-ions and hemin the formation of the hemin/G-quadruplex DNAzyme structure is energetically favored, thus, yielding the open configuration of the tweezers, T<sub>2</sub>, and the displacement of the bridging strand, (71). The catalytic hemin/G-quadruplex units catalyze the H<sub>2</sub>O<sub>2</sub>-mediated oxidation of Amplex Red to the fluorescent product resofurin. The resulting fluorescence provides then the readout signal for the open state of the tweezers. Treatment of the tweezers T<sub>2</sub> with [2.2.2]-cryptand eliminates the stabilizing K<sup>+</sup>-ions from the G-quadruplex, resulting in its separation. This leads to the rehybridization of the bridging strand, (70), and regeneration of the closed tweezers configuration, T<sub>1</sub>. In these nanostructures the system is catalytically inactive. Re-addition of K<sup>+</sup>-ions to the system re-opens the tweezers, resulting in the catalytically active hemin/G-quadruplex DNAzyme structure. By the cyclic K<sup>+</sup>-induced opening of the tweezers and the reverse closure of the tweezers in the presence of [2.2.2]-cryptand, the molecular device is cycled between “ON” and “OFF” states, Fig. 27(b).

**Table 1.** Amplified sensing platforms of DNA using DNAzyme labels

Method	System	Detection limit, M	Sensing time, h	Ref.
chemiluminescence/fluorescence	polymerase/nicking enzyme machinery generating HRP-mimicking DNAzyme	$1 \times 10^{-14}$	1.5	[75]
fluorescence	rolling circle amplification (RCA) and HRP-mimicking DNAzyme machinery	$1 \times 10^{-14}$	2	[83]
chemiluminescence/colorimetric	DNA analyte-driven autonomous generation of HRP-mimicking DNAzyme	$1 \times 10^{-13}$	4–6	[65]
chemiluminescence	hemin/G-quadruplex DNAzyme-modified electrode	$1 \times 10^{-9}$	3	[45]
fluorescence	Zn(II)-protoporphyrin IX/G-quadruplex complex with Exo III-assisted analyte recycling	$2 \times 10^{-10}$	3	[81]
chemiluminescence	HRP mimicking DNAzyme-functionalized Au nanoparticles	$1 \times 10^{-10}$	6	[84]
colorimetric	a cascade of $Mg^{2+}$ -dependent DNAzyme and HRP-mimicking DNAzyme	$1 \times 10^{-12}$	7	[72]
fluorescence	carbolic regeneration of analyte by $Mg^{2+}$ -dependent DNAzyme	$1 \times 10^{-12}$	12	[69]
electrochemical	recycling of analyte by exonuclease III	$2 \times 10^{-9}$	2	[85]
colorimetric	bifunctional oligonucleotide probe based on a hemin G-quadruplex DNAzyme	$5.4 \times 10^{-9}$	2	[86]
surface enhanced Raman scattering (SERS)	separation-free SERS discriminating assay	$1 \times 10^{-9}$	3	[87]
chemiluminescence resonance energy transfer (CRET)	HRP-mimicking DNAzyme-modified CdSe/ZnS quantum dots	$1 \times 10^{-8}$	3	[56]
fluorescence	graphene oxide molecular beacon	$2 \times 10^{-9}$	3	[88]

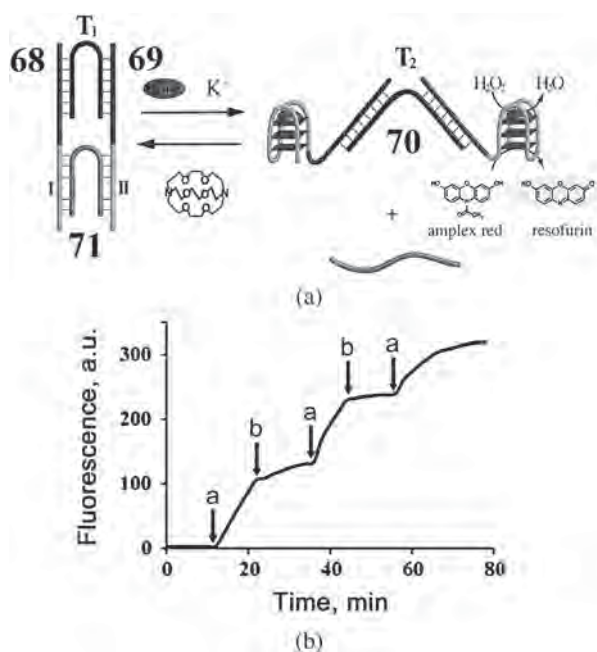
**Table 2.** Sensing platforms for sensing aptamer-ligand complexes

Ligand	Method	System	Detection limit, M	Sensing time, h	Ref.
ATP	colorimetric	Au NPs-modified aptamer	$6 \times 10^{-7}$	0.5	[89]
ATP	chemiluminescence and chemiluminescence resonance energy transfer (CRET)	ATP aptamer G-quadruplex/hemin acts as DNAzyme and the DNAzyme-modified quantum dots	$1 \times 10^{-5}$	3	[35]
ATP	fluorescence (rolling circle amplification, RCA)	aptazyme-coupled RCA	$1 \times 10^{-6}$	2	[90]
ATP	fluorescence	aptamer duplex/ethidium bromide/tetrahedral fluorene complex	$2 \times 10^{-4}$	5.5	[91]
ATP	fluorescence	Zn(II)-protoporphyrin IX/ATP aptamer complex	$1 \times 10^{-5}$	2	[81]
Thrombin	colorimetric	thrombin/hemin/thrombin binding aptamer-G-quadruplex/L-cysteine/agggregation Au NPs	$3 \times 10^{-10}$	4	[79]
Thrombin	chemiluminescence and chemiluminescence resonance energy transfer (CRET)	thrombin/hemin/thrombin binding aptamer-G-quadruplex DNAzyme linked to a QD	$2 \times 10^{-10}$	3	[35]
Thrombin	fluorescence	Ag NCS-labeled thrombin binding aptamer	$1 \times 10^{-9}$	1	[92]
Thrombin	electrochemical	thrombin-thrombin binding aptamer complex-inhibited electron transfer	$6.4 \times 10^{-9}$	3	[93]

**Table 3.** Sensor platforms for the detection of telomerase

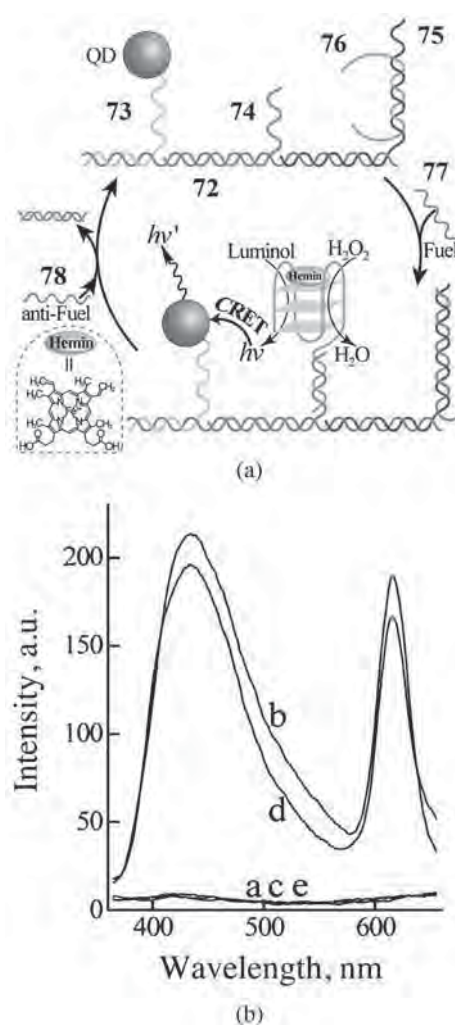
Method	System	Detection limit	Sensing time, h	Ref.
PCR-based assay	telomeric repeat amplification protocol (TRAP)	10–100 cells	24	[94]
colorimetric	HRP-mimic DNAzyme catalytic beacons	500 cells	1.5 h	[95]
fluorescence	molecular probes/telomerase primer/polymerase	4–40 cells	6	[96]
fluorescence	CdSe/ZnS QDs/telomerase primer/Texas red-dUTP	10000 cells	1	[97]
fluorescence	CdSe/ZnS QDs/telomerase primer/hemin	269 cells/ $\mu$ L	3.5	[78]
chemiluminescence	telomerase primer-modified Au electrode/DNAzyme-functionalized Au NPs	1000 cells	17	[98]
surface plasmon resonance	telomerase primer-modified SPR electrode/Au NPs	18 cells/ $\mu$ L	3.5	[78]
electrochemical	telomerase primer-modified Au electrode/Au NPs/hexaamineruthenium(III)	10 cells	2	[99]
electrochemical	telomerase primer-modified ISFET electrode	65 cells/ $\mu$ L	3.5	[78]
electrochemical	telomerase primer-modified Au electrode- $\text{Fe}(\text{CN})_6^{3-}/\text{Fe}(\text{CN})_6^{4-}$	1000 cells	4	[100]
fluorescence	ZnP/telomerase/G-quadruplex	380 cells/ $\mu$ L	3.5	[81]
colorimetric	hemin/telomere-G-quadruplex/L-cysteine/agggregation Au NPs	27 cells/ $\mu$ L	3 h	[80]





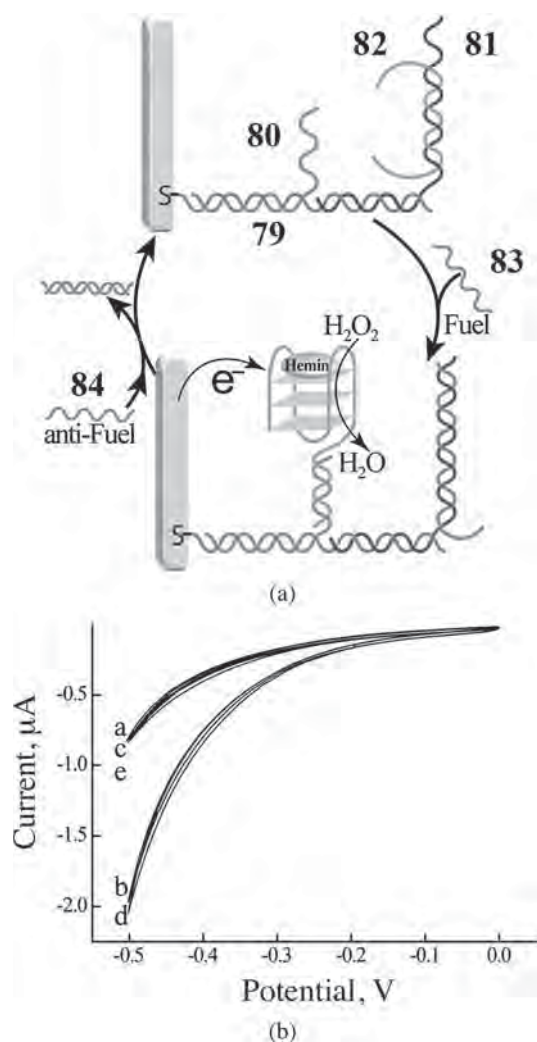
**Fig. 27.** (a) A switchable  $K^+$ /[2.2.2]-cryptand reconfigurable DNA tweezers. The opening of the tweezers by  $K^+$ -ion leads to the formation of “arm”-functionalized hemin/G-quadruplex DNAzyme units. The DNAzyme-containing opened tweezers catalyze the  $H_2O_2$ -mediated oxidation of Amplex Red to the fluorescent resorufin. Elimination of  $K^+$ -ions from the G-quadruplexes by [2.2.2]-cryptand results in the dissociation of the hemin/G-quadruplexes, and to the blockage of the oxidation of Amplex-Red. (b) Time-dependent fluorescence changes of the tweezers system upon: (a) Opening of the tweezers in the presence of  $K^+$ -ions. (b) Closure of the tweezers upon addition of [2.2.2]-cryptand and elimination of  $K^+$  from the G-quadruplex sites (Reprinted with permission from Ref. 122. Copyright (2014) Wiley-VCH)

The CRET-stimulated activation of the luminescence of QDs through the hemin/G-quadruplex-catalyzed generation of chemiluminescence was applied to follow the activity of a DNA “walker” molecular device [123], Fig. 28(a). A DNA scaffold (72) was designed to act as the track of the “walker” system. The CdSe/ZnS QDs modified with the nucleic acid (73) were hybridized with the scaffold (72), and these were used as a reporter site for the walking process. The nucleic acid (74) and (75) were hybridized with the track scaffold and these include protruding tethers acting as footholds for the walker operation. The walker units (76) were hybridized with foothold (75) to form the energetically stabilized duplex. The walker element includes partial complementarity, also, to foothold (74), yet with lower affinity, and includes also the caged sequence of the G-quadruplex. In the presence of the fuel strand, (77), the walker unit is displaced due to the formation of the energetically favored duplex (77)/(75), and this results in the walk-over of the unit (76) to the less favored foothold position, (74). The transition of the walker to foothold (74) is accompanied by the uncaging of the G-quadruplex



**Fig. 28.** (a) Probing the reversible DNA walker operation between two states on a DNA scaffold, using the hemin/G-quadruplex chemiluminescence resonance energy transfer (CRET) to the semiconductor QDs as readout signal for the “walking” process. (b) The luminescence spectra of the system upon the walk-over of the walker (76) from foothold (75) to (74) using the respective fuel and anti-fuel strands. (a) Walker on foothold (76) (b) fuel-stimulated transfer of the walker to foothold (74) (c) Anti-fuel-driven transition of the walker from foothold (74) to (75) (d) and (e) Re-transition of the walker to footholds (74) and (75), respectively. Inset: CRET-induced luminescence intensities of the QDs upon transition between the two states (Reprinted with permission from Ref. 123. Copyright (2013) American Chemical Society)

sequence, and the formation of the hemin/G-quadruplex DNAzyme. This catalyzes the oxidation of luminol by  $H_2O_2$ , and the generation of chemiluminescence — a process that stimulates the chemiluminescence resonance energy transfer (CRET) process to the QDs, resulting in the luminescence of the QDs at  $\lambda_{em} = 620$  nm. The subsequent addition of the anti-fuel strand (78) to the system, displaces the fuel strand (77) from foothold (75), due to the formation of the energetically stabilized duplex (77)/(78). The release of strand (77) from foothold (75)



**Fig. 29.** (a) Electrochemical probing of a fuel/anti-fuel-driven walker system between two states on a DNA scaffold associated with an Au electrode, using the hemin/G-quadruplex-catalyzed reduction of  $\text{H}_2\text{O}_2$  as readout signal for the position of the walker. (b) The electrocatalytic currents corresponding to: (a) Walker positioned on foothold (81). (b) Fuel-driven transition of the walker to foothold (80) while generating the hemin/G-quadruplex electrocatalyst. (c) Anti-fuel-driven transition of the walker to foothold (81), (d) and (e) cyclic re-transition of the walker to footholds (80) and (81), respectively. Inset: Electrocatalytic cathodic currents generated by the walker system upon the fuel/anti-fuel-driven transitions of the walker between the two states (Reprinted with permission from Ref. 123. Copyright (2013) American Chemical Society)

leads to the reverse transition of the walker to foothold (75) due to the formation of an energetically stabilized duplex (76)/(75). This latter process dissociates the G-quadruplex structure, leading to the switching-off of the catalytic properties of the system, and the accompanying CRET process. By the cyclic treatment of the functional DNA structure with the fuel and anti-fuel strands, the “walker” unit is reversibly translocated between the footholds (74) and (75), a process that is transduced by

the CRET-stimulated luminescence properties of the QDs reporter elements, Fig. 28(b). Similarly, the electrocatalytic functions of the hemin/G-quadruplex were used to report the walker functions of the DNA device on electrode surfaces, Fig. 29(a). In this system, the scaffold (79) was assembled on an Au electrode surface, and the nucleic acids (80) and (81) were hybridized with the scaffold track (79). The strand (82), acting as the walker unit, was hybridized with foothold (81) to form the stable duplex structure (81)/(82). The walker unit is partially complementary to foothold (80), and includes in a caged configuration the G-quadruplex sequence. In the presence of the fuel strand (83) the walker unit (82) is displaced from foothold (81), leading to the transition of the walker to foothold (80), where the less energetically stabilized duplex is formed. The translocation of the walker to foothold (80) is accompanied by the self-assembly of the electrocatalytic hemin/G-quadruplex, that catalyzes the electrochemical reduction of  $\text{H}_2\text{O}_2$  and the formation of an electrocatalytic cathodic currents. The subsequent treatment of the system with the anti-fuel strand (84) displaces the fuel strand in the form of the stable duplex structure (83)/(84), and this triggers the reverse transition of the walker unit from foothold (80) to (81). This process dissociates the hemin/G-quadruplex structure, thus switching-off the electrocatalytic function of the system. Accordingly, by the cyclic treatment of these walker nanostructure associated with the electrode, with the fuel and anti-fuel strands, the walker unit is reversibly translocated between footholds (80) and (81) and the process is transduced by the switchable ON-OFF electrocatalytic functions of the hemin/G-quadruplex reporter, Fig. 29(b).

## CONCLUSIONS AND PERSPECTIVES

Metalloporphyrin-functionalized G-quadruplexes and particularly hemin/G-quadruplexes exhibit versatile catalytic, photocatalytic, and electrocatalytic properties. Specifically, the hemin/G-quadruplex-catalyzed processes can proceed either in the presence of added  $\text{H}_2\text{O}_2$  as an oxidant, or under aerobic conditions in the absence of exogenously added  $\text{H}_2\text{O}_2$ . One functional aspect of these DNAzyme-catalyzed processes is their implementation in chemical synthesis, although the catalytic functions of the hemin/G-quadruplex as a DNAzyme are substantially lower as compared to the analogous reactions driven by respective hemeproteins. One reason for this lower activity is the fact that even though hemin/G-quadruplexes include a catalytic site they lack a substrate binding site, an essential component for the high activity of native enzymes. The conjugation of aptamer units to the hemin/G-quadruplex catalyst could provide a means to construct an integrated catalyst, containing both a substrate binding site and a catalytic unit that mimics native enzymes with a higher activity. An additional aspect is the variable activities toward different substrates

exhibited by the different hemin/G-quadruplex structures. At present, the basic understanding of the structure-function relationships that dictates the different substrate-specific activities is slim. A major breakthrough could be envisaged, however, if molecular dynamics simulations could be adapted to predict the optimal structures of the DNazymes for target reactions.

The application of the unique catalytic, electrocatalytic and photophysical properties of hemin/G-quadruplexes has been extensively used to develop a variety of electrical and optical sensing platforms. Specifically, the use of different nucleic acid machineries for the autonomous synthesis of hemin/G-quadruplex catalytic labels, or for the amplified analysis of DNA or aptamer-ligand complexes has been addressed. In this context, it was emphasized that the DNA machineries, such as the rolling circle amplification process (RCA), the hybridization chain reaction (HCR) or the telomerization process, yield long wires composed of the catalytic hemin/G-quadruplex units. The implementation of these wires as catalytic templates for the growth of conductive polymers, *e.g.* polyaniline or polypyrrole, could provide an attractive means for the synthesis of nanoscale electronic materials.

The electron-transfer quenching of semiconductor QDs by conjugated hemin/G-quadruplex labels, and the chemiluminescence resonance energy transfer (CRET) process between hemin/G-quadruplex labels and semiconductor QDs have been introduced as versatile methods for the multiplexed sensing of DNA analytes and aptamer-ligand complexes. In this context, the parallel detection of the analytes was accomplished by using different-sized CdSe/ZnS QDs. Extension of this method to other semiconductor QDs, *e.g.* CdTe or PbSe, could enhance the complexity of multiplexed analysis of targets. Finally, the enhanced fluorescence properties of Zn(II)-protoporphyrin IX/G-quadruplexes have been applied as effective luminescence probes for sensing. These unique properties of the fluorophores/G-quadruplexes could be applied to develop new photoelectrochemical cells, *e.g.* dye-sensitized solar cells.

The progress demonstrated in applying metalloporphyrin/G-quadruplexes in different scientific disciplines promises that these nanostructures will continue to attract future theoretical and experimental scientific efforts.

### Acknowledgements

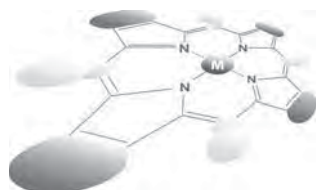
Our research on G-quadruplexes is supported by the Israel Science Foundation and the Future Emerging Technologies project, MULTI (317707), of the European Community Seventh Framework Programme.

### REFERENCES

- Engelhart AE, Plavec J, Persil O and Hud NV. *Nucleic Acid-Metal Ion Interactions*, RSC Publishing: Cambridge, 2009; 118–153.
- Burge S, Parkinson GN, Hazel P, Todd AK and Neidle S. *Nucleic Acids Res.* 2006; **34**: 5402–5415.
- Joachimi A, Benz A and Hartig JS. *Bioorg. Med. Chem.* 2009; **17**: 6811–6815.
- Arora A and Maiti S. *J. Phys. Chem. B.* 2009; **113**: 10515–10520.
- Sen D and Gilbert W. *Curr. Opin. Struct. Biol.* 1991; **1**: 435–438.
- Mergny JL, De Cian A, Ghelab A, Saccà B and Lacroix L. *Nucleic Acids Res.* 2005; **33**: 81–94.
- Gray RD and Chaires JB. *Nucleic Acids Res.* 2007; **36**: 4191–4203.
- Dai J, Carver M, PUNCHIHEWA C, Jones RA and Yang D. *Nucleic Acids Res.* 2007; **35**: 4927–4940.
- Ambrus A, Chen D, Dai J, Bialis T, Jones RA and Yang D. *Nucleic Acids Res.* 2006; **34**: 2723–2735.
- Zhang Z, Dai J, Veliath E, Jones RA and Yang D. *Nucleic Acids Res.* 2010; **38**: 1009–1021.
- Gray RD, Trent JO and Chaires JB. *J. Mol. Biol.* 2014; **426**: 1629–1650.
- Le HT, M, Miller C, Buscaglia R, Dean WL, Holt PA, Chaires JB, and Tren JO. *Org. Biomol. Chem.* 2012; **10**: 9393–9404.
- Hardin CC, Perry AG and White K. *Biopolymers* 2000–2001; **56**: 147–194.
- Lane AN, Chaires JB, Gray RD and Trent JO. *Nucleic Acids Res.* 2008; **36**: 5482–5515.
- Parkinson GN, Lee MPH and Neidle S. *Nature* 2002; **417**: 876–880.
- Wang Y and Patel DJ. *Structure* 1993; **1**: 263–282.
- Bryan TM, Englezou A, Gupta J, Bacchetti S and Reddell RR. *EMBO J.* 1995; **14**: 4240–4248.
- Bodnar AG, Ouellette M, Frolkis M, Holt SE, Chiu CP, Morin GB, Harley CB, Shay JW, Lichtsteiner S and Wright WE. *Science* 1998; **279**: 349–352.
- Harley CB, Futcher AB and Greider CW. *Nature* 1990; **355**: 458–460.
- Shay JW and Bacchetti S. *Eur. J. Cancer* 1997; **33**: 787–791.
- Kim NW. *Eur. J. Cancer* 1997; **33**: 781–786.
- Morin GB. *Cell* 1989; **59**: 521–529.
- Huppert JL and Balasubramanian S. *Nucleic Acids Res.* 2005; **33**: 2908–2916.
- Todd AK, Johnston M and Neidle S. *Nucleic Acids Res.* 2005; **33**: 2901–2907.
- Balasubramanian S and Neidle S. *Curr. Opin. Chem. Biol.* 2009; **13**: 345–353.
- Balasubramanian S, Hurley LH and Neidle S. *Nat. Rev. Drug. Discov.* 2011; **10**: 261–275.
- Bock LC, Griffin LC, Latham JA, Vermaas EH and Toole JJ. *Nature* 1992; **355**: 564–566.
- Macaya RF, Waldron JA, Beutel BA, Gao HT, Joesten ME, Yang MH, Patel R, Bertelsen AH and Cook AF. *Biochemistry* 1995; **34**: 4478–4492.
- Travascio P, Li Y and Sen D. *Chem. Biol.* 1998; **5**: 505–517.

30. Travascio P, Bennet AJ, Wang DY and Sen D. *Chem. Biol.* 1999; **6**: 779–787.
31. Travascio P, Witting PK, Mauk AG and Sen D. *J. Am. Chem. Soc.* 2001; **123**: 1337–1348.
32. Cheng X, Liu X, Bing T, Cao Z and Shangguan D. *Biochemistry* 2009; **48**: 7817–7823.
33. Zhu L, Li C, Zhu Z, Liu D, Zou Y, Wang C, Fu H and Yang CJ. *Anal. Chem.* 2012; **84**: 8383–8390.
34. Li T, Wang E and Dong S. *Chem. Commun.* 2008; **31**: 3654–3656.
35. Liu X, Freeman R, Golub E and Willner I. *ACS Nano* 2011; **5**: 7648–7655.
36. Freeman R, Girsh J, Jou AF, Ho JA, Hug T, Dervedde J and Willner I. *Anal. Chem.* 2012; **84**: 6192–6198.
37. Nakayama S, Wang J and Sintim HO. *Chemistry* 2011; **17**: 5691–5698.
38. Nakayama S and Sintim HO. *Anal. Chim. Acta.* 2012; **747**: 1–6.
39. Nakayama S and Sintim HO. *J. Am. Chem. Soc.* 2009; **131**: 10320–10333.
40. Vummidi B, Alzeer J and Luedtke NW. *ChemBioChem* 2013; **14**: 540–558.
41. Nakayama S, Kelsey I, Wang J and Sintim HO. *Chem. Commun.* 2011; **47**: 4766–4768.
42. Nakayama S, Kelsey I, Wang J, Roelofs K, Stefane B, Luo Y, Lee VT and Sintim HO. *J. Am. Chem. Soc.* 2011; **133**: 4856–4864.
43. Nakayama S and Sintim HO. *Mol. Biosyst.* 2010; **6**: 95–97.
44. Xiao Y, Pavlov V, Gill R, Bourenko T and Willner I. *ChemBioChem.* 2004; **5**: 374–379.
45. Pavlov V, Xiao Y, Gill R, Dishon A, Kotler M and Willner I. *Anal. Chem.* 2004; **76**: 2152–2156.
46. Poon LC, Methot SP, Morabi-Pazooki W, Pio F, Bennet AJ and Sen D. *J. Am. Chem. Soc.* 2011; **133**: 1877–1884.
47. Golub E, Freeman R and Willner I. *Anal. Chem.* 2013; **85**: 12126–12133.
48. Golub E, Freeman R and Willner I. *Angew. Chem. Int. Ed.* 2011; **50**: 11710–11714.
49. Wang ZG, Zhan P and Ding B. *ACS Nano* 2013; **7**: 1591–1598.
50. Pradines V and Pratviel G. *Angew. Chem. Int. Ed.* 2013; **52**: 2185–2188.
51. Wilking M and Hennecke U. *Org. Biomol. Chem.* 2013; **11**: 6940–6945.
52. Pelossof G, Tel-Vered R, Elbaz J and Willner I. *Anal. Chem.* 2010; **82**: 4396–4402.
53. Li T, Wang E and Dong S. *J. Am. Chem. Soc.* 2009; **131**: 15082–15083.
54. Sharon E, Freeman R and Willner I. *Anal. Chem.* 2010; **82**: 7073–7077.
55. Zhang L, Zhu J, Guo S, Li T, Li J and Wang E. *J. Am. Chem. Soc.* 2013; **135**: 2403–2406.
56. Freeman R, Liu X and Willner I. *J. Am. Chem. Soc.* 2011; **133**: 11597–11604.
57. Hu L, Liu X, Ceconello A and Willner I. *Nano Lett.* 2014; **14**: 6030–6035.
58. Pavlov V, Shlyahovsky B and Willner I. *J. Am. Chem. Soc.* 2005; **127**: 6522–6523.
59. Baur J, Gondran C, Holzinger M, Defrancq E, Perrot H and Cosnier S. *Anal. Chem.* 2010; **82**: 1066–1072.
60. Baker BR, Lai RY, Wood MS, Doctor EH, Heeger AJ and Plaxco KW. *J. Am. Chem. Soc.* 2006; **128**: 3138–3139.
61. Kolpashchikov DM. *Chem. Rev.* 2010; **110**: 4709–4723.
62. Niu Y, Zhao Y and Fan A. *Anal. Chem.* 2011; **83**: 7500–7506.
63. Bardea A, Patolsky F, Dagan A and Willner I. *Chem. Commun.* 1999; 21–22.
64. Patolsky F, Weizmann Y and Willner I. *J. Am. Chem. Soc.* 2002; **124**: 770–772.
65. Shimron S, Wang F, Orbach R and Willner I. *Anal. Chem.* 2012; **84**: 1042–1048.
66. Shimron S, Elbaz J, Henning A and Willner I. *Chem. Commun.* 2010; **46**: 3250–3252.
67. Kolpashchikov DM. *J. Am. Chem. Soc.* 2008; **130**: 2934–2935.
68. Li T, Shi L, Wang E and Dong S. *Chem.-Eur. J.* 2009; **15**: 1036–1042.
69. Wang F, Elbaz J, Teller C and Willner I. *Angew. Chem. Int. Ed.* 2011; **50**: 295–299.
70. Liu J, Cao Z and Lu Y. *Chem. Rev.* 2009; **109**: 1948–1998.
71. Wang F, Lu CH, Liu X, Freage L and Willner I. *Anal. Chem.* 2014; **86**: 1614–1621.
72. Li T, Shi L, Wang E and Dong S. *Chem. Eur. J.* 2009; **15**: 3347–3350.
73. Elbaz J, Moshe M, Shlyahovsky B and Willner I. *Chem. Eur. J.* 2009; **15**: 3411–3418.
74. Wang F, Willner B and Willner I. *Top. Curr. Chem.* 2014; **354**: 279–338.
75. Weizmann Y, Beissenhirtz MK, Cheglakov Z, Nowarski R, Kotler M and Willner I. *Angew. Chem. Int. Ed.* 2006; **45**: 7384–7388.
76. Li D, Wieckowska A and Willner I. *Angew. Chem. Int. Ed.* 2008; **47**: 3927–3931.
77. Cheglakov Z, Weizmann Y, Basnar B and Willner I. *Org. Biomol. Chem.* 2007; **5**: 223–225.
78. Sharon E, Freeman R, Riskin M, Gil N, Tzfati Y and Willner I. *Anal. Chem.* 2010; **82**: 8390–8397.
79. Niazov-Elkan A, Golub E, Sharon E, Balogh D and Willner I. *Small* 2014; **10**: 2883–2891.
80. Sharon E, Golube, Niazov-Elkan A, Balogh D and Willner I. *Anal. Chem.* 2014; **86**: 3153–3158.
81. Zhang Z, Sharon E, Freeman R, Liu X and Willner I. *Anal. Chem.* 2012; **84**: 4789–4797.
82. Li T, Dong S and Wang E. *J. Am. Chem. Soc.* 2010; **132**: 13156–13157.
83. Cheglakov Z, Weizmann Y, Basnar B and Willner I. *Org. Biomol. Chem.* 2007; **5**: 223–225.

84. Niazov T, Pavlov V, Xiao Y, Gill R and Willner I. *Nano Lett.* 2004; **4**: 1683–1687.
85. Hsieh K, Xiao Y and Tom SH. *Langmuir* 2010; **26**: 10392–10396.
86. Zhang LB, Zhu JB, Li T and Wang EK. *Anal. Chem.* 2011; **83**: 8871–8876.
87. Lierop DV, Faulds K and Graham D. *Anal. Chem.* 2011; **83**: 5817–5821.
88. Lu CH, Li J, Liu JJ, Yang HH, Chen X and Chen GN. *Chem. Eur. J.* 2010; **16**: 4889–4894.
89. Wang J, Wang LH, Liu XF, Liang ZQ, Song SP, Li WX, Li GX and Fan CH. *Adv. Mater.* 2007; **19**: 3943–3946.
90. Cho EJ, Yang LT, Levy M and Ellington AD. *J. Am. Chem. Soc.* 2005; **127**: 2022–2023.
91. Wang YY and Liu B. *Analyst* 2008; **133**: 1593–1598.
92. Sharma J, Yeh H-C, Yoo H, Werner JH and Martinez JS. *Chem. Commun.* 2011; **47**: 2294–2296.
93. Xiao Y, Lubin AA, Heege AJ and Plaxco KW. *Angew. Chem., Int. Ed.* 2005; **44**: 5456–5459.
94. Kim NW and Wu F. *Nucleic Acids Res.* 1997; **25**: 2595–2597.
95. Xiao Y, Pavlov V, Niazov T, Dishon A, Kotler M and Willner I. *J. Am. Chem. Soc.* 2004; **126**: 7430–7431.
96. Ding C, Li X, Ge Y and Zhang S. *Anal. Chem.* 2010; **82**: 2850–2855.
97. Patolsky F, Gill R, Weizmann Y, Mokari T, Banin U and Willner I. *J. Am. Chem. Soc.* 2003; **125**: 13918–13919.
98. Niazov T, Pavlov V, Xiao Y, Gill R and Willner I. *Nano Lett.* 2004; **4**: 1683–1687.
99. Li Y, Liu B, Li X and Wei Q. *Biosens. Bioelectron.* 2010; **25**: 2543–2547.
100. Yang W, Zhu X, Liu Q, Lin Z, Qiu B and Chen G. *Chem. Commun.* 2011; **47**: 3129–3131.
101. Beissenhirtz MK and Willner I. *Org. Biomol. Chem.* 2006; **4**: 3392–3401.
102. Bath J and Turberfield AJ. *Nat. Biotechnol.* 2007; **2**: 275–284.
103. Krishnan Y and Simmel FC. *Angew. Chem., Int. Ed.* 2011; **50**: 3124–3156.
104. Teller C and Willner I. *Curr. Opin. Biotechnol.* 2010; **21**: 376–391.
105. Niemeyer CM and Adler M. *Angew. Chem. Int. Ed.* 2002; **41**: 3779–3783.
106. Elbaz J, Shimron S and Willner I. *Chem. Commun.* 2010; **46**: 1209–1211.
107. Yurke B, Turberfield AJ, Mills AP Jr, Simmel FC and Neumann JL. *Nature* 2000; **406**: 605–608.
108. Elbaz J, Wang ZG, Orbach R and Willner I. *Nano Lett.* 2009; **9**: 4510–4514.
109. You M, Huang F, Chen Z, Wang RW and Tan W. *ACS Nano* 2012; **6**: 7935–7941.
110. Wang ZG, Elbaz J and Willner I. *Nano Lett.* 2011; **11**: 304–309.
111. Lu CH, Ceconello A, Elbaz J, Credi A and Willner I. *Nano Lett.* 2013; **13**: 2303–2308.
112. Qi XJ, Lu CH, Ceconello A, Yang HH and Willner I. *Chem. Commun.* 2014; **50**: 4717–4720.
113. Tian Y and Mao C. *J. Am. Chem. Soc.* 2004; **126**: 11410–11411.
114. Shimron S, Ceconello A, Lu CH and Willner I. *Nano Lett.* 2013; **13**: 3791–3795.
115. Elbaz J, Ceconello A, Fan Z, Govorov AO and Willner I. *Nat. Commun.* 2013; **4**: 2000.
116. Ceconello A, Lu CH, Elbaz J and Willner I. *Nano Lett.* 2013; **13**: 6275–6280.
117. Fu J and Yan H. *Nat. Biotechnol.* 2012; **30**: 407–408.
118. Wang ZG, Elbaz J and Willner I. *Angew. Chem. Int. Ed.* 2012; **51**: 4322–4326.
119. McKee ML, Milnes PJ, Bath J, Stulz E, Turberfield AJ and O'Reilly RK. *Angew. Chem. Int. Ed.* 2010; **49**: 7948–7951.
120. Hu Y, Wang F, Lu, CH, Girsh J, Golub E and Willner, I. *Chem. Eur. J.* 2014; **20**: 16203–16209.
121. Storhoff JJ, Elghanian R, Mucic RC, Mirkin CA and Letsinger RL. *J. Am. Chem. Soc.* 1998; **120**: 1959–1964.
122. Aleman-Garcia MA, Orbach R and Willner I. *Chem. Eur. J.* 2014; **20**: 5619–5624.
123. Liu X, Niazov-Elkan A, Wang F and Willner I. *Nano Lett.* 2013; **13**: 219–225.



# Effect of axial ligands on electronic structure and O<sub>2</sub> reduction by iron porphyrin complexes: Towards a quantitative understanding of the “push effect”

Subhra Samanta, Pradip Kumar Das, Sudipta Chatterjee and Abhishek Dey\*

Department of Inorganic Chemistry, Indian Association for the Cultivation of Science, Kolkata 700032, India

Dedicated to Professor Shunichi Fukuzumi on the occasion of his retirement

Received 29 November 2014

Accepted 13 January 2015

**ABSTRACT:** Axial ligands play a dominating role in determining the electronic structure and reactivity of iron porphyrin active sites and synthetic models. Several properties unique to the cysteine bound heme enzyme, cytochrome P450, is attributed to the “push effect” of the thiolate axial ligand. In this mini-review the ground state electronic structure of iron porphyrins with imidazole, phenolate and thiolate complexes, derived using a combination of spectroscopy and DFT calculations, are discussed. The differences in kinetics and selectivity of oxygen reduction reaction (ORR), catalyzed by these iron porphyrin complexes with different axial ligands, help elucidate the varying push effects of the different axial ligands on oxygen activation by ferrous porphyrin. The spectroscopic and kinetic data help to develop a quantitative understanding of the “push effect” and, in particular, the electrostatic and covalent contributions to it.

**KEYWORDS:** push effect, iron porphyrin, ORR.

## INTRODUCTION

Several key metallo-enzymes utilize heme cofactors to catalyze chemical transformations [1–4]. Important biological functions such as transport and storage of O<sub>2</sub>, oxidation of organic molecules with O<sub>2</sub>, synthesis of NO and N<sub>2</sub>O and quenching of reactive oxygen species are catalyzed by these active sites [5–8]. Surprisingly, the large gamut of activity can be attenuated by the axial amino acid ligand (proximal ligand). Similarly the 2nd sphere interactions (like H-bonding) can alter reactivity of these active sites and does not entail any change in the heme structure. The effect of axial ligation is beautifully illustrated when one considers the fact that while hemoglobin (Hb) and myoglobin (Mb), both utilizing the imidazole head group of a histidine residue to bind the heme iron, bind O<sub>2</sub> for storage or transport, cytochrome P450 (cyt P450), which utilizes the thiolate group of a cysteine residue to bind heme, not only binds O<sub>2</sub> but

also activates it to oxidize organic substrates [9–13]. The role of 2nd sphere residues in reactivity analogously is evident in the “pull” effect in Poulos–Kraut mechanism amongst others [14].

Inspired by their diverse reactivities, mimicking of these active sites has been a long term goal for many chemists. Synthetic iron porphyrins containing thiolate, imidazole and phenolate axial ligands, some of which can mimic the reactivity of their natural analogs have been amply demonstrated over the last four decades [15–27]. The *meso* phenyl substituents on the phenyl ring are used to conveniently introduce additional chemical moieties like axial ligand or distal super-structures into the design [28, 29]. One of the major advantages of synthetic modeling of active sites is to be able to systematically vary/control structural entities. This allows elucidation of the roles of these additional chemical entities, often unique to a particular enzyme, in determining nuances is reactivity between different active sites which are ostentatiously not very different from each other. Such elegance is often difficult to achieve in a protein

\*Correspondence to: Abhishek Dey, [icad@iacs.res.in](mailto:icad@iacs.res.in)

active site *via* site directed mutagenesis [30, 31]. For example elegant design of distal metal binding site in iron porphyrins and hydrogen bonding to axial thiolate ligand have provided unprecedented insight into the role of these attributes, encountered in active sites, in tuning structure/function of the active site [32–35]. Such efforts have led to successful modeling of O<sub>2</sub> binding in Hb/Mb and peroxide shunt in cyt P450 [16, 36–38].

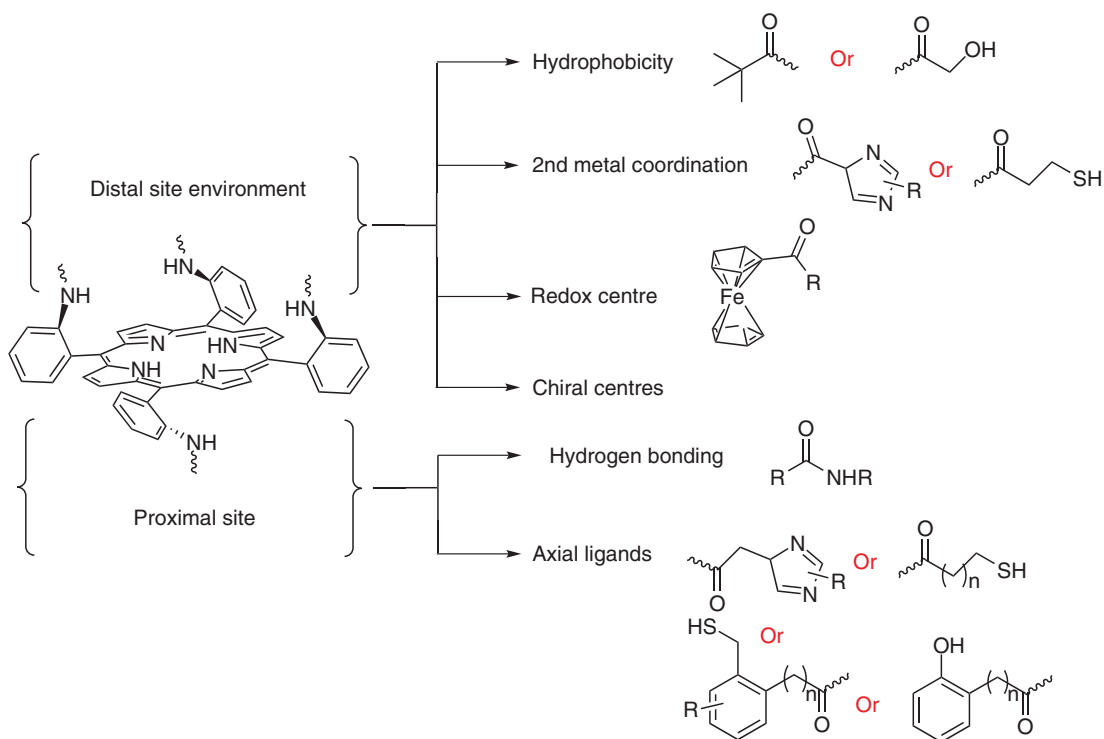
The focus of synthetic inorganic chemists is gradually shifting towards not only designing better synthetic models but also towards investigating the geometric and electronic structures that affect the reactivity of these models [19]. Catalytic O<sub>2</sub> activation and/or reduction by these complexes are significant to the current context of energy generation and storage [39–43]. The mechanistic details of the O<sub>2</sub> reduction reaction (ORR) depends on and how the axial ligands as well as the distal environment affects the reaction coordinate are key information needed to design successful catalysts [44, 45]. Particularly, obtaining higher resolution insight into role of weaker interactions like H-bonding in tuning and, in many cases, determining the function of heme active sites provide major motivation for such academic pursuit [33].

Over the last few years our group has been investigated in synthesizing iron porphyrin complexes with thiolate, phenolate and imidazole axial ligands with goal of understanding the role of these ligands in tuning electronic structure and ORR properties of iron porphyrin complexes [15, 27, 46]. Additionally by

introducing H-bonding residues in the distal site of iron porphyrin complexes, we have illustrated the likely role of these weak interactions in ORR [28, 29]. In this mini-review, we summarize our contribution in understanding the role of axial ligands in determining the ground state (GS) electronic structure and electrocatalytic O<sub>2</sub> reduction properties with an eventual goal of quantifying the “push effect.” The mini-review comprises of three sections; (A) Synthesis, (B) Ground State Properties and (C) Electrocatalytic O<sub>2</sub> Reduction.

## A. SYNTHESIS OF MODEL COMPOUNDS

The scaffold of *meso*-tetra(2-aminophenyl)porphyrin (TAPP) [9, 47] is quite amenable to chemical modifications as an amine group can be functionalized using a diverse set of reactions. Further the ability to enrich specific atropisomers allows controlling the orientation of the incoming functional group with respect to the ring and other functional groups present. These factors have been demonstrated in erstwhile synthetic achievements of several groups [17, 24, 42]. We aspired to use the TAPP architecture to mimic 2nd sphere interactions like H-bonding to the axial ligands and generate a series of complexes with different axial ligands which are biologically relevant. In this review we summarize our efforts of understanding the role of different axial ligands using synthetic models bearing



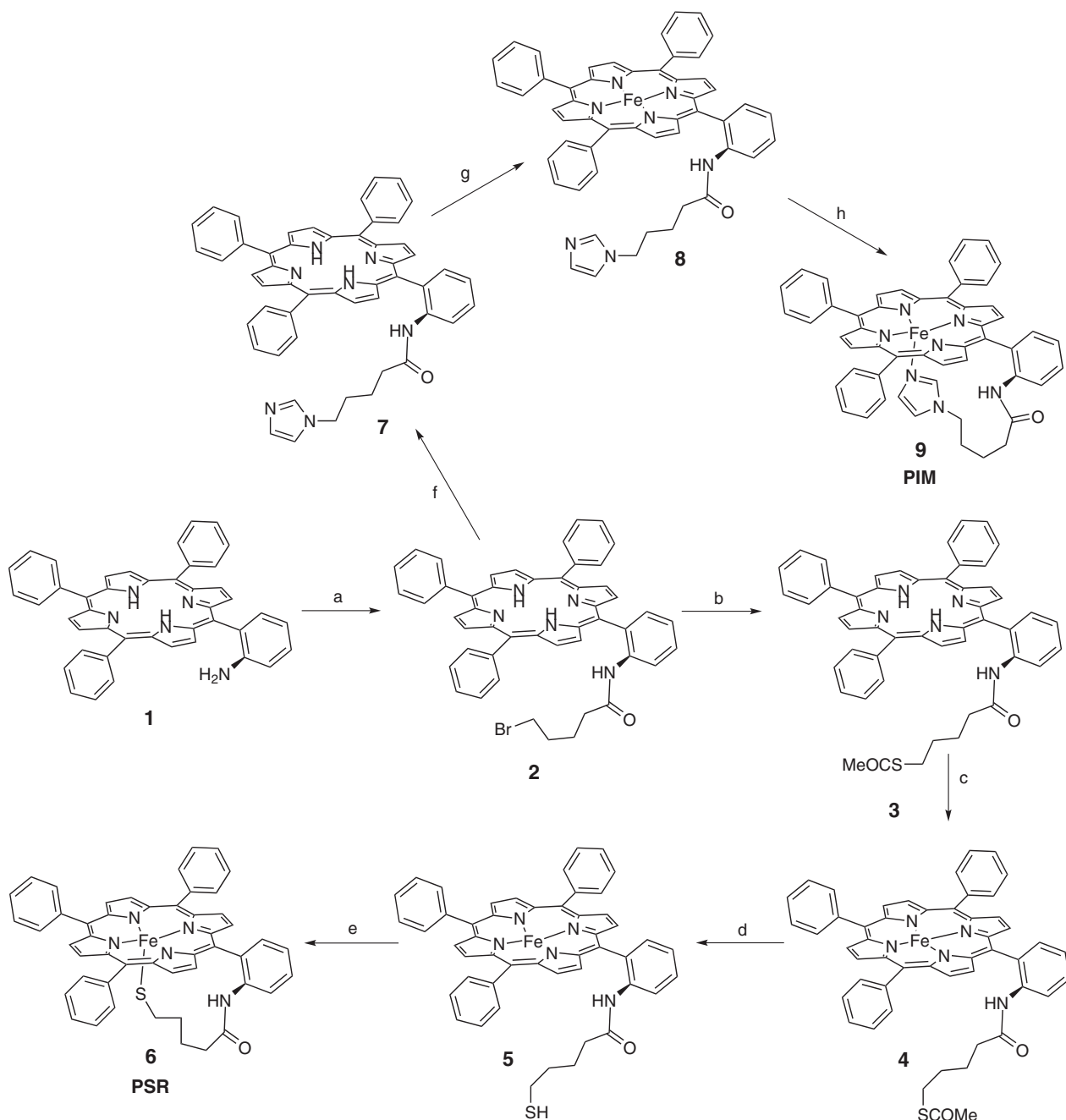
**Fig. 1.** Design of introduction of different functional moieties in distal and proximal site

imidazole, phenolate and thiolate ligands covalently attached to the porphyrin ring.

**(i) Aliphatic and bulky aliphatic thiolate, imidazole model complexes (PSR and PPSR, PIM)**

Recently we have reported a few iron porphyrin complexes with an axial thiolate ligand covalently attached to the porphyrin ring and its analogous imidazole

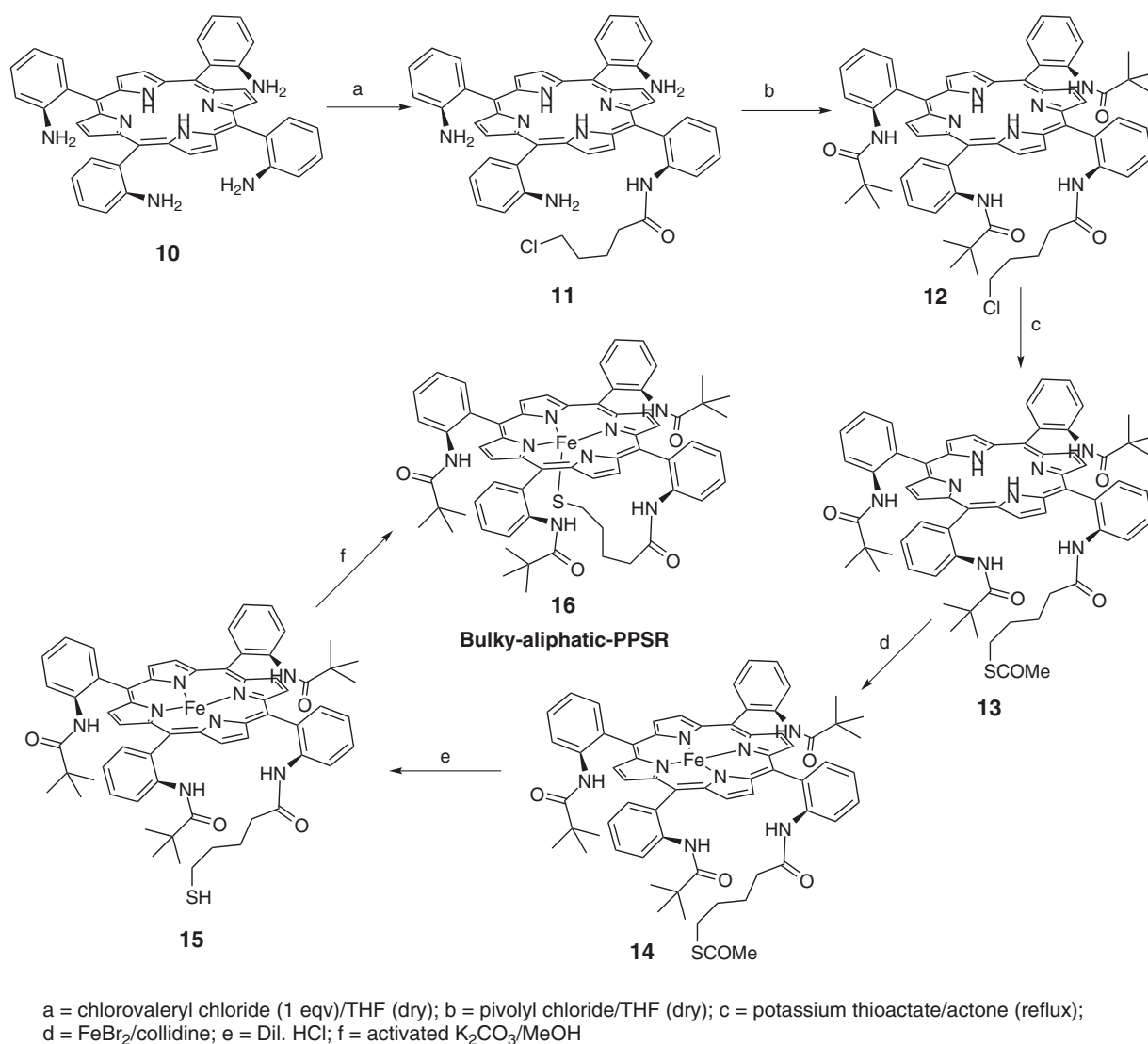
ligand bearing complexes [19]. We have started with *meso*-(2-aminophenyl)-*tris*-phenyl porphyrin (1) [48] and the amino functional group has been utilized to attach bromovaleryl chloride. The terminal bromide group is then functionalized with thiol or imidazole to result in thiolate and imidazole bound iron porphyrin complexes, respectively (Fig. 2). The final thiolate bound iron porphyrin complex is air sensitive in nature. To introduce tolerance in O<sub>2</sub> the thiolate ligand needs to be sterically



a = bromovaleryl chloride/THF (Dry); b = potassium thioacetate/DMF (reflux); c = FeBr<sub>2</sub>/collidine; d = Dil. HCl; e = activated K<sub>2</sub>CO<sub>3</sub>/MeOH; f = imidazole/MeOH (reflux); g = FeBr<sub>2</sub>/collidine; h = NaOMe/MeOH.

**Fig. 2.** General synthetic protocol to aliphatic thiolate (PSR) and its analogue imidazole model (PIM)





**Fig. 3.** Synthetic route of the bulky aliphatic thiolate ligated model complex (PPSR)

protected (Fig. 3). This was achieved by starting with TAPP (10) as the basic scaffolds. One of the *o*-amino functional group is first converted to the corresponding amide linkage (11) by chloroaleryl chloride. The rest of the three amino groups of the porphyrin have been protected by the treatment of pivoyl chloride to (12). The Fe–S bond is formed at the final step of the synthesis by treating the thiol modified porphyrin with activated potassium carbonate to get the target product (16, referred to as PPSR from here on).

### (ii) Benzyl thiolate complex

Apart from aliphatic thiols, benzylic thiols were synthesized as well (complexes 31 and 35) [23, 27]. The synthesis of both the complexes (31) and (35) are detailed in Fig. 5. Only the synthesis of (31), which is more complex, is discussed here. Starting from *p*-iodo cresol (17), the ether linkage is established by treating with ethyl-bromoacetate

in presence of potassium carbonate to give the compound (18) with a higher yield. An alkyne moiety is introduced by Sonogashira coupling reaction using Pd catalyst. To introduce the thiolate functional group, first the brominating of the benzylic position by NBS is achieved which is then converted to thioacetate functionalized compound (21). It is important to keep the thiol group protected as thioacetate in this ligand as thiols groups can complicate the following reactions and are prone to oxidation/degradation. However this automatically implies that to attach this ligand arm to TAPP one has to hydrolyze the ester group to a carboxylic acid in the presence of the thioacetate group. The crucial step of this synthetic scheme is, thus, achieving selective hydrolysis of the ester group in 21 and 26. It is achieved using LiOH in solvent mixture.

The corresponding ligand (22, Lig-A) is then attached to the porphyrin (TAPP) (10) to result in compound (28) by a modified Mukaiyama rearrangement. Generally this reaction is done at elevated temperature which, in this

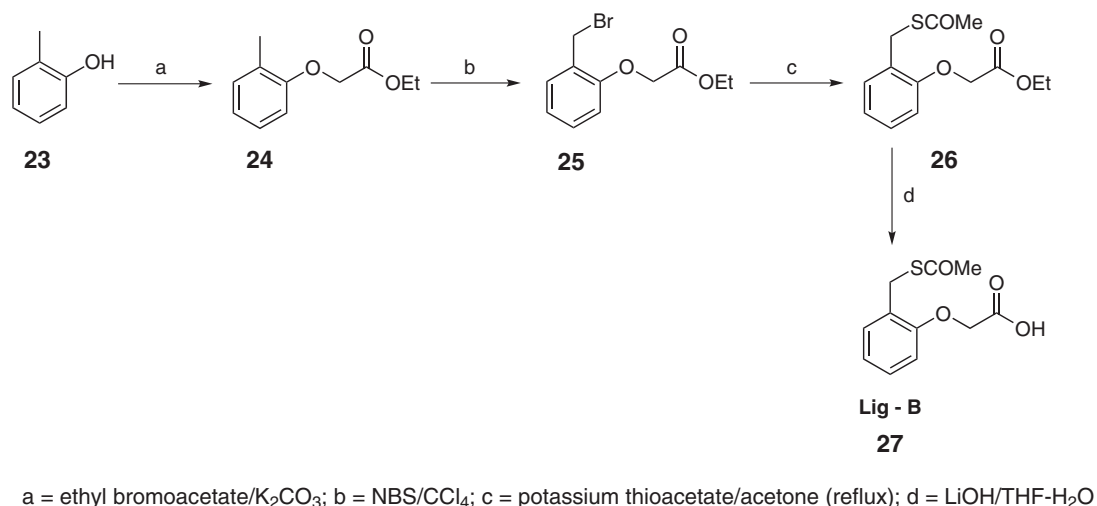
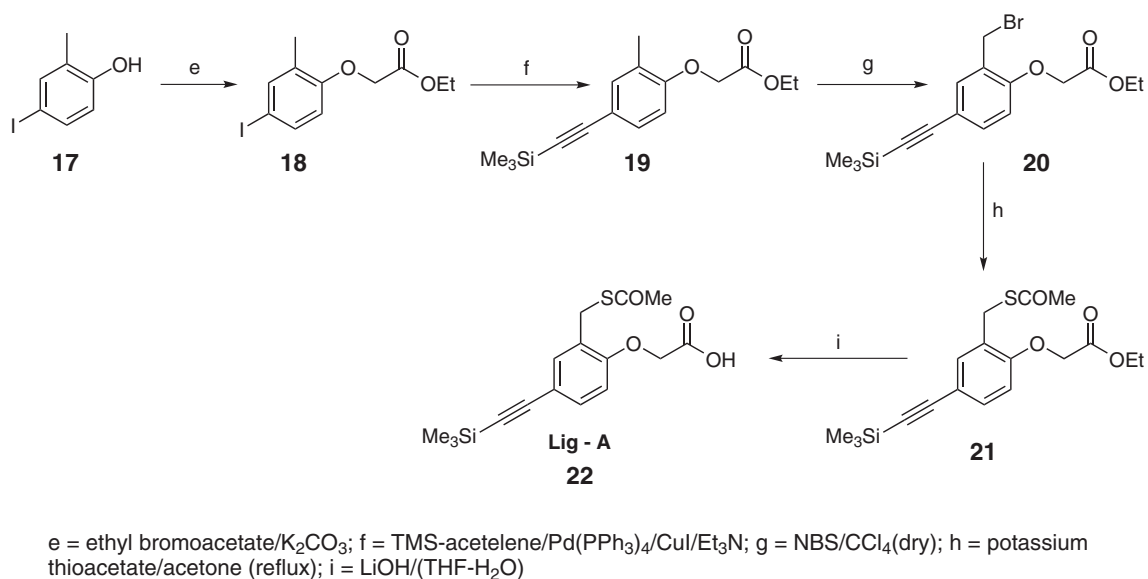


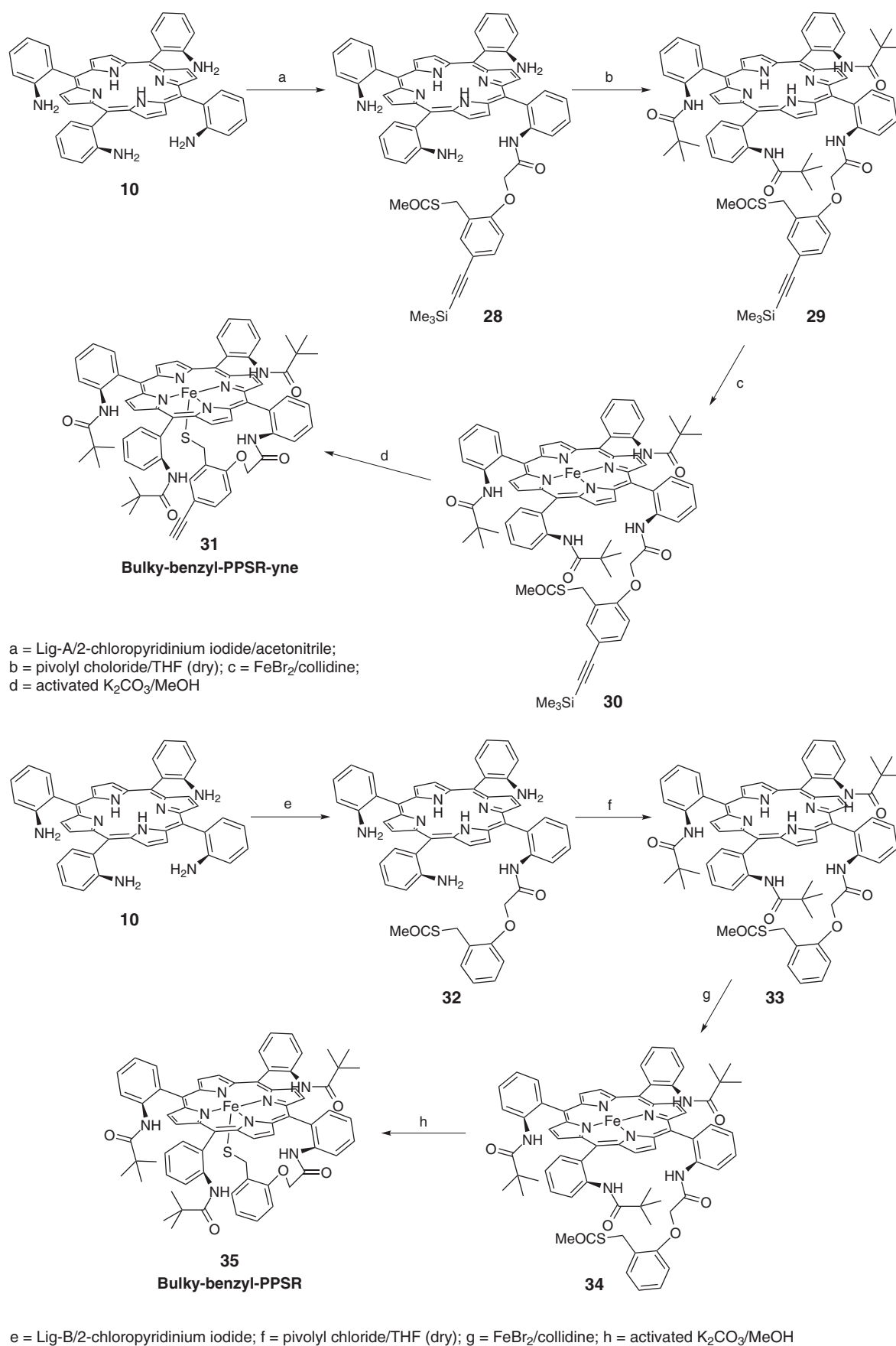
Fig. 4. General synthetic route for alkyne terminated and non-terminated ligands

case, may lead to scrambling or atropisomers. In this case the reaction had to be performed at RT to avoid that. It was observed that the use of mixture of solvent (THF and acetonitrile) instead of acetonitrile allows the reaction to proceed at room temperature. The remaining three amino groups are then protected with pivoly chloride; this protection is used to introduce steric protection around the thiolate. The thioacetate and the TMS groups were de-protected after introducing the iron in the final step to result in the thiolate bound iron center. The target molecule (31), referred to as PPSR-yne from here on, is found to be air stable [27].

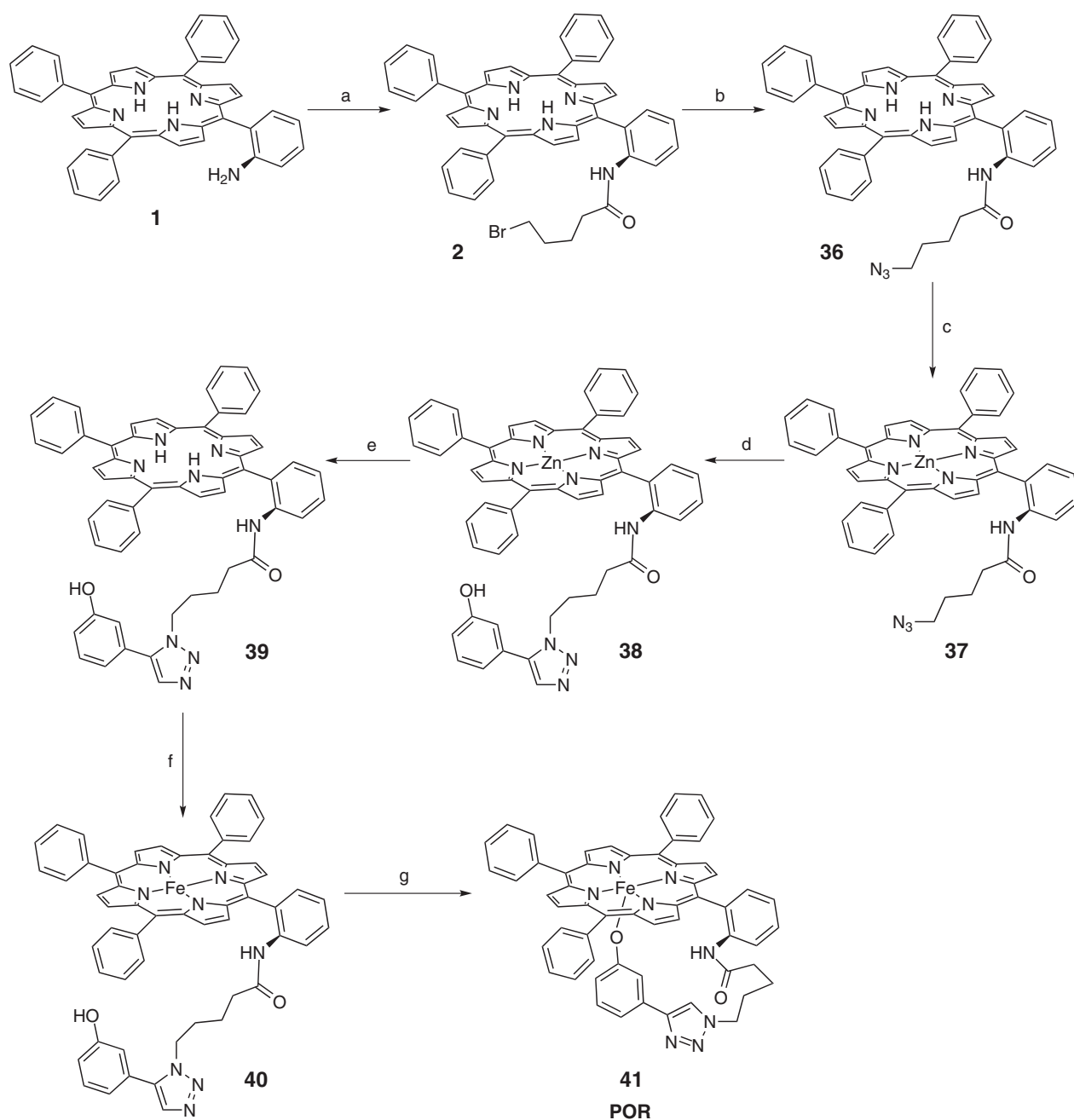
### (iii) Axial phenolate ligand

Introduction of a phenolate linker analogous to the thiolate and imidazole was found to be synthetically

inaccessible as using the approach similar to PPSR-yne will require the use of redox active catechol while using an approach similar to PSR will require C–C coupling. Thus an alternate linker had to be designed (Fig. 6). The amino functional group of *meso*-(2-aminophenyl)-trisphenyl porphyrin was reacted with bromovaleryl chloride. Compound (2) was refluxed with  $NaN_3$  to get the azide terminated compound (36) which was metalated with  $Zn(OAc)_2$  to get the Zn-porphyrin complex (37). The resulting complex (37) is “clicked” with 3-hydroxyphenyl acetylene using Cu(I) catalyzed 1,3-cycloaddition of azides to terminal alkynes [49]. The resultant Zn bound complex (38) is de-metalated in presence of dilute HCl yielding free base porphyrin (39). The iron complex (40) with the phenol ligand is treated with activated  $K_2CO_3$  to get desired phenolate bound iron porphyrin (41, referred to as POR from here on) (Fig. 6) [20, 50].



**Fig. 5.** Synthetic strategy for cyt P450 models PPSR-yne and its analogue without alkyne bulky benzyl-PPSR



a = bromovaleryl chloride/THF (dry); b = NaN<sub>3</sub>/DMF (reflux); c = Zn(OAc)<sub>2</sub>/THF; d = 3-hydroxyphenyl acetelene/CuSO<sub>4</sub>/Na-ascorbate; e = Dil. HCl; f = FeBr<sub>2</sub>/collidine; g = activated K<sub>2</sub>CO<sub>3</sub>/MeOH

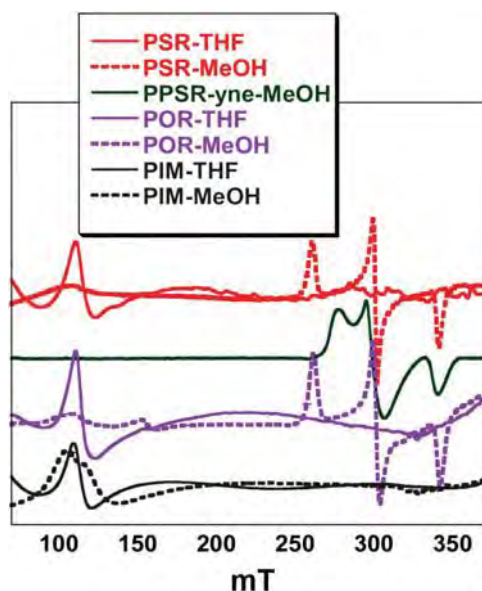
**Fig. 6.** Synthetic route for the phenolate bound heme catalase model POR

## B. GROUND STATE PROPERTIES OF MODEL COMPOUNDS

### (i) EPR

The imidazole bound complex, PIM, is high spin (HS) 5/2 ground state (GS) with an axial signal at  $g = 6.0$  in non-coordinating solvents like CH<sub>2</sub>Cl<sub>2</sub> or THF. In

a coordinating solvent like MeOH a rhombic distortion ( $g = 6.2, 5.4$ ), suggests formation of a six-coordinate (6C) MeOH bound complex (PIM-MeOH) but retaining its  $S = 5/2$  GS (Fig. 7, gray). Hence, the PIM complex mimics the co-ordination and spin state properties of histidine coordinated enzyme active sites *e.g.* hemoglobin, cytochrome *c* oxidase, *etc.* *i.e.* the five coordinate (5C) and the solvent bound 6C state are both HS [19].



**Fig. 7.** The X-band EPR spectra of the synthetic complexes at 77 K

**Table 1.** EPR parameters for the heme complexes

	Spin	$g_1$	$g_2$	$g_3$	$\nu/\lambda$
Cyt P450 [51]	1/2	2.45	2.26	1.91	4.59
Catalase resting [52]	5/2	6.0			
Catalase-N <sub>3</sub> <sup>-</sup> [52, 53]	1/2	2.50	2.26	1.87	3.98
Hb [51]	5/2				
Cyt <i>c</i> oxidase [22]	5/2				
SR complex [23]	1/2	2.32	2.21	1.96	6.43
TCP-TB [42]	1/2	2.33	2.21	1.96	6.55
PPSR-yne-MeOH [27]	1/2	2.33	2.21	1.91	5.68
PPSR in MeOH [19]	1/2	2.49	2.16	1.90	4.07
PSR in MeOH [19]	1/2	2.50	2.16	1.89	3.94
POR [20]	5/2	6.0			
POR-MeOH [20]	1/2	2.49	2.16	1.89	4.02
PIM [19]	5/2				

Both the thiolate bound PSR and phenolate bound POR complexes show axial  $g = 6.0$  signal in a non-coordinating solvents. However in MeOH solvent they both show a  $S = 1/2$  EPR signal at 77 K suggesting conversion to the 5C HS GS to a 6C low spin (LS) GS on binding MeOH. Based on the  $g$  values of the LS thiolate bound iron porphyrin complexes, they can be divided in two categories. The PPSR-yne complex, Naruta *et al.* and Hirobe *et al.* reported benzylic thiolate as axial ligands and have  $V/\lambda$  values close to 6 [23, 42]. The large rhombicity observed in these complexes is consistent with the presence of a strong  $\pi$  anisotropic donor like thiolate. Note that the  $V/\lambda$  for these complexes is significantly higher than that

of the LS active site of cyt P450. Of course this could be due to differences in the donor strength of the axial thiolate or due to 2nd sphere interactions like H-bonding. The  $V/\lambda$  of the more flexible alkyl thiolate linker is around 4.0 and close to 4.55 observed in the LS active site of cyt P450. Considering the fact that both PPSR and PPSR-yne have similar protection of the thiolate, these differences in  $V/\lambda$  likely represents differences in the GS owing to differences between the donor strength of the benzylic thiolate and the alkyl thiolate ligands. However H-bonding from MeOH may affect the  $V/\lambda$  as well.

Similarly, the phenolate bound iron porphyrin complex, POR shows an  $S = 5/2$  GS in a non-coordinating solvent and an  $S = 1/2$  GS with  $g$ -values at 2.49, 2.16, 1.89 at 77 K in a coordinating solvent. The  $g$  values of the LS thiolate complexes are similar to those reported for several cyt-P450 models and the oxidized resting state of the cyt P450 (Table 1). The  $V/\lambda$  of the LS  $S = 1/2$  signal, calculated using the Taylor analysis [54], is similar to those calculated for LS N<sub>3</sub><sup>-</sup> bound catalase and is consistent with the presence of a strong  $\pi$ -anisotropic ligand [51]. Thus both the thiolate and the phenolate bound complexes are HS in their 5C state (non-coordinating solvent) and LS in their 6C state (MeOH solvent) mimicking the properties of cyt P450 and catalase active sites, respectively. The imidazole bound complex, on the other hand, stays HS in both the 5C and 6C states.

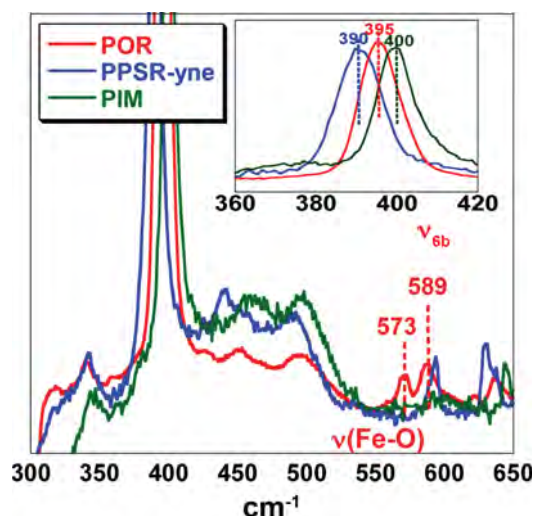
## (ii) Resonance Raman (rR)

The characteristic oxidation state and spin state marker  $\nu_4$  and  $\nu_2$  vibrations for the PIM complex and the HS/LS thiolate and phenolate bound complexes are listed in Table 2. In the low frequency region, vibrations are observed for the MeOH bound PSR complex at 339, 361, 421, 467, 676 and 770 cm<sup>-1</sup>, which are not observed for the methanol bound PIM complex (Table 2) [19]. This suggests that these vibrations possibly originate due to the thiolate coordination to the Fe<sup>III</sup>-porphyrin. The vibrations in the range of 350–470 cm<sup>-1</sup> may have contribution from the Fe<sup>III</sup>-S stretching mode while those in the range of 650–800 cm<sup>-1</sup> may have contribution from the C–S stretching mode (Intra L<sub>ax</sub>, Table 2) [35, 55–58]. While confirmed assignment of these vibrations will require isotopic substitution, DFT calculations were used to support these tentative assignments (*vide infra*). Similarly, the 5C HS aliphatic complex in THF shows additional vibrations at 335, 369 cm<sup>-1</sup>, and 624, 679 and 765 cm<sup>-1</sup>. The rR data of the 5C HS complex POR, show peaks at 573 and 589 cm<sup>-1</sup> corresponding to Fe–Oph vibrations (Fe–O stretch and  $\nu_{6b}$ ) (Table 2), [20] consistent with the values reported for the active site of tyrosine bound heme sites [59–61]. The C–O stretch at 1320 cm<sup>-1</sup> is clearly observed in POR (Table 2, Intra L<sub>ax</sub>).

The  $\nu_8$  vibration, which represents the Fe–N<sub>pyr</sub> (Fe-pyrrole nitrogen) symmetric stretch, is observed at 400 cm<sup>-1</sup> for the  $S = 5/2$  PIM (Fig. 8) [19]. Further the Fe–N<sub>pyr</sub> of the thiolate bound PPSR-yne is at 390 cm<sup>-1</sup>

**Table 2.** rR data of the synthetic complexes

Complex	Fe–L(axial)	Intra L <sub>ax</sub>	$\nu_8$ , cm <sup>-1</sup>	$\nu_4$ , cm <sup>-1</sup>	$\nu_2$ , cm <sup>-1</sup>
PIM			400	1360	1550
PSR 5C/HS	335, 369	624, 679, 765	391	1361	1554
PSR 6C/LS	339, 361, 421, 467	676, 770	387	1366	1566
POR 5C/HS	573, 589	1320	395	1364	1555
POR 6C/LS	560		391	1368	1567



**Fig. 8.** rR data in the low-energy region in THF at 77 K. Laser excitation wavelength = 413.1 nm; power = 10 mW. Inset is showing Fe–N<sub>pyrrole</sub> vibration

which is 5 cm<sup>-1</sup> weaker than the Fe–N<sub>pyr</sub> vibration of the phenolate bound POR complex (395 cm<sup>-1</sup>) [20]. The data thus indicates that the Fe–N<sub>pyr</sub> vibration reflects the relative donor strengths of the axial ligands between complexes having the same spin states. The  $S = 5/2$  PIM complex, which has an axial imidazole ligand, has a higher Fe–N<sub>pyr</sub> vibration relative to the  $S = 5/2$  PPSR-yne and POR complexes, which have a thiolate and phenolate axial ligand, respectively, consistent with the fact that the thiolate and phenolate axial ligands are much better donor than imidazole. Similarly the Fe–N<sub>pyr</sub> vibration of the LS PIM-MeOH, POR-MeOH and PPSR-yne-MeOH complexes are at 395 cm<sup>-1</sup>, 391 cm<sup>-1</sup> and 389 cm<sup>-1</sup>, respectively *i.e.* showing the same trend observed for the 5C HS complexes. DFT calculations have been utilized to understand this effect in detail (*vide infra*).

### (iii) Cyclic voltammetry

PIM has an  $E_{1/2}$  of -0.58 V vs. Fc/Fc<sup>+</sup> in a non-coordination solvent. The  $E_{1/2}$  of the thiolate bound iron porphyrin complexes was found to be at -1.03 V *i.e.* ~500 mV more negative compared to PIM in the non coordinating solvent like THF or DCM [19, 20]. The POR complex was found to

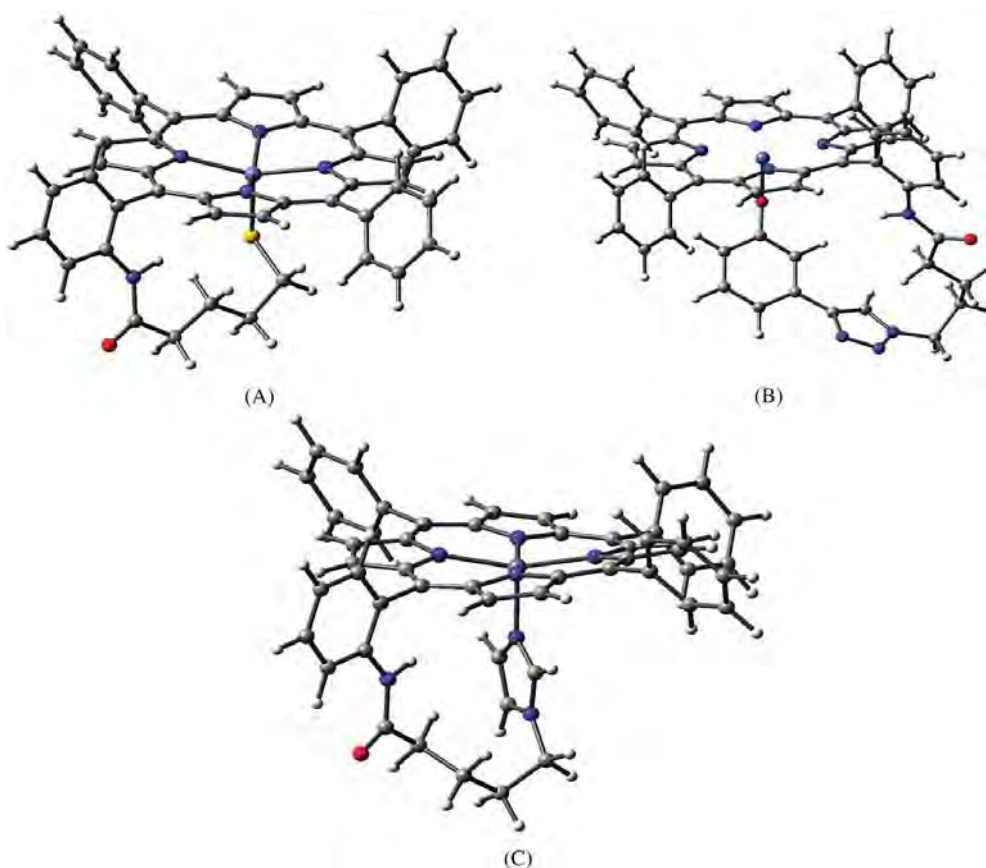
have an  $E_{1/2}$  of -1.14 V vs. Fc<sup>+</sup>/Fc (as an internal reference) in these solvents. Thus the presence of the axial anionic  $\pi$ -donor ligands like thiolate and phenolate lowers the Fe<sup>III/II</sup> potential by ~500 mV relative to the neutral ligand like imidazole. Further the  $E_{1/2}$  of the phenolate bound POR is 110 mV lower than the  $E_{1/2}$  of the thiolate bound PSR. Interestingly, the lower  $E_{1/2}$  of the phenolate bound complex relative to the thiolate bound complex actually reproduces the lower  $E_{1/2}$  of the 5C HS catalase site relative to P450 in aqueous solution [4, 35, 62]. Note that based on the relative magnitude of the Fe–N<sub>pyr</sub> vibration with an axial thiolate ligand and having the lowest Fe–N<sub>pyr</sub> vibration (*i.e.* weakest Fe–N<sub>pyr</sub> bond) may have been expected to have the lower Fe<sup>III/II</sup>  $E^0$  of the three. Contrary to expectations, the phenolate complex is found to have 110 mV lower Fe<sup>III/II</sup>  $E^0$  than the thiolate complex. DFT calculations were found to be very helpful in cogitating these unusual, if not counter-intuitive, trends in the  $E_{1/2}$ .

### (iv) DFT calculations

In the absence of suitable quality crystals, the structure of these complexes could not be determined. However with the vast amount of spectral data available, one could use DFT calculations to obtain an educated guess of the three dimensional structure of these complexes. Optimization of the geometry in the gas phase can be performed using different functional. While most functional will converge on a similar overall geometry, there are always significant differences (up to 0.1 Å) in the optimized metal ligand bond lengths. We found solace in the BP86 [63–65] functional as: (a) the calculated bond lengths (Fig. 9, Table 3) are in good agreement with the reported structures of active sites as well as those of the synthetic model complexes [19] and (b) it reproduced the experimentally observed vibrations [20].

**(a) Vibrations.** The calculated  $\nu_4$  and  $\nu_2$  modes agree quite well when the BP86 functional is used (Table 4). In particular, the calculated  $\nu_8$  vibrations and the experimentally observed trend, PIM > POR > PSR are reproduced in the DFT calculations as well. These are not that well reproduced in the B3LYP functional.

For the 5C HS PSR model, vibrations at 410, 369 and 308 cm<sup>-1</sup> have contributions from the Fe–S stretching mode and consistently a unique vibration is observed at 369 cm<sup>-1</sup> in the rR spectrum of 5C HS PSR complex in THF



**Fig. 9.** DFT optimized structures of complex (A) PSR; (B) POR; (C) PIM

**Table 3.** Optimized bond lengths (Å) of the iron porphyrin models in their oxidized Fe(III) states and relevant Mulliken charges

		Geometry					Mulliken charges	
		Fe–N <sub>pyr</sub>	Fe–L <sup>a</sup>	C–O	Fe–O–C	Fe–X <sub>axial</sub>	q <sub>Fe</sub>	q <sub>O/S/N</sub>
S = 5/2	POR	2.08	1.84	1.33	145		1.54	-0.68
	PSR	2.09	2.31				1.41	-0.41
	PIM	2.05	2.08				1.52	-0.58
S = 1/2	POR	2.00	1.81	1.35	128	2.10	1.26	-0.58
	PSR	1.98	2.18			2.16	1.20	-0.33

<sup>a</sup>L = axial ligand coordinating atom S for PPSR-yne, N for PIM and O for POR.

[19, 35, 55]. The C–S stretching mode is calculated to be at 629 cm<sup>-1</sup> and indeed there are several weak vibrations observed for the 5C PSR (not PIM or POR) complex in this region. The 5C HS POR complex was characterized by two vibrations in this region instead of one; at 573 cm<sup>-1</sup> and the other at 589 cm<sup>-1</sup>. The DFT calculations indicate that as a consequence of a wide Fe–O–C angle (140°), the Fe–O vibration couples (calculated to be at 613 cm<sup>-1</sup>) with the ν<sub>6b</sub> bending mode of the phenolate (calculated to be at 590 cm<sup>-1</sup>) and are both observed in the experimental spectrum. Enhancement of both the Fe–O and ν<sub>6b</sub> of

phenolate in the rR spectra is also observed for a bovine liver catalases which has a Fe–O–C angle of 143°.

**(b) Ground state wave function.** The DFT optimized geometries for the HS and LS complexes are listed in Table 3. The MO contributions (Table 5) of PSR in its 5C HS state reveal that the d<sub>yz</sub> orbital in the PSR model has 28% S<sub>3p</sub> mixed into it while the d<sub>z<sup>2</sup></sub> orbital has 26% S<sub>3p</sub> mixed into it [19, 34, 66]. The GS wavefunction of the 5C HS POR complex has 15% O<sub>2p</sub> mixed into the d<sub>xz</sub>/d<sub>yz</sub> orbital and 4% O<sub>2p</sub> mixed into the d<sub>z<sup>2</sup></sub> orbital [20]. The 5C HS PIM on the other hand has only 7%

**Table 4.** Calculated vibrational frequencies (cm<sup>-1</sup>)

Mode	PSR			POR			PIM		
	rR	BP86	B3LYP <sup>a</sup>	rR	BP86	B3LYP <sup>a</sup>	rR	BP86	B3LYP <sup>a</sup>
$\nu_2$	1554	1551	1477	1555	1550	1525	1551	1533	1482
$\nu_3$	1451	1447	1421	1455	1458	1432	1461	1427	1420
$\nu_4$	1361	1351	1326	1364	1351	1325	1361	1353	1308
$\nu_8$	391	378	373	395	382	378	400	384	366
C–O				1320	1286	1251	—	—	—
Fe–S	336	308	290						
	369	369	303						
		410	351						
Fe–O	—	—	—	573	590	574	—	—	—
				589					
					614	600			

<sup>a</sup> values obtained using B3LYP are scaled by 0.95.

**Table 5.** MO compositions of the  $\beta$  unoccupied orbital

Orbitals	Orbital contribution								
	POR			PSR			PIM		
	Fe <sub>3d</sub>	O <sub>2p,2s</sub>	N <sub>pyr</sub>	Fe <sub>3d</sub>	S <sub>3p</sub>	N <sub>pyr</sub>	Fe <sub>3d</sub>	N <sub>2p,2s</sub>	N <sub>pyr</sub>
$d_{x^2-y^2}$	67.08	0.01	15.42	68.01	0.00	14.92	66.51	0.00	16.49
$\pi^*$	19.56	1.29	7.16	22.74	6.51	7.17	—	—	—
$d_{z^2}$	55.06	3.66	5.19	45.34	15.87	5.84	66.6	6.69	6.19
$d_{yz}$	61.81	9.19	1.89	53.48	28.64	1.8	72.1	0.91	2.89
$d_{xz}$	64.44	5.55	1.84	70.54	1.03	1.52	71.22	2.29	3.1
$d_{xy}$	90.44	0.04	0.43	89.47	0.42	0.42	85.49	0.08	1.32

imidazole nitrogen mixed into the  $d_z^2$  orbital with minor  $\pi$  contribution [10, 34]. Thus the phenolate and thiolate complexes form more covalent Fe–L bonds with both  $\sigma$  and  $\pi$  contributions whereas PIM forms a weakly covalent bond with mostly  $\sigma$  contribution. The strong covalent charge transfer from axial ligand (thiolate and phenolate) to Fe<sup>III</sup> raises the energy of the Fe<sub>3d</sub> orbital due to lowering of the  $Z_{\text{eff}}$  on the Fe. This allows back-bonding interaction between the occupied iron  $t_2$  orbital and the low-lying unoccupied porphyrin  $\pi^*$  orbital. The calculated wavefunctions clearly show that anionic ligands like phenolate and thiolate show >20%  $d_{xz/yz}$  mixing into the porphyrin  $\pi^*$  while the PIM complex shows none. This back-bonding interaction stabilizes the  $t_2$  orbital ( $d_{xz}$  and  $d_{yz}$ ). This helps explain the fact that while 6C Fe(III) porphyrin complexes bound to anionic ligands like thiolate and phenolate and active sites of cyt P450 and catalase show LS GS, the corresponding 6C Fe(III) porphyrin complexes bound to imidazole and active sites of Hb/Mb stabilizes a HS GS state.

(c) **Reduction potential.** The experimental data indicate that the Fe<sup>III/II</sup>  $E_{1/2}$  is most positive for the PIM complex. The calculated potential, both in the gas phase and after solvent correction, shows the same trend *i.e.* the  $E_{1/2}$  of PIM is significantly more positive than those of PSR and POR. The fact that the  $E_{1/2}$  for a complex bound to a neutral ligand (imidazole) is more positive than that of an anionic ligand (phenolate and thiolate) is not surprising and the reasons therein are well understood. What is rather interesting is the observation that the  $E_{1/2}$  for POR is measured to be 110 mV more negative than that of PSR

**Table 6.** DFT calculated reduction potential in volt

Complex	Potential (gas phase)	Potential (DCM)
PSR	-1.917	-0.784
POR	-1.883	-0.791
PIM	1.065	0.085



**Table 7.** Mulliken charges and electrostatic interaction energies

	Fe <sup>III</sup>				Fe <sup>II</sup>				
	q <sub>Fe</sub>	q <sub>S</sub>	r <sub>Fe-L</sub>	E <sub>elec</sub>	q <sub>Fe</sub>	q <sub>S</sub>	r <sub>Fe-L</sub>	E <sub>elec</sub>	ΔE <sub>elec</sub>
Gas phase (ε = 1)									
PSR	1.45	-0.37	2.31	-3.27	1.37	-0.49	2.36	-4.01	+0.74
POR	1.59	-0.62	1.84	-7.55	1.47	-0.62	1.90	-6.76	-0.79
In DCM solution (ε = 8.9)									
PSR	1.46	-0.44	2.31	-3.92	1.38	-0.59	2.36	-4.86	+0.92
POR	1.60	-0.64	1.84	-7.84	1.46	-0.64	1.90	-6.90	-0.94

[20]. Based on the calculated GS wavefunctions of POR and PSR one would have possibly expected that the  $E_{1/2}$  of PSR which fashions a more covalent Fe–L<sub>ax</sub> bond (also reflected in the  $\nu_8$ ) would be lower. Indeed the calculated gas phase  $E_{1/2}$  for PSR is 34 mV lower than that of POR (Table 6). Interestingly, when solvation is included (DCM) the POR complex is calculated to have a more negative potential (7 mV) relative to the PSR complex; qualitatively reproducing the experimental observation. This reflects differences in the nature of bonding between the PSR and POR complex.

The contribution of electrostatic interaction in bonding energy ( $BE_{elec}$ ) can be approximately estimated by Coulomb's law;

$$BE_{elec} = Z_{eff}^{Fe} Z_{eff}^L / r_{Fe-L} \times 14.1 \text{ kcal/mol} \quad (1)$$

The calculated Mulliken charges on the Fe and S atoms for PSR and Fe and O atoms for POR in the gas phase and after solvation are listed in Table 7.

The electrostatic interaction ( $E_{elec}$ , Table 7) of the oxidized state of POR complex is more than that of PSR [20]. This is a result of the strong covalent bonding between the thiolate sulfur and the iron in the oxidized state which reduces the partial charges on the individual centers and the shortened Fe–L bond length of the phenolate ligand. However in the reduced state the  $E_{elec}$  is larger for PSR. When the  $E_{elec}$  for both the oxidized and reduced states are considered, the electrostatic stabilization favors the oxidation of POR complex by 1.53 Kcal/mol relative to the PSR complex. This may be expected to lower the reduction potential of the POR complex relative to the PSR complex by 66 mV. The corresponding calculated  $E^0$  of the PSR is 34 mV more negative in the gas phase. This, of course, represents the combined effect of the covalent and electrostatic contributions to bonding. In this case the large covalency of the Fe–S bond in the oxidized state, as indicated in the reduction of the  $\nu_8$  vibration and the calculated GS wave function, results in a more negative  $E^0$  for the PSR complex relative to the POR complex.

The electrostatic stabilization increases in when a PCM is used as the polarization of the environment favors charge separation in the GS wavefunction. The

enhanced electrostatic stabilization of the POR complex, on including solvation, in its oxidized form relative to the reduced form (0.94 Kcal/mol) is now expected to lower its potential by 81 mV relative to the PSR complex where the oxidized state is now destabilized by 0.92 Kcal/mol relative to the reduced state. Thus the inclusion of the polarized medium is expected to lower the  $E^0$  of the POR complex relative to the PSR complex 80 mV (1.86 Kcal/mol), 14 mV more relative to the gas phase. This is why a more covalent ligand like thiolate has a more positive potential than a less covalent ligand like phenolate in solution.

## C. ELECTROCATALYTIC O<sub>2</sub> REDUCTION

Rotating disc electrochemistry (RDE) is a convenient approach for analyzing electrocatalytic currents using the Kouteky–Levich equation [67]:

$$I^{-1} = i_k(E)^{-1} + i_L^{-1} \quad (2)$$

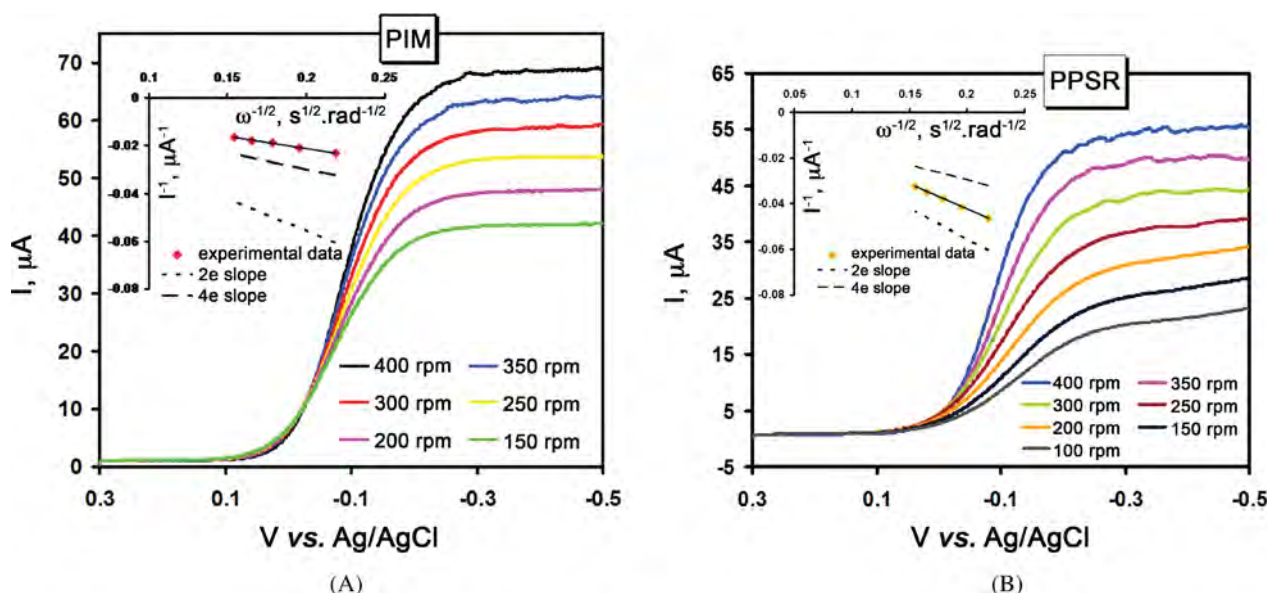
where  $i_k(E)$  is the potential dependent kinetic current,  $i_L$  is the Levich current given by:

$$i_L = 0.62nFA[O_2](D_{O_2})^{2/3}\omega^{1/2}\nu^{-1/6} \quad (3)$$

where  $n$  is the number of electrons transferred to the substrate,  $A$  is the macroscopic area of the disc (0.125 cm<sup>2</sup>),  $[O_2]$  is the concentration of O<sub>2</sub> in an air saturated buffer (0.26 mM) at 25 °C,  $D_{O_2}$  is the diffusion coefficient of O<sub>2</sub> (1.8 × 10<sup>-5</sup> cm<sup>2</sup>.s<sup>-1</sup>) at 25 °C,  $\omega$  is the angular velocity of the disc, and  $\nu$  is the kinematic viscosity of the solution (0.009 cm<sup>2</sup>.s<sup>-1</sup>) at 25 °C [68].

### (i) PIM vs. PPSR

The slopes obtained from the experimental data for PIM closely matches with the theoretical slope predicted for a 4e<sup>-</sup> process (Fig. 10a, inset). However, for the PPSR the slope corresponds to a (3.25 ± 0.25)e<sup>-</sup> process on EPG surface (Fig. 10b, inset). The values of  $n$  obtained indicate that under very fast electron transfer O<sub>2</sub> undergoes almost complete 4e<sup>-</sup> reduction to H<sub>2</sub>O by PIM but not by PPSR. The intercepts of the K-L plots indicate that the 2nd order



**Fig. 10.** LSV of PIM (A) and PPSR (B) physisorbed on EPG in air saturated pH 7 buffer at a scan rate of 50 mV/s at multiple rotations using Ag/AgCl as reference and Pt wire as counter electrodes. K–L plots of the respective catalysts are given in black bold line in the inset of the figures. The theoretical plots for 2e<sup>-</sup> and 4e<sup>-</sup> processes are indicated by the dotted and dashed lines respectively

rate of O<sub>2</sub> reduction is of the order of 10<sup>4</sup> for PIM and 10<sup>6</sup> for PPSR [15, 69, 70].

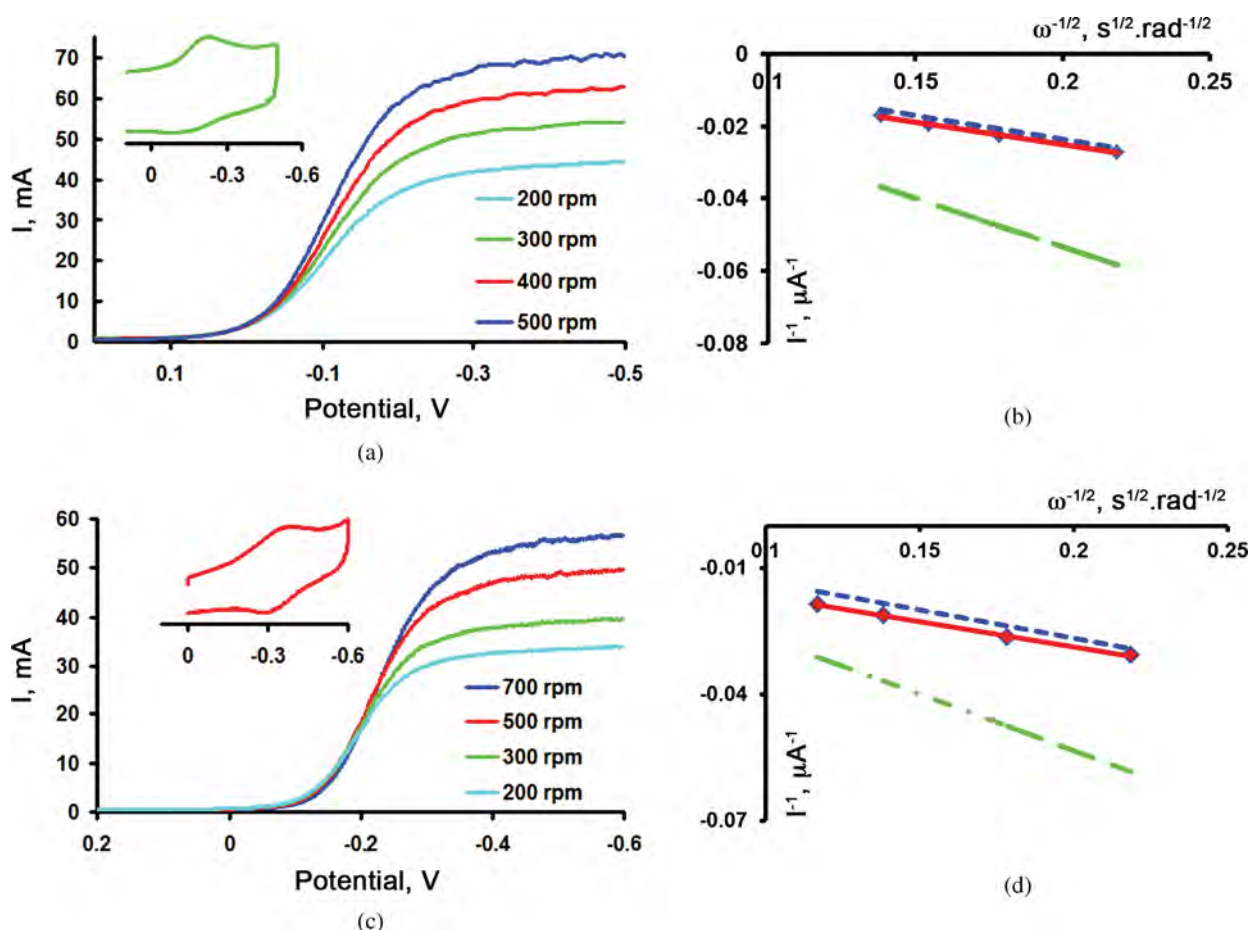
### (ii) Benzyl thiolate and phenolate

The RDE data of the complexes PPSR-yne and POR (Fig. 11), physisorbed on EPG electrodes, indicate that a normal substrate diffusion limited current is observed below -0.4 V. The K-L plot indicates that the experimental data matches closely the theoretical plot for a 4e<sup>-</sup> process. Thus the synthetic P450 mimic and its phenolate analog can reduce O<sub>2</sub> by 4e<sup>-</sup>/4H<sup>+</sup> when absorbed on an EPG electrode. The 2nd order rate of O<sub>2</sub> reduction for POR and PPSR-yne are obtained to be 10<sup>5</sup> and 10<sup>7</sup>, respectively [27].

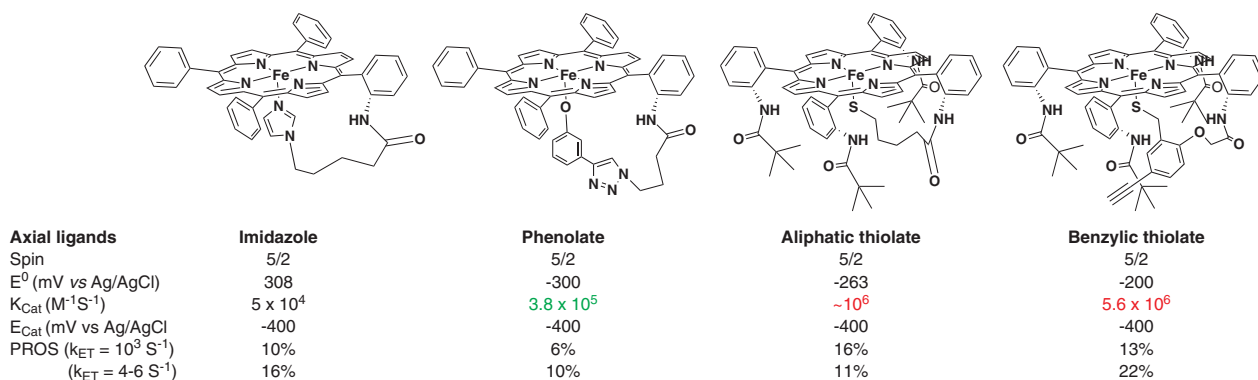
EPG surfaces allow for very facile electron transfer to the catalyst  $k_{ET} > 10^5 \text{ s}^{-1}$ . This is far from physiological conditions where the electron transfer from the reductase component to the active site varies between 4–1000 s<sup>-1</sup> in different WT and mutant cytochrome P450 enzymes [71, 72]. Thus investigation of electrocatalytic O<sub>2</sub> reduction is warranted under physiologically relevant slow electron transfer rates. Hence, gain further insight into ORR mechanism electrocatalytic O<sub>2</sub> reduction by PIM and PPSR at fast (EPG), slow (C<sub>8</sub>SH modified Au) and very slow (C<sub>16</sub>SH modified Au) electron transfer rates were investigated [73].

When absorbed on a thiol self-assembled monolayer (SAM) on Au electrodes, these constructs are not stable enough to allow RDE investigations. Rather rotating ring disc electrochemistry (RRDE) is utilized to investigate these systems. In RRDE partially reduced oxygen species (PROS) produced on the working electrode is detected on

a Pt ring electrode, encircling the working disc electrode, which is held at a potential where it can oxidize the PROS produced to O<sub>2</sub> and this oxidation current can be used to quantitatively determine the amount of PROS generated during O<sub>2</sub> reduction [67]. PIM produces about 3.5 ± 1% PROS at pH 7 when physisorbed on EPG, whereas, PPSR produces 19 ± 1.5% PROS [15]. The higher PROS produced in PPSR during O<sub>2</sub> reduction implies less than 4e<sup>-</sup> reduction of O<sub>2</sub> on an average consistent with the number electrons being less than four in the RDE experiments of PPSR. The higher PROS may reflect the higher *trans* effect of the thiolate ligand, compared to the neutral imidazole ligand, which leads to facile hydrolysis of Fe<sup>III</sup> bound O<sub>2</sub><sup>-</sup> (oxy adduct) or OOH (peroxy adduct) species resulting in H<sub>2</sub>O<sub>2</sub> (a 2e<sup>-</sup>/2H<sup>+</sup> reduction product) during ORR. When physisorbed on C<sub>16</sub>SH SAM, where  $k_{ET} \sim 3\text{--}6 \text{ s}^{-1}$ , the catalysts show an electron transfer limited catalytic current in contrast to mass transfer limited current on EPG and C<sub>8</sub>SH ( $k_{ET} \sim 10^3 \text{ s}^{-1}$ ) SAM. PIM produces 10 ± 0.5% and 16 ± 1% PROS when physisorbed on C<sub>8</sub>SH and C<sub>16</sub>SH SAM, respectively [15]. Thus, with a decrease in the ET rate an increase in the PROS formation is observed for PIM. In the case of PPSR, a decrease in PROS formation is observed with decrease in the ET rate from >10<sup>5</sup> s<sup>-1</sup> on EPG to ~10<sup>3</sup> s<sup>-1</sup> and 3–6 s<sup>-1</sup> in C<sub>8</sub>SH and C<sub>16</sub>SH SAM, respectively (Fig. 12). When physisorbed on C<sub>8</sub>SH SAM PPSR produces ~16 ± 0.5% PROS, while in C<sub>16</sub>SH it shows about 11 ± 1% PROS. Such decrease in PROS with decrease in ET flux has not been observed before *i.e.* this is an opposite trend compared to PIM or other reported O<sub>2</sub> reducing iron porphyrin complexes. This opposite trend in PROS production of PIM and PPSR



**Fig. 11.** (a) LSV data of the PPSR-yne catalyst (**31**) deposited on the EPG surface at multiple rotations in pH 7 buffer, using 100 mM KPF<sub>6</sub> as supporting electrolyte and Pt and Ag/AgCl as counter and reference electrode respectively (top). (Inset) CV of the PPSR-yne catalyst (**31**) at 2 V/s scan rate. (b) K-L plot of the PPSR-yne catalyst (**31**) (black bold line). The theoretical plots for the 4e<sup>-</sup> and 2e<sup>-</sup> processed are indicated by dotted and dashed lines (bottom). (c) LSV data of POR catalyst. (Inset) CV of the catalyst in N<sub>2</sub> atmosphere at 50 mV/s. (d) K-L plot of the catalyst in C (red bold line). The theoretical plots for the 4e<sup>-</sup> and 2e<sup>-</sup> processed are indicated by dashed blue and red lines, respectively



**Fig. 12.** Active site models of iron porphyrins without any distal substituents. The values of imidazole bound complex are obtained from references

suggests that these two complexes, differing in the axial ligation, reduce molecular O<sub>2</sub> in different mechanistic pathways.

To compare the role of ET rate in the selectivity of O<sub>2</sub> reduction of the PPSR-yne and POR complex, RRDE

experiments were performed. The presence of the terminal alkyne group on the PPSR-yne complex allows a covalent attachment of this complex to the surface. Thus the PPSR-yne complex was covalently attached to a mixed SAM containing 10% of azide terminated thiols where

the rate of electron transfer can be attenuated by varying chain length of the thiol used. Naturally such experiments could not be performed with the phenolate bound model which does not bear a terminal alkyne group and thus these experiments were performed by physisorbing this complex on C<sub>8</sub>SH and C<sub>16</sub>SH SAM akin to PIM and PPSR. The benzylic thiolate bound PPSR-yne complex show 13% and 22% PROS on C<sub>8</sub>SH ( $k_{ET} \sim 10^3 \text{ s}^{-1}$ ) and C<sub>16</sub>SH ( $k_{ET} \sim 3\text{--}6 \text{ s}^{-1}$ ) SAM, respectively (Fig. 12) [27]. This is in sharp contrast to the aliphatic thiolate bound PPSR complex which in fact shows *reduction* in PROS with *decrease* in ET rate. The POR complex shows very little effect of ET on PROS production as even on C<sub>16</sub>SH SAM surface the PROS are only 10%!

## CONCLUSION

The effect of axial ligand on the reactivity of iron porphyrin complex has been an interesting area of inorganic chemistry, inspired by the diverse reactivity's exhibited by heme cofactors with varying ligation, which has attracted synthetic chemistry and spectroscopists alike. Several previous groups have investigated potential effects of change in axial ligation on catalytic substrate oxidation using per-acids, peroxides, *etc.* (analogous to the peroxide shunt in cyt P450) [11, 74–77]. We have, over the last few years, investigated the effect of changes in axial ligation in ORR [15, 27]. ORR by definition included the O<sub>2</sub> activation process and hence helps investigate the effect of axial ligation on O<sub>2</sub> activation as well [50]. These differences in O<sub>2</sub> activation and reduction were rationalized with spectroscopic investigations of the GS properties of ferric porphyrin complexes and DFT calculations.

Geometry optimized DFT calculations reproduce the experimental results and trends and provide rationale, based on GS wavefunctions of PIM, POR and PSR, behind these observations [20]. Overall these calculations suggest that while imidazole acts mainly as a neutral  $\sigma$  donor, both phenolate and thiolate are anionic ligands with significant  $\sigma$  and anisotropic  $\pi$ -covalency associated with them. The thiolate ligand is found to be substantially more covalent than the imidazole and significantly more covalent than the anionic phenolate as well. Thus the residual electron density is greater in the phenolate than the thiolate in the complexes anionic ligands. The greater electron density on the phenolate oxygen and the shorter Fe–O bond (relative to a Fe–S bond) results in greater electrostatic contributions to Fe–O bonding relative to Fe–S bonding [19, 20]. Comparison of any spectroscopic, electrochemical and chemical properties of these complexes, thus, require due consideration of electrostatic and covalent contributions to them. Consider the fact that analogous to metal ligand bonding, one can envisage electrostatic and covalent contributions to the “push” effect. The spectroscopic data ( $\nu_8$  in rR) on PIM, POR and PPSR (or PPSR-yne) clearly show that the covalent donation PIM < POR < PSR *i.e.* the thiolate is

the strongest donor of the three [20]. Covalent donation from phenolate and thiolate result in stabilization of the LS GS in MeOH bound 6C POR and PSR, respectively, where the analogous MeOH bound PIM is HS. Similarly the lower potentials of both POR and PSR relative to PIM reflect the role of anionic ligands. Alternatively, the greater electrostatic contribution to bonding in the ferric phenolate complex (*i.e.* less covalent relative to thiolate) is readily presented in the lower Fe<sup>III</sup>/ $E^0$  in the phenolate complex relative to the thiolate bound complex in a non-polar solvent in spite of having a less covalent bond with the Fe in the phenolate.

The rate of ORR by the imidazole, thiolate and phenolate bound iron porphyrin complexes can be compared to each other. These complexes do not bear any distal super structure and only vary in their axial ligation allowing unambiguous comparison of the effect of the three axial ligands. Compared to a neutral ligand, imidazole, the  $k_{cat}$  is one order of magnitude higher in the phenolate bound complex and two orders of magnitude higher in the thiolate bound complex. If these results are viewed in the context of the “push effect” of these *trans* axial ligands on the mechanism of O<sub>2</sub> reduction, a general trend presents itself. The heterolytic O–O bond cleavage in a Fe<sup>III</sup>–OOH intermediate species, formed during O<sub>2</sub> reduction, is likely to be faster in PPSR and POR complexes bearing anionic thiolate or phenolate axial ligand relative to PIM bearing a neutral imidazole ligand, as the additional negative charge in POR it will increase the pK<sub>a</sub> of the bound <sup>•</sup>O<sub>2</sub>H. However the fact that the thiolate bound complex has a  $k_{cat}$  which is an order of magnitude higher than the phenolate bound complex clearly reflects a role of higher covalency of the Fe–S bond, reflected in the lower  $\nu_8$  in the rR data, in addition to the anionic nature of the thiolate axial ligand. These data helps quantify this “push effect” and clearly suggests that, of the three known ligands that bind heme in nature, the thiolate has the greatest push effect promoting enhancing the rate of O–O bond cleavage by 100 times relative to a neutral ligand and 10 times relative to an anionic less covalent phenolate ligand. It also elucidates that there are both electrostatic and covalent contributions to the “push” effect which needs to be considered when rationalizing the role of axial ligands.

## Acknowledgements

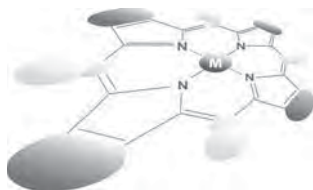
This work is funded by the Department of Science and Technology, India (Grant SB/S1/IC-25/2013). S.S. acknowledges IACS integrated Ph.D. section. P.K.D and S.C acknowledge CSIR SRF fellowship.

## REFERENCES

- ‡ Abbreviations: PSR: aliphatic thiolate; PPSR: bulky aliphatic thiolate; PPSR-yne: benzylic thiolate; PIM: imidazole model; POR: phenolate model.

1. Dawson JH. *Science*. 1988; **240**: 433–439.
2. Denisov IG, Makris TM, Sligar SG and Schlichting I. *Chem. Rev.* 2005; **105**: 2253–2278.
3. Newcomb M, Zhang R, Chandrasena REP, Halgrimson JA, Horner JH, Makris TM and Sligar SG. *J. Am. Chem. Soc.* 2006; **128**: 4580–4581.
4. Sligar SG. *Biochemistry* 1976; **15**: 5399–5406.
5. Averill BA. *Chem. Rev.* 1996; **96**: 2951–2964.
6. Brown WE, Sutcliffe JW and Pulsinelli PD. *Biochemistry* 1983; **22**: 2914–2923.
7. Gross Z, Nimri S, Barzilay CM and Simkhovich L. *J. Biol. Inorg. Chem.* 1997; **2**: 492–506.
8. Kerr EA, Yu NT, Bartnicki DE and Mizukami H. *J. Biol. Chem.* 1985; **260**: 8360–8365.
9. Collman JP, Gagne RR, Reed C, Halbert TR, Lang G and Robinson WT. *J. Am. Chem. Soc.* 1975; **97**: 1427–1439.
10. Green MT. *J. Am. Chem. Soc.* 1998; **120**: 10772–10773.
11. Meunier B, de Visser SP and Shaik S. *Chem. Rev.* 2004; **104**: 3947–3980.
12. Ogliaro FO, Cohen S, de Visser SP and Shaik S. *J. Am. Chem. Soc.* 2000; **122**: 12892–12893.
13. Rittle J and Green MT. *Science* 2010; **330**: 933–937.
14. Derat E and Shaik S. *J. Phys. Chem. B.* 2006; **110**: 10526–10533.
15. Chatterjee S, Sengupta K, Samanta S, Das PK and Dey A. *Inorg. Chem.* 2013; **52**: 9897–9907.
16. Collman JP. *Acc. Chem. Res.* 1977; **10**: 265–272.
17. Collman JP, Devaraj NK, Decreau RA, Yang Y, Yan YL, Ebina W, Eberspacher TA and Chidsey CED. *Science* 2007; **315**: 1565–1568.
18. Collman JP, Yang Y, Dey A, Decreau RA, Ghosh S, Ohta T and Solomon EI. *Proc. Natl. Acad. Sci.* 2008; **105**: 15660–15665.
19. Das PK, Chatterjee S, Samanta S and Dey A. *Inorg. Chem.* 2012; **51**: 10704–10714.
20. Das PK and Dey A. *Inorg. Chem.* 2013; **53**: 7361–7370.
21. Fujii H, Yoshimura T and Kamada H. *Inorg. Chem.* 1997; **36**: 6142–6143.
22. Halime Z, Kotani H, Li Y, Fukuzumi S and Karlin KD. *Proc. Natl. Acad. Sci.* 2011; **108**: 13990–13994.
23. Higuchi T, Uzu S and Hirobe M. *J. Am. Chem. Soc.* 1990; **112**: 7051–7053.
24. Kim E, Chufen EE, Kamaraj K and Karlin KD. *Chem. Rev.* 2004; **104**: 1077–1134.
25. Liu JG, Naruta Y and Tani F. *Angew. Chem. Int. Ed.* 2005; **44**: 1836–1840.
26. Matsu-ura M, Tani F, Nakayama S, Nakamura N and Naruta Y. *Angew. Chem. Int. Ed.* 2000; **39**: 1989–1991.
27. Samanta S, Das PK, Chatterjee S, Sengupta K, Mondal B and Dey A. *Inorg. Chem.* 2013; **52**: 12963–12971.
28. Samanta S, Mitra K, Sengupta K, Chatterjee S and Dey A. *Inorg. Chem.* 2013; **52**: 1443–1453.
29. Samanta S, Sengupta K, Mitra K, Bandyopadhyay S and Dey A. *Chem. Commun.* 2012; **48**: 7631–7633.
30. DiCarlo CM, Vitello LB and Erman JE. *J. Inorg. Biochem.* 2007; **101**: 603–613.
31. Stayton PS and Sligar SG. *Biochemistry* 1990; **29**: 7381–7386.
32. Deng TJ, Macdonald IDG, Simianu MC, Sykora M, Kincaid JR and Sligar SG. *J. Am. Chem. Soc.* 2000; **123**: 269–278.
33. Dey A, Jiang Y, Ortiz de Montellano P, Hodgson KO, Hedman B and Solomon EI. *J. Am. Chem. Soc.* 2009; **131**: 7869–7878.
34. Dey A, Okamura TA, Ueyama N, Hedman B, Hodgson KO and Solomon EI. *J. Am. Chem. Soc.* 2005; **127**: 12046–12053.
35. Suzuki N, Higuchi T, Urano Y, Kikuchi K, Uekusa H, Ohashi Y, Uchida T, Kitagawa T and Nagano T. *J. Am. Chem. Soc.* 1999; **121**: 11571–11572.
36. Das TK, Couture M, Ouellet Y, Guertin M and Rousseau DL. *Proc. Natl. Acad. Sci.* 2001; **98**: 479–484.
37. Tani F, Matsu-ura M, Ariyama K, Setoyama T, Shimada T, Kobayashi S, Hayashi T, Matsuo T, Hisaeda Y and Naruta Y. *Chem. Eur. J.* 2003; **9**: 862–870.
38. Walters MA, Spiro TG, Suslick KS and Collman JP. *J. Am. Chem. Soc.* 1980; **102**: 6857–6858.
39. Gewirth AA and Thorum MS. *Inorg. Chem.* 2010; **49**: 3557–3566.
40. Kahlow MA, Loehr TM, Zuberi TM and Gennis RB. *J. Am. Chem. Soc.* 1993; **115**: 5845.
41. Solomon EI, Chen P, Metz M, Lee SK and Palmer AE. *Angew. Chem., Int. Ed.* 2001; **40**: 4570–4590.
42. Tani F, Matsu-ura M, Nakayama S and Naruta Y. *Coord. Chem. Rev.* 2002; **226**: 219–226.
43. Verkhovskiy MI, Morgan JE and Wikstroem M. *Biochemistry* 1994; **33**: 3079–3086.
44. Babcock GT and Wikstrom M. *Nature* 1992; **356**: 301–309.
45. Sengupta K, Chatterjee S, Samanta S and Dey A. *Proc. Natl. Acad. Sci.* 2013; **110**: 8431–8436.
46. Sengupta K, Chatterjee S, Samanta S, Bandyopadhyay S and Dey A. *Inorg. Chem.* 2013; **52**: 2000–2014.
47. Collman JP, Gagne RR, Halbert TR, Marchon JC and Reed CA. *J. Am. Chem. Soc.* 1973; **95**: 7868–7870.
48. Collman JP, Brauman JI, Doxsee KM, Halbert TR, Bunnenberg E, Linde RE, LaMar GN, Del Gaudio J, Lang G and Spartalian K. *J. Am. Chem. Soc.* 1980; **102**: 4182–4192.
49. Kolb HC, Finn MG and Sharpless KB. *Angew. Chem. Int. Ed.* 2001; **40**: 2004–2021.
50. Das PK, Mitra K and Dey A. *Chem. Commun.* 2013; **50**: 5218–5220.
51. Walker FA. *Coord. Chem. Rev.* 1999; **185**: 471–534.
52. Jacob GS and Orme-Johnson WH. *Biochemistry* 1979; **18**: 2975–2980.

53. Burke JM, Kincaid JR, Peters S, Gagne RR, Collman JP and Spiro TG. *J. Am. Chem. Soc.* 1978; **100**: 6083–6088.
54. Taylor CPS. *Biochim. Biophys. Acta.* 1977; **491**: 137–148.
55. Champion PM, Stallard BR, Wagner GC and Gunsalus IC. *J. Am. Chem. Soc.* 1982; **104**: 5469–5472.
56. Chen Z, Ost TWB and Schelvis JPM. *Biochemistry* 2004; **43**: 1798–1808.
57. Deng TJ, Proniewicz LM, Kincaid JR, Yeom H, Macdonald IDG and Sligar SG. *Biochemistry* 1999; **38**: 13699–13706.
58. Wells AV, Li P, Champion PM, Martinis SA and Sligar SG. *Biochemistry* 1992; **31**: 4384–4393.
59. Nagai K, Kagimoto T, Hayashi A, Taketa F and Kitagawa T. *Biochemistry* 1983; **22**: 1305–1311.
60. Nagai M, Yoneyama Y and Kitagawa T. *Biochemistry* 1989; **28**: 2418–2422.
61. Sharma KD, Andersson LA, Loehr TM, Turner J and Goff HM. *J. Biol. Chem.* 1989; **264**: 12772–12779.
62. Fisher MT and Sligar SG. *J. Am. Chem. Soc.* 1985; **107**: 5018–5019.
63. Becke AD. *Phys. Rev. A* 1988; **38**: 3098–3100.
64. Becke AD. *J. Chem. Phys.* 1993; **98**: 5648–5652.
65. Perdew JP. *Phys. Rev. B* 1986; **33**: 8822–8824.
66. Paulat F and Lehnert N. *Inorg. Chem.* 2007; **46**: 1547–1549.
67. Bard AJ and Faulkner LR. *Electrochemical Methods*, J. Wiley: New York, 1980; 300.
68. McCrory CCL, Devadoss A, Ottenwaelder X, Lowe RD, Stack TDP and Chidsey CED. *J. Am. Chem. Soc.* 2011; **133**: 3696–3699.
69. Boulatov R, Collman JP, Shiryaeva IM and Sunderland CJ. *J. Am. Chem. Soc.* 2002; **124**: 11923–11935.
70. Collman JP, Decreau RA, Dey A and Yang Y. *Proc. Natl. Acad. Sci.* 2009; **106**: 4101–4105.
71. Daff SN, Chapman SK, Holt RA, Govindaraj S, Poulos TL and Munro AW. *Biochemistry* 1997; **36**: 13816–13823.
72. Whitehouse CJC, Bell SG and Wong LL. *Chem. Soc. Rev.* 2012; **41**: 1218–1260.
73. Devaraj NK, Decreau RA, Ebina W, Collman JP and Chidsey CED. *J. Phys. Chem. B.* 2006; **110**: 15955–15962.
74. de Visser SP and Tan LS. *J. Am. Chem. Soc.* 2008; **130**: 12961–12974.
75. Kumar D, Karamzadeh B, Sastry GN and de Visser SP. *J. Am. Chem. Soc.* 2010; **132**: 7656–7667.
76. Shaik S, Kumar D, de Visser SP, Altun A and Thiel W. *Chem. Rev.* 2005; **105**: 2279–2328.
77. Shaik S, Kumar D and de Visser SP. *J. Am. Chem. Soc.* 2008; **130**: 14016.



# Porphyrin-based photosensitizers and the corresponding multifunctional nanoplateforms for cancer-imaging and phototherapy

Avinash Srivatsan<sup>a</sup>, Joseph R. Missert<sup>b</sup>, Santosh K. Upadhyay<sup>c</sup>  
and Ravindra K. Pandey<sup>\*a,b,δ</sup>

<sup>a</sup>Department of Molecular Pharmacology and Cancer Therapeutics and <sup>b</sup>PDT Center, Cell Stress Biology, Roswell Park Cancer Institute, Buffalo, NY 14263, USA

<sup>c</sup>Department of Biotechnology, Kumaun University, Nainital, India

*Dedicated to Professor Shunichi Fukuzumi on the occasion of his retirement*

Received 12 December 2014

Accepted 13 January 2015

**ABSTRACT:** This review article briefly describes: (a) the advantages in developing multifunctional nanoparticles for cancer-imaging and therapy, (b) the advantages and limitations of most of the porphyrin-based compounds in fluorescence imaging and photodynamic therapy (PDT), (c) problems associated with current Food and Drug Administration (FDA) approved photosensitizers, (d) challenges in developing *in vivo* target-specific PDT agents, (e) development of porphyrin-based nuclear-imaging agents (PET, SPECT) with an option of PDT, (f) the importance of light dosimetry in PDT, (g) the role of whole body or local hyperthermia in enhancing tumor-uptake, tumor-imaging and phototherapy and finally, (h) the advantages of photosensitizer-gold nanocages (Ps-Au NC) in photoacoustic and PDT.

**KEYWORDS:** photodynamic therapy, nanoparticles, nanoplateforms, cancer-imaging, multimodality agents, theranostics, fluorescence, nuclear imaging, magnetic resonance imaging.

## INTRODUCTION

The idea of having a single agent that does “all” is the pinnacle of personalized medicine. An agent that allows for visualization of the problem while having the ability to treat the condition is always promising and advantageous. If the agent also has the property to help monitor the response of treatment, that helps with the analyzing the outcome of the treatment. Theranostic research is the area of science trying to integrate therapeutic applications with diagnostic imaging [1, 2], and it requires a strong interaction between various disciplines (Fig. 1). For selecting a particular cancer treatment modality, diagnostic agents play an extremely important role. Before initiating treatment of cancer, it is

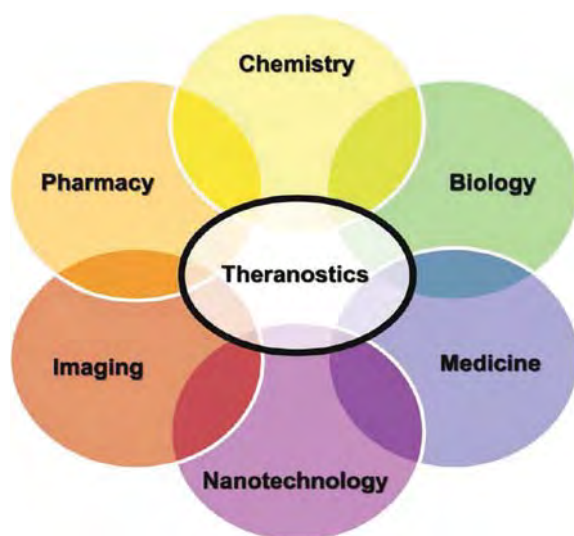
important to understand the location of the tumor, identify the type of cancer, its boundaries, and whether the disease is localized or has metastasized to other organs. Once, the nature of the disease is known, best available treatment options could be selected for controlling the spread of the disease.

The ability to deliver contrast or therapeutic agents selectively to tumors at effective concentrations is a key factor for the efficacy of cancer detection and therapy. In current cancer treatment modalities, the diagnosis and treatment are done separately. This leads to the problems of selectivity with respect to tumors and differences in the biodistribution of the agents within the body.

The theranostic agents can be comprised of chemotherapeutic drugs, radioactive compounds, and/or antibodies targeting the vasculature of the tumor or targeting key pathways required for the growth of the tumor. Gene therapy involving delivery of siRNA, plasmids, antisense oligonucleotides, ribozymes, DNazymes, viral vectors

<sup>δ</sup>SPP full member in good standing

\*Correspondence to: Ravindra K. Pandey, email: Ravindra.pandey@roswellpark.org, tel: +1 716-845-3203



**Fig. 1.** Various fields encompassing development of theranostics for cancer. *Methods* 2011; **55**: 193–195

delivering DNA and RNA to tumor cells are also currently under research for theranostic applications [2]. Nanoparticles such as gold nanorods and nanoshells (Aurolase<sup>®</sup>) are therapeutic in nature by themselves and can lead to tumor destruction by a photothermal effect [3]. This effect is seen wherein light activation of the nanoparticles leads to generation of heat which causes tumor ablation. A similar effect is also seen by use of magnetic nanoparticles as well. Das *et al.* have shown the use of magnetic nanoparticles loaded with a fluorescence dye (RITC) along with methotrexate and a folate moiety to target tumors overexpressing the folate receptor [4]. Imaging of tumors involves use of modalities that help understand the anatomical as well as physiological nature of tumors. These range from use of fluorescence probes for image guided surgical resection of tumors, various radionuclides for Positron Emission Tomography (PET) or Single Photon Emission Computed Tomography (SPECT). The other commonly used imaging modality is Magnetic Resonance Imaging (MRI) which provides high spatial resolution and functional information about soft tissues.

Theranostic agents are generally classified into two groups based of their mode of design. The first approach is the use of nanoparticles which can be functionalized with a variety of imaging and therapeutic moieties for use as theranostic particles [4, 5]. The properties offered by nanoparticles allow for their use as agents to carry both imaging as well as therapeutic drugs. The main advantages of using nanoparticles include their size (in 10–100 nm range), which delays their clearance from the body allowing for increased circulation time. Nanoparticles are capable of delivering good payload of material to the site of the tumor because they escape into the tumor microenvironment as a result of the leaky

vasculature within the tumor. The Enhanced Permeability and Retention (EPR) effect is the property by which nanoparticles such as liposomes; gold nanoparticles, *etc.* tend to accumulate more in the tumor tissues as compared to normal tissues. Tumor tissues have poor lymphatic drainage and this allows for retention of the nanoparticles post extravasation. Nanoparticles also have a high surface to volume ratio; this is advantageous as they can be loaded with large amount of drugs for delivery to the tumor. This allows for simultaneous loading of both diagnostic as well as imaging agents. Nanoparticles are easily customizable and allow for surface functionalization with targeting ligands for increased tumor specificity; can be surface coated with polymers such as polyethylene glycol (PEG) [5] or poly(lactic-co-glycolic acid) (PLGA) [6, 7] for increased circulation times. Nanoparticles also allow for efficient loading of imaging as well as therapeutic agents. It is possible to control the ratio of the imaging agent to the therapeutic agent using nanoparticle chemistry. It has been shown that it is possible to have a single nanoparticle formulation carrying high payload of the therapeutic drug and a lower dose of the imaging agent. Also, theranostic nanoparticles can be modulated to release the drug at site of tumor based on tumor microenvironment conditions, *e.g.* peptide linkages that can be cleaved by matrix metalloproteinases (MMP's) [8–10], which are normally abundant in a variety of tumors. Finally, nanoparticles can also help in delivery of drugs difficult to formulate within water-based solutions, by encapsulation or protective biopolymer coating [6].

In spite of all the advantages provided by nanoparticles, they are still lacking certain properties crucial for which their application in clinical use. The use of nanoparticles for development of theranostics has mainly focused on improving the sensitivity or increasing the image resolution. Macrophages and other phagocytes readily engulf most nanoparticles. This leads to accumulation within the liver, the spleen, and the lymphatic system. The long-term safety of nanoparticles and their clearance from the various organs is still not well-understood. There have been issues with the toxicity induced by nanoparticles after administration. Quantum dots, which are comprised of cadmium salts, might induce toxicity if released in serum after injection [11–14]. Another concern is that the shape and size of the nanoparticles can induce adverse effects on various types of the cells. Different types of nanoparticles have been shown to be cytotoxic to human cells, induce oxidative stress, or elicit an immune response. Lastly, there have been few nanoparticles including Abraxane [15] that have been approved by various health organizations for use in clinic or are under clinical trials (Table 1).

Another approach to develop theranostic agents involves synthesizing a single agent that offers both therapeutic as well as imaging capabilities. The number of single agents which can serve this purpose are few in the literature. Most of the chemotherapeutic agents are



**Table 1.** Examples of nanocarrier-based drugs on the market

Product	Company	Drug	Formulation	Application
Doxil	Sequus Pharmaceuticals	doxorubicin	Pegylated liposome	Matastatic ovarian cancer and Kaposi sarcoma in AIDS patients
Dauno-Xome	NeXstar Pharmaceutica	daunorubicin in citrate	liposome	Kaposi sarcoma in AIDS patients
Emend	Merck/Elan	aprepitant (MK 869)	proprietary Nanocrystal® formulation	Chemotherapy-related side effects (nausea and vomiting)
Abraxane	Abraxis Bioscience Astra Zeneca	Paclitaxel	albumin nanoparticles	Metastatic breast cancer
Myocet	Zeneus Pharma Sopherion Therapeutics	doxorubicin	liposome	Combinatorial therapy of breast cancer, ovarian cancer, and Kaposi sarcoma
Combindex	Adanced Magnetic Inc.	iron oxide	Dextran 10 coated iron oxide nanoparticles	Different tumor imaging
Oncaspar	Enzon	L-asparaginase	Polymer protein conjugate	Leukemia

Source: *Cancers* 2011; **3**: 4024–4045.

not good candidates for synthesis of theranostic agents as the amount of drug required is far higher than the imaging dose, and are not tumor-specific. Attaching tumor-targeted molecules to chemotherapeutic drugs alters their pharmacokinetic profiles with reduced tumor-specificity and long-term survival. Antibodies are a class of molecules which have shown promise as theranostic agents, but they are economically expensive. On the other hand, certain tumor-avid porphyrin-based photosensitizers have the ability to fluoresce when excited by light. This provides an opportunity for tumor imaging prior to or after the therapy. Porphyrin molecules also allow for attaching tumor targeting moieties at the peripheral position(s) to develop tumor specific theranostic agents.

### Photodynamic therapy: A brief history

Photosensitizers are a class of compounds which have been known in the literature for a long time and are being used for the treatment of various medical indications. The earliest record of use of light sensitive compounds comes from ancient texts of the Chinese, Romans and Greeks who used the dyes for treatment of various dermatologic conditions. In the early 1900's, when there was a lot of interest in light therapy, Finsen demonstrated the first example of phototherapy by using UV light to irradiate *lupus vulgaris*. Raab's research investigated the link between light dose and extent of treatment when using light reactive dyes (acridine orange) for destruction of protozoans such as paramecium [16]. He showed that with more the light given to the paramecium, more was the damage. The first example of use of light to treat cancer was seen in the work of Tappeiner and Jesionek [16]. They used a variety of fluorescent compounds such eosin, fluorescein and others for topical treatment of human skin cancers. Most of the compounds used for phototherapy were not successfully transferred to the clinic because of the high skin phototoxicity and low tumor specificity. A new class of photosensitizers derived from hematoporphyrin showed great promise for clinical photodynamic therapy. These compounds showed selectively for tumor tissues. Dr. Lipson and others showed that breast cancer patients responded well to treatment when injected with HpD, an oligomer of hematoporphyrin [17]. But, the mechanism of tumor destruction was not clear. A short time later, Weishaupt *et al.* [18, 19] showed that photodynamic effect was due to the destruction of tumor cells by singlet oxygen, which is generated as a result of photochemical reaction. When light is absorbed by the photosensitizer, it goes to a excited state, which converts the molecular oxygen in proximate tissue to singlet oxygen, a highly reactive species responsible for the cytotoxic effect. Dougherty's initial work at RPCI, Buffalo, NY in early 1980's on a derivative of HpD lead to the development of Photofrin® [20–26]. Photofrin® was eventually approved by the FDA for the treatment of various types of cancers such

as esophageal, certain skin cancers, head/neck cancer and early to late stage lung cancers. Photofrin® is often classified as the first generation photosensitizer. However, Photofrin suffers with some limitations; *e.g.* long-term skin phototoxicity, relatively limited tumor specificity [27, 28] and its inability to treat large and deeply rooted tumors.

It is also important to understand that photodynamic therapy is still not considered a mainstream form of cancer therapy. Most clinicians still consider PDT to be an adjuvant to radiation and chemotherapy, however, the development of new photosensitizers with improved properties could allow for its acceptance by more clinicians and pharmaceutical companies.

### Basics of photodynamic therapy

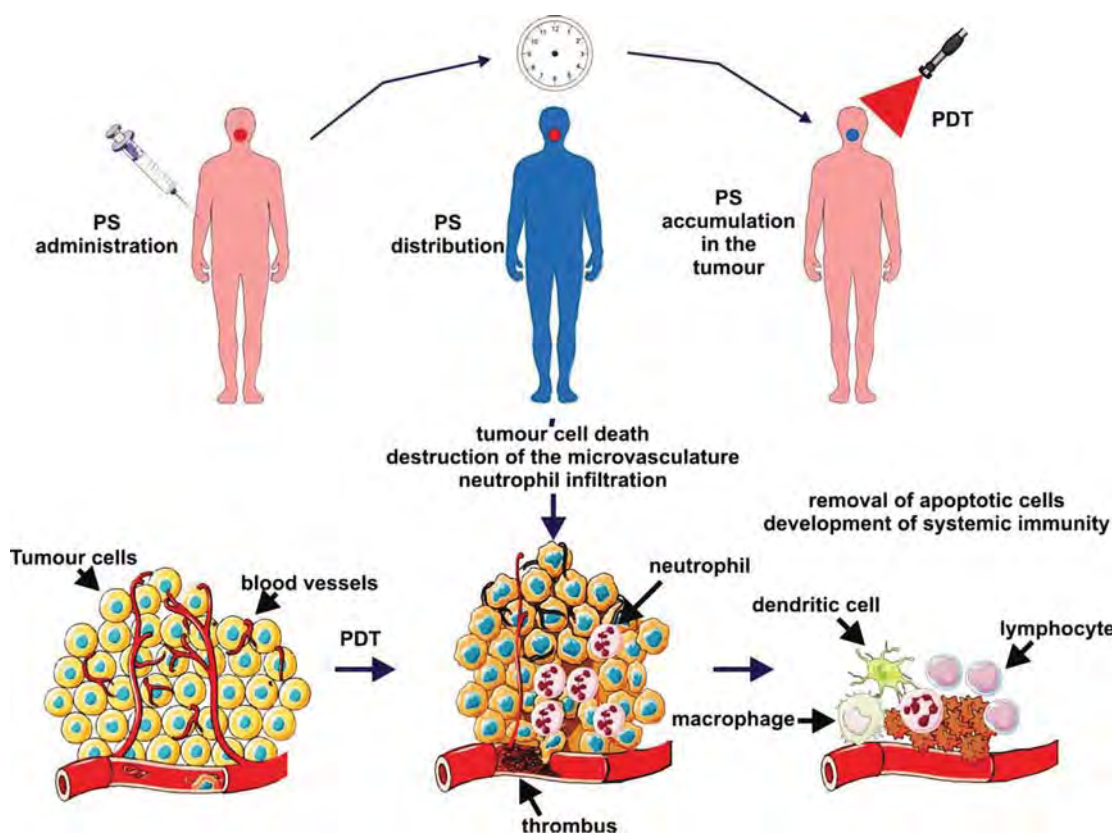
PDT is a 2-stage procedure (Fig. 2). It consists of administering the photosensitizer formulation by intravenous (i.v.) or intraperitoneal (i.p.) injection and waiting for a certain period of time to obtain the maximum uptake of the photosensitizer in tumor with a significant difference in accumulation between the normal and malignant tissue [29]. The tumors are then exposed with local light treatment, which certainly limits systemic toxicities. However, this also prevents the treatment of metastatic lesions, which are the most frequent cause of death in cancer patients. Therefore, efforts are currently underway to investigate the combination of PDT with chemotherapy, radiation, surgery and other cancer treatment modalities. For example, in treating glioblastoma, surgery in combination with PDT has provided long-term survival to patients with improved quality of life. This approach is also being used in treating bulky tumors.

Mechanistic studies on PDT have suggested that the vascular damage combined with the necrotic cells present at the tumor site leads to inflammation activating the immune system. This leads to development of anti-tumor immunity both systemic as well as local. Recent findings show that certain PDT induced apoptotic cell death mechanisms are highly immunogenic and capable of driving antitumor immunity as well.

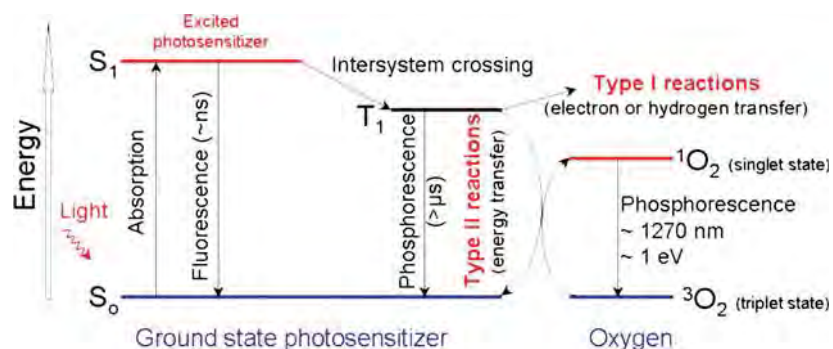
The three major components of PDT are: (i) a photosensitizer (drug), (ii) appropriate wavelength of light and (iii) molecular oxygen ( $^3\text{O}_2$ ). Current research is focused to improve PDT efficacy by optimizing the treatment parameters which could make the best use of these key components.

### Singlet oxygen

Singlet oxygen is the main mediator of tumor cell killing and subsequent effects following the photochemical reaction. The photochemical reaction can be explained by using Jablonski diagram (Fig. 3), which links all the components involved in PDT. Briefly, following the absorption of light, sensitizer is transformed



**Fig. 2.** The Principles of Photodynamic Therapy (PDT). A photosensitizer (PS) is administered systemically or topically. After a period of systemic PS distribution it selectively accumulates in the tumor. Irradiation activates the PS and in the presence of molecular oxygen triggers a photochemical reaction that culminates in the production of singlet oxygen ( $^1O_2$ ). Irreparable damage to cellular macromolecules leads to tumor cell death *via* an apoptotic, necrotic, or autophagic mechanism, accompanied by induction of an acute local inflammatory reaction that participates in the removal of dead cells, restoration of normal tissue homeostasis, and, sometimes, in the development of systemic immunity. *Source: CA Cancer J. Clin.* 2011; **61**: 250–281



**Fig. 3.** Simplified Jablonski diagram. *Source: CA Cancer J. Clin.* 2011; **61**: 250–281.

from its ground singlet state to an electronically excited triplet state *via* a short lived excited singlet state. This triplet state can also readily decay back to ground state through phosphorescence. Alternatively, it can transfer its energy to molecular oxygen ( $^3O_2$ ), thereby generating singlet oxygen ( $^1O_2$ ) [30]. This reaction is called a Type II reaction (Fig. 3). The excited PS in the triplet state can also transfer the energy to any organic molecule

in the vicinity (Type I reaction). This leads to transfer of hydrogen radical or an electron to generate toxic ions such as superoxide radical or hydrogen peroxide which can undergo spontaneous reduction into hydroxyl ion ( $OH^-$ ). It is presumed that the Type II reaction is most predominant of the photochemical reaction [31]. But under hypoxic conditions, it is presumed that there would be more of a Type I type of reaction.

Another phenomenon which occurs during PDT is the destruction of the photosensitizer by the singlet oxygen named as photobleaching [32–35]. The lifetime of  $^1\text{O}_2$  is very short (approximately 10–320 nanoseconds, depending on the environment), limiting its diffusion to only approximately 10 nm in cells [36, 37]. Thus, the destruction of cellular organelles generally happens very close to photosensitizer and is determined by its intracellular localization pattern [38].

A large number of laboratories have focused their attention in determining a correlation (if any) between the photosensitizers site(s) of localization and long-term PDT efficacy. Mitochondria have been proposed as a major subcellular target of the photodynamic effect, although other reported target organelles include plasma membranes, lysosomes and nuclei. It was reported that photodynamic treatment can also result, directly or indirectly, in damage to DNA. However, there is evidence that such damage may not necessarily be lethal to tumor cells. Vascular shutdown has been shown to be a major contributor for PDT efficacy. Other tumor-killing mechanisms induced by PDT as proposed by various research group include direct cell kill and apoptosis [29].

### Light and light dosimetry

Light is an essential component of PDT, and required for activation of the photosensitizer. The wavelength of light used for PDT is usually the longest wavelength in the absorption spectrum of the photosensitizer. Wavelengths of most commonly used photosensitizers range from 600–800 nm to offer adequate light penetration into tissue. It is also important to note that certain tumors such as melanomas are highly pigmented and absorb most of the light which limits the use of PDT for such indications [39].

It is well-established that light at longer wavelength region (700–800 nm) penetrates deeper in tumor-tissue. Therefore, in recent years the emphasis in designing photosensitizers has been focused on long wavelength tetrapyrrolic compounds related to chlorins, bacteriochlorins, phthalocyanines and extended porphyrins (41).

The most frequently light sources for PDT are lasers. They produce highly coherent monochromatic light that can be focused, passed down an optical fiber and directly delivered to the target site through a specially designed illuminator tip. Recently, there has been a lot of interest in light emitting diodes for clinical use as they are readily available and relatively economical. They are easily automated, can be calibrated before and during PDT and have long shelf life. They can be designed to deliver light within a very narrow spectral band and with high fluence rates. Also, recent advances in the field have allowed for attachment of cylindrical or spherical diffusers so as to adjust the power of light being delivered through the fiber. Fibers are also easier to attach to endoscopes used routinely in gastroenterology and could help in detection and subsequent treatment of colon polyps and bile duct tumors.

Light dosimetry is another important factor that makes a remarkable difference in PDT treatment efficacy. It includes two parameters: light fluence and fluence rate. The light fluence is the total energy of exposed light across a sectional area of irradiated spot (energy per unit area exposed to light,  $\text{J}/\text{cm}^2$ ). The fluence rate is the radiant energy incident per second across a sectional area of irradiated spot (power per unit area of light,  $\text{W}/\text{m}^2$ ,  $1 \text{ W} = 1 \text{ J/s}$ ). To give the same fluence (dose) of light, the lower the fluence rate used, the longer exposure time is required. Clinically, high fluence rates are usually chosen to reduce treatment time. However it was reported that high fluence rate may not be appropriate for eliciting the optimal PDT effect. The current standard procedures for PDT dosing can be found in the American Association of Physicists in Medicine report 88 [42]. The overall goal of the PDT dosimetry is to reach the threshold level so as to initiate tumor cell death. The light fluence rate used during the treatment determines the rate of oxygen consumption in tumors. High fluence rates would excite more photosensitizing molecules simultaneously, thereby consume a significant part of available oxygen. It is possible that in such cases single treatment might not be efficient enough as reported by Wilson *et al.* [42]. When fluence rates are high enough, depletion of oxygen can occur to such an extent that it results in a reduced photodynamic effect since there is not an effective production of the cytotoxic species. Low fluence rates might be better suited to achieve more tumor kill as the treatment is prolonged and so the tumor is exposed to more singlet oxygen, especially in hypoxic tumors. Lower fluence rates also help in damaging the vasculature supplying oxygen and nutrients to the tumor. New research in PDT dosimetry provides support for fractionated and metronomic PDT [43]. This involves irradiating the tumor for periods of time at a low fluence rate and stopping in between to allow the tumor to recover and be re-oxygenated. This also translated to better treatment response in the clinic. In cases of actinic keratoses, fractionated PDT with ALA-PDT has shown good clinical response [44–47].

Studies are underway in several laboratories to develop oxygen diffusion models in which lower fluence rates generate singlet oxygen more efficiently so that the tumor is exposed to more singlet oxygen over longer periods of time. Overall, it is critical to understand the kinetics of oxygenation in response to PDT treatment and light dosimetry to better develop optimized PDT protocols. It is also important to understand the role that tissue oxygenation and light dosimetry play in photobleaching of photosensitizers; and these are currently active fields of research in PDT.

### Photosensitizers

Photosensitizers are the most important component of PDT as they are the drugs required for PDT to take

place. While photodynamic therapy has been studied for many years, it is still being optimized. Most of the photosensitizers used have tetrapyrrole structures. An ideal photosensitizer should have the following properties.

1. It should have significant singlet oxygen producing ability, a key component for the destruction of tumor cells [48, 49].
2. Unlike Photofrin and Foscan, it should have limited skin phototoxicity.
3. Its longest wavelength should be in the range of 650–800 nm. Porphyrin based photosensitizer have a strong absorption band around 400 nm called the “Soret” band, and a satellite absorption band (Q-band, the longest wavelength peak between 600 and 800 nm). Only the Q-band is useful for PDT treatment with regards to light penetration in tissue.
4. Pandey *et al.*, in a series of pyropheoporphide, purpurinimides and bacterio purpurinimides have shown that overall lipophilicity makes a significant impact in the ability of a photosensitizer to accumulate within the tumor, which correlates to PDT efficacy [50].
5. Unlike Photofrin, which is a chemically complex mixture, the photosensitizer should be chemically pure, which would help to determine the precise mechanism, PK/PD and toxicity profiles of the molecule.
6. A good photosensitizer should also be easy to synthesize and the starting material should be readily available. This will make PDT more economical.
7. Lastly, but very importantly, an effective photosensitizer should show high tumor selectivity.

To date, many photosensitizers have been developed (Table 2) and investigated but none have demonstrated all of these ‘ideal’ properties. Future development of photosensitizers that possess all or a majority of these characteristics will have significant impact on the efficacy of PDT.

There are two classes of photosensitizers being used for treatment of cancer. The first class incorporates endogenous photosensitizers and includes those which are present or formed inside the body. These include coproporphyrin, uroporphyrin and protoporphyrin IX, a precursor for heme biosynthesis and are derived from  $\delta$ -aminolevulinic acid (ALA). The second category of PDT agents belongs to exogenous photosensitizers including the hemetoporphyrin derivative (HpD) and its purified version Photofrin®. The limitations of these agents as discussed before prompted researchers to develop more effective second generation PDT agents, with reduced skin photosensitivity and longer wavelength absorption [51]. These sensitizers were synthesized from various tetrapyrrole ring structures, *e.g.* porphyrins, chlorins, phthalocyanines, porphycenes, pheophorbides, purpurins and bacteriochlorins & bacteriopurpurins [52,

53]. The inherent highly conjugation ring structure of these molecules allows for absorption of light in the visible and red regions of the spectrum.

The exogenous photosensitizers used in a number of studies by Roswell Park group are derived from chlorophyll-a and bacteriochlorophyll-a. Among the chlorophyll-a analogs, the 2-[1-hexyloxyethyl]-2-devinyl pyropheophorbide-*a* (Photochlor or HPPH) [54, 55] is currently undergoing Phase II human clinical trials of head and neck cancer [56]. HPPH shows a slow clearance from the plasma [57], and when this photosensitizer was administered at clinically relevant doses, it was found to have a reduced period of skin sensitivity (five to six days) compared to Photofrin which shows skin phototoxicity for about six to eight weeks following administration [28]. HPPH is superior to Photofrin in that the absorbance maximum is around 660–665 nm, allowing for deeper tissue penetration of light [58]. In contrast to many porphyrins and chlorins (one of the pyrrole ring of the tetrapyrrolic system is reduced) analogs, HPPH shows two distinct fluorescence peaks (at 675 nm and 710 nm). Thus it presents an opportunity for being used as a fluorescence imaging agent at near infrared region (excitation at 665 nm and emission at 710 nm).

One of the second generation photosensitizers, Verteporfin (QLT Photo Therapeutics, Ciba Vision), causes less skin photosensitivity than porfimer sodium (Photofrin). It is approved for treatment of age related macular degeneration (AMD) worldwide [59, 60] and is finding use clinically for treatment of other indications such as antibacterial PDT. It localizes in tumor vasculature very quickly after *i.v.* injection, and accumulates in tumor vessels 10–15 min post-injection. It is currently being explored for the treatment of a variety of other tumors such as pancreatic, prostate, ovarian cancers *etc.* [61–63]. It is proposed that Verteporfin might be effective for treatment of highly vascularized tumors because of its affinity for tumor vasculature.

de Visscher *et al.* analyzed the clinical trials data conducted with Foscan (*m*-THPC) [64–66]. It showed good response for treatment of actinic keratosis and Bowen’s disease. It was also shown that Barrett’s esophagus, which is a precursor for developing adenocarcinoma could be effectively controlled by use of *m*THPC-PDT. In fact it worked almost 40–50 fold better than ALA or Photofrin when used to treat high grade dysplasia or carcinoma. It cleared almost 100% of the early stage lesions. Recent work also showed that Foscan was effective in combination with surgery or chemotherapy for treatment of malignant mesothelioma [67, 68].

SnEt2 (Purlytin) is another sensitizer which was found to be very promising clinically as PDT agent but was reported to be unstable *in vivo*. The resulting metabolite after the breakdown was found to be toxic. Radachlorin is a mixture of multiple chlorins and has limited application. Not much clinical data are available on other

**Table 2.** Current photosensitizers, their approval status and cancer indications [29]

Photosensitizer	Structure	Wavelength, nm	Approval	Clinical trials	Cancer types
Porfimer sodium (Photofrin) (HPD)	Porphyrin	630	Worldwide		Lung, esophagus, bile duct, bladder, brain, ovarian
ALA	Porphyrin precursor	635	Worldwide		Skin, bladder, brain, esophagus
ALA esters	Porphyrin precursor	635	Europe		Skin, Bladder
Verteporfin	Chlorin	690	Worldwide (AMD)		Ophthalmic, pancreatic, skin
Temoporfin (Foscan) (mTHPC)	Chlorin	652	Europe	United States	Head and neck, lung, brain, skin, bile duct
HPPH	Chlorin	665		United States	Lung, Esophageal, head & neck
SnE42 (Purlytin)	Chlorin	660		United States	Skin, breast
Talaporfin (LS11, MACE, NPe6)	Chlorin	660		United States	Liver, colon, brain
Ce6-PVP (Fotolon), Ce6 derivatives (Radachlorin, Photodithazine)	Chlorin	660		Belarus, Russia	Nasopharyngeal, sarcoma, brain
Silicon phthalocyanine (Pc4)	Phthalocyanine	675		United States	Cutaneous, T-cell lymphoma
Padoporfin (TOOKAD)	Bacteriochlorin	762		United States	Prostate
Motexafin lutetium (Lutex)	Texaphyrin	732		United States	Breast

Source: *CA Cancer J. Clin* 2011; **61**: 250–281.

photosensitizers listed in Table 1 except for TOOKAD, a Pd-bacteriochlorin-based photosensitizer, which exhibits 100% singlet oxygen generation with limited fluorescence property. It has an extremely fast clearance from the body ranging from 2–3 h following injections, and shows low skin photosensitivity (69). It is currently being investigated for treatment of prostate adenocarcinoma and other indications. Despite its high singlet oxygen producing ability, TOOKAD does not retain in tumor for a long time and needs simultaneous perfusion and light treatment. A short treatment window associated with TOOKAD limits its utility in clinical PDT. A list of the photosensitizers approved by the FDA or are at various stages of clinical trials are listed in Table 2.

### Tumor targeting and photodynamic therapy

In spite of all the advances in the development of 2nd generation photosensitizers for improving the singlet oxygen yield and the light absorption of the PS at the near infrared region of the spectrum, there are still limitations to the use of PS for conventional treatment of cancers. One of the main problems has been the nonspecific localization of PS which often leads to incomplete treatment outcomes and unintended toxicity to normal tissues following exposure to light irradiation during PDT.

Numerous attempts have been made to improve the specificity of the photosensitizers. Structure activity relationship studies have focused on altering the hydrophobicity or lipophilicity of the newer photosensitizers so as to increase their uptake within the tumors [50]. There are several published studies that have used various types of nanoparticles to improve the delivery of desired agent(s) to tumor site. These include but are not limited to polyacrylamide nanoparticles [70] silica based nanoparticles [71], gold nanoparticles [72] and liposomal formulations, *etc.* [73]. The nanoparticles, in general are useful in delivering the highly hydrophobic porphyrin-based agents to tumors, but the long-term tumor response (cure) outcome has not improved significantly over the free drug formulations. Therefore, a number of target-specific strategies for PDT have been developed to improve PS specificity for diseased tissue. These include conjugation of photosensitizers or nanoparticles containing the PDT agents to a variety of compounds ranging from antibodies targeting overexpressed reporters on the tumor cell surface, ligands binding cell surface proteins and carbohydrate moieties targeting various transporters. DNA based oligonucleotides have also been used for the conjugation with photosensitizers for development of target sensitive photosensitizers. Low density lipoprotein has been conjugated to various photosensitizers to target LDL receptors which are in abundance in certain tumor types [74].


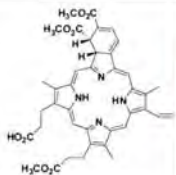
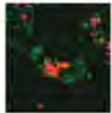

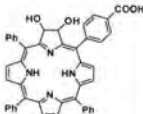
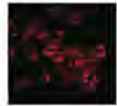

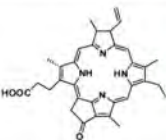
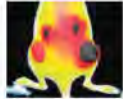

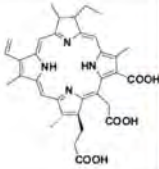
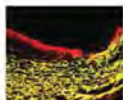



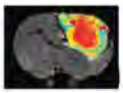
In recent years, attempts are underway to improve upon the limitations of the 2nd generation PS which

mainly involves the tumor specificity and PDT efficacy of the PS (Table 3). The goal of the using targeting agents has been to increase the uptake of the drug within the tumor region relative to the normal tissues. For designing a tumor-specific agent a lot of factors play key roles and should be considered. First and foremost is that the agent should have desired photophysical properties, and the tumor-targeting moiety should show higher tumor-specificity. The attachment of a targeting agent should not increase the aggregation of the photosensitizer and the *in vivo* activity should be maintained. Such a system is often difficult to develop because of tumor heterogeneity, which is characterized by uncontrolled proliferative growth and the unwanted spread of aberrant cells from their site of origin. Such a vast diversity in tumor environment presents a tremendous challenge in development target-specific agents.

One of the first agents to be used for developing a targeted photosensitizer involved the use of antibodies [69]. This approach consists of linking photosensitizer with monoclonal antibodies (MAb) against specific antigens of tumor cells. A number of tumor specific markers have been identified on the surface of the cancer cells and MAbs are available to target many of them. It is also thought internalizing MAbs can be more useful unlike non-internalizing Abs. A study showed that the hydrophilic PS TrisMPyP-Phico(2)H when conjugated to the internalizing antibodies cMAb U36 or mMAb 425, showed good PDT efficacy in A431 cells unlike free drug alone or when conjugated to non-internalizing Ab [75–77]. Hasan *et al.* [78] have developed monoclonal Ab targeting the overexpressed EGFR (Epidermal Growth Factor receptor), which is normally highly expressed in a variety of cancers such as pancreatic, head and neck, and other oral cancers. Conjugation of EGFR targeting MAb to chlorin e6 or Visudyne (BpD) improved PDT efficacy in EGFR overexpressing A431 cell line and OVCAR-5 cell lines [78]. Kobayashi *et al.* used Trastuzumab targeting the HER-2 receptor in combination with hydrophilic phthalocyanine based photosensitizer and achieved excellent selectivity and high PDT efficacy as compared to free phthalocyanine [79].

Certain carbohydrates have long been a focus of research in developing agents to target cancers as almost all tumors require a high amount of energy, more so in the absence of oxygen, sugars can be metabolized through non-tricarboxylic acid (TCA) cycle to generate ATP for growing tumor cells. Sugars such as glucose, galactose, lactose and fructose have been used for development of targeted agents. Fluorodeoxyglucose labeled with <sup>18</sup>Fluorine is used universally for Positron Emission Tomography (PET) for early tumor detection. With the simple chemistry available for conjugation of sugar moieties to either chemotherapeutic drugs or imaging compounds, it is possible to develop targeted photosensitizers conjugated with sugar moieties [80–82].

**Table 3.** Disease-targeted constructs for PFD and PDT, showing the targeting moiety, imaging agent, and biological application

Targeting agent	Imaging agent	Application
<b>A</b> Antibody 	BPD 	 Subcellular localization of BPD in human ovarian cancer cells <i>in vitro</i> <sup>139</sup>
<b>B</b> Peptide 	TPC 	 Peptide-mediated delivery of TPC to human breast carcinoma cells <i>in vitro</i> <sup>142</sup>
<b>C</b> Small Molecule 	Pyro 	 Folate receptor-targeted delivery of Pyro in a subcutaneous murine model for human epidermoid carcinoma <sup>143</sup>
<b>D</b> Antibody 	Ce6 	 PFD of aortic plaques <i>ex vivo</i> with an antibody-Ce6 conjugate in a rabbit model <sup>146</sup>
<b>E</b> Antibody 	Alexa Fluor 680	 Real-time post-PDT imaging of secreted VEGF using an antibody-fluorophore conjugate in a subcutaneous murine model for prostate cancer <sup>147</sup>
<b>F</b> Peptide 	Alexa Fluor 594 Iron oxide	 Peptide-targeted nanoparticle for PFD, PDT, and MRI in an orthopic rat glioma model <sup>24</sup>

Source: *Chem. Rev.* 2010; **110**: 2795–2838.

### Multi-modality imaging

Imaging can play an important role at every stage of PDT, from disease detection, treatment planning (including dosimetry), to real-time monitoring of treatment and its outcome assessment. A theranostic agent could be a single compound that inherently has both imaging and treatment capability. Or it could be a single compound where a photosensitizer is synthetically conjugated to an imaging agent. Finally, if a nanoparticle approach is used, the imaging and therapeutic components could be loaded individually onto a single nanoparticle platform or alternatively, the conjugate imaging-therapy agent could be loaded onto the platform. The best imaging modality would provide both anatomical as well as functional information.

Table 4 lists the advantages and disadvantages of various techniques.

Imaging modalities include a variety of techniques using a number of different characteristics ranging from anatomical, physiological, molecular properties of tumors. Imaging of tumors is achieved using either techniques which involve radioactive compounds which generate a signal on a screen (Computerized Tomography, Positron Emission Tomography or SPECT) or by use of non-radioactive materials which might improve contrast of tumors (Magnetic Resonance Imaging (MRI)), fluorescence signal upon activation and acoustic signal (ultrasound and photoacoustic). More recently, imaging modalities have been combined with each other to get the maximum information about the tumor so as to decide the best course of action.



**Table 4.** Advantages and disadvantages of imaging techniques used with molecularly targeted or non-targeted contrast agents

Technique	Advantages	Disadvantages
Computed tomography	<ul style="list-style-type: none"> <li>— Unlimited depth penetration</li> <li>— High spatial resolution</li> <li>— Whole-body imaging possible</li> <li>— Short acquisition time (minutes)</li> <li>— Moderately expensive</li> <li>— Anatomical imaging</li> </ul>	<ul style="list-style-type: none"> <li>— Radiation exposure</li> <li>— Poor soft-tissue contrast</li> <li>— Probably not used for molecular imaging; currently only anatomical and functional imaging</li> </ul>
Positron emission tomography	<ul style="list-style-type: none"> <li>— Unlimited depth penetration</li> <li>— Whole-body imaging possible</li> <li>— Quantitative molecular imaging</li> <li>— Can be combined with CT or MRI for anatomical information</li> </ul>	<ul style="list-style-type: none"> <li>— Radiation exposure</li> <li>— Expensive</li> <li>— Low spatial resolution (1–2 mm; 4–8 mm<sup>3</sup>)</li> <li>— Long acquisition time (min to h)</li> </ul>
Single photon-emission computed tomography	<ul style="list-style-type: none"> <li>— Unlimited depth penetration</li> <li>— Whole-body imaging possible</li> <li>— Quantitative molecular imaging</li> <li>— Theranostic: can combine imaging and radiotherapy</li> <li>— Can be combined with CT for anatomical information</li> </ul>	<ul style="list-style-type: none"> <li>— Radiation exposure</li> <li>— Low spatial resolution (0.3–1 mm; 12–15 mm<sup>3</sup>)</li> <li>— Long acquisition time</li> </ul>
Magnetic resonance imaging	<ul style="list-style-type: none"> <li>— Unlimited depth penetration</li> <li>— Whole-body imaging possible</li> <li>— No ionizing irradiation</li> <li>— High spatial resolution</li> </ul>	<ul style="list-style-type: none"> <li>— Expensive</li> <li>— Long acquisition time (min-hours)</li> <li>— Limited sensitivity for detection of molecular contrast agents</li> </ul>

(Continued)

Table 4. (Continued)

Technique	Advantages	Disadvantages
Magnetic resonance spectroscopy	<ul style="list-style-type: none"> <li>— Whole-body imaging possible</li> <li>— No ionizing irradiation</li> </ul>	<ul style="list-style-type: none"> <li>— Expensive</li> <li>— Long acquisition time (min-hours)</li> <li>— Low sensitivity</li> </ul>
Ultrasound	<ul style="list-style-type: none"> <li>— No ionizing irradiation</li> <li>— Real-time imaging/short acquisition time (min)</li> <li>— High spatial resolution</li> <li>— Can be applied externally or internally (endoscopy)</li> <li>— Inexpensive</li> <li>— Highly sensitive</li> </ul>	<ul style="list-style-type: none"> <li>— Whole-body imaging not possible</li> <li>— Contrast agents currently limited to vasculature</li> <li>— Operator dependency</li> </ul>
Optical	<ul style="list-style-type: none"> <li>— No ionizing irradiation</li> <li>— Real-time imaging/short acquisition time (sec-min)</li> <li>— Relatively high spatial resolution</li> <li>— Can be applied externally or internally (endoscopy)</li> <li>— Inexpensive</li> <li>— Highly quantitative and sensitive</li> <li>— Multiplexing</li> </ul>	<ul style="list-style-type: none"> <li>— Limited depth penetration (<math>\leq 1</math> cm)</li> <li>— Whole-body imaging not possible</li> </ul>

Source: *Clinical Radiology* 2010; **65**: 500–516.

Based on tumor type, tumor characteristics, location of the tumor stage and grade of tumor, clinicians can design the best treatment course for the patient so as to get the best outcome possible. Imaging is also helpful in monitoring the efficacy of treatment to see if there is tumor shrinkage and during treatment if the properties of the tumor change, a clinician can then reevaluate the treatment paradigm for that particular patient. Also once the treatment is complete, monitoring the patient(s) for long-term basis is also important to assess the treatment modality and change if necessary.

The Roswell Park group has also explored the utility of tumor-avid photosensitizers as vehicles to deliver the desired imaging agents to tumor. For example, conjugation of HPPH with Gadolinium-DTPA moieties [83, 84] or cyanine dye [85] or certain radionuclides [86] has created certain novel multifunctional agents for MR/fluorescence and PET/fluorescence imaging with an option of PDT. Some of the conjugates are currently in advanced stages of preclinical trials.

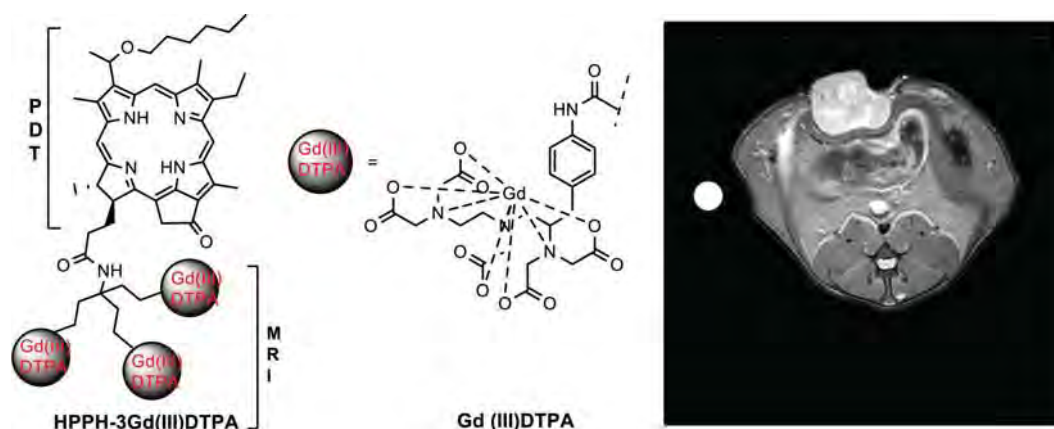
### Magnetic Resonance Imaging (MRI)

Imaging systems have already been an integral part in screening, diagnosis, and staging of many cancers [12]. Among them, Magnetic Resonance Imaging (MRI) has been a popular tool in tumor detection because of its high depth of penetration, spatial resolution and high soft tissue contrast. MRI uses contrast enhancing agents such as Gadolinium ( $Gd^{3+}$ ) based agents [87, 88]. But recent work has found use for nanoparticles such as super paramagnetic iron oxide nanoparticles (SPIO) and regular iron oxide nanoparticles for improving tumor contrast [4, 89]. The advantage of using such nanoparticles is that these allow for delivery of other agents such as chemotherapeutic or other imaging agents. Photosensitizers have also helped in the delivery

of MRI agents. Porphyrin based photosensitizers have been found to be excellent candidates for delivery of MRI contrast agents to tumors. The tumor avid nature of the photosensitizers helps to take the contrast agent to the tumor site. FDA approved MRI contrast agents such as Magnevist, Omniscan and Prohance have a very short plasma half-life ranging from 10–15 min post injection. These agents are not tumor specific and cannot be directed to small tumors or foci in the lymph nodes. Attachment to porphyrins can slow down the clearance of these contrast agents from the body or the tumor. Attaching contrast agents to a tumor targeting vehicle to improve contrast has recently been demonstrated by Pandey *et al.* by conjugating a tumor avid photosensitizer (3-devinyl-3-[1-(hexyloxy)ethyl]pyropheophorbide *a* (HPPH)) to a MRI contrast agent (Gd(III)-aminobenzyl-diethylenetriaminepentaacetic acid (DTPA)) [83, 84]. This agent showed good therapeutic benefit as a photosensitizer as well as an excellent MRI contrast agent, providing a better contrast than Magnevist at 10 times lower concentration (Fig. 4). The histopathology report confirmed that the histological structure of every organ was preserved, and no sign of toxicological lesions were seen at variable doses, even at 2.5-fold of the imaging dose.

### Computerized Tomography (CT)

Computerized Tomography (CT) is another imaging method which has found to be very popular in the clinic. It is used primarily for screening, monitoring and detection of tumors in the clinic. CT is predominantly done using iodine based radionuclides. The main disadvantage with CT is that it uses X-ray for generation of contrast which is risky for patients as there is fear of generation of tumors from prolonged exposure to such type of radiation. But recent work in the field with low dose CT has reduced the risk of secondary tumors and at the same time helped improve early detection of tumors as well [90].



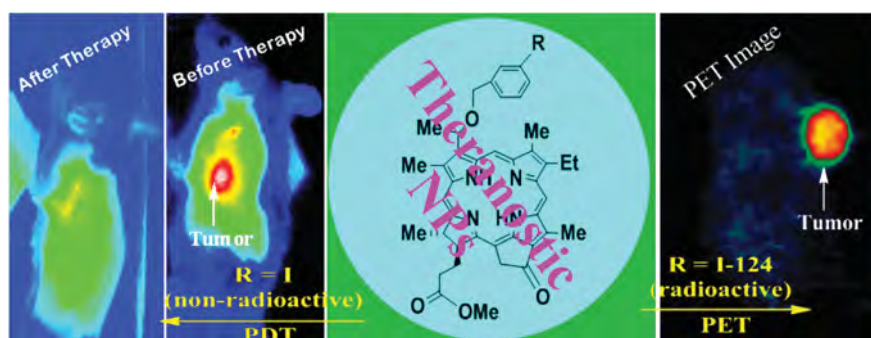
**Fig. 4.** HPPH conjugated with 3Gd(III)DTPA shows significant tumor enhanced image (29%) compared to the surrounding tissues in rats implanted with WardColon tumors. Maximum intensity was observed at 24 h post-injection. MR imaging dose: 10  $\mu\text{mol/kg}$ , a 10-fold lower imaging dose than the dose used for Magnevist, a current clinical standard. *Source: Bioconjugate Chemistry* 2010; **21**: 828–835

### Positron Emission Tomography (PET) and Single Photon Emission Computed Tomography (SPECT)

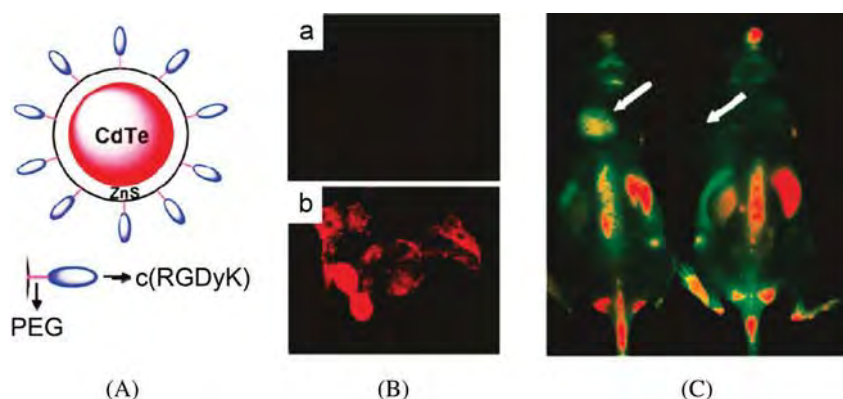
The most popular radioactive based imaging techniques used in the clinic are Positron Emission Tomography (PET) along with Single Photon Emission Computed Tomography (SPECT). There is a general consensus amongst experts in the field of imaging that PET and SPECT provide the best sensitivity to visualize interaction between physiological processes and ligands. With the use of radioactivity the depth of penetration is nearly limitless when using PET and unlike MRI, images are obtained in “real time” with a small dose of the radionuclide (often in picomolar to nanomolar concentrations). But the main issue with PET is the lack of good spatial resolution unlike MRI. These days, however, PET is not used as a standalone towards imaging technique in the clinic but is often used in combination with other modalities such as CT or SPECT. PET-CT and PET-SPECT images provide more information about the tumor and have improved early detection and monitoring of therapeutic intervention for most tumor types. Another prominent feature of nuclear imaging is its ability to image biological processes and metabolic activity in tissues and organs.  $^{18}\text{F}$ Fluorodeoxyglucose ( $^{18}\text{F}$ FDG) is the most popular radionuclide used for PET imaging and has been used in the clinic for detection of primary as well as metastatic tumors. Solid tumors usually have higher uptake of  $^{18}\text{F}$ -FDG due to relatively higher levels of glucose transporters. But this limits its use to detection of tumors in organs which are generally metabolically more active including but not limited to brain and pancreatic cancers. But PET has shown remarkable sensitivity and accuracy. The average FDG PET sensitivity and specificity across all oncology applications is estimated at 84%. Another advantage of using radionuclides is the easy chemistry for development of tumor specific PET agents. Tumors express a lot of receptors on their surface to help them grow independent of growth factors, improve survival under hypoxic conditions, avoid immune surveillance and finally metastasize to distant sites. PET radiochemistry

allows for developing *in vivo* radiolabels which can target some of these receptors, helping in identifying both local as well as metastatic tumors. One of the popular ligands used is cRGD peptide targeting the integrin receptor  $\alpha_v\beta_3$ , which is overexpressed in growing neovasculature as well tumors of the brain, breast, head and neck and many others. Chen *et al.* describe the use of RGD conjugated radionuclides including  $^{89}\text{Zr}$ ,  $^{18}\text{F}$ ,  $^{68}\text{Ga}$  and  $^{64}\text{Cu}$  to target a variety of tumors that includes prostate cancer, pancreatic cancer, and breast tumors [12, 91–97]. They have shown a significant advantage of labeling PRT radionuclides with the RGD as there is high tumor to background noise ratio implying good contrast. Photosensitizers are also being used for developing PET agents. Pandey and group at Roswell Park Cancer Institute, Buffalo have demonstrated development of PET agents using labeled  $^{124}\text{I}$ iodine, which could treat tumors with 100% efficiency [86]. Zheng *et al.* have also recently synthesized a tumor specific porphyrin-peptide folate (PPF) probe with a  $^{64}\text{Cu}$  label for PET imaging.  $^{64}\text{Cu}$ -PPF uptake in FR-positive tumors was visible on small-animal PET images with high tumor-to-muscle ratio ( $8.88 \pm 3.60$ ) observed after 24 h [98]. PET can be used for monitoring efficacy of PDT. It is non-invasive and provides the advantage of doing whole body imaging unlike other techniques. A good example of noninvasive molecular imaging is provided by Subbarayan *et al.*, who used autoradiography imaging to monitor apoptosis after PDT with the compound  $^{99\text{m}}\text{Tc}$ -annexin V as the contrast agent for detection of tumors by SPECT [99]. Along with other nuclides like  $^{111}\text{In}$ -SPECT provides a good adjunct to PET as it uses a lower radioactive dose than  $^{99\text{m}}\text{Tc}$ . This provides benefits to patients as they are exposed to lower radiation dose.

Among the porphyrin-based PET imaging agents, the 3-(1'-*m*- $^{124}\text{I}$ iodo-benzyloxy)ethylpyropheophorbide-a derived from chlorophyll-a developed by Roswell Park group [85] has shown excellent PET-imaging ability of various types of tumors in mice (Fig. 5). As a non-radioactive analog, it shows excellent PDT efficacy. Thus, the combination of a radioactive and a non-radioactive compound (with similar pharmacokinetic



**Fig. 5.** PAA-based biodegradable and biocompatible multifunctional nanoplatform for cancer-imaging and therapy containing both radioactive (I-124) and non-radioactive chlorophyll-a based compound in desired imaging and PDT doses



**Fig. 6.** Quantum Dot Imaging (A) Schematic diagram of QD750-PEG2k-RGD. (B) *In vitro* staining of human breast MCF and human glioblastoma U87MG cells (low and high levels of integrin  $\alpha_v\beta_3$  expression, respectively) using QD750-PEG2k-RGD. (C) *In vivo* NIR fluorescence imaging of U87MG tumor-bearing mice (left shoulder, denoted with white arrows) injected with QD750-PEG2k-RGD (left) and QD750-PEG2k (right). *Source. Nano Lett.* 2006; **6**: 669–676

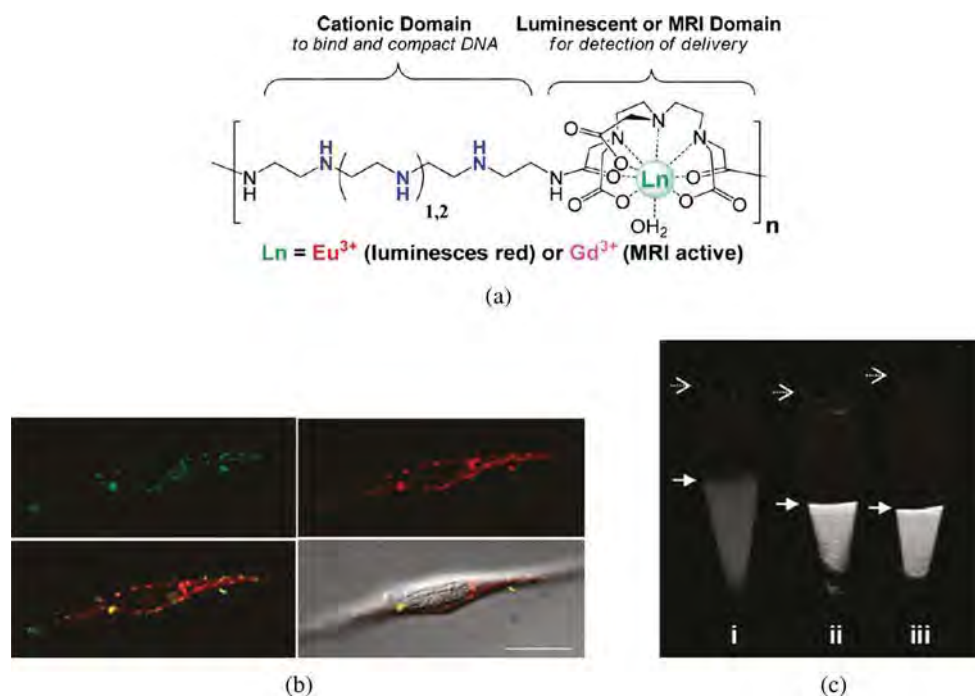
and pharmacodynamics profiles), can be used for dual imaging (PET/fluorescence) and PDT. Interestingly, the post-loading of the iodinated analogs (I-124 labeled and the corresponding non-radioactive compound) in polyacrylamide-based (PAA) nanoparticles (NPs) made a remarkable difference in *in vivo* biodistribution of the imaging and therapy agents with a significant increase in tumor-uptake with reduced uptake in other organs, especially in spleen [100].

### Optical imaging

Among the non-radioactive based imaging modalities, optical imaging is one of the most widely researched and popular modalities of imaging, both at the clinical as well as academic level. Fluorescence microscopy is already well-known for studying and analyzing information at the molecular level (*in vitro* and *ex-vivo*). *In vivo* imaging is gaining interest for preclinical and clinical applications. Some of the major advantages of doing optical imaging over other imaging modalities is the high sensitivity (nanomolar to micromolar for optical imaging) of the technique. The probes used for optical imaging and detection are easy and cheap to synthesize and are safe for use in patients because of the inert nature or most of the probes. Probes used are non-toxic and easily cleared from the various organs. Research in the field has led to the development of new instrumentation which can image whole body or specific tissue in real time. Probes normally used are synthesized in a variety of excitation and emission wavelengths (ranging from 500–900 nm). New instruments can easily image across this broad range. Another major advantage of using optical probes is that they are easy to conjugate to tumor targeting agents such as peptides and sugars. They can also be easily loaded or conjugated with nanoparticles to develop theranostic agents that can help image/treat tumors. Nanoparticles which are loaded with chemotherapeutic drugs or

radiosensitizers can be combined with optical agents to monitor the efficacy of treatment following delivery to tumors. Nanoparticles such as quantum dots are themselves fluorescent when excited under ambient light conditions (Fig. 6). Quantum dots have high quantum yield, are resistant to photobleaching and degradation and have long fluorescence lifetimes. The disadvantages of quantum dots are limited biocompatibility and significant toxicity in animals. But recent work in the field has led to the development of new kind of quantum dots which are biocompatible and are currently used for *in vivo* tracking of cells, for studying cell–cell interactions and also for detection of micrometastasis of various types of tumors [1, 11, 14, 101, 102].

Several types of nanoparticles are reported as carriers for optical probes and have been exploited extensively. Nanoparticles have the potential to preferentially localize to the tumors due to the enhanced perfusion effect (EPR) which allows them to pass through the leaky vasculature of the tumor and into tumor cells. Nanoparticles such as iron oxide nanoparticles have been used for combined MRI and optical imaging of tumors. Various fluorophores are easily conjugated to the surface of the iron oxide nanoparticles to allow real time imaging of tumors post injection (Fig. 7). Recent work has allowed for labeling of stem cells with iron oxide nanoparticles to monitor trafficking, and cell based interactions [82,103–106]. Polymeric nanoparticles when labeled with fluorophores are able to deliver a variety of chemotherapeutic drugs and other agents of interest. Reineke *et al.* have developed a set of polymeric nanoparticles (polyethyleneamine) based nanoparticles which encapsulate a Gd based MRI contrast agent with nucleic acid such as DNA for combined gene therapy and MR imaging. The group uses a lanthanide ( $\text{Eu}^{3+}$ ) instead of regular fluorophores for visualization of efficacy of transfection. Plasmid DNA based transfection experiments show high uptake of these nanoparticles both through high contrast on the MRI in



**Fig. 7.** Theranostic nanoparticles for gene delivery and MRI. (a) Chemical structure of lanthanide- and oligoethyleneamine-containing theranostic polymers for nucleic acid delivery. (b) Deconvoluted confocal microscopy images of HeLa cells transfected with polyplexes containing Eu<sup>3+</sup>-chelated polymer (red) and fluorescein isothiocyanate- (FITC-) labeled pDNA (green), and their overlay with DIC (differential interference contrast), shows accumulation of polyplexes in the perinuclear region and in cytoplasm. (c) Magnetic resonance (MR) images of cells transfected with two different Gd-containing polymers, (ii) and (iii), compared to untreated HeLa cells. Figure adapted from Bryson JM, Fichter KM, Chu W-J, Lee J-H, Li J, Madsen LA, McLendon PM, Reineke TM. Polymer beacons for luminescence and magnetic resonance imaging of DNA delivery. *Source: Proc. Natl. Acad. Sci. USA.* 2009; **106**: 16913–16918

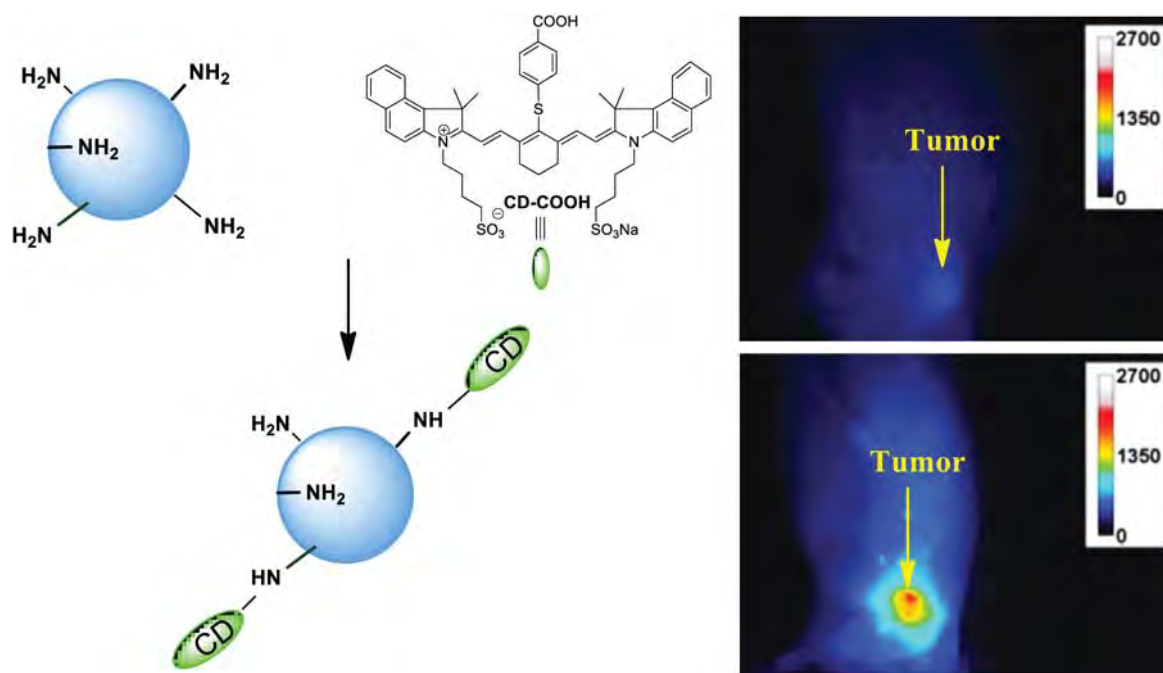
transfected vs. untransfected cells, as well as through optical imaging with the lanthanide which showed higher fluorescence in the transfected cells [107].

Most of the photosensitizers fluoresce, and therefore certain PDT agents with required photophysical properties can benefit from the development of agents for fluorescence-guided PDT. Photosensitizer Fluorescence Detection (PFD), a technique used for demarcation of tumors has been extensively researched at both the laboratory as well as the clinical scale for imaging of tumor. Protoporphyrin IX and  $\delta$ -aminolevulinic acid, a prodrug of protoporphyrin IX have been used for imaging of skin tumor prior to treatment [44, 108–113]. PFD has been used for detection of bladder cancer and found great success when using ALA or more recently lipophilic ALA. In a Phase III clinical trial, ALA based PFD for bladder cancer 61.5% of patients in the fluorescence endoscopy group were tumor-free at the time of follow-up, compared with only 40.6% in the white-light group, with no noted difference in side effects from the procedure. Since 2003 onwards, studies of fluorescence cystoscopy for detection of bladder cancer using HAL (hexyl aminolevulinic acid) instead of free ALA reported a similar marked improvement in sensitivity over white-light imaging [114].

One limitation of the fluorescent property of most porphyrin photosensitizers is the small wavelength difference between the longest wavelength absorption peak and the fluorescence emission wavelength. Thus, they are not “ideal” candidates for fluorescence-imaging. However, the cyanine dyes on the other hand show desired properties for imaging, but most of them are not tumor-avid. The Roswell Park group has previously shown that the postloading of a photosensitizer and the cyanine dye in a desired ratio into nanoparticles can be used as bifunctional agents for both cancer-imaging and therapy [115, 116]. Interestingly by conjugation of a non-tumor avid cyanine dye with amino functionalized polyacrylamide-based NPs produced remarkable tumor-images of Colon26 tumors implanted in BALB/C mice, which further confirmed the tumor-avidity of these NPs (Fig. 8).

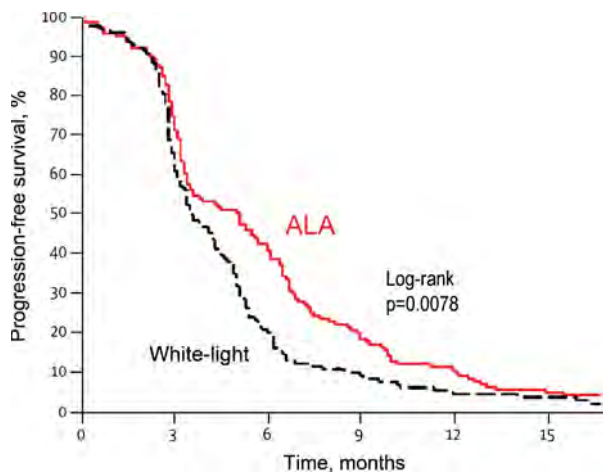
#### Photosensitizer based Fluorescence Detection (PFD) for tumor imaging and therapy

Fluorescence guided resection (FGR) using PS precursors has received considerable attention in the treatment of brain cancer. The ability to optimally resect malignant tissue with minimal damage to surrounding



**Fig. 8.** Compared to a free cyanine dye the corresponding formulation in which the dye was postloaded to polyacrylamide (PAA) NPs show enhanced tumor-imaging ability in BALB/c mice bearing Colon26 tumors at 24 h post-injection (dye dose:  $0.3 \mu\text{mol/kg}$ , an un-optimized imaging dose). *Source: ACS Nano.* 2012; **6**: 6843–6851

normal areas is a critical determinant of meaningful improvement in progression-free survival and quality of life for patients with brain cancer. ALA, which found great success in detection of malignant lesions of bladder cancer, has also been investigated in detection of tumor margins in brain cancer. Stummer *et al.* found that there was significant accumulation of ALA in malignant glioma cells which eventually lead to a large multi-center Phase III clinical trial for use of ALA based PFD of malignant gliomas during intraoperative surgery (Fig. 9). This highly successful trial was terminated at the interim analysis of the first 270 patients, when 65% of those in the FGR group were without residual disease at postoperative MRI, compared with 36% in the white-light group. Though there was no overall survival benefit for patients who got the treatment, it is important to note that there was higher population of patients who showed progression free survival as compared to patients who did not undergo ALA based resection of malignant glioma. This study prompted the use of other photosensitizers for tumor delineage such as mTHPC. Further, it was noted that the presence of the photosensitizer offered the opportunity to perform PDT during or after surgery. This might offer a survival benefit to patients as residual tumor can be destroyed following surgery and might be a safer option as compared to radiation or chemotherapy. In an effort led by Kostron and colleagues mTHPC guided fluorescence guided resection (FGR) with adjuvant PDT was evaluated in 26 patients with malignant brain tumors. Kostron *et al.* also reported that there was an increase in



**Fig. 9.** Progression-free survival data by treatment group for the large multicenter trial reported by Stummer W *et al.* *Lancet Oncol.* 2006; **7**: 392 which compared white-light and fluorescence-guided resection for treatment of malignant glioma. After 6 months there was a significant enhancement in progression-free survival in the 5-ALA group as compared to white light. *Source: Chem. Rev.* 2010; **110**: 2795–2838

the median survival from 3.5 months to 9 months in the group of patients which received the *m*-THPC based FGR [117, 118]. PFD has also been explored in metastatic ovarian cancer, skin cancer, oral cancer and also recently found success in head and neck cancer at Roswell Park Cancer Institute under the guidance of Rigual *et al.* [72,

119–125]. While PFD has made a significant clinical impact as an intraoperative imaging modality for guidance of surgical resection, it has not been extensively explored as a non-invasive approach. One of the main limitations of PFD is the source of lower wavelength of light used for excitation. Therefore, the penetration of light is not deep enough to get the complete extent of the tumor especially with the tumors that are deeply seated. Still PFD can really help all aspects of PDT. It can also help in determining dosimetry and feedback during and after treatment of tumors. Combining it with other modalities such as Optical Coherence Tomography or Photoacoustic Tomography (PAT) could push the boundaries in using PFD for improving patient care and patient treatment of various tumor types [126].

### Gold nanoparticles and Photoacoustic Tomography (PAT)

Photoacoustic Tomography is a new and upcoming technique which utilizes the ability of light to generate acoustic signals through photon scattering by various tissues. One of main advantages is that ultrasonic wave is able to overcome the optical diffusion limit. Photoacoustic images are generated by detecting those pressure waves which are collected by an ultrasonic detector used routinely in ultrasonography imaging. Thus PAT is able to generate multispectral high-resolution imaging of biological structures, ranging in size from organelles to organs. PAT has the ability to excite various tissues at different wavelengths and hence will generate good contrast amongst different organs. PAT also has higher sensitivity as compared to other techniques such as OCT and confocal microscopy. Lastly, the PAT image is a background free image as anything which does not absorb the light will not generate a PAT signal and hence will not show up on the screen. Thus, PAT is able to generate high resolution images and with good contrast is able to differentiate between a variety of tissue types. PAT is being actively researched in a variety of areas ranging from vascular biology, oncology, cardiovascular diseases, ophthalmology, neurology and gastroenterology. Hemoglobin in the blood is strong absorber of light and can be used to generate a lot of anatomical and physiological information using PAT. External contrast enhancers provide the opportunity to get more information using PAT. Commonly used contrast agents include metallic nanoparticles, popularly gold nanoparticles, nanocages and nanorods, dyes, and even gene reporters. Gold based nanoparticles are the most popular amongst the agents investigated for use as PAT contrast agents. They are biocompatible, do not generate an immune response, are easily customized for use in various scenarios and have deep NIR absorption, which helps maximizing imaging depth. Gold nanocages are the most popular gold based PAT contrast agents and

they offer good imaging capability even for deeply seated tumors. They can be conjugated with a variety of tumor specific ligands for high uptake within the tumor and can be loaded with therapeutic agents for development of theranostic agents that can deliver drugs to the tumor and also help image therapeutic efficacy following drug delivery. Kim *et al.* [127] have demonstrated detection of pigmented melanoma tumors (B16 F10) using PAT through gold nanocages. Gold nanocages used for the detection of melanoma tumors (Fig. 10) showed remarkable contrast at concentrations far lower than normally used for other contrast agents such as single walled carbon nanotubes (SWCNT) and gold nanorods. Conjugation with melanoma targeting ligand improved the efficiency of the gold nanocages by almost 300% indicating active targeting of the tumor by the gold nanocages.

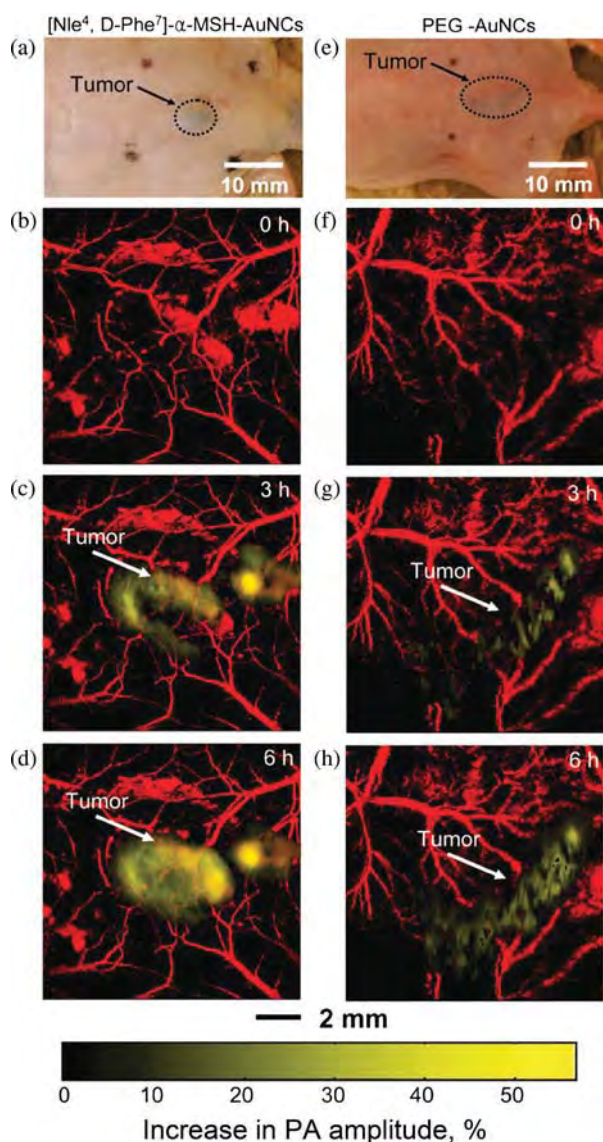
Gold nanocages have proven to be versatile agents to image sentinel lymph nodes, which are amongst the primary sites for metastatic cells and helping to delineate infected lymph nodes against clean lymph nodes. This will help clinicians to predict the spread of the disease along with biopsy and removal of lymph nodes. Using a rat model, Wang *et al.* [127] investigated the use of gold nanocage-based PAT mapping of lymph nodes and were able to image to about a depth of 33 mm below the surface of the skin which is greater than any optical resolution depth.

Clearance of these gold nanocages from the various organs and the toxicity studies in small animals are underway. Dyes and other fluorophores can also be used as contrast agents with and without gold NPs. In theory, all fluorophores (including porphyrin-based photosensitizers) can generate PAT signal at appropriate wavelengths. Fluorescent probes generate fluorescence through decay of photons from higher energy orbital level. But often the fluorescent efficiency is not 100% and some amount of the energy is lost to thermal emission. This energy can be detected by PAT; hence certain porphyrin-based fluorophores are unique as they can be simultaneously used for optical as well as PAT imaging. These compounds can also be loaded on gold nanomaterials, for developing agents for PAT and fluorescence imaging [128, 129] with and without the option of PDT.

### Photothermal Therapy (PTT)

Another unique advantage of using gold nanomaterials is the ability to generate heat through the LSPR (longitudinal surface plasmon resonance) effect. Gold nanocages and nanorods can absorb light and convert it into heat which can be used for treatment of tumor cells, which is also called the photothermal effect [130–132]. Gold nanocages are excellent candidates for irradiating with light at the absorbance wavelength at 0.7 W/cm<sup>2</sup>, which is able to increase the intratumoral temperature





**Fig. 10.** *In vivo* noninvasive PA time-course coronal MAP images of B16 melanomas using [Nle<sup>4</sup>,D-Phe<sup>7</sup>]- $\alpha$ -MSH and PEG-AuNCs. (a, e) Photographs of nude mice transplanted with B16 melanomas before injection of (a) [Nle<sup>4</sup>,D-Phe<sup>7</sup>]- $\alpha$ -MSH- and (e) PEG-AuNCs. Time-course PA images of the B16 melanomas after intravenous injection with 100  $\mu$ L of 10 nM (b–d) [Nle<sup>4</sup>,D-Phe<sup>7</sup>]- $\alpha$ -MSH and (f–h) PEG-AuNCs through the tail vein. The background vasculature images were obtained using the PA microscope at 570 nm (ultrasonic frequency = 50 MHz), and the melanoma images were obtained using the PA microscope at 778 nm (ultrasonic frequency = 10 MHz). Color schemes: red for blood vessels and yellow for the increase in PA amplitude. *Source: ACS Nano*. 2010; 4: 4559–4564

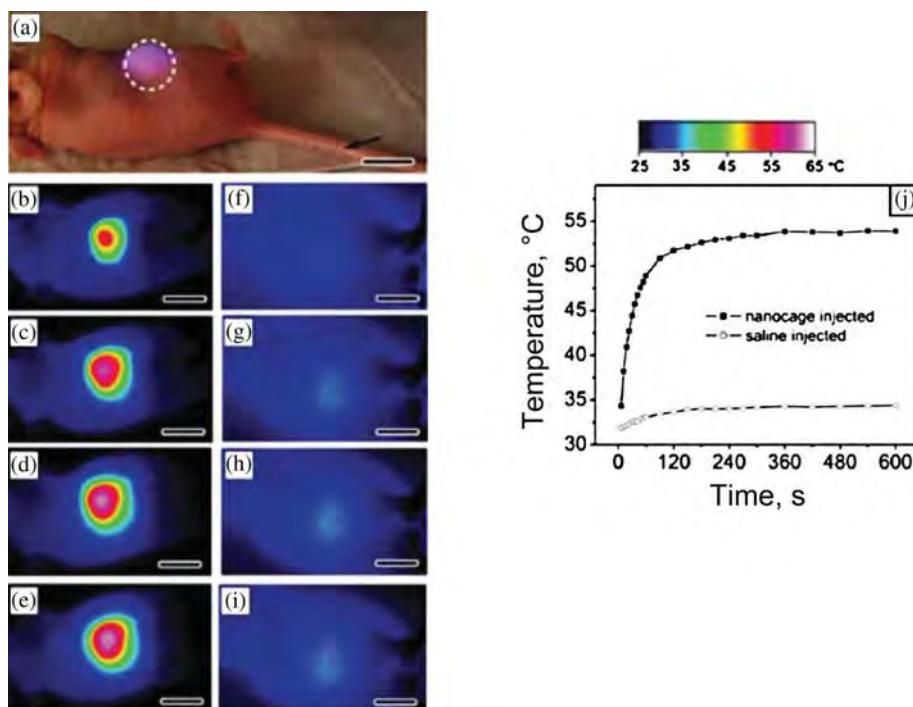
to as high as 55 °C (Fig. 11). At that temperature, a significant tumor killing and a decrease in tumor size was observed following the treatment. Gold nanocages can help monitor tumor destruction following PTT by PAT imaging [133]. However, in contrast to fluorescence the amount of material required for *in vivo*-PAT imaging is much higher.

## Hyperthermia with and without PDT

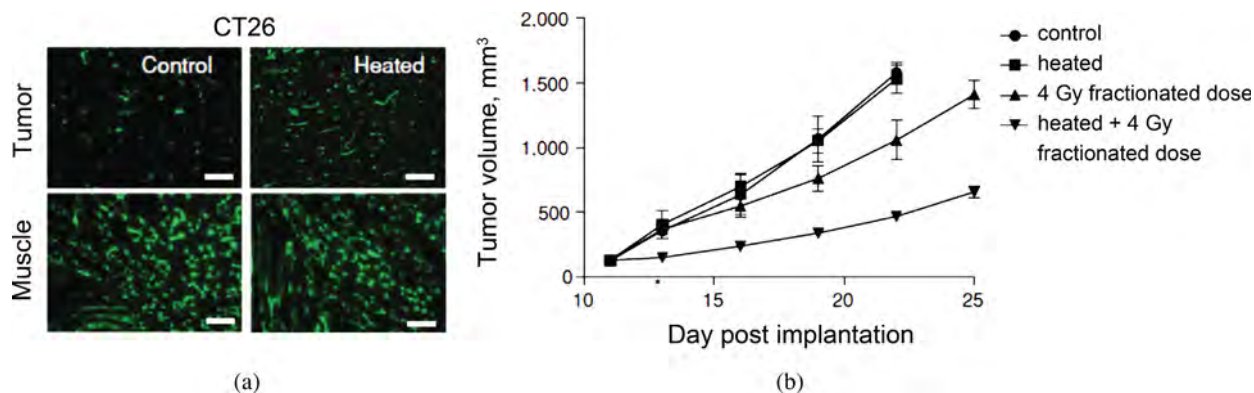
Hyperthermia can influence tumor-control in two different ways. The first is direct killing of cells by heat which involves heating the tumor and the surrounding regions to high temperature (45 °C or higher). Thermal killing of tumor has been accomplished using a number of techniques from using radio-frequency waves (RF) to high frequency ultrasound (HIFU) [134–136] which requires focused ultrasound delivery (around 2.25 MHz) into the tumor. Delivery of such energy results in a fast rise of temperature within the tumor to about 55–60 °C, and causes killing of tumor cells. This type of hyperthermia based treatment is currently in clinical trials for a variety of soft tissue tumors. Tumors of the kidney, prostate, liver, and breast have been targeted with promising results (Fig. 12).

The research by the hypothermia group at Roswell Park Cancer Institute involves fever range hyperthermia (40–41 °C). Hypoxia is correlated to radioresistance, it has been proposed that the abnormal vascularization of tumors leads to increased hypoxia whereas re-perfusion fever is an evolutionary conserved mechanism which often follows inflammation after an infection. Fever provides survival benefits by limiting the growth of pathogens and modulating the growth of effector T cells which help in control of infections. Tumors in both patients and xenograft models in mice express a high interstitial fluid pressure (IFP) which limits the efficacy of a variety of drugs as there is resistance to uptake of drugs into the tumor [137–139]. Furthermore, elevated IFP compromises the response of tumor to radiotherapy (140).

Because hypoxia is clearly related to radioresistance, it has been reported that the abnormal vascularization of tumors leads to increased hypoxia whereas re-perfusion could improve radiosensitivity of tumors. Mild hyperthermia provides benefits both at the cellular level as well as the tissue level. Mild hyperthermia has shown to boost anti-tumor immunity in an IL-6 dependent manner. It also boosts anti-tumor immunity by enhancing the expression of effector CD8 T cells as well as IFN  $\gamma$  production. Hyperthermia has also shown to boost the levels of Natural Killer (NK) cells which are one of the main mediators of anti-tumor immunity. As compared to control animals, whole body hyperthermia increased NK cell infiltration at the site of the tumor. Hyperthermia is also known to regulate the expression of Treg cells. Immature myeloid cells (iMCs) when exposed to mild hyperthermia show increased maturation into dendritic cells that acted as potent stimulators of CD8 T cells [8, 141, 142]. Hyperthermia is also known to increase lymphocyte and leukocyte trafficking. This can promote immune surveillance and allow for naive cells to encounter antigens presented circulating dendritic cells [141]. Clinical trials have shown increased survival benefit following hyperthermia because of increased response to chemotherapy and radiotherapy [143]. PDT efficacy



**Fig. 11.** (a) Photograph of a tumor-bearing mouse under the photothermal treatment. 100 mL of PEGylated nanocages at a concentration of  $9 \times 10^{12}$  particles/mL or saline was administered intravenously through the tail vein as indicated by an arrow. After the nanocages had been cleared from the circulation (72 h after injection), the tumor on the right flank was irradiated by the diode laser at  $0.7 \text{ W.cm}^2$  with a beam size indicated by the dashed circle. (b–g) Thermographic images of (b–e) nanocage-injected and (f–i) saline-injected tumor-bearing mice at different time points: (b, e) 1 min, (c, f) 3 min, (d, g) 5 min, and (e, i) 10 min. (j) Plots of average temperature within the tumors (dashed circle) as a function of irradiation time. *Source: Small. 2010; 6: 811–817*



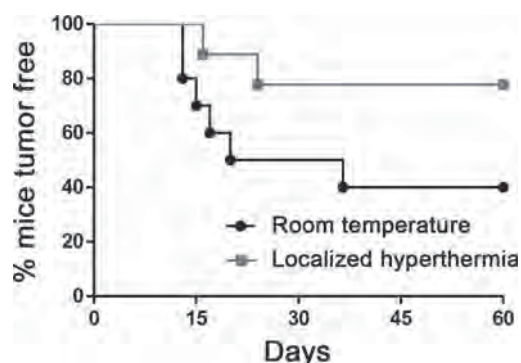
**Fig. 12.** (a) Elevated body temperature increases tumor blood vessel perfusion in BALB/c mice bearing CT26 tumors. A, representative fluorescence micrographs (at  $5\times$ ) of CT26 tumor implanted s.c. on the hind leg (volume 300–600 mm<sup>3</sup>; top pair) and muscle (bottom pair) showing perfused blood vessels following tail vein injection of the cyanine dye DiOC<sub>7</sub>(3). The micrographs on the left are those obtained from tissue excised from unheated control mice and the 2 micrographs on the right are from mice after 6 h of heating. The increased number of perfused vessels in a tumor from a heated mouse (160 vessels per field) is apparent in comparison with that of an untreated mouse (82 vessels per field). There is no visible difference in the number of perfused vessels in muscles from unheated control mice and that from heated animals. Scale bars 500 mm. (b) Heat treatment enhances the efficacy of radiation therapy. A, CT26 tumors were implanted s.c. on the flank of BALB/c mice. Tumor growth was then monitored in the following groups (n/45 per group): control untreated mice (\*), mice that were only heated (&), mice that received only radiation (1 Gy/d for 4 days, days 12–15;~), and mice that were heated and followed 24 h later by 4 consecutive radiation treatments (1 Gy/d for 4 days). Tumor growth rates in the unheated control and the heat-only groups were indistinguishable. The slowest growth rate was observed in tumors of mice that received the combination of heating followed by fractionated radiation. Statistical test using one-way ANOVA with Dunnett’s multiple comparison tests for comparative analysis of the means of the treated groups to the mean of the control group shows significant difference only for the group of mice that received combined heating and radiation. *Source: Cancer Research. 2011; 71: 3872–3880*

can also be enhanced following hyperthermia. The increased perfusion and lower IFP can allow for higher photosensitizer concentration within the tumor as well as higher tumor reoxygenation. This might increase PDT efficacy following light treatment. Also, PDT anti-tumor immunity is mediated through neutrophils, lymphocytes and natural killer cells [142–146]. Hyperthermia can help boost anti-tumor immunity following PDT by increased trafficking of immune cells in to the tumor and helping antigen presentation following PDT.

The photodynamic therapy (PDT) efficacy of 3-(1'-hexyloxy)ethyl-pyropheophorbide-*a* (HPPH), a chlorophyll based photosensitizer (PS), currently in Phase I/II human clinical trials and being developed by Photolitec, LLC for the use in head and neck, and lung cancers, was investigated for a long-term tumor cure in combination with mild heating. Both systemic and local heating in combination with PDT showed enhanced PDT efficacy in BALB/c and in nude mice implanted with Colon26 and U87 tumors respectively. The improved PDT efficacy (long-term percentage tumor cure) in combination with heating was due to an increase in tumor-uptake of the photosensitizer (PS) (Fig. 13, Pandey *et al.*, unpublished results).

Nanoparticles such as gold nanocages and nanorods, magnetic iron oxide nanoparticles have also shown promise for hyperthermia based killing of tumor cells. Gold nanomaterials can achieve photothermal killing of tumors by various mechanisms. The first mechanism is the mild temperature increase (*i.e.* from 3 to 6 °C) that often proceeds *via* apoptotic pathways. This mode of killing takes a longer time and there are minimal side effects. The results are often dramatic and the treatments are prolonged and recurrent. This effect is often called as the Lance Armstrong effect [136]. If there is a rapid increase in temperature, the necrotic damage is more prominent.

Using HPPH as the photosensitizer, the RPCI group in collaboration with Dr. Chen, University of Arkansas, Fayetteville, AR and Dr. Kim, Pohang University of Science and Technology, Pohang, Republic of Korea, demonstrated a controlled release of hydrophobic drugs from exterior and interior of poly(ethylene glycol) covered gold nanocages [147]. Two encapsulation routes were investigated: one utilizing PEG to entrap HPPH within the AuNC void (HPPH-in-AuNC) and the other utilizing hydrophobic interactions to load HPPH within the PEG-monolayer coating the AuNC (AuNC-HPPH). After loading, the physical, fluorescence, and Raman properties were characterized along with drug release. HPPH-in-AuNC loading was diffusion-based and could be manipulated by changing concentrations; no drug release was observed (Fig. 11). AuNC-HPPH was found to have a maximum loading of  $\sim 2.5 \times 10^5$  HPPHs/AuNC, with  $K_d$  between PEG and HPPH of  $\sim 17$   $\mu$ M. Protein mediated release from the exterior conjugate was observed in a serum mimetic environment, the rate was found to be sensitive to surface modification and

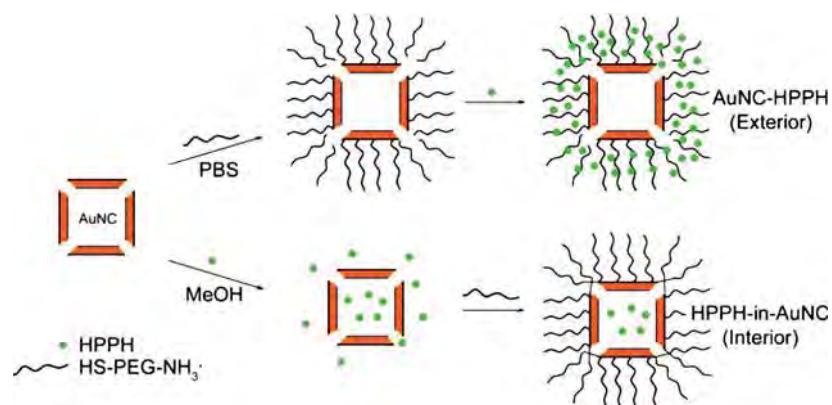


**Fig. 13.** Kaplan-Meier survival plot for HPPH-PDT response under room temperature and localized hyperthermia conditions at a drug dose of  $0.47 \mu\text{mol/kg}$  in BALB/c mice bearing Colon 26 tumor on shoulder (10 and 9 mice/group, respectively): light dose,  $135 \text{ J/cm}^2$ ,  $75 \text{ mW/cm}^2$  at 24 h post-injection, statistically significant with  $P < 0.05$  (Mantel-Cox test). Srivatsan & Pandey *et al.*, unpublished results

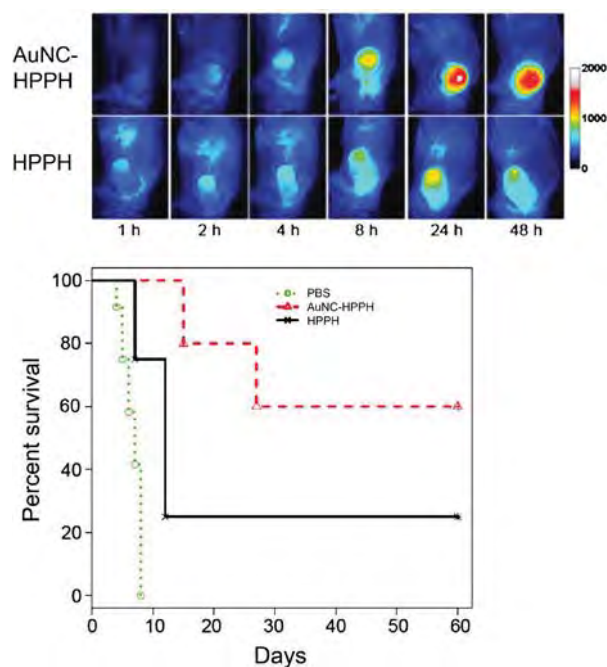
surface charge. The photothermal effect was used to initiate burst release, and the presence or absence of light was found to impart significant control of the release kinetics from the system, demonstrating on-demand release (Fig. 14).

The *in vitro in vivo* efficacy of HPPH alone and the gold nanocage-HPPH (ANNC-HPPH) was compared under similar treatment parameters and the nanocages showed improved PDT efficacy. The *in vivo* results are summarized in Fig. 15. For a proof-of-principle study, two groups of tumor-bearing mice were intravenously injected with HPPH ( $0.3 \mu\text{mol/kg}$ ) as free HPPH or AuNC-HPPH. As a control group, five mice were intravenously injected with PBS. Guided by fluorescence imaging, the mice were treated with 665-nm laser irradiation for 30 min with a total light dose of  $135 \text{ J/cm}^2$  at 24-h post-injection when the accumulation of the conjugates reached its peak.

After the PDT treatment, tumor growth was monitored by measuring the tumor size for up to 60 days. The mice were euthanized when the tumor grew to  $400 \text{ mm}^3$ . Of the mice treated with free HPPH, only one of the five mice remained alive with tumor size  $< 400 \text{ mm}^3$  (20% survival) at 60 days post-treatment. Of the mice treated with AuNC-HPPH, three of five mice survived with complete tumor cure at 60 days post-treatment. In contrast, no mouse in the control group with PBS injection survived beyond 15 days post-treatment. These results suggest that the survival rate of the AuNC-HPPH treated mice is higher than the HPPH-treated mice under the same irradiation condition, indicating the higher potency of AuNC-HPPH as compared to the equal amount of free HPPH. *In vivo* toxicity has been one of the main issues in generating NPs-based therapeutic/imaging agents. A short-term study on AuNC-HPPH by RPCI group also demonstrated that there were neither toxicity nor phenotypical changes in mice at therapeutic dose of the conjugates or even at



**Fig. 14.** Schematic illustration of two strategies for entrapment of hydrophobic molecules using PEG-covered AuNCs. The drug can be loaded onto (top) the exterior (AuNC-HPPH) or (bottom) the interior (HPPH-in-AuNC) of the AuNC at 24 h post-injection (i.v.)



**Fig. 15.** Top: fluorescence imaging to monitor the delivery process of HPPH. Bottom: Kaplan-Meier plot of percent survival (tumor-free) of Colon-26 tumor-bearing mice after intravenous injection of PBS (green), HPPH (0.3  $\mu\text{mol}$  HPPH/kg, black), and AuNC-HPPH (0.3  $\mu\text{mol}$  HPPH/kg, red), followed by light irradiation with a fluence of 135 J/cm<sup>2</sup>. Source: *Theranostics*, 2014; **4**: 163–174

100-fold higher than therapeutic dose of gold nanocages. This study is of critical importance in developing therapeutic/imaging agents related to gold-nanocages.

## CONCLUSION

The idea of developing a single theranostic agent that can integrate real-time evaluation of tumor burden with improved treatment is highly desirable. These agents can help circumvent the current problems associated

with combining multiple agents for tumor detection and subsequent therapy. Certain tumor-avid porphyrin-based photosensitizers (PS) used as drugs in PDT, with multi-functional groups, provide an opportunity to introduce desired key moieties in designing improved theranostic agents. It has also been demonstrated that gold nanocage-photosensitizer conjugates can enable dual image-guided delivery of photosensitizer and significantly improve the efficacy of photodynamic therapy in a murine model — for example, the photosensitizer, 3-devinyl-3-(1'-hexyloxyethyl)-pyropheophorbide (HPPH), noncovalently entrapped in the poly(ethylene glycol) monolayer coated on the surface of gold nanocages can be monitored optically by fluorescence and by photoacoustic imaging. The slow nature of the release in turn results in an increase in accumulation of the drug within implanted tumors due to the passive delivery of gold nanocages. Furthermore, the conjugate was found to generate more therapeutic singlet oxygen and have a lower IC<sub>50</sub> value than the free drug alone. Thus the conjugate resulted significant suppression of tumor growth as compared to the free drug *in vivo*, and provides a possible opportunity of developing improved cancer imaging and therapeutic agents not limited to PDT.

## Acknowledgements

The data presented (in part) in this review article from our laboratories were financially supported by the NIH (CA119358, PO1 CA55791, RO1 CA127369 and R21 CA176154), which is highly appreciated. The authors also acknowledge the financial support received by Photolitec, LLC, Roswell Park Alliance and the NCI Cancer Support Grant CA016156.

## REFERENCES

1. Kelkar SS and Reineke TM. *Bioconjug. Chem.* 2011; **22**: 1879–1903.
2. Juweid ME and Mottaghy FM. *Methods* 2011; **55**: 193–195.

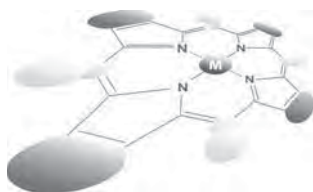
3. Panchapakesan B, Book-Newell B, Sethu P, Rao M and Irudayaraj J. *Nanomedicine* 2011; **6**: 1787–1811.
4. Das M, Mishra D, Dhak P, Gupta S, Maiti TK, Basak A and Pramanik P. *Small*, **5**, 2883–2893.
5. Jokerst JV, Lobovkina T, Zare RN and Gambhir SS. *Nanomedicine* 2011; **6**: 715–728.
6. Danhier F, Ansorena E, Silva JM, Coco R, Le Breton A and Préat V. *J. Control Release* 2012; **161**: 505–522.
7. Danhier F, Ansorena E, Silva JM, Coco R, Le Breton A and Préat V. *J. Control Release* 2009; **133**: 1–7.
8. Scherer RL, McIntyre O and Matrisian LM. *Cancer Metastasis Rev.* 2008; **27**: 679–690.
9. Scherer RL, VanSaun MN, McIntyre JO and Matrisian LM. *Mol Imaging*, 2008; **7**: 118–131.
10. Van de Wiele C and Oltenfreiter R. *Cancer Biother. Radiopharm.* 2006; **21**: 409–417.
11. Bentolila LA, Michalet X, Pinaud FF, Tsay JM, Doose S, Li JJ, Sundaresan G, Wu AM, Gambhir SS and Weiss S. *Discov. Med.* 2005; **5**: 213–218.
12. Cai W, Shin DW, Chen K, Gheysens O, Cao Q, Wang SX, Gambhir SS and Chen X. *Nano. Lett.* 2006; **6**: 669–676.
13. Chen N, He Y, Su Y, Li X, Huang Q, Wang H, Zhang X, Tai R and Fan C. *Biomaterials* 2012; **33**: 1238–1244.
14. Michalet X, Pinaud FF, Bentolila LA, Tsay JM, Doose S, Li JJ, Sundaresan G, Wu AM, Gambhir SS and Weiss S. *Science* 2005; **307**: 538–544.
15. Elsadek B and Kratz F. *J. Control Release* 2012; **157**: 4–28.
16. Moan J and Peng Q. *Anticancer Res.* 2003; **23**: 3591–3600.
17. Lipson RL, Baldes, EJ and Olsen AM. *J. Natl. Cancer Inst.* 1961; **26**: 1–11.
18. Dougherty TJ, Gomer CJ and Weishaupt KR. *Cancer Res.* 1976; **36**: 2330–2333.
19. Weishaupt KR, Gomer CJ and Dougherty TJ. *Cancer Res.* 1976; **36**: 2326–2329.
20. Dougherty TJ. *Oncology* 1989; **3**: 67–78.
21. Dougherty TJ. *Seminars in Surgical Oncology* 1989; **5**: 6–16.
22. Dougherty TJ. *Crit. Rev. Oncol. Hematol.* 1984; **2**: 83–116.
23. Khan SA, Dougherty TJ and Mang TS. *European Journal of Cancer*, 1993; **29A**: 1686–1690.
24. Pandey PK, Smith KM and Dougherty TJ. *Med. Chem.* 1990; **33**: 2032–2038.
25. Waldow SM, Henderson BW and Dougherty TJ. *Lasers Surg. Med.* 1987; **7**: 12–22.
26. Yang VX, Muller PJ, Herman P and Wilson BC. *Lasers Surg. Med.* 2003; **32**: 224–232.
27. Bellnier DA, Greco WR, Loewen GM, Nava H, Oseroff AR and Pandey RK. *Cancer Res.* 2003; **63**: 1806–1813.
28. Bellnier DA, Greco WR, Loewen GM, Nava H, Oseroff AR and Pandey RK. *Cancer Chemother. Pharmacol.* 2006; **57**: 40–45.
29. Agostinis P, Berg K, Cengel KA, Foster TH, Girotti AW, Gollnick SO, Hahn SM, Hamblin MR, Juzeniene A, Kessel D, Korbelik M, Moan J, Mroz P, Nowis D, Piette J, Wilson BC and Golab J. *CA Cancer J. Clin.* 2011; **61**: 250–281.
30. Ochsner MJ. *Photochem. Photobiol. B.* 1997; **3**: 1–18.
31. Foote CS. *Science* 1968; **162**: 963–970.
32. Iinuma S, Schomacker KT, Wagnieres G, Rajadhyaksha M, Bamberg M, Momma T and Hasan T. *Cancer Res.* 1999; **59**: 6164–6170.
33. Mang TS, Dougherty TJ, Potter WR, Boyle DG, Somer S and Moan J. *Photochem. Photobiol.* 1987; **45**: 501–506.
35. Wang L, Gu Y, Li XS, Liu FG and Yu CQ. *Guang Pu Xue Yu Guang Pu Fen Xi*, 2007; **27**: 2073–2078.
36. Dysart JS and Patterson MS. *Phys. Med. Biol.* 2005; **50**: 2597–2616.
37. Dysart JS Singh G and Patterson MS. *Photochem. Photobiol.* 2005; **81**: 196–205.
38. Moan J, Berg K, Kvam E, Western A, Malik Z, Rück A and Schneckenburger H. *Ciba Found. Symp.* 1989; **146**: 95–111.
39. Nowak-Sliwinska P, Karocki A, Elas M, Pawlak A, Stochel G and Urbanska K. *Biochem. Biophys. Res. Commun.* 2006; **349**: 549–555.
40. Pandey RK, Goswami LN, Chen Y, Gryshuk A, Missert JR, Oseroff A and Dougherty TJ. *Lasers Surg. Med.* 2006; **38**: 445–467.
41. Williams MP, Ethirajan M, Ohkubo K, Chen P, Pera P, Morgan J, White WH 3rd, Shibata M, Fukuzumi S, Kadish KM and Pandey RK. *Bioconjug. Chem.* 2011; **2**: 2283–2295.
42. Wilson BC and Patterson MS. *Phys. Med. Biol.* 2008; **53**: 61–109.
43. Bogaards A, Varma A, Zhang K, Zach D, Bisland SK, Moriyama EH, Lilge L, Muller PJ and Wilson BC. *Photochem. Photobiol. Sci.* 2005; **4**: 438–442.
44. Goldman M and Atkin D. *J. Cosmet. Laser Ther.* 2003; **5**: 107–110.
45. Avram DK and Goldman MP. *J. Drugs Dermatol.* **3**: 2004; 36–39.
46. Goldberg LH, Landau JM, Moody MN, Marquez D, Jih M, Kimyai-Asadi A, Friedman PM, Busch A and Vergilis-Kalner IJ. *J. Drugs Dermatol.* 2012; **11**: 593–597.
47. Dirschka T, Radny P, Dominicus R, Mensing H, Brüning H, Jenne L, Karl L, Sebastian M, Oster-Schmidt C, Klövekorn W, Reinhold U, Tanner M, Gröne D, Deichmann M, Simon M, Hübinger F, Hofbauer G, Krähn-Senftleben G, Borrosch F, Reich K, Berking C, Wolf P, Lehmann P, Moers-Carpi M, Hönigsmann H, Wernicke-Panten K, Helwig C,

- Foguet M, Schmitz B, Lübbert H and Szeimies RM; AK-CT002 Study Group. *Br. J. Dermatol.* 2012; **166**: 137–146.
48. Koudinova NV, Pinthus JH, Brandis A, Brenner O, Bendel P, Ramon J, Eshhar Z, Scherz A and Salomon Y. *Int. J. Cancer*, 2003; **104**: 782–789.
  49. Framme C, Sachs HG, Flucke B, Theisen-Kunde D and Birngruber R. *Sci.* 2006; **47**: 5443–5446.
  50. Pandey RK, Goswami LN, Chen Y, Gryshuk A, Missert JR, Oseroff A and Dougherty T. *J. Lasers in Surgery and Medicine* 2006; **38**: 445–467.
  51. O'Connor AE, Gallagher WM and Byrne AT. *Photochem. Photobiol.* 2009; **85**: 1053–1074.
  52. De Rosa FS and Bentley MV. *Pharm Res.* 2000; **17**: 1447–1455.
  53. Gold MH and Goldman MP. *Dermatol. Surg.* 2004; **30**: 1077–1084.
  54. Pandey RK, Sumlin A, Potter WR, Bellnier D, Henderson BW, Cpnstantine S, Aoudia M, Rodgers MR, Smith KM and Dougherty T. *J. Photochem. Photobiol.* 1996; **63**: 194–205.
  55. Henderson BW, Bellnier DA, Graco WR, Sharma A, Pandey RK, Vaughan L, Weishaupt KR and Dougherty TJ. *Cancer Res.* 1997; **57**: 4000–4007.
  56. Bellnier DA, Freco WR, Loewen GM, Nava V, Oseroff AO, Pandey RK, Tsuchida T and Dougherty T. *J. Cancer Res.* 2003; **63**: 1806–1813.
  57. Bellnier DA, Greco WR, Loewen GM, Nava H, Oseroff AR and Dougherty TJ. *Lasers Surgery and Medicine* 2006; **38**: 439–444.
  58. Lobel J, MacDonald IJ, Ciesielski MJ, Barone T, Potter WR, Pollina J, Plunkett RJ, Fenstermaker RA and Dougherty TJ. *Lasers Surg. Med.* 2001; **29**: p. 397–405.
  59. Schmidt-Erfurth U and Hasan T. *Survey of Ophthalmology* 2000; **45**: 195–214.
  60. Kaiser RS, Berger JW, Williams GA, Tolentino MJ, Maguire AM, Alexander J, Madjarov B and Margherio RM. *Retina* 2002; **22**: 683–690.
  61. Chen B, Pogue BW, Goodwin IA, O'Hara JA, Wilmot CM, Hutchins JE, Hoopes PJ and Hasan T. *Radiat. Res.* 2003; **160**: 452–459.
  62. Samkoe KS, Chen A, Rizvi I, O'Hara JA, Hoopes PJ, Pereira SP, Hasan T and Pogue BW. *International J. Radiation Oncology Biology Physics.* 2010; **76**: 251–259.
  63. Celli JP, Solban N, Liang A, Pereira SP and Hasan T. *Lasers Surg. Med.* 2011; **43**: 565–574.
  64. de Visscher SAHJ, Dijkstro PU, Tan IB, Roodenburg JLN and Witjes MJH. *Oral Oncology* 2013; **49**: 192–210.
  65. Fan KF, Hopper C, Speight PM, Buonaccorsi GA and Bown SG. *Int. J Cancer* 1997; **73**: 25–32.
  66. Senge MO. *Photodyn. Ther.* 2012; **9**: 170–179.
  67. Ris HB, Krueger T, Giger A, Lim CK, Stewart JC, Althaus U and Altermatt HJ. *Br. J. Cancer*, 1999; **79**: 1061–1066.
  68. Krueger T, Altermatt HJ, Mettler D, Scholl B, Magnusson L and Ris HB. *Lasers Surg. Med.* 2003; **32**: 61–68.
  69. Pandey RK and Zheng G. In *Porphyryns as Photosensitizers in Photodynamic Therapy, The Porphyrin Handbook* Vol. 6, Kadish KM, Smith KM and Guillard R. (Eds.) Academic Press: San Diego, 2000.
  70. Gupta A, Wang S, Pera P, Rao KVR, Patel N, Ohulchanskyy T, Missert J, Morgan J, Kopelman R and Pandey RK. *Nanomedicine: Nanotechnology, Biology and Medicine* 2013; **8**: 941–950.
  71. Kim S, Ohulchanskyy TY, Pudavar HE, Pandey RK and Prasad PN. *J. Am. Chem. Soc.* 2007; **129**: 2669–2675.
  72. Cheng Y, Samia AC, Meyers J, Panagopoulos I, Fei B and Burda C. *J. Am. Chem. Soc.* 2008; **130**: 10643–10647.
  73. Carter KA, Shao S, Hoopes MI, Luo D, Ahsan B, Grigoryants VM, Song W, Huang H, Zhang G, Pandey RK, Geng J, Pfeifer BA, Scholes CP, Ortega J, Karttunen M and Lovell JF. *Nature Commun.* 2014; DOI: 1038/ncomms4546.
  74. Celli JP, Spring BQ, Rizvi I, Evans CL, Samkoe KS, Verma S, Pogue BW and Hasan T. *Chem. Rev.* 2010; **110**: 2795–2838.
  75. Vrouenraets MB Visser GW, Stigter M, Oppelaar H, Snow GB and van Dongen GA. *Cancer Res.* 2001; **61**: 1970–1975.
  76. Vrouenraets MB *et al.* *Int. J. Cancer* 2002; **98**: 793–798.
  77. van Dongen GAMS, Visser GWM and Vrouenraets MB. *Advanced Drug Delivery Reviews* 2004; **46**: 31–52 and references therein.
  78. Savellano MD, Hasan T. *Clin Cancer Res.* 2005 Feb 15; **11**(4): 1658–1668.
  79. Mitsunaga M, Ogawa M, Kosaka N, Rosenblum LT, Choyke PL and Kobayashi H. *Nature Medicine* 2011; **17**: 1685–1710.
  80. Zheng G, Graham A, Shibata M, Missert JR, Oseroff AR, Dougherty TJ and Pandey RK. *J. Org. Chem.* 2001; **66**: 8709–8716.
  81. Zheng X and Pandey RK. *Anticancer Agents Med. Chem.* 2008; **8**: 241–268.
  82. Zheng X, Morgan J, Pandey SK, Chen Y, Tracy E, Baumann H, Missert JR, Batt C, Jackson J, Bellnier DA, Henderson BW and Pandey RK. *J. Med. Chem.* 2009; **52**: 4306–4318.
  83. Sperryak JA, White WH 3rd, Ethirajan M, Patel NJ, Goswami L, Chen Y, Turowski S, Missert JR, Batt C, Mazurchuk R and Pandey RK. *Bioconjug. Chem.* 2010; **21**: 828–835.
  84. Li G, Slansky A, Dobhal MP, Goswami LN, Graham A, Chen Y, Kanter P, Alberico RA, Sperryak J, Morgan J, Mazurchuk R, Oseroff A, Grossman Z and Pandey RK. *Bioconjug. Chem.* 2005; **16**: 32–42.

85. Chen Y, Gryshuk A, Achilefu S, Ohulchansky T, Potter W, Zhong T, Morgan J, Chance B, Prasad PN, Henderson BW, Oseroff A and Pandey RK. *Bioconjug. Chem.* 2005; **16**: 1264–1274.
86. Pandey SK, Gryshuk AL, Sajjad M, Zheng X, Chen Y, Abouzeid MM, Morgan J, Charamisinau I, Nabi HA, Oseroff A and Pandey RK. *J. Med. Chem.* 2005; **48**: 6286–6295.
87. Caravan P, Ellison JJ, McMurry TJ and Lauffer RB. *Chem. Rev.* 1999; **99**: 2293–2352.
88. Aime S, Cabella C, Colombatto S, Geninatti Crich S, Gianolio E and Maggioni F. *J. Magn. Reson. Imaging* 2002; **16**: 394–406.
89. Arbab AS, Bashaw LA, Miller BR, Jordan EK, Lewis BK, Kalish H and Frank JA. *Radiology* 2003; **229**: 838–846.
90. Iyer AK and He J. *Current Medicinal Chemistry* 2012; **19**: 3230–3240.
91. Chen X, Liu S, Hou Y, Tohme M, Park R, Bading JR and Conti PS. *Eur. J. Nucl. Med. Mol. Imaging* 2004; **6**: 350–359.
92. Chen X, Park R, Hou Y, Khankaldyyan V, Gonzales-Gomez I, Tohme M, Bading JR, Laug WE and Conti PS. *Eur. J. Nucl. Med. Mol. Imaging* 2004; **31**: 1081–1089.
93. Chen X, Park R, Tohme M, Shahinian AH, Bading JR and Conti PS. *Bioconjug. Chem.* 2004; **15**: 41–49.
94. Liu S, Hsieh WY, Jiang Y, Kim YS, Sreerama SG, Chen X, Jia B and Wang F. *Bioconjug. Chem.* 2007; **18**: 438–446.
95. Lee HY, Li Z, Chen K, Hsu AR, Xu C, Xie J, Sun S and Chen X. *J. Nucl. Med.* 2008; **49**: 1371–1379.
96. Li ZB, Chen K and Chen X. *Eur. J. Nucl. Med. Mol. Imaging* 2008; **35**: 1100–1108.
97. Liu Z, Yan Y, Liu S, Wang F and Chen X. *Bioconjug. Chem.* 2009; **20**: 1016–1025.
98. Shi J, Liu TW, Chen J, Green D, Jaffray D, Wilson BC, Wang F and Zheng G. *Theranostics* 2011; **1**: 363–370.
99. Subbarayan M, Häfeli UO, Feyes DK, Unnithan J, Emancipator SN and Mukhtar H. *J. Nucl. Med.* 2003; **44**: 650–656.
100. Gupta A, Wang S, Marko A, Joshi P, Ethirajan M, Chen Y, Yao R, Sajjad M, Kopelman R and Pandey RK. *Theranostics* 2014; **4**: 614–628.
101. Chen LD, Liu J, Yu XF, He M, Pei XF, Tang ZY, Wang QQ, Pang DW and Li Y. *Biomaterials* 2008; **29**: 4170–4176.
102. Smith BR, Cheng Z, De A, Koh AL, Sinclair R and Gambhir SS. *Nano Lett.* 2008; **8**: 2599–2606.
103. Chung TH, Hsiao JK, Hsu SC, Yao M, Chen YC, Wang SW, Kuo MY, Yang CS and Huang DM. *ACS Nano*, 2011; **5**: 9807–9816.
104. Xu C, Miranda-Nieves D, Ankrum JA, Matthiesen ME, Phillips JA, Roes I, Wojtkiewicz GR, Juneja V, Kultima JR, Zhao W, Vemula PK, Lin CP, Nahrendorf M and Karp JM. *Nano Lett.* 2012; **12**: 4131–4139.
105. Sun JH, Zhang YL, Qian SP, Yu XB, Xie HY, Zhou L and Zheng SS. *Nano Lett.* 2012; **12**: 4131–4139.
106. Sun JH, Zhang YL, Qian SP, Yu XB, Xie HY, Zhou L and Zheng SS. *Mol. Med. Report* 2012; **5**: 317–320.
107. Bryson JM, Fichter KM, Chu WJ, Lee JH, Li J, Madsen LA, McLendon PM and Reineke TM. *Proc. Natl. Acad. Sci.* 2009; **106**: 16913–16918.
108. Stummer W, Novotny A, Stepp H, Goetz C, Bise K and Reulen HJ. *J. Neurosurg.* 2000; **9**: p. 1003–1013.
109. Zaak D, Hungerhuber E, Schneede P, Stepp H, Frimberger D, Corvin S, Schmeller N, Kriegmair M, Hofstetter A and Knuechel R. *Cancer* 2002; **95**: 1234–1238.
110. Betz CS, Stepp H, Janda P, Arbogast S, Grevers G, Baumgartner R and Leunig A. *Int. J. Cancer* 2002; **97**: 245–252.
111. Moriyama EH, Bisland SK, Lilge L and Wilson BC. *Photochem. Photobiol.* 2004; **80**: p. 242–249.
112. Fradet Y, Grossman HB, Gomella L, Lerner S, Cookson M, Albala D and Droller MJ; PC B302/01 Study Group. *J. Urol.* 2007; **178**: p. 68–73.
113. Nava HR, Allamaneni SS, Dougherty TJ, Cooper MT, Tan W, Wilding G and Henderson BW. *Surg. Med.* 2011; **43**: p. 705–712.
114. Yung A, Stables GI, Fernandez C, Williams J, Bojar RA and Goulden V. *Clin. Exp. Dermatol.* 2007; **32**: 716–721.
115. Gupta A, Wang S, Pera P, Rao KVR, Patel N, Ohulchansky TY, Missert J, Morgan J, Koo-Lee Y-E, Kopelman R and Pandey RK. *Nanomedicine: Nanotechnology, Biology and Medicine* 2012; **8**: 941–950.
116. Wang S, Kim G, Koo-Lee Y-E, Hah HJ, Ethirajan M, Pandey RK and Kopelman R. *ACS Nano*. 2012; **8**: 6843–6851.
117. Zimmermann A. *Photochem. Photobiol.* 2001; **74**: 611–616.
118. Zimmermann A. *Photochem. Photobiol.* 2002; **75**: 335–338.
119. Kostron Hand Rossler K. *Wien. Med. Wochenschr.* 2006; **156**: 338–441.
120. Jayaprakash V, Sullivan M, Merzianu M, Rigual NR, Loree TR, Popat SR, Moysich KB, Ramananda S, Johnson T, Marshall JR, Hutson AD, Mang TS, Wilson BC, Gill SR, Frustino J, Bogaards A and Reid ME. *Cancer Prevention Research* 2009; **2**: 966–974.
121. Rigual NR, Thankappan K, Cooper M, Sullivan MA, Dougherty T, Popat SR, Loree TR, Biel MA and Henderson B. *Archives of Otolaryngology Head & Neck Surgery* 2009; **135**: 784–788.
122. Sunar U, Rohrbach D, Rigual N, Tracy E, Keymel K, Cooper MT, Baumann H and Henderson BH. *Opt Express* 2010; **18**: 14969–14978.
123. Löning M, Diddens H, Küpker W, Diedrich K and Hüttmann G. *Cancer* 2004; **100**: 1650–1656.

124. de Visscher SA, Dijkstra PU, Tan IB, Roodenburg JL and Witjes MJ. *Oral Oncol* 2012.
125. Karakullukcu B, Stoker SD, Wildeman AP, Copper MP, Wildeman MA and Tan IB. *Eur Arch Otorhinolaryngol.* 2012.
126. Song KH, Kim C, Cobley CM, Xia Y and Wang LV. *Nano Lett.* 2009; **9**: 183–188.
127. Kim C, Cho EC, Chen J, Song KH, Au L, Favazza C, Zhang Q, Cobley CM, Gao F, Xia and Y Wang LV. *ACS Nano* 2010; **4**: 4559–4564.
128. Jokerst JV and Gambhir SS. *Acc. Chem. Res.* 2011; **44**: 1050–1060.
129. Wang LV and Hu S. *Science* 2012; **335**: 1458–1462.
130. Nam J, Nam H, Jung S, Hwang S, Wang T, Hur J, Im K, Park N, Kim KH and Kim S. *Chemphyschem.* 2012.
131. Wang J, Dong B, Chen B, Jiang Z and Song H. *Dalton Trans.* 2012; **41**: 11134–11144.
132. Jin H, Yang P, Cai J, Wang J and Liu M. *Appl. Microbiol. Biotechnol.* 2012; **94**: p. 1199–1208.
133. Chen J, Glaus C, Laforest R, Zhang Q, Yang M, Gidding M, Welch MJ and Xia Y. *Small* 2010; **6**: 811–817.
134. Li W, Cai X, Kim C, Sun G, Zhang Y, Deng R, Yang M, Chen J, Achilefu S, Wang LV and Xia Y. *Nanoscale* 2011; **3**: 1724–1730.
135. Wang YH, Liao AH, Chen JH, Wang CR and Li PC. *J. Biomed. Opt.* 2012; **17**: 045001.
136. Coffey DS, Getzenberg RH and DeWeese TL. *JAMA* 2006; **296**: p. 445–448.
137. Dayanc BE, Beachy SH, Ostberg JR and Repasky EA. *Int. J. Hyperthermia* 2008; **24**: 41–56.
138. Skitzki JJ, Repasky EA and Evans SS. *Curr. Opin. Investig. Drugs* 2009; **10**: 550–558.
139. Peer AJ, Grimm MJ, Zynda ER and Repasky EA. *Immunol Res.*, 2010; **46**: 137–154.
140. Peer AJ, Grimm MJ, Zynda ER and Repasky EA. *Cancer Res.* 2011; **71**: 3872–3880.
141. Mace TA, Zhong L, Kilpatrick C, Zynda E, Lee CT, Capitano M, Minderman H and Repasky EA. *J. Leukoc. Biol.* 2011; **90**: 951–962.
142. Fisher DT, Chen Q, Skitzki JJ, Muhitch JB, Zhou L, Appenheimer MM, Vardam TD, Weis EL, Passanese J, Wang WC, Gollnick SO, Dewhirst MW, Rose-John S, Repasky EA, Baumann H and Evans SS. *J. Clin. Invest.* 2011; **121**: 3846–3859.
143. Beachy SH and Repasky EA. *Int. J. Hyperthermia* 2011; **27**: 344–352.
144. Gollnick S and Brackett CM. *Immunol. Res.* 2010; **46**: 216–226.
145. Brackett CM and Gollnick SO. *Photochem. Photobiol. Sci.* 2011; **10**: 649–652.
146. Gollnick S. *J. Natl. Compr. Cancer Network* 2012; **10**: S40–43.
147. Srivatsan A, Jenkins SV, Jeon M, Wu Z, Kim C, Chen J and Pandey RK. *Theranostics*, 2014; **4**: 163–174.





# Macrocyclic dipyririn dimer bridged by ethylene and dioxyphenylene linkers

Ji-Young Shin<sup>\*◇</sup>, Satoru Hiroto<sup>◇</sup> and Hiroshi Shinokubo<sup>◇</sup>

Department of Applied Chemistry, Graduate School of Engineering, Nagoya University, Furo-cho, Chikusa-ku, Nagoya 464-8603, Japan

*Dedicated to Professor Shunichi Fukuzumi on the occasion of his retirement*

Received 29 August 2014

Accepted 17 September 2014

**ABSTRACT:** A tetrapyrrolic macrocycle containing ethylene and dioxyphenylene bridges was obtained through the reaction of a dipyririn-DDQ adduct with triethylamine. The structure of the macrocycle was elucidated by X-ray diffraction analysis. The macrocycle exhibited solvent-dependent absorption spectra due to intramolecular charge transfer interactions.

**KEYWORDS:** dipyririn, DDQ oxidation, intramolecular charge transfer.

## INTRODUCTION

2,3-Dichloro-5,6-dicyano-1,4-benzoquinone (DDQ) is a convenient dehydrogenating agent, which has been commonly used in numerous chemical reactions [1–10]. In particular, DDQ is the first choice for the oxidative conversion of porphyrinogens and dipyrromethanes to the corresponding porphyrins and dipyririns. However, DDQ sometimes induces unexpected reactions to provide DDQ adducts. In 1965, H.-D. Becker reported the formation of hydroquinone ethers in the oxidations of phenols through radical pathways [11]. In our previous research, we have reported that DDQ afforded a series of DDQ-adducts upon treatment with dipyrromethanes [12, 13]. Namely, DDQ could act not only as a simple oxidant but also as a coupling partner with dipyririns. In addition, bisdipyririn-DDQ adduct **1** was converted to novel dicyanoethylene-bridged bisdipyririn **2** in the presence of an excess amount of Et<sub>3</sub>N (>1.5 equiv.) in a few minutes (Scheme 1) [13]. We then found that the use of a decreased amount of Et<sub>3</sub>N changed the reaction outcome. Here we disclose the details of the structure and the characteristic absorption spectra of the product.

<sup>◇</sup> SPP full member in good standing

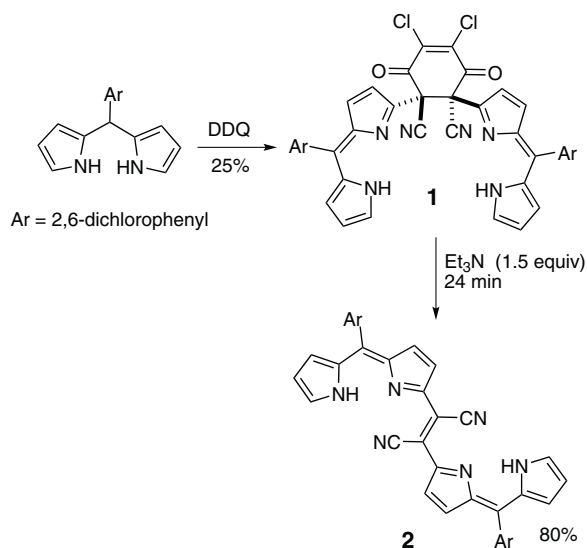
\*Correspondence to: Ji-Young Shin, email: jyshin@apchem.nagoya-u.ac.jp, tel/fax: +81 52-789-6771

## RESULTS AND DISCUSSION

We found that treatment of bisdipyririn-DDQ adduct **1** with 0.9 equiv. of Et<sub>3</sub>N resulted in the formation of the new polypyrrolic product **3** in 31% yield (Scheme 2). Formation of bisdipyririn **2** was not observed in this case. <sup>1</sup>H NMR of **3** displayed broad β-pyrrole proton signals which were hard to assign to the product.

Fortunately, we succeeded in growing plate-shaped single crystals of **3**. The structure of **3** was elucidated by X-ray diffraction analysis [14] and HR-MS derived accurate masses for the corresponding molecular formulae. Figure 1 shows the crystal structure of compound **3**. Interestingly, dioxyphenylene and ethylene moieties bind two dipyririn units into a macrocyclic structure. In the crystal packing, two conformers (**A** and **B** in Fig. 1) were observed as a set of unit. While the conformer **B** shows a tilted structure on the main skeleton of the macrocycle, the other conformer **A** exhibits rather planar structure. Mean deviation of **A** is 0.225 Å, which indicates its highly planar structure. Dihedral angles of two dipyririn moieties in each macrocycle were measured with 4.57° and 21.0° for **A** and **B**, respectively. In both structures, the dioxyphenylene ring is perpendicular to the main plane of the macrocycle composed of dicyanoethylene bisdipyririn, due to steric hindrance.

The structure of **3** exhibits intramolecular hydrogen bonding interactions, which induce downfield-shift of two

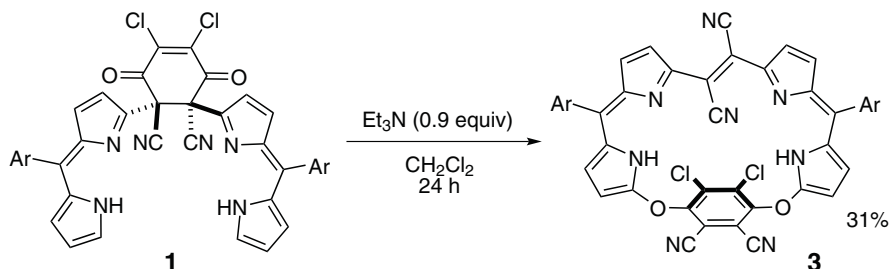


**Scheme 1.** Formation of dicyanoethylene-bridged bisdipyrrin **2** from bisdipyrrin-DDQ adduct **1**

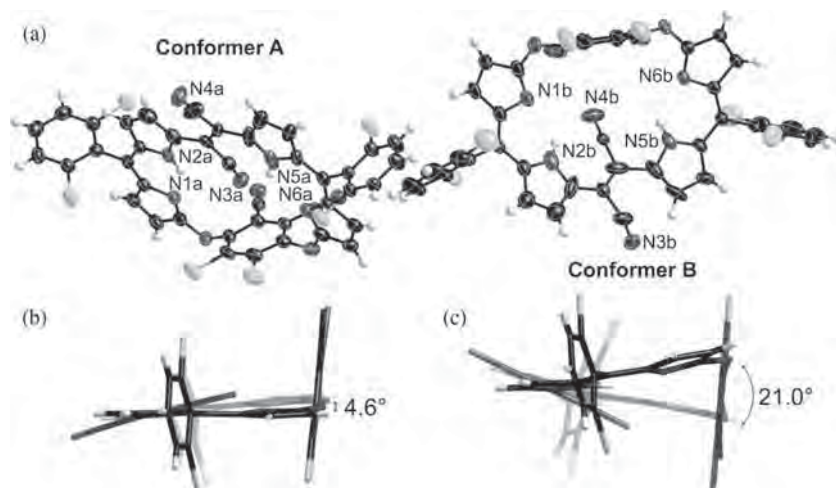
NH peaks in its  $^1\text{H}$  NMR spectrum (12.29 and 12.84 ppm for its  $\text{CD}_2\text{Cl}_2$  solution). The pyrrole proton signals were broadened at rt, which probably suggests tautomerism in the dipyrin moieties. We then measured temperature

dependence of the proton peaks. The overall peaks sharpened to give their individual coupling constant as the temperature decreased (Fig. 2). The peaks which appeared as broad singlets at rt started being split and sharpened. Finally, those peaks were observed as sets of respective double-doublet or doublets at  $-50^\circ\text{C}$ : two sets of pyrrole  $\beta$ -proton peaks (each set is two double-doublet peaks) were found at 7.20 and 6.77 ppm and at 6.16 and 6.07 ppm, respectively. Another two sets of pyrrole  $\beta$ -proton peaks were found as doublets at 6.77 and 6.55 ppm and at 6.70 and 6.54 ppm, respectively.

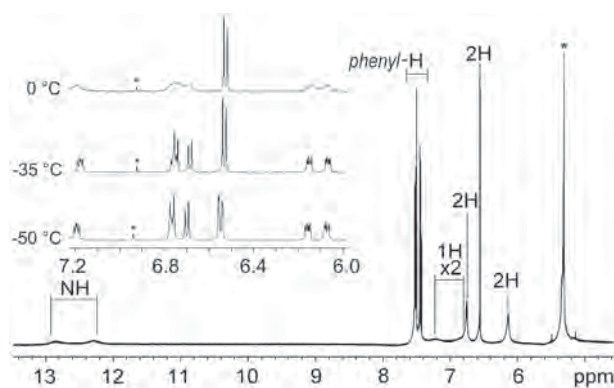
Compared to a typical absorption band of dipyrins, the absorption bands of **2** and **3** which contain dicyanoethylene linkers were largely bathochromic-shifted due to the extended  $\pi$ -conjugation through the ethylene-bridge (Fig. 3:  $\lambda_{\text{max}} = 736$  and  $662$  nm for **2** and **3**, respectively). Similarly, the emission bands of **2** and **3** were also observed at substantially long wavelength ranges ( $\lambda_{\text{em}} = 778$  and  $705$  nm for **2** and **3**, respectively). Furthermore, the addition of the dioxyphenylene-bridge induced hypsochromic shifts in both absorption and emission bands. This change is fairly consistent with the result of cyclic voltammetry for those compounds in which the gap of the first oxidation and reduction potentials decreased. The differences between  $E_{\text{ox}}^1$  and  $E_{\text{red}}^1$  for **2**



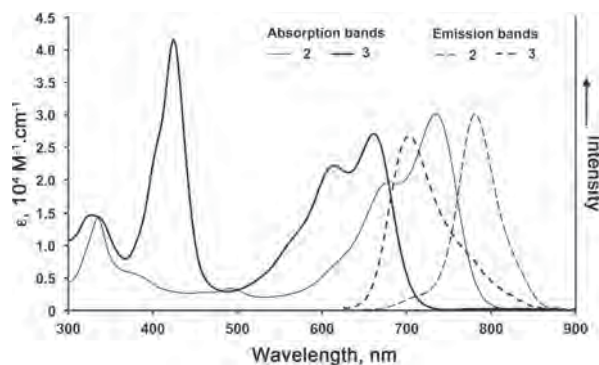
**Scheme 2.** Formation of macrocyclic bisdipyrrin **3** from bisdipyrrin-DDQ adduct **1**: Ar = 2,6-dichlorophenyl



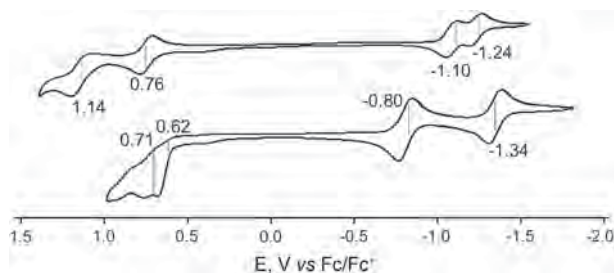
**Fig. 1.** Crystal structure of the macrocycle **3**. (a) Structures of conformers **A** and **B** and side views of (b) conformer **A** and (c) conformer **B**. Thermal ellipsoids are scaled with 50% probability level. Dihedral angles of two dipyrin moieties are shown in (b) and (c)



**Fig. 2.**  $^1\text{H}$  NMR spectra of macrocycle **3** in  $\text{CD}_2\text{Cl}_2$  at various temperatures



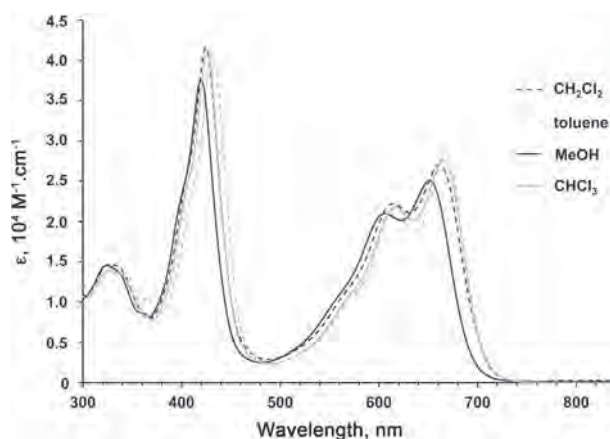
**Fig. 3.** Optical spectra of compounds **2** and **3** in  $\text{CH}_2\text{Cl}_2$



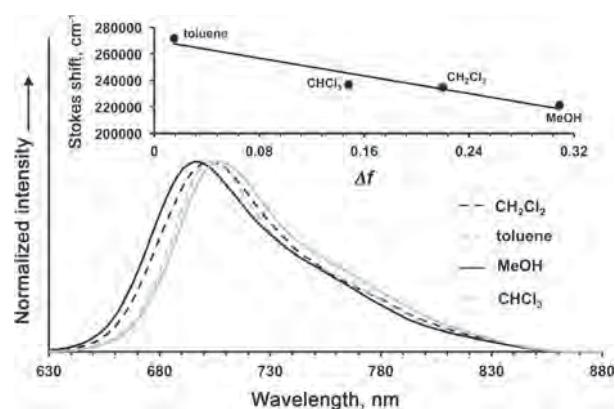
**Fig. 4.** Cyclic voltammograms of **2** (bottom) and **3** (top) in  $\text{CH}_2\text{Cl}_2$  containing  $\text{Bu}_4\text{NPF}_6$  at rt: working electrode = glassy carbon, counter electrode = Pt wire, reference electrode =  $\text{Ag}/\text{Ag}^+$  and scan rate =  $50 \text{ mV}\cdot\text{s}^{-1}$



**Fig. 7.** Frontier orbitals of compound **3** calculated at the B3LYP/6-31G(d) level



**Fig. 5.** Absorption spectral dependence of **3** on the selected organic solvents



**Fig. 6.** Dependence of fluorescence spectra of **3** on polarity of selected solvents and its Lippert–Mataga plot (inset).  $\Delta f$  denotes orientation polarizability

and **3** were found to be 1.42 V and 1.86 V, respectively (Fig. 4). Interestingly, a high solvent dependence was observed in the absorption spectra of **3**. Fig. 5 shows UV-vis absorption spectra of **3** in four selected solvents where the dependency of the spectra on solvent polarity was observed. The absorption band near the longest wavelength gradually bathochromic-shifts in accordance with decreases in solvent polarity. The solvent dependence

was also observed in emission spectra of **3** (Fig. 6). The spectral changes dependent on the solvent-polarity were analyzed by Lippert–Mataga plot [15, 16]. Relatively large slope of  $-167140\text{ cm}^{-1}$  indicates an intramolecular charge transfer interaction in **3**.

To investigate the observed intramolecular charge transfer character in **3**, we carried out molecular orbital calculations by the DFT method at the B3LYP/6-31G(d) level of theory. As shown in Fig. 7, LUMO in **3** is localized at the dioxyphenylene moiety, while HOMO is delocalized at both the dicyanoethylene-bridge and dipyrin units, suggesting the existence of the intramolecular charge transfer interactions.

## EXPERIMENTAL

### General

$^1\text{H}$  NMR (500 MHz) and  $^{13}\text{C}$  NMR (126 MHz) spectra were recorded on a Varian INOVA-500 spectrometer. The chemical shifts,  $\delta$ s, were reported in ppm relative to the solvent taken for the measurement ( $\text{CDCl}_3$ ,  $\delta = 7.26$  ppm for  $^1\text{H}$  NMR and  $\delta = 77.0$  ppm for  $^{13}\text{C}$  NMR, respectively;  $\text{CD}_2\text{Cl}_2$ ,  $\delta = 5.32$  ppm for  $^1\text{H}$  NMR). UV-vis absorption spectrum was recorded on a Shimadzu UV2550 spectrometer. Mass spectrum was recorded on a Bruker micrOTOF using the ESI-TOF method with a  $\text{CH}_3\text{CN}$  solution of the compound. X-ray diffraction data were collected on a Bruker SMART APEX XRD equipped with a large area CCD detector and the collected data was integrated by using the Bruker SAINT software package. The refined structure was afforded by using the SHELX crystallographic program in the Bruker-AXS software package. Calculation was assessed on the Gaussian03 program. Commercially acquired chemicals were used without further purification.

### Synthesis of cyclic bisdipyrin **3**

*Meso*-2,6-dichlorophenyldipyrromethane was prepared according to the reference method [17]. Column chromatography on silica gel followed by recrystallization from  $\text{CH}_2\text{Cl}_2$ /hexane yielded an off-white solid. DDQ adduct **1** was prepared from *meso*-2,6-dichlorophenyldipyrromethane following the reference method [12, 18] and purified by column chromatography (using silica gel and neat  $\text{CH}_2\text{Cl}_2$ ) and recrystallization (from  $\text{CH}_2\text{Cl}_2$ /hexane). Compound **3** was obtained from the treatment of a  $\text{CH}_2\text{Cl}_2$  (75 mL) solution of **1** (30 mg,  $37.4\text{ }\mu\text{mol}$ ) with  $\text{Et}_3\text{N}$  (5  $\mu\text{L}$ ,  $34.3\text{ }\mu\text{mol}$ ) and purified by column chromatography on silica gel using neat  $\text{CH}_2\text{Cl}_2$  as eluent. Green color in regular organic solvent. Yield 10 mg ( $11.4\text{ }\mu\text{mol}$ , 31%).  $^1\text{H}$  NMR (500 MHz;  $\text{CD}_2\text{Cl}_2$ , rt):  $\delta_{\text{H}}$ , ppm 6.15 (bs, 2H,  $\beta\text{H}$ ), 6.56 (d, 2H,  $J = 5.0$ ,  $\beta\text{H}$ ), 6.76 (bs, 3H,  $\beta\text{H}$ ), 7.22 (bs, 1H,  $\beta\text{H}$ ), 7.44 (t, 2H,  $J = 8.0$ , Aryl-H), 7.53 (m, 4H, Aryl-H), 12.29 (bs, 1H, NH),

12.84 (bs, 1H, NH).  $^{13}\text{C}$  NMR (125 MHz;  $\text{CD}_2\text{Cl}_2$ ):  $\delta_{\text{C}}$ , ppm 111.1, 114.2, 118.0, 119.7, 128.2, 128.3, 129.5, 130.8, 136.4, 137.9, 140.0, 171.6. HR-MS (ESI-MS):  $m/z$  874.9478 (calcd. for  $[\text{M} - \text{H}]^-$ : 874.9419,  $\text{C}_{42}\text{H}_{15}\text{N}_8\text{Cl}_6\text{O}_2^-$ ). UV-vis ( $\text{CH}_2\text{Cl}_2$ ):  $\lambda_{\text{max}}$ , nm (log  $\epsilon$ ), 325.5 (4.33), 424.5 (5.77), 613.5 (4.49), 661 (4.58).

## CONCLUSION

In conclusion, treatment of the bisdipyrin-DDQ adduct **1** with  $\text{Et}_3\text{N}$  afforded a unique macrocycle **3** containing a dicyanoethylene bridge and a dioxyphenylene moiety. As compared to acyclic bisdipyrin **2**, the existence of the dioxyphenylene moiety in **3** increases the HOMO–LUMO gap and induces hypsochromic shifts in both the absorption and emission bands. Both optical spectra exhibit significant solvent-dependence due to an intramolecular charge transfer interaction. Cyclic/acyclic compounds derived from dipyrins provide a diversity of chemophysical and metal-complexation properties, which makes them applicable to various chemistry fields such as molecular recognition and coordination polymers [19]. Elucidation of the reaction mechanism for the formation of **3** and study of these application of these dicyanoethylene-bridged bisdipyrins are underway.

### Acknowledgements

This research was supported by a Grant-in-Aid for Scientific Research (C) (No. 26410042) from MEXT (Japan). We also acknowledge G30 program of Nagoya university for support of this work.

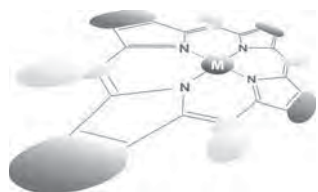
### Supporting information

Crystallographic data for compound **3** have been deposited at the Cambridge Crystallographic Data Centre (CCDC) under number CCDC-953877. Copies can be obtained on request, free of charge, via [www.ccdc.cam.ac.uk/data\\_request/cif](http://www.ccdc.cam.ac.uk/data_request/cif) or from the Cambridge Crystallographic Data Centre, 12 Union Road, Cambridge CB2 1EZ, UK (fax: +44 1223-336-033 or email: [deposit@ccdc.cam.ac.uk](mailto:deposit@ccdc.cam.ac.uk)).

## REFERENCES

- Walker D and Hiebert JD. *Chem. Rev.* 1967; **67**: 153–195.
- Lindsey JS, Schreiman IC, Hsu HC, Kearney PC and Marguerettaz AM. *J. Org. Chem.* 1987; **52**: 827–836.
- Yu L, Muthukumar K, Sazanovich IV, Kirmaier C, Hindin E, Diers JR, Boyle PD, Bocian Df, Holten D and Lindsey JS. *Inorg. Chem.* 2003; **42**: 6629–6647.
- Geier GR III, Chick JF, Callinan JB, Reid CG and Auguscinski WP. *J. Org. Chem.* 2004; **69**: 4159–4169.

5. Capella L, Montevecchi PC and Nanni D. *J. Org. Chem.* 1994; **59**: 7379–7382.
6. Brückner C, Karunaratne V, Rettig SJ and Dolphin D. *Can. J. Chem.* 1996; **74**: 2182–2193.
7. Lindsey JS. In *The Porphyrin Handbook*, Vol. 1, Kadish KM, Smith KM and Guillard R. (Eds.) Academic Press: San Diego, CA, 2000.
8. Gross Z, Galili N and Saltsman I. *Angew. Chem. Int. Ed.* 1999; **38**: 1427–1429.
9. Shin JS, Furuta H, Yoza K, Igarashi S and Osuka A. *J. Am. Chem. Soc.* 2001; **123**: 7190–7191.
10. Wood TE and Thompson A. *Chem. Rev.* 2007; **107**: 1831–1861.
11. Becker HD. *J. Org. Chem.* 1965; **30**: 982–989.
12. Shin JS, Hepperle SS, Patrick BO and Dolphin D. *Chem. Commun.* 2009; 2323–2325.
13. Shin JS, Patrick BO and Dolphin D. *Org. Biomol. Chem.* 2009; **7**: 2032–2035.
14. The crystallographic data for **3** has been deposited with the Cambridge Crystallographic Data Centre (CCDC–953877).
15. Huang Y, Cheng T, Li F, Luo C, Huang CH, Cai Z, Zeng X and Zhou J. *J. Phys. Chem. B* 2002; **106**: 10031–10040.
16. Smallwood IM. *Handbook of Organic Solvent Properties*, Arnold: London, UK, 1996.
17. Lee CH and Lindsey JS. *Tetrahedron* 1994; **50**: 11427–11440.
18. Shin JS and Dolphin D. *New J. Chem.* 2011; **35**: 2483–2487.
19. (a) Korobkov I, Gambarotta S and Yap GPA. *Angew. Chem. Int. Ed.* 2002; **41**: 3433–3436. (b) Gale PA, Anzenbacher P and Sessler JL. *Coord. Chem. Rev.* 2001; **222**: 57–102. (c) Love JB. *Chem. Commun.* 2009; 3154–3165. (d) Dong B, Sakurai T, Honsho Y, Seki S and Maeda H. *J. Am. Chem. Soc.* 2013; **135**: 1284–1287. (e) Wang Q, Xie Y, Ding Y, Li X and Zhu W. *Chem. Commun.* 2010; **46**: 3669–3671.



# Synthesis of push–pull porphyrin with two electron-donating and two electron-withdrawing groups and its application to dye-sensitized solar cell

Tomohiro Higashino<sup>a</sup>, Yamato Fujimori<sup>a</sup>, Kenichi Sugiura<sup>a</sup>, Yukihiro Tsuji<sup>a</sup>,  
Seigo Ito<sup>b</sup> and Hiroshi Imahori<sup>\*a,c,d</sup>

<sup>a</sup>Department of Molecular Engineering, Graduate School of Engineering, Kyoto University, Nishikyo-ku, Kyoto 615-8510, Japan

<sup>b</sup>Department of Electrical Engineering and Computer Sciences, Graduate School of Engineering, University of Hyogo, 2167 Shosha, Himeji, Hyogo 671-2280, Japan

<sup>c</sup>Institute for Integrated Cell-Material Sciences (WPI-iCeMS), Kyoto University, Nishikyo-ku, Kyoto 615-8510, Japan

*Dedicated to Professor Shunichi Fukuzumi on the occasion of his retirement*

Received 2 September 2014

Accepted 29 September 2014

**ABSTRACT:** We synthesized for the first time a push–pull porphyrin dye bearing two diarylamino groups and two carboxyphenylethynyl groups as electron-donating and electron-withdrawing anchoring groups, respectively. The absorption spectrum displayed broad and red-shifted absorption, achieving panchromatic light-harvesting in visible and NIR regions. Introduction of multiple push–pull groups into *meso*-positions is a promising strategy for the rational design of porphyrin sensitizers for light-harvesting applications. The preliminary photovoltaic performance is moderate (3.0%), but the extensive photocurrent generation matches with the excellent light-harvesting ability. Further modulation of the photovoltaic properties of porphyrin DSSCs will be possible by suitable selection of electron-donating and electron-withdrawing groups as well as introduction of the substituents into the porphyrin core.

**KEYWORDS:** porphyrin, solar cell, titanium oxide.

## INTRODUCTION

In recent years, the increasing energy consumption and concern about environmental issues strongly demand utilization of sunlight as alternative, clean and renewable energy resource. In this regard, photovoltaic cells are promising technologies that directly convert solar energy into electricity. Since the seminal paper was reported by Grätzel and co-workers in 1991 [1], dye-sensitized solar cells (DSSCs) have attracted much attention as an alternative to silicon-based solar cells because of their low cost production and high power conversion

efficiency. Numerous organometallic/organic dyes have been investigated for their application to DSSCs [2–21]. Among these, porphyrins are regarded as a promising candidate due to their intense absorption in visible and near-infrared (NIR) regions, and versatile molecular design. However, typical porphyrins have a limited light-harvesting ability at 450–500 nm and >600 nm. To overcome this drawback, various porphyrin dyes exhibiting broad and red-shifted absorption have been assessed for DSSCs [10–21]. The development of novel porphyrins possessing excellent light-harvesting ability is crucial to high-performance DSSC as well as light-harvesting devices. In fact, high power conversion efficiency ( $\eta$ ) more than 10% has been demonstrated in DSSCs based on push–pull type porphyrin dyes [15–21]. Importantly, the  $\eta$  value has increased up to *ca.* 13% by

<sup>d</sup>SPP full member in good standing

\*Correspondence to: Hiroshi Imahori, email: imahori@scl.kyoto-u.ac.jp

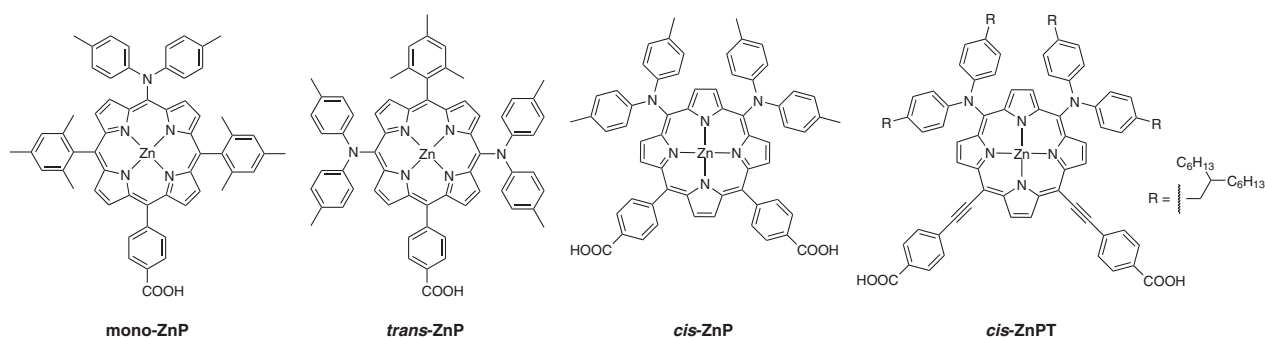
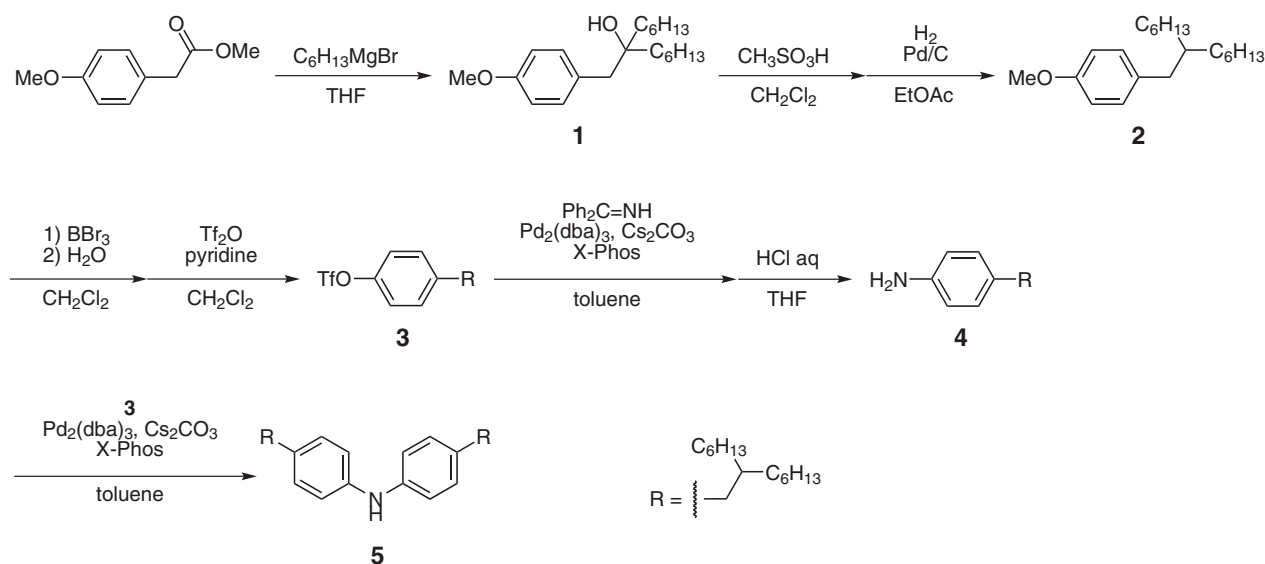


Fig. 1. Molecular structures of porphyrins in previous [22] and this work



Scheme 1. Synthesis of diarylamine 5

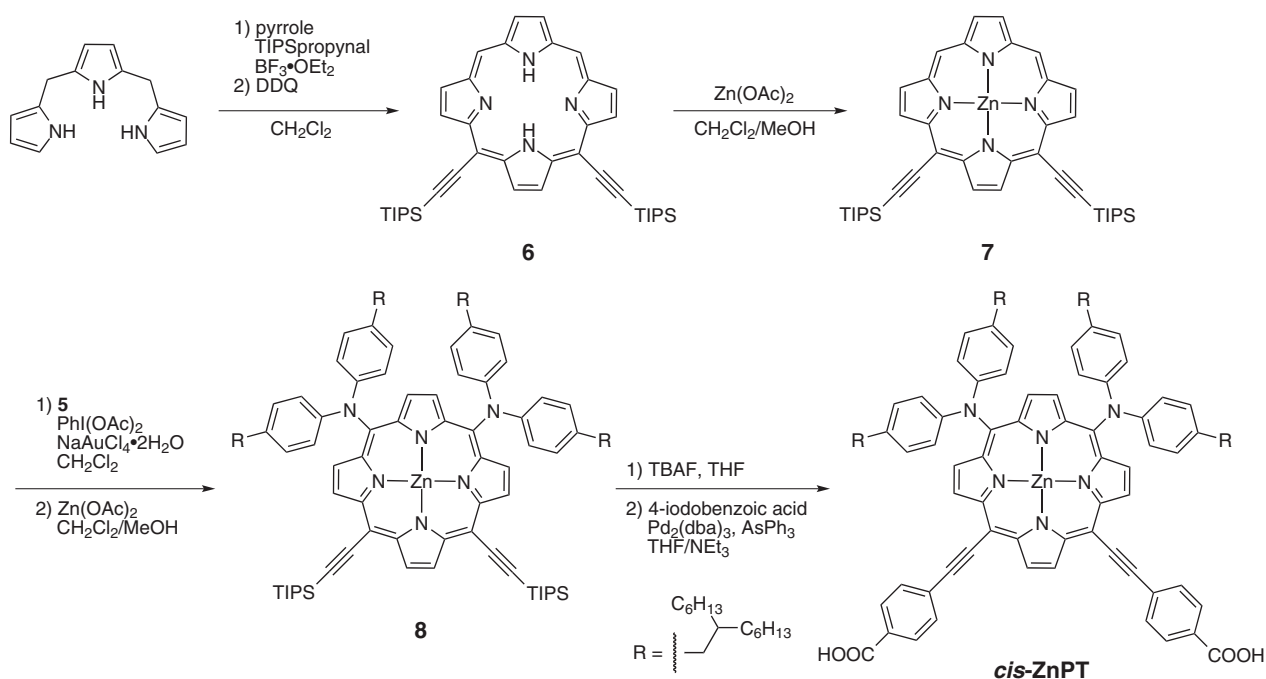
using cobalt-based redox shuttle [19, 20]. We previously reported the influences of the number and substitution position of diarylamino groups at the *meso*-positions of carboxyphenylporphyrins on the optical and photovoltaic properties (Fig. 1) [22]. Porphyrin dyes bearing two diarylamino groups (*trans*-ZnP, *cis*-ZnP) displayed better light-harvesting abilities than porphyrin bearing one diarylamino group (*mono*-ZnP). In contrast, the  $\eta$ -values of the cells with *trans*-ZnP and *cis*-ZnP were inferior to that with *mono*-ZnP. This can be attributed at least partially to the lower electron density distribution of the electron-withdrawing anchoring group in LUMO, resulting in insufficient electron injection into conduction band (CB) of TiO<sub>2</sub> from the excited porphyrin singlet state. Introduction of phenylethynyl group into the *meso*-position is known to induce a more effective  $\pi$ -conjugation with the porphyrin core than that of phenyl group [18]. Therefore, we thought that replacement of carboxyphenyl group with carboxyphenylethynyl group at the *meso*-position would lead to efficient electron injection to TiO<sub>2</sub> as well as improvement of the light-harvesting ability.

Herein, we report the synthesis of novel push-pull porphyrin *cis*-ZnPPT bearing two diarylamino groups as electron-donating substituents and two carboxyphenylethynyl groups as electron-withdrawing anchoring groups with *cis*-configurations (Fig. 1). Optical and electrochemical properties of *cis*-ZnPPT were examined in comparison with *cis*-ZnP. Preliminary photovoltaic properties of *cis*-ZnPPT DSSC were also investigated.

## RESULTS AND DISCUSSION

### Synthesis

Solubility of sensitizer dyes is a key factor to ensure the adsorption on TiO<sub>2</sub>. Thus, we used 2-hexyloctyl group into the *meso*-position of diarylamino moieties of *cis*-ZnPPT as solubilizing groups. First, functionalized diarylamine 5 as an important intermediate precursor was prepared, as illustrated in Scheme 1.

Scheme 2. Synthesis of porphyrin dye *cis-ZnPT*

The reaction of methyl 2-(4-methoxyphenyl)acetate with hexylmagnesium bromide provided alcohol **1**. Dehydration of **1** with methanesulfonic acid followed by hydrogenation gave anisole **2** bearing the branched alkyl chain. The methoxy group of **2** was converted to triflate of **3** by demethylation and subsequent reaction with trifluoromethanesulfonic anhydride. Then, palladium-catalyzed cross coupling reaction with benzophenone imine furnished aniline **4** after treatment with diluted hydrochloric acid. Diarylamine **5** was obtained by further palladium-catalyzed cross coupling of **4** with triflate **3**.

In the next step, porphyrin dye *cis-ZnPT* was synthesized according to Scheme 2. Porphyrin precursor **6** with two ethynyl groups at *cis*-configuration was prepared by acid-catalyzed condensation of tripyrrane [23], triisopropylsilylpropynal [24] and pyrrole. After zinc insertion, oxidative amination of **7** [25] with diarylamine **5** yielded *meso*-bis(diarylaminoporphyryne) **8**. Finally, deprotection of triisopropylsilyl (TIPS) groups of **8** by tetrabutylammonium fluoride (TBAF) followed by Sonogashira coupling reaction afforded desired porphyrin dye *cis-ZnPT*, bearing the two electron-donating diarylamino groups and the two electron-withdrawing anchoring carboxyphenylethynyl groups.

### Optical and electrochemical properties

The UV-vis absorption spectrum of *cis-ZnPT* in ethanol is depicted in Fig. 2. The Soret band is split and broadened covering wavelengths from 400 nm to 550 nm. The Q-bands are also broadened and red-shifted compared with *cis-ZnP* [22] due to the extension of  $\pi$ -conjugation

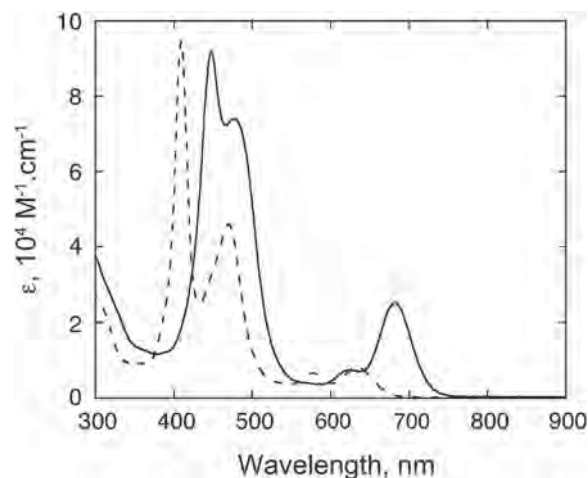


Fig. 2. UV-vis absorption spectra of *cis-ZnPT* in ethanol (solid line) and *cis-ZnP* in dichloromethane (dashed line) [22]

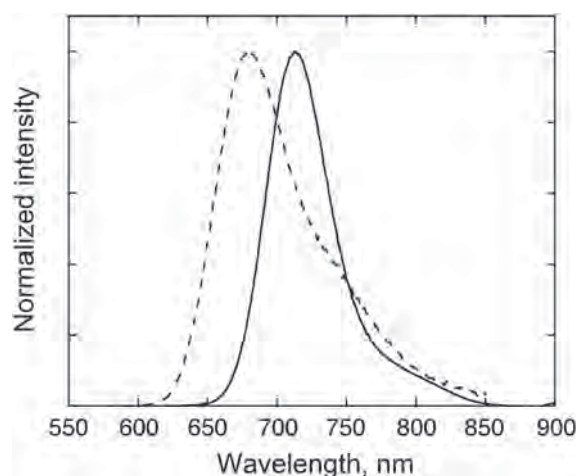
by the additional ethynyl moieties. The lowest-energy Q-band absorption of *cis-ZnPT* (684 nm) is even more red-shifted than that of porphyrin dye SM315 (668 nm) that recorded the highest  $\eta$  value of 13% [20]. The steady-state fluorescence spectrum of *cis-ZnPT* was measured in ethanol (Fig. 3). In accordance with the absorption properties, the emission maximum of *cis-ZnPT* (713 nm) is shifted toward longer wavelength in comparison with *cis-ZnP* (680 nm) [22]. From the intersection of the normalized absorption and emission spectra, the zero-zero excitation energy ( $E_{0-0}$ ) is determined to be 1.78 eV (Table 1), which is smaller than that of *cis-ZnP* (1.89 eV).



**Table 1.** Optical and electrochemical data and driving forces for electron transfer processes on TiO<sub>2</sub>

	$\lambda_{\text{abs}}^{\text{a}}$ , nm ( $\epsilon$ , 10 <sup>3</sup> M <sup>-1</sup> .cm <sup>-1</sup> )	$\lambda_{\text{em}}^{\text{b}}$ , nm	$E_{\text{ox}}^{\text{c}}$ , V	$E_{\text{red}}^{\text{c}}$ , V	$E_{0-0}^{\text{d}}$ , V	$E_{\text{ox}}^{*\text{e}}$ , V	$\Delta G_{\text{inj}}^{\text{f}}$ , eV	$\Delta G_{\text{reg}}^{\text{g}}$ , eV
<i>cis</i> -ZnPT	448 (91.5) <sup>a</sup>	713	0.89	-0.85	1.78	-0.89	-0.39	-0.49
	478 (74.1) <sup>a</sup>							
	624 (7.57) <sup>a</sup>							
	684 (25.2) <sup>a</sup>							
<i>cis</i> -ZnP <sup>h</sup>	408 (96)	680	0.77	-1.13	1.89	-1.12	-0.62	-0.37
	476 (35)							
	577 (6)							
	636 (8)							

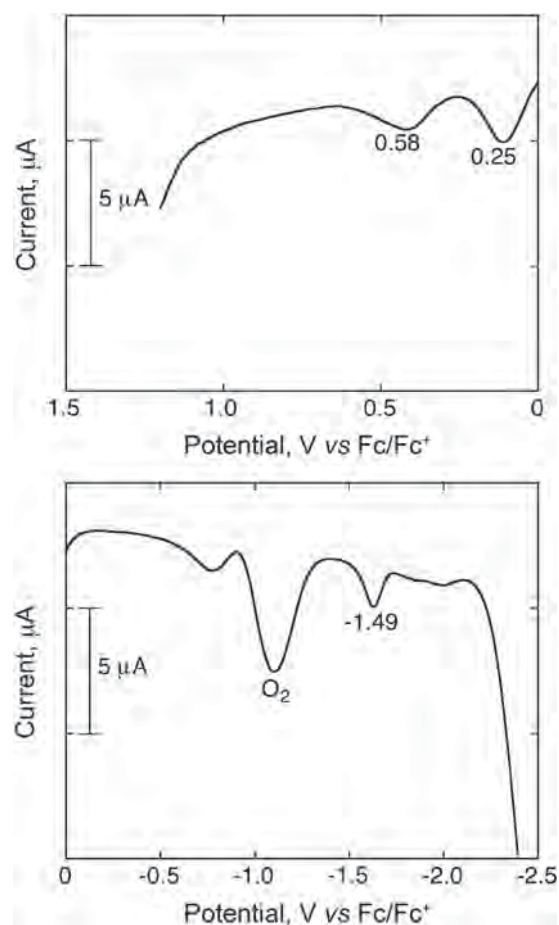
<sup>a</sup>Wavelengths for Soret and Q-bands maxima in ethanol. <sup>b</sup>Wavelength for emission maximum by exciting at Soret band. <sup>c</sup>Determined by using DPV (vs. NHE). <sup>d</sup>Determined from intersection of the normalized absorption and emission spectra. <sup>e</sup>Determined by adding  $E_{0-0}$  to  $E_{\text{ox}}$  (vs. NHE). <sup>f</sup>Driving force for electron injection from the porphyrin singlet excited state into the CB of TiO<sub>2</sub> (-0.5 V vs. NHE). <sup>g</sup>Driving force for dye regeneration by I/I<sub>3</sub><sup>-</sup> redox shuttle (0.4 V vs. NHE). <sup>h</sup>Taken from Ref. 22.



**Fig. 3.** Normalized fluorescence spectra of *cis*-ZnPT in ethanol (solid line) and *cis*-ZnP in dichloromethane (dashed line) [22]. The samples were excited at Soret band

These results corroborate that replacement of the carboxyphenyl groups with the carboxyphenylethynyl groups at the *meso*-positions improves the light-harvesting ability of the porphyrin dye in visible and NIR regions.

To determine the first oxidation potential ( $E_{\text{ox}}$ ) and reduction potential ( $E_{\text{red}}$ ) of *cis*-ZnPT, differential pulse voltammetry (DPV) measurements were conducted in CH<sub>2</sub>Cl<sub>2</sub> containing 0.1 M tetrabutylammonium hexafluorophosphate (Bu<sub>4</sub>N<sup>+</sup>PF<sub>6</sub><sup>-</sup>) as an electrolyte (Fig. 4). The  $E_{\text{ox}}$  value of *cis*-ZnPT (0.89 V vs. NHE) is slightly higher than that of *cis*-ZnP (0.77 V vs. NHE [22]), whereas the  $E_{\text{red}}$  value of *cis*-ZnPT (-0.85 V vs. NHE) is significantly shifted to positive direction relative to *cis*-ZnP (-1.13 V vs. NHE [22]). These results imply that the replacement of the carboxyphenyl groups with the carboxyphenylethynyl groups at the *meso*-positions largely affects the  $E_{\text{red}}$  value because of the more



**Fig. 4.** Differential pulse voltammetry (DPV) curves of *cis*-ZnPT. The sweeps are shown in (a) oxidation and (b) reduction regions with a sweep rate of 40 mV.s<sup>-1</sup>. The peaks at 0.25 V and 0.58 V vs. Fc/Fc<sup>+</sup> originate from the first and second oxidation of *cis*-ZnPT, whereas that at -1.49 V vs. Fc/Fc<sup>+</sup> from the first reduction of *cis*-ZnPT. The DPV measurements were performed in dichloromethane containing 0.1 M Bu<sub>4</sub>NPF<sub>6</sub> as a supporting electrolyte

electron-withdrawing nature of the carboxyphenylethynyl groups. The electrochemical HOMO–LUMO gap of *cis*-ZnPT (1.74 eV) is smaller than that of *cis*-ZnP (1.90 eV), which agrees with the trend on the optical bandgaps. From the spectroscopic and electrochemical measurements, the driving forces for electron injection ( $\Delta G_{\text{inj}}$ ) from the porphyrin singlet excited state into the CB of TiO<sub>2</sub> (-0.5 V vs. NHE [18]), and for regeneration of the porphyrin dye ( $\Delta G_{\text{reg}}$ ) by I<sup>-</sup>/I<sub>3</sub><sup>-</sup> redox shuttle (+0.4 V vs. NHE [18]) are calculated (Table 1). Since these driving forces are more negative than -0.3 eV, electron injection and dye regeneration processes are thermodynamically feasible and the driving forces are sufficient for efficient electron transfer.

To gain insight into the ground state geometry of *cis*-ZnPT and electron density distribution of HOMO and LUMO, we performed DFT calculations (B3LYP/6-31G\*) [26]. *cis*-ZnPT is found to possess a planar porphyrin ring to which the diarylamino groups are almost perpendicular, avoiding the steric congestion around the *meso*-positions. The calculated HOMO–LUMO gap of *cis*-ZnPT (2.12 eV) is smaller than that of *cis*-ZnP (2.49 eV), which is consistent with the trends on the optical and electrochemical HOMO–LUMO gaps. The electron density of the carboxylic acid anchoring group in the LUMO of *cis*-ZnPT is remarkably larger than that of *cis*-ZnP [22] (Fig. 5). The electron density distribution of LUMO around an anchoring group is known to influence the electronic coupling between the excited adsorbed dye and 3d orbital of TiO<sub>2</sub> [22]. Thus, we can anticipate efficient electron injection from the dye excited state to the CB of TiO<sub>2</sub> compared with that of *cis*-ZnP.

### Photovoltaic properties of porphyrin-sensitized solar cell

Preliminary photovoltaic measurements were carried out by using the porphyrin dye *cis*-ZnPT. A TiO<sub>2</sub> electrode was immersed in 0.2 mM EtOH solution of *cis*-ZnPT at 25 °C for 1 h and DSSC was fabricated with the TiO<sub>2</sub> electrode stained with *cis*-ZnPT. The absorption spectrum of *cis*-ZnPT adsorbed TiO<sub>2</sub> electrode reveals intense absorption profile in visible and NIR regions (Fig. 6), ensuring high surface coverage of the TiO<sub>2</sub> surface by *cis*-ZnPT. The current-voltage characteristic was measured under standard AM 1.5 condition using an electrolyte solution consisting of 1.0 M 1,3-dimethylimidazolium iodide, 0.03 M I<sub>2</sub>, 0.05 M LiI, 0.1 M guanidinium thiocyanate and 0.50 M 4-*tert*-butylpyridine in 85:15 mixture of acetonitrile and valeronitrile (Fig. 7). The DSSC based on *cis*-ZnPT exhibits a short circuit current ( $J_{\text{sc}}$ ) of 7.65 mA.cm<sup>-2</sup>, an open circuit voltage ( $V_{\text{oc}}$ ) of 0.59 V, and a fill factor ( $ff$ ) of 0.67, corresponding to an overall  $\eta$  value of 3.0%. Unexpectedly, this  $\eta$ -value is lower than that of DSSC with *cis*-ZnP ( $J_{\text{sc}} = 13.0$  mA.cm<sup>-2</sup>,  $V_{\text{oc}} = 0.64$  V,  $ff = 0.67$ ,  $\eta = 5.5\%$ ) [22]. The photocurrent action spectrum follows

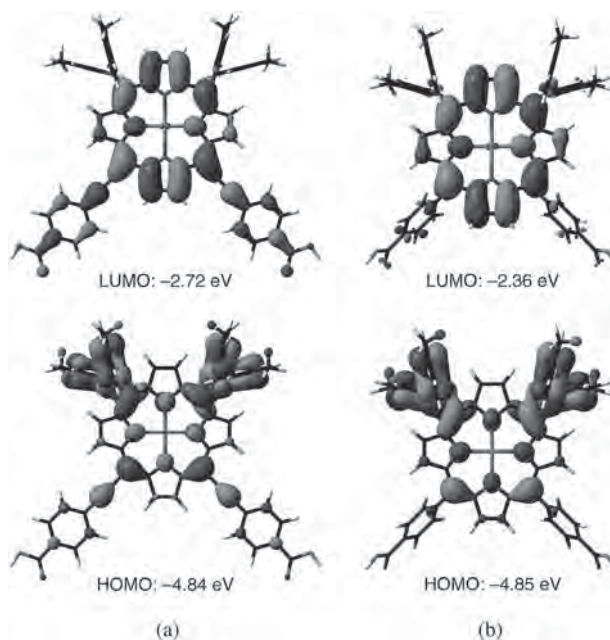


Fig. 5. Selected Kohn-Sham orbitals for (a) *cis*-ZnPT and (b) *cis*-ZnP obtained by DFT calculations with B3LYP/6-31G\*

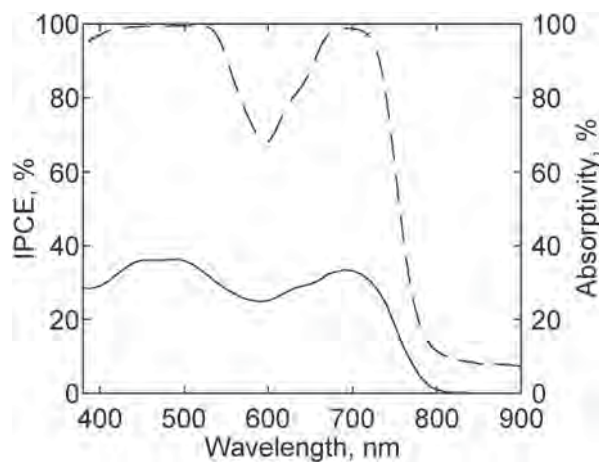
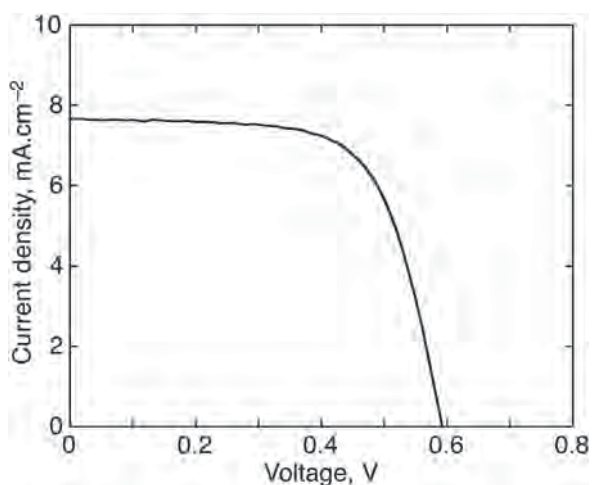


Fig. 6. Photocurrent action spectrum of the DSSC with *cis*-ZnPT (solid line) and absorption spectrum (dashed line) of *cis*-ZnPT adsorbed TiO<sub>2</sub> electrode. For the absorption spectrum the scattering TiO<sub>2</sub> layer was not applied to the TiO<sub>2</sub> electrode to obtain the absorption profile accurately

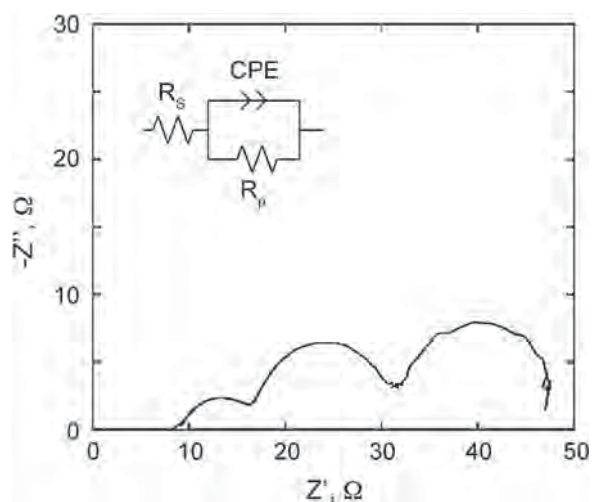
the corresponding absorption spectrum of the porphyrin adsorbed on the TiO<sub>2</sub> electrode (Fig. 6). Although the photocurrent generation response is relatively flat in visible region and exceeds the wavelength more than 800 nm, the IPCE values are moderate (maximum value of 36% at 500 nm). The IPCE value is calculated from the following equation:  $\text{IPCE} = \text{LHE} \times \phi_{\text{inj}} \times \eta_{\text{col}}$ , where LHE (light-harvesting efficiency) is the number of absorbed photons per the number of incident photons,  $\phi_{\text{inj}}$  is the quantum yield for electron injection, and  $\eta_{\text{col}}$  is the efficiency of charge collection. Considering that both



**Fig. 7.** Photocurrent-voltage characteristic of the DSSC with *cis*-ZnPT

the light-harvesting and electron injection efficiencies are likely to be high as described above, the low IPCE values result from the low charge collection efficiency. Zhang *et al.* reported that the length of the alkyl chain on the donor-group of push-pull porphyrins exerts a significant effect on the photovoltaic properties [27]. They found that too long alkyl chain on the electron-donating substituent tends to decrease the  $J_{SC}$  and resultant  $\eta$  values. We revealed that longer sensitizer dyes along the molecular axis are likely to be inclined onto  $TiO_2$  [28–30]. We have also demonstrated that more tilted geometry of adsorbed porphyrins to  $TiO_2$  is responsible for the faster electron injection and charge recombination as well as the smaller ratio of long-lived porphyrin radical cation due to the stronger through-space electronic coupling between the porphyrin and the  $TiO_2$ , resulting in small  $J_{SC}$  and  $\eta$  values [28, 29]. Although the origin is not clear at this stage, the long 2-hexyloctyl chains on the electron-donating diarylamino groups of *cis*-ZnPT would adopt the more tilt geometry on the  $TiO_2$  surface than *cis*-ZnPT, leading to fast charge recombination between the porphyrin radical cation and electron in the CB of the  $TiO_2$  and eventual small  $J_{SC}$  and  $\eta$  values.

To obtain further insight into the relationship between the charge recombination resistance and the photovoltaic performance, we applied electrical impedance spectroscopy (EIS) to the solar cell. The EIS Nyquist plot for the DSSC based on *cis*-ZnPT was obtained under standard AM 1.5 illumination at open-circuit conditions (Fig. 8). The small semicircle at the left side, large semicircle in the middle, and large semicircle at the right side of Fig. 8 correspond to the electron transfer processes at the Pt electrode, at the  $TiO_2$ -dye-electrolyte interface ( $R_p$ ), and in the electrolyte, respectively. A small  $R_p$  implies small charge recombination resistance between the  $TiO_2$  and the electrolyte. Actually, a  $R_p$  value of the DSSC based on *cis*-ZnPT (16.7  $\Omega$ ) is smaller than



**Fig. 8.** The EIS Nyquist plot for DSSCs based on *cis*-ZnPT under AM 1.5 illumination at open-circuit conditions. The inset is an equivalent Randles circuit impedance model.  $R_s$  is the series resistance accounting for transport resistance of transparent conducting oxide (TCO);  $R_p$  is the charge transfer resistance for charge recombination at the FTO/ $TiO_2$ /electrolyte interfaces; while CPE is the constant phase element representing capacitance at the  $TiO_2$ /electrolyte/interface. The interfacial electron transfer resistance ( $R_p$ ) at the  $TiO_2$ /dye/electrolyte interface was determined as 16.7  $\Omega$

that (20.06  $\Omega$ ) based on analogous push-pull porphyrin YD2 exhibiting a higher photovoltaic performance ( $J_{SC} = 17.05 \text{ mA.cm}^{-2}$ ,  $V_{OC} = 0.742 \text{ V}$ ,  $ff = 0.718$ ,  $\eta = 9.1\%$ ) under the similar conditions [18]. Therefore, the result of the EIS measurements is also consistent with the lower  $V_{OC}$  value (0.59 V) of the DSSC with *cis*-ZnPT than *cis*-ZnPT (0.64 V) and YD2 (0.742 V).

## EXPERIMENTAL

### General

Commercially available solvents and reagents were used without further purification unless otherwise mentioned. Triethylamine was distilled from  $CaH_2$ . Silica-gel column chromatography and alumina column chromatography were performed with UltraPure Silica Gel (230–400 mesh, SiliCycle) and Alumina, Activated (about 300 mesh, Wako). Thin-layer chromatography (TLC) was performed with Silica gel 60  $F_{254}$  (Merck). Size exclusion gel permeation chromatography (GPC) was conducted with Bio-Beads S-X1 (Bio-Rad).  $^1H$  NMR spectra were recorded with a JEOL EX-400 spectrometer (operating at 400 MHz). High-resolution mass spectra (HRMS) were measured on a Thermo Fischer Scientific EXACTIVE spectrometer for ESI measurements. UV-vis absorption spectrum was measured with a Perkin-Elmer Lambda 900 UV-vis/NIR spectrometer. Steady-state fluorescence spectrum was obtained by a HORIBA

SPEX Fluoromax-3 spectrofluorometer. Attenuated total reflectance-Fourier transform infrared (ATR-FTIR) spectra were taken with the golden gate diamond anvil ATR accessory (NICOLET 6700, Thermo scientific), using typically 256 scans at a resolution of 2  $\text{cm}^{-1}$ . All samples were placed in contact with the diamond window using the same mechanical force. Electrical impedance spectra were measured on SP-150 (Bio-Logic) spectrometer.

## Synthesis

Tripyrrane[23] and triisopropylsilylpropynal[24] were prepared according to literature.

**7-(4-Methoxybenzyl)tridecan-7-ol (1).** To a stirred suspension of hexylmagnesium bromide [31.4 mmol, prepared from magnesium (800 mg, 32.9 mmol) and 1-bromohexane (4.4 mL, 31.4 mmol) in dry THF (16.2 mL)], a solution of methyl 2-(4-methoxyphenyl)acetate (1.7 mL, 10.5 mmol) in dry THF (30 mL) was added dropwise at 0 °C. The reaction mixture was allowed to warm to room temperature over 1 h, followed by refluxing overnight. The reaction was quenched with aqueous saturated  $\text{NH}_4\text{Cl}$  at room temperature. The reaction mixture was diluted with ethyl acetate and layers were separated. Organic layer was washed with brine, dried over  $\text{Na}_2\text{SO}_4$ , and concentrated. The crude mixture was purified by silica-gel column chromatography (24:1 hexane-ethyl acetate) to give **1** as a colorless oil. Yield 2.6 g (67%).  $^1\text{H}$  NMR (400 MHz;  $\text{CDCl}_3$ ;  $\text{Me}_4\text{Si}$ ):  $\delta_{\text{H}}$ , ppm 0.89 (6H, t,  $-\text{CH}_2\text{CH}_3$ ), 1.28–1.51 (20H, m,  $-(\text{CH}_2)_5\text{CH}_3$ ), 2.68 (2H, s, benzyl), 3.80 (3H, s,  $-\text{OCH}_3$ ), 6.85 (2H, d, Ph), 7.12 (2H, s, Ph). IR (ATR):  $\nu$ ,  $\text{cm}^{-1}$  836, 1039, 1178, 1248, 1300, 1465, 1512, 1611, 2858, 2930, 2953, 3472. MS (ESI):  $m/z$  343.2599 (calcd. for  $[\text{M} + \text{Na}]^+$  343.2608).

**4-(2-Hexyloctyl)anisole (2).** To a stirred solution of **1** (2.0 g, 6.2 mmol) in dry  $\text{CH}_2\text{Cl}_2$  (44 mL), methanesulfonic acid (0.9 mL, 13.9 mmol) was added at 0 °C. After 1 h, the reaction was quenched with aqueous saturated  $\text{NaHCO}_3$  at 0 °C. Organic layer was separated, dried over  $\text{Na}_2\text{SO}_4$ , and concentrated. To the residue, 10% Pd/C (245 mg, 0.2 mmol) and ethyl acetate (10 mL) were added, and the mixture was stirred overnight under  $\text{H}_2$  atmosphere. The reaction mixture was filtered through Celite and concentrated. The crude mixture was purified by silica-gel column chromatography (hexane) to give **2** as a colorless oil. Yield 1.5 g (79%).  $^1\text{H}$  NMR (400 MHz;  $\text{CDCl}_3$ ;  $\text{Me}_4\text{Si}$ ):  $\delta_{\text{H}}$ , ppm 0.87 (6H, t,  $-\text{CH}_2\text{CH}_3$ ), 1.23 (20H, m,  $-(\text{CH}_2)_5\text{CH}_3$ ), 1.53 (1H, m,  $-\text{CH}(\text{C}_6\text{H}_{13})_2$ ), 2.45 (2H, d, benzyl), 3.79 (3H, s,  $-\text{OCH}_3$ ), 6.81 (2H, d, Ph), 7.04 (2H, d, Ph). IR (ATR):  $\nu$ ,  $\text{cm}^{-1}$  818, 1041, 1177, 1247, 1300, 1465, 1512, 1612, 2855, 2925, 2954. MS (ESI):  $m/z$  304.2762 (calcd. for  $[\text{M}]^+$  304.2766).

**4-(2-Hexyloctyl)phenyltrifluoromethanesulfonate (3).** To a stirred solution of **2** (1.4 g, 4.8 mmol) in dry  $\text{CH}_2\text{Cl}_2$  (10 mL),  $\text{BBr}_3$  (5.3 mL, 1 M in  $\text{CH}_2\text{Cl}_2$ ) was added dropwise at  $-78^\circ\text{C}$ . The reaction mixture was allowed to

warm to room temperature for overnight. The reaction was quenched with  $\text{H}_2\text{O}$  at 0 °C and layers were separated. Organic layer was dried over  $\text{Na}_2\text{SO}_4$  and concentrated. To a stirred mixture of the residue and pyridine (0.6 mL) in dry  $\text{CH}_2\text{Cl}_2$  (7.2 mL), trifluoromethanesulfonic anhydride (1.0 mL, 5.9 mmol) was added. After 1 h, the reaction was quenched with aqueous 1 M HCl and layers were separated. Organic layer was dried over  $\text{Na}_2\text{SO}_4$  and concentrated. The crude mixture was purified by silica-gel column chromatography (24:1 hexane-ethyl acetate) to give **3** as a colorless oil. Yield 1.8 g (89%).  $^1\text{H}$  NMR (400 MHz;  $\text{CDCl}_3$ ;  $\text{Me}_4\text{Si}$ ):  $\delta_{\text{H}}$ , ppm 0.87 (6H, t,  $-\text{CH}_2\text{CH}_3$ ), 1.23–1.29 (20H, m,  $-(\text{CH}_2)_5\text{CH}_3$ ), 1.59 (1H, m,  $-\text{CH}(\text{C}_6\text{H}_{13})_2$ ), 2.54 (2H, d, benzyl), 7.16 (2H, d, Ph), 7.20 (2H, d, Ph). IR (ATR):  $\nu$ ,  $\text{cm}^{-1}$  558, 632, 889, 1143, 1214, 1250, 1427, 1501, 2857, 2929, 2957. MS (ESI):  $m/z$  421.2031 (calcd. for  $[\text{M} - \text{H}]^-$  421.2030).

**4-(2-Hexyloctyl)aniline (4).** A mixture of **3** (1.0 g, 2.4 mmol), benzophenone imine (0.48 mL, 2.9 mmol),  $\text{Pd}_2(\text{dba})_3$  (108 mg, 0.12 mmol), XPhos (225 mg, 0.47 mmol) and  $\text{Cs}_2\text{CO}_3$  (3.9 g, 11.8 mmol) in dry toluene (10 mL) was freeze-pump-thaw degassed and stirred at 90 °C overnight. The reaction mixture was cooled to room temperature and concentrated. The crude mixture was purified by silica-gel column chromatography (24:1 hexane-ethyl acetate) to give imine adduct as yellow oil. To a stirred solution of imine adduct in THF (30 mL), aqueous 1 M HCl (10 mL) was added. After 1 h, the reaction was quenched with aqueous saturated  $\text{NaHCO}_3$ . The reaction mixture was diluted with ethyl acetate and layers were separated. Organic layer was washed with brine, dried over  $\text{Na}_2\text{SO}_4$ , and concentrated. The crude mixture was purified by silica-gel column chromatography (4:1 hexane-ethyl acetate) to give **4** as a orange oil. Yield 610 mg (89%).  $^1\text{H}$  NMR (400 MHz;  $\text{CDCl}_3$ ;  $\text{Me}_4\text{Si}$ ):  $\delta_{\text{H}}$ , ppm 0.87 (6H, t,  $-\text{CH}_2\text{CH}_3$ ), 1.23 (20H, m,  $-(\text{CH}_2)_5\text{CH}_3$ ), 1.52 (1H, m,  $-\text{CH}(\text{C}_6\text{H}_{13})_2$ ), 2.41 (2H, d, benzyl), 3.46 (2H, s,  $-\text{NH}_2$ ), 6.61 (2H, d, Ph), 6.92 (2H, d, Ph). IR (ATR):  $\nu$ ,  $\text{cm}^{-1}$  558, 632, 1274, 1466, 1516, 1625, 2855, 2925, 2955, 3355. MS (ESI):  $m/z$  290.2839 (calcd. for  $[\text{M} + \text{H}]^+$  290.2842).

**Bis[4-(2-Hexyloctyl)phenyl]amine (5).** A mixture of **3** (800 mg, 1.9 mmol), **4** (500 mg, 1.7 mmol),  $\text{Pd}_2(\text{dba})_3$  (79 mg, 0.086 mmol), XPhos (165 mg, 0.35 mmol) and  $\text{Cs}_2\text{CO}_3$  (2.8 g, 8.6 mmol) in dry toluene (10 mL) was freeze-pump-thaw degassed and stirred at 90 °C overnight. The reaction mixture was cooled to room temperature and concentrated. The crude mixture was purified by silica-gel column chromatography (24:1 hexane-ethyl acetate) to give **5** as a orange oil. Yield 600 mg (62%).  $^1\text{H}$  NMR (400 MHz;  $\text{CDCl}_3$ ;  $\text{Me}_4\text{Si}$ ):  $\delta_{\text{H}}$ , ppm 0.87 (12H, t,  $-\text{CH}_2\text{CH}_3$ ), 1.29 (40H, m,  $-(\text{CH}_2)_5\text{CH}_3$ ), 1.56 (2H, m,  $-\text{CH}(\text{C}_6\text{H}_{13})_2$ ), 2.46 (4H, d, benzyl), 5.53 (1H, s,  $-\text{NH}$ ), 6.98 (4H, d, Ph), 7.04 (4H, d, Ph). IR (ATR):  $\nu$ ,  $\text{cm}^{-1}$  559, 632, 1310, 1459, 1516, 1609, 2856, 2924, 2957, 3398. MS (ESI):  $m/z$  562.5333 (calcd. for  $[\text{M} + \text{H}]^+$  562.5346).

**5,10-Bis(triisopropylsilylethynyl)porphyrin (6).** A mixture of tripyrrane (500 mg, 2.2 mmol), pyrrole (0.15 mL, 2.2 mmol) and triisopropylsilylpropynal (934 mg, 4.4 mmol) in  $\text{CH}_2\text{Cl}_2$  (260 mL) was stirred under Ar and shielded from light for 15 min, then  $\text{BF}_3 \cdot \text{OEt}_2$  (0.18 mL, 1.4 mmol) was added. After 45 min, 2,3-dichloro-5,6-dicyano-1,4-benzoquinone (DDQ) (1.5 g, 6.6 mmol) was added and the reaction mixture was stirred for 10 min. The reaction mixture was passed through a short alumina column and concentrated. The crude mixture was purified by silica-gel column chromatography (3:1 hexane- $\text{CH}_2\text{Cl}_2$ ) to give **6** as a purple solid. Yield 95 mg (6.4%).  $^1\text{H}$  NMR (400 MHz;  $\text{CDCl}_3$ ;  $\text{Me}_4\text{Si}$ ):  $\delta_{\text{H}}$ , ppm -4.21 (2H, s, pyrrole-NH), 1.53 (42H, m, TIPS), 8.86 (2H, s,  $\beta$ ), 8.97 (2H, d,  $\beta$ ), 9.50 (4H, m,  $\beta$ ), 9.62 (2H, s, *meso*). IR (ATR):  $\nu$ ,  $\text{cm}^{-1}$  560, 656, 671, 694, 713, 766, 788, 848, 880, 964, 993, 1052, 1156, 1245, 1459, 2133, 2861, 2939. MS (ESI):  $m/z$  671.3942 (calcd. for  $[\text{M} + \text{H}]^+$  671.3960). mp > 300 °C.

**[5,10-Bis(triisopropylsilylethynyl)porphyrinato]zinc(II) (7).** To a stirred solution of **6** (200 mg, 0.30 mmol) in  $\text{CH}_2\text{Cl}_2$  (30 mL) and MeOH (15 mL),  $\text{Zn}(\text{OAc})_2$  (273 mg, 1.5 mmol) was added. After 5 h, the reaction mixture was concentrated and passed through a short silica-gel column ( $\text{CH}_2\text{Cl}_2$ ). Reprecipitation from  $\text{CH}_2\text{Cl}_2/\text{MeOH}$  to give **7** as a purple solid. Yield 212 mg (97%).  $^1\text{H}$  NMR (400 MHz;  $\text{CDCl}_3$ ;  $\text{Me}_4\text{Si}$ ):  $\delta_{\text{H}}$ , ppm 1.58 (42H, m, TIPS), 8.96 (2H, s,  $\beta$ ), 9.00 (2H, d,  $\beta$ ), 9.51 (2H, d,  $\beta$ ), 9.55 (2H, s,  $\beta$ ), 9.57 (2H, s, *meso*). IR (ATR):  $\nu$ ,  $\text{cm}^{-1}$  582, 674, 697, 725, 769, 790, 855, 883, 997, 1056, 1182, 1212, 1463, 2138, 2864, 2889, 2942. MS (ESI):  $m/z$  733.3071 (calcd. for  $[\text{M} + \text{H}]^+$  733.3095). mp > 300 °C.

**[5,10-Bis(*N,N*-bis(4-(2-hexyloctyl)phenyl)amino)-15,20-bis(triisopropylsilylethynyl)porphyrinato]zinc(II) (8).** To a stirred solution of **7** (35 mg, 0.048 mmol) and **5** (130 mg, 0.23 mmol) in  $\text{CH}_2\text{Cl}_2$  (40 mL), phenyliodine diacetate (PIDA) (31 mg, 0.096 mmol) and  $\text{NaAuCl}_4 \cdot 2\text{H}_2\text{O}$  (46 mg, 0.12 mmol) was added. After 30 min, the reaction was quenched with aqueous saturated  $\text{Na}_2\text{S}_2\text{O}_3$  and layers were separated. Organic layer was washed with brine, dried over  $\text{Na}_2\text{SO}_4$ , and concentrated. To a stirred solution of the residue in  $\text{CH}_2\text{Cl}_2$  (16 mL) and MeOH (8 mL),  $\text{Zn}(\text{OAc})_2$  (87 mg, 0.47 mmol) was added. After 2 h, the reaction mixture was concentrated. The crude mixture was purified by silica-gel column chromatography (1:4 hexane- $\text{CH}_2\text{Cl}_2$ ) to give **8** as a dark green solid. Yield 30 mg (34%).  $^1\text{H}$  NMR (400 MHz;  $\text{CDCl}_3$ ;  $\text{Me}_4\text{Si}$ ):  $\delta_{\text{H}}$ , ppm 0.83 (24H, t,  $-\text{CH}_2\text{CH}_3$ ), 1.20–1.25 (80H, m,  $-(\text{CH}_2)_5\text{CH}_3$ ), 1.48–1.57 (46H, m,  $-\text{CH}(\text{C}_6\text{H}_{13})_2$  and TIPS), 2.39 (8H, d, benzyl), 6.92 (8H, d, Ph), 7.15 (8H, d, Ph), 9.08 (2H, s,  $\beta$ ), 9.23 (2H, d,  $\beta$ ), 9.53 (2H, d,  $\beta$ ), 9.66 (2H, s,  $\beta$ ). IR (ATR):  $\nu$ ,  $\text{cm}^{-1}$  634, 795, 883, 1061, 1216, 1260, 1297, 1340, 1463, 1506, 1606, 2139, 2360, 2856, 2925, 2956. MS (ESI):  $m/z$  1851.3262 (calcd. for  $[\text{M}]^+$  1851.3251). mp > 300 °C.

**[5,10-Bis(*N,N*-bis(4-(2-hexyloctyl)phenyl)amino)-15,20-bis(4-carboxyphenyl)ethynyl]porphyrinato**

**zinc(II) (*cis*-ZnPT).** To a stirred solution of **8** (25 mg, 0.013 mmol) in dry THF (3.0 mL), TBAF (0.10 mL, 1 M in THF) was added. After 30 min, the reaction was quenched with  $\text{H}_2\text{O}$  and the reaction mixture was diluted with  $\text{CH}_2\text{Cl}_2$ . Layers were separated and organic layer was dried over  $\text{Na}_2\text{SO}_4$  and concentrated. A solution of the residue, 4-iodobenzoic acid (14 mg, 0.056 mmol),  $\text{Pd}_2(\text{dba})_3$  (6.0 mg, 0.0066 mmol), triphenylarsine (17 mg, 0.056 mmol) and  $\text{NEt}_3$  (0.67 mL) in dry THF (3.3 mL) was freeze-pump-thaw degassed and stirred at 80 °C overnight. The reaction mixture was cooled to room temperature and concentrated. The crude mixture was passed through a short silica-gel column (MeOH) and GPC (toluene). Reprecipitation from  $\text{CH}_2\text{Cl}_2/\text{acetonitrile}$  to give *cis*-ZnPT as a dark green solid. Yield 10 mg (42%). UV-vis (EtOH):  $\lambda_{\text{max}}$ , nm (log  $\epsilon$ ) 448 (4.96), 478 (4.87), 624 (3.88), 684 (4.40).  $^1\text{H}$  NMR (400 MHz;  $\text{CDCl}_3/\text{pyridine-d}_5$ ;  $\text{Me}_4\text{Si}$ ):  $\delta_{\text{H}}$ , ppm 0.86 (24H, t,  $-\text{CH}_2\text{CH}_3$ ), 1.23–1.27 (80H, m,  $-(\text{CH}_2)_5\text{CH}_3$ ), 1.56 (4H, m,  $-\text{CH}(\text{C}_6\text{H}_{13})_2$ ), 2.42 (8H, d, benzyl), 6.93 (8H, d, Ph), 7.15 (8H, d, Ph), 8.07 (4H, d, Ph), 8.37 (4H, d, Ph), 9.02 (2H, s,  $\beta$ ), 9.22 (2H, d,  $\beta$ ), 9.53 (2H, d,  $\beta$ ), 9.76 (2H, s,  $\beta$ ). IR (ATR):  $\nu$ ,  $\text{cm}^{-1}$  709, 792, 854, 1029, 1098, 1175, 1213, 1258, 1312, 1344, 1417, 1453, 1506, 1604, 1688, 2191, 2359, 2853, 2924, 2957, 3472. MS (ESI):  $m/z$  1802.0874 (calcd. for  $[\text{M} + \text{Na}]^+$  1802.0902). mp > 300 °C.

## Electrochemistry

Electrochemical measurements were made using an ALS 630a electrochemical analyzer. Redox potentials were determined by differential pulse voltammetry (DPV) in  $\text{CH}_2\text{Cl}_2$  containing 0.1 M tetrabutylammonium hexafluorophosphate ( $\text{Bu}_4\text{NPF}_6$ ). A glassy carbon (3 mm diameter) working electrode,  $\text{Ag}/\text{AgNO}_3$  reference electrode, and Pt wire counter electrode were employed. Ferrocene (+0.64 V vs. NHE) was used as an external standard for the DPV measurements.

## Preparation of porphyrin-sensitized $\text{TiO}_2$ electrode and photovoltaic measurements

The preparation of  $\text{TiO}_2$  electrodes and the fabrication of the sealed cells for photovoltaic measurements were performed according to literature [18, 31]. The details of this work were described as follows.

Nanocrystalline  $\text{TiO}_2$  particles (20 nm, CCIC: PST23NR, JGC-CCIC) and submicrocrystalline  $\text{TiO}_2$  particles (400 nm, CCIC: PST400C, JGC-CCIC) were used as the transparent and the light-scattering layers of the photoanode, respectively. To prepare the working electrodes, FTO glasses (solar 4 mm thickness, 10  $\Omega/\square$ , Nippon Sheet Glass) were first cleaned in a detergent solution using an ultrasonic bath for 15 min and then rinsed with distilled water and ethanol. After UV- $\text{O}_3$  irradiation for 18 min, the FTO glass plates were immersed into a 40 mM aqueous  $\text{TiCl}_4$  solution at 70 °C for 30 min and washed with distilled water and ethanol. A layer of the

nanocrystalline TiO<sub>2</sub> paste was coated on the FTO glass plate by a screen-printing method, kept in a clean box for a few minutes, and then dried over 6 min at 125 °C. This screen-printing procedure with the nanocrystalline TiO<sub>2</sub> paste was repeated to reach a thickness of 12 μm. After drying the films at 125 °C, a layer of the sub-microcrystalline TiO<sub>2</sub> paste was further deposited by screen-printing in the same method as the fabrication of the nanocrystalline TiO<sub>2</sub> layer, resulting in formation of a light-scattering TiO<sub>2</sub> film of 4 μm on the transparent TiO<sub>2</sub> film of 12 μm. Finally, the electrodes coated with the TiO<sub>2</sub> pastes were gradually heated under an airflow at 325 °C for 5 min, at 375 °C for 5 min, at 450 °C for 15 min, and at 500 °C for 15 min. The thickness of the films was determined using a surface profiler (SURFCOM 130A, ACCRETECH). The size of the TiO<sub>2</sub> film was 0.16 cm<sup>2</sup> (4 × 4 mm). The TiO<sub>2</sub> electrode was treated again with 40 mM TiCl<sub>4</sub> solution at 70 °C for 30 min and then rinsed with distilled water and ethanol, sintered at 500 °C for 30 min, and cooled to 70 °C before dipping into the dye solution. The TiO<sub>2</sub> electrode was immersed into an ethanol solution of the porphyrin (0.20 mM) at 25 °C for 1 h.

The counter electrode was prepared by drilling a small hole in an FTO glass (solar 1 mm thickness, 10 Ω/□, Nippon Sheet Glass), rinsing with distilled water and ethanol followed by treatment with 0.1 M HCl solution in 2-propanol using an ultrasonic bath for 15 min. After heating in air for 15 min at 400 °C, the platinum was deposited on the FTO glass by coating with a drop of H<sub>2</sub>PtCl<sub>6</sub> solution (2 mg in 1 mL of ethanol) twice. Finally, the FTO glass was heated at 400 °C for 15 min to obtain the counter Pt electrode. A sandwich cell was prepared by using the dye-anchored TiO<sub>2</sub> film as a working electrode and a counter Pt electrode, which were assembled with a hotmelt-ionomer film Surlyn polymer gasket (DuPont, 50 μm), and the superimposed electrodes were tightly held and heated at 110 °C to seal the two electrodes. The aperture of the Surlyn frame was 2 mm larger than that of the area of the TiO<sub>2</sub> film, and its width was 1 mm. The hole in the counter Pt-electrode was sealed by a film of Surlyn. A hole was then made in the film of Surlyn covering the hole with a needle. A drop of an electrolyte was put on the hole in the back of the counter Pt electrode. It was introduced into the cell via vacuum backfilling. Finally, the hole was sealed using Surlyn film and a cover glass (0.13–0.17 mm thickness). A solder was applied on each edge of the FTO electrodes. The electrolyte solution used was 1.0 M 1,3-dimethylimidazolium iodide, 0.03 M I<sub>2</sub>, 0.05 M LiI, 0.1 M guanidinium thiocyanate and 0.50 M 4-*tert*-butylpyridine in 85:15 mixture of acetonitrile and valeronitrile.

Incident photon-to-current efficiency (IPCE) and photocurrent–voltage (I–V) performance were measured on an action spectrum measurement setup (CEP-2000RR, BUNKOUKEIKI) and a solar simulator (PEC-L10, Peccell Technologies) with a simulated sunlight of AM

1.5 (100 mW.cm<sup>-2</sup>), respectively: IPCE (%) = 100 × 1240 ×  $i/(W_{in} \times \lambda)$ , where  $i$  is the photocurrent density (A.cm<sup>-2</sup>),  $W_{in}$  is the incident light intensity (W.cm<sup>-2</sup>), and  $\lambda$  is the excitation wavelength (nm). During the photovoltaic measurements, a black plastic tape was attached on the back of the TiO<sub>2</sub> electrode except for the TiO<sub>2</sub> film region to reduce scattering light.

## CONCLUSION

We synthesized for the first time a porphyrin dye *cis*-ZnPT with enhanced push–pull character, by introducing two diarylamino groups and two carboxyphenylethynyl groups as electron-donating and electron-withdrawing anchoring groups, respectively. The absorption spectrum displayed broad and red-shifted absorption compared with the reference porphyrin without the triple bonds in the anchoring groups, achieving panchromatic light-harvesting in visible and NIR regions. This exemplifies that introduction of multiple electron-donating and electron-withdrawing groups into a porphyrin core is a potential strategy for the rational design of porphyrin sensitizers for light-harvesting applications. Unfortunately, the preliminary photovoltaic performance ( $\eta = 3.0\%$ ) is moderate, but the extensive photocurrent generation matches with the excellent light-harvesting property of *cis*-ZnPT. We believe that further modulation of the photovoltaic properties of porphyrin DSSCs will be possible by selecting suitable electron-donating and electron-withdrawing groups as well as introducing the substituents into the porphyrin core in an elaborated manner.

## Acknowledgements

This work was financially supported by Advanced Low Carbon Technology Research and Development Program (ALCA, JST) and WPI Initiative (MEXT, Japan).

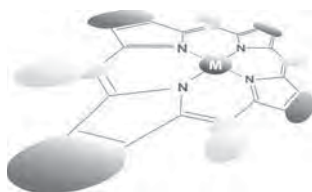
## Supporting information

Figures S1–S9 are given in the supplementary material. This material is available free of charge *via* the Internet at <http://www.worldscinet.com/jpp/jpp.shtml>.

## REFERENCES

- O'Regan B and Grätzel M. *Nature* 1991; **353**: 737–740.
- Nazeeruddin MK, De Angelis F, Fantacci S, Selloni A, Viscardi G, Liska P, Ito S, Takeru B and Grätzel M. *J. Am. Chem. Soc.* 2005; **127**: 16835–16847.
- Gao F, Wang Y, Shi D, Zhang J, Wang M, Jing X, Humphry-Baker R, Wang P, Zakeeruddin SM and Grätzel M. *J. Am. Chem. Soc.* 2008; **130**: 10720–10728.

4. Chen C, Wang M, Li J, Pootrakulchote N, Alibabaei L, Ngoc-le CH, Decoppet J, Tsai J, Grätzel C, Wu C, Zakeeruddin SM and Grätzel M. *ACS Nano* 2009; **3**: 3103–3109.
5. Han L, Islam A, Chen H, Malapaka C, Chiranjeevi B, Zhang S, Yang X and Yanagida M. *Energy Environ. Sci.* 2012; **5**: 6057–6060.
6. Mishra A, Fischer MKR and Bäuerle P. *Angew. Chem. Int. Ed.* 2009; **48**: 2474–2499.
7. Ooyama Y and Harima Y. *Eur. J. Org. Chem.* 2009; 2903–2934.
8. Zeng W, Cao Y, Bai Y, Wang Y, Shi Y, Zhang M, Wang F, Pan C and Wang P. *Chem. Mater.* 2010; **22**: 1915–1925.
9. Tan LL, Huang JF, Shen Y, Xiao LM, Liu JM, Kuang DB and Su CY. *J. Mater. Chem. A* 2014; **2**: 8988–8994.
10. Campbell WM, Burrell AK, Officer DL and Jolley KW. *Coord. Chem. Rev.* 2004; **248**: 1363–1379.
11. Imahori H, Umeyama T and Ito S. *Acc. Chem. Res.* 2009; **42**: 1809–1818.
12. Martínez-Díaz MV, de la Torre G and Torres T. *Chem. Commun.* 2010; **46**: 7090–7108.
13. Li LL and Diau EWG. *Chem. Soc. Rev.* 2013; **42**: 291–304.
14. Ladomenou K, Kitsopoulos TN, Sharma GD and Coutsolelos AG. *RSC Adv.* 2014; **4**: 21379–21404.
15. Lu HP, Tsai CY, Yen WN, Hsieh CP, Lee CW, Yeh CY and Diau EWG. *J. Phys. Chem. C* 2009; **113**: 20990–20997.
16. Bessho T, Zakeeruddin SM, Yeh CY, Diau EWG and Grätzel M. *Angew. Chem. Int. Ed.* 2010; **49**: 6646–6649.
17. Yella A, Lee HW, Tsao HN, Yi C, Chandiran AK, Nazeeruddin MK, Diau EWG, Yeh CY, Zakeeruddin SM and Grätzel M. *Science* 2011; **334**: 629–634.
18. Kurotobi K, Toude Y, Kawamoto K, Fujimori Y, Ito S, Chabera P, Sundström V and Imahori H. *Chem. Eur. J.* 2013; **19**: 17075–17081.
19. Yella A, Mai CL, Zakeeruddin SM, Chang SN, Hsieh CH, Yeh CY and Grätzel M. *Angew. Chem. Int. Ed.* 2014; **53**: 2973–2977.
20. Mathew S, Yella A, Gao P, Humphry-Baker R, Curchod BFE, Ashari-Astani N, Tavernelli I, Rothlisberger U, Nazeeruddin MK and Grätzel M. *Nature Chem.* 2014; **6**: 242–247.
21. Luo J, Xu M, Li R, Huang KW, Jiang C, Qi Q, Zeng W, Zhang J, Chi C, Wang and Wu J. *J. Am. Chem. Soc.* 2014; **136**: 265–272.
22. Imahori H, Matsubara Y, Iijima H, Umeyama T, Matano Y, Ito S, Niemi M, Tkachenko NV and Lemmetyinen H. *J. Phys. Chem. C* 2010; **114**: 10656–10665.
23. Taniguchi S, Hasegawa H, Yanagiya S, Tabeta Y, Nakano Y and Takahashi M. *Tetrahedron* 2001; **57**: 2103–2108.
24. Robles O and McDonald FE. *Org. Lett.* 2008; **10**: 1811–1814.
25. Shen DM, Liu C, Chen XG and Chen QY. *J. Org. Chem.* 2009; **74**: 206–211.
26. Frisch MJ *et al.* *Gaussian 09, revision C.01*, Gaussian, Inc., Wallingford, CT, 2010.
27. Xue X, Zhang W, Zhang N, Ju C, Peng X, Yang Y, Liang Y, Feng Y and Zhang B. *RSC Adv.* 2014; **4**: 8894–8900.
28. Imahori H, Kang S, Hayashi H, Haruta M, Kurata H, Isoda S, Canton SE, Infahsaeng Y, Kathiravan A, Pascher T, Chábera P, Yartsev AP and Sundström V. *J. Phys. Chem. A* 2011; **115**: 3679–3690.
29. Ye S, Kathiravan A, Hayashi H, Tong Y, Infahsaeng Y, Chabera P, Pascher T, Yartsev AP, Isoda S, Imahori H and Sundström V. *J. Phys. Chem. C* 2013; **117**: 6066–6080.
30. Hayashi H, Touchy AS, Kinjo Y, Kurotobi K, Toude Y, Ito S, Saarenpää H, Tkachenko NV, Lemmetyinen H and Imahori H. *ChemSusChem* 2013; **6**: 508–517.
31. Ito S, Murakami TN, Comte P, Liska P, Grätzel C, Nazeeruddin MK and Grätzel M. *Thin Solid Films* 2008; **516**: 4613–4619.



# Preparation and characterization of a tungsten(V) corrole dichloride complex

Rosa Padilla, Heather L. Buckley, Ashleigh L. Ward and John Arnold\*

Department of Chemistry, University of California, Berkeley, California 94720, USA

Dedicated to Professor Shunichi Fukuzumi on the occasion of his retirement

Received 17 August 2014

Accepted 30 September 2014

**ABSTRACT:** The first example of a tungsten(V) corrole complex,  $(\text{Mes}_2(p\text{-OMePh})\text{corrole})\text{WCl}_2$ , has been prepared through a metathesis reaction of a lithium corrole  $(\text{Mes}_2(p\text{-OMePh})\text{corrole})\text{Li}_3 \cdot 6\text{THF}$  and  $\text{WCl}_6$ . The product constitutes the first example of a tungsten(V) corrole complex synthesized under mild conditions and only the second example of a tungsten corrole complex.

**KEYWORDS:** corrole, tungsten, early transition metal, air sensitive.

## INTRODUCTION

Reports of early transition metal complexes of conjugated macrocycles are becoming increasingly common. These compounds are of interest in part due to their utility for organometallic transformations [1], as oxygen reduction catalysts [2, 3], and for applications in light harvesting [4] and fluorescence [5]. Interest has also grown in the development of new methodologies that make reliable synthesis of both the starting ligands and their air-sensitive metal complexes feasible.

In particular, the preparation of metallocorrole complexes has developed considerably in the past decade. Preparation of a range of *meso*-substituted corroles became broadly accessible with the publication of a number of papers by Paolesse [6], Gross [7, 8], and Gryko [9, 10]. This has led to the preparation of corrole complexes from across the periodic table, including complexes of iridium [11], gold [12], lead [13], and bismuth [14]. Our work in this area has focused on the development of lithium corrole as a metathesis reagent [15] which has allowed the preparation of a series of group 4 [15, 16], lanthanide [17], and actinide [18] corrole complexes.

Recent work by Gross and coworkers led to the preparation of the only example of a tungsten corrole

complex [19]. This species is a high-valent tungsten(VI)  $\mu$ -oxo bridged dimeric complex, and is one of only a handful of third row transition metal corrole complexes prepared to-date. Also of great interest is the recent preparation and crystallographic characterization of a molybdenum(IV) oxo corrole complex [20]. Along with the spectroscopic identification of mononuclear (oxo)-molybdenum(IV) corroles and previous reports of (oxo)-molybdenum(V) corroles [21–23], these species suggest a wealth of unexplored reactivity of early transition metal corrole complexes where both the ligand and the metal have potential redox activity.

Here we present the preparation and full structural characterization of the first tungsten(V) corrole complex, based on a metathesis reaction with a trilithium corrole complex.

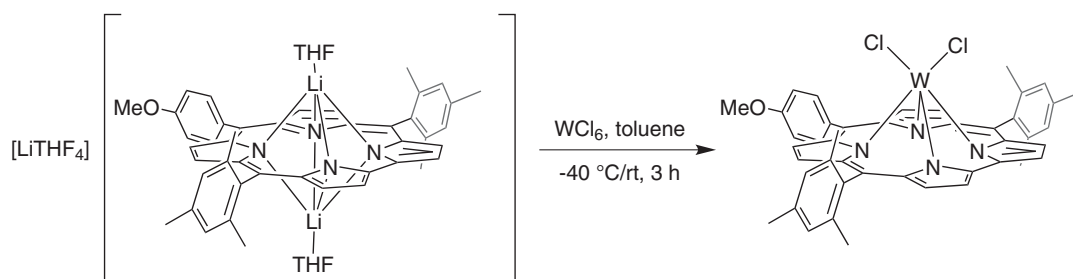
## RESULTS AND DISCUSSION

The tungsten(V) corrole dichloride complex  $(\text{Mes}_2(p\text{-OMePh})\text{corrole})\text{WCl}_2$  was prepared in toluene by the combination of  $(\text{Mes}_2(p\text{-OMePh})\text{corrole})\text{Li}_3 \cdot 6\text{THF}$  with 1.5 equivalents of tungsten hexachloride at  $-40^\circ\text{C}$  (Scheme 1). Evaporation of the solvent under vacuum, followed by extraction and recrystallization in hexanes, afforded dark brown crystals of the product in 70% yield (Scheme 1).

The UV-visible spectrum in dichloromethane is shown in Fig. 1 (absorption maxima are listed in the Experimental

\*Correspondence to: John Arnold, email: [arnold@berkeley.edu](mailto:arnold@berkeley.edu)





Scheme 1. Synthesis of  $(\text{Mes}_2(p\text{-OMePh})\text{corrole})\text{WCl}_2$

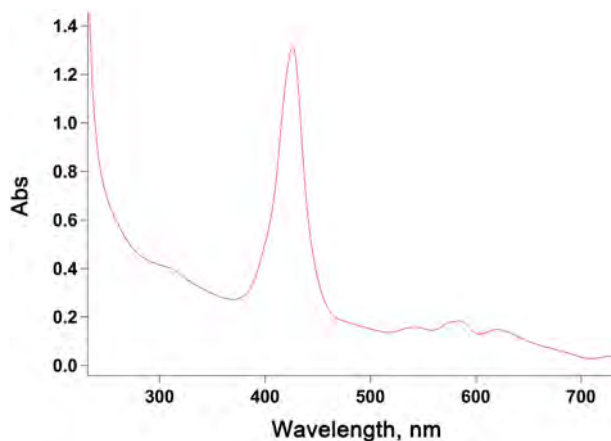


Fig. 1. UV-visible absorption spectrum of  $(\text{Mes}_2(p\text{-OMePh})\text{corrole})\text{WCl}_2$  in dichloromethane

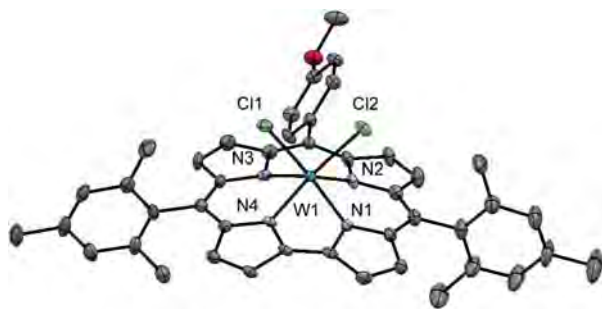


Fig. 2. Molecular structure of  $(\text{Mes}_2(p\text{-OMePh})\text{corrole})\text{WCl}_2$ , determined by single-crystal X-ray diffraction. H atoms and non-coordinated solvent omitted for clarity; thermal ellipsoids at 50% probability level

section). The spectrum includes one strong, intense Soret band around 426 nm and three less intense Q-bands (or  $\alpha$  bands) [24] between 540 and 625 nm. In the ESI-MS, peaks attributable to tungsten-oxo species were seen, no doubt due to facile hydrolysis by the matrix used to solubilize the air- and moisture-sensitive complex (see Experimental). As expected for a W(V),  $d^1$  system,  $^1\text{H}$  NMR spectroscopy revealed only broad, poorly defined signals.

Crystals suitable for X-ray diffraction were grown by slow evaporation in hexane at room temperature (see Fig. 2). Despite the lower oxidation state, the W-N<sub>4</sub>

plane distance of 0.867 Å is shorter than those observed in the bridged  $\mu$ -oxo dimer tungsten(VI) corrole complex [19] (0.961(4)–0.970(4) Å), perhaps due to steric repulsion between the two corrole ligands in the latter. The distance is longer than for the corresponding Mo(V) [21] and Mo(IV) [20] species (0.729(1) Å) and 0.78 Å respectively), consistent with the slightly larger radius of tungsten vs. molybdenum.

## EXPERIMENTAL

### General considerations

All reactions were performed using standard Schlenk and N<sub>2</sub>-atmosphere glovebox techniques. Glassware was stored in an oven at *ca.* 180 °C. Solvents were dried by passing through a column of activated alumina and degassed with nitrogen [25]. UV-visible spectra were determined with a Varian Cary 50 UV-vis spectrophotometer using a 1 mm quartz cell. Mass spectral data (ESI-MS, positive mode) were obtained at the University of California, Berkeley Microanalytical Facility, using vacuum-dried samples dissolved in dry THF. X-ray crystal diffraction analyses were performed at the University of California, Berkeley CHEXRAY facility. Melting points were determined using sealed capillaries prepared under nitrogen and are uncorrected.

Trilithium 5,15-bis(2,4,6-trimethylphenyl)-10-(4-methoxyphenyl)corrole hexakis (tetrahydrofuran) ( $\text{Mes}_2(p\text{-OMePh})\text{corroleLi}_3\cdot 6\text{THF}$ ) was prepared according to a previously reported procedure [15]. Tungsten hexachloride was obtained from Aldrich.

### Synthesis

**Tungsten(V) 5,15-bis(2,4,6-trimethylphenyl)-10-(4-methoxyphenyl)corrole dichloride  $\text{Mes}_2(p\text{-OMePh})\text{corrole}(\text{WCl}_2)$**  was prepared as follows.  $\text{Mes}_2(p\text{-OMePh})\text{corroleLi}_3\cdot 6\text{THF}$  (120 mg, 0.110 mmol) and  $\text{WCl}_6$  (65 mg, 0.165 mmol) were combined in toluene (20 mL) and stirred at -40 °C for 10 min. The solution was then allowed to warm to room temperature and stirred for 3 h. After this time, the solvent was removed under vacuum and the solid was extracted with hexanes (2 × 3 mL),

**Table 1.** Crystallographic data for (Mes<sub>2</sub>(*p*-OMePh) corrole)WCl<sub>2</sub>

	(Mes <sub>2</sub> ( <i>p</i> -OMePh) corrole)WCl <sub>2</sub>
Formula	C <sub>45</sub> H <sub>37</sub> Cl <sub>4</sub> N <sub>4</sub> O <sub>1</sub> W <sub>1</sub>
Form. wt., amu	975.43
Wavelength, Å	0.71073
Space group	P2 <sub>1</sub> /n
<i>a</i> , Å	8.1411 (8)
<i>b</i> , Å	18.6966 (18)
<i>c</i> , Å	26.845 (3)
α, °	90
β, °	93.389 (5)
γ, °	90
<i>V</i> , Å <sup>3</sup>	4078.9 (7)
<i>Z</i>	4
ρ <sub>calcd</sub> , g/cm <sup>3</sup>	1.588
<i>F</i> <sub>000</sub>	1940
μ, mm <sup>-1</sup>	3.135
<i>T</i> <sub>min</sub> / <i>T</i> <sub>max</sub>	0.859/0.940
Refl'ns collected	34,341
Indep. refl'ns	7454
<i>R</i> <sub>int</sub>	0.0476
<i>R</i> <sub>1</sub> , <i>wR</i> <sub>2</sub>	0.0476, 0.1169
<i>R</i> <sub>1</sub> , (all data)	0.0570
GoF	0.936
Res. peak/hole, e <sup>-</sup> /Å <sup>3</sup>	3.826/-1.796

filtered through Celite®, concentrated until saturation and allowed to stand to afford the product as dark brown blocks (69 mg, 70% yield). Single crystals suitable for X-ray diffraction were obtained by slow evaporation of a solution of the product in hexanes at room temperature. UV-vis (dichloromethane): λ, nm 426, 542, 584, 621. ESI-MS (+): *m/z* calcd. for C<sub>44</sub>H<sub>37</sub>N<sub>4</sub>O<sub>3</sub>W-[W(corrole)] O<sub>2</sub><sup>+</sup>: 853.2370; found 853.2390. mp decomposition above 300 °C.

#### Determination of molecular structure by single-crystal X-ray diffraction

X-ray structural determinations were performed on a Bruker APEX II Quazar diffractometer. The instrument is Kappa Geometry with DX and is a 3-circle diffractometer that couples a CCD detector [26] with a sealed-tube source of monochromated Mo Kα radiation. A crystal of appropriate size was coated in Paratone-N oil and mounted on a Kaptan® loop. The loop was transferred to the diffractometer, centered in the beam, and cooled by a nitrogen flow low-temperature apparatus

that had been previously calibrated by a thermocouple placed at the same position as the crystal. Preliminary orientation matrices and cell constants were determined by collection of 60 10 s frames, followed by spot integration and least-squares refinement. The reported cell dimensions were calculated from all reflections with *I* > 10 σ. The data were corrected for Lorentz and polarization effects; no correction for crystal decay was applied. An empirical absorption correction based on comparison of redundant and equivalent reflections was applied using SADABS [27]. All software used for diffraction data processing and crystal-structure solution and refinement are contained in the APEX2 program suite (Bruker AXS, Madison, WI) [28]. Thermal parameters for all non-hydrogen atoms were refined anisotropically. For all structures,  $R_1 = \Sigma(|F_o| - |F_c|)/\Sigma(|F_o|)$ ;  $wR_2 = [\Sigma\{w(F_o^2 - F_c^2)^2\}/\Sigma\{w(F_o^2)^2\}]^{1/2}$ . ORTEP diagrams were created using the ORTEP-3 software package and POV-ray [29]. Table 1 shows crystallographic data for (Mes<sub>2</sub>(*p*-OMePh)corrole)WCl<sub>2</sub>.

## CONCLUSION

In summary, the first tungsten(V) corrole complex has been prepared. By analogy to previously prepared monomeric corrole and porphyrin chloride complexes, this new compound has the potential to further broaden the scope of metallocorrole chemistry. Further studies aimed at exploring the reactivity of this unusual corrole complex are in progress and will be reported in due course.

## Acknowledgements

RP Acknowledges the UC-MEXUS Fellowship. HLB acknowledges the International Fulbright Science and Technology Fellowship. We are grateful to Antonio DiPasquale (XRD) and Zhongrui Zhou (MS) for assistance with instrumentation.

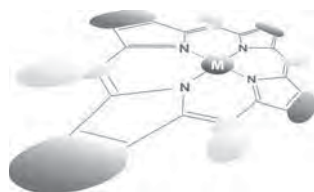
## Supporting information

Crystallographic data have been deposited at the Cambridge Crystallographic Data Centre (CCDC) under number CCDC-1019500. Copies can be obtained on request, free of charge, via [www.ccdc.cam.ac.uk/data\\_request/cif](http://www.ccdc.cam.ac.uk/data_request/cif) or from the Cambridge Crystallographic Data Centre, 12 Union Road, Cambridge CB2 1EZ, UK (fax: +44 1223-336-033 or email: [deposit@ccdc.cam.ac.uk](mailto:deposit@ccdc.cam.ac.uk)).

## REFERENCES

1. Aviv I and Gross Z. *Chem. Commun.* 2006; **42**: 4477.
2. Kadish KM, Frémond L, Ou Z, Shao J, Shi C, Anson FC, Burdet F, Gros CP, Barbe J-M and Guillard R. *J. Am. Chem. Soc.* 2005; **127**: 5625.

3. Dogutan DK, Stoian SA, McGuire R, Schwalbe M, Teets TS and Nocera DG. *J. Am. Chem. Soc.* 2011; **133**: 131.
4. Brizet B, Desbois N, Bonnot A, Langlois A, Dubois A, Barbe J-M, Gros CP, Goze C, Denat F and Harvey PD. *Inorg. Chem.* 2014; **53**: 3392.
5. Liang X, Mack J, Zheng L, Shen Z and Kobayashi N. *Inorg. Chem.* 2014; **53**: 2797.
6. Paolesse R, Mini S, Sagone F, Boschi T, Jaquinod L, Nurco DJ and Smith KM. *Chem. Commun.* 1999; **2**: 1307.
7. Gross Z, Galili N, Simkhovich L, Saltsman I, Botoshnsky M, Blaser D, Boese R and Goldberg I. *Org. Lett.* 1999; **1**: 599.
8. Gross Z, Galili N and Saltsman I. *Angew. Chem. Int. Ed.* 1999; **38**: 1427.
9. Koszarna B and Gryko DT. *J. Org. Chem.* 2006; **71**: 3707.
10. Gryko DT. *J. Porphyrins Phthalocyanines* 2008; **12**: 906.
11. Palmer JH, Durrell AC, Gross Z, Winkler JR and Gray HB. *J. Am. Chem. Soc.* 2010; **132**: 9230.
12. Rabinovich E, Goldberg I and Gross Z. *Chem. Eur. J.* 2011; **17**: 12294.
13. Schöfberger W, Lengwin F, Reith LM, List M and Knör G. *Inorg. Chem. Commun.* 2010; **13**: 1187.
14. Reith LM, Stiftinger M, Monkowius U, Knör G and Schoefberger W. *Inorg. Chem.* 2011; **50**: 6788.
15. Buckley HL, Chomitz WA, Koszarna B, Tasiar M, Gryko DT, Brothers PJ and Arnold J. *Chem. Commun.* 2012; **48**: 10766.
16. Padilla R, Buckley HL, Ward AL and Arnold J. *Chem. Commun.* 2014; **50**: 2922.
17. Buckley HL, Anstey MR, Gryko DT and Arnold J. *Chem. Commun.* 2013; **49**: 3104.
18. Ward AL, Buckley HL, Lukens WW and Arnold J. *J. Am. Chem. Soc.* 2013; **135**: 13965.
19. Nigel-Etinger I, Goldberg I and Gross Z. *Inorg. Chem.* 2012; **51**: 1983.
20. Nigel-Etinger I, Goldberg I and Gross Z. *Inorg. Chem.* 2013; **52**: 4139.
21. Luobeznova I, Raizman M, Goldberg I and Gross Z. *Inorg. Chem.* 2006; **45**: 386.
22. Johansen I, Norheim H-K, Larsen S, Alemayehu AB, Conradie J and Ghosh A. *J. Porphyrins Phthalocyanines* 2011; **15**: 1335.
23. Mody VV, Fitzpatrick MB, Zabaneh SS, Czernuszczyk RS, Gałeczowski M and Gryko DT. *J. Porphyrins Phthalocyanines* 2009; **13**: 1040.
24. Palmer JH. *Struct. Bond.* 2012; **142**: 49.
25. Alaimo PJ, Peters DW, Arnold J and Bergman RG. *J. Chem. Ed.* 2001; **78**: 64.
26. SMART: Area Detector Software Package, Bruker Analytic X-ray Systems I. Madison, WI, 2003.
27. SADABS: Bruker-Nonius Area Detector Scaling and Absorption V2.05 Bruker Analytical X-ray System, I. Madison, WI, 2003.
28. Sheldrick GM. *Acta. Crystallogr. A.* 2008; **64**: 112.
29. Farrugia LJ. *Appl. Crystallogr.* 1997; **30**: 565.



# A novel terbium-cobalt tetra(4-sulfonatophenyl)porphyrin: Synthesis, structure and photophysical and electrochemical properties

Wen-Tong Chen<sup>\*a,b</sup>, Jian-Gen Huang<sup>a</sup>, Qiu-Yan Luo<sup>a</sup>, Ya-Ping Xu<sup>a</sup>  
and Hong-Ru Fu<sup>b</sup>

<sup>a</sup>Institute of Applied Chemistry, School of Chemistry and Chemical Engineering, Jiangxi Province Key Laboratory of Coordination Chemistry, Jingtangshan University, Ji'an, Jiangxi 343009, China

<sup>b</sup>State Key Laboratory of Structural Chemistry, Fujian Institute of Research on the Structure of Matter, Chinese Academy of Sciences, Fuzhou, Fujian 350002, China

*Dedicated to Professor Shunichi Fukuzumi on the occasion of his retirement*

Received 1 October 2014

Accepted 16 October 2014

**ABSTRACT:** A novel terbium-cobalt porphyrin  $\{[\text{Tb}(\text{H}_2\text{O})_3][\text{Co}(\text{TPPS})]\}_n \cdot n\text{H}_2\text{O}$  (**1**) (TPPS = tetra(4-sulfonatophenyl)porphyrin) has been synthesized *via* a hydrothermal reaction and structurally characterized by X-ray single crystal diffraction. Compound **1** is characterized by a three-dimensional (3-D) porous open framework, which is originated from the Co(TPPS) moieties interconnected by the terbium ions. The fluorescence study shows that compound **1** displays an emission band in the blue region. Nanosecond transient spectra reveals that the fluorescence lifetime is 1.14 ms. The cyclic voltammetry (CV) and differential pulse voltammetry (DPV) experiments discovers one reversible wave with  $E_{1/2} = -0.80$  V.

**KEYWORDS:** crystal structure, hydrothermal reaction, framework, fluorescence, porphyrin.

## INTRODUCTION

Porphyrins broadly exist in nature and they are a key factor in photosynthesis process and red blood cells carrying dioxygen [1]. Because porphyrins have special physiological activity and unique properties, they can be widely used in the areas such as catalysts, electrochemical sensors, medicine, solar energy conversion, and so on [2–4]. The peripheral organic groups and nitrogen atoms of porphyrin core can coordinate with metal ions, so porphyrins can act as a multifunctional ligand to construct metalloporphyrinic frameworks (MPFs). MPFs have recently received more and more interest because they exhibit important applications in the fields of optical, adsorption, catalysis, energy and electron transfer [5–8]. Up to date, many non-metallated porphyrins have been applied as a second building unit

(SBU) to prepare new MPFs, for example, tetrakis(4-carboxyphenyl)porphyrin (TCPP), *meso*-tetra(4-pyridyl)porphyrin (TPyP), tetrakis(4-(carboxymethyleneoxy)phenyl)porphyrin (TCMOPP), tetrakis(3,5-dicarboxyphenyl)porphyrin (TDCPP) [9–14].

Similar to these nonmetallated porphyrins, the tetra(4-sulfonatophenyl)porphyrin (TPPS) is also known as a rigid, large and square planar symmetrical ligand with many coordination sites, one is the center of the 24-membered macrocyclic porphyrin core, the others are the 12 oxygen atoms on the peripheral sulfonic groups. As a result, TPPS is probably a useful SBU to design and construct MPFs. However, TPPS has been rarely found in synthesizing MPFs and there are only two MPFs containing TPPS have been documented up to date [15, 16]. Therefore, the crystal structures and properties of MPFs containing TPPS are still needed to be investigated. In recent years, our interest is mainly focused on the TPPS-containing MPFs, which might

\*Correspondence to: Wen-Tong Chen, email: wtchen\_2000@aliyun.com, tel/fax: +86 796-811-9239

have interesting structural motifs and properties like fluorescence and magnetism. We report in this work the hydrothermal synthesis, crystal structure and properties of a terbium-cobalt TPPS porphyrinic compound, *i.e.*  $\{[\text{Tb}(\text{H}_2\text{O})_3][\text{Co}(\text{TPPS})]\}_n \cdot n\text{H}_2\text{O}$  (**1**) (TPPS = tetra(4-sulfonatophenyl)-porphyrin), which shows a 3-D porous open framework. Compound **1** was investigated by X-ray single-crystal diffraction, FT-IR, UV-vis, fluorescence, luminescence lifetime, CV and DPV.

## EXPERIMENTAL

### Materials and instrumentation

All chemical reagents were commercially available and used without further purification. FT-IR was conducted on a Nicolet 5DX spectrometer. UV-vis spectra were obtained on a PE Lambda 900 spectrometer. Fluorescence was measured on an Edinburgh FLS920 apparatus. Fluorescent lifetime was carried out by a Photon Technology International GL-3300 nitrogen laser. Cyclic voltammetry (CV) and differential pulse voltammetry (DPV) were performed on a BAS 100W electrochemical analyzer in deaerated methanol solution with 0.1 M tetra-*n*-butylammonium hexafluorophosphate (TBAPF6) as a supporting electrolyte under argon atmosphere. A three-electrode cell was adopted with a platinum wire and a platinum working electrode as a counter electrode.

### Synthesis of $\{[\text{Tb}(\text{H}_2\text{O})_3][\text{Co}(\text{TPPS})]\}_n \cdot n\text{H}_2\text{O}$ (**1**)

It was synthesized by loading  $\text{TbCl}_3 \cdot 6\text{H}_2\text{O}$  (0.5 mmol, 187 mg),  $\text{CoCl}_2 \cdot 6\text{H}_2\text{O}$  (0.5 mmol, 119 mg), TPPS (0.1 mmol, 94 mg) and 10 mL distilled water into a 23 mL Teflon-lined stainless steel reactor and heating it at 473 K for three days. The product was then cooled to room temperature and purple crystals were collected by filtration and washed with distilled water. The yield is 16% (based on terbium). FT-IR (KBr):  $\nu$ ,  $\text{cm}^{-1}$  3424(vs), 2365(w), 1632(vs), 1446(m), 1393(m), 1173(vs), 1125(s), 1039(s), 998(vs), 809(m), 741(s) and 641(m).

### X-ray structure determination

A single crystal was carefully selected and mounted on a glass fiber for X-ray diffraction experiment. The intensity data were gathered on a Rigaku Mercury CCD X-ray diffractometer equipped with graphite-monochromatic Mo- $K\alpha$  radiation ( $\lambda = 0.71073 \text{ \AA}$ ) by using a  $\omega$  scan method. CrystalClear program was applied to data reduction and empirical absorption correction [17]. By means of Siemens SHELXTL™ Version 5 program, the crystal structure was solved by the direct methods and refined by full-matrix least-squares on  $F^2$  [18]. The non-hydrogen atoms were yielded by difference Fourier maps and refined with anisotropic

**Table 1.** Summary of crystallographic data and structure analysis

Empirical formula	$\text{C}_{44}\text{H}_{33}\text{CoN}_4\text{O}_{16}\text{S}_4\text{Tb}$
Formula weight	1219.83
Crystal system	Triclinic
Space group	$P\bar{1}$
Unit cell dimensions	
$a$ , $\text{\AA}$	11.1637 (15)
$b$ , $\text{\AA}$	13.4231 (12)
$c$ , $\text{\AA}$	19.713 (2)
$\alpha$ , $^\circ$	71.9640 (10)
$\beta$ , $^\circ$	74.6130 (10)
$\gamma$ , $^\circ$	75.7640 (10)
Volume, $\text{\AA}^3$	2664.7 (5)
$Z$	2
Density, calculated, $\text{Mg}\cdot\text{m}^{-3}$	1.520
Crystal size, mm	$0.14 \times 0.10 \times 0.08$
Color	Purple
Shape	Block
Theta range for data collection, $^\circ$	3.30–25.03
Index ranges	$-13 \leq h \leq 13$ , $-15 \leq k \leq 15$ , $-17 \leq l \leq 23$
Reflections collected	15,230
Independent reflections	8717
Reflections with $[I > 2\sigma(I)]$	4177
Refinement method	Full-matrix least-squares on $F^2$
Goodness-of-fit on $F^2$	0.996
Final $R$ indices (obs.)	$R_1 = 0.0755$ , $wR_2 = 0.1556$
$R$ indices (all)	$R_1 = 0.1182$ , $wR_2 = 0.1784$
$\mu$ , $\text{mm}^{-1}$	1.851
$F(000)$	1218
Largest and mean $\Delta/\sigma$	0.001, 0
$\Delta\rho(\text{max, min})$ , $\text{e}/\text{\AA}^3$	1.241, -1.070

thermal parameters. Hydrogen atoms, except for those on the water molecules, were theoretically generated and allowed to ride on their respective parent atoms, but were not refined. Tables 1 and 2 list the crystallographic data as well as the selected bond lengths and angles.

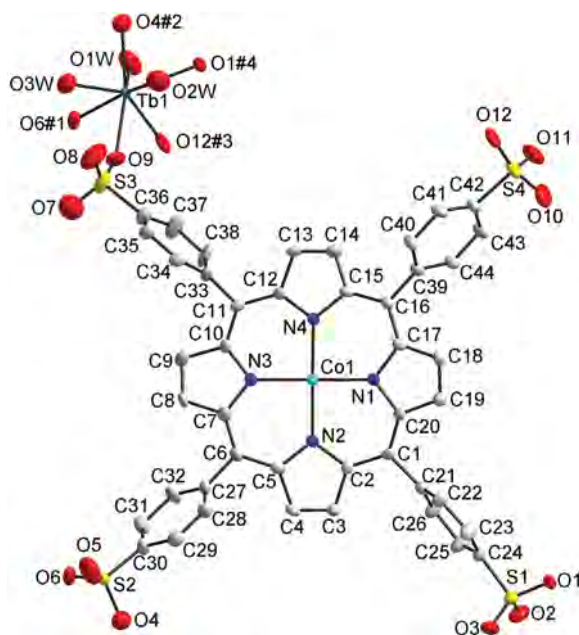
## RESULTS AND DISCUSSION

As shown in Table 1, compound **1** is crystallized in the  $P\bar{1}$  space group of the triclinic system with two formula units in one cell. An ORTEP drawing with atomic labels of the crystal structure of **1** is given in Fig. 1.

**Table 2.** Selected bond lengths (Å) and bond angles (°)

Tb(1)-O(6)#1	2.162 (3)	O(4)#2-Tb(1)-O(9)#4	138.8 (1)
Tb(1)-O(4)#2	2.238 (3)	O(1W)-Tb(1)-O(9)#4	145.0 (1)
Tb(1)-O(12)#3	2.371 (3)	O(3W)-Tb(1)-O(9)#4	72.9 (1)
Tb(1)-O(1)#4	2.533 (3)	O(12)#3-Tb(1)-O(9)#4	75.5 (1)
Tb(1)-O(9)	2.479 (3)	O(6)#1-Tb(1)-O(2W)	145.9 (1)
Tb(1)-O(1W)	2.296 (4)	O(4)#2-Tb(1)-O(2W)	74.2 (1)
Tb(1)-O(2W)	2.501 (4)	O(1W)-Tb(1)-O(2W)	136.7 (1)
Tb(1)-O(3W)	2.347 (4)	O(3W)-Tb(1)-O(2W)	77.8 (2)
Co(1)-N(1)	1.969 (3)	O(12)#3-Tb(1)-O(2W)	111.6 (1)
Co(1)-N(2)	1.966 (3)	O(9)#4-Tb(1)-O(2W)	74.2 (1)
Co(1)-N(3)	1.972 (3)	O(6)#1-Tb(1)-O(1)	144.1 (1)
Co(1)-N(4)	1.950 (3)	O(4)#2-Tb(1)-O(1)	73.5 (1)
O(6)#1-Tb(1)-O(4)#2	116.5 (1)	O(1W)-Tb(1)-O(1)	73.6 (1)
O(6)#1-Tb(1)-O(1W)	76.1 (1)	O(3W)-Tb(1)-O(1)	139.0 (1)
O(4)#2-Tb(1)-O(1W)	75.3 (1)	O(12)#3-Tb(1)-O(1)	73.89 (9)
O(6)#1-Tb(1)-O(3W)	74.7 (1)	O(9)#4-Tb(1)-O(1)	117.5 (1)
O(4)#2-Tb(1)-O(3W)	75.1 (1)	O(2W)-Tb(1)-O(1)	68.8 (1)
O(1W)-Tb(1)-O(3W)	122.3 (2)	N(4)-Co(1)-N(2)	176.5 (1)
O(6)#1-Tb(1)-O(12)#3	80.7 (1)	N(4)-Co(1)-N(1)	90.2 (1)
O(4)#2-Tb(1)-O(12)#3	141.6 (1)	N(2)-Co(1)-N(1)	89.8 (1)
O(1W)-Tb(1)-O(12)#3	76.5 (2)	N(4)-Co(1)-N(3)	90.1 (1)
O(3W)-Tb(1)-O(12)#3	143.0 (1)	N(2)-Co(1)-N(3)	90.2 (1)
O(6)#1-Tb(1)-O(9)#4	78.9 (1)	N(1)-Co(1)-N(3)	174.6 (1)

Symmetry codes: #1  $x-1, y-1, z$ ; #2  $-x+2, -y+1, -z$ ; #3  $-x+1, -y, -z+1$ ; #4  $-x+1, -y+1, -z+1$ .



**Fig. 1.** An ORTEP drawing of **1** with 20% ellipsoid probability. The lattice water molecules and hydrogen atoms were omitted for clarity

X-ray single-crystal diffraction analysis discovers that compound **1** is characteristic of a 3-D porous open framework. The molecular structure of **1** is comprised of  $\{[\text{Tb}(\text{H}_2\text{O})_3][\text{Co}(\text{TPPS})]\}_n^{n-}$  anions and protonated water molecules. The  $\text{Tb}^{3+}$  ions are bound by eight oxygen atoms from five sulfonic groups and three coordinating water molecules, constructing a slightly distorted square anti-prism geometry. Two neighboring  $\text{Tb}^{3+}$  ions are interlinked by two  $\mu_2$ -sulfonic groups to give a  $\text{Tb}_2\text{O}_{14}$  moiety. The shortest distance between two neighboring  $\text{Tb}^{3+}$  ions is 4.6888(4) Å. The bond lengths of Tb–O are in the range of 2.162(3) Å–2.533(3) Å with a mean value of 2.366(4) Å, which is normal and comparable with those documented in the references [19–24]. The bond angles of O–Tb–O are in the wide span of 68.8(1)°–145.9(1)°.

The cobalt ions are resided in the center of the 24-membered macrocyclic porphyrin core. Each cobalt ion is surrounded by four nitrogen atoms of the porphyrin core, forming a slightly distorted square. The bond lengths of Co–N are between 1.950(3) Å and 1.972(3) Å, which is also normal and comparable with those reported previously [25–30]. The shortest distance between two neighboring cobalt ions is 6.2263(6) Å. Each  $\text{Tb}_2\text{O}_{14}$

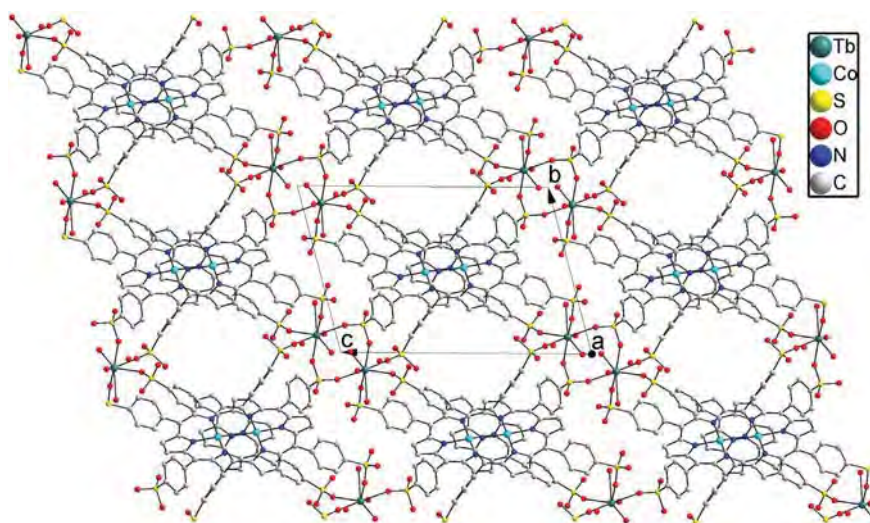


Fig. 2. A packing diagram of **1**

moiety connects eight Co(TPPS) molecules to complete a 3-D porous open framework with the channels parallel to the *a* direction, as shown in Fig. 2. The lattice water molecules locate in the voids of the 3-D porous open framework.

The porphyrin macrocycle in **1** exhibits a saddle-distorted geometry and the four pyrrole rings slightly distort in an alternant mode either upward or downward with respect to the mean plane of the saddle-like porphyrin macrocycle. The displacement of the atoms on the 24-membered porphyrin macrocycle is from  $-0.413 \text{ \AA}$  to  $0.380 \text{ \AA}$ . The displacement of the four pyrrole nitrogen atoms is  $\pm 0.077 \text{ \AA}$  from their mean plane. With respect to the plane of four pyrrole nitrogen atoms which might represent the average plane of the macrocyclic porphyrin core, the distortion angles of the aryl rings are  $55.55^\circ$ ,  $62.81^\circ$ ,  $72.82^\circ$  and  $101.22^\circ$ , respectively. It should be pointed out that compound **1** exhibits a large void space being  $320 \text{ \AA}^3$  which is 12% of the unit-cell volume.

Gouterman has put forward a four orbital's theory [31], *i.e.* the UV-vis absorption spectrum of a metalloporphyrin generally displays two kinds of absorption bands, one strong B-band (or Soret band) at around 400 nm and several weaker Q-bands locating at 500–650 nm. The UV-vis absorption spectrum of **1** carried out in methanol solutions at room temperature is shown in Fig. 3. The B-band is found at 433 nm with a molar absorption coefficient  $\epsilon$  being of  $4.74 \times 10^4 \text{ M}^{-1}\cdot\text{cm}^{-1}$ . From the UV-vis absorption spectrum we also observe one Q-band residing at 549 nm. As for a free-base porphyrin, it generally possesses three or four Q-bands. Therefore, the Q-band number of **1** is less than a normal free-base porphyrin. Such discrepancy in the Q-band number could be ascribable to the increase of the molecular symmetry of porphyrins, which is originated from the metalation of the porphyrins.

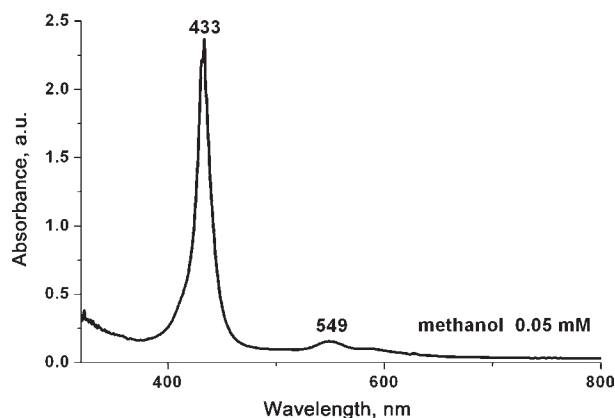


Fig. 3. UV-vis absorption spectrum

In general, the terbium ion can exhibit good fluorescence properties. Considering this, we measured the fluorescence of **1** under room temperature. To our knowledge, because of the concentration quenching effect, porphyrins in solid state can not emit fluorescence. As a result, the fluorescent spectra of **1** were conducted in methanol solutions. The fluorescent measurements reveal that the excitation spectra of **1** have effective energy absorption in the range of 300–400 nm, as shown in Fig. 4. The excitation spectra of **1** display a maximum value at 355 nm. We also carried out the emission spectra of **1** by using a photo-excitation of 355 nm and, the emission spectra exhibit a narrow and sharp emission band in the blue region with a maximum value being of 461 nm.

This fluorescent emission band is obviously not ascribable to the characteristic emissions of terbium. For terbium ions, the emission spectra generally display four emission bands at around 492, 548, 588 and

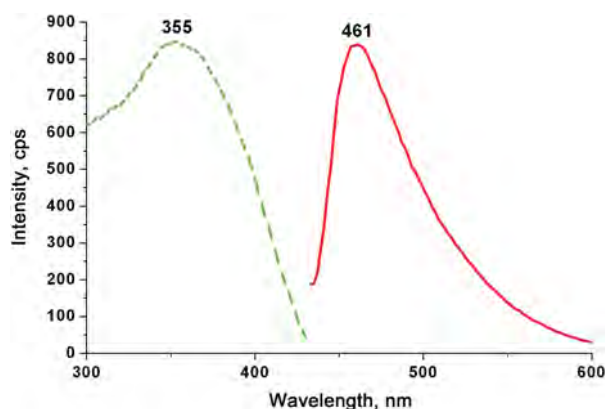


Fig. 4. The excitation (green) and emission (red) spectra

623 nm, corresponding to the characteristic emission  $^5D_4$ - $^7F_J$  transitions ( $J = 6, 5, 4$  and  $3$ , respectively) of  $Tb^{3+}$  ions [32–35]. The absence of the characteristic emissions of the  $Tb^{3+}$  ions suggests that TPPS cannot effectively transfer the absorbed energy to the  $Tb^{3+}$  ions. On the other hand, it is well-known that porphyrins usually exhibit emissions at wavelengths longer than 600 nm. Hence, the peak at 461 nm is not originated from the porphyrin ligand, either. As a result, it is proposed that the peak at 461 nm is probably due to the metal to ligand charge transfer (MLCT). By means of a time-correlated single-photon counting technique, we performed the fluorescence lifetime experiment in methanol solutions. The time-resolved nanosecond transient spectra of **1** are shown in Fig. 5 and the spectra are fitted as a single exponential. The fluorescence lifetime of **1** is determined to be 1.14 ns in methanol solutions.

Kadish and his co-workers have pointed out that some vital factors, which mainly decide the redox potentials of a porphyrin, include the supporting electrolytes, the solvents, and porphyrin itself [36]. The redox potentials sometimes can be different up to 1.0 V, depending on different conditions. The cyclic voltammetry (CV) and differential pulse voltammetry (DPV) of compound **1** were performed in methanol solutions and  $TBAPF_6$  (0.1 M) at room temperature in argon atmosphere. A slow scan CV curve of compound **1** shows one reversible couples ( $-0.86$  V and  $-0.74$  V) with  $E_{1/2}$  being of  $-0.80$  V, which is very close to the value of  $-0.79$  V on DPV diagram, as shown in Fig. 6. The reversible redox potentials should be ascribed to the first oxidation of the porphyrin moieties. Besides the reversible couple waves, there are two more reductive peaks locating at  $-0.30$  V and  $-1.32$  V in the CV diagram, which are also in good agreement with the values of  $-0.32$  V and  $-1.31$  V in the DPV diagram, respectively.

In this work we report a novel terbium-cobalt porphyrin  $\{[Tb(H_2O)_3][Co(TPPS)]\}_n \cdot nH_2O$ , which is prepared *via* a hydrothermal reaction. The title compound is characterized by a 3-D porous open framework.

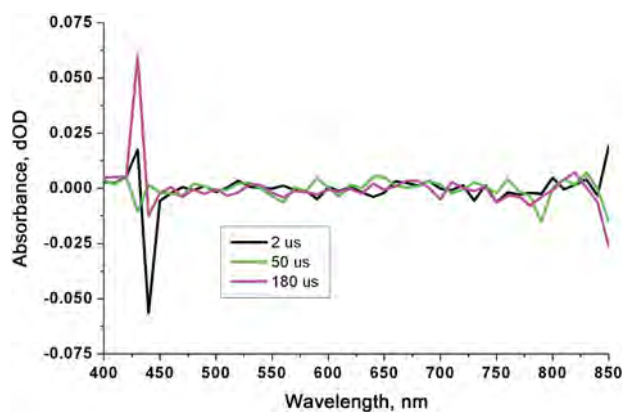


Fig. 5. Nanosecond transient spectra

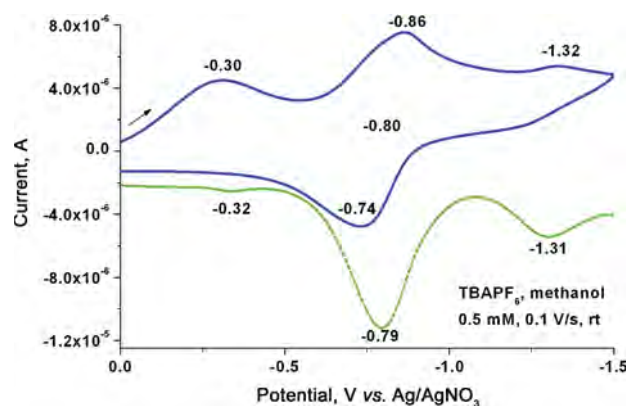


Fig. 6. CV (blue solid) and DPV (green dashed) curves

Compound **1** displays a large void space being of  $320 \text{ \AA}^3$  which is 12% of the unit-cell volume. It displays a fluorescence emission band in the blue region and the fluorescence lifetime is 1.14 ns in methanol solutions. The CV and DPV measurements discover a reversible couple waves with  $E_{1/2} = -0.80$  V.

### Acknowledgements

This work was supported by the NSF of China (21361013), the NSF of Jiangxi Province (20132BAB203010), the science and technology project of Jiangxi Provincial Department of Education (GJJ14554) and the open foundation (No. 20130014) of the State Key Laboratory of Structural Chemistry, Fujian Institute of Research on the Structure of Matter, Chinese Academy of Sciences.

### Supporting information

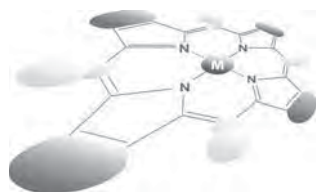
Crystallographic data for the structural analysis have been deposited at the Cambridge Crystallographic Data Center (CCDC) under number CCDC-982022 for (**1**). Copies can be obtained on request, free of charge,



via [www.ccdc.cam.ac.uk/data\\_request/cif](http://www.ccdc.cam.ac.uk/data_request/cif) or from the Cambridge Crystallographic Data Center, 12 Union Road, Cambridge CB2 1EZ, UK (fax: +44 1223-336-033 or email: [data\\_request@ccdc.cam.ac.uk](mailto:data_request@ccdc.cam.ac.uk)).

## REFERENCES

- Kadish KM, Van Caemelbecke E and Royal G. *The Porphyrin Handbook*, Vol. 8, Kadish KM, Smith KM and Guilard R. (Eds.) Academic Press: San Diego, CA, 2000; pp 1–114.
- Jiang J and Ng DKP. *Acc. Chem. Res.* 2009; **42**: 79–88.
- Drain CM, Varotto A and Radivojevic I. *Chem. Rev.* 2009; **109**: 1630–1658.
- Bucher C, Devillers CH, Moutet JC, Royal G and Saint-Aman E. *Coord. Chem. Rev.* 2009; **253**: 21–36.
- Zou C and Wu CD. *Dalton Trans.* 2012; **41**: 3879–3888.
- Fateeva A, Chater PA, Ireland CP, Tahir AA, Khimyak YZ, Wiper PV, Darwent JR and Rosseinsky MJ. *Angew. Chem., Int. Ed.* 2012; **51**: 7440–7444.
- Wang XS, Chrzanowski M, Kim C, Gao WY, Wojtas L, Chen YS, Zhang XP and Ma S. *Chem. Commun.* 2012; **48**: 7173–7175.
- Fateeva A, Devautour-Vinot S, Heymans N, Devic T, Grenèche JM, Wuttke S, Miller S, Lago A, Serre C, Weireld GD, Maurin G, Vimont A and Férey G. *Chem. Mater.* 2012; **23**: 4641–4646.
- Morris W, Voloskiy B, Demir S, Gándara F, McGrier PL, Furukawa H, Cascio D, Stoddart JF and Yaghi OM. *Inorg. Chem.* 2012; **51**: 6443–6445.
- Zou C, Xie MH, Kong GQ and Wu CD. *CrystEngComm.* 2012; **14**: 4850–4856.
- Smythe NC, Butler DP, Moore CE, McGowan WR, Rheingold AL and Beauvais LG. *Dalton Trans.* 2012; **41**: 7855–7858.
- Matsunaga S, Endo N and Mori W. *Eur. J. Inorg. Chem.* 2011; **29**: 4550–4557.
- Zha Q, Rui X, Wei T and Xie Y. *CrystEngComm.* 2014; **16**: 7371–7384.
- Zha Q, Ding C, Rui X and Xie Y. *Cryst. Growth Des.* 2013; **13**: 4583–4590.
- Chen WT, Yamada Y, Liu GN, Kubota A, Ichikawa T, Kojima Y, Guo GC and Fukuzumi S. *Dalton Trans.* 2011; **40**: 12826–12831.
- Demel J, Kubát P, Millange F, Marrot J, Císařová I and Lang K. *Inorg. Chem.* 2013; **52**: 2779–2786.
- CrystalClear ver. 1.35, (Rigaku Corporation) 2002.
- SHELXTLTM ver. 5, Reference Manual, (Siemens Energy & Automation Inc, Madison, Wisconsin, USA) 1994.
- Cai SL, Zheng SR, Fan J, Tan JB, Xiao TT and Zhang WG. *J. Solid State Chem.* 2011; **184**: 3172–3178.
- Zheng SR, Cai SL, Yang QY, Xiao TT, Fan J and Zhang WG. *Inorg. Chem. Commun.* 2011; **14**: 826–830.
- Stojanovic M, Robinson NJ, Assefa Z and Sykora RE. *Inorg. Chim. Acta* 2011; **376**: 422–427.
- Yan X, Li Y, Wang Q, Huang X, Zhang Y, Gao C, Liu W, Tang Y, Zhang H and Shao Y. *Cryst. Growth Des.* 2011; **11**: 4205–4212.
- Cristovao B, Klak J, Miroslaw B and Mazur L. *Inorg. Chim. Acta* 2011; **378**: 288–296.
- Chen MS, Zhao Y, Okamura TA, Su Z, Sun WY and Ueyama N. *Supramol. Chem.* 2011; **23**: 117–124.
- Muniappan S, Lipstman S, George S and Goldberg I. *Inorg. Chem.* 2007; **46**: 5544–5554.
- Annoni E, Pizzotti M, Ugo R, Quici S, Morotti T, Casati N and Macchi P. *Inorg. Chim. Acta* 2006; **359**: 3029–3041.
- Hodgson MC, Burrell AK, Boyd PDW, Brothers PJ and Rickard CEF. *J. Porphyrins Phthalocyanines* 2002; **6**: 737–747.
- Wang K, Poon CT, Wong WK, Wong WY, Choi CY, Kwong DWJ, Zhang H and Li ZY. *Eur. J. Inorg. Chem.* 2009; **7**: 922–928.
- Konarev DV, Khasanov SS, Saito G and Lyubovskaya RN. *Cryst. Growth Des.* 2009; **9**: 1170–1181.
- Konarev DV, Neretin IS, Saito G, Slovokhotov YL, Otsuka A and Lyubovskaya RN. *Eur. J. Inorg. Chem.* 2004; **9**: 1794–1798.
- Gouterman M. *The Porphyrins*, Vol. III; Dolphin D. (Ed.) Academic Press: New York, 1978.
- Yan B and Zhu HX. *J. Fluoresc.* 2007; **17**: 331–337.
- Viswanathan S and Bettencourt-Dias A. *Inorg. Chem. Commun.* 2006; **9**: 444–448.
- Chen W and Fukuzumi S. *Inorg. Chem.* 2009; **48**: 3800–3807.
- Horiuchi T, Iki N, Hoshino H, Kabuto C and Miyano S. *Tetrahedron Lett.* 2007; **48**: 821–825.
- Kadish KM, Van Caemelbecke E, D'Souza F, Lin M, Nurco DJ, Medforth CJ, Forsyth TP, Krattinger B, Smith KM, Fukuzumi S, Nakanishi I and Shelnutt JA. *Inorg. Chem.* 1999; **38**: 2188–2198.



# Systematic studies on side-chain structures of phthalocyaninato-polysiloxanes: Polymerization and self-assembling behaviors

Satoru Yoneda<sup>a</sup>, Tsuneaki Sakurai<sup>\*a,b,†</sup>, Toru Nakayama<sup>†b</sup>, Kenichi Kato<sup>c</sup>, Masaki Takata<sup>c</sup> and Shu Seki<sup>\*a</sup>

<sup>a</sup> Graduate School of Engineering, Osaka University, 2-1 Yamadaoka, Suita, Osaka 565-0871, Japan

<sup>b</sup> School of Engineering, The University of Tokyo, 7-3-1 Hongo, Bunkyo-ku, Tokyo 113-8656, Japan

<sup>c</sup> RIKEN SPring-8 Center, 1-1-1 Kouto, Sayo-cho, Sayo-gun, Hyogo 679-5148, Japan

*Dedicated to Professor Shunichi Fukuzumi on the occasion of his retirement*

Received 26 October 2014

Accepted 5 November 2014

**ABSTRACT:** A series of dihydroxysilicon phthalocyanines having soluble side chains were synthesized and their bulk-state polymerization capability was investigated. Detailed spectroscopic study of the obtained phthalocyaninato-polysiloxanes revealed that strong electron donating ability and small steric hindrance of the peripheral substituents are the dominant factors to afford high-molecular weight polymers. The polymers show the behaviors of columnar liquid crystal (LC), which is clarified by the presence of clear X-ray diffraction patterns with a hexagonal lattice and birefringent textures in polarized optical microscopy. Because of the siloxane covalent bonds through central silicon atoms, phthalocyaninato-polysiloxanes accommodate one-dimensional phthalocyanine arrays with strong  $\pi$ -electronic couplings, thus exhibiting columnar LC property even for the derivatives carrying short peripheral chains and leading to the relatively higher density of  $\pi$ -electron systems in the materials. This tendency is different from typical discotic small molecules that require optimum side chain structures for LC formation.

**KEYWORDS:** phthalocyanine, one-dimensional polymer, liquid crystal, columnar phase.

## INTRODUCTION

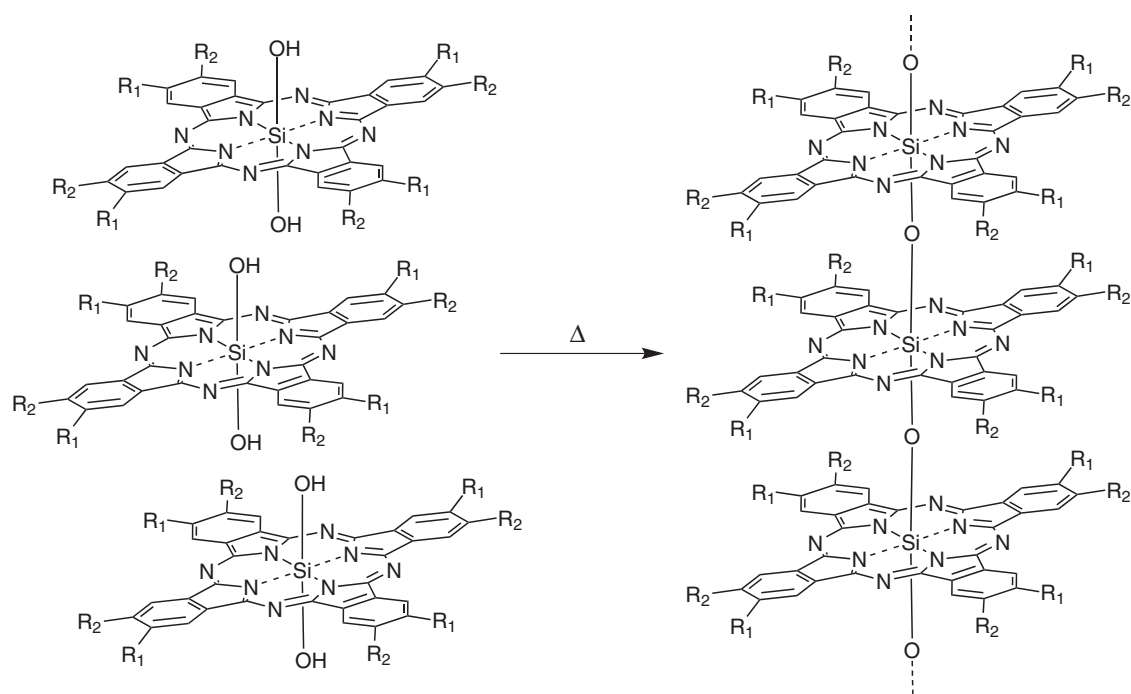
Along with the recent progress in organic electronics, researchers have increasingly focused on the solid-state assembly of  $\pi$ -electron-rich conjugated molecules [1, 2]. In developing a novel semiconducting material, synthetic approaches are useful for manipulating the electronic property in a molecular level. However, at the same time, changing the molecular structure often results in

the drastic change of its assembled (packing) structure that eventually affects the charge carrier transporting property [3, 4]. Consequently, we have always difficulty in predicting and controlling the charge transport properties of the organic materials in the assembled state. In that sense, columnar assembly of disc-shaped molecules allowing well-defined one-dimensional charge carrier transport pathways are interesting for tailoring organic semiconductors. Phthalocyaninato-polysiloxane (PcPS) is one of such compounds, where phthalocyanine rings are cofacially arranged at the distance of  $\sim 3.3$  Å  $\pi$ -stacking periodicity (Scheme 1) [5–7]. Due to this characteristic structure, PcPS has often been called as “Shish-kebab polymer”. The non-substituted propotype compound was reported in 1962 by Joyner and Kenney [8]. On the other hand, Wegner and coworkers developed soluble derivatives with high molecular weight [9, 10],

<sup>†</sup>SPP full member in good standing

\*Correspondence to: Tsuneaki Sakurai, email: t-sakurai@chem.eng.osaka-u.ac.jp, tel: +81 6-6879-4588; Shu Seki, email: seki@chem.eng.osaka-u.ac.jp, tel: +81 6-6879-4586

<sup>†</sup>Current address: Division of Materials Science, Faculty of Pure and Applied Sciences, University of Tsukuba, 1-1-1 Tennodai, Tsukuba, Ibaraki 305-8573, Japan



**Scheme 1.** Dihydroxysilicon phthalocyanine and its polymerization reaction

while Nolte and coworkers recently reported more complex systems [11, 12]. These derivatives form a Langmuir–Blodgett film that shows anisotropic conductive property upon carrier doping [13, 14]. In the most recent decade, analogous heterochromophore arrays based on pyrrole-based macrocycles was reported [15, 16]. While normal  $\pi$ -conjugated disc-shaped molecules can self-assemble into columnar structures only when they carry appropriate side chains [17], PcPS has a polysiloxane chains that keeps columnar stacking of Pc rings with strong electronic coupling, in principle for any derivatives. This distinguishing feature must allow PcPSs to be attractive for molecular electronics and device applications. Although development of a soluble PcPS with ultrahigh degree of polymerization is worth investigating since it affords long-range hole transporting materials [18–20], nevertheless, the variety of reported PcPS molecules was quite limited [21–23]. Namely, the relationship between peripheral groups and polymerization behaviors has remained unclear to date, herein we newly synthesized a series of dihydroxysilicon phthalocyanines (SiPcs) with various type of side chains and investigated their polymerization capability, liquid crystallinity [24, 25] and self-assembled structures. As a consequence, we found that strong electron donating ability and small steric hindrance of the peripheral substituents enhance the condensation reaction of the axial hydroxyl groups to form high molecular-weight polymers. Besides, we revealed that PcPSs tend to form a columnar liquid crystal (LC) with a hexagonal packing, even for the derivatives carrying small side chains, which

is a characteristic behavior compared to usual small molecules-based discotic LCs.

## EXPERIMENTAL

### Chemicals and instruments

Unless otherwise noted, all commercial reagents were purchased from Wako Pure Chemical Industries Ltd., Tokyo Chemical Industry Co. Ltd. and Sigma–Aldrich Co. and used as received. The detailed synthetic schemes are described in the supplementary material. Column chromatography was performed on Silica Gel 60N (spherical, neutral) from Kanto Chemicals, or silica gel PSQ 60B (spherical, neutral) from Fuji Silysia Chemical Ltd. TLC analyses were carried out on aluminum sheets coated with silica gel 60 (Merck 5554). Recycling preparative size-exclusion chromatography (SEC) was performed by using JAIGEL 1H and 2H polystyrene-gel columns on a JAI model LC-9210NEXT recycling preparative HPLC system.

### Characterization of compounds

$^1\text{H}$  NMR spectra were recorded in  $\text{CDCl}_3$  on a JEOL model 400SS spectrometer, operating at 400 MHz, where chemical shifts were determined with respect to tetramethylsilane (TMS) as an internal reference. Matrix-assisted laser desorption/ionization time-of-flight (MALDI-TOF) mass spectrometry was performed on a Bruker model Autoflex III spectrometer using dithranol as

a matrix. Electronic absorption spectra were recorded on a JASCO model V-570 UV/VIS/NIR spectrophotometer.

### Polarized optical microscopy (POM)

Polarized optical micrographs were recorded on a Nikon model ECLIPSE E600FN polarized optical microscope equipped with a hand-made hot stage and KPI model TC02 temperature controller. Thin film samples were fabricated on a glass plate and heated to *ca.* 150 °C. After 10 min annealing, they were allowed to room temperature and observed by the microscope.

### Differential scanning calorimetry (DSC)

DSC measurements were performed on a Mettler model DSC 822e differential scanning calorimeter. Cooling and heating profiles were recorded and analyzed with a Mettler model STARE system. Polymer samples were put into an aluminum pan and allowed to a measurement under N<sub>2</sub> gas flow.

### X-ray diffraction analysis (XRD)

X-ray diffraction measurements were carried out using a synchrotron radiation X-ray beam with a wavelength

of 0.108 nm on BL44B2 at the Super Photon Ring (SPring-8, Hyogo, Japan) [26]. A large Debye–Scherrer camera was used in conjunction with an imaging plate as a detector, and all diffraction patterns were recorded with a 0.01° step in 2θ. During the measurements, samples were put into a 0.5-mm thick glass capillary and rotated to obtain a homogeneous diffraction pattern. The exposure time to the X-ray beam was 1.5 min. The temperature was controlled by high-temperature N<sub>2</sub> gas flow. Heating and cooling process was carried out at a rate of 10 °C min<sup>-1</sup> and annealed at the target temperature for 2 min prior to the beam exposure.

## RESULTS AND DISCUSSION

### Synthesis of dihydroxysilicon phthalocyanines

In this study, 13 dihydroxysilicon phthalocyanine derivatives were prepared in total as shown in Fig. 1. They include linear alkoxy, branched alkoxy, alkyl, thioalkyl, alkynyl, and phenoxy groups, where the number of side chains per Pc unit is four or eight. These side chains were introduced into the peripheral (2, 3, 9, 10, 16, 17, 23 and 24) position of Pc rings since non-peripherally

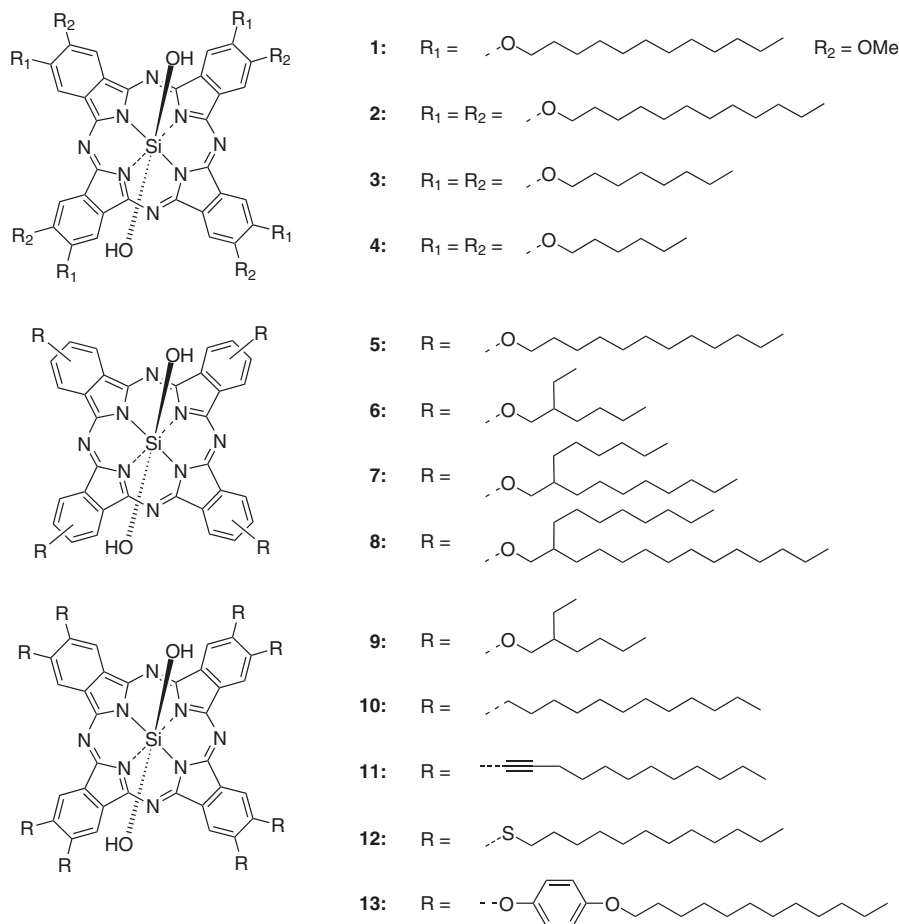
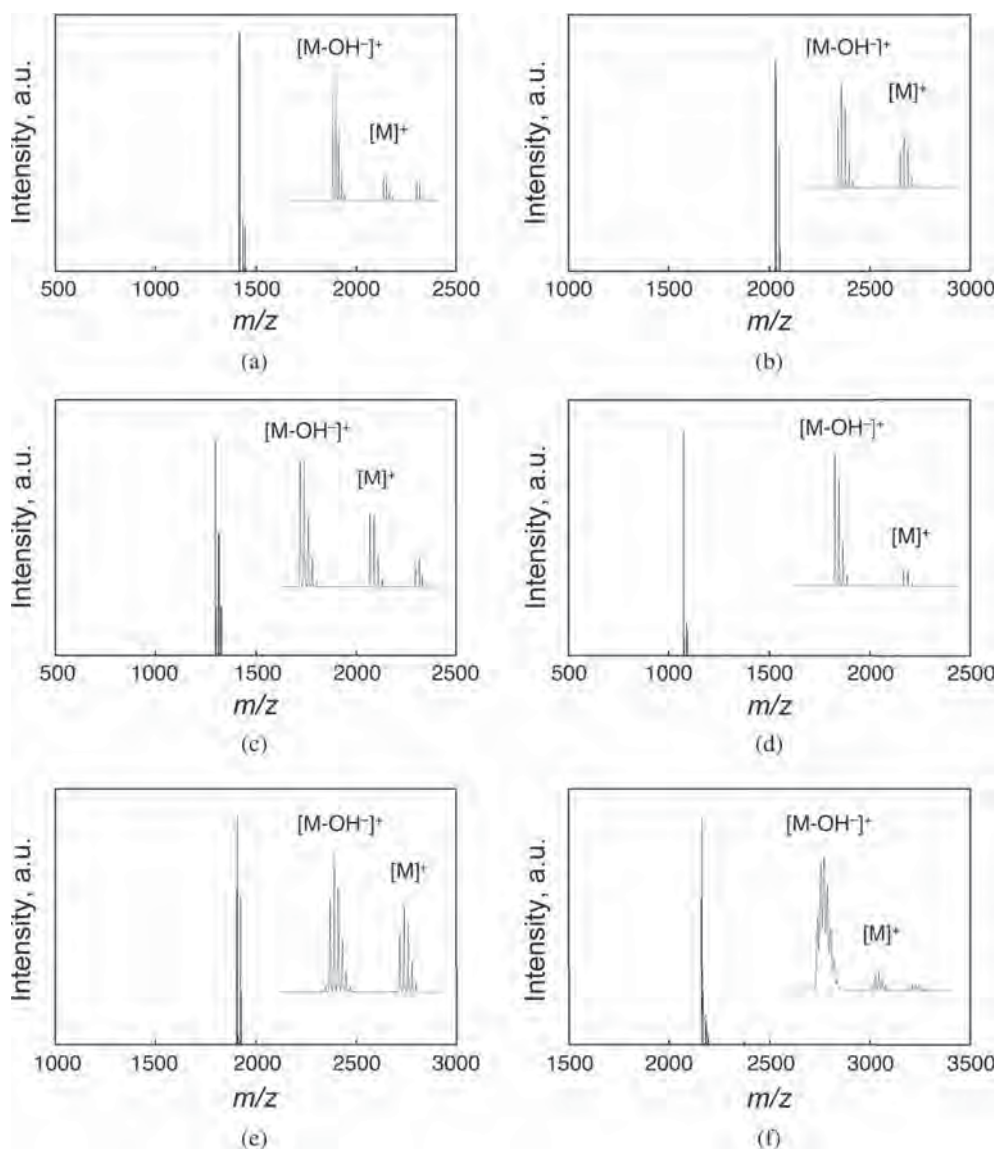


Fig. 1. Chemical structures of dihydroxysilicon phthalocyanine derivatives



**Fig. 2.** MALDI-TOF-MS spectra of (a) **1**, (b) **2**, (c) **5**, (d) **6**, (e) **10** and (f) **12**. Mass peak at around  $[M + 10]^+$  in (a), (c) and (f) indicate a fragment that tends to appear upon high laser intensity

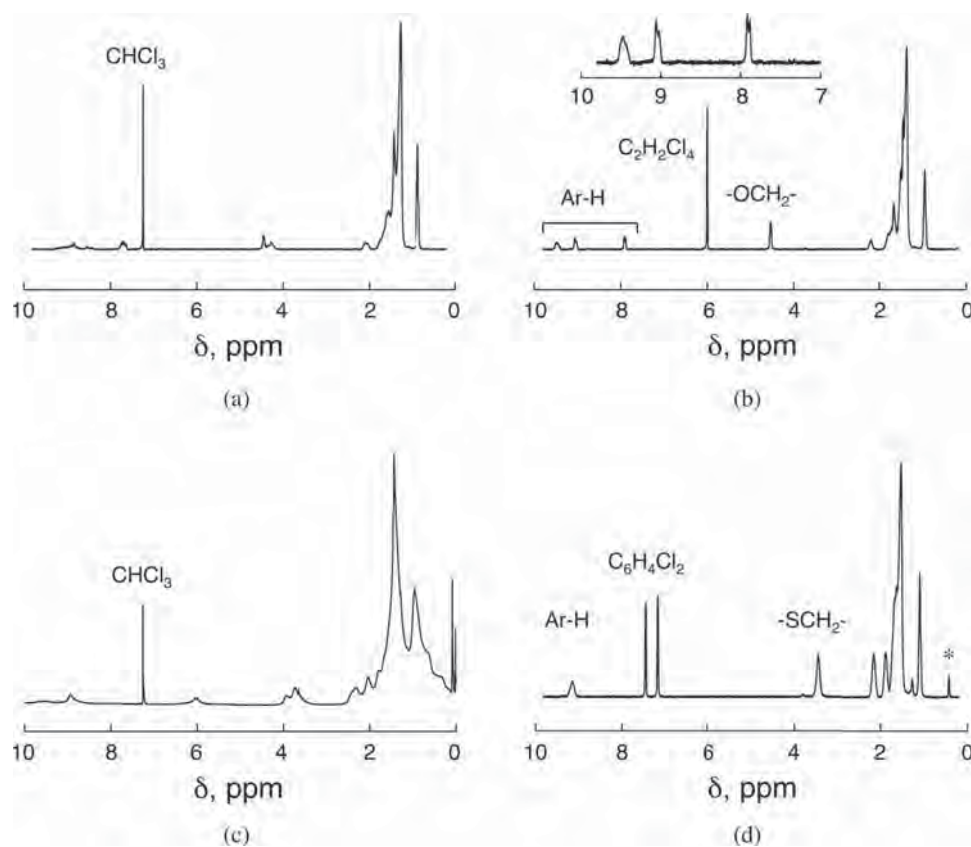
substituted SiPcs are known to stop polymerization [27]. Compounds **1–4** were synthesized according to the reported procedures with a slight modification, while **5–13** were newly synthesized as shown in the supplementary material. The isolation of these SiPcs was confirmed by thin-layer chromatography and MALDI-TOF-MS spectrometry (Fig. 2). Strong aggregation tendency of SiPcs did not allow clear  $^1\text{H}$  NMR spectra in  $\text{CDCl}_3$  at room temperature. However, some derivatives enable to show clear spectra in  $\text{C}_2\text{D}_2\text{Cl}_4$  or  $\text{C}_6\text{D}_4\text{Cl}_2$  at high temperature without oligomerization (Fig. 3). At the same time, alcoxy derivatives such as **2** easily form oligomers in a NMR tube in such a high-temperature condition, which becomes evident by preparative size-exclusion chromatography of the resultant solution followed by MALDI-TOF-MS analysis of the eluted fractions.

### Polymerization of dihydroxysilicon phthalocyanines

Polymerization reaction was carried out under vacuum by elevating up to  $200^\circ\text{C}$  the temperature of the bulk **1–13** in a glass vial, respectively, where the reaction time was set at 24 h. After 24 h, we checked the polymerization progress by blue shift of Q-band in absorption spectra. If there are residual monomers in the system, then further 24 h reaction was performed. When the absorption spectra was saturated, the sample was allowed to room temperature and used as the polymer named as poly-**1**, poly-**2**, and so on.

### Role of side chains on polymerization behaviors

In the earlier works, degree of polymerization for PcPS was estimated by various analytical methods including size-exclusion chromatography (SEC), IR

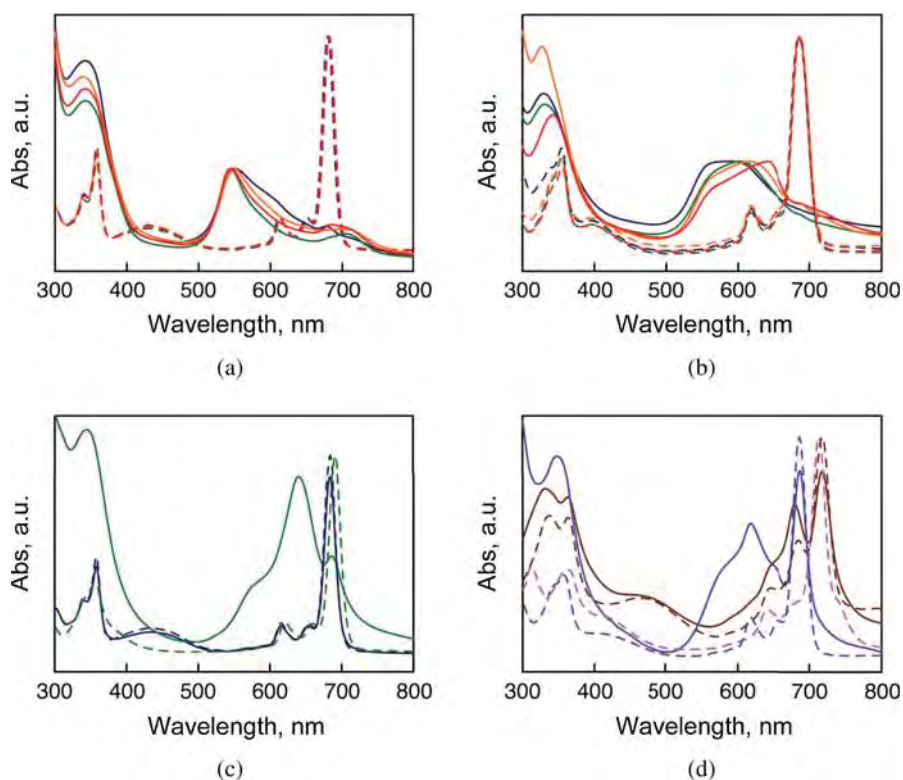


**Fig. 3.**  $^1\text{H}$  NMR spectra of (a) **8** in  $\text{CDCl}_3$  at  $60^\circ\text{C}$ , (b) **8** in  $\text{CD}_2\text{Cl}_4$  at  $120^\circ\text{C}$ , (c) **12** in  $\text{CDCl}_3$  at  $60^\circ\text{C}$  and (d) **12** in  $\text{C}_6\text{D}_4\text{Cl}_2$ . Spectra (a) and (c) indicate the aggregation behavior. The asterisk in (d) shows an impurity

spectroscopy focusing on terminal hydroxyl groups, absorption spectral shift of Q-band upon  $\pi$ -stacking, and small-angle X-ray scattering (SAXS) in solution [25, 28, 29]. Although SAXS analysis seems most suitable for the absolute evaluation of the rod-shaped polymer length, we used UV-vis spectroscopic method for convenience and simplicity. Due to the strong electronic coupling among Pc rings with *H*-type stacking configuration [30], PcPS generally shows a remarkable blue shift of its Q-band even in dilute solution, which is clearly demonstrated by the isolation and spectroscopic study of soluble SiPc discrete oligomers [31, 32]. Based on this blue-shift value, it is possible to estimate the degree of polymerization and easily compare its degree among different derivatives.

After absorption spectral saturation upon heating up to  $200^\circ\text{C}$ , reported compounds **2–4** as well as its analog **1** looked purple and showed an obvious blue shift of Q-band ( $\Delta\lambda = 130\text{--}137\text{ nm}$ ) (Fig. 4a and Table 1), which well agrees with the previous result of **2** [25]. The average degree of polymerization ( $P_w$ ) from the observed blue shift ( $0.43\text{--}0.45\text{ eV}$ ), leading to the lower limit of 25, is considered to be *ca.* 100 [28, 29]. Although huge aromatic compounds are more difficult to ionize than low-molecular weight chemicals, we detected the molecular mass of *e.g.* over 10 mer for Poly-**1** ( $M_w \sim 20000$ ) in MALDI-TOF-MS spectrometry (Fig. 5). Of

interest, it took a much shorter reaction time for **2** to show spectral saturation than that for **4**, while **3** took a time between them. This order implies that **2** is more fluidic and provides higher molecular mobility thanks to the peripheral dodecyloxy chains, which results in the shorter required time until the condensation reaction between axial hydroxyl groups. Meanwhile, as already described, the absorption spectra of Poly-**1–4** are almost identical. These observations predict that the final  $P_w$  value is determined by the local electronic density of Pc cores, whereas the fluidity of side chains may affect the required reaction time to complete the polymerization. In sharp contrast, tetra-alcoxy-substituted Poly-**5** showed a smaller blue shift of its Q-band ( $\Delta\lambda = 103\text{ nm}$ ) than Poly-**1–4** (Fig. 4b). Considering the negligible effect of fluidity on the eventual absorption spectra, this small shift originates from the substitution pattern of the Pc core. In fact, Poly-**6**, Poly-**7**, and Poly-**8**, tetra-substituted derivatives having branched alcoxy chains afford similar spectra to Poly-**5** rather than Poly-**1–4**, indicating that local electronic density is the dominant factor to determine  $P_w$ . More specifically, the order of Q-band shift was Poly-**5** > Poly-**6** > Poly-**7** > Poly-**8**. In other words, when electronic states of monomers resemble each other, the monomer having side chains with smaller volume leads to higher  $P_w$  due to their steric effect on the reactivity of hydroxyl



**Fig. 4.** UV-vis spectra of polymer (solid lines) and monomer (dashed lines) of (a) **1** (navy), **2** (green), **3** (yellow), **4** (red), (b) **5** (navy), **6** (green), **7** (yellow), **8** (red), (c) **9** (navy), **10** (green) and (d) **11** (pink), **12** (purple), **13** (brown) in  $\text{CHCl}_3$  diluted solutions

**Table 1.** Summary of the observed absorption maxima and blue shift of Q-bands, birefringence in optical images and phase structures determined from XRD measurements

Compound	Absorption maxima of Q-band for monomer, nm	Absorption maxima of Q-band for polymer, nm	Blue-shift value, eV	Birefringence in POM for monomer	Birefringence in POM for polymer	Self-organized structure for monomer at rt	Self-organized structure for polymer at rt
<b>1</b>	680	550	0.431	Yes	Yes	$\text{Col}_h$	$\text{Col}_h$
<b>2</b>	683	549	0.443	Yes	Yes	$\text{Col}_h$	$\text{Col}_h$
<b>3</b>	682	549	0.440	Yes	Yes	$\text{Col}_h$	$\text{Col}_h$
<b>4</b>	682	545	0.457	Yes	Yes	$\text{Col}_h$	$\text{Col}_h$
<b>5</b>	686	583	0.319	Yes	Yes	$\text{Col}_h$	$\text{Col}_h$
<b>6</b>	687	602	0.255	No	Yes	Amorphous	$\text{Col}_h$
<b>7</b>	687	615	0.211	No	Yes	Amorphous	$\text{Col}_h$
<b>8</b>	687	644	0.121	No	Yes	Amorphous	$\text{Col}_h$
<b>9</b>	683	683	0	No	— <sup>a</sup>	— <sup>b</sup>	— <sup>a</sup>
<b>10</b>	690	640	0.140	Yes	No	$\text{Col}_r$	Amorphous
<b>11</b>	713	— <sup>c</sup>	— <sup>c</sup>	Yes	— <sup>c</sup>	— <sup>b</sup>	— <sup>c</sup>
<b>12</b>	718	718	0	Yes	Yes	$\text{Col}_x$	$\text{Col}_x$
<b>13</b>	686	618	0.199	Yes	Yes	$\text{Col}_h$	$\text{Col}_h$

<sup>a</sup>**9** did not polymerize. <sup>b</sup>We did not check because of their undesirable polymerization behaviors. <sup>c</sup>**11** was insoluble after heating for 24 h. Phase notation:  $\text{Col}_h$ , hexagonal columnar phase;  $\text{Col}_r$ , rectangular columnar phase;  $\text{Col}_x$ , unidentified columnar phase, respectively.

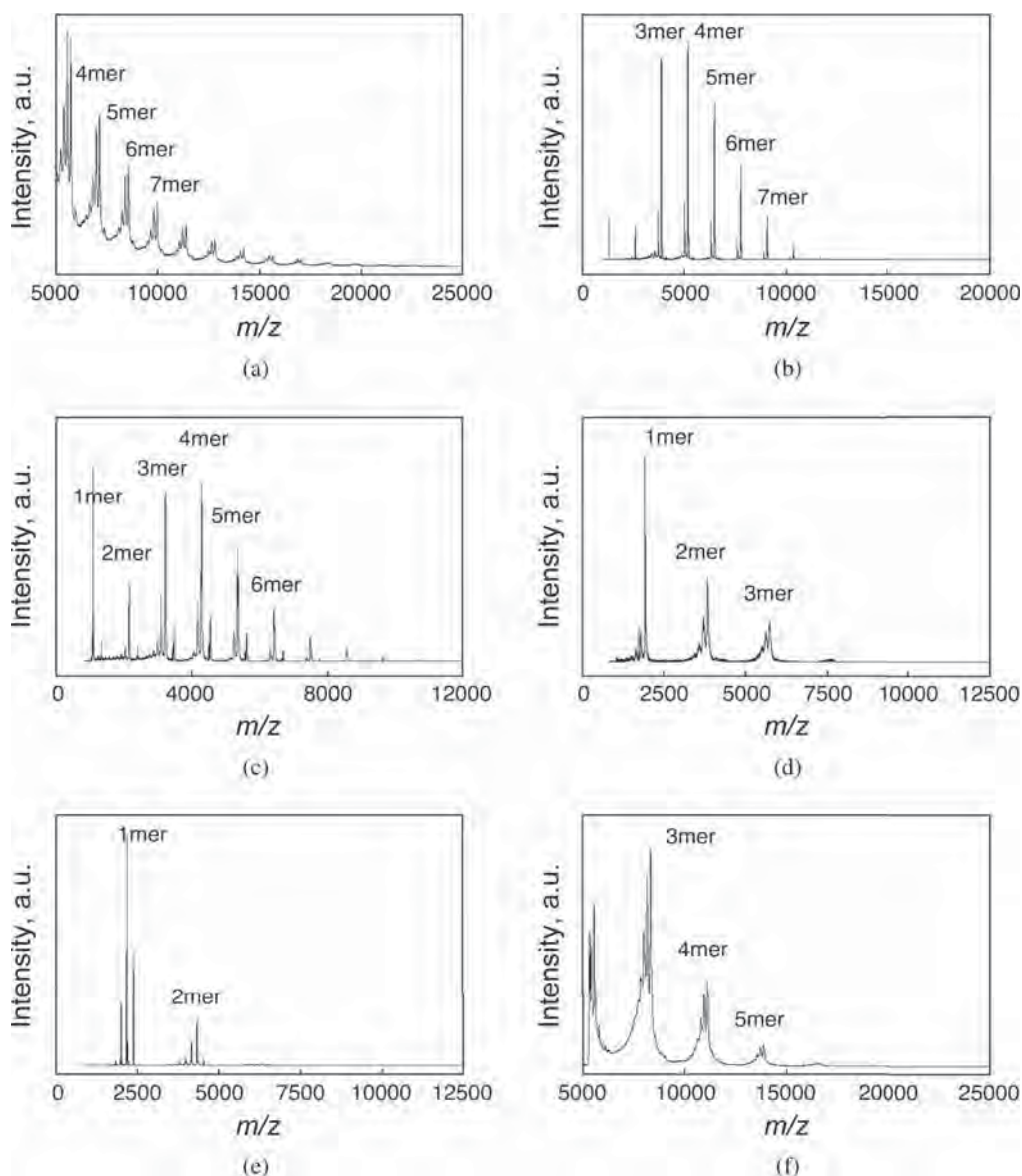


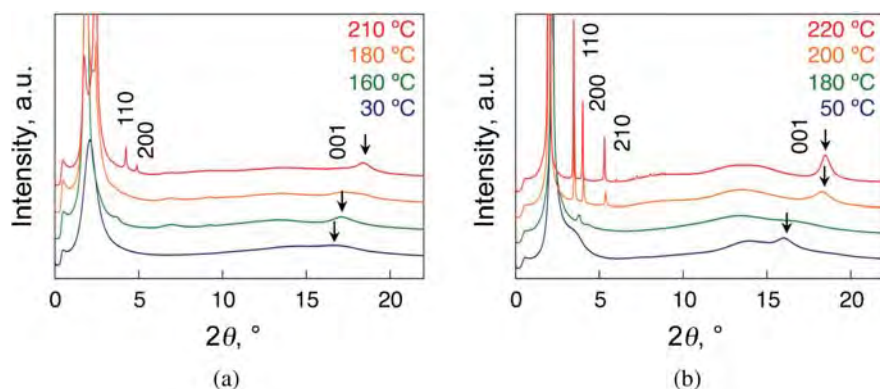
Fig. 5. MALDI-TOF-MS spectra of (a) Poly-1, (b) Poly-5, (c) Poly-6, (d) Poly-10, (e) Poly-12 and (f) Poly-13

groups (Fig. 4b). It is more obvious by seeing the fact that compound **9**, whose electronic density distribution must resemble **1–4**, hardly change its absorption spectra before and after the heating treatment (Fig. 4c). Eight branched chains prevent the access of hydroxyl groups by their huge steric effect.

Then, we investigated the effect of other types of side chains such as alkyl, thioalkyl, alkynyl, and phenoxy groups. As a result, all **10–13** show no significant blue shift of their Q-band after heating (Fig. 4d), while the obtained Poly-**10–13** just showed a sign of small oligomeric products in MALDI-TOF-MS such as dimer and trimer (Fig. 5). The observed smaller spectral shift of Poly-**10** than that of Poly-**2** strongly supports our hypothesis that electron-donating ability of peripheral substituents increases the saturated  $P_w$  value. In fact, an earlier report

proved that a methylhydroxy SiPc with octapentyloxy chains can dimerize in solution at the lower temperature than the analogous octapentyl derivative [33]. As discussed in that literature, the difference between alkyl and alkoxy substituents hardly affects their oxidation potentials of Pc rings, thus resulting in the change in reactivity of axial hydroxyl groups. Meanwhile, **11** afforded an insoluble substance after heating. We gave up to investigate further on this compound. Compound **12**, a thioalkyl analog of **2**, seemed to form small oligomeric products. On the other hand, a derivative **13** has phenoxy groups with electron donating capability. However, judging from absorption and MALDI-TOF-MS spectra, a large steric effect by phenyl rings operates and prevents its sufficient polymerization. Overall, through the approach of synthesizing a series of SiPc libraries, we newly found





**Fig. 6.** *In situ* variable-temperature X-ray diffraction patterns of (a) **1** from 30 to 210 °C and (b) **2** from 50 to 220 °C upon heating. **1** at 210 °C and **2** at 220 °C indicate the formation of Poly-1 and Poly-2, respectively. Arrows show diffraction peaks corresponding to the  $\pi$ -stacking distances

**Table 2.** Observed and calculated  $d$ -spacing values for Poly-1-8 from their XRD patterns at 30 °C

Compound <sup>a</sup>	Assignment of phase structure	Cell parameters, Å	$hkl = 100$ $d_{\text{obs}} (d_{\text{cal}}), \text{Å}$	$hkl = 110$ $d_{\text{obs}} (d_{\text{cal}}), \text{Å}$	$hkl = 200$ $d_{\text{obs}} (d_{\text{cal}}), \text{Å}$	$hkl = 210$ $d_{\text{obs}} (d_{\text{cal}}), \text{Å}$	$hkl = 001$ $d_{\text{obs}}, \text{Å}$
<b>Poly-1</b>	Col <sub>h</sub>	$a = 28.7, c = 3.33$	24.9 (24.9)	14.4 (14.4)	12.5 (12.5)	— <sup>b</sup>	3.33
<b>Poly-2</b>	Col <sub>h</sub>	$a = 34.6, c = 3.32$	30.0 (30.0)	17.2 (17.3)	14.9 (15.0)	11.4 (11.3)	3.32
<b>Poly-3</b>	Col <sub>h</sub>	$a = 29.8, c = 3.33$	25.9 (25.8)	14.9 (14.9)	12.9 (12.9)	9.75 (9.76)	3.33
<b>Poly-4</b>	Col <sub>h</sub>	$a = 26.8, c = 3.33$	23.3 (23.2)	13.4 (13.4)	11.6 (11.6)	8.77 (8.77)	3.33
<b>Poly-5</b>	Col <sub>h</sub>	$a = 28.6, c = 3.34$	24.9 (24.8)	14.2 (14.3)	12.4 (12.4)	— <sup>b</sup>	3.34
<b>Poly-6</b>	Col <sub>h</sub>	$a = 23.4, c = 3.35$	20.2 (20.3)	11.7 (11.7)	10.3 (10.2)	— <sup>b</sup>	3.35
<b>Poly-7</b>	Col <sub>h</sub>	$a = 28.4, c = 3.42$	24.8 (24.6)	14.2 (14.2)	12.3 (12.3)	9.30 (9.30)	3.42
<b>Poly-8</b>	Col <sub>h</sub>	$a = 32.9, c = 3.47$	28.2 (28.2)	16.3 (16.3)	14.1 (14.1)	10.7 (10.7)	3.47 <sup>c</sup>

<sup>a</sup>PcPSs exhibiting featureless XRD patterns at 30 °C are not shown here. <sup>b</sup>No clear peak was observed. <sup>c</sup>Corresponding diffraction peak was very broad.

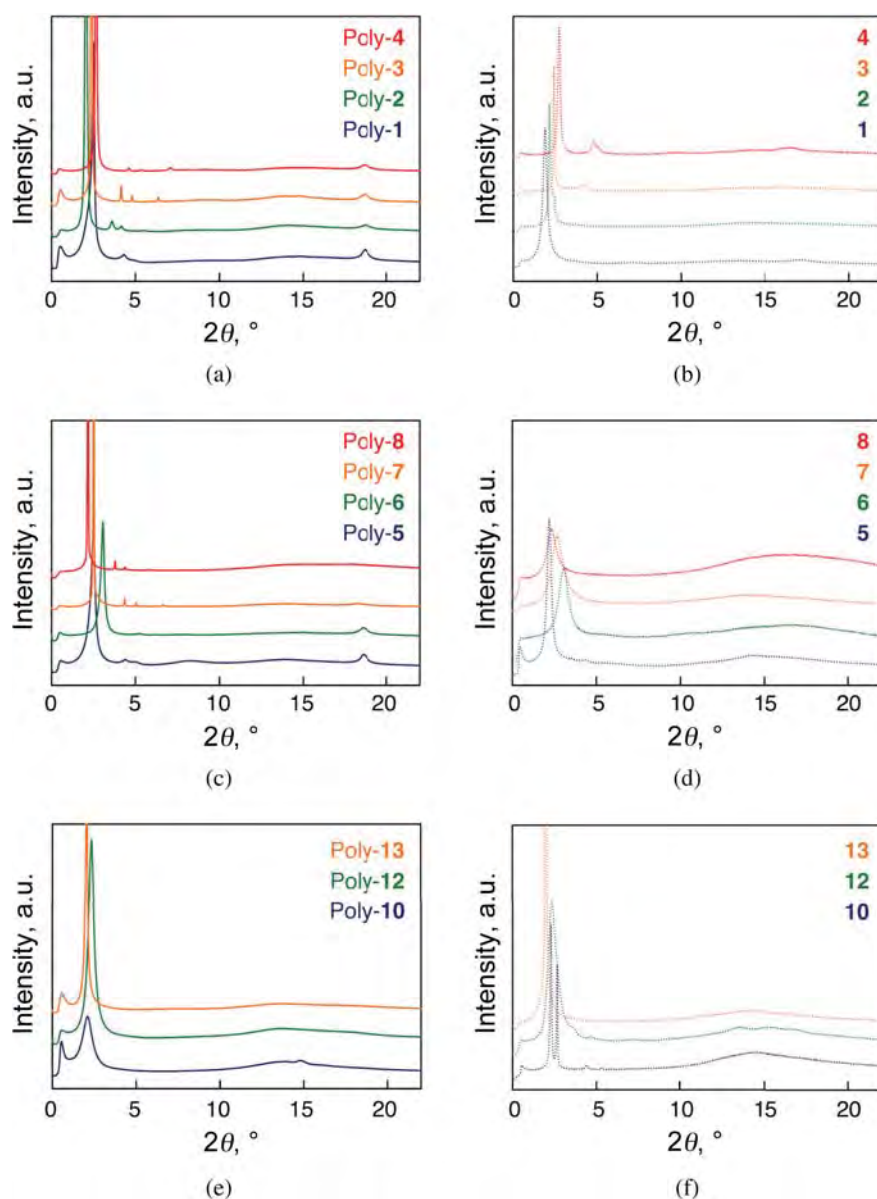
not only (i) small steric hindrance of the peripheral substituents but also (ii) strong electron donating ability are the important factors to obtain high-molecular weight PcPS polymers.

### Self-organized structures

Liquid crystalline materials of  $\pi$ -electron systems are interesting because they serve as a soft organic semiconductor with directional charge carrier transporting property [17, 34]. As reported in previous researches, both the monomer and polymer of alkoxy derivatives such as **1–4** and Poly-1–4 are known to exhibit a columnar phase [25]. In the case of monomeric SiPcs,  $\pi$ - $\pi$  interactions among Pc rings and intermolecular hydrogen bonding by hydroxyl groups contribute to stabilize a hexagonal or rectangular columnar phase [35]. In contrast, PcPSs self-assemble into hexagonal columnar phases due to the face-to-face  $\pi$ -stacking with no columnar-isotropic liquid phase transition. We confirmed this tendency by *in situ* variable-temperature X-ray diffraction (XRD) analysis.

For example, as shown in Fig. 6b, the initial powder sample of **2** displayed a  $\pi$ -stacking periodicity of  $d = 3.88 \text{ Å}$ . Upon heating up to 220 °C, Poly-2 was formed and showed a set of sharp peaks in XRD that can be assigned to a hexagonal lattice together with a decreased Pc-to-Pc distance of  $d = 3.32 \text{ Å}$  due to the formation of siloxane bonds.

Next, our new libraries were characterized by XRD and POM. All of Poly-5–8 on a glass plate showed a birefringent texture in POM under crossed Nicols condition as (Fig. 8). In addition, a set of diffraction peaks, assignable to a hexagonal packing, appeared in XRD of all these polymers, where the observed lattice parameter  $a$  is 28.6, 23.4, 28.4 and 32.9 Å for Poly-5–8, respectively (Table 2). The  $\pi$ -stacking distances were also confirmed, giving the lattice parameter  $c$  of 3.34, 3.35, 3.42 and 3.47 Å, respectively. Although all the PcPSs have the polysiloxane backbone, the Si–O–Si distance was modulated in response to the volume of side chains. Interestingly, as clarified by the dark images in POM (Figs 8k, 8m and 8o) and featureless XRD patterns



**Fig. 7.** X-ray diffraction patterns of (a) Poly-1 (navy), Poly-2 (green), Poly-3 (yellow), Poly-4 (red), (b) **1** (navy), **2** (green), **3** (yellow), **4** (red), (c) Poly-5 (navy), Poly-6 (green), Poly-7 (yellow), Poly-8 (red), (d) **5** (navy), **6** (green), **7** (yellow), **8** (red), (e) Poly-10 (navy), Poly-12 (green), Poly-13 (yellow) and (f) **10** (navy), **12** (green), **13** (yellow) at 30°C

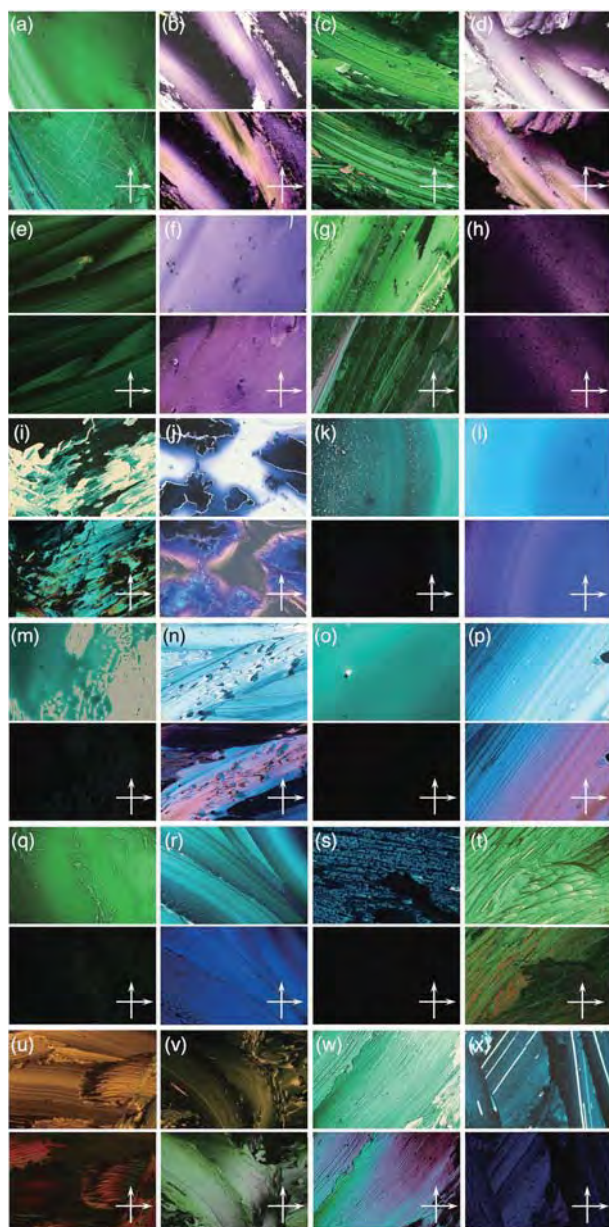
(Fig. 7d), monomeric **6–8** give amorphous materials. Based on this fact, we consider that the branched side chains destabilize the  $\pi$ -stacking interaction due to the remarkable steric effect. Taking into account that Poly-**6–8** adopt hexagonal columnar phases, it is explained that the covalently assembled Pc rings by the siloxane bond leads to form a column and such rod-shaped PcPSs were eventually packed into a hexagonal lattice. By contrast, **10** having eight dodecyl chains shows a rectangular columnar phase, exhibiting the tendency of not a face-to-face but slipped  $\pi$ -stacking (Fig. 7 and Table 3). Its oligomer, Poly-**10**, displayed broad peaks in XRD and a dark image in POM (Figs 7c and 8s). With these experimental results, we suppose that Poly-**10** indicates a

low degree of polymerization ( $P_w$ ) not to form a column. Moreover, owing to the nature of polycondensation systems, Poly-**10** consists of a mixture of different length oligomers, which decreases the structural order in the solid-state packing to result in an amorphous substance. The monomers **12** and **13**, as well as oligomeric Poly-**13**, all showed a birefringent image in POM (Figs 8u–8x). Nevertheless, Poly-**12** and Poly-**13** gave featureless broad peaks in XRD that are not enough for determining their packing structure (Fig. 7c).

It is revealed that SiPcs having at least four alkoxy chains at the peripheral positions let their axial hydroxyl groups be reactive to polymerize in the condensed phase. The obtained PcPSs with a sufficiently high  $P_w$  are

**Table 3.** Observed and calculated  $d$ -spacing values for **10** from its XRD pattern at 30 °C

Compound	Assignment of phase structure	Cell parameters, Å	$hkl = 110$	$hkl = 200$	$hkl = 020$	$hkl = 310$	$hkl = 400$
			$d_{\text{obs}} (d_{\text{cal}}), \text{Å}$	$d_{\text{obs}} (d_{\text{cal}}), \text{Å}$	$d_{\text{obs}} (d_{\text{cal}}), \text{Å}$	$d_{\text{obs}} (d_{\text{cal}}), \text{Å}$	$d_{\text{obs}} (d_{\text{cal}}), \text{Å}$
<b>10</b>	Col <sub>1</sub>	$a = 47.0, b = 33.1$	27.0 (27.1)	23.3 (23.5)	16.6 (16.6)	14.0 (14.2)	11.6 (11.8)



**Fig. 8.** Optical (top) and crossed polarized (bottom) images of (a) **1**, (b) Poly-**1**, (c) **2**, (d) Poly-**2**, (e) **3**, (f) Poly-**3**, (g) **4**, (h) Poly-**4**, (i) **5**, (j) Poly-**5**, (k) **6**, (l) Poly-**6**, (m) **7**, (n) Poly-**7**, (o) **8**, (p) Poly-**8**, (q) **9**, (r) **10**, (s) Poly-**10**, (t) **11**, (u) **12** (v) Poly-**12**, (w) **13** and (x) Poly-**13**

composed of face-to-face  $\pi$ -stacking of Pc arrays that self-assemble into a two-dimensional hexagonal packing structure. Accordingly, all the observed  $\pi$ -stacking peaks in XRD look broad that is different from the nature of

single crystalline oligomers. Namely, Pc rings in PcPSs are dynamically fluctuated regardless of being fixed by a siloxane bond, which exactly provides the liquid crystalline character over a wide temperature range. Our results disclosed the generality of such an effect of siloxane bonds, as is evident by the fact that compounds **6–8** form amorphous state but Poly-**6–8** self-assemble into a columnar LC. In usual discotic liquid crystals based on small molecules, large aromatic cores should be subjected to multisubstitution by long alkyl chains for liquid crystallization [17, 36]. Consequently, the volume of semiconducting units become too small in the resultant materials, which often leads to poor performance as an organic semiconductor. In sharp contrast, PcPSs are able to behave as a liquid crystalline material having one-dimensional hole-transporting property, with minimizing the volume of the peripheral insulating chains. This feature is quite promising for developing soft materials with high density of electronic functional sites.

## CONCLUSION

Inspired by the unique structure of phthalocyaninato-polysiloxane (PcPS) that enables a one-dimensional hole-transporting pathway fixed by siloxane bonds, we have explored the structural requirement of peripheral chains of the phthalocyanine core for affording high molecular weight polymers. Through the approach of newly synthesized dihydroxysilicon phthalocyanine libraries, we noticed that the key factors are strong electron donating ability and small steric hindrance of the peripheral substituents. Furthermore, we revealed that PcPSs with a sufficient degree of polymerization generally self-assemble into a hexagonal columnar LC. This is even the case for the PcPSs having four ethylhexyl chains whose monomeric precursors cannot form a columnar LC. The behavior most likely originates from the polysiloxane backbone that fixes the  $\pi$ -stacked array and stabilizes the columnar assembly. Therefore, we believe that PcPSs would come back, unlike normal disc-shaped small molecules, as a soft material affording both high density of functional units and anisotropic ordered structures.

## Acknowledgements

We thank Prof. Takuzo Aida and Mr. Yoshiki Shibuya in The University of Tokyo for DSC measurements and Dr. Atsuya Muranaka in RIKEN for helpful discussions.

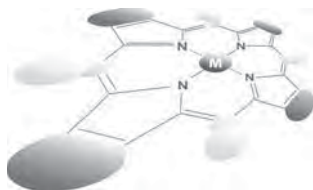
The synchrotron radiation XRD experiments were performed at BL44B2 in SPring-8 with the approval of RIKEN (Proposal No. 20120100). T.S. thanks the Japan Society for the Promotion of Science for a Young Scientist Fellowship.

### Supporting information

Detailed synthetic procedures and differential scanning calorimetry charts of Poly-1 and Poly-2 are given in the supplementary material. This material is available free of charge via the Internet at <http://www.worldscinet.com/jpp/jpp.html>.

### REFERENCES

- Engelkamp H, van Nostrum CF, Picken SJ and Nolte RJM. *Supramolecular Soft Matter: Applications in Materials and Organic Electronics*, Nakanishi T. (Ed.) John Wiley & Sons: Hoboken, NJ, 2011.
- Supramolecular Chemistry from Molecules to Nanomaterials*, Gale PA and Steed JW. (Eds.) John Wiley & Sons: Hoboken, NJ, 2012.
- Delgado MCR, Kim EG, da Silva Filho DA and Bredas JL. *J. Am. Chem. Soc.* 2010; **132**: 3375–3387.
- Mas-Torrent M and Rovira C. *Chem. Rev.* 2011; **111**: 4833–4856.
- Kroenke W, Kenney M, Joyner R and Sutton L. *Inorg. Chem.* 1963; **2**: 1064–1065.
- Dirk C, Inabe T, Schoch K and Marks T. *J. Am. Chem. Soc.* 1983; **105**: 1539–1550.
- Kleinwachter J and Hanack M. *J. Am. Chem. Soc.* 1997; **119**: 10684–10695.
- Joyner RD and Kenney ME. *Inorg. Chem.* 1962; **1**: 717–718.
- Orthmann E and Wegner G. *Angew. Chem. Int. Ed.* 1986; **25**: 1105–1107.
- Caseri W, Sauer T and Wegner G. *Makromol. Chem. Rapid Commun.* 1988; **9**: 651–657.
- Sielcken O, Vandekuyl L, Drenth W, Schoonman J and Nolte RJM. *J. Am. Chem. Soc.* 1990; **112**: 3086–3093.
- Vannostrum C, Picken S, Schouten A and Nolte RJM. *J. Am. Chem. Soc.* 1995; **117**: 9957–9965.
- Rengel H, Gattinger P, Silerova R and Neher, D. *J. Phys. Chem. B* 1999; **103**: 6858–6862.
- Gattinger P, Rengel H, Neher D, Gurka M, Buck M, Van de Craats A and Warman J. *J. Phys. Chem. B* 1999; **103**: 3179–3186.
- Zhao Z, Cammidge AN and Cook MJ. *Chem. Commun.* 2009; **48**: 7530–7532.
- Zhao Z, Cammidge AN, Hughes DL and Cook MJ. *Org. Lett.* 2010; **12**: 5138–5141.
- Laschat S, Baro A, Steinke N, Giesselmann F, Haegele C, Scalia G, Judele R, Kapatsina E, Sauer S, Schreivogel A and Tosoni M. *Angew. Chem. Int. Ed.* 2007; **46**: 4832–4887.
- Almeida M, Gaudiel JG, Kellogg GE, Tetrick SM, Marcy HO, McCarthy WJ, Butler JC, Kannewurf CR and Mark TJ. *J. Am. Chem. Soc.* 1989; **111**: 5271–5284.
- Schouten PG, Warman JM, Dehaas MP, Vanderpol JF and Zwikker JW. *J. Am. Chem. Soc.* 1992; **114**: 9028–9034.
- Tans S, Miedema R, Geerligs L, Dekker C, Wu J and Wegner G. *Synthetic Metals*, 1997; **84**: 733–734.
- Martinez-Diaz M, Ruau-del-Teixier A and Torres T. *Thin Solid Films*, 1996; **284**: 284–288.
- Engelkamp H, van Nostrum CF, Picken SJ, and Nolte RJM. *Chem. Commun.* 1998; **34**: 979–980.
- Gurek A, Appel G, Mikalo R and Schmeisser D. *J. Porphyrins Phthalocyanines* 2001; **5**: 751–757.
- Sirlin C, Bosio L and Simon J. *Mol. Cryst. Liq. Cryst.* 1988; **155**: 231–238.
- Vanderpol J, Zwikker J, Warman J and Dehaas M. *Recl Trav Chim Pay B* 1990; **109**: 208–215.
- Kato K, Hirose R, Takemoto M, Ha S, Kim J, Higuchi M, Matsuda R, Kitagawa S and Takata M. *AIP Conf. Proc.* 2010; **1234**: 875–878.
- Cammidge AN, Nekelson F, Hughes DL, Zhao Z and Cook MJ. *J. Porphyrins Phthalocyanines* 2010; **14**: 1001–1011.
- Caseri W, Sauer T and Wegner G. *Makromol. Chem. Rapid Commun.* 1988; **9**: 651–657.
- Sauer T and Wegner G. *Macromolecules* 1991; **24**: 2240–2252.
- Kasha M, Rawls H and El-Bayoumi M. *Pure Appl. Chem.* 1965; **11**: 371–392.
- Gunaratne T, Kennedy VO, Kenney ME and Rodgers MAJ. *J. Phys. Chem. A* 2004; **108**: 2576–2582.
- Yang Y, Samas B, Kennedy VO, Macikenas D, Chaloux BL, Miller JA, Speer RL, Protasiewicz J, Pinkerton AA and Kenney ME. *J. Phys. Chem. A* 2011; **115**: 12474–12485.
- Li Z and Lieberman M. *Inorg. Chem.* 2001; **40**: 932–939.
- Fleischmann EK and Zentel R. *Angew. Chem. Int. Ed.* 2013; **52**: 8810–8827.
- Sauer T and Wegner G. *Mol. Cryst. Liq. Cryst.* 1988; **162**: 97–118.
- Sergeyev S, Pisula W and Geerts YH. *Chem. Soc. Rev.* 2007; **36**: 1902–1929.



## Dimeric 1:2 adduct of $\beta,\beta'$ -bis(diphenylphosphino)porphyrin with silver(I) chloride

Keisuke Fujimoto<sup>a,∞</sup>, Hideki Yorimitsu<sup>\*a,b,∞</sup> and Atsuhiko Osuka<sup>\*a,∞</sup>

<sup>a</sup>Department of Chemistry, Graduate School of Science, Kyoto University, Sakyo-ku, Kyoto 606-8502, Japan

<sup>b</sup>ACT-C, Japan Science and Technology Agency, Japan

Dedicated to Professor Shunichi Fukuzumi on the occasion of his retirement

Received 16 October 2014

Accepted 5 November 2014

**ABSTRACT:** A 2,18-bis(diphenylphosphino)porphyrin ligand undergoes complexation with silver(I) chloride to afford a stable phosphine-silver complex. X-ray crystallographic analysis of the complex revealed a dimeric structure of a 1:2 adduct of the diphosphine and silver(I) chloride, where each phosphorus atom coordinates a silver atom. The four AgCl units construct a distorted cubic cluster with small metallophilic interaction. Variable temperature <sup>31</sup>P NMR study exhibited a slow ligand exchange process between <sup>107</sup>Ag and <sup>109</sup>Ag at high temperature.

**KEYWORDS:** porphyrin, diphosphine, silver complex, cubic cluster.

### INTRODUCTION

All group 11 metals in the oxidation state +1 often form clusters with a variety of configurations depending on geometric and electronic nature of their ligands and metals [1]. Among interactions working in metal complexes, electrostatic contributions, such as dipole–dipole interactions, are dominant in clusters of coordinated silver(I) halides. In the case of simple triphenylphosphine-silver halides (PPh<sub>3</sub>)AgX, cubane-like tetrameric clusters (**A**) and ladder-like tetrameric clusters (**B**) were experimentally characterized (Chart 1) [2]. The cubane-like tetrameric cluster (**A**) was revealed to be the most stable configuration by single crystal analysis as well as theoretical calculations [3]. Diphosphine ligands show more diverse coordination ability. In addition to **A** and **B** [4], various configurations have been seen in the solid state structure of group 11 metal halides, for example, quadrangular dimeric cluster with monodentate

coordination (**C**) [5] or bidentate coordination (**D**) [6], trigonal bipyramidal trimeric cluster (**E**) [7], and drum-like hexameric cluster (**F**) [8].

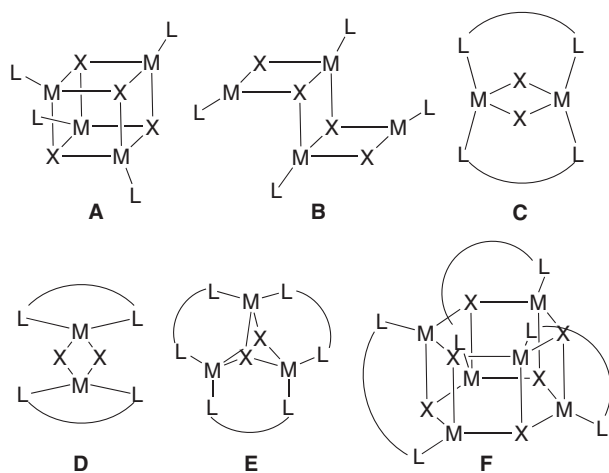
We have developed a rigid porphyrin-based diphosphine ligand **1**, which shows tridentate coordination to group 10 metals to form PCP-pincer complexes with a *meso*-carbon–metal bond [9]. To investigate further coordination behavior of the porphyrin-based diphosphine ligand, we have tested complexation with silver(I) chloride with an expectation of cluster formation.

### RESULTS AND DISCUSSION

We prepared 2,18-bis(diphenylphosphino)porphyrin **1** according to our previous report [9]. Diphosphine ligand **1** was treated with an excess amount of silver(I) chloride in *N,N*-dimethylformamide (DMF)/toluene. After consumption of **1**, filtration of the residual silver salt with Celite<sup>®</sup> followed by recrystallization from CH<sub>2</sub>Cl<sub>2</sub>/methanol afforded a stable silver complex **2** in 80% yield as pure red solids (Scheme 1). The <sup>31</sup>P NMR spectrum of **2** in CDCl<sub>3</sub> at 25 °C showed two sets of doublets, characteristic in phosphine-silver complexes [10], at -6.54 ppm (Fig. 1). The doublets were observed in a downfield range compared to the signal of the parent

<sup>∞</sup> SPP full and <sup>∞∞</sup> student member in good standing

\*Correspondence to: Atsuhiko Osuka, email: osuka@kuchem.kyoto-u.ac.jp, tel: +81 075-753-4008, fax: +81 075-753-3970; Hideki Yorimitsu, email: yori@kuchem.kyoto-u.ac.jp, tel: +81 075-753-4010, fax: +81 075-753-3970

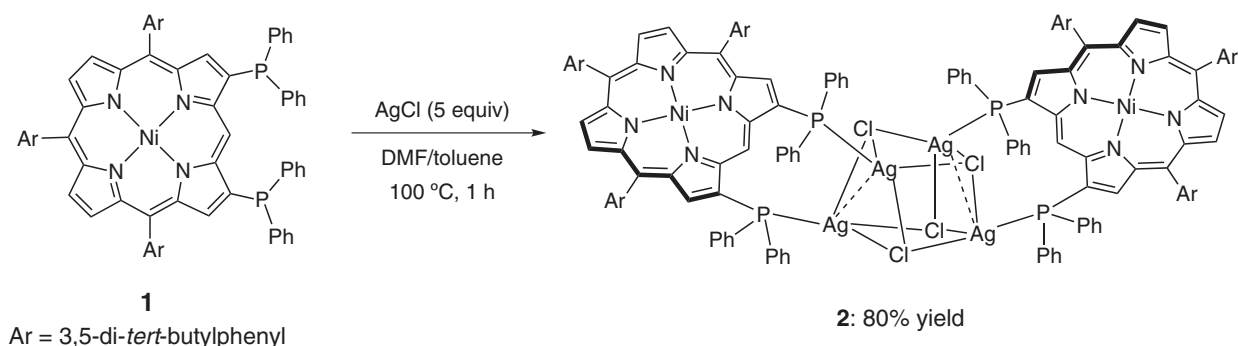


**Chart 1.** Structural types observed for phosphine complexes of group 11 metal halides

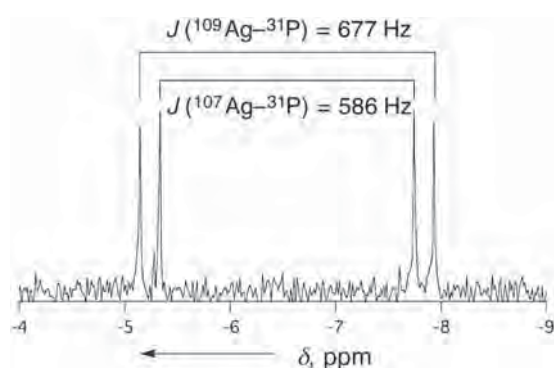
ligand **1** of  $-25.36$  ppm, because of the coordination to a silver atom. The coupling constants of the inner and outer doublets are 586 Hz and 677 Hz, respectively. These two doublets are assigned to  $^{107}\text{Ag}-^{31}\text{P}$  and  $^{109}\text{Ag}-^{31}\text{P}$  coupling, respectively, considering the gyromagnetic ratio and isotopic ratio of  $^{107}\text{Ag}/^{109}\text{Ag}$  in the literature [10]. The high-resolution electrospray-ionization time-of-flight

(HR-ESI-TOF) mass spectrum of **2** indicated the base ion peak at  $m/z = 2849.9814$  of  $[\text{M}-2\text{Ag}-3\text{Cl}]^+$  (calcd. for  $\text{C}_{172}\text{H}_{180}\text{N}_8^{35}\text{Cl}_1^{109}\text{Ag}_2^{58}\text{Ni}_2\text{P}_4$ ; 2849.9794) suggesting a facile dimeric assembly of **2** in an acetonitrile solution. The UV-vis absorption spectrum of **2** in  $\text{CH}_2\text{Cl}_2$  exhibited a strong Soret-band at 430 nm and a weak Q-band at 538 nm (Fig. 2). The slight red-shifts indicate that electronic interaction between assembled two porphyrin units is negligible in a  $\text{CH}_2\text{Cl}_2$  solution.

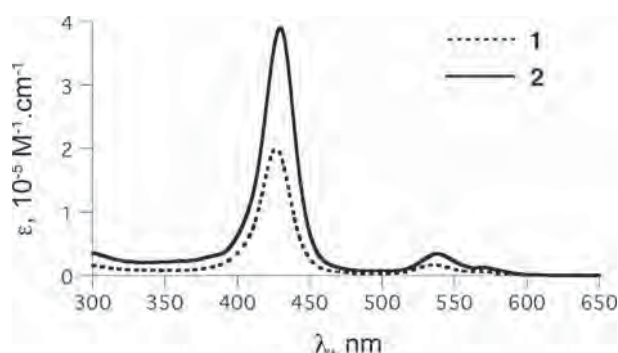
The explicit solid state structure of **2** was determined by X-ray crystallographic analysis (Fig. 3). Single crystals for the measurement were grown by vapor diffusion of acetonitrile in a benzene solution of **2**. Each silver atom is coordinated by one phosphine ligand and three  $\mu_3$ -chloride ligands. Four silver centers aggregate to construct a distorted  $\text{Ag}_4\text{Cl}_4$  cubic cluster. Two porphyrin units were proved to be assembled through the  $\text{Ag}_4\text{Cl}_4$  core. Each phosphorus atom of **1** coordinates to one silver atom, the two silver atoms being coordinated by one molecule of **1**. The distances between the two silver atoms coordinated by the same **1** were determined to be 3.1028(11) Å for Ag(1)–Ag(2) and 3.0895(10) Å for Ag(3)–Ag(4). Generally,  $d^{10}-d^{10}$  closed-shell interaction, so-called metallophilic interaction, is too small to be dominant in the coordination chemistry of copper and silver compounds [11]. However, these Ag–Ag bonds are



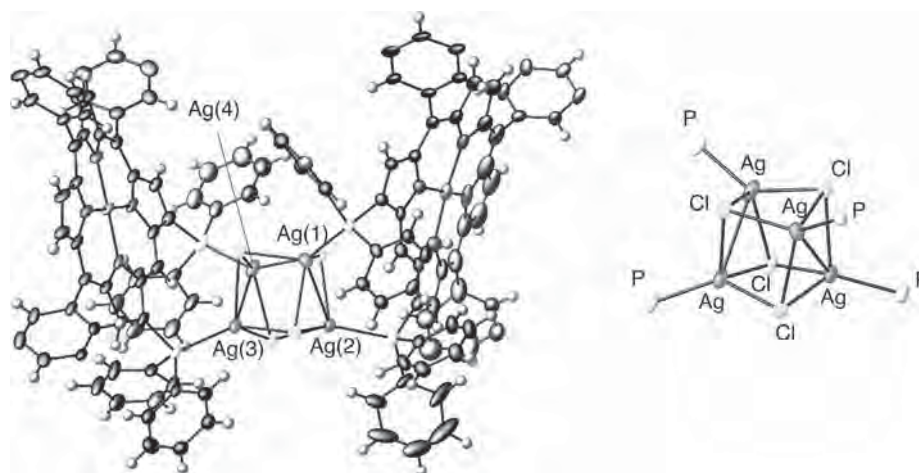
**Scheme 1.** Synthesis of silver complex **2**



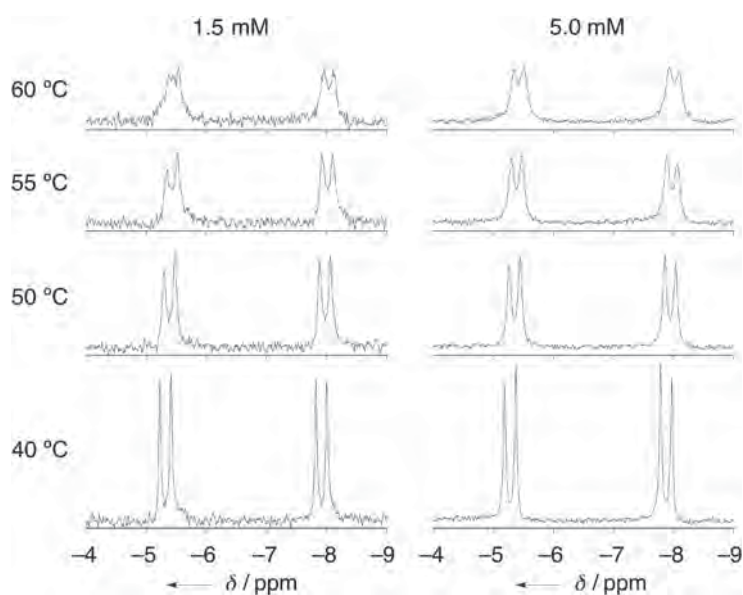
**Fig. 1.**  $^{31}\text{P}$  NMR spectrum of **2** in  $\text{CDCl}_3$  at 25 °C



**Fig. 2.** UV-vis absorption spectra of **1** and **2** in  $\text{CH}_2\text{Cl}_2$



**Fig. 3.** X-ray crystal structure of **2**. The thermal ellipsoids are scaled to 30% probability. Solvent molecules and *tert*-butyl groups are omitted for clarity



**Fig. 4.** Variable temperature  $^{31}\text{P}$  NMR spectra of 1.5 mM and 5.0 mM  $\text{CDCl}_3$  solutions of **2** from 40 °C to 60 °C

significantly shorter than twice the van der Waals radius of Ag of 1.72 Å, suggesting the existence of metallophilic interaction, although the other Ag–Ag distances are in a range of 3.55–3.72 Å.

The dynamic behavior of **2** was examined through variable temperature  $^{31}\text{P}$  NMR study. As mentioned above, two sets of sharp doublets were observed at 25 °C in  $\text{CDCl}_3$ . This is different from the fact that sharp signals are seen only below -30 °C in the case of monophosphine-silver halide system. The ligand exchange process between  $^{107}\text{Ag}$  and  $^{109}\text{Ag}$  is usually rapid on a  $^{31}\text{P}$  NMR time scale to exhibit broad signal at room temperature [10]. Figure 4 shows the  $^{31}\text{P}$  NMR spectra of **2** at higher temperatures. With increase of the temperature from

40 °C to 60 °C, the original sharp signals gradually changed to broad signals. After cooling the heated solution, the sharp signals of **2** were observed again. This tendency was independent of the concentration of **2** and the same spectra were obtained from 1.5 mM and 5.0 mM solutions. These results indicate that an intramolecular ligand dissociation-recombination process would proceed at high temperature and that the dimeric structure is fairly stable.

## EXPERIMENTAL

### General

All reagents were of the commercial reagent grade and were used without further purification except where noted. Dry DMF was distilled from  $\text{P}_2\text{O}_5$ . Dry toluene was distilled from  $\text{CaH}_2$ . UV-vis absorption spectra were recorded on a Shimadzu UV-2550 spectrometer.  $^1\text{H}$  NMR (600 MHz),  $^{13}\text{C}$  NMR (151 MHz), and  $^{31}\text{P}$  NMR (243 MHz) spectra were recorded on a JEOL ECA-600 spectrometer. Chemical shifts were reported as the delta scale in ppm relative to  $\text{CHCl}_3$  ( $\delta = 7.26$ ) for  $^1\text{H}$  NMR, to  $\text{CDCl}_3$  ( $\delta = 77.16$ ) for  $^{13}\text{C}$  NMR, and to  $\text{H}_3\text{PO}_4$  ( $\delta = 0.00$ ) for  $^{31}\text{P}$  NMR. High-resolution electrospray-ionization time-of-flight mass spectrometry (HR-ESI-TOF-MS) was recorded on a BRUKER micrOTOF model using positive mode for acetonitrile solutions of samples. X-ray crystallographic data were collected on a Rigaku XtaLAB P200 apparatus at -180 °C using graphite-monochromated  $\text{CuK}\alpha$  radiation ( $\lambda = 1.54187$  Å). The structures were solved by direct method SIR-97 and refined by SHELXL-97 program [12].

## Silver complex 2

A Schlenk tube containing 2,18-bis(diphenylphosphino)porphyrin **1** (52 mg, 40  $\mu\text{mol}$ ) and AgCl (29 mg, 200  $\mu\text{mol}$ ) was purged with argon, and then charged with dry DMF (2.0 mL) and dry toluene (2.0 mL). The reaction mixture was stirred for 1 h at 100 °C. After removal of the solvents under reduced pressure, the residue was dissolved in  $\text{CH}_2\text{Cl}_2$  and then filtrated with Celite®. Recrystallization from  $\text{CH}_2\text{Cl}_2$ /methanol gave **2** as red solids (51 mg, 16  $\mu\text{mol}$ , 80%).  $^1\text{H}$  NMR ( $\text{CDCl}_3$ , 600 MHz, 25 °C):  $\delta$ , ppm 10.07 (s, 2H, *meso*), 8.70 (d,  $J = 5.0$  Hz, 4H,  $\beta$ ), 8.63 (d,  $J = 5.0$  Hz, 4H,  $\beta$ ), 8.18 (d,  $J_{\text{P-H}} = 4.6$  Hz, 4H,  $\beta$ ), 7.81 (br-s, 4H, Ar-*o*), 7.69 (t,  $J = 1.8$  Hz, 2H, Ar-*p*), 7.62–58 (m, 24H, Ar-*p* and Ph-*o*), 7.52 (t,  $J = 1.8$  Hz, 4H, Ar-*p*), 7.14 (t,  $J = 7.2$  Hz, 8H, Ph-*p*), 7.08 (t,  $J = 7.2$  Hz, 16H, Ph-*m*), 1.45 (s, 36H, *t*Bu), 1.30 (s, 72H, *t*Bu).  $^{13}\text{C}$  NMR ( $\text{CDCl}_3$ , 151 MHz, 25 °C):  $\delta$ , ppm 149.11, 148.89, 143.39, 143.16, 142.41 ( $J_{\text{P-C}} = 18.7$  Hz), 141.40 ( $J_{\text{P-C}} = 10.1$  Hz), 139.93, 139.80, 139.20, 136.21 ( $J_{\text{P-C}} = 33.2$  Hz), 134.66 ( $J_{\text{P-C}} = 17.4$  Hz), 133.01, 132.52, 132.07 ( $J_{\text{P-C}} = 33.2$  Hz), 130.36, 128.75, 128.67, 128.25, 121.36, 121.23, 120.74, 120.05, 105.7–105.4 (broad) 35.12, 34.94, 31.80, 31.74.  $^{31}\text{P}$  NMR (243 MHz,  $\text{CDCl}_3$ , 25 °C,  $^1\text{H}$ -decoupling):  $\delta$ , ppm -6.54 (two sets of doublet,  $J_{\text{inner}} = 586$  Hz and  $J_{\text{outer}} = 677$  Hz). HR-ESI-TOF-MS:  $m/z$  2849.9814 [ $\text{M}-2\text{Ag}-3\text{Cl}$ ] $^+$  (calcd. for  $\text{C}_{172}\text{H}_{180}\text{N}_8^{35}\text{Cl}_1^{109}\text{Ag}_2^{58}\text{Ni}_2\text{P}_4$ ; 2849.9794). UV-vis ( $\text{CH}_2\text{Cl}_2$ ):  $\lambda$ , nm ( $\epsilon$ ,  $\text{M}^{-1}\cdot\text{cm}^{-1}$ ) 430 (390000), 538 (34000). Crystal data:  $\text{C}_{198}\text{H}_{191.53}\text{O}_1\text{N}_{12}\text{Ag}_4\text{Cl}_4\text{Ni}_2\text{P}_4$ ,  $M_w = 3569.74$ , triclinic, space group  $P-1$  (No. 2),  $a = 19.362(6)$  Å,  $b = 22.300(6)$  Å,  $c = 24.143(7)$  Å,  $\alpha = 99.486(6)^\circ$ ,  $\beta = 107.037(4)^\circ$ ,  $\gamma = 97.763(11)^\circ$ ,  $V = 9643(5)$  Å $^3$ ,  $T = 93$  K,  $\rho_{\text{calcd}} = 1.229$  g.cm $^{-3}$ ,  $Z = 2$ ,  $R_1 = 0.1125$  ( $I > 2\sigma(I)$ ),  $R_w = 0.3252$  (all data), GOF = 1.122.

## SUMMARY

We have investigated the coordination behavior of porphyrin-based diphosphine **1** toward silver(I) chloride. X-ray analysis revealed the tetrameric cubic cluster structure of  $\text{Ag}_4\text{Cl}_4$  core bridging two porphyrin units. Variable temperature  $^{31}\text{P}$  NMR study indicated the presence of an intramolecular ligand exchange process at high temperature. Further investigations on the coordination properties of the diphosphine ligand are currently underway.

## Acknowledgements

This work was supported by Grant-in-Aid for Scientific Research (no. 25220802(S)) from MEXT of Japan.

## Supporting information

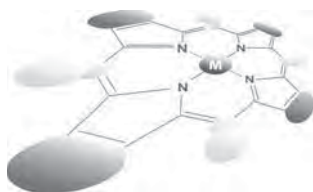
Figures S1–S3 (NMR spectra of **2**) are given in the supplementary material. This material is available free of charge via the Internet at <http://www.worldscinet.com/jpp/jpp.shtml>.

Crystallographic data have been deposited at the Cambridge Crystallographic Data Centre (CCDC) under number CCDC-1028076. Copies can be obtained on request, free of charge, via [www.ccdc.cam.ac.uk/data\\_request/cif](http://www.ccdc.cam.ac.uk/data_request/cif) or from the Cambridge Crystallographic Data Centre, 12 Union Road, Cambridge CB2 1EZ, UK (fax: +44 1223-336-033 or email: [data\\_request@ccdc.cam.ac.uk](mailto:data_request@ccdc.cam.ac.uk)).

## REFERENCES

- (a) Artigas MM, Crespo O, Gimeno MC, Jones PG, Laguna A and Villacampa MD. *Inorg. Chem.* 1997; **36**: 6454–6456. (b) Cingolani A, Effendy, Pellei M, Pettinari C, Santini C, Skelton BW and White AH. *Inorg. Chem.* 2002; **41**: 6633–6645. (c) Cingolani A, Effendy, Hanna JV, Pellei M, Pettinari C, Santini C, Skelton BW and White AH. *Inorg. Chem.* 2003; **42**: 4938–4948. (d) Partyka DV and Deligonul N. *Inorg. Chem.* 2009; **48**: 9463–9475. (e) Fliedel C and Braunstein C. *Organometallics* 2010; **29**: 5614–5626.
- (a) Teo B-K and Calabrese JC. *J. Am. Chem. Soc.* 1975; **97**: 1256–1257. (b) Teo B-K and Calabrese JC. *Inorg. Chem.* 1976; **15**: 2474–2486.
- Schwerdtfeger P, Krawczyk RP, Hammerl A and Brown R. *Inorg. Chem.* 2004; **43**: 6707–6716.
- Fu W-F, Gan X, Che C-M, Cao Q-Y, Zhou Z-Y and Zhu NN-Y. *Chem. Eur. J.* 2004; **10**: 2228–2236.
- (a) Barrow M, Bürgi H-B, Camalli M, Caruso F, Fischer E, Venanzi LM and Zambonelli L. *Inorg. Chem.* 1983; **22**: 2356–2362. (b) Caruso F, Camalli M, Rimml H and Venanzi LM. *Inorg. Chem.* 1985; **24**: 673–679.
- Bayler A, Schier A and Schmidbaur H. *Inorg. Chem.* 1998; **37**: 4353–4359.
- Zhou W-B, Dong Z-C, Song J-L, Zeng H-Y, Cao R, Guo G-C, Huang J-S and Li J. *J. Cluster Sci.* 2002; **13**: 119–136.
- Yang X-Y, Li Y and Pullarkat SA. *Inorg. Chem.* 2014; **53**: 10232–10239.
- Fujimoto K, Yoneda T, Yorimitsu H and Osuka A. *Angew. Chem. Int. Ed.* 2014; **53**: 1127–1130.
- (a) Muettterties EL and Alegranti CW. *J. Am. Chem. Soc.* 1972; **94**: 6386–6391. (b) Bergbreiter DE and Yang Y-C. *J. Org. Chem.* 2010; **75**: 873–878.
- (a) Jansen M. *Angew. Chem., Int. Ed. Engl.* 1987; **26**: 1098–1110. (b) Hermann HL, Boche G and Schwerdtfeger P. *Chem. Eur. J.* 2001; **7**: 5333–5342. (c) Schwerdtfeger P, Hermann HL and Schmidbaur H. *Inorg. Chem.* 2003; **42**: 1334–1342.
- SHELXL-97 and SHELXS-97, Program for the Refinement of Crystal Structures from Diffraction Data, University of Göttingen, Göttingen (Germany); Sheldrick GM and Schneider TR, *Methods Enzymol.* 1997; **277**: 319–343.





## Donor- $\pi$ -acceptor, triazine-linked porphyrin dyads as sensitizers for dye-sensitized solar cells

Ganesh D. Sharma<sup>\*a</sup>, Galateia E. Zervaki<sup>b</sup>, Kalliopi Ladomenou<sup>b</sup>,  
Emmanuel N. Koukaras<sup>c</sup>, Panagiotis P. Angaridis<sup>e</sup> and Athanassios G. Coutsolelos<sup>\*c,d</sup>

<sup>a</sup>R&D Center for Engineering and Science, JEC Group of Colleges, Jaipur Engineering College, Kukas, Jaipur (Raj.) 303101, India

<sup>b</sup>Laboratory of Bioinorganic Chemistry, Department of Chemistry, University of Crete, Voutes Campus, P. O. Box 2208, 71003 Heraklion, Crete, Greece

<sup>c</sup>Institute of Chemical Engineering Sciences, Foundation for Research & Technology Hellas (FORTH/ICE-HT), Stadiou Str. Platani, Patras 26504, Greece

<sup>d</sup>Molecular Engineering Laboratory, Department of Physics, University of Patras, Patras, 26500, GR, Greece

<sup>e</sup>Department of Chemistry, Aristotle University of Thessaloniki, Thessaloniki 54124, Greece

*Dedicated to Professor Shunichi Fukuzumi on the occasion of his retirement*

Received 27 October 2014

Accepted 6 November 2014

**ABSTRACT:** Two porphyrin dyads with the donor- $\pi$ -acceptor molecular architecture, namely (ZnP)-[triazine-gly]-(H<sub>2</sub>PCOOH) and (ZnP)-[triazine-Npip]-(H<sub>2</sub>PCOOH), which consist of a zinc-metallated porphyrin unit and a free-base porphyrin unit covalently linked at their peripheries to a central triazine group, substituted either by a glycine in the former or a *N*-piperidine group in the latter, have been synthesized *via* consecutive amination substitution reactions of cyanuric chloride. The UV-vis absorption spectra and cyclic-voltammetry measurements of the two dyads, as well as theoretical calculations based on Density Functional Theory, suggest that they have suitable frontier orbital energy levels for use as sensitizers in dye-sensitized solar cells. Dye-sensitized solar cells based on (ZnP)-[triazine-gly]-(H<sub>2</sub>PCOOH) and (ZnP)-[triazine-Npip]-(H<sub>2</sub>PCOOH) have been fabricated, and they were found to exhibit power conversion efficiency values of 5.44 and 4.15%, respectively. Photovoltaic measurements (*J*-*V* curves) and incident photon to current conversion efficiency spectra of the two solar cells suggest that the higher power conversion efficiency value of the former solar cell is a result of its enhanced short circuit current, open circuit voltage, and fill factor values, as well as higher dye loading. This is ascribed to the existence of two carboxylic acid anchoring groups in (ZnP)-[triazine-gly]-(H<sub>2</sub>PCOOH), compared to one carboxylic acid group in (ZnP)-[triazine-Npip]-(H<sub>2</sub>PCOOH), which leads to a more effective binding onto the TiO<sub>2</sub> photoanode. Electrochemical impedance spectra show evidence that the (ZnP)-[triazine-gly]-(H<sub>2</sub>PCOOH) based solar cell exhibits a longer electron lifetime and more effective suppression of charge recombination reactions between the injected electrons and electrolyte.

**KEYWORDS:** DSSC, porphyrin dyad, triazine, piperidine, glycine.

<sup>†</sup>SPP full member in good standing

\*Correspondence to: Athanassios G. Coutsolelos, email: [coutsole@chemistry.uoc.gr](mailto:coutsole@chemistry.uoc.gr); Ganesh D. Sharma, email: [gdsharma273@gmail.com](mailto:gdsharma273@gmail.com)

## INTRODUCTION

Among the various types of solar cells, dye sensitized solar cells (DSSCs) with are considered to be very promising, since due to their low cost and are considered

facile manufacturing processes [1], they have the potential to provide an economic alternative over silicon based solar cells. The sensitizer of a DSSC plays a key role in absorbing sunlight and injecting electrons into the semi-conductor photoanode. Initial research work was devoted on sensitizers based on Ru(II) complexes and resulted in power conversion efficiency (PCE) values higher than 11% [2]. However, due to low molar absorption coefficients, instability, high cost, and environmental concerns, their wide application was limited, encouraging research for new types, noble metal-free molecular sensitizers [3]. An ideal molecular sensitizer for DSSC is required to exhibit high molar absorption coefficients with a broad spectral coverage up to the near infrared region of solar spectrum, as well as chemical and photochemical stability [4].

Inspired by the natural process of photosynthesis, in which the photosynthetic cores of bacteria and plants capture solar energy by using chromophores which are based on porphyrin structures [5] and, through complex biological redox processes, convert it into chemical energy. Additionally, due to the strong absorption of porphyrins (with Soret and Q-bands in the visible region of the solar spectrum), a large number of these compounds has been employed as sensitizers for DSSCs [6]. Interestingly, the energy levels and, hence, the spectral properties of porphyrins can be tuned by appropriate functionalization of their *meso* and  $\beta$ -positions. Moreover, the absorption spectra of porphyrins can be red shifted and broadened by elongation of the  $\pi$ -conjugated ring, as well as by enhancement of the push-pull character of porphyrins [7]. Diau, Yeh and coworkers introduced the idea of porphyrin sensitizers with the D- $\pi$ -A or "push-pull" molecular architecture, featuring a zinc-porphyrin as  $\pi$  aromatic bridge, as well as donor (D) and acceptor (A) moieties at the *meso* positions [8]. By utilizing porphyrin sensitizers of this type, in combination with an electrolyte containing the redox couple  $I^-/I_3^-$ , Bessho and coworkers reported a DSSC with a PCE value of 11% [9]. Employment of a "push-pull" zinc porphyrin sensitizer with long alkoxy chains as side substituents, in combination with an organic dye as co-sensitizer and a  $[Co(bipy)_3]^{2+/3+}$  based electrolyte, Yella *et al.* reported a remarkable PCE of 12.3% [10]. More recently a new benchmark in DSSCs with overall PCE of 13% was achieved by using a similar D- $\pi$ -A porphyrin with appropriate D and A substituents [11]. However, the synthesis of this type of porphyrins requires several synthetic steps, including the use of expensive reagents for catalytic reactions, such as Sonogashira and Buchwald-Hartwig cross-coupling reactions, which makes their commercial applications infeasible.

Another way to further improve the PCE values of porphyrin based DSSCs is to extend the light harvesting ability of porphyrin sensitizers to the near infrared region. This can be accomplished by covalently linking porphyrin macrocycles to other chromophores or other

porphyrin units, either through  $\pi$ -conjugated groups or directly. Porphyrin arrays held together by ethynyl groups at the *meso* positions have been found to exhibit strong electronic coupling between the porphyrin units, resulting in the splitting of their Soret bands and broadening of the Q-bands [12]. Additionally, directly linked porphyrin dyads through their *meso* positions are found to exhibit slightly higher light harvesting efficiencies than the corresponding single porphyrin units [13], while doubly and triply fused porphyrin arrays show wide absorption covering the visible and near IR regions [14].

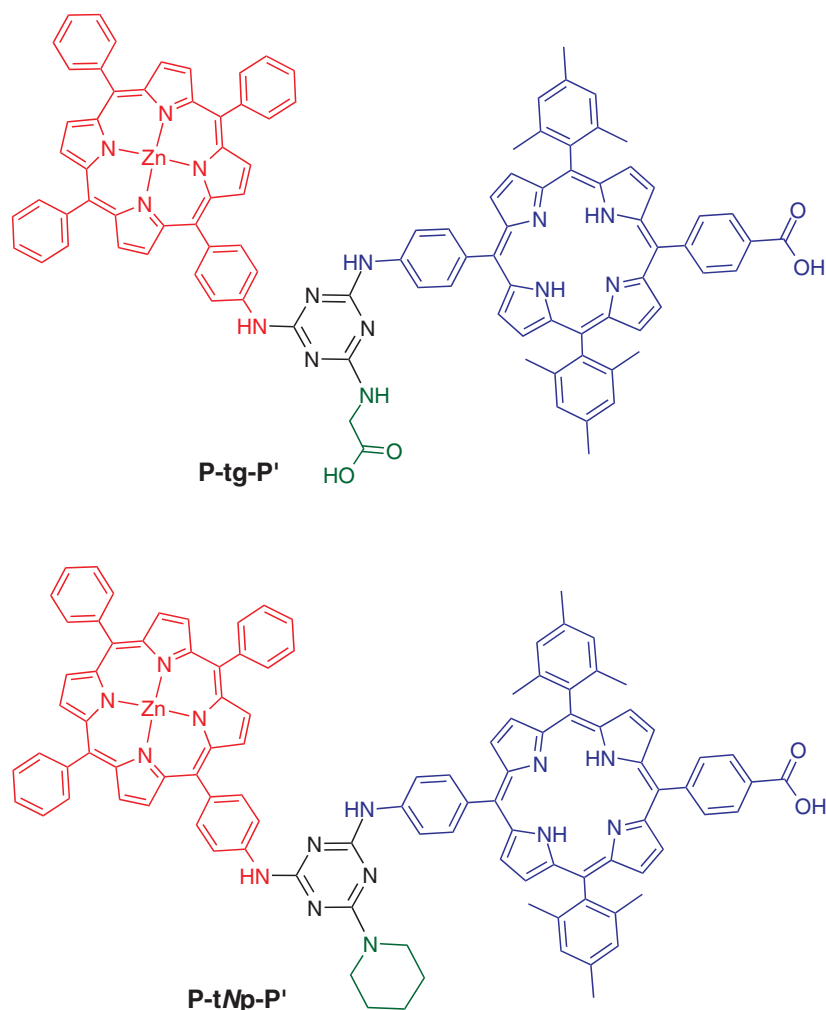
A conjugated group recently employed as linker for the synthesis of metal free organic dyes for DSSCs and other photoconductive materials applications is 1,3,5-triazine [15]. For example, triazine-bridged porphyrin triads have been recently reported and used as electron donors, together with fullerene derivatives as electron acceptors, in bulk heterojunction (BHJ) solar cells by Luechai *et al.* [16] and our group [17]. In the area of DSSCs, You *et al.* reported a DSSC sensitized by triazine bridged D- $\pi$ -A metal free organic dye exhibiting a PCE value of 3.63% [18]. Furthermore, we recently reported sensitization of DSSCs by triazine-bridged porphyrin dyads bearing different anchoring units at various positions achieving PCE values in the range of 3.5 to 5.28% [19, 20].

Herein, we present the synthesis of two new triazine-bridged porphyrin dyads with the D- $\pi$ -A molecular architecture, namely (ZnP)-[triazine-gly]-(H<sub>2</sub>PCOOH) or P-tg-P' (**4a**) and (ZnP)-[triazine-Npip]-(H<sub>2</sub>PCOOH) or P-tNp-P' (**4b**) (Scheme 1). Both compounds were used as sensitizers in DSSCs, resulting in PCE values of 5.44 and 4.15%, respectively. The higher value of PCE of the former solar cell is ascribed to a higher dye loading, longer electron life time and reduced charge recombination, which are related to the more effective binding of dyad P-tg-P' onto the TiO<sub>2</sub> surface, due to the presence of two carboxylic acid anchoring groups in its molecular structure, compared to one carboxylic acid anchoring unit and a piperidine binding site of the P-tNp-P' dyad.

## EXPERIMENTAL

### General methods, materials, and techniques

All manipulations were carried out using standard Schlenk techniques under nitrogen atmosphere. 2,4,6-Trichloro-1,3,5-triazine (cyanuric chloride), diisopropylethylamine (DIPEA), glycine methyl ester hydrochloride, KOH and other chemicals and solvents were purchased from usual commercial sources and used as received, unless otherwise stated. Tetrahydrofuran (THF) was freshly distilled from Na/benzophenone. 5-(4-Aminophenyl)-10,15,20-triphenyl-porphyrin zinc (Zn[TPPNH<sub>2</sub>]) and



Scheme 1. The porphyrin dyads

5-(4-carbomethoxyphenyl)-15-(4-aminophenyl)-10,20-bis(2,4,6-trimethylphenyl)-porphyrin ( $H_2$ [Porph1]) were prepared according to literature procedures [20, 21].

### Synthesis

**Synthesis of dyad (ZnP)-[triazine-gly]-( $H_2$ PCOOH) or P-tg-P' (4a).** To a THF solution (1 mL) of cyanuric chloride (0.0096 g, 0.052 mmol) and DIPEA (11  $\mu$ L, 0.062 mmol) a THF solution (1 mL) of porphyrin  $H_2$ [Porph] (0.040 g, 0.052 mmol) was added, under Ar at 0°C. The mixture was stirred at 0°C for 15 min, and upon reaction completion (monitored by TLC), it was left to warm at room temperature. Next, a THF solution (2 mL) of Zn[TPPNH<sub>2</sub>] (0.072 g, 0.104 mmol) and DIPEA (22  $\mu$ L, 0.124 mmol) was added and the mixture was stirred at room temperature overnight. An excess of glycine methylester (0.065 g, 0.52 mmol) and DIPEA (180  $\mu$ L, 1.04 mmol) were added and the mixture was stirred at 65°C for 24 h. The volatiles were removed under reduced pressure and after

dilution in  $CH_2Cl_2$ ; the residue was purified by column chromatography (silica gel,  $CH_2Cl_2$ /ethanol 5%). The product **3a** was isolated as a purple solid. Yield 0.052 g (61.5%). <sup>1</sup>H NMR (300 MHz,  $CDCl_3$ ):  $\delta$ , ppm 9.04 (*s br*, 2H), 8.93 (*s br*, 8H), 8.71 (*m*, 6H), 8.39 (*m*, 2H), 8.30 (*m*, 2H), 8.19 (*s br*, 9H), 8.00 (*d*,  $J = 8.1$  Hz, 4H), 7.93 (*d*,  $J = 7.5$  Hz, 1H), 7.72 (*m*, 9H), 7.52 (*m*, 1H), 7.20 (*m*, 5H), 4.08 (*s*, 3H), 3.75 (*s*, 3H), 2.58 (*s*, 6H), 1.78 (*s*, 12H), -2.62 (*s*, 2H). HRMS (MALDI-TOF): *m/z* calcd. for  $C_{102}H_{79}N_{14}O_4Zn$ , 1627.5622 [ $M + H$ ]<sup>+</sup>: found 1627.5637. UV-vis ( $CH_2Cl_2$ ):  $\lambda$ , nm 421, 515, 550, 591, 648. Anal. calcd. for  $C_{102}H_{78}N_{14}O_4Zn$ : C, 75.20; H, 4.83; N, 12.04. Found C, 75.43; H, 4.88; N, 12.15.

**Ester hydrolysis.** To a THF solution (22 mL) of **3a** (0.030 g, 0.018 mmol), 6 mL MeOH, 7.5 mL  $H_2O$  and KOH (0.450 g, 0.008 mol) were added. After stirring the reaction mixture at room temperature overnight, the organic solvents were removed under reduced pressure and then a solution of HCl (0.5 M) was added dropwise, until pH 6. The precipitate was filtered, washed with water, extracted with  $CH_2Cl_2$  and purified by column

chromatography (silica gel, CH<sub>2</sub>Cl<sub>2</sub>/EtOH 10%). The product P-tg-P' (**4a**) was isolated as a purple solid. Yield 0.025 g (89%). <sup>1</sup>H NMR (300 MHz, DMSO-d<sub>6</sub>): δ, ppm 9.80 (*s br*, 2H), 8.97 (*s br*, 5H), 8.78 (*s br*, 7H), 8.65 (*s br*, 4H), 8.42 (*s br*, 4H), 8.32 (*s br*, 2H), 8.22 (*s br*, 8H), 7.83 (*s br*, 7H), 7.32 (*s br*, 6H), 6.91 (*m*, 1H), 6.62 (*s*, 1H), 4.00 (*s*, 2H), 3.40 (*s*, 6H), 1.25 (*s*, 12H), -2.68 (*s*, 2H). <sup>13</sup>C NMR (125 MHz, DMSO-d<sub>6</sub>): δ, ppm 171.8, 168.2, 165.7, 164.5, 149.7, 149.2, 145.7, 142.8, 138.4, 137.7, 134.5, 134.2, 131.5, 130.2, 129.0, 128.7, 127.8, 127.4, 126.6, 120.2, 120.1, 117.7, 62.6, 52.0, 34.0, 29.2, 22.1, 21.1. HRMS (MALDI-TOF): *m/z* calcd. for C<sub>100</sub>H<sub>75</sub>N<sub>14</sub>O<sub>4</sub>Zn: 1599.5309 [M + H]<sup>+</sup>, found 1599.5291. UV-vis (DMSO): λ, nm (ε × 10<sup>-3</sup> M<sup>-1</sup>.cm<sup>-1</sup>) 429 (527.7), 517 (14.1), 560 (19.5), 601 (11.8), 647 (4.6). Anal. calcd. for C<sub>100</sub>H<sub>74</sub>N<sub>14</sub>O<sub>4</sub>Zn: C, 75.01; H, 4.66; N, 12.25. Found C, 75.14; H, 4.57; N, 12.42.

**Synthesis of dyad (ZnP)-[triazine-Npip]-(H<sub>2</sub>PCOOH) or P-tNp-P' (**4b**).** To a THF solution (1 mL) of cyanuric chloride (0.0096 g, 0.052 mmol) and DIPEA (11 μL, 0.062 mmol) a THF solution (1 mL) of porphyrin H<sub>2</sub>[Porph] (0.040 g, 0.052 mmol) was added, under Ar at 0 °C. The mixture was stirred at 0 °C for 15 min, and upon reaction completion (monitored by TLC), it was left to warm at room temperature. Next, a THF solution (2 mL) of Zn[TPPNH<sub>2</sub>] (0.072 g, 0.104 mmol) and DIPEA (22 μL, 0.124 mmol) was added and the mixture was stirred at room temperature overnight. An excess of piperidine (78 μL, 0.52 mmol) and DIPEA (180 μL, 1.04 mmol) were added and the mixture was stirred at 65 °C for 24 h. The volatiles were removed under reduced pressure and after dilution in CH<sub>2</sub>Cl<sub>2</sub>, the residue was purified by column chromatography (silica gel, CH<sub>2</sub>Cl<sub>2</sub>/ethanol 2%). The product **3b** was isolated as a purple solid. Yield 0.055 g (65%). <sup>1</sup>H NMR (300 MHz, CDCl<sub>3</sub>): δ, ppm 9.11 (*d*, *J* = 4.8 Hz, 2H), 8.97 (*t*, *J* = 4.8 Hz, 7H), 8.74 (*m*, 7H), 8.41 (*m*, 3H), 8.34 (*m*, 3H), 8.24 (*m*, 9H), 8.04 (*d*, *J* = 8.1 Hz, 4H), 7.76 (*m*, 8H), 7.30 (*s*, 4H), 4.08 (*s*, 3H), 3.94 (*s br*, 5H), 2.62 (*s*, 6H), 1.84 (*s*, 12H), -2.57 (*s*, 2H). HRMS (MALDI-TOF): *m/z* calcd. for C<sub>104</sub>H<sub>83</sub>N<sub>14</sub>O<sub>2</sub>Zn: 1623.6037 [M + H]<sup>+</sup>, found 1623.6055. UV-vis (CH<sub>2</sub>Cl<sub>2</sub>): λ, nm 421, 515, 551, 590, 648. Anal. calcd. for C<sub>104</sub>H<sub>82</sub>N<sub>14</sub>O<sub>2</sub>Zn: C, 76.86; H, 5.09; N, 12.07. Found C, 77.05; H, 5.02; N, 12.16.

**Ester hydrolysis.** To a THF solution (22 mL) of **3b** (0.030 g, 0.018 mmol), 6 mL MeOH, 7.5 mL H<sub>2</sub>O and KOH (0.450 g, 0.008 mol) were added. After stirring the reaction mixture at room temperature overnight, the organic solvents were removed under reduced pressure and then a solution of HCl (0.5 M) was added dropwise, until pH 6. The precipitate was filtered, washed with water, extracted with CH<sub>2</sub>Cl<sub>2</sub> and purified by column chromatography (silica gel, CH<sub>2</sub>Cl<sub>2</sub>/EtOH 5%). The product P-tNp-P' (**4b**) was isolated as a purple solid. Yield 0.025 g (86%). <sup>1</sup>H NMR (300 MHz, THF-d<sub>8</sub>): δ,

ppm 8.98 (*d*, *J* = 4.5 Hz, 2H), 8.94 (*d*, *J* = 4.2 Hz, 2H), 8.83 (*s br*, 6H), 8.76 (*s br*, 2H), 8.66 (*s br*, 4H), 8.43 (*d*, *J* = 8.1 Hz, 2H), 8.29 (*m*, 6H), 8.16 (*m*, 7H), 7.72 (*m*, 6H), 7.30 (*m*, 6H), 6.92 (*s*, 5H), 6.59 (*s*, 1H), 5.88 (*s*, 2H), 2.59 (*s br*, 10H), 2.21 (*s*, 6H), 1.73 (*s*, 12H), -2.49 (*s*, 2H). <sup>13</sup>C NMR (75 MHz, THF-d<sub>8</sub>): δ, ppm 168.2, 166.4, 151.8, 151.2, 147.7, 146.7, 144.9, 140.3, 139.8, 139.0, 138.5, 136.0, 135.7, 132.8, 132.4, 129.2, 128.9, 128.3, 127.4, 126.2, 121.6, 119.2, 118.9, 118.8, 118.4, 31.1, 30.1, 22.0. HRMS (MALDI-TOF): *m/z* calcd. for C<sub>103</sub>H<sub>81</sub>N<sub>14</sub>O<sub>2</sub>Zn 1609.5880 [M + H]<sup>+</sup>, found 1609.5910. UV-vis (THF): λ, nm (ε × 10<sup>-3</sup> M<sup>-1</sup>.cm<sup>-1</sup>) 424 (514.6), 515 (16.2), 555 (18.8), 596 (9.3), 649 (3.8). Anal. calcd. for C<sub>103</sub>H<sub>80</sub>N<sub>14</sub>O<sub>2</sub>Zn: C, 76.78; H, 5.00; N, 12.17. Found C, 76.69; H, 4.86; N, 12.34.

### NMR spectra

<sup>1</sup>H NMR spectra were recorded on a Bruker DPX-300 MHz and <sup>13</sup>C NMR spectra on both Bruker DPX-75 MHz and Bruker AMX-125 MHz spectrometers, as solutions in deuterated solvents by using the solvent peak as the internal standard.

### Mass spectra

High-resolution mass spectra were recorded on a Bruker UltrafleXtreme MALDI-TOF/TOF spectrometer.

### Photophysical measurements

UV-vis absorption spectra were measured on a Shimadzu UV-1700 spectrophotometer using 10 mm path-length cuvettes. Emission spectra were measured on a JASCO FP-6500 fluorescence spectrophotometer equipped with a red sensitive WRE-343 photomultiplier tube (wavelength range: 200–850 nm).

### Electrochemistry measurements

Cyclic and square wave voltammetry experiments were carried out at room temperature using an AutoLab PGSTAT20 potentiostat and appropriate routines available in the operating software (GPES, version 4.9). Measurements were carried out in freshly distilled and deoxygenated THF, with scan rate 100 mV.s<sup>-1</sup>, with a solute concentration of 1.0 mM in the presence of tetrabutylammonium hexafluorophosphate (0.1 M) as supporting electrolyte. A three-electrode cell setup was used with a platinum working electrode, a saturated calomel (SCE) reference electrode, and a platinum wire as counter electrode. The system was calibrated by ferrocene.

### Computational methods

Theoretical calculations were performed within the framework of density functional theory (DFT). For the initial gas-phase geometry optimizations, the gradient

corrected functionals PBE [22] of Perdew, Burke and Ernzerhof and the triple- $\zeta$  quality TZVP basis set [23], were employed for all calculations. Several rotamers were used as initial geometries. At this stage the resolution of the identity method [24] was used for the treatment of the two-electron integrals to increase the computational efficiency (without loss in accuracy). The resulting structures were further optimized using both the hybrid exchange–correlation functional PBE0 [25] (without adjustable parameters), as well as the hybrid functional B3LYP [26], using the same basis set. Tight convergence criteria were placed for the SCF energy (up to  $10^{-7}$  Eh) and the one-electron density (rms of the density matrix up to  $10^{-8}$ ) as well as for the norm of the Cartesian gradient (residual forces both average and maximum smaller than  $1.5 \times 10^{-5}$  a.u.) and residual displacements (both average and maximum smaller than  $6 \times 10^{-5}$  a.u.). The optical band gaps of the porphyrin dyads were calculated by TD-DFT excited state calculations, using the same functionals and basis set on the corresponding ground state structures. The corresponding UV-vis spectra were calculated using the B3LYP functional. The first round of geometry optimizations was performed using the Turbomole package [27], while for the following calculations the Gaussian package was employed [28].

### Preparation of TiO<sub>2</sub> electrodes and DSSCs

DSSCs were fabricated with electrodes based on fluorine-doped tin oxide (FTO)-coated glass substrates, which were pre-cleaned with deionized water, acetone, and ethanol and then dried in air. The working electrodes were prepared by firstly forming a blocking layer from 0.2 M di-isopropoxy titanium bis (acetylacetonate) in isopropanol by spray pyrolysis. This was then followed by the deposition of a nano-crystalline layer of TiO<sub>2</sub> with the doctor blade technique using dye sol TiO<sub>2</sub> paste (DSL 18NR-T) on a pre-cleaned FTO coated glass substrate. The TiO<sub>2</sub> coated FTO electrodes were heated at 500 °C for 30 min. The TiO<sub>2</sub> electrodes were then dipped in 0.02 M aqueous TiCl<sub>4</sub> for 20 min, rinsed with water and ethanol and annealed at 500 °C for 20 min. The thickness of the TiO<sub>2</sub> electrode was measured using a thin film thickness measurement system (Nano calc XR Ocean Optics Germany) and found to be in the range of 10–12  $\mu$ m. Finally, it was immersed in a porphyrin solution (200  $\mu$ M in THF) for 12 h to give the porphyrin-sensitized TiO<sub>2</sub> working electrode. The platinum wire counter electrode was prepared by spin-coating drops of a H<sub>2</sub>PtCl<sub>6</sub> solution onto a FTO-coated glass substrate and heating at 350 °C for 15 min. The DSSCs were assembled by separating the working electrode from the counter electrode by a 20  $\mu$ m thick Surlyn hot-melt gasket. In the space between the working and counter electrodes, the electrolyte (consisting of 0.05 M I<sub>2</sub>, 0.5 M

LiI, 0.6 M dimethylpropyl-benzimidazole iodide, 0.5 M 4-*tert*-butylpyridine in an acetonitrile solution) was introduced through a hole and sealed with Surlyn.

### Photovoltaic measurements

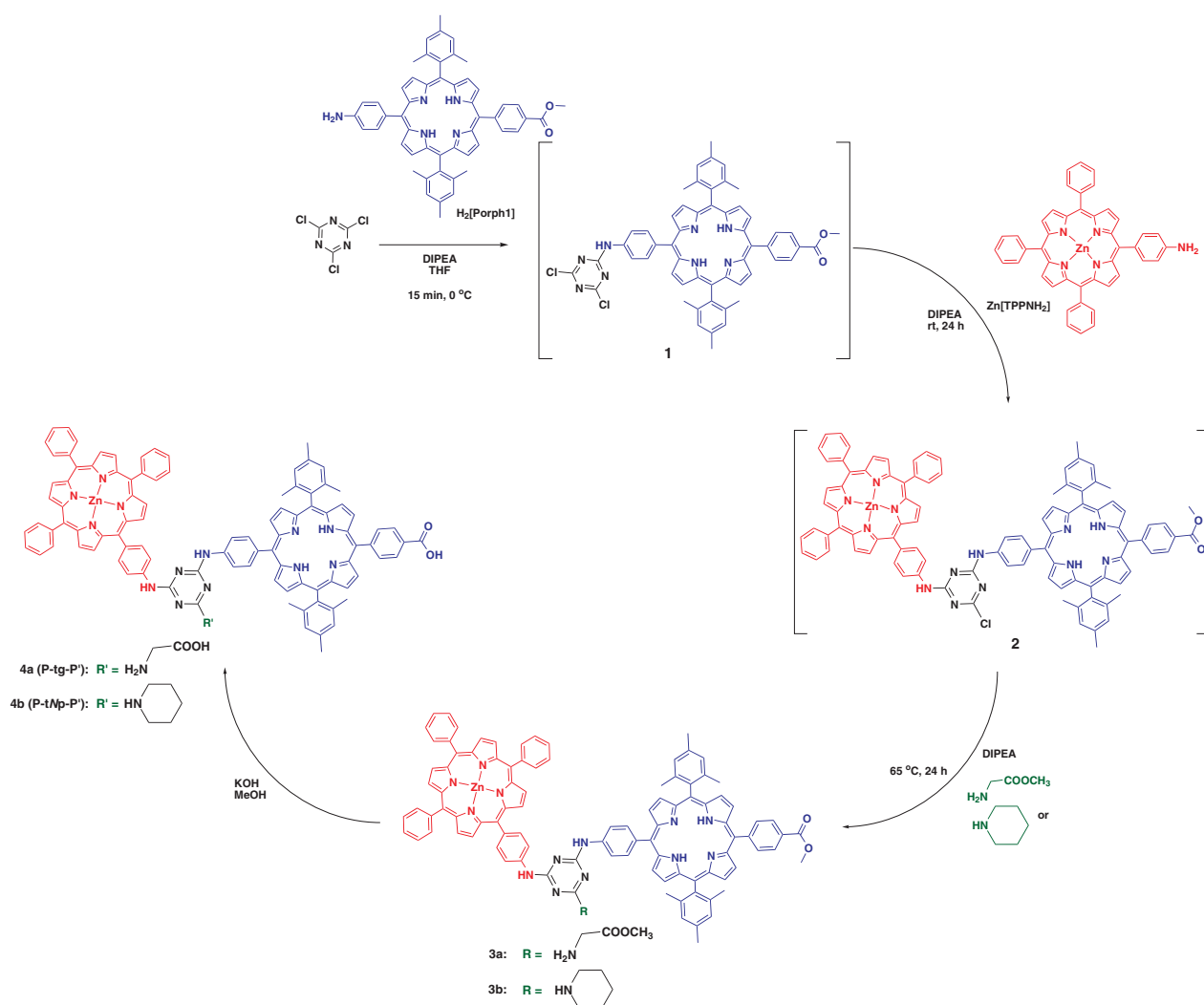
The current-voltage ( $J$ - $V$ ) characteristics of the DSSCs under illumination were measured by a Keithley source meter and a solar simulator coupled with a 150 W xenon lamp and an AM optical filter to give an illumination intensity of 100 mW cm<sup>-2</sup> at the DSSC surface. The electrochemical impedance spectra (EIS) in the dark were recorded by using an electrochemical workstation (Auto lab PGSTAT) with a frequency response analyzer. The frequency range was from 10 mHz to 100 KHz, and an AC potential of 10 mV was used. A dc bias equivalent to the open-circuit voltage of the DSSC was applied. The impedance data were analyzed using Z-View software with an appropriate equivalent circuit. The incident photon to current conversion efficiency (IPCE) was measured as a function of wavelength with a xenon lamp, monochromator, and Keithley source meter at 10 mW.cm<sup>-2</sup>. The intensity calibration for the IPCE measurement was performed by using a standard silicon photodiode.

## RESULTS AND DISCUSSION

### Synthesis and characterization

As shown in Scheme 1, porphyrin dyads (ZnP)-[triazine-gly]-(H<sub>2</sub>PCOOH) (**4a**) and (ZnP)-[triazine-Npip]-(H<sub>2</sub>PCOOH) (**4b**), abbreviated as P-tg-P' and P-tNp-P', respectively, consist of a *meso* aryl-substituted zinc-metallated porphyrin unit P (namely 5-(4-aminophenyl)-10,15,20-triphenylporphyrin zinc) and a free-base porphyrin unit P' (namely 5-(4-carboxyphenyl)-15-(4-aminophenyl)-10,20-bis(2,4,6-trimethylphenyl) porphyrin) which are connected, through aryl-amino groups at their peripheries, by a central 1,3,5-triazine moiety (t). In the former, the triazine ring is further functionalized by a glycine group, while in the latter by an *N*-piperidine group. Both porphyrin dyads contain potential anchoring groups for attachment onto the TiO<sub>2</sub> surface of DSSC electrodes: the former two carboxylic acid groups, while the latter one carboxylic acid and one *N*-substituted piperidine group.

The syntheses of two dyads, shown in Scheme 2, was accomplished *via* stepwise amination reactions of cyanuric chloride, which is the precursor of the bridging 1,3,5-triazine group of both dyads. The potential of cyanuric chloride to provide access to a variety of triazine-bridged assemblies, such as macrocycles [29], dendrimers [30], and multiporphyrin arrays [31], has been demonstrated in the past. Furthermore, we recently



**Scheme 2.** Syntheses of porphyrin dyads P-tg-P' and P-tNp-P'

reported symmetrical and unsymmetrical triazine-bridged porphyrin dyads and triads [19, 20].

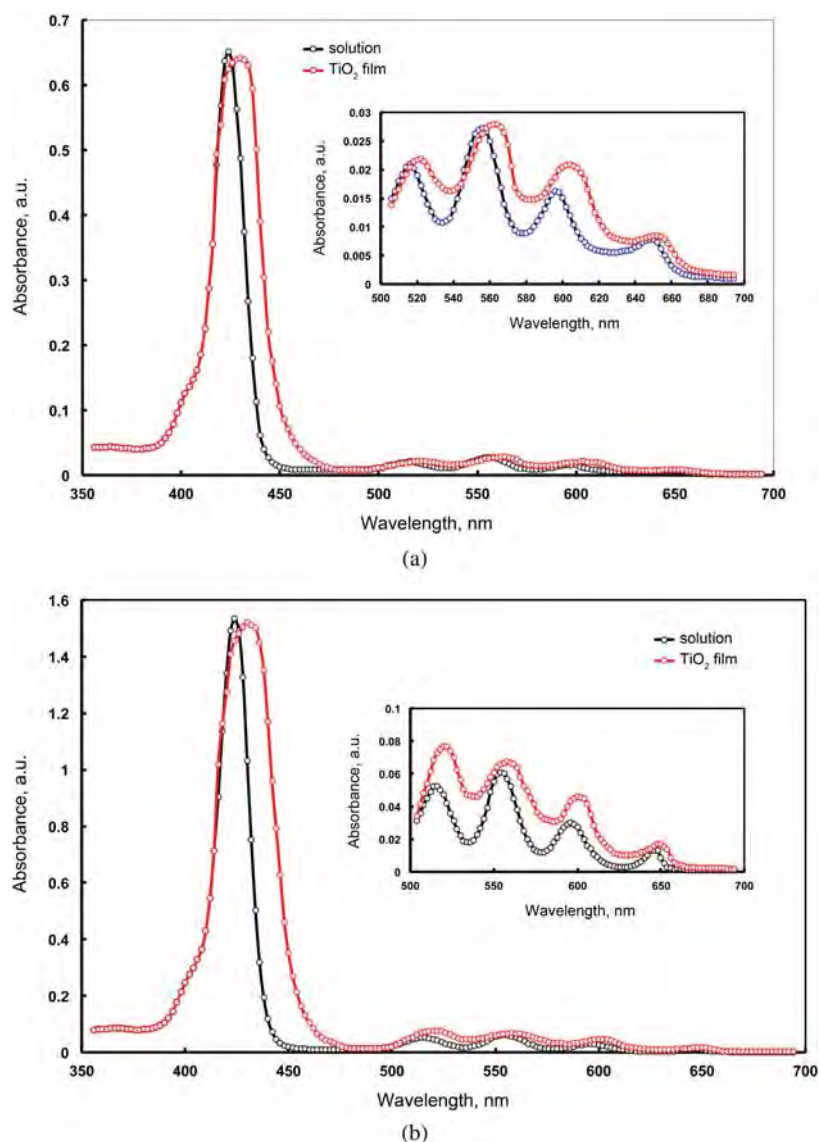
The initial step for the syntheses of both dyads involves the reaction of cyanuric chloride with H<sub>2</sub>[Porph] in the presence of the base DIPEA at 0 °C in THF (Scheme 2). The reaction was monitored by TLC indicating the disappearance of the reactants and the formation of the mono-porphyrin-triazine adduct **1**. The latter was not isolated but further reacted at room temperature with Zn[TPP-NH<sub>2</sub>] affording the di-porphyrin-triazine adduct **2**. The third chlorine atom of cyanuric chloride was substituted by a glycine-methyl ester moiety in a one-pot reaction at 65 °C resulting in the di-porphyrin-triazine-glycine methyl ester adduct **3a**, as confirmed by <sup>1</sup>H NMR spectroscopy and MALDI-TOF spectrometry. In the <sup>1</sup>H NMR spectrum of **3a**, the signals of the aromatic H's *ortho* to the amino groups of Zn[TPP-NH<sub>2</sub>], after attachment to the triazine ring, are downfield displaced compared to those of free Zn[TPP-NH<sub>2</sub>]. Basic hydrolysis of the methyl ester groups of **3a** resulted in the formation of porphyrin dyad P-tg-P' (**4a**), in almost quantitative

yield, as indicated by <sup>1</sup>H NMR spectroscopy, MALDI-TOF spectrometry, UV-vis absorption spectroscopy, and elemental analysis. In the <sup>1</sup>H NMR spectrum of **4a**, with respect to that of **3a**, it should be noted the absence of the signal attributed to the methyl-ester H's after hydrolysis reaction.

Porphyrin dyad P-tNp-P' (**4b**) was synthesized in a similar manner, following the above mentioned sequence of reactions. Piperidine group was introduced in a substitution reaction of the third chlorine atom of cyanuric chloride yielding the di-porphyrin-triazine-piperidine adduct **3b**. Hydrolysis reaction resulted in the formation of the desired porphyrin dyad **4b**. <sup>1</sup>H and <sup>13</sup>C NMR spectroscopy, MALDI-TOF spectrometry, UV-vis absorption spectroscopy, and elemental analysis confirmed the identity and purity of the product.

### Photophysical studies

The UV-vis absorption spectra of dyads P-tg-P' and P-tNp-P' in THF solutions are shown in Figs 1a and 1b,



**Fig. 1.** Normalized UV-vis absorption spectra of dyads (a) P-tg-P' and (b) P-tNp-P' in THF solutions (black color lines) and after adsorbed onto TiO<sub>2</sub> films (red color lines)

respectively (black color). The absorption spectra of both dyads exhibit the typical porphyrin absorption bands, with an intense Soret band in the 400–450 nm range and four moderate bands in the 500–700 nm with no additional features. This indicates that in ground states of the dyads there is no significant electronic interaction between the two porphyrin units attached to the triazine ring. The absorption spectra of P-tg-P' and P-tNp-P' adsorbed onto TiO<sub>2</sub> film (Figs 1a and 1b, red color) show the usual porphyrin Soret and Q-bands. In general, when porphyrins are adsorbed onto the TiO<sub>2</sub> surface, they form either *H*- or *J*-aggregates. The broader and red shifted bands of both porphyrin dyads may be attributed to intermolecular interactions that result in the formation of *J*-type aggregates [32]. As can be seen from Fig. 1b, the red shift and broadening are more pronounced for dyad P-tg-P', suggesting a stronger electronic coupling,

which may be due to the presence of two carboxylic acid anchoring units in its molecular structure [33]. Furthermore, it is an indication of an enhanced light harvesting ability of P-tg-P' compared to P-tNp-P'. The optical band gaps  $E_g^{\text{opt}}$  of porphyrin dyads P-tg-P' and P-tNp-P' were estimated using the expression;

$$E_g^{\text{opt}} = 1240/\lambda_{\text{onset}} \quad (1)$$

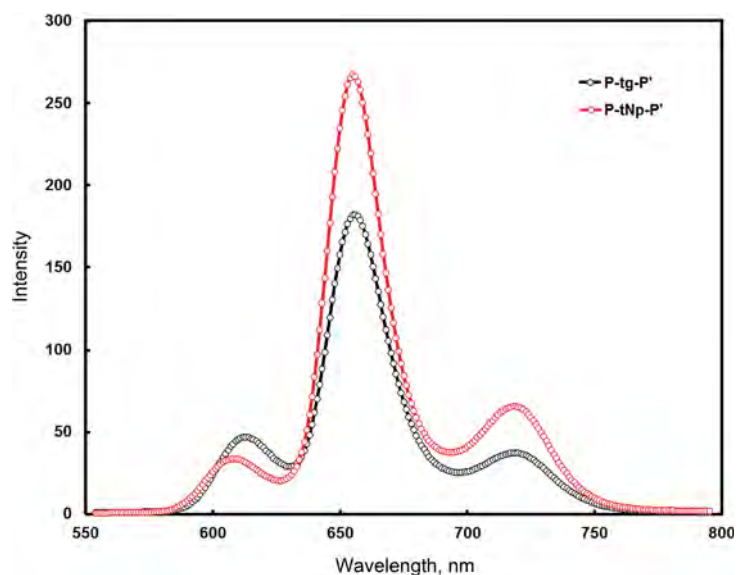
where  $\lambda_{\text{onset}}$  is the absorption onset edge, and they were found to be 1.84 and 1.86 eV, respectively (Table 1).

In Fig. 2 the steady-state fluorescence spectra of the two dyads P-tg-P' and P-tNp-P' in THF solutions are shown. Exciting the porphyrin dyads at the Soret band (424 nm) results in photoluminescence with three peaks of unequal intensities: 612, 656 and 718 nm for the former (black color line), and 608, 655 and 717 nm for the latter (red color line), respectively. Since both dyads

**Table 1.** Photophysical data, and calculated optical band gaps  $E_g^{\text{opt}}$  for dyads P-tg-P' and P-tNp-P'

Compound	Absorption $\lambda_{\text{max}}$ , nm ( $\epsilon \times 10^{-5} \text{ M}^{-1} \cdot \text{cm}^{-1}$ ) in solution <sup>a</sup>	Absorption $\lambda_{\text{max}}$ , nm on TiO <sub>2</sub> film	Emission $\lambda_{\text{max}}$ , nm in solution <sup>a</sup>	$E_g^{\text{opt}}$ , eV
P-tg-P'	424 (5.277), 517 (0.141), 560 (0.195), 601 (0.118), 647 (0.046)	430, 522, 564, 604, 654	612, 656, 717	1.84
P-tNp-P'	424 (5.146), 515 (0.162), 555 (0.188), 596 (0.093), 649 (0.038)	430, 522, 560, 600, 648	608, 655, 718	1.88

<sup>a</sup>Measured in THF at 298 K. <sup>b</sup>Calculated by onset absorption edge  $\lambda_{\text{onset}}$  of the Q-bands and the expression.  $E_g^{\text{opt}} = 1240/\lambda_{\text{onset}}$ .

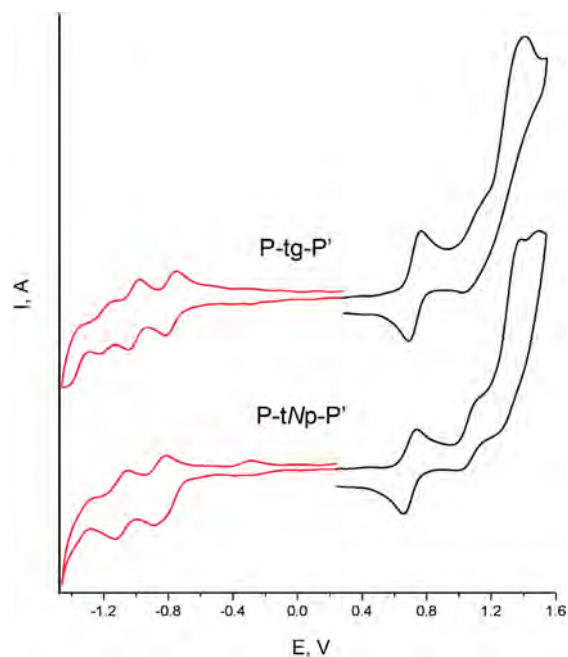
**Fig. 2.** Isoabsorbing fluorescence spectra of dyads P-tg-P' (black color line) and P-tNp-P' (black color line) in THF solutions

contain free-base and zinc-metalated porphyrin units, their fluorescence spectra result from the superposition of the fluorescence spectra of these two moieties.

### Electrochemical studies

The electrochemical behavior of P-tg-P' and P-tNp-P' porphyrin dyads was investigated with cyclic and square-wave voltammetry measurements [34]. The corresponding cyclic and square-wave voltammograms are presented in Fig. 3 and Fig. S19, respectively, while the relevant electrochemical data are listed in Table 2. The first oxidation for both dyads is a reversible process occurring at  $E_{\text{ox}}^1 = +1.07 \text{ V vs. NHE}$ , while the first reductions are reversible processes observed at  $E_{\text{red}}^1 = -0.86$  and  $E_{\text{red}}^1 = -0.85 \text{ V vs. NHE}$  for P-tg-P' and P-tNp-P', respectively. In general, both dyads exhibit the typical electrochemical processes of assemblies consisted of aryl-substituted Zn-metalated and free-base porphyrin units.

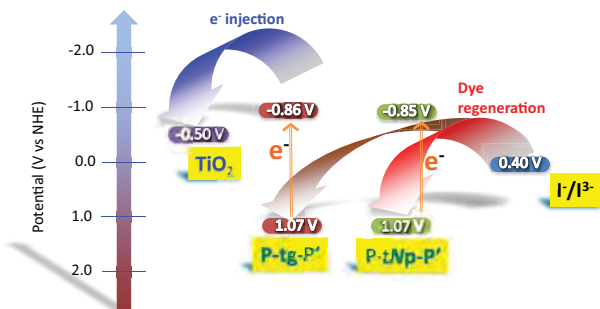
An efficient sensitizer should have HOMO and LUMO energy levels which are compatible with the redox potential of electrolyte and conduction band (CB) edge of TiO<sub>2</sub>, respectively, so that efficient electron injection

**Fig. 3.** Cyclic voltammograms of dyads P-tg-P' and P-tNp-P' in DMSO vs. NHE. The ferrocene/ferrocenium (Fc/Fc<sup>+</sup>) redox couple wave is observed at 0.69 V



**Table 2.** Electrochemical data, and calculated band gaps  $E_g^{\text{elec}}$  for dyads P-tg-P' and P-tNp-P'

Compound	$E_{\text{ox}}^1$ , V	$E_{\text{ox}}^2$ , V	$E_{\text{red}}^1$ , V	$E_{\text{red}}^2$ , V	$E_{\text{red}}^3$ , V	$E_{\text{red}}^4$ , V	$E_g^{\text{elec}}$ , eV
P-tg-P'	1.07	1.36	-0.86	-1.10	-1.28	-1.50	1.93
P-tNp-P'	1.07	1.32	-0.85	-1.08	-1.32	-1.49	1.92

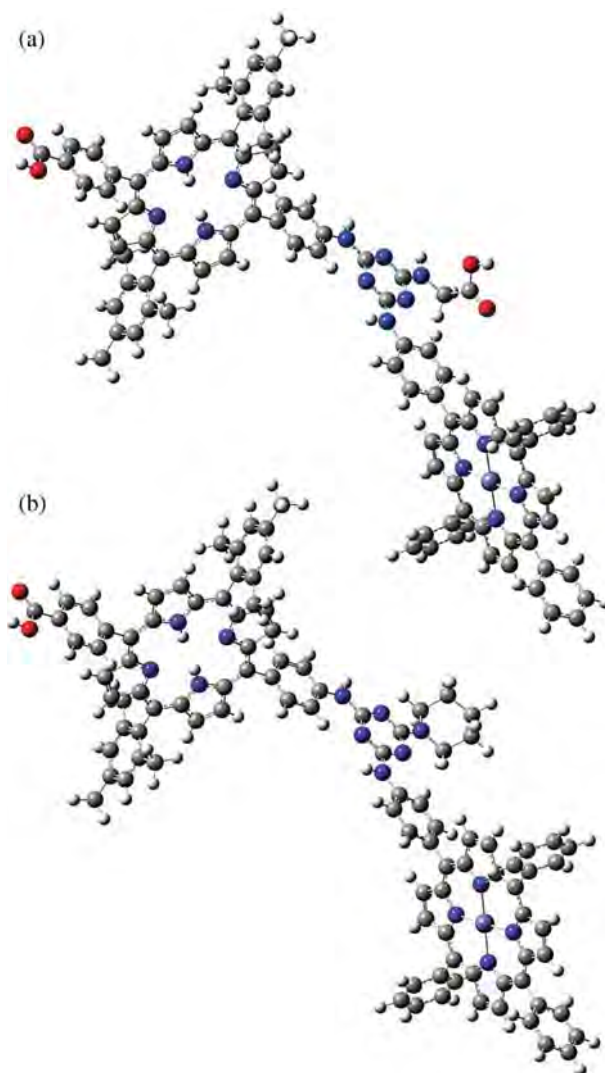
**Scheme 3.** Energy diagram depicting HOMO and LUMO potentials of the dyads

and regeneration processes are enabled. For efficient electron injection from the photoexcited sensitizer into the  $\text{TiO}_2$  CB, the LUMO energy level of the sensitizer should be higher than the  $\text{TiO}_2$  CB edge (-0.5 V vs. NHE). In addition, for efficient electron regeneration of the sensitizer radical cation (after photoinduced electron injection), the HOMO energy level of the sensitizer should be lower than the potential of the electrolyte redox  $\text{I}^-/\text{I}_3^-$  couple (+0.4 V vs. NHE). As mentioned above, the first oxidation potential for both dyads is +1.07 V vs. NHE, while the first reduction potentials are -0.86 and -0.85 V vs. NHE for P-tg-P' and P-tNp-P', respectively, which means that there is sufficient driving force for efficient electron injection and dye regeneration processes for the P-tg-P' and P-tNp-P' sensitized solar cells. This is also depicted schematically in the energy diagram shown in Scheme 3 [35].

Based on the above mentioned electrochemical data, the HOMO–LUMO band gaps  $E_g^{\text{elec}}$  of P-tg-P' and P-tNp-P' were found to be 1.93 and 1.92 eV, respectively (Table 2). The fact that these are larger than the corresponding optical band gaps  $E_g^{\text{opt}}$  calculated from the photophysical measurements (Table 1) can be attributed to solvent effects [36].

### Theoretical calculations

In order to gain an insight into the molecular geometries and electronic structures of P-tg-P' (**4a**) and P-tNp-P' (**4b**) porphyrin dyads, theoretical studies were performed within the framework of DFT [37]. Geometry optimizations were carried out in the gas-phase using the PBE, PBE0, and B3LYP functionals. The structures of the two compounds optimized using the B3LYP functional

**Fig. 4.** Optimized structure of porphyrin dyads (a) P-tg-P' and (b) P-tNp-P'. Carbon, nitrogen, hydrogen, oxygen and zinc atoms correspond to grey, blue, white, red and green spheres, respectively

are shown in Fig. 4, while their optimized coordinates are provided in Table S1 in Supporting information. The dyads exhibit “butterfly like” structures with the triazine moiety being nearly co-planar with the bridging, amino-substituted phenyl groups of the two porphyrin units P and P'. The non-planar orientation of the two porphyrin units, which results in breaking of conjugation by the twisted bridging phenyl rings, together with the relatively large interporphyrin distance, do not favor the electronic

**Table 3.** DFT calculated properties of dyads P-tg-P' and P-tNp-P': HOMO and LUMO energies, HOMO–LUMO gaps, optical gaps ( $E_g^{\text{calc}}$ ), oscillator strengths ( $f$ ), orbital contribution assignments, and dipole moments ( $\mu$ )

	HOMO, eV	LUMO, eV	HL, eV	$E_g^{\text{calc}}$ , eV	$f$	Assignment	$\mu$ , D
P-tg-P'							
PBE	-4.78	-3.09	1.69	1.67	$5.00 \times 10^{-4}$	H→L 99.3%	4.09
PBE0	-5.43	-2.51	2.92	2.20	$3.35 \times 10^{-2}$	H-1→L 33.0%; H-1→L+1 32.1%; H-3→L 17.5%; H-3→L+1 16.4%	3.82
B3LYP	-5.28	-2.60	2.68	2.15	$2.71 \times 10^{-2}$	H-1→L 55.8%; H-3→L+1 28.5%; H-1→L+1 9.6%; H-3→L 5.2%	3.76
P-tNp-P'							
PBE	-4.71	-3.02	1.69	1.71 (1.96)	$9.00 \times 10^{-4}$	H-1→L 85.8%; H→L 14.1% (H→L 40.0%; H→L+1 23.3%; H-3→L+1 14.1%; H-3→L 9.5% H-1→L 6.7%)	5.15
PBE0	-5.40	-2.47	2.93	2.19	$3.57 \times 10^{-2}$	H-1→L 32.2%; H-1→L+1 28.2%; H-3→L+1 17.1%; H-3→L 16.5%	4.78
B3LYP	-5.27	-2.56	2.71	2.15	$2.67 \times 10^{-2}$	H-1→L 45.8%; H-3→L+1 28.9%; H→L 10.9%; H-1→L+1 7.1%	4.79

communication between the two  $\pi$ -electronic systems P and P', which is consistent with the UV-vis absorption spectra, and cyclic voltammograms of the two dyads.

For the optimized structures of the two porphyrin dyads P-tg-P' and P-tNp-P', the corresponding optical gaps were calculated employing the PBE, PBE0, and B3LYP functionals. The results are listed in Table 3, along with the HOMO and LUMO energies, the HOMO–LUMO gaps, the optical gaps  $E_{\text{opt}}^{\text{calc}}$  and the main contributions to the first (allowed) excitation. Results are provided for all three functionals, which can additionally be used for comparison with the literature. It has been shown [38, 39] that the PBE0 functional performs efficiently for calculating excitation energies (average absolute deviation of 0.14 eV). The hybrid functionals overestimate only slightly the optical gaps for both structures by approximately 0.3 eV. The character of the first allowed excitations only for configurations with a contribution larger than 4% is also provided in Table 3. For dyad P-tNp-P' in the case of the PBE functional we additionally provide the values (given in parentheses) that correspond to the first excitation with a significantly higher larger oscillator strength. Both structures exhibit a clear multi-configurational character for the first excitation (for the hybrid functionals). The hybrid functionals produce contributions from the same — near frontier — orbitals with some variation on the percentages. The contributions include transitions between the HOMO down to HOMO–3 and LUMO up to LUMO+3. The near HOMOs and near LUMOs are energetically very near to the HOMO and LUMO with maximum energy differences about 0.30 eV and 0.15 eV for the near HOMOs and near LUMOs, respectively.

In Fig. 5 the isosurfaces (isovalue = 0.02) of all of the MOs that appear in the configuration assignments

of Table 3, namely from HOMO down to HOMO–3 and LUMO up to LUMO+3 calculated using the B3LYP functional, have been plotted. All orbitals are highly localized on one (or the other) of the porphyrin units. In the case of P-tg-P' all of the (main) contributing transitions to the first excitation are between orbitals localized on the same porphyrin of the dyad. To quantify the contributions of the moieties to the frontier orbitals, the total and partial density of states (PDOS) have been calculated. The PDOS for the dyads P-tg-P' and P-tNp-P' are shown in Fig. S1. We denote the porphyrin with the phenyl groups as porphyrin-1 and the porphyrin with the 2,4,6-methyl phenyl groups, *i.e.* without the central Zn atom, as porphyrin-2. We further partition the remaining atoms of the structure to the 2,6-diamine-1,3,5-triazine and the glycine or piperidine groups. The triazine contributions are first noted at lower energies around -6.2 eV for P-tg-P' and -6.0 eV for P-tNp-P'. The most noticeable difference is that the glycine moiety first contributions to states is at -7.0 eV with a percentage of 7.8% and the piperidine at -6.5 eV with a percentage of 13.8%. Further contributions of piperidine are noted only at much lower energies at -9.2 eV and below and of glycine at -8.3 eV and below. The second virtual state peaks (located about 0.7 and 0.8 eV for P-tg-P' and P-tNp-P', respectively, higher than the corresponding LUMO peak) for both dyads are well separated from other energetically either higher or lower states and are dominated by contributions from porphyrin-2.

The UV-vis absorption spectra of the two dyads P-tg-P' and P-tNp-P' have also been calculated at the TD-DFT/B3LYP level (Fig. S2). The spectra have been produced by convoluting Gaussian functions with HWHM = 0.05 eV centered at the excitation wavenumbers. The UV-vis spectra of the dyads are overall similar. They exhibit a high

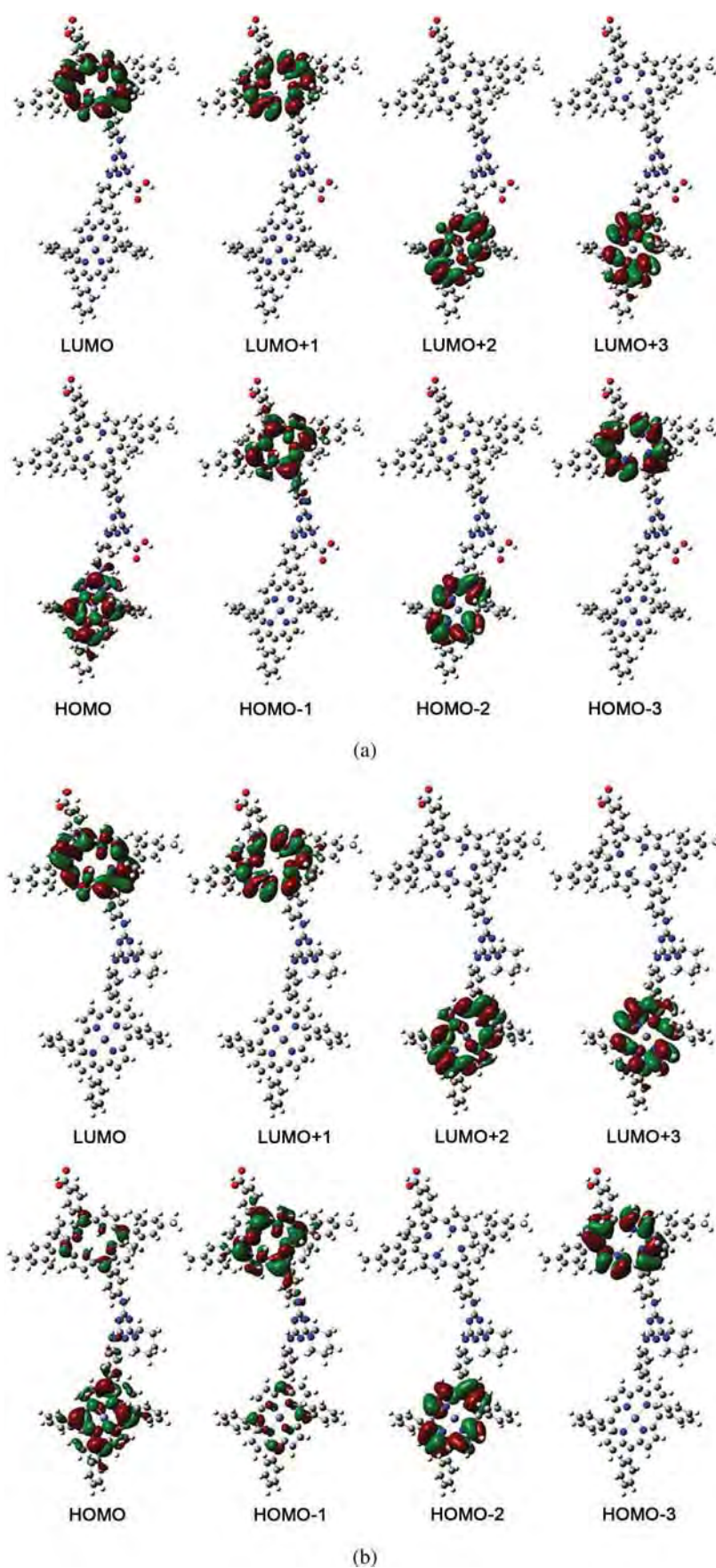
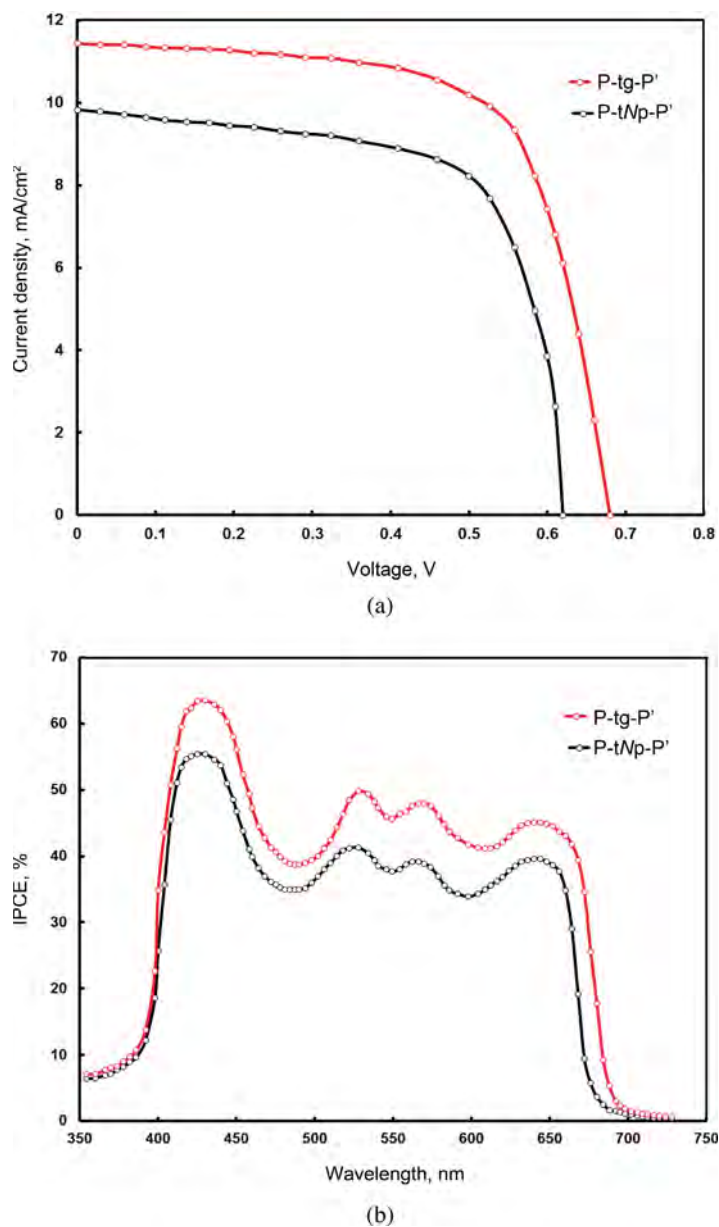


Fig. 5. Frontier and near-frontier orbitals of porphyrin dyads (a) P-tg-P' and (b) P-tNp-P'



**Fig. 6.** (a) Current-voltage ( $J$ - $V$ ) characteristics, and (b) IPCE spectra of DSSCs based on P-tg-P' (red color lines) and P-tNp-P' (black color lines)

intensity band with three peaks at small wavenumbers, a low intensity band at larger wavenumbers and a very low intensity band at even larger wavenumbers around 575 nm. The high intensity band's peaks are centered at 375 nm (3.31 eV), 389 nm (3.19 eV) and 410 nm (3.02 eV), and 376 nm (3.30 eV), 401 nm (3.09 eV) and 418 nm (2.97 eV) for structures P-tg-P' and P-tNp-P' respectively.

### Photovoltaic properties

Porphyrin dyads P-tg-P' (**4a**) and P-tNp-P' (**4b**) were used as sensitizers for the fabrication of DSSCs. The current-voltage ( $J$ - $V$ ) characteristics under illumination

(AM 1.5, 100 mW/cm<sup>2</sup>) of the two DSSCs are presented in Fig. 6a while the corresponding photovoltaic parameters are summarized in Table 4. The device based on the P-tg-P' dyad exhibits short circuit photocurrent ( $J_{sc}$ ), open circuit voltage ( $V_{oc}$ ), and fill factor ( $FF$ ) values of 11.44 mA/cm<sup>2</sup>, 0.68 V and 0.70, respectively, resulting in an overall PCE of 5.44%, while the values of the corresponding photovoltaic parameters of the P-tNp-P' based solar cell are 9.84 mA/cm<sup>2</sup>, 0.62 V, and 0.68, giving a PCE of 4.15%.

A major reason for the higher PCE value of the P-tg-P' based solar cell is its enhanced  $J_{sc}$  value. This is reflected in the IPCE spectral responses of the P-tg-P' and P-tNp-P' sensitized DSSCs, which, as shown in Fig. 6b, extend up

**Table 4.** Photovoltaic parameters of DSSCs sensitized by dyads P-tg-P' and P-tNp-P'

DSSC sensitized by	$J_{sc}^a$ , mA/cm <sup>2</sup>	$V_{oc}^b$ , V	FF <sup>c</sup>	PCE <sup>d</sup> , %
P-tg-P'	11.44	0.68	0.70	5.44
P-tNp-P'	9.84	0.62	0.68	4.15

<sup>a</sup>Short circuit current, <sup>b</sup>open circuit voltage, <sup>c</sup>fill factor, <sup>d</sup>photoconversion efficiency.

to ~680 nm for both solar cells. P-tg-P'-based solar cell exhibits a stronger and more extended IPCE response than the latter solar cell, which accounts for its higher  $J_{sc}$  value.

Furthermore, analysis of the amounts of dye adsorbed onto the TiO<sub>2</sub> surface of the photoanodes of the two DSSCs by desorption method [40], revealed that the dye loading for the P-tg-P' based TiO<sub>2</sub> photoanode is higher than that of the P-tNp-P' based photoanode. This might be related to the more effective binding of the former dyad onto the TiO<sub>2</sub> surface, due to the presence of two carboxylic acid anchoring groups on its structure, compared to one carboxylic acid group and a hindered *N*-piperidine binding site in the latter. Therefore, P-tg-P' is supposed to exhibit a lower tendency to form  $\pi$ - $\pi$  stacked dye aggregates onto the TiO<sub>2</sub> surface than that of P-tNp-P', resulting in an increased electron injection efficiency into the TiO<sub>2</sub> CB and an increased overall PCE [41].

In addition, the  $V_{oc}$  value of the solar cell based on dyad P-tg-P' is higher than that of the P-tNp-P'-based device (0.68 vs. 0.62 V, respectively). In general, differences in the  $V_{oc}$  values of DSSCs originate from two factors: (a) differences in the TiO<sub>2</sub> CB edge with respect to electrolyte potential, and (b) differences in the charge transfer processes at the electrode/electrolyte interfaces, *i.e.* charge recombination reactions of the injected electrons with the electrolyte, which affect the corresponding electron lifetimes of the DSSCs. In order to shed light into these electron transfer processes in the P-tg-P' and P-tNp-P'-sensitized solar cells, their electrochemical impedance spectra (EIS) were recorded in the dark, using a forward bias of 0.66 V. The Nyquist plots of EIS of the two DSSCs are presented in Fig. 7. The semicircles in the high- and middle-frequency regions are associated with the charge transfer processes at the Pt counter electrode/electrolyte and the TiO<sub>2</sub>/dye/electrolyte interfaces, respectively [42]. The charge recombination resistance ( $R_{ct}$ ) related to the charge recombination rate between the injected electron and electron acceptor I<sub>3</sub><sup>-</sup> of the electrolyte was estimated from the radius of the middle-frequency semicircle. It was found that the DSSC sensitized by P-tg-P' exhibits a significantly larger  $R_{ct}$  value (= 39.24  $\Omega$ ) compared to that of P-tNp-P' (= 27.64  $\Omega$ ), thus implying a slower rate of charge recombination at the TiO<sub>2</sub>/electrolyte interface, which leads to a higher  $V_{oc}$  value. Correspondingly, the lower  $R_{ct}$  value of the latter solar cell indicates a higher charge loss in the TiO<sub>2</sub>/electrolyte interface and consequently a lower value  $V_{oc}$ . The difference in the  $V_{oc}$  values of the two DSSCs may

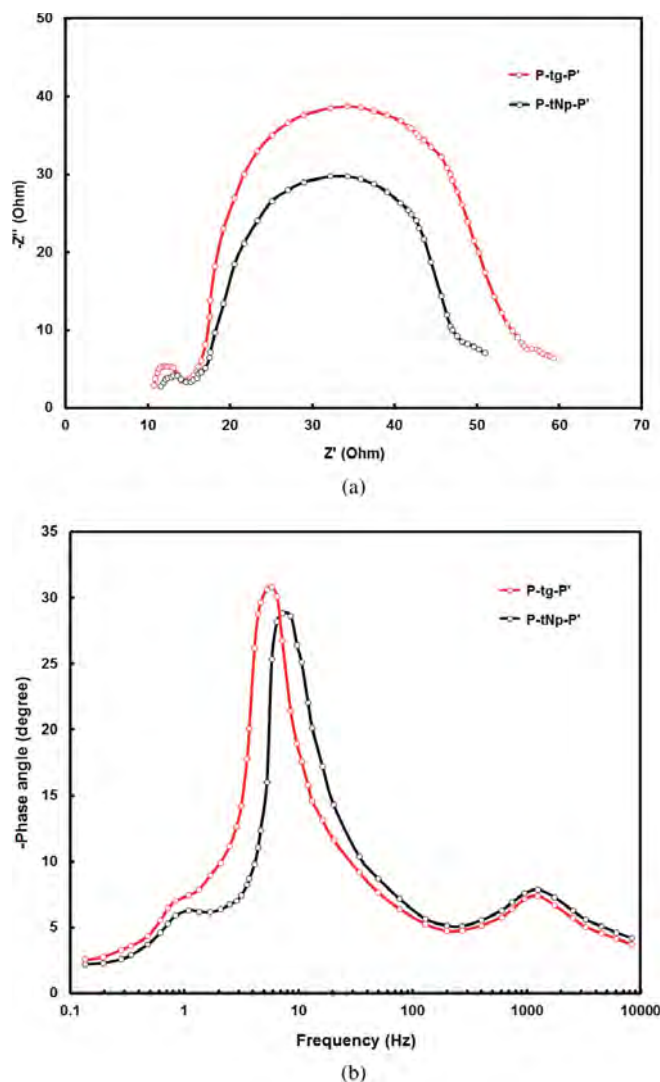
also be related to their corresponding electron lifetimes ( $\tau_e$ ). In Fig. 7, the Bode phase plots of EIS of DSSCs based on P-tg-P' and P-tNp-P' dyads are presented. In such as plot, the frequency  $f_{max}$  at the maximum of the middle frequency region semicircle is associated with the charge transfer process at the TiO<sub>2</sub>/dye/electrolyte interface and it is related to electron lifetime  $\tau_e$ :

$$\tau_e = \frac{1}{2\pi f_{max}} \quad (2)$$

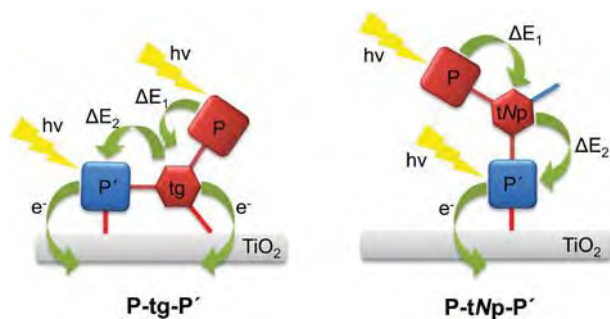
The  $\tau_e$  value for the DSSC sensitized by P-tg-P' was calculated to be higher (= 27.34 ms) than that for the P-tNp-P'-sensitized solar cell (= 22.56 ms), which is consistent with the higher  $V_{oc}$  value of the former solar cell. This is consistent with a more effective suppression of the recombination of the injected electrons with the I<sub>3</sub><sup>-</sup> in the electrolyte, which leads to an enhancement of both  $J_{sc}$  and  $V_{oc}$  values and improvement in the overall PCE value of the P-tg-P'-sensitized solar cell.

From the abovementioned data, it is obvious that both dyads P-tg-P' and P-tNp-P' are effective sensitizers for DSSCs. The PCE values of the corresponding solar cells are higher than the PCE values of the solar cells that we recently reported using similar but symmetrical dyads P-tg-P and P-tNp-P [19]. This can be related to the fact that in the present case the sensitizing dyes P-tg-P' and P-tNp-P' can be described as D- $\pi$ -A systems, where D (donor) is a zinc-metallated porphyrin unit,  $\pi$  is the triazine linker, and A (acceptor) is a free-base porphyrin unit with a carboxylic acid anchoring group, which result in more effective electron flow into the TiO<sub>2</sub> CB.

The different photovoltaic performances of the P-tg-P'- and P-tNp-P'-based solar cells can be related to the fact that dyad P-tg-P' contains two carboxylic acid anchoring group, while dyad P-tNp-P' contains only one carboxylic acid anchoring group and an *N*-piperidine binding site. Considering that *N*-piperidine binding site is hindered and not as effectively binding site as carboxylic acids, the attachment of P-tg-P' and P-tNp-P' onto the TiO<sub>2</sub> surface can be depicted by a branched system bound through two carboxylic acid groups and a linear system bound through one carboxylic acid group, respectively (Scheme 4). In the former case, this leads to the formation of a more compact layer of dye adsorbed onto the TiO<sub>2</sub> film (as evidenced by the higher dye loading), and results in a



**Fig. 7.** (a) Nyquist plots and (b) Bode phase plots of electrochemical impedance spectra of DSSCs based on dyads P-tg-P' (red color lines) and P-tNp-P' (black color lines), measured with a bias voltage of 0.66 V under dark conditions



**Scheme 4.** Binding sites that are placed on the dyads

cooperative electron transfer to the TiO<sub>2</sub> surface and more efficient electron injection (as evidenced by the longer electron lifetime and higher charge recombination resistance).

The different efficiencies of the P-tg-P' and P-tNp-P'-sensitized solar cells may also be attributed to energy related factors, *i.e.* transfer of absorbed solar energy from the porphyrin units to the TiO<sub>2</sub> CB. Assuming that each transfer between the porphyrin units and the triazine group is associated with a minimum energy requirement  $\Delta E_i$ ,  $i = 1, 2$ , (Scheme 4), the electron injection into the TiO<sub>2</sub> CB would be more energetically demanding for the solar cell based on P-tNp-P' (due to the presence of only one carboxylic acid anchoring group) and would lead to a lower photovoltaic performance than the P-tg-P'-based DSSC.

## CONCLUSION

In summary, we have designed and synthesized two porphyrin dyads P-tg-P' and P-tNp-P' with the D- $\pi$ -A molecular architecture, which contain two and

one carboxylic acid anchoring units, respectively. The synthesis of the compounds was achieved *via* temperature dependent amination reactions of cyanuric chloride. Photophysical and electrochemical studies suggest that the dyads have suitable frontier orbital energies in order to be used as sensitizers in DSSCs. The DSSC sensitized by P-tg-P' showed a better photovoltaic performance with an overall PCE of 5.44% compared to the P-tNp-P'-based solar cell which showed a PCE of 4.15%. The higher PCE value of the P-tg-P' sensitized solar cell results from its enhanced photovoltaic parameters, *i.e.* short circuit current ( $J_{sc}$ ), open circuit voltage ( $V_{oc}$ ), and fill factor ( $FF$ ) values, as well as a larger dye loading. This is attributed to the more effective binding of P-tg-P' onto the TiO<sub>2</sub> surface of the photoanode, due to the fact that it contains two carboxylic acid anchoring groups (compared to one carboxylic acid anchoring group of P-tNp-P'), which lead to a longer electron lifetime ( $\tau_e$ ) and larger recombination resistance.

### Supporting information

Cartesian coordinates, total and partial density of states of structures, and theoretically calculated UV-vis spectra of **4a** and **4b**, <sup>1</sup>H NMR and <sup>13</sup>C NMR spectra of **3a**, **4a**, **3b**, and **4b**, square-wave voltammograms of **4a** and **4b** are given in the supplementary material. This material is available free of charge *via* the Internet at <http://www.worldscinet.com/jpp/jpp.shtml>.

### Acknowledgements

Financial support from the European Commission (FP7-REGPOT-2008-1, Project BIOSOLENUTI no. 229927) is greatly acknowledged. This research has also been co-financed by the European Union (European Social Fund) and Greek national funds (Heraklitos II) through the Operational Program "Education and Lifelong Learning" of the National Strategic Reference Framework Research Funding Program (THALIS-UOA-MIS 377252).

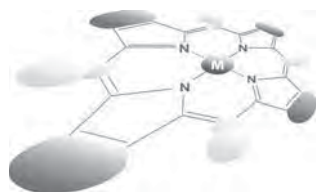
### REFERENCES

- (a) O'Regan B and Grätzel M. *Nature* 1991; **353**: 737–740. (b) Kazim S, Nazeeruddin MK, Grätzel M and Ahmad S. *Angew. Chem. Int. Ed.* 2014; **53**: 2812–2824. (c) Nayak PK and Cahen D. *Adv. Mater.* 2014; **26**: 1622–1628.
- (a) Chen CY, Wang MK, Li JY, Pootrakulchote N, Alibabaei L, Ngoc-le CH, Decoppet JD, Tsai JH, Grätzel C, Wu CG, Zakeeruddin SM and Grätzel M. *ACS Nano* 2009; **3**: 3103–3109. (b) Cao K, Lu JF, Cui J, Shen Y, Chen W, Alemu G, Wang Z, Yuan HL, Xu J, Wang MK and Cheng YB. *J. Mater. Chem. A* 2014; **2**: 4945–4953. (c) Han L, Islam A, Chen H, Malapaka C, Chiranjeevi B, Zhang S, Yang X and Yanagida M. *Energy Environ. Sci.* 2012; **5**: 6057–6060.
- (a) Mishra A, Fischer MKR and Bauerle P. *Angew. Chem. Int. Ed.* 2009; **48**: 2474–2499. (b) Cao K and Wang MK. *Front. Optoelectron.* 2013; **6**: 373–385. (c) Singh SP, Roy MS, Thomas KRJ, Balaiah S, Bhanuprakash K and Sharma GD. *J. Phys. Chem. C* 2012; **116**: 5941–5950. (d) Haid S, Marszalek M, Mishra A, Wielopolski M, Teuscher J, Zakeeruddin SM, Grätzel M and Bäuerle P. *Adv. Funct. Mater.* 2012; **22**: 1291–1302. (e) Kim B-G, Chung K and Kim J. *Chem.–Eur. J.* 2013; **19**: 5220–5230. (f) Qin C, Wong W-Y and Han L. *Chem.–Asian J.* 2013; **8**: 1706–1719. (g) Chang S, Wang H, Hua Y, Li Q, Xiao X, Wong W-K, Wong WY, Zhu X and Chen T. *J. Mater. Chem. A* 2013; **1**: 11553–11558. (h) Hua Y, Chang S, Huang D, Zhou X, Zhu X, Zhao J, Chen T, Wong W-Y and Wong W-K. *Chem. Mater.* 2013; **25**: 2146–2153.
- Robertson N. *Angew. Chem. Int. Ed.* 2006; **45**: 2338–2345.
- Hasobe T, Imahori H, Kamat PV, Ahn TK, Kim SK, Kim D, Fujimoto A, Hirakawa T and Fukuzumi S. *J. Am. Chem. Soc.* 2005; **127**: 1216–1228.
- (a) Li LL and Diau EWG. *Chem. Soc. Rev.* 2013; **42**: 291–304. (b) Pellejà L, Kumar CV, Clifford JN and Palomares E. *J. Phys. Chem. C* 2014; **118**: 16504–16509. (c) Yella A, Mai C-L, Zakeeruddin SM, Chang S-N, Hsieh C-H, Yeh C-Y and Grätzel M. *Angew. Chem. Int. Ed.* 2014; **53**: 1–6. (d) Imahori H, Umeyama T and Ito S. *Acc. Chem. Res.* 2009; **42**: 1809–1818. (e) Walter MG, Rudine AB and Wamser CC. *J. Porphyrins Phthalocyanines* 2010; **14**: 759–792. (f) Liu Y, Lin H, Dy JT, Tamaki K, Nakazaki J, Nakayama D, Uchida S, Kubo T and Segawa H. *Chem. Commun.* 2011; **47**: 4010–4012. (g) Imahori H, Matsubara Y, Iijima H, Umeyama TH, Matano Y, Ito S, Niemi M, Tkachenko NV and Lemmetyinen H. *J. Phys. Chem. C* 2010; **114**: 10656–10665. (h) Wang Y, Li X, Liu B, Wu W, Zhua W and Xie Y. *RSC Adv.* 2013; **3**: 14780–14790. (i) Lu J, Liu S, Li H, Shen Y, Xu J, Cheng Y and Wang M. *J. Mater. Chem. A* 2014; **2**: 17495–17501.
- Kurotobi K, Toude Y, Kawamoto K, Fujimori Y, Ito S, Chabera P, Sundström V and Imahori H. *Chem.–Eur. J.* 2013; **19**: 17075–17081. (b) Ball JM, Davis NKS, Wilkinson JD, Kirkpatrick J, Teuscher J, Gunning R, Anderson HL and Snaith HJ. *RSC Adv.* 2012; **2**: 6846–6853. (c) Luo J, Xu MF, Li RZ, Huang KW, Jiang CY, Qi QB, Zeng WD, Zhang J, Chi CY, Wang P and Wu JS. *J. Am. Chem. Soc.* 2014; **136**: 265–272.
- Lee CW, Lu HP, Lan CM, Huang YL, Liang YR, Yen WN, Liu YC, Lin YS, Diau EWG and Yeh CY. *Chem.–Eur. J.* 2009; **15**: 1403–1412.
- Bessho T, Zakeeruddin SM, Yeh CY, Diau EWG and Grätzel M. *Angew. Chem. Int. Ed.* 2010; **49**: 6646–6649.
- Yella A, Lee HW, Tsao HN, Yi C, Chandiran AK, Nazeeruddin MK, Diau EWG, Yeh CY, Zakeeruddin SM and Grätzel M. *Science* 2011; **334**: 629–634.

11. Mathew M, Yella A, Humphry-Baker PR, Curchod BFE, Ashari-Astani N, Tavernelli I, Rothlisberger U, Nazeeruddin MK and Grätzel M. *Nat. Chem.* 2014; **6**: 242–247.
12. Angiolillo PJ, Lin VSY, Vanderkooi JM and Therien MJ. *J. Am. Chem. Soc.* 1995; **117**: 12514–12527.
13. Mozer AJ, Griffith MJ, Tsekouras G, Wagner P, Wallace GG, Mori S, Sunahara K, Miyashita M, Earles JC, Gordon KC, Du LC, Katoh R, Furube A and Officer DL. *J. Am. Chem. Soc.* 2009; **131**: 15621–15623.
14. (a) Park JK, Chen JP, Lee HR, Park SW, Shinokubo H, Osuka A and Kim D. *J. Phys. Chem. C* 2009; **113**: 21956–21963. (b) Martinson ABF, Hamann TW, Pellin MJ and Hupp JT. *Chem.–Eur. J.* 2008; **14**: 4458–4467. (c) Tsuda A and Osuka A. *Science* 2001; **293**: 79–82.
15. (a) Zhong H, Xu E, Zeng D, Du J, Sun J, Ren S, Jiang B and Fang Q. *Org. Lett.* 2008; **10**: 709–712. (b) Pang J, Tao Y, Freiberg S, Yang XP, D'Iorio M and Wang S. *J. Mater. Chem.* 2002; **12**: 206–212. (c) Kang JW, Lee DS, Park HD, Park YS, Kim JW, Jeong WI, Yoo KM, Go K, Kim SH and Kim JJ. *J. Mater. Chem.* 2007; **17**: 3714–3719. (d) Kulkarni AP, Tonzola CJ, Babel A and Jenekhe SA. *Chem. Mater.* 2004; **16**: 4556–4573.
16. Luechai A, Gasiorowski J, Petsom A, Neugebauer H, Sariciftci NS and Thamyongkit P. *J. Mater. Chem.* 2012; **22**: 23030–23037.
17. Sharma GD, Zervaki GE, Angaridis PA, Kitsopoulos TN and Coutsolelos AG. *J. Phys. Chem. C* 2014; **118**: 5968–5977.
18. Liu J, Wang K, Zhnag X, Li C and You X. *Tetrahedron* 2013; **69**: 190–200.
19. (a) Zervaki GE, Roy MS, Panda MK, Angaridis PA, Chrissos E, Sharma GD and Coutsolelos AG. *Inorg. Chem.* 2013; **52**: 9813–9825. (b) Zervaki GE, Angaridis PA, Koukaras EN, Sharma GD and Coutsolelos AG. *Inorg. Chem. Front.* 2014; **1**: 256–270.
20. Zervaki GE, Papastamatakis E, Angaridis PA, Singh M, Kurchania R, Kitsopoulos TN, Sharma GD and Coutsolelos AG. *Eur. J. Inorg. Chem.* 2014; **6**: 1020–1033.
21. Ladomenou K, Lazarides T, Panda MK, Charalambidis G, Daphnomili D and Coutsolelos AG. *Inorg. Chem.* 2012; **51**: 10548–10556.
22. Perdew JP, Burke K and Ernzerhof M. *Phys. Rev. Lett.* 1996; **77**: 3865–3868.
23. Schäfer A, Huber C and Ahlrichs R. *J. Chem. Phys.* 1994; **100**: 5829–5835.
24. Eichkorn K, Treutler O, Öhm H, Häser M and Ahlrichs R. *Chem. Phys. Lett.* 1995; **240**: 283–290.
25. Adamo C and Barone V. *J. Chem. Phys.* 1999; **110**: 6158–6169.
26. (a) Becke AD. *J. Chem. Phys.* 1993; **98**: 5648–5652. (b) Lee C, Yang W and Parr RG. *Phys. Rev. B* 1988; **37**: 785–789.
27. *TURBOMOLE* (version 5.6), Universität Karlsruhe: 2000.
28. Frisch MJ, Trucks GW, Schlegel HB, Scuseria GE, Robb MA, Cheeseman JR, Scalmani G, Barone V, Mennucci B, Petersson GA, Nakatsuji H, Caricato M, Li X, Hratchian HP, Izmaylov AF, Bloino J, Zheng G, Sonnenberg JL, Hada M, Ehara M, Toyota K, Fukuda R, Hasegawa J, Ishida M, Nakajima T, Honda Y, Kitao O, Nakai H, Vreven T, Montgomery Jr JA, Peralta JE, Ogliaro F, Bearpark M, Heyd JJ, Brothers E, Kudin KN, Staroverov VN, Kobayashi R, Normand J, Raghavachari K, Rendell A, Burant JC, Iyengar SS, Tomasi J, Cossi M, Rega N, Millam JM, Klene M, Knox JE, Cross JB, Bakken V, Adamo C, Jaramillo J, Gomperts R, Stratmann RE, Yazyev O, Austin AJ, Cammi R, Pomelli C, Ochterski JW, Martin RL, Morokuma K, Zakrzewski VG, Voth GA, Salvador P, Dannenberg JJ, Dapprich S, Daniels AD, Farkas Ö, Foresman JB, Ortiz JV, Cioslowski J and Fox DJ. *Gaussian 03* (revision C.01), Gaussian, Inc.: Wallingford CT, 2004.
29. Löwik DWPM and Lowe CR. *Eur. J. Org. Chem.* 2001; **15**: 2825–2839.
30. (a) Steffensen MB and Simanek EE. *Org. Lett.* 2003; **5**: 2359–2361. (b) Zhang W and Simanek EE. *Org. Lett.* 2000; **2**: 843–845.
31. (a) Carofiglio T, Varotto A and Tonellato U. *J. Org. Chem.* 2004; **69**: 8121–8124. (b) Ichihara K and Naruta Y. *Chem. Lett.* 1995; **8**: 631–632. (c) Carofiglio T, Lubian E, Menegazzo I, Saielli G and Varotto A. *J. Org. Chem.* 2009; **74**: 9034–9043. (d) Lazarides T, Charalambidis G, Vuillamy A, Reglier M, Klontzas E, Froudakis G, Kuhri S, Guldi DM and Coutsolelos AG. *Inorg. Chem.* 2011; **50**: 8926–8936.
32. (a) Lin CY, Wang YC, Hsu SJ, Lo CF and Diao EWG. *J. Phys. Chem. C* 2010; **114**: 687–693. (b) Lin CY, Lo CF, Luo L, Lu HP, Hung CS and Diao EWG. *J. Phys. Chem. C* 2009; **113**: 755–764. (c) Lo CF, Luo L, Diao EWG, Chang IJ and Lin CY. *Chem. Commun.* 2006; **13**: 1430–1432.
33. He H, Gurung A, Si L and Sykes AG. *Chem. Commun.* 2012; **48**: 7619–7621.
34. Hagfeldt A, Boschloo G, Sun L, Kloo L and Pettersson H. *Chem. Rev.* 2010; **110**: 6595–6663.
35. Snaith HJ. *Adv. Funct. Mater.* 2010; **20**: 13–19.
36. Imahori H, Iijima H, Hayashi H, Toude Y, Umeyama T, Matano Y and Ito S. *Chem. Sus. Chem.* 2011; **4**: 797–805.
37. Warnan J, Favereau L, Meslin F, Severac M, Blart E, Pellegrin Y, Jacquemin D and Odobel F. *ChemSusChem* 2012; **5**: 1568–1577.



38. Jacquemin D, Perpète EA, Scuseria GE, Ciofini I and Adamo C. *J. Chem. Theory Comput.* 2008; **4**: 123–135.
39. Wong BM. *J. Phys. Chem. C* 2009; **113**: 21921–21927.
40. Nazeeruddin MK, Angelis FD, Fantacci S, Selloni A, Viscardi G, Liska P, Ito S, Takeru B and Grätzel M. *J. Am. Chem. Soc.* 2005; **127**: 16835–16847.
41. Pastore M and Angelis FD. *J. Phys. Chem. Lett.* 2013; **4**: 956–974.
42. (a) Wang Q, Moser JE and Grätzel M. *J. Phys. Chem. B* 2005; **109**: 14945–14953. (b) Halme J, Vahermaa P, Miettunen K and Lund P. *Adv Mater.* 2010; **22**: E210–E234.



# Optical limiting and singlet oxygen generation properties of phosphorus triazatetrabenzcorroles

Colin Mkhize, Jonathan Britton<sup>◇</sup>, John Mack<sup>◇</sup> and Tebello Nyokong<sup>\*◇</sup>

Department of Chemistry, Rhodes University, Grahamstown 6140, South Africa

Dedicated to Professor Shunichi Fukuzumi on the occasion of his retirement

Received 27 October 2014

Accepted 7 November 2014

**ABSTRACT:** Novel phosphorus triazatetrabenzcorrole (TBC) tetrasubstituted at the  $\alpha$ - and  $\beta$ -positions of the peripheral fused benzene rings with *t*-butylphenoxy substituents have been prepared and characterized. The effect of the substituents on the electronic structures and optical properties is investigated with TD-DFT calculations and MCD spectroscopy. The optical limiting properties have been investigated to examine whether the lower symmetry that results from the direct pyrrole–pyrrole bond and hence the permanent dipole moment that is introduced result in higher safety thresholds, relative to the values that have been reported for phthalocyanines. The suitability of the compounds for singlet oxygen applications has also been examined.

**KEYWORDS:** triazatetrabenzcorrole, singlet oxygen, optical limiting, MCD spectroscopy.

## INTRODUCTION

Triazatetrabenzcorroles (TBCs) are a relatively recent addition to the low-symmetry phthalocyanine analog family [1]. When Pc complexes are prepared in the presence of a reducing agent, the phthalocyanine ligand can lose an aza-nitrogen atom to instead form a triazatetrabenzcorrole (TBC) complex. Due to their smaller cavity size, TBCs have been shown to preferentially incorporate main group element ions of high oxidative state such as P(V), Ge(IV) and Si(IV) [2, 3]. The formation of Sn(III) and Rh(III) TBCs [4, 5] has also been reported. The first example of a phosphorus TBC complex was reported by Gouterman and coworkers in 1981 [6], but was incorrectly characterized as a P<sup>III</sup>Pc complex. Subsequently in 1986, Fujiki demonstrated that this complex was actually a P<sup>V</sup>TBC [7]. The structure and properties of P<sup>V</sup>TBC were later elucidated by Liu *et al.* [8] and Goldberg and coworkers [9], while those of P<sup>III</sup>TBCs in cold concentrated H<sub>2</sub>SO<sub>4</sub> have been investigated by Jianbo *et al.* [10]. The optical properties of TBCs differ markedly from those of Pcs.

There is a narrowing and red shift of the B-band to *ca.* 450 nm and three intense bands are observed in the Q region between 580–700 nm, which have been used to monitor the formation of the compound [11]. Since the Q-band lies at the edge of the optical window for tissue penetration, TBC complexes are potentially suitable for use as photosensitizers in photodynamic therapy (PDT). In the context of PDT research, TBCs can be regarded as a fourth generation derivative of the porphyrin family. P<sup>V</sup>TBC derivatives have been reported to have moderately high singlet oxygen quantum yields [8, 10]. Oxophosphorus triazatetrabenzcorroles have also been shown to possess good photodynamic efficiency toward HeLa cells [12]. To further explore the utility of TBCs for biomedical applications, we recently reported a study of the photocytotoxicity of a novel P<sup>V</sup>TBC complex with eight peripheral *t*-butylphenoxy substituents [13], after a very high singlet oxygen quantum yield value had been reported by Kobayashi and coworkers [14]. In this paper, the photophysical and singlet oxygen generation properties of  $\beta$ -octa- and  $\beta$ -tetrasubstituted isomers are compared to those of  $\alpha$ -tetrasubstituted isomers.

Interest in the P<sup>V</sup>TBC compounds extends beyond their possible utility for PDT. The C<sub>2v</sub> symmetry of TBC ligand results in a permanent electric dipole, which makes

<sup>◇</sup>SPP full member in good standing

\*Correspondence to: Tebello Nyokong, email: t.nyokong@ru.ac.za, fax: +27 46-603-8801

TBCs possible candidates for third order nonlinear optics research, since this requires an electric dipole within the active moiety. Optical limiting (OL) materials have become the subject of considerable research interest due to the need to protect human eyes and sensitive optical devices from high intensity light sources such as lasers [15–18]. When exposed to very intense light, OL materials limit the output energy of the emerging beam, due to their excited triplet state becoming more populated than their ground state resulting in what is known as reverse saturable absorption (RSA) when there is strong triplet–triplet absorption. Although the OL properties of many organic molecules have been examined, in recent years an increasing amount of research has been carried out on phthalocyanines and their derivatives due to the high absorption cross section ratio of the triplet excited state relative to the ground state in the 400–600 nm region, which includes the second harmonic of the Nd:YAG laser at 532 nm that is often utilized in laser applications [19–22]. The nonlinear optical (NLO) properties of MPCs have been modified by substituting different metal atoms into the ring or altering the peripheral and axial functionalities [23–26]. The large singlet oxygen quantum yields that have been reported suggest that the triplet state quantum yields should also be very high. Although P<sup>V</sup>TBC complexes possess the properties that are normally required to form a good optical limiter, little work has been done to quantify their suitability for OL applications [27]. In this paper, the OL properties of novel  $\alpha$ - and  $\beta$ -tetrasubstituted dihydroxyphosphorus(V) TBCs (Scheme 1) are examined along with those of the corresponding  $\beta$ -octasubstituted TBC that was studied previously with the Shen group [13].

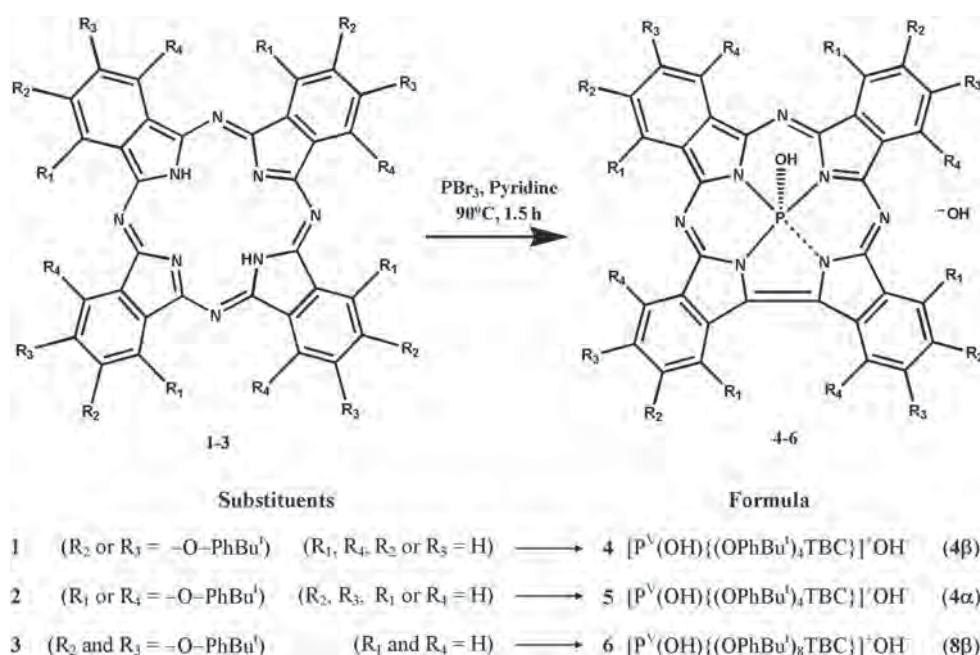
## EXPERIMENTAL

### Materials

Pyridine was purchased from Sigma–Aldrich and dried using molecular sieves (0.4 nm, rods). Spectroscopic grade dimethyl sulfoxide (DMSO) and silica gel were purchased from Merck. Reagent grade chloroform, dichloromethane and methanol were obtained from Minema. Phosphorus tribromide, phosphorus oxybromide, Poly(bisphenol A carbonate)(PBC), average molecular weight ~28,200 g/mol were purchased from Sigma–Aldrich. The unmetallated phthalocyanines (**1–3**) were synthesized according to literature methods [28].

### Equipment

Electronic absorption spectra were recorded on a Shimadzu UV-2550 spectrophotometer. Magnetic circular dichroism (MCD) spectra were measured with a Chirascan plus spectrodichrometer equipped with a 1 T (tesla) permanent magnet by using both the parallel and antiparallel fields. The conventions of Piepho and Schatz are used to describe the sign of the MCD signal and the Faraday terms [29]. Fluorescence emission and excitation spectra were collected on a Varian Eclipse spectrofluorimeter. The absorbance ranged between 0.04 and 0.05 at the excitation wavelength for all samples. Infra-red spectra were collected on a Perkin–Elmer Universal ATR Sampling accessory spectrum 100 FT-IR spectrometer. Fluorescence lifetimes were measured with a FluoTime 300 EasyTau spectrometer (PicoQuant GmbH) using a time correlated single photon counting



Scheme 1. Synthetic pathway for forming the triazetetraazacorroles

(TCSPC) technique. The samples were excited at 670 nm with a diode laser (LDH-P-670, 20 MHz repetition rate, 44 ps pulse width, PicoQuant GmbH). The detector employed was a Peltier cooled Photomultiplier (PMA-C 192-M, PicoQuant GmbH).  $^1\text{H}$  NMR spectra were obtained using a Bruker AVANCE 600 MHz NMR spectrometer in DMSO- $d_6$ . Elemental analyses were done using a Vario-Elementar Microcube ELIII, while mass spectra data were collected in the positive ion mode with  $\alpha$ -cyanocinamic acid as the matrix on a Bruker AutoFLEX III Smart-beam TOF/TOF mass spectrometer. Scanning electron microscope (SEM) images were recorded using a TESCAN Vega TS 5136LM microscope.

An ultra sensitive germanium detector (Edinburgh Instruments, El-P) combined with a 1000 nm long pass filter (Omega, RD 1000 CP) and a 1270 nm band-pass filter (Omega, C1275, BP50) was used to detect the phosphorescence decay of singlet oxygen at 1270 nm. Measurements were made in the presence and absence of sodium azide ( $\text{NaN}_3$ ) as a physical quencher for singlet oxygen. DMSO solutions of **4** and **5** were excited using a Quanta-Ray Nd:YAG laser providing 400 mJ, 9 ns pulses of laser light at 10 Hz pumping a Lambda-Physik FL3002 dye (Pyridin 1 dye in methanol). The same laser setup was used for the determination of triplet decay kinetics as has been described previously [30]. All Z-scan experiments described in this study were performed using a frequency-doubled Quanta-Ray Nd:YAG laser as the excitation source. The laser was operated in a near Gaussian transverse mode at 532 nm (second harmonic), with a pulse repetition rate of 10 Hz and energy range of 0.1  $\mu\text{J}$ –0.1 mJ, limited by the energy detectors (Coherent J5–09). The low repetition rate of the laser prevents cumulative thermal nonlinearities. The beam was spatially filtered to remove higher order modes and tightly focused with a 15 cm focal length lens. No damage was detected between runs when the sample was moved or replaced.

### General procedure for synthesis of phosphorus(V) triazatetrabenzcorroles

A solution of 0.2 mL  $\text{PBr}_3$  in 2 mL pyridine was added to a suspension of free base phthalocyanine (**1**, **2**) (57.5 mg, 0.052 mmol) in 15 mL pyridine. This was refluxed at 90 °C for 1.5 h under an inert atmosphere. The product was cooled to about 20 °C and was poured into water and then filtered. The precipitate was washed with 3  $\times$  30 mL methanol and then purified further on a silica column, with the product of interest coming out following elution with a 7:3 chloroform/MeOH solvent system.

**Dihydroxyphosphorus(V) (2, 9(or 10), 16(or 17), 23(or 24)-*t*-butylphenoxy)triazatetrabenzcorrole (4).** A dark green product was obtained. Yield 40.3 mg (68%). Anal. calcd. for  $\text{C}_{72}\text{H}_{66}\text{N}_7\text{O}_6\text{P}\cdot 12\text{H}_2\text{O}$ : C, 62.91; H, 6.75; N, 7.13. Found C, 62.25; H, 5.89; N, 7.33. UV-vis (DMSO):  $\lambda_{\text{max}}$ , nm (log  $\epsilon$ ) 664 (4.82), 632 (4.55), 602

(4.31), 448 (5.09), 419 (4.68). IR:  $\nu_{\text{max}}$ ,  $\text{cm}^{-1}$  3306 (O–H), 3071 (aromatic C–H), 2957, 2924 (aromatic C–H), 1596, 1504 (C–C); 1274, 1239, 1171, 1106 (C–O–C), 1359, 1014 (C–N), 958, 876, 825, 747, 680 (TBC skeletal).  $^1\text{H}$  NMR ( $\text{CDCl}_3$ ):  $\delta_{\text{H}}$ , ppm 7.36–7.48 (12H, m, Pc-H), 6.83–7.19 (16H, m, Phenyl-H), 2.21 (2H, s, O–H), 1.22–1.40 (36H, m, methyl-H). MS (MALDI-TOF):  $m/z$  (calcd. for  $[\text{M} + \text{H}]^+$  1140.3; found 1141.8).

**Dihydroxyphosphorus(V) (1, 8(or 11), 15(or 18), 22(or 25)-*t*-butylphenoxy)triazatetrabenzcorrole (5).** The final product was dark green. Yield 27.8 mg (47%). Anal. calcd. for  $\text{C}_{72}\text{H}_{66}\text{N}_7\text{O}_6\text{P}\cdot 4\text{H}_2\text{O}$ : C, 69.27; H, 6.30; N, 7.85. Found C, 69.75; H, 6.15; N, 7.30. UV-vis (DMSO):  $\lambda_{\text{max}}$ , nm (log  $\epsilon$ ) 676 (4.98), 632 (4.55), 602 (4.31), 448 (5.09), 419 (4.68). IR:  $\nu_{\text{max}}$ ,  $\text{cm}^{-1}$  1610, 1574, 1506, 1483 (aromatic C–C stretch), 1249, 1214, 1174, 1129 (C–O–C), (C–O), 1342 (C–N), 1054 (C–H bend), 3027 (aromatic C–H), 2958 (alkyl C–H), 886, 826, 746, 723, 682 (TBC skeletal).  $^1\text{H}$  NMR ( $\text{CDCl}_3$ ):  $\delta_{\text{H}}$ , ppm 7.38–7.54 (16H, m, Phenyl-H), 6.72–7.12 (12H, m, Pc-H), 2.1 (2H, s, OH) 0.81–1.49 (36H, m, methyl-H). MS (MALDI-TOF):  $m/z$  (calcd. for  $[\text{M} - 3\text{H}]^+$  1140.3; found 1137.6).

### Preparation of thin films of 4 and 5

Solutions of  $\alpha$ - and  $\beta$ -tetrasubstituted TBCs with Q-band absorbances of 1.5 were prepared in dichloromethane. 0.5 g of PBC was added to 5 mL of these solutions. The film was prepared by placing 1 mL of the PBC/TBC solution in a small glass petri dish (diameter = 5 cm), and placing it under vacuum ( $\sim 10^{-3}$  Torr) until the solvent was completely removed.

### Theoretical calculations

Geometry optimization and TD-DFT calculations were carried out using the B3LYP functional of the Gaussian09 software packages [31] with 6-31G(d) basis sets. The B3LYP optimized geometries were then used to carry out TD-DFT calculations using the Coulomb-attenuated B3LYP (CAM-B3LYP) functional with 6-31G(d) basis sets. The CAM-B3LYP functional was used to calculate the electronic absorption properties based on the time-dependent (TD-DFT) method, since it includes a long-range correction of the exchange potential, which incorporates an increasing fraction of Hartree–Fock (HF) exchange as the interelectronic separation increases. This has been demonstrated to make it more suitable for studying porphyrinoid compounds where there is significant charge transfer in the electronic excited states [32, 33] as is likely to be the case with TBC complexes.

### Nonlinear optical parameters

Z-scan experiments were performed according to the method described by Sheik–Bahae [34–36]. Assuming

a Gaussian-shaped spatial and temporal pulse, and using the open aperture Z-scan theory for multi-photon absorption (*n*PA) that was reported by Sutherland *et al.* [37], the general expression for open aperture normalized transmittance can be written as:

$$T_{OA(2PA)} = \frac{1}{1 + \beta_2 L_{\text{eff}} (I_{00} / (1 + (z/z_0)^2))} \quad (1)$$

where  $I_{00}$  is the on-focus intensity (peak input intensity),  $\beta_2$  is the two photon absorption coefficient,  $L_{\text{eff}}$ ,  $z$  and  $z_0$  are the effective pathlength in the sample, the translation distance of the sample relative to the focus and the Rayleigh length respectively. The Rayleigh length is defined as  $\pi w_0^2/\lambda$  where  $\lambda$  is the wavelength of the laser and  $w_0$  is the beam waist at the focus, ( $z = 0$ ).  $L_{\text{eff}}$  is given by:

$$L_{\text{eff}} = \frac{1 - e^{-\alpha L}}{\alpha} \quad (2)$$

where  $\alpha$  is the linear absorption coefficient.

The imaginary component of the third order susceptibility ( $\text{Im}[\chi^{(3)}]$ ) is given by [38]:

$$I_m[\chi^{(3)}] = n^2 \epsilon_0 c \lambda \beta_2 / 2\pi \quad (3)$$

where  $n$  and  $c$  are the linear refractive index and the speed of light respectively,  $\epsilon_0$  is the permittivity of free space,  $\lambda$  and  $\beta_2$  terms are as described above.

Second order hyperpolarizability ( $\gamma$ ) of the material was determined using [38]:

$$\gamma = \frac{\text{Im}[\chi^{(3)}]}{f^4 C_{\text{mol}} N_A} \quad (4)$$

where  $N_A$  is the Avogadro constant,  $C_{\text{mol}}$  is the concentration of the active species in the triplet state per mole and  $f$  is the Lorentz local field factor given as,  $f = (n^2 + 2)/3$ .

## RESULTS AND DISCUSSION

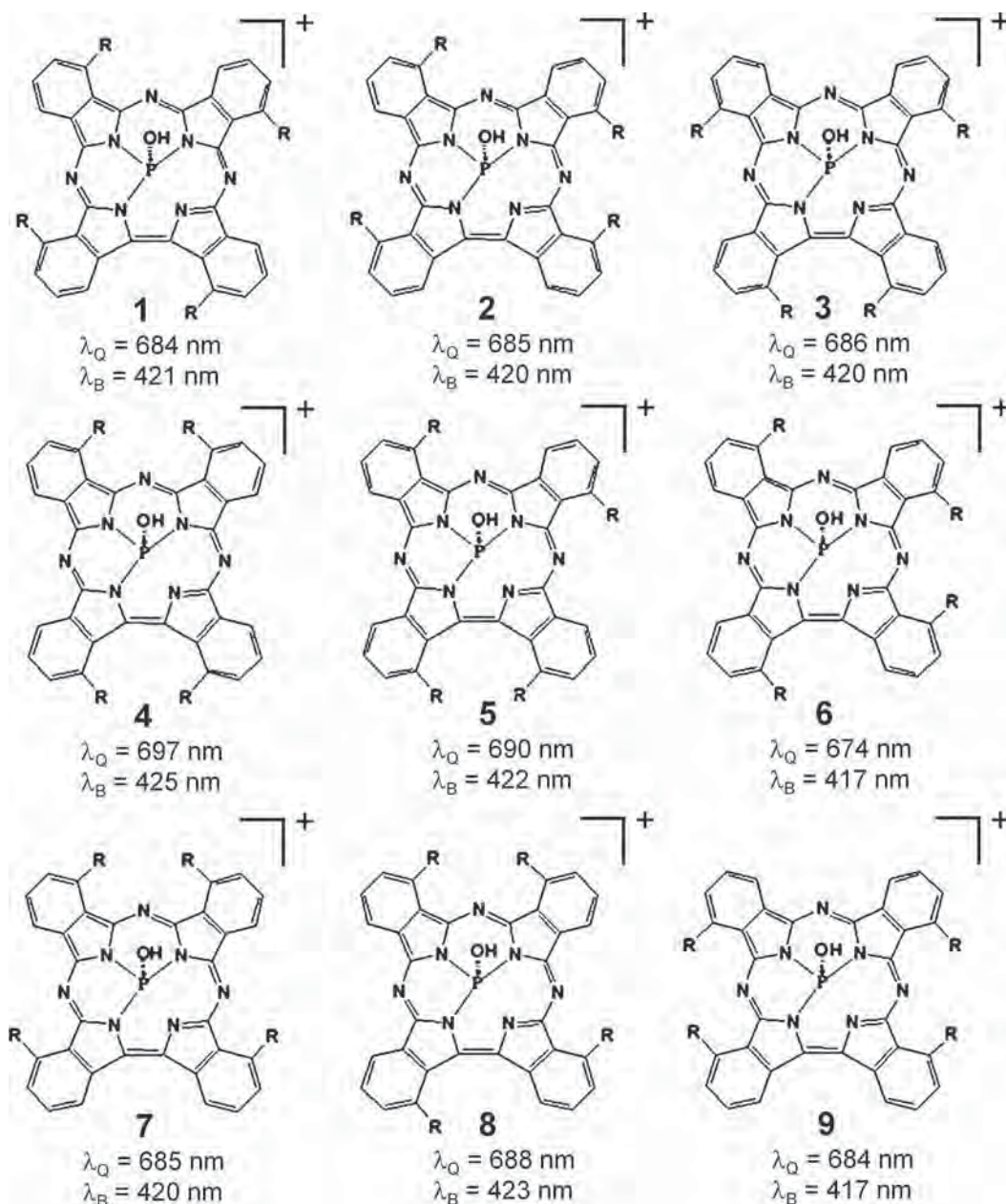
### Synthesis and characterization

Scheme 1 shows the synthetic pathway for compounds **4–6** using starting materials **1–3**. The full characterization of **6** has been reported previously [13]. Although only one isomer is possible for **6**, mixtures of positional isomers are likely to be formed for tetra-substituted complexes **4** and **5**. Kobayashi's use of  $\alpha$ - and  $\beta$ -terminology [1] to refer to substitution at the non-peripheral and peripheral positions of the benzo rings, respectively, is used throughout. No attempt has been made to further separate the positional isomers by column chromatography. As has been reported previously for phthalocyanines [1], positional isomerism

is not likely to make a significant difference to the optical spectroscopy in the context of  $\beta$ -substitution, since there is no scope for steric hindrance between neighboring substituents and there are small MO coefficients on the peripheral carbons of the benzo rings on the frontier  $\pi$ -MOs, but is likely to have a larger effect in the context of  $\alpha$ -substitution (Fig. 1). The novel P<sup>V</sup>TBC compounds were analyzed using elemental analysis, NMR, magnetic circular dichroism and -IR spectroscopy and MALDI-TOF mass spectrometry. All theoretical predictions were made assuming that only one hydroxyl group was axially coordinated to the phosphorus central atom, as was recently reported for **6** based on the analysis of <sup>31</sup>P NMR spectral data [13] in the manner that had earlier been carried out for other P<sup>V</sup>TBCs by Goldberg and coworkers [9].

### Optical spectroscopy and TD-DFT calculations

Electronic absorption spectroscopy is one of the most useful methods for characterizing Pcs and its analogs, due to the presence of the intense Q and B-bands of Gouterman's 4-orbital model [39] in the 600–750 and 300–400 nm regions, respectively. Magnetic circular dichroism (MCD) spectroscopy can be used to identify the main electronic Q(0,0) and B(0,0) bands of porphyrinoids, due to the presence of intense Faraday  $\mathcal{A}_1$  terms or coupled pairs of oppositely-signed Faraday  $\mathcal{B}_0$  terms [1, 40]. A C<sub>16</sub>H<sub>16</sub><sup>2+</sup> cyclic polyene corresponding to the inner ligand perimeter can be regarded as being the parent perimeter for describing and rationalizing the optical properties. The  $\pi$ -system contains a series of MOs arranged in ascending energy with  $M_L = 0, \pm 1, \pm 2, \pm 3, \pm 4, \pm 5, \pm 6, \pm 7$  and 8 nodal properties based on the magnetic quantum number for the cyclic perimeter,  $M_L$ . The frontier  $\pi$ -MOs have  $M_L = \pm 4$  and  $\pm 5$  nodal properties, respectively. The four spin-allowed  $M_L = \pm 4 \rightarrow \pm 5$  excitations give rise to two orbitally degenerate <sup>1</sup>E<sub>u</sub> excited states, on the basis of the  $\Delta M_L = \pm 9$ , and  $\Delta M_L = \pm 1$  transitions. This results in the forbidden and allowed Q and B-bands of Gouterman's 4-orbital model for porphyrins [39], since an incident photon can provide only one quantum of orbital angular momentum. Michl [41] introduced an **a**, **s**, **-a** and **-s** terminology (Fig. 2) for the four MOs derived from the HOMO and LUMO of the parent perimeter so that  $\pi$ -systems of porphyrinoids with differing molecular symmetry such as Pcs and TBCs and relative orderings of the four frontier  $\pi$ -MOs in energy terms can be readily compared. One MO derived from the HOMO of a C<sub>16</sub>H<sub>16</sub><sup>2+</sup> parent hydrocarbon perimeter and another derived from the LUMO have nodal planes which coincide with the *yz*-plane and are referred to, respectively, as the **a** and **-a** MOs, while the corresponding MOs with antinodes on the *yz*-plane are referred to as the **s** and **-s** MOs (Fig. 2). Since the **a** and **s** MOs have angular nodal planes on alternating sets of atoms, the incorporation of the

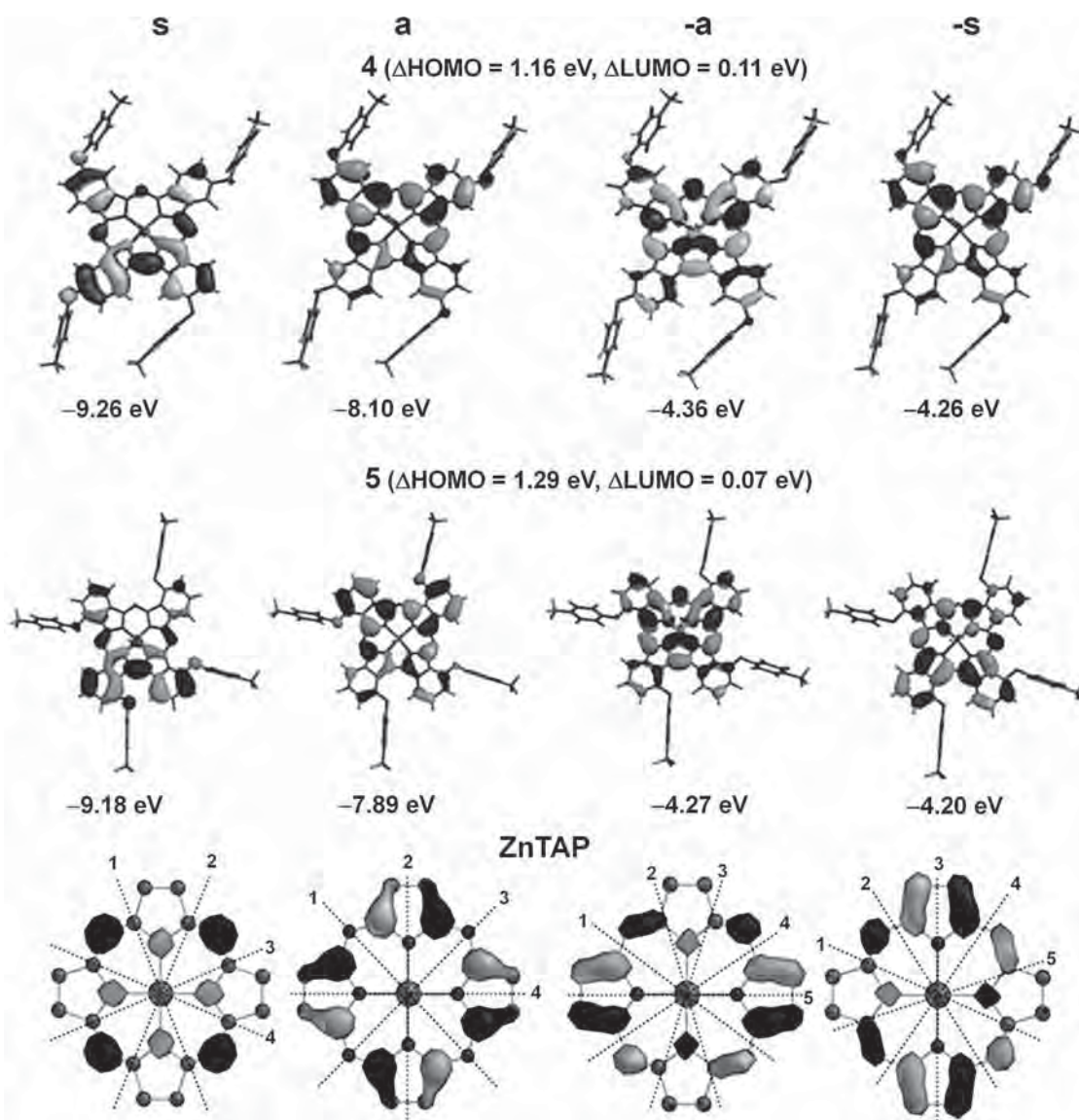


**Fig. 1.** Structures of the nine positional isomers of the  $\alpha$ -tetrasubstituted TBC (**5**) with the calculated values for the more intense Q and B-band components

aza-nitrogen atoms have a much larger stabilizing effect on the energy of the *s* MO resulting in a large separation of the *a* and *s* MOs (the  $\Delta$ HOMO value in the context of Michl's perimeter model [41]) and Q(0,0) bands that are dominated by the *a*  $\rightarrow$  *-a* and *a*  $\rightarrow$  *-s* one-electron transitions (Table 1) rather than having near equal contributions from the *s*  $\rightarrow$  *-a* and *s*  $\rightarrow$  *-s* one-electron transitions [42]. This leads to a mixing of the allowed and forbidden properties of the Q and B-bands.

While the spectra of the  $\beta$ -octa- and  $\beta$ -tetrasubstituted compounds **4** and **6** are very similar (Fig. 3), more significant changes are observed in the spectra of the  $\alpha$ -tetrasubstituted compound **5**. The  $\pi$ -systems of free base ligands of TBC complexes would have at most  $C_{2v}$

symmetry and hence lack four-fold axes of symmetry. There is a minor lifting of the degeneracy of the *-a* and *-s* MOs (the  $\Delta$ LUMO value in the context of Michl's perimeter model [39], while the gap between the *a* and *s* MOs is referred to as the  $\Delta$ HOMO value) in addition to the far larger splitting of the *a* and *s* MOs caused by the large MO coefficients on the aza-nitrogens in the context of the *s* MO (Fig. 4). This results in two symmetry-split Q(0,0) bands in the electronic absorption spectra of **4** (at 666 and 638 nm) and **5** (at 676 and 642 nm) (Fig. 3), with coupled pairs of Faraday  $\mathcal{B}_0$  terms replacing the positive Faraday  $\mathcal{A}_1$  terms that dominate the MCD of most  $D_{4h}$  symmetry metal porphyrin and phthalocyanine complexes [1, 40, 43]. The Q(0,0)



**Fig. 2.** Nodal patterns of the four frontier  $\pi$ -MOs of zinc tetraazaporphyrin (ZnTAP) with the angular nodal planes highlighted to describe the  $M_L = \pm 4$  and  $\pm 5$  nodal patterns, and the nodal patterns and MO energies for one of the positional isomers of **4** and **5** at an isosurface value of 0.04 a.u. Michl [40] introduced a, s, -a and -s nomenclature to describe the four frontier  $\pi$ -MOs based on whether there is a nodal plane (a and -a) or an antinode (s and -s) on the y-axis. Once the alignment of the angular nodal planes has been clearly defined the effect of different structural perturbations can be readily conceptualized on a qualitative basis through a consideration of the relative size of the MO coefficients on each atom on the perimeter

bands of **5** are red-shifted by *ca.* 10 nm compared to **4**, since the substituents at the  $\alpha$ -positions result in a narrowing of the HOMO–LUMO gap, due to the larger MO coefficients at these positions in the **a** MO (Fig. 4). The most intense B-bands of **4** and **5** are markedly red shifted to 450 and 463 nm relative to the B1/B2 bands of MPc complexes. The Stillman group [44] used the simultaneous spectral band deconvolution of the electronic absorption and MCD spectra of phthalocyanines to identify the presence of a second intense absorption band close in the B-band region, so the band nomenclature for phthalocyanines was modified to, in ascending energy, the Q (*ca.* 670 nm),

B1 (*ca.* 370 nm), B2 (*ca.* 330 nm), N (*ca.* 275 nm), L (*ca.* 245 nm) and C (*ca.* 210 nm) bands [39, 44b].

As has been reported previously [13, 40], the alignment of the nodal planes in the frontier  $\pi$ -MOs of the TBC complex are broadly similar to those of the parent phthalocyanine. The loss of one of the aza-nitrogens results in a marked destabilization of s MO but has a much smaller impact on the **a** MO (Fig. 5), which has nodal planes on or near the bridging atoms. The resulting decrease in the  $\Delta$ HOMO value leads to a decrease in the mixing of the allowed and forbidden properties of the Q and B-bands (Table 1). The loss of an aza-nitrogen atom also destabilizes the -**a** and -**s** MOs of **4** and **5** to a greater

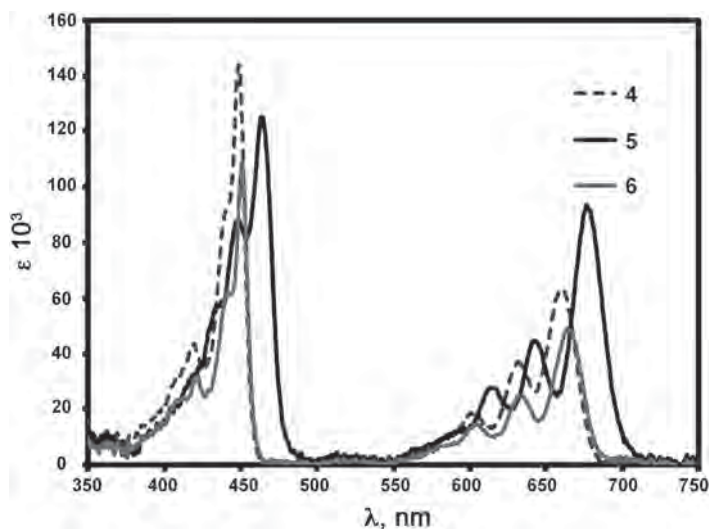


Fig. 3. Electronic absorption spectra of the  $P^VTBC$  complexes 4–6 in  $CHCl_3$

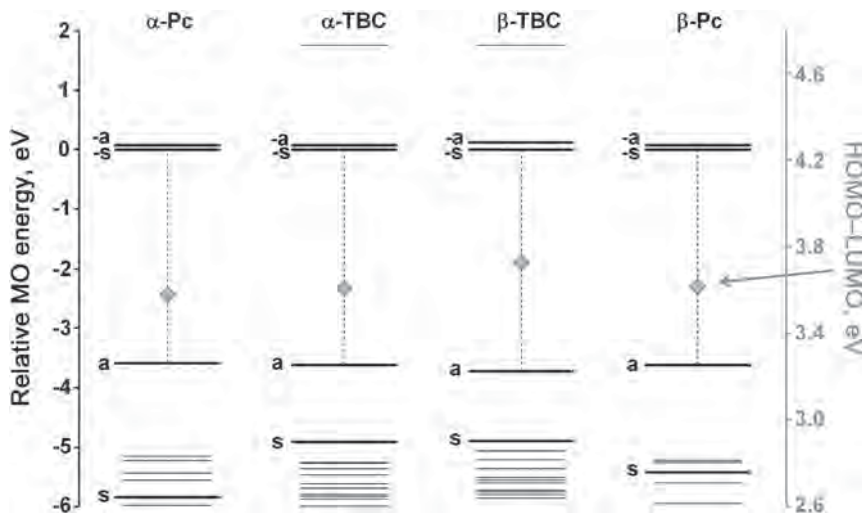


Fig. 4. Relative MO energies of the  $C_4$  symmetry  $\alpha$ - (2,  $\alpha$ -Pc) and  $\beta$ -tetrasubstituted Pcs (1,  $\beta$ -Pc) and the analogous positional isomers (Fig. 2) for a- (5,  $\alpha$ -TBC) and b-tetrasubstituted (4,  $\beta$ -TBC) TBCs in TD-DFT calculations (Table 1) with the CAM-B3LYP functional with the energy of the LUMO set to zero in each case. The a, s, -a and -s of Michl's perimeter model are highlighted in bold black. The diamonds represent the HOMO–LUMO energy difference and the gray dashed lines highlight the HOMO–LUMO gap

extent than the **a** MO relative to the electronic structures of **1** and **2** (Fig. 5) and this leads to an increase in the HOMO–LUMO gap and hence in a significant blue-shift of the  $Q(0,0)$  bands relative to those of the analogous phthalocyanines [1, 40]. Michl [41] has demonstrated that when  $\Delta LUMO < \Delta HOMO$ , as is the case with most tetraazaporphyrinoids, a  $-ve/+ve$  sequence is anticipated in  $B_0$  term intensity in ascending energy terms in the MCD spectra, while a  $+ve/-ve$  sequence is anticipated when  $\Delta LUMO > \Delta HOMO$ . The  $-/+/-/+$  sign sequence observed for the Q and B-bands in the MCD spectra (Figs 6 and 7) is consistent with what would be anticipated based on the predicted  $\Delta HOMO$  and  $\Delta LUMO$  values (Fig. 1). The

spectra of **4** and **5** are somewhat similar to that of a porphyrin complex, therefore, since there is a weakening of the  $Q(0,0)$  bands relative to the B-band and a relatively narrow and well-resolved B-band is observed beyond 400 nm. This is more pronounced in the spectrum of **5**, due to the smaller  $\Delta HOMO$  value (Figs 2 and 5). Relatively narrow band widths are observed in the Q-band regions of the optical spectra of **4** and **5**, while a range of *ca.* 20 nm is predicted for the  $Q(0,0)$  bands of the nine possible positional isomers of **5** (Fig. 1) in TD-DFT calculations with the CAM-B3LYP functional for B3LYP optimized geometries. It seems probable therefore that the more sterically hindered isomers  $\alpha$ -tetrasubstituted isomers are formed in significantly lower yields.

### Photophysical properties

The absorption, excitation and fluorescence emission spectra of **4** and **5** in DMSO are shown in Fig. 8. The main fluorescence emission bands are approximate mirror images of the lower energy  $Q(0,0)$  absorption and excitation bands, so the geometries of the ground and excited states are clearly similar as would normally be anticipated for a complex with a heteroaromatic  $\pi$ -system. The main fluorescence emission peaks for **4** and **5** lie at 669 and 686 nm in DMSO (Table 2). The Stokes shift values of 9 and 8 nm, lie within the usual range of values that have been reported previously for Pc derivatives [45]. The fluorescence quantum yield values ( $\Phi_F$ ) of **4** and **5** in DMSO were determined by the comparative method [46, 47] and were found to be similar to or

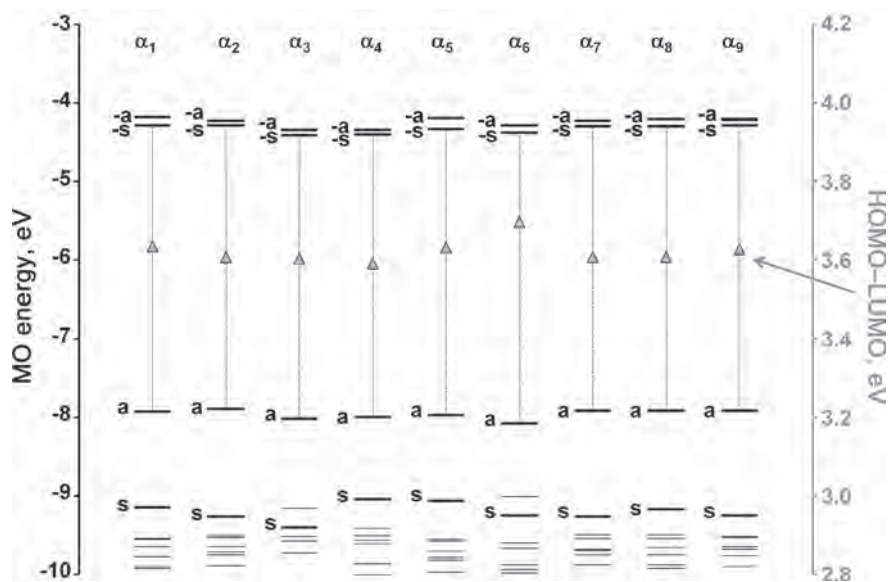
lower than that of the ZnPc standard ( $\Phi_F = 0.20$ ) [48]. Mono-exponential luminescence decay curves with  $\tau_F$  values of 2.34 and 2.91 ns were observed for **4** and **5** suggesting that only one fluorescing species is present in solution in each case. Laser flash photolysis was used to determine the triplet state quantum yields ( $\Phi_T$ ) and lifetimes ( $\tau_T$ ) of **4** and **5** (Table 2). The triplet decay curves were found to obey second order kinetics due to the effect of triplet–triplet recombination [49], and are hence consistent with the data observed previously for MPC complexes at high concentrations ( $>1 \times 10^{-4} M$ ). In DMSO, **4** and **5** have triplet state quantum yields ( $\Phi_T = 0.64$



**Table 1.** TD-DFT spectra of the B3LYP optimized geometries of **4** and **5** calculated with the CAM-B3LYP functional and 6-31G(d) basis sets

Band <sup>a</sup>	# <sup>b</sup>	Calcd. <sup>c</sup>			5 ( $\alpha$ )		
					Exp <sup>d</sup>	Wavefunction = <sup>e</sup>	
—	1	—	—	—	—	—	Ground state
Q	2	14.6	684.5	(0.28)	14.8	676	<b>91% a</b> $\rightarrow$ <b>-s</b> ; <b>5% s</b> $\rightarrow$ <b>-a</b> ; ...
Q	3	16.2	618.1	(0.34)	15.5	644	<b>85% a</b> $\rightarrow$ <b>-a</b> ; <b>12% s</b> $\rightarrow$ <b>-s</b> ; ...
—	4	23.7	421.1	(0.08)	—	—	67% a $\rightarrow$ L+2; <b>18% s</b> $\rightarrow$ <b>-a</b> ; ...
B	5	24.8	402.7	(0.56)	21.4	467	<b>86% s</b> $\rightarrow$ <b>-s</b> ; <b>9% a</b> $\rightarrow$ <b>-a</b> ; ...
B	6	25.5	392.5	(0.72)	22.2	450	<b>64% s</b> $\rightarrow$ <b>-a</b> ; 20% s $\rightarrow$ L+2; <b>5% a</b> $\rightarrow$ <b>-s</b> ;
Band	#	Calcd.			4 ( $\beta$ )		
—	1	—	—	—	—	—	Ground state
Q	2	15.1	664	(0.20)	15.2	660	<b>90% a</b> $\rightarrow$ <b>-s</b> ; <b>7% s</b> $\rightarrow$ <b>-a</b> ; ...
Q	3	16.6	401	(0.30)	15.8	633	<b>88% a</b> $\rightarrow$ <b>-a</b> ; <b>8% s</b> $\rightarrow$ <b>-s</b> ; ...
—	4	24.3	412	(0.09)	—	—	66% a $\rightarrow$ L+2; <b>23% s</b> $\rightarrow$ <b>-a</b> ; ...
B	5	25.3	395	(0.99)	22.2	451	<b>86% s</b> $\rightarrow$ <b>-s</b> ; <b>9% a</b> $\rightarrow$ <b>-a</b> ; ...
B	6	26.4	378	(0.79)	22.7	440	<b>64% s</b> $\rightarrow$ <b>-a</b> ; 20% s $\rightarrow$ L+2; <b>5% a</b> $\rightarrow$ <b>-s</b> ; ...

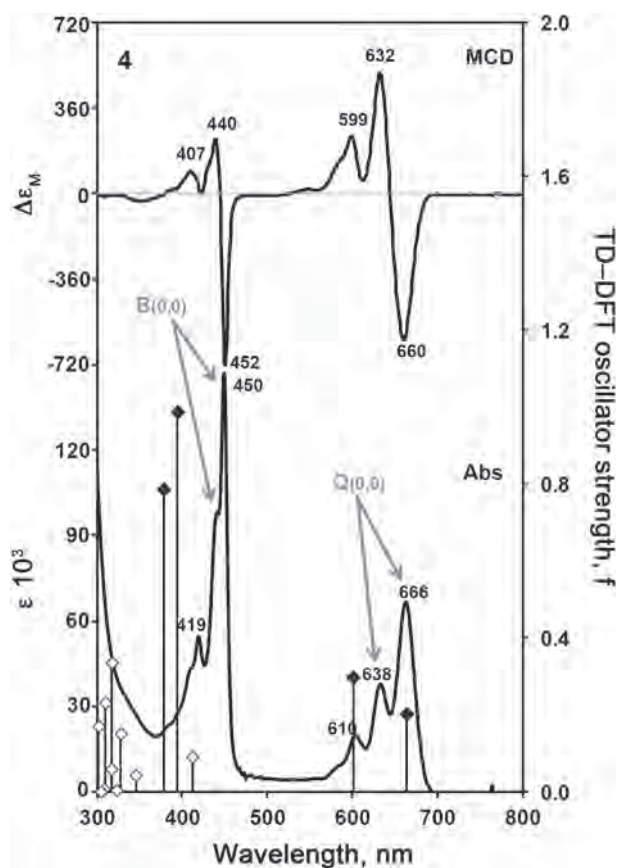
<sup>a</sup>Band assignment described in the text. <sup>b</sup>The number of the state assigned in terms of ascending energy within the TD-DFT calculation. <sup>c</sup>Calculated band energies ( $10^3 \cdot \text{cm}^{-1}$ ), wavelengths (nm) and oscillator strengths in parentheses (f). <sup>d</sup>Observed energies ( $10^3 \cdot \text{cm}^{-1}$ ) and wavelengths (nm) in Figs 6 and 7. <sup>e</sup>The wave functions based on the eigenvectors predicted by TD-DFT. One-electron transitions associated with the four frontier  $\pi$ -MOs of Gouterman's 4-orbital model [39] are highlighted in bold. H and L refer to the HOMO and LUMO, respectively.



**Fig. 5.** MO energies of the nine  $\alpha$ -tetrasubstituted TBC isomers (Fig. 1). The **a**, **s**, **-a**, and **-s** MOs of Michl's perimeter model MOs are shown with thick black lines. The diamonds represent the HOMO–LUMO gap difference and the gray dashed lines represent the HOMO–LUMO gap

and 0.89) that are comparable to or higher than that of the ZnPc standard ( $\Phi_T = 0.65$ ) [50] (Table 2) and have significantly longer triplet state lifetimes ( $\tau_T = 882$  and  $1228 \mu\text{s}$  for **4** and **5**, respectively, and  $350 \mu\text{s}$  for ZnPc).

The triplet state quantum yield represents the fraction of absorbing molecules that undergo intersystem crossing to the metastable triplet excited state. These results, and the cell cytotoxicity studies that were reported recently



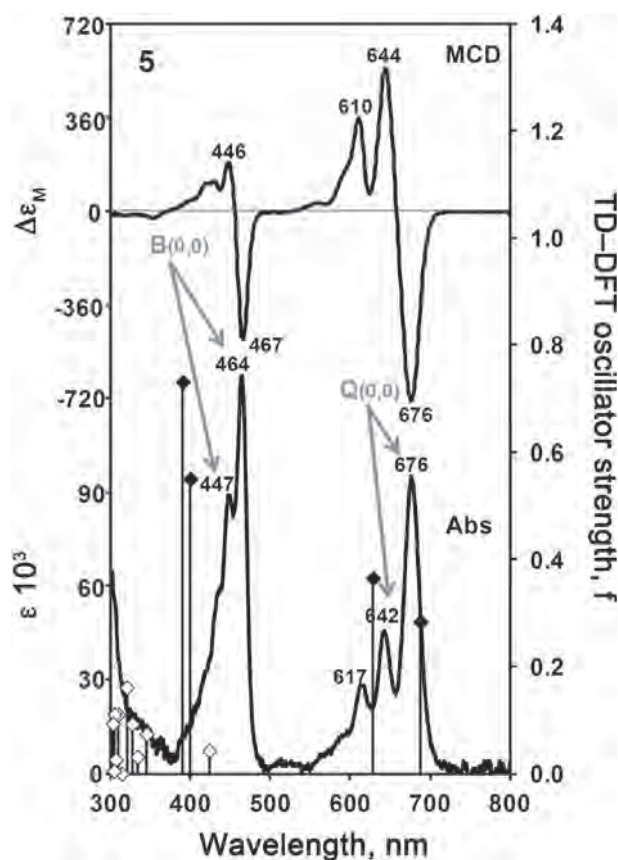
**Fig. 6.** MCD (top) and electronic absorption spectra (bottom) of the  $\beta$ -tetrasubstituted TBC (**4**) in DMSO. The TD-DFT oscillator strengths (Table 1) are plotted against a secondary axis. The Q and B-band transitions which are described by Gouterman's 4-orbital model [39] are highlighted with black diamonds

for **6** [13], further demonstrate the potential utility of P<sup>V</sup>TBCs for PDT applications.

### Photochemical properties

Singlet oxygen is generated when there is energy transfer between the T<sub>1</sub> state of the photosensitizer and molecular dioxygen. It has been reported that the Type II mechanism is more prevalent in photoinitiated oxidation; thus the magnitude of the  $\Phi_{\Delta}$  value, is often the main criterion for selecting a photosensitizer. The value can vary based on the triplet excited state energy, the ability of solvents to quench the singlet oxygen, the triplet excited state lifetime and the efficiency of the energy transfer between the triplet excited state of the sensitizer and the ground state of oxygen. Time resolved phosphorescence decay curve of singlet oxygen was used to determine singlet oxygen quantum yield of **4–6** in DMSO [49]:

$$I(t) = B \frac{\tau_D}{\tau_T - \tau_D} [e^{-t/\tau_T} - e^{-t/\tau_D}] \quad (5)$$

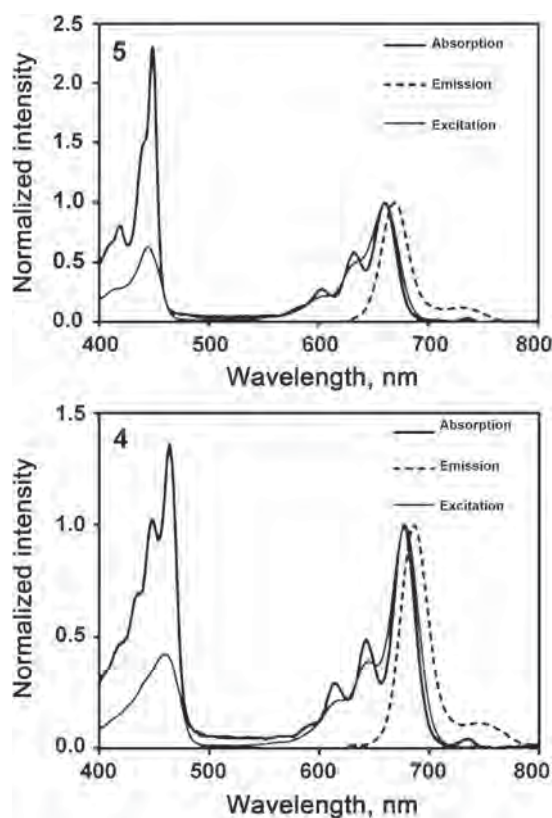


**Fig. 7.** MCD spectrum (top) and ground state electronic absorption spectrum (bottom) of the  $\alpha$ -tetrasubstituted TBC (**5**) in DMSO. The TD-DFT oscillator strengths (Table 1) are plotted on the secondary axis. The Q and B-band transitions which are described by Gouterman's 4-orbital model [39] are highlighted with black diamonds

where,  $I(t)$  is the phosphorescence intensity of <sup>1</sup>O<sub>2</sub> at time  $t$ ,  $\tau_D$  is the lifetime of <sup>1</sup>O<sub>2</sub> phosphorescence decay,  $\tau_T$  is the triplet state lifetime of the standard or sample and  $B$  is a coefficient related to sensitizer concentration and <sup>1</sup>O<sub>2</sub> quantum yield. The singlet oxygen quantum yield,  $\Phi_{\Delta}$ , of the complex was then determined using a comparative method:

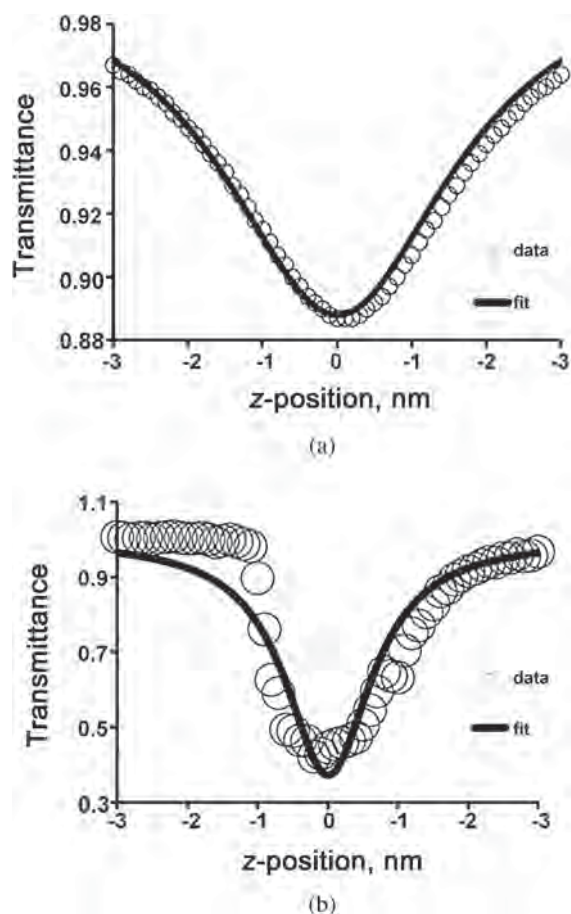
$$\Phi_{\Delta} = \Phi_{\Delta}^{\text{Std}} \cdot \frac{B \cdot A^{\text{Std}}}{B^{\text{Std}} \cdot A} \quad (6)$$

where  $\Phi_{\Delta}^{\text{Std}}$  is the singlet oxygen quantum yields for the ZnPc standard ( $\Phi_{\Delta}^{\text{Std}} = 0.67$  in DMSO) [50],  $B$  and  $B^{\text{Std}}$  refer to coefficient involved in sensitizer concentration and <sup>1</sup>O<sub>2</sub> quantum yield for the sample and standard, respectively; while  $A$  and  $A^{\text{Std}}$  refer to the absorbances of the sample and standard, respectively at the excitation wavelength. Although relatively high  $\Phi_{\Delta}$  values were obtained for **4–6** (Table 2), when the photobleaching stabilities were determined in DMSO by monitoring the decrease in the intensity of the Q-band over time during irradiation with incident



**Fig. 8.** Absorption, excitation and fluorescence emission spectra of the  $\alpha$ -tetrasubstituted TBC (**5**) in DMSO (conc  $\sim 2.8 \times 10^{-6}$  M) (TOP), and the absorption, fluorescence excitation and emission spectra of  $\beta$ -tetrasubstituted TBC (**4**) in DMSO (conc  $\sim 3 \times 10^{-6}$  M) (BOTTOM)

light [49, 51, 52], the photodegradation quantum yield ( $\Phi_{pd}$ ) values ranged from  $3.7 \times 10^{-2}$  for **4** to  $4.5 \times 10^{-4}$  for **6**. This demonstrates that the P<sup>v</sup>TBCs are of low stability in the solvent used and hence may not be suitable for singlet oxygen applications. Stable Pc complexes typically have values in the  $10^{-6}$  range, while values in the  $10^{-3}$  range have been reported for the most unstable Pc complexes [53]. Bulky aryloxy substituents are typically introduced to enhance the solubility of Pc complexes and their analogs. Their electron donating properties destabilize the frontier  $\pi$ -MOs and hence may be problematic from a photostability standpoint [54], so different strategies may have to be adopted to enhance the stability of TBC complexes for use in singlet oxygen applications in future.



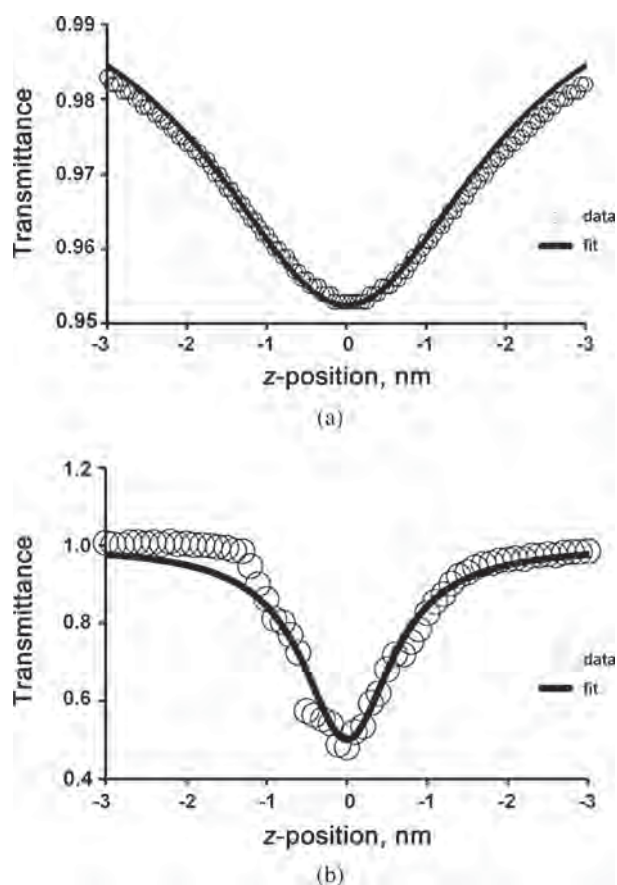
**Fig. 9.** Z-scan of the  $\alpha$ -tetrasubstituted TBC (**5**) in (a) DMSO and (b) poly(bisphenol A carbonate)

### Nonlinear optical parameters

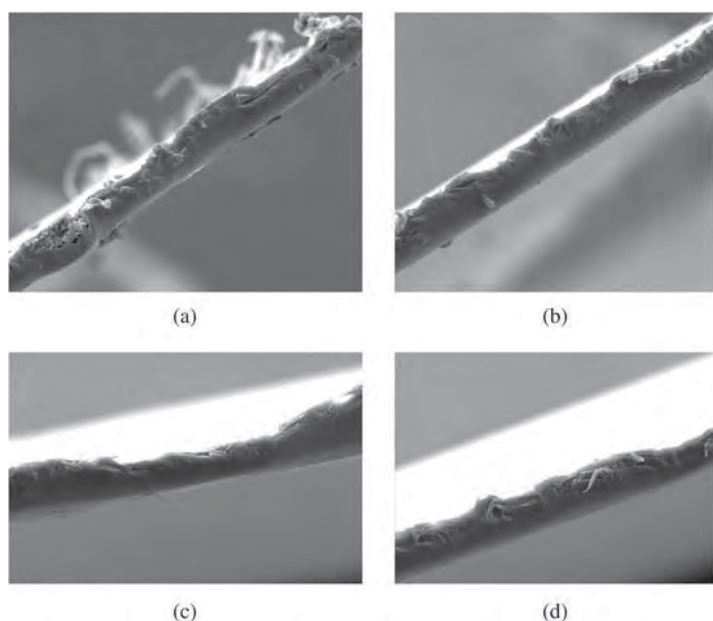
Only a limited amount of research has been carried out on the nonlinear optical properties of TBCs [27]. It was suspected that the lack of a center of symmetry and the presence of a permanent dipole moment would make TBCs effective nonlinear optical materials. Z-scan studies were conducted both in solution (DMSO) and in polymer media (poly bisphenol A carbonate). The energy used for solution studies was  $\sim 35 \mu\text{J}$  and for the films  $\sim 25 \mu\text{J}$ . Figures 9 and 10 show the results of both the solution and film studies. The profiles fit with those of reverse saturable absorbers using equations that were used previously for a series of main group metal phthalocyanine complexes [55]. The reduction in light

**Table 2.** Photophysical/chemical properties of **4–6** in DMSO

	$\lambda_{\text{abs}}$ , nm	$\lambda_{\text{em}}$ , nm	$\lambda_{\text{ex}}$ , nm	$\Phi_{\text{F}}$	$T_{\text{F}}$ , ns	$\Phi_{\text{T}}$	$T_{\text{T}}$ , $\mu\text{s}$	$\Phi_{\Delta}$	$\Phi_{\text{PD}}$
<b>4</b>	660	669	660	0.20	2.34	0.64	$882 \pm 7$	0.66	$3.7 \times 10^{-2}$
<b>5</b>	676	686	678	0.12	2.91	0.89	$1228 \pm 5$	0.52	$2.4 \times 10^{-3}$
<b>6</b>	664	673	665	0.19	2.28	0.81	$877 \pm 5$	0.74	$4.5 \times 10^{-4}$



**Fig. 10.** Z-scan of the  $\beta$ -tetrasubstituted TBC (**4**) in (a) DMSO and (b) poly(bisphenol A carbonate)



**Fig. 11.** Scanning electron microscopy images of the PBC thin films. (a) and (b) show clearly the edge of the thin film, whereas (c) and (d) show the edge and part of the surface. In (C), it can be seen that the film is not of uniform thickness

**Table 3.** Nonlinear optical parameters of the  $\alpha$ - and  $\beta$ -tetrasubstituted TBCs embedded in thin films. The limiting intensity ( $I_{\text{lim}}$ ) is judged against the safety threshold of  $0.945 \text{ J.cm}^{-2}$

Compound (films)	$\gamma$ , esu	$\text{Im}[\chi^{(3)}]/\alpha$ , esu	$I_{\text{lim}}$ , $\text{J.cm}^{-2}$
<b>4</b> ( $\alpha$ )	$2.1 \times 10^{-25}$	$2.9 \times 10^{-10}$	0.16
<b>5</b> ( $\beta$ )	$1.2 \times 10^{-26}$	$1.9 \times 10^{-11}$	0.58

transmission in the TBC solutions is not as great as that seen in the films, as has been demonstrated previously for phthalocyanines. This can be attributed to the denser packing of molecules with reverse saturable absorption properties in the path of the light and their immobility. For a useful limiter, the transmission needs to drop to 50% or below, and ideally the transmission curve should be perfectly symmetrical around the focal point ( $z = 0$ ). For the solutions (Figs 9a and 10a), this is almost achieved due to the homogeneity of the sample, but the curves are asymmetric for the films (Figs 9b and 10b) due to the low homogeneity and uneven film surface (Fig. 11). During the z-scan measurements, the film is slightly deformed, so issues such as light defocusing and stray light can be encountered. Multiple scans were run at different film positions and an average curve was utilized for the calculations to address this. The  $\text{Im}[\chi^{(3)}]/\alpha$  values for the TBCs embedded in PBC lie in the order of magnitude of  $10^{-11}$ – $10^{-10}$  (Table 3). Complexes with promising OL properties typically exhibit values in the  $10^{-15}$ – $10^{-9}$  range. Although these values are comparable to those of phthalocyanine films reported previously [55] and hence suggest that a wider range of TBC complexes

merits further study in this regard, when the limiting intensity values are examined, it becomes clear that they lie below the safety threshold of  $0.95 \text{ J.cm}^{-2}$  stipulated by the International Commission on Non-Ionizing Radiation Protection and are lower than those reported for the PBC films of Pc complexes [55]. It is noteworthy that a significantly higher limiting intensity value was obtained for the  $\beta$ -tetrasubstituted compound (Table 3).

## CONCLUSION

As has been reported previously for the  $\beta$ -octasubstituted  $\text{P}^{\text{V}}$ TBC [13], the  $\alpha$ - and  $\beta$ -tetrasubstituted complexes have relatively high singlet oxygen quantum yields. Higher values are obtained for the  $\beta$ -tetrasubstituted complex than for the corresponding  $\alpha$ -substituted complex, probably due to the greater conformational flexibility that is likely to be encountered when substituents are introduced at the  $\alpha$ -positions. Although the optical limiting properties of thin films containing **4** and **5** were not as promising

as those that have been reported previously for comparable phthalocyanine complexes [54], in depth studies of the OL properties of a wider range of TBCs is merited given the permanent dipole moment and relatively high triplet state quantum yields of these complexes. The photodegradation quantum yields for TBCs 4–6 demonstrate that the P<sup>V</sup>TBC complexes readily degrade in solution, and would not be suitable for use in products which are meant to stand up to prolonged high intensity light conditions. Further studies of novel TBC complexes will be required to identify combinations of peripheral substituents and axially ligated central ions, which enhance the solubility of the complexes without having a negative impact on the photostability and OL properties of the complex.

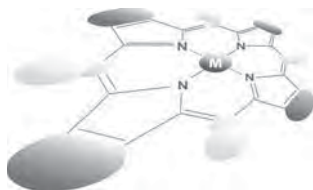
### Acknowledgements

This work was supported by the Department of Science and Technology (DST) Innovation and National Research Foundation (NRF), South Africa through DST/NRF South African Research Chairs Initiative (UID 62620) and by the CSIR National Laser Centre, Rental Pool Programme. The theoretical calculations were carried out at the Centre for High Performance Computing in Cape Town, South Africa.

### REFERENCES

- Mack J and Kobayashi N. *Chem. Rev.* 2011; **111**: 281–321.
- Breusova MO, Pushkarev VE and Tomilova LG. *Russ. Chem. Bull.* 2007; **46**: 1456–1460.
- Li J, Subramanian LR and Hanack M. *J. Chem. Soc. Chem. Commun.* 1997; 2010: 679–680.
- Chen MJ, Klingler RJ and Rathke JW. *J. Porphyrins Phthalocyanines* 2001; **5**: 442–448.
- Khene S, Ogunsipe A, Antunes E and Nyokong T. *J. Porphyrins Phthalocyanines* 2007; **11**: 109–117.
- Gouterman M, Sayer P, Shankland E and Smith JP. *Inorg. Chem.* 1981; **20**: 87–92.
- Fujiki M, Tabei H and Isa K. *J. Am. Chem. Soc.* 1986; **108**: 1532–1536.
- Liu J, Zhao Y, Zhao F, Zhang F, Song X and Chau F-T. *J. Photochem. Photobiol. A: Chem.* 1996; **99**: 115–119.
- (a) Fox JP and Goldberg DP. *Inorg. Chem.* 2003; **42**: 8181–8191. (b) Goldberg DP. *Acc. Chem. Res.* 2007; **40**: 626–634.
- Jianbo L, Fushi Z, Fuqun Z, Yingwu T, Xinqi S and Guangqing Y. *J. Photochem. Photobiol. A: Chem.* 1995; **91**: 99–104.
- Zhang X, Chang Y, Peng Y and Zhang F. *Aust. J. Chem.* 2009; **62**: 434–440.
- Tang Y, Chan S-K, Zhao F, Li X, Zhang F and Song Z. *J. Porphyrins Phthalocyanines* 2002; **6**: 484–488.
- Maohu S, Jiangwei T, Mkhize C, Kubheka G, Jinfeng Z, Mack J, Nyokong T and Shen Z. *J. Porphyrins Phthalocyanines* 2014; **18**: 698–707.
- Furuyama T, Sugiya Y and Kobayashi N. *Chem. Commun.* 2014; **50**: 4312–4314.
- Tutt LW and Kost A. *Nature* 1992; **356**: 225–226.
- Perry JW, Mansour K, Lee I-YS, Wu X-L, Bedworth PV, Wada CT, Tian M and Sasabe H. *Science* 1996; **273**: 1533–1536.
- Hsrilal SS, Bindhu CV, Nampoori VPN and Vallabhan CPG. *J. Appl. Phys.* 1999; **86**: 1388–1393.
- Li C, Zhang L, Yang M, Wang H and Wang Y. *Phys. Rev. A* 1994; **49**: 1149–1157.
- Shirk J, Pong RGS, Bartoli FJ and Snow AW. *Appl. Phys. Lett.* 1993; **63**: 1880–1883.
- Perry JW, Mansour K, Marder SR, Perry KJ, Alvarez Jr. D and Choong I. *Opt. Lett.* 1994; **19**: 625–627.
- Hughes S, Spruce G, Wherrett BS and Kobayashi T. *J. Appl. Phys.* 1997; **81**: 5905–5913.
- Shirk JS, Pong RGS, Flom SR, Heckmann H and Hanack M. *J. Phys. Chem. A* 2000; **104**: 1438–1449.
- De la Torre G, Vazquez P, Lopez FA and Torres T. *Chem. Rev.* 2004; **104**: 3723–3750.
- Dini D, Calvete MJF, Hanack M and Meneghetti M. *J. Phys. Chem. A* 2008; **112**: 8515–8522.
- Gu YZ, Liang ZJ and Gan FX. *Opt. Mater.* 2001; **17**: 471–475.
- Liu C, Wang X, Gong G, Liu Y, Qiu W and Zhu D. *Chem. Phys. Lett.* 2001; **347**: 378–382.
- Huang L, Li Z, Fushi Zhang F, Tung C-H and Kasatani K. *Opt. Commun.* 2008; **281**: 1275–1279.
- Nyokong T and Antunes EM. *J. Porphyrins Phthalocyanines* 2009; **13**: 153–160.
- Piepho SB and Schatz PN. In *Group Theory in Spectroscopy with Applications to Magnetic Circular Dichroism*, Wiley: New York, 1983.
- Fashina A, Antunes E and Nyokong T. *Polyhedron* 2013; **53**: 278–285.
- Gaussian 09, Revision A.02, Frisch MJ, Trucks GW, Schlegel HB, Scuseria GE, Robb MA, Cheeseman JR, Scalmani G, Barone V, Mennucci B, Petersson GA, Nakatsuji H, Caricato M, Li X, Hratchian HP, Izmaylov AF, Bloino J, Zheng G, Sonnenberg JL, Hada M, Ehara M, Toyota K, Fukuda R, Hasegawa J, Ishida M, Nakajima T, Honda Y, Kitao O, Nakai H, Vreven T, Montgomery JA, Jr, Peralta JE, Ogliaro F, Bearpark M, Heyd JJ, Brothers E, Kudin KN, Staroverov VN, Kobayashi R, Normand J, Raghavachari K, Rendell A, Burant JC, Iyengar SS, Tomasi J, Cossi M, Rega N, Millam JM, Klene M, Knox JE, Cross JB, Bakken V, Adamo C, Jaramillo J, Gomperts R, Stratmann RE, Yazyev O, Austin AJ, Cammi R, Pomelli C, Ochterski JW, Martin RL, Morokuma K, Zakrzewski VG, Voth GA, Salvador P, Dannenberg JJ, Dapprich S, Daniels AD, Farkas Ö, Foresman JB, Ortiz JV, Cioslowski J and Fox DJ. Gaussian, Inc., Wallingford CT, 2009.

32. Cai Z-L, Crossley MJ, Reimers JR, Kobayashi R and Amos RD. *J. Phys. Chem. B* 2006; **110**: 15624–15632.
33. Mack J, Stone J and Nyokong T. *J. Porphyrins Phthalocyanines* 2014; **18**: 630–641.
34. Sheik-Bahae M, Said AA and Van Stryland EW. *Opt. Lett.* 1989; **14**: 955–957.
35. Sheik-Bahae M, Said AA, Wei TH, Hagan DJ and Van Stryland EW. *IEEE J. Quantum Electron.* 1990; **26**: 760–769.
36. Kuzyk MG, Dirk CW and Van Stryland EW. In *Characterization Techniques and Tabulations for Organic Nonlinear Materials*, Kuzyk MG and Dirk CW. (Eds) Marcel Dekker, Inc.: New York, USA, 1998; pp 655–692.
37. Sutherland RL, Mclean DG and Kirkpatrick S. *Handbook of Nonlinear Optics*, Second Ed., Marcel Dekker, Inc.: New York, USA, 2003.
38. Dini D and Hanack M. In *The Porphyrin Handbook: Physical Properties of Phthalocyanine based Materials*, Kadish KM, Smith KM and Guillard R. (Eds) Academic Press: New York, USA, 1999; pp 22–31.
39. Gouterman M. In *The Porphyrins, Optical Spectra and Electronic Structure of Porphyrins and Related Rings*, Vol. III, Dolphin D. (Ed.) Academic Press: New York, 1978; pp 1–165.
40. Mack J, Bunya M, Lansky D, Goldberg DP and Kobayashi N. *Heterocycles* 2008; **76**: 1369–1380.
41. (a) Michl J. *J. Am. Chem. Soc.* 1978; **100**: 6801–6811. (b) Michl J. *J. Am. Chem. Soc.* 1978; **100**: 6812–6818. (c) Michl J. *Pure Appl. Chem.* 1980; **52**: 1549–1563. (d) Michl J. *Tetrahedron* 1984; **40**: 3845–3934.
42. Mack J, Asano Y, Kobayashi N and Stillman MJ. *J. Am. Chem. Soc.* 2005; **127**: 17697–17711.
43. (a) Mack J, Stillman MJ and Kobayashi N. *Coord. Chem. Rev.* 2007; **251**: 429–453. (b) Kobayashi N, Muranaka A and Mack J. *Circular Dichroism and Magnetic Circular Dichroism Spectroscopy for Organic Chemists*, Royal Society of Chemistry: London, UK, 2011.
44. (a) Nyokong T, Gasyna Z and Stillman MJ. *Inorg. Chem.* 1987; **26**: 548–553. (b) Nyokong T, Gasyna Z and Stillman MJ. *Inorg. Chem.* 1987; **26**: 1087–1095. (c) Ough EA, Nyokong T, Creber KAM and Stillman MJ. *Inorg. Chem.* 1988; **27**: 2724–2732. (d) Mack J and Stillman MJ. *J. Phys. Chem.* 1995; **95**: 7935–7945. (e) Mack J and Stillman MJ. *Inorg. Chem.* 1997; **36**: 413–425.
45. Kuznetsova N, Gretsova N, Kalmykova E, Makarova E, Dashkevich S, Negrimovskii V, Kaliya O and Luk'yanets E. *Russ. J. Gen. Chem.* 2000; **70**: 133–140.
46. Senge MO, Renner MW, Kalisch WW and Fajer J. *J. Chem. Soc. Dalton Trans.* 2000: 381–386.
47. Fery-Forgues S and Lavabre DJ. *Chem. Ed.* 1999; **76**: 1260–1264.
48. (a) Ogunsipe A, Chen JY and Nyokong T. *New J. Chem.* 2004; **28**: 822–827. (b) Tau P, Ogunsipe A, Maree S, Maree MD and Nyokong T. *J. Porphyrins Phthalocyanines* 2003; **7**: 439–446.
49. Spiller W, Kliesch H, Wöhrle D, Hackbarth S, Röder B and Schnurpfeil G. *J. Porphyrins Phthalocyanines* 1998; **2**: 145–158.
50. (a) Tran-Thi TH, Desforge C and Thiec CC. *J. Phys. Chem.* 1989; **93**: 1226–1233. (b) Canlica M, Altdal A and Nyokong T. *J. Porphyrins Phthalocyanines* 2012; **16**: 826–832.
51. Fu J, Li XY, Ng DKP and Wu C. *Langmuir* 2002; **18**: 3843–3847.
52. (a) Erdoğan A and Nyokong T. *Inorg. Chim. Acta* 2009; **362**: 4875–4883. (b) Seotsanyana-Mokhosi I, Kuznetsova N and Nyokong T. *J. Photochem. Photobiol. A: Chem.* 2001; **140**: 215–222.
53. Nyokong T. *Coord. Chem. Rev.* 2007; **251**: 1707–1722.
54. Mack J, Kobayashi N and Stillman MJ. *J. Inorg. Biochem.* 2009; **104**: 310–317.
55. Mkhize C, Britton J and Nyokong T. *Polyhedron* 2014; **81**: 607–613.



# Design of diethynyl porphyrin derivatives with high near infrared fluorescence quantum yields

Kimihiro Susumu<sup>a,c,d</sup> and Michael J. Therien<sup>\*b</sup>

<sup>a</sup> Department of Chemistry, 231 South 34th Street, University of Pennsylvania, Philadelphia, PA 19104-6323, USA

<sup>b</sup> Department of Chemistry, French Family Science Center, 124 Science Drive, Duke University, Durham, NC 27708-0346, USA

Dedicated to Professor Shunichi Fukuzumi on the occasion of his retirement

Received 6 October 2014

Accepted 11 November 2014

**ABSTRACT:** A design strategy for (porphinato)zinc-based fluorophores that possess large near infrared fluorescence quantum yields is described. These fluorophores are based on a (5,15-diethynylporphinato)zinc(II) framework and feature symmetric donor or acceptor units appended at the *meso*-ethynyl positions via benzo[*c*][1,2,5]thiadiazole moieties. These (5,15-bis(benzo[*c*][1',2',5']thiadiazol-4'-ylethynyl)-10,20-bis[2',6'-bis(3'',3''-dimethyl-1''-butyloxy)phenyl]porphinato)zinc(II) (**4**), (5,15-bis[4'-(*N,N*-dihexylamino)benzo[*c*][1',2',5']thiadiazol-7'-ylethynyl]-10,20-bis[2',6'-bis(3'',3''-dimethyl-1''-butyloxy)phenyl]porphinato)zinc(II) (**5**), (5,15-bis([7'-(4''-*n*-dodecyloxyphenylethynyl)benzo[*c*][1',2',5']thiadiazol-4'-yl]ethynyl)-10,20-bis[2',6'-bis(3'',3''-dimethyl-1''-butyloxy)phenyl]porphinato)zinc(II) (**6**), (5,15-bis([7'-(4''-*n*-dodecyloxyphenyl)benzo[*c*][1'',2'',5'']thiadiazol-4''-yl]ethynyl)benzo[*c*][1',2',5']thiadiazol-4'-yl]ethynyl)-10,20-bis[2',6'-bis(3'',3''-dimethyl-1''-butyloxy)phenyl]porphinato)zinc(II) (**7**), 5,15-bis([7'-(4''-*N,N*-dihexylaminophenylethynyl)benzo[*c*][1',2',5']thiadiazol-4'-yl]ethynyl)-10,20-bis[2',6'-bis(3'',3''-dimethyl-1''-butyloxy)phenyl]porphinato)zinc(II) (**8**), and (5,15-bis([7'-(4''-*N,N*-dihexylaminophenylethynyl)benzo[*c*][1',2',5']thiadiazol-4'-yl]ethynyl)-10,20-bis[2',6'-bis(3'',3''-dimethyl-1''-butyloxy)phenyl]porphinato)zinc(II) (**9**) chromophores possess red-shifted absorption and emission bands that range between 650 and 750 nm that bear distinct similarities to those of the chlorophylls and structurally related molecules. Interestingly, the measured radiative decay rate constants for these emitters track with the integrated oscillator strengths of their respective *x*-polarized Q-band absorptions, and thus define an unusual family of high quantum yield near infrared fluorophores in which emission intensity is governed by a simple Strickler–Berg dependence.

**KEYWORDS:** diethynylporphyrin, benzo[*c*][1,2,5]thiadiazole, near infrared, fluorescence quantum yield, Strickler–Berg.

## INTRODUCTION

The design and synthesis of near infrared (NIR) absorption materials that possess large absorptive

oscillator strengths and high fluorescence quantum yields are important to molecular imaging [1–5] and solar energy conversion technologies [6–10]. Likewise, the efficient utilization of NIR sunlight is a key feature of natural photosynthesis, which exploits NIR-absorbing dyes such as chlorophylls and pheophytins [11]. Relative to the tremendous attention that has been paid to the design and synthesis of low band gap chromophores and materials [12–19], much less focus has been given to the development of strategies that channel enhanced oscillator strength into the low energy optical transitions

<sup>†</sup>SPP full member in good standing

\*Correspondence to: Michael J. Therien, tel: +1 919-660-1670, email: michael.therien@duke.edu

Current address: <sup>c</sup>Optical Sciences Division, U.S. Naval Research Laboratory, Washington, DC 20375, USA; <sup>d</sup>Sotera Defense Solutions, Inc., Columbia, MD 21046, USA

of such compositions. For example, only a limited number of conjugated organic structures possess both high oscillator strength NIR ( $S_0 \rightarrow S_1$ ) absorptions and corresponding high ( $S_1 \rightarrow S_0$ ) fluorescence quantum yields [20, 21]. In general, a higher  $S_0 \rightarrow S_1$  absorptive extinction coefficient should correlate with a larger  $S_1 \rightarrow S_0$  radiative rate constant, congruent with the Strickler–Berg relationship [22]; most strongly absorbing organic NIR dyes, however, are not impressive emitters, due in many cases to large magnitude  $S_1$  state non-radiative rate constants that are readily rationalized within the context of the energy gap law [23].

Porphyryns are tetrapyrrole  $\pi$ -conjugated systems, and the lowest energy absorption bands of simple tetraphenylporphyrin or octaethylporphyrin monomers range typically over the 600 to 650 nm spectral regime and feature modest absorptive extinction coefficients ( $\epsilon < 10^4 \text{ M}^{-1} \cdot \text{cm}^{-1}$ ). Modification of the porphyrin  $\pi$ -skeleton can further reduce the HOMO–LUMO gap; the electronic structures of such reduced band gap porphyrins can in general be rationalized using Gouterman's four orbital model [24]. In a simple (porphinato)metal complex having  $D_{4h}$  symmetry, the LUMO is doubly degenerate, and the HOMO and HOMO-1 are nearly degenerate in energy; as a result, substantial configuration interaction mixes the ( $a_{1u} \rightarrow e_g$ ) and ( $a_{2u} \rightarrow e_g$ ) transitions. Constructive and destructive combinations of these one-electron transitions give rise to an intense shorter-wavelength Soret band and a weakly absorbing longer-wavelength Q-band. While removal of frontier orbital (HOMO/HOMO-1, LUMO/LUMO+1) degeneracy is expected to result in augmentation of the Q-band absorptive extinction coefficient, relatively few examples exist of low band gap porphyrin derivatives that possess intense NIR Q-bands [25–29].

In contrast, the chlorophylls, natural porphyrin derivatives, possess lowest energy Q-bands with significant extinction coefficients ( $\epsilon: 0.5 \sim 1 \times 10^5 \text{ M}^{-1} \cdot \text{cm}^{-1}$ ) [30, 31]; some chlorophyll derivatives and related macrocycles feature substantial fluorescence quantum yields that range from  $\sim 0.05$  to  $0.3$  [32, 33]. While significant strides have been made in recent years regarding chlorophyll synthesis [33–35], the more involved nature of their fabrication limits many possible applications of these structures. Chromophores within the phthalocyanine family also exhibit intense low energy electronic absorption bands ( $\epsilon: 1 \sim 2 \times 10^5 \text{ M}^{-1} \cdot \text{cm}^{-1}$ ); while a few examples of these chromophores are known that feature both substantial NIR absorptivity and significant fluorescence quantum yield ( $0.1 \sim 0.8$ ) [36, 37], it is important to point out that extensive modulation of phthalocyanine absorptive properties and photophysics is limited by the modest frontier orbital electron density localized at the periphery of the macrocycle-fused benzene rings [38].

We have explored synthesis and electronic properties of *meso*-ethynyl porphyrin derivatives [39–62] for nonlinear optics [60, 63–81], optoelectronic devices [82–87], and fluorescence-based optical imaging technologies [88–97].

Ethyne groups fused to the porphyrin *meso*-positions provide significant electronic interaction with the macrocycle  $a_{2u}$ -derived HOMO and remove the degeneracy of the low-lying empty  $e_g$  orbitals [39, 42, 45, 50, 55]. Here we report the synthesis and optical properties of conjugated 5,15-diethynyl(porphinato)zinc(II) complexes that feature conjugated terminal groups having varying degrees of proquinoidal character (Fig. 1) that drive intense Q-band absorptions; the uncommon emissive properties of these new fluorophores based on a (5,15-diethynylporphinato)zinc(II) framework are discussed within the context of the Strickler–Berg relationship.

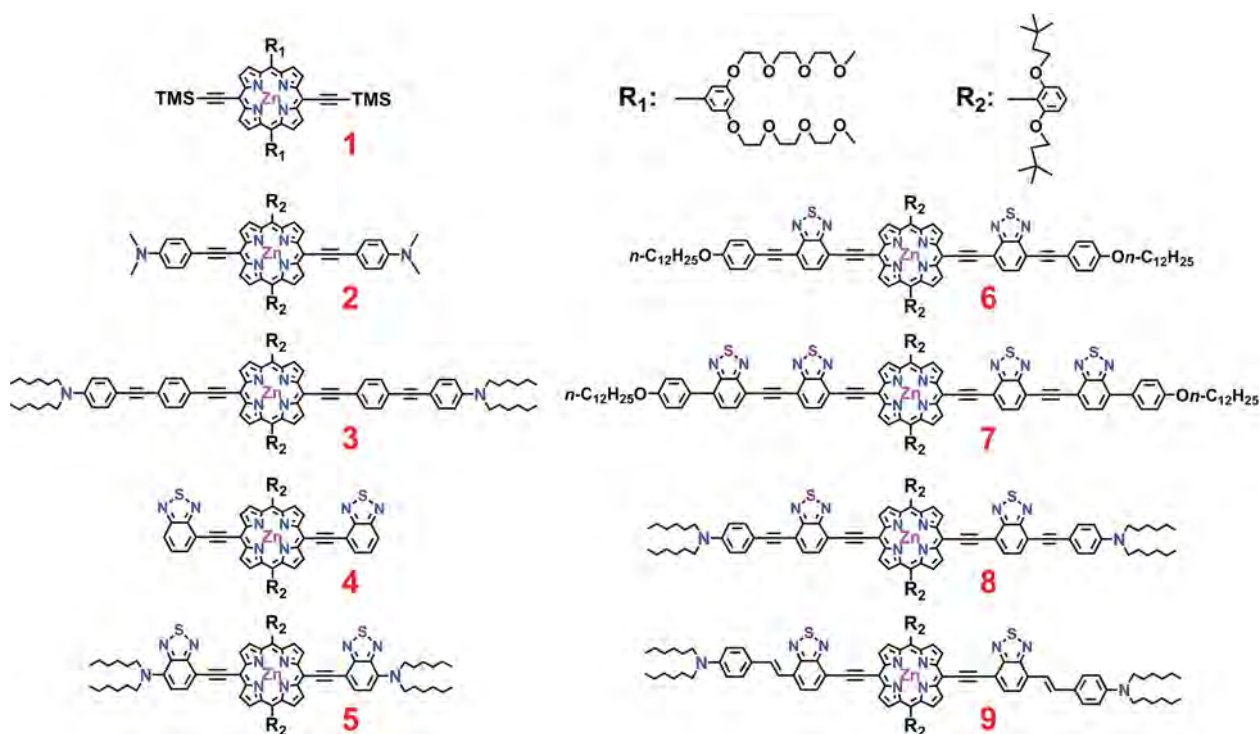
## EXPERIMENTAL

### Materials

All manipulations were carried out under nitrogen previously passed through an  $O_2$  scrubbing tower (Schweitzerhall R3-11 catalyst) and a drying tower (Linde 3-Å molecular sieves) unless otherwise stated. Air sensitive solids were handled in a Braun 150-M glove box. Standard Schlenk techniques were employed to manipulate air-sensitive solutions. Tetrahydrofuran (THF) was distilled from K/4-benzoylbiphenyl under  $N_2$ . Triethylamine and MeOH were distilled from  $CaH_2$  under  $N_2$ . The catalysts  $Pd(PPh_3)_4$ ,  $Pd(PPh_3)_2Cl_2$ , dichloro[1,1'-bis(diphenylphosphino)ferrocene]palladium(II) dichloromethane adduct,  $P(t-Bu)_3$  (10 wt% solution in hexanes), tris(dibenzylideneacetone)dipalladium(0) ( $Pd_2dba_3$ ), CuI and triphenylarsine ( $AsPh_3$ ) were purchased from Strem Chemicals and used as received. 4-Bromobenzo[c][1,2,5]thiadiazole, and 4,7-dibromobenzo[c][1,2,5]thiadiazole were prepared by literature methods [98]. (5,15-Bis[trimethylsilylethynyl]-10,20-bis[3',5'-bis(9"-methoxy-1",4",7"-trioxanonyl)phenyl]porphinato)zinc(II) (**1**), (5,15-dibromo-10,20-bis[2',6'-bis(3",3"-dimethyl-1"-butyloxy)phenyl]porphinato)zinc(II), (5,15-diethynyl-10,20-bis[2',6'-bis(3",3"-dimethyl-1"-butyloxy)phenyl]porphinato)zinc(II), and (5,15-bis(4'-(*N,N*-dimethylamino)phenylethynyl)-10,20-bis[2',6'-bis(3",3"-dimethyl-1"-butyloxy)phenyl]porphinato)zinc(II) (**2**) were synthesized as described previously [50, 54, 66]. A number of key precursors were synthesized as reported earlier [99]. All NMR solvents, and all other chemicals, were used as received.

Chemical shifts for  $^1H$  NMR spectra are relative to the tetramethylsilane (TMS) signal in deuterated solvent (TMS,  $\delta = 0.00$  ppm). All  $J$  values are reported in Hertz. Flash and size exclusion column chromatography were performed on the bench top, using respectively silica gel (EM Science, 230–400 mesh) and Bio-Rad Bio-Beads SX-1 as media. CI mass spectra were acquired at the Mass Spectrometry Center at the University of Pennsylvania. MALDI-TOF mass spectroscopic data were obtained with a Voyager-DE RP instrument





**Fig. 1.** Structures of the TMS-protected (5,15-diethynyl-10,20-bis[3',5'-bis(9''-methoxy-1'',4'',7''-trioxanyl)phenyl]porphinato) zinc(II) reference monomer (**1**), and NIR fluorophores **2–9**

(PerSeptive Biosystems); samples for these experiments were prepared as micromolar solutions in either  $\text{CH}_2\text{Cl}_2$  or THF, and dithranol (Sigma–Aldrich) was utilized as the matrix.

### Instrumentation

$^1\text{H}$  NMR spectra were recorded on either 250 MHz AC-250, 300 MHz DMX-300, or 500 MHz AMX-500 Bruker spectrometers. Electronic absorption spectra were recorded on a Shimadzu PharmaSpec UV1700 spectrophotometer. Fluorescence spectra were obtained with a Spex Fluorolog-3 spectrophotometer (Jobin Yvon Inc., Edison, NJ) that utilized a T-channel configuration with red sensitive R2658 Hamamatsu PMT and liquid nitrogen cooled InGaAs detectors. The obtained fluorescence spectra were corrected using the spectral output of a calibrated light source supplied by the National Bureau of Standards. Fluorescence quantum yields were measured on  $\text{N}_2$ -purged solutions at room temperature. Tetraphenylporphyrin in benzene ( $\Phi_f = 0.13$ ) was used as a standard [100]. The fluorescence quantum yields of each sample were calculated using the following equation (Equation 1)

$$\frac{\Phi_{f(s)}}{\Phi_{f(r)}} = \frac{F_s \cdot A_r \cdot n_s^2}{F_r \cdot A_s \cdot n_r^2} \quad (1)$$

where  $\Phi_f$  is the fluorescence quantum yield,  $F$  is the area under the corrected fluorescence band (expressed

in number of photons),  $A$  is the absorbance at the excitation wavelength, and  $n$  is the refractive index of the solvents used. Subscripts  $s$  and  $r$  refer to the sample and reference, respectively. Time-correlated single-photon counting (TCSPC) experiments to measure fluorescence lifetimes were performed using an Edinburgh Analytical Instruments FL/FS 900 spectrofluorimeter. The excitation sources for TCSPC measurements were either a nanosecond flash lamp operating under an atmosphere of  $\text{H}_2$  gas (0.50–0.55 bar, 0.7 nm fwhm, 40 kHz repetition rate) or a blue ( $450 \pm 15$  nm) light-emitting diode (Picoquant PLS 450/PDL 800-B) triggered at a frequency of 100 kHz by a Berkeley Nucleonics 555 pulse generator. TCSPC data were analyzed by iterative convolution of the fluorescence decay profile with the instrument response function using software provided by Edinburgh Instruments.

### Synthesis

**(5,15-Bis[4'-(4''-N,N-dihexylaminophenylethynyl)phenylethynyl]-10,20-bis[2',6'-bis(3'',3''-dimethyl-1''-butyloxy)phenyl]porphinato)zinc(II) (3).** 1-(4'-N,N-dihexylaminophenylethynyl)-4-iodobenzene [99] (55.5 mg,  $1.14 \times 10^{-4}$  mol), (5,15-diethynyl-10,20-bis[2',6'-bis(3'',3''-dimethyl-1''-butyloxy)phenyl]porphinato) zinc(II) (50.4 mg,  $5.17 \times 10^{-5}$  mol),  $\text{Pd}(\text{PPh}_3)_4$  (13.2 mg,  $1.14 \times 10^{-5}$  mol),  $\text{CuI}$  (1.0 mg,  $5.3 \times 10^{-6}$  mol) and dry THF (7.0 mL) were added to a 100-mL round-bottom flask. Ar was bubbled into the reaction mixture for 5 min before

piperidine (0.50 mL) was added. The reaction mixture was stirred at 45 °C for 3.5 h under Ar. After the solvent was evaporated, the residue was chromatographed on silica gel with 8:1 hexanes:THF as the eluent. Yield 0.063 g (72% based on 50.4 mg of (5,15-diethynyl-10,20-bis[2',6'-bis(3'',3''-dimethyl-1''-butyloxy)phenyl]porphinato)zinc(II)). <sup>1</sup>H NMR (300 MHz; CDCl<sub>3</sub>): δ, ppm 9.67 (d, 4H, *J* = 4.6 Hz, β-H), 8.86 (d, 4H, *J* = 4.6 Hz, β-H), 7.96 (d, 4H, *J* = 8.4 Hz, Ph-H), 7.72 (t, 2H, *J* = 8.4 Hz, Ph-H), 7.65 (d, 4H, *J* = 8.4 Hz, Ph-H), 7.43 (d, 4H, *J* = 8.8 Hz, Ph-H), 7.02 (d, 4H, *J* = 8.5 Hz, Ph-H), 6.61 (d, 2H, *J* = 9.0 Hz, Ph-H), 3.92 (t, 8H, *J* = 7.3 Hz, -O-CH<sub>2</sub>-C), 3.30 (t, 8H, *J* = 7.6 Hz, -N-CH<sub>2</sub>-C), 1.60 (m, 8H, -N-C-CH<sub>2</sub>-C), 1.2–1.4 (m, 24H, -CH<sub>2</sub>-), 0.92 (t, 8H, *J* = 6.8 Hz, O-C-CH<sub>2</sub>-), 0.89 (t, 12H, *J* = 7.3 Hz, -CH<sub>3</sub>), 0.27 (s, 36H, -C-CH<sub>3</sub>). MS (MALDI-TOF): *m/z* 1690.92 (calcd. for [M]<sup>+</sup> 1690.976).

**4-(Trimethylsilylethynyl)benzo[c][1,2,5]thiadiazole.** 4-Bromobenzo[c][1,2,5]thiadiazole (0.378 g, 1.76 × 10<sup>-3</sup> mol), Pd(PPh<sub>3</sub>)<sub>4</sub> (0.125 g, 1.08 × 10<sup>-4</sup> mol), CuI (14 mg, 7.4 × 10<sup>-5</sup> mol) and dry THF (20 mL) were added to a 100-mL round-bottom flask. Ar was bubbled into the reaction mixture for 5 min before diisopropylamine (1.0 mL) and (trimethylsilyl)acetylene (1.00 mL, 7.1 × 10<sup>-3</sup> mol) were added. The reaction mixture was stirred at 45 °C for 11 h under Ar. After cooling, the solvent was evaporated. The residue was chromatographed on silica gel column with 1:1 hexanes:CHCl<sub>3</sub> as the eluent. Yield 0.406 g (99% based on 0.378 g of 4-bromobenzo[c][1,2,5]thiadiazole). <sup>1</sup>H NMR (300 MHz; CDCl<sub>3</sub>): δ, ppm 7.99 (dd, 1H, *J* = 1.0, 8.8 Hz, Ph-H), 7.77 (dd, 1H, *J* = 1.0, 7.0 Hz, Ph-H), 7.55 (dd, 1H, *J* = 7.0, 8.8 Hz, Ph-H), 0.34 (s, 9H, -Si-CH<sub>3</sub>). MS (CI): *m/z* 232.048 (calcd. for [M]<sup>+</sup> 232.049).

**4-Ethynylbenzo[c][1,2,5]thiadiazole.** 4-(Trimethylsilylethynyl)benzo[c][1,2,5]thiadiazole (0.100 g, 4.30 × 10<sup>-4</sup> mol), K<sub>2</sub>CO<sub>3</sub> (78.6 mg, 5.7 × 10<sup>-4</sup> mol), THF (3.0 mL), and MeOH (2.0 mL) were added to a 100-mL round-bottom flask. The reaction mixture was stirred at room temperature for 1.5 h under Ar. The reaction mixture was filtered and the solvent was evaporated. Yield quantitative. <sup>1</sup>H NMR (300 MHz; CDCl<sub>3</sub>): δ, ppm 8.04 (d, 1H, *J* = 8.8 Hz, Ph-H), 7.81 (d, 1H, *J* = 6.9 Hz, Ph-H), 7.58 (t, 1H, *J* = 8.0 Hz, Ph-H), 3.59 (s, 1H, ethynyl-H). MS (CI): *m/z* 160.009 (calcd. for [M]<sup>+</sup> 160.010).

**(5,15-Bis(benzo[c][1,2,5]thiadiazol-4-ylethynyl)-10,20-bis[2',6'-bis(3'',3''-dimethyl-1''-butyloxy)phenyl]-porphinato)zinc(II) (4).** 4-Ethynylbenzo[c][1,2,5]thiadiazole (40.0 mg, 2.50 × 10<sup>-4</sup> mol), (5,15-dibromo-10,20-bis[2',6'-bis(3'',3''-dimethyl-1''-butyloxy)phenyl]porphinato)zinc(II) (71.0 mg, 2.50 × 10<sup>-4</sup> mol), Pd(PPh<sub>3</sub>)<sub>4</sub> (22.6 mg, 2.0 × 10<sup>-5</sup> mol), CuI (2.0 mg, 1.1 × 10<sup>-5</sup> mol) and dry THF (10 mL) were added to a 100-mL round-bottom flask. Ar was bubbled into the reaction mixture for 5 min before piperidine (0.50 mL) was added. The reaction mixture was stirred at 48 °C for 24 h under Ar. After cooling, the solvent was evaporated. The

residue was chromatographed on silica gel column with 5:1 hexanes:THF as the eluent. The product was further purified by size exclusion column chromatography (Bio Rad Bio-Beads SX-1 packed in THF, gravity flow). Yield 40.7 mg (50% based on 71.0 mg of (5,15-dibromo-10,20-bis[2',6'-bis(3'',3''-dimethyl-1''-butyloxy)phenyl]porphinato)zinc(II)). <sup>1</sup>H NMR (300 MHz; CDCl<sub>3</sub>): δ, ppm 9.91 (d, 4H, *J* = 4.5 Hz, β-H), 8.87 (d, 4H, *J* = 4.5 Hz, β-H), 8.18 (d, 2H, *J* = 7.0 Hz, Ph-H), 8.07 (d, 2H, *J* = 8.8 Hz, Ph-H), 7.76 (dd, 2H, *J* = 7.0, 8.8 Hz, Ph-H), 7.72 (t, 2H, *J* = 8.4 Hz, Ph-H), 7.03 (d, 4H, *J* = 8.4 Hz, Ph-H), 3.92 (t, 8H, *J* = 7.6 Hz, -O-CH<sub>2</sub>-C), 0.83 (t, 8H, *J* = 7.5 Hz, -O-C-CH<sub>2</sub>-C), 0.37 (s, 36H, -C-CH<sub>3</sub>). MS (MALDI-TOF): *m/z* 1240.7 (calcd. for [M]<sup>+</sup> 1240.441).

**(5,15-Bis[4'-(*N,N*-dihexylamino)benzo[c][1',2',5']thiadiazole-7'-ylethynyl]-10,20-bis[2',6'-bis(3'',3''-dimethyl-1''-butyloxy)phenyl]porphinato)zinc(II) (5).** 4-Bromo-7-(*N,N*-dihexylamino)benzo[c][1,2,5]thiadiazole [99] (53.8 mg, 1.35 × 10<sup>-4</sup> mol), (5,15-diethynyl-10,20-bis[2',6'-bis(3'',3''-dimethyl-1''-butyloxy)phenyl]porphinato)zinc(II) (41.0 mg, 4.2 × 10<sup>-5</sup> mol), Pd(PPh<sub>3</sub>)<sub>4</sub> (12.8 mg, 1.1 × 10<sup>-5</sup> mol), CuI (1.1 mg, 5.8 × 10<sup>-6</sup> mol) and dry THF (5.0 mL) were added to a 100-mL round-bottom flask. Ar was bubbled into the reaction mixture for 5 min before piperidine (0.20 mL) was added. The reaction mixture was stirred at 45 °C for 24 h under Ar. After the solvent was evaporated, the residue was chromatographed on silica gel with 8:1 hexanes: THF as the eluent. Yield 22.0 mg (33% based on 41.0 mg of (5,15-diethynyl-10,20-bis[2',6'-bis(3'',3''-dimethyl-1''-butyloxy)phenyl]porphinato)zinc(II)). <sup>1</sup>H NMR (300 MHz; CDCl<sub>3</sub>): δ, ppm 9.94 (d, 4H, *J* = 4.6 Hz, β-H), 8.86 (d, 4H, *J* = 4.6 Hz, β-H), 8.07 (d, 2H, *J* = 8.2 Hz, Ph-H), 7.70 (t, 2H, *J* = 8.4 Hz, Ph-H), 7.00 (d, 4H, *J* = 8.5 Hz, Ph-H), 6.59 (d, 2H, *J* = 8.3 Hz, Ph-H), 3.91 (t, 8H, *J* = 7.2 Hz, -O-CH<sub>2</sub>-C), 3.86 (t, 8H, *J* = 8.3 Hz, -N-CH<sub>2</sub>-C), 1.79 (m, 8H, -N-C-CH<sub>2</sub>-C), 1.1–1.5 (m, 24H, -CH<sub>2</sub>-), 0.94 (t, 8H, *J* = 7.0 Hz, O-C-CH<sub>2</sub>-), 0.88 (t, 12H, *J* = 7.2 Hz, -CH<sub>3</sub>), 0.26 (s, 36H, -C-CH<sub>3</sub>). MS (MALDI-TOF): *m/z* 1607.08 (calcd. for [M]<sup>+</sup> 1606.838).

**4-Bromo-7-(4'-*n*-dodecyloxyphenylethynyl)benzo[c][1,2,5]thiadiazole.** 4-*n*-Dodecyloxyethynylbenzene [99] (0.620 g, 2.16 × 10<sup>-3</sup> mol), 4,7-dibromobenzo[c][1,2,5]thiadiazole (1.91 g, 6.50 × 10<sup>-3</sup> mol), Pd(PPh<sub>3</sub>)<sub>2</sub>Cl<sub>2</sub> (0.162 g, 2.31 × 10<sup>-4</sup> mol), CuI (21 mg, 1.1 × 10<sup>-4</sup> mol), and dry toluene (10 mL) were added to a 100-mL round-bottom flask. Ar was bubbled into the reaction mixture for 5 min before triethylamine (10 mL) was added. The reaction mixture was stirred at 45 °C for 3 h under Ar. After the solvent was evaporated, the reaction mixture was chromatographed on silica gel with 2:1 hexanes:CH<sub>2</sub>Cl<sub>2</sub>. Yield 0.496 g (46% based on 0.620 g of 4-*n*-dodecyloxyethynylbenzene). <sup>1</sup>H NMR (300 MHz; CDCl<sub>3</sub>): δ, ppm 7.83 (d, 1H, *J* = 7.6 Hz, Ph-H), 7.63 (d, 1H, *J* = 7.6 Hz, Ph-H), 7.59 (d, 2H, *J* = 8.9 Hz, Ph-H), 6.91 (d, 2H, *J* = 8.9 Hz, Ph-H), 3.99 (t, 2H, *J* = 6.6 Hz, -OCH<sub>2</sub>-), 1.80 (quint, 2H, -OC-CH<sub>2</sub>-), 1.45 (m, 2H,

–CH<sub>2</sub>–), 1.2–1.4 (m, 16H, –CH<sub>2</sub>–), 0.88 (t, 3H, *J* = 6.7 Hz, –CH<sub>3</sub>). MS (CI): *m/z* 498.133 (calcd. for [M]<sup>+</sup> 498.134).

**(5,15-Bis([7'-(4'-*n*-dodecyloxyphenylethynyl)benzo[c][1,2,5]thiadiazol-4'-yl)ethynyl)-10,20-bis[2',6'-bis(3'',3''-dimethyl-1''-butyloxy)phenyl]porphinato)zinc(II) (6).** 4-Bromo-7-(4'-*n*-dodecyloxyphenylethynyl)benzo[c][1,2,5]thiadiazole (40.9 mg, 8.19 × 10<sup>-5</sup> mol), (5,15-diethynyl-10,20-bis[2',6'-bis(3'',3''-dimethyl-1''-butyloxy)phenyl]porphinato)zinc(II) (35.7 mg, 3.66 × 10<sup>-5</sup> mol), Pd(PPh<sub>3</sub>)<sub>4</sub> (10.1 mg, 8.7 × 10<sup>-6</sup> mol), CuI (1.3 mg, 6.8 × 10<sup>-6</sup> mol), and dry THF (6.0 mL) were added to a 100-mL round-bottom flask. Ar was bubbled into the reaction mixture for 10 min before piperidine (0.50 mL) was added. The reaction mixture was stirred at 44 °C for 17.5 h under Ar. After cooling, the solvent was evaporated. The residue was chromatographed on silica gel with 5:1 hexanes:THF as the eluent. The product was further purified by size exclusion column chromatography (BioRad Bio-Beads SX-1 packed in THF, gravity flow). Yield 45.5 mg (69% based on 35.7 mg of 5,15-diethynyl-10,20-bis[2',6'-bis(3'',3''-dimethyl-1''-butyloxy)phenyl]porphinato)zinc(II)). <sup>1</sup>H NMR (300 MHz; 1 drop pyridine-d<sub>5</sub> in CDCl<sub>3</sub>): δ, ppm 9.90 (d, 4H, *J* = 4.6 Hz, β-H), 8.86 (d, 4H, *J* = 4.6 Hz, β-H), 8.15 (d, 2H, *J* = 7.4 Hz, Ph-H), 7.92 (d, 2H, *J* = 7.4 Hz, Ph-H), 7.72 (t, 2H, *J* = 8.4 Hz, Ph-H), 7.65 (d, 4H, *J* = 8.8 Hz, Ph-H), 7.03 (d, 4H, *J* = 8.5 Hz, Ph-H), 6.94 (d, 4H, *J* = 8.9 Hz, Ph-H), 4.01 (t, 4H, *J* = 6.6 Hz, –O–CH<sub>2</sub>–C), 3.93 (t, 8H, *J* = 7.5 Hz, –O–CH<sub>2</sub>–C), 1.82 (quint, 4H, *J* = 6.8 Hz, –O–CH<sub>2</sub>–C), 1.48 (m, 4H, –CH<sub>2</sub>–), 1.15–1.40 (m, 32H, –CH<sub>2</sub>–), 0.89 (t, 6H, *J* = 6.7 Hz, –CH<sub>3</sub>), 0.83 (t, 8H, *J* = 7.5 Hz, –OC–CH<sub>2</sub>–), 0.37 (s, 36H, –C–CH<sub>3</sub>). MS (MALDI-TOF): *m/z* 1809.0 (calcd. for [M]<sup>+</sup> 1808.869).

**4-*n*-Dodecyloxyphenyl-4',4',5',5'-tetramethyl-1',3',2'-dioxaborolane.** 4-*n*-Dodecyloxyiodobenzene [99] (1.00 g, 2.58 × 10<sup>-3</sup> mol), dichloro[1,1'-bis(diphenylphosphino)ferrocene]palladium(II)-dichloromethane adduct (0.106 g, 1.30 × 10<sup>-4</sup> mol) were added to 1,2-dichloroethane (5.0 mL) and Et<sub>3</sub>N (1.0 mL, 7.2 × 10<sup>-3</sup> mol). 4,4,5,5-Tetramethyl-1,3,2-dioxaborolane (0.56 mL, 3.9 × 10<sup>-3</sup> mol) was added, and the reaction mixture was stirred at 75 °C for 1.5 h under Ar. After cooling, the solvent was evaporated. The residue was chromatographed on silica gel with 2:1 hexanes:CHCl<sub>3</sub> as the eluent. Yield 0.674 g (67% based on 1.00 g of 4-*n*-dodecyloxyiodobenzene). <sup>1</sup>H NMR (250 MHz; CDCl<sub>3</sub>): δ, ppm 7.73 (d, 2H, *J* = 8.7 Hz, Ph-H), 6.88 (d, 2H, *J* = 8.7 Hz, Ph-H), 3.97 (t, 2H, *J* = 6.6 Hz, –OCH<sub>2</sub>–), 1.78 (quint, 2H, *J* = 6.6 Hz, –OC–CH<sub>2</sub>–), 1.45 (m, 2H, –CH<sub>2</sub>–), 1.33 (s, 12H, –CH<sub>3</sub>), 1.26 (m, 16H, –CH<sub>2</sub>–), 0.88 (t, 3H, *J* = 6.5 Hz, –CH<sub>3</sub>). MS (CI): *m/z* 388.317 (calcd. for [M]<sup>+</sup> 388.315).

**4-Bromo-7-(4'-*n*-dodecyloxyphenyl)benzo[c][1,2,5]thiadiazole.** 4-*n*-Dodecyloxyphenyl-4',4',5',5'-tetramethyl-1',3',2'-dioxaborolane (0.313 g, 8.06 × 10<sup>-4</sup> mol), 4,7-dibromobenzo[c][1,2,5]thiadiazole (0.474 g, 1.61 × 10<sup>-3</sup> mol), Pd(PPh<sub>3</sub>)<sub>4</sub> (97 mg, 8.4 × 10<sup>-5</sup> mol), K<sub>2</sub>CO<sub>3</sub>

(0.347 g, 2.51 × 10<sup>-3</sup> mol), DMF (25 mL), and H<sub>2</sub>O (3.0 mL) were added to a 100-mL round-bottom flask. Ar was bubbled into the reaction mixture for 5 min at room temperature. The reaction mixture was warmed up to 86 °C and stirred for 7.5 h under Ar. After cooling, 200 mL of dilute aq. HCl was added to the reaction mixture, and the product was extracted with CHCl<sub>3</sub> and dried over Na<sub>2</sub>SO<sub>4</sub>. The solvent was evaporated, and the residue was chromatographed on silica gel with 1:1 hexanes:CHCl<sub>3</sub>. The product was further purified by size exclusion column chromatography (BioRad Bio-Beads SX-1 packed in THF, gravity flow). Yield 0.295 g (77% based on 0.313 g of 4-*n*-dodecyloxyphenyl-4',4',5',5'-tetramethyl-1',3',2'-dioxaborolane). <sup>1</sup>H NMR (300 MHz; CDCl<sub>3</sub>): δ, ppm 7.90 (d, 1H, *J* = 7.6 Hz, –CH<sub>2</sub>–), 7.85 (d, 2H, *J* = 8.8 Hz, Ph-H), 7.53 (d, 1H, *J* = 7.6 Hz, Ph-H), 7.05 (d, 2H, *J* = 8.8 Hz, Ph-H), 4.04 (t, 2H, *J* = 6.5 Hz, –OCH<sub>2</sub>–), 1.83 (quint, 2H, *J* = 6.5 Hz, –OC–CH<sub>2</sub>–), 1.49 (m, 2H, –CH<sub>2</sub>–), 1.2–1.4 (m, 16H, –CH<sub>2</sub>–), 0.88 (t, 3H, *J* = 6.6 Hz, –CH<sub>3</sub>). MS (CI): *m/z* 474.133 (calcd. for [M]<sup>+</sup> 474.134).

**4-(4'-*n*-Dodecyloxyphenyl)-7-(trimethylsilyl-ethynyl)benzo[c][1,2,5]thiadiazole.** 4-Bromo-7-(4'-*n*-dodecyloxyphenyl)benzo[c][1,2,5]thiadiazole (0.2364 g, 4.97 × 10<sup>-4</sup> mol), Pd(PPh<sub>3</sub>)<sub>4</sub> (55.4 mg, 4.79 × 10<sup>-5</sup> mol), CuI (3.4 mg, 1.8 × 10<sup>-5</sup> mol), and dry THF (10 mL) were added to a 100-mL round-bottom flask. Ar was bubbled into the reaction mixture for 5 min before (trimethylsilyl)acetylene (0.25 mL, 1.8 × 10<sup>-3</sup> mol) and diisopropylamine (1.0 mL) were added. The reaction mixture was stirred at 50 °C for 17.5 h under Ar. After cooling, the solvent was evaporated. The residue was chromatographed on silica gel with 8:1 hexanes:THF. Yield 0.240 g (98% based on 0.2364 g of 4-bromo-7-(4'-*n*-dodecyloxyphenyl)benzo[c][1,2,5]thiadiazole). <sup>1</sup>H NMR (300 MHz; CDCl<sub>3</sub>): δ, ppm 7.90 (d, 2H, *J* = 8.9 Hz, Ph-H), 7.82 (d, 1H, *J* = 7.4 Hz, Ph-H), 7.61 (d, 1H, *J* = 7.4 Hz, Ph-H), 7.05 (d, 2H, *J* = 8.9 Hz, Ph-H), 4.04 (t, 2H, *J* = 6.5 Hz, –OCH<sub>2</sub>–), 1.82 (quint, 2H, *J* = 6.9 Hz, –OC–CH<sub>2</sub>–), 1.49 (m, 2H, –CH<sub>2</sub>–), 1.2–1.4 (m, 16H, –CH<sub>2</sub>–), 0.88 (t, 3H, *J* = 6.7 Hz, –CH<sub>3</sub>), 0.34 (s, 9H, –Si–CH<sub>3</sub>). MS (CI): *m/z* 493.272 (calcd. for [M + H]<sup>+</sup> 493.271).

**4-(4'-*n*-Dodecyloxyphenyl)-7-ethynylbenzo[c][1,2,5]thiadiazole.** 4-(4'-*n*-Dodecyloxyphenyl)-7-(trimethylsilyl-ethynyl)benzo[c][1,2,5]thiadiazole (0.223 g, 4.53 × 10<sup>-4</sup> mol) was dissolved in a mixture of THF (7.0 mL) and MeOH (3.0 mL). K<sub>2</sub>CO<sub>3</sub> (85 mg, 6.2 × 10<sup>-4</sup> mol) was added, and the reaction mixture was stirred for 2 h under Ar. The reaction mixture was filtered and the filtrate evaporated. Yield 0.190 g (99.7% based on 0.223 g of 4-(4'-*n*-dodecyloxyphenyl)-7-(trimethylsilyl-ethynyl)benzo[c][1,2,5]thiadiazole). <sup>1</sup>H NMR (300 MHz; CDCl<sub>3</sub>): δ, ppm 7.90 (d, 2H, *J* = 8.9 Hz, Ph-H), 7.86 (d, 1H, *J* = 7.3 Hz, Ph-H), 7.63 (d, 1H, *J* = 7.4 Hz, Ph-H), 7.06 (d, 2H, *J* = 8.9 Hz, Ph-H), 4.04 (t, 2H, *J* = 6.5 Hz, –OCH<sub>2</sub>–), 3.60 (s, 1H, ethynyl-H), 1.83 (quint, 2H,

$J = 6.9$  Hz,  $-\text{OC}-\text{CH}_2-$ ), 1.49 (m, 2H,  $-\text{CH}_2-$ ), 1.2–1.4 (m, 16H,  $-\text{CH}_2-$ ), 0.88 (t, 3H,  $J = 6.7$  Hz,  $-\text{CH}_3$ ). MS (ESI):  $m/z$  421.233 (calcd. for  $[\text{M} + \text{H}]^+$  421.231).

**4-([4'-(4''-*n*-Dodecyloxyphenyl)benzo[c][1,2,5]thiadiazol-7'-yl)ethynyl)-7-iodobenzo[c][1,2,5]thiadiazole.** 4-(4'-*n*-Dodecyloxyphenyl)-7-ethynylbenzo[c][1,2,5]thiadiazole (0.120 g,  $2.85 \times 10^{-4}$  mol), 4,7-diiodobenzo[c][1,2,5]thiadiazole [99] (0.232 g,  $5.98 \times 10^{-4}$  mol),  $\text{Pd}_2\text{dba}_3$  (32.8 mg,  $3.6 \times 10^{-5}$  mol),  $\text{AsPh}_3$  (92.4 mg,  $3.0 \times 10^{-4}$  mol), and dry THF (15 mL) were added to a 100-mL round-bottom flask. Ar was bubbled into the reaction mixture for 5 min before diisopropylethylamine (1.0 mL) was added. The reaction mixture was stirred at 48 °C for 12.5 h under Ar. After cooling, the solvent was evaporated. The residue was chromatographed on silica gel with 8:1 hexanes:THF. The product was further purified by size exclusion column chromatography (BioRad Bio-Beads SX-1 packed in THF, gravity flow). Yield 69.8 mg (36% based on 0.120 g of 4-(4'-*n*-dodecyloxyphenyl)-7-ethynylbenzo[c][1,2,5]thiadiazole).  $^1\text{H}$  NMR (300 MHz;  $\text{CDCl}_3$ ):  $\delta$ , ppm 8.16 (d, 1H,  $J = 7.5$  Hz, Ph-H), 8.03 (d, 1H,  $J = 7.4$  Hz, Ph-H), 7.96 (d, 2H,  $J = 8.9$  Hz, Ph-H), 7.71 (d, 1H,  $J = 7.4$  Hz, Ph-H), 7.70 (d, 1H,  $J = 7.5$  Hz, Ph-H), 7.08 (d, 2H,  $J = 8.9$  Hz, Ph-H), 4.05 (t, 2H,  $J = 6.5$  Hz,  $-\text{OCH}_2-$ ), 1.84 (quint, 2H,  $J = 7.0$  Hz,  $-\text{OC}-\text{CH}_2-$ ), 1.49 (m, 2H,  $-\text{CH}_2-$ ), 1.2–1.4 (m, 16H,  $-\text{CH}_2-$ ), 0.88 (t, 3H,  $J = 6.6$  Hz,  $-\text{CH}_3$ ). MS (MALDI-TOF):  $m/z$  680.09 (calcd. for  $[\text{M}]^+$  680.110).

**(5,15-Bis([7'-(4''-*n*-dodecyloxyphenyl)benzo[c][1'',2'',5'']thiadiazol-4''-yl)ethynyl)benzo[c]-[1',2',5']thiadiazol-4'-yl)ethynyl)-10,20-bis[2',6'-bis(3'',3''-dimethyl-1''-butyloxy)phenyl]porphinato)zinc(II) (7).** 4-([4'-(4''-*n*-dodecyloxyphenyl)benzo[c][1',2',5']thiadiazol-7'-yl)ethynyl)-7-iodobenzo[c][1,2,5]thiadiazole (31.0 mg,  $4.55 \times 10^{-5}$  mol), 5,15-diethynyl-10,20-bis[2',6'-bis(3'',3''-dimethyl-1''-butyloxy)phenyl]porphinato)zinc(II) (22.2 mg,  $2.28 \times 10^{-5}$  mol),  $\text{Pd}(\text{PPh}_3)_4$  (9.1 mg,  $7.9 \times 10^{-6}$  mol),  $\text{CuI}$  (1.7 mg,  $8.9 \times 10^{-6}$  mol), and dry THF (8.0 mL) were added to a 100-mL round-bottom flask. Ar was bubbled into the reaction mixture for 5 min before piperidine (0.50 mL) was added. The reaction mixture was stirred at 50 °C for 3.5 h under Ar. After cooling, the solvent was evaporated. The residue was chromatographed on silica gel with 3:1 hexanes:THF as the eluent. The product was further purified by size exclusion column chromatography (BioRad Bio-Beads SX-1 packed in THF, gravity flow). Yield 30.2 mg (64% based on 31.0 mg of 4-([4'-(4''-*n*-dodecyloxyphenyl)benzo[c][1',2',5']thiadiazol-7'-yl)ethynyl)-7-iodobenzo[c][1,2,5]thiadiazole).  $^1\text{H}$  NMR (300 MHz; 1 drop pyridine- $d_5$  in  $\text{CDCl}_3$ ):  $\delta$ , ppm 9.92 (d, 4H,  $J = 4.6$  Hz,  $\beta$ -H), 8.89 (d, 4H,  $J = 4.5$  Hz,  $\beta$ -H), 8.21 (d, 2H,  $J = 7.4$  Hz, Ph-H), 8.13 (d, 2H,  $J = 7.4$  Hz, Ph-H), 8.09 (d, 2H,  $J = 7.4$  Hz, Ph-H), 7.98 (d, 4H,  $J = 8.7$  Hz, Ph-H), 7.75 (d, 2H,  $J = 7.3$  Hz, Ph-H), 7.73 (t, 2H,  $J = 8.3$  Hz, Ph-H), 7.09 (d, 4H,  $J = 8.8$  Hz, Ph-H), 7.04 (d, 4H,  $J = 8.5$  Hz, Ph-H), 4.06 (t,

4H,  $J = 6.4$  Hz,  $-\text{O}-\text{CH}_2-\text{C}$ ), 3.94 (t, 8H,  $J = 7.5$  Hz,  $-\text{O}-\text{CH}_2-\text{C}$ ), 1.85 (quint, 4H,  $J = 7.0$  Hz,  $-\text{O}-\text{CH}_2-\text{C}$ ), 1.50 (m, 4H,  $-\text{CH}_2-$ ), 1.15–1.40 (m, 32H,  $-\text{CH}_2-$ ), 0.89 (t, 6H,  $-\text{CH}_3$ ), 0.85 (t, 8H,  $J = 7.5$  Hz,  $-\text{OC}-\text{CH}_2-$ ), 0.39 (s, 36H,  $-\text{C}-\text{CH}_3$ ). MS (MALDI-TOF):  $m/z$  2076.99 (calcd. for  $[\text{M}]^+$  2076.857).

**5,15-Bis([7'-(4''-*N,N*-dihexylaminophenylethynyl)benzo[c][1',2',5']thiadiazol-4'-yl)ethynyl)-10,20-bis[2',6'-bis(3'',3''-dimethyl-1''-butyloxy)phenyl]porphinato)zinc(II) (8).** 4-(4'-*N,N*-Dihexylaminophenylethynyl)-7-iodobenzo[c][1,2,5]thiadiazole [99] (73.6 mg,  $1.35 \times 10^{-4}$  mol), 5,15-diethynyl-10,20-bis[2',6'-bis(3'',3''-dimethyl-1''-butyloxy)phenyl]porphinato)zinc(II) (59.0 mg,  $6.05 \times 10^{-5}$  mol),  $\text{Pd}(\text{PPh}_3)_4$  (15.6 mg,  $1.35 \times 10^{-5}$  mol),  $\text{CuI}$  (1.0 mg,  $5.3 \times 10^{-6}$  mol), and dry THF (6.0 mL) were added to a 100-mL round-bottom flask. Ar was bubbled into the reaction mixture for 5 min before piperidine (0.50 mL) was added. The reaction mixture was stirred at 49 °C for 20 h under Ar. After cooling, the solvent was evaporated. The residue was chromatographed on silica gel with 5:1 hexanes:THF as the eluent. The product was further purified by size exclusion column chromatography (BioRad Bio-Beads SX-1 packed in THF, gravity flow). Yield 0.107 g (98% based on 59.0 mg of 5,15-diethynyl-10,20-bis[2',6'-bis(3'',3''-dimethyl-1''-butyloxy)phenyl]porphinato)zinc(II)).  $^1\text{H}$  NMR (300 MHz;  $\text{CDCl}_3$ ):  $\delta$ , ppm 9.99 (d, 4H,  $J = 4.6$  Hz,  $\beta$ -H), 8.94 (d, 4H,  $J = 4.6$  Hz,  $\beta$ -H), 8.17 (d, 2H,  $J = 7.4$  Hz, Ph-H), 7.89 (d, 2H,  $J = 7.4$  Hz, Ph-H), 7.73 (t, 2H,  $J = 8.4$  Hz, Ph-H), 7.56 (d, 4H,  $J = 7.7$  Hz, Ph-H), 7.03 (d, 4H,  $J = 8.5$  Hz, Ph-H), 6.64 (d, 4H,  $J = 9.0$  Hz, Ph-H), 3.94 (t, 8H,  $J = 7.3$  Hz,  $-\text{O}-\text{CH}_2-\text{C}$ ), 3.32 (t, 8H,  $J = 7.6$  Hz,  $-\text{N}-\text{CH}_2-\text{C}$ ), 1.5–1.7 (m, 4H,  $-\text{CH}_2-$ ), 1.25–1.45 (m, 24H,  $-\text{CH}_2-$ ), 0.8–1.0 (m, 20H,  $-\text{O}-\text{C}-\text{CH}_2-$  and  $-\text{CH}_3$ ), 0.26 (s, 36H,  $-\text{C}-\text{CH}_3$ ). MS (MALDI-TOF):  $m/z$  1807.1 (calcd. for  $[\text{M}]^+$  1806.901).

**4-(4'-(*N,N*-Dihexylamino)phenylethenyl)-7-iodobenzo[c][1,2,5]thiadiazole.** *N,N*-Dihexylamino-4-vinylbenzene [99] (0.154 g,  $5.36 \times 10^{-4}$  mol), 4,7-diiodobenzo[c][1,2,5]thiadiazole [99] (0.309 g,  $7.96 \times 10^{-4}$  mol),  $\text{Pd}_2\text{dba}_3$  (50.4 mg,  $5.5 \times 10^{-5}$  mol), and dry 1,4-dioxane (7.0 mL) were added to a 100-mL round-bottom flask. Ar was bubbled into the reaction mixture for 5 min before dicyclohexylmethylamine (0.50 mL) and  $\text{P}(\text{t-Bu})_3$  (10 wt% in hexanes, 1.00 mL,  $3.3 \times 10^{-4}$  mol) were added. The reaction mixture was stirred at 57 °C for 48 h under Ar. After the solvent was evaporated, the reaction mixture was chromatographed on silica gel with 8:1 hexanes:THF. The product was further purified by size exclusion column chromatography (BioRad Bio-Beads SX-1 packed in THF, gravity flow). Yield 42.2 mg (14% based on 0.154 g of *N,N*-dihexylamino-4-vinylbenzene).  $^1\text{H}$  NMR (300 MHz;  $\text{CDCl}_3$ ):  $\delta$ , ppm 8.04 (d, 1H,  $J = 7.6$  Hz, Ph-H), 7.84 (d, 1H,  $J = 16.4$  Hz, vinyl-H), 7.50 (d, 2H,  $J = 8.8$  Hz, Ph-H), 7.38 (d, 1H,  $J = 16.2$  Hz, vinyl-H), 7.37 (d, 1H,  $J = 7.8$  Hz, Ph-H), 6.64 (d, 2H,  $J = 8.9$  Hz, Ph-H), 3.30 (t, 4H,  $J = 7.6$  Hz,  $-\text{NCH}_2-$ ), 1.61 (m, 4H,

–NC–CH<sub>2</sub>–), 1.15–1.45 (m, 12H, –CH<sub>2</sub>–), 0.91 (t, 6H, *J* = 6.7 Hz, –CH<sub>3</sub>). MS (CI): *m/z* 547.1481 (calcd. for [M]<sup>+</sup> 547.148).

**(5,15-Bis([7'-(4''-*N,N*-dihexylaminophenylethenyl)benzo[c][1',2',5']thiadiazol-4'-yl]ethynyl)-10,20-bis[2',6'-bis(3'',3''-dimethyl-1''-butyloxy)phenyl]porphinato)zinc(II) (9).** 4-(4'-*N,N*-Dihexylaminophenylethenyl)-7-iodobenzo[c][1,2,5]thiadiazole (42.2 mg, 7.71 × 10<sup>-5</sup> mol), 5,15-diethynyl-10,20-bis[2',6'-bis(3'',3''-dimethyl-1''-butyloxy)phenyl]porphinato zinc(II) (38.0 mg, 3.90 × 10<sup>-5</sup> mol), Pd(PPh<sub>3</sub>)<sub>4</sub> (10.5 mg, 9.1 × 10<sup>-6</sup> mol), CuI (1.0 mg, 5.3 × 10<sup>-6</sup> mol), and dry THF (5.0 mL) were added to a 100-mL round-bottom flask. Ar was bubbled into the reaction mixture for 5 min before piperidine (0.50 mL) was added. The reaction mixture was stirred at 47 °C for 43 h under Ar. After cooling, the solvent was evaporated. The residue was chromatographed on silica gel with 5:1 hexanes:THF as the eluent. The product was further purified by size exclusion column chromatography (BioRad Bio-Beads SX-1 packed in THF, gravity flow). Yield 30.4 mg (43% based on 42.2 mg of 4-(4'-*N,N*-dihexylaminophenylethenyl)-7-iodobenzo[c][1,2,5]thiadiazole). <sup>1</sup>H NMR (500 MHz; 1 drop pyridine-d<sub>5</sub> in CDCl<sub>3</sub>): δ, ppm 9.90 (d, 4H, *J* = 4.5 Hz, β-H), 8.84 (d, 4H, *J* = 4.5 Hz, β-H), 8.14 (d, 2H, *J* = 7.2 Hz, Ph-H), 7.99 (d, 2H, *J* = 16.1 Hz, vinyl-H), 7.77 (d, 2H, *J* = 7.4 Hz, Ph-H), 7.71 (t, 2H, *J* = 8.5 Hz, Ph-H), 7.57 (d, 4H, *J* = 8.4 Hz, Ph-H), 7.55 (d, 2H, *J* = 16.0 Hz, vinyl-H), 7.02 (d, 4H, *J* = 8.6 Hz, Ph-H), 6.68 (d, 4H, *J* = 8.7 Hz, Ph-H), 3.92 (t, 8H, *J* = 7.4 Hz, –O–CH<sub>2</sub>–C), 3.33 (t, 8H, *J* = 7.6 Hz, –N–CH<sub>2</sub>–C), 1.63 (m, 8H, –CH<sub>2</sub>–), 1.3–1.4 (m, 24H, –CH<sub>2</sub>–), 0.93 (t, 12H, *J* = 6.7 Hz, –CH<sub>3</sub>), 0.84 (t, 8H, *J* = 7.5 Hz, –O–C–CH<sub>2</sub>–), 0.39 (s, 36H, –C–CH<sub>3</sub>). MS (MALDI-TOF): *m/z* 1811.0 (calcd. for [M]<sup>+</sup> 1810.932).

## RESULTS AND DISCUSSION

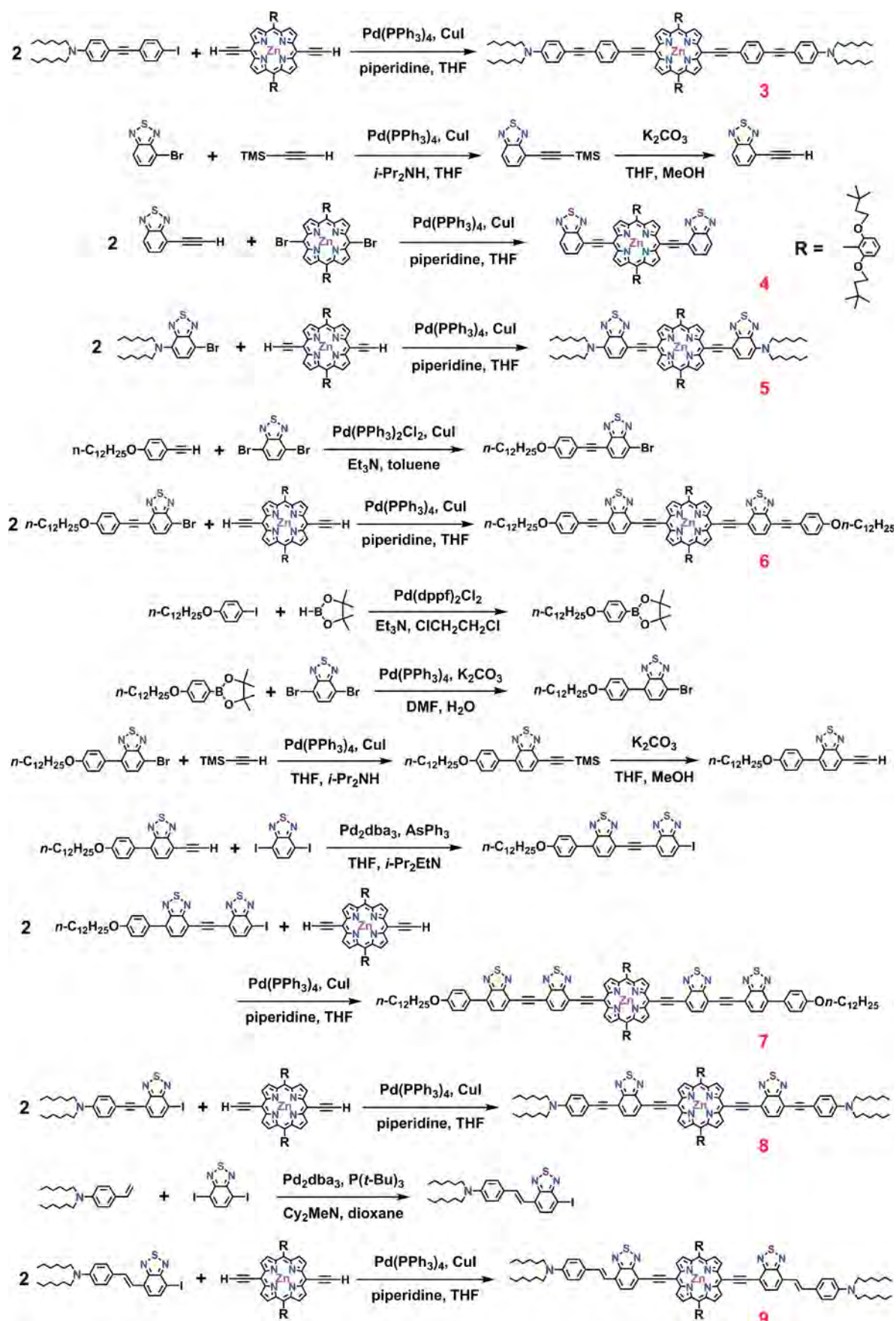
### Synthesis

Chromophores **2–9** are based on a (5,15-diethynylporphinato)zinc(II) framework and feature symmetric donor or acceptor units appended at the *meso*-ethynyl positions that derive from phenylene and benzo[c][1,2,5]thiadiazole building blocks; these structures, along with the TMS-protected (5,15-diethynyl-10,20-bis[3',5'-bis(9''-methoxy-1'',4'',7''-trioxanonyl)phenyl]porphinato)zinc(II) reference monomer (**1**), are shown in Fig. 1. Scheme 1 details the syntheses of fluorophores **3–9**. The proquinoidal spacer unit, benzo[c][1,2,5]thiadiazole, which extends π-conjugation from the porphyrin core for **4–9**, has been used not only as a common building block to enhance electronic delocalization within π-conjugated oligomers and polymers, but also as an electron accepting moiety [55, 99, 101, 102]. Incorporation of benzo[c][1,2,5]thiadiazole into conjugated organic networks is made

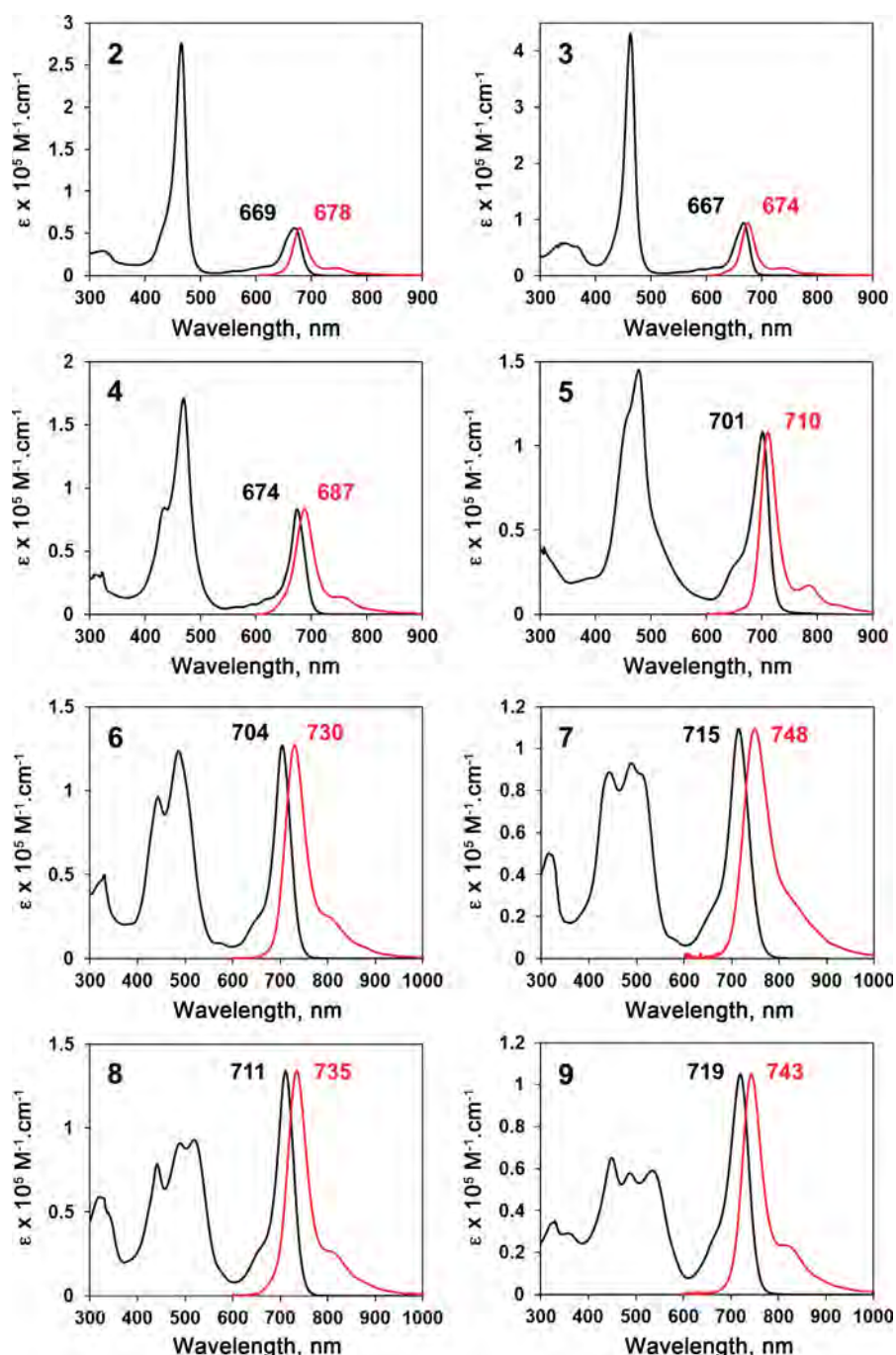
facile through the agency of palladium-catalyzed cross-coupling reactions. In **2–9**, each aromatic unit is linked by either ethyne or ethene units through Sonogashira or Heck coupling reactions. The 10- and 20-*meso*-positions of the (porphinato)zinc cores of **1–9** feature either 3,5-bis(9'-methoxy-1',4',7'-trioxanonyl)phenyl (**1**) or 2,6-bis(3',3'-dimethyl-1'-butyloxy)phenyl substituents (**2–9**) to ensure high solubility. Fluorophores **2–9** were synthesized by Pd-mediated cross-coupling reactions involving appropriately modified terminal substituents and 5,15-dibromo- or 5,15-diethynyl(porphinato)zinc(II) synthons (Experimental Section).

### Steady-state electronic absorption spectra

Electronic absorption spectra of NIR fluorophores **2–9** recorded in THF solvent are displayed in Fig. 2. These chromophores feature lowest energy Q absorption bands that are significantly red-shifted (1985–3070 cm<sup>-1</sup>) and intensified (~20 to 50-fold enhanced in oscillator strength) relative to the analogous transition manifold of [5,10,15,20-tetraphenyl(porphinato)]zinc(II) (**TPPZn**) [100]. While chromophores **2** and **3** manifest spectral signatures akin to other closely related, [5,15-bis(aryl)ethynyl]-10,20-diphenylporphinato]zinc(II) complexes [42], note that structures **4–9**, which incorporate benzo[c][1,2,5]thiadiazole units, manifest spectra that bear distinct similarities to chlorophylls and structurally related molecules [103]. The extinction coefficients of the x-polarized Q-band [Q<sub>x</sub>(0,0)] transitions for **4–9** are significantly enhanced relative to **2** and **3**, which bear 5,15-bis(arylethynyl) macrocycle substituents (Fig. 2, Table 1). As conjugation is expanded at the porphyrin (5,15-bis(benzo[c][1',2',5']thiadiazol-4'-ylethynyl) moieties [**4**→**5**→(**6**, **7**, **8**, **9**)] (Fig. 2, Table 1), increasingly pronounced B-state (Soret) transition manifold splitting is evident; note that the Q<sub>x</sub>(0,0) transition extinction coefficients for fluorophores **6–9** surpass those of their most intense respective B-band absorption, and exceed 10<sup>5</sup> M<sup>-1</sup>.cm<sup>-1</sup>, a value comparable to Q-state absorptions characteristic of chlorophylls and phthalocyanines [30, 37]. In contrast to the full widths at half maximum (FWHM) values for the B-band manifolds of **6–9**, which span 4430–6480 cm<sup>-1</sup> and greatly exceed that of the **TPPZn** benchmark (660 cm<sup>-1</sup>), the FWHMs of their respective Q<sub>x</sub>(0,0) transitions range from 812 to 940 cm<sup>-1</sup>. Compounds **3** and **8** highlight the qualitative impact of 5,15-bis(benzo[c][1',2',5']thiadiazol-4'-ylethynyl) substituents relative to corresponding 5,15-bis(aryl)ethynyl groups upon the (porphinato)zinc chromophore long-wavelength absorption maximum: note the x-polarized Q-state absorption maximum for **8** is 928 cm<sup>-1</sup> red-shifted relative to that for **3**. The enhanced π-conjugation afforded by the benzo[c][1,2,5]thiadiazolyl group is consistent with its proquinoidal character [104], and earlier work which establishes that *meso* (benzo[c][1,2,5]thiadiazol-4-ylethynyl) substituents



Scheme 1. Synthetic routes to 5,15-diethynyl-(porphinato)zinc(II)-based fluorophores 3–9 and to key precursor compounds



**Fig. 2.** Absorption (black line) and fluorescence (red line) spectra of 5,15-diethynyl-(porphinato)zinc(II)-based fluorophores **2–9** recorded in THF solvent

drive pronounced  $S_1$  state cumuleninc character for (porphinato)zinc-based chromophores [55].

### Fluorescence spectra

Figure 2 also highlights the fluorescence spectra recorded for chromophores **2–9** in THF solvent; these spectra mirror the respective lowest energy Q-state absorption manifolds for these chromophores. The fluorescence energy maxima red-shift with increasing

degrees of conjugation [**4**→**5**→(**6**, **7**, **8**, **9**)] (Fig. 2, Table 1); note in this regard that fluorophore **7** features an emission band maximum centered at 748 nm, and that structures **2–9** feature narrow fluorescence bands ( $620 \text{ cm}^{-1} < \text{FWHM}(S_1 \rightarrow S_0) < 1130 \text{ cm}^{-1}$ ) that are significantly reduced with respect to the  $S_1 \rightarrow S_0$  FWHM value determined for **TPPZn** ( $1924 \text{ cm}^{-1}$ ). Note also that the narrow fluorescence bands of **2–9** resemble the spectral breadths of their respective lowest energy Q-state absorption manifolds (Table 1) and feature low-magnitude

**Table 1.** Comparative electronic absorption and steady-state fluorescence spectral data determined for chromophores **1–9** in THF solvent relative to the **TPPZn** benchmark

	$\lambda_{\max}(S_0 \rightarrow S_1)$ , nm <sup>a</sup>	$\epsilon_{\max}(S_0 \rightarrow S_1)$ , M <sup>-1</sup> .cm <sup>-1a</sup>	FWHM ( $S_0 \rightarrow S_1$ ), cm <sup>-1a</sup>	$\lambda_{\max}$ ( $S_1 \rightarrow S_0$ ), nm	FWHM ( $S_1 \rightarrow S_0$ ), cm <sup>-1</sup>	Stokes shift, cm <sup>-1c</sup>
<b>TPPZn</b> (in benzene)	589	3680	577	605	1924 <sup>b</sup>	449
<b>1</b>	632	33,200	438	638	626	149
<b>2</b>	669	57,000	824	678	656	198
<b>3</b>	667	94,000	704	674	618	156
<b>4</b>	674	84,000	654	687	809	281
<b>5</b>	701	108,000	737	710	649	181
<b>6</b>	704	127,000	812	730	922	506
<b>7</b>	715	109,400	939	748	1131	617
<b>8</b>	711	134,000	818	735	890	459
<b>9</b>	719	105,000	940	743	870	449

<sup>a</sup>For **1–9**, the value reported corresponds to that for the x-polarized ( $S_0 \rightarrow S_1$ ) absorption. Note that for the **TPPZn** chromophore, the value reported corresponds to that for the Q(0,0) transition. <sup>b</sup>The value reported corresponds to that for the Q-state manifold. <sup>c</sup>The difference in energy between the absorption ( $S_0 \rightarrow S_1$ ) and fluorescence ( $S_1 \rightarrow S_0$ ) band maxima.

**Table 2.** Comparative x-polarized [ $S_0 \rightarrow S_1$ ;  $Q_x(0,0)$ ] integrated absorptive oscillator strengths, fluorescence quantum yields, fluorescence lifetimes, experimental and calculated radiative rate constants, and experimental non-radiative rate constants determined for chromophores **1–9** in THF solvent relative to the **TPPZn** benchmark

	Oscillator strength <sup>a</sup>	$\Phi_f^b$	$\tau_f$ , ns	$k_r$ ( $\times 10^7$ s <sup>-1</sup> )	$k_{nr}$ ( $\times 10^7$ s <sup>-1</sup> )	$k_r(\text{calc})^d$ ( $\times 10^7$ s <sup>-1</sup> )
<b>TPPZn</b> (in benzene)	0.00977	0.033 <sup>c</sup>	2.09	1.58	46.27	1.78
<b>1</b>	0.0669	0.058 (0.021)	1.99	2.91	47.34	4.30
<b>2</b>	0.216	0.22 (0.044)	2.04	10.78	38.24	7.72
<b>3</b>	0.304	0.25 (0.043)	1.63	15.34	46.01	11.1
<b>4</b>	0.253	0.15 (0.013)	1.42	10.56	59.86	9.23
<b>5</b>	0.366	0.19 (0.012)	1.20	15.83	67.50	11.3
<b>6</b>	0.474	0.32 (0.020)	1.97	16.24	34.52	13.0
<b>7</b>	0.473	0.35 (0.035)	1.87	18.72	34.76	11.8
<b>8</b>	0.504	0.36 (0.032)	1.71	21.05	37.43	13.8
<b>9</b>	0.454	0.26 (0.029)	1.37	18.98	54.01	11.5

<sup>a</sup> $f = 4.6 \times 10^{-9} \cdot \epsilon_{\max} \cdot \Delta\nu_{1/2}$ ; the oscillator strengths were calculated for the x-polarized ( $S_0 \rightarrow S_1$ ) absorption. Note that for the **TPPZn** chromophore, the reported integrated oscillator strength corresponds to that for the Q-state transition manifold. <sup>b</sup>Fluorescence quantum yields determined relative to free base TPP in benzene ( $\Phi_f = 0.13$ ); parenthetical values represent standard deviations from the mean. <sup>c</sup>From Ref. 100. <sup>d</sup>Calculated using Equation 2.

Stokes shifts (155–620 cm<sup>-1</sup>), congruent with a minimal degree of excited-state structural relaxation relative to the ground-state conformation for these chromophores.

### Strickler–Berg analysis of the $S_1$ -state photophysics of fluorophores **2–9**

Relative to the (porphinato)zinc chromophore **TPPZn** ( $\Phi_f = 0.033$ ), the fluorescence quantum yields of fluorophores **2–9** are particularly dramatic (0.15 <

$\Phi_f < 0.36$ ; Table 2). Further, given the shape and intensity of the steady-state fluorescence spectra of these monomeric (porphinato)zinc chromophores that bear either 5,15-bis[(ary)ethynyl] or 5,15-bis(benzo[c][1',2',5']thiadiazol-4'-ylethynyl) substituents, coupled with the fact that the emission band maxima of these species are significantly red-shifted (1690–3160 cm<sup>-1</sup>) with respect to the **TPPZn** benchmark (Table 1), suggest an analysis of the  $S_1$  state photophysics within the context of the Strickler–Berg model, which relates increases in



the integrated oscillator strength of the lowest-energy ground-state absorption band with a corresponding augmentation of the radiative decay rate constant ( $k_r$ , Equation 2) [22].

$$k_r = 2.880 \times 10^{-9} n^2 \langle \tilde{\nu}_f^{-3} \rangle_{Av}^{-1} \frac{g_l}{g_u} \int \epsilon d \ln \tilde{\nu} \quad (2)$$

Here  $k_r$  is radiative decay rate constant,  $n$  is the refractive index of the solvent,  $g_l$  and  $g_u$  are the respective degeneracies of the ground and excited states,  $\epsilon$  is the molar extinction coefficient,  $\nu$  is the frequency of the transition in  $\text{cm}^{-1}$ . The term  $\langle \tilde{\nu}_f^{-3} \rangle_{Av}^{-1}$  is expressed as;

$$\langle \tilde{\nu}_f^{-3} \rangle_{Av}^{-1} = \frac{\int I(\nu) d\nu}{\int \nu^{-3} I(\nu) d\nu} \quad (3)$$

where  $I$  is the intensity of the fluorescence spectrum, measured in terms of relative numbers of quanta at each frequency. The fluorescence quantum yield ( $\Phi_f$ ) is simply described by Equation 4;

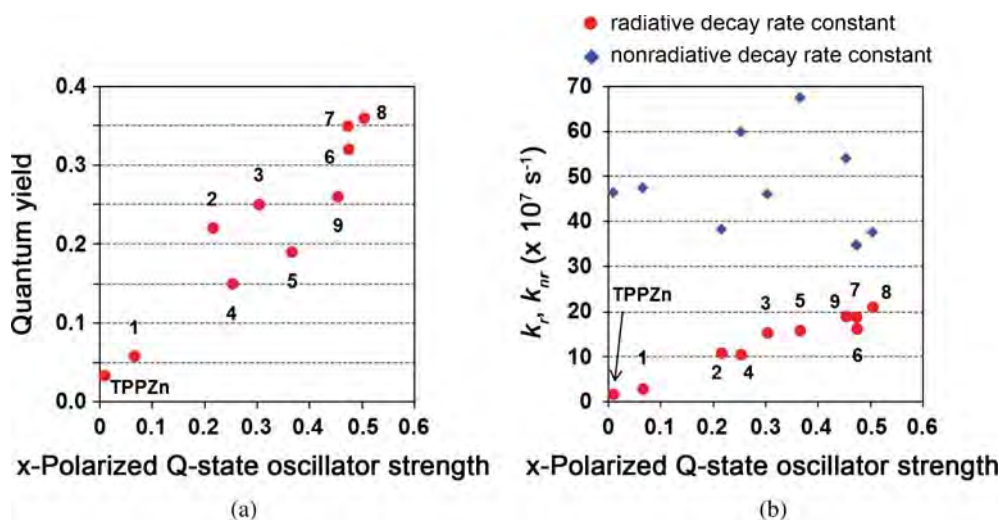
$$\Phi_f = \frac{k_r}{k_r + k_{nr}} \quad (4)$$

where  $k_{nr}$  describes the magnitude of the non-radiative decay rate constant, which corresponds to the sum of the internal conversion ( $k_{ic}$ ) and intersystem crossing ( $k_{isc}$ ) rate constants. Provided that the magnitudes of the non-radiative rate remain approximately constant within a family of closely related chromophores, an increase in the integrated oscillator strength results in a corresponding increase in the fluorescence quantum yield.

Figure 3 highlights the x-polarized Q-state oscillator strength dependent fluorescence quantum yields, radiative

rate constants, and non-radiative rate constants of fluorophores **1–9** relative to the **TPPZn** benchmark. Note the distinct increase in the magnitude of the radiative rate constant with increasing x-polarized Q-state oscillator strength (Fig. 3B), and that the measured  $k_r$  values for fluorophores **5–9** exceed that of the **TPPZn** by more than an order of magnitude. This apparent Stricker–Berg dependence of the radiative rate constant upon the integrated lowest energy  $S_0 \rightarrow S_1$  oscillator strength gives rise to a family of porphyrin-based NIR fluorophores in which the longest wavelength emitter (**7**, 748 nm) features a fluorescence quantum yield ( $\Phi_f = 0.35$ ; Tables 1 and 2) that exceeds that of chromophores **1–6** and **9**, which emit to the blue of this wavelength.

As emission wavelengths approach the NIR spectral domain, the simple Stricker–Berg predicted dependence of the radiative rate constant upon the magnitude of the integrated oscillator strength is generally mitigated by expected energy gap law effects [23], where increasing magnitudes of the  $S_0-S_1$  internal conversion rate constant ( $k_{ic}$ ) track with diminishing  $S_0-S_1$  energy gaps and thus sharply decrease  $\Phi_f$ . In these chromophores, two factors conspire to enhance  $\Phi_f$  as emission wavelength increases over the 650–750 nm spectral domain. The first of these derives from the fact that the proquinoidal benzo[c][1,2,5]thiadiazole unit minimizes the extent of excited-state structural relaxation relative the ground-state conformation [55] for chromophores **4–9**, reflected by the narrow fluorescence bands and modest Stokes shifts determined for these species (Fig. 2; Tables 1 and 2), and thereby reduces  $S_1-S_0$  Franck–Condon overlap important for determining the magnitude of  $k_{ic}$ . The second factor that drives this unusual dependence of  $\Phi_f$  upon emission wavelength stems from the fact that for these ethyne-elaborated (porphinato)zinc derivatives, intersystem



**Fig. 3.** x-Polarized Q-state [ $S_0(S_0 \rightarrow S_1)$ ] oscillator strength dependent fluorescence quantum yields, radiative rate constants ( $k_r$ ), and non-radiative rate constants ( $k_{nr}$ ) of diethynyl(porphinato)zinc(II) derivatives (**1–9**) relative to the [5,10,15,20-tetraphenyl-(porphinato)]zinc(II) (**TPPZn**) benchmark. (a) x-Polarized Q-state oscillator strength dependence of the fluorescence quantum yield. (b) x-Polarized Q-state oscillator strength dependence of the radiative and non-radiative decay rate constant magnitudes

crossing into the triplet manifold generates  $T_1$  states that manifest more spatially confined excitations relative to the globally delocalized  $S_1$  states of these chromophores [41, 45, 47, 54, 62]. This diminished overlap of  $S_1$  and  $T_1$  state wavefunctions mitigates  $S_1$ - $T_1$  intersystem crossing rate constants ( $k_{isc}$  values), and thus serves to counter-balance the effect of augmented Franck–Condon mediated internal conversion that typically accompanies  $S_0$ - $S_1$  energy gap reductions; this effect has been detailed previously for closely related compounds [57]. Thus, for **4–9**, extension of x-polarized conjugation of the (5,15-diethynylporphinato)zinc(II) framework *via* the benzo[c][1,2,5]thiadiazole moiety causes the magnitude of  $k_r$  to increase faster than does the magnitude of  $k_{nr}$  as emission wavelength increases, providing substantial fluorescence quantum yields that manifest a weak energy gap law [23] dependence over this spectral regime.

## CONCLUSION

We describe a design strategy for (porphinato)zinc-based chromophores that possess large NIR fluorescence quantum yields. These fluorophores are based on a (5,15-diethynylporphinato)zinc(II) framework and feature symmetric donor or acceptor units appended at the *meso*-ethynyl positions *via* benzo[c][1,2,5]thiadiazole moieties. These chromophores possess red-shifted absorption and emission bands relative to **TPPZn** and (5,15-diethynyl-10,20-arylporphinato)zinc(II) benchmarks that range between 650 and 750 nm and bear distinct spectral similarities to those manifest by chlorophylls and structurally related molecules.

Interestingly, the measured radiative decay rate constants for these emitters track with the integrated oscillator strengths of their respective x-polarized Q-band absorptions, and thus define an unusual family of high quantum yield NIR fluorophores in which emission intensity is governed by a simple Strickler–Berg dependence. These photophysical properties derive from the facts that: (i) the proquinoidal benzo[c][1,2,5]thiadiazole unit minimizes the extent of excited-state structural relaxation relative the ground-state conformation [55], and (ii) *meso*-ethynyl elaborated (porphinato)zinc compounds are characterized by  $T_1$  states that are more spatially confined than their globally delocalized  $S_1$  states [41, 45, 47, 54, 62], which result in diminished  $S_1$ - $T_1$  intersystem crossing rate constants relative to conventional (porphinato)zinc chromophores. For these NIR fluorophores, these effects cause the magnitude of  $k_r$  to increase faster than does the magnitude of  $k_{nr}$  as emission wavelength increases, providing substantial fluorescence quantum yields that manifest a weak energy gap law [23] dependence over the spectral regime (685–750 nm) spanned by these emitters. These designs that take advantage of these photophysical properties make possible broadly absorptive and strongly

emissive NIR fluorophores that derive from a monomeric (5,15-diethynyl-porphinato)zinc framework.

## Acknowledgements

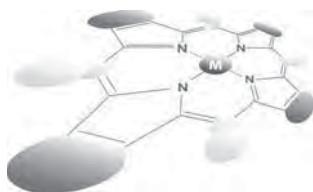
This work was supported through the Department of Defense (W81XWH-13-1-0086). The authors thank Professor Felix N. Castellano and Dr. Radiy Islangulov for their assistance with fluorescence lifetime measurements.

## REFERENCES

- Weissleder R. *Nat. Biotechnol.* 2001; **19**: 316–317.
- Weissleder R and Ntziachristos V. *Nat. Med.* 2003; **9**: 123–128.
- Bremer C, Ntziachristos V and Weissleder R. *Eur. Radiol.* 2003; **13**: 231–243.
- Frangioni JV. *Curr. Opin. Chem. Biol.* 2003; **7**: 626–634.
- Hilderbrand SA and Weissleder R. *Curr. Opin. Chem. Biol.* 2010; **14**: 71–79.
- Martínez-Díaz MV, de la Torre G and Torres T. *Chem. Commun.* 2010; **46**: 7090–7108.
- Liu Y, Lin H, Dy JT, Tamaki K, Nakazaki J, Nakayama D, Uchida S, Kubo T and Segawa H. *Chem. Commun.* 2011; **47**: 4010–4012.
- Chang Y-C, Wang C-L, Pan T-Y, Hong S-H, Lan C-M, Kuo H-H, Lo C-F, Hsu H-Y, Lin C-Y and Diao EW-G. *Chem. Commun.* 2011; **47**: 8910–8912.
- Mathew S, Yella A, Gao P, Humphry-Baker R, Curchod BFE, Ashari-Astani N, Tavernelli I, Rothlisberger U, Nazeeruddin MK and Grätzel M. *Nature Chem.* 2014; **6**: 242–247.
- D'Souza F, Amin AN, El-Khouly ME, Subbaiyan NK, Zandler ME and Fukuzumi S. *J. Am. Chem. Soc.* 2012; **134**: 654–664.
- Balzani V, Credi A and Venturi M. *ChemSusChem* 2008; **1**: 26–58.
- Roncali J. *Chem. Rev.* 1997; **97**: 173–205.
- van Müllekom HAM, Vekemans JAJM, Havinga EE and Meijer EW. *Mater. Sci. Eng.* 2001; **32**: 1–40.
- Tsuda A and Osuka A. *Science* 2001; **293**: 79–82.
- Kiyose K, Kojima H and Nagano T. *Chem. Asian J.* 2008; **3**: 506–515.
- Escobedo JO, Rusin O, Lim S and Strongin RM. *Curr. Opin. Chem. Biol.* 2010; **14**: 64–70.
- Qian G and Wang ZY. *Chem. Asian J.* 2010; **5**: 1006–1029.
- Luo S, Zhang E, Su Y, Cheng T and Shi C. *Biomaterials* 2011; **32**: 7127–7138.
- Mori H, Tanaka T and Osuka A. *J. Mater. Chem. C* 2013; **1**: 2500–2519.
- Zhao W and Carreira EM. *Angew. Chem. Int. Ed.* 2005; **44**: 1677–1679.
- Umezawa K, Nakamura Y, Makino H, Citterio D and Suzuki K. *J. Am. Chem. Soc.* 2008; **130**: 1550–1551.

22. Strickler SJ and Berg RA. *J. Chem. Phys.* 1962; **37**: 814–822.
23. Englman R and Jortner J. *Mol. Phys.* 1970; **18**: 145–164.
24. Gouterman M. *J. Mol. Spectrosc.* 1961; **6**: 138–163.
25. Finikova OS, Cheprakov AV and Vinogradov SA. *J. Org. Chem.* 2005; **70**: 9562–9572.
26. Nakamura J, Okujima T, Tomimori Y, Komobuchi N, Yamada H, Uno H and Ono N. *Heterocycles* 2010; **80**: 1165–1175.
27. Davis NKS, Thompson AL and Anderson HL. *Org. Lett.* 2010; **12**: 2124–2127.
28. Davis NKS, Thompson AL and Anderson HL. *J. Am. Chem. Soc.* 2011; **133**: 30–31.
29. Diev VV, Schlenker CW, Hanson K, Zhong Q, Zimmerman JD, Forrest SR and Thompson ME. *J. Org. Chem.* 2012; **77**: 143–159.
30. Sauer K, Smith JRL and Schultz AJ. *J. Am. Chem. Soc.* 1966; **88**: 2681–2688.
31. Connolly JS, Samuel EB and Janzen AF. *Photochem. Photobiol.* 1982; **36**: 565–574.
32. Forster LS and Livingston R. *J. Chem. Phys.* 1952; **20**: 1315–1320.
33. Kee HL, Kirmaier C, Tang Q, Diers JR, Muthiah C, Taniguchi M, Laha JK, Ptaszek M, Lindsey JS, Bocian DF and Holten D. *Photochem. Photobiol.* 2007; **83**: 1110–1124.
34. Taniguchi M, Cramer DL, Bhise AD, Kee HL, Bocian DF, Holten D and Lindsey JS. *New J. Chem.* 2008; **32**: 947–958.
35. Kozyrev A, Ethirajan M, Chen P, Ohkubo K, Robinson BC, Barkigia KM, Fukuzumi S, Kadish KM and Pandey RK. *J. Org. Chem.* 2012; **77**: 10260–10271.
36. Seybold PG and Gouterman M. *J. Mol. Spectrosc.* 1969; **31**: 1–13.
37. Kobayashi N, Ogata H, Nonaka N and Luk'yanets EA. *Chem. Eur. J.* 2003; **9**: 5123–5134.
38. Susumu K, Maruyama H, Kobayashi H and Tanaka K. *J. Mater. Chem.* 2001; **11**: 2262–2270.
39. Lin VS-Y, DiMugno SG and Therien MJ. *Science* 1994; **264**: 1105–1111.
40. Lin VS-Y and Therien MJ. *Chem. Eur. J.* 1995; **1**: 645–651.
41. Angiolillo PJ, Lin VS-Y, Vanderkooi JM and Therien MJ. *J. Am. Chem. Soc.* 1995; **117**: 12514–12527.
42. LeCours SM, DiMugno SG and Therien MJ. *J. Am. Chem. Soc.* 1996; **118**: 11854–11864.
43. LeCours SM, Philips CM, de Paula JC and Therien MJ. *J. Am. Chem. Soc.* 1997; **119**: 12578–12589.
44. Kumble R, Palese S, Lin VS-Y, Therien MJ and Hochstrasser RM. *J. Am. Chem. Soc.* 1998; **120**: 11489–11498.
45. Shediak R, Gray MHB, Uyeda HT, Johnson RC, Hupp JT, Angiolillo PJ and Therien MJ. *J. Am. Chem. Soc.* 2000; **122**: 7017–7033.
46. Fletcher JT and Therien MJ. *J. Am. Chem. Soc.* 2000; **122**: 12393–12394.
47. Angiolillo PJ, Susumu K, Uyeda HT, Lin VS-Y, Shediak R and Therien MJ. *Synth. Met.* 2001; **116**: 247–253.
48. Fletcher JT and Therien MJ. *Inorg. Chem.* 2002; **41**: 331–341.
49. Fletcher JT and Therien MJ. *J. Am. Chem. Soc.* 2002; **124**: 4298–4311.
50. Susumu K and Therien MJ. *J. Am. Chem. Soc.* 2002; **124**: 8550–8552.
51. Rubtsov IV, Susumu K, Rubtsov GI and Therien MJ. *J. Am. Chem. Soc.* 2003; **125**: 2687–2696.
52. Redmore NP, Rubtsov IV and Therien MJ. *J. Am. Chem. Soc.* 2003; **125**: 8769–8778.
53. Rubtsov IV, Redmore NP, Hochstrasser RM and Therien MJ. *J. Am. Chem. Soc.* 2004; **126**: 2684–2685.
54. Angiolillo PJ, Uyeda HT, Duncan TV and Therien MJ. *J. Phys. Chem. B* 2004; **108**: 11893–11903.
55. Susumu K, Duncan TV and Therien MJ. *J. Am. Chem. Soc.* 2005; **127**: 5186–5195.
56. Susumu K, Frail PR, Angiolillo PJ and Therien MJ. *J. Am. Chem. Soc.* 2006; **128**: 8380–8381.
57. Duncan TV, Susumu K, Sinks LE and Therien MJ. *J. Am. Chem. Soc.* 2006; **128**: 9000–9001.
58. Duncan TV, Wu SP and Therien MJ. *J. Am. Chem. Soc.* 2006; **128**: 10423–10435.
59. Frail PR, Susumu K, Huynh M, Fong J, Kikkawa JM and Therien MJ. *Chem. Mater.* 2007; **19**: 6062–6064.
60. Duncan TV, Ishizuka T and Therien MJ. *J. Am. Chem. Soc.* 2007; **129**: 9691–9703.
61. Duncan TV, Frail PR, Miloradovic IR and Therien MJ. *J. Phys. Chem. B* 2010; **114**: 14696–14702.
62. Angiolillo PJ, Rawson J, Frail PR and Therien MJ. *Chem. Commun.* 2013; **49**: 9722–9724.
63. LeCours SM, Guan H-W, DiMugno SG, Wang CH and Therien MJ. *J. Am. Chem. Soc.* 1996; **118**: 1497–1503.
64. Priyadarshy S, Therien MJ and Beratan DN. *J. Am. Chem. Soc.* 1996; **118**: 1504–1510.
65. Karki L, Vance FW, Hupp JT, LeCours SM and Therien MJ. *J. Am. Chem. Soc.* 1998; **120**: 2606–2611.
66. Uyeda HT, Zhao Y, Wostyn K, Asselberghs I, Clays K, Persoons A and Therien MJ. *J. Am. Chem. Soc.* 2002; **124**: 13806–13813.
67. Duncan TV, Rubtsov IV, Uyeda HT and Therien MJ. *J. Am. Chem. Soc.* 2004; **126**: 9474–9475.
68. Zhang T-G, Zhao Y, Asselberghs I, Persoons A, Clays K and Therien MJ. *J. Am. Chem. Soc.* 2005; **127**: 9710–9720.
69. Zhang T-G, Zhao Y, Song K, Asselberghs I, Persoons A, Clays K and Therien MJ. *Inorg. Chem.* 2006; **45**: 9703–9712.
70. Xu T, Wu SP, Miloradovic I, Therien MJ and Blasie JK. *Nano Lett.* 2006; **6**: 2387–2394.
71. Duncan TV, Song K, Hung S-T, Miloradovic I, Nayak A, Persoons A, Verbiest T, Therien MJ and Clays K. *Angew. Chem. Int. Ed.* 2008; **47**: 2978–2981.

72. Keinan S, Therien MJ, Beratan DN and Yang W. *J. Phys. Chem. A* 2008; **112**: 12203–12207.
73. Therien MJ. *Nature* 2009; **458**: 716–717.
74. Hu X, Xiao D, Keinan S, Asselberghs I, Therien MJ, Clays K, Yang W and Beratan DN. *J. Phys. Chem. C* 2010; **114**: 2349–2359.
75. Gonella G, Dai H-L, Fry HC, Therien MJ, Krishnan V, Tronin A and Blasie JK. *J. Am. Chem. Soc.* 2010; **132**: 9693–9700.
76. Krishnan V, Tronin A, Strzalka J, Fry HC, Therien MJ and Blasie JK. *J. Am. Chem. Soc.* 2010; **132**: 11083–11092.
77. Singh-Rachford TN, Nayak A, Muro-Small ML, Goeb S, Therien MJ and Castellano FN. *J. Am. Chem. Soc.* 2010; **132**: 14203–14211.
78. Ishizuka T, Sinks LE, Song K, Hung S-T, Nayak A, Clays K and Therien MJ. *J. Am. Chem. Soc.* 2011; **133**: 2884–2896.
79. Jiang N, Zuber G, Keinan S, Nayak A, Yang W, Therien MJ and Beratan DN. *J. Phys. Chem. C* 2012; **116**: 9724–9733.
80. Fry HC, Lehmann A, Sinks LE, Asselberghs I, Tronin A, Krishnan V, Blasie JK, Clays K, DeGrado WF, Saven JG and Therien MJ. *J. Am. Chem. Soc.* 2013; **135**: 13914–13926.
81. Deria P, Bargaen CDV, Olivier J-H, Kumbhar AS, Saven JG and Therien MJ. *J. Am. Chem. Soc.* 2013; **135**: 16220–16234.
82. Ostrowski JC, Susumu K, Robinson MR, Therien MJ and Bazan GC. *Adv. Mater.* 2003; **15**: 1296–1300.
83. Banerjee P, Conklin D, Nanayakkara S, Park T-H, Therien MJ and Bonnell DA. *ACS Nano* 2010; **4**: 1019–1025.
84. Conklin D, Park T-H, Nanayakkara S, Therien MJ and Bonnell DA. *Adv. Funct. Mater.* 2011; **21**: 4712–4718.
85. Conklin D, Nanayakkara S, Park T-H, Lagadec MF, Stecher JT, Therien MJ and Bonnell DA. *Nano Lett.* 2012; **12**: 2414–2419.
86. Li Z, Park T-H, Rawson J, Therien MJ and Borguet E. *Nano Lett.* 2012; **12**: 2722–2727.
87. Conklin D, Nanayakkara S, Park T-H, Lagadec MF, Stecher JT, Chen X, Therien MJ and Bonnell DA. *ACS Nano* 2013; **7**: 4479–4486.
88. Ghoroghchian PP, Frail PR, Susumu K, Blessington D, Brannan AK, Bates FS, Chance B, Hammer DA and Therien MJ. *Proc. Natl. Acad. Sci. USA* 2005; **102**: 2922–2927.
89. Ghoroghchian PP, Frail PR, Susumu K, Park T-H, Wu SP, Uyeda HT, Hammer DA and Therien MJ. *J. Am. Chem. Soc.* 2005; **127**: 15388–15390.
90. Wu SP, Lee I, Ghoroghchian PP, Frail PR, Zheng G, Glickson JD and Therien MJ. *Bioconjugate Chem.* 2005; **16**: 542–550.
91. Ghoroghchian PP, Lin JJ, Brannan AK, Frail PR, Bates FS, Therien MJ and Hammer DA. *Soft Matter* 2006; **2**: 973–980.
92. Ghoroghchian PP, Frail PR, Li G, Zupancich JA, Bates FS, Hammer DA and Therien MJ. *Chem. Mater.* 2007; **19**: 1309–1318.
93. Christian NA, Milone MC, Ranka SS, Li G, Frail PR, Davis KP, Bates FS, Therien MJ, Ghoroghchian PP, June CH and Hammer DA. *Bioconjugate Chem.* 2007; **18**: 31–40.
94. Duncan TV, Ghoroghchian PP, Rubtsov IV, Hammer DA and Therien MJ. *J. Am. Chem. Soc.* 2008; **130**: 9773–9784.
95. Ghoroghchian PP, Therien MJ and Hammer DA. *Wiley Interdiscip. Rev.: Nanomed. Nanobiotechnol.* 2009; **1**: 156–167.
96. Christian NA, Benencia F, Milone MC, Li G, Frail PR, Therien MJ, Coukos G and Hammer DA. *Mol. Imaging Biol.* 2009; **11**: 167–177.
97. Kamat NP, Liao Z, Moses LE, Rawson J, Therien MJ, Dmochowski IJ and Hammer DA. *Proc. Natl. Acad. Sci. U.S.A.* 2011; **108**: 13984–13989.
98. Pilgram K, Zupan M and Skiles R. *J. Heterocycl. Chem.* 1970; **7**: 629–633.
99. Susumu K, Fisher JAN, Zheng J, Beratan DN, Yodh AG and Therien MJ. *J. Phys. Chem. A* 2011; **115**: 5525–5539.
100. Quimby DJ and Longo FR. *J. Am. Chem. Soc.* 1975; **97**: 5111–5117.
101. Velusamy M, Justin Thomas KR, Lin JT, Hsu Y-C and Ho K-C. *Org. Lett.* 2005; **7**: 1899–1902.
102. Bundgaard E and Krebs FC. *Sol. Energy Mater. Sol. Cells* 2007; **91**: 954–985.
103. Linnanto J and Korppi-Tommola J. *J. Phys. Chem. A* 2001; **105**: 3855–3866.
104. Neto BAD, Lapis AAM, Júnior ENdS and Dupont J. *Eur. J. Org. Chem.* 2013: 228–255.



# Synthesis and photodynamics of diphenylethynyl-bridged porphyrin-quinoidal porphyrin hybrids

Shuhei Sakatani<sup>a</sup>, Takuya Kamimura<sup>a◇◇</sup>, Kei Ohkubo<sup>b◇</sup>, Shunichi Fukuzumi<sup>b◇</sup>  
and Fumito Tani<sup>\*a◇</sup>

<sup>a</sup>Institute for Materials Chemistry and Engineering, Kyushu University, Fukuoka 812-8581, Japan

<sup>b</sup>Department of Material and Life Science, Graduate School of Engineering, Osaka University, ALCA, Japan Science and Technology (JST), Suita, Osaka 565-0871, Japan

*Dedicated to Professor Shunichi Fukuzumi on the occasion of his retirement*

Received 28 October 2014

Accepted 12 November 2014

**ABSTRACT:** As new donor–acceptor hybrids for energy and/or electron transfer, zinc complex and free-base of a porphyrin-quinoidal porphyrin dyad linked by a diphenylethynyl bridge were prepared *via* Sonogashira and subsequent Takahashi coupling reactions. The quinoidal porphyrin units have two dicyanomethylene groups at the opposite *meso*-positions. The UV-vis absorption spectra of the dyads were almost linear summations of the absorption spectra of each component in comparison with those of the monomeric reference compounds, indicating very weak electronic interactions between the chromophores at the ground state. Both zinc complex and free-base of the reference porphyrin exhibited fluorescence in the range of *ca.* 600–700 nm upon photoexcitation, while the quinoidal porphyrin monomers showed no fluorescence. The considerable quenching (more than 99%) of the porphyrin fluorescence in the dyads suggested significant electronic communications between the subunits of the excited state. The electrochemical analysis confirmed that the first oxidations of the dyads occur at the porphyrin units and the first reductions take place at the quinoidal porphyrin units. Femtosecond laser flash photolysis of the zinc dyad with photoexcitation at 393 nm showed both ultrafast (<1 ps) energy and electron transfer from the porphyrin unit to the quinoidal porphyrin one, which processes resulted in the quenching of the porphyrin fluorescence. On the other hand, the free-base dyad underwent only energy transfer.

**KEYWORDS:** porphyrin, quinoidal porphyrin, donor–acceptor, energy transfer, electron transfer.

## INTRODUCTION

The versatility of chlorophylls to play roles as donors and acceptors in both energy and electron transfer in natural photosynthesis [1] makes porphyrinoids promising for the components in artificial photosynthesis systems [2]. A large variety of donor–acceptor hybrids including porphyrinoids have been designed with the aim to elucidate the mechanism of photoinduced energy and electron transfer and realize efficient processes as

observed in the natural systems [3, 4]. For preparing a new donor–acceptor hybrid, bis-dicyanomethylene-substituted quinoidal porphyrin [5], which is a nonaromatic electron-deficient compound having porphyrin core just as tetracyanoquinodimethane (TCNQ) is a quinoidal form of benzene, is an intriguing candidate for an energy and/or electron acceptor against porphyrinic donors, because it has absorption bands of longer wavelength and a much stronger electron accepting ability than those of normal porphyrins. Although the monomers and homo-dimers of quinoidal porphyrin have been studied by Anderson *et al.* to show near-IR absorption and non-linear optoelectronic properties [5], a hetero-dimer composed of porphyrin and quinoidal porphyrin has never been prepared so

◇ SPP full and ◇◇ student member in good standing

\*Correspondence to: Fumito Tani, email: tanif@ms.ifoc.kyushu-u.ac.jp, tel: +81 92-642-2732, fax: +81 92-642-2732

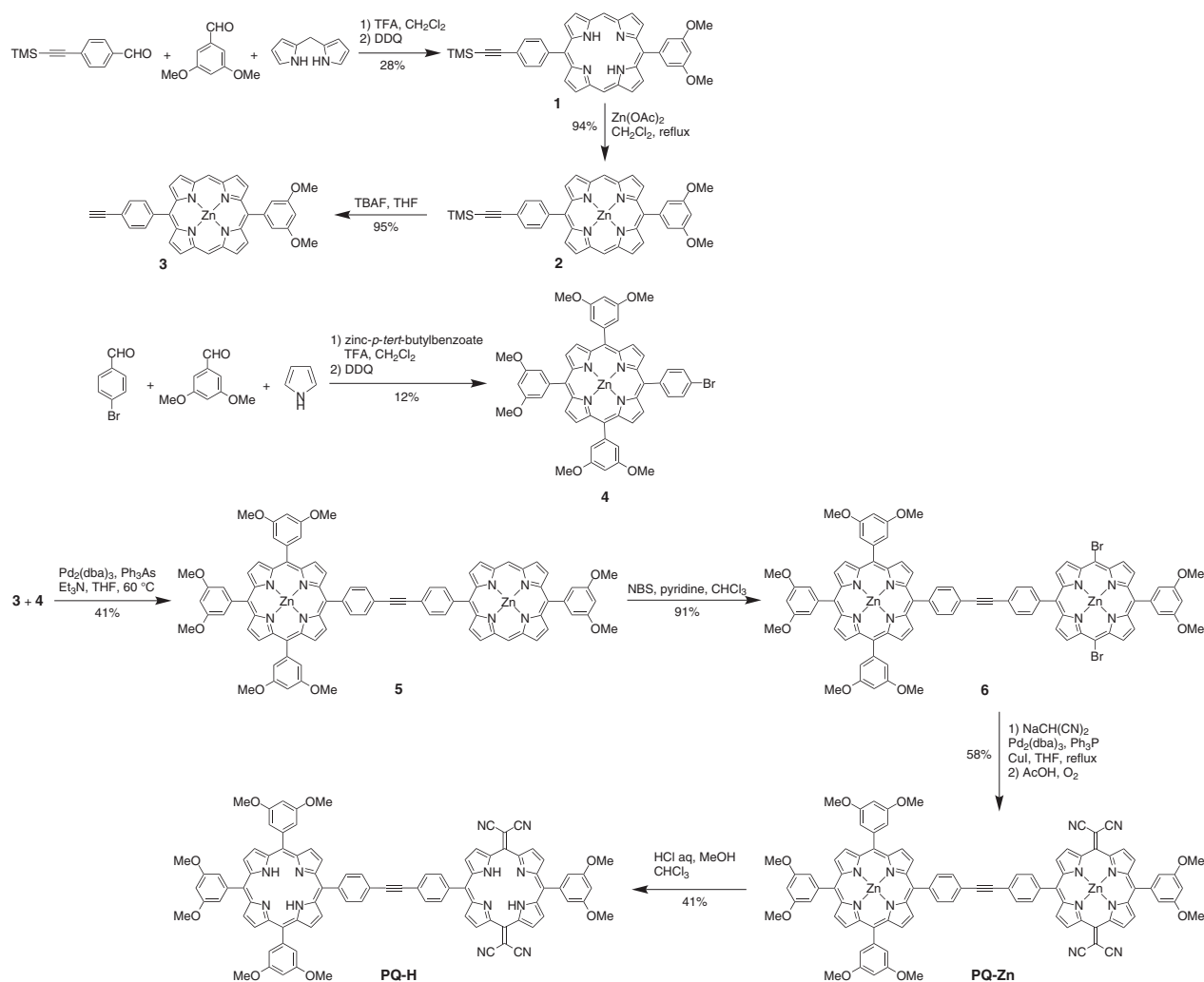
far. Therefore, we have designed zinc complex and free-base of a porphyrin-quinoidal porphyrin dyad linked by a rigid diphenylethynyl group [6] taking into account the knowledge that the most effective system for understanding energy and electron transfer processes is a donor-acceptor dyad of a well-defined relative arrangement. We herein report their synthesis and photophysical properties investigated by spectroscopic and electrochemical methods.

## RESULTS AND DISCUSSION

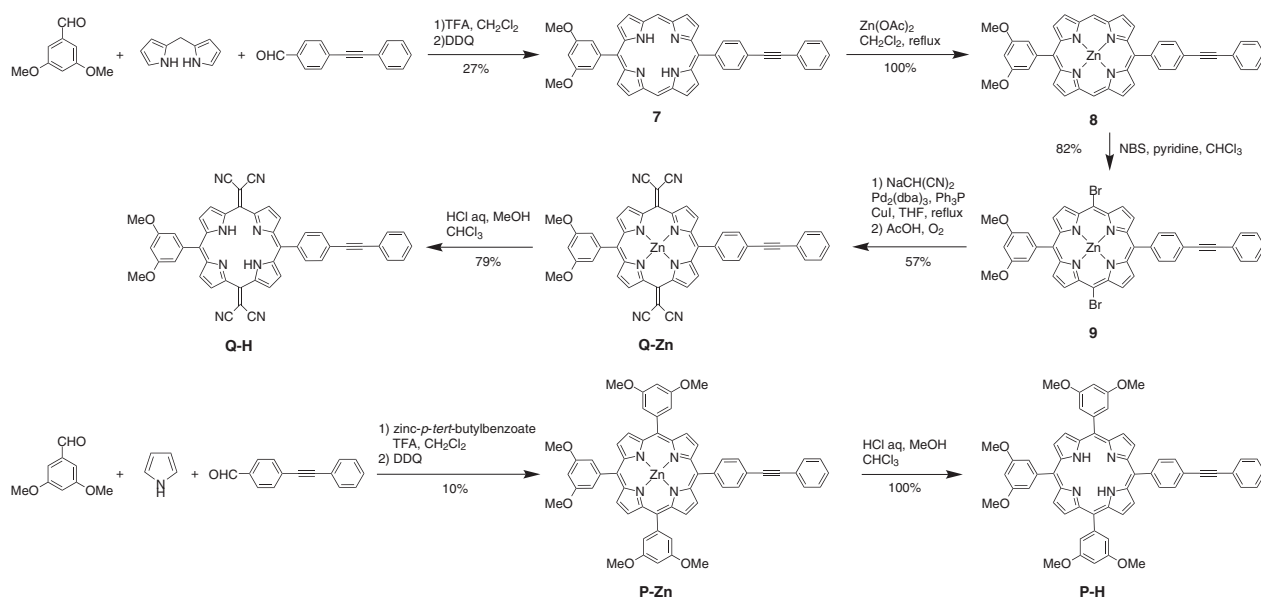
### Synthesis and structures

The synthetic pathways for the dyads and the reference compounds are shown in Schemes 1 and 2. 3,5-Dimethoxyphenyl groups were introduced at the *meso*-positions of the porphyrins **1** and **4** for the efficient

chromatographic separation from other porphyrinic by-products. The polarity of the methoxy group affected the affinity of the produced compounds toward silica-gel to enable the separation. The dimeric framework was obtained by Sonogashira coupling reaction [7] of ethynylphenyl-substituted 5,15-diarylporphyrin **3** and 4-bromophenyl-substituted *meso*-tetraarylporphyrin **4**. The desired dyad **PQ-Zn** was prepared by bromination of the *meso*-positions with NBS and Pd, Cu-catalyzed Takahashi coupling reaction [8] followed by aerobic oxidation. The reference quinoidal porphyrin **Q-Zn** and porphyrin **P-Zn** were synthesized in the similar pathways except the use of 4-(phenylethynyl)benzaldehyde [9] at the step of the porphyrin formation. The free-base compounds were obtained by acidic demetallation of the corresponding zinc complexes. All synthesized compounds were fully characterized by  $^1\text{H}$  NMR,  $^{13}\text{C}$  NMR, high-resolution FAB mass, and IR and UV-vis absorption spectroscopies. The non-aromaticity of the



Scheme 1. Synthesis of porphyrin-quinoidal porphyrin dyads



Scheme 2. Synthesis of monomeric reference compounds

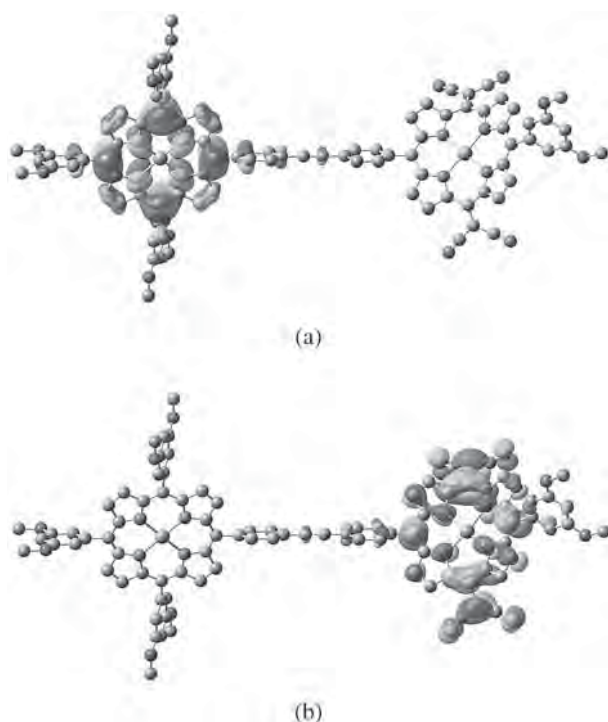


Fig. 1. The selected molecular orbitals of **PQ-Zn** determined by DFT(6-31G/d,p), (a) HOMO, (b) LUMO

quinoidal cores was confirmed by the  $^1\text{H}$  NMR spectra; high-field shifted signals of the pyrrole  $\beta$ -protons ( $\delta = ca. 6.6\text{--}7.2$  ppm) and low-field shifted signals of the central NH ( $\delta = ca. 13.7$  ppm).

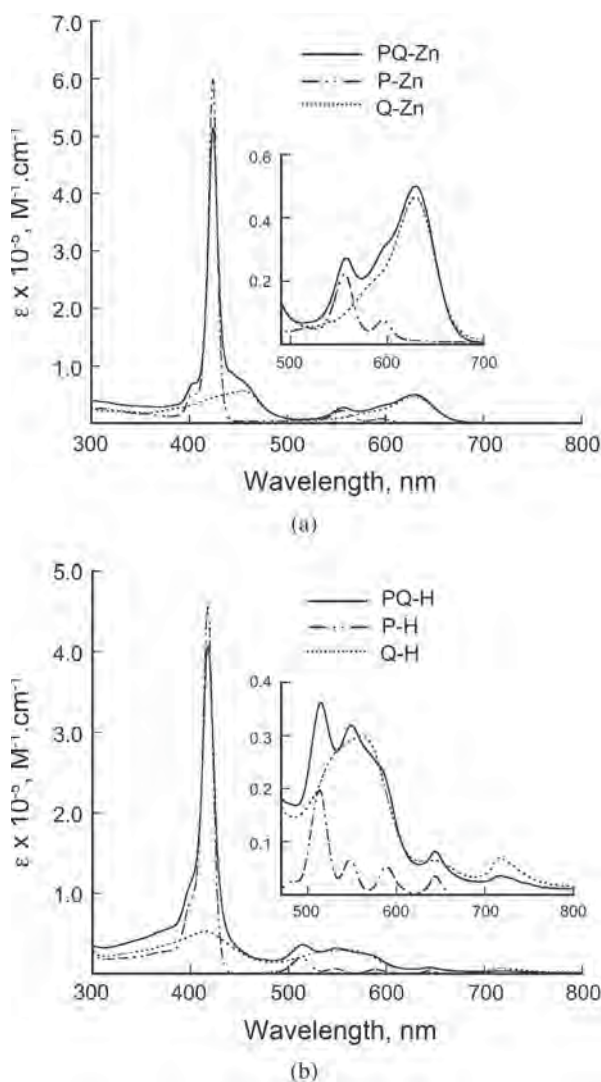
The molecular structure of **PQ-Zn** was modeled by DFT (B3LYP/6-31G(d,p)) calculation (Fig. 1) [10]. The center-to-center distance was estimated to be 19.6 Å. The quinoidal core shows nonplanar saddle-shaped

distortion similar to the crystal structure of the reported quinoidal porphyrin [5a]. The two phenyl groups in the linker are almost coplanar each other, while the dihedral angle between the phenyl plane and the porphyrin core is *ca.* 70°. Hence, the conjugation of the  $\pi$ -system of each chromophore is not extended to the other. The HOMO orbital of **PQ-Zn** is located exclusively on the porphyrin moiety on the basis of the DFT calculation. In contrast, the LUMO exists only on the quinoidal porphyrin core. These structural and electronic features are also observed for the calculated model of **PQ-H**.

### UV-vis absorption and fluorescence spectroscopic analysis

The ground state absorption spectra of the dyads in acetonitrile are compared to those of the corresponding reference compounds in Fig. 2. The spectra of the dyads are almost the linear combination of the spectra of the components (Table 1), although the slight broadenings of the absorption bands are present, indicating the very weak interactions between the porphyrin and quinoidal porphyrin moieties at the ground states. The quinoidal porphyrins have mainly two comparable absorption bands ( $\lambda_{\text{max}} = 455, 630$  nm for **Q-Zn**,  $\lambda_{\text{max}} = 415, 562$  nm for **Q-H**), which are weaker than the Soret bands of the porphyrins, but stronger than the Q-bands. Moreover, their longest-wavelength absorption bands ( $\lambda_{\text{max}} = 630$  nm for **Q-Zn**,  $\lambda_{\text{max}} = 719$  nm for **Q-H**) are more bathochromic than those of the corresponding porphyrins.

Upon photoexcitation at the Soret or Q-bands, the zinc complex and free-base of the reference porphyrin exhibit fluorescence emission in the visible region as shown in Fig. 3. On the other hand, quinoidal porphyrins



**Fig. 2.** UV-vis absorption spectra of the dyads and the reference compounds in acetonitrile, (a) zinc complexes, (b) free-bases

**Table 1.** UV-vis absorption data of the dyads and the reference compounds in acetonitrile

Compound	$\lambda_{\max}$ , nm				
<b>PQ-Zn</b>	424	455 (sh)	558	595 (sh)	630
<b>P-Zn</b>	424		556	596	
<b>Q-Zn</b>		455			630
<b>PQ-H</b>	418	515	550	590 (sh)	644
<b>P-H</b>	418	513	548	589	644
<b>Q-H</b>	415		562		719

have no fluorescence within the detection limit of the spectrometer. Interestingly, upon the photoexcitation of the dyads at the absorption bands of the porphyrins, the fluorescence intensities are significantly reduced (less than 1%) compared with those of the reference porphyrin

compounds. The excitation ratios were estimated based on the extinction coefficients of the reference compounds: **PQ-Zn** P/Q = 0.93/0.07 at 424 nm, **PQ-H** P/Q = 0.90/0.10 at 418 nm. Hence, some strong electronic interactions between the chromophores are anticipated in the dyads in the excited states, being contrary to the results observed for the ground states. Because the fluorescence spectra of the porphyrins have substantial overlapping with the absorption spectra of the quinoidal porphyrins, energy transfer from the excited porphyrin parts to the quinoidal porphyrin moieties in the dyads is supposed to be a possible reason for the fluorescence quenching of the dyads.

### Electrochemical analysis

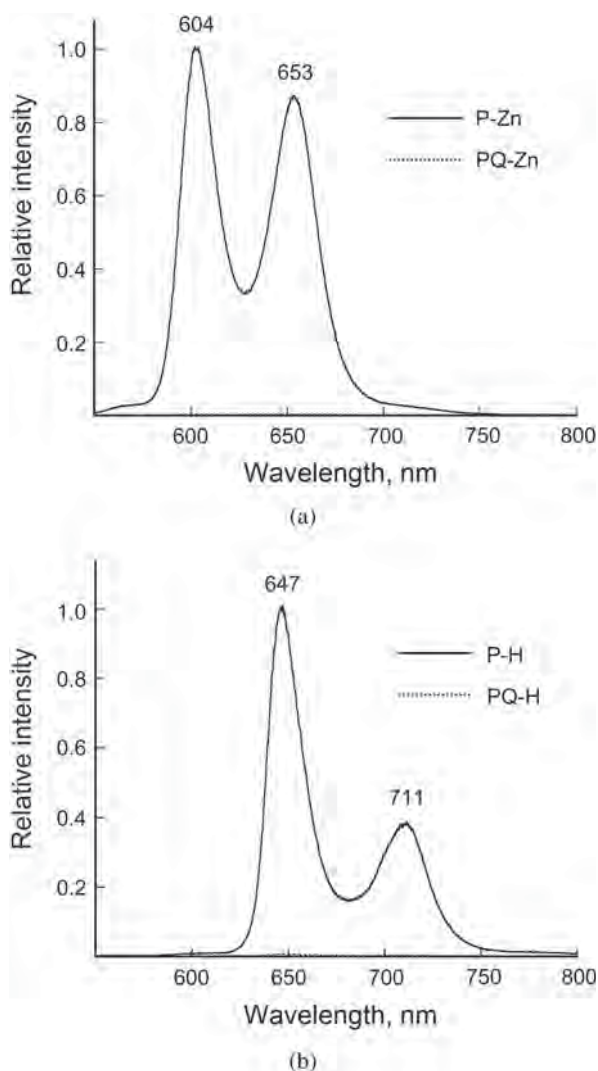
The cyclic voltammograms of the dyads and the reference compounds are shown in Fig. 4. The comparison of the redox potentials implies that the first oxidations of the dyads occur on the porphyrin moieties and the first reductions arise on the quinoidal porphyrin cores (Table 2), as suggested by the DFT calculation. The energy levels of the putative charge-separated (CS) states, which are composed of porphyrin radical cations and quinoidal porphyrin radical anions, are determined from the potential differences between the first oxidation and reduction potentials, which are 0.88 eV for **PQ-Zn** and 1.09 eV for **PQ-H**. Both values are lower than the singlet energy level of each chromophore determined from the spectroscopic data (2.07 eV for **P-Zn**, *ca.* 1.75 eV for **Q-Zn**, 1.92 eV for **P-H**, *ca.* 1.55 eV for **Q-H**), suggesting the possibility of photoinduced electron transfer from the porphyrin parts to the quinoidal porphyrin moieties *via* the singlet excited states of the dyads.

The quinoidal porphyrin monomers were photometrically titrated with a two-electron reductant (1-benzyl-1,4-dihydro-nicotinamide dimer) [11] to obtain absorption spectra of their radical anions (Fig. 5). Upon addition of 0.5 mole equivalent of the reductant, characteristic spectra were observed with absorption maxima at 527, 720, 944, 1135 nm for **Q-Zn** and 520, 733, 987, 1180 nm for **Q-H**. The spectra of the radical anions were stable under ambient conditions, being in good agreement with the reversible reduction waves in the cyclic voltammograms of the quinoidal porphyrins. These are the first measurements of the absorption spectra of the quinoidal porphyrin radical anions.

### Laser flash photolysis

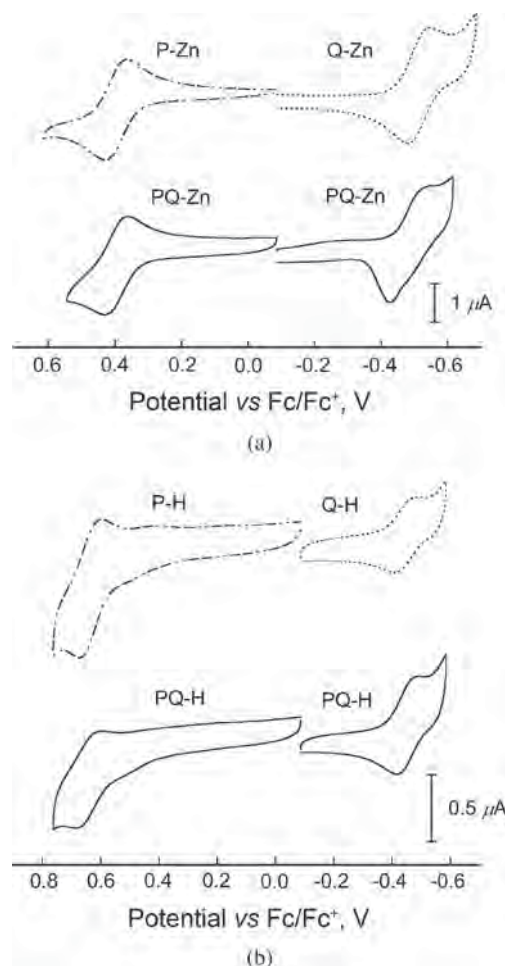
Photoinduced events of the dyads and the reference compounds were investigated to provide an information on the quenching of the porphyrin fluorescence in the





**Fig. 3.** Fluorescence spectra of the dyads and the porphyrinic reference compounds in acetonitrile, (a) zinc complexes excited at 424 nm, (b) free-bases excited at 418 nm. The relative intensity was obtained by dividing the measured intensity by the absorbance at the excitation wavelength and normalizing the maximum intensity of the porphyrin to 1.0.  $[\text{PQ-Zn}] = 1.2 \times 10^{-7} \text{ M}^{-1}$ ,  $[\text{P-Zn}] = 1.2 \times 10^{-7} \text{ M}^{-1}$ ,  $[\text{PQ-H}] = 2.3 \times 10^{-7} \text{ M}^{-1}$ ,  $[\text{P-H}] = 1.5 \times 10^{-7} \text{ M}^{-1}$

dyads. The time-resolved transient absorption spectra in acetonitrile solution were obtained by femtosecond laser flash photolysis after photoexcitation at 393 nm (Figs 6, 7). The spectra of **P-Zn** at both 1 and 400 ps showed a broad singlet-singlet absorption band from visible to near-IR region overlapped with sharp negative absorption bands (Fig. 6a). The negative bands are due to the ground state bleaching at 550 and 600 nm as well as fluorescence at 600 and 650 nm. The singlet excited state of **P-Zn** was transformed to the triplet excited state by intersystem crossing with a rate constant of  $2.1 \times 10^9 \text{ s}^{-1}$  [12]. In contrast, the spectra of **Q-Zn** as shown in Fig. 6b exhibited ground state bleaching at 630 nm only at



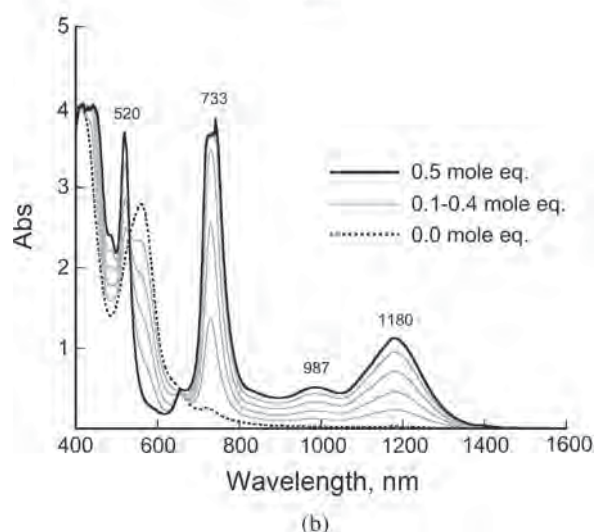
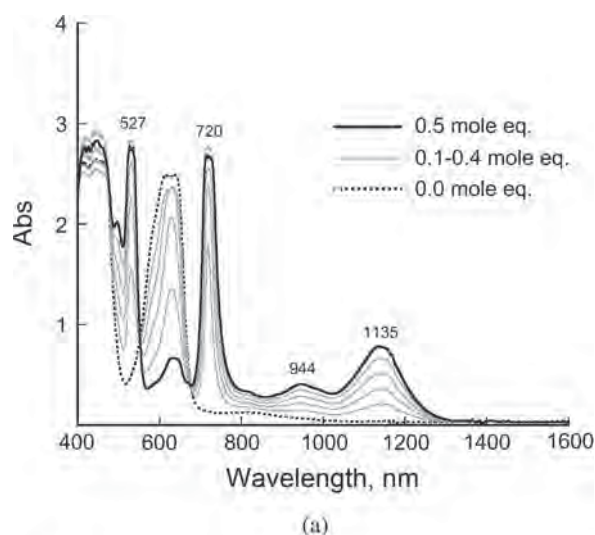
**Fig. 4.** Cyclic voltammograms of the dyads and the reference compounds in deaerated acetonitrile containing 0.1 M  $\text{Bu}_4\text{NPF}_6$ , (a) zinc complexes, (b) free-bases. Concentrations were all  $4.0 \times 10^{-4} \text{ M}^{-1}$  except **P-Zn** ( $2.0 \times 10^{-4} \text{ M}^{-1}$ ). Scan speeds were all  $100 \text{ mV.s}^{-1}$

**Table 2.** Redox potentials ( $E^{1/2}$  vs.  $\text{Fc/Fc}^+$ ) of the dyads and the reference compounds in acetonitrile containing 0.1 M  $\text{Bu}_4\text{NPF}_6$

Compound	$E^{1/2}$ (ox), V	$E^{1/2}$ (red), V
<b>PQ-Zn</b>	0.39	-0.49
<b>P-Zn</b>	0.40	<i>a</i>
<b>Q-Zn</b>	<i>a</i>	-0.52
<b>PQ-H</b>	0.64	-0.45
<b>P-H</b>	0.64	<i>a</i>
<b>Q-H</b>	<i>a</i>	-0.45

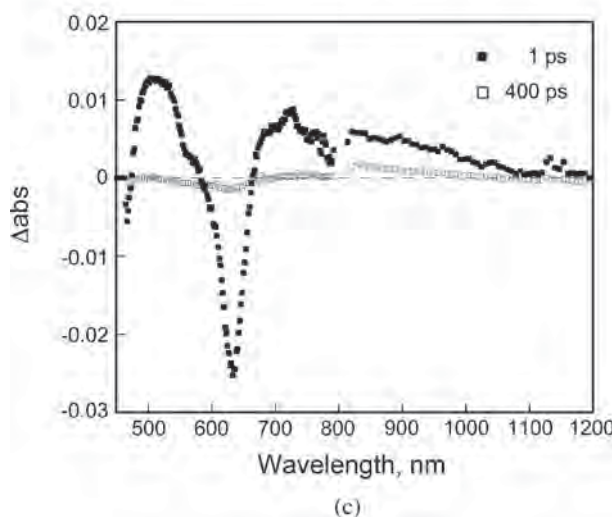
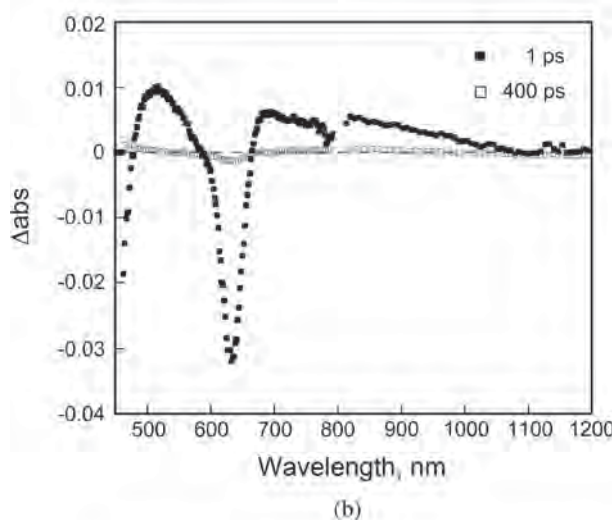
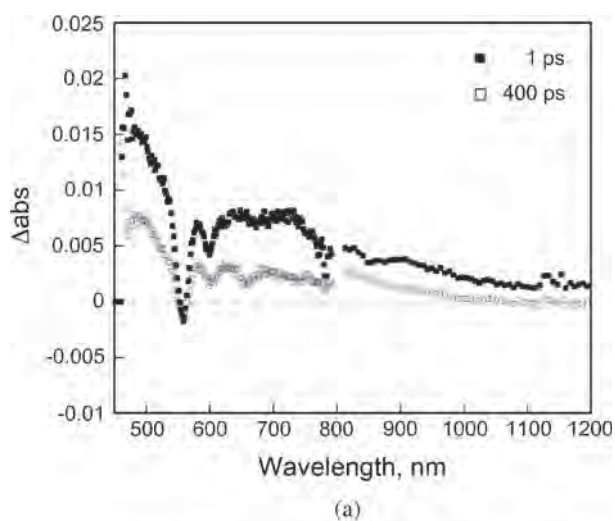
<sup>a</sup>Redox wave was not observed in the range of +0.8 V to -0.8 V vs.  $\text{Fc/Fc}^+$ .

earlier stage and changed very fast directly to a base line with a rate constant of  $3.1 \times 10^{11} \text{ s}^{-1}$ . There was no characteristic absorption in the spectra at 400 ps, indicating the restoration of the ground state. Next, we

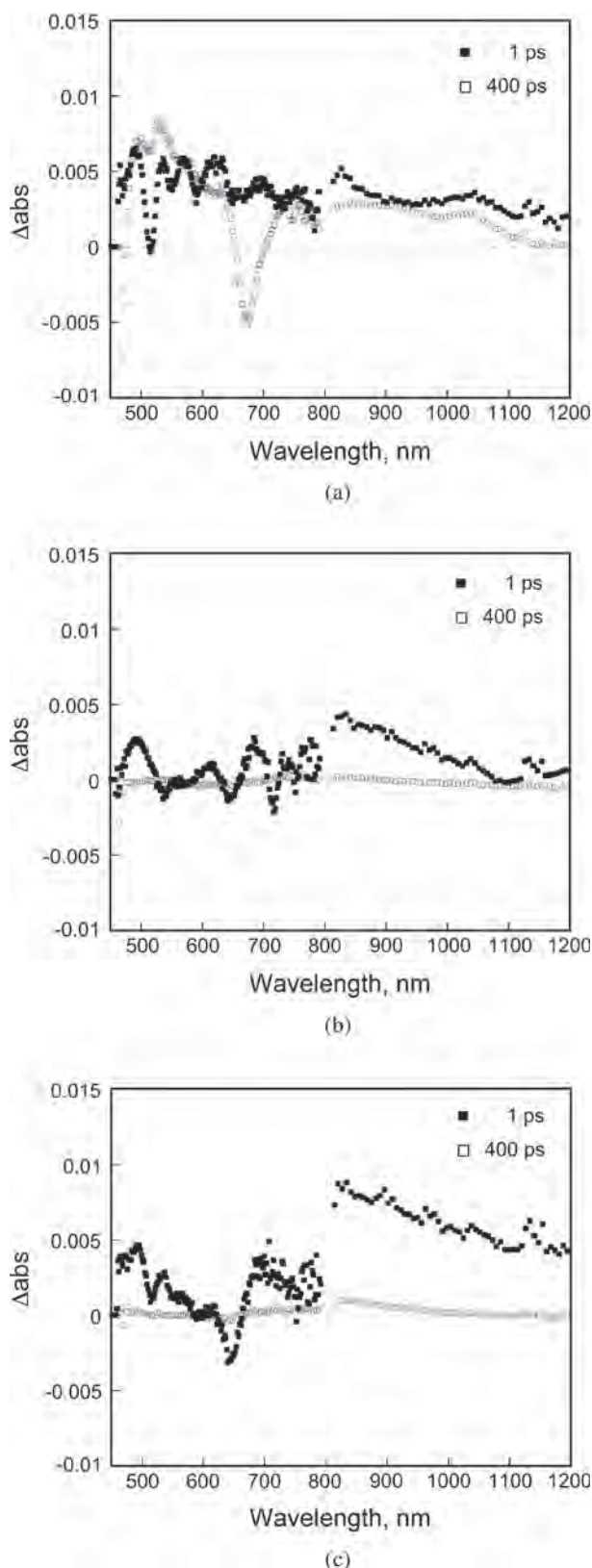


**Fig. 5.** Absorption spectral changes of the quinoidal porphyrins upon titration of 1-benzyl-1,4-dihydro-nicotineamide dimer in acetonitrile. (a) **Q-Zn**, (b) **Q-H**.  $[Q-Zn] = [Q-H] = 1.0 \times 10^{-4} M^{-1}$

measured the transient spectra of **PQ-Zn** to compare with those of **P-Zn** and **Q-Zn** (Fig. 6c). From the extinction coefficients of **P-Zn** and **Q-Zn**, the excitation ratio for **PQ-Zn** at 393 nm was estimated to be  $P/Q = 0.40/0.60$ . It is notable that the spectra of **PQ-Zn** were very similar to those of **Q-Zn** although *ca.* 40% of light was absorbed by the porphyrin units. The absorption features for the porphyrin unit were absent even at 1 ps. In addition, the characteristic absorption bands assignable to the quinoidal radical anion, though they were weaker than the singlet bleaching of the quinoidal unit, were found at 724, 965 and 1132 nm, indicating formation of a CS state. Hence, these results imply that **PQ-Zn** undergoes both ultrafast energy transfer as a major pathway and electron transfer as a minor one from the porphyrin unit to the quinoidal porphyrin. The resulting excited quinoidal moiety decays with the same rate ( $3.0 \times 10^{11} s^{-1}$ ) as **Q-Zn**.



**Fig. 6.** Transient absorption spectra of the zinc complexes of the dyads and the reference compounds in deaerated acetonitrile at room temperature taken at 1 and 400 ps after femtosecond laser excitation at 393 nm. (a) **P-Zn**, (b) **Q-Zn**, (c) **PQ-Zn**.  $[P-Zn] = 3.0 \times 10^{-5} M^{-1}$ ,  $[Q-Zn] = 2.0 \times 10^{-5} M^{-1}$ ,  $[PQ-Zn] = 1.4 \times 10^{-5} M^{-1}$



**Fig. 7.** Transient absorption spectra of the free-bases of the dyads and the reference compounds in deaerated acetonitrile at room temperature taken at 1 and 400 ps after femtosecond laser excitation at 393 nm. (a) **P-H**, (b) **Q-H**, (c) **PQ-H**. [**P-H**] =  $7.9 \times 10^{-6} \text{ M}^{-1}$ , [**Q-H**] =  $5.0 \times 10^{-6} \text{ M}^{-1}$ , [**PQ-H**] =  $6.4 \times 10^{-6} \text{ M}^{-1}$

On the other hand, the rate of the charge recombination in the CS state is difficult to determine from the transient spectra, because the electron transfer is a rather minor pathway. The efficient porphyrin fluorescence quenching in **PQ-Zn** results from fast energy- and electron-transfer processes. The efficient energy transfer process is caused by the good overlapping (600–650 nm) of the porphyrin fluorescence spectrum with the absorption of the quinoidal porphyrin. As mentioned above, the photoinduced electron transfer *via* the singlet excited states of the zinc porphyrin unit or quinoidal one is also energetically possible. The present conclusion is supported by analogous results of previous studies: (i) ultrafast energy transfer (2.0 ps) for the Zn-chlorophyll dimer having the same diphenylethynyl linker [6h], (ii) ultrafast electron transfer (<1 ps) in  $S_2$ -excited states of Zn, Sb and Ge porphyrins [13]. The minor CS state would be formed *via* the  $S_2$  state of the zinc-porphyrin unit. The excited quinoidal unit resulting from the energy transfer does not afford an expected CS state due to its intrinsic short lifetime.

Slightly different results were obtained in the femtosecond photolysis experiments of the free-base compounds. The singlet–singlet absorption of **P-H** at 1 ps was observed with the ground state bleaching at 510 nm and the fluorescence bleaching at 650 nm (Fig. 7a). The singlet excited state of **P-H** was transformed to the triplet excited state with a rate constant of  $2.5 \times 10^{10} \text{ s}^{-1}$ . The spectra of **Q-H** at 1 ps exhibited ground state bleaching at 550, 650, 710 nm, but the spectra decayed very fast directly to a base line with a rate constant of  $3.0 \times 10^{11} \text{ s}^{-1}$  (Fig. 7b). There was almost no specific absorption band in the spectra at 400 ps due to the restoration of the ground state. The transient absorption spectra of **PQ-H** upon the photoexcitation ( $P/Q = 0.57/0.43$ ) had common features with those of **Q-H**, being much different from those of **P-H** (Fig. 7c). The absorption bands assignable to the quinoidal radical anion were not clearly detected in the transient spectra of **PQ-H** [14]. These results suggest that only the very fast energy transfer from the porphyrin unit to the quinoidal part in **PQ-H** causes the quenching of the porphyrin fluorescence and photoinduced electron transfer may not occur in the excited state of **PQ-H**. The resulting excited state of the quinoidal unit decays to the ground state without formation of an intermediate such as a CS state due to its intrinsic short lifetime.

## EXPERIMENTAL

### General

Reagents and solvents of best grade available were purchased from commercial suppliers and were used without further purification unless otherwise noted. Dry acetonitrile was purchased from Wako Pure Chemical Industries, Ltd. Dry tetrahydrofuran (THF) was obtained

by distillation from Na and benzophenone under N<sub>2</sub> atmosphere. Dry triethylamine (Et<sub>3</sub>N) and pyridine were obtained by distillation from CaH<sub>2</sub> under N<sub>2</sub> atmosphere after being stirred with KOH overnight. Nuclear magnetic resonance (NMR) spectra were recorded on a Bruker AVANCE III 600 (151 MHz for <sup>13</sup>C) spectrometer. Chemical shifts were reported as δ values in ppm relative to tetramethylsilane. High-resolution fast atom bombardment mass spectra (HR-FAB-MS) were measured with 3-nitrobenzyl alcohol (NBA) as a matrix and recorded on a JEOL LMS-HX-110 spectrometer. Ultraviolet-visible (UV-vis) absorption and infrared (IR) spectra were recorded on Shimadzu UV-3100PC and BIO RAD FTS6000 spectrophotometers, respectively. Fluorescence spectra were measured on a Shimadzu RF-5300PC spectrofluorophotometer with a quartz cuvette (path length = 10 mm) at 298 K.

**5-(3,5-Dimethoxyphenyl)-15-[4-(trimethylsilyl-ethynyl)phenyl]porphine (1).** A solution of dipyrromethane (439 mg, 3.00 mmol) [15], 4-(trimethylsilyl-ethynyl)benzaldehyde (303 mg, 1.50 mmol) [16] and 3,5-dimethoxybenzaldehyde (249 mg, 1.50 mmol) in CH<sub>2</sub>Cl<sub>2</sub> (600 mL) was bubbled with N<sub>2</sub> for 30 min in dark. To the solution was added trifluoroacetic acid (0.14 mL, 1.9 mmol) and the solution was stirred at room temperature for 2 h. Then, 2,3-dichloro-5,6-dicyano-1,4-benzoquinone (1.02 g, 4.50 mmol) dissolved in THF was added and the solution was stirred for another 1 h. The resulting solution was neutralized with triethylamine (0.50 mL, 3.6 mmol). After evaporation, the mixture was filtered through a short alumina column and the alumina was washed with CH<sub>2</sub>Cl<sub>2</sub>. After removal of the solvent, the residue was purified by silica-gel column chromatography (hexane/CH<sub>2</sub>Cl<sub>2</sub> = 1/1, v/v) and recrystallized from CH<sub>2</sub>Cl<sub>2</sub>/MeOH to give brown solid (261 mg, 28%), mp > 300 °C. <sup>1</sup>H NMR (600 MHz, CDCl<sub>3</sub>): δ<sub>H</sub>, ppm -3.13 (s, 2H, -NH), 0.43 (s, 9H, -Si(CH<sub>3</sub>)<sub>3</sub>), 4.01 (s, 6H, -OCH<sub>3</sub>), 6.96 (s, 1H, Ar-H), 7.47 (d, *J* = 2.4 Hz, 2H, Ar-H), 7.95 (d, *J* = 7.8 Hz, 2H, Ar-H), 8.23 (d, *J* = 7.8 Hz, 2H, Ar-H), 9.05 (d, *J* = 4.8 Hz, 2H, pyrrole β-H), 9.19 (d, *J* = 4.2 Hz, 2H, pyrrole β-H), 9.38 (d, *J* = 4.8 Hz, 4H, pyrrole β-H), 10.30 (s, 2H, *meso*-H). <sup>13</sup>C NMR (151 MHz, CDCl<sub>3</sub>): δ<sub>C</sub>, ppm 0.3, 55.8, 95.8, 100.2, 105.2, 105.5, 105.6, 114.2, 118.3, 119.1, 122.8, 130.8, 130.9, 131.3, 131.8, 131.9, 134.9, 141.9, 143.4, 145.4, 145.5, 146.9, 147.2, 159.3. IR (KBr): ν<sub>max</sub>, cm<sup>-1</sup> 655, 691, 741, 790, 853, 928, 959, 1022, 1063, 1153, 1203, 1248, 1345, 1417, 1453, 1493, 1589, 2156, 2835, 2954. UV-vis (acetonitrile): λ<sub>max</sub>, nm (ε, M<sup>-1</sup>·cm<sup>-1</sup>) 404 (370000), 501 (16000), 535 (6300), 574 (5200), 629 (2100). HR-FAB-MS (NBA): *m/z* calcd. for C<sub>39</sub>H<sub>34</sub>N<sub>4</sub>O<sub>2</sub>Si: 618.2451. Found 618.2464. Anal. calcd. for C<sub>39</sub>H<sub>34</sub>N<sub>4</sub>O<sub>2</sub>Si: C, 75.70; H, 5.54; N, 9.05%. Found C, 75.55; H, 5.46; N, 8.85.

**{5-[3,5-Dimethoxyphenyl]-15-[4-(trimethylsilyl-ethynyl)phenyl]porphinato}zinc(II) (2).** Zinc acetate dihydrate (1.32 g, 6.00 mmol) dissolved in MeOH was added to a solution of **1** (371 mg, 0.600 mmol) in CH<sub>2</sub>Cl<sub>2</sub>

(600 mL) and the mixture was refluxed under N<sub>2</sub> for 2 h. The reaction mixture was washed with water twice. The organic layer was dried over Na<sub>2</sub>SO<sub>4</sub> and evaporated. The crude product was recrystallized from CH<sub>2</sub>Cl<sub>2</sub>/MeOH to give red solid (384 mg, 94%), mp > 300 °C. <sup>1</sup>H NMR (600 MHz, CDCl<sub>3</sub>): δ<sub>H</sub>, ppm 0.41 (s, 9H, -Si(CH<sub>3</sub>)<sub>3</sub>), 3.98 (s, 6H, -OCH<sub>3</sub>), 6.91 (s, 1H, Ar-H), 7.44 (s, 2H, Ar-H), 7.92 (d, *J* = 7.2 Hz, 2H, Ar-H), 8.19 (d, *J* = 7.2 Hz, 2H, Ar-H), 9.07 (d, *J* = 3.6 Hz, 2H, pyrrole β-H), 9.23 (d, *J* = 3.6 Hz, 2H, pyrrole β-H), 9.41 (dd, *J* = 4.8 Hz, 4H, pyrrole β-H), 10.27 (s, 2H, *meso*-H). <sup>13</sup>C NMR (151 MHz, CDCl<sub>3</sub>): δ<sub>C</sub>, ppm 0.3, 55.8, 95.5, 100.1, 105.4, 106.4, 106.5, 114.1, 119.3, 120.0, 122.5, 130.5, 132.0, 132.0, 132.3, 132.7, 134.6, 143.1, 144.6, 149.6, 149.7, 149.8, 150.1, 159.0. IR (KBr): ν<sub>max</sub>, cm<sup>-1</sup> 656, 702, 733, 783, 810, 862, 937, 993, 1041, 1061, 1155, 1203, 1250, 1290, 1327, 1392, 1419, 1458, 1498, 1522, 1591, 2156, 2835, 2956. UV-vis (acetonitrile): λ<sub>max</sub>, nm (ε, M<sup>-1</sup>·cm<sup>-1</sup>) 411 (480000), 543 (19000), 580 (4300). HR-FAB-MS (NBA): *m/z* calcd. for C<sub>39</sub>H<sub>32</sub>N<sub>4</sub>O<sub>2</sub>SiZn: 680.1586. Found 680.1583. Anal. calcd. for C<sub>39</sub>H<sub>32</sub>N<sub>4</sub>O<sub>2</sub>SiZn: C, 68.67; H, 4.73; N, 8.21%. Found C, 68.60; H, 4.71; N, 8.15.

**[5-(3,5-Dimethoxyphenyl)-15-(4-ethynylphenyl)porphinato]zinc(II) (3).** A 300 mL flask containing **2** (342 mg, 0.500 mmol) was purged with N<sub>2</sub> and dry THF (170 mL) was added to the flask. The solution was bubbled with N<sub>2</sub> for 30 min. To the solution was added TBAF (1 M solution in THF, 0.60 mL), the solution was stirred at room temperature for 30 min and quenched with deionized water. The mixture was purified by silica-gel column chromatography (hexane/CH<sub>2</sub>Cl<sub>2</sub> = 1/2, v/v) and recrystallized from CH<sub>2</sub>Cl<sub>2</sub>/MeOH to give red solid (292 mg, 95%), mp > 300 °C. <sup>1</sup>H NMR (600 MHz, CDCl<sub>3</sub>): δ<sub>H</sub>, ppm 3.35 (s, 1H, -C≡CH), 3.99 (s, 6H, -OCH<sub>3</sub>), 6.93 (s, 1H, Ar-H), 7.45 (s, 2H, Ar-H), 7.94 (d, *J* = 7.2 Hz, 2H, Ar-H), 8.22 (d, *J* = 7.8 Hz, 2H, Ar-H), 9.10 (d, *J* = 4.2 Hz, 2H, pyrrole β-H), 9.25 (d, *J* = 3.6 Hz, 2H, pyrrole β-H), 9.43 (d, *J* = 4.2 Hz, 4H, pyrrole β-H), 10.31 (s, 2H, *meso*-H). <sup>13</sup>C NMR (151 MHz, THF-d<sub>8</sub>): δ<sub>C</sub>, ppm 55.6, 79.5, 84.3, 100.0, 106.3, 106.3, 114.8, 119.0, 120.3, 122.4, 130.8, 132.0, 132.1, 132.2, 132.7, 135.4, 144.8, 145.8, 150.3, 150.3, 150.5, 150.6, 159.9. IR (KBr): ν<sub>max</sub>, cm<sup>-1</sup> 702, 733, 784, 809, 859, 939, 993, 1062, 1155, 1204, 1289, 1327, 1393, 1420, 1453, 1521, 1600, 2835, 2936, 3093, 3288. UV-vis (acetonitrile): λ<sub>max</sub>, nm (ε, M<sup>-1</sup>·cm<sup>-1</sup>) 411 (490000), 543 (18000), 580 (3500). HR-FAB-MS (NBA): *m/z* calcd. for C<sub>36</sub>H<sub>24</sub>N<sub>4</sub>O<sub>2</sub>Zn: 608.1191. Found 608.1193. Anal. calcd. for C<sub>36</sub>H<sub>24</sub>N<sub>4</sub>O<sub>2</sub>Zn: C, 70.88; H, 3.97; N, 9.18%. Found C, 70.84; H, 3.93; N, 9.07.

**[5-(4-Bromophenyl)-10,15,20-(3,5-dimethoxyphenyl)porphinato]zinc(II) (4).** 4-Bromobenzaldehyde (462 mg, 2.50 mmol), 3,5-dimethoxybenzaldehyde (1.25 g, 7.50 mmol), pyrrole (0.84 mL, 12 mmol) and zinc-*p-tert*-butylbenzoate (1.26 g, 3.00 mmol) were dissolved in CH<sub>2</sub>Cl<sub>2</sub> (1.20 L). The solution was bubbled with N<sub>2</sub> for 30 min in dark. To the solution was added trifluoroacetic acid (0.28 mL, 3.6 mmol) and

the solution was stirred at room temperature for 4 h. Then, 2,3-dichloro-5,6-dicyano-1,4-benzoquinone (1.79 g, 8.00 mmol) dissolved in THF was added and the solution was stirred for another 1 h. The resulting solution was neutralized with triethylamine (1.0 mL, 7.0 mmol). After evaporation of the solvent, the mixture was purified by silica-gel column chromatography ( $\text{CH}_2\text{Cl}_2$ ) to give purple solid (293 mg, 12%), mp > 300 °C.  $^1\text{H}$  NMR (600 MHz,  $\text{CDCl}_3$ ):  $\delta_{\text{H}}$ , ppm 3.92 (s, 18H,  $-\text{OCH}_3$ ), 6.85 (s, 3H, Ar-H), 7.37 (d,  $J = 1.8$  Hz, 6H, Ar-H), 7.88 (d,  $J = 7.8$  Hz, 2H, Ar-H), 8.08 (d,  $J = 7.8$  Hz, 2H, Ar-H), 8.90 (d,  $J = 4.2$  Hz, 2H, pyrrole  $\beta$ -H), 9.03 (s, 4H, pyrrole  $\beta$ -H), 9.05 (d,  $J = 4.8$  Hz, 2H, pyrrole  $\beta$ -H).  $^{13}\text{C}$  NMR (151 MHz,  $\text{CDCl}_3$ ):  $\delta_{\text{C}}$ , ppm 55.8, 100.2, 113.9, 119.6, 121.1, 122.3, 129.9, 131.7, 132.2, 132.3, 135.9, 142.0, 144.7, 150.0, 150.1, 150.2, 150.3, 158.8. IR (KBr):  $\nu_{\text{max}}$ ,  $\text{cm}^{-1}$  699, 721, 761, 799, 938, 1001, 1066, 1154, 1203, 1348, 1420, 1453, 1592, 1705, 2835, 2935, 2998. UV-vis (acetonitrile):  $\lambda_{\text{max}}$ , nm ( $\epsilon$ ,  $\text{M}^{-1}\cdot\text{cm}^{-1}$ ) 423 (550000), 555 (19000), 595 (5300). HR-FAB-MS (NBA):  $m/z$  calcd. for  $\text{C}_{50}\text{H}_{39}\text{N}_4\text{O}_6\text{ZnBr}$ : 934.1344. Found 934.1342. Anal. calcd. for  $\text{C}_{50}\text{H}_{39}\text{N}_4\text{O}_6\text{ZnBr}$ : C, 64.08; H, 4.19; N, 5.98%. Found C, 64.22; H, 4.31; N, 5.80.

**4-[Zinc(II) 5-(3,5-dimethoxyphenyl)-15-porphinyl]-4'-[zinc(II) 5,10,15-tri(3,5-dimethoxyphenyl)-20-porphinyl]diphenylethyne (5).** The alkynylphenyl porphyrin **3** (122 mg, 0.200 mmol), the bromophenyl porphyrin **4** (375 mg, 0.400 mmol),  $\text{Pd}_2(\text{dba})_3$  (73 mg, 0.080 mmol) and triphenylarsine (220 mg, 0.720 mmol) were placed in 25 mL flask and dried under high vacuum. The flask was filled with  $\text{N}_2$ . Then dry THF (6.5 mL) and dry triethylamine (6.5 mL) bubbled with argon for 20 min were added to the flask and the mixture was stirred at 60 °C overnight. After evaporation of the solvent, the reaction mixture was diluted with  $\text{CH}_2\text{Cl}_2$  and washed with sat. NaCl aq twice. The organic layer was dried over  $\text{Na}_2\text{SO}_4$  and evaporated. The residue was purified by silica-gel column chromatography ( $\text{CH}_2\text{Cl}_2/\text{AcOEt} = 100/1$ , v/v) to give reddish violet solid (122 mg, 41%), mp > 300 °C.  $^1\text{H}$  NMR (600 MHz,  $\text{CDCl}_3$ ):  $\delta_{\text{H}}$ , ppm 3.95 (s, 6H,  $-\text{OCH}_3$ ), 3.96 (s, 12H,  $-\text{OCH}_3$ ), 3.99 (s, 6H,  $-\text{OCH}_3$ ), 6.88 (s, 1H, Ar-H), 6.90 (s, 2H, Ar-H), 6.92 (s, 1H, Ar-H), 7.41–7.46 (m, 8H, Ar-H), 8.11 (dd,  $J = 7.8$  Hz, 4H, Ar-H), 8.33 (dd,  $J = 7.2$  Hz, 4H, Ar-H), 9.04 (d,  $J = 4.8$  Hz, 2H, pyrrole  $\beta$ -H), 9.06 (s, 4H, pyrrole  $\beta$ -H), 9.12 (d,  $J = 4.8$  Hz, 2H, pyrrole  $\beta$ -H), 9.22 (d,  $J = 4.2$  Hz, 2H, pyrrole  $\beta$ -H), 9.26 (d,  $J = 4.2$  Hz, 2H, pyrrole  $\beta$ -H), 9.46 (d,  $J = 4.2$  Hz, 2H, pyrrole  $\beta$ -H), 9.49 (d,  $J = 4.2$  Hz, 2H, pyrrole  $\beta$ -H), 10.35 (s, 2H, *meso*-H).  $^{13}\text{C}$  NMR (151 MHz,  $\text{CDCl}_3$ ):  $\delta_{\text{C}}$ , ppm 55.7, 55.7, 55.8, 90.7, 90.8, 100.0, 100.2, 106.4, 106.4, 114.0, 114.2, 119.3, 119.9, 120.5, 121.1, 121.1, 122.7, 122.8, 130.2, 130.2, 131.9, 132.0, 132.2, 132.3, 132.4, 132.7, 134.7, 134.9, 143.1, 143.3, 144.6, 144.8, 149.5, 149.7, 149.8, 150.1, 150.1, 150.1, 150.2, 150.3, 158.8, 158.8. IR (KBr):  $\nu_{\text{max}}$ ,  $\text{cm}^{-1}$  695, 720, 797, 854, 937, 998, 1026, 1060, 1153, 1203, 1287, 1344, 1393, 1419, 1451, 1521, 1589, 2833, 2931. UV-vis

(acetonitrile):  $\lambda_{\text{max}}$ , nm ( $\epsilon$ ,  $\text{M}^{-1}\cdot\text{cm}^{-1}$ ) 412 (390000), 425 (690000), 549 (32000), 594 (8800). HR-FAB-MS (NBA):  $m/z$  calcd. for  $\text{C}_{86}\text{H}_{62}\text{N}_8\text{O}_8\text{Zn}_2$ : 1462.3274. Found 1462.3270. Anal. calcd. for  $\text{C}_{86}\text{H}_{62}\text{N}_8\text{O}_8\text{Zn}_2+0.50\text{CH}_2\text{Cl}_2$ : C, 69.26; H, 4.21; N, 7.43%. Found C, 69.01; H, 4.22; N, 7.43.

**4-[Zinc(II) 5,15-dibromo-10-(3,5-dimethoxyphenyl)-20-porphinyl]-4'-[zinc(II) 5,10,15-tri(3,5-dimethoxyphenyl)-20-porphinyl]diphenylethyne (6).** A solution of **5** (58.6 mg, 0.0400 mmol) and pyridine (0.032 mL, 0.40 mmol) in  $\text{CHCl}_3$  (35 mL) was cooled to 0 °C. Then NBS (15.7 mg, 0.0880 mmol) dissolved in  $\text{CHCl}_3$  (5 mL) was added to the solution, and the solution was stirred at 0 °C for 15 min before quenching with acetone. After evaporation, the reaction mixture was purified by silica-gel column chromatography ( $\text{CH}_2\text{Cl}_2/\text{AcOEt} = 100/1$ , v/v) to give purple solid (59 mg, 91%), mp > 300 °C.  $^1\text{H}$  NMR (600 MHz,  $\text{CDCl}_3$ ):  $\delta_{\text{H}}$ , ppm 3.87 (s, 6H,  $-\text{OCH}_3$ ), 3.92 (s, 6H,  $-\text{OCH}_3$ ), 3.93 (s, 12H,  $-\text{OCH}_3$ ), 6.76 (s, 1H, Ar-H), 6.83 (s, 1H, Ar-H), 6.85 (s, 2H, Ar-H), 7.30 (d,  $J = 2.4$  Hz, 2H, Ar-H), 7.35 (d,  $J = 1.8$  Hz, 2H, Ar-H), 7.41 (d,  $J = 2.4$  Hz, 4H, Ar-H), 8.01 (d,  $J = 7.8$  Hz, 2H, Ar-H), 8.07 (d,  $J = 7.8$  Hz, 2H, Ar-H), 8.17 (d,  $J = 7.8$  Hz, 2H, Ar-H), 8.31 (d,  $J = 7.8$  Hz, 2H, Ar-H), 8.97 (d,  $J = 4.2$  Hz, 2H, pyrrole  $\beta$ -H), 9.04–9.06 (m, 8H, pyrrole  $\beta$ -H), 9.11 (d,  $J = 4.8$  Hz, 2H, pyrrole  $\beta$ -H), 9.71 (d,  $J = 4.2$  Hz, 2H, pyrrole  $\beta$ -H), 9.73 (d,  $J = 4.8$  Hz, 2H, pyrrole  $\beta$ -H).  $^{13}\text{C}$  NMR (151 MHz,  $\text{THF}-d_6$ ):  $\delta_{\text{C}}$ , ppm 55.6, 55.6, 90.9, 91.3, 100.2, 100.2, 105.2, 114.5, 114.6, 114.8, 120.3, 121.4, 121.4, 121.9, 122.9, 123.3, 123.8, 130.4, 130.5, 131.7, 132.1, 132.3, 133.3, 133.5, 133.5, 134.0, 135.4, 135.5, 143.8, 144.9, 145.1, 146.0, 150.5, 150.6, 150.8, 150.8, 150.8, 151.0, 151.2, 151.5, 159.8, 159.8, 159.9. IR (KBr):  $\nu_{\text{max}}$ ,  $\text{cm}^{-1}$  696, 736, 762, 792, 939, 999, 1024, 1064, 1154, 1203, 1286, 1345, 1419, 1451, 1590, 2834, 2932. UV-vis (acetonitrile):  $\lambda_{\text{max}}$ , nm ( $\epsilon$ ,  $\text{M}^{-1}\cdot\text{cm}^{-1}$ ) 424 (420000), 433 (440000), 560 (24000), 604 (11000). HR-FAB-MS (NBA):  $m/z$  calcd. for  $\text{C}_{86}\text{H}_{60}\text{N}_8\text{O}_8\text{Zn}_2\text{Br}_2$ : 1618.1484. Found 1618.1471. Anal. calcd. for  $\text{C}_{86}\text{H}_{60}\text{N}_8\text{O}_8\text{Zn}_2\text{Br}_2+\text{CH}_2\text{Cl}_2$ : C, 61.85; H, 3.66; N, 6.56%. Found C, 62.08; H, 3.90; N, 6.36.

**PQ-Zn.** The dibromo porphyrin dimer **6** (41 mg, 0.025 mmol), malononitrile (17 mg, 0.25 mmol), triphenylphosphine (26 mg, 0.10 mmol),  $\text{Pd}_2(\text{dba})_3$  (23 mg, 0.025 mmol) and CuI (10 mg, 0.050 mmol) were placed in 100 mL flask. The flask was dried under high vacuum and filled with  $\text{N}_2$ . Then dry THF (10 mL) was added to the flask and the mixture was bubbled with argon for 20 min. Argon-bubbled dry pyridine (0.08 mL) was added to the flask. NaH (min. 60% in paraffin liquid, 20 mg, 0.50 mmol) was placed in another 25 mL flask and washed with dry THF. The 25 mL flask was dried under high vacuum and filled with  $\text{N}_2$ . The mixture in the 100 mL flask was moved to the 25 mL flask and refluxed overnight. Then, acetic acid (29  $\mu\text{L}$ , 0.50 mmol) was added to the reaction mixture at room temperature and stirred under air for 30 min. After evaporation, the

residue was diluted with  $\text{CH}_2\text{Cl}_2$  and washed with sat.  $\text{NaHCO}_3$  aq and sat.  $\text{NaCl}$  aq. The organic layer was dried over  $\text{Na}_2\text{SO}_4$  and evaporated. The residue was purified by silica-gel column chromatography ( $\text{CHCl}_3/\text{MeCN} = 100/2$ , v/v) to give green solid (24 mg, 58%), mp > 300 °C.  $^1\text{H}$  NMR (600 MHz,  $\text{CDCl}_3$ ):  $\delta_{\text{H}}$ , ppm 3.84 (s, 6H,  $-\text{OCH}_3$ ), 3.95 (s, 18H,  $-\text{OCH}_3$ ), 6.60 (s, 3H, Ar-H), 6.63 (d,  $J = 4.2$  Hz, 2H, pyrrole  $\beta$ -H), 6.66 (d,  $J = 4.2$  Hz, 2H, pyrrole  $\beta$ -H), 6.89 (t,  $J = 1.8$  Hz, 3H, Ar-H), 7.08 (d,  $J = 4.8$  Hz, 2H, pyrrole  $\beta$ -H), 7.11 (d,  $J = 4.2$  Hz, 2H, pyrrole  $\beta$ -H), 7.39 (m, 6H, Ar-H), 7.52–7.53 (m, 2 H, Ar-H), 7.78 (d,  $J = 7.8$  Hz, 2H, Ar-H), 7.96 (d,  $J = 7.8$  Hz, 2H, Ar-H), 8.24 (d,  $J = 8.4$  Hz, 2H, Ar-H), 8.92 (d,  $J = 4.8$  Hz, 2H, pyrrole  $\beta$ -H), 9.01 (s, 4H, pyrrole  $\beta$ -H), 9.04 (d,  $J = 4.2$  Hz, 2H, pyrrole  $\beta$ -H).  $^{13}\text{C}$  NMR (151 MHz,  $\text{CDCl}_3$ ):  $\delta_{\text{C}}$ , ppm 55.7, 89.6, 92.0, 100.0, 101.6, 108.7, 114.0, 115.1, 120.0, 120.9, 122.0, 122.1, 122.2, 125.3, 129.1, 130.0, 131.1, 131.2, 131.6, 132.1, 132.2, 132.3, 133.3, 133.4, 134.7, 137.5, 139.2, 143.9, 145.0, 147.1, 147.1, 149.9, 150.0, 150.1, 150.2, 151.0, 151.6, 154.5, 154.6, 155.2, 158.8, 160.2, 167.9. IR (KBr):  $\nu_{\text{max}}$ ,  $\text{cm}^{-1}$  697, 733, 760, 795, 833, 937, 1020, 1072, 1154, 1204, 1271, 1301, 1344, 1420, 1464, 1495, 1562, 1599, 1723, 2215, 2836, 2933. UV-vis (acetonitrile):  $\lambda_{\text{max}}$ , nm ( $\epsilon$ ,  $\text{M}^{-1}\cdot\text{cm}^{-1}$ ) 424 (510000), 558 (27000), 630 (50000). HR-FAB-MS (NBA):  $m/z$  calcd. for  $\text{C}_{92}\text{H}_{60}\text{N}_{12}\text{O}_8\text{Zn}_2$ : 1588.3240. Found 1588.3273. Anal. calcd. for  $\text{C}_{92}\text{H}_{60}\text{N}_{12}\text{O}_8\text{Zn}_2 + 0.30 \text{CHCl}_3$ : C, 68.09; H, 3.73; N, 10.32%. Found C, 67.87; H, 4.12; N, 9.97.

**PQ-H.** A solution of 35% HCl aq (2.4 mL) in MeOH (8 mL) was added to a solution of **PQ-Zn** (96 mg, 0.060 mmol) in  $\text{CHCl}_3$  (120 mL) and the solution was stirred at room temperature for 20 min. The reaction mixture was washed with sat.  $\text{NaHCO}_3$  aq twice and sat.  $\text{NaCl}$  aq once. The organic layer was dried over  $\text{Na}_2\text{SO}_4$  and evaporated. The crude product was purified by silica-gel column chromatography ( $\text{CHCl}_3/\text{MeCN} = 100/2$ , v/v) followed by recrystallization from  $\text{CH}_2\text{Cl}_2/\text{MeOH}$  to give deep purple solid (36 mg, 41%), mp > 300 °C.  $^1\text{H}$  NMR (600 MHz,  $\text{CDCl}_3$ ):  $\delta_{\text{H}}$ , ppm -2.80 (s, 2H,  $-\text{NH}$ ), 3.84 (s, 6H,  $-\text{OCH}_3$ ), 3.97 (s, 18H,  $-\text{OCH}_3$ ), 6.60 (s, 2H, Ar-H), 6.64 (s, 1H, Ar-H), 6.74 (d,  $J = 4.2$  Hz, 2H, pyrrole  $\beta$ -H), 6.77 (d,  $J = 4.8$  Hz, 2H, pyrrole  $\beta$ -H), 6.91 (s, 3H, Ar-H), 7.21 (d,  $J = 4.2$  Hz, 2H, pyrrole  $\beta$ -H), 7.25 (d,  $J = 4.2$  Hz, 2H, pyrrole  $\beta$ -H), 7.41 (s, 6H, Ar-H), 7.53 (d,  $J = 8.4$  Hz, 2H, Ar-H), 7.80 (d,  $J = 7.8$  Hz, 2H, Ar-H), 7.98 (d,  $J = 8.4$  Hz, 2H, Ar-H), 8.25 (d,  $J = 7.8$  Hz, 2H, Ar-H), 8.86 (d,  $J = 4.2$  Hz, 2H, pyrrole  $\beta$ -H), 8.95 (s, 4H, pyrrole  $\beta$ -H), 8.98 (d,  $J = 4.2$  Hz, 2H, pyrrole  $\beta$ -H), 13.76 (s br, 2H,  $-\text{NH}$ ).  $^{13}\text{C}$  NMR (151 MHz,  $\text{CDCl}_3$ ):  $\delta_{\text{C}}$ , ppm 55.8, 80.2, 89.6, 92.4, 100.3, 102.0, 109.3, 114.0, 114.2, 114.2, 119.2, 120.2, 120.2, 122.3, 122.8, 123.0, 126.0, 130.3, 131.3, 131.6, 134.8, 136.0, 137.8, 143.0, 144.1, 144.1, 144.9, 145.4, 152.4, 159.0, 160.5. IR (KBr):  $\nu_{\text{max}}$ ,  $\text{cm}^{-1}$  693, 729, 800, 929, 971, 1019, 1064, 1155, 1204, 1346, 1391, 1420, 1457, 1521, 1589, 2218, 2852, 2925, 3321. UV-vis (acetonitrile):  $\lambda_{\text{max}}$ , nm ( $\epsilon$ ,  $\text{M}^{-1}\cdot\text{cm}^{-1}$ ) 418

(410000), 515 (37000), 550 (34000), 644 (6500), 713 (1700). HR-FAB-MS (NBA):  $m/z$  calcd. for  $\text{C}_{92}\text{H}_{65}\text{N}_{12}\text{O}_8$  [ $\text{MH}^+$ ]: 1465.5048. Found 1465.5084. Anal. calcd. for  $\text{C}_{92}\text{H}_{64}\text{N}_{12}\text{O}_8 + 2.70 \text{CH}_4\text{O}$  (MeOH): C, 73.28; H, 4.86; N, 10.83%. Found C, 73.64; H, 4.74; N, 10.18.

**5-(3,5-Dimethoxyphenyl)-15-[4-(phenylethynyl)phenyl]porphine (7).** A solution of dipyrromethane (439 mg, 3.00 mmol) [14], 4-(phenylethynyl)benzaldehyde (309 mg, 1.50 mmol) [9] and 3,5-dimethoxybenzaldehyde (249 mg, 1.50 mmol) in  $\text{CH}_2\text{Cl}_2$  (600 mL) was bubbled with  $\text{N}_2$  for 30 min in dark. To the solution was added trifluoroacetic acid (134  $\mu\text{L}$ , 1.80 mmol) and the solution was stirred at room temperature for 2 h. Then, 2,3-dichloro-5,6-dicyano-1,4-benzoquinone (1.02 g, 4.50 mmol) dissolved in THF was added and the solution was stirred for another 1 h. The resulting solution was neutralized with triethylamine (0.50 mL, 3.6 mmol). After evaporation, the mixture was filtered through a short silica-gel column and the silica-gel was washed with  $\text{CH}_2\text{Cl}_2$ . After removal of the solvent, the residue was purified by silica-gel column chromatography (hexane/ $\text{CH}_2\text{Cl}_2 = 1/2$ , v/v) to give purple solid (254 mg, 27%), mp > 300 °C.  $^1\text{H}$  NMR (600 MHz,  $\text{CDCl}_3$ ):  $\delta_{\text{H}}$ , ppm -3.12 (s br, 2H,  $-\text{NH}$ ), 4.01 (s, 6H,  $-\text{OCH}_3$ ), 6.94 (s, 1H, Ar-H), 7.46 (m, 5H, Ar-H), 7.72 (d,  $J = 7.2$  Hz, 2H, Ar-H), 8.00 (d,  $J = 7.2$  Hz, 2H, Ar-H), 8.28 (d,  $J = 7.2$  Hz, 2H, Ar-H), 9.10 (d,  $J = 4.2$  Hz, 2H, pyrrole  $\beta$ -H), 9.19 (d,  $J = 4.2$  Hz, 2H, pyrrole  $\beta$ -H), 9.41 (dd,  $J = 4.8$  Hz, 4H, pyrrole  $\beta$ -H), 10.33 (s, 2H, *meso*-H).  $^{13}\text{C}$  NMR (151 MHz,  $\text{THF-d}_8$ ):  $\delta_{\text{C}}$ , ppm 55.6, 89.9, 91.1, 100.7, 105.9, 114.5, 118.7, 119.8, 123.7, 124.2, 129.2, 130.9, 131.1, 131.5, 132.3, 132.5, 135.6, 142.5, 143.9, 146.2, 146.3, 147.6, 147.9, 160.3. IR (KBr):  $\nu_{\text{max}}$ ,  $\text{cm}^{-1}$  691, 744, 793, 858, 926, 959, 1022, 1066, 1156, 1209, 1238, 1350, 1418, 1464, 1590, 2835, 2931, 3285. UV-vis (acetonitrile):  $\lambda_{\text{max}}$ , nm ( $\epsilon$ ,  $\text{M}^{-1}\cdot\text{cm}^{-1}$ ) 405 (350000), 501 (15000), 535 (6800), 575 (5000), 629 (2400). HR-FAB-MS (NBA):  $m/z$  calcd. for  $\text{C}_{42}\text{H}_{30}\text{N}_4\text{O}_2$ : 622.2369. Found 622.2339. Anal. calcd. for  $\text{C}_{42}\text{H}_{30}\text{N}_4\text{O}_2$ : C, 81.01; H, 4.86; N, 9.00%. Found C, 80.68; H, 4.84; N, 8.76.

**{5-[3,5-Dimethoxyphenyl]-15-[4-(phenylethynyl)phenyl]porphinato}zinc(II) (8).** Zinc acetate dihydrate (659 mg, 3.00 mmol) dissolved in MeOH was added to a solution of **7** (187 mg, 0.300 mmol) in  $\text{CH}_2\text{Cl}_2$  (300 mL) and the mixture was refluxed under  $\text{N}_2$  for 2 h. The reaction mixture was washed with water twice. The organic layer was dried over  $\text{Na}_2\text{SO}_4$  and evaporated. The crude product was recrystallized from  $\text{CH}_2\text{Cl}_2/\text{MeOH}$  to give red solid (208 mg, 100%), mp > 300 °C.  $^1\text{H}$  NMR (600 MHz,  $\text{CDCl}_3$ ):  $\delta_{\text{H}}$ , ppm 3.99 (s, 6H,  $-\text{OCH}_3$ ), 6.93 (s, 1H, Ar-H), 7.46 (m, 5H, Ar-H), 7.72 (d,  $J = 6.6$  Hz, 2H, Ar-H), 7.98 (d,  $J = 7.2$  Hz, 2H, Ar-H), 8.26 (d,  $J = 7.2$  Hz, 2H, Ar-H), 9.16 (d,  $J = 3.6$  Hz, 2H, pyrrole  $\beta$ -H), 9.25 (d,  $J = 4.2$  Hz, 2H, pyrrole  $\beta$ -H), 9.45 (dd,  $J = 4.8$  Hz, 4H, pyrrole  $\beta$ -H), 10.33 (s, 2H, *meso*-H).  $^{13}\text{C}$  NMR (151 MHz,  $\text{THF-d}_8$ ):  $\delta_{\text{C}}$ , ppm 55.6, 90.2, 90.8, 100.0, 106.3, 106.4, 114.8, 119.2, 120.3, 123.1, 124.4, 129.1,

129.2, 130.3, 132.0, 132.2, 132.2, 132.3, 132.7, 135.5, 144.5, 145.8, 150.3, 150.5, 150.6, 159.9. IR (KBr):  $\nu_{\max}$ ,  $\text{cm}^{-1}$  691, 732, 754, 783, 808, 862, 938, 993, 1063, 1155, 1207, 1289, 1328, 1345, 1393, 1418, 1464, 1522, 1590, 2834, 2931. UV-vis (acetonitrile):  $\lambda_{\max}$ , nm ( $\epsilon$ ,  $\text{M}^{-1}\cdot\text{cm}^{-1}$ ) 412 (480000), 543 (19000), 581 (4500). HR-FAB-MS (NBA):  $m/z$  calcd. for  $\text{C}_{42}\text{H}_{28}\text{N}_4\text{O}_2\text{Zn}$ : 684.1504. Found 684.1507. Anal. calcd. for  $\text{C}_{42}\text{H}_{28}\text{N}_4\text{O}_2\text{Zn}$ : C, 73.53; H, 4.11; N, 8.17%. Found C, 73.46; H, 4.13; N, 7.96.

**[5,15-Dibromo-10-[3,5-dimethoxyphenyl]-20-[4-(phenylethynyl)phenyl]porphinato}zinc(II) (9).**

A solution of **8** (274 mg, 0.400 mmol) and pyridine (0.32 mL, 4.0 mmol) in  $\text{CHCl}_3$  (360 mL) was cooled to  $0^\circ\text{C}$ . Then NBS (142 mg, 0.800 mmol) dissolved in  $\text{CHCl}_3$  (40 mL) was added to the solution and the solution was stirred at  $0^\circ\text{C}$  for 15 min before quenching with acetone. After evaporation, the reaction mixture was purified by silica-gel column chromatography (hexane/ $\text{CH}_2\text{Cl}_2 = 1/2$ , v/v) to give purple solid (280 mg, 82%), mp  $> 300^\circ\text{C}$ .  $^1\text{H}$  NMR (600 MHz,  $\text{THF-d}_8$ ):  $\delta_{\text{H}}$ , ppm 3.96 (s, 6H,  $-\text{OCH}_3$ ), 6.95 (t,  $J = 1.8$  Hz, 1H, Ar-H), 7.34 (d,  $J = 2.4$  Hz, 2H, Ar-H), 7.42–7.46 (m, 3H, Ar-H), 7.68 (d,  $J = 7.2$  Hz, 2H, Ar-H), 7.95 (d,  $J = 7.8$  Hz, 2H, Ar-H), 8.19 (d,  $J = 7.8$  Hz, 2H, Ar-H), 8.89 (d,  $J = 4.2$  Hz, 2H, pyrrole  $\beta$ -H), 8.97 (d,  $J = 4.2$  Hz, 2H, pyrrole  $\beta$ -H), 9.65 (d,  $J = 4.8$  Hz, 2H, pyrrole  $\beta$ -H), 9.68 (d,  $J = 4.2$  Hz, 2H, pyrrole  $\beta$ -H).  $^{13}\text{C}$  NMR (151 MHz,  $\text{THF-d}_8$ ):  $\delta_{\text{C}}$ , ppm 55.6, 89.9, 91.0, 100.2, 105.1, 114.8, 121.8, 122.8, 123.6, 124.2, 129.2, 129.2, 130.4, 132.3, 133.3, 133.4, 133.5, 133.9, 135.4, 143.7, 145.1, 150.8, 150.9, 151.2, 151.5, 159.9. IR (KBr):  $\nu_{\max}$ ,  $\text{cm}^{-1}$  692, 737, 756, 790, 867, 941, 1001, 1023, 1076, 1153, 1204, 1286, 1320, 1345, 1418, 1452, 1500, 1589, 2834, 2931. UV-vis (acetonitrile):  $\lambda_{\max}$ , nm ( $\epsilon$ ,  $\text{M}^{-1}\cdot\text{cm}^{-1}$ ) 430 (200000), 566 (7900), 607 (5000). HR-FAB-MS (NBA):  $m/z$  calcd. for  $\text{C}_{42}\text{H}_{26}\text{N}_4\text{O}_2\text{ZnBr}_2$ : 839.9714. Found 839.9722. Anal. calcd. for  $\text{C}_{42}\text{H}_{26}\text{N}_4\text{O}_2\text{ZnBr}_2 + 0.5 \text{C}_6\text{H}_{14}$  (hexane): C, 60.94; H, 3.75; N, 6.32%. Found C, 60.68; H, 3.65; N, 6.00.

**Q-Zn.** The dibromo porphyrin **9** (21 mg, 0.025 mmol), malononitrile (17 mg, 0.25 mmol), triphenylphosphine (26 mg, 0.10 mmol),  $\text{Pd}_2(\text{dba})_3$  (23 mg, 0.025 mmol) and  $\text{CuI}$  (10 mg, 0.050 mmol) were placed in 100 mL flask. The flask was dried under high vacuum and filled with  $\text{N}_2$ . Then dry THF (8 mL) was added to the flask, and the mixture was bubbled with argon for 20 min. Argon-bubbled dry pyridine (0.08 mL) was added to the flask.  $\text{NaH}$  (min. 60% in paraffin liquid, 20 mg, 0.50 mmol) was placed in another 25 mL flask and washed with dry THF. The 25 mL flask was dried under high vacuum and filled with  $\text{N}_2$ . The mixture in the 100 mL flask was moved to the 25 mL flask and refluxed overnight. Then, acetic acid (29  $\mu\text{L}$ , 0.50 mmol) was added to the reaction mixture at room temperature and stirred under air for 30 min. After evaporation, the residue was diluted with  $\text{CH}_2\text{Cl}_2$  and washed with sat.  $\text{NaHCO}_3$  aq and sat.  $\text{NaCl}$  aq. The organic layer was dried over  $\text{Na}_2\text{SO}_4$  and evaporated. The residue was purified by silica-gel

column chromatography ( $\text{CH}_2\text{Cl}_2/\text{MeCN} = 100/2$ , v/v) to give green solid (12 mg, 57%), mp  $> 300^\circ\text{C}$ .  $^1\text{H}$  NMR (600 MHz,  $\text{CDCl}_3$ ):  $\delta_{\text{H}}$ , ppm 3.79 (s, 6H,  $-\text{OCH}_3$ ), 6.40 (s, 2H, Ar-H), 6.49–6.53 (m, 4H, pyrrole  $\beta$ -H), 6.57 (s, 1H, Ar-H), 7.03 (d,  $J = 4.2$  Hz, 4H, pyrrole  $\beta$ -H), 7.30 (d,  $J = 6.0$  Hz, 2H, Ar-H), 7.36–7.37 (m, 3H, Ar-H), 7.55 (dd,  $J = 7.2$  Hz, 4H, Ar-H).  $^{13}\text{C}$  NMR (151 MHz,  $\text{CDCl}_3$ ):  $\delta_{\text{C}}$ , ppm 55.7, 88.7, 91.9, 101.8, 108.6, 115.3, 122.1, 122.3, 122.9, 125.3, 126.4, 128.6, 128.8, 130.4, 131.1, 131.9, 133.3, 133.5, 137.0, 138.9, 140.5, 147.5, 148.6, 151.1, 151.7, 154.4, 155.7, 160.1. IR (KBr):  $\nu_{\max}$ ,  $\text{cm}^{-1}$  691, 733, 759, 793, 834, 1021, 1077, 1156, 1205, 1270, 1305, 1331, 1369, 1465, 1494, 1560, 1591, 2216, 2840, 2933. UV-vis (acetonitrile):  $\lambda_{\max}$ , nm ( $\epsilon$ ,  $\text{M}^{-1}\cdot\text{cm}^{-1}$ ) 455 (56000), 630 (47000). HR-FAB-MS (NBA):  $m/z$  calcd. for  $\text{C}_{48}\text{H}_{26}\text{N}_8\text{O}_2\text{Zn}$ : 810.1470. Found 810.1475. Anal. calcd. for  $\text{C}_{48}\text{H}_{26}\text{N}_8\text{O}_2\text{Zn} + 0.56\text{CH}_2\text{Cl}_2$ : C, 67.84; H, 3.18; N, 13.03%. Found C, 68.22; H, 3.50; N, 12.64.

**Q-H.** A solution of 35%  $\text{HCl}$  aq (0.32 mL) in  $\text{MeOH}$  (1.3 mL) was added to a solution of **Q-Zn** (26 mg, 0.032 mmol) in  $\text{CHCl}_3$  (32 mL), and the solution was stirred at room temperature for 3 h. The reaction mixture was washed with sat.  $\text{NaHCO}_3$  aq twice and sat.  $\text{NaCl}$  aq once. The organic layer was dried over  $\text{Na}_2\text{SO}_4$  and evaporated. The crude product was purified by silica-gel column chromatography ( $\text{CH}_2\text{Cl}_2/\text{MeCN} = 100/2$ , v/v) to give deep purple solid (19 mg, 79%), mp  $> 300^\circ\text{C}$ .  $^1\text{H}$  NMR (600 MHz,  $\text{CDCl}_3$ ):  $\delta_{\text{H}}$ , ppm 3.83 (s, 6H,  $-\text{OCH}_3$ ), 6.58 (d,  $J = 1.8$  Hz, 2H, Ar-H), 6.62 (s, 1H, Ar-H), 6.67 (d,  $J = 4.8$  Hz, 2H, pyrrole  $\beta$ -H), 6.74 (d,  $J = 4.8$  Hz, 2H, pyrrole  $\beta$ -H), 7.18 (d,  $J = 4.2$  Hz, 2H, pyrrole  $\beta$ -H), 7.21 (d,  $J = 4.8$  Hz, 2H, pyrrole  $\beta$ -H), 7.38–7.39 (m, 3H, Ar-H), 7.44 (d,  $J = 7.8$  Hz, 2H, Ar-H), 7.57–7.58 (m, 2H, Ar-H), 7.66 (d,  $J = 7.8$  Hz, 2H, Ar-H), 13.72 (s br, 2H,  $-\text{NH}$ ).  $^{13}\text{C}$  NMR (151 MHz,  $\text{CDCl}_3$ ):  $\delta_{\text{C}}$ , ppm 55.8, 80.2, 88.4, 92.4, 102.0, 109.3, 114.1, 114.2, 122.8, 126.0, 128.6, 129.0, 131.2, 131.4, 131.9, 135.8, 137.7, 144.9, 145.3, 152.4, 160.5. IR (KBr):  $\nu_{\max}$ ,  $\text{cm}^{-1}$  690, 729, 756, 798, 817, 931, 952, 970, 1020, 1067, 1157, 1204, 1337, 1391, 1421, 1467, 1519, 1580, 2218, 2840, 2932, 3325. UV-vis (acetonitrile):  $\lambda_{\max}$ , nm ( $\epsilon$ ,  $\text{M}^{-1}\cdot\text{cm}^{-1}$ ) 415 (57000), 562 (33000), 719 (1900). HR-FAB-MS (NBA):  $m/z$  calcd. for  $\text{C}_{48}\text{H}_{29}\text{N}_8\text{O}_2$  [ $\text{MH}^+$ ]: 749.2413. Found 749.2386. Anal. calcd. for  $\text{C}_{48}\text{H}_{28}\text{N}_8\text{O}_2 + 0.24 \text{CH}_2\text{Cl}_2$ : C, 75.33; H, 3.77; N, 14.57%. Found C, 75.67; H, 3.99; N, 13.86.

**[5,10,15-(3,5-Dimethoxyphenyl)-20-[4-(phenylethynyl)phenyl]porphinato}zinc(II) (P-Zn).** 4-(phenylethynyl)benzaldehyde (516 mg, 2.50 mmol) [**9**], 3,5-dimethoxybenzaldehyde (1.25 g, 7.50 mmol), pyrrole (0.83 mL, 12 mmol) and zinc-*p-tert*-butylbenzoate (1.26 g, 3.00 mmol) were dissolved in  $\text{CH}_2\text{Cl}_2$  (1.20 L). The solution was bubbled with  $\text{N}_2$  for 30 min in dark. To the solution was added trifluoroacetic acid (0.27 mL, 3.6 mmol) and the solution was stirred at room temperature for 4 h. Then, 2,3-dichloro-5,6-dicyano-1,4-benzoquinone (1.82 g, 8.00 mmol) dissolved in THF was added and the solution was stirred for another 1 h. The

resulting solution was neutralized with triethylamine (1.0 mL, 7.0 mmol). After evaporation, the mixture was filtered through a short silica-gel column and the silica-gel was washed with  $\text{CH}_2\text{Cl}_2$ . After removal of the solvent, the residue was purified by silica-gel column chromatography ( $\text{CH}_2\text{Cl}_2$ ) to give purple solid (243 mg, 10%), mp > 300 °C.  $^1\text{H}$  NMR (600 MHz,  $\text{CDCl}_3$ ):  $\delta_{\text{H}}$ , ppm 3.94 (s, 18H,  $-\text{OCH}_3$ ), 6.88 (t,  $J = 1.8$  Hz, 3H, Ar-H), 7.40 (d,  $J = 1.8$  Hz, 6H, Ar-H), 7.41–7.44 (m, 3H, Ar-H), 7.69 (d,  $J = 7.2$  Hz, 2H, Ar-H), 7.93 (d,  $J = 8.4$  Hz, 2H, Ar-H), 8.21 (d,  $J = 7.8$  Hz, 2H, Ar-H), 8.95 (d,  $J = 4.8$  Hz, 2H, pyrrole  $\beta$ -H), 9.04 (s, 4H, pyrrole  $\beta$ -H), 9.06 (d,  $J = 4.8$  Hz, 2H, pyrrole  $\beta$ -H).  $^{13}\text{C}$  NMR (151 MHz,  $\text{CDCl}_3$ ):  $\delta_{\text{C}}$ , ppm 55.8, 89.6, 90.6, 100.2, 113.9, 120.4, 121.1, 121.1, 122.7, 123.5, 128.5, 128.6, 128.6, 130.0, 131.9, 131.9, 132.2, 132.3, 134.6, 143.1, 144.8, 150.1, 150.1, 150.2, 150.2, 158.9. IR (KBr):  $\nu_{\text{max}}$ ,  $\text{cm}^{-1}$  693, 720, 761, 798, 860, 938, 1001, 1027, 1064, 1154, 1204, 1348, 1420, 1452, 1495, 1591, 2835, 2934, 2997. UV-vis (acetonitrile):  $\lambda_{\text{max}}$ , nm ( $\epsilon$ ,  $\text{M}^{-1}\cdot\text{cm}^{-1}$ ) 424 (600000), 556 (22000), 596 (7800). HR-FAB-MS (NBA):  $m/z$  calcd. for  $\text{C}_{58}\text{H}_{44}\text{N}_4\text{O}_6\text{Zn}$ : 956.2552. Found 956.2553. Anal. calcd. for  $\text{C}_{58}\text{H}_{44}\text{N}_4\text{O}_6\text{Zn}$ : C, 72.69; H, 4.63; N, 5.85%. Found C, 72.46; H, 4.90; N, 5.63.

**5,10,15-(3,5-Dimethoxyphenyl)-20-[4-(phenylethynyl)phenyl]porphine (P-H).** A solution of 35% HCl aq (0.50 mL) in MeOH (2.0 mL) was added to a solution of **P-Zn** (48 mg, 0.050 mmol) in  $\text{CHCl}_3$  (50 mL) and the solution was stirred at room temperature for 4 h. The reaction mixture was washed with sat.  $\text{NaHCO}_3$  aq twice and sat.  $\text{NaCl}$  aq once. The organic layer was dried over  $\text{Na}_2\text{SO}_4$  and evaporated. The crude product was purified by silica-gel column chromatography ( $\text{CH}_2\text{Cl}_2$ ) to give purple solid (46 mg, 100%), mp > 300 °C.  $^1\text{H}$  NMR (600 MHz,  $\text{CDCl}_3$ ):  $\delta_{\text{H}}$ , ppm -2.80 (s, 2H,  $-\text{NH}$ ), 3.97 (s, 18H,  $-\text{OCH}_3$ ), 6.91 (t,  $J = 1.8$  Hz, 3H, Ar-H), 7.41 (d,  $J = 1.8$  Hz, 6H, Ar-H), 7.43–7.45 (m, 3H, Ar-H), 7.70 (d,  $J = 6.6$  Hz, 2H, Ar-H), 7.95 (d,  $J = 7.8$  Hz, 2H, Ar-H), 8.22 (d,  $J = 7.8$  Hz, 2H, Ar-H), 8.86 (d,  $J = 4.2$  Hz, 2H, pyrrole  $\beta$ -H), 8.95 (s, 4H, pyrrole  $\beta$ -H), 8.97 (d,  $J = 4.8$  Hz, 2H, pyrrole  $\beta$ -H).  $^{13}\text{C}$  NMR (151 MHz,  $\text{CDCl}_3$ ):  $\delta_{\text{C}}$ , ppm 55.8, 89.5, 90.7, 100.3, 114.0, 119.5, 120.1, 120.1, 122.9, 123.5, 128.6, 130.1, 131.9, 134.7, 142.4, 144.1, 159.0. IR (KBr):  $\nu_{\text{max}}$ ,  $\text{cm}^{-1}$  691, 734, 757, 801, 918, 972, 1018, 1063, 1154, 1204, 1355, 1420, 1453, 1590, 2835, 2932, 2997, 3315. UV-vis (acetonitrile):  $\lambda_{\text{max}}$ , nm ( $\epsilon$ ,  $\text{M}^{-1}\cdot\text{cm}^{-1}$ ) 418 (460000), 513 (20000), 548 (7100), 589 (5800), 644 (3600). HR-FAB-MS (NBA):  $m/z$  calcd. for  $\text{C}_{58}\text{H}_{46}\text{N}_4\text{O}_6$ : 894.3417. Found 894.3420. Anal. calcd. for  $\text{C}_{58}\text{H}_{46}\text{N}_4\text{O}_6$ : C, 77.83; H, 5.18; N, 6.26%. Found C, 77.51; H, 5.44; N, 5.97.

### Electrochemical measurements

Electrochemical measurements were performed on an ALS630C electrochemical analyzer in deaerated acetonitrile containing 0.1 M  $\text{Bu}_4\text{NPF}_6$  as the supporting

electrolyte at 298 K. A conventional three-electrode cell was used with a platinum working electrode (surface area of 0.3  $\text{mm}^2$ ) and a platinum wire as a counter electrode. The platinum working electrodes (BAS) were routinely polished with BAS polishing alumina suspension and rinsed with acetone and acetonitrile before use. The measured potentials were recorded with respect to an  $\text{Ag}/\text{AgNO}_3$  (0.01 M in acetonitrile) reference electrode. All potentials (vs.  $\text{Ag}/\text{Ag}^+$ ) were converted to values vs. ferrocene/ferrocenium as an internal reference. All electrochemical measurements were carried out under an  $\text{N}_2$  atmosphere.

### Laser flash photolysis

Femtosecond transient absorption spectroscopy experiments were conducted using an ultrafast source: Integra-C (Quantronix Corp.), an optical parametric amplifier: TOPAS (Light Conversion Ltd) and a commercially available optical detection system: Helios provided by Ultrafast Systems LLC. The source for the pump and probe pulses were derived from the fundamental output of Integra-C ( $\lambda = 786$  nm, 2 mJ per pulse and fwhm = 130 fs) at a repetition rate of 1 kHz. 75% of the fundamental output of the laser was introduced into a second harmonic generation (SHG) unit: Apollo (Ultrafast Systems) for excitation light generation at  $\lambda = 393$  nm, while the rest of the output was used for white light generation. The laser pulse was focused on a sapphire plate of 3 mm thickness and then white light continuum covering the visible region from  $\lambda = 410$  nm to 800 nm was generated *via* self-phase modulation. A variable neutral density filter, an optical aperture, and a pair of polarizer were inserted in the path in order to generate stable white light continuum. Prior to generating the probe continuum, the laser pulse was fed to a delay line that provides an experimental time window of 3.2 ns with a maximum step resolution of 7 fs. In our experiments, a wavelength at  $\lambda = 393$  nm of SHG output was irradiated at the sample cell with a spot size of 1 mm diameter where it was merged with the white probe pulse in a close angle ( $<10^\circ$ ). The probe beam after passing through the 2 mm sample cell was focused on a fiber optic cable that was connected to a CMOS spectrograph for recording the time-resolved spectra ( $\lambda = 410$ –800 nm). Typically, 1500 excitation pulses were averaged for 3 s to obtain the transient spectrum at a set delay time. Kinetic traces at appropriate wavelengths were assembled from the time-resolved spectral data. All measurements were conducted at room temperature, 295 K.

### CONCLUSION

We have prepared newly designed zinc complex and free-base of a porphyrin-quinoidal porphyrin dyad linked by a diphenylethynyl bridge as new donor-acceptor hybrids. The UV-vis absorption spectra of the dyads were almost linear combinations of the absorption spectra of



each component. Namely, there are very weak electronic interactions between the chromophores at the ground state. The diphenylethynyl linker is considered to suppress electronic communication due to the large dihedral angle between the phenyl group and the porphyrin plane, as suggested by the DFT-calculated model structure. On the other hand, in the fluorescence spectra of the dyads, the porphyrin emissions were significantly quenched, indicating the presence of strong interactions between the two units at the excited states. The electrochemical analysis revealed that the first oxidations and reductions of the dyads occur at the porphyrin units and the quinoidal porphyrin units, respectively. Femtosecond laser flash photolysis of the zinc dyad suggested both ultrafast (<1 ps) energy and electron transfer from the porphyrin unit to the quinoidal part to afford the singlet excited state of the quinoidal unit and the CS state, respectively. The former was considered to be a major intermediate. These ultrafast processes resulted in the quenching of the porphyrin fluorescence in the dyad. On the other hand, the free-base dyad underwent only energy transfer from the porphyrin unit to the quinoidal porphyrin part to quench the fluorescence of the porphyrin unit and give the quinoidal excited state, which decayed without formation of a CS state due to its intrinsic short lifetime. In order to use quinoidal porphyrins as efficient acceptors in photoinduced electron transfer, it is necessary to elongate the lifetimes of their excited states by structural modifications. Once this problem is solved, quinoidal porphyrins will be attractive chromophores on account of their additional merit that they strongly absorb visible light that normal porphyrins do not.

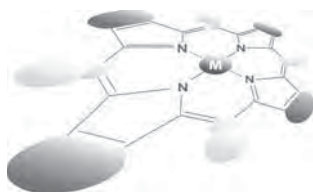
### Acknowledgements

This work was supported by Grants-in-Aid (Nos. 20108009 to F. T., 20108010 to S. F. and 26620154 and 26288037 to K. O.) from Ministry of Education, Culture, Sports, Science and Technology of Japan and Research Grants to F. T. from Tokuyama Science and Technology Foundation and Iketani Science and Technology Foundation. We acknowledge Prof. T. Shinmyozu of Kyushu University for his kind cooperation.

### REFERENCES

- (a) Milgrom LR. *The Colours of Life: An Introduction to the Chemistry of Porphyrins and Related Compounds*, Oxford University Press: New York, 1997. (b) *Photosynthesis in Relation to Model Systems*, Vol. 3, Barber J. (Ed.) Elsevier Scientific Publishing Company: Amsterdam, 1979. (c) *The Photosynthetic Reaction Center*, Vols 1 and 2, Deisenhofer J and Norris JR. (Eds.) Academic Press: San Diego, 1993. (d) *Molecular Mechanism of Photosynthesis*, Blankenship RE. (Ed.) Wiley-Blackwell: Dordrecht, 2002. (e) Collings AF and Critchley C. *Artificial Photosynthesis: From Basic Biology to Industrial Application*, Wiley-VCH: Weinheim, 2005. (f) Balzani V. *Electron Transfer in Chemistry*, Wiley-VCH: Weinheim, 2001.
- (a) Gust D and Moore TA. *The Porphyrin Handbook*, Vol. 8, Kadish KM, Smith KM and Guillard R. (Eds.) Academic Press: San Diego, 2000; pp 153–190. (b) Harvey PD. *The Porphyrin Handbook*, Vol. 18, Kadish KM, Smith KM and Guillard R. (Eds.) Academic Press: San Diego, 2003; pp 63–250. (c) *Handbook of Porphyrin Science*, Kadish KM, Smith KM and Guillard R. (Eds.) World Scientific: Singapore, 2010.
- (a) Gust D, Moore TA and Moore AL. *Acc. Chem. Res.* 2001; **34**: 40–48. (b) Fukuzumi S. *Org. Biomol. Chem.* 2003; **1**: 609–620. (c) El-Khouly ME, Ito O, Smith PM and D'Souza F. *J. Photochem. Photobiol. C: Photochemistry Reviews* 2004; **5**: 79–104. (d) Fukuzumi S. *Phys. Chem. Chem. Phys.* 2008; **10**: 2283–2297. (e) Gust D, Moore TA and Moore A. *Acc. Chem. Res.* 2009; **42**: 1890–1898. (f) Hasobe T. *Phys. Chem. Chem. Phys.* 2010; **12**: 44–57. (g) D' Souza F, Sandanayaka AS. D and Ito O. *J. Phys. Chem. Lett.* 2010; **1**: 2586–2593. (h) Fukuzumi S and Ohkubo K. *J. Mater. Chem.* 2012; **22**: 4575–4587. (i) Hasobe T. *J. Phys. Chem. Lett.* 2013; **4**: 1771–1780. (j) Guldi DM. *Chem. Soc. Rev.* 2002; **31**: 22–36. (k) Imahori H, Mori Y and Matano Y. *J. Photochem. Photobiol. C: Photochemistry Reviews* 2003; **4**: 51–83. (l) D'Souza F and Ito O. *Coord. Chem. Rev.* 2005; **249**: 1410–1422. (m) Fukuzumi S, Ohkubo K and Suenobu T. *Acc. Chem. Res.* 2014; **47**: 1455–1464.
- (a) Fukuzumi S. *Bull. Chem. Soc. Jpn.* 2006; **79**: 177–195. (b) Imahori H. *Bull. Chem. Soc. Jpn.* 2007; **80**: 621–636. (c) Fukuzumi S and Kojima T. *J. Mater. Chem.* 2008; **18**: 1427–1439. (d) D'Souza F and Ito O. *Chem. Commun.* 2009; 4913–4928. (e) Fukuzumi S, Honda T, Ohkubo K and Kojima T. *Dalton Trans.* 2009; 3880–3889. (f) Wasielewski MR. *Acc. Chem. Res.* 2009; **42**: 1910–1921. (g) Ohkubo K and Fukuzumi S. *Bull. Chem. Soc. Jpn.* 2009; **82**: 303–315. (h) Bottari G, de la Torre G, Guldi DM and Torres T. *Chem. Rev.* 2010; **110**: 6768–6816. (i) D'Souza F and Ito O. *Chem. Soc. Rev.* 2012; **41**: 86–96. (j) Imahori H, Umeyama T, Kurotobi K and Takano Y. *Chem. Commun.* 2012; **48**: 4032–4045. (k) Gust D, Moore TA and Moore AL. *Faraday Discuss.* 2012; **155**: 9–26. (l) Bottari G, Trukhina O, Ince M and Torres T. *Coord. Chem. Rev.* 2012; **256**: 2453–2477. (m) Ito O and D'Souza F. *Molecules* 2012; **17**: 5816–5835. (n) Schuster DI. *J. Org. Chem.* 2013; **78**: 6811–6841. (o) Fukuzumi S and Ohkubo K. *Dalton Trans.* 2013; **42**: 15846–15858.
- (a) Blake IM, Anderson HL, Beljonne D, Brédas JL and Clegg W. *J. Am. Chem. Soc.* 1998; **120**: 10764–10765. (b) Blake IM, Rees LH, Claridge TDW

- and Anderson HL. *Angew. Chem. Int. Ed.* 2000; **39**: 1818–1821. (c) Blake IM, Krivokapic A, Katterle M and Anderson HL. *Chem. Commun.* 2002; 1662–1663. (d) McEwan KJ, Fleitz PA, Rogers JE, Slagle JE, McLean DG, Akdas H, Katterle M, Blake IM and Anderson HL. *Adv. Mater.* 2004; **16**: 1933–1935. (e) Smith MJ, Clegg W, Nguyen KA, Rogers JE, Pachter R, Fleitz PA and Anderson HL. *Chem. Commun.*, 2005; 2433–2435.
6. The examples of intramolecular energy and electron transfer in diphenylethynyl-bridged dimers composed of tetrapyrrole derivatives have been reported so far. (a) Osuka A, Tanabe N, Kawabata S, Yamazaki I and Nishimura Y. *J. Org. Chem.* 1996; **60**: 7177–7185. (b) Hsiao JS, Krueger BP, Wagner RW, Johnson TE, Delaney JK, Mauzerall DC, Fleming GR, Lindsey JS, Bocian DF and Donohoe RJ. *J. Am. Chem. Soc.* 1996; **118**: 11181–11193. (c) Seth J, Palaniappan V, Wagner RW, Johnson TE, Lindsey JS and Bocian DF. *J. Am. Chem. Soc.* 1996; **118**: 11194–11207. (d) Strachan JP, Gentemann S, Seth J, Kalsbeck WA, Lindsey JS, Holten D and Bocian DF. *J. Am. Chem. Soc.* 1997; **119**: 11191–11201. (e) Strachan JP, Gentemann S, Seth J, Kalsbeck WA, Lindsey JS, Holten D and Bocian DF. *Inorg. Chem.* 1998; **37**: 1191–1201. (f) Hascoat P, Yang SI, Lammi RK, Alley J, Bocian DF, Lindsey JS and Holten D. *Inorg. Chem.* 1999; **38**: 4849–4853. (g) Lammi RK, Ambroise A, Balasubramanian T, Wagner RW, Bocian DF, Holten D and Lindsey JS. *J. Am. Chem. Soc.* 2000; **122**: 7579–7591. (h) Kelley RF, Tauber MJ, Wilson TM and Wasielewski MR. *Chem. Commun.* 2007; 4407–4409.
  7. (a) Fortage J, Scarpaci A, Viau L, Pellegrin Y, Blart E, Falkenström M, Hammarström L, Asselberghs I, Kellens R, Libaers W, Clays K, Eng MP and Odobel F. *Chem. Eur. J.* 2009; **15**: 9058–9067. (b) Ryan A, Gehrold A, Perusitti R, Pintea M, Fazekas M, Locos OB, Blaikie F and Senge MO. *Eur. J. Org. Chem.* 2011; 5817–5844. (c) Liu Y, Lin H, Li J, Dy JT, Tamaki K, Nakazaki J, Nakayama D, Nishiyama C, Uchida S, Kubo T and Segawa H. *Phys. Chem. Chem. Phys.* 2012; **14**: 16703–16712.
  8. Uno M, Seto M, Masuda M, Ueda W and Takahashi S. *Tetrahedron Lett.* 1985; **26**: 1553–1556.
  9. Leadbeater NE and Tominack BJ. *Tetrahedron Lett.* 2003; **44**: 8653–8656.
  10. Gaussian 09, Revision D.01, Frisch MJ, Trucks GW, Schlegel HB, Scuseria GE, Robb MA, Cheeseman JR, Scalmani G, Barone V, Mennucci B, Petersson GA, Nakatsuji H, Caricato M, Li X, Hratchian HP, Izmaylov AF, Bloino J, Zheng G, Sonnenberg JL, Hada M, Ehara M, Toyota K, Fukuda, R, Hasegawa J, Ishida M, Nakajima T, Honda Y, Kitao O, Nakai H, Vreven T, Montgomery JAJ, Peralta JE, Ogliaro F, Bearpark M, Heyd JJ, Brothers E, Kudin KN, Staroverov VN, Keith T, Kobayashi R, Normand J, Raghavachari K, Rendell A, Burant JC, Iyengar SS, Tomasi J, Cossi M, Rega N, Millam JM, Klene M, Knox JE, Cross JB, Bakken V, Adamo C, Jaramillo J, Gomperts R, Stratmann RE, Yazyev O, Austin AJ, Cammi R, Pomelli C, Ochterski JW, Martin RL, Morokuma K, Zakrzewski VG, Voth GA, Salvador P, Dannenberg JJ, Dapprich S, Daniels AD, Farkas Ö, Foresman JB, Ortiz JV, Cioslowski J and Fox DJ. Gaussian, Inc., Wallingford CT, 2013.
  11. (a) Fukuzumi S, Suenobu T, Patz M, Hirasaka T, Itoh S, Fujitsuka M and Ito O. *J. Am. Chem. Soc.* 1998; **120**: 8060–8068. (b) Fukuzumi S, Suenobu T, Hirasaka T, Sakurada N, Arakawa R, Fujitsuka M and Ito O. *J. Phys. Chem. A* 1999; **103**: 5935–5941.
  12. The lifetime of the singlet excited state of **P-Zn** (0.48 ns) is shorter than the value of typical zinc porphyrin (*e.g.* ZnTPP: 2.0–2.5 ns). The excited state may be quenched by the electron-donating 3,5-dimethoxyphenyl groups or the 1,2-diphenylethynyl moiety.
  13. (a) Mataga N, Chosrowjan H, Shibata Y, Yoshida N, Osuka A, Kikuzawa T and Okada T. *J. Am. Chem. Soc.* 2001; **123**: 12422–12423. (b) Mataga N, Chosrowjan H, Taniguchi S, Shibata Y, Yoshida N, Osuka A, Kikuzawa T and Okada T. *J. Phys. Chem. A* 2002; **106**: 12191–12201. (c) Mataga N, Taniguchi S, Chosrowjan H, Osuka A and Yoshida N. *Chem. Phys.* 2003; **295**: 215–228. (d) Fujitsuka M, Shiragami T, Cho DW, Tojo S, Yasuda M and Majima T. *J. Phys. Chem. A* 2014; **118**: 3926–3933.
  14. Unidentified small peaks in the earlier transient spectra of **PQ-H** were found at 894, 976, 1044 and 1135 nm, which values are slightly different from those of the free-base quinoidal radical anion.
  15. Laha JK, Dhanalekshmi S, Taniguchi M, Ambroise A and Lindsey JS. *Organic Process Research & Development* 2003; **7**: 799–812.
  16. Lembo A, Tagliatesta P and Guldi DM. *J. Phys. Chem. A* 2006; **110**: 11424–11434.



# Molecular structures, redox properties, and photosubstitution of ruthenium(II) carbonyl complexes of porphycene

Toru Okawara<sup>a,†,‡</sup>, Masaaki Abe<sup>\*b</sup>, Shiho Ashigara<sup>a</sup> and Yoshio Hisaeda<sup>\*b,c,§</sup>

<sup>a</sup>Department of Chemistry and Biochemistry, Graduate School of Engineering, Kyushu University, 744 Moto-oka, Nishi-ku, Fukuoka 819-0395, Japan

<sup>b</sup>Department of Applied Chemistry, Graduate School of Engineering, Kyushu University, 744 Moto-oka, Nishi-ku, Fukuoka 819-0395, Japan

<sup>c</sup>Center for Molecular Systems (CMS), Kyushu University, 744 Moto-oka, Nishi-ku, Fukuoka 819-0395, Japan

Dedicated to Professor Shunichi Fukuzumi on the occasion of his retirement

Received 30 October 2014

Accepted 12 November 2014

**ABSTRACT:** Two ruthenium(II) carbonyl complexes of porphycene, (carbonyl)(pyridine)(2,7,12,17-tetra-*n*-propylporphycenato)ruthenium(II) (**1**) and (carbonyl)(pyridine)(2,3,6,7,12,13,16,17-octaethylporphycenato)ruthenium(II) (**2**), have been structurally characterized by single-crystal X-ray diffraction analysis. Cyclic voltammetry has revealed that the porphycene complexes undergo multiple oxidations and reductions in dichloromethane and the reduction potentials are highly positive compared to porphyrin analogs. UV-light irradiation (400 nm or shorter wavelength region) of a benzene solution of **1** and **2** containing external pyridine leads to dissociation of the carbonyl ligand from the ruthenium(II) centers to give the corresponding bis-pyridine complexes. The identical reaction has been also studied for a porphyrin derivative (carbonyl)(pyridine)(2,3,7,8,12,13,17,18-octaethylporphyrinato)ruthenium(II) (**3**). The first-order kinetic analysis has revealed that the photosubstitution of all of the compounds occurs in the order of  $10^{-3} \text{ s}^{-1}$  at 298 K but proceeds faster for complexes of porphycene (**1** and **2**) than that of porphyrin (**3**).

**KEYWORDS:** porphycene, ruthenium, crystal structures, redox properties, photosubstitution.

## INTRODUCTION

Axial ligand substitution reactions of ruthenium(II) porphyrins [1–3] and also phthalocyanines [4] have been studied extensively and are important in relevance for their catalysis and the formation of coordination polymers through axial binding [5–10]. For the axial ligand transformation, photosubstitution of CO in  $[\text{Ru}^{\text{II}}(\text{P})(\text{CO})\text{L}]$  where P =

porphyrinato or phthalocyanato dianion; L = monodentate ligands such as methanol and pyridine derivatives is the first step to obtain  $[\text{Ru}^{\text{II}}(\text{P})(\text{L})_2]$  derivatives [1]. Hopf *et al.* reported UV-photosubstitution of CO for  $[\text{Ru}(\text{OEP})(\text{CO})(\text{pyridine})]$  (OEP = 2,3,7,8,12,13,17,18-octaethylporphyrinato dianion) in pyridine to give  $[\text{Ru}(\text{OEP})(\text{pyridine})_2]$  [1] and later the identical photosubstitution has been applied to many cases [1–3, 5–10]. Hoshino *et al.* studied the identical photosubstitution reaction by using steady-light and laser flash photolysis techniques and discussed in detail the ligand-substitution mechanism [2]. More recently, Ishii *et al.* described visible excitation of ruthenium phthalocyanine molecules to release CO in a stepwise manner by two-photon excitation using a nanosecond-pulsed laser technique [4].

Porphycene, which is a constitutional isomer of porphyrin, has a rectangular coordination cavity [11–13]. In

<sup>§</sup>SPP full and <sup>∞</sup> student member in good standing

\*Correspondence to: Masaaki Abe, email: mabe@mail.cstm.kyushu-u.ac.jp, tel: +81 92-802-2828, fax: +81 92-802-2828; Yoshio Hisaeda, email: yhisatem@mail.cstm.kyushu-u.ac.jp, tel: +81 92-802-2826, fax: +81 92-802-2826

<sup>†</sup>Current address: Department of Materials Chemistry and Chemical Engineering, National Institute of Technology, Kitakyushu College, 5-20-1 Shi-i, Kokuraminami-ku, Kitakyushu 802-0985, Japan

the past few decades, porphycene and metalloporphycene have been widely investigated because of their unique properties arising from the rectangular structure of the tetrapyrrolic macrocycle [14–23]. In particular, porphycene is characterized by its superior physicochemical properties over porphyrins such as more intense absorption in the visible region [24, 25], higher singlet oxygen generation efficiency [26–32], and catalytic activities [33–36]. Photochemistry of porphycene and metalloporphycenes has been of considerable interest in their potential use as photodynamic therapy (PDT) agents [26, 27] and also as photocatalysts [37], in which a higher molar absorption coefficient ( $\epsilon$  in  $M^{-1}\cdot cm^{-1}$ ) for porphycene over that for porphyrin is apparently a strong advantage and thus triggers the motivation for the study. In our previous paper [38], we have described the synthesis and spectroscopic characterizations of a series of six-coordinate ruthenium complexes of porphycene,  $[Ru(Pc)(CO)(L)]$  and  $[Ru(Pc)(L)_2]$  where Pc represents 2,7,12,17-tetra-*n*-propylporphycenato dianion (TPrPc<sup>2-</sup>) and 2,3,6,7,12,13,16,17-octaethylporphycenato dianion (OEPc<sup>2-</sup>) and L represents pyridine derivatives. It is noted that Sessler *et al.* have described a somewhat different type of “organometallic” ruthenium porphycenes [39].

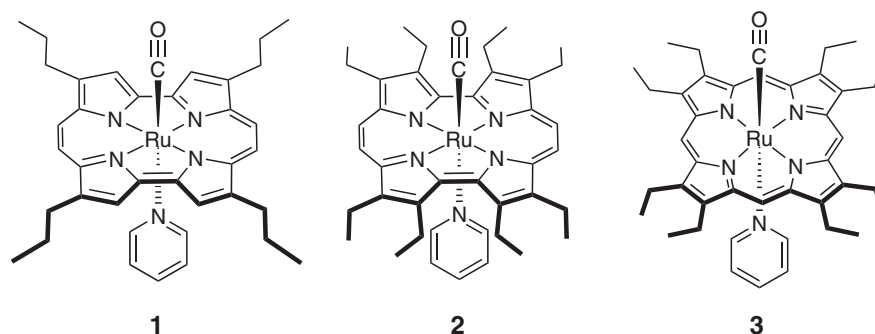
In the current study, we have unambiguously determined molecular structures of two ruthenium(II) carbonyl porphycenes **1** and **2** as illustrated in Chart 1, and examined

their redox properties and photosubstitution reactions. The photosubstitution reactions examined in this study are depicted in Scheme 1. For comparison, the photosubstitution of a porphyrin analog **3** (Chart 1) was also studied. We show that the UV-light excitation of **1–3** in benzene containing external pyridine leads to photosubstitution of CO to give the corresponding six-coordinate bis-pyridine complexes  $[Ru(Pc)(pyridine)_2]$ . The first-order kinetic analysis has shown that the photosubstitution of all of the compounds occurs in the order of  $10^{-3} s^{-1}$  at 298 K and proceeds faster for the porphycene complexes **1** and **2** than the porphyrin complex **3**.

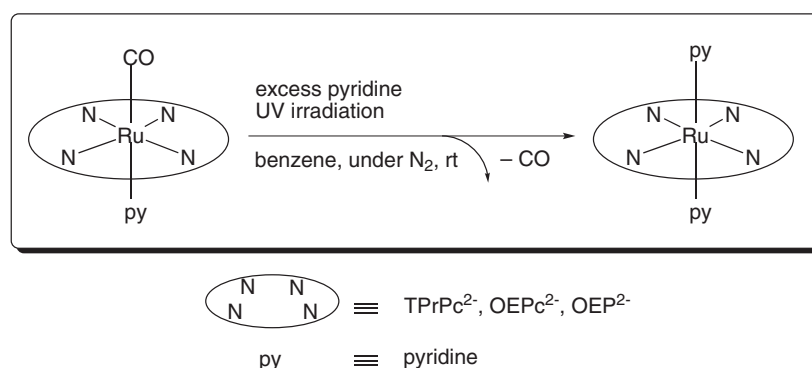
## EXPERIMENTAL

### General

All solvents and reagents used in this work were of commercially available grade and used as received unless otherwise stated. Benzene used for the photochemical reactions was distilled over NaH prior to the measurements. Complexes **1–3** were prepared according to the previous reports [1, 16, 38]. UV-vis absorption spectra were recorded on a Hitachi U-3310 spectrophotometer using  $CH_2Cl_2$  or benzene as solvents. Fourier-transform infrared



**Chart 1.** Chemical structures of **1–3** examined in this study. **1**,  $[Ru(TPrPc)(CO)(pyridine)]$  where TPrPc = 2,7,12,17-tetra-*n*-propylporphycenato dianion. **2**,  $[Ru(OEPc)(CO)(pyridine)]$  where OEPc = 2,3,6,7,12,13,16,17-octaethylporphycenato dianion. **3**,  $[Ru(OEP)(CO)(pyridine)]$  where OEP = 2,3,7,8,12,13,17,18-octaethylporphycenato dianion



**Scheme 1.** Photosubstitution of **1–3**

(FT-IR) spectra were obtained on a JASCO FT/IR-460 Plus spectrometer with a KBr method. Elemental analysis was performed by the Service Center of Elementary Analysis of Organic Compounds at Kyushu University. Cyclic voltammetry was performed by ALS-630 with a three-electrode cell by using Pt (1.6 mm in diameter), Pt coil, and Ag/AgCl as a working, counter, and reference electrodes, respectively. Each complex (1 mM) was dissolved in dry CH<sub>2</sub>Cl<sub>2</sub> containing 0.1 M tetra-*n*-butylammonium perchlorate as a supporting electrolyte. The solution for cyclic voltammetry was flushed by nitrogen prior to the measurement. Under our experimental conditions, ferrocene/ferricinium redox couple was observed at a half-wave potential  $E_{1/2} = 0.48$  V vs. Ag/AgCl. **Caution!** *The perchlorate salt should always be handled with great caution due to its potential nature of explosion.*

### Single-crystal X-ray diffraction study

Single crystals of **1** and **2** suitable for X-ray diffraction study were grown from CH<sub>2</sub>Cl<sub>2</sub>/CH<sub>3</sub>OH/pyridine (49/49/2)

at 293 K. The crystal was mounted on a glass fiber and the diffraction data were collected at 273 and 173 K for **1** and **2**, respectively, with a Bruker SMART APEX CCD diffractometer equipped with graphite-monochromated Mo *K*α radiation ( $\lambda = 0.71073$  Å) from a fine-focus sealed tube operated at 50 kV and 30 mA. The data frames were integrated using SAINT [40] and merged to give a unique data set for the structure determination. Absorption corrections by SADABS [41] were carried out. The structures were solved by a direct method and refined by the full-matrix least-squares method on all  $F^2$  data using the SHELXL-97 [42] suite of programs. All non-hydrogen atoms were anisotropically refined. Hydrogen atoms were located at geometrically idealized, calculated positions and constrained to ride on their parent atoms with  $U_{\text{iso}}(\text{H}) = 1.2U_{\text{eq}}(\text{CH and CH}_2)$ ,  $U_{\text{iso}}(\text{H}) = 1.5U_{\text{eq}}(\text{CH}_3)$ . For **2**, isotropic restraints were used for convergence in the refinement cycles, and SIMU and ISOR commands of the program Shelxtl [42] were applied to Ru1, C37, and O1 by applying an s.u. value of 0.002. The crystallographic data of **1** and **2** are collected in Table 1. Attempts to

**Table 1.** Crystallographic and refinement data for **1** and **2**

Compound	<b>1</b>	<b>2</b>
Formula	C <sub>38</sub> H <sub>41</sub> N <sub>5</sub> ORu	C <sub>42</sub> H <sub>49</sub> N <sub>5</sub> ORu
<i>F</i> <sub>w</sub>	684.85	740.93
<i>T</i> , K	273	173
Wavelength, Å	0.71073	0.71073
Crystal system	Orthorhombic	Triclinic
Space group	<i>Fdd</i> 2	<i>P</i> 1
<i>a</i> , Å	20.658(5)	9.4733(7)
<i>b</i> , Å	21.877(5)	10.0151(8)
<i>c</i> , Å	14.784(4)	10.6698(8)
$\alpha$ , deg	90	82.4340(10)
$\beta$ , deg	90	86.8440(10)
$\gamma$ , deg	90	64.9670(10)
<i>V</i> , Å <sup>3</sup>	6682(3)	909.23(12)
<i>Z</i>	8	1
Density (calcd), Mg.m <sup>-3</sup>	1.362	1.353
Absorption coefficient, mm <sup>-1</sup>	0.504	0.471
<i>F</i> (000)	2712	388
$\theta$ , deg	1.93 to 24.50	1.93 to 30.41
Reflections collected	7635	6770
Independent reflections	2612 [ <i>R</i> (int) = 0.0403]	5681 [ <i>R</i> (int) = 0.0185]
Data/restraints/parameters	2612/1/209	5681/27/450
Goodness-of-fit on $F^2$	1.027	0.877
<i>R</i> 1 [ <i>I</i> > 2σ( <i>I</i> )]	0.0397	0.0506
<i>wR</i> <sub>2</sub> (all data) <sup>a</sup>	0.1093	0.1427
Largest diff. peak and hole, e.Å <sup>-3</sup>	1.056 and -0.239	0.722 and -1.233

<sup>a</sup>  $w = 1/[\sigma^2(F_o^2) + (0.08P)^2 + 0.75P]$  where  $P = (F_o^2 + 2F_c^2)/3$  for **1** and  $w = 1/[\sigma^2(F_o^2) + (0.10P)^2 + 1.50P]$  where  $P = (F_o^2 + 2F_c^2)/3$  for **2**.

obtain high-resolution molecular structure of **3** were so far unsuccessful due to a severe disorder problem. Reflection data of **3** were obtained by identical methods to those for **1** and **2**, and isotropic restraints were employed for convergence in the refinement cycles. Preliminary crystallographic and refinement data of **3** are as follows: triclinic space group *P1* (at 223 K);  $a = 10.411(5)$  Å,  $b = 10.472(4)$  Å,  $c = 20.558(9)$  Å,  $\alpha = 92.691(7)^\circ$ ,  $\beta = 91.898(8)^\circ$ ,  $\gamma = 115.358(7)^\circ$ ,  $V = 2019.6(15)$  Å<sup>3</sup>, and  $Z = 2$  with  $R1$  ( $I > I(2\sigma)$ ) = 0.0531 and  $wR2$  (all data) = 0.1583.

### Photosubstitution of CO and kinetic analysis

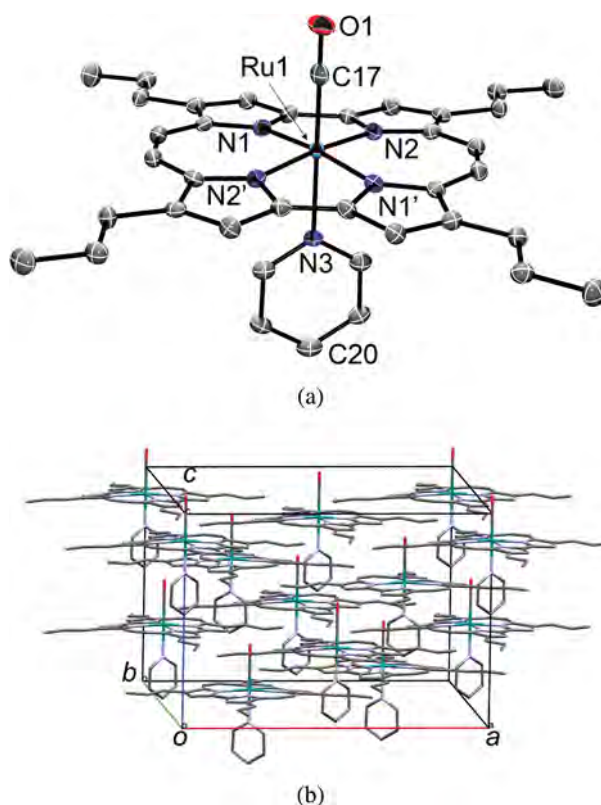
Photosubstitution of CO in **1–3** in benzene was studied by UV-vis spectroscopy at 298 K using an optical cuvette (optical path length, 1.0 cm) with a vacuum-cooked reservoir. A benzene solution of **1–3** was prepared for the kinetic study where the concentration of the complex was typically 3 μM to adjust  $Abs = 0.080$  at the irradiation wavelength  $\lambda_{ex} = 360$  nm. A large excess of pyridine was also added to the solution as an external ligand (0.2%, >1000 equiv). The solution was degassed by the freeze-pump-thaw method. The photosubstitution was studied by UV-vis spectroscopy at 298 K with photoirradiation from JASCO HM-25 equipped with a 150-W Xe lamp, which was monochromated by SO-X150LC monochromator and photon quality measurement unit S1337-1010BQ. The first-order kinetic treatment was employed for the absorbance  $A_t$  at 383, 385, and 397 nm for **1**, **2**, and **3**, respectively, at a given irradiation time with  $t = 30, 60, 120, 300, 600,$  and  $1200$  s. Rate constants for the photoinduced CO dissociation were obtained with the first-order treatment,  $\ln[(A_t - A_\infty)/(A_0 - A_\infty)]$  vs. the irradiation time ( $t$ ), where  $A_0$  and  $A_\infty$  are the initial and final absorbance, respectively, during the photolytic reactions. The  $A_\infty$  was obtained from the UV-vis spectra of extended time of photoirradiation, typically 5-min additional irradiation. The wavelength dependence was studied for **1** by photo-excitation at different wavelengths ( $\lambda_{ex} = 360, 380, 400,$  and  $600$  nm).

## RESULTS AND DISCUSSION

### X-ray crystallography

The synthesis and spectroscopic characterizations of **1** and **2** have been reported previously [16, 38]. In the current study, structural determination of the two compounds has been carried out by single-crystal X-ray crystallography. ORTEP drawings and crystal packing diagrams for **1** and **2** are shown in Figs 1 and 2, respectively. More detailed data are provided in the Supporting information (Tables S1–S4).

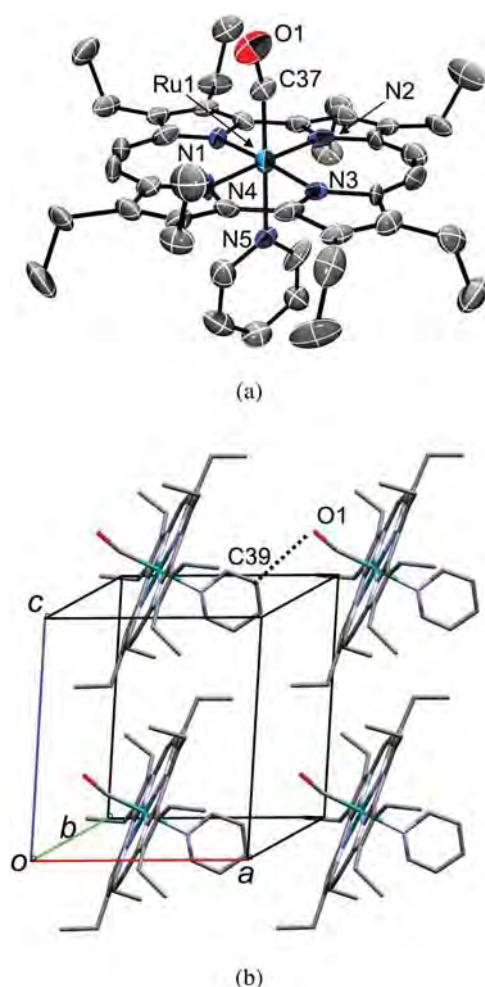
(a) Molecular structure of **1**. Compound **1** crystallizes in an orthorhombic space group *Fdd2* with  $Z = 8$ . Compound **1** has a centrosymmetric structure with



**Fig. 1.** The molecular structure of **1**. (a) An ORTEP drawing of **1** with thermal ellipsoids at a 50% probability level. Hydrogen atoms are omitted for clarity. (b) A crystal packing diagram

a  $C_2$  axis passing through O1–C17–Ru1–N3–C20 to give a linear axial coordination with Ru1–C17–O1 =  $180^\circ$  (Fig. 1a). The central ruthenium atom adopts a distorted octahedral geometry with RuN<sup>Pc</sup><sub>4</sub>N<sup>Py</sup>C donor set, where N<sup>Pc</sup> and N<sup>Py</sup> represent nitrogen donors from basal TPrPc<sup>2-</sup> and axial pyridine ligands, respectively. The axial carbonyl and pyridine ligands coordinate to the ruthenium center with Ru1–C17 = 1.852(13) and Ru1–N3 = 2.177(9) Å. The porphycene ring is almost planar and the four pyrrole nitrogen atoms form a near rectangular shape (see below). Four *n*-Pr substituents lie nearly on the porphycene macrocyclic plane. The molecular packing diagram (Fig. 1b) shows that the molecules exist as the pyridine–Ru–CO axis parallels to the *c* axis and the porphycene plane on the *ab* plane. No significant intermolecular interactions are seen in the solid state.

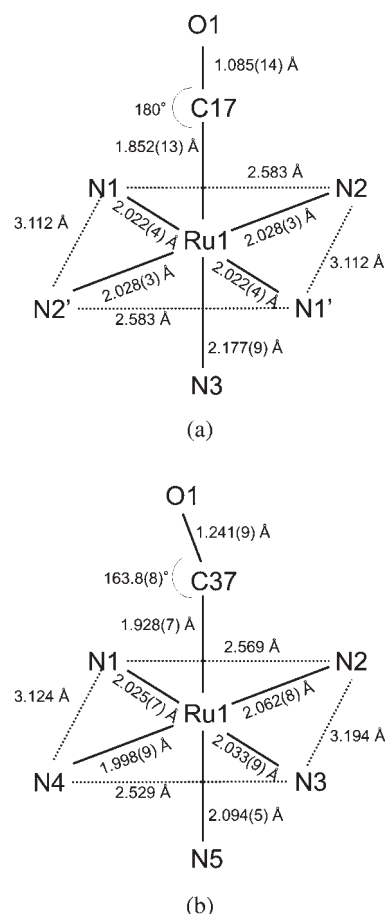
(b) Molecular structure of **2**. Compound **2** crystallizes in a triclinic space group *P1* with  $Z = 1$ . The central ruthenium atom adopts a distorted octahedral geometry with RuN<sup>Pc</sup><sub>4</sub>N<sup>Py</sup>C donor set, where N<sup>Pc</sup> and N<sup>Py</sup> represent nitrogen donors from basal OEPc<sup>2-</sup> and axial pyridine ligands, respectively (Fig. 2a). Principal structural features of **2** are closely similar to those of **1** but there are notable characteristics arising from crystal packing. Compound **2** possesses a highly bent Ru–C–O bonding in



**Fig. 2.** The molecular structure of **2**. (a) An ORTEP drawing of **2** with thermal ellipsoids at a 50% probability level. Hydrogen atoms are omitted for clarity. (b) A crystal packing diagram and intermolecular interaction (a broken line)

the axial coordination ( $\text{Ru1-C37-O1} = 163.8(8)^\circ$ ). This bent structure apparently comes from an intermolecular interaction observed in the solid state, where a hydrogen-bonding interaction is observed between O atom in the carbonyl ligand and one of hydrogen atoms of the pyridine ligand in the neighboring molecule ( $\text{O1} \cdots \text{C39} = 3.376 \text{ \AA}$ , Fig. 2b). This intermolecular interaction also leads to a remarkable increase in the Ru–CO length in **2** ( $\text{Ru1-C37} = 1.928(7) \text{ \AA}$ ) over that in the Ru–CO length in **1** ( $1.852(13) \text{ \AA}$ ) which involves no intermolecular interactions. As is consistent with the Ru–CO lengths in the solid state, infrared vibrational frequency of  $\nu(\text{CO})$  for **2** (KBr method,  $1930 \text{ cm}^{-1}$ ) was found to shift to the lower energy than that for **1** ( $1935 \text{ cm}^{-1}$ ). This structural deviation in **2** also gives a significant influence in the Ru–pyridine bonds trans to CO, giving a shorter Ru–N<sup>Py</sup> distance for **2** ( $2.094(5) \text{ \AA}$ ) than **1** ( $2.177(9) \text{ \AA}$ ).

As demonstrated for many other structures of metalloporphyrines [13], the macrocyclic skeletal geometry of ruthenium(II) porphyrines in **1** and **2**

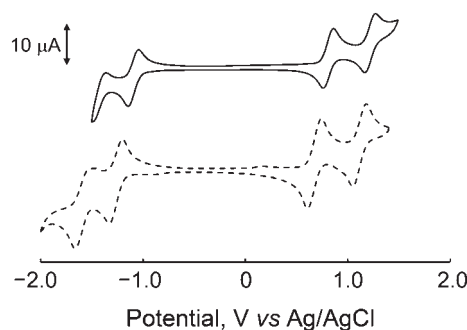


**Fig. 3.** Coordination geometry of (a) **1** and (b) **2** with selected interatomic distances and angles

are significantly altered from that of their free-base precursors,  $\text{H}_2\text{TPrPc}$  and  $\text{H}_2\text{OEPc}$  [12, 18]. Figure 3 shows schematic representation of the coordination geometry of **1** and **2** with selected interatomic distances and angles. In both complexes, four nitrogen atoms ( $\text{N}^{\text{Pc}}$ ) form rectangular coordination cavity with  $\text{N}^{\text{Pc}} \cdots \text{N}^{\text{Pc}}$  separations of 2.583 and 3.112  $\text{ \AA}$  for **1** and 2.549 and 3.159  $\text{ \AA}$  (on average) for **2**. Similar atomic separations are reported for  $[\text{Zn}(\text{OEPc})]$  [18],  $[\text{Pt}(\text{TPrPc})]$  [19], and  $[\text{Re}_2(\text{TPrPc})(\text{CO})_6]$  [20], but shorter separations are also found for  $[\text{Co}(\text{TPrPc})(\text{pyridine})_2](\text{ClO}_4)$  [43] and  $[\text{Ni}(\text{TPrPc})]$  [12].

### Redox properties

Redox properties of **1** and **2** were studied by cyclic voltammetry in  $\text{CH}_2\text{Cl}_2$  containing 0.1 M tetra-*n*-butylammonium perchlorate as a supporting electrolyte. The voltammograms and the electrochemical data, including half-wave potential ( $E_{1/2}$ ) and peak-to-peak separation ( $\Delta E_p$ ), are shown in Fig. 4 and Table 2, respectively. According to the literature [44], all redox waves observed for **1** and **2** in the potential window studied can be assigned to the ligand-centered processes. Since



**Fig. 4.** Cyclic voltammograms of 1 mM of **1** (a solid line) and **2** (a broken line) in  $\text{CH}_2\text{Cl}_2$  containing 0.1 M tetra-*n*-butylammonium perchlorate. Scan rate =  $100 \text{ mV}\cdot\text{s}^{-1}$

*d* orbital energy of the central ruthenium is significantly stabilized by strong back-donation of the axial CO, no metal-based processes are observed. Complex **1** showed reversible redox waves at  $E_{1/2} = -1.10, +0.81, \text{ and } +1.25 \text{ V}$  along with a quasi-reversible wave at  $E_{1/2} = -1.40 \text{ V}$  vs. Ag/AgCl (Fig. 4, a solid line). These values are negatively shifted from the free-base porphycene [45] as a result of an electron donation from the central ruthenium. Complex **2** showed three reversible redox waves at  $-1.28, +0.67, \text{ and } +1.11 \text{ V}$  vs. Ag/AgCl and a quasi-reversible wave at  $-1.57 \text{ V}$  vs. Ag/AgCl (Fig. 4, a broken line). Both compounds show two reduction processes to form anion radical and dianion species between  $-1.0$  and  $-1.6 \text{ V}$  and also two oxidation processes to form cation radical and dication species between  $+0.6$  and  $+1.3 \text{ V}$  vs. Ag/AgCl. In contrast to the porphycenes, the reduction processes of porphyrin complex **3** were found at highly negative potentials ( $-1.72$  and  $-2.09 \text{ V}$  vs. SCE) [46]. The obvious difference arises from the energy level of  $\pi^*$  orbital of the macrocyclic tetrapyrrole ligands, in which LUMO of porphycene is lower than that of porphyrin.

### Photosubstitution

Photosubstitution of CO in ruthenium-porphyrins [1–3] and -phthalocyanines [4], and other transition-metal coordination compounds [47–52] have been studied

extensively and provided important basis for syntheses, supramolecular construction, reaction mechanisms, and catalysis. Compounds **1–3** undergo CO dissociation upon UV excitation ( $\lambda_{\text{ex}} = 360 \text{ nm}$ ) in the presence of excess amount of pyridine (Scheme 1). UV-vis spectral changes during the photoirradiation of **1–3** are shown in Fig. 5. Figure 5a shows the spectral change for **1**. Prior to photoirradiation, the compound exhibits peak maxima at 383 and 610 nm, which correspond to the Soret and Q-bands of the porphycene ring. As the photoreaction proceeded, new absorption bands appeared at  $\lambda_{\text{max}} = 316, 340, 450, 602, \text{ and } 622 \text{ nm}$ . Isosbestic points were observed at 356, 418, 564, 606, 616, and 628 nm, confirming a clean transformation of the parent molecule to a single photoproduct. The peak at 450 nm can be assigned to a metal-to-ligand charge-transfer (MLCT) band ascribed to transition from the *d*(Ru) to the  $\pi^*(\text{pyridine})$  orbitals [7]. Figures 5b and 5c show sequential spectral changes for **2** and **3**, respectively, during photosubstitution. In all cases, the final photoproduct  $[\text{Ru}^{\text{II}}(\text{Pc})(\text{pyridine})_2]$  is proposed on the basis of UV-vis spectroscopy showing identical spectra to those of isolated  $[\text{Ru}(\text{Pc})(\text{pyridine})_2]$  complexes [38]. Also, IR spectra of the photoproduct do not show absorption ascribed to  $\nu_{\text{CO}}$ . It is noted here that in the presence of lower concentrations of pyridine (10 and 100 equiv.) the final spectra were inconsistent with the spectrum of the bis-pyridine complex (Supporting information, Figs S1 and S2).

Absorbance change of the Soret band ( $\lambda_{\text{max}} = 383, 385, \text{ and } 397 \text{ nm}$  for **1**, **2**, and **3**, respectively) was used for the kinetic analysis. As shown in Fig. 6, photosubstitution of CO in **1–3** is well described by the first-order kinetics. Full data of kinetic analysis of **1–3** under various conditions are given in the Supporting information (Tables S5–S9). As compiled in Table 3, the rate constants at 298 K range in the order of  $10^{-3} \text{ s}^{-1}$  for all of the compounds, but it is clear that the photosubstitution proceeds faster for porphycene complexes **1** and **2** than the porphyrin complex **3**.

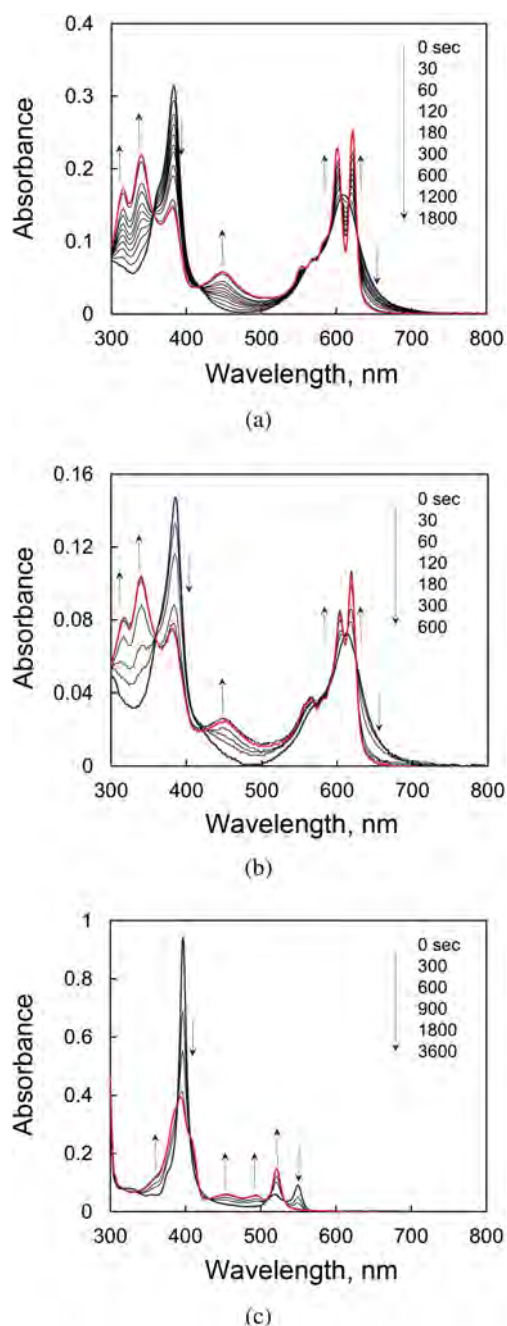
Reaction rate constants were further obtained at different wavelengths of the photoexcitation in order to find active absorption bands for the

**Table 2.** Electrochemical data of **1–3**

Compounds	$E_{1/2}, \text{ V vs. Ag/AgCl } (\Delta E_p, \text{ mV})$				References
	$\text{Pc}^{2-}/\text{Pc}^{\bullet-}$	$\text{Pc}^{\bullet-}/\text{Pc}$	$\text{Pc}/\text{Pc}^{+}$	$\text{Pc}^{+}/\text{Pc}^{2+}$	
<b>1</b> <sup>a</sup>	-1.40 (110)	-1.10 (102)	+0.81 (100)	+1.25 (109)	This work
<b>2</b> <sup>a</sup>	-1.57 (193)	-1.28 (130)	+0.67 (132)	+1.11 (129)	This work
<b>3</b> <sup>b</sup>	-2.09 <sup>c</sup>	-1.72 <sup>c</sup>	+0.68	+1.28	46

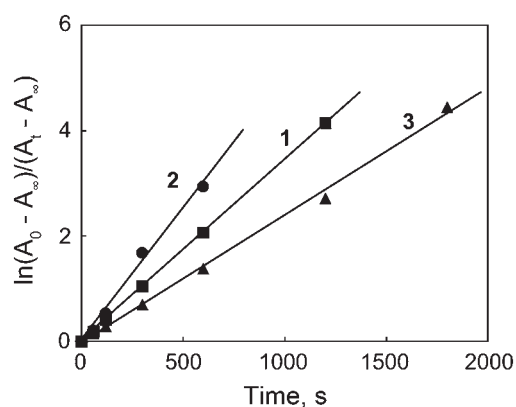
<sup>a</sup>[Complex] = 1 mM. Working electrode: Pt ( $\phi = 1.6 \text{ mm}$ ); counter electrode: Pt coil; reference electrode: Ag/AgCl. Solvent: dichloromethane. Supporting electrolyte: 0.1 M tetra-*n*-butylammonium perchlorate. Scan rate =  $0.1 \text{ V}\cdot\text{s}^{-1}$ . <sup>b</sup>Working electrode: Pt ( $\phi = 25 \mu\text{m}$ ); counter electrode: Pt; reference electrode: saturated calomel electrode (SCE). Solvent:  $\text{CH}_2\text{Cl}_2$ . Supporting electrolyte: 0.1 M tetra-*n*-butylammonium perchlorate. Scan rate =  $10 \text{ V}\cdot\text{s}^{-1}$ . <sup>c</sup>Scan rate =  $50 \text{ V}\cdot\text{s}^{-1}$ .





**Fig. 5.** UV-vis spectral changes during the course of photosubstitution of CO in (a) **1** (3.5  $\mu\text{M}$ ), (b) **2** (1.9  $\mu\text{M}$ ), and (c) **3** (4.0  $\mu\text{M}$ ) at 298 K in a degassed benzene solution containing 0.2% pyridine. Blue and red spectra indicate the initial and final spectra, respectively. Upward and downward arrows indicate the increase and decrease in the absorbance, respectively

photosubstitution. Figure 7 depicts the plot of rate constants for **1** at different excitation wavelengths along with the absorption spectrum of **1**. The observed rate constants are given in Table 4. As clearly seen, the photosubstitution occurs faster as the ruthenium porphyrine was excited by UV-light at an increasing energy. The visible excitation does not lead to the

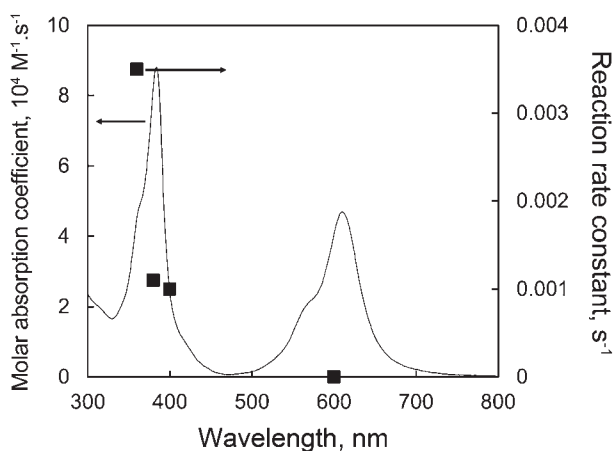


**Fig. 6.** The first-order plot for the photosubstitution of CO in **1** (■), **2** (●), and **3** (▲) in benzene containing 0.2% pyridine at 298 K

**Table 3.** Rate constants of photosubstitution ( $k_{\text{obs}}$ ) of **1–3** at 298 K<sup>a</sup>

Compounds	$k_{\text{obs}}, 10^{-3} \text{ s}^{-1}$
<b>1</b>	3.5
<b>2</b>	5.0
<b>3</b>	2.4

<sup>a</sup>The concentration of compounds was adjusted so that absorbance at the irradiation wavelength was 0.080: [**1**] = 1.7  $\mu\text{M}$ ; [**2**] = 2.0  $\mu\text{M}$ ; [**3**] = 4.8  $\mu\text{M}$ . Solvent: benzene containing 0.2% pyridine (0.62 mM).



**Fig. 7.** UV-vis spectrum of **1** in benzene (a solid line) and rate constants (■) for the photosubstitution of CO in **1** observed at four distinct wavelengths of excitation with  $\lambda_{\text{ex}} = 600, 400, 380,$  and 360 nm

photosubstitution at all. Hoshino and co-workers has reported [2] that the CO dissociation reaction of [Ru(OEP)(CO)] in acetonitrile occurs *via* a photoexcitation of the ground-state complex to a singlet  $\pi-\pi^*$  excited state and

**Table 4.** Rate constants of photosubstitution ( $k_{\text{obs}}$ ) of **1** at 298 K upon irradiation at different wavelengths ( $\lambda_{\text{ex}}$ )<sup>a</sup>

$\lambda_{\text{ex}}$ , nm	$k_{\text{obs}}$ , $10^{-3} \text{ s}^{-1}$
360	3.5
380	1.1
400	1.0
600	<sup>b</sup>

<sup>a</sup>The concentration of **1** was adjusted so that absorbance at the irradiation wavelength was 0.080: [**1**] = 1.7  $\mu\text{M}$  for  $\lambda_{\text{ex}}$  = 360 nm; 0.9  $\mu\text{M}$  for  $\lambda_{\text{ex}}$  = 380 nm; 3.3  $\mu\text{M}$  for  $\lambda_{\text{ex}}$  = 400 nm; 1.9  $\mu\text{M}$  for  $\lambda_{\text{ex}}$  = 600 nm. Solvent: benzene containing 0.2% pyridine (0.62 mM). <sup>b</sup>No reaction proceeded.

then it eventually turns into a high-energy triplet ruthenium-to-porphyrin MLCT state of the complex. We infer that the photosubstitution for the metalloporphycenes proceed similarly, in which a transient Ru<sup>III</sup> species in the MLCT excited state affords a weaker Ru–CO bond due to the lack of  $\pi$ -back donation, thereby facilitating the axial CO to be substituted. The faster reaction in porphycenes can be explained by accessibility to the high-energy MLCT state. This is supported by the presence of a low-lying  $\pi^*$  orbital of porphycene as confirmed by the electrochemical analyses described above. A more detailed mechanistic study is in progress to elucidate the photolytic pathway.

## CONCLUSION

In this paper, the first crystallographic structural determination has been successfully shown for the six-coordinate, ruthenium(II) carbonyl complexes of porphycene [Ru(TPrPc)(CO)(pyridine)] (**1**) and [Ru(OEPc)(CO)(pyridine)] (**2**). Cyclic voltammetry of **1** and **2** revealed that they undergo two-step oxidations and two-step reductions in  $\text{CH}_2\text{Cl}_2$  and the reduction potentials are much more positive than that of the porphyrin analog [Ru(OEP)(CO)(pyridine)] (**3**). UV-excitation ( $\lambda_{\text{ex}}$  = 400 nm or shorter wavelengths) of **1** and **2** dissolved in benzene containing a large excess of pyridine as an entering ligand gave the corresponding bis-pyridine derivatives [Ru(TPrPc)(pyridine)<sub>2</sub>] and [Ru(OEPc)(pyridine)<sub>2</sub>], respectively, in a quantitative manner with rate constants in the order of  $10^{-3} \text{ s}^{-1}$  at 298 K. Remarkably, the photosubstitution occurs faster for complexes of porphycene (**1** and **2**) than porphyrin (**3**). The excitation spectra indicated that the active band for photosubstitution is located at 400 nm or shorter wavelength region, which is most likely associated with an MLCT band (ruthenium to porphycene). The photosubstitution does not proceed at all with a visible band (Q-band) excitation.

## Acknowledgements

This work was supported by Grants-in-Aid for Scientific Research on Innovative Areas ‘‘Molecular Activation’’ (No. 25105537) and ‘‘Coordination Programming’’ (No. 24108730), Grants-in-Aid for Scientific Research (A) (No. 21245016) and (B) (No. 25288031), the Global COE Program ‘‘Science for Future Molecular Systems’’, and Nanotechnology Platform (No. NPS13103) from MEXT. MA also acknowledges the financial support from Tokuyama Science Foundation.

## Supporting information

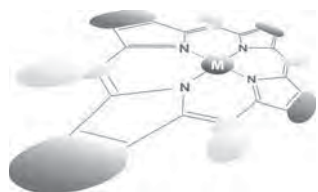
Selected bond distances and angles for **1** and **2** (Tables S1–S4); detailed kinetic analysis data under various conditions (Tables S5–S9); UV-vis spectral changes during 360-nm irradiation in the presence of a small excess of pyridine (Figs S1 and S2) are given in the supplementary material. This material is available free of charge *via* the Internet at <http://www.worldscinet.com/jpp/jpp.shtml>.

Crystallographic data for compounds **1** and **2** have been deposited at the Cambridge Crystallographic Data Centre (CCDC) under numbers CCDC-1031496 and CCDC-1031495, respectively. Copies can be obtained on request, free of charge, *via* [www.ccdc.cam.ac.uk/data\\_request/cif](http://www.ccdc.cam.ac.uk/data_request/cif) or from the Cambridge Crystallographic Data Centre, 12 Union Road, Cambridge CB2 1EZ, UK (fax: +44 1223-336-033 or email: [data\\_request@ccdc.cam.ac.uk](mailto:data_request@ccdc.cam.ac.uk)).

## REFERENCES

- Hopf FR, O’Brien TP, Scheidt WR and Whitten DG. *J. Am. Chem. Soc.* 1975; **97**: 277–281.
- Hoshino M and Kashiwagi Y. *J. Phys. Chem.* 1990; **94**: 673–678.
- Ishii K, Hoshino S and Kobayashi N. *Inorg. Chem.* 2004; **43**: 7969–7971.
- Ishii K, Shiine M, Shimizu Y, Hoshino S, Abe H, Sogawa K and Nagao K. *J. Phys. Chem. B* 2008; **112**: 3138–3143.
- Zhang R, Huang Y, Abebrese C, Thompson H, Vanover E and Webb C. *Inorg. Chim. Acta* 2011; **376**: 152–157.
- Offord DA, Sachs SB, Ennis MS, Eberspacher TA, Griffin JH, Chidsey CED and Collman JP. *J. Am. Chem. Soc.* 1998; **120**: 4478–4487.
- Marvaud V and Launay J-P. *Inorg. Chem.* 1993; **32**: 1376–1382.
- Ikonen M, Guez D, Marvaud V and Markovitsi D. *Chem. Phys. Lett.* 1994; **231**: 93–97.
- Stulz E, Scott SM, Bond AD, Otto S and Sanders JKM. *Inorg. Chem.* 2003; **42**: 3086–3096.
- Imamura T and Fukushima K. *Coord. Chem. Rev.* 2000; **198**: 133–156.

11. Vogel E, Köcher M, Schmickler H and Lex J. *Angew. Chem. Int. Ed. Engl.* 1986; **25**: 257–259.
12. Vogel E, Balci M, Pramod K, Koch P, Lex J and Ermer O. *Angew. Chem. Int. Ed. Engl.* 1987; **26**: 928–931.
13. Fowler CJ, Sessler JL, Lynch VM, Waluk J, Gebauer A, Lex J, Heger A, Zuniga-y-Rivero F and Vogel E. *Chem. Eur. J.* 2002; **8**: 3485–3496.
14. D'Souza F, Boulas PL, Kisters M, Sambrotta L, Aukauloo AM, Guillard R and Kadish KM. *Inorg. Chem.* 1996; **35**: 5743–5746.
15. Fita P, Garbacz P, Nejbauer M, Radzewicz C and Waluk J. *Chem. Eur. J.* 2007; **17**: 3672–3678.
16. Li Z-Y, Huang S and Che C-M. *Inorg. Chem.* 1992; **31**: 2670–2672.
17. D'Souza F, Boulas PL, Aukauloo AM, Guillard R, Kisters M, Vogel E and Kadish KM. *J. Phys. Chem.* 1994; **98**: 11885–11891.
18. Vogel E, Koch P, Hou X-L, Lex J, Lausmann M, Kisters M, Aukauloo MA, Richard P and Guillard R. *Angew. Chem. Int. Ed. Engl.* 1993; **32**: 1600–1604.
19. Che C-M, Cheung K-K, Li Z-Y and Wong K-Y. *Polyhedron* 1994; **13**: 2563–2567.
20. Che C-M, Li Z-Y, Guo C-X, Wong K-Y, Chern S-S and Peng S-M. *Inorg. Chem.* 1995; **34**: 984–987.
21. Okawara T, Abe M, Shimakoshi H and Hisaeda Y. *Bull. Chem. Soc. Jpn.* 2011; **84**: 718–728.
22. Okawara T, Abe M, Shimakoshi H and Hisaeda Y. *Res. Chem. Intermed.* 2013; **39**: 161–176.
23. Taneda M, Tanaka A, Shimakoshi H, Ikegami A, Hashimoto K, Abe M and Hisaeda Y. *Tetrahedron Lett.* 2013; **54**: 5727–5729.
24. Hasegawa J, Takata K, Miyahara T, Neya S, Frisch MJ and Nakatsuji H. *J. Phys. Chem. A* 2005; **109**: 3187–3200.
25. Braslavsky SE, Müller M, Mártire DO, Pörting S, Bertolotti SG, Chakravorti S, Koç-Weier G, Knipp B and Schaffner K. *J. Photochem. Photobiol. B: Biology* 1996; **40**: 191–198.
26. Bonnett R. *Chem. Soc. Rev.* 1995; **24**: 19–33.
27. Stockert JC, Canete M, Juarranz A, Vallanueva A, Horobin RW, Borrell JI, Teixido J and Nonell S. *Curr. Med. Chem.* 2007; **14**: 997–1026.
28. Shimakoshi H, Baba T, Iseki Y, Aritome I, Endo A, Adachi C and Hisaeda Y. *Chem. Commun.* 2008; **44**: 2882–2884.
29. Maeda D, Shimakoshi H, Abe M and Hisaeda Y. *Inorg. Chem.* 2009; **48**: 9853–9860.
30. Shimakoshi H, Sasaki K, Iseki Y and Hisaeda Y. *J. Porphyrins Phthalocyanines* 2012; **16**: 530–536.
31. Sánchez-García D and Sessler JL. *Chem. Soc. Rev.* 2008; **37**: 215–238.
32. Arad O, Rubio N, Sánchez-García D, Borrell JI and Nonell S. *J. Porphyrins Phthalocyanines* 2009; **13**: 376–381.
33. Hayashi T, Okazaki K, Urakawa N, Shimakoshi H, Sessler JL, Vogel E and Hisaeda Y. *Organometallics* 2001; **20**: 3074–3078.
34. Lo W-C, Che C-M, Cheng KF and Mak TCW. *Chem. Commun.* 1997; 1205–1206.
35. Matsuo T, Dejima H, Hirota S, Murata D, Sato H, Ikegami T, Hori H, Hisaeda Y and Hayashi T. *J. Am. Chem. Soc.* 2004; **126**: 16007–16017.
36. Okawara T, Hashimoto K, Abe M, Shimakoshi H and Hisaeda Y. *Chem. Commun.* 2012; **48**: 5413–5415.
37. Maeda D, Shimakoshi H, Abe M and Hisaeda Y. *Dalton Trans.* 2009; **1**: 140–145.
38. Okawara T, Abe M, Shimakoshi H and Hisaeda Y. *Chem. Lett.* 2008; **37**: 906–907.
39. Cuesta L, Karnas E, Lynch VM, Chen P, Shen J, Kadish KM, Ohkubo K, Fukuzumi S and Sessler JL. *J. Am. Chem. Soc.* 2009; **131**: 13538–13547.
40. Bruker AXS, SAINT, Bruker AXS Inc., Madison, WI, USA. 2009.
41. Bruker AXS, SADABS, Bruker AXS Inc., Madison, WI, USA. 2008.
42. Sheldrick GM. *Acta Cryst.* 2008; **A64**: 112–122.
43. Shimakoshi H, Aritome I, Hirota S and Hisaeda Y. *Bull. Chem. Soc. Jpn.* 2005; **78**: 1619–1623.
44. Brown GM, Hopf FR, Meyer TJ and Whitten DG. *J. Am. Chem. Soc.* 1975; **97**: 5385–5390.
45. Bernard C, Gisselbrecht JP, Gross M, Vogel E and Lausmann M. *Inorg. Chem.* 1994; **33**: 2393–2401.
46. Kadish KM, Tagliatesta P, Hu Y, Deng YJ, Mu XH and Bao LY. *Inorg. Chem.* 1991; **30**: 3737–3743.
47. Farrell IR and Vlček Jr A. *Coord. Chem. Rev.* 2000; **208**: 87–101.
48. Koike K, Okoshi N, Hori H, Takeuchi K, Ishitani O, Tsubaki H, Clark IP, George MW, Johnson FPA and Turner JJ. *J. Am. Chem. Soc.* 2002; **124**: 11448–11455.
49. Akashi D, Kido H, Abe M, Sasaki Y and Ito T. *Dalton Trans.* 2004; 2883–2889.
50. Abe M, Masuda T, Kondo T, Uosaki K and Sasaki Y. *Angew. Chem. Int. Ed.* 2005; **44**: 416–419.
51. Zhang Y, Tong Y, Abe M, Uosaki K, Osawa M, Sasaki Y and Ye S. *J. Mater. Chem.* 2009; **19**: 261–267.
52. Abe M, Inatomi A and Hisaeda Y. *Dalton Trans.* 2011; **40**: 2289–2298.



# Supramolecular photovoltaic cells utilizing inclusion complexes composed of $\text{Li}^+@C_{60}$ and cyclic porphyrin dimer

Hayato Sakai<sup>a</sup>, Takuya Kamimura<sup>b</sup><sup>◇◇</sup>, Fumito Tani<sup>\*b</sup><sup>◇</sup> and Taku Hasobe<sup>\*a</sup><sup>◇</sup>

<sup>a</sup>Department of Chemistry, Faculty of Science and Technology, Keio University, Yokohama 223-8522, Japan

<sup>b</sup>Institute for Materials Chemistry and Engineering, Kyushu University, Fukuoka 812-8581, Japan

Dedicated to Professor Shunichi Fukuzumi on the occasion of his retirement

Received 27 October 2014

Accepted 14 November 2014

**ABSTRACT:** We have newly constructed supramolecular photovoltaic cells using inclusion complexes of lithium-ion-encapsulated [60]fullerene ( $\text{Li}^+@C_{60}$ ) and cyclic porphyrin dimers ( $M\text{-CPD}_{\text{Py}}$ ,  $M = \text{H}_4$  and  $\text{Ni}_2$ ). First, supramolecular inclusion complexes of  $\text{Li}^+@C_{60}$  and  $M\text{-CPD}_{\text{Py}}$  were prepared in MeCN/PhCN (3/1, v/v) by rapid injection method. The molecular aggregates with spherical nanoparticles demonstrated a broad absorption property in the visible region. The macroscopic structures were also estimated to be ca. 200 nm in diameter by transmission electron microscope (TEM) and dynamic light scattering (DLS) measurements. The photoelectrochemical solar cells composed of these assemblies on nanostructured  $\text{SnO}_2$  electrode were fabricated by electrophoretic deposition method. The photoelectrochemical behavior of the nanostructured  $\text{SnO}_2$  film of supramolecular nanoassemblies of  $\text{Li}^+@C_{60}$  and  $M\text{-CPD}_{\text{Py}}$  is significantly higher than those of the single component films ( $\text{Li}^+@C_{60}$  or  $M\text{-CPD}_{\text{Py}}$ ) and supramolecular inclusion complexes of pristine  $C_{60}$  and  $M\text{-CPD}_{\text{Py}}$ .

**KEYWORDS:** porphyrin, endohedral fullerene, supramolecular assembly, photovoltaic cell.

## INTRODUCTION

Supramolecular strategy is a useful method to construct highly organized molecular architectures with appropriate size and shape because of a simple and convenient way [1–4]. The utilization of non-covalent interactions has important advantage over the synthetic organization based on many covalent bonds because of the self-assembling features of molecules by non-covalent interactions. These assemblies can give rise to the new phenomena and properties in comparison with the corresponding monomer. The driving forces for the construction of supramolecular assemblies are mainly due to the spontaneous process through non-covalent interactions such as van der Waals forces and hydrogen bonding [5–10]. Consequently, such a method has

gained increased importance in the fields of chemistry and material science as a bottom-up strategy [1, 2]. Especially, these organized structures may meet the requirement in technological fields such as electronic and electrochemical devices [11–19].

Porphyrins have contributed as attractive building blocks for construction of photofunctional nanomaterials since they have characteristic photophysical and electrochemical properties, which can be readily fine-tuned by substituents or by metal ions [13–16, 20]. From the viewpoint of the chemical structures, porphyrins also possess an extensively two-dimensional planar  $\pi$ -system and are therefore useful not only for synthetic light-harvesting systems, but also for efficient electron transfer because of small reorganization energy [21–25]. Consequently, covalent or non-covalent systems (*i.e.* molecular dyad and triad *etc.*) have been extensively synthesized to examine sequential energy- and electron-transfer processes, as seen in natural photosynthetic systems [25–34]. Moreover, porphyrins are also good candidates for construction of organized supramolecular

<sup>◇◇</sup>SPP full and <sup>◇◇</sup>student member in good standing

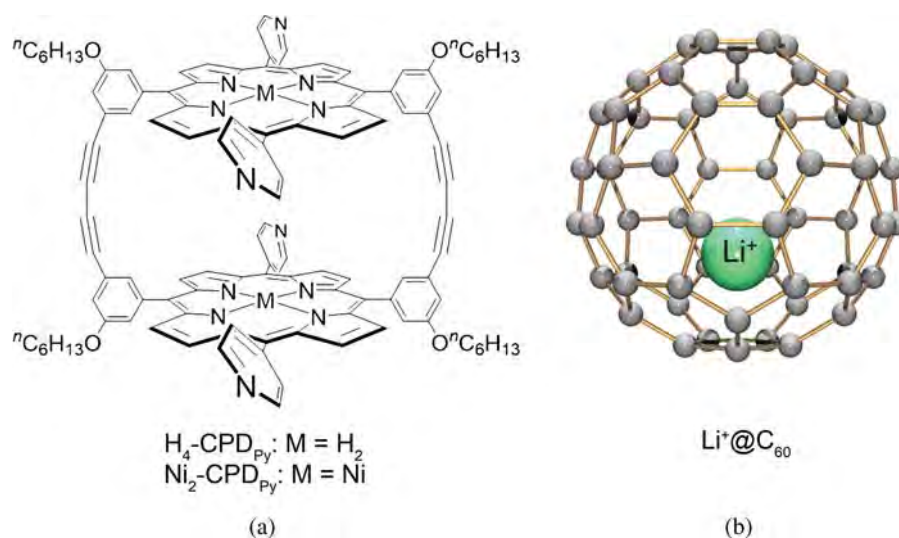
\*Correspondence to: Taku Hasobe, email: hasobe@chem.keio.ac.jp, fax: +81 45-566-1697; Fumito Tani, email: tanif@ms.ifoc.kyushu-u.ac.jp, fax: +81 92-642-2732

architectures. So far, a variety of supramolecular architectures composed of porphyrins from spherical particles to anisotropic long fibers have been reported [35–44]. These photofunctional supramolecular architectures of porphyrins are also promising for electronics and solar energy conversion [45–53].

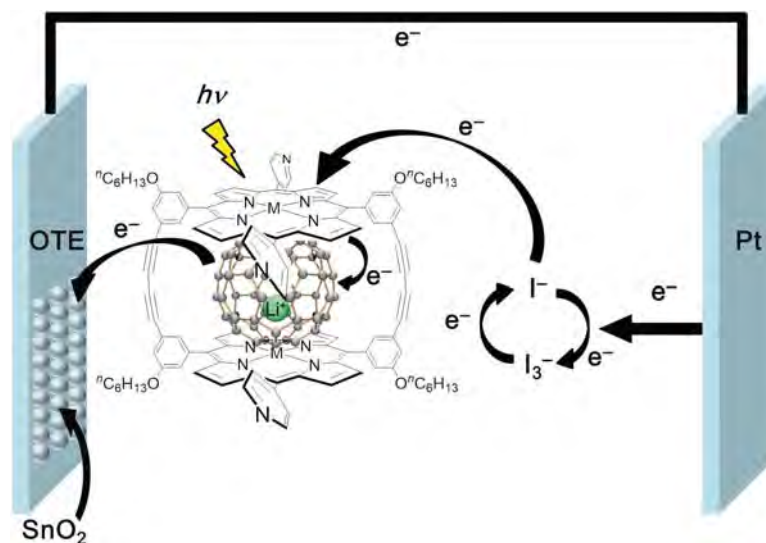
Concerning electron acceptors, fullerene, which is an extensively conjugated three-dimensional spherical  $\pi$ -system, is an ideal electron acceptor because of the minimal changes of structure and solvation associated with the electron-transfer reduction. Additionally, a combination between porphyrins and fullerenes accelerates photoinduced electron transfer and slows charge recombination, leading to the generation of a long-lived charge-separated state with a high quantum yield [22, 23, 27, 28, 33, 54]. Fullerene is also well-known to form electrostatic host–guest supramolecular complexes with

porphyrin [55, 56]. In particular, our reported receptor molecules composed of multiple porphyrin units, *i.e.* free-base and nickel cyclic porphyrin dimers ( $M\text{-CPD}_{\text{Py}}$ ,  $M = \text{H}_4$  and  $\text{Ni}_2$ ), which are shown in Fig. 1, are suitable for the inclusion of pristine  $C_{60}$  and its derivatives because of the strong binding by  $\pi$ – $\pi$  interaction [57–59]. The inclusion complex of  $C_{60}$  and the free-base porphyrin dimer ( $C_{60} \subset \text{H}_4\text{-CPD}_{\text{Py}}$ ) underwent photoinduced electron transfer from the porphyrin to  $C_{60}$ . However, the corresponding inclusion complex of  $C_{60}$  and the nickel cyclic porphyrin dimer ( $C_{60} \subset \text{Ni}_2\text{-CPD}_{\text{Py}}$ ) did not show the expected charge-separated (CS) state in the time-resolved transient absorption spectra upon photoexcitation because the estimated energy level of the CS state (1.98 eV) is higher than that of  ${}^3\text{Ni}_2\text{-CPD}_{\text{Py}}^*$  (1.50 eV) or  ${}^3C_{60}^*$  (1.57 eV) [59].

A lithium ion encapsulated fullerene ( $\text{Li}^+@C_{60}$ ) is a strong electron acceptor as compared to the pristine  $C_{60}$



**Fig. 1.** Chemical structures of cyclic porphyrin dimers and lithium-ion-encapsulated fullerene used in this study



**Scheme 1.** A schematic illustration of photoelectrochemical solar cell of  $\text{SnO}_2/(\text{Li}^+@C_{60} \subset M\text{-CPD}_{\text{Py}})_n$

[60–65]. The high reduction potential of  $\text{Li}^+\text{@C}_{60}$  relative to that of  $\text{C}_{60}$  makes the energy levels of the resulting CS states lower than the triplet excited energy. Actually,  $\text{Li}^+\text{@C}_{60}$  is included within a free base and nickel complex of a cyclic porphyrin dimer to afford supramolecules in a polar solvent with large association constants. In both cases, we can clearly observe photoinduced electron transfer to produce the CS state. The lifetimes of the resulting CS states are 0.50 ms for  $\text{Li}^+\text{@C}_{60} \subset \text{H}_4\text{-CPD}_{\text{Py}}$  and 0.67 ms for  $\text{Li}^+\text{@C}_{60} \subset \text{Ni}_2\text{-CPD}_{\text{Py}}$  [66]. These results indicate that the inclusion complex of  $\text{Li}^+\text{@C}_{60}$  and cyclic porphyrin dimers are promising for solar energy conversion systems.

We report herein preparation and light energy conversion property of supramolecular photovoltaic cells using inclusion complexes of the cyclic porphyrin dimers and  $\text{Li}^+\text{@C}_{60}$  (Fig. 1). The photoelectrochemical behavior of supramolecular nanoassemblies of  $\text{Li}^+\text{@C}_{60}$  and the cyclic porphyrin dimers [denoted as  $(\text{Li}^+\text{@C}_{60} \subset \text{M-CPD}_{\text{Py}})_n$ ] on the nanostructured  $\text{SnO}_2$  film on an optically transparent conducting glass electrode (denoted as OTE) is significantly higher than the single component films of  $\text{M-CPD}_{\text{Py}}$  or  $\text{Li}^+\text{@C}_{60}$  nanoassemblies [denoted as  $(\text{M-CPD}_{\text{Py}})_n$  or  $(\text{Li}^+\text{@C}_{60})_n$ , respectively] (Scheme 1). Especially, the incident photon-to-photocurrent generation efficiency (IPCE) of  $(\text{Li}^+\text{@C}_{60} \subset \text{Ni}_2\text{-CPD}_{\text{Py}})_n$ -deposited film is two times larger than that of our reported  $(\text{C}_{60} \subset \text{Ni}_2\text{-CPD}_{\text{Py}})_n$ -deposited film because of occurrence of the efficient photoinduced electron transfer process.

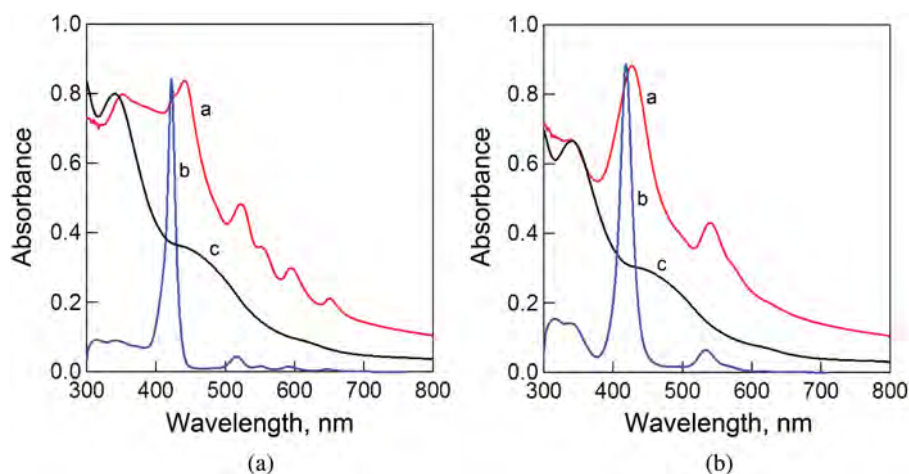
## RESULTS AND DISCUSSION

Supramolecular assemblies of  $\text{Li}^+\text{@C}_{60}$  and cyclic porphyrin dimers [denoted as  $(\text{Li}^+\text{@C}_{60} \subset \text{M-CPD}_{\text{Py}})_n$ ] were prepared as follows [65, 67–69] although the details were described in the experimental section. Briefly, a mixture

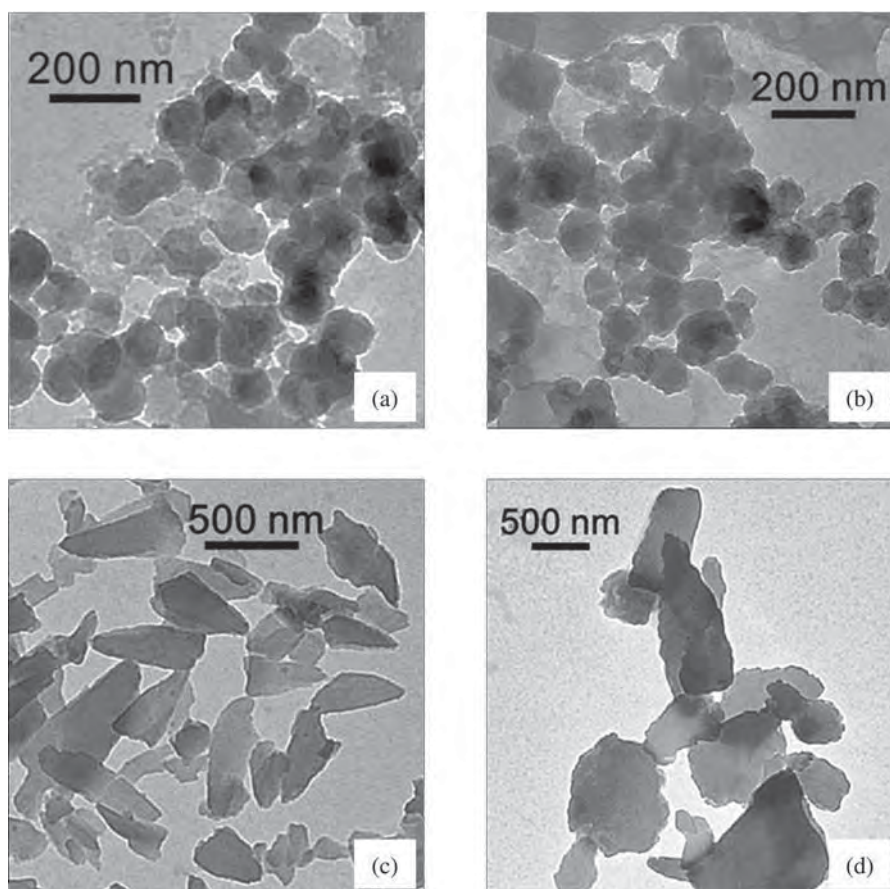
of  $\text{Li}^+\text{@C}_{60} \text{PF}_6^-$  (0.25 mM) and  $\text{M-CPD}_{\text{Py}}$  (0.25 mM) in PhCN solution (good solvent) was injected into three times volume of MeCN (poor solvent). The final concentrations of  $\text{Li}^+\text{@C}_{60}$  and  $\text{M-CPD}_{\text{Py}}$  are 63  $\mu\text{M}$  in MeCN/PhCN (3/1, v/v), respectively. The reference single component system  $[(\text{Li}^+\text{@C}_{60})_n$  or  $(\text{M-CPD}_{\text{Py}})_n$ ] was also prepared by the same manner. It should be emphasized that the initial process [*i.e.* preparation of a mixture of  $\text{Li}^+\text{@C}_{60} \text{PF}_6^-$  (0.25 mM) and  $\text{M-CPD}_{\text{Py}}$  (0.25 mM) in PhCN] successfully ensured the formation of inclusion complexes between  $\text{Li}^+\text{@C}_{60}$  and  $\text{M-CPD}_{\text{Py}}$  [66].

To discuss the aggregate trends, UV-vis absorption spectra of  $(\text{Li}^+\text{@C}_{60} \subset \text{H}_4\text{-CPD}_{\text{Py}})_n$  and  $(\text{Li}^+\text{@C}_{60} \subset \text{Ni}_2\text{-CPD}_{\text{Py}})_n$  were measured as shown in Figs 2a and 2b, respectively. In Fig. 2a, the spectrum *a* shows  $(\text{Li}^+\text{@C}_{60} \subset \text{H}_4\text{-CPD}_{\text{Py}})_n$  in MeCN/PhCN (3/1, v/v). As compared to the spectra of monomeric forms of  $\text{H}_4\text{-CPD}_{\text{Py}}$  and  $\text{Li}^+\text{@C}_{60}$  in PhCN (spectra *b* and *c*), the spectrum of  $(\text{Li}^+\text{@C}_{60} \subset \text{H}_4\text{-CPD}_{\text{Py}})_n$  largely became broadened and red-shifted. Actually, the Soret band of  $(\text{Li}^+\text{@C}_{60} \subset \text{H}_4\text{-CPD}_{\text{Py}})_n$  is red-shifted by 20 nm relative to that of monomeric form:  $\text{H}_4\text{-CPD}_{\text{Py}}$ . Such broadening behavior indicates that the molecular environment is significantly perturbed because of the aggregation of porphyrin molecules or the supramolecules by  $\pi$ -stacking. The trend of  $(\text{Li}^+\text{@C}_{60} \subset \text{Ni}_2\text{-CPD}_{\text{Py}})_n$  is also similar to that of  $(\text{Li}^+\text{@C}_{60} \subset \text{H}_4\text{-CPD}_{\text{Py}})_n$  as shown in Fig. 2b.

To evaluate the macroscopic aggregate formation of  $(\text{Li}^+\text{@C}_{60} \subset \text{M-CPD}_{\text{Py}})_n$  and reference compounds, transmission electron microscope (TEM) measurements were performed as shown in Fig. 3. As solvents were evaporated on the copper TEM grid, the nanoassemblies formed in well-defined shapes and sizes. Figures 3a and 3b show TEM images of  $(\text{Li}^+\text{@C}_{60} \subset \text{H}_4\text{-CPD}_{\text{Py}})_n$  and  $(\text{Li}^+\text{@C}_{60} \subset \text{Ni}_2\text{-CPD}_{\text{Py}})_n$ , respectively. In both cases, we can clearly see spherical and arranged *ca.* 200 nm-sized nanoparticles, whereas the single component



**Fig. 2.** UV-vis absorption spectra of molecular assemblies and reference monomers. (a) (a) 630  $\mu\text{M}$   $(\text{Li}^+\text{@C}_{60} \subset \text{H}_4\text{-CPD}_{\text{Py}})_n$  in MeCN/PhCN (3/1, v/v), (b)  $\text{H}_4\text{-CPD}_{\text{Py}}$  (monomer) in PhCN and (c)  $\text{Li}^+\text{@C}_{60}$  (monomer) in PhCN. (b) (a) 630  $\mu\text{M}$   $(\text{Li}^+\text{@C}_{60} \subset \text{Ni}_2\text{-CPD}_{\text{Py}})_n$  in MeCN/PhCN (3/1, v/v), (b)  $\text{Ni}_2\text{-CPD}_{\text{Py}}$  (monomer) in PhCN and (c)  $\text{Li}^+\text{@C}_{60}$  (monomer) in PhCN



**Fig. 3.** TEM images of (a)  $(\text{Li}^+@C_{60} \subset \text{H}_4\text{-CPDpy})_n$ , (b)  $(\text{Li}^+@C_{60} \subset \text{Ni}_2\text{-CPDpy})_n$ , (c)  $(\text{H}_4\text{-CPDpy})_n$  and (d)  $(\text{Ni}_2\text{-CPDpy})_n$

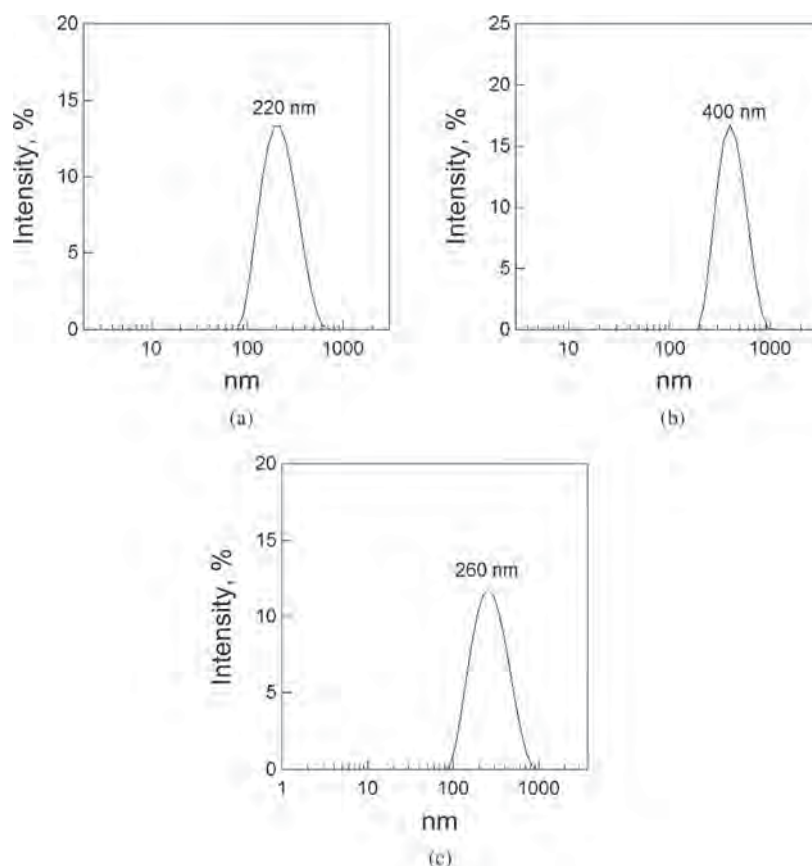
systems such as  $(\text{H}_4\text{-CPDpy})_n$  and  $(\text{Ni}_2\text{-CPDpy})_n$  have much larger polygonal structures (*ca.* 500–600 nm) (Figs 3c and 3d). Judging from the molecular scale of porphyrins and  $\text{Li}^+@C_{60}$ , one can conclude that porphyrin molecules are self-assembled with  $\text{Li}^+@C_{60}$  in the mixed solution to yield large donor–acceptor (D–A) nanoassemblies with an interpenetrating network.

These aggregate features in MeCN/PhCN (3/1, v/v) were also confirmed by dynamic light scattering (DLS) measurement (Fig. 4). The smaller average sizes of  $(\text{Li}^+@C_{60} \subset \text{H}_4\text{-CPDpy})_n$  (220 nm in diameter) were observed as compared to the single component systems such as  $(\text{H}_4\text{-CPDpy})_n$  (400 nm) and  $(\text{Li}^+@C_{60})_n$  (260 nm). The emphasis is placed on that the sizes of nanoassemblies measured from DLS nicely agree with those from TEM. Therefore, we can summarize that these nanoassemblies are formed in MeCN/PhCN, not but in the solute–substrate interface [70].

To evaluate photoelectrochemical performance of  $(\text{Li}^+@C_{60} \subset \text{M-CPDpy})_n$  on nanostructured  $\text{SnO}_2$  films cast on an optically conducting glass electrode (referred as OTE/ $\text{SnO}_2$ ), we prepared  $(\text{Li}^+@C_{60} \subset \text{M-CPDpy})_n$ -deposited film on OTE/ $\text{SnO}_2$  [referred as  $\text{SnO}_2/(\text{Li}^+@C_{60} \subset \text{M-CPDpy})_n$ ]. The preparation procedure is as follows. First, the suspension [ $(\text{Li}^+@C_{60} \subset \text{M-CPDpy})_n$ ]

was transferred into a cuvette, in which the two electrodes, *i.e.* OTE and OTE/ $\text{SnO}_2$ , were placed and kept at a distance of  $\sim 5$  mm using a Teflon spacer. Then, by applying the DC electric field ( $\sim 100 \text{ V}\cdot\text{cm}^{-1}$ ), these nanoassemblies were deposited from the suspension to the OTE/ $\text{SnO}_2$  electrode surface [68]. The reference single component system [ $(\text{Li}^+@C_{60})_n$ , or  $(\text{M-CPDpy})_n$ ] was analogously deposited onto the electrode surface to form  $\text{SnO}_2/(\text{Li}^+@C_{60})_n$  or  $\text{SnO}_2/(\text{M-CPDpy})_n$ . As reported previously [69], charging of porphyrin and  $C_{60}$  composite assemblies in the DC electric field play an important role in the growth and deposition process. These films are quite robust and can be washed with organic solvents to remove any loosely bound porphyrin and fullerene moieties.

Figures 5a and 5b show UV-vis absorption spectra of  $\text{SnO}_2/(\text{Li}^+@C_{60} \subset \text{H}_4\text{-CPDpy})_n$  and  $\text{SnO}_2/(\text{Li}^+@C_{60} \subset \text{Ni}_2\text{-CPDpy})_n$ , respectively. In both cases, the absorption of the  $\text{SnO}_2/(\text{Li}^+@C_{60} \subset \text{M-CPDpy})_n$  (spectrum *a*) is highly enhanced compared with that of the reference system containing only porphyrin units [ $\text{SnO}_2/(\text{M-CPDpy})_n$ ]. These results ensure that incident light is absorbed strongly in the visible and near-IR regions by  $\text{SnO}_2/(\text{Li}^+@C_{60} \subset \text{M-CPDpy})_n$  due to the supramolecular  $\pi$ -complex formation between porphyrin and  $\text{Li}^+@C_{60}$ .



**Fig. 4.** Size distributions of molecular assemblies estimated by dynamic light scattering (DLS) measurement. (a) 630  $\mu\text{M}$  ( $\text{Li}^+\text{@C}_{60} \subset \text{H}_4\text{-CPDpy}_n$ ) in MeCN/PhCN (3/1, v/v), (b) 630  $\mu\text{M}$  ( $\text{H}_4\text{-CPDpy}_n$ ) in MeCN/PhCN (3/1, v/v) and (c) 630  $\mu\text{M}$  ( $\text{Li}^+\text{@C}_{60}$ )<sub>n</sub> in MeCN/PhCN (3/1, v/v)

To evaluate photoelectrochemical performance, we measured photocurrent action spectra by a standard two-electrode system consisting of a working electrode and a Pt wire gauze electrode in MeCN solution including 0.5 M lithium iodide (LiI) and 0.01 M iodine ( $\text{I}_2$ ) (Scheme 1). The incident photon-to-photocurrent generation efficiency (IPCE) values were calculated by normalizing the photocurrent values for incident light energy and intensity and using Equation 1 [71];

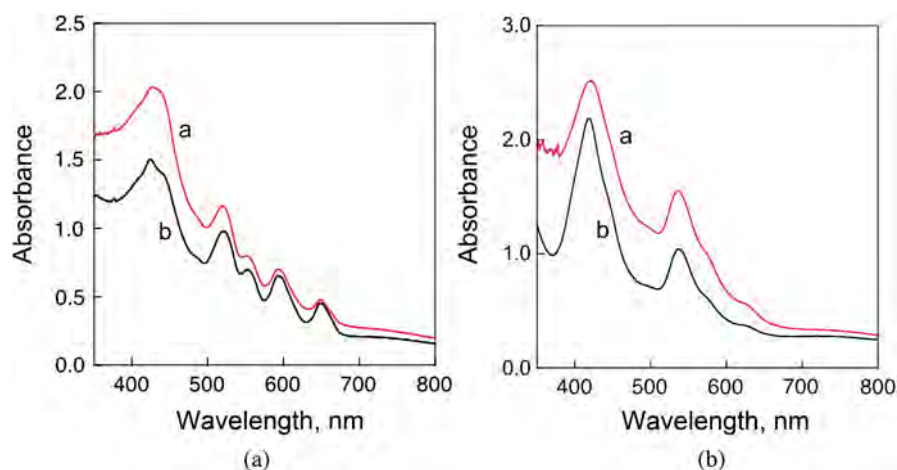
$$\text{IPCE (\%)} = 100 \times 1240 \times i_{\text{sc}} / (I_{\text{inc}} \times \lambda) \quad (1)$$

In the equation,  $i_{\text{sc}}$  is the short circuit photocurrent density ( $\text{A cm}^{-2}$ ),  $I_{\text{inc}}$  is the incident light intensity ( $\text{W.cm}^{-2}$ ) and  $\lambda$  is the wavelength (nm). Figures 6a and 6b show the photocurrent action spectra of  $\text{SnO}_2/(\text{Li}^+\text{@C}_{60} \subset \text{H}_4\text{-CPDpy}_n)$  and  $\text{SnO}_2/(\text{Li}^+\text{@C}_{60} \subset \text{Ni}_2\text{-CPDpy}_n)$ , respectively. In Fig. 6a,  $\text{SnO}_2/(\text{Li}^+\text{@C}_{60} \subset \text{H}_4\text{-CPDpy}_n)$  demonstrate a broad photoresponse in the visible region. The maximum IPCE of  $\text{SnO}_2/(\text{Li}^+\text{@C}_{60} \subset \text{H}_4\text{-CPDpy}_n)$  attains 19% at 460 nm, which is much larger than those of  $\text{SnO}_2/(\text{H}_4\text{-CPDpy}_n)$  (4.0%) and  $\text{SnO}_2/(\text{Li}^+\text{@C}_{60})_n$  (5.5%), respectively. Additionally, the maximum IPCE of  $\text{SnO}_2/(\text{Li}^+\text{@C}_{60} \subset \text{H}_4\text{-CPDpy}_n)$  (19%) is slightly larger than that of  $\text{SnO}_2/(\text{C}_{60} \subset \text{H}_4\text{-CPDpy}_n)$  (17%), which is previously reported by our group [59]. These results

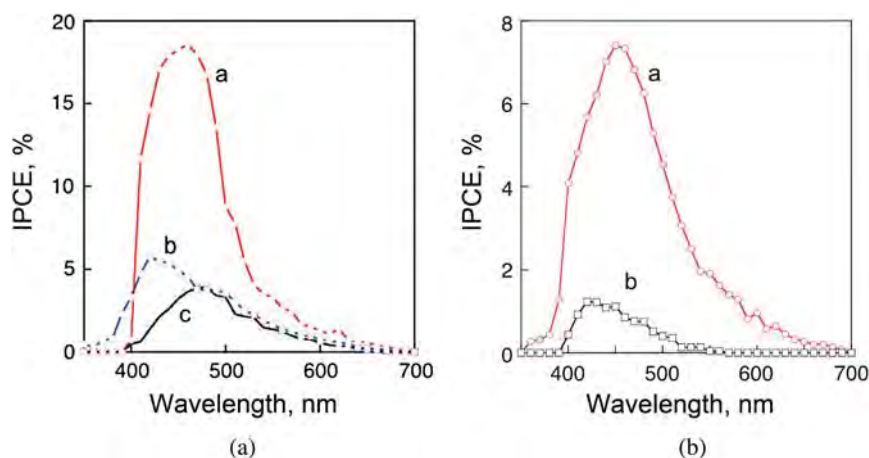
successfully indicate that D–A nanoassemblies with an interpenetrating network contribute to the enhanced photocurrent generation *via* photoinduced electron transfer. On the other hand,  $\text{SnO}_2/(\text{Li}^+\text{@C}_{60} \subset \text{Ni}_2\text{-CPDpy}_n)$  also possesses a broad photoresponse in the visible region, which parallels with the corresponding absorption spectrum (Fig. 5b). The maximum IPCE is 7.5% at 450 nm, which is much larger than that of  $\text{SnO}_2/(\text{Ni}_2\text{-CPDpy}_n)$  (1.3%). Previously, we already reported the maximum IPCE (~4%) of  $\text{SnO}_2/(\text{C}_{60} \subset \text{Ni-CPDpy}_n)$  [59]. Therefore, by replacing  $\text{C}_{60}$  with  $\text{Li}^+\text{@C}_{60}$ , the maximum IPCE of  $\text{SnO}_2/(\text{Li}^+\text{@C}_{60} \subset \text{Ni}_2\text{-CPDpy}_n)$  became two times larger than that of  $\text{SnO}_2/(\text{C}_{60} \subset \text{Ni-CPDpy}_n)$ .

The photocurrent generation mechanism of  $\text{SnO}_2/(\text{Li}^+\text{@C}_{60} \subset \text{M-CPDpy}_n)$  can be discussed based on the established photodynamics as shown in Scheme 2 [66]. The photocurrent generation in the present system may be mainly initiated by photoinduced electron transfer as follows in the nanoassemblies to produce the CS state,  $\text{M-CPDpy}^{\bullet+} - \text{Li}^+\text{@C}_{60}^{\bullet-}$ . In case of  $\text{Li}^+\text{@C}_{60} \subset \text{H}_4\text{-CPDpy}$ , electron transfer from singlet or triplet excited state ( $^1\text{H}_4\text{-CPDpy}^*$  or  $^3\text{H}_4\text{-CPDpy}^*$ ) [ $E(^1\text{H}_4\text{-CPDpy}^*/\text{H}_4\text{-CPDpy}^{\bullet+}) = -0.69 \text{ V}$  or  $E(^3\text{H}_4\text{-CPDpy}^*/\text{H}_4\text{-CPDpy}^{\bullet+}) = -0.30 \text{ V vs. SCE}$ ] [66] to ground state  $\text{Li}^+\text{@C}_{60}$  [ $E(\text{Li}^+\text{@C}_{60}/\text{Li}^+\text{@C}_{60}^{\bullet-}) = 0.14 \text{ V vs. SCE}$ ] [62]. Similarly, in  $\text{Li}^+\text{@}$





**Fig. 5.** UV-vis absorption spectra of (a) (a)  $\text{SnO}_2/(\text{Li}^+@C_{60} \subset \text{H}_4\text{-CPDpy})_n$  and (b)  $\text{SnO}_2/(\text{H}_4\text{-CPDpy})_n$ , and (b) (a)  $\text{SnO}_2/(\text{Li}^+@C_{60} \subset \text{Ni}_2\text{-CPDpy})_n$  and (b)  $\text{SnO}_2/(\text{Ni}_2\text{-CPDpy})_n$



**Fig. 6.** Photocurrent action spectra of (a) (a)  $\text{SnO}_2/(\text{Li}^+@C_{60} \subset \text{H}_4\text{-CPDpy})_n$ , (b)  $\text{SnO}_2/(\text{H}_4\text{-CPDpy})_n$  and (c)  $\text{SnO}_2/(\text{Li}^+@C_{60})_n$ , and (b) (a)  $\text{SnO}_2/(\text{Li}^+@C_{60} \subset \text{Ni}_2\text{-CPDpy})_n$ , (b) and  $\text{SnO}_2/(\text{Ni}_2\text{-CPDpy})_n$

$C_{60} \subset \text{Ni}_2\text{-CPDpy}$ , electron transfer occurs from singlet or triplet excited state ( $^1\text{Ni}_2\text{-CPDpy}^*$  or  $^3\text{Ni}_2\text{-CPDpy}^*$ ) [ $E(\text{H}_4\text{-CPDpy}^*/\text{H}_4\text{-CPDpy}^{**}) = -0.63 \text{ V}$  or  $E(^3\text{Ni}_2\text{-CPDpy}^*/\text{Ni}_2\text{-CPDpy}^{**}) = -0.16 \text{ V}$  vs. SCE] [66] to ground state  $\text{Li}^+@C_{60}$  [ $E(\text{Li}^+@C_{60}/\text{Li}^+@C_{60}^{\bullet-}) = 0.14 \text{ V}$  vs. SCE)] [62]. The reduced  $\text{Li}^+@C_{60}$  ( $\text{Li}^+@C_{60}^{\bullet-}$ ) [ $E(\text{Li}^+@C_{60}/\text{Li}^+@C_{60}^{\bullet-}) = 0.14 \text{ V}$  vs. SCE)] [62] injects electrons into the conduction band of  $\text{SnO}_2$  ( $\sim 0.2 \text{ V}$  vs. SCE) [69], whereas the oxidized  $\text{M-CPDpy}$  [ $E(\text{H}_4\text{-CPDpy}^{**}/\text{H}_4\text{-CPDpy}) = 1.21 \text{ V}$  and  $E(\text{Ni}_2\text{-CPDpy}^{**}/\text{Ni}_2\text{-CPDpy}) = 1.34 \text{ V}$  vs. SCE] [66] undergoes the electron-transfer reduction with the iodide ( $\text{I}_3^-/\text{I}^- = 0.7 \text{ V}$  vs. SCE) [69] in the electrolyte solution. Thus, the enhanced light energy conversion properties of  $\text{SnO}_2/(\text{Li}^+@C_{60} \subset \text{M-CPDpy})_n$  were successfully observed as compared to the corresponding single component systems and our reported pristine  $C_{60}$  and  $\text{M-CPDpy}$  based systems [59].

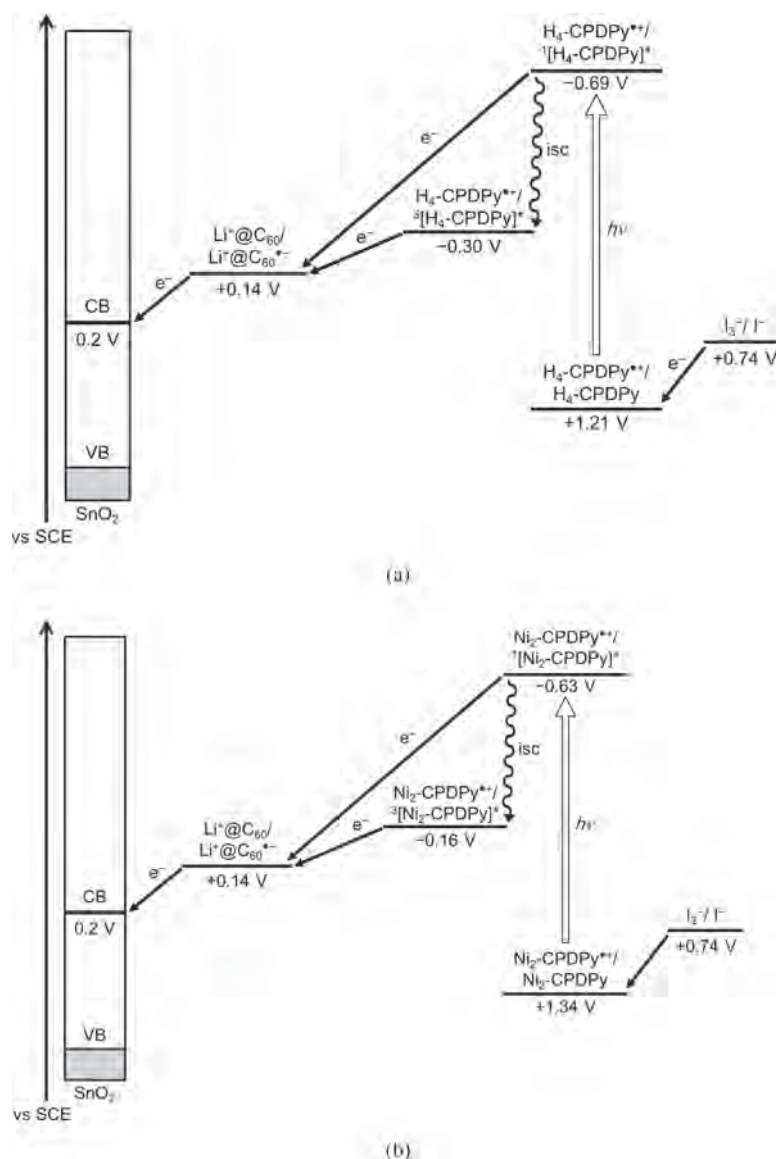
In conclusion, this paper demonstrates new supramolecular photovoltaic cells using inclusion complexes of lithium-ion-encapsulated [60]fullerene

[ $\text{Li}^+@C_{60}$ ] and cyclic porphyrin dimers. The light energy conversion properties of the supramolecular nanoassemblies of  $\text{Li}^+@C_{60}$  and  $\text{M-CPDpy}$ -deposited  $\text{SnO}_2$  films are higher than those of the single component films and supramolecular nanoassemblies of pristine  $C_{60}$  and cyclic porphyrin dimers. Such a supramolecular assemblies utilizing inclusion complexes of donor and acceptor molecules provide a new perspective for the construction of solar energy conversion systems.

## EXPERIMENTAL

### Materials

Chemicals were purchased from commercial sources and used without further purification, unless otherwise stated. Lithium ion-encapsulated fullerene



**Scheme 2.** Proposed photocurrent generation scheme of  $\text{Li}^+\text{@C}_{60}$  + M-CPDPy (a)  $\text{Li}^+\text{@C}_{60}$  +  $\text{H}_4\text{-CPDPy}$  and (b)  $\text{Li}^+\text{@C}_{60}$  +  $\text{Ni}_2\text{-CPDPy}$

hexafluorophosphate salt ( $\text{Li}^+\text{@C}_{60}$   $\text{PF}_6^-$ , Idea International Corporation) was commercially obtained from Wako Pure Chemicals, Japan. The synthesis of cyclic porphyrin dimers was previously reported [57]. An optically transparent conducting glass electrode (OTE) was purchased from Touki Co. Ltd., Japan.

#### Dynamic light scattering (DLS) measurements

The particle size and distribution were measured in MeCN/PhCN (3:1 v/v) using light-scattering equipment (Zetasizer nano ZS).

#### TEM measurements

Transmission electron micrograph (TEM) measurements were recorded on Tecnai spirit (FEI company) by

applying a drop of the sample to a copper grid. TEM images were recorded on a transmission electron microscope an accelerating voltage of 120 kV for imaging.

#### Spectroscopic measurements

UV-vis absorption spectra were recorded on Perkin Elmer (Lambda 750) UV-vis-NIR spectrophotometer.

#### Preparation of supramolecular assemblies of $\text{Li}^+\text{@C}_{60}$ and cyclic porphyrin dimers

A mother solution was prepared by mixing  $\text{Li}^+\text{@C}_{60}$   $\text{PF}_6^-$  (0.25 mM) and M-CPDPy (0.25 mM) in PhCN (good solvent). This process successfully ensured the formation of inclusion complexes between  $\text{Li}^+\text{@C}_{60}$  and M-CPDPy [66]. Then, the mother solution (1 mL) was injected to MeCN

(3 mL) as a poor solvent. Finally, the suspended solution containing the supramolecular assemblies were obtained.

### Preparation of supramolecular assemblies of cyclic porphyrin dimers

A mother solution of M-CPD<sub>py</sub> (0.25 mM) was prepared in PhCN. Then, the mother solution (1 mL) was injected to MeCN (3 mL) as a poor solvent. Finally, the suspended solution containing the supramolecular assemblies were obtained.

### Preparation of supramolecular assemblies of $\text{Li}^+\text{@C}_{60}$

A mother solution of  $\text{Li}^+\text{@C}_{60}$  PF<sub>6</sub><sup>-</sup> (0.25 mM) was prepared in PhCN. Then, the mother solution (1 mL) was injected to MeCN (3 mL) as a poor solvent. Finally, the suspended solution containing the supramolecular assemblies were obtained.

### Preparation of $(\text{Li}^+\text{@C}_{60} \subset \text{M-CPD}_{\text{py}})_n$ -deposited films

Nanostructured SnO<sub>2</sub> films were cast on an optically transparent conducting glass electrode (OTEs) by applying a colloidal solution obtained from Sigma–Aldrich. The air-dried films were annealed at 673 K. Details on preparation of SnO<sub>2</sub> films on conducting glass substrates are reported elsewhere [47].  $(\text{Li}^+\text{@C}_{60} \subset \text{M-CPD}_{\text{py}})_n$  composite films were simply prepared by electrophoretic deposition method. A known amount of  $\text{Li}^+\text{@C}_{60}$  PF<sub>6</sub><sup>-</sup>, M-CPD<sub>py</sub> or the mixture solution in PhCN/MeCN (1/3, v/v, ~4 mL) was transferred to a 1 cm cuvette in which two OTEs were kept at a distance of ~6 mm using a Teflon spacer. A DC electric field (~100 V/cm) for 1 min was applied between these two electrodes using a PowerPac HV (Bio-Rad). The deposition of the film can be visibly seen as the solution becomes colorless with simultaneous brown coloration of the OTE electrode. The SnO<sub>2</sub> film coated with  $(\text{Li}^+\text{@C}_{60} \subset \text{M-CPD}_{\text{py}})_n$  is referred to SnO<sub>2</sub>/( $\text{Li}^+\text{@C}_{60} \subset \text{M-CPD}_{\text{py}})_n$ .

### Photoelectrochemical measurements

Photoelectrochemical measurements were carried out in a standard two-compartment cell consisting of a working electrode, a Pt wire gauze counter electrode. A KEITHLEY 2400 was used for photocurrent generation density. For the IPCE measurements, a monochromator (SM-25, Bunkoh Keiki Co., LTD) was introduced into the path of the excitation beam (150 W xenon lamp, Bunkoh Keiki Co., LTD) for the selected wavelength. The lamp intensity at each wavelength was determined using a Si photodiode (Hamamatsu Photonics S1337-1010BQ) and corrected.

### Acknowledgements

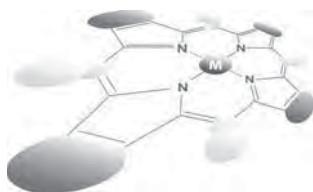
This work was partially supported by Grant-in-Aids for Scientific Research (Nos. 26286017 & 26620159 to TH

and 20108009 to FT) and from the Ministry of Education, Culture, Sports, Science and Technology (MEXT), Japan and the Murata Science Foundation.

### REFERENCES

- Whitesides GM and Boncheva M. *Proc. Natl. Acad. Sci. USA*. 2002; **99**: 4769–4774.
- Bowden NB, Weck M, Choi IS and Whitesides GM. *Acc. Chem. Res.* 2000; **34**: 231–238.
- Lehn J-M. *Angew. Chem., Int. Ed. Engl.* 1990; **29**: 1304–1319.
- Aida T, Meijer EW and Stupp SI. *Science* 2012; **335**: 813–817.
- Stoddart JF. *Nat. Chem.* 2009; **1**: 14–15.
- Fukuzumi S, Honda T and Kojima T. *Coordin Chem Rev* 2012; **256**: 2488–2502.
- Northrop BH, Zheng Y-R, Chi K-W and Stang PJ. *Acc. Chem. Res.* 2009; **42**: 1554–1563.
- Li S-S, Northrop BH, Yuan Q-H, Wan L-J and Stang PJ. *Acc. Chem. Res.* 2009; **42**: 249–259.
- Bottari G, Trukhina O, Ince M and Torres T. *Coordin Chem Rev* 2012; **256**: 2453–2477.
- Lee J, Farha OK, Roberts J, Scheidt KA, Nguyen ST and Hupp JT. *Chem. Soc. Rev.* 2009; **38**: 1450–1459.
- Brune A, Jeong G, Liddell PA, Sotomura T, Moore TA, Moore AL and Gust D. *Langmuir* 2004; **20**: 8366–8371.
- Xiao S, Myers M, Miao Q, Sanaur S, Pang K, Steigerwald ML and Nuckolls C. *Angew. Chem. Int. Ed.* 2005; **44**: 7390–7394.
- Hasobe T. *J. Phys. Chem. Lett.* 2013; **4**: 1771–1780.
- Hasobe T. *Phys. Chem. Chem. Phys.* 2012; **14**: 15975–15987.
- Hasobe T and Sakai H. *ECS J. Solid State Sci. Technol.* 2013; **2**: M3015–M3022.
- Hasobe T. *Phys. Chem. Chem. Phys.* 2010; **12**: 44–57.
- Hasobe T, Murata H, Fukuzumi S and Kamat PV. *Mol. Cryst. Liq. Cryst.* 2007; **471**: 39–51.
- Hasobe T and Sakai H. *J. Porphyrins Phthalocyanines* 2011; **15**: 301–311.
- Hasobe T, Murata H, Kamat PV and Fukuzumi S. *Jpn. J. Appl. Phys.* 2008; **47**: 1223–1229.
- Shi Y, Sánchez-Molina I, Cao C, Cook TR and Stang PJ. *Proc. Natl. Acad. Sci. USA*. 2014; **111**: 9390–9395.
- Fukuzumi S, Ohkubo K and Suenobu T. *Acc. Chem. Res.* 2014; **47**: 1455–1464.
- Fukuzumi S. *Phys. Chem. Chem. Phys.* 2008; **10**: 2283–2297.
- Fukuzumi S. In *Pure Appl. Chem.*, 2003; Vol. 75, p. 577.
- Hasobe T, Hattori S, Kamat PV and Fukuzumi S. *Tetrahedron* 2006; **62**: 1937–1946.

25. Fukuzumi S and Kojima T. *J. Mater. Chem.* 2008; **18**: 1427–1439.
26. Fukuzumi S. *Pure Appl. Chem.* 2003; **75**: 577–587.
27. Kirner S, Sekita M and Guldi DM. *Adv. Mater.* 2014; **26**: 1482–1493.
28. Bottari G, de la Torre G, Guldi DM and Torres T. *Chem. Rev.* 2010; **110**: 6768–6816.
29. Gust D, Moore TA and Moore AL. *Acc. Chem. Res.* 2001; **34**: 40–48.
30. Gust D, Moore TA and Moore AL. *Acc. Chem. Res.* 1993; **26**: 198–205.
31. Wasielewski MR. *Acc. Chem. Res.* 2009; **42**: 1910–1921.
32. D'Souza F and Ito O. *Chem. Soc. Rev.* 2012; **41**: 86–96.
33. Umeyama T and Imahori H. *J. Phys. Chem. C* 2012; **117**: 3195–3209.
34. Imahori H, Mori Y and Matano Y. *J. Photochem. Photobiol. C: Photochem. Rev.* 2003; **4**: 51–83.
35. Drain CM, Varotto A and Radivojevic I. *Chem. Rev.* 2009; **109**: 1630–1658.
36. Drain CM, Batteas JD, Flynn GW, Milic T, Chi N, Yablon DG and Sommers H. *Proc. Natl. Acad. Sci. USA.* 2002; **99**: 6498–6502.
37. Hasobe T, Oki H, Sandanayaka ASD and Murata H. *Chem. Commun.* 2008: 724–726.
38. Hasobe T, Sandanayaka ASD, Wada T and Araki Y. *Chem. Commun.* 2008: 3372–3374.
39. Nakanishi T, Kojima T, Ohkubo K, Hasobe T, Nakayama K and Fukuzumi S. *Chem. Mater.* 2008; **20**: 7492–7500.
40. Sandanayaka ASD, Araki Y, Wada T and Hasobe T. *J. Phys. Chem. C* 2008; **112**: 19209–19216.
41. Hasobe T, Fukuzumi S and Kamat PV. *J. Am. Chem. Soc.* 2005; **127**: 11884–11885.
42. Hasobe T, Fukuzumi S and Kamat PV. *J. Phys. Chem. B* 2006; **110**: 25477–25484.
43. Hasobe T, Kamat PV, Absalom MA, Kashiwagi Y, Sly J, Crossley MJ, Hosomizu K, Imahori H and Fukuzumi S. *J. Phys. Chem. B* 2004; **108**: 12865–12872.
44. Sakuma T, Sakai H and Hasobe T. *Chem. Commun.* 2012; **48**: 4441–4443.
45. Hasobe T, Sakai H, Mase K, Ohkubo K and Fukuzumi S. *J. Phys. Chem. C* 2013; **117**: 4441–4449.
46. Maligaspe E, Sandanayaka ASD, Hasobe T, Ito O and D'Souza F. *J. Am. Chem. Soc.* 2010; **132**: 8158–8164.
47. Sandanayaka ASD, Murakami T and Hasobe T. *J. Phys. Chem. C* 2009; **113**: 18369–18378.
48. Hasobe T, Imahori H, Kamat PV, Ahn TK, Kim SK, Kim D, Fujimoto A, Hirakawa T and Fukuzumi S. *J. Am. Chem. Soc.* 2005; **127**: 1216–1228.
49. Hasobe T, Kamat PV, Troiani V, Solladié N, Ahn TK, Kim SK, Kim D, Kongkanand A, Kuwabata S and Fukuzumi S. *J. Phys. Chem. B* 2005; **109**: 19–23.
50. Hasobe T, Kashiwagi Y, Absalom MA, Sly J, Hosomizu K, Crossley MJ, Imahori H, Kamat PV and Fukuzumi S. *Adv. Mater.* 2004; **16**: 975–979.
51. Hasobe T, Imahori H, Kamat PV and Fukuzumi S. *J. Am. Chem. Soc.* 2003; **125**: 14962–14963.
52. Hasobe T, Rabbani MG, Sandanayaka ASD, Sakai H and Murakami T. *Chem. Commun.* 2010; **46**: 889–891.
53. Hasobe T, Hattori S, Kamat PV, Urano Y, Umezawa N, Nagano T and Fukuzumi S. *Chem. Phys.* 2005; **319**: 243–252.
54. Fukuzumi S. *Bull. Chem. Soc. Jpn.* 2006; **79**: 177–195.
55. Boyd PDW and Reed CA. *Acc. Chem. Res.* 2004; **38**: 235–242.
56. Tashiro K and Aida T. *Chem. Soc. Rev.* 2007; **36**: 189–197.
57. Nobukuni H, Shimazaki Y, Tani F and Naruta Y. *Angew. Chem., Int. Ed.* 2007; **46**: 8975–8978.
58. Nobukuni H, Tani F, Shimazaki Y, Naruta Y, Ohkubo K, Nakanishi T, Kojima T, Fukuzumi S and Seki S. *J. Phys. Chem. C* 2009; **113**: 19694–19699.
59. Nobukuni H, Shimazaki Y, Uno H, Naruta Y, Ohkubo K, Kojima T, Fukuzumi S, Seki S, Sakai H, Hasobe T and Tani F. *Chem. Eur. J.* 2010; **16**: 11611–11623.
60. Aoyagi S, Nishibori E, Sawa H, Sugimoto K, Takata M, Miyata Y, Kitaura R, Shinohara H, Okada H, Sakai T, Ono Y, Kawachi K, Yokoo K, Ono S, Omote K, Kasama Y, Ishikawa S, Komuro T and Tobita H. *Nat. Chem.* 2010; **2**: 678–683.
61. Fukuzumi S, Ohkubo K, Kawashima Y, Kim DS, Park JS, Jana A, Lynch VM, Kim D and Sessler JL. *J. Am. Chem. Soc.* 2011; **133**: 15938–15941.
62. Ohkubo K, Kawashima Y and Fukuzumi S. *Chem. Commun.* 2012; **48**: 4314–4316.
63. Kawashima Y, Ohkubo K and Fukuzumi S. *J. Phys. Chem. A* 2012; **116**: 8942–8948.
64. Aoyagi S, Sado Y, Nishibori E, Sawa H, Okada H, Tobita H, Kasama Y, Kitaura R and Shinohara H. *Angew. Chem. Int. Ed.* 2012; **51**: 3377–3381.
65. Ohkubo K, Kawashima Y, Sakai H, Hasobe T and Fukuzumi S. *Chem. Commun.* 2013; **49**: 4474–4476.
66. Kamimura T, Ohkubo K, Kawashima Y, Nobukuni H, Naruta Y, Tani F and Fukuzumi S. *Chem. Sci.* 2013; **4**: 1451–1461.
67. Kamat PV, Barazzouk S and Hotchandani S. *Adv. Mater.* 2001; **13**: 1614–1617.
68. Hasobe T, Imahori H, Fukuzumi S and Kamat PV. *J. Mater. Chem.* 2003; **13**: 2515–2520.
69. Hasobe T, Imahori H, Fukuzumi S and Kamat PV. *J. Phys. Chem. B* 2003; **107**: 12105–12112.
70. Sakai H, Rabbani MG and Hasobe T. *J. Porphyrins Phthalocyanines* 2011; **15**: 639–651.
71. Hasobe T, Hattori S, Kotani H, Ohkubo K, Hosomizu K, Imahori H, Kamat PV and Fukuzumi S. *Org. Lett.* 2004; **6**: 3103–3106.



# *N*-confused meso-tetraaryl-substituted free-base porphyrins: determination of protonation and deprotonation constants in nonaqueous media

Zhongping Ou<sup>\*a</sup>∞, Xueyan Chen<sup>a</sup>, Lina Ye<sup>a</sup>, Songlin Xue<sup>a</sup>, Yuanyuan Fang<sup>b</sup>∞, Xiaoqin Jiang<sup>b</sup> and Karl M. Kadish<sup>\*b</sup>∞

<sup>a</sup>School of Chemistry and Chemical Engineering, Jiangsu University, Zhenjiang 212013, China

<sup>b</sup>Department of Chemistry, University of Houston, Houston TX 77204-5003, USA

Dedicated to Professor Shunichi Fukuzumi on the occasion of his retirement

Received 28 September 2014

Accepted 17 November 2014

**ABSTRACT:** The protonation and deprotonation reactions for a series *N*-confused meso-tetraaryl-substituted free-base porphyrins containing electron-donating or electron-withdrawing substituents was monitored in CHCl<sub>3</sub> and DMF by UV-visible spectroscopy during titrations with trifluoroacetic acid or tetra-*n*-butylammonium hydroxide. The spectroscopic data was also used to calculate equilibrium constants for these reactions. The examined compounds are represented as (XPh)<sub>4</sub>NCPH<sub>2</sub>, where “NCP” represents the *N*-confused porphyrin  $\pi$ -conjugated macrocycle and X is a CH<sub>3</sub>O, CH<sub>3</sub>, H or Cl *para*-substituent on the four meso-phenyl rings (Ph) of the compound. The porphyrins can exist in two tautomeric forms depending upon the solvent and each tautomer undergoes two stepwise protonation reactions leading to formation of the mono- and bis-protonated porphyrins, [(XPh)<sub>4</sub>NCPH<sub>3</sub>]<sup>+</sup> and [(XPh)<sub>4</sub>NCPH<sub>4</sub>]<sup>2+</sup>. A single step deprotonation is observed for the same compounds in DMF and the product is assigned as [(XPh)<sub>4</sub>NCPH]. Comparisons are made between UV-visible spectra of the protonated, neutral and deprotonated forms of the porphyrin and the effect of the porphyrin ring substituents and tautomeric form of the neutral porphyrin on the UV-visible spectra and protonation constants is discussed along with data from DFT calculations.

**KEYWORDS:** *N*-confused free-base porphyrins, protonation, deprotonation, determination of equilibrium constants.

## INTRODUCTION

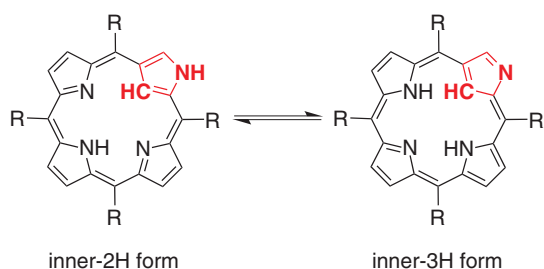
The chemical and physical properties of *N*-confused porphyrins have attracted a great deal of interest [1–26] since the first discovery of these compounds in 1994 [27, 28]. *N*-confused porphyrins have the same chemical composition as normal porphyrins but they possess an inverted pyrrole so that a carbon atom of the pyrrole is

located within the core of the macrocycle and a nitrogen atom from the pyrrole resides at the macrocycle periphery. A notable feature of the *N*-confused free-base porphyrins is that two NH tautomers can be observed in solution, the exact form of which will depend upon the proton-accepting ability of the solvent [20–26, 29]. These forms are shown in Chart 1 where the inner-2H of the porphyrin is mainly observed in strongly proton-accepting solvents such as dimethylformamide (DMF), dimethylacetamide (DMAc) and dimethyl sulfoxide (DMSO), and the inner-3H form is exclusively observed in aprotic solvents such as CH<sub>2</sub>Cl<sub>2</sub>, CHCl<sub>3</sub> and toluene [1, 22].

Most free-base tetraarylporphyrins (PorH<sub>2</sub>) can be easily protonated and this reaction almost invariably

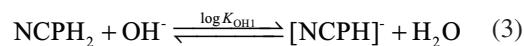
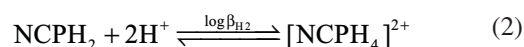
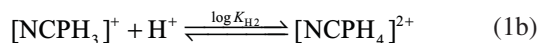
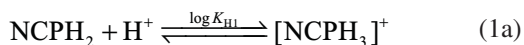
∞ SPP full and ∞ student member in good standing

\*Correspondence to: Zhongping Ou, email: zpou2003@yahoo.com, tel: +86 511-88791800, fax: +86 0511-88791800; Karl M. Kadish, email: kkadish@uh.edu, tel: +1 (713)-743-2740, fax: +1 (713)-743-2745



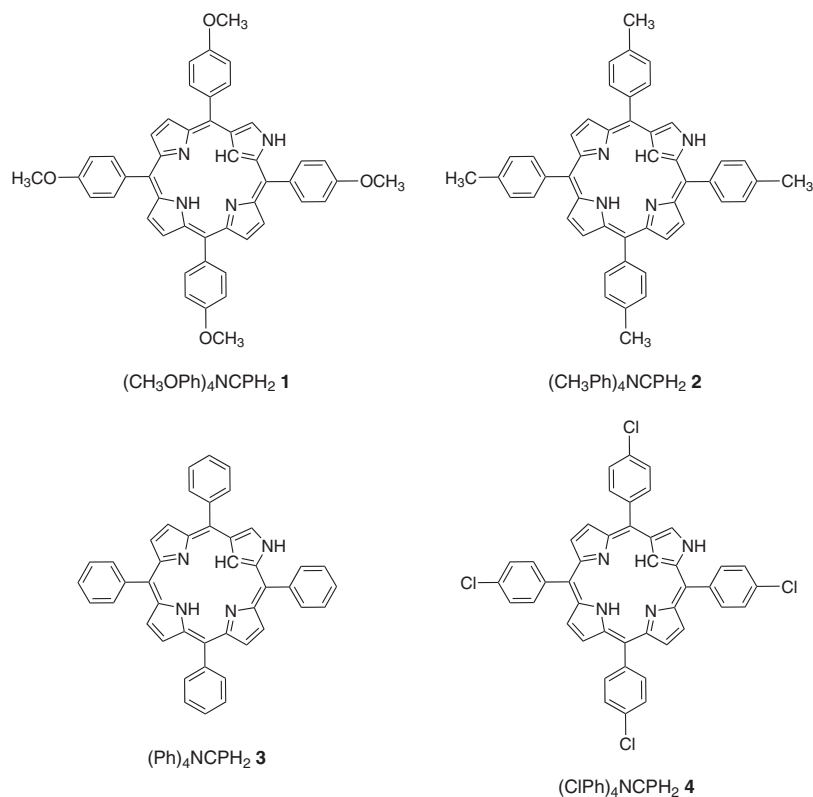
**Chart 1.** Structures of the two tautomeric forms for *N*-confused free-base *meso*-substituted tetraarylporphyrins

occurs in a single one step process to give the porphyrin dication,  $[\text{PorH}_4]^{2+}$  [30]. In the case of *N*-confused free-base tetraarylporphyrins ( $\text{NCPH}_2$ ), two stepwise one-proton addition reactions are observed to give the *mono*- and *bis*-protonated species,  $[\text{NCPH}_3]^+$  and  $[\text{NCPH}_4]^{2+}$  as shown in Equations 1a, 1b, and 2, where Equation 2 represents the overall bis-protonation constant,  $\log\beta_{\text{H}_2}$ . Deprotonation of the neutral *N*-confused free-base porphyrins can also occur [22] and this leads to  $[\text{NCPH}]^-$  as shown in Equation 3.



Protonation constants have been determined for a few *N*-confused free-base porphyrins [20, 36] but there have been no reported values for deprotonation constants of the same compounds. In addition, no comparisons have been made between protonation constants of the inner-3H and inner 2H forms of the *N*-confused free-base porphyrins or between protonation/deprotonation constants of *N*-confused free-base porphyrins and structurally related free-base corroles or free-base porphyrins in nonaqueous media.

This is addressed in the present paper where the protonation and deprotonation reactions were spectroscopically monitored in  $\text{CHCl}_3$  during titrations with trifluoroacetic acid (TFA) or tetra-*n*-butylammonium hydroxide (TBAOH) for a series of *N*-confused free-base tetraarylporphyrins in their inner-3H form and in DMF for the same porphyrins in their inner-2H form. The investigated compounds are represented as  $(\text{XPh})_4\text{NCPH}_2$ , where “NCP” is a *N*-confused free-base porphyrin macrocycle and X is a  $\text{OCH}_3$ ,  $\text{CH}_3$ , H or Cl substituent on the *para*-positions of four phenyl rings (Ph) of the macrocycle (Chart 2). The resulting spectroscopic data were used to calculate the protonation and deprotonation equilibrium constants,  $\log K_{\text{H}_1}$ ,  $\log K_{\text{H}_2}$ .



**Chart 2.** Structures of examined *N*-confused free-base porphyrins (only the tautomer in its inner-2H form is shown for each compound)

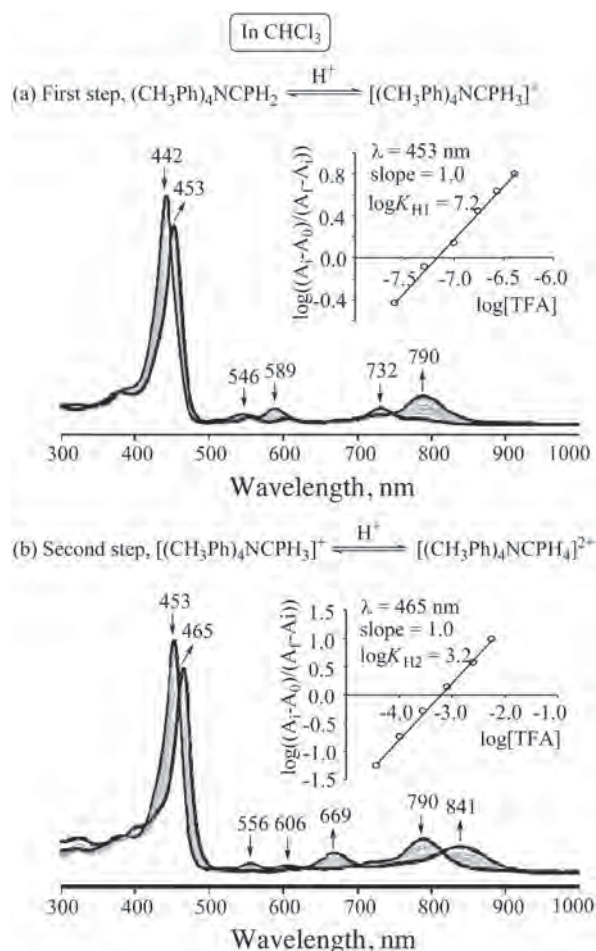
$\log\beta_{H_2}$  and  $\log K_{OH1}$  as shown in Equations 1–3. The site of each protonation (and type of tautomer in solution) is suggested both by the magnitude of the first protonation constant and UV-visible spectra of the neutral and *mono*-protonated porphyrins, as well as by DFT calculations.

## RESULTS AND DISCUSSION

### Protonation of the inner-3H and inner-2H forms

Two solvents were selected for investigating the protonation reactions of compounds **1–4**. One was  $\text{CHCl}_3$  where  $(\text{XPh})_4\text{NCPH}_2$  exists in its inner-3H form and the other was DMF where the porphyrin is in its inner-2H form as shown in Chart 1 and earlier demonstrated by NMR and UV-visible measurements in these solvents [20, 27]. Both tautomeric forms of the *N*-confused porphyrins have two nitrogens available for protonation (see Chart 1), but because the inverted pyrrole has its nitrogen on different positions of the macrocycle, differences are observed in the magnitude of the  $\log K_{H1}$  values with changes in the solvent. Small differences are also observed in the UV-visible spectra and  $\log K$  values with changes the electron-donating or electron-withdrawing group on the four *meso*-phenyl rings of the macrocycle. This is discussed on the following pages.

**Inner-3H forms in  $\text{CHCl}_3$ .** An example of the spectral changes which occur during the two step protonation of  $(\text{XPh})_4\text{NCPH}_2$  is shown in Fig. 1 for  $(\text{CH}_3\text{Ph})_4\text{NCPH}_2$  **2** in  $\text{CHCl}_3$  with increasing concentration of TFA. The initial porphyrin in its inner-3H form is characterized by a Soret band at 442 nm and three visible bands at 546, 589 and 732 nm. In the first protonation step, the Soret band shifts



**Fig. 1.** UV-visible spectral changes during stepwise titration of  $(\text{CH}_3\text{Ph})_4\text{NCPH}_2$  **2** (inner-3H form) with TFA in  $\text{CHCl}_3$  (insert shows the Hill plot used to determine the number of protons added and the protonation equilibrium constants)

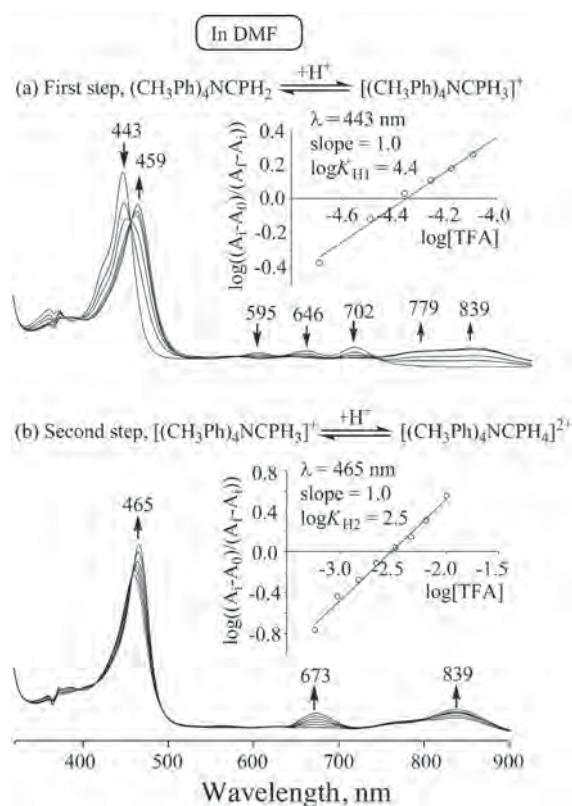
**Table 1.** UV-visible spectral data ( $\lambda_{\text{max}}$ , nm) of the neutral, *mono*- and bis-protonated compounds **1–4** in  $\text{CHCl}_3$  and DMF. The most intense bands in each spectrum are shown in bold print

Type of cpd	Form of cpd	in $\text{CHCl}_3$				in DMF				
neutral	$(\text{CH}_3\text{OPh})_4\text{NCPH}_2$ <b>1</b>	<b>444</b>	543	582	<b>735</b>	<b>443</b>	593	646	<b>703</b>	
	$(\text{CH}_3\text{Ph})_4\text{NCPH}_2$ <b>2</b>	<b>442</b>	546	589	<b>732</b>	<b>443</b>	595	646	<b>702</b>	
	$(\text{Ph})_4\text{NCPH}_2$ <b>3</b>	<b>440</b>	543	584	<b>728</b>	<b>441</b>	596	643	<b>698</b>	
	$(\text{ClPh})_4\text{NCPH}_2$ <b>4</b>	<b>441</b>	543	586	<b>730</b>	<b>443</b>	595	644	<b>700</b>	
<i>mono</i> -protonated	$[(\text{CH}_3\text{OPh})_4\text{NCPH}_3]^+$	<b>461</b>	557	611	<b>795</b>	<b>458</b>	568	628	<b>779</b>	838
	$[(\text{CH}_3\text{Ph})_4\text{NCPH}_3]^+$	<b>453</b>	556	606	<b>790</b>	<b>459</b>	567	628	<b>779</b>	839
	$[(\text{Ph})_4\text{NCPH}_3]^+$	<b>450</b>	553	600	<b>780</b>	<b>456</b>	569	630	<b>770</b>	831
	$[(\text{ClPh})_4\text{NCPH}_3]^+$	<b>452</b>	553	602	<b>780</b>	<b>456</b>	568	629	<b>770</b>	829
bis-protonated	$[(\text{CH}_3\text{OPh})_4\text{NCPH}_4]^{2+}$	<b>474</b>		687	<b>864</b>	<b>466</b>		673	<b>837</b>	
	$[(\text{CH}_3\text{Ph})_4\text{NCPH}_4]^{2+}$	<b>465</b>		669	<b>841</b>	<b>465</b>		673	<b>839</b>	
	$[(\text{Ph})_4\text{NCPH}_4]^{2+}$	<b>461</b>		662	<b>829</b>	<b>462</b>		662	<b>825</b>	
	$[(\text{ClPh})_4\text{NCPH}_4]^{2+}$	<b>465</b>		666	<b>838</b>	<b>465</b>		667	<b>829</b>	

**Table 2.** Protonation constants of *N*-confused free-base tetraarylporphyrins

Compound	4σ <sup>a</sup>	Inner-3H form (CHCl <sub>3</sub> )			Inner-2H form (DMF)		
		logK <sub>H1</sub>	logK <sub>H2</sub>	logβ <sub>H2</sub>	logK <sub>H1</sub>	logK <sub>H2</sub>	logβ <sub>H2</sub>
(CH <sub>3</sub> Oph) <sub>4</sub> NCPH <sub>2</sub> <b>1</b>	-1.08	6.3	2.8	9.1	4.5	2.2	6.7
(CH <sub>3</sub> Ph) <sub>4</sub> NCPH <sub>2</sub> <b>2</b>	-0.68	7.2	3.2	10.4	4.4	2.5	6.9
(Ph) <sub>4</sub> NCPH <sub>2</sub> <b>3</b>	0.00	7.0	3.0	10.0	4.3	2.1	6.4
(ClPh) <sub>4</sub> NCPH <sub>2</sub> <b>4</b>	0.92	5.0	3.1	8.1	4.0	2.0	6.0

<sup>a</sup>Hammett substituent constant taken from Ref. 39 for the para-substituents on the four phenyl rings of the compound.



**Fig. 2.** UV-visible spectral changes of (CH<sub>3</sub>Ph)<sub>4</sub>NCPH<sub>2</sub> **2** (inner-2H form) during a titration with TFA in DMF (insert is the Hill plot for determination of the number of protons and protonation equilibrium constants)

to 453 nm and three new Q-bands appear at 556, 606 and 790 nm, as shown in Fig. 1a. Multiple isobestic points (at 449, 490 and 745) are observed in the conversion of (CH<sub>3</sub>Ph)<sub>4</sub>NCPH<sub>2</sub> to [(CH<sub>3</sub>Ph)<sub>4</sub>NCPH<sub>3</sub>]<sup>+</sup>. Multiple isobestic points at λ = 460, 510, 620 and 819 nm are also observed in the spectra during the second step of the titration, with the Soret band shifting from 453 to 465 nm and two major Q-bands appearing at 669 and 841 nm in the final spectrum.

The spectral changes in Figs 1a and 1b were analyzed as a function of the added TFA concentration using the

Hill equation [37]. In both steps of the titration, a linear relationship is seen in the plots of log[(A<sub>T</sub>-A<sub>0</sub>)/(A<sub>T</sub>-A<sub>1</sub>)] vs. log[TFA]. The slope of the line is 1.0 for each protonation step, thus confirming that one proton is stepwise added to the porphyrin in CHCl<sub>3</sub> to generate the *mono*- and *bis*-protonated derivatives, respectively. The stepwise protonation constants of **2** were calculated from the zero intercept of the Hill plots as logK<sub>H1</sub> = 7.2 and logK<sub>H2</sub> = 3.2 (see inserts in Fig. 1). Similar spectral changes were seen in CHCl<sub>3</sub> for the other three investigated porphyrins and the spectral data for each *mono*- and *bis*-protonated porphyrin are summarized in Table 1. The calculated protonation constants (logK<sub>H1</sub>, logK<sub>H2</sub> and logβ<sub>H2</sub>) are summarized in Table 2.

As seen in Table 1, and also in Fig. 1, the conversion of (CH<sub>3</sub>Ph)<sub>4</sub>NCPH<sub>2</sub> to [(CH<sub>3</sub>Ph)<sub>4</sub>NCPH<sub>3</sub>]<sup>+</sup> and then to [(CH<sub>3</sub>Ph)<sub>4</sub>NCPH<sub>4</sub>]<sup>2+</sup> results in a ~12 nm shift of the Soret band for each added proton. At the same time there is a red shift of 50–60 nm in the longest wavelength Q-band with increase in the number of added protons. This is discussed further in a later section of the manuscript.

**Inner-2H forms in DMF.** Two stepwise protonations were also observed for each investigated porphyrin in DMF and examples of the two sets of spectral changes which occur during a titration of (CH<sub>3</sub>Ph)<sub>4</sub>NCPH<sub>2</sub> **2** with TFA are shown in Fig. 2. Again, the slope of the Hill plot for each protonation step of **2** is 1.0, indicating that one proton is added to the inner-2H form of the porphyrin in each step to generate first the *mono*-protonated porphyrin [(CH<sub>3</sub>Ph)<sub>4</sub>NCPH<sub>3</sub>]<sup>+</sup> and then the *bis*-protonated derivative [(CH<sub>3</sub>Ph)<sub>4</sub>NCPH<sub>4</sub>]<sup>2+</sup>, with the equilibrium constants being calculated as logK<sub>H1</sub> = 4.4, logK<sub>H2</sub> = 2.5 and logβ<sub>H2</sub> = 6.9.

As seen in Fig. 2 the *mono*-protonation of **2** in DMF, with formation of [(CH<sub>3</sub>Ph)<sub>4</sub>NCPH<sub>3</sub>]<sup>+</sup>, results in a red-shift of the Soret band from 443 to 459 nm and the appearance of a broad Q-band with maxima at 779 and 839 nm. Further additions of TFA to solution then lead to generation of the *bis*-protonated porphyrin [(CH<sub>3</sub>Ph)<sub>4</sub>NCPH<sub>4</sub>]<sup>2+</sup>, which exhibits a spectrum having a Soret band at 465 nm and two well-defined Q-bands at 673 and 839 nm. This spectrum is almost identical to the spectrum of the *bis*-protonated **2** in CHCl<sub>3</sub>. The UV-visible spectrum of compounds **3** as well as **4** are



also similar to each other in DMF and  $\text{CHCl}_3$  after the addition of two protons but this is not the case for the  $\text{OCH}_3$  derivative (cpd **1**) where different UV-spectra are observed in the two solvents. This is true both in the case of the initial neutral compound and the protonated form of the porphyrin.

With the one exception mentioned above, five different types of UV-visible spectra are observed for each *N*-confused porphyrin depending upon the specific solvent and the degree of protonation. There are two types of spectra for the neutral porphyrins (one for each tautomer) and two types for the *mono*-protonated porphyrins as shown in Fig. 3 (again, one for each tautomer). However, the bis-protonated porphyrins in  $\text{CH}_2\text{Cl}_2$  and DMF are characterized by the same spectrum, independent of solvent. This is consistent with the fact that there are different locations on the macrocycle for the nitrogens being protonated in the first step but not in the second where the conversion of  $[(\text{CH}_3\text{Ph})_4\text{NCPH}_3]^+$  to  $[(\text{CH}_3\text{Ph})_4\text{NCPH}_4]^{2+}$  involves the addition of one proton to a single unprotonated nitrogen within the porphyrin core. Quite similar  $\log K_{\text{H}2}$  values are also observed in DMF and  $\text{CHCl}_3$  (see Table 2) but the measured value of  $\log K_{\text{H}1}$  is larger in  $\text{CHCl}_3$  than in DMF due to the

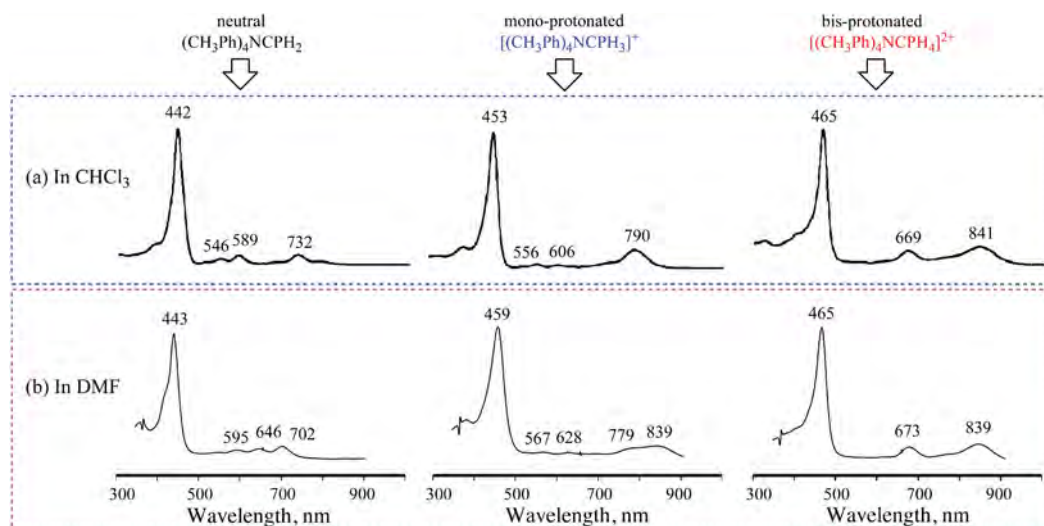
fact that the outer nitrogen on the inverted pyrrole in the inner-3H form of the porphyrin is more easily accessible than the nitrogens within the core of the macrocycle in its inner-2H form.

The five types of spectra are shown in Fig. 3 and a summary of the reactions which occur for each tautomer is given in Scheme 1.

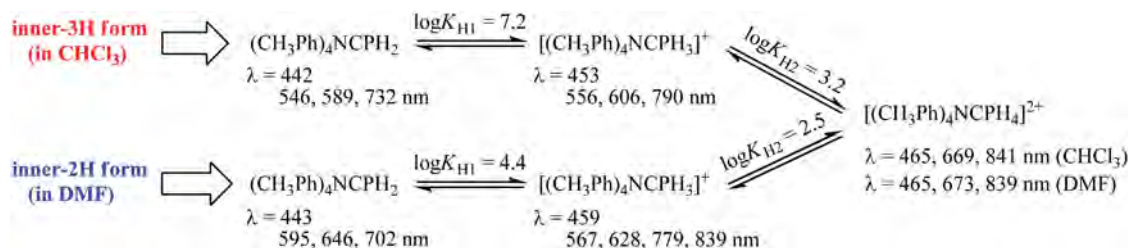
### Deprotonation in DMF

Figure 4 illustrates the spectral changes which occur when TBAOH is added to a solution of  $(\text{CPh})_4\text{NCPH}_2$  **4** in DMF. As the reaction of **4** with TBAOH proceeds, the Soret band is red-shifted from 443 to 454 nm while the most intense Q-band at 700 nm decreases in intensity and three new Q-bands grow in at 593, 638 and 688 nm. A linear Hill plot with a slope of 1.0 is obtained in the titration (see insert in Fig. 4), thus indicating generation of *mono*-deprotonated  $[(\text{CPh})_4\text{NCPH}]^-$  under the given solution conditions. The equilibrium constant was then obtained from the zero intercept of the Hill plot and the  $\log K_{\text{OH}1}$  value calculated as 4.8.

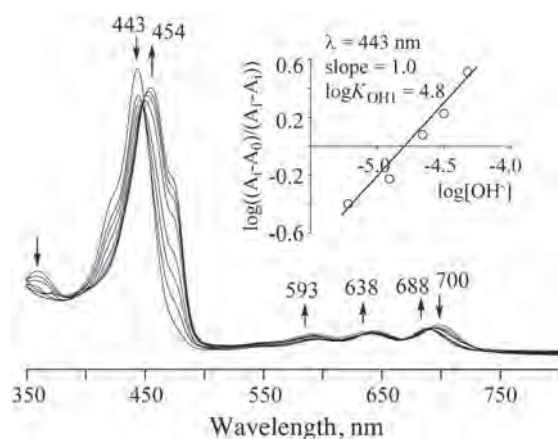
The *N*-confused free-base porphyrins, **1–3**, also react with TBAOH in a similar manner to quantitatively



**Fig. 3.** UV-visible spectra of the neutral, *mono*-protonated and bis-protonated compound **2** in (a)  $\text{CHCl}_3$  and (b) DMF



**Scheme 1.** Stepwise protonation of  $(\text{CH}_3\text{Ph})_4\text{NCPH}_2$  in its inner-3H and inner-2H forms



**Fig. 4.** UV-visible spectral changes of  $(\text{CIPh})_4\text{NCPH}_2$  **4** during a titration with TBAOH in DMF (insert is the Hill plot for determination of the dissociation number of protons and deprotonation equilibrium constants)

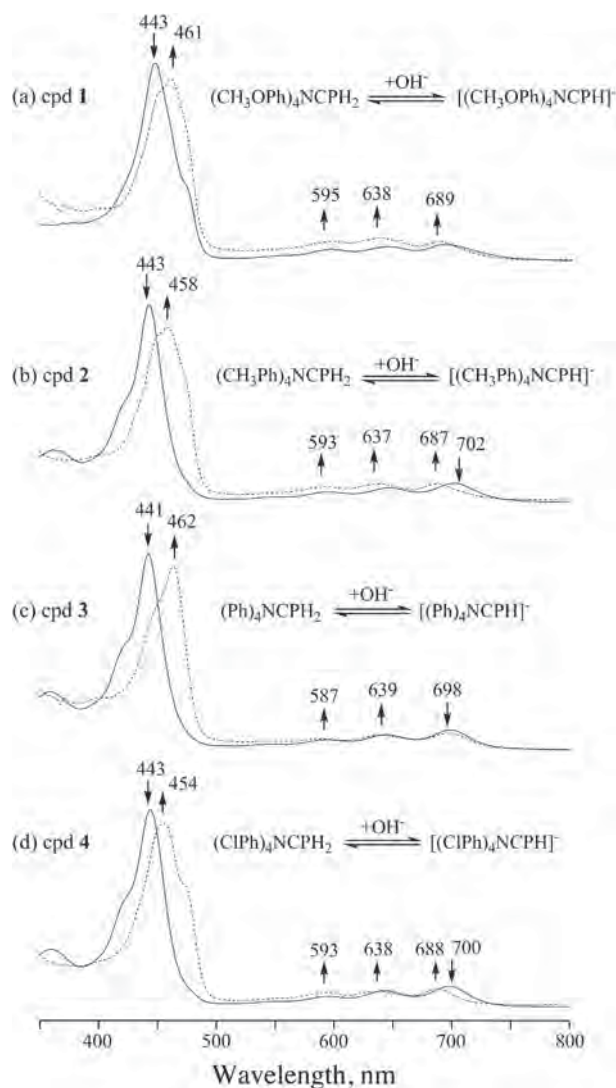
generate  $[(\text{XPh})_4\text{NCPH}]^-$  under the same solution conditions. The spectrum of the four examined *N*-confused porphyrins are shown in Fig. 5 before (—) and after (---) deprotonation and a summary of the spectral data for each  $[(\text{XPh})_4\text{NCPH}]^-$  species along with the experimentally determined deprotonation constants are listed in Table 3. The deprotonation constants range from  $\log K_{\text{OH}1} = 4.5$  for compound **1** to  $\log K_{\text{OH}1} = 4.8$  for compounds **3** and **4**. The small differences in  $\log K_{\text{OH}1}$  for compounds **1–4** suggests a weak substituent effect on the central nitrogens of the investigated *N*-confused porphyrins.

### Effect of proton addition on UV-visible spectra

Independent of the solvent, a linear correlation is seen between the number of protons added to the porphyrin macrocycle and the maximum absorbance of bands in the UV-visible spectrum. A plot of  $\lambda_{\text{max}}$  vs. number of protons added to the nitrogens of the initial porphyrin is given in Fig. 6. The shift of  $\lambda_{\text{max}}$  per each added proton amounts to 12 nm for the Soret band and 53 nm for the selected Q-band in  $\text{CHCl}_3$ . A similar linear correlation is seen in DMF where the Soret band shifts by 11 nm per added proton and the Q-band by 66 nm per added proton. This correlation is shown in Fig. 6b. Red-shifts of the absorption bands upon protonation have also been observed for structurally related corroles [38].

### Effect of substituent on protonation constants

It is known that the relative acidity of porphyrins and corroles can be directly related to the electron-withdrawing or electron-donation properties of substituents on the *meso*-phenyl groups of the macrocycle [38]. This is also the case for the currently examined compounds in DMF but not in  $\text{CHCl}_3$ , as shown in Fig. 7 where the measured



**Fig. 5.** UV-visible spectra of compounds **1–4** in their neutral (—) and *mono*-deprotonated (---) forms after titration with TBAOH in DMF

protonation constants are plotted vs.  $4\sigma$ ,  $\sigma$  being the Hammett substituent constant taken from the literature [39]. Linear relationships are seen for the plots of  $\log K_{\text{H}1}$  and  $\log K_{\text{H}2}$  vs.  $4\sigma$  in DMF (Fig. 7b), with the larger  $\log K_{\text{H}}$  values being obtained for the porphyrins with electron-donating substituents. However, no evident correlation is seen between  $\log K_{\text{H}}$  values and  $4\sigma$  in  $\text{CHCl}_3$  (Fig. 7a). The first proton addition in  $\text{CHCl}_3$  is much larger than the first proton addition in DMF, consistent with two different types of nitrogens being involved in the first protonation step, an outer pyrrole nitrogen in  $\text{CHCl}_3$  and an inner core pyrrole nitrogen in DMF.

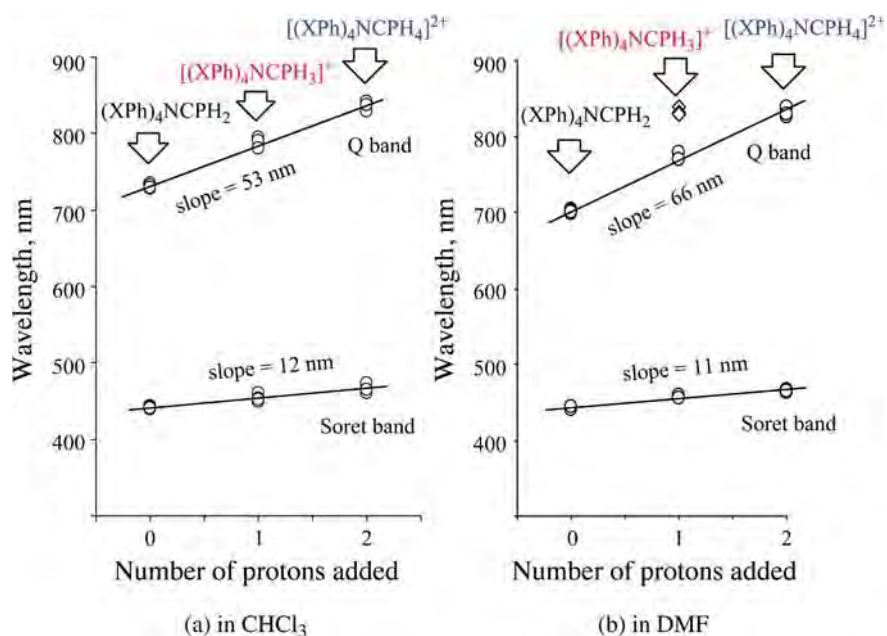
### Proposed site of the protonation and deprotonation

As discussed above, protonation of the *N*-confused free-base porphyrins with TFA occurs in two steps, both

**Table 3.** UV-visible spectral data ( $\lambda_{\max}$ , nm) of *mono*-deprotonated compounds **1–4** in DMF with added tbaoh and the deprotonation constants

Macrocycle	Compound	Deprotonation constant
<i>N</i> -confused porphyrin	$(\text{XPh})_4\text{NCPH}_2 + \text{OH}^- \rightleftharpoons [(\text{XPh})_4\text{NCPH}]^- + \text{H}_2\text{O}$	
	$(\text{CH}_3\text{OPh})_4\text{NCPH}_2$ <b>1</b>	$\log K_{\text{OH1}} = 4.5$
	$(\text{CH}_3\text{Ph})_4\text{NCPH}_2$ <b>2</b>	$\log K_{\text{OH1}} = 4.6$
	$(\text{Ph})_4\text{NCPH}_2$ <b>3</b>	$\log K_{\text{OH1}} = 4.8$
	$(\text{ClPh})_4\text{NCPH}_2$ <b>4</b>	$\log K_{\text{OH1}} = 4.8$
Corrole <sup>a</sup>	$(\text{Cor})\text{H}_3 + \text{OH}^- \rightleftharpoons [(\text{Cor})\text{H}_2]^- + \text{H}_2\text{O}$	
	$(\text{CH}_3\text{Ph})_3\text{CorH}_3$	$\log K_{\text{OH1}} = 3.6$
	$(\text{CF}_3\text{Ph})_3\text{CorH}_3$	$\log K_{\text{OH1}} = 4.9$
	$(\text{CNPh})_3\text{CorH}_3$	$\log K_{\text{OH1}} = 5.0$
	$(\text{CNPh})(\text{Cl}_2\text{Ph})_2\text{CorH}_3$	$\log K_{\text{OH1}} = 4.7$
	$(\text{CNPh})((\text{CH}_3)_3\text{Ph})_2\text{CorH}_3$	$\log K_{\text{OH1}} = 4.4$
	$(\text{F}_5\text{Ph})_3\text{CorH}_3$	$\log K_{\text{OH1}} = 6.4$

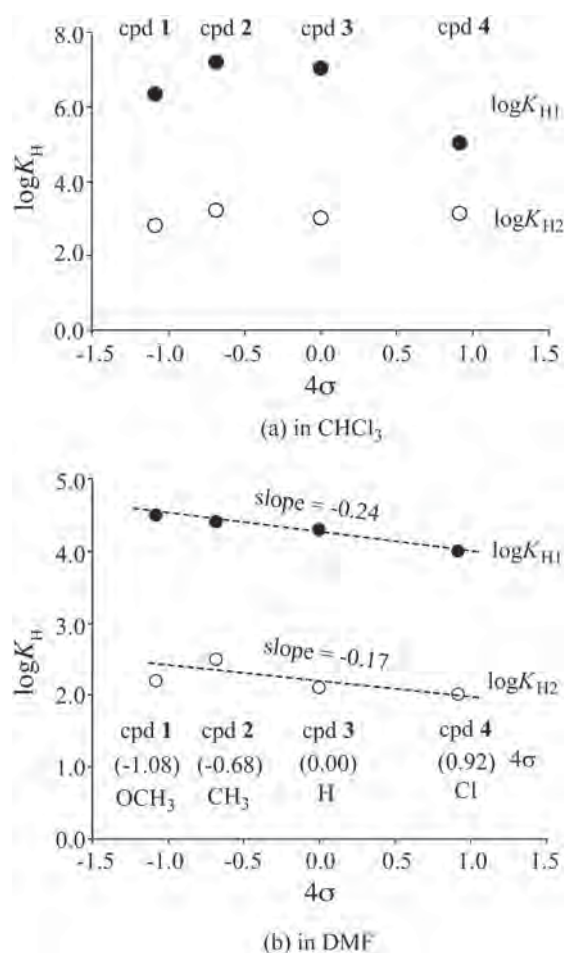
<sup>a</sup>Data measured in PhCN by titration with piperidine (Ref. 38).

**Fig. 6.** Plots of the Soret and Q-band wavelengths (nm, bold data in Table 1) vs. the number of protons added to  $(\text{XPh})_4\text{NCPH}_2$  in (a)  $\text{CHCl}_3$  and (b) DMF

in  $\text{CHCl}_3$  and DMF but the UV-visible spectrum of the neutral and *mono*-protonated porphyrins depends upon the solvent, as does the magnitude of the first protonation constants. This difference is due to the fact that different tautomers are seen in the two solvents, an inner 3H-form in  $\text{CHCl}_3$  and an inner 2H-form in DMF.

Although the protonation constants and spectroscopic data seem definitive, a theoretical calculation of the ESP (electrostatic potential) atomic charge is useful in

some cases for determination of the electrophilic and nucleophilic reaction sites [40]. Thus, in order to better assign the protonation and deprotonation sites of the *N*-confused free-base porphyrins, the ESP atomic charge ( $e$ ) of the four nitrogen atoms (labeled as N2, N21, N23 and N24 in Table 4) for each compound was calculated at the B3LYP/6-31+G(d,p) level with the B3LYP/6-31G(d) geometries in  $\text{CHCl}_3$  and DMF and the data are given in Table 4.



**Fig. 7.** Plots of protonation constants ( $\log K_a$ ) for compounds **1–4** vs. the Hammett substituent constant ( $4\sigma$ ) in (a)  $\text{CHCl}_3$  and (b) DMF

As seen from Table 4, the calculated charge on N2 is more positive than that on N23 in DMF, suggesting that the hydrogen on N2 is easiest to deprotonate.

**Table 4.** Calculated electrostatic potential (ESP) atomic charge (e) on nitrogen atoms of *N*-confused free-base tetraarylporphyrins

Compound	N2	N21	N23	N24
<b>in <math>\text{CHCl}_3</math></b>				
	1 <sup>st</sup> protonated		2 <sup>nd</sup> protonated	
( $\text{OCH}_3\text{Ph}$ ) <sub>4</sub> NCPH <sub>2</sub> 1	-0.640	-0.234	-0.642	-0.236
( $\text{CH}_3\text{Ph}$ ) <sub>4</sub> NCPH <sub>2</sub> 2	-0.650	-0.132	-0.562	-0.162
(Ph) <sub>4</sub> NCPH <sub>2</sub> 3	-0.797	-0.477	-0.528	-0.460
(ClPh) <sub>4</sub> NCPH <sub>2</sub> 4	-0.609	-0.131	-0.528	-0.111
<b>in DMF</b>				
	1 <sup>st</sup> deprotonated	2 <sup>nd</sup> protonated		1 <sup>st</sup> protonated
( $\text{OCH}_3\text{Ph}$ ) <sub>4</sub> NCPH <sub>2</sub> 1	-0.118	-0.596	-0.710	-0.597
( $\text{CH}_3\text{Ph}$ ) <sub>4</sub> NCPH <sub>2</sub> 2	-0.005	-0.567	-0.507	-0.590
(Ph) <sub>4</sub> NCPH <sub>2</sub> 3	-0.072	-0.508	-0.299	-0.550
(ClPh) <sub>4</sub> NCPH <sub>2</sub> 4	-0.042	-0.545	-0.490	-0.530

Comparisons between the calculated charge on N2 and that on N23, show that N2 is easier to protonate than N23 for the inner-3H form of the porphyrins **2–4** in  $\text{CHCl}_3$ . In the case of the inner-2H forms of the porphyrin in DMF, the N24 atom should be the first to protonate because it has a more negative charge than N21 which is the other possible nitrogen protonation site in compounds **1–3**.

The second protonation of **1–4** should occur on the N23 atom in  $\text{CHCl}_3$  and on the N21 atom in DMF. The *mono*- and *bi*-protonated sites of the *N*-confused free-base porphyrins in these two solvents are then proposed to be protonated as shown in Scheme 2. It should again be pointed out that two different tautomeric forms of the porphyrin can exist in solution and the schematically illustrated structures shown in Scheme 2 are the most probable forms in  $\text{CHCl}_3$  and DMF, as suggested by the spectroscopic data as well as by DFT calculations.

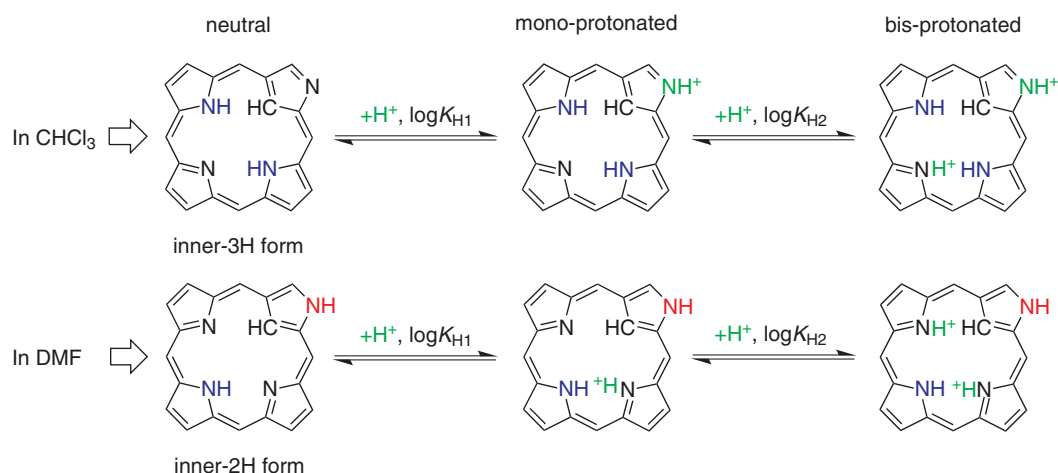
## EXPERIMENTAL

### Chemicals

Dichloromethane ( $\text{CH}_2\text{Cl}_2$ ), *N,N'*-dimethylformamide (DMF), trifluoroacetic acid (TFA, 99.9%) and tetra-*n*-butylammonium hydroxide (TBAOH, 1.0 M in methanol) were purchased from Sigma–Aldrich Chemical Co. and used as received for experiments.

### Determination of protonation and deprotonation equilibrium constants

A series of  $\text{CHCl}_3$  or DMF solutions containing TFA (TBAOH) in different concentrations was prepared and used as the acid-titration reagent. Microliter quantities of TFA (TBAOH) in  $\text{CHCl}_3$  or DMF were added gradually to a 6.0 mL  $\text{CHCl}_3$  or DMF solution of the *N*-confused free-base porphyrin in a 1.0 cm home-made cell and the spectral changes monitored after each addition.



**Scheme 2.** Proposed protonation sites of the *N*-confused free-base porphyrins in  $\text{CHCl}_3$  and DMF

UV-visible spectra were recorded with a Hewlett-Packard Model 8453 diode array spectrophotometer at 298 K. Changes in spectra during the titration with TFA or TBAOH were analyzed as a function of the concentration of added acid and base, using the Hill equation [37] to calculate equilibrium constants for proton addition or dissociation in the nonaqueous solvent,  $\text{CHCl}_3$  and DMF.

### Theoretical calculations

Density functional theory (DFT) calculations were performed with the Gaussian 09 program [41]. Geometry optimizations were carried out within unconstrained C1 symmetry. All structures in  $\text{CH}_2\text{Cl}_2$  solution (dielectric constant,  $\epsilon = 8.93$ ) and DMF solution (dielectric constant,  $\epsilon = 36.7$ ) were tested to be stable using the polarized continuum model (PCM) [42–47] with the 6-31G(d) basis set at the B3LYP level. The electrostatic potential (ESP) atomic charges [48] at the B3LYP/6-31+G (d, p) level were performed to obtain more accurate charges with the B3LYP/6-31G(d) geometries in solution.

### CONCLUSION

The investigated *N*-confused free-base porphyrins can be stepwise protonated to give *mono*- and *bis*-protonated porphyrins upon addition of acid into the nonaqueous solvent. A two step protonation process occurs for both the inner-3H form of the porphyrin in  $\text{CHCl}_3$  and the inner-2H form in DMF but only a single step deprotonation process is observed for the same porphyrins in DMF. The inner-3H form of the porphyrin is easier to protonate than the same porphyrin in its inner-2H form. As is expected, protonation and/or deprotonation of the *N*-confused porphyrins has a significant effect on the UV-visible spectra of the compounds. The two tautomers have different UV-visible spectra and this fact might be used to predict the form of the porphyrin in a given solvent.

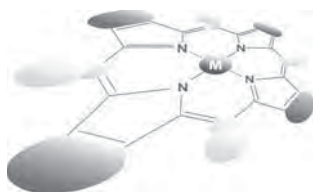
### Acknowledgements

This work was supported by grants from the Natural Science Foundation of China (Grant No. 21071067) and the Robert A. Welch Foundation (KMK, grant no. E-680).

### REFERENCES

1. Toganoh M and Furuta H. *Chem. Commun.* 2012; **48**: 937–954.
2. Li XF, Liu HC, Zheng AT, Yu XY and Yi PG. *Youji Huaxue* 2011; **31**: 166–175.
3. Harvey JD and Ziegler CJ. *J. Inorg. Biochem.* 2006; **100**: 869–880.
4. Maeda H and Furuta H. *Pure Appl. Chem.* 2006; **78**: 29–44.
5. Chmielewski PJ and Latos-Grazynski L. *Coord. Chem. Rev.* 2005; **249**: 2510–2533.
6. Srinivasan A and Furuta H. *Acc. Chem. Res.* 2005; **38**: 10–20.
7. Harvey JD and Ziegler CJ. *Coord. Chem. Rev.* 2003; **247**: 1–19.
8. Furuta H, Maeda H and Osuka A. *Chem. Commun.* 2002; 1795–1804.
9. Toganoh M and Furuta H. In *Handbook of Porphyrin Science*, Vol. 2, Kadish KM, Smith KM and Guilard R. (Eds.) World Scientific: New Jersey, 2010; pp 295–367.
10. Maeda H, Osuka A, Ishikawa Y, Aritome I, Hisaeda Y and Furuta H. *Org. Lett.* 2003; **5**: 1293–1296.
11. Furuta H, Ogawa T, Uwatoko Y and Araki K. *Inorg. Chem.* 1999; **38**: 2676–2682.
12. Zilbermann I, Maimon E, Ydgar R, Shames AI, Korin E, Soifer L and Bettelheim A. *Inorg. Chem. Commun.* 2004; **7**: 1238–1241.
13. Maeda H, Ishikawa Y, Matsuda T, Osuka A and Furuta H. *J. Am. Chem. Soc.* 2003; **125**: 11822–11823.

14. Chen WC and Hung CH. *Inorg. Chem.* 2001; **40**: 5070–5071.
15. Scott Bohle D, Chen WC and Hung CH. *Inorg. Chem.* 2002; **41**: 3334–3336.
16. Wang YC, Chen JH, Wang SS and Tung JY. *Inorg. Chem.* 2013; **52**: 10711–10713.
17. Fields KB, Engle JT, Sripothongnak S, Kim C, Zhang XP and Ziegler CJ. *Chem. Commun.* 2011; **47**: 749–751.
18. Harvey JD and Ziegler CJ. *Chem. Commun.* 2004; 1666–1667.
19. Ikawa Y, Touden S, Katsumata S and Furuta H. *Bioorg. Med. Chem.* 2013; **21**: 6501–6505.
20. Furuta H, Ishizuka T, Osuka A, Dejima H, Nakagawa H and Ishikawa Y. *J. Am. Chem. Soc.* 2001; **123**: 6207–6208.
21. Ghosh A. *Angew. Chem., Int. Ed. Engl.* 1995; **34**: 1028–1030.
22. Ziegler CJ, Erickson NR, Dahlby MR and Nemykin VN. *J. Phys. Chem. A* 2013; **117**: 11499–11508.
23. Aleman EA, Rajesh CS, Ziegler CJ and Modarelli DA. *J. Phys. Chem. A* 2006; **110**: 8605–8612.
24. Aleman EA, Rocha JM, Wongwitwichote W, Mora-Tovar LAM and Modarelli DA. *J. Phys. Chem. A* 2011; **115**: 6456–6471.
25. Belair JP, Ziegler CJ, Rajesh CS and Modarelli DA. *J. Phys. Chem. A* 2002; **106**: 6445–6451.
26. Furuta H, Morimoto T and Osuka A. *Org. Lett.* 2003; **5**: 1427–1430.
27. Furuta H, Asano T and Ogawa T. *J. Am. Chem. Soc.* 1994; **116**: 767–768.
28. Chemielewski PJ, Latos-Grażyński L, Rachlewicz K and Glowiak T. *Angew. Chem., Int. Ed. Engl.* 1994; **33**: 779–781.
29. Xue SL, Ou ZP, Ye LN, Fang YY, Jiang XQ and Kadish KM. *Chem. Eur. J.* 2015; DOI:10.1002/chem.201405570.
30. (a) Fang YY, Bhyrappa P, Ou ZP and Kadish KM. *Chem. Eur. J.* 2014; **20**: 524–532; (b) Inisan C, Sailard JY, Guillard R, Tabard A and Mest YL. *New J. Chem.* 1998; 823–830.
31. De Luca G, Romeo A, Scolaro LM, Ricciardi G and Rosa A. *Inorg. Chem.* 2007; **46**: 5979–5988.
32. Su B, Li F, Partovi-Nia R, Gros C, Barbe JM, Samec Z and Girault HH. *Chem. Commun.* 2008; 5037–5038.
33. Honda T, Kojima T and Fukuzumi S. *Chem. Commun.* 2009; 4994–4996.
34. Chemielewski PJ and Latos-Grażyński L. *J. Chem. Soc., Perkin Trans. 2* 1995; 503–509.
35. Chemielewski PJ, Siczek M and Szterenbergl L. *Inorg. Chem.* 2011; **50**: 6719–6736.
36. Shaw JL, McMurry JL, Salehi P and Stovall A. *J. Porphyrins Phthalocyanines* 2014; **18**: 231–239.
37. Ellis PE, Linard JE, Szymanski T, Jones RD, Budge JR and Basolo F. *J. Am. Chem. Soc.* 1980; **102**: 1889–1896.
38. Shen J, Ou ZP, Shao JG, Galezowski M, Gryko DT and Kadish KM. *J. Porphyrins Phthalocyanines* 2007; **11**: 269–276.
39. Zuman P. *Substituents Effects in Organic Polarography*, Plenum Press: New York, 1967.
40. Lu T and Chen FW. *Acta Phys. Chem. Sin.* 2012; **28**: 1–18.
41. Frisch MJ. *Gaussian 09, Revision A. 02*, Gaussian, Inc., Wallingford, CT, 2009.
42. Tomasi J and Persico M. *Chem. Rev.* 1994; **94**: 2027–2094.
43. Cossi M, Barone V, Cammi R and Tomasi J. *Chem. Phys. Lett.* 1996; **255**: 327–335.
44. Barone V, Cossi M and Tomasi J. *J. Chem. Phys.* 1997; **107**: 3210–3221.
45. Cossi M and Barone V. *J. Chem. Phys.* 1998; **109**: 6246–6254.
46. Barone V, Cossi M and Tomasi J. *J. Comput. Chem.* 1998; **19**: 404–417.
47. Cramer CJ and Truhlar DG. *Chem. Rev.* 1999; **99**: 2161–2200.
48. Chirlian LE and Francl MM. *J. Comp. Chem.* 1987; **8**: 894–905.



## Energy-transfer studies on phthalocyanine–BODIPY light harvesting pentad by laser flash photolysis

Mohamed E. El-Khouly<sup>a</sup>, Cem Göl<sup>b</sup>, Morad M. El-Hendawy<sup>a</sup>, Serkan Yeşilot<sup>b</sup> and Mahmut Durmuş<sup>\*b</sup>

<sup>a</sup>Department of Chemistry, Faculty of Science, Kafrelsheikh University, Kafr El-Sheikh 33516, Egypt

<sup>b</sup>Gebze Technical University, Department of Chemistry, PO Box 141, Gebze 41400, Kocaeli, Turkey

*Dedicated to Professor Shunichi Fukuzumi on the occasion of his retirement*

Received 15 October 2014

Accepted 17 November 2014

**ABSTRACT:** A molecular pentad, comprised of zinc phthalocyanine (ZnPc) with four boron dipyrromethene units (BODIPY) have been examined by femtosecond and nanosecond laser flash photolysis to explore its photoinduced intramolecular events from the excited BODIPY. The geometry optimization showed that the phthalocyanine moiety is completely symmetric and form perfect square planar complex with zinc. The absorption spectrum of ZnPc-BODIPY pentad covers most of the visible region (*ca.* 300–750 nm), which clearly is an advantage for capturing solar energy. The excitation transfer from the singlet BODIPY to ZnPc is envisioned due to good spectral overlap of the BODIPY emission and ZnPc absorption spectra. Femtosecond laser flash photolysis studies provided concrete evidence for the occurrence of energy transfer from the singlet excited BODIPY to ZnPc in tetrahydrofuran. The kinetic study of energy transfer measured by monitoring the decay of the BODIPY emission revealed fast energy transfer ( $5.90 \times 10^{10} \text{ s}^{-1}$ ) in the molecular pentad. Since the electron transfer from the singlet ZnPc to BODIPY is thermodynamically not feasible, the singlet ZnPc decayed to populates the triplet ZnPc, in addition to the ground state. These findings suggest the potential of the examined ZnPc-BODIPY pentad to be efficient photosynthetic antenna in the artificial photosynthetic systems.

**KEYWORDS:** boron dipyrromethene (BODIPY), phthalocyanine, energy transfer, light harvesting, laser photolysis.

## INTRODUCTION

Energy-transfer cassette consists of two or more fluorescent units attached to the same (or similar) molecule. One unit acts as an energy donor and the other as an energy acceptor. The energy donor absorbs light and this energy is then transferred to the acceptor, which then emits the light at a longer wavelength. The efficiency of the energy-transfer process depends on the spectral overlap of the donor emission with the acceptor absorbance, the distance between the donor and the

acceptor, the relative orientation of donor and acceptor, and the effectiveness of other de-excitation modes [1]. Toward the goal of constructing artificial photosynthetic systems that have ability to convert the light into chemical energy, BF<sub>2</sub>-chelated dipyrromethene compounds (abbreviated as BODIPY), which are derived from 4,4-difluoro-1,3,5,7-tetramethyl-4-bora-3a, 4-adiaza *s*-indacene, have attracted much attention in the recent years as antenna molecules. Due to their intense fluorescence, BODIPYs have found useful in building new energy-transfer cassettes [2]. Because of the similarity of their structures, energy-transfer cassettes containing BODIPY and porphyrin [3–11] units have received much attention for their applications as solar energy harvesting systems. The unique features of BODIPYs make them useful in a

\*Correspondence to: Mohamed E. El-Khouly, email: mohamedelkhouly@yahoo.com; Mahmut Durmuş, email: durmus@gyte.edu.tr

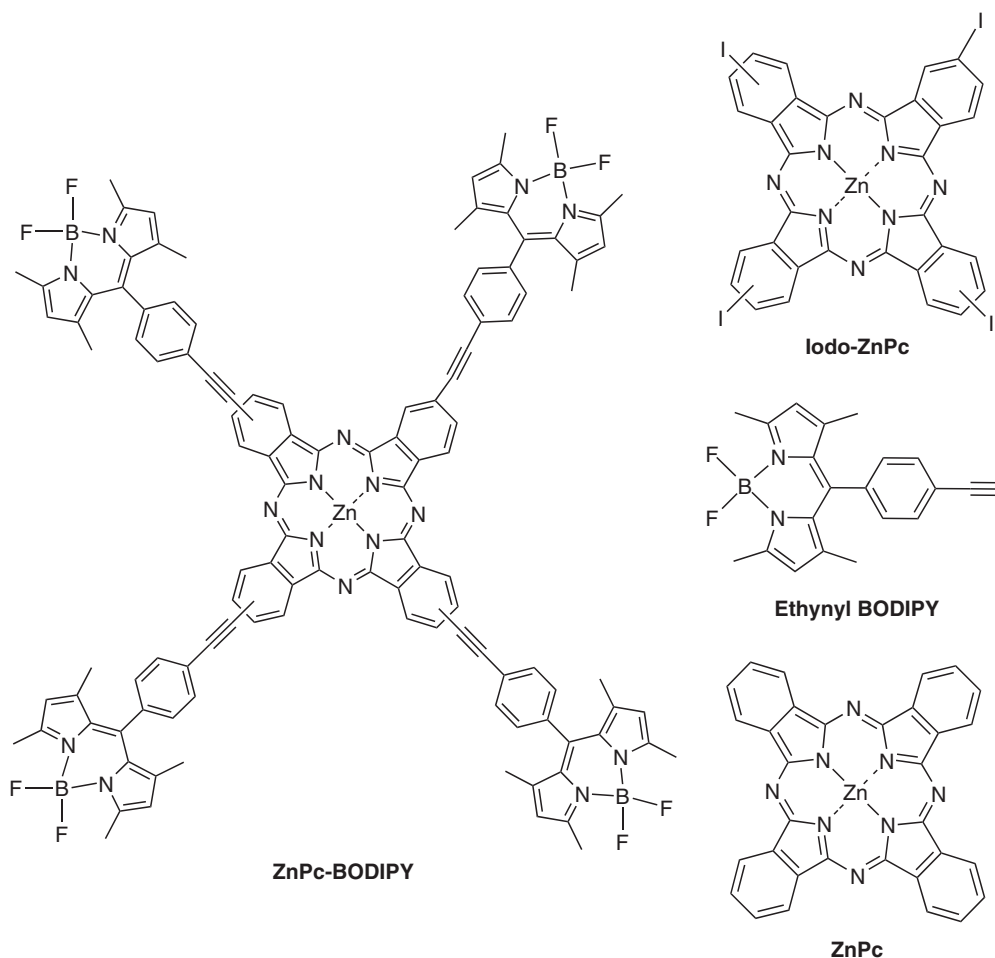
range of applications including artificial photosynthesis, luminescent labeling agents [12–14], fluorescent switches [15, 16], chemosensors [17–20], holographic systems for digital information storage [21–23], and laser dyes [24].

Phthalocyanine (Pc) compounds have mostly taken part in many fields ranging from industrial [25], technological [26] to biomedical applications [27] owing to their suitable properties such as high solubility of substituted derivatives in most common solvents, long wavelength absorption (near IR), high triplet quantum yields, and long triplet lifetime [28–31]. Addition to these appropriate properties, capability of efficient singlet oxygen generation make phthalocyanines as significant photosensitizers [32, 33] for photodynamic therapy (PDT) cancer applications [34].

In literature, a few studies are known about compounds containing BODIPY and phthalocyanine on the same molecule. Most of these compounds are axially BODIPY substituted boron subphthalocyanines or silicon phthalocyanines [35–38]. Another study is unsymmetrical zinc phthalocyanine derivative bearing one BODIPY group at the peripheral position [39].

Addition to these works, the photophysical and photochemical properties of a novel dye compound contains four BODIPY groups at the peripheral positions of the phthalocyanine framework was studied in our previous work [40]. We have recently reported the synthesis, photophysical and photochemical properties of unsymmetrical zinc phthalocyanines containing one, two or three BODIPY groups on the phthalocyanine core [41]. Preliminary results of this study were shown that the ZnPc-BODIPY pentad dye systems exhibited efficient energy transfer from the excited BODIPY units to the phthalocyanine core. Furthermore, the pentad produced efficiently singlet oxygen ( $\Phi_{\Delta} = 0.69$ ) suggesting its potential as good photosensitizer in photodynamic therapy (PDT) applications for cancer treatment [40].

In this report, the energy transfer process for symmetrical pentad bearing four BODIPY units connected to the phthalocyanine core *via* an ethynyl linkage at peripheral positions (ZnPc-BODIPY; Fig. 1) was deeply investigated by femtosecond and nanosecond laser flash photolysis to explore photoinduced intramolecular events of the light harvesting pentad.



**Fig. 1.** Molecular structures of ZnPc-BODIPY pentad, as well as the reference compounds



## RESULTS AND DISCUSSION

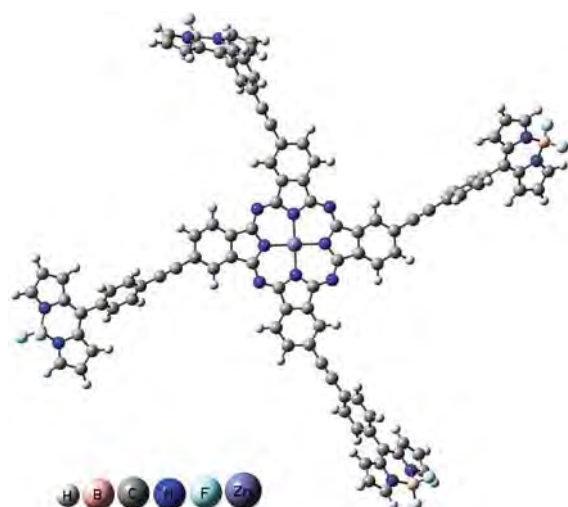
The geometry of ZnPc-BODIPY pentad was optimized in the gas phase using the long range correlated hybrid functional wB97xD that implemented in Gaussian 09 [42]. 6-311g(d,p) basis set was used for all atoms. The calculations showed that the phthalocyanine moiety is completely symmetric and form perfect square planar complex with zinc (Fig. 2). The dihedral angle between BODIPY and phenyl ring is about 125°. The center-to-center distance between the zinc atom of phthalocyanine and boron atom of BODIPY was found to be around 17.7 Å.

### Steady-state electronic absorption measurements

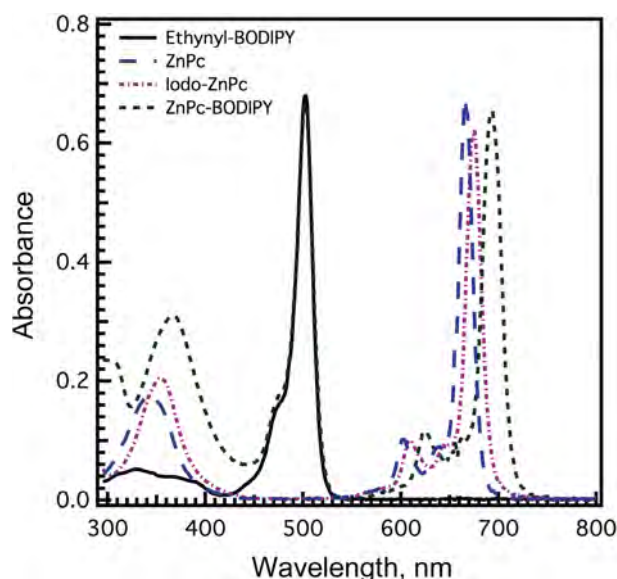
Figure 3 shows the normalized electronic absorption spectra of the ZnPc-BODIPY pentad as well ZnPc and Ethynyl-BODIPY reference compounds in tetrahydrofuran (THF). The spectrum of Ethynyl-BODIPY exhibited a sharp Q-band at 502 nm with a vibronic band at 474 nm and weak B-bands at the around 300–400 nm. The absorption bands of Iodo-ZnPc reference were observed at 354, 609, 644 and 675 nm, which is around 10 nm red shifted compared to the unsubstituted ZnPc. When turning to the ZnPc-BODIPY pentad, one can note that Q-band of ZnPc is red shifted by about 19 nm compared with that of the iodo-ZnPc, suggesting significant ground-state interactions between ZnPc and BODIPY units in the pentad. The absorption spectrum of ZnPc-BODIPY pentad covers most of the visible region (*ca.* 300–750 nm), which clearly is an advantage for capturing solar energy.

### Steady-state fluorescence measurements

Upon excitation at 480 nm, Ethynyl-BODIPY exhibited a strong fluorescence emission at 517 nm



**Fig. 2.** wB97xD/6-311g(d,p)-optimized geometry of ZnPc-BODIPY pentad. The symbols of atoms are depicted in the figure



**Fig. 3.** Electronic absorption spectra of Ethynyl-BODIPY, ZnPc, Iodo-ZnPc and ZnPc-BODIPY pentad in THF. The spectra of BODIPY and ZnPc-BODIPY were normalized at the BODIPY absorption maxima

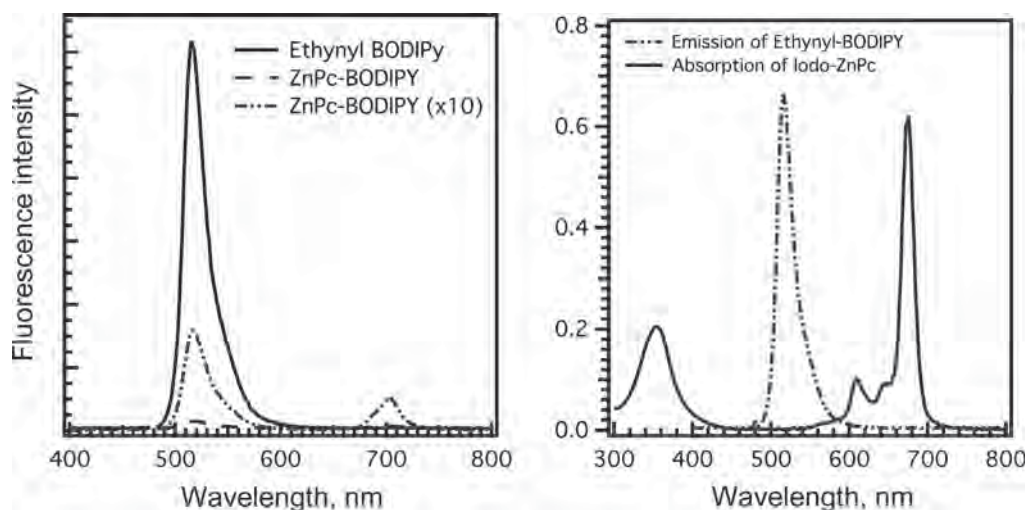
(Fig. 4) with a fluorescence quantum yield ( $\Phi_f$ ) of 0.55 [43] in tetrahydrofuran. Upon excitation with 620 nm, the fluorescence bands of the ZnPc and Iodo-ZnPc were observed in the visible light at 675 and 683 nm, respectively. The lower fluorescence intensity of Iodo-ZnPc compared to ZnPc can be rationalized by the increasing in the intersystem crossing caused by the heavy atom effect of four iodine atoms on the phthalocyanine framework.

For ZnPc-BODIPY pentad, in which the BODIPY is linked to ZnPc, the BODIPY emission was greatly reduced yield ( $\Phi_f = 0.08$ ). Concomitantly, a strong fluorescence at 701 nm appeared. By making reference to the fluorescence spectrum of ZnPc reference (Fig. S1, Supporting information), this band can be assigned to the ZnPc unit of the pentad. This observation clearly showed energy transfer from the singlet-excited state of Ethynyl-BODIPY (2.40 eV) moiety to the lower energy state of ZnPc unit (1.76 eV).

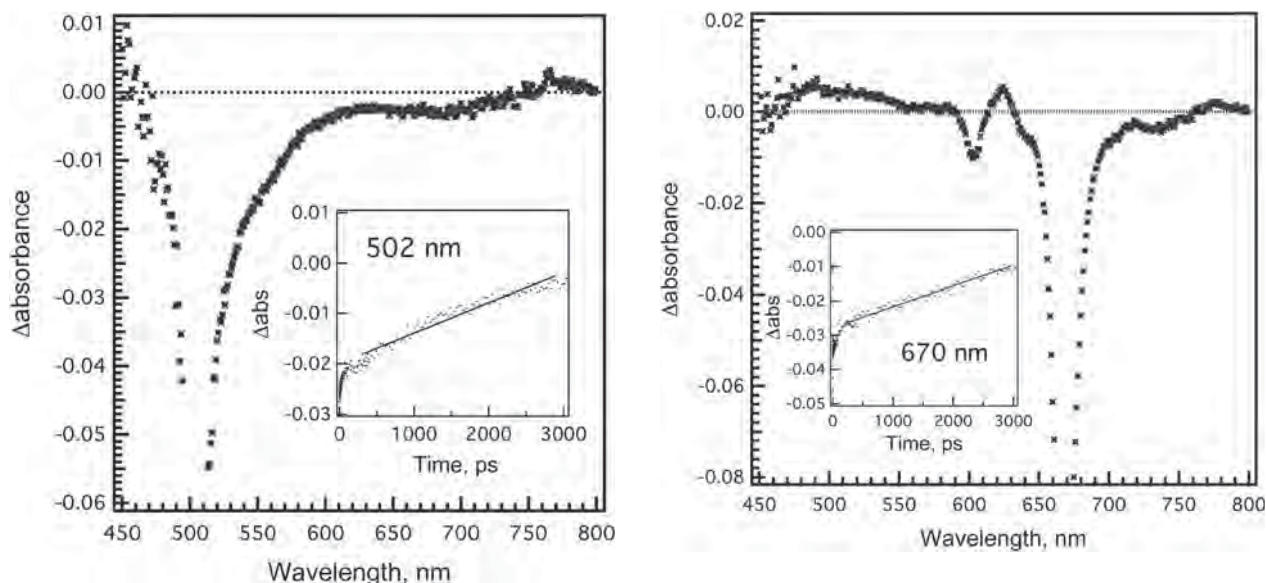
Further, excitation spectrum for the ZnPc-BODIPY pentad was recorded by fixing the emission monochromator to the ZnPc emission peak maxima. The excitation spectrum revealed the absorption band of not only ZnPc at  $\lambda = 687$  nm but also BODIPY at  $\lambda = 503$  nm, which provides direct proof for singlet-singlet energy transfer (Fig. S2, Supporting information).

### Femtosecond and nanosecond transient absorption studies

Femtosecond transient absorption spectroscopy was used to obtain further insight into the excited state interactions in ZnPc-BODIPY pentad. To this end, the



**Fig. 4.** (Left) steady-state fluorescence spectra of ZnPc-BODIPY and the reference Ethynyl-BODIPY in THF;  $\lambda_{\text{ex}} = 480$  nm. (Right) overlap between the fluorescence spectrum of BODIPY and absorption spectrum of ZnPc entities

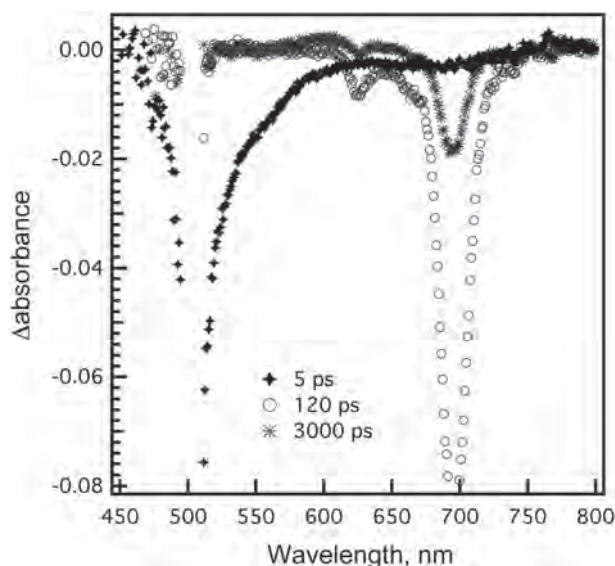


**Fig. 5.** Differential absorption spectra obtained upon femtosecond flash photolysis ( $\lambda_{\text{ex}} = 480$  nm) of Ethynyl-BODIPY in deaerated THF. The inset shows the time profiles of the singlet-excited state of BODIPY at 502 nm

spectra of the model compounds BODIPY and ZnPc were first examined. Figure 5 shows the differential absorption spectra of Ethynyl-BODIPY in THF upon excitation at 480 nm. The strong bleaching of the band at *ca.* 502 nm revealed the instantaneous formation of the singlet excited BODIPY [9, 44–46]. The lifetime was found to be 3.74 ns and a slow intersystem crossing to the triplet-excited state also occurred ( $k = 2.67 \times 10^8 \text{ s}^{-1}$ ). Similar features were observed in the spectra of ZnPc. The spectra were dominated by pronounced bleaching at 670 nm (Fig. 6). By monitoring the decay of the 670 nm band, the lifetime of the singlet ZnPc ( $^1\text{ZnPc}^*$ ) was found to be 5.55 ns and the rate constant

of the intersystem crossing of ZnPc was determined to be  $1.80 \times 10^8 \text{ s}^{-1}$ .

The spectral features in the visible region, which are seen immediately (*i.e.* 5 ps) upon excitation of the ZnPc-BODIPY pentad in THF (Fig. 7) are almost same as those recorded for BODIPY singlet excited state ( $^1\text{BODIPY}^*$ ). The absorption of the singlet BODIPY at  $\lambda = 502$  nm is greatly diminished in intensity over time, with concomitant formation of the singlet ZnPc band at 700 nm, which provide quite clear evidence for energy transfer between the photoexcited BODIPY and the singlet ground state of ZnPc. The kinetics of BODIPY to ZnPc energy transfer was determined by exponential



**Fig. 7.** Differential absorption spectra obtained upon femto-second laser flash photolysis ( $\lambda_{\text{ex}} = 480$  nm) of ZnPc-BODIPY pentad in THF at the indicated time intervals

fitting of the decay profile of the  $^1\text{BODIPY}^*$  at 502 nm ( $k_{\text{ENT}} = 5.90 \times 10^{10} \text{ s}^{-1}$ ), which is close to formation of the singlet ZnPc at around 700 nm ( $6.30 \times 10^{10} \text{ s}^{-1}$ ) (Fig. 8). This process is comparable with that of the reported ZnPc-BODIPY dyad [39], but it is much faster than the reported energy transfer from the singlet BODIPY to zinc porphyrin [4, 5, 11].

By extending the time window to 3 ns, one can see clearly the slow decay of the formed  $^1\text{ZnPc}^*$  ( $1.77 \times 10^8 \text{ s}^{-1}$ ), which is close to that of the Iodo-ZnPc reference, indicating that the  $^1\text{ZnPc}^*$  is not quenched by the attached BODIPY in THF. Such absence of electron-transfer reaction from ZnPc to BODIPY was confirmed by recording the spectrum of ZnPc-BODIPY pentad in the NIR region. From the recorded spectrum, one could not see clear evidence about the formation of ZnPc radical cation (at around 840 nm) and/or BODIPY radical anion indicating that the

electron transfer *via* the singlet ZnPc is not likely occur in the light harvesting ZnPc-BODIPY pentad. This finding is in a good agreement with the electrochemical measurements of ZnPc-BODIPY pentad in deaerated THF, containing tetra-*n*-butylammonium hexafluorophosphate (TBAPF<sub>6</sub>, 0.1 M) as the supporting electrolyte. As seen from Fig. 9, the cyclic voltammogram exhibited the first one-electron oxidation of ZnPc at 820 mV *vs.* SCE and the one-electron reduction of BODIPY at -920 mV *vs.* SCE. Based on the redox values and the energy of singlet ZnPc, the driving force for charge separation ( $-\Delta G_{\text{CS}}$ ) was determined as  $< 0.02$  eV, suggesting that the electron transfer is not thermodynamically feasible from the singlet ZnPc to the attached BODIPY [47].

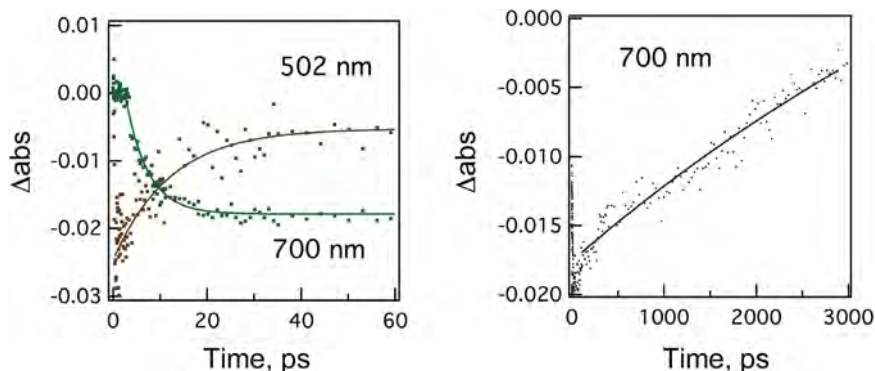
The observed fast energy transfer from the singlet excited state of BODIPY to ZnPc may be explained either *via* Dexter's exchange mechanism [48] or Förster's dipole-dipole mechanism [49]. The former mechanism involves a double-electron exchange involving one electron from the LUMO of the excited donor to the empty LUMO of the acceptor with a simultaneous transfer of another electron from the HOMO of the acceptor to the half-filled HOMO of the donor. In this case, the rate constant is given by Equation 1:

$$k_{\text{D}} = 4\pi^2 H^2 J_{\text{D}}/h \quad (1)$$

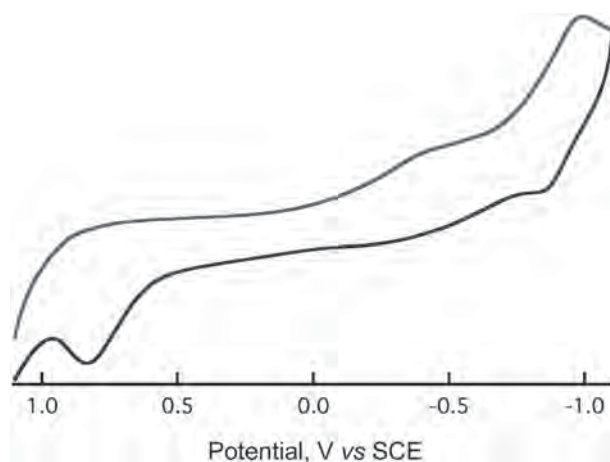
where  $h$  is the Planck's constant,  $H$  is the electronic exchange parameter, and  $J_{\text{D}}$  is the Dexter spectral overlap integral [48]. The spectroscopic studies revealed that such an electronic interaction is largely negligible. Therefore, the results of the present study were analyzed according to Förster's mechanism, in which the rate constant of excitation energy transfer ( $k_{\text{Förster}}$ ) is given by Equation 2 [49].

$$k_{\text{Förster}} = [8.8 \times 10^{-25} k^2 \Phi_{\text{D}} J_{\text{Förster}}]/[n^4 \tau_{\text{D}} R^6] \quad (2)$$

where  $n$  is the solvent refractive index,  $\Phi_{\text{D}}$  and  $\tau_{\text{D}}$  are the fluorescence quantum yield (0.55) and the fluorescence



**Fig. 8.** (Left) fast decay of the singlet BODIPY ( $\lambda = 502$  nm) and fast formation of the singlet ZnPc ( $\lambda = 700$  nm) upon exciting the ZnPc-BODIPY pentad with 480 nm laser light. (Right) slow decay of the formed singlet ZnPc ( $\lambda = 700$  nm) within 3000 ps



**Fig. 9.** Cyclic voltammogram of ZnPc-BODIPY pentad in deaerated THF containing tetra-*n*-butylammonium hexafluorophosphate (TBAPF<sub>6</sub>, 0.1 M). Scan rate = 40 mV.s<sup>-1</sup>

lifetime (1.65 ns) of the isolated donor, respectively,  $J_{\text{Förster}}$  is the Förster's overlap integral representing the emission of the donor and absorption of the acceptor, and  $R$  is the donor-acceptor center-to-center distance (17.7 Å). In Equation 2,  $k^2$  is the orientation factor and for flexible systems of the type discussed here, a value of  $k^2 = 2/3$  is generally used [50].

The  $J_{\text{Förster}}$  spectral overlap integral is given by Equation 3:

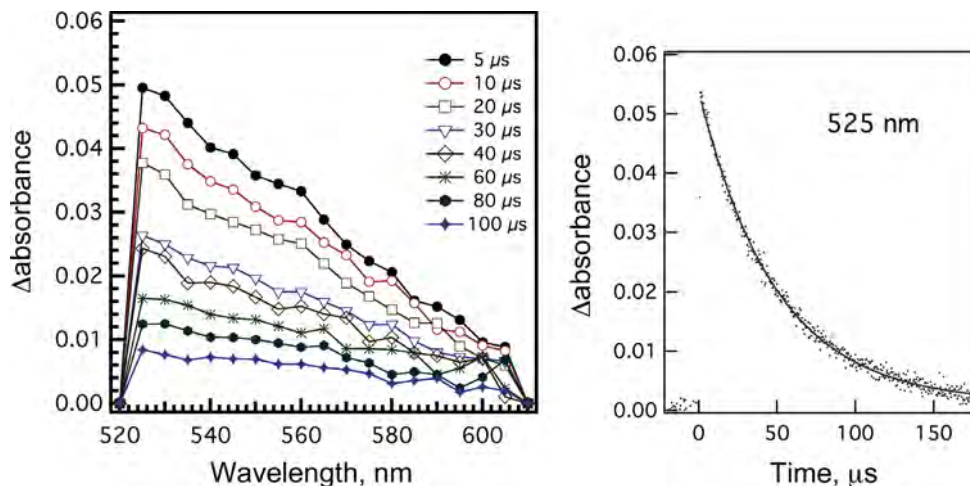
$$J_{\text{Förster}} = \int F_{\text{D}}(\lambda)\epsilon_{\text{A}}(\lambda)\lambda^4 d\lambda \quad (3)$$

where  $F_{\text{D}}(\lambda)$  is the fluorescence intensity of the donor with total intensity normalized to unity,  $\epsilon_{\text{A}}(\lambda)$  is the molar extinction coefficient of the acceptor expressed in

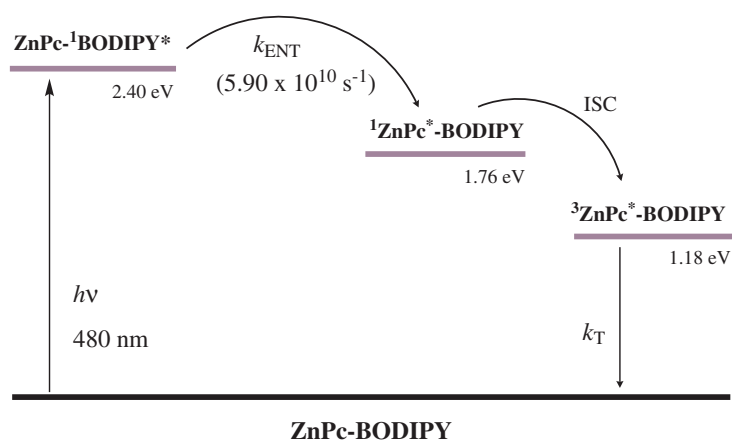
the unit of M<sup>-1</sup>.cm<sup>-1</sup> and  $\lambda$  in nanometers. Analysis of the data according to Equation 3 gave a  $J_{\text{Förster}}$  value of  $1.10 \times 10^{-12}$  M<sup>-1</sup>.cm<sup>3</sup> for the ZnPc-BODIPY pentad. The  $k_{\text{Förster}}$  value was then calculated to be  $5.60 \times 10^{10}$  s<sup>-1</sup> according to Equation 2, revealing a fast excitation energy transfer process. This is consistent with the observed fast energy transfer with  $k_{\text{ENT}} = 6.30 \times 10^{10}$  s<sup>-1</sup>.

Further nanosecond transient absorption spectra were recorded to get another proof for the singlet-singlet energy transfer from BODIPY to ZnPc. Upon excitation of ZnPc-BODIPY pentad in deaerated THF with 480 nm laser light, which is exclusively excited the BODIPY entity, the recorded transient absorption spectra exhibited absorption in the range of 500–600 nm with maxima at 525 nm that unambiguously assigned to the triplet state of ZnPc (Fig. 10) [28–31]. The finding that one can see only the formation the triplet ZnPc, but not the triplet BODIPY, can be explained by the efficient energy transfer from the singlet BODIPY to form the singlet ZnPc, which is relaxed to form the triplet state of ZnPc (<sup>3</sup>ZnPc\*) *via* intersystem crossing process with a rate of  $2.04 \times 10^4$  s<sup>-1</sup>.

Figure 11 summarizes the photochemical events in the form of an energy level diagram for the investigated ZnPc-BODIPY pentad. Selective excitation of the BODIPY entity of the ZnPc-BODIPY populates the singlet-excited state of BODIPY, which transfers its energy to the attached ZnPc. In the absence of the electron transfer pathway, the formed singlet ZnPc was decayed to populate the low lying triplet excited state of ZnPc (1.18 eV) [51] *via* intersystem crossing process. It should be noted that reverse energy transfer from the singlet ZnPc to BODIPY is thermodynamically not feasible. Finally, the triplet state of ZnPc decay to populate the ground state.



**Fig. 10.** (Left panel) nanosecond transient absorption spectra by the 480 nm laser light excitation of ZnPc-BODIPY in deaerated THF. (Right panel) decay time profile of the triplet ZnPc at 525 nm



**Fig. 11.** Energy level diagram depicting the intramolecular photoinduced processes in the ZnPc-BODIPY pentad

## EXPERIMENTAL

### Chemicals

4,4'-difluoro-8-(4-ethynyl)-phenyl-1,3,5,7-tetramethyl-4-bora-3a,4a-diaza-s-indacene (Etynyl-BODIPY) [52], 2(3), 9(10),16(17),23(24)-tetrakis(iodo) zinc(II) phthalocyanine (Iodo-ZnPc) [53] and 2(3), 9(10), 16(17), 23(24)-tetrakis-[4,4'-difluoro-8-(4-ethynyl)-phenyl-1,3,5,7-tetramethyl-4-bora-3a,4a-diaza-s-indacene phthalocyaninato] zinc(II) (ZnPc-BODIPY) [40] were synthesized and purified according to literature procedures. Unsubstituted zinc phthalocyanine (ZnPc) was purchased from Aldrich.

### Instruments

The UV-visible spectral measurements were carried out with a Shimadzu Model 2550 double monochromator UV-visible spectrophotometer. The fluorescence emission was monitored by using a Varian Eclipse spectrometer. A right angle detection method was used.

Cyclic voltammogram (CV) of pentad was recorded on an EG&G PARSTAT electrochemical analyzer using a three electrode system. A platinum button electrode was used as the working electrode. A platinum wire served as the counter electrode. A saturated calomel electrode (SCE) was used as the reference electrode. All measurements were carried out in tetrahydrofuran containing tetra-*n*-butylammonium hexafluorophosphate (TBAPF<sub>6</sub>, 0.1 M) as the supporting electrolyte. Scan rate = 40 mV.s<sup>-1</sup>. All the solutions were purged prior to electrochemical and spectral measurements using argon gas.

The studied compounds were excited by a Panther OPO pumped by Nd:YAG laser (Continuum, SLII-10, 4–6 ns fwhm) with the powers of 1.5 and 3.0 mJ *per* pulse. The transient absorption measurements were performed using a continuous xenon lamp (150 W) and an InGaAs-PIN photodiode (Hamamatsu 2949) as

a probe light and a detector, respectively. The output from the photodiodes and a photomultiplier tube was recorded with a digitizing oscilloscope (Tektronix, TDS3032, 300 MHz). Femtosecond transient absorption spectroscopy experiments were conducted using an ultrafast source: Integra-C (Quantronix Corp.), an optical parametric amplifier: TOPAS (Light Conversion Ltd.) and a commercially available optical detection system: Helios provided by Ultrafast Systems LLC. The source for the pump and probe pulses were derived from the fundamental output of Integra-C (780 nm, 2 mJ/pulse and fwhm = 130 fs) at a repetition rate of 1 kHz. 75% of the fundamental output of the laser was introduced into TOPAS which has optical frequency mixers resulting in tunable range from 285 nm to 1660 nm, while the rest of

the output was used for white light generation. Typically, 2500 excitation pulses were averaged for 5 seconds to obtain the transient spectrum at a set delay time. Kinetic traces at appropriate wavelengths were assembled from the time-resolved spectral data. All measurements were conducted at 298 K. The transient spectra were recorded using fresh solutions in each laser excitation.

## CONCLUSION

The spectroscopic studies of light harvesting symmetrical pentad bearing four BODIPY units connected to the phthalocyanine core *via* an ethynyl linkage at peripheral positions have been accomplished. The geometry optimization showed that the phthalocyanine moiety is completely symmetric and form perfect square planar complex with zinc. The distance between the zinc atom of ZnPc and boron atom of BODIPY is about 17.7 Å. The dihedral angle between BODIPY and phenyl ring is about 125°. The redox states were examined by using voltammetry studies, and the free-energy calculations suggested that the charge separation *via* the singlet-excited states of BODIPY and ZnPc entities is not energetically feasible. However, selective excitation of the BODIPY entity of ZnPc-BODIPY pentad in polar tetrahydrofuran revealed quantitative quenching of the BODIPY fluorescence with simultaneous emission from the ZnPc entity in the near-IR region. The energy-transfer reaction was characterized by the femtosecond laser flash photolysis studies. The kinetics of energy transfer, measured by monitoring the decay of BODIPY emission or the rise of the ZnPc, revealed fast energy transfer ( $5.90 \times 10^{10} \text{ s}^{-1}$ ) in the pentad, which agrees well with the theoretical estimations. The present study successfully demonstrates utilization of the examined pentad as efficient light harvesting material.

## Acknowledgements

Dr. El-Khouly is very much grateful to professor Shunichi Fukuzumi (Osaka University) for his kind support this work. This work was supported by Scientific and Technological Research Council of Turkey (TUBITAK) (Project no. TBAG-111T066).

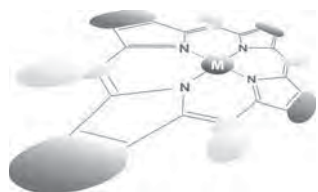
## Supporting information

The cartesian coordinates of the wb97xd/6-311g(d,p)-optimized geometry of ZnPc-BODIPY pentad, fluorescence spectra of the phthalocyanine references, and nanosecond transient spectra of Ethynyl-BODIPY in deaerated tetrahydrofuran (Figs S1–S3) are given in the supplementary material. This material is available free of charge via the Internet at <http://www.worldscinet.com/jpp/jpp.shtml>.

## REFERENCES

1. *Principles Applications of Photochemistry*, Wardle B. (Ed.) Jon Wiley & Sons, Ltd.: UK, 2009.
2. El-Khouly ME, Fukuzumi S and D'Souza F. *ChemPhysChem* 2014; **15**: 30.
3. Shiragami T, Tanaka K, Andou Y, Tsunami SI, Matsumoto J, Luo H, Araki Y, Ito O, Inoue H and Yasuda M. *J. Photochem. Photobiol. A* 2005; **170**: 287.
4. Lazarides T, Charalambidis G, Vuillamy A, Réglier M, Klontzas E, Froudakis G, Kuhri S, Guldi DM and Coutsolelos AG. *Inorg. Chem.* 2011; **50**: 8926.
5. D'Souza F, Smith PM, Zandler ME, McCarty AL, Ito M, Araki Y and Ito O. *J. Am. Chem. Soc.* 2004; **126**: 7898.
6. El-Khouly ME, Wijesinghe CA, Nesterov VN, Zandler ME, Fukuzumi S and D'Souza F. *Chem. Eur. J.* 2012; **18**: 13844.
7. Maligaspe E, Kumpulainen T, Subbaiyan NK, Zandler ME, Lemmetyinen H, Tkachenko NV and D'Souza F. *Phys. Chem. Chem. Phys.* 2010; **12**: 7434.
8. Eggenspieler A, Takai A, El-Khouly ME, Ohkubo K, Gros CP, Bernhard C, Goze C, Denat F, Barbe JM and Fukuzumi S. *J. Phys. Chem. A* 2012; **116**: 3889.
9. D'Souza F, Amin AN, El-Khouly ME, Subbaiyan NK, Zandler ME and Fukuzumi S. *J. Am. Chem. Soc.* 2012; **134**: 654.
10. D'Souza F, Wijesinghe CA, El-Khouly ME, Hudson J, Niemi M, Lemmetyinen H, Tkachenko NV, Zandler ME and Fukuzumi S. *Phys. Chem. Chem. Phys.* 2011; **13**: 18168.
11. Liu JY, El-Khouly ME, Fukuzumi S and Ng DKP. *Chem. Eur. J.* 2011; **17**: 1605.
12. Haugland RP. *Handbook of Fluorescent Probes and Research Chemicals*, Molecular Probes; 6th edition, (1996).
13. Yee MC, Fas SC, Stohlmeyer MM, Wandless TJ and Cimprich KA. *J. Biol. Chem.* 2005; **280**: 29053.
14. Fa M, Bergstrom F, Hagglof P, Wilczynska M, Johansson LBA and Ny T. *Structure* 2000; **8**: 397.
15. Golovkova TA, Kozlov DV and Neckers DC. *J. Org. Chem.* 2005; **70**: 5545.
16. Trieflinger C, Rurack K and Daub J. *Angew. Chem. Int. Ed.* 2005; **44**: 2288.
17. Zhang X, Wang H, Li JS and Zhang HS. *Anal. Chim. Acta* 2003; **481**: 101.
18. Rurack K, Kollmannsberger M and Daub J. *Angew. Chem. Int. Ed.* 2001; **40**: 385.
19. Baki CN and Akkaya EU. *J. Org. Chem.* 2001; **66**: 1512.
20. Gabe Y, Urano Y, Kikuchi K, Kojima H and Nagano T. *J. Am. Chem. Soc.* 2004; **126**: 3357.
21. Blaya S, Acebal P, Carretero L and Fimia A. *Opt. Commun.* 2003; **228**: 55.
22. Lam SY and Damzen MJ. *Opt. Commun.* 2003; **218**: 365.
23. Jakubiak R, Natarajan LV, Tondiglia V, He GS, Prasad PN, Bunning TJ and Vaia RA. *Appl. Phys. Lett.* 2004; **85**: 6095.
24. Arbeloa TL, Arbeloa FL, Arbeloa IL, Garcia-Moreno I, Costela A, Sastre R and Amat-Guerri F. *Chem. Phys. Lett.* 1999; **299**: 315.
25. Gregory P. *J. Porphyrins Phthalocyanines* 2000; **4**: 432.
26. Tracz A, Makowski T, Masirek S, Pisula W and Geerts YH. *Nanotechnology* 2007; **18**: 485303.
27. Priola SA, Raines A and Caughey WS. *Science* 2000; **287**: 1503.
28. El-Khouly ME, Ito O, Smith PM and D'Souza F. *J. Photochem. Photobiol. C* 2004; **5**: 79.
29. El-Khouly ME, Islam SDM, Fujitsuka M and Ito O. *J. Porphyrins Phthalocyanines* 2000; **4**: 713.
30. El-Khouly ME, Kang ES, Kay KY, Choi CS, Araki Y and Ito O. *Chem. Eur. J.* 2007; **13**: 2854.
31. El-Khouly ME, Kim JH, Kay KY, Choi CS, Araki Y and Ito O. *Chem. Eur. J.* 2009; **15**: 5301.
32. Bonnet R. *Chem. Soc. Rev.* 1995; **24**: 19.
33. Lovell JF and Lo PC. *Theranostics* 2012; **9**: 815.
34. Durmuş M. In *Photochemical and Photophysical Characterization, Photosensitizers in Medicine, Environment, and Security*, Nyokong T and Ahsen V. (Eds.) Springer, New York, 2012; pp 135.
35. Liu JY, Yeung HS, Xu W, Li X and Ng DKP. *Org. Lett.* 2008; **10**: 5421.
36. Liu JY, Ermilov EA, Röder B and Ng DKP. *Chem. Commun.* 2009; **12**: 1517.
37. Ermilov EA, Liu JY, Ng DKP and Röder B. *Phys. Chem. Chem. Phys.* 2009; **11**: 6430.
38. Liu JY, Huang Y, Menting R, Röder B, Ermilov EA and Ng DKP. *Chem. Commun.* 2013; **49**: 2998.
39. Rio Y, Seitz W, Gouloumis A, Vazquez P, Sessler JL, Guldi DM and Torres T. *Chem. – Eur. J.* 2010; **16**: 1929.

40. Göl C, Malkoç M, Yeşilot S and Durmuş M. *Dalton Trans.* 2014; **43**: 7561.
41. Göl C, Malkoç M, Yeşilot S and Durmuş M. *Dyes Pigm.* 2014; **111**: 81.
42. Chai JD and Head-Gordon M. *Phys. Chem. Chem. Phys.* 2008; **10**: 6615.
43. Yin X, Li Y, Zhu Y, Jing X, Li Y and Zhu D. *Dalton Trans.* 2010; **39**: 9929.
44. El-Khouly ME, Amin AN, Zandler ME, Fukuzumi S and D'Souza F. *Chem. Eur. J.* 2012; **18**: 5239.
45. Shi WJ, El-Khouly ME, Ohkubo K, Fukuzumi S and Ng DKP. *Chem. Eur. J.* 2013; **19**: 11332.
46. Ulrich G, Ziessel R and Harriman A. *Angew. Chem. Int. Ed.* 2008; **47**: 1184.
47. The driving force for charge separation ( $-\Delta G_{CS}$ ) was calculated from the following equation:  $-\Delta G_{CS} = \Delta E_{0-0} - E_{ox} + E_{red}$ ; where  $\Delta E_{0-0}$  is the energy of the singlet ZnPc,  $E_{ox}$  is the first one-electron oxidation of ZnPc, and  $E_{red}$  is the first one-electron reduction of BODIPY.
48. Dexter DL. *J. Chem. Phys.* 1953; **21**: 836.
49. Förster T. *Discuss. Faraday Soc.* 1959; **27**: 7.
50. Principles of Fluorescence Spectroscopy, 3rd ed., Lakowicz JR. (Ed.) Springer: Singapore, 2006.
51. Fukuzumi S, Ohkubo K, Ortiz J, Gutierrez AM, Fernandez-Lazaro F and Sastre-Santos A. *J. Phys. Chem. A* 2008; **112**: 10744.
52. Godoy J, Vives G and Tour JM. *Organic Letters* 2010; **12**: 1464.
53. Maya EM, Haisch P, Vazquez P and Torres T. *Tetrahedron* 1998; **54**: 4397.



# Charge separation in supramolecular ferrocene(s)-zinc porphyrin-fullerene triads: A femtosecond transient absorption study

Gary N. Lim, Whitney A. Webre and Francis D'Souza\*<sup>‡</sup>

Department of Chemistry, University of North Texas, 1155 Union Circle, #305070, Denton, TX 76203-5017, USA

Dedicated to Professor Shunichi Fukuzumi on the occasion of his retirement

Received 28 October 2014

Accepted 21 November 2014

**ABSTRACT:** Mechanistic aspects of photoinduced charge separation in supramolecular triads, constructed using covalently linked zinc porphyrin-ferrocene(s) dyads — self-assembled *via* axial coordination to either pyridine or phenylimidazole appended fulleropyrrolidine ( $\text{Fc}_x\text{-ZnP:PyC}_{60}$  or  $\text{Fc}_x\text{-ZnP:ImC}_{60}$ ;  $x = 1$  or  $2$ ), has been investigated using femtosecond pump-probe transient spectroscopy. Upon photoexcitation of ZnP, charge separation from ferrocene to  $^1\text{ZnP}^*$  to yield the initial  $\text{Fc}^+\text{-ZnP}^*:\text{C}_{60}$  radical ion-pair or charge separation from  $^1\text{ZnP}^*$  to  $\text{C}_{60}$  to yield the initial  $\text{Fc-ZnP}^{*\cdot}:\text{C}_{60}^{\cdot-}$  radical ion-pair, depending upon the ferrocene-zinc porphyrin intermolecular distance, was observed. These radical ion-pairs resulted in the formation of ultimate distantly separated  $\text{Fc}^+\text{-ZnP}:\text{C}_{60}^{\cdot-}$  radical ion-pairs either *via* an electron migration (former case) or hole shift (latter case) process. Kinetics of charge separation as a function of spacer connecting the ferrocene and porphyrin, and spacer between the porphyrin and fullerene is reported. In agreement with our earlier study (*J. Phys. Chem. B* 2004; **108**: 11333–11343), the  $\text{Fc}^+\text{-ZnP}:\text{C}_{60}^{\cdot-}$  radical ion-pair persisted beyond the monitoring time window of our instrument, suggesting charge stabilization in these supramolecular triads.

**KEYWORDS:** charge separation, supramolecular triad, zinc porphyrin, fullerene, ferrocene, femtosecond transient spectroscopy.

## INTRODUCTION

Understanding the mechanistic details and evaluation of kinetic information of photoinduced charge separation in artificial photosynthetic donor–acceptor conjugates is important for light energy harvesting, both in terms of efficiency and the cost of production [1–24]. Consequently, studies on photoinduced electron transfer in multi-modular molecular and supramolecular donor–acceptor systems have seen a rapid growth in recent years mainly to address the mechanistic details of electron transfer as applicable towards light energy harvesting [25–33], and also, to the development of molecular optoelectronic devices [34].

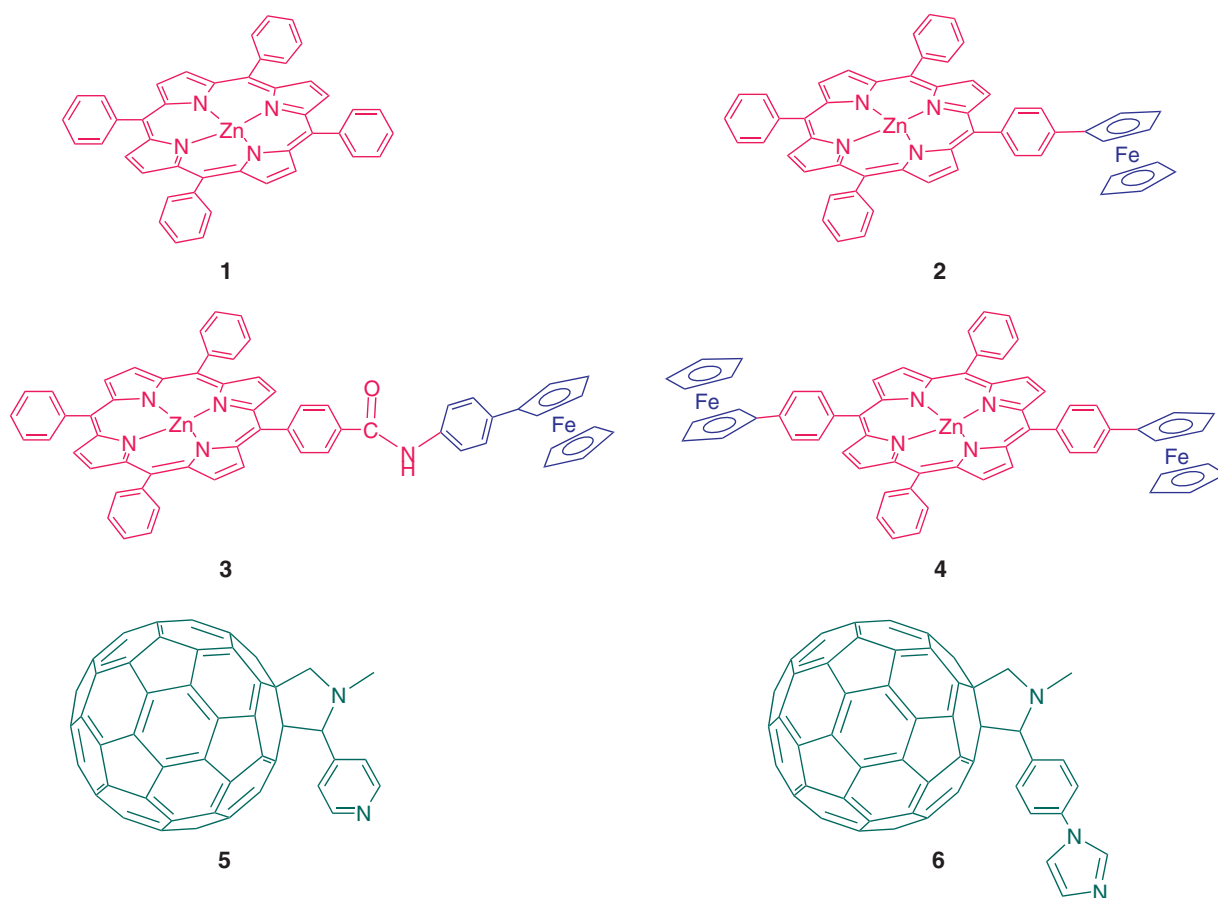
In the construction of such donor–acceptor systems, fullerenes [35] and porphyrins [36] have traditionally been utilized as constituents owing to their rich and well-understood redox, optical, and photochemical properties. Fullerenes ( $\text{C}_{60}$  and  $\text{C}_{70}$ ) in donor–acceptor dyads are known to accelerate forward electron transfer ( $k_{\text{CS}}$ ) and slow down backward electron transfer ( $k_{\text{CR}}$ ), due to their small reorganization energy in electron transfer reactions [37, 38]. Consequently, a number of metallotetrapyrrole-fullerene donor–acceptor systems have been synthesized and studied to probe the effect of molecular topology, and distance and orientation effects on the charge separation and recombination processes [1–24].

In an effort to further stabilize the charge separated states, recently, elegantly designed multi-modular polyads (*viz.*, triads, tetrads, pentads, *etc.*) have also been synthesized and studied [1–24]. In some of these systems, using

<sup>‡</sup>SPP full member in good standing

\*Correspondence to: Francis D'Souza, email: Francis.DSouza@unt.edu, tel: +1 940-369-8832, fax: +1 940-565-4318

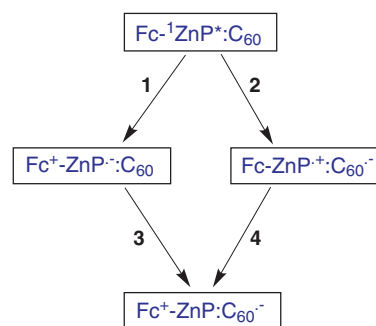




**Fig. 1.** Structure of the donors (**1** to **4**) and acceptors (**5** and **6**) utilized to form supramolecular dyads (**1:5** or **1:6**) and triads (binding of **2, 3**, or **4** to **5** or **6**) *via* metal-ligand axial coordination of zinc porphyrin. The symbol ‘:’ refers to metal-ligand axial coordination bond

photosynthetic reaction center concepts [33], distinctly separated donor–acceptor radical ion pairs are generated upon initial electron transfer by charge migration reactions along the well-tuned redox gradients. In these studies, covalently or self-assembled ferrocene-porphyrin-fullerene triads are one of the well-studied polyads [39, 40]. Among the different strategies, one of the designs developed in our laboratory involved utilizing covalently linked ferrocene(s)-zinc porphyrin self-assembled *via* metal-ligand axial coordination to zinc center (Fig. 1) [40a]. Here, zinc porphyrin was functionalized with one or two ferrocene entities with different spacer units. Also, fulleropyrrolidine having a pyridine or phenylimidazole coordinating ligands was employed as an electron acceptor. The different ligands on fullerene varied the ZnP–fullerene donor–acceptor distance. In these triads, it was possible to establish photoinduced electron transfer leading to charge stabilization using time-resolved fluorescence and nanosecond transient studies.

As shown in Scheme 1, in the triads, the initial electron transfer from the singlet excited zinc porphyrin ( $^1\text{ZnP}^*$ ) could involve ferrocene (route 1) or fullerene (route 2) to yield the respective  $\text{Fc}^+-\text{ZnP}^{\bullet+}:\text{C}_{60}$  or  $\text{Fc}-\text{ZnP}^{\bullet+}:\text{C}_{60}^{\bullet-}$  intermediate radical ion-pair species. The former would



**Scheme 1.** Routes for formation of  $\text{Fc}^+-\text{ZnP}:\text{C}_{60}^{\bullet-}$  charge separated state from  $\text{Fc}-^1\text{ZnP}^*:\text{C}_{60}$  in the investigated supramolecular triads

undergo an electron migration to fullerene (route 3) to yield  $\text{Fc}^+-\text{ZnP}:\text{C}_{60}^{\bullet-}$  as the final charge separated species while the latter would undergo a hole shift involving neighboring ferrocene (route 4) to yield the same final charge separated species with distantly separated cation and radical anion species. In our previous work [40a], based on steady-state and time-resolved fluorescence studies, we proposed route 1 as the initial step involved in the triads formed by **2** or **4** coordinated to fullerene

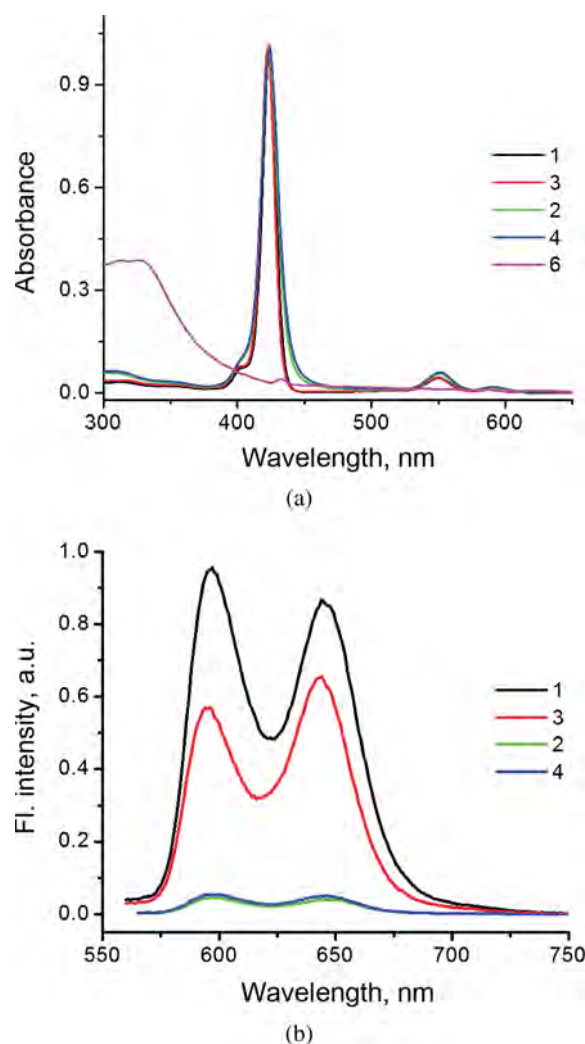
(5 or 6), while route 2 as the initial step involved in the triads formed by 3 coordinated to fullerene (5 or 6), but could not offer any spectroscopic evidence to support this claim. In the present study, we have accomplished this task by performing systematic studies using femtosecond transient absorption in toluene, as discussed in the following sections.

## RESULTS AND DISCUSSION

The ferrocene-zinc porphyrin and fulleropyrrolidine derivatives were synthesized according to our previous procedure [40a, 41a]. Purity of these compounds were checked by thin-layer chromatography and were stored in dark to avoid any photodecomposition. Freshly prepared solutions, degassed using argon, were used in spectral investigations.

Figure 2a shows the normalized absorption spectrum of the porphyrin and fullerene derivatives in toluene. Appended ferrocene had no significant effect on the peak maxima of both Soret and visible bands, however, slight broadening of the spectrum was observed. The spectrum of ImC<sub>60</sub> (6) reveals considerable absorption in the 400 nm region with peak maxima at 324 and 432 nm. Similar spectral features were observed for PyC<sub>60</sub>, 5. This suggests that at the 400 nm excitation wavelength where our femtosecond transient spectrometer operates, both ZnP (about 60–70%) and fullerene (about 30–40%) are getting excited. Figure 2b shows the fluorescence spectrum of the porphyrin derivatives, excited at 550 nm corresponding to the visible band. The 0,0 emission band of zinc porphyrin in compound 3 in which the ferrocene and porphyrin are held together by a phenyl amide bond was quenched nearly 40%, however, in compounds 2 and 4, having direct linkage, the quenching was over 95% in toluene. As reported earlier [40a], in *o*-dichlorobenzene (DCB), this quenching was over 70% for 3 and over 98% for compounds 2 and 4. These results indicate occurrence of efficient excited state events in 2 and 4, and to a lesser extent in 3.

The binding of fullerenes, 5 and 6 to zinc porphyrins 1–4 was studied in DCB in which red-shifted Soret and visible bands accompanied by one or more isosbestic points,



**Fig. 2.** Normalized absorption and fluorescence spectrum ( $\lambda_{\text{ex}} = 550$  nm) of zinc porphyrin, 1 and ferrocene-zinc porphyrin derivatives (2–4) and phenylimidazole functionalized fullerene, 6 in N<sub>2</sub> saturated toluene

expected for penta-coordinated zinc porphyrin complex, were observed [41]. Job's plots confirmed 1:1 stoichiometry for these dyads. The binding constants,  $K$  evaluated by constructing Scatchard plot of the absorbance data, are given in Table 1. The magnitude of these values suggest moderate

**Table 1.** Binding constants for axial coordination of fullerene ligands to ferrocene-zinc porphyrin dyads in DCB at 298 K

Porphyrin	$K, \text{M}^{-1}$ <sup>a</sup>			Ref.
	Pyridine	PyC <sub>60</sub> , 5	ImC <sub>60</sub> , 6	
1	$7.8 \times 10^3$	$7.2 \times 10^3$	$11.6 \times 10^3$	41a
2	$7.7 \times 10^3$	$26.8 \times 10^3$	$29.6 \times 10^3$	40a
3	$5.3 \times 10^3$	$20.5 \times 10^3$	$22.6 \times 10^3$	40a
4	$5.8 \times 10^3$	$23.4 \times 10^3$	$24.6 \times 10^3$	40a

<sup>a</sup>Error =  $\pm 10\%$ .

**Table 2.** Electrochemical half-wave potentials (*vs.* Fc/Fc<sup>+</sup>) of the Fc-ZnP:C<sub>60</sub> triads in *o*-dichlorobenzene, 0.1 M (TBA)ClO<sub>4</sub>, geometric parameters from B3LYP/3-21G(\*) calculations, and free-energy change associated for different radical ion-pairs formation from the initial singlet excited zinc porphyrin (redox potential data and computational distances were taken from reference 40a)

Compound	ZnP <sup>0/+</sup>	Fc <sup>0/+</sup>	C <sub>60</sub> <sup>0/+</sup>	ZnP <sup>0/+</sup>	R <sub>cc</sub> <sup>1a</sup>	R <sub>cc</sub> <sup>2b</sup>	R <sub>ee</sub> <sup>1c</sup>	ΔG <sub>cs</sub> <sup>d</sup>	ΔG <sub>cs</sub> <sup>e</sup>	ΔG <sub>HS</sub> <sup>f</sup>
<b>1:6</b> <sup>c</sup>	0.29	-0.01	-1.10	-1.91	12.3	—	—	-0.12	-0.65	-0.30
<b>2:6</b> <sup>c</sup>	0.21	-0.03	-1.17	-1.93	12.1	10.4	2.6	-0.09	-0.66	-0.24
<b>3:5</b>	0.28	-0.01	-1.14	-1.91	9.98	16.8	3.7	-0.12	-0.62	-0.29
<b>3:6</b> <sup>c</sup>	0.27	-0.01	-1.13	-1.91	13.0	16.9	3.8	-0.12	-0.64	-0.28
<b>4:6</b> <sup>c</sup>	0.23	-0.01	-1.19	-1.94	13.0	10.5	2.8	-0.10	-0.62	-0.24

<sup>a</sup>Center-to-center distance between ZnP and C<sub>60</sub> entities; <sup>b</sup>center-to-center distance between ZnP and ferrocene entities; <sup>c</sup>edge-to-edge distance (through-space) between ferrocene and fullerene entities; <sup>d</sup>for formation of Fc<sup>+</sup>-ZnP<sup>•</sup>:C<sub>60</sub> radical ion-pair from <sup>1</sup>ZnP\*<sup>•</sup>; <sup>e</sup>for formation of Fc-ZnP<sup>•+</sup>:C<sub>60</sub><sup>•-</sup> radical ion-pair from <sup>1</sup>ZnP\*<sup>•</sup>; <sup>f</sup>for formation of Fc<sup>+</sup>-ZnP:C<sub>60</sub><sup>•+</sup> from Fc-ZnP<sup>•+</sup>:C<sub>60</sub><sup>•-</sup> radical ion-pair.

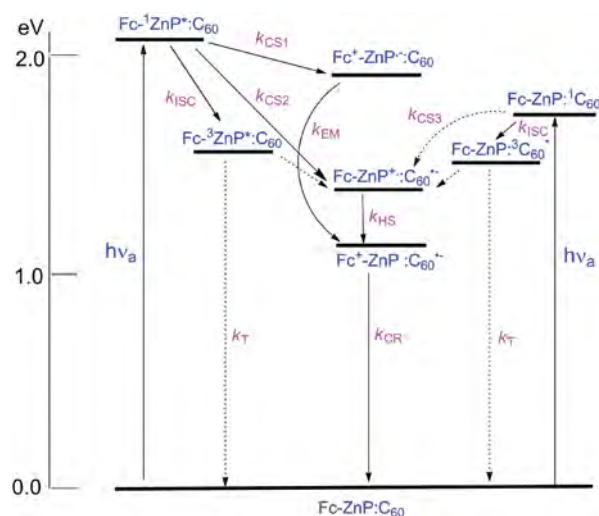
level of binding. Generally, *K* for **6** binding to a given zinc porphyrin is higher than that observed for the binding of **5** to the same zinc porphyrin derivative. Introducing one or two ferrocene entities on the zinc macrocycle improved the binding by 2–3 times compared to that observed for pristine ZnP binding of **5** or **6** [40a].

Table 2 summarizes the free-energy data for various charge separated states discussed in Scheme 1 originated from the initial singlet excited state of zinc porphyrin. The electrochemical redox potentials and key geometry factors deduced from B3LYP/3-21G(\*) geometry optimization studies of the dyads and triads were adapted from our previous study [40a]. It may be mentioned here that in the optimized structures, the fullerene entity was closer to the ferrocene entity, perhaps due to the electron deficient and electron rich nature of the respective entities. Consequently, the measured edge-to-edge distance (Table 2) in most of the cases were within the van der Waals interacting distances. The free-energy calculations were performed according to Rehm–Weller approach [42] using oxidation potential of the donor and reduction potential of the acceptor, and spectroscopic data, according to the following equation.

$$\Delta G_{cs}^0 = E_{1/2}(D^{+}/D) - E_{1/2}(A/A^{•-}) - \Delta E_{0-0} \quad (1)$$

where  $E_{1/2}(D^{+}/D)$  is the first one-electron oxidation potential of the donor porphyrin or ferrocene,  $E_{1/2}(A/A^{•-})$  is the first one-electron reduction potential of the C<sub>60</sub> electron acceptor,  $\Delta E_{0-0}$  is the energy of the 0–0 transition energy gap between the lowest excited state and the ground state, being 2.04 eV for zinc porphyrin. The solvation energy is omitted in these calculations for simplicity.

An energy level diagram revealing the possible photochemical events was constructed by utilizing the calculated energy of each radical ion-pair from Table 2, and the reported singlet and triplet energies ( $E^S = 2.04$  for ZnP and 1.75 eV for C<sub>60</sub>;  $E^T = 1.55$  eV for ZnP and 1.50 eV for C<sub>60</sub>) [40d, 43] of the sensitizers, as shown



**Fig. 3.** Energy level diagram showing the different photochemical events of the supramolecular triad composed of ferrocene, zinc porphyrin and fullerene entities ( $\lambda_{ex} = 400$  nm) in DCB. Abbreviations: *k* stands for different kinetic processes. HS = hole shift, CS = charge separation, ISC = intersystem crossing, and CR = charge recombination. Thick and solid arrows — most probable process, and dashed arrow — less likely process

in Fig. 3. It is important to note that the formation of Fc<sup>+</sup>-ZnP<sup>•</sup>:C<sub>60</sub> radical ion-pair is only possible from <sup>1</sup>ZnP\* ( $k_{CS1}$ ) and not from <sup>1</sup>C<sub>60</sub>\* while formation of Fc-ZnP<sup>•+</sup>:C<sub>60</sub><sup>•-</sup> radical ion-pair is possible from both <sup>1</sup>ZnP\* ( $k_{CS2}$ ) and <sup>1</sup>C<sub>60</sub>\* ( $k_{CS3}$ ) or even from their triplet excited states, <sup>3</sup>ZnP\* and <sup>3</sup>C<sub>60</sub>\* (shown in dashed arrows), resulted after the sensitizers had undergone an intersystem crossing process ( $k_{ISC}$ ). The final charge separated state, Fc<sup>+</sup>-ZnP:C<sub>60</sub><sup>•+</sup>, could be formed either by an electron migration process involving Fc<sup>+</sup>-ZnP<sup>•</sup>:C<sub>60</sub> ( $k_{EM}$ ) or a hole shift process involving Fc-ZnP<sup>•+</sup>:C<sub>60</sub><sup>•-</sup> ( $k_{HS}$ ). These processes are in competition with Fc<sup>+</sup>-ZnP<sup>•</sup>:C<sub>60</sub> and Fc-ZnP<sup>•+</sup>:C<sub>60</sub><sup>•-</sup> radical ion-pairs relaxing directly to the ground state. In the present donor–acceptor conjugates,

singlet–singlet energy transfer from the  $^1\text{ZnP}^*$  to the ground state  $\text{C}_{60}$  is considered to be noncompetitive due to latter's lack of absorption in the emission region of zinc porphyrin (575–700 nm) [44]. A similar argument could be applied for singlet–singlet energy transfer involving  $^1\text{ZnP}^*$  to the ground state ferrocene.

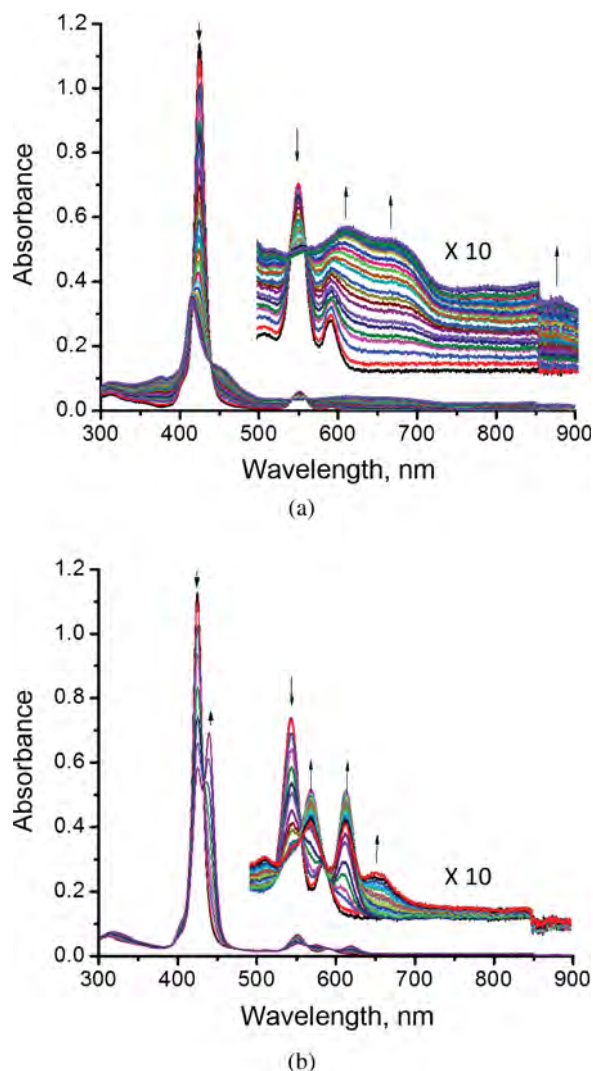
Femtosecond transient absorption studies were performed to unravel electron transfer pathways in these triads. In the present study, photochemically more stable toluene has been used instead of DCB. In such a case, the energy of the various charge separated states would be 100–200 mV higher than that shown in Fig. 3. However, it is important to note that the energy levels of both  $\text{Fc}^+-\text{ZnP}^{++}:\text{C}_{60}^{\bullet-}$  and  $\text{Fc}^+-\text{ZnP}:\text{C}_{60}^{\bullet-}$  would be lower than both  $^3\text{ZnP}^*$  and  $^3\text{C}_{60}^*$ , not affecting the electron transfer path that has been originally established in DCB.

Prior performing transient absorption studies, spectroelectrochemical studies were performed to characterize one-electron reduced, and one- and two-electron oxidized products of a ferrocene-zinc porphyrin dyad (**2**) to help in characterizing photochemical electron transfer products. During one-electron oxidation to form  $\text{Fc}^+-\text{ZnP}$  (applied potential = 0.63 V vs. Ag/AgCl), no significant changes were observed indicating lack of strong absorption of ferrocenium cation in the visible region. However, during the second electron oxidation (applied potential = 0.90 V vs. Ag/AgCl), the Soret and Q-bands of ZnP decreased in intensity with the appearance of new peaks at 374, 414, 448(sh), 610, 667, and 873 nm corresponding to the formation of  $\text{Fc}^{++}-\text{ZnP}^{++}$  species in which the spectral changes in the visible region are mainly of that of  $\text{ZnP}^{++}$  (Fig. 4a). These spectral changes were found to be reversible with the appearance of an isosbestic point at 443 nm. Figure 4b shows the spectral changes associated during one-electron reduction of dyad, **2** at an applied potential of -1.36 V vs. Ag/AgCl. The Soret band located at 425 nm and the Q-band at 550 nm decreased in intensity accompanied by new bands at 314, 440, 514, 576, 619 and 660 nm corresponding to the formation of  $\text{Fc}^--\text{ZnP}^{\bullet-}$ . Isosbestic points at 433 and 564 nm were observed indicating the existence of only one equilibrium process.

The overall peak positions and shapes were similar to that reported for radical anion and radical cation of ZnP in literature [45] with some differences due to the presence of directly linked ferrocene and experimental solution conditions.

### Femtosecond transient absorption studies

First, the probe zinc porphyrin, **1** and the dyads, **2–4** were investigated in toluene using 400 nm laser of 100 fs pulse width. As shown in Fig. 5a, excitation of **1** instantly populated the  $\text{S}_1$  and  $\text{S}_2$  states of the porphyrins with maximum in the ~447 nm region. At higher wavelength region, a depleted signal in the Q-band region of zinc porphyrin (550 nm), opposite mimic of the ground state



**Fig. 4.** Spectral changes observed for compound **2** during (a) second oxidation corresponding to the formation of  $\text{Fc}^{++}-\text{ZnP}^{++}$  and (b) first reduction corresponding to the formation of  $\text{Fc}^--\text{ZnP}^{\bullet-}$  species in DCB containing 0.2 M (TBA)ClO<sub>4</sub>. Please note that first oxidation corresponding to the formation of  $\text{Fc}^+-\text{ZnP}$  revealed no significant spectral changes in the monitored spectral window. Figure inset are spectra in the visible region enlarged vertically by a factor of 10

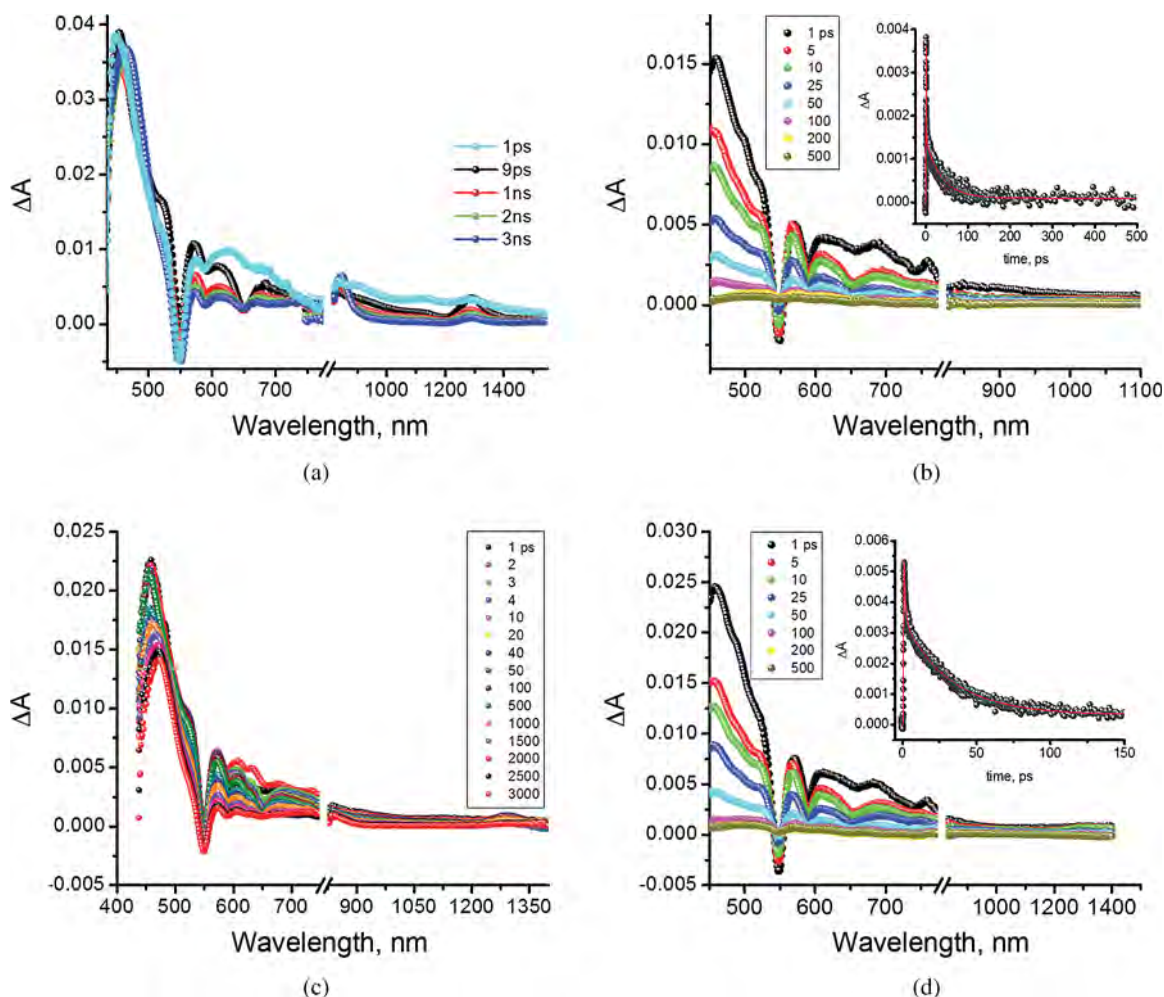
absorption of the Q-band was observed. In addition, depleted bands at 590 and 648 nm, corresponding to stimulated emission of zinc porphyrin were also observed [41c]. Interestingly, in the near-IR region, an additional peak at 1288 nm was observed. The decay rate of this peak was close to that of excited lifetime of  $^1\text{ZnP}^*$  (1.85 ns) suggesting that this peak is indeed due to the singlet excited state of zinc porphyrin. Decay of singlet peaks were accompanied by new peaks at 465 and 845 nm corresponding to the triplet excited state of zinc porphyrin [41c]. The spectral features for  $\text{Fc}^+-\text{ZnP}$  dyad, **2** are shown in Fig. 5b. The instantaneously formed singlet features decayed faster than that observed for the ZnP probe in addition to a new peak at 685 nm at early

time scales corresponding to  $\text{ZnP}^*$ . Also, no clear peak of triplet zinc porphyrin at higher time scales was observed. The time profile of  $\text{ZnP}^*$  shown in Fig. 5b inset shows the charge separation and recombination processes to be very fast. The estimated rate of charge separation,  $k_{\text{CS}}$ , and rate of charge recombination,  $k_{\text{CR}}$ , by analyzing the decay curves, were found to be  $7.90 \times 10^{11} \text{ s}^{-1}$  and  $2.67 \times 10^{10} \text{ s}^{-1}$ , respectively.

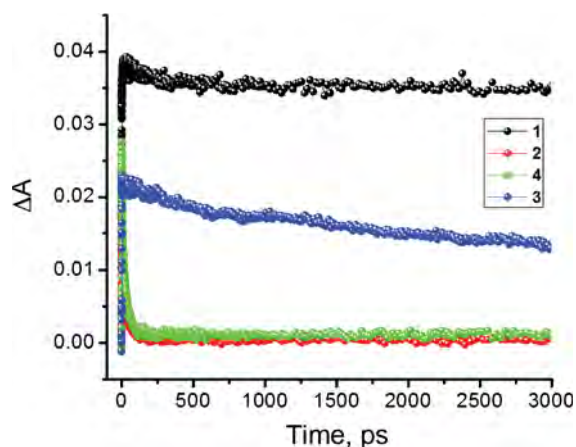
For dyad **3**, in which the zinc porphyrin and ferrocene are held a phenylamide linker, the spectral features resembled close to that of the probe, **1**. However, in agreement with the steady-state fluorescence results, the rate of decay of the singlet state monitored at 460 nm was in between that of **1** and **3** (see Fig. 6), suggesting occurrence of slow electron transfer due to increased distance between the ferrocene and porphyrin entities. The spectral features of  $\text{ZnP}^*$  at 680 nm were rather weak, and under these conditions,  $k_{\text{CS}}$  and  $k_{\text{CR}}$  were found to be difficult to establish. As predicted, for compound **4** with two ferrocene entities connected to zinc porphyrin,

the transient spectral features were similar to that of dyad **2**. That is, rapid decay of singlet peaks with the appearance of  $\text{ZnP}^*$  at 680 nm, were observed. The measured  $k_{\text{CS}}$  and  $k_{\text{CR}}$  by analyzing the decay of 680 nm peak, were found to be  $8.64 \times 10^{11} \text{ s}^{-1}$  and  $3.20 \times 10^{10} \text{ s}^{-1}$ , respectively, slightly higher than that observed in **2** due to the presence of two ferrocene units. It may be mentioned here that the measured  $k_{\text{CS}}$  values for **2** and **3** were nearly an order of magnitude smaller than that reported by Kubo *et al.* [46] for directly linked ferrocene-zinc porphyrin dyads (no phenyl spacer; ferrocene directly linked to the *meso*-position) due to close proximity of the entities ( $k_{\text{CS}} > 10^{12} \text{ s}^{-1}$ ).

Femtosecond transient studies of **1:5** and **1:6** dyads is reported in our recent publication where photoinduced electron transfer leading to  $\text{ZnP}^{*+}:\text{C}_{60}^{\bullet-}$  radical ion-pair was established [41c]. In this case, it was possible to spectrally characterize both  $\text{ZnP}^{*+}$  in the 660–680 nm range and  $\text{C}_{60}^{\bullet-}$  in the 1020 nm range. The measured  $k_{\text{CS}}$  for these dyads by monitoring the growth of  $\text{C}_{60}^{\bullet-}$  was



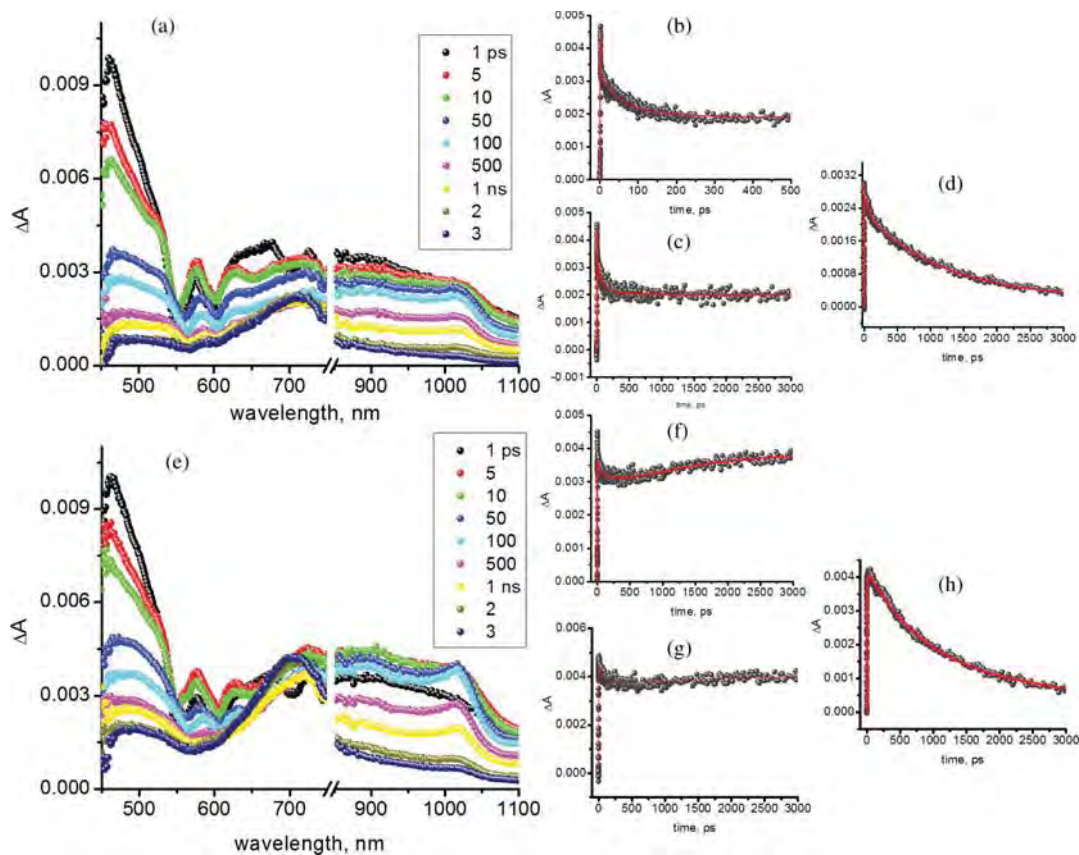
**Fig. 5.** Femtosecond transient absorption spectra of (a) **1**, (b) **2**, (c) **3** and (d) **4** in toluene at the excitation wavelength of 400 nm. Figure inset in b and d shows time profile of the 680 nm peak corresponding to  $\text{ZnP}^*$



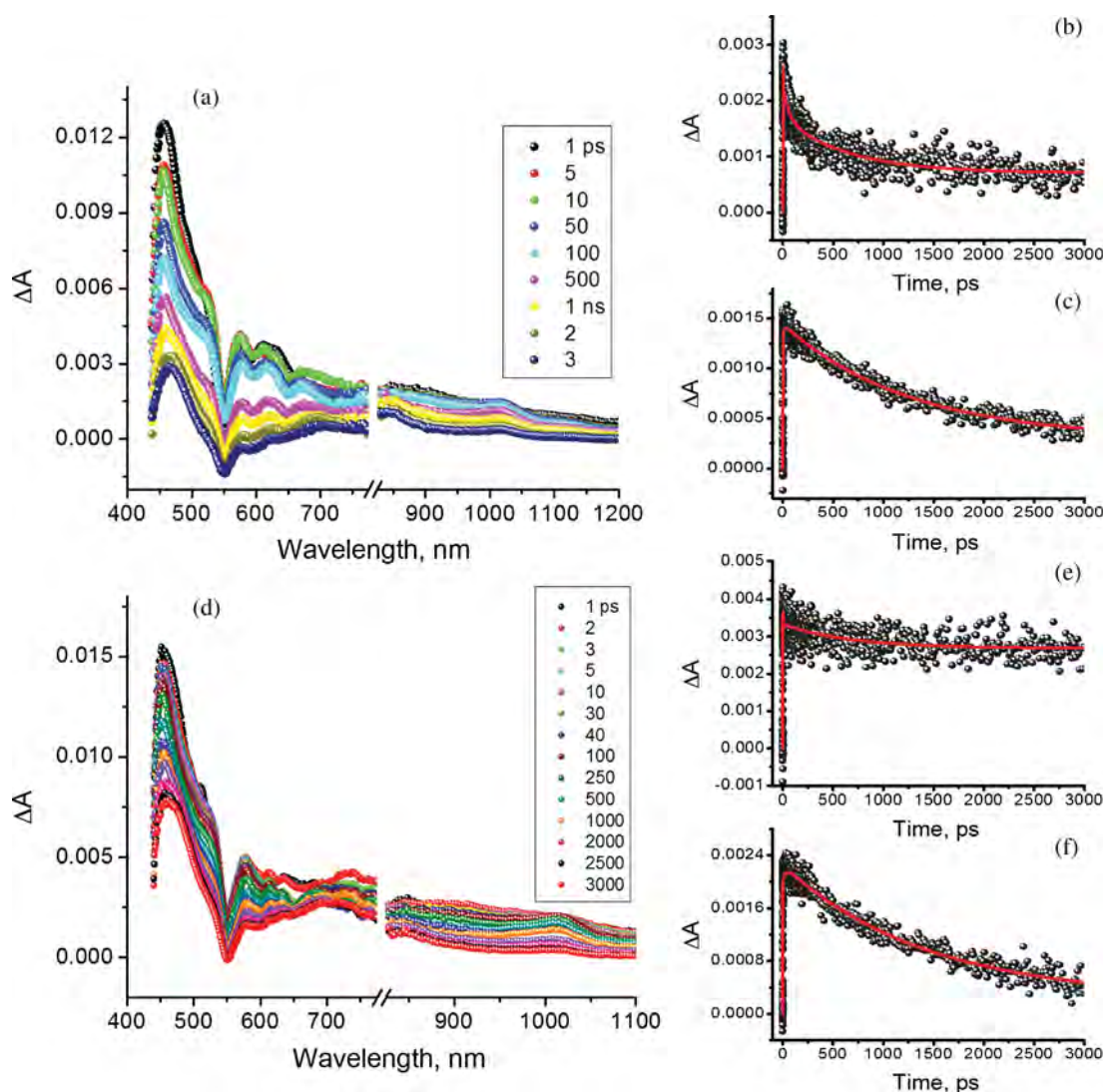
**Fig. 6.** Time profile of the 460 nm peak representing decay of zinc porphyrin singlet excited state in pristine zinc porphyrin and ferrocene-zinc porphyrin dyads in toluene

found to be  $7.90 \times 10^9 \text{ s}^{-1}$  and  $5.7 \times 10^9 \text{ s}^{-1}$ , respectively, for **1:5** and **1:6** dyads. Figure 7 shows femtosecond transient spectra of **2:5** and **2:6** triads in toluene along with the time profiles of key transient peaks. The spectral features at 1 ps were similar to that observed for the dyad, **2**. That is, the instantly formed singlet ZnP developed the

characteristic peak of  $\text{ZnP}^*$  at 680 nm suggesting that the initial charge separation in these triads follow route 1 in Scheme 1. The time constant for the formation of  $\text{ZnP}^*$  was 1.24 ps for **2:5** and 1.29 ps for **2:6** dyads which resulted a  $k_{\text{CS}}$  values of  $8.06 \times 10^{11} \text{ s}^{-1}$  and  $7.75 \times 10^{11} \text{ s}^{-1}$ , respectively for the **2:5** and **2:6** triads. In addition, there was a broad peak in the 850–910 nm range characteristic of singlet excited fulleropyrrolidine [43]. With time, a new band at 1020 nm characteristic of  $\text{C}_{60}^{\bullet-}$  radical anion appeared (time constant = 24.4 and 33.68 ps, respectively, for **2:5** and **2:6** triads) while the peak of  $\text{ZnP}^{*+}$  radical cation expected at 650 nm range was hidden with other spectral bands in this wavelength region. The rate of electron migration,  $k_{\text{EM}}$ , from the initial  $\text{ZnP}^*$  to  $\text{C}_{60}$  was found to be  $7.65 \times 10^{11} \text{ s}^{-1}$  and  $7.45 \times 10^{11} \text{ s}^{-1}$ , respectively for the **2:5** and **2:6** triads. The  $k_{\text{EM}}$  rates were found to be higher than the  $k_{\text{CS}}$  rates reported for **1:5** and **1:6** dyads, being  $7.90 \times 10^9 \text{ s}^{-1}$  and  $5.7 \times 10^9 \text{ s}^{-1}$ , respectively. The fact that  $k_{\text{EM}}$  in the triads is faster than  $k_{\text{CS}}$  in the dyads suggest that electron migration from  $\text{ZnP}^*$  to  $\text{C}_{60}$  to produce the final charge separated state,  $\text{Fc}^+-\text{ZnP}:\text{C}_{60}^{\bullet-}$  is the main electron transfer route (process 1 followed by 3 in Scheme 1) in **2:5** and **2:6** triads. Appearance of a new band at 720 nm corresponding to triplet  $\text{C}_{60}$  was also observed (see Figs 7c and 7g for time profiles). This



**Fig. 7.** Femtosecond transient absorption spectra of (a) **2:5** (0.05 mM each) and (e) **2:6** (0.05 mM each) in toluene at the excitation wavelength of 400 nm. Figures b, c and d show the time profile of the 680, 726 and 1020 nm bands of **2:5**, respectively. Figures f, g and h show the time profile of the 680, 722 and 1020 nm bands of **2:6**, respectively



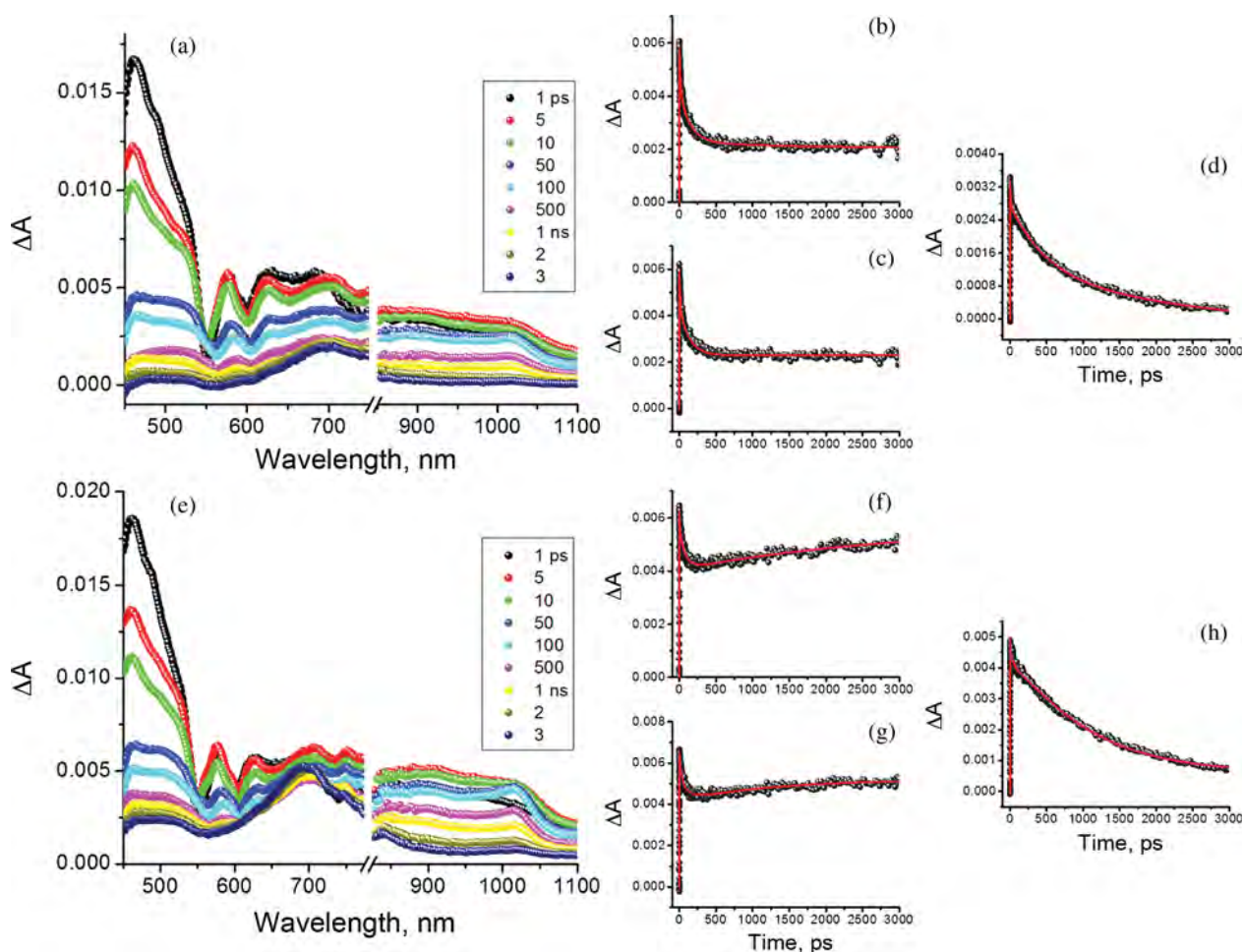
**Fig. 8.** Femtosecond transient absorption spectra of (a) **3:5**, and (d) **3:6** in toluene at the excitation wavelength of 400 nm. Figures b and c show the time profile of the 710 and 1020 nm bands of **3:5**, respectively. Figures e and f show the time profile of the 723 and 1020 nm bands of **3:6**, respectively

could be a product of intersystem crossing of  $^1\text{C}_{60}^*$  since the energy of  $\text{Fc-ZnP}^{*+}:\text{C}_{60}^{\bullet-}$  radical ion-pair is lower than that of  $^3\text{C}_{60}^*$  and  $^3\text{ZnP}^*$  states as shown in Fig. 3. As shown in Figs 7d and 7h, decay of the fullerene anion radical persisted beyond the 3 ns time window of our instrument.

Figure 8 shows the transient spectra of the **3:5** and **3:6** triads along with the time profile of key transient bands. Similar to pristine **3**, peaks corresponding to  $^1\text{ZnP}^*$  decayed at a much slower rate than that observed for pristine **2** or the **2:5** and **2:6** triads. Spectral evidence for the formation of  $\text{ZnP}^*$  in the 680 nm range was bleak. These observations suggest that process 1 in Scheme 1 is not the main initial electron transfer route and route 2 could be the predominant one. Importantly, evidence for the formation of charge separated state was obtained with the characteristic peak of  $\text{C}_{60}^{\bullet-}$  radical anion at 1020 nm. The expected, short-lived as a result of hole

migration to Fc;  $\text{ZnP}^{*+}$  band was overlapped with other bands in the 650–680 nm range. Assuming route 2 is the initial electron transfer step,  $k_{\text{CS}}$  values of  $6.16 \times 10^{10} \text{ s}^{-1}$  and  $2.83 \times 10^{10} \text{ s}^{-1}$ , respectively for the **3:5** and **3:6** triads which were slightly higher than that obtained for **1:5** and **1:6** dyads. Additionally,  $k_{\text{CS}}$  for **3:5** was higher than that for **3:6** due to close disposition (see Table 2 for donor–acceptor distances). A new band in the 720 nm range was also developed with time which was attributed to the formation of  $^3\text{C}_{60}^*$  from the initially formed  $^1\text{C}_{60}^*$ . Additionally, for both of these triads, due to the occurrence of hole shift to Fc to yield final  $\text{Fc}^+:\text{ZnP}^+:\text{C}_{60}^{\bullet-}$  radical ion-pair, the decay of fullerene radical anion persisted beyond 3 ns as shown in Figs 8c and 8f, respectively, for **3:5** and **3:6** triads.

As shown in Fig. 9, the femtosecond transient spectral features of triads **4:5** and **4:6** were similar to those of corresponding **2:4** and **2:6** triads. That is, the singlet



**Fig. 9.** Femtosecond transient absorption spectra of (a) **4:5**, and (e) **4:6** in toluene at the excitation wavelength of 400 nm. Figures b, c and d show the time profile of the 680, 710 and 1020 nm bands of **4:5**, respectively. Figures f, g and h show the time profile of the 685, 710 and 1020 nm bands of **4:6**, respectively.

ZnP transient bands decayed with the initial appearance of  $\text{ZnP}^*$  at 680 nm suggesting route 1 in Scheme 1 to produce  $\text{Fc}^+-\text{ZnP}^*-\text{C}_{60}$  is the main quenching pathway. By monitoring the growth of this band,  $k_{\text{CS}}$  values of  $7.16 \times 10^{11} \text{ s}^{-1}$  and  $6.54 \times 10^{11} \text{ s}^{-1}$ , respectively, for the **4:5** and **4:6** triads were obtained. The rapid decay of  $\text{ZnP}^*$  resulted in the appearance of  $\text{C}_{60}^*$  peak at 1020 nm implying electron migration from the initially formed  $\text{ZnP}^*$  to  $\text{C}_{60}$  to produce  $\text{Fc}^+-\text{ZnP}-\text{C}_{60}^*$  is the main route. The estimated rate of electron migration,  $k_{\text{EM}}$ , from the initial  $\text{ZnP}^*$  to  $\text{C}_{60}$  was found to be  $7.38 \times 10^{11} \text{ s}^{-1}$  and  $6.16 \times 10^{11} \text{ s}^{-1}$ , respectively for the **4:5** and **4:6** triads. These values are higher than those obtained for charge separation in the **1:5** and **1:6** dyads at least by an order of magnitude suggesting route 1 followed by route 3 in Scheme 1 is the main electron transfer path in these triads also. Between **4:5** and **4:6**,  $k_{\text{EM}}$  value was higher for **4:5** due to close disposition of fullerene entity compared to that in **4:6** (see Table 1 for donor–acceptor distances). Additionally, a new band in the 720 nm range appeared with time which was attributed to the formation of  ${}^3\text{C}_{60}^*$

from the initially formed  ${}^1\text{C}_{60}^*$ . Similar to the triads formed by **2** and **3** with **5** and **6**, due to the formation of  $\text{Fc}^+-\text{ZnP}:\text{C}_{60}^*$  radical ion-pair, the decay of fullerene radical anion persisted beyond 3 ns as shown in Fig. 9c and 9f, respectively, for **4:5** and **4:6** triads.

## EXPERIMENTAL

The investigated compounds were synthesized according to our earlier published methods [40a, 41a]. Purity of the compound was checked on thin-layer chromatography prior running the experiments.

### Instrumentation

The UV-visible and near-IR spectral measurements were carried out with a Shimadzu 2550 UV-vis spectrophotometer or Jasco V-670 spectrophotometer. The steady-state fluorescence emission was monitored by using a Varian (Cary Eclipse) Fluorescence Spectrophotometer or a Horiba Jobin Yvon Nanolog spectrofluorometer



equipped with PMT (for UV-visible) and InGaAs (for near-IR) detectors. A right angle detection method was used for fluorescence measurements at room temperature. All the solutions were purged prior to spectral measurements using argon gas. Spectroelectrochemical studies were performed using a thin-layer setup from BAS, West Lafayette, IN that included a platinum gauze working electrode, Ag/AgCl reference electrode and platinum wire auxiliary electrode. A Princeton Applied Research potentiostat/galvanostat Model 263A was used to apply desired potentials to generate radical anion and cation species.

### Femtosecond transient absorption spectral measurements

Femtosecond transient absorption spectroscopy experiments were performed using an Ultrafast Femtosecond Laser Source (Libra) by Coherent incorporating diode-pumped, mode locked Ti:Sapphire laser (Vitesse) and diode-pumped intra cavity doubled Nd:YLF laser (Evolution) to generate a compressed laser output of 1.45 W. For optical detection, a Helios transient absorption spectrometer coupled with femtosecond harmonics generator both provided by Ultrafast Systems LLC was used. The source for the pump and probe pulses were derived from the fundamental output of Libra (Compressed output 1.45 W, pulse width 100 fs) at a repetition rate of 1 kHz. 95% of the fundamental output of the laser was introduced into harmonic generator which produces second and third harmonics of 400 and 267 nm besides the fundamental 800 nm for excitation, while the rest of the output was used for generation of white light continuum. In the present study, the second harmonic 400 nm excitation pump was used in all the experiments. Kinetic traces at appropriate wavelengths were assembled from the time-resolved spectral data. Data analysis was performed using Surface Explorer software supplied by Ultrafast Systems. All measurements were conducted in degassed toluene at 298 K.

### SUMMARY

Primary electron transfer from the  $^1\text{ZnP}^*$  to either ferrocene or fullerene in the supramolecular Fc-ZnP- $\text{C}_{60}$  triads was established from femtosecond transient absorption studies in toluene. As speculated from our previous study [40a], formation of initial  $\text{Fc}^+\text{-ZnP}^{\bullet-}\text{:C}_{60}$  radical ion-pair in the case of closely spaced, covalently linked ferrocene-zinc porphyrin, while formation of initial  $\text{Fc-ZnP}^{\bullet+}\text{:C}_{60}^{\bullet-}$  radical ion-pair in the case of covalently linked ferrocene-zinc porphyrin with higher separation distance, has been established in the present study. These radical ion-pair yielded the final  $\text{Fc}^+\text{-ZnP:C}_{60}^{\bullet-}$  charge separated species either *via* an electron migration (in the case of **2:5**, **2:6**, **4:5** and **4:6** triads) or hole shift (in the case of **3:5** and **3:6** triads). In agreement

with our previous study, due to distant separation of cation and radical anion species, the radical ion-pair persisted beyond 3 ns, the time window of our instrument (the final radical ion-pair persisted over 100–200 ns in DCB [40a]). The present study demonstrates the effect of the distance between ferrocene and zinc porphyrin entities in the supramolecular triads formed by axial coordination of fullerene on the primary and secondary electron transfer events.

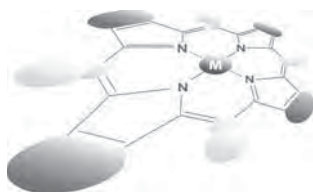
### Acknowledgements

This work is financially supported by the National Science Foundation (Grant nos. 1110942 and 1401188 to FD).

### REFERENCES

1. Gust D, Moore TA and Moore AL. *Acc. Chem. Res.* 2009; **42**: 1890–1898.
2. Gust D, Moore TA and Moore AL. *Acc. Chem. Res.* 2001; **34**: 40–48.
3. Wasielewski MR. *Acc. Chem. Res.* 2009; **42**: 1910–1921.
4. Guldi DM, Rahman GMA, Sgobba V and Ehli C. *Chem. Soc. Rev.* 2006; **35**: 471–487.
5. Schuster DI, Li K and Guldi DM. *C. R. Chimie* 2006; **9**: 892–908.
6. Gottari G, Trukhina O, Ince M and Torres T. *Coord. Chem. Rev.* 2012; **256**: 2453–2477.
7. Dirian K, Herranz MA, Katsukis G, Malig J, Rodriguez-Perez L, Romero-Nieto C, Strauss V, Martin N and Guldi DM. *Chem. Sci.* 2013; **4**: 4335–4353.
8. Sessler JL, Lawrence CM and Jayawickramarajah J. *Chem. Soc. Rev.* 2007; **36**: 314–325.
9. Fukuzumi S, Ohkubo K, D'Souza F and Sessler JL. *Chem. Commun.* 2012; **48**: 9801–9815.
10. Umeyama T and Imahori H. *Energy Environ. Sci.* 2008; **1**: 120–133.
11. Hasobe T. *Phys. Chem. Chem. Phys.* 2010; **12**: 44–57.
12. Imahori H, Umeyama T, Kei K and Yuta T. *Chem. Commun.* 2012; **48**: 4032–4045.
13. D'Souza F and Ito O. *Coord. Chem. Rev.* 2005; **249**: 1410–1422.
14. D'Souza F and Ito O. *Chem. Commun.* 2009; 4913–4928.
15. El-Khouly ME, Ito O, Smith PM and D'Souza F. *J. Photochem. Photobiol. C* 2004; **5**: 79–104.
16. D'Souza F and Ito O. *Chem. Soc. Rev.* 2012; **41**: 86–96.
17. D'Souza F and Ito O. *Molecules*, 2012; **17**: 5816–5835.
18. Fukuzumi S. *Org. Biomol. Chem.* 2003; **1**: 609–620.
19. Fukuzumi S. *Bull. Chem. Soc. Jpn.* 2006; **79**: 177–195.

20. Fukuzumi S. *Phys. Chem. Chem. Phys.* 2008; **10**: 2283–2297.
21. Fukuzumi S and Kojima T. *J. Mater. Chem.* 2008; **18**: 1427–1439.
22. Fukuzumi S, Honda T, Ohkubo K and Kojima T. *Dalton Trans.* 2009; 3880–3889.
23. Fukuzumi S and Ohkubo K. *J. Mater. Chem.* 2012; **22**: 4575–4587.
24. El-Khouly ME, Fukuzumi S and D'Souza F. *ChemPhysChem* 2014; **15**: 30–47.
25. Lewis NS and Nocera DG. *Proc. Natl. Acad. Sci. U.S.A.* 2006; **103**: 15729–15735.
26. Turner JA. *Science* 1999; **285**: 687–689.
27. Barber J. *Chem. Soc. Rev.* 2009; **38**: 185–196.
28. Scholes GD, Fleming GR, Olaya-Castro A and van Grondelle R. *Nat. Chem.* 2011; **3**: 763–774.
29. Kamat PV. *J. Phys. Chem. C* 2007; **111**: 2834–2860.
30. Fukuzumi S. *Eur. J. Inorg. Chem.* 2008; **9**: 1351–1362.
31. Fukuzumi S and Yamada Y. *J. Mater. Chem.* 2012; **22**: 24284–24296.
32. *The Photosynthetic Reaction Center*, Deisenhofer J and Norris JR. (Eds.) Academic Press: San Diego, 1993.
33. Deisenhofer J, Epp O, Miki K, Huber R and Michel H. *J. Mol. Biol.* 1984; **180**: 385–398.
34. (a) *Introduction of Molecular Electronics*, Petty MC, Bryce MR and Bloor D. (Eds.) Oxford University Press: New York, 1995. (b) *Molecular Switches*, Feringa BL. (Ed.) Wiley-VCH GmbH: Weinheim, 2001.
35. (a) Kroto HW, Heath JR, O'Brien SC, Curl RF and Smalley RE. *Nature* 1985; **318**: 162–163. (b) Kratschmer W, Lamb LD, Fostiropoulos F and Huffman DR. *Nature* 1990; **347**: 345–347. (c) *Fullerene and Related Structures*, Vol. 199, Hirsch A. (Ed.) Springer: Berlin, 1999. (d) Xie Q, Perez-Cordero E and Echegoyen L. *J. Am. Chem. Soc.* 1992; **114**: 3978–3980.
36. *The Porphyrin Handbook*, Vol. 1–10, Kadish KM, Smith KM and Guilard R. (Eds.) Academic Press: Burlington, MA, 2000.
37. Imahori H, Hagiwara K, Akiyama T, Akoi M, Taniguchi S, Okada T, Shirakawa M and Sakata Y. *Chem. Phys. Lett.* 1996; **263**: 545–550.
38. Marcus RA and Sutin N. *Biochim. Biophys. Acta* 1985; **811**: 265–273.
39. (a) Imahori H, Tamaki K, Guldi DM, Luo C, Fujitsuka M, Ito O, Sakata Y and Fukuzumi S. *J. Am. Chem. Soc.* 2001; **123**: 2607–2617. (b) Imahori H, Guldi DM, Tamaki K, Yoshida Y, Luo CP, Sakata Y and Fukuzumi S. *J. Am. Chem. Soc.* 2001; **123**: 6617–6628. (c) Imahori H, Tamaki K, Araki Y, Sekiguchi Y, Ito O, Sakata Y and Fukuzumi S. *J. Am. Chem. Soc.* 2002; **124**: 5165–5174. (d) Imahori H, Sekiguchi Y, Kashiwagi Y, Sato T, Araki Y, Ito O, Yamada H and Fukuzumi S. *Chem. Eur. J.* 2004; **10**: 3184–3196. (e) Guldi DM, Imahori H, Tamaki K, Kashiwagi Y, Yamada H, Sakata Y and Fukuzumi S. *J. Phys. Chem. A* 2004; **108**: 541–548. (f) Imahori H, Norieda H, Yamada H, Nishimura Y, Yamazaki I, Sakata Y and Fukuzumi S. *J. Am. Chem. Soc.* 2001; **123**: 100–110. (g) Kashiwagi Y, Imahori H, Araki Y, Ito O, Yamada K, Sakata Y and Fukuzumi S. *J. Phys. Chem. A* 2003; **107**: 5515–5522.
40. (a) D'Souza F, Smith PM, Gadde S, McCarty AL, Kullman MJ, Zandler ME, Ito O, Araki Y and Ito O. *J. Phys. Chem. B* 2004; **108**: 11333–11343. (b) D'Souza F, Chitta R, Gadde S, Islam DMS, Schumacher AL, Zandler ME, Araki Y and Ito O. *J. Phys. Chem. B* 2006; **110**: 25240–25250. (c) D'Souza F, El-Khouly ME, Gadde S, Zandler ME, McCarty AL, Araki Y and Ito O. *Tetrahedron* 2006; **62**: 1967–1978. (d) D'Souza F, Gadde S, Islam S, Wijesinghe CA, Schumacher AL, Zandler ME, Araki Y and Ito O. *J. Phys. Chem. A* 2007; **111**: 8552–8560. (e) Subbaiyan NK, Wijesinghe CA and D'Souza F. *J. Am. Chem. Soc.* 2009; **131**: 14646–14647. (f) Wijesinghe CA, El-Khouly ME, Zandler ME, Fukuzumi S and D'Souza F. *Chem. Eur. J.* 2013; **19**: 9629–9638. (g) Lim GN, Maligaspe E, Zandler ME and D'Souza F. *Chem. Eur. J.* 2014; **20**: 17089–17099.
41. (a) D'Souza F, Deviprasad GR, Zandler ME, Hoang VT, Klykov A, Perera M, van Stipdonk MJ, El-Khouly ME, Fujitsuka M and Ito O. *J. Phys. Chem. A* 2002; **106**: 3243–3252. (b) D'Souza F, Deviprasad GR, Rahman MS and Choi JP. *Inorg. Chem.* 1999; **38**: 2157–2160. (c) Das SK, Song B, Mahler A, Nesterov VN, Wilson AK, Ito O and D'Souza F. *J. Phys. Chem. C* 2014; **118**: 3994–4006. (d) Das SK, Mahler A, Wilson AK and D'Souza F. *ChemPhysChem* 2014; **15**: 2462–2472.
42. Rehm D and Weller A. *Isr. J. Chem.* 1970; **7**: 259.
43. Guldi DM and Kamat PV. In *Fullerenes*, Kadish KM and Ruoff RS. (Eds.) John Wiley & Sons: New York, 2000; Chapter 5, pp 225–281.
44. *Principles of Fluorescence Spectroscopy*, 3rd ed., Lakowicz JR. (Ed.) Springer: Singapore, 2006.
45. (a) Closs GL and Closs LE. *J. Am. Chem. Soc.* 1963; **85**: 818–819. (b) Kadish KM and Rhodes RK. *Inorg. Chem.* 1981; **20**: 2961–2966. (c) Neta P, Scherz A and Levanon H. *J. Am. Chem. Soc.* 1979; **101**: 3624–3629.
46. Kubo M, Mori Y, Otani M, Murakami M, Ishibashi Y, Yasuka M, Hosomizu K, Miyasaka H, Imahori H and Nakashima S. *J. Phys. Chem. A* 2007; **111**: 5136–5143.



# Nondestructive readout fluorescence memory based on a gallium(III) corrole complex and photochromic *cis*-1,2-dithienylethene

Jijoon Kang and Youngmin You<sup>\*◇</sup>

Department of Advanced Materials Engineering for Information and Electronics, Kyung Hee University, Yongin, Gyeonggi-do 446-701, Korea

Dedicated to Professor Shunichi Fukuzumi on the occasion of his retirement

Received 30 October 2014

Accepted 24 November 2014

**ABSTRACT:** Photochromic switching of fluorescence emission provides a viable principle to creation of all optical molecular memory. Successful operation of the fluorescence memory requires deliberate control of the energetics between a fluorophore and a photochrome. One essential requirement is that photoexcitation for fluorescence emission does not interfere with the photochromic processes. Gallium(III) corrole complexes outfit the condition because their fluorescence emissions display large Stokes shifts, permitting photoexcitation at the optical window where the photochromism of *cis*-1,2-dithienylethene is not executed. To demonstrate the capability for fluorescence memory, we prepared molecularly dispersed poly(methyl methacrylate) (PMMA) films of a gallium corrole complex and *cis*-1,2-dithienylethene. The memory cycle comprising fluorescence readout and reversible photochromic switching of the fluorescence emission is fully reversible without suffering from fatigue during repeated operation. The corresponding fluorescence on/off ratio is greater than those of previous memory based on porphyrins. Fluorescence lifetime measurements employing time-correlated single photon counting techniques reveal occurrence of fast energy transfer ( $\sim 10^9$  s<sup>-1</sup>) which is effectively gated by the photochromism.

**KEYWORDS:** fluorescence memory, corroles, photochromism, energy transfer.

## INTRODUCTION

Photochromism refers to a reversible interconversion between two isomers under alternating photoirradiation at different wavelengths. Among a variety of photochromic molecules, *cis*-1,2-dithienylethene is the most successful as its photochromism carries advantages, including ultrafast rates (<8 ps), full reversibility, thermal stability, and outstanding fatigue resistance [1–3]. *Cis*-1,2-dithienylethene undergoes a reversible [6 $\pi$ ] electrocyclic reaction, which consists of cyclization (*i.e.* open form  $\rightarrow$  closed form) and cycloreversion (*i.e.* closed form  $\rightarrow$  open form) occurring under UV and visible photoirradiation, respectively. The photochromism alters electronic

structures in the photoisomers, producing optical changes. The utility of modulating optical properties by selecting photoirradiation wavelengths is appealing for creation of molecular devices [4–6]. Of particular interest is fluorescence memory, since capability for remote access and high-contrast readout enables fully optical memory. Operation of the fluorescence memory is usually based on photochromic modulation of energy transfer between a fluorophore and *cis*-1,2-dithienylethene. Specifically, a fluorescence-off state is achieved due to nonradiative energy transfer to the closed form of *cis*-1,2-dithienylethene displaying strong absorption in the visible region, whereas the energy transfer is abolished by cycloreversion to the open form having high energy electronic states (*i.e.* fluorescence-on state).

To facilitate the photochromic modulation of fluorescence, a fluorophore should satisfy several criteria: (1) A large spectral overlap of the fluorescence emission

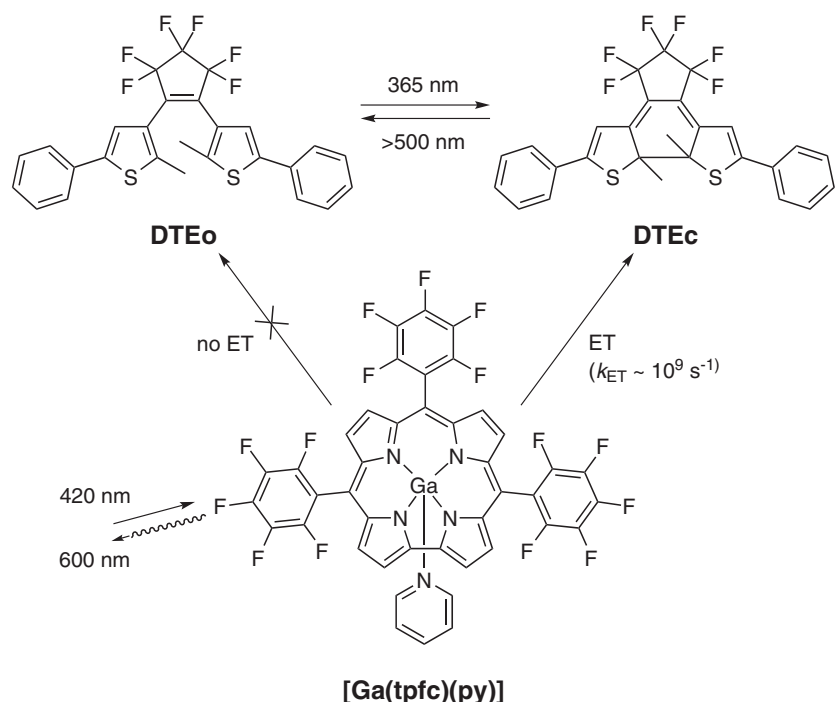
<sup>◇</sup>SPP full member in good standing

\*Correspondence to: Youngmin You, email: odds2@khu.ac.kr, tel: +82 31-201-3328, fax: +82 31-204-8114

with the absorption band of the closed form of *cis*-1,2-dithienylethene, and (2) the photoexcitation wavelength that does not interfere with the photochromic processes of *cis*-1,2-dithienylethene. Porphyrins are valuable platforms for creating fluorescence memory, because they display red fluorescence emissions which overlap with the strong visible absorption spectrum of the closed form of *cis*-1,2-dithienylethene. Furthermore, large Stokes shifts in the fluorescence emission enable spectral separation for selective photoexcitation of porphyrins. Indeed, several pioneering works by the research groups of Branda [7, 8], Andréasson [9], and Kim [10] have elegantly demonstrated utility of red-fluorescent porphyrins for constructing molecular fluorescence memories. The approach has recently been extended by the group of Shustova to preparation of photofunctional metal–organic frameworks comprised of zinc tetra(4-carboxylphenyl)porphyrin and a *cis*-1,2-dithienylethene compound having distal 4-pyridyl moieties [11]. In addition, fluorescence switching behaviors of triads involving *cis*-1,2-dithienylethene cores and two terminal porphyrin units have also been reported [12].

Corroles belong to a family of porphyrinoids, and are characteristic of a smaller core cavity due to the absence of one methine unit [13]. Syntheses and photophysical investigations of free-base and metalcorroles have been pioneered by Gross and co-workers, and the studies have shown that fluorescence properties of metalcorroles of light metal cores are superior to those of the porphyrin congeners [14–23]. Especially, aluminum and gallium

corroles possess fluorescence quantum yields greater than that of zinc porphyrin, with substantial molar absorbance values at the photoexcitation wavelengths [24–27]. The bright fluorescence emission retains large Stokes shifts, as fast internal conversion enables strong emission from the Q-band electronic state upon photoexcitation at the Soret band [27]. It is notable that the Soret absorption band is located within the spectral window where both the open and closed forms of *cis*-1,2-dithienylethene do not absorb. Therefore, it is anticipated that fluorescence memory based on metalcorroles can outperform those relying on porphyrins. Despite the promise, however, photochromic fluorescence memory involving metalcorroles has yet to be demonstrated to date. Herein, we report high contrast fluorescence memory with full capability for nondestructive readout of fluorescence information. The memory system consisted of a bimolecular mixture of 3,3'-(hexafluorocyclopent-1-ene-1,2-diyl)bis(2-methyl-5-phenylthiophene) (DTE) and a gallium complex of 5,10,15-tris(pentafluorophenyl)corrole and pyridine ([Ga(tpfc)(py)]) (Scheme 1). We chose [Ga(tpfc)(py)] because gallium(III) corrole complexes were established to display outstanding air stability and fluorescence performance [26, 28, 29]. In addition, the weak Lewis acidity of the gallium core conferred fluorescence properties insusceptible to coordinating media [28]. We directly monitored intermolecular energy transfer occurring from [Ga(tpfc)(py)] to the closed form of DTE by employing time-correlated single photon counting techniques, which provided compelling evidence that



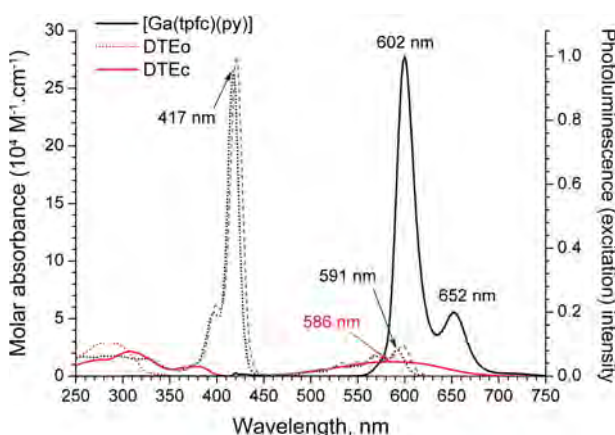
**Scheme 1.** Structures and schematic representation of the photophysical behaviors of [Ga(tpfc)(py)] and the open (DTEo) and closed (DTEc) forms of DTE

modulation of the unidirectional energy transfer served as the key mechanism of the memory.

## RESULTS AND DISCUSSION

DTE (10 wt% in a PMMA film) underwent cyclization under photoirradiation at 365 nm (4 W) to reach a photostationary state of the closed form (DTEc) within three min. Cycloreversion was relatively slow under our condition that employed white LEDs (7 W) and a cut-on filter ( $\lambda > 500$  nm). Although our experiments were not significantly impeded by the sluggish cyclization, use of high power lamps may improve the conversion rate. UV-vis absorption spectrum of the open form of DTE (DTEo, 10 wt% in a PMMA film) displayed a peak wavelength at 286 nm, and had no band in the visible region (Fig. 1). In contrast, the DTEc film showed blue absorption color with a strong absorption band at 586 nm. Cyclization and cycloreversion yields for DTE in PMMA films were determined to be 98% and 87%, respectively, using the molar absorbance value of DTEc at 586 nm ( $\epsilon = 1.2 \times 10^4 \text{ M}^{-1} \cdot \text{cm}^{-1}$ ) [30]. These values were comparable to the yields obtained in acetonitrile solutions [30, 31], indicating that the high yield photochromic properties were retained in the polymer films.

As shown in Fig. 1, a PMMA film containing 10 wt% [Ga(tpfc)(py)] exhibited strong red fluorescence. The fluorescence spectrum possessed two peaks occurring at  $\lambda_{\text{em}} = 602$  nm and 652 nm. The fluorescence quantum yield ( $\Phi_{\text{F}}$ ) determined using an integrating sphere was  $0.39 \pm 0.05$ . Photoluminescence excitation spectrum recorded at  $\lambda_{\text{em}} = 605$  nm matched perfectly with the UV-vis absorption spectrum (Fig. 1). This photophysical

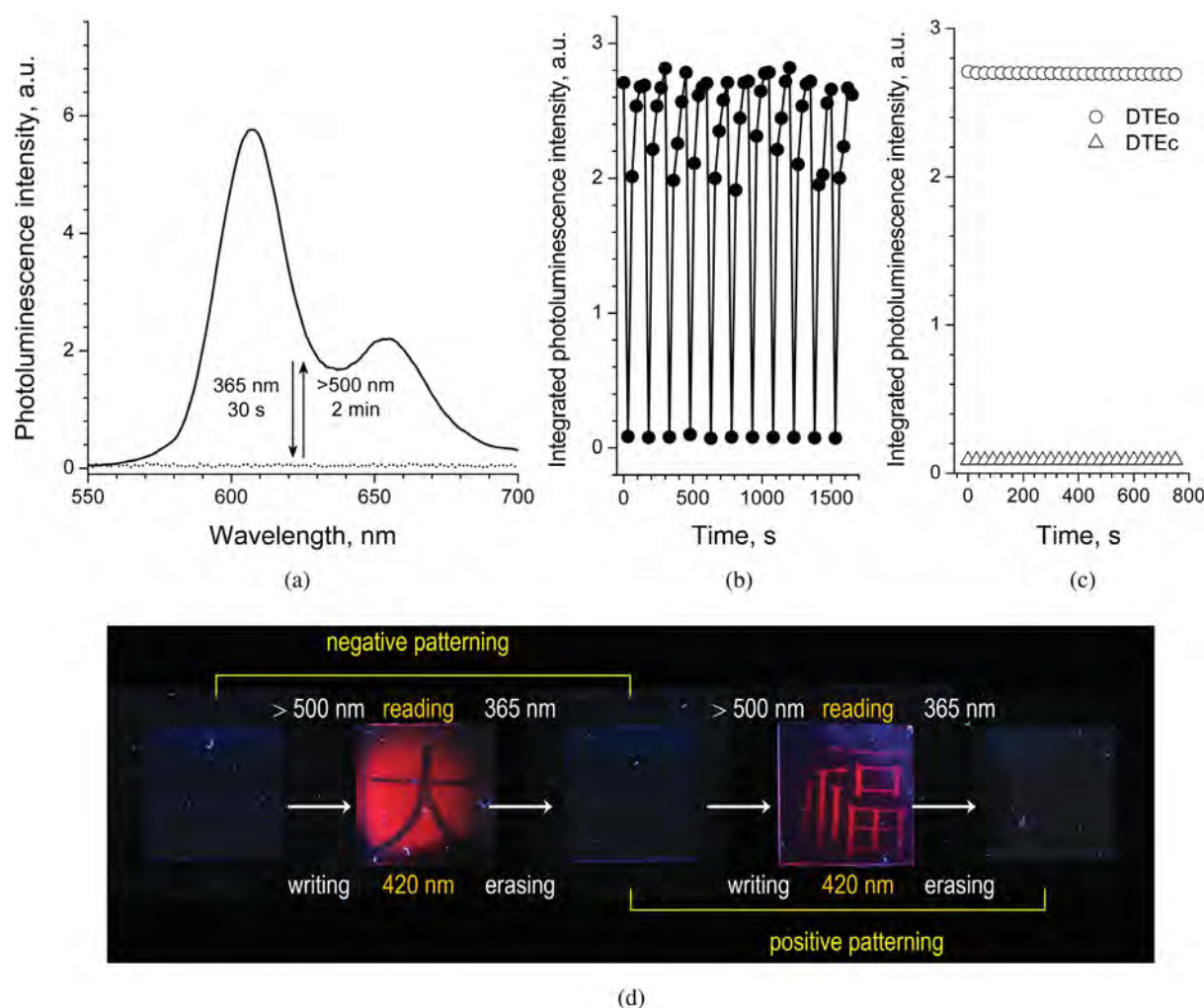


**Fig. 1.** UV-vis absorption spectra of DTEo (dotted red line), DTEc (solid red line), and [Ga(tpfc)(py)] (dotted black line), and photoluminescence (solid black line;  $\lambda_{\text{ex}} = 420$  nm) and photoluminescence excitation (dashed grey line;  $\lambda_{\text{obs}} = 605$  nm) spectra of [Ga(tpfc)(py)]. The photoluminescence and photoluminescence excitation spectra were normalized to their maximum values. DTE and [Ga(tpfc)(py)] were doped into PMMA films at 10 wt%

signature was consistent with the previous assignment that the red fluorescence originated from the first singlet excited ( $S_1$ ) state associated with the Q-band [27]. Nevertheless, stronger Soret absorption and ultrafast internal conversion from the second singlet excited ( $S_2$ ) state of the Soret band to the  $S_1$  state conferred a larger photoexcitation intensity on the Soret band. The Stokes shift between the Soret excitation and Q fluorescence was as large as  $7257 \text{ cm}^{-1}$ . The fluorescence spectrum of [Ga(tpfc)(py)] overlapped with the absorption band of DTEc with a spectral overlap integral of  $1.7 \times 10^{14} \text{ M}^{-1} \cdot \text{cm}^{-1} \cdot \text{nm}^4$ . The corresponding Förster radius was  $29 \text{ \AA}$ , being comparable with the value ( $30 \text{ \AA}$ ) for the zinc porphyrin coordinated with 3,3'-(hexafluorocyclopent-1-ene-1,2-diyl)bis(2-methyl-5-(4-pyridyl)thiophene)) [11]. It was also noted that both DTEo and DTEc had negligible absorption in the Soret absorption region (*i.e.*  $\lambda = 400\text{--}450$  nm). Taken together, the steady-state photophysical results suggest that the [Ga(tpfc)(py)] and DTE couple can perform nondestructive fluorescence memory with on/off ratios greater than porphyrin-based ones.

As the first demonstration of validity of our strategy, fluorescence memory behaviors were evaluated for a PMMA film doped with [Ga(tpfc)(py)] and DTE (2:1, mole/mole; [Ga(tpfc)(py)] concentration = 10 wt%). The full reversibility of the photochromism of DTE was retained in the binary mixture using the closing and opening photoirradiation wavelengths of  $\lambda_{\text{O} \rightarrow \text{C}} = 365$  nm and  $\lambda_{\text{C} \rightarrow \text{O}} > 500$  nm, respectively. Strong fluorescence emission from [Ga(tpfc)(py)] was observed in the DTEo state upon the photoirradiation at  $\lambda_{\text{ex}} = 420$  nm. In sharp contrast, the [Ga(tpfc)(py)] emission was quenched completely by cyclization to DTEc (Fig. 2a). The corresponding fluorescence on/off ratio estimated from the integrated fluorescence intensities was as high as 40. Subsequent cycloreversion by exposure to visible light  $\lambda_{\text{C} \rightarrow \text{O}} > 500$  nm restored to the original spectrum. The memory cycle comprising writing ( $\lambda_{\text{C} \rightarrow \text{O}} > 500$  nm), reading ( $\lambda_{\text{ex}} = 420$  nm), and erasing ( $\lambda_{\text{O} \rightarrow \text{C}} = 365$  nm) was fully reversible with fatigue resistance for more than 10 times (Fig. 2b). Indeed, the fluorescence intensities in both DTEo and DTEc states were not influenced by the prolonged exposure to the photoexcitation beam ( $\lambda_{\text{ex}} = 420$  nm; Fig. 2c). The demonstration unequivocally showed the full ability for fluorescence memory with nondestructive readout capability.

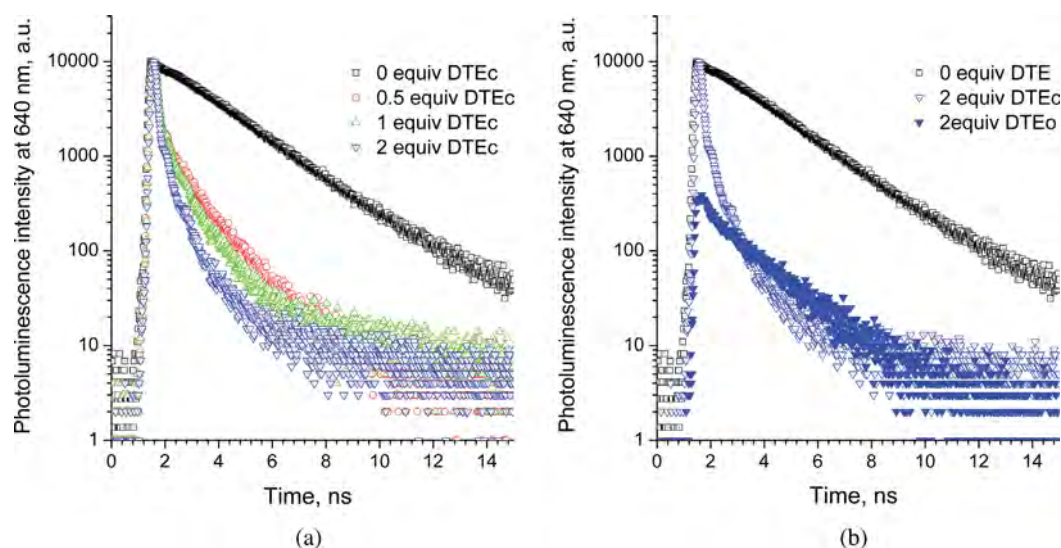
To establish the photophysical mechanism for the photochromic fluorescence modulation, we monitored the fluorescence decay traces ( $\lambda_{\text{obs}} = 640$  nm) of the PMMA films containing 10 wt% [Ga(tpfc)(py)] and varying concentrations (0–2 equiv. to [Ga(tpfc)(py)]) of DTEc after picosecond pulsed photoexcitation at 377 nm (Fig. 3a). Exposure to the 377 nm laser was kept as brief as possible to minimize cyclization of DTE. The fluorescence decay trace of [Ga(tpfc)(py)] followed a monoexponential decay model in the absence of DTEc.



**Fig. 2.** Demonstration of the nondestructive fluorescence memory. [Ga(tpfc)(py)] and DTE (2:1, by mole/mole; [Ga(tpfc)(py)] concentration = 10 wt%) were doped into PMMA films. (a) Photoluminescence spectra ( $\lambda_{\text{ex}} = 420 \text{ nm}$ ) of the PMMA film after cyclization (dotted line;  $\lambda_{\text{O} \rightarrow \text{C}} = 365 \text{ nm}$ ) and cycloreversion (solid line;  $\lambda_{\text{C} \rightarrow \text{O}} > 500 \text{ nm}$ ) of DTE. (b) Repetitive fluorescence switching of the PMMA film during the alternated photoirradiation at  $\lambda_{\text{O} \rightarrow \text{C}} = 365 \text{ nm}$  and  $\lambda_{\text{C} \rightarrow \text{O}} > 500 \text{ nm}$ . Fluorescence intensities were recorded under photoexcitation at  $\lambda_{\text{ex}} = 420 \text{ nm}$ . (c) Nondestructivity of the fluorescence-on (circles) and -off (triangles) states under prolonged photoirradiation at  $\lambda_{\text{ex}} = 420 \text{ nm}$ . (d) Photos showing the fluorescence memory behaviors consisting of the writing ( $\lambda_{\text{C} \rightarrow \text{O}} > 500 \text{ nm}$ ), reading ( $\lambda_{\text{ex}} = 420 \text{ nm}$ ), and erasing ( $\lambda_{\text{O} \rightarrow \text{C}} = 365 \text{ nm}$ ) cycle

The fluorescence lifetime was 2.59 ns, similar to the value (2.39 ns) for a 50  $\mu\text{M}$  [Ga(tpfc)(py)] solution in deaerated  $\text{CH}_3\text{CN}$ . Increasing the DTEc concentration in the PMMA films shortened the fluorescence lifetime. The decay traces for the mixture of [Ga(tpfc)(py)] and DTEc were best fitted to a biexponential decay model. Fit parameters, including fluorescence lifetimes and preexponential factors, are piled in Table S1 in the Supporting information. Weighted average values of the fluorescence lifetimes were, thus, calculated to be 0.89, 0.67, and 0.50 ns for the films containing 0.50, 1.0, and 2.0 equiv. DTEc, respectively. The decrease in the fluorescence lifetimes should be ascribed to intermolecular energy transfer to DTEc, because photoinduced electron transfer for generation of a nonemissive charge-separated species would be unlikely in the doped polymer films.

The energy transfer rate ( $k_{\text{ET}}$ ) for the 2:1 mixture for DTEc and [Ga(tpfc)(py)] was calculated to be  $1.6 \times 10^9 \text{ s}^{-1}$ , using the relationship,  $k_{\text{ET}} = 1/\tau - 1/\tau_0$ , where  $\tau$  and  $\tau_0$  are the fluorescence lifetimes of [Ga(tpfc)(py)] in the presence and absence of DTEc, respectively. This energy transfer rate was comparable to the intramolecular energy transfer rates for dyads consisting of [Ga(tpfc)(py)] and BODIPY compounds [32]. The  $k_{\text{ET}}$  value was one order of magnitude greater than the radiative rate constant ( $k_r$ ,  $k_r = \Phi_{\text{F}}/\tau_0$ ) and the nonradiative rate constant ( $k_{\text{nr}}$ ,  $k_{\text{nr}} = (1 - \Phi_{\text{F}})/\tau_0$ ) of [Ga(tpfc)(py)], which were  $1.5 \times 10^8 \text{ s}^{-1}$  and  $2.4 \times 10^8 \text{ s}^{-1}$ , respectively. The corresponding quantum yield for energy transfer ( $\Phi_{\text{ET}}$ ,  $\Phi_{\text{ET}} = k_{\text{ET}}/(k_{\text{ET}} + k_r + k_{\text{nr}})$ ) reached as large as 0.80. The energy transfer was abolished by cycloreversion to DTEo. As shown in Fig. 3b, the fluorescence lifetime of the decay trace ( $\lambda_{\text{obs}} = 640 \text{ nm}$ )



**Fig. 3.** (a) Photoluminescence decay traces ( $\lambda_{\text{obs}} = 640 \text{ nm}$ ) for PMMA films doped with 10 wt% [Ga(tpfc)(py)] and increased concentrations (0, 0.50, 1.0, and 2.0 equiv.) of DTEc after picosecond pulsed laser photoexcitation (temporal resolution = 16 ps) at 377 nm. (b) Comparison of the photoluminescence decay traces ( $\lambda_{\text{obs}} = 640 \text{ nm}$ ) of 10 wt% [Ga(tpfc)(py)] (empty black squares) and 10 wt% [Ga(tpfc)(py)] in the closed (empty blue triangles) and open (filled blue triangles) states of DTE (2.0 equiv.). Acquisition of the decay trace for the film containing 2 equiv. DTEo was kept as brief as possible (<3 s) to minimize cyclization. Fit parameters to a biexponential decay model are piled in Tables S1 and S2 in the Supporting information

for a PMMA film containing a 2:1 ratio of DTEo and [Ga(tpfc)(py)] was 2.50 ns, being practically identical to that for the unperturbed [Ga(tpfc)(py)] (*i.e.* 2.59 ns).

## EXPERIMENTAL

### Materials

[Ga(tpfc)(py)] was prepared according to the protocols established by Gross and Bendix *et al.* [14, 26]. Further purification using preparative TLC techniques was carried out to improve purity of the compound. Spectroscopic identification results of the gallium corrole complex, including  $^1\text{H}$  and  $^{19}\text{F}$  NMR and ESI MS spectra, were consistent with the proposed structure, while the ESI MS spectrum revealed detachment of the pyridine ligand under the ESI conditions. Synthesis of 3,3'-(hexafluorocyclopent-1-ene-1,2-diyl)bis(2-methyl-5-phenylthiophene) (DTE) was reported earlier by us [30]. Commercially available chemicals, including poly(methyl methacrylate) (PMMA;  $M_w = 120,000$ , Aldrich) were used as received without additional purification.  $\text{CH}_2\text{Cl}_2$  and THF were purified by filtering over anhydrous alumina columns prior to use. Reactions were monitored using thin layer chromatography (TLC). Commercial TLC plates (silica gel 60 F254, Merck Co.) were developed and the spots were visualized under UV illumination at 254 or 365 nm. Silica gel column chromatography was performed using silica gel 60 (particle size 0.040–0.063 mm, Merck Co.).  $^1\text{H}$ ,  $^{13}\text{C}$ , and  $^{19}\text{F}$  NMR spectra were collected with a Bruker Ultrashield 400 plus NMR spectrometer, and the

$^1\text{H}$  and  $^{13}\text{C}$  NMR spectra were referenced to deuterated solvents. ESI MS spectra were recorded using a Thermo Electronics Co. Finnigan LCQ Advantage Max spectrometer. High resolution mass spectra were acquired by employing a JEOL JMS-600W/JMS-700GC and an Applied Biosystems Tempo nano HPLC/QSTAR Elite spectrometers.

### Synthesis

**[Ga(tpfc)(py)].** Violet powder. Yield 5%.  $^1\text{H}$  NMR ( $\text{CDCl}_3$ , 400 MHz):  $\delta$ , ppm 2.89 (d,  $J = 4.6 \text{ Hz}$ , 2H), 5.77 (t,  $J = 6.7 \text{ Hz}$ , 2H), 6.54 (t,  $J = 7.7 \text{ Hz}$ , 1H), 8.63 (d,  $J = 4.2 \text{ Hz}$ , 2H), 8.78 (m, 2H), 8.84 (d,  $J = 3.8 \text{ Hz}$ , 2H), 9.20 (d,  $J = 4.0 \text{ Hz}$ , 2H).  $^{19}\text{F}$  NMR ( $\text{CDCl}_3$ , 376 MHz):  $\delta$ , ppm -162.36 (m, 6F), -153.81 (m, 3F), -137.75 (m, 6F). MS (ESI, positive):  $m/z$  945.5 (calcd. for [Ga(tpfc)( $\text{NCCH}_3$ ) $_2$  +  $\text{H}$ ] $^+$ , 945.0). UV-vis ( $\text{CH}_3\text{CN}$ ):  $\lambda_{\text{abs}}$ , nm ( $\epsilon$ ,  $\text{M}^{-1}\cdot\text{s}^{-1}$ ) 417 (264000), 548 (8980), 567 (18200), 591 (22500).

**3,3'-(Hexafluorocyclopent-1-ene-1,2-diyl)bis(2-methyl-5-phenylthiophene) (DTE).** White powder. Yield 38%.  $^1\text{H}$  NMR (400 MHz,  $\text{CD}_3\text{CN}$ ):  $\delta$ , ppm 2.02 (s, 6H), 7.33 (t,  $J = 7.2 \text{ Hz}$ , 2H), 7.38–7.43 (m, 6H), 7.60 (d,  $J = 7.2 \text{ Hz}$ , 4H).  $^{13}\text{C}$  NMR (100 MHz,  $\text{CDCl}_3$ ):  $\delta$ , ppm 14.8, 122.7, 125.9, 126.1, 128.1, 129.2, 133.6, 141.5, 143.5. HR MS (FAB, positive):  $m/z$  311.9819 (calcd. for  $\text{C}_{27}\text{H}_{18}\text{F}_6\text{S}_2$ , 311.9820).

### Preparation of PMMA films

1,2-dichloroethane solution containing 5 wt% of solute (PMMA, [Ga(tpfc)(py)], and DTE) was sonicated for 15 min. The total concentration of the dopants (*i.e.*

[Ga(tpfc)(py)] and DTE) was kept to 10 wt% relative to PMMA, unless otherwise stated. The solution was passed through a 0.45  $\mu\text{m}$  PVDF disposable syringe filter to remove insoluble fractions prior to spincoating. The polymer solution was delivered onto a 2.5 cm  $\times$  2.5 cm glass substrate using a micropipette to cover the whole surface of the substrate. Spincoating was performed at 2000 rpm for 30 s using a WON corporation HANA-150D spincoater.

### Spectroscopic measurements

The photostationary states of the open and closed forms of DTE were achieved by irradiating at  $\lambda > 500$  nm (a white light from 7 W LEDs was allowed to pass a cut-on filter) and  $\lambda = 365$  nm (4 W, VL-4.LC, VILBER LOURMAT), respectively. UV-vis absorption spectra were collected on an Agilent Cary 300 UV-vis spectrophotometer at room temperature. Photoluminescence spectra were obtained using a Quanta Master 400 scanning spectrofluorimeter at room temperature. The samples were excited at 420 nm throughout the photoluminescence measurements. The absolute photoluminescence quantum yields of the films were determined using an integrating sphere. The measurements were performed in triplicate. Photoluminescence decay traces of the films were acquired based on time-correlated single photon counting (TCSPC) techniques using a FluoTime 200 instrument (PicoQuant, Germany). A picosecond 377 nm diode laser (PicoQuant, Germany; temporal resolution = 16 ps) was used as the excitation source. The photoluminescence signals at 640 nm were obtained using an automated motorized monochromator. Photoluminescence decay profiles were analyzed (OriginPro 8.0, OriginLab) using mono- or biexponential decay models. The measurements were performed in duplicate using fresh films.

### CONCLUSION

To summarize, we successfully demonstrated the nondestructive readout fluorescence memory by uniquely combining the photochromic molecule (DTE) and red-fluorescent gallium(III) corrole complex, [Ga(tpfc)(py)]. The fluorescence memory was fabricated by doping [Ga(tpfc)(py)] and DTE into a PMMA matrix. The erasing and writing cycle of the memory involved photochromic cyclization ( $\lambda_{\text{O} \rightarrow \text{C}} = 365$  nm) and cycloreversion ( $\lambda_{\text{C} \rightarrow \text{O}} > 500$  nm), respectively, while fluorescence acquisition ( $\lambda_{\text{ex}} = 420$  nm) served as the readout process. The all-optical cycle of write-read-erase was fully reversible, and the fluorescence reading did not alter the information recorded by the photochromism. The photochromic modulation of the fluorescence intensities was investigated by monitoring fluorescence decay traces of [Ga(tpfc)(py)] with varying the concentration of DTE. Photochromic cyclization of DTE significantly shortened the fluorescence lifetime

of [Ga(tpfc)(py)], whereas cycloreversion restored the original fluorescence decay profiles. The rate constant for the energy transfer from [Ga(tpfc)(py)] to the closed form of DTE was one order of magnitude greater than the rate constants for radiative and nonradiative transition of [Ga(tpfc)(py)], supporting the notion that the photochromically gated energy transfer served as the key mechanism of the fluorescence memory.

### Acknowledgements

This work was supported by a grant from Samsung Research Funding Center for Future Technology (SRFC-MA1301-01 to Y.Y.).

### Supporting information

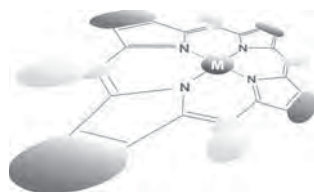
Figures S1–S5 and Tables S1–S2 are given in the supplementary material. This material is available free of charge *via* the Internet at <http://www.worldscinet.com/jpp/jpp.shtml>.

### REFERENCES

1. Perrier A, Maurel F and Jacquemin D. *Acc. Chem. Res.* 2012; **45**: 1173–1182.
2. Nakamura S, Yokojima S, Uchida K, Tsujioka T, Goldberg A, Murakami A, Shinoda K, Mikami M, Kobayashi T, Kobatake S, Matsuda K and Irie M. *J. Photochem. Photobiol. A* 2008; **200**: 10–18.
3. Matsuda K and Irie M. *J. Photochem. Photobiol. C* 2004; **5**: 169–182.
4. Irie M. *Chem. Rev.* 2000; **100**: 1685–1716.
5. Tian H and Yang S. *Chem. Soc. Rev.* 2004; **33**: 85–97.
6. Yun C, You J, Kim J, Huh J and Kim E. *J. Photochem. Photobiol. C* 2009; **10**: 111–129.
7. Norsten TB and Branda NR. *Adv. Mater.* 2001; **13**: 347–349.
8. Norsten TB and Branda NR. *J. Am. Chem. Soc.* 2001; **123**: 1784–1785.
9. Kärnbratt J, Hammarson M, Li S, Anderson HL, Albinsson B and Andréasson J. *Angew. Chem., Int. Ed.* 2010; **49**: 1854–1857.
10. Kim HJ, Jang JH, Choi H, Lee T, Ko J, Yoon M and Kim H-J. *Inorg. Chem.* 2008; **47**: 2411–2415.
11. Williams DE, Rietman JA, Maier JM, Tan R, Greytak AB, Smith MD, Krause JA and Shustova NB. *J. Am. Chem. Soc.* 2014; **136**: 11886–11889.
12. Osuka A, Fujikane D, Shinmori H, Kobatake S and Irie M. *J. Org. Chem.* 2001; **66**: 3913–3923.
13. Johnson AW and Kay IT. *J. Chem. Soc.* 1965: 1620–1629.
14. Gross Z, Galili N and Saltsman I. *Angew. Chem., Int. Ed.* 1999; **38**: 1427–1429.
15. Gross Z, Golubkov G and Simkhovich L. *Angew. Chem., Int. Ed.* 2000; **39**: 4045–4047.



16. Gross Z, Simkhovich L and Galili N. *Chem. Commun.* 1999: 599–600.
17. Paolesse R, Jaquinod L, Nurco DJ, Mini S, Sagone F, Boschi T and Smith KM. *Chem. Commun.* 1999: 1307–1308.
18. Simkhovich L, Mahammed A, Goldberg I and Gross Z. *Chem. Eur. J.* 2001; **7**: 1041–1055.
19. Paolesse R, Licoccia S and Boschi T. *Inorg. Chim. Acta* 1990; **178**: 9–12.
20. Saltsman I, Mahammed A, Goldberg I, Tkachenko E, Botoshansky M and Gross Z. *J. Am. Chem. Soc.* 2002; **124**: 7411–7420.
21. Sorasaene K, Taqavi P, Henling LM, Gray HB, Tkachenko E, Mahammed A and Gross Z. *J. Porphyrins Phthalocyanines* 2007; **11**: 189–197.
22. Gryko DT and Koszarna B. *Org. Biomol. Chem.* 2003; **1**: 350–357.
23. Gross Z, Galili N, Simkhovich L, Saltsman I, Botoshansky M, Bläser D, Boese R and Goldberg I. *Org. Lett.* 1999; **1**: 599–602.
24. Weaver JJ, Sorasaene K, Sheikh M, Goldschmidt R, Tkachenko E, Gross Z and Gray HB. *J. Porphyrins Phthalocyanines* 2004; **8**: 76–81.
25. Agadjanian H, Ma J, Rentsendorj A, Valluripalli V, Hwang JY, Mahammed A, Farkas DL, Gray HB, Gross Z and Medina-Kauwe LK. *Proc. Natl. Acad. Sci., USA* 2009; **106**: 6105–6110.
26. Bendix J, Dmochowski IJ, Gray HB, Mahammed A, Simkhovich L and Gross Z. *Angew. Chem., Int. Ed.* 2000; **39**: 4048–4051.
27. Liu X, Mahammed A, Tripathy U, Gross Z and Steer RP. *Chem. Phys. Lett.* 2008; **459**: 113–118.
28. Kowalska D, Liu X, Tripathy U, Mahammed A, Gross Z, Hirayama S and Steer RP. *Inorg. Chem.* 2009; **48**: 2670–2676.
29. Ding T, Alemán EA, Modarelli DA and Ziegler CJ. *J. Phys. Chem. A* 2005; **109**: 7411–7417.
30. Lee S, You Y, Ohkubo K, Fukuzumi S and Nam W. *Org. Lett.* 2012; **14**: 2238–2241.
31. Lee S, You Y, Ohkubo K, Fukuzumi S and Nam W. *Angew. Chem., Int. Ed.* 2012; **51**: 13154–13158.
32. Brizet B, Desbois N, Bonnot A, Langlois A, Dubois A, Barbe J-M, Gros CP, Goze C, Denat F and Harvey PD. *Inorg. Chem.* 2014; **53**: 3392–3403.



## Photophysical properties of Sn(IV)tetraphenylporphyrin-pyrene dyad with a $\beta$ -vinyl linker

P. Silviya Reeta<sup>\*a</sup>, Adis Khetubol<sup>a</sup>, Tejaswi Jella<sup>b</sup>, Vladimir Chukharev<sup>a</sup>,  
Fawzi Abou-Chahine<sup>a</sup>, Nikolai V. Tkachenko<sup>a $\diamond$</sup> , L. Giribabu<sup>\*b</sup>  
and Helge Lemmetyinen<sup>\*a $\diamond$</sup>

<sup>a</sup>Department of Chemistry and Bioengineering, Tampere University of Technology, P.O. Box 541,  
FIN-33101 Tampere, Finland

<sup>b</sup>Inorganic & Physical Chemistry Division, CSIR-Indian Institute of Chemical Technology, Uppal Road,  
Tarnaka, Hyderabad 500007, Telangana, India

*Dedicated to Professor Shunichi Fukuzumi on the occasion of his retirement*

Received 30 October 2014

Accepted 25 November 2014

**ABSTRACT:** A Sn(IV)tetraphenylporphyrin (T) has been functionalized with a  $\beta$ -vinyl pyrene (P) and the photophysical properties of the formed dyad (T-P) with its corresponding precursors were studied in three solvents with different polarities using steady-state and time-resolved measurements in ps and fs timescales. When the pyrene moiety is excited at  $\lambda_{\text{ex}} = 340$  nm, the fluorescence spectroscopy experiments indicate in all the studied solvents, an efficient quenching of the pyrene emission. When excited at either  $\lambda_{\text{ex}} = 340$  nm or  $\lambda_{\text{ex}} = 405$  nm, where porphyrin absorbs, a new emissive excited state complex (T-P)\* is observed at wavelengths close to the parent porphyrin emission. The emission is more pronounced in nonpolar hexane showing a mono-exponential decay, but bi-exponential decays are observed in more polar dichloromethane and acetonitrile. When the porphyrin moiety is excited at  $\lambda_{\text{ex}} = 425$  nm, the fs transient absorption analysis shows two different intermediate species ( $\sim 7$ –11 ps and 80–100 ps) with broad absorption in the near-IR region. This implies either the existence of two different excited conformers (T-P)\*, which decay to the ground state *via* a charge separated state (CSS), or the formation of the (T-P)\* state *via* the second excited state of the porphyrin moiety, yielding first an excited emissive  $\nu$ (T-P)\* state, with a lifetime of 80–100 ps.

**KEYWORDS:** Sn(IV)tetraphenylporphyrin,  $\beta$ -vinyl pyrene donor, optical properties, fs transient absorption, kinetics.

### INTRODUCTION

Porphyrin and their metallo derivatives render as potential chromophores in a wide variety of organo-electronic applications [1–8]. While their close resemblance with the natural photosynthetic reaction center [9–13] represent them as unique model systems to understand the more complex photoinduced electron and energy transfer reactions occurring in nature [7].

Though extensive reports are available describing the intramolecular excitation energy transfer (EET) and photoinduced electron transfer (PET) in a variety of porphyrin-based donor-acceptor (D-A) systems with a donor/acceptor attached either at a peripheral (*-meso* [14–19] or  $\beta$ -pyrrolic [20–24]) or at axial position of resident metallo/metalloid center [27–31], there endures a continual interest in exploring the excited state behavior of such D-A systems. Markedly, functionalizing the pyrrole- $\beta$  position with donors/acceptors has gained special importance due to the favorable in-plane orbital overlap of the peripheral donor with the  $\pi$ -conjugated macrocycle, which sequentially enhances the effective

<sup>$\diamond$</sup>  SPP full member in good standing

\*Correspondence to: Helge Lemmetyinen, email: helge.lemmetyinen@tut.fi, tel: +358 40-581-1347

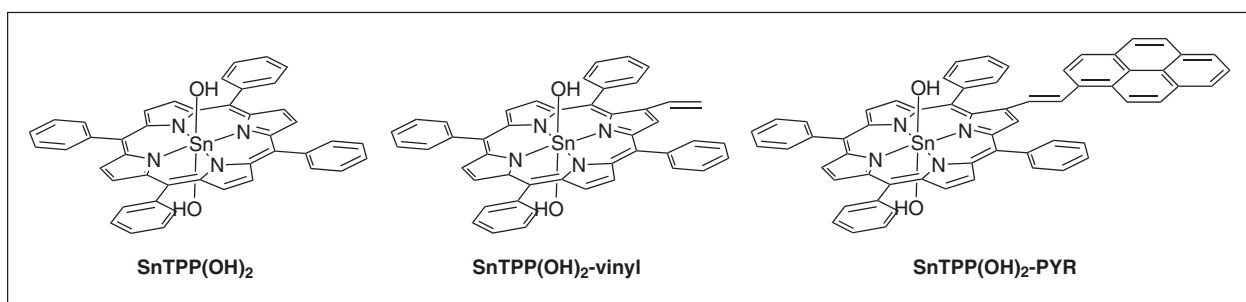


Fig. 1. Molecular structure of the Sn(IV)porphyrin-pyrene dyad and its precursors

electron/energy transfer between the peripheral substitution with the porphyrin ring [20–24].

The fascinating photophysical aspects of Sn(IV) porphyrin supramolecular architectures were investigated previously [29] by employing a wide range of axially ligated donors and acceptors. Recently, we investigated photophysical properties of porphyrin-pyrene dyad in which pyrene is connected at  $\beta$ -pyrrolic position of either a free-base or Zn(II) porphyrin [24]. In this report, the macrocyclic Sn(IV)porphyrin conjugation is extended with a pyrene chromophore *via* a vinylene spacer at the  $\beta$ -pyrrolic position (Fig. 1) and its influence on the structural, redox, and excited state properties of the macrocycle have been dealt in detail using various spectroscopic techniques in the subsequent sections. Further research on axial substitution of the Sn(IV) porphyrin-pyrene dyad with specific acceptor moieties is being continued in our laboratory.

## EXPERIMENTAL

### General

All the reagents and solvents used for the reactions were purchased from Sigma-Aldrich. The solvents utilized for the electrochemical and spectral analysis were further purified by following standard procedures [32]. Moisture sensitive reactions were performed under an inert atmosphere of nitrogen. Chromatographic purifications were performed using Silica gel (60–120 mesh) and neutral or basic alumina (activity grade I).

The UV-visible spectra were recorded on a Shimadzu (Model UV-3600) spectrophotometer using  $1 \times 10^{-6}$  M concentrations. The steady-state fluorescence measurements were performed on a Fluorolog-3 spectrofluorometer (Spex Model, JobinYvon). The concentration of the solutions were maintained constantly at OD < 0.1 for all the compounds in order to eliminate the possibility of quenching caused by the aggregation and to minimize nonlinear absorption and re-absorption effects.

The time correlated single photon counting (TCSPC) method was used for measuring the fluorescence lifetime of the molecules in their excited state. The base (PicoQuant

GmbH) system consisted of PicoHarp-200 controller, a PDL-800-B driver and pulsed LED (PLS-8-2-295) and pulsed diode (LDH-P-C-405B) exciting samples at 340 and 405 nm, respectively. The detection part consisted of micro-channel photomultiplier tube (R3809u-50 Hamamatsu) coupled with a monochromator. The time resolution of the system was roughly 300 and 60 ps with excitation at 340 and 405 nm, respectively. The data were analyzed using a freely available software package Decfit. The quality of the fit was ascertained from the  $\chi^2$  values and the distribution of residuals. Differential pulse voltammetric (DPV) technique was performed using a PC-controlled electrochemical analyzer (CH instrument model CHI620C) using Ferrocene as the standard and 0.1 M TBAP (*vs.*) SCE under standard experimental conditions.

The fluorescence decay associated spectra (DAS) were obtained by global fitting of the fluorescence decays, measured at every 10 nm over the region of the emission spectrum (550–800 nm) ( $\chi^2 \sim 1.1$ ), at a fixed excitation intensity and measurement time. The relative amplitudes of the decay components were further corrected by a function corresponding to the detector sensitivity [33].

Ultrafast fluorescence decays were measured using an up-conversion method described elsewhere [34] with a temporal resolution of  $\sim 150$  fs. In brief, fundamental pulses of 840 nm produced by a Ti:Sapphire laser (TiF50, CDP-Avesta) at 80 MHz repetition rate were split into two beams. One portion underwent second harmonic generation to excite the sample at 420 nm, generating emission. The second portion of the fundamental pulse beam was passed to a delay line and then mixed with the emission to achieve frequency up-conversion. The resulting UV photons were detected by a photon counting photomultiplier coupled with a monochromator with a typical averaging of 10 s at each delay time.

For transient absorption measurements, a sub-picosecond resolution setup was used and described in detail elsewhere [34, 35]. Briefly, 800 nm laser pulses at 1 kHz repetition rate were generated by a Ti:Sapphire laser system (Libra F, Coherent Inc.). The fundamental pulses were split into two beams; one pump beam was guided through an optical parametric amplifier (Topas C, Light Conversion Ltd.) to generate the excitation pulses

at 340 and 425 nm. The pump beam and the rest of fundamental were delivered to a pump-probe measurement system (ExciPro, CDP Inc.). The system generated a white light continuum (WLC) from the 800 nm beam which was used as a probe pulse. The probe was guided through a delay line with a moving right angle reflector that changed the optical path length of the probe with respect to the pump beam. The maximum time scale available to monitor absorption changes was *ca.* 6 ns. The probe pulse was split into two to obtain signal and reference beams that both passed through the sample. The signal beam was overlapped with the pump beam while the reference beam was not. The excitation was modulated by a chopper synchronized excitation pulses to detect probe pulse spectra with and without the excitation and to calculate differential transient absorbance for each excitation pulse. Measurements were recorded with a 10 s average for each delay time, *i.e.* averaging 10000 excitation shots. The spectra were acquired in two ranges, 460–780 nm and 850–1050 nm. The measurements around fundamental wavelength, 800 nm, were unreliable since the continuum was very uneven close to the fundamental.

The raw data were fit globally by a sum of exponents to perform data analysis, a procedure which has been described in more detail previously [34]. Briefly, the number of exponents needed for a reasonable fit quality yielded the number of transient species in the photo-induced processes. The rate constants for the formation or relaxation of transient species can be calculated from the respective lifetimes of each component. The results of the fits are presented as decay component spectra with the amplitudes of the exponents plotted as functions of wavelength.

## Synthesis

The 5,10,15,20-tetraphenylporphyrinato tin(IV) [**SnTPP(OH)<sub>2</sub>**] [36], 2-vinyl-5,10,15,20-tetraphenylporphyrinato tin(IV) [**SnTPP(OH)<sub>2</sub>-vinyl**] [37], and 2-pyrenyl-5,10,15,20-tetraphenylporphyrinato tin(IV) [**SnTPP(OH)<sub>2</sub>-PYR**] [20, 22] were synthesized by following the literature reported procedures. The synthetic details are presented in the experimental procedure below.

## General procedure for the synthesis of dihydroxy Sn(IV)porphyrins

The dihydroxy tin(IV) porphyrins were synthesized by refluxing the corresponding free-base porphyrin (2.0 g, 3 mM, for representative H<sub>2</sub>TPP) and SnCl<sub>2</sub>·2H<sub>2</sub>O (3.0 g, 13 mM) dissolved in 50 mL of pyridine for 2 h. Then the mixture was cooled and pyridine was removed under reduced pressure. The solid obtained was dissolved in CHCl<sub>3</sub> and washed several times with water. The organic layer was dried by passing through anhydrous Na<sub>2</sub>SO<sub>4</sub> and chromatographed over basic alumina. Elution with CHCl<sub>3</sub>/CH<sub>3</sub>OH (98:2 V/V) gave the corresponding dichloro tin(IV) porphyrins. Yield upto 95%.

A 10% aqueous NaOH solution was added to the CHCl<sub>3</sub> solution of the corresponding dichloro Sn(IV) porphyrin and the mixture was stirred at room temperature for 2 h. The organic layer was separated and dried to get violet solid of the corresponding dihydroxy Sn(IV) porphyrin, which were recrystallized from CH<sub>2</sub>Cl<sub>2</sub>-hexane. Yield upto 90%.

**SnTPP(OH)<sub>2</sub>.** Yield 90%. ESI-MS: *m/z* C<sub>44</sub>H<sub>30</sub>N<sub>4</sub>O<sub>2</sub>Sn, (765.44): [M + H<sup>+</sup>] 766 (85%). <sup>1</sup>H NMR (CDCl<sub>3</sub>): δ, ppm 9.15 (s, 8H), 8.18 (m, 8H), 7.80 (m, 12H).

**SnTPP(OH)<sub>2</sub>-vinyl.** Yield 87%. ESI-MS: *m/z* C<sub>46</sub>H<sub>32</sub>N<sub>4</sub>O<sub>2</sub>Sn, (791.50): [M + 2H<sup>+</sup>] 793 (100%). <sup>1</sup>H NMR (CDCl<sub>3</sub>): δ, ppm 8.75 (multiplet, 7H), 8.15 (m, 8H), 7.75 (multiplet, 12H), 6.49 (dd, 1H, *J* = 1.0 Hz, *J* = 10.8 Hz, *J* = 17.1 Hz), 5.90 (dd, 1H, *J* = 2.0 Hz, *J* = 17.1 Hz), 5.15 (dd, 1H, *J* = 2.4 Hz, *J* = 10.8 Hz).

**SnTPP(OH)<sub>2</sub>-PYR.** Yield 90%. ESI-MS: *m/z* C<sub>62</sub>H<sub>40</sub>N<sub>4</sub>O<sub>2</sub>Sn, (991.44): [M + H<sup>+</sup>] 991 (50%). <sup>1</sup>H NMR (CDCl<sub>3</sub>): δ, ppm 9.45 (s, 1H), 9.11 (m, 6H), 8.56 (s, 1H), 8.38 (m, 8H), 8.21 (m, 4H), 8.12 (s, 2H), 8.01 (m, 2H), 7.86 (m, 12H), 7.32 (d, 1H, *J* = 15.9), 7.16 (d, 1H, *J* = 15.9 Hz).

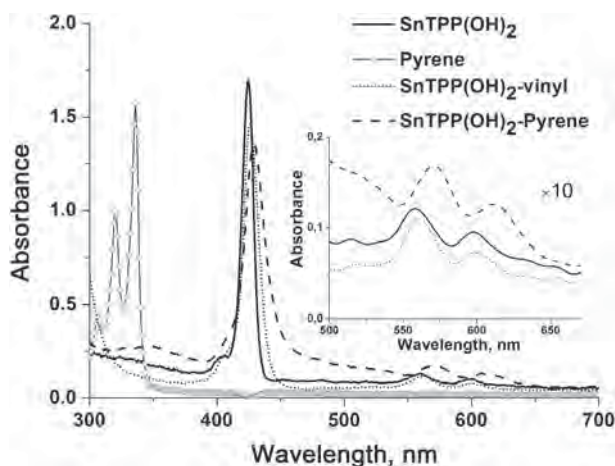
## RESULTS AND DISCUSSION

Preliminary characterization of the molecules synthesized was performed with ESI-MS, <sup>1</sup>H NMR, and UV-visible absorption spectroscopy. Mass spectral data *m/z*, (Rel.Int.%) of [**SnTPP(OH)<sub>2</sub>-vinyl**]: [M + 2H]<sup>+</sup>, 793 (100) and [**SnTPP(OH)<sub>2</sub>-PYR**]: [M + H]<sup>+</sup>, 991 (50) and the corresponding <sup>1</sup>H NMR spectra recorded in CDCl<sub>3</sub> were shown in supplementary material (Fig. S1 to S3) and the chemical shift data in δ, ppm using tetramethylsilane (TMS) as the internal standard was summarized in the experimental section. Both the molecules [**SnTPP(OH)<sub>2</sub>-vinyl**] and [**SnTPP(OH)<sub>2</sub>-PYR**] displayed the characteristic β-pyrrolic and *meso*-proton resonance positions of corresponding **SnTPP(OH)<sub>2</sub>** precursor. Resonance due to –CH=CH<sub>2</sub> in [**SnTPP(OH)<sub>2</sub>-vinyl**] appear at δ 6.49 (dd, 1H, *J* = 1.0 Hz, *J* = 10.8 Hz, *J* = 17.1 Hz), 5.90 (dd, 1H, *J* = 2.0 Hz, *J* = 17.1 Hz), 5.15 (dd, 1H, *J* = 2.4 Hz, *J* = 10.8 Hz). In [**SnTPP(OH)<sub>2</sub>-PYR**], the pyrene protons appear as more overlapping peaks along with the signals of porphyrin-*meso* protons in the aromatic region while the two vinylic protons appear as doublets at δ 7.32 (d, 1H, *J* = 15.9) and 7.16 (d, 1H, *J* = 15.9 Hz).

## Optical properties

The UV-visible absorption spectrum of the dyad is compared with those of its precursors in Fig. 2 and the data are summarized in Table 1. The absorption of pyrene is mainly at the 300–350 nm region. For **SnTPP(OH)<sub>2</sub>-vinyl** and **SnTPP(OH)<sub>2</sub>** the absorption bands are displayed at the very same wavelength regions with intense Soret bands appearing at around 425 nm and two less intense Q-bands around 500 to 620 nm region.

The absorption peaks are slightly broadened and red shifted by ~5–6 nm for the **SnTPP(OH)<sub>2</sub>-PYR** dyad



**Fig. 2.** UV-visible absorption spectra of pyrene and the studied Sn(IV)porphyrin derivatives in  $\text{CH}_2\text{Cl}_2$

**Table 1.** UV-visible data ( $1 \times 10^{-6}$  M for Soret and  $1 \times 10^{-3}$  M for Q-bands)

Compound	Absorption, $\lambda_{\text{max}}$ , nm (log $\epsilon$ , $\text{M}^{-1}\cdot\text{cm}^{-1}$ ) <sup>a</sup>					
	Porphyrin bands			Pyrene bands		
<b>SnTPP(OH)<sub>2</sub></b>	425 (5.07)	560 (4.10)	600 (3.85)	—		
<b>SnTPP(OH)<sub>2</sub>-vinyl</b>	426 (5.01)	562 (4.05)	601 (3.05)	—		
<b>SnTPP(OH)<sub>2</sub>-PYR</b>	426 (5.06)	557 (4.03)	597 (3.54)	239 (3.30)	290 (4.30)	347 (4.39)
<b>Pyrene</b>	—			290 (4.55)	333 (4.39)	376 (4.34)

<sup>a</sup>Solvent  $\text{CH}_2\text{Cl}_2$ , error limits:  $\lambda_{\text{max}}$ ,  $\pm 1$  nm, log  $\epsilon$ ,  $\pm 10\%$ .

due to the presence of extended conjugation *via* the vinyl spacer. The results indicate a weak ground state interaction between the porphyrin and pyrene moieties in **SnTPP(OH)<sub>2</sub>-PYR**.

### Electrochemical properties

The redox curves of the reported Sn(IV)porphyrins with their corresponding precursors were measured by differential pulse voltammetry with  $\text{CH}_2\text{Cl}_2$  solvent and 0.1 M TBAP as supporting electrolyte and the data are summarized in supplementary material (Table S1 and Fig. S5). Figure S5 and data in Table S1 indicate that the dyad shows up to two reduction and three oxidation peaks under the experimental conditions employed in this study. Wave analysis suggested that, in general, while the first two reduction steps and the first two oxidation steps are reversible ( $i_{pc}/i_{pa} = 0.9\text{--}1.0$ ) and diffusion-controlled ( $i_{pc}/\nu^{1/2} = \text{constant}$  in the scan rate ( $\nu$ ) range 50–500 mV/s) one-electron transfer ( $\Delta E_p = 60\text{--}70$  mV;

$\Delta E_p = 65 \pm 3$  mV for ferrocenium/ferrocene couple) reactions. The peaks occurring at anodic potentials are ascribed to successive one-electron oxidations of the porphyrin parts of **SnTPP(OH)<sub>2</sub>/SnTPP(OH)<sub>2</sub>-PYR**. As seen in Fig. S5, the pyrene redox potential appears as overlapped peaks in **SnTPP(OH)<sub>2</sub>-PYR** compared to the precursor **SnTPP(OH)<sub>2</sub>**. Quite interestingly, when appended with peripheral pyrene (**SnTPP(OH)<sub>2</sub>-PYR**), the first oxidation potential of porphyrin, shows a cathodic shift by nearly 80 mV compared to its precursor **SnTPP(OH)<sub>2</sub>**. This observation accounts for the influence of attaching a peripheral electron donating pyrene in **SnTPP(OH)<sub>2</sub>-PYR** on the redox properties of Sn(IV) porphyrins.

The spectroscopic and electrochemical features of the Sn(IV)porphyrin-pyrene dyad described above suggest that in the ground state, an electronic communication between the porphyrin and pyrene chromophores, though not significant, but could not be completely ruled out. Nevertheless, the excited state properties of individual chromophores could be more deeply exploited by selective excitation of the individual chromophore units.

### Fluorescence quantum yields

The emission spectra of the Sn(IV)porphyrin precursors and dyads were measured in different solvents with increasing polarity, in hexane (Hex), dichloromethane (DCM), and acetonitrile (AcCN). The recorded emission spectra are displayed in Figs 3 and 4, and the data are summarized in Table 2. The fluorescence quantum yields of the reported compounds were calculated with reference to ZnTPP ( $\phi = 0.036$  in  $\text{CH}_2\text{Cl}_2$ ) [38]. The efficiency of fluorescence quenching was measured by employing Equation 1;

$$Q = \frac{\Phi(D) - \Phi(DA)}{\Phi(D)} \quad (1)$$

where  $\phi(D)$  refers to the fluorescence quantum yield of pyrene or **SnTPP(OH)<sub>2</sub>**, whereas  $\phi(DA)$  refers to the quantum yield of **SnTPP(OH)<sub>2</sub>-PYR**.

The emission measurements of the precursor porphyrin were performed at  $\lambda_{\text{ex}} = 425$  nm while the dyad molecule was excited at two different wavelengths, *i.e.*  $\lambda_{\text{ex}} = 340$  nm or 425 nm, where the individual subunits pyrene and porphyrin, respectively, absorb predominantly. Considering the dyad molecule, the peripheral pyrene emission ( $\lambda_{\text{em}} = 350\text{--}500$  nm) overlaps with the porphyrin absorption maximum ( $\lambda_{\text{abs}} = 420$  nm) as shown in Fig. S4, which shows the possible occurrence of the energy transfer from the pyrene to the Sn(IV)porphyrin moiety, which is supported by the efficient quenching of pyrene emission (Fig. 3) upto 98% in the dyad at  $\lambda_{\text{ex}} = 340$  nm. This is also supported by the spectral overlap of the excitation spectra of the dyad with its UV-visible absorption spectra in Hex and AcCN (Figs S6 and S7). More importantly, at

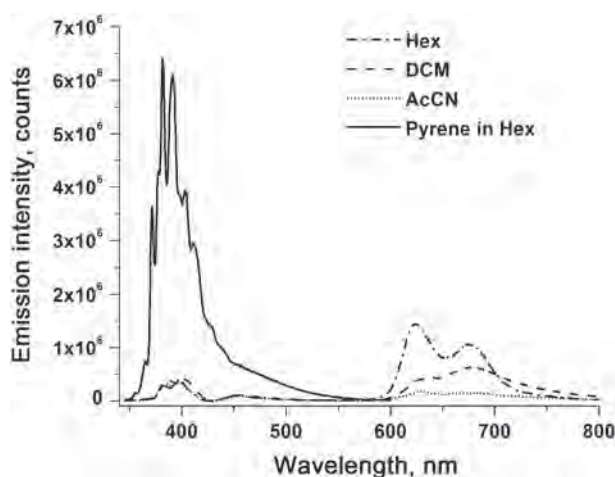


Fig. 3. Fluorescence spectra of pyrene in hexane and  $\text{SnTPP(OH)}_2\text{-PYR}$  in three different solvents.  $\lambda_{\text{ex}} = 340 \text{ nm}$

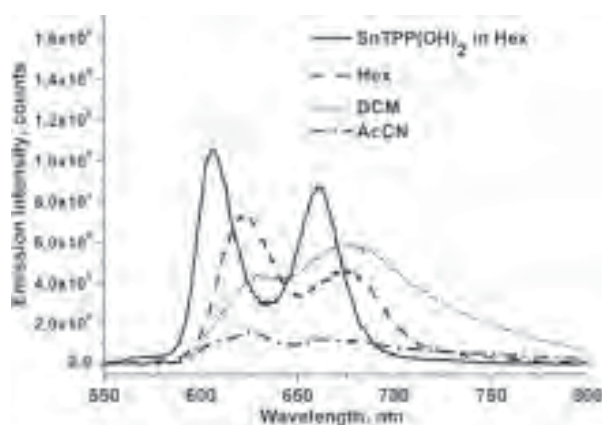


Fig. 4. Fluorescence spectra of  $\text{SnTPP(OH)}_2$  in Hex and  $\text{SnTPP(OH)}_2\text{-PYR}$  in Hex, DCM, and AcCN.  $\lambda_{\text{ex}} = 425 \text{ nm}$

600–750 nm the emission is enhanced with a variation in the intensity ratios accompanied with pronounced broadening and red-shifted maxima compared to that of the  $\text{SnTPP(OH)}_2$  emission (Fig. 3). A similar trend is also observed when the porphyrin chromophore was excited at  $\lambda_{\text{ex}} = 425 \text{ nm}$  (Fig. 4).

Thus, irrespective of the chromophore being excited the dyad shows distinct emission features, which could be possibly due to the formation of an intermediate species, which does not exactly have the emission properties of the neat porphyrin moiety, but is also influenced by the pyrene, covalently linked to it by a double bond. This new intramolecular emissive transient state is a noticeable interesting phenomena in this report. The occurrence of this intermediate species is investigated by the time-resolved measurements at ps and fs time scales, the details of which will be described in the subsequent sections.

### Time-resolved fluorescence experiments

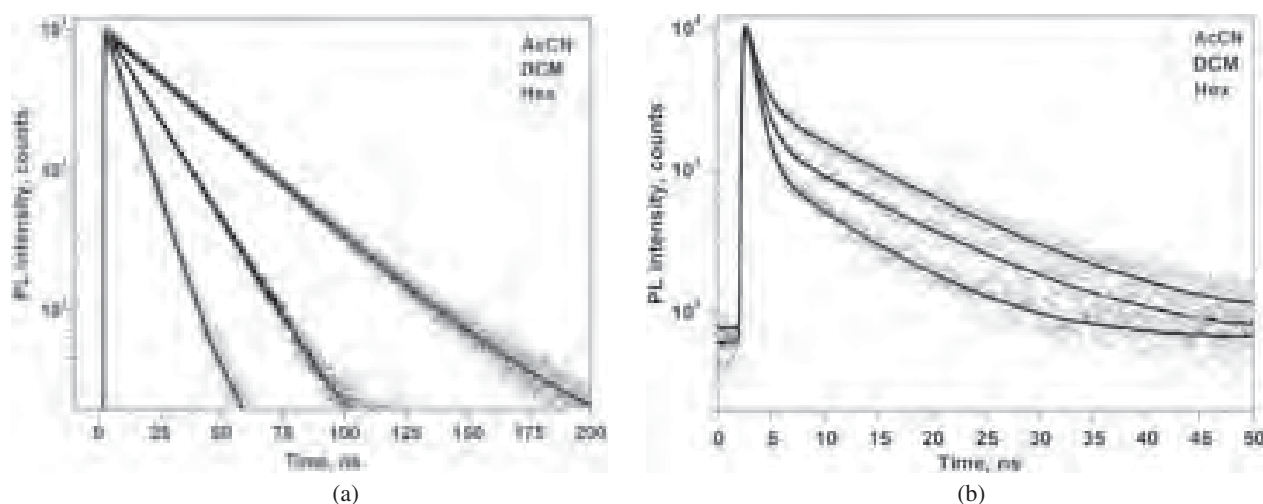
As evidenced from the fluorescence quantum yield (QY) data, a relatively efficient quenching of pyrene monomer emission possibly due to energy transfer, was observed in the  $\text{SnTPP(OH)}_2\text{-PYR}$ . This leads to the formation of a “new emission band” at a longer wavelength, which is no longer characteristic of the pyrene monomer. This new emission band reflects the formation of new excited state which combines properties of both pyrene and porphyrin monomers and could be described as an intramolecular transient state with dual fluorescence properties (see Figs 3 and 4).

To gain further insight of the intramolecular photophysical processes between the pyrene and porphyrin moieties in the dyad, time-correlated single photon counting (TCSPC) experiments were performed

Table 2. Fluorescence data<sup>a</sup> of the studied compounds

Compound	$\lambda_{\text{em}}$ , nm ( $\phi$ , % $Q^b$ )					
	$\lambda_{\text{ex}} = 425 \text{ nm}$			$\lambda_{\text{ex}} = 340 \text{ nm}$		
	Hexane	$\text{CH}_2\text{Cl}_2$	$\text{CH}_3\text{CN}$	Hexane	$\text{CH}_2\text{Cl}_2$	$\text{CH}_3\text{CN}$
$\text{SnTPP(OH)}_2$	605, 669 (0.043)	605, 661 (0.048)	604, 659 (0.066)			
$\text{SnTPP(OH)}_2\text{-Vinyl}$	606, 661 (0.037)	605, 661 (0.040)	606, 660 (0.045)			
$\text{SnTPP(OH)}_2\text{-PYR}$	630, 679 (0.056)	622, 674 (0.039)	626, 664 (0.020)	383, 394, 456 (0.001, 95)	386, 397, 456 (0.002, 98)	385, 397, 455 (0.001, 98)
				624, 676 (0.083)	637, 677 (0.077)	630, 673 (0.023)
Pyrene	—	—	—	381, 391, 403 (0.021)	372, 383, 392 (0.087)	372, 382, 392 (0.047)

<sup>a</sup>Error limits:  $\lambda_{\text{ex}}$ ,  $\pm 2 \text{ nm}$ ,  $\phi \pm 10\%$ . <sup>b</sup> $Q$  is defined in Equation 1 (see text).



**Fig. 5.** Fluorescence decays of (a) **pyrene** and (b) the **SnTPP(OH)<sub>2</sub>-PYR** in Hex, DCM, and AcCN.  $\lambda_{\text{ex}} = 340$  nm and  $\lambda_{\text{em}} = 385$  nm

in three different solvents with varied static dielectric constants. First, we collected the fluorescence decays of the solutions of the dyad and compared them with those of the corresponding reference compounds, *i.e.* **pyrene** and **SnTPP(OH)<sub>2</sub>** (Figs 5 and 6) and **SnTPP(OH)<sub>2</sub>-vinyl** (Fig. S8). Each sample was excited either at 340 nm (pyrene absorption) or at 405 nm (porphyrin absorption) and the decay times were measured at their corresponding emission maxima in three different solvents. The corresponding decay curves are shown in Figs 5 and 6 and the data are summarized in Tables 3 and 4 (complete data in Table S2 of supplementary material).

From Fig. 5 and Table 3, when excited at  $\lambda_{\text{ex}} = 340$  nm and monitored the pyrene emission at 385 nm in both polar and nonpolar solvents, the decays of the dyad are bi-exponential and the fluorescence lifetimes shorter than that for the pyrene monomer. The shorter ( $\sim 1$  ns) decay component, contributes 75–91% to the fluorescence.

The decreased lifetimes correspond to efficient excitation energy transfer (EET) from pyrene  $\rightarrow$  porphyrin. Moreover, the quenching is more efficient in the nonpolar solvent (hexane) where the larger contribution (91%) of

this component is observed. The quenching rate constants were calculated using Equation 2.

$$k_q = \frac{1}{\tau_f^0} \left( \frac{\Phi_f^0}{\tau_f k_f} - 1 \right) = \frac{1}{\tau_f} - \frac{1}{\tau_f^0} \quad (2)$$

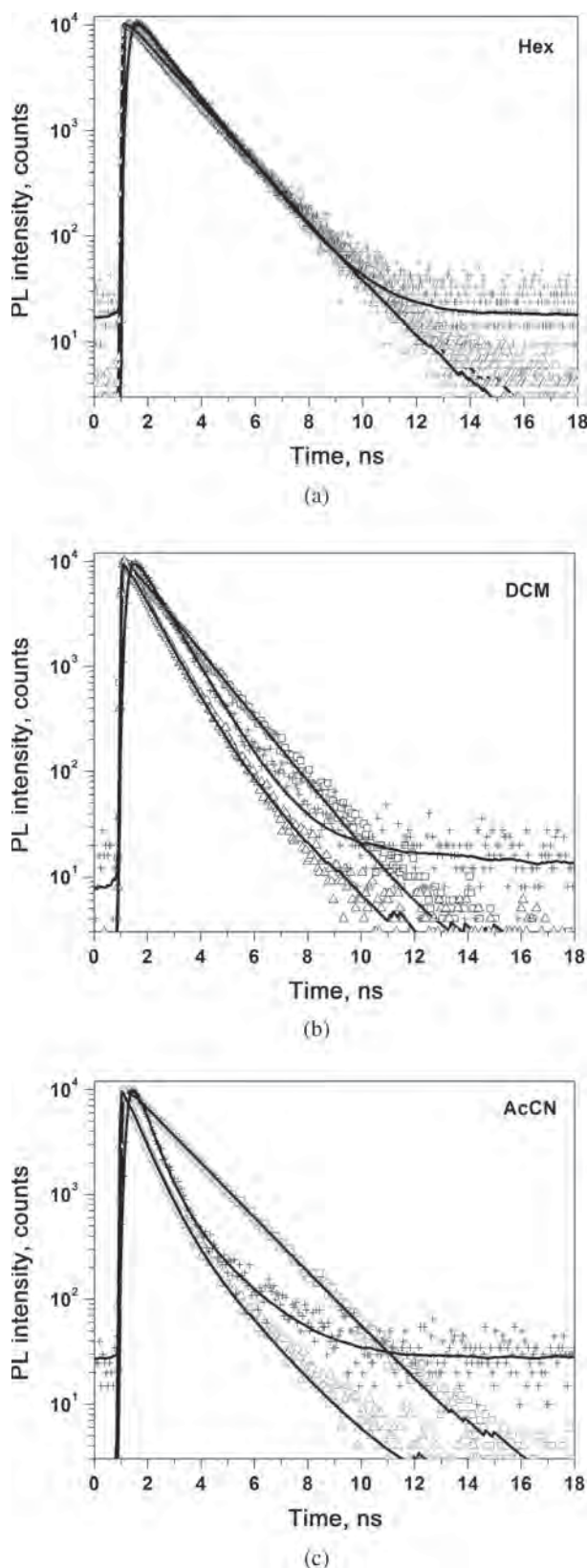
Here  $\Phi_f^0$  is the fluorescence quantum yield of the donor in the absence of acceptor.  $k_f$  is the fluorescence decay rate constant of the donor.  $\tau_f$  and  $\tau_f^0$  are the decay times of the donor in the presence and absence of the acceptor, respectively. The time  $\tau_f$  corresponds to the lifetime of the shorter living component observed for the dyad, while  $\tau_f^0$  corresponds to the lifetime of the single exponential decay observed for the monomer. The calculated rate constants are summarized in Table 3.

The results in Table 3 are in a relatively good agreement with the quantum yield data collected from the steady-state emission experiment (Table 2). Furthermore, the decay of the dyad emission by two different time constants might be due to an equilibrium formed between the excited monomer in the dyad and the excited emissive state, as will be discussed later. On the other hand it

**Table 3.** Fluorescence decay times, amplitudes and quenching rate constants ( $k_q$ ,  $\text{s}^{-1}$ )<sup>‡</sup> at  $\lambda_{\text{ex}} = 340$  nm and  $\lambda_{\text{em}} = 385$  nm analyzed from the fluorescence decay curves in Fig. 5

Compound	Solvent	$\tau_1$ , ns	$\tau_2$ , ns	$k_q$ , $\text{s}^{-1}$
<b>Pyrene</b>	Hexane	8.20 (100%)	—	—
	DCM	28.81 (100%)	—	—
	AcCN	15.12 (100%)	—	—
<b>SnTPP(OH)<sub>2</sub>-PYR</b>	Hexane	0.77 (90.8%)	7.59 (9.2%)	$1.18 \times 10^9$
	DCM	1.12 (75.3%)	10.91 (24.7%)	$0.86 \times 10^9$
	AcCN	0.94 (86.3%)	10.27 (13.7%)	$1.00 \times 10^9$

<sup>‡</sup> $k_q$  is the quenching rate constant of the pyrene emission observed for the **SnTPP(OH)<sub>2</sub>-PYR** dyad calculated according to Equation 2. Error limits of  $\tau$  and  $k_q \sim 10\%$ . Values in parenthesis are the relative amplitudes of corresponding decay components.



**Fig. 6.** Fluorescence decays of  $\text{SnTPP(OH)}_2$  ( $\square\square\square$ ,  $\lambda_{\text{ex}} = 405$  nm,  $\lambda_{\text{em}} = 650$  nm) and  $\text{SnTPP(OH)}_2\text{-PYR}$  ( $\triangle\triangle\triangle$ ,  $\lambda_{\text{ex}} = 405$  nm,  $\lambda_{\text{em}} = 675$  nm) and  $\text{SnTPP(OH)}_2\text{-PYR}$  ( $+++$ ,  $\lambda_{\text{ex}} = 340$  nm,  $\lambda_{\text{em}} = 675$  nm) in (a) Hex, (b) DCM, and (c) AcCN

might imply the formation of two distinguished excited states, which decay to the ground state with different time constants, which is probably caused by a change of the molecular conformation [18].

From Fig. 6 and Table 4, when excited at  $\lambda_{\text{ex}} = 405$  nm, and monitored at the porphyrin emission maxima, 650 nm–675 nm, the decay curves of the dyad were bi-exponential in DCM and AcCN, with the shorter lifetime component having the major amplitude. Whereas in hexane the decay was mono-exponential. Thus, in DCM and AcCN, irrespective of the wavelength of the chromophore being excited, *i.e.*  $\lambda_{\text{ex}} = 340$  nm (where the absorption ratio is about 1.7:1 for pyrene:porphyrin) or 405 nm (which excites selectively porphyrin chromophore), the fluorescence decays can be analyzed as a sum of two exponentials. The decay times and amplitudes are presented in Table 4.

Comparing the lifetimes in Tables 3 and 4, one can observe that monitoring either at 385 nm (pyrene emission) or at  $>650$  nm (porphyrin emission), the decays for  $\text{SnTPP(OH)}_2\text{-PYR}$  are bi-exponential in all solvents, when monitored at the pyrene or porphyrin emission wavelengths, except the porphyrin emissions in hexane. In the case of nonpolar hexane, the decay is mono-exponential and the lifetime is the same as that of  $\text{SnTPP(OH)}_2$ . The results suggest that the final excited state of the dyad combines the properties of both pyrene and porphyrin monomers and can no longer be considered as individual monomers. The relative amplitudes of the decay components however are slightly different at different excitation wavelengths. Especially the longer decay times in the later case ( $\lambda_{\text{ex}} = 405$  nm) are considerably shorter.

For the emission at wavelength  $>410$  nm the time constants are very close to each other regardless of the chromophore being excited, *i.e.* in pyrene or porphyrin absorption band. This could be attributed to the stabilization of only one intermediate species in nonpolar hexane, whereas in polar solvents, there is a probability for the formation of different excited states, *e.g.* a charge separated or a conformeric state, which both could account for the two decay components.

### Decay associated spectra

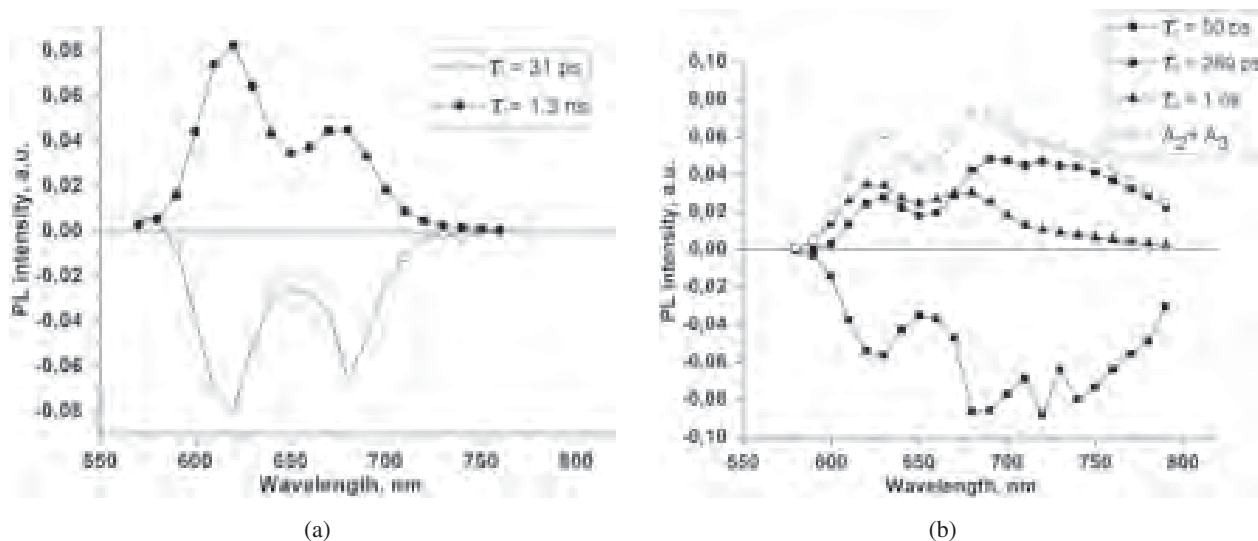
As mentioned above the final excited state of the dyad combines properties of both the chromophores and can no longer be considered as pyrene (P) or porphyrin (T) moieties individually. The relative amplitudes of the decay components are slightly different at different excitation wavelengths. Namely, the shorter living component has little larger contribution when excitation occurred at 340 nm, while the longer living component has little larger contribution when excitation occurred at 405 nm. The decay of the  $\text{SnTPP(OH)}_2\text{-PYR}$  (T-P) dyad emission by two different time constants might be due, on



**Table 4.** Fluorescence decay times, amplitudes and quenching rate constant ( $k_q$ ,  $s^{-1}$ )<sup>‡</sup> at  $\lambda_{ex}$  = 340 or 405 nm, and  $\lambda_{em}$  at porphyrin emission maxima analyzed from the fluorescence decay curve in Fig. 6

Compound	Solvent	$\lambda_{exc}$ , nm	$\lambda_{em}$ , nm	$\tau_1$ , ns	$\tau_2$ , ns	$k_q$ , $s^{-1}$
<b>SnTPP(OH)<sub>2</sub></b>	Hexane	405	650	1.54 (100)	—	—
	DCM			1.39 (100)	—	—
	AcCN			1.67 (100)	—	—
<b>SnTPP(OH)<sub>2</sub>-PYR</b>	Hexane	340	675	1.36 (100)	—	No quenching
		405	675	1.52 (100)	—	No quenching
	DCM	340	675	0.91 (88.8)	2.07 (11.2)	$0.38 \times 10^9$
		405	675	0.63 (52.5)	1.22 (47.5)	$0.87 \times 10^9$
	AcCN	340	675	0.50 (84.5)	1.67 (15.5)	$1.40 \times 10^9$
		405	675	0.57 (87.4)	1.65 (12.6)	$1.15 \times 10^9$

$k_q$ <sup>‡</sup> is the quenching rate constant of the pyrene emission observed for the **SnTPP(OH)<sub>2</sub>-PYR** dyad calculated according to Equation 2. Error limits of  $\tau$  and  $k_q \sim 10\%$ . Values in parenthesis are the relative amplitudes of corresponding decay components.

**Fig. 7.** The fluorescence decay associated spectra of T-P dyad in Hex (a) and in AcCN (b) at 405 nm excitation. The time constants with negative amplitudes, about 30 and 50 ps, are on the limit of the time resolution of the instruments

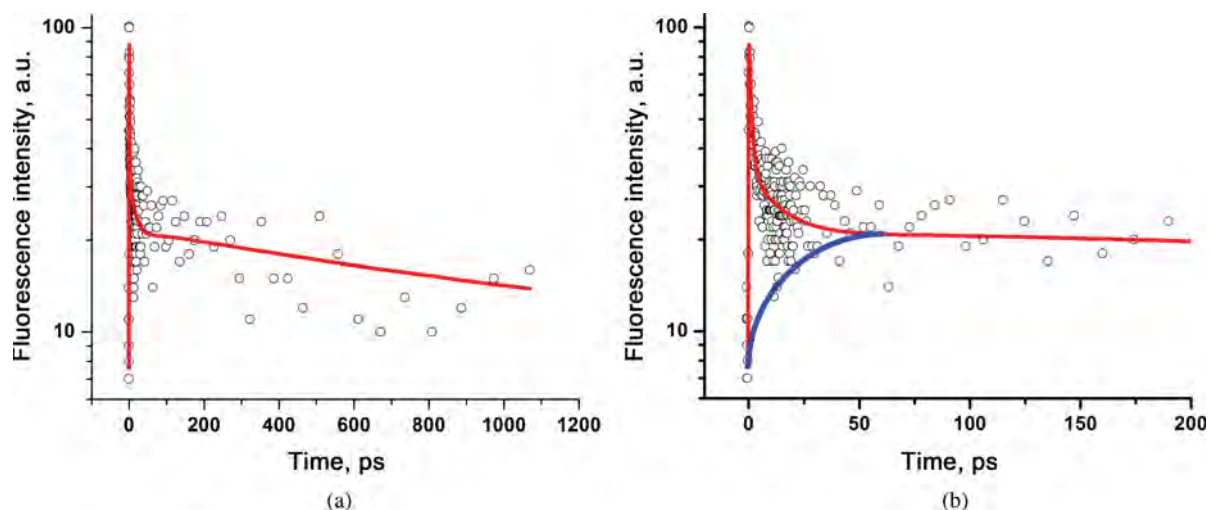
one hand, to an equilibrium formed between the excited monomer in the dyad and the excited emissive state. This could be especially in the case of pyrene emission (Table 3). On the other hand it might imply the formation of two distinguished excited states, which decay to the ground state with different time constants, which could be caused either by a change of the molecular conformation [18] or by reactions of different excited state, *e.g.* the first and second excited state.

Since the two distinguished decay components were observed from the dyad in the polar solvents, it is worth to further investigate how these species contribute over the range of the emission band. Hence the fluorescence decay associated spectra (DAS) of the T-P dyad in hexane and AcCN were measured.

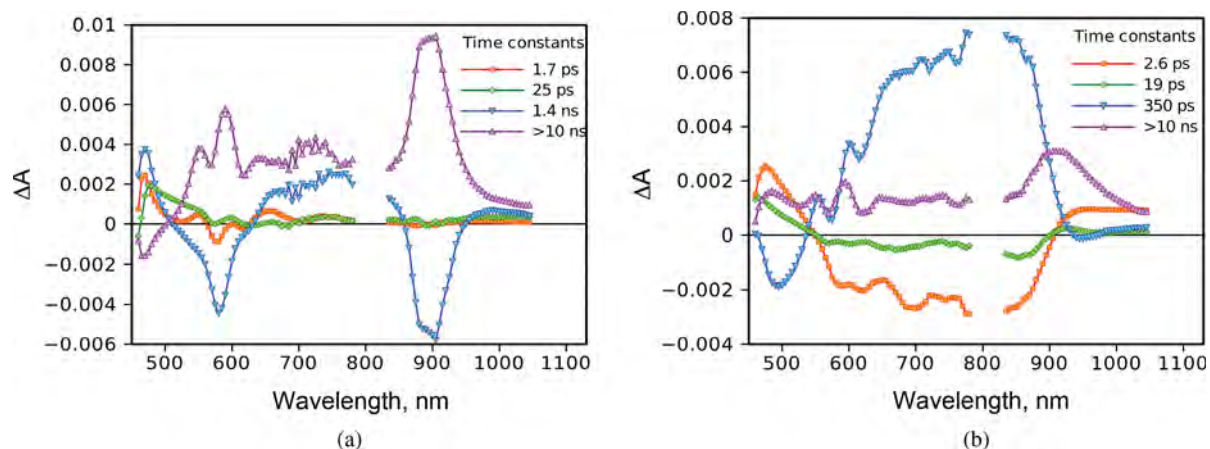
The results of DAS measurements are shown in Fig. 7. Two different components are formed in times of few tens of picosecond (31 and 50 ps) and decay mono-exponentially (1.3 ns) in hexane, whereas bi-exponentially (280 ps and 1 ns) in AcCN. Although the formation times of 30–50 ps are on the limit of the time resolution of TCSPC-method, and thus that of the DAS-method, these components could imply a formation of the (T-P)\* state from the primary excited T\*-P state.

### Fluorescence up-conversion experiments

The fluorescence up-conversion lifetime measurements for T-P dyad in AcCN gave decay curves with three major decay components; a fast component, 10 ps, a



**Fig. 8.** The fluorescence up-conversion decay curves of T-P dyad in Hex, excited at 420 nm and monitored at 615 nm, with time windows of (a) 1.1 ns and (b) 200 ps. The decay can be analysed as three-exponential, yielding  $\tau_1 = 10$  ps (84%),  $\tau_2 = 25$  ps (-36%), and  $\tau_3 = 1.3$  ns (52%). The growing of 25 ps component is indicated by the blue curve



**Fig. 9.** Transient component spectra of T-P dyad in Hex (a) and AcCN (b) at  $\lambda_{\text{exc}} = 340$  nm

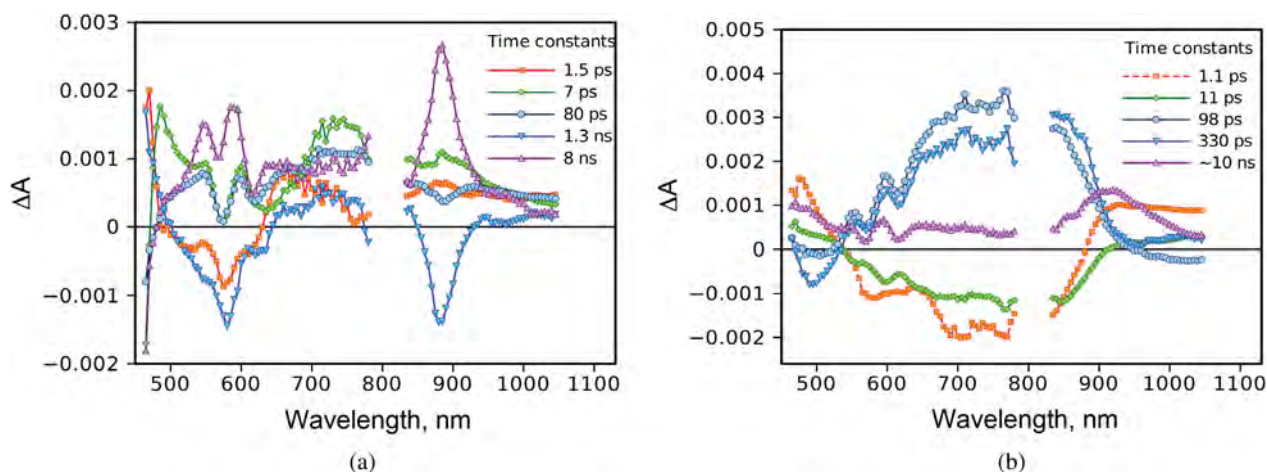
longer-living component, about 1.3 ns, and a component with a negative amplitude, 25 ps (see Fig. 8 and its caption). The determined lifetimes coincide reasonably well with those obtained by the DAS-method. The very fast component (10 ps, in up-conversion) could be the fluorescence lifetime of the T moiety, while the longer-living (about 1.3 ns) component should correspond to the emission of the (T-P)\* complex. Moreover this 1.3 ns component fits very well with the single-exponential decay of the dyad in hexane, observed in TCSPC experiment. The additional intermediate component with a negative amplitude and lifetime of ~25 ps resembles the 30–50 ps components observed in the DAS experiments and corresponds to the formation of (T-P)\*.

### Ultra-fast pump-probe experiments

The transient absorption behavior of T-P compound was studied by the femtosecond pump-probe method

with excitation both at 340 nm (pyrene absorption) and at 425 nm (porphyrin absorption). The transient absorption component spectra, at 340 nm excitation, in hexane and acetonitrile are shown in Fig. 9.

In hexane (Fig. 9(a)) a ~2 ps component corresponds to the singlet excited state of the pyrene moiety. This is followed by a 25 ps component, and a formation of the excited dyad, (T-P)\*. This fits very well with the 25 ps component observed in the fluorescence up-conversion experiment. (T-P)\* has a broad absorption from 620 nm to 850 nm, with a lifetime of 1.4 ns. These results also coincide well with fluorescence up-conversion and TCSPC results. The negative bands (1.4 ns) at 500–620 nm and 860–940 nm describe the formation of the final transient state, with lifetime longer than 6 ns, the upper limit of the instrument, and a broad intense absorption from 500 to 950 nm, with two main maxima. This state could be cation radical (at shorter wavelength) of SnTPP and anion radical (at longer wavelength) of pyrene moieties.



**Fig. 10.** Transient component spectra of T-P dyad in Hex (a) and AcCN (b) at  $\lambda_{\text{ex}} = 425$  nm

In acetonitrile (Fig. 9(b)) the two fast components correspond, as previously mentioned, to the singlet state decay (2.6 ps) of the porphyrin moiety and the simultaneous formation (19 ps) of the excited dyad, (T-P)\*. It has a broad absorption band from 600 nm to 910 nm and considerably shorter (350 ps) lifetime than in hexane. The final state is the charge transfer state with the absorption characteristic for porphyrin cation (600–800 nm) and that of the pyrene anion (870–950 nm).

The transient absorption component spectra, at 425 nm excitation, in hexane and acetonitrile are shown in Fig. 10. In hexane (Fig. 10(a)) the result shows a strong and broad absorption band with a lifetime of 7 ps and the maximum at *ca.* 750 nm, and clear bleaching of the ground state SnTPP absorption at 580 and 630 nm. This could correspond to the singlet excited state of the porphyrin. The next component, 80 ps, does not exist at 340 nm excitation, neither in fluorescence experiments. It has a very broad absorption band from the visible to the NIR region. That is followed by 1.3 ns and 8 ns components, which are similar to those observed with the 340 nm excitation, and assigned to the (T-P)\* state (1.3 ns) and the cation and anion radical (8 ns) of the SnTPP and pyrene moieties, respectively.

At 425 nm excitation (Fig. 10(b)) in AcCN the transient absorption responses are quite similar to those in hexane. A broad absorption with about 100 ps lifetime was not observed at the 340 nm excitation nor in the fluorescence experiments.

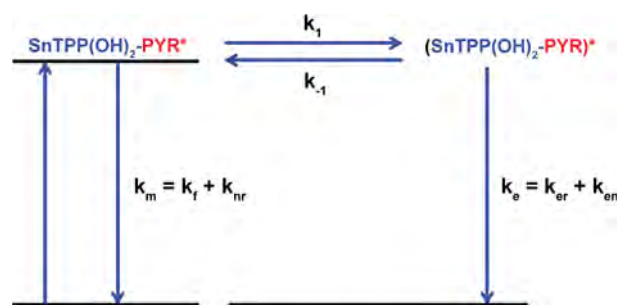
## FLUORESCENCE KINETICS

In the nonpolar solvent (hexane), independent of the excitation wavelengths, the fluorescence decays of the dyad at the porphyrin emission wavelength, can be analyzed as a single exponential decay with the time constant around 1.4–1.7 ns, which resembles that of

the porphyrin monomer [SnTPP(OH)<sub>2</sub>]. Moreover, the single component decay could also suggest that in a nonpolar solvent the excited state can be regarded as a state, in which the excitation is located in the porphyrin moiety, although the emission is red-shifted compared to that of SnTPP(OH)<sub>2</sub> and is less perturbed by the surrounding solvent molecules.

When the pyrene moiety is excited at 340 nm and monitored at the pyrene emission wavelength at 385 nm, the bi-exponential emission decay of the T-P dyad indicates an equilibrium between the excited ground state complex, (T-P)\*, and a newly formed excited complex between T and P. Energetically this is possible because the energy of the first excited state of pyrene is about the same as the energy of the Soret band of the porphyrin moiety. This is actually shown quite clearly in Fig. 5, where the decay of the fluorescence monitored at 385 nm is evidently bi-exponential with lifetimes of about 1 and 10 ns.

The dynamics when monitored at the pyrene emission wavelength could be described by an “equilibrium” kinetics as in Fig. 11.



**Fig. 11.** The “equilibrium” dynamics when excited and monitored at the pyrene absorption and emission wavelengths, respectively

**Table 5.** Kinetic parameters calculated for **SnTPP(OH)<sub>2</sub>-PYR** monitored at pyrene emission.  $\lambda_{\text{ex}} = 340$  nm. All the rate constants are presented in  $\times 10^8 \text{ s}^{-1}$ 

Solvent	$A_1$	$A_2$	$\beta_1$	$\beta_2$	$k_m$	X	Y	$k_1[B]$	$k_{-1}$	$k_e$
Hexane	0.91	0.09	13.0	1.32	1.22	11.90	2.39	10.70	1.06	1.33
DCM	0.75	0.25	8.93	0.92	0.35	6.95	2.90	6.60	1.81	1.09
AcCN	0.86	0.14	10.6	0.97	0.66	9.31	2.30	8.65	1.28	1.02

By using the data in Table 3, the kinetic parameters in Fig. 11 could be calculated based upon Equations 3–5:

$$[A^*] = \frac{[A^*]_0}{\beta_1 - \beta_2} \left[ (X - \beta_2)e^{-\beta_1 t} + (\beta_1 - X)e^{-\beta_2 t} \right] \quad (3)$$

$$[E^*] = \frac{k_1 [A^*]_0}{\beta_1 - \beta_2} \left[ e^{-\beta_2 t} - e^{-\beta_1 t} \right] \quad (4)$$

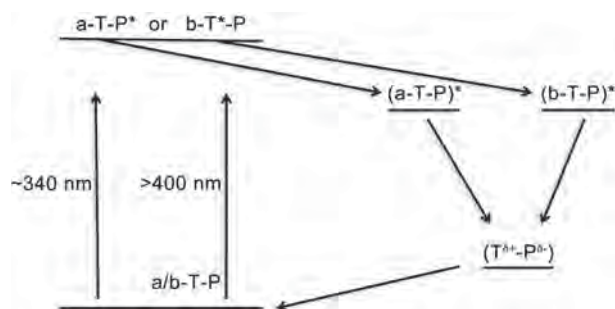
$$\beta_{1,2} = \frac{1}{2} \left[ X + Y \mp \sqrt{(Y - X)^2 + 4k_1 k_{-1}} \right] \quad (5)$$

In Equations 3–5,  $X = k_m + k_1$  and  $Y = k_e + k_{-1}$ , where  $k_m$  is a relaxation rate (radiative + non-radiative) of the excited pyrene monomer, (T-P\*);  $k_1$  is the formation rate of the excited dyad, (T-P)\*;  $k_e$  and  $k_{-1}$  are the relaxation (radiative + non-radiative) rates of the excited dyad, (T-P)\*. The calculated kinetic parameters are presented in Table 5.

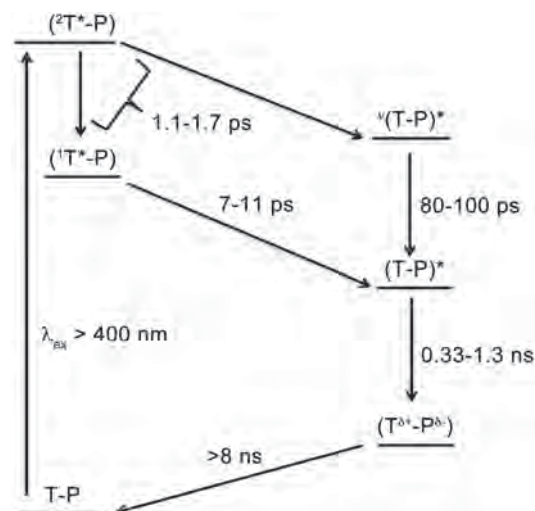
With the excitation at 405 nm, where the pyrene moiety absorbs significantly less than porphyrin, the time resolved fluorescence decays were also bi-exponential, but the longer-living components were 5–6 times shorter in time, 1.6–2.1 ns (Table 4), than those obtained by the P absorption and emission (Table 3). Thus the emission at >600 nm does not originate from the equilibrium state, which was formed and observed with the P excitation and emission, respectively. Also the relative amplitudes of the two emission bands (Fig. 4) at about 625 nm and 675 nm varied depending on solvent polarity and monitoring wavelength.

## MECHANISMS

The processes followed after the excitation of the T-P dyad can be described in all the solvents with practically the same mechanism (Fig. 12). First, when mainly the pyrene moiety in the T-P dyad is excited, the excitation is followed by an energy transfer to the porphyrin moiety. Then an excited dyad is formed and decays to a partial charge transfer complex, more efficiently in polar DCM and acetonitrile, than in nonpolar hexane. The existence of two different conformers and their influence on the ground and excited state properties of a porphyrin dimer linked by a vinylene spacer has been studied previously [18]. Thus, two possible conformers due to the vinyl chain, should be taken into account.



**Fig. 12.** The kinetic scheme for the decay processes followed the excitation of the pyrene moiety of the T-P dyad based on assumption on two conformers of the T-P dyad



**Fig. 13.** The mechanisms at the 425 nm excitation. The scheme is based on the assumption on the electron transfer from the second excited state of porphyrin and the results of the pump-probe measurements shown in Fig. 10

Namely, two types of excited dyads, (a-T-P)\* and (b-T-P)\* are formed depending on the relative ground state concentration ratio of the conformers. The excited dyads have different lifetimes, from about 0.6 to 1.6 ns, depending on the environment. Finally the excited state dyads relax to charge transfer complexes and to the ground state.

Based on the time-resolved fluorescent (Figs 5 and 6) and pump-probe measurements (Figs 9 and 10) with

either pyrene or porphyrin excitation, it seems evident, that the mechanisms differ from each other at the very beginning of the photo-induced processes. The differences between 340 nm and 425 nm excitations can be qualitatively explained as follows (Fig. 13). The porphyrin excitation yields the excitation of the second excited state of porphyrin in the dyad, ( $^2T^*$ -P). This opens a possibility for an intramolecular charge transfer to occur from  $^2T^*$  state of the porphyrin to the pyrene moiety. This is quantitatively discussed by Mataga *et al.* [39] and recently by Fujitsuka *et al.* [40], and explains well the observed differences depending on the excitation wavelength. As the electron transfer would take place from the  $^2T^*$  state, it decays, in 1.1–1.7 ps (Fig. 10) to the  $^1T^*$  state, ( $^1T^*$ -P), and to an excited dyad,  $^V(T-P)^*$ . This state, which is not observed with the 340 nm excitation (Fig. 9), relaxes in 80–100 ps to a longer living excited dyad,  $(T-P)^*$ , which also is formed *via* the ( $^1T^*$ -P) state in 7–11 ps.  $(T-P)^*$  relaxes in 0.33–1.3 ns to the charge separated state,  $(T^{\delta+}-P^{\delta-})$ . The mechanism presented in Fig. 13 explains well the observation of five different component spectra in Fig. 10.

Analogically to the porphyrin excitation, the pyrene excitation (Fig. 9) could create an excited complex  $^U(T-P)^*$  in few picosecond, which relaxes to the  $(T-P)^*$  state in 19–25 ps. The latter has lifetime 0.3–1.4 ns, depending on the solvent. The CT state formed after  $(T-P)^*$  has a lifetime >10 ns.

The properties of the transient states of  $^V(T-P)^*$ ,  $^U(T-P)^*$ , and  $(T-P)^*$  resemble those known as intramolecular exciplexes, because they have emission bands, which differ from those of porphyrin or pyrene (Figs 4 and 8). The exciplexes, however, do not have fine structure, as the emission of the  $(T-P)^*$  state has two bands. This could be explained by the formations of two types of  $(T-P)^*$  states due to the different conformers [18] of the dyad in solution (Fig. 12). More intriguing explanation is, however, formation of different kinds of intramolecular exciplexes *via* the  $^1T^*$  and  $^2T^*$  states of the porphyrin moiety, as shown in Fig. 13.

## CONCLUSION

In conclusion, a Sn(IV)porphyrin-pyrene dyad has been synthesized showing photophysical behavior radically different from that of the constituent chromophores. Time-resolved fluorescence measurements show the existence of an intermediate emissive species, which is observed to be more stabilized in nonpolar hexane and shows a mono-exponential decay of 1.36 ns ( $\lambda_{ex} = 340$  nm) or 1.52 ns ( $\lambda_{ex} = 425$  nm), when observed at the porphyrin emission wavelength. Whereas, as the solvent polarity increases, a bi-exponential decay is observed with a variation in the component amplitudes, which could be due to the formation of charge separated state (CSS) as

an additional contributing species. However, from the pump-probe measurements, when excited at 425 nm, two different intermediate species are observed (~7–11 ps and 80–100 ps) with broad absorptions in the near-IR region, which imply the existence of two different conformers, which decays to the ground state *via* a CSS. An alternative explanation is that the intramolecular electron transfer and the formation of the final CSS state occurs *via* the second excited state of the porphyrin. The dyad synthesized serves as a molecular platform to demonstrate the influence of the flexible vinyl spacer on the excited state photophysics of the chromophores involved. Moreover, the presence of Sn(IV) metal center could assist in extending the axial coordination of the dyad molecules, further studies of which is in progress.

## Acknowledgements

HL acknowledges the financial support from the Academy of Finland (UVIADDEM) and the Finnish Funding Agency for Technology and Innovation (Biosphere). And LG acknowledges the Department of Science and Technology (DST, SB/S1/IC-14/2014) for financial support of this work.

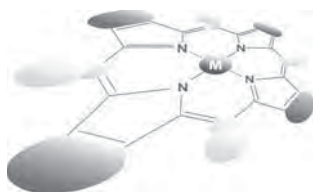
## Supporting information

Figures S1–S8 and Tables 1–2 are given in the supplementary material. This material is available free of charge *via* the Internet at <http://www.worldscinet.com/jpp/jpp.shtml>.

## REFERENCES

1. *The Handbook of Porphyrin Science*, Kadish K, Smith K and Guillard R. (Eds.) World Scientific: Hackensack, NJ, 2010.
2. Imahori H, Umeyama T and Ito S. *Acc. Chem. Res.* 2009; **42**: 1809–1818.
3. Campbell WM, Burrell AK, Officer DL and Jolley KW. *Coord. Chem. Rev.* 2004; **248**: 1363–1369.
4. Walter MG, Rudine AB and Wamser CC. *J. Porphyrins Phthalocyanines* 2010; **14**: 759–792.
5. Perez MD, Borek C, Forrest SR and Thompson ME. *J. Am. Chem. Soc.* 2009; **131**: 9281–9286.
6. Kira A, Matsubara Y, Iijima H, Umeyama T, Matano Y, Ito S, Niemi M, Tkachenko NV, Lemmetyinen H and Imahori H. *J. Phys. Chem. C* 2010; **114**: 11293–11304.
7. Baldo MA, O' Brien DF, You Y, Shoustikov A, Sibley S, Thompson ME and Forrest SR. *Nature* 1998; **395**: 151–154.
8. Murphy AR and Fréchet MJ. *Chem. Rev.* 2007; **107**: 1066–1096.
9. McConnell I, Li G and Brudvig GW. *Chem. Biol.* 2010; **17**: 434–447.

10. Gust D, Moore TA and Moore AL. *Acc. Chem. Rev.* 2009; **42**: 1890–1898.
11. Liu JY, El-Khouly ME, Fukuzumi S and Ng DKP. *Chem. Eur. J.* 2011; **17**: 1605–1613.
12. Aratani N, Kim D and Osuka A. *Acc. Chem. Res.* 2009; **42**: 1922–1934.
13. Albinsson B and Mårtensson J. *J. Photochem. Photobiol. C: Photochem. Rev.* 2008; **9**: 138–155.
14. Aratani N, Cho HY, Ahn TK, Cho S, Kim D, Sumi H and Osuka A. *J. Am. Chem. Soc.* 2003; **125**: 9668–9681.
15. Tsuda A, Nakamura Y and Osuka A. *Chem. Commun.* 2003; **9**: 1096–1097.
16. Osuka A, Tanabe N, Nakajima S and Maruyama K. *J. Chem. Soc. Perkin Trans.* 1996; **2**: 199–204.
17. Susumu K, Shimidzu T, Tanaka K and Segawa H. *Tetrahedron Lett.* 1996; **37**: 8399–8402.
18. Chachisvilis M, Chirvony VS, Shulga AM, Källebring B, Larsson S and Sundström V. *J. Phys. Chem.* 1996; **100**: 13867–13873.
19. Flamigni L, Johnston MR and Giribabu L. *Chem. Eur. J.* 2002; **8**: 3938–3947.
20. Bonfantini EE, Burrell AK, Campbell WM, Crossley MJ, Gosper JJ, Harding MM, Officer DL and Reid DCW. *J. Porphyrins Phthalocyanines* 2002; **6**: 708–719.
21. Ventura B, Barigelletti F, Lodato F, Officer DL and Flamigni L. *Phys. Chem. Chem. Phys.* 2009; **11**: 2166–2176.
22. Bonfantini EE, Burrell AK, Officer DL and Reid DCW. *Inorg. Chem.* 1997; **36**: 6270–6278.
23. Lembo A, Tagliatesta P and Guild DM. *J. Phys. Chem. A* 2006; **110**: 11424–11434.
24. Reeta PS, Ravikumar K and Giribabu L. *J. Chem. Sci.* 2013; **125**: 259–266.
25. Kandhadi J, Kanaparthi RK and Giribabu L. *J. Porphyrins Phthalocyanines* 2012; **16**: 282–289.
26. Vijendra SS and Mangalampalli R. *Inorg. Chem.* 2011; **50**: 1713–1722.
27. Giribabu L, Kumar CV and Reddy PY. *Chem. Asian J* 2007; **2**: 1574–1580.
28. Giribabu L, Kumar CV and Reddy PY. *J. Porphyrins Phthalocyanines* 2006; **10**: 1007–1016.
29. Arnold DP and Janet B. *Coord. Chem. Rev.* 2004; **248**: 299–319.
30. Poddutoori PK, Zarrabi N, Moiseev AG, Brisa RG, Vassiliev S and Van der Est A. *Chem. Eur. J.* 2013; **19**: 3148–3161.
31. Giribabu L, Ashok Kumar A, Neeraja V and Maiya BG. *Angew. Chem. Int. Ed.* 2001; **40**: 3621–3624.
32. Perrin DD, Armarego WLF and Perrin DR. *Purification of Laboratory Chemicals*, Oxford: Pergamon, 1986.
33. Kesti TJ, Tkachenko NV, Vehmanen V, Yamada H, Imahori H, Fukuzumi S and Lemmetyinen H. *J. Am. Chem. Soc.* 2002; **124**: 8067–8077.
34. Tkachenko NV, Rantala L, Tauber AY, Helaja J, Hynninen PH and Lemmetyinen H. *J. Am. Chem. Soc.* 1999; **121**: 9378–9387.
35. Stranius K, Iashin V, Nikkonen T, Muuronen M, Helaja J and Tkachenko NV. *J. Phys. Chem. A* 2014; **118**: 1420–1429.
36. Kadish KM, Xu QY, Maiya GB, Barbe J-M and Guillard R. *J. Chem. Soc., Dalton Trans.* 1989; **8**: 1531–1536.
37. Berezovskii VV, Wöhrle D, Tsaryova O, Makarov SG, Pomogailo SI, Glagolev NN, Zhilina ZI, Voloshanovskii IS, Roshchupkin VP and Pomogailo AD. *Russ. Chem. Bull. Int. Ed.* 2007; **56**: 160–167.
38. Reddy RD and Maiya BG. *J. Porphyrins Phthalocyanines* 2002; **6**: 3–11.
39. Mataga N, Taniguchi S, Chosrowjan H, Osuka A and Yoshida N. *Chem. Phys.* 2003; **295**: 215–228.
40. Fujitsuka M, Shiragami T, Cho DW, Tojo S, Yasuda M and Majima T. *J. Phys. Chem. A* 2014; **118**: 3926–3933.



## Effects of heme modification on oxygen affinity and cooperativity of human adult hemoglobin

Tomokazu Shibata<sup>a</sup>, Eisuke Furuichi<sup>a</sup>, Kiyohiro Imai<sup>b</sup>, Akihiro Suzuki<sup>c</sup>  
and Yasuhiko Yamamoto<sup>\*a,d</sup>

<sup>a</sup>Department of Chemistry, University of Tsukuba, Tsukuba 305-8571, Japan

<sup>b</sup>Department of Frontier Bioscience, Faculty of Bioscience and Applied Chemistry, Hosei University, Tokyo 184-8584 Japan

<sup>c</sup>Department of Materials Engineering, Nagaoka National College of Technology, Nagaoka 940-8532, Japan

<sup>d</sup>Life Science Center of Tsukuba Advanced Research Alliance, University of Tsukuba, Tsukuba 305-8577, Japan

*Dedicated to Professor Shunichi Fukuzumi on the occasion of his retirement*

Received 18 October 2014

Accepted 28 November 2014

**ABSTRACT:** We substituted strongly electron-withdrawing trifluoromethyl (CF<sub>3</sub>) group(s) as heme side chain(s) of human adult hemoglobin (Hb) to achieve large alterations of the heme electronic structure, in order to elucidate the relationship between the oxygen (O<sub>2</sub>) binding properties of Hb and the electronic properties of heme peripheral side chains. The obtained results were compared with those of similar studies performed on myoglobin (Mb), *e.g.* (Nishimura R, Matsumoto D, Shibata T, Yanagisawa S, Ogura T, Tai H, Matsuo T, Hirota S, Neya S, Suzuki A, and Yamamoto Y. *Inorg. Chem.* 2014; **53**: 9156–9165). These two proteins shared the common feature of a decrease in O<sub>2</sub> affinity upon the CF<sub>3</sub> substitution(s). Using the  $P_{50}$  value, which is the partial pressure of O<sub>2</sub> required for 50% oxygenation of a protein, and the equilibrium constant ( $pK_a$ ) of the “acid-alkaline transition” in the met form of a protein as measures of the O<sub>2</sub> affinity and the electron density of heme Fe atom of the protein, respectively, a linear  $pK_a$ - $\log(1/P_{50})$  relationship was demonstrated for the Hb and Mb systems. The native Hb, however, deviated from the  $pK_a$ - $\log(1/P_{50})$  relationship, while the native Mb followed it. These results highlighted the significance of the vinyl side chains of the heme cofactor in the functional control of Hb through tertiary and quaternary structural changes upon the oxygenation of the protein.

**KEYWORDS:** acid-alkaline transition, cooperativity, heme electronic structure, hemoglobin, oxygen affinity.

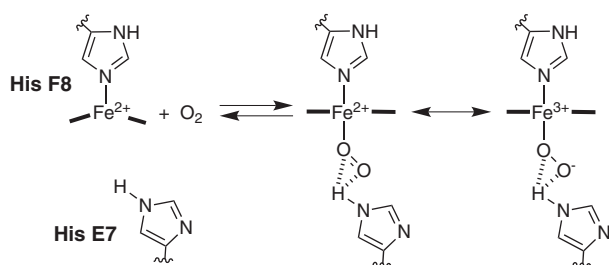
## INTRODUCTION

Human adult hemoglobin (Hb) is an oxygen transport tetrameric hemoprotein consisting of two  $\alpha$  and two  $\beta$  subunits, and has long been a paradigm for cooperative ligand binding and allostery [1–4]. Hb reversibly and cooperatively binds oxygen molecules (O<sub>2</sub>) *via* its ferrous heme Fe atoms. The oxygenation of the protein is quite often represented by means of a Hill plot, *i.e.* a log-log

plot of the ratio of the fraction of O<sub>2</sub>-bound sites to that of unbound ones,  $x$ , *vs.* the partial pressure of O<sub>2</sub>,  $p$ , and the O<sub>2</sub> affinity and cooperativity of the protein are generally represented by the  $P_{50}$  value, which is the  $p$  value at  $x = 1$ , and the maximal slope of the plot, known as the Hill coefficient,  $n$ , respectively [2]. The O<sub>2</sub> binding properties of Hb are thought to be controlled at multiple interdependent and hierarchically organized levels in the protein structure, the higher levels ultimately acting on the lower ones [4]. The first level is the control of the heme Fe reactivity, which is achieved through the heme environment furnished by nearby amino acid residues, and subtle tuning of the intrinsic heme Fe reactivity, followed

<sup>†</sup>SPP full member in good standing

\*Correspondence to: Yasuhiko Yamamoto, email: yamamoto@chem.tsukuba.ac.jp, tel/fax: +81 29-853-6521



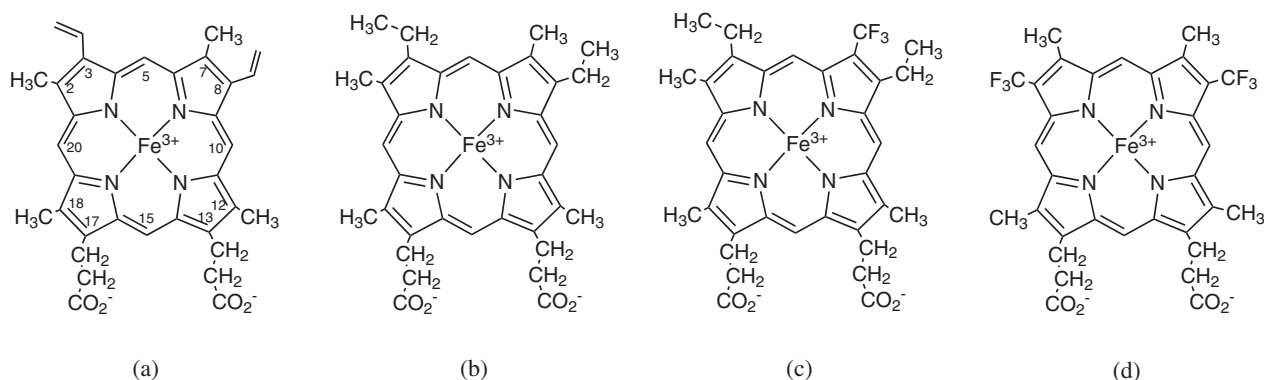
**Scheme 1.** Oxygenation of deoxy Mb and Hb

by the tertiary and quaternary structural changes. The first control level has been exhaustively explored in myoglobin (Mb), a monomeric oxygen storage hemoprotein [5–15]. We recently revealed that the  $O_2$  affinity of Mb is controlled through electronic tuning of the intrinsic heme Fe reactivity through the electron density of the heme Fe atom ( $\rho_{Fe}$ ) [13–15]. The relationship between the  $\rho_{Fe}$  value and the  $O_2$  affinity of Mb is reasonably interpreted in terms of the effect of a change in the  $\rho_{Fe}$  value on the resonance process between the  $Fe^{2+}-O_2$  and  $Fe^{3+}-O_2^-$ -like species (Scheme 1) [16–18], and, for example, a decrease in the  $\rho_{Fe}$  value stabilizes the  $Fe^{2+}-O_2$  species over the  $Fe^{3+}-O_2^-$ -like one, resulting in an increase in the  $O_2$  dissociation rate constant, which in turn lowers the  $O_2$  affinity [13–15].

In this study, we have investigated the effects of a change in the  $\rho_{Fe}$  value on the  $O_2$  binding properties of Hb in order to elucidate the differences in the functional consequences of a change in the  $\rho_{Fe}$  value between Hb and Mb. As in the cases of our previous Mb studies [13–15], we substituted strongly electron-withdrawing perfluoromethyl ( $CF_3$ ) group(s), as heme side chain(s), to achieve large and stepwise alterations of the heme electronic structure using the reported procedure [19, 20]. Meso-heme (Meso), 13,17-bis(2-carboxylatoethyl)-3,8-diethyl-2,12,18-trimethyl-7-trifluoromethylporphyrinato iron(III) (7-PF) [19], and 13,17-bis(2-carboxylatoethyl)-3,7-diethyl-12,18-trimethyl-2,8-ditrifluoromethylporphyrinato iron(III) (2,8-DPF) [13] were incorporated into

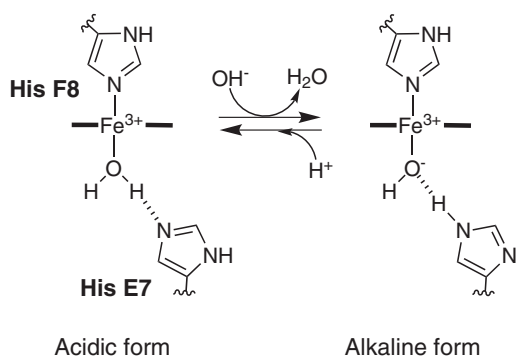
the apoprotein of Hb to prepare reconstituted Hbs, *i.e.* Hb(Meso), Hb(7-PF), and Hb(2,8-DPF), respectively. These heme cofactors differ in the numbers of  $CF_3$ ,  $CH_3$ , and  $C_2H_5$  side chains (Fig. 1). The use of these heme cofactors affords great variation in the electronic structure of the porphyrin moiety of the heme cofactor, and hence the  $\rho_{Fe}$  value. The  $\rho_{Fe}$  value is semiquantitatively manifested in the equilibrium constant,  $pK_a$ , of the so-called “acid-alkaline transition” in the met-form of the protein (Scheme 2) [13, 21]. The heme active sites of the met-forms of Hb and Mb (metHb and metMb, respectively) exhibit characteristic pH-dependent structure changes collectively known as the acid-alkaline transition [1]. MetHb and metMb possessing highly conserved distal His E7 (E7 represents an alphanumeric code referring to the positions of amino acid residues in the helices and turns of Mb, E7 denoting the 7th residue in the E helix) have  $H_2O$  and  $OH^-$  as coordinated external ligands under low and high pH conditions, respectively [22]. The  $\rho_{Fe}$  value is manifested in the  $pK_a$  one through its effect on the  $H^+$  affinity of the  $Fe^{3+}$ -bound  $OH^-$ .

We report herein the results of  $O_2$  binding studies on Hb(Meso), Hb(7-PF), and Hb(2,8-DPF), involving measurements of the  $P_{50}$  and  $n$  values. As in the case of Mb [13–15], comparison of the  $pK_a$  and  $P_{50}$  values among the reconstituted Hbs demonstrated that the  $pK_a$  and  $P_{50}$  values of the proteins correlate well with each other in such a manner that the latter increases, and hence the  $O_2$  affinity decreases, with a decrease in the former. On the other hand, the native Hb deviated from the  $pK_a$ - $P_{50}$  relationship demonstrated through studies of the reconstituted Hbs and Mbs, while the native Mb followed the  $pK_a$ - $P_{50}$  relationship [13–15]. This finding could be due to the cooperativity of the native Hb, as reflected in the  $n$  value of 3.0 [1, 2, 23], because the reconstituted Hbs exhibited relatively low cooperativities, *i.e.* the  $n$  values of Hb(Meso), Hb(7-PF), and Hb(2,8-DPF) were 1.7, 1.6 and 1.6. These findings provide novel insights into the structure-function relationships in oxygen binding hemoproteins.



**Fig. 1.** Molecular structures of protoheme (Proto) (a), mesoheme (Meso) (b), 13,17-bis(2-carboxylatoethyl)-3,8-diethyl-2,12,18-trimethyl-7-trifluoromethylporphyrinato-iron(III) (7-PF) (c), and 13,17-bis(2-carboxylatoethyl)-3,7-diethyl-12,18-trimethyl-2,8-ditrifluoromethylporphyrinato-iron(III) (2,8-DPF) (d). The numbering system for the heme cofactor is indicated with (A)





**Scheme 2.** Acid-alkaline transition in metMb and metHb

## RESULTS

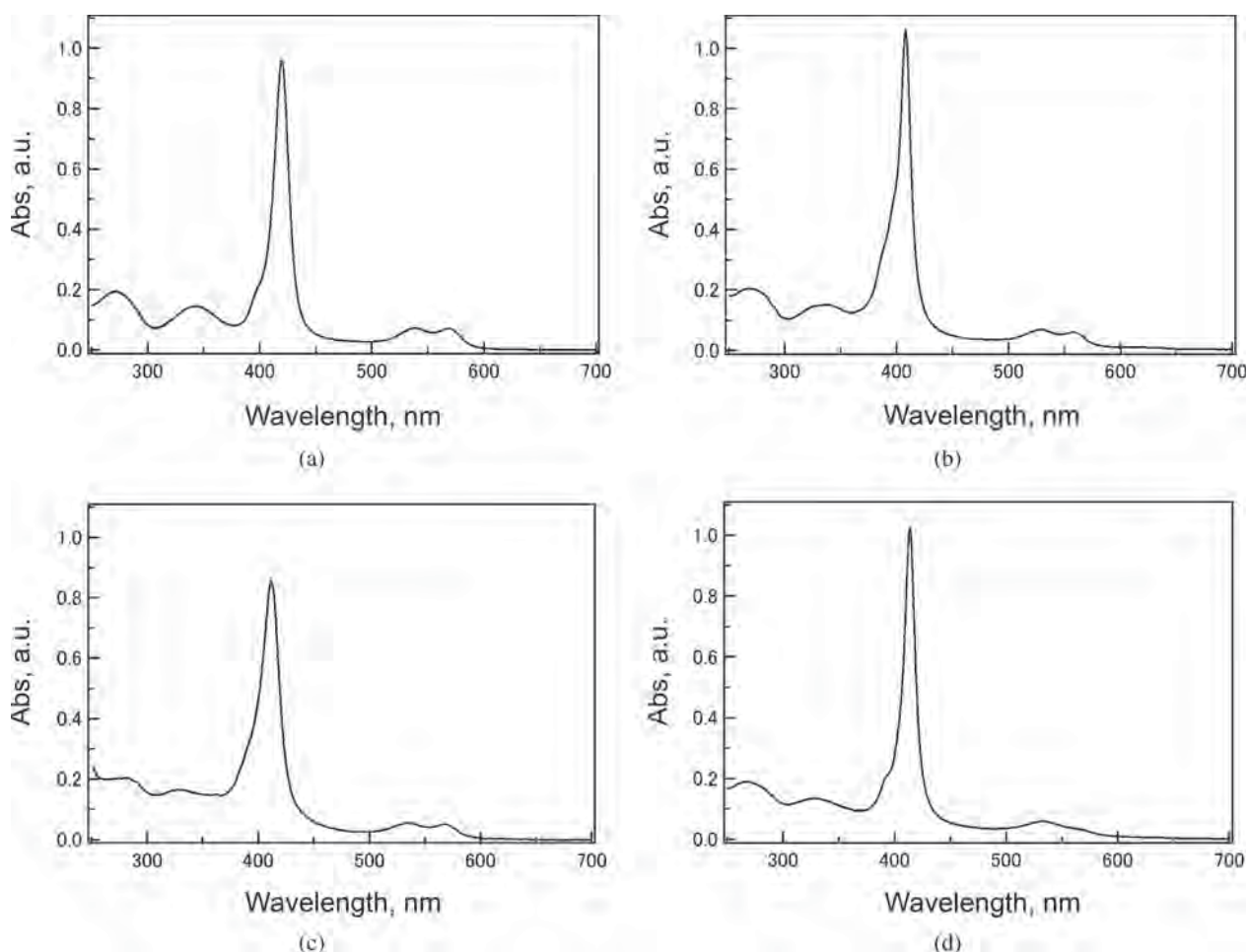
### Absorption spectra of the reconstituted Hbs

Absorption spectra have been used extensively to characterize the structural properties of hemoproteins. In particular, the Soret band characteristic of the porphyrin

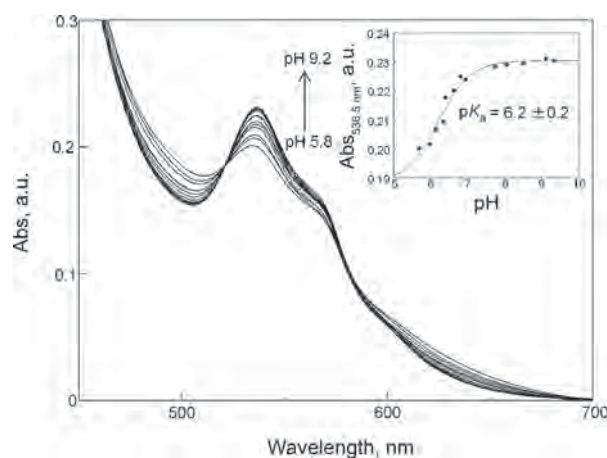
$\pi$ -system of heme has been shown to be highly sensitive to the heme environment [1]. Absorption spectra of the CO adducts of native Hb, Hb(Meso), Hb(7-PF), and Hb(2,8-DPF) are compared in Fig. 2. The wavelengths of Soret bands at maximum absorption ( $\lambda_{\max}$ ) were 420, 408, 412 and 414 nm for the CO adducts of native Hb, Hb(Meso), Hb(7-PF) and Hb(2,8-DPF), respectively. The similarity in the  $\lambda_{\max}$  values among the proteins supported that the heme cofactors of the reconstituted Hbs were accommodated properly like that of the native protein.

### $pK_a$ values of the acid-alkaline transition in metHb(2,8-DPF)

We determined the  $pK_a$  value for the acid-alkaline transition of metHb(2,8-DPF) at 25°C through fitting of the pH-dependent 536.5 nm absorption with the Henderson–Hasselbalch equation (Fig. 3), the value of  $6.2 \pm 0.2$  being obtained. Due to the low stability of metHb(2,8-DPF) under low pH conditions, the precision of the  $pK_a$  determination in this protein was not as high as that for the other metHbs. The  $pK_a$  values of various metHbs [28] and metMbs [13] are listed in Table 1.



**Fig. 2.** UV-vis spectra of CO adducts of native Hb (a), Hb(Meso) (b), Hb(7-PF) (c), and Hb(2,8-DPF) (d) in 20 mM potassium phosphate buffer, pH 7.4, at 25°C



**Fig. 3.** Absorption spectra, 445–750 nm, of methHb(2,8-DPF) at 25 °C and various pH values, 5.8–9.2, with a plot of the 536.5 nm absorbance against pH in the inset. A  $pK_a$  value of  $6.2 \pm 0.2$  was obtained from fitting of the plots to the Henderson–Hasselbalch equation

Comparison of the values among the methHbs indicated that the introduction of one  $CF_3$  group decreased the  $pK_a$  value by  $\sim 1$  pH unit. This finding was similar to that obtained through studies of the metMbs [13]. The systematic  $pK_a$  decrease in these proteins with increasing number of  $CF_3$  groups is due to the withdrawal of electron density from the porphyrin moiety of the heme factor toward these electron-attracting peripheral side chains. Furthermore, with a given heme cofactor, the  $pK_a$  value of the metHb was smaller by  $\sim 1$  pH unit relative to that of the metMb [13]. The  $\sim 1$  pH unit difference between the  $pK_a$  values of the metHbs and metMbs possessing identical heme cofactors supported the accuracy of the  $pK_a$  determination for methHb(2,8-DPF).

### $O_2$ binding properties of the reconstituted Hbs

The  $O_2$  binding properties of the reconstituted Hbs were characterized through determination of the  $P_{50}$  and  $n$  values obtained from the OECs. The values of 0.68, 1.4, and 8.9 mmHg were determined for the  $P_{50}$  values of Hb(Meso), Hb(7-PF), and Hb(2,8-DPF), respectively, at

pH 7.40 and 20 °C (Table 1). Thus, the  $P_{50}$  value increased consistently with increasing number of  $CF_3$  substitutions, indicating that the  $O_2$  affinity of a protein decreases with increasing electron-withdrawing power of its heme peripheral side chains. The relationship between the  $O_2$  affinity and the  $CF_3$  substitutions in Hb was consistent with that in Mb previously reported [13–15].

The  $n$  values for Hb(Meso), Hb(7-PF), and Hb(2,8-DPF) were determined to be 1.7, 1.6, and 1.6, respectively (Table 1), which were smaller than that of the native Hb, *i.e.* 3.0 [1, 2, 28]. Hence the reconstituted Hbs exhibited lower cooperativity than the native Hb does, as has been reported for other reconstituted Hbs [29–32]. On the other hand, the similarity in the  $n$  value among the reconstituted Hbs indicated that the cooperativity of Hb was not affected by the  $CF_3$  substitution(s).

## DISCUSSION

### $pK_a$ values of the acid-alkaline transition in the reconstituted metHbs

The  $pK_a$  value of methHb(2,8-DPF) was determined to be  $6.2 \pm 0.2$ . Therefore, based on the  $pK_a$  values of the metHbs (Table 1), the proteins are ranked as Hb(2,8-DPF) < Hb(7-PF) < native Hb < Hb(Meso), which is as expected from the electronic nature of the peripheral side chains of the heme cofactors. Comparison of the  $pK_a$  values between the metHb and metMb systems indicated that the values of the metHbs were smaller by  $\sim 1$  pH unit compared with those of the metMbs possessing identical heme cofactors (Table 1). The  $pK_a$  value is thought to be affected by the heme environment, as is the  $\rho_{Fe}$  value [28]. Ferriheme carries a net positive-charge, and hence needs to be stabilized by neutralization through electrostatic interaction with near-by polar groups in the hydrophobic heme environment of a protein. Hence, as far as the stability of the ferriheme in the protein is concerned, the alkaline form is more stable than the acidic one because of neutralization of the cationic character of the ferriheme by the coordinated  $OH^-$  (Scheme 1). Using the average value of the hydrophathy indices [33] of 36 amino acid residues

**Table 1.**  $pK_a$ ,  $P_{50}$  and  $n$  values of Hbs, and  $pK_a$  and  $P_{50}$  values of Mbs

		Proto	Meso	7-PF	2,8-DPF
Hb	$pK_a^a$	$7.90 \pm 0.05$	$8.52 \pm 0.05$	$7.52 \pm 0.05$	$6.2 \pm 0.2$
	$P_{50}^b$ (mmHg)	5.3	0.65	1.4	8.9
	$n^b$	3.0	1.7	1.6	1.6
Mb	$pK_a^c$	$8.90 \pm 0.05^c$	$9.43 \pm 0.03^c$	$8.57 \pm 0.03^c$	$7.41 \pm 0.05^c$
	$P_{50}^b$ (mmHg)	$0.58^c$	$0.38^c$	$1.10^c$	$2.80^c$

<sup>a</sup>Determined through analysis of the pH dependence of the absorption spectra at 25 °C.

<sup>b</sup>Determined from the oxygen equilibrium curve obtained at 7.40 and 20 °C.

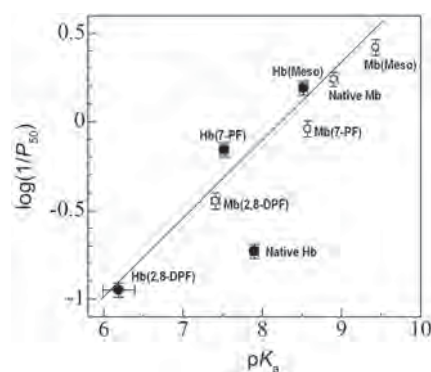
<sup>c</sup>Taken from Ref. 13.

in close proximity to the heme cofactor as a measure of the hydrophobicity of the heme environment (see Table S1 and Figures S1–S3 in the Supporting information), the heme active sites of Mb, and the  $\alpha$  and  $\beta$  subunits of Hb are ranked as Mb <  $\alpha$  subunit <  $\beta$  subunit, in order of increasing hydrophobicity of the heme environment of the protein, thus determined ranking being identical to that of the proteins, in order of decreasing  $pK_a$  value, *i.e.*  $8.32 \pm 0.05$ ,  $7.48 \pm 0.05$ , and  $8.90 \pm 0.05$  for the  $\alpha$  and  $\beta$  subunits of metHb and metMb, respectively [13, 28]. Consequently, for a give heme cofactor, the smaller  $pK_a$  value for the metHb than that for the metMb could be due to the higher hydrophobicity of the heme environment in the former.

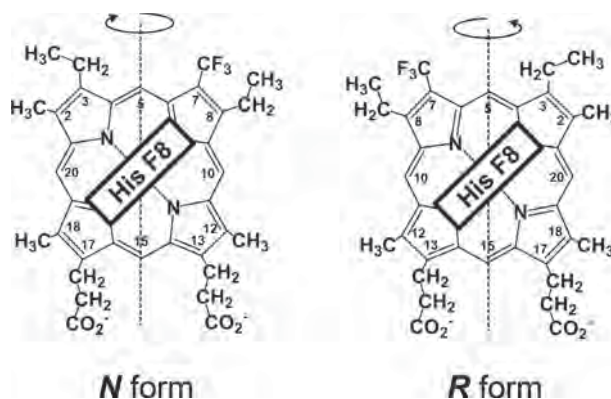
### Effects of a change in the $\rho_{Fe}$ value on the O<sub>2</sub> binding properties of Hb

Using the quantity  $1/P_{50}$  and the  $pK_a$  value as measures of the O<sub>2</sub> affinity and the  $\rho_{Fe}$  value of the protein, respectively, the effect of a change in the  $\rho_{Fe}$  value on the O<sub>2</sub> affinity of Hb was examined. For the reconstituted proteins, the  $pK_a$  value correlated well with  $\log(1/P_{50})$  in such a manner that the  $1/P_{50}$  value increased by a factor of 3 with an increase of 1  $pK_a$  unit (Fig. 4). Similar results have been obtained through studies of Mbs possessing these chemically-modified heme cofactors [13]. In the case of the Mbs, the decrease in  $\log(1/P_{50})$ , and hence the O<sub>2</sub> affinity, with decreasing  $pK_a$  value, and hence the  $\rho_{Fe}$  one, has been shown to be due to an increase in the O<sub>2</sub> dissociation rate [13–15]. The relationship between the  $\rho_{Fe}$  value and the O<sub>2</sub> dissociation rate could be interpreted in terms of the effect of a change in the  $\rho_{Fe}$  value on the resonance process between the  $Fe^{2+}-O_2$  and  $Fe^{3+}-O_2^-$ -like species (Scheme 1) [13–15]. A decrease in the  $\rho_{Fe}$  value hinders the formation of the  $Fe^{3+}-O_2^-$ -like species through obstruction of the Fe–O bond polarization, leading to stabilization of the  $Fe^{2+}-O_2$  species over the  $Fe^{3+}-O_2^-$ -like one, which in turn results in an increase in the O<sub>2</sub> dissociation rate, because O<sub>2</sub> dissociation from the heme Fe atom occurs only at the  $Fe^{2+}-O_2$  bond. Therefore, the correlation between the O<sub>2</sub> affinity and the  $\rho_{Fe}$  value of the reconstituted Hbs could be similarly interpreted.

The incorporation of 7-PF into the subunits of the apoprotein in two orientations differing by 180° rotation about the 5,10-*meso* axis results in the well-documented heme orientational disorder, *i.e.* *N* and *R* forms [34] (Fig. 5). The *N* form:*R* form ratio for the  $\alpha$  subunit of Hb(7-PF) is about 1:3, but, on the other hand, *N* form dominates in the  $\beta$  subunit [28]. In addition, the *N* and *R* forms of the  $\alpha$  subunit, and the  $\beta$  subunit exhibited  $pK_a$  values of  $7.55 \pm 0.05$ ,  $7.59 \pm 0.05$ , and  $7.38 \pm 0.05$ , respectively [28]. Based on the linear  $pK_a$ - $\log(1/P_{50})$  relationship,  $P_{50}$  values of  $1.7 \pm 0.1$ ,  $1.6 \pm 0.1$ , and  $2.1 \pm 0.1$  mmHg were obtained for the *N* and *R* forms of the  $\alpha$  subunit, and the  $\beta$  subunit, respectively, from their  $pK_a$



**Fig. 4.** Plots of the  $pK_a$  values against the quantity  $\log(1/P_{50})$  for Hbs (filled circles) and Mbs (open circles) possessing the heme cofactors in Fig. 1. The  $pK_a$  values were determined at 25°C, and the  $P_{50}$  values were measured at 20°C and pH 7.40. The straight line in the plots was obtained on linear least-squares fitting of all the data points of the Hbs and Mbs excluding that of native Hb



**Fig. 5.** The two 7-PF orientations, *N* and *R* forms, differing by 180° about the 5-H-15-H axis, with respect to His F8

values. The sensitivity of the measurement was not high enough to differentiate these  $P_{50}$  values.

Although the reconstituted Hbs exhibited a linear  $pK_a$ - $\log(1/P_{50})$  relationship (Fig. 4), the  $P_{50}$  value of  $1.2 \pm 0.1$  mmHg estimated from the  $pK_a$  value of  $7.90 \pm 0.05$  for the native metHb [28] was considerably smaller than the observed value of 5.3 mmHg (Fig. 4). The disagreement between the estimated and observed  $P_{50}$  values for the native Hb may be due to its high cooperativity, as manifested in the *n* value of 3.0 [1, 2, 23], because the reconstituted Hbs exhibited relatively low cooperativity, *i.e.* *n* values of 1.6–1.7 (Table 1). In contrast to the functional control of Mb, which is achieved through the heme environment furnished by nearby amino acid residues, and subtle tuning of the intrinsic heme Fe reactivity, the O<sub>2</sub> binding properties of Hb are significantly affected by the tertiary and quaternary structural changes upon oxygenation of the protein. Consequently, the linear  $pK_a$ - $\log(1/P_{50})$  relationship shown in Fig. 4 is thought to

be applicable to Hbs exhibiting low cooperativity. These results highlighted the significance of the vinyl side chains of the heme cofactor in the functional control of Hb through the tertiary and quaternary structural changes upon oxygenation of the protein.

## MATERIALS AND METHODS

### Sample preparation

Hb was prepared from blood obtained from the Medical Center of the University of Tsukuba. CO gas (Japan Air Gases) was slowly bubbled through the blood, and the protein was prepared as a carbon monoxide (CO) adduct using the reported procedure [24]. MetHb was prepared from the CO adduct of the protein under a stream of O<sub>2</sub> gas with strong illumination in the presence of a five-fold molar excess of potassium ferricyanide (Wako Chemical Co.). The protein was separated from the residual chemicals using a Sephadex G-50 (Sigma Chemical Co.) column equilibrated with 50 mM Bis-Tris (Sigma Chemical Co.), pH 6.5. 7-PF and 2,8-DPF were synthesized as previously described [13, 19]. Mesoheme was prepared from mesoporphyrin IX dimethyl ester (Aldrich Chemical Co.). The apoprotein of Hb was prepared at 4 °C according to the procedure of Teale [25], and reconstitution of the apoprotein with heme was carried out by the standard procedure [24]. The pH of the sample was measured with a Horiba F-22 pH meter equipped with a Horiba type 6069-10c electrode, and was adjusted using 0.2 M NaOH or HCl.

### Absorption and circular dichroism measurements

Absorption spectra of the proteins were recorded at 25 °C with a Beckman DU 640 spectrophotometer and the protein concentration of 10 μM in 20 mM potassium phosphate buffer, pH 7.4.

### Oxygen equilibrium curves

Oxygen equilibrium curves (OECs) of the proteins were measured with 30 μM protein in 100 mM phosphate buffer, pH 7.4, and 100 mM Cl<sup>-</sup> at 20 °C, using the previously described automatic oxygenation apparatus [26].  $P_{50}$  and  $n$  values were determined through non-linear least-squares fitting of the OEC data [27].

## CONCLUSION

The effects of the CF<sub>3</sub> substitutions on the  $\rho_{\text{Fe}}$  value for Hb were manifested in the  $pK_a$  value. For a give heme cofactor, the  $pK_a$  value of Hb, which is smaller by ~1 pH unit relative to that of Mb, was attributed to the more hydrophobic nature of its heme active site. As has been demonstrated for the Mbs [13–15], the O<sub>2</sub> affinity of Hb decreases with decreasing  $\rho_{\text{Fe}}$  value in such a manner that

the  $P_{50}$  value increases by a factor of ~3 with a decrease of 1  $pK_a$  unit. The native Hb deviated from the linear  $pK_a$ - $\log(1/P_{50})$  relationship, while the native Mb followed it [13]. In contrast to the functional control of Mb, which is achieved through the heme environment furnished by nearby amino acid residues, and tuning of the intrinsic heme Fe reactivity, the O<sub>2</sub> binding properties of Hb are significantly affected by the tertiary and quaternary structural changes upon oxygenation of the protein. Consequently, the deviation of the native Hb from the  $pK_a$ - $\log(1/P_{50})$  relationship suggested the significance of the vinyl side chains of the heme cofactor in the control of the cooperative O<sub>2</sub> binding of the protein.

### Acknowledgements

This work was supported by Grants-in-Aid for Scientific Research from the Ministry of Education, Culture, Sports, Science and Technology, Japan, the Yazaki Memorial Foundation for Science and Technology, and the NOVARTIS Foundation (Japan) for the Promotion of Science.

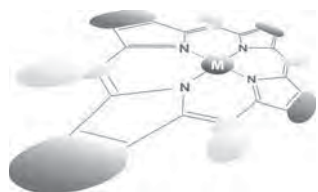
### Supporting information

Figures S1–S3 and Table S1 are given in the supplementary material. This material is available free of charge via the Internet at <http://www.worldscinet.com/jpp/jpp.shtml>.

## REFERENCES

1. Antonini E and Brunori M. *Hemoglobins and Myoglobins and their Reactions with Ligands*, North Holland Publishing: Amsterdam, 1971.
2. Imai K. *Allosteric Effects in Haemoglobin*, Cambridge University Press: Cambridge, 1982.
3. Barrick D, Ho NT, Simplaceanu V, Dahlquist FW and Ho C. *Nat. Struc. Biol.* 1997; **4**: 78–83.
4. Bellelli A, Burunori M, Miele AE, Panetta G and Vallone B. *Curr. Protein Peptide Sci.* 2006; **7**: 17–45.
5. Olson JS, Mathews AJ, Rohlfs RJ, Springer BA, Egeberg KD, Sliger SG, Tame J, Renaud JP and Nagai K. *Nature* 1988; **336**: 265–266.
6. Springer BA, Egeberg KD, Sliger SG, Rohlfs RJ, Mathews AJ and Olson JS. *J. Biol. Chem.* 1989; **264**: 3057–3060.
7. Rohlfs RJ, Mathews AJ, Carver TE, Olson JS, Springer BA, Egeberg KD and Sliger SG. *J. Biol. Chem.* 1990; **265**: 3168–3176.
8. Egeberg KD, Springer BA, Sliger SG, Carver TE, Rohlfs RJ and Olson JS. *J. Biol. Chem.* 1990; **265**: 11788–11795.
9. Carver TE, Rohlfs RJ, Olson JS, Gibson QH, Blackmore RS, Springer BA and Sliger SG. *J. Biol. Chem.* 1990; **265**: 20007–20020.

10. Springer BA, Sligar SG, Olson JS and Phillips GN Jr. *Chem. Rev.* 1994; **94**: 699–714.
11. Olson JS and Phillips GN Jr. *J. Biol. Inorg. Chem.* 1997; **2**: 544–552.
12. Capece L, Marti MA, Crespo A, Doctorovich F and Estrin DA. *J. Am. Chem. Soc.* 2006; **128**: 12455–12461.
13. Shibata T, Nagao S, Fukaya M, Tai H, Nagatomo S, Morihashi K, Matsuo T, Hirota S, Suzuki A, Imai K and Yamamoto Y. *J. Am. Chem. Soc.* 2010; **132**: 6091–6098.
14. Nishimura R, Shibata T, Ishigami I, Ogura T, Tai H, Nagao S, Matsuo T, Hirota S, Shoji O, Watanabe Y, Imai K, Neya S, Suzuki A and Yamamoto Y. *Inorg. Chem.* 2014; **53**: 1092–1099.
15. Nishimura R, Matsumoto D, Shibata T, Yanagisawa S, Ogura T, Tai H, Matsuo T, Hirota S, Neya S, Suzuki A and Yamamoto Y. *Inorg. Chem.* 2014; **53**: 9156–9165.
16. Pauling L. *Nature* 1964; **203**: 182–183.
17. Weiss JJ. *Nature* 1964; **202**: 83–84.
18. Jensen KP, Roos BO and Ryde U. *J. Inorg. Biochem.* 2005; **99**: 45–54, 978.
19. Toi H, Homma M, Suzuki A and Ogoshi H. *J. Chem. Soc. Chem. Commun.* 1985; 1791–1792.
20. Ono N, Kawamura H and Maruyama K. *Bull. Chem. Soc. Jpn.* 1989; **62**: 3386–3388.
21. Nishimura R, Shibata T, Tai H, Ishigami I, Ogura T, Nagao S, Matsuo T, Hirota S, Imai K, Neya S, Suzuki A and Yamamoto Y. *Inorg. Chem.* 2013; **52**: 3349–3355.
22. Shu F, Ramakrishnan V and Schoenborn BP. *Proc. Natl. Acad. Sci. USA* 2000; **97**: 3872–3877.
23. Imai K. *J. Mol. Biol.* 1979; **133**: 233–247.
24. La Mar GN, Yamamoto Y, Jue T, Smith KM and Pandey RK. *Biochemistry* 1985; **24**: 3826–3831.
25. Teale FWJ. *Biochim. Biophys. Acta* 1959; **35**: 543.
26. Imai K. *Methods Enzymol.* 1981; **76**: 438–449.
27. Imai K. *Methods Enzymol.* 1981; **76**: 470–486.
28. Shibata T, Nagao S, Tai H, Nagatomo S, Hamada H, Yoshikawa H, Suzuki A and Yamamoto Y. *J. Biochem.* 2010; **148**: 217–229.
29. Asakura T and Sono M. *J. Biol. Chem.* 1974; **249**: 7087–7093.
30. Kawabe K, Imaizumi K, Yoshida Z, Imai K and Tyuma I. *J. Biochem.* 1982; **92**: 1713–1722.
31. Sugita Y and Yoneyama Y. *J. Biol. Chem.* 1971; **246**: 389–394.
32. Yonetani T, Yamamoto H and Woodrow G.V.III. *J. Biol. Chem.* 1974; **249**: 682–690.
33. Kyte J and Doolittle RF. *J. Mol. Biol.* 1982; **157**: 105–132.
34. La Mar GN, Budd DL, Viscio DB, Smith KM and Langry LC. *Proc. Natl. Acad. Sci. USA* 1978; **75**: 5755–5759.



# Photocurrent enhancements in a porphyrin-viologen linked compound under plasmonic and magnetic fields

Hiroaki Yonemura<sup>\*a</sup>†, Tomoki Niimi<sup>b</sup> and Sunao Yamada<sup>a</sup>

<sup>a</sup> Department of Applied Chemistry, Faculty of Engineering, Kyushu University, 744 Motoooka, Nishi-ku, Fukuoka 819-0395, Japan

<sup>b</sup> Department of Materials Physics and Chemistry, Graduate School of Engineering, Kyushu University, 744 Motoooka, Nishi-ku, Fukuoka 819-0395, Japan

*Dedicated to Professor Shunichi Fukuzumi on the occasion of his retirement*

Received 24 October 2014

Accepted 28 November 2014

**ABSTRACT:** Zinc-porphyrin(ZnP)–viologen(V<sup>2+</sup>) linked compound containing six methylene group (ZnP(6)V)–silver nanoparticle (AgNP) composite films was fabricated by combining electrostatic layer-by-layer adsorption and the Langmuir–Blodgett method. The incident photo to photocurrent efficiency (IPCE) values of the ZnP(6)V–AgNP composite films are higher than those of the ZnP(6)V films and much higher than those of ZnP derivative films without V<sup>2+</sup> moiety as a reference. The large increase in the IPCE values of the ZnP(6)V–AgNP composite films likely comes from a combination of localized surface plasmon resonance (LSPR) from AgNPs and photoinduced intramolecular electron-transfer upon linking to a V<sup>2+</sup> moiety. The photocurrents of the ZnP(6)V–AgNP composite films and the ZnP(6)V films increase upon application of a magnetic field. Magnetic field effects (MFEs) were clearly observed for both ZnP(6)V–AgNP composite films and the ZnP(6)V films. Photocurrents increase with magnetic field under low magnetic fields ( $B \leq 150\text{--}300$  mT) and are constant under high magnetic fields ( $B > 150\text{--}300$  mT). MFEs can be explained by a radical pair mechanism. The magnitude of the MFEs in the ZnP(6)V–AgNP composite films is higher than that in the ZnP(6)V films. A remarkable increase in photocurrent for the ZnP(6)V–AgNP composite films was observed because of LSPR from the AgNPs in the presence of a magnetic field when compared with the ZnP(6)V films in the absence of a magnetic field.

**KEYWORDS:** photocurrent, magnetic field effect, silver nanoparticle, localized surface plasmon resonance, photoinduced intramolecular electron-transfer, radical pair mechanism.

## INTRODUCTION

Donor–acceptor (D–A) linked compounds in various organized molecular environments are expected to serve as model systems for investigations into electron-transfer reactions in biochemical systems such as photosynthesis. Fabricating organized molecular assemblies in which the D and the A are elaborately arranged at the molecular level on an electrode surface is a useful method to achieve highly

efficient photoelectric conversion [1]. Using covalently bonded D–A systems, a number of modified electrodes have been designed for use as photosensitive electrodes [2]. Well-defined self-assembled coaxial nanowires consisting of D–A linked compounds are expected to become next generation photofunctional nanodevices [3, 4]. However, the reaction mechanism of the photoelectrochemical process of modified electrodes or self-assembled nanostructures has not yet been determined. One reason for this is the shortage of appropriate means to verify the complicated mechanisms at work in modified electrodes.

The mechanisms of photochemical reactions in the gas phase, the liquid phase, and the solid phase have been explained in terms of magnetic field effects (MFEs)

† SPP full member in good standing

\*Correspondence to: Hiroaki Yonemura, tel: +81 92-802-2814, fax: +81 92-802-2815, e-mail: yonemura@mail.cstm.kyushu-u.ac.jp

on reaction kinetics or yields [5–7]. Consequently, the magnetic field is expected to provide a novel method of controlling photoinduced electron-transfer and subsequent processes.

A number of studies on the effect of MFEs on photoconductivity in organic films have been reported, the first being by Sokolik and Frankevich [8]. The photoconductivity of organic films increases in the presence of a magnetic field and MFEs have been explained in terms of an isotropic  $g$ -value ( $\Delta g$ ) mechanism operating on electron-hole pairs (excitons). Singlet-triplet transitions are assumed to occur owing to the different electron and hole  $g$ -values. The MFEs on the photoconductivity of poly(*N*-vinylcarbazole) films has also been studied by Okamoto *et al.* [9]. They reported that the photocurrent increases with magnetic field under low strength magnetic fields (<0.1 T) and reaches saturation under high strength magnetic fields (>0.1 T). MFEs increase when using dimethylterephthalate as the doping agent. The MFEs on photoconductivity in an organic polymer (poly-phenylene vinylene derivative) with  $C_{60}$  as the dopant was examined by Frankevich *et al.* [10]. They found that the photocurrent increases with magnetic field under low strength magnetic fields (<0.15 T) and saturation is reached under high strength magnetic fields (>0.15 T). However, no MFEs on photoinduced discharge rates were observed for  $C_{60}$ -doped poly(*N*-vinylcarbazole) [11]. By contrast, the spin dynamics of carrier generation in a photoconductive material were examined by Ogiwara *et al.* for a  $C_{60}$ -doped poly(*N*-vinylcarbazole) film [12]. In this study, MFEs were found to influence photoconductivity. The MFEs on photoconductivity in poly(*N*-vinylcarbazole) films doped with lumichrome have been investigated at up to 10 T [13].

Recently, the MFEs on various processes in organic semiconductors has been actively studied. Organic semiconductors are interesting materials for spintronics applications because of their long spin lifetimes. Organic spintronics allows magnetic functionality in organic electronics [14].

Studying the MFEs on photoelectrochemical reactions in photosensitive electrodes is expected to provide useful insights into their complicated reaction mechanisms and thus promote research into the application of MFEs in molecular devices. The MFEs under high magnetic fields ( $\sim 8$  T) on the photoelectrochemical reactions of photosensitive electrodes modified with poly(*N*-methylpyrrole) has been reported by Konno *et al.* [15]. However, little is known about the MFEs on photoelectrochemical reactions in photosensitive electrodes.

We examined the MFEs on the photoelectrochemical reactions of photosensitive electrodes modified with zinc-tetraphenylporphyrin (ZnP)–viologen ( $V^{2+}$ ) linked compounds [ZnP(*n*)V ( $n = 4, 6, 8$ )] with four, six, or eight methylene groups [16–18] and containing semiconductor nanoparticles [19, 20]. We also examined the MFEs on

the photoelectrochemical reactions of photosensitive electrodes modified with nanoclusters containing a  $C_{60}$  derivative and a methylphenothiazine group to demonstrate the use of  $C_{60}$  in a photonic nanodevice [21]. We also examined the MFEs on the photoelectrochemical reactions of ZnP(*n*)V ( $n = 4, 6, 8$ ) in an ionic liquid (1-butyl-3-methylimidazolium tetrafluoroborate) using a two-electrode cell [22, 23]. Recently, we determined the MFEs on the photoelectrochemical reactions of electrodes modified with nanowires consisting of poly(3-hexylthiophene) (P3HT), disordered P3HT films with and without annealing, and poly[2-methoxy-5-(2-ethylhexyloxy)-1,4-phenylenevinylene] (MEH-PPV) films [24, 25].

Photocurrent generation devices composed of organic compounds are expected to become next generation solar cells. However, improving the efficiency of photoelectric conversion is the most important. One method to improve these devices is the use of localized surface plasmon resonance (LSPR) induced by the coupling of an incident electric field with free electrons in metal nanoparticles [26–38].

We have reported the use of electrostatic layer-by-layer adsorption for fabricating multi-structures of silver nanoparticles (AgNPs) [28, 32–37] and gold nanoparticles (AuNPs) [31, 38]. This technique is convenient and sophisticated equipment such as vacuum systems are not required. The control of the deposition density of charged metal nanoparticles (MNPs) by changing the immersion time of the substrate in a corresponding colloidal solution is easily done. Previously, we found a remarkable enhancement in the photocurrent response based on the photoexcitation of tetraphenyl porphyrin, a zinc-tetraphenyl porphyrin (ZnTPP), a palladium phthalocyanine derivative, and poly(3-hexylthiophene) as organic dyes adsorbed onto the surfaces of AgNPs. The dye–AgNP assemblies were prepared using the layer-by-layer technique for the organic dye–AgNP composite films [26, 31–36]. Recently, we also found a remarkable enhancement in cathodic photocurrent responses for composite films of a ZnP– $V^{2+}$ -linked compound [ZnP(6)V] as a D–A-linked compound with AgNPs or AuNPs on ITO-electrodes. This was attributed to a combination of LSPR and photoinduced intramolecular electron-transfer [37, 38]. However, the MFEs on the photocurrents of ZnP(6)V–AgNP composite films and the large increase in the anodic photocurrent response because of LSPR has not been investigated yet. This is important to clarify the influence of the orientation and conformation of ZnP(6)V on the photoelectrochemical reactions of ZnP(6)V–AgNP composite films. However, the orientation and conformation of ZnP(*n*)V was not controlled previously because of the use of the spin-coating method [37, 38].

In this study, we examined the effects of enhanced electric fields because of LSPR on the photocurrents

of ZnP(6)V-linked compound–AgNP composite films using a combination of the electrostatic layer-by-layer adsorption technique and the Langmuir–Blodgett method. We investigated how AgNPs affect the MFEs on photocurrents in ZnP(6)V–AgNP composite films.

## EXPERIMENTAL

### General

Silver nitrate ( $\text{AgNO}_3$ , Wako Pure Chemical Industries, Ltd.), trisodium citrate dihydrate (Wako Pure Chemical Industries, Ltd.), Poly(ethyleneimine) (PEI, Mw = 50,000–1100,000, Wako Pure Chemical Industries, Ltd.), arachidic acid (AA) (Tokyo kasei) and the other chemicals were used as received. The amphiphilic ZnP– $\text{V}^{2+}$ -linked compound containing six methylene groups [ZnP(6)V] (Fig. 1) was synthesized as reported previously [39–42]. The amphiphilic ZnP compound without a  $\text{V}^{2+}$  moiety [ZnP(6)AB] (Fig. 1), as a reference, was also synthesized in our laboratory [39–42]. The purity of ZnP(6)V and ZnP(6)AB was confirmed by  $^1\text{H}$  NMR spectra and elemental analysis. AgNPs capped with citrate were prepared according to the reported procedure [28, 32–37, 43]. A AgNP surface plasmon peak was present at 403 nm. The average diameter of the AgNPs was 50 nm, as determined from transmission electron microscope (TEM) images. Water was deionized using a Milli-Q system (Millipore) and we used indium tin oxide (ITO) electrodes ( $10 \Omega/\text{sq.}$ ).

The steady-state absorption spectra of the solutions and the films were recorded on a Shimadzu UV-3150 spectrometer. TEM images were measured on a TEM (JEOL JEM-2010). Scanning electron microscope (SEM) images were taken on a Hitachi High-Tech SU8000 after drying the sample under vacuum for more than 6 h.

### Preparation of the modified ITO-electrodes

ITO-electrodes modified with ZnP(6)V–AgNP composite films, ZnP(6)AB–AgNP composite films, ZnP(6)V films, and ZnP(6)AB films were prepared by a combination of electrostatic layer-by-layer adsorption and the standard Langmuir–Blodgett (LB) method. First, the modified ITO-electrodes were prepared by depositing a mixed monolayer consisting of ZnP(6)V or ZnP(6)AB and AA (1:10) on ITO-electrodes (1 layer) using the LB technique [16–18]. A chloroform solution containing the porphyrin derivatives [ZnP(6)V and ZnP(6)AB] (0.2 mM) mixed with AA (2 mM) at a molar ratio of 1:10 was spread over a water subphase containing  $\text{CaCl}_2$  (0.3 mM) and  $\text{NaHCO}_3$  (0.05 mM, pH 7.0). Surface pressure-molecular area isotherms ( $\pi$ -A curves) were measured using a film balance controller (USI System, USI-3-22-QY) at a compression speed of  $0.05 \text{ mm}\cdot\text{s}^{-1}$  and a controlled temperature of 298 K. For monolayer deposition using ZnP(6)V or ZnP(6)AB and AA (1:10), we stopped the barrier at  $30 \text{ mN}\cdot\text{m}^{-1}$  and the monolayer was transferred onto an ITO substrate using a Z-type deposition (withdrawal) process at  $30 \text{ mN}\cdot\text{m}^{-1}$ . The deposition speed was  $0.05 \text{ mm}\cdot\text{s}^{-1}$ .

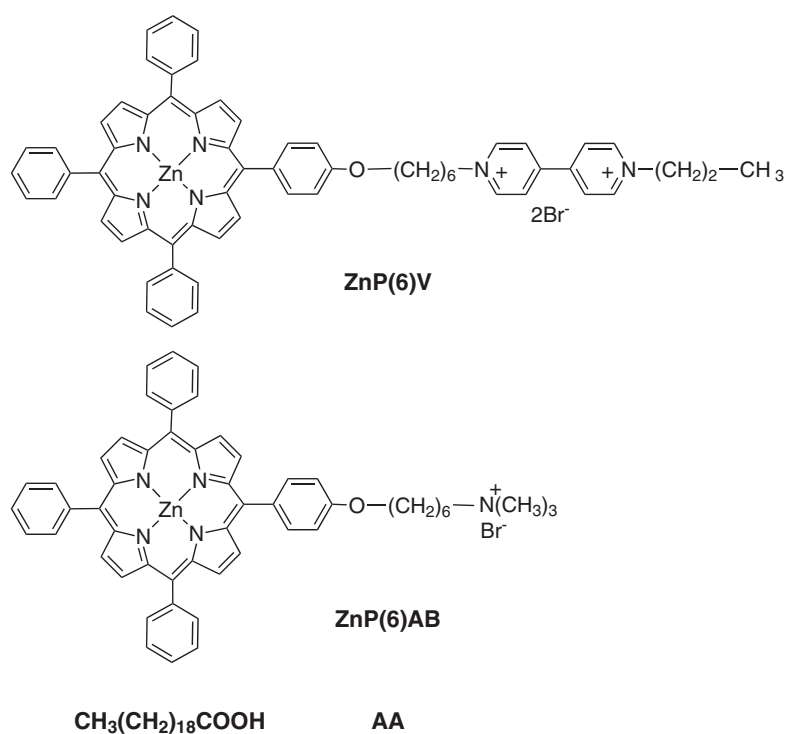


Fig. 1. Chemical structures of the amphiphilic porphyrin derivatives [ZnP(6)V and ZnP(8)AB] and arachidic acid (AA)



ZnP(6)V films (PEI/ZnP(6)V/ITO) and ZnP(6)AB films (PEI/ZnP(6)AB/ITO) were prepared as reported [44]. After depositing the mixed LB monolayer (1 layer), the LB-electrode (ZnP(6)V/ITO or ZnP(6)AB/ITO) was immersed in an aqueous PEI solution (45 mg/mL) for 20 min at 303 K to produce a LB-electrode modified with PEI (PEI/ZnP(6)V/ITO or PEI/ZnP(6)AB/ITO).

ZnP(6)V–AgNP composite films (AgNP/PEI/ZnP(6)V/ITO) or ZnP(6)AB–AgNP composite films (AgNP/PEI/ZnP(6)AB/ITO) were prepared by electrostatic layer-by-layer adsorption as reported previously [28, 32–36]. The positively-charged LB ITO-electrode (PEI/ZnP(6)V/ITO or the PEI/ZnP(6)AB/ITO) electrode was then immersed in an aqueous colloidal solution of negatively-charged AgNPs for 2 h to immobilize AgNPs on the positively-charged ITO-electrode by electrostatic adsorption (AgNP/PEI/ZnP(6)V/ITO or AgNP/PEI/ZnP(6)AB/ITO).

### Electrochemical and photoelectrochemical measurements

Electrochemical and photoelectrochemical measurements were carried out using a three-electrode cell containing the ITO-electrode modified with ZnP(6)V–AgNP composite films, ZnP(6)AB–AgNP composite films, ZnP(6)V films, or ZnP(6)AB films as a working electrode, a platinum electrode as a counter electrode, and a Ag/AgCl (sat. KCl) electrode as a reference electrode using an ALS 420 model EQCM instrument (BAS). The measurements were performed under a nitrogen atmosphere. NaClO<sub>4</sub> (0.1 M) was used as the supporting electrolyte.

Photoelectrochemical measurements for the photocurrent action spectra of incident photo to photocurrent efficiency (IPCE) values were performed using the same three electrode cells as those used for the CV measurements in an aqueous solution containing 0.1 M NaClO<sub>4</sub> in the presence of triethanolamine (TEOA; 50–150 mM) as a sacrificial electron donor under a nitrogen atmosphere. The light intensity was monitored by an optical power meter (ADVANTEST, Q8230). Photocurrent action spectra of IPCE values were obtained using light through a monochromator from a 150 W Xe lamp (Hamamatsu Photonics L2274) and measured with a potentiostat (Huso HECS-318C) at 0 V vs. Ag/AgCl.

### MFEs on photocurrents

The MFEs on the photocurrent was determined in a manner similar to that in our previous studies [16–25]. The electrode cell was placed in the pole gap of an electromagnet and an electric field was applied perpendicular to the magnetic field [19–23]. MFE measurements for different photocurrents were also obtained using the same three electrode cells and the same experimental conditions as those for the photocurrent action spectra measurements. MFE measurements were obtained using 150 W Xe lamp irradiation (Hamamatsu Photonics

L2274) through two filters (THORLABS, 400 nm long pass FGL400S and 900 nm short pass FGS900S) and a light guide (Sigma Koki) with a potentiostat (Huso HECS-318C) at 0 V vs. Ag/AgCl in the presence of triethanolamine (TEOA; 50 mM) as a sacrificial electron donor under a nitrogen atmosphere.

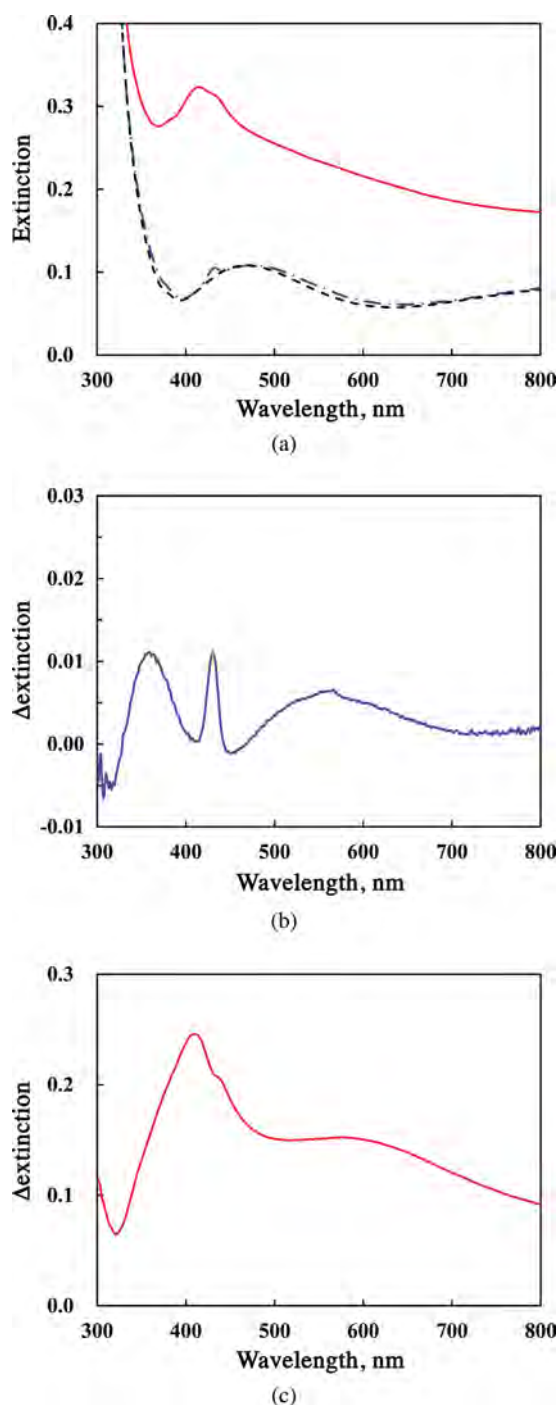
## RESULTS AND DISCUSSION

### Characterization of the ZnP(6)V–AgNP composite films, the ZnP(6)AB–AgNP composite films, the ZnP(6)V films, and the ZnP(6)AB films

The  $\pi$ -A isotherm for ZnP(6)V and AA (1:10) shows that no appreciable expanded phase is present and a stable condensed phase is formed, as described in previous papers [16–18]. A similar  $\pi$ -A isotherm was observed when the ratio of porphyrin derivative [ZnP(6)AB] to AA was 1:10. These results indicate that stable condensed phases form at a molar ratio of [ZnP(6)V or ZnP(6)AB] to AA of 1:10.

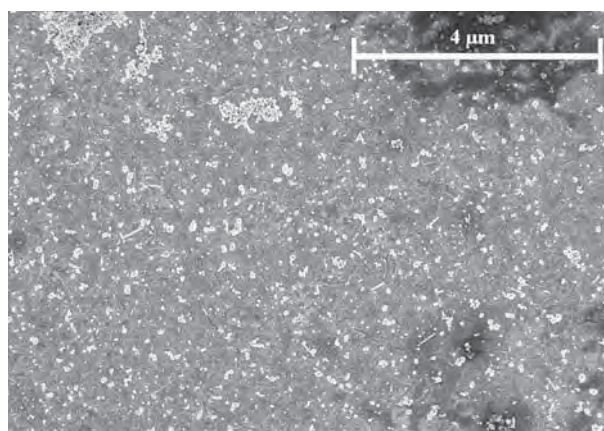
Figure 2 shows extinction spectra for AgNP/PEI/ZnP(6)V/ITO (ZnP(6)V–AgNP composite film), ZnP(6)V/ITO (ZnP(6)V film), and ITO and the difference extinction spectra between ZnP(6)V/ITO and ITO, and between AgNP/PEI/ZnP(6)V/ITO and ZnP(6)V/ITO. The ZnP(6)V–AgNP composite films (AgNP/PEI/ZnP(6)V/ITO) contain two SP bands (Figs 2a and 2c). One broad absorption band ( $\lambda_{\text{max}} = 410$  nm) at approximately 400–500 nm is assignable to the SP band of isolated AgNPs, or the band of the transverse oscillation mode of coupled particles. Broad and small bands ( $\lambda_{\text{max}} = 575$  nm) at approximately 500–800 nm are assignable to the SP band and the plasmon band of AgNP aggregates in addition to the longitudinal oscillation mode band of coupled particles, as reported previously [28, 33–37, 45]. In the SEM image of AgNP/PEI/ZnP(6)V/ITO, a number of isolated AgNPs are present and hardly any aggregation of AgNPs is observed (Fig. 3). The density of the AgNPs was estimated to be 13% from the SEM image of AgNP/PEI/ZnP(6)V/ITO (Fig. 3). The result obtained from the extinction spectrum (Fig. 2c) is consistent with that from the SEM image (Fig. 3). Similar extinction spectra and a similar SEM image were obtained for AgNP/PEI/ZnP(6)AB/ITO. The results indicate that the density of the AgNPs in AgNP/PEI/ZnP(6)AB/ITO are similar to that in AgNP/PEI/ZnP(6)V/ITO.

The absorption band around 430–460 nm in the extinction spectra and the difference extinction spectrum (Fig. 2b) comes from the Soret band of the ZnP moiety of ZnP(6)V. The Soret band peak of ZnP(6)V is present at 430 nm (Fig. 2b). It is red-shifted compared with that of the ZnP moiety of ZnP(6)V in toluene (423 nm). This result may be attributed to the aggregation of ZnP(6)V in the LB modified electrode (ZnP(6)V/ITO) and/or the electronic interaction between AgNPs and the ZnP



**Fig. 2.** (a) Extinction spectra of AgNP/PEI/ZnP(6)V/ITO (ZnP(6)V-AgNP composite film) (red unbroken line), ZnP(6)V/ITO (ZnP(6)V film) (blue dash-dotted line), and ITO (black broken line). (b) Difference extinction spectra between ZnP(6)V/ITO and ITO (blue unbroken line). (c) Difference extinction spectra between AgNP/PEI/ZnP(6)V/ITO and ZnP(6)V/ITO (red unbroken line)

moiety of ZnP(6)V. The difference extinction spectra between ZnP(6)AB/ITO and ITO is similar to that between ZnP(6)V/ITO and ITO (Fig. 2b). On the basis of our observations, the amounts of immobilized ZnP(6)V



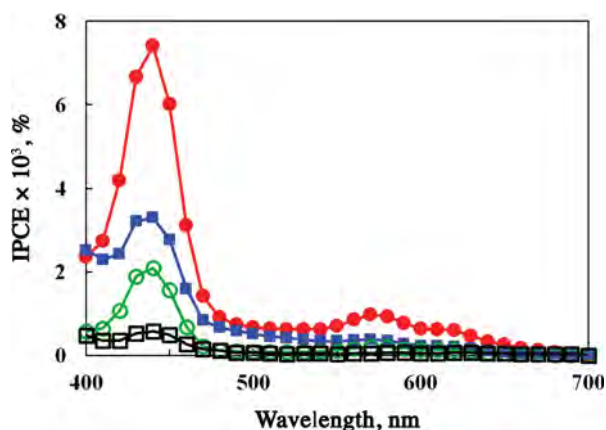
**Fig. 3.** SEM image of AgNP/PEI/ZnP(6)V/ITO (ZnP(6)V-AgNP composite film)

or ZnP(6)AB in AgNP/PEI/ZnP(6)V/ITO, AgNP/PEI/ZnP(6)AB/ITO, PEI/ZnP(6)V/ITO, and PEI/ZnP(6)AB/ITO are similar. Therefore, we can compare the IPCE values of AgNP/PEI/ZnP(6)V/ITO, AgNP/PEI/ZnP(6)AB/ITO, ZnP(6)V/ITO, and ZnP(6)AB/ITO without dividing the IPCE values by the amount of ZnP(6)V or ZnP(6)AB.

The redox potentials of the ZnP(6)V-AgNP composite films (AgNP/PEI/ZnP(6)V/ITO), the ZnP(6)AB-AgNP composite films (AgNP/PEI/ZnP(6)AB/ITO), the ZnP(6)V films (PEI/ZnP(6)V/ITO), and the ZnP(6)AB films (PEI/ZnP(6)AB/ITO) were examined by CV and DPV measurements. For AgNP/PEI/ZnP(6)V/ITO, the peak corresponding to the first reduction of the  $V^{2+}$  moiety is present at  $-0.65$  V vs. Ag/AgCl while the peak that corresponds to the re-oxidation of the viologen radical ( $V^{•+}$ ) moiety is present at  $-0.52$  V vs. Ag/AgCl. The reduction potential of the  $V^{2+}$  moiety in AgNP/PEI/ZnP(6)V/ITO is estimated to be  $-0.59$  V vs. Ag/AgCl. Similar results were obtained for the CV and DPV measurements of PEI/ZnP(6)V/ITO. The reduction potential of the  $V^{2+}$  moiety in PEI/ZnP(6)V/ITO is also estimated to be  $-0.58$  V vs. Ag/AgCl.

However, the current peaks from the oxidation of ZnP and the re-reduction of the porphyrin radical (ZnP $^{•+}$ ) are not clearly present in AgNP/PEI/ZnP(6)V/ITO, AgNP/PEI/ZnP(6)AB/ITO, ZnP(6)V/ITO, and ZnP(6)AB/ITO. This result is attributed to the suppression of electron-transfer from ZnP to the ITO-electrode. In other words, the ZnP moieties are located far from the electrode and within the LB films in the ZnP(6)V-AgNP composite films, the ZnP(6)AB-AgNP composite films, the ZnP(6)V films, and the ZnP(6)AB films, as described in a previous paper [18].

Thermodynamic data for the intramolecular electron-transfer reactions in ZnP( $n$ )V ( $n = 4, 6, 8$ ) have been evaluated previously [46, 47]. In ZnP(6)V-modified electrodes, the Gibbs free energy driving force  $\Delta G$  [ $\Delta G_{CR}$ ,  $\Delta G_{CS}(S)$ , and  $\Delta G_{CS}(T)$ ] for the intramolecular



**Fig. 4.** Photocurrent action spectra of IPCE values of AgNP/PEI/ZnP(6)V/ITO (ZnP(6)V-AgNP composite film) (●), AgNP/PEI/ZnP(6)AB/ITO (ZnP(6)AB-AgNP composite film) (■), PEI/ZnP(6)V/ITO (ZnP(6)V film) (○), and PEI/ZnP(6)AB/ITO (ZnP(6)V film) (□) at 0 V vs. Ag/AgCl in TEOA (50 mM)

charge recombination (CR) process from  $V^{*+}$  to  $ZnP^{*+}$  and for the intramolecular charge separation (CS) process from the singlet excited state [ $^1ZnP^*$  (S)] and the triplet excited state [ $^3ZnP^*$  (T)] of ZnP to  $V^{2+}$  can be calculated using the redox potentials of ZnP (0.78 V vs. Ag/AgCl) [18] and  $V^{2+}$  (-0.59 V or -0.58 V vs. Ag/AgCl; ZnP(6)V-AgNP composite films or ZnP(6)V films).

The thermodynamic values ( $-\Delta G_{CS}(S) = 0.64$  eV or 0.65 eV,  $-\Delta G_{CS}(T) = 0.13$  eV or 0.14 eV, and  $-\Delta G_{CR} = 1.37$  eV or 1.36 eV; ZnP(6)V-AgNP composite films or ZnP(6)V films) indicate that intramolecular electron-transfer from  $^1ZnP^*$  or  $^3ZnP^*$  to  $V^{2+}$  and the reverse electron-transfer in ZnP(6)V is thermodynamically favorable.

#### Photoelectrochemical reactions of the ZnP(6)V-AgNP composite films, the ZnP(6)AB-AgNP composite films, the ZnP(6)V films, and the ZnP(6)AB films

The photocurrent action spectra of IPCE values of the ZnP(6)V-AgNP composite films, the ZnP(6)AB-AgNP composite films, the ZnP(6)V films, and the ZnP(6)AB films were measured to investigate the effects of AgNPs on the photoelectrochemical responses of the ZnP(6)V-AgNPs composite films. Irradiating the ITO-electrodes modified with four films [ZnP(6)V-AgNPs composite films, ZnP(6)AB-AgNPs composite films, ZnP(6)V films, and ZnP(6)AB films] with visible light (>400 nm) resulted in stable anodic photocurrents at 0 V vs. Ag/AgCl in TEOA (50 mM) (Fig. 4). Effect of TEOA concentration on photocurrent action spectra of IPCE values of PEI/ZnP(6)V/ITO (ZnP(6)V film) was measured typically. The IPCE values changed with

increasing TEOA concentration from 50 mM to 150 mM. The IPCE values of Soret band (430 nm) increased 1.40 times in TEOA (100 mM) and 1.18 times in TEOA (150 mM) as comparison with that in TEOA (50 mM). On the other hand, the IPCE values of Soret band (430 nm) of the Q-band (560 nm) increased 1.10 times in TEOA (100 mM), but decreased 0.75 times as comparison with that in TEOA (50 mM). We measured all the samples in TEOA (50 mM) as a sacrificial electron donor, as same experimental condition in the previous papers, because we compared between the results in present paper and those in the previous papers [16–18]. The photocurrent action spectra of IPCE values of all the samples (Fig. 4) were in good agreement with the absorption spectra of the ZnP moieties of ZnP(6)AB or ZnP(6)V in ethanol or with the difference extinction spectra between ZnP(6)AB/ITO or ZnP(6)V/ITO and ITO (Fig. 2b). These results strongly indicate that the photocurrents of the ITO-electrodes modified with the ZnP(6)V-AgNPs composite films, the ZnP(6)AB-AgNPs composite films, the ZnP(6)V films, and the ZnP(6)AB films can be attributed to the photoexcitation of the ZnP moiety of ZnP(6)V or ZnP(6)AB.

The IPCE value ratios of the Soret band (430 nm) and the Q-band (560 nm) are summarized in Table 1. The IPCE values of PEI/ZnP(6)V/ITO are higher than those of PEI/ZnP(6)AB/ITO (Fig. 4). The IPCE value ratios (ZnP(6)V/ZnP(6)AB) of the Soret band (430 nm) and the Q-band (560 nm) are 3.6 and 4.2, respectively (Table 1). The PCE values of AgNP/PEI/ZnP(6)V/ITO are higher than those of AgNP/PEI/ZnP(6)AB/ITO (Fig. 4). The IPCE value ratios (AgNP-ZnP(6)V/AgNP-ZnP(6)AB) of the Soret band (430 nm) and the Q-band (560 nm) are 2.1 and 2.4, respectively (Table 1). These results are in good agreement with those reported previously [37]. Therefore, the increase in IPCE values for ZnP(6)V compared with the IPCE values of ZnP(6)AB are attributed to photoinduced electron-transfer from the excited state of ZnP ( $ZnP^*$ ) ( $^1ZnP^*$  and  $^3ZnP^*$ ) to  $V^{2+}$  and subsequent electron-transfer from the reduced  $V^{2+}$  ( $V^{*+}$ ) to the ITO-electrode. This occurs in both PEI/ZnP(6)V/ITO and AgNP/PEI/ZnP(6)V/ITO because the orientation of

**Table 1.** IPCE value ratios of the Soret band (430 nm) and the Q-band (560 nm)

IPCE value ratio	Soret band (430 nm)	Q-band (560 nm)
ZnP(6)V/ZnP(6)AB	3.6	4.2
AgNP-ZnP(6)AB/ZnP(6)AB	6.1	9.3
AgNP-ZnP(6)V/ZnP(6)AB	13	22
AgNP-ZnP(6)V/ZnP(6)V	3.9	5.2
AgNP-ZnP(6)V/AgNP-ZnP(6)AB	2.1	2.4
ZnP(6)AB: PEI/ZnP(6)AB/ITO, ZnP(6)V: PEI/ZnP(6)V/ITO, AgNP-ZnP(6)AB: AgNP/PEI/ZnP(6)AB/ITO, AgNP-ZnP(6)V: AgNP/PEI/ZnP(6)V/ITO.		

ZnP(6)V was confirmed and the conformation of ZnP(6)V extends into the LB films.

The IPCE values of AgNP/PEI/ZnP(6)V/ITO are higher than those of PEI/ZnP(6)V/ITO (Fig. 4). The IPCE value ratios (AgNP-ZnP(6)V/ZnP(6)V) of the Soret band (430 nm) and the Q-band (560 nm) are 3.9 and 5.2, respectively (Table 1). Additionally, the IPCE values of AgNP/PEI/ZnP(6)AB/ITO are higher than those of PEI/ZnP(6)AB/ITO (Fig. 4). The IPCE value ratios of the Soret band (430 nm) and the Q-band (560 nm) were 6.1 and 9.3, respectively (Table 1). Finally, the IPCE values of AgNP/PEI/ZnP(6)V/ITO were much higher than those of PEI/ZnP(6)AB/ITO (Fig. 4). The IPCE value ratios (AgNP-ZnP(6)V/ZnP(6)AB) of the Soret band (430 nm) and the Q-band (560 nm) were 13 and 22, respectively (Table 1). In the presence of AgNPs the increase in IPCE values at 560 nm in the Q-band region was approximately 1.3–1.7 times that at 430 nm in the Soret band region (Table 1).

On the basis of these observations, the increase in IPCE values in the Q-band region are higher than those in the Soret band region in the presence of AgNPs (AgNP/PEI/ZnP(6)AB/ITO and AgNP/PEI/ZnP(6)V/ITO). The increase in IPCE value at 560 nm in the Q-band region is similar to that at 430 nm in the Soret band region in PEI/ZnP(6)V/ITO.

If the photocurrent from AgNP/PEI/ZnP(6)AB/ITO or AgNP/PEI/ZnP(6)V/ITO is generated only through a simple photoexcitation of the ZnP moieties of the immobilized ZnP(6)AB or ZnP(6)V molecules, the IPCE value ratios should be independent of irradiation wavelength. However, the relative increases are dependent on the irradiation wavelength in AgNP/PEI/ZnP(6)AB/ITO and AgNP/PEI/ZnP(6)V/ITO compared with the IPCE values of PEI/ZnP(6)AB/ITO as a reference (Table 1).

The Q-band (500–700 nm) absorption of the ZnP moiety in ZnP(6)AB or ZnP(6)V is similar to the plasmon bands of aggregated AgNPs (Fig. 2c). Therefore, the significant increase in IPCE value at 560 nm is most likely responsible for the surface plasmons of the AgNPs aggregates. These results are similar to those of the photocurrents in porphyrin/gold nanostructures [27, 29, 30] and in dye-MNPs (AgNPs or AuNPs) composite films [28, 31–38].

We recently reported that a large increase in the cathodic photocurrents in ZnP(6)V–AgNP composite [37] and ZnP(6)V–AuNP composite films [38] are observed compared with that in ZnP(6)V films. These increases most likely come from LSPR because of the AgNPs and AuNPs, respectively. The anodic direction of the photocurrents was opposite to that obtained in previous papers [16–18]. Similar increases in the photocurrents were observed for the ZnP(6)V–AgNP composite in this study. The large increase in photocurrent in the ZnP(6)V–AgNP composite in this study is in fair agreement with that of ZnP(6)V–AgNP

composite films and ZnP(6)V–AuNP composite films immobilized by spin-coating [37, 38]. Therefore, increases in photocurrents because of the AgNPs in the ZnP(6)V–AgNP composite films and the ZnP(6)AB–AgNP composite films in this study strongly suggest that local electric fields appear in the vicinity of the AgNPs surface. This contributes to the anodic increase in photocurrent generation based on the immobilized ZnP moiety in ZnP(6)V or ZnP(6)AB (LSPR enhanced excitation) as shown in Fig. 4. The increase in anodic photocurrent in the ZnP(6)V–AgNP composite films compared with that in the ZnP(6)AB–AgNP composite films also suggests a contribution by photoinduced intramolecular electron-transfer from ZnP\* (<sup>1</sup>ZnP\* and/or <sup>3</sup>ZnP\*) to V<sup>2+</sup> in the ZnP(6)V–AgNP composite films. This is similar to that obtained during a comparison between ZnP(6)V films and ZnP(6)AB films.

On the basis of these observations, the higher increases in anodic photocurrents in the ZnP(6)V–AgNP composite films (AgNP/PEI/ZnP(6)V/ITO) can most likely be attributed to the combination of LSPR from the AgNPs and photoinduced intramolecular electron-transfer because of V<sup>2+</sup> moiety linkages. This result strongly suggests that the higher increases in cathodic photocurrents in the ZnP(6)V–AgNP composite films and the ZnP(6)V–AuNP composite films can be attributed to a combination of LSPR from AgNPs and photoinduced intramolecular electron-transfer. This is despite the orientation of the conformation of ZnP(6)V on ITO-modified electrodes, which could not be controlled because of the use of spin-coating [37, 38].

#### MFEs on the photocurrents of the ZnP(6)V–AgNP composite films, the ZnP(6)AB–AgNP composite films, the ZnP(6)V films, and the ZnP(6)AB films

We examined the MFEs on the photoelectrochemical reactions of the ZnP(6)V–AgNP composite, ZnP(6)V, and the ZnP(6)AB films to verify the influence of the AgNPs and the MFEs on photocurrents in the ZnP(6)V–AgNP composite films.

In the ZnP(6)V–AgNP composite and the ZnP(6)V films, the photocurrent clearly increases in the presence of a magnetic field (Fig. 6).

The magnitude of the MFE influence on the photocurrent can be expressed as:

$$Q = (I(B) - I(0))/I(0) \times 100 \quad (1)$$

where I(0) and I(B) are the photocurrents in the absence and presence of the magnetic field (B), respectively, as reported previously [16–25].

In the ZnP(6)V films (PEI/ZnP(6)V/ITO), Q increases gradually under low magnetic fields ( $B \leq 300$  mT) and it is constant under high magnetic fields ( $B \geq 300$  mT), as shown in Fig. 6. The magnetic field dependence agrees with that of the ZnP(6)V-modified electrode used as a LB film previously [16–18]. The magnitude of the MFE

( $Q_{\max} \approx 25\%$ ) in this study (PEI/ZnP(6)V/ITO) was larger than that ( $Q_{\max} \approx 15\%$ ) reported previously (ZnP(6)V/ITO) [17, 18]. This result can probably be attributed to the effect of PEI.

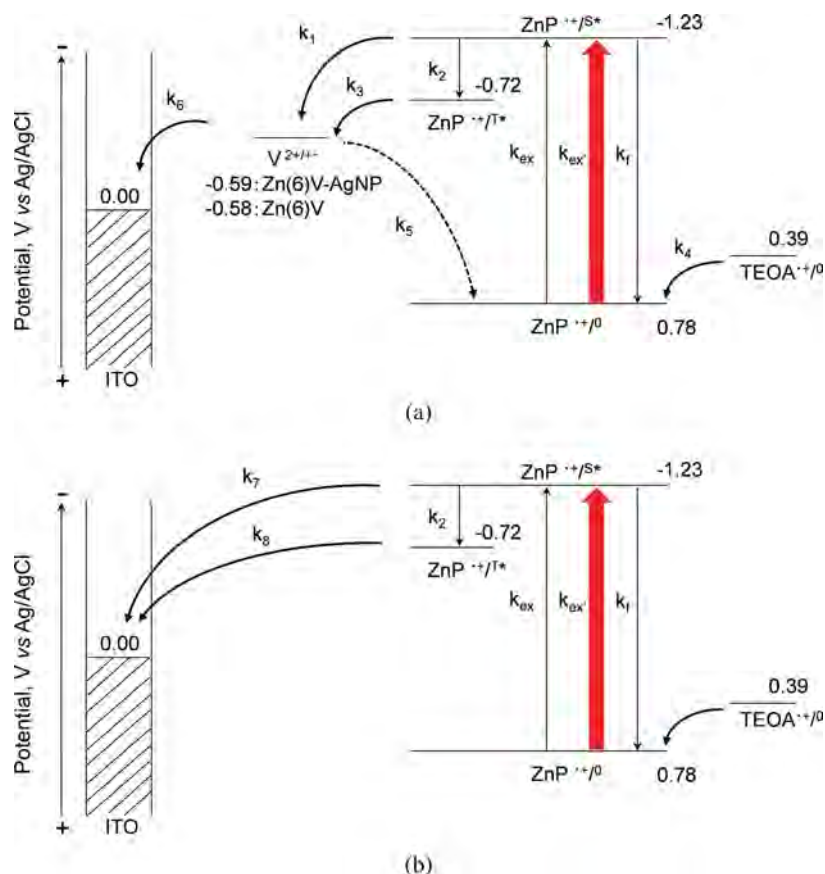
Conversely,  $Q$  increases sharply under low magnetic fields ( $B \leq 150$  mT) and is constant under high magnetic fields ( $B \geq 150$  mT) for the ZnP(6)V–AgNP composite (AgNP/PEI/ZnP(6)V/ITO), as shown in Fig. 6. Interestingly, the magnitude of the MFE ( $Q_{\max} \approx 40\%$ ) of the ZnP(6)V–AgNP composite film was higher than that ( $Q_{\max} \approx 25\%$ ) of the ZnP(6)V films (PEI/ZnP(6)V/ITO). Additionally, the magnetic field dependence of the  $Q$  values in the ZnP(6)V–AgNP composite films is different from that in the ZnP(6)V films. The difference is the influence of the AgNPs, as discussed later.

Significant increases in the photocurrents of the ZnP(6)V–AgNP composite films (AgNP/PEI/ZnP(6)AB/ITO) were observed for the first time as a result of LSPR from the AgNPs and because of magnetic field effects in the radical pair mechanism.

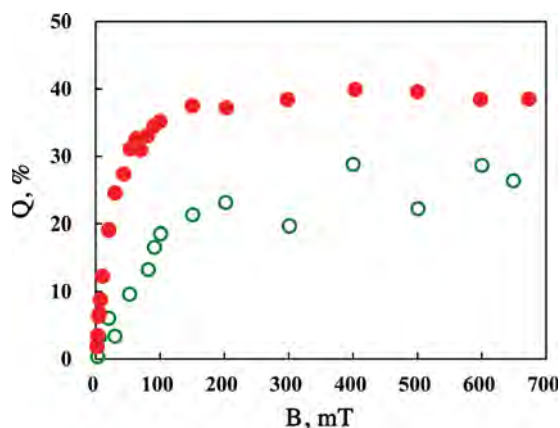
In contrast, no magnetic field effects were observed for the photocurrent of the ZnP(6)AB films (PEI/ZnP(6)AB/ITO) and the ZnP(6)AB–AgNP composite films

(AgNP/PEI/ZnP(6)AB/ITO) because radical pairs were not generated in the photoelectrochemical reaction of the ZnP(6)AB films or the ZnP(6)AB–AgNP composite films. These results are in fair agreement with those of a ZnP(8)AB-modified electrode used as a LB film [16–18]. Therefore, the MFEs on photocurrents can be explained by a radical pair mechanism, as described below.

Reaction schemes for the photoelectrochemical reaction of the ZnP(6)V–AgNP composite films, the ZnP(6)AB–AgNP composite films, the ZnP(6)V films, and the ZnP(6)AB films, and the photochemical reaction of ZnP(6)V are summarized in Figs 5 and 7, respectively. These were reported in previous papers [18]. The MFEs on the photocurrents in the ZnP(6)V–AgNP composite films and the ZnP(6)V films come from the photogeneration of triplet radical pairs,  $^3(\text{ZnP}^{*+}-\text{V}^{*+})$  via a photoinduced intramolecular electron-transfer process from  $^3\text{ZnP}^*$  to  $\text{V}^{2+}$  at the ITO-electrode surface. This process (Fig. 7) is also suggested by the obtained thermodynamic values ( $-\Delta G_{\text{CS}}(T) = 0.13$  eV or  $0.14$  eV; ZnP(6)V–AgNP composite films or the ZnP(6)V films) as described above. Intersystem crossing of the photogenerated radical pair ( $k_{\text{isc}}$  in Fig. 7) is the rate-determining step for radical pair



**Fig. 5.** Schematic reaction scheme for the photoelectrochemical reaction of (a) AgNP/PEI/ZnP(6)V/ITO (ZnP(6)V–AgNP composite film) and PEI/ZnP(6)V/ITO (ZnP(6)V film) and (b) AgNP/PEI/ZnP(6)AB/ITO (ZnP(6)AB–AgNP composite film) and PEI/ZnP(6)AB/ITO (ZnP(6)AB film).  $k_{\text{ex}}$ : rate constant of excitation of ZnP,  $k'_{\text{ex}}$ : rate constant for the excitation of ZnP in the presence of AgNP (LSPR enhanced excitation),  $k_f$ : rate constant of the fluorescence emission process of ZnP\*



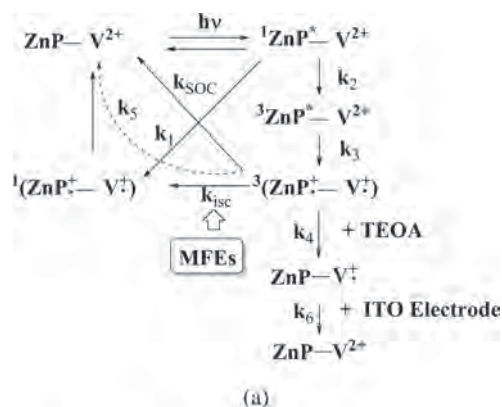
**Fig. 6.** Magnetic field dependence of the Q values in AgNP/PEI/ZnP(6)V/ITO (ZnP(6)V-AgNP composite film) (●) and PEI/ZnP(6)V/ITO (ZnP(6)V film) (○)

decay via reverse electron-transfer [ $k_5$  in Figs 5a and 7] to the ground state. Under sufficiently strong magnetic fields ( $B \geq 50$  mT), intersystem crossing is controlled by relaxation from the triplet sublevels to the corresponding singlet levels [5–7]. As intersystem crossing is suppressed by the magnetic field, the probability of electron-transfer increases for the reduced viologen ( $V^{+\bullet}$ ) in the triplet radical pair to the ITO-electrode. As a consequence, the photocurrent increases in the presence of a magnetic field, as shown in Fig. 6.

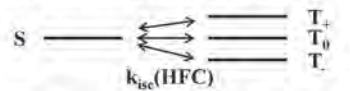
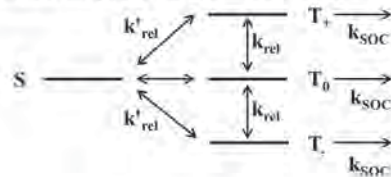
In the ZnP(6)AB–AgNP composite films (AgNP/PEI/ZnP(6)AB/ITO) and the ZnP(6)AB films (PEI/ZnP(6)AB/ITO), direct electron-transfer occurs from  $^1\text{ZnP}^*$  or  $^3\text{ZnP}^*$  [ $k_7$  and  $k_8$  in Fig. 5b] to the ITO-electrode. No photocurrent MFEs were observed for the ZnP(6)AB–AgNP composite films or the ZnP(6)AB films because photogenerated triplet radical pairs were not generated by intramolecular electron-transfer. These results are consistent with those obtained for the use of a ZnP(8)AB-modified electrode as a LB film [16–18].

Direct electron-transfer from  $^1\text{ZnP}^*$  or  $^3\text{ZnP}^*$  to the ITO-electrode as is the case for the ZnP(6)AB–AgNP composite films and the ZnP(6)AB films (Fig. 5b) may partly contribute to the photocurrents of the ZnP(6)V–AgNP composite and the ZnP(6)V films (Fig. 5a). However, the photocurrent MFEs are experimental evidence for a photoelectrochemical response from the ZnP(6)V–AgNP composite films and the ZnP(6)V films. This comes from a sequential electron-transfer from the ZnP moiety to the ITO-electrode with the  $V^{2+}$  moiety serving as a mediator.

The MFEs in a biradical can be explained by spin rephrasing ( $\Delta g$ ), hf coupling (hfc) and spin-lattice relaxation (SLR) mechanisms in the radical pair mechanism [5–7]. The  $\Delta g$  mechanism is ineffective for the MFEs of ZnP(6)V in the ZnP(6)V–AgNP composite films and the ZnP(6)V films under the low magnetic field strengths ( $\leq 700$  mT) used in this study [48]. The



(a)

(1) Zero magnetic field ( $B=0$  mT)(2) Low magnetic field ( $B < \text{ca. } 4$  mT)(3) Higher magnetic field ( $B > \text{ca. } 4$  mT)

(b)

**Fig. 7.** (a) Reaction scheme showing the MFEs on the photoelectrochemical reactions of AgNP/PEI/ZnP(6)V/ITO (ZnP(6)V-AgNP composite film) and PEI/ZnP(6)V/ITO (ZnP(6)V film). (b) Schematic representation of the effect of Zeeman splitting on intersystem crossing ( $k_{\text{isc}}$ ) leading to reverse electron transfer ( $k_5$ ) from  $^1(\text{ZnP}^+ \bullet - \text{V}^{+\bullet})$

rate constant of the  $\Delta g$  mechanism was estimated using the g-values of the  $\text{ZnP}^{+\bullet}$  ( $g = 2.0025$ ) [49] and  $\text{V}^{+\bullet}$  ( $g = 2.0052$ ) [50] radicals. The hfc mechanism can be discussed in terms of the semi-theoretical value ( $B_{1/2}$ ), which is half width of the MFE where  $B_{1/2}$  is given by  $B_{1/2} = 2(B_1^2 + B_2^2)/(B_1 + B_2)$ .  $B_1$  and  $B_2$  refer to the hf interactions between the nuclear spins and the unpaired electron spins of each radical [5–7]. The  $B_{1/2}$  value is estimated to be 2.0 mT using the hfc constants of  $\text{ZnP}^{+\bullet}$  [49] and  $\text{V}^{+\bullet}$  [50]. The  $B_{1/2}$ -value (2.0 mT) is smaller than the experimental values (*ca.* 20 mT; ZnP(6)V–AgNP composite films, and *ca.* 80 mT; ZnP(6)V films) (Fig. 6). These results indicate that the MFE obtained for low magnetic fields ( $\leq 150$  mT; ZnP(6)V–AgNP composite films and  $\leq 300$  mT; ZnP(6)V films) cannot be explained by only considering the isotropic hfc mechanism.

However, it can be interpreted in terms of the hfc ( $B < ca. 4$  mT) and SLR mechanisms because of anisotropic hf and dipole-dipole interactions ( $ca. 4$  mT  $< B < 150$  mT; ZnP(6)V–AgNP composite films or  $ca. 4$  mT  $< B \leq 300$  mT; ZnP(6)V films) [16–18, 24, 25, 48]. The MFEs on the photocurrents under low magnetic fields for the ZnP(6)V–AgNP composite films ( $B \leq 150$  mT) and the ZnP(6)V films ( $B \leq 300$  mT) cannot be explained by only considering the isotropic hfc mechanism. However, it can be interpreted in terms of the hfc ( $B < ca. 4$  mT) and SLR mechanisms because of anisotropic hf and dipole-dipole interactions ( $ca. 4$  mT  $< B < 150$  mT; ZnP(6)V–AgNP composite films or 300 mT; ZnP(6)V films), which is similar to previous reports [16–18, 24, 25, 48]. MFEs under high magnetic fields become constant at higher than 150 mT (ZnP(6)V–AgNP composite films) or 300 mT (ZnP(6)V films). The saturation behavior is dominated by SOC-induced ISC processes ( $k_{SOC}$  in Fig. 7). The Q values become constant under high magnetic fields ( $B > 150$  mT; ZnP(6)V–AgNP composite films or 300 mT; ZnP(6)V films) since SOC-induced ISC processes are independent of the magnetic field.

Differences in the magnetic field dependence of the Q values can be attributed to the contribution of the SLR mechanisms to the MFEs of the ZnP(6)V–AgNP composite films and the ZnP(6)V films. The results most likely come from the fast relaxation time ( $k_{rel}$  and  $k'_{rel}$  in Fig. 7b) of the AgNPs in the ZnP(6)V–AgNP composite films. Consequently, the contribution of the SLR mechanism to the MFEs in the ZnP(6)V–AgNP composite films probably decreases more than that in the ZnP(6)V films. Both the isotropic hfc and the SLR mechanisms thus contribute to the MFEs of the photocurrent in the ZnP(6)V films while the MFEs are mostly dominated by the isotropic hfc mechanism in the ZnP(6)V–AgNP composite films.

The magnitude of the MFE ( $Q_{max} \approx 40\%$ ) in the ZnP(6)V–AgNP composite films is much higher than that ( $Q_{max} \approx 25\%$ ) in the ZnP(6)V films (PEI/ZnP(6)V/ITO) (Fig. 6). These results can most likely be attributed to the contribution of AgNPs to the MFEs and the photochemical reactions including the photoinduced electron-transfer reactions of ZnP(6)V. The effect of AgNPs on MFEs can be explained by considering several effects of the reaction processes. First, the magnitudes of the MFEs are controlled by the saturation behavior of the Q values ( $Q_{max}$ ). The  $Q_{max}$  values are dominated by a SOC-induced ISC process ( $k_{SOC}$  in Fig. 7). However, the magnitude of the MFE decreases in the presence of AgNPs because the SOC-induced ISC process accelerates in the presence of AgNPs. This is similar to the effect of temperature on MFEs [50–52]. In other words,  $Q_{max}$  increases in the presence of AgNPs because the SOC-induced ISC processes probably accelerate as a result of the heavy atom effect of the AgNPs during SOC-induced ISC processes. Second, the magnitude of the MFEs is controlled by the relaxation process ( $k_{rel}$  and  $k'_{rel}$  in Fig. 7b) of the photogenerated

radical pairs in the SLR mechanism. The magnitude of the MFE decreases in the presence of AgNPs since the relaxation time accelerates in the presence of AgNPs, as described above. Third, the magnitude of the MFEs is controlled by the contribution of the singlet radical pair,  $^1(\text{ZnP}^{+\bullet}-\text{V}^{+\bullet})$ , via a photoinduced intramolecular electron-transfer process from  $^1\text{ZnP}^*$  to  $\text{V}^{2+}$  at the ITO-electrode surface ( $k_1$  in Figs 5 and 7), and/or the influence of the direct electron-transfer process from  $^1\text{ZnP}^*$  and/or  $^3\text{ZnP}^*$  to the ITO-electrode without a mediator ( $k_7$  and/or  $k_8$  in Fig. 5b) on the photocurrents. Therefore, the magnitude of the MFE increases in the presence of AgNPs because of the contribution of the triplet radical pair,  $^3(\text{ZnP}^{+\bullet}-\text{V}^{+\bullet})$ , which increases the photocurrents more than is the case for the singlet radical pair,  $^1(\text{ZnP}^{+\bullet}-\text{V}^{+\bullet})$ . Intersystem crossing in  $^3\text{ZnP}^*$  ( $k_1$  in Figs 5 and 7) accelerates because of the heavy atom effect of the AgNPs. The magnitude of the MFE increases in the presence of AgNPs because of photoinduced intramolecular electron-transfer from  $^3\text{ZnP}^*$  to  $\text{V}^{2+}$  ( $k_2$  in Figs 5 and 7) and this may be enhanced by LSPR in the AgNPs.

On the basis of these considerations the effect of AgNPs on MFEs can be explained by the third contribution (increase in the intersystem crossing of  $^3\text{ZnP}^*$  because of the heavy atom effect and/or AgNPs and increases in the photoinduced intramolecular electron-transfer from  $^3\text{ZnP}^*$  to  $\text{V}^{2+}$  because of LSPR in the presence of AgNPs). This contribution is more important than the first and second contributions.

## CONCLUSION

In this study, a large increase in the anodic photocurrents of ZnP(6)V–AgNP composite films that were prepared by a combination of electrostatic layer-by-layer adsorption and the Langmuir-Blodgett method were observed compared to ZnP(6)AB films. These large increases most likely come from a combination of LSPR from AgNPs and photoinduced intramolecular electron-transfer from ZnP\* ( $^1\text{ZnP}^*$  and  $^3\text{ZnP}^*$ ) to  $\text{V}^{2+}$  in ZnP(6)V.

The photocurrents in the ZnP(6)V–AgNP composite films increased upon the application of a magnetic field. A remarkable increase in the anodic photocurrent was observed when combining LSPR and magnetic field effects. This study indicates that a combination of LSPR from AgNPs and MFEs is useful in increasing the photocurrents of modified electrodes in, for example, D–A linked compounds.

Further investigations into the mechanism of the influence of LSPR from MNPs (AgNPs or AuNPs) on photocurrents in D–A-linked compound–MNP composite films are now in progress.

## Acknowledgements

The authors thank the Center of Advanced Instrumental Analysis, Kyushu University for performing SEM

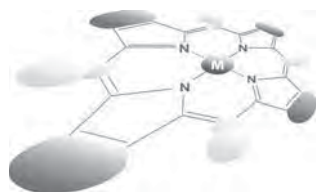
measurements. This study was financially supported by Grants-in-Aid for Scientific Research C (No. 21550135), by a grant from Challenging Exploratory Research (Nos. 25600006 and 24651145), and by the Nanotechnology Network Project (Kyushu Area Nanotechnology Platform) from the Ministry of Education, Culture, Sports, Science and Technology (MEXT) of Japan.

## REFERENCES

- Fujihira M. *Mol. Cryst. Liq. Cryst.* 1990; **183**: 59–69.
- Imahori H, Mori Y and Matano Y. *J. Photochem. Photobiol. C* 2003; **4**: 51–83.
- Hara T, Furukawa K, Nakamura T, Yamamoto Y, Kosaka A, Jin W, Fukushima T and Aida T. *J. Phys. Soc. Jpn.* 2008; **77**: 034710(1–5).
- Yamamoto Y, Fukushima T, Jin W, Kosaka A, Hara T, Nakamura T, Saeki A, Seki S, Tagawa S and Aida T. *Adv. Mater.* 2006; **18**: 1297–1300.
- Steiner UE and Ulrich T. *Chem. Rev.* 1989; **89**: 51–147.
- Nagakura S, Hayashi H and Azumi T. *Dynamic Spin Chemistry*, Kodansha-Wiley: Tokyo/New York, 1998.
- Tanimoto Y and Fujiwara Y. *Handbook of Photochemistry and Photobiology*, Vol. 1, Nalwa HS. (Ed.) American Scientific Publishers: 2003; pp 413–446.
- Sokolik IA and Frankevich EL. *Usp. Fiz. Nauk* 1973; **111**: 261–288.
- Okamoto K, Oda N, Itaya A and Kusabayashi S. *Chem. Phys. Lett.* 1975; **35**: 483–486.
- Frankevich E, Zakhidov A, Yoshino K, Maruyama Y and Yakushi K. *Phys. Rev. B* 1996; **53**: 4498–4508.
- Wang Y and Suna A. *J. Phys. Chem. B* 1997; **101**: 5627–5618.
- Konno A, Mogi I and Watanabe K. *J. Electroanal. Chem.* 2001; **507**: 202–205.
- Ogiwara T, Ikoma T, Akiyama K and Tero-Kubota S. *Chem. Phys. Lett.* 2005; **411**: 378–383.
- Ikoma T, Ogiwara T, Takahashi Y, Akiyama K, Tero-Kubota S, Takahashi Y, Suzuki T and Wakikawa Y. *Synth. Met.* 2009; **160**: 285–290.
- Konno A, Mogi I and Watanabe K. *J. Electroanal. Chem.* 2001; **507**: 202–205.
- Yonemura H, Ohishi K and Matsuo T. *Chem. Lett.* 1996; **25**: 661–662.
- Yonemura H, Ohishi K and Matsuo T. *Mol. Cryst. Liq. Cryst.* 1997; **294**: 221–294.
- Yonemura H, Tahara H, Ohishi K, Iida S and Yamada S. *Jpn. J. Appl. Phys.* 2010; **49**: 01AD04(1–7).
- Yonemura H, Yoshida M, Mitake S and Yamada S. *Electrochemistry* 1999; **67**: 1209–1210.
- Yonemura H, Yoshida M and Yamada S. *Stud. Surf. Sci. Catal.* 2001; **132**: 741–744.
- Yonemura H, Kuroda N and Yamada S. *Sci. Technol. Adv. Mater.* 2006; **7**: 643–648.
- Tahara H, Yonemura H, Harada S and Yamada S. *Mol. Cryst. Liq. Cryst.* 2011; **539**: 121–124.
- Tahara H, Yonemura H, Harada S and Yamada S. *Jpn. J. Appl. Phys.* 2011; **50**: 081605(1–6).
- Yonemura H, Takata M and Yamada S. *Mol. Cryst. Liq. Cryst.* 2013; **579**: 120–123.
- Yonemura H, Takata M and Yamada S. *Jpn. J. Appl. Phys.* 2014; **53**: 01AD06(1–11).
- Atwater HA and Polman A. *Nat. Mater.* 2010; **9**: 205–213.
- Akiyama T, Nakada M, Terasaki N and Yamada S. *Chem. Commun.* 2006; 395–397.
- Arakawa T, Munaoka T, Akiyama T and Yamada S. *J. Phys. Chem. C* 2009; **113**: 11830–11835.
- Sugawa K, Akiyama T, Kawazumi H and Yamada S. *Langmuir* 2009; **25**: 3887–3893.
- Akiyama T, Aiba K, Hoashi K, Wang M, Sugawa K and Yamada S. *Chem. Commun.* 2010; **46**: 306–308.
- Takahashi Y, Taura S, Akiyama T and Yamada S. *Langmuir* 2012; **28**: 9155–9160.
- You J, Takahashi Y, Yonemura H, Akiyama T and Yamada S. *Jpn. J. Appl. Phys.* 2012; **51**: 02BK04(1–4).
- Matsumoto R, Yonemura H and Yamada S. *J. Phys. Chem. C* 2013; **117**: 2486–2493.
- Matsumoto R, Yamada S and Yonemura H. *Jpn. J. Appl. Phys.* 2013; **52**: 04CK07(1–7).
- Leonard K, Takahashi Y, You J, Yonemura H and Yamada S. *Chem. Phys. Lett.*, 2013; **584**: 130–134.
- You J, Leonard K, Takahashi Y, Yonemura H and Yamada S. *Phys. Chem. Chem. Phys.* 2014; **16**: 1166–1173.
- Matsumoto R, Yamada S and Yonemura H. *Mol. Cryst. Liq. Cryst.* 2013; **579**: 115–119.
- Matsumoto R, Yamada S and Yonemura H. *Mol. Cryst. Liq. Cryst.* 2014; **598**: 86–91.
- Nakamura H, Uehata A, Motonaga A, Ogata T and Matsuo T. *Chem. Lett.* 1987; **16**: 543–546.
- Uehata A, Nakamura H, Usui S and Matsuo T. *J. Phys. Chem.* 1989; **93**: 8197–8203.
- Ito T, Ujiie T, Naka M and Nakamura H. *Chem. Phys. Lett.* 2001; **340**: 308–316.
- Ito T, Naka M, Miura A, Ujiie T, Nakamura H and Matsuo T. *Bull. Chem. Soc. Jpn.* 2001; **74**: 657–665.
- Lee PC and Meisel D. *J. Phys. Chem.* 1982; **86**: 3391–3395.
- Schmitt J, Decher G, Dressick WJ, Brandow SL, Geer RE, Shashidhar R and Calvert JM. *Adv. Mater.* 1997; **9**: 61.
- Goulet PJG, dos Santos DS, Alvarez-Puebla RA, Oliveira ON and Aroca RF. *Langmuir* 2005; **21**: 5576–5581.
- Yonemura H, Nobukuni H, Moribe S, Yamada S, Fujiwara Y and Tanimoto Y. *Chem. Phys. Lett.* 2004; **385**: 417–422.



47. Yonemura H, Harada S, Moribe S, Yamada S, Fujiwara Y, Tanimoto Y and Nakamura H. *Mol. Phys.* 2006; **104**: 1559–1572.
48. Fajer J, Borg DC, Forman A, Dorphin D and Felton RH. *J. Am. Chem. Soc.* 1970; **92**: 3451–3459.
49. Johnson CS and Gutowsky Jr. HS. *J. Chem. Phys.* 1963; **39**: 58–62.
50. Tahara H, Yonemura H, Harada S, Nakashima A and Yamada S. *Chem. Phys. Lett.* 2012; **524**: 42–48.
51. Moribe S, Yonemura H, Wakita Y, Yamashita T and Yamada S. *Mol. Phys.* 2010; **108**: 1929–1940.
52. Moribe S, Yonemura H and Yamada S. *Chem. Phys.* 2007; **334**: 242–252.



## Cholesteryl oleate-appended phthalocyanines as potential photosensitizers in the treatment of leishmaniasis

Laura E. Sánchez Contreras<sup>a,d</sup>, Johannes Zirzmeier<sup>b</sup>, Sabrina V. Kirner<sup>b,♦♦</sup>,  
Francesca Setaro<sup>a</sup>, Fernando Martínez<sup>c</sup>, Stefany Lozada<sup>d</sup>, Patricia Escobar<sup>d</sup>,  
Uwe Hahn<sup>a,e</sup>, Dirk M. Guldi<sup>\*b,♦</sup> and Tomás Torres<sup>\*a,f,♦</sup>

<sup>a</sup>Departamento de Química Orgánica (Modulo 01), Facultad de Ciencias, Universidad Autónoma de Madrid, Cantoblanco, 28049 Madrid, Spain

<sup>b</sup>Department of Chemistry and Pharmacy, Interdisciplinary Center for Molecular Materials (ICMM), Friedrich-Alexander-Universität Erlangen-Nürnberg, Egerlandstrasse 3, 91058 Erlangen, Germany

<sup>c</sup>Centro de Investigación en Catálisis, Escuela de Química, Universidad Industrial de Santander, Colombia

<sup>d</sup>Centro de Investigación en Enfermedades Tropicales (CINTROP), Escuela de Medicina, Departamento de Ciencias Básicas, Universidad Industrial de Santander, Bucaramanga, Colombia

<sup>e</sup>Laboratoire de Chimie des Matériaux Moléculaires, Université de Strasbourg et CNRS (UMR 7509), Ecole Européenne de Chimie, Polymères et Matériaux (ECPM), 25 rue Becquerel, 67087 Strasbourg Cedex 2, France

<sup>f</sup>IMDEA-Nanociencia, c/Faraday 9, Campus de Cantoblanco, 28049 Madrid, Spain

*Dedicated to Professor Shunichi Fukuzumi on the occasion of his retirement*

Received 13 November 2014

Accepted 3 December 2014

**ABSTRACT:** Two phthalocyanines (Pcs) with either a zinc or a ruthenium metal at the center of the macrocycle have been functionalized by a cholesteryl oleate moiety. The potential photosensitizers (PSs) for the treatment of cutaneous leishmaniasis have been studied on their photophysical properties and their ability to generate singlet oxygen. These experiments corroborate that solvent mixtures containing variable ratios of THF and water impact the excited state deactivation. The compounds were used preloaded into LDL particles and their phototoxic activity was evaluated in a preliminary way.

**KEYWORDS:** phthalocyanines, steroids, cholesterol, leishmaniasis, singlet oxygen.

### INTRODUCTION

According to the WHO, leishmaniasis is among the 17 neglected tropical diseases [1]. This parasitic disease is caused by protozoan parasites from more than 20 leishmania species and is prevalent in more than 88 countries [2]. It is transmitted to humans by the bites of infected female phlebotomine sandflies. Whereas at the beginning of the treatment of leishmaniasis, pentavalent antimony compounds have been administered [3], drug resistance [4] to this type of drugs displaced the focus

towards antifungal macrolide polyenes and more recently to anticancer alkylphosphocholines [5]. It is this evolving resistance with the concomitant proliferation of specific diseases that is the strong motivation to develop new approaches for medical treatment.

Photodynamic therapy (PDT) is an emerging therapeutic modality that employs the combination of photosensitive compounds and light to generate a cytotoxic effect for the targeted treatment of cancer and other diseased tissues. This approach has received growing popularity over the last decades [6–8]. The fact, that PDT is dependent on the presence of molecular oxygen supports the general idea that singlet oxygen (<sup>1</sup>O<sub>2</sub>) generated by the photosensitization of molecular triplet oxygen is one of the principal toxic species formed

♦ SPP full and ♦♦ student member in good standing

\*Correspondence to: Dirk M. Guldi, email: [dirk.guldi@fau.de](mailto:dirk.guldi@fau.de);  
Tomás Torres, email: [tomas.torres@uam.es](mailto:tomas.torres@uam.es)

during PDT. Porphyrin- and phthalocyanine (Pc)-derived photosensitizers (PSs) are among the compounds that have demonstrated their ability to generate singlet oxygen and thus are able to act as PSs. However, the use of Pcs in PDT requires their adequate functionalization or incorporation into nanocarriers, in order to render them water-soluble and biocompatible [9]. In this respect, a number of Pc derivatives comprising for instance zinc [10–13], silicon [14–17], or ruthenium [18–20] as central metal atom in the macrocyclic scaffold have shown good PDT activity. Apart from the generation of  $^1\text{O}_2$ , the substance class of Pcs features some remarkable properties originating not last from the exceptionally high absorption that lies typically in the visible region of the UV/vis spectrum between 630 to 750 nm [21, 22]. This so-called Q-band is the reason that makes such chromophores valuable in different fields of science and technology [23].

We herein describe two Pcs functionalized with cholesteryl oleate moieties. Whereas the steroidal unit is linked covalently at the periphery in case of the ZnPc, it is placed at the axial position of the RuPc upon coordination of the pyridyl ligand to the ruthenium metal center. The photophysical properties have been studied and have evidenced a solvent dependent excited state deactivation of ZnPc and RuPc.

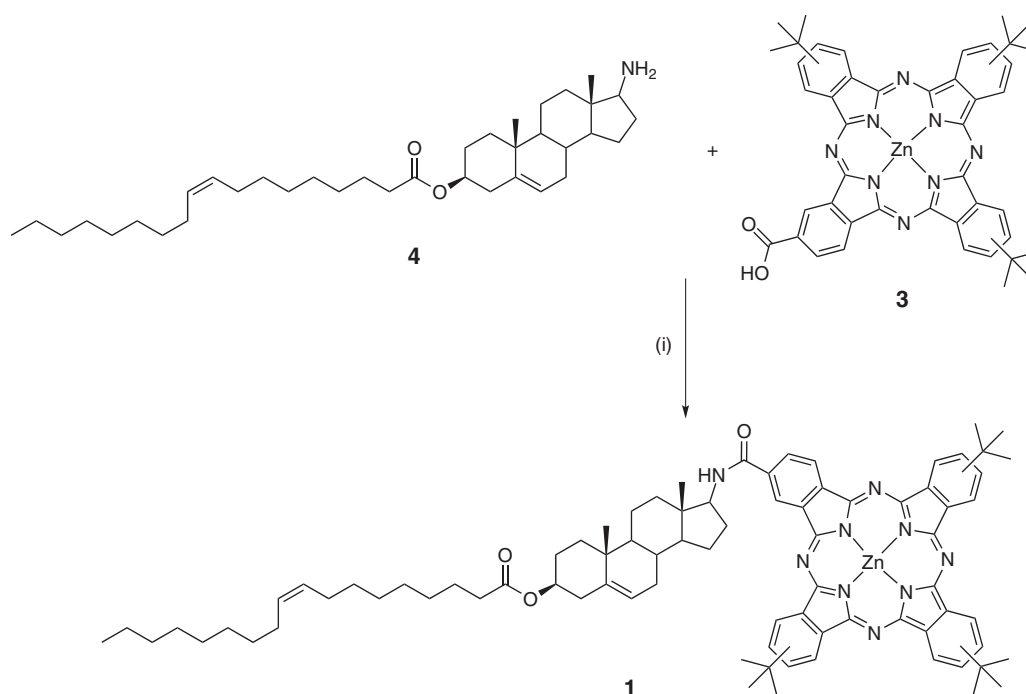
## RESULTS AND DISCUSSION

The synthesis of the two new Pc-derived PSs ZnPc (**1**) and RuPc (**2**) is depicted in Schemes 1 and 2. ZnPc **3**,

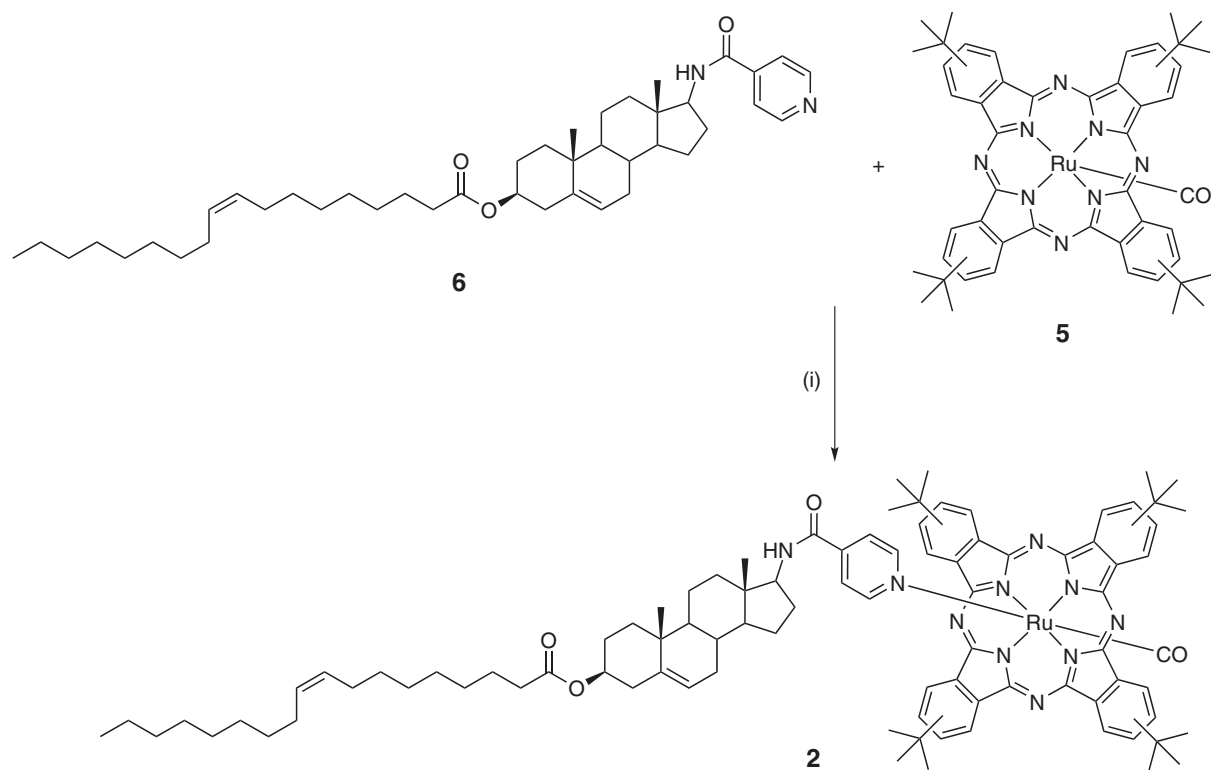
also known as TT1 [24], and cholesteryl oleate **4** [25] have been prepared according to literature protocols. The precursors have then been linked covalently under the use of a *N,N'*-dicyclohexylcarbodiimide (DCC)-mediated amide coupling reaction in the presence of a catalytic amount of 1-hydroxybenzotriazol (HOBt) to provide **1** as a solid (Scheme 1). Likewise, the terminal amino group of **4** served to introduce a pyridine moiety. Accordingly, reaction of building block **4** with isonicotinoic acid hydrochloride led to the formation of pyridine-based ligand **6**. On the other hand, ruthenium phthalocyanine **5** comprising a CO moiety as axial ligand has been synthesized again following a procedure developed in our group [26]. Consequently, simply mixing Pc-derivative **5** with N-type ligand **6** at elevated temperature furnished RuPc **2** as a blue solid (Scheme 2).

The position of functionalization has a tremendous impact on the aggregation properties. This phenomenon can in turn be effectively tuned through the appropriate choice of the Pc metal center and its availability for axial substitution. As a consequence, modification at the periphery of ZnPcs has been demonstrated to not severely suppress aggregation, while placing the ligand at the axial position is viable when aiming at non-aggregated Pcs. This is however only possible with certain metal Pcs including silicon, aluminum or ruthenium, which can coordinate specific ligands orthogonally.

One of the major drawbacks brought about by Pcs is their hydrophobicity, which prevents their direct administration into the bloodstream, necessitating the



**Scheme 1.** Preparation of cholesteryl oleate appended zinc phthalocyanine **1**. Reagents and conditions: (i) DCC, HOBt,  $\text{CH}_2\text{Cl}_2$ ,  $0^\circ\text{C}$  to room temperature, 1d

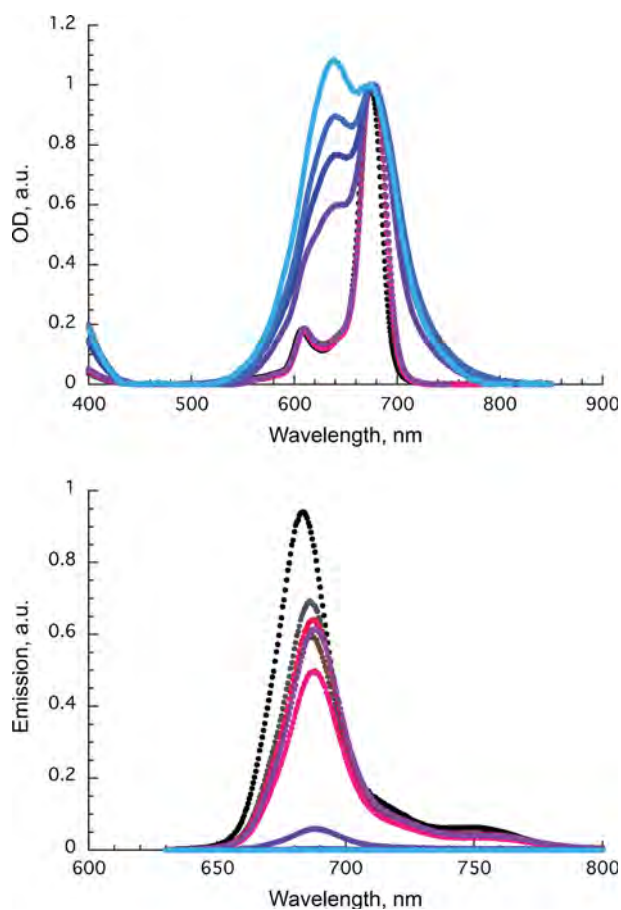


**Scheme 2.** Preparation of cholesteryl oleate appended ruthenium phthalocyanine **2**. Reagents and conditions: (i) THF, 50 °C, 18 h

use of organic solvents. Though modification by pure chemical means is a feasible method, thus giving rise to hydrophilic Pcs, the use of vehicles renders possible a more selective transport. When referring to vehicles able to transport and deliver drugs into cells the reconstitution of low density lipoproteins (LDL) as described by Krieger *et al.* is a rather simple yet effective method [27]. The LDL particle consists of a nonpolar core of neutral lipids such as cholesterol esters that are surrounded by a polar shell of phospholipids, unesterified cholesterols, and apolipoprotein B100. The latter is recognized by cell surface LDL receptors causing internalization by cells. Consequently, the native cholesteryl esters have to be extracted from LDL particles and then to be replaced by cholesterol ester-appended drugs or PSs. Lipoproteins in general confer several advantages such as their natural composition showing low cytotoxicity, a small size that favors diffusion through the vascular membrane, and the above described apolar core able to accommodate lipophilic drugs, which are thus protected from the blood environment during transport. In addition, the localization of the PS inside the lipophilic core of lipoproteins does not alter their recognition by cell receptors. Relying on this approach, the delivery of hydrophobic drugs can be accomplished. Hence, in line with these reports, the modification of **1** and **2** with cholesteryl oleate presented herein is anticipated to play a crucial role and to assist the incorporation of the PS conjugates into the LDL lipid core.

The photophysical properties will be discussed hereafter. Despite their amphiphilic structures, **1** and **2** proved to be water insoluble. In light of the latter, **1** and **2** were probed in different tetrahydrofuran (THF) to water ratios, that is, increasing the water content in 10 vol% increments from 0 vol% to 90 vol%, by means of absorption and fluorescence (Fig. 1). For example, **1** features in pure THF a Soret-type absorption at 350 nm and a set of Q-type absorptions at 607 and 673 nm. Mirror imaged to the long wavelength absorption, a short wavelength fluorescence maximum evolves around 684 nm with a fluorescence quantum yield of about 27%. All of these features are in perfect agreement with the well-known characteristics of Pcs. Once water is added the long wavelength absorption and the short wavelength fluorescence red shift due to a more polar environment. Interesting is an appreciable lowering of the fluorescence intensity to about 70% of the initial intensity when up to 50 vol% of water are present. It is, however, when going to a 40 to 60 v/v THF/H<sub>2</sub>O ratio and beyond that more drastic changes are discernable in the absorption and fluorescence spectra. In terms of absorption, the Soret-type absorption intensities blue shifts by 10 nm and, in addition, the Q-type absorption at 640 nm intensifies. In terms of fluorescence, a significant quenching sets in, which reaches a factor of more than 500 when 90 vol% water is added.

Generally speaking a similar trend is noted for **2**. In pure THF, absorption maxima are noted at 345, 585, and



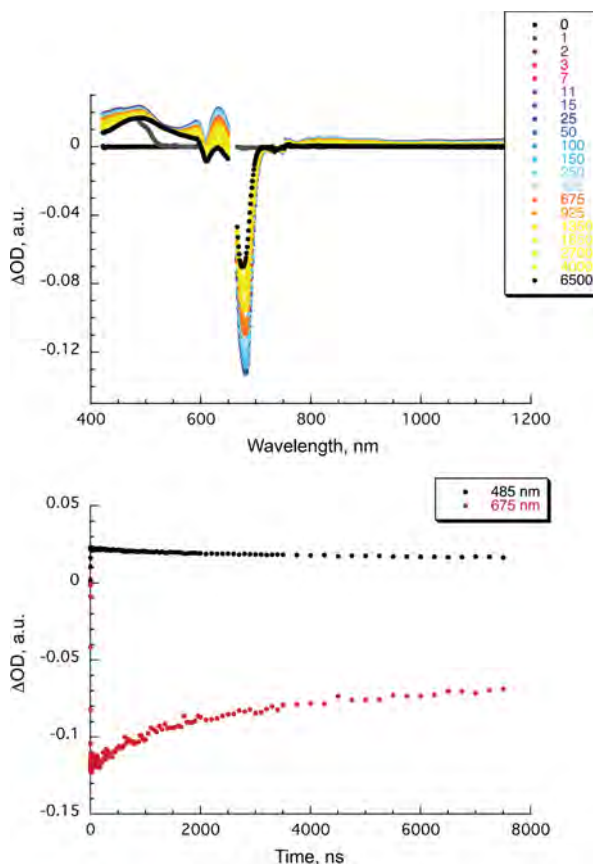
**Fig. 1.** Upper part — absorption spectra of a dilute solution of **1** ( $1 \times 10^{-6}$  M) with variable ratios of THF and water (100/0, 90/10, 80/20, 70/30, 60/40, 50/50, 40/60, 30/70, 20/80, 10/90 from black and brown to red, purple, and blue). Lower part — fluorescence spectra of a dilute solution of **1** ( $5 \times 10^{-7}$  M) with variable ratios of THF and water (100/0, 90/10, 80/20, 70/30, 60/40, 50/50, 40/60, 30/70, 20/80, 10/90 from black and brown to red, purple, and blue)

647 nm. These red shift, for example, from 647 to 652 nm in the presence of 10, 20, 30, 40, 50, and 60 vol% water. Going beyond 60 vol%, the blue part of the absorption increases in intensity and in the red part of the absorption an additional feature develops at 625 nm. All of the aforementioned characteristics are accompanied by a broad tailing absorption, which reaches out to 750 nm. Similarly, the fluorescence with a quantum yield of 0.2%, which maximizes at 650 nm in the absence of any water, only red shifts but not weakens significantly when up to 60 vol% water are added. In stark contrast, 70, 80, and 90 vol% water lead to a substantial quenching of the fluorescence with factors of up to 100. Additionally, a phosphorescence maximum at 950 nm is observed in pure THF.

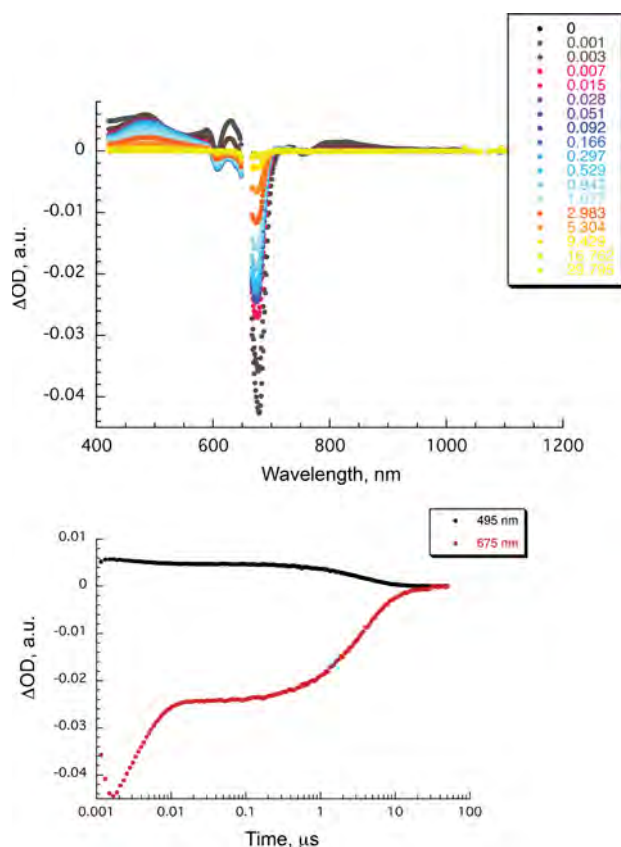
In time resolved emission experiments (TCSPC), a single component with a lifetime of 2.6 ns was noted for **1** in THF. Upon addition of up to 60 vol% water, still the same fluorescence lifetime of 2.6 ns was determined.

However, the significant fluorescence quenching seen in the steady state experiments leads to the hypothesis that the actual lifetime is shorter than the detection limit of our TCSPC setup, that is, 150 ps. In other words, the fluorescence decay must be biphasic and all that we are observing is the long-lived component, which matches that in pure THF. When even more water is added, the fluorescence becomes so weak that it drops below the detection limit. In contrast, the fluorescence lifetime of **2** is — even in pure THF — shorter than 150 ps.

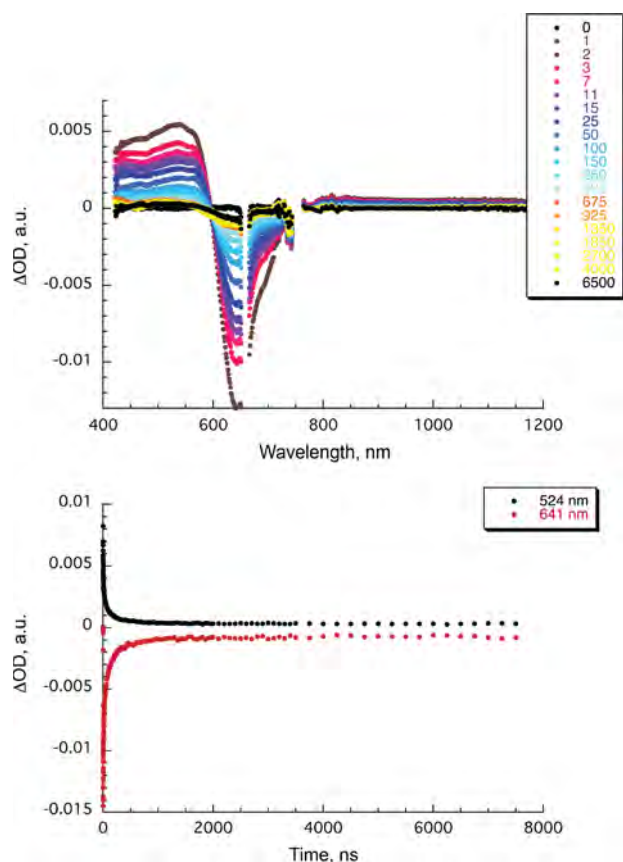
To shed light onto the water dependent changes in the absorption and fluorescence features we turned to femtosecond pump probe experiments (Figs 2–5). To this end, **1** and **2** were first probed in pure THF with 656 nm excitation. In terms of spectroscopy, commencing with the photoexcitation their singlet excited state features are noted. For **1**, these are maxima at 449, 488, 592, 633, 840, 908, and 1015 nm and minima at 610 and 681 nm, while maxima at 453, 522, 607, 922, and 1028 nm and minima at 589 nm and around 660 nm are registered for **2**. In both cases, the singlet excited states intersystem cross to the corresponding triplet manifolds. In particular,



**Fig. 2.** Upper part — differential absorption spectra (visible and near-infrared) obtained upon femtosecond flash photolysis (656 nm) of **1** in THF with time delays between 0 and 6500 ps at room temperature. Lower part — time-absorption profiles at 485 and 675 nm, reflecting the triplet excited state formation and singlet excited state formation/decay, respectively



**Fig. 3.** Upper part — differential absorption spectra (visible and near-infrared) obtained upon femtosecond flash photolysis (656 nm) of **1** in THF with time delays between 0 and 29.795 μs at room temperature. Lower part — time-absorption profiles at 495 and 675 nm, reflecting the triplet excited state formation/decay and singlet excited state formation/decay, respectively

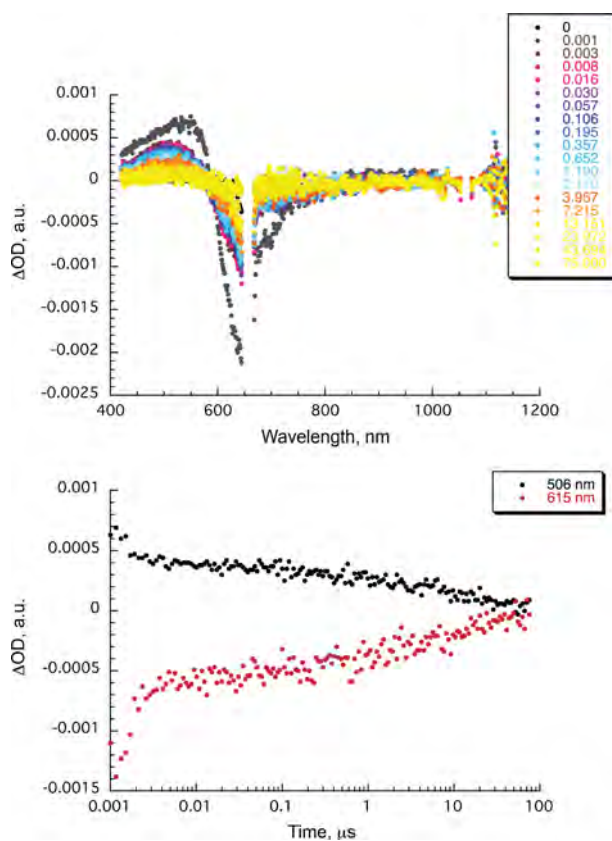


**Fig. 4.** Upper part — differential absorption spectra (visible and near-infrared) obtained upon femtosecond flash photolysis (656 nm) of **1** in 10 to 90 v/v ratio of THF and water with time delays between 0 and 6500 ps at room temperature. Lower part — time-absorption profiles at 524 and 641 nm, reflecting the triplet excited state formation and singlet excited state formation/decay, respectively

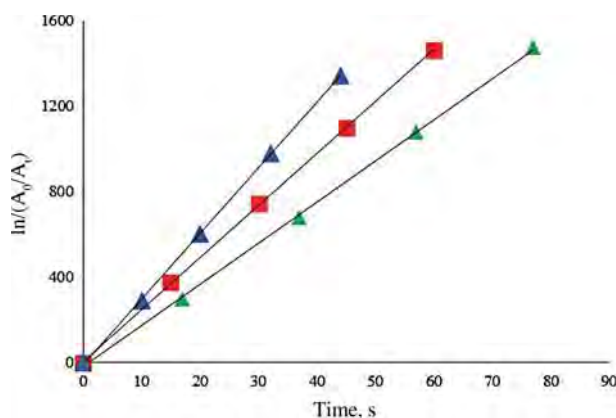
a maximum at 492 and minima at 610, and 675 nm relate to the triplet excited state of **1** and a maximum at 525 and minima at 589 nm, and around 660 nm to that of **2**. In terms of kinetics the singlet and triplet excited state lifetimes are  $2.8 \pm 0.1$  ns/ $3.7 \pm 0.1$  μs and  $7.5 \pm 0.3$  ps/ $9.4 \pm 0.1$  μs for **1** and **2**, respectively.

Going to an extreme, **1** and **2** were probed in a 10 to 90 v/v ratio of THF and water. Upon 656 nm excitation, the singlet excited state bleaching in the form of a minimum at 643 nm for **1** and at 628 and 690 nm for **2** is, on one hand, different from the THF studies, and, on the other hand, a good reflection of the ground state absorption. The latter are accompanied by maxima at 433 and 538 nm with a broad band in the NIR for **1** and at 530 nm with a broad NIR band for **2**. A kinetic analysis reveals that the excited state decay is multiphasic for **1** with lifetimes of  $1.4 \pm 0.1$ / $22.6 \pm 0.1$  ps and  $12.3 \pm 2.2$  μs. In line with what has been gathered for **1** in just THF the two components are ascribed to the singlet and the triplet excited state deactivations. A resembling, multiphasic decay evolved for photoexcited **2**, where the lifetimes are  $3.3 \pm 0.3$ / $61.9 \pm 6.4$  ps and  $0.08 \pm 0.01$ / $0.95 \pm 0.01$  μs.

Singlet oxygen ( $^1O_2$ ) is considered of supreme importance in PDT, and therefore its rate of production represents a crucial parameter to characterize all new PSs. Singlet oxygen quantum yields ( $\phi_{\Delta}$ ) of **1** and **2** were determined in THF following a procedure reported in the literature using 1,3-diphenylisobenzofuran (DPBF) as chemical quencher for singlet oxygen [28]. Decrease of DPBF concentration in solution with irradiation time was monitored at 414 nm and non-substituted ZnPc was used as reference compound ( $\phi_{\Delta(\text{THF})} = 0.53$ ) [29]. No significant changes in Q-band shape or intensity were observed, indicating that **1** and **2** are not decomposing or aggregating within the experimental period. Interestingly, **1** and **2** have shown good ability to photosensitize  $^1O_2$ , as revealed by its quantum yield values ( $\phi_{\Delta}$ ): 0.56 and 0.45, respectively. In Fig. 6 the decrease of DPBF absorption induced by the reference (ZnPc) and by the samples **1** and **2** after irradiation is plotted. From the data, it becomes evident that **1** performs better than **2**. Plotting of dependence of  $\ln(A_0/A_t)$  on irradiation time ( $t$ ) (with  $A_0$  and  $A_t$  being the respective scavenger absorbance values



**Fig. 5.** Upper part — differential absorption spectra (visible and near-infrared) obtained upon femtosecond flash photolysis (656 nm) of **1** in 10 to 90 v/v ratio of THF and water with time delays between 0 and 75  $\mu s$  at room temperature. Lower part — time-absorption profiles at 506 and 615 nm, reflecting the triplet excited state formation/decay and singlet excited state formation/decay, respectively



**Fig. 6.** Plot of decrease in DPBF absorption induced by (non-substituted) ZnPc (red squares), **1** (in blue triangles) and **2** (green triangles), upon irradiation over time ( $t$ ) in THF

at monitoring wavelength before and after irradiation time) affords a straight line whose slope illustrates the PS efficacy to generate  $^1O_2$ , and from which  $\phi_\Delta$  can be calculated.

Once the ability of **1** and **2** to produce  $^1O_2$  was assessed, their efficiency to act as PSs *in vitro* was examined preliminary. Apart from intracellular amastigotes of *L. panamensis* parasites experiments using monocytic cell line THP-1 have been performed in order to gather also information on the potential of the two new PSs for the treatment of leukemia. The compounds were preloaded into LDL particles through direct incubation and their phototoxic activity was evaluated on intracellular amastigotes of *L. panamensis* parasites and mammalian tumoral human monocytic cell line THP-1, irradiated at a light dose of 5 J/cm<sup>2</sup> and  $\lambda = 400\text{--}700$  nm. The toxicity was calculated after 72 h or 24 h (for *L. panamensis* parasites and mammalian THP-1 cells, respectively) and the results were expressed as percent of inhibition of infection for parasites and growth for cells at the concentration of Pc used in each experiment (at a range of 0–5  $\mu M$ ). For THP-1 cells, the **2** preloaded in LDL resulted more phototoxic than **1** in the concentration range used (% inhibition maximum = 25 and 19.7, respectively). For both compounds, **1** and **2** preloaded into LDL the  $CC_{50} > 5 \mu M$ . Intracellular amastigotes of *L. panamensis* were not photosensitive to **1** and **2** in the concentration range used, but we observed a significant inhibition of infection in the order to 6.31% for **1** and 2.41% for **2** at 5  $\mu M$ . On the other hand, the percentage of inhibition of infection was increased 6 fold for **1** and **2** when these were preloaded into LDL particles (at 5  $\mu M$  solution **1** and 1.6  $\mu M$  solution **2**) when compared to the corresponding compound being not incorporated into reconstituted LDL. THP-1 cells were more susceptible to treatment with compounds than intracellular amastigotes and use of LDL as a vehicle enhanced the phototoxic effect of the Pc-based PSs.

To conclude, two Pcs, *i.e.* zinc and ruthenium Pcs, respectively, endowed with cholesteryl oleate moieties were successfully synthesized. The photophysical properties corroborate a solvent dependent deactivation of the ZnPc and RuPc excited states as the solvent composition, namely the relative ratio between THF and water, has been systematically changed. Preliminary studies of reconstitution of LDL with the new PS-cholesteryl ester conjugates have been successfully carried out. These Pc-containing vehicles have been tested in biological assays, thus aiming at studying the phototoxic action of these assemblies in cells infected with leishmania or likewise in the treatment of cutaneous leishmaniasis. Both compounds have been proved to possess great potential as PSs candidates, showing low toxicity and high efficiency.

## EXPERIMENTAL

### General

All reagents and solvents were used as purchased from commercial sources without further purification.

Compounds **3** [24], **4** [25], and **5** [26] have been prepared according to literature protocols. All reactions were performed in standard glassware under an inert argon atmosphere. Reactions were monitored by thin-layer chromatography using TLC plates precoated with silica gel 60F<sub>254</sub> (Merck). Column chromatography was carried out on Merck silica gel 60, 40–63 μm (230–400 mesh). Gel permeation chromatography was performed using Biorad, Biobeads SX-1 and tetrahydrofuran as eluent. <sup>1</sup>H NMR spectra were recorded using Bruker Avance 300 MHz instruments with the solvent signal as reference (H<sub>pc</sub>: phthalocyanine protons, H<sub>py</sub>: pyridine protons, H<sub>db</sub>: double bond vinyl or olefinic protons, H<sub>tBu</sub>: *tert*-butyl protons). Mass spectra were recorded using a MS-50 from A.E.I., Manchester, GB (EI), a Concept 1H from Kratos Analytical Ltd., Manchester, GB (FAB), and a MALDI-TofSpec-E from MICROMASS, GB (MALDI).

### Singlet oxygen quantum yields

Singlet oxygen (<sup>1</sup>O<sub>2</sub>) quantum yields (φ<sub>Δ</sub>) of compounds **1** and **2** were measured in THF [28]. The experiments were conducted in the dark. In detail, the procedure was as follows: 2 mL of a stock solution of scavenger (with an absorbance of *ca.* 1) in THF was transferred into a 1 × 1 cm quartz optical cell and bubbled with oxygen for 1 min. A stock solution of the Pc in the same solvent was then added, in a defined amount to reach a final Q-band absorbance value of about 0.1. The solution was stirred and irradiated for defined time intervals, using a halogen lamp (300 W). Incident light was filtered through a water filter (6 cm) and an additional filter to remove light under 530 nm (Newport filter FSQ-OG530). The experiments for each sample were performed three times and the obtained data represent mean values of those three experiments; the estimated error is ± 10%. Singlet oxygen quantum yield (φ<sub>Δ</sub>) was calculated through the following equation:

$$\phi_{\Delta}^S = \phi_{\Delta}^R \frac{k^S I_{aT}^R}{k^R I_{aT}^S} \quad (1)$$

where *k* is the slope of a plot of ln (*A*<sub>0</sub>/*A*<sub>t</sub>) vs. irradiation time *t*, with *A*<sub>0</sub> and *A*<sub>t</sub> being the absorbance of scavenger at the monitoring wavelength before and after irradiation time *t*, respectively. *I*<sub>aT</sub> is the total amount of light absorbed by the dye. Superscripts *R* and *S* indicate reference and sample, respectively. *I*<sub>aT</sub> is calculated as a sum of intensities of the absorbed light *I*<sub>a</sub> at wavelengths from the filter cutoff to 800 nm (step 0.5 nm). *I*<sub>a</sub> at given wavelength is calculated using Beer's law:

$$I_a = I_0 (1 - e^{-2.3A}) \quad (2)$$

where transmittance of the filter at a given wavelength stays for *I*<sub>0</sub> and the absorbance of the dye at this wavelength stays for *A*.

### Synthesis

**Compound 1.** To a solution of ZnPc **3** (45 mg, 57 μmol) and amine **4** (29 mg, 52 μmol) in CH<sub>2</sub>Cl<sub>2</sub> (6 mL) under argon and at 0 °C were added in succession HOBT (8.1 mg, 53 μmol) and *N,N'*-dicyclohexylcarbodiimide (12.9 mg, 62 μmol). After stirring for 1 h at 0 °C the mixture was allowed to warm to room temperature and was stirred for 18 h. The solvent was evaporated to dryness and the crude was purified by column chromatography on silica gel (eluent mixture: hexane/dioxane 3:1) followed by size exclusion chromatography on Biorad, Biobeads SX-1 (eluent: tetrahydrofuran) to yield ZnPc **1** as blue solid (25 mg, 36%). <sup>1</sup>H NMR (300 MHz, CDCl<sub>3</sub>): δ, ppm 9.51 (m, 4H, H<sub>pc</sub>), 9.29 (m, 4H, H<sub>pc</sub>), 8.32 (m, 4H, H<sub>pc</sub>), 5.43–5.34 (m, 3H, H<sub>vi</sub>), 4.63 (m, 1H), 3.58 (s, 1H), 2.27–2.20 (m, 6H), 2.05–1.90 (m, 10H), 1.72 (m, 6H), 1.64 (m, 27H, H<sub>tBu</sub>), 1.31–1.36 (m, 25H), 0.97 (m, 3H), 0.91 (m, 3H), 0.11 (m, 3H). MALDI-TOF-MS (ditanol): *m/z* (%) calcd. for C<sub>82</sub>H<sub>102</sub>N<sub>9</sub>O<sub>3</sub>Zn: 1325 [M + H]<sup>+</sup>, found 1326.

**Compound 6.** Amine **4** (68 mg, 123 μmol) was dissolved in CH<sub>2</sub>Cl<sub>2</sub> (5 mL) under argon and at 0 °C NEt<sub>3</sub> (26 μL, 184 μmol) and isonicotinoylchloridehydrochloride (32.8 mg, 184 μmol) were added. The mixture was allowed to warm to room temperature and stirred for 40 h. The solvent was evaporated to dryness and the crude was purified by gradient column chromatography on silica gel (eluent mixture: CH<sub>2</sub>Cl<sub>2</sub>/MeOH 20:1 to 8:1) to yield **6** as yellowish oil (161 mg, 86%). <sup>1</sup>H NMR (300 MHz, CDCl<sub>3</sub>): δ, ppm 8.73 (d, *J* = 9 Hz, 2H, H<sub>py</sub>), 7.60 (d, *J* = 9 Hz, 2H, H<sub>py</sub>), 6.08 (m, 1H, NH), 5.33 (m, 3H, H<sub>db</sub>), 4.60 (m, 1H), 4.11 (m, 1H), 2.25 (m, 6H), 2.10–1.99 (m, 6H), 1.62 (m, 10H), 1.50–1.29 (m, 25H), 1.03 (s, 3H, CH<sub>3</sub>), 0.87 (t, *J* = 10 Hz, 3H, CH<sub>3</sub>), 0.79 (s, 3H, CH<sub>3</sub>).

**Compound 2.** A solution of RuPc **5** (90 mg, 104 μmol) and compound **6** (63 mg, 96 μmol) in THF (5 mL) under argon was heated at 50 °C for 18 h. The solvent was evaporated to dryness and the crude was purified by size exclusion chromatography on Biorad, Biobeads SX-1 (eluent: tetrahydrofuran) to yield RuPc **2** as blue solid (52 mg, 36%). <sup>1</sup>H NMR (300 MHz, CDCl<sub>3</sub>): δ, ppm 9.40 (m, 4H, H<sub>pc</sub>), 9.30 (m, 4H, H<sub>pc</sub>), 8.15 (4H, H<sub>pc</sub>), 5.56 (d, *J* = 5 Hz, 2H, H<sub>py</sub>), 5.32 (m, 3H, H<sub>db</sub>), 4.67 (m, 1H, NH), 4.47 (m, 1H), 3.39 (m, 1H), 2.25 (m, 6H), 2.18 (d, *J* = 5 Hz, 2H, H<sub>py</sub>), 2.02 (m, 2H), 1.78 (s, 36H, H<sub>tBu</sub>), 1.59 (m, 5H), 1.42 (m, 18H), 1.22–1.36 (m, 17H), 0.85 (m, 6H, CH<sub>3</sub>), 0.11 (s, 3H, CH<sub>3</sub>).

### Photophysical characterization

For the photophysical characterization the samples were placed in fluorometric cuvettes with different pathways and, when necessary purged with argon. Steady-state UV-vis absorption spectroscopy was performed on a Lambda2 spectrometer (Perkin Elmer). Steady state fluorescence spectra were carried out at a FluoroMax3



spectrometer (Horiba) in the visible detection range and at a FluoroLog3 spectrometer (Horiba) with an IGA Symphony detector ( $512 \times 1 \times 1 \mu\text{m}$ ) in the NIR detection range. Fluorescence lifetimes were determined by the time correlated single photon counting (TCSPC) technique using a FluoroLog3 emission spectrometer (Horiba JobinYvon) equipped with an R3809U-58 MCP (Hamamatsu) and a SuperK Extreme high power supercontinuum fiber laser (NKT) with an attached SuperK Varia (NKT) exciting at 610 nm (150 ps fwhm). Femtosecond transient absorption (TA) experiments were carried out with an amplified Ti:Sapphire laser system CPA-2110 fs laser (Clark MXR: output 775 nm, 1 kHz, 150 fs pulse width) using transient absorption pump/probe detection systems (Helios and Eos, Ultrafast Systems). The 656 nm excitation wavelength was generated with a noncolinear optical parametric amplifier (NOPA, Clark MXR).

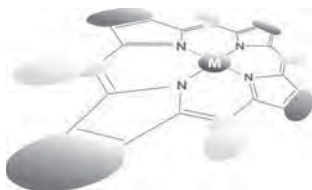
### Acknowledgements

This work was supported by the EU (projects CosmoPHOS-nano, FP7-NMP-2012-LARGE-6, 310337-2 and SO<sub>2</sub>S, FP7-PEOPLE-2012-ITN, 316975), the Spanish MICINN (CTQ-2011-24187/BQU), the Comunidad de Madrid (S2013/MIT-2841 FOTOCARBON) and the Instituto Colombiano para el Desarrollo de la Ciencia y la Tecnología “Francisco José de Caldas” COLCIENCIAS (Grant no. 110240820556).

### REFERENCES

1. <http://www.who.int/leishmaniasis/en/>
2. (a) Kumar A. *Leishmania and Leishmaniasis*, Vol. 3, Springer Science+Business Media: New York, 2013. (b) Herwaldt BL. *Lancet* 1999; **354**: 1191–1199.
3. (a) Murray HW, Berman JD, Davies CR and Saravia NG. *Lancet* 2005; **366**: 1561–1577. (b) Mishra J, Saxena A and Singh S. *Front. Med. Chem.* 2012; **6**: 97–130.
4. (a) Croft SL, Sundar S and Fairlamb AH. *Clin. Microbiol. Rev.* 2006; **19**: 111–126. (b) Yasinzaï M, Khan M, Nadhman A and Shahnaz G *Future Med. Chem.* 2013; **5**: 1877–1888. (c) Vanaerschot M, Dumetz F, Roy S, Ponte-Sucre A, Arevalo J and Dujardin JC. *Expert Rev. Anti-Infect. Ther.* 2014; **12**: 937–946.
5. Croft SL and Coombs GH. *Trends Parasitol.* 2003; **19**: 502–508. (b) Singh N, Kumar M and Singh RK. *Asian Pac. J. Trop. Med.* 2012; **5**: 485–497. (c) Monge-Maillo B and López-Vélez R. *Drugs* 2013; **73**: 1889–1920.
6. Dolmans D, Fukumura D and Jain RK. *Nat. Rev. Cancer* 2003; **3**: 380–387.
7. Celli JP, Spring BQ, Rizvi I, Evans CL, Samkoe KS, Verna S, Pogue BW and Hasan T. *Chem. Rev.* 2010; **110**: 2795–2838.
8. Lowell JF, Liu TWB, Chen J and Zheng G. *Chem. Rev.* 2010; **110**: 2839–2857.
9. Ethirajan M, Chen Y, Joshi P and Pandey RK. *Chem. Soc. Rev.* 2011; **40**: 340–362.
10. Ng ACH, Li XY and Ng DKP. *Macromolecules* 1999; **32**: 5292–5298.
11. Nishiyama N, Iriyama A, Jang WD, Miyata K, Itaka K, Inoue Y, Takahashi H, Yanagi Y, Tamaki Y, Koyama H and Kataoka K. *Nat. Mater.* 2005; **4**: 934–941.
12. Nishiyama N, Marimoto Y, Jang WD and Kataoka K. *Adv. Drug Delivery Rev.* 2009; **61**: 327–338.
13. Wang A, Zhou L, Fang KL, Zhou L, Lin Y, Zhou JH and Wei SH. *Eur. J. Med. Chem.* 2012; **58**: 12–21.
14. Hofman JW, van Zeeland F, Turker S, Talsma H, Lambrechts SAG, Sakharov DV, Hennink WE and van Nostrum CF. *J. Med. Chem.* 2007; **50**: 1485–1494.
15. Mao J, Zhang Y, Zhu J, Zhang C and Guo Z. *Chem. Commun.* 2009; **49**: 908–910.
16. Jiang X, Lo P and Ng DKP. *J. Med. Chem.* 2011; **54**: 320–330.
17. Doane TL, Chuang CH, Chomas A and Burda C. *ChemPhysChem* 2013; **14**: 321–330.
18. Ishii K, Shiine M, Shimizu Y, Hoshino SI, Abe H, Sogawa K and Kobayashi N. *J. Phys. Chem. B* 2008; **112**: 3138–3143.
19. Hahn U, Setaro F, Ragas X, Gray-Weale A, Nonell S and Torres T. *Phys. Chem. Chem. Phys.* 2011; **13**: 3385–3393.
20. Setaro F, Ruiz-González R, Nonell S, Hahn U and Torres T. *J. Inorg. Biochem.* 2014; **136**: 170–176.
21. (a) *Handbook of Porphyrin Science*, Vols. 1–5, Kadish KM, Smith KM and Guillard R. (Eds.) World Scientific: Singapore, 2010. (b) *The Porphyrin Handbook*, Vols. 16–20, Kadish KM, Smith KM and Guillard R. (Eds.) Academic Press: New York, 1999.
22. (a) Bottari G, de la Torre G, Guldi DM and Torres T. *Chem. Rev.* 2010; **110**: 6768–6816. (b) Torres T. *Angew. Chem. Int. Ed.* 2006; **45**: 2834–2837. (c) Claessens CG, de la Torre and Torres T. *Chem. Commun.* 2007; 2000–2015. (d) Claessens CG, Hahn U and Torres T. *Chem. Rec.* 2008; **8**: 75–97. (e) de la Torre G, Bottari G, Hahn U and Torres T. *Struct. Bond.* 2010; **135**: 1–44.
23. Rio Y, Rodríguez-Morgade MS and Torres T. *Org. Biomol. Chem.* 2008; **6**: 1877–1894.
24. Cid JJ, Yum JH, Jang SR, Nazeeruddin MK, Ferrero EM, Palomares E, Ko J, Grätzel M and Torres T. *Angew. Chem. Int. Ed.* 2007; **46**: 8358–8362.
25. (a) Wu SP, Lee I, Ghoroghchian PP, Frail PR, Zheng G, Glickson JD and Therien MJ. *Bioconjugate Chem.* 2005; **16**: 542–550. (b) Zheng G, Li H, Zhang M, Lund-Katz S, Chance B and Glickson JD. *Bioconjugate Chem.* 2002; **13**: 392–396.
26. Rodríguez-Morgade MS, Torres T, Atienza-Castellanos C and Guldi DM. *J. Am. Chem. Soc.* 2006; **128**: 15145–15154.

27. Krieger M, McPhaul MJ, Goldstein JL and Brown MS. *J. Biol. Chem.* 1979; **254**: 3845–3853.
28. (a) Wilkinson F, Helman WP and Ross AB. *J. Phys. Chem. Ref. Data* 1993; **22**: 113–118. (b) Agboola B, Ozoemena K and Nyokong T. *J. Mol. Catal. A: Chem.* 2006; **248**: 84–92. (c) Makhseed S, Tuhl A, Samuel J, Zimcik J, Al-Awadi N and Novakova V. *Dyes Pigm.* 2012; **95**: 351–357.
29. Kaestner L, Cesson M, Kassab K, Christensen T, Edminson PD, Cook MJ, Chambrier I and Jori G. *Photochem. Photobiol. Sci.* 2003; **2**: 660–667.



# Highly efficient hydroxylation of gaseous alkanes at reduced temperature catalyzed by cytochrome P450BM3 assisted by decoy molecules

Norifumi Kawakami<sup>a</sup>, Zhiqi Cong<sup>b</sup>, Osami Shoji<sup>\*b</sup> and Yoshihito Watanabe<sup>\*c</sup>

<sup>a</sup>Department of Biosciences and Informatics, Keio University, 3-14-1 Hiyoshi, 223-8522 Yokohama, Japan

<sup>b</sup>Department of Chemistry, Graduate School of Science, Nagoya University, Furo-cho, Chikusa-ku, Nagoya, 464-8602, Japan

<sup>c</sup>Research Center for Materials Science Nagoya University, Furo-cho, Chikusa-ku, Nagoya, 464-8602, Japan

Dedicated to Professor Shunichi Fukuzumi on the occasion of his retirement

Received 9 November 2014

Accepted 4 December 2014

**ABSTRACT:** Cytochrome P450BM3 functions as a small-alkane hydroxylase upon the addition of perfluorocarboxylic acids (PFs) as decoy molecules. The coupling efficiency (product formation rate per NADPH consumption rate) for the hydroxylation of small alkanes was improved by reducing the reaction temperature to 0 °C.

**KEYWORDS:** cytochrome P450, gaseous alkanes, perfluorocarboxylic acids, decoy molecules.

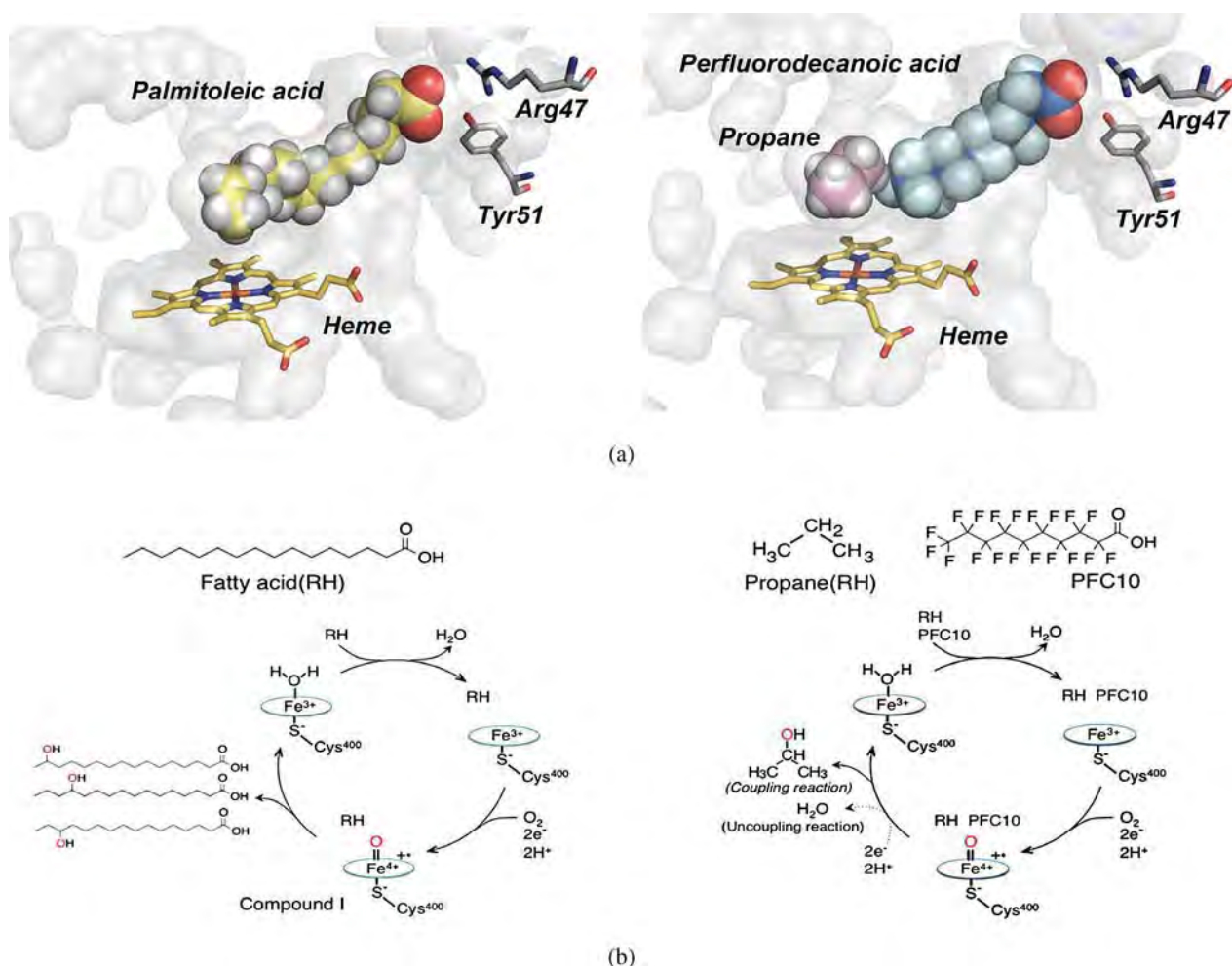
## INTRODUCTION

Hydroxylation of small alkanes catalyzed by enzymes has been recognized as an important process for producing precursors of fine chemicals and feedstocks. Several small alkane hydroxylases, such as methane monooxygenase and omega alkane hydroxylase AlkB, have been widely studied in the context of industrial applications [1–6]. In addition, a variety of engineered enzymes that catalyze the hydroxylation of small alkanes has also been successfully prepared by site-directed and/or random mutagenesis [7, 8]. For example, cytochrome P450BM3, which catalyzes the hydroxylation of fatty acids having an alkyl chain length from 12 to 20 (C12–20) carbon units, has been engineered to catalyze the hydroxylation of gaseous alkanes such as ethane, propane, and butane [9–11]. Although wild-type P450BM3 selectively catalyzes the hydroxylation of long-alkyl-chain fatty acids (Fig. 1b, left), our research

group and Zilly *et al.* recently reported that even wild-type P450BM3 can catalyze the hydroxylation of small alkanes in the presence of a series of perfluorocarboxylic acids (PFs) with alkyl chain lengths from 5 to 14 (PFC5–14); the latter perfluorinated compounds were named “decoy molecules” (Fig. 1b, right) [12, 13]. According to the reaction mechanism of fatty acid hydroxylation by P450BM3 (Fig. 1b, left), fatty acid binding induces a positive redox potential shift of the heme iron by removing a ligated water molecule, which is crucial for initiating the catalytic cycle. Molecular oxygen is then reductively activated by utilizing two electrons from NADPH to form an oxoferryl(IV) porphyrin  $\pi$  cation radical (so-called Compound I), which is responsible for the hydroxylation of substrates (Fig. 1) [14–17]. We found that because PFs have structures that are similar to those of fatty acids, it is also possible to initiate the catalytic cycle to form Compound I [12]; however, the PFs are not hydroxylated because of the high dissociation energy of C–F bonds. By adding small alkanes to the reaction mixture, the produced Compound I can hydroxylate the small alkanes instead of PFs (Fig. 1b, right). Interestingly, the catalytic activities of the alkane hydroxylation depend on the alkyl chain length of the PFs. For example,

<sup>†</sup> SPP full member in good standing

\*Correspondence to: Osami Shoji, email: [shoji.osami@a.mbox.nagoya-u.ac.jp](mailto:shoji.osami@a.mbox.nagoya-u.ac.jp); Yoshihito Watanabe, email: [p47297a@nucc.cc.nagoya-u.ac.jp](mailto:p47297a@nucc.cc.nagoya-u.ac.jp), tel: +81 52-789-3557, fax: +81 52-789-2953



**Fig. 1.** (a) The active site of P450BM3 containing palmitoleic acid (left; PDB code: 1FAG) and the plausible active-site structure of P450BM3 containing PFC10 and propane (right). (b) General reaction mechanism of P450BM3 (left) and the reaction mechanism of propane hydroxylation catalyzed by P450BM3 with perfluorodecanoic acid (PFC10) as a decoy molecule (right). In the presence of PFC10, although uncoupling reaction produces water molecule (dotted line in the reaction cycle), propane is converted to 2-propanol (solid line in the reaction cycle)

the highest catalytic activities for propane and butane hydroxylation reactions were observed in the presence of PFC10 and PFC9, respectively. Therefore, we concluded that the PFs partially occupy the active site of P450BM3, leaving a small amount of space that was suitable for accommodating small alkanes (Fig. 1a, right). Although small alkanes are hydroxylated in the presence of PFs, the coupling efficiency (product formation rate per NADPH consumption rate) was low: 18 and 55% for propane and butane hydroxylation reactions, respectively. As reported previously [18], Compound I, generated from P450BM3 in the presence of PFs, is also reduced back to the resting state through a further two-electron reduction leading to the production of H<sub>2</sub>O. This unproductive consumption of Compound I competes with the hydroxylation of small alkanes (Fig. 1b, right) [12, 19]. By increasing the propane pressure from 8 kPa to 0.5 MPa, the coupling efficiency was improved to 50% [19], indicating that the concentration of small alkanes is a key parameter that

affects coupling efficiency. We reasoned that the coupling efficiency could be improved if the enzymatic reaction was performed at lower temperature because this would lead to an increase in the concentration of gaseous alkanes in the aqueous solution. We herein report that the effect of temperature on the catalytic activity and coupling efficiency of propane and butane hydroxylation reactions catalyzed by wild-type P450BM3 in the presence of PFs is indeed significant.

## EXPERIMENTAL

### Materials

P450BM3 was prepared according to the method previously reported [12]. The concentration of the enzyme was determined by CO-difference spectra. The details of purification of P450BM3 are shown in below.

*E. coli* cells expressing P450BM3 suspended in 20 mM Tris-HCl (pH 7.4) are disrupted by using an ultrasonicator at 4 °C. After removing cell debris by centrifugation, the supernatant was applied to DE-52 column (*Whatman*). The proteins weakly bound to DE-52 are washed out with 20 mM Tris-HCl containing 50 mM KCl (pH 7.4) and tightly bound proteins including P450BM3 are eluted with the Tris-buffer containing 250 mM KCl. The P450BM3 fraction was collected and further purified by DEAE 650S (TOSOH). P450BM3 was eluted with the Tris-HCl buffer with KCl concentration gradient from 0 to 120 mM. To remove the bound substrates, NADPH was added immediately before applying to gel filtration column, Sephacryl S-300 (GE Healthcare), equilibrated with 20 mM Tris buffer with 100 mM KCl (pH 7.4) and the P450BM3 fraction was collected. All chemical reagents were purchased from commercial sources and used without further purification. *o*-Cresol, *m*-cresol, and perfluorononanoic acid (PEC9) were obtained from Tokyo Chemical Industry Co. (Tokyo, Japan). Benzylalcohol, *p*-cresol, and perfluorooctanoic acid (PFC8) were purchased from Sigma-Aldrich Co., (St. Louis, MO). Toluene were obtained from Kanto Chemical Co., Inc. (Tokyo, Japan). The following chemicals were purchased from WAKO Pure Chemical Industries, Ltd (Osaka, Japan): benzene, and perfluorodecanoic acid (PFC10). Gaseous alkanes are purchased from Taiyo Nippon Sanso Corp. NADPH was purchased from Nakalai tesque, Inc.

### Measurement

UV-vis spectra were recorded on a Shimadzu UV-2400 PC spectrophotometer. GC analysis was performed by GC2014 (Shimadzu Corp.) with Rtx-1 column (Restek Corp.). HPLC analysis was performed using an Inertsil® ODS-3 column (4.6 mm × 250 mm; GL Sciences, Inc., Tokyo, Japan) installed on a Shimadzu SCL-10AVP system controller equipped with Shimadzu LC-10ADVP pump systems, a Shimadzu RF-10AXL fluorescence spectrometer, a Shimadzu CTO-10AVP column oven, and a Shimadzu DGU-12A degasser.

### Gaseous alkane hydroxylation reactions

Reaction mixture containing 500 nM P450BM3, 100 μM PFs was prepared in the gaseous alkane saturated buffer at 20 or 0 °C. The reaction temperature was kept by water bath and iced water for the reaction at 20 and 0 °C, respectively. PFs for stock solution were dissolved in DMSO and adjusted to 20 mM. Gaseous alkane saturated buffer was also prepared at each temperature. Immediately after adding 5 mM NADPH (for the long-term reaction, 20 mM of NADPH was used), the reaction mixture was pressured by a balloon containing gaseous alkane and molecular oxygen with the ratio of 4 to 1. The remaining air in the reaction vessel was replaced by making gas flow from balloon to the out *via* the vessel for

1 min. One hour later, the amount of remaining NADPH was estimated by measuring the absorbance at 340 nm.

### Propanol and butanol detection

After one-hour reaction, 1 mL of reaction mixture was transferred to new glass vial containing 0.15 g of sodium nitrite for derivatization, and then 1 mM 3-pentanol was added as internal standard. Before putting the sample on ice, 1 mL of hexane (for propanol) or dichloromethane (for butanol) were added. To the resulting reaction mixture, 150 μL of aqueous solution of sulfuric acid (20%) was gently added. The glass vial was kept on ice for 15 min. The derivatized products, 2-propylnitrite or 2-butylnitrite, were extracted and analyzed by Gas Chromatography (GC). The analytical conditions were as follows: column temperature, 323 K (holding 5 min) to 523 K (25 K/min, holding 3 min); the injection port and FID detector temperature were 523 K; carrier gas, helium. The products were identified based on the retention time of authentic samples. The concentration of the products was determined by using the ratio of peak area of the product to the area of the internal standard (3-pentanol).

### Hydroxylation of benzene

Benzene hydroxylation by P450BM3 was carried out in 20 mM Tris-HCl (pH = 7.4) buffer containing 100 mM KCl at 0 °C for 1 h in the presence of 0.5 μM P450BM3, 10 mM benzene, 5 mM NADPH, and 100 μM PFC9. PFC9 was dissolved in DMSO and added to the reaction mixture. After 1 h reaction, a solution of hydrochloric acid (1 M) was added to the reaction mixture to quench the reaction followed by neutralization with a solution of KOH (1 M). The resulting solution was filtrated and analyzed by reverse phase HPLC. The HPLC analytical conditions were as follows: flow rate, 0.5 mL/min; acetonitrile/water = 1/1; column temperature, 30 °C; monitoring absorption at 210 and 270 nm. Phenol was identified using authentic samples. Reaction was performed at least three times.

### Hydroxylation of toluene

The reaction was carried out in the same manner as for the hydroxylation of benzene. The reaction was evaluated by reverse phase HPLC. Products were identified using authentic samples.

### NADPH consumption

Immediately after preparing reaction mixture containing 0.5 μM P450BM3, 10 mM benzene, and 100 μM perfluorinated carboxylic acids, reaction was initiated by the addition of 5 mM NADPH. The absorbance of NADPH at 340 nm was monitored. The concentration of the NADPH was estimated using its molar extinction coefficient at 340 nm, 6220 M<sup>-1</sup> · cm<sup>-1</sup>.

**Table 1.** The catalytic activity of propane and butane hydroxylations by P450BM3 with PFs at 0 °C and 20 °C. The amount of 2-propanol and 2-butanol after 1 h reaction are given in [ $\mu\text{M}$ ]. The amount of NADPH consumed and the coupling efficiency are given in [ $\mu\text{M}$ ] and [Product]/[NADPH consumed]  $\times$  100, respectively

	Propane 2-propanol, $\mu\text{M}^{\text{a,b}}$	NADPH consumption, $\mu\text{M}^{\text{a,b}}$	Coupling efficiency, % <sup>a</sup>	Butane 2-butanol, $\mu\text{M}^{\text{a,b}}$	NADPH consumption, $\mu\text{M}^{\text{a,b}}$	Coupling efficiency, % <sup>a</sup>	<i>ee</i> , %	No alkanes NADPH consumption, $\mu\text{M}^{\text{a,b}}$
PFC8 0 °C	160 $\pm$ 20 (320)	590 $\pm$ 130 (1180)	27 $\pm$ 5	1110 $\pm$ 220 (2220)	1320 $\pm$ 60 (2640)	84 $\pm$ 12	18	200 $\pm$ 30 (400)
PFC8 20 °C	500 $\pm$ 80 (1000)	1930 $\pm$ 70 (3860)	26 $\pm$ 5	2170 $\pm$ 310 (4340)	3180 $\pm$ 430 (6360)	68 $\pm$ 1	14	400 $\pm$ 110 (800)
PFC9 0 °C	660 $\pm$ 120 (1320)	1160 $\pm$ 170 (2320)	57 $\pm$ 10	2620 $\pm$ 230 (5240)	2730 $\pm$ 110 (5460)	96 $\pm$ 9	20	410 $\pm$ 180 (820)
PFC9 20 °C	1310 $\pm$ 270 (2620)	4190 $\pm$ 100 (8380)	31 $\pm$ 7	2820 $\pm$ 480 (5640)	3610 $\pm$ 580 (7220)	78 $\pm$ 2	14	2100 $\pm$ 60 (4200)
PFC10 0 °C	480 $\pm$ 40 (960)	1110 $\pm$ 160 (2220)	44 $\pm$ 5	1140 $\pm$ 50 (2280)	1510 $\pm$ 80 (3020)	75 $\pm$ 1	16	660 $\pm$ 80 (1320)
PFC10 20 °C	1620 $\pm$ 80 (3240)	4240 $\pm$ 70 (8480)	38 $\pm$ 2	2830 $\pm$ 360 (5660)	4050 $\pm$ 290 (8100)	70 $\pm$ 6	16	3860 $\pm$ 130 (7720)

<sup>a</sup>Values are averages  $\pm$  standard deviation calculated from three different experiments. <sup>b</sup>Values in the parentheses are turnover frequency (nmol/hour/nmol-P450BM3).

## RESULTS AND DISCUSSION

We first investigated whether the use of P450BM3 in conjunction with PFs catalyzed the hydroxylation of propane and butane gas at 0 °C (Table 1) and confirmed that, even at this low temperature, the P450BM3–PF complexes functioned as a monooxygenase to selectively yield 2-propanol and 2-butanol, respectively. To understand the effect of reaction temperature, hydroxylation of propane and butane was also carried out at 20 °C and the coupling efficiency and hydroxylation rate were compared with those measured at 0 °C [20]. The coupling efficiency of propane hydroxylation improved slightly from 38 to 44% in the presence of PFC10, upon reducing the reaction temperature, whereas the hydroxylation rate decreased from 3240 to 960 nmol/h/nmol-P450BM3. Similarly, a small improvement in the coupling efficiency and a decrease in the catalytic activity were observed for butane hydroxylation in the presence of PFC10 at 0 °C. The coupling efficiency for propane hydroxylation upon lowering the temperature showed a more significant improvement, from 31 to 57%, in the presence of PFC9. Furthermore, the coupling efficiency of butane hydroxylation was also drastically improved at lower temperature, from 78 to 96%, in the presence of PFC9. Notably, butane hydroxylation with PFC9 at 0 °C resulted in almost complete coupling (96%) while maintaining a catalytic activity comparable to that measured for the reaction performed at 20 °C. The uncoupling reaction in the absence of alkane gas was also dramatically suppressed, from 4200 to 820 turnover frequency, by lowering the temperature (Table 1), suggesting that P450BM3 was activated when the PFC9 and gaseous alkanes occupied the active-site space simultaneously. Although the uncoupling reaction in the absence of alkane gas was also suppressed in the case of PFC10 (from 7720 to 1320 turnover frequency), the coupling efficiency was not much improved. We reasoned that PFC10 is too effective for initiating the generation of active species even at 0 °C. Because PFC10 alone was sufficient enough for the generation of active species, the uncoupling reaction was predominant even in the presence of alkane gas.

**Table 2.** The catalytic activity of propane hydroxylation by P450BM3 with PFC10 at 0 and 20 °C for 24 h. The amount of 2-propanol and NADPH consumed after 24 h reaction are given in [μM]. The total turnover number (TON) and the coupling efficiency are given in nmol/nmol-P450BM3, and [Product]/[NADPH consumed] × 100, respectively

	2-propanol, μM	NADPH consumption, μM	Coupling efficiency, %	Turnover number (TON)
20 °C	2380	14 100	17	4760
0 °C	4920	12 400	40	9840

Given that the solubility of gaseous molecules is inversely proportional to solvent temperature, the concentration of gaseous molecules in the buffer solution increases upon lowering the reaction temperature and thus the coupling efficiency is improved by performing the reaction at 0 °C rather than at 20 °C. In fact, the solubilities of propane and butane in water at 4 °C are reported to be 3.46 and 3.21 M, respectively, which are twice as large as those of propane at 19.8 °C (1.74 M) and butane at 20 °C (1.46 M) [21]. In addition to these results, propane hydroxylation in the presence of PFC9 over a longer period showed a total turnover number (TON) of 9840, with 40% coupling efficiency for 24 h reaction at 0 °C, whereas the same reaction performed at 20 °C had a TON of 4760, with 18% coupling efficiency, indicating that cooling the reaction mixture was also effective with respect to the total amount of product formed (Table 2). The enantioselectivity for the formation of 2-butanol increased slightly, especially in the presence of PFC9 (from 14 to 20% *ee*, Table 1), but the small difference suggests that the orientation of butane in the active site is not significantly affected by the reaction temperature. Although improved butane hydroxylation by engineered P450BM3 at 0 °C was recently described, the effect of temperature upon the enantioselectivity was not reported [22]. To investigate the effect of performing the reaction at 0 °C upon hydroxylation of substrates other than gaseous alkane, we also conducted the hydroxylation reaction with benzene and toluene [23] at 0 and at 20 °C for 1 h (Table 3).

**Table 3.** The catalytic activity of benzene and toluene hydroxylations by P450BM3 with PFC9 at 0 °C and 20 °C for 1 h. The amount of products after 1 h reaction are given in [μM]. The amount of NADPH consumed and the coupling efficiency are given in [μM] and [Product]/[NADPH consumed] × 100, respectively

Substrate	Product, μM <sup>a</sup>		NADPH consumption, μM <sup>a</sup>	Coupling efficiency, %
	Major	Minor		
Benzene 0 °C	980 ± 180 (Phenol)		3070 ± 20	32 ± 6
Benzene 20 °C	2030 ± 480 (Phenol)		8270 ± 420	25 ± 7
Toluene 0 °C	1830 ± 70 ( <i>o</i> -Cresol)	280 ± 30 (Benzyl alcohol)	4200 ± 140	50 ± 4
Toluene 20 °C	4100 ± 260 ( <i>o</i> -Cresol)	510 ± 50 (Benzyl alcohol)	9860 ± 30	47 ± 3

<sup>a</sup> Values are averages ± standard deviation calculated from at least three different experiments.

The coupling efficiency for the hydroxylation of benzene (25%) and toluene (47%) at 20 °C was improved to 32% and 50%, respectively, by reducing the temperature to 0 °C. Because the regioselectivity of toluene hydroxylation was not affected significantly by the reaction temperature, we presume the orientation of toluene in the cavity of P450BM3 at 0 °C would be not much different from that at 20 °C. The improved coupling efficiency observed for the benzene and toluene hydroxylation using PFC9 as a decoy molecule could be attributed to suppression of the uncoupling reaction in the absence of substrate at 0 °C.

Given that the coupling efficiency was clearly improved with gaseous alkane hydroxylation, the improved solubility of gaseous alkanes at 0 °C in the buffer solution together with the suppression of the uncoupling reaction in the absence of substrate at 0 °C contribute to efficient reactions catalyzed by P450BM3 with the assistance of decoy molecules.

## CONCLUSION

We have demonstrated that the coupling efficiency of propane and butane hydroxylation catalyzed by the P450BM3-decoy molecule system is significantly improved by performing the reaction at 0 °C. The coupling efficiency for propane and butane reached 57 and 96%, respectively. Conducting the reaction at low temperature is beneficial not only for the coupling efficiency but also for the total amount of product formed through small alkane hydroxylation. Although the turnover rate at 0 °C clearly decreased, performing the reaction at 0 °C could be one of the strategies to improve the efficiency of gaseous alkane hydroxylation catalyzed by P450BM3 with the assistance of decoy molecules.

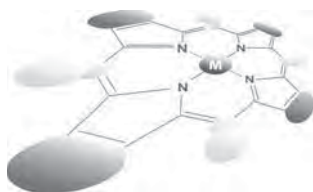
## Acknowledgements

This work was supported by Grants-in-Aid for Scientific Research (S) to Y.W. (24225004), Grant-in-Aid for Scientific Research on Innovative Areas "Molecular Activation Directed toward Straightforward Synthesis" to O.S. (25105724), and a Grant-in-Aid for Young Scientists (A) to O.S. (21685018) from the Ministry of Education, Culture, Sports, Science, and Technology (Japan).

## REFERENCES

- Merkx M, Kopp DA, Sazinsky MH, Blazyk JL, Muller J and Lippard SJ. *Angew. Chem. Int. Ed.* 2001; **40**: 2782–2807.
- Lee SJ, McCormick MS, Lippard SJ and Cho US. *Nature* 2013; **494**: 380–384.
- Koch DJ, Chen MM, van Beilen JB and Arnold FH. *Appl. Environ. Microbiol.* 2009; **75**: 337–344.
- Nieder M and Shapiro J. *J. Bacteriol.* 1975; **122**: 93–98.
- Staijen IE, van Beilen JB and Witholt B. *Eur. J. Biochem.* 2000; **267**: 1957–1965.
- Jiang Y and Dalton H. *Biochim. Biophys. Acta, Gen. Subj.* 1994; **1201**: 76–84.
- Bell SG, Stevenson JA, Boyd HD, Campbell S, Riddle AD, Orton EL and Wong LL. *Chem. Commun.* 2002; 490–491.
- Xu F, Bell SG, Lednik J, Insley A, Rao ZH and Wong LL. *Angew. Chem. Int. Ed.* 2005; **44**: 4029–4032.
- Boddupalli SS, Pramanik BC, Slaughter CA, Estabrook RW and Peterson JA. *Arch. Biochem. Biophys.* 1992; **292**: 20–28.
- Meinhold P, Peters MW, Chen MMY, Takahashi K and Arnold FH. *ChemBioChem* 2005; **6**: 1765–1768.
- Fasan R, Meharena YT, Snow CD, Poulos TL and Arnold FH. *J. Mol. Biol.* 2008; **383**: 1069–1080.
- Kawakami N, Shoji O and Watanabe Y. *Angew. Chem. Int. Ed.* 2011; **50**: 5315–5318.
- Zilly FE, Acevedo JP, Augustyniak W, Deege A, Hausig UW and Reetz MT. *Angew. Chem. Int. Ed.* 2011; **50**: 2720–2724.
- Rittle J and Green MT. *Science* 2010; **330**: 933–937.
- Makris TM, von Koenig K, Schlichting I and Sligar SG. *J. Inorg. Biochem.* 2006; **100**: 507–518.
- Murataliev MB and Feyereisen R. *Biochemistry* 1996; **35**: 15029–15037.
- Perera R, Sono M, Raner GM and Dawson JH. *Biochem. Biophys. Res. Commun.* 2005; **338**: 365–371.
- Pons N, Pipino S and De Matteis F. *Biochem. Pharmacol.* 2003; **66**: 405–414.
- Kawakami N, Shoji O and Watanabe Y. *Chem. Sci.* 2013; **4**: 2344–2348.
- We found that air was still remained in the reaction vessel in our previous method [12]. Incomplete replacement of air with small alkane causes the low concentration of small alkanes in the reaction mixture. By thoroughly replacing the remaining air by small alkanes, we obtained the higher coupling efficiency of propane and butane hydroxylation than those of the previous results [12].
- Yalkowsky SH, He Y and Jain P. *Handbook of Aqueous Solubility Data*, 2nd ed., CRC Press: Boca Raton, 2010; pp 75 and 127.
- Staudt S, Muller CA, Marienhagen J, Boing C, Buchholz S, Schwaneberg U and Groger H. *Beilstein Journal of Organic Chemistry* 2012; **8**: 186–191.
- Shoji O, Kunitatsu T, Kawakami N and Watanabe Y. *Angew. Chem. Int. Ed.* 2013; **52**: 6606–6610.





## Synthesis and characterization of a sulfur-containing phthalocyanine-gold nanoparticle hybrid

Vicente M. Blas-Ferrando, Javier Ortiz, Fernando Fernández-Lázaro<sup>◇</sup>  
and Ángela Sastre-Santos<sup>\*◇</sup>

Área de Química Orgánica, Instituto de Bioingeniería, Universidad Miguel Hernández, 03202 Elche, Spain

*Dedicated to Professor Shunichi Fukuzumi on the occasion of his retirement*

Received 18 November 2014

Accepted 4 December 2014

**ABSTRACT:** This work reports on the synthesis and characterization of a new gold nanoparticle-zinc phthalocyanine system, AuNP-S('Bu)<sub>3</sub>ZnPc, prepared by a ligand exchange reaction of tetraoctylammonium bromide with a novel unsymmetrically substituted zinc phthalocyanine which contains one thioester group in the peripheral position [AcS('Bu)<sub>3</sub>ZnPc]. The AuNP-S('Bu)<sub>3</sub>ZnPc hybrid was characterized using UV-vis and <sup>1</sup>H NMR spectroscopies. Transmission electron microscopy allowed the estimation of the size, which was calculated to be ~5 nm. AuNPs-S('Bu)<sub>3</sub>ZnPc conjugate showed much lower fluorescence quantum yield values than the AcS('Bu)<sub>3</sub>ZnPc demonstrating either an energy or electron transfer from the ZnPc to the AuNP. The AuNP-S('Bu)<sub>3</sub>ZnPc hybrid has been anchored to a TiO<sub>2</sub> semiconducting layer using lipoic acid. A solid configuration of TiO<sub>2</sub>-lipoic acid-AuNP-S('Bu)<sub>3</sub>ZnPc has been prepared by anchoring lipoic acid to the TiO<sub>2</sub> (TiO<sub>2</sub>-LA) and introducing later the TiO<sub>2</sub>-LA with free thiol groups in a toluene solution of AuNP-S('Bu)<sub>3</sub>ZnPc. We have also observed by UV-vis and fluorescence measurements the importance of the ZnPc in avoiding AuNP aggregation on the TiO<sub>2</sub> surface.

**KEYWORDS:** zinc phthalocyanine, gold nanoparticle.

### INTRODUCTION

In recent years, chromophore-functionalized nanoparticles have generated a great deal of interest due to their application in optoelectronics [1, 2], electronic devices [3, 4], chemical and biological sensors, [5] and targeted drug delivery agents [6, 7]. In photovoltaics, dye-sensitized solar cells (DSSCs) have emerged as a cheap alternative to silicon cells [8, 9]. The need for improving light harvesting in DSSCs has led to the search for new dyes or combinations of dyes that absorb strongly in the full solar spectrum [10–17]. Among all of these dyes, gold nanoparticles (AuNPs) [18] and phthalocyanines [19] are two good candidates to be married for DSSC improvement.

AuNPs present an intense plasmon resonance band around 520 nm whose characteristics can be tuned by controlling the shape, size and ligands surrounding the nanoparticle, opening the door to their use as antennas in photovoltaic devices [20, 21]. They can enhance the photocurrent of the cell in, at least, three ways, namely: (i) increasing the probability of photon absorption due to scattering by the interaction with their electric field [22], (ii) through direct induction of electron-hole pairs in the semiconductor [23] and (iii) by injection of photoexcited charge carriers upon the phenomenon of localized surface plasmon resonance (LSPR) [24]. Moreover, the functionality of the gold nanoparticles can be enhanced by assembling with photoactive chromophores. On the other hand, phthalocyanines (Pcs) have been successfully used in DSSCs because of their high chemical and photochemical stabilities and their strong absorption in the red-near IR. Their optical and electrochemical properties can be tuned by choosing the appropriate

<sup>◇</sup>SPP full member in good standing

\*Correspondence to: Ángela Sastre-Santos, email: [asastre@umh.es](mailto:asastre@umh.es), tel: +34 96665-8408, fax: +34 96665-8351

central metal and peripheral substituents [25–28] allowing them to have the adequate LUMO energy to inject into the titanium dioxide conduction band. Their application in dye-sensitized solar cells has been studied extensively, although moderate efficiencies have been achieved to date [29, 30].

Recent studies point to AuNPs as promising materials for the light-harvesting process in DSSCs. Kamat *et al.* have recently observed a mesoscopic TiO<sub>2</sub> film modified with gold clusters delivering a stable photocurrent of 3.96 mA.cm<sup>-2</sup> with a power conversion efficiency of 2.3% [31]. Moreover, plasmonic effects have been successfully incorporated in DSSCs by core-shell nanoparticles. The insulating layer of silicon oxide prevents the recombination of electrons at the surface of nanoparticles with the dye and the electrolyte. Furthermore, the presence of the nanoparticles increases the absorption of the dye [32, 33]. In order to both prevent the electron recombination and to get a panchromatic effect in DSSC, we decided to anchor ZnPcs to AuNPs to later study their photovoltaic properties. The photophysical dynamics of AuNPs functionalized with Pcs has been studied [34–36], however, to the best of our knowledge, no such DSSCs have been performed till now. For this purpose, we have prepared one bulky zinc phthalocyanine with three *tert*-butyl groups in the periphery and with one aliphatic side chain functionalized with a sulfur rest [AcS(*Bu*)<sub>3</sub>ZnPc] to allow binding to gold nanoparticles. Moreover, we have developed a method for anchoring the AuNP capped with ZnPc to TiO<sub>2</sub>, which had been previously functionalized with lipoic acid (LA), in order to get a solid configuration to study in DSSC.

## EXPERIMENTAL

### General methods

All chemicals were reagent-grade, purchased from commercial sources, and used as received, unless otherwise specified. Column chromatography was performed on silica gel 60 ACC 40–63 μm. Thin layer chromatography was carried out on TLC plates coated with SiO<sub>2</sub> (40–63 μm) 60F254 and they were visualized by UV light. NMR spectra were measured with a Bruker AC 300. UV-vis spectra were recorded with a Helios Gamma spectrophotometer. Fluorescence spectra were recorded with a Perkin Elmer LS 55 Luminiscence Spectrometer and IR spectra with a Nicolet Impact 400D spectrophotometer. Mass spectra were obtained from a Bruker Microflex matrix-assisted laser desorption/ionization time of flight (MALDI-TOF). Transmission electron microscope (TEM) images were obtained using a JEOL JEM1400 Plus transmission electron microscope at 120 kV accelerating voltage.

### Electrochemical measurements

CV measurements were performed in a conventional three-electrode cell using a μ-AUTOLAB type III

potentiostat/galvanostat at 298 K, over PhCN and deaerated sample solutions (~0.5 mM), containing 0.10 M tetrabutylammonium hexafluorophosphate (TBAPF<sub>6</sub>) as supporting electrolyte. A platinum working electrode, Ag/AgNO<sub>3</sub> reference electrode and a platinum wire counter electrode were employed. Ferrocene/ferrocenium couple was used as an internal standard for all measurements.

### Gold nanoparticles (AuNPs-TOABr)

Gold nanoparticles were prepared by a method similar to that described by Brust *et al.* [37]. The core diameter of tetraoctylammonium bromide-gold nanoparticles (AuNP-TOABr) was estimated from transmission electron microscopy (TEM) images. The gold nanoparticles have a diameter of *ca.* 5 nm. The absorption coefficient of the nanoparticles at 522 nm was estimated according to the relationship between the absorbance and the diameter of the nanoparticle [38].

### Synthesis

**2-{2'-[(5''-Acetylthiopentyl)oxo]amino}ethoxy}-9(10),16(17),23(24)-tri-*tert*-butylphthalocyaninate Zn(II) [AcS(*Bu*)<sub>3</sub>ZnPc].** 5.4 mg (0.03 mmol) of 6-bromohexanoic acid, 6.3 mg (0.03 mmol) of 2-chloro-4,6-dimethoxy-1,3,5-triazine (CDMT) and 8 μL (0.04 mmol) of 4-methylmorpholine (NMM) were dissolved and stirred in 1 mL of dried THF under argon atmosphere. Then, 23 mg (0.03 mmol) of 2'-aminoethoxy-9(10), 16(17), 23(24)-tri-*tert*-butylphthalocyaninate Zn(II) [39, 40] were added and the reaction was allowed to proceed for 16 h at room temperature. The crude was diluted in AcOEt and washed with NaHCO<sub>3</sub>, H<sub>2</sub>O and brine. The organic layer was dried with MgSO<sub>4</sub> and concentrated in vacuum. 61 mg (0.066 mmol) of 2-{2'-[(5''-bromopentyl)oxo]amino}ethoxy}-9(10),16(17),23(24)-tri-*tert*-butylphthalocyaninate Zn(II) and 34 mg (0.3 mmol) of potassium thioacetate were diluted in a mixture (1:1) of THF/EtOH under argon atmosphere and heated at 70 °C. After 3 h of reaction, DCM was added and the organic layer was washed with H<sub>2</sub>O, dried with MgSO<sub>4</sub> and concentrated in vacuum. The compound was purified by column chromatography (DCM:MeOH/99:1), affording 29 mg of AcS(*Bu*)<sub>3</sub>ZnPc (75%). <sup>1</sup>H NMR (TFA-*d*<sub>1</sub>): δ, ppm 1.25–1.55 [m, 4H, 2 × CH<sub>2</sub>], 1.71 [s, 27H, 3 × (CH<sub>3</sub>)<sub>3</sub>C], 1.92 (m, 2H, CH<sub>2</sub>), 2.36 (s, 3H, CH<sub>3</sub>CO), 2.79 (t, *J* = 7.2 Hz, 2H, CH<sub>2</sub>CO), 2.94 (t, *J* = 7.2 Hz, 2H, CH<sub>2</sub>S) 4.22 (br s, 2H, CH<sub>2</sub>N), 4.74 (br s, 2H, CH<sub>2</sub>O), 7.91 (d, *J* = 8.1, 1H, HPc), 8.54 (m, 3H, HPc), 9.02 (s, 1H, HPc), 9.34–9.42 (m, 4H, HPc), and 9.52–9.57 (m, 3H, HPc). IR (KBr): ν, cm<sup>-1</sup> 3400, 2954, 2860(OCH<sub>2</sub>), 1720 (CONH), 1648, 1609, 1488, 1462, 1390, 1330, 1256, 1131, 1089 (C=COC), 1046, 920, 748 (SC) and 673. UV-vis (THF): λ<sub>max</sub>, nm (log ε) 348 (4.82), 612 (4.37) and 679 (5.12).

HR-MS (MALDI-TOF, dithranol):  $m/z$   $[M]^+$  calcd. for  $C_{54}H_{57}N_9O_3SZn$  calc. 975.359; found 975.377.

**Covalent linking of  $AcS(^tBu)_3ZnPc$  to AuNPs.** 1 mg (1  $\mu$ mol) of  $AcS(^tBu)_3ZnPc$  and 500  $\mu$ L (0.04  $\mu$ mol) of a  $5 \times 10^{-5} M^{-1} \cdot L^{-1}$  toluene solution of TOABr-AuNP were dissolved in 2 mL of toluene and stirred for 24 h under argon atmosphere. After this time, the reaction mixture was precipitated in pentane and subsequently centrifuged at 14500 rpm for 20 min. After washing several times with pentane, till no blue color was observed in the solution, 1.44 mg of a brownish precipitate of AuNP- $S(^tBu)_3ZnPc$  was obtained.

## RESULTS AND DISCUSSION

### Synthesis and characterization

The synthesis of the new sulfur-containing  $ZnPc$  [ $AcS(^tBu)_3ZnPc$ ] was accomplished by condensation reaction of the aminoethoxytri-*tert*-butylphthalocyanine zinc [( $NH_2C_2H_4O$ ) $(^tBu)_3ZnPc$ ] with 6-bromohexanoic acid and subsequent nucleophilic substitution with potassium thioacetate in 75% yield (Scheme 1).

$AcS(^tBu)_3ZnPc$  was fully characterized by  $^1H$  NMR, FT-IR, UV-vis and HR-MALDI-TOF-MS. The  $^1H$  NMR spectrum of  $AcS(^tBu)_3ZnPc$  in TFA (Fig. 1a) shows three multiplets at 9.57–9.52, 9.42–9.34 and 8.54–8.52 ppm ( $H_A$ ,  $H_B$  and  $H_C$ , respectively) corresponding to the aromatic hydrogens of the  $^tBu$ -substituted rings and one from the fourth ring. Furthermore, at 9.02 and 7.91 ppm appear two signals, which integrate for one proton, assigned to the two hydrogen atoms in the neighbourhood of the ethoxy chain ( $H_D$  and  $H_E$ , respectively) and at 7.16 ppm, one singlet accounts for the proton of the amide group ( $H_F$ ). At 4.74 and 4.22 ppm appear the methylene groups attached to the oxygen ( $H_G$ ) and to the amide nitrogen ( $H_H$ ), respectively. In the aliphatic region of the spectrum, at 2.94 ppm can be identified a triplet corresponding to the methylene linked to the sulfur atom ( $H_I$ ), at 2.79 ppm shows a triplet that correspond to the methylene linked to the amide group ( $H_J$ ), at 2.36 ppm is found the methyl

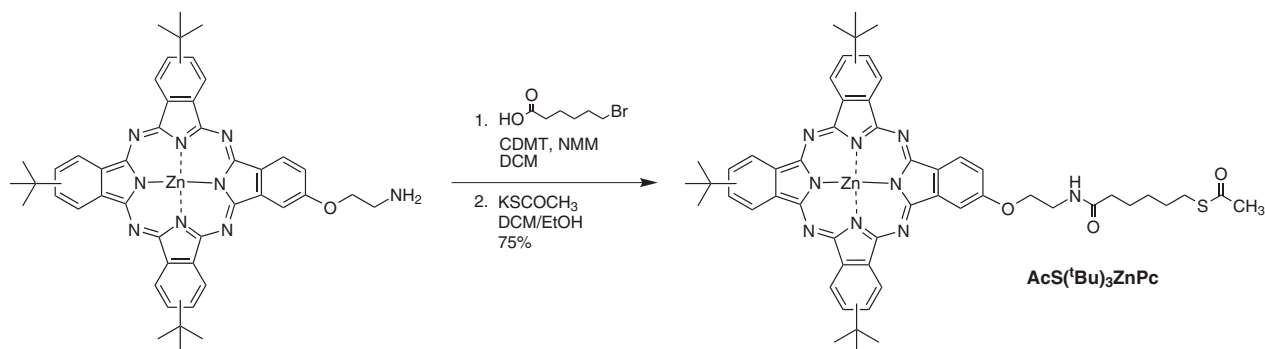
group of the thioester ( $H_K$ ), at 1.81–1.36 ppm appears the rest of the methylene groups of the alkyl chain ( $H_L$ ,  $H_M$  and  $H_N$ ) and, finally, at 1.71 ppm the *tert*-butyl groups in the peripheral positions of the phthalocyanine ( $H_O$ ). To assure the correct assignation of the signals of the phthalocyanine core, we also carried out a temperature-dependent  $^1H$  NMR spectrum of  $AcS(^tBu)_3ZnPc$  in  $DMSO-d_6$  (Fig. 1b). At 25 °C the aromatic region of the spectrum exhibits a broad multiplet at 8.32 ppm, which integrates for four hydrogens assigned to the three peripheral hydrogens adjacent to the *tert*-butyl groups ( $H_C$ ) and to the NH of the amide group. To check this assumption, we increased the temperature looking for the expected displacement of the NH signal. At 40 °C the multiplet splits emerging a broad triplet integrating for one hydrogen, which appears at 8.23 ppm, while a broad multiplet integrating for three hydrogen keeps the original position. At 50 °C this new triplet maintains the integral and shifts further to 8.15 ppm.

The FT-IR spectrum of  $AcS(^tBu)_3ZnPc$  (see Supporting information) shows broad carbonyl bands at 1688  $cm^{-1}$  (thioester) and 1648  $cm^{-1}$  (amide), and also bands at 1089  $cm^{-1}$  (C–O vibration of the ethoxy group) and at 748  $cm^{-1}$  (C–S vibration). Final evidence of the structure of  $AcS(^tBu)_3ZnPc$  was given by HR-MALDI-TOF mass spectrometry where the molecular ion peak at 975.377 daltons is observed, in accordance with the expected theoretical value (see SI).

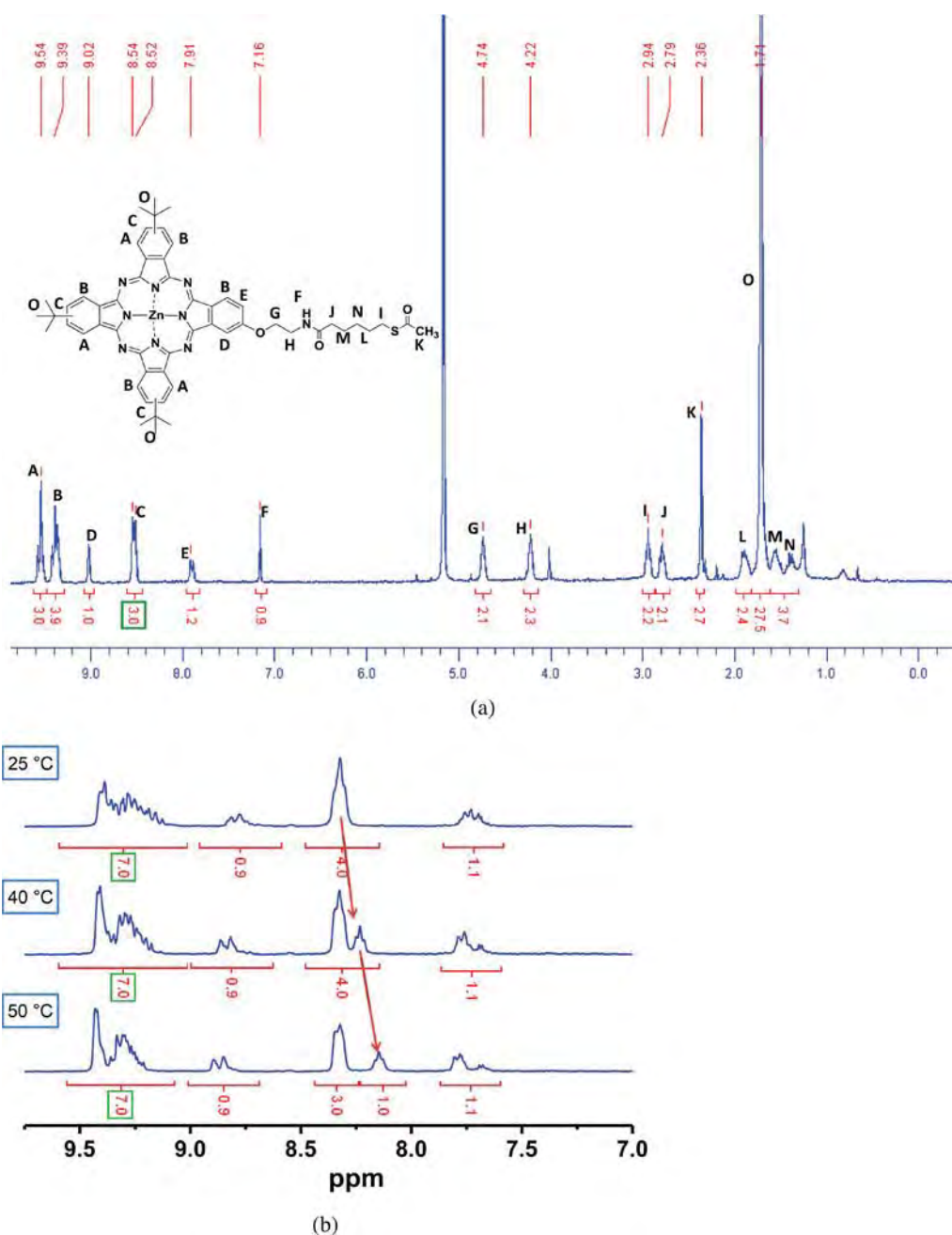
Gold Nanoparticles were prepared using the Brust method [37]. Briefly, hydrogen tetrachloroaurate(III), as Au source, was dissolved in toluene with the aid of tetraoctylammonium bromide in the presence of sodium borohydride. Subsequently, a ligand-exchange reaction with  $AcS(^tBu)_3ZnPc$  in toluene as solvent yielded the AuNP- $S(^tBu)_3ZnPc$  hybrid (Scheme 2).

### Optical and electrochemical measurements

The UV-vis absorption spectrum of  $AcS(^tBu)_3ZnPc$  in THF is displayed in Fig. 2a. The absorption spectrum presents an intense well-defined Q-band centered at 680 nm and a B-band at 349 nm. The steady state



Scheme 1. Synthesis of  $AcS(^tBu)_3ZnPc$



**Fig. 1.** (a) <sup>1</sup>H NMR of AcS('Bu)<sub>3</sub>ZnPc in TFA-d<sub>1</sub> as solvent. (b) Enlargement of the aromatic region of the <sup>1</sup>H NMR of AcS('Bu)<sub>3</sub>ZnPc in DMSO-d<sub>6</sub> as solvent at different temperatures

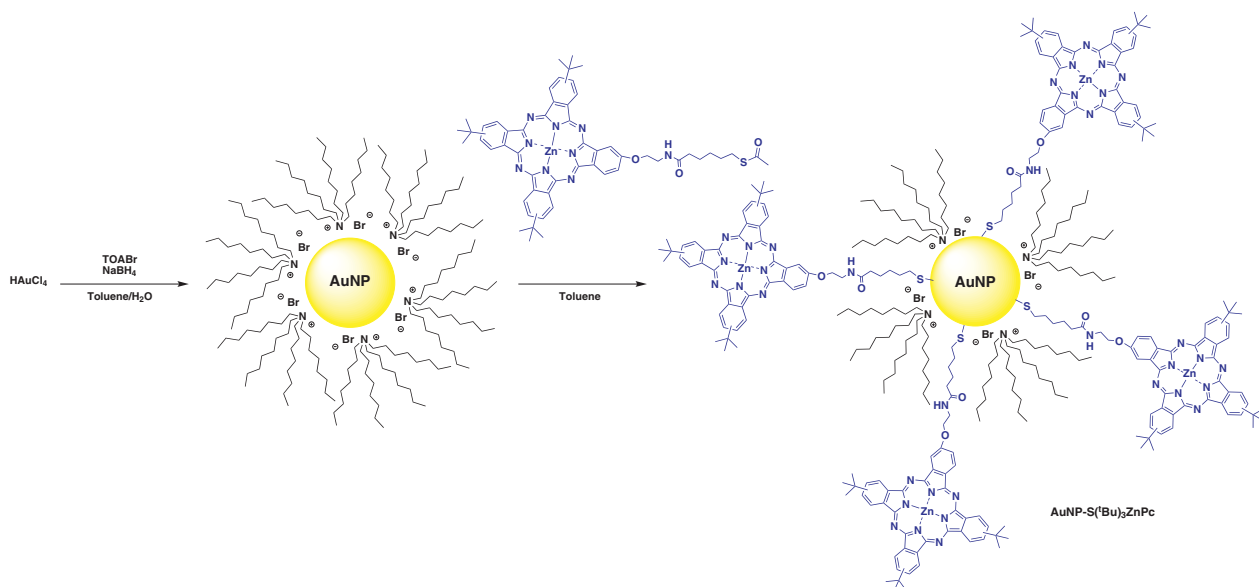
fluorescence spectrum was also measured in THF ( $\lambda_{\text{exc}}$  610 nm) observing emission at 685 nm. From the intersection of the normalized absorption and emission spectra, the zero-zero excitation energy ( $E_{0-0}$ ) can be determined as 1.81 eV (Fig. 2b) [41].

The electrochemical characterization of AcS('Bu)<sub>3</sub>ZnPc was performed using cyclic voltammetry in PhCN as solvent containing 0.1 M tetrabutylammonium hexafluorophosphate (TBAPF<sub>6</sub>) as supporting electrolyte (Fig. 3). The sulfur-substituted phthalocyanine presents one oxidation and two one-electron reduction waves,

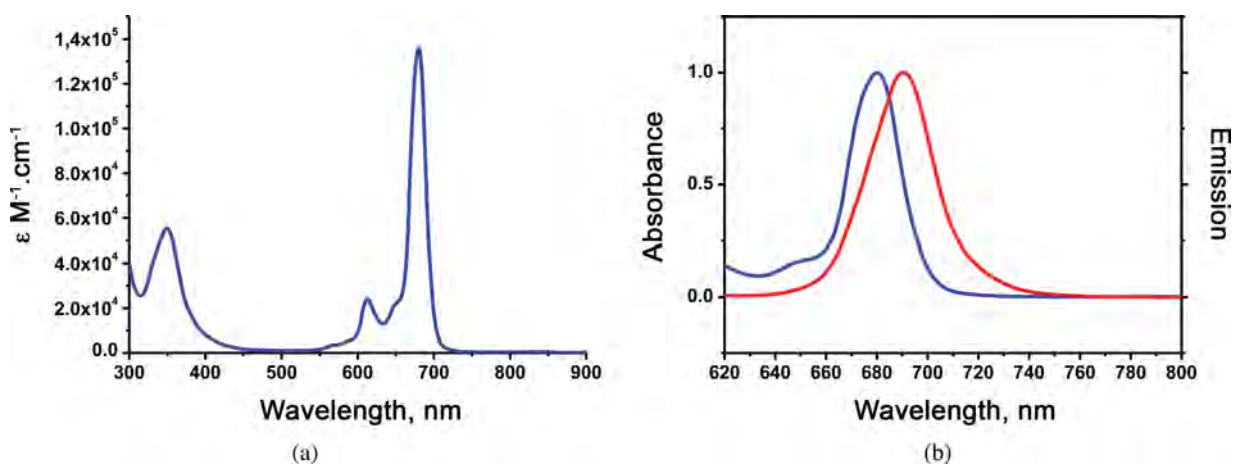
which are centered at  $E_{\text{ox}} = 0.13$  V,  $E_{\text{red}} = -1.45$  V and  $E_{\text{red}} = -1.59$  V (all vs. Fc/Fc<sup>+</sup>).

### Absorption, fluorescence spectra and TEM images of AuNP-S('Bu)<sub>3</sub>ZnPc

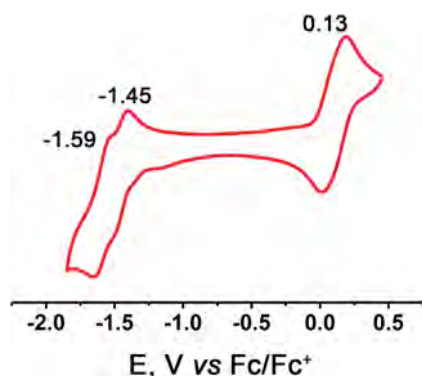
All spectroscopic studies were carried out using toluene as solvent. UV-vis spectrum of AuNP-S('Bu)<sub>3</sub>ZnPc hybrid system clearly confirms that the reaction between the gold nanoparticle and the phthalocyanine took place. We observe an intense plasmonic band centered at



**Scheme 2.** Ligand-exchange reaction and synthesis of the AuNP-S'(Bu)<sub>3</sub>ZnPc hybrid

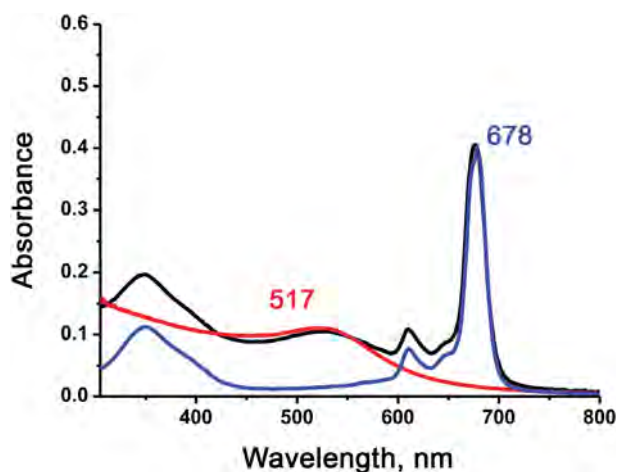


**Fig. 2.** (a) UV-vis absorption spectrum of AcS'(Bu)<sub>3</sub>ZnPc in THF as solvent. (b) Enlarged UV-vis absorption spectrum (blue line) vs. emission spectrum (red line) of AcS'(Bu)<sub>3</sub>ZnPc in THF as solvent

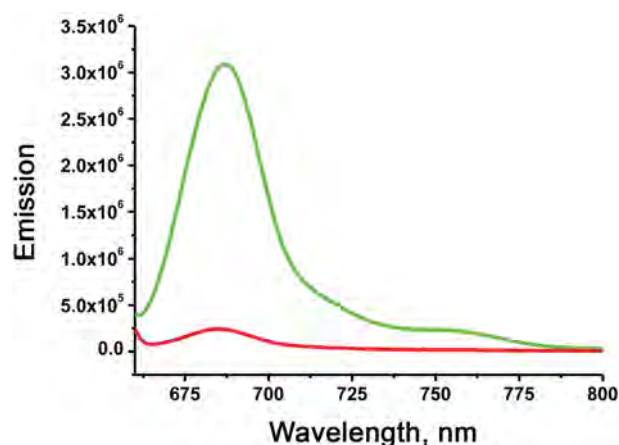


**Fig. 3.** Cyclic voltammogram (100 mV.s<sup>-1</sup>) of AcS'(Bu)<sub>3</sub>ZnPc ~0.5 mM in deaerated PhCN containing 0.10 M of TBAPF<sub>6</sub> as supporting electrolyte

517 nm and the Q-band at 675 nm of the phthalocyanine (Fig. 4). A tiny hypsochromic shift of 3 nm in the Q-band and the lack of any shift in the plasmonic band of the AuNP-S'(Bu)<sub>3</sub>ZnPc hybrid vs. the Q-band of the AcS'(Bu)<sub>3</sub>ZnPc and the plasmonic band of the TOABr-AuNP indicate a very small, if any, interaction between the ZnPc and the AuNP. Taking into account the molar extinction coefficient of the AcS'(Bu)<sub>3</sub>ZnPc hybrid ( $1.32 \times 10^5 \text{ M}^{-1} \cdot \text{cm}^{-1}$  at 679 nm) and the molar extinction coefficient of the TOABr-AuNP ( $3.70 \times 10^5 \text{ M}^{-1} \cdot \text{cm}^{-1}$  at 517 nm) and assuming that the absorption coefficient of the ZnPc in the Q-band region does not change significantly upon assembling phthalocyanines on gold nanoparticles, the number of ZnPcs *per* AuNP is calculated to be around 13. This estimated load is lower



**Fig. 4.** Absorption spectra of AuNP-TOABr (red line), AcS('Bu)<sub>3</sub>ZnPc (blue line) and AuNP-S('Bu)<sub>3</sub>ZnPc (black line) in toluene as solvent



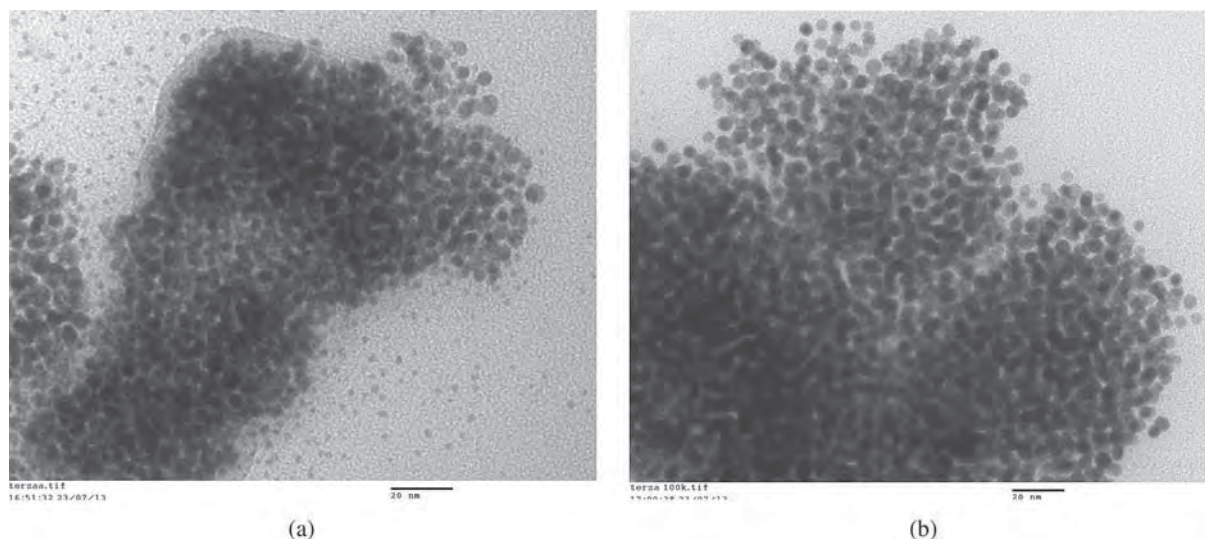
**Fig. 5.** Fluorescence spectra of AcS('Bu)<sub>3</sub>ZnPc (green line) and AuNP-S('Bu)<sub>3</sub>ZnPc (red line) in toluene as solvent

than the obtained by Lemmetyinen *et al.* for a metal free phthalocyanine with two anchoring sulfur atoms in the non-peripheral positions [34]. The number of sulfur atoms in the molecule may be the reason of the different load. Further studies are needed to prove this assumption.

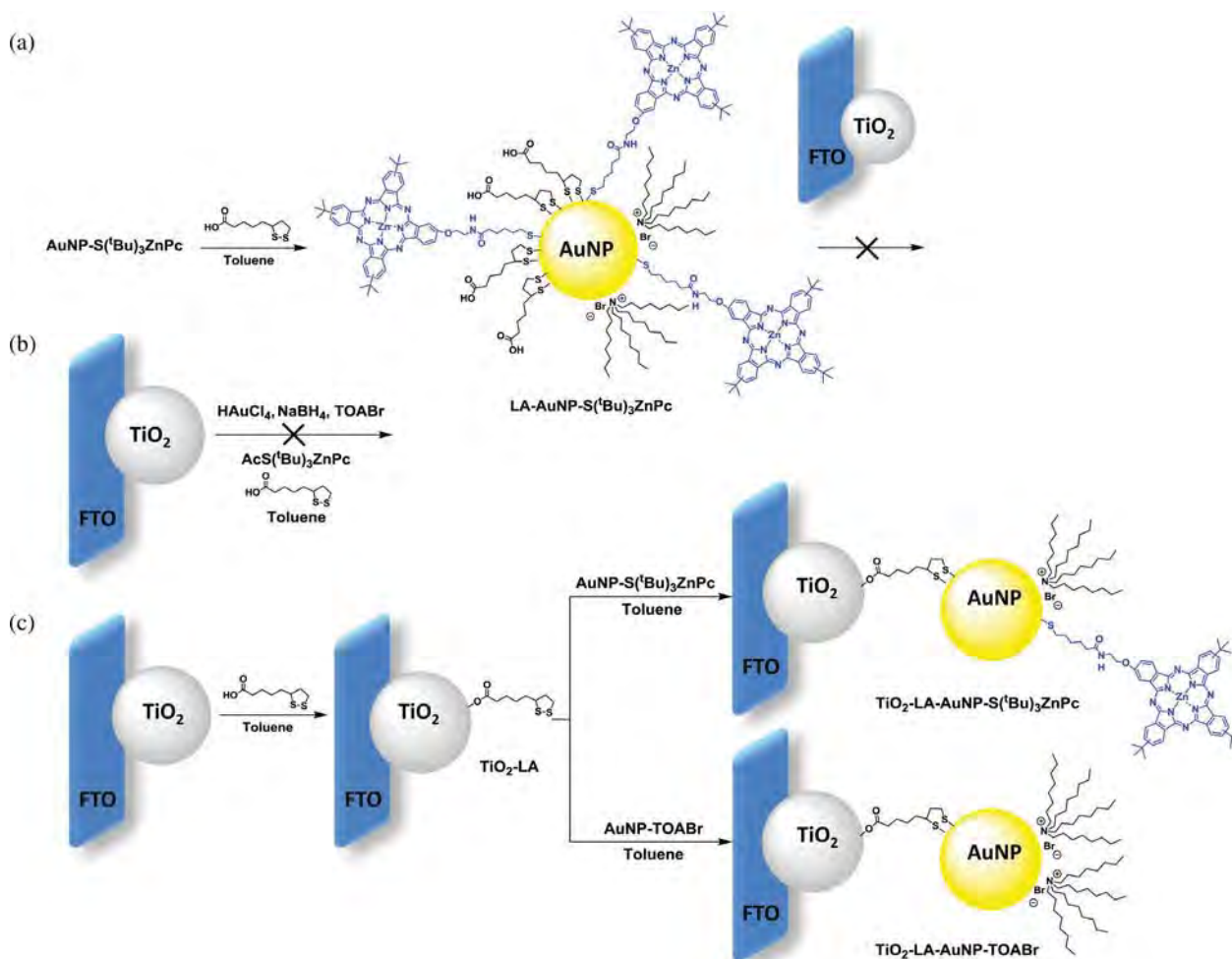
AcS('Bu)<sub>3</sub>ZnPc has a broad fluorescence band in toluene with the maximum at 685 nm (green line) and a quantum efficiency of 0.05%. This fluorescence is almost totally quenched (92%) in the case of the AuNP-S('Bu)<sub>3</sub>ZnPc (Fig. 5), although the position and shape of the spectrum remain unchanged (red line). The direct union between Pc and the AuNP facilitates the phenomenon of intersystem crossing and it could cause a direct energy transfer from the phthalocyanine to the gold nanoparticle. It is clear from the literature that the fluorescence behavior of phthalocyanines in the presence of AuNPs depends on the nature of both the macrocycle and the linker. Time-resolved fluorescence and absorption spectroscopies are underway to investigate the electron injection and recombination processes occurring in the AuNP-S('Bu)<sub>3</sub>ZnPc hybrid.

The TEM images of the AuNP-S('Bu)<sub>3</sub>ZnPc hybrid in comparison with the AuNP-TOABr show a highly ordered arrangement with a particle size average of 5 nm (Fig. 6).

We have studied the capability of anchoring the AuNP-S('Bu)<sub>3</sub>ZnPc hybrid to a TiO<sub>2</sub> semiconducting film to evaluate DSSC parameters (Scheme 3). Using lipoic acid (LA) we have been able to anchor the AuNP to the TiO<sub>2</sub> and also to anchor the AuNP-S('Bu)<sub>3</sub>ZnPc hybrid. Our first strategy was to functionalize a freshly prepared AuNP-S('Bu)<sub>3</sub>ZnPc with LA to latter anchor it to the TiO<sub>2</sub> surface (Scheme 3a). However, the LA-AuNP-S('Bu)<sub>3</sub>ZnPc hybrid resulted only soluble in water, making it impossible to be adsorbed into the TiO<sub>2</sub>. Secondly, we tried to anchor the hybrid to the TiO<sub>2</sub>



**Fig. 6.** TEM images of (a) AuNP-TOABr, and (b) AuNP-S('Bu)<sub>3</sub>ZnPc hybrid



**Scheme 3.** Anchoring the AuNP-S('Bu)<sub>3</sub>ZnPc hybrid to TiO<sub>2</sub> semiconducting film

mixing the latter with a toluene solution of a mixture of HAuCl<sub>4</sub>, NaBH<sub>4</sub>, TOABr, AcS('Bu)<sub>3</sub>ZnPc and LA in a one pot reaction, as previously described, [36] without success (Scheme 3b). Finally, a two step process was carried out, first anchoring LA to the TiO<sub>2</sub> (TiO<sub>2</sub>-LA) and later introducing the TiO<sub>2</sub>-LA with free thiol groups in a toluene solution of AuNP-S('Bu)<sub>3</sub>ZnPc to obtain TiO<sub>2</sub>-LA-AuNP-S('Bu)<sub>3</sub>ZnPc. In a similar way, TiO<sub>2</sub>-LA-AuNP-TOABr was also prepared to be used as reference (Scheme 3c).

The UV-vis spectrum of TiO<sub>2</sub>-LA-AuNP-S('Bu)<sub>3</sub>ZnPc in the film shows the Q-band of the ZnPc at 684 nm and the surface plasmonic band (SPB) of the AuNP centered at 540 nm. The SPB also appears in the TiO<sub>2</sub>-LA-AuNP-TOABr reference, but much to our surprise, it is centered at 577 nm, this means 37 nm red shifted in comparison to that of the film of the ZnPc-containing hybrid (Fig. 7). This red-shift of the SPB is indicative of a closer interparticle proximity, *i.e.* the AuNps are somehow aggregated at the TiO<sub>2</sub> surface [42, 43]. To present more evidences that the ZnPc might reduce the aggregation of the nanoparticle on the TiO<sub>2</sub> surface, we have performed

fluorescence measurements to support our conclusions. First, upon irradiation on the ZnPc at 600 nm, we have compared the emission of the ZnPc in toluene solution (green line) with the emission of the drop-casted ZnPc on the TiO<sub>2</sub> surface (purple line) (Fig. 8a). AcS('Bu)<sub>3</sub>ZnPc did not anchor to TiO<sub>2</sub> due to the lack of an adequate anchoring group. The emission of the AcS('Bu)<sub>3</sub>ZnPc in solution is 38 nm red-shifted, from 699 nm to 737 nm, after adsorption on TiO<sub>2</sub> which indicates the typical aggregation in solid state. A quenching of this band is observed in the TiO<sub>2</sub>-LA-AuNP-S('Bu)<sub>3</sub>ZnPc hybrid (blue line), indicating an energy or electron transfer from the ZnPc to the covalently bonded AuNP. Secondly, upon irradiation on the AuNP at 500 nm, we have studied the emission of the AuNP in three different media: in toluene solution, supported in the TiO<sub>2</sub>-LA-AuNP-TOABr solid and in the TiO<sub>2</sub>-LA-AuNP-S('Bu)<sub>3</sub>ZnPc hybrid (Fig. 8b). A strong quenching, together with a 61 nm red-shift of the emission, is observed when comparing the AuNP emission band in toluene solution (pink line, 573 nm) with the one supported on the TiO<sub>2</sub> surface (red line, 634 nm) indicating the aggregation of the nanoparticles on the

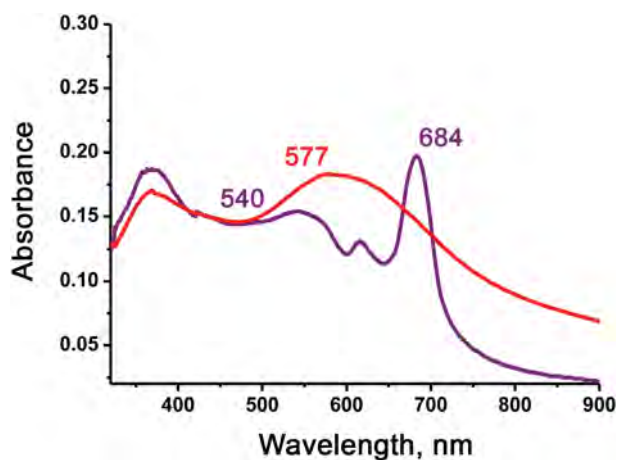


Fig. 7. UV-vis absorption spectra of films of  $\text{TiO}_2\text{-LA-AuNP-S(Bu)}_3\text{ZnPc}$  (purple line) and  $\text{TiO}_2\text{-LA-AuNP-TOABr}$  (red line)

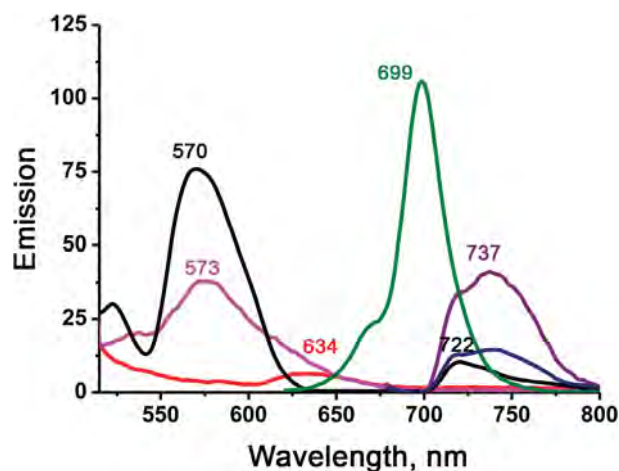


Fig. 8. (a) Fluorescence spectra ( $\lambda_{\text{exc}} = 600 \text{ nm}$ ) of  $\text{AcS(Bu)}_3\text{ZnPc}$  in toluene as solvent (green line),  $\text{TiO}_2\text{-AcS(Bu)}_3\text{ZnPc}$  (purple line) and  $\text{TiO}_2\text{-LA-AuNP-S(Bu)}_3\text{ZnPc}$  (blue line). (b) Fluorescence spectra ( $\lambda_{\text{exc}} = 500 \text{ nm}$ ) of  $\text{AuNP-TOABr}$  in toluene as solvent (pink line),  $\text{TiO}_2\text{-LA-AuNP}$  (red line) and  $\text{TiO}_2\text{-LA-AuNP-S(Bu)}_3\text{ZnPc}$  (black line)

semiconductor surface. Surprisingly, the fluorescence of the AuNp is totally recovered when the ZnPc is covalently bounded in the  $\text{TiO}_2\text{-LA-AuNP-S(Bu)}_3\text{ZnPc}$  hybrid (black line, 570 nm), unequivocally probing that ZnPc promotes the disaggregation of the AuNps, as it was also observed by absorption spectroscopical data (Fig. 7). The emission of the ZnPc is also observed at 722 nm in the  $\text{TiO}_2\text{-LA-AuNP-S(Bu)}_3\text{ZnPc}$  hybrid. This unexpected result make even more valuable the role to be played by the ZnPc in a AuNP-ZnPc-based DSSC, as it will act not only as light harvester, but also as preventer of nanoparticle aggregation on the  $\text{TiO}_2$  surface. DSSC devices using the  $\text{TiO}_2\text{-LA-AuNP-S(Bu)}_3\text{ZnPc}$  configuration are underway and the results will be published in due course.

## CONCLUSION

A new unsymmetrically substituted zinc phthalocyanine with a thioester group in the peripheral position [ $\text{AcS(Bu)}_3\text{ZnPc}$ ] has been synthesized and chemically characterized. This compound has been covalently linked to gold nanoparticles of 5 nm,  $\text{AuNP-S(Bu)}_3\text{ZnPc}$ , by a ligand exchange reaction on  $\text{TOABr-AuNP}$ . We have developed a two-steps methodology to anchor  $\text{AuNP-S(Bu)}_3\text{ZnPc}$  hybrid to  $\text{TiO}_2$  semiconducting films using lipoic acid. We have also observed by UV-vis and fluorescence measurements the importance of the ZnPc in avoiding AuNP aggregation on the  $\text{TiO}_2$  surface. This method opens the way to covalently attach different kind of chromophore-functionalized nanoparticles onto  $\text{TiO}_2$  to study their DSSC performances.

## Acknowledgements

This work has been supported by the Spanish Ministerio de Economía y Competitividad, Generalitat Valenciana and the European FEDER funds (CTQ2011-26455, PROMETEO 2012/010 and ISIC/2012/008).

## Supporting information

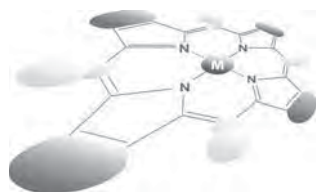
Figures S1–S3 are given in the supplementary material. This material is available free of charge via the Internet at <http://www.worldscinet.com/jpp/jpp.shtml>.

## REFERENCES

- Ozby E. *Science* 2006; **311**: 189.
- Bozhevolnyi SI, Volkov VS, Devaux E, Laluet JY and Ebbesen TW. *Nature* 2006; **440**: 508.
- Herderick ED, Tresback JS, Vasiliev AL and Padture NP. *Nanotechnology* 2007; **18**: 155204/1.
- Blumel A, Klug A, Eder S, Scherf U, Moderegger E and List EJW. *Org. Electron.* 2007; **8**: 389.
- Howes PD, Chandrawati R and Stevens MM. *Science* 2014; **346**: 1247390.
- Yoon HJ and Jang WD. *J. Porphyrins Phthalocyanines* 2013; **17**: 16–26.
- Sapsford KE, Algar WR, Berti L, Boeneman Gemmill K, Casey BJ, Oh E, Stewart MH and Medintz IL. *Chem. Rev.* 2013; **113**: 1904–2074.
- O'Regan B and Grätzel M. *Nature* 1991; **353**: 737–740.
- Butler D. *Nature* 2008; **454**: 558–559.
- Planells M, Céspedes-Guirao FJ, Forneli A, Sastre-Santos Á, Fernández-Lázaro F and Palomares E. *J. Mat. Chem.* 2008; **18**: 5802–5808.
- Yu Q, Wang Y, Yi Z, Zu N, Zhang J, Zhang M and Wang P. *ACS Nano* 2010; **4**: 6032–6038.
- Nazeeruddin MK, De Angelis F, Fantacci S, Selloni A, Viscardi G, Liska P, Ito S, Takeru B and Grätzel M. *J. Am. Chem. Soc.* 2005; **127**: 16835–16847.



13. Mathew S, Yella A, Gao P, Humphry-Baker R, Curchod BFE, Ashari-Astani N, Tavernell L, Rothlisberger U, Nazeeruddin MdK and Grätzel M. *Nat. Chem.* 2014; **6**: 242–247.
14. Ragoussi ME, Cid JJ, Yum JH, de la Torre G, Di Censo D, Grätzel M, Nazeeruddin MK and Torres T. *Angew. Chem. Int. Ed.* 2012; **51**: 4375–4378.
15. Ikeuchi T, Nomoto H, Masaki N, Griffith MJ, Mori M and Kimura M. *Chem. Commun.* 2014; **50**: 1941–1943.
16. Barea EM, Ortiz J, Payá FJ, Fernández-Lázaro F, Fabregat-Santiago F, Sastre-Santos A and Bisquert J. *Energy Environ. Sci.* 2010; **3**: 1985–1994.
17. Kramer IJ and Sargent EH. *ACS Nano* 2011; **5**: 8506–8514.
18. Stewart ME, Anderton CR, Thompson LB, Maria J, Gray SK, Rogers JA and Nuzzo RG. *Chem. Rev.* 2008; **108**: 494–521.
19. Leznoff CC and Lever ABP. *Phthalocyanines: Properties and Applications*, Vols. 1–4, VCH: Weinheim, Germany, 1989, 1993, 1996.
20. Mayer KM and Hafner JH. *Chem. Rev.* 2011; **111**: 3828–3857.
21. Ng SP, Lu XQ, Ding N, Lawrence Wua CH and Lee CH. *Solar Energy* 2014; **99**: 115–125.
22. Ferry VE, Sweatlock LA, Pacifici D and Atwater HA. *Nano Lett.* 2008; **8**: 4391–4397.
23. Long R and Prezhdo OV. *J. Am. Chem. Soc.* 2014; **136**: 4343–4354.
24. Rockstuhl C, Fahr S and Lederer F. *J. Appl. Phys.* 2008; **104**: 123102.
25. McKeown NB. *Phthalocyanines: Materials Synthesis Structure and Function*, Cambridge University Press: Cambridge, 1998.
26. de la Torre G, Vázquez P, Agulló-López F and Torres T. *Chem. Rev.* 2004; **104**: 3723.
27. de la Torre G, Claessens CG and Torres T. *Chem. Commun.* 2007: 2000.
28. Mack J and Kobayashi N. *Chem. Rev.* 2011; **111**: 281.
29. Martín-Gomis L, Fernández-Lázaro F and Sastre-Santos A. *J. Mater. Chem. A* 2014; **2**: 15672–15682.
30. Ragoussi ME, Ince M and Torres T. *Eur. J. Org. Chem.* 2013: 6475–6489.
31. Chen Y.-S, Choi H and Kamat PV. *J. Am. Chem. Soc.* 2013; **135**: 8822–8825.
32. Qi J, Dang X, Hammond PT and Belcher AM. *ACS Nano* 2011; **5**: 7108–7116.
33. Brown MD, Suteewong T, Sai Santosh Kumar R, D’Innocenzo V, Petrozza A, Lee MM, Wiesner U and Snaith HJ. *Nano Lett.* 2011; **11**: 438–445.
34. Kotiaho A, Lahtinen R, Efimov A, Metsberg HK, Sariola E, Lehtivuori H, Tkachenko NV and Lemmetyinen H. *J. Phys. Chem. C* 2010; **114**: 162–168.
35. Nyokong T and Antunes E. *Coord. Chem. Rev.* 2013; **257**: 2401–2418.
36. Ashokkumar R, Kathiravan A and Ramamurthy P. *Phys. Chem. Chem. Phys.* 2014; **16**: 14139.
37. Brust M, Walker M, Bethell D, Schiffrin DJ and Whyman R. *J. Chem. Soc., Chem. Commun.* 1994: 801.
38. Rance GA, Marsh DH and Khlobystov AN. *Chem. Phys. Lett.* 2008; **460**: 230–236.
39. Fukuzumi S, Ohkubo K, Ortiz J, Gutiérrez AM, Fernández-Lázaro F and Sastre-Santos Á. *Chem. Commun.* 2005: 3814–3816.
40. Fukuzumi S, Ohkubo K, Ortiz J, Gutiérrez AM, Fernández-Lázaro F and Sastre-Santos A. *J. Phys. Chem. A* 2008; **112**: 10744–10752.
41. Gierschner J, Cornil J and Egelhaaf HJ. *Adv. Mater.* 2007; **19**: 173–191.
42. Ghosh SK and Pal T. *Chem. Rev.* 2007; **107**: 4797
43. Zotti G, Vercelli B, Battagliarin M, Berlin A, Hernandez V and Lopez Navarrete JT. *J. Phys. Chem. C* 2007; **111**: 5886.



# Metal-induced dynamic conformational and fluorescence switch of quinone-appended Zn-porphyrin

Yasuyuki Yamada<sup>a,b</sup>, Kosuke Hiraga<sup>a</sup> and Kentaro Tanaka<sup>\*a</sup>

<sup>a</sup>Department of Chemistry, Graduate School of Science, Nagoya University, Furo-cho, Chikusa-ku, Nagoya 464-8602, Japan

<sup>b</sup>Research Institute of Materials Science, Nagoya University, Furo-cho, Chikusa-ku, Nagoya 464-8602, Japan

*Dedicated to Professor Shunichi Fukuzumi on the occasion of his retirement*

Received 19 November 2014

Accepted 4 December 2014

**ABSTRACT:** In this report, we have designed and synthesized a novel switching molecule whose fluorescence can be switched *via* dynamic conformational change between expanded and shrunk states induced by metal complexation and decomplexation. The switching molecule is composed of three kinds of components, namely, a Zn<sup>2+</sup>-porphyrin fluorophore, two quinone quenchers, and their linkers containing a 4,4'-bipyridine moiety. UV-vis and fluorescence titration studies revealed that metal complexation of the bipyridine units with Zn<sup>2+</sup> ions induced the dynamic structural change of the molecular shape and simultaneous enhancement of fluorescence of the Zn<sup>2+</sup>-porphyrin fluorophore.

**KEYWORDS:** porphyrin, fluorescence switching, folding, bipyridine, quinone.

## INTRODUCTION

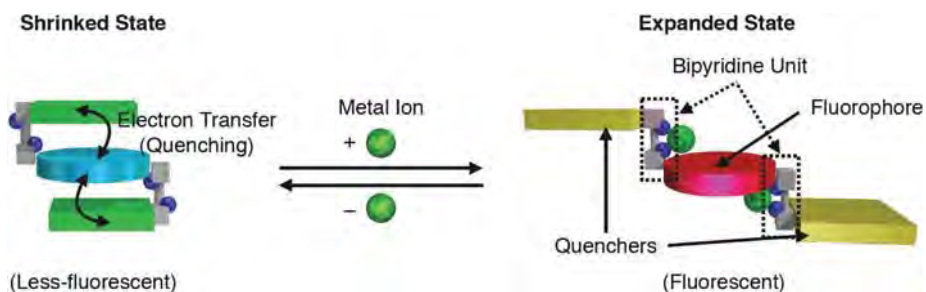
Development of nano scale molecular actuators whose structures can be dynamically switched by external stimuli have attracted considerable interests for their potential application to the molecular machines, sensors, information storage, and so on [1–3]. In nature, it is well-recognized that dynamic structural changes of the biomolecules such as proteins produces the mechanical and electrochemical energy as the results of chemical, photochemical, and electrochemical reactions to maintain the living systems. Artificial molecular systems have also achieved such an energy conversion to gain structural and functional switches. Recent progress of supramolecular chemistry has contributed to them and many contrivances have been proposed for the dynamic molecular switches induced by external stimuli such as light [4, 5], redox [6, 7], pH [8, 9], ion binding [10], and so on.

As the way to induce the reversible transformation, metal coordination chemistry has been widely used as a powerful

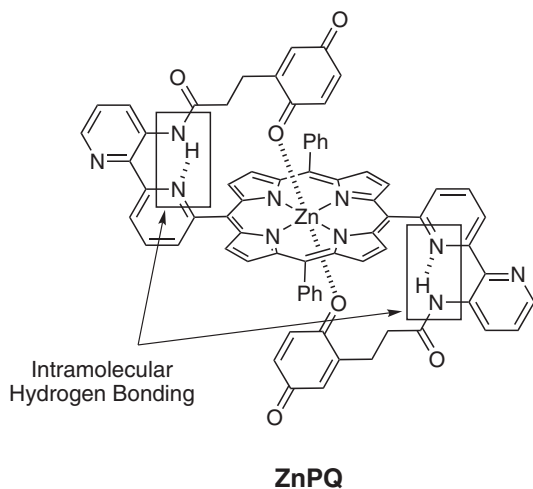
tool because of adjustable binding affinity and kinetics between a metal ion and a ligand as well as predictable structural geometry. For example, the early generation of the supramolecular systems emerged from Rebek's work in which metal binding affinity of a crown ether was allosterically regulated by another metal binding to a bipyridine unit as a part of the crown ether ring [11]. Lehn has introduced an ion-triggered switch in nanomechanical butterfly-type bis(porphyrin)terpyridines [12–14]. These studies obviously demonstrated the powerfulness and usefulness of the oligopyridine unit for the metal-induced dynamic mechanical switch of molecular interactions.

In this report, we have designed and synthesized molecular machines whose fluorescence can be switched through dynamic structural switch induced via metal complexation. Schematic representation of our concept for the molecular switch is summarized in Fig. 1. Our designed molecules are composed of a fluorophore and two quenchers on the side-arms which were connected by bipyridine units to the central fluorophore. These molecules can exhibit both expanded and shrunk states corresponding to metal-complexed and -decomplexed forms, respectively. When the quenchers are proximal of the fluorophore, efficient electron transfer would

\*Correspondence to: Kentaro Tanaka, email: [kentaro@chem.nagoya-u.ac.jp](mailto:kentaro@chem.nagoya-u.ac.jp)



**Fig. 1.** Schematic representation of the reversible fluorescent switch *via* metal-induced dynamic structural transformation



**Fig. 2.** Chemical structure of a quinone-sandwiched  $Zn^{2+}$ -porphyrin **ZnPQ**

occur to quench the fluorescence of the fluorophore. Metal complexation by the bipyridine units would result in transformation into the expanded state in which the quencher and the fluorophore become separated, resulting in the increase of the fluorescence.

Recently, we have reported the synthesis of **ZnPQ** composed of a  $Zn^{2+}$ -porphyrin as the fluorophore, two quinone moieties as the quenchers on the side-arms, and the bipyridine connectors (Fig. 2) [15]. The crystal structure of **ZnPQ** clearly represented the folded structure when there were no coordinated metals on the bipyridine connectors and the keto oxygen atoms of the two quinone moieties coordinated to the axial positions of the  $Zn^{2+}$  ion. Since the folded structure seems to be adequate for efficient quenching of the fluorescent emission of the  $Zn^{2+}$ -porphyrin, we assumed that this structural character of the molecule is suitable for the switchable fluorescent molecular system.

## EXPERIMENTAL

### General

Synthetic procedures were carried out under dry nitrogen atmosphere, unless otherwise specified. All reagents

and solvents were purchased at the highest commercial quality available and used without further purification, unless otherwise stated. 5,15-bis(6-bromopyridin-2-yl)-10,20-diphenylporphyrin **3** [15], *trans*-4-((*tert*-butoxy carbonyl)amino)-cyclohexylamine **5** [16], *p*-benzoquinone-2-ethyl-2'-carboxylic acid **8** [17], and a quinone-appended  $Zn^{2+}$ -porphyrin **ZnPQ** [15] were prepared according to the literature procedures.  $^1H$ ,  $^{13}C$  NMR spectra were recorded on a JEOL JNM-A600 (600 MHz for  $^1H$ ; 150 MHz for  $^{13}C$ ) spectrometer or a JEOL JNM-A400 (400 MHz for  $^1H$ ; 100 MHz for  $^{13}C$ ) spectrometer at a constant temperature of 298 K. Tetramethylsilane (TMS) was used as an internal reference for  $^1H$  and  $^{13}C$  NMR measurements in  $CDCl_3$ . Elemental analyses were performed on a Yanaco MT-6 analyzer. Silica gel column chromatographies and thin-layer (TLC) chromatography were performed using Merck silica gel 60 and Merck silica gel 60 (F254) TLC plates, respectively. GPC was performed using a JAI LC-9204 equipped with JAIGEL 1H-40/2H-40 columns. ESI mass spectrometry was performed with a Waters LCT-Premier XE Spectrometer controlled using Masslynx software.

The absorption spectra were recorded with a Hitachi U-4100 spectrophotometer in  $CH_2Cl_2$  solutions at  $20 \pm 0.1$  °C in 1.0 cm quartz cells. The fluorescent spectra were recorded with a Hitachi F-4500 fluorescence spectrophotometer in  $CH_2Cl_2$  solutions at  $20 \pm 0.1$  °C in 1.0 cm quartz cells.

### Synthesis

**2-Bromoisonicotinic acid 4.** 2-Chloroisonicotinic acid (0.51 g, 3.2 mmol) was suspended in a mixture of AcOH (8 mL) and 48% aqueous HBr (1 mL). The suspension was refluxed for 7 h, during which the suspension became homogenous. Additional amount of 48% aqueous HBr (7 mL) was added during the reflux. After evaporation of the solvent, saturated aqueous  $NH_4Cl$  (100 mL) was added. The mixture was extracted with EtOAc (100 mL  $\times$  2). The combined organic layer was dried over anhydrous  $Na_2SO_4$ , filtered, and concentrated to obtain colorless solid (0.59 g). This crude product was suspended in a mixture of AcOH (8 mL) and 48% aqueous HBr (8 mL). The mixture was heated again

at reflux temperature for further 21 h. After evaporation of the solvent, saturated aqueous  $\text{NH}_4\text{Cl}$  (50 mL) was added and the mixture was extracted with EtOAc (50 mL  $\times$  2). The pH of the aqueous layer was adjusted to approximately 5 with saturated aqueous  $\text{NaHCO}_3$  and the layer was extracted with EtOAc (40 mL  $\times$  2). The combined organic layer was dried over anhydrous  $\text{Na}_2\text{SO}_4$ , filtered, and concentrated to obtain the desired compound as a colorless solid. Yield 0.30 g (46%).  $^1\text{H}$  NMR (270 MHz; DMSO- $d_6$ ; TMS):  $\delta_{\text{H}}$ , ppm 8.59 (dd,  $J = 4.9$  Hz, 0.6 Hz, 1H), 7.96 (dd,  $J = 1.3$  Hz, 0.6 Hz, 1H), 7.85 (dd,  $J = 4.9$  Hz, 1.3 Hz, 1H).  $^{13}\text{C}$  NMR (100 MHz; DMSO- $d_6$ ; TMS):  $\delta_{\text{C}}$ , ppm 164.7, 151.6, 142.0, 141.3, 127.1, 122.5. IR (ATR/ZnSe):  $\nu$ ,  $\text{cm}^{-1}$  3100, 2922, 2771, 2451, 1848, 1705.

***N*-(*trans*-4-(*tert*-Butoxycarbonylamino)-cyclohexyl)-2-bromoisonicotinamide 6.** *trans*-4-((*tert*-Butoxycarbonyl)amino)-cyclohexylamine **5** (1.5 g, 6.9 mmol) was added to a mixture of  $\text{CH}_2\text{Cl}_2$  (20 mL), 2-bromoisonicotinic acid **4** (1.3 g, 6.7 mmol), BOP (3.0 g, 6.8 mmol), and  $\text{Et}_3\text{N}$  (2.3 mL, 16 mmol). The solution was stirred for 21 h at room temperature. After evaporation of the solvent,  $\text{CHCl}_3$  (500 mL) was added. The resulting mixture was washed with saturated aqueous  $\text{NaHCO}_3$  (250 mL) and water (250 mL  $\times$  2) successively, dried over anhydrous  $\text{MgSO}_4$ , filtered, and concentrated to obtain pale brown solid (3.3 g). The crude product was purified by silica gel column chromatography (4.5 cm  $\phi$   $\times$  21 cm,  $\text{CHCl}_3$ :MeOH = 24:1–19:1) to give colorless solid (3.1 g). Recrystallization from  $\text{CHCl}_3$ :MeOH = 4:1 ((v/v) 100 mL) and hexane (500 mL) afforded the target compound as a colorless solid. Yield 2.0 g (74%).  $^1\text{H}$  NMR (400 MHz;  $\text{CDCl}_3$ ; TMS):  $\delta_{\text{H}}$ , ppm 8.48 (d,  $J = 5.1$  Hz, 1H), 7.77 (s, 1H), 7.54 (dd,  $J = 5.1$  Hz, 1.4 Hz, 1H), 5.97 (br, 1H, exchangeable), 4.43 (br, 1H), 3.94–3.91 (m, 1H), 3.46 (br, 1H), 2.13–2.07 (m, 4H), 1.45 (s, 9H), 1.40–1.24 (m, 4H).  $^{13}\text{C}$  NMR (100 MHz;  $\text{CDCl}_3$ ; TMS):  $\delta_{\text{C}}$ , ppm 163.4, 155.2, 150.9, 144.4, 143.0, 125.6, 120.0, 79.4, 48.8, 48.7, 31.9, 31.6, 28.4. IR (ATR/ZnSe):  $\nu$ ,  $\text{cm}^{-1}$  3279, 2981, 2933, 2857, 1686, 1645, 1536. MS (ESI-TOF):  $m/z$  420.1 (calcd. for  $[\text{M} + \text{Na}]^+$ ). Found 420.0.

**5,15-Bis[4'-[*N*-(*trans*-4-(*tert*-butoxycarbonylamino)-cyclohexyl)-2-bromoisonicotinamide 6 (0.26 g, 0.65 mmol),  $\text{Pd}(\text{PPh}_3)_4$  (38 mg, 33  $\mu\text{mol}$ ),  $\text{Me}_3\text{SnSnMe}_3$  (0.15 mL, 0.72 mmol) and toluene (20 mL) was refluxed for 8 h. After **6** was completely consumed, 5,15-bis(6-bromopyridin-2-yl)-10,20-diphenylporphyrin **3** (0.10 g, 0.13 mmol),  $\text{Pd}(\text{PPh}_3)_4$  (31 mg, 27  $\mu\text{mol}$ ), and toluene (10 mL) were added to the mixture at room temperature. The suspension was refluxed for 13 h. After the solvent was removed, a mixture of  $\text{CH}_2\text{Cl}_2$  and MeOH were added and the resulting solution was filtrated through a Celite pad. The filtrate was concentrated under reduced pressure to**

give black solid (0.37 g). The crude product was purified by silica gel column chromatography (3 cm  $\phi$   $\times$  25 cm,  $\text{CH}_2\text{Cl}_2$ :acetone = 7:1) to give violet solid (87 mg), which was further purified by GPC to obtain the title compound as a violet solid. Yield 79 mg (47%).  $^1\text{H}$  NMR (400 MHz;  $\text{CDCl}_3$ ; TMS):  $\delta_{\text{H}}$ , ppm 8.91–8.87 (m, 12H), 8.63 (br, 1H), 8.35–8.22 (m, 8H), 7.78–7.76 (m, 8H), 6.04–6.02 (m, 2H), 3.69 (br, 2H), 3.08 (br, 2H), 1.78 (br, 8H), 1.31 (s, 18H), 1.04–0.95 (m, 8H). IR (ATR/ZnSe):  $\nu$ ,  $\text{cm}^{-1}$  3307, 3058, 2932, 2857, 1683, 1640. MS (ESI-TOF):  $m/z$  1273.6 (calcd. for  $[\text{M} + \text{Na}]^+$ ). Found 1273.4.

### A quinone-appended porphyrin 1

*Deprotection of the Boc groups of 7.* 5,15-bis[4'-[*N*-(*trans*-4-(*tert*-butoxycarbonylamino)-cyclohexyl)-carbamoyl]-[2,2']-bipyridin-6-yl]-10,20-diphenylporphyrin **7** (0.13 g, 0.10 mmol), was dissolved in a mixture of 4 M HCl in 1,4-dioxane (0.5 mL) and MeOH (2.0 mL). The mixture was stirred for 3 h at room temperature. After the solution was neutralized with saturated aqueous  $\text{Na}_2\text{CO}_3$  (5 mL), the solvents were evaporated.  $\text{CHCl}_3$  (200 mL) was added to the resulting mixture. The solution was washed with saturated aqueous  $\text{Na}_2\text{CO}_3$  (10 mL), water (50 mL  $\times$  6), dried over anhydrous  $\text{Na}_2\text{SO}_4$ , filtered, and concentrated under reduced pressure to obtain a purple residue (0.12 g). The crude product was purified by reprecipitation from  $\text{CHCl}_3$ :MeOH = 4:1 ((v/v), 3 mL) and hexane (40 mL) to obtain 5,15-bis[4'-[*N*-(*trans*-4-aminocyclohexyl)-carbamoyl]-[2,2']-bipyridin-6-yl]-10,20-diphenylporphyrin as a violet solid. Yield 0.11 g (100%). This product was used for the next reaction without further purification.  $^1\text{H}$  NMR (400 MHz; DMSO- $d_6$ ; TMS):  $\delta_{\text{H}}$ , ppm 8.95–8.88 (m, 12H), 8.66 (s, 2H), 8.47–8.45 (m, 6H), 8.26–8.25 (m, 4H), 7.84–7.82 (m, 8H), 3.50 (br, 3H (including  $\text{H}_2\text{O}$ )), 2.29 (br, 2H), 1.59–1.56 (m, 8H), 1.13–1.10 (m, 4H), 0.92–0.89 (m, 4H), -2.88 (br, 2H).  $^{13}\text{C}$  NMR (400 MHz;  $\text{CDCl}_3$ ; TMS):  $\delta_{\text{C}}$ , ppm 173.8, 164.6, 162.6, 160.0, 156.6, 154.1, 150.1, 142.9, 141.6, 135.9, 134.5, 131.7, 130.8, 130.2, 127.9, 126.8, 122.1, 120.7, 120.2, 118.5, 117.6, 48.3, 34.6, 30.9, 29.7. IR (ATR/ZnSe):  $\nu$ ,  $\text{cm}^{-1}$  3313, 2932, 2854, 1648, 1548. MS (ESI-TOF):  $m/z$  1051.5, (calcd. for  $[\text{M} + \text{Na}]^+$ ). Found 1051.4.

*Coupling reaction with 6.* 5,15-Bis[4'-[*N*-(*trans*-4-Aminocyclohexyl)-carbamoyl]-[2,2']-bipyridin-6-yl]-10,20-diphenylporphyrin (0.11 g, 0.10 mmol) prepared above was added to the solution of *p*-benzoquinone-2-ethyl-2'-carboxylic acid **8** (37 mg, 0.20 mmol), BOP (90 mg, 0.20 mmol), and  $\text{Et}_3\text{N}$  (75  $\mu\text{L}$ , 0.53 mmol) in  $\text{CH}_2\text{Cl}_2$  (20 mL). The mixture was stirred for 1.5 h at room temperature, and then, a mixture of  $\text{CH}_2\text{Cl}_2$  and MeOH (4:1 (v/v), 100 mL) was added. The resulting solution was washed with saturated aqueous  $\text{NaHCO}_3$  (500 mL) and water (500 mL  $\times$  4). The organic layer was dried over anhydrous  $\text{Na}_2\text{SO}_4$ , filtered, and concentrated under reduced pressure to give a purple solid (0.13 g).

The crude product was purified by silica gel column chromatography twice (1st: 3 cm  $\phi$   $\times$  25 cm, CH<sub>2</sub>Cl<sub>2</sub>:MeOH = 49:1–9:1; 2nd: 3 cm  $\phi$   $\times$  22 cm, CH<sub>2</sub>Cl<sub>2</sub>:MeOH = 49:1–97:3), to give purple residue (69 mg), which was further purified by reprecipitation from CHCl<sub>3</sub>:MeOH = 4:1 ((v/v), 8 mL) and hexane (200 mL) to give a title compound as a purple solid. Yield 61 mg (44%). <sup>1</sup>H NMR (400 MHz; CDCl<sub>3</sub>: CD<sub>3</sub>OD = 1:1 (v/v); TMS):  $\delta_{\text{H}}$ , ppm 8.91–8.83 (m, 12H), 8.75 (s, 2H), 8.39–8.38 (m, 4H), 8.24 (d,  $J$  = 7.6 Hz, 2H), 7.81–7.79 (m, 8H), 6.71 (d,  $J$  = 10.0 Hz, 2H), 6.66 (dd,  $J$  = 10.4 Hz, 2.4 Hz, 2H), 6.48 (br, 2H), 3.65 (br, 2H), 2.60 (t,  $J$  = 7.5 Hz, 4H), 2.26 (t,  $J$  = 7.3 Hz, 4H), 1.76–1.66 (m, 8H), 1.02–1.04 (m, 8H). IR (ATR/ZnSe):  $\nu$ , cm<sup>-1</sup> 3308, 3063, 2925, 2853, 1654, 1634. MS (ESI-TOF):  $m/z$  1397.5 (calcd. for [M + Na]<sup>+</sup>). Found 1397.6.

**A Zn<sup>2+</sup> complex of 1 (Zn-1).** A mixture of a quinone-appended porphyrin **1** (4.7 mg, 3.4  $\mu$ mol), 2 mM solution of Zn(OAc)<sub>2</sub> in a mixture of MeOH (1.7 mL), and CHCl<sub>3</sub> (1.7 mL) was refluxed for 1 h. After the solution was evaporated, the residue was purified by silica gel column chromatography (2 cm  $\phi$   $\times$  15 cm, CHCl<sub>3</sub>:MeOH = 39:1), to give a violet solid, which was further purified by GPC (JAI-LC9204, CHCl<sub>3</sub>), followed by recrystallization from CHCl<sub>3</sub>/Et<sub>2</sub>O to obtain the title compound as a violet solid. Yield 3.8 mg (77%). <sup>1</sup>H NMR (400 MHz; CDCl<sub>3</sub>:DMSO-*d*<sub>6</sub> = 1:1; TMS):  $\delta_{\text{H}}$ , ppm 8.90–8.85 (m, 12H), 8.70 (br, 1H), 8.40–8.33 (m, 6H), 8.22–8.20 (m, 4H), 7.82–7.75 (m, 8H), 6.74 (d,  $J$  = 10.0 Hz, 2H), 6.67 (dd,  $J$  = 10.0 Hz, 2.4 Hz, 2H), 6.49 (d,  $J$  = 2.4 Hz, 2H), 2.55–2.54 (m, 49H (including DMSO)), 2.22 (t,  $J$  = 7.2 Hz, 4H), 1.69–1.66 (m, 8H), 1.20–1.08 (m, 8H). IR (ATR/ZnSe):  $\nu$ , cm<sup>-1</sup> 3306, 2922, 2822, 1652. MS (ESI-TOF):  $m/z$  1459.4 (calcd. for [M + Na]<sup>+</sup>). Found 1459.5. Anal. calcd. for C<sub>88</sub>H<sub>78</sub>N<sub>12</sub>O<sub>9</sub>Zn (Zn-1·Et<sub>2</sub>O): C, 69.86; H, 5.20; N, 11.11. Found C, 70.00; H, 5.00; N, 11.05.

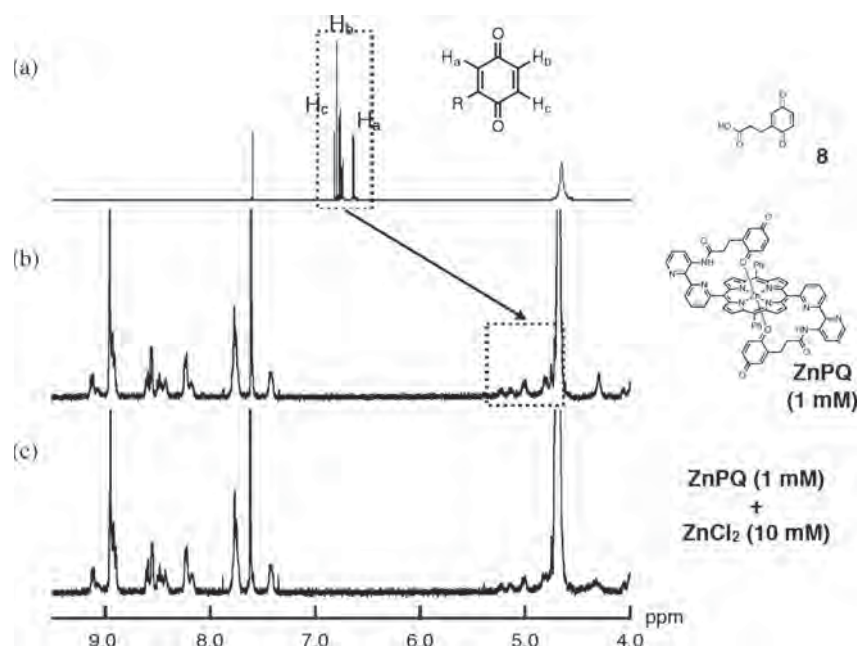
**A Zn<sup>2+</sup> complex of 7 (Zn-7).** A mixture of 5,15-Bis[4'-[N-(*trans*-4-(*tert*-butoxycarbonylamino)-cyclohexyl)-carbamoyl]-[2,2']-bipyridin-6-yl]-10,20-diphenylporphyrin **7** (38 mg, 31  $\mu$ mol), Zn(OAc)<sub>2</sub> (6.6 mg, 36  $\mu$ mol), CHCl<sub>3</sub> (5 mL), and MeOH (1 mL) was stirred for 21.5 h at room temperature. Additional amount of Zn(OAc)<sub>2</sub> (1.6 mg, 8.8  $\mu$ mol) was added and the solution was stirred for 18 h. After the solvents were evaporated, the residue was dissolved in CHCl<sub>3</sub> (100 mL). The solution was washed with saturated aqueous NaHCO<sub>3</sub> (100 mL) and water (100 mL), dried over Na<sub>2</sub>SO<sub>4</sub>, filtered, and concentrated under reduced pressure. The crude solid was purified by silica gel column chromatography (2 cm  $\phi$   $\times$  18 cm, CHCl<sub>3</sub>:acetone = 9:1) to give the title compound as a violet solid. Yield 28 mg (68%). <sup>1</sup>H NMR (400 MHz; CDCl<sub>3</sub>:DMSO-*d*<sub>6</sub> = 1:1; TMS):  $\delta_{\text{H}}$ , ppm 8.89–8.86 (m, 12H), 8.70 (br, 1H), 8.38–8.33 (m, 6H), 8.22–8.20 (m, 4H), 7.81–7.77 (m, 8H), 6.24 (br, 2H), 3.57 (br, 2H), 1.68 (br, 8H), 1.32 (s, 18H), 1.19–1.08 (m, 8H). IR (ATR/ZnSe): 3307, 2936,

1889, 1641. MS (ESI-TOF):  $m/z$  1313.5 (calcd. for [M + Na]<sup>+</sup>). Found 1313.9. Anal. calcd. for C<sub>76</sub>H<sub>72</sub>N<sub>12</sub>O<sub>6</sub>Zn (Zn-7): C, 69.42; H, 5.52; N, 12.78. Found C, 69.46; H, 5.58; N, 12.94.

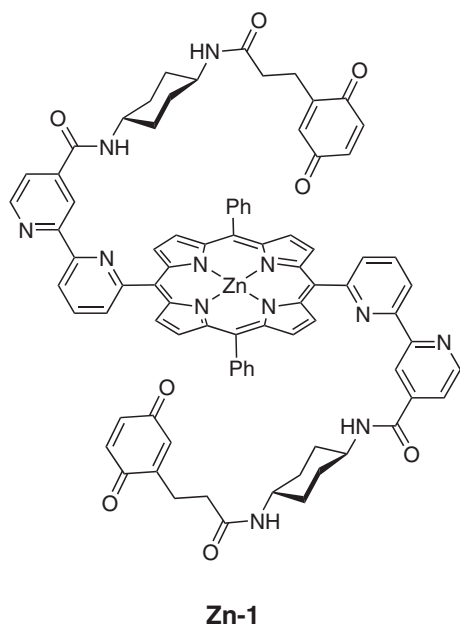
## RESULTS AND DISCUSSION

### <sup>1</sup>H NMR study of ZnPQ

We first attempted to observe the conformational change of a quinone-appended Zn<sup>2+</sup> porphyrin **ZnPQ** in the presence of Zn<sup>2+</sup> ion, which is expected to bind to bipyridine connectors. **ZnPQ** showed simple <sup>1</sup>H NMR signals in CDCl<sub>3</sub> (Fig. S1 in the Supporting information), all of which can be assignable to those of one C<sub>2</sub>-symmetrical complex (Fig. 2) expected from the crystal structure [15]. However, we decided to investigate the effect of additive Zn<sup>2+</sup> ion in a 1:1 mixture of CDCl<sub>3</sub> and MeOH-*d*<sub>4</sub> (v/v) because of the solubility of ZnCl<sub>2</sub>. Figure 3 shows the comparison of the <sup>1</sup>H NMR spectra of 3-(*p*-benzoquinone-3-yl)propionic acid **8**, **ZnPQ** (1 mM) with no additive Zn<sup>2+</sup> ion, and **ZnPQ** (1 mM) in the presence of 10 mM ZnCl<sub>2</sub> at 20 °C. **ZnPQ** in the mixed solvent showed rather complex <sup>1</sup>H NMR spectra. This is probably because of the existence of conformational isomers mainly due to the rotation of the bipyridine unit at the *meso* positions of the Zn<sup>2+</sup>-porphyrin center (*cis*- and *trans*-isomers as shown in Fig. S2 in the Supporting information). We assume that the coordination bonds between an oxygen on the quinones and Zn<sup>2+</sup> ions were weakened in the solution containing MeOH which can potentially coordinate to the Zn<sup>2+</sup> center, allowing the bipyridine units to rotate at the *meso* positions. In spite of these isomers, comparison of the <sup>1</sup>H NMR showed that three aromatic protons of the benzoquinone ring of **ZnPQ** (H<sub>a</sub>, H<sub>b</sub>, and H<sub>c</sub>, see Fig. 3a) showed significant upfield shifts compared to those of quinone unit **8** (Figs 3a and 3b), implying that the quinone moieties of **ZnPQ** also locate in the shielded region of the porphyrin ring in this solvent system. Upon addition of ZnCl<sub>2</sub> to the solution of **ZnPQ**, no apparent shifts of the <sup>1</sup>H NMR signals were observed at room temperature (Figs 3b and 3c) as well as at refluxing temperature for two days. Moreover, Zn(OAc)<sub>2</sub>, HgCl<sub>2</sub>, and Pd(OAc)<sub>2</sub> did not affect the signals. These results apparently indicate that metal ions did not coordinate to the bipyridine units. As suggested by the results of single crystal X-ray structural analysis and <sup>1</sup>H NMR study, the bipyridine units of **ZnPQ** contains strong intramolecular hydrogen bonds between the amido-NH protons at the C6 position of the outer pyridine rings and the N1' nitrogens of the inner pyridine rings (highlighted by dashed squares in Fig. 2) [15]. Presumably, these hydrogen bonds prevent the bipyridine units to coordinate to the metal ions in chelate fashion.



**Fig. 3.** Comparison of the partial  $^1\text{H}$  NMR spectra of (a) 3-(*p*-benzoquinone-3-yl)propionic acid **8**, (b) a quinone-appended Zn $^{2+}$ -porphyrin **ZnPQ** (1 mM) with no additive Zn $^{2+}$  ion, and (c) **ZnPQ** in the presence of 10 mM ZnCl $_2$  in a 1:1 mixture of CDCl $_3$  and MeOH- $d_4$  (v/v) at 20 °C



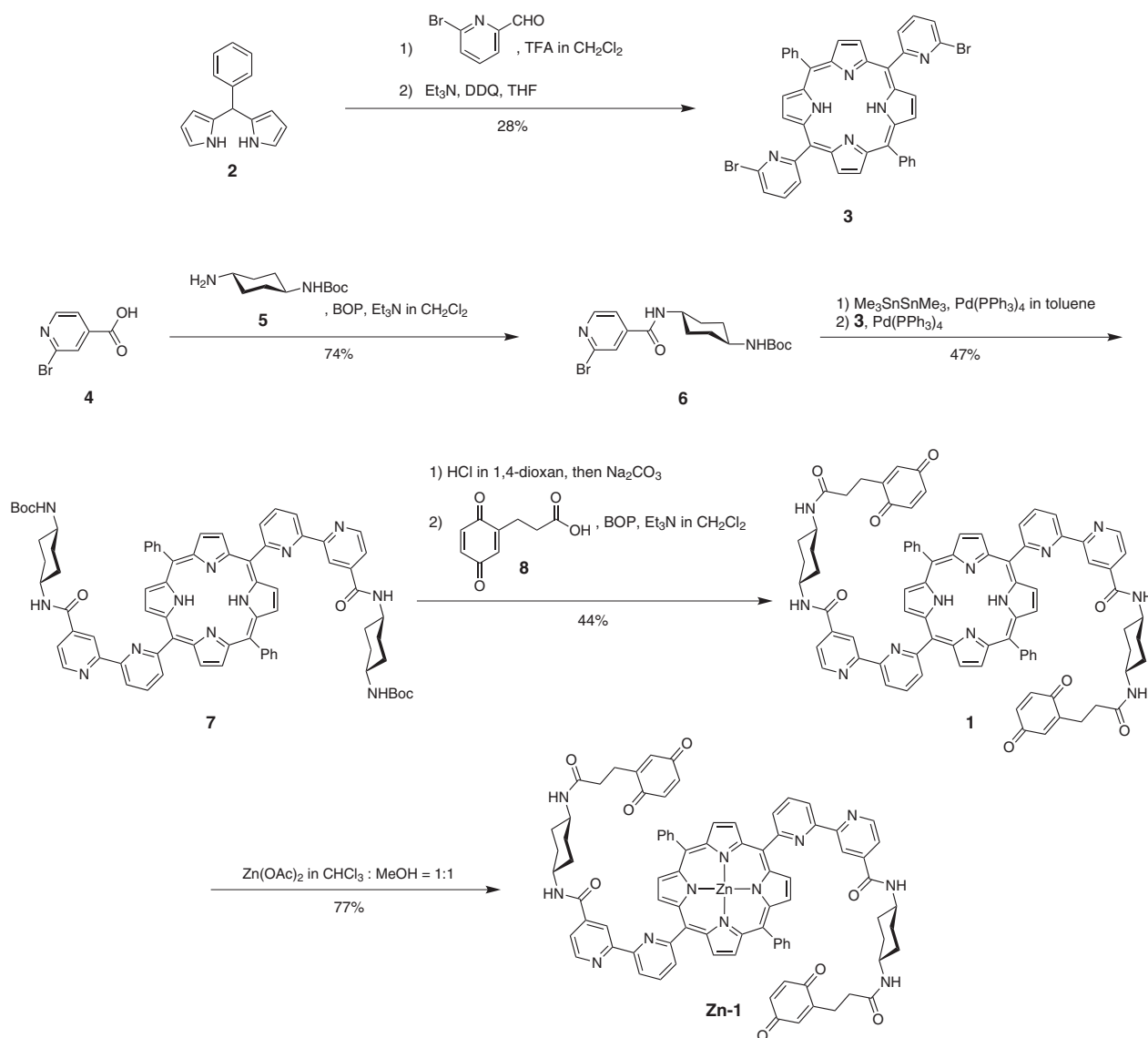
**Fig. 4.** Chemical structure of a quinone-sandwiched Zn $^{2+}$ -porphyrin **Zn-1**

### Design and synthesis of a quinone-appended Zn $^{2+}$ -porphyrin (**Zn-1**)

Taking the results of  $^1\text{H}$  NMR study on **ZnPQ** into consideration, we decided to synthesize a novel quinone-appended Zn $^{2+}$ -porphyrin **Zn-1** possessing a different-type of bipyridine linker as shown in Fig. 4. Compared

to **ZnPQ**, quinone moieties of **Zn-1** are connected at the C5'-positions of the outer pyridyl rings of the bipyridine units through rigid *trans*-bis(1,4-acylamino) cyclohexane moieties whose amide NH protons seem to be hard to form hydrogen bonds with the pyridine units. The molecular model generated by SCIGRESS software indicated that quinone moieties of **Zn-1** could coordinate to the Zn $^{2+}$ -porphyrin center in the folded structure, where the two pyridine rings of the bipyridine moieties become almost *trans*-planar conformation as depicted in Fig. S3 in the Supporting information. We expected that the fluorescence intensity of **Zn-1** would be increased by increase of the distances between Zn $^{2+}$ -porphyrin and quinone units through the conformational change into the expanded form.

**Zn-1** was synthesized according to Scheme 1. The structure of **Zn-1** was constructed based on the *trans*-A $_2$ B $_2$ -type porphyrin **3**, which was prepared by the condensation of 2-bromopyridine-6-carboxaldehyde and 5-phenyl dippyromethane **2** in the presence of TFA, followed by oxidation by DDQ as reported previously [15]. On the other hand, 2-bromoisonicotinic acid **4** was condensed with *trans*-4-((*tert*-butoxycarbonyl)amino)cyclohexyl-1-amine **5** by using (benzotriazol-1-yloxy)-tris(dimethylamino)phosphonium hexafluorophosphate (BOP) as a coupling reagent to afford the linker unit **6**. Bipyridine units of **Zn-1** was constructed by Stille coupling reaction based on the procedure reported by Lehn *et al.* [12] First, **6** was stannylated by Pd-mediated coupling reaction with hexamethylditin, followed by condensation with a porphyrin moiety **3** in toluene using



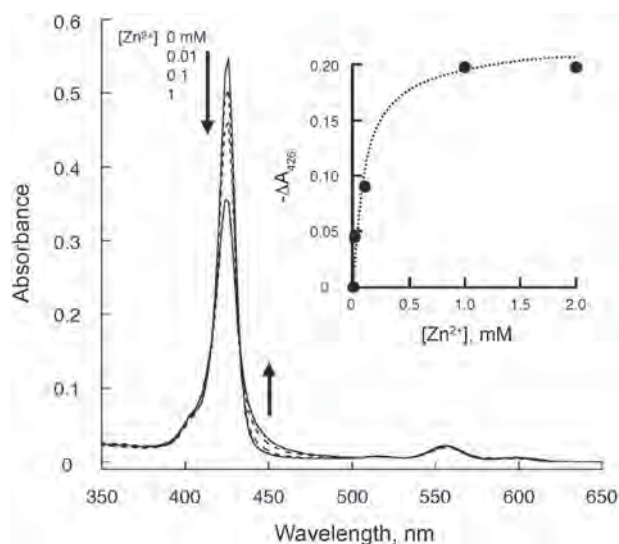
**Scheme 1.** Synthesis of a quinone-appended  $Zn^{2+}$ -porphyrin **Zn-1**

$Pd(PPh_3)_4$  as a catalyst to give **7** containing two bipyridine moieties in a moderate yield (47% in two steps). To construct **7**, we also attempted a Stille coupling reaction between **4** and **5**, 15-diphenyl-10,20-bis(trimethylstannyl) porphyrin generated by trimethylstannylation of **3**. However, the desired compound **7** was not obtained because the trimethylstannylation by hexamethylditin did not proceed successfully. After removal of Boc protective group of the peripheral amine moieties of **7**, quinone units were introduced through amide bond formation with **8** using BOP as a coupling reagent to give a quinone-appended porphyrin **1** in 44% yield in two steps. Finally, we introduced a  $Zn^{2+}$  ion into the porphyrin center to afford the desired  $Zn^{2+}$  complex **Zn-1**. Although **Zn-1** has three different metal coordination sites, namely, a porphyrin center and two peripheral bipyridine units, condensation with just one equivalent of  $Zn^{2+}$  ion against

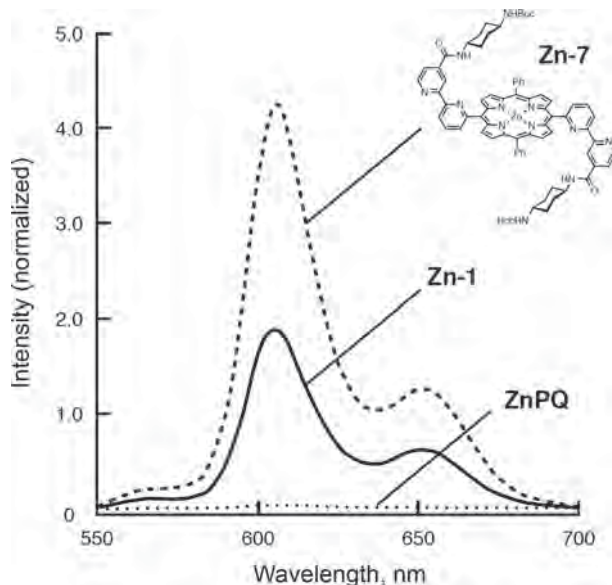
**Zn-1** allowed us to introduce a  $Zn^{2+}$  ion into the porphyrin center to afford **Zn-1** in 77% yield. **Zn-1** was identified by  $^1H$  NMR, ESI-TOF MS. Especially diagnostic is the disappearance of the pyrrolic NH proton of the porphyrin unit after introduction of  $Zn^{2+}$  ion (see Experimental Section).

#### UV-vis spectrometric and fluorescence titration of a quinone-appended $Zn^{2+}$ -porphyrin **Zn-1**

UV-vis titration was performed in a mixture of CHCl3 and MeOH (1:1 (v/v)) at 20 °C. A quinone-appended  $Zn^{2+}$ -porphyrin **Zn-1** has the absorption maximum at 428 nm corresponding to the Soret band of  $Zn^{2+}$ -porphyrin and other absorptions at 558 nm and 599 nm corresponding to the Q-bands of the  $Zn^{2+}$ -porphyrin, as indicated in Fig. 5. Upon addition of  $Zn^{2+}$ , the intensity of the Soret band was



**Fig. 5.** Absorption spectra of a quinone-appended  $\text{Zn}^{2+}$ -porphyrin **Zn-1** in the presence of increasing amount of  $\text{ZnCl}_2$  in a mixture of  $\text{CHCl}_3$ : $\text{MeOH} = 1:1$  (v/v) at  $20^\circ\text{C}$ .  $[\text{Zn-1}] = 1.0 \mu\text{M}$ . Inset: A plot of  $-\Delta A_{425}$  vs.  $[\text{Zn}^{2+}]$



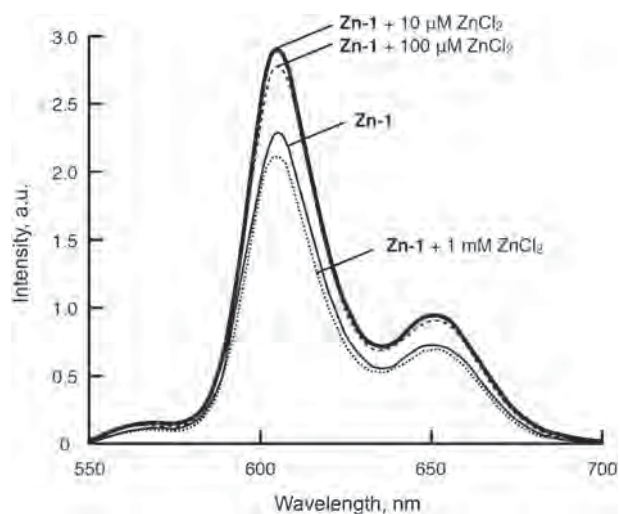
**Fig. 6.** Fluorescence spectra of a quinone-appended  $\text{Zn}^{2+}$ -porphyrins **Zn-1** (solid line) and **ZnPQ** (dotted line) and a quinone-free  $\text{Zn}^{2+}$ -porphyrin **Zn-7** (dash line) in a mixture of  $\text{CHCl}_3$ : $\text{MeOH}$  (1:1 (v/v)) at  $20^\circ\text{C}$ .  $\lambda_{\text{ex}} = 425 \text{ nm}$ . These spectra were normalized based on the absorbance at 425 nm.  $[\text{Zn-1}] = [\text{Zn-PQ}] = [\text{Zn-7}] = 1.0 \mu\text{M}$

gradually lowered without apparent shift of the absorption maximum as shown in the inset of Fig. 5, while Q-bands were almost unchanged. This spectral change was caused by coordination of  $\text{Zn}^{2+}$  ions to the two bipyridine units followed by the structural expansion. After addition of up to 1 mM of  $\text{Zn}^{2+}$  ion against the  $1.0 \mu\text{M}$  of **Zn-1**, the spectral change was almost saturated. Although the

spectral change includes the two complexation steps, which are hard to separate, between the bipyridine units and  $\text{Zn}^{2+}$  ions, the association constant of at least one of them can be expected to be in the order of  $10^3$  (inset of Fig. 4).

Fluorescence studies for **Zn-1**, **ZnPQ**, and a reference compound **Zn-7** which does not contain quinone moieties were performed in a mixture of  $\text{CHCl}_3$  and  $\text{MeOH}$  (1:1 (v/v)) at  $20^\circ\text{C}$ . As shown in Fig. 6, **Zn-1** showed fluorescence characteristic of the  $\text{Zn}^{2+}$ -porphyrin with two emission maxima (606 and 650 nm) by excitation at 425 nm. The fluorescence emission of **Zn-1** was smaller than that of quinone-free  $\text{Zn}^{2+}$ -porphyrin **Zn-7**, implying that the quinone units act as quenchers *via* electron transfer. Moreover, **ZnPQ**, in which quinone moieties directly coordinate to the  $\text{Zn}^{2+}$  center, showed more efficient quenching, compared to **Zn-1**. These results clearly indicate that the distance between the quinone quenchers and the  $\text{Zn}^{2+}$ -porphyrin fluorophore is the key to control the quenching of the fluorescence.

Fluorescence titration of **Zn-1** in the presence of increasing amount of  $\text{Zn}^{2+}$  was carried out as shown in Fig. 7. In accordance with an increase of the concentration of  $\text{Zn}^{2+}$  ion, the fluorescence intensities at 606 and 650 nm were gradually decreased. After addition of  $10 \mu\text{M}$  of  $\text{Zn}^{2+}$  against  $1 \mu\text{M}$  of **Zn-1**, the intensity was reached to approximately 1.3 times larger than that in the absence of  $\text{Zn}^{2+}$  ion. We assumed that the increase in the fluorescence intensity of **Zn-1** after addition of  $\text{Zn}^{2+}$  ion is due to the conformational change of the peripheral bipyridine unit *via* complexation with  $\text{Zn}^{2+}$ , causing the increase of the distance between  $\text{Zn}^{2+}$ -porphyrin center



**Fig. 7.** Fluorescence spectra of a quinone-appended  $\text{Zn}^{2+}$ -porphyrin **Zn-1** (solid line) in the presence of increasing amount of  $\text{ZnCl}_2$  in a mixture of  $\text{CHCl}_3$ : $\text{MeOH}$  (1:1 (v/v)) at  $20^\circ\text{C}$ .  $\lambda_{\text{ex}} = 425 \text{ nm}$ .  $[\text{Zn-1}] = 1.0 \mu\text{M}$ . **Zn-1** showed almost identical absorbance at 425 nm in the presence of increasing amount of  $\text{ZnCl}_2$



and the quinone moieties to result in the suppression of the electron transfer from Zn<sup>2+</sup>-porphyrin to quinone moieties. Upon the titration of ZnCl<sub>2</sub>, the <sup>1</sup>H NMR signals of the quinone moieties on **Zn-1** shifted to downfield, although the signals became rather complex after addition of ZnCl<sub>2</sub>. This indicates that the peripheral quinone moieties got away from the shielded region of the central porphyrin as a result of complexation of the peripheral bipyridine units with Zn<sup>2+</sup> ions in spite of generation of some conformational isomers of the peripheral sidechains (Fig. S4 in the Supporting information). Addition of more than 10 μM of Zn<sup>2+</sup> ions gradually decreased the fluorescence intensity, which became smaller than that in the absence of ZnCl<sub>2</sub> after addition of 1 mM of ZnCl<sub>2</sub>. This is probably because of the quenching of fluorescence by heavy metal effect of the excess amount of Zn<sup>2+</sup> ion.

## CONCLUSION

In conclusion, we synthesized a Zn<sup>2+</sup>-porphyrin **Zn-1** possessing two peripheral quinone moieties at the *trans-meso* positions, in which porphyrin and quinones are bridged by bipyridine linkers. This quinone-appended Zn<sup>2+</sup>-porphyrin was designed to form a sandwich-type folded structure which promotes donor–acceptor interaction between Zn<sup>2+</sup>-porphyrin and two peripheral quinones to afford quenching of the fluorescence of Zn<sup>2+</sup>-porphyrin unit. It was revealed that the fluorescence of the Zn<sup>2+</sup>-porphyrin center of **Zn-1** was significantly quenched compared to that of a quinone-free Zn<sup>2+</sup>-porphyrin **Zn-7**. As we expected, complexation of the peripheral bipyridine units of **Zn-1** with Zn<sup>2+</sup> ions induced the recovery of fluorescence intensity, which is presumably because the distances between the Zn<sup>2+</sup>-porphyrin center and quinone moieties were increased *via* conformational change of the bipyridine linker by metal complexation. Thus, it was demonstrated that proper molecular design of the Zn<sup>2+</sup>-porphyrin with folded structure can produce the supramolecular machine whose fluorescence intensity can be switched by metal complexation. This system has a potential to be mechanical switching devices or molecular sensors.

## Acknowledgements

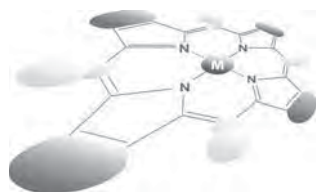
This work was financially supported by Grant-in-Aids for Scientific Research on Innovative Areas “Coordination Programming” (area 2107, No. 21108012) to K.T. from the Ministry of Education, Culture, Sports, Science, and Technology, Japan.

## Supporting information

Figures S1–S4 are given in the supplementary material. This material is available free of charge *via* the Internet at <http://www.worldscinet.com/jpp/jpp.shtml>.

## REFERENCES

1. Sauvage J-P and Gaspard P. *From Non-Covalent Assemblies to Molecular Machines*, Wiley-VCH: Weinheim, 2011.
2. Feringa B. *Molecular Switches*, Wiley-VCH: Weinheim, 2001.
3. Bruns CJ and Stoddart JF. *Acc. Chem Res.* 2014; **47**: 2186–2199.
4. Li H, Fahrenbach AC, Coskun A, Zhu Z, Barin G, Zhao Y-L, Rotros YY, Sauvage J-P and Stoddart JF. *Angew. Chem. Int. Ed.* 2011; **50**: 6782–6788.
5. Lohmann F, Ackermann D and Famulok M. *J. Am. Chem. Soc.* 2012; **134**: 11884–11887.
6. Fahrenbach AC, Zhu Z, Cao D, Liu W-G, Li H, Dey SK, Basu S, Trabolsi A, Botros YY, Goddard III WA and Stoddart JF. *J. Am. Chem. Soc.* 2012; **134**: 16275–16288.
7. Andersen SS, Share AI, Poulsen BLC, Kørner M, Duedal T, Benson CR, Hansen SW, Jeppesen JO and Flood AH. *J. Am. Chem. Soc.* 2014; **136**: 6373–6384.
8. Grunder S, McGrier PL, Whalley AC, Boyle MM, Stern C and Stoddart JF. *J. Am. Chem. Soc.* 2013; **135**: 17691–17694.
9. Clavel C, Romuald C, Brabet E and Coutrot F. *Chem. Eur. J.* 2013; **19**: 2982–2989.
10. Huang Y-L, Hung W-C, Lai C-C, Liu Y-H, Peng S-M and Chiu S-H. *Angew. Chem. Int. Ed.* 2007; **46**: 6629–6633.
11. Rebek Jr. J, Trend JE, Wattley RV and Chakravorti S. *J. Am. Chem. Soc.* 1979; **101**: 4333–4337.
12. Linke-Schaetzel M, Anson CE, Powell AK, Buth G, Palomares E, Durrant JD, Balaban TS and Lehn J-M. *Chem. Eur. J.* 2006; **12**: 1931–1940.
13. Petitjean A, Khoury RG, Kyritsakas N and Lehn J-M. *J. Am. Chem. Soc.* 2004; **126**: 6637–6647.
14. Barboju M, Prodi L, Montalti M, Zaccheroni N, Kyritsakas N and Lehn J-M. *Chem. Eur. J.* 2004; **10**: 2953–2959.
15. Yamada Y and Tanaka K. *J. Inorg. Organomet. Polym.* 2013; **23**: 180–185.
16. Ducruet AP, Rice RL, Tamura K, Yokokawa F, Yokokawa S, Wipf P and Lazo JS. *Bioorg. Med. Chem.* 2000; **8**: 1451–1466.
17. Epiert M, Maichle-Mössmer C and Maier ME. *J. Org. Chem.* 2002; **67**: 8692–8695.



## Reactions of a heme-superoxo complex toward a cuprous chelate and $\bullet\text{NO}_{(g)}$ : CcO and NOD chemistry

Savita K. Sharma, Patrick J. Rogler and Kenneth D. Karlin<sup>\*◇</sup>

Department of Chemistry, Johns Hopkins University, Baltimore, MD 21218, USA

Dedicated to Professor Shunichi Fukuzumi on the occasion of his retirement

Received 18 November 2014

Accepted 13 December 2014

**ABSTRACT:** Following up on the characterization of a new (heme)Fe<sup>III</sup>-superoxide species formed from the cryogenic oxygenation of a ferrous-heme (P<sup>Py</sup>)Fe<sup>II</sup> (**1**) (P<sup>Py</sup> = a tetraarylporphyrinate with a covalently tethered pyridine group as a potential axial base), giving (P<sup>Py</sup>)Fe<sup>III</sup>-O<sub>2</sub><sup>-</sup> (**2**) (Li Y *et al.*, *Polyhedron* 2013; **58**: 60–64), we report here on (i) its use in forming a cytochrome *c* oxidase (CcO) model compound, or (ii) in a reaction with nitrogen monoxide ( $\bullet\text{NO}$ ; nitric oxide) to mimic nitric oxide dioxygenase (NOD) chemistry. Reaction of (**2**) with the cuprous chelate [Cu<sup>I</sup>(AN)][B(C<sub>6</sub>F<sub>5</sub>)<sub>4</sub>] (AN = bis[3-(dimethylamino)propyl]amine) gives a *meta*-stable product [(P<sup>Py</sup>)Fe<sup>III</sup>-(O<sub>2</sub><sup>-</sup>)-Cu<sup>II</sup>(AN)][B(C<sub>6</sub>F<sub>5</sub>)<sub>4</sub>] (**3a**), possessing a high-spin iron(III) and Cu(II) side-on bridged peroxo moiety with a  $\mu$ - $\eta^2$ : $\eta^2$ -binding motif. This complex thermally decays to a corresponding  $\mu$ -oxo complex [(P<sup>Py</sup>)Fe<sup>III</sup>-(O<sup>2-</sup>)-Cu<sup>II</sup>(AN)][B(C<sub>6</sub>F<sub>5</sub>)<sub>4</sub>] (**3**). Both (**3**) and (**3a**) have been characterized by UV-vis, <sup>2</sup>H NMR and EPR spectroscopies. When (**2**) is exposed to  $\bullet\text{NO}_{(g)}$ , a ferric heme nitrate compound forms; if 2,4-di-*tert*-butylphenol is added prior to  $\bullet\text{NO}_{(g)}$  exposure, phenol *ortho*-nitration occurs with the iron product being the ferric hydroxide complex (P<sup>Py</sup>)Fe<sup>III</sup>(OH) (**5**). The latter reactions mimic the action of NOD's.

**KEYWORDS:** heme-superoxo, high spin heme-copper peroxo, heme-copper- $\mu$ -oxo, peroxy nitrite, nitrate.

## INTRODUCTION

Metalloenzymes form an essential component of the various biological and physiological functions that are essential for life [1]. Hemoproteins are perhaps the best-known class of metalloenzymes, and their reactions with dioxygen are foundational to aerobic life. These proteins are critical to dioxygen storage and transport (myoglobin and hemoglobin) [2], substrate oxygenation (cytochrome P-450 family), as well as dioxygenation [3] and peroxidation [4]. Heme-copper proteins are critical to cellular respiration (*e.g.* in cytochrome *c* oxidase). Nitric oxide is biosynthesized and interacts with hemoproteins as part for this molecule's involvement in inflammatory responses, cellular signaling, and vasodilation. Nitric

oxide dioxygenase (NOD) [5] and nitric oxide reductase (NOR) [6] enable cellular NO regulation/removal when it is present in excess.

It has been shown that CcO functionality is inhibited in the presence of NO [7, 8] *via* competition with O<sub>2</sub> for binding at the binuclear center. Under certain physiological conditions the NO concentration *in vivo* can reach levels that significantly affect the reaction rate of CcO [9]. To compensate, myoglobin (Mb) and/or hemoglobin (Hb) play a major role in scavenging  $\bullet\text{NO}$ , helping to keep respiratory homeostasis. This maintains the proton gradient over the mitochondrial inner membrane, driving ATP synthesis. When  $\bullet\text{NO}$  is overproduced *in vivo* as a component of inflammatory response, reactive nitrogen species (RNS) can be formed by the reaction of NO with reactive oxygen species (ROS) such as superoxide, to generate a peroxy nitrite (O=NOO<sup>-</sup>). Peroxy nitrite [10, 11] is a strong oxidant and nitrating

<sup>◇</sup> SPP full member in good standing

\*Correspondence to: Kenneth D. Karlin, email: karlin@jhu.edu

agent, and reacts with a number of biological substrates such as thiols [12], tyrosine residues [13], lipids,  $\text{CO}_2$ , DNA [14–16] and metalloproteins [17]. Hence,  $\bullet\text{NO}$  and peroxynitrite scavenging by Hb/Mb, is critical not only to respiration, but also for the mitigation of oxidative damage *via* NOD activity [18, 19].

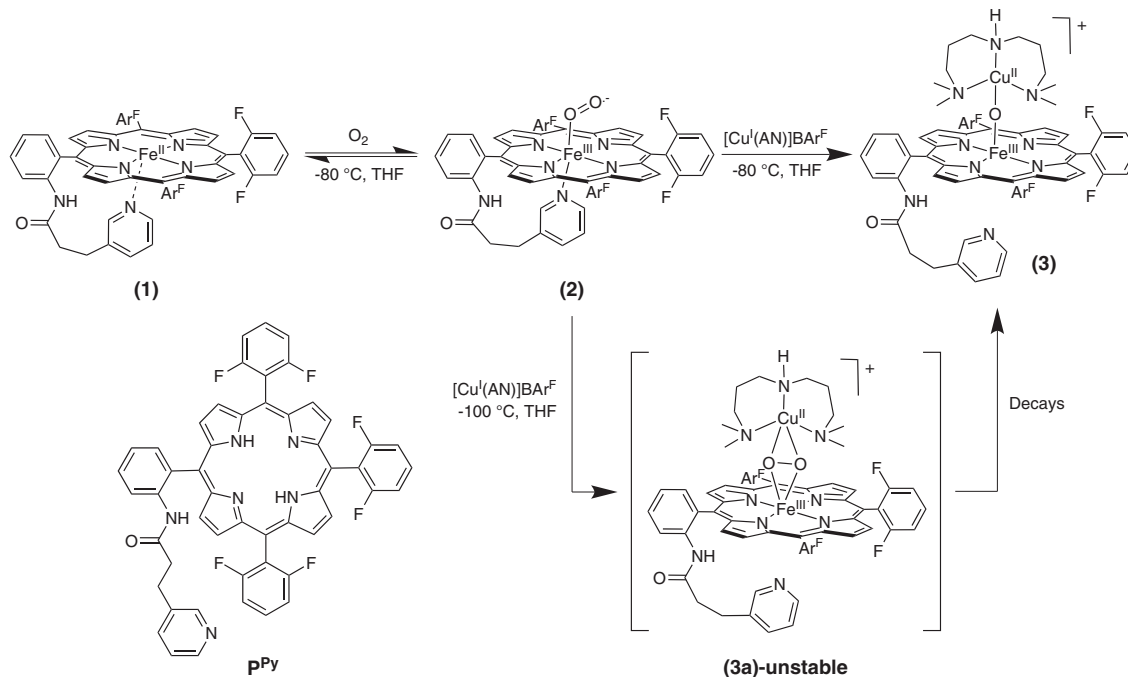
Our own research group is particularly interested in providing basic coordination chemistry insights into the possible reactive intermediates formed during CcO turnover by using synthetic functional models [20–24]. CcO is responsible for the reduction of  $\text{O}_2$  to water as a terminal step of the respiratory chain of mitochondria and many aerobic bacteria [25–27]. A ferric superoxo species is the most well studied dioxygen intermediate generated upon initial  $\text{O}_2$ -reaction with the fully reduced active-site heme Fe(II)–Cu(I) center [28]. This species forms prior to O–O bond cleavage and as such has attracted considerable interest [29–31]. Here, we describe the reactivity of an iron(III)-superoxo species (**2**) towards (i) a cuprous-chelated complex  $[\text{Cu}^{\text{I}}(\text{AN})][\text{B}(\text{C}_6\text{F}_5)_4]$  and (ii)  $\bullet\text{NO}$ , these reactions representing synthetic functional models for CcO and NOD, respectively.

## RESULTS AND DISCUSSION

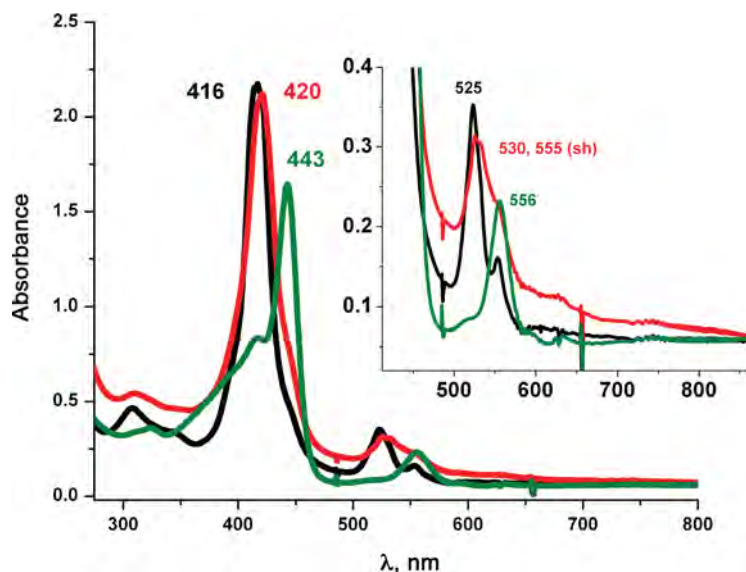
### Reactivity of the iron(III)-superoxo complex (**2**) towards $[\text{Cu}^{\text{I}}(\text{AN})][\text{B}(\text{C}_6\text{F}_5)_4]$

Earlier work in our group [31] described the synthesis and characterization of  $(\text{P}^{\text{Py}})\text{Fe}^{\text{II}}$  (**1**) [ $\text{P}^{\text{Py}}$ ] = pyridyl tailed

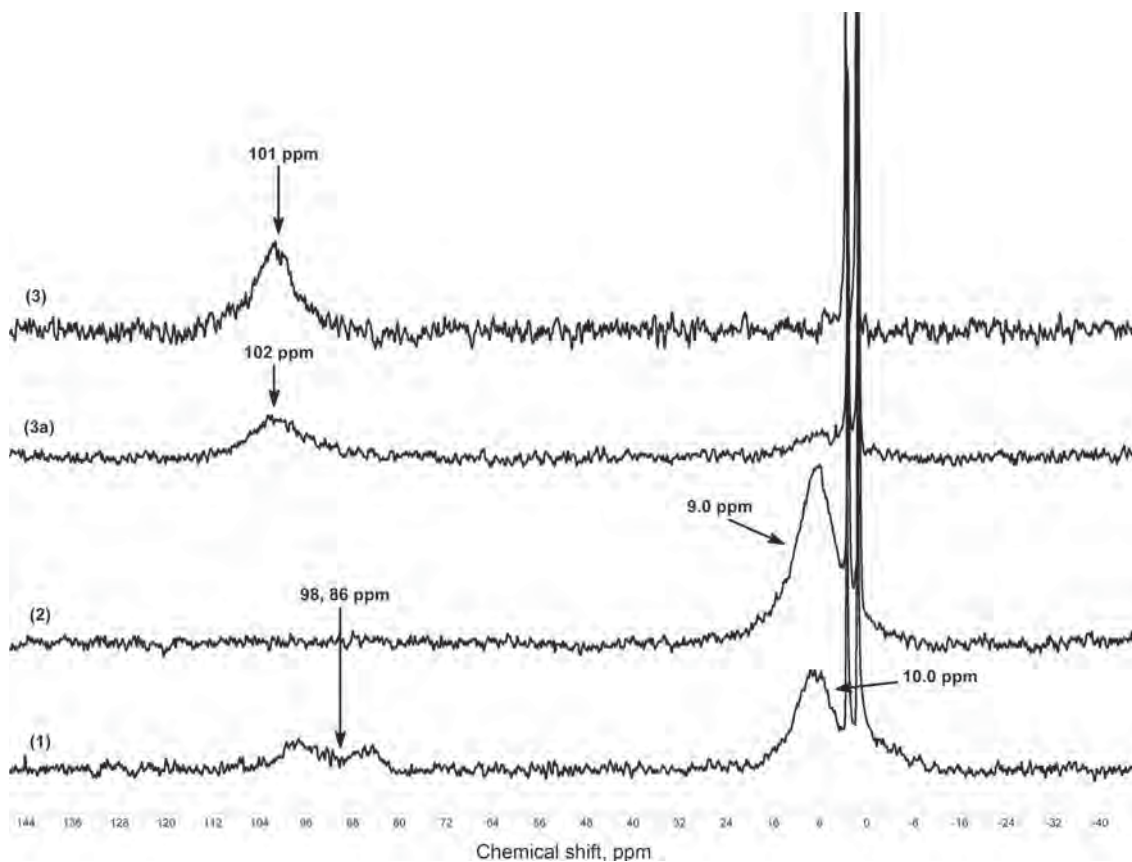
porphyrinate (2-)] ( $\lambda_{\text{max}} = 416, 525, 554$  (sh) nm) which reacts reversibly with dioxygen to give a diamagnetic iron(III)-superoxo species  $(\text{P}^{\text{Py}})\text{Fe}^{\text{III}}(\text{O}_2^{\bullet-})$  (**2**) (UV-vis,  $\lambda_{\text{max}} = 419, 535$  nm; EPR, silent). This is stable in solution below  $-30^\circ\text{C}$  in coordinating solvents such as tetrahydrofuran (THF), acetone, or acetonitrile as well as in non-coordinating solvents like dichloromethane (DCM). The use of copper ion complexes with tridentate alkylamino ligand AN has previously been useful [23, 32–34] and as such this copper chelate was employed here. Addition of one equivalent of  $[\text{Cu}^{\text{I}}(\text{AN})][\text{B}(\text{C}_6\text{F}_5)_4]$  (Scheme 1) to the superoxo compound (**2**) in THF at  $-100^\circ\text{C}$ , monitored by UV-vis spectroscopy, leads to the immediate formation of a heme-copper- $\text{O}_2$  adduct (**3a**) [ $\lambda_{\text{max}} = 420, 530, 555$  (sh) nm], see Fig. 1. The UV-vis spectrum of (**3a**) is very similar to our previously described high-spin  $[(\text{heme})\text{Fe}^{\text{III}}(\text{O}_2^2-)\text{Cu}^{\text{II}}(\text{L})]^+$  species where L is a tri- or tetradentate alkylamino or pyridylalkylamino ligand; these possess a side-on binding of peroxide to both metal ions, as depicted in Scheme 1 [35–37]. Thermal decomposition of (**3a**) leads to the formation of complex (**3**) with a red shifted Soret band at 443 nm and Q-band at 556 nm (Fig. 1). These are characteristic features for  $\mu$ -oxo  $\text{Fe}^{\text{III}}\text{-O-Cu}^{\text{II}}$  like species, such as the previously structurally and spectroscopically characterized complex  $[(\text{F}_8)\text{Fe}^{\text{III}}(\text{O}^2-)\text{Cu}^{\text{II}}(\text{TMPA})]^+$  [38] (TMPA = tris(2-pyridylmethyl)amine). Complex (**3**) can also be obtained by direct bubbling of dioxygen to a 1:1 mixture of  $(\text{P}^{\text{Py}})\text{Fe}^{\text{II}}$  (**1**) and  $[\text{Cu}^{\text{I}}(\text{AN})][\text{B}(\text{C}_6\text{F}_5)_4]$  at  $-80^\circ\text{C}$  in THF. The  $\mu$ -oxo complex  $[(\text{P}^{\text{Py}})\text{Fe}^{\text{III}}(\text{O}^2-)\text{Cu}^{\text{II}}(\text{AN})]^+$  (**3**) (or rather a protonated  $\mu$ -hydroxo conjugate acid form),



**Scheme 1.** Formation of  $(\text{P}^{\text{Py}})\text{Fe}^{\text{III}}(\text{O}_2^{\bullet-})$  (**2**) *via* oxygenation of  $(\text{P}^{\text{Py}})\text{Fe}^{\text{II}}$  (**1**) and subsequent reaction with  $[\text{Cu}^{\text{I}}(\text{AN})]^+$  to give the *meta*-stable intermediate, the high-spin heme-peroxo-copper complex (**3a**), which decays to give the  $\mu$ -oxo complex  $[(\text{P}^{\text{Py}})\text{Fe}^{\text{III}}(\text{O}^2-)\text{Cu}^{\text{II}}(\text{AN})]^+$  (**3**)



**Fig. 1.** UV-vis spectra of (1, black) a reduced  $(P^{Py})Fe^{II} + [Cu^I(AN)]^+$  1:1 mixture; (3a, red) high spin peroxo complex  $[(P^{Py})Fe^{III}-(O_2^-)Cu^II(AN)]^+$ ; (3, green)  $\mu$ -oxo complex  $[(P^{Py})Fe^{III}-(O_2^-)-Cu^II(AN)]^+$



**Fig. 2.**  $^2H$  NMR spectra at  $-80^\circ C$  in THF (1)  $(d_8-P^{Py})Fe^{II}$ -THF, (2)  $(d_8-P^{Py})Fe^{III}-O_2^{2-}$ ; (3a)  $[(d_8-P^{Py})Fe^{III}-(O_2^-)-Cu^II(AN)]^+$  and (3)  $[(d_8-P^{Py})Fe^{III}-(O_2^-)-Cu^II(AN)]^+$

are of interest since such species derive from dioxygen reactivity, thus perhaps related to  $CcO$  reaction chemistry [39, 40].

Further characterization of  $\mu$ -oxo complex (3) was provided by low temperature  $^2H$  NMR spectroscopy of

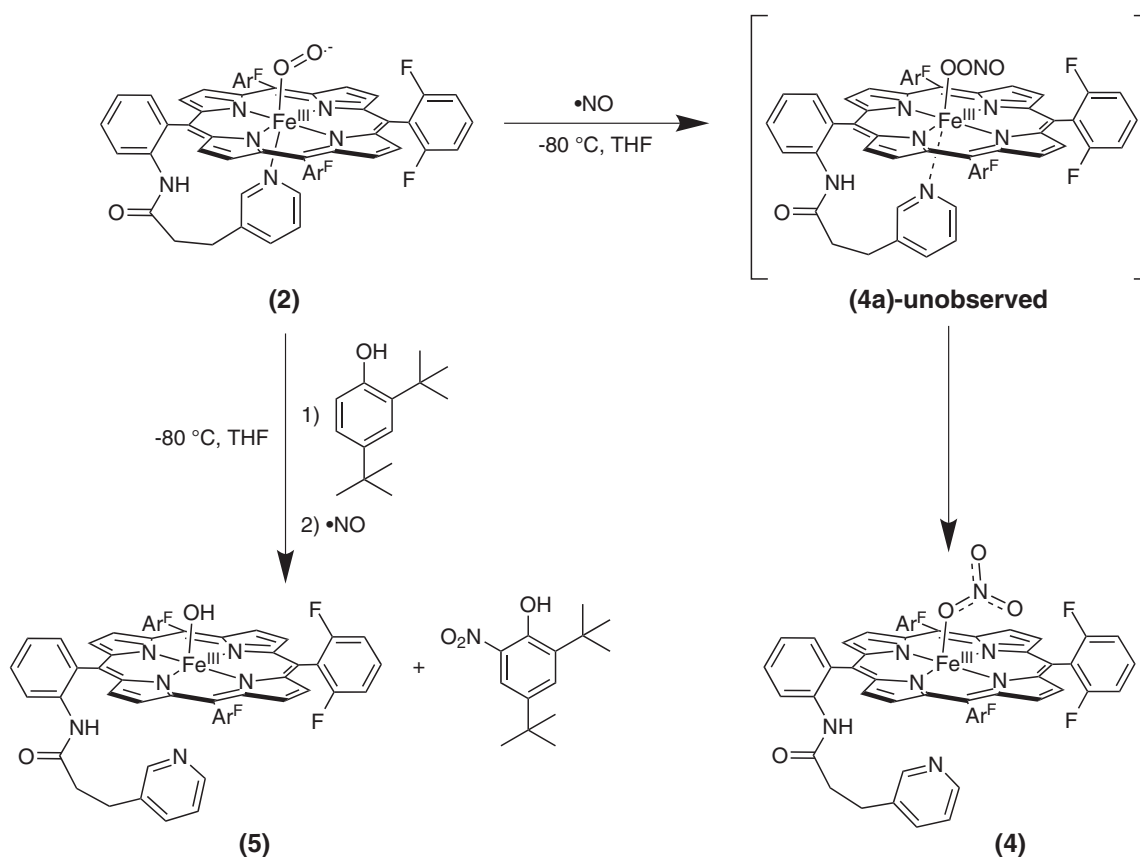
the pyrrole deuterated analogue of  $(P^{Py})Fe^{II}$  (1),  $(d_8-P^{Py})Fe^{II}$ . Figure 2 shows  $^2H$  NMR spectra of the oxygenation reaction of a  $(P^{Py})Fe^{II}$ -THF (1) exhibits a pyrrole resonance at  $\delta$  10 ppm, indicative of a low-spin ( $S = 0$ ) six-coordinate ferrous heme at low temperature, but we also

observe pyrrole resonances at  $\delta$  98 and 86 ppm, which are characteristic of a penta-coordinated high spin heme. We interpret this observed NMR spectroscopic data as indicating that complex (1) is a mixture of 6-coordinate (pyridyl + THF) low-spin iron(II) and 5 or 6-coordinate high-spin iron(II) (e.g. pyridyl arm off, THF bound, or *vice versa*, and also possibly a bis-THF ligated ferrous heme). Direct bubbling of dioxygen to (1) gives superoxo complex (2) where a pyrrole resonance occurs in the diamagnetic region, at  $\delta$  9.0 ppm. Subsequent addition of one equiv. of  $[\text{Cu}^{\text{I}}(\text{AN})]^+$  to the cold solution of superoxo complex (2) in an NMR tube leads to the formation of  $[(\text{P}^{\text{Py}})\text{Fe}^{\text{III}}(\text{O}_2^-)\text{-Cu}^{\text{II}}(\text{AN})]^+$  (3), with a downfield shifting of the pyrrole resonance to  $\delta$  102 ppm (Fig. 2), indicative of a high-spin ferric heme (also, see below). Complex (3) is stable at room temperature. We have previously reported this characteristic pattern of a downfield shifted pyrrole resonance for  $(\text{P})\text{Fe}^{\text{III}}\text{-X-Cu}^{\text{II}}$  ( $\text{X} = \text{O}_2^-$  or  $\text{O}^{2-}$ ) systems having overall  $S = 2$  spin states [37, 41–43], which arise from the antiferromagnetic coupling of the  $S = 5/2$  high-spin heme-Fe(III) center to an  $S = 1/2$  copper(II) moiety, through the bridging X ligand in (3) or (3a). When monitoring peroxo complex (3a) by  $^2\text{H}$  NMR spectroscopy, a clean thermal transformation to (3) is observed. EPR spectroscopic interrogation of (3) and

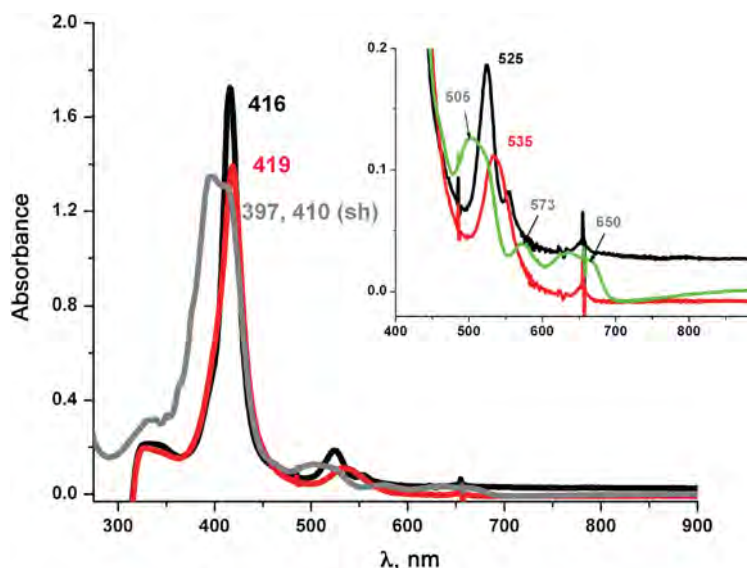
(3a) revealed that both are EPR inactive, consistent with their formulations.

### Reactivity of iron(III)-superoxo complex (2) towards $\bullet\text{NO}_{(g)}$

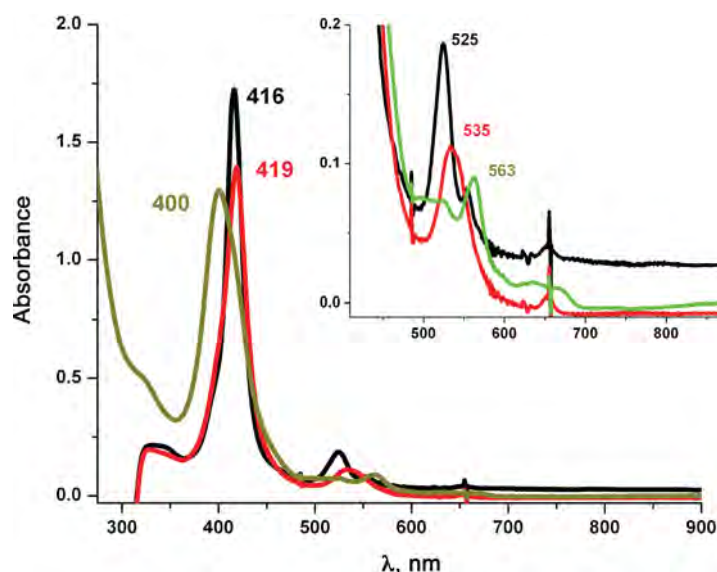
Using a gas-tight three way syringe, addition of  $\bullet\text{NO}_{(g)}$  to superoxo species  $(\text{P}^{\text{Py}})\text{Fe}^{\text{III}}(\text{O}_2^-)$  (2) at  $-80^\circ\text{C}$  in THF, as monitored by UV-vis spectroscopy, led to the immediate formation of a five-coordinate nitrato compound  $(\text{P}^{\text{Py}})\text{Fe}^{\text{III}}(\text{ONO}_2)$  (4) [UV-vis,  $\lambda_{\text{max}} = 397, 410$  (sh), 505, 573, 650 nm; EPR,  $g = 6, 14$  K, high-spin iron(III)], as indicated in Scheme 2 and with spectra shown in Fig. 3. Product (4) yields a positive test for nitrate ion, as determined using semiquantitative QUANTOFIX nitrate ( $\text{NO}_3^-$ )/nitrite ( $\text{NO}_2^-$ ) test paper; no  $\text{NO}_2^-$  ion was detected and the yield of nitrate ion was estimated to be  $> 75\%$  (see Experimental). These results are very similar to what we observed in a previous study of  $(\text{F}_8)\text{Fe}^{\text{II}}$  ( $\text{F}_8 = \text{tetrakis}(2,6\text{-difluorophenyl})\text{porphyrinate}(2-)$ ) where addition of  $\bullet\text{NO}_{(g)}$  to the superoxo complex  $(\text{F}_8)\text{Fe}^{\text{III}}(\text{O}_2^-)$ , yields a five-coordinate nitrato heme complex [44]. While no transient species were detected following addition of  $\bullet\text{NO}_{(g)}$  to (2) and isolation of (4), the formation of a nitrite complex supports the intermediacy



**Scheme 2.** Reaction sequence where  $\bullet\text{NO}_{(g)}$  is added to superoxo complex (2) to give nitrato complex (4). In the presence of a phenolic substrate, the same reaction gives (5) as a final product along with the *ortho*-nitrated phenol



**Fig. 3.** UV-vis spectra showing superoxo (**2**, red) formed from reduced ( $(P^{Py})Fe^{II}$  (**1**, black) by bubbling  $O_{2(g)}$  at  $-80^\circ C$ ; nitrate complex ( $(P^{Py})Fe^{III}-ONO_2$  (**4**, grey) generated immediately after addition of  $\bullet NO_{(g)}$



**Fig. 4.** UV-vis spectroscopy in THF at  $-80^\circ C$ . The black spectrum is reduced  $(P^{Py})Fe^{II}$  (**1**); red is (**2** + DTBP), and green is (**5**)

of a peroxyinitrite  $\cdot OON=O$  species (**4a**) which formed during the reaction (Scheme 2), indicating an NOD type of reaction mechanism (see below).

Thus, we sought chemical evidence which might support our supposition involving the formation of a peroxyinitrite species during the reaction of (**2**) with  $\bullet NO_{(g)}$ . Here, a tyrosine analog, 2,4-di-*tert*-butylphenol (DTBP), was added into the solution of superoxo complex  $(P^{Py})Fe^{III}-(O_2^{\bullet-})$  (**2**). When  $\bullet NO_{(g)}$  was subsequently added, we observed the immediate formation of  $(P^{Py})Fe^{III}(OH)$  (**5**) [ $\lambda_{max} = 400, 563$  nm] as indicated by the Q-band feature in the UV-vis spectrum (Fig. 4). We then isolated the pure  $(P^{Py})Fe^{III}(OH)$  (**5**) ( $\lambda_{max} = 410, 563$ ) from

this mixture (see Experimental). An authentic sample of  $(P^{Py})Fe^{III}(OH)$  (**5**) ( $\lambda_{max} = 412, 563$ ) was prepared (see Experimental), and has nearly identical UV-vis features as those observed for the reaction product. The UV-vis and EPR spectroscopic features observed here also closely match those known for  $(F_8)Fe^{III}(OH)$  ( $\lambda_{max} = 408, 572$  nm high-spin, EPR,  $g = 6.0$ ) [44] (Fig. 4). Workup of the reaction solution revealed that the product (**5**) forms along with high yields (>85%) of 2,4-di-*tert*-butyl-6-nitrophenol ( $NO_2$ -DTBP), as confirmed *via* gas-chromatography. This reaction mixture was also tested for the presence of any  $NO_3^-/NO_2^-$  ions and yielded a negative result for both.

These studies indicate the involvement of a heme-peroxynitrite like intermediate  $[(\text{P}^{\text{Py}})\text{Fe}^{\text{III}}\text{-OONO}]$  (**4a**), which we could not detect, but that formed when superoxo complex  $(\text{P}^{\text{Py}})\text{Fe}^{\text{III}}\text{-}(\text{O}_2^{\bullet-})$  (**2**) was reacted with  $\bullet\text{NO}_{(g)}$  (Scheme 2). There were previous reports that suggested the detection of heme-peroxynitrite species in the reaction of oxy-heme (*i.e.* ferric superoxo) with  $\bullet\text{NO}_{(g)}$ , either *via* UV-vis or EPR spectroscopy [18, 45]. However these results were refuted by Moënné-Loccoz and co-workers [46] using rapid freeze quench resonance Raman spectroscopy with Mb, which revealed that such intermediates were in fact iron-bound nitrate species formed prior to their decay to metMb. Still, the generally accepted mechanism of  $\bullet\text{NO}$  dioxygenase involves direct reaction of the  $\text{Fe}^{\text{III}}\text{-}(\text{O}_2^{\bullet-})$  oxy complex with  $\bullet\text{NO}$ , giving a peroxynitrite intermediate. Subsequent homolytic O–O bond cleavage produces an oxo-ferryl ( $\text{Fe}^{\text{IV}}\text{=O}$ ) species and the free radical nitrogen dioxide ( $\bullet\text{NO}_2$ ); the latter attacks the ferryl O-atom to produce a N–O bond, yielding nitrate [47–50]. Recent work with oxy-coboglobin models [51, 52] exhibiting NOD-like activity has led to the detection of peroxynitrite intermediates using low temperature FTIR, this work has helped to shed light onto favorable conditions for generating peroxynitrite intermediates. Also, recent work by Nam and Karlin [53] has shown an alternative method for mimicking NOD activity that is isoelectronic to the methods discussed above. In this case, NOD activity was exhibited using a nitrosonium ion added to a non-heme iron peroxo species. Following these literature precedents, we can hypothesize that (**4a**) undergoes homolysis to give a ferryl +  $\bullet\text{NO}_2$  radical, which can be captured by phenol present in solution. The ferryl would oxidize the phenol to a phenoxyl radical which will further react with  $\bullet\text{NO}_2$  to give *ortho*-nitration of the phenol and form a very stable ferric hydroxo complex (**4**), as we observed (Scheme 2).

## EXPERIMENTAL

### General

All reagents and solvents used were of commercially available analytical quality except as noted. Dioxygen was dried by passing through a short column of supported  $\text{P}_4\text{O}_{10}$  (Aquasorb, Mallinkrodt). Nitrogen monoxide ( $\bullet\text{NO}$ ) gas was obtained from Matheson Gases (High Purity Grade, Full cylinder  $\sim 500$  psig @ 70 °F) and purified as follows: it was first passed through multiple columns containing Ascarite II (Thomas Scientific) to remove higher nitrogen oxide impurities. Further purification by distillation was completed by warming frozen  $\bullet\text{NO}$  (as crystalline  $\text{N}_2\text{O}_2$ ) from 78 K in a liquid  $\text{N}_2$  cooled vacuum trap to 193 K through use of an acetone/dry-ice ( $-78^\circ\text{C}$ ) bath, and collection in a second liquid  $\text{N}_2$  cooled evacuated vacuum trap. This secondary flask

was again warmed to 193 K and the purified  $\bullet\text{NO}$  was collected in an evacuated Schlenk flask (typically 50 mL) closed with a rubber septum secured tightly by copper wire. The  $\bullet\text{NO}$  in the Schlenk flask is collected and kept at higher pressures ( $>1$  atm). Addition of  $\bullet\text{NO}$  and  $\text{O}_2$  to the metal complex solutions was accomplished using a three-way long needle syringe connected to a Schlenk line.

THF and Pentane were distilled over Na/benzophenone ketyl or calcium hydride. 2,4-di-*tert*-butylphenol (DTBP) was purchased from Sigma-Aldrich and purified by multiple recrystallizations in toluene under Ar. All other reagents were used as received.

Preparation and handling of air-sensitive compounds were performed under an argon atmosphere using standard Schlenk techniques or in an MBraun Labmaster 130 inert atmosphere ( $<1$  ppm  $\text{O}_2$ ,  $<1$  ppm  $\text{H}_2\text{O}$ ) drybox filled with nitrogen gas. Solvents were purged with Ar prior to use. All UV-vis measurements were carried out by using a Hewlett Packard 8453 diode array spectrophotometer with a 10 mm path quartz cell. The spectrometer was equipped with HP Chemstation software and a Unisoku thermostated cell holder for low temperature experiments. All NMR spectra were recorded in 7 inch, 5 mm o.d. NMR tubes. Low-temperature  $^1\text{H}$  NMR (Bruker 300 MHz spectrometer equipped with a tunable deuterium probe to enhance deuterium detection) measurements were performed at  $-80^\circ\text{C}$  under a  $\text{N}_2$  atmosphere. The  $^2\text{H}$  chemical shifts are calibrated to natural abundance deuterium solvent peaks. EPR measurements of the frozen solutions were carried out at 14K on an X-Band Bruker EMX CW EPR spectrometer controlled with a Bruker ER 041 XG microwave bridge operating at the X-band ( $\sim 9$  GHz). Gas chromatography (GC) was performed on an Agilent 6890 gas chromatograph fitted with a HP-5 (5%-phenyl)-methylpolysiloxane capillary column (30 m  $\times$  0.32 mm  $\times$  0.25 mm) and equipped with a flame-ionization detector.

### Synthesis

$(\text{P}^{\text{Py}})\text{Fe}^{\text{II}}/(\text{d}_8\text{-P}^{\text{Py}})\text{Fe}^{\text{II}}$  (**1**) and  $[\text{Cu}^{\text{I}}(\text{AN})]\text{BAR}^{\text{F}}$  were synthesized as previously described [31, 32].

#### Preparation of $^2\text{H}$ NMR and EPR samples

**In-situ generation of complexes (3a) and (3).** In a typical experiment, 0.57 mL of a  $(\text{d}_8\text{-P}^{\text{Py}})\text{Fe}^{\text{II}}$  (5 mM) solution in THF was placed in a 5 mm rubber septum capped NMR tube. After cooling down the NMR tube to  $-80^\circ\text{C}$  (acetone/ $\text{N}_{2(\text{liq})}$  bath), dioxygen was bubbled through the solution mixture to form the  $(\text{d}_8\text{-P}^{\text{Py}})\text{Fe}^{\text{III}}(\text{O}_2^{\bullet-})$  complex (**2**). The NMR tube was transferred rapidly into the NMR instrument which was precooled to  $-85^\circ\text{C}$ . Similar to our UV-vis experiments, complex (**3a**) was prepared by removing any excess of dioxygen by vacuum/Ar cycles from (**2**) and careful addition of 1 equiv. of  $[\text{Cu}^{\text{I}}(\text{AN})]\text{BAR}^{\text{F}}$  complex. Finally, Complex (**3a**) was warmed to RT to obtain decomposed product (**3**).

EPR samples were prepared in a similar way by using 9 mm EPR tube.

**In-situ generation of complex (4).** In a typical experiment, 0.650 mL of  $(P^{Py})Fe^{II}$  (1 mM) in THF was placed in a 9 mm rubber septum capped EPR tube. After cooling down the EPR tube to  $-80^{\circ}C$  (acetone/ $N_{2(liq)}$  bath), 3 mL dioxygen was bubbled through the solution mixture to form the  $(P^{Py})Fe^{III}(O_2^{\bullet-})$  complex (2). Similar to our UV-vis experiments, complex (4) was prepared by removing excess of dioxygen by vacuum/Ar cycles from (2) and careful addition of 2 mL  $\bullet NO_{(g)}$  via 3-way gas tight syringe. Excess gas was removed by vacuum/Ar cycles. After generation of all complexes, the tubes were frozen in  $N_{2(liq)}$  and brought to the spectrometer for measurement.

**Synthesis of  $(P^{Py})Fe^{III}-OH$  (5).**  $(P^{Py})Fe^{III}-OH$  (5) was prepared using a modified procedure for the synthesis of its previously published [31] chloride analog,  $(P^{Py})Fe^{III}-Cl$ . In this case  $(P^{Py})Fe^{III}-Cl$  was dissolved in  $\sim 250$  mL DCM, and this DCM layer was then stirred vigorously with  $\sim 250$  mL of 3.0 M NaOH in a 1000 mL round-bottom flask for 3 h. Separation of the organic layer, followed by drying with magnesium sulfate, and solvent removal yielded the  $(P^{Py})Fe^{III}-OH$  (5) Yield 600 mg (57.8%). This compound was then characterized by UV-vis, and  $^1H$  NMR spectroscopies as well as ESI-MS. UV-vis (THF):  $\lambda_{max}$ , nm 412, 563, room temperature.  $^1H$  NMR (300 MHz;  $CD_2Cl_2$ ):  $\delta_{pyrrole}$  80.63 ppm. MS (ESI):  $m/z$  924. EPR  $g = 6$ .

#### Procedure for nitrate/nitrite test

In a 25 mL-Schlenk flask compound (1) was prepared in 10 mL THF (0.1 mM solution, inside dry box). In a typical bench top reaction, the flask was cooled to  $-80^{\circ}C$  (Acetone/dry ice bath) and dioxygen was bubbled through complex 1, resulting in the formation of the superoxo species, (2). Excess  $O_{2(g)}$  was removed by several cycles of Ar bubble followed by vacuum. Addition of  $\bullet NO_{(g)}$  to (2) resulted in formation of (4), immediately. The reaction mixture was for 10 min at  $-80^{\circ}C$ . After 10 mins, solvent was removed and solid product was isolated in 5 mL of DCM and extracted with 10 mL of aqueous NaCl solution (6 mM). The presence of a significant amount of nitrate ion in the aqueous layer was confirmed by semiquantitative QUANTOFIX nitrate/nitrite test strips.

#### Nitration of the 2,4-di-tert-butylphenol (DTBP)

The formation of the superoxo complex (2) in THF at  $-80^{\circ}C$  was carried out as described above for (1) (0.1 mM) in a schlenk cuvette, and the reaction was monitored by UV-vis. Excess  $O_{2(g)}$  was removed by bubbling the solution with Ar and vacuum purge cycles as before. Two equivalents of 2,4-di-tert butylphenol (DTBP) (0.1 mmol) were added. Upon addition of the DTBP no change in the UV-vis spectrum was observed.  $\bullet NO_{(g)}$  was added by using a three-way gas tight syringe,

leading to the formation of (5). The resulting solution was concentrated *in vacuo* and pentane was added to precipitate the Fe product. The pentane solution was collected by decanting. The Fe product was washed several times with pentane, and the pentane solution was removed and collected by decanting after each wash. The solid Fe product  $(P^{Py})Fe^{III}-S$  ( $S = \text{solvent, } H_2O, ^-OH$ ) was dried *in vacuo*, redissolved in THF and its UV-vis spectrum was recorded [ $\lambda_{max} = 410, 563$  nm; a small change in the Soret position compared to the reaction mixture is observed, possibly due to the different solution conditions and different temperature for the spectra recorded]; these spectral parameters matched those of authentically synthesized  $(P^{Py})Fe^{III}(OH)$  (see above). The pentane solution containing the phenolic products was filtered to remove any trace of Fe product and the solvent was removed *in vacuo*. The resulting solid was re-dissolved in MeOH and dodecane used as internal standard and injected into a GC. This showed 2,4-di-*t*-butyl-6-nitrophenol ( $NO_2$ -DTBP) (82% yield) and unreacted DTBP as the only products of the reaction. These were identified by comparison to the spectra obtained from commercial 2,4-di-*t*-butyl-6-nitrophenol, and 2,4-di-*t*-butylphenol respectively.

## CONCLUSION

From this investigation we can conclude that our present ferric superoxo complex (2) can show cytochrome *c* oxidase reactivity (*CcO*) in the presence of a cuprous complex, generating a peroxo-bridged heme-Cu intermediate which can thermally transform to a heme- $(O^2-)-Cu(L)$   $\mu$ -oxo product, which is derived from dioxygen reactivity. Alternatively, (2) can also function as a  $\bullet NO$  scavenger by oxidizing it to the biologically benign nitrate ion, complex (4). Further work is going on in our laboratory using this system.

## Acknowledgements

We are grateful to the US National Institutes of Health for support of this research (GM60353).

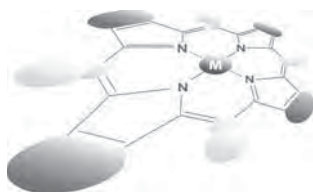
## REFERENCES

1. Holm RH, Kennepohl P and Solomon EI. *Chem. Rev.* 1996; **96**: 2239–2314.
2. Perutz MF. *Annu. Rev. Physiol.* 1990; **52**: 1–25.
3. Sono M, Roach MP, Coulter ED and Dawson JH. *Chem. Rev.* 1996; **96**: 2841–2888.
4. English AM and Tsaprailis G. *Advances in Inorganic Chemistry*, Sykes AG. (Ed.) Academic Press: 1995; pp 79–125.
5. Gardner PR, Gardner AM, Martin LA and Salzman AL. *Proc. Natl. Acad. Sci. USA.* 1998; **95**: 10378–10383.



6. Wasser IM, De Vries S, Moenne-Loccoz P, Schroder I and Karlin KD. *Chem. Rev.* 2002; **102**: 1201–1234.
7. Cleeter MWJ, Cooper JM, Darley-Usmar VM, Moncada S and Schapira AHV. *FEBS Letters* **345**: 50–54.
8. Brown GC and Cooper CE. *FEBS Letters* **356**: 295–298.
9. Brown GC. *FEBS Letters* **369**: 136–139.
10. Radi R. *Proc. Natl. Acad. Sci. USA.* 2004; **101**: 4003–4008.
11. Szabo C, Ischiropoulos H and Radi R. *Nat Rev Drug Discov.* 2007; **6**: 662–680.
12. Radi R, Beckman JS, Bush KM and Freeman BA. *J. Biol. Chem.* 1991; **266**: 4244–4250.
13. Ischiropoulos H. *Arch. Biochem. Biophys.* 1998; **356**: 1–11.
14. Radi R, Beckman JS, Bush KM and Freeman BA. *Arch. Biochem. Biophys.* 1991; **288**: 481–487.
15. Denicola A, Freeman BA, Trujillo M and Radi R. *Arch. Biochem. Biophys.* 1996. **333**: 49–58.
16. King PA, Anderson VE, Edwards JO, Gustafson G, Plumb RC and Suggs JW. *J. Am. Chem. Soc.* 1992; **114**: 5430–5432.
17. Radi R. *Chem. Res. Toxicol.* 1996; **9**: 828–835.
18. Herold S, Exner M and Nauser T. *Biochemistry* 2001; **40**: 3385–3395.
19. Herold S, Shivashankar K and Mehl M. *Biochemistry* 2002; **41**: 13460–13472.
20. Kim E, Helton ME, Wasser IM, Karlin KD, Lu S, Huang HW, Moenne-Loccoz P, Incarvito CD, Rheingold AL, Honecker M, Kaderli S and Zuberbuhler AD. *Proc. Natl. Acad. Sci. USA.* 2003; **100**: 3623–3628.
21. Kim E, Chufan EE, Kamaraj K and Karlin KD. *Chem. Rev.* 2004; **104**: 1077–1133.
22. Chufan EE, Puiu SC and Karlin KD. *Acc. Chem. Res.* 2007; **40**: 563–572.
23. Halime Z, Kieber-Emmons MT, Qayyum MF, Mondal B, Gandhi T, Puiu SC, Chufan EE, Sarjeant AA, Hodgson KO, Hedman B, Solomon EI and Karlin KD. *Inorg. Chem.* 2010; **49**: 3629–3645.
24. Halime Z, Kotani H, Li Y, Fukuzumi S and Karlin KD. *Proc. Natl. Acad. Sci. USA.* 2011; **108**: 3990–3994.
25. Ferguson-Miller S and Babcock GT. *Chem. Rev.* 1996; **96**: 2889–2908.
26. Tsukihara T, Aoyama H, Yamashita E, Tomizaki T, Yamaguchi H, Shinzawa-Itoh K, Nakashima R, Yaono R and Yoshikawa S. *Science* 1995; **269**: 1069–1074.
27. Iwata S, Ostermeier C, Ludwig B and Michel H. *Nature* 1995; **376**: 660–669.
28. Varotsis C, Zhang Y, Appelman EH and Babcock GT. *Proc. Natl. Acad. Sci. USA.* 1993; **90**: 237–241.
29. Collman JP, Sunderland CJ, Berg KE, Vance MA and Solomon EI. *J. Am. Chem. Soc.* 2003; **125**: 6648–6649.
30. Momenteau M and Reed CA. *Chem. Rev.* 1994; **94**: 659–698.
31. Li Y, Sharma SK and Karlin KD. *Polyhedron.* 2013; **58**: 190–196.
32. Liang HC, Zhang CX, Henson MJ, Sommer RD, Hatwell KR, Kaderli S, Zuberbuhler AD, Rheingold AL, Solomon EI and Karlin KD. *J. Am. Chem. Soc.* 2002; **124**: 4170–4171.
33. Kieber-Emmons MT, Qayyum MF, Li Y, Halime Z, Hodgson KO, Hedman B, Karlin KD and Solomon EI. *Angew. Chem. Int. Ed. Engl.* 2012; **51**: 168–172.
34. Kieber-Emmons MT, Li Y, Halime Z, Karlin KD and Solomon EI. *Inorg. Chem.* 2011; **50**: 11777–11786.
35. Chufan EE, Mondal B, Gandhi T, Kim E, Rubie ND, Moenne-Loccoz P and Karlin KD. *Inorg. Chem.* 2007; **46**: 6382–6394.
36. Del Rio D, Sarangi R, Chufan EE, Karlin KD, Hedman B, Hodgson KO and Solomon EI. *J. Am. Chem. Soc.* 2005; **127**: 11969–11978.
37. Kim E, Helton ME, Lu S, Moenne-Loccoz P, Incarvito CD, Rheingold AL, Kaderli S, Zuberbuhler AD and Karlin KD. *Inorg. Chem.* 2005; **44**: 7014–7029.
38. Karlin KD, Nanthakumar A, Fox S, Murthy NN, Ravi N, Huynh BH, Orosz RD and Day EP. *J. Am. Chem. Soc.* 1994; **116**: 4753–4763.
39. Sharma V, Karlin KD and Wikström M. *Proc. Natl. Acad. Sci. USA* 2013; **110**: 16844–16849.
40. Fox S, Nanthakumar A, Wikstrom M, Karlin KD and Blackburn NJ. *et al. J. Am. Chem. Soc.* 1996; **118**: 24–34.
41. Ghiladi RA and Karlin KD. *Inorg. Chem.* 2002; **41**: 2400–2407.
42. Ghiladi RA, Huang H-W, Moenne-Loccoz P, Stasser J, Blackburn NJ, Woods AS, Cotter RJ, Incarvito CD, Rheingold AL and Karlin KD. *J. Biol. Inorg. Chem.* 2005; **10**: 63–77.
43. Ghiladi RA, Chufan EE, Rio DD, Solomon EI, Kerbs C, Huynh BH, Huang H-W, Moenne-Loccoz P, Kaderli S, Honecker M, Zuberbuhler AD, Marzilli L, Cotter RJ and Karlin KD. *Inorg. Chem.* 2007; **46**: 3889–3902.
44. Schopfer MP, Mondal B, Lee DH, Sarjeant AA and Karlin KD. *J. Am. Chem. Soc.* 2009; **131**: 11304–11305.
45. Olson JS, Foley EW, Rogge C, Tsai AL, Doyle MP and Lemon DD. *Free Radic. Biol. Med.* 2004; **36**: 685–697.
46. Yukl ET, De Vries S and Moenne-Loccoz P. *J. Am. Chem. Soc.* 2009; **131**: 7234–7235.
47. Herold S and Koppenol WH. *Coord. Chem. Rev.* 2005; **249**: 499–506.

48. Gunaydin H and Houk KN. *J. Am. Chem. Soc.* 2008; **130**: 10036–10037.
49. Pacher P, Beckman JS and Liaudet L. *Physiol. Rev.* 2007; **87**: 315–424.
50. Boccini F and Herold S. *Biochemistry.* 2004; **43**: 16393–16404.
51. Kurtikyan TS, Eksuzyan SR, Goodwin JA and Hovhannisyan GS. *Inorg. Chem.* 2013; **52**: 12046–12056.
52. Kurtikyan TS, Eksuzyan SR, Hayrapetyan VA, Hovhannisyan GS and Goodwin JA. *J. Am. Chem. Soc.* 2012; **134**: 13861–13870.
53. Yokoyama A, Han JE Karlin KD and Nam W. *Chem. Commun.* 2014; **50**: 1742–1744.



## Near-infrared luminescent Sn(IV) complexes of N-confused tetraphenylporphyrin: Effect of axial anion coordination

Arghya Basu<sup>a</sup>, Motoki Kitamura<sup>a</sup>, Shigeki Mori<sup>b</sup><sup>◇</sup>, Masatoshi Ishida<sup>a</sup><sup>◇</sup>, Yongshu Xie<sup>c</sup> and Hiroyuki Furuta<sup>\*a</sup><sup>◇</sup>

<sup>a</sup>Department of Chemistry and Biochemistry, Graduate School of Engineering and Education Center for Global Leaders in Molecular Systems for Device, Kyushu University, Fukuoka 819-0395, Japan

<sup>b</sup>Integrated Center for Science, Ehime University, Matsuyama 790-8577, Japan

<sup>c</sup>Key Laboratory for Advanced Materials and Institute of Fine Chemicals, East China University of Science & Technology, Shanghai 200237, P.R. China

*Dedicated to Professor Shunichi Fukuzumi on the occasion of his retirement*

Received 16 November 2014

Accepted 15 December 2014

**ABSTRACT:** Novel tin(IV) halo complexes of an N-confused tetraphenylporphyrin with different axial ligands have been synthesized and characterized by various spectroscopic methods including X-ray crystallographic analysis. The molecular structures of the dichloro and dibromo derivatives possess perfect octahedral geometries, which are nearly comparable to the corresponding regular porphyrin complexes. In contrast, the iodide/triiodide complex obtained by a same reaction manner, demonstrated that the tin(IV) cation is slightly displaced towards axially coordinated iodide anion, giving rise to the different electronic structure due to the tautomeric form of N-confused porphyrin ligand. These structural differences reflected to the distinct photophysical and electrochemical properties. The Sn(IV) complexes are near IR luminescent, however the unsymmetrical axial coordination of iodide and triiodide anions in the tin(IV) N-confused porphyrin complex allows, in particular, the longer emission lifetimes and a smaller singlet-triplet energy gap, which were investigated by steady-state and time-resolved spectroscopies as well as theoretical calculations.

**KEYWORDS:** N-confused porphyrin, tin(IV) complex, photophysical properties, DFT calculations.

## INTRODUCTION

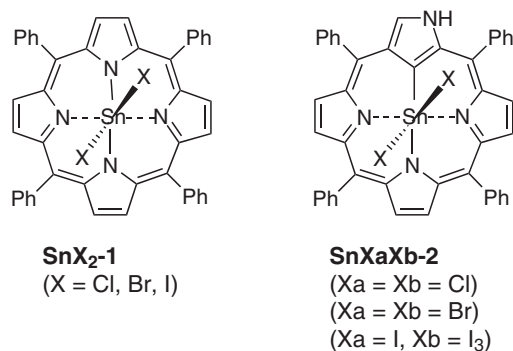
Porphyrinoids and their metal derivatives being larger  $\pi$ -conjugated aromatic compounds are one of the ubiquitous variants as photoactive materials, *e.g.* near-infrared (NIR) chromophores and emitters, sensitizers for solar cells and photodynamic therapy, *etc.* [1] Many porphyrin-based compounds have been recognized as the structural motifs: for example, in natural biological systems, Mg-chlorophylls play an important role in the photosynthetic light-harvesting antenna complexes for energy transfer processes [2]. In this regard, the optical

properties such as the intense Soret (B-) band and resolved Q-bands reaching to the far red region in the absorption spectrum and the corresponding luminescent nature are particularly attractive. These properties retain in the other metalloporphyrins if the central metal is chosen appropriately.

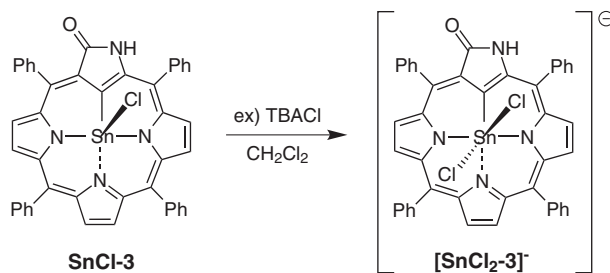
One of the representative example is a tin(IV) porphyrin complex (**SnCl<sub>2</sub>-1**) (Fig. 1), since the tin(IV) ion is diamagnetic and can be accommodated in the porphyrin core without distorting the planarity of the macrocycles [3]. Their electronic transitions can also be interpreted by the typical Goutermann's orbital model as similar to the zinc(II) congeners [4]. Another structural characteristic of tin(IV) porphyrins is octahedral coordination configurations with two axial anionic ligands on the tin center to neutralize the metal valence state. In fact,

<sup>◇</sup>SPP full member in good standing

\*Correspondence to: Hiroyuki Furuta, email: hfuruta@cstf.kyushu-u.ac.jp, fax: +81 92-802-2865



**Fig. 1.** Chemical structures of Sn(IV) complexes used in this study



**Scheme 1.** Anion binding of **SnCl-3** occurring at the tin center gives an anionic complex, **[SnCl<sub>2</sub>-3]<sup>-</sup>**

the axially coordinated ligands are easily replaceable by simple chemical reactions [3], which can therefore fine-tune their optical characters by suitable choices of the external ligands. It has been noted that the axial coordination reactivity (*i.e.* oxophilicity) of the tin(IV) center also plays in the vital roles in having unique higher excited state character that violates “Kasha’s rule” [5], construction of the beautiful supramolecular assemblies [6], photophysical properties [7a, 7b], photocatalysts [7c–7e] and phototherapeutic agents [7f, 7g].

As potential approaches for chemical tunings of the photophysical properties of the porphyrinoids and their metal complexes, we have been extensively investigating on structural modifications, so-called, “*N*-confusion” of the porphyrin backbones. The generating *N*-confused porphyrins (termed as NCPs) are isomers of porphyrin derivatives embedded a confused pyrrole that is connected to the neighboring *meso*-carbons at the  $\alpha$ - and  $\beta'$ -pyrrolic positions. NCPs provide unique NIR absorbing and emitting properties as well as a coordination environment, “NNNC” involving a C–H moiety on the inward, thereby forming various organometallic complexes [8]. A Sn(IV) *N*-confused oxoporphyrin (**SnCl-3**) has been reported previously by us and demonstrated the anion binding capability for various halide anions *via* taking advantage of the Lewis acidity of the vacant axial tin cation center (Scheme 1) [9]. The unexpected finding that the emission intensities of the neutral **SnCl-3** were enhanced even upon

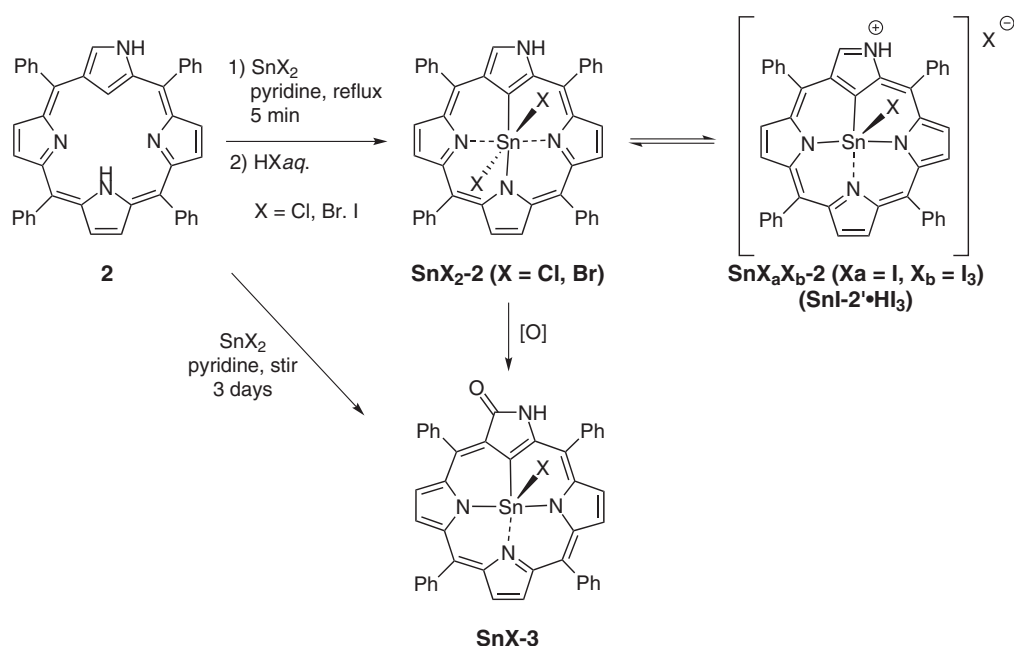
complexation with heavy atomic anions (*e.g.* bromide or iodide) inspired us to investigate the effects of the axial ligands on the photophysical properties of Sn(IV) NCP complexes. In addition, the inherent thermally activated delayed fluorescence (TADF) property of Sn(IV) difluoride porphyrin complexes [10] further motivated us to examine the detailed photophysical properties of genuine Sn(IV) NCP complexes.

In this study, we have synthesized and characterized a series of Sn(IV) NCP complexes (**SnX<sub>2</sub>-2**; X = Cl, Br and I<sub>3</sub>) and investigated axial anion effects on their photophysical properties by spectroscopic means (Fig. 1). The X-ray crystal structures of the chloride and bromide derivatives, **SnCl<sub>2</sub>-2** and **SnBr<sub>2</sub>-2** revealed the similar octahedral complexes to those of the regular **SnX<sub>2</sub>-1**, whereas the unsymmetric structure of **Sn(I)<sub>3</sub>-2** obtained by the same reaction manner exhibited a distorted square-pyramidal coordination geometry. These structural differences in Sn(IV) NCP complexes gave rise to the distinct photophysical properties (*e.g.* NIR emission and the lifetime), which were well accounted by DFT (B3LYP)-based calculations. The axial anions also play roles for electrochemical nature of the complexes. The redox-rich character of the anions (*e.g.* iodide) bound to the Sn(IV) center was seen in the cyclic voltammetry, which is in agreement of the frontier molecular orbital behaviors.

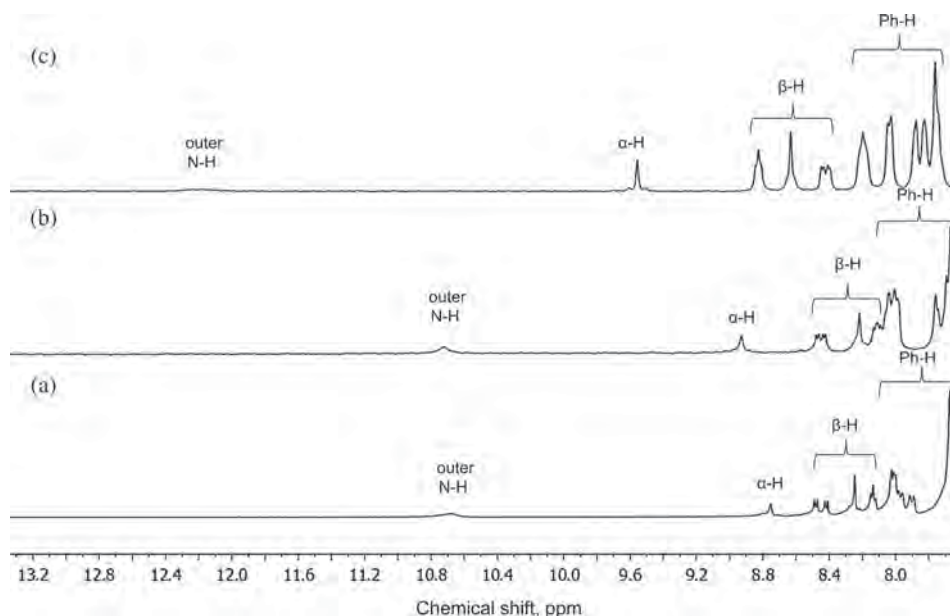
## RESULTS AND DISCUSSION

### Synthesis and structural characterization of Sn(IV) halo complexes of *N*-confused porphyrin

It has been reported that an NCP ligand **2** can form different type of Sn(IV) complexes depending on the reaction conditions (Scheme 2) [9]. Upon stirring ligand **2** with excess tin(II) chloride salts in pyridine for 3 days, the tin(IV) chloride complex of *N*-confused oxoporphyrin **SnCl-3** was dominantly formed. In contrast, short refluxing **2** with a 200 equiv of tin(II) chloride for 5 min in pyridine followed by acidic workup (aq. HCl) gave the desired tin(IV) dichloride complex, **SnCl<sub>2</sub>-2** as a main product. The complex **SnCl<sub>2</sub>-2** was converted to the oxidized form **SnCl-3** under oxidative conditions. As proved by the observation of characteristic peripheral pyrrolic NH signals at 10.67 ppm in the <sup>1</sup>H NMR spectrum and two chloride axial ligands on the Sn(IV) center of **SnCl<sub>2</sub>-2** through the X-ray single crystallographic analysis (*vide infra*), the ligand **2** is present in its dianionic form and captures a Sn(IV) cation in its core, yielding indeed the Sn(IV) complex **SnCl<sub>2</sub>-2** with same coordination manner of the regular porphyrin (*i.e.* **SnCl<sub>2</sub>-1**). It is noteworthy that none of the trianionic behavior of the ligand **2** (supporting in **SnCl<sub>2</sub>-2**) was seen through the intrinsic NH tautomeric ability as seen for Ag(III) and Sb(V) NCP complexes [8]. The DFT-supported energetic comparison of two tautomeric



**Scheme 2.** Synthesis of Sn(IV) halo complexes derived from NCP 2

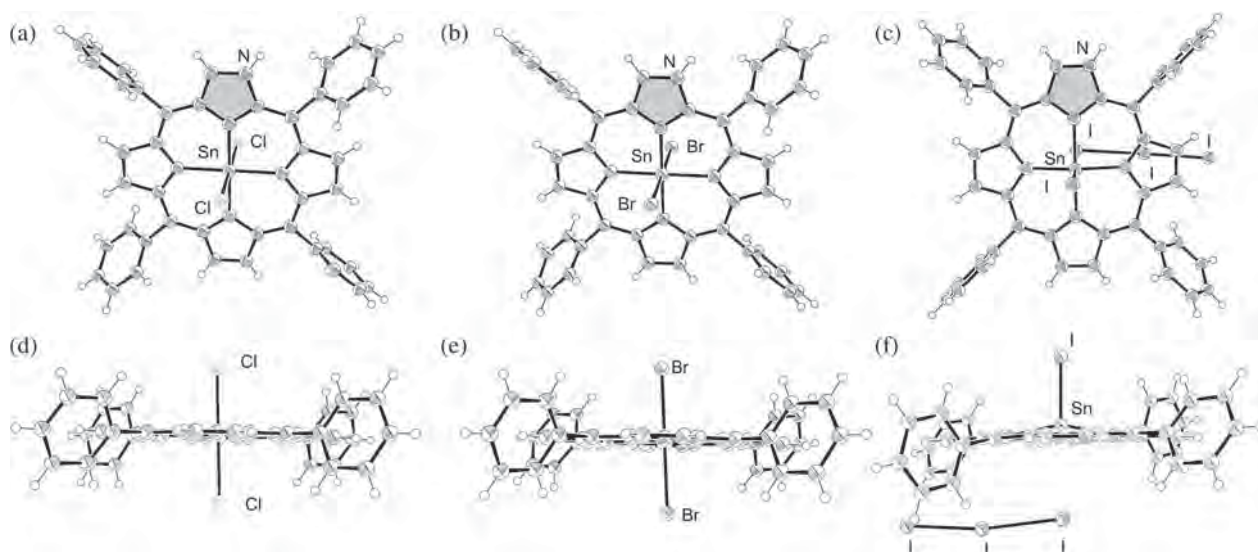


**Fig. 2.** Partial  $^1\text{H}$  NMR spectra of (a)  $\text{SnCl}_2\text{-2}$ , (b)  $\text{SnBr}_2\text{-2}$  and (c)  $\text{Sn(I)I}_3\text{-2}$  complexes in  $\text{CDCl}_3$

complexes suggested that the complex  $\text{SnCl}_2\text{-2}$  is more stable with energy difference of 11.53 kcal/mol than the complex ( $\text{SnCl}_2\text{-2}\cdot\text{HCl}$ ) (Scheme 2). The combination of stronger Lewis acidity of the electron deficient tin(IV) cation and the intrinsic electronegativity of chloride anion may be attributed to the stabilization of six-coordinated electronic structures of  $\text{SnCl}_2\text{-2}$  [11].

The metal complexation reaction with different salts,  $\text{SnBr}_2$  and  $\text{SnI}_2$  afforded the corresponding complexes,  $\text{SnBr}_2\text{-2}$  and  $\text{Sn(I)I}_3\text{-2}$ , respectively (Scheme 2) as

inferred from the mass and  $^1\text{H}$  NMR spectroscopies. The parent peaks of  $m/z = 811.0495$  and  $859.0381$  for cationic  $[\text{SnBr}_2\text{-2}]^+$  (calcd. 811.0519) and  $[\text{SnI}_2\text{-2}]^+$  (calcd. 859.0380) were detected by electron spray ionization-time of flight (ESI-TOF) mass spectroscopies. The spectroscopic feature of  $^1\text{H}$  NMR spectra of  $\text{SnBr}_2\text{-2}$  is comparable to that of  $\text{SnCl}_2\text{-2}$ ; the characteristic outer NH signal is observed at 10.74 ppm and the resonances of  $\beta\text{-H}$ s and *meso*-phenyl CHs appear in the similar patterns (Fig. 2). In contrast, significant downfield shifts in the



**Fig. 3.** ORTEP views of the X-ray crystal structures of (a)  $\text{SnCl}_2\text{-2}$  (b)  $\text{SnBr}_2\text{-2}$  and (c)  $\text{Sn(I)(I}_3\text{)-2}$ . Front (top) and side views (bottom) of the complexes are shown. Thermal ellipsoids set to the 50% probability level

peak positions of the hydrogen atoms of the four pyrrole rings are observed for  $\text{Sn(I)(I}_3\text{)-2}$ , which is ascribed by the broken molecular symmetry of  $\text{Sn(I)(I}_3\text{)-2}$  with the non-identical axially coordinated anionic ligands (proved by X-ray crystallography, *vide infra*) as well as the distinct electronic structure. The downfield shift of NH proton is also pronounced, which is presumably due to the strong hydrogen bonding interaction between weakly coordinated  $\text{I}_3$  anion and NH proton in solution. Therefore the formation of axially unsymmetrical Sn(IV) iodide/triiodide complex,  $\text{Sn(I)(I}_3\text{)-2}$ , were speculated. During the recrystallization process, triiodide anions were formed *via* reaction of the native iodide with iodine ( $\text{I}_2$ ) under aerobic conditions [12]. The resulting triiodide is actually less nucleophilic, therefore present nearby the complex without metal coordination.

The coupling constants to the  $\alpha\text{-H}$  of the confused pyrrole ring,  $^4J(\text{Sn-H})$  could manifest the structural difference (Fig. 2 and Table S3). This parameter is relatively sensitive to the basicity nature of the axial ligands on the tin center. The coupling constants of  $\text{SnCl}_2\text{-2}$  and  $\text{SnBr}_2\text{-2}$  were determined to be 28.8 and 28.5 Hz, respectively, whereas the value of  $\text{Sn(I)(I}_3\text{)-2}$  is 30.3 Hz. The reference values of regular  $\text{SnX}_2\text{-1}$  ( $\text{X} = \text{Cl, Br, I}$ ) are reported to be 15.2, 15.0 and 13.7 Hz, respectively [3b]. On this basis, the basicity trend of the axial coordinated ligands of  $\text{SnX}_2\text{-2}$  ( $\text{X} = \text{Cl, Br}$ ) are in agreement, however, the case of  $\text{Sn(I)(I}_3\text{)-2}$  bearing the non-identical iodide and triiodide anions exhibited the opposite trend. In addition, the absolute value of  $^4J(\text{Sn-H})$  for the tin NCP complexes is significantly larger than those of the regular complexes (generally in the range of 8–22 Hz). This may be attributed to the stronger electronic interaction between the tin center and the confused pyrrolic CH.

### X-ray crystal structures of Sn(IV) NCP complexes

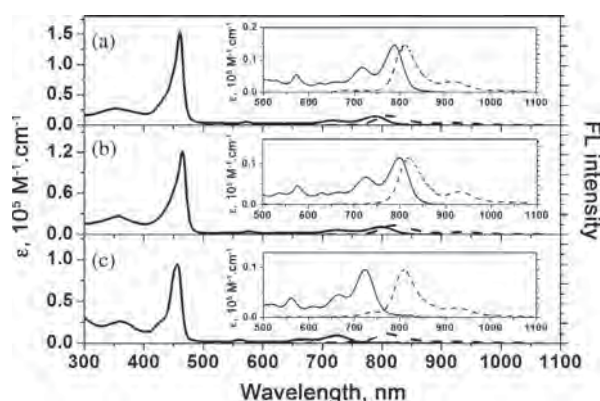
The structures of a series of tin(IV) complexes used in this study were unambiguously characterized by X-ray crystallographic analysis (Fig. 3 and Table S1). The crystals suitable for X-ray crystallographic analysis were obtained from diffusion method with a mixture of dichloromethane/hexane under ambient conditions. The crystal structure of  $\text{SnCl}_2\text{-2}$  revealed the octahedral geometry, where a Sn(IV) cation was accommodated in the NCP core and two axially positions of the cation center are occupied by two chloride anions. The bond angles for Cl–Sn–N (or Cl–Sn–C) are approximately  $90^\circ$  also support the tetragonal bis-pyramidal configuration. The structure is well comparable with the reported complex,  $\text{SnCl}_2\text{-1}$  (Table S2). Specifically, it was found that the Sn–C bond lengths are estimated to be 2.077 Å, which is relatively shorter than that of mean Sn–N bond (2.125 Å) as seen in other metal complexes of NCP derivatives [8]. The Sn–Cl bond length is also significantly longer (*i.e.* 2.523 Å) compared to that of  $\text{SnCl}_2\text{-1}$  (2.420 Å) [13]. For the dibromide complex,  $\text{SnBr}_2\text{-2}$ , the coordination environment of the Sn(IV) cation was elucidated to be almost identical to  $\text{SnCl}_2\text{-2}$  (Fig. 3b). The average bond length of Sn–Br was determined to be 2.676 Å, which is longer than that of  $\text{SnCl}_2\text{-2}$  (Table S2). The slight change in structural parameters observed between the complexes,  $\text{SnCl}_2\text{-2}$  and  $\text{SnBr}_2\text{-2}$  might be due to the less electronegative nature of the bromide anion present at the axial positions.

As speculated by  $^1\text{H}$  NMR spectroscopy (*vide supra*), the crystal structure of  $\text{Sn(I)(I}_3\text{)-2}$  was found to be different from those of  $\text{SnCl}_2\text{-2}$  and  $\text{SnBr}_2\text{-2}$ . Although the crystal structure of  $\text{Sn(I)(I}_3\text{)-2}$  is partially disordered, the presence of two kinds of external ligands, iodide and

triiodide anions, was elucidated in the complex (Fig. 3c). The triiodide anion is vibrated nearby the axial positions of the cation center [14]. Accordingly, the tin(IV) center was slightly displaced from the mean plane (24 core atoms) towards the axial iodide anion, which causes a core distortion (mean plane deviation: 0.037 Å) with the clear difference of bond distances of Sn–I (2.614 Å) and Sn•••I<sub>3</sub> (3.559 Å). The less ionic bonding nature of triiodide anions may induce the non-covalent interaction of the Sn(IV) cation and triiodide anion, and hence alternations of the electronic structure of Sn(I)(I<sub>3</sub>)-2 with unsymmetric π-conjugated macrocycle in Sn(I)(I<sub>3</sub>)-2. The overall crystal structure analysis of all the three complexes revealed that the axially coordinated anions have significant effect on coordination environment of the Sn(IV) cation, which may effect to the photophysical and redox properties of the complexes.

### Photophysical properties

In accord with the structural differences between the tin(IV) complexes, each complex revealed the characteristic features in the steady-state UV-vis-NIR absorption and fluorescence spectra (Fig. 4 and Table 1). The UV-vis-NIR absorption spectra of the complexes in dichloromethane exhibited a characteristic Soret absorption bands around 460 nm with high extinction coefficients ( $\epsilon > 100\,000 \text{ M}^{-1}\cdot\text{cm}^{-1}$ ) with vibronic Q-band structures, which is indicative of the aromatic nature of the macrocycles. The complexes, SnCl<sub>2</sub>-2 and SnBr<sub>2</sub>-2, showed clear Q-bands in the NIR region with peaks at 788, 717, 658, 625 nm for SnCl<sub>2</sub>-2 and 717, 726, 663, 629 nm for SnBr<sub>2</sub>-2. The red-shifts of the Q(0,0)-band of SnBr<sub>2</sub>-2 is well in consistency with the observation for the regular SnX<sub>2</sub>-1, which is attributed to the basicity of the axially coordinated anionic ligands as observed in the SnX<sub>2</sub>-1 [3b]. According to the theoretical aspect,



**Fig. 4.** UV-vis-NIR absorption (solid line) and fluorescence (broken line) spectra of the complexes, (a) SnCl<sub>2</sub>-2, (b) SnBr<sub>2</sub>-2 and (c) Sn(I)(I<sub>3</sub>)-2 in dichloromethane at 298 K. Insets show the magnified Q-bands region. Excitation wavelength is  $\lambda = 440 \text{ nm}$

the iodide derivative, Sn(I)(I<sub>3</sub>)-2, was expected to show further red-shift of the lower energy bands. However, the complex Sn(I)(I<sub>3</sub>)-2 represented the opposite absorption spectral tendency; both the Soret band and Q-bands were rather blue-shifted than those of SnCl<sub>2</sub>-2 and SnBr<sub>2</sub>-2, which implies the different electronic transitions in Sn(I)(I<sub>3</sub>)-2 (*vide infra*).

It is noteworthy that three complexes show NIR emissions around 800 nm upon excitation at the Soret band in dichloromethane solution at room temperature (Fig. 4). The positions of the emission maxima are shifted in the order of Sn(I)(I<sub>3</sub>)-2, SnCl<sub>2</sub>-2 and SnBr<sub>2</sub>-2, which is well agreed with the lowest absorption energies. The fluorescence intensities were likewise dependent upon the axial counter anions as compared to the quantum yield ( $\Phi_{\text{FL}}$ ) of the complexes (*e.g.* 0.005 for SnCl<sub>2</sub>-2, 0.002 for SnBr<sub>2</sub>-2 and 0.001 for Sn(I)(I<sub>3</sub>)-2) (Table 1). It is likely that the heavy atom effect (*e.g.* spin-orbit

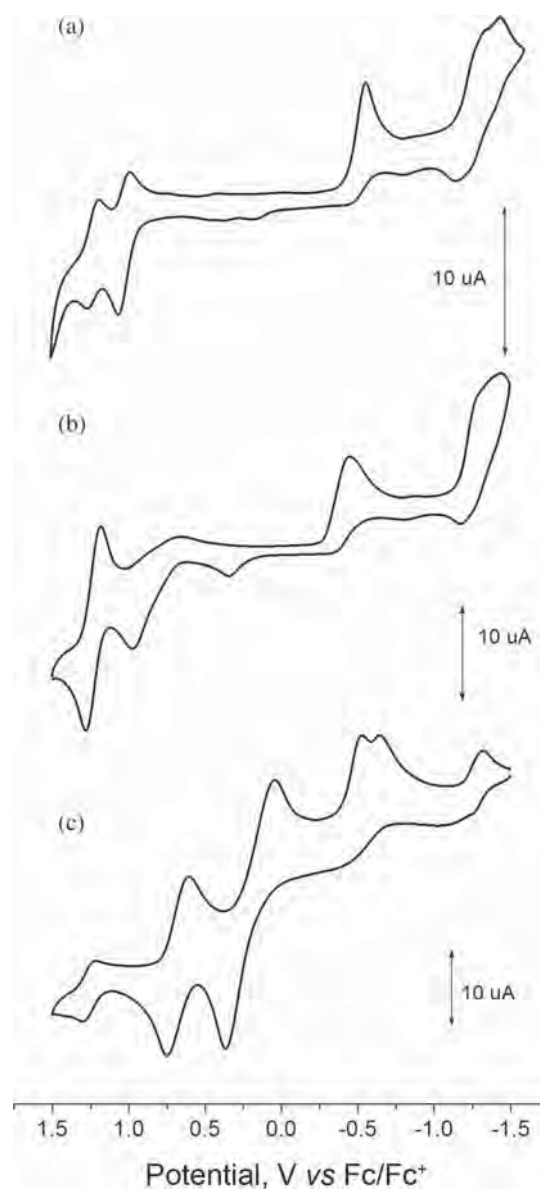
**Table 1.** Photophysical properties of the Sn(IV) complexes<sup>a</sup>

Compound	$\lambda_{\text{abs}}$ , nm ( $\epsilon$ , $10^5 \text{ M}^{-1}\cdot\text{cm}^{-1}$ ) <sup>b</sup>	$\lambda_{\text{FL}}$ , nm <sup>c</sup>	$\tau_{\text{FL}}$ , ns <sup>d</sup>	$\Phi_{\text{FL}}$ <sup>e</sup>	$\lambda_{\text{PL}}$ , nm <sup>f</sup>	Stokes shift, cm <sup>-1</sup>	$E_{\text{S}}$ , eV <sup>g</sup>	$\Delta E_{\text{S,T}}$ , eV <sup>h</sup>
SnCl <sub>2</sub> -2	353 (0.27), 461 (1.53), 572 (0.54), 625 (0.02), 658 (0.03), 717 (0.07), 788 (0.14)	811	0.32 (100)	0.005	—	161.31	1.55	0.71
SnBr <sub>2</sub> -2	357 (0.26), 465 (1.21), 576 (0.04), 629 (0.02), 663 (0.03), 726 (0.06), 800 (0.11)	819	0.082 (65.8) 0.26 (34.2)	0.002	—	241.97	1.53	0.66
Sn(I)(I <sub>3</sub> )-2	329 (0.26), 456 (0.93), 600 (0.93), 560 (0.03), 609 (0.02), 665 (0.04), 724 (0.09)	805	0.31 (80.2) 2.24 (19.8)	0.001	920	1371.17	1.63	0.33

<sup>a</sup>In CH<sub>2</sub>Cl<sub>2</sub>, <sup>b</sup>absorption maximum along with absorption extinction coefficient, <sup>c</sup>fluorescence maximum, <sup>d</sup>fluorescence lifetime with excitation at 440 nm, <sup>e</sup>fluorescence quantum yield values based on the relative yield of **2** ( $\Phi_{\text{FL}} = 0.015$ ), <sup>f</sup>phosphorescence maximum measured at 233 K, <sup>g</sup>lowest excited singlet energies estimated from the intersection of the absorption and fluorescence spectra, <sup>h</sup>theoretical singlet and triplet energy gaps obtained by the B3LYP/LANL2DZ calculations.

coupling coefficient of the ligands, Cl<sup>-</sup> ( $\zeta = 587 \text{ cm}^{-1}$ ), Br<sup>-</sup> ( $\zeta = 2460 \text{ cm}^{-1}$ ) and I<sup>-</sup> ( $\zeta = 5069 \text{ cm}^{-1}$ ) [15]) on the optical properties is remarkable, which altered the excited state dynamics, that is, accelerated the internal conversion or intersystem crossing rates of the excited state species. Compared to the regular **SnCl<sub>2</sub>-1**, the complex **SnCl<sub>2</sub>-2** showed an NIR fluorescence at the longer wavelength with  $\lambda_{\text{max}} = 810 \text{ nm}$ , however the quantum yield is significantly lower than that of **SnCl<sub>2</sub>-1** ( $\Phi_{\text{FL}} = 0.03$ ). This result is probably due to the cross conjugated nature through the nitrogen atom of the confused pyrrole ring on the  $\pi$ -conjugated circuit as it is effected to the freebase species ( $\Phi_{\text{FL}} = 0.015$ ). The temporal fluorescence emission profiles of the complexes were determined by time-correlated single-photon counting (TCSPC) method in the CH<sub>2</sub>Cl<sub>2</sub> solution (Fig. S4 and Table 1). The lifetime ( $\tau_{\text{FL}}$ ) of **SnCl<sub>2</sub>-2** obtained by the fitting by exponential decay function is 0.32 ns, which is relatively shorter than that of regular **SnCl<sub>2</sub>-1** ( $\tau_{\text{FL}} = 0.6 \text{ ns}$ ). The fluorescence rate constant ( $k_{\text{f}}$ , s) was thus estimated to be  $1.5 \times 10^7$ . As considering the lower singlet energy of **SnCl<sub>2</sub>-2** ( $E_{\text{s}} = 1.55 \text{ eV}$  vs.  $2.04 \text{ eV}$  for **SnCl<sub>2</sub>-1**), the internal deactivation rate could be faster. In the case of **SnBr<sub>2</sub>-2**, the quantum yield of fluorescence emission is smaller and the lifetime ( $\tau_{\text{FL1}}$  and  $\tau_{\text{FL2}}$ ) obtained by biexponential decay curve fitting is likewise shorter (Table 1). The two-decay profile could be originated from two vibronic states, which is contributed from the rapid deactivation of the excited singlet state due to the heavy atom effect of the axial anions (rate constant,  $k_{\text{FL}} = 1.7 \times 10^6 \text{ s}$ ). These results are attributed to the fact that the introduction of confused pyrrole unit in the core leads to the significant electronic perturbations of the distinct  $\pi$ -conjugated framework and the emission nature of the complexes is therefore optically sensitive toward the internal axial coordinated anions.

On the contrary, it was found that the emission wavelength of **Sn(I)(I<sub>3</sub>)-2** is blue shifted and the fluorescence lifetime ( $\tau_{\text{FL}}$ ) is much longer by comparison with those of dichloride and dibromide complexes (Table 1). In comparison with the **SnX<sub>2</sub>-2** (X = Cl or Br), the Stokes shift of **Sn(I)(I<sub>3</sub>)-2** is determined to be larger (*i.e.*  $1371 \text{ cm}^{-1}$ ), which suggests the large difference in the structure between the ground state and excited one. Upon lowering the temperature, the second vibrated spectral band  $E(0-1)$  of emission was significantly increased in the iodide complex, **Sn(I)(I<sub>3</sub>)-2**, while the shape of first band,  $E(0-0)$  was not changed (Fig. S3). The long lived excited state could be relevant to the phosphorescence emission, since the quantum yields of triplet ( $T_1$ ) formation are larger than 0.9 in the tin(IV) porphyrin complex [16]. The narrower singlet and triplet excitation energy gap ( $\Delta E_{\text{s-T}}$ ) for **Sn(I)(I<sub>3</sub>)-2** was determined to be 0.23 eV from the emission wavelengths, which imply the participation of the TADF process from the triplet state could be reasonably considered for relatively longer fluorescence emission ( $\tau_{\text{FL2}}$ ).



**Fig. 5.** Cyclic voltammograms of (a) **SnCl<sub>2</sub>-2**, (b) **SnBr<sub>2</sub>-2** and (c) **Sn(I)(I<sub>3</sub>)-2** in CH<sub>2</sub>Cl<sub>2</sub> containing 0.1 M *n*-TBAPF<sub>6</sub> as supporting electrolyte under identical conditions: 100 mV/s scan rate and [compound] = 1 mM

### Redox properties

The redox properties of the Sn(IV) complexes were investigated using cyclic voltammetry (CV) and differential pulse voltammetry (DPV) in CH<sub>2</sub>Cl<sub>2</sub> containing 0.1 M *n*-tetrabutylammonium hexafluorophosphate (TBAPF<sub>6</sub>) as a supporting electrolyte (Fig. 5 and Table 2). The facile reduction nature of **SnCl<sub>2</sub>-1** has been characterized where  $\pi$ -anion radical and dianion species are easily generated upon tin(IV) metal coordination [17]. The overall basicity of the axial ligand could alter the redox properties of the complexes. The CV of **SnCl<sub>2</sub>-2** revealed two quasi-reversible oxidation waves at 1.21 and 0.98 (V vs. ferrocene/



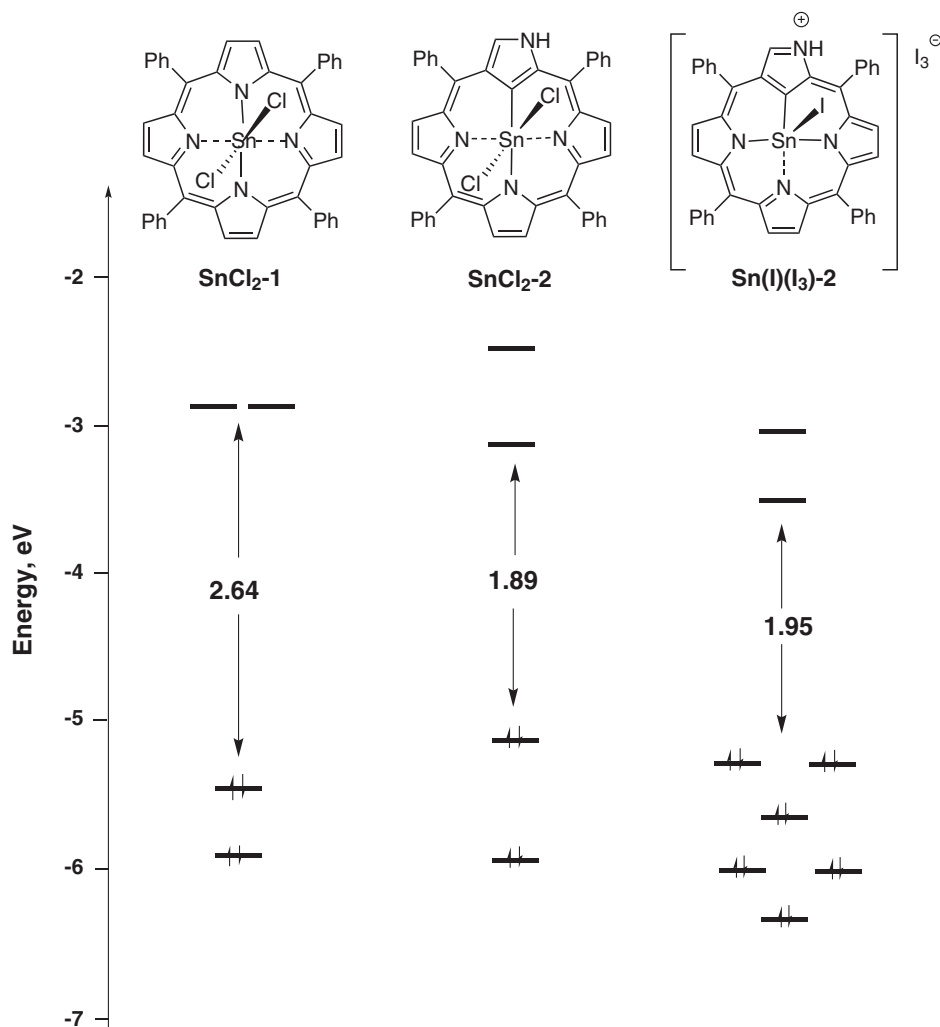


Fig. 6. Comparative energy diagram of **SnCl<sub>2</sub>-1**, **SnCl<sub>2</sub>-2** and **Sn(I)(I<sub>3</sub>)-2** obtained by the B3LYP/LANL2DZ calculations

ferrocenium) and irreversible and quasi-reversible reduction waves were seen at -0.47 and -1.20 V, respectively. Compared to the regular **SnCl<sub>2</sub>-1**, the facile oxidation and reduction potentials of **SnCl<sub>2</sub>-2** were elucidated, therefore indicating the narrower HOMO–LUMO gaps of 1.45 V [17]. Relative to **SnCl<sub>2</sub>-2**, the similarity of the redox nature of **SnBr<sub>2</sub>-2** was elucidated as inferred by the redox behaviors (Table 2). The slight narrower HOMO–LUMO gap of 1.34 V was obtained compared to that of **SnCl<sub>2</sub>-2**. In the case of **Sn(I)(I<sub>3</sub>)-2**, the electrochemical behavior is relatively complicated. The redox coupled waves of the iodide and triiodide anions (*e.g.* I<sub>3</sub>/I, I<sup>•</sup>/I, I<sub>2</sub><sup>•</sup>/I) are overlapped with the inherent electrochemical waves of the Sn(IV) NCP complex [18]. Therefore, although it is difficult to distinguish the origins of the NCP redox character, the relatively separated HOMO–LUMO gaps of **Sn(I)(I<sub>3</sub>)-2** may be estimated. The different choice of the axial coordination anions in **SnX<sub>2</sub>-2** reflected to the change in the oxidation and reduction properties.

### Theoretical calculations

The in-depth analysis of the spectroscopic and electrochemical results indicated that the axially coordinated anionic ligands have crucial effect on both the ground state and excited state, and thus on the photophysical properties of the Sn(IV) NCP complexes. In an effort to gain further theoretical insight into the electronic effects of the anions in the Sn(IV) complexes, DFT (B3LYP/LanL2DZ) calculations were carried out (Fig. 6 and Figs S5–S10). The optimized structures of all complexes well reproduced the results of the X-ray crystallographic observation (Fig. S5). In particular, the complex **Sn(I)(I<sub>3</sub>)-2** revealed the deformed plane with mean deviation value of 0.064 Å, whereas the highly planar conformation was demonstrated in **SnX<sub>2</sub>-2** (X = Cl and Br). The frontier molecular orbital (MO) of **SnCl<sub>2</sub>-2** shows the typical electron density distributions (*i.e.* a<sub>1u</sub>, a<sub>2u</sub> and e<sub>g</sub>) based on the Gouterman's theory [19]. However both the HOMO and LUMO pairs are

**Table 2.** Redox potentials and electrochemical HOMO–LUMO gaps  $\Delta E$  of Sn(IV) NCP complexes

Compound	$E^{1/2}_{\text{ox3}}$ <sup>a</sup>	$E^{1/2}_{\text{ox2}}$ <sup>a</sup>	$E^{1/2}_{\text{ox1}}$ <sup>a</sup>	$E^{1/2}_{\text{red1}}$ <sup>a</sup>	$E^{1/2}_{\text{red2}}$ <sup>a</sup>	$\Delta E^b$	$\Delta E_{\text{H-L}}^c$
<b>SnCl<sub>2</sub>-2</b>	—	1.21	0.98	-0.47	-1.20	1.45	1.89
<b>SnBr<sub>2</sub>-2</b>	—	1.19	0.87	-0.47	-1.31	1.34	1.84
<b>Sn(I)(I<sub>3</sub>)-2</b>	1.24	0.66 <sup>d</sup>	0.25 <sup>d</sup>	-0.43 <sup>d</sup>	-1.27	0.68	1.95

<sup>a</sup>Potentials (unit; V), <sup>b</sup> $\Delta E$  (V) =  $E^{1/2}_{\text{ox1}} - E^{1/2}_{\text{red1}}$ , <sup>c</sup> $\Delta E_{\text{H-L}}$  (eV) =  $E^{(\text{HOMO})} - E^{(\text{LUMO})}$  obtained by DFT(B3LYP) calculations.

<sup>d</sup>The redox couples of the iodide/triiodide species are involved; Ref. 18.

non-degenerated, respectively, due to the unsymmetric electronic structures of NCP macrocycle, therefore the HOMO–LUMO energy gap became narrower relative to that of **SnCl<sub>2</sub>-1** (*i.e.*  $\Delta E = 1.89$  eV vs. 2.64 eV) (Fig. 6). In the cases of **SnBr<sub>2</sub>-2** and **Sn(I)(I<sub>3</sub>)-2**, the LUMO and LUMO+1 are predominantly consisted of the porphyrin's MOs ( $\pi^*$  orbitals) for both. The HOMOs of **SnBr<sub>2</sub>-2** however indicate the presence of the axial ligand dominant four MOs in the HOMO–1 to HOMO–4, which provide the intramolecular charge transfer (ICT) character (Fig. S7). This ICT nature of the unsymmetric **Sn(I)(I<sub>3</sub>)-2** is also seen in the HOMOs admixing with the porphyrin's MOs (HOMO–2) (Fig. S8). By comparing the MO energy profile, the electronic structure of **Sn(I)(I<sub>3</sub>)-2** is heterogeneously different with those of **SnX<sub>2</sub>-2** (X = Cl and Br). This hypothesis was analyzed by evaluation of the distinct aromaticity. The extent of aromaticity was quantified by using nucleus-independent chemical shifts (NICS(0)) and harmonic oscillator model of aromaticity (HOMA) values. The HOMA of 0.630 for **Sn(I)(I<sub>3</sub>)-2** and the NICS(0) values at the inner macrocycles of approximately -7 ppm are larger than those of **SnCl<sub>2</sub>-2** and **SnBr<sub>2</sub>-2**, indicating the stronger aromaticity despite the core distortion (Fig. S9) [20]. Due to the unsymmetrical coordination fashion of **Sn(I)(I<sub>3</sub>)-2**, the trianionic “*type A*” configuration of the supporting ligand could be stabilized with a distinct  $18\pi$  aromaticity through the interconversion of “valence-coupled NH-tautomerism” occurring in the NCP derivatives. (Fig. 6) [21].

The time dependent (TD) DFT calculations of the Sn(IV) complexes demonstrated a reasonable agreement with the experimental spectra (Fig. S10). Although the molecular symmetries of the tin(IV) complexes are broken, the electronic spectra of the complexes, **SnX<sub>2</sub>-2** and **Sn(I)(I<sub>3</sub>)-2**, could be essentially described by a classical Gouterman's four-orbital model, which involves configuration interaction between the  $a_{1u}$ ,  $a_{2u}$  and  $e_g$  symmetric MOs. The calculated energy gaps between the singlet and triplet states ( $\Delta E_{\text{S-T}}$ ) of the tin(IV) complexes were clearly dependent on the conjugated electronic structures (Table 2). This could be due to the decrement of the exchange interaction integral of the HOMO (dominant on I<sub>3</sub> molecule) and LUMO (on porphyrin core) wavefunctions of **Sn(I)(I<sub>3</sub>)-2**. The values of *ca.* 0.7 eV were estimated for **SnCl<sub>2</sub>-2** and **SnBr<sub>2</sub>-2**, whereas the

**Sn(I)(I<sub>3</sub>)-2** possesses a smaller gap of 0.33 eV, suggesting that excitons may be harvested by the triplet  $\rightarrow$  singlet upconversion. The further detailed photophysical study on the NCP-based complexes would be requisite to confirm this possibility.

## EXPERIMENTAL

### General

All of the reactions were performed in oven-dried reaction vessels under Ar or N<sub>2</sub>. Commercially available solvents and reagents were used without further purification unless otherwise mentioned. CH<sub>2</sub>Cl<sub>2</sub> was dried by passing through a pad of alumina. Thin-layer chromatography (TLC) was carried out on aluminum sheets coated with silica gel 60 F<sub>254</sub> (Merck). Preparative separation was performed by silica gel flash column chromatography (KANTO Silica Gel 60 N, spherical, neutral, 40–50  $\mu\text{m}$ ) or silica gel gravity column chromatography (KANTO Silica Gel 60 N, spherical, neutral, 63–210  $\mu\text{m}$ ). <sup>1</sup>H NMR spectra were recorded in CDCl<sub>3</sub> solution on a JNM-AL SERIES FT-NMR spectrometer (JEOL) at 300 MHz, and chemical shifts were reported relative to a residual proton of a deuterated solvent, CHCl<sub>3</sub> ( $\delta = 7.26$ ) in ppm. Mass spectra were recorded on an autoflex MALDI-TOF mass spectrometer (Bruker Daltonics) and ESI-TOF mass spectrometer, JMS-T100CS (JEOL) using CH<sub>3</sub>OH as a solvent. Cyclic voltammograms (CVs) were measured in a three-electrode cell consisting of a glassy carbon working electrode, a platinum counter electrode, and an Ag/AgCl reference electrode. Measurements were carried out with an ALS 620B instrument (ALS Co., Ltd.) under an Ar atmosphere at room temperature. CVs were recorded in 0.1 M *n*-Bu<sub>4</sub>NPF<sub>6</sub> in CH<sub>2</sub>Cl<sub>2</sub>. The redox potentials were calibrated by the ferrocene/ferrocenium (Fc/Fc<sup>+</sup>) couple.

### Photophysical measurements

UV-vis-NIR absorption spectra were recorded on a UV-3150PC spectrometer (Shimadzu) with a photomultiplier tube detector (190–750 nm) and a PbS detector (750–3200 nm). Emission spectra were recorded

on a HORIBA SPEX Fluorolog-3 spectrometer. The temperature-dependent spectra were obtained with use of cryostat CoolSpeK UV USP-203-B (UNISOKU). Time-resolved photoluminescence lifetime measurements were carried out by using time-correlated single photon counting lifetime spectroscopy system, HAMAMATSU Quantaaurus-Tau C11567-01. A light-emitting diode (LED) at 370 nm was used for the excitation. The fluorescence lifetimes ( $\tau_s$ ) were determined by curve fitting method.

## Synthesis

Tin(IV) tetraphenylporphyrin complexes were prepared according to the reported methods; **SnCl<sub>2</sub>-1**, **SnBr<sub>2</sub>-1** and **SnI<sub>2</sub>-1** [3b]. The freebase NCP was prepared by the reported method [22].

**General synthetic procedures for SnX<sub>2</sub>-2 (X = Cl, Br, I/I<sub>3</sub>)**. A mixture of freebase NCP **2** (61 mg, 0.1 mmol) and tin(II) halide (X = Cl, Br, I) salts (20 mmol) was reflux in pyridine (15 mL) at 110 °C under N<sub>2</sub> for 5 min and the hot reaction mixture was instantly poured into cold hexane (50 mL). The precipitates were filtered under *vacuum* and the dark green solid was washed with hexane (3 × 10 mL) and then dissolved in a minimum amount of dichloromethane (CH<sub>2</sub>Cl<sub>2</sub>). The resulting dichloromethane solution was evaporated under reduced pressure. After column chromatographic purification using CH<sub>2</sub>Cl<sub>2</sub>/MeOH (4%) as the eluent, work up with corresponding acid (HX; X = Cl, Br, I) give crystalline solid of **SnX<sub>2</sub>-2** (X = Cl, Br, I/I<sub>3</sub>) complexes.

**SnCl<sub>2</sub>-2**. Yield 35%. <sup>1</sup>H NMR (CDCl<sub>3</sub>, 300 MHz, 298 K):  $\delta_H$ , ppm 10.67 (br, 1H, outer NH), 8.74 (s, 1H,  $\alpha$ -H), 8.41 (d,  $J$  = 4.5 Hz, 1H,  $\beta$ -H), 8.35 (d,  $J$  = 4.5 Hz, 1H,  $\beta$ -H), 8.17 (s, 2H,  $\beta$ -H), 8.10 (t,  $J$  = 4.8 Hz, 2H,  $\beta$ -H), 7.94 (m, 8H, *o*-Ph), 7.61 (m, 12H, *m*-Ph and *p*-Ph). ESI-TOF MS:  $m/z$  767.1032 (ex. mass calcd. for C<sub>44</sub>H<sub>28</sub>ClN<sub>4</sub>Sn [M<sup>+</sup> – Cl], 767.1024). UV-vis (CH<sub>2</sub>Cl<sub>2</sub>):  $\lambda_{max}$ , nm (log  $\epsilon$ ) 353 (4.44), 461 (5.19), 572 (3.74), 625 (3.46), 658 (3.51), 717 (3.89), 788 (4.17).

**SnBr<sub>2</sub>-2**. Yield 32%. <sup>1</sup>H NMR (CDCl<sub>3</sub>, 300 MHz, 298 K):  $\delta_H$ , ppm 10.74 (br, 1H, outer NH), 8.94 (s, 1H,  $\alpha$ -H), 8.48 (d,  $J$  = 5.1 Hz, 1H,  $\beta$ -H), 8.42 (d,  $J$  = 4.2 Hz, 1H,  $\beta$ -H), 8.23 (s, 2H,  $\beta$ -H), 8.10 (t,  $J$  = 4.8 Hz, 2H,  $\beta$ -H), 8.06 (m, 8H, *o*-Ph), 7.67–7.77 (m, 12H, *m*-Ph and *p*-Ph). ESI-TOF MS:  $m/z$  811.0495 (ex. mass calcd. for C<sub>44</sub>H<sub>28</sub>BrN<sub>4</sub>Sn [M<sup>+</sup> – Br], 811.0519). UV-vis (CH<sub>2</sub>Cl<sub>2</sub>):  $\lambda_{max}$ , nm (log  $\epsilon$ ) 357 (4.43), 465 (5.08), 576 (3.67), 629 (3.48), 663 (3.49), 726 (3.83), 800 (4.06).

**Sn(I)(I<sub>3</sub>)-2**. Yield 15%. <sup>1</sup>H NMR (CDCl<sub>3</sub>, 300 MHz, 298 K):  $\delta_H$ , ppm 12.2 (br, 1H, outer NH), 9.62 (s, 1H,  $\alpha$ -H), 8.85 (t,  $J$  = 4.8 Hz, 2H,  $\beta$ -H), 8.68 (s, 2H,  $\beta$ -H), 8.49 (d,  $J$  = 4.5 Hz, 1H,  $\beta$ -H), 8.46 (d,  $J$  = 3.9 Hz, 1H,  $\beta$ -H), 8.25 (m, 4H, *o*-Ph), 8.09 (m, 4H, *o*-Ph), 7.65–7.78 (m, 12H, *m*-Ph and *p*-Ph). ESI-TOF MS:  $m/z$  859.0381 (ex. mass calcd. for C<sub>44</sub>H<sub>28</sub>I<sub>4</sub>Sn [M<sup>+</sup> – I<sub>3</sub>], 859.0380). UV-vis (CH<sub>2</sub>Cl<sub>2</sub>):  $\lambda_{max}$ , nm (log  $\epsilon$ ) 359 (4.41), 456 (4.97), 560 (3.57), 609 (3.34), 665 (3.65), 724 (3.98).

## X-ray crystallography

X-ray analyses of **SnCl<sub>2</sub>-2**, **SnBr<sub>2</sub>-2** and **Sn(I)(I<sub>3</sub>)-2** were performed on a Saturn 724 diffractometer equipped with a CCD detector (RIGAKU) using MoK $\alpha$  (graphite, monochromated,  $\lambda$  = 0.710747 Å) radiation. The structures were solved by direct method on SIR2004 and expanded using Fourier techniques. All of the positional parameters and thermal parameters of non-hydrogen atoms were refined anisotropically on  $F^2$  by the full-matrix least-squares method. Hydrogen atoms were placed at the calculated positions and refined riding on their corresponding carbon atoms. All calculations were performed using the CrystalStructure 4.0 [23] crystallographic software package except for refinement, which was performed using SHELXL-97 [24].

## Computational methods

DFT calculations were performed with a Gaussian09 program package without symmetry assumption [25]. Initial structures are based on the X-ray structures of the related compounds. The geometries were fully optimized at the Becke's three-parameter hybrid functional combined with the Lee–Yang–Parr correlation functional abbreviated as the B3LYP level of density functional theory with LANL2DZ basis set for all the calculations [26].

## CONCLUSION

In summary, novel tin(IV) complexes of N-confused tetraphenylporphyrin, **SnX<sub>2</sub>-2** (X = Cl, Br, I/I<sub>3</sub>) possessing different axial ligands were synthesized and characterized by spectroscopic method including X-ray single crystallographic analysis. The chloride or bromide derivatives being genuine isomers of the tin(IV) halo porphyrinato complexes are different in terms of the electronic and photophysical properties with the iodide complex, **Sn(I)(I<sub>3</sub>)-2** bearing nonidentical axial ligands. Due to the unsymmetric coordination mode, the DFT-based theoretical analysis resulted in the fact that the formally trianionic structure of **Sn(I)(I<sub>3</sub>)-2** with a distinct 18 $\pi$  conjugated circuit could be considered as inferred by the indices of NICS and HOMA assessments. These electronic properties allow a small singlet and triplet excited state energy gap ( $\Delta E_{S-T}$ ), which could contribute to the longer emission lifetime through exciton upconversion from T<sub>1</sub> → S<sub>1</sub>. The manipulation of the axial coordination on the tin(IV) center of the complexes would offer efficient NIR emissive luminophores for lighting applications. The further exploration of opt-electronic organic materials under “N-confusion” concept is in progress our laboratory.

## Acknowledgements

The present work is supported by Grant-in-Aid for Scientific Research (25248039 to HF) and Young

Scientist (26810024 to MI) from the Japan Society for the Promotion of Science (JSPS).

### Supporting information

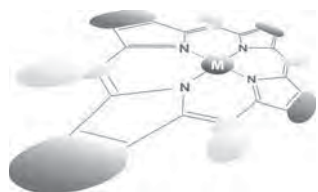
The chart of NMR and MS spectra, crystallographic details, and theoretical calculations are given in the supplementary material. This material is available free of charge via the Internet at <http://www.worldscinet.com/jpp/jpp.shtml>.

Crystallographic data for compounds **SnCl<sub>2</sub>-2**, **SnBr<sub>2</sub>-2** and **Sn(I)(I<sub>3</sub>)-2** have been deposited at the Cambridge Crystallographic Data Centre (CCDC) under numbers CCDC-1033331, 1033332 and 1033333, respectively. Copies can be obtained on request, free of charge, via [www.ccdc.cam.ac.uk/data\\_request/cif](http://www.ccdc.cam.ac.uk/data_request/cif) or from the Cambridge Crystallographic Data Centre, 12 Union Road, Cambridge CB2 1EZ, UK (fax: +44 1223-336-033 or email: [data\\_request@ccdc.cam.ac.uk](mailto:data_request@ccdc.cam.ac.uk)).

### REFERENCES

1. *The Porphyrin Handbook*, Kadish KM, Smith KM and Guillard R. (Eds.) Academic Press: San Diego, CA, 2000.
2. (a) *Chlorophylls and Bacteriochlorophylls*, Grimm B, Porra RJ, Rüdiger W and Scheer H. (Eds.) Springer: Dordrecht, Netherlands, 2006; pp 1–26. (b) Chen M, Schliep M, Willows RD, Cai Z-L, Neilan BA and Scheer H. *Science* 2010; **329**: 1318–1319. (c) Björn LO, Papageorgiou GC, Blankenship RE and Govindjee. *Photosynth. Res.* 2009; **99**: 85–98.
3. (a) Arnold DP and Blok J. *Coord. Chem. Rev.* 2004; **248**: 299–319. (b) Arnold DP. *Polyhedron* 1986; **5**: 1957–1963.
4. Ceulemans A, Oldenhof W, Gorller-Walrand C and Vanquickenborne LG. *J. Am. Chem. Soc.* 1986; **108**: 1155–1163.
5. Some papers reported the observations of S<sub>2</sub> fluorescence. See; (a) Ghiggion KP, Giri NK, Hanrieder J, Martell JD, Muller J, Paige MF, Robotham B, Szymkowski J and Steer RP. *J. Phys. Chem. A* 2013; **117**: 7833–7840. (b) Jang JH, Kim HJ, Kim H-J, Kim CH, Joo T, Cho DW and Yoon M. *Bull. Korean. Chem. Soc.* 2007; **28**: 1967–1972.
6. (a) Shetti VS, Pareek Y and Ravikanth M. *Coord. Chem. Rev.* 2012; **256**: 2816–2842. (b) Dvivedi A, Pareek Y and Ravikanth M. *Chem. Eur. J.* 2014; **20**: 4481. (c) Kim HJ, Bampos N and Sanders JKM. *J. Am. Chem. Soc.* 1999; **121**: 8120–8121. (d) Redman JE, Feeder N, Teat SJ and Sanders JKM. *Inorg. Chem.* 2001; **40**: 2486–2499. (e) Kumar AA, Giribabu L, Reddy DR and Maiya BG. *Inorg. Chem.* 2001; **40**: 6757–6766. (f) Hunter CA and Tomas S. *J. Am. Chem. Soc.* 2006; **128**: 8975–8979.
7. (a) Solntsev PV, Sabin JR, Dammer SJ, Gerasimchuk NN and Nemykin VN. *Chem. Commun.* 2010; **46**: 6581–6583. (b) Maeda D, Shimakoshi H, Abe M and Hisaeda Y. *Inorg. Chem.* 2009; **48**: 9853–9860. (c) Moghadam M, Tangestaninejad S, Mirkhani V and Shaibani R. *Tetrahedron* 2004; **60**: 6105–6111. (d) Handman J, Harriman A and Porter G. *Nature* 1984; **307**: 534–535. (e) Jang JH, Jeon K-S, Oh S, Kim H-J, Asahi T, Masuhra H and Yoon M. *Chem. Mater.* 2007; **19**: 1984–1991. (f) Philippova TO, Galkin BN, Golovenko NY, Zhilina ZI and Vodzinskii SV. *J. Porphyrins Phthalocyanines* 2000; **4**: 243–247. (g) Embleton ML, Nair SP, Cookson BD and Wilson M. *J. Antimicrob. Chemother.* 2002; **50**: 857–864.
8. Toganoh M and Furuta H. *Chem. Commun.* 2012; **48**: 937–954.
9. Xie Y, Morimoto T and Furuta H. *Angew. Chem. Int. Ed.* 2006; **45**: 6907–6910.
10. Endo A, Ogasawara M, Takahashi A, Yokoyama D, Kato Y and Adachi C. *Adv. Mater.* 2009; **21**: 4802–4806.
11. Brown ID and Skowron A. *J. Am. Chem. Soc.* 1990; **112**: 3401–3403.
12. (a) Turner DH, Flynn GW, Sutin N and Beitz JV. *J. Am. Chem. Soc.* 1972; **94**: 1554–1559. (b) Ruasse MF, Aubard J, Galland B and Adenier A. *J. Phys. Chem.* 1986; **90**: 4382–4388.
13. Collins DM, Scheidt WR and Hard JL. *J. Am. Chem. Soc.* 1972; **94**: 6689–6696.
14. A Sn(IV) cation is also vibrated by the occupation at two positions in the macrocyclic core.
15. Mcpherson GL, Koch RC and Stucky GD. *J. Chem. Phys.* 1974; **60**: 1424–1431.
16. Indelli MT, Chiorboli C, Ghirotti M, Orlandi M, Scandola F, Kim HJ and Kim H-J. *J. Phys. Chem. B* 2010; **114**: 14273–14282.
17. Ou Z, E W, Zhu W, Thordarson P, Santic PJ, Crossley MJ and Kadish KM. *Inorg. Chem.* 2007; **46**: 10840–10849.
18. The redox potentials (V vs. Fc/Fc<sup>+</sup> in MeCN) of iodide-triiodide system have been reported; the redox potentials of E<sup>0</sup>(I<sub>2</sub><sup>•-</sup>/I<sup>-</sup>), E<sup>0</sup>(I<sup>•</sup>/I<sup>-</sup>) and E<sup>0</sup>(I<sub>3</sub><sup>-</sup>/I<sup>-</sup>) are estimated at +0.30, +0.60 and -0.34 V, respectively. See; Boschloo G and Hagfeldt A. *Acc. Chem. Res.* 2009; **42**: 1819–1826.
19. Goutermann M. In *The Porphyrins*, Dolphin D. (Ed.) Academic: New York, 1978.
20. The NICS and HOMA values of the freebase **2** are -6.335 ppm and 0.5392, respectively, which supports the dianionic properties of **SnCl<sub>2</sub>-2**.
21. Furuta H, Ishizuka T, Osuka A, Dejima H, Nakagawa H and Ishikawa Y. *J. Am. Chem. Soc.* 2001; **123**: 6207–6208.
22. Geier III GR, Ciringh Y, Li F, Haynes DM and Lindsey JS. *Org. Lett.* 2000; **2**: 1745–1748.

23. CrystalStructure 4.0: Crystal Structure Analysis Package, Rigaku Corporation (2000–2010). Tokyo 196–8666, Japan.
24. SHELX97: Sheldrick GM. *Acta Cryst.* 2008; **A 64**: 112–122.
25. Gaussian 09, Revision A.1, Frisch MJ, Trucks GW, Schlegel HB, Scuseria GE, Robb MA, Cheeseman JR, Scalmani G, Barone V, Mennucci B, Petersson GA, Nakatsuji H, Caricato M, Li X, Hratchian HP, Izmaylov AF, Bloino J, Zheng G, Sonnenberg JL, Hada M, Ehara M, Toyota K, Fukuda R, Hasegawa J, Ishida M, Nakajima T, Honda Y, Kitao O, Nakai H, Vreven T, Montgomery Jr.-JA, Peralta JE, Ogliaro F, Bearpark M, Heyd JJ, Brothers E, Kudin KN, Staroverov VN, Kobayashi R, Normand J, Raghavachari K, Rendell A, Burant JC, Iyengar SS, Tomasi J, Cossi M, Rega N, Millam NJ, Klene M, Knox JE, Cross JB, Bakken V, Adamo C, Jaramillo J, Gomperts R, Stratmann RE, Yazyev O, Austin AJ, Cammi R, Pomelli C, Ochterski JW, Martin RL, Morokuma K, Zakrzewski VG, Voth GA, Salvador P, Dannenberg JJ, Dapprich S, Daniels AD, Farkas Ö, Foresman JB, Ortiz JV, Cioslowski J and Fox DJ. Gaussian, Inc., Wallingford CT, 2009.
26. (a) Becke AD. *Phys. Rev. A* 1988; **38**: 3098–3100.  
(b) Lee C, Yang W and Parr RG. *Phys. Rev. B* 1988; **37**: 785–789.



# Preparation and characterization of cobalt(II) phthalocyanine complex-encapsulated zeolite-X

Nayumi Ohata<sup>a</sup>, Yurie Ito<sup>a</sup>, Daisuke Nakane<sup>a</sup>, Hideki Kitamura<sup>b</sup> and Hideki Masuda<sup>\*a</sup>

<sup>a</sup> Department of Frontier Materials, Graduate School of Engineering, Nagoya Institute of Technology, Gokiso-cho, Showa-ku, Nagoya 466-8555, Japan

<sup>b</sup> Sinanen Zeomic Co., Ltd., 1-1, Nakagawa Honmachi, Minato-ku, Nagoya 455-0051, Japan

*Dedicated to Professor Shunichi Fukuzumi on the occasion of his retirement*

Received 30 November 2014

Accepted 15 December 2014

**ABSTRACT:** Cobalt(II) phthalocyanine has been encapsulated into the supercage of X-type zeolite as an active monomer (CoPc-X) by the “ship-in-bottle” synthesis method, and furthermore the CoPc-X has been ion-exchanged with secondary metals ( $M^{n+} = Na^+, Ag^+, Cu^{2+}, Zn^{2+}$ ) to obtain CoPc- $M^{n+}$ -X. They have been characterized by elemental analysis, fluorescent X-ray, UV-vis, diffuse reflectance, physisorption analysis, and ESR spectroscopic methods, and their deodorant behaviors for smell gasses, 2-nonenal and indole, have been examined.

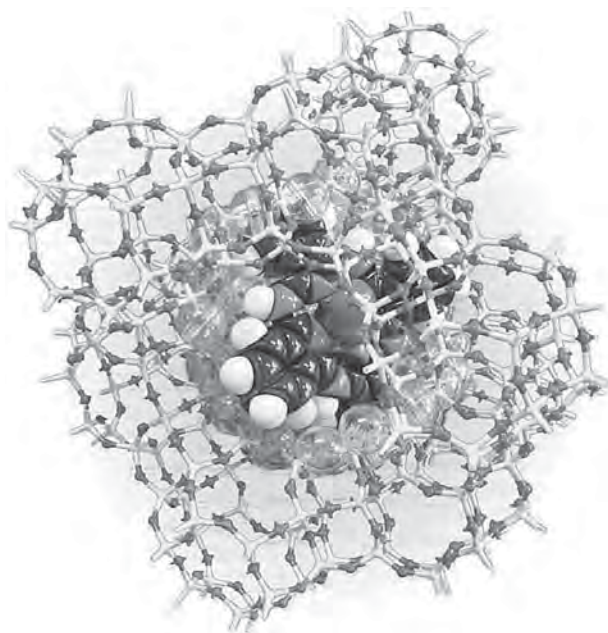
**KEYWORDS:** cobalt phthalocyanine, X-type zeolite, cobalt phthalocyanine-encapsulated zeolite, deodorant behavior, ship-in-bottle synthesis, ion-exchange method.

## INTRODUCTION

Metallophthalocyanine complex is known to have a unique structure/function similar to metalloporphyrins that play essential roles in biological metabolic systems. However, it is very difficult to employ metallophthalocyanine complexes as a catalytically active species without any modifications, because they form stable and inactive aggregates. One of the most effective methods to make use of metallophthalocyanine as an active metal complex is the encapsulation of phthalocyanine molecules inside the pores of appropriate porous materials such as zeolites. In 1977, the first study on encapsulation of metallophthalocyanine in faujasite zeolite was published [1]. Thereafter, a number of catalytic materials and analogous systems have been studied as a heterogeneous catalyst [2–7]. Faujasite zeolite is an attractive material to hold the metallophthalocyanine, because it has a supercage of crystalline pores consisting of four spherical windows with a diameter of 7.4 Å and spherical cages of 13 Å. The

X-type zeolite is one of the systematic aluminosilicate zeolite of Faujasite family. The framework induces a negative net charge per one aluminum, and various small cations can be inserted to compensate the negative charges, which give rise to ion-exchange properties of zeolite. The metal ion ( $M^{n+}$ ) in the metal ion-exchanged zeolite ( $M^{n+}$ -X) play the role of template reagent when  $M^{n+}$ -X are reacted with 1,2-Dicyanobenzene as a starting compound of phthalocyanine. 1,2-Dicyanobenzene is loaded into nanopores because its molecular size is smaller than the pore size of the supercage window of zeolite. The metallophthalocyanine complex synthesized inside the supercage can not get away from the supercage. The synthetic method is so-called “ship-in-bottle” method [8, 9]. Previously we also studied the catalytic oxidative reactivity by using nickel(II) phthalocyanine complex-encapsulated zeolite, and examined the effect of secondary metal ions incorporated into the zeolite with an expectation of novel high-performance material [10]. In this study, we synthesized the cobalt(II) phthalocyanine complex (CoPc) encapsulated into the supercages of X-type zeolite by the “ship-in-bottle” method (Scheme 1), and prepared the secondary ion-exchanged zeolite-X

\*Correspondence to: Hideki Masuda, email: [masuda.hideki@nitech.ac.jp](mailto:masuda.hideki@nitech.ac.jp), +81 52-735-5228



**Scheme 1.** Structure of CoPc-encapsulated zeolite

by the ion-exchanged method with another metal ions  $M^{n+}$  ( $M^{n+} = Ag^+, Zn^+, Cu^{2+}$ ), where the former and the latter have been named to CoPc-X and CoPc- $M^{n+}$ -X, respectively. They were identified and characterized by the elemental and fluorescent analyses, UV-vis, reflectance, ESR spectroscopic, and physisorption analysis methods.

## EXPERIMENTAL

### Reagents

Reagents used in this study were purchased as a reagent grade from Wako Pure Chemical Industry Inc. or Tokyo Kasei Kogyo Inc. and were used without further purification. Reagent grade solvents were obtained from Wako Pure Chemical Industry Inc. and Kanto Kagaku Inc. and were doubly distilled before use.

### Preparation of CoPc- $M^{n+}$ -X ( $M^{n+} = Na^+, Ag^+, Cu^{2+}$ , and $Zn^{2+}$ )

Cobalt(II) phthalocyanine encapsulated in the supercage of zeolite-X, CoPc-X, was prepared by following the procedure treated previously for the corresponding zeolite-Y [8, 9]. The  $Co^{2+}$ -exchanged zeolite-X ( $Co = \sim 1$  wt.%) was heated with excess amount of 1,2-dicyanobenzene at 493 K for 6 h in inert solvent of ethylene glycol. The crude CoPc-X was washed with acetone, methanol, pyridine, and acetone, repeatedly, in the Soxhlet extractor to remove unreacted and incomplete compounds in and/or on the supercage of zeolite and external phthalocyanine generated on the outside surface

of the zeolite [7]. Subsequently, the purified CoPc-X was stirred in  $Na^+$ -containing solution to replace unreacted  $Co^{2+}$  ion to  $Na^+$  one and give CoPc- $Na^+$ -X. The other metal ion-exchanged CoPc- $M^{n+}$ -X were also prepared by the 'secondary ion-exchange' reaction of CoPc-X with  $M^{n+}$  ion ( $M^{n+} = Na^+, Ag^+, Cu^{2+}$ , and  $Zn^{2+}$ ). They were characterized by elemental analysis, UV-vis, diffuse reflectance (DR), fluorescent X-ray analysis (EDX), physisorption analysis, and ESR spectroscopic methods. Deodorant effect for some smell gasses was estimated from the rate of reduction of smell gas in the presence of CoPc- $M^{2+}$ -X (1 g), which was analyzed with GC/MS method.

### Measurements

Elemental analysis was carried out using a Parkin Elmer PE2400 II elemental analyzer. Electronic absorption spectra in UV-vis region were measured by a JASCO UV-vis spectrophotometer V-570 using 1 cm quartz cell. DR spectra were recorded with a JASCO UV-vis spectrophotometer V-570 equipped with ISN-470 integrating sphere. The spectra of complexes encapsulated into the zeolite were recorded against zeolite-X background. Energy dispersive X-ray fluorescence (EDX) analysis was carried out using a Shimadzu EDX-800HS fluorescence spectrometer with a calibration curve methods for metal atoms. Specific surface analyses were performed on a BEL Japan BELSORP-max with nitrogen as the absorption gas at liquid nitrogen temperature by Brunauer-Emmett-Teller (BET) method. Gas chromatograms were measured by a Shimadzu GC-8APF gas chromatography with a Shimadzu C-R6A Chromatopack integrator. Solid state ESR spectra were measured with a JEOL RE-1X ESR spectrometer at 77 K. Depdorant behavior of CoPc- $M^{2+}$ -X was carried out for nonenal and indole. The sample (1 g) of CoPc- $M^{n+}$ -X was put in the tedlar bag<sup>®</sup> to which the smell gas of nonenal (200 ppm) or indole (100 ppm) was flowed. The decreasing rates of residual gas were determined by GC/MS spectroscopy after 1 and 3 h.

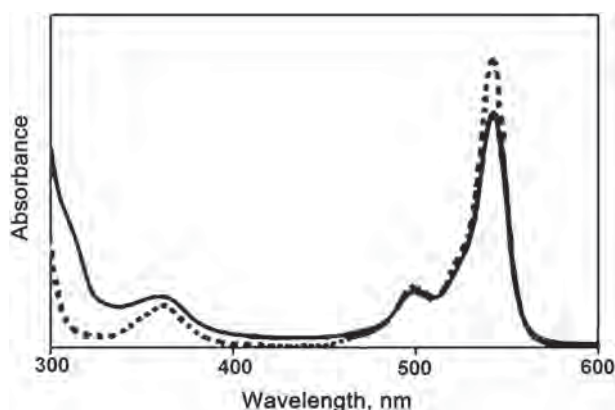
## RESULTS AND DISCUSSION

### Preparation and characterization of CoPc- $M^{n+}$ -X

The X-type zeolite exhibited a color change from white to pale blue through the "ship-in-bottle" synthesis and secondary ion-exchange processes. The elemental analyses of some zeolites CoPc- $M^{n+}$ -X gave a C/N ratio of  $\sim 4$ , which corresponds to the C/N ratio for neat CoPc, 4.0. The data of EDX analyses for CoPc-X are summarized in Table 1. The number of Pc molecules per unit cell of zeolite including eight supercages was about 1.6, which was estimated from C/N analysis. The number of cobalt atoms in a unit cell of zeolite-X was found to be more

**Table 1.** The components of heavy elements of CoPc-Na<sup>+</sup>-X determined by EDX method

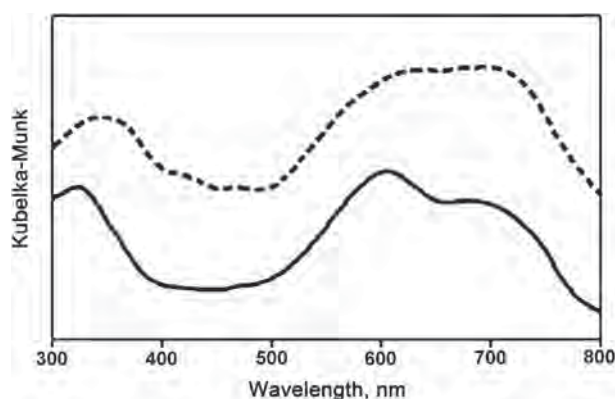
	CoPc-Na-X wt. %	CoPc-Ag-X wt. %	CoPc-Cu-X wt. %	CoPc-Zn-X wt. %
O	47.8	47.6	47.7	47.7
Si	20.7	19.8	20.6	20.5
Al	17.5	16.8	17.5	17.4
Na	12.0	11.1	11.2	11.4
Co	0.746	0.661	0.711	0.722
Ag	—	0.851	—	—
Cu	—	—	1.100	—
Zn	—	—	—	1.180

**Fig. 1.** UV-vis spectra of CoPc-Na<sup>+</sup>-X system (dotted line) and CoPc complex (solid line) in H<sub>2</sub>SO<sub>4</sub> solution

than Pc ligands, although the secondary ion-exchange method was treated to remove unreacted cobalt ions.

In order to demonstrate the formation of CoPc inside zeolite, we measured UV-vis spectrum of CoPc-Na<sup>+</sup>-X dissolved in H<sub>2</sub>SO<sub>4</sub> solution, because zeolite is decomposed in H<sub>2</sub>SO<sub>4</sub> whereas CoPc is not decomposed but dissolved. As expected, the spectrum (Q-bands at 697 and 785 nm, and Soret or B-band at 423 nm) of CoPc-Na<sup>+</sup>-X in H<sub>2</sub>SO<sub>4</sub> solution is almost the same as that (Q-bands at 696 and 784 nm, and Soret or B-band at 422 nm) of CoPc complex in H<sub>2</sub>SO<sub>4</sub> solution (Fig. 1), indicating the CoPc complex was formed inside nanopores of zeolite-X by “ship-in-bottle.”

DR spectrum of powder CoPc-Na<sup>+</sup>-X is shown together with the sum of those of neat CoPc and zeolite-X in Fig. 2. The DR spectrum of CoPc-Na<sup>+</sup>-X gave two broad bands at around 606 and 674 nm and one broad band at around 323 nm, and the sum of the spectra of neat CoPc and zeolite-X afforded similar three broad bands at around 635 and 696 and 345 nm. These bands were assigned as follows; the former two and the latter one broad bands are characteristic of Q- and B-bands of metallophthalocyanine complex, respectively [6, 7]. This

**Fig. 2.** DR spectra of powder CoPc-Na<sup>+</sup>-X (dashed line) and a mixture (block line) of neat CoPc and zeolite-X

spectrum is similar to that of CoPc-Y reported previously (two intense bands centered at 610 and 675 nm), although a shoulder band at around 730 nm observed in CoPc-encapsulated zeolite-Y was not detected in that of CoPc-Na<sup>+</sup>-X (Fig. 2). In that of CoPc-Y, the red shifts of B and Q-bands in comparison with those of neat CoPc suggest a distortion from a planarity of CoPc molecule by the encapsulation into zeolite. This means that the symmetry of CoPc structure was lowered from *D*<sub>4h</sub> for example to *D*<sub>2h</sub> by the encapsulation of CoPc inside zeolite, because the reduction in planarity of the phthalocyanine molecule is known to lead to an increased separation of the Q<sub>x</sub> and Q<sub>y</sub> components [11, 12].

In order to determine that CoPc molecule is encapsulated inside the nanopores of X-type zeolite, we carried out N<sub>2</sub> adsorption measurements for NaX and CoPc-Na<sup>+</sup>-X. As expected, the BET specific surface area (675.5 m<sup>2</sup>.g) and pore volume (0.23 cm<sup>3</sup>.g) of CoPc-Na<sup>+</sup>-X were both evidently smaller than those (836.8 m<sup>2</sup>.g and 0.30 cm<sup>3</sup>.g, respectively) of NaX, indicating that CoPc molecule is incorporated inside the nanopores of zeolite.

Interestingly, the solid state ESR spectrum of CoPc-Na<sup>+</sup>-X at 77 K gave a sharp intense resonance line in the lower-field region (*g*<sub>||</sub> = 1.88) and a weak resonance line in the higher-field region (*g*<sub>⊥</sub> = 2.99) as shown in Fig. 3. The lower-field lines are composed of eight equally spaced peaks (a peak separation of 19 mT) varying in intensity, and the higher-field set also consists of eight weak peaks, equally spaced with a separation of 20 mT gauss. These hyperfine splittings correspond to the nuclear spin of cobalt ion, *I* = 7/2. Such an ESR spectrum with a clear hyperfine splitting is quite similar to that of the cobalt(II) phthalocyanine magnetically diluted in metal-free, zinc and nickel phthalocyanines that was reported previously [13]. Such a clearly splitting peak has not been observed in CoPc only, a mixture of CoPc and zeolite, and zeolite inserted with Co<sup>2+</sup> ion, all of which gave broad bands. These findings strongly suggest that CoPc is encapsulated independently in the nanopore of zeolite.



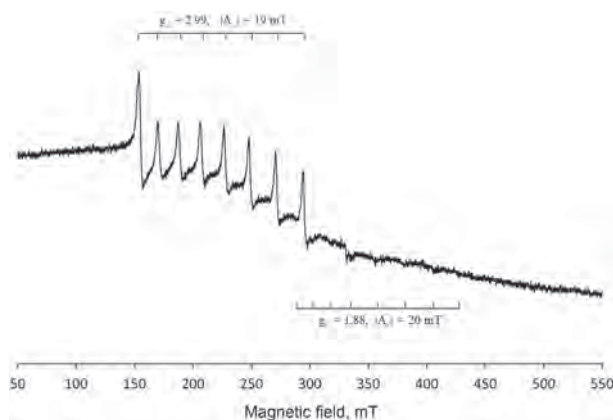


Fig. 3. Solid state ESR spectrum of CoPc-Na<sup>+</sup>-X

Table 2. Deodorant behaviors for smell gases, 2-nonenal<sup>a</sup> and indole<sup>a</sup>, after 1 and 3 h

Samples	Smell gases	Decreasing rate of smell gas, %	
		1 h	3 h
CoPc-Na <sup>+</sup> -X	nonenal	71	72
	indole	12	60
CoPc-Ag <sup>+</sup> -X	2-nonenal	10	84
	indole	65	100
CoPc-Zn <sup>2+</sup> -X	2-nonenal	24	85
	indole	78	100
CoPc-Cu <sup>2+</sup> -X	2-nonenal	83	94
	indole	65	100
Na <sup>+</sup> X	2-nonenal	60	70
	indole	52	64

<sup>a</sup>200 and 100 ppm of 2-nonenal and indole, respectively, were put in the tetrabag.

### Deodorant behaviors of CoPc-Na<sup>+</sup>-X

It is well-known that zeolites have a deodorant function for a long time, so we tried to study on the deodorant behaviors of cobalt(II) phthalocyanine-encapsulating zeolite. Using CoPc-X and its second-ion exchanged CoPc-X, CoPc-M<sup>n+</sup>-X, we evaluated the time-dependency of decreasing rate of smell gases, 2-nonenal and indole, which are a component of distinctive body odor and excretion smell, respectively, by GC/MS spectrometry. Table 2 shows a summary of the decreasing rates of small gasses after 1 and 3 h. Both smells were decreased by all of the zeolites used; where the decrease of blank was within 5% after 3 h. Especially, indole was reduced in CoPc-M<sup>n+</sup>-X containing cobalt phthalocyanine complex in zeolite, although it was also decreased in zeolite-X (Na<sup>+</sup>-X).

This may be explained to have been pulled into zeolite by a attractive  $\pi$ - $\pi$  interaction between phthalocyanine and indole molecules. On the other hand, the deodorant behaviors of 2-nonenal did not show a significant difference between CoPc-M<sup>n+</sup>-X and Na<sup>+</sup>-X, although a slightly larger decrease was found in CoPc-M<sup>n+</sup>-X with M = Ag<sup>+</sup>, Zn<sup>2+</sup>, and Cu<sup>2+</sup>. The decreasing in 2-nonenal may have been induced by electrostatic interaction between 2-nonenal and metal ions in zeolite, because 2-nonenal has an aldehyde group. The large decrease found in CoPc-M<sup>n+</sup>-X with M = Ag<sup>+</sup>, Zn<sup>2+</sup>, and Cu<sup>2+</sup> may be due to somewhat weak interaction between metal ion of cobalt phthalocyanine and 2-nonenal. Na<sup>+</sup>-X and CoPc-Na<sup>+</sup>-X did not show a significant deodorant behavior for indole and 2-nonenal. This may mean that the Na<sup>+</sup> ion as the second ion is strongly surrounded by water molecules to disturb the approach of smell gas.

### SUMMARY

In order to prepare a metallophthalocyanine as an active monomer (CoPc-X), we synthesized cobalt(II) phthalocyanine complexes encapsulated into the supercage of X-type zeolite by the “ship-in-bottle” synthesis method. Because a phthalocyanine usually aggregates in the solid state and is very difficult to make its peculiar function to appear. They have been characterized by elemental analysis, fluorescent X-ray, UV-vis, diffuse reflectance, physisorption analysis, and ESR spectroscopic methods. Furthermore the CoPc-X has been ion-exchanged with secondary metal ions (M<sup>n+</sup> = Na<sup>+</sup>, Ag<sup>+</sup>, Cu<sup>2+</sup>, Zn<sup>2+</sup>) to obtain CoPc-M<sup>n+</sup>-X. The deodorant behavior for smell gasses, 2-nonenal and indole, has also been examined, and significant adsorption of indole to the CoPc-M<sup>n+</sup>-X systems has been explained in terms of  $\pi$ - $\pi$  interaction between indole and phthalocyanine.

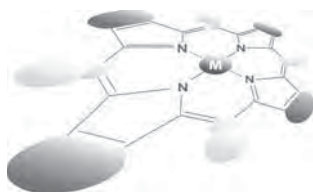
### Acknowledgements

We gratefully acknowledge for the support of this work by a Grant-in-Aid for Scientific Research from the Ministry of Education, Culture, Sports, Science, Sports and Technology, by the Knowledge Cluster Project, and from the Strategic Young Researcher Overseas Visits Program for Accelerating Brain Circulation.

### REFERENCES

1. Korol'kova TV, Zakharov AN and Romanovskii BV. *Ves. Mosk. Univ. Ser. Khim.* 1984; **25**: 362–364.
2. Diegruber H, Plath PJ and Schulz-Ekloff G. *J. Mol. Catal.* 1984; **24**: 115–126.
3. Herron N, Stucky GD and Tolman CA. *J. Chem. Soc., Chem. Commun.* 1986; 1521–1522.

4. Seelan S and Sinha AK. *Appl. Catal. A.: Gen.* 2003; **238**: 201–2009.
5. Haber J, Pamin K and Poltowics J. *J. Mol. Catal. A.* 2004; **224**: 153–159.
6. Paez-Mozo E, Gabriumas N, Lucaccioni F, Acosta DD, Patrono P, Ginestra AL, Ruiz P and Delmon B. *J. Phys. Chem.* 1993; **97**: 12819–12827.
7. Ray S and Vasudevan S. *Inorg. Chem.* 2003; **42**: 1711–1719.
8. Meyer G, Wöhrle D, Mohl M and Schulz-Ekloff G. *Zeolite*. 1984; **4**: 30–34.
9. Seelan S, Sinha AK, Srinivas D and Sivasanker S. *J. Mol. Catal. A.* 2000; **157**: 163–171.
10. Ohata N, Ito Y, Gomibuchi D, Kitamura H, Funahashi Y, Ozawa T and Masuda H. *Adv. Mat. Res.* 2006; **11–12**: 281–284.
11. Dodsworth ES, Lever ABP, Seymour P and Leznoff CC. *J. Chem. Phys.* 1985; **89**: 5698–5705.
12. Orti E, Bredas JL and Clarisse C. *J. Chem. Phys.* 1990; **92**: 1228–1235.
13. Assour JM and Kahn W. *J. Am. Chem. Soc.* 1965; **87**: 207–212.



## Redox behavior of novel nickel and palladium complexes supported by trianionic non-innocent ligand containing $\beta$ -diketiminato and phenol groups

Yuma Morimoto, June Takaichi, Shinichi Hanada, Kei Ohkubo<sup>◇</sup>, Hideki Sugimoto, Nobutaka Fujieda, Shunichi Fukuzumi<sup>◇</sup> and Shinobu Itoh\*

Department of Material and Life Science, Division of Advanced Science and Biotechnology,  
Graduate School of Engineering, Osaka University, 2-1 Yamadaoka, Suita, Osaka 565-0871, Japan

Dedicated to Professor Shunichi Fukuzumi on the occasion of his retirement

Received 5 November 2014

Accepted 18 December 2014

**ABSTRACT:** A new type of nickel and palladium complexes with non-innocent  $\beta$ -diketiminato ligand having redox active phenol groups, 2,4-di-*tert*-butyl-6-(((1*E*,2*E*)-3-((3,5-di-*tert*-butyl-2-hydroxyphenyl)amino)-2-nitroallylidene)amino)phenol ( $LH_3$ , fully protonated form) have been developed, and the structure, physical properties, and reactivity of their one-electron and two-electron oxidized complexes,  $[M^{II}(L^{\bullet 2})]$  and  $[M^{II}(L^-)]^+$  ( $M = Ni^{II}$  or  $Pd^{II}$ ) have been examined in detail. The two-electron oxidized forms of both complexes,  $[M^{II}(L^-)]^+$ , exhibited hydrogen atom abstraction ability from 1,4-cyclohexadiene (CHD) comparable to its copper analog  $[Cu^{II}(L^-)]^+$  (*Dalton Trans.* 2013; **42**: 2438-2444). The one-electron oxidized form of palladium complex,  $[Pd^{II}(L^{\bullet 2})]$ , was also found to oxidize CHD, whereas the nickel analog,  $[Ni^{II}(L^{\bullet 2})]$ , exhibited photo-induced oxidation ability of CHD.

**KEYWORDS:** nickel complex, palladium complex,  $\beta$ -diketiminato ligand, non-innocent ligand.

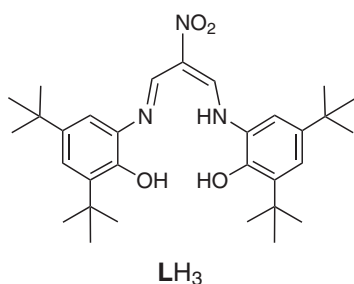
## INTRODUCTION

Transition metal complexes supported by redox non-innocent ligands such as porphyrin and phthalocyanine derivatives have long been attracting much attention due to their relevance to enzymatic catalysis and a variety of functional materials [1, 2]. The capability of an electron release from highly conjugated  $\pi$ -orbitals of porphyrin and phthalocyanine are regarded as important factor to facilitate multi-electron transfer such as hydroxylation of aliphatic substrates occurring in cytochrome P450 (CYP) and its models [3–10]. Recently, phenol-containing ligand also have received much interest as an active site model of metalloenzymes containing a redox-active organic cofactor such as tyrosine or its derivatives

[11–14]. Galactose oxidase is a typical example of such enzymes, which contains a copper(II)-tyrosyl (phenoxy) radical as the key reactive intermediate for the oxidation of primary alcohols to aldehydes [15–19]. In this enzyme, the copper center is further ligated by an additional tyrosyl residue to construct a Tyr–Cu–Tyr motif. In order to mimic such an active site structure, salen-type ligands consisting with two phenol groups connected by diamine derivatives have been tested [13, 14]. In most cases, ligand effects as well as metal ion effects on the electronic structures of one-electron oxidized mix-valent systems have been investigated, but little attention has been focused on the reactivity of the phenoxy radical transition-metal complexes. In this respect, Stack and co-workers have investigated the direct reaction between the  $Cu^{II}$ -phenoxy radical complexes and benzyl alcohol to demonstrate the importance of substrate coordination to the metal center prior to the C–H bond activation of the substrates [20–22]. In parallel, the electronic

<sup>◇</sup> SPP full member in good standing

\*Correspondence to: Shinobu Itoh, email: [shinobu@mls.eng.osaka-u.ac.jp](mailto:shinobu@mls.eng.osaka-u.ac.jp), tel: +81 6-6879-7932, fax: +81 6-6879-7935



**Scheme 1.** Molecular structure of the ligand

structures and chemical properties of the group 10 element complexes, Ni, Pd, and Pt, supported by salen type ligands have also been investigated in detail [23–32]. In those studies, unambiguously demonstrated are the ability of salen-type ligands modulating the multi-electron redox processes of the metal center.

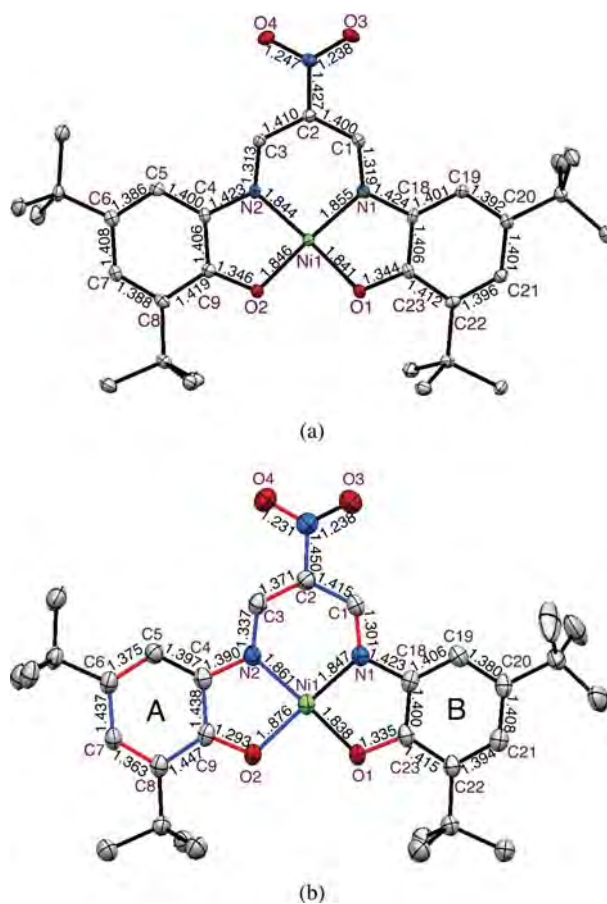
Recently, we have examined the reactivity of a discreet Cu<sup>II</sup>-phenoxy radical complex generated by using a new type of diphenol ligand consisting with a  $\beta$ -diketiminato bridging moiety as shown in Scheme 1 [33]. In this study, we have further examined the spectroscopic property and reactivity of phenoxy radical complexes to evaluate the metal ion effects using Ni- and Pd-complexes supported by the same ligand.

## RESULTS AND DISCUSSION

### Synthesis and characterization

The nickel(II) and the palladium(II) complexes were prepared by treating the neutral ligand LH<sub>3</sub> (Scheme 1) with an equimolar amount of nickel(II) acetate or palladium(II) acetate in the presence of a base (NEt<sub>4</sub>OH or Et<sub>3</sub>N). The single crystals were obtained as described in the Experimental section. In the case of Pd-complex, the counter cation was exchanged from Et<sub>3</sub>NH<sup>+</sup> to Bu<sub>4</sub>N<sup>+</sup> to facilitate crystallization (see Experimental section). Figures 1(a) and 2(a) show the crystal structures of (Et<sub>4</sub>N)[Ni<sup>II</sup>(L<sup>3-</sup>)] and (Bu<sub>4</sub>N)[Pd<sup>II</sup>(L<sup>3-</sup>)], respectively (the counter cations are omitted for simplicity, the crystallographic data are presented in Supporting information, Table S1). In both complexes, the ligand takes the tri-anionic form (fully deprotonated form L<sup>3-</sup>), since there is one counter cation (R<sub>4</sub>N<sup>+</sup>) per one complex molecule (not shown in Fig. 1(a) and 2(a)), and the negative mode ESI-MS gave an intense peak cluster at 578.30 and 626.15, respectively, which are assignable to the molecular formula of the anionic complexes [M<sup>II</sup>(L<sup>3-</sup>)]<sup>-</sup> (M = Ni and Pd) (Fig. 3). The peak distribution patterns are also consistent with those expected for the respective complexes.

The metal centers of [Ni<sup>II</sup>(L<sup>3-</sup>)]<sup>-</sup> and [Pd<sup>II</sup>(L<sup>3-</sup>)]<sup>-</sup> exhibited square planar geometries with the N<sub>2</sub>O<sub>2</sub> donor

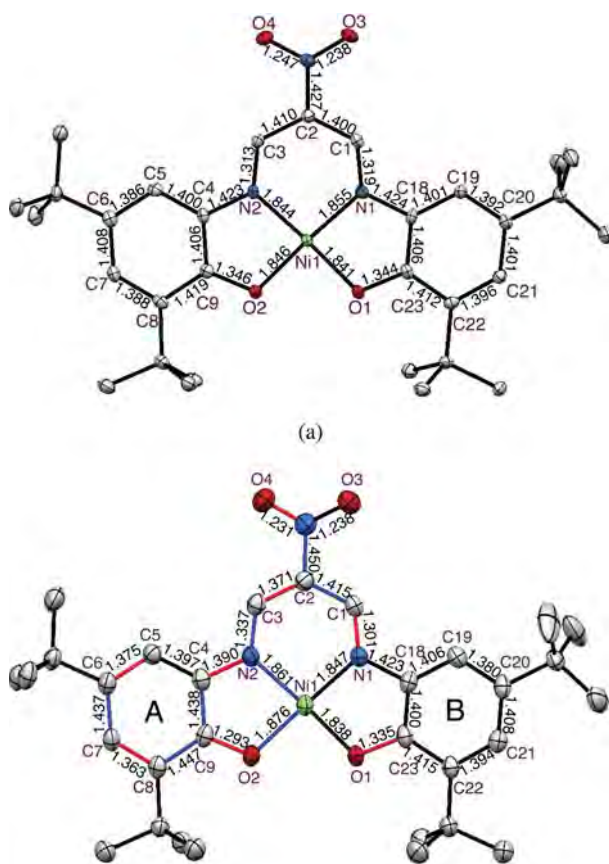


**Fig. 1.** ORTEP drawings of (a) (Et<sub>4</sub>N)[Ni<sup>II</sup>(L<sup>3-</sup>)] and (b) [Ni<sup>II</sup>(L<sup>2-</sup>)] showing 50% probability thermal ellipsoids. Hydrogen atoms, counter cation, and solvent molecules are omitted for clarity. For the structure of [Ni<sup>II</sup>(L<sup>2-</sup>)], elongated bonds (more than 0.01 Å) are indicated in blue color, and shortened bonds (more than 0.01 Å) are indicated in red color

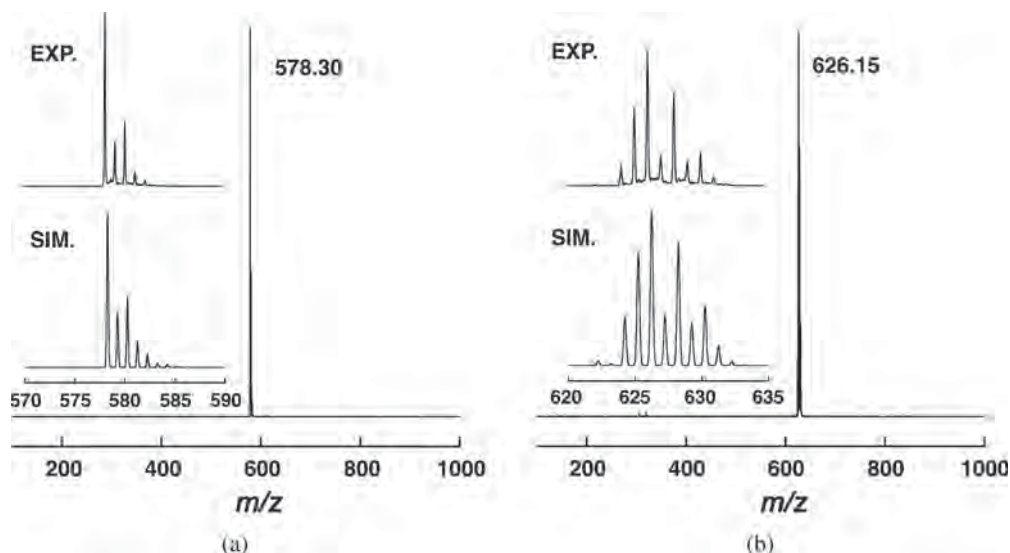
set of the ligand, where the torsion angles between the O1–M1–N1 and O2–M1–N2 planes are 2.3° and 0.4°, respectively. The bond length of Ni–O (1.841 and 1.846 Å) and Ni–N (1.855 and 1.844 Å) are slightly shorter than those of Ni<sup>II</sup>-salen complex [Ni<sup>II</sup>(sal<sup>2-</sup>)] (sal<sup>2-</sup> = diphenolate form of salH<sub>2</sub>, *N,N'*-bis(3,5-di-*tert*-butylsalicylidene)-1,2-cyclohexane-(1*R*,2*R*)-diamine, Ni–O, 1.852 and 1.854 Å; Ni–N, 1.852 and 1.860 Å) [35]. The Pd–O bond lengths (1.997 and 1.999 Å) are slightly longer than those of [Pd<sup>II</sup>(sal<sup>2-</sup>)] (Pd–O, 1.970 and 1.969 Å), whereas the Pd–N bond lengths (1.957 and 1.954 Å) are almost the same to those of [Pd<sup>II</sup>(sal<sup>2-</sup>)] (Pd–N, 1.959 and 1.946 Å) [28]. Apparently, the M–O and M–N bonds of the Ni-complex are shorter than those of the Pd-complex, which is due to the difference in the ionic radius between the two metal ions; Ni(II) 0.63 Å, Pd(II) 0.78 Å.

### Redox property

The redox properties of [M<sup>II</sup>(L<sup>3-</sup>)]<sup>-</sup> were examined using cyclic voltammetry (CV) as shown in Fig. 4.



**Fig. 2.** ORTEP drawings of (a)  $(\text{Bu}_4\text{N})[\text{Pd}^{\text{II}}(\text{L}^{3-})]$  and (b)  $[\text{Pd}^{\text{II}}(\text{L}^{2-})]$  showing 50% probability thermal ellipsoids. Hydrogen atoms, counter cation, and solvent molecules are omitted for clarity. For the structure of  $[\text{Pd}^{\text{II}}(\text{L}^{2-})]$ , elongated bonds (more than  $0.01 \text{ \AA}$ ) are indicated in blue color, and shorten bonds (more than  $0.01 \text{ \AA}$ ) are indicated in red color

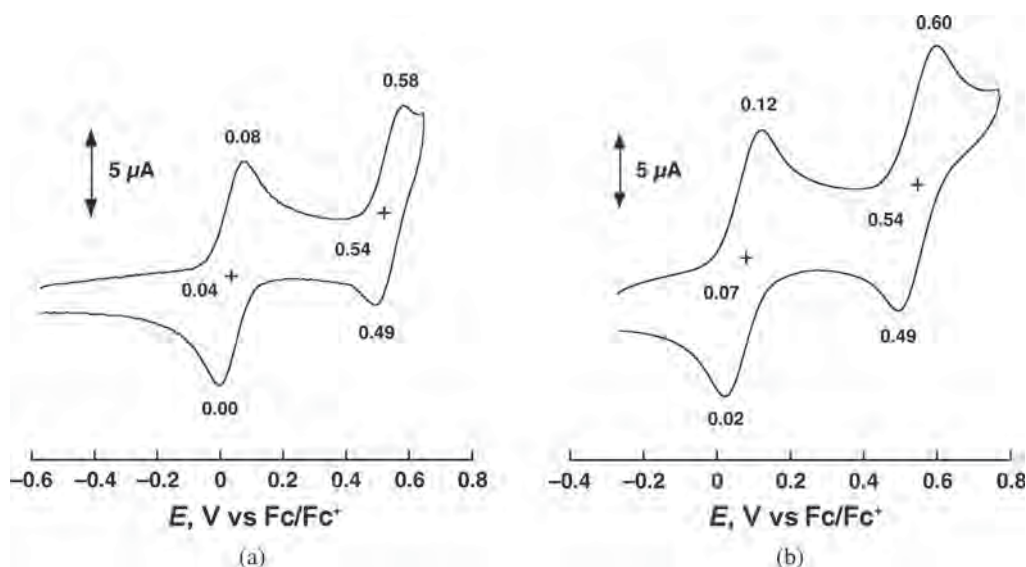


**Fig. 3.** ESI-MS (negative mode) of (a)  $[\text{Ni}^{\text{II}}(\text{L}^{3-})]^-$  and (b)  $[\text{Pd}^{\text{II}}(\text{L}^{3-})]^-$  in  $\text{CH}_2\text{Cl}_2$ . Inset: expanded spectra (EXP) and their simulation spectra (SIM)

Both complexes exhibited two reversible redox couples ( $E_{1/2}^1$  and  $E_{1/2}^2$ ) due to the first and second one-electron oxidation of the anionic complexes. The redox potential of the  $\text{Ni}^{\text{II}}$ - and  $\text{Pd}^{\text{II}}$ -complexes are summarized in Table 1 together with those of the  $\text{Cu}^{\text{II}}$ -complex of the same ligand  $[\text{Cu}^{\text{II}}(\text{L}^{3-})]$  and  $[\text{M}^{\text{II}}(\text{sal}^{2-})]$  ( $\text{M} = \text{Cu}, \text{Ni}, \text{and Pd}$ ) for comparison (reference papers for the reported data are indicated in the table footnote).

It appears that the  $E_{1/2}^1$  and  $E_{1/2}^2$  values as well as the  $\Delta E_{1/2}$  ( $E_{1/2}^1 - E_{1/2}^2$ ) values of all the  $\text{L}^{3-}$  complexes ( $\text{M}^{\text{II}} = \text{Cu}, \text{Ni}, \text{and Pd}$ ) are fairly similar as  $E_{1/2}^1 = -0.07 \sim +0.07 \text{ V}$ ,  $E_{1/2}^2 = +0.46 \sim +0.54 \text{ V}$  vs Ferrocene/Ferrocenium ion ( $\text{Fc}/\text{Fc}^+$ ) and  $\Delta E_{1/2} = 0.47 \sim 0.50 \text{ V}$ , which are largely negative as compared to those of the salen complexes. The largely negative shifts of the  $E_{1/2}$  values of  $[\text{M}^{\text{II}}(\text{L}^{3-})]^-$  as compared to those of  $[\text{M}^{\text{II}}(\text{sal}^{2-})]$  can be attributed to the higher HOMO level of the trianionic  $\text{L}^{3-}$  as compared to that of the dianionic  $\text{sal}^{2-}$  [33].

In the salen system, it has been reported that the electronic coupling between the redox active phenolate groups correlates strongly with difference in the metal  $d$  orbital energy and ligand MO energy [20]. In the present ligand system, on the other hand, the degree of electronic coupling is independent on the metal ions as indicated by the similar  $E_{1/2}$  and  $\Delta E_{1/2}$  values among the three complexes ( $\text{Cu}, \text{Ni}, \text{and Pd}$ ). This may be due to the conjugation between the two phenolate groups through the  $\beta$ -diketiminato backbone. SOMO 155a of  $[\text{Cu}^{\text{II}}(\text{L}^{2-})]$  calculated by using DFT method, which mainly consists of  $\pi$ -orbitals on the ligand, clearly shows that the two phenolate groups are electronically bridged by the conjugated  $\beta$ -diketiminato moiety [33]. In the salen system, there is no such conjugative interaction between the two phenolate groups, since the phenolate groups are connected by the saturated alkyl diamine moiety.



**Fig. 4.** Cyclic voltammograms of (a)  $[\text{Ni}^{\text{II}}(\text{L}^{3-})]^-$  ( $5.0 \times 10^{-4}$  M) and (b)  $[\text{Pd}^{\text{II}}(\text{L}^{3-})]^-$  ( $5.0 \times 10^{-4}$  M) in  $\text{CH}_2\text{Cl}_2$  containing  ${}^n\text{Bu}_4\text{NPF}_6$  (0.10 M); working electrode: glassy carbon, counter electrode: Pt, reference: ferrocene, scan rate 100 mV/s

**Table 1.** Electrochemical data of the oxidation of  $[\text{M}^{\text{II}}(\text{L}^{3-})]^-$  and  $[\text{M}^{\text{II}}(\text{sal}^{2-})]^-$

Complex	$E_{1/2}^1, \text{V}^a$	$E_{1/2}^2, \text{V}^a$	$\Delta E_{1/2} (E_{1/2}^1 - E_{1/2}^2), \text{V}$
$[\text{Cu}^{\text{II}}(\text{L}^{3-})]^-$ <sup>b</sup>	-0.06	+0.46	0.50
$[\text{Ni}^{\text{II}}(\text{L}^{3-})]^-$	+0.04	+0.54	0.50
$[\text{Pd}^{\text{II}}(\text{L}^{3-})]^-$	+0.07	+0.54	0.47
$[\text{Cu}^{\text{II}}(\text{sal}^{2-})]^-$ <sup>c</sup>	+0.45	+0.65	0.20
$[\text{Ni}^{\text{II}}(\text{sal}^{2-})]^-$ <sup>d</sup>	+0.37	+0.85	0.48
$[\text{Pt}^{\text{II}}(\text{sal}^{2-})]^-$ <sup>e</sup>	+0.45	+0.80	0.35

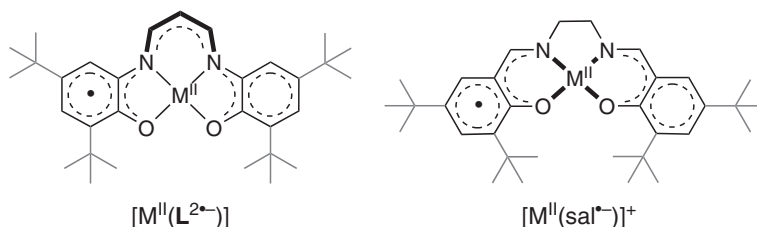
<sup>a</sup> vs Fc/Fc<sup>+</sup>. <sup>b</sup> from Ref. 15. <sup>c</sup> from Ref. 19. <sup>d</sup> from Ref. 20. <sup>e</sup> from Ref. 18.

Therefore, the electronic coupling can only be mediated by the metal ion (Scheme 2).

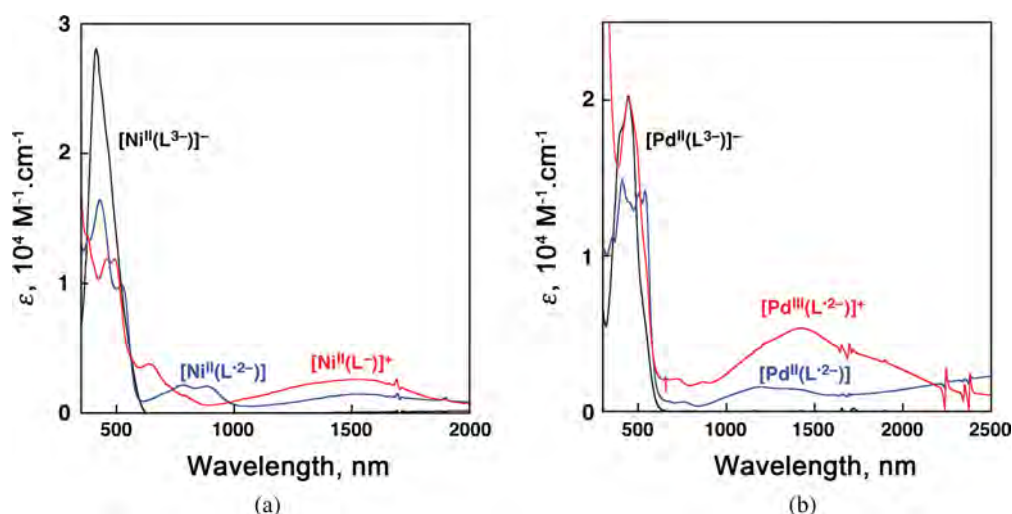
### One-electron oxidation product

The one-electron oxidation products can also be generated by the chemical oxidation using an equimolar amount of  $\text{AgSbF}_6$  in  $\text{CH}_2\text{Cl}_2$ , and their single crystals suitable for X-ray crystallographic analysis were

successfully obtained by recrystallization from  $\text{CH}_2\text{Cl}_2/n$ -hexane. Crystal structures of the neutral complexes  $[\text{Ni}^{\text{II}}(\text{L}^{2-})]$  and  $[\text{Pd}^{\text{II}}(\text{L}^{2-})]$  are shown in Fig. 1(b) and Fig. 2(b), respectively. The crystallographic data are presented in Table S2. The crystal structure of  $[\text{Ni}^{\text{II}}(\text{L}^{2-})]$  clearly indicates that one-electron oxidation of  $[\text{Ni}^{\text{II}}(\text{L}^{3-})]^-$  caused a distinctive structural change in the aminophenol moiety of ring A and  $\beta$ -diketiminato moiety. Namely, structures of the aminophenol moiety of rings A and B are nearly identical in  $[\text{Ni}^{\text{II}}(\text{L}^{3-})]^-$  (Fig. 1(a)), whereas contribution of a quinonoid canonical form increases in the aminophenol moiety of ring A in the oxidized complex  $[\text{Ni}^{\text{II}}(\text{L}^{2-})]$  (Fig. 1(b)). The distance of Ni1–O2 (1.876 Å) increases as compared with that of Ni1–O1 (1.838 Å). In addition, such structural changes occurred on  $\beta$ -diketiminato moiety as well, e.g. the bond distances of C4–N2 and C3–C2 are shrunk from 1.423 and 1.410 to 1.390 and 1.371, respectively. These structural features of the oxidized complex are consistent with the conclusion that the one-electron oxidation takes place at the conjugated  $\pi$ -orbital consisting of phenolate and  $\beta$ -diketiminato part to give  $\text{L}^{2-}$  rather than at the metal. One-electron oxidation product  $[\text{Pd}^{\text{II}}(\text{L}^{2-})]$  showed a similar structural features to  $[\text{Ni}^{\text{II}}(\text{L}^{2-})]$  as shown in Fig. 2(b). The notable structural change was



**Scheme 2.** Conjugation of  $\pi$ -orbital in  $[\text{M}^{\text{II}}(\text{L}^{2-})]$  and  $[\text{M}^{\text{II}}(\text{sal}^{1-})]^+$



**Fig. 5.** (a) Absorption spectra of  $[\text{Ni}^{\text{II}}(\text{L}^{3-})]^-$  (black line),  $[\text{Ni}^{\text{II}}(\text{L}^{2-})]$  (blue line) and  $[\text{Ni}^{\text{II}}(\text{L}^-)]^+$  (red line) in  $\text{CH}_2\text{Cl}_2$  at  $-10^\circ\text{C}$ . (b) Absorption spectra of  $[\text{Pd}^{\text{II}}(\text{L}^{3-})]^-$  (black line),  $[\text{Pd}^{\text{II}}(\text{L}^{2-})]$  (blue line) and  $[\text{Pd}^{\text{III}}(\text{L}^{2-})]^+$  (red line) in  $\text{CH}_2\text{Cl}_2$  at  $30^\circ\text{C}$

observed at the aminophenol moiety of ring A as well as the  $\beta$ -diketiminato moiety upon one-electron oxidation of  $[\text{Pd}^{\text{II}}(\text{L}^{3-})]^-$ .

In Fig. 5(a), the absorption spectrum of the one-electron oxidized complex  $[\text{Ni}^{\text{II}}(\text{L}^{2-})]$  is shown in the blue line together with that of the starting material  $[\text{Ni}^{\text{II}}(\text{L}^{3-})]^-$  in the black line. The  $\lambda_{\text{max}}$  value of the absorption band at 429 nm of  $[\text{Ni}^{\text{II}}(\text{L}^{2-})]$  is close to that of the strong absorption band at 414 nm of the starting complex  $[\text{Ni}^{\text{II}}(\text{L}^{3-})]^-$ , whereas the intensity of the former ( $\epsilon = 16,400 \text{ M}^{-1}\cdot\text{cm}^{-1}$ ) is largely reduced as compared to that of the latter ( $28,100 \text{ M}^{-1}\cdot\text{cm}^{-1}$ ). Thus, the absorption band at 429 nm together with the shoulder around 524 nm ( $9,860 \text{ M}^{-1}\cdot\text{cm}^{-1}$ ) could be attributed to metal-to-phenolate charge transfer (MLCT) bands as in the case of the copper complex with the same ligand system [33].

The reduction of the intensity of this band in  $[\text{Ni}^{\text{II}}(\text{L}^{2-})]$  is consistent with the fact that one of the phenolate rings is oxidized to the phenoxyl radical as suggested by the X-ray structure shown in Fig. 2(b). Then, the broad absorption bands at 784 nm ( $2,180 \text{ M}^{-1}\cdot\text{cm}^{-1}$ ), 883 nm ( $2,090 \text{ M}^{-1}\cdot\text{cm}^{-1}$ ), and 1530 nm ( $1,470 \text{ M}^{-1}\cdot\text{cm}^{-1}$ ) of  $[\text{Ni}^{\text{II}}(\text{L}^{2-})]$  in the visible to near IR (vis-NIR) region could be attributed to the phenoxyl radical moiety. Existence of such a broad absorption band at 1530 nm may be due to the expanded  $\pi$ -conjugation system through the  $\beta$ -diketiminato moiety as indicated by the X-ray structure (see Fig. 2(b)). This electronic communication between the phenoxyl radical and the phenolate rings through the expanded  $\pi$ -conjugated system is also suggested by the electrochemical data presented in Table 1.

The absorption spectrum of the one-electron oxidized complex  $[\text{Pd}^{\text{II}}(\text{L}^{2-})]$  is also shown in the blue line together with that of the starting material  $[\text{Pd}^{\text{II}}(\text{L}^{3-})]^-$  in the black line in Fig. 5(b). The relatively intense absorption bands at 409 nm ( $\epsilon = 14,900 \text{ M}^{-1}\cdot\text{cm}^{-1}$ ), 503 nm ( $14,000 \text{ M}^{-1}\cdot\text{cm}^{-1}$ ),

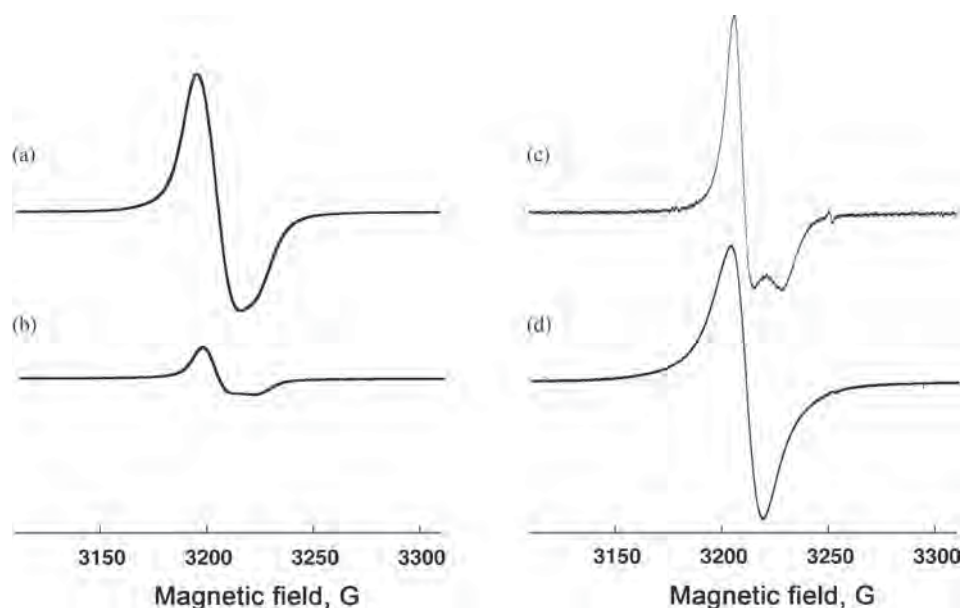
and 540 nm ( $14,200 \text{ M}^{-1}\cdot\text{cm}^{-1}$ ) could also be attributed to the MLCT transitions, and the broad absorption bands in the NIR region (above 800 nm) are due to the phenoxyl radical species.

In frozen  $\text{CH}_2\text{Cl}_2$  at 77 K, the starting materials  $[\text{Ni}^{\text{II}}(\text{L}^{3-})]^-$  and  $[\text{Pd}^{\text{II}}(\text{L}^{3-})]^-$  were EPR silent (data are not shown). The  $^1\text{H-NMR}$  spectra of  $[\text{Ni}^{\text{II}}(\text{L}^{3-})]^-$  and  $[\text{Pd}^{\text{II}}(\text{L}^{3-})]^-$  in  $\text{CH}_2\text{Cl}_2$  at 298 K exhibited well-resolved proton signals in the diamagnetic region ( $\delta = 0\text{--}10$  ppm) (Supporting Fig. S1). These results clearly demonstrated that the metal(II) centers have low-spin state ( $S = 0$ ) in both complexes.

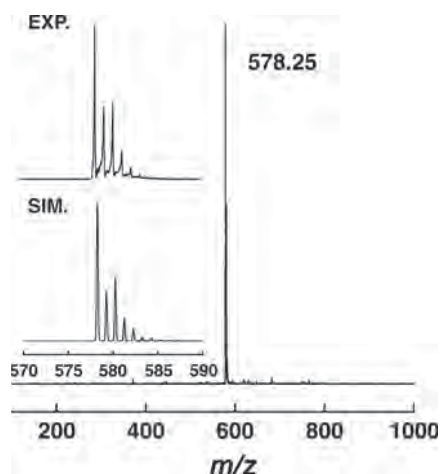
On the other hand, the EPR measurement of the one-electron oxidation complexes  $[\text{Ni}^{\text{II}}(\text{L}^{2-})]$  and  $[\text{Pd}^{\text{II}}(\text{L}^{2-})]$  gave relatively broad axial signals at  $g_{\perp} = 1.989$  and  $g_{\parallel} = 1.979$  ( $g_{\perp} = 1.986$ ), and  $g_{\parallel} = 2.006$  and  $g_{\parallel} = 1.991$  ( $g_{\infty} = 2.001$ ), respectively (Figs 6(a) and 6(c)). These signals are attributed to the metal-coordinating phenoxyl radical species  $\text{L}^{2\cdot-}$ .

### Two-electron oxidation product

Further oxidation of  $[\text{Ni}^{\text{II}}(\text{L}^{2-})]$  by  $\text{N}(\text{Ph-Br})_3\cdot\text{SbCl}_6$  ( $E_{1/2} = 0.70 \text{ V vs Fc/Fc}^+$ ) [36] in  $\text{CH}_2\text{Cl}_2$  gave a two-electron oxidized cationic complex exhibiting intense absorption bands at 460 nm ( $11,900 \text{ M}^{-1}\cdot\text{cm}^{-1}$ ) and 494 nm ( $11,800 \text{ M}^{-1}\cdot\text{cm}^{-1}$ ) together with a relatively weak band at 640 nm ( $3,800 \text{ M}^{-1}\cdot\text{cm}^{-1}$ ) and a broad NIR band around 1525 nm ( $2,610 \text{ M}^{-1}\cdot\text{cm}^{-1}$ ) (red line spectrum in Fig. 5(a)). The ESI-MS measured in the positive mode matches the chemical formulation of  $[\text{Ni}^{\text{II}}(\text{L}^-)]^+$  (Fig. 7). The EPR signals of the neutral complex of nickel,  $[\text{Ni}^{\text{II}}(\text{L}^{2-})]$  (Fig. 6(a)), were significantly weakened upon the one-electron oxidation with  $\text{N}(\text{Ph-Br})_3\cdot\text{SbCl}_6$  as shown in Fig. 6(b). This clearly indicated that the *main* component of two-electron oxidized cationic complex



**Fig. 6.** EPR spectra of (a)  $[\text{Ni}^{\text{II}}(\text{L}^{\bullet 2-})]$  ( $5.0 \times 10^{-4}$  M), (b)  $[\text{Ni}^{\text{II}}(\text{L}^{\bullet})]^+$  ( $5.0 \times 10^{-4}$  M), (c)  $[\text{Pd}^{\text{II}}(\text{L}^{\bullet 2-})]$  ( $5.0 \times 10^{-4}$  M), and (d)  $[\text{Pd}^{\text{III}}(\text{L}^{\bullet 2-})]^+$  ( $5.0 \times 10^{-4}$  M) at 77 K

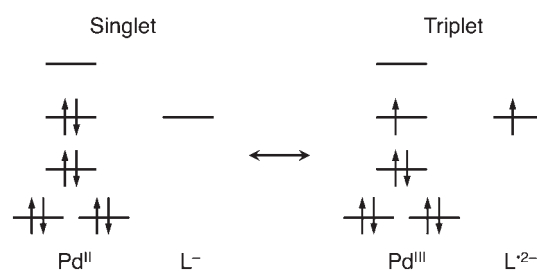


**Fig. 7.** ESI-MS (positive mode) of  $[\text{Ni}^{\text{II}}(\text{L}^{\bullet})]^+$  in  $\text{CH}_2\text{Cl}_2$ . Inset: expanded spectrum (EXP) and its simulation spectrum (SIM)

was an EPR-silent diamagnetic species,  $[\text{Ni}^{\text{II}}(\text{L}^-)]$  ( $S = 0$ ), where  $\text{L}^-$  denotes two-electron oxidized ligand with a quinonoid canonical form.

In the case of palladium complex, oxidation of the neutral complex  $[\text{Pd}^{\text{II}}(\text{L}^{\bullet 2-})]$  using  $\text{N}(\text{Ph}-\text{Br})_3 \cdot \text{SbCl}_6$  gave a relatively intense EPR signal at  $g = 2.003$  (Fig. 6(d)). The result suggests formation of a triplet species ( $S = 1$ ) by the oxidation of doublet neutral complex. The number of un-paired electron of the two-electron oxidized complex was estimated to be 1.66 using Evans method (Supporting Fig. S2), which is assignable to the average of singlet species (17%) and triplet species (83%) (Scheme 3) [37–39].

Thus the main locus of the second oxidation is thought to be the metal center in the palladium system to give mainly



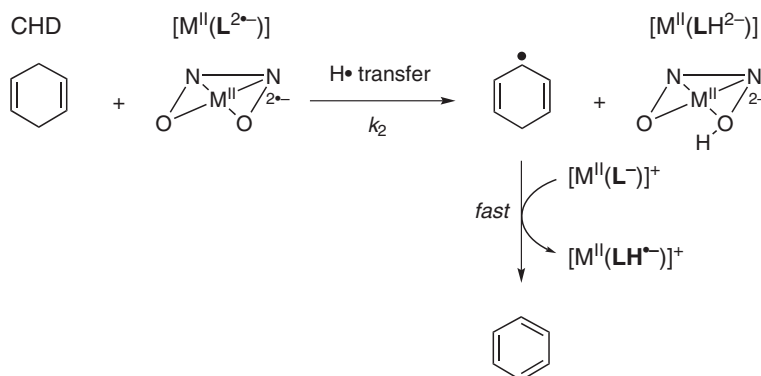
**Scheme 3.** Schematic energy diagram of two-electron oxidized Pd-complex at 77 K

$[\text{Pd}^{\text{III}}(\text{L}^{\bullet 2-})]^+$  (Scheme 3). Then, the small EPR signal observed in the two-electron oxidation of the nickel system shown in Fig. 6(b) may be due to the larger contribution of singlet species  $[\text{Ni}^{\text{II}}(\text{L}^{\bullet})]^+$ , in which the redox locus is on the ligand moiety as discussed above [40].

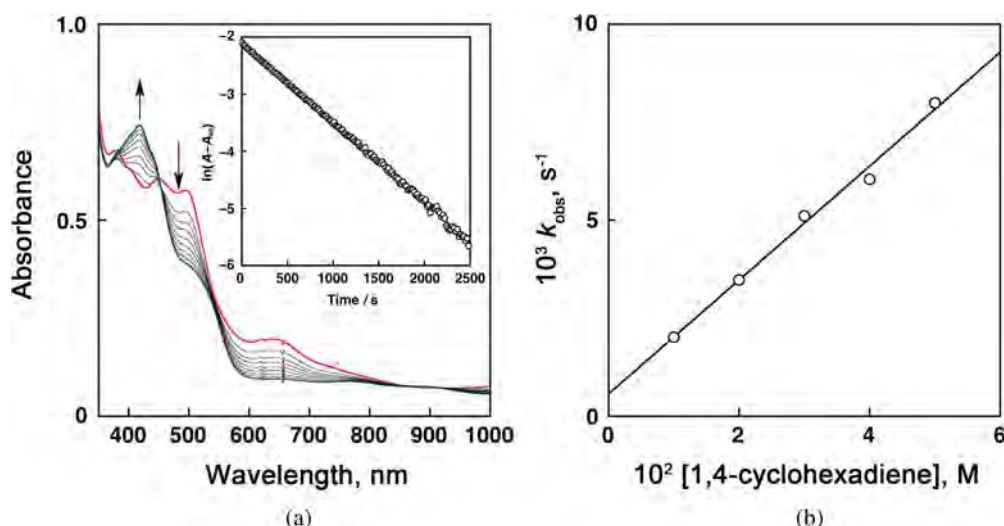
### Reactivity of two-electron oxidized complexes

In our previous study of the copper complexes, reactivity toward hydrogen atom donor was examined using 1,4-cyclohexadiene (CHD) as a model substrate [33]. The cationic complex  $[\text{Cu}^{\text{II}}(\text{L}^{\bullet})]^+$  (two-electron oxidized complex) underwent hydrogen atom abstraction reaction from CHD to give  $[\text{Cu}^{\text{II}}(\text{LH}^{\bullet})]^+$  (protonated form of  $[\text{Cu}^{\text{II}}(\text{L}^{\bullet 2-})]$ ) and cyclohexenyl radical intermediate, the later of which further donated hydrogen atom to another molecule of  $[\text{Cu}^{\text{II}}(\text{L}^{\bullet})]^+$  to give benzene and one more  $[\text{Cu}^{\text{II}}(\text{LH}^{\bullet})]^+$  (Scheme 4). Thus, the stoichiometry of the reaction was  $[\text{Cu}^{\text{II}}(\text{L}^{\bullet})]^+:\text{CHD} = 2:1$ , where  $[\text{Cu}^{\text{II}}(\text{L}^{\bullet})]^+$  acted as a one-electron oxidant (Scheme 4). Addition of





**Scheme 4.** Reaction of  $[M^{II}(L^{2*})]$  with 1,4-cyclohexadiene (CHD)



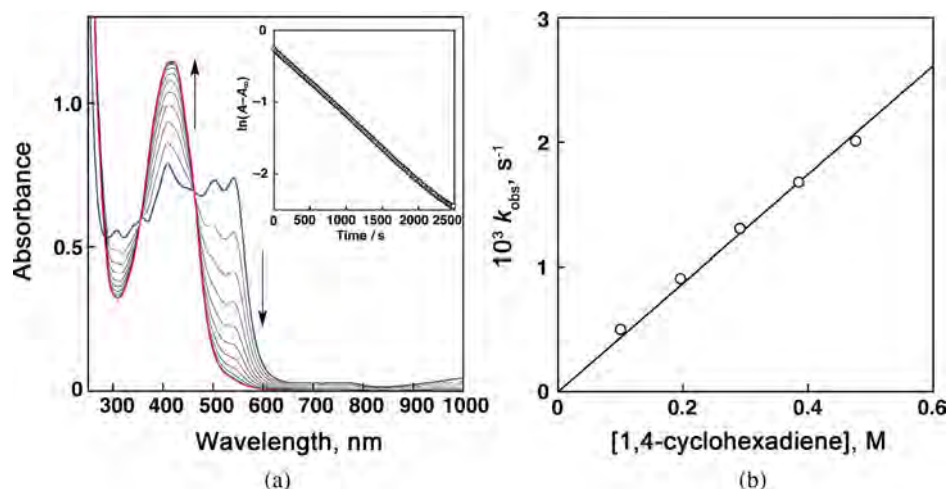
**Fig. 8.** (a) Spectral change observed upon addition of 1,4-cyclohexadiene ( $2.0 \times 10^{-2}$  M) to  $[Ni^{II}(L^{\bullet-})]^+$  ( $5.0 \times 10^{-5}$  M) in  $CH_2Cl_2$  at  $30^\circ C$ . Inset: first-order plot based on the time-dependent absorption change at 640 nm. (b) Plot of  $k_{obs}$  vs. [1,4-cyclohexadiene]

a base such as triethylamine to the final reaction mixture generated  $[Cu^{II}(L^{2*})]$ .

In this study, reactivity of the cationic complexes,  $[Ni^{II}(L^{\bullet-})]^+$  and  $[Pd^{III}(L^{2*})]^+$ , was also examined under the same experimental conditions. Addition of an excess amount of 1,4-cyclohexadiene (CHD) to a  $CH_2Cl_2$  solution of  $[Ni^{II}(L^{\bullet-})]^+$  ( $5.0 \times 10^{-5}$  M) readily resulted in the spectral changes as shown in Fig. 8(a). The products given by the oxidation reaction were determined to be benzene with GC-MS. The final spectrum of the reaction did not match the spectrum of  $[Ni^{II}(L^{2*})]$  itself, but addition of 1 equiv of triethylamine (base) to the final solution resulted in the appearance of absorption bands due to  $[Ni^{II}(L^{2*})]$  as shown in Fig. S3(a).  $[Pd^{III}(L^{2*})]^+$  was also confirmed to show similar reactivity to that of  $[Ni^{II}(L^{\bullet-})]^+$  (Fig. S3(b)). Thus, the reaction consequences of the both nickel and palladium complex are the same with those of the copper complex (Scheme 4) [33]. The reaction of nickel complex obeyed first-order kinetics in the presence of excess amount of CHD as shown in the inset of Fig. 8(a), and

the pseudo-first-order rate constant ( $k_{obs}$ ) increased with increasing the concentration of CHD. Plot of  $k_{obs}$  against the substrate concentration gave a straight line with a small intercept (Fig. 8(b)), from which the second-order rate constant  $k_2$  and self-decomposition rate constant  $k_{dec}$  were determined as  $0.15 M^{-1} \cdot s^{-1}$  and  $5.7 \times 10^{-4} s^{-1}$  as the slope and the intercept, respectively. The reactivity of  $[Pd^{III}(L^{2*})]^+$  toward CHD was also examined in the same way, and the second-order rate constant  $k_2$  and the self-decomposition rate constant  $k_{dec}$  were determined as  $0.52 M^{-1} \cdot s^{-1}$  and  $2.8 \times 10^{-3} s^{-1}$ , respectively (Fig. S4). The self-decomposition rate constants  $k_{dec}$  determined were nearly equal to those directly determined by following the decrease of the absorption bands due to the cationic complex in the absence of the substrate ( $6.2 \times 10^{-4} s^{-1}$  for  $[Ni^{II}(L^{\bullet-})]^+$  and  $2.4 \times 10^{-3} s^{-1}$  for  $[Pd^{III}(L^{2*})]^+$ ).

The rate constant  $k_2$  ( $0.76 M^{-1} \cdot s^{-1}$ ) of the copper complex  $[Cu^{II}(L^{\bullet-})]^+$  is larger than those of the nickel and palladium complexes ( $0.15 M^{-1} \cdot s^{-1}$  and  $0.52 M^{-1} \cdot s^{-1}$ ), which is not consistent with its negative value of  $E^2_{1/2}$  as



**Fig. 9.** (a) Spectral change observed upon addition of 1,4-cyclohexadiene (0.20 M) to  $[\text{Pd}^{\text{II}}(\text{L}^{\bullet 2-})]$  ( $5.0 \times 10^{-5}$  M) in  $\text{CH}_2\text{Cl}_2$  at  $30^\circ\text{C}$ . Inset: first-order plot based on the time-dependent absorption change at 540 nm. (b) Plot of  $k_{\text{obs}}$  vs. [1,4-cyclohexadiene]

compared to those of the nickel and palladium complexes (Table 1). Reactivity of  $[\text{Pd}^{\text{III}}(\text{L}^{\bullet 2-})]^+$  is somewhat larger than that of  $[\text{Ni}^{\text{II}}(\text{L}^-)]^+$ , even though the  $E_{1/2}^2$  values of these complexes are identical (Table 1). These differences in reactivity may be due to the different electronic configuration between the cationic complexes as discussed above.

### Reactivity of one-electron oxidized complexes

$[\text{Cu}^{\text{II}}(\text{L}^{\bullet 2-})]$  itself showed essentially no reactivity toward CHD, but it disproportionated into  $(1/2)[\text{Cu}^{\text{II}}(\text{L}^{\bullet 3-})]$  and  $(1/2)[\text{Cu}^{\text{II}}(\text{L}^-)]^+$  in the treatment with CHD [33]. Thus, CHD was also converted to benzene by the reaction with generated  $[\text{Cu}^{\text{II}}(\text{L}^-)]^+$  [33]. In this case, reaction followed second-order kinetics with respect to the concentration of the copper complex, indicating that the disproportionation process is the rate-determining step.

The neutral complex of nickel(II),  $[\text{Ni}^{\text{II}}(\text{L}^{\bullet 2-})]$ , did not show reactivity toward CHD under ambient conditions. In this case, photo irradiation induced the oxidation of CHD to give benzene and the starting nickel(II) complex  $[\text{Ni}^{\text{II}}(\text{L}^{\bullet 3-})]$  (after base treatment of the final reaction mixture). Details of this photochemical reaction will be reported elsewhere.

In the case of  $[\text{Pd}^{\text{II}}(\text{L}^{\bullet 2-})]$ , addition of CHD into the  $\text{CH}_2\text{Cl}_2$  solution of the neutral complex ( $5.0 \times 10^{-5}$  M) at  $30^\circ\text{C}$  resulted in a spectral change shown in Fig. 9(a). The characteristic absorption bands due to  $[\text{Pd}^{\text{II}}(\text{L}^{\bullet 2-})]$  decrease with a concomitant increase in the new absorption bands represented by the peak at 417 nm ( $\epsilon = 23,300 \text{ M}^{-1} \cdot \text{cm}^{-1}$ ). The reaction obeyed first-order kinetics in the presence of a large excess of CHD as shown in the inset of Fig. 9(a). Plot of the first-order rate constant  $k_{\text{obs}}$  against the substrate concentration gave a linear line passing through the origin, from which the second-order rate constant  $k_2$  was determined as  $4.4 \times 10^{-3} \text{ M}^{-1} \cdot \text{s}^{-1}$  (Fig. 9(b)). Addition

of 1 equiv of triethylamine to the final reaction mixture resulted in quantitative generation of the spectrum of  $[\text{Pd}^{\text{II}}(\text{L}^{\bullet 3-})]$  (starting material) (Fig. S5(a)). Contrary, addition of 1 equiv of 10-camphorsulfonic acid to  $[\text{Pd}^{\text{II}}(\text{L}^{\bullet 3-})]$  generated spectrum identical to that of the final reaction mixture of CHD and  $[\text{Pd}^{\text{II}}(\text{L}^{\bullet 2-})]$  (Fig. S5(b)). The reactivity of one-electron oxidized complexes  $[\text{Pd}^{\text{II}}(\text{L}^{\bullet 2-})]$  in the C–H bond activation reaction of CHD was two orders of magnitude lower, when compared to that of two-electron oxidized complex  $[\text{Pd}^{\text{III}}(\text{L}^{\bullet 2-})]^+$ .

It is also interesting to note that  $E_{1/2}^1$  values of all complexes are fairly similar as  $E_{1/2}^1 = -0.06 \sim +0.07$  V, nevertheless, each one-electron oxidized complex  $[\text{Cu}^{\text{II}}(\text{L}^{\bullet 2-})]$ ,  $[\text{Ni}^{\text{II}}(\text{L}^{\bullet 2-})]$ , and  $[\text{Pd}^{\text{II}}(\text{L}^{\bullet 2-})]$  exhibited different reactivity. It is likely to be due to the energy difference of O–H bonds of protonated aminophenol moiety [41].

## EXPERIMENTAL

### Materials and methods

The reagents and solvents used in this study except for the ligand and the complexes were commercial products of the highest available purity and were further purified by the standard methods, if necessary [34]. The ligand  $\text{LH}_3$  was prepared according to the reported methods [33]. FT-IR spectra were recorded with a Shimadzu FTIR-8200PC. Electronic absorption spectra were measured using a Hewlett-Packard HP8453 diode array spectrophotometer or a Jasco V-570 UV/VIS/NIR spectrophotometer equipped with a Unisoku thermostated cell holder USP-203 designed for low temperature measurements. Mass spectra were recorded with a JEOL JMS-700T Tandem MS station or a JEOL JMS-700. NMR spectra were recorded on a JEOL ECP400, a JEOL ECS400, or a Varian UNITY INOVA 600 MHz. A concentric double tube was utilized to perform Evans

method. EPR spectra were taken on a JEOL X-band spectrometer (JES-RE1XE) under non-saturating microwave power conditions (1.0 mW) operating at 9.2 GHz. The magnitude of the modulation was chosen to optimize the resolution and the signal to noise ratio (S/N) of the observed spectrum. The  $g$  values were calibrated using an  $Mn^{2+}$  marker. Elemental analyses were recorded with a PerkinElmer or a Fisons Instruments EA1108 Elemental Analyzer.

### X-ray structure determination

Each single crystal was mounted on a loop. Data from X-ray diffraction were collected at  $-170^{\circ}C$  by a VariMax with RAPID imaging plate two-dimensional area detector, using graphite-monochromated Mo  $K\alpha$  radiation ( $\lambda = 0.71069 \text{ \AA}$ ) to  $2\theta_{max}$  of  $55^{\circ}$ . All of the crystallographic calculations were performed using the Crystal Structure software package of the Molecular Structure Corporation (Crystal Structure: Crystal Structure Analysis Package version 3.8.1. Molecular Structure Corp. and Rigaku Corp. (2005)). The structures were solved with SIR2008 or SHELX97 and refined with CRYSTALS. All non-hydrogen atoms and hydrogen atoms were refined anisotropically and isotropically, respectively.

### Synthesis

**$(NBu_4)[Ni^{II}(L^3)]$** . To an ethanol solution (1.0 mL) containing  $LH_3$  (10.5 mg, 20  $\mu\text{mol}$ ) and  $Ni^{II}(CH_3COO)_2 \cdot 4H_2O$  (5.0 mg, 20  $\mu\text{mol}$ ) was added 1.5 M tetraethylammonium hydroxide in methanol (40  $\mu\text{l}$ , 60  $\mu\text{mol}$ ), and the mixture was stirred for 1 h at room temperature. Then, the solvent was removed by evaporation, and the product was recrystallized from the resulting residue using EtOH/*n*-hexane to give single crystals suitable for X-ray crystallographic analysis (6.1 mg, 43%). IR (KBr):  $\nu$ ,  $\text{cm}^{-1}$  2951 (C–H), 1531, 1361 ( $NO_2$ ).  $^1H$  NMR ( $CDCl_3$ , 400 MHz):  $\delta$ , ppm 1.06 (t, 12H,  $J = 7.2$  Hz,  $(CH_3CH_2)_4N^+$ ), 1.29 (s, 18H,  $CH_3$ ), 1.44 (s, 18H,  $CH_3$ ), 3.23 (q, 8H,  $J = 7.2$  Hz,  $(CH_3CH_2)_4N^+$ ), 6.97 (d, 2H,  $J = 2.0$  Hz, aromatic protons), 7.36 (d, 2H,  $J = 2.0$  Hz, aromatic protons), 9.00 (s, 2H,  $H$ ). MS (ESI):  $m/z$  578.30, calcd. for  $C_{30}H_{25}N_6NiO_4$  578.25. Anal. calcd. for  $C_{39}H_{62}N_4O_4Ni \cdot EtOH$ : C, 65.16; H, 9.07; N, 7.41. Found C, 65.11; H, 9.31; N, 7.49.

**$[Ni^{II}(L^{2-})]$** .  $(Et_3NH)[Ni^{II}L]$  (27.3 mg, 40  $\mu\text{mol}$ ) in  $CH_2Cl_2$  (1.0 mL) was added to a  $CH_2Cl_2$  solution (1.0 mL) containing  $AgSbF_6$  (98%, 13.5 mg, 40  $\mu\text{mol}$ ) with stirring at room temperature. The mixture was added dropwise to hexane (100 mL) with vigorous stirring. After reducing the volume of the resulting solution to 3 mL, the precipitates were filtered off. Evaporation of the filtrate gave dark red material, from which  $[Ni^{II}(L^{2-})]$  was obtained as black crystals by recrystallization from hexane (15.1 mg, 65%). IR (KBr):  $\nu$ ,  $\text{cm}^{-1}$  2953 (C–H), 1561, 1360 ( $NO_2$ ). Anal. calcd. for  $C_{31}H_{42}N_3O_4Ni$ : C, 64.26; H, 7.31; N, 7.25. Found C, 64.12; H, 7.25; N, 7.14.

**$(NBu_4)[Pd^{II}(L^3)]$** . To a  $CH_2Cl_2$  solution (3.0 mL) containing  $LH_3$  (52.4 mg, 100  $\mu\text{mol}$ ) and  $Pd^{II}(CH_3COO)_2$  (22.5 mg, 100  $\mu\text{mol}$ ) was added triethylamine (42 mL, 300  $\mu\text{mol}$ ) and the mixture was stirred for an hour at room temperature. The reaction mixture was added dropwise to *n*-hexane (60 mL) to give orange powder. The collected powder and  $(Bu)_4NBr$  (322 mg, 1.0 mmol) was dissolved in MeOH- $CH_2Cl_2$  ( $v:v = 1:1$ ), and slow evaporation of the solvent gave orange crystals suitable for X-ray crystallographic analysis (44.0 mg, 51%). IR (KBr):  $\nu$ ,  $\text{cm}^{-1}$  2957 (C–H), 1540, 1361 ( $NO_2$ ).  $^1H$  NMR ( $CDCl_3$ , 400 MHz):  $\delta$ , ppm 0.76 (t, 12H,  $J = 7.2$  Hz ( $CH_3CH_2CH_2CH_2)_4N^+$ ), 1.01 (m, 8H,  $(CH_3CH_2CH_2CH_2)_4N^+$ ), 1.34 (m, 27H,  $CH_3$  and  $(CH_3CH_2CH_2CH_2)_4N^+$ ), 2.99 (t, 8H,  $J = 8.4$  Hz,  $(CH_3CH_2CH_2CH_2)_4N^+$ ), 7.08 (s, 2H, aromatic protons), 7.54 (s, 2H, aromatic protons), 9.30 (s, 2H,  $H$ ). MS (ESI):  $m/z$  626.15, calcd. for  $C_{30}H_{25}N_6NiO_4$  626.22. Anal. calcd. for  $C_{47}H_{78}N_4O_4Pd \cdot 0.5H_2O$ : C, 64.25; H, 9.06; N, 6.38. Found C, 64.17; H, 9.29; N, 6.43.

**$[Pd^{II}(L^{2-})]$** .  $(Et_3NH)[Pd^{II}L]$  (6.0 mg, 8.2  $\mu\text{mol}$ ) in  $CH_2Cl_2$  (0.50  $\mu\text{L}$ ) was added to a  $CH_2Cl_2$  solution (0.50 mL) containing  $AgSbF_6$  (98%, 2.8 mg, 8.2  $\mu\text{mol}$ ) with stirring at room temperature. The mixture was added dropwise to hexane (30 mL) with vigorous stirring. After reducing the volume of the resulting solution to 3 mL, the precipitates were filtered off. Evaporation of the filtrate gave dark red material, from which  $[Pd^{II}(L^{2-})]$  was obtained as black crystals by recrystallization from hexane (mg, 49%). IR (KBr):  $\nu$ ,  $\text{cm}^{-1}$  2952 (C–H), 1547, 1362 ( $NO_2$ ). Anal. calcd. for  $C_{31}H_{42}N_3O_4Pd$ : C, 59.37; H, 6.75; N, 6.70. Found C, 59.60; H, 6.84; N, 6.59.

### CONCLUSION

In this study, a new type of Ni and Pd complexes supported by the non-innocent  $\beta$ -diketiminato ligand containing two phenol groups has been developed and the structures, physical properties, and redox behaviors of the nickel(II) and the palladium(II) complexes,  $[M^{II}(L^3)]$ , have been examined in detail. The one-electron oxidation of  $[Ni^{II}(L^3)]$  gave  $[Ni^{II}(L^{2-})]$ , where the supporting ligand is oxidized to provide nickel(II)-phenoxy radical complexes exhibiting the characteristic absorption spectra in the visible-to-NIR region. Further one-electron oxidation of  $[Ni^{II}(L^{2-})]$  gave the two-electron oxidation product  $[Ni^{II}(L)]^+$ , where the oxidation also takes place at the ligand moiety. The one- and two-electron oxidation of  $[Pd^{II}(L^3)]$  gave  $[Pd^{II}(L^{2-})]$  and  $[Pd^{III}(L^{2-})]^+$ , respectively, where the supporting ligand is oxidized in the former, whereas the metal center is mainly oxidized in the later.

The two-electron-oxidation complexes  $[Ni^{II}(L)]^+$  and  $[Pd^{III}(L^{2-})]^+$  exhibited hydrogen atom abstraction ability from CHD as in the case of the copper complex with same ligand. However, the reactivity was slightly lower than

that of the Cu-complex. The reaction of one-electron-oxidation complex  $[\text{Ni}^{\text{II}}(\text{L}^{\bullet 2})]$  with CHD included photo-induced oxidation of CHD, whereas one-electron-oxidation complex  $[\text{Pd}^{\text{II}}(\text{L}^{\bullet 2})]$  showed thermal hydrogen atom abstraction ability from CHD. The reactivity of two-electron oxidized complexes  $[\text{Ni}^{\text{II}}(\text{L})]^+$  and  $[\text{Pd}^{\text{II}}(\text{L}^{\bullet 2})]^+$  in the C–H bond activation reaction of CHD is much higher than that of the one-electron oxidized complex  $[\text{Ni}^{\text{II}}(\text{L}^{\bullet 2})]$  and  $[\text{Pd}^{\text{II}}(\text{L}^{\bullet 2})]$ . These results will provide further insights into the redox functions of transition-metal organic radical species.

### Acknowledgements

This work was supported by a Grant-in-Aid for Scientific Research on Innovative Areas “Molecular Activation Directed toward Straightforward Synthesis” (No. 22105007) and “Stimuli-responsive Chemical Species” (No. 24109015) and a Grant-in-Aid for Exploratory Research (No. 25620044) from the Ministry of Education, Culture, Sports, Science and Technology, Japan. Y.M., N.F., and S.I. also express their special thanks to the JSPS Japanese-German Graduate Externship Program on “Environmentally Benign Bio- and Chemical Processes” for financial support of the stay in RWTH Aachen.

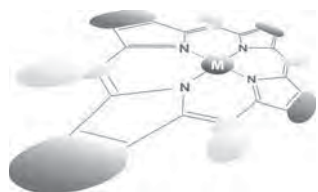
### Supporting information

Crystallographic data (Tables S1 and S2) and additional spectroscopic and kinetic data (Figs S1–S5) are given in the supplementary material. This material is available free of charge via the Internet at <http://www.worldscinet.com/jpp/jpp.shtml>.

### REFERENCES

- Luca OR and Crabtree RH. *Chem. Soc. Rev.* 2013; **42**: 1440–1459.
- Praneeth VKK, Ringenberg MR and Ward TR. *Angew. Chem., Int. Ed.* 2012; **51**: 10228–10234.
- Rittle J and Green MT. *Science* 2010; **330**: 933–937.
- Dunford HB. *Peroxidases and Catalases: Biochemistry, Biophysics, Biotechnology and Physiology*, Wiley: 2010.
- de Montellano PRO. *Cytochrome P450: Structure, Mechanism, and Biochemistry*, Springer: 1995.
- Meunier B. *Chem. Rev.* 1992; **92**: 1411–1456.
- Sono M, Roach MP, Coulter ED and Dawson JH. *Chem. Rev.* 1996; **96**: 2841–2888.
- Lombardi A, Nistri F and Pavone V. *Chem. Rev.* 2001; **101**: 3165–3190.
- Meunier B, de Visser SP and Shaik S. *Chem. Rev.* 2004; **104**: 3947–3980.
- Sorokin AB. *Chem. Rev.* 2013; **113**: 8152–8191.
- Itoh S, Taki M and Fukuzumi S. *Coord. Chem. Rev.* 2000; **198**: 3–20.
- Jazdzewski BA and Tolman WB. *Coord. Chem. Rev.* 2000; **200**: 633–685.
- Thomas F. *Eur. J. Inorg. Chem.* 2007; **2007**: 2379–2404.
- Lyons CT and Stack TDP. *Coord. Chem. Rev.* 2013; **257**: 528–540.
- Ito N, Phillips SEV, Stevens C, Ogel ZB, McPherson MJ, Keen JN, Yadav KDS and Knowles PF. *Nature* 1991; **350**: 87–90.
- Whittaker MM, Kersten PJ, Nakamura N, Sanders-Loehr J, Schweizer ES and Whittaker JW. *J. Biol. Chem.* 1996; **271**: 681–687.
- Krüger H-J. *Angew. Chem., Int. Ed.* 1999; **38**: 627–631.
- Rogers MS and Dooley DM. *Curr. Opin. Chem. Biol.* 2003; **7**: 189–196.
- Whittaker JW. *Arch. Biochem. Biophys.* 2005; **433**: 227–239.
- Pratt RC and Stack TDP. *J. Am. Chem. Soc.* 2003; **125**: 8716–8717.
- Pratt RC and Stack TDP. *Inorg. Chem.* 2005; **44**: 2367–2375.
- Asami K, Tsukidate K, Iwatsuki S, Tani F, Karasawa S, Chiang L, Storr T, Thomas F and Shimazaki Y. *Inorg. Chem.* 2012; **51**: 12450–12461.
- Rotthaus O, Thomas F, Jarjayes O, Philouze C, Saint-Aman E and Pierre J-L. *Chem.-Eur. J.* 2006; **12**: 6953–6962.
- Storr T, Wasinger EC, Pratt RC and Stack TDP. *Angew. Chem., Int. Ed.* 2007; **46**: 5198–5201.
- Storr T, Verma P, Shimazaki Y, Wasinger EC and Stack TDP. *Chem.-Eur. J.* 2010; **16**: 8980–8983.
- Chiang L, Kochem A, Jarjayes O, Dunn TJ, Vezin H, Sakaguchi M, Ogura T, Orio M, Shimazaki Y, Thomas F and Storr T. *Chem.-Eur. J.* 2012; **18**: 14117–14127.
- Shimazaki Y, Arai N, Dunn TJ, Yajima T, Tani F, Ramogida CF and Storr T. *Dalton Trans.* 2011; **40**: 2469–2479.
- Shimazaki Y, Stack TDP and Storr T. *Inorg. Chem.* 2009; **48**: 8383–8392.
- de Bellefeuille D, Askari MS, Lassalle-Kaiser B, Journaux Y, Aukauloo A, Orio M, Thomas F and Ottenwaelder X. *Inorg. Chem.* 2012; **51**: 12796–12804.
- Kawai M, Yamaguchi T, Masaoka S, Tani F, Kohzuma T, Chiang L, Storr T, Mieda K, Ogura T, Szilagy RK and Shimazaki Y. *Inorg. Chem.* 2014; **53**: 10195–10202.
- Shimazaki Y, Tani F, Fukui K, Naruta Y and Yamauchi O. *J. Am. Chem. Soc.* 2003; **125**: 10512–10513.
- Shimazaki Y, Yajima T, Tani F, Karasawa S, Fukui K, Naruta Y and Yamauchi O. *J. Am. Chem. Soc.* 2007; **129**: 2559–2568.
- Takaichi J, Ohkubo K, Sugimoto H, Nakano M, Usa D, Maekawa H, Fujieda N, Nishiwaki N, Seki S, Fukuzumi S and Itoh S. *Dalton Trans.* 2013; **42**: 2438–2444.

34. Perrin DD, Armarego WLF and Perrin DR. *Purification of Laboratory Chemicals 4th Edition*, 4th ed., Pergamon Press: Elmsford, NY, 1996.
35. Shimazaki Y, Tani F, Fukui K, Naruta Y and Yamauchi O. *J. Am. Chem. Soc.* 2003; **125**: 10512–10513.
36. Connelly NG and Geiger WE. *Chem. Rev.* 1996; **96**: 877–910.
37. Evans DF. *Journal of the Chemical Society (Resumed)* 1959: 2003–2005.
38. Garland CW, Nibler JW and Shoemaker DP. *Experiments in physical chemistry*, 8th ed., McGraw-Hill Higher Education: Boston, 2009.
39. EPR spectrum due to the two-electron oxidized triplet species  $[\text{Pd}^{\text{III}}(\text{L}^{\bullet 2-})]$  generated by further oxidation of the one-electron oxidized doublet species  $[\text{Pd}^{\text{II}}(\text{L}^{\bullet 2-})]$  was broad and obscure. This may be caused by the equilibrium between  $S = 0$  and 1 states.
40. Evans method was not applicable to two-electron oxidized species of nickel complex due to instability of the species under room temperature.
41. Warren JJ, Tronic TA and Mayer JM. *Chem. Rev.* 2010; **110**: 6961–7001.



## Electrochemistry and spectroelectrochemistry of $\beta$ -pyrazino-fused tetraarylporphyrins in nonaqueous media

Yuanyuan Fang<sup>a</sup>, Federica Mandoj<sup>b</sup>, Lihan Zeng<sup>a</sup>, Rajesh Pudi<sup>b</sup>, Manuela Stefanelli<sup>b</sup>, Roberto Paolesse<sup>\*b,c,d</sup> and Karl M. Kadish<sup>\*a,d</sup>

<sup>a</sup> Department of Chemistry, University of Houston, Houston, Texas, 77204-5003, USA

<sup>b</sup> Dipartimento di Scienze e Tecnologie Chimiche, Università di Roma Tor Vergata, via della Ricerca Scientifica 1, 00133 Rome, Italy

<sup>c</sup> CNR IDASC, via Fosso del Cavaliere, 00133 Rome, Italy

*Dedicated to Professor Shunichi Fukuzumi on the occasion of his retirement*

Received 26 November 2014

Accepted 18 December 2014

**ABSTRACT:** Bis-porphyrins containing a  $\beta,\beta'$ -fused pyrazino (Pz) linking group were examined by electrochemistry and thin-layer UV-visible spectroelectrochemistry in PhCN containing 0.1 M tetra-*n*-butylammonium perchlorate (TBAP) as supporting electrolyte. The investigated compounds are represented as M(TPP)-Pz-(TPP)M, where TPP is the dianion of tetraphenylporphyrin and M = Zn(II), Cu(II) or Ag(II). The effect of the linking Pz group on the redox potentials and UV-visible spectra of the neutral, electroreduced and electrooxidized bis-porphyrins is discussed and the data compared to what is observed for related monoporphyrins and earlier characterized bis-porphyrins containing a tetraazaanthracene (TA) linking group and the same central metal ions. The Cu(II) and Zn(II) Pz linked bis-porphyrins exhibit a relatively strong interaction between the two equivalent porphyrin macrocycles as evidenced by UV-visible spectra of the neutral compounds and characteristic splitting of redox processes for three of the four electron transfer reactions, the one exception being the first oxidation, where no splitting of potentials is observed in the formation of the bisporphyrin bis-cation radical, [M(TPP)-Pz-(TPP)M]<sup>2+</sup>. The first oxidation and first reduction of the bis-porphyrin with two Ag(II) central metal ions occurs *via* two overlapping one-electron transfer steps in each process indicating equivalent, but non-interacting redox centers. This difference in redox behavior is due to differences in the site of electron transfer, metal centered for the Ag(II) bisporphyrins, which undergo Ag(II)/Ag(III) and Ag(II)/Ag(I) processes as compared to only ring centered electron transfers for the Cu(II) and Zn(II) derivatives. The Pz-linked Zn(II) bis-porphyrins have a larger average HOMO–LUMO gap (2.01 V) as compared to related tetraazaanthracene linked bis-porphyrins (1.67 V), which were earlier characterized in the literature, but the gap is smaller than that for the mono-porphyrins with the same central metal ions (2.17 V). Each redox reaction of the investigated bisporphyrins was characterized by thin-layer spectroelectrochemistry.

**KEYWORDS:** bisporphyrin, electrochemistry, spectroelectrochemistry, metal center effect.

<sup>d</sup> SPP full member in good standing

\*Correspondence to: Karl M. Kadish, email: [kkadish@uh.edu](mailto:kkadish@uh.edu), tel: +1 (713)-743-2740, fax: +1 (713)-743-2745; Roberto Paolesse, email: [roberto.paolesse@uniroma2.it](mailto:roberto.paolesse@uniroma2.it), tel/fax: +39 06-72594328

## INTRODUCTION

Extended porphyrinoid molecules have attracted much attention because of their fundamental, theoretical interest, and their use for diverse applications in the fields of biology, technology and medicine [1–4].

$\beta,\beta'$ -appended and linked porphyrins have been proposed as key components for applications in building electron- and energy-transfer devices, and many such molecules have been reported [5–11].

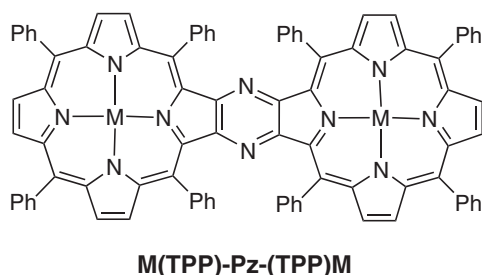
An extension of the porphyrin core aromaticity generally leads to a decrease in the electrochemical HOMO–LUMO gap [12–16], and strong red shifts of absorption bands in the optical spectrum of the neutral compounds [4, 17, 18]. As a result of these changes there are also changes in the linear and nonlinear optical properties of the compounds. Understanding the most important factors that affect the site of electron transfer in bis-porphyrins, as well as the magnitude of interaction between equivalent redox active centers in these compounds is of vital interest to tune and direct the chemical reactivity of expanded porphyrins and larger arrays [7].

A number of previously characterized bis-porphyrins have contained fused linking groups at the *meso* or  $\beta$ -pyrrole positions of the macrocycle [4, 13,

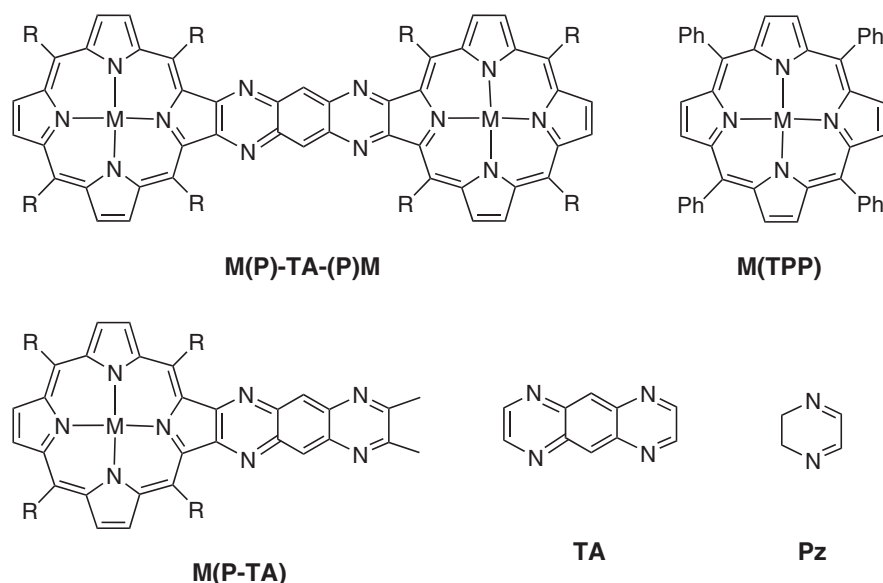
15, 19]. In the case of transition metal derivatives with redox active central metal ions, the porphyrin metal oxidation state could sometimes be stepwise cycled between its  $M^I$ ,  $M^{II}$ ,  $M^{III}$ ,  $M^{IV}$  or even  $M^V$  forms, as a function of the applied potential and variations in the type and number of bound axial ligands [16]. It is well-documented in the literature that the site of electron transfer in metalloporphyrins can be tuned by appropriate selection of solvent, axial ligand binding, and/or porphyrin ring substituents [16], and this is also the case for bis-porphyrins.

Electrochemical characterization of covalently linked symmetrical and unsymmetrical bis-metalloporphyrin dyads such as  $M(\text{TPP-TriPP})M$  and  $M(\text{TPP-DEHMP})M$  have been reported [20], where TPP-TriPP and TPP-DEHMP are the tetraanions of 1,4-bis-[5'-(10',15', 20'-triphenylporphyrinyl)]benzene and 1-[5-(10,15,20-triphenylporphyrinyl)]-4-[10-(2,18-diethyl-3,7,8,12,13,17-hexamethylporphyrinyl)] benzene, respectively. In each dyad, the two porphyrin macrocycles are linked by a

(a) Investigated bis-porphyrins



(b) Reference porphyrins



**Chart 1.** Structures of (a) investigated bis-porphyrins with Zn(II), Cu(II) and Ag(II) central metal ions and (b) related reference compounds where R is a tri-*t*-butylphenyl group

single bond and, in the case of  $M(\text{TPP-TriPP})M$ , might be considered as two triphenylporphyrins bridged by a single linking phenyl group. The UV-visible spectra of the neutral bisporphyrin dyads linked by a single phenyl group are almost identical to the superimposed spectra of the two corresponding monomeric units [20] and this indicates that little or no interaction occurs between the two macrocycles in their neutral form. Evidence of non-interacting macrocycles is also given by the electrochemical data where redox potentials of the bis-porphyrins are almost identical to  $E_{1/2}$  values for oxidation or reduction of the combined individual monoporphyrin units and no “splitting” of the redox processes are observed which would occur for equivalent interacting redox centers [20].

There are numerous examples in the literature where oxidation or reduction of bis-porphyrins and bis-corroles exhibit split redox processes in oxidation or reduction [21–27]. The separation between the values of  $E_{1/2}$  in the split processes will reflect the degree of interaction between the two macrocycles in the dyad, with the measured  $\Delta E_{1/2}$  values ranging from as small as several millivolts for small interactions to almost 500 mV for large interactions, one example of the latter being given for tetraazaanthracene (TA) linked porphyrins such as  $M(\text{P-TA-P})M$ , where  $M = \text{H}_2, \text{Cu}(\text{II}), \text{Zn}(\text{II})$  or  $\text{Pd}(\text{II})$  [13].

Another series of bisporphyrins which are structurally related to the TA-linked derivatives are the pyrazine linked bis-porphyrins, whose synthesis and brief electrochemistry were described in a recent publication [19]. A split redox process was reported for oxidation of the  $\text{Zn}(\text{II})$  bisporphyrin, but the overall redox behavior was complicated by the presence of side reactions that occurred in  $\text{CH}_2\text{Cl}_2$  and none of the other bisporphyrins were electrochemically characterized in the manuscript. Furthermore, the spectra of the oxidized or reduced  $\text{Zn}(\text{II})$  bisporphyrin were not measured and thus a more detailed analysis of this compound's redox behavior and spectroscopic properties after oxidation or reduction is needed. This is addressed in the current paper, where we present the electrochemistry and spectroelectrochemistry of  $\text{Zn}(\text{II}), \text{Cu}(\text{II})$  and  $\text{Ag}(\text{II})$   $\beta,\beta$ -pyrazino fused bisporphyrins in benzonitrile (PhCN) containing 0.1 M tetrabutylammonium perchlorate (TBAP). The first two compounds undergo only ring centered electron transfer reactions, while the  $\text{Ag}(\text{II})$  bisporphyrin exhibits both a metal-centered oxidation and a metal-centered reduction prior to oxidation or reduction at the conjugated bisporphyrin macrocycle. The examined porphyrins are represented as  $M(\text{TPP})\text{-Pz-(TPP)}M$  and shown in Chart 1 along with several reference compounds containing linked pyrazine and tetraazaanthracene groups. The electrochemical behavior of the currently investigated dyads are examined as a function of the type and oxidation state of the central metal ion and the type of linking group.

## EXPERIMENTAL

### Instrumentation

Cyclic voltammetry was carried out at 298 K by using an EG&G Princeton Applied Research (PAR) 173 potentiostat/galvanostat. A homemade three-electrode cell was used for cyclic voltammetric measurement and consisted of a glassy carbon working electrode, a platinum counter electrode and a homemade saturated calomel reference electrode (SCE). The SCE was separated from the bulk of the solution by a fritted bridge of low porosity which contained the solvent/supporting electrolyte mixture.

Thin-layer UV-visible spectroelectrochemical experiments were performed with a home-built thin-layer cell which has a light transparent platinum net working electrode. Potentials were applied and monitored with an EG&G PAR Model 173 potentiostat. Time-resolved UV-visible spectra were recorded with a Hewlett-Packard Model 8453 diode array spectrophotometer. High purity  $\text{N}_2$  from Trigas was used to deoxygenate the solution and kept over the solution during each electrochemical and spectroelectrochemical experiment.

### Chemicals

Reagents and solvents (Aldrich, Fluka) were of the highest grade available and were used without further purification. Silica gel 60 (70–230 mesh, Sigma Aldrich) was used for column chromatography. UV-visible spectra were recorded on a Cary 50 spectrophotometer. Mass spectra (FAB mode) were recorded on a VGQuattro spectrometer in the positive-ion mode using *m*-nitrobenzyl alcohol (Aldrich) as a matrix.

Benzonitrile (PhCN) was obtained from Aldrich Co., and distilled over  $\text{P}_2\text{O}_5$  under vacuum prior to use. Tetra-*n*-butylammonium perchlorate (TBAP) was purchased from Sigma Chemical or Fluka Chemika Co., recrystallized from ethyl alcohol, and dried under vacuum at 40 °C for at least one week prior to use.

**Zn(TPP)-Pz-(TPP)Zn** and **Cu(TPP)-Pz-(TPP)Cu** were synthesized according to literature methods [19].

**Synthesis of Ag(TPP)-Pz-(TPP)Ag.** To a stirred mixture of  $\text{H}_2(\text{TPP})\text{-Pz-(TPP)}\text{H}_2$  (20 mg, 0.016 mmol) in pyridine (5 mL),  $\text{Ag}(\text{OAc})$  (26 mg, 0.16 mmol) was added, and the solution was refluxed for 1 h. The progress of the reaction was monitored by TLC and UV-visible spectroscopy. When the reaction was complete, the mixture was cooled to room temperature and an equal volume of water was added to precipitate the silver complex. The resulting precipitate was separated by filtration and then purified by chromatography on a silica gel column, eluting with dichloromethane. The major fraction was collected and crystallized from dichloromethane/methanol affording  $\text{Ag}(\text{TPP})\text{-Pz-(TPP)}\text{Ag}$  (8 mg, 33.3%). UV-visible ( $\text{CH}_2\text{Cl}_2$ ):  $\lambda_{\text{max}}$ , nm



(log  $\epsilon$ ) 408 (4.12), 486 (4.61), 578 (4.08). MS:  $m/z$  1464  $[M]^+$ . Calcd. for  $C_{88}H_{52}N_{10}Ag_2$ : C, 72.1; H, 3.6; N, 9.6. Found C, 72.3; H, 3.5; N, 9.8.

## RESULTS AND DISCUSSION

### UV-visible absorption spectra of neutral compounds

UV-visible spectra of  $M(TPP)\text{-Pz}\text{-(TPP)}M$  in PhCN are shown in Fig. 1 for the Zn(II) and Cu(II) derivatives. Both bisporphyrins are characterized by a split Soret band, located at 411/500 nm for  $M = Zn$  and 425/495 nm for  $M = Cu$ . There is also a single relatively intense Q-band at 600 nm (Zn) or 590 nm (Cu). A similar spectrum is seen for the  $Ag(TPP)\text{-Pz}\text{-(TPP)}Ag$  in PhCN, which is characterized by bands at 415, 489

and 578 nm. By way of comparison, the three related monometallic  $M(TPP)$  complexes in PhCN are each characterized by an unsplit Soret band at 419 to 428 nm and two weak Q-bands at 537 to 600 nm. The spectral data for these mono and bisporphyrins are summarized in Table 1 for the related TA-linked porphyrins under the same solution conditions. As seen in the table and figure, the separation between the split Soret bands of the  $M(TPP)\text{-Pz}\text{-(TPP)}M$  bisporphyrins is 70 nm for  $M = Cu(II)$ , 74 nm for  $M = Ag(II)$  and 89 nm for  $M = Zn(II)$ . These values are much larger than the separation in  $\lambda_{max}$  for the split Soret bands of the Cu and Zn TA linked porphyrins (see Table 1) but, as discussed below, the TA linked complexes exhibit a greater interaction between the two redox active macrocycles upon reduction as compared to the related Pz-linked derivatives.

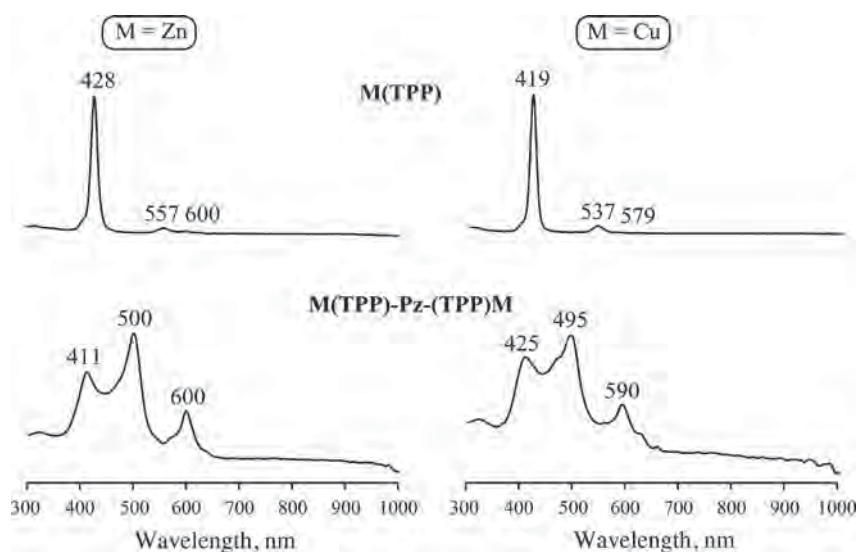
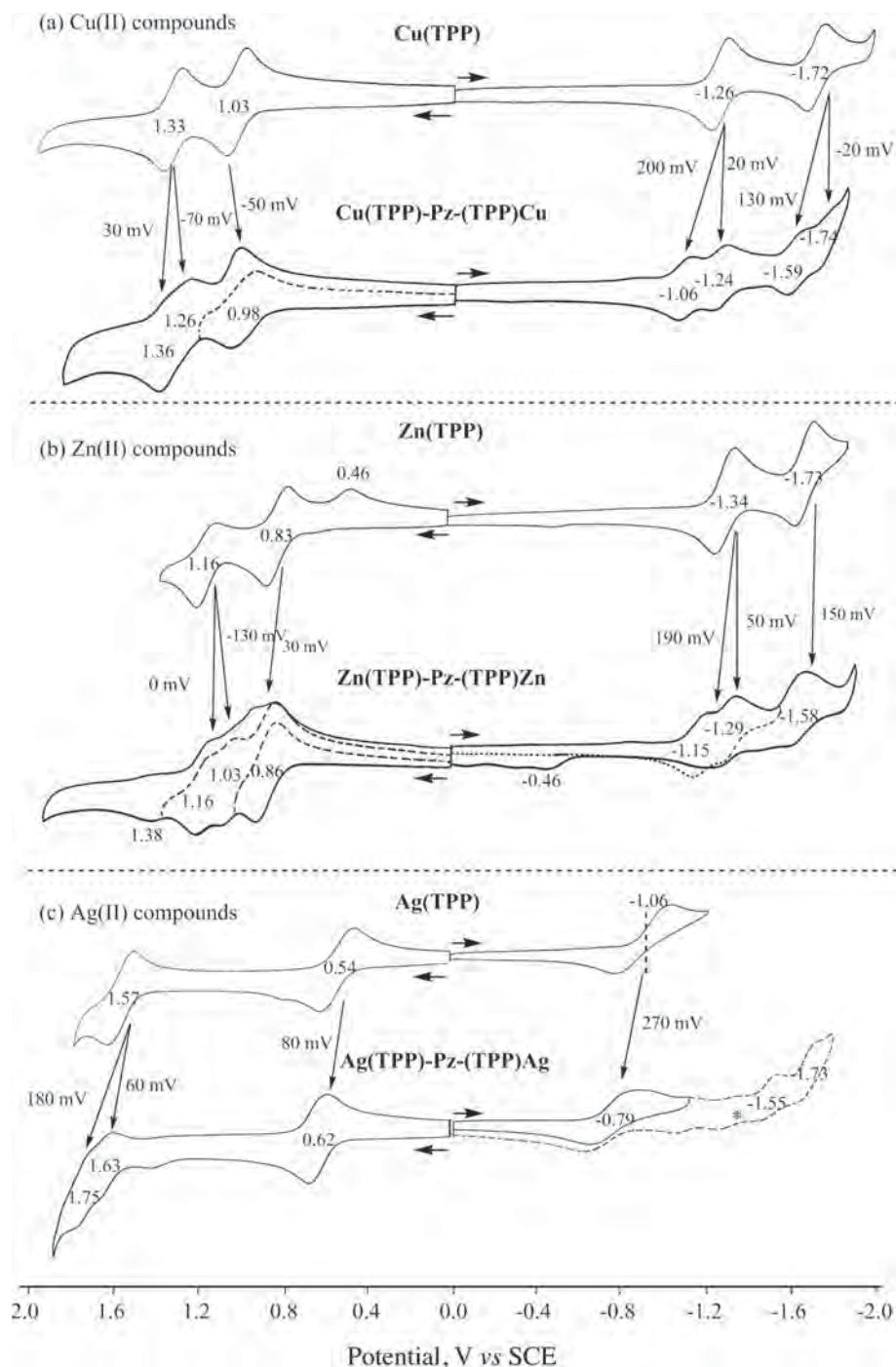


Fig. 1. UV-vis spectra of  $M(TPP)$  and  $M(TPP)\text{-Pz}\text{-(TPP)}M$  in PhCN

Table 1. UV-visible spectral data ( $\lambda_{max, nm}$ ) of investigated  $M(TPP)\text{-Pz}\text{-(TPP)}M$  and related compounds in PhCN

Macrocycle	M	Soret band, nm		Q-band, nm	
$M(TPP)$	Zn	428		557	600
	Cu	419		537	579
	Ag	423		539	569
$M(TPP)\text{-Pz}\text{-(TPP)}M$	Zn	411	500	600	
	Cu	425	495	590	
	Ag	415	489	578	
$M(P)\text{-TA}\text{-(P)}M$	Zn	435	467	527	
	Cu	431	444	552	



**Fig. 2.** Cyclic voltammograms of M(TPP) and M(TPP)-Pz-(TPP)M in PhCN containing 0.1 M TBAP where M equals (a) Cu(II), (b) Zn(II) and (c) Ag(II)

### Electrochemistry

The electrochemistry of each M(TPP)-Pz-(TPP)M complex was characterized in PhCN containing 0.1 M TBAP. Cyclic voltammograms of the three bisporphyrins and reference M(TPP) compounds with the same central metal ions are shown in Fig. 2, and a summary of half-wave potentials for each redox reaction is given in Table 2.

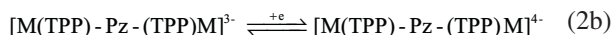
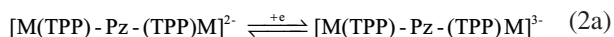
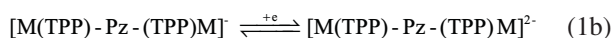
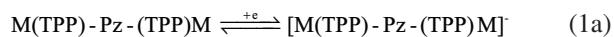
The M(TPP)-Pz-(TPP)M derivatives exhibit multiple reductions and oxidations in PhCN containing 0.1 M TBAP. Four reversible reductions are seen for Cu(TPP)-Pz-(TPP)Cu (Fig. 2a) and three for Zn(TPP)-Pz-(TPP)Zn (Fig. 2b). The first two one electron reductions are assigned as formation of a bisporphyrin monoanion radical, and bisporphyrin diradical as shown in Equations 1a and 1b, while the next two reductions involve formation of the bisporphyrin with three and four added electrons,

**Table 2.** Half-wave potentials (V vs. SCE) of porphyrins M(TPP)-Pz-(TPP)M, M(P)-TA-(P)M, M(P-TA) and M(TPP), where M = Zn, Cu and Ag in PhCN containing 0.1 M TBAP

Compound	Ring oxidation			Ring reduction			H-L Gap <sup>f</sup>	Ref.	
	2nd	1st		1st	2nd				
Cu(TPP)-Pz-(TPP)Cu	1.36	1.26	0.98	-1.06	-1.24	-1.59	-1.74	2.04	<i>tw</i>
Zn(TPP)-Pz-(TPP)Zn	1.16	1.03	0.86	-1.15	-1.29	-1.58	-1.58	2.01	<i>tw</i>
Ag(TPP)-Pz-(TPP)Ag	1.73	1.63	0.62 <sup>b</sup>	-0.79 <sup>b</sup>		-1.55	-1.73		<i>tw</i>
Cu(P)-TA-(P)Cu	1.20		1.00	-0.70	-1.18	-1.47	-1.92 <sup>a</sup>	1.70	[13]
Zn(P)-TA-(P)Zn	1.04		0.84	-0.83	-1.33 <sup>a</sup>	-1.48	-1.83 <sup>a</sup>	1.67	[13]
Cu(P-TA)	1.19		1.01	-0.92		-1.37		1.93	[13]
Zn(P-TA)	1.04		0.84	-1.00		-1.40		1.84	[13]
Cu(TPP)	1.33		1.03	-1.26		-1.72		2.29	<i>tw</i>
Zn(TPP)	1.16		0.83	-1.34		-1.73		2.17	<i>tw</i>
Ag(TPP)	1.57		0.54 <sup>b</sup>	-1.06 <sup>b</sup>		-1.67 <sup>c</sup>			[29]
Pz				-2.07 <sup>d</sup>					[28]
TA				-0.96 <sup>d,e</sup>		-1.54 <sup>d,e</sup>			[28]

<sup>a</sup>Irreversible peak potential at scan rate of 0.1 V/s; <sup>b</sup>Metal-centered reaction; <sup>c</sup>Data measured in pyridine; <sup>d</sup>Potentials reported in CH<sub>3</sub>CN, 0.1 M TBAP vs. an Ag/AgCl reference electrode; <sup>e</sup>Two overlapped one-electron transfers in single step; <sup>f</sup>H-L gap represents the HOMO–LUMO gap which is the potential difference between the first ring-centered oxidation and first ring-centered reduction.

as written in Equations 2a and 2b. The last two reductions of the Cu(II) bisporphyrin are well-separated ( $E_{1/2} = -1.59$  and  $-1.74$  V) in PhCN, but the same processes (given by Equations 2a and 2b) are overlapped in potential for the Zn(II) derivative as seen in Fig. 2b.



The above four one-electron reductions of the Cu(II) and Zn(II) bisporphyrins can be compared with the two one-electron reductions of monometallic Cu(TPP) and Zn(TPP) to give porphyrin  $\pi$  anion radicals and dianions. The first reduction of the M(TPP) compounds is located at  $E_{1/2} = -1.26$  V (Cu) or  $-1.34$  V (Zn) and the second at  $-1.72$  or  $-1.73$  V, respectively. Each ring-centered reduction of the monoporphyrin is split into two separate processes in the dyad, as shown in Fig. 2 where, for example, the Cu(II) Pz complex is reversibly reduced at  $-1.06$ ,  $-1.24$ ,  $-1.59$  and  $-1.74$  V. The difference in  $E_{1/2}$  between the first two sets of Cu(TPP)-Pz-(TPP)Cu reductions amounts to 180 and 150 mV, respectively, and a similar 140 mV separation in  $\Delta E_{1/2}$  is seen between the first two reductions of the Zn pyrazine-linked dyad ( $E_{1/2} = -1.15$  and  $-1.29$  V).

The 140–180 mV separation between  $E_{1/2}$  values for Equations 1a and 1b is consistent with a moderate interaction between the two redox active macrocycles, but it is much less than the 480–500 mV separation between the first two reductions of Cu(P)-TA-(P)Cu and Zn(P)-TA-(P)Zn (see Table 2) where a strong interaction is observed.

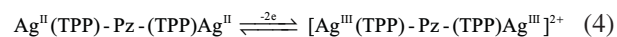
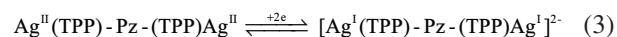
Tetraazaanthracene (TA) has a larger  $\pi$  system than pyrazine (Pz) and it is also easier to reduce than Pz [28]. Thus one might expect to have a greater electron density on the linking TA group than on the linking Pz group of the singly reduced dyads. The TA-linked dyads should also be easier to reduce by a single electron than the Pz-linked dyads. In addition, the porphyrin dyads in both series should be easier to reduce than the unlinked M(TPP) derivatives in the same solvent. This is indeed the case, as seen in Table 2 where the  $E_{1/2}$  values of the Cu(II) porphyrins follows the trend:  $-0.70$  V (TA dyad) >  $-1.06$  V (Pz dyad) >  $-1.26$  V (Cu(TPP)). The same trend in  $E_{1/2}$  for the first reduction is seen for the Zn(II) compounds, where  $E_{1/2}$  follows the order:  $-0.83$  V (TA dyad) >  $-1.15$  V (Pz dyad) >  $-1.34$  V (Zn(TPP)). Both sets of data suggested that the difference in electrochemical behavior between the two series of TA and Pz dyads is related to the electron density on the singly reduced compounds, which in the case of the TA-linked porphyrins is partially on the fused TA group, as described in an earlier publication [13].

In contrast to what occurs for the fused TA and Pz dyads of Cu(II) and Zn(II), there is no splitting in  $E_{1/2}$

values for the first reduction of Ag(TPP)-Pz-(TPP)Ag. This can be accounted for by the fact that the initial reduction of this porphyrin occurs not at the macrocycle or at the linked Pz group, but rather at the two Ag(II) metal ions, both of which accept one electron at the same half-wave potential of -0.79 V, thus indicating equivalent, but noninteracting redox centers for the *metal centered reductions*. In this regard it should be noted that Ag(TPP)-Pz-(TPP)Ag is easier to reduce than Ag(TPP) by 270 mV and this positive shift of reduction potential can be accounted for by the extended  $\pi$  conjugation of the dyad formed upon fusion of the Pz group to the two TPP macrocycles.

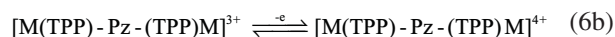
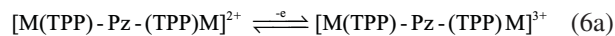
The second reduction of Ag(TPP) could not be measured in PhCN due to demetalation but  $E_{1/2}$  for the ring-centered reduction of  $[\text{Ag}^{\text{I}}(\text{TPP})]^-$  has been reported as -1.67 V in pyridine [29]. This potential is close to the average  $E_{1/2}$  for the two, presumably ring-centered, one-electron reductions of Ag(TPP)-Pz-(TPP)Ag at -1.55 and -1.73 V in PhCN (see Fig. 2). The peak current for each of the two ring-centered reductions is approximately half that of the Ag(II)/Ag(I) process of the dyad, consistent with two one-electron transfers, separated by 180 mV. A similar potential separation is seen between the first split ring centered reduction of the dyads with Cu(II) (180 mV) or Zn(II) (140 mV) metal ions. Also, as would be expected for the case of two equivalent interacting redox centers, the first *ring-centered reduction* of  $[\text{Ag}^{\text{I}}(\text{TPP})\text{-Pz-(TPP)Ag}^{\text{I}}]^{2-}$  to give the “half reduced” dyad is easier than the potential for the ring-centered reduction of monomeric  $[\text{Ag}^{\text{I}}(\text{TPP})]^-$  under the same solution conditions.

Focusing further on the redox behavior of the Ag(II) dyad, it should be noted that the first oxidation of Ag(TPP)-Pz-(TPP)Ag at  $E_{1/2} = 0.62$  V is shifted positively from the  $E_{1/2}$  of 0.54 V for oxidation of Ag(TPP) and this process is unsplit like the reduction. This lack of splitting is attributed to the site of electron transfer, which involves the two Ag(II) metal ion to give a bis-Ag(III) bisporphyrin. The peak current for the metal-centered oxidation of Ag(TPP)-Pz-(TPP)Ag in PhCN is equal to the peak current for the metal-centered reduction (see CV in Fig. 2), thus indicating a transfer of two electrons in each process as shown by Equations 3 and 4.



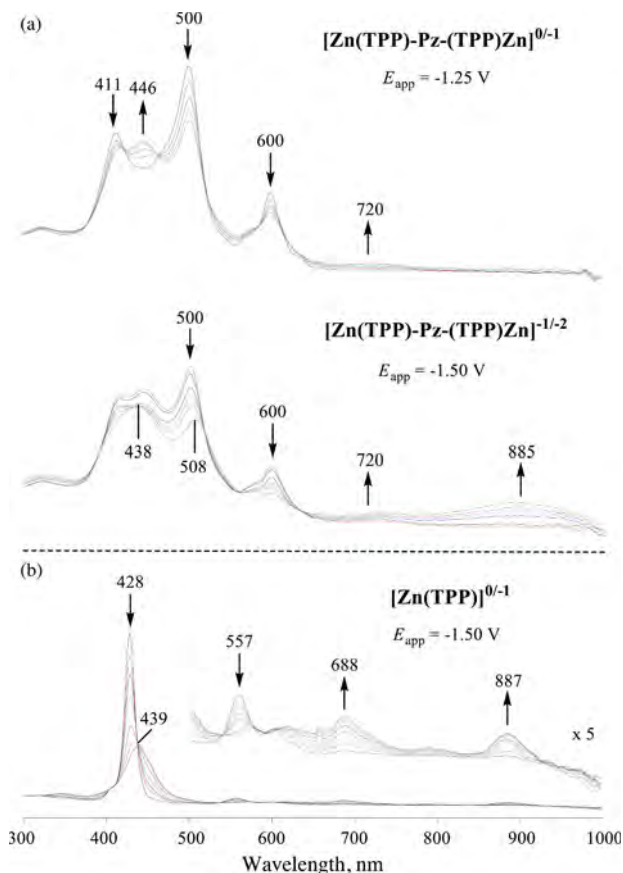
Finally, it should be pointed out that the first ring-centered oxidation of Ag(TPP)-Pz-(TPP)Ag occurs in two steps (at  $E_{1/2} = 1.63$  and 1.75 V), which are separated by 120 mV. Similar separations are observed for the second ring-centered oxidation of Cu(TPP)-Pz-(TPP)Cu (100 mV) and Zn(TPP)-Pz-(TPP)Zn (130 mV). Thus, the +2 charge on the porphyrin may be related to the

splitting and the redox processes for oxidation of the three dyads can be written as shown in Equations 5 and 6, where the overall charges on the porphyrin are +2, +3 and +4, respectively.



### Spectroelectrochemical monitoring of reduction and oxidation products

*M(TPP)-Pz-(TPP)M*,  $M = \text{Zn or Cu}$ . UV-visible spectra obtained during controlled potential reduction of Zn(TPP)-Pz-(TPP)Zn in PhCN containing 0.1 M TBAP are shown in Fig. 3. The neutral Zn(II) bisporphyrin has a split Soret band at 411 and 500 nm and single strong Q-band at 600 nm. All three peaks decrease in intensity during the first reduction by one electron (Equation 1a) as a new peak grows in at 446 nm, along with a broad band at 720 nm (Fig. 3a). Further reduction of the “half reduced”  $[\text{Zn}(\text{TPP})\text{-Pz-(TPP)Zn}]^-$  dyad at a controlled potential at -1.50 V leads to the bisporphyrin



**Fig. 3.** UV-visible spectral changes during the controlled potential reduction of (a) Zn(TPP)-Pz-(TPP)Zn and (b) Zn(TPP) in PhCN, 0.1 M TBAP

$[\text{Zn}(\text{TPP})\text{-Pz}(\text{TPP})\text{Zn}]^{2-}$ , which is assigned as a bis-anion radical (Equation 1b). This spectrum is seen in the lower half of Fig. 3a and is characterized by bands at 438, 508, 720 and 885 nm. A very similar UV-visible spectrum is seen after reduction of Zn(TPP) to its  $\pi$  anion radical form at a controlled potential of -1.50 V. This spectrum has bands at 439, 688 and 887 nm (Fig. 3b), but lacks the 508 nm band, which is present in the reduced Zn(II) dyad, but not in the reduced Zn(II) monoporphyrin  $\pi$  anion radical.

Similar UV-visible bands are also seen in the spectra of electrogenerated  $[\text{Zn}(\text{TPP})\text{-Pz}(\text{TPP})\text{Zn}]^{2+}$  and  $[\text{Zn}(\text{TPP})]^+$ . These spectra are shown in Fig. 4. The oxidized dyad, which has lost two electrons, has bands at 413 and 500 nm and a broad band between 600 and 900 nm (Fig. 4a). The monoporphyrin  $\pi$ -cation radical has bands at 415 and 458 nm and a broad band between 550 and 750 nm. The major difference between the two spectra is the intensity of the band at 500 nm for the oxidized dyad.

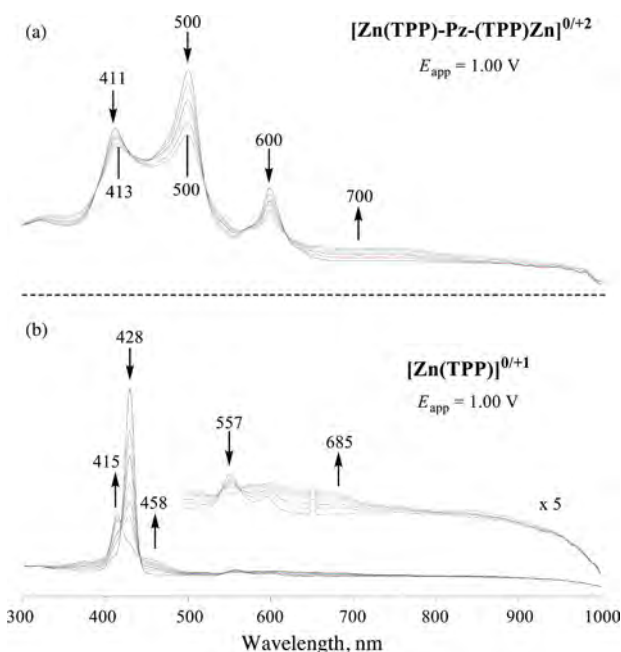
**Ag(TPP)-Pz-(TPP)Ag.** The first reduction and first oxidation of Ag(TPP)-Pz-(TPP)Ag were monitored by thin-layer spectroelectrochemistry in PhCN. The spectral changes observed during reduction are shown in Fig. 5a and those during oxidation in Fig. 5b. The spectrum of the neutral Ag(II) bisporphyrin is characterized by a split Soret band at 415/489 nm and a strong Q-band at 578 nm. This spectrum is similar to that of the Cu(II) and Zn(II) bisporphyrins as seen in Table 1.

All three absorption bands of Ag(TPP)-Pz-(TPP)Ag decrease in intensity during the first controlled potential reduction at -1.05 V as a new peak for the reduced dyad grows in at 446 nm (Fig. 5a). No major absorbances are seen between 700 and 1000 nm, consistent with the site of electron addition being located at the two metal ions and not at the conjugated macrocycles. The spectral changes in Fig. 5a are different than those reported for reduction of Ag(TPP) [29], consistent with a strong interaction between the two Ag(I) metallomacrocycles.

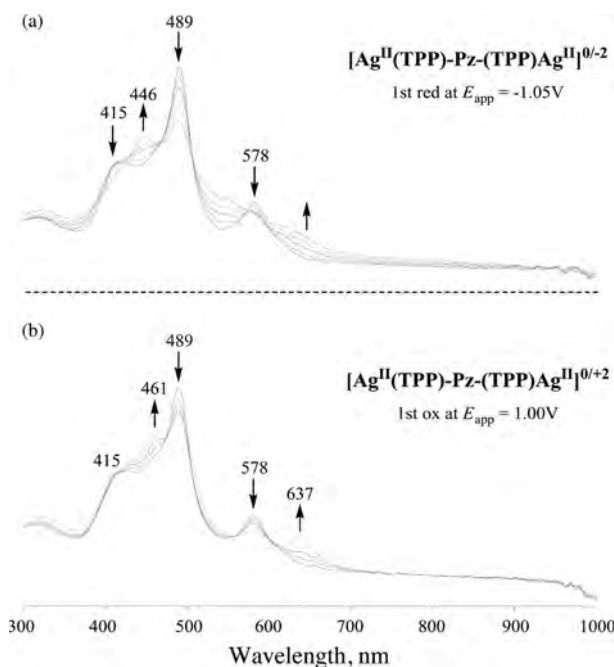
The spectral changes associated with conversion of Ag(TPP)-Pz-(TPP)Ag to  $[\text{Ag}(\text{TPP})\text{-Pz}(\text{TPP})\text{Ag}]^{2+}$  are illustrated in Fig. 5b. The bis-Ag(II) bisporphyrin is characterized by bands at 415, 489 and 578 nm. The 415 nm band remains unchanged upon the abstraction of two electrons and conversion of Ag(II) to Ag(III) and while the 489 and 578 nm bands disappear and new bands are seen at 461 and 637 nm. There are no absorptions from 700–1000 nm consistent with a metal-centered electron transfer.

### Summary and final comments on redox reactions of M(TPP)-Pz-(TPP)M

In summary, the linking of two porphyrins by a fused pyrazine group leads to a splitting of reduction potentials for ring centered reactions, but not for reduction at the central metal ion that occurs in the case of the Ag(II)

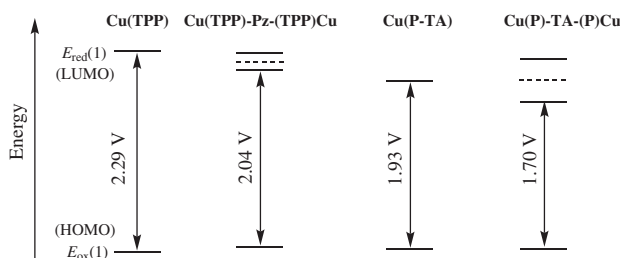


**Fig. 4.** UV-visible spectral changes during the controlled potential oxidation of (a) Zn(TPP)-Pz-(TPP)Zn and (b) Zn(TPP) in PhCN, 0.1 M TBAP

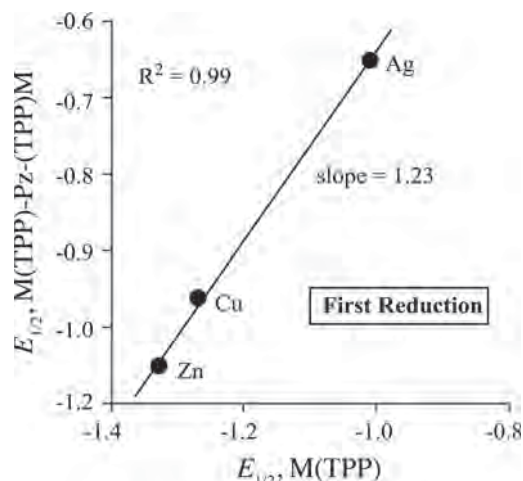


**Fig. 5.** UV-visible spectral changes for Ag(TPP)-Pz-(TPP)Ag during controlled potential (a) reduction and (b) oxidation in PhCN, 0.1 M TBAP

bisporphyrin. The difference between the two  $E_{1/2}$  values for formation of the half reduced and fully reduced macrocycle of the dyad ranges from 140–180 mV, consistent with a moderate interaction between the two redox active  $\pi$  ring systems of the bisporphyrins. There



**Fig. 6.** Measured HOMO–LUMO gap for related Cu(II) porphyrins in PhCN, containing 0.1 M TBAP



**Fig. 7.** Correlation of reduction potential (V vs. SCE) between M(TPP) and M(TPP)-Pz-(TPP)M

is no significant difference in  $\Delta E_{1/2}$  with changes in the metal ion from Cu<sup>II</sup> to Zn<sup>II</sup>, and also seems to be the case for the TA-linked dyads of Cu<sup>II</sup> and Zn<sup>II</sup>, which show a very large interaction between the two equivalent redox active macrocycles, as indicated by a  $\Delta E_{1/2}$  between the split redox processes of close to 500 mV (see Table 2).

The fused Pz and TA linking groups are both electroactive in the absence of a fused porphyrin, with  $E_{1/2}$  values being reported as -2.07 and -0.96 V vs. Ag/AgCl [28], respectively. Because TA itself is easier to reduce than any of the three investigated monoporphyrins (see Table 2), the site of the first added electron in the TA-linked bisporphyrins should be located on the linker far more than in the case of the Pz group of the M(TPP)-Pz-(TPP)M derivatives. No separation in half wave potentials is observed for the reduction at the two metal centers of Ag(TPP)-Pz-(TPP)Ag and this is consistent with the added electron being on the metal center and not on the fused linking Pz group.

As earlier indicated, the ease of the first reduction for the metalloporphyrins in Table 2 follows the order: M(P)-TA-(P)M > M(P-TA) > M(TPP)-Pz-(TPP)M > M(TPP). As also seen in this table, the easier the ring-centered reduction of the metalloporphyrin, the smaller the HOMO–LUMO gap, which ranges from 1.70 to 2.29 V

as shown in Fig. 6. No splitting of the redox processes are seen for the first oxidation of the three examined M(TPP)-Pz-(TPP)M compounds. However, the second oxidation of each bisporphyrin is split into two processes, with  $\Delta E_{1/2}$  values ranging from 100 to 130 mV for the reactions given by Equations 5 and 6. Finally, it should be noted that a plot of  $E_{1/2}$  for the first reduction of M(TPP)-Pz-(TPP)M vs.  $E_{1/2}$  for the first reduction of M(TPP) in PhCN is linear with a slope of 1.23 and a correlation coefficient of 0.99 (see Fig. 7). The larger than unity slope of 1.23 indicates that the degree of interaction between the macrocycles of M(TPP)-Pz-(TPP)M upon reduction depends upon the type of central metal ion.

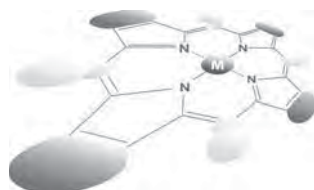
## Acknowledgements

We gratefully acknowledge support from the Robert A. Welch Foundation (K.M.K., Grant E-680), and Italian MIUR (FIRB project RBFR12WB3W).

## REFERENCES

- Martinez-Diaz VM and Torres T. In *Handbook of Porphyrin Science*, Vol. 10, Kadish KM, Smith KM and Guillard R. (Eds.) World Scientific: Singapore, 2010; Chapter 45, pp 141–181.
- Duclairoir F and Marchon J-C. In *Handbook of Porphyrin Science*, Vol. 10, Kadish KM, Smith KM and Guillard R. (Eds.) World Scientific: Singapore, 2010; Chapter 47, pp 245–311.
- Ethirajan M, Patel NJ and Pandey RK. In *Handbook of Porphyrin Science*, Vol. 4, Kadish KM, Smith KM and Guillard R. (Eds.) World Scientific: Singapore, 2010; Chapter 19, pp 249–323.
- Lewtak JP and Gryko DT. *Chem. Commun. (Cambridge, U. K.)* 2012; **48**: 10069–10086.
- Sintic PJ, E W, Ou Z, Shao J, McDonald JA, Cai Z-L, Kadish KM, Crossley MJ and Reimers JR. *Phys. Chem. Chem. Phys.* 2008; **10**: 268–280.
- Armstrong RS, Foran GJ, Hough WA, D'Alessandro DM, Lay PA and Crossley MJ. *Dalton Trans.* 2006; **40**: 4805–4813.
- Crossley MJ, Sintic PJ, Walton R and Reimers JR. *Org. Biomol. Chem.* 2003; **1**: 2777–2787.
- Sendt K, Johnston LA, Hough WA, Crossley MJ, Hush NS and Reimers JR. *J. Am. Chem. Soc.* 2002; **124**: 9299–9309.
- Reimers JR, Hall LE, Crossley MJ and Hush NS. *J. Phys. Chem. A* 1999; **103**: 4385–4397.
- Chou J-H, Nalwa HS, Kosal ME, Rakow NA and Suslick KS. In *The Porphyrin Handbook*, Vol. 6, Kadish KM, Smith KM and Guillard R. (Eds.) Academic Press: San Diego, 2000; Chapter 41, pp 45–118.
- Malinski T. In *The Porphyrin Handbook*, Vol. 6, Kadish KM, Smith KM and Guillard R. (Eds.) Academic Press: San Diego, 2000; Chapter 44, pp 231–256.

12. Kadish KM, Ou Z, Zhan R, Khoury T, E W and Crossley MJ. *J. Porphyrins Phthalocyanines* 2010; **14**: 866–876.
13. Ou Z, Zhu W, Sintic PJ, Fang Y, Crossley MJ and Kadish KM. *J. Porphyrins Phthalocyanines* 2012; **16**: 674–684.
14. Fukuzumi S, Ohkubo K, Zhu W, Sintic M, Khoury T, Sintic PJ, E W, Ou Z, Crossley MJ and Kadish KM. *J. Am. Chem. Soc.* 2008; **130**: 9451–9458.
15. Zhu W, Sintic M, Ou Z, Sintic PJ, McDonald JA, Brotherhood PR, Crossley MJ and Kadish KM. *Inorg. Chem.* 2010; **49**: 1027–1038.
16. Kadish KM, Van Caemelbecke E and Royal G. In *The Porphyrin Handbook*, Vol. 8, Kadish KM, Smith KM and Guillard R. (Eds.) Academic Press: New York, 2000; Chapter 55, pp 1–114.
17. Davis NKS, Pawlicki M and Anderson HL. *Org. Lett.* 2008; **10**: 3945–3947.
18. Davis NKS, Thompson AL and Anderson HL. *Org. Lett.* 2010; **12**: 2124–2127.
19. Mandoj F, Nardis S, Pudi R, Lvova L, Fronczek FR, Smith KM, Prodi L, Genovese D and Paolesse R. *Dyes Pigm.* 2013; **99**: 136–143.
20. Kadish KM, Guo N, Van Caemelbecke E, Paolesse R, Monti D and Tagliatesta P. *J. Porphyrins Phthalocyanines* 1998; **2**: 439–450.
21. Guillard R, Jerome F, Barbe J-M, Gros CP, Ou Z, Shao J, Fischer J, Weiss R and Kadish KM. *Inorg. Chem.* 2001; **40**: 4856–4865.
22. Chen P, Lau H, Habermeyer B, Gros CP, Barbe J-M and Kadish KM. *J. Porphyrins Phthalocyanines* 2011; **15**: 467–479.
23. Barbe J-M, Habermeyer B, Khoury T, Gros CP, Richard P, Chen P and Kadish KM. *Inorg. Chem.* 2010; **49**: 8929–8940.
24. Guillard R, Gros CP, Barbe J-M, Espinosa E, Jerome F, Tabard A, Latour J-M, Shao J, Ou Z and Kadish KM. *Inorg. Chem.* 2004; **43**: 7441–7455.
25. Kadish KM, Ou Z, Shao J, Gros CP, Barbe J-M, Jerome F, Bolze F, Burdet F and Guillard R. *Inorg. Chem.* 2002; **41**: 3990–4005.
26. Ngameni E, Laouenan A, L'Her M, Hinnen C, Hendricks NH and Collman JP. *J. Electroanal. Chem. Interfacial Electrochem.* 1991; **301**: 207–226.
27. Guillard R, Brandes S, Tardieux C, Tabard A, L'Her M, Miry C, Gouerec P, Knop Y and Collman JP. *J. Am. Chem. Soc.* 1995; **117**: 11721–11729.
28. Fogel Y, Kastler M, Wang Z, Andrienko D, Bodwell GJ and Muellen K. *J. Am. Chem. Soc.* 2007; **129**: 11743–11749.
29. Kadish KM, Lin XQ, Ding JQ, Wu YT and Araullo C. *Inorg. Chem.* 1986; **25**: 3236–3242.



# Synthesis and anti-cancer activities of a water soluble gold(III) porphyrin

Aaron D. Lammer, Melissa E. Cook and Jonathan L. Sessler\*<sup>◇</sup>

Department of Chemistry, The University of Texas at Austin, 105 E. 24th Street-A5300, Austin, TX 78712-1224, USA

Dedicated to Professor Shunichi Fukuzumi on the occasion of his retirement

Received 6 December 2014

Accepted 19 December 2014

**ABSTRACT:** Gold(III) compounds continue to be explored for their potential utility as anticancer agents. A recognized limitation is the reactivity of gold(III), which is typically reduced to the more labile gold(I) state under physiological conditions. The use of porphyrins can overcome this problem. However, to date the stabilization provided by the use a strongly chelating porphyrin is offset by the poor solubility of the resulting complex in aqueous media. In this work, we describe the synthesis and *in vitro* anti-cancer activity of a gold(III)porphyrin complex with relatively good aqueous solubility. As judged from standard antiproliferation assays, this complex displays an  $IC_{50}$  of 9  $\mu$ M for the A2780 human ovarian cancer cell line. This is a higher level of potency than displayed by two related control systems.

**KEYWORDS:** gold, porphyrin, anti-cancer, solubility.

## INTRODUCTION

As cancers continue to develop resistance to traditional chemotherapies, such as cisplatin and its derivatives, there is a corresponding need to develop novel drugs that operate by different mechanisms of action [1]. One approach involves testing other metal complexes. In this context, significant effort has been devoted towards use of gold(III) species for the treatment of cancer, as well as many other illnesses [2]. However, in most ligand environments gold(III) is unstable under physiological conditions, and is reduced quickly to the more labile gold(I). A number of stabilizing ligand have been explored in order to avoid reduction and retain the presumably more active Au(III) oxidation state, a number of stabilizing ligand have been explored [3]. A particular attractive complexing agent would be a porphyrin due to its known ability to stabilize otherwise labile metal centers, as well as the recognized cancer targeting capabilities demonstrated by many porphyrin derivatives [4]. One major drawback of most easy-to-prepare porphyrins is their poor solubility

in aqueous media. Various synthetic strategies have been utilized to overcome this latter deficiency, including the use of methylated pyridine-, sulfate-, and polysaccharide-modified porphyrins. However, these modifications affect the biological properties of the core porphyrin species, including if or how it triggers cell death [5]. In this study, we report the synthesis of a water soluble, hydroxyl modified tetraphenyl gold porphyrin and show that it has antiproliferative activity against the human ovarian cancer cell line, A2780.

Gold compounds have been used since 2500 B.C. for the treatment of smallpox and measles [6]. Gold complexes were incorporated into the modern pharmacopeia in the 1920's by Koch when he used them for the treatment of tuberculosis, with an eventual shift to gold(I) thiolates to mediate toxicity [2a and 2b]. Since then, gold-containing agents have been extensively studied for the treatment of rheumatoid arthritis, and recently HIV [2h–2j]. In 1965 Lorber and coworkers reported the anti-cancer activity of auranofin (**1**) against strains of cancer derived from the HeLa cell line Fig. 1 [7]. Berners-Price and Sadler studied the ligand exchange of gold(I) and gold(III) complexes in 1996 [8]. In that same year, Kelland and co-workers reported *in vivo* studies of 2-[(dimethylamino)methyl] phenylgold(III) against a panel of human cancer

<sup>◇</sup>SPP full member in good standing

\*Correspondence to: Jonathan L. Sessler, email: [ssessler@cm.utexas.edu](mailto:ssessler@cm.utexas.edu)



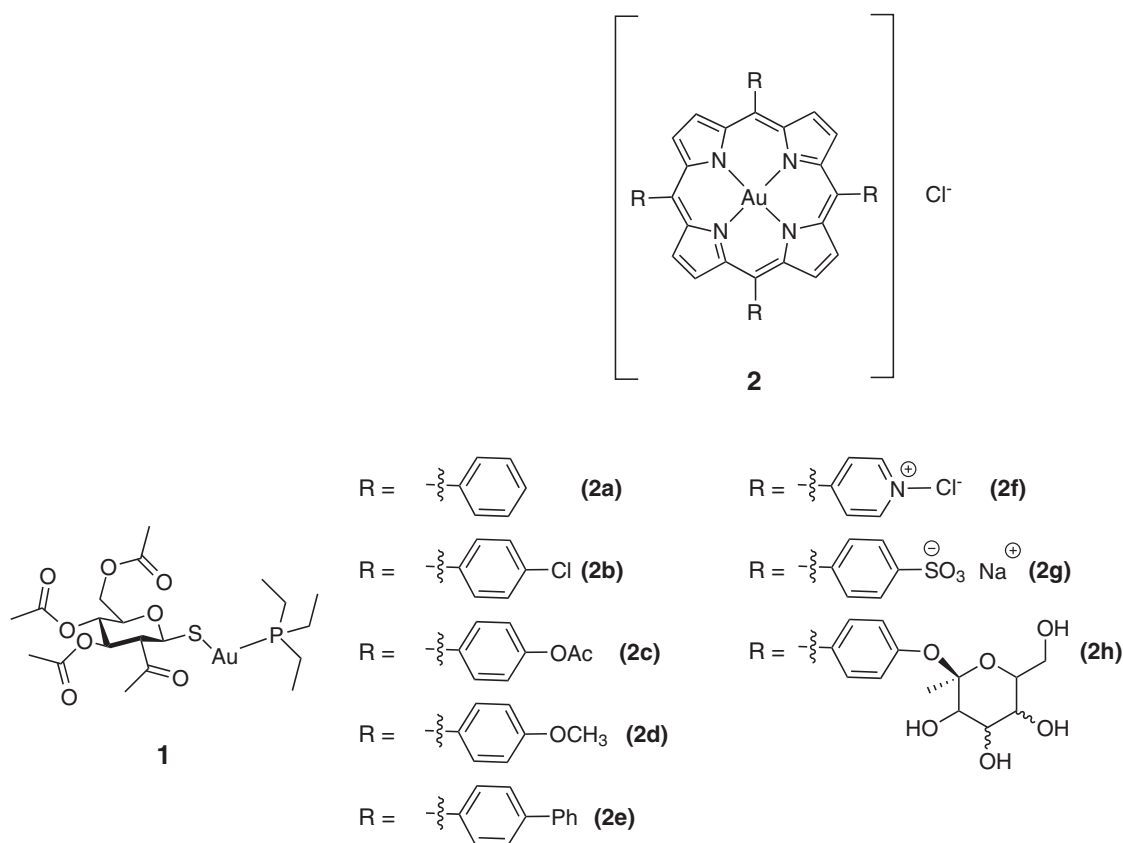


Fig. 1. Aurofin 1 [7] and several known gold(III) porphyrin systems [3, 4]

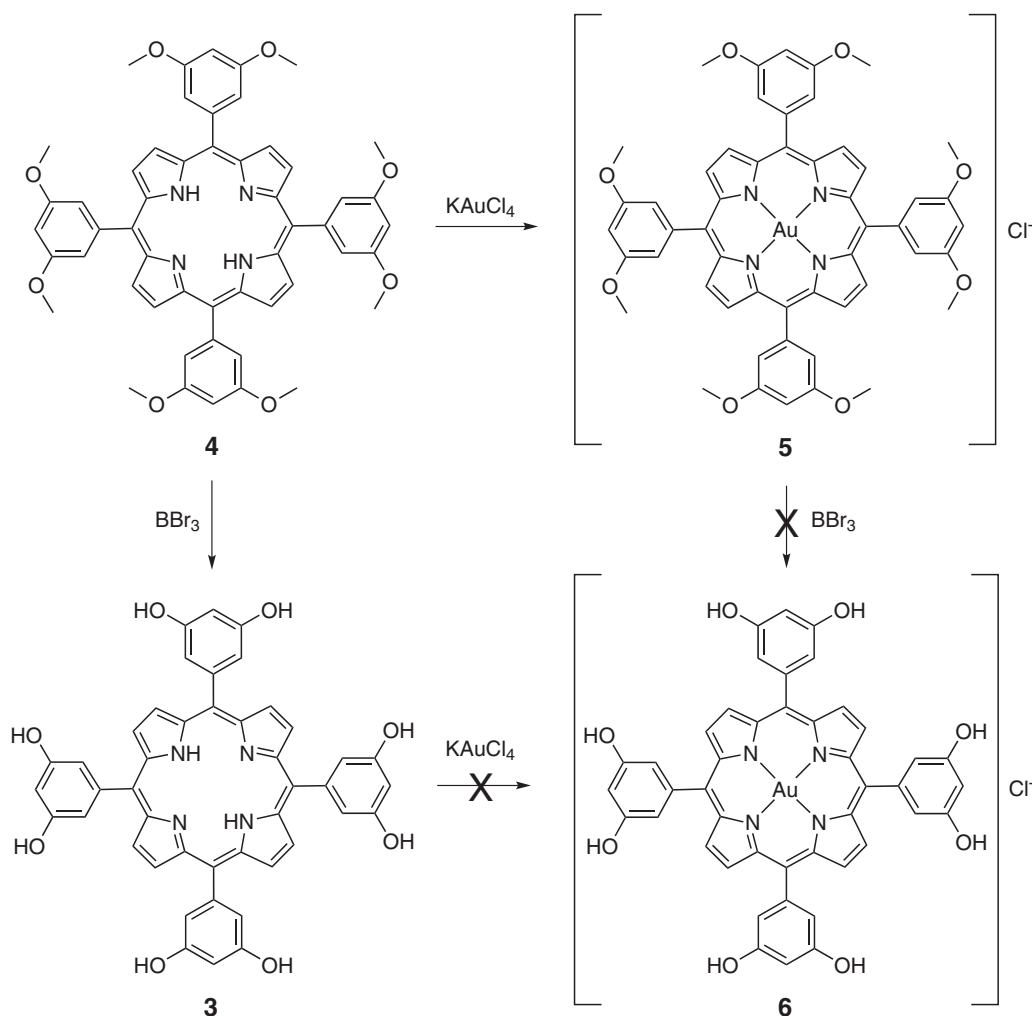
cell lines including colon, breast, ovarian and bladder. Unfortunately, this complex was characterized by limited activity, an effect ascribed to poor aqueous solubility [9]. Since that time, a number of groups have developed a wide range of gold complexes and have reported varying degrees of efficacy against a variety of cancer cell lines, both *in vivo* and *in vitro* [2, 10].

Many researchers have been attracted to gold(III) porphyrins as possible drugs due to the high stability and relative ease of synthesis typical of porphyrins [3]. A commonly studied system is *meso*-tetraphenylporphyrin gold chloride (**2a**) [3, 4]. Among other benefits complex **2a** binds non-covalently to human serum albumin (HSA) [4n]. Many metal-based drugs, including oxaliplatin and auranofin, bind strongly with plasma proteins, predominately HAS, which makes gold(III) porphyrins further attractive in the context of pharmaceutical lead development.

Compound **2a** has shown significant cytotoxicity against numerous cell lines, including KB-3-1 and the multi-drug resistant variant, KB-V1 [4i]. The effectiveness against KB-V1 was taken as evidence that the P-glycoproteins, proteins that remove foreign substances including drugs from the cell, have little effect on **2a**. These studies also revealed a ten-fold increase in the cytotoxicity towards tumor cells as compared to healthy cells. Additionally, it is worth noting that the

zinc derivative (ZnTPP) proved at least 100 fold less cytotoxic than the corresponding gold porphyrin, **2a** [4]. *In vivo* studies involving the human ovarian A2780 and A2780cis (cisplatin resistant) cell line-derived xenografts in nude mice revealed severely retarded tumor growth, and higher concentration of apoptotic cells [4o]. Similar results were seen with **2a** in the case of other studies, as noted in several recent reviews [4a, 4b and 5].

Although **2a** displays many attributes that make it attractive as a potential anti-cancer agent, it is severely limited by its poor solubility in aqueous media. To address this deficiency, a number of other gold porphyrins (*e.g.* **2b–2h**) have been prepared [3, 4]. Among the most widely studied of these are those containing methylated pyridine- (**2f**), phenyl sulfate- (**2g**), and polysaccharide subunits. While showing greatly increased solubility, as a general rule, the cytotoxicity of these compounds is generally diminished relative to **2a** [4n]. In fact, the cytotoxicity of the charged species is all but eliminated, a finding attributed to the decreased lipophilicity of the complexes in question [4n]. On the other hand, the polysaccharide functionalized system (**2h**) displays attractive anti-angiogenic properties [4n]. This leads us to suggest that new gold(III) systems with good aqueous solubility may show significant anticancer activity. We report here one such system, the gold(III) porphyrin complex **6** derived from the polyhydroxylated porphyrin **3**.



**Scheme 1.** Attempted synthesis of octahydroxy gold(III) tetraphenylporphyrin **6**

## EXPERIMENTAL

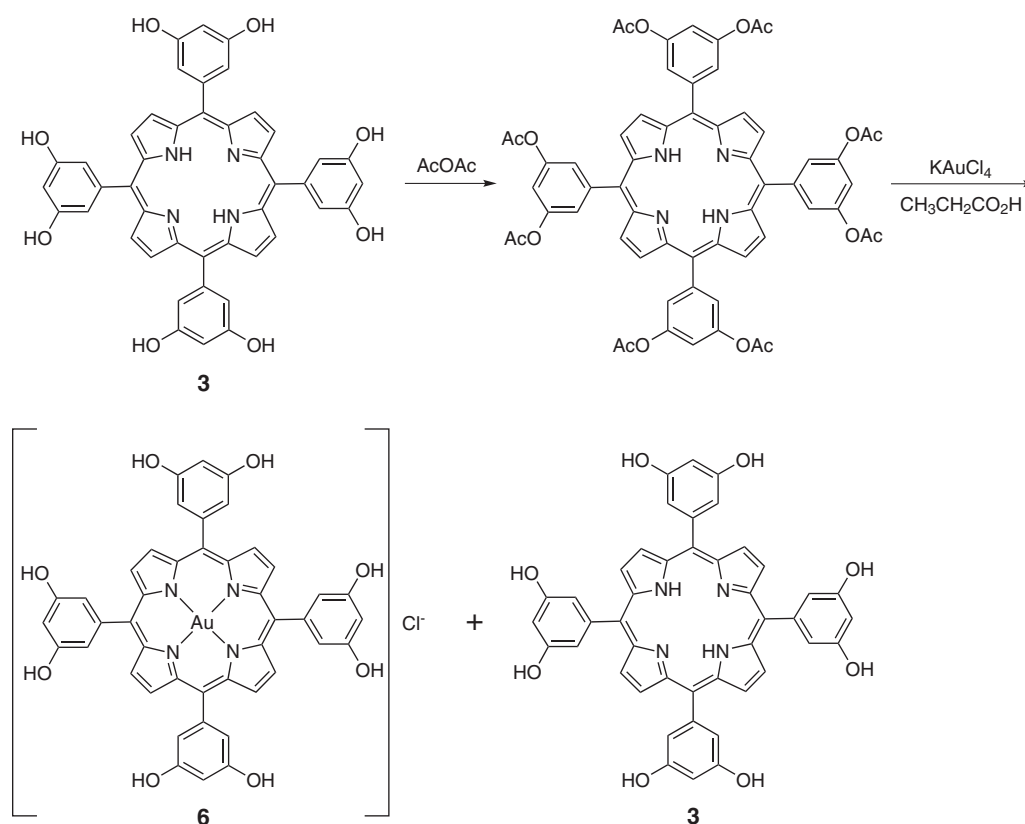
Octahydroxy tetraphenylporphyrin (**3**) was synthesized from octamethoxytetraphenyl porphyrin (**4**) by subjecting the methoxy group to boron tribromide-mediated cleavage [11]. Carrying out this bond scission using a pre-formed gold(III) octamethoxy tetraphenylporphyrin resulted in demetalation. Equally unsuccessful was a strategy wherein the cleavage step was carried out prior to metalation and then metalation was attempted using with potassium tetrachloride aurate. Under these conditions, only starting material was recovered (Scheme 1). However, the desired gold(III) complex could be obtained by protecting the hydroxyl groups by treating with acetic anhydride prior to metalation. This protection was found to proceed in near quantitative yield. Metalation, concomitant with deprotection, was then accomplished by heating the porphyrin with potassium tetrachloroaurate at reflux in propionic acid [12]. The desired, deprotected product was isolated in 20% yields, along with the octahydroxy freebase porphyrin (**3**) (Scheme 2). No evidence of the

corresponding acetoxy protected metalated porphyrin was observed after the reaction.

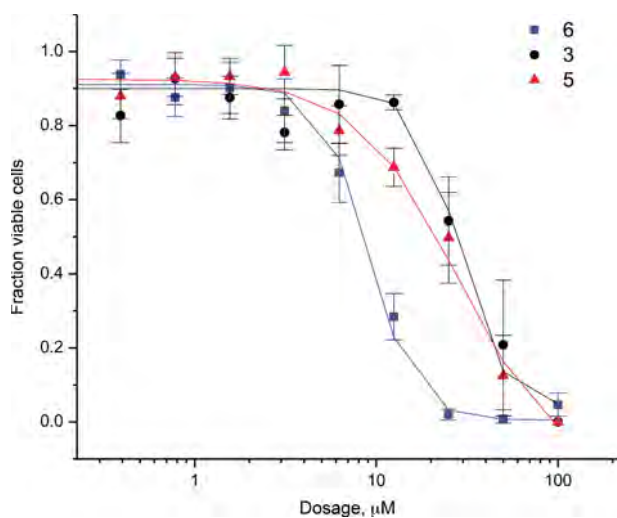
Gold porphyrin complexes were characterized by high-resolution mass spectrometry, in addition to UV/Vis and NMR spectroscopy. Compared to the metal-free form **3**, the Soret band of the gold complex **6** is hypsochromically shifted by 6 nm compared in ethyl acetate solution. This shift has been explained by Jamin and Iwamoto in terms of a stabilization of the HOMO orbitals as the result of strong Au-N interactions[13]. The  $^1\text{H}$  NMR spectrum of the Au(III) complex **6** recorded in  $\text{CD}_3\text{OD}$  showed all the expected CH signals. However, the hydroxyl protons proved difficult to identify; presumably, this reflects  $-\text{OH}$  to  $-\text{OD}$  exchange. Analysis by HPLC shows one peak with a slight shoulder. This peak is thought to be due to ligand exchange with acetate under the conditions of HPLC analysis.

### *In vitro* cytotoxicity studies

The cytotoxicity of octahydroxy gold(III) porphyrin (**6**), octamethoxy gold(III) porphyrin (**5**) and the



**Scheme 2.** Synthesis of Au(III) octahydroxytetraphenylporphyrin. Also shown is the demetallated freebase porphyrin (3) obtained as a side product during the reaction sequence



**Fig. 2.** A2780 cells dosed with either compounds 3, 5, and 6 at 100 μM, followed by 50% serial dilutions. Antiproliferative activity was determined from MTT assays. Error bars are the standard deviations for measurements performed in triplicate

metal-free octahydroxy porphyrin (3) were evaluated using the human ovarian cancer cell line A2780. Cells were incubated with varying dosages at 37 °C for five days before treatment with thianol blue for 4 h.

The above cell studies revealed an IC<sub>50</sub> value of 9 μM in the A2780 cell line for the octahydroxy gold(III) porphyrin (6). Under analogous conditions, IC<sub>50</sub> values of 29 μM and 28 μM were found for the octamethoxy (5) and freebase (3) derivatives respectively. These results are shown in Fig. 2, which includes the error bars reflecting reproducibility (standard deviation) across at least three separate measurements.

## RESULTS AND DISCUSSION

The mechanism by which the gold porphyrins trigger cell death is not completely understood. It was initially thought to be similar to cisplatin in that it involves dative binding to DNA [3]. However, more recently it has been proposed that gold complexes interact with proteasomes and thioredoxin reductase [4a, 4d]. More generally, lipophilic planar cations have been proposed as mitochondria targeting agents [4n]. Gold(III) porphyrins bearing only neutral substituents (and thus bearing only a single cationic charge in the case of a poorly coordinating axial ligand) are thus of particular interest since they would allow the limits of this latter postulate to be tested in an operational sense within the context of anticancer drug discovery efforts. The system we report here, complex 6, was designed with such considerations in mind. It incorporates multiple hydroxyphenyl substituents.

Gratifyingly, it displays good solubility in aqueous media without the high net charge characteristic of many solubilized gold porphyrins. As part of the synthetic effort leading to **6**, the free base form **3**, as well as the gold complex of a protected version, **5**, were obtained.

The A2780 cell line was used to test the antiproliferative activity of **6** and two related species. Standard MTT assays were used. These revealed an IC<sub>50</sub> value of 9 μM for the octahydroxy gold(III) porphyrin (**6**). In contrast, IC<sub>50</sub> values of 28 μM, and 29 μM were recorded for the octamethoxy (**5**) gold(III) complex and the freebase porphyrin (**3**), respectively. On this basis, we conclude that the complexation of a gold(III) center in a water solubilized porphyrin ligand can produce a system with more favorable cytotoxic features than the constituents from whence it is formally derived.

## CONCLUSION

We have developed a gold(III) porphyrin with increased water solubility relative to tetraphenyl gold porphyrin (**1a**). This increase in solubility, combined with the fundamental complexation features inherent in the use of gold porphyrins, produces a species, complex **6**, that shows promising anticancer activity as judged from initial cellular antiproliferative studies. Importantly, complex **6** retains the stability and ease of synthesis of previously reported porphyrin systems [4]. In marked contrast to many of the previous strategies used to increase the aqueous solubility of gold porphyrins through use of ionic substituents, no increase in charge is associated with the use of **6** as compared to gold(III) tetraphenyl-porphyrin. No reduction in the anticancer activity nor, presumably, a change in the mode of action was thus expected. In fact, the use of neutral substituents produces an increased *in vitro* anticancer activity relative to the corresponding methylated gold porphyrin system B5. Moreover, the higher antiproliferative activity seen for the gold(III) porphyrin complex **6** relative to the corresponding freebase system **3**, is consistent with the overall cytotoxicity being the result of both the gold center as well as the choice hydrophilic porphyrin. The fortuitous combination of both enhanced aqueous solubility and antiproliferative activity seen in **6** leads us to suggest that this class of complex may have a role to play in the treatment of neoplastic diseases. Currently, complex **6** is being tested against a number of cancer cells lines with the goal of commencing near-term *in vivo* efficacy and toxicity studies.

## Acknowledgements

This work was supported by the National Institutes of Health (grant CA 68682 to J.L.S.).

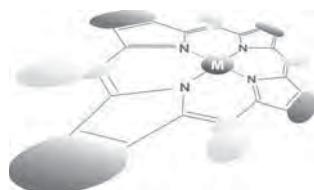
## Supporting information

Supplementary material is available free of charge via the Internet at <http://www.worldscinet.com/jpp/jpp.shtml>.

## REFERENCES

- (a) Stordal B, Pavlakis N and Davey R. *Cancer Treat. Rev.* 2007; **33**: 688. (b) Siddik ZH. *Oncogene* 2003; **22**: 7165.
- (a) Huanzi Z and Yuantao N. *Gold Bull.* 2001; **34**: 24. (b) Orvig C and Abrams MJ. *Chem. Rev.* 1999; **99**: 2201. (c) Koch R. *Dtsch. Med. Wochenschr.* 1890; **16**: 756. (d) Forestier JJ and Lab J. *Clin. Med.* 1935; **20**: 827. (e) Sneader W. *Drug Discovery: A History*, John Wiley & Sons Ltd: Chichester, England, 59–61; (f) Shaw CF III. *Chem. Rev.* 1999; **99**: 2589. (g) Abrams MJ and Murrer BA. *Science* 1993; **261**: 725. (h) Brown CH and Smith WE. *Chem. Soc. Rev.*, 1980; **9**: 217. (i) Fonteh PN, Keter FK and Meyer D. *BioMetals* 2010; **23**: 185. (j) Sun R W-Y, Yu W-Y, Sun H and Che C-M. *Chem.Bio. Chem.* 2004; **5**: 1293. (k) Che C-M and Sun W-Y. *Chem. Commun.* 2011; **47**: 9554.
- (a) McKeage MJ, Maharaj L and Berners-Price BJ. *Coord. Chem. Rev.* 2002; **232**: 127. (b) Calamai P, Carotti S, Guerri A, Mazzei A, Messori L, Mini E, Orioli P and Speroni GP. *Anticancer Drug Des.* 1998; **13**: 67. (c) Fricker SP. *Met. Based Drugs* 1999; **6**: 291. (d) Ronconi L, Marzano C, Zanello P, Corsini M, Miolo G, Macca C, Trevisan A and Fregona D. *J. Med. Chem.* 2006; **49**: 1648. (e) Messori L, Marcon G and Orioli P. *Bioinorg. Chem. Appl.* 2003; **1**: 177. (f) Messori L, Abbate F, Marcon G, Orioli P, Fontani M, Mini E, Mazzei T, Carotti S, O'Connell T and Zanello P. *J. Med. Chem.* 2000; **43**: 3541. (g) Marcon G, Carotti S, Coronello M, Messori L, Mini E, Orioli P, Mazzei T, Cinellu MA and Minghetti G. *J. Med. Chem.* 2002; **45**: 1672. (h) Bruni B, Guerri A, Marcon G, Messori L and Orioli P. *Croat. Chem. Acta.* 1999; **72**: 221. (i) Aldinucci D, Lorenzon D, Stefani L, Giovagnini L, Colombatti A and Fregona D. *Anticancer Drugs* 2007; **18**: 323. (j) Casas JS, Castano MV, Cifuentes MC, García-Monteagudo JC, Sánchez A, Sordo J and Abram U. *J. Inorg. Biochem.* 2004; **98**: 1009. (k) Buckley RG, Elsome AM, Fricker SP, Henderson GR, Theobald BR, Parish RV, Howe BP and Kelland LR. *J. Med. Chem.* 1996; **39**: 5208. (l) Rigobello MP, Scutari G, Folda A, Bindoli A. *Biochem. Pharmacol.* 2004; **67**: 689. (m) Kim NH, Lee MY, Park SJ, Choi JS, Oh MK and Kim IS. *Immunol.* 2007; **122**: 607. (n) Hirano T. *Int. Rev. Immunol.* 1998; **16**: 249. (o) Kisselev AF and Goldberg AL. *Chem. Biol.* 2001; **8**: 739. (n) Goldberg AL. *Science* 1995; **268**: 522. (p) Adams J. *Drug Discov. Today* 2003; **8**: 307. (q) Almond JB and Cohen GM. *Leukemia* 2002; **16**: 433. (r) Adams J, Palombella VJ, Sausville EA, Johnson J, Destree A, Lazarus DD, Maas J, Pien CS, Prakash S and Elliott PJ. *Cancer Res.* 1999; **59**: 2615. (s) Lightcap ES, McCormack TA, Pien CS, Chau V, Adams J and Elliott PJ. *Clin. Chem.* 2000;

- 46:** 67. (t) Tan C, Waldmann TA, *Cancer Res.* 2002; **62:** 1083.
4. (a) Milacic V and Dou QP. *Coord. Chem. Rev.* 2009; **253:** 1649. (b) Ott I. *Coord. Chem. Rev.* 2009; **253:** 1670. (c) Milacic V, Fregona D and Dou QP. *Histol. Histopathol.* 2008; **23:** 101. (d) Wang X and Guo Z. *Dalton Trans.* 2008; 1521. (e) Kostova I. *Anti-Cancer Agents Med. Chem.* 2006; **6:** 19. (f) Tiekink ERT. *Crit. Rev. Oncol. Hematol.* 2002; **42:** 225. (g) Shaw CF III. *Chem. Rev.* 1999; **99:** 2589. (h) Sun R W-Y, Yu W-Y, Sun H and Che C-M, *Chem. Bio. Chem.* 2004; **5:** 129. (i) Che C-M, Sun R W-Y, Yu W-Y, Ko C-B, Zhu N and Sun H. *Chem. Commun.* 2003; 1718. (j) Chow K H-M, Sun R W-Y, Lam JBB, Li C K-L, Xu A, Ma D- L, Abagyan R, Wang Y and Che C-M. *Cancer Res.* 2010; **70:** 329. (k) Wang D and Lippard SJ. *Nat. Rev. Drug Discovery* 2005; **4:** 307. (l) Takahara PM, Rosenzweig AC, Frederick CA and Lippard JS. *Nature* 1995; **377:** 649. (m) Chu G. *J. Biol. Chem.* 1994; **269:** 787. (n) Sun R W-Y, Li C K-L, Ma DL, Yan JJ, Lok CN, Leung CH, Zhu N and Che C-M. *Chem. Eur. J.* 2010; **16:** 3097. (o) Lum CT, Sun R W-Y, Zou T and Che C-M. *Chem. Sci.*, 2014; **5:** 1579.
5. Bindoli A, Rigobello MP, Scutari G, Gabbiani C, Casini A and Messori L. *Coord. Chem. Rev.* 2009; **253:** 1692.
6. Fricker SP. *Gold Bull.* 1996; **29:** 53.
7. Simon TM, Kunishima DH, Vibert GJ and Lorber A. *Cancer* 1979; **44:** 1965.
8. Berners-Price SJ and Sadler SJ. *Coord. Chem. Rev.* 1996; **151:** 1.
9. Buckley RG, Elsome AM, Fricker SP, Henderson GR, Theobald BRC, Parish RV, Howe BP and Kelland LR. *J. Med. Chem.* 1996; **39:** 5208.
10. (a) Cattaruzza L, Fregona D, Mongiat M, Ronconi L, Fassina A, Colombatti A and Aldinucci D. *Int. J. Cancer* 2011; **128:** 206. (b) Fregona D, Ronconi L and Aldinucci D. *Drug Discovery Today* 2009; **14:** 1075. (c) Ronconi L and Fregona D. *Dalton Trans.* 2009; 10670. (d) Saggioro D, Rigobello MP, Paloschi L, Folda A, Moggach SA, Parsons S, Ronconi L, Fregona D and Bindoli A. *Chem. Biol.* 2007; **14:** 1128. (e) Milacic V, Chen D, Ronconi L, Landis-Piwowar KR, Fregona D and Dou QP. *Cancer Res.* 2006; **66:** 10478. (f) Ronconi L, Giovagnini L, Marzano C, Bettio F, Graziani R, Piloni G and Fregona D. *Inorg. Chem.* 2005; **44:** 1867. (g) Giovagnini L, Ronconi L, Aldinucci D, Lorenzon D, Sitran S and Fregona D. *J. Med. Chem.* 2005; **48:** 1588.
11. Oar MA, Dichtel WR, Serin JM, Fréchet JMJ, Rogers JE, Slagle JE, Fleitz PA, Tan L-S, Ohulchansky TY and Prasad PN. *Chem. Mater.* 2006; **18:** 3682.
12. Sun L, Chen H, Zhang Z, Yang Q, Tong H, Xu A and Wang C. *J. Inorg. Biochem.* 2012; **108:** 47.
13. Jamin ME and Iwamoto RT. *Inorg. Chim. Acta* 1978; **27:** 135.



# Free-base porphyrin and [60]fullerene linked by oligomeric ethylenedioxythienylenevinylene bridge

Beatriz Pelado<sup>a</sup>, Julieta Coro<sup>a,b</sup>, Pilar de la Cruz<sup>a</sup> and Fernando Langa<sup>\*a</sup>†

<sup>a</sup> Instituto de Nanociencia, Nanotecnología y Materiales Moleculares (INAMOL), Universidad Castilla-La Mancha, Campus de la Fábrica de Armas, 45072 Toledo, Spain

<sup>b</sup> Laboratorio de Síntesis Orgánica, Facultad de Química, Universidad de La Habana, 10400 La Habana, Cuba

*Dedicated to Professor Shunichi Fukuzumi on the occasion of his retirement*

Received 5 December 2014

Accepted 24 December 2014

**ABSTRACT:** The synthesis and structural characterization and the study of the electronic properties of two novel porphyrin-bridge-fullerene molecules, where a free-based porphyrin and [60]fullerene are connected through one and two units of ethylenedioxythienylenevinylene  $\pi$ -conjugated bridges, is reported. The absorption studies, voltamperometric measurements and theoretical calculations at DFT level are presented. A HOMO–LUMO gap as low as 1.41 eV has been found for compound **6**.

**KEYWORDS:** porphyrin, EDOT, fullerene, molecular wire.

## INTRODUCTION

Study of donor–acceptor (D–A) systems is a topic of high interest because of their application of such systems in artificial photosynthesis, organic solar cells, sensors and organic field-effect transistors devices [1]. Due to its exceptional properties as absorption spectrum extending over most of the visible spectral region, three-dimensional structure, reduction potentials comparable to quinones and low value for re-organization energy in electron-transfer reactions, fullerene C<sub>60</sub> has proved to behave as an ideal acceptor in D–A systems as fullerenes stabilize the charge separated state in comparison with other related systems [2]. In the other hand, porphyrins, as synthetic analog of natural chlorophyll, has been widely used as electron donor and light harvesting moiety in electron-transfer processes as their significant redox chemistry. These macrocycles present an intense Soret band at around 400 nm (with extinction coefficients as high as 10<sup>5</sup> M<sup>-1</sup>.cm<sup>-1</sup>) and the Q-bands at nearby 600 nm [3]. Covalent architectures formed by porphyrins and fullerenes linked by a huge variety

of bridging groups have been the subject of numerous studies in recent years [4].  $\pi$ -Conjugated oligomers as oligothiophene (OT) [5] and oligophenylenevinylene (OPV) [6] moieties have been shown to act as long distance molecular wires in the efficient photoinduced electron transfer from the porphyrin chromophore to the fullerene. Recently, we have described the use of oligothiophenevinylene oligomers (*n*TVs) [7], where the thiophene moieties was substituted by alkyl chains, as efficient bridges in donor–donor [8], acceptor–acceptor [9] or donor–acceptor [10] systems showing an attenuation factor for electron transfer as low as 0.016 Å<sup>-1</sup> [11]. The functionalization of thiophenes with ethylenedioxy groups produced the well known 3,4-ethylenedioxythiophene (EDOT). EDOT has attracted the most attention because of its high stability, low oxidation potential and the electron-rich ethylenedioxy group, making it an excellent structural unit. Although EDOT derivatives are key players in organic electronics, however, their thienylenevinylene (EDOTV) oligomer derivatives have received scarce attention. We have prepared the first series of three ethylenedioxythienylenevinylene oligomers of increasing size. Their optical, electrochemical and chemical properties have been studied in detail and in comparison with their non-EDO and non-vinylene parents [12].

†SPP full member in good standing

\*Correspondence to: Fernando Langa, email: Fernando.Langa@uclm.es, tel: +34 925-268843, fax: +34 925-268840

Aimed by this results, in this manuscript, we present here the first initiative to explore the role of EDOTV oligomers as bridges between porphyrins and [60]fullerene, describing the synthesis, electronic and electrochemical characterization, as well as theoretical calculations of two novel electroactive molecules where a free-base porphyrin and  $C_{60}$  are covalently connected through one and two units of ethylenedioxythiophenevinylene (EDOTVs)  $\pi$ -conjugated bridges.

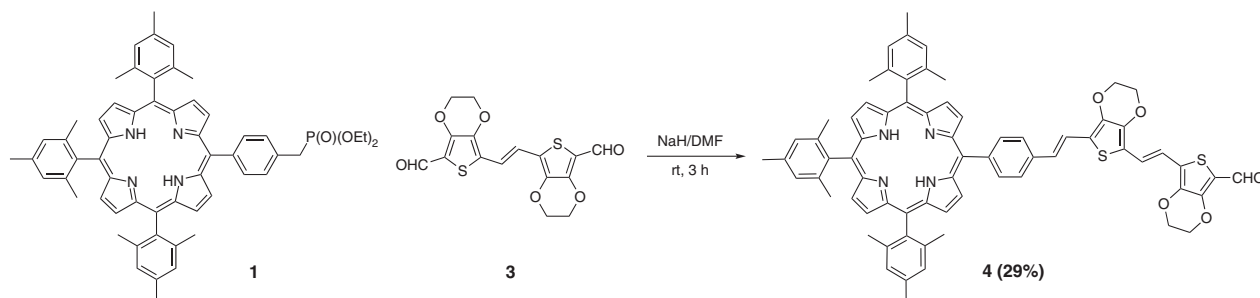
## RESULTS AND DISCUSSION

Precursor aldehyde **4** was prepared in 29% yield by Horner–Wadsworth–Emmons reaction between porphyrin phosphonate **1** [13] and *trans*-bis-(3,4-ethylenedioxythiophene)vinylenebis-carbaldehyde (**3**) [14] at room temperature in the presence of NaH as base and under careful stoichiometric conditions (Scheme 1). Compound **4** was fully characterized by spectroscopic techniques; the  $^1\text{H}$  NMR showed, the formyl proton at  $\delta = 9.91$  ppm and all the rest of the expected signals; particularly interesting is that the *E* configuration of both double bonds are confirmed by the measured coupling constant values ( $J = 16$  Hz in both cases).

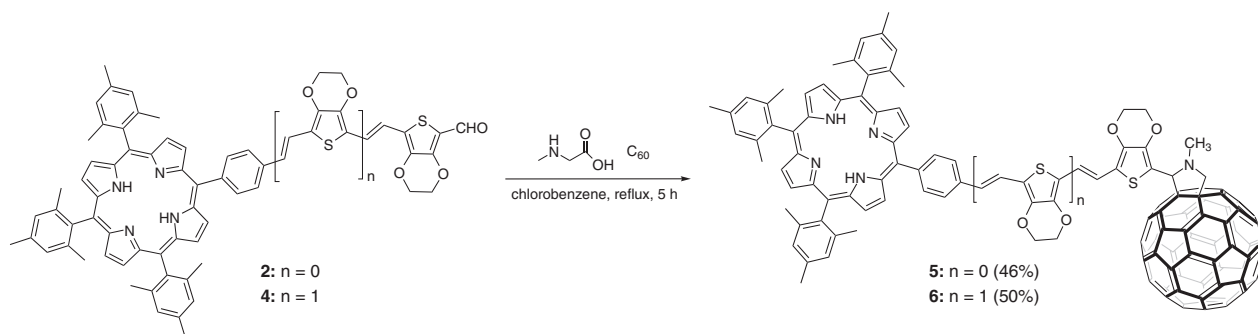
Triads **5** and **6** were obtained in 46% and 50% yield respectively by means of a 1,3-dipolar cycloaddition of compounds **2** [15] and **4** and *N*-methylglycine to fullerene  $C_{60}$  in refluxing chlorobenzene (Scheme 2). Compounds **5** and **6** were purified by column chromatography in silica gel (eluent: toluene/*n*-hexane 1:1) followed by

centrifugation several times with methanol and *n*-pentane. The structures of cycloadducts **5** and **6** were confirmed by analytical and spectroscopic data. The  $^1\text{H}$  NMR spectra, recorded in  $\text{CDCl}_3$ , of both triads exhibit all expected signals corresponding to the porphyrin core, as well as those attributed to the ethylenedioxythiophenevinylene  $\pi$ -conjugated bridges whose vinyl hydrogens show coupling constant values around  $J = 16$  Hz confirming their *E* geometries. The characteristic pyrrolidine signature between  $\delta = 3.92$  and  $4.93$ , as two doublets (AB system), and one singlet at  $\delta = 4.90$  ppm can be observed as well in both molecules. Finally, the structure of **5** and **6** were confirmed by MALDI-TOF mass spectra which show the expected  $M^+$  peaks at  $m/z = 1681.18$  (for **5**) and  $1162.47$  (for **6**) together with the peak at  $m/z = 720$  corresponding to  $C_{60}$ .

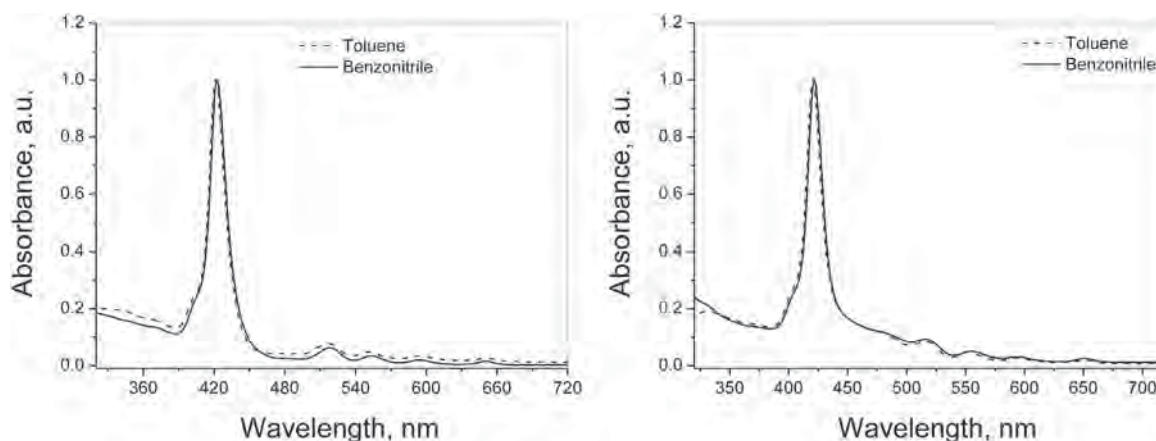
The electronic properties were studied by UV-vis and emission spectroscopies. The absorption spectra of both triads, **5** and **6**, are a linear combination of the spectra of compounds **2** or **4**, respectively and  $C_{60}$ , indicating the absence of electronic interactions between the organic addend and the fullerene cage in the ground state; both spectra are dominated by the Soret and Q-bands characteristic of the free-base porphyrin systems [16]. When the absorption spectra were studied in solvents with different polarity (toluene and benzonitrile), a slight bathochromic shift was observed with increasing solvent polarity (Fig. 1), thus confirming the absence of electronic interactions (*vide supra*). Interestingly, despite the longer conjugated bridge in triad **6**, its Soret band is



Scheme 1. Synthesis of precursor aldehyde **4**



Scheme 2. Synthesis of triads **5** and **6**



**Fig. 1.** Normalized absorption spectra of triad **5** (left) and triad **6** (right) in toluene (...) and benzonitrile (-) as solvent ( $[ ] = 10^{-7}$  M)

**Table 1.** Absorption<sup>a</sup> and electrochemical data (OSWV)<sup>b</sup> of compounds **5** and **6**

Compound	$\lambda_{\text{abs}}^a$ , nm	$\log \epsilon$	$E_{\text{red}}^1$ , V	$E_{\text{red}}^2$ , V	$E_{\text{red}}^3$ , V	$E_{\text{red}}^4$ , V	$E_{\text{ox}}^1$ , V	$E_{\text{ox}}^2$ , V
$C_{60}$			-1.05	-1.46	-1.92			
<b>H<sub>2</sub>Por<sup>c</sup></b>			-1.75	-2.05			+0.53	+0.79
<b>2EDOTV</b>							+0.27	+0.56
<b>5</b>	422.5	5.6	-1.18	-1.61	-1.93 (b)	-2.29	+0.58	+1.07 <sup>d</sup>
<b>6</b>	422.0	5.5	-1.16	-1.54	-1.82 (b)	-2.17	+0.25	+0.60 <sup>d</sup>

<sup>a</sup> Measured in benzonitrile in a concentration of  $10^{-7}$  M. <sup>b</sup> V vs. Fc/Fc<sup>+</sup>; GCE as working electrode; 0.1 M TBAP; *o*-dichlorobenzene:MeCN (4:1); scan rate: 100 mV/s. <sup>c</sup> Data collected from literature [17]. <sup>d</sup> Broad, corresponding to two electrons.

slightly hypsochromically shifted with respect to that in **5**, either in toluene ( $\approx 1.0$  nm) or benzonitrile ( $\approx 0.5$  nm) (Fig. 1), indicating the lack of conjugation between the porphyrin and the ethylenedioxythiophenevinylene  $\pi$ -conjugated bridge in both systems.

Orsteyoung Square Wave Voltammetry measurements (in *o*-dichlorobenzene:acetonitrile 4:1 solution, using glassy carbon as working electrode; Ag/AgNO<sub>3</sub> as reference electrode; Pt as counter-electrode; 0.1 M Bu<sub>4</sub>NClO<sub>4</sub>, a scan rate of 100 mV/s at room temperature) were used to evaluate the electrochemical characteristics of compounds **5** and **6**. Relevant data are provided in Table 1.

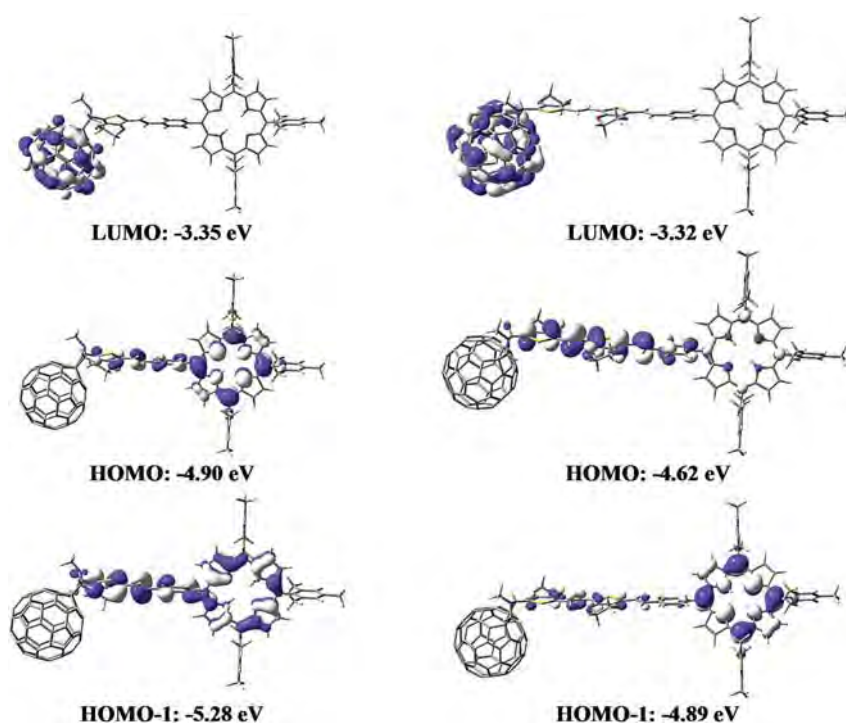
In the cathodic zone of the voltammogram, compound **5** shows a first reduction potential at -1.18 V corresponding to the first C<sub>60</sub> reduction; at -1.61 V appears the second reduction of fulleropyrrolidine entity and next, at 1.93 V, two one-electron process due to the overlap of the first reduction of free-base porphyrin [17] and the third reduction of fulleropyrrolidine entities; appears one more reduction wave at -2.28 V, attributed to the second reduction potential of the porphyrin. As expected, the reduction potential values for **5** are cathodically shifted in comparison with those of pristine C<sub>60</sub>, which has been

accounted for by the saturation of a double bond of the C<sub>60</sub> sphere which raises the LUMO energy level. Similarly, compound **6** shows the first reductive wave of the C<sub>60</sub> unit at -1.16 V, which is in good agreement with values typically observed for C<sub>60</sub> derivatives, the other reduction waves for the fullerene core of **6** appearing at -1.54 V and -1.82 V, the last wave is broad as simultaneously appears the first reduction of the porphyrin.

In the anodic zone, compound **5** shows a first oxidation potential at +0.58 V, attributed to the porphyrin core, and a broad second oxidation potential (maximum at +1.07 V) which should correspond to two electrons due to the simultaneous oxidation of the  $\pi$ -conjugated bridge and the second oxidation of the porphyrin macrocycle. On the other hand, in compound **6**, the first oxidation potential is observed at +0.25 V, ascribed to the more extended  $\pi$ -conjugated bridge, now having two units of ethylenedioxythiophenevinylene; the second oxidation wave appears at +0.59 V as a broad wave, corresponding to the second oxidation potential of the conjugated bridge and the first of the free-base porphyrin. These results are in agreement to theoretical calculations (*vide infra*).

The HOMO–LUMO gap determined by difference between the first reduction and the first oxidation





**Fig. 2.** Electronic density contours ( $0.02 \text{ eBohr}^{-3}$ ) and energy values for HOMO and LUMO calculated at the B3LYP/3-21G level of triads **5** (left) and **6** (right)

potentials is much lower for compound **6** (1.41 eV) than for **5** (1.76 eV) as a consequence of the more extended conjugation.

In order to get insight of the electronic properties and more stable geometry of dyads **5** and **6**, theoretical calculations at DFT/B3LYP level using a 3-21G basis set were performed with Gaussian03. Figure 2 shows the more stable geometries of compounds **5** and **6**. As expected, the porphyrin macrocycle presents a dihedral angle around with  $60^\circ$  respect to the conjugated bridge suggesting the absence of electronic communication between both moieties. On the other hand, the conjugated system acting as bridge is almost planar with all dihedral angles smaller than  $2^\circ$ .

In frontier orbital examination, the LUMO is fully localized in the electron-acceptor unit of  $\text{C}_{60}$  in both compounds (Fig. 2). Nevertheless, the HOMO location is different in both compounds **5** and **6**. In compound **5**, with the shorter conjugated bridge, the HOMO is mainly centered in the porphyrin macrocycle with some contribution from the thienylenevinylene bridge and similar distribution is observed for the HOMO-1 orbital in the agreement with the two electrons oxidation observed in electrochemical measurements; for compound **6** the electronic distribution of HOMO is completely different, as the HOMO is centered in the conjugated oligomer without significant participation of the porphyrin. Next, the HOMO-1 is centered on the porphyrin macrocycle and these facts are in good agreement with the electrochemical results. As expected, the energy

of the LUMO is similar in both compounds while the HOMO energy is higher in **6**, with larger conjugated systems, than in **5**. As consequence, compound **6** has a calculated HOMO–LUMO gap as low as 1.30 eV in good agreement with the experimental value determined by electrochemistry (*vide supra*).

## EXPERIMENTAL

### General remarks

Synthetic procedures were carried out under inert argon atmosphere, in dry solvent unless otherwise noted. All reagents and solvents were reagent grade and were used without further purification.  $\text{C}_{60}$  was purchased from MER Corporation. Chromatographic purifications were performed using silica gel 60 SDS (particle size 0.040–0.063 mm). Analytical thin-layer chromatography was performed using Merck TLC silica gel 60 F254.  $^1\text{H}$  NMR spectra were obtained on Bruker TopSpin AV-400 (400 MHz) spectrometer. Chemical shifts are reported in parts per million (ppm) relative to the solvent residual peak ( $\text{CDCl}_3$ , 7.27 ppm).  $^{13}\text{C}$  NMR chemical shifts are reported relative to the solvent residual peak ( $\text{CDCl}_3$ , 77.00 ppm). UV-vis measurements were carried out on a Shimadzu UV 3600 spectrophotometer. For extinction coefficient determination, solutions of different concentrations were prepared in benzonitrile, HPLC grade, with absorption between 0.1–1 of absorbance using a 1 cm UV cuvette.

The emission measurements were carried out on Cary Eclipse fluorescence spectrophotometer. Mass spectra (MALDI-TOF) were recorded on a VOYAGER DE™ STR mass spectrometer using dithranol as matrix. Melting points are uncorrected. Cyclic voltammetry was performed in *o*-dichlorobenzene/acetonitrile 4:1 solutions. Tetrabutylammonium perchlorate (0.1 M as supporting electrolyte) were purchased from Acros and used without purification. Solutions were deoxygenated by argon bubbling prior to each experiment which was run under argon atmosphere. Experiments were done in a one-compartment cell equipped with a glassy carbon working electrode ( $\varnothing = 2$  mm) and a platinum wire counter electrode. An Ag/AgNO<sub>3</sub> (0.01 M in the supporting electrolyte) electrode was used as reference and checked against the ferrocene/ferrocenium couple (Fc/Fc<sup>+</sup>) before and after each experiment.

The molecular geometries and frontier molecular orbitals of these new dyes have been optimized by density functional theory (DFT) calculations at the DFT/B3LYP level using a 3-21G basis set in the Gaussian 0.3 program [18].

## Synthesis

**Synthesis of 4.** In a round-bottomed flask, under argon atmosphere, phosphonate **1** [17] (200 mg, 0.22 mmol) was added, at 0 °C, over a NaH (21 mg, 0.89 mmol) in dry DMF (30 mL). After 15 min stirring, a solution of *trans*-bis-(3,4-ethylenedioxythiophene)vinylenebiscarbaldehyde (**3**) [18] in dry DMF (30 mL) was added and the reaction mixture was stirred for 3 h. Water and ethyl ether were added, the organic phase was dried over MgSO<sub>4</sub>. The obtained solid, after evaporation of the solvent under reduce pressure, was purified by column chromatography (silica-gel, *n*-hexane/AcOEt 1:1) to give compound **4** in a 29% yield (70 mg, 0.06 mmol). FT-IR (KBr):  $\nu_{\max}$ , cm<sup>-1</sup> 2982, 2913, 1645, 1445, 1069, 993. <sup>1</sup>H NMR (400 MHz, CDCl<sub>3</sub>):  $\delta$ , ppm 9.91 (1H, s), 8.86 (2H, d, *J* = 4.6 Hz), 8.72 (2H, d, *J* = 4.6 Hz), 8.66 (4H, s), 8.20 (2H, d, *J* = 8.0 Hz), 7.85 (2H, d, *J* = 8.0 Hz), 7.49 (1H, d, *J* = 16.0 Hz), 7.31 (6H, s), 7.28 (1H, d, *J* = 16.0 Hz), 7.20 (1H, d, *J* = 16.0 Hz), 6.95 (1H, d, *J* = 16.0 Hz), 4.40 (8H, m), 2.65 (9H, s), 1.89–1.88 (18 H, m), -2.52 (2H, s). <sup>13</sup>C NMR (100 MHz, CDCl<sub>3</sub>):  $\delta$ , ppm 179.2, 148.7, 141.4, 141.0, 139.9, 139.4, 138.4, 138.3, 138.2, 137.7, 136.5, 135.0, 129.0, 127.8, 127.0, 124.6, 121.0, 119.0, 118.3, 118.0, 117.8, 117.4, 115.3, 115.2, 115.0, 65.4, 65.1, 65.0, 64.6, 29.7, 21.8, 21.7, 21.5. MS-MALDI-TOF: *m/z* 1100.53 (calcd. for [M]<sup>+</sup> 1100.40).

**Synthesis of triad 5.** In a round-bottomed flask, under argon atmosphere, a solution of **2** (60 mg, 0.06 mmol), C<sub>60</sub> (92 mg, 0.13 mmol) and *N*-methylglycine (17 mg, 0.19 mmol) in 15 mL of dry chlorobenzene was kept refluxing for 2.5 h. At room temperature, the solvent was evaporated under vacuum and the product was purified by column chromatography (silica-gel, toluene/*n*-hexane

1:1) followed by a gel permeation chromatography (Bio-Beads S-X1, Bio-Rad, using toluene as eluant). Finally, the solid was centrifugated twice with methanol and twice with *n*-pentane affording the triad **5** in 46% yield (50 mg, 0.03 mmol). FT-IR (KBr):  $\nu_{\max}$ , cm<sup>-1</sup> 2945, 2914, 2850, 1604, 1438, 1184, 1086, 968, 801, 733. <sup>1</sup>H NMR (400 MHz, CDCl<sub>3</sub>):  $\delta$ , ppm 8.85 (2H, d, *J* = 4.6 Hz), 8.70 (2H, d, *J* = 4.6 Hz), 8.66 (4H, s), 8.18 (2H, d, *J* = 7.9 Hz), 7.84 (2H, d, *J* = 7.9 Hz), 7.47 (1H, d, *J* = 16.2 Hz), 7.29 (6H, s), 7.23 (d, 1H, *J* = 16.2 Hz), 5.50 (bs, 1H), 4.99 (d, 1H, *J* = 9.2 Hz), 4.37–4.20 (m, 4H), 4.27 (d, 1H, *J* = 9.2 Hz), 3.02 (s, 3H), 2.65 (s, 9H), 1.88–1.87 (m, 18 H). <sup>13</sup>C NMR (100 MHz, CDCl<sub>3</sub>):  $\delta$ , ppm 156.1, 153.8, 153.7, 153.2, 145.2, 145.1, 144.6, 144.3, 143.1, 142.9, 142.6, 142.5, 142.3, 142.1, 142.1, 142.0, 142.0, 141.9, 141.8, 141.6, 141.1, 140.1, 139.8, 139.7, 139.5, 138.4, 138.2, 137.7, 137.2, 136.6, 135.8, 135.5, 135.0, 127.8, 126.3, 124.5, 119.0, 118.7, 118.0, 117.7, 69.9, 69.0, 65.1, 65.0, 40.6, 21.8, 21.5. UV-vis (BCN):  $\lambda_{\max}$ , nm (log  $\epsilon$ ) 422.5 (5.63), 518 (4.43), 554 (4.17), 595 (3.93), 651 (3.83). MS-MALDI-TOF: *m/z* 1681.18 (calcd. for [M]<sup>+</sup> 1681.44).

**Synthesis of triad 6.** In a round-bottomed flask, under argon atmosphere, a solution of aldehyde **4** (30 mg, 0.03 mmol), C<sub>60</sub> (20 mg, 0.03 mmol) and *N*-methylglycine (73 mg, 0.08 mmol) in 20 mL of dry chlorobenzene was kept refluxing for 3 h. At room temperature, the solvent was evaporated under vacuum and the product was purified by column chromatography (silica-gel, toluene) and the solid was centrifugated twice with methanol and twice with *n*-pentane to give triad **6** in 50% yield (25 mg, 0.02 mmol). FT-IR (KBr):  $\nu_{\max}$ , cm<sup>-1</sup> 2915, 1850, 1656, 1438, 1360, 1082, 997, 797, 721. <sup>1</sup>H NMR (400 MHz, CHCl<sub>3</sub>):  $\delta$ , ppm 8.84 (2H, d, *J* = 4.6 Hz), 8.69 (2H, d, *J* = 4.6 Hz), 8.64 (4H, s), 8.16 (2H, d, *J* = 8.0 Hz), 7.81 (2H, d, *J* = 8.0 Hz), 7.46 (1H, d, *J* = 16.0 Hz), 7.28 (6H, s), 7.11 (1H, d, *J* = 16.0 Hz), 7.00 (1H, d, *J* = 16.0 Hz), 6.93 (1H, d, *J* = 16.0 Hz), 5.44 (1H, bs), 4.97 (1H, d, *J* = 9.6 Hz), 4.39–4.13 (8H, m), 4.23 (1H, d, *J* = 9.6 Hz), 2.97 (3H, s), 2.63 (9H, s), 1.87–1.86 (18H, m), -2.54 (2H, s). <sup>13</sup>C NMR (100 MHz, CDCl<sub>3</sub>):  $\delta$ , ppm 156.1, 153.8, 153.7, 153.2, 147.3, 146.7, 146.4, 146.3, 146.1, 146.1, 146.0, 145.9, 145.8, 145.5, 145.4, 145.3, 145.2, 145.1, 144.6, 144.3, 143.1, 143.0, 143.0, 142.6, 142.6, 142.5, 142.5, 142.3, 142.2, 142.1, 142.0, 142.0, 141.6, 141.0, 140.1, 140.1, 139.9, 139.7, 139.3, 138.4, 138.2, 137.7, 137.2, 136.7, 136.7, 135.8, 135.5, 135.0, 127.7, 125.7, 124.4, 119.0, 118.5, 118.0, 117.6, 116.3, 116.2, 116.1, 115.5, 69.8, 69.0, 65.0, 65.0, 21.7, 21.7, 21.5. UV-vis (BCN):  $\lambda_{\max}$ , nm (log  $\epsilon$ ) 422 (5.52), 516 (4.49), 555 (4.23), 596 (4.01), 650.5 (3.94). MS-MALDI-TOF: *m/z* 1876.37 (calcd. for [M]<sup>+</sup> 1876.58).

## CONCLUSION

In summary, we have synthesized two novel porphyrin-bridge-fullerene molecules, where a free-based porphyrin

and [60]fullerene are connected through one and two units of EDOTVs  $\pi$ -conjugated bridges. Absorption spectroscopy indicates that the absence of electronic interactions between the free-base porphyrin, the EDOTV based bridge and [60]fullerene. Electrochemical studies and theoretical calculations show that the porphyrin macrocycle show the larger electron-donating ability in compound **5**; in contrast, in compound **6**, the main donor is the thienylenevinylene based oligomer. Finally, A HOMO–LUMO gap as low as 1.41 eV has been found for compound **6**.

### Acknowledgements

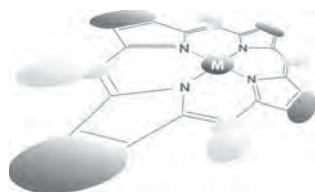
Financial support from MINECO (Project reference CTQ2013-48252-P) and from JCCM (Project reference PEII-2014-014-P) is gratefully acknowledged. BP thanks to the MINECO for a FPI grant.

### REFERENCES

- (a) Wasielewski MR. *Chem. Rev.* 1992; **92**: 435–461. (b) Gust D, Moore TA and Moore LA. *Acc. Chem. Res.* 2001; **34**: 40–48. (c) Balzani V, Credi A and Venturi M. In *Molecular Devices and Machines*, Wiley-VCH Verlag GmbH & Co. KGaA: 2008; pp 171–207.
- (a) Echegoyen L and Echegoyen LE. *Acc. Chem. Res.* 1998; **31**: 593–601. (b) Guldi DM and Prato M. *Acc. Chem. Res.* 2000; **33**: 695–703. (c) Langa F and Nierengarte JF. *Fullerenes: Principles and Applications*, Royal Society of Chemistry: 2011.
- (a) *The Porphyrin handbook*, Kadish K, Smith KM and Guillard R. (Eds.) Academic Press: San Diego, London, 2000. (b) Imahori H, Umeyama T and Ito O. *Acc. Chem. Res.* 2001; **34**: 40–48. (b) Gust D, Moore TA and Moore AL. *Acc. Chem. Res.* 2009; **42**: 1809–1818.
- (a) Guldi DM, Rahman GMA, Sgobba V and Ehli C. *Chem. Soc. Rev.* 2006; **35**: 471–487. (b) Delgado JL, de la Cruz P, López-Arza V, Langa F, Kimball DB, Haley MM, Araki Y and Ito O. *J. Org. Chem* 2004; **69**: 2661–2668. (c) Villegas C, Delgado JL, Bouit PA, Grimm B, Seitz W, Martin N and Guldi DM. *Chem. Sci.* 2011; **2**: 1677–1681. (d) Wijesinghe CA, El-Khouly ME, Zandler ME, Fukuzumi S and D'Souza F. *Chem. Eur. J.* 2013; **19**: 9629–9638. (e) Imahori H. *Org. Biomol. Chem.* 2004; **2**: 1425–1433.
- (a) Ikemoto J, Takimiya K, Otsubo T, Fujitsuka M and Ito O. *Org. Lett.* 2002; **4**: 309–311. (b) Nakamura T, Fujitsuka M, Araki Y, Ito O, Ikemoto J, Takimiya K, Aso Y and Otsubo T. *J. Phys. Chem. B* 2004; **108**: 10700–10710. (c) Oike T, Kurata T, Takimiya K, Otsubo T, Aso Y, Zhang H, Araki Y and Ito O. *J. Am. Chem. Soc.* 2005; **127**: 15372–15373. (d) Nakamura T, Ikemoto J, Fujitsuka M, Araki Y, Ito O, Takimiya K, Aso Y and Otsubo T. *J. Phys. Chem. B* 2005; **109**: 14365–14374.
- de la Torre G, Giacalone F, Segura JL, Martín N and Guldi DM. *Chem. Eur. J.* 2005; **11**: 1267–1280.
- Roncali J. *Acc. Chem. Res.* 2000; **33**: 147–156.
- (a) Casado J, Rodríguez-Gonzalez S, Ruiz-Delgado MC, Moreno Oliva M, Lopez-Navarrete JT, Caballero R, de la Cruz P and Langa F. *Chem. Eur. J.* 2009; **15**: 2548–2559. (b) Rodríguez González S, Ruiz Delgado MC, Caballero R, de la Cruz P, Langa F, López Navarrete JT and Casado J. *J. Am. Chem. Soc.* 2012; **134**: 5675–5681.
- Urbani M, Pelado B, de la Cruz P, Yamanaka K, Ito O and Langa F. *Chem. Eur. J.* 2011; **17**: 5432–5444.
- (a) Oswald F, Islam DMS, Araki Y, Troiani V, de la Cruz P, Moreno A, Ito O and Langa F. *Chem. Eur. J.* 2007; **13**: 3924–3933. (b) Oswald F, Islam DMS, Araki Y, Troiani V, Caballero R, de la Cruz P, Moreno A, Ito O and Langa F. *Chem. Commun.* 2007; 4498–4500. (c) Barea EM, Caballero R, López-Arroyo L, Guerrero A, de la Cruz P, Langa F and Bisquert J. *ChemPhysChem.* 2011; **12**: 961–965.
- Oswald F, Islam DMS, El-Khouly ME, Araki Y, Caballero R, de la Cruz P, Ito O and Langa F. *Phys-ChemChemPhys.* 2014; **16**: 2443–2451.
- Mayorga-Burrezo P, Pelado B, Ponce Ortiz R, de la Cruz P, López-Navarrete JT, Langa F and Casado J. *Chem. Eur. J.* 2015; **21**: 1713.
- Loewe RS, Ambroise A, Muthukumar K, Padmaja K, Lysenko AB, Mathur GLQ, Bocian DF, Misra V and Lindsey JS. *J. Org. Chem.* 2004; **69**: 1453–1460.
- Pelado B, de la Cruz P, González-Pedro V, Barea EM and Langa F. *Tetrahedron Lett.* 2012; **53**: 6665–6669.
- The synthesis of **2** will be described elsewhere.
- (a) Echeverria CA, Tigrerosa A, Ortiza A, Insuasty B and Martín N. *J. Porphyrins Phthalocyanines* 2011; **15**: 1232–1238. (b) Chen C, Zhu YZ, Zhao HY and Zheng JY. *Tetrahedron Lett.* 2013; **54**: 1607–1611. (c) Konev AS, Khlebnikov AF, Nikiforova TG, Virtsev AA and Frauendorf H. *J. Org. Chem.* 2013; **78**: 2542–2552. (d) Rego LGC, Hames BC, Mazon KT and Joswig JO. *J. Phys. Chem. C* 2014; **118**: 126–134. (e) Ballatore MB, Spesia MB, Milanese ME and Durantini EN. *Eur. J. Med. Chem.* 2014; **83**: 685–694.
- D'Souza F, Deviprasad GR, Zandler ME, El-Khouly ME, Fujitsuka M and Ito O. *J. Phys. Chem. B* 2002; **106**: 4952–4962.
- Gaussian 03, Revision D.02, Frisch MJ, Trucks GW, Schlegel HB, Scuseria GE, Robb MA, Cheeseman JR, Montgomery Jr JA, Vreven T, Kudin KN, Burant JC, Millam JM, Iyengar SS, Tomasi J, Barone V, Mennucci B, Cossi M, Scalmani G, Rega N, Petersson GA, Nakatsuji H, Hada M, Ehara M, Toyota K, Fukuda R, Hasegawa J, Ishida M, Nakajima T, Honda Y, Kitao O, Nakai H, Klene M, Li X, Knox JE, Hratchian HP,

Cross JB, Bakken V, Adamo C, Jaramillo J, Gomperts R, Stratmann RE, Yazyev O, Austin AJ, Cammi R, Pomelli C, Ochterski JW, Ayala PY, Morokuma K, Voth GA, Salvador P, Dannenberg JJ, Zakrzewski VG, Dapprich S, Daniels AD, Strain MC, Farkas O, Malick DK, Rabuck AD, Raghavachari K, Foresman JB, Ortiz JV, Cui Q, Baboul AG, Clifford S,

Cioslowski J, Stefanov BB, Liu G, Liashenko A, Piskorz P, Komaromi I, Martin RL, Fox DJ, Keith T, Al-Laham MA, Peng CY, Nanayakkara A, Challacombe M, Gill PMW, Johnson B, Chen W, Wong MW, Gonzalez C and Pople JA. Gaussian, Inc., Wallingford CT, 2004.



# Efficient oxidation of ethers with pyridine *N*-oxide catalyzed by ruthenium porphyrins

Nobuki Kato, Yu Hamaguchi, Naoki Umezawa and Tsunehiko Higuchi\*<sup>◇</sup>

Graduate School of Pharmaceutical Sciences, Nagoya City University, 3-1 Tanabe-dori, Mizuho-ku, Nagoya 467-8603, Japan

Dedicated to Professor Shunichi Fukuzumi on the occasion of his retirement

Received 16 November 2014

Accepted 24 December 2014

**ABSTRACT:** We found that oxidation of cyclic ethers with the Ru porphyrin-heteroaromatic *N*-oxide system gave lactones or/and ring-opened oxidized products with regioselectivity. A relatively high kinetic isotope effect was observed in the ether oxidation, suggesting that the rate-determining step is the first hydrogen abstraction.

**KEYWORDS:** ruthenium catalyst, porphyrin, pyridine *N*-oxide, ether, oxidation.

## INTRODUCTION

Metalloporphyrin-catalyzed oxidations have been extensively investigated because of their relevance to the chemistry and biochemistry of cytochrome P450 and other heme-containing oxidizing enzymes [1]. Although enormous numbers of catalytic oxidizing systems have been reported, only a few are suitable for organic synthesis from the viewpoint of yield based on substrate [2]. We have found that ruthenium porphyrin efficiently catalyzes oxygen transfer from heteroaromatic *N*-oxides, including pyridine *N*-oxide derivatives, to alkanes, alkenes and aromatic rings to afford oxidized products in generally high yields under mild conditions [3]. Uniquely, *N*-acyl cyclic amines are oxidatively ring-opened to afford *N*-acyl-amino acids in high yields [3h]. Here, we describe an examination of the oxidation of ethers with the Ru porphyrin-heteroaromatic *N*-oxide system as part of an evaluation of the scope and limitations of this system. Ether moieties are often seen in natural products and pharmaceuticals, and selective oxidation of ether should afford novel oxygenated derivatives and/or compounds identical with natural metabolites. We report here the oxidation of

various cyclic ethers with 2,6-dichloropyridine *N*-oxide catalyzed by Ru porphyrins.

## EXPERIMENTAL

### General

NMR spectra were recorded on a JEOL JNM-GSX400 (400 MHz for <sup>1</sup>H) spectrometer, a JEOL JNM-LA500 (500 MHz for <sup>1</sup>H) or a Varian VNMR5 500 spectrometer (500 MHz for <sup>1</sup>H) spectrometer. Chemical shifts are reported in  $\delta$  ppm relative to tetramethylsilane ( $\delta = 0.00$ ) or CHCl<sub>3</sub> ( $\delta = 7.26$ ) for <sup>1</sup>H NMR unless otherwise stated. Multiplicity is expressed as s = singlet, d = doublet, t = triplet, m = multiplet, br = broad, *etc.* Mass spectra were determined on a JEOL JMS-LCmate spectrometer or a JEOL JMS-AX505 spectrometer. IR spectra were obtained using a FT/IR-680 plus Fourier-transform infrared spectrometer.

Reagents and solvents were of commercial grade, and were used without purification unless otherwise stated. Oxygen- or moisture-sensitive reactions were carried out under an argon atmosphere. Solvents were dried as follows for moisture-sensitive reactions. Dehydrated THF and Et<sub>2</sub>O were purchased from Kanto Chemical Co., Inc. and used as received. 1,2-dichloroethane was treated with MS4A. Oxygen- or moisture-sensitive compounds were introduced *via* a syringe or stainless

<sup>◇</sup> SPP full member in good standing

\*Correspondence to: Tsunehiko Higuchi, email: [higuchi@phar.nagoya-cu.ac.jp](mailto:higuchi@phar.nagoya-cu.ac.jp), tel: +81 52-836-3435, fax: +81 52-836-3435

steel cannula through a rubber septum. Analytical TLC was performed using 0.025 mm Merck Kiesegel TLC plates (60 F<sub>254</sub>). Bands were visualized by exposure to UV light (254 nm), or to 10% aqueous phosphomolybdic acid or 8% *p*-anisaldehyde solution in ethanol containing 6% sulfonic acid and 1% acetic acid, followed by heating on a hot plate. Flash column chromatography was performed using Fuji Silysia BW 300 (300 mesh).

## Synthesis

**Preparation of Ru<sup>IV</sup>(TMP)Cl<sub>2</sub> 1 and Ru<sup>IV</sup>(TPFPP)Cl<sub>2</sub> 2.** The insertion of ruthenium atom into TMP and the oxidation of the resulting carbonyl complex was done according to the method reported by Groves' group [4] for the synthesis of Ru<sup>II</sup>(TMP)CO and Ru<sup>VI</sup>(TMP)O<sub>2</sub>. To a solution of Ru<sup>VI</sup>(TPFPP)(O)<sub>2</sub> (20.0 mg, 18.0 μmol) in 18 mL of benzene was added activated molecular sieves 4A (1.81 g) under Ar and added dropwise *conc.* HCl (720 μL). After the addition was completed, the mixture was stirred at room temperature for 3.5 h. The reaction mixture was filtered through a pad of celite to remove the sieves. Recrystallization (*n*-hexane/CH<sub>2</sub>Cl<sub>2</sub>) gave Ru<sup>IV</sup>(TPFPP)(Cl)<sub>2</sub> (14.0 mg, 65%) as a red solid. FAB-MS: *m/z* 1108 [M<sup>+</sup> - Cl].

Ru<sup>IV</sup>(TPFPP)Cl<sub>2</sub> 2 was synthesized according to the literature procedure [5].

**General procedure for oxidation of ethers with pyridine *N*-oxide catalyzed by ruthenium porphyrins (from 3a to 4a).** To a solution of catalyst 1 (2.5 mg, 2.6 μmol) and 2,6-dichloropyridine *N*-oxide (328 mg, 2.00 mmol) in 1,2-dichloroethane (5 mL) was added substrate 3a (83.0 μL, 800 μmol) at room temperature under Ar atmosphere. After stirring for 20 h at 40 °C, the reaction mixture was concentrated *in vacuo*. The residue was purified by silica gel column chromatography (CH<sub>2</sub>Cl<sub>2</sub>/hexane = 1:1) to afford 4a (66.0 mg, 83%) as a colorless oil. <sup>1</sup>H NMR (400 MHz, CDCl<sub>3</sub>) δ 1.24 (s, 6H), 3.60 (s, 2H). EI-MS: *m/z* 100 ([M]<sup>+</sup>).

**γ-Butyrolactone 4b.** <sup>1</sup>H NMR (400 MHz, CDCl<sub>3</sub>): δ, ppm 2.24–2.32 (m, 2H), 2.50 (t, *J* = 7.8 Hz, 2H), 4.36 (t, *J* = 7.0 Hz, 2H). EI-MS: *m/z* 86 ([M]<sup>+</sup>).

**Succinic anhydride 5b.** <sup>1</sup>H NMR (400 MHz, CDCl<sub>3</sub>): δ, ppm 2.90 (s, 4H). EI-MS: *m/z* 100 ([M]<sup>+</sup>).

**δ-Valerolactone 4c.** <sup>1</sup>H NMR (400 MHz, CDCl<sub>3</sub>): δ, ppm 1.84–1.95 (m, 4H), 2.56 (t, *J* = 6.8 Hz, 2H), 4.35 (t, *J* = 5.6 Hz, 2H). EI-MS: *m/z* 100 ([M]<sup>+</sup>).

**Glutaric acid 5c.** <sup>1</sup>H NMR (500 MHz, CDCl<sub>3</sub>): δ, ppm 2.05 (quintet, *J* = 6.7 Hz, 2H), 2.46 (t, *J* = 6.7 Hz, 2H). EI-MS: *m/z* 132 ([M]<sup>+</sup>).

**ε-Caprolactone 4e.** <sup>1</sup>H NMR (500 MHz, CDCl<sub>3</sub>): δ, ppm 1.74–1.80 (m, 4H), 1.85–1.89 (m, 2H), 2.63–2.66 (m, 2H), 4.22–4.24 (m, 2H). EI-MS: *m/z* 114 ([M]<sup>+</sup>).

**Hydroxy carboxylic acid 5e.** <sup>1</sup>H NMR (500 MHz, CDCl<sub>3</sub>): δ, ppm 1.25–1.40 (m, 2H), 1.48–1.65 (m, 4H), 2.30 (t, 2H, *J* = 7.5 Hz), 3.59 (t, 2H, *J* = 6.4 Hz), 7.67 (s, 1H). EI-MS: *m/z* 132 ([M]<sup>+</sup>).

**Adipic acid 6e.** <sup>1</sup>H NMR (500 MHz, DMSO-*d*<sub>6</sub>): δ, ppm 1.50–1.56 (m, 4H), 2.22–2.26 (m, 4H), 12.05 (s, 2H). EI-MS: *m/z* 146 ([M]<sup>+</sup>).

**Epoxide 6f.** <sup>1</sup>H NMR (400 MHz, acetone-*d*<sub>6</sub>): δ, ppm 1.88–2.17 (m, 2H), 3.58–3.98 (m, 3H), 5.17 (d, *J* = 2.0 Hz, 1H).

**Epoxide 6g.** <sup>1</sup>H NMR (400 MHz, acetone-*d*<sub>6</sub>): δ, ppm 1.35–1.65 (m, 2H), 1.87–2.13 (m, 2H), 3.13 (m, 1H), 3.47–3.61 (m, 2H), 4.67 (d, *J* = 2.4 Hz, 1H). EI-MS: *m/z* 100 ([M]<sup>+</sup>).

**Sclearolide 4i.** IR (KBr): ν, cm<sup>-1</sup>. 1770. <sup>1</sup>H NMR (500 MHz, CDCl<sub>3</sub>): δ, ppm 0.80–0.91 (m, 6H), 1.00–1.70, 1.84–1.97 (m, 17H), 2.33–2.38 (m, 2H), 2.51 (dd, *J* = 6.4, 6.4 Hz, 1H). FAB-MS: *m/z* 251 [M + H]<sup>+</sup>.

**Preparation of 3j.** To a suspension of NaBD<sub>4</sub> (41.0 mg, 1.10 mmol) in THF (2 mL) was added a solution of *cis*-1,2-cyclohexanedicarboxylic anhydride (170 mg, 1.10 mmol) at 0 °C and the reaction mixture was stirred at room temperature for 2 h. *p*-toluenesulfonic acid monohydrate (37.9 mg, 220 μmol) was added cautiously, then the resulting mixture was stirred for 2.5 h and concentrated *in vacuo*. Water (20 mL) was added and the water layer was extracted with ethyl acetate. The combined organic layers were dried over Na<sub>2</sub>SO<sub>4</sub>, and concentrated *in vacuo*. The residue was purified by distillation to afford the lactone (144 mg, 92%). IR (KBr): ν, cm<sup>-1</sup>. 3219 (C–H), 2260 (C–D), 1772 (–COO–). <sup>1</sup>H NMR (500 MHz, CDCl<sub>3</sub>): δ, ppm 1.14–1.30 (m, 3H), 1.57–1.67 (m, 3H), 1.79–1.85 (m, 1H), 2.10–2.14 (m, 1H), 2.42–2.48 (m, 1H), 2.62–2.66 (m, 1H). EI-MS: *m/z* 142 ([M]<sup>+</sup>).

To a suspension of LiAlH<sub>4</sub> (125 mg, 3.30 mmol) in THF (10 mL) was added a solution of the lactone (155 mg, 1.10 mmol) in THF (15 mL) at 0 °C. The reaction mixture was stirred at reflux temperature for 10 h, then cooled to 0 °C and quenched with AcOEt (2 mL) and water to destroy excess LiAlH<sub>4</sub>. The mixture was filtered and the filtrate was dried. Evaporation of the solvent furnished a crude product that was filtered through a short silica gel column to obtain the diol (85.0 mg, 53%). <sup>1</sup>H NMR (500 MHz, CDCl<sub>3</sub>): δ, ppm 1.38–1.55 (m, 10H), 1.94 (brs, 2H), 3.58 (d, *J* = 8.5 Hz, 1H), 3.76 (d, *J* = 8.5 Hz, 1H). EI-MS: *m/z* 146 ([M]<sup>+</sup>).

To a solution of the diol (53.0 mg, 360 μmol) in pyridine (4 mL) was added *p*-toluenesulfonic acid (69.1 mg, 360 μmol) at 0 °C. The reaction mixture was stirred for 4 h at reflux temperature, and then the reaction was quenched with water (10 mL). The aqueous layer was extracted with chloroform. The combined organic layers were washed with brine, dried over Na<sub>2</sub>SO<sub>4</sub> and concentrated *in vacuo*. The crude product was purified by silica-gel column chromatography to afford 3j (30.2 mg, 66%). <sup>1</sup>H NMR (500 MHz, CDCl<sub>3</sub>): δ, ppm 1.37–1.55 (m, 8H), 1.91 (m, 2H), 3.55 (dd, *J* = 3.6, 11.2 Hz, 1H), 3.73 (dd, *J* = 8.6, 11.2 Hz, 1H). EI-MS: *m/z* 128 ([M]<sup>+</sup>). EI-HRMS: *m/z* calcd. for C<sub>8</sub>H<sub>12</sub>H<sub>2</sub>O ([M]<sup>+</sup>) 128.1170, found 128.1156.

### Deuterium kinetic isotope study

To a solution of catalyst **1** (2.5 mg, 2.6  $\mu\text{mol}$ ) and 2,6-dichloropyridine *N*-oxide (96.7 mg, 590  $\mu\text{mol}$ ) in 1,2-dichloroethane (1.5 mL) was added substrate **3j** (30.2 mg, 236  $\mu\text{mol}$ ) at room temperature under an Ar atmosphere. The reaction mixture was stirred for 20 h at 40 °C, and then concentrated *in vacuo*. The ratio of **4j/4j-d2** was determined by  $^1\text{H}$  NMR spectroscopy.

## RESULTS AND DISCUSSION

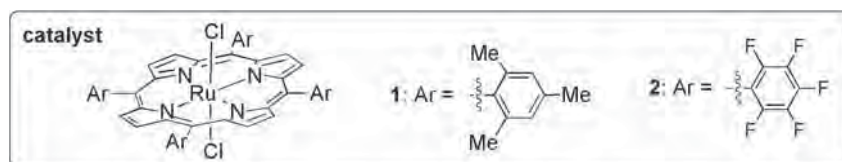
The results of oxidation of cyclic ethers using the ruthenium porphyrin-2,6-dichloropyridine *N*-oxide (abbreviated as RuP-DCPO) system are summarized in Table 1.  $\text{Ru}^{\text{IV}}(\text{TMP})\text{Cl}_2$  **1** or  $\text{Ru}^{\text{IV}}(\text{TPFPP})\text{Cl}_2$  **2** was used (TMP: tetramesitylporphyrinato; TPFPP: tetrakis(pentafluorophenyl)porphyrinato). Both complexes (0.3 mol.%)

efficiently converted 3,3-dimethyloxetane **3a** and THF **3b** into the corresponding lactone (entries 2-5), accompanied in the case of entries 4 and 5 with small amounts of secondary oxidized products **5b** and lactol **6b**. On the other hand, the reaction did not proceed at all in the absence of catalyst (entry 1). The ruthenium porphyrin catalysts are essential for this oxidation. Tetrahydropyran **3c** gave both lactone **4c** and ring-opened, secondary-oxidized product **5c** (entries 6 and 7); **4c** may be formed by further oxidation at the hemiacetal C-H bond of intermediate lactol **3d**, while **5c** may be formed by further oxidation of 5-hydroxypentalanal, *i.e.* the open form of **3d**. Therefore, we examined direct oxidation of **3d** with our system (entries 8 and 9). The product profiles in entries 6 and 7 were similar to that in entries 8 and 9. This result is consistent with the idea that lactol **3d** is a common intermediate of **4c** and **5c** in the oxidation pathway of **3c**. Oxidation of oxepane **3e** mainly

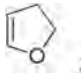
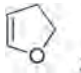
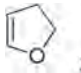
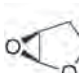
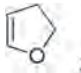
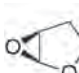
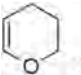
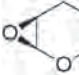
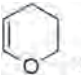
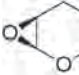
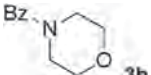
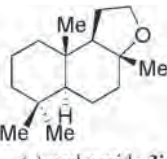
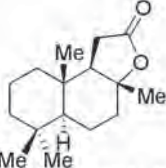
**Table 1.** Oxidation of cyclic ethers by ruthenium porphyrin-2,6-dichloropyridine *N*-oxide system<sup>a</sup>

Entry	Substrate	Catalyst	<i>N</i> -oxide	Product, Isolated yield	
1		—	2.5 eq		0%
2		<b>1</b>	2.5 eq		83%
3		<b>2</b>	2.5 eq		90%
4		<b>1</b>	2.5 eq		75%
5		<b>2</b>	2.5 eq		69%
					2%
					5%
					20%
					22%
6		<b>1</b>	2.5 eq		38%
7		<b>2</b>	2.5 eq		56%
					38%
					16%
8		<b>1</b>	1.3 eq		32%
9		<b>2</b>	1.3 eq		51%
					30%
					19%
10		<b>1</b>	2.5 eq		6%
11		<b>2</b>	2.5 eq		3%
					13%
					18%
					44%
					48%

<sup>a</sup>Reaction conditions: substrate (0.16 M) and 2,6-dichloropyridine *N*-oxide (0.40 M; 2.5 eq) unless otherwise noted. Yields are based on the substrate used. <sup>b</sup>not isolated.



**Table 2.** Functional group selectivity in the oxidation of cyclic ethers by ruthenium porphyrin-2,6-dichloropyridine *N*-oxide system<sup>a</sup>

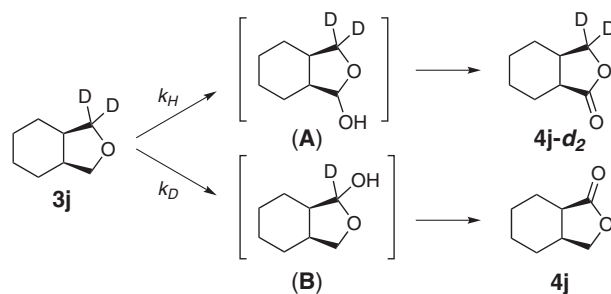
Entry	Substrate	Catalyst	Time	Product, Isolated yield
1		—	21 h	 0%
2		<b>1</b>	21 h	 <b>6f</b> 71%
3		<b>2</b>	21 h	 17%
4		<b>1</b>	46 h	 85%
5		<b>2</b>	46 h	 20%
6		<b>2</b>	4 h	complex mixture
7	 (-)-ambroxide <b>3i</b>	<b>2</b>	24 h	 80% (+)-sclareolide <b>4i</b>

<sup>a</sup>Reaction conditions: substrate (0.16 M), catalyst (0.3 mol %) and 2,6-dichloropyridine *N*-oxide (0.40 M) were stirred in 1,2-dichloroethane at 40 °C. Yields are based on the substrate used.

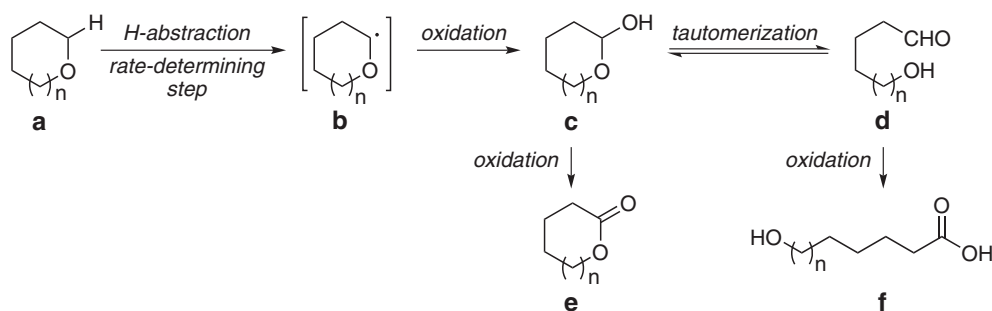
gave ring-opened, multi-oxidized products (**5e** and **6e**), with lactone **4e** as a minor product (entries 10 and 11). This selectivity in product profile is probably due to a marked shift of the equilibrium between 7-membered lactol and 6-hydroxyhexanal towards the latter form under the reaction conditions. White *et al.* developed an excellent catalytic oxidizing system and applied it to ether oxidation. The product profiles in the case of **3b**, **3c** and **3e** differ slightly from those in the case of White's catalytic system with an iron complex [6]. Catalytic amounts of RuCl<sub>3</sub> or RuO<sub>2</sub> and an excess of NaIO<sub>4</sub> couple have often been used for ether oxidation [7]. These systems form highly reactive RuO<sub>4</sub> as an active intermediate and are convenient for organic synthesis. However, our oxidation system shows a higher selectivity for lactone formation than the RuO<sub>2</sub>/NaIO<sub>4</sub> system [8]. As mentioned above, the RuP-DCPO system is also applicable to regioselective oxidation of ethers. There are no previous reports describing catalytic oxidation of ethers using metalloporphyrin catalysts.

Next, we evaluated chemoselectivity in the oxidation with the RuP-DCPO system (Table 2). The corresponding epoxide was obtained with good chemoselectivity when the substrate was cyclic ether with a C–C double bond (entries 2–5). Epoxidation is considered to proceed faster than oxidation of the  $\alpha$ -ethereal C–H bonds in the RuP-DCPO system. When catalyst **2** was used, the yields dramatically decreased (entries 3 and 5). Fluorinated complex **2** should have higher Lewis acidity than **1**. Therefore, it is considered that most of the epoxides **6f** and **6g** would be decomposed by Lewis acid catalysis in the presence of **2**.

Actually, a complex mixture of products was formed in addition to the corresponding epoxide, and the starting material and the corresponding lactone were not observed. In the absence of catalyst, the epoxidation did not proceed (entry 1). Oxidation of *N*-benzylmorpholine **3h** gave a complex mixture (entry 6). Considering this result, there seems to be almost no difference between the reactivity of the amide part and that of the ether part toward the active species formed in the oxidizing system [3h], although the structures of the products were not determined. We also examined oxidation of (-)-ambroxide **3i**, which is a natural product, as a further application (entry 7). The oxidation afforded (+)-sclareolide **4i** in good yield, *i.e.* the natural product was regioselectively oxidized. Even reaction for two days did not give any other product, even though the product has two reactive tertiary carbons, and the catalyst was still active.

**Scheme 1.** Kinetic isotope effect





Scheme 2. Proposed reaction mechanism

To obtain mechanistic insight into our oxidation, the kinetic isotope effect was examined using *syn*-octahydro[1,1- $d_2$ ]isobenzofuran **3j** (Scheme 1). The intramolecular kinetic isotope effect in the reaction of **3j** with this oxidation system was evaluated from the product ratio of **4j-d<sub>2</sub>** vs. **4j** as **A/B**. The **A/B** ratio was determined to be 5.5. The  $k_H/k_D$  value could be extrapolated to 5.5, since the lactol oxidation step (hydrogen abstraction-OH rebound step or through-bond electron transfer step) is considered to be much faster than the ethereal hydrogen abstraction. The relatively high  $k_H/k_D$  value strongly suggests that the rate-determining step is the first hydrogen abstraction, in the same way as in the reaction of amides [3h]. The oxidation step of lactol is considered to be faster.

The ring-opened compound **5c** was not observed in the reaction of lactone **4c** in the RuP-DCPO system. Therefore, the ring-opened compounds were not obtained from lactones. Instead, the ring-opened compounds are considered to be generated by oxidation of aldehydes, which are tautomers of the lactones, since we previously showed that the RuP-DCPO system efficiently oxidized aldehydes to afford the corresponding carboxylic acids [3h].

The proposed reaction mechanism based on the above results is summarized in Scheme 2. First, cleavage of the  $\alpha$ -ethereal C-H bond, which was deduced to be the rate-determining step from the kinetic isotope study, takes place, and the resulting radical **b** rebounds to a putative compound II-type intermediate to afford the lactol **c**. Then **c** is directly oxidized to give the lactone form **e**. On the other hand, the formyl group on ring-opened form **d**, a tautomer of lactol **c**, is readily oxidized to form hydroxycarboxylic acid **f**. The product yield ratio of **e** and **f** may reflect deviation of the equilibrium between **c** and **d** depending on the ring size. By analogy with the known chemistry of cytochrome P450 and its model compounds [1], the role of the catalyst may be as follows: An active intermediate formed by the reaction of 2,6-dichloropyridine *N*-oxide with Ru(IV) porphyrin abstracts the H atom from the  $\alpha$ -ethereal C-H bond and the resulting hydroxyl radical equivalent on the Ru rapidly rebounds to radical intermediate **b**. The lactol **c** is also oxidized by the active intermediate to give lactone **e**.

In summary, we have shown that the RuP-DCPO system is applicable to regioselective oxidation of ethers. This reaction system converts most 4- and 5-membered cyclic ethers to lactones with good regioselectivity and efficiency. Tetrahydropyran, a 6-membered cyclic ether, gave both lactone and ring-opened oxidized products in comparable yields. Most products were ring-opened ones in the case of oxepane, a 7-membered cyclic ether. The efficient conversion of (-)-ambroxide to (+)-sclareolide is a good example of regioselective oxidation of a cyclic ether moiety in a complex natural product. We expect that the RuP-DCPO system will provide direct access from natural products to diverse new biologically active compounds. Further investigation of the scope of this reaction is in progress.

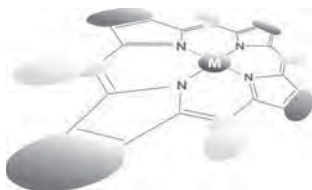
### Acknowledgements

This work was partly supported by Grants-in-Aid for Scientific Research on Priority Areas (No. 19028054, No. 20037056, "Chemistry of Concerto Catalysis") and Platform for Drug Discovery, Informatics, and Structural Life Science from the Ministry of Education, Culture, Sports, Science and Technology, Japan.

### REFERENCES

- (a) Meunier B, Robert A, Pratviel G and Bernadou J. In *The Porphyrin Handbook*, Vol. 4, Kadish KM, Smith KM and Guillard R. (Eds.) Academic Press: San Diego, 2000; pp 119–187. (b) Groves JT, Shalyaev K and Lee J. In *The Porphyrin Handbook*, Vol. 4, Kadish KM, Smith KM and Guillard R. (Eds.) Academic Press: San Diego, 2000; pp 17–40. (c) Mansuy D. *C. R. Chim.* 2007; **10**: 392–413.
- In *Handbook of Reagents for Organic Synthesis: Catalytic Oxidation Reagents*, Fuchs PL. (Ed.) John Wiley & Sons: Chichester, 2013.
- (a) Higuchi T, Ohtake H and Hirobe M. *Tetrahedron Lett.* 1989; **30**: 6545–6548. (b) Higuchi T, Ohtake H and Hirobe M. *Tetrahedron Lett.* 1991; **32**: 7435–7438. (c) Ohtake H, Higuchi T and Hirobe M. *Tetrahedron Lett.* 1992; **33**: 2521–2524. (d) Ohtake H,

- Higuchi T and Hirobe M. *J. Am. Chem. Soc.* 1992; **114**: 10660–10662. (e) Ohtake H, Higuchi T and Hirobe M. *Heterocycles*. 1995; **40**: 867–903. (f) Shingaki T, Miura K, Higuchi T, Hirobe M and Nagano T. *Chem. Commun.* 1997; 861–862. (g) Higuchi T, Satake C and Hirobe M. *J. Am. Chem. Soc.* 1995; **117**: 8879–8880. (h) Ito R, Umezawa N and Higuchi T. *J. Am. Chem. Soc.* 2005; **127**: 834–835.
4. Groves JT and Quinn R. *Inorg. Chem.* 1984; **23**: 3844–3846.
  5. Wang C, Shalyaev KV, Bonchio M, Carofiglio T and Groves JT. *Inorg. Chem.* 2006; **45**: 4769–4782.
  6. Chen MS and White MC. *Science* 2010; **327**: 566–571.
  7. (a) In *Encyclopedia of Reagents for Organic Synthesis*, Vol. 6, Paquette LA. (Ed.) John Wiley & Sons: Chichester, 1995; pp 4420. (b) In *Ruthenium Oxidation Complexes*, Griffith WP. (Ed.) Springer: New York, 2011.
  8. Smith III AB and Scarborough RM. *Synth. Commun.* 1980; **10**: 205–211.



## Mechanistic study of methanol oxidation by Ru<sup>IV</sup>–oxo complexes

Yoshihito Shiota<sup>\*a</sup>, Shoya Takahashi<sup>a</sup>, Shingo Ohzu<sup>b</sup>, Tomoya Ishizuka<sup>b</sup>,  
Takahiko Kojima<sup>b</sup> and Kazunari Yoshizawa<sup>\*a,c</sup>

<sup>a</sup>Institute for Materials Chemistry and Engineering, Kyushu University, Nishi-ku, Fukuoka 819-0395, Japan

<sup>b</sup>Department of Chemistry, Graduate School of Pure and Applied Sciences, University of Tsukuba, Ibaraki 305-8577, Japan

<sup>c</sup>Elements Strategy Initiative for Catalysts & Batteries, Kyoto University, Nishi-ku, Kyoto 615-8520, Japan

*Dedicated to Professor Shunichi Fukuzumi on the occasion of his retirement*

Received 8 December 2014

Accepted 24 December 2014

**ABSTRACT:** The catalytic conversion of methanol to formaldehyde by three kinds of non-porphyrin Ru complexes, Ru<sup>IV</sup>O(TPA) (TPA = tris(2-pyridylmethyl)amine) (**1a**), Ru<sup>IV</sup>O(6-COO-TPA) (6-COO-TPA = 2-(6-carboxyl-pyridyl)methyl-bis(2-pyridylmethyl)amine) (**1b**), and Ru<sup>IV</sup>O(N4Py) (N4Py = *N,N*-bis(2-pyridyl-methyl)-*N*-bis(2-pyridyl)methylamine) (**1c**), is discussed by using density functional theory (DFT) calculations. There are two possible reaction pathways for the oxidation of methanol to formaldehyde with respect to the first hydrogen abstraction from the methyl group (path 1) and the hydroxyl group (path 2). Path 1 and path 2 involve the hydroxymethyl radical ( $\bullet\text{CH}_2\text{OH}$ ) and the methoxyl radical ( $\text{CH}_3\text{O}\bullet$ ), respectively, as an intermediate. DFT calculations demonstrate that the two pathways are energetically comparable in the reactions by the three Ru<sup>IV</sup>–oxo complexes. The reactions with **1a** and **1c** are initiated by the C–H bond dissociation with activation barriers of 22.2 and 21.4 kcal/mol, respectively, while the reaction with **1b** is initiated by the O–H bond dissociation with an activation barrier of 18.1 kcal/mol. However, the calculations showed that the rate-determining step is the H-atom abstraction from the CH<sub>3</sub> group of methanol in all the pathways. These results are in good agreement with kinetic analysis of the reactions by the Ru<sup>IV</sup>–oxo complexes, being useful for considering the mechanism of methanol oxidation.

**KEYWORDS:** catalytic mechanism, C–H activation, DFT calculation, methanol oxidation, Ru–oxo complex.

## INTRODUCTION

High-valent metal–oxo species play important roles in natural enzymatic systems as key reactive intermediates for the oxidation of organic compounds; for example, iron-oxo and manganese–oxo complexes [1–3]. Applications of such an efficient catalytic oxidation of organic compounds in aqueous solution are effective in the design

of greener chemical processes [4, 5]. According to Kojima and co-workers, the selective and efficient oxygenations of alcohols and olefins with water as an oxygen source are catalyzed by Ru<sup>IV</sup>–oxo complexes, for example, [Ru<sup>IV</sup>(O)(TPA)(H<sub>2</sub>O)]<sup>2+</sup> (TPA = tris(2-pyridylmethyl)amine) (**1a**), [Ru<sup>IV</sup>(O)(6-COO-TPA)]<sup>+</sup> (6-COO-TPA = 2-(6-carboxyl-pyridyl)methyl-bis(2-pyridylmethyl)amine) (**1b**), and [Ru<sup>IV</sup>(O)(N4Py)]<sup>2+</sup> (N4Py = *N,N*-bis(2-pyridylmethyl)-*N*-bis(2-pyridyl)methylamine) (**1c**), as shown in Chart 1 [6]. These Ru<sup>IV</sup>–oxo complexes are formed by proton-coupled electron transfer (PCET) [7], in which the deprotonation of a coordinated water molecule and the oxidation of the metal center are considered to occur in a concerted

<sup>†</sup>SPP full member in good standing

\*Correspondence to: Yoshihito Shiota, email: shiota@ms.ifoc.kyushu-u.ac.jp; Kazunari Yoshizawa, email: kazunari@ms.ifoc.kyushu-u.ac.jp

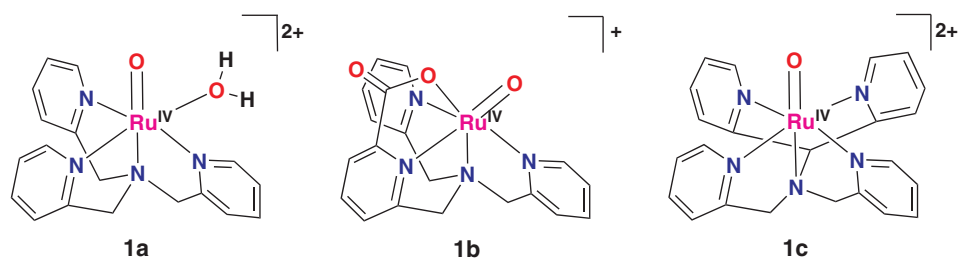


Chart 1.

manner. The experimental observations indicate that the three complexes have essentially identical catalytic activity for the oxidation of organic compounds.

Oxidation reactions catalyzed by Ru<sup>IV</sup>-oxo complexes have been extensively studied because of a wide range of substrates and a variety of reaction mechanisms. Transfers of e<sup>-</sup>, H•, and H<sup>+</sup> have been implicated in various reactions mediated by [Ru<sup>IV</sup>O]<sup>2+</sup> [8–12]. Rocker and Meyer provided detailed mechanistic insights into the oxidation of alcohols by [Ru<sup>IV</sup>(bpy)<sub>2</sub>(py)(O)]<sup>2+</sup> (bpy = 2,2'-bipyridine and py = pyridine) [13]. A great deal of attention has been focused on a better understanding of the catalytic oxidation of organic compounds by Ru<sup>IV</sup>-oxo species from a theoretical point of view [14–17]. From generalized valence bond calculations, Carter and Goddard [18] pointed out that the ground state of the bare RuO<sup>+</sup> complex has a double bond similar to that of dioxygen. They expect the RuO<sup>+</sup> species to be reactive because of the radical character on the O atom. Cundari and Drago [14] reported using the INDO/1 method that the C–H bond to be activated is orthogonal to the RuO π MOs for the oxidation of alcohol by a six-coordinate Ru<sup>IV</sup>-oxo complex.

In the course of the oxidation of methanol to formaldehyde, two hydrogen atoms should be abstracted from methanol in two steps. In a detailed DFT study, Yoshizawa and Kagawa calculated two competitive pathways for the gas phase oxidation of methanol by the bare FeO<sup>+</sup> complex [19]. In the first pathway the C–H bond dissociation initially occurs with the formation of an intermediate complex Fe(OH)(OHCH<sub>2</sub>)<sup>+</sup> while in the second pathway the O–H bond dissociation initially occurs with another intermediate complex Fe(OH)(OCH<sub>3</sub>)<sup>+</sup>. In the methanol oxidation by various Fe-oxo species such as the [FeO<sub>4</sub>]<sup>2-</sup>, [FeO]<sup>2+</sup>, and [(tpa)Fe<sup>IV</sup>O]<sup>2+</sup> complexes, the initial C–H bond dissociation is favorable in energy in comparison with the initial O–H bond dissociation [20]. On the other hand, Zhao *et al.* reported that the initial O–H bond activation is energetically more favorable in the oxidation of methanol catalyzed by VO<sub>2</sub><sup>+</sup> than the initial C–H bond activation [21]. A vanadium oxide cluster OV(OH)<sub>3</sub> gives rise to methanol oxidation with the formation of a methoxide intermediate, as confirmed by experimental and theoretical studies [22]. In a previous study [23] we reported the mechanism of

the catalytic conversion of 1,2-cyclohexanediol to adipic anhydride by **1a** using DFT calculations. Although there is no significant difference between the activation barriers for the two kinds of H-atom abstraction from the substrate, the energies of the subsequent intermediates lead us to conclude that the C–H bond dissociation should take place in the first step. Although the kinetic analysis with the three Ru<sup>IV</sup>-oxo complexes were carried out for the oxidation of methanol [6c], the reaction mechanism by the Ru<sup>IV</sup>-oxo complexes is still not fully understandable. Here, we report the mechanism for the conversion of methanol to formaldehyde by the three Ru<sup>IV</sup>-oxo complexes, **1a**, **1b**, and **1c**, using DFT calculations to better understand effects of the coordination environment on the reaction mechanism.

## METHOD OF CALCULATION

We used the hybrid B3LYP DFT method [24, 25] implemented with the Gaussian 09 program [26]. The Hay–Wadt basis set [27] was used for the Ru atom, and the D95\*\* basis set [28] for the H, C, N, and O atoms to obtain optimized geometries. All energies were subsequently estimated by using a larger basis set, SDD [29] for the Ru atom and 6-311+G\*\* [30] for the other atoms. The dielectric effect of water solvent was incorporated by using the polarized continuum model (PCM) [31]. Vibrational-frequency calculations were systematically performed to verify each optimized geometry corresponding to a local minimum with no imaginary frequency or a saddle point with only one imaginary frequency. Zero-point vibrational energy corrections were taken into account in calculating the total energies of the reaction species.

## RESULTS AND DISCUSSION

### Optimized structures and electronic states of the Ru<sup>IV</sup>O complexes

We first calculated the structures and electronic states in the triplet ground state of the Ru<sup>IV</sup>O complexes, **1a**, **1b** and **1c**, and their corresponding aqua complexes, Ru<sup>II</sup>(H<sub>2</sub>O), which are a part of the final products in the

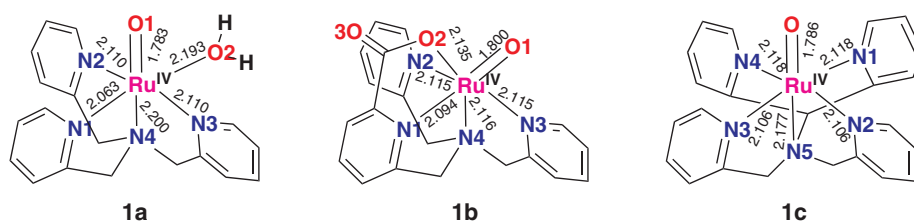
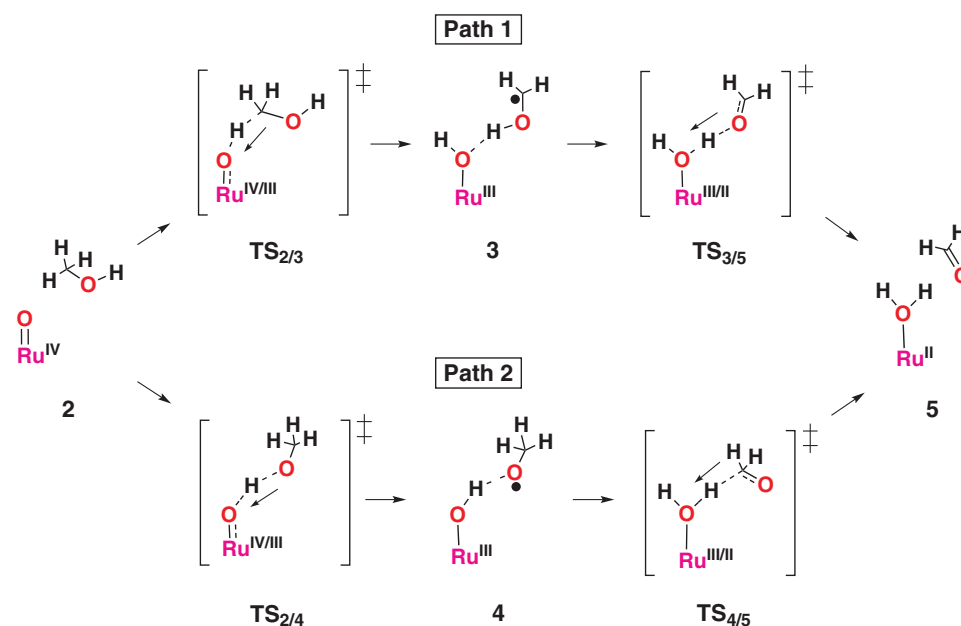


Fig. 1. Optimized geometries of the Ru<sup>IV</sup>-oxo complexes in the triplet state



Scheme 1.

oxidation of methanol to formaldehyde. Computations at the B3LYP/LANL2DZ level of theory demonstrated that all of the Ru<sup>IV</sup>-oxo complexes have six-coordinated structures. Figure 1 shows optimized geometries of the Ru<sup>IV</sup>-oxo complexes in the triplet state. The Ru–O bond distances of complexes **1a**, **1b**, and **1c** are 1.783, 1.800, and 1.786 Å, respectively; the  $\nu(\text{Ru}-\text{O})$  vibrations of **1a**, **1b** and **1c** are reasonably calculated to be 823 cm<sup>-1</sup>, 809 cm<sup>-1</sup>, and 824 cm<sup>-1</sup>. Thus, complex **1b** has a weaker Ru–O bond than the others, due to a significant *trans* effect of the axial pyridine ligand [32]. Since the Ru–O bond involves the  $\pi^*$  orbitals between the Ru atom and the oxo ligand, these results suggest that the Ru–O bond in **1b** is influenced by the  $\pi$ -type interaction of the pyridine nitrogen at the *trans* position with the oxo ligand. In contrast, the  $\sigma$  bonding interaction by the tertiary amino nitrogen is almost independent of the Ru–O bond distances in **1a** and **1c**.

The energy difference between the closed-shell singlet and triplet states,  $\Delta E_{ST} = E_S - E_T$ , is 18.4 kcal/mol in **1a**, 14.9 kcal/mol in **1b**, and 23.4 kcal/mol in **1c**. In addition, the open-shell singlet state lies about 7 kcal/mol above the triplet state in these complexes. Therefore

DFT computations indicate that the triplet spin state is the ground state in these Ru<sup>IV</sup>-oxo complexes in the six-coordinate octahedral coordination environments. On the other hand,  $\Delta E_{ST}$  is –30 kcal/mol in all of the Ru<sup>II</sup>(H<sub>2</sub>O) complexes; thus, the singlet spin state is the ground state in the Ru<sup>II</sup>(H<sub>2</sub>O) complexes. As a consequence, we expect that there should be at least one crossing point between the triplet and singlet potential energy surfaces in the course of the oxidation process.

### Oxidation of methanol by the Ru<sup>IV</sup>O complexes

Here let us look at the conversion of methanol to formaldehyde by the Ru<sup>IV</sup>-oxo complexes. The dehydrogenation of methanol is initiated by an H-atom abstraction, followed by the formation of a radical intermediate. Then, another H atom of methanol is abstracted by the hydroxo ligand of a Ru<sup>III</sup>(OH) complex to form the final products formaldehyde and a Ru<sup>II</sup>(H<sub>2</sub>O) complex. As mentioned earlier in this manuscript, there are two possible reaction pathways, as shown in Scheme 1.

In path 1, an H atom of the CH<sub>3</sub> group is first abstracted by the oxo ligand of **2** to form the intermediate complex

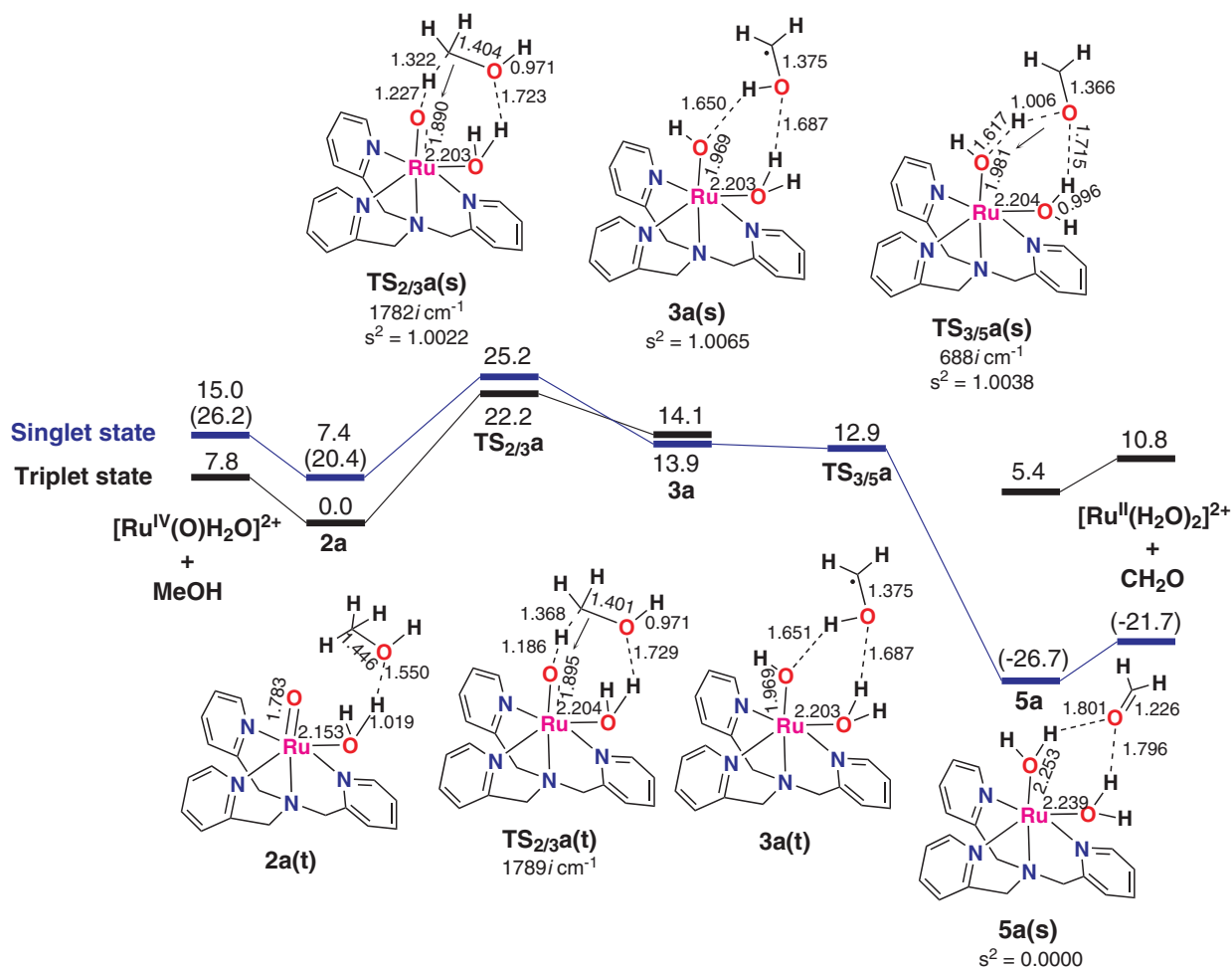
**3**, and then another H atom of the OH group is abstracted by the hydroxo ligand resulting in the formation of the product complex **5**, together with formaldehyde. On the other hand, in path 2, the H atom of the OH group is first abstracted by the oxo ligand of **2** to form the intermediate complex **4**, and after that, an H atom of the CH<sub>3</sub> group is abstracted by the hydroxo ligand resulting in the formation of **5** and formaldehyde. The difference in the reaction mechanism between path 1 and path 2 is how the H-atom abstraction takes place in the CH<sub>3</sub> group and the OH group. In this way, we analyzed these reaction mechanisms about the three kinds of Ru<sup>IV</sup>-oxo complexes.

### Reaction by complex **1a**

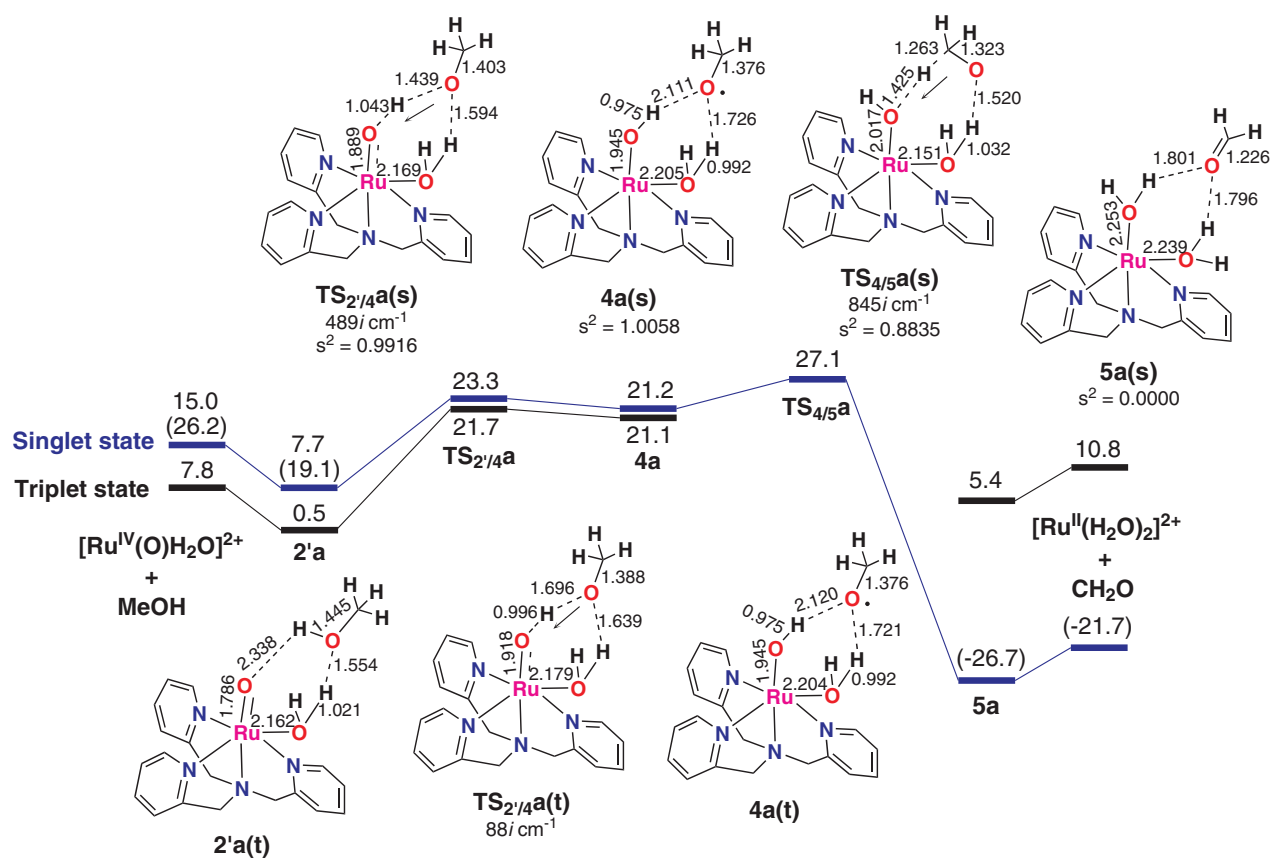
We next considered the reaction of **1a** with methanol along path 1. Figure 2 shows computed energy diagrams for the triplet and singlet reaction pathways. After the first transition state the general profile of these diagrams is downhill toward the product direction and the reaction

is exothermic accordingly. We therefore expect that the first transition state should play an important role in this oxidation process.

In the initial stages of the reaction, **1a** and methanol form an association complex **2a** with a binding energy of 20.3 kcal/mol in the gas phase, which is decreased to 7.8 kcal/mol in water solution. The hydroxyl group of the substrate is anchored to the aqua ligand through a hydrogen bond of 1.550 Å. A cationic complex and a neutral molecule have a strong binding energy in the gas phase in general. Thus, the binding energy of 20.3 kcal/mol comes from the Coulombic attraction and the hydrogen bond, whereas the binding energy of 7.8 kcal/mol in solution mainly comes from the hydrogen bond, due to a decrease in Coulombic attraction. In path 1 the first transition state on the triplet surface connects **2a** and **3a** with an imaginary frequency mode of 1789i cm<sup>-1</sup>. This high frequency is a direct consequence of a C–H bond cleavage as well as an O–H bond formation, as the vibrational mode suggests. The transition-state structure involves a C–H bond of 1.368 Å and an O–H



**Fig. 2.** Computed energy diagrams for the conversion of methanol to formaldehyde by complex **1a** via path 1 at the B3LYP level including zero-point vibrational energy corrections. Units are in kcal/mol and Angstroms. Values in parentheses are the closed-shell singlet state



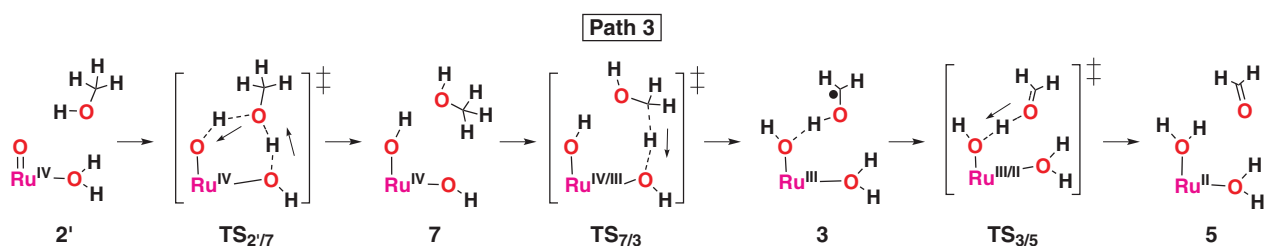
**Fig. 3.** Computed energy diagrams for the conversion of methanol to formaldehyde by complex **1a** via path 2 at the B3LYP level including zero-point vibrational energy corrections. Units are in kcal/mol and Angstroms. Values in parentheses are the closed-shell singlet state

bond of 1.186 Å. The Ru–O bond distance is increased to 1.895 Å in  $\text{TS}_{2/3a}$  from 1.783 Å in **2a**. The hydrogen-bond distance is increased to 1.729 Å in  $\text{TS}_{2/3a}$  from 1.550 Å in **2a**. The C–H bond dissociation produces a radical species; calculated spin densities of the carbon atom bonded to the hydroxo ligand are 0.49 in  $\text{TS}_{2/3a}$  and 0.94 in **3a**. Thus, **3a** can be assigned as a diradical species, in which the Ru<sup>III</sup>OH complex is weakly coupled with a hydroxymethyl radical. Intermediate **3a** is then transformed into **5a** with almost no activation barrier after the spin transition from the triplet state to the singlet state, followed by the dissociation of the complex into formaldehyde and a Ru<sup>II</sup> complex. Thus, there is no transition state between **3a** and **5a** in the triplet state.

Figure 3 shows computed energy diagrams for path 2. Since path 2 is initiated by the cleavage of the OH bond of methanol leading to the formation of methoxyl radical, we considered another reactant complex **2'a** as an initial structure. Calculated relative energy of **2'a** is only 0.5 kcal/mol, and therefore the interconversion between **2a** and **2'a** is likely to occur with the movement of **1a** and methanol. Complex **2'a** as well as **2a** has an interaction between the aqua ligand and the oxygen atom of methanol. The O–H bond distance is 1.554 Å in **2'a**, which is comparable to 1.550 Å in **2a**. In addition

**2'a** has another interaction between the oxo ligand and the hydroxyl group of methanol, the other O–H bond distance being 2.338 Å. The two interactions determine the orientation of methanol and induce the OH bond cleavage along path 2. The first transition state  $\text{TS}_{2/4a}$  is related to the H-atom abstraction from the OH group of methanol to form intermediate **4a**.  $\text{TS}_{2/4a}$  has an imaginary frequency mode of 88i cm<sup>-1</sup> in the triplet state. The transition-state structure involves an O–H bond of 1.696 Å and a RuO–H bond of 0.996 Å. Taking account of the two bond distances along the reaction coordinate,  $\text{TS}_{2/4a}$  is a late transition state. The Ru–O bond distance is increased to 1.918 Å in  $\text{TS}_{2/4a}$  from 1.786 Å in **2'a**. The hydrogen bond is increased to 1.639 Å in  $\text{TS}_{2/4a}$  from 1.554 Å in **2'a**. Intermediate **4a** is also a radical complex that corresponds to a Ru<sup>III</sup>OH complex and methoxyl radical. Calculated spin densities of the relevant oxygen atom are 0.36 in  $\text{TS}_{2/4a}$  and 0.87 in **4a**.

Intermediate **4a** undergoes a spin crossover from the triplet state to the open-shell singlet state to abstract the second hydrogen in  $\text{TS}_{4/5a}$ , which connects **4a** and **5a** as a transition state with an imaginary frequency mode of 845i cm<sup>-1</sup>. This transition state has a C–H bond of 1.263 Å and a RuO–H bond of 1.425 Å. The short C–H bond and the long O–H bond in  $\text{TS}_{4/5a}$  suggest it to be an early



Scheme 2.

transition state, whereas  $\text{TS}_{2/4}\mathbf{a}$  is a late transition state. Note that a calculated  $\langle S^2 \rangle$  value of 1.00 corresponds to a biradical species in the open-shell singlet state. Therefore a calculated  $\langle S^2 \rangle$  value of 0.8572 in  $\text{TS}_{4/5}\mathbf{a}$  suggests that the antiferromagnetic coupling between the two radical centers in the open-shell singlet state is lost with the formation of  $\mathbf{5a}$  in the closed-shell singlet state.

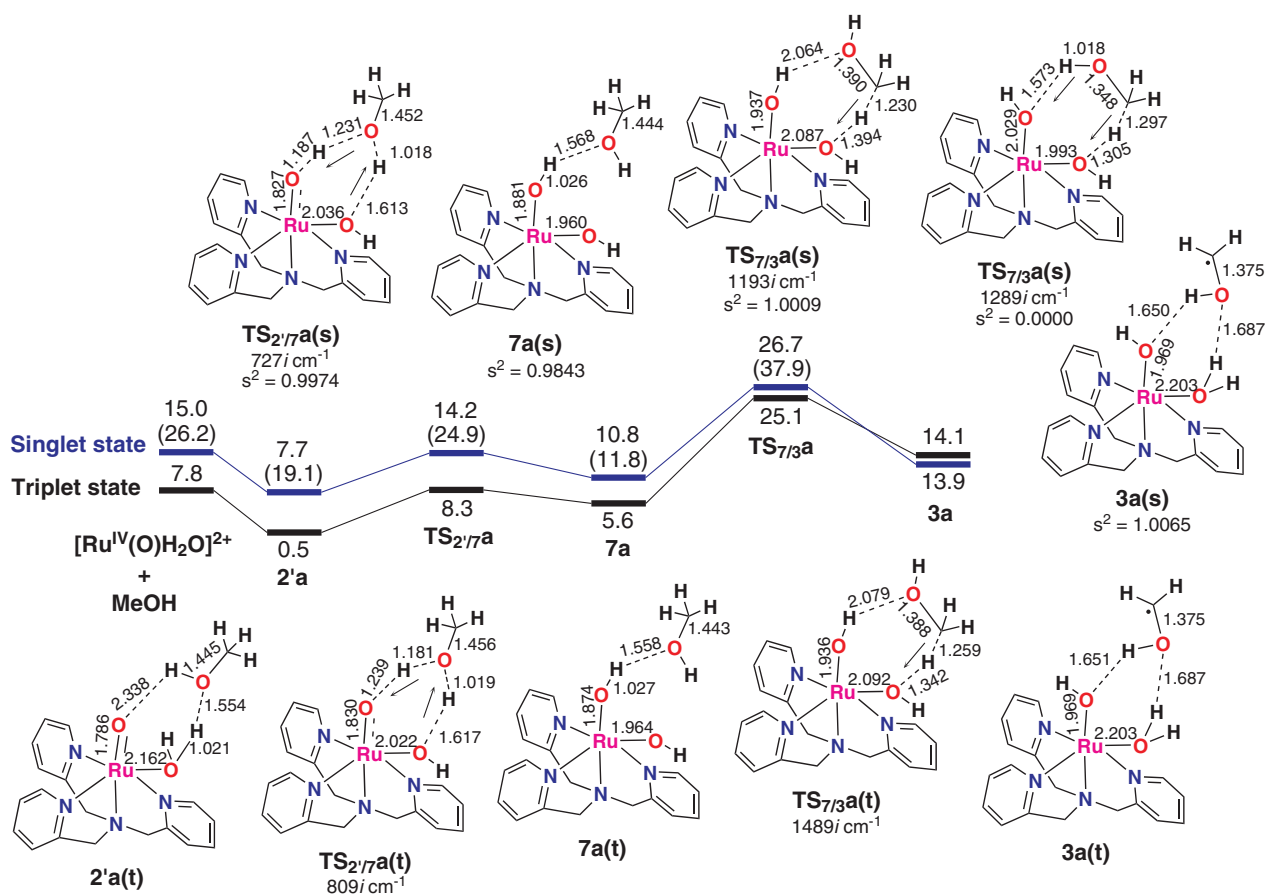
Computed energies of  $\text{TS}_{2/3}\mathbf{a}$  and  $\text{TS}_{2/4}\mathbf{a}$  are 22.2 and 21.7 kcal/mol relative to complex  $\mathbf{2a}$ , respectively. Although the two transition states are energetically comparable, the relative energies of the intermediates are quite different;  $\mathbf{4a}$  is energetically unstable compared to  $\mathbf{3a}$ . Moreover, there is a second transition state with an activation barrier of 6.0 kcal/mol in path 2, whereas there is no activation barrier between  $\mathbf{3a}$  and  $\mathbf{5a}$  in path 1. After the first transition state the spin crossover from the triplet state to the open-shell singlet state plays an important role in the formation of  $\mathbf{5a}$ . The potential energy diagrams demonstrate that the surface crossing between the triplet and the singlet states can occur in the vicinity of  $\mathbf{3a}$  and  $\mathbf{4a}$ . Optimized structures of  $\mathbf{3a}$  and  $\mathbf{4a}$  in the singlet state are almost identical to that in the triplet state, and each point corresponds to a crossing seam between the triplet and singlet potential energy surfaces. Therefore we can view  $\mathbf{3a}$  and  $\mathbf{4a}$  as an approximate minimum energy crossing point (MECP) in each reaction pathway. The spin crossover is likely to occur in the vicinity of  $\mathbf{3a}$  and  $\mathbf{4a}$  corresponding to crossing seams. After the spin crossover the singlet state  $\mathbf{3a}$  is not stable in energy, whereas  $\mathbf{4a}$  remains as a stable complex. Once the spin transition occurs, the singlet potential energy surface with  $\mathbf{3a}$  directly leads to the formation of the relevant product. Shaik and co-workers<sup>33</sup> suggested that spin inversion effects can dramatically affect reaction mechanisms, rate constants, branching ratio, and temperature behaviors of organometallic transformations. We studied the surface crossing and spin crossover in detail in the activation of C–H bond especially for methane hydroxylation by  $\text{FeO}^+$  and related bare transition-metal oxide ions [34] Harvey and co-workers [35] also pointed out that reaction rates of spin blocking strongly depend on details of the potential energy surfaces and of the topology associated with their crossing. These computational results lead us to conclude that path 1 is energetically favored in the oxidation of methanol by complex  $\mathbf{1a}$ .

We found another possible pathway (path 3) to  $\mathbf{3a}$  from  $\mathbf{2'a}$ , as shown in Scheme 2. In path 3 the reaction involves a new intermediate ( $\mathbf{7a}$ ) that corresponds to a complex of  $\text{Ru}^{\text{IV}}(\text{OH})_2$  ( $\mathbf{6a}$ ) and methanol. Complex  $\mathbf{6a}$  is an isomer of  $\mathbf{1a}$ . The transformation from  $\mathbf{1a}$  to  $\mathbf{6a}$  by a concerted proton transfer can occur through methanol as well as through water molecule. The  $\text{Ru}^{\text{IV}}$  complex requires an aqua ligand for this reaction, and therefore we take no account of path 3 in the methanol oxidation by  $\mathbf{1b}$  and  $\mathbf{1c}$ . Complex  $\mathbf{1a}$  is first converted to  $\mathbf{6a}$ , and then  $\mathbf{6a}$  abstracts an H atom from the  $\text{CH}_3$  group of methanol to form  $\mathbf{3a}$ . Water molecule as well as methanol molecule can catalyze the interconversion between  $\mathbf{1a}$  and  $\mathbf{6a}$ . Complex  $\mathbf{6a}$  is energetically unstable compared to  $\mathbf{1a}$  by 3.9 kcal/mol. The activation barrier for the concerted proton transfer through water molecule in the conversion from  $\mathbf{1a}$  to  $\mathbf{6a}$  is 10.4 kcal/mol. In the presence of methanol, this transformation is likely to occur, a calculated activation barrier being 8.3 kcal/mol. In contrast, the activation barrier for this transformation in the absence of water or methanol is 26.0 kcal/mol. Thus, methanol molecule or water molecule is important for the occurrence of this transformation.

To consider methanol oxidation along path 3, we considered computed energy diagrams and optimized structures from  $\mathbf{2'a}$  to  $\mathbf{3a}$  via  $\mathbf{7a}$  (the complex of  $\mathbf{6a}$  and methanol), as shown in Fig. 4. An H atom of the  $\text{CH}_3$  group of methanol is abstracted by the hydroxo ligand of  $\mathbf{6a}$  corresponding to the aqua ligand of  $\mathbf{1a}$  to form  $\mathbf{3a}$ , and then another H atom of the hydroxymethyl radical is shifted to the hydroxo ligand resulting in the formation of  $\text{CH}_2=\text{O}$ . A calculated energy gap is 5.6 kcal/mol between  $\mathbf{2'a}$  and  $\mathbf{7a}$ . As mentioned above, the activation barrier of  $\text{TS}_{2/7}\mathbf{a}$  is only 8.3 kcal/mol, which is smaller than the energy of  $\text{TS}_{2/4}\mathbf{a}$ . Thus, this transformation is likely to occur compared to the simple H-atom abstraction. The Ru–O bond distance is increased to 1.874 Å in  $\mathbf{7a}$  from 1.786 Å in  $\mathbf{2'a}$ . Calculated spin densities in the oxygen atom located in the oxo moiety are 0.93 in  $\mathbf{2'a}$  and 0.41 in  $\mathbf{7a}$  in the triplet state.

The second transition state connects  $\mathbf{7a}$  and  $\mathbf{3a}$  with an imaginary frequency mode of  $1489i \text{ cm}^{-1}$  in the triplet state. Since the transition state of the triplet state lies 1.5 kcal/mol below that of the open-shell singlet state, the spin state is still conserved. The transition-state





**Fig. 4.** Computed energy diagrams for the conversion of methanol to formaldehyde by complex **7a** via Path 3 at the B3LYP level including zero-point vibrational energy corrections. Units are in kcal/mol and Angstroms. Values in parentheses are the closed-shell singlet state

structure has a C–H bond of 1.259 Å and an O–H bond of 1.342 Å. The Ru–O bond distance is increased to 1.936 Å in **TS<sub>7/3a</sub>** from 1.874 Å in **7a**. The hydrogen bond is elongated to 2.079 Å in **TS<sub>7/3a</sub>** from 1.558 Å in **7a**. After **TS<sub>7/3a</sub>** the reaction proceeds in an almost identical way as path 1. On the other hand, **TS<sub>7/3a</sub>** also calculated in the closed-shell singlet state directly connects **3a** and **5a** with a relative energy of 37.9 kcal/mol. This direct pathway needs a higher activation barrier than the two-step pathway. This result indicates that the oxidation of methanol with the Ru<sup>IV</sup>-oxo complexes *via* a H• transfer rather than a direct hydride abstraction.

The transition states of **TS<sub>2/7a</sub>** in Fig. 4 and **TS<sub>2/4a</sub>** in Fig. 3 are similar to that of a proton shift from methanol to the oxidant. An activation barrier for **TS<sub>2/7a</sub>**, however, is smaller than the energy of **TS<sub>2/4a</sub>**. Therefore this transformation occurs preferentially and interferes with the H-atom abstraction from the OH group of methanol. Complex **7a** can easily come back to **2a** thermodynamically. Thus, we conclude that path 1 is a dominant pathway in the oxidation of methanol by the Ru<sup>IV</sup>-oxo complex with an aqua ligand.

Both path 1 and path 3 begin with an H-atom abstraction from the CH<sub>3</sub> group of methanol to form

intermediate **3** in the course of methanol oxidation. There is one step between **2** and **3** in path 1, while there are two steps with intermediate **7** in path 3. Since a computed energy of the rate-determining step is 22.2 kcal/mol in path 1 and 25.1 kcal/mol in path 3, there is a small energy difference between path 1 and path 3. Moreover, a computed activation barrier of **TS<sub>7/3a</sub>** is 17.9 kcal/mol, which is smaller than that of **TS<sub>2/3a</sub>**. Thus, **1a** and **6a**, which are important active species in path 1 and path 3, have almost the same oxidizing ability for C–H activation. If there is complex **6a** in water, **6a** should also play an important role in the oxidation of the substrate.

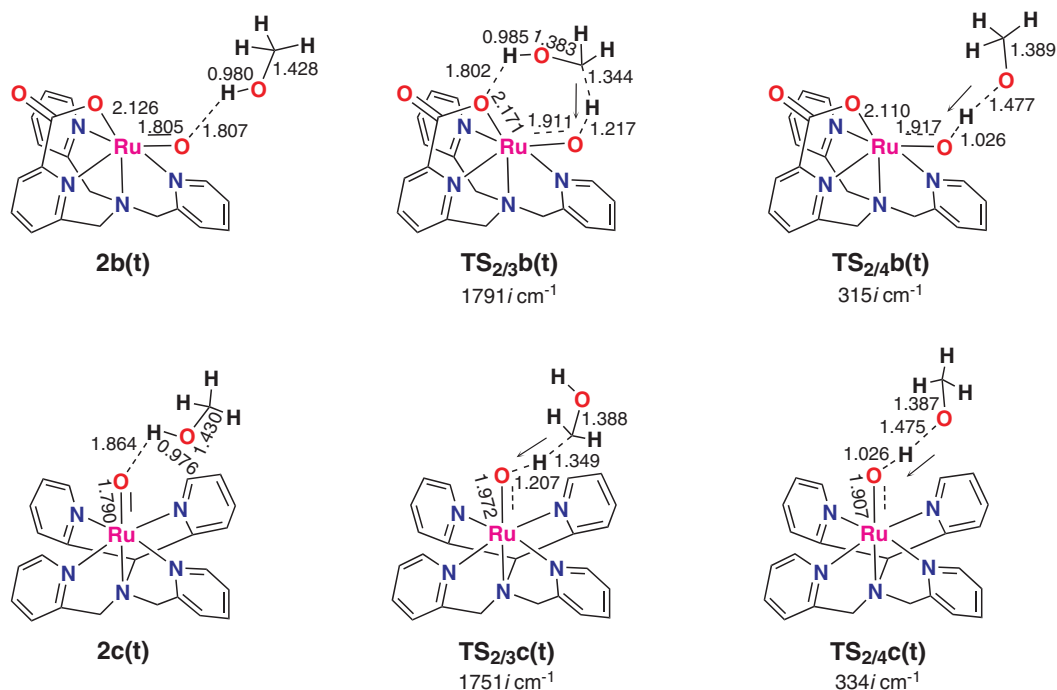
### Reaction by complexes **1b** and **1c**

We next look into the reaction pathways catalyzed by **1b** and **1c**. In experiments, the three complexes have almost the same catalytic activity [6]. The radical intermediates and transition states along path 1 and path 2 about **1b** and **1c** were also obtained by DFT calculations. There are no significant difference among **1a**, **1b** and **1c** in the reaction step of path 1 and path 2. Computed energies for the conversion of methanol to formaldehyde by complexes **1b** and **1c** are summarized in Table 1.

**Table 1.** Computed energies for the conversion of methanol to formaldehyde by complex **1b** and **1c** at the B3LYP level including zero-point vibrational energy corrections. Energies are in units of kcal/mol

	<b>2b</b>	<b>TS<sub>2/3b</sub></b>	<b>3b</b>	<b>TS<sub>2/4b</sub></b>	<b>4b</b>	<b>TS<sub>4/5b</sub></b>	<b>5b</b>
triplet state	0.0	21.2	5.9	18.7	18.1		
singlet state	6.4 (13.9) <sup>a</sup>	22.4	5.9 <sup>b</sup>	20.1	18.1	19.7	(-29.3)
	<b>2c</b>	<b>TS<sub>2/3c</sub></b>	<b>3c</b>	<b>TS<sub>2/4c</sub></b>	<b>4c</b>	<b>TS<sub>4/5c</sub></b>	<b>5c</b>
triplet state	0.0	21.4	12.2	21.1	20.6		
singlet state	7.2 (24.1)	22.9	12.2 <sup>b</sup>	22.8	20.6	25.9	(-30.7)

<sup>a</sup>Values in parentheses are the closed-shell singlet state. <sup>b</sup>Single point calculation.

**Fig. 5.** Optimized structures for reactant complexes and transition states of the triplet state for the conversion of methanol to formaldehyde by **1b** and **1c**. Units are in Angstroms

In view of the computed energy in the rate-determining step, there is only a small difference between path 1 and path 2 in **1b** and **1c**. The two pathways are possible to occur from an energetic point of view. In addition the triplet and singlet energy surfaces have no significant difference without the reactant complexes. The relative energy of **TS<sub>2/3b</sub>** is 21.2 kcal/mol and that of **TS<sub>2/3c</sub>** is 21.4 kcal/mol, which are very close to that of **TS<sub>2/3a</sub>**. On the other hand, the energy of **TS<sub>4/5b</sub>** is much lower than that of **TS<sub>4/5a</sub>** and **TS<sub>4/5c</sub>**. Only in the case of **1b**, the energy of **TS<sub>4/5</sub>** is lower than that of **TS<sub>2/3</sub>**. Consequently, path 2 is a dominant pathway in **1b**, whereas path 1 is a dominant pathway in **1a** and **1c**. The relative energy of the second transition state in path 2 plays an important role in determining the energetically low-lying pathway for the oxidation of methanol. We therefore conclude that the two possible reaction pathways of methanol oxidation

by the Ru<sup>IV</sup>-oxo complexes are energetically comparable and that the coordination environment determines which pathway is dominant by controlling the reaction rate of path 2.

Relative energies of **TS<sub>4/5</sub>** are correlated with the strength of the Ru–O bond. Calculated Ru–OH bond distances of Ru<sup>III</sup>OH complexes **8a**, **8b**, and **8c**, which form intermediate complexes with substrate in **3** and **4**, are 1.945, 1.966, and 1.950 Å, respectively (Table S76–S78) in the Supporting Information). The  $\nu(\text{Ru–OH})$  vibration is calculated to be 618 cm<sup>-1</sup> in **1a**, 594 cm<sup>-1</sup> in **1b**, and 611 cm<sup>-1</sup> in **1c**. Therefore complex **8b** has a weak Ru–OH bond compared to the others. According to a *trans* effect, the  $\pi$  type interaction by the pyridine nitrogen provides the weak Ru–O bond in **1b**. This weakening of the Ru–O bond enhances the facility of the H-atom abstraction from substrate. On the other hand,

our calculations show that the relative energy of **TS**<sub>2/3</sub> is almost the same among the three Ru<sup>IV</sup>-oxo complexes. Looking at the strength of C–H bond, that of methoxyl radical is activated compared with that of methanol. The length of a C–H bond of methoxyl radical is lengthened from that of methanol, 1.095 Å to 1.115 Å. Thus, the C–H bond cleavage catalyzed by the Ru–O bond is effective for **TS**<sub>4/5</sub>, but not for **TS**<sub>2/3</sub>. Consequently, the coordination environment of Ru<sup>IV</sup>-oxo complex **1b** may only affect the reaction rate of path 2.

The geometry of the reactant complex is slightly different. Complex **1a** forms a hydrogen bond between the OH group of methanol and the aqua ligand, whereas complexes **1b** and **1c** form a hydrogen bond between the OH group of methanol and the oxo ligand. In **1a**, there are two types of initial complexes. One has no interaction between the oxo ligand and the OH group, while another has a direct interaction between them. On the other hand, there is only one type of initial complex in **1b** and **1c**, which have a direct interaction between the oxo ligand and the OH group of methanol. In **1b** and **1c** path 2 is more likely to occur than path 1 because the oxo ligand is placed close to the OH group of methanol but not the CH<sub>3</sub> group of methanol in the initial complexes. However, in **1b** and **1c** the interaction with methanol is not so strong. The binding energies of methanol are 7.8 kcal/mol in **1a**, 3.4 kcal/mol in **1b**, and 2.4 kcal/mol in **1c**. The hydrogen bonds of complexes **1b** and **1c** are 1.807 and 1.864 Å, respectively, which are longer than that of complex **1a**. Moreover, complex **1a** forms a hydrogen bond between the OH group of methanol and the aqua ligand in the first transition state, whereas complexes **1b** and **1c** form no hydrogen bond between the substrate and the oxidant except **TS**<sub>2/3b</sub>, as shown in Fig 5.

The DFT calculations show that the rate-determining step is the H-atom abstraction from the CH<sub>3</sub> group of methanol in all pathways, which is consistent with the results of the kinetic analysis with the three Ru<sup>IV</sup>-oxo complexes. Looking at the number of reaction step, **TS**<sub>3/5</sub> includes almost no activation barrier, and there is also almost no energy gap between **TS**<sub>2/4</sub> and **4** in all the three Ru complexes. These results indicate that intermediate complexes **3** and **4** are unstable and short-lived. Thus, the oxidation reaction of methanol with the Ru<sup>IV</sup>-oxo complexes can be considered to occur in almost one step rather than in two steps.

## CONCLUSION

We have discussed mechanisms for the conversion of methanol to formaldehyde by three kinds of non-porphyrin Ru<sup>IV</sup>-oxo complexes bearing different pyridylamine ligands on the basis of DFT calculations at the B3LYP level of theory. We computed and analyzed two possible reaction pathways about the Ru<sup>IV</sup>-oxo complexes. There are two types of initial complexes through the hydrogen bond between the aqua ligand and the OH group of

methanol. One has a direct interaction between the oxo ligand and the CH<sub>3</sub> group of methanol, while another has an interaction between the oxo ligand and the OH group of methanol. The difference in the competitive reaction pathways is in whether the initial H-atom abstraction from the CH<sub>3</sub> group of methanol takes place (path 1) or that from the OH group occurs (path 2). Thus, path 1 and path 2 involve the hydroxymethyl radical (•CH<sub>2</sub>OH) and the methoxyl radical (CH<sub>3</sub>O•), respectively, as an intermediate. DFT calculations demonstrated that the two possible reaction pathways of methanol oxidation by the Ru<sup>IV</sup>-oxo complexes are energetically comparable. Path 1 is a dominant pathway for **1a** and **1c**, whereas path 2 is dominant for **1b**. The calculations also showed that the rate-determining step is the H-atom abstraction from the CH<sub>3</sub> group of methanol in all the pathways, which is consistent with the results of the kinetic analysis with the three Ru<sup>IV</sup>-oxo complexes [6d]. In this study, we clarified the mechanism for the conversion of methanol to formaldehyde by the Ru<sup>IV</sup>-oxo complexes and effects of the coordination environment on the mechanism of methanol oxidation.

## Acknowledgements

Y.S. and K.Y. thank Grants-in-Aid for Scientific Research (Nos. 21750063, 2245028, and 24109014) from the Japan Society for the Promotion of Science and the Ministry of Education, Culture, Sports, Science and Technology (MEXT) of Japan and the MEXT Projects of “Integrated Research on Chemical Synthesis” and “Elements Strategy Initiative” for their support of this work. T.K. thanks financial support through Grants-in-Aid for Scientific Research (Nos. 24245011 and 25109507) from the Japan Society for the Promotion of Science and that provided by the Mitsubishi Foundation.

## Supporting information

Complete reference 26 and atomic Cartesian coordinates for all the structures optimized in the present study (Tables S1–S79) are given in the supplementary material. This material is available free of charge *via* the Internet at <http://www.worldscinet.com/jpp/jpp.shtml>.

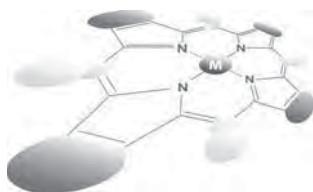
## Notes

The authors declare no competing financial interest.

## REFERENCES

- Ortiz de Montellano PR. *Cytochrome P450*, 2ed., Plenum Press: New York, 1995.
- Schlichting I, Berendzen J, Chu K, Stock AM, Maves SA, Benson DE, Sweet RM, Ringe D, Petsko GA and Sligar SG. *Science* 2000; **287**: 1615–1622.
- Poulos TL. *Phil. Trans. R. Soc. A* 2005; **363**: 793–806.

4. Shilov AE and Shul'pin GB. *Chem. Rev.* 1997; **97**: 2879–2932.
5. Punniyamurthy T, Velusamy S and Iqbal J. *Chem. Rev.* 2005; **105**: 2329–2363.
6. (a) Hirai Y, Kojima T, Mizutani Y, Shiota Y, Yoshizawa K and Fukuzumi S. *Angew. Chem., Int. Ed.* 2008; **47**: 5772–5776. (b) Kojima T, Hirai Y, Ishizuka T, Shiota Y, Yoshizawa K, Ikemura K, Ogura T and Fukuzumi S. *Angew. Chem., Int. Ed.* 2010; **49**: 8449–8453. (c) Ohzu S, Ishizuka T, Hirai Y, Jiang H, Sakaguchi M, Ogura T, Fukuzumi S and Kojima T. *Chem. Sci.* 2012; **3**: 3421–3431. (d) Ishizuka T, Ohzu S, Kotani H, Shiota Y, Yoshizawa K and Kojima T. *Chem. Sci.*, 2014; **5**: 1429–1436.
7. (a) Huynh MHV and Meyer TJ. *Chem. Rev.* 2007; **107**: 5004–5064. (b) Meyer TJ, Huynh MHV and Thorp HH. *Angew. Chem., Int. Ed.* 2007; **46**: 5284–5304.
8. Meyer TJ and Huynh MHV. *Inorg. Chem.* 2003; **42**: 8140–8160.
9. Che C–M and Yam VWW. *Adv. Transition Met. Coord. Chem.* 1996; **1**: 209–237.
10. (a) Bryant JR and Mayer JM. *J. Am. Chem. Soc.* 2003; **125**: 10351–10361. (b) Bryant JR, Matsuo T and Mayer JM. *Inorg. Chem.* 2004; **43**: 1587–1592.
11. (a) Ebersson L and Nilsson M. *Acta Chem. Scand.* 1990; **44**: 1062–1070. (b) Bockman TM, Hubig SM and Kochi JK. *J. Am. Chem. Soc.* 1998; **120**: 2826–2830.
12. (a) Moyer BA and Meyer TJ. *Inorg. Chem.* 1981; **20**: 436–444. (b) Dobson JC, Helms JH, Doppelt P, Sullivan BP, Hatfield WE and Meyer TJ. *Inorg. Chem.* 1989; **28**: 2200–2204.
13. Rucker L and Meyer TJ. *J. Am. Chem. Soc.* 1987; **109**: 746–754.
14. Cundari TR and Drago RS. *Inorg. Chem.* 1990; **29**: 3904–3907.
15. (a) Sharma PK, de Visser SP, Oglario F and Shaik S. *J. Am. Chem. Soc.* 2003; **125**: 2291–2300. (b) Dhuri SN, Seo MS, Lee Y-M, Hirao H, Wang Y, Nam W and Shaik S. *Angew. Chem., Int. Ed.* 2008; **47**: 3356–3359.
16. Lujan S, Slocik JM, Chatterjee D, Mitra A and Shepherd RE. *Inorg. Chim. Acta* 2004; **357**: 785–796.
17. Zierkiewicz W and Privalov T. *Dalton Trans.* 2006; **15**: 1867–1874.
18. Carter EA and Goddard III WA. *J. Phys. Chem.* 1988; **92**: 2109–2115.
19. Yoshizawa K and Kagawa Y. *J. Phys. Chem. A* 2000; **104**: 9347–9355.
20. (a) Kamachi T, Kouno T and Yoshizawa K. *J. Org. Chem.* 2005; **70**: 4380–4388. (b) Louwse MJ, Vassilev P and Baerends EJ. *J. Phys. Chem. A* 2008; **112**: 1000–1012. (c) Cheng L, Wang J, Wang M and Wu Z. *Phys. Chem. Chem. Phys.* 2010; **12**: 4092–4103.
21. González-Navarrete P, Gracia L, Calatayud M and Andrés J. *J. Comput. Chem.* 2010; **31**: 2493–2501.
22. Zhao L, Tan M, Chen J, Ding Q, Lu X, Chi Y, Yang G, Guo W and Fu Q. *J. Phys. Chem. A* 2013; **117**: 5161–5170.
23. Shiota Y, Herrera JM, Juhász G, Abe T, Ohzu S, Ishizuka T, Kojima T and Yoshizawa K. *Inorg. Chem.* 2011; **50**: 6200–6209.
24. Becke AD. *Phys. Rev. A* 1988; **38**: 3098–3100.
25. Lee C, Yang W and Parr RG. *Phys. Rev. B* 1988; **37**: 785–789.
26. Frisch MJ *et al.* Gaussian 09, revision C.01; Gaussian, Inc.: Wallingford, CT, 2010.
27. Hay PJ and Wadt WR. *J. Chem. Phys.* 1985; **82**: 299–310.
28. Dunning TH and Hay PJ. *In Modern Theoretical Chemistry*; Schaefer HF, III, Ed.; Plenum: New York, 1976; Vol. 3, p 1–27.
29. Dolg M, Stoll H and Preuss H. *Theor. Chim. Acta.* 1993; **85**: 441–450.
30. Krishnan P, Binkley JS, Seeger R and Pople JA. *J. Chem. Phys.* 1980; **72**: 650–654.
31. (a) Miertu S, Scrocco E and Tomasi J. *Chem. Phys.* 1981; **55**: 117–129. (b) Cancès E, Mennucci B, Tomasi J. *J. Chem. Phys.* 1997; **107**: 3032–3041. (c) Mennucci B, Cancès E, Tomasi J. *J. Phys. Chem. B* 1997; **101**: 10506–10517.
32. Che, C-M, Lai, T-F and Wong K-Y. *Inorg. Chem.* 1987; **26**: 2289–2299.
33. (a) Fiedler A, Schröder D, Shaik S and Schwarz H. *J. Am. Chem. Soc.*, 1994; **116**: 10734–10741. (b) Schröder D, Shaik S and Schwarz H. *Acc. Chem. Res.* 2000; **33**: 139–145. (c) Shaik S, Hirao H and Kumar D. *Acc. Chem. Res.* 2007; **40**: 532–542.
34. (a) Yoshizawa K, Shiota Y and Yamabe T. *Chem. Eur. J.* 1997; **3**: 1160–1169. (b) Yoshizawa K, Shiota Y and Yamabe, T. *J. Am. Chem. Soc.* 1998; **120**: 564–572. (c) Yoshizawa K, Shiota Y and Yamabe T. *Organometallics* 1998; **17**: 2825–2831. (d) Yoshizawa K, Shiota Y and Yamabe T. *J. Chem. Phys.* 1999; **111**: 538–545. (e) Shiota Y and Yoshizawa K. *J. Am. Chem. Soc.* 2000; **122**: 12317–12326. (f) Shiota Y and Yoshizawa K. *J. Chem. Phys.* 2003; **118**: 5872–5879. (g) Yoshizawa K. *Acc. Chem. Res.* 2006; **39**: 375–382. (h) Yoshizawa K. *Bull. Chem. Soc. Jpn.* 2013; **86**: 1086–1116.
35. Carreón-Macedo J-L and Harvey JN. *J. Am. Chem. Soc.*, 2004; **126**: 5789–5797. (b) Harvey JN. *WIREs. Comput. Mol. Sci.* 2014; **4**: 1–14.



# Very fast singlet and triplet energy transfers in a tri-chromophoric porphyrin dyad aided by the truxene platform

Adam Langlois<sup>a</sup>, Hai-Jun Xu<sup>b</sup>, Paul-Ludovic Karsenti<sup>a</sup>, Claude P. Gros<sup>\*b</sup> and Pierre D. Harvey<sup>\*a</sup>

<sup>a</sup>Département de Chimie, Université de Sherbrooke, Sherbrooke, Québec J1K 2R1, Canada

<sup>b</sup>Université de Bourgogne, ICMUB (UMR 6302), 9, Avenue Alain Savary, BP 47870, 21078 Dijon Cedex, France

Dedicated to Professor Shunichi Fukuzumi on the occasion of his retirement

Received 3 November 2014

Accepted 26 December 2014

**ABSTRACT:** A trichromophoric dyad composed of an octa- $\beta$ -alkyl-palladium(II)porphyrin (donor) and two tri-*meso*-aryl-zinc(II)porphyrins (acceptors) held by a truxene spacer exhibits very fast rates for triplet energy transfers at 77 ( $k_{ET}(T_1) = 1.63 \times 10^8 \text{ s}^{-1}$ ) and 298 K ( $k_{ET}(T_1) = 3.44 \times 10^8 \text{ s}^{-1}$ ), whereas the corresponding singlet energy transfer rates,  $k_{ET}(S_1) = 3.9 \times 10^{10} \text{ s}^{-1}$  (77 K) and  $k_{ET}(S_1) = 6.0 \times 10^{10} \text{ s}^{-1}$  (298 K), are also considered fast. The interpretation for these results is that the energy transfer processes proceed *via* a through bond Dexter mechanism (*i.e.* double electron exchange) supported by comparison with literature data and evidence for a moderate MO coupling between the donor and acceptor chromophores in the frontier MOs.

**KEYWORDS:** energy transfer, MO coupling, palladium(II)porphyrin, zinc(II)porphyrin, Dexter mechanism, ultrafast fluorescence lifetime.

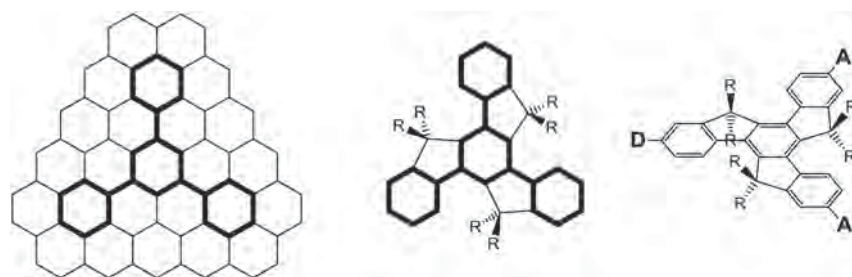
## INTRODUCTION

Graphene and graphene-oxide are 2-dimensional materials that have attracted tremendous attention due to their extraordinary electronic and optical properties, which accommodate a large potential in optoelectronic applications [1–7]. Truxene is a  $C_3$ -symmetry aromatic platform that shares a common structural feature with graphene (Fig. 1), which found potential applications in the area of solar cells [8–18] and organic light emitting diodes [19–25], mainly due to its hole transport properties [25]. On the photophysical point of view, this triangular aromatic fragment was investigated for photo-induced electron transfers, notably with  $C_{60}$

groups (truxene\*  $\rightarrow C_{60}$ ) [26, 27], and for both singlet ( $S_1$ ) and triplet ( $T_1$ ) energy transfer processes whether this planar unit is used as a chromophoric energy donor [28–38], or simply as a scaffolding for the design of dyads and triads [39–45]. One common denominator in the latter studies, notably those reported by Ziessel and his collaborators [39–42] and our group [43–45], is that the rates for energy transfer,  $k_{ET}$ , are always fast or very fast when using truxene as the spacer between the donor(s) and acceptors (Fig. 1, right). This is also true for porphyrin and BODIPY-containing assemblies (fast;  $10^9 < k_{ET} < 10^{10} \text{ s}^{-1}$ ; very fast  $k_{ET} > 10^{10} \text{ s}^{-1}$ ) [43–45], but surprisingly and to the best of our knowledge, no example for  $T_1$  energy transfer was reported so far for this rather common chromophore. This observation is rather pertinent to the extraordinary electronic conductivity of graphene (see Ref. [1] and the references therein) and to the fact that energy transfer in the  $T_1$  state is dominated (but not exclusively) by the Dexter

<sup>◇</sup>SPP full member in good standing

\*Correspondence to: Claude P. Gros, email: Claude.Gros@u-bourgogne.fr; Pierre D. Harvey, email: Pierre.Harvey@USherbrooke.ca



**Fig. 1.** Structural comparison of a segment of graphene (left) stressing on the common triangular sub-skeleton (in bold) of truxene (middle). Right: example of a view of the relative positions of the energy donor (D) and acceptors (A) in the literature multiyads built with truxene as the spacer. The *R* groups are commonly alkane chains, often used to improve the solubility

mechanism (double electron exchange) [46] over the Förster one (*i.e.* long range dipole–dipole interactions) [47]. If this is true,  $T_1$  energy transfers between two porphyrin units should be rather fast as previously observed for polypyridyl-containing coordination complexes as donors and acceptors ( $k_{ET} > 10^8 \text{ s}^{-1}$ ) [39–42]. We now report the synthesis of a dyad containing a palladium(II)-porphyrin (Fig. 1) as both  $S_1$  ( $k_{ET} > 10^{10} \text{ s}^{-1}$ ) and  $T_1$  ( $k_{ET} > 10^8 \text{ s}^{-1}$ ) donor and two zinc(II) porphyrin as acceptors (Chart 1). Both rates are found fast at 298 and 77 K.

## EXPERIMENTAL

### Materials

Unless otherwise noted, all chemicals and solvents were of analytical reagent grade and used as received. Absolute dichloromethane ( $\text{CH}_2\text{Cl}_2$ ) was obtained from Carlo Erba. Silica gel (Merck; 70–120 mm) was used for column chromatography. Analytical thin-layer chromatography was performed with Merck 60 F254 silica gel (precoated sheets, 0.2 mm thick). Reactions were monitored by thin-layer chromatography, UV-vis spectroscopy and MALDI/TOF mass spectrometry. Monocarbaldehydedibromohexabutyltruxene was prepared as previously described in the literature [43]. Borolanylporphyrin **3** was prepared following a recently reported procedure [48]. Truxene **1** was synthesized as previously reported in the literature [43].

### Synthesis

**2-(13,17-Diethyl-2,3,7,8,12,18-hexamethylporphyrin-5-yl)-7,12-dibromo-5,5',10,10',15,15'-hexabutyltruxene (2).** 2-(Zn-13,17-Diethyl-2,3,7,8,12,18-hexamethylporphyrin-5-yl)-7,12-dibromo-5,5',10,10',15,15'-hexabutyltruxene **1** (220 mg, 0.163 mmol) was dissolved in 180 mL of  $\text{CHCl}_3$ . 100 mL of 6 M HCl was added. The reaction mixture was stirred for 10 min quickly and monitored by MALDI-TOF mass. The organic layer was separated by separatory funnel and washed with saturated  $\text{NaHCO}_3$  solution, water two times.

The product was purified by column chromatography on silica gel with  $\text{CH}_2\text{Cl}_2$ ,  $\text{CH}_2\text{Cl}_2$ - $\text{CHCl}_3$ . The pure free base porphyrin **2** was obtained from recrystallization from  $\text{CHCl}_3/\text{CH}_3\text{OH}$ . Yield 193 mg, 92%.  $^1\text{H NMR}$  ( $\text{CDCl}_3$ ):  $\delta$ , ppm 10.21 (s, 2H, *meso-H*), 9.99 (s, 1H, *meso-H*), 8.73 (d, 1H,  $J = 9.0 \text{ Hz}$ , Ar-H), 8.29 (m, 3H, Ar-H), 8.07 (d, 1H,  $J = 6.0 \text{ Hz}$ , Ar-H), 7.69–7.53 (m, 4H, Ar-H), 4.10 (q, 4H, pyrro- $\text{CH}_2\text{CH}_3$ ), 3.68 (s, 6H, pyrro- $\text{CH}_3$ ), 3.56 (s, 6H, pyrro- $\text{CH}_3$ ), 3.26 (m, 2H, Truxene- $\text{CH}_2$ -), 2.97 (m, 4H, Truxene- $\text{CH}_2$ -), 2.57 (s, 6H, pyrro- $\text{CH}_3$ ), 2.20 (m, 6H,  $-\text{CH}_2$ -), 1.91 (t, 6H,  $J = 9.0 \text{ Hz}$ , pyrro- $\text{CH}_2\text{CH}_3$ ), 1.09–0.98 (m, 12H,  $-\text{CH}_2$ -), 0.85–0.56 (m, 30H,  $-\text{CH}_2\text{CH}_3$ ). HRMS (MALDI-TOF):  $m/z$  1282.6037  $[\text{M}]^+$ , 1282.5996 calcd. for  $\text{C}_{81}\text{H}_{96}\text{Br}_2\text{N}_4$ . UV-vis ( $\text{CH}_2\text{Cl}_2$ ):  $\lambda_{\text{max}}$ , nm ( $\epsilon \times 10^{-3} \text{ M}^{-1}\text{cm}^{-1}$ ) 285.0 (63.3), 301.9 (65.3), 314.0 (98.1), 404.0 (254.2), 503.0 (19.4), 537.0 (7.8), 571.0 (8.5), 625.0 (2.8), 653.9 (2.3).

**2-(Pd(II)-13,17-Diethyl-2,3,7,8,12,18-hexamethylporphyrin-5-yl)-7,12-dibromo-5,5',10,10',15,15'-hexabutyltruxene ([Pd]).** 2-(13,17-Diethyl-2,3,7,8,12,18-hexamethylporphyrin-5-yl)-7,12-dibromo-5,5',10,10',15,15'-hexabutyltruxene **2** (100 mg, 0.078 mmol) was dissolved in 40 mL of  $\text{CHCl}_3$ . Bis(benzonitrile)dichloropalladium(II)  $[\text{PdCl}_2(\text{PhCN})_2]$  (120 mg, 0.312 mmol) was added. The reaction mixture was heated to reflux overnight at room temperature. Cooled to the room temperature, the solvent was removed under reduced pressure. The residue was chromatographed on silica gel with 80% DCM-heptane. Yield 82 mg, 76%.  $^1\text{H NMR}$  ( $\text{CDCl}_3$ ):  $\delta$ , ppm 10.14 (s, 2H, *meso-H*), 10.08 (s, 1H, *meso-H*), 8.66 (d, 1H,  $J = 6.0 \text{ Hz}$ , truxene-H), 8.29 (t, 2H,  $J = 6.0 \text{ Hz}$ , truxene-H), 8.17 (m, 1H, truxene-H), 8.03 (m, 1H, truxene-H), 7.69–7.51 (m, 4H, H-phenyl), 4.37 (q, 4H, pyrro- $\text{CH}_2\text{CH}_3$ ), 3.62 (s, 6H, pyrro- $\text{CH}_3$ ), 3.51 (s, 6H, pyrro- $\text{CH}_3$ ), 3.22 (m, 2H, Truxene- $\text{CH}_2$ -), 2.98 (m, 6H, Truxene- $\text{CH}_2$ -), 2.51 (s, 6H, pyrro- $\text{CH}_3$ ), 1.92 (t, 6H,  $J = 6.0 \text{ Hz}$ , pyrro- $\text{CH}_2\text{CH}_3$ ), 1.28–0.99 (m, 12H,  $-\text{CH}_2$ -), 0.70–0.55 (m, 30H,  $-\text{CH}_2\text{CH}_3$ ), HRMS (MALDI-TOF):  $m/z$  1386.4918  $[\text{M}]^+$ , 1386.4977 calcd. for  $\text{C}_{81}\text{H}_{94}\text{BrN}_4\text{Pd}$ . UV-vis ( $\text{CH}_2\text{Cl}_2$ ):  $\lambda_{\text{max}}$ , nm ( $\epsilon \times 10^{-3} \text{ M}^{-1}\text{cm}^{-1}$ ) 285.0 (66.8), 301.9 (80.8), 314.0 (123.9), 399.0 (302.1), 514.9 (24.2), 548.0 (49.1).

**2-(Pd(II)-13,17-diethyl-2,3,7,8,12,18-hexamethylporphyrin-5-yl)-7,12-di(zinc(II) 5,15-*p*-tolyl-10-phenylporphyrin)-5,5',10,10',15,15'-hexabutyltruxene ([Pd-Zn<sub>2</sub>]).** A DMF/toluene (1/2) solution (15 mL) of a mixture of 2-(Pd-13,17-diethyl-2,3,7,8,12,18-hexamethylporphyrin-5-yl)-7,12-dibromo-5,5',10,10',15,15'-hexabutyltruxene (67.0 mg, 0.0482 mmol) [Pd], zinc(II) 5,15-*p*-tolyl-10-phenyl-20-(4',4',5',5'-tetramethyl-[1',2',3'-dioxaborolan-2'-yl])porphyrin (95.0 mg, 0.125 mmol) **3**, Cs<sub>2</sub>CO<sub>3</sub> (100.0 mg, 0.246 mmol, 5 equiv.) and Pd(PPh<sub>3</sub>)<sub>4</sub> (5.56 mg, 10% equiv., 0.00482 mmol) was degassed by freeze-pump-thaw cycles and then stirred for 40 h at 96 °C under Ar. The organic solvent was removed under reduced pressure. The residue was chromatographed on silica gel with 50% CHCl<sub>3</sub>-heptane. The pure product [Pd-Zn<sub>2</sub>] was obtained by recrystallization from CH<sub>2</sub>Cl<sub>2</sub>/CH<sub>3</sub>OH. Yield 52 mg, 44%. <sup>1</sup>H NMR (CDCl<sub>3</sub>): δ, ppm 10.16 (s, 4H, *meso*-H), 10.07 (s, 2H, *meso*-H), 9.19 (m, 4H, H-pyrro), 9.10 (m, 4H, H-pyrro), 9.03 (m, 4H, H-pyrro), 8.98 (m, 4H, H-pyrro), 8.88 (t, 3H, *J* = 9.0 Hz, truxene-H), 8.51 (m, 2H, truxene-H), 8.36–8.24 (m, 7H, H-phenyl and truxene-H), 8.18–8.08 (m, 9H, H-phenyl), 7.79 (m, 6H, H-phenyl), 7.60 (d, 8H, *J* = 6.0 Hz, H-phenyl), 4.06 (q, 4H, pyrro-CH<sub>2</sub>CH<sub>3</sub>), 3.62 (s, 6H, pyrro-CH<sub>3</sub>), 3.56 (s, 6H, pyrro-CH<sub>3</sub>), 3.49 (m, 6H, H-truxene), 2.75 (s, 12H, phenyl-CH<sub>3</sub>), 2.65 (s, 6H, pyrro-CH<sub>3</sub>), 2.49 (m, 6H, Truxene-CH<sub>2</sub>-), 1.39–1.16 (m, 24H, -CH<sub>2</sub>-), 0.90 (m, 18H, -CH<sub>3</sub>). HRMS (MALDI-TOF): *m/z* 2482.9559 [M]<sup>+</sup>, 2482.9568 calcd. for C<sub>151</sub>H<sub>157</sub>N<sub>12</sub>Zn. UV-vis (CH<sub>2</sub>Cl<sub>2</sub>): λ<sub>max</sub>, nm (ε × 10<sup>-3</sup> M<sup>-1</sup>.cm<sup>-1</sup>) 311.0 (74.6), 399.9 (257.1), 423.0 (892.9), 514.0 (24.9), 549.0 (76.0), 592.1 (15.9).

## Instruments

<sup>1</sup>H NMR spectra were recorded with a Bruker DRX-300 AVANCE transform spectrometer at the “Pôle Chimie Moléculaire (Welience, UB-Filiale)”; chemical shifts are expressed in ppm relative to chloroform. Molar extinction coefficients were measured with a Varian Cary 1 spectrophotometer (Université de Bourgogne). Mass spectra were obtained with a Bruker Daltonics Ultraflex II spectrometer in the MALDI/TOF reflectron mode using dithranol as a matrix. The measurements were made at the “Pôle Chimie Moléculaire (Welience, UB-Filiale)”. Absorption spectra were measured on a Varian Cary 300 Bio UV-vis spectrometer at 298 K and on a Hewlett-Packard 8452A diode array spectrometer with a 0.1 s integration time at 77 K (Université de Sherbrooke). Steady state fluorescence and excitation spectra were acquired on an Edinburgh Instruments FLS980 phosphorimeter equipped with single monochromators. All fluorescence spectra were corrected for instrument response. Fluorescence lifetime measurements were made with the FLS908 phosphorimeter using a 378 nm picosecond pulsed diode laser (fwhm = 78 ps) as an excitation source. Phosphorescence lifetime

measurements were acquired on the FLS980 using a microsecond flashlamp set with a 515 nm excitation. Data collection on the FLS980 system is done by time correlated single photon counting (TCSPC).

## DFT calculation procedure

All density functional theory (DFT) calculations were performed with Gaussian 09 [49] at the Université de Sherbrooke with the Mammouth supercomputer supported by Le Réseau Québécois De Calculs Hautes Performances. The DFT geometry optimisations and Time dependant DFT (TD-DFT) calculations [50–59] were carried out using the B3LYP method. A 6-31g\* basis set was used for C, H, N atoms [60–65]. VDZ (valence double z) with SBKJC effective core potentials were used for all Zn and Pd atoms [60–65]. Theoretical UV-visible absorption spectra were obtained using GaussSum [66].

## Femtosecond transient absorption spectroscopy

The fs transient spectra and decay profiles were acquired on a homemade setup with a Ti-sapphire source (Soltice, Spectra Physics). The measurements were made using the output of an OPA (OPA-800 CF, Spectra-Physics) operating at λ<sub>exc</sub> = 400, 515 or 550 nm, a pulse width of ~90 fs, rep. rate = 1 kHz, spot size ~500 μm, a white light continuum generated inside a sapphire window and a custom made dual CCD camera of 64 × 1024 pixels sensitive between 200 and 1100 nm (S7030, Spectronic Devices). The pulse energy was varied according to the samples (See report in SI). The delay line permitted to probe up to 4 ns with an accuracy of ~4 fs. The results were analyzed with the program Glotaran (<http://glotaran.org>) permitting to extract a sum of independent exponentials ( $I(\lambda, t) = C_1(\lambda) \times e^{-\frac{t}{\tau_1}} + C_2(\lambda) \times e^{-\frac{t}{\tau_2}} + \dots$ ) that fits the whole 3D transient map.

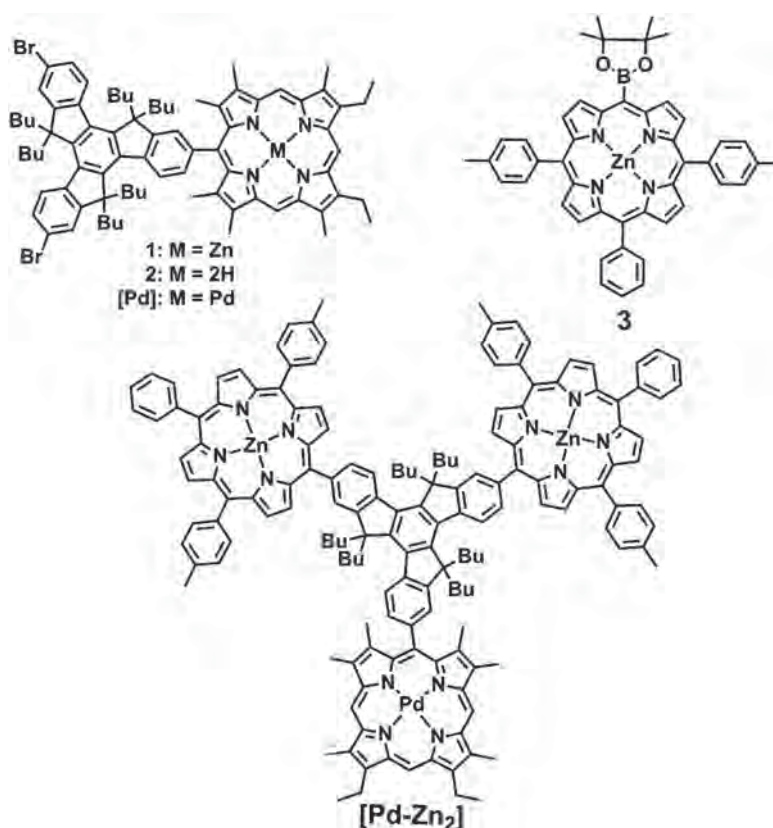
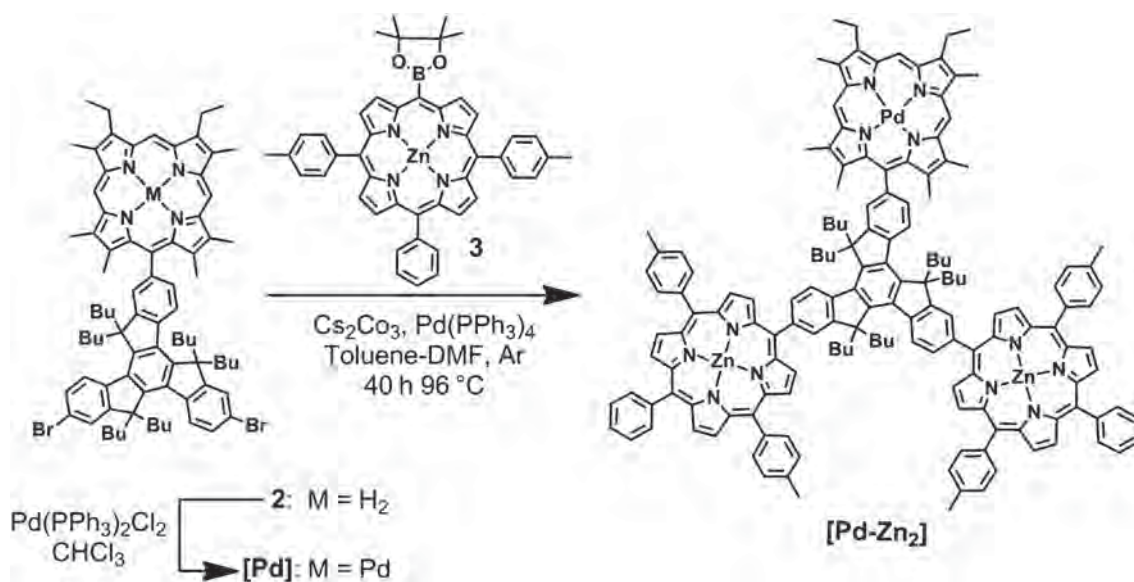
## Fast kinetic fluorescence measurements

The short components of the fluorescence decays were measured using the SHG of a Soltice (Spectra-Physics) Ti-sapphire laser (λ<sub>exc</sub> = 398 nm; fwhm = ~100 fs; pulse energy = 0.1 μJ per pulse, rep. rate = 1 kHz; spot size ~2 mm) and a Streak camera (Axis-TRS, Axis Photonique Inc.) with less than 8 ps resolution. The results were also globally analyzed with the program Glotaran (<http://glotaran.org>) permitting to extract a sum of independent exponentials ( $I(\lambda, t) = C_1(\lambda) \times e^{-\frac{t}{\tau_1}} + C_2(\lambda) \times e^{-\frac{t}{\tau_2}} + \dots$ ).

## RESULTS AND DISCUSSION

### Synthesis

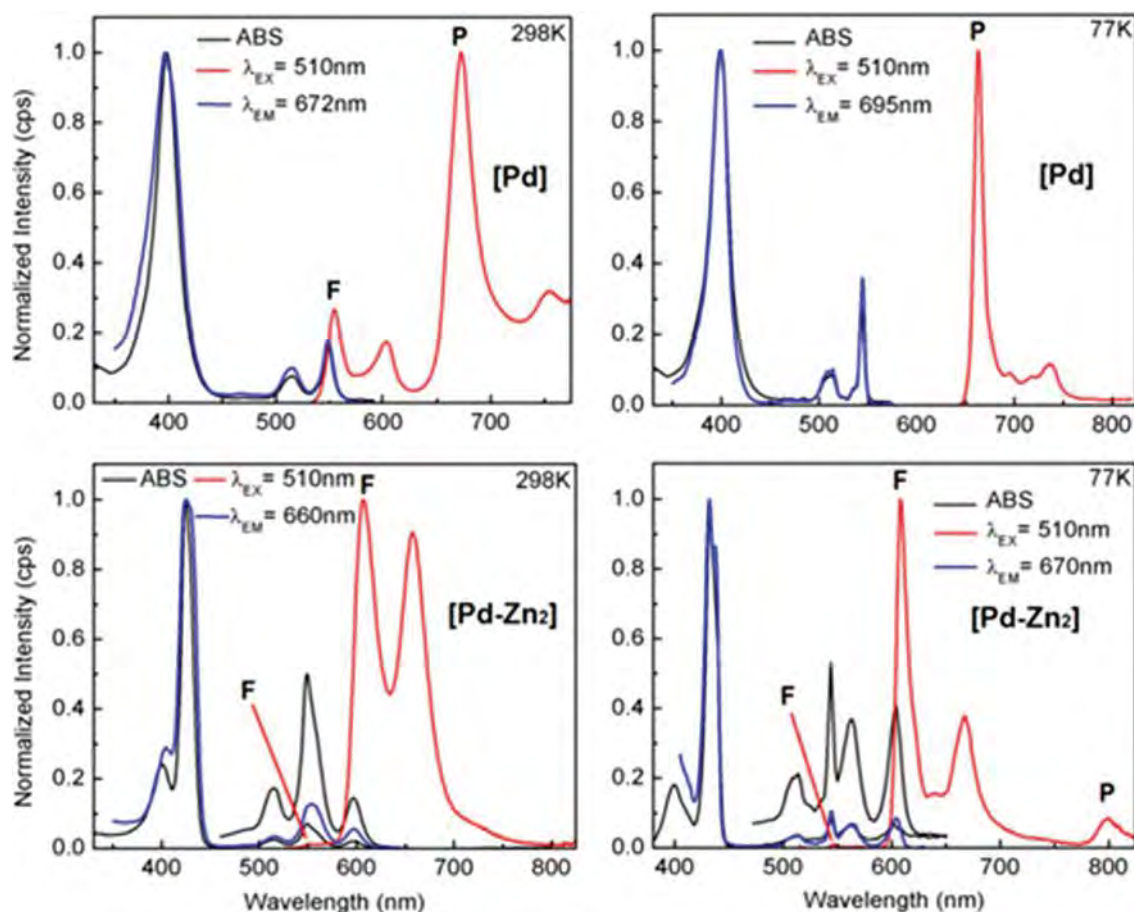
The synthetic route to access to porphyrin derivative [Pd-Zn<sub>2</sub>] is outlined in Scheme 1. Palladium complex [Pd] was firstly prepared by reacting the free base porphyrin **2** with bis(benzonitrile)dichloropalladium(II)

Chart 1. Structures of [Pd], porphyrin **3** and [Pd-Zn<sub>2</sub>]Scheme 1. Synthesis of [Pd] and [Pd-Zn<sub>2</sub>]

in refluxing chloroform overnight. The subsequent Suzuki cross-coupling reaction of [Pd] (1 equivalent) with boronated porphyrin **3** (2.6 equiv.) catalyzed by Pd(PPh<sub>3</sub>)<sub>4</sub> in a mixture of DMF-toluene and Cs<sub>2</sub>CO<sub>3</sub> as a base provided [Pd-Zn<sub>2</sub>] in 44% yield.

**Absorption and luminescence spectroscopy.** The absorption spectra (Fig. 2) of both [Pd] and [Pd-Zn<sub>2</sub>] exhibit the presence of the expected Soret bands and Q-bands (the peak positions and absorptivity data are placed in the Experimental section).





**Fig. 2.** Absorption (black) emission (red) and excitation (blue) spectra for **[Pd]** (up) and **[Pd-Zn<sub>2</sub>]** (down) in 2MeTHF at 298 and 77 K (F = fluorescence; P = phosphorescence). For **[Pd-Zn<sub>2</sub>]**, the fluorescence and phosphorescence arise from the [Zn]-chromophore, except for the very weak signal near 550 nm, which is due to [Pd]-fluorescence

The absorption spectrum of **[Pd]** shows a Soret band at approximately 400 nm with two Q-band absorptions centered at 515 and 546 nm (0–0 peak). The absorption spectrum of **[Pd-Zn<sub>2</sub>]** exhibits two Soret bands at 400 and 431 nm corresponding to the [Pd] and [Zn] chromophores, respectively. Intuitively, one would expect the appearance of four Q-bands in the absorption spectrum of **[Pd-Zn<sub>2</sub>]** due to the presence of two different metallo-porphyrins. However at 298 K, only three absorption Q-bands are depicted, centered at 515, 550 and 596 nm, presumably due to the overlap of one Q-band from the **[Pd]** moiety with one Q-band from the **[Zn]** moieties. This assumption was indeed confirmed by measuring the absorption spectrum at 77 K where four Q-bands were clearly resolved, centered at 514, 544, 560 and 603 nm (0–0 peak of the [Zn]-chromophore; Fig. 2). The role of the S<sub>1</sub> and T<sub>1</sub> energy donor was assigned based on the position of the 0–0 bands in the absorption (from the lowest energy vibronic peak), emission (fluorescence and phosphorescence; from the highest energy vibronic peaks respectively labelled by F and P in Fig. 2 for convenience) spectra. In this case, the S<sub>1</sub> and T<sub>1</sub> energy donor is the **[Pd]** moiety of **[Pd-Zn<sub>2</sub>]**.

The assignment of **[Pd]** as the donor is further confirmed when analyzing the luminescence spectra of **[Pd-Zn<sub>2</sub>]**. Upon a selective excitation of the [Pd]-moiety at 515 nm at 298 K, the emission spectrum is found to be dominated by the fluorescence of the [Zn]-chromophore exhibiting emission peaks at 606 and 656 nm. The emission spectrum also does not clearly show a low intensity shoulder in the vicinity of 670 nm for the expected phosphorescence of the [Pd]-chromophore by comparing with the **[Pd]** spectra. However, the measurements of time-resolved spectra show evidence for a long-lived component (see below) at this wavelength. The very weak fluorescence of [Pd]-unit compared to the [Zn]-fragment can also be depicted at 551 nm (see Supporting information for expanded emission spectrum). The same feature is also depicted in the emission spectrum of **[Pd-Zn<sub>2</sub>]** at 77 K. Moreover, a new emission band centered at 800 nm is also noted. This new emission band can readily be attributed to the T<sub>1</sub> emission of the [Zn]-moiety [67]. The low intensity of the fluorescence and phosphorescence of the [Pd]-unit relative to the [Zn]-fragment strongly suggests the presence of S<sub>1</sub> and T<sub>1</sub> energy transfers. The occurrence of the [Zn]-phosphorescence may

be attributed to three additive effects. First, the large decrease of the [Pd]-phosphorescence may allow a better visualization of the [Zn]-component. Second, the heavy atom effect exerted by the Pd-atom may populate the  $T_1$  state of the [Zn]-chromophore, and third, the presence of  $T_1$  energy transfer may also promote this  $T_1$  population. Evidence for efficient  $S_1$  and  $T_1$  energy transfers ( $[Pd]^* \rightarrow [Zn]$ ) is unambiguously provided by the measurements of the excitation spectra of the fluorescence and phosphorescence components of the [Zn]-unit. Indeed in all cases, the excitation spectra superpose perfectly the absorption ones (Fig. 2), which are composed of the absorption features of both residues (more excitation spectra showing the monitoring the [Zn]-fluorescence and phosphorescence are provided in the SI).

#### **Lifetime measurements and energy transfer kinetics.**

The excited state kinetics associated with the  $S_1$  and  $T_1$  energy transfers in **[Pd-Zn<sub>2</sub>]** were addressed by fluorescence and phosphorescence lifetime measurements (Table 1). All decay traces are placed in the SI.

The acceptor properties are first characterized. The measurements of the phosphorescence lifetimes,  $\tau_p$ , of the emission band at 800 nm depicted at 77 K for **[Pd-Zn<sub>2</sub>]** confirmed the identification of this emission as the [Zn]-phosphorescence (*i.e.* in the ms time scale) [67]. In this case, the emission decay at 77 K is biphasic indicating the presence of two emissive species. These entities are most likely due to the presence of two conformations or groups of conformations of the [Zn]-chromophores associated with rotations about the truxene- $C_{meso}$  single bonds. Consistent with this observation, a similar bi-exponential behavior of the [Zn]-fluorescence decay monitored at ~610 nm, exhibiting a similar component ratio, is also

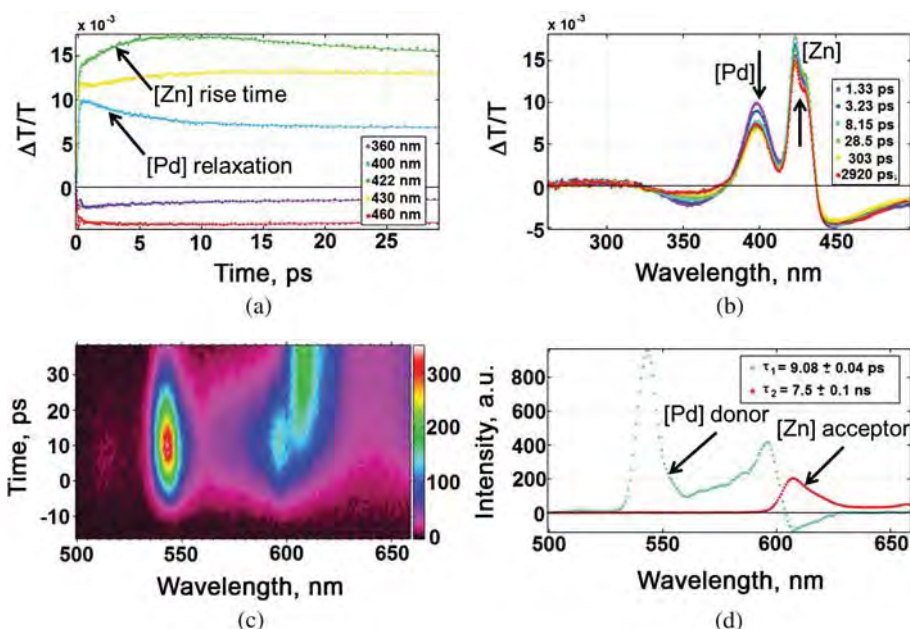
observed at 77 K (Table 1). This hypothesis is further supported by the fact that the decay trace of the **[Zn]**-fluorescence becomes mono-exponential upon warming to 298 K. In this case, an “averaging” of rotational conformations occurs. Moreover, when the fluorescence decay of [Zn]-chromophore at 77 K is analyzed by the exponential series method (ESM), a large distribution of lifetimes, spreading from 1.2 to 3.3 ns centered at 2.1 ns is obtained (see SI; note that this value is not reported in Table 1). Using DFT computations, the total energy of a structurally related dyad (dyad **21** to be described below) [44] is plotted against the dihedral angle formed by the [Zn]- and truxene-planes (placed in the SI for convenience). The graph exhibits a double minimum at 72 and 117° with inter-conversion barriers of respectively 0.82 and 1.42 kJ.mol<sup>-1</sup>. This computational result indicates that there is enough thermal activation (*i.e.* 2.49 kJ.mol<sup>-1</sup>) for facile inter-conversion at 298 K. However at 77 K, the available thermal energy is only 0.64 kJ.mol<sup>-1</sup>, so inter-conversion is not possible, especially in a glassy medium. Consequently, these computations support adequately the model for a single “average”  $\tau_F$  describing many simultaneous configurations when emitting at 298 K, and two conformations or narrow distributions of groups of conformations characterized by a double exponential fits and a large distributions of  $\tau_F$  values (from ESM analysis) at 77 K.

The donor properties are now addressed. In this case, one can exclude the possibility of various conformations as the methyl groups at the  $\beta$ -positions prevent rotations about the truxene- $C_{meso}$  bond. Due to its weak (298) or very weak (77 K) fluorescence intensity (Fig. 2) and its very short excited state lifetime, the  $\tau_F$  data of

**Table 1.** Fluorescence and phosphorescence lifetimes for **[Pd-Zn<sub>2</sub>]** and **[Pd]** in 2MeTHF<sup>a</sup>

Comp.	T, K	chrom <sup>a</sup>	$\lambda_{exc}$ , nm <sup>a</sup>	$\lambda_{em}$ , nm <sup>a</sup>	$\tau_F$ or $\tau_P$ <sup>a</sup>	$\chi^2$
<b>[PdZn<sub>2</sub>]</b>	77	[Pd]-	400	580 (F)	9.1 ± 0.1 ps <sup>b</sup>	2.9
		[Pd]-	378	700 (P)	6.13 ± 0.25 ns	1.042
		[Zn]-	378	608 (F)	1.87 ± 0.05 ns (60%) 2.84 ± 0.05 ns (40%)	1.079
		[Zn]-	545	800 (P)	16.0 ± 1.0 ms (72.5%) 33.0 ± 1.0 ms (27.5%)	1.301
	298	[Pd]-	515	— (F)	4.8 ± 0.1 ps <sup>c</sup>	1.55
		[Pd]-	378	720 (P)	2.9 ± 0.2 ns	1.056
		[Zn]-	378	610 (F)	1.84 ± 0.10 ns	1.059
		<b>[Pd]</b>	77	[Pd]-	550	580 (F)
298	[Pd]-	515	667 (P)	1.8 ± 0.3 ms	1.149	
		400	— (F)	6.7 ± 0.1 ps <sup>c</sup>	1.08	
		515	667 (P)	3.0 ± 0.7 $\mu$ s	1.648	

<sup>a</sup>Chrom. = chromophore; exc = excitation; em = monitored emission; F = fluorescence; P = phosphorescence; the values in brackets are the relative contributions. <sup>b</sup>Value obtained by ultrafast streak camera measurement. <sup>c</sup>Value obtained by ultrafast transient absorption measurement.



**Fig. 3.** Ultrafast kinetic measurements of **[Pd-Zn<sub>2</sub>]**: (a) Kinetic profiles obtained by fs transient absorption spectroscopy showing a clear energy transfer from the [Pd]- (fast decay) to the [Zn]-chromophores (rise) at 298 K. (b) Spectral profiles as a function of time after excitation of **[Pd-Zn<sub>2</sub>]** at 515 nm at 298 K. (c) Photoluminescence map of **[Pd-Zn<sub>2</sub>]** at 77 K showing the fast appearance of the donor (540 nm) and the rise of the acceptor (near 600 nm). (d) Decay-associated spectra of **[Pd-Zn<sub>2</sub>]** obtained by global analysis. The times in the inset indicate the lifetimes obtained by global analysis

the [Pd]-chromophore could not be obtained through traditional fluorescence lifetime measurements (*i.e.* TCSPC). In order to extract the fluorescence lifetimes of the [Pd]-chromophore ultrafast measurements were carried out using two analysis methods (a full report of all ultrafast measurements is provided in the SI). First, the streak camera was used in order to examine the photoluminescence of the [Pd]-chromophore as a function of time. This allowed us to confirm that the fluorescence lifetime was in fact very short ( $\sim 9.4$  ps at 298 K) and unambiguously provide evidence for singlet energy transfer. Given that, this value was very close to the IRF of the streak measurement the fluorescence lifetime was further investigated fs transient absorption measurements which yielded a 6.7 ps component that was assigned to the  $\tau_F$  of **[Pd]** at 298 K. Time resolved photoluminescence provided a 14.1 ps lifetime at 77 K for **[Pd]** but unfortunately in the absence of a cryostat, transient absorption measurements could only be performed at 298 K.

Time resolved photoluminescence measurements of **[Pd-Zn<sub>2</sub>]** yielded  $\tau_{FS}$  of 7.1 and 9.1 ps at 298 and 77 K, respectively. Once again transient absorption kinetic measurements were used in order to confirm the  $\tau_{FS}$  of the [Pd]-chromophore but more importantly to take advantage of the time resolution ( $\sim 150$  fs). These measurements yielded a component with a 4.8 ps lifetime which was assigned to the [Pd]-chromophore that has been quenched by singlet energy transfer (Table 1). The short ps time scale is consistent with a singlet excited

state lifetime for **PdTPP** as a reference. Indeed, the singlet excited state lifetime measurements of **PdTPP** yielded a value of 11 ps (298 K) extracted from transient absorption spectroscopy, which compares favorably to 13.5 ps at 298 K and to 26 ps at 77 K obtained by time-resolved fluorescence measurements (Streak camera).

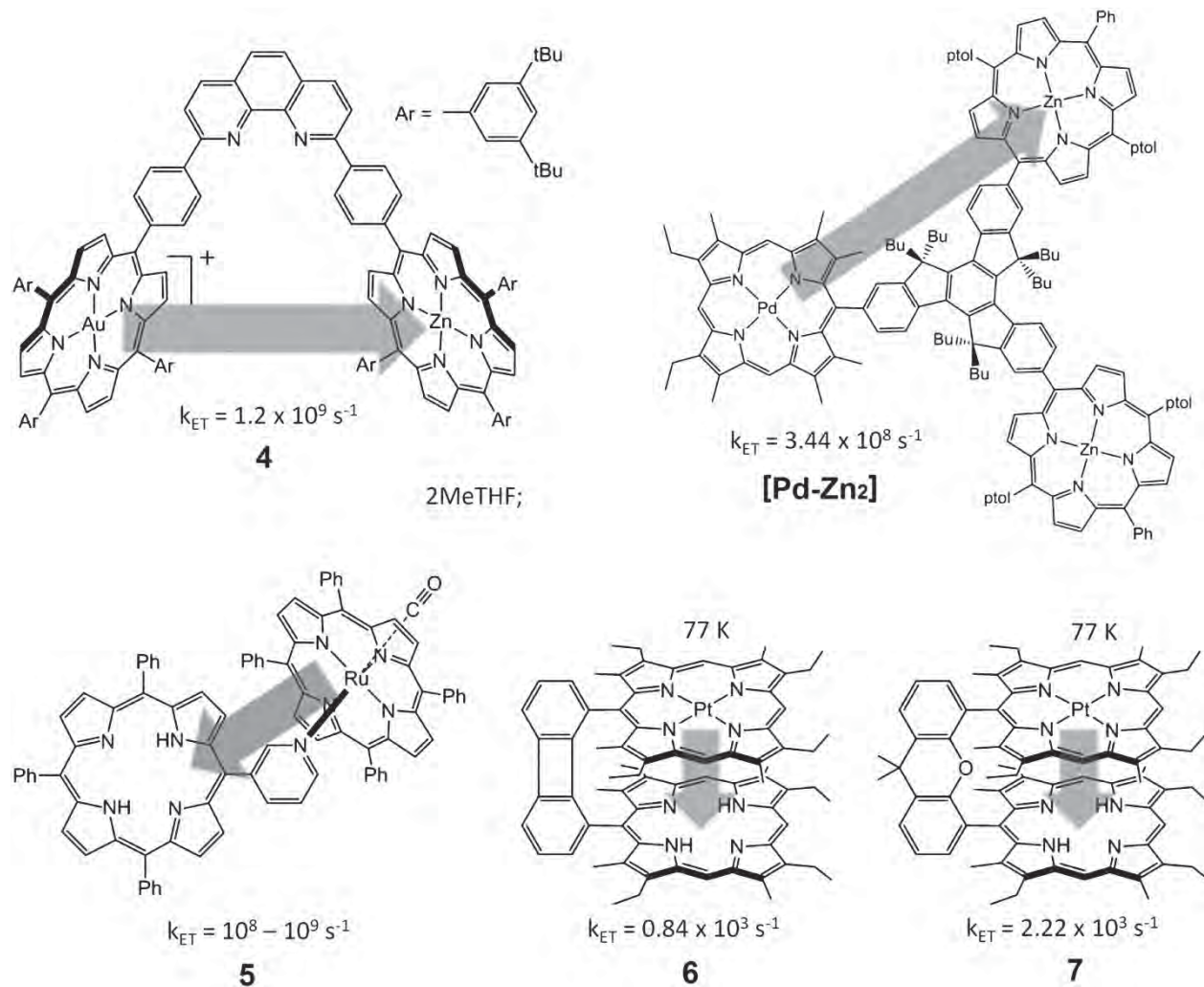
The  $\tau_p$  data of the [Pd]-moiety of **[Pd-Zn<sub>2</sub>]** were measured by monitoring the emission intensity after 700 nm. The resulting  $\tau_p$  values of 6.13 and 2.9 ns at 77 and 298 K can be attributed to the [Pd]-chromophore due to the fact that they are obviously too long to be associated with the [Zn]-unit. For the comparison molecule **[Pd]**, the  $\tau_p$  values are 1.8 ms and 3.0  $\mu$ s at 77 and 298 K, respectively. These values are in line with  $\tau_p$  values reported for Pd-porphyrin compounds [68].

Irrefutable evidence for energy transfer from the [Pd]-chromophore to the [Zn]-chromophore is provided at both 298 and 77 K by fs transient absorption spectroscopy and ultrafast photoluminescence spectroscopy respectively (Fig. 3). In Fig. 3 (frame A) the kinetic traces obtained by transient absorption at 298 K when selectively exciting the [Pd]-chromophore ( $\lambda_{probe} = 515$  nm) are shown. In this graph, one can clearly identify the rapid relaxation of the [Pd]-Soret band at 400 nm and the rise time of the [Zn]-Soret band caused by the [Pd]  $\rightarrow$  [Zn] energy transfer. A rise time can be explained as a continued population of the excited state of a chromophore after the excitation source has been shut off. This phenomenon can only occur when a chromophore is obtaining its excitation energy from an alternate source such as energy transfer.

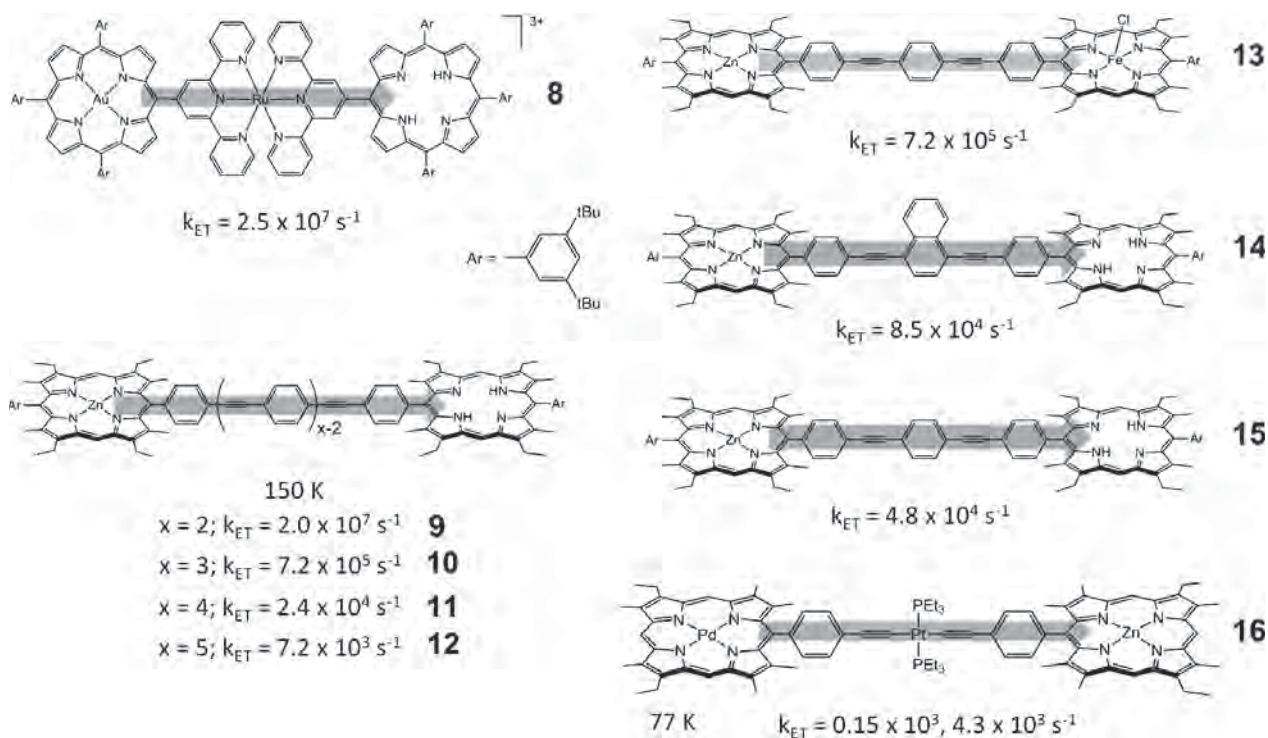
In frame B (Fig. 3), the spectral profiles of the Soret bands are shown, where again we can see the “feeding” of the [Zn]-chromophore by the [Pd]-chromophore. Transient absorption at 77 K was not possible however ultrafast photoluminescence of [Pd-Zn<sub>2</sub>] (Fig. 3, frame C) shows a clear donor–acceptor system where the [Pd]-chromophore is giving its energy to the [Zn]-chromophore (Fig. 3, frame D).

The decrease in  $\tau_p$  and  $\tau_F$  going from the monoporphyrin [Pd] to the dyad [Pd-Zn<sub>2</sub>] also illustrate the obvious efficient energy transfers. The efficiency of energy transfer,  $\text{eff}(\%) = ((1/\tau_e) - (1/\tau_e^\circ)) / (1/\tau_e)$  with  $\tau_e$  and  $\tau_e^\circ$  being the emission lifetime (fluorescence or phosphorescence) of the donor in the presence and absence of an acceptor, respectively. For [Pd-Zn<sub>2</sub>],  $\text{eff}(\%)$  for S<sub>1</sub> energy transfer is 28 and 35% at 298 and 77 K, respectively, while the  $\text{eff}(\%)$  for T<sub>1</sub> energy transfers are 99.9 and ~100% at 298 and 77 K, which is fully consistent with the rather good match between the excitation and

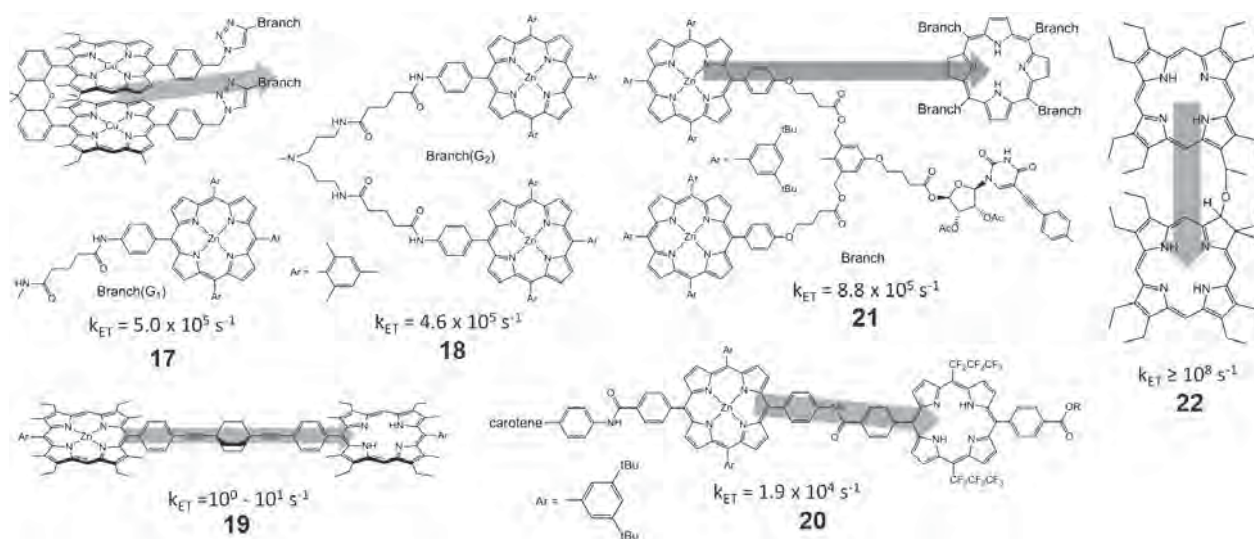
absorption spectra (Fig. 2). The much higher T<sub>1</sub> energy transfer efficiency clearly indicates that the truxene core favors the through bond triplet energy transfer process which is Dexter dominant. The rates for S<sub>1</sub> and T<sub>1</sub> energy transfers,  $k_{\text{ET}}(\text{S}_1)$  and  $k_{\text{ET}}(\text{T}_1)$ , respectively, can be obtained from  $k_{\text{ET}} = (1/\tau_e) - (1/\tau_e^\circ)$  where again “e” refers to emission for fluorescence (S<sub>1</sub>) and phosphorescence (T<sub>1</sub>). The values of  $k_{\text{ET}}(\text{S}_1)$  were determined from the ultrafast lifetime measurements. They were found to be  $3.9 \times 10^{10}$  and  $6.0 \times 10^{10} \text{ s}^{-1}$  at 77 and 298 K respectively. These values were found to compare favorably with the singlet energy transfer rates that were measured by us for similar compounds built upon a truxene spacer (see compounds **23** and **24** in Fig. 7) [43, 44] For  $k_{\text{ET}}(\text{T}_1)$ , the values are  $3.44 \times 10^8$  and  $1.6 \times 10^8 \text{ s}^{-1}$  at 77 and 298 K, respectively. These rates are indeed fast but may compare favorably with some of the fastest ever reported for bis- and multi-porphyrin dyads. Figures 4–6 summarize three series of such species [67, 69–79]. This list is



**Fig. 4.** Comparison of triplet–triplet  $k_{\text{ET}}$ 's for [Pd-Zn<sub>2</sub>], **4**, **5**, **6**, and **7** (at room temperature unless stated otherwise) [67, 69–70]. The arrows indicate the direction of the energy transfers. Dyad **7** includes a non-conjugated spacer but is placed there for comparison with dyad **6**



**Fig. 5.** Comparison of triplet–triplet  $k_{ET}$ 's for **8–16** (at room temperature unless stated otherwise) [71–75]. The arrows indicate the direction of the energy transfers. Note that dyads **10** and **15** are the same but the rates were not measured under the same experimental conditions by the authors

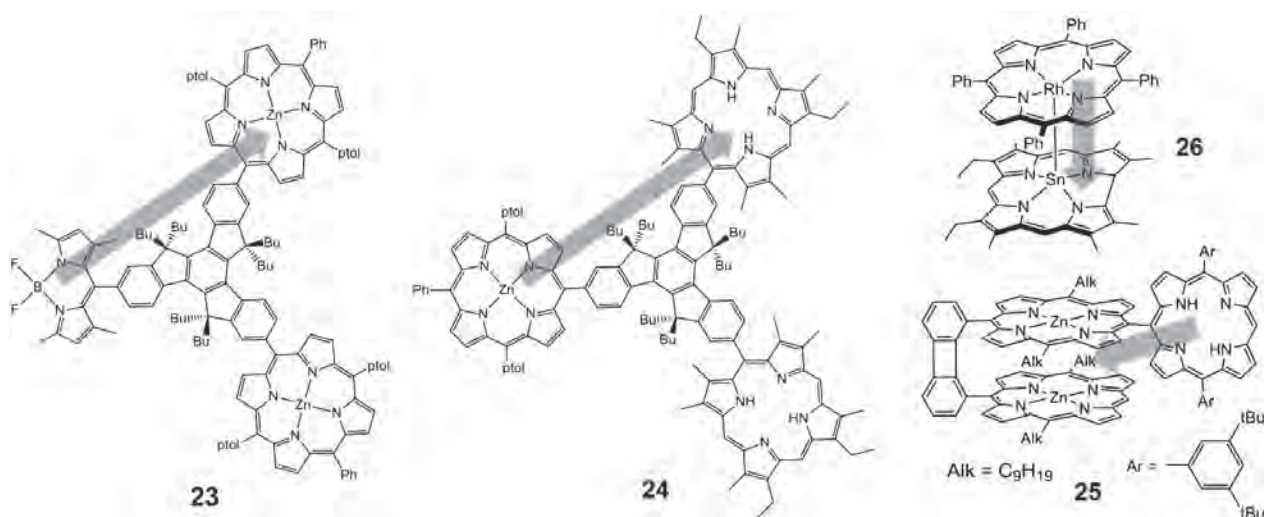


**Fig. 6.** Comparison of triplet–triplet  $k_{ET}$ 's for **17–22** [76–79]. The arrows indicate the direction of the energy transfers. Note that dyad **22** is composed of a porphyrin and a chlorin

not exhaustive but assembles representative examples for the fastest rates along with others for comparison purposed. These figures exhibit respectively three dyad categories: (1) dyads: separated by non-linear conjugated bridges, (2) by linear conjugated bridges, and (3) by non-conjugated spacers, in order to address through bond and through space processes.

[Pd–Zn<sub>2</sub>] is a dyad that belongs to the first category and its triplet–triplet  $k_{ET}$  value ranks among the fastest

ones. In an attempt to correlate structures with rates, dyads separated by a linear conjugated spacer are also compared (Fig. 5). Two features are striking. First, the extensively bent structure found in dyad **6** impacts tremendously negatively on the rate. Seemingly, this dyad behaves as there was no conjugation promoting electronic communication between the chromophores (see dyad **7**). This observation relates onto 120° relationship between the C<sub>meso</sub>(donor)–bridge–C<sub>meso</sub>(acceptor). Second, the



**Fig. 7.** Structures of dyads **23** ( $k_{ET}(S_1) = 4.5 \times 10^{10}$  (298);  $2.6 \times 10^{10} \text{ s}^{-1}$  (77 K)) [43], **24** ( $k_{ET}(S_1) = 0.71 \times 10^{10}$  (298);  $>0.96 \times 10^{10} \text{ s}^{-1}$  (77 K)) [44], **25** ( $k_{ET}(S_1) = 20 \times 10^{10} \text{ s}^{-1}$  (298 K)) [87], and **26** ( $k_{ET}(T_1) \sim 3.4 \times 10^8 \text{ s}^{-1}$  (77 K)) [88]. The arrows indicate the direction of the energy transfer

**Table 2.** Energy transfer kinetic data for [Pd-Zn<sub>2</sub>] at 298 and 77 K (D = donor = [Pd]-unit)

	298 K $\tau_D, \text{s}$	$\tau_D^0, \text{s}$	$k_{ET}, \text{s}^{-1}$	77 K $\tau_D, \text{s}$	$\tau_D^0, \text{s}$	$k_{ET}, \text{s}^{-1}$
$k_{ET}(S_1)$	$4.8 \times 10^{-12}$	$6.7 \times 10^{-12}$	$6.0 \times 10^{10}$	$9.1 \times 10^{-12}$	$1.41 \times 10^{-11}$	$3.9 \times 10^{10}$
$k_{ET}(T_1)$	$2.90 \times 10^{-9}$	$3.00 \times 10^{-6}$	$3.44 \times 10^8$	$6.13 \times 10^{-9}$	$1.80 \times 10^{-3}$	$1.63 \times 10^8$

use of a metallic center in the bridge also reduces  $k_{ET}$ . This effect (by  $\sim 2$  orders of magnitude) is obvious when comparing dyad **10** (also identical to **14** but measured under different conditions) with **16** (replacement of a  $\text{C}_6\text{H}_4$  group by *trans*-Pt( $\text{PEt}_3$ )<sub>2</sub>). However, increasing the number of  $\pi$ -conjugation in the bridge such a dyad **15** vs. **14** also increases the rate (almost double). It seems that truxene may fall into this category. Moreover, the decrease of  $k_{ET}$  vs. the distance is well illustrated by dyads **9–12**. Because through space processes are also possible, Figure 6 compares some donor–acceptor system held together by a chain that does not promote conjugation.

There is no surprise to note that the  $k_{ET}$ 's for this series are significantly slower than that for the conjugated bridge. The  $k_{ET}$  value of dyad **19** strongly suggests that almost no triplet–triplet energy transfer should take place in non-conjugated system. Moreover, it has been shown that through space energy transfer operating *via* a Dexter mechanism (double electron transfer) should operate in a cofacial geometry with an inter-planar distance of  $<5 \text{ \AA}$  [67, 80]. Because of the chain flexibility of the spacer, folding is often possible and may explain the faster rate [81], notably for dyad **22**. These data strongly indicate that the fast rates reported for [Pd-Zn<sub>2</sub>] is not likely due to a through space process, but rather a through bond. This conclusion corroborates that previously made

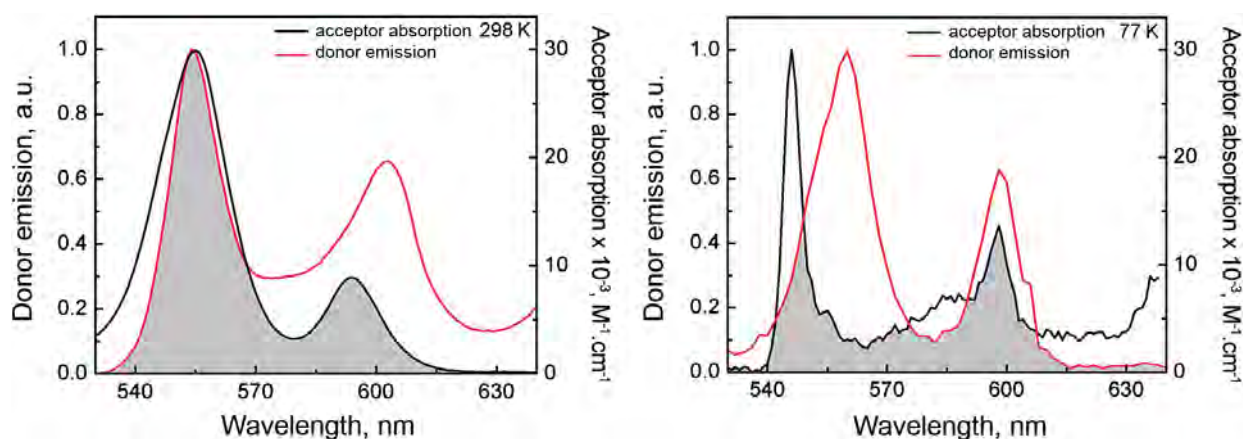
for the related truxene/porphyrin-containing dyad **23** concerning the singlet–singlet energy transfer [43]. The singlet–singlet energy transfer rate,  $k_{ET}(S_1) = 3.9 \times 10^{10} \text{ s}^{-1}$  at 77 and  $6.0 \times 10^{10} \text{ s}^{-1}$  298 K are consistent with those reported for dyads **23** and **24** (Fig. 7) [43, 44]. The kinetic parameters for the reported energy transfers are summarized in Table 2.

**Analysis of the energy transfer kinetics.** Most research groups uses the Förster (dipole–dipole interactions) and Dexter (double electron transfer) theories to provide an interpretation of their energy transfer processes. Basically, the rates (in  $\text{s}^{-1}$ ) are described according these theories are given in Equations 1 and 2:

$$k_{\text{Förster}} \cong 8.785 \times 10^{-25} \cdot \left( \frac{k_F^{\circ}(D)\kappa^2}{r^6 n^4} \right) \cdot J \quad (1)$$

$$k_{\text{Dexter}} = K \cdot J \cdot e^{\left(\frac{-2r}{L}\right)} \quad (2)$$

where  $k_F^{\circ}(D)$  is the radiative rate constant of the donor in the absence of an acceptor,  $\kappa^2$  is an orientation factor (fully described in the SI),  $r$  is the donor–acceptor center-to-center separation,  $n$  is the refractive index,  $K$  is a pre-exponential factor,  $L$  is the van der Waals radii of the donor chromophore and  $J$  is an overlap integral described below and is a key parameter for both processes.



**Fig. 8.** Comparison of the normalized fluorescence spectrum and absorption spectrum of ZnTPP of [Pd] at 298 and 77 K. The grey areas represent the  $J$ -integrals

Based on the shorter  $\tau_f$  datum for [Pd-Zn<sub>2</sub>] at 298 K (excluding the uncertainties) in comparison with that at 77 K, the corresponding  $k_{ET}(S_1)$  (298 K) is  $> k_{ET}(S_1)$  (77 K). To address this difference in energy transfer rates, the  $J$ -integral was calculated using a method previously described by us [82]. Noteworthy, this parameter operates in both the Förster and Dexter mechanism (more detail below). This method applies Equation 3 where  $F_D^*$  is the emission spectrum of the donor (here the [Pd]-chromophore) for which the area under the curve has been normalized to unity,  $\epsilon_A$  is the absorption spectrum of the acceptor in its absorbivity (here the [Zn]-chromophore), and  $\lambda$  is the wavelength (in nm). For a qualitative analysis, ZnTPP, tetra-(*meso*-phenyl)-zinc(II) porphyrin, was used for this analysis (Fig. 8).

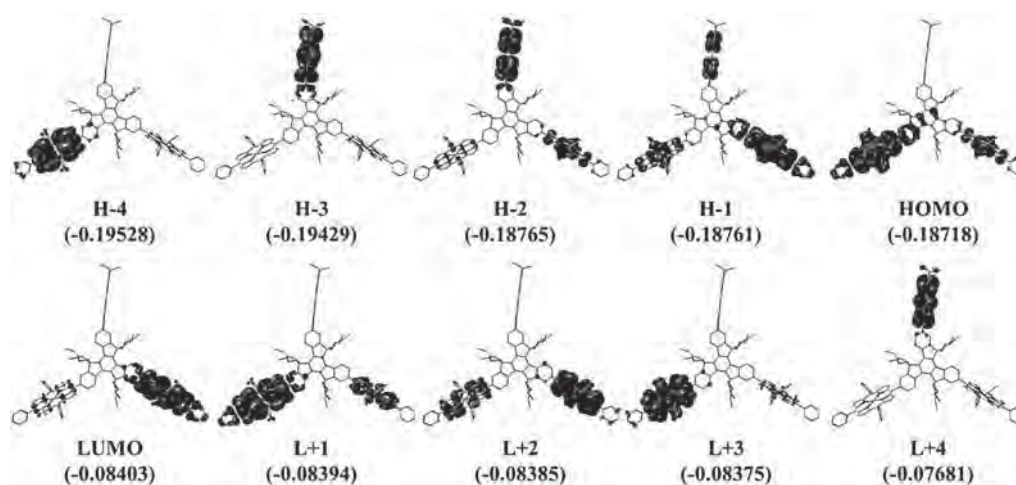
$$J(M^{-1}cm^{-1}nm^{-1}) = \int_0^{\infty} F_D(\lambda)\epsilon_A(\lambda)\lambda^4 d\lambda \quad (3)$$

$$\int_0^{\infty} F_D^*(\lambda)d\lambda = \int_0^{\infty} F_D^*(\lambda)\epsilon_A(\lambda)\lambda^4 d\lambda$$

In these cases, the calculated values of the  $J$ -integral are  $1.22 \times 10^{15} M^{-1} \cdot cm^{-1} \cdot nm^4$  at 298 K and  $9.94 \times 10^{14} M^{-1} \cdot cm^{-1} \cdot nm^4$  at 77 K. Noteworthy, there is approximately a 25% increase when the temperature is raised from 77 to 298 K. This observation is consistent with the experimental trend:  $k_{ET}(S_1)$  (298 K) must be  $> k_{ET}(S_1)$  (77 K). It should also be noted that the calculation of the  $J$ -integral indicates that there should not be a large difference between the singlet energy transfer rates as we change from 77 to 298 K (*i.e.* both rates should be in the same order of magnitude). This calculation supports the calculated singlet energy transfer rates which show a  $\sim 53\%$  increase between 77 and 298 K. The discrepancies between the  $J$ -integral prediction and the measured rates are most likely caused by the large level of unavoidable noise in the 77 K spectral measurements that are used to calculate the  $J$ -integral.

**MO couplings vs. rates for energy transfers.** Other groups [72, 83, 84] and one of us [85–87] pointed out that fast energy transfer rates are often associated with large MO couplings between the donor and acceptor, which is notably obvious when examining the frontier MOs. For [Pd-Zn<sub>2</sub>], the  $k_{ET}$ -s suggest fast rates, but faster rates exist such as dyads **4** and **25** [69, 87]. Consequently, MO couplings is also expected, but in a moderate manner. This point is addressed by DFT and TDDFT computations. The MO representations of the frontier MOs for [Pd-Zn<sub>2</sub>] (Fig. 9) exhibit obvious coupling between the donor and acceptor, notably for HOMO-1 and HOMO-2. Moreover, MO coupling between the two acceptors is also computed (HOMO, HOMO-1, LUMO+1, LUMO+2). The atomic contributions for each fragment of the dyads for each frontier MOs are provided in Table 3. The HOMO-1, HOMO, LUMO and LUMO+1-3 are located on the [Zn]-chromophores. Their small energy gaps are consistent with their role as acceptors. Conversely, the HOMO-2,3 and LUMO-4,5 (LUMO-5 not shown) exhibit major atomic contributions of the [Pd]-chromophore, hence also confirming the energy donor assignment. TDDFT calculations (Table 4) confirm that the lowest energy electronic transitions are centered on the [Zn]-chromophores, and then at higher energy on the [Pd]-one. The computed energy gap between the two lowest energy transitions of the [Zn]- and [Pd]-chromophores ( $\sim 40$  nm) corroborates reasonably well the experimental value ( $\sim 58$  nm).

The MO coupling is evident from the non-nil atomic contributions from other residues, which may vary from 0.0 to 10.0%. Interestingly, the truxene platform also contributes to the MO for all frontier MOs. These computations indicate that an energy transfer operating *via* the Dexter mechanism is facilitated for [Pd-Zn<sub>2</sub>] in comparison with a dyad system composed of an unconjugated bridge. However, the level of coupling is lower than other systems, and so as the relative level of



**Fig. 9.** MO representations of the frontier MOs for  $[\text{Pd-Zn}_2]$  (optimized geometries; DFT; B3LYP). H = HOMO, L = LUMO. The  $[\text{Pd}]$ -chromophore placed at the top. The MO energies are in a.u. The donor–acceptors center-to-center distances are 18.19 and 18.28 Å

**Table 3.** Percent contributions of the frontier MO's as a function of molecular fragment

Mol. frag.	H-4	H-3	H-2	H-1	HOMO	LUMO	L+1	L+2	L+3	L+4
E, eV	-5.3	-5.3	-5.1	-5.1	-5.1	-2.3	-2.3	-2.3	-2.3	-2.1
truxene	1.4	4.2	0.7	4.6	6.6	4.6	4.6	1.9	1.8	0.5
$[\text{Pd}]$	0.0	<b>92.9</b>	<b>83.7</b>	10.0	0.1	0.0	0.0	0.0	0.0	<b>91.6</b>
$[\text{Zn}_1]$	<b>94.4</b>	0.0	1.5	7.2	<b>71.5</b>	2.0	<b>79.1</b>	7.5	<b>86.8</b>	0.0
$[\text{Zn}_2]$	0.6	0.0	8.4	<b>65.4</b>	8.2	<b>85.3</b>	8.1	<b>80.7</b>	1.2	0.0
alkyl/aryl	3.6	2.9	5.6	12.8	13.6	8.1	8.2	10.0	10.2	7.9

**Table 4.** The six computed lowest energy electronic transitions for  $[\text{Pd-Zn}_2]$  and their major contributions ( $f$  = oscillator strength). The 100 first electronic transitions are placed in the SI

No.	$\lambda$ , nm	$f$	Major contributions, %
1	542.4	0.0739	H-4→L+3 (32), HOMO→L+1 (50)
2	541.7	0.0424	H-4→L+1 (31), HOMO→L+3 (55)
3	541.5	0.0457	H-5→L+2 (28), H-1→LUMO (42)
4	541.0	0.0442	H-5→LUMO (32), H-1→L+2 (41)
5	504.8	0.0576	H-3→L+5 (33), H-2→L+4 (59)
6	504.1	0.0355	H-3→L+4 (37), H-2→L+5 (55)

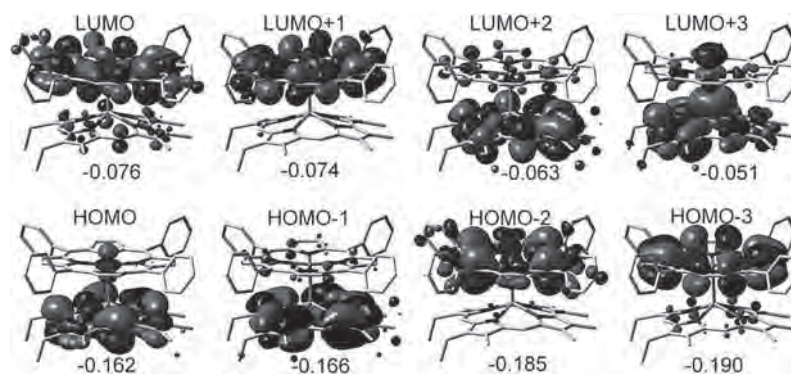
atomic contribution mixing is higher. This is particularly true for dyad **25** ( $k_{\text{ET}}(\text{S}_1) = 20 \times 10^{10} \text{ s}^{-1}$  (298 K)) [87].

Moreover, in order to further support the relationship between MO coupling and the  $k_{\text{ET}}(\text{T}_1)$  values, we qualitatively examined the MO representations of a M–M' bonded dyad (see dyad **26** in Fig. 7) that was investigated several years ago [88]. The conclusion was that depending on how the rate was calculated,  $k_{\text{ET}}(\text{T}_1)$  must range between  $5.0 \times 10^6$  and  $3.3 \times 10^8 \text{ s}^{-1}$ . Because of the reliability of the model complex used, the latter

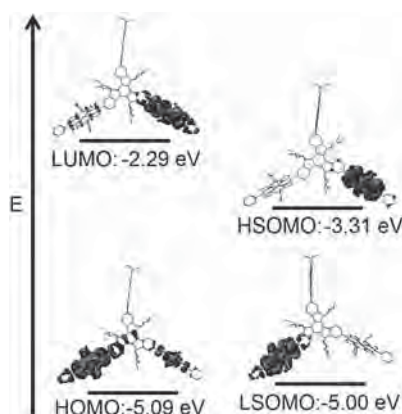
value is the most reliable. This is also considered very fast for an energy transfer occurring at the triplet state and therefore MO coupling must be present. Indeed, this is exactly as it is observed (Fig. 10; unpublished). This conclusion is interesting since the presence of metal atoms in the bridge (here the bridge is the Rh–Sn bond) has the tendency of decreasing  $k_{\text{ET}}$ .

*Nature of the triplet state.* DFT computations allow for the calculations of the optimized geometry in the lowest energy triplet state. The representations of the





**Fig. 10.** MO representations of the frontier MOs for dyad **25** shown in Fig. 5 [88]. The energies (under the MOs) are in a.u. (unpublished)



**Fig. 11.** MO representations of the HSOMO and LSOMO of  $[\text{Pd-Zn}_2]$

highest and lowest semi-occupied MO (HSOMO and LSOMO, respectively) compare favorably to that of the HOMO and LUMO (Fig. 11) indicating that the nature of the lowest energy triplet state is not altered in a major way with respect to the corresponding singlet state. The slight difference that can be noticed is the decrease in computed minor atomic contributions that account for the MO coupling.

## CONCLUSION

This new truxene-bridge multi-chromophoric dyad exhibits a very fast  $k_{\text{ET}}(T_1)$  value (in the order of  $10^8 \text{ s}^{-1}$ ). This time scale places this type of dyad in a group of very fast assemblies (see **4**, **5** and **26** for instance) where  $k_{\text{ET}}(T_1)$  is placed within  $10^8$  and  $10^9 \text{ s}^{-1}$ , regardless of the donor–acceptor center-to-center distances. Based on comparisons with literature data establishing a structure–property relationship in donor–bridge–acceptor systems, and on DFT and TDDFT computations, the dominant mechanism for this triplet energy transfer process is found to be Dexter. With a long donor–acceptor center-to-center

separation of  $\sim 18.2 \text{ \AA}$ , and an eff(%) of nearly 100% at both temperatures, the truxene bridge is unquestionably an excellent spacer for a double electron transfer (*i.e.* Dexter) where moderate MO couplings is also computed for  $[\text{Pd-Zn}_2]$ . This triangular structure is reminiscent of a sub-structure of the 2D lamellar structure of graphene, for which exceptional electronic properties, including conductivity, have been reported. The design of photonic devices, although still in its infancy, should be expanding in the near future.

## Acknowledgements

This research was supported by the Natural Sciences and Engineering Research Council of Canada (NSERC). AL also thanks NSERC for a graduate scholarship.

## Supporting information

Figures S1–S23 and Tables S1–S2 are given in the supplementary material. This material is available free of charge *via* the Internet at <http://www.worldscinet.com/jpp/jpp.shtml>.

## REFERENCES

1. Yazyev OV and Chen YP. *Nature Nanotechnology*. 2014; **9**: 755–767.
2. Muellen K. *ACS Nano*. 2014; **8**: 6531–6541.
3. Eigler S and Hirsch A. *Angew. Chem., Int. Ed.* 2014; **53**: 7720–7738.
4. Cummings AW, Duong DL, Nguyen VL, Tuan DV, Kotakoski J, Barrios Vargas JE, Lee YH and Roche S. *Adv. Mat.* 2014; **26**: 5079–5094.
5. Tsukagoshi K, Li S-L, Miyazaki H, Aparecido-Ferreira A and Nakaharai S. *J. Phys. D: App. Phys.* 2014; **47**: 094003/1-094003/17. DOI: 10.1088/0022-3727/47/9/094003 *In press*.
6. Otsuji T, Popov V, Ryzhii V, Li J, Niu L, Zheng Z and Yan F. *Adv. Mat.* 2014; **26**: 5239–5273.
7. Sun Z and Chang H. *ACS Nano*. 2014; **8**: 4133–4156.

8. Wang Z, Wang H, Liang M, Tan Y, Cheng F, Sun Z and Xue S. *ACS App. Mat. & Inter.* 2014; **6**: 5768–5778.
9. Wang Z, Liang M, Wang H, Wang P, Cheng F, Sun Z and Song X. *ChemSusChem.* 2014; **7**: 795–803.
10. Hao Y, Liang M, Wang Z, Cheng F, Wang C, Sun Z and Xue S. *Tetrahedron.* 2013; **69**: 10573–10580.
11. Hao Y, Liang M, Wang Z, Wang L, Sun Y, Sun Z and Xue S. *Phys. Chem. Chem. Phys.* 2013; **15**: 15441–15449.
12. Yang X, Zheng Q, Tang C, Cai D, Chen S-C and Ma Y. *Dyes Pigments.* 2013; **99**: 366–373.
13. Shi Y, Liang M, Wang L, Han H, You L, Sun Z and Xue S. *ACS App. Mat. Inter.* 2013; **5**: 144–153.
14. Tsuji H, Ota Y, Furukawa S, Mitsui C, Sato Y and Nakamura E. *Asian J. Org. Chem.* 2012; **1**: 34–37.
15. Zong X, Liang M, Chen T, Jia J, Wang L, Sun Z and Xue S. *ChemComm.* 2012; **48**: 6645–6647.
16. Zong X, Liang M, Fan C, Tang K, Li G, Sun Z and Xue S. *J. Phys. Chem. C.* 2012; **116**: 11241–11250.
17. Liang M, Lu M, Wang Q-L, Chen W-Y, Han H-Y, Sun Z and Xue S. *J. Power Sources.* 2011; **196**: 1657–1664.
18. Wang J-L, He Z, Wu H, Cui H, Li Y, Gong Q, Cao Y and Pei J. *Chem. Asian J.* 2010; **5**: 1455–1465.
19. Choi KM, Kim K-Y, Kim T-D, Das RR, Choi BK, Park JJ, Kim J-M and Lee K-S. *J. Nanosci. Nanotech.* 2010; **10**: 6916–6919.
20. Huang J, Xu B, Su J-H, Chen CH and Tian H. *Tetrahedron.* 2010; **66**: 7577–7582.
21. Wu Y, Hao X, Wu J, Jin J and Ba X. *Macromolecules.* 2010; **43**: 731–738.
22. Wu M, Gong Z, Kuehne AJC, Kanibolotsky AL, Chen YJ, Perepichka IF, MacKintosh AR, Gu E, Skabara PJ, Pethrick RA and Dawson MD. *Optics Express.* 2009; **17**: 16436–16443.
23. Yang Z, Xu B, He J, Xue L, Guo Q, Xia H and Tian W. *Org. Electronics.* 2009; **10**: 954–959.
24. Kimura M, Kuwano S, Sawaki Y, Fujikawa H, Noda K, Taga Y and Takagi K. *J. Mat. Chem.* 2005; **15**: 2393–2398.
25. Cao X-Y, Liu X-H, Zhou X-H, Zhang Y, Jiang Y, Cao Y, Cui Y-X and Pei J. *J. Org. Chem.* 2004; **69**: 6050–6058.
26. Sanchez L, Martin N, Gonzalez-Cantalapiedra E, Echavarren AM, Rahman GMA and Guldi DM. *Org. Letters.* 2006; **8**: 2451–2454.
27. Wang J-L, Duan X-F, Jiang B, Gan L-B, Pei J, He C and Li Y-F. *J. Org. Chem.* 2006; **71**: 4400–4410.
28. Pina J, Seixas de Melo JS, Koenen J-M, Jung S and Scherf U. *J. Phys. Chem. C.* 2013; **117**: 3718–3728.
29. Du B, Fortin D and Harvey PD. *J. Inorg. Organomet. Polym. Mat.* 2013; **23**: 81–88.
30. Montgomery NA, Hedley GJ, Ruseckas A, Denis J-C, Schumacher S, Kanibolotsky AL, Skabara PJ, Galbraith I, Turnbull GA and Samuel IDW. *Phys. Chem. Chem. Phys.* 2012; **14**: 9176–9184.
31. Du B and Harvey PD. *ChemCommun.* 2012; **48**: 2671–2673.
32. Koenen J-M, Jung S, Patra A, Helfer A and Scherf U. *Adv. Mat.* 2012; **24**: 681–686.
33. Du B, Fortin D and Harvey PD. *Inorg. Chem.* 2011; **50**: 11493–11505.
34. Du B, Yuan S-C and Pei J. *Aust. J. Chem.* 2011; **64**: 1209–1218.
35. Wang J-Y, Han J-M, Yan J, Ma Y and Pei J. *Chem. Eur. J.* 2009; **15**: 3585–3594.
36. Wang J-L, Yan J, Tang Z-M, Xiao Q, Ma Y and Pei J. *J. Am. Chem. Soc.* 2008; **130**: 9952–9962.
37. Wang J-L, Luo J, Liu L-H, Zhou Q-F, Ma Y and Pei J. *Org. Lett.* 2006; **8**: 2281–2284.
38. Duan X-F, Wang J-L and Pei J. *Org. Lett.* 2005; **7**: 4071–4074.
39. Diring S, Ziessel R, Barigelletti F, Barbieri A and Ventura B. *Chemistry.* 2010; **16**: 9226–9236.
40. Ventura B, Barbieri A, Barigelletti F, Diring S and Ziessel R. *Inorg. Chem.* 2010; **49**: 8333–8346.
41. Diring S, Puntoriero F, Nastasi F, Campagna S and Ziessel R. *J. Am. Chem. Soc.* 2009; **131**: 6108–6110.
42. Diring S, Ventura B, Barbieri A and Ziessel R. *Dalton Trans.* 2012; **41**: 13090–13096.
43. Xu H-J, Bonnot A, Karsenti P-L, Langlois A, Abdelhameed M, Barbe J-M, Gros CP and Harvey PD. *Dalton Trans.* 2014; **43**: 8219–8229.
44. Langlois A, Xu H-J, Brizet B, Denat F, Barbe J-M, Gros CP and Harvey PD. *J. Porphyrins Phthalocyanines.* 2014; **18**: 94–106.
45. Xu H-J, Du B, Gros CP, Richard P, Barbe J-M and Harvey PD. *J. Porphyrins Phthalocyanines.* 2013; **17**: 44–55.
46. Dexter DL. *J. Chem. Phys.* 1953; **21**: 836–850.
47. Förster T. *Ann. Phys.* 1948; **2**: 55–75.
48. Habermeyer B, Takai A, Gros CP, El Ojaimi M, Barbe J-M and Fukuzumi S. *Chem. Eur. J.* 2011; **17**: 10670–10681.
49. Frisch MJ. Wallingford CT, 2004.
50. Bauernschmitt R and Ahlrichs R. *Chem. Phys. Lett.* 1996; **256**: 454–464.
51. Becke AD. *J. Chem. Phys.* 1993; **98**: 5648–5652.
52. Casida ME, Jamorski C, Casida KC and Salahub DR. *J. Chem. Phys.* 1998; **108**: 4439–4449.
53. Hohenberg P and Kohn W. *J. Phys. Rev.* 1964; **136**: B864–B871.
54. Hohenberg P and Kohn W. *J. Phys. Rev.* 1965; **140**: A1133–A1138.
55. Lee C, Yang W and Parr RG. *Phys. Rev. B* 1988; **37**: 785–789.
56. Michlich B, Savin A, Stoll H and Preuss H. *Chem. Phys. Lett.* 1989; **157**: 200–206.
57. Parr RG and Yang W. *Density-Functional Theory of Atoms and Molecules*, Oxford Univ. Press: Oxford, 1989.
58. Salahub DR and Zerner MC. *The Challenge of d and f Electrons*; Amer. Chem. Soc.: Washington, D.C., 1989.

59. Stratmann RE, Scuseria GE and Frisch MJ. *J. Chem. Phys.* 1998; **109**: 8218–8224.
60. Binkley JS, Pople JA and Hehre WJ. *J. Am. Chem. Soc.* 1980; **102**: 939–947.
61. Dobbs KD and Hehre WJ. *J. Comput. Chem.* 1986; **7**: 359–378.
62. Dobbs KD and Hehre WJ. *J. Comput. Chem.* 1987; **8**: 861–879.
63. Dobbs KD and Hehre WJ. *J. Comput. Chem.* 1987; **8**: 880–893.
64. Gordon MS, Binkley JS, Pople JA, Pietro WJ and Hehre WJ. *J. Am. Chem. Soc.* 1982; **104**: 2797–2803.
65. Pietro WJ, Francl MM, Hehre WJ, Defrees DJ, Pople JA and Binkley JS. *J. Am. Chem. Soc.* 1982; **104**: 5039–5048.
66. O'Boyle NM, Tenderholt AL and Langner KM. *J. Comp. Chem.* 2008; **29**: 839–845.
67. Faure S, Stern C, Espinosa E, Douville J, Guillard R and Harvey PD. *Chem. Eur. J.* 2005; **11**: 3469–3481.
68. Bolze F, Gros CP, Harvey PD and Guillard R. *J. Porphyrins Phthalocyanines.* 2001; **5**: 569–574.
69. Brun AM, Harriman A, Heitz V and Sauvage J-P. *J. Am. Chem. Soc.* 1991; **113**: 8657–8663.
70. Prodi A, Indelli MT, Kleverlaan CJ, Scandola F, Alessio E, Gianferrara T and Marzilli LG. *Chem. Eur. J.* 1999; **5**: 2668–2679.
71. Flamigni L, Barigelletti F, Armaroli N, Ventura B, Collin J-P, Sauvage J-P and Garth Williams JA. *Inorg. Chem.* 1999; **38**: 661–667.
72. Eng MP, Ljungdahl T, Mrtensson J and Albinsson B. *J. Phys. Chem. B.* 2006; **110**: 6438–6491.
73. Zhang K, Wang Z, Wang F, Zhu B, Gu Y and Guo L. *Acta. Optica Sinica.* 2008; **28**: 320–325.
74. Andreasson J, Kyrchenko A, Martensson J and Albinsson B. *Photochem. Photobiol. Sci.* 2002; **1**: 111–119.
75. Bellows D, Aly SM, Gros CP, El Ojaimi M, Barbe J-M, Guillard R and Harvey PD. *Inorg. Chem.* 2009; **48**: 7613–7629.
76. Bregier F, Aly SM, Gros CP, Barbe J-M, Rousselin Y and Harvey PD. *Chem. Eur. J.* 2011; **17**: 14643–14662.
77. Palacios RE, Kodis G, Gould SL, de la Garza L, Brune A, Gust D, Moore TA and Moore AL. *ChemPhysChem.* 2005; **6**: 2359–2370.
78. Flamigni L, Talarico AM, Ventura B, Sooambar C and Solladie N. *Eur. J. Inorg. Chem.* 2006; **11**: 2155–2165.
79. Knyukshto VN, Zen'kevich EI, Kuz'mitskii VA, Gael' VI, Shul'ga AM, Levinson EG and Mironov AF. *J. Appl. Spectrosc.* 1998; **65**: 75–83.
80. Faure S, Stern C, Guillard R and Harvey PD. *J. Am. Chem. Soc.* 2004; **126**: 1253–1261.
81. Brizet B, Desbois N, Bonnot A, Langlois A, Dubois A, Barbe J-M, Gros CP, Goze C, Denat F and Harvey PD. *Inorg. Chem.* 2014; **53**: 3392–3403.
82. Langlois A and Harvey PD. *J. Porphyrins Phthalocyanines.* 2014; **18**: 666–674.
83. Kycychenko A and Albinsson B. *Chem. Phys. Lett.* 2002; **366**: 291–299.
84. You Z-Q and Hsu C-P. *J. Chem. Phys.* 2010; **133**: 074105.
85. Harvey PD, Langlois A, Filatov M, Fortin D, Ohkubo K, Fukuzumi S and Guillard R. *J. Porphyrins Phthalocyanines* 2012; **16**: 685–694.
86. Harvey PD, Filatov MA and Guillard R. *J. Porphyrins Phthalocyanines* 2011; **15**: 1150–1171.
87. Filatov M, Laquai F, Fortin D, Guillard R and Harvey PD. *ChemComm.* 2010; **48**: 9176–9178.
88. Poulin J, Stern C, Guillard R and Harvey PD. *Photochem. Photobio.* 2006; **82**: 171–176.



# Synthesis and wire-like performance of diruthenium molecular wire with a C≡C-porphyrin-C≡C linker

Yuya Tanaka, Masanori Ono and Munetaka Akita\*

Chemical Resources Laboratory, Tokyo Institute of Technology, RI-27, 4259 Nagatsuta Midori-ku Yokohama 226-8503, Japan

*Dedicated to Professor Shunichi Fukuzumi on the occasion of his retirement*

Received 1 December 2014

Accepted 26 December 2014

**ABSTRACT:** A diruthenium complex with a free-base porphyrin linker **1** is synthesized and characterized by  $^1\text{H}$  and  $^{31}\text{P}$  NMR, IR, and ESI-TOF-MS spectroscopy. A cyclic voltammogram of **1** shows two reversible waves attributed to the redox processes at the ruthenium centers, and a comproportionation constant ( $K_C$ ) has been determined to be  $1.8 \times 10^5$ , indicating that a mixed valence state of **1**<sup>+</sup> is thermodynamically stable. The monocationic complex **1**<sup>+</sup> obtained by chemical oxidation of **1** by  $[\text{Cp}_2\text{Fe}]\text{PF}_6$  shows an intervalence charge transfer (IVCT) band in the NIR region. On the basis of the electronic coupling ( $V_{ab}$ ) of  $2644 \text{ cm}^{-1}$  obtained by analysis of the IVCT band, complex **1**<sup>+</sup> is assigned as a Class III compound according to the Robin–Day classification. DFT calculation and IR study suggest that the strength of  $\pi$ -back donation is one of key determinants for a strong electronic coupling between the two metal centers.

**KEYWORDS:** electron transfer, molecular wire, ruthenium, mixed valence.

## INTRODUCTION

In recent years, there has been increasing interest in molecular electronics because of the difficulty in and the large cost for downsizing silicon-based semiconductors. Single molecule devices are essential components for molecular electronics [1]. In particular, organometallic complexes with two redox active metal units linked by a  $\pi$ -conjugated spacer are considered to be nano-scale conducting wires, because a hole or an unpaired electron generated at the metal center upon a redox process could be delocalized over and/or transferred through the spacer *via* thermal- and/or photo-excited processes [2]. In order to construct an efficient organometallic wire, M-BL-M, a variety of transition metal fragments (M) and bridging ligands (BL) have been examined and several review articles have appeared so far [3].

Performance of molecular wire is dependent on strength of the electronic interaction between the terminal metal fragments, and, in general, is sensitive to the balance of the orbital energy levels between the metal fragments and the bridging ligands [3i, j]. For example, the series of the organometallic molecular wires with the redox-active  $\text{RuCp}^*(\text{dppe})$  fragments and various diethynylarene bridging ligands, **2–4** (Fig. 1), show similar metal–metal interactions as indicated by the electronic coupling ( $V_{ab}$ ) (see Table 3), and are categorized into class II compounds according to the Robin–Day classification [4]. For development of better molecular-wire systems, we anticipated that incorporation of a much more extended aromatic system into the bridging ligand should change the electronic structure of the organometallic wire to lead to an enhancement of the interaction between the metal fragments and the bridging ligand. Therefore, porphyrins, which have been frequently used as key components for electron and energy transfer devices both in the natural and artificial systems [5], are expected to be promising candidates for the bridging unit. Although, several examples of such systems have been reported so

\*Correspondence to: Munetaka Akita, email: makita@res.titech.ac.jp, fax +81 45-924-5230

far, most of them are confined to the ferrocenyl systems (**5** and **6**) [6], and few examples are found for the systems bearing other redox pendants. Herein, we report synthesis of a molecular wire **1** with the electron-rich  $-\text{C}\alpha\text{C}-\text{RuCp}^*(\text{dppe})$  fragments linked by a free-base porphyrin (Fig. 1) and its wire-like performance.

## RESULT AND DISCUSSION

### Synthesis

Free-base ruthenium porphyrin complex **1** was synthesized by the two-step one-pot reaction *via* a vinylidene intermediate (Scheme 1) [3a]. Reaction of the terminal alkyne precursor **8** with a cationic ruthenium species,  $[\text{RuCp}^*(\text{dppe})]\text{BF}_4$ , generated by treatment of  $\text{RuCp}^*(\text{dppe})\text{Cl}$  with  $\text{AgBF}_4$ , afforded the vinylidene intermediate, which was further deprotonated by DBU to give complex **1** in 20% yield. Complex **1** has been fully characterized by  $^1\text{H}$  and  $^{31}\text{P}$  NMR, ESI-TOF-MS, and IR spectroscopy, which provided spectra consistent with the

desired structure. Singlet signals for the  $\text{Cp}^*$  ( $^1\text{H}$  NMR) and  $\text{dppe}$  ( $^{31}\text{P}$  NMR) ligands indicate a symmetrical structure of **1**, and the  $\text{C}\equiv\text{C}$  vibration appears at  $2016\text{ cm}^{-1}$ .

### Electrochemistry

Electrochemical measurement was carried out for a  $\text{CH}_2\text{Cl}_2$  solution of complex **1** (Fig. 2, Table 1). Two successive reversible waves were observed at  $-550\text{ mV}$  ( $E_1$ ) and  $-250\text{ mV}$  ( $E_2$ ), and one quasi-reversible wave ( $E_3$ ) was observed at  $550\text{ mV}$  (*vs.*  $\text{Fc}/\text{Fc}^+$  couples). The first and second waves are attributed to 1e-redox processes at the two Ru centers and the third one is assigned to the redox process at the porphyrin part as determined by comparison with the reference compounds **2–4** and **7** (Table 1) [7]. The separation between the first two redox waves ( $\Delta E$ ) comparable to those of the ruthenium-based complexes **1** and **2–4** ( $\sim 300\text{ mV}$ ) indicates that the comproportionation constants ( $K_C \sim 10^5$ ), which reflect thermodynamic stability of the 1e-oxidized mixed valence species ( $\text{M}^+$ ) over the neutral ( $\text{M}$ ) and the dicationic ( $\text{M}^{2+}$ ) species,

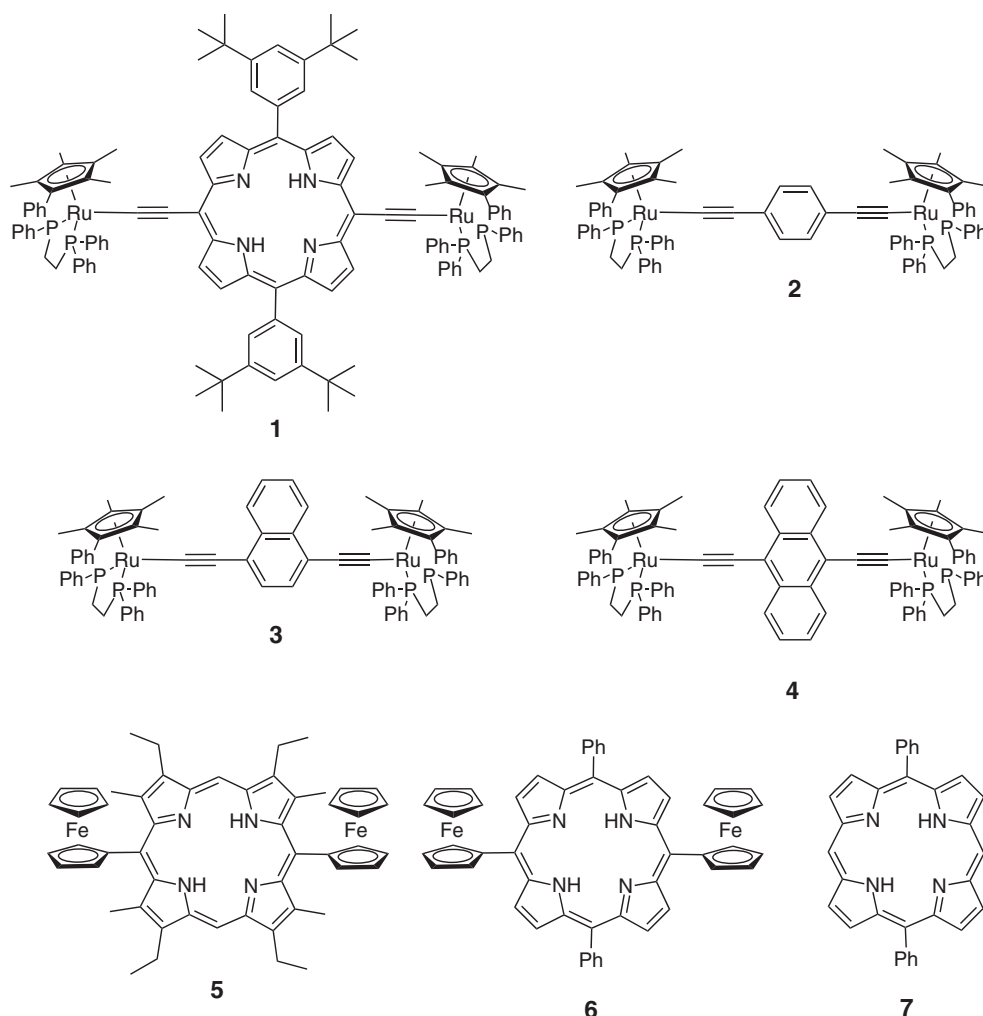
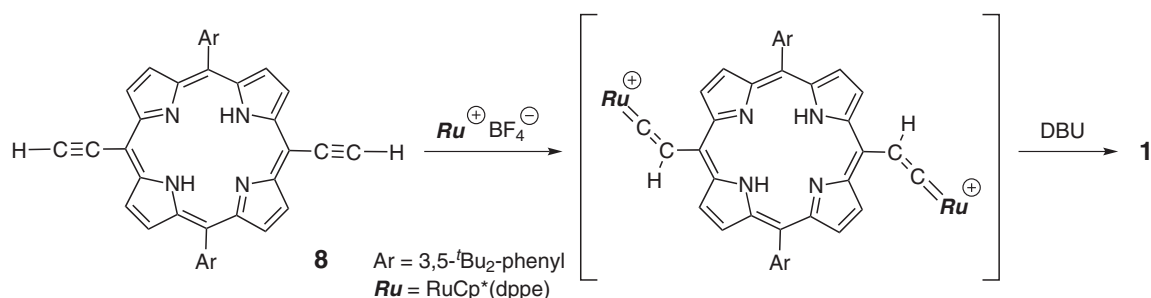
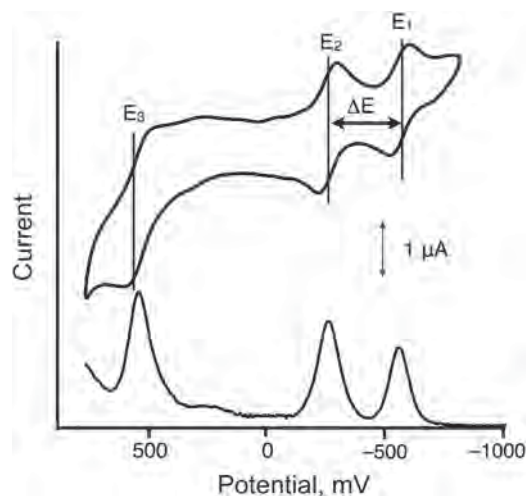


Fig. 1. Molecular structures of **1–7**

Scheme 1. Synthetic route for complex **1**

**Fig. 2.** CV and DPV charts for **1** obtained in CH<sub>2</sub>Cl<sub>2</sub> (1 × 10<sup>-3</sup> M). Supporting electrolyte: *n*-Bu<sub>4</sub>NPF<sub>6</sub> (0.1 M), scan rate: 100 mV/s for CV and 25 mV/s for DPV

Table 1. CV data for **1–7**

Complex	E <sub>1</sub> , V <sup>c</sup>	E <sub>2</sub> , V <sup>c</sup>	ΔE <sup>f</sup> , V <sup>c</sup>	K <sub>C</sub> <sup>g</sup>	E <sub>3</sub> , V <sup>e</sup>
<b>1</b> <sup>a</sup>	-0.55	-0.25	0.31	1.8 × 10 <sup>5</sup>	0.55 <sup>h</sup>
<b>2</b> <sup>a</sup>	-0.45	-0.16	0.29	8.0 × 10 <sup>4</sup>	0.78 <sup>i</sup>
<b>3</b> <sup>a</sup>	-0.52	-0.22	0.30	1.2 × 10 <sup>5</sup>	0.83 <sup>i</sup>
<b>4</b> <sup>a</sup>	-0.63	-0.33	0.30	1.2 × 10 <sup>5</sup>	0.83 <sup>i</sup>
<b>5</b> <sup>b</sup>	-0.31	-0.10	0.21	3.6 × 10 <sup>3</sup>	0.63 <sup>i</sup>
<b>6</b> <sup>c</sup>	0	0.15	0.15	3.5 × 10 <sup>2</sup>	0.84 <sup>i</sup>
<b>7</b> <sup>d</sup>					0.51 <sup>h</sup>

<sup>a</sup>In CH<sub>2</sub>Cl<sub>2</sub>; [complex] = 0.001 M, [NBu<sub>4</sub>PF<sub>6</sub>] = 0.1 M; working electrode (W.E.): Pt; counter electrode (C.E.): Pt; reference electrode (R.E.): Ag/AgNO<sub>3</sub>. Scan rate = 100 mV/s. <sup>b</sup>In CH<sub>2</sub>Cl<sub>2</sub>; [complex] = 0.001 M [NBu<sub>4</sub>ClO<sub>4</sub>] = 0.1 M; R.E.: Ag/AgCl. Scan rate = 100 mV/s. <sup>c</sup>In CH<sub>2</sub>Cl<sub>2</sub>; [NBu<sub>4</sub>BF<sub>4</sub>] = 0.05 M; W.E. Pt. <sup>d</sup>In CH<sub>2</sub>Cl<sub>2</sub>; [complex] = 0.001 M [NBu<sub>4</sub>(B(C<sub>6</sub>F<sub>5</sub>)<sub>4</sub>)] = 0.1 M; W.E.: Pt; C.E.: Pt; R.E.: Ag/AgNO<sub>3</sub>. Scan rate = 100 mV/s. <sup>e</sup>vs. Fc/Fc<sup>+</sup> couple. <sup>f</sup>ΔE = E<sub>2</sub> - E<sub>1</sub>. <sup>g</sup>K<sub>C</sub> = exp(F·ΔE/RT). <sup>h</sup>Quasi-reversible. <sup>i</sup>Irreversible.

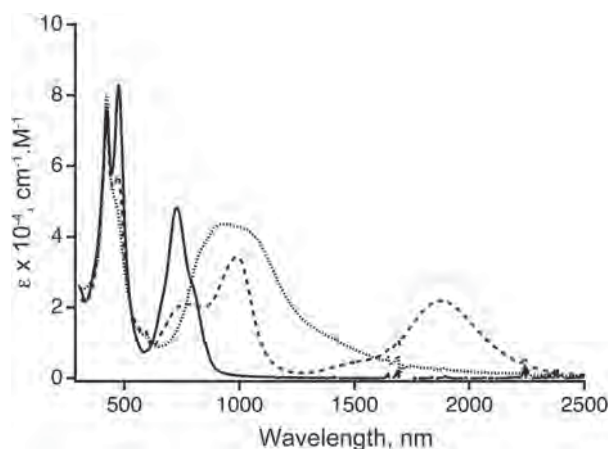
are similar. The insensitivity of the bridging ligand to the K<sub>C</sub> value is in stark contrast to the corresponding derivatives containing the corresponding iron fragments,

FeCp\*(dppe), for which the molecular wire with a larger π-system in the bridging ligand shows a larger K<sub>C</sub> value [3i, 8]. Because the K<sub>C</sub> value is dependent not only on the term of electronic coupling (V<sub>ab</sub>) but also on those of ion pairing, solvation, electrostatic repulsion, and so on [9], the ruthenium molecular wires with a larger π-system may be strongly influenced by such factors compared with the iron derivatives. The ferrocenyl porphyrin complexes **5** [6d] and **6** [6c] were reported previously and they showed two well-separated redox waves, though the ΔE values (210 and 150 mV, respectively) were smaller than that of **1**. Moreover, the redox potential of the porphyrin part (E<sub>3</sub>) for **1** (0.55 mV) is shifted cathodically compared to the ferrocenyl complexes **5** (0.63 mV) and **6** (0.84 mV), indicating the electron donating ability of the -C≡C-RuCp\*(dppe) fragment being stronger than that of the ferrocenyl group.

### UV-Vis-NIR spectroscopy

For complex **1**, intense absorptions are observed at 423, 474 and 727 nm. The former two bands are attributed to Soret-bands and the third one is assigned as a Q-band, to both of which the metal acetylide part contributes to a considerable extent, as indicated by the red-shifts compared to **8** (Soret band at 432 nm and Q-band at 679 nm) as well as the DFT study (*vide infra*). Considering that the arene derivatives **2–4** show the lowest-energy absorption bands at 370 (**2**), 430 (**3**), and 560 nm (**4**) (*cf.* 727 nm (**1**)), the expansion of the π-system in the bridging ligand decreases the HOMO–LUMO energy gap of the molecular wire system.

Monocationic and dicationic species of **1** were prepared *via* chemical oxidation of **1** with ferrocenium hexafluorophosphate in THF solutions. UV-vis-NIR spectra of **1**<sup>n+</sup> (n = 0–2) in CH<sub>2</sub>Cl<sub>2</sub> are shown in Fig. 3. Upon 1e-oxidation of the neutral complex **1**, the original Soret band at 474 nm is weakened and the Q-band is shifted to lower energies (984 nm), indicating that the aromatic character of the porphyrin core is strongly perturbed by the oxidation [10]. Additionally, a new broad NIR band appears around 1892 nm. The electronic coupling V<sub>ab</sub> of molecular wires can be evaluated from an IVCT (intervalence charge transfer) band usually appearing in the NIR region. NIR bands of transition

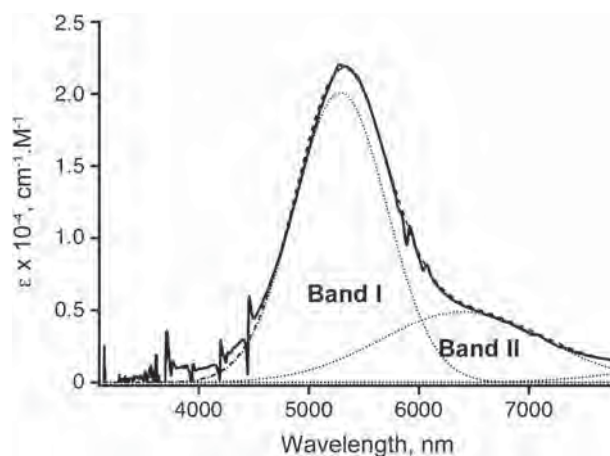


**Fig. 3.** UV-vis-NIR spectra for  $[1^{n+}](PF_6)_n$  ( $n = 0-2$ ) observed in  $CH_2Cl_2$  (plane: neutral, dashed: monocation, dotted: dication)

**Table 2.** UV-vis-NIR data for  $[1^{n+}](PF_6)_n$  ( $n = 0-2$ ) observed in  $CH_2Cl_2$

Complex	$\lambda_{max}$ , nm ( $\epsilon \times 10^{-4}$ , $M^{-1} \cdot cm^{-1}$ )
<b>1</b>	260 (6.00), 423 (7.70), 474 (8.28), 727 (4.82)
$[1^+]PF_6$	422 (7.20), 472 (5.72), 771 (2.10), 984 (3.43), 1891 (2.21)
$[1^{2+}](PF_6)_2$	425 (7.91), 933 (4.35)
<b>8</b>	432 (30.1), 542 (0.79), 583 (0.11), 620 (0.40), 679 (1.67)

metal mixed-valence species are observed as a sum of multiple bands including an IVCT band. A couple of reasons for emergence of multiple NIR bands are as follows: (1) spin-orbit coupling breaking degeneracy of the d orbitals [11], (2) overlapping with ligand field transitions of the transition metal centers [12], and (3) the presence of rotamers giving different IVCT energies [13]. According to deconvolution analysis of the NIR bands of  $1^+$ , the spectrum is divided into two Gaussian bands (band I and II), and the band I is assigned as the IVCT band and used for the  $V_{ab}$  determination (Fig. 4, Table 3).



**Fig. 4.** A NIR absorption spectrum for  $[1^+]PF_6$  observed in  $CH_2Cl_2$  (plane) and the deconvoluted Gaussian curves (dashed)

Following careful analysis of band I leads to assignment of  $1^+$  as a Class III compound according to the Robin-Day classification: (1) The band I ( $\nu^{exp} = 841 \text{ cm}^{-1}$ ) is much narrower than the calculated band width ( $\nu^{calc} = 3495 \text{ cm}^{-1}$ ) when estimated as a class II compound [14]; (2) The IVCT band is independent on the solvent polarity (See Supporting information). Thus the  $V_{ab}$  value for  $1^+$  is determined to be  $2644 \text{ cm}^{-1}$ . The value is much larger than those found for complexes **2**, **3** and **4** ( $588-697 \text{ cm}^{-1}$ ), which are classified as class II species [4]. Moreover, the ferrocenylporphyrin derivative **6** is also classified as a class II system with a  $V_{ab}$  value of  $1300 \text{ cm}^{-1}$ , although the metal-metal distances for **2-4** (ca.  $12 \text{ \AA}$ ) and **6** ( $<13 \text{ \AA}$ ) are much shorter than that for **1** ( $16.2 \text{ \AA}$ ).

### DFT calculations

To clarify the reasons why complex **1** shows the wire-like performance better than the others, DFT calculations have been conducted for the model complexes **1'**, **2'** and **4'**, where the  $Cp^*$  and dppe ligands and the *tert*-butyl groups are replaced by the Cp and the dmpe ligands and the hydrogen atoms, respectively (Fig. 5). The HOMOs of **1'**, **2'** and **4'** are delocalized over the M-BL-M structures,

**Table 3.** NIR data for  $[1^+]PF_6 - [4^+]PF_6$  observed in  $CH_2Cl_2$

Complex	$\nu_{max}$ , $cm^{-1}$	$\epsilon_{max}$ , $M^{-1} \cdot cm^{-1}$	$\nu_{1/2}^{exp}$ , $cm^{-1}$	$\nu_{1/2}^{calc}$ , $cm^{-1}$ <sup>a</sup>	$V_{ab}^{ClassII}$ , $cm^{-1}$ <sup>b</sup>	$V_{ab}^{ClassIII}$ , $cm^{-1}$ <sup>c</sup>
$[1^+]PF_6$	5287	20000	841	3495	379	2644
$[2^+]PF_6$	8300	4400	4200	4380	661	4150
$[3^+]PF_6$	8300	4900	4200	4380	697	4150
$[4^+]PF_6$	8100	5000	3000	4320	588	4050
$[6^+]PF_6$	11700	16000	3400	5200	1300	5850

<sup>a</sup> Calculated according to the Hush formula when assumed as a class II compound ( $\nu_{1/2}^{calc} = (2310\nu_{max})^{1/2}$  ( $cm^{-1}$ )).

<sup>b</sup> Calculated as a Class II compound.  $V_{ab}^{ClassII} = 2.06 \times 10^{-2} (\nu_{max} \epsilon_{max} \nu_{1/2}^{exp})^{1/2} / r$  ( $cm^{-1}$ ). <sup>c</sup> Calculated as a class III compound  $V_{ab}^{ClassIII} = \lambda_{max} / 2$  ( $cm^{-1}$ ).

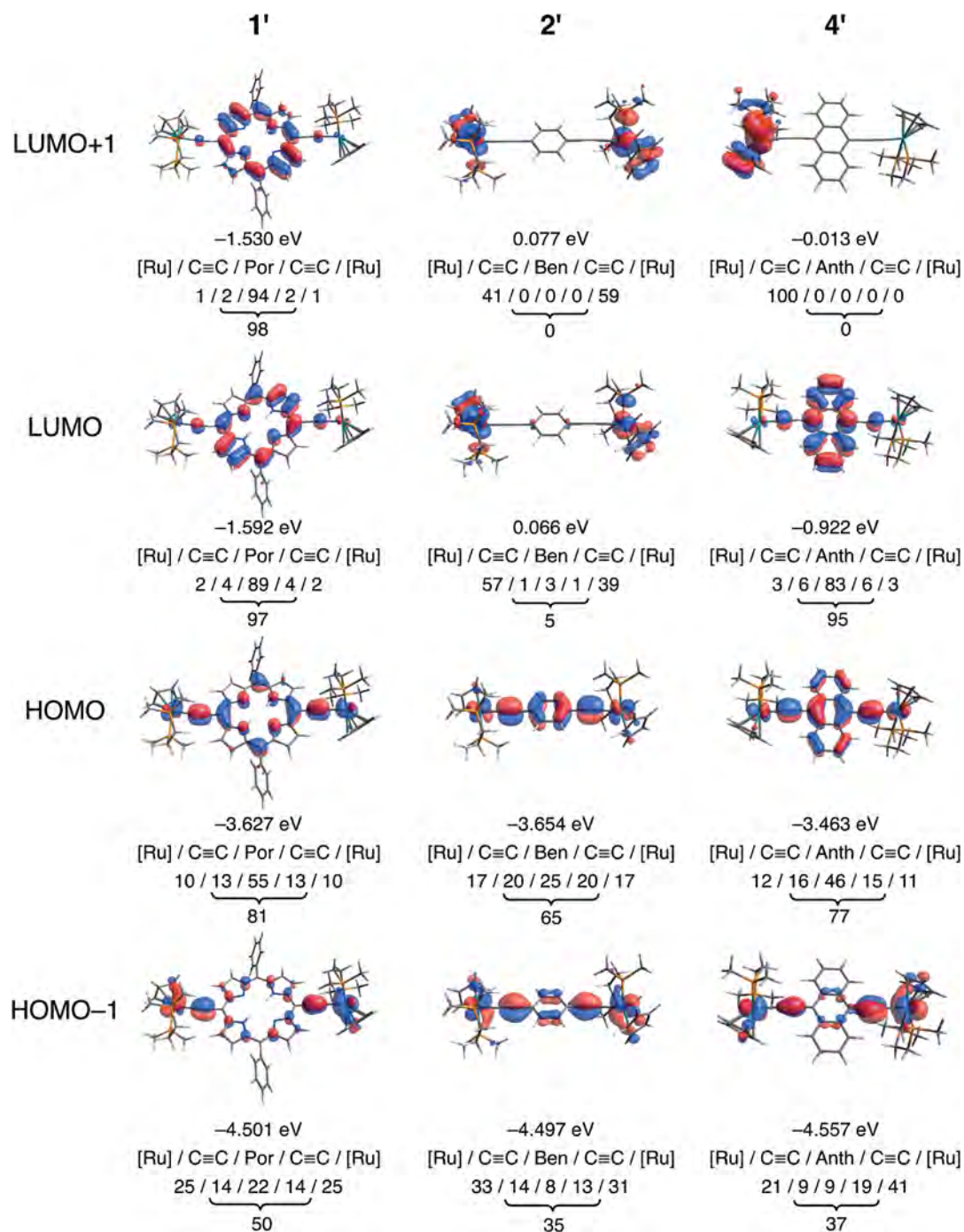


Fig. 5. Contour plots, energies, and percentage contributions of the Kohn–Sham orbitals of 1', 2', and 4'

whereas the LUMOs of 1' and 4' are mainly localized on the bridging ligands and the LUMO of 2' is localized on the metal center. LUMO+1 of 1 is almost degenerated with LUMO, while LUMO as well as LUMO+1 of 2' and LUMO+1 of 4' are localized on the Ru fragments. The most significant feature is that the LUMO level of 1' is much lower in energy than those of 2' and 4' (>0.5 eV), while the energy levels of the HOMOs with the dominant contributions from the Ru fragments remain similar. As a result, the significantly reduced HOMO–LUMO

gap of 1' (2.04 eV) causes the red-shift of the above-mentioned lowest energy UV-vis absorption maxima compared to 2' (3.59 eV) and 4' (2.54 eV). Mulliken population analysis provides a further insight into the electronic structure of the HOMOs. When the HOMOs of 1', 2' and 4' are compared, contribution of the bridging diethynylporphyrin part in 1' (81%) is larger than that of the diethynylarene parts in 2' (65%) and 4' (77%). These data reveal more significant contribution of the bridging ligand character to the frontier orbitals of 1'. This feature



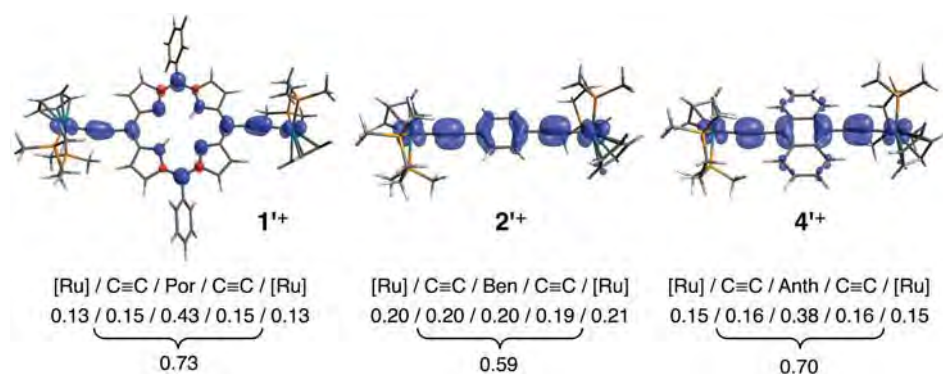


Fig. 6. Distributions of computed spin densities and distributions of spin densities on  $1'^+$ ,  $2'^+$ , and  $4'^+$

Table 4. Bond lengths and Mulliken charges of  $1'^{n+}$ ,  $2'^{n+}$  and  $4'^{n+}$  ( $n = 0, 1$ )<sup>a</sup>

Complex	Ru–C≡, Å	C≡C, Å	≡C–C(por), Å	Mulliken charge at Ru
$1'$	2.015	1.235	1.423	-0.393
$1'^+$	1.970	1.246	1.398	
$2'$	2.022	1.232	1.427	-0.404
$2'^+$	1.963	1.246	1.399	
$4'$	2.020	1.234	1.423	-0.395
$4'^+$	1.967	1.248	1.392	

<sup>a</sup>Averaged values for the two units.

Table 5. Experimental and calculated IR data for neutral and monocationic species of  $1^{(n)}$ ,  $2^{(n)}$ , and  $4^{(n)}$

Complex	Neutral, cm <sup>-1</sup>	Monocation, cm <sup>-1</sup>
$1^a$	2016 (s)	1940 (s)
$1'^b$	2035 (asym, 4164), 2040 (sym, 27)	1974 (asym, 11245), 1989 (sym, 0)
$2^c$	2068 (m)	2061 (w), 1997 (s), 1974 (vs), 1915 (w, sh)
$2'^b$	2062 (sym, 0), 2064 (asym, 1175)	1981 (sym, 3), 1987 (asym, 5442)
$4^c$	2031 (m), 2045 (m)	2020 (w), 1954 (vs), 1898 (w,sh)
$4'^b$	2042 (sym, 523), 2043 (asym, 1252),	1973 (asym, 6415), 1981 (sym, 0)

<sup>a</sup>In KBr. <sup>b</sup>Calculated vibrational frequency corrected by a scaling factor of 0.950. Vibrational mode and computed intensity are shown in parentheses. <sup>c</sup>In CH<sub>2</sub>Cl<sub>2</sub>/NBu<sub>4</sub>PF<sub>6</sub> [4].

should come from lowering of MOs associated with the arene moieties as the size of the arene moiety increases. For example, in the case of  $2'$ , the vacant orbitals associated with the benzene ring lie higher in energy and, as result, the LUMO is mainly based on the Ru fragment. As the size of the  $\pi$ -systems expands as in the cases of  $1'$  and  $4'$ , however, MOs associated with the arene moieties are lowered in energy so as to be involved in the frontier orbitals, *i.e.* LUMO.

Computed bond lengths for  $1'$ ,  $2'$ , and  $4'$  associated with the Ru–C≡C–por moieties including the C≡C lengths are very similar, while the calculated C≡C vibrational

frequencies of  $1'$ ,  $2'$  and  $4'$ , which are in good agreements with the experimental data (Table 5), are rather sensitive to the aromatic systems in the bridging ligands. The single C≡C vibrational frequency of  $1'$  located at 2035 cm<sup>-1</sup> (for  $1$ , 2016 cm<sup>-1</sup>) is attributed to the asymmetric vibrational mode and is much lower in energy than those of the benzene and anthracene derivatives (2068 ( $2$ ): 2064 ( $2'$ ), and 2045 ( $4$ ): 2043 cm<sup>-1</sup>( $4'$ )) [4]. These data indicate that  $\pi$ -back donation from the metal centers to the bridging ligand becomes significant as the size of the  $\pi$ -system in the bridging ligand increases, as is also in agreement with the dependence of the Mulliken charges

at the Ru atoms on the size of the  $\pi$ -aromatic rings in the linkers ( $1'$ : -0.393 >  $4'$ : -0.395 >  $2'$ : -0.404, Table 4).

For the monocationic species  $1^+$ ,  $2^+$  and  $4^+$ , the Ru–C $\equiv$  and  $\equiv$ C–C(por) distances are shortened and the C $\equiv$ C distance is elongated owing to contribution of the cumulenic character (Ru=C=C=C(por)) when compared to the neutral counterparts (Table 4). The spin densities calculated for the monocationic species  $1^+$ ,  $2^+$  and  $4^+$  (Fig. 6) are distributed over the Ru–BL–Ru moieties [15], and the shapes of the distributions are similar to those of the HOMOs of the neutral species. The sum of the spin densities over the diethynylporphyrin part (0.73e) in  $1^+$  is larger than those of the diethynylbenzene part (0.59e) in  $2^+$  and the diethynylanthracene part (0.70e) in  $4^+$ , indicating more extensive delocalization of the radical cation of  $1^+$ . The trend of the spin distribution over the bridging ligands is in accord with that of the lower energy shifts of the C $\equiv$ C vibrations of the monocationic species ( $1^+$ : 1940/ $4^+$ : 1954/ $2^+$ : 1974 cm $^{-1}$ ), suggesting that the  $\pi$ -back donation is crucial for the delocalization (stabilization) of the radical cation. Therefore the radical cation tends to be delocalized over the Ru–BL–Ru part as the size of the  $\pi$ -system in the bridging ligand (BL) increases.

## EXPERIMENTAL

### General procedures

5,15-Dibromo-10,20-bis(3,5-di-*tert*-butylphenyl)porphyrin [16] and RuCp\*(dppe)Cl [17] were prepared according to the reported procedures. THF, ether, CH $_2$ Cl $_2$  were purified by a solvent purification system [18]. Benzene and MeOH were purchased from Kanto Chemicals and degassed prior to use. Other chemicals were purchased and used without further purification. NMR spectra were recorded on a JEOL EX-300 spectrometer ( $^1$ H, 300 MHz) and a Bruker AVANCE II 400 MHz spectrometer ( $^1$ H, 400 MHz;  $^{31}$ P, 162 MHz). Chemical shifts (downfield from TMS ( $^1$ H) and H $_3$ PO $_4$  ( $^{31}$ P)) and coupling constants are reported in ppm and in Hz, respectively. Solvents for NMR measurements were dried over molecular sieves, degassed, and stored under N $_2$ . IR and UV-vis-near IR spectra were recorded on JASCO FT/IR 4200 and JASCO V-670 spectrometers, respectively. High resolution ESI-TOF mass spectra were obtained with a Bruker micrOTOF II. Electrochemical measurements were recorded on a Hokutodenkou HZ-5000 analyzer (observed in CH $_2$ Cl $_2$ ; [complex] = 0.001 M [NBu $_4$ PF $_6$ ] = 0.1 M; Ag/AgCl: electrode; reported with respect to the [FeCp $_2$ ]/[FeCp $_2$ ] $^+$  couple). Elemental analyses were performed at the Center for Advanced Materials Analysis, Technical Department, Tokyo Institute of Technology.

### Synthesis

**Preparation of 5,15-bis(ethynyl)-10,20-bis(3,5-di(*tert*-butyl)phenyl)porphyrin 8.** The title compound was

prepared by desilylation of the silylated precursor **9**, 5,15-bis(trimethylsilylethynyl)-10,20-bis(3,5-di(*tert*-butyl)phenyl)porphyrin, which was previously synthesized by the condensation reaction of (3,5-bis-*tert*-butylphenyl)-2,2-dipyrrylmethane and 3-trimethyl-silylprop-2-ynal [19] but we prepared the compound by another route including Sonogashira coupling followed by desilylation as reported in Ref. 20. To a mixture of 5,15-dibromo-10,20-bis(3,5-di(*tert*-butyl)phenyl)porphyrin (220.4 mg, 0.261 mmol, 1 equiv.), Pd(dba) $_2$  (30.0 mg, 0.0108 mmol, 0.2 equiv.), Bu $_4$ NOAc (26.2 mg, 0.0522 mmol, 0.2 equiv.) and THF (30 mL) was added trimethylsilylacetylene (184 mL, 1.30 mmol, 5 equiv.) and the solution was stirred for 12 h at room temperature. Then the reaction mixture was quenched by brine and the organic layer was extracted with dichloromethane, dried over Na $_2$ SO $_4$ , passed through a neutral alumina pad. The solvent was removed *in vacuo* to give crude **9** (235.5 mg, 0.268 mmol), which was used without further purification. The spectroscopic data were identical to the previously reported data [19]. To a solution of **9** (373.7 mg, 0.425 mmol) dissolved in THF (5 mL) was added a MeOH solution (20 mL) of K $_2$ CO $_3$  (235 mg, 1.7 mmol), and the mixture was stirred for 3 h. To the resultant reaction mixture was added H $_2$ O, and the product was extracted with CH $_2$ Cl $_2$ , and dried over Na $_2$ SO $_4$ . The filtrate was passed through a neutral alumina column and the solvent was removed under reduced pressure to give **8** (190.6 mg, 0.259 mmol, 61%) as a green solid. IR (KBr):  $\nu$ , cm $^{-1}$  2094 ( $\nu_{C\equiv C}$ ), 3451 (N–H).  $^1$ H NMR (300 MHz, C $_6$ D $_6$ , rt):  $\delta$ , ppm -2.25 (s, -NH, 2H), 1.43 (s, *t*-Bu, 36H), 4.20 (s, RC $\equiv$ CH, 2H), 7.84 (s, *p*-ArH, 2H), 8.05 (s, *o*-ArH 4H), 8.90 (d,  $J$  = 4.8 Hz,  $\beta$ -CH 4H), 9.66 (d,  $J$  = 4.8 Hz,  $\beta$ -CH 4H). HR-MS (ESI-TOF MS, CsI):  $m/z$  calcd. for 787.3567 [M] $^+$ , found 787.3580 [M] $^+$ .

**RuCp\*(dppe) free base porphyrin complex 1.** To a solution of RuCp\*(dppe)Cl (196.6 mg, 0.293 mmol) in CH $_2$ Cl $_2$  (15 mL) was added AgPF $_6$  (56.2 mg, 0.289 mmol) and the mixture was stirred at room temperature under N $_2$  atmosphere. After 20 min, the resultant solution was added to a CH $_2$ Cl $_2$  solution (30 mL) of **8** (90.4 mg, 0.114 mmol) *via* a cannula and the mixture was stirred for 16 h at room temperature. The reaction mixture was concentrated *in vacuo* and the residue was filtered through a Celite pad, which was washed with CH $_2$ Cl $_2$ . The filtrate was concentrated *in vacuo* to give the ruthenium vinylidene intermediate as a black solid, which was dissolved in CH $_2$ Cl $_2$  (10 mL) and treated with DBU (68.2  $\mu$ L, 0.456 mmol). The mixture was stirred for 4 h and then the product was extracted with benzene from the black solid. The volatiles were removed under reduced pressure and the residue was washed with MeOH. The resulting black solid was dissolved in benzene and the product was precipitated by addition of methanol. The residue was recrystallized from CH $_2$ Cl $_2$ -diethyl ether added to give **1** (45.7 mg, 0.0228 mmol, 20% yield) as a dark green powder. IR (KBr):  $\nu$ , cm $^{-1}$  2016 ( $\nu_{C\equiv C}$ ), 3309 (N–H).  $^1$ H NMR (400 MHz, C $_6$ D $_6$ , rt):  $\delta$ , ppm -2.18 (brs, NH, 2H)

1.50 (s, *t*-Bu, 36H), 1.85 (s, Cp\*, 30H), 2.11 (br, dppe-CH<sub>2</sub>, 4H), 3.15 (br, dppe-CH<sub>2</sub>, 4H), 6.90–7.35 (m, dppe-Ph, 32H), 7.91 (t, *J* = 2.0 Hz, *p*-ArH, 2H), 7.98–8.10 (m, dppe-Ph, 8H), 8.18 (d, *J* = 2.0 Hz, *o*-ArH, 4H), 8.56 (d, *J* = 4.5 Hz, β-CH, 4H), 8.80 (d, *J* = 4.5 Hz, β-CH, 4H). <sup>31</sup>P NMR (162 MHz, C<sub>6</sub>D<sub>6</sub>, rt): δ, ppm 82.0. Anal. calcd. for (1-2CH<sub>2</sub>Cl<sub>2</sub>): C 69.67, H 6.22, N: 2.58, found C 69.45, H 6.52, N 3.08. HR-MS (ESI-TOF MS, CsI): *m/z* calcd. for 2002.7375 [M]<sup>+</sup>, found 2002.7371 [M]<sup>+</sup>.

**Preparation of cationic complexes of 1<sup>+</sup> and 1<sup>2+</sup>.** To a THF solution of **1** was added [FeCp<sub>2</sub>]PF<sub>6</sub> (0.9 equiv. or 1.9 equiv.) at -78 °C, and the mixture was stirred for 1 h. The volatiles were removed under reduced pressure to give dark-colored precipitates, which were collected and washed with diethyl ether. [1<sup>+</sup>]PF<sub>6</sub>. Dark green (59%). IR (KBr): ν, cm<sup>-1</sup> 1940 (RC≡CRu). HR-MS (ESI-TOF MS, CsI): *m/z* calcd. for 2002.7375 [M]<sup>+</sup>, found 2002.7302 [M]<sup>+</sup>. [1<sup>2+</sup>](PF<sub>6</sub>)<sub>2</sub>. Dark brown (68%). IR (KBr): ν, cm<sup>-1</sup> 1908 (RC≡CRu). HR-MS (ESI-TOF MS, CsI): *m/z* calcd. for 1001.3685 [M]<sup>2+</sup>, found 1001.3699 [M]<sup>2+</sup>.

### DFT calculation

DFT calculations were performed by using the Gaussian 09 (D01) program package [21]. Full optimizations of geometry, single point calculations and spin density calculations were carried out with the (U) B3LYP/LanL2DZ (for Ru) and 6-31G(d) (for C, H, N, P) levels of theory. No imaginary vibrational frequency was found in the vibrational frequency analysis for the optimized geometry.

### CONCLUSION

In this paper, we have reported synthesis and characterization, and wire-like performance of an organometallic molecular wire consisting of the ruthenium fragments and a free-base porphyrin linker (**1**). Electrochemical analysis of **1** gives a large comproportionation constant of  $1.8 \times 10^5$ . Monocationic species 1<sup>+</sup> shows an intense absorption band in the NIR region, which is attributed to an IVCT band. The quite narrow bandwidth and no solvent dependence of the IVCT band of complex 1<sup>+</sup> reveals that 1<sup>+</sup> is a class III compound according to the Robin–Day classification, whereas 2<sup>+</sup>–4<sup>+</sup> are class II compounds. It is notable that, although the M–M separation of **1** is much longer than those of the related wires **2–4** with the smaller aromatic rings in the bridges and the ferrocenyl derivative **6**, electronic coupling of **1** is much larger than those of the others. Analysis of the IR and UV-vis data for **1** and 1<sup>+</sup> and DFT calculations for 1<sup>+</sup> and 1<sup>2+</sup> reveal, that (1) the central arene moiety prominently participates in the frontier orbitals, in particular, in LUMOs, as the π-arene moiety is extended in the size and (2) such effects cause increased π-back donation from the metal to the bridging ligand to lead to a more efficient molecular wire. Thus the

present study provides a guiding principle for molecular design of efficient molecular wires to achieve a long-range electron transfer system.

### Acknowledgements

This work was financially supported by a Grant-in-Aid for Scientific Research on Innovative Areas (“Coordination Programming” Area 2017, No. 24108101) from the Ministry of Education, Culture, Sport, Science and Technology and a Grant-in-Aid for Scientific Research (22350026) from the Japan Society for Promotion of Science.

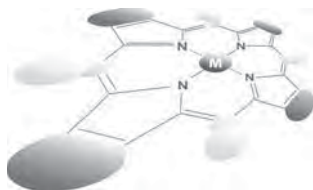
### Supporting information

NIR spectrum of 1<sup>+</sup> in CH<sub>3</sub>CN, <sup>1</sup>H and <sup>31</sup>P NMR spectra of **1** and Cartesian coordinates of the optimized geometry of 1<sup>+</sup>, 2<sup>+</sup>, and 4<sup>+</sup> (n = 0, 1), (Figures S1–S3 and Tables S1–S6), are given in the supplementary material. This material is available free of charge via the Internet at <http://www.worldscinet.com/jpp/jpp.shtml>.

### REFERENCES

- (a) Aviram A and Ratner MA. *Chem. Phys. Lett.* 1974; **29**: 277. (b) Nemykin VN, Rohde GT, Barrett CD, Hadt RG, Bizzarri C, Galloni P, Floris B, Nowik I, Herber RH, Marrani AG, Zanoni R and Loim NM. *J. Am. Chem. Soc.* 2009; **131**: 14969.
- (a) Ward MD. *Chem. Soc. Rev.* 1995; **24**: 121. (b) Launay JP. *Coord. Chem. Rev.* 2013; **257**: 1544. (c) Nemykin VN, Purchel AA, Spaeth AD and Barybin MV. *Inorg. Chem.* 2013; **52**: 11004.
- (a) Paul F and Lapinte C. *Coord. Chem. Rev.* 1998; **178**: 431. (b) Bruce MI and Low PJ. *Adv. Organomet. Chem.* 2004; **50**: 179. (c) Szaferst S and Gladysz JA. *Chem. Rev.* 2003; **103**: 4175. (d) Schwab PFH, Smith JR and Michl J. *Chem. Rev.* 2005; **105**: 1197. (e) Zalis S, Winter RF and Kaim W. *Coord. Chem. Rev.* 2010; **254**: 1383. (f) Akita M and Koike T. *Dalton Trans.* 2008; 3523. (g) Xi B and Ren T. *C. R. Chim.* 2009; **12**: 321. (h) Costuas K and Rigaut S. *Dalton Trans.* 2011; **40**: 5643. (i) Halet JF and Lapinte C. *Coord. Chem. Rev.* 2013; **257**: 1584. (j) Low PJ. *Coord. Chem. Rev.* 2013; **257**: 1507. (k) Hildebrandt A and Lang H. *Organometallics* 2013; **32**: 5640. (l) Rainer WF. *Organometallics* 2014; **33**: 4517.
- Fox MA, Le Guennic B, Roberts RL, Brue DA, Yufit DS, Howard JAK, Manca G, Halet JF, Hartl F and Low PJ. *J. Am. Chem. Soc.* 2011; **133**: 18433.
- (a) Niwa S, Yu LJ, Takeda K, Hirano Y, Kawakami T, Wang-Otomo ZY and Miki K. *Nature* 2014; **508**: 228. (b) Guldi DM and Fukuzumi S. *J. Porphyrins*

- Phthalocyanines* 2002; **6**: 289. (c) Imahori H and Fukuzumi S. *Adv. Funct. Mater.* 2004; **14**: 525.
6. (a) Burrell AK, Campbell WM, Jameson GB, Officer DL, Boyd PDW, Zhao Z, Cocks PA and Gordon KC. *Chem. Commun.* 1999; **7**: 637. (b) Auger A and Swarts JC. *Organometallics* 2007; **26**: 102. (c) Nemykin VN, Rohde GT, Barrett CD, Hadt RG, Sabin JR, Reina G, Galloni P and Floris B. *Inorg. Chem.* 2010; **49**: 7497. (d) Rhee SW, Na YH, Do Y and Kim J. *Inorg. Chim. Acta* 2000; **309**: 49. (e) Nemykin VN, Barrett CD, Hadt RG, Subbotin RI, Maximov AY, Polshin EV and Kuposov AY. *Dalton Trans.* 2007; **31**: 3378. (f) Nemykin VN, Rohde GT, Barrett CD, Hadt RG, Bizzarri C, Galloni P, Floris B, Nowik I, Herber RH, Marrani AG, Zanoni R and Loim NM. *J. Am. Chem. Soc.* 2009; **131**: 14969. (g) Vecchi A, Galloni P, Floris B and Nemykin VN. *J. Porphyrins Phthalocyanines* 2013; **17**: 165.
  7. Auger A, Muller AJ and Swarts JC. *Dalton Trans.* 2007; 3623.
  8. (a) De Montigny F, Argouarch G, Costuas K, Halet JF, Roisnel T, Toupet L and Lapinte C. *Organometallics* 2005; **24**: 4558. (b) Tanaka Y, Shaw-Taberlet JA, Justaud F, Cador O, Roisnel T, Akita M, Hamon JR and Lapinte C. *Organometallics* 2009; **28**: 4656.
  9. (a) Richardson DE and Taube H. *Coord. Chem. Rev.* 1984; **60**: 107. (b) Barrière F and Geiger WE. *J. Am. Chem. Soc.* 2006; **128**: 3980.
  10. Chang D, Malinski T, Ulman A and Kadish KM. *Inorg. Chem.* 1984; **23**: 817.
  11. Demadis KD, Hartshorn CM and Meyer TJ. *Chem. Rev.* 2001; **101**: 2655.
  12. Ghazala SI, Paul F, Toupet L, Roisnel T, Hapiot P and Lapinte C. *J. Am. Chem. Soc.* 2006; **128**: 2463.
  13. Parthey M, Gluyas JBG, Fox MA, Low PJ and Kaupp M. *Chem. Eur. J.* 2014; **20**: 6895.
  14. D'Alessandro DM and Keene FR. *Chem. Rev.* 2006; **106**: 2270.
  15. According to computed IR vibrational frequencies of  $1^+$ ,  $2^+$  and  $4^+$ , all complexes mainly shows single IR band ascribed to asymmetric  $C\equiv C$  vibrational mode. On the contrary, only  $1^+$  shows single vibrational frequency and complexes  $2^+$  and  $4^+$  show multiple bands. Therefore the spin distributions of  $2^+$  and  $4^+$  are over-estimated. Thus the spin densities of  $2^+$  and  $4^+$  should be more localized than computed predictions. It is known that DFT calculation at B3LYP level of theory over-estimate delocalization states. See Renz M, Theilacker K, Lambert C and Kaupp M. *J. Am. Chem. Soc.* 2009; **131**: 16292.
  16. Balaban TS, Goddard R, Linke-Schaetzel M and Lehn JM. *J. Am. Chem. Soc.* 2003; **125**: 4233.
  17. (a) Oshima N, Suzuki H and Moro-Oka Y. *Chem. Lett.* 1984; 1161. (b) Bruce MI, Ellis BG, Low PJ, Skelton BW and White SH. *Organometallics* 2003; **22**: 3184.
  18. Pangborn AB, Giardello MA, Grubbs RH, Rosen RK and Timmers FJ. *Organometallics* 1996; **15**: 1518.
  19. Plater JM, Aiken S and Bourhill G. *Tetrahedron* 2002; **58**: 2415.
  20. Balaban TS, Bhise AD, Fischer M, Linke-Schaetzel M, Roussel C and Vanthuyne N. *Angew. Chem. Int. Ed.* 2003; **42**: 2140.
  21. Gaussian 09, Revision D.01, Frisch MJ, Trucks GW, Schlegel HB, Scuseria GE, Robb MA, Cheeseman JR, Scalmani G, Barone V, Mennucci B, Petersson GA, Nakatsuji H, Caricato M, Li X, Hratchian HP, Izmaylov AF, Bloino J, Zheng G, Sonnenberg JL, Hada M, Ehara M, Toyota K, Fukuda R, Hasegawa J, Ishida M, Nakajima T, Honda Y, Kitao O, Nakai H, Vreven T, Montgomery JA, Peralta Jr. JE, Ogliaro F, Bearpark M, Heyd JJ, Brothers E, Kudin KN, Staroverov VN, Kobayashi R, Normand J, Raghavachari K, Rendell A, Burant JC, Iyengar SS, Tomasi J, Cossi M, Rega N, Millam JM, Klene M, Knox JE, Cross JB, Bakken V, Adamo C, Jaramillo J, Gomperts R, Stratmann RE, Yazyev O, Austin AJ, Cammi R, Pomelli C, Ochterski JW, Martin RL, Morokuma K, Zakrzewski VG, Voth GA, Salvador P, Dannenberg JJ, Dapprich S, Daniels AD, Farkas Ö, Foresman JB, Ortiz JV, Cioslowski J and Fox DJ. Gaussian, Inc., Wallingford CT, 2009.



# Diporphyrin magnesium complex with long-wavelength light absorption for organic solar cells

Takenari Sato, Takafumi Nakagawa, Hiroshi Okada and Yutaka Matsuo<sup>\*†</sup>

Department of Chemistry, School of Science, The University of Tokyo, 7-3-1 Hongo, Bunkyo-ku, Tokyo 113-0033, Japan

Dedicated to Professor Shunichi Fukuzumi on the occasion of his retirement

Received 2 December 2014

Accepted 26 December 2014

**ABSTRACT:** We synthesized a diporphyrin compound [4,7-bis[5-[arylethynyl]-10,20-bis{(triisopropylsilyl)ethynyl}porphyrin-15-yl]-2,1,3-benzothiadiazole dimagnesium(II)], in which two porphyrin units were linked using a benzothiadiazole unit as an electron-withdrawing moiety. These diporphyrins have low-lying HOMO and LUMO levels with long-wavelength light absorption property. Power conversion efficiency of the organic solar cell using this diporphyrin and mix-PCBM (a 85:15 mixture of [6,6]-phenyl-C<sub>61</sub>-butyric acid methyl ester (PC<sub>61</sub>BM) and [6,6]-phenyl-C<sub>71</sub>-butyric acid methyl ester (PC<sub>71</sub>BM) was 2.75% with short-circuit current density of 8.79 mA/cm<sup>2</sup>, open-circuit voltage of 0.80 V, and fill factor of 0.39. Photocurrent conversion in the near infrared region was demonstrated by the incident photon-to-current efficiency spectrum.

**KEYWORDS:** porphyrin, magnesium, low-bandgap, organic solar cells, photovoltaics.

## INTRODUCTION

The porphyrin framework is used for photosynthesis in nature, and has advantageous photophysical and electrochemical properties. Porphyrins are good organic dyes possessing large absorption coefficient, high stability and high susceptibility in electron transfer reactions for organic photovoltaics [1]. Soluble porphyrin derivatives as electron donor materials that have the long-wavelength absorption property are drawing much attention for high performance of small molecule organic solar cells (OSCs) [2]. In this decade, power conversion efficiency (PCE) of porphyrin-based solution-processed OSCs was increased to 7.2% when low-bandgap porphyrin derivative was employed [3]. Previously in our group, we synthesized soluble porphyrin derivatives that have acetylene linkers with triisopropylsilyl (TIPS) solubilizing units for solution processability, aryl  $\pi$ -extending units for

efficient charge mobility, and a center magnesium atom for increasing solubility by coordinating solvent molecules [4]. The expansion of  $\pi$ -conjugated system is an effective way to obtain materials showing long-wavelength light absorption. Porphyrin dimers are known not only as chiral sensors [5] but also as donor materials in dye-sensitized solar cells because *meso-meso* linked porphyrin shows wide-range light absorption covering the near-IR region [6]. The donor-acceptor structures bridged by  $\pi$ -conjugated systems were well investigated to control the highest occupied molecular orbital (HOMO) and lowest unoccupied molecular orbital (LUMO) levels, and hence to have long-wavelength light absorbing low-bandgap materials [7, 8].

Herein, we report synthesis of the diporphyrin compound linked by an electron-withdrawing 2,1,3-benzothiadiazole unit for long-wavelength light absorption and photovoltaic performance in organic thin-film solar cells. A normal-structured bulk heterojunction device showed PCE of 2.75% with high open-circuit voltage ( $V_{OC} = 0.80$  V) and near IR photocurrent conversion. In addition,

<sup>†</sup>SPP full member in good standing

\*Correspondence to: Yutaka Matsuo, email: matsuo@chem.s.u-tokyo.ac.jp, tel/fax: +81 3-5841-1476

smooth surface morphology for the blended thin-film of diporphyrin compound and fullerene derivatives was observed. These desirable features are attributed to low-lying energy levels, low-bandgap nature, and flexible diporphyrins structures. This molecular design will contribute to developing electron donor materials in small molecule OSCs.

## RESULTS AND DISCUSSION

### Synthesis

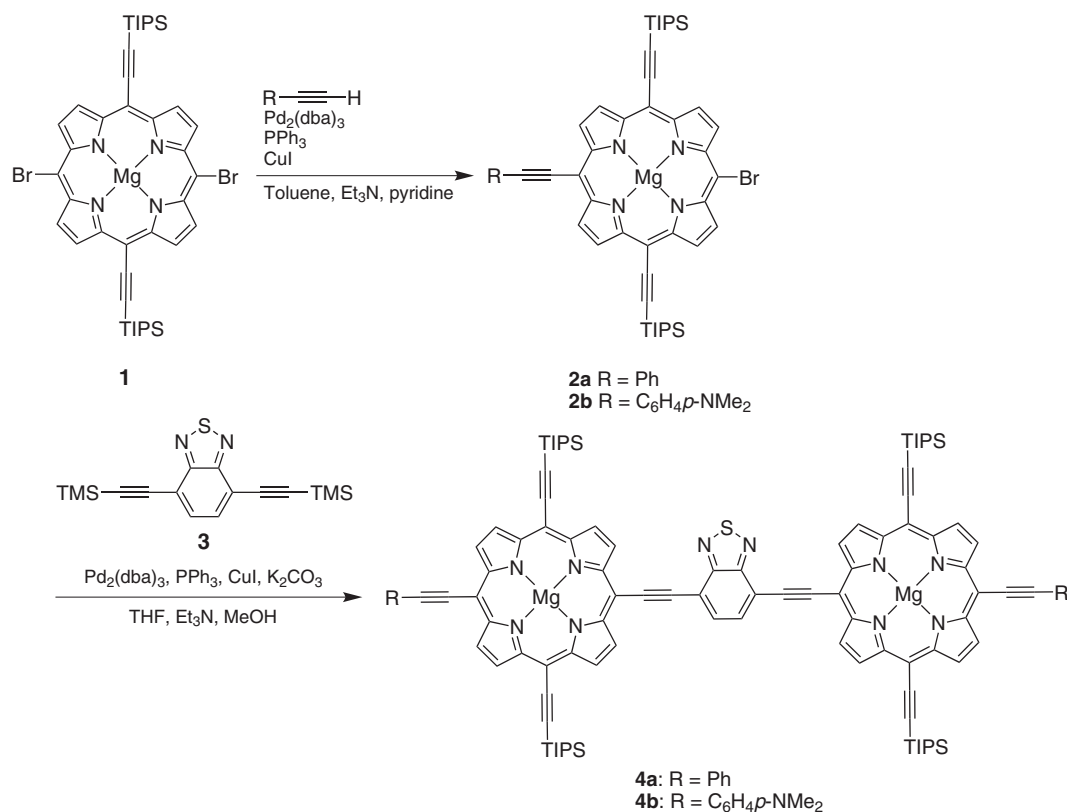
We designed 4,7-diethynyl-2,1,3-benzothiadiazole-linked diporphyrin for the low-bandgap diporphyrin compound, which have an electron-withdrawing benzothiadiazole unit (Scheme 1). Electron deficient 2,1,3-benzothiadiazole is often used as an electron-withdrawing unit in low-bandgap donor-acceptor polymers for high performance organic solar cells [9]. The synthetic route for this diporphyrin compound is shown in Scheme 1. Magnesium dibromoporphyrin **1** and 4,7-bis(trimethylsilylethynyl)-2,1,3-benzothiadiazole **3** were prepared according to the literature methods [10, 11]. First, we synthesized magnesium bromoporphyrin **2** as a starting material for the synthesis of the target compound. We synthesized bromo(dimethylaminophenylethynyl)porphyrin **2b**, which was successfully isolated by using normal silica gel column

chromatography. On the other hand, bromo(phenylethynyl)porphyrin **2a** was purified using a middle pressure column, because **2a** was difficult to be isolated by the silica gel column chromatography technique. This is attributable to the difference in polarity between the phenyl and dimethylaminophenyl groups. Finally, diporphyrin **4a** and **4b** were synthesized by deprotection of the trimethylsilyl group of **3** and following double Sonogashira coupling reaction in one pot, and successfully purified with silica gel column chromatography. Reprecipitation from THF/methanol gave analytically pure diporphyrins **4** as dark red powder. Compounds **4** were characterized by  $^1\text{H}$  NMR and mass spectrometry.

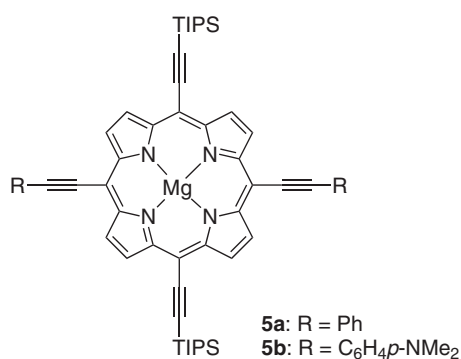
Compounds **4** were stable in air, and were not problematic in purification and device fabrication. In addition, compounds **4** had enough solubility for various organic aromatic solvents in the presence of THF. We consider that THF can serve as an axial ligand to the magnesium metal center to prevent the diporphyrins from intermolecular stacking in solution. We surmise that this THF ligand can be removed with thermal annealing process in the OSC device fabrication [4c].

### Photophysical and electrochemical properties

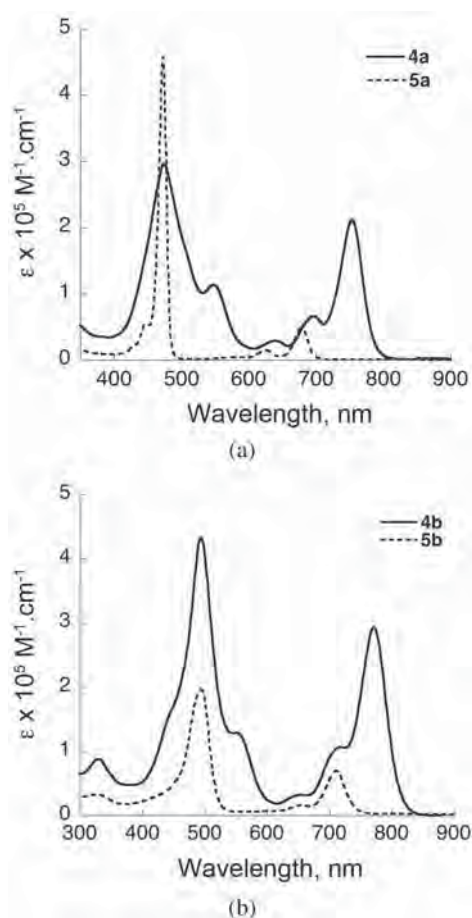
The UV-vis absorption spectra of diporphyrin compounds **4** and reference compounds **5** (Fig. 1) are shown in Fig. 2. Compound **4a** showed a broad Soret band at



**Scheme 1.** Synthesis of benzothiadiazole-linked magnesium diporphyrins **4**



**Fig. 1.** Structures of reference compounds, mono-porphyrins **5**



**Fig. 2.** UV-vis absorption spectra. (a) Diporphyrin **4a** in THF and porphyrin **5a** in  $\text{CH}_2\text{Cl}_2$  [4a]. (b) Diporphyrin **4b** in THF and porphyrin **5b** in  $\text{CH}_2\text{Cl}_2$  [4a]

474 nm. This is almost the same wavelength to the previously reported magnesium[*trans*-bis(triisopropylsilylethynyl)-bis(phenylethynyl)-porphyrin] **5a** (473 nm), while its shape is different from that for **5a**. On the other hand, Q-band at 754 nm that was red-shifted compared with compound **5a** (679 nm) (Table 1). In compound **4b**, similar tendency was observed. The Soret band of **4b** was observed at the same absorption maximum

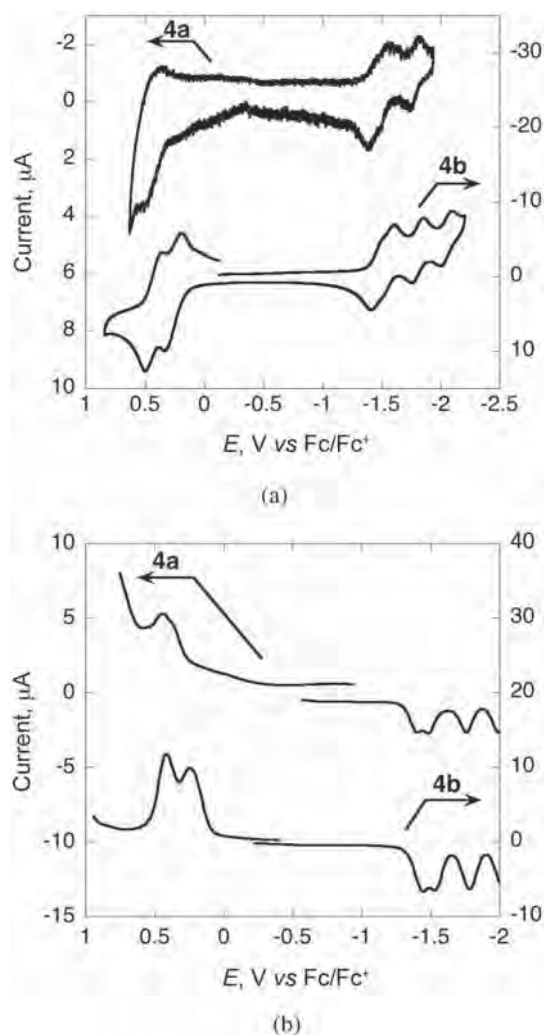
**Table 1.** Peak wavelength of Soret band and Q-band

Compound	$\lambda_{\text{Soret}}$ , nm ( $\epsilon$ , $\text{dm}^3 \cdot \text{mol}^{-1} \cdot \text{cm}^{-1}$ )	$\lambda_{\text{Q}}$ , nm ( $\epsilon$ , $\text{dm}^3 \cdot \text{mol}^{-1} \cdot \text{cm}^{-1}$ )
diporphyrin <b>4a</b> <sup>a</sup>	474 ( $3.0 \times 10^5$ )	754 ( $2.2 \times 10^5$ )
porphyrin <b>5a</b> <sup>b</sup>	473 ( $4.6 \times 10^5$ )	679 ( $4.8 \times 10^5$ )
diporphyrin <b>4b</b> <sup>a</sup>	494 ( $4.3 \times 10^5$ )	771 ( $2.9 \times 10^5$ )
porphyrin <b>5b</b> <sup>b</sup>	496 ( $2.4 \times 10^5$ )	704 ( $8.6 \times 10^4$ )

<sup>a</sup> in THF, <sup>b</sup> in  $\text{CH}_2\text{Cl}_2$  [3a]

as magnesium[*trans*-bis(triisopropylsilylethynyl)-bis(dimethylaminophenylethynyl)-porphyrin] **5b** at 494 nm with different shape, and Q-band of **4b** was red-shifted from 704 nm (**5b**) to 771 nm (**4b**). This long-wavelength light absorption is ascribed to expanded  $\pi$ -conjugated system in diporphyrins **4**. In the thin films, broad and red-shifted spectra were observed because of strong intermolecular interaction between adjacent molecules. The diporphyrins **4** realizes both good solubility and intermolecular interaction in the solid state; these properties are desirable for application to small molecule OSCs.

Electrochemical properties were investigated by cyclic voltammetry (CV) and differential pulse voltammetry (DPV). Diporphyrins **4** showed pseudo-reversible oxidation and reduction waves in CV (Fig. 3a). This result suggests that electrochemical stability of these compounds is acceptable for OSCs application. In CV and DPV of **4b**, the first and second overlapped one-electron reduction waves as well as separated third and fourth ones were observed on the cathodic scan. We surmise that the first and second ones are due to reduction of the two porphyrin cores, which are electronically interacted each other with peak separation of 80 mV through the  $\pi$ -electron conjugated diethynyl benzothiadiazole linker. We assigned the third reduction wave to reduction of the benzothiadiazole unit. This is supported by the data from literature [6a], where bis(trimethylsilylethynyl) benzothiadiazole shows  $-1.66 \text{ V vs. Fc/Fc}^+$  in its reduction potential. On the anodic scan for **4b**, two waves of two-electron oxidation were observed. We consider that electronic communication between two porphyrin units through the benzothiadiazole are not effective on the oxidation state. For the compound **4a**, similar redox pattern was observed, but the oxidation waves were rather irreversible. For more details, frontier orbital energy levels, *i.e.* HOMO and LUMO levels were estimated from the DPV data (Fig. 3b, Table 2). The HOMO and LUMO levels of diporphyrin **4a** ( $-5.17$  and  $-3.40 \text{ eV}$ , respectively) were found to be lower than those of porphyrin **5a** ( $-5.11$  and  $-3.25 \text{ eV}$ , respectively). Compound **4b** showed same manner with HOMO and LUMO levels of  $-5.04$  and  $-3.35 \text{ eV}$ , respectively, which were lower than mono-porphyrin **5b** ( $-4.89$  and  $-3.21 \text{ eV}$ , respectively). Considering the HOMO and LUMO levels



**Fig. 3.** Electrochemical properties of compounds **4**. (a) Cyclic voltammogram. (b) Differential pulse voltammogram. Measurements were performed in THF solution containing TBAPF<sub>6</sub> (0.1 M) as a supporting electrolyte at 25 °C with a scan rate of 100 mV/s. Glassy-carbon, platinum wire, and Ag/AgClO<sub>4</sub> electrodes were used as working, counter, and reference electrodes, respectively

of [6,6]-phenyl-C<sub>61</sub>-butyric acid methyl ester (PC<sub>61</sub>BM), which is a commonly used electron acceptor having HOMO and LUMO levels at *ca.* -6.1 eV and -3.8 eV, respectively, these diporphyrins are expected to act as

suitable electron donors in OSCs. Moreover, with the lower-lying HOMO level of diporphyrins **4**, we expected that the devices using diporphyrins **4** give high  $V_{OC}$ .

### Photovoltaic performance of diporphyrins

Bulk heterojunction OSCs were fabricated by solution process with a general device structure of indium tin oxide (ITO)/poly(styrenesulfonate)-doped poly(ethylenedioxythiophene) (PEDOT:PSS)/porphyrins:PC<sub>61</sub>BM/Ca/Al and their performance were measured under AM 1.5 illumination with incident light power of 100 mW/cm<sup>2</sup>. These results are summarized in Table 3, and  $J$ - $V$  curves is shown in Fig. 4a. The device using **4b** with a porphyrin(D):fullerene(A) ratio of 1:4 gave PCE of 1.6% with short-circuit current density ( $J_{SC}$ ) of 5.1 mA/cm<sup>2</sup>,  $V_{OC}$  of 0.66 V, and fill factor (FF) of 0.47. When we changed the solvent from chlorobenzene to 1,2-dichlorobenzene, PCE dropped from 1.6% to 0.68%. In comparison to the mono-porphyrin compound **5b**, the photovoltaic parameters,  $J_{SC}$ ,  $V_{OC}$  and FF, were increased from 3.3 to 5.1 mA/cm<sup>2</sup>, from 0.55 to 0.66, and from 0.33 to 0.47, respectively and accordingly PCE increased from 0.57 to 1.6. When we used **4a**, PCE reached 1.95% with  $J_{SC}$  of 6.38 mA/cm<sup>2</sup>,  $V_{OC}$  of 0.80 V, and FF of 0.38 on the D:A = 1:3 device. Then we employed mix-PCBM electron acceptor that is a mixture of PC<sub>61</sub>BM and [6,6]-phenyl-C<sub>71</sub>-butyric acid methyl ester (PC<sub>71</sub>BM) in a ratio of *ca.* 85:15. We obtained PCE of 2.75% with  $J_{SC}$  of 8.79 mA/cm<sup>2</sup>,  $V_{OC}$  of 0.80 V, and FF of 0.39. This PCE value was higher than what we previously obtained with compound **5a** (2.5%) [4a]. In comparison of **4a** and **4b**, lower  $V_{OC}$  was obtained for **4b** because of its high HOMO level due to electron-donating dimethylaminophenyl groups. Even though diporphyrin **4b** has better light harvesting property owing to the enhanced push-pull structure, we think exceeding overall performance of the **4b** device over the **4a** device is difficult due to this  $V_{OC}$  issue.

We ascribe this improvement to the lower-lying HOMO level and long-wavelength light absorption property of diporphyrins **4** as well as good phase separation in the organic photocurrent conversion active layer of the devices using **4**. In association with the HOMO level of **4**, we obtained decent  $V_{OC}$  of 0.80 V. In addition, incident photon-to-current efficiency (IPCE) spectra for

**Table 2.** Electrochemical properties<sup>a</sup>

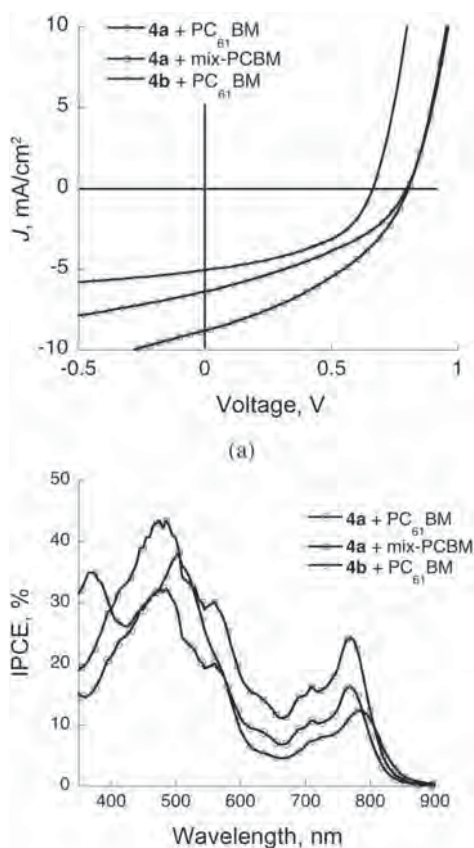
Compound	$E_{1/2}$ (ox 1), V	$E_{1/2}$ (ox 2), V	$E_{1/2}$ (red 1), V	$E_{1/2}$ (red 2), V	$E_{1/2}$ (red 3), V	HOMO, eV	LUMO, eV
diporphyrin <b>4a</b>	0.37	0.46	-1.40	-1.48	-1.76	-5.17	-3.40
porphyrin <b>5a</b>	0.31	—	-1.55	—	—	-5.11	-3.25
diporphyrin <b>4b</b>	0.24	0.42	-1.45	-1.53	-1.78	-5.04	-3.35
porphyrin <b>5b</b>	0.09	—	-1.59	—	—	-4.89	-3.21

<sup>a</sup>The potential was corrected against Fc/Fc<sup>+</sup>. The HOMO and LUMO levels were estimated by the following equation; HOMO =  $-(4.8 + E_{1/2}(\text{ox}))$ , LUMO =  $-(4.8 + E_{1/2}(\text{red}))$ . The data for compounds **5** were taken from reference 4a.



**Table 3.** Device performane of OSCs using diporphyrin **4**

Active layer	$V_{OC}$ , V	$J_{SC}$ , mA/cm <sup>2</sup>	FF	PCE, %
<b>4a</b> + PC <sub>61</sub> BM	0.80	6.38	0.38	1.95
<b>4a</b> + mix-PCBM	0.80	8.79	0.39	2.75
<b>4b</b> + PC <sub>61</sub> BM	0.66	5.05	0.47	1.57

**Fig. 4.** Photovoltaic properties of diporphyrin **4**. (a)  $J$ - $V$  curve of OSC devices: diporphyrin **4a** with PCBM, diporphyrin **4a** with mix-PCBM, and diporphyrin **4b** with PCBM. (b) IPCE spectra for the device using **4**

the devices (Fig. 4b) exhibited photocurrent conversion at the near-IR region up to 900 nm. The Q-band of **4** contributed to this long-wavelength photocurrent conversion. Furthermore, atomic force microscope (AFM) images for the active layers of the diporphyrins **4** devices showed smooth surface morphology (see Supporting Information). These were smoother than that for the mono-porphyrin **5** device. Surface roughness,  $R_a$  for the **4a**:PC<sub>61</sub>BM, **4a**:mix-PCBM, and **4b**:PC<sub>61</sub>BM devices were 0.31, 0.29, and 0.32, respectively, which was smaller than that for the **5a**:PC<sub>61</sub>BM device ( $R_a = 0.76$ ). We surmise that flexibility of the diporphyrin structure compared with the monomeric structure contributes to having good miscibility of the electron donor and

acceptor molecules in the blended bulk heterojunction thin-films.

## EXPERIMENTAL

### General

All reactions dealing with air- or moisture-sensitive compounds were carried out in a dry reaction vessel under nitrogen or argon. Analytical thin-layer chromatography was performed on glass plates coated with 0.25 nm 230–400 mesh silica gel containing a fluorescent indicator (Merck). Silica gel column chromatography was performed on silica gel (for flash chromatography, Wako, Wakogel® C-300 and KANTO, silicagel 60N) or with packed glass column (for medium pressure liquid chromatography, YAMAZEN, ultrapack Si-40D). The NMR spectra were measured on JEOL ECA-500 or ECX-400 spectrometers and reported in parts per million from tetramethylsilane. Mass spectra were acquired by Shimadzu MALDI-TOF-MASS Axima-CFR+. UV-vis absorption spectra were recorded on a JASCO V-670 spectrometer. Electrochemical measurements were performed using a HOKUTO DENKO HZ-5000 voltammetric analyzer. All CV and DPV measurements were carried out in a one-compartment cell under argon gas, equipped with a glassy-carbon working electrode, a platinum wire counter electrode, and an Ag/Ag<sup>+</sup> reference electrode. The supporting electrolyte was a 0.1 M THF solution of tetrabutylammonium hexafluorophosphate (TBAPF<sub>6</sub>).

### Materials

Compound **1** was prepared according to the literature [10]. The other materials were purchased from Tokyo Kasei Co., Sigma Aldrich Inc. and other commercial suppliers and used without further purification. Solvents were purchased from KANTO CHEMICAL CO., INC and purified by a solvent purification system (GlassContour) equipped with columns of activated alumina and supported copper catalyst (Q-5) prior to use.

### Synthesis

**[5-Bromo-15-phenylethynyl-10,20-bis{(triisopropylsilyl)ethynyl}porphyrinato]magnesium(II) (2a).** Compound **1** (504 mg, 0.59 mmol), phenylacetylene (94.1 mg, 0.92 mmol), Pd<sub>2</sub>(dba)<sub>3</sub> (34.2 mg, 0.037 mmol), PPh<sub>3</sub> (78.2 mg, 0.30 mmol) and CuI (28.2 mg, 0.15 mmol) were dissolved in toluene (200 mL), Et<sub>3</sub>N (50 mL) and pyridine (4 mL) under argon, and the mixture was stirred at 60 °C for 12 h. The mixture was washed with water (100 mL) three times and then dried over anhydrous Na<sub>2</sub>SO<sub>4</sub>. The solvent was evaporated, and the residue was purified by silica gel column chromatography (CH<sub>2</sub>Cl<sub>2</sub>:hexane, gradient from 1:1) and MPLC (silica

gel, THF:hexane = 3:97). Reprecipitation from CH<sub>2</sub>Cl<sub>2</sub>/MeOH gave the title compound as green solid (100 mg, 19%). <sup>1</sup>H NMR (400 MHz, CDCl<sub>3</sub>): δ, ppm 1.47 (m, 42H, TIPS), 7.53 (t, *J* = 6.9 Hz, 1H, *p*-phenyl), 7.59 (pseudo t, *J* = 7.3 Hz, 2H, *o*-phenyl), 8.05 (d, *J* = 7.3 Hz, 2H, *o*-phenyl), 9.60 (d, *J* = 4.1 Hz, 2H, β-pyrrolic), 9.64 (d, *J* = 4.6 Hz, 2H, β-pyrrolic), 9.67 (d, *J* = 4.1 Hz, 2H, β-pyrrolic), 9.70 (d, *J* = 4.6 Hz, 2H, β-pyrrolic). <sup>13</sup>C NMR (100 MHz, CDCl<sub>3</sub>): δ, ppm 11.9, 19.1, 92.6, 96.4, 98.6, 102.7, 103.4, 108.7, 109.4, 124.1, 125.5, 128.7, 131.6, 131.9, 132.1, 133.7, 135.7, 149.1, 152.2, 152.4, and 152.6. MS (MALDI<sup>+</sup>): *m/z* 870.00 (calcd. 870.30 for [M]<sup>+</sup>).

**Dimagnesium(II) complex of 4,7-bis[5-phenylethynyl]-10,20-bis((triisopropylsilyl)ethynyl)porphyrin-15-yl]-2,1,3-benzothiadiazole (4a).** Compound **2a** (100 mg, 0.12 mmol), compound **3** (17.9 mg, 0.055 mmol), Pd<sub>2</sub>(dba)<sub>3</sub> (10.2 mg, 0.011 mmol), PPh<sub>3</sub> (23.0 mg, 0.088 mmol), CuI (8.5 mg, 0.044 mmol) and K<sub>2</sub>CO<sub>3</sub> (57.0 mg, 0.42 mmol) were dissolved in THF (40 mL), Et<sub>3</sub>N (2 mL) and MeOH (4 mL) under argon, and the mixture was stirred at 80 °C for 13 h. The solvent was evaporated and then short pass silica gel column chromatography (THF:hexane = 1:1). After evaporation of solvent, the residue was purified by silica gel column chromatography (THF:hexane = 2:8). Reprecipitation from THF/MeOH gave the title compound as a reddish-brown solid (18.5 mg, 18%). <sup>1</sup>H NMR (400 MHz, THF-*d*<sub>8</sub>): δ, ppm 1.38 (m, 84H, TIPS), 7.52 (t, *J* = 7.3 Hz, 2H, *p*-phenyl), 7.60 (pseudo t, *J* = 7.3 Hz, 4H, *m*-phenyl), 8.11 (d, *J* = 7.3 Hz, 4H, *o*-phenyl), 8.63 (s, 2H), 9.63 (d, *J* = 4.6 Hz, 4H, β-pyrrolic), 9.67 (d, *J* = 4.1 Hz, 4H, β-pyrrolic), 9.70 (d, *J* = 4.1 Hz, 2H, β-pyrrolic), 10.01 (d, *J* = 4.6 Hz, 4H, β-pyrrolic). <sup>13</sup>C NMR (100 MHz, THF-*d*<sub>8</sub>): δ, ppm 13.2, 19.8, 85.4, 101.1, 111.6, 129.8, 132.4, 132.6, 132.7, 152.1, 152.3, 152.8, 152.8, and 152.9. UV-vis (THF): λ<sub>max</sub>, nm (ε) 474 (2.2 × 10<sup>5</sup>), 754 (1.6 × 10<sup>5</sup>). MS (MALDI<sup>+</sup>): *m/z* 1764.79 (calcd. 1764.76 for [M]<sup>+</sup>).

**[5-Bromo-15-[(4'-*N,N*-dimethylamino)phenyl]ethynyl]-10,20-bis((triisopropylsilyl)ethynyl)porphyrinato]magnesium(II) (2b).** Compound **1** (1.901 g, 2.233 mmol), 4-ethynyl-*N,N*-dimethylaniline (355.6 mg, 2.449 mmol), Pd<sub>2</sub>(dba)<sub>3</sub> (127.2 mg, 0.1389 mmol), PPh<sub>3</sub> (293.5 mg, 1.119 mmol) and CuI (106.8 mg, 0.5608 mmol) were dissolved in toluene (600 mL), Et<sub>3</sub>N (150 mL) and pyridine (7.5 mL) under argon, and the mixture was stirred at 80 °C for 2.5 h. The mixture was washed with water (3 × 500 mL) and then dried over anhydrous Na<sub>2</sub>SO<sub>4</sub>. The solvent was evaporated, and the residue was purified by silica gel column chromatography (CH<sub>2</sub>Cl<sub>2</sub>:hexane, gradient from 1:2 to 3:1). Reprecipitation from CH<sub>2</sub>Cl<sub>2</sub>/MeOH gave the title compound as green solid (757.9 mg, 37%). <sup>1</sup>H NMR (400 MHz, CDCl<sub>3</sub>): δ, ppm 1.43–1.56 (m, 42H, TIPS), 3.08 (s, 6H, CH<sub>3</sub>), 6.84 (d, *J* = 8.6 Hz, 2H, *m*-phenyl), 7.90 (d, *J* = 8.6 Hz, 2H, *o*-phenyl), 9.58 (d, *J* = 4.7 Hz, 2H, β-pyrrolic), 9.63 (d, *J* = 4.4 Hz, 2H, β-pyrrolic), 9.67 (d, *J* = 4.4 Hz, 2H, β-pyrrolic), 9.70 (d,

*J* = 4.4 Hz, 2H, β-pyrrolic). <sup>13</sup>C NMR (100 MHz, CDCl<sub>3</sub>): δ, ppm 11.9, 19.1, 40.2, 90.9, 98.4, 98.5, 103.3, 104.9, 108.0, 109.5, 111.3, 112.3, 131.9, 132.1, 132.1, 132.6, 133.5, 149.2, 152.0, 152.3, and 152.6. MS (MALDI<sup>+</sup>): *m/z* 913.34 (calcd. 913.03 for [M]<sup>+</sup>).

**4,7-Bis[5-[(4'-*N,N*-dimethylamino)phenyl]ethynyl]-10,20-bis((triisopropylsilyl)ethynyl)porphyrin-15-yl]-2,1,3-benzothiadiazole (4b).** Compound **2b** (200.1 mg, 0.2185 mmol), compound **3** (35.82 mg, 0.1090 mmol), Pd<sub>2</sub>(dba)<sub>3</sub> (19.95 mg, 0.02179 mmol), PPh<sub>3</sub> (45.98 mg, 0.1753 mmol), CuI (16.93 mg, 0.08889 mmol) and K<sub>2</sub>CO<sub>3</sub> (113.7 mg, 0.8229 mmol) were dissolved in THF (55 mL), Et<sub>3</sub>N (4 mL) and MeOH (8 mL) under argon, and the mixture was stirred at 80 °C for 23 h. The solvent was evaporated, and then the residue was purified by silica gel column chromatography (THF:hexane = 1:5 to THF). Reprecipitation from THF/MeOH gave the title compound as green solid (68.92 mg, 34%). <sup>1</sup>H NMR (400 MHz, THF-*d*<sub>8</sub>): δ, ppm 1.50–1.61 (m, 84H, TIPS), 3.12 (s, 12H, CH<sub>3</sub>), 6.95 (d, *J* = 8.3 Hz, 4H, *m*-phenyl), 7.94 (d, *J* = 7.8 Hz, 4H, *o*-phenyl), 8.60 (s, 2H), 9.58 (d, *J* = 3.1 Hz, 4H, β-pyrrolic), 9.63 (d, *J* = 3.4 Hz, 4H, β-pyrrolic), 9.68 (d, *J* = 4.4 Hz, 2H, β-pyrrolic), 10.01 (d, *J* = 4.4 Hz, 4H, β-pyrrolic). <sup>13</sup>C NMR (100 MHz, THF-*d*<sub>8</sub>): δ, ppm 13.0, 19.6, 40.3, 92.3, 94.5, 97.8, 100.1, 102.5, 103.6, 104.4, 107.7, 111.6, 112.9, 118.6, 129.2, 131.7, 132.2, 132.3, 132.5, 132.6, 133.6, 151.6, 151.9, 152.2, 152.4, 152.9, and 156.3. UV-vis (THF): λ<sub>max</sub>, nm (ε) 494 (4.3 × 10<sup>5</sup>), 771 (2.9 × 10<sup>5</sup>). MS (MALDI<sup>+</sup>): *m/z* 1850.84 (calcd. 1850.84 for [M]<sup>+</sup>).

## Fabrication and evaluation of OSC devices

PEDOT:PSS (H.C. Starck, Clevios PVP AI4083) were purchased from Aldrich and H.C. Starck, respectively, and used as received. Active-layer solutions were prepared by using Porphyrins and PC<sub>61</sub>BM or mix-PCBM in 1:3 or 1:4 weight ratio in chlorobenzene or 1,2-dichlorobenzene (concentration, 5 mg/mL or 10 mg/mL vs. donor materials). These blended solutions were stirred for 2 h under nitrogen atmosphere, and filtered with poly(tetrafluoroethylene) (pore size, 0.20 μm) prior to use.

All the devices were fabricated on patterned ITO substrates that were ultrasonically cleaned using a surfactant, deionized water, acetone, 2-propanol and subjected to UV-ozone treatment for 15 min. A thin layer of PEDOT:PSS was spin-coated onto the ITO glass by using an aqueous dispersion of PEDOT:PSS to obtain a smooth 40 nm thick film. The PEDOT:PSS-coated substrate was dried in air for 10 min at 120 °C, and then devices were moved in glove box (moisture and O<sub>2</sub> are <0.1 ppm). A blended solution was spin-coated onto the PEDOT:PSS layer to obtain an active layer. Thermal annealing was performed at 65 °C or 120 °C for 10 min. The Ca/Al electrode (Ca = 20 nm; Al = 80 nm) was evaporated onto the film through a shadow mask, giving a device with an active area of 0.25 cm<sup>2</sup>.

The encapsulated solar cells were subjected to  $J$ - $V$  measurements under both dark and irradiated conditions. Current-voltage sweeps were taken with a Keithley 2400 source measurement unit controlled by a computer. The light source used to determine PCE was an AM1.5G solar simulator system (Sumitomo Heavy Industries Advanced Machinery) with intensity of 100 mW/cm<sup>2</sup>. The IPCE spectrum was measured under a constant power generated by monochromatized photons using a xenon lamp.

## CONCLUSION

We synthesized low bandgap diporphyrin compound **4** containing two magnesium tetraethynylporphyrins and an electron-withdrawing 2,1,3-benzothiadiazole connecting unit through the double Sonogashira-coupling reaction. The obtained diporphyrin has long-wavelength light absorption property with the Soret band at 474 and 794 nm for **4a** and **4b**, respectively, and the Q-band at 754 and 771 nm for **4a** and **4b**, respectively. This property provided long-wavelength photocurrent conversion at the near-IR region up to 900 nm. Compound **4** showed both oxidation and reduction processes, giving estimated HOMO levels of -5.17 and -5.04 eV for **4a** and **4b**, respectively, and LUMO levels of -3.40 and -3.35 eV for **4a** and **4b**, respectively. These values are lower lying than that for the reference mono-porphyrin compound. These low-lying energy levels contributed to having high  $V_{oc}$  (0.80 V). Overall, OSC devices using the diporphyrins as electron donors showed better performance than the device using corresponding reference mono-porphyrin compounds. Further optimization of the molecular design with this diporphyrin framework will give some insights to have efficient OSCs with long-wavelength photocurrent conversion.

## Acknowledgements

This work was supported by the Tokuyama Science Foundation, and partly by the Strategic Promotion of Innovative Research and Development from the Japan Science and Technology Agency, JST and the Funding Program for Next-Generation World-Leading Researchers.

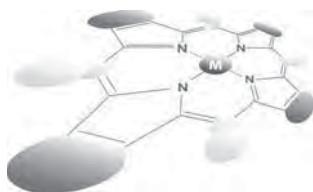
## Supporting information

AFM images (Figs S1–S13) are given in the supplementary material. This material is available free of charge via the Internet at <http://www.worldscinet.com/jpp/jpp.shtml>.

## REFERENCES

- (a) Martínez-Díaz MV, Torre G and Torres T. *Chem. Commun.* 2010; **46**: 7090–7108. (b) Imahori H, Umeyama T, Kurotobi K and Takano Y. *Chem. Commun.* 2012; **48**: 4032–4045. (c) Luo J, Xu M, Li R, Huang K-W, Jiang C, Qi Q, Zeng W, Zhang J, Chi C, Wang P and Wu J. *J. Am. Chem. Soc.* 2014; **136**: 265–272. (d) Kurotobi K, Toude Y, Kawamoto K, Fujimori Y, Ito S, Chabera P, Sundström V and Imahori H. *Chem. Eur. J.* 2013; **19**: 17075–17081. (e) Yella A, Mai C-L, Zakeeruddin SM, Chang S-N, Hsieh C-H, Yeh C-Y and Grätzel M. *Angew. Chem.* 2014; **126**: 3017–3021. (f) Mathew S, Yella A, Gao P, Humphry-Baker R, Curchod BFE, Ashari-Astani N, Tavernelli I, Rothlisberger U, Nazeeruddin MK and Grätzel M. *Nature Chem.* 2014; **6**: 242–247.
- For example; (a) Yella A, Lee H-W, Tsao HN, Yi C, Chandiran AK, Nazeeruddin MK, Diao EW-G, Yeh C-Y, Zakeeruddin SM and Grätzel M. *Science* 2011; **334**: 629–634. (b) Khan SM, Kaur M, Heflin JR and Sayyad MHJ. *Phys. Chem. Solids.* 2011; **72**: 1430–1435 (c) Li L-L and Diao EW-G. *Chem. Soc. Rev.* 2013; **42**: 291–304. (d) Lu J, Zhang B, Yuan H, Xu X, Cao K, Cui J, Liu S, Shen Y, Cheng Y, Xu J and Wang M. *J. Phys. Chem. C* 2014; **118**: 14739–14748.
- (a) Waltera MG, Rudineb AB and Wamser CC. *J. Porphyrins Phthalocyanines* 2010; **14**: 759–792. (b) Li L, Huang Y, Peng J, Cao Y and Peng X. *J. Mater. Chem. A* 2013; **1**: 2144–2150. (c) Qin H, Li L, Guo F, Su S, Peng J, Cao Y and Peng X. *Energy Environ. Sci.* 2014; **7**: 1397–1401.
- (a) Hatano J, Obata N, Yamaguchi S, Yasuda T and Matsuo Y. *J. Mater. Chem.* 2012; **22**: 19258–19263. (b) Yamamoto T, Hatano J, Nakagawa T, Yamaguchi S and Matsuo Y. *Appl. Phys. Lett.* 2013; **102**: 013305. (c) Matsuo Y, Hatano J and Nakagawa T. *J. Phys. Org. Chem.* 2014; **27**: 87–93. (d) Nakagawa T, Hatano J and Matsuo Y. *J. Porphyrins Phthalocyanines* 2014; **18**: 735–740.
- (a) Borovkov V. *Symmetry* 2014; **6**: 256–294. (b) Anyika M, Gholami H, Ashtekar KD, Acho R and Borhan B. *J. Am. Chem. Soc.* 2014; **136**: 550–553.
- (a) Susumu K, Duncan TV and Therien MJ. *J. Am. Chem. Soc.* 2005; **127**: 5186–5195. (b) Balaz M, Collins HA, Dahlstedt E and Anderson HL. *Org. Biomol. Chem.* 2009; **7**: 874–888. (c) Fisher JAN, Susumu K, Therien MJ and Yodh AG. *J. Chem. Phys.* 2009; **130**: 134506. (d) Mai C-L, Huang W-K, Lu H-P, Lee C-W, Chiu C-L, Liang Y-R, Diao EW-G and Yeh C-Y. *Chem. Commun.* 2010; **46**: 809–811.
- Walker B, Kim C and Nguyen T-Q. *Chem. Mater.* 2011; **23**: 470–482.
- (a) Taylor PN, Wylie AP, Huuskonen J and Anderson HL. *Angew. Chem. Int. Ed.* 1998; **37**: 986–989 (b) Davis NKS, Thompson AL and Anderson HL. *J. Am. Chem. Soc.* 2011; **133**: 30–31. (c) Yella A, Mai C-L, Zakeeruddin SM, Chang S-N, Hsieh C-H, Yeh C-Y and Grätzel M. *Angew. Chem. Int. Ed.* 2014; **126**: 3017–3021. (d) Wang C-L, Hu J-Y, Wu C-H, Kuo H-H, Chang Y-C, Lan Z-J, Wu H-P, Diao EW-G and Lin C-Y. *Energy Environ. Sci.* 2014; **7**: 1392–1396.

9. (a) Cheng YJ, Yang SH and Hsu CS. *Chem. Rev.* 2009; **109**: 5868–5923.
10. Screen TEO, Lawton KB, Wilson GS, Dolney N, Ispasoiu R, Goodson III T, Martin SJ, Bradley DDC and Anderson HL. *J. Mater. Chem.* 2001; **11**: 312–320.
11. Huang X, Meng J, Dong Y, Cheng Y and Zhu C-J. *Polym. Sci. Part A; Polym. Chem.* 2010; **48**: 997–1006.



# Formate dehydrogenase catalyzed CO<sub>2</sub> reduction in a chlorin-e<sub>6</sub> sensitized photochemical biofuel cell

Yutaka Amao<sup>\*a,b,c</sup> and Naho Shuto<sup>c,d</sup>

<sup>a</sup>Advanced Research Institute for Natural Science and Technology, Osaka City University, Sugimoto 3-3-138, Sumiyoshi-ku, Osaka 558-8585, Japan

<sup>b</sup>Research Center for Artificial Photosynthesis (ReCAP), Osaka City University, Sugimoto 3-3-138, Sumiyoshi-ku, Osaka 558-8585, Japan

<sup>c</sup>Precursory Research for Embryonic Science and Technology (PRESTO), Japan Science and Technology Agency, 4-1-8 Honcho Kawaguchi, Saitama 332-0012, Japan

<sup>d</sup>Department of Applied Chemistry, Oita University, Dannoharu 700, Oita 870-1192, Japan

*Dedicated to Professor Shunichi Fukuzumi on the occasion of his retirement*

Received 31 October 2014

Accepted 29 December 2014

**ABSTRACT:** The new visible-light operated CO<sub>2</sub>-glucose biofuel cell consisting of chlorin-e<sub>6</sub> immobilized on TiO<sub>2</sub> thin layer film onto optical transparent conductive glass electrode (OTE) as an anode, formate dehydrogenase (FDH) and viologen with long alkyl chain co-immobilized OTE as a cathode, and the solution containing glucose, glucose dehydrogenase (GDH) and NAD<sup>+</sup> as a fuel was developed. The short-circuit photocurrent and the open-circuit photovoltage of this cell are 37 μA.cm<sup>-2</sup> and 390 mV, respectively. The maximum power is estimated to be 57 μW.cm<sup>-2</sup>. The overall photoenergy conversion efficiency is estimated to be 0.057%. After 2 h irradiation to this cell, 0.65 μmol of formic acid was produced. During irradiation, the photocurrent was constant value of 32 ± 10 μA.cm<sup>-2</sup> in the cell. Thus, CO<sub>2</sub> reduces and formic acid produces while generating electricity with visible light irradiation to this biofuel cell.

**KEYWORDS:** chlorin-e<sub>6</sub>, formate dehydrogenase, biofuel cell, CO<sub>2</sub> reduction, solar energy, biomass.

## INTRODUCTION

Energy utilization of the saccharide based biomass resources is important in the environmental science and the development of new energy source research fields [1–3]. Biofuel cells using saccharide based biomass resources have been paid much attention for utilization of renewable energy [4–13]. We previously reported some visible-light operated saccharide-O<sub>2</sub> biofuel cell. In these reports, the visible-light operated glucose and sucrose-O<sub>2</sub> biofuel cells using chlorophyll-*a* derivative chlorin-e<sub>6</sub> (Chl-e<sub>6</sub>) immobilized onto TiO<sub>2</sub> layer with optical transparent conductive glass plate electrode (OTE), platinum layer coated OTE and solution with enzymatic

saccharide hydrolysis [14, 15]. Chlorophylls, which act as effective visible-light sensitizer in photosynthesis of green plant, have absorption maximum around 650 nm [16]. Thus, chlorophylls are attractive compound as a visible-light photosensitizer. As the carboxyl group establishes an electronic coupling with the 3d conduction band orbital manifold of Ti, the carboxyl group in photosensitizers is essential for anchoring the photosensitizing molecule on the surface of TiO<sub>2</sub>. As native chlorophylls do not have the carboxyl group, the effective electron injection from the photoexcited state of chlorophyll to the conduction band orbital of Ti is not achieved. On the other hand, Chl-e<sub>6</sub> has three carboxyl groups in molecule as shown in Fig. 1. As the absorption spectrum of Chl-e<sub>6</sub> is similar to that of chlorophyll, Chl-e<sub>6</sub> is suitable visible light photosensitizer compared with the other sensitizers [17–20].

\*Correspondence to: Yutaka Amao, email: [amao@ocarina.osaka-cu.ac.jp](mailto:amao@ocarina.osaka-cu.ac.jp), tel: +81 6-6605-3726, fax: +81 6-6605-3726

In contrast, CO<sub>2</sub> conversion to organic molecule with visible light irradiation is potential technology for the realization of catalytic CO<sub>2</sub> reduction. Some studies on the visible-light induced CO<sub>2</sub> conversion to organic molecules with enzyme and photo-redox system have been reported [21–29]. For example, formic acid production from HCO<sub>3</sub><sup>-</sup> or CO<sub>2</sub> with the system of methylviologen (MV<sup>2+</sup>) photoreduction using a system containing ruthenium(II) coordination compound as a photosensitizer and mercaptoethanol (RSH) as an electron donor in the presence of formate dehydrogenase (FDH) has also been reported [21–25]. We also previously reported the visible-light induced enzymatic formic acid production from HCO<sub>3</sub><sup>-</sup> or CO<sub>2</sub> with FDH using the photosensitization of water-soluble zinc porphyrin or chlorophyll-*a* [26–29]. In these reaction, reduced form of MV<sup>2+</sup> acts as a co-enzyme for FDH, catalyzed CO<sub>2</sub> to formic acid.

By using FDH and viologen co-immobilized electrode instead of platinum electrode, thus, visible-light operated saccharide-CO<sub>2</sub> enzyme fuel cell with formic acid production will be developed. CO<sub>2</sub> reduces and the fuel produces while generating electricity with visible light irradiation to this biofuel cell.

In this work, new visible-light operated CO<sub>2</sub>-glucose biofuel cell consisting of Chl-*e*<sub>6</sub> immobilized on TiO<sub>2</sub> thin layer onto OTE as an anode, FDH and viologen co-immobilized OTE as a cathode, and the solution containing glucose, glucose dehydrogenase (GDH) and NAD<sup>+</sup> as a fuel as shown in Fig. 1 are developed, and photovoltaic and formic acid production properties are studied.

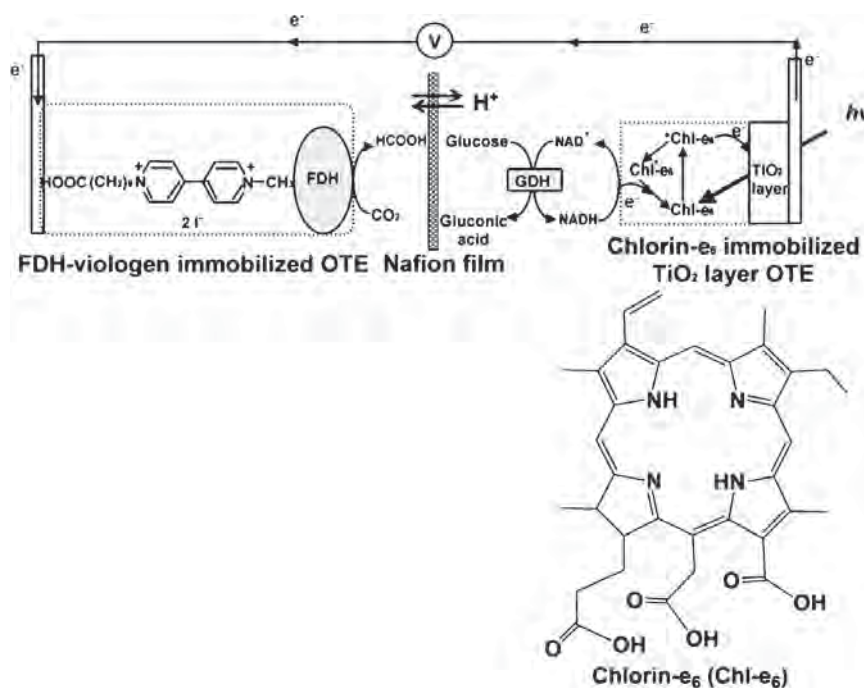
## EXPERIMENTAL

### Materials

Chl-*e*<sub>6</sub> and GDH from *Bacillus* sp. were purchased from Wako Pure Chemical Industries Ltd. (Osaka, Japan). NAD<sup>+</sup> was purchased from Oriental Yeast Co. Ltd. Titanium dioxide nano-powder (P25) was purchased from Degussa. Optical transparent conductive glass plate electrode (OTE) (10–15 Ω/square SnO<sub>2</sub>: fluorine coated) was obtained from Nihon Sheet Glass Co. Ltd. Indium-tin oxide (ITO) nanoparticle (particle shape: angular, average particle size: 30 nm) was obtained from C.I Kasei Co., Ltd. FDH from *Saccharomyces cerevisiae* and proton permeable membrane, Nafion<sup>®</sup> 115 film was obtained from Sigma-Aldrich Co. Ltd. The other chemicals were analytical grade or the highest grade available.

### Preparation of TiO<sub>2</sub> thin layer film onto OTE

The TiO<sub>2</sub> thin layer onto OTE was prepared by a similar procedure to that described in the literature for the studies on dye-sensitized solar cells [30–38]. TiO<sub>2</sub> nano-powder was dispersed by grinding HNO<sub>3</sub> aqueous solution including polyethylene glycol. The viscous suspension was spread to 1 cm<sup>2</sup> onto OTE (1 × 5 cm) at room temperature. A thin layer film was obtained by raking off the excess of suspension with a glass rod. The electrode substrate was dried using hot plate at 80 °C for 30 min, this substrate was annealed at 450 °C for 30 min under ambient condition to form a TiO<sub>2</sub> thin layer film onto OTE. The thickness of the



**Fig. 1.** Schematic drawing of visible-light operated CO<sub>2</sub>-glucose biofuel cell consisting of Chl-*e*<sub>6</sub> immobilized on TiO<sub>2</sub> thin layer film onto OTE as an anode, FDH and viologen co-immobilized OTE as a cathode, and the solution containing glucose, GDH and NAD<sup>+</sup> as a fuel

layer of TiO<sub>2</sub> onto OTE was about 10 μm, determined by using a micron-sensitive caliper.

### Preparation of Chl-e<sub>6</sub> immobilized to TiO<sub>2</sub> thin layer on OTE

Chl-e<sub>6</sub> immobilized to TiO<sub>2</sub> thin layer on OTE was prepared by following method [39]. An OTE with a TiO<sub>2</sub> thin layer film was dipped into 0.2 mM Chl-e<sub>6</sub> in methanol solution at room temperature for 6 h. After dipping, the substrate was washed with methanol several times and then the substrate was dried under vacuum overnight. Chl-e<sub>6</sub> immobilized to TiO<sub>2</sub> thin layer on OTE was defined as Chl-e<sub>6</sub>/TiO<sub>2</sub> electrode.

### Synthesis of 1-carboxyundecanoyl-1'-methyl-4,4'-bipyridinium bromide, iodide (CH<sub>3</sub>V(CH<sub>2</sub>)<sub>9</sub>COOH)

1-Methyl-4,4'-bipyridinium iodide (CH<sub>3</sub>V) was synthesized by following the method from Refs. 40 and 41. 4,4'-Bipyridine (0.16 mol) was dissolved in 400 mL of acetone and then methyl iodide (0.18 mol) was added to the reaction mixture with stirring at room temperature for 24 h. CH<sub>3</sub>V was produced as a yellow precipitate. The precipitate was collected by suction filtration and washed with acetone. The desired product was recrystallized from ethanol and water and dried under vacuum overnight.

1-Carboxyundecanoyl-1'-methyl-4,4'-bipyridinium bromide, iodide (CH<sub>3</sub>V(CH<sub>2</sub>)<sub>9</sub>COOH) was synthesized by refluxing CH<sub>3</sub>V with about 10 times the molar equivalent of 1-bromoundecanoic acid in 100 mL acetonitrile at 90 °C for 24 h. CH<sub>3</sub>V(CH<sub>2</sub>)<sub>9</sub>COOH was produced as a yellow precipitate. The precipitate was collected by suction filtration and washed with acetonitrile. The desired product was recrystallized from ethanol and water and dried under vacuum overnight.

### Preparation of FDH-CH<sub>3</sub>V(CH<sub>2</sub>)<sub>9</sub>COOH co-immobilized onto OTE

The viscous suspension containing indium-tin oxide nanoparticle was spread to 1 cm<sup>2</sup> onto OTE (1 × 5 cm) at room temperature. An ITO thin layer film was obtained by raking off the excess of suspension with a glass rod. The substrate was dried using hot plate at 80 °C for 30 min, was annealed at 450 °C for 30 min under ambient condition to form an ITO thin layer film onto OTE. The active area of electrode was 1.0 cm<sup>2</sup>. To immobilize the CH<sub>3</sub>V(CH<sub>2</sub>)<sub>9</sub>COOH onto the ITO thin layer film onto OTE, the substrate was dipped into methanol solution containing CH<sub>3</sub>V(CH<sub>2</sub>)<sub>9</sub>COOH (300 μM) for 68 h at 25 °C. To physically remove adsorbed CH<sub>3</sub>V(CH<sub>2</sub>)<sub>9</sub>COOH, the electrode was washed with methanol. This was defined as CH<sub>3</sub>V(CH<sub>2</sub>)<sub>9</sub>COOH/ITO electrode. Finally, FDH was immobilized onto the CH<sub>3</sub>V(CH<sub>2</sub>)<sub>9</sub>COOH/ITO electrode. The electrode was dipped into the sodium pyrophosphate buffer solution (pH 7.4) containing FDH (0.75 μM) for 1 h at 4 °C and then was washed with sodium

pyrophosphate buffer solution (pH 7). This was defined as FDH-CH<sub>3</sub>V(CH<sub>2</sub>)<sub>9</sub>COOH/ITO electrode.

### Characterization of photoelectrochemical biofuel cell

The anode with the Chl-e<sub>6</sub>/TiO<sub>2</sub> electrode was gently squeezed together with a FDH-CH<sub>3</sub>V(CH<sub>2</sub>)<sub>9</sub>COOH/ITO electrode (cathode) *via* the proton transparent membrane (PEM), Nafion® 115 using spring and irradiated from the electrode side of anode. The anodic solution consisted of 0.1 M glucose, 3.5 mM NAD<sup>+</sup> and 10 μM GDH in 50 mM in 10 mM Tris-HCl buffer (pH 7.0). The CO<sub>2</sub> saturated 10 mM Tris-HCl buffer (pH 7.0) solution was used as cathodic reaction. This cell was defined as visible-light operated glucose-CO<sub>2</sub> biofuel cell.

A solar simulator (YSS-40, Yamashita Denso) was used as a light source (A.M. 1.5 100 mW.cm<sup>-2</sup>). The photovoltage and photocurrent responses were measured with a digital multimeter with model 34401A (Agilent) under dark and irradiation cycles.

The photocurrent-photovoltage characteristic of the cell was measured with the two digital multimeters. The photocurrent and photovoltage were changed with 500-W variable resistor. The active electrode area was 1.0 cm<sup>2</sup>.  $I_{\text{Ph(max)}}$  and  $V_{\text{Ph(max)}}$  are the photocurrent and photovoltage for output of maximum power ( $P_{\text{max}}$ ).  $I_{\text{SC}}$  and  $V_{\text{OC}}$  are indicated the closed-circuit photocurrent and open-circuit photovoltage. The overall photoenergy conversion efficiency ( $\lambda$ ) is defined by the following equation:

$$h = P_{\text{max}}/P_{\text{in}} \quad (1)$$

where  $P_{\text{in}}$  is the power of incident light source (100 mW.cm<sup>-2</sup>).

The concentration of formic acid produced in cell during irradiation was measured with an ionic chromatograph system (Dionex IC2000).

A 400 W Xe lamp with a monochromator was used as light source for the measurement of photocurrent action spectrum in the short-circuit mode. The incident photon-to-current conversion efficiency (IPCE) values were determined between 400 and 750 nm, calculated according to the following equation:

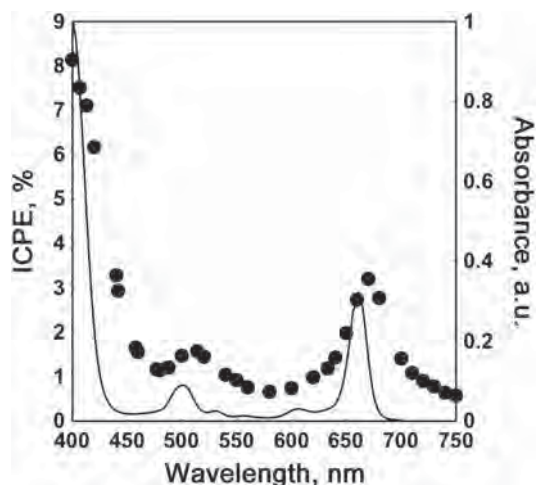
$$\text{IPCE} = 1240 i_{\text{ph}}(\text{mA})/P(\text{mW}) \lambda (\text{nm}) \quad (2)$$

where  $i_{\text{ph}}$  and  $P$  are the photocurrent and power of the incident radiation and  $\lambda$  is the wavelength of monochromatic light.

## RESULTS AND DISCUSSION

### Photocurrent action spectrum

The effect of wavelength of light source on the photocurrent of visible-light operated glucose-CO<sub>2</sub> biofuel cell was investigated. Figure 2 shows the



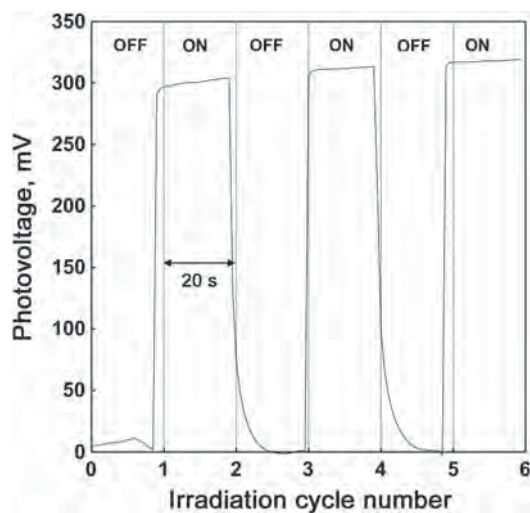
**Fig. 2.** Photocurrent action spectra of visible-light operated  $\text{CO}_2$ -glucose biofuel cell (closed circle). The IPCE is plotted as a function of wavelength. The solid line is UV-vis absorption spectrum of Chl- $e_6$  in methanol solution

photocurrent action spectrum of visible-light operated glucose- $\text{CO}_2$  biofuel cell (closed circle), where the IPCE is plotted as a function of wavelength. The photocurrent action spectrum was similar to that of the UV-vis absorption spectrum of Chl- $e_6$  in methanol solution as shown in Fig. 2 (solid line). IPCE values were reached a maximum around the wavelength of absorption maximum. IPCE values of visible-light operated glucose- $\text{CO}_2$  biofuel cell at 400, 541 and 661 nm are 8.0, 1.8 and 3.8%, respectively. Thus, the biofuel cell using visible light sensitization of  $\text{TiO}_2$  film by Chl- $e_6$  was developed.

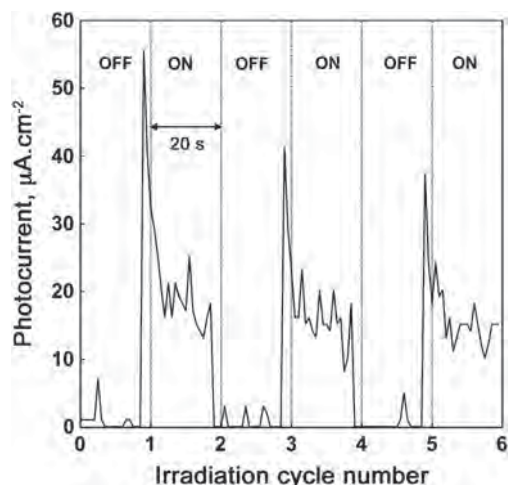
### Photovoltage and photocurrent responses

Figure 3 shows the photovoltage response of visible-light operated  $\text{CO}_2$ -glucose biofuel cell under dark and irradiation cycles. The voltage increased under irradiation and decreased under dark conditions. Under irradiation condition, photovoltage was estimated to be *ca.*  $330 \pm 30$  mV. The voltage changes were fully reversible and hysteresis was not observed during the measurements.

Figure 4 shows the photocurrent response of visible-light operated  $\text{CO}_2$ -glucose biofuel cell under dark and irradiation conditions. The current also increased under irradiation and decreased under dark conditions. When the visible-light was irradiated to cell, photocurrent was increased and then was reached to constant value. This is caused by back electron transfer between the viologen unit and the ITO electrode in  $\text{CH}_3\text{V}(\text{CH}_2)_9\text{COOH}/\text{ITO}$  electrode. Under irradiation condition, photocurrent was estimated to be *ca.*  $27 \pm 10 \mu\text{Acm}^{-2}$ . The current changes were also fully reversible and hysteresis was not observed during the measurements.



**Fig. 3.** Photovoltage response of visible-light operated  $\text{CO}_2$ -glucose biofuel cell under dark and irradiation cycles with  $100 \text{ mW}\cdot\text{cm}^{-2}$  light



**Fig. 4.** Photocurrent response of visible-light operated  $\text{CO}_2$ -glucose biofuel cell under dark and irradiation cycles with  $100 \text{ mW}\cdot\text{cm}^{-2}$  light

### Photocurrent-photovoltage profile

Figure 5 shows the photocurrent-photovoltage characteristics of visible-light operated glucose- $\text{CO}_2$  biofuel cell irradiated with the light intensity of  $100 \text{ mW}\cdot\text{cm}^{-2}$ . The short-circuit photocurrent ( $I_{\text{SC}}$ ) was  $37 \mu\text{A}\cdot\text{cm}^{-2}$ , and the open-circuit photovoltage ( $V_{\text{OC}}$ ) is 390 mV, respectively. The power output of cell as a function of photovoltage also is shown in Fig. 5. The maximum power,  $P_{\text{max}}$  is estimated to be  $57 \mu\text{W}\cdot\text{cm}^{-2}$ .  $\eta$  value calculated by Equation 1 is estimated to be 0.057%. In contrast,  $I_{\text{SC}}$  and  $V_{\text{OC}}$  under the dark condition in this cell are *ca.* zero. Thus, this cell is operated with the visible-light photosensitization of  $\text{TiO}_2$  thin layer film by Chl- $e_6$ . These results show that visible-light operated glucose- $\text{CO}_2$  biofuel cell based on the visible-light



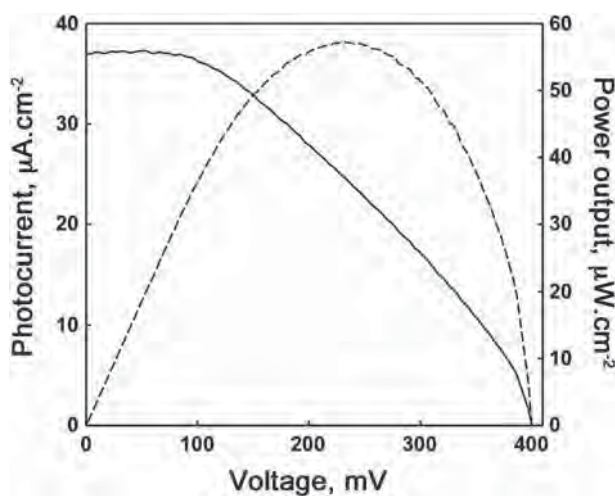


Fig. 5. Photocurrent-photovoltage characteristic and power output curves of visible-light operated CO<sub>2</sub>-glucose biofuel cell under 100 mW.cm<sup>-2</sup> irradiation

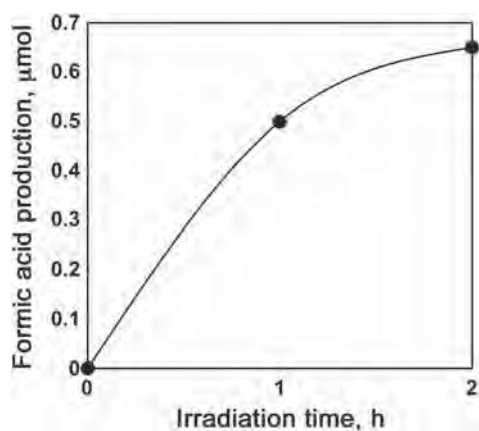


Fig. 6. Time dependence of formic acid production in visible-light operated CO<sub>2</sub>-glucose biofuel cell under 100 mW.cm<sup>-2</sup> irradiation

photosensitization of TiO<sub>2</sub> thin layer film by Chl-e<sub>6</sub> and FDH-CH<sub>3</sub>V(CH<sub>2</sub>)<sub>9</sub>COOH/ITO electrode was developed.

#### Formic acid production in the CO<sub>2</sub>-glucose biofuel cell with visible-light irradiation

Next let us focus on the formic acid production from CO<sub>2</sub> in the CO<sub>2</sub>-glucose biofuel cell with visible-light irradiation. Figure 6 shows the time dependence of formic acid production in the CO<sub>2</sub>-glucose biofuel cell with visible-light irradiation. After 2 h irradiation, 0.65 μmol of formic acid was produced. During irradiation, the photocurrent was constant value of 32 ± 10 μA.cm<sup>-2</sup> in the cell. Thus, CO<sub>2</sub> is reduced and formic acid is produced while generating electricity with visible light irradiation to this biofuel cell.

## CONCLUSION

In conclusion, the new visible-light operated CO<sub>2</sub>-glucose biofuel cell consisting of chlorin-e<sub>6</sub> immobilized on TiO<sub>2</sub> thin layer film onto OTE as an anode, FDH and viologen with long alkyl chain co-immobilized OTE as a cathode, and the solution containing glucose, GDH and NAD<sup>+</sup> as a fuel is developed and photovoltaic properties are studied. In this cell, the short-circuit photocurrent and the open-circuit photovoltage are estimated to be 37 μA.cm<sup>-2</sup> and 390 mV, respectively. The maximum power and the overall photoenergy conversion efficiency are estimated to be 57 μW.cm<sup>-2</sup> and 0.057%, respectively. During irradiation, the photocurrent was a constant value of 32 ± 10 μA.cm<sup>-2</sup> and 0.65 μmol of formic acid was produced after 2 h irradiation to the cell. Thus, CO<sub>2</sub> is reduced and formic acid is produced while generating electricity with visible light irradiation to this biofuel cell.

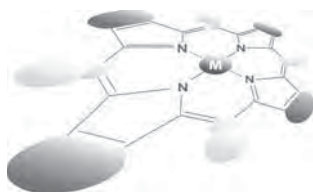
## Acknowledgements

This work was partially supported by Precursory Research for Embryonic Science and Technology (PRESTO, Japan Science and Technology Agency JST), Grants-in-Aid for Scientific Research (C) (Japan Society for the Promotion of Science) (23560947), and Grant-in-Aid for Scientific Research on Innovative Areas "Artificial Photosynthesis (2406)."

## REFERENCES

1. Wang D. *Fuel Energy Abstract* 1998; **39**: 188.
2. Minowa T and Inoue S. *Renew. Energ.* 1999; **16**: 1114–1117.
3. Rustamov VR, Abdullayev KM, Aliyev FG and Kerimov VK. *Int. J. Hydro. Energ.* 1998; **23**: 649–652.
4. Bullen RA, Arnot TC, Lakeman JB and Walsh FC. *Biosens. Bioelectron.* 2006; **21**: 2015–2045.
5. Ramanavicius A, Kausaite A and Ramanaviciene A. *Biosens. Bioelectron.* 2005; **20**: 1962–1967.
6. Davis F and Higson SPJ. *Biosens. Bioelectron.* 2007; **22**: 1224–1235.
7. Akers NL, Moore CM and Minteer SD. *Electrochim. Acta* 2006; **50**: 2521–2525.
8. Inamuddin, Shin KM, Kim SI, So I and Kim SJ. *Electrochim. Acta* 2009; **54**: 3979–3983.
9. Wang SC, Yang F, Silva M, Zarow A, Wang Y and Iqbal Z. *Electrochem. Commun.* 2009; **11**: 34–37.
10. Taylor G. *Energy Policy* 2008; **36**: 4406–4409.
11. Barbosa MJ, Rocha MJ, Tramper J and Wijffels RH. *J. Biotechnol.* 2001; **85**: 25–33.
12. Garcia L, French R, Czernik S and Chornet E. *Appl. Catal. A: General.* 2001; **201**: 225–239.
13. Hambourger M, Gervaldo M, Svedruzic D, King PW, Gust D, Ghirardi M, Moore AL and Moore TA. *J. Am. Chem. Soc.* 2008; **130**: 2015–2022.

14. Amao Y and Takeuchi Y. *Int. J. Glob. Energ. Issue.* 2007; **28**: 295–303.
15. Amao Y and Takeuchi Y. *Int. J. Hydro. Energ.* 2008; **33**: 2845–2849.
16. Scheer H. *Chlorophylls*, CRC Press: London, 1991.
17. Kamat PV, Chauvet JP and Fessenden RW. *J. Phys. Chem.* 1986; **90**: 1389–1394.
18. Komori T and Amao Y. *Electrochemistry* 2003; **71**: 174–176.
19. Amao Y, Yamada Y and Aoki K. *J. Photochem. Photobiol. A: Chem.* 2004; **164**: 47–51.
20. Amao Y and Komori T. *Biosens. Bioelectron.* 2004; **19**: 843–847.
21. Mandler D and Willner I. *J. Chem. Soc. Perkin Trans 2.* 1998; 997–1003.
22. Willner I and Mandler D. *J. Am. Chem. Soc.* 1989; **111**: 1330–1336.
23. Willner I, Lapidot N, Riklin A, Kasher R, Zahavy E and Katz E. *J. Am. Chem. Soc.* 1994; **116**: 1428–1441.
24. Willner I and Lapidot N. *J. Am. Chem. Soc.* 1990; **112**: 6438–6439.
25. Kodaka M and Kubota Y. *J. Chem. Soc. Perkin Trans 2.* 1999; 891–894.
26. Miyatani R and Amao Y. *Biotechnol. Lett.* 2002; **24**: 1931–1934.
27. Miyatani R and Amao Y. *J. Mol. Catal. B. Enzym.* 2004; **27**: 121–125.
28. Miyatani R and Amao Y. *J. Jpn. Petrol. Inst.* 2004; **47**: 27–31.
29. Tsujisho I, Toyoda M and Amao Y. *Catal. Commun.* 2006; **7**: 173–176.
30. O'Regan B and Grätzel M. *Nature* 1991; **353**: 737–740.
31. Nazeeruddin MK, Kay A, Rodicio I, Humphry-Baker R, Muller E, Vlachopoulos N and Grätzel M. *J. Am. Chem. Soc.* 1993; **115**: 6382–6390.
32. Pechy P, Rotzinger FP, Nazeeruddin MK, Kohle O, Zakeeruddin SM, Humphry-Baker R and Grätzel M. *J. Chem. Soc. Chem. Commun.* 1995; 65–66.
33. Papageorgiou N, Athanassov Y, Bonhote P, Pettersson H, Azam A and Grätzel M. *J. Electrochem. Soc.* 1996; **143**: 3099–3108.
34. Wada Y, Tomita K, Murakoshi K and Yanagida S. *J. Chem. Res. (S).* 1996; 320–321.
35. Murakoshi K, Kogure R, Wada Y and Yanagida S. *Chem. Lett.* 1997; 471–472.
36. Nakade S, Kambe S, Kitamura T, Wada Y and Yanagida S. *J. Phys. Chem. B.* 2001; **105**: 9150–9152.
37. Zhang D, Ito S, Wada Y, Kitamura T and Yanagida S. *Chem. Lett.* 2001; 1042–1043.
38. Kitamura T, Maitani M, Matsuda M, Wada Y and Yanagida S. *Chem. Lett.* 2001; 1054–1055.
39. Amao Y and Yamada Y. *Langmuir* 2005; **21**: 3008–3012.
40. Amao Y, Shuto N, Furuno K, Obata A, Fuchino Y, Uemura K, Kajino T, Sekito T, Iwai S, Miyamoto Y and Matsuda M. *Faraday Discuss.* 2012; **155**: 289–296.
41. Amao Y and Shuto N. *Res.Chem. Intermed.* 2014; **40**: 3267–3276.



## Effect of alkyl substituents: 5,15-bis(trimethylsilylethynyl)-vs. 5,15-bis(triisopropylsilylethynyl)-tetrabenzoporphyrins and their metal complexes

Kohtaro Takahashi<sup>a</sup>, Naoya Yamada<sup>b</sup>, Daichi Kumagai<sup>b</sup>, Daiki Kuzuhara<sup>a,†</sup>,  
Mitsuharu Suzuki<sup>a</sup>, Yuji Yamaguchi<sup>b</sup>, Naoki Aratani<sup>a</sup>, Ken-ichi Nakayama<sup>\*b</sup>  
and Hiroko Yamada<sup>\*a,†</sup>

<sup>a</sup> Graduate School of Materials Science, Nara Institute of Science and Technology, 8916-5, Ikoma, Nara 630-0192, Japan

<sup>b</sup> Department of Organic Device Engineering, Graduate School of Science and Engineering, Yamagata University, Yonezawa 992-8510, Japan

<sup>c</sup> CREST, Japan Science and Technology Agency (JST), 4-1-8 Honcho, Kawaguchi, Saitama 332-0012, Japan

Dedicated to Professor Shunichi Fukuzumi on the occasion of his retirement

Received 4 November 2014

Accepted 29 December 2014

**ABSTRACT:** The copper(II), nickel(II), *etc.* complexes of 5,15-bis(trimethylsilylethynyl)tetrabenzoporphyrin (**TMS-H<sub>2</sub>BP**) and 5,15-bis(triisopropylsilylethynyl)tetrabenzoporphyrin (**TIPS-H<sub>2</sub>BP**) have been prepared from the corresponding bicycle[2.2.2]octadiene(BCOD)-fused precursors by the retro-Diels–Alder reaction. X-ray diffraction (XRD) analyses show that **TMS-H<sub>2</sub>BP** and its metal complexes of zinc(II) (**TMS-ZnBP**) and copper(II) (**TMS-CuBP**) adopt flat molecular conformations and form herringbone-type packing structures in the single crystalline state. **TIPS-H<sub>2</sub>BP** and the zinc(II) and copper(II) complexes (**TIPS-ZnBP** and **TIPS-CuBP**) are similar to the TMS derivatives in molecular conformation, but these TIPS derivatives form one-dimensional slipped-stack structures. The nickel complexes **TMS-NiBP** and **TIPS-NiBP** have U-shaped structures because of the small size of nickel(II) ion. Solution processed organic thin-film transistors of the benzoporphyrins were fabricated and **TMS-H<sub>2</sub>BP** showed the highest hole mobility of 0.11 cm<sup>2</sup>.V<sup>-1</sup>.s<sup>-1</sup>. Bulk heterojunction organic solar cells based on **TMS-** or **TIPS-H<sub>2</sub>BP** and their metal complexes as *p*-type and PC<sub>71</sub>BM as *n*-type materials were fabricated by solution process. Atomic force microscopy and thin-film XRD measurements indicated that the film crystallinities were increased by raising the annealing temperature over 180 °C or by changing the substituents from triisopropylsilyl to trimethylsilyl. The best power-conversion efficiency (PCE) of 1.49% was achieved with **TMS-ZnBP** by annealing at 180 °C with a moderate crystallinity and smooth surface.

**KEYWORDS:** benzoporphyrin, metal complexes, crystal structure, organic solar cells.

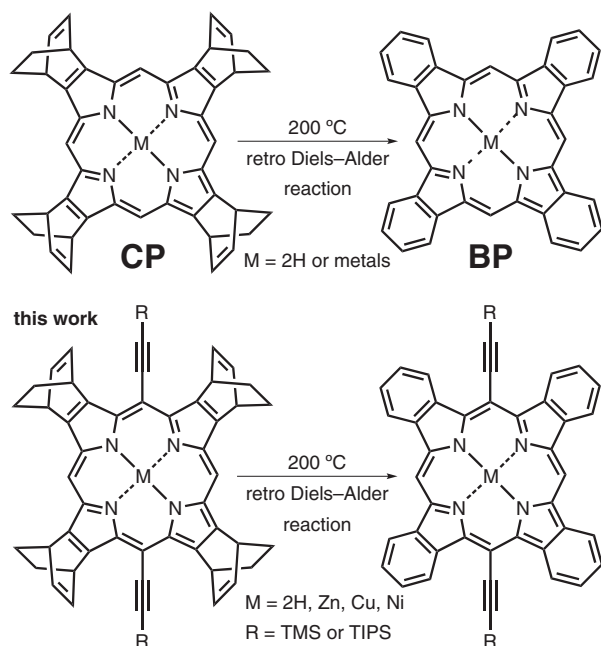
## INTRODUCTION

Organic semiconducting materials have attracted much attention for the development of organic electronics such as organic thin-film transistors (OTFTs) and organic solar cells

(OSCs). These organic electronic devices are expected to be flexible, light-weight, large area and low cost. Recently, high mobilities of over 10 cm<sup>2</sup>.V<sup>-1</sup>.s<sup>-1</sup> have been attained in OTFTs, which are close to or over the performances of amorphous silicon devices [1, 2]. The power-conversion efficiencies of OSCs have been reported to reach almost 10% with single and tandem systems using polymers as active layers [3]. Tetrabenzoporphyrin (**BP**) has been reported as one of the excellent organic semiconducting

<sup>†</sup> SPP full member in good standing

\*Correspondence to: Hiroko Yamada, email: hyamada@ms.naist.jp, Fax: +81 743-72-6042



**Fig. 1.** Synthesis of **BPs** by the retro Diels–Alder reaction

materials. However, the solubility of **BP** is low in common organic solvents, and thus **BP** is not compatible with solution-based deposition processes. In order to apply **BP** to solution-process, Ono and his colleagues have developed a soluble precursor of **BP**, bicyclo[2.2.2]octadiene-fused (or annulated) porphyrin (**CP**), which is soluble in common organic solvents such as chloroform, toluene and chlorobenzene [4]. The precursor **CP** can be quantitatively converted to **BP** upon heating through the retro Diels–Alder reaction (Fig. 1) in solution and in the solid state without chemical reagents and purification. This thermal conversion method thus has allowed us not only to synthesize  $\pi$ -expanded porphyrins and related compounds [5], phthalocyanines [6], BODIPYs [7], isothianaphthenes [8], thioindigo [9] and acenes [10], but also to apply the materials to solution-processed OTFTs and OSCs. Ono, Kanicki, and coworkers have achieved a carrier mobility of  $0.1 \text{ cm}^2 \cdot \text{V}^{-1} \cdot \text{s}^{-1}$  in a top-gate-bottom-contact OTFT device [11]. In addition, the precursor method enables fabrication of multi-layer organic films by solution process owing to the insolubilization of thin films after the thermal conversion. Using this “precursor approach,” Nakamura *et al.* fabricated *p*–*i*–*n*-type OSC devices based on **BP** as *p*-type material and bis(dimethylphenylsilylmethyl)[60]fullerenes (SIMEF) as *n*-type material to achieve the maximum photo-conversion efficiency (PCE) of 5.2% [12]. More recently, we have reported the synthesis of a **BP**–fullerene dyad for use as the inter (*i*)-layer material in *p*–*i*–*n*-type OSCs, in which we obtained PCEs up to 1.98% [13].

To improve the performance of organic electronic devices, molecular design of semiconducting materials is among the most important considerations. Pentacene

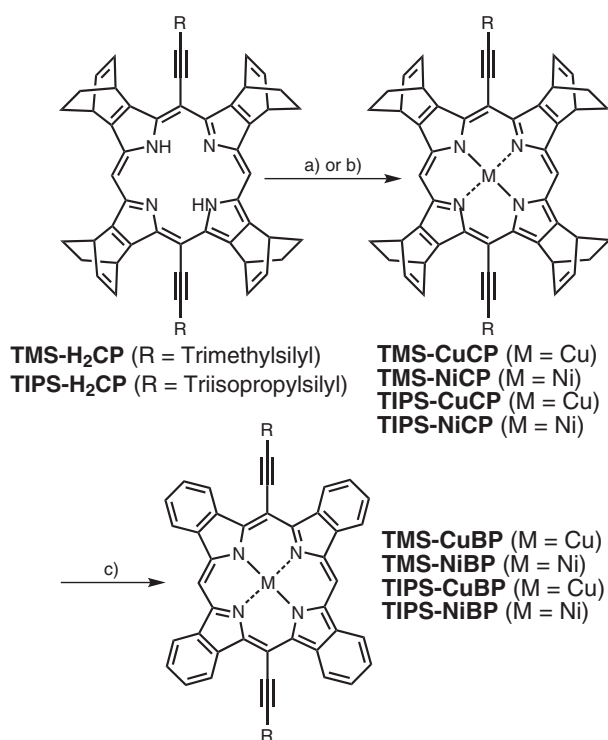
is one of the most promising organic semiconducting materials showing good carrier mobilities of over  $1 \text{ cm}^2 \cdot \text{V}^{-1} \cdot \text{s}^{-1}$  in OTFT devices, but it is hardly soluble in common organic solvents and unstable in ambient conditions. In contrast, 6,13-triisopropylsilylethynyl-pentacene (TIPS-PEN) represents a good solubility and chemical stability owing to the introduction of the bulky triisopropylsilyl (TIPS)-ethynyl groups to the most reactive 6,13-positions. The pristine pentacene packs to form a herringbone motif, while TIPS-PEN forms a two-dimensional-slipped-stack column structure [14]. TIPS-PEN-based OTFTs show superior carrier mobilities of up to  $11 \text{ cm}^2 \cdot \text{V}^{-1} \cdot \text{s}^{-1}$  in solution-processed single-crystalline film [15]. Motivated by these results, various TIPS and related trialkylsilyl substituted acene derivatives have been developed as organic FET materials [16].

Based on these precedent contributions, we have designed and synthesized 5,15-bis(trimethylsilylethynyl) tetrabenzoporphyrin (**TMS-H<sub>2</sub>BP**), 5,15-bis(triisopropylsilylethynyl)tetrabenzoporphyrin (**TIPS-H<sub>2</sub>BP**) and their zinc complexes [17]. Trialkylsilylethynyl groups were introduced to the 5- and 15-positions of **BP** to expand  $\pi$ -conjugation effectively. **TMS-H<sub>2</sub>BP** and **TIPS-H<sub>2</sub>BP** were prepared by the retro Diels–Alder reaction of BCOD-fused 5,15-bis(trimethylsilylethynyl)porphyrin (**TMS-H<sub>2</sub>CP**) and 5,15-bis(triisopropylsilylethynyl)porphyrin (**TIPS-H<sub>2</sub>CP**), respectively. The absorption of **TMS-H<sub>2</sub>BP** is redshifted as compared to **BP** and its absorption edge reaches 710 nm. Such a redshift is favorable for OSC materials, and a similar redshift was observed for **TIPS-H<sub>2</sub>BP**. At the same time, the solubility and crystal structures are different depending on the introduced substituent. Herein, we will describe the synthesis, optical properties, electrochemical properties and crystal structures of zinc(II), copper(II) and nickel(II) complexes of **TMS-H<sub>2</sub>BP** and **TIPS-H<sub>2</sub>BP** in order to discuss the substituent effect of trimethylsilyl (TMS) and TIPS groups on **BP**. The performances of OTFT and bulk heterojunction (BHJ) OSC devices of **TMS-H<sub>2</sub>BP**, **TIPS-H<sub>2</sub>BP** and their zinc and copper complexes as *p*-type materials and [6,6]-phenyl C<sub>71</sub> butyric acid methyl ester (PC<sub>71</sub>BM) as an *n*-type material will be also discussed.

## RESULTS AND DISCUSSION

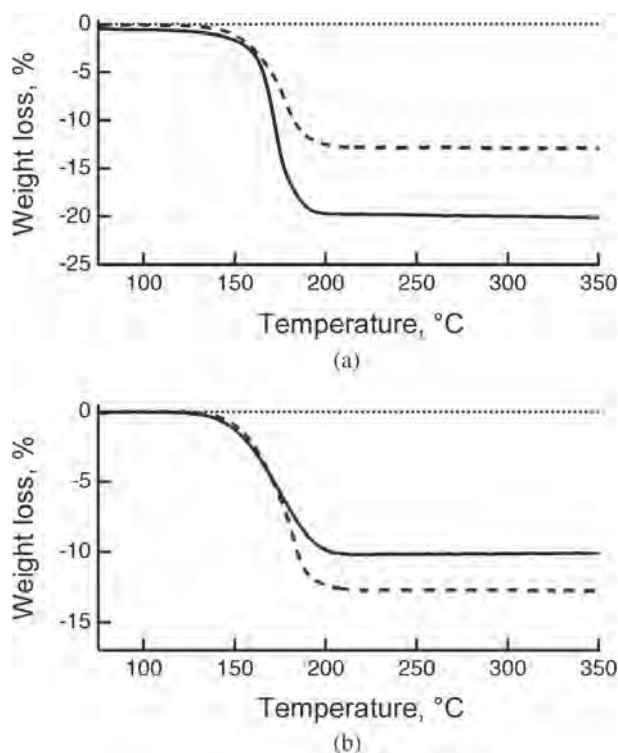
### Synthesis and characterization of TMS-BP and TIPS-BP metal complexes

**TMS-H<sub>2</sub>CP**, **TMS-H<sub>2</sub>BP**, **TIPS-H<sub>2</sub>CP** and **TIPS-H<sub>2</sub>BP** and the corresponding zinc(II) complexes were prepared according to the literature [17a–17c]. The synthesis of metal complexes of **TMS-BP** and **TIPS-BP** is shown in Scheme 1. The copper and nickel complexes of **TMS-CP** and **TIPS-CP** were synthesized from **TMS-H<sub>2</sub>CP** and **TIPS-H<sub>2</sub>CP** by general metal insertion methods. **TMS-H<sub>2</sub>CP** and **TIPS-H<sub>2</sub>CP** were



**Scheme 1.** Synthesis of **TMS-BP** and **TIPS-BP** metal complexes. Reagents and conditions: (a)  $\text{Cu}(\text{OAc})_2 \cdot \text{H}_2\text{O}$ ,  $\text{CHCl}_3$ , MeOH; (b)  $\text{Ni}(\text{OAc})_2 \cdot 4\text{H}_2\text{O}$ ,  $\text{CHCl}_3$ , MeOH

reacted with  $\text{Cu}(\text{OAc})_2 \cdot \text{H}_2\text{O}$  in  $\text{CHCl}_3$  and MeOH to give **TMS-CuCP** in 84% and **TIPS-CuCP** in 91% yields. The nickel complexes were also prepared from **TMS-H<sub>2</sub>CP** and **TIPS-H<sub>2</sub>CP** through the reactions with  $\text{Ni}(\text{OAc})_2 \cdot 4\text{H}_2\text{O}$  in  $\text{CHCl}_3$  and MeOH, by which **TMS-NiCP** and **TIPS-NiCP** were obtained in 87% and 93% yields, respectively. The thermal conversion of copper and nickel complexes of **TMS-CP** and **TIPS-CP** was analyzed by thermogravimetric analysis (TGA) with a heating rate of  $10^\circ\text{C} \cdot \text{min}^{-1}$  under a nitrogen atmosphere (Fig. 2). The mass loss of all metal complexes started at around  $150^\circ\text{C}$  and finished at around  $200^\circ\text{C}$ . The observed mass loss of 12.8% for **TMS-CuCP** is in agreement with the calculated value of 12.8% for the loss of the four ethylene units per molecule. The mass loss for **TMS-NiCP** (12.9%) and **TIPS-NiCP** (10.2%) are also in agreement with the calculated values of 12.8% and 10.8%. On the other hand, the observed mass loss of **TIPS-CuCP** is 19.7%, which is consistent with the loss of four ethylene molecules and a chloroform molecule per one **TIPS-CuCP** molecule (calculated value: 19.9%). The TGA results suggested that the precursor **CPs** could be converted to the corresponding **BPs** quantitatively by heating at  $200^\circ\text{C}$  in the solid state. The **TMS-CuBP** and **TMS-NiBP** exhibited low solubilities in common organic solvents, while **TIPS-CuBP** and **TIPS-NiBP** were soluble in halogenated solvents, THF and toluene.



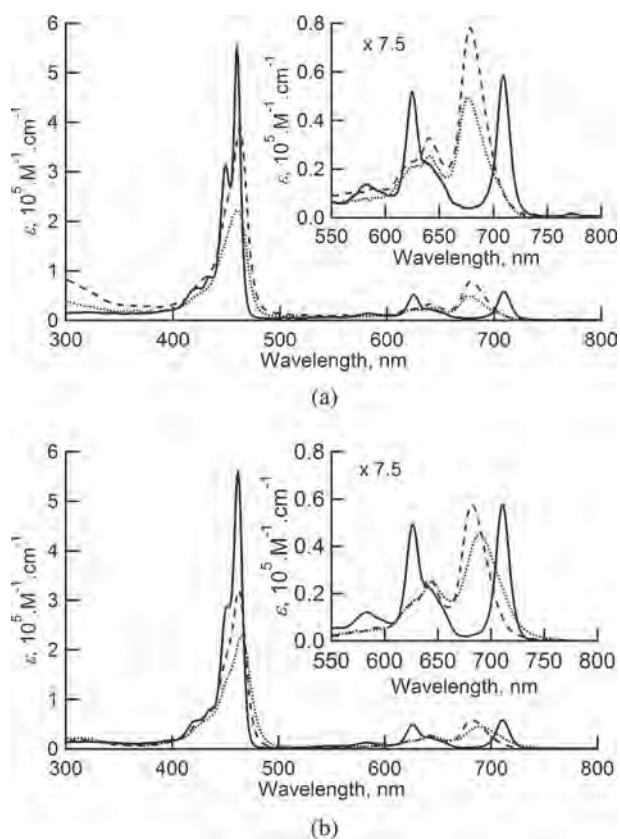
**Fig. 2.** Thermogravimetric analyses of (a) **TMS-CuCP** (broken line) and **TIPS-CuCP** (solid line). (b) **TMS-NiCP** (broken line) and **TIPS-NiCP** (solid line). Data was taken with a heating rate of  $10^\circ\text{C} \cdot \text{min}^{-1}$  under a nitrogen atmosphere

The structures of **TMS-NiBP** and **TIPS-NiBP** were characterized by  $^1\text{H}$  and  $^{13}\text{C}$  NMR spectroscopy, high-resolution mass spectrometry (HRMS) and single-crystal X-ray diffraction (XRD) analysis. **TMS-CuBP** and **TIPS-CuBP** were also characterized by HRMS and single-crystal XRD analysis.

### Photophysical and electrochemical properties

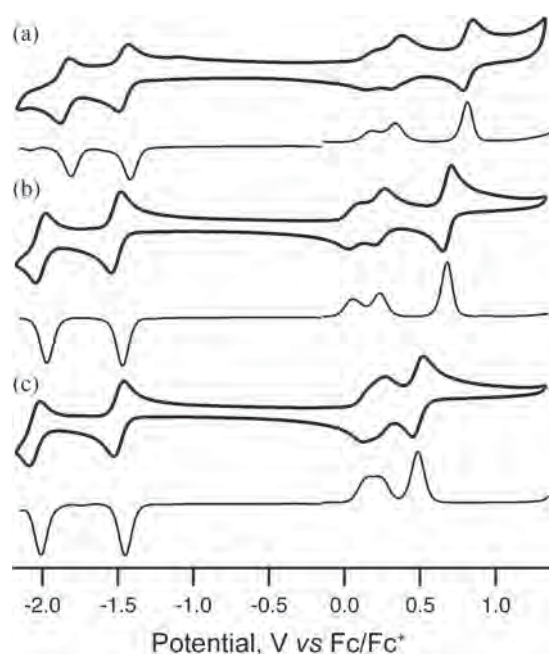
The UV-vis absorption spectra of **TMS-BPs** in DMF and **TIPS-BPs** in  $\text{CH}_2\text{Cl}_2$  are shown in Fig. 3. The obtained optical data are summarized in Table 1. We previously reported the absorption of **TMS-H<sub>2</sub>BP**, **TMS-ZnBP** [17c], **TIPS-H<sub>2</sub>BP** and **TIPS-ZnBP** [17a] in  $\text{CH}_2\text{Cl}_2$ . **TMS-H<sub>2</sub>BP** shows peak top of the Soret-band at 462 nm and the longest wavelength of Q-band at 711 nm and **TIPS-H<sub>2</sub>BP** shows at 460 and 710 nm. The absorption spectra of **TMS-BPs** and **TIPS-BPs** are redshifted from **TMS-CPs** and **TIPS-CPs** because of the  $\pi$ -expansion (Fig. S1). The Soret band peaks of metal porphyrins are almost the same as those of free-base porphyrins, but the longest Q-band peaks are blueshifted compared to the free-base porphyrins.

To investigate the electrochemical properties of **TIPS-H<sub>2</sub>BP** and its metal complexes, we performed the cyclic voltammetry (CV) and differential pulse voltammetry (DPV) in  $\text{CH}_2\text{Cl}_2$  with 0.1 M *n*-Bu<sub>4</sub>NPF<sub>6</sub> as an electrolyte



**Fig. 3.** Absorption spectra of (a) **TMS-CuBP** (broken line), **TMS-NiBP** (dotted line) and **TMS-H<sub>2</sub>BP** (solid line) in DMF and (b) **TIPS-CuBP** (broken line), **TIPS-NiBP** (dotted line) and **TIPS-H<sub>2</sub>BP** (solid line) in CH<sub>2</sub>Cl<sub>2</sub>

at room temperature. The results are shown in Fig. 4 and Table 1. The electrochemical properties of **TMS-BP** metal complexes could not be measured because of the insolubility. The reversible three oxidation peaks were observed for **TIPS-H<sub>2</sub>BP** (0.18, 0.22 and 0.48 V vs.



**Fig. 4.** Cyclic voltammograms (solid lines) and differential pulse voltammograms (thin lines) of (a) **TIPS-H<sub>2</sub>BP**, (b) **TIPS-ZnBP**, (c) **TIPS-CuBP** and (d) **TIPS-NiBP** in CH<sub>2</sub>Cl<sub>2</sub> for **TIPS-H<sub>2</sub>BP**, in benzonitrile for **TIPS-ZnBP**, **TIPS-CuBP** and **TIPS-NiBP** with 0.1 M *n*-Bu<sub>4</sub>NPF<sub>6</sub>. Scan rate = 100 mV.s<sup>-1</sup>

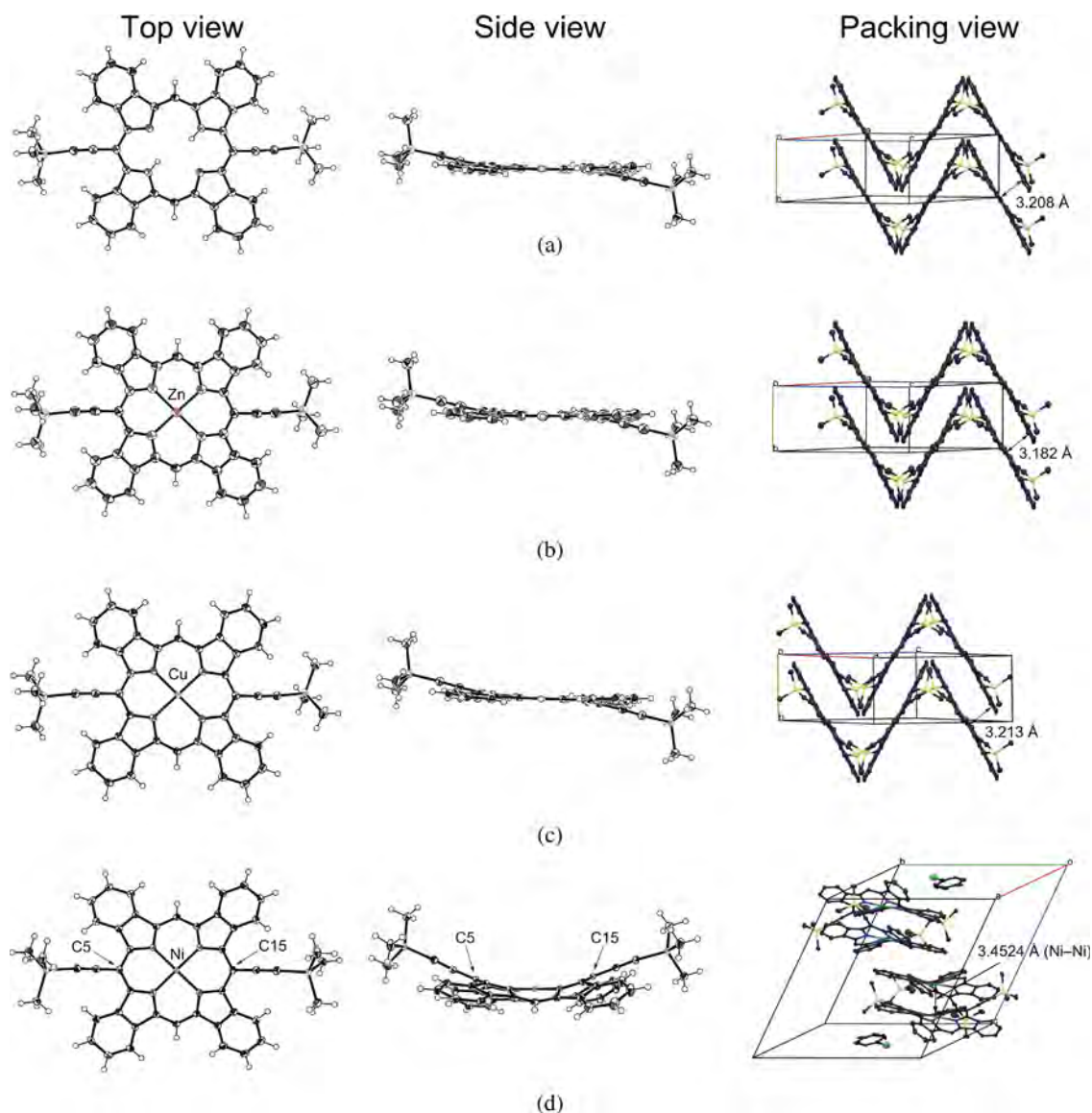
ferrocene/ferrocenium), **TIPS-CuBP** (0.06, 0.23 and 0.68 V), **TIPS-NiBP** (0.17, 0.22 and 0.37 V) and two oxidation peaks were observed for **TIPS-ZnBP** (0.07 and 0.59 V) while the reversible two reduction peaks were observed for **TIPS-H<sub>2</sub>BP** (-1.42 and -1.81 V), **TIPS-CuBP** (-1.34 and -1.48 V), **TIPS-NiBP** (-1.30 and -2.01 V) and **TIPS-ZnBP** (-1.64 and -2.06 V). The first and second oxidation peaks of **TIPS-H<sub>2</sub>BP**, **TIPS-CuBP** or **TIPS-NiBP** correspond to one electron oxidation in total, and the ratio of the two peaks changes depending

**Table 1.** Optical and electrochemical properties

Compounds	$\lambda_{\text{abs}}$ , nm	$E_{\text{ox}}$ , V <sup>d</sup>	$E_{\text{red}}$ , V <sup>d</sup>	$E_{\text{g}}$ , eV <sup>e</sup>	$E_{\text{HOMO}}$ , eV <sup>f</sup>	$E_{\text{LUMO}}$ , eV <sup>g</sup>
<b>TMS-H<sub>2</sub>BP</b>	450, 460, 583, 625, 710 <sup>a</sup>	—	—	1.56	-5.18	-3.61
<b>TMS-ZnBP</b>	467, 633, 649, 682 <sup>b</sup>	—	—	1.60	-5.25	-3.62
<b>TMS-CuBP</b>	462, 641, 678 <sup>b</sup>	—	—	1.61	-5.10	-3.49
<b>TMS-NiBP</b>	462, 642, 677 <sup>b</sup>	—	—	—	—	—
<b>TIPS-H<sub>2</sub>BP</b>	452, 462, 583, 626, 711 <sup>a</sup>	0.18, 0.34, 0.81	-1.42, -1.81	1.59	-5.20	-3.61
<b>TIPS-ZnBP</b>	468, 632, 647, 681 <sup>c</sup>	0.08, 0.59	-1.64, -2.06	1.61	-5.37	-3.76
<b>TIPS-CuBP</b>	463, 642, 682 <sup>a</sup>	0.06, 0.23, 0.68	-1.34, -1.48	1.62	-4.88	-3.26
<b>TIPS-NiBP</b>	465, 645, 689 <sup>a</sup>	0.17, 0.22, 0.37	-1.30, -2.01	—	—	—

<sup>a</sup>In CH<sub>2</sub>Cl<sub>2</sub>, <sup>b</sup>in DMF, <sup>c</sup>in THF. <sup>d</sup>Potential values were measured by DPV in CH<sub>2</sub>Cl<sub>2</sub> for **TIPS-H<sub>2</sub>BP**, in benzonitrile for **TIPS-ZnBP**, **TIPS-CuBP** and **TIPS-NiBP** with 0.1 M *n*-Bu<sub>4</sub>NPF<sub>6</sub>. The ferrocene/ferrocenium cation redox couple was used as the internal standard. Scan rate = 100 mV.s<sup>-1</sup>. [sample] = 0.5 mM. Working electrode: glassy carbon. Counter electrode: Pt wire. Reference electrode: Ag/AgNO<sub>3</sub>. <sup>e</sup>Determined by optical gaps from the absorption onsets in the films.

<sup>f</sup>Determined by photoelectron spectroscopy in air. <sup>g</sup> $E_{\text{LUMO}} = E_{\text{HOMO}} + E_{\text{g}}$ .



**Fig. 5.** Crystal structures of **TMS-H<sub>2</sub>BP**, **TMS-ZnBP**, **TMS-CuBP** and **TMS-NiBP**. Top (left column) and side (center column) and packing (right column) views of (a) **TMS-H<sub>2</sub>BP**, (b) **TMS-ZnBP** (c) **TMS-CuBP** and (d) **TMS-NiBP**. Thermal ellipsoids represent the 50% probability for top view and side view. Hydrogen atoms were omitted for clarity for packing view

on the concentration of the sample (Fig. S2). We assume that the first oxidation potential belongs to the formation of dimeric cation radical and the second peak is corresponding to the oxidation to monomeric cation. The third peak of **TIPS-H<sub>2</sub>BP**, **TIPS-CuBP** and **TIPS-NiBP** is one electron oxidation and corresponds to the second oxidation of BP compounds. This phenomenon was also observed for a BP-C<sub>60</sub> dyad [13].

#### Crystal structures of TMS-BP and TIPS-BP metal complexes

Single crystals of **TMS-H<sub>2</sub>BP**, **TMS-ZnBP**, **TMS-CuBP** and **TMS-NiBP** suitable for X-ray analysis were obtained by recrystallization in *o*-dichlorobenzene (**TMS-H<sub>2</sub>BP**, **TMS-ZnBP** and **TMS-CuBP**) or slow

diffusion of heptane into a chlorobenzene solution (**TMS-NiBP**). **TMS-H<sub>2</sub>BP** adopts a sigmoidal-shape in the single-crystalline state and is packed in one-dimensional slipped-stack structures (Fig. 5a). The neighboring columns are arranged to form a herringbone motif which is different from **TIPS-H<sub>2</sub>BP** which form a one-dimensional columnar array. The distance associated with the  $\pi$ - $\pi$  stacking between porphyrin cores is 3.208 Å. **TMS-ZnBP** and **TMS-CuBP** afforded similar herring-bone-type packing structures comprising of sigmoidal-shaped molecules. The shortest distance between neighboring porphyrin cores are 3.182 Å for **TMS-ZnBP** and 3.213 Å for **TMS-CuBP** (Figs 5b and 5c). On the other hand, the BP framework in **TMS-NiBP** adopts a saddle-shaped conformation reflecting the small radius of nickel(II) atom in comparison with

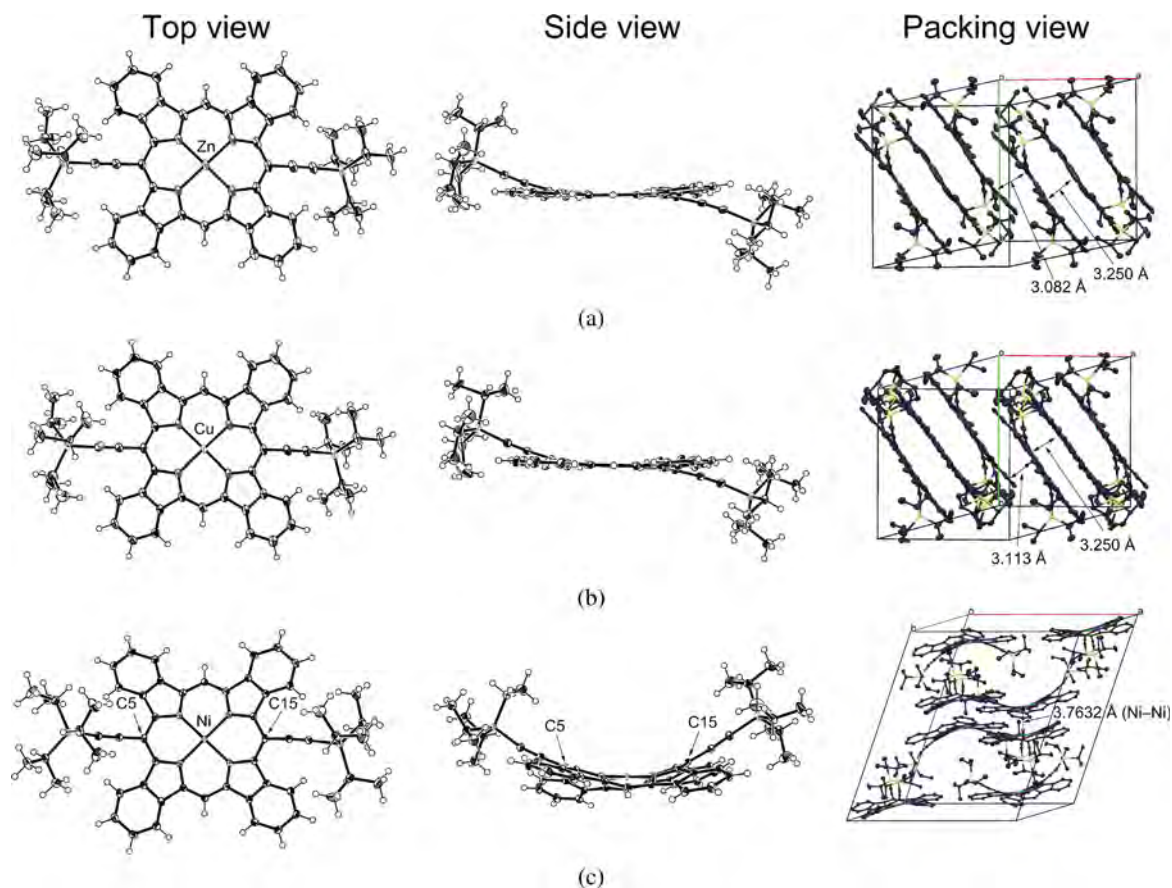
the cavity size of porphyrin (Fig. 5d). The intramolecular C5–C15 distances are 6.657(2) and 6.656(3) Å, and the TMS substituents orient to the same direction so that the overall molecular conformation is V-shaped when viewed from the side. Molecules of **TMS-NiBP** form a face-to-face dimeric motif, in which the two molecules are stacked orthogonally with their curved porphyrin surfaces fitting well to each other. Two chlorobenzene molecules are located in the unit cell to occupy the space between the face-to-face dimeric motifs. The TMS groups of each molecule are oriented toward its partner in the dimeric structure. The associated Ni–Ni distance in the dimer is 3.4524(3) Å. Neighboring dimers are related by an inversion center to form a slipped-stack structure extending along the  $\langle 0\bar{1}1 \rangle$  direction.

Single crystals of **TIPS-ZnBP** and **TIPS-CuBP** were obtained by slow diffusion of heptane into a chlorobenzene solution and by slow diffusion of methanol into a chloroform solution, respectively (Figs 6a and 6b). **TIPS-ZnBP** and **TIPS-CuBP** have a planar benzoporphyrin core and two ethynyl groups bent from the benzoporphyrin plane sigmoidally as similar to the case of **TIPS-H<sub>2</sub>BP**. In the packing structures of **TIPS-ZnBP** and **TIPS-CuBP**, molecules form a triad-like structures where the

molecules are stacked orthogonally. The minimum plane-to-plane distance of each molecule is 3.250 Å for both **TIPS-ZnBP** and **TIPS-CuBP**, which distance is shorter than that of **TIPS-H<sub>2</sub>BP** (3.295 Å) [17a]. The triad units are packed parallel to make one-dimensional slip-stacked structures with the plane-to-plane distances of 3.082 Å for **TIPS-ZnBP** and 3.113 Å for **TIPS-CuBP**, respectively. Single crystals of **TIPS-NiBP** were obtained by slow diffusion of ethanol into a 1,2-dichloroethane solution. The crystal structure of **TIPS-NiBP** is similar to **TMS-NiBP** (Fig. 6c). **TIPS-NiBP** molecules show a saddle-shaped conformation with the intramolecular C5–C15 distances are 6.645(2) or 6.671(2) Å, and form a face-to-face dimeric motif. The curved porphyrin surfaces are fitted well to each other, but TIPS groups of each molecule are oriented against its partner in the dimeric structure. The associated Ni–Ni contact is 3.7632(3) Å.

### Fabrication and evaluation of OTFTs

We have fabricated OTFT devices utilizing the free-base and the corresponding zinc(II) and copper(II) complexes of **TMS-BP** and **TIPS-BP** to investigate the effect of the substituent structure and metalation on the performance



**Fig. 6.** Crystal structures of **TIPS-ZnBP**, **TIPS-CuBP** and **TIPS-NiBP**. Top (left column) and side (center column) and packing (right column) view of (a) **TIPS-ZnBP**, (b) **TIPS-CuBP** and (c) **TIPS-NiBP**. Thermal ellipsoids represent the 50% probability for top view and side view. Hydrogen atoms were omitted for clarity for packing view



**Table 2.** OTFT characteristics of TMS- and TIPS-BPs

Compounds	$\mu_{\text{FET}}$ , $\text{cm}^2 \cdot \text{V}^{-1} \cdot \text{s}^{-1}$	$I_{\text{on}}/I_{\text{off}}$	$V_{\text{th}}$ , V
TMS-H <sub>2</sub> BP	0.11	$2.4 \times 10^6$	-12.3
TMS-ZnBP	$5.56 \times 10^{-5}$	$8.0 \times 10^1$	19.4
TMS-CuBP	$4.49 \times 10^{-4}$	$9.4 \times 10^4$	-11.9
TIPS-H <sub>2</sub> BP	$4.36 \times 10^{-5}$	$4.3 \times 10^4$	-17.8
TIPS-ZnBP	$1.11 \times 10^{-5}$	$6.6 \times 10^3$	1.2
TIPS-CuBP	$5.61 \times 10^{-3}$	$1.9 \times 10^4$	-12.2

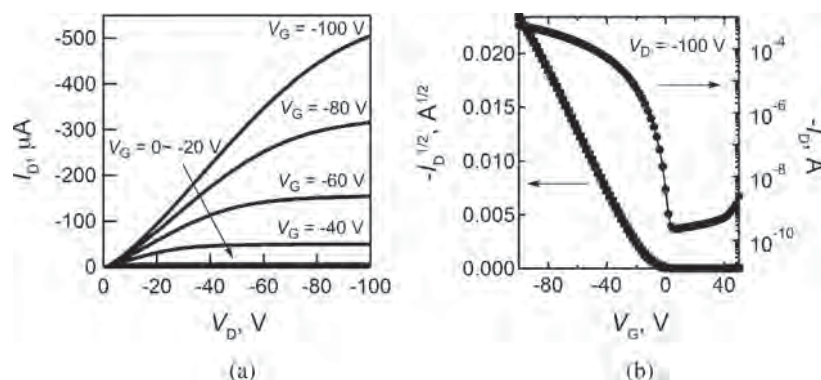
of OTFT devices. The TMS-BP or TIPS-BP films were fabricated by heating thin-films which were fabricated by spin-coating of the precursors, TMS-CP or TIPS-CP, on *n*-doped Si substrates followed by heating. Bottom-gate-top-contact structures were by evaporating the Au source and draining electrodes on the organic film. Performance parameters of each OTFT device estimated from the saturation regime are summarized in Table 2. The best performance was obtained with TMS-H<sub>2</sub>BP, which gave a hole mobility ( $\mu_{\text{FET}}$ ) of  $0.11 \text{ cm}^2 \cdot \text{V}^{-1} \cdot \text{s}^{-1}$  with an on/off ratio was  $2.4 \times 10^6$ . The output and transfer curves of this device are shown in Fig. 7. The XRD patterns of the films heated at 180 °C suggested the edge-on configuration for these films (Fig. S6).

### Fabrication and evaluation of OSCs

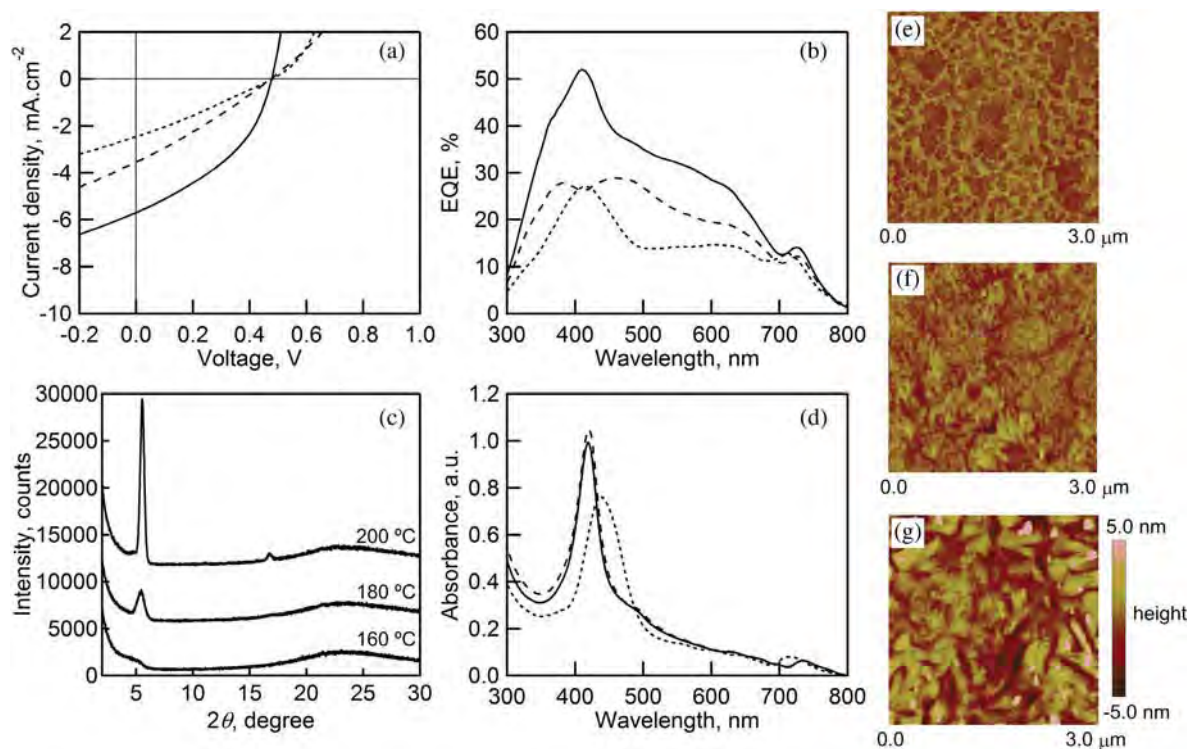
We have also fabricated OSCs utilizing the free-base and the corresponding zinc(II) and copper(II) complexes of TMS-BP and TIPS-BP as *p*-type materials with PC<sub>71</sub>BM as *n*-type material to investigate the effect of the substituent structure and metalation on the performance of OSC devices. To fabricate TMS- and TIPS-BP-based OSCs, we have initially investigated the ionization energy of thin-films on ITO-glass substrates by photoelectron spectroscopy in air to estimate the HOMO levels ( $E_{\text{HOMO}}$ ) of materials. The ionization energies are 5.22 eV for TMS-H<sub>2</sub>BP, 5.25 eV for TMS-ZnBP, 5.10 eV

for TMS-CuBP, 5.24 eV for TIPS-H<sub>2</sub>BP, 5.37 eV for TIPS-ZnBP and 4.88 eV for TIPS-CuBP (Table 1 and Fig. S3). The LUMO levels ( $E_{\text{LUMO}}$ ) were estimated by adding the optical bandgaps to the IPs. The optical bandgaps were determined from the absorption onset of the thin-films (Table 1 and Fig. S4). The LUMO levels were calculated to be -3.61 eV for TMS-H<sub>2</sub>BP, -3.62 eV for TMS-ZnBP, -3.49 eV for TMS-CuBP, -3.61 eV for TIPS-H<sub>2</sub>BP, -3.76 eV for TIPS-ZnBP and -3.26 eV for TIPS-CuBP. The typical OPV structure was glass/ITO/PEDOT:PSS (30 nm)/TMS- or TIPS-BP:PC<sub>71</sub>BM/BCP (7 nm)/Al (100 nm). Active layers were deposited by spin-coating (2500 rpm for TMS-CPs or 800 rpm for TIPS-CPs) of a solution containing a precursor (TMS-CPs or TIPS-CPs) and PC<sub>71</sub>BM (1:1 (w/w)) in a chloroform solution for TMS-CPs ( $20 \text{ mg} \cdot \text{mL}^{-1}$ ) or a mixture of chloroform:chlorobenzene (1:1(v/v)) solution for TIPS-CPs ( $10 \text{ mg} \cdot \text{mL}^{-1}$ ). Each of the deposited film was then heated at 160, 180 or 200 °C for 30 min to generate the corresponding benzoporphyrin *in situ*. It is known that the thermal conversion temperature largely affects the device properties because of the change in film morphology and crystallinity [19].

The *J*-*V* curves of the devices having TMS-H<sub>2</sub>BP:PC<sub>71</sub>BM or TIPS-H<sub>2</sub>BP:PC<sub>71</sub>BM as active layer are shown in Figs 8a and 9a. The values of short circuit current density ( $J_{\text{SC}}$ ), open circuit voltage ( $V_{\text{OC}}$ ), fill factor (FF), and power conversion efficiency (PCE) are summarized in Table 3. When the TMS-H<sub>2</sub>BP:PC<sub>71</sub>BM film was annealed at 160 °C, a PCE of 0.33% was obtained. By increasing the annealing temperature to 180 °C, PCE was improved to 1.09% with  $J_{\text{SC}} = 5.07 \text{ mA} \cdot \text{cm}^{-2}$ ,  $V_{\text{OC}} = 0.48 \text{ V}$  and FF = 0.40. However, further increase of the annealing temperature to 200 °C resulted in a decreased PCE of 0.47%. The TIPS-H<sub>2</sub>BP:PC<sub>71</sub>BM system showed a similar tendency to TIPS-H<sub>2</sub>BP:PC<sub>71</sub>BM and the highest PCE of 1.02% was obtained by annealing at 180 °C associated with  $J_{\text{SC}} = 5.22 \text{ mA} \cdot \text{cm}^{-2}$ ,  $V_{\text{OC}} = 0.61 \text{ V}$  and FF = 0.28. The other annealing temperatures (160 and 200 °C) gave lower PCE values (0.57% and 0.19%). The TMS-H<sub>2</sub>BP:PC<sub>71</sub>BM and TIPS-H<sub>2</sub>BP:PC<sub>71</sub>BM devices are comparable in  $J_{\text{SC}}$  and FF values, while



**Fig. 7.** OTFT characteristics of bottom-gate and top-contact device based on TMS-H<sub>2</sub>BP. (a) Out pot curves at different gate voltages. (b) Transfer curves in the saturated region at a drain voltage of -100 V



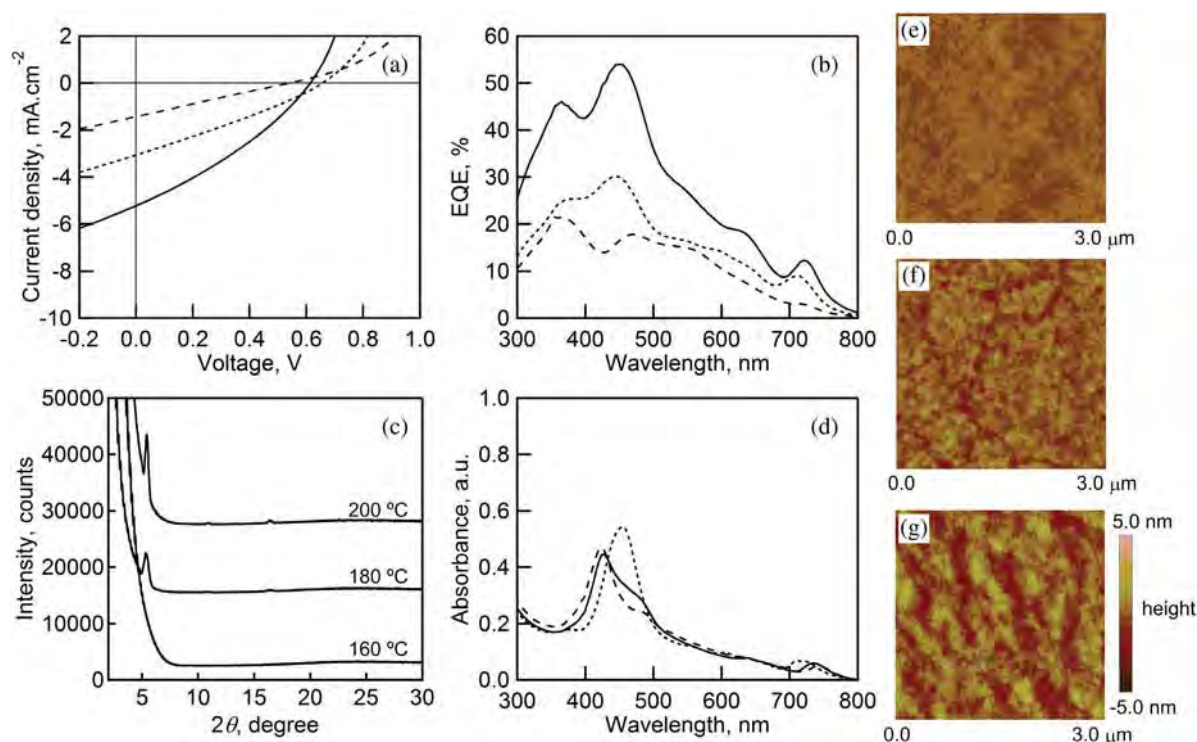
**Fig. 8.** (a)  $J$ - $V$  curves of BHJ solar cells based on **TMS-H<sub>2</sub>BP:PC<sub>71</sub>BM** produced at 160 (dotted), 180 (solid) and 200 °C (dashed). (b) EQE spectra of BHJ solar cells based on **TMS-H<sub>2</sub>BP:PC<sub>71</sub>BM** produced at 160 (dotted), 180 (solid) and 200 °C (dashed). (c) XRD patterns of **TMS-H<sub>2</sub>BP:PC<sub>71</sub>BM** composite films. (d) Absorption spectra of **TMS-H<sub>2</sub>BP:PC<sub>71</sub>BM** film produced at 160 (dotted), 180 (solid) and 200 °C (dashed). Tapping-mode AFM height images of the **TMS-H<sub>2</sub>BP:PC<sub>71</sub>BM** composite films produced at (e) 160, (f) 180, and (g) 200 °C

the  $V_{OC}$  values are considerably different. The external quantum efficiency (EQE) (Figs 8b and 9b) of the devices prepared by heating at 180 °C is higher as compared to those obtained by heating at 160 and 200 °C, although the absorption spectra of the blend films are similar between the 180 and 200 °C devices (Figs 8d and 9d).

Active-layer structures of these devices were investigated by out-of-plane XRD and tapping-mode atomic force microscopy (AFM). Figures 8c and 9c show XRD patterns of the **TMS-H<sub>2</sub>BP:PC<sub>71</sub>BM** and **TIPS-H<sub>2</sub>BP:PC<sub>71</sub>BM** blend films annealed at 160, 180, and 200 °C. Diffraction peaks are observed at  $2\theta = 5.43^\circ$  and  $5.44^\circ$  for the **TMS-H<sub>2</sub>BP:PC<sub>71</sub>BM** blend films annealed at 180 and 200 °C, respectively. In the case of **TIPS-H<sub>2</sub>BP:PC<sub>71</sub>BM** films annealed at 180 and 200 °C, diffraction peaks are observed at  $5.45^\circ$  and  $5.50^\circ$ , respectively. These peaks correspond to the (001) diffraction of **TIPS-H<sub>2</sub>BP** considering the corresponding peak observed for a **TIPS-H<sub>2</sub>BP** neat film (Fig. S6b). The peak intensity increased with raising the annealing temperature from 180 to 200 °C. The film annealed at 160 °C showed no specific diffraction peaks. This observation implies that **TMS-H<sub>2</sub>BP** and **TIPS-H<sub>2</sub>BP** films become crystalline over 180 °C, while the annealing at 160 °C affords amorphous films. The similarity between the absorption spectra of the films annealed at 180 and 200 °C is in agreement with the results of XRD. Figures

8e–8g and 9e–9g show the AFM images of **TMS-H<sub>2</sub>BP:PC<sub>71</sub>BM** and **TIPS-H<sub>2</sub>BP:PC<sub>71</sub>BM** blend films. The **TMS-H<sub>2</sub>BP:PC<sub>71</sub>BM** blend films show large domains at all annealing temperatures. These phase separation is promoted by increasing the annealing temperature. In particular, domains as large as 1  $\mu\text{m}$  and large cracks were observed for the film annealed at 200 °C. On the contrary, the **TIPS-H<sub>2</sub>BP:PC<sub>71</sub>BM** blend films annealed at 160 and 180 °C show smooth surface with smaller roughness, indicating the formation of micro-domains. In the case of the film annealed at 200 °C, cracks were found on the surface. As the results of XRD, the higher crystallinity films of **TMS-H<sub>2</sub>BP** and **TIPS-H<sub>2</sub>BP** were obtained by annealing at 200 °C, and these crystalline films have large grains. In general, the organic materials have the exciton diffusion length within 20–30 nm. To attain the high PCE values, efficient charge separation is necessary and the grain size should be in the same order as the exciton diffusion length. Therefore, the larger grain size leads to lower PCEs [20]. The film annealed at 180 °C has the highest PCE owing to the smooth surface and moderate crystallinity of **TMS-H<sub>2</sub>BP** and **TIPS-H<sub>2</sub>BP**. These results indicate that the bulky TIPS groups and moderate annealing temperature inhibited the growth of large domains in blend films with PC<sub>71</sub>BM.

The OSC using **TMS-ZnBP** or **TIPS-ZnBP** as p-type material with PC<sub>71</sub>BM as an n-type material were



**Fig. 9.** (a)  $J$ - $V$  curves of BHJ solar cells based on **TIPS-H<sub>2</sub>BP:PC<sub>71</sub>BM** produced at 160 (dotted), 180 (solid) and 200 °C (dashed). (b) EQE spectra of **TIPS-H<sub>2</sub>BP:PC<sub>71</sub>BM** produced at 160 (dotted), 180 (solid) and 200 °C (dashed). (c) XRD patterns of **TIPS-H<sub>2</sub>BP:PC<sub>71</sub>BM** composite films. (d) Absorption spectra of **TIPS-H<sub>2</sub>BP:PC<sub>71</sub>BM** films produced at 160 (dotted), 180 (solid) and 200 °C (dashed). Tapping-mode AFM height images of the **TIPS-H<sub>2</sub>BP:PC<sub>71</sub>BM** composite films produced at (e) 160, (f) 180, and (g) 200 °C

**Table 3.** Device performances of **TMS-** and **TIPS-BP**-based OSCs

<i>p</i> -type materials	Temperature, °C	$J_{SC}$ , mA.cm <sup>-2</sup>	$V_{OC}$ , V	FF	PCE, %
<b>TMS-H<sub>2</sub>BP</b>	160	2.46	0.48	0.28	0.33
	180	5.70	0.48	0.40	1.09
	200	3.53	0.47	0.28	0.47
<b>TMS-ZnBP</b>	160	6.79	0.45	0.37	1.13
	180	7.81	0.46	0.41	1.49
	200	7.86	0.47	0.39	1.44
<b>TMS-CuBP</b>	160	4.51	0.43	0.38	0.72
	180	1.83	0.43	0.18	0.14
	200	1.49	0.42	0.30	0.19
<b>TIPS-H<sub>2</sub>BP</b>	160	3.06	0.66	0.29	0.57
	180	5.22	0.61	0.32	1.02
	200	1.43	0.54	0.24	0.19
<b>TIPS-ZnBP</b>	160	2.12	0.68	0.30	0.44
	180	5.03	0.61	0.37	1.13
	200	4.29	0.64	0.36	0.99
<b>TIPS-CuBP</b>	160	3.85	0.65	0.34	0.86
	180	3.22	0.37	0.28	0.33
	200	3.64	0.42	0.28	0.42

also fabricated. The results are summarized in Table 3, Figs S7a and S7b. **TMS-ZnBP** and **TIPS-ZnBP** showed the best performances with the annealing temperature at 180 °C. The  $J_{SC}$  and FF values of **TMS-ZnBP** were improved compared to **TMS-H<sub>2</sub>BP**, and a PCE of 1.49% was attained. The  $V_{OC}$  value of **TMS-ZnBP** was comparable to **TMS-H<sub>2</sub>BP**, although the  $E_{HOMO}$  of **TMS-ZnBP** is lower than that of **TMS-H<sub>2</sub>BP**. The increase in  $J_{SC}$  is probably due to form the face-on  $\pi$ - $\pi$  stacking of **TMS-ZnBP** in **TMS-ZnBP:PC<sub>71</sub>BM** films (180 and 200 °C). This is indicated by the observation peaks at  $2\theta = 28.5$  and  $28.6^\circ$  ( $d = 3.13$  and  $3.12$  Å) in the XRD patterns as shown in Fig. S6b. These peaks correspond to the distance of  $\pi$ - $\pi$  stacking as supported by the crystal structure of **TMS-ZnBP** (Fig. 5b). **TIPS-ZnBP** also showed the improvement of the PCE compared to **TIPS-H<sub>2</sub>BP**, and the 1.13% of PCE was attained.

The OSC using **TMS-CuBP** or **TIPS-CuBP** as p-type material with PC<sub>71</sub>BM as an n-type material were also fabricated. The copper porphyrins are known to exhibit short fluorescence lifetimes compared with the free-base porphyrins and are not suitable for the OSC, since the exciton diffusion length becomes shorter [21]. The results are summarized in Table 3 and Figs S7c and S7d. The best annealing temperature was 160 °C and the PCE values are 0.72 and 0.86% for **TMS-CuBP** and **TIPS-CuBP**, respectively. **TMS-CuBP** and **TIPS-CuBP** single films are crystalline (Fig. S4f), but the crystallinity of the blend films with PC<sub>71</sub>BM are lower than **H<sub>2</sub>BP** and **ZnBP** films. The AFM images of **TMS-CuBP:PC<sub>71</sub>BM** blend films showed larger domains for the films annealed at 180 and 200 °C, although the XRD patterns showed small peaks. The AFM images of **TIPS-CuBP:PC<sub>71</sub>BM** blend films look smooth and amorphous. These will be one of the reasons why the  $J_{SC}$  of the devices with **TMS-CuBP** and **TIPS-CuBP** are relatively low.

## EXPERIMENTAL

### General

<sup>1</sup>H NMR and <sup>13</sup>C NMR spectra were recorded on a JEOL ECX 400P spectrometer at ambient temperature using tetramethylsilane as an internal standard. ESI mass spectra were measured on a JEOL JMS-700 spectrometer. UV-vis spectra were measured on a JASCO UV/vis/NIR spectrophotometer V-570. All solvents and chemicals were reagent grade quality, obtained commercially and used without further purification. For spectral measurements, spectral grade solvents were purchased from Nacalai Tesque Inc. X-ray crystallographic data were recorded at 103 K (**TMS-H<sub>2</sub>BP**, **TMS-ZnBP**, **TMS-CuBP**, **TMS-NiBP**) and 123 K (**TIPS-CuBP**, **TIPS-NiBP**) on a Rigaku CCD detector (Saturn 724) mounted on a Rigaku rotating anode X-ray generator (Micro-Max-007HF) using Mo-K $\alpha$  radiation from the

corresponding set of confocal optics. The structures were solved by direct methods and refined on F2 by full-matrix least-squares using the CrystalClear and SHELXS-2000 program. Ionization potential was determined by atmospheric photoelectron spectroscopy (Riken Keiki, AC-3). Materials **TMS-H<sub>2</sub>CP** [17b], **TMS-ZnCP**, **TMS-ZnBP** [17c], **TIPS-H<sub>2</sub>CP**, **TIPS-ZnCP** and **TIPS-ZnBP** [17a] were prepared according to the procedures described in literature. PC<sub>71</sub>BM was purchased from Luminescence Technology Corp. and used as received. Thermogravimetric analysis were performed on a Seiko Thermal Analyser Exstar TG/DTA 6200. X-ray diffraction (XRD) was recorded on a Rigaku Smartlab system. AFM image were recorded on Bruker D8 and Veeco Dimension Icon.

### Synthesis

**[5,15-Bis(trimethylsilylethynyl)tetrakis-(bicycle[2,2,2]octadieno)porphyrinato]copper(II) (TMS-CuCP)**. A saturated solution of Cu(OAc)<sub>2</sub>·H<sub>2</sub>O in methanol (18 mL) was added to a solution of **TMS-H<sub>2</sub>CP** (0.118 g, 0.145 mmol) in CHCl<sub>3</sub> (50 mL). After stirring for 2 h at room temperature, the reaction mixture was poured into water and extracted with CHCl<sub>3</sub>. The organic layer was washed with water and brine, then dried over Na<sub>2</sub>SO<sub>4</sub>, and the solvent was removed under a reduced pressure. The residue was purified by recrystallization CHCl<sub>3</sub>/MeOH to give **TMS-CuCP** as purple crystals in 84% (0.106 g, 0.121 mmol). UV-vis (CH<sub>2</sub>Cl<sub>2</sub>):  $\lambda_{max}$ , nm ( $\epsilon \times 10^4$ ) 431 (39.9), 563 (1.47), 591 (2.23), 605 (2.31). HRMS (ESI):  $m/z$  876.3119, calcd. for C<sub>54</sub>H<sub>53</sub>N<sub>4</sub>CuSi<sub>2</sub>: 876.3105 [M + H]<sup>+</sup>. Elemental analysis: anal. calcd. for C<sub>54</sub>H<sub>52</sub>CuN<sub>4</sub>Si<sub>2</sub>: C, 73.98; H, 5.98; N, 6.39. Found C, 73.92; H, 5.97; N, 6.41.

**[5,15-Bis(trimethylsilylethynyl)tetrakis-(bicycle[2,2,2]octadieno)porphyrinato]nickel(II) (TMS-NiCP)**. A saturated solution of Ni(OAc)<sub>2</sub>·4H<sub>2</sub>O in methanol (10 mL) was added to a solution of **TMS-H<sub>2</sub>CP** (0.113 g, 0.138 mmol) in CHCl<sub>3</sub> (50 mL) at room temperature. The mixture was refluxed for 3 h. After being cooled to room temperature, the reaction mixture was poured into water and extracted with CHCl<sub>3</sub>. The organic layer was washed with water and brine, then dried over Na<sub>2</sub>SO<sub>4</sub>, and the solvent was removed under a reduced pressure. The residue was purified by recrystallization (CHCl<sub>3</sub>/MeOH) to give **TMS-NiCP** as purple crystals in 87% (105 mg, 0.120 mmol). <sup>1</sup>H NMR (400 MHz; CDCl<sub>3</sub>; Me<sub>4</sub>Si):  $\delta_H$ , ppm 9.55 (m, 2H), 6.97 (m, 8H), 6.35 (m, 4H), 5.39 (m, 4H), 2.04–1.83 (m, 16H), 0.57 (m, 18 H). <sup>13</sup>C NMR (100 MHz; CDCl<sub>3</sub>; Me<sub>4</sub>Si):  $\delta_C$ , ppm 206.36, 151.68, 151.65, 151.59, 150.12, 150.02, 149.98, 137.16, 136.55, 136.53, 135.75, 133.36, 133.31, 106.28, 106.26, 106.20, 106.17, 98.10, 95.33, 77.20, 50.05, 38.90, 35.87, 27.25, 27.19, 27.01, 0.27, 0.09. UV-vis (CH<sub>2</sub>Cl<sub>2</sub>):  $\lambda_{max}$ , nm ( $\epsilon \times 10^4$ ) 430 (29.6), 603 (1.95). HRMS (ESI):  $m/z$

871.3168, calcd. for  $C_{54}H_{53}N_4NiSi_2$ : 871.3162  $[M + H]^+$ . Elemental analysis: anal. calcd. for  $C_{54}H_{52}N_4NiSi_2 \cdot 1/2 H_2O$ : C, 73.63; H, 6.06; N, 6.39. Found C, 73.68; H, 5.96; N, 6.60.

**[5,15-Bis(triisopropylsilylethynyl)tetrakis(bicyclo[2,2,2]octadieno)porphyrinato]copper(II) (TIPS-CuCP).** A solution of  $Cu(OAc)_2 \cdot H_2O$  (407 mg, 2.04 mmol) in methanol (15 mL) was added to a solution of **TIPS-H<sub>2</sub>CP** (101 mg, 0.103 mmol) in  $CHCl_3$  (50 mL). After stirring for 2 h at room temperature, the reaction mixture was washed with saturated  $NaHCO_3$  aq., and water. The mixture was then dried over  $Na_2SO_4$ , and the solvent was removed under reduced pressure. The residue was purified by recrystallization ( $CHCl_3/MeOH$ ) to give **TIPS-CuCP** as purple crystals in 91% (97.7 mg, 0.0935 mmol). UV-vis ( $CH_2Cl_2$ ):  $\lambda_{max}$ , nm ( $\epsilon \times 10^4$ ) 431 (41.1), 562 (1.74), 592 (2.64), 604 (2.47). HRMS (ESI):  $m/z$  1044.4984, calcd. for  $C_{66}H_{77}Cu N_4Si_2$ : 1044.4983  $[M + H]^+$ .

**[5,15-Bis(triisopropylsilylethynyl)tetrakis(bicyclo[2,2,2]octadieno)porphyrinato]nickel(II) (TIPS-NiCP).** A solution of  $Ni(OAc)_2 \cdot 4H_2O$  (0.507 g, 2.04 mmol) in methanol (15 mL) was added to a solution of **TIPS-H<sub>2</sub>CP** (101 mg, 0.103 mmol) in  $CHCl_3$  (50 mL) at room temperature. The mixture was refluxed for 3 h. After being cooled to room temperature, the reaction mixture was washed with saturated  $NaHCO_3$  aq., and water. The mixture was then dried over  $Na_2SO_4$ , and the solvent was removed under reduced pressure. The residue was purified by recrystallization ( $CHCl_3/MeOH$ ) to give **TIPS-NiCP** as purple crystals in 93% (98.6 mg, 0.0948 mmol).  $^1H$  NMR (400 MHz;  $CDCl_3$ ;  $Me_4Si$ ):  $\delta_H$ , ppm 9.51 (m, 2H), 6.94 (m, 8H), 6.41 (m, 4H), 5.37 (m, 4H), 2.10–1.76 (m, 16H), 1.53–1.42 (m, 6H), 1.36–1.33 (m, 36H).  $^{13}C$  NMR (100 MHz;  $CDCl_3$ ;  $Me_4Si$ ):  $\delta_C$ , ppm 151.91, 151.87, 151.83, 151.80, 151.77, 150.55, 150.52, 150.50, 137.19, 137.15, 136.40, 136.38, 136.36, 135.90, 135.86, 135.82, 135.78, 133.06, 133.03, 107.28, 104.73, 104.66, 98.14, 95.30, 95.26, 38.66, 38.63, 35.90, 35.88, 27.23, 27.20, 27.15, 18.86, 11.78. UV-vis ( $CH_2Cl_2$ ):  $\lambda_{max}$ , nm ( $\epsilon \times 10^4$ ) 432 (23.8), 594 (1.65), 601 (1.62). HRMS (ESI):  $m/z$  1039.5042, calcd. for  $C_{66}H_{77}N_4NiSi_2$ : 1039.5040  $[M + H]^+$ .

**5,15-Bis(trimethylsilylethynyl)tetrabenzoporphyrin (TMS-H<sub>2</sub>BP).** **TMS-H<sub>2</sub>BP** was prepared according to the procedures described in literature [17c]. Crystallographic data:  $C_{46}H_{38}N_4Si_2$ ,  $M_w = 702.98$ , monoclinic, space group  $C2/c$ ,  $a = 37.5744$  (10),  $b = 6.47957$  (16),  $c = 15.2073$  (4) Å,  $\beta = 100.5070$  (10),  $V = 3640.37$  (17) Å<sup>3</sup>,  $T = 103$  K,  $Z = 4$ ,  $R_1 = 0.0478$ ,  $wR_2 = 0.1282$ , GOF = 1.064.

**[5,15-Bis(trimethylsilylethynyl)tetrabenzoporphyrinato]zinc(II) (TMS-ZnBP).** **TMS-ZnBP** was prepared according to the procedures described in literature [17c]. Crystallographic data:  $C_{46}H_{36}N_4Si_2Zn$ ,  $M_w = 766.34$ , monoclinic, space group  $C2/c$ ,  $a = 37.029$ (3),  $b = 6.5615$  (4),  $c = 15.1517$  (4) Å,  $\beta = 100.2749$  (15),  $V = 3610.6$  (4) Å<sup>3</sup>,  $T = 103$  K,  $Z = 4$ ,  $R_1 = 0.0596$ ,  $wR_2 = 0.1596$ , GOF = 1.030.

**[5,15-Bis(trimethylsilylethynyl)tetrabenzoporphyrinato]copper(II) (TMS-CuBP).** **TMS-CuBP** was heated at 200 °C for 1 h in a sample tube under reduced pressure to give **TMS-CuBP** quantitatively. UV-vis (DMF):  $\lambda_{max}$ , nm ( $\epsilon \times 10^4$ ) 462 (38.6), 641 (3.27), 678 (7.81). HRMS (MALDI):  $m/z$  763.1769, calcd. for  $C_{46}H_{36}CuN_4Si_2$ : 763.1775  $[M]^+$ . Crystallographic data:  $C_{46}H_{36}CuN_4Si_2$ ,  $M_w = 764.54$ , monoclinic, space group  $C2/c$ ,  $a = 37.0934$  (9),  $b = 6.5331$  (2),  $c = 15.2433$  (4) Å,  $\beta = 101.1999$  (7)°,  $V = 3623.6$  (2) Å<sup>3</sup>,  $T = 103$  K,  $Z = 4$ ,  $R_1 = 0.0410$ ,  $wR_2 = 0.1064$ , GOF = 1.069.

**[5,15-Bis(trimethylsilylethynyl)tetrabenzoporphyrinato]nickel(II) (TMS-NiBP).** **TMS-NiBP** was heated at 200 °C for 1 h in a sample tube under reduced pressure to give **TMS-NiBP** quantitatively.  $^1H$  and  $^{13}C$  NMR spectra could not record because of the low solubility. UV-vis (DMF):  $\lambda_{max}$ , nm ( $\epsilon \times 10^4$ ) 462 (30.0), 642 (2.53), 677 (4.94). HRMS (MALDI):  $m/z$  758.1827, calcd. for  $C_{46}H_{36}N_4NiSi_2$ : 758.1832  $[M]^+$ . Crystallographic data:  $2(C_{46}H_{36}N_4NiSi_2) \cdot C_6H_5Cl$ ,  $M_w = 3146.27$ , triclinic, space group  $P-1$ ,  $a = 13.9807$  (3),  $b = 17.5488$  (4),  $c = 18.7217$  (4) Å,  $\alpha = 63.4700$  (7),  $\beta = 76.3869$  (7),  $\gamma = 67.1216$  (7)°,  $V = 3775.7$  (2) Å<sup>3</sup>,  $T = 103$  K,  $Z = 1$ ,  $R_1 = 0.0352$ ,  $wR_2 = 0.0955$ , GOF = 1.091.

**[5,15-Bis(triisopropylsilylethynyl)tetrabenzoporphyrinato]zinc(II) (TIPS-ZnBP).** **TIPS-ZnBP** was prepared according to the procedures described in literature [17a]. UV-vis (THF):  $\lambda_{max}$ , nm ( $\epsilon \times 10^4$ ) 468 (61.7), 632 (1.96), 647 (1.87), 681 (9.96). Crystallographic data:  $C_{174}H_{180}N_{12}Si_6Zn_3$ ,  $M_w = 2083.95$ , triclinic, space group  $P-1$ ,  $a = 12.9138$  (2),  $b = 15.6986$  (3),  $c = 19.0118$  (4) Å,  $\alpha = 101.5960$  (10),  $\beta = 108.2190$  (10),  $\gamma = 97.6090$  (10),  $V = 3506.44$  (11) Å<sup>3</sup>,  $T = 103$  K,  $Z = 1$ ,  $R_1 = 0.0476$ ,  $wR_2 = 0.1275$ , GOF = 1.069.

**[5,15-Bis(triisopropylsilylethynyl)tetrabenzoporphyrinato]copper(II) (TIPS-CuBP).** **TIPS-CuBP** was heated at 200 °C for 1 h in a sample tube under reduced pressure to give **TIPS-CuBP** quantitatively. UV-vis ( $CH_2Cl_2$ ):  $\lambda_{max}$ , nm ( $\epsilon \times 10^4$ ) 682 (5.75), 642 (2.64), 463 (32.0), 314 (1.75). HRMS (ESI):  $m/z$  954.3551, calcd. for  $C_{58}H_{60}CuN_4Si_2$ : 954.3550  $[M]^+$ . Crystallographic data:  $C_{58}H_{60}CuN_4Si_2$ ,  $M_w = 932.82$ , triclinic, space group  $P-1$ ,  $a = 12.9931$  (3),  $b = 15.6209$  (4),  $c = 19.0424$  (4) Å,  $\alpha = 101.3190$  (10),  $\beta = 108.7220$  (10),  $\gamma = 97.5070$  (10)°,  $V = 3510.32$  (14) Å<sup>3</sup>,  $T = 123$  K,  $Z = 3$ ,  $R_1 = 0.0410$ ,  $wR_2 = 0.1006$ , GOF = 1.070.

**[5,15-Bis(triisopropylsilylethynyl)tetrabenzoporphyrinato]nickel(II) (TIPS-NiBP).** **TIPS-NiBP** was heated at 200 °C for 1 h in a sample tube under reduced pressure to give **TIPS-NiBP** quantitatively.  $^1H$  NMR (400 MHz;  $CDCl_3$ ;  $Me_4Si$ ):  $\delta_H$ , ppm 9.98 (m, 4H), 8.97 (m, 2H), 8.71 (m, 4H), 7.91 (m, 4H), 7.81 (m, 4H), 1.53–1.43 (m, 6H), 1.38–1.32 (m, 36H).  $^{13}C$  NMR (100 MHz;  $CDCl_3$ ;  $Me_4Si$ ):  $\delta_C$ , ppm 138.25, 137.34, 136.58, 133.58, 126.19, 125.95, 124.66, 119.69, 108.51, 106.41, 94.18, 92.37, 18.96, 11.71. UV-vis ( $CH_2Cl_2$ ):  $\lambda_{max}$ , nm ( $\epsilon \times 10^4$ ) 689 (4.51), 645 (2.48), 465 (22.6), 314 (2.08). HRMS (ESI):

$m/z$  927.3787, calcd. for  $C_{58}H_{60}N_4NiSi_2$ : 927.3788 [M + H]<sup>+</sup>. Crystallographic data:  $C_{58}H_{60}N_4NiSi_2$ ,  $M_w = 928.01$ , monoclinic, space group  $P2_1/n$ ,  $a = 23.6378$  (5),  $b = 16.8788$  (3),  $c = 26.1340$  (5) Å,  $\beta = 113.5099$  (7)°,  $V = 9561.4$  (3) Å<sup>3</sup>,  $T = 123$  K,  $Z = 8$ ,  $R_1 = 0.0363$ ,  $wR_2 = 0.0965$ , GOF = 1.033.

### Electrochemical measurements

CV and DPV measurements were conducted in a solution of 0.1 M  $n$ -Bu<sub>4</sub>NPF<sub>6</sub> in CH<sub>2</sub>Cl<sub>2</sub> (**TIPS-H<sub>2</sub>BP**) or benzonitrile (**TIPS-ZnBP**, **TIPS-CuBP** and **TIPS-NiBP**) with a scan rate of 100 mV.s<sup>-1</sup> at room temperature in an argon-filled cell. A glassy carbon electrode and a Pt wire were used as a working and a counter electrode, respectively. An Ag/AgNO<sub>3</sub> electrode was used as a reference electrode, which was normalized with the half-wave potential of ferrocene/ferrocenium cation (Fc/Fc<sup>+</sup>) redox couple.

### Fabrication and evaluation of organic thin-film transistor

The heavily doped  $n$ -type Si substrates with 300 nm thick thermally grown SiO<sub>2</sub> layer as the gate dielectric Si substrates were cleaned sequentially with H<sub>2</sub>O, acetone and 2-propanol in an ultrasonic bath, and treated with UV-ozone plasma for 20 min. Chloroform solutions of precursors (**TMS-CPs** or **TIPS-CPs**, 7 mg.mL<sup>-1</sup>) were spin coated at 1000 rpm for 40 s on Si substrates in a nitrogen glove box, where H<sub>2</sub>O and O<sub>2</sub> concentrations were <0.5 ppm. **TIPS-CPs** or **TMS-CPs** films were annealed at 180 °C for 30 min. Au source and drain electrodes (70 nm) were vacuum deposited through a metal shadow mask. The channel length ( $L$ ) and width ( $W$ ) were 50 μm and 5.5 mm, respectively.

Transfer ( $I_D$ - $V_G$ ) and output ( $I_D$ - $V_D$ ) curves of OTFT devices were measured using an Agilent HP4155C semiconductor parameter analyzer in a glove box at room temperature. Field-effect mobility ( $\mu_{FET}$ ) was estimated from the saturation regime at drain voltage  $V_{DS} = -100$  V, using the equation:

$$I_{DS} = (\mu WC_i/2L)(V_G - V_{th})^2 \quad (1)$$

where  $I_{DS}$  is the drain-source current,  $\mu$  the field-effect mobility,  $W$  the channel width,  $L$  the channel length,  $C_i$  the capacitance per unit area of the gate dielectric layer, and  $V_{th}$  the threshold voltage.

### Fabrication and evaluation of organic cell

The typical spin-coated BHJ devices of **TIPS-H<sub>2</sub>BP** or **TMS-H<sub>2</sub>BP** and PC<sub>71</sub>BM [ITO/PEDOT:PSS(30nm)/**TIPS-H<sub>2</sub>BP**:PC<sub>71</sub>BM or **TMS-H<sub>2</sub>BP**:PC<sub>71</sub>BM/BCP (7nm)/Al (100 nm)] were fabricated as follows; ITO-coated glass substrates were cleaned stepwisely in Semico clean 56, water, acetone, and 2-propanol under ultrasonication for 10 min each. After the UV/O<sub>3</sub> treatment for 20 min,

the poly(3,4-ethylenedioxythiophene):poly(4-styrenesulfonate) layer (PEDOT:PSS, Clevious, Al4083) was spin-coated onto a cleaned ITO surface. After being backed at 120 °C in air for 20 min, the substrates were transferred into a nitrogen filled glove box (< 0.5 ppm O<sub>2</sub> and H<sub>2</sub>O). **TIPS-H<sub>2</sub>CP**:PC<sub>71</sub>BM = 1:1 (w/w) (10 mg.mL<sup>-1</sup> chloroform:chlorobenzene = 1:1 (v/v), 250 μl, 800 rpm) or **TMS-H<sub>2</sub>CP**:PC<sub>71</sub>BM = 1:1 (w/w) (20 mg.mL<sup>-1</sup> chloroform, 250 μL, 2500 rpm) spin-coated for 40 s in a glove box, then heated at by the various temperatures for 30 min followed by the continuous vacuum deposition of BCP (7 nm) and Al (100 nm). The device was then tested in air after the encapsulation in the glove box. The current-voltage ( $J$ - $V$ ) curves were measured using a Keithley 2400 source measure unit under AM 1.5G illumination at an intensity of 100 mW.cm<sup>-2</sup> using a solar simulator (Bunko-keiki, CEP-2000TF). The external quantum efficiency (EQE) spectra were measured with a Xe lamp and monochromator using a CEP-2000 integrated system by Bunko-keiki Co.

## CONCLUSION

We have succeeded in the preparation of the **TMS**- and **TIPS-BP** metal complexes by the retro Diels-Alder reaction of the corresponding precursors, **TMS**- and **TIPS-CP**, respectively. **TMS**- and **TIPS-BPs** exhibited very similar absorption properties with little effects from the **TMS**- and **TIPS**-groups. We revealed that the two alkylsilyl groups induced the different crystal structures. **TMS-H<sub>2</sub>BP**, **TMS-ZnP** and **TMS-CuBP** showed the herringbone-type packing structures, while **TIPS-H<sub>2</sub>BP**, **TIPS-ZnP** and **TIPS-CuBP** showed the one-dimensional slip stacked structures. OTFT devices of these benzoporphyrins were fabricated by solution process and the best performance was obtained for **TMS-H<sub>2</sub>BP** with a  $\mu_{FET}$  of 0.11 cm<sup>2</sup>. V<sup>-1</sup>.s<sup>-1</sup>. The BHJ-type OSCs based on **TMS-H<sub>2</sub>BP** or **TIPS-H<sub>2</sub>BP** with PC<sub>71</sub>BM were also fabricated. The best performance among these OSC systems was obtained with a **TMS-H<sub>2</sub>BP**:PC<sub>71</sub>BM blend film annealed at 180 °C with a PCE of 1.09%. The film structures evaluated by the AFM and XRD measurements suggested the critical effect of the annealing temperature to the film structure and thus the device performance. By annealing at 180 °C, the crystallinity of **TMS-H<sub>2</sub>BP** and **TIPS-H<sub>2</sub>BP** was increased as opposed to annealing at 160 °C which resulted to the formation of amorphous films. However, annealing at 200 °C promoted large phase separation and cracking to provide the considerably lower PCEs. The films annealed at 180 °C have moderate crystallinities and smooth surfaces, and are suitable for OSC devices in the case of **TMS-H<sub>2</sub>BP** and **TIPS-H<sub>2</sub>BP**. The BHJ OSC devices based on zinc(II) and copper(II) complexes as  $p$ -type materials were also fabricated. The blend films of **TMS-ZnBP** or **TIPS-ZnBP** and PC<sub>71</sub>BM showed better molecular orientations, and afforded improved of the OSC performances as compared

to free-base and copper(II) complex. Investigations of a wider variety of benzoporphyrin derivatives with different substituents are in progress, with the aim of achieving further improved performance in benzoporphyrin-based OSCs.

### Acknowledgements

This work was supported by a Grant-in-Aid (Nos. 25288092 and 26105004 to H.Y. and No. 25288113 to K.N.), the Green Photonics Project in NAIST and the program for promoting the enhancement of research universities in NAIST sponsored by the Ministry of Education, Culture, Sports, Science and Technology, Japan. We acknowledge the Nippon Synthetic Chem. Ind. (Osaka, Japan) for a gift of ethyl isocyanoacetate, which was used for the preparation of the starting pyrroles.

### Supporting information

Figures S1–S8 and Tables S1–S7 are given in the supplementary material. This material is available free of charge via the Internet at <http://www.worldscinet.com/jpp/jpp.shtml>.

Crystallographic data for compounds **TMS-H<sub>2</sub>BP**, **TMS-ZnBP**, **TMS-CuCP**, **TMS-NiCP**, **TIPS-ZnBP**, **TIPS-CuCP** and **TIPS-NiCP** have been deposited at the Cambridge Crystallographic Data Centre (CCDC) under numbers CCDC-1031711, 1039260, 1031710, 1031712, 1040808, 1031708 and 1031709, respectively. Copies can be obtained on request, free of charge, via [www.ccdc.cam.ac.uk/data\\_request/cif](http://www.ccdc.cam.ac.uk/data_request/cif) or from the Cambridge Crystallographic Data Centre, 12 Union Road, Cambridge CB2 1EZ, UK (fax: +44 1223-336-033 or email: [data\\_request@ccdc.cam.ac.uk](mailto:data_request@ccdc.cam.ac.uk)).

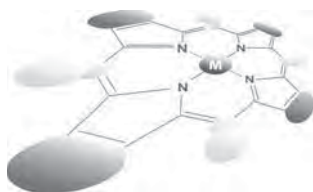
### REFERENCES

1. Yuan Y, Giri G, Ayzner AL, Zoombelt AP, Mannsfeld SCB, Chen J, Nordlund D, Toney MF, Huang J and Bao Z. *Nat. Commun.* 2014; **5**: 3005.
2. Luo C, Kyaw AKK, Perez LA, Patel S, Wang M, Brimm B, Bazan GC, Kramer EJ and Heeger AJ. *Nano Lett.* 2014; **14**: 2764–2771.
3. Kan B, Zhang Q, Li M, Wan X, Wan N, Long G, Wang Y, Yang X, Feng H and Chen Y. *J. Am. Chem. Soc.* 2014; **136**: 15529–15532.
4. Ito S, Murashima T, Ono N and Uno H. *Chem. Commun.* 1998; 1661–1662.
5. (a) Ono N, Yamada H and Okujima T. *Handbook of Porphyrin Science*, Vol. 2, World Scientific: Singapore, 2010; 1–102. (b) Carvalho CMBC, Brocksom TJ and Oliveira KT. *Chem. Soc. Rev.* 2013; **42**: 3302–3317 and reference cited therein. (c) Roznyatovskiy VV, Lee C-H and Sessler JL.

6. (a) Ono N, Yamada H and Okujima T. *Chem. Soc. Rev.* 2013; **42**: 1921–1933 and reference cited therein. (d) Yamada H, Okujima T and Ono N. *Chem. Commun.* 2008; 2957–2974 and reference cited therein. (e) Ishida S-I, Kuzuhara D, Yamada H and Osuka A. *Asia. J. Org. Chem.* 2014; **3**: 716–722.
6. Hirao A, Akiyama T, Okujima T, Yamada H, Uno H, Sakai Y, Aramaki S and Ono N. *Chem. Commun.* 2008; **39**: 4714–4716.
7. (a) Nakamura M, Kitatsuka M, Takahashi K, Nagata T, Mori S, Kuzuhara D, Okujima T, Yamada H, Nakae T and Uno H. *Org. Biomol. Chem.* 2014; **12**: 1309–1317. (b) Nakamura M, Tahara H, Takahashi K, Nagata T, Uoyama H, Kuzuhara D, Mori S, Okujima T, Yamada H and Uno H. *Org. Biomol. Chem.* 2012; **10**: 6840–6849. (c) Tomimori Y, Okujima T, Yano T, Mori S, Ono N, Yamada H and Uno H. *Tetrahedron* 2011; **67**: 3187–3193. (d) Okujima T, Tomimori Y, Nakamura J, Yamada H, Uno H and Ono N. *Tetrahedron* 2010; **66**: 6895–6900. (e) Uno H, Ito S, Wada M, Watanabe H, Nagai M, Hayashi A, Murashima T and Ono N. *J. Chem. Soc., Perkin Trans.* 2000; **1**: 4347–4355.
8. (a) Liu Q, Kong F-T, Tetsuo O, Yamada H, Dai S-Y, Uno H, Ono N, You X-Z and Shen Z. *Tetrahedron Lett.* 2012; **53**: 3264–3267. (b) Liu Q, Feng Q-Y, Yamada H, Wang Z-S, Ono N, You X-Z and Shen Z. *Chem. Asia. J.* 2012; **7**: 1312–1319. (c) Shimizu Y, Shen Z, Ito S, Uno H, Daube J and Ono N. *Tetrahedron Lett.* 2002; **43**: 8485–8488.
9. Uno H, Moriyama K, Ishikawa T, Ono N and Yahiro H. *Tetrahedron Lett.* 2004; **45**: 9083–9086.
10. (a) Tanaka K, Aratani N, Kuzuhara D, Sakamoto S, Okujima T, Ono N, Uno H and Yamada H. *RSC Adv.* 2013; **3**: 15310–15315. (b) Herwig PT and Mullen K. *Adv. Mater.* 1999; **11**: 480–483. (c) Uno H, Takiue T, Uoyama H, Okujima T, Yamada H and Masuda G. *Heterocycles* 2010; **82**: 791–802.
11. Shea PB, Kanicki J, Pattison LR, Petroff P, Kawano M, Yamada H and Ono N. *J. Appl. Phys.* 2006; **100**: 034502.
12. Matsuo Y, Sato Y, Niinomi T, Soga I, Tanaka H and Nakamura E. *J. Am. Chem. Soc.* 2009; **131**: 16048–16050.
13. Tamura Y, Saeki H, Hashizume J, Okazaki Y, Kuzuhara D, Suzuki M, Aratani N and Yamada H. *Chem. Commun.* 2014; **50**: 10379–10381.
14. Anthony JE. *Chem. Rev.* 2006; **106**: 5028–5048 and reference cited therein.
15. Diao Y, Tee BC-K, Giri G, Xu J, Kim DH, Becerril HA, Stoltenberg RM, Lee TH, Xue G, Mannsfeld SCB and Bao Z. *Nat. Mater.* 2013; **12**: 665–671.
16. (a) Bunz UHF, Engelhart JU, Lindner BD and Schaffroth M. *Angew. Chem. Int. Ed.* 2013; **52**: 3810–3821 and reference cited therein. (b) Wang C, Dong H, Hu W, Liu Y and Zhu D. *Chem. Rev.* 2012; **112**: 2208–2267 and reference cited therein.

17. (a) Takahashi K, Kuzuhara D, Aratani N and Yamada H. *J. Photopol. Sci. Tech.* 2013; **26**: 213–216. (b) Yamada H, Kushibe K, Mitsuogi S, Okujima T, Uno H and Ono N. *Tetrahedron Lett.* 2008, **49**, 4731–4733. (c) Yamada H, Kushibe K, Okujima T, Uno H and Ono N. *Chem. Commun.* 2006; 383–385.
18. (a) Lin Y-F, Shu Y, Parkin SR, Anthony JE and Malliaras GG. *J. Mater. Chem.* 2009; **19**: 3049–3056. (b) Payne MM, Parkin SR, Anthony JE, Kuo C-C and Jackson TN. *J. Am. Chem. Soc.* 2005; **127**: 4986–4987. (c) Anthony JE, Eaton DL and Parkin SR. *Org. Lett.* 2002; **4**: 15–18.
19. Saeki H, Kurimoto O, Nakaoka H, Misaki M, Kuzuhara D, Yamada H, Ishida K and Ueda. *Y. J. Mater. Chem. C* 2014; **2**: 5357–5364.
20. Peumans P, Yakimov Aharon and Forrest SR. *J. Appl. Phys.* 2003; **93**: 3693–3723 and reference cited therein.
21. Guide M, Lin JDA, Proctor CM, Chen J, García-Cervera C and Nguyen T-Q. *J. Mater. Chem. A* 2014; **2**: 7890–7896.





## Corrole–imide dyads — Synthesis and optical properties

Roman Voloshchuk<sup>a</sup>, Mariusz Tasior<sup>a</sup>, Adina I. Ciuciu<sup>b</sup>, Lucia Flamigni<sup>\*b</sup>  
and Daniel T. Gryko<sup>\*a</sup><sup>◇</sup>

<sup>a</sup>Institute of Organic Chemistry of the Polish Academy of Sciences, Kasprzaka 44/52, 01-224 Warsaw, Poland

<sup>b</sup>Istituto per la Sintesi Organica e Fotoreattività (ISOF), CNR, Via P. Gobetti 101, 40129 Bologna, Italy

Dedicated to Professor Shunichi Fukuzumi on the occasion of his retirement

Received 10 November 2014

Accepted 29 December 2014

**ABSTRACT:** Two rarely seen building blocks have been incorporated into light absorbing arrays: corroles and 2,3-naphthalimides. General synthetic strategy consisting in direct condensation of formyl substituted aromatic imides with dipyrroles led to diverse range of *trans*-A<sub>2</sub>B-corroles in acceptable yields. Spectroscopic properties of all five dyads studied suggest that regardless the imide's structure, components are weakly electronically coupled. Positioning 2,3-naphthalimide unit partially above the corrole core leads to slight alteration of their optical properties. Dyads bearing blue-absorbing imide components display different behavior depending on their structure. In corrole linked with naphthalenyl-naphthalene-1,8-carboximide a 100% effective energy transfer reaction from the imide component to the corrole component occurred. On the contrary, in small, strongly polarized amino-cyano-phthalimide neither efficient energy-nor electron-transfer could be detected and excitation leads to fluorescence from both components.

**KEYWORDS:** corroles, imide, synthesis, fluorescence, dipyrroles.

### INTRODUCTION

The synthesis and photophysical characterization of multichromophoric arrays capable of energy and/or electron transfer have been one of the most exciting and fruitful areas of research in the last few decades [1]. The study of model systems mimicking the basic photochemical events in natural photosynthesis, often called “artificial photosynthesis,” together with the crystallization of natural photosynthetic membrane complexes, considerably helped to establish the rules that govern the photoinduced processes observed in Nature [2]. Recently this basic subject has developed into a more advanced field which aims at light-driven water splitting and carbon-free fuel hydrogen production [3]. The interest in artificial photosynthesis is still growing,

because an efficient conversion of sunlight into chemical energy or electricity might solve the rising environmental and energy supply problems. Furthermore, this research area is providing a deep insight into processes like photoinduced electronic energy transfer and electron transfer, which are of interest for a wide range of applications, from material chemistry to biology.

The majority of chromophores involved into natural photosynthesis belongs to the porphyrinoid class. Nature has chosen these tetrapyrrolic macrocycles to play such an important role because of their unique structure (aromatic 18  $\pi$ -electron [18]-diazaannulene system), spectroscopic and redox properties, the ability of charge delocalization and formation of complexes with many metal cations. It is not surprising that the most frequently used building blocks for the construction of artificial multichromophoric arrays are *meso*-substituted porphyrins [4]. However, other porphyrinoids like chlorins [5], phthalocyanines [6] and subporphyrins [7] have been also used for this purpose. We recently incorporated another member of porphyrinoid family — corroles, into light harvesting

<sup>◇</sup> SPP full member in good standing

\*Correspondence to: Daniel T. Gryko, email: daniel.gryko@icho.edu.pl, tel: +48 22-3433063, fax: +48 22-6326681; Lucia Flamigni, email: lucia.flamigni@isof.cnr.it

arrays [8]. Corroles are one carbon short analogs of porphyrins with three *meso*-carbons between the four pyrrole rings. Because of structural similarity to corrin (macrocycle found in vitamin B<sub>12</sub>) they attracted attention since early 60s of the last century [9], however, lack of efficient synthetic methodologies strongly hampered the progress in their chemistry. Nevertheless, recent discoveries in this area made them readily available [10], opening the door for various applications [11]. The analysis of spectroscopic, photophysical and electrochemical properties of *meso*-substituted corroles reveals that they exhibit more intense absorption of red light, larger Stokes shift, higher fluorescence quantum yields [12] and lower oxidation potentials [13], when compared to similarly substituted porphyrins. By taking advantage of these properties, we were able to achieve ultra-fast and efficient energy and electron transfer in corrole-fullerene [8f], corrole-aromatic imide [8b, 8i] and (aromatic) bisimide dyads and triads [8c, 8e, 8j, 8m]. Fullerenes and aromatic imides and bisimides are particularly convenient building blocks for multichromophoric arrays, because the former dye secures excellent charge separation lifetimes, whereas the latter is amenable for structural modifications, thus allowing an easy alteration of the properties of the resulting model systems. While working with the corrole-aromatic imide dyads and triads, we focused our attention on the very rare 2,3-naphthalimides. This type of chromophore, to the best of our knowledge, has never been used in the construction of light absorbing arrays, despite the structural similarity to broadly used 1,8-naphthalimides [8b, 14] and naphthalene-4,5:1,8-bis(dicarboximides) [15]. Attracted by the interesting photophysical properties of corrole-imide dyads, we set ourselves the difficult task of incorporation, for the first time, of 2,3-naphthalimides and few other less common aromatic imides into multichromophoric array. In spite of the development of new methodologies towards the synthesis of *meso*-substituted corroles, this could be a serious synthetic challenge, mostly due to solubility problems. In this paper we present the results of our synthetic efforts, the spectroscopic characterization of the prepared dyads and the basic photophysical properties.

## RESULTS AND DISCUSSION

### Design and synthesis

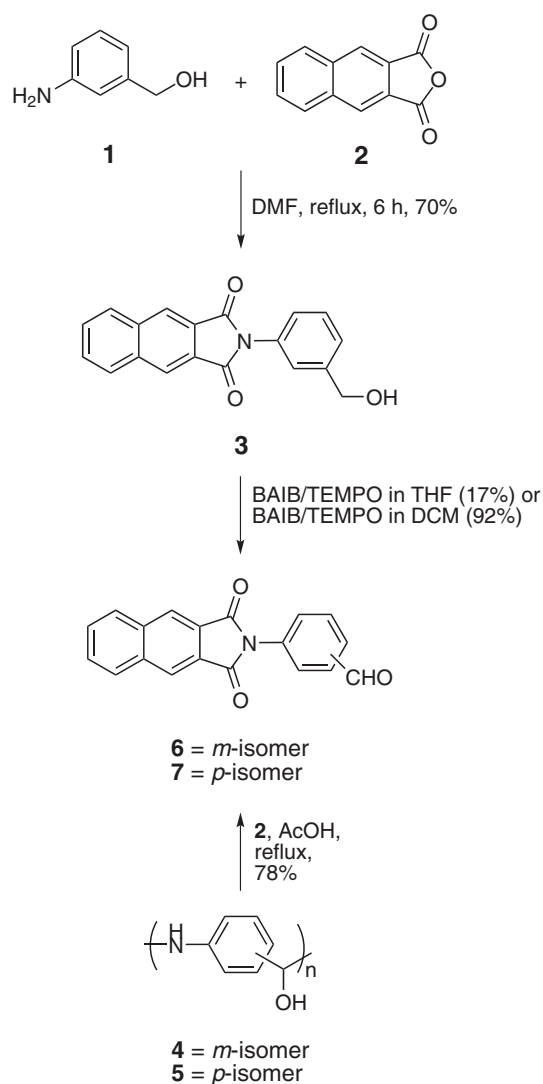
We were curious how spatial arrangement, especially strained face-to-face orientation of the dyad counterparts will influence its spectroscopic and photophysical properties. We required chromophore with elongated shape and absorption below 400 nm, so its absorption will not entirely overlap with Soret band of corroles. Consequently, we have chosen naphthalene-2,3-carboxyimide as a key structural element. In addition, we also designed to imides absorbing in violet-blue

region. We would like one of them to possess large  $\pi$ -system without strong electron-withdrawing character and the second one very small but still possessing strong absorption between 400 and 450 nm. In order to synthesize *trans*-A<sub>2</sub>B-corrole-imide dyads we decided to utilize the well-developed [2+1] condensation between dipyrroles and aldehydes. Given the moderate stability of corroles, we followed the general strategy starting from the preparation of an elaborated aldehyde which would then be used in the corrole forming reaction. Therefore our strategy was as follows: the synthesis of imide-derived aldehyde followed by final condensation with dipyrrole. In all cases 5-(pentafluorophenyl)dipyrrole was chosen, since previous studies showed that electron-withdrawing substituents are necessary to secure reasonable stability of final corrole [8b].

The shortest approach towards the necessary aldehydes would be to use aminobenzaldehydes and perform their direct condensation with the corresponding anhydrides. Such compounds, however, are generally unstable and even traces of acids initiate their polymerization. Therefore some kind of protection of an aldehyde functionality has to be used. We decided to investigate two approaches: protection of aldehyde in the form of acetal and the use of aminobenzyl alcohols as one oxidation level lower precursors for corresponding aldehydes. The latter option is justified by the fact that such alcohols are readily oxidized to corresponding aldehydes by a variety of methods. Thus, 2,3-naphthalenedicarboxylic acid anhydride (**2**) was reacted with 3-aminobenzyl alcohol in a boiling DMF and, after aqueous workup and flash chromatography purification, the desired alcohol **3** was obtained in 70% yield as a readily crystallizing solid. The solubility of the prepared alcohol in common organic solvents was rather low, presumably due to  $\pi$ -stacking and intermolecular hydrogen bond formation, and this fact complicated the search for appropriate conditions for oxidation reaction. The brief survey of oxidizing systems was made and in most cases either conversion was incomplete or complex mixtures arose. Surprisingly, oxidation of alcohol **3** with [bis(acetoxy)-iodo]benzene (BAIB)/TEMPO system [16] in dichloromethane gave target aldehyde **6** in a yield of 92%, though substrate was never dissolved and the reaction was performed in solid-to-solid regime, whereas better solubilizing solvent (THF) gave the expected product in much lower yield (17%) (Scheme 1).

Some time ago we found that 3-aminobenzaldehyde polymer reacts readily with 1,8-naphthalenedicarboxylic acid anhydride, forming the desired imidoaldehyde in one step [8b]. To our delight, anhydride of 2,3-naphthalenedicarboxylic acid exhibited similar reactivity against both 3-aminobenzaldehyde polymer (**4**) and 4-aminobenzaldehyde polymer (**5**), thus allowing straightforward, one step synthesis of aldehydes **6** and **7**.

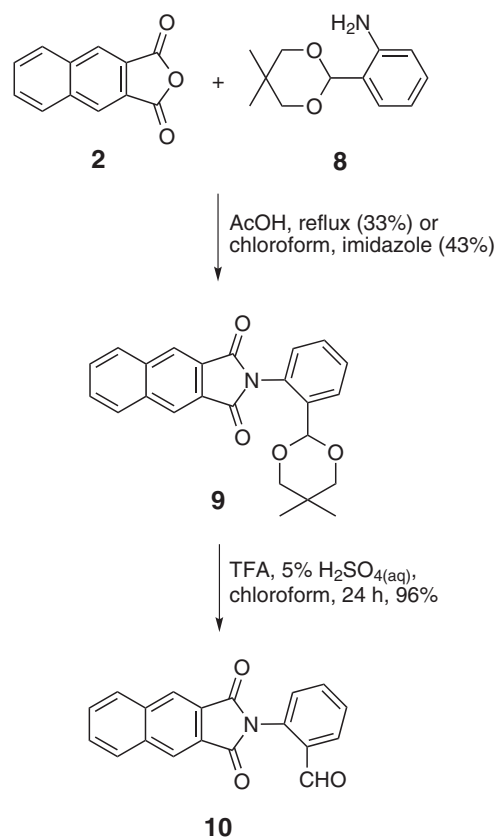
According to our plan, *ortho*-substituted isomer of aldehydes **6** and **7** was one of the crucial substrates.



Scheme 1.

Therefore we synthesized acetal **9**, by the condensation of **8** with anhydride **2**. Among tested reaction conditions, boiling substrates in chloroform with an excess of imidazole gave the best results [17]. Subsequent deprotection of aldehyde function gave desired compound **10** (Scheme 2).

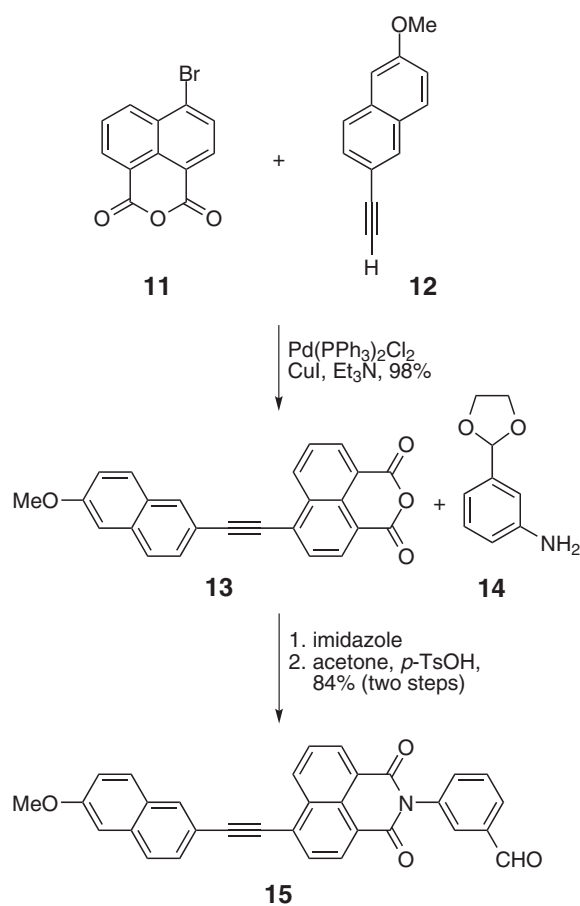
Aldehyde **15**, possessing skeleton unknown before, is particularly interesting, as its  $\pi$ -expanded structure can be characterized by strong donor–acceptor character, resulting in significant bathochromic shift of both absorption and emission maxima. Its synthesis was achieved in two steps starting from anhydride **11**. Sonogashira coupling with commercially available naphthalene-based arylacetylene **12**, followed by condensation of newly prepared anhydride **13** with 3-aminobenzaldehyde ethylene acetal (**14**) in imidazole/chloroform mixture, and deprotection step gave desired aldehyde **15** in excellent overall yield (Scheme 3).



Scheme 2.

Finally, continuing the search towards new small chromophores with interesting optical properties, derivatives of 3-amino-4-cyano-5,6-diphenylphthalimide were synthesized. Corresponding anhydride **19** was prepared according to published procedure [18]. Simple derivatives of this anhydride (phthaloyl hydrazide and *N*-hydroxy phthalimide) were described in the literature exclusively from the point of view of their biological activity (antitumor agents). Their spectroscopic properties were never studied and *N*-aryl-substituted imides of such type were unknown before our work. The combination of electron-withdrawing and electron-donating groups alters the electronic structure of organic chromophore decreasing the difference between HOMO and LUMO. As a result, anhydride **19** strongly absorbs violet-blue light. Assuming that free amino group will not cause complications during imide formation due to the combined effect of steric hindrance and its electron-poor character, anhydride **19** was used in further steps without modifications. In order to synthesize the necessary aldehyde, the mixture of anhydride **19** and *p*-aminobenzaldehyde polymer (**5**) was refluxed in acetic acid. Aldehyde **20** was obtained with good yield and acceptable purity without chromatographic purification (Scheme 4).

With a small library of aromatic aldehydes, precursors for corrole synthesis, we began a dyads' synthesis. We have chosen the reaction conditions optimized for corroles



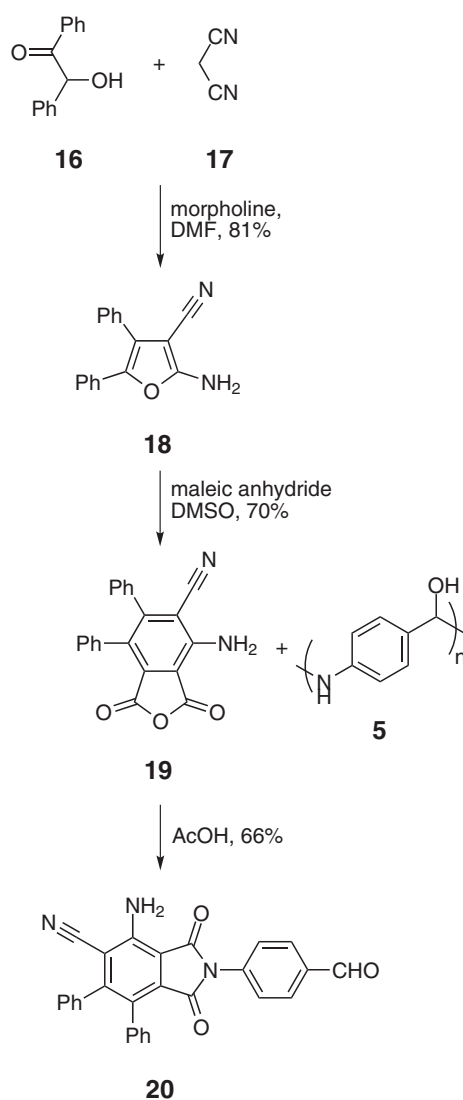
Scheme 3.

bearing electron-withdrawing substituents, which were elaborated in our group [10j]. The reactions were performed in dichloromethane as a solvent with TFA concentration of *ca.* 13 mM. After bilane (the linear tetrapyrrolic corrole precursor) formation, the oxidation step was performed with DDQ. Under these conditions we were able to obtain five corrole-aromatic imide dyads, usually in moderate yield (14–18%). Only corrole **26** was formed in lower yield (6%, Table 1). Among possible unfavorable factors, free amino group of aldehyde was considered to be a site which is capable to bind acidic catalyst and hence reduce its active concentration in the reaction mixture. Having this in mind, reaction was repeated with doubled concentration of TFA (*ca.* 27 mM) but, unfortunately, it did not improve outcome of the experiment.

Finally, imides **28** and **29** and corrole **30** were prepared and used for photophysical studies as model compounds lacking additional chromophore (Scheme 5). All prepared corroles were sufficiently stable both in solid state and in solution, thus allowing their spectroscopic characterization.

### Spectroscopic characterization of prepared dyads

The five corrole-based dyads have been studied in toluene (TOL) solutions at room temperature along



Scheme 4.

with their imides and corrole models, **28**, **29**, **13** and **30** respectively. Corrole **30** has been previously extensively investigated by our groups [12a] and often used as model for corrole containing multi-component systems [8a, 8c, 8e].

**Dyads 22, 23, 24.** The absorption spectra of dyads **22–24** are reported in Fig. 1 overlaid to those of the corresponding models. These dyads differ for the linking position (*ortho*, *meta*, *para*) of the imide to the corrole and one of the aims of our study was to detect differences in their spectroscopic and photophysical properties. Naphthalene-imide **28** displays a structured absorption band with maxima at 358 and 341 nm with a molar absorption coefficient  $< 3,000 \text{ M}^{-1} \cdot \text{cm}^{-1}$ , whereas corrole **30** has an intense Soret band at 419 nm ( $\epsilon = 120,000 \text{ M}^{-1} \cdot \text{cm}^{-1}$ ) and weaker Q-bands at 523, 562, 617 and 640 nm ( $\epsilon < 20,000 \text{ M}^{-1} \cdot \text{cm}^{-1}$ ). As can be seen from Fig. 1, the spectra of the *meta* and *para* dyads **22** and **23** are

**Table 1.** Synthesis of corrole–aromatic imide dyads

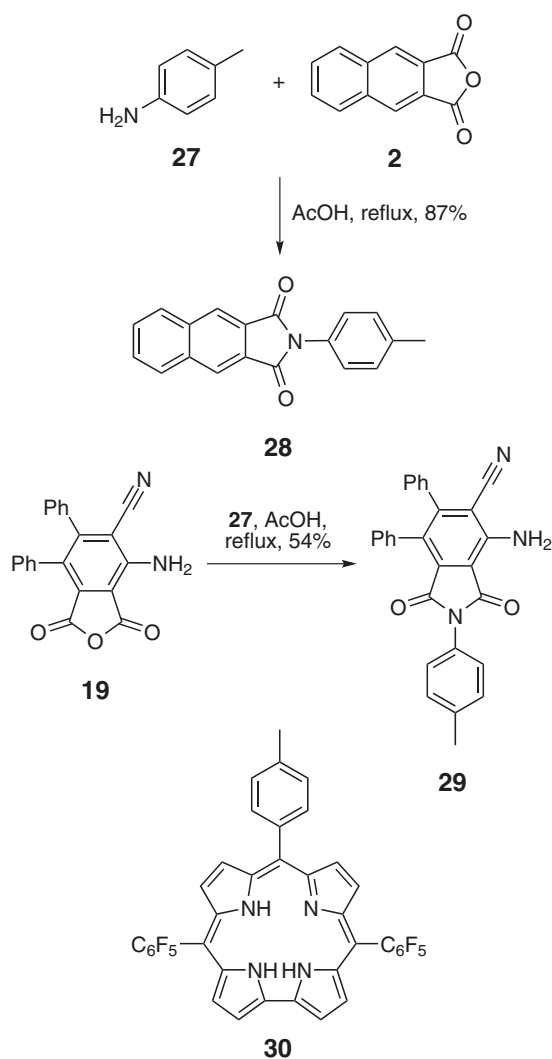
Aldehyde	Corrole	R	Yield, %
6	22		16
7	23		14
10	24		17
15	25		18
20	26		6

perfectly superimposable to the plain superposition of the component models **28** and **30** (Figs 1a and 1b). They in fact display additivity both in the UV, where the imide **28** bands position and intensity are well-reproduced and at lower energies, where the Soret and Q-bands of corrole **30** are perfectly overlapped. This is an indication of a poor electronic coupling of the component units in the dyads. On the contrary the *ortho* isomer **24** displays poor additivity (Fig. 1c) which can be noticed predominantly in the region of corrole absorbance, in the intensity of the 419 nm Soret band and in the lowest energy Q-band at 640 nm, which is missing in the dyad. However, also in the UV region where the imide bands are discernible, the total absorbance is lower than expected on the basis of a plain additivity. The behavior of the *ortho* dyad **24** is ascribed to a perturbation induced by the positioning of aromatic system over the corrole ring.

The luminescence properties of dyads **22–24** were examined in detail in order to ascertain whether the

photoinduced processes were affected by the substitution type. The imide model **28** displays a broad emission spectrum with maximum at 501 nm and a weak luminescence yield with  $\Phi_{fl} = 0.011$  and corrole **30** shows a more intense luminescence with  $\Phi_{fl} = 0.14$  after excitation on the respective bands (Table 2).

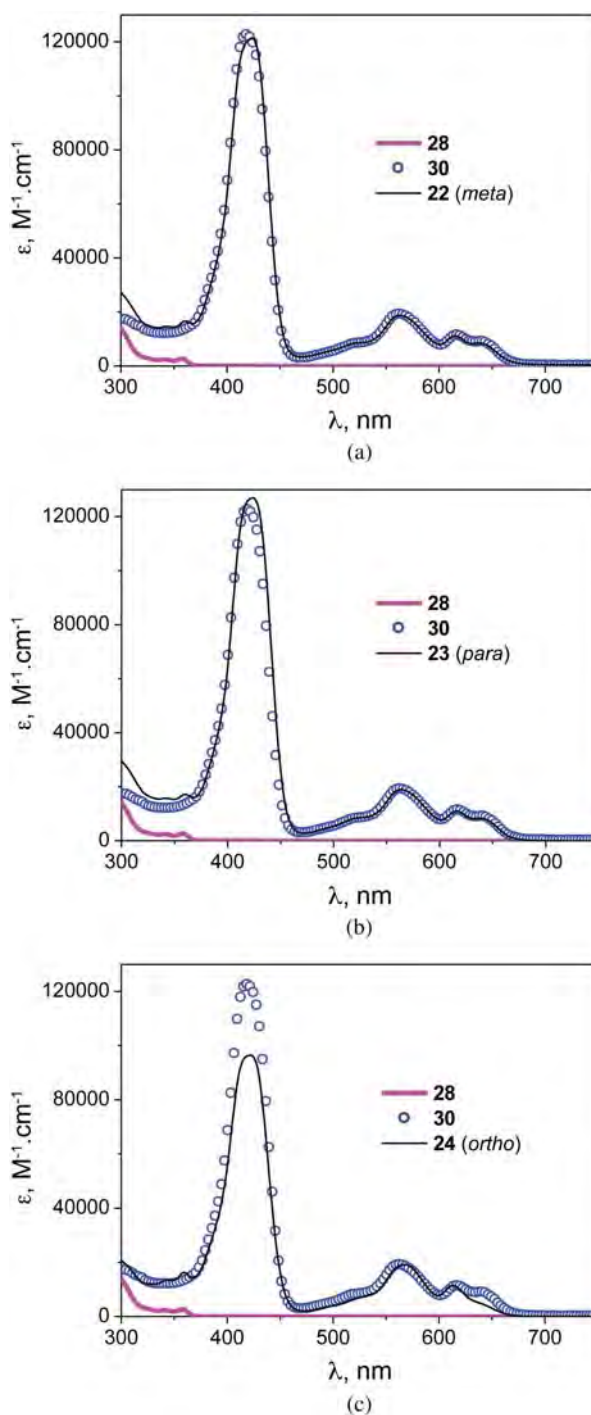
The dyads, after excitation in the imide band at 358 nm displayed a luminescence which was essentially that of corrole (Fig. 2). The luminescence of the imide moiety is almost completely quenched (<97%) whereas the corrole band appears sensitized by a value of *ca.* 20% in the isomers **22** and **23**. On the contrary, the emission of the corrole unit in the *ortho* isomer **24** has an intensity identical to that of corrole. This indicates that in the decoupled dyads **22** and **23** a complete energy transfer from the imide moiety to the corrole occurs, in fact 20% is also the amount of photons absorbed by the donor imide at the excitation wavelength, see absorption spectra. For dyad **24**, characterized as discussed above



Scheme 5.

by some electronic interaction because of the geometric arrangement, the sensitization is not clearly detected. However, an excitation spectrum registered at 660 nm, where only corrole moiety emits, indicate the presence of the bands of the imide (Fig. 3), showing that also in this case energy transfer occurs.

Excitation of the corrole unit in the dyads leads to an emission identical to that of the model in dyads **22** and **23**, whereas in the *ortho* derivative **24** there is a quenching of the order of 20% (data not shown). Time resolved experiments after 355 nm excitation shows that in all dyads the lifetime of the model imide measured at 500 nm, 1.6 ns in the model, is reduced to  $55 \pm 5$  ps, identical within experimental uncertainty, whereas the lifetime of corrole moiety measured at 660 nm is identical to that of the models for all dyads,  $3.85 \pm 0.5$  ns. These data allow to calculate a rate of energy transfer from the imide to the corrole moiety of the order of  $1.8 \times 10^{10} \text{ s}^{-1}$  for all dyads. Such a high rate is not surprising given the strong overlap



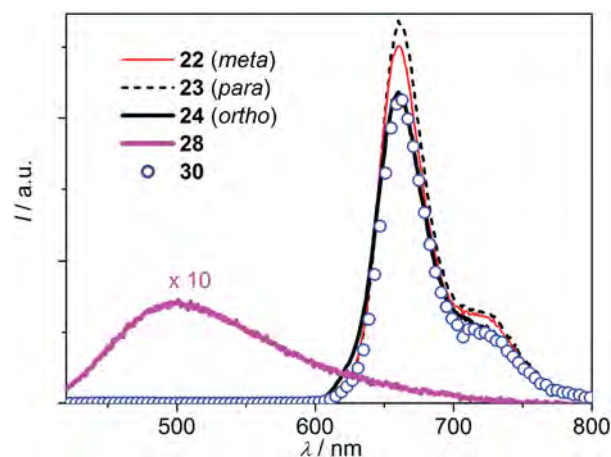
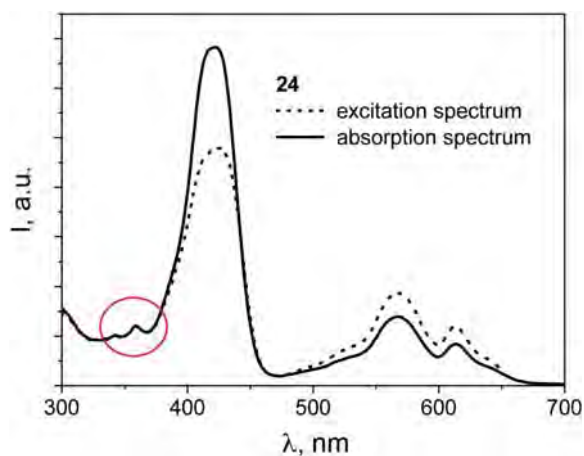
**Fig. 1.** Absorption spectra of dyads **22**, **23** and **24** in TOL overlaid with those of the models **28** and **30**

between the emission of donor **28** and the absorption of acceptor **30**, a critical parameter for the occurrence of energy transfer. The “strange” behavior of the *ortho* dyad **24**, which appears to have a lower emission yield from the corrole unit than the model and the other dyads might be ascribable to the electronic perturbation brought about by the close packing of the two chromophores which are expected to alter the radiative parameters. However we cannot completely exclude the hypothesis that a through

**Table 2.** Luminescence parameters of dyads **22–24** and pertinent models in TOL at room temperature

	$\lambda_{\text{max}}^{\text{em}}$ , nm <sup>a</sup>	$\Phi_{\text{fl}}^{\text{b}}$	$\Phi_{\text{fl}}^{\text{c}}$	$\tau$ , ns
<b>28</b>	501	0.011		1.6
<b>30</b>	656, 716		0.14 <sup>d</sup>	3.8 <sup>d</sup>
<b>22</b>	660, 716	<0.0001, 0.16	0.14	0.054; 3.8
<b>23</b>	661, 717	<0.0001, 0.17	0.14	0.060; 3.9
<b>24</b>	661, 715	0.0003, 0.14	0.11	0.050; 3.9

<sup>a</sup>Data from corrected spectra. <sup>b</sup>Luminescence quantum yield, excitation in the imide band (350 nm). <sup>c</sup>Luminescence quantum yield, excitation in the corrole band (560 nm). <sup>d</sup>Data from Ref. 12a.

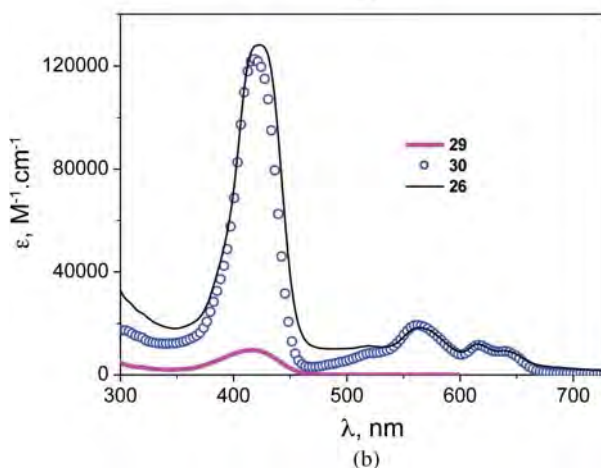
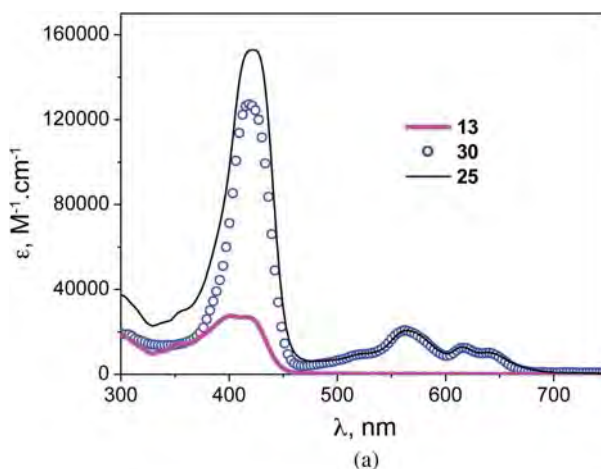
**Fig. 2.** Fluorescence spectra in TOL of dyads **22**, **23** and **24** and models after excitation at 358 nm (optically matched solutions with  $A = 0.09$ )**Fig. 3.** Arbitrarily scaled absorption and excitation spectra of **24** in TOL. The excitation spectrum has been recorded at 660 nm

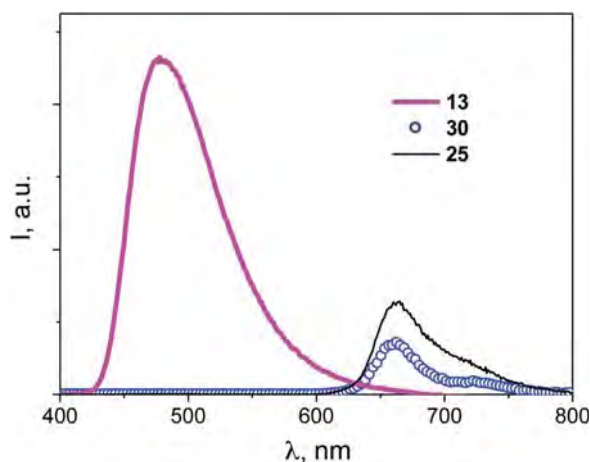
space electron transfer can occur with low efficiency in such a close packing of donor (**30**) and acceptor (**28**) both *via* LUMO–LUMO (when corrole is excited) than *via* HOMO–HOMO (when the imide is excited) mechanisms.

Therefore, from the present data there is no clear evidence that the different types of substitution either *ortho*, *meta* or *para*, affect the nature or the rate of the photoinduced processes. It can however be noticed that in the *ortho* isomer **24** the proximity of the electronic clouds of the two moieties due to the positioning of the imide over the tetrapyrrolic ring, induces an electronic interaction leading to a variation in spectroscopic parameters.

**Dyads 25 and 26.** The absorption spectra of the dyads and the related models **13**, **29** and **30** are reported in Fig. 4. Due to the low amount of compound available, the molar absorption coefficients might be affected by some uncertainty. Imide **13** displays a structured band with maxima at 403 and 417 nm ( $\epsilon$  ca. 27,000 M<sup>-1</sup>.cm<sup>-1</sup>) and **29** displays a broad absorption band around 415 nm, with an  $\epsilon = 10,000$  M<sup>-1</sup>.cm<sup>-1</sup>, in agreement with similar compounds [19]. The dyad spectra appear to be the simple superposition of the component units within experimental errors, indicating that the level of electronic interaction between the components is weak.

The photophysics of these dyads was examined with a lower detail in comparison to the former ones. The

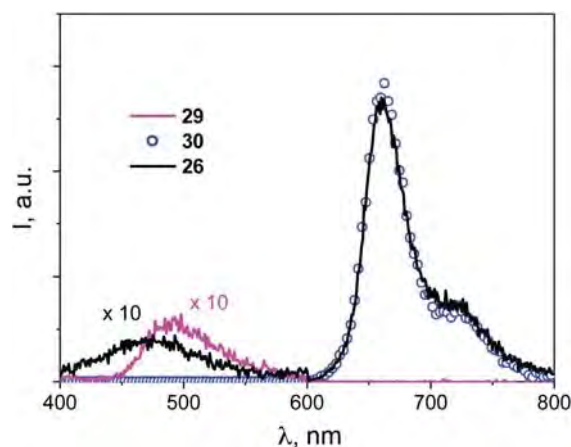
**Fig. 4.** Absorption spectra of dyads **25** and **26** in TOL overlaid with those of the models **13**, **29** and **30**



**Fig. 5.** Fluorescence spectra in TOL of dyad **25** and models after excitation at 350 nm (optically matched solutions with  $A = 0.07$ )

emission spectra of dyad **25** and of optically matched models **13** and **30** after excitation at 350 nm are reported in Fig. 5. The fluorescence of reference **13** maximizes at 478 nm and is quite high compared to the other imide components (luminescence quantum yield close to 1), but not unusual for this type of structures [19]. The luminescence of the imide is totally quenched in the dyad whereas the luminescence of the corrole unit is sensitized by a factor of 2. By taking into account that at 350 nm the imide component absorbs *ca.* 50% of the incident photons (see Fig. 4a), the observed phenomena can be interpreted by a 100% effective energy transfer reaction from the imide component to the corrole component. Selective excitation of the dyad on the corrole band at 560 nm leads to a luminescence identical to that of the model corrole (data not shown).

Figure 6 illustrates the luminescence spectra of **26** and model components. The imide **29** displays a very weak luminescence, with  $\lambda_{\text{max}}$  at 495 nm, similar to the one of the previously seen model **28**. Excitation of **26** at 350 nm leads to a luminescence from the imide units reduced to about 80% of that of the model **29**, accompanied by a 20 nm hypsochromic shift. No sensitization or quenching was noticed in the luminescence of the corrole moiety with respect to **30** upon excitation at the same wavelength. A selective excitation at 560 nm where only the corrole absorbs, led to a luminescence decrease of this unit in the dyad to *ca.* 80% compared to the model (data not shown). The results are not so clear-cut as the former one. The photoinduced processes, which might be a combination of energy and electron transfer are however rather inefficient, leaving the luminescence of both components almost unaffected. A more detailed examination involving time resolved absorption techniques would be necessary in order to elucidate the detailed mechanism.



**Fig. 6.** Fluorescence spectra in TOL of dyad **26** and models after excitation at 350 nm (optically matched solutions with  $A = 0.07$ ). The luminescence intensity of **26** is multiplied by 10 only in the 400–600 nm range

## EXPERIMENTAL

### General

All commercially available compounds were used without additional purification, unless otherwise noted. Organic solvents were purified according to generally accepted literature methods [20]. Reactions involving air and/or moisture sensitive reagents were performed under inert atmosphere (argon). Reactions progress was controlled by thin layer chromatography (TLC), performed on commercially available aluminum plates covered with silica gel or neutral aluminum oxide (60 F254, Merck). All  $R_f$  values are referred to  $\text{SiO}_2$ . For the purification by the means of column chromatography silica gel 60 (Merck) was used. Dry column vacuum chromatography was performed on MN-Silica gel P/UV254 for preparative chromatography. Size exclusion column (SEC) was filled with BioRad Bio-Beads SX-1 and eluted with either THF or toluene. Melting points were measured on Automatic Melting Point Apparatus (EZ-Melt, Stanford Research Systems) and are presented without correction. Structure and purity of synthesized compounds was confirmed using  $^1\text{H}$ ,  $^{13}\text{C}$  NMR, MS and elemental analysis (all values are given as percentages). NMR spectra were obtained on Varian Mercury 400 MHz, Bruker DRX500 MHz, Varian VNMR5 500 MHz or 600 MHz. Reported chemical shifts ( $\delta$ , ppm) were determined relative to TMS as the internal reference. Mass spectra were obtained on AMD-604 (AMD Intectra GmbH), Mariner (Perseptive Biosystems, Inc.), 4000 Q-TRAP (Applied Biosystems) or GCT Premier (Waters). Some compounds were synthesized following literature procedures: **8** [21], **14** [22], **19** [18], **30** [10j]. Compounds **1**, **2**, **4**, **5**, **11**, **12**, **16**, **17**, **27** were commercially available and used without further purification.



## Synthesis

**Preparation of 2-(3-(hydroxymethyl)phenyl)-benzo-[f]isoindole-1,3-dione (3).** The solution of 2,3-naphthalenedicarboxylic acid anhydride (**2**, 1.98 g, 10 mmol) and 3-aminobenzyl alcohol (**1**, 1.23 g, 10 mmol) in DMF (50 mL) was heated under reflux for 6 h. After cooling the reaction mixture to ambient temperature water (50 mL) was added. The precipitate was filtered off, washed with small amount of EtOH and chromatographed (SiO<sub>2</sub>, CH<sub>2</sub>Cl<sub>2</sub> + 2%MeOH) affording **3** (2.11 g, 70%) as colorless crystals. mp 214–215 °C. <sup>1</sup>H NMR (500 MHz, DMSO-*d*<sub>6</sub>, TMS): δ, ppm 4.59 (2H, d, *J* = 5.8 Hz, CH<sub>2</sub>), 5.35 (1H, t, *J* = 5.8 Hz, OH), 7.36 (1H, d, *J* = 8.0 Hz, C<sub>6</sub>H<sub>4</sub>), 7.42 (1H, d, *J* = 8.0 Hz, C<sub>6</sub>H<sub>4</sub>), 7.45 (1H, s, C<sub>6</sub>H<sub>4</sub>), 7.51 (1H, t, *J* = 8.0 Hz, C<sub>6</sub>H<sub>4</sub>), 7.81 (2H, m, naphth), 8.30 (2H, m, naphth), 8.60 (2H, s, naphth). <sup>13</sup>C NMR (125 MHz, DMSO-*d*<sub>6</sub>, TMS): δ, ppm 62.9, 125.2, 125.7, 126.1, 126.6, 127.8, 129.0, 129.8, 130.7, 132.4, 135.6, 144.0, 167.2. Anal. calcd. for C<sub>19</sub>H<sub>13</sub>NO<sub>3</sub>: C, 75.24; H, 4.32; N, 4.62; found C, 75.23; H, 4.45; N, 4.54. HRMS-EI: *m/z* [M]<sup>+</sup> calcd. for C<sub>19</sub>H<sub>13</sub>NO<sub>3</sub>, 303.0895; found 303.0900.

**Preparation of 3-(1,3-dioxo-1,3-dihydrobenzo[f]isoindol-2-yl)benzaldehyde (6).** **Method A.** Alcohol **3** (660 mg, 2.18 mmol) was suspended in the solution of TEMPO (34 mg, 10% mol) in DCM (5 mL). Subsequently, BAIB (772 mg, 2.4 mmol) was added and the reaction mixture was stirred until the alcohol was fully consumed (nearly 3 h). The reaction mixture was diluted with DCM to dissolve solid product, washed with saturated Na<sub>2</sub>S<sub>2</sub>O<sub>3</sub> aq and extracted with DCM (3 × 10 mL). The combined organic extracts were washed with NaHCO<sub>3</sub> and brine, dried over Na<sub>2</sub>SO<sub>4</sub> and concentrated under reduced pressure. Flash column chromatography (silica, DCM/hexanes 4:1) afforded title compound as a colorless crystalline solid (610 mg, 92%). **Method B.** 2,3-naphthalenedicarboxylic acid anhydride (**2**, 991 mg, 5 mmol) and 3-aminobenzaldehyde polymer (**4**, 605 mg, 5 mmol) were suspended in acetic acid (12 mL) and stirred at reflux overnight. The precipitate, formed after cooling to rt, was filtered off, washed with AcOH and dried under vacuum (1.18 g, 78%). *R<sub>f</sub>* 0.4 (DCM). mp 281 °C (decomposed). <sup>1</sup>H NMR (600 MHz, DMSO-*d*<sub>6</sub>, TMS): δ, ppm 7.78–7.85 (3H, m, C<sub>6</sub>H<sub>4</sub> + naphth), 7.87 (1H, m, C<sub>6</sub>H<sub>4</sub>), 8.02 (1H, m, C<sub>6</sub>H<sub>4</sub>), 8.07 (1H, m, C<sub>6</sub>H<sub>4</sub>), 8.33 (2H, m, naphth), 8.67 (2H, s, naphth), 10.10 (1H, s, CHO). <sup>13</sup>C NMR (150 MHz, DMSO-*d*<sub>6</sub>, TMS): δ, ppm 124.9, 127.3, 127.3, 129.3, 129.7, 130.2, 132.9, 133.0, 135.1, 136.7, 166.4, 192.5. Anal. calcd. for C<sub>19</sub>H<sub>11</sub>NO<sub>3</sub>: C, 75.74; H, 3.68; N, 4.65; found C, 75.63; H, 3.71; N, 4.58. HRMS-EI: *m/z* [M]<sup>+</sup> calcd. for C<sub>19</sub>H<sub>11</sub>NO<sub>3</sub>, 301.0739; found 301.0724.

**Preparation of 4-(1,3-dioxo-1,3-dihydrobenzo[f]isoindol-2-yl)benzaldehyde (7).** 2,3-Naphthalenedicarboxylic acid anhydride (**2**, 1.98 g, 10 mmol) and 4-aminobenzaldehyde polymer (**5**, 1.21 g, 10 mmol) were suspended in acetic acid (25 mL) and stirred at reflux

overnight. Orange color disappeared (reaction mixture becomes yellow). The precipitate, formed after cooling to rt, was filtered off, washed with AcOH and dried under vacuum (2.38 g, 79%). *R<sub>f</sub>* 0.3 (DCM). <sup>1</sup>H NMR (500 MHz, DMSO-*d*<sub>6</sub>, TMS): δ, ppm 7.79 (2H, d, *J* = 8.4 Hz, C<sub>6</sub>H<sub>4</sub>), 7.82 (2H, m, naphth.), 8.10 (2H, d, *J* = 8.4 Hz, C<sub>6</sub>H<sub>4</sub>), 8.33 (2H, m, naphth.), 8.67 (2H, s, naphth.), 10.09 (1H, s, CHO). <sup>13</sup>C NMR (125 MHz, DMSO-*d*<sub>6</sub>, TMS): δ, ppm 125.5, 127.7, 128.0, 130.0, 130.4, 130.8, 135.6, 135.7, 137.8, 166.7, 192.9. Anal. calcd. for C<sub>19</sub>H<sub>11</sub>NO<sub>3</sub>: C, 75.74; H, 3.68; N, 4.65; found C, 75.68; H, 3.68; N, 4.63. HRMS-EI: *m/z* [M]<sup>+</sup> calcd. for C<sub>19</sub>H<sub>11</sub>NO<sub>3</sub>, 301.0739; found 301.0729.

**Preparation of 2-[2-(5,5-dimethyl-[1,3]dioxan-2-yl)-phenyl]benzo[f]isoindole-1,3-dione (9).** **Method A.** The mixture of 2,3-naphthalenedicarboxylic acid anhydride (**2**, 420 mg, 2.12 mmol) and 2-aminobenzaldehyde acetal **8** (482 mg, 2.33 mmol) in AcOH (5 mL) was stirred at 110 °C overnight. After cooling to rt and solvent evaporation, the residue was dissolved in DCM, washed with NaHCO<sub>3</sub> aq, dried over Na<sub>2</sub>SO<sub>4</sub> and chromatographed (AcOEt/hexanes 1:3) giving 273 mg (33%) of acetal **9**. **Method B.** 2,3-naphthalenedicarboxylic acid anhydride (**2**, 990 mg, 5 mmol), acetal **8** (1.55 g, 7.5 mmol) and imidazole (6.8 g, 0.1 mol) were loaded into 100 mL round-bottom flask and chloroform (40 mL) was added. The mixture was stirred at gentle reflux for 2 h and then cooled to rt. The solvent was removed on rotary evaporator and the residue was taken up in small amount of absolute ethanol. The resulting suspension was sonicated for 15 min and then filtered. Filter cake was washed with cold ethanol and air-dried. Column chromatography (DCM/hexanes 3:1) afforded 838 mg (43%) of **9** as a colorless solid. *R<sub>f</sub>* 0.5 (DCM/hexanes 3:1). <sup>1</sup>H NMR (500 MHz, CDCl<sub>3</sub>, TMS): δ, ppm 0.61 (3H, s, CH<sub>3</sub>), 1.10 (3H, s, CH<sub>3</sub>), 3.39 (2H, d, *J* = 10.9 Hz, CH<sub>2</sub>), 3.55 (2H, d, *J* = 11.1 Hz, CH<sub>2</sub>), 5.42 (1H, s, CH), 7.29 (1H, m, C<sub>6</sub>H<sub>4</sub>), 7.51 (2H, m, C<sub>6</sub>H<sub>4</sub>), 7.74 (2H, m, naphth.), 7.85 (1H, m, C<sub>6</sub>H<sub>4</sub>), 8.11 (2H, m, naphth.), 8.47 (2H, s, naphth.). <sup>13</sup>C NMR (125 MHz, CDCl<sub>3</sub>, TMS): δ, ppm 21.7, 23.0, 30.1, 77.6, 99.0, 125.2, 127.7, 127.9, 129.3, 129.4, 129.5, 129.6, 129.7, 130.3, 135.6, 136.2, 167.2. Anal. calcd. for C<sub>24</sub>H<sub>21</sub>NO<sub>4</sub>: C, 74.40; H, 5.46; N, 3.62; found C, 74.13; H, 5.36; N, 3.58. HRMS-EI: *m/z* [M]<sup>+</sup> calcd. for C<sub>24</sub>H<sub>21</sub>NO<sub>4</sub>, 387.1471; found 387.1478.

**Preparation of 2-(1,3-dioxo-1,3-dihydro-benzo[f]isoindol-2-yl)-benzaldehyde (10).** TFA (8 mL) and 5% H<sub>2</sub>SO<sub>4</sub> were added to acetal **9** (1 mmol) dissolved in 20 mL of chloroform and the reaction mixture was stirred for 24 h at rt. The reaction mixture was diluted with water (50 mL) and allowed to stir for the next 30 min. The mixture was extracted with chloroform (3 × 10 mL), washed with 2 M NaHCO<sub>3</sub>, dried over MgSO<sub>4</sub> and concentrated. Residue was recrystallized from chloroform to give crystalline product (96%). <sup>1</sup>H NMR (500 MHz, DMSO-*d*<sub>6</sub>, TMS): δ, ppm 7.67 (1H, d, *J* = 7.8 Hz, C<sub>6</sub>H<sub>4</sub>), 7.76 (1H, t, *J* = 7.5 Hz, C<sub>6</sub>H<sub>4</sub>), 7.83 (2H, m, naphth.), 7.89 (1H, m, C<sub>6</sub>H<sub>4</sub>), 8.08 (1H, m, C<sub>6</sub>H<sub>4</sub>), 8.33

(2H, m, naphth.), 8.67 (2H, s, naphth.), 10.04 (1H, s, CHO).  $^{13}\text{C}$  NMR (125 MHz, DMSO- $d_6$ , TMS):  $\delta$ , ppm 125.6, 128.0, 130.0, 130.1, 130.7, 130.8, 131.5, 132.5, 132.7, 135.2, 135.7, 167.4, 191.7. HRMS-EI:  $m/z$   $[\text{M}]^{+}$  calcd. for  $\text{C}_{19}\text{H}_{11}\text{NO}_3$ , 301.0739; found 301.0743.

**Preparation of 4-(6-methoxynaphthalen-2-ylethynyl)-1,8-naphthalenedicarboxylic anhydride (13).** A 100 mL round-bottom flask containing a magnetic stirbar was charged with 4-bromo-1,8-naphthalic anhydride (**11**, 830 mg, 3 mmol), triphenylphosphine (16 mg, 0.06 mmol), copper(I) iodide (5.7 mg, 0.03 mmol), bis(triphenylphosphine)palladium dichloride (2.1 mg, 3  $\mu\text{mol}$ ), and 15 mL of triethylamine. 2-Ethynyl-6-methoxynaphthalene (**12**, 656 mg, 3.6 mmol) was added to the flask with 30 mL of toluene. A condenser containing a nitrogen inlet was placed attached, and the reaction mixture was heated to reflux for 14 h. The reaction mixture was cooled and filtered. The filtercake was washed with toluene and dried at 80 °C under vacuum. At this point the yield of a crude product, yellow amorphous solid contaminated with small amount of starting anhydride, was 1.11 g (98%) and it was used in the next step without any further purification. HRMS-EI:  $m/z$   $[\text{M}]^{+}$  calcd. for  $\text{C}_{25}\text{H}_{14}\text{O}_4$ , 378.0892; found 378.0900.

**Preparation of aldehyde 15.** The mixture anhydride **13** (756 mg, 2 mmol), 3-aminobenzaldehyde ethylene acetal (**14**, 396 mg, 2.4 mmol) and imidazole (6.8 g, 0.1 mol) in chloroform (40 mL) was stirred at gentle reflux for 12 h and then cooled to rt. The solvent was removed on rotary evaporator and the residue was taken up in small amount of absolute ethanol. The resulting suspension was sonicated for 10 min, filtered, washed with cold ethanol and dried under vacuum. NMR analysis revealed the mixture of aldehyde and acetal and the sample was fully deprotected by stirring it with excess of acetone in the presence of *p*-TsOH (35 mmol/L). The product was purified by gravity column chromatography (DCM/acetone 98:2), furnishing aldehyde **15** as a bright yellow solid (811 mg, 84%). mp 222–3 °C. Anal. calcd. for  $\text{C}_{34}\text{H}_{23}\text{NO}_5$ : C, 77.70; H, 4.41; N, 2.68; found C, 77.85; H, 4.34; N, 2.66. HRMS-EI:  $m/z$   $[\text{M}]^{+}$  calcd. for  $\text{C}_{34}\text{H}_{23}\text{NO}_5$ , 525.1576; found 525.1564.

**Preparation of 4-amino-1,3-dioxo-6,7-diphenyl-2-p-formylphenyl-2,3-dihydro-1H-isoindole-5-carbonitrile (20).** Anhydride **19** (1.8 g, 5.3 mmol) and *p*-aminobenzaldehyde polymer (**5**, 770 mg 6.36 mmol) were suspended in AcOH (14 mL) and the reaction mixture was stirred at reflux overnight. Orange color of aminobenzaldehyde disappeared and reaction was cooled to rt. Yellow solid was filtered off, washed with small amount of AcOH and dried under vacuum, giving 1.54 g (66%) of aldehyde **20**.  $R_f$  0.4 (DCM).  $^1\text{H}$  NMR (400 MHz,  $\text{CDCl}_3$ , TMS):  $\delta$ , ppm 6.20 (2H, br s,  $\text{NH}_2$ ), 7.00–7.05 (2H, m, Ph), 7.09–7.14 (2H, m, Ph), 7.17–7.24 (3H, m, Ph), 7.24–7.31 (3H, m, Ph), 7.65 (2H, m,  $\text{C}_6\text{H}_4$ ), 7.97 (2H, m,  $\text{C}_6\text{H}_4$ ), 10.03 (1H, s, CHO).  $^{13}\text{C}$  NMR (100 MHz,  $\text{CDCl}_3$ , TMS):  $\delta$ , ppm 104.0, 110.4, 114.9, 126.3, 127.7,

128.2, 128.9, 129.1, 129.4, 129.7, 130.2, 130.3, 131.6, 133.4, 135.1, 135.8, 136.6, 146.6, 154.4, 165.0, 167.1, 191.1. Anal. calcd. for  $\text{C}_{28}\text{H}_{17}\text{N}_3\text{O}_3$ : C, 75.84; H, 3.86; N, 9.48; found C, 75.94; H, 3.88; N, 9.44. HRMS-EI:  $m/z$   $[\text{M}]^{+}$  calcd. for  $\text{C}_{28}\text{H}_{17}\text{N}_3\text{O}_3$ , 443.1270; found 443.1257.

**Preparation of corrole dyad 22.** Aldehyde **6** (0.6 g, 2 mmol) and 5-(pentafluorophenyl)dipyrrane (**21**, 1.25 g, 4 mmol) were suspended in 30 mL of DCM and 330  $\mu\text{L}$  of preprepared TFA solution (from now on this solution will be referred as “TFA stock solution,” 10 mL of TFA in 100 mL of DCM) was added. The reaction course was controlled by TLC and after 30 min, the reaction was quenched by triethylamine addition (60  $\mu\text{L}$ ). The reaction mixture was diluted to 200 mL with DCM and poured into solution of DDQ (1.18 g, 5.2 mmol) in 300 mL of DCM stirred vigorously. After 2 h, the reaction mixture was slightly concentrated and passed through 2 cm silica pad. Product-containing fractions (contaminated by dipyrin) were combined and solvent was removed under reduced pressure. Residue was washed with small amount of methanol, suspended in boiling cyclohexane and after cooling, crystals were filtered off and dried under vacuum giving 288 mg of corrole **22** (16%).  $R_f$  0.4 (DCM/hexanes 3:2). UV-vis (DCM):  $\lambda_{\text{max}}$ , nm ( $\epsilon \times 10^{-3}$ ) 613 (13.5), 563 (13.5), 422 (127.7).  $^1\text{H}$  NMR (500 MHz, THF- $d_8$ , TMS):  $\delta$ , ppm (–4)–(–1.5) (3H, br s, NH), 7.72 (2H, m, naphth.), 7.90–7.97 (2H, m,  $\text{C}_6\text{H}_4$ ), 8.19 (2H, m, naphth.), 8.25 (1H, m,  $\text{C}_6\text{H}_4$ ), 8.47 (1H, m,  $\text{C}_6\text{H}_4$ ), 8.55 (2H, s, naphth.), 8.59 (2H, br s,  $\beta$ -H), 8.84 (2H, br s,  $\beta$ -H), 8.87 (2H, d,  $J = 4.5$  Hz,  $\beta$ -H), 9.09 (2H, d,  $J = 3.7$  Hz,  $\beta$ -H). HRMS-ESI:  $m/z$   $[\text{M} + \text{H}]^{+}$  calcd. for  $\text{C}_{49}\text{H}_{22}\text{N}_5\text{O}_2\text{F}_{10}$ , 902.1608; found 902.1646.

**Preparation of corrole dyad 23.** Aldehyde **7** (0.6 g, 2 mmol) and 5-(pentafluorophenyl)dipyrrane (**21**, 1.25 g, 4 mmol) were suspended in 30 mL of DCM and 330  $\mu\text{L}$  of TFA stock solution (see above) was added. The reaction course was controlled by TLC and after 30 min, the reaction was quenched by triethylamine addition (60  $\mu\text{L}$ ). The reaction mixture was diluted to 200 mL and poured into solution of DDQ (1.18 g, 5.2 mmol) in 300 mL DCM stirred vigorously. After 2 h, the reaction mixture was slightly concentrated and passed through 2 cm silica pad. Product-containing fractions were combined and solvent was removed under reduced pressure. Residue was washed with small amount of methanol, suspended in boiling cyclohexane and after cooling, crystals were filtered off and dried under vacuum giving 244 mg of corrole **23** (14%).  $R_f$  0.33 (DCM/hexanes 2:1). UV-vis (DCM):  $\lambda_{\text{max}}$ , nm ( $\epsilon \times 10^{-3}$ ) 615 (12.4), 564 (11.3), 419 (118.3).  $^1\text{H}$  NMR (500 MHz, THF- $d_8$ , TMS):  $\delta$ , ppm (–4)–(–1.5) (3H, br s, NH), 7.78 (2H, m, naphth.), 8.02 (2H, m,  $\text{C}_6\text{H}_4$ ), 8.25 (2H, m, naphth.), 8.35 (2H, m,  $\text{C}_6\text{H}_4$ ), 8.63 (4H, m, naphth.+ $\beta$ -H), 8.74 (2H, br s,  $\beta$ -H), 8.82 (2H, br s,  $\beta$ -H), 9.10 (2H, br s,  $\beta$ -H). HRMS-ESI:  $m/z$   $[\text{M} + \text{H}]^{+}$  calcd. for  $\text{C}_{49}\text{H}_{22}\text{N}_5\text{O}_2\text{F}_{10}$ , 902.1608; found 902.1618.

**Preparation of corrole dyad 24.** The mixture of aldehyde **10** (311 mg, 1.03 mmol) and

5-(pentafluorophenyl)dipyrrane (**21**, 645 mg, 2.06 mmol) in 15 mL of DCM was treated with 170  $\mu$ L of TFA stock solution (see above). After 20 min, the reaction was quenched with 30  $\mu$ L of triethylamine, diluted with DCM to 130 mL and DDQ (608 mg, 2.68 mmol) dissolved in a minimal amount of toluene was added. After 2 h of stirring, the reaction mixture was passed through silica pad, evaporated with Celite and chromatographed (DCM/hexanes 1:4  $\rightarrow$  1:1). Product-containing fractions were collected and evaporated. Crystallization from DCM afforded 157 mg (17%) of corrole **24** as a crystalline solid.  $R_f$  0.4 (DCM/hexanes 3:2). UV-vis (THF):  $\lambda_{max}$ , nm ( $\epsilon \times 10^{-3}$ ) 296 (22.9), 419 (11.7), 561 (19.4), 611 (11.0).  $^1\text{H NMR}$  (500 MHz,  $\text{CDCl}_3$ , TMS):  $\delta$ , ppm 7.27 (m, naphth.), 7.48 (2H, m, naphth.), 7.61 (2H, s, naphth.), 7.82 (1H, m,  $\text{C}_6\text{H}_4$ ), 7.89 (1H, m,  $\text{C}_6\text{H}_4$ ), 7.97 (1H, m,  $\text{C}_6\text{H}_4$ ), 8.25 (1H, m,  $\text{C}_6\text{H}_4$ ), 8.42 (2H, br s,  $\beta$ -H), 8.66 (2H, d,  $J = 5.9$  Hz,  $\beta$ -H), 8.81 (2H, d,  $J = 6.0$  Hz,  $\beta$ -H), 8.91 (2H, br s,  $\beta$ -H). HRMS-ESI:  $m/z$  [ $\text{M} + \text{H}$ ] $^+$  calcd. for  $\text{C}_{49}\text{H}_{22}\text{N}_5\text{O}_2\text{F}_{10}$ , 902.1608; found 902.1579.

**Preparation of corrole dyad 25.** To the mixture of aldehyde **15** (770 mg, 1.6 mmol) and 5-(pentafluorophenyl)dipyrrane (**21**, 1 g, 3.2 mmol) in 24 mL of DCM, 260  $\mu$ L of TFA stock solution (see above) was added while stirring. The reaction was very slow and it was left to stir overnight, then quenched with 45  $\mu$ L of triethylamine. After dilution with DCM to 300 mL, DDQ (944 mg, 4.16 mmol), dissolved in a minimal amount of toluene, was added and the reaction mixture was stirred for 2 h. Subsequently, the reaction mixture was passed through silica pad, evaporated with Celite and chromatographed (DCM/hexanes 3:1). There were additional spots with similar polarity and the sample was submitted to SEC purification (eluted with THF). Product-containing fractions were collected and evaporated. Crystallization from DCM afforded 320 mg (18%) of corrole **25** as a crystalline solid.  $R_f$  0.4 (DCM/hexanes 3:1). UV-vis (toluene):  $\lambda_{max}$ , nm ( $\epsilon \times 10^{-3}$ ) 431 (157), 561 (17.1), 614 (12.2), 647 (7.9).  $^1\text{H NMR}$  (400 MHz,  $\text{CDCl}_3$ , TMS):  $\delta$ , ppm (-4)–(-1.5) (3H, br s, NH), 3.95 (3H, s,  $\text{OCH}_3$ ), 7.15 (1H, m,  $\text{C}_{10}\text{H}_6$ ), 7.20 (1H, m,  $\text{C}_{10}\text{H}_6$ ), 7.67 (1H, m,  $\text{C}_{10}\text{H}_6$ ), 7.76 (3H, m,  $\text{C}_6\text{H}_4 + \text{C}_{10}\text{H}_6$ ), 7.89–8.00 (2H, m,  $\text{C}_6\text{H}_4 + \text{naphth.}$ ), 8.04 (1H, d,  $J = 7.6$  Hz, naphth.), 8.13 (1H, s,  $\text{C}_{10}\text{H}_6$ ), 8.22 (1H, m,  $\text{C}_6\text{H}_4$ ), 8.30 (1H, m,  $\text{C}_6\text{H}_4$ ), 8.57 (2H, br s,  $\beta$ -H), 8.70 (1H, d,  $J = 7.6$  Hz, naphth.), 8.78 (4H, m, naphth.+ $\beta$ -H), 8.97 (2H, d,  $J = 4.4$  Hz,  $\beta$ -H), 9.11 (2H, d,  $J = 4.4$  Hz,  $\beta$ -H). HRMS-ESI:  $m/z$  [ $\text{M} + \text{H}$ ] $^+$  calcd. for  $\text{C}_{62}\text{H}_{31}\text{F}_{10}\text{N}_5\text{O}_3$ , 1082.2111; found 1082.2142.

**Preparation of corrole dyad 26.** Aldehyde **20** (1.54 g, 3.47 mmol) and 5-(pentafluorophenyl)dipyrrane (**21**, 2.17 g, 6.95 mmol) were dissolved in 50 mL of DCM and 0.57 mL of TFA stock solution (see above) was added. The reaction mixture was stirred at rt for 20 min and then the reaction was quenched by the addition of triethylamine (0.1 mL). The reaction mixture was diluted with DCM to 450 mL and DDQ (2.05 g, 9 mmol; dissolved in minimal

amount of toluene) was added. After 2 h of stirring at rt, the reaction mixture was passed through silica pad, and then chromatographed (DCM/hexanes 1:1). The product was contaminated with additional fluorescent compounds which were successfully removed by the chromatography on SEC (eluted with toluene). Product-containing fractions were collected and evaporated. After crystallization, corrole **26** was obtained as dark fine powder (211 mg, 6%).  $R_f$  0.4 (DCM/hexanes 1:1). UV-vis (toluene):  $\lambda_{max}$ , nm ( $\epsilon \times 10^{-3}$ ) 429 (153), 563 (15.2), 613 (11.6), 645 (6.9).  $^1\text{H NMR}$  (500 MHz,  $\text{THF}-d_8$ ):  $\delta$ , ppm (-4)–(-1.5) (3H, br s, NH), 6.90 (2H, br s,  $\text{NH}_2$ ), 7.02–7.36 (10H, m, Ph), 7.93 (2H, d,  $J = 8$  Hz,  $\text{C}_6\text{H}_4$ ), 8.33 (2H, d,  $J = 8$  Hz,  $\text{C}_6\text{H}_4$ ), 8.63 (2H, br s,  $\beta$ -H), 8.71 (2H, m,  $\beta$ -H), 8.83 (2H, br s,  $\beta$ -H), 9.14 (2H, br s,  $\beta$ -H). HRMS-ESI:  $m/z$  [ $\text{M} + \text{H}$ ] $^+$  calcd. for  $\text{C}_{58}\text{H}_{28}\text{F}_{10}\text{N}_7\text{O}_2$ , 1044.2139; found 1044.2171.

**Preparation of 2-(p-tolyl)-benzo[f]isoindole-1,3-dione (28).** Anhydride **2** (396 mg, 2 mmol) and *p*-toluidine (**27**, 214 mg, 2 mmol) were heated under reflux in 10 mL of AcOH overnight. After cooling, the resulting precipitate was filtered off and washed with AcOH and EtOH, affording 499 mg (87%) of **28** as off-white powder.  $^1\text{H NMR}$  (500 MHz,  $\text{CDCl}_3$ , TMS):  $\delta$ , ppm 2.42 (3H, s,  $\text{CH}_3$ ), 7.33, 7.37 (4H, AA'BB',  $J = 8.3$  Hz), 7.71–7.74 (2H, m,  $\text{C}_{10}\text{H}_6$ ), 8.07–8.11 (2H, m,  $\text{C}_{10}\text{H}_6$ ), 8.44 (2H, s,  $\text{C}_{10}\text{H}_6$ ).  $^{13}\text{C NMR}$  (125 MHz,  $\text{CDCl}_3$ , TMS):  $\delta$ , ppm 21.2, 125.2, 126.5, 127.5, 129.2, 129.3, 129.8, 130.3, 135.7, 138.3, 167.2. Anal. calcd. for  $\text{C}_{19}\text{H}_{13}\text{NO}_2$ : C, 79.43; H, 4.56; N, 4.88; found C, 79.42; H, 4.55; N, 4.81. HRMS-ESI:  $m/z$  [ $\text{M} + \text{H}$ ] $^+$  calcd. for  $\text{C}_{19}\text{H}_{14}\text{NO}_2$ , 288.1025; found 288.1028.

**Preparation of 4-amino-1,3-dioxo-6,7-diphenyl-2-p-tolyl-2,3-dihydro-1H-isoindole-5-carbonitrile (29).** Anhydride **19** (511 mg, 1.5 mmol) and *p*-toluidine (**27**, 193 mg, 1.8 mmol) were heated under reflux in 5 mL of AcOH overnight. After cooling, solvent was evaporated off, the residue was dissolved in chloroform, washed with  $\text{NaHCO}_3$ , water and brine. The organic layer was separated and dried over  $\text{MgSO}_4$ . Flash column chromatography (DCM/hexanes 1:3  $\rightarrow$  2:1) and crystallization (chloroform/hexanes) afforded 350 mg (54%) of **29** as yellow crystals.  $R_f$  0.3 (DCM/hexanes 1:2).  $^1\text{H NMR}$  (500 MHz,  $\text{CDCl}_3$ , TMS):  $\delta$ , ppm 2.37 (3H, s,  $\text{CH}_3$ ), 6.14 (2H, br s,  $\text{NH}_2$ ), 7.01 (2H, m,  $\text{C}_6\text{H}_4$ ), 7.03 (2H, m,  $\text{C}_6\text{H}_4$ ), 7.11 (3H, m, Ph), 7.15 (7H, m, Ph).  $^{13}\text{C NMR}$  (125 MHz,  $\text{CDCl}_3$ , TMS):  $\delta$ , ppm 21.2, 103.7, 111.0, 115.1, 126.3, 127.6, 127.7, 128.2, 128.5, 128.8, 129.4, 129.5, 129.6, 130.4, 132.0, 133.6, 136.1, 138.2, 146.4, 153.9, 165.7, 167.8; Anal. calcd. for  $\text{C}_{28}\text{H}_{19}\text{N}_3\text{O}_2$ : C, 78.31; H, 4.46; N, 9.78; found C, 78.37; H, 4.44; N, 9.83. HRMS-ESI:  $m/z$  [ $\text{M} + \text{Na}$ ] $^+$  calcd. for  $\text{C}_{28}\text{H}_{19}\text{N}_3\text{O}_2\text{Na}$ , 452.1370; found 452.1392.

## Spectroscopy and photophysics

Spectroscopic grade toluene (C. Erba) was used without further purification. The absorption spectra

were recorded by a Perkin-Elmer Lambda 950 UV-vis spectrophotometer and the emission spectra corrected for the photomultiplier response were detected by an Edinburgh FLSP920 fluorimeter equipped with a R928P Hamamatsu photomultiplier with a spectral coverage from 200 nm to *ca.* 820 nm. Fluorescence quantum yields, when reported, were calculated from the corrected luminescence spectra against a reference with the following Equation 1:

$$\phi_{em} = \frac{A_r n^2 I}{n_r^2 I_r A} \phi_r \quad (1)$$

The reference used for **28** emission quantum yield was air-equilibrated quinine sulphate in 1N H<sub>2</sub>SO<sub>4</sub> with  $\phi_{fl} = 0.546$  [23], whereas the reported value of 0.14 for **30** was used as reference to calculate the emission quantum yield of the corrole units [12a].

Fluorescence lifetimes in the nanosecond region were detected by a Time Correlated Single Photon Counting apparatus (IBH) with excitation at 331 or 465 nm. A system based on a Streak Camera Hamamatsu C1587 equipped with M1952 and a Nd-YAG laser (Continuum PY62/10, 35 ps pulse, 1 mJ at 355 nm) was used for detecting luminescence with picosecond resolution [24]. Estimated errors are 10% on lifetimes, molar extinction coefficients and quantum yields. The working temperature, if not otherwise specified, is  $295 \pm 2$  K.

## CONCLUSION

The comparison of three different methodologies leading to various small aromatic imides bearing formyl groups has proven that both reaction with commercially available polymers of aminobenzaldehydes and utilization of aminobenzyl alcohols are the best strategies in terms of overall efficiency. We proved that regardless the orientation of naphthalene-2,3-imide moiety *vs.* corrole ring the interaction between these chromophores is small. Still placing it above the corrole ring induces small changes in photophysical behavior. We also have shown that while altering the size and electron density in blue-absorbing aromatic imides one can manipulate the behavior of bichromophoric systems. While large, slightly polarized imides tend to lead to energy transfer, small and strongly polarized derivatives of phthalimide induced more complex behavior.

## Acknowledgements

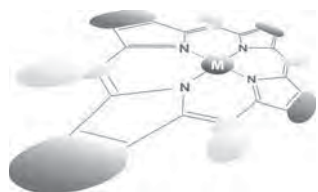
This research has been financially supported by the Polish National Science Center (844/N-ESF-EuroSolarFuels/10/2011/0) and the Italian National Research Council (CNR) in the framework of the

European Science Foundation (ESF-EUROCORES-EuroSolarFuels-10-FP-006). A.I.C acknowledges the European Community's Seventh Framework Programme (TOPBIO project-grant agreement no. 264362) for an ESR grant.

## REFERENCES

- Balzani V, Ceroni P and Juris A. *Photochemistry and Photophysics: Concepts, Research, Applications*, Wiley-VCH: 2014.
- Scholes GD, Fleming GR, Olaya-Castro A and van Grondelle R. *Nat. Chem.* 2011; **3**: 763–774.
- Andreiadis ES, Chavarot-Kerlidou M, Fontcave M and Artero V. *Photochem. Photobiol.* 2011; **87**: 946–964.
- Gust D and Moore TA. In *The Porphyrin Handbook, Electron Transfer*, Vol. 8, Kadish KM, Smith KM and Guillard R. (Eds.) Academic Press: 1999; pp 153–184.
- Ohkubo K, Kotani H, Shao J, Ou Z, Kadish KM, Li G, Pandey RK, Fujitsuka M, Ito O, Imahori H and Fukuzumi S. *Angew. Chem., In. Ed.* 2004; **43**: 853–856.
- (a) Bottari G, de la Torre G, Guldi DM and Torres T. *Chem. Rev.* 2010; **110**: 6768–6816. (b) Göransson E, Boixel J, Fortage J, Jacquemin D, Becker H-C, Blart E, Hammarström L and Odobel F. *Inorg. Chem.* 2012; **51**: 11500–11512.
- (a) Oh J, Sung J, Kitano M, Inokuma Y and Osuka A. Kim D. *Chem. Commun.* 2014; **50**: 10424–10426. (b) Osuka A, Tsurumaki E and Tanaka T. *Bull. Chem. Soc. Jpn.* 2011; **84**: 679–697.
- (a) Flamigni L, Ventura B, Tasiar M and Gryko DT. *Inorg. Chim. Acta* 2007; **360**: 803–813. (b) Tasiar M, Gryko DT, Cembor M, Jaworski JS, Ventura B and Flamigni L. *New J. Chem.* 2007; **31**: 247–259. (c) Flamigni L, Ventura B, Tasiar M, Becherer T, Langhals H and Gryko DT. *Chem. Eur. J.* 2008; **14**: 169–183. (d) Gros CP, Brisach F, Meristoudi A, Espinoza E, Guillard R and Harvey PD. *Inorg. Chem.* 2007; **46**: 125–135. (e) Tasiar M, Gryko DT, Shen J, Kadish KM, Becherer T, Langhals H, Ventura B and Flamigni L. *J. Phys. Chem. C* 2008; **112**: 19699–19709. (f) D'Souza F, Chitta R, Ohkubo K, Tasiar M, Subbaiyan NK, Zandler ME, Rogacki MK, Gryko DT and Fukuzumi S. *J. Am. Chem. Soc.* 2008; **130**: 14263–14272. (g) Tasiar M, Gryko DT, Pielacińska DJ, Zanelli A and Flamigni L. *Chem. Asian J.* 2010; **1**: 130–140. (h) Tasiar M, Voloshchuk R, Poronik YM, Rowicki T and Gryko DT. *J. Porphyrins Phthalocyanines* 2011; **15**: 1011–1023. (i) Ciuciu AI, Flamigni L, Voloshchuk R and Gryko DT. *Chem. Asian J.* 2013; **8**: 1004–1014. (j) Voloshchuk R, Gryko DT, Chotkowski M, Ciuciu AI and Flamigni L. *Chem. Eur. J.* 2012; **18**: 14845–14859. (k) Flamigni L, Ciuciu AI, Langhals H, Böck B

- and Gryko DT. *Chem. Asian J.* 2012; **7**: 582–592.
- (l) Flamigni L and Gryko DT. *Chem. Soc. Rev.* 2009; **38**: 1635–1646. (m) Flamigni L, Vyrostek D, Voloshchuk R and Gryko DT. *Phys Chem. Chem. Phys.* 2010; **12**: 474–483.
9. (a) Paolesse R. In *The Porphyrin Handbook*, Vol. 2, Kadish KM, Smith KM and Guillard R. (Eds.) Academic Press: San Diego, CA, 2000; pp 201. (b) Sessler JL and Weghorn SJ. In *Expanded, Contracted & Isomeric Porphyrins*, Pergamon: Oxford, 1997; pp 11. (c) Erben C, Will S and Kadish KM. In *The Porphyrin Handbook*, Vol. 2, Kadish KM, Smith KM and Guillard R. (Eds.) Academic Press: San Diego, CA, 2000; pp 233. (d) Montforts F-P, Glasenapp-Breiling M and Kusch D. In *Houben-Weyl Methods of Organic Chemistry*, Vol E9d, Schaumann E. (Ed.) Thieme: Stuttgart, New York, 1998; pp 665–672. (e) Gryko DT. *Eur. J. Org. Chem.* 2002; 1735–1743. (f) Guillard R, Kadish KM, Barbe J-M and Stern C. In *The Porphyrin Handbook*, Vol 18, Kadish KM, Smith KM and Guillard R. (Eds.) Academic Press: 2003; pp 303–351. (g) Gryko DT, Fox JP and Goldberg DP. *J. Porphyrins Phthalocyanines* 2004; **8**: 1091–1105. (h) Nardis S, Monti D and Paolesse R. *Mini-Rev. Org. Chem.* 2005; **2**: 355–372. (i) Goldberg DP. *Acc. Chem. Res.* 2007; **40**: 626–634. (j) Aviv I and Gross Z. *Chem. Commun.* 2007; 1987–1999. (k) Johnson AW and Kay IT. *Proc. Chem. Soc. London* 1964; 89–90.
10. (a) Gross Z, Galili N and Saltsman I. *Angew. Chem. Int. Ed.* 1999; **38**: 1427–1429. (b) Paolesse R, Nardis S, Sagone F and Khoury RM. *J. Org. Chem.* 2001; **66**: 550–556. (c) Briñas RP and Brückner C. *Synlett* 2001; 442–444. (d) Gryko DT and Jadach K. *J. Org. Chem.* 2001; **66**: 4267–4275. (e) Sakow D, Böker B, Brandhorst K, Burghaus O and Bröring M. *Angew. Chem. Int. Ed.* 2013; **52**: 4912–4915. (f) Gryko DT, Tasior M and Koszarna B. *J. Porphyrins Phthalocyanines* 2003; **7**: 239–248. (g) Geier GR III, Chick JFB, Callinan JB, Reid CG and Auguscinski WP. *J. Org. Chem.* 2004; **69**: 4159–4169. (h) Jeandon C, Ruppert R and Callot HJ. *Chem. Commun.* 2004; 1090–1091. (i) Koszarna B and Gryko DT. *J. Org. Chem.* 2006; **71**: 3707–3717. (j) Gryko DT and Koszarna B. *Synthesis* 2004; 2205–2209. (k) Stefanelli M, Nardis S, Tortora L, Fronczek FR, Smith KM, Licocchia S and Paolesse R. *Chem. Commun.* 2011; **47**: 4255–4257. (l) Tortora L, Nardis S, Fronczek FR, Smith KM and Paolesse R. *Chem. Commun.* 2011; **47**: 4243–4245. (m) Barata JFB, Silva AMG, Neves MGPMS, Tomé AC, Silva AMS and Cavaleiro JAS. *Tetrahedron Lett.* 2006; **47**: 8171–8174.
11. (a) Kupersmidt L, Okun Z, Amit T, Mandel S, Saltsman I, Mahammed A, Bar-Am O, Gross Z and Youdim MBH. *J. Neurochem.* 2010; **113**: 363–373. (b) Kanamori A, Catrinescu M-M, Mahammed A, Gross Z and Levin LA. *J. Neurochem.* 2010; **114**: 488–498.
12. (a) Ventura B, Degli Esposti A, Koszarna B, Gryko DT and Flamigni L. *New J. Chem.* 2005; **29**: 1559–1566. (b) Ding T, Alemán EA, Mordarelli DA and Ziegler CJ. *J. Phys. Chem. A* 2005; **109**: 7411–7417. (c) Kowalska D, Liu X, Tripathy U, Mahammed A, Gross Z, Hirayama S and Steer RP. *Inorg. Chem.* 2009; **48**: 2670–2676.
13. Shao J, Shen J, Z Ou, Wenbo E, Koszarna B, Gryko DT and Kadish KM. *Inorg. Chem.* 2006; **45**: 2251–2265.
14. (a) Wallin S, Monnereau C, Blart E, Gankou J-R, Odobel F and Hammarström L. *J. Phys. Chem. A* 2010; **114**: 1709–1721. (b) Miller SE, Lukas AS, Marsh E, Bushard P and Wasielewski MR. *J. Am. Chem. Soc.* 2000; **122**: 7802–7810.
15. (a) Röger C, Miloslavina Y, Brunner D, Holzwarth AR and Würthner F. *J. Am. Chem. Soc.* 2008; **130**: 5929–5939. (b) Gunderson VL, Smeigh AL, Hoon Kim C, Co DT and Wasielewski MR. *J. Am. Chem. Soc.* 2012; **134**: 4363–4372. (c) Guha S, Goodson FS, Roy S, Corson LJ, Gravenmier CA and Saha S. *J. Am. Chem. Soc.* 2011; **133**: 15256–15259.
16. (a) De Mico A, Margarita M, Parlanti M, Vescovi A and Piancatelli G. *J. Org. Chem.* 1997; **62**: 6974–6977. (b) Nowak-Król A, Koszarna B, Yoo SY, Chromiński J, Węclawski MK, Lee C-H and Gryko DT. *J. Org. Chem.* 2011; **76**: 2627–2634.
17. Lukas AS, Bushard PJ, Weiss EA and Wasielewski MR. *J. Am. Chem. Soc.* 2003; **125**: 3921–3930.
18. Gewald K. *Chem. Ber.* 1996; **99**: 1002–1007.
19. Flamigni L, Ventura B, You C-C, Hippicus C and Würthner F. *J. Phys. Chem. C* 2007; **111**: 622–630.
20. Armarego WLF and Chai CLL. *Purification of Laboratory Chemicals* (4th edn), Elsevier Science: 2003.
21. Imahori H, Azuma T, Ozawa S, Yamada H, Ajavakom A, Norieda H, Sakata Y and Ushida K. *Chem. Commun.* 1999; **35**: 557–558.
22. Clayden J, Pickworth M and Jones LH. *Chem. Commun.* 2009; **45**: 547–549.
23. Eaton DF. *Pure Appl. Chem.* 1988; **60**: 1107–1114.
24. Flamigni L, Talarico AM, Chambron JC, Heitz V, Linke M, Fujita N and Sauvage J-P. *Chem. Eur. J.* 2004; **1**: 2689–2699.



## Mechanistic study of a manganese porphyrin catalyst for on-demand production of chlorine dioxide in water

Scott D. Hicks<sup>a</sup>, Silei Xiong<sup>b</sup>, Curt J. Bougher<sup>a</sup>, Grigori A. Medvedev<sup>b</sup>, James Caruthers<sup>b</sup> and Mahdi M. Abu-Omar<sup>\*a,b,†</sup>

<sup>a</sup> Brown Laboratory, Negishi Brown Institute, and Department of Chemistry, Purdue University, 560 Oval Drive, West Lafayette, Indiana 47907, USA

<sup>b</sup> School of Chemical Engineering, Purdue University, Forney Hall of Chemical Engineering, 480 Stadium Mall Drive, West Lafayette, Indiana 47907, USA

Dedicated to Professor Shunichi Fukuzumi on the occasion of his retirement

Received 24 November 2014

Accepted 30 December 2014

**ABSTRACT:** A water-soluble manganese porphyrin complex was examined for the catalytic formation of chlorine dioxide from chlorite under ambient temperature at pH 5.00 and 6.90. Quantitative kinetic modeling allowed for the deduction of a mechanism that accounts for all experimental observations. Catalysis is initiated *via* an OAT (Oxygen Atom Transfer) reaction resulting in formation of a putative manganese(V) oxo species, which undergoes ET (Electron Transfer) with chlorite to form chlorine dioxide. As chlorine dioxide accumulates in solution, chlorite consumption slows down and ClO<sub>2</sub> reaches a maximum as the system reaches equilibrium. In phosphate buffer at pH 6.90, manganese(IV) oxo accumulates and its reaction with ClO<sub>2</sub> gives ClO<sub>3</sub><sup>-</sup>. However, at pH 5.00 acetate buffer proton coupled electron transfer (PCET) from chlorite to manganese(IV) oxo is fast and irreversible leading to chlorate formation only *via* the putative manganese(V) oxo species. These differences underscore how PCET rates affect reaction pathways and mechanism. The ClO<sub>2</sub> product can be collected from the aqueous reaction mixture *via* purging with an inert gas, allowing for the preparation of chlorine dioxide on-demand.

**KEYWORDS:** manganese, porphyrin, chlorine dioxide, kinetics, catalysis.

## INTRODUCTION

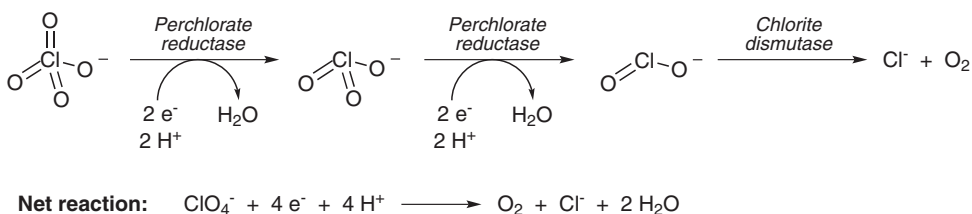
The removal of chlorine oxyanions (ClO<sub>n</sub><sup>-</sup>, *n* = 1–4) from drinking water and the environment has received much attention in recent years [1–3]. Their wide range of applications and high solubility has led to a severe contamination of water sources by these anthropogenic pollutants. Perchlorate (ClO<sub>4</sub><sup>-</sup>) is commonly used in rocket fuel, missiles, and fireworks. Despite its strong oxidizing potential, perchlorate is quite inert in aqueous solution, which results in its accumulation in the environment [4]. Chlorate (ClO<sub>3</sub><sup>-</sup>) is primarily used for the production of

chlorine dioxide (ClO<sub>2</sub>) used in pulp bleaching [5] and less commonly as herbicide. Chlorite (ClO<sub>2</sub><sup>-</sup>) is primarily used as a source of ClO<sub>2</sub>, and hypochlorite (ClO<sup>-</sup>) is primarily used as disinfectant. While the applications of chlorine oxyanions have changed over time as a result of new markets and environmental concerns, it is obvious that chlorine oxyanions are essential chemicals in modern life.

Biologically, there are two enzymes that catalyze the remediation of chlorine oxyanions to innocuous chloride (Cl<sup>-</sup>) and dioxygen (O<sub>2</sub>) as shown in Scheme 1 [4, 6]. Perchlorate reductase (PR), a molybdenum enzyme, is responsible for catalyzing the reduction of perchlorate, (Cl<sup>VII</sup>), to chlorite (Cl<sup>III</sup>) presumably *via* chlorate (Cl<sup>V</sup>) intermediate. Despite a favorable reduction potential, perchlorate reductase does not further reduce ClO<sub>2</sub><sup>-</sup>.

<sup>†</sup> SPP full member in good standing

\*Correspondence to: Mahdi M. Abu-Omar, email: mabuomar@purdue.edu, tel: +1 (765)-494-5302, fax: +1 (765)-494-0239



**Scheme 1.** Proposed biological route for the degradation/remediation of chlorine oxyanions

Instead, chlorite is further reduced to innocuous chloride ( $\text{Cl}^-$ ) and dioxygen ( $\text{O}_2$ ) by a highly conserved, soluble heme containing enzyme known as chlorite dismutase (Cld) [7–9]. The chemistry of this enzyme is of considerable interest as a result of photosystem II being the only other known enzymatically catalyzed process for O–O bond formation.

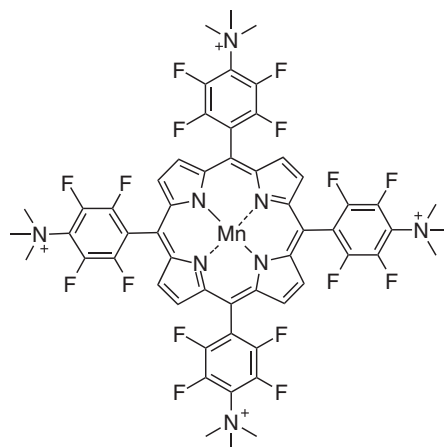
Dubois and coworkers have studied the mechanism of Cld and proposed a rebound pathway between iron-oxo Compound I (formed from the reaction of  $\text{Fe}^{\text{III}}$ -heme and chlorite) and hypochlorite to give dioxygen and chloride [8, 9]. The reaction chemistry of chlorite and chlorous acid,  $\text{Cl}^{\text{III}}$ , has been studied extensively and recently reviewed by Fábíán [10]. Collman and Braumann have reported on the electrochemical reduction of chlorite catalyzed by metalloporphyrins [11], as well as on the use of chlorite with manganese porphyrin for catalytic alkane oxidations [12].

Our group has reported on the dismutation of chlorite under physiological pH using water-soluble ferric porphyrins [13, 14]. In these model systems, the reaction proceeds for the most part to disproportionation products, chloride and chlorate, in 1:2 stoichiometry. One exception was the fluorinated complex  $[\text{Fe}^{\text{III}}(\text{TF}_4\text{TMAP})]^+$ , which afforded moderate  $\text{O}_2$  yields. More recently, a computational study on  $[\text{Fe}^{\text{III}}(\text{Por})]^+$  supports the formation of  $\text{Fe}^{\text{IV}}(\text{O})$  (Compound II) and chlorine monoxide intermediate *via* homolytic bond cleavage of chlorite [15]. Unlike the fluorinated ferric porphyrin, the manganese analog favors the formation of chlorine dioxide as opposed to dioxygen. Recently, we reported the conversion of chlorite to chlorine dioxide in good yields catalyzed by  $[\text{Mn}^{\text{III}}(\text{TF}_4\text{TMAP})]^+$  under physiological pH at room temperature [16]. Groves and co-workers have also independently shown that  $[\text{Mn}^{\text{III}}(\text{TDMImp})]^+$  among other manganese porphyrin catalysts also convert chlorite to chlorine dioxide [17, 18]. We have also reported on two non-heme manganese complexes,  $[\text{Mn}^{\text{II}}(\text{N4Py})]^{2+}$  and  $[\text{Mn}^{\text{II}}(\text{Bn-TPEN})]^{2+}$ , that catalyze the conversion of chlorite to  $\text{ClO}_2$  in moderate yields under room temperature at pH 5.00 [19]. Lau and co-workers have reported on a ruthenium bisphenanthroline complex that produces  $\text{ClO}_2$  [20].

Industrially, there are several methods for the production of chlorine dioxide [21]. The majority of methods involve highly corrosive conditions and harsh oxidants, which raise health and environmental/safety

concerns. Of the chlorine oxyanions used for  $\text{ClO}_2$  production, chlorate is the most common source *via* the reaction with methanol in the presence of concentrated sulfuric acid [21]. However, the one-electron electrochemical oxidation of chlorite offers an alternative route to  $\text{ClO}_2$  but requires substantial energy input. The primary commercial use of chlorine dioxide is as an oxidizing agent for pulp bleaching [5] and more recently for water disinfection/treatment [21]. For disinfection applications, chlorine dioxide is prepared by the chlorite-hypochlorite reaction in the presence of hydrochloric acid; see for example Du Pont's Oxychlor® II generator. Chlorine dioxide is preferred over chlorine gas ( $\text{Cl}_2$ ) for water treatment as it exhibits superior antimicrobial activity and generates less harmful by-products [22]. One major drawback; however, is the instability of  $\text{ClO}_2$  at high pressure, a fact that effectively prohibits its transport as a gas. Hence, on-site production of  $\text{ClO}_2$  is a prerequisite for any practical application.

In this work, we examine the kinetics and mechanism of the  $[\text{Mn}^{\text{III}}(\text{TF}_4\text{TMAP})]^{5+}$  complex (Fig. 1) for chlorine dioxide production from chlorite at pH 5.00 and 6.90. The reaction proceeds efficiently reaching completion within 3 h with as little as 0.10 mol% catalyst loading under ambient temperature and noncorrosive pH. The complex  $[\text{Mn}^{\text{III}}(\text{TF}_4\text{TMAP})]^{5+}$  initiates catalysis by oxygen-atom transfer (OAT) followed by electron transfer (ET) and



**Fig. 1.** Structure of  $[\text{Mn}^{\text{III}}(\text{TF}_4\text{TMAP})]^{5+}$ . The counteranion is trifluoromethane sulfonate

proton coupled electron transfer (PCET). Chlorine dioxide is produced and high-valent  $\text{Mn}^{\text{IV}}(\text{O})$  accumulates until the reaction system reaches equilibrium. The rate of PCET to  $\text{Mn}^{\text{IV}}(\text{O})$  is significantly affected by pH resulting in different mechanistic pathways at the two investigated pH values. A comprehensive mechanism that satisfies all experimental observations is obtained from quantitative kinetics modeling.

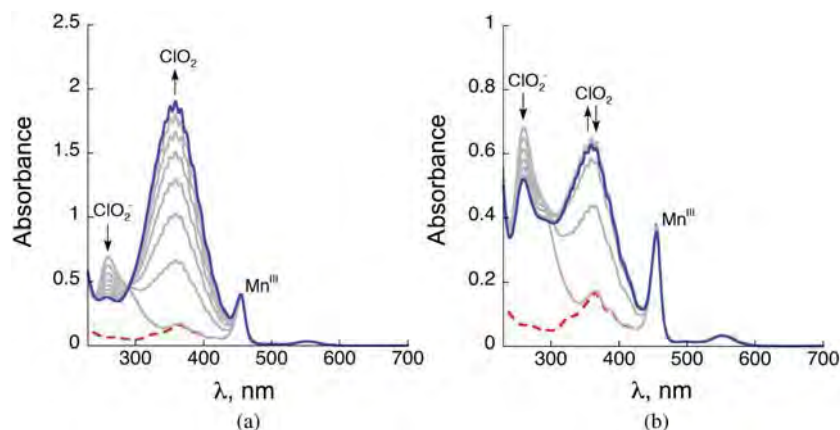
## RESULTS AND DISCUSSION

### Results

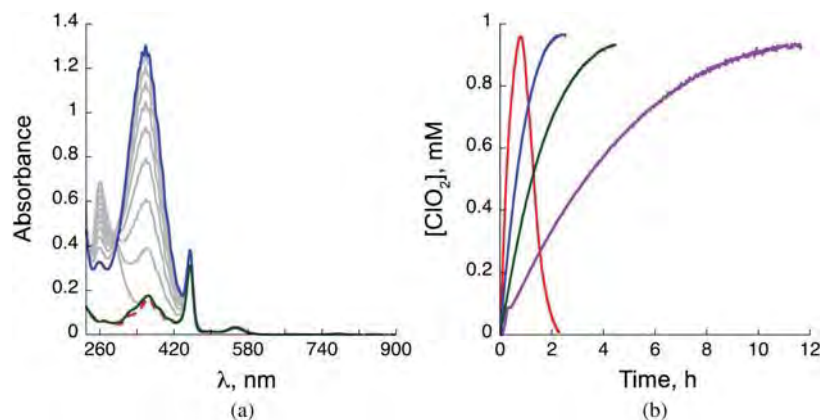
**Formation of  $\text{ClO}_2$ .** The catalytic activity of  $[\text{Mn}^{\text{III}}(\text{TF}_4\text{TMAP})]^{5+}$  for  $\text{ClO}_2$  production starting from  $\text{ClO}_2^-$  was examined at 25.0 °C in 50.0 mM acetate buffer (pH 5.00) and 50.0 mM phosphate buffer (pH 6.90) (Fig. 2). The reactivity was also examined in 50.0 mM

borate buffer (pH 9.00); however, the production of  $\text{ClO}_2$  was not observed at high pH with the disproportionation of chlorite to chloride and chlorate instead being favored. This observation suggests the process for  $\text{ClO}_2$  production is proton dependent and, if produced, is quickly converted to chloride and chlorate in basic medium. Hence, for pH 5.00 and 6.90 the formation of  $\text{ClO}_2$  was monitored following its characteristic absorption band at  $\lambda_{\text{max}} = 360 \text{ nm}$  ( $\epsilon = 1250 \text{ M}^{-1}\text{cm}^{-1}$ ). To confirm the formation of chlorine dioxide, diethyl ether was added to a typical reaction upon maximum absorbance at 360 nm and  $\text{ClO}_2$  extracted into the organic ether phase. UV-vis and MS spectra of the organic ether layer confirmed  $\text{ClO}_2$  by comparison to authentic samples (Fig. S2). The formation of dioxygen ( $\text{O}_2$ ) was not observed in any of the reactions performed.

**Temperature dependence.** The change in reaction rate and  $\text{ClO}_2$  yield at different temperatures (5.0 to 35.0 °C) was examined in 50.0 mM acetate buffer (pH 5.00) as shown in Fig. 3. The maximum concentration of chlorine



**Fig. 2.** Characteristic UV-vis spectral changes during catalysis over 3 h. Starting catalyst (red dashed), maximum  $\text{ClO}_2$  (blue). (a) Experiment conducted in 50.0 mM acetate buffer (pH = 5.00). Reaction conditions:  $[\text{Mn}^{\text{III}}(\text{TF}_4\text{TMAP})]_0 = 3.98 \mu\text{M}$ ;  $[\text{ClO}_2^-]_0 = 4.00 \text{ mM}$ . (b) Experiment conducted in 50.0 mM phosphate buffer (pH = 6.90). Reaction conditions:  $[\text{Mn}^{\text{III}}(\text{TF}_4\text{TMAP})]_0 = 3.98 \mu\text{M}$ ;  $[\text{ClO}_2^-]_0 = 4.00 \text{ mM}$



**Fig. 3.** Temperature effect on the formation of  $\text{ClO}_2$  from  $\text{ClO}_2^-$  using  $[\text{Mn}^{\text{III}}(\text{TF}_4\text{TMAP})]^{5+}$  in 50.0 mM acetate buffer (pH 5.00). (a) UV-vis spectra changes when the reaction was conducted at 35.0 °C. Starting catalyst (red dashed), maximum  $\text{ClO}_2$  (blue, 50 min), consumption of  $\text{ClO}_2$  (green, 2 h). Reactions conditions:  $[\text{Mn}^{\text{III}}(\text{TF}_4\text{TMAP})] = 3.99 \mu\text{M}$ ;  $[\text{ClO}_2^-] = 4.01 \text{ mM}$ . (b) Chlorine dioxide vs. time at 35.0 °C (red), 25.0 °C (blue), 15.0 °C (green) and 5.00 °C (purple)



dioxide was not affected by temperature while the rate of formation increased as temperature increased. When the reaction was conducted above room temperature, a noticeable decrease in  $\text{ClO}_2$  concentration was observed over time after the maximum chlorine dioxide was reached.

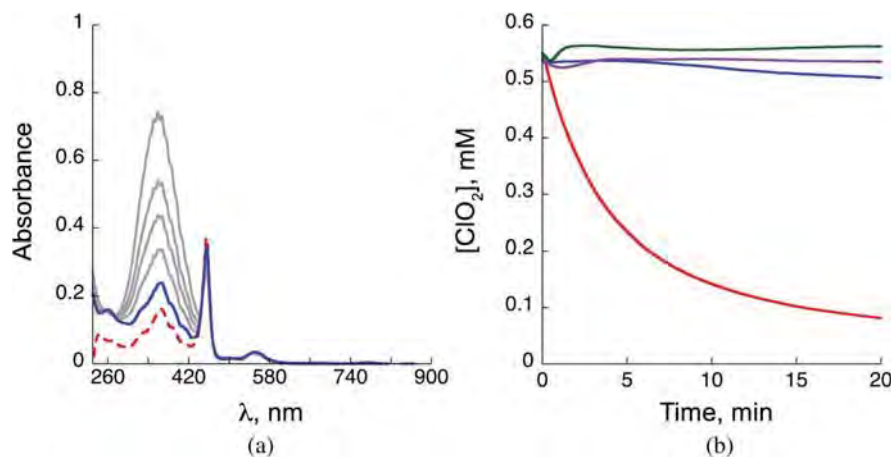
**Products analysis by Ion Chromatography (IC).** In order to determine the concentration of other chlorine containing products, ion chromatography was performed on reaction mixtures upon maximum yield/concentration of  $\text{ClO}_2$ . IC confirms that the chlorite reactant was consumed and both  $\text{Cl}^-$  and  $\text{ClO}_3^-$  were also formed. When the concentration of chlorite or catalyst was increased, more chlorate was formed. Longer reaction times led to the complete decomposition of chlorite, while the concentration of chlorine dioxide remained relatively constant in 50.0 mM acetate buffer (pH 5.00). The concentration of  $\text{ClO}_2$  decreased over time in 50.0 mM phosphate buffer (pH 6.90) leading to larger concentrations of chloride and chlorate. The exact yields of anions for selected reaction conditions are summarized in Table 1. Ion chromatograms and exact yields of anions for all reactions are provided in the Supporting Information (Figs S3–S17 and Tables S1–S4).

**Reactivity of independently prepared chlorine dioxide with  $[\text{Mn}^{\text{III}}(\text{TF}_4\text{TMAP})]^{5+}$ .** To probe for the effect of product on reaction kinetics,  $\text{ClO}_2$  was collected in 50.0 mM acetate buffer (pH 5.00) and 50.0 mM phosphate buffer (pH 6.90) from a separate reaction and the reactivity of the catalyst with freshly prepared  $\text{ClO}_2$  was examined at 25.0 °C (Fig. 4). Chlorine dioxide (550  $\mu\text{M}$ ) in the absence of catalyst in both buffers led to a minimal decrease in concentration. The reaction of  $\text{ClO}_2$  with  $\text{Mn}^{\text{III}}$  catalyst (3.98  $\mu\text{M}$ ) in acetate buffer resulted in a minimal decrease in  $\text{ClO}_2$  concentration. However, when the reaction was examined in phosphate buffer

in the presence of  $\text{Mn}^{\text{III}}$  porphyrin,  $\text{ClO}_2$  was consumed within 30 min with an increase in chlorite and chlorate concentrations (Table S5).

**Reactivity of hypochlorite with  $[\text{Mn}^{\text{III}}(\text{TF}_4\text{TMAP})]^{5+}$ .** Hypochlorite is a known two-electron oxidant and is a proposed intermediate of the reaction. Therefore the reaction between  $[\text{Mn}^{\text{III}}(\text{TF}_4\text{TMAP})]^{5+}$  and hypochlorite ( $\text{ClO}^-$ ) was monitored at 5.00 °C. The manganese(V) oxo species was not observed in acetate or phosphate buffer as a result of rapid comproportionation with  $[\text{Mn}^{\text{III}}]^{5+}$  to form  $\text{Mn}^{\text{IV}}(\text{O})$  (Fig. S29). In borate buffer; however, the rapid formation of the  $[\text{Mn}^{\text{V}}(\text{O})]^+$  species was observed with slow conversion to  $\text{Mn}^{\text{IV}}(\text{O})$  over time (Fig. S29). As a result of the rapid formation of  $\text{Mn}^{\text{IV}}(\text{O})$  in acetate and phosphate buffers, the reactivity was examined using stop-flow UV-vis spectroscopy at 455 nm ( $\text{Mn}^{\text{III}}$  soret) and 417 nm ( $\text{Mn}^{\text{IV}}(\text{O})$  soret). Examination of the reaction time highlights the rapid consumption of hypochlorite in both acetate and phosphate buffers. However, when conducted in phosphate buffer, the hypochlorite was consumed more rapidly as a result of a higher concentration of the anionic form ( $\text{pK}_a = 7.53$ ). The resulting absorbance changes over time are found in Fig. S30 for acetate buffer and Fig. S31 for phosphate buffer (Supporting information).

**Absorption spectroscopy and kinetics.** The consumption of chlorite was monitored by the decrease in absorbance at 260 nm ( $\epsilon = 154 \text{ M}^{-1}\text{cm}^{-1}$ ) and the production of chlorine dioxide was monitored by the increase in absorbance at 360 nm ( $\epsilon = 1250 \text{ M}^{-1}\text{cm}^{-1}$ ). The catalyst has an absorbance at 260 nm ( $18267 \text{ M}^{-1}\text{cm}^{-1}$ ); however, the concentrations of chlorite used contributed more to the intensity at this wavelength. The catalyst also has an absorbance at 360 nm ( $42376 \text{ M}^{-1}\text{cm}^{-1}$ ) and its absorbance was subtracted relative to the  $\text{Mn}^{\text{III}}$  soret peak at 455 nm ( $95747 \text{ M}^{-1}\text{cm}^{-1}$ ). While the time



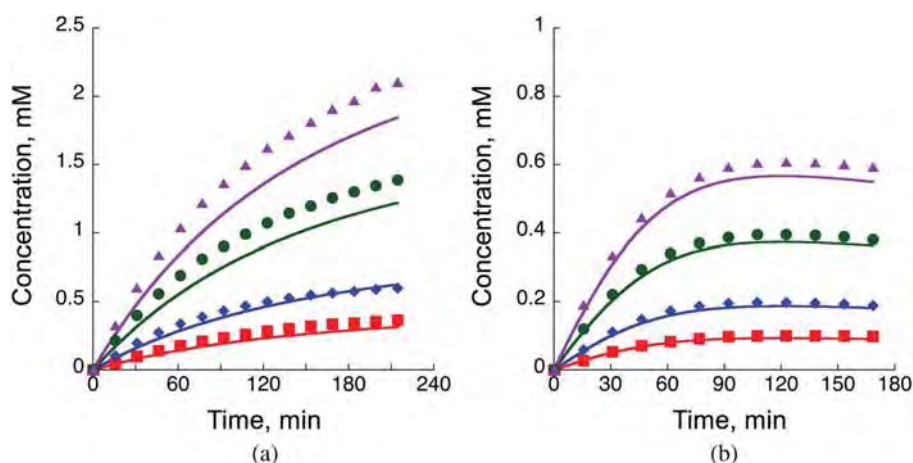
**Fig. 4.** Examination of product inhibition by reacting  $\text{ClO}_2$  with  $[\text{Mn}^{\text{III}}(\text{TF}_4\text{TMAP})]^{5+}$  in acetate (pH 5.00) and phosphate (pH 6.90) buffer. (a) The reaction of  $[\text{Mn}^{\text{III}}(\text{TF}_4\text{TMAP})]^{5+}$  (3.98  $\mu\text{M}$ ) and chlorine dioxide (550  $\mu\text{M}$ ) in 50.0 mM phosphate buffer results in the disappearance of  $\text{ClO}_2$  and a decrease in the  $\text{Mn}^{\text{III}}$  soret. (b) Chlorine dioxide vs. time for chlorine dioxide in the absence of catalyst in acetate (purple) and phosphate (blue) buffer and in the presence of catalyst in acetate (green) and phosphate (red)

profiles at 260 nm ( $\text{ClO}_2^-$ ) and 360 nm ( $\text{ClO}_2$ ) fit a single exponential equation to a first approximation, the time profiles exhibit features of more complex kinetics (Fig. 5). Ion chromatography confirms that most of the starting chlorite is consumed when the maximum concentration of  $\text{ClO}_2$  is reached.

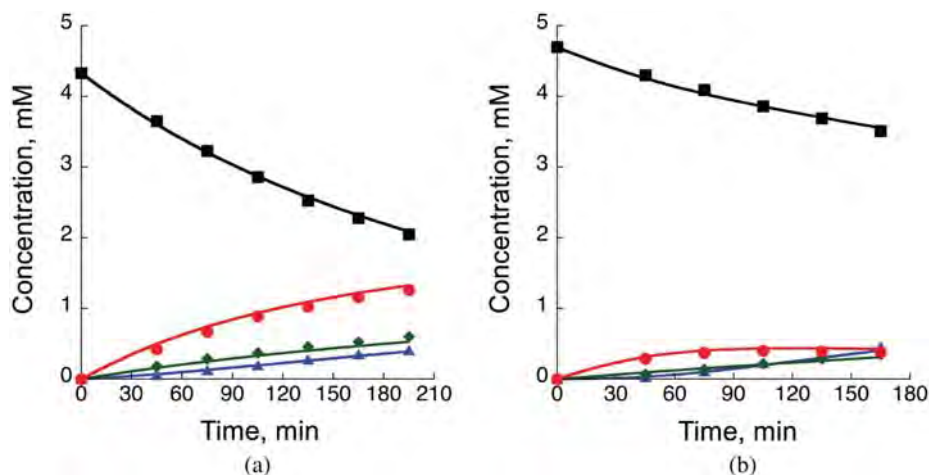
The amount of  $\text{ClO}_2$  produced is dependent on  $[\text{ClO}_2^-]$  in a linear fashion (Table 1) with a maximum yield of ca. 61% and 33% at pH 5.00 and 6.90, respectively. The sensitivity of  $\text{ClO}_2$  yield indicates product inhibition or further decomposition of  $\text{ClO}_2$  at high concentrations.

**Time-dependent product distribution.** To further elucidate the mechanism for chlorine dioxide formation,

the concentrations of all chlorine-containing species were analyzed at 30 min intervals by ion chromatography ( $\text{ClO}_2^-$ ,  $\text{Cl}^-$ ,  $\text{ClO}_3^-$ ) and UV-vis spectroscopy ( $\text{ClO}_2$ ) and fit by quantitative kinetic modeling. As expected, the reaction products chloride, chlorate, and chlorine dioxide are produced as chlorite is consumed (Fig. 6). Chlorine dioxide reaches a plateau within 3 h while the concentration of both chloride and chlorate continue to increase over time. These observations as well as the proposed reaction steps (Scheme 2) were used to predict the concentrations of all chlorine containing species over the course of the reaction using a mathematical model.



**Fig. 5.** Kinetics of  $\text{ClO}_2$  formation using  $[\text{Mn}^{\text{III}}(\text{TF}_4\text{TMAP})]^{5+}$  as a catalyst at pH 5.00 and 6.90 at 25.0 °C. (a) Changes in concentration of  $\text{ClO}_2^-$  vs. time in 50.0 mM acetate buffer (pH = 5.00). Solid lines represent kinetic modeling fits. Conditions:  $[\text{Mn}^{\text{III}}(\text{TF}_4\text{TMAP})]_0 = 3.98 \mu\text{M}$ ;  $[\text{ClO}_2^-]_0 = 5.78, 3.92, 1.96, 0.98 \text{ mM}$  (top to bottom). (b) Changes in concentration of  $\text{ClO}_2^-$  vs. time in 50.0 mM phosphate buffer (pH = 6.90). Solid lines represent kinetic modeling fits. Conditions:  $[\text{Mn}^{\text{III}}(\text{TF}_4\text{TMAP})]_0 = 3.99 \mu\text{M}$ ;  $[\text{ClO}_2^-]_0 = 6.10, 4.03, 2.01, 1.00 \text{ mM}$  (top to bottom)



**Fig. 6.** Time-dependent concentrations of chlorine containing species during catalysis.  $\text{ClO}_2^-$  (black),  $\text{Cl}^-$  (green),  $\text{ClO}_3^-$  (blue), and  $\text{ClO}_2$  (red). Solid lines represent kinetic modeling fits. (a) Reaction conducted in acetate buffer (pH = 5.00). Conditions:  $[\text{Mn}^{\text{III}}(\text{TF}_4\text{TMAP})]_0 = 4.00 \mu\text{M}$ ;  $[\text{ClO}_2^-]_0 = 4.33 \text{ mM}$ . (b) Reaction conducted in phosphate buffer (pH = 6.90). Conditions:  $[\text{Mn}^{\text{III}}(\text{TF}_4\text{TMAP})]_0 = 4.00 \mu\text{M}$ ;  $[\text{ClO}_2^-]_0 = 4.70 \text{ mM}$

**Table 1.** Results for the catalytic conversion of chlorite to chlorine dioxide in 50.0 mM acetate buffer (pH 5.00) and 50.0 mM phosphate buffer (pH 6.90)<sup>a</sup>

[Mn-Cat], $\mu\text{M}$	pH	$[\text{ClO}_2^-]_0$	$[\text{ClO}_2^-]_f$	$\Delta[\text{Cl}^-]$	$\Delta[\text{ClO}_3^-]$	$[\text{ClO}_2]$	% $\text{ClO}_2^b$
3.98	5.00	6.73	3.16	0.84	0.72	1.97	55%
3.98	5.00	1.05	0.49	0.13	0.08	0.34	61%
8.02 <sup>c</sup>	5.00	2.28	0.73	0.36	0.34	0.83	54%
3.99	6.90	6.62	4.77	0.54	0.71	0.59	32%
3.99	6.90	1.04	0.74	0.09	0.11	0.10	33%
6.01	6.90	2.19	1.40	0.24	0.38	0.17	22%

<sup>a</sup>All concentrations are mM unless otherwise stated. Chlorine dioxide concentrations were quantified by using UV-vis spectroscopy on the reaction mixture. Ion chromatography was used to quantify the concentrations of other chlorine-containing species. Ion chromatograms were performed at 3 h unless otherwise stated. <sup>b</sup>Percentage calculated by using the final concentration of chlorine dioxide divided by the concentration of reacted chlorite. <sup>c</sup>Ion chromatography was performed at maximum chlorine dioxide.

## Discussion

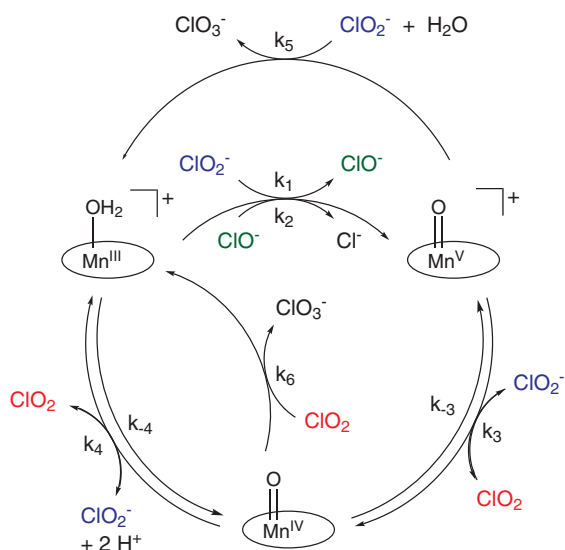
The catalytic formation of chlorine dioxide from chlorite using the catalyst  $[\text{Mn}^{\text{III}}(\text{TF}_4\text{TMAP})]^{5+}$  was examined in 50.0 mM acetate buffer (pH 5.00) and 50.0 mM phosphate buffer (pH 6.90) at 25.0°C. Good yields of  $\text{ClO}_2$  were observed using as little as 0.10 mol% of  $[\text{Mn}^{\text{III}}(\text{TF}_4\text{TMAP})]^{5+}$  with turnover frequencies (TOF), defined as  $[\text{ClO}_2]$  produced per mole of catalyst loading per hour, of 105 and 32  $\text{h}^{-1}$  at pH 5.00 and 6.90, respectively. The consumption of chlorite was monitored by the decrease in absorbance at 260 nm ( $\epsilon = 154 \text{ M}^{-1} \text{ cm}^{-1}$ ). The UV charge transfer (CT) bands for  $[\text{Mn}^{\text{III}}]^+$  are minimal compared to the intensity of chlorite used in experiments. The formation of chlorine dioxide (product) was monitored by the increase in absorbance at 360 nm ( $\epsilon = 1250 \text{ M}^{-1} \text{ cm}^{-1}$ ). The UV charge transfer (CT) bands for  $[\text{Mn}^{\text{III}}]^+$  are more pronounced at 360 than at 260 nm and were subtracted from the calculation of chlorine dioxide concentration. In addition to reaction kinetics following chlorite consumption and chlorine dioxide formation by UV-vis, all other chlorine containing species,  $\text{ClO}_2^-$ ,  $\text{ClO}_3^-$ , and  $\text{Cl}^-$ , were profiled at different time intervals during the reaction by ion chromatography, allowing for complete mass action kinetic analysis. Neither catalyst bleaching nor dioxygen formation was observed for any of the reaction conditions investigated. In the absence of catalyst in acetate buffer, chlorite forms chlorine dioxide but over several days. In phosphate buffer, no chlorine dioxide formation was observed even after several days. Thus the manganese catalyst is necessary and plays a major role in conversion.

While in acetate buffer the catalyst is accounted for in its entirety by the  $\text{Mn}^{\text{III}}$  soret band, at higher pH in phosphate buffer some of the catalyst is present as  $\text{Mn}^{\text{IV}}(\text{O})$ . After 3 h, the absorbance at 260 nm continues to decrease over time while the concentration of chlorine dioxide either remains constant or decreases depending on the pH of the solution. The reaction at the lower pH 5.00 has four distinguishing features in comparison

to that at pH 6.90: (1) the rate of chlorite consumption is higher (Fig. 6), (2) the chlorine dioxide product does not react at pH 5.00 with the resting state of the catalyst,  $\text{Mn}^{\text{III}}$  (Fig. 4, also Fig. S27 vs. Fig. S28), (3)  $\text{Mn}^{\text{IV}}(\text{O})$  is more reactive at pH 5.00 and thus it does not accumulate at lower pH, and (4)  $\text{ClO}_3^-$  is formed at the offset of the reaction while at pH 6.90  $\text{ClO}_3^-$  formation is sigmoidal (Fig. 6).

Any proposed mechanism must be consistent with all experimental observations. Furthermore, the soret band shows that throughout the reaction the catalyst is not degraded and can be accounted for fully. High-valent  $\text{Mn}^{\text{IV}}(\text{O})$  forms concurrently with chlorine dioxide formation and chlorite consumption and accumulates only at higher pH 6.90. While not observed, a  $[\text{Mn}^{\text{V}}(\text{O})]^+$  species is postulated as the intermediate en route to  $\text{Mn}^{\text{IV}}(\text{O})$  because at pH = 5.00  $\text{ClO}_3^-$  is formed at the offset of the reaction and must arise from chlorite. Since oxidation of chlorite by  $\text{Mn}^{\text{IV}}(\text{O})$  to give chlorate would afford a  $\text{Mn}^{\text{II}}$  porphyrin, a thermodynamically unfavorable reaction, a putative  $[\text{Mn}^{\text{V}}(\text{O})]^+$  must be formed and be responsible for  $\text{ClO}_3^-$  formation at pH 5.00. The proposed sequence of reactions that satisfies all experimental observations and used in quantitative kinetics modeling (see Supporting information) is given in Scheme 2. The individual reactions that make up the catalytic cycle in Scheme 2 are provided in Equations 1–6.

The manganese(III) porphyrin  $[\text{Mn}^{\text{III}}(\text{TF}_4\text{TMAP})]^{5+}$ , referred to as  $[\text{Mn}^{\text{III}}]^+$ , reacts with chlorite *via* OAT to afford  $[\text{Mn}^{\text{V}}(\text{O})]^+$  and hypochlorite (Equation 1). The subsequent reaction of  $\text{ClO}^-$  with  $[\text{Mn}^{\text{III}}]^+$  is rapid and gives  $\text{Cl}^-$  as the end product (Equation 2). In the kinetic modeling, the rate constant ( $k_2$ ) for the reaction of hypochlorite is much larger than  $k_1$  and can be considered instantaneous. In both buffers, reaction (2) is complete in seconds (Figs S30 and S31). The catalytic reactions, in comparison, are on the hour timescale.  $k_1$  at pH 5.00 is 2x that at pH 6.90. The rate of electron transfer (ET) from chlorite to the putative  $[\text{Mn}^{\text{V}}(\text{O})]^+$  ( $k_3$ ) (Equation 3) is independent of pH. In phosphate buffer, reaction



**Scheme 2.** Proposed mechanism for the conversion of  $\text{ClO}_2^-$  to  $\text{ClO}_2$ ,  $\text{ClO}_3^-$ , and  $\text{Cl}^-$  using a water-soluble manganese porphyrin catalyst

**Table 2.** Rate constants for the catalytic conversion of chlorite to chlorine dioxide<sup>a</sup>

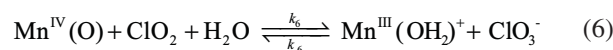
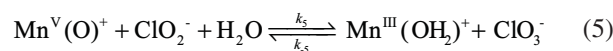
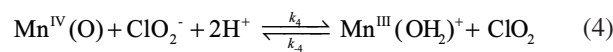
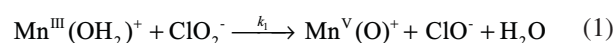
pH <sup>b</sup>	$k_1$	$k_3$	$k_{-3}$	$k_4$	$k_{-4}$	$k_5$	$k_6$
5.00	4.0	480	1600	140	0	75	0
6.90	2.0	>500 <sup>c</sup>	0	2900	645	d	1350

<sup>a</sup>All rate constants are  $\text{M}^{-1}\cdot\text{s}^{-1}$ . <sup>b</sup>pH 5.00 50 mM acetate buffer and pH 6.90 50 mM phosphate buffer. <sup>c</sup>Conversion to  $[\text{Mn}^{\text{IV}}(\text{O})]$  is fast and only a lower bound can be determined. <sup>d</sup>Pathway (5) is negligible as  $k_5/k_3 < 10^{-2}$  from global kinetic fitting.

(3) is irreversible. This is determined from studying independently the reaction of chlorine dioxide with  $[\text{Mn}^{\text{III}}]^+$ , which forms  $[\text{Mn}^{\text{IV}}(\text{O})]$ ,  $\text{ClO}_2^-$ , and  $\text{ClO}_3^-$ . The kinetic data for chlorine dioxide consumption at pH 6.90 cannot be modeled properly if  $k_{-3}$  is added. However, in acetate buffer at pH 5.00, reaction (3) must be reversible otherwise  $\text{ClO}_3^-$  and  $\text{ClO}_2$  would always be produced in a constant ratio, which is not observed experimentally. Furthermore, only if reaction (3) is reversible, the production rate of  $\text{ClO}_2$  slows down as  $\text{ClO}_3^-$  continues to be produced from chlorite.

The subsequent step is proton coupled electron transfer (PCET) to  $[\text{Mn}^{\text{IV}}(\text{O})]$  ( $k_4$ ) (Equation 4), which is faster at pH 5.00 and irreversible. In comparison at pH 6.90 the reaction is reversible ( $K_4$  at pH 6.90  $\cong$  5). This differentiating feature has been confirmed independently by studying the reaction of the resting catalyst  $[\text{Mn}^{\text{III}}]^+$  with freshly prepared  $\text{ClO}_2$  (Figs S27 and S28). A consequence of this significant difference in PCET rates for reaction (4) is that  $[\text{Mn}^{\text{IV}}(\text{O})]$  does not accumulate at pH 5.00 and the only route to chlorate is *via* the putative  $[\text{Mn}^{\text{V}}(\text{O})]^+$  ( $k_5$ ) (Equation 5). Conversely,

at pH 6.90  $\text{Mn}^{\text{IV}}(\text{O})$  accumulates and chlorate is formed *via* sigmoidal kinetics through  $k_6$  (Equation 6) from  $\text{ClO}_2$  rather than chlorite. The rate constants  $k_6$  and  $k_4$  are well-established because they are obtained from the independent study of the kinetics of  $\text{ClO}_2$  consumption in the presence of  $[\text{Mn}^{\text{III}}]^+$  in phosphate buffer (Fig 4, and Figs S27 and S28). The values of rate constants are obtained from numerical fitting by solving the ordinary differential equations, which assume constant  $[\text{H}_3\text{O}^+]$  at each buffered pH value, for all species involved (Supporting information) and are presented in Table 2. The simulated profiles from the kinetic modeling are presented by solid lines in all figures throughout the manuscript as well as the extensive data in the Supplementary material. Agreement between the kinetic simulations and experimental data is a testimony to the ability of the presented model to accommodate all the salient features observed for this catalytic reaction.



## CONCLUSION

In contrast to the iron(III)  $[\text{Fe}^{\text{III}}(\text{TF}_4\text{TMAP})]^{5+}$  catalyzed reaction [13, 14], the analogous manganese complex investigated herein does not produce dioxygen. Instead chlorine dioxide ( $\text{ClO}_2$ ) is formed with accumulation of  $\text{Mn}^{\text{IV}}(\text{O})$  at pH 6.90. The reaction features striking differences at the two studied pH values of 5.00 and 6.90. At neutral pH the PCET reaction between  $\text{Mn}^{\text{IV}}(\text{O})$  and  $\text{ClO}_2^-$  is reversible and chlorate formation originates from the reaction of  $\text{Mn}^{\text{IV}}(\text{O})$  and the  $\text{ClO}_2$  product. In contrast, PCET between  $\text{Mn}^{\text{IV}}(\text{O})$  and  $\text{ClO}_2^-$  at pH 5.00 is irreversible. Chlorate at pH 5.00 is formed at the offset of the reaction from the putative  $[\text{Mn}^{\text{V}}(\text{O})]^+$  and  $\text{ClO}_2^-$  rather than the product chlorine dioxide. The outcome is higher and more persistent chlorine dioxide production at pH 5.00 vs. 6.90. This constitutes another example of the importance of PCET rates and how they dictate the underlying reaction mechanism, a hallmark of Professor Fukuzumi's research and career in this very fundamental and central area of research in chemistry [23–25]. Our results parallel and complement many of the observations noted for iron(III) and mercury(II) mediated chlorite decomposition in aqueous medium *via* redox Fenton type chemistry [10, 26–28].

## Acknowledgements

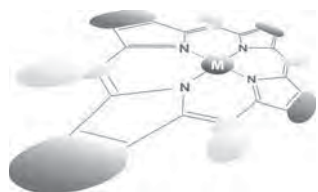
This research was supported by NSF (CHE-1110475). We dedicate this paper to Professor Shunichi Fukuzumi in celebration of his 65th birthday, and the many contributions he has made over the decades to physical inorganic and organic chemistry.

## Supporting information

The synthesis and characterization of the  $[\text{Mn}^{\text{III}}(\text{TF}_4\text{TMAP})]^{5+}$  complex, ion chromatograms for all of the reactions performed as well as details on the proposed mechanism and predicted concentrations of the different oxidation states of manganese during catalysis based on mathematical kinetic modeling of the mechanism (Figs S1–S31, Tables S1–S5) are given in the supplementary material. This material is available free of charge via the Internet at <http://www.worldscinet.com/jpp/jpp.shtml>.

## REFERENCES

- Roberson JA. *Environ. Sci. Tech.* 2010; **45**: 154–160.
- Calder RSD and Schmitt KA. *Environ. Sci. Tech.* 2010; **44**: 8008–8014.
- Karanfil T, Krasner Stuart W, Westerhoff P and Xie Y. In *Disinfection By-Products in Drinking Water*, Vol. 995, American Chemical Society: 2008; pp 2.
- Coates JD and Achenbach LA. *Perchlorate, Environmental Occurrence, Interactions and Treatment*, Springer: New York, 2006.
- Vogt H, Balej J, Bennett JE, Wintzer P, Sheikh SA and Gallone P. In *Ullmann's Encyclopedia of Industrial Chemistry*, Wiley-VCH Verlag GmbH & Co. KGaA: 2000.
- Thorell HD, Stenklo K, Karlsson J and Nilsson T. *Appl. Environ. Microbiol.* 2003; **2**: 569–580.
- Thorell HD, Beyer NH, Heegaard NHH, Öhman M and Nilsson T. *Eur. J. Biochem.* 2004; **271**: 3539–3546.
- Streit BR and DuBois JL. *Biochemistry* 2008; **47**: 5271–5280.
- Lee AQ, Streit BR, Zdilla MJ, Abu-Omar MM and DuBois JL. *PNAS* 2008; **105**: 15654–15659.
- Fábián I. *Coord. Chem. Rev.* 2001; **216–217**: 449–472.
- Collman JP, Boulatov R, Sunderland CJ, Shiryayeva IM and Berg KE. *J. Am. Chem. Soc.* 2002; **124**: 10670–10671.
- Slaughter LM, Collman JP, Eberspacher TA and Brauman JI. *Inorg. Chem.* 2004; **43**: 5198–5204.
- Zdilla MJ, Lee AQ and Abu-Omar MM. *Inorg. Chem.* 2009; **48**: 2260–2268.
- Zdilla MJ, Lee AQ and Abu-Omar MM. *Angew. Chem., Int. Ed.* 2008; **47**: 7697–7700.
- Keith JM, Abu-Omar MM and Hall MB. *Inorg. Chem.* 2011; **50**: 7928–7930.
- Hicks SD, Petersen JL, Bougher CJ and Abu-Omar MM. *Angew. Chem., Int. Ed.* 2011; **50**: 699–702.
- Umile TP, Wang D and Groves JT. *Inorg. Chem.* 2011; **50**: 10353–10362.
- Umile TP and Groves JT. *Angew. Chem., Int. Ed.* 2011; **50**: 695–698.
- Hicks SD, Kim D, Xiong S, Medvedev GA, Caruthers JM, Hong S, Nam W and Abu-Omar MM. *J. Am. Chem. Soc.* 2014; **136**: 3680–3686.
- Hu Z, Du H, Man W-L, Leung C-F, Liang H and Lau T-C. *Chem. Commun.* 2012; **48**: 1102–1104.
- Vogt H, Balej J, Bennett JE, Wintzer P, Sheikh SA, Gallone P, Vasudevan S and Pelin K. In *Ullmann's Encyclopedia of Industrial Chemistry*, Wiley-VCH Verlag GmbH & Co. KGaA: 2010; pp 55.
- Ogata N and Shibata T. *J. Gen. Virol.* 2008; **89**: 60–67.
- Nishida Y, Morimoto Y, Lee Y-M, Nam W and Fukuzumi S. *Inorg. Chem.* 2013; **52**: 3094–3101.
- Fukuzumi S and Karlin KD. *Coord. Chem. Rev.* 2013; **257**: 187–195.
- Fukuzumi S. *Coord. Chem. Rev.* 2013; **257**: 1564–1575.
- Fábián I and Gordon G. *Inorg. Chem.* 1992; **31**: 2144–2150.
- Fábián I and van Eldik R. *Inorg. Chem.* 1993; **32**: 3339–3342.
- Lednický LA and Stanbury DM. *J. Am. Chem. Soc.* 1983; **105**: 3098–3101.



# Structural changes in non-planar octaaryl substituted phthalocyanine phosphorus complexes

Taniyuki Furuyama<sup>◇</sup>, Ryosuke Harako and Nagao Kobayashi<sup>\*◇</sup>

Department of Chemistry, Graduate School of Science, Tohoku University, Sendai 980-8578, Japan

Dedicated to Professor Shunichi Fukuzumi on the occasion of his retirement

Received 28 October 2014

Accepted 7 January 2015

**ABSTRACT:** Phosphorus complexes of non-planar  $\alpha$ -octaaryl phthalocyanine derivatives ( $(\alpha\text{-Ar})_8\text{Pc}$ ), **3a** and **3b** have been synthesized by introduction of phosphorus(V) ions into free-base Pcs **2a** and **2b**. **3a** and **3b** were characterized by MS,  $^1\text{H}$  and  $^{31}\text{P}$  NMR spectra. The solid state structure of **3a** indicated a ruffled Pc structure due to the small atomic radius of phosphorus, although the corresponding free-base Pc **2a** has a saddled Pc structure. The phosphorus complexes showed intense absorption bands (Q-bands) in the near-IR region, while the introduction of electron-donating groups at the peripheral phenyl groups was efficient for additional red-shifting of the Q-band. Electrochemical data revealed that the red-shift of the Q-band is attributable to a decrease in the HOMO–LUMO gap due to significant and moderate stabilization of the LUMO and HOMO, respectively. MO calculations suggested that the phosphorus(V) ion intensified the electronic interaction between the peripheral aryl moieties and the Pc macrocyclic core.

**KEYWORDS:** phosphorus phthalocyanine, ruffled structure, electronic structure, near-infrared absorption.

## INTRODUCTION

Phthalocyanines (Pcs) are some of the most well-known and successful artificial dyes and pigments in modern materials chemistry. Pcs have a symmetrical  $18\pi$  electron aromatic macrocycle, and an intense absorption band (the so-called Q-band) appears in the visible (650–700 nm) region. The optical properties of Pcs often correlate with their function in practical applications, so that changing the absorption properties of Pcs is one of the most attractive research topics in their chemistry [1]. Recently, we reported that the introduction of phosphorus(V) ions into appropriate Pcs can shift their Q-band beyond 1000 nm [2]. Interestingly, the effect of the phosphorus atom is completely different between Pcs and tetraazaporphyrins (TAPs) [3], the congeners of Pc. Hence, the combination of a central phosphorus ion,

peripheral substituents, and the macrocyclic core appears critical, in order to obtain novel absorption properties.

A rigid planar structure for the macrocycle is also a feature of Pcs. However, we [4], Cook [5], and McKeown [6] reported “non-planar Pcs” with bulky peripheral substituents at the so-called  $\alpha$  positions of Pcs. X-ray crystallography revealed that this type of derivative has a highly-saddled conformation due to the steric hindrance of the peripheral substituents. These Pcs also retain  $18\pi$  aromaticity, namely curved  $\pi$ -conjugation [7], and an intense Q absorption band still appears. In the case of octaaryl-substituted non-planar Pcs, these show a significantly red-shifted Q-band (at around 800 nm) [4a], while the Q-bands of octaalkyl-substituted non-planar Pcs appear at a similar wavelength to typical Pcs (at around 700 nm) [5]. On the other hand, Kojima and Fukuzumi demonstrated that the saddled structure of Pcs could assemble with protonated porphyrins, and that the resulting complex undergoes photoinduced intrasupramolecular electron transfer [8]. Moreover, unique effects dependent on phenyl substitution [9] and the central element [10]

<sup>◇</sup> SPP full member in good standing

\*Correspondence to: Nagao Kobayashi, email: [nagaok@m.tohoku.ac.jp](mailto:nagaok@m.tohoku.ac.jp), tel/fax +81 22-795-7719

of octaphenyl-substituted non-planar Pcs have also been reported by our group. Although the effect of aryl groups is still not completely clear, the modified octaaryl-substituted non-planar Pcs may be attractive targets in materials chemistry. In this paper, we report the synthesis and properties of phosphorus(V) complexes of non-planar  $\alpha$ -octaaryl phthalocyanine derivatives ( $\alpha$ -Ar)<sub>8</sub>Pc. The crystallographic structures of Pc [2] and TAP [3a] phosphorus complexes show ruffled configurations due to the small atomic radius of the phosphorus. Peripheral substitution effects in the phosphorus complexes are also significant, where the absorption envelope of phosphorus TAP was proven to be changed markedly by changing the peripheral moieties, since the aryl substituents are directly linked to the TAP core. Hence, phosphorus(V) complexes of arylated non-planar Pc (( $\alpha$ -Ar)<sub>8</sub>PcP(V)) appear to be attractive subjects for examining their structural and spectroscopic properties.

## EXPERIMENTAL

### Measurements

Electronic absorption spectra were recorded on a JASCO V-570 spectrophotometer. Magnetic circular dichroism (MCD) spectra were obtained on a JASCO J-725 spectrodichromometer equipped with a JASCO electromagnet capable of producing magnetic fields of up to 1.03 T (1 T = 1 tesla) with both parallel and antiparallel fields. The magnitudes were expressed in terms of molar ellipticity per tesla ( $[\theta]_M$ , deg.M<sup>-1</sup>.cm<sup>-1</sup>.T<sup>-1</sup>). NMR spectra were obtained on a Bruker AVANCE III 500 spectrometer using CDCl<sub>3</sub> as solvent unless otherwise noted. Chemical shifts and coupling constants are expressed in  $\delta$ (ppm) values and in hertz (Hz), respectively. <sup>1</sup>H NMR spectra were referenced to the residual solvent as an internal standard. <sup>31</sup>P NMR spectra were referenced to external 85% H<sub>3</sub>PO<sub>4</sub> solution (0.0 ppm). The following abbreviations are used: s = singlet, d = doublet, and m = multiplet. High-resolution mass spectra (HRMS) were recorded on a Bruker Daltonics Apex-III spectrometer. CV measurements were recorded with a Hokuto Denko HZ5000 potentiostat under a nitrogen atmosphere in *o*-dichlorobenzene (*o*-DCB) with 0.1 M of tetrabutylammonium perchlorate (TBAP) as a supporting electrolyte. Measurements were made with a glassy carbon electrode (area = 0.07 cm<sup>2</sup>), an Ag/AgCl reference electrode, and a Pt wire counter electrode. The concentration of the solution was fixed at 1.0 mM and the sweep rates were set to 100 mV/s. The ferrocenium/ferrocene (Fc<sup>+</sup>/Fc) couple was used as an internal standard.

### Crystallographic data collection

A red, plate shaped single crystal of **3a** 0.20 × 0.10 × 0.05 mm, was selected for measurement. The diffraction data were collected using a Bruker APEXII CCD

diffractometer with Bruker Helios multilayered confocal mirror monochromatized MoK $\alpha$  radiation ( $\lambda = 0.71073 \text{ \AA}$ ) at -173 °C. The structures were solved by a direct method (SIR2004) [11] and refined using a full-matrix least squares technique (SHELXL-97) [12]. Yadokari-XG 2009 software was used as a GUI for SHELXL-97 [13]. All non-hydrogen atoms were refined anisotropically. The positions of all hydrogen atoms were calculated geometrically, and refined by applying riding models. Some large electron peaks due to solvent molecule(s) were found in the unit cell. As we failed to model these properly, the rest of the molecules were refined without the effect of the solvent molecules by the Platon squeeze technique [14].

### Synthesis

Free-base phthalocyanines **2a** [4] and **2b** [9] were prepared according to the literature.

**Preparation of ( $\alpha$ -Ph)<sub>8</sub>Pc phosphorus(V) complex (3a).** POBr<sub>3</sub> (150 mg, excess) was added to a solution of **2a** (30 mg, 26.7  $\mu$ mol) in 2 mL of pyridine and stirred for 1 h at room temperature. After removing the solvent *in vacuo*, the residue was dissolved in a solution of CH<sub>2</sub>Cl<sub>2</sub>/MeOH (2/1 v/v) and stirred for 1 h at room temperature. The organic layer was collected, washed with water, and the solvent removed, to yield a dark red product (phosphorus(V) Pc). The resulting solid was dissolved in CH<sub>3</sub>CN/CH<sub>2</sub>Cl<sub>2</sub> (1/1 v/v), then KPF<sub>6</sub> (25 mg, 140  $\mu$ mol) added. After stirring the mixture for 3 h at room temperature, the solvent was removed, and the residue recrystallized from CH<sub>2</sub>Cl<sub>2</sub>/*n*-hexane. The title compound was obtained (20 mg, 55%) as a red powder. <sup>1</sup>H NMR (500 MHz, CDCl<sub>3</sub>):  $\delta$ , ppm 7.89 (s, 8H), 7.37–7.33 (m, 24H), 7.28–7.26 (m, 16H), 0.01 (d, 6H, <sup>3</sup>J<sub>PH</sub> = 28.5 Hz). <sup>31</sup>P NMR (200 MHz, CDCl<sub>3</sub>):  $\delta$ , ppm -144 (septet, PF<sub>6</sub>, *J* = 700 Hz), -173 (s, P(OMe)<sub>2</sub>). HRMS-MALDI: *m/z* calcd. for C<sub>82</sub>H<sub>54</sub>N<sub>8</sub>O<sub>2</sub>P [M – PF<sub>6</sub>]<sup>+</sup> 1213.4102. Found 1213.4101. Anal. calcd. for C<sub>82</sub>H<sub>54</sub>F<sub>6</sub>N<sub>8</sub>O<sub>2</sub>P<sub>2</sub>: C, 72.46; H, 4.00; N, 8.24. Found C, 72.40; H, 4.37; N, 7.98. UV-vis (CH<sub>2</sub>Cl<sub>2</sub>):  $\lambda_{\text{max}}$ , nm (10<sup>-5</sup>  $\epsilon$ ) 852 (1.10).

**Preparation of ( $\alpha$ -4-OMe-Ph)<sub>8</sub>Pc phosphorus(V) complex (3b).** The procedure described for **3a** was used with **2b**, to give the title compound as a gray powder (72%). <sup>1</sup>H NMR (500 MHz, CDCl<sub>3</sub>):  $\delta$ , ppm 7.87 (s, 8H), 7.41 (d, 16H, *J* = 8.5 Hz), 6.79 (d, 16H, *J* = 8.5 Hz), 3.97 (s, 24H), 0.16 (d, 6H, <sup>3</sup>J<sub>PH</sub> = 28.5 Hz). <sup>31</sup>P NMR (200 MHz, CDCl<sub>3</sub>):  $\delta$ , ppm -144 (septet, PF<sub>6</sub>, *J* = 700 Hz), -172 (s, P(OMe)<sub>2</sub>). HRMS-MALDI: *m/z* calcd. for C<sub>90</sub>H<sub>70</sub>N<sub>8</sub>O<sub>10</sub>P [M – PF<sub>6</sub>]<sup>+</sup> 1453.4947. Found 1453.4948. UV-vis (CH<sub>2</sub>Cl<sub>2</sub>):  $\lambda_{\text{max}}$ , nm (10<sup>-5</sup>  $\epsilon$ ) 916 (1.01).

### Computational details

Geometry optimization for all molecules was performed at the DFT level, by means of the hybrid Becke3LYP[15] (B3LYP) functional, as implemented in Gaussian 2009 [16]. The 6-31G\* basis set was used

for all atoms. After the geometry optimization, time-dependent (TD) DFT calculations [17] were performed to evaluate the stick absorption spectrum employing BLYP functionals with long-range correction (LC) [18] (LC-BLYP) using the same basis set. All stationary points were optimized without any symmetry assumptions, and characterized by normal coordinate analysis at the same level of the theory (number of imaginary frequency,  $\text{Nimag}$ , 0).

## RESULTS AND DISCUSSION

### Synthesis

The synthetic procedures for the phosphorus(V) complexes are shown in Scheme 1. Free-base Pcs **2a** and **2b** were first prepared according to the literature procedures in moderate yields. For the introduction of a phosphorus ion into the macrocyclic core, phosphorus oxybromide was used, as previously reported. Finally, the desired complexes **3a** ( $\alpha$ -octa(phenyl)) and **3b** ( $\alpha$ -octa(*p*-methoxyphenyl)) were isolated as the hexafluorophosphate salts. The color of **3a** and **3b** is red and gray, respectively, rather than the typical blue-green color of Pc. **3a** and **3b** showed excellent solubility in general organic solvents, and could be fully characterized by NMR and HR-MALDI-FT-ICR mass spectroscopy. The observed MS spectrum of **3a** and calculated isotropic distributions are shown in Fig. 1. The strongest peak was found at  $m/z = 1213.4101$ , and the isotropic distribution patterns provided a reasonable match with experiment for the compound whose molecular formula is  $\text{C}_{82}\text{H}_{54}\text{N}_8\text{O}_2\text{P}$  as a cationic part of **3a** ( $[\text{M} - \text{PF}_6]^+$ ). The  $^1\text{H}$  NMR spectra show only one kind of peripheral aryl group, at the  $\beta$ -position of the Pc macrocycle, and a doublet assignable to axial methoxy groups at high field (*ca.* 0 ppm); hence the conformation of the phosphorus(V) complexes appears to retain a highly symmetrical, unaggregated

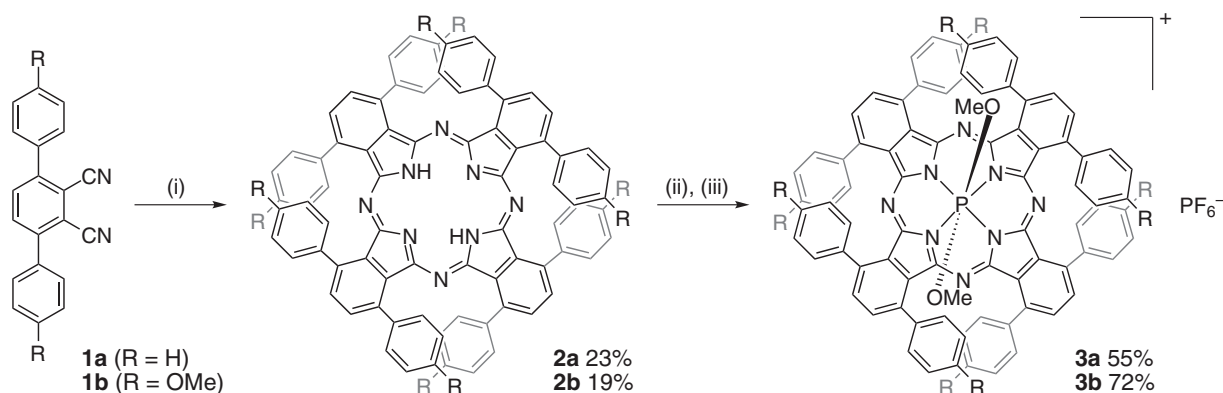
structure in solution. The  $^{31}\text{P}$  NMR spectra exhibit only one peak at -173 ppm for **3a** and -172 ppm for **3b**, supporting hexa-coordinated phosphorus representations [19] lying within the central cavity of the Pc macrocycle.

### Solid-state structure

The structure of **3a** was unambiguously elucidated by X-ray diffraction analysis of crystals obtained from the diffusion of *n*-pentane into a  $\text{CH}_2\text{Cl}_2$  solution of **3a**. The X-ray crystallographic structure of **3a** is shown in Fig. 2. Figure 3 shows the displacement of the 24 core atoms from the  $4N$  mean plane of **2a** (crystallographic data was taken from Ref. 4b) and **3b**. The degree of distortion of the core ( $\Delta r$ ), which was calculated as the square root of the sum of square of the deviation of each atom from the mean plane, rationalizes the nonplanarity of the Pcs. Although the  $\Delta r$  value of **3a** (0.57) is close to that of **2a** (0.58), the type of distortion is different. **3a** has a ruffled structure rather than the typical saddled structure reported for non-planar Pcs. The distances between the two pyrrole-nitrogen atoms at opposite sides in the core (3.675(4) and 3.685(4) Å) for **3a** are shorter than those of **2a** (3.804(5) and 3.983(4) Å) and reported metallo and free-base Pcs (3.8–4.0 Å) [2a]. The small macrocyclic Pc core of **3a** originates from the small atomic radius (106 pm) of the phosphorus(V) atom, resulting in a bond length of 1.84 Å between phosphorus and nitrogen in the core of **3a**, which is reasonable for a single bond of hexacoordinated phosphorus(V)–nitrogen [20]. Therefore, the structural influence of only one phosphorus(V) atom is stronger than the bulky phenyl substituents at the peripheral position.

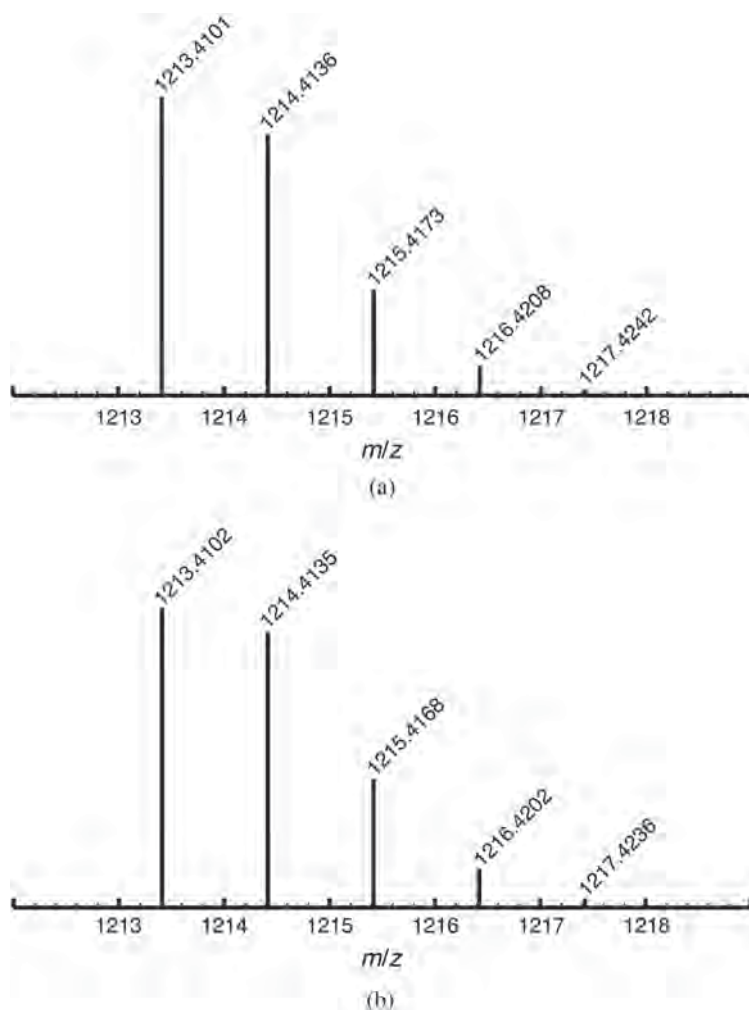
### Electronic absorption and MCD spectroscopy

The absorption and MCD spectra of the Pcs in  $\text{CH}_2\text{Cl}_2$  are shown in Fig. 4. The absorption spectra of all compounds show intense Q-bands in the near-IR

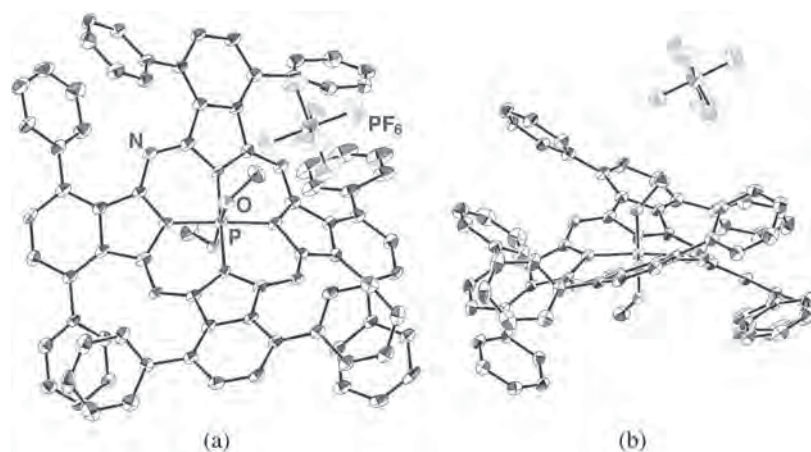


**Scheme 1.** Synthesis of octaaryl substituted phthalocyanine phosphorus(V) complexes. *Reagents and conditions:* (i)  $n\text{-BuOLi}$  (4 eq),  $n\text{-BuOH}$ , reflux, 1 h; (ii)  $\text{POBr}_3$  (20 eq), pyridine, rt, 1 h, then MeOH, rt, 1 h; (iii)  $\text{KPF}_6$ ,  $\text{CH}_3\text{CN}/\text{CH}_2\text{Cl}_2$ , rt, 3 h





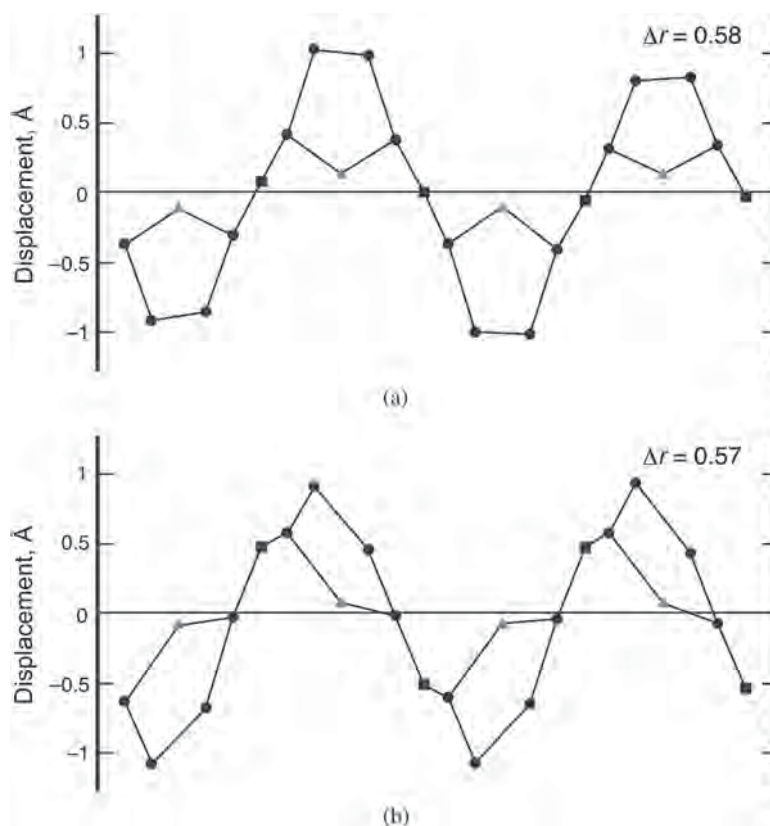
**Fig. 1.** Observed high-resolution mass spectrum (a) of **3a** and the theoretical distribution pattern for  $C_{82}H_{54}N_8O_2P ([M - PF_6]^+)$  (b)



**Fig. 2.** X-ray crystal structure of **3a**. The thermal ellipsoids were scaled to the 50% probability level. (a) top view; (b) side view. H atoms, and solvent molecules have been omitted for clarity

region. The Q-bands of free-base Pc **2a** and **2b** might be split theoretically into four peaks, but they show only two peaks or shoulders ( $Q_{00}$  and  $Q_{01}$  bands). In the MCD spectra of **2a** and **2b**, dispersion-type signals

were observed corresponding to their  $Q_{00}$  bands. It is considered that the splitting of the Q-band is so small that the superimposition of two oppositely signed Faraday  $B$  terms give seemingly  $A$  term-like MCD signals, the



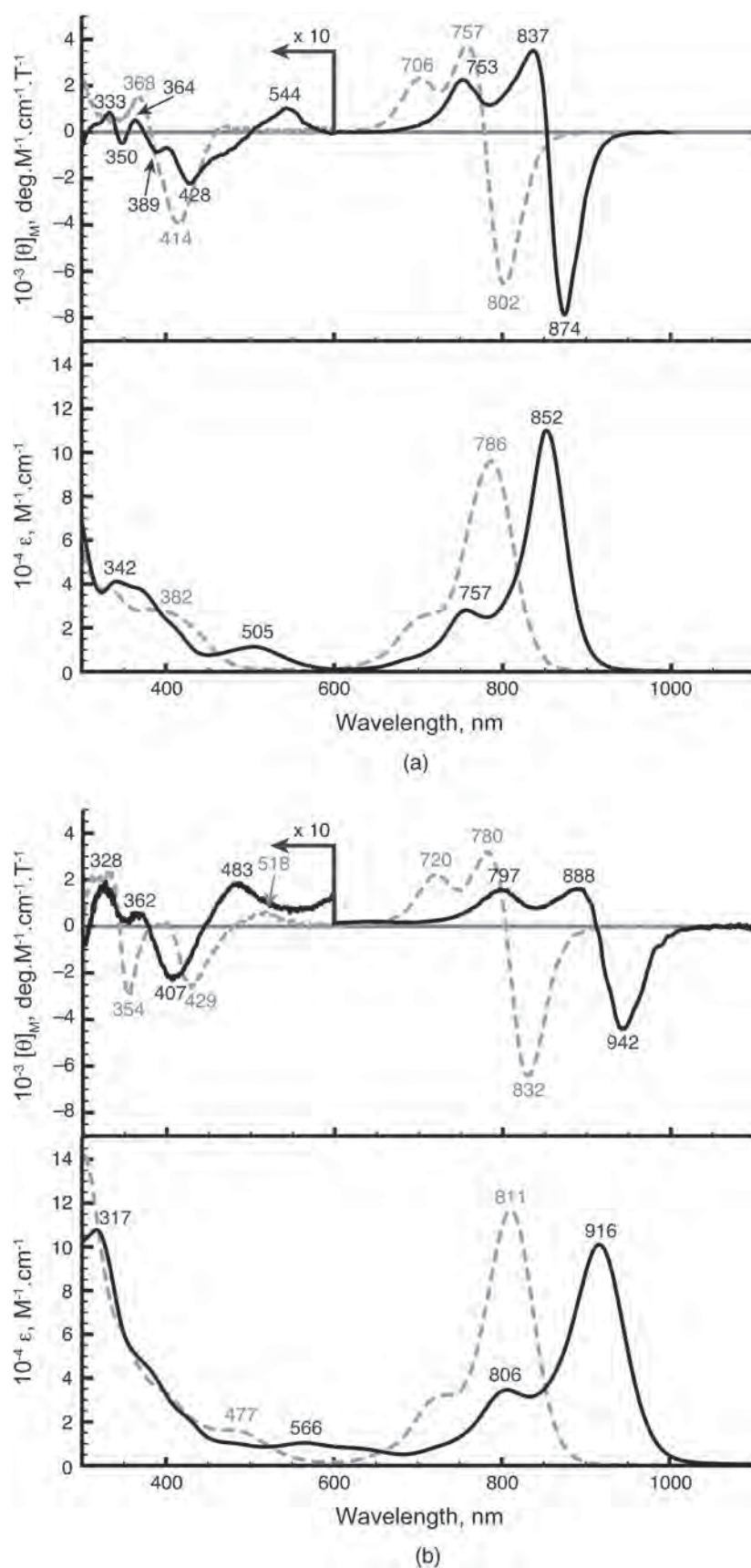
**Fig. 3.** Views of the skeletal deviation of the atoms from the 4N mean plane for (a) **2a** (crystallographic data was taken from Ref. 4b) and (b) **3a**. The black circles indicate carbon atoms. The black squares and gray triangles indicate nitrogen atoms at the *meso*-position and coordinating nitrogen atoms, respectively

so-called pseudo Faraday A term. As we previously reported [4, 9], the introduction of eight aryl groups at the  $\alpha$  positions can shift the Q-band to the near-IR region; in particular, **2b** has a sharp Q-band in the region beyond 800 nm. The insertion of a phosphorus(V) ion into **2a** produces a red-shift of *ca.* 70 nm (*ca.* 990  $\text{cm}^{-1}$ ), while the difference between the free-base  $\alpha$ -(ArS)<sub>8</sub>Pc and its phosphorus(V) complex is *ca.* 210 nm (*ca.* 2500  $\text{cm}^{-1}$ ) [2]. The extent of the red-shift upon phosphorus insertion into the core of the Pc was different from substituent to substituent, so that octaaryl substitution at the  $\alpha$  position is not efficient for further red-shifting beyond 1000 nm by the phosphorus(V) ion, which is different from the case of  $\alpha$ -octathioaryl group substituted Pc [2]. In contrast, the substitution effect at the aryl group is enhanced by phosphorus insertion. The difference in Q-band position between methoxy substituted **3a** and **3b** (64 nm, *ca.* 820  $\text{cm}^{-1}$ ) is significantly larger than that between unsubstituted **2a** and **2b** (25 nm, *ca.* 390  $\text{cm}^{-1}$ ). The Q-band of **3b** appears at 916 nm, which is sufficiently long enough for application in the near-IR photodynamic therapy of cancer [21]. Since Pcs having a Q-band at around 900 nm are still rare, the combination of a central phosphorus atom and appropriate aryl groups at the  $\alpha$  position appears to be an efficient method for accessing near-IR light at around 900 nm. The Faraday A MCD term

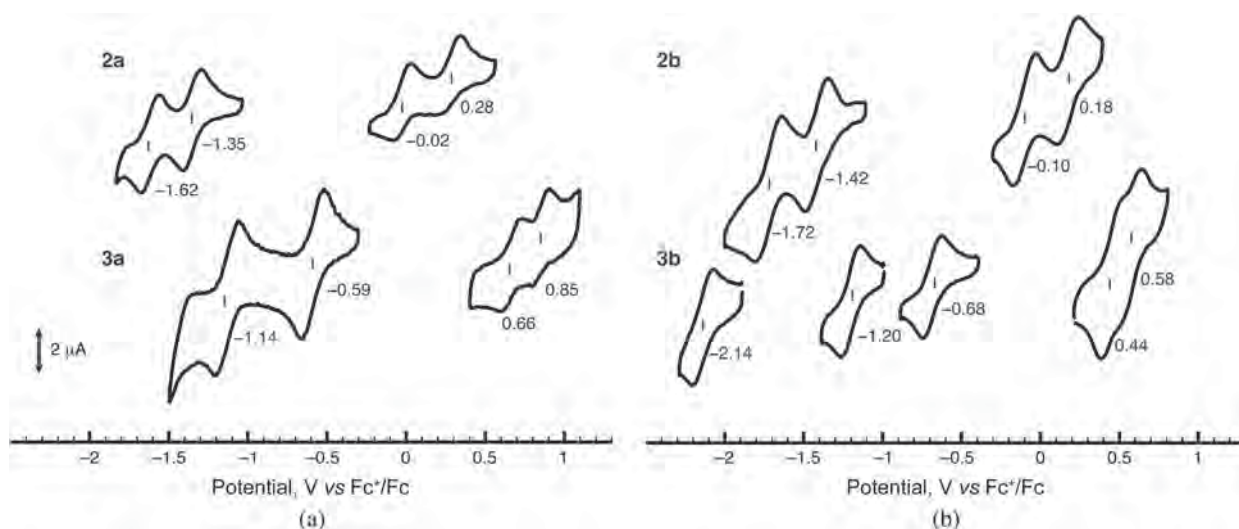
of **3a** and **3b** in the Q-band region further indicates that the practical chromophore symmetry of these complexes is close to  $D_{4h}$ , similarly to typical metallo Pcs. A broad, weak absorption band appeared between the Soret and Q-bands (at around 500 nm) for the phosphorus complexes. The MCD spectra corresponding to these absorptions cannot be interpreted simply, since their complex character suggests an overlap of several transitions. Although the detailed assignment will be discussed later, these bands could be assigned to a charge-transfer (CT) band from peripheral aryl groups to the macrocyclic Pc core. Emission of phosphorus(V) complexes are very weak ( $\Phi_F < 0.01$ ), so that the fluorescence spectra of both **3a** and **3b** could not be obtained.

### Electrochemistry

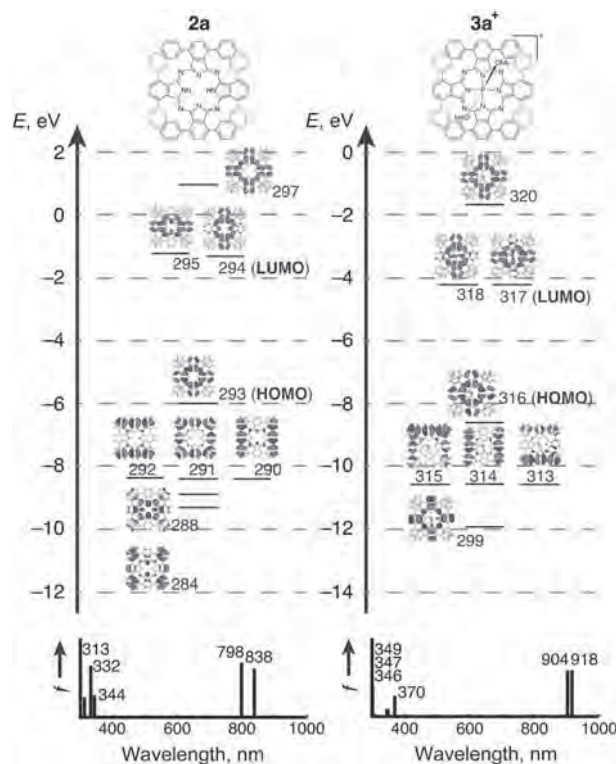
It is well-established that the HOMO and LUMO energies of Pc derivatives correlate well with their first oxidation and reduction potentials [22]. Estimating the values of the redox potentials is also important in order to determine the origins of the effect of phosphorus insertion. Fig 5 displays cyclic voltammograms of the Pcs in *o*-dichlorobenzene (DCB) with 0.1 M *n*-Bu<sub>4</sub>NClO<sub>4</sub> as the supporting electrolyte. The gap between the first redox potentials ( $E_{1\text{ox}} - E_{1\text{red}}$ ) correlate well with the



**Fig. 4.** UV-vis-NIR absorption (bottom) and MCD (top) spectra of Pcs in  $\text{CH}_2\text{Cl}_2$ . (a): **2a** (gray dashed line) and **3a** (black solid line). (b): **2b** (gray dashed line) and **3b** (black solid line)



**Fig. 5.** Cyclic voltammetry data for (a) **2a** and **3a**, and (b) **2b** and **3b**. Cyclic voltammograms were acquired from 1.0 mM solutions of analyte in 0.1 M  ${}^n\text{Bu}_4\text{NClO}_4/o\text{-DCB}$ . Ferrocene was used as an internal standard and set to 0 V



**Fig. 6.** Partial molecular energy diagram and orbitals of **2a** and cationic part of **3a**<sup>+</sup> (top) and their calculated absorption spectra (bottom). Calculations were performed at the LC-BLYP/6-31G\*\*/B3LYP/6-31G\* level

positions of the Q-bands. Both of the redox potentials of **2b** are shifted cathodically from those of **2a**, so that it is concluded that the electron donating group (OMe) on the exterior of the  $\pi$ -conjugated system of the Pc ligand can affect the electronic structure of  $\alpha$ -octaarylated Pc. After the introduction of a phosphorus(V) ion into the Pc, both the redox potentials are shifted anodically. For

**2a** and **3a**, the first reduction potential, which is related to the LUMO level, shifted from -1.35 V to -0.59 V, while the first oxidation potential, which is related to the HOMO level, shifted from -0.02 to 0.66 V. These potentials indicate that the stabilization of the LUMO is larger than that of the HOMO after the phosphorus introduction. Similar changes in redox potentials were

**Table 1.** Calculated excited wavelength ( $\lambda$ ) and oscillator strengths ( $f$ ) for components of selected transition energies

Compound	$\lambda$ , nm	$f$	Composition, % <sup>a</sup>
<b>2a</b>	838.0	0.43	288→294 (7%), 293→295 (92%)
	798.4	0.49	288→295 (4%), 293→294 (94%)
	343.8	0.20	290→295 (11%), 292→294 (11%), 293→297 (66%)
	332.3	0.46	284→294 (12%), 288→294 (58%), 293→295 (6%)
	312.4	0.18	284→295 (3%), 288→295 (31%), 291→294 (31%) 292→297 (3%), 293→298 (10%)
<b>3a<sup>+</sup></b>	917.8	0.42	299→318 (3%), 316→317 (91%), 316→318 (4%)
	904.0	0.41	299→317 (3%), 316→317 (4%), 316→318 (91%)
	370.0	0.19	313→318 (29%), 314→317 (33%), 316→320 (21%)
	349.2	0.07	313→317 (10%), 313→318 (22%), 313→320 (2%) 314→317 (13%), 314→318 (4%), 315→317 (26%)
	346.8	0.07	313→317 (6%), 313→318 (18%), 314→317 (17%) 314→320 (2%), 315→317 (26%), 315→318 (6%)
	345.8	0.06	313→317 (4%), 314→317 (8%), 315→317 (9%) 315→318 (51%), 315→320 (3%), 316→319 (4%)

observed on going from **2b** to **3b**. In particular, the cathodic shift (0.22 V) of the first oxidation potential on going from phosphorus-containing **3a** (0.66 V) to **3b** (0.44 V) is larger than that observed (0.08 V) on going from free-base **2a** (-0.02 V) to **2b** (-0.10 V), supporting the conclusion that the substitution effect is enhanced by the phosphorus introduction.

### Molecular orbital calculations

In order to enhance the interpretation of the electronic structures of  $(\alpha\text{-Ar})_8\text{PcP(V)}$ , MO calculations of free-base Pc **2a** and the cationic part of the phosphorus complex **3a** (**3a<sup>+</sup>**) have been performed. The molecular geometries were first optimized at the DFT level using B3LYP/6-31G(d). Since a CT interaction between peripheral aryl groups and the Pc macrocyclic core can be expected from the observed absorption spectrum of **3a**, we applied the LC-BLYP [3, 18]/6-31G(d) level to the calculations for the molecular orbitals and excited states of **2a** and **3a<sup>+</sup>**. Partial MO energy diagrams showing the calculated absorption spectra are shown in Fig. 6, with the calculated transition energies, oscillator strengths ( $f$ ), and configurations summarized in Table 1. The lowest-energy bands (the Q-bands) of **2a** are calculated to lie at 838 and 798 nm, while those of **3a<sup>+</sup>** are calculated to lie at 918 and 904 nm, supporting the experimental absorption spectra. These bands are composed mainly of HOMO → LUMO or HOMO → LUMO+1 transitions (*ca.* 90%), and the HOMO, LUMO, and LUMO+1 orbitals included in the transitions correspond to the  $a_{1u^-}$ ,  $e_{gy^-}$ , and  $e_{gx^-}$ -like

orbitals in Gouterman's model [23], respectively. The central phosphorus(V) ion significantly stabilizes both the HOMO and LUMO, with a higher extent for the LUMO, as expected from the CVs of **2a** and **3a** (Fig. 5). The calculated bands (370, 349, 347 and 346 nm) of **3a<sup>+</sup>** are composed of transitions from the HOMO-1, HOMO-2 and HOMO-3 to the nearly-degenerate LUMOs. The HOMO-1 to HOMO-3 transitions are localized on the peripheral phenyl rings, so that these bands can be assigned to CT transitions. The complicated transitions in the calculated spectrum indicate quite complicated MCD signals of **3a** at around 500 nm. We also calculated the absorption spectrum and molecular orbitals of  $[\beta\text{-Ph}_8\text{PcP(OMe)}_2]^+$  [**3a**], which is a positional isomer of  $[\alpha\text{-Ph}_8\text{PcP(OMe)}_2]^+$  having phenyl groups at eight  $\beta$ -positions, however, the positions of these transitions were estimated to lie in a shorter wavelength region (356–336 nm) than those of **3a<sup>+</sup>**, supporting the conclusion that the substitution effect of  $\alpha$ -arylated Pc (**3a** vs. **3b**) is larger than  $\beta$ -arylated Pc.

### CONCLUSION

Non-planar  $\alpha$ -octaaryl phthalocyanine phosphorus(V) complexes have been prepared in order to estimate the effect of peripheral substituents and a central phosphorus(V) ion. The non-planar structure of  $\alpha$ -octaaryl free-base Pcs does not prevent the introduction of the phosphorus ion into the core of the Pc. The synthesized phosphorus(V) Pcs can be fully characterized by MS and NMR spectra; moreover, the X-ray crystallographic

structure of **3a** could be obtained. The crystal of **3a** has a distorted, ruffled structure, while that of non-metalated **2a** adopts a saddled structure, supporting the premise that the small atomic radius of the phosphorus ion can switch the structure of the macrocyclic core, even in Pcs with bulky substituents. The Q-bands of the phosphorus(V) complexes show a significant red shift from those of free-base Pcs. The introduction of an electron-donating methoxy group into the peripheral aryl groups at eight  $\alpha$ -positions is quite efficient for shifting the Q-band, so that the Q-band of **3b** appeared beyond 900 nm. Cyclic voltammograms of the Pcs also support the red-shifted Q-bands and the substitution effect of phosphorus(V) Pcs, while MO calculations can explain the experimental results. Thus, the combination of  $\alpha$ -octaaryl Pcs and a central phosphorus ion can manipulate both the near-IR absorption properties and the solid-state structures, indicating that this strategy can be applied for developing novel near-IR absorbing functional dyes and pigments.

### Acknowledgements

This work was partly supported by Grant-in-Aids for Scientific Research on Innovative Areas (25109502, “Stimuli-responsive Chemical Species”), Scientific Research (B) (No. 23350095), Challenging Exploratory Research (No. 25620019) and Young Scientist (B) (No. 24750031) from the Ministry of Education, Culture, Sports, Science, and Technology (MEXT). The authors thank Prof. Takeaki Iwamoto and Dr. Shintaro Ishida (Tohoku University) for X-ray measurements. Some of the calculations were performed using supercomputing resources at the Cyberscience Center of Tohoku University.

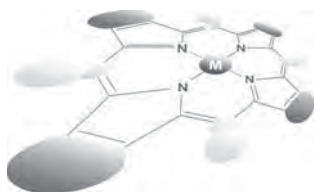
### Supporting information

Crystallographic data have been deposited at the Cambridge Crystallographic Data Centre (CCDC) under number CCDC-1030507. Copies can be obtained on request, free of charge, via [www.ccdc.cam.ac.uk/data\\_request/cif](http://www.ccdc.cam.ac.uk/data_request/cif) or from the Cambridge Crystallographic Data Centre, 12 Union Road, Cambridge CB2 1EZ, UK (fax: +44 1223-336-033 or email: [data\\_request@ccdc.cam.ac.uk](mailto:data_request@ccdc.cam.ac.uk)).

### REFERENCES

1. *Handbook of Porphyrin Science*, Kadish KM, Smith KM and Guillard R. (Eds.) World Scientific: 2010.
2. (a) Furuyama T, Satoh K, Kushiya T and Kobayashi N. *J. Am. Chem. Soc.* 2014; **136**: 765–776. (b) Kobayashi N, Furuyama T and Satoh K. *J. Am. Chem. Soc.* 2011; **133**: 19642–19645.
3. (a) Furuyama T, Yoshida T, Hashizume D and Kobayashi N. *Chem. Sci.* 2014; **5**: 2466–2474. (b) Furuyama T, Asai M and Kobayashi N. *Chem. Commun.* 2014; **50**: 15101–15104.
4. (a) Fukuda T, Homma S and Kobayashi N. *Chem. Eur. J.* 2005; **11**: 5205–5216. (b) Kobayashi N, Fukuda T, Ueno K and Ogino H. *J. Am. Chem. Soc.* 2001; **123**: 10740–10741.
5. Chambrier I, Cook MJ and Wood PT. *Chem. Commun.* 2000; 2133–2134.
6. McKeown NB, Li H and Helliwell M. *J. Porphyrin Phthalocyanines* 2005; **9**: 841–845.
7. Luo J, Xu X, Mao R and Miao Q. *J. Am. Chem. Soc.* 2012; **134**: 13796–13803.
8. Kojima T, Honda T, Ohkubo K, Shiro M, Kusukawa T, Fukuda T, Kobayashi N and Fukuzumi S. *Angew. Chem. Int. Ed.* 2008; **47**: 6712–6716.
9. Fukuda T, Ishiguro T and Kobayashi N. *Tetrahedron Lett.* 2005; **46**: 2907–2909.
10. (a) Fukuda T, Yamamoto K and Kobayashi N. *J. Porphyrin Phthalocyanines* 2013; **17**: 756–762. (b) Fukuda T, Homma S and Kobayashi N. *Chem. Commun.* 2003; 1574–1575. (c) Fukuda T, Ono K, Homma S and Kobayashi N. *Chem. Lett.* 2003; **32**: 736–737.
11. Burla MC, Caliendo R, Camalli M, Carrozzini B, Cascarano GL, De Caro L, Giacovazzo C, Polidori G and Spagna R. *J. Appl. Cryst.* 2005; **38**: 381–388.
12. Sheldrick GM. SHELXL-97, Program for the Solution and Refinement of Crystal Structures, University of Göttingen, Göttingen, Germany, 1997.
13. (a) Wakita K. *Yadokari-XG, Software for Crystal Structure Analyses*, 2001. (b) Kabuto C, Akine S, Nemoto T and Kwon E. *J. Cryst. Soc. Jpn.* 2009; **51**: 218.
14. (a) Spek AL. *J. Appl. Cryst.* 2003; **36**: 7–13. (b) van der Sluis P and Spek AL. *Acta Crystallogr. Sect. A* 1990; **46**: 194–201.
15. (a) Becke AD. *Phys. Rev.* 1988; **A38**: 3098–3100. (b) Becke AD. *J. Chem. Phys.* 1993; **98**: 1372–1377. (c) Becke AD. *J. Chem. Phys.* 1993; **98**: 5648–5652. (d) Lee C, Yang W and Parr RG. *Phys. Rev.* 1988; **B37**: 785–788.
16. Gaussian 09, Revision D.01, Frisch MJ, Trucks GW, Schlegel HB, Scuseria GE, Robb MA, Cheeseman JR, Scalmani G, Barone V, Mennucci B, Petersson GA, Nakatsuji H, Caricato M, Li X, Hratchian HP, Izmaylov AF, Bloino J, Zheng G, Sonnenberg JL, Hada M, Ehara M, Toyota K, Fukuda R, Hasegawa J, Ishida M, Nakajima T, Honda Y, Kitao O, Nakai H, Vreven T, Montgomery, Jr. JA, Peralta JE, Ogliaro F, Bearpark M, Heyd JJ, Brothers E, Kudin KN, Staroverov VN, Keith T, Kobayashi R, Normand J, Raghavachari K, Rendell A, Burant JC, Iyengar SS, Tomasi J, Cossi M, Rega N, Millam JM, Klene M, Knox JE, Cross JB, Bakken V, Adamo C, Jaramillo J, Gomperts R, Stratmann RE, Yazyev O, Austin AJ, Cammi R, Pomelli C, Ochterski JW, Martin RL, Morokuma K, Zakrzewski VG, Voth GA, Salvador P, Dannenberg JJ, Dapprich S, Daniels AD, Farkas Ö, Foresman JB, Ortiz JV, Cioslowski J and Fox DJ. Gaussian, Inc., Wallingford CT, 2013.

17. (a) Bauernschmitt Rd and Ahlrichs R. *Chem. Phys. Lett.* 1996; **256**: 454–464. (b) Dreuw A and Head-Gordon M. *Chem. Rev.* 2005; **105**: 4009–4037.
18. Iikura H, Tsuneda T, Yanai T and Hirao K. *J. Chem. Phys.* 2001; **115**: 3540–3544.
19. Holmes RR. *Chem. Rev.* 1996; **96**: 927–950.
20. Wong CY, Kennepohl DK and Cavell RG. *Chem. Rev.* 1996; **96**: 1917–1952.
21. (a) Schmitt J, Heitz V, Sour A, Bolze F, Ftouni H, Nicoud J-F, Flamigni L and Ventura B. *Angew. Chem. Int. Ed.* 2015; **54**: 169–173. (b) Tian J, Ding L, Xu H-J, Shen Z, Ju H, Jia L, Bao L and Yu J-S. *J. Am. Chem. Soc.* 2013; **135**: 18850–18858.
22. Kobayashi N, Miwa H and Nemykin VN. *J. Am. Chem. Soc.* 2002; **124**: 8007–8020.
23. Gouterman M. In *The Porphyrins*, Vol. 3, Part A, Dolphin D. (Ed.) Academic Press: USA, 1978; pp 1.



## Myoglobin-based non-precious metal carbon catalysts for an oxygen reduction reaction

Akira Onoda<sup>\*a◇</sup>, Yuta Tanaka<sup>a</sup>, Toshikazu Ono<sup>a†</sup>, Shotaro Takeuchi<sup>b</sup>, Akira Sakai<sup>b</sup> and Takashi Hayashi<sup>\*a◇</sup>

<sup>a</sup> Department of Applied Chemistry, Graduate School of Engineering, Osaka University, Suita, Osaka 565-0871, Japan

<sup>b</sup> Department of Systems Innovation, Graduate School of Engineering Science, Osaka University, Toyonaka, Osaka 560-8531, Japan

*Dedicated to Professor Shunichi Fukuzumi on the occasion of his retirement*

Received 1 December 2014

Accepted 7 January 2015

**ABSTRACT:** A non-precious metal catalyst (NPMC) promoting a four-electron oxygen reduction reaction (ORR) was synthesized by heat treatment of myoglobin (Mb) containing a heme (iron protoporphyrin IX) as a source of iron, nitrogen, and carbon atoms. Samples of the mixture of Mb and carbon black (Vulcan XC72R: VC) were pyrolyzed at 740, 840, 940, 1040 or 1140 °C under N<sub>2</sub> flow. The microstructures of the carbonized Mb catalysts were characterized by XRD, Raman spectroscopy, XPS, and TEM. Results indicate that the iron-containing active site is embedded within the surface structure in an amorphous domain of the carbon materials. The catalyst ink in a 0.05 wt% Nafion solution in isopropanol was coated onto a glassy carbon electrode and the ORR activity of Mb-based NPMCs was evaluated in a rotating disk electrode experiment in an O<sub>2</sub>-saturated 0.1 M HClO<sub>4</sub> solution at 25 °C. The catalyst synthesized at 940 °C has the highest ORR activity in terms of the onset potential and the current density. In contrast, pyrolytic temperatures above 940 °C decrease the activity, suggesting that the active structure of the catalyst apparently decomposes at higher temperatures. The Koutecky–Levich plots indicate that the Mb-based catalyst prepared at 940 °C catalyzes four-electron ORR ( $n = ca. 4$ ). The catalysts prepared at other temperatures have  $n$  values of 3.6 at 740 °C, 3.7 at 840 °C, and 2.9 at 1040 °C. The ORR of Mb/VC is diffusion-controlled at potentials lower than 0.3 V (vs. RHE) and the onset potential is  $0.84 \pm 0.01$  V.

**KEYWORDS:** non-precious metal catalyst, carbon catalyst, oxygen reduction reaction, myoglobin, heme.

### INTRODUCTION

Polymer electrolyte fuel cells (PEFCs) currently represent one of the most promising technologies for

energy conversion. It is desirable to replace the Pt catalysts used at both of the fuel cell electrodes with non-precious metal catalysts (NPMCs) [1]. In particular provision of an NPMC cathodic catalyst for the oxygen reduction reaction (ORR) would be expected to drive the development of new PEFCs. The development of NPMCs with high ORR activity has thus been a focal point of PEFC studies. Since Jasinski discovered that a simple metal-N<sub>4</sub> complex, cobalt phthalocyanine, catalyzes an ORR [2], other CoN<sub>4</sub>- and FeN<sub>4</sub> macrocycles have been found to be suitable for use as ORR catalysts [3]. The stability and activity of a series of macrocycle-based

◇ SPP full member in good standing

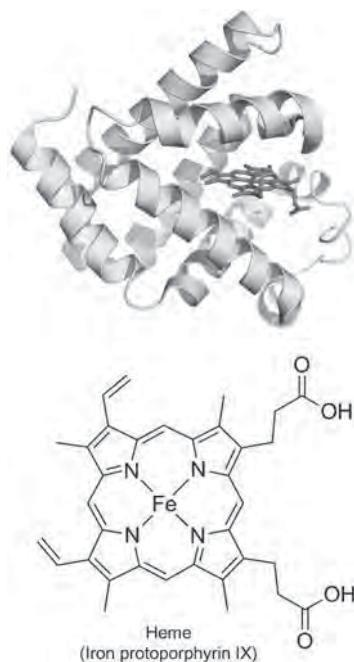
\*Correspondence to: Akira Onoda, email: onoda@chem.eng.osaka-u.ac.jp, tel: +81 6-6879-7929; Takashi Hayashi, email: thayashi@chem.eng.osaka-u.ac.jp, tel: +81 6-6879-7928

†Current address: Department of Chemistry and Biochemistry, Graduate School of Engineering, Kyushu University, 744 Motooka, Nishi, Fukuoka, 819-0395, Japan



carbon catalysts were then significantly improved after heat treatment between 500 and 900 °C under an inert atmosphere [4–17]. Promising NPMCs synthesized from a metal ion, a source of carbon, and a source of nitrogen atom by heat treatment have been reported [18–22].

Natural N4-macrocyclic metal complexes such as heme (iron protoporphyrin IX) are used in the active site of a wide range of enzyme-driven redox reactions [23]. In particular, cytochrome *c* oxidase contains heme in the active site and catalyzes an ORR in conjunction with a neighboring Cu site [24–26]. Model complexes and biomimetic models including a heme cofactor have thus been studied to unravel the intriguing four-electron reduction process [27–32]. Heme has also been recognized as an attractive building block for construction of NPMCs because they are easily obtained from natural sources. Several groups have reported the preparation of heme-based NPMCs and investigated their electrocatalytic activity [33, 34]. Direct carbonization from a hemoprotein is expected to be advantageous. Maruyama *et al.* reported that NPMCs prepared from hemoproteins such as catalase and hemoglobin have ORR activity [35–37]. Our group has been engaged in engineering of myoglobin (Mb), another representative hemoprotein (Fig. 1) [38–43] which has not yet been explored as a possible NPMC precursor. Herein, we report the characterization of NPMCs prepared from Mb by heat treatment and an investigation of the ORR activity of these NPMCs under acidic conditions.



**Fig. 1.** Crystal structure of horse heart myoglobin (PDB ID: 1WLA) and chemical structure of heme (iron protoporphyrin IX)

## EXPERIMENTAL

### Materials and methods

Carbon black (Vulcan XC72R) (VC) was purchased from MOUBIC INC. Horse heart myoglobin was purchased from Sigma-Aldrich. Myoglobin was dissolved in water and the precipitates were removed by centrifugation (10000 rpm, 10 min, 4 °C) before use. Cobalt protoporphyrin IX and reconstituted Mb with the cobalt complex were prepared according to the previous methods [44, 45]. The solution of the purified Mb (100 mg/10 mL) was mixed with VC (10 mg) and the suspension was incubated for 4 h at 4 °C. The mixture was freeze-dried to prepare a catalyst precursor. About 100 mg of the ground powder on an alumina boat (length 80 mm, width 16 mm, height 10 mm) was placed in a quartz tube (diameter 50 mm, length 800 mm), which was then installed in a hinge split tube furnace (Koyo Thermo Systems Co. Ltd., KTF045N1). The samples were heated from ambient temperature to each of the target temperatures of 740, 840, 940, 1040 and 1140 °C for 1 h under N<sub>2</sub> flow (0.2 L.min<sup>-1</sup>), and incubated for 2 h. The temperature of the sample inside the furnace was recorded with a thermocouple equipped with a data logger (CHINO MC3000). After cooling, the heat-treated catalysts were ground, and washed with 1 M HCl<sub>aq</sub> and then with excess volumes of water twice. The dried catalysts were used for the experiments.

The catalyst sample (4.0 mg) was suspended in a 0.05 wt% Nafion solution in isopropanol (100 μL) and the catalyst ink was sonicated in an ultrasonic bath at 100 W at 35 kHz for 30 min. The ink (10 μL) was coated onto a glassy carbon electrode (GCE) with an area of 0.196 cm<sup>2</sup> and dried slowly at room temperature. Electrochemical measurements were carried out in a three-electrode cell connected to a potentiostat (ALS, electrochemical analyzer model 610B). A glassy carbon electrode (GCE) was used as the working electrode, Pt foil was employed as the counter electrode, and Ag/AgCl (+0.199 vs. SHE) was used as the reference electrode. Rotating disk electrode (RDE) experiments were performed in an O<sub>2</sub> or N<sub>2</sub> saturated 0.1 M HClO<sub>4</sub> solution at 25 °C. Electrode rotation rates were controlled using a Pine Instruments AFMSRCE rotator with a Pine MSR motor controller.

### Physical measurements

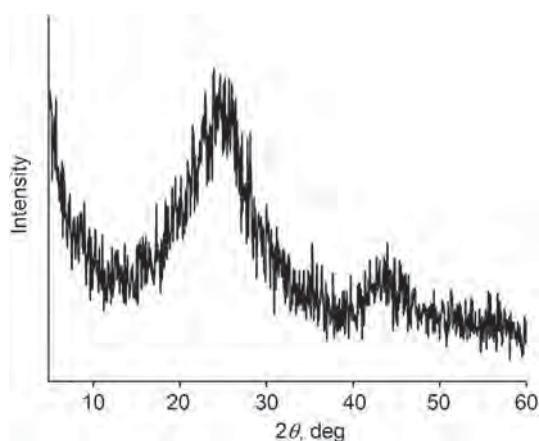
X-ray diffraction (XRD) measurements were performed using a Rigaku SmartLab diffractometer with CuKα radiation. XRD patterns were recorded in the 2θ range from 5° to 60°. Raman spectra were obtained using a Jasco NRS-3100 spectrometer with an excitation wavelength of 532 nm. The powder sample was measured on the glass plates. X-ray photoelectron spectroscopy (XPS) measurements were performed with Shimadzu KRAROS AXIS-165x instrument using monochromatic

Mg K $\alpha$  radiation (1253.6 eV). The system was calibrated with a C1s peak at 284.5 eV. The samples were fixed as powder on a stainless steel sample holder with a double adhesive carbon tape. Transmission electron microscopy (TEM) measurements were performed using Hitachi HF-2000 with an acceleration voltage of 100 kV. The samples were prepared by adding 1.0 mg of the catalyst, Mb/VC pyrolyzed at 940°C, into a solution, with subsequent ultrasonication for 5 min. The sample ink was loaded onto a 150-mesh molybdenum microgrid (Okenshoji Co., Ltd.) and the sample was dried at room temperature.

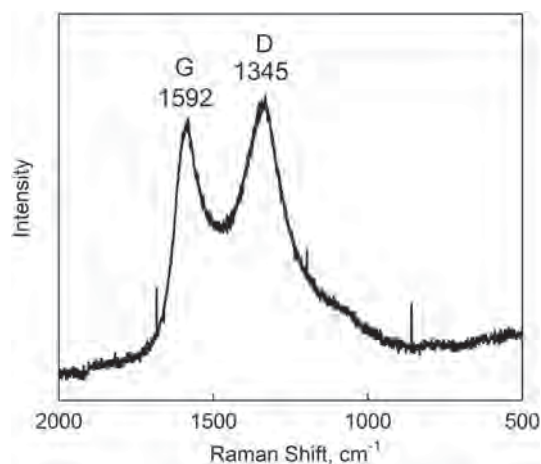
## RESULTS AND DISCUSSION

### Characterization of Mb-based NPMC by XRD

The turbostratic structure with random layers of a graphitic lattice in the Mb/VC catalyst pyrolyzed at 940°C was analyzed by X-ray diffraction (XRD) as shown in Fig. 2. In general, powder samples of carbons in a turbostratic structure provide diffraction peaks for 002 ( $2\theta = 25.5\text{--}26.6^\circ$ ), 004 ( $2\theta = 53.2\text{--}54.7^\circ$ ), and a two-dimensional 10 line at *ca.*  $44^\circ$ . Previous XRD analyses on carbonized materials of catalase and hemoglobin showing two broad peaks at *ca.*  $25^\circ$  and  $44^\circ$  confirmed the amorphous structure of the materials [36, 37]. The Mb/VC catalyst was found to exhibit a strong and broad peak at *ca.*  $25^\circ$  and very weak peak at  $44^\circ$ . These observations confirm the turbostratic and amorphous structure. Heat treatment of the iron-containing precursor often generates Fe<sub>2</sub>O<sub>3</sub>, which is identified by diffraction at  $35^\circ$ . The absence of the peak assignable to Fe<sub>2</sub>O<sub>3</sub> suggests that Fe<sub>2</sub>O<sub>3</sub> is not included in the Mb/VC catalyst pyrolyzed at 940°C, which was washed with an acidic solution.



**Fig. 2.** X-ray diffraction spectrum of the Mb/VC catalyst pyrolyzed at 940°C



**Fig. 3.** Raman spectrum of the Mb/VC catalyst pyrolyzed at 940°C

### Raman spectroscopy

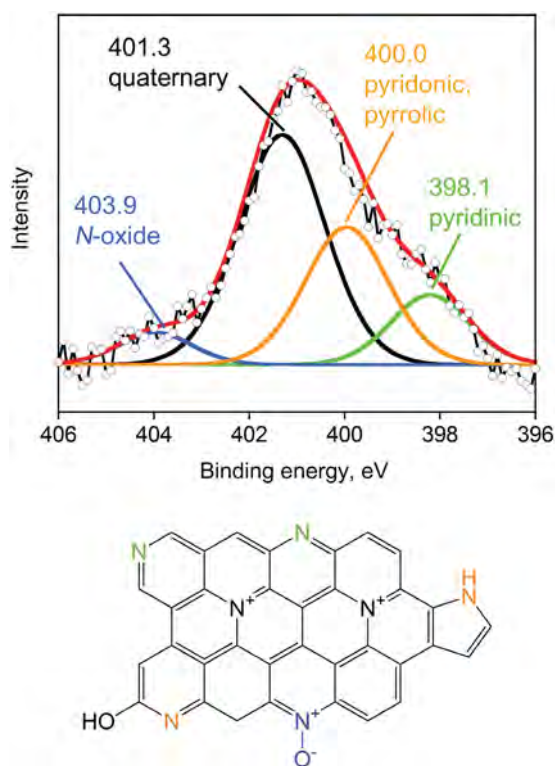
Raman spectroscopic analysis provides valuable information on the microstructure of carbon materials. It is known that highly ordered graphite presents a band between 1100 and 1700  $\text{cm}^{-1}$ , whereas disordered carbons show significantly different spectra with a D (disorder) band in the vicinity of 1350  $\text{cm}^{-1}$  and graphitized carbons give rise to a G (graphite) band at 1580  $\text{cm}^{-1}$ , which is assignable to in-plane displacement of the carbons strongly coupled in the hexagonal sheets [46, 47]. The Raman spectrum of the carbonized Mb presenting typical D- and G-bands indicates that the disordered carbonous structure is included in the catalyst (Fig. 3). The microcrystalline planar crystal size ( $L_a$ ) was calculated from  $I(D)$  and  $I(G)$ , which represent the integrated intensities of D and G bands, respectively (Equation 1) [46, 47].

$$L_a = 44[I(D)/I(G)]^{-1} \quad (1)$$

From Equation 1, the  $L_a$  value was estimated to be 1.9 nm for the Mb-based catalyst. The small  $L_a$  value indicates that the crystalline domain does not grow sufficiently and that the amorphous domain is abundant in the catalysts.

### XPS

The XPS analysis for the N1s state was performed to determine the chemical structure of the nitrogen-containing graphitic layer (Fig. 4). Previous experimental and theoretical studies reported that three types of nitrogen atoms appear as the N1s peak in the range of 398 and 403 eV binding energy [48–50]. The N1s peak at 398.3–399.5 eV is assigned to the pyridinic N atom at the edge of a graphene layer and the peak at 399.9–400.7 eV is assigned to the pyrrolic N atom. The N1s peak at 401–403 eV is assigned to the graphitic nitrogen atom bound



**Fig. 4.** N1s XPS spectrum of the Mb/VC catalyst pyrolyzed at 940 °C (circles). The deconvoluted spectra are shown in green, orange, black, and blue lines and the simulated spectrum is shown in a red line

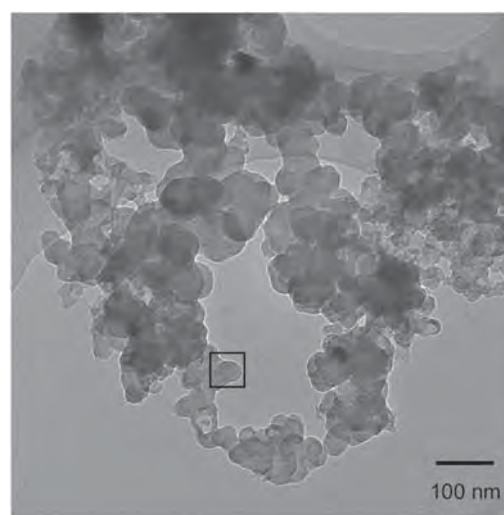
to three carbon atoms. Therefore, after the heat treatment, the Mb/VC catalysts were found to predominantly contain the pyridinic and pyrrolic N atoms in the carbon framework (Fig. 4), which would remain to provide a binding site for the iron atom.

## TEM

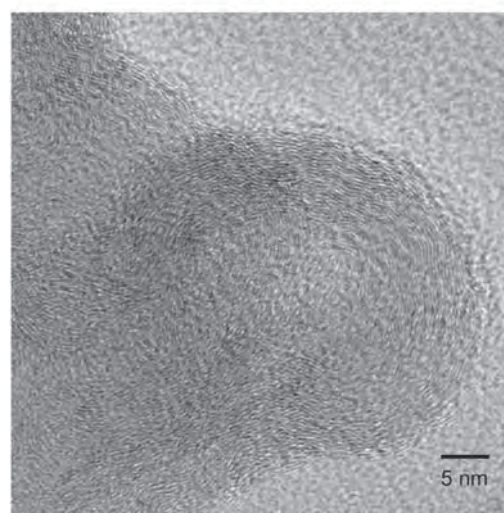
TEM images of the Mb/VC catalyst synthesized after the heat treatment at 940 °C are shown in Fig. 5a. The graphitic nanostructures are formed on the carbon aggregate after the carbonization of protoporphyrin embedded within the Mb protein matrix (Fig. 5b). In addition, large iron oxide aggregates were rarely observed, suggesting that the iron atoms are well-dispersed and embedded as the Fe active sites within the carbon surface. Therefore, the myoglobin matrix could contribute to dispersal of the Fe macrocycle moieties on the carbon structures.

## Electrochemical performance of ORR

The ORR activities of the different samples of Mb-based carbon catalysts synthesized by heat treatment at 740, 840, 940, 1040, and 1140 °C were analyzed by hydrodynamic voltammetry. The Mb/VC catalyst was suspended in a Nafion solution/isopropanol solution and the catalyst



(a)



(b)

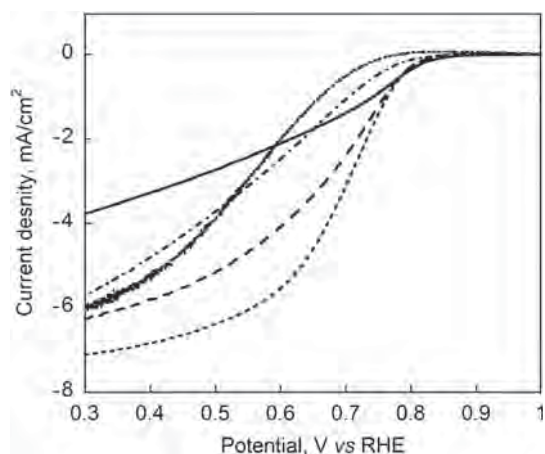
**Fig. 5.** (a) TEM image of the Mb/VC catalyst pyrolyzed at 940 °C. (b) HR-TEM image of the boxed region in Fig. 5a

ink was immobilized on the GCE. This electrode was used as a working electrode in the RDE experiments in an O<sub>2</sub>-saturated 0.1 M HClO<sub>4</sub> solution. The measured current was subtracted from the background current under an N<sub>2</sub>-saturated atmosphere. The polarization curves of the catalysts are shown in Fig. 6. The ORR activity of the catalyst was also analyzed by hydrodynamic voltammetry under the similar conditions at different rotating rates (Fig. 7), and the results were analyzed using the Koutechy–Levich equation (Equations 2 and 3) [51].

$$I^{-1} = I_K^{-1} + I_L^{-1} \quad (2)$$

$$I_L = 0.620 n F A D_0^{2/3} \omega^{1/2} \nu^{-1/6} C_0 \quad (3)$$

where  $I$ ,  $I_K$ , and  $I_L$  represent the measured, kinetically-controlled, and diffusion-limited currents, respectively.  $\omega$  is the electrode rotation rate,  $n$  is the overall number of electrons transferred in the half reaction,  $F$  is the Faraday



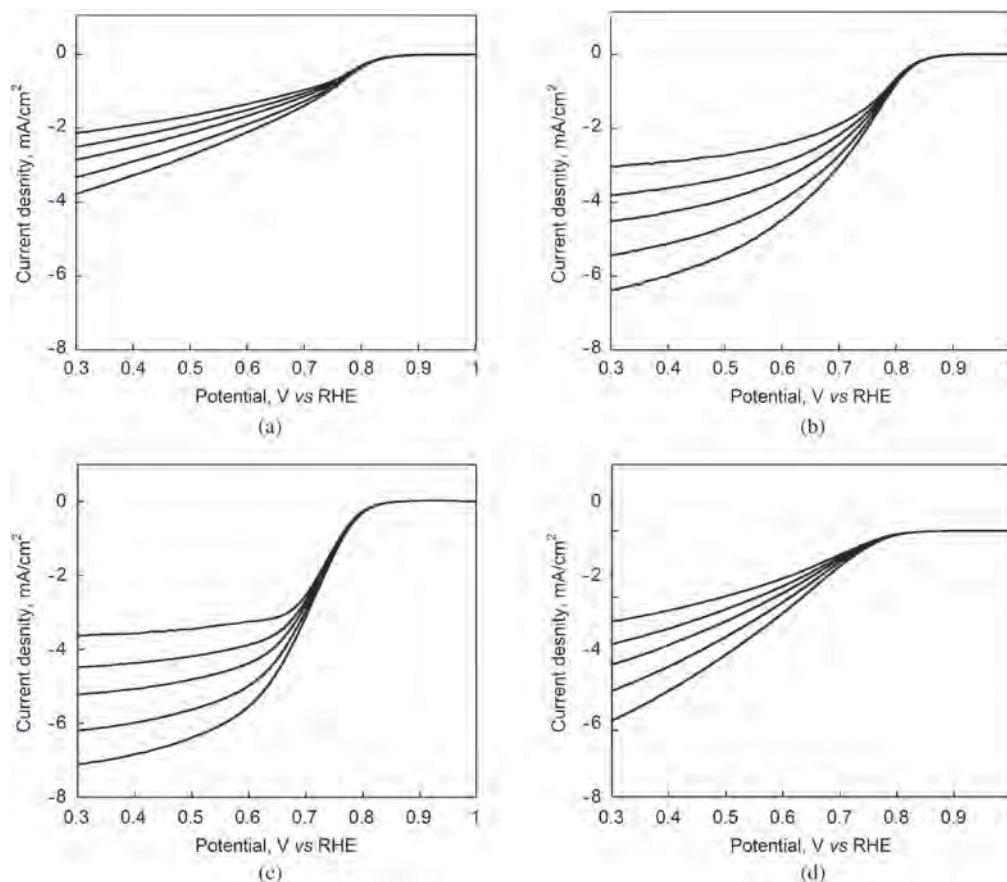
**Fig. 6.** Polarization curves of Mb/VC catalysts synthesized at different temperatures of 740 °C (solid line), 840 °C (long dashed line), 940 °C (dashed line), 1040 °C (dot dashed line), and 1140 °C (dotted line) coated on GCE in O<sub>2</sub> saturated 0.1 M HClO<sub>4</sub> solution. Scan rate: 10 mV/s. Rotation rate: 2000 rpm

constant ( $96,485 \text{ C}\cdot\text{mol}^{-1}$ ),  $C_0$  is the bulk concentration of O<sub>2</sub> dissolved in the electrolyte ( $1.18 \times 10^{-6} \text{ mol}\cdot\text{cm}^{-3}$ ),  $A$  is the electrode surface ( $0.196 \text{ cm}^2$ ),  $D_0$  is the O<sub>2</sub> diffusion coefficient ( $1.9 \times 10^{-5} \text{ cm}^2\cdot\text{s}^{-1}$ ), and  $\nu$  is the kinematic

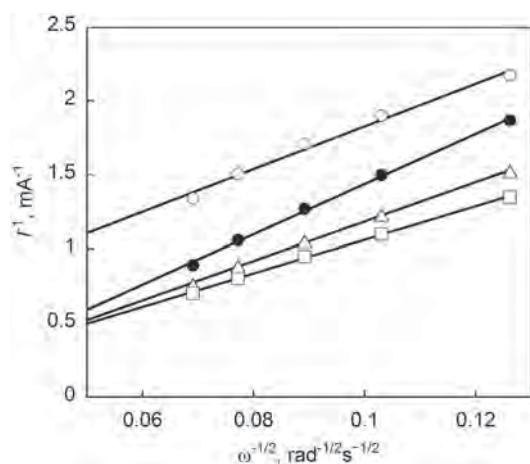
viscosity of the electrolyte ( $9.87 \times 10^{-3} \text{ cm}^2\cdot\text{s}^{-1}$ ). The plot of the inverse of the current vs.  $\omega^{-1/2}$  yields a straight line with the intercept corresponding to  $I_k$  and the slopes reflecting the  $I_L$ , which was used to calculate the number of electrons involved in the ORR (Fig. 8).

The results on the polarization curve show that the ORR activity is dependent on the pyrolytic temperature: (i) The ORR activity increases as the heat-treatment temperature increases until 940 °C; (ii) the highest catalytic activity is obtained for the sample produced at 940 °C; (iii) samples produced at higher temperatures (>940 °C) have decreased activity in terms of the onset potential and the current density; (iv) the Koutecky–Levich equation indicates that the Mb-based catalysts synthesized at 940 °C have the highest activity for four-electron ORR ( $n = ca. 4$ ) the  $n$  values for the catalysts produced at other temperatures are 3.6 at 740 °C, 3.7 at 840 °C, and 2.9 at 1040 °C; and (v) the ORR catalyzed by Mb/VC prepared at 940 °C is diffusion-controlled at a lower potential than 0.3 V (vs. RHE) and the onset potential is 0.84 V. The decrease in the activity for the samples prepared at higher temperatures would derive from the loss of the active sites [36].

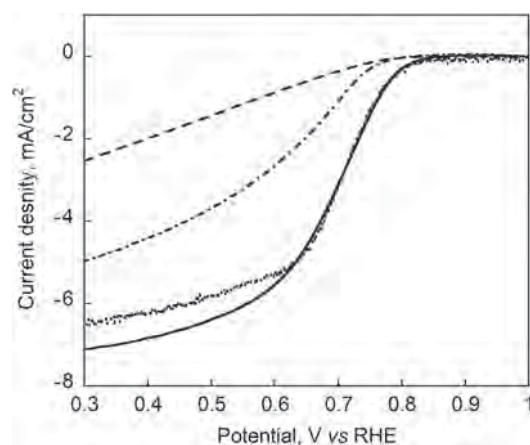
To determine the effective component in the source materials of the pyrolyzed catalyst, Mb/VC, the ORR



**Fig. 7.** Polarization curves of Mb/VC catalysts synthesized at (a) 740 °C, (b) 840 °C, (c) 940 °C, and (d) 1040 °C coated on GCE in O<sub>2</sub> saturated 0.1 M HClO<sub>4</sub> solution with different rotation rates of 600, 900, 1200, 1600, 2000 rpm. Scan rate: 10 mV/s



**Fig. 8.** (a) Koutecky-Levich plots at 0.3 V for the Mb/VC catalysts synthesized at different temperatures of 740°C (circles), 840°C (triangles), 940°C (squares), and 1040°C (filled circles)°C



**Fig. 9.** Polarization curves of the catalysts synthesized from apoMb (dashed line), heme (dotted line), Co-substituted Mb (dash-dotted line), and Mb (solid line) at 940°C coated on GCE in O<sub>2</sub> saturated 0.1 M HClO<sub>4</sub> solution. Scan rate: 10 mV/s. Rotation rate: 2000 rpm

activities of two catalysts were evaluated; the catalyst pyrolyzed from an apo form of Mb (apoMb) in which the heme was removed (apoMb/VC) and the catalyst pyrolyzed from heme without the Mb matrix (heme/VC) (Fig. 9). The apoMb/VC catalyst clearly showed lower ORR activity, while the heme/VC catalyst showed high activity similar to that of Mb/VC. In addition, the heme/VC catalyst efficiently catalyzes four-electron reduction of O<sub>2</sub>. These results suggest that the key component required for high ORR activity is derived from the carbonized Fe–N<sub>x</sub> species pyrolyzed from the heme moiety. We also investigated cobalt-substituted Mb, which was prepared by the reconstitution of apoMb with cobalt protoporphyrin IX as a source of NPMC (CoMb/VC). Although the number of electron ( $n$ ) involved in the ORR of CoMb/VC ( $n = 3.1$ ) is higher than that of the

metal-free catalyst, apoMb/VC, it is lower relative to the Mb/VC containing Fe.

## CONCLUSION

We developed a high performance NPMC for four-electron ORR, which is appropriate for use at the cathode in PEFCs. Myoglobin, which contains heme, a natural iron N4-macrocyclic cofactor is used as the catalyst source. It is found that the Mb-based NPMC pyrolyzed at 940°C has the highest activity toward four-electron ORR with an onset potential of 0.84 V. Our study demonstrates that myoglobin has excellent potential for use as a precursor of NPMCs in construction of PEFCs.

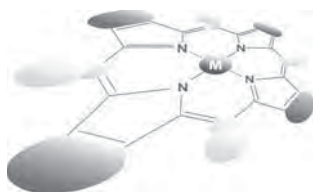
## Acknowledgements

This work was supported by a Grant-in-Aid for Young Scientists (A), KAKENHI 25708031. A.O. acknowledges a support from Japan Association of Chemical Innovation (JACI). T.O. acknowledges a support from Research Fellowship of JSPS. Y.T. acknowledges support from the Interactive Material Science Cadet program (IMSC). The authors wish to thank Dr. Tadashi Sento and Dr. Yuji Shimasaki at Nippon Shokubai Co. Ltd. for their expert assistance with XPS measurements and for helpful discussions of the results. We acknowledge Dr. Shinji Tamura and Prof. Nobuhito Imanaka at Department of Applied Chemistry, Graduate School of Science, Osaka University for XRD and Raman measurements.

## REFERENCES

1. Debe MK. *Nature* 2012; **486**: 43–51.
2. Jasinski R. *Nature* 1964; **201**: 1212–1213.
3. Anson FC, Shi C and Steiger B. *Acc. Chem. Res.* 1997; **30**: 437–444.
4. Jahnke H, Schönborn M and Zimmerman G. *Top. Curr. Chem.* 1978; **61**: 133–181.
5. Bagotzky VS, Tarasevich MR, Radyushkina KA, Levina OA and Andrusyova SI. *J. Power Sources* 1978; **2**: 233–240.
6. Holze R, Vogel I and Vielstich W. *J. Electroanal. Chem. Interfacial Electrochem.* 1986; **210**: 277–286.
7. Tanaka AA, Fierro C, Scherson D and Yeager EB. *J. Phys. Chem., B* 1987; **91**: 3799–3807.
8. van Veen JAR, Colijn HA and van Baar JF. *Electrochim. Acta* 1988; **33**: 801–804.
9. Widelöv A and Larsson R. *Electrochim. Acta* 1992; **37**: 187–197.
10. Widelöv A. *Electrochim. Acta* 1993; **38**: 2493–2502.
11. Lalande G, Faubert G, Côté R, Guay D, Dodelet JP, Weng LT and Bertrand P. *J. Power Sources* 1996; **61**: 227–237.
12. Bouwkamp-Wijnoltz AL, Visscher W and van Veen JAR. *Electrochim. Acta* 1998; **43**: 3141–3152.

13. Gojković SL, Gupta S and Savinell RF. *J. Electroanal. Chem.* 1999; **462**: 63–72.
14. Lefèvre M, Dodelet JP and Bertrand P. *J. Phys. Chem., B* 2000; **104**: 11238–11247.
15. Bouwkamp-Wijnoltz AL, Visscher W, van Veen JAR, Boellaard E, van der Kraan AM and Tang SC. *J. Phys. Chem., B* 2002; **106**: 12993–13001.
16. Lefèvre M and Dodelet J-P. *Electrochim. Acta* 2003; **48**: 2749–2760.
17. Schulenburg H, Stankov S, Schünemann V, Radnik J, Dorbandt I, Fiechter S, Bogdanoff P and Tributsch H. *J. Phys. Chem., B* 2003; **107**: 9034–9041.
18. Bashyam R and Zelenay P. *Nature* 2006; **443**: 63–66.
19. Lefèvre M, Proietti E, Jaouen F and Dodelet J-P. *Science* 2009; **324**: 71–74.
20. Wu G, More KL, Johnston CM and Zelenay P. *Science* 2011; **332**: 443–447.
21. Chung HT, Won JH and Zelenay P. *Nat. Commun.* 2013; **4**: 1922.
22. Proietti E, Jaouen F, Lefèvre M, Larouche N, Tian J, Herranz J and Dodelet J-P. *Nat Commun* 2011; **2**: 416.
23. *Handbook of Metalloproteins*, Vol. 1, John Wiley & Sons, Ltd.: Chichester, 2001.
24. Tsukihara T, Aoyama H, Yamashita E, Tomizaki T, Yamaguchi H, Shinzawa-Itoh K, Nakashima R, Yaono R and Yoshikawa S. *Science* 1995; **269**: 1069–1074.
25. Tsukihara T, Aoyama H, Yamashita E, Tomizaki T, Yamaguchi H, Shinzawa-Itoh K, Nakashima R, Yaono R and Yoshikawa S. *Science* 1996; **272**: 1136–1144.
26. Kaila VRI, Verkhovsky MI and Wikström M. *Chem. Rev.* 2010; **110**: 7062–7081.
27. Collman JP, Boulatov R, Sunderland CJ and Fu L. *Chem. Rev.* 2003; **104**: 561–588.
28. Kim E, Chufán EE, Kamaraj K and Karlin KD. *Chem. Rev.* 2004; **104**: 1077–1134.
29. Thorseth MA, Tornow CE, Tse ECM and Gewirth AA. *Coord. Chem. Rev.* 2013; **257**: 130–139.
30. Liu X, Yu Y, Hu C, Zhang W, Lu Y and Wang J. *Angew. Chem., Int. Ed.* 2012; **51**: 4312–4316.
31. Mukherjee S, Sengupta K, Das MR, Jana SS and Dey A. *J. Biol. Inorg. Chem.* 2012; **17**: 1009–1023.
32. Mukherjee S, Bandyopadhyay S, Chatterjee S and Dey A. *Chem. Commun.* 2014; **50**: 12304–12307.
33. Jiang R, Tran DT, McClure JP and Chu D. *Electrochim. Acta* 2012; **75**: 185–190.
34. Xu JB, Zho TS and Zeng J. *Inter. J. Hydrogen Energy* 2012; **37**: 15976–15982.
35. Maruyama J, Okamura J, Miyazaki K, Uchimoto Y and Abe I. *J. Phys. Chem., C* 2008; **112**: 2784–2790.
36. Maruyama J and Abe I. *Chem. Mater.* 2006; **18**: 1303–1311.
37. Maruyama J and Abe I. *Chem. Mater.* 2005; **17**: 4660–4667.
38. Hayashi T, Hitomi Y, Takimura T, Tomokuni A, Mizutani T, Hisaeda Y and Ogoshi H. *Coord. Chem. Rev.* 1999; **190**: 961–974.
39. Sato H, Watanabe M, Hisaeda Y and Hayashi T. *J. Am. Chem. Soc.* 2005; **127**: 56–57.
40. Matsuo T, Hayashi A, Abe M, Matsuda T, Hisaeda Y and Hayashi T. *J. Am. Chem. Soc.* 2009; **131**: 15124–15125.
41. Onoda A, Himiyama T, Ohkubo K, Fukuzumi S and Hayashi T. *Chem. Commun.* 2012; **48**: 8054–8056.
42. Oohora K, Kihira Y, Mizohata E, Inoue T and Hayashi T. *J. Am. Chem. Soc.* 2013; **135**: 17282–17285.
43. Hayashi T, Onoda A and Sano Y. *Israel J. Chem.* 2014: in press.
44. Matsuo T, Tsuruta T, Maehara K, Sato H, Hisaeda Y and Hayashi T. *Inorg. Chem.* 2005; **44**: 9391–9396.
45. Yonetani T, Yamamoto H and Woodrow III. GV. *J. Biol. Chem.* 1974; **249**: 682–690.
46. Jawhari T, Roid A and Casado J. *Carbon* 1995; **33**: 1561–1565.
47. Wang Y, Alsmeyer DC and McCreery RL. *Chem. Mater.* 1990; **2**: 557–563.
48. Faubert G, Côté R, Dodelet JP, Lefèvre M and Bertrand P. *Electrochim. Acta* 1999; **44**: 2589–2603.
49. Casanovas J, Ricart JM, Rubio J, Illas F and Jiménez-Mateos JM. *J. Am. Chem. Soc.* 1996; **118**: 8071–8076.
50. Pels JR, Kapteijn F, Moulijn JA, Zhu Q and Thomas KM. *Carbon* 1995; **33**: 1641–1653.
51. Bard AJ and Faulkner LR. *Electrochemical Methods: Fundamentals and Applications*, John Wiley & Sons: New York, 2001



# Synthesis of carboxylated chlorophylls and their application as functional materials

Shin-ichi Sasaki<sup>a,b</sup>, Xiao-Feng Wang<sup>c</sup>, Toshitaka Ikeuchi<sup>b</sup> and Hitoshi Tamiaki<sup>\*a</sup>

<sup>a</sup>Graduate School of Life Sciences, Ritsumeikan University, Kusatsu, Shiga 525-8577, Japan

<sup>b</sup>Nagahama Institute of Bio-Science and Technology, Nagahama, Shiga 526-0829, Japan

<sup>c</sup>Key Laboratory of Physics and Technology for Advanced Batteries (Ministry of Education), College of Physics, Jilin University, Changchun 130012, P. R. China

Dedicated to Professor Shunichi Fukuzumi on the occasion of his retirement

Received 27 October 2014

Accepted 8 January 2015

**ABSTRACT:** A series of chlorophyll derivatives possessing a carboxy group were synthesized aiming at their application as sensing materials and to dye-sensitized solar cells (DSSCs). Their absorption and fluorescence responses to amine concentrations in THF and photovoltaic performance of DSSCs on TiO<sub>2</sub> films were investigated.

**KEYWORDS:** chlorin, tetrapyrrole, visible absorption spectrum, dye-sensitized solar cell.

## INTRODUCTION

Chlorophylls (Chls) are representative dye molecules in nature. They play crucial roles such as light-harvesting and energy-transfer in the initial stage of photosynthesis [1]. Many model compounds have been developed to investigate the mechanism of energy/electron-transferring processes [2, 3] or to mimic supramolecular structures based on self-assembling abilities [4–6]. On the other hand, characteristics of Chl molecules are also fascinating as functional materials for any practical application. For example, Pandey *et al.* have synthesized a series of Chl derivatives for photodynamic therapy [7]. We recently reported Chl derivatives possessing C3-trifluoroacetyl group **1** (see Fig. 1) as an amine/alcohol sensor [8], C3-ureido group **2** as an anion sensor [9], and carboxy group at various positions **3–6** as components for dye-sensitized solar cells (DSSCs) [10]. Although the carboxy group in **3–6** was introduced to bind dye molecules on TiO<sub>2</sub> in a solar cell device, acidic COOH is also expected to act as a sensing moiety toward bases such as organic amines. In this

study, we report the synthesis of a series of carboxylated Chl derivatives and their application to DSSCs as well as being analytical reagents for amine detection.

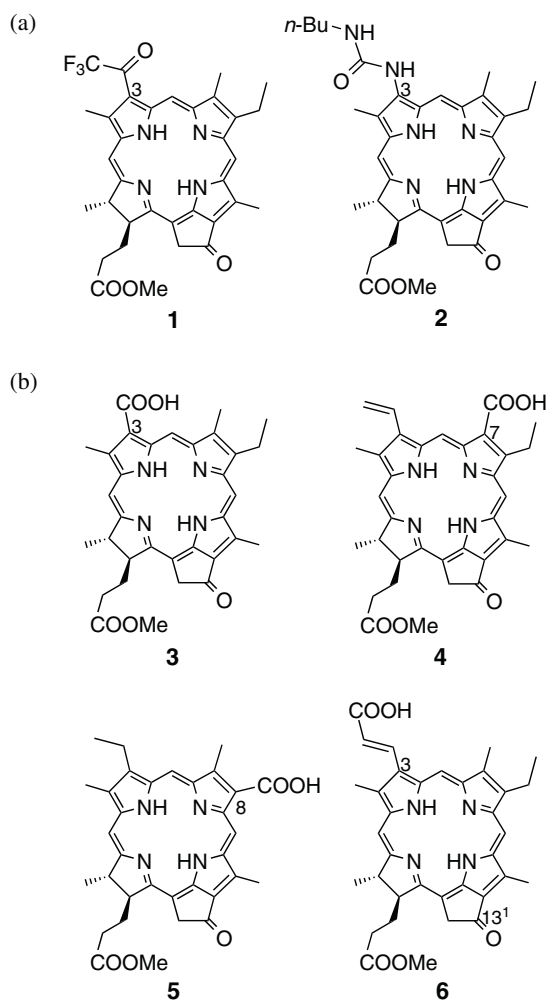
## RESULTS AND DISCUSSION

Because the longest absorption (Q<sub>y</sub>) band in Chl derivatives is sensitive to the C3-functional group [11] and the DSSC performance of **3** was better than those of C7- **4** and C8-carboxylated chlorins **5** [10e], target compounds were designed to possess a carboxy group in the C3-substituent along with different peripheral substituents on the chlorin ring. Their synthetic routes are outlined in Schemes 1 and 2.

Methyl pyropheophorbide-*a* (**7**) and methyl pyropheophorbide-*d* (**8**) were prepared by the reported procedures [12]. A *p*-carboxyphenyl unit at the C3<sup>2</sup>-position of **7** was introduced by Wittig reaction between the C3-formyl group of **8** and the corresponding phosphonium salt under similar conditions reported previously [13] to give **9** in 45% yield. Knoevenagel reaction of **8** with cyanoacetic acid in piperidine/THF gave monocarboxylated chlorin **10** [14], while its reaction with malonic acid in piperidine/pyridine gave dicarboxylated chlorin **11**. For the synthesis of

<sup>†</sup>SPP full member in good standing

\*Correspondence to: Hitoshi Tamiaki, email: tamiaki@fc.ritsumei.ac.jp, fax: +81 77-561-2890



**Fig. 1.** Chemical structures of chlorophyll derivatives possessing (a) C3-functional groups for molecular recognition and (b) a carboxylic acid moiety for application to dye-sensitized solar cells

C20-substituted chlorins, the C3-formyl group of **8** was reduced to the C3-hydroxymethyl group, then treated with pyridinium tribromide to give 20-bromo-chlorin **13** [15]. Successively, its Suzuki–Miyaura cross-coupling reaction with 3,5-dimethylphenylboronic acid using palladium catalyst (57%), oxidation to the C3-formyl group (66%), Wittig reaction with  $\text{Ph}_3\text{P}=\text{CHCOOBu}^t$  (89%), and acidic hydrolysis of the *tert*-butyl ester (90%) gave 20-aryl-chlorin **16**. In the similar manner,  $\alpha$ -thienyl-chlorin **17** was prepared from **13** in four steps (67%  $\times$  69%  $\times$  83%  $\times$  95%), and 20-bromo-chlorin **18** in three steps without the cross-coupling reaction. On the other hand, Knoevenagel reaction was used to convert the C13<sup>1</sup>-oxo group in **12** to a dicyanomethylene group [16], then the *tert*-butyl ester was hydrolyzed to give the corresponding carboxylic acid **19**. 13<sup>1</sup>-Deoxo-chlorin **21** was prepared from the corresponding 3-formyl-chlorin **20** [17]. Finally, zinc-metalation of free-base chlorins **6**, **10**, **11**, and **19** was performed as previously reported in quantitative yields [18].

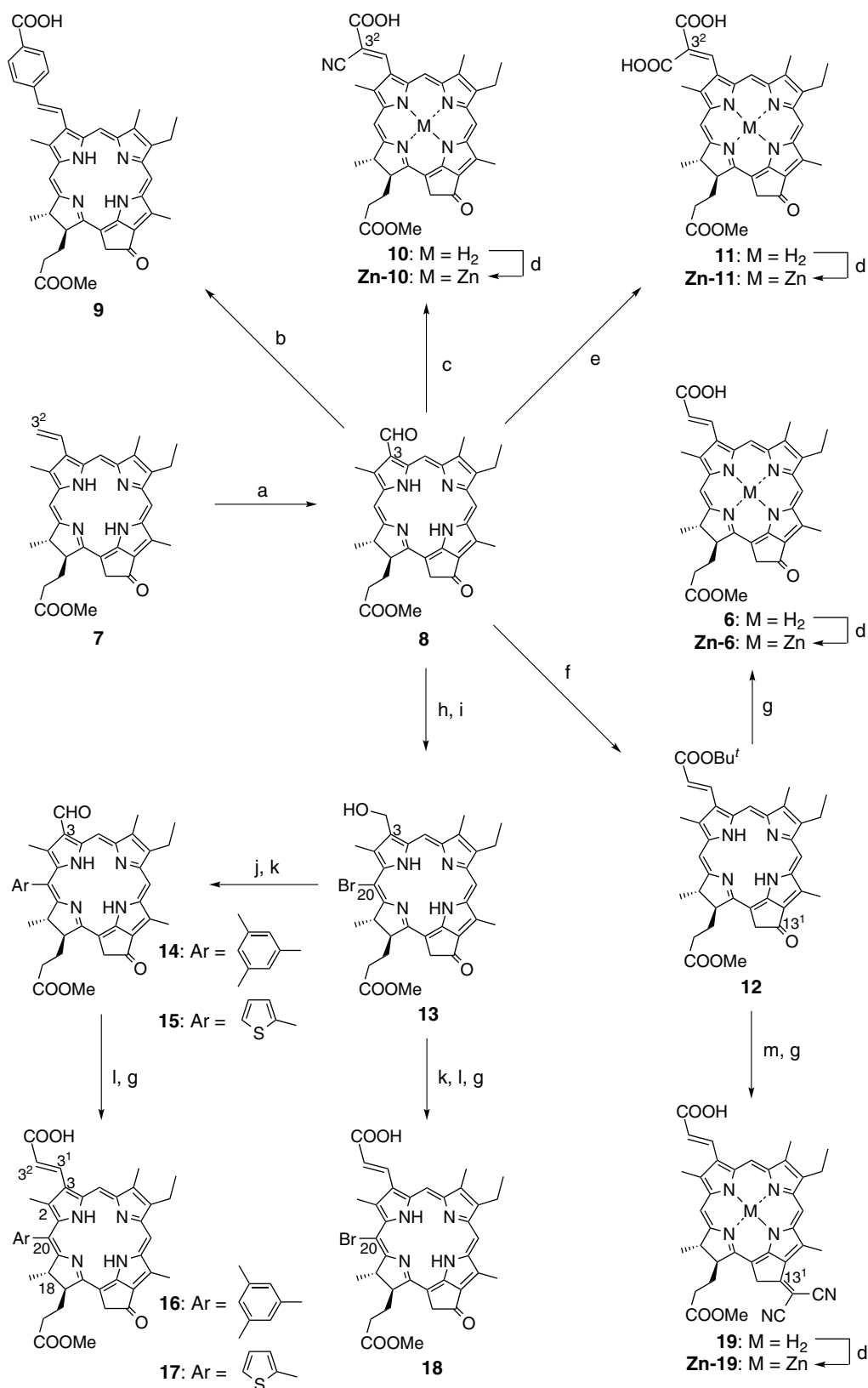
In the initial stage of this study, visible spectra of carboxylated Chl derivatives **3–6** and **9** in different solvents were measured and the results are summarized in Tables 1 and S1. Since a reference compound **7** showed almost the same spectra both in THF and  $\text{Et}_3\text{N}$  [see also Ref. 8a for solvatochromism of **1**], a chlorin skeleton possessing the inner NH groups seems to be less sensitive to solvent polarity. Therefore, spectral differences of **3–6** and **9** in THF and  $\text{Et}_3\text{N}$  can be ascribed to the change of form in the carboxylic acid moiety. The  $Q_y$  peak shift value of **3** in THF and  $\text{Et}_3\text{N}$  is 7 nm, which is larger than those of **4** and **5** possessing a C7/C8-carboxy group. The value is also larger than those of **6** (2 nm) and **9** (1 nm), which is in accordance with the order of distance between the carboxy group and chlorin ring. A similar tendency is observed in  $\text{CHCl}_3$  and pyridine (Table S1). Electron-withdrawing groups at the C3-position are known to cause a red-shift of the  $Q_y$  peak [11]. Therefore, negative charge of the carboxylate anion in basic solvents is considered to partially make up the electron density at the C3-carbonyl carbon atom of **3**, causing a blue-shift of the  $Q_y$  peak compared to its carboxylic acid form in THF or  $\text{CHCl}_3$ .

Figure 2 compares the absorption spectra of free-base chlorins **3**, **6**, and **9** in THF. The  $Q_y$  peak position of **6** (681 nm) is the same as that of **3** in spite of its  $\pi$ -extension at the C3-double bond, while **9** possessing a styryl spacer between the COOH and chlorin ring showed a slight blue-shift (677 nm). When  $\text{Et}_3\text{N}$  was added to a THF solution of **6**, a blue-shift of the  $Q_y$  peak was observed with an increase of  $\text{Et}_3\text{N}$  concentration. The shift was saturated at *ca.* 2%(v/v) (681 nm  $\rightarrow$  677 nm) as shown in Fig. 3. When the solution was excited at 417 nm, the main fluorescence emission maximum was a similar function of the  $\text{Et}_3\text{N}$  concentration (685 nm  $\rightarrow$  681 nm). Although the equilibrium complexation between carboxylic acids and amines in organic solvents is complicated [19], chlorin **6** has been demonstrated to be used as a sensing reagent for amine concentration both in electronic absorption and fluorescence emission spectroscopies.

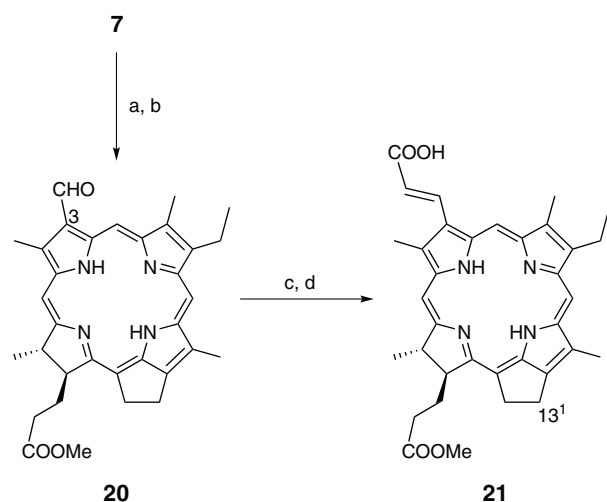
Carboxylated chlorins **3–6** were successfully used in DSSCs [10], among which chlorin **6** possessing C3-acrylic acid moiety and its related compounds showed the best performances in this series [20]. Therefore, DSSCs based on newly synthesized chlorins were compared to **6** under the same conditions. Figure 4 compares the incident photon-to-current conversion efficiency (IPCE) profiles and  $I$ - $V$  curves of DSSCs based on chlorins **3**, **6**, and **9**. Energy-to-electron conversion efficiency ( $\eta$ ) of **6** (6.1%) is better than that of **3** (3.4%), while the character of **9** possessing an additional benzene ring spacer is a little disappointing (1.4%).

In view of the mechanism of electron injection from the Chl pigments into  $\text{TiO}_2$ , the cyano group adjacent to COOH in **10** or two carboxy groups in **11** at the C3<sup>2</sup>-position might facilitate the electron-withdrawing from the chlorin  $\pi$ -skeleton. To investigate the electronic



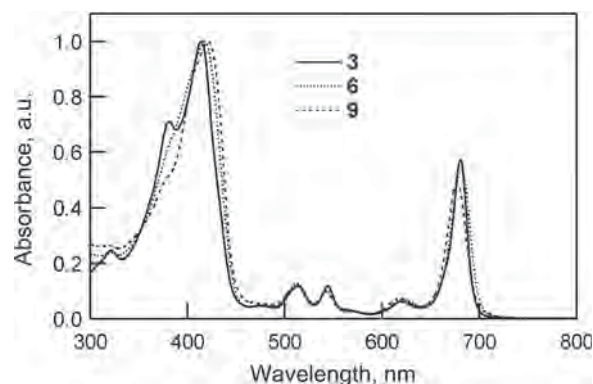


**Scheme 1.** Synthesis of carboxylated chlorophylls by modifying methyl pyropheophorbides-ald (**7/8**): (a) OsO<sub>4</sub>, NaIO<sub>4</sub>, THF-aq. AcOH; (b) Br<sup>-</sup>Ph<sub>3</sub>P<sup>+</sup>CH<sub>2</sub>-C<sub>6</sub>H<sub>4</sub>-COOH, K<sub>2</sub>CO<sub>3</sub>, 18-crown-6, THF; (c) NCCH<sub>2</sub>COOH, piperidine-THF; (d) Zn(OAc)<sub>2</sub>·2H<sub>2</sub>O, MeOH-CH<sub>2</sub>Cl<sub>2</sub>; (e) CH<sub>2</sub>(COOH)<sub>2</sub>, piperidine-pyridine, (f) Ph<sub>3</sub>P=CHCOOBu', CH<sub>2</sub>Cl<sub>2</sub>; (g) CF<sub>3</sub>COOH; (h) Bu'<sup>-</sup>NH<sub>2</sub>·BH<sub>3</sub>, CH<sub>2</sub>Cl<sub>2</sub>; (i) pyridinium tribromide, CH<sub>2</sub>Cl<sub>2</sub>; (j) Ar-B(OH)<sub>2</sub>, PdCl<sub>2</sub>(dppf), Cs<sub>2</sub>CO<sub>3</sub>, THF; (k) PDC, CH<sub>2</sub>Cl<sub>2</sub>; (l) Ph<sub>3</sub>P=CHCOOBu', toluene; (m) CH<sub>2</sub>(CN)<sub>2</sub>, Et<sub>3</sub>N-THF

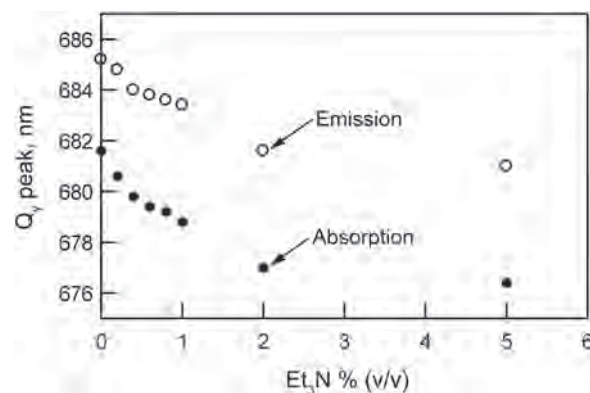


**Scheme 2.** Synthesis of a carboxylated 13<sup>1</sup>-deoxy-chlorophyll derivative **21** by modifying **7**: (a) NaBH<sub>4</sub>, CF<sub>3</sub>COOH, CH<sub>2</sub>Cl<sub>2</sub>; (b) OsO<sub>4</sub>, NaIO<sub>4</sub>, THF-aq. AcOH; (c) Ph<sub>3</sub>P=CHCOOBu<sup>t</sup>, CH<sub>2</sub>Cl<sub>2</sub>; (d) CF<sub>3</sub>COOH

effects at the diagonal position, C13<sup>1</sup>-oxo group in **6** was changed to a dicyanomethylene group as a stronger electron-withdrawing moiety (**19**) or reduced to two hydrogen atoms as an electron-donating moiety (**21**). Introduction of a cyano group at the C3/C13-positions is known to bring a peak broadening of Soret band with a red-shift of Q<sub>y</sub> peak [16], which seems to be an advantage for efficient light-absorption in a wide range. Figure 5 compares the absorption spectra of the above chlorins, among which chlorin **19** possessing the C13<sup>1</sup>-dicyanomethylene unit showed the largest red-shift of the Q<sub>y</sub> peak (714 nm) with a broad Soret band reaching



**Fig. 2.** Electronic absorption spectra of **3** (solid line), **6** (dotted line), and **9** (dashed line) in THF. All spectra were normalized at their Soret peaks

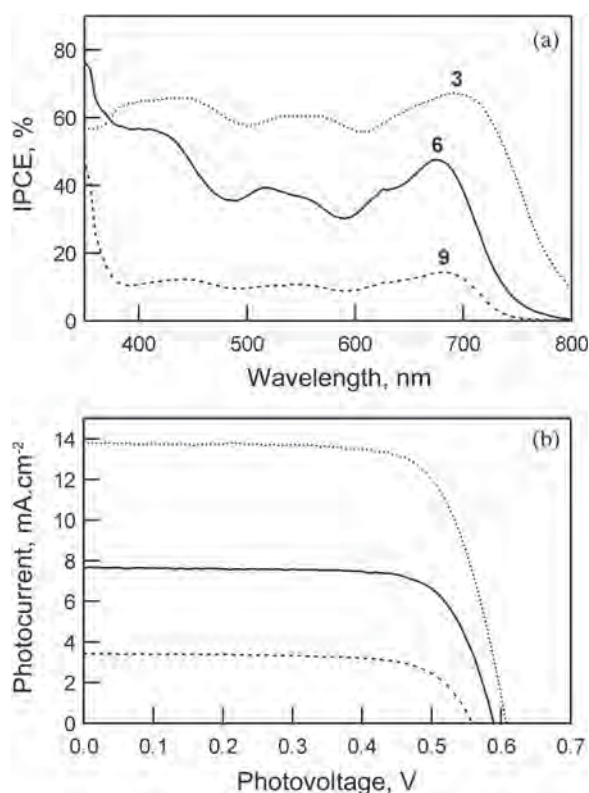


**Fig. 3.** Shifts of Q<sub>y</sub> absorption (closed circles) and main fluorescence emission maxima (opened circles, excited at 417 nm) of chlorin **6** in THF with the addition of triethylamine

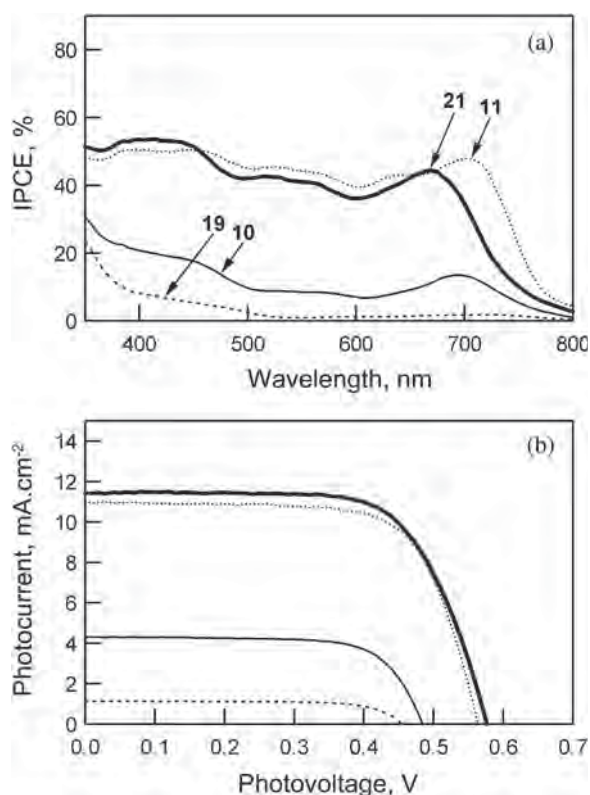
**Table 1.** Spectral characteristics of carboxylated chlorins in different solvents

Compound	Solvent	$\lambda_{\max}$ , nm			$\Delta\lambda(Q_y)^a$
		Soret	Q <sub>x</sub>	Q <sub>y</sub>	
<b>3</b> (3-COOH)	THF	414	513/544	681	7
	Et <sub>3</sub> N	412	511/541	674	
<b>4</b> (7-COOH)	THF	429	521/555	657	-3
	Et <sub>3</sub> N	426	518/551	660	
<b>5</b> (8-COOH)	THF	424	514/556	655	-1
	Et <sub>3</sub> N	421	511/551	656	
<b>6</b> (3-CH=CH-COOH)	THF	417	513/543	681	2
	Et <sub>3</sub> N	415	511/540	679	
<b>7</b> (Reference compound)	THF	411	508/536	668	0
	Et <sub>3</sub> N	410	507/535	668	
<b>9</b> (3-CH=CH-C <sub>6</sub> H <sub>4</sub> -COOH)	THF	421	513/543	677	1
	Et <sub>3</sub> N	418	512/541	676	

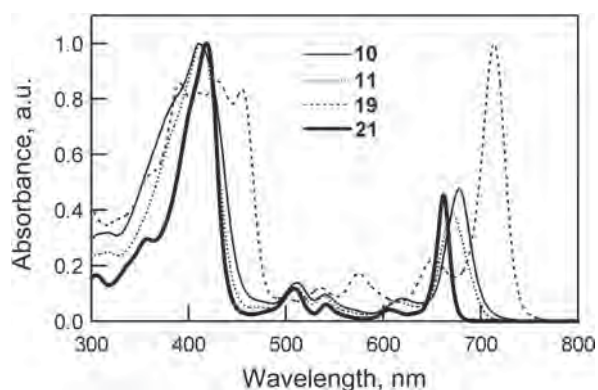
<sup>a</sup> $\Delta\lambda(Q_y) = \lambda_{\max}[Q_y(\text{THF})] - \lambda_{\max}[Q_y(\text{Et}_3\text{N})]$ .



**Fig. 4.** (a) IPCE profiles and (b) *I*-*V* curves of DSSCs based on **3** (solid line), **6** (dotted line), and **9** (dashed line) sensitizers on a TiO<sub>2</sub> electrode



**Fig. 6.** (a) IPCE profiles and (b) *I*-*V* curves of DSSCs based on **10** (solid thin line), **11** (dotted line), **19** (dashed line), and **21** (solid thick line) sensitizers on a TiO<sub>2</sub> electrode



**Fig. 5.** Electronic absorption spectra of **10** (solid thin line), **11** (dotted line), **19** (dashed line), and **21** (solid thick line) in THF. All spectra were normalized at their most intense peaks

to 480 nm, while chlorin **21** lacking the C13<sup>1</sup>-oxo group showed a slight blue-shift of the Q<sub>y</sub> peak (661 nm) with a relatively sharp Soret peak at 416 nm.

Figure 6 shows the IPCE profiles and *I*-*V* curves of DSSCs based on chlorins **10**, **11**, **19**, and **21**. It was found that the introduction of cyano group(s) drastically decreased the *J*<sub>sc</sub> and *V*<sub>oc</sub> values (**6** → **10/19**), resulting in worse efficiencies. Introduction of an additional carboxy group in **11** and keto-carbonyl reduction in **21** also

decreased the performance of DSSCs compared to **6**. It is reported that one of the reasons for lower performance of DSSCs is dye-aggregation during the adsorption on TiO<sub>2</sub> [10a]. Thus, bulky substituents at the C20-position as in **16**-**18** were introduced to prevent the stacking of chlorin rings. Finally, several free-base chlorins were zinc-metalated to change the HOMO/LUMO levels of dye molecules. However, as summarized in Table 2, the performance of DSSCs based on these new chlorins was not improved (for IPCE profiles and *I*-*V* curves, see Figs S12 and S13). The bulky C20-substituent could cause a twist of the C3-C3<sup>1</sup> bond [21], which would be a disadvantage for electron injection from the chlorin ring to C3<sup>2</sup>-carboxy group. It is interesting to note that insertion of central zinc decreased the η values in **Zn-6** and **Zn-11** compared to free-base chlorins **6** and **11**, while the opposite effect was observed in the case of cyano-chlorins **10/Zn-10** (1.5 → 1.7%) and **19/Zn-19** (0.4 → 1.8%).

## EXPERIMENTAL

### General

Electronic absorption and fluorescence emission spectra were measured on Hitachi U-3500 and F-4500

**Table 2.** Photovoltaic performance of DSSCs based on the carboxylated chlorins

Compound	$J_{sc}$ , mA.cm <sup>-2</sup>	$V_{oc}$ , V	FF	$\eta$ , %
<b>3</b>	7.7	0.59	0.74	3.4
<b>6</b>	13.8	0.61	0.73	6.1
<b>9</b>	3.4	0.56	0.71	1.4
<b>10</b>	4.3	0.48	0.71	1.5
<b>11</b>	11.0	0.56	0.70	4.3
<b>16</b>	8.5	0.55	0.65	3.0
<b>17</b>	4.2	0.52	0.69	1.5
<b>18</b>	2.6	0.46	0.75	0.9
<b>19</b>	1.1	0.46	0.72	0.4
<b>21</b>	11.4	0.58	0.69	4.5
<b>Zn-6</b>	8.0	0.62	0.71	3.6
<b>Zn-10</b>	4.6	0.52	0.73	1.7
<b>Zn-11</b>	8.0	0.55	0.68	3.0
<b>Zn-19</b>	4.8	0.53	0.71	1.8

spectrometers, respectively. Fluorescence quantum yields in THF were determined by using a Hamamatsu Photonics C9920-02 spectrometer. All melting points were measured with a Yanagimoto micro melting apparatus and were uncorrected. <sup>1</sup>H NMR spectra were recorded on a JEOL JNM-600HR spectrometer in CDCl<sub>3</sub>. Chemical shifts are reported relative to the residual solvent peak:  $\delta = 7.26$  ppm (CHCl<sub>3</sub>). Proton peaks were assigned by <sup>1</sup>H-<sup>1</sup>H COSY as well as NOESY or ROESY spectra. Atmospheric pressure chemical ionization (APCI) quadrupole mass spectra (MS) and laser desorption ionization time of flight (TOF) MS were measured by Shimadzu LCMS-2010 EV and AXIMA-CFR+ apparatus, respectively; methanol solutions were injected for APCI-MS and no matrix was used for TOF-MS. Flash column chromatography (FCC) was performed with silica gel (Merck, Kieselgel 60). GPC was performed with recycling preparative high-performance liquid chromatography LC-908 (Japan Analytical Industry) with three connected polystyrene packed columns (Jaigel 1H, 2H, and 3H).

Methyl *trans*-3<sup>2</sup>-carboxy-pyropheophorbide-*a* (**6**) [10e], methyl pyropheophorbide-*a* (**7**) [12], methyl pyropheophorbide-*d* (**8**) [12], methyl 3<sup>2</sup>-carboxy-3<sup>2</sup>-cyano-pyropheophorbide-*a* (**10**) [10b], methyl *trans*-3<sup>2</sup>-(*tert*-butoxycarbonyl)-pyropheophorbide-*a* (**12**) [10e], methyl 3-devinyl-3-hydroxymethyl-20-bromo-pyropheophorbide-*a* (**13**) [15], and methyl 13-deoxy-pyropheophorbide-*d* (**20**) [17] were prepared as previously reported. THF was distilled over CaH<sub>2</sub> before use. Other solvents and reagents were used as purchased without further purification. Zinc-metalation of free-base chlorins was done according to the reported procedure in

quantitative yields [18], and pure samples were obtained after simple recrystallization from CH<sub>2</sub>Cl<sub>2</sub> and hexane. All synthetic procedures were done in the dark under nitrogen.

### Fabrication of dye-sensitized solar cells and photovoltaic measurements

An optically transparent electrode (OTE) with 0.25 cm<sup>2</sup> working area was prepared by screen-printing fluorine-doped tin oxide (FTO) glass (Nippon Sheet Glass 10  $\Omega$ .cm<sup>-2</sup>) with 18 nm and 400 nm TiO<sub>2</sub> nanoparticles with thicknesses of 10  $\mu$ m and 4  $\mu$ m, for light-harvesting and light-scattering, respectively. Each DSSC was fabricated using this OTE, the counter electrode of Pt-sputtered FTO glass, and an electrolyte containing 0.1 M LiI, 0.05 M I<sub>2</sub>, and 0.6 M 1-propyl-3-methylimidazolium iodide in a mixture of acetonitrile and valeronitrile (1:1, v/v). The details of fabrication of DSSCs were described earlier [20b]. Both *I*-*V* curves and IPCE characterizations of DSSCs were carried out on a CEP-2000 integrated system (Bunkou Keiki) under standard measurement conditions.

### Synthesis

**Zinc methyl *trans*-3<sup>2</sup>-carboxy-pyropheophorbide-*a* (Zn-6).** Zinc-metalation of free-base **6** gave **Zn-6**: mp > 300 °C. UV-vis (THF):  $\lambda_{max}$ , nm 671 (relative intensity, 0.96), 623 (0.14), 576 (0.07), 532 (0.05), 437 (1.00), 384 (0.47). Flu (THF:  $\lambda_{ex} = 436$  nm):  $\lambda_{em} = 678$  nm;  $\Phi_{Flu}$  (THF:  $\lambda_{ex} = 436$  nm) = 20%. <sup>1</sup>H NMR (1% pyridine-*d*<sub>5</sub>-CDCl<sub>3</sub>):  $\delta$ , ppm 9.55 (1H, s, 10-H), 9.50 (1H, s, 5-H), 9.21 (1H, d, *J* = 16 Hz, 3-CH), 8.43 (1H, s, 20-H), 7.32 (1H, d, *J* = 16 Hz, 3<sup>1</sup>-CH), 5.19, 5.07 (each 1H, d, *J* = 19 Hz, 13<sup>1</sup>-CH<sub>2</sub>), 4.39 (1H, dq, *J* = 2, 7 Hz, 18-H), 4.20 (1H, dt, *J* = 8, 2 Hz, 17-H), 3.70 (2H, q, *J* = 8 Hz, 8-CH<sub>2</sub>), 3.68 (3H, s, 12-CH<sub>3</sub>), 3.55 (3H, s, 17<sup>2</sup>-CO<sub>2</sub>CH<sub>3</sub>), 3.49 (3H, s, 2-CH<sub>3</sub>), 3.28 (3H, s, 7-CH<sub>3</sub>), 2.54, 2.25 (each 1H, m, 17-CH<sub>2</sub>), 2.36, 1.93 (each 1H, m, 17<sup>1</sup>-CH<sub>2</sub>), 1.70 (3H, d, *J* = 7 Hz, 18-CH<sub>3</sub>), 1.67 (3H, t, *J* = 8 Hz, 8<sup>1</sup>-CH<sub>3</sub>). MS (APCI): *m/z* found 655, calcd. for C<sub>35</sub>H<sub>35</sub>N<sub>4</sub>O<sub>5</sub>Zn [MH]<sup>+</sup>, 655.

**Methyl *trans*-3<sup>2</sup>-(4-carboxyphenyl)-pyropheophorbide-*a* (9).** To a solution of **8** (55 mg, 0.10 mmol) in THF (20 mL) was added [(4-carboxyphenyl)methyl]-triphenylphosphonium bromide (72 mg, 1.5 mmol), K<sub>2</sub>CO<sub>3</sub> (21 mg, 1.5 mmol), and 18-crown-6 (5 mg, 0.02 mmol). The mixture was refluxed and the reaction was monitored by TLC and UV-vis spectrum. Each mixture of phosphonium bromide (150 mg), K<sub>2</sub>CO<sub>3</sub> (40 mg), and 18-crown-6 (10 mg) was added after 3-, 5-, and 7-h reflux. The reaction mixture was refluxed for 9 h and cooled to room temperature, poured into an aqueous diluted HCl solution, and extracted with CH<sub>2</sub>Cl<sub>2</sub>. The extract was washed with brine and concentrated *in vacuo*. To the residue MeOH (40 mL) was added and the insoluble solid was filtered, washed with Et<sub>2</sub>O (20 mL), and dried *in vacuo* to give chlorin **9** (30 mg, 45%) as a black solid: mp

>300 °C. UV-vis (THF):  $\lambda_{\text{max}}$ , nm 677 (relative intensity, 0.51), 618 (0.08), 543 (0.10), 513 (0.12), 422 (1.00). Flu (THF:  $\lambda_{\text{ex}} = 422$  nm):  $\lambda_{\text{em}} = 684$  nm;  $\Phi_{\text{Flu}}$  (THF:  $\lambda_{\text{ex}} = 422$  nm) = 23%.  $^1\text{H NMR}$  (3% pyridine- $d_5$ - $\text{CDCl}_3$ ):  $\delta$ , ppm 9.48 (1H, s, 10-H), 9.35 (1H, s, 5-H), 8.59 (1H, s, 20-H), 8.34 (1H, d,  $J = 16$  Hz, 3-CH), 8.29, 7.84 (each 2H, d,  $J = 8$  Hz, 3 $^2$ - $\text{C}_6\text{H}_4$ ), 7.56 (1H, d,  $J = 16$  Hz, 3 $^1$ -CH), 5.27, 5.11 (each 1H, d,  $J = 19$  Hz, 13 $^1$ - $\text{CH}_2$ ), 4.50 (1H, dq,  $J = 2, 7$  Hz, 18-H), 4.30 (1H, dt,  $J = 9, 2$  Hz, 17-H), 3.67 (2H, q,  $J = 8$  Hz, 8- $\text{CH}_2$ ), 3.64, 3.62 (each 3H, s, 12- $\text{CH}_3$ , 17 $^2$ - $\text{CO}_2\text{CH}_3$ ), 3.44 (3H, s, 2- $\text{CH}_3$ ), 3.21 (3H, s, 7- $\text{CH}_3$ ), 2.71 (1H, m, 17-CH), 2.59 (1H, m, 17 $^1$ -CH), 2.31 (2H, m, 17-CHCH), 1.83 (3H, d,  $J = 7$  Hz, 18- $\text{CH}_3$ ), 1.69 (3H, t,  $J = 8$  Hz, 8 $^1$ - $\text{CH}_3$ ), 0.42 (1H, br, NH), -1.71 (1H, s, NH). MS (APCI):  $m/z$  found 669, calcd. for  $\text{C}_{41}\text{H}_{41}\text{N}_4\text{O}_5$   $[\text{MH}]^+$ , 669.

**Zinc methyl 3 $^2$ -carboxy-3 $^2$ -cyano-pyropheophorbide-a (Zn-10).** Zinc-metalation of free-base chlorin **10** gave **Zn-10**: mp >300 °C. UV-vis (THF):  $\lambda_{\text{max}}$ , nm 675 (relative intensity, 0.86), 581 (0.18), 441 (1.00), 401 (0.74). Flu (THF:  $\lambda_{\text{ex}} = 441$  nm):  $\lambda_{\text{em}} = 694$  nm;  $\Phi_{\text{Flu}}$  (THF:  $\lambda_{\text{ex}} = 441$  nm) = 11%.  $^1\text{H NMR}$  (3% pyridine- $d_5$ - $\text{CDCl}_3$ ):  $\delta$ , ppm 9.87 (1H, s, 3-CH), 9.54 (1H, s, 10-H), 9.28 (1H, s, 5-H), 8.50 (1H, s, 20-H), 5.20, 5.08 (each 1H, d,  $J = 19$  Hz, 13 $^1$ - $\text{CH}_2$ ), 4.42 (1H, br-q,  $J = 7$  Hz, 18-H), 4.22 (1H, br-d,  $J = 9$  Hz, 17-H), 3.67 (3H, s, 12- $\text{CH}_3$ ), 3.63 (2H, br, 8- $\text{CH}_2$ ), 3.55 (3H, s, 17 $^2$ - $\text{CO}_2\text{CH}_3$ ), 3.50 (3H, s, 2- $\text{CH}_3$ ), 3.22 (3H, s, 7- $\text{CH}_3$ ), 2.57, 2.26 (each 1H, m, 17- $\text{CH}_2$ ), 2.38, 1.95 (each 1H, m, 17 $^1$ - $\text{CH}_2$ ), 1.71 (3H, d,  $J = 7$  Hz, 18- $\text{CH}_3$ ), 1.67 (3H, br-t, 8 $^1$ - $\text{CH}_3$ ). MS (TOF):  $m/z$  found 680, calcd. for  $\text{C}_{36}\text{H}_{34}\text{N}_5\text{O}_5\text{Zn}$   $[\text{MH}]^+$ , 680.

**Methyl 3 $^2$ ,3 $^2$ -dicarboxy-pyropheophorbide-a (11).** To a solution of **8** (110 mg, 0.20 mmol) in pyridine (10 mL) and piperidine (1 mL) was added malonic acid (208 mg, 2.0 mmol), and the mixture was stirred for 2 days at room temperature. The reaction mixture was poured into an aqueous diluted HCl solution and extracted with  $\text{CH}_2\text{Cl}_2$ . The extract was washed with water, dried over anhydrous  $\text{Na}_2\text{SO}_4$ , filtered, and concentrated *in vacuo*. The residue was dissolved in  $\text{CH}_2\text{Cl}_2$  and excess hexane was added to form a precipitate, which was filtered and dried *in vacuo* to give chlorin **11** (123 mg, 97%) as a black solid: mp >300 °C. UV-vis (THF):  $\lambda_{\text{max}}$ , nm 673 (relative intensity, 0.49), 615 (0.08), 539 (0.11), 510 (0.13), 412 (1.00). Flu (THF:  $\lambda_{\text{ex}} = 413$  nm):  $\lambda_{\text{em}} = 682$  nm;  $\Phi_{\text{Flu}}$  (THF:  $\lambda_{\text{ex}} = 413$  nm) = 21%.  $^1\text{H NMR}$  (3% pyridine- $d_5$ - $\text{CDCl}_3$ ):  $\delta$ , ppm 9.39 (1H, s, 10-H), 9.27 (1H, s, 3-CH), 9.24 (1H, s, 5-H), 8.58 (1H, s, 20-H), 5.25, 5.09 (each 1H, d,  $J = 19$  Hz, 13 $^1$ - $\text{CH}_2$ ), 4.46 (1H, dq,  $J = 2, 7$  Hz, 18-H), 4.27 (1H, dt,  $J = 8, 2$  Hz, 17-H), 3.61, 3.58 (each 3H, s, 12- $\text{CH}_3$ , 17 $^2$ - $\text{CO}_2\text{CH}_3$ ), 3.54 (2H, q,  $J = 8$  Hz, 8- $\text{CH}_2$ ), 3.35 (3H, s, 2- $\text{CH}_3$ ), 3.06 (3H, s, 7- $\text{CH}_3$ ), 2.67 (1H, m, 17-CH), 2.55 (1H, m, 17 $^1$ -CH), 2.27 (2H, m, 17-CHCH), 1.78 (3H, d,  $J = 7$  Hz, 18- $\text{CH}_3$ ), 1.58 (3H, t,  $J = 8$  Hz, 8 $^1$ - $\text{CH}_3$ ), 0.20 (1H, br, NH), -1.86 (1H, br-s, NH). MS (TOF):  $m/z$  found 637, calcd. for  $\text{C}_{36}\text{H}_{37}\text{N}_4\text{O}_7$   $[\text{MH}]^+$ , 637.

**Zinc methyl 3 $^2$ ,3 $^2$ -dicarboxy-pyropheophorbide-a (Zn-11).** Zinc-metalation of free-base chlorin **11** gave **Zn-11**: mp >300 °C. UV-vis (THF):  $\lambda_{\text{max}}$ , nm 664 (relative intensity, 0.69), 530 (0.10), 432 (1.00), 384 (0.63). Flu (THF:  $\lambda_{\text{ex}} = 434$  nm):  $\lambda_{\text{em}} = 679$  nm;  $\Phi_{\text{Flu}}$  (THF:  $\lambda_{\text{ex}} = 434$  nm) = 9%.  $^1\text{H NMR}$  (pyridine- $d_5$ , 80 °C):  $\delta$ , ppm 9.97 (1H, br-s, 5-H), 9.80 (1H, s, 10-H), 9.17 (1H, br-s, 3-CH), 8.54 (1H, s, 20-H), 5.35, 5.16 (each 1H, d,  $J = 19$  Hz, 13 $^1$ - $\text{CH}_2$ ), 4.45 (1H, br, 18-H), 4.26 (17-H overlap with  $\text{H}_2\text{O}$ ), 3.78 (3H, s, 12- $\text{CH}_3$ ), 3.65 (2H, br, 8- $\text{CH}_2$ ), 3.53 (3H, s, 17 $^2$ - $\text{CO}_2\text{CH}_3$ ), 3.35 (3H, s, 2- $\text{CH}_3$ ), 3.13 (3H, s, 7- $\text{CH}_3$ ), 2.68, 2.36 (each 1H, br, 17- $\text{CH}_2$ ), 2.56, 2.27 (each 1H, br, 17 $^1$ - $\text{CH}_2$ ), 1.71 (3H, br, 18- $\text{CH}_3$ ), 1.60 (3H, br, 8 $^1$ - $\text{CH}_3$ ). MS (APCI):  $m/z$  found 701, calcd. for  $\text{C}_{36}\text{H}_{35}\text{N}_4\text{O}_7\text{Zn}$   $[\text{MH}]^+$ , 701.

**Methyl trans-3 $^2$ -carboxy-20-(3,5-dimethylphenyl)-pyropheophorbide-a (16).** To a solution of 20-bromochlorin **13** (126 mg, 0.20 mmol) in THF (20 mL) was added 3,5-dimethylphenylboronic acid (450 mg, 3.0 mmol), [1,1'-bis(diphenylphosphino)ferrocene]palladium(II) dichloride ( $\text{PdCl}_2(\text{dppf})$ , 29 mg, 0.04 mmol),  $\text{Cs}_2\text{CO}_3$  (652 mg, 2.0 mmol), and the mixture was refluxed for 24 h. The reaction mixture was poured into an aqueous diluted HCl solution and extracted with  $\text{CH}_2\text{Cl}_2$ . The organic phase was washed with brine and concentrated *in vacuo*. The crude product was purified by FCC ( $\text{MeOH}/\text{CH}_2\text{Cl}_2 = 1:99$ ) followed by GPC to give the corresponding 20-(3,5-dimethylphenyl)-chlorin (75 mg, 57%). To the above 3-hydroxymethyl-20-(3,5-dimethylphenyl)-chlorin (66 mg, 0.10 mmol) in  $\text{CH}_2\text{Cl}_2$  (10 mL) and benzene (10 mL) was added pyridinium dichromate (PDC, 300 mg, 0.80 mmol), and the mixture was stirred for 5 h at room temperature. The reaction mixture was poured into an aqueous diluted HCl solution and extracted with  $\text{CH}_2\text{Cl}_2$ . The organic phase was washed with brine and concentrated *in vacuo*. The crude product was purified by FCC ( $\text{Et}_2\text{O}/\text{CH}_2\text{Cl}_2 = 1:19$ ) to give the corresponding 3-formyl-chlorin (43 mg, 66%). To the above 3-formyl-chlorin (39 mg, 0.060 mmol) in  $\text{CH}_2\text{Cl}_2$  (20 mL) was added (*tert*-butoxycarbonylmethylene)-triphenylphosphorane (75 mg, 0.20 mmol), and the mixture was stirred for 3 h at room temperature. The solution was subjected to FCC ( $\text{Et}_2\text{O}/\text{CH}_2\text{Cl}_2 = 1:19$ ) to give the corresponding 3-[2-(*tert*-butoxycarbonyl)ethenyl]-chlorin (40 mg, 89%). The above *tert*-butyl ester (35 mg, 0.046 mmol) was dissolved in  $\text{CF}_3\text{COOH}$  (5 mL) and the solution was stirred for 30 min at room temperature. The reaction mixture was diluted with water and extracted with  $\text{CH}_2\text{Cl}_2$ , and the organic phase was concentrated *in vacuo*. The residue was dissolved in  $\text{CH}_2\text{Cl}_2$  and excess hexane was added to form a precipitate, which was filtered and dried *in vacuo* to give chlorin **16** (29 mg, 90%) as a black solid: mp >300 °C. UV-vis (THF):  $\lambda_{\text{max}}$ , nm 686 (relative intensity, 0.50), 627 (0.07), 552 (0.14), 521 (0.12), 421 (1.00). Flu (THF:  $\lambda_{\text{ex}} = 421$  nm):  $\lambda_{\text{em}} = 696$  nm;  $\Phi_{\text{Flu}}$  (THF:  $\lambda_{\text{ex}} = 421$  nm) = 22%.  $^1\text{H NMR}$  (3% pyridine- $d_5$ - $\text{CDCl}_3$ ):  $\delta$ , ppm 9.59 (1H, s,

5-H), 9.51 (1H, s, 10-H), 9.03 (1H, d,  $J = 16$  Hz, 3-CH), 7.71, 7.21 (each 1H, s, *o*-H of 20-Ph), 7.31 (1H, s, *p*-H of 20-Ph), 6.95 (1H, d,  $J = 16$  Hz, 3<sup>1</sup>-CH), 5.25, 5.20 (each 1H, d,  $J = 19$  Hz, 13<sup>1</sup>-CH<sub>2</sub>), 4.39 (1H, q,  $J = 7$  Hz, 18-H), 4.111/4.105 (1H, d,  $J = 9$  Hz, 17-H), 3.69 (2H, q,  $J = 8$  Hz, 8-CH<sub>2</sub>), 3.67, 3.55 (each 3H, s, 12-CH<sub>3</sub>, 17<sup>2</sup>-CO<sub>2</sub>CH<sub>3</sub>), 3.45 (3H, s, 2-CH<sub>3</sub>), 3.27 (3H, s, 7-CH<sub>3</sub>), 2.61, 2.47 (each 3H, s, *m*-CH<sub>3</sub> of 20-Ph), 2.49 (3H, s, 2-CH<sub>3</sub>), 2.57, 2.25 (each 1H, m, 17-CH<sub>2</sub>), 2.48, 2.20 (each 1H, m, 17<sup>1</sup>-CH<sub>2</sub>), 1.70 (3H, t,  $J = 8$  Hz, 8<sup>1</sup>-CH<sub>3</sub>), 1.07 (3H, d,  $J = 7$  Hz, 18-CH<sub>3</sub>), -1.58 (1H, s, NH) [another NH was too broad to be observed]. MS (APCI):  $m/z$  found 697, calcd. for C<sub>43</sub>H<sub>45</sub>N<sub>4</sub>O<sub>5</sub> [MH]<sup>+</sup>, 697.

**Methyl *trans*-3<sup>2</sup>-carboxy-20-(2-thienyl)-pyropheophorbide-a (17).** Similar to the synthesis of **16**, reaction of **13** (126 mg, 0.20 mmol) with 2-thiophenboronic acid (256 mg, 2.0 mmol) in THF (40 mL) in the presence of PdCl<sub>2</sub>(dppf) (29 mg, 0.04 mmol) and Cs<sub>2</sub>CO<sub>3</sub> (652 mg, 2.0 mmol) gave 20-thienyl-chlorin (85 mg, 67%) after preparative TLC (acetone/dichloroethane = 3:17). Oxidation of the 3-hydroxymethyl group of the product (80 mg, 0.13 mmol) with PDC (350 mg, 0.93 mmol) in CH<sub>2</sub>Cl<sub>2</sub> (15 mL) and benzene (15 mL) gave the corresponding 3-formyl-chlorin (55 mg, 69%) after FCC (Et<sub>2</sub>O/CH<sub>2</sub>Cl<sub>2</sub> = 1:19) followed by preparative TLC (acetone/benzene = 1:9). Wittig reaction of the chlorin (50 mg, 0.079 mmol) with (*tert*-butoxycarbonylmethylene)triphenylphosphorane (90 mg, 0.24 mmol) in CH<sub>2</sub>Cl<sub>2</sub> gave the adduct (48 mg, 83%) after FCC (Et<sub>2</sub>O/CH<sub>2</sub>Cl<sub>2</sub> = 1:19). Cleavage of the *tert*-butyl ester (45 mg, 0.062 mmol) in CF<sub>3</sub>COOH gave **17** (40 mg, 95%) as a black solid: mp >300 °C. UV-vis (THF): λ<sub>max</sub>, nm 687 (relative intensity, 52), 627 (0.07), 552 (0.14), 520 (0.11), 420 (1.00). Flu (THF: λ<sub>ex</sub> = 420 nm): λ<sub>em</sub> = 698 nm; Φ<sub>Flu</sub> (THF: λ<sub>ex</sub> = 420 nm) = 17%. <sup>1</sup>H NMR (3% pyridine-*d*<sub>5</sub>-CDCl<sub>3</sub>): δ, ppm 9.564/9.557 (1H, s, 5-H), 9.48/9.47 (1H, s, 10-H), 9.02/9.00 (1H, d,  $J = 16$  Hz, 3-CH), 7.73–7.34 (3H, m, α, β, β-H of 20-α-thienyl), 6.97/6.94 (1H, d,  $J = 16$  Hz, 3<sup>1</sup>-CH), 5.21, 5.20 (each 1H, d,  $J = 19$  Hz, 13<sup>1</sup>-CH<sub>2</sub>), 4.62/4.51 (1H, q,  $J = 7$  Hz, 18-H), 4.12 (1H, m, 17-H), 3.67 (2H, q,  $J = 8$  Hz, 8-CH<sub>2</sub>), 3.65/3.64, 3.55/3.54, 2.69/2.67 (each 3H, s, 2-CH<sub>3</sub>, 12-CH<sub>3</sub>, 17<sup>2</sup>-CO<sub>2</sub>CH<sub>3</sub>), 3.23 (3H, s, 7-CH<sub>3</sub>), 2.59, 2.22 (each 1H, m, 17-CH<sub>2</sub>), 2.47, 2.15 (each 1H, m, 17<sup>1</sup>-CH<sub>2</sub>), 1.68 (3H, t,  $J = 8$  Hz, 8<sup>1</sup>-CH<sub>3</sub>), 1.20/1.16 (3H, d,  $J = 7$  Hz, 18-CH<sub>3</sub>), -1.41 (1H, s, NH) [another NH was too broad to be observed]. MS (APCI):  $m/z$  found 675, calcd. for C<sub>39</sub>H<sub>39</sub>N<sub>4</sub>O<sub>5</sub>S [MH]<sup>+</sup>, 675.

**Methyl *trans*-3<sup>2</sup>-carboxy-20-bromo-pyropheophorbide-a (18).** Methyl 20-bromo-pyropheophorbide-*d* was prepared by oxidation of the 3-hydroxymethyl group of **13** similar to the synthesis of **14**. Wittig reaction of the 3-formyl-chlorin (63 mg, 0.10 mmol) with (*tert*-butoxycarbonylmethylene)triphenylphosphorane (56 mg, 0.15 mmol) in refluxing toluene gave the product (70 mg, 96%) after FCC (Et<sub>2</sub>O/CH<sub>2</sub>Cl<sub>2</sub> = 1:19). Cleavage of the *tert*-butyl ester (51 mg, 0.070 mmol) in CF<sub>3</sub>COOH gave

**17** (44 mg, 94%) as a black solid: mp >300 °C. UV-vis (THF): λ<sub>max</sub>, nm 685 (relative intensity, 0.48), 626 (0.05), 553 (0.15), 521 (0.10), 417 (1.00). Flu (THF: λ<sub>ex</sub> = 418 nm): λ<sub>em</sub> = 692 nm; Φ<sub>Flu</sub> (THF: λ<sub>ex</sub> = 418 nm) = 2%. <sup>1</sup>H NMR (10% pyridine-*d*<sub>5</sub>-CDCl<sub>3</sub>): δ, ppm 9.36 (1H, s, 5-H), 9.32 (1H, s, 10-H), 8.84 (1H, d,  $J = 16$  Hz, 3-CH), 6.81 (1H, d,  $J = 16$  Hz, 3<sup>1</sup>-CH), 5.10 (2H, s, 13<sup>1</sup>-CH<sub>2</sub>), 4.74 (1H, q,  $J = 7$  Hz, 18-H), 4.12 (1H, d,  $J = 9$  Hz, 17-H), 3.48 (3H, s, 12-CH<sub>3</sub>), 3.46 (3H, s, 2-CH<sub>3</sub>), 3.43 (3H, s, 17<sup>2</sup>-CO<sub>2</sub>CH<sub>3</sub>), 3.44 (2H, 8-CH<sub>2</sub> overlapped with 17<sup>2</sup>-CO<sub>2</sub>CH<sub>3</sub>), 3.01 (3H, s, 7-CH<sub>3</sub>), 2.48, 2.11 (each 1H, m, 17-CH<sub>2</sub>), 2.36, 2.01 (each 1H, m, 17<sup>1</sup>-CH<sub>2</sub>), 1.50 (3H, t,  $J = 8$  Hz, 8<sup>1</sup>-CH<sub>3</sub>), 1.46 (3H, d,  $J = 7$  Hz, 18-CH<sub>3</sub>), 0.66 (1H, br, NH), -2.10 (1H, s, NH). MS (APCI):  $m/z$  found 671, calcd. for C<sub>35</sub>H<sub>36</sub>BrN<sub>4</sub>O<sub>5</sub> [MH]<sup>+</sup>, 671.

**Methyl *trans*-3<sup>2</sup>-carboxy-13<sup>1</sup>-deoxo-13<sup>1</sup>-(dicyanomethylene)pyropheophorbide-a (19).** A mixture of chlorin **12** (130 mg, 0.20 mmol), malononitrile (660 mg, 10 mmol), and Et<sub>3</sub>N (607 mg, 6.0 mmol) in THF (25 mL) was refluxed for 6 h. The solution was cooled to room temperature, poured into an aqueous 1% HCl solution, and extracted with CH<sub>2</sub>Cl<sub>2</sub>. The extract was washed with brine, dried over anhydrous Na<sub>2</sub>SO<sub>4</sub>, filtered, and concentrated. The crude product was purified by FCC (Et<sub>2</sub>O/CH<sub>2</sub>Cl<sub>2</sub> = 1:49) followed by recrystallization from CH<sub>2</sub>Cl<sub>2</sub>/hexane to give the corresponding 13<sup>1</sup>-dicyanomethylene-chlorin (105 mg, 76%). Cleavage of the *tert*-butyl ester (80 mg, 0.11 mmol) in CF<sub>3</sub>COOH gave **19** (62 mg, 89%) as a green solid: mp > 300 °C. UV-vis (THF): λ<sub>max</sub>, nm 714 (relative intensity, 1.00), 651 (0.23), 574 (0.17), 536 (0.12), 455 (0.83), 430 (0.87), 391 (0.85). Flu (THF: λ<sub>ex</sub> = 429 nm): λ<sub>em</sub> = 724 nm; Φ<sub>Flu</sub> (THF: λ<sub>ex</sub> = 429 nm) = 23%. <sup>1</sup>H NMR (10% pyridine-*d*<sub>5</sub>-CDCl<sub>3</sub>): δ, ppm 9.01 (1H, s, 10-H), 8.99 (1H, s, 5-H), 8.75 (1H, d,  $J = 16$  Hz, 3-CH), 8.37 (1H, s, 20-H), 6.84 (1H, d,  $J = 16$  Hz, 3<sup>1</sup>-CH), 5.41, 5.27 (each 1H, d,  $J = 20$  Hz, 13<sup>1</sup>-CH<sub>2</sub>), 4.31 (1H, q,  $J = 7$  Hz, 18-H), 4.09 (1H, d,  $J = 9$  Hz, 17-H), 3.55 (3H, s, 17<sup>2</sup>-CO<sub>2</sub>CH<sub>3</sub>), 3.40 (3H, s, 12-CH<sub>3</sub>), 3.40 (2H, 8-CH<sub>2</sub> overlapped with 12-CH<sub>3</sub>), 3.22 (3H, s, 2-CH<sub>3</sub>), 2.95 (3H, s, 7-CH<sub>3</sub>), 2.51 (2H, m, 17-CHCH), 2.23, 2.08 (each 1H, m, 17-CHCH), 1.72 (3H, d,  $J = 7$  Hz, 18-CH<sub>3</sub>), 1.50 (3H, t,  $J = 8$  Hz, 8<sup>1</sup>-CH<sub>3</sub>), 0.75, -1.34 (each 1H, s, NH×2). MS (TOF):  $m/z$  found 641, calcd. for C<sub>38</sub>H<sub>37</sub>N<sub>6</sub>O<sub>4</sub> [MH]<sup>+</sup>, 641.

**Zinc methyl *trans*-3<sup>2</sup>-carboxy-13<sup>1</sup>-deoxo-13<sup>1</sup>-(dicyanomethylene)pyropheophorbide-a (Zn-19).** Zinc-metalation of free-base chlorin **19** gave **Zn-19**: mp >300 °C. UV-vis (THF): λ<sub>max</sub>, nm 715 (relative intensity, 1.00), 659 (0.30), 464 (0.70), 441 (0.65), 394 (0.70). Flu (THF: λ<sub>ex</sub> = 441 nm): λ<sub>em</sub> = 726 nm; Φ<sub>Flu</sub> (THF: λ<sub>ex</sub> = 441 nm) = 15%. <sup>1</sup>H NMR (3% pyridine-*d*<sub>5</sub>-CDCl<sub>3</sub>): δ, ppm 9.36 (1H, s, 10-H), 9.22 (1H, s, 5-H), 9.04 (1H, d,  $J = 16$  Hz, 3-CH), 8.24 (1H, s, 20-H), 7.23 (1H, d,  $J = 16$  Hz, 3<sup>1</sup>-CH), 5.64, 5.51 (each 1H, d,  $J = 20$  Hz, 13<sup>1</sup>-CH<sub>2</sub>), 4.29 (1H, q,  $J = 7$  Hz, 18-H), 4.09 (1H, d,  $J = 9$  Hz, 17-H), 3.83 (3H, s, 12-CH<sub>3</sub>), 3.62 (2H, q,  $J = 8$  Hz, 8-CH<sub>2</sub>), 3.58 (3H, s, 17<sup>2</sup>-CO<sub>2</sub>CH<sub>3</sub>), 3.39 (3H, s, 2-CH<sub>3</sub>), 3.17 (3H, s, 7-CH<sub>3</sub>), 2.50, 2.18 (each 1H, m, 17-CH<sub>2</sub>), 2.40, 1.98 (each 1H, m,

17<sup>1</sup>-CH<sub>2</sub>), 1.66 (3H, d, *J* = 7 Hz, 18-CH<sub>3</sub>), 1.63 (3H, t, *J* = 8 Hz, 8<sup>1</sup>-CH<sub>3</sub>). MS (APCI): *m/z* found 703, calcd. for C<sub>38</sub>H<sub>35</sub>N<sub>6</sub>O<sub>4</sub>Zn [MH]<sup>+</sup>, 703.

**Methyl *trans*-3<sup>1</sup>-carboxy-13<sup>1</sup>-deoxy-pyropheophorbide-a (21).** Similar to the synthesis of **16**, Wittig reaction of **20** (54 mg, 0.10 mmol) with (*tert*-butoxy-carbonylmethylene)triphenylphosphorane (188 mg, 0.50 mmol) in refluxing toluene gave the adduct (60 mg, 95%) after FCC (Et<sub>2</sub>O/CH<sub>2</sub>Cl<sub>2</sub> = 1:19). Cleavage of the *tert*-butyl ester (51 mg, 0.080 mmol) in CF<sub>3</sub>COOH gave **21** (43 mg, 93%) as a black solid: mp >300 °C. UV-vis (THF): λ<sub>max</sub>, nm 661 (relative intensity, 0.40), 605 (0.04), 541 (0.05), 508 (0.12), 416 (1.00). Flu (THF: λ<sub>ex</sub> = 417 nm): λ<sub>em</sub> = 664 nm; Φ<sub>Flu</sub> (THF: λ<sub>ex</sub> = 417 nm) = 18%. <sup>1</sup>H NMR (3% pyridine-*d*<sub>5</sub>-CDCl<sub>3</sub>): δ, ppm 10.01 (1H, s, 5-H), 9.52 (1H, s, 10-H), 9.47 (1H, d, *J* = 16 Hz, 3-CH), 8.98 (1H, s, 20-H), 7.23 (1H, d, *J* = 16 Hz, 3<sup>1</sup>-CH), 4.91, 4.79 (each 1H, m, 13<sup>1</sup>-CH<sub>2</sub>), 4.64 (1H, q, *J* = 7 Hz, 18-H), 4.46 (1H, d, *J* = 9 Hz, 17-H), 4.06 (2H, m, 13-CH<sub>2</sub>), 3.83 (2H, q, *J* = 8 Hz, 8-CH<sub>2</sub>), 3.68 (3H, s, 2-CH<sub>3</sub>), 3.56 (3H, s, 17<sup>2</sup>-CO<sub>2</sub>CH<sub>3</sub>), 3.47 (3H, s, 12-CH<sub>3</sub>), 3.44 (3H, s, 7-CH<sub>3</sub>), 2.78, 2.33 (each 1H, m, 17-CH<sub>2</sub>), 2.60, 2.21 (each 1H, m, 17<sup>1</sup>-CH<sub>2</sub>), 1.84 (3H, d, *J* = 7 Hz, 18-CH<sub>3</sub>), 1.75 (3H, t, *J* = 8 Hz, 8<sup>1</sup>-CH<sub>3</sub>), -1.50 (1H, br, NH), -3.10 (1H, s, NH). MS (TOF): *m/z* found 578, calcd. for C<sub>35</sub>H<sub>38</sub>N<sub>4</sub>O<sub>4</sub> [M]<sup>+</sup>, 578.

## CONCLUSION

In conclusion, a series of carboxylated chlorins were synthesized and their applications as components in DSSCs as well as sensing reagents were investigated. The detection of additional amine in THF was demonstrated by both visible absorption and fluorescence emission spectroscopies in the near-infrared region (>650 nm), which would be an advantageous point for analysis of bio-related materials. On the other hand, the photovoltaic performance of DSSCs was evaluated using chlorin-adsorbed TiO<sub>2</sub> films. Although the newly developed chlorins did not improve the energy-to-electron conversion efficiency, the obtained data are useful for the molecular design of dye-sensitizers with a higher performance.

## Acknowledgements

This work was partially supported by Grants-in-Aid for Scientific Research (A) (No. 2245030 to H.T) and (C) (No. 25410152 to S.S), and for Young Scientists (A) (23686138 to X.-F.W) as well as for Scientific Research on Innovation Areas, “Artificial Photosynthesis” (No. 24107002 to H.T) from the Japan Society for the Promotion of Science (JSPS).

## Supporting information

Spectral characteristics of **3–7** and **9** (Table S1) as well as <sup>1</sup>H NMR spectra of newly synthesized chlorins (Figs S1–S11), IPCE profiles and *I–V* curves of DSSCs based on **16–18** and **Zn-6/10/11/19** (Figs S12 and S13),

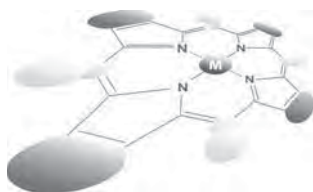
and electronic absorption and fluorescence emission spectra of chlorins listed in Tables 1 and 2 (Figs S14–S30) are given in the supplementary material. This material is available free of charge via the Internet at <http://www.worldscinet.com/jpp/jpp.shtml>.

## REFERENCES

- (a) Chen M and Scheer H. *J. Porphyrins Phthalocyanines* 2013; **17**: 1–15. (b) Orf GS and Blankenship RE. *Photosynth. Res.* 2013; **116**: 315–331. (c) König C and Neugebauer J. *ChemPhysChem.* 2012; **13**: 386–425.
- (a) Kawashima Y, Ohkubo K, Mase K and Fukuzumi S. *J. Phys. Chem. C* 2013; **117**: 21166–21177. (b) Mase K, Ohkubo K and Fukuzumi S. *J. Am. Chem. Soc.* 2013; **135**: 2800–2808.
- (a) Gunderson VL and Wasielewski MR. *Chem. Phys. Lett.* 2013; **556**: 303–307. (b) Gunderson VL, Smeigh AL, Kim CH, Co DT and Wasielewski MR. *J. Am. Chem. Soc.* 2012; **134**: 4363–4372. (c) Gunderson VL and Wasielewski MR. *Handbook of Porphyrin Science*, Vol. 20, Kadish KM, Smith KM and Guillard R. (Eds.) World Scientific: Singapore, 2012; pp 45–105.
- Balaban TS. *Handbook of Porphyrin Science*, Vol. 1, Kadish KM, Smith KM and Guillard R. (Eds.) World Scientific: Singapore, 2010; pp 221–306.
- Sengupta S and Würthner F. *Acc. Chem. Res.* 2013; **46**: 2498–2512.
- Miyatake T and Tamiaki H. *Coord. Chem. Rev.* 2010; **254**: 2593–2602.
- (a) Srivatsan A, Wang Y, Joshi P, Sajjad M, Chen Y, Liu C, Thankppan K, Missert JR, Tracy E, Morgan J, Rigual N, Baumann H and Pandey RK. *J. Med. Chem.* 2011; **54**: 6859–6873. (b) Joshi P, Ethirajan M, Goswami LN, Srivatsan A, Missert JR and Pandey RK. *J. Org. Chem.* 2011; **76**: 8629–8640.
- (a) Sasaki S, Kotegawa Y and Tamiaki H. *Tetrahedron Lett.* 2006; **47**: 4849–4852. (b) Sasaki S, Kotegawa Y and Tamiaki H. *Bull. Chem. Soc. Jpn.* 2009; **82**: 267–271. (c) Sasaki S, Kotegawa Y, Azuma K, Kunieda M and Tamiaki H. *Chem. Lett.* 2009; **38**: 796–797. (d) Takano K, Sasaki S, Citterio D, Tamiaki H and Suzuki K. *Analyst* 2010; **135**: 2334–2339. (e) Tamiaki H, Azuma K, Kinoshita Y, Monobe R, Miyatake T and Sasaki S. *Tetrahedron* 2013; **69**: 1987–1993.
- Sasaki S, Mizutani K, Kunieda M, Azuma K and Tamiaki H. *Chem. Lett.* 2013; **42**: 1212–1213.
- (a) Wang XF, Xiang J, Wang P, Koyama Y, Yanagida S, Wada Y, Hamada K, Sasaki S and Tamiaki H. *Chem. Phys. Lett.* 2005; **408**: 409–414. (b) Wang XF, Kakitani Y, Xiang J, Koyama Y, Rondonuwu FS, Nagae H, Sasaki S and Tamiaki H. *Chem. Phys. Lett.* 2005; **416**: 229–233. (c) Wang XF, Matsuda A,

- Koyama Y, Nagae H, Sasaki S, Tamiaki H and Wada Y. *Chem. Phys. Lett.* 2006; **423**: 470–475. (d) Wang XF, Koyama Y, Nagae H, Wada Y, Sasaki S and Tamiaki H. *J. Phys. Chem. C* 2008; **112**: 4418–4426. (e) Wang XF, Kitao O, Zhou H, Tamiaki H and Sasaki S. *Chem. Commun.* 2009; 1523–1525. (f) Wang XF and Tamiaki H. *Energy Environ. Sci.* 2010; **3**: 94–106.
11. (a) Tamiaki H and Kouraba M. *Tetrahedron* 1997; **53**: 10677–10688. (b) Sasaki S and Tamiaki H. *J. Org. Chem.* 2006; **71**: 2648–2654. (c) Tamiaki H and Kunieda M. *Handbook of Porphyrin Science*, Vol. 11, Kadish KM, Smith KM and Guillard R. (Eds.) World Scientific: Singapore, 2011; pp 223–290. (d) Tamiaki H, Ohata M, Kinoshita Y and Machida S. *Tetrahedron* 2014; **70**: 1629–1634. (e) Yamamoto Y and Tamiaki H. *Tetrahedron* 2014; **70**: 2731–2737.
  12. Tamiaki H, Amakawa M, Shimono Y, Tanikaga R, Holzwarth AR and Schaffner K. *Photochem. Photobiol.* 1996; **63**: 92–99.
  13. Porcal W, Hernández P, Aguirre G, Boiani L, Boiani M, Merlino A, Ferreira A, Maio RD, Castro A, González M and Cerecetto H. *Bioorg. Med. Chem.* 2007; **15**: 2768–2781.
  14. Wang XF, Koyama Y, Wada Y, Sasaki S and Tamiaki H. *Chem. Phys. Lett.* 2007; **439**: 115–120.
  15. Tamiaki H, Matsunaga S, Taira Y, Wada A, Kinoshita Y and Kunieda M. *Tetrahedron Lett.* 2014; **55**: 3351–3354.
  16. (a) Sasaki S, Yoshizato M, Kunieda M and Tamiaki H. *Eur. J. Org. Chem.* 2010; 5287–5291. (b) Tamiaki H, Kuno M and Ohata M. *Photochem. Photobiol.* 2014; **90**: 1277–1286.
  17. Wiederrecht GP, Svec WA, Niemczyk MP and Wasielewski MR. *J. Phys. Chem.* 1995; **99**: 8918–8926.
  18. Tamiaki H, Yagai S and Miyatake T. *Bioorg. Med. Chem.* 1998; **6**: 2171–2178.
  19. DeTar DF and Novak RW. *J. Am. Chem. Soc.* 1970; **92**: 1361–1365.
  20. (a) Wang XF, Kitao O, Zhou H, Tamiaki H and Sasaki S. *J. Phys. Chem. C* 2009; **113**: 7954–7961. (b) Wang XF, Wang L, Tamai N, Kitao O, Tamiaki H and Sasaki S. *J. Phys. Chem. C* 2011; **115**: 24394–24402. (c) Wang XF, Tamiaki H, Kitao O, Ikeuchi T and Sasaki S. *J. Power Sources* 2013; **242**: 860–864.
  21. Rotation of the aromatic ring at the C20-position is restricted due to the steric effect of C2- and C18-methyl groups, and <sup>1</sup>H NMR signals of the C20-benzene ring in **16** is distinguished as the upper and lower sides of the chlorin  $\pi$ -plane. Similarly, chlorin **17** possessing the C20-thiophene ring showed two sets of signals for several protons of the chlorin macrocycle. Such a steric repulsion between C20- and C2-position is expected to suspend the coplanar conformation of the C3-double bond with the chlorin ring; see Tamiaki H, Kotegawa Y and Mizutani K. *Bioorg. Med. Chem.* 2008; **18**: 6037–6040.





## Electroabsorption spectra of push–pull porphyrins in solution and in solid films

Kamlesh Awasthi<sup>a</sup>, Hung-Yu Hsu<sup>b</sup>, Hung-Chu Chiang<sup>a</sup>, Chi-Lun Mai<sup>c</sup>,  
Chen-Yu Yeh<sup>\*c</sup>, Eric Wei-Guang Diau<sup>\*b</sup> and Nobuhiro Ohta<sup>\*a<sup>◇</sup></sup>

<sup>a</sup> Research Institute for Electronic Science, Hokkaido University, Sapporo 001-0020, Japan

<sup>b</sup> Department of Applied Chemistry and Institute of Molecular Science, National Chiao Tung University, Hsinchu 30010, Taiwan

<sup>c</sup> Department of Chemistry and Center of Nanoscience & Nanotechnology, National Chung Hsing University, Taichung 402, Taiwan

*Dedicated to Professor Shunichi Fukuzumi on the occasion of his retirement*

Received 30 October 2014

Accepted 8 January 2015

**ABSTRACT:** Polarized electroabsorption (E-A) spectra of highly efficient porphyrin sensitizers (YD2 and YD2-oC8) have been measured in benzene solution. Polarized E-A spectra of these push–pull porphyrins embedded in poly(methyl methacrylate) films or sensitized on TiO<sub>2</sub> films are also observed. Based on the analysis of the E-A spectra, the magnitude of the electric dipole moment both in the ground state and in the lowest excited state have been evaluated in solution and in solid films. The electric dipole moment in the excited state of these compounds is very large on TiO<sub>2</sub> films, suggesting the interfacial charge transfer on TiO<sub>2</sub> surface following photoexcitation of porphyrin dyes. The electric dipole moment in the excited state evaluated from the E-A spectra is very different from the one evaluated from the electrophotoluminescence spectra on TiO<sub>2</sub>, suggesting that the strong local field of TiO<sub>2</sub> films is applied to the fluorescing dyes attached to TiO<sub>2</sub> films.

**KEYWORDS:** Stark shift, electric dipole moment, dye-sensitized solar cell, push–pull porphyrins.

## INTRODUCTION

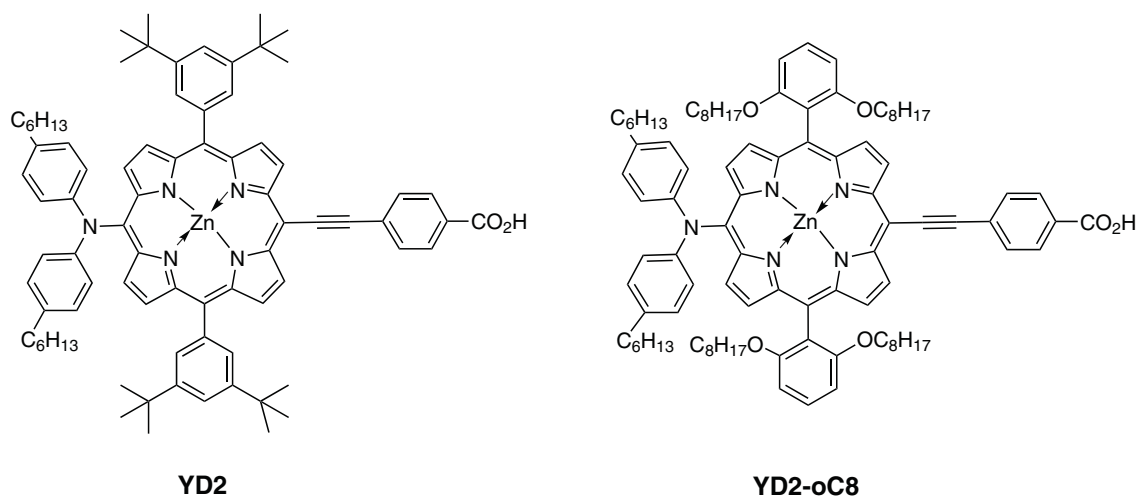
Electric dipole moment, whose value reflects the molecular structure as well as electronic structure in each electronic state, is important not only as the fundamental physical parameter of molecules and molecular aggregates but also as the parameter which decides material functions such as nonlinear optical property or Kerr effect [1, 2]. In optoelectronic devices such as solar cell, charge separated character, that is, the magnitude of the electric dipole moment following photoexcitation is important because the primary process of dye-sensitized solar cell (DSSC) following photoirradiation is charge separation

in dye molecules. This kind information can be obtained from the measurements of electroabsorption spectra and electrophotoluminescence spectra [3–6], where plots of the field-induced change in absorption intensity and photoluminescence intensity are shown, respectively, as a function of wavelength or wavenumber. The effects of local electric fields on the optical properties, which may play an important role on DSSC [7–9], can be also obtained from the measurements of electroabsorption and electrophotoluminescence spectra. Hereafter, electroabsorption and electrophotoluminescence spectra are abbreviated to be E-A and E-PL spectra, respectively.

Porphyrins have a significant potential as sensitizers for highly efficient DSSC, owing to their photostability and high light-harvesting capabilities [10, 11]. In our previous paper [12], electric field effects on photoluminescence spectra, *i.e.* E-PL spectra, were reported for push–pull porphyrins YD2 and YD2-oC8, which give highly

<sup>◇</sup> SPP full member in good standing

\*Correspondence to: Nobuhiro Ohta, email: nohta@es.hokudai.ac.jp; Eric Wei-Guang Diau, email: diau@mail.nctu.edu.tw; Chen-Yu Yeh, email: cyeh@dragon.nchu.edu.tw



**Fig. 1.** Molecular structure of YD2 and YD2-oC8

efficient photon energy conversion [13]. The molecular structures of these compounds are shown in Fig. 1. The dye-sensitized solar cell made of YD2-oC8 in a cobalt electrolyte attained efficiency more than 12% of power conversion [14]. Fluorescence of YD2 and YD2-oC8 is quenched in poly(methyl methacrylate) (PMMA) films by application of electric field, suggesting that the relaxation from the fluorescent state to a nonfluorescent charge-separated state is accelerated by electric field. The field-induced quenching becomes extremely large, when sensitized dyes are attached to TiO<sub>2</sub> films. Then, it was suggested that the electric field-induced quenching of fluorescence, which probably results from the field-induced charge separation to the nonfluorescent state, is related to the efficiency of the photon energy conversion in solar cells. It was also shown that the magnitude of the change in electric dipole moment following the fluorescence emission, which was evaluated from the E-PL spectra, is much larger in dyes attached to TiO<sub>2</sub> than that in dyes embedded in a PMMA film, suggesting that the charge-separated character of porphyrins is much larger on TiO<sub>2</sub> films than that in PMMA films. This observation further implies that the interfacial charge transfer occurs from the dyes to the TiO<sub>2</sub> surface as a result of the strong coupling between dyes and TiO<sub>2</sub> film.

The difference in electric dipole moment between the excited state and the ground state evaluated from the E-PL spectra was reported [12]. Hereafter, electric dipole moment and its change following optical transition are denoted by  $\mu$  and  $\Delta\mu$ , respectively. E-PL spectra give the value of  $\Delta\mu$  ( $= |\Delta\mu|$ ) between the fluorescent relaxed state and the ground state, while E-A spectra give the  $\Delta\mu$  value between the ground state and the photoexcited Franck-Condon state. Therefore, it seems to be very important to know whether the value of  $\Delta\mu$  evaluated from the E-PL spectra is different from the one evaluated from the E-A spectra. If the exact value of  $\mu$  ( $= |\mu|$ ) can be obtained in each electronic state, further, a comparison among

different dyes can be made concerning the relation between the electric dipole moment and the solar energy conversion efficiency.

In the presence of electric fields, molecular reorientation occurs along the applied electric field, depending on the magnitude of  $\mu$  of molecules. Then, the  $\mu$  value both in the ground state and in the excited state can be obtained from the polarized E-A spectra in solution [15, 16]. In the present study, polarized E-A spectra of YD2 and YD2-oC8 have been measured in benzene solution. By evaluating the change in intensity of the E-A spectra resulting from the field-induced reorientation, the value of  $\mu$  in the ground state of each molecule has been determined. The magnitude of  $\Delta\mu$  following excitation into the lowest excited state of these compounds embedded in PMMA film or attached on TiO<sub>2</sub> films has been also evaluated, based on the measurements of the E-A spectra. By combining both results in solution and in solid films, the magnitudes of  $\mu$  both in the ground state, *i.e.*  $\mu_g$ , and in the lowest excited state, *i.e.*  $\mu_e$ , have been evaluated. These magnitudes of  $\mu$  of different porphyrin dyes obtained in PMMA and on TiO<sub>2</sub> films have been compared with each other to examine the role of the TiO<sub>2</sub> surface which plays in DSSC. The results of the E-A spectra are also compared with the ones obtained from the E-PL spectra reported in our previous paper [12].

## THEORETICAL BACKGROUND

Energy levels and transition dipole moments of a molecule are influenced by an electric field. In the presence of an applied electric field ( $F$ ), the shift of the transition energy ( $\Delta E$ ) is related to the difference in dipole moment ( $\Delta\mu$ ) and molecular polarizability ( $\Delta\alpha$ ) between the excited state and the ground state.

$$\Delta E = -\Delta\mu \cdot F - F \cdot \Delta\alpha \cdot F/2 \quad (1)$$

As a result, optical spectra show a shift or/and a broadening upon the application of  $F$ . By assuming an isotropic distribution of the molecules in the absence of  $F$ , the intensity of the E-A spectrum at wavenumber  $\bar{\nu}$ , *i.e.*  $\Delta A(\bar{\nu})$  can be expressed as the sum of the zeroth, first and second derivatives of the absorption spectrum as follows [23]:

$$\Delta A(\bar{\nu}) = (fF)^2 \left[ A_\chi A(\bar{\nu}) + B_\chi \bar{\nu} \frac{d}{d\bar{\nu}} \left\{ \frac{A(\bar{\nu})}{\bar{\nu}} \right\} + C_\chi \bar{\nu} \frac{d^2}{d\bar{\nu}^2} \left\{ \frac{A(\bar{\nu})}{\bar{\nu}} \right\} \right] \quad (2)$$

where  $A_\chi$ ,  $B_\chi$  and  $C_\chi$  are coefficients. Note that  $\chi$  represents the angle between the field direction and the polarization direction of the excitation light. If the field-induced change in transition moment is negligible, each coefficient can be expressed as follows [17]:

$$A_\chi = \frac{(3 \cos^2 \chi - 1)}{30k^2 T^2} \left[ \mu_g^2 (3 \cos^2 \zeta - 1) + 3kT(\alpha_m - \bar{\alpha}) \right] \quad (3)$$

$$B_\chi = \frac{\Delta \bar{\alpha}}{2hc} + \frac{\mu_g \Delta \mu \cos \gamma}{3hckT} + \frac{(3 \cos^2 \chi - 1)}{15hc} \left\{ \frac{\mu_g \Delta \mu (3 \cos \zeta \cos \eta - \cos \gamma)}{kT} + \frac{3(\Delta \alpha_m - \Delta \bar{\alpha})}{2} \right\} \quad (4)$$

$$C_\chi = |\Delta \mu|^2 \left\{ \frac{5 + (3 \cos^2 \chi - 1)(3 \cos^2 \eta - 1)}{30h^2 c^2} \right\} \quad (5)$$

where  $c$  is the velocity of light,  $k$  is Boltzmann's constant,  $h$  is Planck's constant,  $T$  is temperature,  $\mu_g$  and  $\Delta \mu$  are the magnitudes of the ground state dipole moment and the change in electric dipole moment following photoexcitation, respectively.  $\alpha_m$  is the polarizability in the ground state with respect to the direction of the transition dipole moment.  $\bar{\alpha}$  represents the average of the trace of the polarizability tensor.  $\zeta$  is the angle between  $\mu$  and the transition dipole moment ( $d$ ).  $\gamma$  is the angle between  $\mu_g$  and  $\Delta \mu$ .  $\eta$  is the angle between  $\Delta \mu$  and  $d$ . Then, the derivative components of the E-A spectra observed with  $\chi = 54.7^\circ$  can be written as follows:

$$A_{54.7} = 0 \quad (6)$$

$$B_{54.7} = \frac{\Delta \bar{\alpha}}{2hc} + \frac{\mu \Delta \mu \cos \gamma}{3hckT} \quad (7)$$

$$C_{54.7} = \frac{|\Delta \mu|^2}{6h^2 c^2} \quad (8)$$

A comparison between Equations 3 and 6 shows that the magnitude of  $\mu_g$  can be evaluated from the difference between the E-A spectra obtained with  $\chi = 90^\circ$  and  $54.7^\circ$ . It is also noted that the temperature dependent term can be neglected even in the presence of  $F$ , if the molecules

are fixed. In the above discussion, the transition moment is assumed to be independent of the applied electric field. If the transition dipole moment itself is affected by  $F$ , the transition moment in the presence of  $F$ ,  $d^F$ , can be written as:

$$d^F = d + X \cdot F + F \cdot Y \cdot F \quad (9)$$

where  $d$  is the transition dipole moment vector in the absence of  $F$ , and  $X$  and  $Y$  are the transition moment polarizability and hyperpolarizability tensors, respectively. In randomly distributed system, the coefficients of the zeroth and first derivative components of the E-A spectra observed with a magic angle of  $\chi$  which results from  $X$  and  $Y$  can be given using the tensor components of  $X$  and  $Y$  as follows [18]:

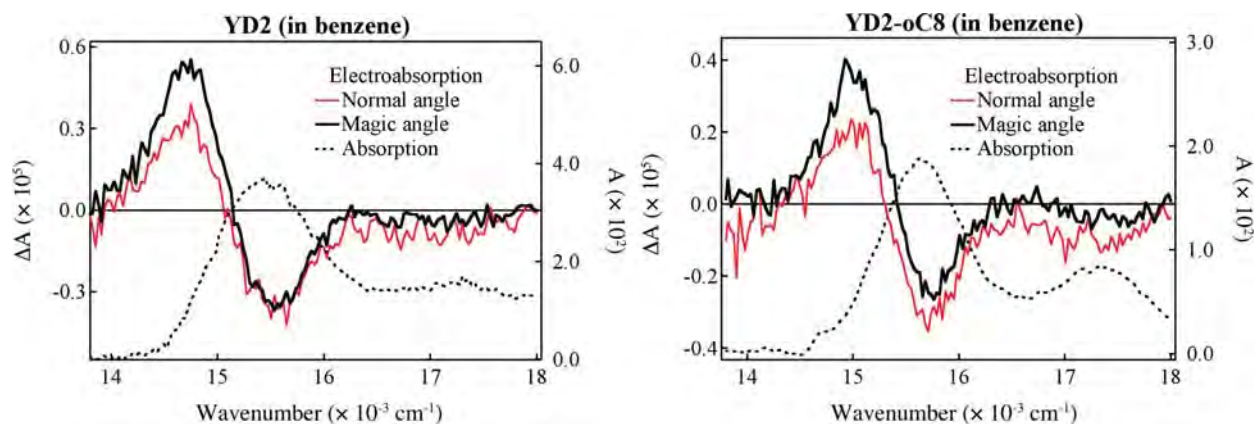
$$A_{54.7} = \frac{1}{3|d|^2} \sum_{i,j} X_{ij}^2 + \frac{2}{3|d|^2} \sum_{i,j} d_i Y_{ij}^2 \quad (10)$$

$$B_{54.7} = \sum_{i,j} d_i X_{ij} \Delta \mu_j$$

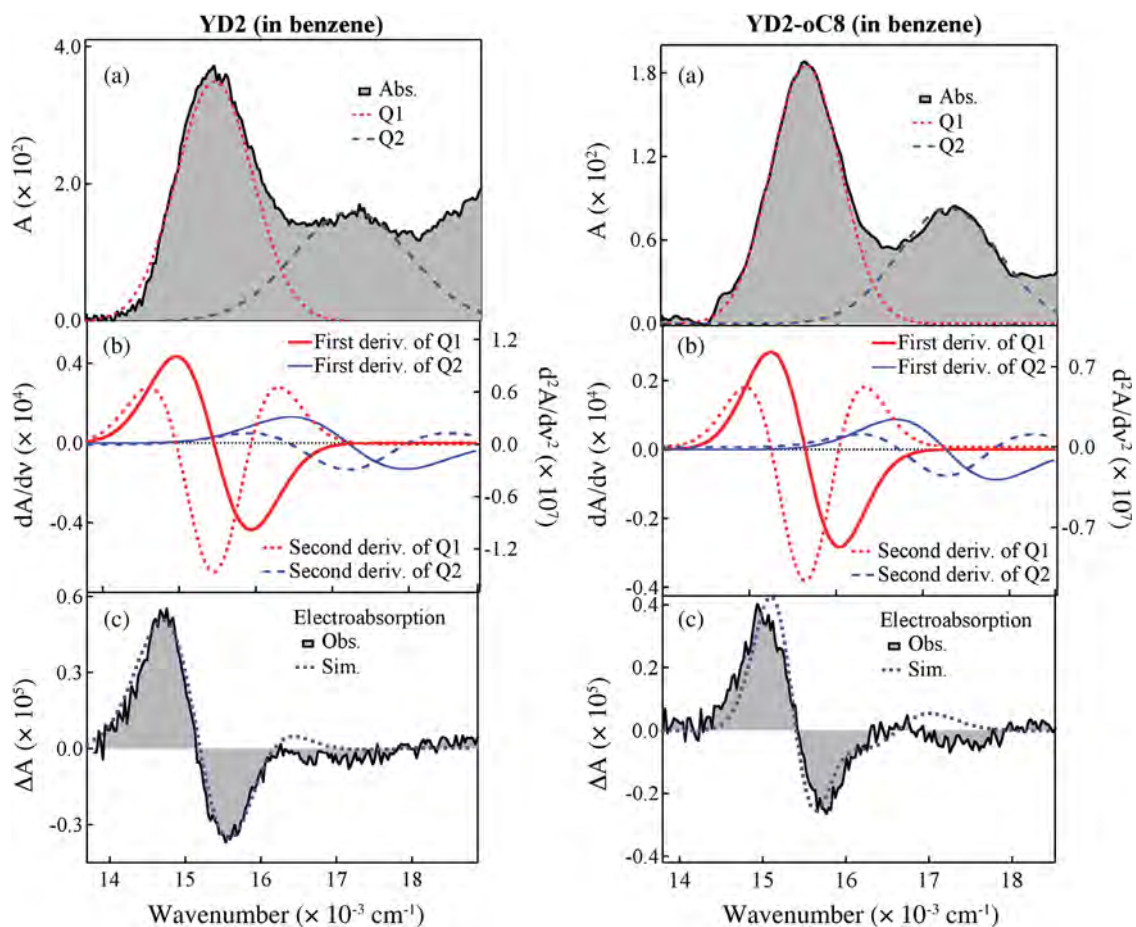
The subscripts  $i$  and  $j$  refer to components of the vectors or tensors. Thus, the coefficient  $A_\chi$  is not zero even with the magic angle of  $\chi$ , if the transition moment is affected by  $F$ .

## RESULTS AND DISCUSSION

E-A spectra of YD2 and YD2-oC8 in benzene solution observed for the Q-bands are shown in Fig. 2, together with the absorption spectrum. The E-A spectra were obtained with  $\chi = 90^\circ$  and  $54.7^\circ$  (magic angle). As shown later, E-A spectra in solid films are independent of the angle of  $\chi$ . In contrast with the E-A spectra in solid films, E-A spectra in solution observed with  $\chi = 90^\circ$  and  $54.7^\circ$  are different from each other, which is attributed to the field-induced reorientation of the molecules in solution. As shown in Fig. 2, the difference in intensity of the E-A spectra is attributed to the band located in the longer wavelength region, which is called as Q1-band, and the difference in the next lowest band located in the wavelength region shorter than the Q1-band, which is called as Q2-band, is very small. Then, it is assumed that the difference is observed only for the Q1-band, and that this difference corresponds to the  $A_\chi$  term of Equation 3. By assuming that the anisotropy of the polarizability is negligible, *i.e.*  $\alpha_m = \bar{\alpha}$  and that the difference of the E-A spectra observed with  $\chi = 90^\circ$  and  $54.7^\circ$  corresponds to the first term of Equation 3, the magnitude of  $\mu_g$  of YD2 and YD2-oC8 is determined to be 2.9 and 5.1 D, respectively. Here, it is assumed that both the direction of the electric dipole moment in the ground state and the direction of the transition moment of the Q1-band are along the direction of the push-pull substituents, *i.e.*  $\zeta = 0$ . The negligible difference of the E-A intensity with different angles of  $\chi$  for the Q2-band may indicate that the angle of  $\zeta$  is close to the magic angle. The E-A



**Fig. 2.** Electroabsorption spectra of YD2 (left) and YD2-oC8 (right) in benzene solution observed for the Q-band region with  $\chi = 90^\circ$  and  $54.7^\circ$ . The applied field strength was  $0.16 \text{ MV}\cdot\text{cm}^{-1}$  in both cases



**Fig. 3.** The analysis of the E-A spectra of YD2 (left) and YD2-oC8 (right) observed with a magic angle of  $\chi$  in solution with a field strength of  $0.16 \text{ MV}\cdot\text{cm}^{-1}$ . Absorption spectra (top), its first and second derivative spectra (middle) and E-A and simulated spectra (bottom)

spectra observed in solution with  $\chi = 54.7^\circ$  are simulated by a linear combination of the zeroth, first and second derivative spectra, as shown in Fig. 3. From the second derivative component in the E-A spectra observed with the magic angle of  $\chi$ , the magnitude of  $\Delta\mu$  was evaluated to be 5.6 and 4.5 D, respectively, for the Q1-band of YD

2 and YD2-oC8. By combining  $\mu_g$  and  $\Delta\mu$  thus obtained, the magnitudes not only of  $\mu_g$  but also of  $\mu_e$  in the excited state reached by the Q1-band excitation are determined by assuming that the electric dipole moment in the excited state is larger than that in the ground state. The results are shown in Table 1.

**Table 1.** Magnitudes of  $\Delta\mu$  following absorption to the Q1-band,  $\mu_g$  and  $\mu_e$  of YD2 and YD2-oC8 in benzene, in PMMA film and on TiO<sub>2</sub> film evaluated from the E-A spectra<sup>a</sup>

	YD2	YD2-oC8
$\Delta\mu$ (D)		
in benzene	5.6	4.5
in PMMA	3.2 (8.6) <sup>b</sup>	4.0 (7.0) <sup>b</sup>
on TiO <sub>2</sub>	8.3 (41.3) <sup>b</sup>	12.5 (77.3) <sup>b</sup>
$\mu_g$ (D)		
in benzene	2.9	5.1
$\mu_e$ (D)		
in benzene	8.5	9.6
in PMMA	6.1	9.1
on TiO <sub>2</sub>	11.2	17.6

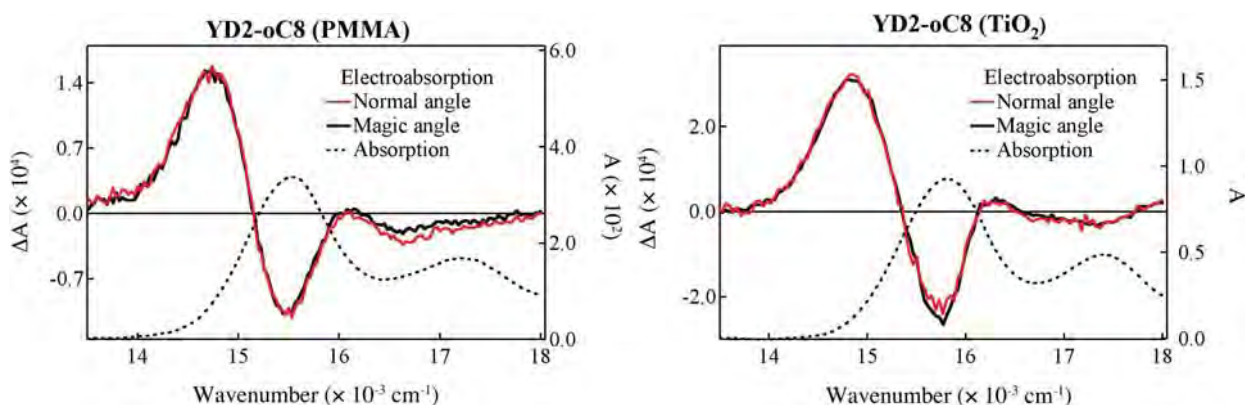
<sup>a</sup>Internal field factor ( $f$ ) is assumed to be unity, and errors are regarded as  $\pm 15\%$  in all values. <sup>b</sup>The magnitude of  $\Delta\mu$  estimated from the E-PL spectra [10].

Polarized E-A spectra of YD2 and YD2-oC8 embedded in a PMMA film or attached on TiO<sub>2</sub> films were obtained both with  $\chi = 90^\circ$  and  $54.7^\circ$ . The results of YD2-oC8 are shown in Fig. 4. Both spectra are essentially the same, indicating that the consideration on the field-induced orientation is not necessary in solid films. Then, the temperature dependent term in Equations 3, 4 and 7 can be neglected in solid films. As shown in Fig. 4, however, the integration of the E-A spectra along the wavenumber from  $14000\text{ cm}^{-1}$  to  $18000\text{ cm}^{-1}$ , that is, along the Q1 and G2-bands, gives nonzero value, *i.e.* positive value, indicating that the absorption intensity of the Q1-band increases in the presence of  $F$ . As mentioned above, this value does not come from the field-induced reorientation. Then, the field-induced increase of the absorption intensity is attributed to the change in transition moment,

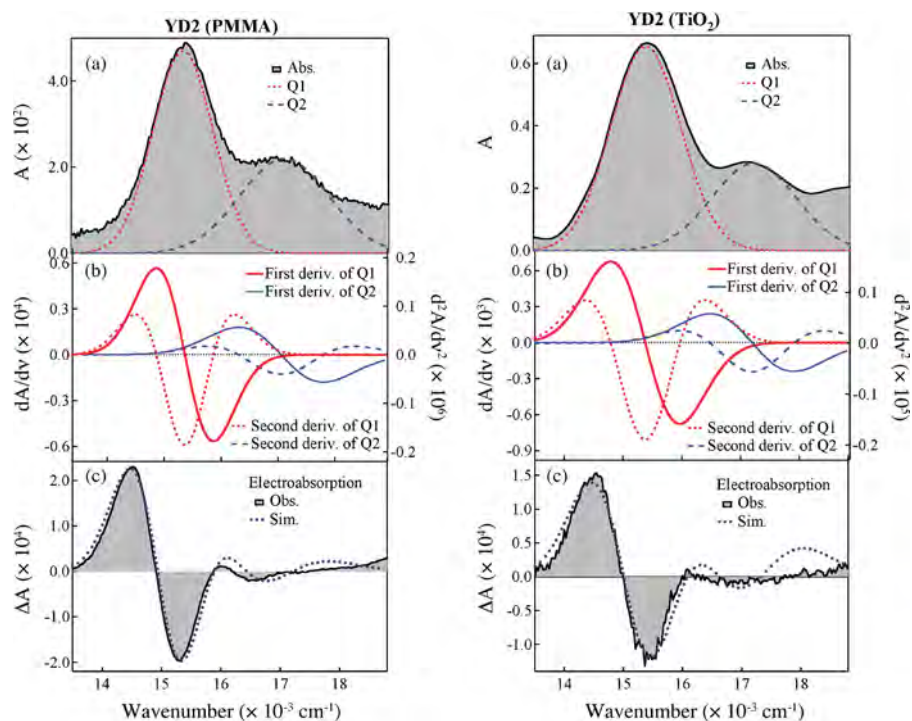
that is, the transition moment polarizability, *i.e.*  $A_{54.7}$  given in Equation 10, is not negligible. It is noted that the integrated intensity relative to the absorption intensity is  $\sim 0.00015$  with a field strength of  $0.1\text{ MV}\cdot\text{cm}^{-1}$ . This value is proportional to the square of the applied electric field, and the field-induced increase in absorption intensity with a field strength of  $1.0\text{ MV}\cdot\text{cm}^{-1}$  is expected to be about 1.5%. As in the case of E-A spectra in solution, the E-A spectra of porphyrin dyes in solid film obtained with  $\chi = 54.7^\circ$  are analyzed by a linear combination of the zeroth, first and second derivatives of the absorption spectra, by assuming that absorption spectra are composed by the Q1 and Q2-bands. The results are shown in Figs 5 and 6, respectively, for YD2 and YD2-oC8. In the present study, the attention is paid only to the Q1-band, and the magnitude of  $\Delta\mu$  following excitation into the Q1-band was obtained, based on the second derivative component of absorption spectra in the E-A spectra. The results are shown in Table 1.

The  $\Delta\mu$  values in PMMA are roughly the same as the ones obtained in solution. On the other hand, the  $\Delta\mu$  values on TiO<sub>2</sub> are much larger than the ones in PMMA or in solution. E-PL spectra also show that the magnitudes of  $\Delta\mu$  of both YD2 and YD2-oC8 attached on TiO<sub>2</sub> films are much larger than that obtained in PMMA films (see Table 1). These results imply that the charge separated state of YD2 and YD2-oC8 is extended over TiO<sub>2</sub> surface, as we have already suggested in our previous paper [12]. Also the value of  $\Delta\mu$  both of YD2 and of YD2-oC8 on TiO<sub>2</sub> obtained from the E-PL spectra are much larger than that obtained from the E-A spectra on TiO<sub>2</sub>. This result may suggest that the local field produced by the TiO<sub>2</sub> surface on which excited molecules of porphyrins are attached is much larger than the field produced by the TiO<sub>2</sub> surface to which the ground state molecules of porphyrins are simply attached. It is noted that the internal field factor was assumed to be unity in the results shown in Table 1.

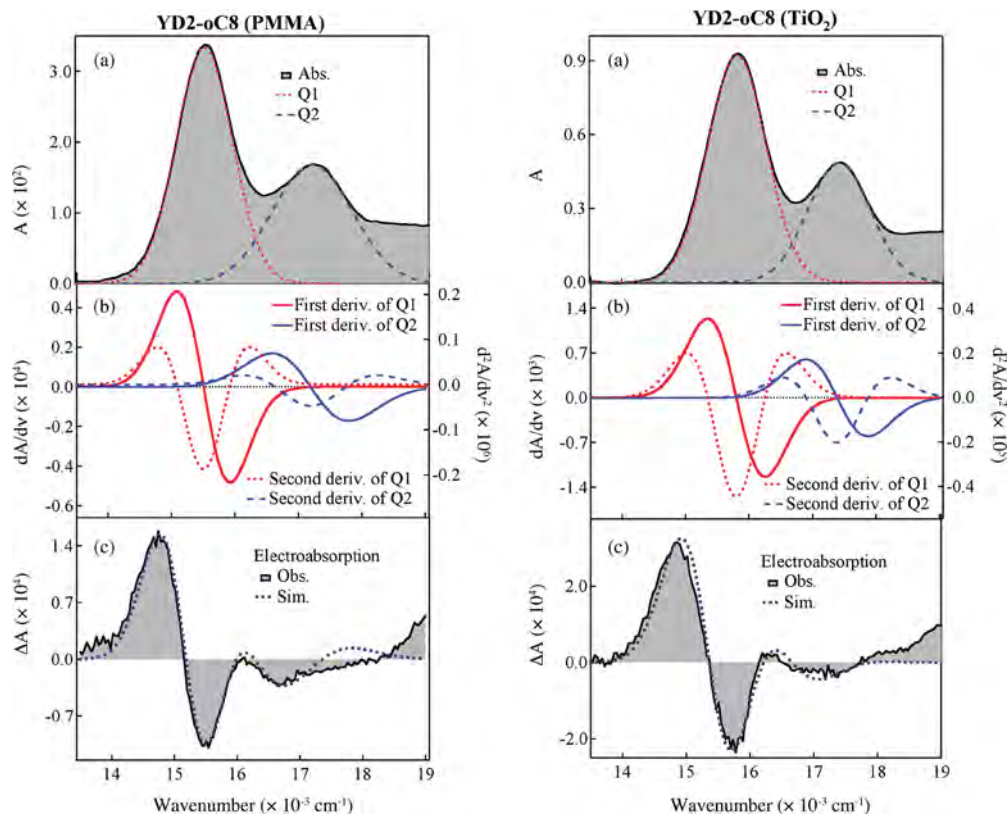
The magnitude of  $\mu$  of YD2-oC8 is larger than that of YD2 both in the ground state and in the excited state, as shown in Table 1. The long alkoxy chains attached at



**Fig. 4.** E-A spectra in the Q-band region of YD2-oC8 embedded in a PMMA film (left) and attached on TiO<sub>2</sub> films (right) with  $\chi = 90^\circ$  and  $54.7^\circ$ . The field strength was 1.0 and  $0.1\text{ MV}\cdot\text{cm}^{-1}$ , respectively



**Fig. 5.** The analysis of the E-A spectra of YD2 embedded in a PMMA film (left) and attached to  $\text{TiO}_2$  films (right) observed with a magic angle of  $\chi$  with a field strength of 1.0 and 0.1  $\text{MV}\cdot\text{cm}^{-1}$ , respectively. Absorption spectra (top), its first and second derivative spectra (middle) and E-A and simulated spectra (bottom)



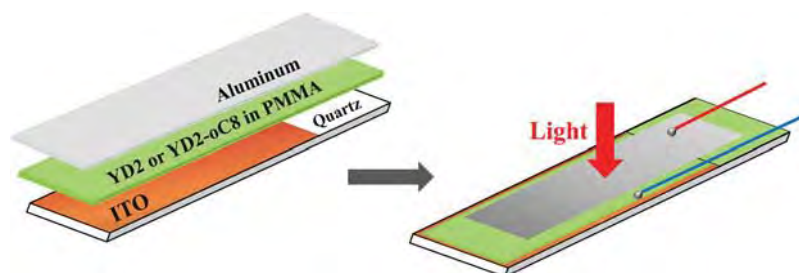
**Fig. 6.** The analysis of the E-A spectra of YD2-oC8 embedded in a PMMA film (left) and attached to  $\text{TiO}_2$  films (right) observed with a magic angle of  $\chi$  with a field strength of 1.0 and 0.1  $\text{MV}\cdot\text{cm}^{-1}$ , respectively. Absorption spectra (top), its first and second derivative spectra (middle) and E-A and simulated spectra (bottom)

the *ortho*-positions of the *meso*-phenyls of the porphyrin seems to reduce the planarity between porphyrin and phenyls, which may play a role to increase the polar character of YD2-oC8 both in the ground state and in the excited state, in comparison with YD2. The substitution of the long alkoxy chains at the *ortho*-position may also protect the dye aggregation of the porphyrin cores. Then, the high performance of DSSC with YD2-oC8 may result from the large value of  $\mu$  in the excited state and also from the protection of the porphyrin cores from the dye aggregation.

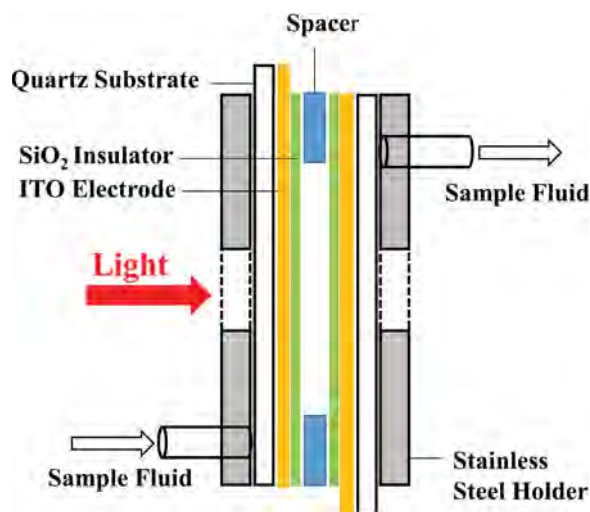
## EXPERIMENTAL

Solution sample of YD2 or YD2-oC8 was prepared with benzene as a solvent. Anhydrous benzene (Wako Chem.) was used without further purification. The sample was circulated through sandwich-type cell by using a peristaltic pump with a constant low flow rate. The liquid cell consisted of two ITO-coated quartz windows and a polymer spacer (6  $\mu\text{m}$ ). The schematic illustration of the solution cell is shown in Fig. 7. ITO layers were used as the semitransparent electrodes. A silicon-dioxide film was coated on the ITO layer as an insulator film with a thickness of 0.58  $\mu\text{m}$ . AC voltage (4 kHz) was applied to the liquid cell. The strength of the applied electric field was evaluated from the applied voltage divided by the gap between two electrodes of the cell, which was evaluated from interferogram. Hereafter, applied electric field is represented as  $F$ . The sample solution was used at ambient pressure at room temperature.

The synthetic details of YD2 and YD2-oC8 are reported elsewhere [19–21]. For the YD2: PMMA or YD2-oC8: PMMA thin films, the porphyrin embedded in PMMA was deposited on an ITO-coated quartz substrate with a spin-coating technique from toluene solution in which a mixture of porphyrin and PMMA (weight ratio = 1:40) was dissolved. The thickness of the sample was  $\sim 0.5 \mu\text{m}$  measured with an interferometric microscope (Nano Spec/AFT-010-0180, Nanometric). A semitransparent Al film was further deposited on the sample film with vacuum vapor deposition. The scheme of the solid sample of porphyrins embedded in PMMA is shown in Fig. 8.



**Fig. 8.** Schematic illustration of the solid sample of YD2 or YD2-oC8 embedded in PMMA film. ITO and Al films were used as the electrodes



**Fig. 7.** Design of the solution cell used in the present study for the E-A measurements

$\text{TiO}_2$  nanoparticles (NP) were prepared according to the conventional synthetic procedure reported by Grätzel and co-workers [22, 23], and then prepared as a paste for screen printing according to the procedure reported elsewhere [24]. The  $\text{TiO}_2$  NP was coated on a  $\text{TiCl}_4$  treated FTO glass substrate (TEC 7, Hartford) to obtain a film with the thickness  $\sim 15 \mu\text{m}$ . For the porphyrin/ $\text{TiO}_2$  thin films, the porphyrin adsorbed on transparent  $\text{TiO}_2$  layer on FTO glass substrate with thickness  $\sim 3 \mu\text{m}$  and then a PMMA thin film  $\sim 0.5 \mu\text{m}$  was deposited on the  $\text{TiO}_2$  film as an insulator. Furthermore, there was an Al film deposited on the PMMA thin film. ITO/FTO and Al films were served as electrodes in solid samples.

E-A spectra were obtained using electric field modulation spectroscopy. Both home-made E-A spectrometer and the commercially available E-A spectrometer (JASCO EMV-200) were used. Details of these apparatus are described elsewhere [5, 6, 15, 16]. Briefly, the modulated transmitted light intensity from the sample detected by the photomultiplier was sent to an amplifier, and then ac and dc signals were separated. The dc signal ( $I$ ), which corresponds to the total intensity of the transmitted light, was recorded by an analog-to-digital converter. The ac signal ( $\Delta I$ ) was detected by a lock-in

amplifier at the second harmonic of the modulation frequency of the applied voltage. Then, the field-induced change in absorbance,  $\Delta A$ , was obtained by the following equation:  $\Delta A = -(2\sqrt{2}/\ln 10)\Delta I/I$ . The electric field was determined in every case, as the ratio of applied voltage divided by the distance between two electrodes, *i.e.* between ITO and ITO films in solution and between ITO/FTO and Al films in solid films.

## CONCLUSION

Electroabsorption (E-A) spectra of push–full porphyrins, YD2 and YD2-oC8, have been measured in solution. Based on the polarization dependence of the E-A spectra, which results from the field-induced reorientation of dye molecules, electric dipole moment in the ground state and the magnitude of the change in electric dipole moment following excitation into the Q1-band of these compounds have been obtained. E-A spectra of these compounds embedded in PMMA films or attached on TiO<sub>2</sub> films are also observed, and the corresponding magnitudes of the change in electric dipole moment following excitation into the Q1-band were also obtained in solid films. The large electric dipole moment in the excited state of the porphyrins on TiO<sub>2</sub> probably correspond to the high energy conversion of the DSSC constructed using these porphyrin sensitizers. The electric dipole moment in the excited state of the dyes on TiO<sub>2</sub> evaluated from the E-A spectra are very different from those evaluated from the E-PL spectra, suggesting that the strong local field of TiO<sub>2</sub> films is applied to the fluorescing dyes attached to TiO<sub>2</sub> films.

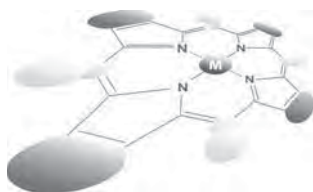
## Acknowledgements

We thank Prof. Y.-P. Lee of NCTU for helpful discussions. Ministry of Science and Technology of Taiwan and Ministry of Education of Taiwan, under the ATU program, provided support for this project. Japan Science and Technology Agency (JST) also supported this project.

## REFERENCES

- Shen YR. *Optics, Rev. Mod. Phys.* 1976; **48**: 1–32.
- Michl J and Thulstrup EW. *Spectroscopy with Polarized Light Solute Alignment by Photoselection, in Liquid Crystals, Polymers, and Membranes*, Wiley: New York, 1986.
- Zdyb A and Krawczyk S. *Appl. Surf. Sci.* 2010; **256**: 4854–4858.
- Krawczyk S and Zdyb A. *J. Phys. Chem. C* 2011; **115**: 22328–22335.
- Mehata MS, Hsu CS, Lee YP and Ohta N. *J. Phys. Chem. C* 2009; **113**: 11907–11915.
- Mehata MS, Hsu CS, Lee YP and Ohta N. *J. Phys. Chem. B* 2010; **114**: 6258–6265.
- Ardo S, Sun Y, Castellano FN and Meyer GJ. *J. Phys. Chem. B* 2010; **114**: 14596–14604.
- Pastore M and Angelis FD. *J. Phys. Chem. Lett.* 2011; **2**: 1261–1267.
- Cappel UB, Feldt SM, Schöneboom J, Hagfeldt A and Boschloo G. *J. Am. Chem. Soc.* 2010; **132**: 9096–9101.
- Imahori H, Umeyama T and Ito S. *Acc. Chem. Res.* 2009; **42**: 1809–1818.
- Martinez-Diaz MV, Torre Gdl and Torres T. *Chem. Commun.* 2010; **46**: 7090–7108.
- Hsu HY, Chiang HC, Hu JY, Awasthi K, Mai CL, Yeh CY, Ohta N and Diao EWG. *J. Phys. Chem. C* 2013; **117**: 24761–24766.
- Li LL and Diao EWG. *Chem. Soc. Rev.* 2013; **42**: 291–304.
- Yella A, Lee HW, Tsao HN, Yi C, Chandiran AK, Nazeeruddin MK, Diao EWG, Yeh CY, Zakeeruddin SM and Grätzel M. *Science* 2011; **334**: 629–634.
- Tayama J, Iimori T and Ohta N. *J. Chem. Phys.* 2009; **131**: 244509-1–244509-7.
- Chiang HC, Iimori T, Onodera T, Oikawa H and Ohta N. *J. Phys. Chem. C* 2012; **116**: 8230–8235.
- Jalviste E and Ohta N. *J. Photochem. photobiol., C* 2007; **8**: 30–46.
- Locknar SL, Chowdhury A and Peteanu LA. *J. Phys. Chem. B* 2000; **104**: 5816–5824.
- Lee CW, Lu HP, Lan CM, Huang YL, Liang YR, Yen WN, Liu YC, Lin YS, E. Diao EWG and Yeh CY. *Chem. Eur. J.* 2009; **15**: 1403–1412.
- Lu HP, Tsai CY, Yen WN, Hsieh CP, Lee CW, Yeh CY and Diao EWG. *J. Phys. Chem. C* 2009; **113**: 20990–20997.
- Bessho T, Zakeeruddin SM, Yeh CY, Diao EWG and Grätzel M. *Angew. Chem. Int. Ed.* 2010; **49**: 6646–6649.
- Barbé CJ, Arendse F, Comte P, Jirousek M, Lenzmann F, Shklover V and Grätzel M. *J. Am. Ceram. Soc.* 1997; **80**: 3157–3171.
- Ito S, Murakami TN, Comte P, Liska P, Grätzel C, Nazeeruddin MK and Grätzel M. *Thin Solid Films* 2008; **516**: 4613–4619.
- Ito S, Chen P, Comte P, Nazeeruddin MK, Liska P, Pechy P and Grätzel M. *Prog. Photovoltaics* 2007; **15**: 603–612.





# Pre-organized dinucleosides with pendant porphyrins for the formation of sandwich type complexes with DABCO with high association constants

Sonja Merkas<sup>a,b</sup>, Souhaila Bouatra<sup>a</sup>, Régis Rein<sup>a</sup>, Ivo Piantanida<sup>b</sup>, Mladen Zinic<sup>b</sup> and Nathalie Solladié<sup>\*a $\diamond$</sup>

<sup>a</sup> CNRS, LCC (Laboratoire de Chimie de Coordination), 205 route de Narbonne, 31077 Toulouse, France and Université de Toulouse, UPS, INPT, 31077 Toulouse, France

<sup>b</sup> Laboratory of Supramolecular and Nucleoside Chemistry, Rudjer Boskovic Institute, Bijenicka cesta 54, HR-10002 Zagreb, Croatia

*Dedicated to Professor Shunichi Fukuzumi on the occasion of his retirement*

Received 1 December 2014

Accepted 12 January 2015

**ABSTRACT:** We report herein the synthesis of a dinucleotide bearing pendant porphyrins dedicated to adopt a pre-organized coformation with face-to-face porphyrins, and capable to self-organize in a stable sandwich type complex with bidentate base such as DABCO. Earlier studies demonstrated that a peptidic linker does not provide sufficient pre-organization to enhance significantly the association constant with bidentate bases such as DABCO on the contrary of some other flexible linkers such as uridine or 2'-deoxyuridine. We document herein that the gain in stability for the formation of sandwich type host-guest complex with DABCO can be even greater when a dinucleotide linker is used. Such pre-organization increases the association constants by one to two orders of magnitude when compared to the association constants of the same bidentate ligands with a reference Zn(II) porphyrin. Comparison of these results with those obtained for rigid tweezers shows a better efficiency of the flexible nucleosidic dimers. We thus document the fact that the choice of rigid spacers is not the only way to pre-organize bisporphyrins, and that some well-chosen nucleosidic linkers offer an interesting option for the synthesis of such devices. Furthermore, the chirality and enantio-purity of the nucleosidic linkers paves the way toward the selective complexation of enantio-pure bidentate guests and the resolution of racemates.

**KEYWORDS:** porphyrins, nucleosides, binding studies, supramolecular complexes.

## INTRODUCTION

Chemistry “beyond the molecule” is epitomized in nature by a plethora of relatively weak noncovalent interactions [1, 2]. The three-dimensional structures of most biopolymers are controlled with noncovalent interactions, either between different parts of the same strand (as in protein  $\alpha$ -helices) or between two separate

strands (as in the DNA duplex and protein  $\beta$ -sheet). While nature has refined the construction of biopolymers, our mastery of the subtle noncovalent interactions as synthetic tools is in an early stage of development. Only in past two decades scientists began to develop ways of mimicking the natural light-harvesting complexes by noncovalent assembly of porphyrin units aiming to obtain favored spacing and orientation between the chromophores [3–21]. The construction of multi-chromophoric assemblies has led to resurgence of interest in coordination chemistry due to formation of ordered arrays directed through molecular recognition events [22–26]. As a module in the construction of supramolecular assemblies

$\diamond$  SPP full member in good standing

\*Correspondence to: Nathalie Solladié, email: [nathalie.solladie@lcc-toulouse.fr](mailto:nathalie.solladie@lcc-toulouse.fr), tel: +33 (0)5-6133-3202, fax: +33 (0)5-6155-3003

porphyrins and metalloporphyrins can be exploited in two different ways: porphyrins can behave as donor building blocks insofar as they comprise *meso*-substituents, such as pyridyl groups, which can act as ligands that can suitably coordinate to metal cations, while metalloporphyrins can act as acceptor building blocks as soon as the metal atom inside the porphyrin core has at least one axial site available for coordination. The interest in metalloporphyrins lays in the ease of exchange of various metals and ligands, which allow spatial control of porphyrin macrocycles. The coordination bond formed by metalloporphyrins has been explored in understanding how metal–ligand interactions are directing formation of supramolecular porphyrin arrays. In this respect a vast array of supramolecular systems have been prepared, such as cyclic oligomers [7, 15, 27, 28], linear oligomers [29–31] and polymers [32–34], squares [35], tapes [36, 37] and other geometries [8, 38]. Important work on nucleotide-porphyrin or DNA-porphyrin conjugates for self-assembly and multi-porphyrin arrays has also been done in the last decade [39].

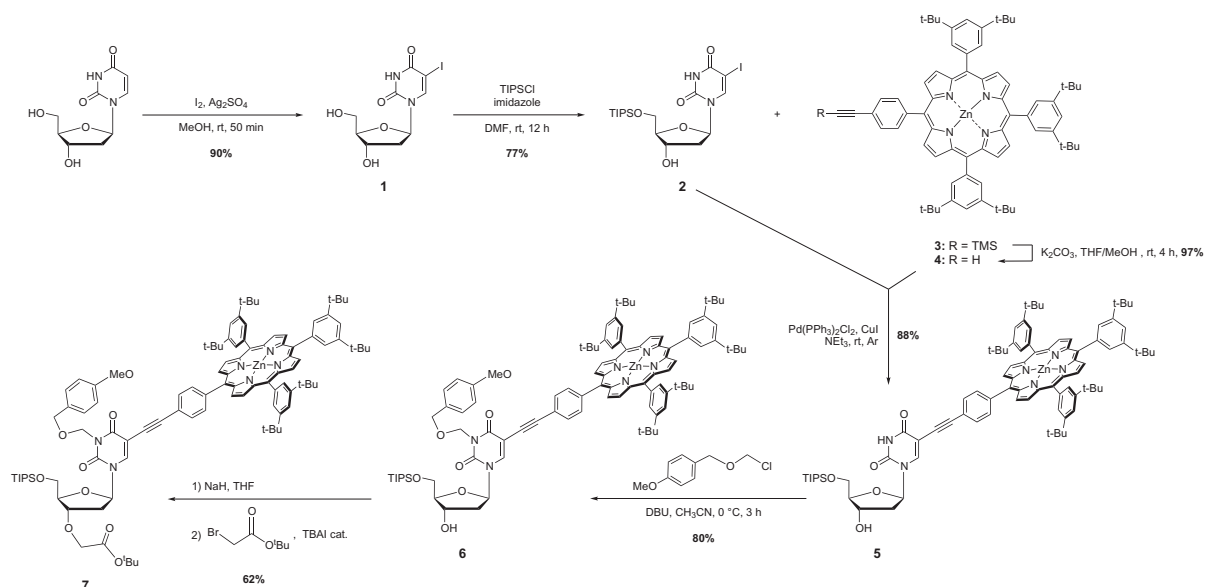
For the last few years, we have focussed on cofacial bis-porphyrin tweezers for host/guest interactions and investigated the possibility to obtain self-coordinated molecular systems with predictable spectral and redox characteristics [40]. We report here the synthesis of a di-nucleotide bearing pendant porphyrins dedicated to adopt a pre-organized conformation with face-to-face porphyrins, and capable to self-organize in a stable sandwich type complex with bidentate base such as DABCO. Using a similar strategy as the one used in antisense research, an artificial nucleotidic backbone was built from modified deoxy-uridine units linked with a more rigid linker than the phosphodiester moieties found in natural oligonucleotides. Antisense research

uses modified oligonucleotides, less flexible than natural strands, to pre-organize the system toward the obtaining of stable double helices between synthesized and natural oligonucleotides. A modified oligonucleotidic backbone was here used to target a parallel conformation of the porphyrins appended to each deoxy-uridine moiety. To provide a rigid environment for the porphyrins, the uridine units were coupled in 3'-5' stepwise fashion using ether-ester type of spacer of suitable length, and porphyrins were anchored to the uridine by means of robust carbon–carbon bonds. This is a first step toward the elaboration of longer oligonucleotides with pendant porphyrins and pre-defined conformation.

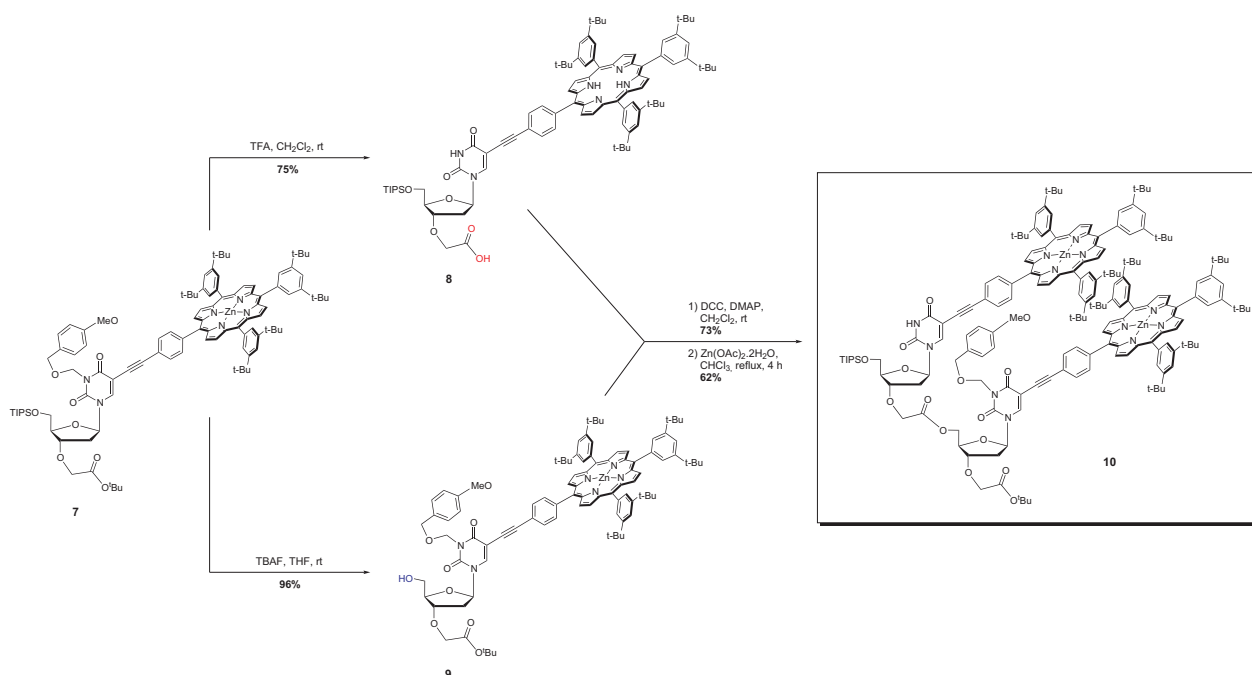
## RESULTS AND DISCUSSION

### Synthesis of a dinucleotide with pendant porphyrins

The preparation of the porphyrin-uridine conjugate **10** is based on the dimerization of a derivative of 2'-deoxyuridine, as a building unit, functionalized by a porphyrin at C-5 position of the nucleic base. The synthesis of dimer **10** is depicted in Schemes 1 and 2. The 2'-deoxyuridine has thus to be functionalized at both C-3' and C-5' positions of the ribose and at C-5 position of the uracil nucleic base where the porphyrin will be appended. The first step for obtaining monomer **7** is based on iodination of commercially available 2'-deoxyuridine at C-5 position under classical conditions [41]. For selective protection of the ribose primary hydroxyl group, a triisopropylsilyl (TIPS) protecting group, stable under various conditions and easily cleaved by treatment with fluoride-ion source, was chosen. The porphyrin-uridine conjugate **5** was obtained in 88% yield



Scheme 1. Synthesis of monomer **7**



**Scheme 2.** Synthesis of di-nucleotide **10**

by Sonogashira coupling of the terminal alkyne function of the A<sub>3</sub>B type Zn(II) porphyrin **4** and the 5-iodo-*O*-5'-triisopropylsilyl-2'-deoxyuridine **2**. The *meso*-substituted tetraarylporphyrin bearing peripheral ethynyl and 3,5-di-*tert*-butyl groups **4** was synthesized by deprotection of the trimethylsilyl (TMS) group of porphyrin **3**, which was obtained using the conditions developed by Lindsey *et al.* [42]. In order to avoid any side reaction during the functionalization of monomer **5** at the *O*-3' position, which is prerequisite for the oligomerization process, the *N*-3 position of the uracil nucleic base of monomer **5** was protected by a *p*-methoxybenzyl chloromethyl ether group (pMeOBOM), stable to both basic and nucleophilic reagents [43]. After having quantitatively protected monomer **5**, a selective etherification of compound **6** was realized by direct alkylation at the *O*-3' position with *tert*-butyl 2-bromoacetate under basic conditions in the presence of a catalytic amount of tetrabutylammonium iodide [44]. Monomer **7**, bearing both a TIPS protecting group at *O*-5' position of the ribose and an ester functionalization at *O*-3' position, was then used for the preparation of dimer **10** (Scheme 2).

The oligomerization is based on the choice of mild conditions for the selective deprotection of both *tert*-butyl and triisopropylsilyl groups. The *tert*-butyl group of **7** was cleaved in 75% yield upon treatment with a 2.2 M solution of trifluoroacetic acid (TFA) in dichloromethane. This synthetic method, based on acidic conditions, was anticipated to provoke demetalation of the Zn(II) porphyrin, positioning the desired metalated porphyrin (energy donor) at the *O*-3' end of the

dinucleotide. In the meanwhile, treatment of monomer **7** with *tert*-butylammonium fluoride in tetrahydrofuran produced removal of triisopropylsilyl group in 96% yield to give a free hydroxylic group at *O*-5' position of compound **9**. A nucleosidic 3'–5' coupling reaction was then realized between the carboxylic acid function of free-base monomer **8** and the primary hydroxyl group of Zn(II) monomer **9** in dichloromethane in the presence of *N,N'*-dicyclohexylcarbodiimide (DCC) and *N,N*-dimethylaminopyridine (DMAP) for one night at room temperature. Dimer **10**, bearing two Zn(II) porphyrins, was obtained in 73% yield after purification of the dimer with one free-base and one Zn(II) porphyrins by column chromatography on silica gel and gel permeation chromatography (GPC) in toluene, followed by subsequent metalation of the free-base porphyrin under classical conditions.

#### **Binding studies of DABCO by dinucleotide **10**: formation of a sandwich type molecular complex with a high association constant**

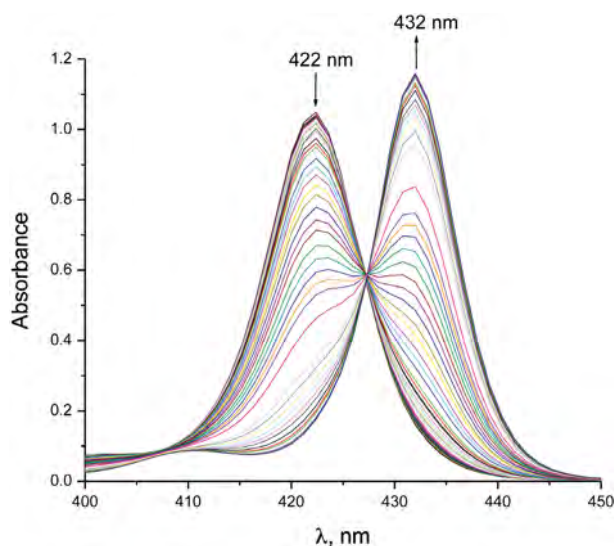
The ability of di-nucleotide **10** to accommodate guests was investigated through binding studies carried out in dichloromethane with 1,4-diazabicyclo[2.2.2]octane (DABCO) as bidentate base. The coordination of DABCO was probed by UV-visible titration. It is based on the use of host–guest interactions for the formation of supramolecular assemblies between the multiporphyrinic arrays and small bidentate ligand (DABCO) through axial coordination. We chose DABCO because this ligand is

known to lead to stable complexes [11], although some other linear bidentate ligands would probably behave the same way. As reported in some of our previous publications [45], it was assumed that the dinucleosidic bis-porphyrin could be preorganized and thus facilitate the coordination of this rigid bifunctional ligand. The synthesized molecular system is amenable to preorganization, because its architecture is based on combination of rigid and flexible linkers. The architecture of multiporphyrinic systems is important because the covalent connectivity between the interacting centers commands the geometry of resulting assembly and the relative orientation of chromophores dictates the strength of the interaction with ligands. As already noted, the geometry of porphyrins in supramolecular assembly is crucial in design of artificial light-harvesting complexes [3–21].

UV-visible absorption titrations were carried out to probe the structure and stability of zinc porphyrin-DABCO complexes. They were performed in dichloromethane at room temperature by adding small aliquots of DABCO solution of discrete concentration to the solution of the porphyrinic array. The approximate concentration of the zinc porphyrin solution was determined by peak absorbance which should be in the range between 0.9–1.1. The several DABCO solutions in dichloromethane with exact concentrations were prepared. 3 mL of the porphyrin solution was placed in a cuvette and the absorption spectrum was recorded. 1–10  $\mu\text{L}$  aliquots of accurately determined DABCO solution were sequentially added to the porphyrin solution and the spectra were recorded after each addition. Data obtained by UV-visible titrations were analysed by using the values of the absorbance at fixed wavelengths, which method is exclusively valid for the complexes with stoichiometry 1/1 [46], and by simultaneous fitting of the whole series of spectra collected at 1 nm intervals using the software SPECFIT [47–49].

Before examining the supramolecular complex of DABCO with the porphyrin array, the properties of simple porphyrin **3** were investigated. This system was employed as a reference since the zinc center can coordinate only to one nitrogen of DABCO. The coordination of DABCO to monomer **3** was probed by UV-visible titration, by using the coordination shift of the Soret absorption as well as the Q-bands. The Soret band absorption was measured at the concentration of  $1.75 \times 10^{-6}$  M which corresponds to peak absorbance of 1.05 at 422 nm. Under these dilute conditions binding of DABCO resulted in a shift of the Soret band from 422 to 432 nm. The clean isobesticity of these spectra demonstrates that the spectroscopically active species in the solution are simple porphyrin **3** and one type of its complex with DABCO. Any further changes in the absorption spectra of this model system were not observed, even with addition of many more equivalents of DABCO (Fig. 1).

The titrations data were analysed with both methods delineated previously, by using the selected wavelengths

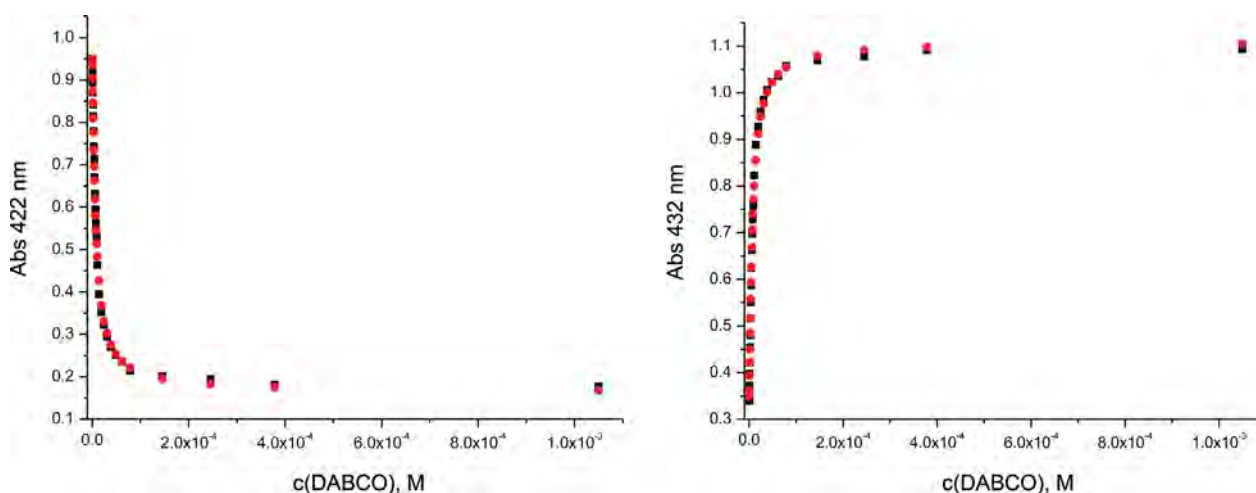


**Fig. 1.** UV-visible titration of simple porphyrin **3** with DABCO in  $\text{CH}_2\text{Cl}_2$  at rt

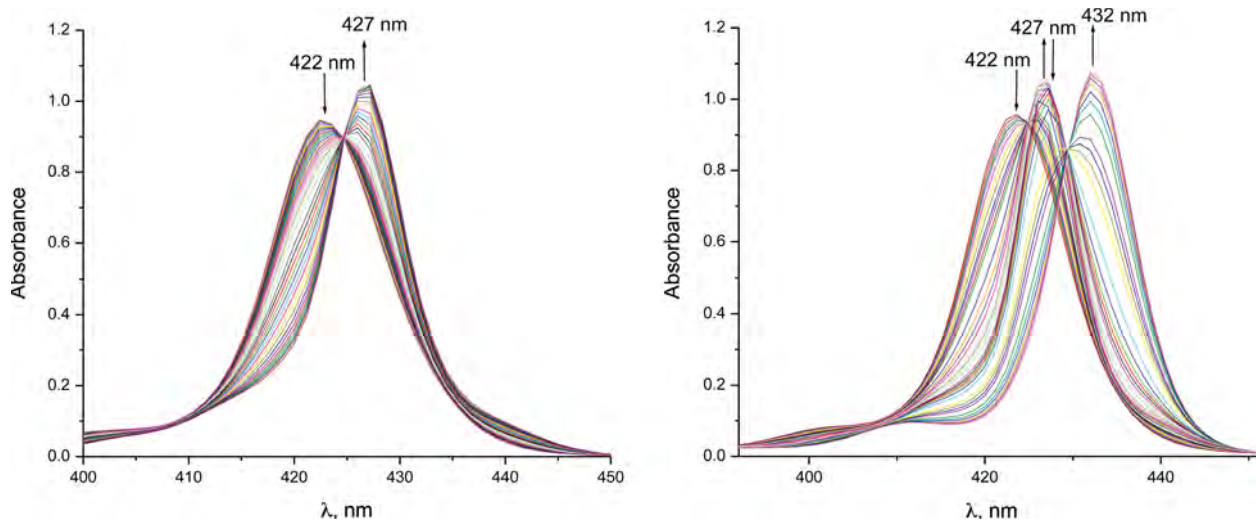
and by fitting the whole spectra using SPECFIT. The first method could be applied only to the model system of zinc porphyrins that forms a 1/1 complex with DABCO. Hence, the binding constant for 1/1 monomer/DABCO complex calculated by this method was found to be  $1.7 \times 10^5 \text{ M}^{-1}$  ( $\log K_{11} = 5.2$ ). Multivariate global factor analysis of the whole series of spectra showed that the titration can be analysed in terms of two colored species, free **3** and 1/1 stoichiometric model. The excellent fit of the titration data to the 1/1 binding model (Fig. 2) provided the stoichiometric binding constant of  $\log K_{11} = 5.27 \pm 0.01$ .

The excellent fit of experimental and calculated data and great agreement in the binding constants obtained by data analysis corroborated that the formation of the 1/1 monomer/DABCO complex was the only process in the titration. Hence, simple porphyrin **3** as the acceptor unit complemented the donor ligand, DABCO, by coordination of electron deficient zinc to the one nitrogen of the base. The zinc porphyrin-DABCO systems have been widely studied by Sanders, Hunter, Anderson and co-workers. They found that a red shift in the Soret band for 10 nm is typical for the 1/1 complex [30, 50–58]. In addition, they described that a simple zinc porphyrin at micromolar concentrations with DABCO forms exclusively 1/1 complex with corresponding binding constant of about  $10^5 \text{ M}^{-1}$ . Thus, our result is in excellent agreement with their observations.

After examining the complexation of the simple porphyrin with DABCO, we studied the binding of the same ligand to dimer **10**, the bis-porphyrinic tweezer appended to an appropriate position of the flexible uridinic scaffold by the rigid acetylene group. The titration of the dimer with DABCO was measured by using the coordination shift of the Soret absorption as well as the Q-bands. The Soret band absorption was



**Fig. 2.** UV-visible titration data (change in absorbance at two wavelengths, 422 nm (black squares) and 432 nm (red dots)) for the binding of simple porphyrin **3** with DABCO, fitted to the calculated curves for the only reliable equilibrium which corresponds to 1/1 complex

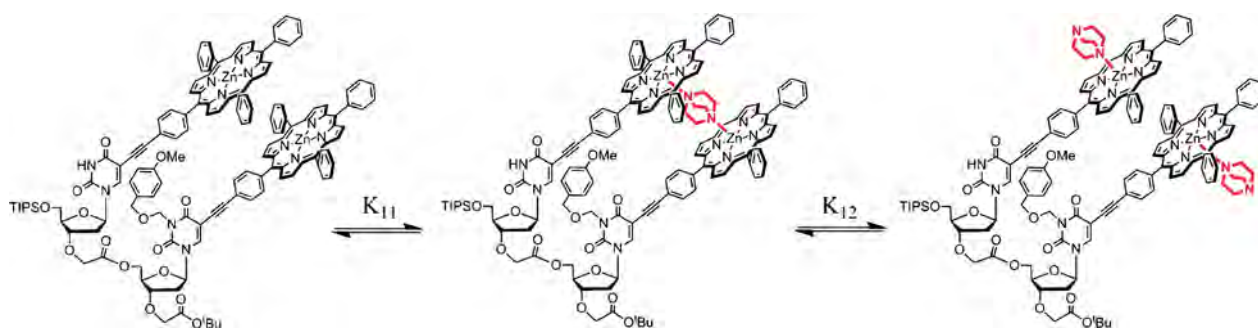


**Fig. 3.** UV-visible titration of bis-porphyrinic tweezer **10** with DABCO in  $\text{CH}_2\text{Cl}_2$  at rt. On the left hand side first part of the titration and on the right the complete titration

measured at the concentration of  $1.04 \times 10^{-6}$  M which corresponds to an absorbance of 0.95 at 422 nm. The titration was performed in two parts to be analysed in terms of two-state equilibria. The first part of the titration was processed until two equivalents of DABCO were added per porphyrin. The complete titration that involved an addition of DABCO until 6000 equivalents per porphyrin was performed separately, Fig. 3.

The clean isobesticity of spectra obtained in the first part of the titration demonstrates that the only colored species present in solution are free dimer **10** and one type of its complex with DABCO. The observed spectral changes are quite similar to those obtained in the titration of monomer **3**. However, there are some minor spectral changes, *i.e.* smaller red shift of the Soret peak, from 422

to 427 nm, as well as intensified and sharpened form of the titration spectrum. A shift in the Soret band of 5 nm is exactly two times smaller than the shift obtained for the 1/1 monomer/DABCO complex. Accordingly, it was reasonable to anticipate formation of the intramolecular 1/1 sandwich complex. On addition of more DABCO, intensity of the absorption band at 427 nm decreased, and a new absorption band appeared at 432 nm. As observed in the titration spectrum of monomer **3**, the Soret absorption at 432 nm is typical for the simple 1/1 porphyrin/DABCO complex. On the basis of the changes in absorption spectra, the possible two consecutive two-state equilibria with corresponding stepwise constants in the binding of DABCO to bis-porphyrinic tweezer **10** are shown in Fig. 4.



**Fig. 4.** Representation of the proposed equilibria involved in the binding of DABCO to bis-porphyrinic tweezer **10**. For clarity reasons *tert*-butyls on *meso*-phenyls are omitted

Spectrophotometric titration of dimer **10** with DABCO was repeated at concentration of  $2.17 \times 10^{-5}$  M, which corresponds to absorbance of 0.98 at 549 nm. At this wavelength the coordination shift of the Q-band was probed. Spectral changes in the titration spectrum involved a progressive decline of the bands characteristic for the free dimer and appearance of new red-shifted bands. This titration spectrum with sharp isosbestic points indicated the presence of an independent spectroscopically active species.

The first method for calculation of the binding constant by using titration data at selected wavelengths was applied only to the first part of the titration characterized by sharp isosbestic point. This analysis could be performed because the complexation by 1/1 binding model was envisaged in the first equilibrium. The binding constant for the 1/1 dimer/DABCO complex was found to be  $7.4 \times 10^6$  M<sup>-1</sup> ( $\log K_{11} = 6.9$ ). The formation of this type of a complex was verified by analysis of the whole set of spectra which correspond to the first part of the titration by using SPECFIT. The analysis resulted with only one possible 1/1 complex with corresponding binding constant  $\log K_{11} \times 6.42 \pm 0.03$ . It is interesting to note that calculated  $\log K_{11}$  for 1/1 dimer/DABCO complex is more than one order of magnitude higher than  $\log K_{11}$  for 1/1 monomer/DABCO complex. Taken together, these results strongly support formation of 1/1 dimer/DABCO sandwich complex through the chelate effect. The whole spectra obtained by the complete titration was analyzed in terms of three possible colored species: free dimer **10**, 1/1 sandwich complex, and 1/2 open complex (Fig. 4). Fitting of the titration data revealed that 1/1 and 1/2 binding models for dimer/DABCO are only possible, Fig. 5.

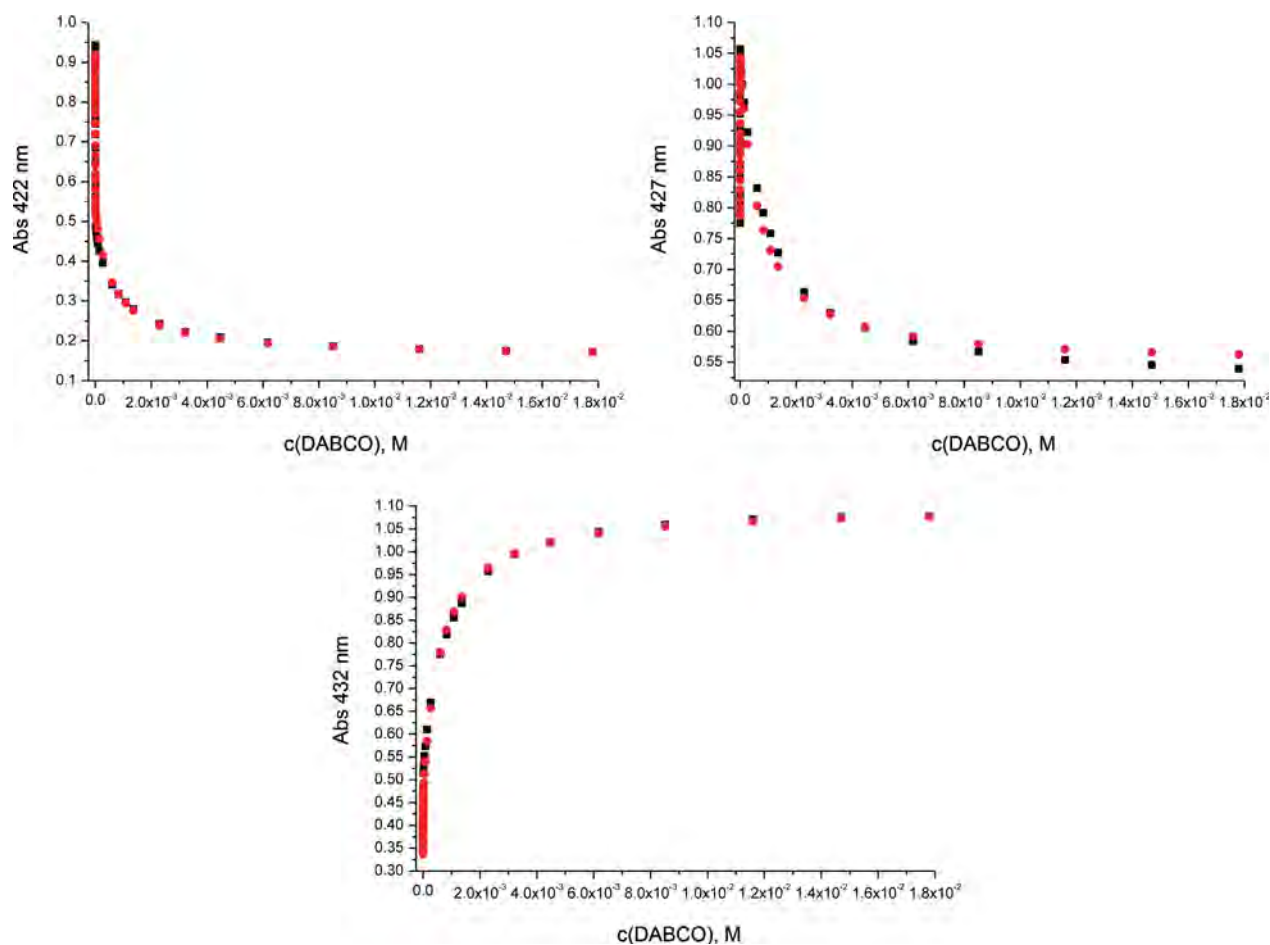
Fitting to 1/1 binding isotherm yielded the stoichiometric binding constant  $\log K_{11} = 6.65 \pm 0.08$ , while the fit to 1/2 binding model provided  $\log K_{12} = 3.21 \pm 0.10$ . The calculated  $\log K_{11}$  is almost identical to  $\log K_{11}$  value obtained in the analysis of the first part of the titration. Moreover, calculated  $\log K_{12}$  value is three orders of magnitude lower than  $\log K_{11}$  value. Therefore, dissociation of the more stable chelated 1/1 complex

is followed by coordination of second DABCO and by that formation of the 1/2 complex in which two DABCO molecules are coordinated to two porphyrins of the dimer. Both, 1/1 and 1/2 complexes involved in these consecutive two-state equilibria are in agreement with the species represented in Fig. 4.

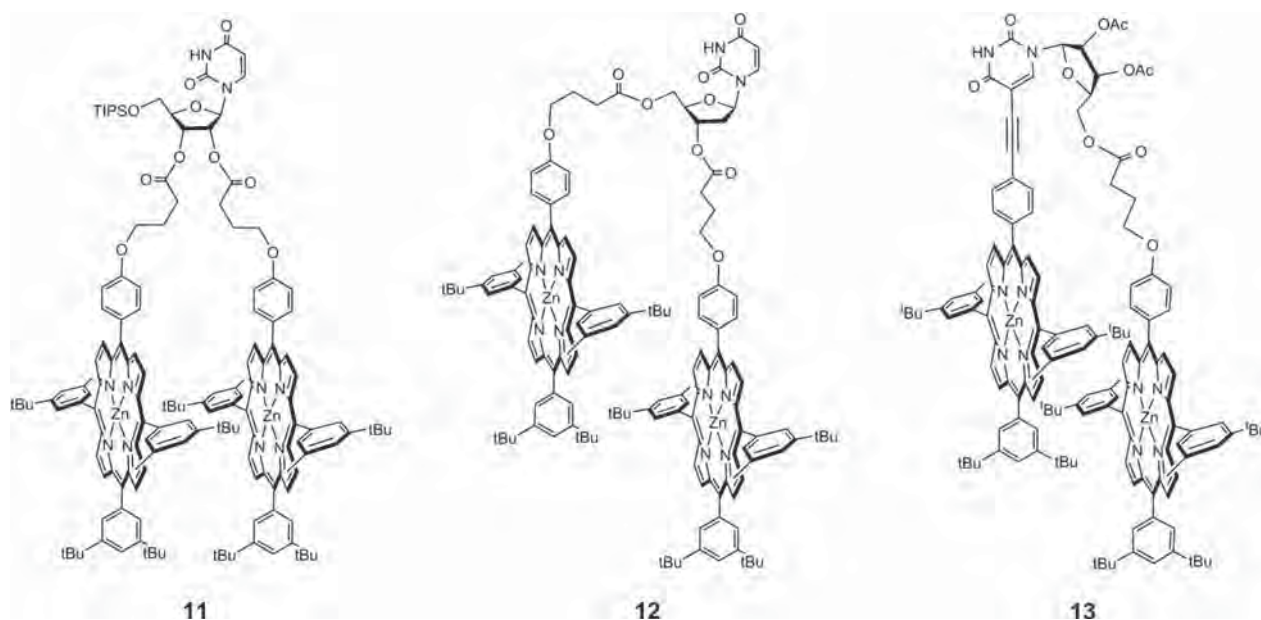
Similar formation of sandwich complexes was evidenced by Sanders, Hunter, Anderson and co-workers [50, 30, 51–58]. These studies show that sandwich complex formation is in concert with the parallel orientation of two porphyrin macrocycles. In this respect, the shifts in titration spectra are caused by proximity of the porphyrins and in this line increased interporphyrinic electronic interaction. The Soret band of the free dimer **10** has hwhm 15 nm, and the Soret band of the dimer/DABCO sandwich complex 11 nm. It is believed that this narrowing indicate a significant increase in the center-to-center distance between the two porphyrins, due to the insertion of DABCO into the bis-porphyrinic cavity. This hypothesis is in great agreement with the half width at half maximum of 13 nm for the 1/2 dimer DABCO open complex. The outer coordination of DABCO allows a shorter center-to-center distance between the porphyrins.

#### Advantage of nucleosidic linkers for the pre-organization of dimers and formation of highly stable complexes with DABCO in regard to some other flexible or rigid spacers

We reported a few years ago the binding studies of three bis-porphyrinic tweezers bearing nucleosidic linkers (Fig. 6) [60]. These dimers differ by the attachment positions of the two porphyrins. For bis-porphyrinic dimers **11** and **12**, both porphyrins are attached to the ribose, in the O-2' and O-3' positions of uridine for dimer **11** and in the O-3' and O-5' positions of 2'-deoxyuridine for dimer **12**. For dimer **12** and **13**, the anchoring position of one Zn(II) porphyrin at the O-5' position of the sugar moiety is conserved, while the second chromophore is attached either at the O-3' position of the 2'-deoxyuridine for dimer **12** or at the C-5 position of the nucleic base for dimer **13** (Fig. 6).



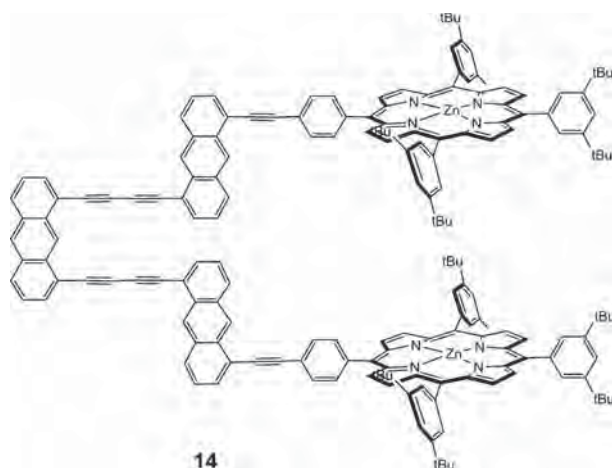
**Fig. 5.** UV-visible titration data (change in absorbance at three wavelengths, 422, 427 and 432 nm) for the binding of bis-porphyrinic tweezer **10** with DABCO, fitted to the calculated curves for the equilibria in Fig. 4



**Fig. 6.** Three new bis-porphyrins bearing a flexible nucleosidic linker and differing by the attachment positions of the two porphyrins

The ability of tweezers **11**, **12** and **13** to accommodate guests was investigated through binding studies carried out in dichloromethane with DABCO as bidentate base. The complexations were monitored by UV-visible spectrophotometric titration of a solution of tweezers in  $\text{CH}_2\text{Cl}_2$  [60]. The association constants for the formation of the complexes were calculated from UV-visible spectroscopic data. A value of  $2.5 \times 10^4 \text{ M}^{-1}$  ( $\log K = 4.4$ ) was found for tweezers **11**, which is similar to the association constant of DABCO with a reference Zn(II) porphyrin 5,10,15,20-tetra-di-*tert*-butyl-phenyl-porphyrin  $\text{A}_4$  ( $2.5 \times 10^4 \text{ M}^{-1}$ ), thus indicating as expected that no well-defined pre-organized conformation exists for bis-porphyrin **11**. However, much higher binding constants were found for the formation of host-guest complexes between tweezers **12** and **13** and DABCO. Values of  $6.3 \times 10^5 \text{ M}^{-1}$  ( $\log K = 5.8$ ) and  $2.0 \times 10^6 \text{ M}^{-1}$  ( $\log K = 6.3$ ) were found. These association constants are increased by 1.5 or 2 orders of magnitude as compared to the association constants of the same bidentate ligand with the above cited reference Zn(II) porphyrin. This enhanced stability of the complex may be ascribed to a pre-organization of the bis-porphyrinic tweezers **12** and **13** forming a cavity and provides convincing evidence that the bidentate base is inserted into the cavity of both dimers *via* host-guest interactions.

To rationalize the pre-organization of these flexible dimers and their capability to behave as tweezers to complex bidentate guests, it is interesting to compare the obtained results with those of a rigid cofacial bis-porphyrinic tweezers (**14**) we synthesized a few years ago (Fig. 7) [12, 60]. More specifically, this rigid dimer was designed in order to force the cofacial orientation of the porphyrins to create a cavity between the two chromophores, thus making them capable of hosting bidentate guests of appropriate size. Poly-anthracenes was chosen as rigid spacer for the construction of this tweezers. The tris-anthracenic spacer used in **14** forces a



**Fig. 7.** Rigid cofacial bis-porphyrinic tweezers with tris-anthracenic spacer **14**

cofacial orientation of the chromophores while allowing a free rotation around the acetylenic axis, thus adjusting the cavity size to accommodate a large variety of guests. The ability of **14** to accommodate guests was investigated through binding studies carried out in dichloromethane with DABCO as bidentate base. The complexations were monitored by a UV-visible spectrophotometric titration in  $\text{CH}_2\text{Cl}_2$ . The association constant ( $K$ ) between tweezers **14** and DABCO was calculated from the UV-visible spectroscopic data and a value of  $3.9 \times 10^5 \text{ M}^{-1}$  ( $\log K = 5.6$ ) was found. This association constant is increased by one order of magnitude, when compared to the association constant for the binding of the same bidentate ligands with a reference Zn(II) porphyrin 5,10,15,20-tetra-di-*tert*-butyl-phenyl-porphyrin  $\text{A}_4$  ( $2.5 \times 10^4 \text{ M}^{-1}$ ,  $\log K = 4.4$ ). The enhanced stability of the complex is ascribed to the pre-organization of the bis-porphyrinic tweezers **14**.

Earlier studies demonstrated that a peptidic linker does not provide sufficient pre-organization to enhance significantly the association constant with bidentate bases such as DABCO [60]. However, other flexible linkers such as uridine or 2'-deoxyuridine generate blocked conformers bringing the two porphyrins in a face-to-face position. We reported herein that the gain in stability for the formation of sandwich type host-guest complex with DABCO can be even greater when a dinucleotide linker is used. Such pre-organization increases the association constants by one to two orders of magnitude when compared to the association constants of the same bidentate ligands with a reference Zn(II) porphyrin. Comparison of these results with those obtained for rigid tweezers **14** shows a better efficiency of the flexible nucleosidic dimers. We thus document the fact that the choice of rigid spacers is not the only way to pre-organize bis-porphyrins, and that some well-chosen nucleosidic linkers offer an interesting option for the synthesis of such devices. Furthermore, the chirality and enantio-purity of the nucleosidic linkers paves the way toward the selective complexation of enantio-pure bidentate guests and the resolution of racemates.

## EXPERIMENTAL

**Preparation of porphyrin-uridine conjugate 5.** The reaction was performed in four batches due to yields acquired at this scale. Thus, 5'-*O*-triisopropylsilyl-5-iodo-2'-deoxyuridine (**2**, 0.31 g, 0.61 mmol) and zinc(II) porphyrin with terminal acetylene (**4**, 0.77 g, 0.74 mmol) were dissolved in triethylamine (15 mL), freshly distilled and deoxygenized by bubbling with argon during 3 h. To this solution  $\text{Pd}(\text{PPh}_3)_2\text{Cl}_2$  (0.011 g, 0.015 mmol) and  $\text{CuI}$  (0.006 g, 0.031 mmol) were added under an argon atmosphere. The mixture was stirred at rt for 60 h and then the batches were combined and concentrated under vacuum. The dark brown residue was dissolved in



dichloromethane and successively extracted with EDTA disodium salt (2% solution), Na<sub>2</sub>S<sub>2</sub>O<sub>3</sub> (0.35 M), saturated solution of NH<sub>4</sub>Cl, and water. The organic phase was concentrated and to the slurry SiO<sub>2</sub> was added, and then evaporated to dryness. The obtained composite was dried in vacuum overnight and then purified by silica-gel column chromatography ( $\varnothing = 5$  cm, h = 19 cm; *n*-hexane/ethyl acetate (8:2)), yielding the compound **5** as a violet solid (3.07 g, 2.16 mmol, 88%). <sup>1</sup>H NMR (CDCl<sub>3</sub>, 500 MHz):  $\delta$ , ppm 9.00 (d, 2H, <sup>3</sup>J = 4.5 Hz, H<sub>β2</sub>), 8.99 (s, 4H, H<sub>β3</sub>), 8.90 (d, 2H, <sup>3</sup>J = 4.5 Hz, H<sub>β1</sub>), 8.21 (d, 2H, H<sub>α</sub>, <sup>3</sup>J = 8.5 Hz), 8.13 (s, 1H, H<sub>6</sub>), 8.09 (dd, 6H, *J* = 2.0 and 4.0 Hz, H<sub>α'</sub>), 7.87 (d, 2H, <sup>3</sup>J = 8.0 Hz, H<sub>m</sub>), 7.79 (td, 3H, <sup>4</sup>J = 2.0 and 6.5 Hz, H<sub>p+pp'</sub>), 6.30 (dd, 1H, H<sub>1</sub>, <sup>3</sup>J = 6.5 and 7.0 Hz), 4.62 (m, 1H, H<sub>3</sub>), 4.03 (m, 1H, H<sub>4</sub>), 3.97 (m, 2H, H<sub>5</sub>), 2.45 (ddd, 1H, H<sub>2</sub>, <sup>3</sup>J = 3.1 and 6.0 Hz and <sup>2</sup>J = 13.6 Hz), 2.26 (ddd, 1H, H<sub>2</sub>, <sup>3</sup>J = 5.8 and 7.3 Hz and <sup>2</sup>J = 13.9 Hz), 1.53 (s, 36H, <sup>t</sup>Bu), 1.52 (s, 18H, <sup>t</sup>Bu), 1.26 (s, 3H, CH<sub>3</sub>TIPS), 1.15 (d, 9H, CH<sub>3</sub>TIPS, <sup>3</sup>J = 3.5 Hz), 1.13 (d, 9H, CH<sub>3</sub>TIPS, <sup>3</sup>J = 3.6 Hz). Elemental analysis (%) for C<sub>88</sub>H<sub>106</sub>N<sub>6</sub>O<sub>5</sub>SiZn (1421.30): calcd. C 74.36, H 7.52, N 5.91; found C 74.21, H 7.72, N 5.21. UV-vis (CH<sub>2</sub>Cl<sub>2</sub>):  $\lambda_{\text{abs}}$ , nm ( $\epsilon$ ) 423 (569 120 M<sup>-1</sup>.cm<sup>-1</sup>), 549 (21 793 M<sup>-1</sup>.cm<sup>-1</sup>), 589 (6 173 M<sup>-1</sup>.cm<sup>-1</sup>).

**Preparation of porphyrin-uridine conjugate protected at N-3 6.** Porphyrin-uridine conjugate **5** (1.00 g, 0.70 mmol) was suspended in acetonitrile (50 mL) and obtained mixture was allowed to stir for 15 min. This homogeneous solution was deaerated and flushed with argon, and then cooled down to 0 °C. To this mixture DBU (0.23 mL, 1.55 mmol) was added and then chloromethyl *p*-methoxybenzyl ether (0.26 mL, 1.41 mmol) was added in portions under argon atmosphere. After an addition was completed the solution was stirred for another 3 h at 0 °C. The product formation was followed by TLC in *n*-hexane/ethyl acetate (5:5) as an eluent, *R<sub>f</sub>* = 0.52. After the reaction mixture was concentrated, the residue was dissolved in dichloromethane. This solution was washed with three portions of water, then evaporated and dried in vacuum overnight. The crude product was purified by column chromatography (SiO<sub>2</sub>;  $\varnothing = 2$  cm, h = 28 cm; *n*-hexane/ethyl acetate (from 8:2 to 2:8)), yielding the compound **6** as a violet solid (0.88 g, 0.56 mmol, 80%). <sup>1</sup>H NMR (CDCl<sub>3</sub>, 300 MHz):  $\delta$ , ppm 9.02 (d, 2H, <sup>3</sup>J = 4.6 Hz, H<sub>β2</sub>), 9.00 (s, 4H, H<sub>β3</sub>), 8.92 (d, 2H, <sup>3</sup>J = 4.7 Hz, H<sub>β1</sub>), 8.22 (d, 2H, H<sub>α</sub>, <sup>3</sup>J = 8.2 Hz), 8.13 (s, 1H, H<sub>6</sub>), 8.09 (d, 4H, <sup>4</sup>J = 1.8 Hz, H<sub>α'</sub>), 8.08 (d, 2H, <sup>4</sup>J = 1.8 Hz, H<sub>α'</sub>), 7.89 (d, 2H, <sup>3</sup>J = 8.2 Hz, H<sub>m</sub>), 7.79 (td, 3H, <sup>4</sup>J = 1.8 and 4.8 Hz, H<sub>p+pp'</sub>), 7.38 (d, 2H, <sup>3</sup>J = 8.8 Hz, H<sub>d</sub>), 6.90 (d, 2H, <sup>3</sup>J = 8.8 Hz, H<sub>c</sub>), 6.30 (t, 1H, H<sub>1</sub>, <sup>3</sup>J = 6.5 Hz), 5.55 (s, 2H, H<sub>a</sub>), 4.71 (s, 2H, H<sub>b</sub>), 4.60 (m, 1H, H<sub>3</sub>), 4.00 (ABM, 2H, H<sub>5</sub>, <sup>3</sup>J = 1.9 and 2.4 Hz and <sup>2</sup>J = 8.9 Hz), 3.99 (m, 1H, H<sub>4</sub>), 3.82 (s, 3H, H<sub>e</sub>), 2.46 (ddd, 1H, H<sub>2</sub>, <sup>3</sup>J = 3.0 and 5.7 Hz and <sup>2</sup>J = 13.5 Hz), 2.20 (ddd, 1H, H<sub>2</sub>, <sup>3</sup>J = 6.0 and 7.7 Hz and <sup>2</sup>J = 13.8 Hz), 1.54 (s, 36H, <sup>t</sup>Bu), 1.53 (s, 18H, <sup>t</sup>Bu), 1.26 (s, 3H, CH<sub>3</sub>TIPS), 1.18 (d, 9H, CH<sub>3</sub>TIPS, <sup>3</sup>J = 3.5 Hz), 1.15 (d, 9H, CH<sub>3</sub>TIPS, <sup>3</sup>J = 3.5 Hz). Elemental analysis (%) for

C<sub>97</sub>H<sub>116</sub>N<sub>6</sub>O<sub>7</sub>SiZn (1571.47): calcd. C 74.14, H 7.44, N 5.35; found C 73.41, H 7.56, N 5.08 (+ 1 ethyl acetate).

**Preparation of monomer 7.** The whole system, round-bottom flask equipped with a magnetic stirring bar and an addition funnel was extra dried, deaerated and flushed with argon. The suspension of NaH (0.005 g, 0.12 mmol) in dry THF (2.0 mL) was cooled using an ice-salt bath, and then charged with the uridine-porphyrin conjugate **6** (0.10 g, 0.064 mmol). The mixture was stirred at 0 °C for 1 h and then at rt for 4 h to complete deprotonation. Again the reaction was cooled using an ice-salt bath and charged with TBAI (0.007 g, 0.0191 mmol), and then an addition funnel was filled with the solution of *tert*-butyl 2-bromoacetate (0.012 mL, 0.083 mmol) in dry THF (0.1 mL), which was added dropwise into the reaction under an argon atmosphere. The mixture was then stirred overnight, allowing it to slowly warm to rt. The product formation was followed by TLC in *n*-hexane/ethyl acetate (7.5:2.5) as an eluent, *R<sub>f</sub>* = 0.40. Removal of solvent *via* rotaevaporation afforded residue which was then dissolved in dichloromethane. The corresponding solution was washed with one portion of saturated solution of NH<sub>4</sub>Cl and two portions of water, before it was evaporated to dryness. The crude product was purified by using column chromatography (SiO<sub>2</sub>;  $\varnothing = 1$  cm, h = 22 cm; *n*-hexane/ethyl acetate (from 9:1 to 6:4)), to yield monomer **7** as a violet solid (0.067 g, 0.040 mmol, 62%) together with residual unreacted **6** (0.03 g, 0.020 mmol, 29%). <sup>1</sup>H NMR (CDCl<sub>3</sub>, 300 MHz):  $\delta$ , ppm 9.02 (d, 2H, <sup>3</sup>J = 4.4 Hz, H<sub>β2</sub>), 9.01 (s, 4H, H<sub>β3</sub>), 8.92 (d, 2H, <sup>3</sup>J = 4.7 Hz, H<sub>β1</sub>), 8.21 (d, 2H, H<sub>α</sub>, <sup>3</sup>J = 8.4 Hz), 8.19 (s, 1H, H<sub>6</sub>), 8.09 (d, 4H, <sup>4</sup>J = 2.0 Hz, H<sub>α'</sub>), 8.08 (d, 2H, <sup>4</sup>J = 2.0 Hz, H<sub>α'</sub>), 7.88 (d, 2H, <sup>3</sup>J = 8.2 Hz, H<sub>m</sub>), 7.79 (td, 3H, <sup>4</sup>J = 1.8 and 4.7 Hz, H<sub>p+pp'</sub>), 7.39 (d, 2H, <sup>3</sup>J = 8.8 Hz, H<sub>d</sub>), 6.91 (d, 2H, <sup>3</sup>J = 8.7 Hz, H<sub>c</sub>), 6.38 (dd, 1H, H<sub>1</sub>, <sup>3</sup>J = 7.9 and 5.7 Hz), 5.57 (s, 2H, H<sub>a</sub>), 4.72 (s, 2H, H<sub>b</sub>), 4.34 (m, 1H, H<sub>3</sub>), 4.30 (m, 1H, H<sub>4</sub>), 4.06 (dd, 2H, H<sub>5</sub>, <sup>3</sup>J = 2.0 and 3.0 Hz and <sup>2</sup>J = 9.0 Hz), 4.04 (AB, 2H, CH<sub>2</sub>,<sup>ether</sup>, <sup>2</sup>J = 16.38 Hz), 3.82 (s, 3H, H<sub>e</sub>), 2.63 (ddd, 1H, H<sub>2</sub>, <sup>3</sup>J = 1.9 and 5.6 Hz and <sup>2</sup>J = 13.8 Hz), 2.12 (ddd, 1H, H<sub>2</sub>, <sup>3</sup>J = 6.6 and 8.1 Hz and <sup>2</sup>J = 14.4 Hz), 1.53 (s, 36H, <sup>t</sup>Bu), 1.52 (s, 18H, <sup>t</sup>Bu), 1.51 (s, 9H, <sup>t</sup>Bu), 1.26 (s, 3H, CH<sub>3</sub>TIPS), 1.18 (d, 9H, CH<sub>3</sub>TIPS, <sup>3</sup>J = 3.3 Hz), 1.16 (d, 9H, CH<sub>3</sub>TIPS, <sup>3</sup>J = 3.4 Hz). Elemental analysis (%) for C<sub>103</sub>H<sub>126</sub>N<sub>6</sub>O<sub>9</sub>SiZn (1685.61): calcd. C 73.39, H 7.53, N 4.99; found C 73.13, H 7.44, N 4.62.

**Preparation of monomer-acid 8.** Monomer **7** (1.00 g, 0.59 mmol) was dissolved in CH<sub>2</sub>Cl<sub>2</sub> stabilized with amylene (25 mL) and solution was cooled using an ice-salt bath, and then TFA (5.0 mL, 0.065 mol) was added. The mixture was flushed with argon, and then left to stir. After 1 h at 0 °C, the bath was removed and the mixture allowed to warm to rt. The reaction was stirred for 5 h at rt when it was judged complete by TLC analysis in the mixture of ethyl acetate/methanol (8.5:1.5) with few drops of acetic acid (*R<sub>f</sub>* (**8**) = 0.48). The reaction solution was diluted and successively washed with water until pH

of an aqueous phase was 7. The solvent from the organic phase was removed by evaporation, and subsequently the crude product was dried in vacuum overnight. Finally the pure product was isolated by silica-gel column chromatography ( $\varnothing = 2$  cm,  $h = 30$  cm; ethyl acetate + 0.1% of acetic acid and gradually increased methanol up to 5%), to yield monomer-acid **8** as a violet solid (0.63 g, 0.445 mmol, 75%).  $^1\text{H NMR}$  ( $\text{CDCl}_3$ , 300 MHz):  $\delta$ , ppm 8.90 (d, 2H,  $^3J = 4.3$  Hz,  $\text{H}_{\beta 2}$ ), 8.89 (s, 4H,  $\text{H}_{\beta 3}$ ), 8.80 (d, 2H,  $^3J = 4.8$  Hz,  $\text{H}_{\beta 1}$ ), 8.21 (d, 2H,  $\text{H}_o$ ,  $^3J = 8.0$  Hz), 8.22 (s, 1H,  $\text{H}_6$ ), 8.08 (d, 4H,  $^4J = 1.8$  Hz,  $\text{H}_o$ ), 8.07 (d, 2H,  $^4J = 2.2$  Hz,  $\text{H}_o$ ), 7.88 (d, 2H,  $^3J = 8.2$  Hz,  $\text{H}_m$ ), 7.79 (td, 3H,  $^4J = 1.7$  and  $3.3$  Hz,  $\text{H}_{p+p'}$ ), 6.38 (dd, 1H,  $\text{H}_1$ ,  $^3J = 5.7$  and  $8.0$  Hz), 4.39 (m, 1H,  $\text{H}_3$ ), 4.31 (m, 1H,  $\text{H}_4$ ), 4.23 (s, 2H,  $\text{CH}_{2,\text{ether}}$ ), 4.06 (ABM, 2H,  $\text{H}_5$ ,  $^3J = 1.4$  and  $3.0$  Hz and  $^2J = 9.6$  Hz), 2.67 (ddd, 1H,  $\text{H}_2$ ,  $^3J = 1.5$  and  $5.6$  Hz and  $^2J = 13.3$  Hz), 2.18 (ddd, 1H,  $\text{H}_2$ ,  $^3J = 6.4$  and  $7.9$  Hz and  $^2J = 14.3$  Hz), 1.52 (s, 54H,  $^t\text{Bu}$ ), 1.26 (s, 3H,  $\text{CH}_{\text{TIPS}}$ ), 1.19 (d, 9H,  $\text{CH}_{3,\text{TIPS}}$ ,  $^3J = 3.6$  Hz), 1.16 (d, 9H,  $\text{CH}_{3,\text{TIPS}}$ ,  $^3J = 3.7$  Hz),  $-2.7$  (s, 2H, NH).

**Preparation of monomer-alcohol 9.** Monomer **7** (1.00 g, 0.59 mmol) was dissolved in THF (30 mL), and TBAF (2.0 mL, 1.19 mmol, 1 M solution in THF) was added. The mixture was deaerated and flushed with argon, and then left to stir at rt for 5 h under an argon atmosphere. The formation of the product was followed by TLC in *n*-hexane/ethyl acetate (6.5:3.5) as an eluent,  $R_f = 0.44$ . The solvent was removed by evaporation and the residue was dissolved in dichloromethane. The obtained solution was washed with three portions of water, and organic phase was removed under reduced pressure. Finally the pure product was isolated by silica-gel column chromatography ( $\varnothing = 3$  cm,  $h = 23$  cm; *n*-hexane/ethyl acetate (8:2)), to afford monomer-alcohol **9** as a violet solid (0.86 g, 0.565 mmol, 96%).  $^1\text{H NMR}$  ( $\text{CDCl}_3$ , 300 MHz):  $\delta$ , ppm 9.05 (d, 2H,  $^3J = 4.1$  Hz,  $\text{H}_{\beta 2}$ ), 9.04 (s, 4H,  $\text{H}_{\beta 3}$ ), 9.00 (d, 2H,  $^3J = 4.7$  Hz,  $\text{H}_{\beta 1}$ ), 8.25 (d, 2H,  $\text{H}_o$ ,  $^3J = 8.1$  Hz), 8.13 (d, 4H,  $^4J = 1.8$  Hz,  $\text{H}_o$ ), 8.12 (d, 2H,  $^4J = 1.8$  Hz,  $\text{H}_o$ ), 8.04 (s, 1H,  $\text{H}_6$ ), 7.94 (d, 2H,  $^3J = 8.1$  Hz,  $\text{H}_m$ ), 7.83 (m, 3H,  $\text{H}_{p+p'}$ ), 7.36 (d, 2H,  $^3J = 6.9$  Hz,  $\text{H}_d$ ), 6.89 (d, 2H,  $^3J = 7.0$  Hz,  $\text{H}_e$ ), 6.04 (t, 1H,  $\text{H}_1$ ,  $^3J = 6.4$  Hz), 5.53 (s, 2H,  $\text{H}_a$ ), 4.70 (s, 2H,  $\text{H}_b$ ), 4.18 (td, 1H,  $\text{H}_3$ ,  $^3J = 4.2$  and  $8.1$  Hz), 4.00 (AB, 2H,  $\text{CH}_{2,\text{ether}}$ ,  $^2J = 16.5$  Hz), 3.95–3.71 (m, 3H,  $\text{H}_4+\text{H}_5$ ), 3.81 (s, 3H,  $\text{H}_c$ ), 2.44 (ddd, 1H,  $\text{H}_2$ ,  $^3J = 4.2$  and  $6.0$  Hz and  $^2J = 13.5$  Hz), 2.27 (td, 1H,  $\text{H}_2$ ,  $^3J = 6.3$  Hz and  $^2J = 13.2$  Hz), 1.56 (s, 36H,  $^t\text{Bu}$ ), 1.55 (s, 18H,  $^t\text{Bu}$ ), 1.50 (s, 9H,  $^t\text{Bu}$ ).

**Preparation of free-base dimer.** Monomer-alcohol **9** (0.66 g, 0.430 mmol) and monomer-acid **8** (0.61 g, 0.430 mmol) were dissolved in dichloromethane (without ethanol and dried over molecular sieves, 40 mL) and to this solution DMAP (0.11 g, 0.903 mmol) and DCC (0.12 g, 0.602 mmol) were added, respectively. The obtained mixture was allowed to stir at rt overnight under an argon atmosphere. The reaction progress was followed by TLC analysis examining the disappearance of the both starting materials and formation of the product (*n*-hexane/ethyl

acetate (6.5:3.5),  $R_f = 0.31$ ). The solvent was removed to dryness *via* rotaevaporation and afforded residue was suspended in minimum volume of toluene. The slurry was placed in refrigerator for 3 h to precipitate DCU. The precipitated white solid was collected by filtration and washed with small portions of chilled toluene. The obtained filtrate was evaporated *in vacuo* and then left to dry in vacuum overnight. The crude product was purified by using column chromatography ( $\text{SiO}_2$ ;  $\varnothing = 3$  cm,  $h = 30$  cm; *n*-hexane/ethyl acetate (from 8:2 to 6:4)) and preparative size exclusion chromatography (Bio-Beads, toluene), yielding the free-base dimer as a violet solid (0.92 g, 0.314 mmol, 73%).  $^1\text{H NMR}$  ( $\text{CDCl}_3$ , 500 MHz,  $c = 3.027 \times 10^{-3}$  M):  $\delta$ , ppm 9.01 (d, 2H,  $^3J = 4.6$  Hz,  $\text{Zn-H}_{\beta 2}$ ), 8.99 (s, 4H,  $\text{Zn-H}_{\beta 3}$ ), 8.92 (d, 2H,  $^3J = 4.7$  Hz,  $\text{Zn-H}_{\beta 1}$ ), 8.89 (s, 4H,  $2\text{H-H}_{\beta 3}$ ), 8.88 (d, 2H,  $^3J = 4.6$  Hz,  $2\text{H-H}_{\beta 2}$ ), 8.76 (d, 2H,  $^3J = 4.7$  Hz,  $2\text{H-H}_{\beta 1}$ ), 8.25 (d, 2H,  $\text{Zn-H}_o$ ,  $^3J = 8.5$  Hz), 8.16 (d, 2H,  $2\text{H-H}_o$ ,  $^3J = 8.0$  Hz), 8.10 (t, 4H,  $^4J = 1.3$  Hz,  $\text{Zn-H}_o$ ), 8.08 (d, 2H,  $^4J = 1.8$  Hz,  $\text{Zn-H}_o$ ), 8.07 (d, 6H,  $^4J = 1.8$  Hz,  $2\text{H-H}_o$ ), 8.06 (s, 1H,  $2\text{H-H}_d$ ), 7.93 (d, 2H,  $^3J = 8.0$  Hz,  $\text{Zn-H}_m$ ), 7.92 (s, 1H,  $\text{Zn-H}_d$ ), 7.78 (td, 5H,  $^4J = 1.5$  and  $3.5$  Hz,  $\text{H}_p$ ), 7.76 (t, 1H,  $^4J = 2.0$  Hz,  $\text{H}_p$ ), 7.75 (d, 2H,  $^3J = 8.0$  Hz,  $2\text{H-H}_m$ ), 7.39 (d, 2H,  $^3J = 9.0$  Hz,  $\text{H}_d$ ), 6.92 (d, 2H,  $^3J = 8.5$  Hz,  $\text{H}_e$ ), 6.31 (t, 1H,  $\text{Zn-H}_1$ ,  $^3J = 6.5$  Hz), 6.28 (dd, 1H,  $2\text{H-H}_1$ ,  $^3J = 8.0$ ,  $^4J = 5.0$  Hz), 5.57 (s, 2H,  $\text{H}_a$ ), 4.73 (s, 2H,  $\text{H}_b$ ), 4.55 (ABM, 2H,  $2\text{H-CH}_{2,\text{ether}}$ ,  $^3J = 3.5$  and  $4.3$  Hz and  $^2J = 7.8$  Hz), 4.45 (q, 1H,  $\text{Zn-H}_4$ ,  $^3J = 4.0$  Hz), 4.41 (d, 1H,  $2\text{H-H}_3$ ,  $^3J = 5.5$  Hz), 4.39 (s, 2H,  $\text{Zn-CH}_{2,\text{ether}}$ ), 4.31 (m, 1H,  $2\text{H-H}_4$ ), 4.29 (m, 1H,  $\text{Zn-H}_3$ ), 4.07 (AB, 2H,  $\text{Zn-H}_5$ ,  $^2J = 16.5$  Hz), 4.02 (ABM, 2H,  $2\text{H-H}_5$ ,  $^3J = 1.0$  and  $1.8$  Hz and  $^2J = 10.0$  Hz), 3.82 (s, 3H,  $\text{H}_c$ ), 2.68 (ddd, 1H,  $2\text{H-H}_2$ ,  $^3J = 3.0$  and  $5.5$  Hz and  $^2J = 14.3$  Hz), 2.60 (ddd, 1H,  $\text{Zn-H}_2$ ,  $^3J = 5.3$  and  $6.8$  Hz and  $^2J = 13.8$  Hz), 2.27 (dd, 1H,  $\text{Zn-H}_2$ ,  $^3J = 7.5$  Hz and  $^2J = 14.3$  Hz), 2.11 (ddd, 1H,  $2\text{H-H}_2$ ,  $^3J = 6.2$  and  $8.6$  Hz and  $^2J = 13.9$  Hz), 1.53 (s, 72H,  $^t\text{Bu}$ ), 1.52 (s, 36H,  $^t\text{Bu}$ ), 1.51 (s, 9H,  $^t\text{Bu}$ ), 1.25 (s, 3H,  $\text{CH}_{\text{TIPS}}$ ), 1.12 (d, 9H,  $\text{CH}_{3,\text{TIPS}}$ ,  $^3J = 4.0$  Hz), 1.11 (d, 9H,  $\text{CH}_{3,\text{TIPS}}$ ,  $^3J = 3.5$  Hz),  $-2.70$  (s, 2H, NH).

**Preparation of zinc(II) porphyrin dimer 10.** The solution of  $\text{Zn}(\text{OAc})_2 \cdot 2\text{H}_2\text{O}$  (0.11 M) was prepared separately by dissolving the corresponding salt (0.0042 g, 0.019 mmol) in methanol (0.18 mL). Such solution was added to the mixture of free-base dimer (0.028 g, 0.0096 mmol) in chloroform (7 mL), and such obtained homogenous mixture was flushed with argon and heated to reflux. The progress of metallation was monitored by UV-visible spectroscopy showing that the reaction was terminated after 4 h of reflux under an argon atmosphere. The solvent was removed by evaporation, the residue was dissolved in dichloromethane and the solution was washed with water. The crude product was purified by column chromatography ( $\text{SiO}_2$ ;  $\varnothing = 1$  cm,  $h = 10$  cm; *n*-hexane/ethyl acetate (7:3)) yielding **10** (0.018 g, 0.0059 mmol, 62%).  $^1\text{H NMR}$  ( $\text{CDCl}_3$ , 250 MHz):  $\delta$ , ppm 9.02 (d, 2H,  $^3J = 4.7$  Hz,  $\text{H}_{\beta 2}$ ), 9.00 (s, 8H,  $\text{H}_{\beta 3}$ ), 8.99 (d, 2H,  $^3J = 4.7$  Hz,  $\text{H}_{\beta 2}$ ), 8.94 (d, 2H,  $^3J = 4.7$  Hz,  $\text{H}_{\beta 1}$ ), 8.87 (d, 2H,  $^3J =$

4.7 Hz, H<sub>β1</sub>), 8.26 (d, 2H, H<sub>o</sub>, <sup>3</sup>J = 8.2 Hz), 8.17 (d, 2H, H<sub>o</sub>, <sup>3</sup>J = 8.1 Hz), 8.11 (d, 4H, <sup>4</sup>J = 1.7 Hz, H<sub>o</sub>'), 8.09 (d, 8H, <sup>4</sup>J = 1.7 Hz, H<sub>o</sub>'), 8.05 (s, 1H, H<sub>6</sub>), 7.94 (d, 2H, <sup>3</sup>J = 8.2 Hz, H<sub>m</sub>), 7.91 (s, 1H, H<sub>6</sub>), 7.79 (s, 6H, H<sub>p</sub>'), 7.75 (d, 2H, <sup>3</sup>J = 8.4 Hz, H<sub>m</sub>), 7.39 (d, 2H, <sup>3</sup>J = 8.7 Hz, H<sub>d</sub>), 6.91 (d, 2H, <sup>3</sup>J = 8.7 Hz, H<sub>c</sub>), 6.29 (t, 1H, H<sub>1</sub>', <sup>3</sup>J = 6.7 Hz), 6.26 (t, 1H, H<sub>1</sub>', <sup>3</sup>J = 6.9 Hz), 5.57 (s, 2H, H<sub>a</sub>), 4.73 (s, 2H, H<sub>b</sub>), 4.55 (ABM, 2H, CH<sub>2,ether</sub>, <sup>3</sup>J = 3.8 and 5.1 Hz and <sup>2</sup>J = 8.1 Hz), 4.42 (m, 2H, H<sub>4</sub>+H<sub>3</sub>), 4.38 (s, 2H, CH<sub>2,ether</sub>), 4.30 (m, 2H, H<sub>4</sub>+H<sub>3</sub>), 4.06 (AB, 2H, H<sub>5</sub>', <sup>2</sup>J = 14.2 Hz), 4.05 (m, 2H, H<sub>5</sub>'), 3.82 (s, 3H, H<sub>e</sub>), 2.64 (m, 2H, H<sub>2</sub>'), 2.27 (q, 1H, H<sub>2</sub>'), <sup>3</sup>J = 7.0 Hz), 2.11 (m, 1H, H<sub>2</sub>'), 1.52 (s, 108H, 'Bu), 1.50 (s, 9H, 'Bu), 1.26 (s, 3H, CH<sub>TIPS</sub>), 1.14 (d, 9H, CH<sub>3,TIPS</sub>, <sup>3</sup>J = 1.3 Hz), 1.11 (d, 9H, CH<sub>3,TIPS</sub>, <sup>3</sup>J = 1.4 Hz). UV-vis (CH<sub>2</sub>Cl<sub>2</sub>): λ<sub>abs</sub>, nm (ε) 422 (1 008 610 M<sup>-1</sup>.cm<sup>-1</sup>), 550 (45 606 M<sup>-1</sup>.cm<sup>-1</sup>), 589 (14 398 M<sup>-1</sup>.cm<sup>-1</sup>). MALDI-TOF MS: m/z 2989.9 ([M]<sup>+</sup> calcd. 2990.6).

## CONCLUSION

We report herein the synthesis of a dinucleotide bearing pendant porphyrins dedicated to adopt a pre-organized coformation with face-to-face porphyrins, and capable to self-organize in a stable sandwich type complex with bidentate base such as DABCO. Earlier studies demonstrated that a peptidic linker does not provide sufficient pre-organization to enhance significantly the association constant with bidentate bases such as DABCO on the contrary of some other flexible linkers such as uridine or 2'-deoxyuridine. We document herein that the gain in stability for the formation of sandwich type host-guest complex with DABCO can be even greater when a dinucleotide linker is used. Such pre-organization increases the association constants by one to two orders of magnitude when compared to the association constants of the same bidentate ligands with a reference Zn(II) porphyrin. Comparison of these results with those obtained for rigid tweezers shows a better efficiency of the flexible nucleosidic dimers. We thus document the fact that the choice of rigid spacers is not the only way to pre-organize bis-porphyrins, and that some well-chosen nucleosidic linkers offer an interesting option for the synthesis of such devices. Furthermore, the chirality and enantio-purity of the nucleosidic linkers paves the way toward the selective complexation of enantio-pure bidentate guests and the resolution of racemates.

## Acknowledgements

This work was supported by the CNRS and the French Ministry of Research.

## NOTES AND REFERENCES

1. Lehn JM. *Angew. Chem. Int. Ed. Engl.* 1988; **27**: 89.
2. Lehn JM. *Science* 2002; **295**: 2400.

3. Fukuzumi S, Saito K, Ohkubo K, Troiani V, Qiu H, Gadde S, D'Souza F and Solladié N. *Phys. Chem. Chem. Phys.* 2011; **13**: 17019.
4. Piet JJ, Taylor PN, Anderson HL, Osuka A and Warman JM. *J. Am. Chem. Soc.* 2000; **122**: 1749.
5. Satake A and Kobuke Y. *Tetrahedron* 2005; **61**: 13.
6. Choi M, Yamazaki T, Yamazaki I and Aida T. *Angew. Chem., Int. Ed.* 2004; **43**: 150.
7. Tomizaki K, Yu L, Wei L, Bocian DF and Lindsey JS. *J. Org. Chem.* 2003; **68**: 8199.
8. Hwang IW, Kamada T, Ahn TK, Ko DM, Nakamura T, Tsuda A, Osuka A and Kim D. *J. Am. Chem. Soc.* 2004; **126**: 16187.
9. Mak CC, Bampos N, Darling SL, Montalti M, Prodi L and Sanders JKM. *J. Org. Chem.* 2001; **66**: 476.
10. Haycock RA, Yartsev A, Michelsen U, Sundström V and Hunter CA. *Angew. Chem. Int. Ed.* 2000; **39**: 3616.
11. Bretar J, Gieselbrecht JP, Gross M and Solladié N. *Chem. Commun.* 2001; 733.
12. Rein R, Gross M and Solladié N. *Chem. Commun.* 2004; 1992.
13. Flamigni L, Talarico AM, Ventura B, Rein R and Solladié N. *Chem. Eur. J.* 2006; **12**: 701.
14. Ikeda C, Tanaka Y, Fujihara T, Ishii Y, Ushiyama T, Yamamoto K, Yoshioka N and Inoue H. *Inorg. Chem.* 2001; **40**: 3395.
15. Ikeda C, Satake A and Kobuke Y. *Org. Lett.* 2003; **5**: 4935.
16. Kameyama K, Satake A and Kobuke Y. *Tetrahedron Lett.* 2004; **45**: 7617.
17. Schmittel M and Kishore RSK. *Org. Lett.* 2004; **6**: 1923.
18. Balaban TS, Goddard R, Linke-Schaetzel M and Lehn JM. *J. Am. Chem. Soc.* 2003; **125**: 4233.
19. Iengo E, Zangrando E and Alessio E. *Eur. J. Inorg. Chem.* 2003; 2371.
20. Iengo E, Zangrando E, Alessio E, Chambron JC, Hitz V, Flamigni L and Sauvage JP. *Chem. Eur. J.* 2003; **9**: 5879.
21. Sugou K, Sasaki K, Kitajima K, Iwaki T and Kuroda Y. *J. Am. Chem. Soc.* 2002; **124**: 1182.
22. Wojaczynski J and Latos-Grazynski L. *Coord. Chem. Rev.* 2000; **204**: 113.
23. Holliday BJ and Mirkin CA. *Angew. Chem. Int. Ed.* 2001; **40**: 2022.
24. Robertson A and Shinkai S. *Coord. Chem. Rev.* 2000; **205**: 157.
25. Toma HE and Araki K. *Coord. Chem. Rev.* 2000; **196**: 307.
26. Leininger S, Oleyuk B and Stang PJ. *Chem. Rev.* 2000; **100**: 853.
27. Anderson HL and Sanders JKM. *J. Chem. Soc., Perkin Trans. 1* 1995; 2223.
28. Vidal-Ferran A, Bampos N and Sanders JKM. *Inorg. Chem.* 1997; **36**: 6117.
29. Anderson HL. *Inorg. Chem.* 1994; **33**: 972.

30. Taylor PN and Anderson HL. *J. Am. Chem. Soc.* 1999; **121**: 11538.
31. Wilson GS and Anderson HL. *Chem. Commun.* 1999; 1539.
32. Michelsen U and Hunter CA. *Angew. Chem. Int. Ed.* 2000; **39**: 764.
33. Gardner M, Guerin AJ, Hunter CA, Michelsen U and Rotger C. *New. J. Chem.* 1999; 309.
34. Fleischer EB and Shachter AM. *Inorg. Chem.* 1991; **30**: 3763.
35. Slone RV and Hupp JH. *Inorg. Chem.* 1997; **36**: 5422.
36. Drain CM, Nifiatis F, Vasenko A and Batteas JD. *Angew. Chem. Int. Ed.* 1998; **37**: 2344.
37. Milic TN, Chi N, Yablon DG, Flynn GW, Batteas JD and Drain CM. *Angew. Chem. Int. Ed.* 2002; **41**: 2117.
38. (a) Reek JNH, Schenning APHJ, Bosman AW, Meijer EW and Crossley MJ. *Chem. Commun.* 1998; 11. (b) Baldini L, Ballester P, Casnati A, Gomila RM, Hunter CA, Sansone F and Ungaro R. *J. Am. Chem. Soc.* 2003; **125**: 14181.
39. (a) Solladié N and Gross M. *Tetrahedron Letters* 1999; **40**: 3369. (b) Solladié N, Gross M, Gisselbrecht JP and Sooambar C. *Chem. Commun.* 2001: 2206. (c) Solladié N, Aubert N, Bouatra S, Bourgogne C, Bregier F, Brettar J, Gisselbrecht JP, Gross M, Rein R, Sooambar C, Troiani V and Walther M. *J. Porphyrins Phthalocyanines* 2003; **7**: 270. (d) Flamigni L, Talarico AM, Ventura B, Marconi G, Sooambar C and Solladié N. *Eur. J. Inorg. Chem.* 2004: 2557. (e) Solladié N, Sooambar C, Herschbach H, Strub JM, Leize E, Van Dorsselaer A, Talarico AM, Ventura B and Flamigni L. *New J. Chem.* 2005; **29**: 1504. (f) Flamigni L, Talarico AM, Ventura B, Sooambar C and Solladié N. *Eur. J. Inorg. Chem.* 2006: 2155. (g) Solladié N, Aziat F, Bouatra S and Rein R. *J. Porphyrins Phthalocyanines* 2008; **12**: 1250. (h) Endo M, Shiroyama T, Fujitsuka M and Majima T. *J. Org. Chem.* 2005; **70**: 7468. (i) Balaz M, Steinkruger JD, Ellestad A and Berova N. *Org. Lett.* 2005; **7**: 5613. (j) Balaz M, Li BC, Jockusch S, Ellestad GA and Berova N. *Angew. Chem. Int. Ed.* 2006; **45**: 3530. (k) Fendt LA, Bouamaied I, Thoni S, Amiot N and Stulz E. *J. Am. Chem. Soc.* 2007; **129**: 15319. (l) Mammana A, Asakawa T, Bitsch-Jensen K, Wolfe A, Chaturantabut S, Otani Y, Li X, Li Z, Nakanishi K, Balaz M, Ellestad GA and Berova N. *Bioorg. Med. Chem.* 2008; **16**: 6544. (m) Bouamaied I, Nguyen TN, Rühl T and Stulz E. *Org. Biomol. Chem.* 2008; **6**: 3888.
40. Solladié N, Hamel A and Gross M. *Chirality* 2001; **13**: 736 and unpublished results.
41. Choi MS, Yamazaki T, Yamazaki I and Aida T. *Angew. Chem. Int. Ed.* 2004; **43**: 150.
42. (a) Lindsey JS, Schreiman IC, Hsu HC, Kearney PC and Marguerettaz AM. *J. Org. Chem.* 1987; **52**: 827. (b) Lindsey JS and Wagner RW. *J. Org. Chem.* 1989; **54**: 828.
43. Lebreton J, De Mesmaeker A and Waldner A. *Synlett* 1993; 54.
44. Wendeborn S, Jouanno C, Wolf RM and De Mesmaeker A. *Tetrahedron Lett.* 1996; **37**: 5511.
45. (a) Barber J and Andersson B. *Nature* 1994; **370**: 31. (b) Kühlbrandt W. *Nature* 1995; **374**: 497. (c) McDermott G, Prince SM, Freer AA, Hawthornthwaite-Lawless AM, Papiz MZ, Cogdell RJ and Isaacs NW. *Nature* 1995; **374**: 517. (d) Pullerits T and Sundström V. *Acc. Chem. Res.* 1996; **29**: 381.
46. Hirose K. *J. Inclusion Phenom. Macrocyclic Chem.* 2001; **39**: 193.
47. SPECFIT, Global Least Squares fitting by Factor Analysis and Marquart Minimization.
48. Gampp H, Maeder M, Meyer CJ and Zuberbühler AD. *Talanta* 1986; **33**: 943.
49. Gampp H, Maeder M, Meyer CJ and Zuberbühler AD. *Talanta* 1985; **32**: 95.
50. Mak CC, Bampos N and Sanders JKM. *Angew. Chem. Int. Ed.* 1998; **37**: 3020.
51. Ballester P, Costa A, Castilla AM, Deyà PM, Frontera A, Gomila RM and Hunter CA. *Chem. Eur. J.* 2005; **11**: 2196.
52. Hunter CA, Meah MN and Sanders JKM. *J. Am. Chem. Soc.* 1990; **112**: 5773.
53. Anderson HL, Hunter CA, Meah MN and Sanders JKM. *J. Am. Chem. Soc.* 1990; **112**: 5780.
54. Kim HJ, Bampos N and Sanders JKM. *J. Am. Chem. Soc.* 1999; **121**: 8120.
55. Hunter CA and Tregonning R. *Tetrahedron* 2002; **58**: 691.
56. Mak CC, Pomeranc D, Montelti M, Prodi L and Sanders JKM. *Chem. Commun.* 1999; 1083.
57. Wilson GS and Anderson HL. *Chem. Commun.* 1999; 1539.
58. Baldini L, Ballester P, Casnati A, Gomila RM, Hunter CA, Sansone F and Ungaro R. *J. Am. Chem. Soc.* 2003; **125**: 14181.
59. Solladié N, Aziat F, Bouatra S and Rein R. *J. Porphyrins Phthalocyanines* 2008; **12**: 1250.

# CONTENTS

Proton-coupled electron transfer chemistry of hangman macrocycles: Hydrogen and oxygen evolution reactions	1
<i>Dilek K. Dogutan, D. Kwabena Bediako, Daniel J. Graham, Christopher M. Lemon and Daniel G. Nocera*</i>	
A new biological function of heme as a signaling molecule	9
<i>Norifumi Muraki, Chihiro Kitatsuji and Shigetoshi Aono*</i>	
Meso-N-arylamino- and N,N-diarylaminoporphyrinoids: Syntheses, properties and applications	21
<i>Ryota Sakamoto*, Suzaliza Mustafar and Hiroshi Nishihara*</i>	
Molecular assemblies based on strong axial coordination in metal complexes of saddle-distorted dodecaphenylporphyrins	32
<i>Tomoya Ishizuka, Shunichi Fukuzumi and Takahiko Kojima*</i>	
A review of iron and cobalt porphyrins, phthalocyanines and related complexes for electrochemical and photochemical reduction of carbon dioxide	45
<i>Gerald F. Manbeck* and Etsuko Fujita*</i>	
Metalloporphyrin/G-quadruplexes: From basic properties to practical applications	65
<i>Eyal Golub, Chun-Hua Lu and Itamar Willner*</i>	
Effect of axial ligands on electronic structure and O <sub>2</sub> reduction by iron porphyrin complexes: Towards a quantitative understanding of the “push effect”	92
<i>Subhra Samanta, Pradip Kumar Das, Sudipta Chatterjee and Abhishek Dey*</i>	
Porphyrin-based photosensitizers and the corresponding multifunctional nanoplatfoms for cancer-imaging and phototherapy	109
<i>Avinash Srivatsan, Joseph R. Missert, Santosh K. Upadhyay and Ravindra K. Pandey*</i>	
Macrocyclic dipyrin dimer bridged by ethylene and dioxyphenylene linkers	135
<i>Ji-Young Shin*, Satoru Hiroto and Hiroshi Shinokubo</i>	
Synthesis of push–pull porphyrin with two electron-donating and two electron-withdrawing groups and its application to dye-sensitized solar cell	140
<i>Tomohiro Higashino, Yamato Fujimori, Kenichi Sugiura, Yukihiro Tsuji, Seigo Ito and Hiroshi Imahori*</i>	
Preparation and characterization of a tungsten(V) corrole dichloride complex	150
<i>Rosa Padilla, Heather L. Buckley, Ashleigh L. Ward and John Arnold*</i>	
A novel terbium-cobalt tetra(4-sulfonatophenyl)porphyrin: Synthesis, structure and photophysical and electrochemical properties	154
<i>Wen-Tong Chen*, Jian-Gen Huang, Qiu-Yan Luo, Ya-Ping Xu and Hong-Ru Fu</i>	
Systematic studies on side-chain structures of phthalocyaninato-polysiloxanes: Polymerization and self-assembling behaviors	160
<i>Satoru Yoneda, Tsuneaki Sakurai*, Toru Nakayama, Kenichi Kato, Masaki Takata and Shu Seki*</i>	

Dimeric 1:2 adduct of $\beta,\beta'$ -bis(diphenylphosphino)porphyrin with silver(I) chloride <i>Keisuke Fujimoto, Hideki Yorimitsu* and Atsuhiko Osuka*</i>	171
Donor- $\pi$ -acceptor, triazine-linked porphyrin dyads as sensitizers for dye-sensitized solar cells <i>Ganesh D. Sharma*, Galatea E. Zervaki, Kalliopi Ladomenou, Emmanuel N. Koukaras, Panagiotis P. Angaridis and Athanassios G. Coutsolelos*</i>	175
Optical limiting and singlet oxygen generation properties of phosphorus triazatetrazabenzcorroles <i>Colin Mkhize, Jonathan Britton, John Mack and Tebello Nyokong*</i>	192
Design of diethynyl porphyrin derivatives with high near infrared fluorescence quantum yields <i>Kimihiro Susumu and Michael J. Therien*</i>	205
Synthesis and photodynamics of diphenylethynyl-bridged porphyrin-quinoidal porphyrin hybrids <i>Shuhei Sakatani, Takuya Kamimura, Kei Ohkubo, Shunichi Fukuzumi and Fumito Tani*</i>	219
Molecular structures, redox properties, and photosubstitution of ruthenium(II) carbonyl complexes of porphycene <i>Toru Okawara, Masaaki Abe*, Shiho Ashigara and Yoshio Hisaeda*</i>	233
Supramolecular photovoltaic cells utilizing inclusion complexes composed of $\text{Li}^+@C_{60}$ and cyclic porphyrin dimer <i>Hayato Sakai, Takuya Kamimura, Fumito Tani* and Taku Hasobe*</i>	242
<i>N</i> -confused <i>meso</i> -tetraaryl-substituted free-base porphyrins: Determination of protonation and deprotonation constants in nonaqueous media <i>Zhongping Ou*, Xueyan Chen, Lina Ye, Songlin Xue, Yuanyuan Fang, Xiaoqin Jiang and Karl M. Kadish*</i>	251
Energy-transfer studies on phthalocyanine–BODIPY light harvesting pentad by laser flash photolysis <i>Mohamed E. El-Khouly*, Cem Göl, Morad M. El-Hendawy, Serkan Yeşilot and Mahmut Durmuş*</i>	261
Charge separation in supramolecular ferrocene(s)-zinc porphyrin-fullerene triads: A femtosecond transient absorption study <i>Gary N. Lim, Whitney A. Webre and Francis D'Souza*</i>	270
Nondestructive readout fluorescence memory based on a gallium(III) corrole complex and photochromic <i>cis</i> -1,2-dithienylethene <i>Jijoon Kang and Youngmin You*</i>	281
Photophysical properties of Sn(IV)tetraphenylporphyrin-pyrene dyad with a $\beta$ -vinyl linker <i>P. Silviya Reeta*, Adis Khetubol, Tejaswi Jella, Vladimir Chukharev, Fawzi Abou-Chahine, Nikolai V. Tkachenko, L. Giribabu* and Helge Lemmetyinen*</i>	288
Effects of heme modification on oxygen affinity and cooperativity of human adult hemoglobin <i>Tomokazu Shibata, Eisuke Furuichi, Kiyohiro Imai, Akihiro Suzuki and Yasuhiko Yamamoto*</i>	301
Photocurrent enhancements in a porphyrin-viologen linked compound under plasmonic and magnetic fields <i>Hiroaki Yonemura*, Tomoki Niimi and Sunao Yamada</i>	308
Cholesteryl oleate-appended phthalocyanines as potential photosensitizers in the treatment of leishmaniasis <i>Laura E. Sánchez Contreras, Johannes Zirzmeier, Sabrina V. Kirner, Francesca Setaro, Fernando Martínez, Stefany Lozada, Patricia Escobar, Uwe Hahn, Dirk M. Guldi* and Tomás Torres*</i>	320
Highly efficient hydroxylation of gaseous alkanes at reduced temperature catalyzed by cytochrome P450BM3 assisted by decoy molecules <i>Norifumi Kawakami, Zhiqi Cong, Osami Shoji* and Yoshihito Watanabe*</i>	329

Synthesis and characterization of a sulfur-containing phthalocyanine-gold nanoparticle hybrid <i>Vicente M. Blas-Ferrando, Javier Ortiz, Fernando Fernández-Lázaro and Ángela Sastre-Santos*</i>	335
Metal-induced dynamic conformational and fluorescence switch of quinone-appended Zn-porphyrin <i>Yasuyuki Yamada, Kosuke Hiraga and Kentaro Tanaka*</i>	344
Reactions of a heme-superoxo complex toward a cuprous chelate and $\bullet\text{NO}_{(g)}$ : CcO and NOD chemistry <i>Savita K. Sharma, Patrick J. Rogler and Kenneth D. Karlin*</i>	352
Near-infrared luminescent Sn(IV) complexes of N-confused tetraphenylporphyrin: Effect of axial anion coordination <i>Arghya Basu, Motoki Kitamura, Shigeki Mori, Masatoshi Ishida, Yongshu Xie and Hiroyuki Furuta*</i>	361
Preparation and characterization of cobalt(II) phthalocyanine complex-encapsulated zeolite-X <i>Nayumi Ohata, Yurie Ito, Daisuke Nakane, Hideki Kitamura and Hideki Masuda*</i>	372
Redox behavior of novel nickel and palladium complexes supported by trianionic non-innocent ligand containing $\beta$ -diketiminato and phenol groups <i>Yuma Morimoto, June Takaichi, Shinichi Hanada, Kei Ohkubo, Hideki Sugimoto, Nobutaka Fujieda, Shunichi Fukuzumi and Shinobu Itoh*</i>	377
Electrochemistry and spectroelectrochemistry of $\beta$ -pyrazino-fused tetraarylporphyrins in nonaqueous media <i>Yuanyuan Fang, Federica Mandoj, Lihan Zeng, Rajesh Pudi, Manuela Stefanelli, Roberto Paolesse* and Karl M. Kadish*</i>	388
Synthesis and anti-cancer activities of a water soluble gold(III) porphyrin <i>Aaron D. Lammer, Melissa E. Cook and Jonathan L. Sessler*</i>	398
Free-base porphyrin and [60]fullerene linked by oligomeric ethylenedioxythienylenevinylene bridge <i>Beatriz Pelado, Julieta Coro, Pilar de la Cruz and Fernando Langa*</i>	404
Efficient oxidation of ethers with pyridine <i>N</i> -oxide catalyzed by ruthenium porphyrins <i>Nobuki Kato, Yu Hamaguchi, Naoki Umezawa and Tsunehiko Higuchi*</i>	411
Mechanistic study of methanol oxidation by Ru <sup>IV</sup> -oxo complexes <i>Yoshihito Shiota*, Shoya Takahashi, Shingo Ohzu, Tomoya Ishizuka, Takahiko Kojima and Kazunari Yoshizawa*</i>	417
Very fast singlet and triplet energy transfers in a tri-chromophoric porphyrin dyad aided by the truxene platform <i>Adam Langlois, Hai-Jun Xu, Paul-Ludovic Karsenti, Claude P. Gros* and Pierre D. Harvey*</i>	427
Synthesis and wire-like performance of diruthenium molecular wire with a C $\equiv$ C-porphyrin-C $\equiv$ C linker <i>Yuya Tanaka, Masanori Ono and Munetaka Akita*</i>	442
Diporphyrin magnesium complex with long-wavelength light absorption for organic solar cells <i>Takenari Sato, Takafumi Nakagawa, Hiroshi Okada and Yutaka Matsuo*</i>	451
Formate dehydrogenase catalyzed CO <sub>2</sub> reduction in a chlorin-e <sub>6</sub> sensitized photochemical biofuel cell <i>Yutaka Amao* and Naho Shuto</i>	459
Effect of alkyl substituents: 5,15-bis(trimethylsilylethynyl)- vs. 5,15-bis(triisopropylsilylethynyl)-tetrabenzoporphyrins and their metal complexes <i>Kohtaro Takahashi, Naoya Yamada, Daichi Kumagai, Daiki Kuzuhara, Mitsuharu Suzuki, Yuji Yamaguchi, Naoki Aratani, Ken-ichi Nakayama* and Hiroko Yamada*</i>	465
Corrole-imide dyads — Synthesis and optical properties <i>Roman Voloshchuk, Mariusz Tasiór, Adina I. Ciuciu, Lucia Flamigni* and Daniel T. Gryko*</i>	479

Mechanistic study of a manganese porphyrin catalyst for on-demand production of chlorine dioxide in water <i>Scott D. Hicks, Silei Xiong, Curt J. Bougher, Grigori A. Medvedev, James Caruthers and Mahdi M. Abu-Omar*</i>	492
Structural changes in non-planar octaaryl substituted phthalocyanine phosphorus complexes <i>Taniyuki Furuyama, Ryosuke Harako and Nagao Kobayashi*</i>	500
Myoglobin-based non-precious metal carbon catalysts for an oxygen reduction reaction <i>Akira Onoda*, Yuta Tanaka, Toshikazu Ono, Shotaro Takeuchi, Akira Sakai and Takashi Hayashi*</i>	510
Synthesis of carboxylated chlorophylls and their application as functional materials <i>Shin-ichi Sasaki, Xiao-Feng Wang, Toshitaka Ikeuchi and Hitoshi Tamiaki*</i>	517
Electroabsorption spectra of push–pull porphyrins in solution and in solid films <i>Kamlesh Awasthi, Hung-Yu Hsu, Hung-Chu Chiang, Chi-Lun Mai, Chen-Yu Yeh*, Eric Wei-Guang Diau* and Nobuhiro Ohta*</i>	527
Pre-organized dinucleosides with pendant porphyrins for the formation of sandwich type complexes with DABCO with high association constants <i>Sonja Merkas, Souhaila Bouatra, Régis Rein, Ivo Piantanida, Mladen Zinic and Nathalie Solladié*</i>	535



## Transfer of Copyright Agreement and Publishing Agreement

The transfer of copyright from the Author(s) should be explicitly stated to enable the Publisher to disseminate the Work to the fullest extent. The following transfer must be signed and returned to the Publisher's office. The work will not be published until reception of the signed agreement.

World Scientific Publishing Co Pte Ltd  
5 Toh Tuck Link,  
Singapore 596224.  
Fax: +65 6467 7667 - Email: [wspc@wspc.com.sg](mailto:wspc@wspc.com.sg)

The work entitled:

-----  
-----  
-----

The Author(s) guarantees that the above article is the Author(s)' original Work, and has never been published elsewhere before and that the text, the illustrations, and any other materials included in the article do not infringe upon any existing copyright.

The Author(s) transfers to JPP, during the full term of copyright, free of charge, the exclusive rights comprised in the copyright of the Work, including but not limited to the right to publish the Work and the material contained therein throughout the world, in all languages, and in all media of expression now known or later developed, and to license or permit others to do so. However, the following rights are reserved by Author(s):

- the right to use, free of charge, all or part of this article in future Works of their own, such as books or lectures;
- the right to reproduce the article for their own purposes provided the copies are not offered for sale;
- the right to make copies of all or part of the Work for the Author(s)' use in classroom teaching.

The Author(s) indemnifies the Publisher and the Editors of the Journal of Porphyrins and Phthalocyanines for, and holds them harmless from, any loss, expense or damage occasioned by a claim or suit by a third party for copyright infringement, or any suit arising out of any breach of the foregoing warranties as a result of publication of his article.

Note: corrections, additions or deletions introduced at the proof stage which constitute a departure from the originally submitted and accepted work will be incorporated at the Authors' expense.

Signature\* \_\_\_\_\_ Date: \_\_\_\_\_

Printed name: \_\_\_\_\_

**\*If signed by only one author on behalf of all coauthors, the additional statement must be signed.**

« I represent and warrant that I am authorized to execute this copyright on behalf of all the authors of the article referred above »

Signature \_\_\_\_\_ Date: \_\_\_\_\_